

ACE2026

16th International Congress on Advances in Civil Engineering

PROCEEDINGS BOOK

12-14 October 2026
Trabzon, Türkiye

Karadeniz Technical University
Department of Civil Engineering
Trabzon, Türkiye

ACE2026

16th International Congress on Advances in Civil Engineering

12-14 October 2026 · Trabzon, Türkiye

EDITORS

Şevket ATEŞ, Ph.D., Professor

Serhat DEMİR, Ph.D., Professor

Barbaros ATMACA, Ph.D., Associate Professor

Publication Information

Title:	ACE2026 - Proceedings Book
Congress:	16th International Congress on Advances in Civil Engineering
Date:	12-14 October 2026
Venue:	Trabzon, Türkiye
Editors:	Şevket ATEŞ, Ph.D., Professor · Serhat DEMİR, Ph.D., Professor · Barbaros ATMACA, Ph.D., Associate Professor
Publisher:	Karadeniz Technical University · Department of Civil Engineering · Trabzon, Türkiye
Year:	2026

All papers in this volume have been peer-reviewed by at least two independent referees. The authors are solely responsible for the content of their contributions. No part of this publication may be reproduced, stored or transmitted in any form without the prior written permission of the publisher.

Preface

Dear Colleagues,

It is our great pleasure to present the Proceedings of ACE2026, the 16th International Congress on Advances in Civil Engineering.

The congress was hosted by the Department of Civil Engineering of Karadeniz Technical University and held on 12–14 October 2026.

The ACE congress series has long brought together researchers, academics, practitioners and graduate students to share recent advances across the whole field of civil engineering. ACE2026 continued this tradition in a hybrid format:

- The first two days were held on campus in Trabzon, in three parallel halls.
- The third day was held entirely online, in three virtual rooms.

This format allowed colleagues who could not travel to Trabzon to present their work and take part in the discussions.

Over the three days, 160 papers were presented in 27 sessions, together with three keynote lectures and five posters. The contributions covered the main branches of the discipline:

- Structures
- Construction Materials
- Transportation
- Construction Management
- Hydraulics
- Geotechnics

The authors came from more than 60 universities, research institutions and companies. Besides Türkiye, they were based in Algeria, Australia, Bangladesh, Canada, India, Iran, Japan, Northern Cyprus, Palestine and the United Arab Emirates. Machine learning and digital tools, low-carbon and sustainable materials, seismic performance and resilient infrastructure were among the themes that ran through the programme.

We are grateful to our keynote speakers for their inspiring lectures:

- Prof. Dr. Faiz Shaikh (Curtin University)
- Dr. Shahab Yasrebi (Geomaple Geotechnics Inc.)
- Prof. Dr. Ahmet Türer (Middle East Technical University)

We also sincerely thank:

- all authors and presenters for their valuable contributions;
- the members of the Scientific Committee and the reviewers for their careful evaluation of the papers;
- the session chairs, who guided the sessions and discussions.

The congress was organised in collaboration with Boğaziçi University, Middle East Technical University, Istanbul Technical University, Yıldız Technical University, Ege University, Eastern Mediterranean University, the Chamber of Civil Engineers of Türkiye (TMMOB İMO) and its Trabzon Branch. We acknowledge their support with gratitude.

We are equally indebted to our sponsors for their generous support:

- TAV Construction
- Pasifik Holding
- ES Denizcilik
- ideCAD
- Trabzon Metropolitan Municipality

Finally, we thank the members of the Organising Committee, our administrative staff and our students, who worked with great dedication behind the scenes.

This volume contains the full papers presented at the congress, published after the authors' final corrections. We hope it will be a useful reference for researchers and practitioners and will encourage new collaborations. We look forward to welcoming you at the next ACE congress.

On behalf of the Organising Committee

Prof. Dr. Şevket Ateş

Head, Department of Civil Engineering, Karadeniz Technical University

Trabzon, October 2026

Committees

ORGANIZING COMMITTEE

Mustafa Tiryaki (Chair)

Şevket Ateş (Co-Chair)

Zekai Angın

Barbaros Atmaca

Serhat Demir

Tuğçe Anılan

Gökhan Adıyaman

Ali İhsan Karakaş

Fatih Yesevi Okur

Vahiddin Alperen Baki

Hüseyin Böler

EXECUTIVE BOARD

Eriş Uygar - Eastern Mediterranean University, Head of Civil Engineering Department

Serdar Soyöz - Boğaziçi University, Head of Civil Engineering Department

Şemsi Yazıcı - Ege University, Head of Civil Engineering Department

Alper İlki - Istanbul Technical University, Head of Civil Engineering Department

Erdem Canbay - Middle East Technical University, Head of Civil Engineering Department

Şevket Ateş - Karadeniz Technical University, Head of Civil Engineering Department

Bilge Doran - Yıldız Technical University, Head of Civil Engineering Department

SCIENTIFIC COMMITTEE

Assoc. Prof. Eriş Uygar - Eastern Mediterranean University

Prof. Arkadiusz Kwiecien - Cracow University of Technology

Prof. Maksym Grzywiński - Czestochowa University of Technology

Prof. Giray Özay - Eastern Mediterranean University

Prof. Misko Cubrinovski - University of Canterbury

Moacir Kripka - University of Passo Fundo

Prof. Khaled Marar - Eastern Mediterranean University

Prof. Peter Mark - Ruhr University Bochum

Prof. Víctor Yepes - Universitat Politècnica de València

Prof. Mahmood Hosseini - Eastern Mediterranean University

Prof. Faiz Shaikh - Curtin University

Prof. Ravipudi Venkata Rao - Sardar Vallabhbhai National Institute of Technology

Assoc. Prof. Mehmet Cemal Geneş - Eastern Mediterranean University

Assoc. Prof. Mehmet Metin Kunt - Eastern Mediterranean University

Prof. Mürüde Çelikağ - Eastern Mediterranean University

Prof. Mustafa Ergil - Eastern Mediterranean University

Prof. Özgür Eren - Eastern Mediterranean University

Prof. Serhan Şensoy - Eastern Mediterranean University

Prof. Tolga Çelik - Eastern Mediterranean University

Prof. Tülin Akçaoğlu - Eastern Mediterranean University

Prof. Umut Türker - Eastern Mediterranean University

Assoc. Prof. Umut Yıldırım - Eastern Mediterranean University

Prof. Zalihe Nalbantoğlu Sezai - Eastern Mediterranean University

Prof. Hafzullah Aksoy - Istanbul Technical University

Prof. Esin Ergen - Istanbul Technical University

Prof. Özkan Şengül - Istanbul Technical University

Prof. Ercan Yüksel - Istanbul Technical University

Dr. Cem Demir - Istanbul Technical University

Prof. Halit Özen - Istanbul Technical University

Prof. Recep İyisan - Istanbul Technical University

Prof. Kutay Orakçal - Boğaziçi University

Prof. Hilmi Luş - Boğaziçi University

Prof. Özer Çinioğlu - Boğaziçi University

Prof. Emre Otay - Boğaziçi University

Prof. Nilüfer Özyurt Zihnioğlu - Boğaziçi University

Prof. Ilgın Yaşar - Boğaziçi University

Prof. Beliz Özorhon - Boğaziçi University

Prof. Şemsi Yazıcı - Ege University

Prof. Selim Altun - Ege University

Prof. Emre Ercan - Ege University

Prof. Ebru Eriş - Ege University

Prof. Gülben Çalış - Ege University

Prof. Yalçın Alver - Ege University

Prof. Metin Hüsem - Karadeniz Technical University

Prof. Ömer Yüksek - Karadeniz Technical University

Prof. Sabriye Banu İkizler - Karadeniz Technical University

Prof. Vedat Toğan - Karadeniz Technical University

Prof. Şeref Oruç - Karadeniz Technical University

Assoc. Prof. Şirin Kurbetci - Karadeniz Technical University

Prof. Ahmet Türer - Middle East Technical University

Prof. Ahmet Birinci - Karadeniz Technical University

Prof. Ahmet Can Altunışık - Karadeniz Technical University

Prof. Osman Sivrikaya - Karadeniz Technical University

Prof. Süleyman Adanur - Karadeniz Technical University

Prof. Murat Günaydın - Karadeniz Technical University

Prof. Abdulkadir Cüneyt Aydın - Atatürk University

Prof. Ali Danandeh Mehr - Antalya Bilim University

Prof. Yusuf Cengiz Toklu - Istanbul Aydın University

Prof. Cenk Alhan - Istanbul University-Cerrahpaşa

Prof. İlker Kazaz - Erzurum Technical University

Assist. Prof. Dr. Amjad Al-Mudhafer - Iraq Al-Mustansiriyah University

Keynote Speakers



Prof. Dr. Faiz Shaikh

School of Civil and Mechanical Engineering, Curtin University, Perth, Australia

KEYNOTE LECTURE

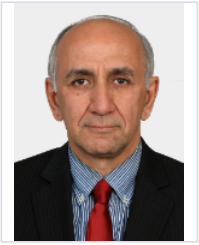
Fresh state, rheological and harden properties of 3D printed concrete made by lithium refinery residue (lithium slag) as partial cement replacement

Faiz Shaikh, SM Arifur Rahman, Prabir Sarker

The lecture presents the use of lithium refinery residue (lithium slag) as a partial cement replacement in 3D printed concrete. Mix design, rheology and printability, buildability, and mechanical and microstructural properties are discussed, together with the reduction in embodied carbon and the prospects for sustainable applications.

ABOUT THE SPEAKER

Prof. Shaikh is a Professor at the School of Civil and Mechanical Engineering, Curtin University. He has more than 220 peer-reviewed publications, including over 170 journal papers, two books and seven book chapters. His research covers engineered geopolymer and cementitious composites, nanomaterials in concrete, supplementary cementitious materials, recycled aggregates and industrial by-products, durability, repair and strengthening of reinforced concrete, and numerical modelling.



Dr. Shahab Yasrebi, PhD, P.Eng

President, Geomaple Geotechnics Inc., Toronto, Canada

KEYNOTE LECTURE

Urban Tunneling Challenges in Rapidly Developing Cities: Risk, Ground Uncertainty, and Digital Transformation in Underground Construction

The lecture examines the growing demand for underground space in megacities and the challenges of tunnelling in dense urban settings: geotechnical uncertainty and risk management, the interaction of new tunnels with existing infrastructure, and construction constraints in metropolitan areas. Lessons from international tunnelling and deep excavation projects are discussed, together with the role of artificial intelligence, monitoring systems and digital twins in underground construction.

ABOUT THE SPEAKER

Dr. Yasrebi is a geotechnical consultant with more than 37 years of international experience in underground infrastructure, deep excavations, ground improvement and site investigation across North America, the Middle East and Asia. He has led complex urban tunnelling projects, is a specialist in the New Austrian Tunnelling Method (NATM), and has authored more than 250 technical publications.



Prof. Dr. Ahmet Türer

Department of Civil Engineering, Middle East Technical University (METU), Ankara, Türkiye

KEYNOTE LECTURE

Snow Damage Patterns at Solar Power Plants: Structural Failures, Snow Drifting and Design Challenges in Ground-Mounted PV Systems

Drawing on forensic evidence from solar power plants damaged under heavy snow in Türkiye, the lecture discusses snow accumulation and drifting around PV arrays, the limitations of TS 498 for ground-mounted systems, aerodynamic gap and balanced snow depth concepts, wind–snow interaction and snow trapped beneath panels, buckling of cold-formed C-section supports, and failures caused by poor connections and workmanship. Lessons from insurance and forensic investigations and the application of ASCE 7-22 and EN 1991-1-3:2025 to solar infrastructure are presented.

ABOUT THE SPEAKER

Prof. Türer is a structural engineer and a full-time faculty member of the Department of Civil Engineering at METU. His work focuses on structural engineering, forensic investigations and structural health monitoring.

Sponsors

ANA SPONSOR

TAV Construction

PASİFİK HOLDİNG

ES DENİZCİLİK

ideCAD®

TMMOB İNŞAAT MÜHENDİSLERİ ODASI

Collaborating Institutions

Karadeniz Teknik Üniversitesi
Karadeniz Technical University
EST. 1955

Boğaziçi Üniversitesi
Boğaziçi University
EST. 1863

Orta Doğu Teknik Üniversitesi
Middle East Technical University
EST. 1956

İstanbul Teknik Üniversitesi
Istanbul Technical University
EST. 1773

Yıldız Teknik Üniversitesi
Yıldız Technical University
EST. 1911

Ege Üniversitesi
Ege University
EST. 1955

Doğu Akdeniz Üniversitesi
Eastern Mediterranean University
EST. 1979

TMMOB İnşaat Mühendisleri Odası
Chamber of Civil Engineers of Turkey

İMO Trabzon Şubesi
Chamber of Civil Engineers, Trabzon Branch

Acknowledgements

We would like to express our sincere gratitude to the session chairs, who guided the sessions and discussions, and to the research assistants and students of the Department of Civil Engineering, Karadeniz Technical University, who worked with great dedication in the preparation and running of the congress.

SESSION CHAIRS

- Prof. Dr. Süleyman Adanur
- Assoc. Prof. Dr. Gökhan Adıyaman
- Prof. Dr. Muhammet Vefa Akpınar
- Prof. Dr. Ahmet Can Altunışık
- Assoc. Prof. Dr. Tuğçe Anılan
- Assoc. Prof. Dr. Barbaros Atmaca
- Asst. Prof. Dr. Alperen Baki
- Assoc. Prof. Dr. Hasan Basri Başağa
- Asst. Prof. Dr. Hüseyin Böler
- Prof. Dr. Ayşe Daloğlu
- Prof. Dr. Tayfun Dede
- Prof. Dr. Serhat Demir
- Prof. Dr. Şakir Erdoğdu
- Prof. Dr. Kemal Hacıefendioğlu
- Prof. Dr. Volkan Kahya
- Asst. Prof. Dr. Ali İhsan Karakaş
- Asst. Prof. Dr. Safa Nayır
- Prof. Dr. Osman Sivrikaya
- Asst. Prof. Dr. Sebahat Şimşek
- Prof. Dr. Vedat Toğan
- Prof. Dr. Ömer Yüksek

RESEARCH ASSISTANTS

- Yılmaz Yılmaz
- Fatih Cebir
- Arife Günay
- Serhan Koç
- Mahir Kumantaş

- Betül Mete Baki
- Aleyna Begüm Taşdemir
- Tolga Barış Terzi
- Büşra Yakak Vatandaş
- Muhammed Fatih Yüksel
- Mehmet Halil Çalım
- Mahmut Cenk Sayıl
- Selenay Gençcelep
- Betül Üstüner
- Sertaç Alperen Koçak

STUDENTS

- Bilal Koş
- Sena Bahar
- Büşra Süeda Arslantaş
- Emre Yılmaz
- Mısra Tavlı
- Muhammet Mehmet Uzun
- Arda Asar
- Rahime Gözde Arık
- Aysun Seyidli

Table of Contents

Invited Lectures — Keynote Speakers 26

ACE-KEY-001 Fresh State, Rheology, Buildability and Mechanical Properties of 3D Printed Concrete Containing Lithium Slag 27
Faiz Shaikh, SM Arifur Rahman and Prabir Sarker

ACE-KEY-002 Urban Tunneling Challenges in Rapidly Developing Cities: Managing Ground Uncertainty, Risk, and Digital Transformation 36
Shahab Yasrebi

ACE-STR-035 Snow Damage Patterns at Solar Power Plants 46
Ahmet Turer

Chapter 1 — Structures 56

ACE-STR-001 Cyclic In-Plane Behavior of AAC Load-Bearing Panel Walls under Varying Axial Stress Levels and Panel Configurations 57
Koray Ugurlu, Omer Faruk Halici, Cem Demir, Mustafa Comert and Alper Ilki

ACE-STR-002 Iterative Damper Optimization for Seismic Retrofit of a Cliff-Mounted Steel Observation Platform 69
Adnan Kiral, Zeliha Tonyali, Maziar Fahimi Farzam

ACE-STR-003 COMPARATIVE SEISMIC DESIGN AND PERFORMANCE EVALUATION OF SPECIAL CONCENTRICALLY BRACED FRAMES AND BUCKLING-RESTRAINED BRACED FRAMES 79
Kazım Burç CİVELEK, Elifsu KAYRAK

ACE-STR-004 The Effect of Steel Fiber Length and Content on the Some Flexural Behavior Properties of the High-strength Concrete Beams 89
Hamdi ÖZTÜRK

ACE-STR-005 The Effect of Rigid Basement Shear Walls on Seismic Behaviour of Reinforced Concrete Structures according to TBEC 2018 97
Hurmet Kucukgoncu

ACE-STR-006 Seismic Performance Assessment of a 100-M-Span Steel Bridge Using Fluid Viscous Dampers 107
Sadi Özsaraç and Fatih Yılmaz

ACE-STR-007 Effect of Opening Location on GFRP-RC Deep Beam Shear Behavior 117
Farid Abed, Anas Saber, Aroob Alateyat, Tamer El-Maaddawy

ACE-STR-008 Corner Radius Effect on Confined Strengths of FRP-Wrapped Rectangular Concrete Members 123
Onur Gedik

ACE-STR-009 Automated Equivalent Frame Modelling and Seismic Assessment of URM Buildings Using MATLAB – SAP2000 Integration 132
Y. Semerdoken and M.A. Erberik

ACE-STR-010 Mechanical Behavior of Timber Folded Plate Joints: An Experimental Comparison of Adhesive and Mechanical Fasteners 142
Muhammed Emin Akyürek, Cenk Aksoylar, Nihan Doğramacı Aksoylar, Mehmet Selim Ökten, Muhammet Ali İpekçi, Haşim Çayır

Table of Contents (cont.)

ACE-STR-011 Mapping Research on AI-Enhanced Mechanical Behavior of Laminated Glass: A Scientometric Analysis 151
Ebru Dural, G.B.O. Öztürk

ACE-STR-012 Comparative Linear and Nonlinear Seismic Analysis of a Historical Masonry Arch Bridge: Dynamic Response and Damage Evolution 162
Emre ALPASLAN and Muhammed Mustafa ÖZTÜRK

ACE-STR-013 SSI Analysis of a NPP Building for FWN Ground Motion Model 173
Gizem Çağlar Dal and Kurtuluş Soyluk

ACE-STR-014 Nonlinear Time History Analysis of a 2.5 MW Onshore Wind Turbine Under Earthquake Loads 184
Ecmel Eylül Naz Özdoğan and Özgür Özçelik

ACE-STR-015 Application of CatBoost Gradient Boosting for Precise Shear Capacity Assessment of Exterior RC Beam-Column Joints 195
Selin ESFENDİYAR and Gamze DOĞAN

ACE-STR-016 Micromechanical Explicit Finite Element Analysis of the Fracture Evolution in Structures under Crack Parallel Stress Condition 203
Sedat Kömürcü and Ferhun C. Caner

ACE-STR-017 The Solution of the Optimal Sensor Placement Problem for Planar Truss System 210
Barbaros ATMACA, Hülya PİR, Büşra YAKAK VATANDAŞ and Tayfun DEDE

ACE-STR-018 A Comparative Study on the Seismic and Environmental Performance of Geopolymer and Conventional Reinforced Concrete Buildings 220
İffet Gamze Mütevelli Özkan and İhsan Türkel

ACE-STR-019 A Data-Driven Framework for Assessing the Energy Dissipation Characteristics of Reinforced Concrete Columns 230
Ziya Muderrisoglu and Yaşar Avcı

ACE-STR-020 Structural Performance of Reinforced Concrete Frames with Lightweight Steel Wall Panels 238
Hussien Alkasim SOALIH, Fatih CEBİR, Serhat DEMİR, Metin HÜSEM and Ramazan LİVAOĞLU

ACE-STR-021 Monitoring the Transformation of Residential Typology from Building Permit Data in Trabzon (2010–2025) 245
Abdullah BOSTANCI and Sina ATABEY

ACE-STR-022 Design Considerations for Concrete Structures Under Fire Exposure 255
Furkan Varinlioglu, Huseyin Okan Anadut, Fuat Koksal

ACE-STR-023 Effect of Structural Steel Profile Geometry on the Cyclic Behavior of SRC Columns: A Numerical Investigation 265
Halit Erdem ÇOLAKOĞLU

ACE-STR-024 Performance-Based Optimization of Buckling-Restrained Braces for RC Structures Using Nonlinear Response History Analysis 276
Clifford Phiri and Çağlayan Hızal

ACE-STR-025 Numerical Prediction of the Seismic Behavior of Steel Plate Reinforced Concrete Squat Shear Walls: A Python-Based Parametric Study 286
Mustafa Ozdemir and Muslum Kilinc

Table of Contents (cont.)

ACE-STR-026 Recent Progress in Geopolymer-Based Applications for Bridge Structures: From Material Feasibility to Deployment Readiness 297
Oğuzhan Çetindemir

ACE-STR-027 Bridge Damage during the 2023 Kahramanmaraş Earthquake Sequence: Failure Mechanisms and Seismic Risk-Reduction Strategies 306
Oğuzhan Çetindemir

ACE-STR-028 Performance of Metaheuristic Algorithms in Cost Optimization of Precast Segmental Circular Tunnel Linings 316
Semiha Hayrioğlu and Hasan Tahsin Öztürk

ACE-STR-029 Vision-Based Unsupervised Anomaly Detection and Regional Damage-Sensitive Mapping of Masonry Minarets: Laboratory Validation and Field Demonstration 326
Tunahan Aslan, Kemal Hacıefendioğlu, Ali Motamedi, Cemile Duman

ACE-STR-030 Architecture and Implementation of an AI- and ROS 2-Based Quadrupedal Platform for Post-Earthquake Crack Inspection 336
Ali Motamedi and Kemal Hacıefendioğlu

ACE-STR-031 Seismic Retrofit of Slender Observation Platforms: An Optimized Tuned Mass Damper Approach 346
Maziar Fahimi Farzam, Adnan Kiral and Zeliha Tonyali

ACE-STR-032 Investigation of Thermal Stresses in Composite Structural Elements Using the Photoelasticity Method: Mechanical Modeling and Preliminary Validation Study 356
Omer Canbey Cucemen and Osman Bulut

ACE-STR-033 Effect of Material Degradation on Structural Performance: A Pushover-Based Assessment 366
Berna İstegün, Erkan Çelebi, Julia Eberl and Alexander Stark

ACE-STR-034 Multi-Modal Seismic Response of RC Buildings with Combined Soft-Story and Torsional Irregularities: A Performance-Based Perspective for Rapid Assessment 378
Berna İstegün, Erkan Çelebi, Julia Eberl and Alexander Stark

ACE-STR-036 Analytical Timber Spaced-Column P-M Interaction Diagram 390
Rabia Izol and Ahmet Turer

ACE-STR-037 Performance Comparison of Fiber-Based and Lumped Plasticity Models in Nonlinear Time-History Analysis of RC Frames 400
Siamak Aghaei, Mehmet Ada, Yusuf Ayvaz

ACE-STR-038 Parametric Analysis of Load-Carrying Capacity and Reinforcement Optimization in Slab-on-Grade Foundations 411
Mehmet Sefa Orak

ACE-STR-039 Free Vibration Response of Homogeneous Porous Beams with Edge Cracks Using Finite Element Method 419
Serhan Koç, Muhittin Turan, Gökhan Adıyaman and Volkan Kahya

ACE-STR-040 A Modified Beam-End Test Method for Bond Behavior of Reinforced Concrete Elements 429
Ahmet Akif Akcora, Serhan Sensoy, Ozgur Eren

Table of Contents (cont.)

ACE-STR-041 Evaluation of Acceleration, Velocity, and Displacement Response Spectra of the February 6, 2023 Kahramanmaraş Earthquakes in the Hatay Region Considering Local Site Classes 439
Merve ARLI SÖNMEZ and Ali KOÇAK

ACE-STR-042 Experimental study of cold-formed steel stud's cyclic axial response 452
Hiba MEDDAH, Nouredine BOURAHLA, Hakim BECHTOULA and Hassan AKNOUCHE

ACE-STR-043 Optimal Sizing and Post-Tensioning Force Design of Cable-Stayed Footbridges via the Rao-2 Algorithm 462
Chiraz FAZZAA, Barbaros ATMACA, Büşra YAKAK VATANDAŞ and Şevket ATEŞ

ACE-STR-044 Optimum Redesign of a Real-World Large-Span Steel Truss Roof in One Overnight Run 472
Hasan Eser and Oğuzhan Hasançebi

ACE-STR-045 Progressive Collapse of RC Buildings with Ground-Floor Slab Discontinuity 479
Alaaddin ALJUNEED, Temel TÜRKER

ACE-STR-046 Toward Unified Machine Learning Models for Reinforced Concrete Columns and Shear Walls: Digital Twin Framework and Preliminary Validation 490
Şevket ATEŞ

ACE-STR-048 Three-Dimensional Elasticity-Based Buckling Analysis of Functionally Graded Sandwich Plates on Kerr Foundation Using State-Space Differential Quadrature Method 498
Sebahat Şimşek and Magd Abdel Wahab

Chapter 2 — Construction Materials **506**

ACE-CME-001 Role of Nano Silica Dispersion Methods in the Mechanical and Physical Performance of High-Performance Concrete 507
Irem Bagca and Kutalmış Recep Akça

ACE-CME-002 Performance-Based Comparison of Fly Ash and Recycled Glass Powder in Low-Carbon Concrete: A Carbon Reduction Efficiency Approach 517
Ebru Dural, Gulmira Adzhygulova, Gulnara Karadeniz, Mehmet Karadeniz

ACE-CME-003 Life Cycle Assessment of Reinforced Concrete Structures using Pozzolanic Materials 524
Ali Danandeh Mehr, Emirhan Yener and Kaan Beyazkılıç

ACE-CME-005 Evaluation of ImageJ-Based Image Processing Workflows for Aggregate Particle Size Distribution Analysis of Hardened Concrete Sections 536
Pınar Yıldırım

ACE-CME-006 Effects of Partial Fine Aggregate Replacement with Crumb Rubber on the Mechanical and Durability Properties of Concrete 546
İsmail Onur Öztürk, Arda Ziya, Umut Yüksel, Beyza Güngör, Sidar Nihat Bıçakçı, Hasan Nuri Türkmenoğlu, Mesut Küçük and Hakan Nuri Atahan

ACE-CME-007 Tetraethyl Orthosilicate-Based Fiber-Reinforced Geopolymer Mortars under Comparative Evaluation of Different Curing Methods 557
Beyza AYGUN, Mucteba UYSAL, Turgay COSGUN, Turhan BILIR

ACE-CME-008 Durability Performance of TEOS-Modified Fiber-Reinforced Geopolymer Mortars under High Temperature Effects 568
Beyza AYGUN, Mucteba UYSAL, Turgay COSGUN, Turhan BILIR

Table of Contents (cont.)

ACE-CME-009 Effects of Disinfectant and Oxidizing Agent Exposure on Mechanical and Physical Properties of Concrete 579
Yılmaz M., Bilici S., Badawi B., Mutlu İ. F., Akbay Arama Z.

ACE-CME-010 Use of Kufeki Stone Powder as a Cement and Limestone Replacement in OPC and LC3 Mortars 589
Mahmut Cenk SAYIL and Şirin KURBETCİ

ACE-CME-011 Mechanical properties of engineered cementitious composites incorporating waste tire rubber 598
Akbar Mikaeelnezhad, Reza Saleh Ahari

ACE-CME-012 Effect of zeolite on the mechanical properties of polypropylene fiber-reinforced mortars under different curing temperatures 609
Mohammad Mahdi Milani, Reza Saleh Ahari

ACE-CME-013 Effect of fibre type and content on the interlayer bond strength of fibre-reinforced self-consolidating concrete cast in distinct layers 620
Meysam Khalilzadeh and Reza Saleh Ahari

ACE-CME-014 Effect of Powder and Colloidal Nano-Silica on the Mechanical and Rheological Properties of Cementitious Composites 630
Tugba Kuru, Hasan Nuri Turkmenoglu, Omer Canbey Cucemen, Osman Bulut

ACE-CME-015 Strength Development under Intermittent Sprinkler Curing: A Comparative Study of Plain and Slag-Blended Concrete 640
Senem Bilici, Arif Tufan Salva, Muhittin Tarhan, Erdal Önkol and Cihan Tayyar Ahı

ACE-CME-016 Moisture Optimization of Roller-Compacted Concrete Pavements Incorporating Recycled Materials 648
Ola Aljumaili, Yunus Emre Demir, Yeşim Arslantürk, Emine Özdoğru, Oğuzhan Şahin, Emin Şengün

ACE-CME-017 Technical and Environmental Evaluation of Electric Arc Furnace Slag as Fine Aggregate Replacement in Cement Mortar 658
Emircan Özçelikci, Hussein Abdullahi Ali, Mehmet Baran

ACE-CME-018 Effect of Activator Type and Dosage on the Mechanical Performance of One-Part Calcined Clay Geopolymer Mortars 665
Nur Demir, Enes Hamidoğlu, Ünal Anıl Doğan

ACE-CME-019 Mechanical and High-Temperature Performance of Geopolymer Foam Concrete Substituted with Marble Powder and Reinforced with PVA Fibers 676
Rümeysa Atmaca, Damla Nur Çelik, Rüya Kılıç Demircan, Gökhan Kaplan

ACE-CME-020 Investigation of the Usability of Hemp Powders in Cementitious Composites 690
Abdulrezzak Alkan, Yunus Gündüz and Yuşa Şahin

ACE-CME-021 Performance assessment of geopolymer mortar using industrial by-product components 699
Alara Girgin, Mihriban Sarı, Kaan Aksoy and Zeynep Başaran Bundur

ACE-CME-022 Use of Recycled Concrete Powders as Supplementary Cementitious Materials in Mortar Mixtures 709
Kadircan Varan, Ünal Anıl Doğan, Aleyna Dinçer, Ayşegül Koyunlular, Beyza Uslu, Kağan Sevinç, Tarık İlyas Özyurt, Tuba Gündoğdu, İsmail Gökalp

Table of Contents (cont.)

ACE-CME-023 Effect of Carbonation Treatment on the Reuse of Concrete Sludge as a Clinker-Reducing Mineral Additive in Cementitious Materials 718
Kadircan Varan, İsmail Gökalp, Teoman Erenoğlu, Senem Bilici, Büşra Çınar Ernek

ACE-CME-024 Early-age strength development in slag-fly ash geopolymers: effect of varying ohmic heating curing durations 726
Mazem Yılmaz and Mucteba Uysal

ACE-CME-025 Effects of Reactive Magnesia in Portland Cements Including Fly Ash and GGBFS for Different Curing Regimes in Short Term 734
M. Kemal Ardoğa, İ. Özgür Yaman and Mustafa Tokyay

ACE-CME-026 The Usability of Metakaolins Produced from Kaolinitic Raw Materials in Green Cement Production 744
Kadircan Varan, Fatma Zehra Toker, İsmail Gökalp, Teoman Erenoğlu, Pınar Uysal, Tüten, Yıldız Yıldırım, Hasan Ahmet Uzunoğlu, Hasan Ergin

ACE-CME-027 Neural Network-Driven Forecasting of Concrete Compressive Strength 752
Mehmet Nadir and Mehmet Sefa Orak

ACE-CME-028 Mechanical Properties of Cements Produced with Construction and Demolition Waste in Accordance with TS EN 197-6 760
Yasemen Polat, Özer Sevim, M. Kemal Ardoğa, Mustafa Şahmaran

ACE-CME-029 Fresh-State Performance and Printability of Brick Powder-Based 3D Printable Concrete with GGBFS and Fly Ash 770
Muhammed Çeçen, Derya Kurt, Yeşim Tarhan, İsmail Hakkı Tarhan

ACE-CME-030 Effect of Supplementary Cementitious Materials on Hemp Fiber-Reinforced Structural Lightweight Concrete with Pumice Aggregate 779
Mehmet Kara and Zehra Canan Girgin

ACE-CME-031 Influence of GGBFS and Fly Ash on the Mechanical Performance of 3D Printable Concrete Incorporating Brick Powder as Fine Aggregate 787
Derya Kurt, Muhammed Çeçen, İsmail Hakkı Tarhan, Yeşim Tarhan

ACE-CME-032 Engineering Sustainable Magnesium Oxalate Cements Using Olivine as a Substitute for Dead-Burned Magnesia 796
Buse Öztürk, Sinan T. Erdoğan

ACE-CME-033 Determination Of The Fracture Energy Of Natural Stone From The Cappadocia Region 805
Harun Yahya SÜNDÜ, Ayşe ERDÖLEN, Nabi YÜZER

ACE-CME-034 Assessment of the Combined Effect of Plastic Aggregate and Silica Fume on Concrete 814
Safa NAYIR, Yılmaz YILMAZ, Doğukan ŞAHİNER, Memduh NAS, Vahiddin Alperen

ACE-CME-035 Flexural Performance of Overlap Configurations for Textile-Reinforced Cementitious Composites 822
Bedirhan Enes Kelek and Esat Selim Kocaman

ACE-CME-036 Clinker Reduction in Portland Limestone Cement through the Incorporation of Mechanochemically Activated Natural Pozzolans 832
Amal Chakir, Vahiddin Alperen Baki, Memduh Nas, Yilmaz Yilmaz, Safa Nayır, Muhammad Ahmad, Fatma Ayvaz, Murathan Bulut, Ayten Çaputcu

Table of Contents (cont.)

ACE-CME-037 Dry Ice-Driven Mechanochemical Carbonation for Enhanced CO? Capture and Reactivity of Bottom Ash 844
Muhammad Ahmad, Vahiddin Alperen Baki, Memduh Nas, Yilmaz Yilmaz, Safa Nayır, Amal Chakir, Fatma Ayvaz, Murathan Bulut, Ayten Çaputcu

ACE-CME-040 Increasing the Reactivity of Natural Pozzolans in Cementitious Systems 853
Sevgi Özen

Chapter 3 — Geotechnics **858**

ACE-GEO-001 3D Numerical Analysis for the Hydraulic Performance of Contemporary Weep Holes in Retaining Structures 859
Burak ÖZÇÖREKÇİ, Mustafa HATİPOĞLU

ACE-GEO-002 Response-Based Sensitivity Analysis of Barcelona Basic Model Parameters for Pile Heave in Expansive Ankara Clay 868
Sefa Yıldırım and Erdal Çokça

ACE-GEO-003 Osterberg Cell (O-Cell) Load Testing for Deep Foundation Capacity Assessment: Principles, Instrumentation, and Case Studies 878
Hasan Altawil and Özcan Tan

ACE-GEO-004 Investigation of the Geotechnical Properties of Sandy Soils Stabilized with Granular Shingle Waste 886
Inci Develioglu and Rumeysa Bulut

ACE-GEO-005 Experimental Comparison of Seismic Behavior in Fixed-Base and Soil–Structure Interaction Systems Using Shaking Table Tests 896
Olguhan Şevket KARAHASAN and Zekai ANGIN

ACE-GEO-006 Investigation of Consolidation and Swelling Behavior of Fiber-Reinforced Clays 905
Ehsan Etminan, Kaveh Dehghanian, Beste Koçak Dinç, Beste Seyla Göçkün and Alperhan Kapucu

ACE-GEO-007 3D lithology and soil modeling in urban areas: the case of Fatih District 914
İzel Yıldız Sertgöz, İbrahim Fırat Mutlu, Meryem Yılmaz, Zülal Akbay Arama

ACE-GEO-008 A Web-Based Tool for Energy-Corrected SPT Evaluation of Soil Liquefaction Potential 925
Oguz K. Sivri and Mustafa Tolun

ACE-GEO-009 Effect of EPS Geofoam on Soil Arching and Deflection Behavior of Small-Diameter Buried HDPE Pipes under High Fill Conditions 932
Perihan Biçer, Sercan Bozkurt, Havvanur Kılıç

ACE-GEO-010 Dynamic Soil Characterization of Alluvial Deposits in Gölbaşı (Adıyaman) Following the 6 February 2023 Kahramanmaraş Earthquakes 942
Muhammed Emin Aytekin, İhsan Yılmaz, Eray Birinci, Erhan Tekin, Eren Pamuk, Kemal Önder Çetin, Nihat Sinan Işık, Seyhan Fırat

ACE-GEO-011 Numerical Investigation of Active Earth Pressure on a Cantilever Retaining Wall with a Shear Key in Cohesive-Frictional Backfill 955
Dina Aqra and Erol Şadoğlu

ACE-GEO-012 A Discrete Element Modeling of the Vibration of a Horizontal Granular Deposit Harmonically Excited at the Base 965
Mouloud MANSOURI and Said DERBANE

Table of Contents (cont.)

ACE-GEO-013 In-Situ Behavior of Massive Twin Pneumatic Caissons During Close-Proximity Simultaneous Sinking: A Case Study 976
Feyzullah Gulsen, Makoto Tone, Naoya Watanabe and Hideo Komine

ACE-GEO-014 Numerical Investigation of Seismic Behavior of Piled Raft Foundation (PRF) and Unconnected Piled Raft Foundation (UPRF) Systems 986
Burak AKÇAY, Osman SİVRİKAYA, Esin ERTÜRK ATMACA, Berk DİKMENOĞLU, Murat GÜNAYDIN, M. Kubilay KELEŞOĞLU, Esra Ece BAYAT, Fezayil SUNCA, Ertuğrul TACİROĞLU, Kemal Önder ÇETİN, Ahmet Can ALTUNIŞIK

Chapter 4 — Hydraulics **998**

ACE-HYD-001 Development of an Artificial Intelligence-Based Water Consumption Forecasting Model for İzmir Province 999
Ergun Uzlu

ACE-HYD-002 Assessing Agricultural Water Allocation in Türkiye: A Multi-Level Stakeholder Assessment Based on the EU Water Allocation Framework 1007
Elif ERDEM and Elcin KENTEL ERDOGAN

ACE-HYD-003 Investigating the effect of channel slope on flow characteristics in open channel experiments 1017
Arife Günay, Tuğçe Anılan and Attila Dedeoğlu

ACE-HYD-004 Numerical Modeling of Cavitation Damage in Spillway Using Finite Volume Method 1024
Yasin YATAGANBABA, Mehmet SORGUN

ACE-HYD-006 Is Türkiye Drying? Regional and Seasonal Drought Trends from High-Resolution SPEI 1034
Ahmet Faruk İpek and Ercan Kahya

ACE-HYD-007 Investigation of Uncertainties in 2D Dam Break Simulations by Monte Carlo Simulations 1040
Muhammed Furkan Kart and Ali Ercan

ACE-HYD-008 Comparison of Climate Model Performances of the Same Institutes using Hydrological Model Outputs: A Case Study with CMIP5 GCM, CMIP6 GCM, and CMIP5 RCM over Göksu Basin 1050
Murat Yegin, O. Burak Akgun and Elcin Kentel

ACE-HYD-009 Prediction of Reservoir Sedimentation by RUSLE Incorporating the Effects of DEM Selection and Spatial Resolution 1060
Yakup Darama, Kutay Yilmaz, Sarp Toprakkale, Meric Yilmaz

ACE-HYD-010 Economic Feasibility Of Rainwater Harvesting Systems In Trabzon, Türkiye: A Water Balance And Cost–Benefit Analysis 1072
Osman Tuğrul BAKİ

ACE-HYD-012 Prediction of Jet Length in Spillways Using Advanced Machine Learning Algorithms 1079
Pelin İlker, Ziya Cem Öztürk and Mehmet Sorgun

ACE-HYD-013 Evaluation of the Performance of Various Machine Learning Methods in Rainfall-Runoff Modeling: A Case Study of the Meriç River 1089
Ceydanur Aydın, Nira Nur Demir and Nurcan Öztürk

Table of Contents (cont.)

ACE-HYD-014 Modeling the Rainfall-Runoff Interaction Using LSBoost, MARS, M5-tree, and ANN: A Case of Çağlayan Creek 1098
Derya Kılıç, Nurcan Öztürk and Hasan Tahsin Öztürk

ACE-HYD-015 Development of New Software for Feasibility Studies of Hydropower Plants 1108
Onur Kemalli, Zafer Bozkuş and T. Kutay Çelebioğlu

ACE-HYD-016 Experimental and Numerical Investigation of Flow Characteristics and Water Surface Profiles Under a Vertically Moving Cylindrical Gate Using HEC-RAS 1118
Kağan CEBE, Yusuf Buğra AKSOY, Bilgin Furkan BAYRAK and Aslı ÜLKE KESKİN

ACE-HYD-017 Spatiotemporal Characteristics of Compound Dry Hot Stress Events in Trabzon Province 1130
Burak Çırağ, İlteriş Taşkolu, Reşat Acar, Mahmut Güngör

ACE-HYD-018 Uncertainty Arising from Effective Rainfall Methods in Agricultural Water Footprint Calculations: A Comparative Analysis at the National Scale 1141
Muhammed Sungur DEMİR and Abdullah MURATOĞLU

ACE-HYD-026 Experimental Investigation of Morphological Equilibrium at a Symmetrical Mobile-Bed River Confluence with a Guiding Wall 1148
Zehra Büyüker and Gökçen Bombar

ACE-HYD-027 A Comparative Assessment of Gravity-Based Block-Type and Conventional Dolphin Systems 1158
Şenol Demirbaş, Erdal Kesgin

Chapter 5 — Transportation **1164**

ACE-TRA-001 Determinants of Driver Rejection of Ride Requests in Ride-Hailing Services 1165
Nihat Can Karabulut, Mustafa Gursoy, Halit Ozen

ACE-TRA-003 Urban Air Mobility in Türkiye: Opportunities, Challenges, and Future Perspectives 1174
Selim Dündar and Barış Akdemir

ACE-TRA-004 Comparative Analysis of Choice Models and Machine Learning Methods for Synthetic Population-Based Mode Choice Modeling of E-Scooter Users 1184
Selim Dündar, Gökçe Yurtseven and Gürkan Günay

ACE-TRA-005 Modeling and Prediction of Traffic Delay in Closely Spaced Roundabouts 1194
Nurdan AKBAŞ, Ruti POLİTİ, Serhan TANYEL

ACE-TRA-006 Effects of Autonomous Vehicle Driving Strategies on Passenger Car–Heavy Vehicle Interactions in Mixed Traffic Flow 1202
Selim Dündar, Ilgin Gokasar, Serhan Tanyel

ACE-TRA-007 Analysis of the Ballast Porosity Variations in British A, B, C, and D Gradations using the Discrete Element Method 1213
Huseyin Boler and Hüseyin Köse

ACE-TRA-008 Evaluating Fare Structure with Best–Worst Method: Istanbul Metro Example 1221
Ömer Murat Urhan and Mustafa Gürsoy

ACE-TRA-009 Lane Changing Behavior at Highway Diverging Areas: A Safety Analysis Based on Time-to-Collision (TTC) 1233
Alpaslan Bozkurt, Ali Topal, Pelin Önelçin and Serhan Tanyel

Table of Contents (cont.)

ACE-TRA-010 A Bibliometric Analysis of Asphalt Mixtures Subjected to Short-and Long-Term Aging 1243
Öznur KARADAĞ, Gizem KAÇAROĞLU, Mehmet SALTAN

ACE-TRA-011 Effects of Pedestrian Demand on the Operational Performance of Unsignalized Intersections 1253
Duygu ŞENOL and Serhan TANYEL

ACE-TRA-012 Evaluation of Physical Properties of POE/Nanoclay Composite Modified Bitumen 1266
Ersoy Kabadayı, Erman Çavdar, Aytuğ Kumandaş, Mahir Kumantaş, Neslihan Şahan and Şeref Oruç

ACE-TRA-013 Operational Characteristics of Queue Discharge Flow at Closely Spaced Signalized Intersections 1276
Ruti Politi and Serhan Tanyel

ACE-TRA-014 The Role of Built Environment Perceptions in University Students' Travel Mode Choices: A Multinomial Logit Analysis 1286
Raziye Peker, Mustafa Sinan Yardım, Kadir Berkhan Akalın

ACE-TRA-016 Modelling Urban Bicycle Use Intensity Using Penalized Regression Methods: Evidence from Eskişehir 1297
Sıla Cemre Demirci and Çağdaş Kara

ACE-TRA-017 Influence of CLS Modification on the Conventional Properties and Temperature Susceptibility of Bitumen 1307
Aytuğ Kumandaş, Erman Çavdar, Mahir Kumantaş, Ersoy Kabadayı, Neslihan Şahan, Erhan Burak Pancar and Şeref Oruç

ACE-TRA-018 Possible User Effects of Sakarya Adapazari - Serdivan Tram Line on Sakarya Transportation 1317
Aykut TOPÇU, Mustafa GÜRSOY

ACE-TRA-020 Digital Twin Road Corridor Architecture and Maturity Framework in Cooperative Intelligent Transportation Systems 1326
Dilara Usta and Mustafa Sinan Yardım

ACE-TRA-021 A Review on Physico-Chemical Identity and Performance Evaluation of Recycled Aggregates for Sustainable Pavements 1336
Md. Amin Al Noor, Sk. Rakibul Islam, Tasnim Mahin and Oishik Majumder

ACE-TRA-022 Investigation of the Effect of Service Quality Perception at Public Transport Transfer Centers and Vehicles on Passenger Satisfaction 1347
Handenur Keser and Yalçın Alver

ACE-TRA-023 Assessing Campus Travel Behavior and Potential CO? Emission Reductions through a Ring Shuttle System: A Case Study of Muğla Sıtkı Koçman University 1356
Ahmet Taha Koçtaş, Elif Dağlı, Mervegül Uysal

ACE-TRA-024 Smart City and Hospital Location Policy: A Transportation Equity Framework 1370
Zeynep Nur Duman, Mehmet Ali Silgu and Mehmet Yılmaz

ACE-TRA-025 Micromobility and Placemaking: Rethinking Accessibility in Urban Mobility 1380
Ilgin Gokasar, Volkan Yıldız, Evinç Doğan

ACE-TRA-026 Autonomous Public Transport as a Traffic Management Element: A Literature-Based Discussion on Applicability and Feasibility 1389
Ilgin Gokasar and Volkan Yıldız

Table of Contents (cont.)

ACE-TRA-027 Autonomous Buses and Their Social Acceptance: A SWOT Analysis 1397
Volkan Yıldız and Ilgin Gokasar

ACE-TRA-028 Evaluating Pedestrian Safety and Crossing Preferences Along Urban Arterial Corridors 1404
Beyhan Ipekyuz and Funda Ture Kibar

ACE-TRA-029 A Framework for Factor Filtering and Algorithm Selection in Highway Alignment Optimization 1414
Özger İnal, Mehmet Ali Silgu and Abdullah Hilmi Lav

ACE-TRA-031 Investigating Urban Mobility Patterns Using Dolmuş Operational Data: The Case of Diyarbakır, Türkiye 1422
Beyhan Ipekyuz

ACE-TRA-043 Designing a Porous Asphalt Skeleton for Semi-Flexible Pavement Applications 1432
Mert Atakan, Cemalettin Kaplan, Yaren Altay, Recep Orçun İnce, Kürşat Yıldız

Chapter 6 — Construction Management **1442**

ACE-COM-001 Construction Management Risk Simulation for Hybrid Renewable Energy EPC Projects: A Probabilistic Framework for Remote Environments 1443
İlkyaz Ceren Güçlü Yavuz and Gürkan Emre Gürcanlı

ACE-COM-002 Information Compliance and Quantity Consistency in IFC-Based Quantity Take-Off: A Focused Review and Conceptual Verification Workflow 1451
Mahdis Motamedi and Hasan Basri Başağa

ACE-COM-003 Identifying Key Business Survey Indicators to Predict Construction Production and Cost Indices 1461
Serkan Aydınlı

ACE-COM-004 Artificial Intelligence Adoption in Construction Management: A Bibliometric Analysis of Emerging Trends, Opportunities, and Future Directions 1469
Özge ALBOĞA

ACE-COM-005 Integrated Decision Support Model for Project Management Software Selection Using DEMATEL, TODIM, and CODAS 1479
Büşra Ziypak, Ümit Bahadır, Fatemeh Mostofi and Vedat Toğan

ACE-COM-006 Automatic Brick Wall Quantity Estimation from Construction Site Images Using YOLO-Based Object Detection and Multiple Regression 1489
Sertaç Alperen Koçak and Hasan Basri Başağa

ACE-COM-007 A Conceptual Analysis of the Need for Prescriptive Digital Tools and Dynamic Decision Partners in Lean Construction Management in Light of Global Literature 1499
İlkim Güven Balli, Elçin Filiz Taş

ACE-COM-008 Investigation of the Effect of Night Ventilation on Cooling Energy Consumption in Buildings 1509
Reyhan Boz, Semih Caglayan and Sadik Yigit

ACE-COM-009 LSTM-Based Activity Classification of Bricklaying Support Tasks on Construction Sites Using Wearable IMU Sensors 1517
Ibrahim Karatas, Abdulkadir Budak, Şahin Tolga Güvel

Table of Contents (cont.)

ACE-COM-010 AI-Based Decision Support Systems in Construction Management: From Technical Capability to Managerial Decision Quality 1525
Yasemin Bayrakkaya, Ali Erkan Karaman

ACE-COM-011 Engineered Stone Restrictions and Trade: A Comparative Assessment Focused on Turkish Natural Stone 1534
Selahattin Armağan Vurdu and Bahri Akyüz

ACE-COM-012 Investigation of COPRAS and ARAS Methods in Trade-Off Problems of Construction Project Scheduling 1544
Nur Sena Kınalı, Tayfun Dede, H. Abdullah Uçan

ACE-COM-013 Adaptive Mold Technology in Precast Concrete Panel Facilities: Optimization and Analysis 1553
Bedirhan Enes Kelek, Gökçen Karakol, Beni Kohen, Muhammed Maraşlı, Necati Aras, Nilüfer Özyurt

ACE-COM-014 Barriers in adoption of Circular Economy in Construction and Demolition Waste Management in Developing Countries 1563
Manjari Chakraborty, Pooja Singh, Rizwan Kazmi

ACE-COM-015 Environmental Implications of Formwork Systems: A Comprehensive Review from a Circular Economy Perspective 1576
Serkan KARALI, Gülben ÇALIŞ

ACE-COM-016 Modeling Bid/No-Bid Decisions in International Infrastructure Projects Using Graph Neural Networks and Natural Language Processing: A Pilot Study 1583
Uğur Günay and Onur Behzat Tokdemir

ACE-COM-017 BIM Integrated Risk Simulation and Management for Data Center Projects 1594
Şeyma Türkmen and Gürkan Emre Gürcanlı

ACE-COM-018 Development of an Automation-Based Smart Curing Cover for Optimizing the Concrete Curing Process 1604
İpek Naz Semercioğlu Akbulut, Seyedehdorsa Akhtarian, Aleyna Özdemir, Bartuğhan Uzun, Yunus Emrahan Akbulut, Hasan Basri Başağa

ACE-COM-019 Evaluation of Construction Contract Disputes Through Supreme Court Decisions 1614
Eda Bayram and Ömer Giran

INVITED LECTURES

Keynote Speakers

3 lectures

Fresh State, Rheology, Buildability and Mechanical Properties of 3D Printed Concrete Containing Lithium Slag

Faiz Shaikh*[1], SM Arifur Rahman[1] and Prabir Sarker[1]
[1] ORCID IDs: 0000-0002-5234-0619; 0000-0003-3725-3186; 0000-0002-5014-7444;
School of Civil and Mechanical Engineering, Curtin University, Perth, Australia,
*Corresponding author e-mail: s.ahmed@curtin.edu.au

Abstract. 3D printed concrete (3DPC) reduces construction waste, labour and time and enables complex geometries without formwork, but its cement-intensive mixtures remain a sustainability challenge. This keynote paper summarises an investigation into lithium slag (LS), the de-lithiated beta spodumene residue of lithium refining, as a supplementary cementitious material in 3DPC. Four printable mixes were studied: a control mix of cement, fly ash and silica fume, a mix in which 40% of the cement was replaced by LS (40LS), and the same two mixes with 1 vol.% polyvinyl alcohol (PVA) fibre. Flowability, rheology, buildability, heat of hydration, compressive, flexural and interlayer bond strength, crack patterns, microstructure and embodied carbon and energy were evaluated. All mixes remained within the printable flow range. The 40LS mix showed the highest viscosity recovery (82.7%) and creep recovery (37%) and the best buildability, with 28 layers and a 410 mm stack height compared with 21 layers and 305 mm for the control. LS reduced the 7- and 28-day compressive strengths by about 11% and 6%, its 7-day flexural strength loss was recovered at 28 days, and it lowered the interlayer bond strength. PVA fibre increased the flexural strength of the LS mix by about 25% but made the layer interface the weakest plane. Replacing 40% of the cement with LS reduced the embodied carbon by 33% and the embodied energy by 20% relative to the control.

Keywords: 3D concrete printing, Lithium slag, Supplementary cementitious materials, Rheology, Buildability, Embodied carbon.

1 Introduction

3D printed concrete (3DPC) has proven to be a promising technology that reduces construction waste, manpower and time while offering innovative architectural solutions [1]. It enables the fabrication of complex structures without conventional formwork and without the noise associated with on-site compaction. However, printable mixtures are cement-intensive, because they must be pumpable and extrudable yet stiffen quickly enough to carry the weight of the layers above [2, 3]. This high cement content is a major sustainability challenge and motivates the use of high volumes of supplementary cementitious materials (SCMs) such as fly ash, slag, silica fume and metakaolin.

Lithium slag (LS) is a by-product of the lithium extraction process whose use as an SCM is currently being researched for conventional cast concrete. Western Australia has three main lithium refinery operations — the Tianqi Lithium Kwinana refinery, the Albemarle Kemerton plant and the Covalent Lithium Kwinana refinery — with a combined production capacity of approximately 150,000 tonnes per year. Approximately 8–9 tonnes of residue are generated to refine one tonne of battery-grade lithium, so that some 1.2–1.5 million tonnes of lithium refinery residue are produced every year and require sustainable management to prevent environmental pollution. This study investigates, for the first time, the potential of LS as an SCM for the production of decarbonised 3DPC, and evaluates its effect on the fresh state,

rheology, buildability, hydration, mechanical properties, microstructure and environmental impact of printable mixes with and without fibre reinforcement.

2 Materials and Methods

2.1 Lithium Slag and Other Materials

The LS used in this study, also known as de-lithiated beta spodumene (DBS), has flaky and angular particles (Fig. 1) and an as-received water content of 28.3%. The average particle sizes of the cement and the LS were 17 μm and 38 μm, respectively. Table 1 compares the chemical composition and physical properties of the cement (OPC), LS, fly ash (FA) and silica fume (SF). LS is rich in SiO_2 (54.6%) and Al_2O_3 (21.1%) with a low CaO content (7.5%), and its specific gravity of 2.46 is markedly lower than that of cement (3.1).

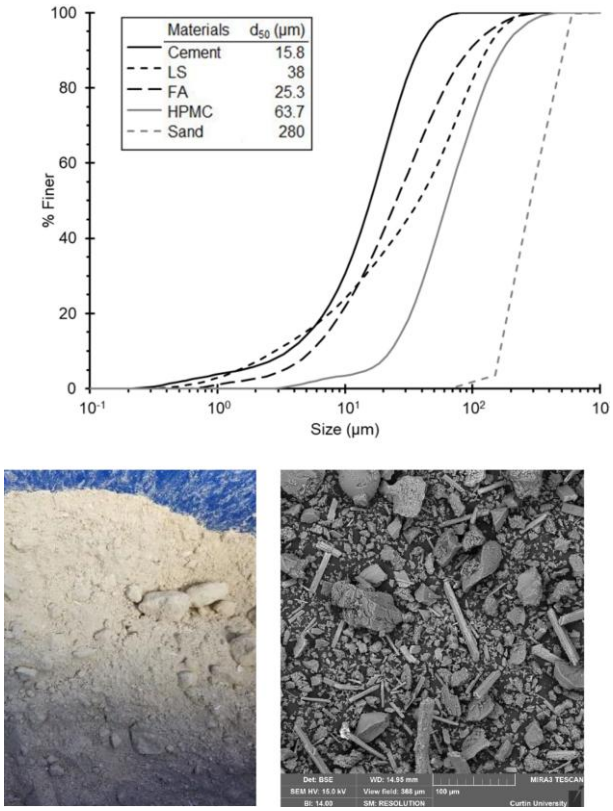


Fig. 1. Lithium slag: particle size distributions of the binder materials and sand (top) (Adopted from [6]), appearance of the as-received LS and SEM image showing its flaky, angular particles (bottom) (Adopted from [7]).

Table 1. Chemical composition and physical properties of the binder materials.

Parameter	OPC	LS	FA	SF
SiO_2 (%)	20.7	54.6	51.1	94.2
Al_2O_3 (%)	5.7	21.1	25.6	–
Fe_2O_3 (%)	2.9	1.5	12.5	–
CaO (%)	63.1	7.5	4.3	–
MgO (%)	1.3	0.6	1.5	–
SO_3 (%)	3.3	5.6	0.2	0.8
K_2O (%)	0.4	0.9	0.7	<0.01
Na_2O (%)	0.3	0.7	0.8	<0.01
LOI at 750 °C (%)	1.9	7.8	0.6	3.2
Specific gravity	3.1	2.46	2.20	2.22
Specific surface area (m^2/kg)	360	342	416	19934

Source: Data from [6]

2.2 Mix Proportions and Printing

Four mixes were designed (Table 2). In the control mix the binder consisted of cement, 20% FA and 10% SF; in the 40LS mix, 40% of the cement was replaced by LS. The binder and sand were combined in a 60:40 mass ratio at a water-to-binder ratio of 0.30. A superplasticiser (SP), a viscosity-modifying admixture (VMA) and hydroxypropyl methylcellulose (HPMC) were used, and the SP dosage was adjusted to maintain the design flow. The fibre-reinforced mixes (Control-F and 40LS-F) contained 1 vol.% PVA fibre.

Table 2. Mix proportions.

Mix ID	OPC	LS	FA	SF	Sand	w/b	SP	VMA	HPMC	PVA
Control	531	–	152	76	506	0.30	0.64	0.60	0.1	–
Control-F	531	–	152	76	506	0.30	1.19	0.60	0.1	1
40LS	319	212	152	76	506	0.30	2.51	0.60	0.1	–
40LS-F	319	212	152	76	506	0.30	3.07	0.60	0.1	1

OPC, LS, FA, SF and sand in kg/m^3; SP, VMA and HPMC in wt.% of binder; PVA in vol.%.

Source: Data from [6]

The mixing and printing protocol is shown in Fig. 2. The dry materials were mixed at 60 rpm; the PVA fibre and HPMC were added after 3 min, and the SP, VMA and water were added in two portions after 4 and 6 min (at 60 and 120 rpm), with scraping of the bowl at 5 min and final mixing at 240 rpm after 10 min. The mixes were then printed with a gantry-type 3D concrete printer for the buildability tests and the preparation of specimens.

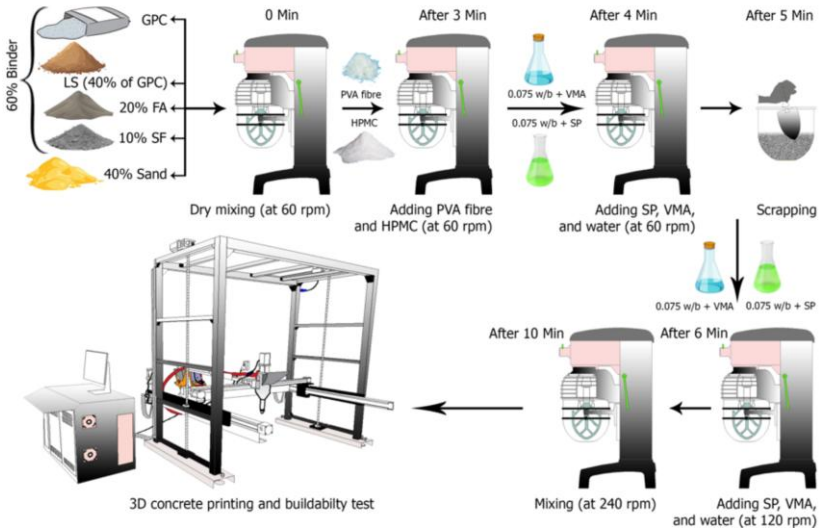


Fig. 2. Mixing protocol and 3D concrete printing (Adopted from [6]).

2.3 Test Methods

The workability of the fresh mixes was measured by the flow test immediately after mixing and after 30 and 60 min. The rheology was measured with a Malvern Kinexus Pro+ rheometer using shear-rate protocols to obtain the plastic viscosity, the viscosity recovery rate (VRR) and the creep recovery. The heat of hydration was measured by isothermal calorimetry. Buildability was assessed by printing cylindrical stacks layer by layer, recording the number of layers and the stack height, and by measuring the deformation ratios of the layers. Compressive, flexural and interlayer bond (tensile) strengths were determined on specimens cut from printed elements at 7 and 28 days, and the microstructure was examined by scanning electron microscopy (SEM) with backscattered electron (BSE) imaging and energy-dispersive X-ray spectroscopy (EDS). Finally, the embodied carbon (EC) and embodied energy (EE) of the mixes were calculated.

3 Results and Discussion

3.1 Flowability and Rheology

The initial flow values of all mixes were within 200 ± 10 mm (Table 3). The flow decreased slightly after 30 min owing to the evaporation of water and markedly after 60 min owing to the onset of hydration, but all mixes remained within the printable flow region of about 140–160 mm reported in the literature.

All printable mixes behaved as pseudo-plastic, shear-thinning non-Newtonian fluids (Fig. 3a). The LS, SP and HPMC enhanced the flocculation and water retention of the mixes, which significantly increased their plastic viscosity and yield stress. The VRR of the control and 40LS mixes was about 73.3% and 82.7%, respectively. The creep recovery was 21.7% for the control and 37% for 40LS, and 28.8% and 15.5% for the corresponding fibre-reinforced mixes (Fig. 3b). A higher creep recovery indicates a greater ability to return to the original shape and thus less deformation under self-weight; the 40LS mix combined the highest VRR and creep recovery of all mixes.

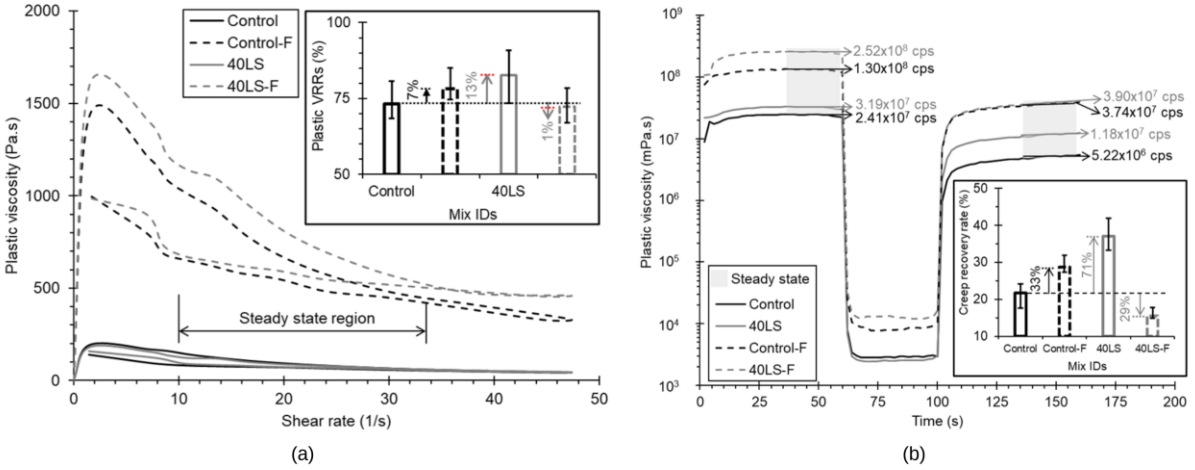


Fig. 3. Rheological behaviour: (a) plastic viscosity versus shear rate with the viscosity recovery rates (inset); (b) viscosity during the creep-recovery protocol with the creep recovery rates (inset). (Adopted from [6])

3.2 Buildability

The control mix could be printed to 21 layers with a stack height of 305 mm, whereas the 40LS mix reached 28 layers and 410 mm (Table 3, Fig. 4). The fibre-reinforced mixes reached 24 layers (360 mm, Control-F) and 21 layers (350 mm, 40LS-F). The better buildability of 40LS can be attributed to its higher VRR and creep recovery and to the lower specific gravity of LS

(2.46), which reduces the gravitational load on the middle and upper layers, limits excessive layer deformation and preserves the structural integrity of the stack.

Table 3. Fresh-state properties and buildability of the mixes.

Property	Control	Control-F	40LS	40LS-F
Flow, initial (mm)	195	200	200	190
Flow after 30 min (mm)	175	165	170	160
Flow after 60 min (mm)	148	138	150	144
Viscosity recovery rate (%)	73.3	n.r.	82.7	n.r.
Creep recovery (%)	21.7	28.8	37.0	15.5
Number of printed layers	21	24	28	21
Stack height (mm)	305	360	410	350

Flow values read from the flow-test chart; n.r. = not reported in the text.
Source: Data from [6]

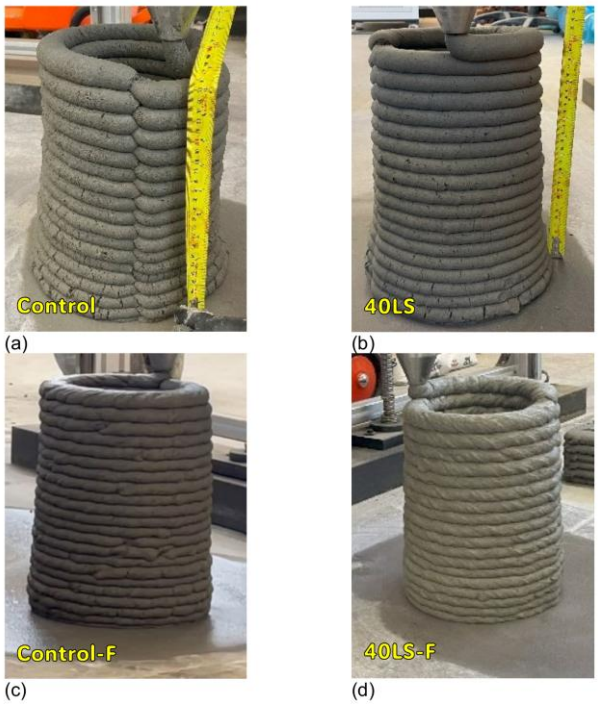


Fig. 4. Buildability tests: (a) Control, (b) 40LS, (c) Control-F and (d) 40LS-F. (Adopted from [6])

3.3 Heat of Hydration

All mixes exhibited a rapid release of heat within the first 60 min owing to wetting and dissolution, followed by a typical dormant phase, during which ettringite (AFt) forms through the interaction between the binder and the pore water (Fig. 5). In the control mix, the C_3S and C_2S of the cement ended the dormant phase and produced the main hydration peak after about 6–7 h. In the 40LS mix, the high LS content and SP dosage diluted the cement clinker and extended the dormant phase: the main peak was delayed by about 21.2 h and its height was reduced by 53%. The cumulative heat at 72 h was about 600 J/g for the control and 370 J/g for 40LS, i.e. 38% lower.

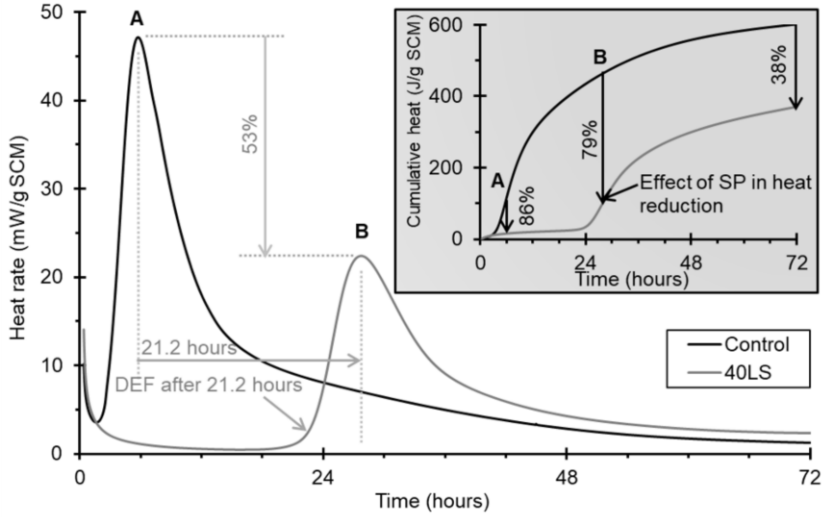


Fig. 5. Heat flow and cumulative heat (inset) of the Control and 40LS mixes, showing the delayed and reduced main hydration peak of 40LS. (Adopted from [6])

3.4 Mechanical Properties

The incorporation of LS reduced the 7- and 28-day compressive strengths by about 11% and 6%, respectively, and the addition of PVA fibre did not improve the compressive strength of either the control or the LS mix (Fig. 6a). The strength activity indices showed that the mixes satisfied the pozzolanicity requirements of ASTM C618 [4], BS 8615-1, AS 3582 and the RILEM TC 267-TRM approach [5]. The flexural strength of the LS mix was about 23% lower than that of the control at 7 days, but this loss was recovered at 28 days (Fig. 6b). PVA fibre increased the flexural strength of the LS mix by about 25% through crack bridging.

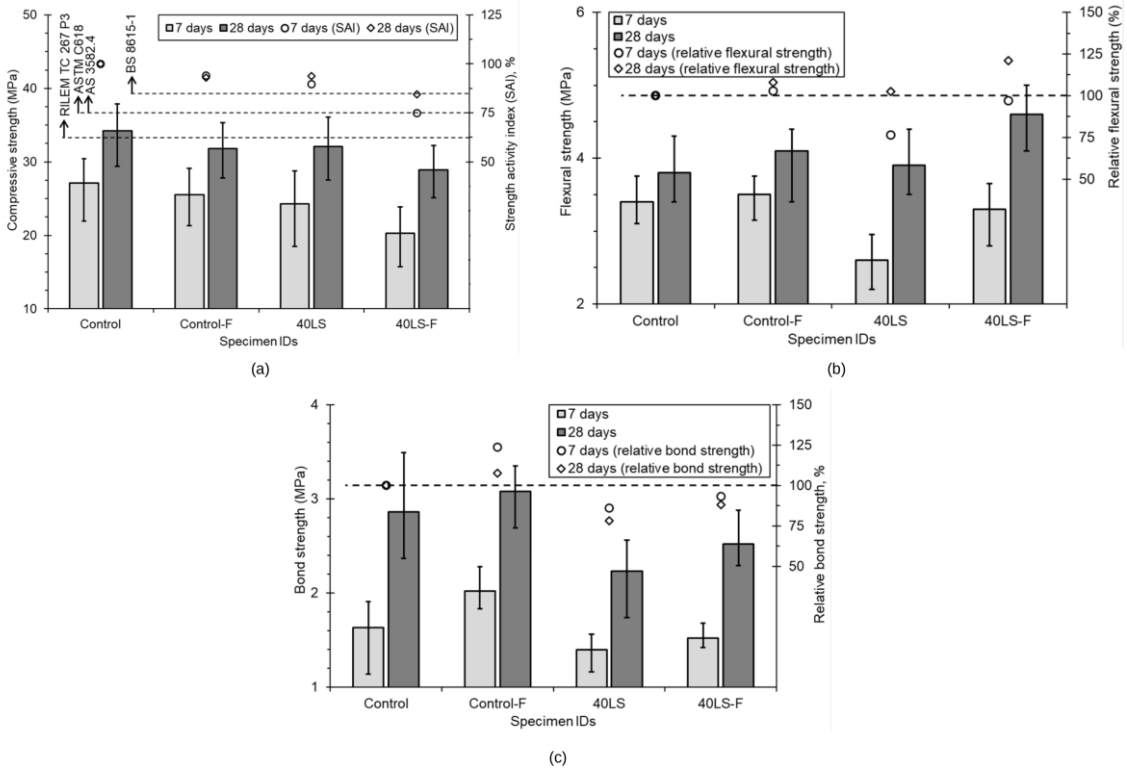


Fig. 6. Strength of the printed specimens at 7 and 28 days: (a) compressive strength with the strength activity index, (b) flexural strength and (c) interlayer bond strength, with values relative to the control. (Adopted from [6])

LS reduced the interlayer bond strength at both ages (Fig. 6c). PVA fibre improved the bond strength of both mixes, by 7% and 10% at 7 and 28 days in the LS mix and by 24% and 8% in the control mix. Because the printer nozzle moves horizontally along the printing direction, the PVA fibres are oriented parallel to the layers. This anisotropy helps to resist crack propagation through fibre bridging and increases the flexural capacity, but in combination with clinker dilution it weakens the interlayer adhesion, so that the bond strength of 40LS-F remained below that of the control.

The crack patterns confirmed this mechanism. In the control and 40LS specimens, the debonding cracks propagated through the middle of the printed layers rather than along the interface, indicating that the layer bond was relatively strong compared with the concrete matrix. In the PVA fibre reinforced specimens, the cracks propagated along the interface between two printed layers, which therefore became the weakest part of the element.

3.5 Microstructure

The BSE images and EDS maps (Fig. 7) show C-S-H and C-A-S-H together with unreacted FA particles in the control mix, AFt needles in the control-F mix, and HPMC, microcracks, pores and partially reacted LS particles in the LS mixes. The 40LS and 40LS-F mixes showed the early-age development of C-A-S-H and amorphous intermediate hydration products.

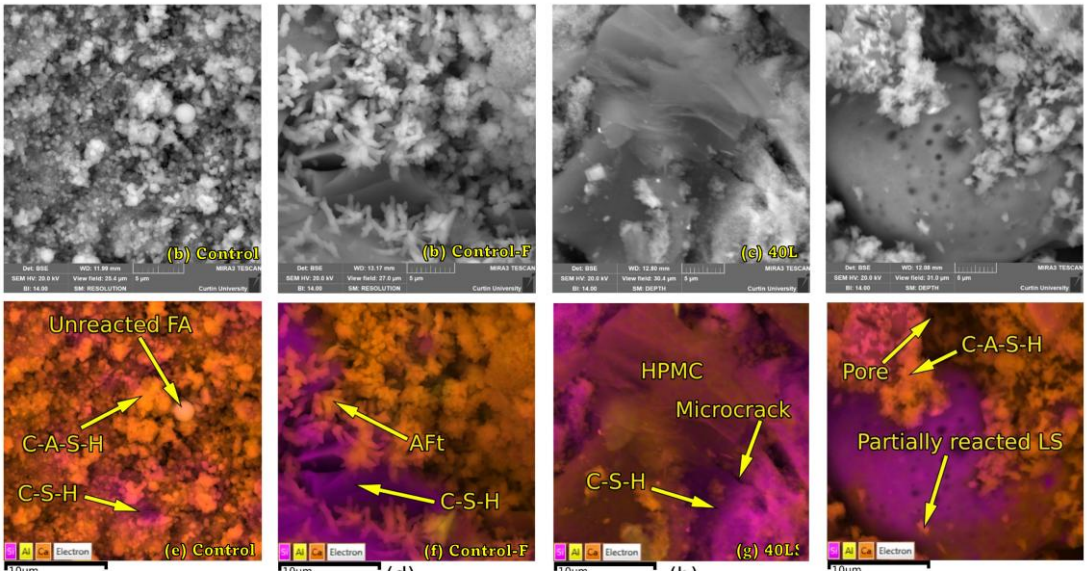


Fig. 7. BSE images (top) and EDS maps (bottom) of the printed mixes, showing C-S-H, C-A-S-H, AFt, unreacted FA, HPMC, microcracks, pores and partially reacted LS. (Adopted from [6])

3.6 Embodied Carbon and Energy

The use of LS as an SCM significantly reduced the environmental impact of the printed concrete (Table 4). The cement was the dominant contributor in all mixes, and the SP and PVA fibre added smaller amounts. The EC of the 40LS mix was 305 kg CO_2-eq/m³, 33% lower than that of the control, and its EE was 2652 MJ/m³, 20% lower. For reference, a conventional 35 MPa concrete has an EC of 375 kg CO_2-eq/m³ and an EE of 2800 MJ/m³, i.e. lower than the cement-rich control mix but higher than the 40LS mix. Besides reducing the environmental footprint, the use of LS encourages the recycling and utilisation of an industrial waste.

Table 4. Embodied carbon (EC) and embodied energy (EE) of the mixes.

Quantity	Control	Control-F	40LS	40LS-F
EC (kg CO_2-eq/m³)	456	468	305	317
Reduction in EC vs. Control	–	–	33%	31%
EE (MJ/m³)	3296	3608	2652	2966
Reduction in EE vs. Control	–	–	20%	10%

Totals of the constituent contributions; reductions relative to the Control mix. Reference 35 MPa concrete: EC = 375 kg CO_2-eq/m³, EE = 2800 MJ/m³.

Source: Data from [6]

4 Conclusions

The following conclusions can be drawn from this study:

- The 40% LS mix exhibited better buildability than the cement-based control (28 versus 21 layers), supported by its higher viscosity recovery and creep recovery and the lower specific gravity of LS. The addition of 1 vol.% PVA fibre reduced the buildability of the LS mix.
- The LS-based 3DPC showed a comparable flexural strength and a slightly lower compressive strength at 28 days, but a lower interlayer bond strength than the cement-based 3DPC.
- 1 vol.% PVA fibre significantly improved the flexural strength and slightly improved the bond strength at both ages, without improving the compressive strength; fibre alignment made the layer interface the weakest plane.
- The control and 40LS mixes released about 600 J/g and 370 J/g of cumulative heat at 72 h. The 40LS mix showed a delayed main hydration peak due to clinker dilution and the high SP content needed to maintain the design flow.
- BSE-EDS analysis of 40LS and 40LS-F showed the early-age development of C-A-S-H and amorphous intermediate hydration products.
- Replacing 40% of the cement with LS in printable mixes reduced the embodied carbon by 33% and the embodied energy by 20% compared with the control mix.

Acknowledgments

The authors acknowledge the Australian Research Council (ARC) for the Discovery Project grant that supported this research.

References

1. Buswell, R.A., Leal de Silva, W.R., Jones, S.Z., Dirrenberger, J.: 3D printing using concrete extrusion: A roadmap for research. Cement and Concrete Research 112, 37–49 (2018). https://doi.org/10.1016/j.cemconres.2018.05.006
2. Le, T.T., Austin, S.A., Lim, S., Buswell, R.A., Gibb, A.G.F., Thorpe, T.: Mix design and fresh properties for high-performance printing concrete. Materials and Structures 45(8), 1221–1232 (2012). https://doi.org/10.1617/s11527-012-9828-z
3. Roussel, N.: Rheological requirements for printable concretes. Cement and Concrete Research 112, 76–85 (2018). https://doi.org/10.1016/j.cemconres.2018.04.005
4. ASTM C618: Standard Specification for Coal Fly Ash and Raw or Calcined Natural Pozzolan for Use in Concrete. ASTM International, West Conshohocken, PA.
5. Li, X., Snellings, R., Antoni, M., et al.: Reactivity tests for supplementary cementitious materials: RILEM TC 267-TRM phase 1. Materials and Structures 51, 151 (2018). https://doi.org/10.1617/s11527-018-1269-x
6. Rahman, SM.A., Khair, S., Shaikh, F.U.A. and Sarker, P.K.: Decarbonized 3D printed concrete incorporating lithium slag and PVA fibre: Buildability, mechanical and

microstructural insights. Materials and Structures 58:245 (2025). https://doi.org/10.1617/s11527-025-02768-w.
7. Rahman, SM.A., Mahmood, A.H., Shaikh, F.U.A. and Sarker, P.K.: Fresh state and Hydration properties of high-volume lithium slag cement paste. Materials and Structures 56:91. https://doi.org/10.1617/s11527-023-02177-x.

Author Contribution Statement

- *Conceptualization:* [[Faiz Shaikh and Prabir Sarker]]
- *Methodology:* [[SM Arifur Rahman, Faiz Shaikh, Prabir Sarker]]
- *Investigation:* [[SM Arifur Rahman, Sanjida Khair]]
- *Writing – Original Draft:* [[SM Arifur Rahman]]
- *Writing – Review & Editing:* [[Faiz Shaikh and Prabir Sarker]]

List of Abbreviations

- **3DPC** — 3D Printed Concrete
- **AFt** — Ettringite
- **BSE** — Backscattered Electron
- **C-(A-)S-H** — Calcium (Alumino-)Silicate Hydrate
- **DBS** — De-lithiated Beta Spodumene
- **EC / EE** — Embodied Carbon / Embodied Energy
- **EDS** — Energy-Dispersive X-ray Spectroscopy
- **FA / SF** — Fly Ash / Silica Fume
- **HPMC** — Hydroxypropyl Methylcellulose
- **LS** — Lithium Slag
- **PVA** — Polyvinyl Alcohol
- **SCM** — Supplementary Cementitious Material
- **SEM** — Scanning Electron Microscopy
- **SP / VMA** — Superplasticiser / Viscosity-Modifying Admixture
- **VRR** — Viscosity Recovery Rate

The authors declare no conflict of interest.

Publication Note

This paper was peer-reviewed, accepted for presentation, and included in the proceedings of the ACE2026 – International Conference on Advances in Civil Engineering, held on 12–14 October 2026 in Trabzon, Türkiye.

This paper may be cited as follows:

F. Shaikh, S.M.A. Rahman and P. Sarker, “Fresh State, Rheology, Buildability and Mechanical Properties of 3D Printed Concrete Containing Lithium Slag,” in Proceedings of the ACE2026 – International Conference on Advances in Civil Engineering, Trabzon, Türkiye, 12–14 October 2026.

Urban Tunneling Challenges in Rapidly Developing Cities: Managing Ground Uncertainty, Risk, and Digital Transformation

Shahab Yasrebi[1]
[1] Geomaple Geotechnics Inc. (GGI), 60 Green Ln, Unit 12A, Thornhill, ON L3T 7P5, Canada,
yasrebi@geomaple.ca

Abstract. Rapid urban growth is pushing transport and utility infrastructure underground, so that tunnels are increasingly built at shallow depth in soft, variable and water-bearing ground beneath sensitive structures. This keynote paper examines how such ground uncertainty can be converted into manageable construction risk. Soft ground is treated as a behavioural category governed by stiffness, strength, drainage and disturbance, and groundwater is identified as a primary design parameter. The principles of the New Austrian Tunnelling Method (NATM) are revisited as an observational design philosophy that links behaviour-based ground classification, support classes, trigger levels and contractual flexibility. Experience from the urban tunnel programme of Tehran is then summarised through four case histories: a 31 m wide bifurcation of the Niayesh tunnel, the cross-passage intersection of the Hakim tunnel, a two-storey tunnel with 3.5 m of cover beneath the Modarres highway, and the 2016 collapse on Tehran Metro Line 6. The cases show that three-dimensional analysis, appropriate constitutive models and monitoring-based back-analysis are needed to predict ground movements reliably. In the two-storey tunnel, only the combination of fore-poling, micro-piles and nailing satisfied the 25.4 mm settlement criterion, reducing the predicted surface settlement by about 51.5%. Finally, a closed-loop digital workflow is outlined in which monitoring, numerical models and data-assisted tools shorten the time between observation and engineering decision.

Keywords: Urban tunnelling, NATM, Ground uncertainty, Observational method, Numerical back-analysis, Digital twin.

1 Introduction

Urban growth, increasing demand for mobility, limited surface space, congested utility corridors and the objectives of sustainability and resilience are moving the infrastructure of megacities underground. As a consequence, tunnelling increasingly takes place in difficult ground and beneath sensitive infrastructure: existing buildings, bridges, highways, lakes and buried services. Under these conditions the performance of a tunnel is governed by the interaction among soil, water, support, construction method and workmanship, rather than by any one of these factors in isolation.

The central question addressed in this paper is how uncertainty in the ground can be converted into manageable construction risk. The discussion follows the sequence *uncertainty* → *control* → *adaptation*. Section 2 describes the sources of ground and groundwater uncertainty in soft-ground tunnelling. Section 3 revisits the principles of the New Austrian Tunnelling Method (NATM) and their implementation through support classes. Section 4 introduces Tehran as a megacity laboratory for urban tunnelling, and Section 5 presents four case histories covering large spans, intersections, very shallow cover and a failure. Section 6 discusses monitoring, numerical back-analysis and digital transformation, and Section 7 summarises the main lessons.

2 Ground Uncertainty and Groundwater in Urban Tunnelling

2.1 Soft Ground as a Behavioural Category

"Soft ground" is a behavioural category rather than a single soil type. It includes soft clays and silts, loose saturated sands, fill and made ground, and mixed ground. Its response to excavation is governed by four behaviours: *stiffness* (low stiffness and limited stand-up time), *strength* (stress-path dependence and non-linearity), *drainage* (dewatering and consolidation effects) and *disturbance* (sensitivity, remoulding and cyclic loading). Urban fill may contain voids, debris and undocumented utilities, and mixed ground can create uneven and locally unstable zones at the face. Design must therefore address a credible range of conditions, not a single deterministic profile.

2.2 Uncertainty in the Ground Model

Ground uncertainty is the first source of tunnel risk. Stratigraphy varies between investigation points; urban ground contains abandoned foundations, wells, voids and services; and groundwater regimes change seasonally and during construction. A useful discipline is to separate explicitly what the site investigation tells us, what must be interpolated between boreholes, and what can still surprise us — voids, utilities, old foundations and changes in permeability. Regional geology defines the framework, but local investigation defines the design.

The history of the city is part of the ground model. Fig. 1 shows an example from Tehran: a watercourse that is visible on a 1956 aerial photograph had been filled with man-made soil by 1966 and later lay across a tunnel alignment. Old waterways, *qanats* (traditional underground water channels) and man-made fill of this kind constitute hidden tunnelling risk unless historical records are systematically included in the investigation.

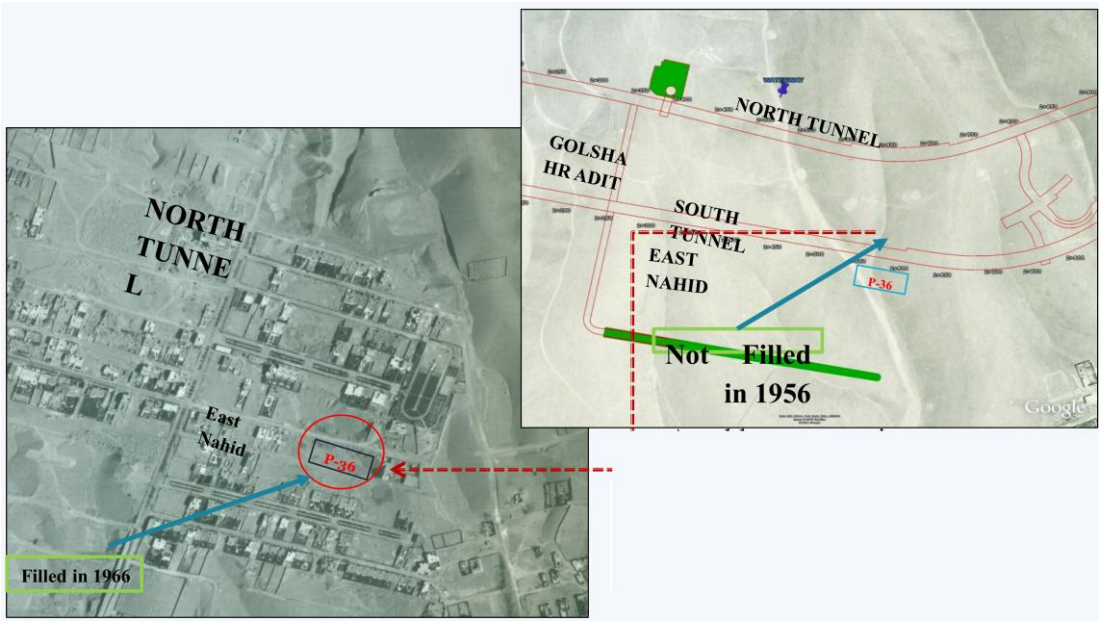


Fig. 1. Urban history as part of the ground model: an old waterway that was open in 1956 and filled with man-made soil by 1966 (aerial photographs) crossing a tunnel alignment in Tehran.

2.3 Groundwater as a Governing Hazard

Groundwater controls four mechanisms of instability in urban tunnels: face instability, piping and internal erosion, drawdown settlement, and blowout or hydraulic fracture. Drawdown increases the effective stress in the surrounding ground and therefore the settlement risk for adjacent structures, even where the tunnel itself remains stable [1, 2]. Groundwater should

therefore be treated as a primary design parameter that is investigated, modelled, controlled and monitored throughout construction.

2.4 The Geotechnical Baseline Report

The Geotechnical Baseline Report (GBR) is one of the most important contractual documents in modern tunnelling because it turns uncertainty into contractual clarity [3]. Its purpose is to define the expected ground conditions, allocate contractual risk, reduce claims, improve communication between the parties and support construction planning. A GBR typically describes the ground and groundwater, states the baseline assumptions, identifies risk zones and sets out the construction expectations. Engineering geology, groundwater, stress redistribution, settlement and site investigation collectively govern tunnel performance and should guide both design and construction decisions.

3 NATM as an Observational Design Philosophy

The New Austrian Tunnelling Method was developed in Austria between 1957 and 1965 by Ladislaus von Rabcewicz, Leopold Müller and Franz Pacher [4]. NATM is a design and construction philosophy, not a fixed excavation sequence or a specific set of excavation and support techniques. The term NATM refers to this philosophy; the sequential excavation method (SEM) describes the sequential excavation approach; sprayed-concrete-lined (SCL) tunnelling is a terminology for the lining technology; and the centre diaphragm method (CDM), side-drift and top heading–bench excavations are excavation sequences. The underlying cycle is: excavate → ground responds → install support → measure → compare with prediction → adjust. Seven principles can be distinguished:

- **Preserve and mobilise ground strength.** Excavation removes confinement; a stress arch forms around the opening when the ground can mobilise its shear resistance, whereas excessive relaxation causes yielding, loosening and a larger support demand. Face effects are three-dimensional and cannot be fully represented by a plane-strain model.
- **Control, not eliminate, deformation.** Too little deformation leads to high support loads; too much leads to deterioration of the ground and surface settlement.
- **Early support and rapid ring closure.** Support is installed close to the face, unsupported time is minimised and the invert is closed early; in shallow soft ground, support timing can be as important as support capacity.
- **Minimise unsupported length and closure time.**
- **Observational method: prediction to action** [5]: predict → monitor → compare → trigger → modify → verify.
- **The contract must permit adaptation**, by defining support classes and decision authority, triggers for changes and commercial mechanisms for approved changes.
- **Behaviour-based ground classification**, in which ground, water, overburden, face stability, deformation potential and nearby assets together determine the support class.

On site, these principles are implemented through a zoning plan of excavation and support classes: investigation → geotechnical zones → expected behaviour → support class → field verification. Table 1 summarises the classes used for the Niayesh tunnel in Tehran, which has a total main-tunnel length of 8100 m, an overburden of 4.7–40 m (18 m on average) and a maximum longitudinal slope of 4.5%. The tunnels were excavated by mechanical excavator following NATM; fan-shaped forepoling (length 6 m, diameter 76 mm) was arranged in the roof in loose ground, and the face was sealed with 3 cm of shotcrete only in poor ground. A modified horseshoe shape was used for the 1.5- and 2.5-lane sections and a mouth-shaped section for the 3.5- and 4-lane sections.

Table 1. Excavation and support classes of the Niayesh tunnel (shotcrete C25/30).

Excavation class	1.5 lanes	2.5 lanes	3.5 lanes	Bifurcation[a]
Area (m²)	87	136	186	470
Width (m)	10.80	14.40	18.00	30.60
Height (m)	9.80	11.90	12.60	19.60
Traffic lanes[b]	1	2	3	4
Shotcrete, main wall (cm)	25	30	35	45–55
Shotcrete, temporary wall (cm)	–	20	25	25
Shotcrete, temporary invert (cm)	25	20	–	20
Shotcrete, main invert (cm)	25	30	35	45–55
Round length, top heading (m)	1–1.5	1–1.5	1–1.5	1
Round length, bench (m)	3–4.5	3–4.5	3–4.5	2

[a] Maximum width and height in the bifurcation area. [b] Main tunnels have one additional 2.5 m wide emergency lane.

4 Tehran: A Megacity Laboratory for Urban Tunnelling

Tehran has an urban area of about 686 km² (approximately 30 km × 25 km), some 10 million residents and about 3 million daytime commuters. The city generates around 15 million trips per day, of which 2.5 million are made on highways, with about 3.5 million cars. The metro network currently spans 310 km with 7 lines and 160 active stations and has carried a total of 820 million trips; the long-term plan aims to extend it to 430 km with eleven lines by 2040. The urban highway tunnels summarised in Table 2 illustrate the range of constraints encountered.

Table 2. Urban highway tunnels in Tehran discussed in this paper.

Tunnel	Total length (m)	Governing constraints
Niayesh	8100	Large spans and bifurcations; bridges, a lake, a highway and high-rise buildings above
Amir Kabir	4060	Shallow cover (4.5–8.5 m) beneath the historic bazaar district
Hakim	1012	Intersections; low cover beneath a sensitive urban park
Arash–Esfandiar	1532	Highway under-passing; commercial buildings, qanats, old waterways and voids

Even small structures can be demanding. The Valiasr underpass, 160 m long with eleven inlets and outlets, was built with only about 3 m of cover beneath one of the busiest intersections of the city. Carefully staged excavation, rapid support installation, protection of adjacent infrastructure and real-time monitoring were essential to maintain both stability and surface serviceability.

5 Case Histories

5.1 Large-Span Bifurcation of the Niayesh Tunnel

The bifurcation chambers of the Niayesh tunnel are about 31 m wide and 19 m high, with an overburden of only 11–14 m. Because of the large span and excavation volume, controlling ground deformation and structural stability was the main challenge. The combination of large span, low cover and non-prismatic geometry produces genuinely three-dimensional behaviour. The chambers were therefore excavated in a multi-stage sequence (Fig. 2), with the excavation and support class selected according to the risk and monitoring plan and verified by back-analysis with PLAXIS models and monitoring data.

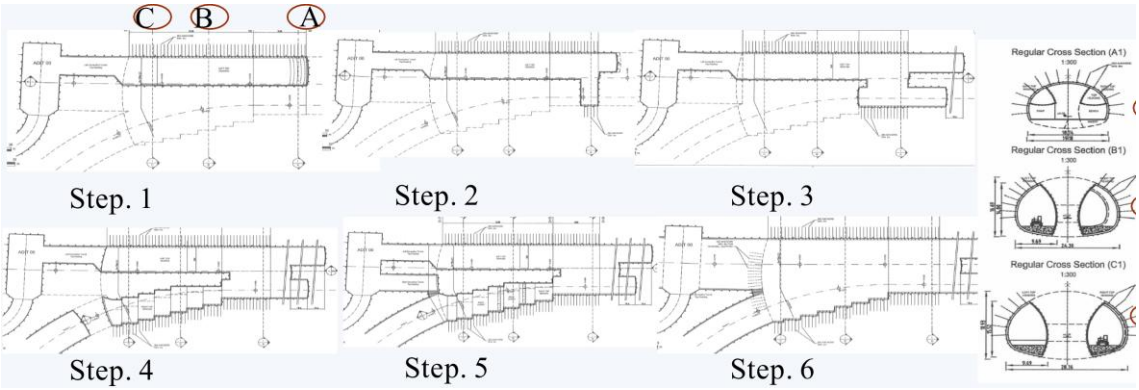


Fig. 2. Six-step excavation sequence for the 31 m bifurcation of the Niayesh tunnel and the regular cross-sections A, B and C.

The study focused on the influence and effectiveness of rib elements during the NATM construction of the bifurcation, built in three phases: pile excavation, rib excavation, and enlargement with final-lining construction. Both 2D and 3D numerical analyses were carried out, and the surface settlements recorded by monitoring were used to assess and validate the 3D predictions (Fig. 3). 3D analysis was necessary because of the non-prismatic geometry, the staged excavation with ribs and the longitudinal load transfer; it showed that the ribs reduced settlement and redistributed the initial-lining forces. Numerical models are predictions; monitoring provides the validation.

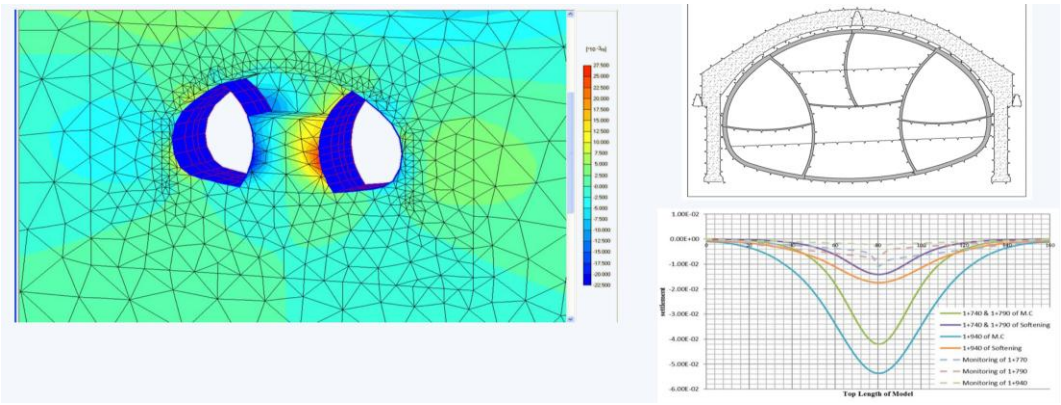


Fig. 3. Numerical modelling of the Niayesh bifurcation (left: 3D model; right: 2D section and comparison of predicted and monitored surface settlement profiles).

Along the alignment, critical positions included the under-passing of the Kurdistan bridge, passages beneath the lake of Mellat Park and beneath the Modarres highway, a cinema and residential high-rise buildings. Beneath the Modarres highway (span of about 18 m and cover of about 5 m), risk was controlled by five integrated measures: a rigid frame, fore-poling, consolidation grouting, short excavation rounds and portal stabilisation with a soil-nailing system.

5.2 Selection of the Constitutive Model

The choice of constitutive model is a crucial and debated aspect of numerical simulation, because it can control the prediction. Tunnelling in cemented soils with strain-softening behaviour is particularly demanding: such materials have distinct peak and residual strength parameters, strength reduces with increasing strain, and the high stiffness of unloading paths around the tunnel combined with the low strain of cemented soils further affects the results [6].

Three questions should be asked of any candidate model: Can it reproduce unloading stiffness? Can it reproduce strain softening? Can its parameters be obtained reliably?

Fig. 4 compares surface settlements recorded at three monitoring sections with predictions from a softening model and from an elastic–perfectly plastic Mohr–Coulomb (MC) model, taking the monitoring records as the reference. The MC model predicted final settlements of roughly 42–54 mm, whereas the softening model predicted about 14–18 mm, much closer to the monitored values. A single elastic modulus or a basic MC parameter set may be adequate for screening, but inadequate for the prediction of movements.

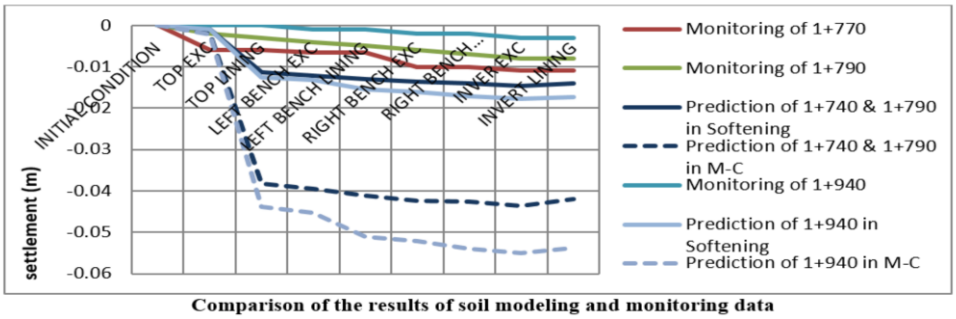


Fig. 4. Surface settlement during the construction stages: monitoring records at chainages 1+770, 1+790 and 1+940 compared with predictions of the softening and Mohr–Coulomb (M-C) models.

5.3 Cross-Passage Intersection of the Hakim Tunnel

The intersection between a cross passage and the main tunnel of the Hakim tunnel (main tunnel about 17.6 m wide and 12.6 m high) has a complex geometry that requires staged 3D analysis, and construction tolerance and sequencing are critical. The analysis also showed that the interaction between the initial and final linings changes the load path. For an 18 m wide, 10.9 m high section (186 m²) with a 35 cm initial lining and a 50 cm final lining, the construction-stage analysis gave a maximum axial force of about 140 t in the initial lining, while the final lining carried a maximum axial force of about 90 t after the assumed degradation of the initial lining. Interface conditions and installation timing strongly influence the final-lining forces and should be modelled explicitly to avoid unrealistic load distributions. The 3D predictions were compared with monitoring data, and the portal was analysed as a three-dimensional boundary problem, since reduced confinement, changing geometry and staged excavation make portals inherently three-dimensional.

5.4 Two-Storey Tunnel beneath the Modarres Highway

The two-storey tunnel of the Arash–Esfandiar project, 13 m high and 12.2 m wide, passes beneath the Modarres highway with only 3.5 m of overburden in fill. The very low cover, large section, relatively straight floor and walls, high walls and the highway above made this the most demanding of the cases. The construction strategy was to reinforce before excavating: fore-poling, micro-piles and nails were installed, followed by staged excavation, structural works and waterproofing (Fig. 5).

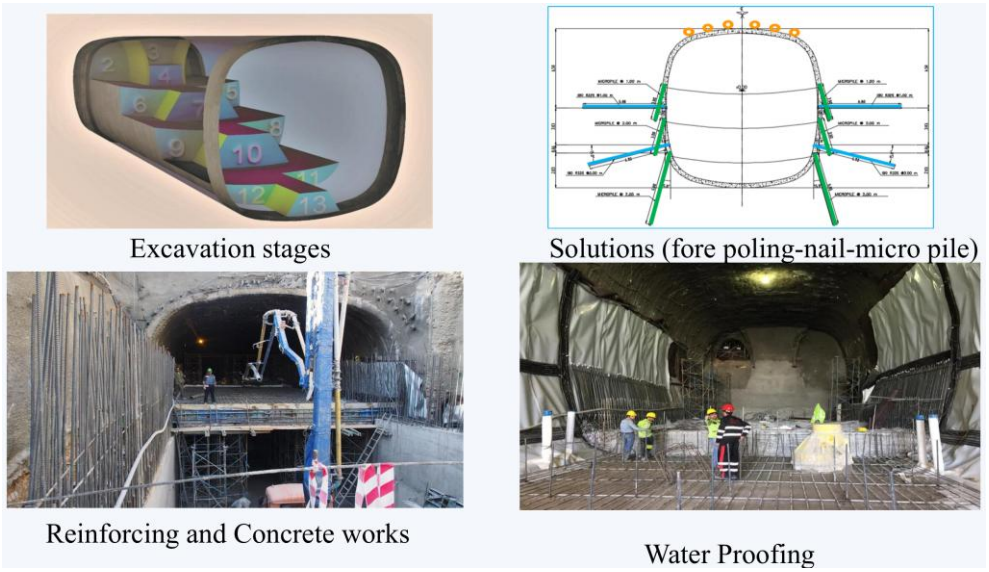


Fig. 5. Construction strategy for the two-storey tunnel: excavation stages, pre-support and reinforcement (fore-poling, nails and micro-piles), reinforcing and concrete works, and waterproofing.

Five numerical cases were evaluated against a maximum surface settlement of 25.4 mm: a baseline without additional support, fore-poles only (60 fore-poles in two rows, 6.0 m long), micro-piles only, nails only, and the combination of all three. The results are listed in Table 3. Only the combined system satisfied the settlement criterion, with a predicted surface settlement of 24.9 mm, a reduction of about 51.5% compared with the baseline. The individual measures reduced settlement by only 10.8–24%.

Table 3. Settlement and initial-lining forces for the five numerical cases of the two-storey tunnel (allowable surface settlement 25.4 mm).

Case	Fore-pole	Micro-pile	Nail	Surface settl. (mm)	Ratio to allow.	Settl. reduct.	Axial force (kN/m)	Bending moment (kN·m/m)	Moment reduct.
1	–	–	–	51.35	2.02	–	603.25	165.39	–
2	✓	–	–	39.03	1.54	24%	651.44	116.25	29.7%
3	–	✓	–	40.41	1.59	21%	712.33	158.34	4.3%
4	–	–	✓	45.79	1.80	10.8%	607.41	148.56	10.2%
5	✓	✓	✓	24.93	0.98	51.5%	714.51	89.95	45.6%

Settlements and axial forces are given as magnitudes. The maximum shear force was practically unchanged (161–164 kN/m) in all cases.

The internal forces show that support does not simply reduce forces but redistributes them: the combined system reduced the maximum bending moment of the initial lining by 45.6%, while the maximum axial force increased from 603 to 715 kN/m and the shear force remained almost constant. During construction, the measured settlements were compared with the predictions of the combined model; the differences between prediction and measurement reveal the remaining uncertainty in the ground model and are used to update it.

5.5 When Control Is Lost: The 2016 Failure on Tehran Metro Line 6

On 17 June 2016, a failure of the tunnel face and lining on Tehran Metro Line 6 produced a sinkhole about 26 m by 17 m in plan, which ruptured a gas pipeline and caused an explosion

(Fig. 6). Three people were killed and the project was delayed by six months. Monitoring records before the failure showed a progressive increase in settlement.

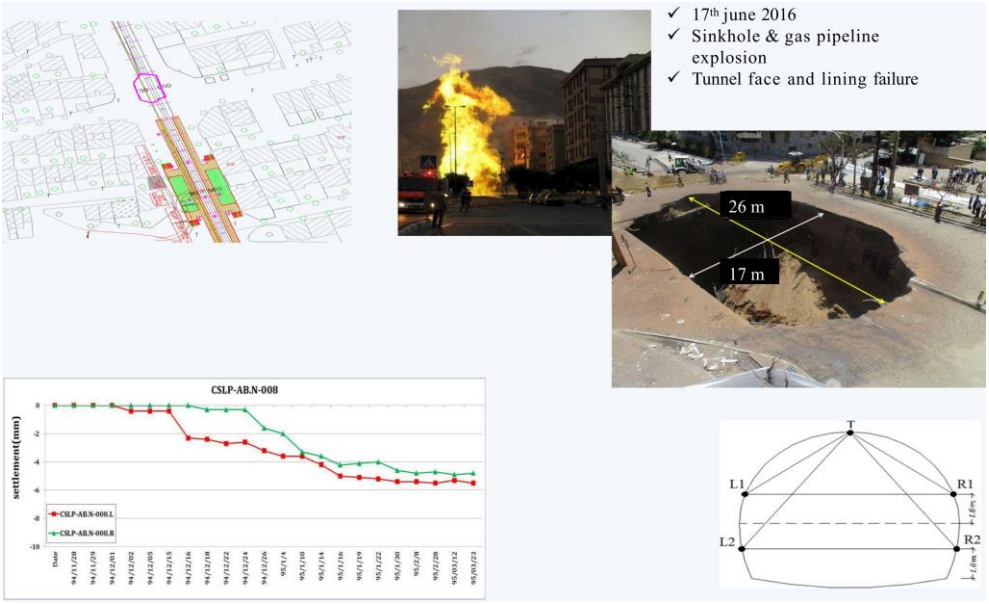


Fig. 6. Failure on Tehran Metro Line 6 (17 June 2016): location plan, gas pipeline explosion, sinkhole of about 26 m × 17 m, and settlement monitoring records before the failure.

After the failure, P.O.R. Consulting Engineers was commissioned to design the excavation and support for passing through the failure zone, to review the design of the rest of Line 6 and to supervise the construction of the temporary and final linings. The design changes included an excavation and support zoning plan based on risk assessment and monitoring results; extensometer and inclinometer monitoring; pre-support by forepoling, micro-piles and face grouting through the failure zone; an increase in face subdivision from two to six drifts; shorter advance lengths; and back-analysis by 3D finite element analysis (FEA) in FLAC under a strict monitoring regime. With a strictly applied risk and monitoring plan, the tunnel was successfully driven through the failure zone. The main lesson for contractor and client was the need for a rigorous monitoring plan and for attention to the risk notes of the consultant.

6 Monitoring, Back-Analysis and Digital Transformation

Monitoring must trigger action and not simply record movement. Trigger levels organised as alert → alarm → action connect monitoring trends, such as crack development on building façades, to predefined engineering responses, which is the practical core of the observational method [5]. After the Line 6 failure, this principle was extended into a closed-loop workflow: physical tunnel → digital model → live data → decision and action. The *physical tunnel* comprises the excavation, support, ground, groundwater and nearby assets; the *digital representation* combines BIM geometry with the geotechnical and numerical models; the *live data* include instrumentation, face mapping, construction progress and support installation; and the *decision layer* contains thresholds, forecasts, scenario testing and corrective actions.

In practice, the workflow is ground model → prediction → monitoring → back-analysis → decision. Near-real-time comparison of predicted and measured deformation, trigger levels linked to engineering actions, and continuous improvement of model parameters by back-analysis increase confidence in the prediction as excavation advances. Data-assisted tools, including artificial intelligence (AI), can add value in three areas: pattern recognition for early warning by identifying abnormal trends and correlations; updating of settlement and risk forecasts as excavation progresses; and comparison of construction alternatives and support

scenarios. AI assists engineering judgement but does not replace it. Digitalisation adds value when it shortens the time between observation and engineering decision.

7 Conclusions

The experience summarised in this paper leads to five conclusions for tunnelling in rapidly developing cities:

- Ground and groundwater govern behaviour; design must address a credible range of conditions, including those inherited from the urban history of the site.
- Deformation must be controlled, not only stability; in shallow soft ground, support timing is as important as support capacity.
- The construction sequence is part of the design, and large spans, intersections and portals require three-dimensional analysis.
- Numerical models predict and monitoring verifies; the constitutive model and its parameters can control the predicted settlement.
- Risk management requires decisions and action, supported by contracts that permit adaptation and by trigger levels linked to predefined responses.

Urban tunnelling therefore requires active control of ground behaviour rather than the execution of a fixed design, following the cycle predict → monitor → compare → update → decide → verify.

Acknowledgments

The author gratefully acknowledges the Organising Committee of ACE2026 for the invitation to deliver this keynote lecture.

References

1. Peck, R.B.: Deep excavations and tunnelling in soft ground. In: Proceedings of the 7th International Conference on Soil Mechanics and Foundation Engineering, State-of-the-Art Volume, pp. 225–290. Sociedad Mexicana de Mecánica de Suelos, Mexico City (1969).
2. Mair, R.J., Taylor, R.N., Bracegirdle, A.: Subsurface settlement profiles above tunnels in clays. Géotechnique 43(2), 315–320 (1993). https://doi.org/10.1680/geot.1993.43.2.315
3. Essex, R.J. (ed.): Geotechnical Baseline Reports for Construction: Suggested Guidelines. American Society of Civil Engineers, Reston, VA (2007).
4. Rabcewicz, L.: The New Austrian Tunnelling Method, part one. Water Power 16(11), 453–457 (1964).
5. Peck, R.B.: Advantages and limitations of the observational method in applied soil mechanics. Géotechnique 19(2), 171–187 (1969). https://doi.org/10.1680/geot.1969.19.2.171
6. Schanz, T., Vermeer, P.A., Bonnier, P.G.: The hardening soil model: formulation and verification. In: Brinkgreve, R.B.J. (ed.) Beyond 2000 in Computational Geotechnics, pp. 281–296. Balkema, Rotterdam (1999).

Author Contribution Statement

- *Conceptualization:* Shahab Yasrebi
- *Methodology:* Shahab Yasrebi
- *Investigation:* Shahab Yasrebi
- *Writing – Original Draft:* Shahab Yasrebi
- *Writing – Review & Editing:* Shahab Yasrebi

List of Abbreviations

- **2D/3D** — Two-/three-dimensional

- **AI** — Artificial Intelligence
- **BIM** — Building Information Modelling
- **CDM** — Centre Diaphragm Method
- **FEA** — Finite Element Analysis
- **GBR** — Geotechnical Baseline Report
- **MC** — Mohr–Coulomb
- **NATM** — New Austrian Tunnelling Method
- **SCL** — Sprayed-Concrete-Lined (tunnelling)
- **SEM** — Sequential Excavation Method

The author declares no conflict of interest.

Publication Note
This paper was peer-reviewed, accepted for presentation, and included in the proceedings of the ACE2026 – International Conference on Advances in Civil Engineering, held on 12–14 October 2026 in Trabzon, Türkiye.

This paper may be cited as follows:
S. Yasrebi, "Urban Tunneling Challenges in Rapidly Developing Cities: Managing Ground Uncertainty, Risk, and Digital Transformation," in Proceedings of the ACE2026 – International Conference on Advances in Civil Engineering, Trabzon, Türkiye, 12–14 October 2026.

Snow Damage Patterns at Solar Power Plants

Ahmet Turer[1]
[1] 0000-0002-2214-1387, Middle East Technical University, Department of Civil Engineering, Ankara, Türkiye, aturer@metu.edu.tr

Abstract. Türkiye's solar capacity reached 25.8 GW in January 2026, representing 20.9% of national installed capacity and supporting its 2053 net-zero strategy. At high-altitude ground-mounted photovoltaic plants (Güneş Enerji Santralleri GES), however, snow may govern structural design. Designers and consultants commonly apply TS498 directly, although it is a "building-based" provision and do not represent the aerodynamic snow behavior of open-frame solar arrays. This study examines root cause of a large number of damage cases and recurring failures documented through field investigations and insurance claims. Wind generally removes snow from exposed roofs, except for local accumulation in roof valleys. On the contrary, wind transports snow from the surrounding ground over the panels at ground mounted GES sites. Once the snow thickness reaches the 0.7-0.8m ground clearance under panels, successive long GES rows act as snow fences, accumulating extra snow on and between arrays. The resulting accumulated and nonuniform snow load can greatly exceed capacity, unlike the TS498 building roof-based loads. Modelling cold-formed C-sections with one-dimensional frame elements cannot capture local plate buckling, torsional instability, eccentricity or connection-region stresses, requiring shell-based representations. Under-torqued bolts in slotted holes, inappropriate self-tapping screws, inadequate detailing, and representing discrete panel reactions as uniformly distributed loads further increase vulnerability. These assumptions and deficiencies cause local and global buckling, connection yielding, and panel bending-punching failure. Assessment of wind-driven snow accumulation, consideration of torsional instability, better connection detailing, and adoption of contemporary provisions such as ASCE 7-22, EN 1991-1-3:2025 for reliable GES in snow-prone regions are underlined.

Keywords: GES; Snow Drifting; Collapse; Buckling, TS498.

1 Introduction

The rapid growth of solar power generation in Türkiye has resulted in the construction of numerous ground-mounted photovoltaic (GMPV) power plants, commonly referred to as Güneş Enerji Santralleri (GES), in regions having widely different climatic, topographic, and geotechnical conditions. Many of these systems consist of lightweight and highly repetitive structural tables assembled from photovoltaic modules, cold-formed steel C-shaped purlins, similar sectioned beams, columns, braces, slotted bolted connections, and driven steel posts. Although their structural layout may appear simple, their response can become considerably more complex when they are installed close to the ground in high-altitude regions exposed to severe snow and wind.

The field evidence examined in this study is based on seven insurance-commissioned forensic investigations conducted by the author between 2017 and 2026, including cases in Kahramanmaraş, Adıyaman, Ağrı, Van, and Bitlis, together with the METU M.S. thesis by Temel [1] concerning the Turkish ground snow-load map and snow-damage prevention for

solar power plants. The most recent investigations were performed at an Ağrı GES in 2025 and at GES facilities in Van and Bitlis in 2026. The investigated portfolio included a plant located above an elevation of 3,100 m and another located adjacent to a ski resort where seasonal snow depths exceeding one meter are common.

Despite differences in structural configuration, elevation, terrain, row spacing, and damage intensity, the investigated facilities exhibited a recurring common feature. Wind-snow interaction caused successive PV rows to behave as snow-retaining obstructions. Snow transported from the surrounding ground and redistributed from the panel surfaces accumulated between the rows and around their lower edges. Sliding snow aggravated the loading condition by faster closing the gap between the ground and lowest panel edge. The resulting snow depths and load distributions could not be represented adequately by applying only a conventional uniformly distributed roof snow load obtained from TS498. In some occasions, designers further reduced the load by factors like C_e (TS EN 1991-1-3 [2]) completely making the structures vulnerable to accumulated snow.

The field observations also showed that 'underestimated' excessive snow accumulation was seldom the sole deficiency but accompanied by other mistakes. Snow demand interacted with thin-walled open C-sections, shear-center eccentricities, concentrated clamp reactions, insufficiently restrained purlins and beams, single-bolt 'slotted connections', construction irregularities, beams connected only by a web plate, and driven posts installed without concrete footings. These interactions produced recurring damage patterns ranging from local member deformation to global buckling modes, PV fracture, and progressive collapse.

The present paper therefore has three principal objectives: (i) to inform designers - engineers regarding the wind induced accumulation of ground mounted GES, evaluate the applicability and limitations of the available Turkish and international design provisions; (ii) to classify the principal structural damage patterns observed during the forensic investigations; and (iii) to identify the physical and structural mechanisms responsible for these failures and propose practical preventive measures. The paper treats the regional ground snow load as an essential climatic input, but not necessarily as the final load magnitude or distribution acting on a low-clearance, multi-row GMPV structure. Wind induced snow accumulation, statistical analysis of 20-50 years satellite based snow data, and General Directorate of Meteorology closest station records must be considered for the GES design.

2 Available National and International Design Provisions

2.1 Turkish Codes

TS498:2021 constitutes the principal starting point for determining snow actions in Türkiye [3]. It provides the regional and elevation-dependent basis for snow loading and refers to TS EN 1991-1-3 for the treatment of roof geometry, balanced and unbalanced loading, and wind-induced snow accumulation [2]. However, its snow-load formulation is primarily framed around roofs of building-type structures. It does not define a dedicated load model for low-clearance, open-frame, multi-row GMPV arrays exposed to snow transported at ground level.

Consequently, TS498 remains necessary for establishing the regional snow hazard, but it should not be regarded as a sufficient stand-alone procedure for determining the final load on a ground-mounted PV array. In particular, the direct application of the commonly used 0.8 roof shape coefficient becomes questionable once the lower edge of the array is obstructed by accumulated snow. The validity of this reduction and the transition from a snow-shedding surface to a snow-retaining obstruction are examined in Section 4.

TS EN 1991-1-3 provides load arrangements for snow drifting at roof steps, parapets, obstructions, valleys, and multi-span roofs [2]. Its provisions for accumulation between successive roof ridges are physically relevant to rows of inclined PV panels because both

configurations contain repeated high points and sheltered zones. Nevertheless, these provisions were developed for building roofs and cannot be transferred directly to GMPV arrays without considering ground proximity, permeability, row spacing, upwind fetch, and the volume of snow that may be transported from the surrounding terrain.

The structural members and connections are generally assessed under the Turkish Regulation on the Design, Calculation and Construction Principles of Steel Structures [4]. Cold-formed members also require the application of TS EN 1993-1-3 [5] or an equivalent thin-walled steel design specification. These provisions are particularly important for the open C-sections widely used as purlins, beams, and columns in GES structures.

The Turkish Regulation on the Design, Calculation and Construction Principles of Light-Gauge Steel Buildings, published in 2026, applies to cold-formed steel sheets having net thicknesses between 0.45 and 4.00 mm [6]. The regulation addresses local, distortional, torsional, flexural-torsional, and lateral-torsional buckling, as well as the separation between the centroid and shear center. Its stated scope is limited to light-gauge steel buildings, and it enters into force on 1 January 2027. It is therefore not a directly governing GES design code for the investigated cases. Nevertheless, the mechanical principles it contains are directly relevant to the cold-formed C-sections used in these systems.

2.2 International Codes

The second-generation EN 1991-1-3:2025 represents an important development because it explicitly considers snow accumulation around rows of tilted PV panels installed on flat roofs [7]. It also relates drift geometry to obstruction height and wind exposure and requires special consideration for low structures to which snow may be transported from the ground. However, its PV provisions are intended primarily for roof-mounted systems. A ground-mounted solar farm may receive snow transported over a much larger terrain than the roof catchment area assumed in such models. The 2025 document is therefore a valuable physical reference but not a complete prescriptive solution for extensive GMPV arrays.

Other international standards and guidelines address individual parts of the problem, as summarized in Table 1.

Table 1. Applicability of principal design documents to ground-mounted PV structures.

Code	Description	Limitation
TS 498:2021 [3]	Regional and elevation-dependent snow action; conventional roof loading	No specific multi-row, ground-level snow-transport model
TS EN 1991-1-3 [2]	Balanced, unbalanced, obstruction and multi-span roof drift loads	Developed principally for building roofs
EN 1991-1-3:2025 [7]	Tilted PV rows on flat roofs; drift related to panel height and exposure	Roof-mounted PV model; not a complete ground-mounted array procedure
ASCE/SEI 7-22 [8]	Risk-targeted ground snow loads and general roof-drift procedures	No dedicated row-to-row drift model for GMPV plants
O'Rourke (2025) [9]	Ground-mounted panels; obstructed and unobstructed lower edges; snow-shedding clearance	Excludes ground snow travelling up a drift and over the module surface
IEC TS 62738 [10]	General design guidance for utility-scale ground-mounted PV plants	Snow recommendations are mainly qualitative
IEC 62938 [11]	Non-uniform module testing with additional loading near the lower edge	Module test only; excludes supporting steel, connections, foundations and row drift
JIS C 8955/NEDO guidance [12, 13]	PV-specific structural and ground-mounted array guidance	Not directly binding in Türkiye but useful for comparison

ASCE/SEI 7-22 provides general snow-load and roof-drift procedures [8]. The more recent ASCE publication Design Snow Loads for Ground Mounted Solar Panels provides a more directly applicable framework by distinguishing unobstructed, partially obstructed, and fully obstructed leading edges [9]. It also relates the required ground clearance to the volume needed to store snow shed from the panels. However, the publication explicitly excludes the mechanism in which ground snow moves up an existing drift and onto the module surface, which is consistent with the mechanism suggested by several of the Turkish field observations.

IEC TS 62738 provides general recommendations for utility-scale ground-mounted PV plants and draws attention to snow accumulation, sliding snow, site conditions, and protection of electrical equipment [10]. It does not prescribe the magnitude or distribution of wind-driven row-to-row drift loads. IEC 62938, in contrast, defines a non-uniform laboratory snow-load test for framed PV modules, including additional loading toward the lower module edge [11]. This test is valuable for module qualification but cannot verify the complete module-clamp-purlin-beam-column-foundation system under site-specific accumulation.

The available documents therefore provide important but separate components of the design problem. None provides a complete procedure integrating regional snow hazard, ground-level snow transport, progressive obstruction of the lower panel edge, row-to-row accumulation, concentrated module reactions, thin-walled member stability, connection slip, and soil-foundation response. A simple approach for considering snow load on GMPV arrays is suggested in the conclusions section.

3 Major Damage Patterns Observed in Ground-Mounted PV Plants

This section classifies the principal physical damage patterns recorded during the forensic investigations. The classification is intentionally based on observable deformation and failure modes. The snow-transport mechanisms, analytical simplifications, and detailing deficiencies that produced or amplified these patterns are discussed separately in Section 4.

Purlin bending and lateral-torsional deformation is the most commonly observed structural damage. The purlins used in GES are commonly made by ‘inclined’, thin-walled open C-sections. Field observations included violently buckled sections (lateral torsional buckling LTB), torsional buckling of the cantilever portion, large vertical and lateral displacement, almost always twisting of the cross-section, rolling deformation towards the slope as the web rotates, and local damage caused at connections such as near module clamps and primary transition between beams. Although snow pressure acts over the module surface, the module transfers this action to the purlins through discrete clamps. The actual purlin loading therefore consists of concentrated or short patch reactions rather than a ‘continuously’ distributed line load as assumed in the FEM. When these reactions act eccentrically relative to the shear center of an inclined C-section, combined bending and torsion will develop. C-sections are usually weak against torsion stresses as they are open channels. The poor connection between purlins add to the poor structural response. Several systems contained purlin splices in which only the thin web of the C-section was connected (Fig. 1). Such details do not provide continuity for the flange forces and very limited resistance to cross-sectional rotation and torsion; they act like moment releases changing the bending moment distribution. Large and multiple slotted holes with lengths in the order of 5*d on the C channel flanges reduced bending capacity and stability of the purlins. Inclined or poorly aligned purlins further increased secondary bending and local force concentrations at these connections.

The primary beams usually support purlins and have suffered similar damage. The beams are connected to the columns in an eccentric manner and some cases used only one bolt. The eccentricity between the beam and column caused rotation, the weakened bema cross section

by slotted hole rotated and torn away from the column. The beam especially suffered more towards the shorter column, since the snow load on that region was higher. Unlike TS498 prediction of even snow load on building-like roofs, the GMPV plants are closer to the ground and snow accumulation is high at the shorter column side. The torn away and buckled beams caused PV to get closer to the columns which are often times contacted, punched through PV, and caused short-circuit and local burning of the panels (Fig. 2 and Fig. 3). The main beams had highest load on the bottom cantilever part as the snow accumulated deeper on that side. Lateral torsional buckling of the cantilever part was dominant in all cases since the analysis did not consider (a) snow accumulation caused by wind on GMPV plants, (b) 1D frame element did not model the shear center being outside the C-channels. Concentrated load applied by the purlins had damaging effects on the beams and purlins. Local buckling was mainly at the short column to beam connection as the shear and bending moment were highest at that connection. The discrete and eccentric purlin reactions, together with insufficient lateral restraint, caused the beams to respond in combined bending and torsion. Concentric beam models may estimate global bending moments but cannot reliably represent torsion and LTB unless the actual load offsets, restraint conditions, connection flexibility, warping, and geometric imperfections are included.

The lower-edge cantilever region of the PV tables was one of the most frequently damaged zones. PV usually connected using 4 pin supports. The bottom row of PV is closest to the ground and wind accumulated snow thickness is highest at this region. The PV panels at the very top are usually exposed because the wind carries snow (unlike even snow assumption by TS498 or designers) and just the opposite side has a lot of snow depth and load acting on it as the snow fills the gap between the ground and lowest row of PVs, then keep on piling meters deep. Most of the GMPV plants had about 25-degree inclination and about 2m vertical height difference between the bottom and top edges. The snow accumulated by wind is compacted denser at the bottom but compaction puts more load on the panels. The PV panels are rated to 5.40 kN/m² and they are mostly cracked in the bottom row, indicating the snow load exceeded this threshold. Since the top row was always exposed, it is not the snow load reached that value evenly throughout the solar field. It was mostly the rows closest to the edge of the solar field where the dominant wind was coming from. Typical evidence included downward displacement of the lower panel line, permanent deformation of the supporting members, separation between adjacent modules, and fracture of module glass or frames. Usually, a few rows work like snow fences and not all of the GMPV rows experience the same snow load. The spatial concentration of damage supports wind-driven redistribution rather than uniform regional overloading. The wind carried snow accumulation has to be considered in the design.

Column punching through PV modules were frequently observed. This was presented as how strong the columns were by the designers; however, it was the weak beam column connection torn apart by poorly evaluated snow accumulation and inadequate connection aggravated by eccentric load transfer and local buckling caused by weakened member using slotted holes causing PV panels to come down and contact with the columns. Beam-column connection slipped, rotated, or tore under load. Many of the examined connections used a single bolt passing through a slotted hole with uncertain torque level (Fig. 4). Once slip or hole elongation occurred, the frame developed a kinematic mechanism and the relative position of the column, beam, and module changed. In several cases, the upper end of a column or an adjoining structural component came into hard contact with the rear surface of a module and penetrated or fractured it. Besides the structural damage, this failure mode damages cables and conductive components and consequently cause insulation failure, short circuits, arcing, and local fire.



Fig. 1. Typical purlin damage (a) poor connection between purlins, (b) combined bending, twist, rolling of inclined cold-formed C-purlins with discrete module-clamp reactions (LTB) and downward movement of PV panels.



Fig. 2. (a) Rotational buckling of the lower-edge cantilever; (b) PV module fractured by column punching with local buckling, connection tearing, slotted single-bolt beam-column connection.



Fig. 3. (a) lateral-torsional deformation of a primary beam, purlin-beam and column-beam interaction; (b) downward penetration of lower columns in softened winter soil, punching of PV.



Fig. 4. (a) buckling of diagonal members as they slide until the end of slotted connections and (b) a long slotted hole with a big head opening on the purlins.

Downward penetration or settlement of driven columns into the soil are observed in a few occasions. GES are like any other load carrying system and the load transfer mechanism is similar to a chain: the system is as strong as the weakest link in a chain. Snow load acts on the PV panels, transferred through pins to purlins, from purlins to beams, beams to columns and to the ground. Some cases where the columns, especially the short ones with the highest axial force, were found to be driven into the ground if the foundation was on weak soil. The columns are generally driven into the ground by impact or axial force during construction. However, the ground conditions during construction are different than the above freezing conditions at the footing level during spring under snow load. As the snow still not fully melted and a lot of snow load acting on the columns, melting snow makes the soil soft and columns on the shorter side may start to penetrate into the ground under snow load. At some facilities, the steel columns or posts without footing, under wet winter/spring conditions, moved vertically by the soil softening. Some posts consequently penetrated further into the ground, settled differentially, or rotated. This movement altered the table geometry and caused all kinds of additional problems with the rest of the members.

4 Wind Induced Snow Accumulation and Conclusions

The damage mechanisms described in Section 3 were amplified by recurring errors in load assessment, structural modelling and connection detailing. Designers frequently applied TS498 roof loads without evaluating ground-level wind-snow redistribution, although wind may remove snow from exposed roofs while successive PV rows trap snow transported across the ground. Structural demand was further underestimated when simplified concentric one-dimensional frame models were used for cold-formed C-sections without adequately representing shear-center eccentricity, torsion, local-global buckling, and concentrated module-clamp reactions. Slotted holes, inadequate washers and complications with bolt torque levels additionally permitted connection slip and rotation. These deficiencies produced recurring rather than genuinely unforeseen damage. As an example, the proportion of damaged PV modules increased from approximately 20% in 2025 to 70% in 2026 at Ağrı GES, because the repairs did not address the governing loading and structural mechanisms. This recurrence demonstrates the need for root-cause design correction rather than repeated component replacement or reliance on insurance recovery.

Site-specific statistical assessment is essential for high-altitude GMPV plants because TS 498 was developed primarily for building roofs and does not represent ground-level snow transport and row-to-row accumulation. On exposed roofs, wind may reduce snow loading; at GMPV sites, however, it redistributes snow across the ground while successive rows act as obstructions that trap the transported mass. Consequently, characteristic ground snow action should be determined from long-term gridded reanalysis SWE and nearby station records, without unjustified exposure reductions, and combined with a separate accumulation model for the obstructed-array condition.

Statistical analysis of satellite-based snow depth at 0.1 degree closest to the GES site indicates that water equivalent snow load on the ground almost every year surpasses the design values provided by TS498 and used in PV load calculations. Some of the designers used factor like exposure coefficient C_e=0.8 to further reduce the snow load and make a more 'economical' design. The ERA5-Land gridded reanalysis estimates of snow water equivalent (SWE) since 1950 is consistently higher than the S_k value used for design during the pre-event period of 1950 – 2024 [14]. The reported characteristic ground snow load in one of the recent studies, S_k = 1.725 kN/m², corresponds to 175.9 mm of snow water equivalent (SWE). This threshold was exceeded in 69 of the 75 years giving an empirical mean recurrence interval of 1.09 years; therefore, it is not an unexpected snow load S_k value, which is expected to be exceed almost every year. The return period of 1.725 kN/m² is about 1.09 years and such a loading cannot be used for design.

When the amount of load for 20 and 50 years return period for Van GES station were calculated, $S_{20,SWE} \approx 4.81\ \mathrm{kN/m^2}$ and $S_{50,SWE} \approx 5.54\ \mathrm{kN/m^2}$ were obtained. These values are 2.79 to 3.21 times larger than the values used considered in the design. Reduction coefficients of 0.8 applied twice for μ_1 and C_e caused a design deviation of about 5 times. Now, considering the snow accumulation and increased snow density adds on top of this deviation since the snow height on the panels are thicker than the snow on the ground because of wind induced accumulation effect.

The climatic record quantifies the snow mass available on the ground, whereas the structural demand on the PV system is governed by its wind-driven redistribution. Blowing snow is transported by creep, saltation and suspension, and is deposited where obstructions or separated-flow regions reduce wind velocity and transport capacity [15]. In the investigated GMPV arrays, the initial 0.70 - 0.80 m clearance allowed airflow beneath the modules and storage of shed snow; however, snowfall, sliding snow and wind-transported deposits progressively closed this gap. Once the lower edge became buried, the snow surface and inclined modules formed a nearly continuous obstruction, causing the rows to behave as

inclined snow fences and promoting further deposition, compaction and filling between successive rows, potentially up to the approximately 2.5 m upper-module elevation (Fig. 5). Perimeter rows intercepted the incoming snow flux first and consequently experienced earlier burial and more severe loading than interior rows. For scale, a 2.5 m drift with an average density of 200 kg/m^3 contains approximately 500 kg/m^2, corresponding to a load of about 4.90 kN/m^2. Design must distinguish between an open-clearance snow-shedding regime and a foreseeable obstructed regime requiring consideration of row-to-row drifting, lower-edge loading and stability of the complete skeletal system.

The forensic evidence indicates that low-clearance GMPV arrays in severe snow climates must be designed for an obstructed condition whenever burial of the lower panel edge is foreseeable. Unless a validated site-specific wind-snow analysis demonstrates a lower demand, the space beneath and between successive arrays should conservatively be assumed to fill with compacted snow up to the upper panel corner, and the resulting non-uniform, lower-edge-dominant actions should be transferred through the complete skeletal load carrying system. Direct application of TS498 roof loads, coefficients, particularly exposure reductions, does not represent this mechanism adequately. Cold-formed open C-sections should be avoided for primary purlins and beams unless their connections, restraints and member stability are explicitly designed for eccentric clamp reactions, combined bending and torsion, local and distortional buckling, warping, and lateral-torsional buckling. Slotted single-bolt connections and concentric frame models that suppress these governing failure modes should not be accepted. If the statistically derived characteristic ground snow depth obtained from ERA5-Land or similar database exceeds the lower panel-edge elevation but remains below the upper panel-edge elevation, loss of the lower-edge clearance should be assumed and the inter-row space should conservatively be considered filled with partially compacted snow at about the upper panel edge level (Fig. 5).

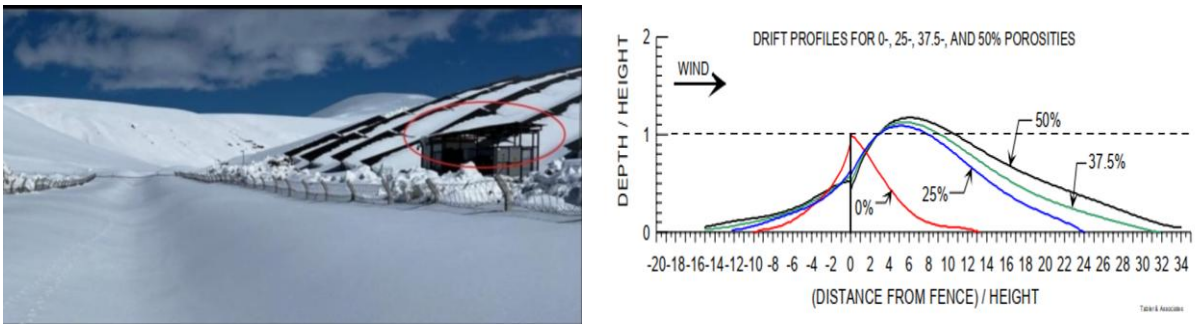


Fig. 5. (a) GMPV rows buried by non-uniform snow approaching 2.5 m, while the adjacent roof remained largely snow-free (b) effect of snow-fence drift profiles over flat terrain (reproduced from Tabler [15], Fig. 3.57).

References

1. Temel, Ö.: A study on new Turkish ground snow load map and snow damage prevention recommendations for solar power plants. M.S. thesis, Middle East Technical University, Ankara (2020). https://hdl.handle.net/11511/45566, last accessed 2026/08/10.
2. Turkish Standards Institution: TS EN 1991-1-3:2007, Eurocode 1: Actions on structures - Part 1-3: General actions - Snow loads. TSE, Ankara (2007).
3. Turkish Standards Institution: TS 498:2021, Design loads for the dimensioning of structural elements. TSE, Ankara (2021).
4. Republic of Türkiye Ministry of Environment and Urbanization: Regulation on Design, Calculation and Construction Principles of Steel Structures. Official Gazette No. 29614, Ankara (2016), amended (2018).

5. Turkish Standards Institution: TS EN 1993-1-3:2007, Eurocode 3: Design of steel structures - Part 1-3: General rules - Supplementary rules for cold-formed members and sheeting. TSE, Ankara (2007).
6. Republic of Türkiye Ministry of Environment, Urbanization and Climate Change: Regulation on Design, Calculation and Construction Principles of Light-Gauge Steel Buildings. Official Gazette No. 33256, Ankara (2026).
7. European Committee for Standardization: EN 1991-1-3:2025, Eurocode 1 - Actions on structures - Part 1-3: Snow loads. CEN, Brussels (2025).
8. American Society of Civil Engineers: Minimum Design Loads and Associated Criteria for Buildings and Other Structures. ASCE/SEI 7-22. ASCE, Reston, VA (2022). https://doi.org/10.1061/9780784415788.
9. O'Rourke, M., Kalush, P.D., Klug, M., Faraone, M.: Design Snow Loads for Ground Mounted Solar Panels. ASCE Press, Reston, VA (2025). https://doi.org/10.1061/9780784486245.
10. International Electrotechnical Commission: IEC TS 62738:2018, Ground-mounted photovoltaic power plants - Design guidelines and recommendations. IEC, Geneva (2018).
11. International Electrotechnical Commission: IEC 62938:2020, Photovoltaic (PV) modules - Non-uniform snow load testing. IEC, Geneva (2020).
12. Japanese Standards Association: JIS C 8955:2017, Load design guide on structures for photovoltaic array. JSA, Tokyo (2017).
13. New Energy and Industrial Technology Development Organization: Ground-Mounted Design Guidelines, revised 2019. NEDO, Kawasaki (2019). https://www.nedo.go.jp/content/800050564.pdf, last accessed 2026/08/16.
14. Copernicus Climate Change Service: ERA5-Land hourly data from 1950 to present. Climate Data Store, ECMWF (2019). https://doi.org/10.24381/cds.e2161bac, last accessed 2026/08/10.
15. Tabler, R.D.: Controlling Blowing and Drifting Snow with Snow Fences and Road Design. Final Report, NCHRP Project 20-7(147), Tabler and Associates, Niwot, CO (2003).

Publication Note

This paper was peer-reviewed, accepted for presentation, and included in the proceedings of the ACE2026 - International Conference on Advances in Civil Engineering, held on 12-14 October 2026 in Trabzon, Türkiye.

This paper may be cited as follows:

Turer A., “Snow Damage Patterns at Solar Power Plants” in Proceedings of the ACE2026 - International Conference on Advances in Civil Engineering, Trabzon, Türkiye, 12-14 October 2026.

CHAPTER 1

Structures

46 papers

Cyclic In-Plane Behavior of AAC Load-Bearing Panel Walls under Varying Axial Stress Levels and Panel Configurations

Koray Ugurlu [1], Omer Faruk Halici [2], Cem Demir [3], Mustafa Comert [4] and Alper Ilki [5]
[1] 0009-0004-9913-9797, Istanbul Technical University, Faculty of Civil Engineering, Istanbul, Türkiye, kugurlu@itu.edu.tr
[2] 0000-0001-8890-8782, MEF University, Department of Civil Engineering, Istanbul, Türkiye, halicio@mef.edu.tr
[3] 0000-0001-8274-5361, Istanbul Technical University, Faculty of Civil Engineering, Istanbul, Türkiye, demirce@itu.edu.tr
[4] 0000-0001-8890-8782, RISE Engineering, Istanbul, Türkiye, mustafa@riseproje.com
[5] 0000-0002-4853-7910, Istanbul Technical University, Faculty of Civil Engineering, Istanbul, Türkiye, ailki@itu.edu.tr

Abstract. Autoclaved Aerated Concrete (AAC) is a versatile cementitious material used to produce both masonry block units and reinforced wall panels. Due to its low self-weight, reinforced AAC load-bearing panel wall systems are particularly suitable for low-rise construction in seismically active regions. This paper presents an experimental investigation of the cyclic in-plane behavior of AAC load-bearing walls comprising two, four, and six panels. The specimens were tested under various axial stress levels and subjected to cyclic displacement reversals. The experimental results showed that the response initiated with separation of the panel bases from the leveling mortar in the form of uplift, followed by visible separation between adjacent panels at lateral drift ratios between 0.50% and 1.00%. In the six-panel specimens, several adjacent panels exhibited monolithic behavior at early drift levels, transitioning to individual panel rocking as the drift increased. The lateral load-carrying capacity of the walls was found to increase with both the applied axial stress and the number of panels. The two-panel walls exhibited a predominantly flexural response, whereas the four- and six-panel walls exhibited a combined flexural–shear response. Overall, the specimens sustained considerable drift demands while maintaining their structural integrity, displaying satisfactory deformation capacity.

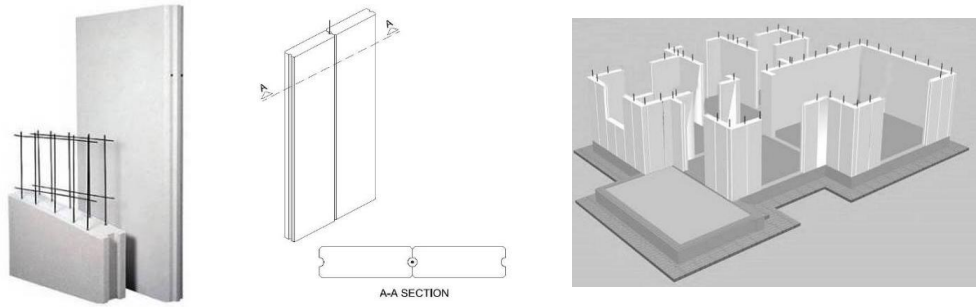
Keywords: AAC panel; load-bearing wall; cyclic experiment

1 Introduction

AAC is a versatile cementitious material used to produce both masonry block units and reinforced panels incorporating wire mesh reinforcement to resist out-of-plane forces (Fig. 1a). Beyond its structural applications in load bearing and infill walls, cladding, floor systems, and insulation boards, it is also distinguished by its lightweight nature, which facilitates rapid construction. Furthermore, AAC offers significant advantages in thermal performance and fire safety.

Structures of two to three stories can be constructed using load-bearing AAC panels alone. In accordance with Turkish Building Earthquake Code (TBEC) [1], the total height of buildings constructed with these panels cannot exceed 10.5 m. When two panels are erected side by side (Fig. 1b) on a foundation over a leveling mortar, the end profiles of the panels form a cylindrical gap between them. Vertical reinforcement bars extending from the foundation run through these gaps to the full height of the wall, after which the gaps are filled with grout. Once all walls are completed (Fig. 1c), a bond beam is cast on top, into which the vertical reinforcement is

embedded via lap splices. AAC floor and roof panels are then laid on these bond beams to form floors and roof.



(a) (b) (c)

Fig. 1. (a) AAC reinforced panel, (b) side by side connection of load-bearing AAC wall panels and (c) Formation of the first story walls [2]

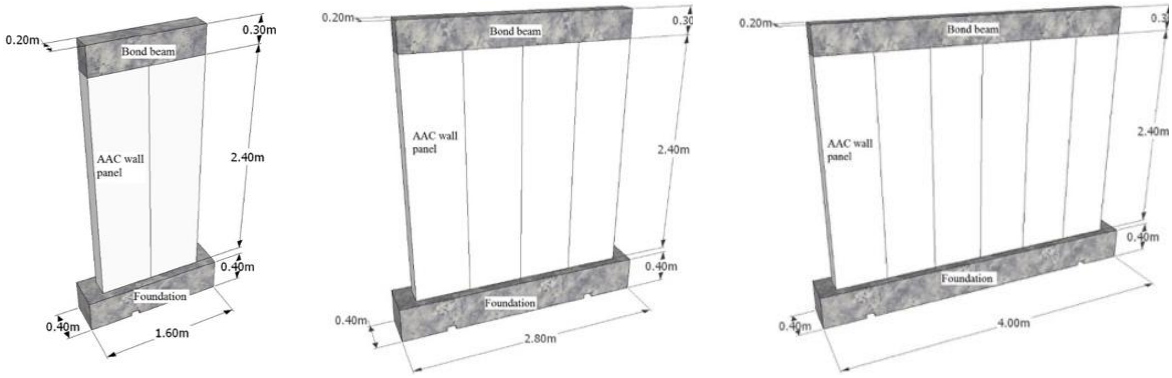
Buildings constructed with this practice in Türkiye since 1970s have exhibited satisfactory seismic performance [3, 4], which is largely attributed to their relatively low self-weight. Several studies have investigated the seismic behavior of AAC load-bearing wall panel systems. Bayulke [5] reported separation of orthogonal walls and corner crushing in a one-story building, while the structure maintained self-centering with minimal residual drift. Tanner [6, 7] and Cancino [8] conducted cyclic in-plane tests on vertically and horizontally oriented panels, recommending the design of vertical panels in interconnected groups. Varela [9, 10] proposed simplified modeling approaches and suggested seismic design factors. Numerical studies using the Concrete Damaged Plasticity model [11] showed good agreement with experiments [12]. Ugurlu et al. [2] reported a significant lateral drift ratio of 2.0%, with a strength degradation of 20% occurring at a drift ratio of 1.5%. Taghipour et al. [13] presented results from the tests conducted at Middle East Technical University (METU), observing ultimate lateral drift ratios of 1.0% and failure modes dominated by flexural and sliding behavior. Gokmen et al. [14] reported an ultimate lateral roof drift ratio of 0.35%, and determined a structural behavior factor (R) of 2.35. More recent studies [15–17] further expanded the experimental database by examining different panel configurations, openings, and boundary conditions under cyclic loading. Despite this growing body of international research, experimental investigation of the seismic behavior of AAC structures within Türkiye had remained limited; prior to 2015, only a single shaking table test [5] had been conducted domestically. To address this gap, a comprehensive research program was initiated in 2015 through a collaboration between Istanbul Technical University (ITU) and Middle East Technical University (METU), funded by Turkish AAC Association (TAACA). This paper presents a part of the results from the experiments carried out as ITU's contribution to that initiative. While a more comprehensive version of this work has been published in Ugurlu et al.[18], the present paper focuses on the experimental observations of the cyclic in-plane behavior, damage progression, and lateral load-carrying capacity of AAC load-bearing panel walls with varying panel configurations and axial stress levels.

2 Experimental Study

2.1 Specimen Geometries and Configuration

Six wall specimens were constructed in the Structural and Earthquake Engineering Laboratory of ITU. The specimens consisted of two, four, and six loadbearing AAC wall panels, each 600 mm in width, designated W2, W4, and W6, respectively (Fig. 2). For each configuration, two identical wall specimens were tested under two different constant axial stress levels (the lower and higher axial stress levels are distinguished by the suffixes -1 and -2, resulting in specimens

W2-1, W2-2, W4-1, W4-2, W6-1, and W6-2). The lower axial stress level was 0.2 MPa and the higher axial stress level was 0.5 MPa. During transportation of W2-1, a cracking sound was heard, which may be indicative of damage sustained prior to testing. Therefore, for this specimen only, the axial stress level was reduced to 0.1 MPa in order not to induce further damage.

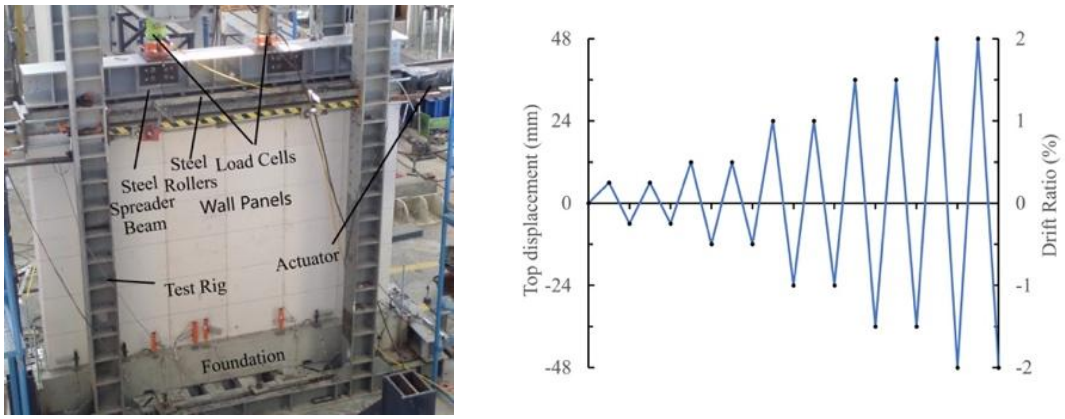


(a) (b) (c)

Fig. 2. Wall specimens (a) Two-panel, (b) Four-panel and (c) Six-panel.

2.2 Specimen Testing and Instrumentation

After construction, the specimens were transported to the test rig (Fig. 3a). Lateral displacements were applied by a hydraulic actuator with a force capacity of 1000 kN and a displacement range of 400 mm, following the loading protocol illustrated in Fig. 3b. The test rig was designed to prevent out-of-plane displacements and foundation uplift. A constant axial load was applied using vertical actuators (one for the W2 specimens and two for the W4 and W6 specimens) and transferred to the specimen through a steel spreader beam. Steel rollers placed beneath the spreader beam allowed free lateral movement of the specimen during testing. Linear potentiometers were used to measure in-plane lateral displacements, panel and foundation uplift and out of plane displacements.



(a) (b)

Fig. 3. (a) Test rig and (b) loading protocol (modified from [18]).

2.3 Test Results

The experimental results are presented as load–displacement curves in Figs. 4,6,8,10,12 and 14. The damage states and the corresponding lateral drift levels are marked on these curves. The damage states are labelled with capital letters from A to E, in chronological order from the earliest to the most advanced damage as the drift amplitude increased. For clarity, these annotations are shown only on the positive envelope, since the damage progression on the negative side was similar and occurred at comparable drift levels. The crack patterns at selected

drift levels for each specimen are illustrated in Figs. 5,7,9,11,13 and 15. In these figures, cracks that developed during the pushing (positive) half-cycle are shown in blue, whereas those that developed during the pulling (negative) half-cycle are shown in red. The measured crack widths in millimeters, are indicated next to each crack or opening. The vertical green lines and the blue dots denote the separation between adjacent panels and the locations of spalled AAC material, respectively. The double-headed arrow indicates the location and direction of the applied lateral load.

W2-1. The load–displacement response of W2-1 is presented in Fig 4. The peak lateral force of 22 kN was attained at a lateral drift ratio of 0.6%, beyond which the strength gradually degraded, and the specimen lost 20% of its load-carrying capacity at a drift ratio of 1.0%.

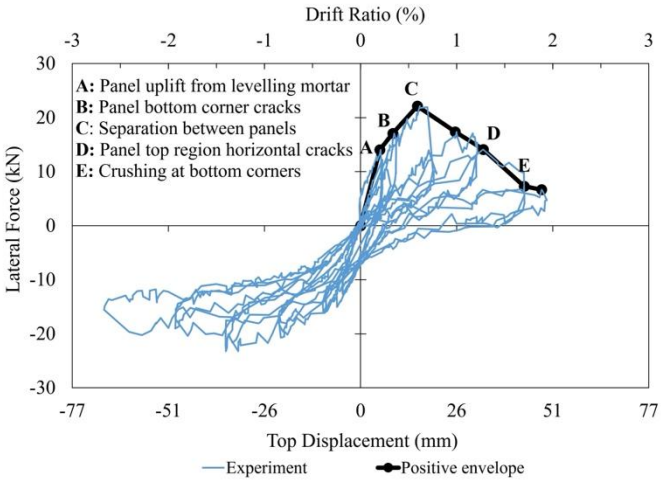
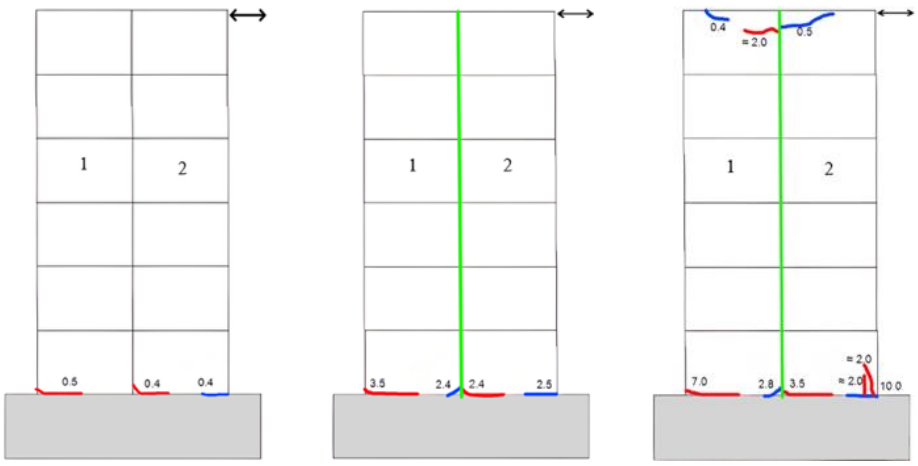


Fig. 4. Lateral load vs. top displacement curve of W2-1 with damage states superimposed (modified from [18]).

The progression of damage in W2-1 is illustrated in Fig. 5. The earliest observed damage was the separation of the panel bases from the leveling mortar, accompanied by uplift at a lateral drift of 0.25 %. The opening associated with this uplift widened progressively as the lateral drift increased. Subsequently, diagonal cracks developed at the bottom corners of the panels. At a target drift ratio of 1.00%, panel-to-panel interface openings along the vertical joints became discernible. As the drift was further increased to 1.50 %, horizontal cracks formed in the upper regions of the panels, and the previously observed corner cracks evolved into localized crushing. No web-shear cracking was observed across the central portion of the panels



(a) (b) (c)

Fig. 5. Observed crack patterns of specimen W2-1 at lateral target drift ratios of (a) 0.25%, (b) 1.00%, and (c) 1.50%.

W2-2. The load–displacement response of W2-2 is presented in Fig. 6. The peak lateral force of 31.5 kN was attained at a lateral drift ratio of 0.5 %, beyond which the strength gradually degraded. The specimen lost 20 % of its load-carrying capacity at a drift ratio of 2.3 %.

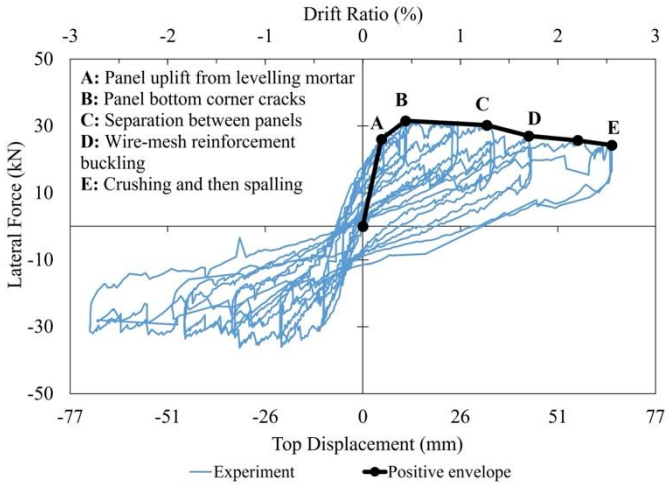
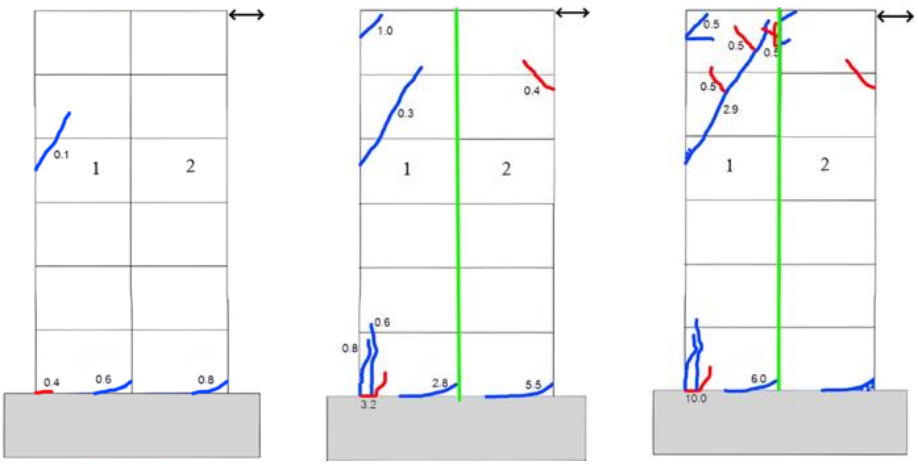


Fig. 6. Lateral load vs. top displacement curve of W2-2 with damage states superimposed (modified from [18]).

The progression of damage in W2-2 is illustrated in Fig. 7. Similar to W2-1, the earliest observed damage at 0.25 % lateral drift, was the separation of the panel bases from the leveling mortar, accompanied by uplift, which widened as the lateral drift increased. Subsequently, diagonal cracks developed at the bottom corners of the panels. At a target drift ratio of 0.50 %, a diagonal shear crack formed near the vertical mid-height of the first panel, on the side opposite to the hydraulic actuator. At the same drift level, panel-to-panel interface openings along the vertical joints became discernible, confirming individual panel rocking behavior, while upper-corner cracks continued to develop and propagate with increasing drift. At a lateral drift ratio of 2.00 %, buckling of the wire mesh reinforcement was observed in the regions where the AAC had crushed and spalled.



(a) (b) (c)

Fig. 7. Observed crack patterns of specimen W2-2 at lateral target drift ratios of (a) 0.25%, (b) 1.00%, and (c) 2.00%. (modified from [18]).

W4-1. The load–displacement response of W4-1 is presented in Fig. 8. The peak lateral force of 81.5 kN was attained at a lateral drift ratio of 0.6 %, beyond which the strength gradually degraded. The specimen lost 20 % of its load-carrying capacity at a drift ratio of 1.1 %.

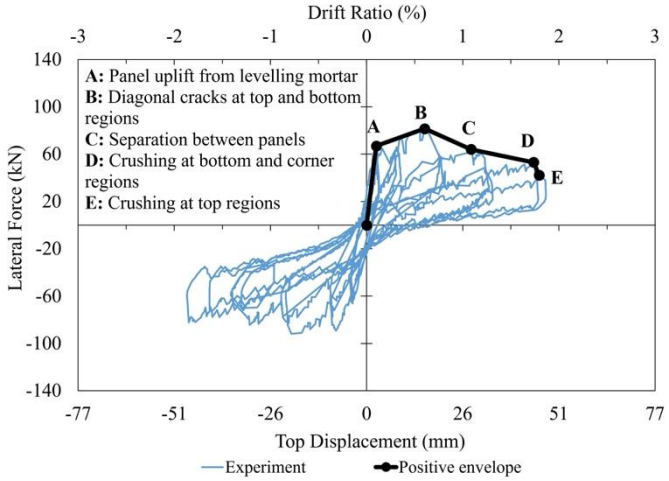
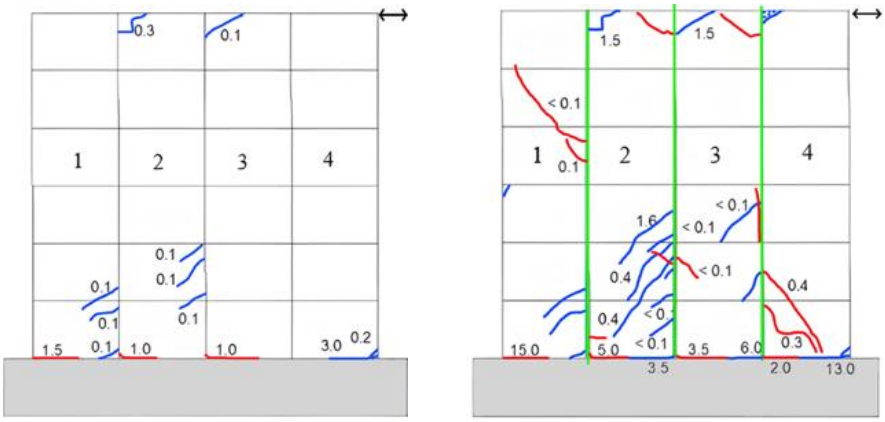


Fig. 8. Lateral load vs. top displacement curve of W4-1 with damage states superimposed (modified from [18]).

The progression of damage in W4-1 is illustrated in Fig. 9. The earliest damage in W4-1 consisted of the separation of the panel bases from the leveling mortar, accompanied by uplift. At a drift ratio of 0.50 %, cracks formed at the upper corners of the panels, and diagonal cracks developed in the lower half of the first and second panels, between the mid-height and the base. As the drift increased to 1.00%, panel-to-panel interface openings became discernible along the vertical joints, while the previously observed cracks grew in both width and number. At a drift ratio of 1.50 %, the diagonal cracks at the mid-height regions and at the upper and lower corners of the panels propagated further, accompanied by crushing at the top and bottom of the panels.



(a) (b)

Fig. 9. Observed crack patterns of specimen W4-1 at lateral target drift ratios of (a) 0.50% and (b) 1.50% (modified from [18]).

W4-2. The load–displacement response of W4-2 is presented in Fig. 10. The peak lateral force of 121.6 kN was attained at a lateral drift ratio of 0.5 %, beyond which the strength gradually degraded. The specimen lost 20 % of its load-carrying capacity at a drift ratio of 1.5 %.

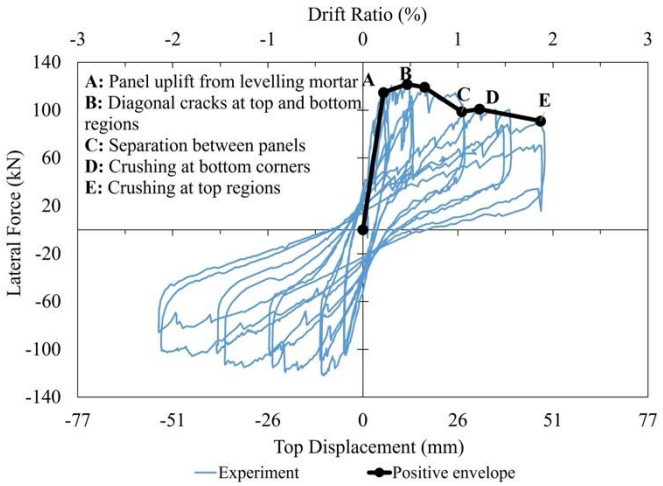
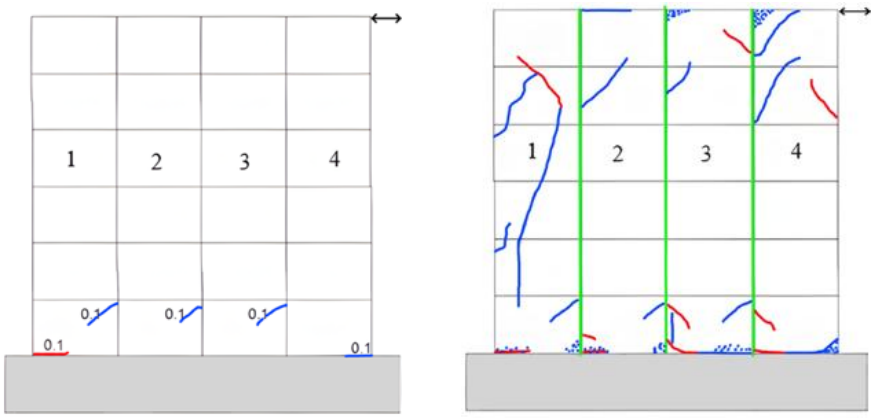


Fig. 10. Lateral load vs. top displacement curve of W4-2 with damage states superimposed (modified from [18]).

The progression of damage in W4-2 is illustrated in Fig. 11. The earliest damage in W4-2 was observed at a drift ratio of 0.25 % and consisted of the separation of the panel bases from the leveling mortar, accompanied by uplift. At a drift ratio of 0.50 %, diagonal cracks were concentrated in the lower and upper regions of the panels. As the drift increased to 1.00%, panel-to-panel interface openings became discernible along the vertical joints, the previously observed cracks grew in both width and number, and new diagonal cracks emerged in the upper regions. At a drift ratio of 1.50 %, the size and number of cracks increased further, and crushing and spalling initiated at the lower and upper corners. At a drift ratio of 2.00%, crushing and spalling intensified, particularly at the lower and upper corners.



(a) (b)

Fig. 11. Observed crack patterns of specimen W4-2 at lateral target drift ratios of (a) 0.25% and (b) 2.00% (modified from [18]).

W6-1. The load–displacement response of W6-1 is presented in Fig. 12. The peak lateral force of 163.6 kN was attained at a lateral drift ratio of 0.3 %, beyond which the strength gradually degraded. The specimen lost 20 % of its load-carrying capacity at a drift ratio of 1.3 %.

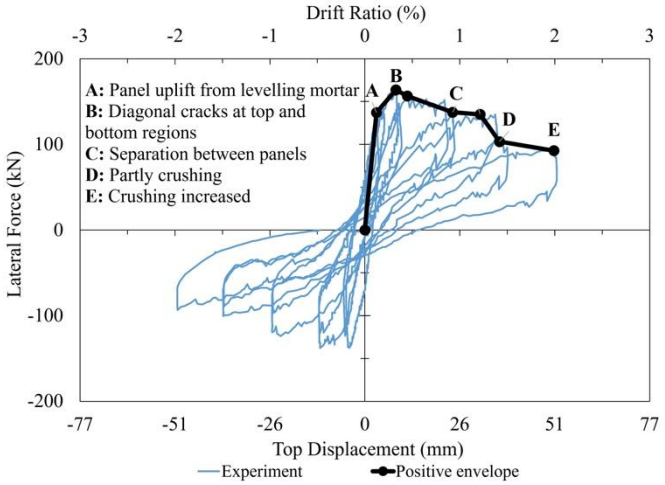
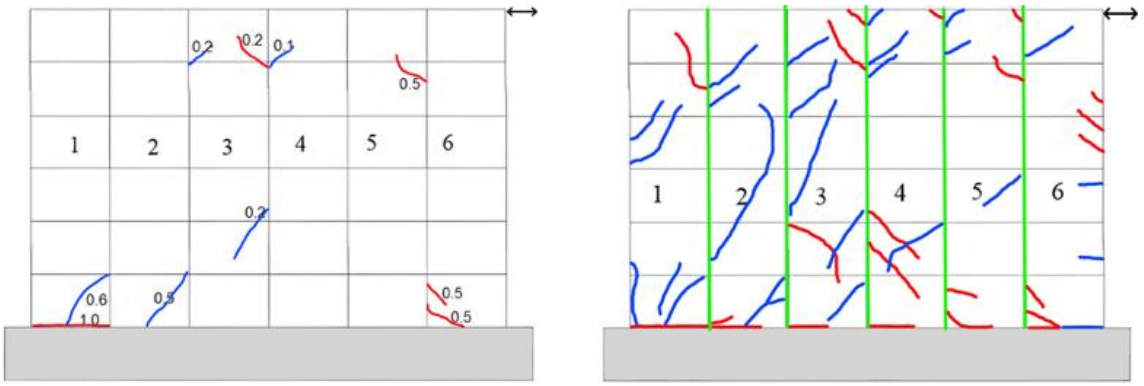


Fig. 12. Lateral load vs. top displacement curve of W6-1 with damage states superimposed (modified from [18]).

The progression of damage in W6-1 is illustrated in Fig. 13. The earliest damage in W6-1 was observed at a drift ratio of 0.25 % and consisted of the separation of the first, second, and sixth panel bases from the leveling mortar, accompanied by uplift. At the same drift level, diagonal cracks formed in the lower and upper regions of the panels. As the drift increased to 0.50 %, these cracks grew in both width and number and propagated into the remaining panels. In addition, web-shear cracks formed in the central regions of the panels, and all panels except the two central ones had separated from the leveling mortar. At a drift ratio of 1.00%, the two remaining central panels also separated from the leveling mortar, the previously observed cracks further increased in both width and number, and panel-to-panel interface openings became discernible along the vertical joints. At a drift ratio of 1.50%, crushing was observed at the panel bases.



(a) (b)

Fig. 13. Observed crack patterns of specimen W6-1 at lateral target drift ratios of (a) 0.25% and (b) 1.50% (modified from [18]).

W6-2. The load–displacement response of W6-2 is presented in Fig. 14. The peak lateral force of 170.0 kN was attained at a lateral drift ratio of 0.4 %, beyond which the strength gradually degraded. The specimen lost 20 % of its load-carrying capacity at a drift ratio of 1.3 %.

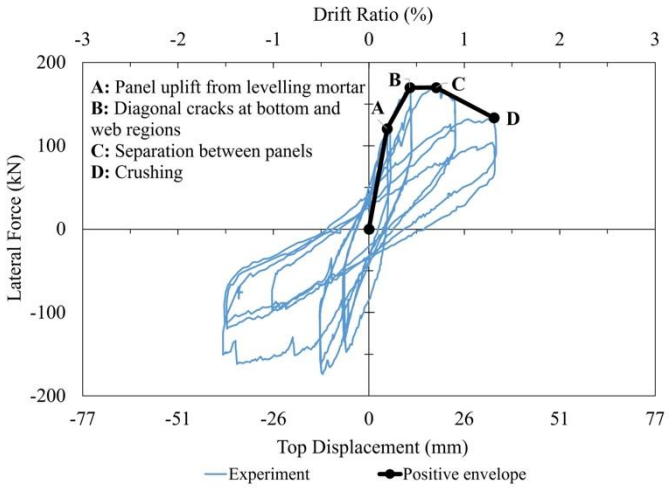
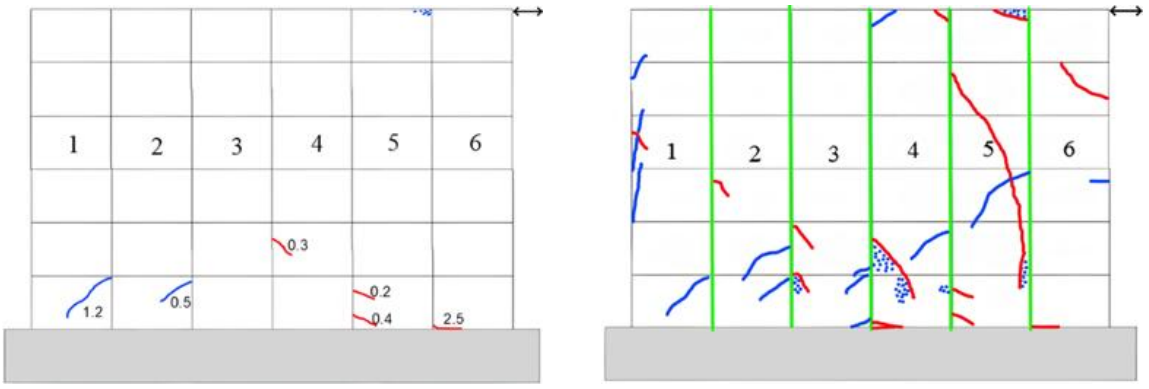


Fig. 14. Lateral load vs. top displacement curve of W6-2 with damage states superimposed (modified from [18]).

The progression of damage in W6-2 is illustrated in Fig. 15. The earliest damage in W6-2 was observed at a drift ratio of 0.25% and consisted of the separation of the panel bases from the leveling mortar, accompanied by uplift. At the same drift level, diagonal cracks formed in the lower regions of the panels. As the drift increased to 0.50%, these cracks grew in both width and number and propagated towards the mid-height of the panels and the upper corners. In addition, web-shear cracks formed in the central regions of the panels. At a drift ratio of 1.00%, the previously observed cracks intensified, panel-to-panel interface openings became discernible along the vertical joints, and crushing and spalling initiated at the lower, mid-height, and upper regions of the panels. At a drift ratio of 1.50%, the crushing and spalling progressed further.



(a) (b)

Fig. 15. Observed crack patterns of specimen W6-2 at lateral target drift ratios of (a) 0.25% and (b) 1.50% (modified from [18]).

2.4 Discussion

In all specimens, the earliest damage was the separation of the panel bases from the leveling mortar, accompanied by uplift, first recorded at a drift ratio of 0.25%, except in W4-1 where this occurred at 0.50%. Corner cracks developed and widened as the uplift increased with drift. At 1.00% drift, panel-to-panel interface openings became discernible along the vertical joints in all specimens, confirming individual panel rocking behavior. Crushing was observed at 1.50% drift, progressing to spalling at 2.00% drift, particularly in the higher axial stress specimens. In W4-2, spalling was concentrated at the panel corners, whereas in W6-2 it

occurred both at the corners and in the vicinity of the diagonal cracks extending toward the central region.

The two-panel specimens exhibited a predominantly flexural response, with damage concentrated at the panel corners and bases. Web-shear cracks developed in the four- and six-panel specimens alongside corner cracking and crushing, indicating a combined flexural–shear response. The more flexural character of the two-panel response may partly reflect the use of a single vertical actuator for axial load application, which provided less rotational restraint to the bond beam compared with the two-actuator configuration used for the four- and six-panel specimens.

In W6-1 and W6-2, diagonal cracks in several adjacent panels followed a similar orientation and extended across panel boundaries up to a drift ratio of 0.50%, suggesting monolithic behavior between these adjacent panels at early drift levels. This tendency was more pronounced in W6-2. As the drift increased, panel-to-panel interface openings became discernible, marking the transition from monolithic to individual panel behavior.

Higher axial stress consistently resulted in greater peak lateral force across all configurations. The peak lateral force increased as the number of panels increased, ranging from 22–31.5 kN for two-panel walls to 163.6–170.0 kN for six-panel walls.

All specimens sustained considerable drift demands while maintaining their structural integrity, with 20% loss of load-carrying capacity observed at drift ratios of 1.0% or greater. The hysteretic response of all specimens remained stable throughout the tests, with no sudden loss of load-carrying capacity, although noticeable pinching was observed particularly after diagonal cracking and interface opening.

3 Conclusions

This study investigated the cyclic in-plane behavior of autoclaved aerated concrete (AAC) load-bearing panel walls consisting of two, four, and six panels through experimental testing. The principal findings are summarized below.

The experimental results confirmed that AAC load-bearing panel walls respond as individual rocking units under cyclic lateral loading, with base separation and panel-to-panel interface opening observed at low drift levels. An exception was noted in the six-panel specimens, where adjacent panels exhibited monolithic behavior up to 0.50% drift before transitioning to individual rocking.

The failure mode was influenced by the panel configuration. Two-panel walls exhibited a predominantly flexural response, while four- and six-panel walls displayed a combined flexural–shear response. It is noted that the difference in the number of vertical actuators used for axial load application may have contributed to this distinction.

Both axial stress level and number of panels had a significant influence on the lateral load-carrying capacity, with higher values of each parameter consistently yielding greater peak lateral force.

All specimens sustained considerable drift demands while maintaining their structural integrity, with 20% loss of load-carrying capacity observed at drift ratios of 1.0% or greater. The hysteretic response remained stable throughout the tests, with no sudden loss of load-carrying capacity, although noticeable pinching was observed after diagonal cracking and interface opening.

Given that the observed response involves both flexural and shear mechanisms, the design of such walls should account for both failure modes and their potential interaction.

Acknowledgments

The financial support by Turkish AAC Association (TAACA) for materials and assemblage workmanship is gratefully acknowledged.

References

1. Turkish Ministry of Interior, Disaster and Emergency Management Presidency: Turkish building earthquake code. Official Gazette of the Republic of Türkiye (2018).
2. Ugurlu, K., Demir, C., Comert, M., Dalgic, K., Ilki, A.: Full-scale seismic testing of a building constructed with AAC panels. In: Proc. of 16th World Conference on Earthquake Engineering. p. 2526. , Santiago, Chile (2017).
3. Karadogan, F.: UNESCO supported post earthquake assessment mission of IPRED members in Van / Turkey. UNESCO (2012).
4. Ugurlu, K., Demir, C., Ilki, A.: Seismic assessment of a school building constructed with AAC panels and experienced 1999 Kocaeli earthquake. In: Proc. SMAR 2013 2nd Conference on Smart Monitoring Assessment and Rehabilitation of Civil Structures. p. 363. , Istanbul, Turkey (2013).
5. Bayülke, N.: Shaking table experiments of structures constructed from AAC materials. General directorate of natural disasters earthquake research center (1987).
6. Tanner, J.E.: Design provisions for autoclaved aerated concrete (AAC) structural systems, (2003).
7. Tanner, J., Varela, J., Brightman, M., Cancino, U., Argudo, J., Klinger, R.: Seismic performance and design of autoclaved aerated concrete (AAC) structural systems. In: Proceedings of 13th World Conference on Earthquake Engineering. p. 541. , Vancouver B.C., Canada (2004).
8. Cancino, U.M.: Behavior of autoclaved aerated concrete shear walls with low-strength AAC, (2003).
9. Varela, J.L., Tanner, J.E., Klingner, R.E.: Development of seismic force reduction and displacement amplification factors for autoclaved aerated concrete structures. Earthq. Spectra. 22, 267–286 (2006). https://doi.org/https://doi.org/10.1193/1.2166034.
10. Varela, J., Bagundo, M., Fernandez, L.: Seismic behavior of AAC structures designed with different flexural capacities. In: Proceedings of the 14th World Conference on Earthquake Engineering. pp. 05-01–0329. , Beijing, China (2008).
11. Lee, J., Fenves, G.L.: Plastic-Damage Model for Cyclic Loading of Concrete Structures. J. Eng. Mech. 124, 892–900 (1998). https://doi.org/10.1061/(ASCE)0733-9399(1998)124:8(892).
12. Taddei, F., Reindl, L., Park, J., Butenweg, C., Karadogan, F.: Numerical investigation of AAC wall panels based on the damage plasticity constitutive law. Cem. Wapno Beton. 7, 86–91 (2011).
13. Taghipour, A., Canbay, E., Binici, B., Aldemir, A., Uzgan, U., Eryurtlu, Z.: Seismic behavior of reinforced autoclaved aerated concrete wall panels. ce/papers. 2, 259–265 (2018). https://doi.org/https://doi.org/10.1002/cepa.818.
14. Gokmen, F., Binici, B., Aldemir, A., Taghipour, A., Canbay, E.: Seismic behavior of autoclaved aerated concrete low rise buildings with reinforced wall panels. Bull. Earthq. Eng. 17, 3933–3957 (2019). https://doi.org/https://doi.org/10.1007/s10518-019-00630-3.
15. Xu, C., Nehdi, M.L., Wang, K., Guo, Y.: Experimental study on seismic behavior of novel AAC prefabricated panel walls. J. Build. Eng. 44, 103390 (2021). https://doi.org/https://doi.org/10.1016/j.jobe.2021.103390.
16. Li, X., Ma, D., Zhang, Q., Zhang, Z., Bao, H., Yao, Y.: Seismic performance of full-scale autoclaved aerated concrete panel-assembled walls: Experimental study and numerical modeling. Buildings. 14, 1333 (2024). https://doi.org/https://doi.org/10.3390/buildings14051333.
17. Sun, Z., Jin, B., Chu, M., Liu, J., Wang, Q., Li, R., Li, X.: Experimental Study on the Seismic Performance of Autoclaved Aerated Concrete Panel Walls. J. Earthq. Eng. 1–24 (2025). https://doi.org/https://doi.org/10.1080/13632469.2025.2575271.

18. Ugurlu, K., Halici, O.F., Demir, C., Comert, M., Ilki, A.: Seismic Behavior and Design of Reinforced Autoclaved Aerated Concrete Load-Bearing Panel Walls. J. Earthq. Eng. 1–35 (2026). https://doi.org/10.1080/13632469.2026.2628027.

Author Contribution Statement

- *Conceptualization:* Koray Ugurlu, Omer Faruk Halici, Cem Demir, Alper Ilki
- *Methodology:* Koray Ugurlu, Omer Faruk Halici, Cem Demir
- *Investigation:* Koray Ugurlu, Omer Faruk Halici, Cem Demir, Mustafa Comert
- *Writing – Original Draft:* Koray Ugurlu
- *Writing – Review & Editing:* Koray Ugurlu, Omer Faruk Halici, Cem Demir, Alper Ilki

Publication Note

This paper was peer-reviewed, accepted for presentation, and included in the proceedings of the ACE2026 – International Conference on Advances in Civil Engineering, held on 12–14 October 2026 in Trabzon, Türkiye.

This paper may be cited as follows:

Ugurlu, K, Halici, O, Demir, C, Comert, M, Ilki, A "Cyclic In-Plane Behavior of AAC Load-Bearing Panel Walls under Varying Axial Stress Levels and Panel Configurations," in Proceedings of the ACE2026 – International Conference on Advances in Civil Engineering, Trabzon, Türkiye, 12–14 October 2026.

Iterative Damper Optimization for Seismic Retrofit of a Cliff-Mounted Steel Observation Platform

Adnan Kiral[1], Zeliha Tonyali[1]*, Maziar Fahimi Farzam[2,3]

[1] Adnan Kiral: 0000-0002-4534-3686; Zeliha Tonyali: 0000-0002-6637-7949, Recep Tayyip Erdogan University, Faculty of Engineering and Architecture, Department of Civil Engineering, Rize, 53100, Türkiye

[2] Maziar Fahimi Farzam: 0000-0001-9635-8186, University of Maragheh, Faculty of Engineering, Department of Civil Engineering, Maragheh 55181-83111, Iran

[3] Maziar Fahimi Farzam, Sahand University of Technology, Faculty of Civil Engineering, Tabriz, Iran

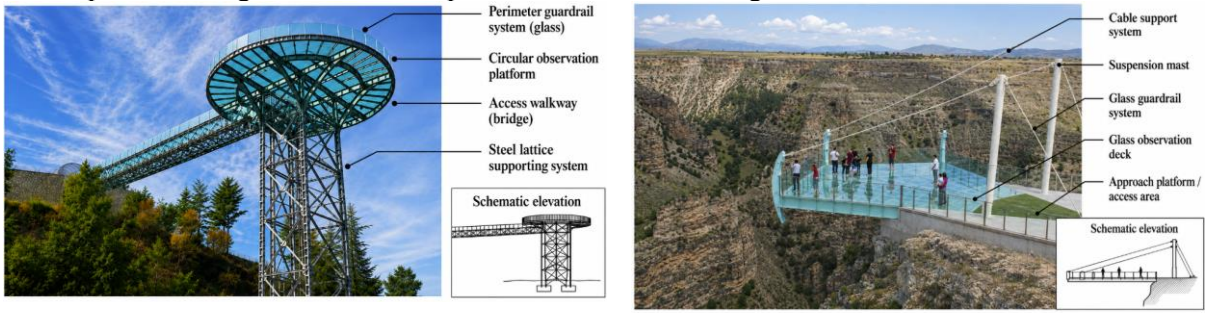
*Corresponding Author E-mail: zeliha.tonyali@erdogan.edu.tr

Abstract. Cliff-mounted glass observation platforms (GOPs) are increasingly constructed as landmark tourist structures; however, their slender steel support systems, low inherent damping, elevated deck mass, and deformation-sensitive circular framing make them vulnerable to near-fault earthquake effects. This study presents a performance-based seismic retrofit approach for a steel GOP using optimized fluid viscous dampers (FVDs) and targeted local strengthening. The GOP in Bursa Province, Türkiye was selected as an example. A three-dimensional structural model was developed in SAP2000 using frame elements. The seismic response was evaluated through bidirectional direct-integration time-history analyses under selected near-fault ground motions from the 2023 Kahramanmaraş earthquake sequence. The proposed retrofit procedure is governed by member-level demand-to-capacity ratios, with a target acceptance limit of $D/C \leq 0.80$. A MATLAB-based iterative design routine was used to update damper coefficients after each time-history analysis until the prescribed performance criterion was satisfied. Within this framework, two practical retrofit alternatives are emphasized: a sequential damper installation strategy, in which the primary support system is first controlled and deck dampers are subsequently optimized, and a hybrid strategy combining FVDs with local cross-sectional enhancement of critical circular ring beams. The results show that the unretrofitted structure develops excessive displacement demand and non-uniform deck deformation, particularly around the outer ring and ramp-connected region. The sequential damper strategy provides a balanced reduction in displacement, acceleration, and base-shear demand, making it attractive when global response control and foundation demand are governing design considerations. In contrast, the hybrid retrofit strategy provides the most effective control of local deck distortion and torsion-sensitive deformation by combining supplemental damping with increased sectional stability of critical deck members. These findings indicate that retrofit design for GOPs should not be based solely on global response reduction, but should also consider local deck deformation, force transfer to the support system, and damper utilization efficiency. The proposed framework provides a practical design-oriented methodology for seismic retrofit of slender steel GOPs located in near-fault regions.

Keywords: Glass observation platform; Viscous damper; Near-fault earthquake; Seismic retrofit

1. Introduction

GOPs have rapidly become landmark tourism structures because they combine scenic visibility, lightweight steel framing, and transparent deck systems. In Türkiye and worldwide, these structures are commonly configured as cliff-mounted or elevated decks with long cantilevered components and irregular plan geometry. Such architectural advantages may also produce low lateral stiffness, low inherent damping, and torsion-sensitive vibration characteristics. Similar lightweight transparent pedestrian and glass-bridge systems have been discussed in recent vibration-serviceability studies [1-3]. Two representative glass observation platforms are shown in Fig. 1.



a) Kirazlıdere glass observation platform (Isparta Province, Türkiye)

b) Ulubey Glass Terrace (Uşak Province, Türkiye)

Fig. 1. Representative glass observation platforms (GOPs)

Despite their growing use in seismically active regions, the seismic retrofit of steel GOPs has received limited attention compared with conventional buildings and bridges. The problem is particularly important for near-fault earthquakes, where strong acceleration pulses and velocity-sensitive demand may simultaneously amplify support-level actions and local deck deformation. Therefore, retrofit design should consider not only global displacement reduction, but also force transfer, torsion-sensitive deck response, and member-level capacity exceedance. This study introduces an iterative viscous-damper optimization framework together with a hybrid retrofit concept that combines supplemental damping with localized section enhancement of critical circular ring beams. To the authors' knowledge, this is the first study to systematically investigate the retrofit of an observation deck using viscous dampers, with particular emphasis on improving seismic performance and controlling dynamic demand in critical structural components.

2 Case Study and Numerical Model

The selected case study is the Oylat GOP located in the İnegöl district of Bursa Province, Türkiye. The platform has an approximate area of 250 m² and is situated on a rocky hilltop. The structure consists of a circular steel deck supported by a spatial lattice tower and connected to the terrain through an access deck. The circular deck is composed of inner and outer ring beams, radial beams, circumferential joists, and primary deck members. Because the deck mass is elevated and the ramp connection introduces geometric eccentricity, the platform is expected to exhibit coupled lateral-torsional behavior under earthquake loading.

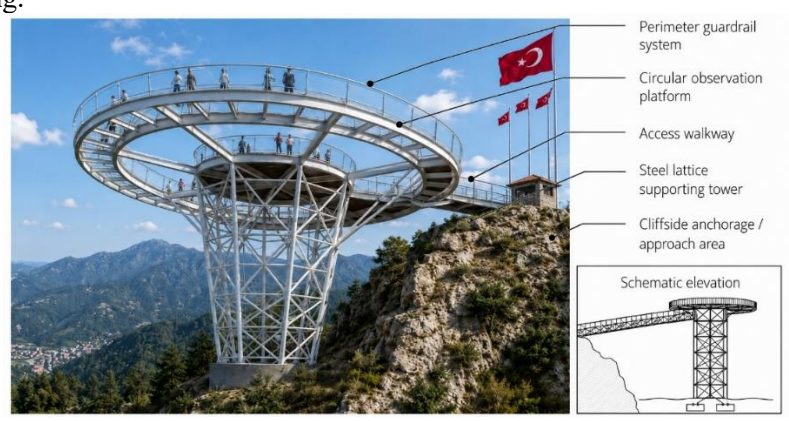


Fig. 2. Oylat GOP and the three-dimensional SAP2000 model

A three-dimensional SAP2000 model was developed using frame elements. The superstructure was mainly represented by HE-series members, whereas the supporting lattice system was modeled using circular hollow sections. In line with the original model description, S275JR steel was assigned to the deck and ramp members, while S235JR steel was assigned to the lattice support members. The model was used for modal analysis and bidirectional direct-integration time-history analyses. Steel member performance was evaluated by the demand-to-capacity (D/C) ratio obtained from member capacity checks. A target D/C limit of 0.80 was adopted as a conservative retrofit acceptance criterion so that all alternatives could be compared using a common performance index [4, 5].

3 Retrofit Strategies and Damper Optimization

Four retrofit strategies were evaluated in order to distinguish the effects of damper distribution, installation sequence, force-transfer control, and local member strengthening. The discussion below summarizes the design logic followed for each strategy before the common optimization procedure and layout figures are presented.

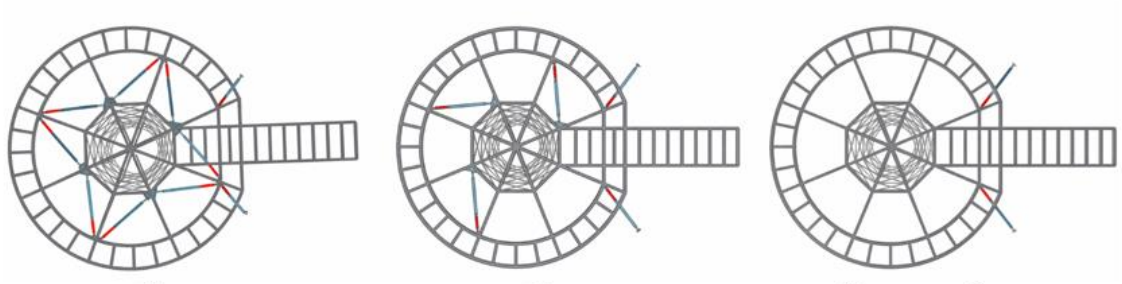
i) Strategy I - distributed damper layout: In this strategy, VDs were placed in a relatively distributed manner between the circular deck system and the supporting members. The purpose of this strategy was to reduce local member demand by increasing energy dissipation at several deck-support interaction points. Therefore, the procedure mainly followed a localized demand-reduction logic: critical regions were identified from the initial D/C distribution, dampers were assigned to these regions, and the damping coefficients were updated iteratively until the target D/C <= 0.80 criterion was approached. This strategy is useful for examining the effect of a broad damper layout, but it may also introduce a less controlled force-transfer mechanism because several dampers act simultaneously around the deck.

ii) Strategy II - sequential column-to-deck optimization: Strategy II was developed as a more systematic damper-only alternative. In this case, the support/column system was controlled first, and the deck-level dampers were optimized after the primary load path had been stabilized. This sequential logic was adopted to prevent the deck dampers from being designed before the main support demand was sufficiently reduced. After each time-history analysis, the MATLAB-based routine updated the damper coefficients and the model was reanalyzed. Compared with Strategy I, this approach provides a clearer design sequence and a more balanced control of displacement, acceleration, and base-shear response.

iii) Strategy III - column-priority damping: Strategy III focused primarily on protecting the main load-bearing support system. The damper layout was therefore more concentrated on the column/support side, while a certain level of deck demand was allowed to remain. This strategy represents a damage-tolerant or support-priority design philosophy in which the main objective is to reduce force demand transferred to the foundation and support members. However, because the circular deck and ramp-connected region are not directly strengthened, this strategy is expected to be less effective in controlling torsion-sensitive local deck deformation.

iv) Strategy IV - hybrid damping and section enhancement. Strategy IV used the practical damper-placement philosophy of Strategy III but added targeted local strengthening of the critical inner and outer circular ring beams. In this hybrid strategy, supplemental viscous damping was used to reduce seismic demand, while section enhancement was used to improve the stiffness, stability, and capacity of the deck members that remained critical after the damper-only stages. The design sequence therefore included column control, deck demand evaluation, section enhancement, and a final coupled verification stage. This strategy directly addresses the main limitation of damper-only schemes by combining global response reduction with local deck-performance improvement.

The strategy layouts and an implementation view of the viscous dampers are given in Figs. 3 and 4. The same D/C-based performance criterion was used in all strategies so that the alternatives could be compared within a consistent performance-based framework.



(b) Str#1 (c) Str#2 (d) Str#3 and Str#4

Fig. 3. Damper layout configurations for the investigated retrofit strategies.

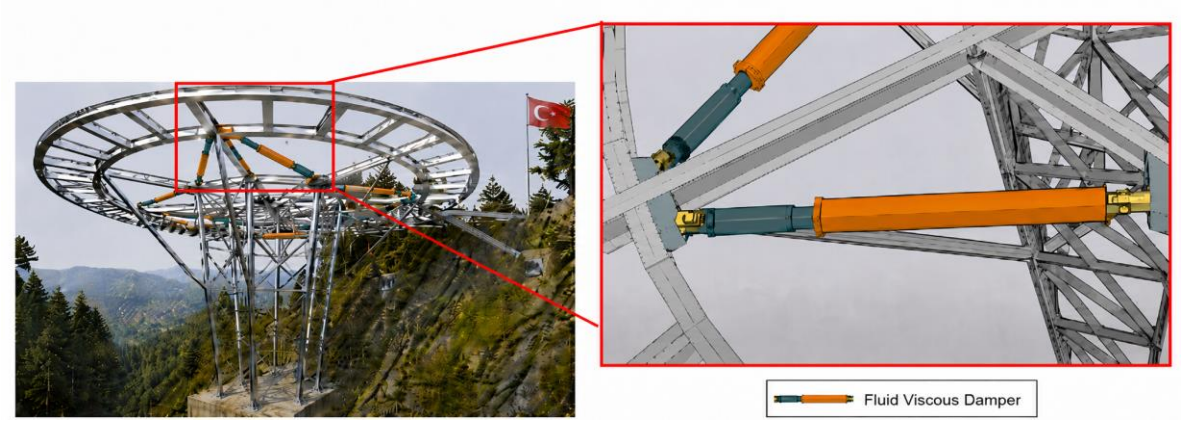


Fig. 4. Applied fluid viscous damper configuration on the observation platform.

The damper force was modeled as a velocity-dependent response using damper-exponential link elements. The viscous dampers were represented by a Maxwell-type link formulation with the damping coefficient treated as the main optimization variable. A MATLAB-based iterative routine was used to update the damping coefficients after each time-history analysis. The loop was repeated until the governing D/C demand satisfied the target threshold. For Strategy 4, the procedure also included a section-enhancement phase and a coupled verification stage, as summarized in Fig. 5.

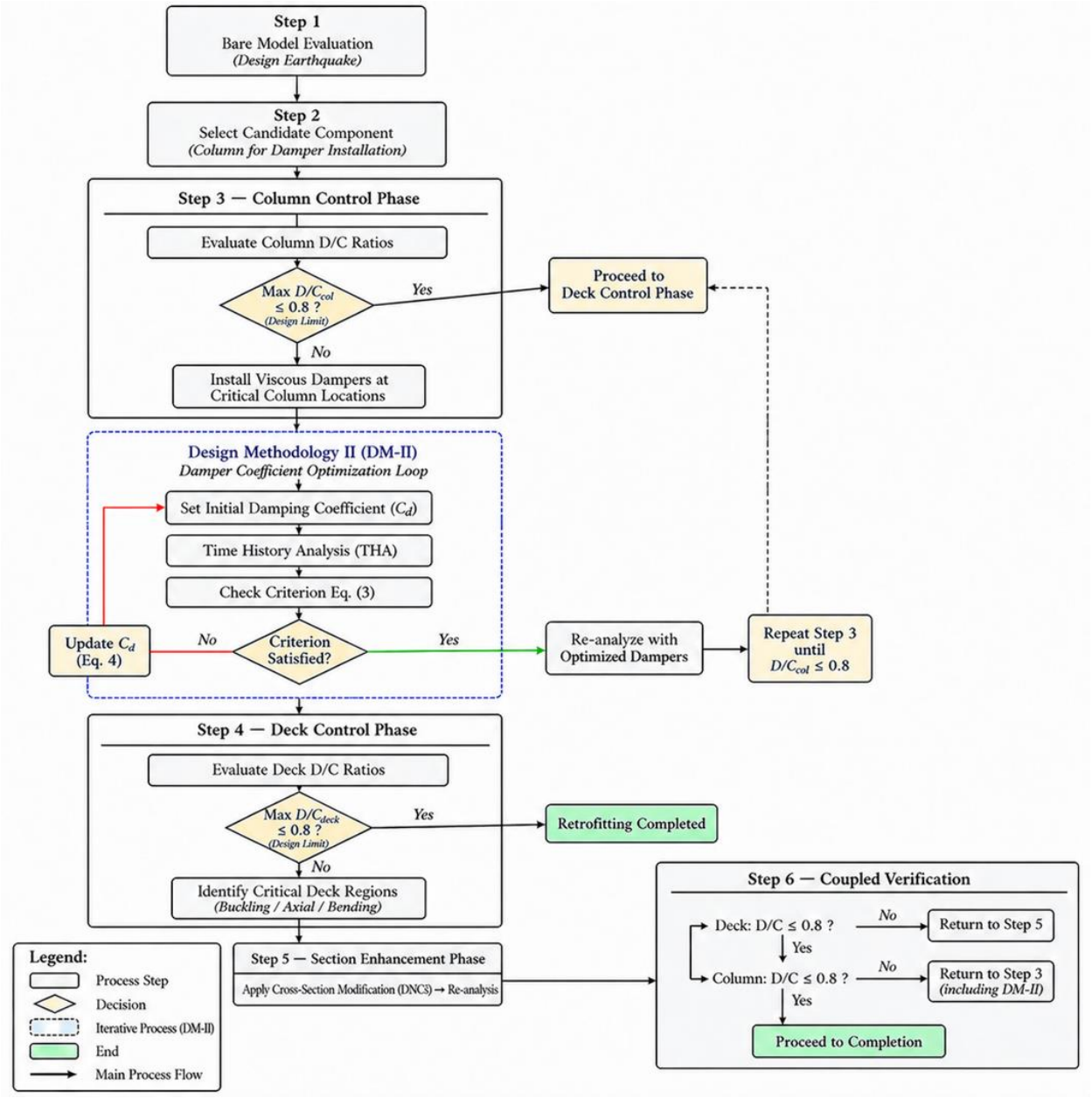


Fig. 5. Flowchart of the proposed Strategy 4 hybrid retrofit methodology.

4 Ground Motions

Three near-fault records from the 2023 Kahramanmaraş earthquake sequence were used: S4614 Pazarcık, S2718 Pazarcık, and S4614 Elbistan, as shown Fig 6. These records were selected to represent near-source conditions and pulse-related demand characteristics relevant to flexible observation platforms [6,7]. The rupture distances range from 2.10 to 8.25 km; S4614 Pazarcık is relatively acceleration dominated, whereas S2718 Pazarcık and S4614 Elbistan have larger PGV/PGA ratios and stronger velocity-sensitive characteristics. The accelerograms were spectrally matched to the target design spectrum using SeismoMatch. The adopted wavelet-based matching procedure follows established response-spectrum matching formulations and was used to obtain spectrum-compatible records while retaining the general time-domain characteristics of the original motions [8-10].

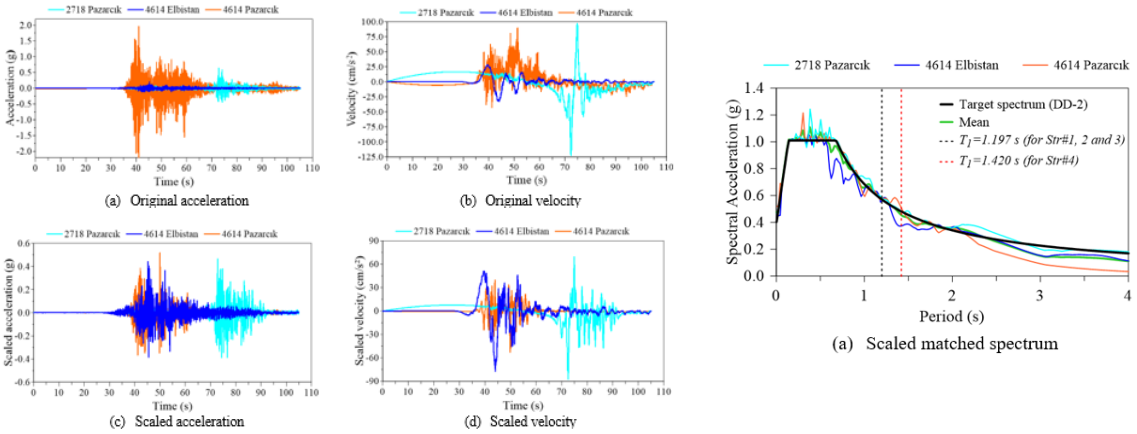


Fig. 6. Ground-motion histories and matched response spectra used in the analyses.

5 Results and Discussion

Fig 7. compares the peak responses of the bare model and the four retrofitted configurations under the selected earthquake records. The bare model developed the highest global response demands and showed extensive member-level D/C exceedance, especially in the circular deck system. This indicates that local deck vulnerability is a governing issue for cliff-mounted observation platforms. Strategies 1 and 2 substantially reduced displacement and acceleration demands. Strategy 2 also provided a balanced base-shear response because the support system was stabilized before the deck dampers were optimized. However, the member-level checks indicate that global response reduction alone is not sufficient unless the circular deck members also satisfy the adopted D/C limit. The peak response results show two distinct retrofit objectives. Strategy 4 achieved the lowest displacement demand, with peak values approximately reduced from about 28-29 cm in the bare structure to about 5-6 cm. However, Strategy 2 provided the most balanced damper-only response in terms of displacement, acceleration, and base-shear reduction. This confirms that peak displacement alone is not sufficient for selecting the optimum retrofit scheme.

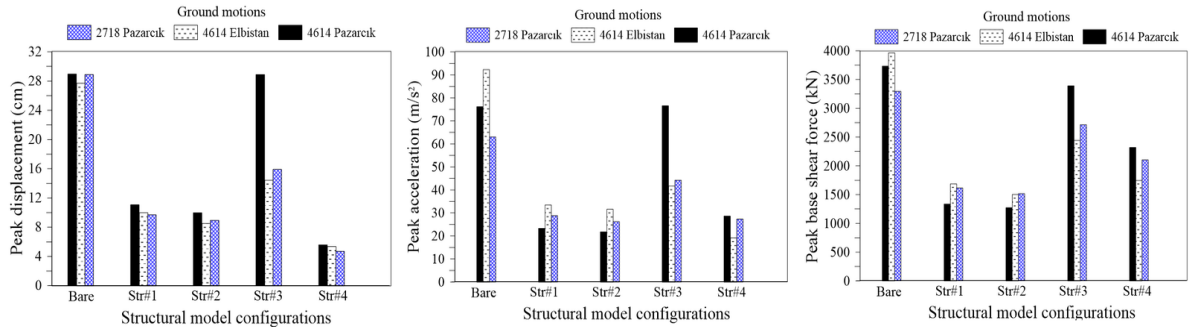


Fig. 7. Peak displacement, acceleration, and base-shear response of the bare and retrofitted configurations.

Fig. 8 presents the RMS values of displacement, acceleration, and base shear for all structural configurations. RMS-based results further indicate that Strategies 1, 2, and 4 reduce the sustained vibration intensity of the platform, whereas Strategy 3 remains less effective. The damper force and hysteresis results confirm that viscous dampers were effectively engaged during the analyses. The hysteresis loops were stable, indicating repeatable energy dissipation and meaningful damper utilization rather than a simple redistribution of structural stiffness.

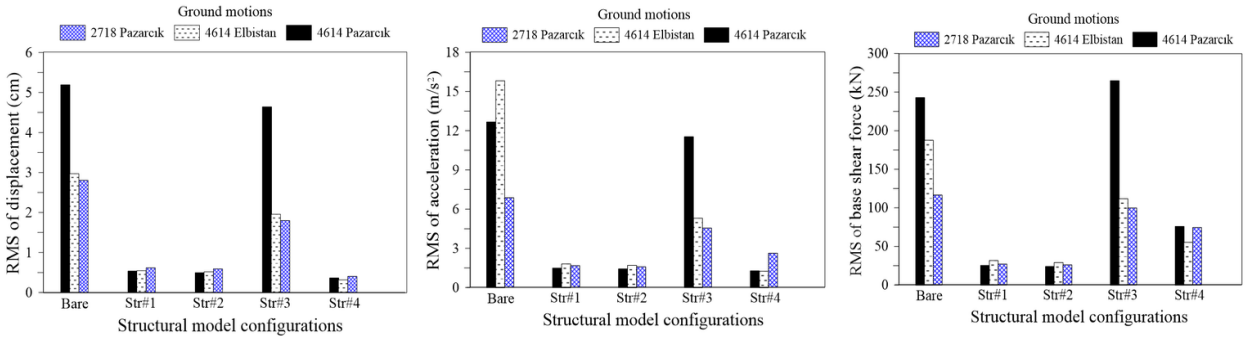
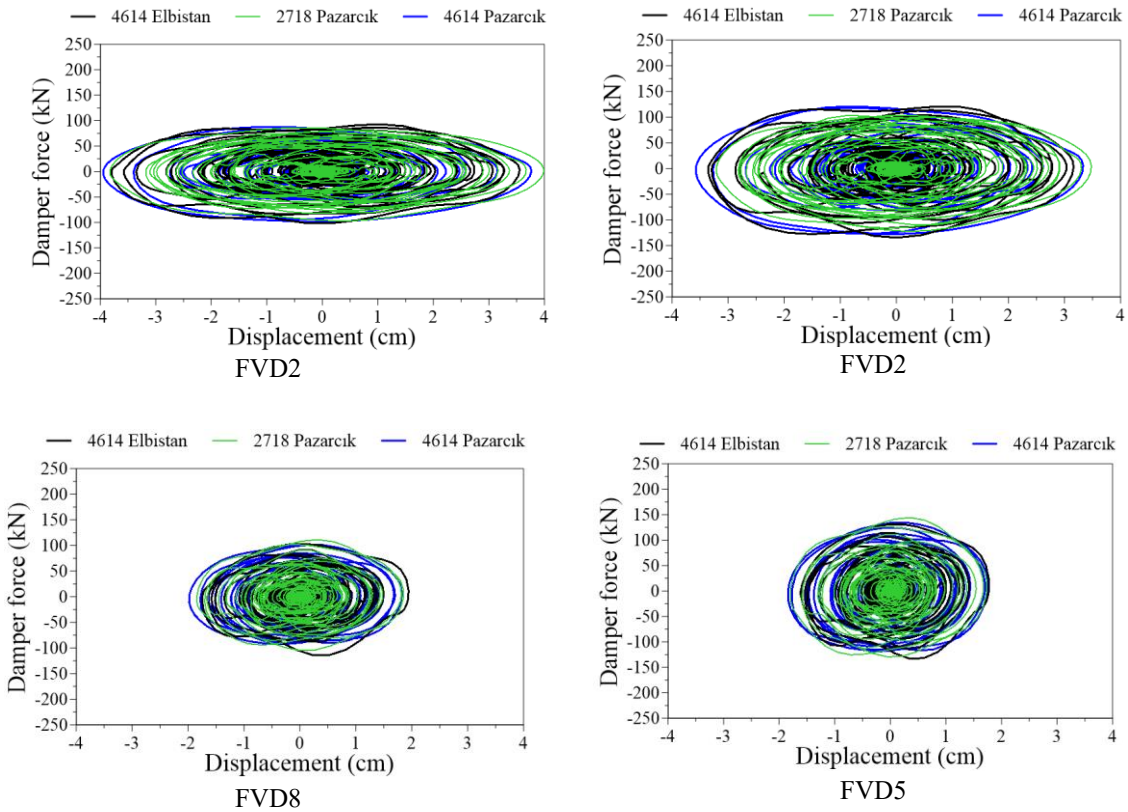
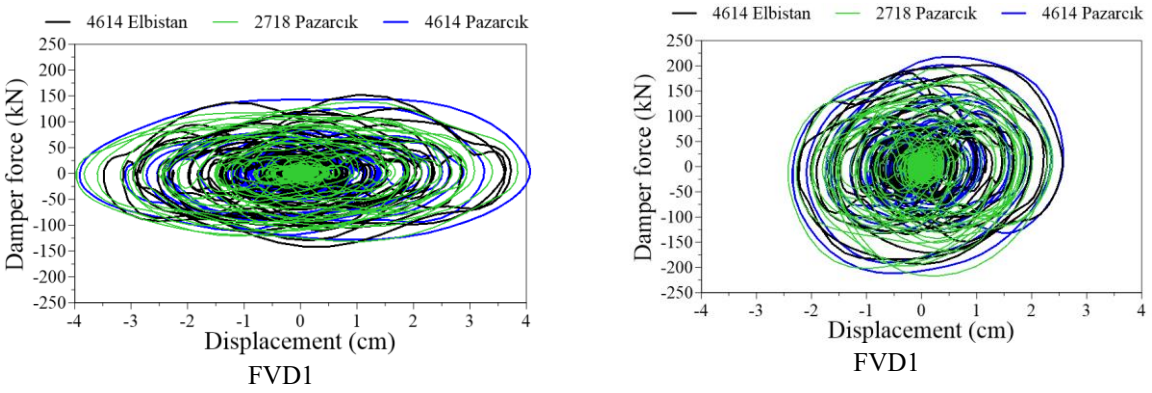


Fig. 8. RMS displacement, acceleration, and base-shear response for the analyzed configurations.

Error! Reference source not found. 9. shows the force–displacement hysteresis behavior of the dampers used in the four retrofit configurations. In all cases, the loops are stable and well developed, indicating that the dampers are effectively engaged and are dissipating seismic input energy in a repeatable manner. For Str#1 and Str#2, the hysteresis loops of the different devices suggest that the damping demand is distributed over more than one response-critical location. The wider loops observed for FVD2 indicate greater displacement demand, whereas the more compact loops of FVD8 and FVD5 indicate more localized motion demand combined with effective force development. This is consistent with the iterative placement logic of the retrofit methodology, in which dampers are assigned according to local structural response rather than uniformly distributed throughout the system. For Str#3 and Str#4, both configurations are represented by FVD1, yet the loop shapes differ noticeably. Str#4 exhibits a more vertically developed hysteretic pattern, which implies a more efficient force response within a relatively controlled displacement range.



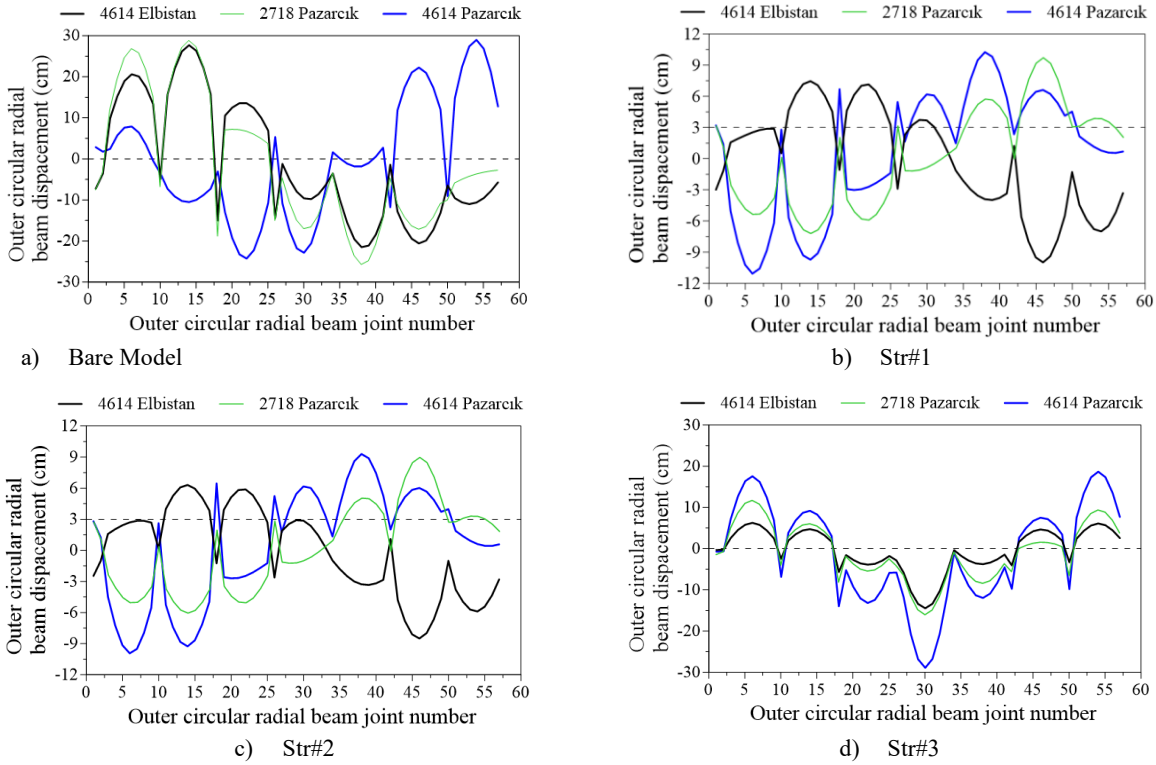
(a) Str#1 (b) Str#2



(c) Str#3 (d) Str#4

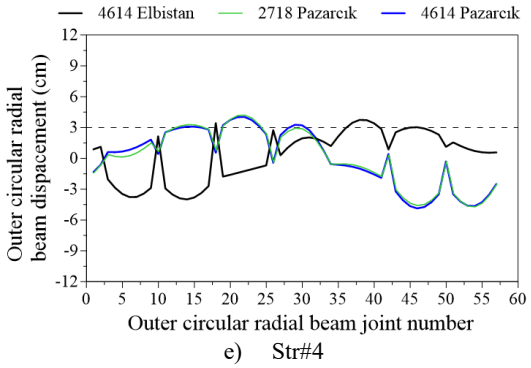
Fig. 9. Representative force-displacement hysteresis loops of the installed viscous dampers.

Fig 10 presents the displacement distribution along the outer circular radial beam line and is arguably the most informative figure regarding local deck behavior. The bare model exhibits large and highly non-uniform oscillatory deformation around the perimeter, indicating pronounced local amplification and torsion-sensitive deck response. Deck-level deformation profiles provide the clearest evidence for the advantage of the hybrid retrofit. The original structure exhibited non-uniform deformation around the outer ring and ramp-connected region. Strategy 4 reduced this irregular deformation by combining supplemental damping with local stiffness and capacity enhancement in the strengthened circular ring beams.



a) Bare Model b) Str#1

c) Str#2 d) Str#3



e) Str#4

Fig. 10. Representative deck deformation profiles for the outer circular/radial beam region.

6 Conclusions

This study developed a performance-based hybrid retrofit strategy for cliff-mounted steel GOPs exposed to near-fault seismic demands. The main contribution lies in combining fluid viscous dampers with selective cross-sectional strengthening of vulnerable circular deck members within a single retrofit scheme. The Oylat GOP was selected as a representative case to evaluate the feasibility of the proposed approach using a three-dimensional SAP2000 model and bidirectional direct-integration time-history analyses. In addition to the hybrid solution, three damper-oriented retrofit configurations were investigated as comparative alternatives. These benchmark cases were used to assess the effectiveness of Str#4 in terms of global seismic response reduction, control of local deck deformation, improvement of member-level capacity, and limitation of force transfer to the supporting system.

- The unretrofitted platform was vulnerable under the selected near-fault records, with excessive displacement demand and local D/C exceedances concentrated in the circular deck system.
- Damper-only strategies reduced global seismic response, but their efficiency depended strongly on damper placement and the resulting force-transfer mechanism.
- The sequential damper strategy provided the most balanced damper-only solution when base-shear limitation and global response reduction were governing objectives.
- The hybrid Strategy 4 provided the best local deck-performance improvement by combining energy dissipation with increased sectional stiffness and stability of critical circular ring beams.
- For steel glass observation platforms, retrofit decisions should combine global response measures, local deck deformation, damper utilization, and member-level capacity indices rather than relying only on peak displacement.

Acknowledgments

The authors acknowledge the support of their institutions and the ACE2026 Organising Committee for the opportunity to present this work.

References

1. Tadeu, A., et al.: Theoretical and experimental analysis of the quasi-static and dynamic behaviour of the world's longest suspension footbridge. Engineering Structures 253, 113830 (2022). https://doi.org/10.1016/j.engstruct.2021.113830.
2. Gong, M., Shen, R., Li, Y., Wang, H., Chen, W., Wei, X.: Practical suggestions for specifications for the vibration serviceability of footbridges. Structural Engineering International 33(4), 659-676 (2023). https://doi.org/10.1080/10168664.2022.2149376.
3. Li, Y., Zhang, X., Wang, C., Zhang, Y., Wei, X.: Human-induced vertical vibration of a glass suspension footbridge. Structure and Infrastructure Engineering 21(4), 656-674 (2025). https://doi.org/10.1080/15732479.2023.2230567.
4. Computers and Structures Inc.: SAP2000: Integrated software for structural analysis and design, Version 25. CSI, Berkeley (2025).

5. American Institute of Steel Construction: Specification for Structural Steel Buildings, ANSI/AISC 360-10. AISC, Chicago (2010).
6. Yazdani, Y., Alembagheri, M.: Nonlinear seismic response of a gravity dam under near-fault ground motions and equivalent pulses. Soil Dynamics and Earthquake Engineering 92, 621-632 (2017). https://doi.org/10.1016/j.soildyn.2016.11.003.
7. Kiral, A., Tonyali, Z., Ergun, M.: A comprehensive analysis of the ground motions of the 2023 Kahramanmaraş, Türkiye earthquakes. Earthquakes and Structures 28(3), 203 (2025). https://doi.org/10.12989/eas.2025.28.3.203.
8. SeismoMatch: A computer program for spectrum matching of earthquake records, Version 2025. Seismosoft Ltd., Pavia, Italy (2025).
9. Hancock, J., Watson-Lamprey, J., Abrahamson, N.A., Bommer, J.J., Markatis, A., McCoy, E., Mendis, R.: An improved method of matching response spectra of recorded earthquake ground motion using wavelets. Journal of Earthquake Engineering 10(S1), 67-89 (2006). https://doi.org/10.1080/13632460609350629.
10. Al Atik, L., Abrahamson, N.: An improved method for nonstationary spectral matching. Earthquake Spectra 26(3), 601-617 (2010). https://doi.org/10.1193/1.3459159.

Author Contribution Statement

- Conceptualization: Adnan Kiral, Zeliha Tonyali
- Methodology: Adnan Kiral, Zeliha Tonyali, Maziar Fahimi Farzam
- Investigation: Adnan Kiral, Zeliha Tonyali
- Writing - Original Draft: Adnan Kiral, Zeliha Tonyali
- Writing - Review & Editing: Adnan Kiral, Zeliha Tonyali, Maziar Fahimi Farzam

Conflict of Interest

The authors declare that there is no conflict of interest.

Data Availability

The numerical data supporting the findings of this study are available from the corresponding author upon reasonable request.

List of Abbreviations

- D/C - Demand-to-capacity ratio
- FVD - Fluid viscous damper
- GOP - Glass observation platform
- RMS - Root mean square
- THA - Time-history analysis

Publication Note

This paper was peer-reviewed, accepted for presentation, and included in the proceedings of the ACE2026 – International Conference on Advances in Civil Engineering, held on 12–14 October 2026 in Trabzon, Türkiye.

This paper may be cited as follows:

Kiral, A., Tonyali, Z., Fahimi Farzam, M., “Iterative Damper Optimization for Seismic Retrofit of a Cliff-Mounted Steel Observation Platform,” in Proceedings of the ACE2026 – International Conference on Advances in Civil Engineering, Trabzon, Türkiye, 12–14 October 2026.

COMPARATIVE SEISMIC DESIGN AND PERFORMANCE EVALUATION OF SPECIAL CONCENTRICALLY BRACED FRAMES AND BUCKLING-RESTRAINED BRACED FRAMES

Kazım Burç CİVELEK[1] ve Elifsu KAYRAK[2]
[1] orcidID, Antalya Bilim University, Civil engineering Department, Antalya, Turkey, burc.civelek@antalya.edu.tr
[2] orcidID, Antalya Bilim University, Civil engineering Department, Antalya, Turkey, elifsu.kayrak@std.antalya.edu.tr

ABSTRACT

Although Special Central Braced Frames (SCBFs) are widely used in the design of multi-story steel structures in high seismic risk areas, they have disadvantages such as element buckling under compression and limited energy dissipation capacity. Buckling-Restrained Braced Frames (BRBFs), exhibiting symmetric hysteretic behavior, offer a superior seismic solution to these structural problems. In this study, the seismic design of a seven-story steel structure was carried out with SCBF and BRBF alternatives according to AISC 341-22 capacity design principles and ASCE 7-22 regulations; The research findings showed that the high coefficient of behavior ($R = 8$) in the BRBF system provided a 25% reduction in the total base shear force seismically. It has been determined that this global seismic demand reduction and the decrease in the unbalanced vertical force (P_{ub}) in the chevron configuration from 558 kN to 117.8 kN prevented mandatory oversizing in beam cross-sections (reduction from HEB 600 profile to HEB 240/340 range) and provided a material optimization of 11.2 tons (19%) in the weight of the frame without braces. In the context of capacity design philosophy, it has been proven that despite the increased excessive strength demand $\Omega_0 = 2.5$), the HEM 360 cross-section can be safely used instead of HEM 400 in the columns thanks to the compensatory effect of the reduced base shear force. In conclusion, this study; Quantitative data demonstrate that the BRB system, with its dramatic material savings and seismic repairability potential offered within a cross-free frame, is an extremely rational and reliable design alternative in high seismic risk areas.

Keywords: Buckling-Restrained Braced Frames, Special Center Braced Frames, Energy Dissipation.

INTRODUCTION

As a country located within a highly active seismic zone, Türkiye faces a critical need to enhance the seismic resistance of its structures to minimize loss of life and property. Recent earthquakes such as the M_w 7.5 Kahramanmaraş Earthquake in 2023 and the M_w 6.2 Istanbul Earthquake have highlighted the necessity for innovative structural systems capable of improving the seismic performance of the existing building stock. In steel structures, Moment-Resisting Frames (MRFs) and Braced Frames are among the most employed lateral force-resisting systems. MRF systems are designed such that beams and columns are connected through moment-resisting joints, providing both stiffness and ductility against lateral loads. Special Moment Frames (SMFs) dissipate seismic energy primarily through the plastic deformation of structural members. However, under severe earthquake loading, large inelastic deformations inevitably result in permanent structural damage and residual deformations, which may adversely affect the post-earthquake functionality and resilience of the structure.

The seismic design philosophy of SMFs is fundamentally based on utilizing the inelastic deformation capacity of structural steel to dissipate earthquake-induced energy.Special Concentrically Braced Frames (SCBFs), on the other hand, enhance the stiffness and strength of structures by transferring lateral loads to the foundation through bracing members installed within the frame. Depending on architectural constraints and stiffness requirements, these systems may be configured in various geometries, including X-bracing, diagonal bracing, and inverted-V (Chevron) bracing. Among these alternatives, X-bracing is generally preferred due to its more effective energy dissipation characteristics at the connection regions under cyclic tension-compression loading. The fundamental design principle of SCBFs is the transformation of lateral loads into axial tensile and compressive forces within the brace members. A distinctive characteristic of SCBF systems is their asymmetric behavior under tension and compression loading. The seismic response of these systems is highly dependent on brace slenderness and differs significantly between tensile and compressive load states. Under tensile loading, brace members undergo strain hardening, whereas under compressive loading, buckling occurs once the critical buckling load is exceeded. Following buckling, a sudden and substantial reduction in load-carrying capacity is observed. Under cyclic loading conditions, the re-straightening of buckled braces results in stiffness degradation, leading to pronounced pinching effects in the force-displacement hysteresis loops and a significant reduction in energy dissipation capacity. Previous studies have concluded that brace slenderness is one of the most influential parameters governing the hysteretic behavior of conventional braces. While tensile loading promotes strain hardening, compressive loading induces buckling once the critical load threshold is exceeded (Figure 1'a). This phenomenon reduces the overall energy dissipation capability of the system and limits its seismic performance. Consequently, conventional braces are unable to dissipate a substantial portion of earthquake energy, and their strength deteriorates rapidly with increasing loading cycles, a phenomenon commonly referred to as strength degradation. Such behavior compromises the seismic safety of structures and may lead to global stability problems, particularly in systems utilizing highly slender braces. Due to these unfavorable behavioral characteristics, modern seismic design provisions, including AISC 341 and the Turkish Building Earthquake Code (TBEC 2018), impose specific limitations on the use of conventional bracing systems. In regions requiring high ductility, brace slenderness ratios are restricted, and special detailing requirements are imposed at connection regions to accommodate brace rotations during buckling, such as the provision of adequate gusset plate free-bending lengths. These limitations and performance concerns have ultimately led to the development of Buckling-Restrained Braces (BRBs), which exhibit stable and symmetric behavior under both tensile and compressive loading. Unlike conventional braces, BRBs eliminate the tendency of brace members to buckle under axial compression, thereby enabling nearly identical hysteretic responses in tension and compression (Figure 1b). As a result, BRBs provide stable energy dissipation, superior ductility, and significantly improved seismic performance under cyclic loading conditions.

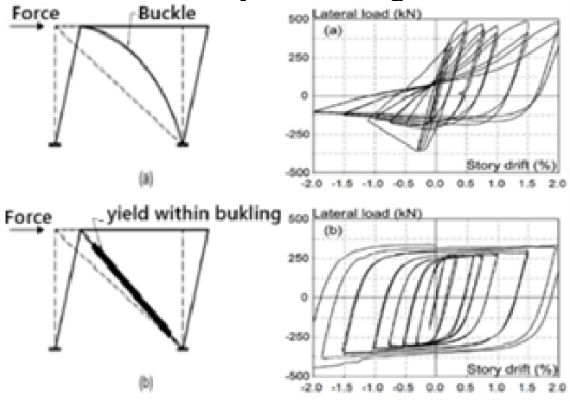


Fig. 1. Lateral load–story drift relationships of (a) a conventional brace (CB) and (b) a buckling-restrained brace (BRB) with diagonal configuration [1].

Buckling-Restrained Braces (BRBs) consist of three primary components: the steel core (SC), the buckling restraint mechanism (BRM), and an unbonded interface layer located between the SC and the BRM. The SC is the component responsible for carrying the axial load. As illustrated in Figure 2, various SC cross-sectional configurations have been proposed and investigated in previous studies. A review of the literature reveals that rectangular [2–4], cruciform [5,6], and H-shaped [7,8] core sections are among the most adopted configurations.The primary function of the BRM is to prevent buckling of the SC under axial compressive loading, thereby enabling the core element to undergo stable post-yield plastic deformation under both tensile and compressive loading conditions. Through this mechanism, the BRB effectively dissipates seismic energy imparted to the structure. BRMs may be manufactured by infilling concrete or mortar into steel tube sections [9], entirely from steel plates [10], or by utilizing advanced composite materials such as glass-fiber-reinforced polymers (GFRP) [11] and carbon-fiber-reinforced polymers (CFRP) [12].The purpose of the unbonded interface layer is to prevent load transfer from the SC to the BRM and to eliminate additional stresses generated by friction between these components during cyclic loading. To achieve this objective, previous studies have investigated methods for determining optimum interface dimensions [13] as well as the use of isolation materials such as butyl tape [14] and silicone sheets [15]. Recent developments in BRB technology have resulted in the emergence of innovative configurations tailored to specific performance requirements. For instance, several studies have proposed replaceable BRB systems in which damaged steel core elements can be readily replaced following a major seismic event [16–18]. Other investigations have introduced all-steel BRB designs incorporating metamaterials and perforated core elements with negative Poisson's ratios [19,20]. Furthermore, dual stage BRB systems have been developed to accommodate large axial deformations without causing structural damage while maintaining stable energy dissipation capabilities at prescribed design drift levels under frequent and moderate earthquake excitations. These advancements demonstrate the continuous evolution of BRB technology toward enhanced seismic resilience, improved reparability, and superior energy dissipation performance compared with conventional bracing systems.

METOT

In this study, two alternative lateral force-resisting systems suitable for multi-story steel buildings located in regions of high seismic hazard were comparatively evaluated. A typical seven-story office building, consisting of six regular stories and one roof level, was selected as the reference structure. The regular story height was taken as 3.5 m, while the roof level height was 2.6 m, resulting in a total building height of 23.6 m. The building has four bays in the X-direction, each with a span length of 9 m, yielding a total plan dimension of 36 m in this direction. Moment-Resisting Frames (MRFs) were employed as the lateral force-resisting system along the X-axis. In the Y-direction, the structure consists of three bays, each measuring 7.5 m in length, resulting in a total building dimension of 22.5 m. The typical floor plan of the building is presented in Fig. 3.

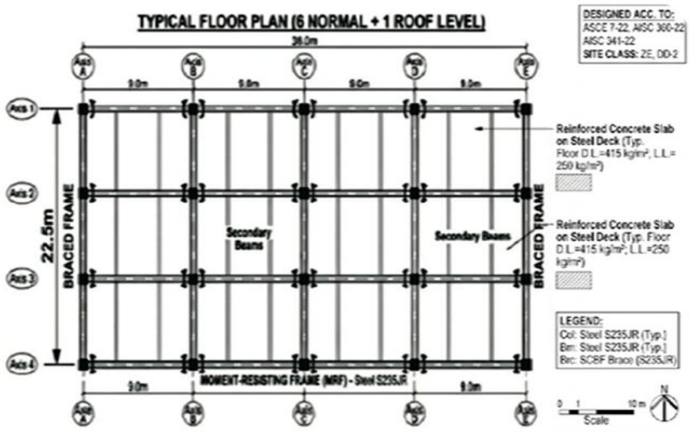


Fig. 3. Typical floor plan.

S235JR structural steel was adopted for the design of the primary load-carrying columns, beams, and bracing members. This steel grade was selected due to its widespread use in construction practice, ease of procurement, cost-effectiveness, and adequate corrosion resistance. Structural analysis and member sizing were performed using the Load and Resistance Factor Design (LRFD) methodology in accordance with the provisions of AISC 360-22 and the seismic detailing requirements of AISC 341-22. Equivalent seismic loads were determined based on the procedures specified in ASCE 7-22. For the comparative analysis, the response modification coefficient was taken as $R = 6$ for the Special Concentrically Braced Frame (SCBF) system and $R = 8$ for the Buckling-Restrained Braced Frame (BRBF) system. Accordingly, the design base shear forces (V_y) were calculated and distributed over the building height. In the capacity design of columns, the system overstrength factors (Ω_0) prescribed by the relevant standards were adopted as 2.0 for the SCBF system and 2.5 for the BRBF system. Within the scope of this study, the DD-2 seismic hazard level, corresponding to a 10% probability of exceedance in 50 years, was selected as the design earthquake level. Furthermore, the ZE site class, representing highly unfavorable soil conditions from a seismic perspective, was adopted. When integrating the seismic parameters defined in the Turkish Seismic Hazard Map into the ASCE 7-22 framework, the structure was assumed to belong to a high seismic risk category corresponding to Seismic Design Category D (SDC D). The design spectral accelerations were taken as $S_{DS} = 1.0g$ and $S_{D1} = 0.6g$.The applied gravity loads consisted of a dead load of 4.07 kN/m^2 and a live load of 2.45 kN/m^2 for typical floors, while the roof level was assigned a dead load of 3.19 kN/m² and a live load of 0.98 kN/m^2. In addition, an exterior cladding load of 0.74 kN/m^2 was considered. Based on these assumptions, the design base shear force in the Y-direction was determined using the Equivalent Lateral Force (ELF) procedure, after which the equivalent seismic story forces and story shear forces were calculated. According to AISC 341-22, the design and detailing requirements for SCBF systems in regions of high seismic hazard (DD-2, SDC D) are governed by stringent provisions intended to ensure satisfactory structural performance and controlled collapse mechanisms. Therefore, the bracing configurations adopted along Grid Lines A–A and E–E were selected to achieve both code compliance and structural economy's 341-22 places restrictions on certain bracing configurations and requires additional design checks to account for unbalanced forces that may develop following brace buckling. In Chevron (V- or inverted V-type) bracing systems, when the compression brace buckles, the force carried by the tension brace generates a significant unbalanced vertical load at the beam intersection point. Consequently, capacity design requirements may lead to substantial beam overdesign. In contrast, the use of a two-story X-

brace configuration allows the tensile and compressive brace forces to balance each other at the connection region, thereby eliminating large, unbalanced forces acting on the beam and resulting in a more economical structural solution. Following this optimization strategy, the brace configuration and member sections were determined first. Subsequently, the brace-to-gusset plate connections, primary beam and column sections, and connection details were designed. The SCBF and BRBF systems located along Grid Lines A–A and E–E are illustrated in Figure 4. After completing the design of the SCBF system, the design of the BRBF system was undertaken. Accordingly, the geometric configuration of the bracing system was modified to better accommodate the unique seismic behavior and performance characteristics of BRBF structures.

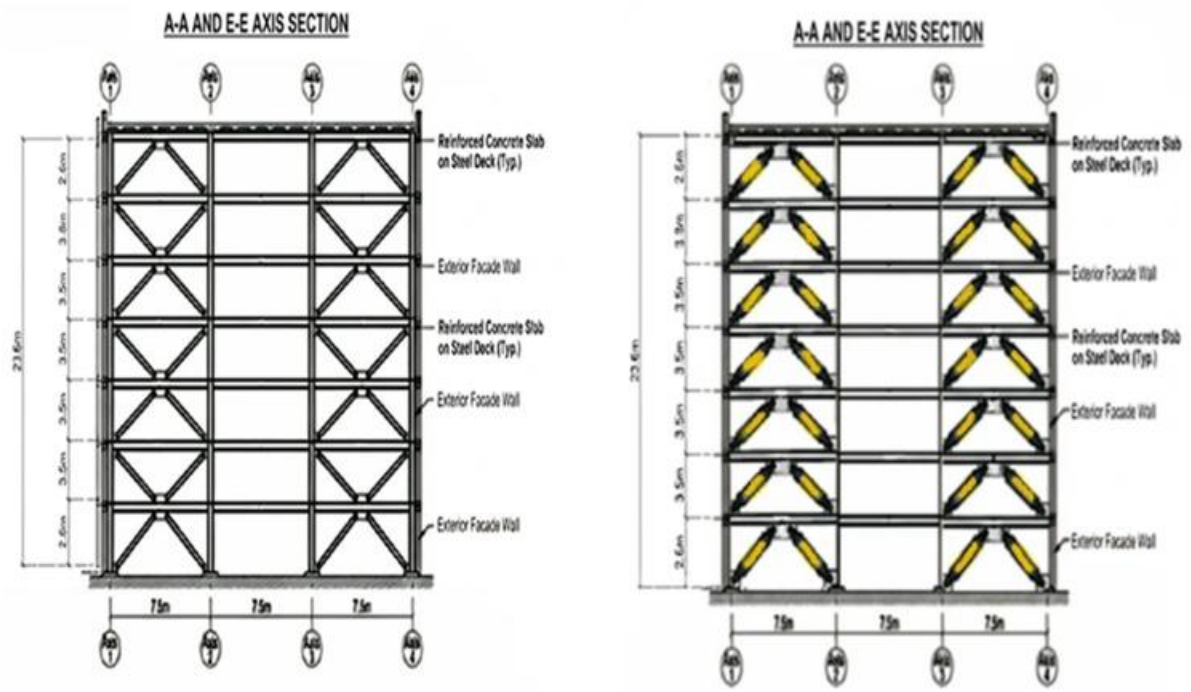


Fig. 4. (a) SCBFs located along Grid Lines A–A and E–E, and (b) BRBFs located along Grid Lines A–A and E–E.

The most significant characteristic of BRB members is their ability to maintain their load-carrying capacity under compressive loading without experiencing global buckling. In a Chevron-configured BRBF system, when one brace reaches its maximum compressive capacity while the opposing brace reaches its maximum tensile capacity, the forces acting at the beam–brace intersection largely balance each other. The remaining force imbalance, typically on the order of 10–15%, is transferred to the beam as an unbalanced vertical force. Consequently, beam sections can be substantially reduced compared to those required in conventional SCBF systems. To provide greater architectural flexibility, Chevron-configured BRBFs were employed in the exterior bays (Bays 1 and 3), while the middle bay was intentionally left unbraced. Although numerous BRB configurations have been proposed in the literature, a conventional BRB system was adopted in this study under the assumption that commercially manufactured BRB units would be procured. This configuration consists of a rectangular steel core encased within a hollow structural section, with the remaining void filled with concrete or mortar. Upon completion of the BRBF design, the brace-to-gusset plate connections were detailed, the primary beam and column sections were selected, and the beam-to-column connections were designed.

RESULT AND DISCUSSION

The analyses revealed significant differences between the SCBF and BRBF systems in terms of seismic force distribution and member sizing requirements. According to ASCE 7-22 (Table 12.2-1), the response modification coefficient (R) is specified as 6 for SCBF systems and 8 for BRBF systems. This difference indicates that BRBFs possess a higher ductility capacity and can dissipate seismic energy more effectively than SCBFs. Based on the Equivalent Lateral Force (ELF) procedure, the design base shear force was calculated as $4048.8\ kN$ for the SCBF system and $3036.6\ kN$ for the BRBF system. Therefore, replacing the SCBF system with a BRBF system resulted in a 25% reduction in the total seismic demand acting on the structure. This reduction directly decreased the seismic demands imposed on all primary structural members, including beams and columns, and enabled significant reductions in member sizes, leading to a more economical design while remaining consistent with capacity design principles. The selection of braced bays was considered a critical aspect of the design due to its influence on both torsional stiffness and architectural functionality. Providing braces in all three bays was expected to produce excessive lateral stiffness and increase overturning demands at the foundation level. To preserve architectural accessibility for corridors, doors, and windows while maintaining structural symmetry, braces were installed only in the exterior bays (Bays 1 and 3), whereas the middle bay (Bay 2) was left unbraced. Furthermore, placing the braces in the exterior bays maximizes the lever arm resisting overturning moments and consequently minimized uplift forces transmitted to the foundation. For the SCBF system, a two-story X-brace configuration was employed throughout the regular floors, while a Chevron configuration was adopted at the roof level where gravity load demands were relatively lower. In contrast, the principal advantage of BRB members lie in their nearly identical tensile and compressive capacities. Owing to this stable hysteretic behavior, considerably more flexible architectural configurations can be achieved without generating large, unbalanced forces in beams. Accordingly, BRB members were also placed in the exterior bays (Bays 1 and 3), while the middle bay remained unbraced for the same structural and architectural reasons adopted in SCBF design. A Chevron bracing configuration was selected for all stories because it provides symmetric lateral stiffness and offers significant practical advantages in fabrication and erection due to the simplicity of the central beam–brace connection. In the SCBF system, the maximum story shear force occurred at the first story. Consequently, the seismic demands acting on the first-story braces governed the brace design. The required axial design force for the first-story braces was determined as $P_u = 692.3\ kN$. Hollow Structural Sections (HSS) with square geometry were selected because they provide identical buckling resistance about both principal axes. An HSS 150×150×10 section was initially chosen as the trial brace section. Subsequent evaluations performed in accordance with AISC 341-22, including axial compression resistance, axial tension resistance, and seismic compactness (local slenderness) checks required for highly ductile members, demonstrated that the selected HSS 150×150×10 section satisfied all applicable limit-state requirements. Unlike conventional brace design in SCBF systems, the steel core areas of BRB members can be adjusted with high precision according to the reduction in story shear forces along the building height. This capability enables highly efficient material optimization. The variation of story shear forces (V_x), steel core cross-sectional areas (A_{sc}), and the dimensions of the square HSS casing sections used as the BRB restraining units throughout the building height are summarized in Table 1.In accordance with the capacity design provisions of AISC 341-22, the maximum expected tensile and compressive strengths of each BRB were calculated based on the selected steel core areas. These calculations incorporated the effects of the strain-hardening adjustment factor ($\omega = 1.4$) and the compression strength adjustment factor ($\beta = 1.15$), thereby accounting for the expected inelastic behavior of the BRB members during severe seismic loading.

Table 1. Cross-sectional distribution of BRB members per story

Story	Story Shear Force ($Vx - kN$)	SC Area ($Asc - (mm^2)$)	SC Plate ($w \times thk - mm$)	SHS outer Casing Dimensions (mm)
7 (roof)	682.2	500	50×10	100×100×5
6th	1396.5	1200	60×20	120×120×6
5th	1975.4	1600	80×20	140×140×6
4th	2423.0	2000	80×25	140×140×6
3rd	2744.3	2250	90×25	150×150×8
2nd	2945.8	2400	100×25	150×150×8
1st	3036.6	2500	100×25	160×160×8

According to the requirements of AISC 341-22, beam design in the SCBF system was categorized into two distinct groups. The first category consisted of beams located in the unbraced middle bay, where the design was governed primarily by gravity loads (dead and live loads). The second category comprised beams located within the braced exterior bays, where design was controlled not only by gravity loads but also by the net unbalanced force transferred to the beam following the buckling of one of the brace members.This concentrated force acting at the beam midpoint generated significant shear forces and bending moments. Although the use of a two-story X-brace configuration effectively reduced force imbalance in the typical stories, the maximum unbalanced force occurred at the roof level where a Chevron bracing configuration was employed. To satisfy these seismic demands, HEB sections, which possess greater cross-sectional area and superior lateral buckling resistance than slender IPE profiles, were selected. For the middle-bay beams (Category 1) and the braced-bay beams in the regular stories (Category 2), HEB 300 sections satisfied all LRFD strength and serviceability requirements. However, for the Chevron-braced roof beam, the excessive unbalanced vertical force ($P_{ub} = 558\,kN$) resulting from one brace reaching its yielding capacity while the opposing brace buckled necessitated the use of an HEB 600 section. Like the SCBF design, beam design in the BRBF system was also divided into two categories in accordance with the capacity design provisions of AISC 341-22. The primary function of the middle-bay beams (Category 1) was to support gravity loads from the floor system and to act as collectors transmitting diaphragm-induced seismic forces to the braced exterior frames. Although HEB 240 sections were found to be adequate when only bending demands were considered, HEB 300 sections were ultimately selected as a standard solution to ensure sufficient stability and reliable transfer of the large axial collector forces generated through beam-column interaction. Even though gravity loads were lower at the roof level, HEB 300 sections were retained in the middle bay to ensure adequate diaphragm force transfer. According to the capacity design philosophy of AISC 341-22, beams located within braced bays are not designed directly for seismic forces; instead, they are proportioned to resist gravity loads together with the net unbalanced vertical forces generated by the connected BRB members at their expected capacities. Consequently, the exterior-bay beams in the regular stories were designed to resist both floor loads and the unbalanced vertical forces associated with the Chevron-configured BRBs. The largest unbalanced vertical force ($P_{ub} = 117.8\,kN$) occurred in the first-story beam. To accommodate the resulting bending and shear demands, an HEB 340 section was selected. At the roof level, however, both the gravity loads and the story shear force were significantly reduced, resulting in smaller BRB capacities and correspondingly lower bending demands. Therefore, an HEB 240 section was found to provide adequate strength for the roof beam. Column design in SCBF systems represents one of the most demanding consequences of the AISC 341-22 capacity design philosophy in terms of structural weight. SCBF columns must

remain stable and capable of resisting the maximum axial forces transmitted through the brace connections after brace yielding and buckling during severe seismic events. To model this critical condition, AISC 341-22 requires seismic loads to be amplified by the system overstrength factor ($\Omega_0 = 2.0$) and included in the governing load combinations. The analyses revealed that the amplified seismic loading condition ($\Omega_0 \, P_{EQ}$) generated extremely large axial compression demands, reaching $6118\,kN$ in the first-story exterior columns. To satisfy the global buckling resistance requirements (KL/r_y) and seismic compactness limits prescribed for highly ductile members ($\lambda_h d$), the use of heavy HEM 400 sections became necessary. The superior energy dissipation capability of the BRBF system results in a higher response modification coefficient ($R = 8$), thereby significantly reducing the design base shear force acting on the structure. Nevertheless, AISC 341-22 requires an even larger overstrength factor ($\Omega_0 = 2.5$) to ensure that columns remain elastic when BRB members develop their maximum expected tensile (T_{max}) and compressive (P_{max}) capacities during severe earthquakes. Despite this stricter overstrength requirement, analyses conducted under the amplified seismic load combination ($\Omega_0 \, P_{EQ}$) indicated that the maximum axial compression demand in the first-story exterior columns was $5833\,kN$, which remained lower than that obtained for the SCBF system. Consequently, HEM 360 sections were sufficient to satisfy both the global buckling resistance requirements (KL/r_y) and the seismic compactness criteria for highly ductile members without compromising structural safety or seismic performance. The findings clearly demonstrate that BRBF systems, owing to their superior energy dissipation capabilities, provide a more robust, reliable, and efficient structural solution for both the design of new steel buildings and the seismic retrofitting of existing structures, particularly in regions exposed to high seismic hazard. Furthermore, the substantial reductions achieved in beam and column sizes highlight the significant economic advantages that can be realized through the adoption of BRBF systems while simultaneously improving seismic resilience and post-earthquake functionality.

ACKNOWLEDGMENTS

The authors would like to express their sincere gratitude to the professors of Civil Engineering at Antalya Bilim University for their valuable guidance, insightful comments, and continuous support throughout the preparation of this study.

LIST OF ABBREVIATIONS

AISC	: American Institute of Steel Construction
ASCE	: American Society of Civil Engineers
A_{sc}	: Steel Core Cross-Sectional Area
BRB	: Buckling-Restrained Brace
BRBF	: Buckling-Restrained Brace Frame
BRM	: Buckling Restraint Mechanism
CB	: Conventional Brace
CBF	: Concentrically Braced Frame
CFRP	: Carbon-Fiber-Reinforced Polymer
DD-2	: Design Earthquake Hazard Level (10% probability of exceedance in 50 years)
ELF	: Equivalent Lateral Force
GFRP	: Glass-Fiber-Reinforced Polymer
HEB	: Wide Flange Beam Profile (European Standard)
HEM	: Heavy Wide Flange Column Profile (European Standard)
HSS	: Hollow Structural Section
LRFD	: Load and Resistance Factor Design

MCV : Main Load-Bearing Elements
MRF : Moment-Resisting Frame
Mw : Moment Magnitude
P_{EQ} : Earthquake Load
P_{ub} : Unbalanced Vertical Force
R : Response Modification Coefficient
SC : Steel Core
SCBF : Special Concentrically Braced Frame
SDC D : Seismic Design Category D
S_{D1} : Design Spectral Acceleration Parameter for 1-Second Period
S_{DS} : Design Spectral Acceleration Parameter for Short Period
SHS : Square Hollow Section
SMF : Special Moment Frame
TBEC : Turkish Building Earthquake Code (TBEC 2018)
V_x : Story Shear Force
V_y : Design Base Shear Force
ZE : Soil Site Class ZE
Ω_0 : System Overstrength Factor

REFERENCES

[1] Hayashi, K., Skalomenos, K.A., Jamshiyas, S., Inamasu, H.: Full-scale testing of naturally buckling steel braces and evaluation of partially rib-strengthened sections to cumulative damage. Soil Dynamics and Earthquake Engineering 147, 106611 (2021).
[2] Celik, O.C., Yuksel, E., Avci-Karatas, C., Bal, A., Gokce, T., Bago, Z., Koller, G.: Component testing of steel-core buckling restrained braces (BRBs) with pinned end connections. In: Proceedings of the 8th International Conference on Advances in Steel Structures, pp. 1–10. Lisbon, Portugal (2015).
[3] Mishra, P., Vyavahare, A.Y.: Experimental and numerical studies on all-steel buckling restrained brace with light-weighted restrainer. International Journal of Steel Structures 24(1), 176–189 (2024).
[4] Lin, P.C., Chang, C.W., Wu, B.C.: Experimental study of high-mode buckling behavior of flat steel core in a buckling-restrained brace. Engineering Structures 314, 118320 (2024).
[5] Luo, L., Sun, X., Song, X., Ou, Z., Zhang, L.: Experimental and numerical study on the hysteretic behavior of a hybrid timber buckling-restrained brace with a cross-shaped steel core. Soil Dynamics and Earthquake Engineering 162, 107461 (2022).
[6] Zheng, S.Y., Yuan, B., Wei, M.S., Liu, X.L., Liu, X.F., Zhou, G.Y., Shi, H.W.: Experimental & numerical investigation of all-steel assembled cruciform buckling-restrained braces. Journal of Constructional Steel Research 207, 107981 (2023).
[7] Kim, D.H., Lee, C.H., Ju, Y.K., Kim, S.D.: Subassemblage test of buckling-restrained braces with H-shaped steel core. The Structural Design of Tall and Special Buildings 24(4), 243–256 (2015).
[8] Yuan, Y., Gao, J., Qing, Y., Wang, C.L.: A new H-section buckling-restrained brace improved by movable steel blocks and stiffening ribs. Journal of Building Engineering 45, 103650 (2022).
[9] Tremblay, R., Bolduc, P., Neville, R., DeVall, R.: Seismic testing and performance of buckling-restrained bracing systems. Canadian Journal of Civil Engineering 33(2), 183–198 (2006).
[10] Ghowsi, A.F., Sahoo, D.R.: Cyclic behavior of all-steel BRBs with bolted angle restrainers: Testing and numerical analysis. Journal of Earthquake Engineering 27(2), 362–388 (2023).

[11] Sun, H., Jia, M., Zhang, S., Wang, Y.: Study of buckling-restrained braces with concrete infilled GFRP tubes. Thin-Walled Structures 136, 16–33 (2019).
[12] Jia, M., Yu, X., Lu, D., Lu, B.: Experimental research of assembled buckling-restrained braces wrapped with carbon or basalt fiber. Journal of Constructional Steel Research 131, 144–161 (2017).
[13] Slama, G.Y., Düğenci, O.: Experimental investigation of effect of changing gap size in buckling restrained braces. Journal of Constructional Steel Research 198, 107532 (2022).
[14] Chen, Q., Wang, C.L., Meng, S., Zeng, B.: Effect of the unbonding materials on the mechanic behavior of all-steel buckling-restrained braces. Engineering Structures 111, 478–493 (2016).
[15] Wei, M., Ma, K., Yuan, B., Zheng, S., Chen, J.: Experimental and numerical studies of the multi-tube assembled buckling-restrained braces. Thin-Walled Structures 195, 111453 (2024).
[16] Wu, A.C., Lin, P.C., Tsai, K.C.: A type of buckling restrained brace for convenient inspection and replacement. Journal of Structural Engineering 12, 20–35 (2012).
[17] Al-Sadoon, Z.A., Karzad, A.S., Sagheer, A., AlHamaydeh, M.: Replaceable fuse buckling-restrained brace (BRB): Experimental cyclic qualification testing and NLFEA modeling. Structures 39, 997–1015 (2022).
[18] Serin, B., Bozkurt, M.B.: Development of replaceable core all-steel buckling-restrained braces. Journal of Constructional Steel Research 226, 109247 (2025).
[19] Zhang, Y., Ren, X., Zhang, X.Y., Huang, T.T., Sun, L., Xie, Y.M.: A novel buckling-restrained brace with auxetic perforated core: Experimental and numerical studies. Engineering Structures 249, 113223 (2021).
[20] Zhu, Y., Wang, J., Cai, X., Xu, Z., Wen, Y.: Cyclic behavior of ellipse and peanut-shaped perforated buckling-restrained braces. Engineering Structures 291, 116432 (2023).

Author Contribution Statement
Author Contribution Statement Conceptualization: Kazım Burç Civelek, Elifsu Kayrak
Methodology: Kazım Burç Civelek
Investigation: Kazım Burç Civelek, Elifsu Kayrak
Writing – Original Draft: Kazım Burç Civelek, Elifsu Kayrak
Writing – Review & Editing: Kazım Burç Civelek

Publication Note
This paper was peer-reviewed, accepted for presentation, and included in the proceedings of the ACE2026 – International Conference on Advances in Civil Engineering, held on 12–14 October 2026 in Trabzon, Türkiye.

This paper may be cited as follows:
Civelek, K.B., Kayrak, E., "Comparative Seismic Design and Performance Evaluation of Special Concentrically Braced Frames and Buckling-Restrained Braced Frames," in Proceedings of the ACE2026 – International Conference on Advances in Civil Engineering, Trabzon, Türkiye, 12–14 October 2026.

The Effect of Steel Fiber Length and Content on the Some Flexural Behavior Properties of the High-strength Concrete Beams

Hamdi ÖZTÜRK[1]
[1] 0000-0003-1015-2932, Karadeniz Technical University, Trabzon Vocational Collage, Trabzon, Türkiye
hozturk@ktu.edu.tr

Abstract. It is well known that the brittleness with low tensile strength and strain capacities of high-strength concrete (HSC) can be overcome by the addition of steel fibers. This paper presents research results of ten high-strength steel fiber concrete beams with steel fiber content of 0.75% and 1% (59 and 78 kg/m^3) by volume. Hooked-end and straight steel fibers with two different length (50 mm and 60 mm) were selected. This research shows that length and volume of steel fibers have significant effect on the load carrying capacity, flexural displacement, maximum strains, energy dissipation capacity, rigidity, and ductility.

Keywords: Flexural behavior, High strength concrete, Steel fiber

1 Introduction

Fiber-reinforced concrete is increasingly being used in civil engineering and taking importance as a structural material. Therefore, there is significant amount of research being carried out to investigate the effect of adding fibres to HSC. The toughness of fibre-reinforced concrete (FRC) materials can be considered as their energy absorption capacity, which is usually characterized by some portion of the area under the load-displacement curve obtained during a flexure test.

A lot of researchers, depending on Romualdi's works [1-2], have showed the usage of the steel fibers in industrial area, at the beginning of 1960. Swamy [3], showed that the addition of steel fibers improves tension, compression, flexural, and first cracking strength of the concrete. Taylor et al.[4], investigated the changes in the strength and toughness of traditional and high strength concrete including steel fibers. They implied that the effects of using steel fiber in the traditional and high strength concrete are similar. Aarup and Jensen [5], showed the possible ductility in the concrete by using short and heavy steel fibers. Materschlager and Bergmeister [6], presented the benefits of the using steel fiber in civil engineering. They investigated some mechanical properties of steel fiber concrete such as changes of ductility, compression and tensile strengths. They implied that using steel fiber-reinforced concrete provides affirmative results on the construction in the seismic areas. Ashour and Wafa [7], implied that using steel fibers in the concrete decreases the crack width while increases the crack number. They observed increasing ductility and delaying ultimate crushing in the concrete. They also implied that dispersion of fibers affects the crack propagation and development and that steel fibers increase the length of plastic hinges. Casanova et al., [8], made some experimental studies investigating the first cracking stress and tensile strength. According to their work, steel fibers increase the tensile strength capacity, which could be explained by the formation of micro cracks and progressing macro cracks. Özyurt et al., [9] showed that steel fiber aspect ratio and content made significant effect on the behavior after the peak stress. Fractural energy enhanced using increasing hooked-end steel fiber. Öztürk [10], Öztürk and Ayvaz [11-13], investigated the flexural behavior of steel-fiber high performance concrete beams. It was showed that steel fibers have significant effect on the load carrying capacity, displacement, maximum strains, energy dissipation capacity, rigidity change, and ductility. Chunxiang and Patnaikuni [14]

implied that the addition of steel fibers can also reduce the deflection of reinforced high strength concrete beams and improve post-cracking behavior significantly.

In this study, it was worked about flexural behavior of test beams made of steel fiber concrete have no reinforcing bars. So, after the work it was able to understand the flexural properties of steel fiber high-strength concrete beams and to compared in as much as for the load carrying capacity, displacement, load-strain variation, energy dissipation capacity, rigidity change, and ductility each other and with non-fibrous concrete beams.

2 Experimental Work

2.1 Materials

Ordinary Portland cement conforming to TS EN 19 [15], with a 28-day compressive strength of 42.5 MPa, crushed limestone sand and aggregate with maximum size of 16 mm, tap water for mixing and curing were used. Silica fume used was a commercially available with a specific gravity of 2.2, a bulk density of 6.0 kN/m^3, and a specific surface of 23 m^2/g, which improved concrete properties in fresh and hardened states. To improve the workability of concrete, a high-range water-reducing admixture (superplasticizer) was employed during mixing operation. The cement, silica fume, water, superplasticizer, crushed limestone sand and aggregate of 500, 50, 150, 13.75, 740 and 903 kg/m^3 were used to make HSC. The slump of the concrete with water/binder (W/B) ratio of 0.27 was 80 mm. Round, hooked-end and straight steel fibers having tensile strength of 1100 MPa were used in this study. The fibers have an average length of 50 and 60 mm with the two volume fractions of 0.75% and 1%. These fibers were available in bundles of about 30 fibers, which were fibrillated with water-soluble glue to ensure immediate dispersion in concrete during mixing.

2.2 Preparation of steel fiber concrete and testing beams

The dry cement and aggregates were mixed for 1 min. in a 0.06 m^3 laboratory mixer. The mixing was continued for further 1 min. while about 80% of water was added. The mixing was continued for another 1 min. and the fibers were then added continuously to the mixer for a period of 2-3 mins.. Finally, the remaining water (or remaining water including super plasticizer) was added and the mixing was continued for an additional 2 mins.. The freshly mix steel steel fiber-reinforced concrete was placed in two equal layers into a beam mold to cast the testing beams for a flexure strength test. Each layers was consolidated using a external vibration. At the end of 24 h after consolidating, the specimen was removed from the mold and cured in laboratory conditions for 28 days. And then flexure tests were performed.

The series of non-fibfous concrete beams (S1), concrete beams (S2) including steel fiber having length of 50 mm with the volume fraction of 0.75%, concrete beams (S3) including steel fiber having length of 60 mm with the volume fraction of 0.75%, concrete beams (S4) including steel fiber having length of 50 mm with the volume fraction of 1%, and concrete beams (S5) including steel fiber having length of 60 mm with the volume fraction of 1% were tested in the experimental study. Each testing beams series, listed in Table1, contains two beams, which have identical cross-section. All the beams have a constant cross-section of 100 mm x 200 mm (width x height) and constant length of 2100 mm. For the purpose of having the same quality concrete, the same concrete mix were used in the production of all test beams produced at different times. Furthermore, it was observed that small changes in concrete compressive strength occurred because of different casting. The average concrete compressive strength was approximately 60 MPa.

Table 1. Steel fiber properties of the test beams

Beam series	Steel fiber	
	Length (mm)	Volume fractions (%)
S1	-	-
S2	50	0.75
S3	60	0.75
S4	50	1
S5	60	1

2.3 The test set-up

The testing beams were simply supported at the both ends and subjected to two-point loads. The distance between the two-point loads was kept constant to be 560 mm. The test set-up used for loading the beam is shown in Figure 1. In this test set-up, the test beams were loaded with increment of 1 kN load by controlling load magnitude. Loading was applied until the load carrying capacity of the test beams was exceeded. In this test set-up, the load is applied to the beam by means of a 200-kN hydraulic testing machine and a dial gauge determines the displacement at the center of the axial line of the test beams. At the end of each load increment, observations and measurements were recorded for the midspan deflection, straingauge readings, and crack development and propagation on the beam surfaces.



Fig.1. A view from the test set-up

3 Results and Discussion

The results obtained from the test beams are given in the following subsections in tables and graphs to compare the results of the beams including the steel fibers having different length and volume fractions with each other and with the results of S1. The comparisons are made separately for the load carrying capacity, displacement, load-strain variation, energy dissipation capacity, rigidity change, and ductility.

3.1 Load-displacement

In this study, high strength non-fibrous concrete beams and steel fiber high-strength concrete beams subjected to flexure were investigated. For the test beams, average loads and displacements at first cracking, at the peak, and at failure are given in Table 2. Load-displacement curves of the test beams including steel fiber are seen in Figure 2.

Table 2. Applied loads and corresponding displacement of the test beams

Test beams	Load (kN)			Displacement (mm)		
	at first cracking	at peak	at failure	at first cracking	at peak	at failure
S1	5.7	5.7	5.7	-	-	-
S2	6.1	6.7	4.3	2.3	3.9	6.4
S3	7.2	8.2	3.8	2.3	6.8	25.4
S4	6.8	7.9	5	2.4	4.6	7.6
S5	8.7	11.2	3.9	2.5	8.2	32

As seen from Table 2 and Figure 2, the load carrying capacities of fibrous concrete beams increase with increasing fiber volume at the first cracking, at the peak, and at failure. Load carrying capacities of S3 and S5 beams are higher than those of S2 and S4 beams, except at failure. Test beams with long fiber were able to carry flexure loads more than those of the test beams with short fiber. So, S3 and S5 beams continued to carrying decreasing loads from peak point to failure. As also seen from the same table and figure, displacements of fibrous concrete beams are almost the same at the first cracking. The displacements of S3 and S5 beams are higher than those of the S2 and S4 beams. In other word, displacement of test beams with long fiber are higher than those of the test beams with short fiber. Displacements of fibrous concrete beams increase with increasing fiber volume at the peak load, and failure.

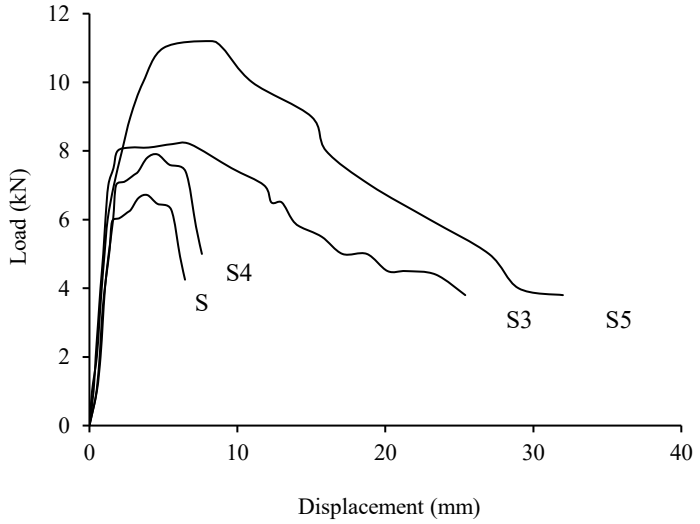


Fig. 2. Load-displacement curves of S2, S3, S4, and S5

3.2 Load-strain

In this study, strains at the center of bottom and top faces of the beams were measured. For the test beams, maximum strains are given in Table 3.As seen from Table 3, the strains of concrete beams increase with increasing steel fiber volume fraction and the fiber length. These strains are higher than that of non-fibrous concrete beam. Maximum strains of concrete beams with long fiber are higher than those of concrete beams with short fiber. Strains of the concrete at the top faces of the beams (compression strains) are higher than those of the concrete at the

bottom faces of the beams (tension strains). The test beams without fiber collapse suddenly after first crack occur, the test beams with fibers do not collapse after the first crack occur. They behave in a ductile manner. That means that steel fibers change the failure pattern of concrete beams from brittle to ductile.

Table 3. Maximum strains of top and bottom faces of concrete beam

Test beams	S1	S2	S3	S4	S5
Strain at the bottom face of beam (10^4 ε)	0.55	1.6	1.8	2.6	3.7
Strain at the top face of beam (10^4 ε)	0.60	1.80	3.30	4	4.3

3.3 Energy dissipation capacity

The energy dissipation capacities of the test beams were determined by calculating the area under the load-displacement curve for each beam. The energy dissipation capacities of the all test beams including steel fibers are given in Table 4.

Table 4. Energy dissipation capacities of the test beams

Test beam	Energy dissipation capacity (kN.mm)
S2	11.50
S3	47
S4	15.50
S5	73.50

As seen from Table 4, energy dissipation capacities of the test beams with long fiber are higher than those of the test beams with short fiber. Energy dissipation capacities of the test beams increase with increasing steel fiber volume fractions. Energy dissipation capacity of S5 is 56.4% higher than that of S3 with respect to that of S3. Energy dissipation capacity of S4 is 34.8% higher than that of S2 with respect to that of S2. Energy dissipation capacity of S3 is 308.7% higher than that of S2 with respect to that of S2. Energy dissipation capacity of S5 is 374.2% higher than that of S4 with respect to that of S4.

3.4 Rigidity change

Rigidity is defined and obtained as the slope of the line drawn from the origin of the load-displacement curve to the intersection of the horizontal line drawn from load chosen with the load-displacement curve. Rigidities of the test beams at the origin, at the first cracking, at the peak, and at failure and decreases in rigidity up to the first cracking, peak, and failure with respect to rigidity at origin are given in Table 5.

As seen from Table 5 and Figure 2, all test beams have the same rigidities at the origin. The rigidities of the fibrous test beams are close to each other for each steel fiber length at the first cracking, at the peak, and at failure. Decreases in rigidities are almost at the same level for each of steel fiber length up to peak load, and failure, except up to the first cracking. The test beams including long fiber lost more rigidity than the test beams including short fiber up to peak and failure, but the test beams including long fiber lost less rigidity than the test beams including short fiber up to the first cracking.

Table 5. Rigidity variations of the test beams

Test beams	Rigidity (kN/mm)				Decrease in rigidity (%)		
	At origin	At first cracking	At peak	At failure	To first cracking	To peak load	To failure
S1	4.2	-	-	-	-	-	-
S2	4.2	2.652	1.718	0.665	36.86	59.09	84.17
S3	4.2	3.130	1.205	0.149	25.48	71.31	96.45
S4	4.2	2.833	1.717	0.658	32.54	59.11	84.33
S5	4.2	3.480	1.374	0.122	17.14	67.28	97.09

Decrease in rigidities of the all test beams change between 17.14% and 36.86% from origin to the first cracking, between 59.09% and 71.31% from origin to peak load, and between 84.17% and 97.09% from origin to failure.

3.5 Ductility

Ductility is one of the main parameters of a structural member under flexure, because the different types of failure patterns for these members are dependent on the reinforcement ratio, and the end restraints.

It is well known that ductility can be expressed by the ductility coefficient. In this study, ductility coefficients given in Table 6 were determined as the ratio of displacement at failure to the displacement at the first cracking. These displacements are determined at the mid-point of the axial line of the test beams. As seen from Table 6, the ductility coefficients take the values from 1 to 12.8. As also seen from this table, the ductility coefficients of the test beams with fibers are larger than those of the test beams without fibers. The same coefficients of the test beams with long fiber are larger than those of the test beams with short fiber.

Ductility coefficients of S2, S3, S4, and S5 are 178%, 1004%, 217%, and 1180% higher than the ductility coefficient of S1, respectively, with respect to ductility coefficient of S1. Ductility coefficient of S5 is 15.94% higher than that of S3 with respect to that of S3. Ductility coefficient of S4 is 14.02% higher than that of S2 with respect to that of S2. Ductility coefficient of S3 is 297.12% higher than that of S2 with respect to that of S2. Ductility coefficient of S5 is 303.78% higher than that of S4 with respect to that of S4.

In addition, steel fibers at the compression zone have delayed the crushing of concrete. So, the test beams including steel fibers can carry additional flexural loads depending on steel fiber volume fractions. Therefore, these test beams displace more up to failure. This means that, as mentioned before, steel fibers change the failure pattern of concrete beams from brittle to ductile.

Table 6. Ductility coefficients of the test beams

Test beams	Displacement at first cracking δ (mm)	Displacement at failure δ_u (mm)	Ductility coefficient δ_u/δ
S1	-	-	1*
S2	2.3	6.4	2.78
S3	2.3	25.4	11.04
S4	2.4	7.6	3.17
S5	2.5	32	12.80

* Since S1 collapses when the first cracking occurs, $\delta_u = \delta$.

4 Conclusions

The main conclusion drawn from the results obtained in this study are given below.

1. Load carrying capacities of the test beams including long fiber are higher than those of the test beams with short fiber. Load carrying capacities increase with increasing fiber content.
2. The displacement of the test beams decreases with increasing steel fiber volume. The maximum displacement of the test beams with long fiber are higher than those of the test beams with short fiber at the peak and the failure.
3. Strains of the test beams increase with increasing steel fiber length and volume fraction. These strains are higher than that of non-fibrous concrete beam.
4. Energy dissipation capacities of the test beams with long fiber are higher than those of the test beams with short fiber and energy dissipation capacities of the test beams increase with increasing steel fiber volume fractions.
5. The test beams including long fiber lost more rigidity than the test beams including short fiber up to peak and failure, but the test beams including long fiber lost less rigidity than the test beams including short fiber up to the first cracking.
6. Test beams with long fiber showed more ductile behavior.

Acknowledgments

This study is supported by the Research Fund of Karadeniz Technical University. Project number: 21.112.001.06. The steel fibers used in this study are provided by BEKSA.

References

1. ACI Committee 544. State-of-the-Art report on fiber reinforced concrete. American Concrete Institute (ACI 544.1R-96), Detroit (1996).
2. Bernhard, RM. Steel Fibre Reinforced Concrete, Ernst & Sohn (1995).
3.Swamy, R.N. Mechanics of fiber reinforced concrete. In: International Symposium of Fiber Reinforced Concrete: SP-44, p.1-28 (1974).
4. Taylor, M., Lydon, F.D., & Barr, B.I.G. (1997). Toughness measurements on steel fiber-reinforced high strength concrete. Cement and Concrete Composites; 19: 329-340 (1997).
5. Aarup, B. & Jensen, B.C. Bond properties of high-strength fiber reinforced concrete. Special Publication (1998).
6. Materschläger, A. & Bergmeister, K. Fibber added concrete, 2nd Int. PhD Symposium in Civil Engineering Budapest (1998).
7. Ashour S.A. & Wafa F.F. Flexural Behavior of High-Strength Fiber Reinforced Concrete Beams. ACI Structural Journal 90(3): 279-287 (1993).
8. Casanova, P., Rossi, P. & Schaller, I. Can Steel Fibers Replace Transverse Reinforced Concrete Beams? ACI Mater. Journal 35(4): 42-52 (1998).

9. Özyurt, N., İlki, A., Taşdemir, C., Taşdemir, M.A. & Yerlikaya, M. Mechanical Behavior of High Strength Steel Fiber Reinforced Concretes with Various Steel Fiber Contents. The Fifth International Congress on Advances in Civil Engineering, Istanbul Technical University, Istanbul, p. 245-258 (2002).
10. Öztürk, H. Comparative investigation of behavior of plain and steel fiber, traditional and high performance concrete produced by one of the aggregates of Eastern Black Sea Region. PhD thesis. Graduate School of Natural and Applied Sciences, Karadeniz Technical University (2005).
11. Öztürk, H., & Ayvaz, Y. Comparative study of flexural behaviour of steel fiber high performance concrete beams. 7th International Congress on Advances in Civil Engineering, October 11-13, Yıldız Technical University, İstanbul, Turkey (2006).
12. Öztürk H., & Ayvaz, Y. Comparative study of flexural behaviour of steel fiber high performance reinforced concrete beams. 8th International Congress on Advances in Civil Engineering, September 15-17, Eastern Mediterranean University, Famagusta, North Cyprus (2008).
13. Öztürk, H., & Ayvaz, Y. (2010) Investigation of Some Mechanical Properties of High-Strength Steel Fiber-Reinforced Concrete. 9th International Congress on Advances in Civil Engineering, September 27-30, Karadeniz Technical University, Trabzon, Turkey (2010).
14. Chunxiang, Q. & Patnaikuni, I. (1999). Properties of high-strength steel fiber-reinforced concrete beams in bending. Cement and Concrete Composites, 21: 73-81 (1999).
15.TS EN 19. Portland cement. Institute of Turkish standard. Ankara, Turkey (1985).

Author Contribution Statement

- *Investigation:* Hamdi ÖZTÜRK

Publication Note

This paper was peer-reviewed, accepted for presentation, and included in the proceedings of the ACE2026 – International Conference on Advances in Civil Engineering, held on 12–14 October 2026 in Trabzon, Türkiye.

This paper may be cited as follows:

Hamdi Öztürk, "The Effect of Steel Fiber Length and Content on the Some Flexural Behavior Properties of the High-strength Concrete Beams," in Proceedings of the ACE2026 – International Conference on Advances in Civil Engineering, Trabzon, Türkiye, 12–14 October 2026.

The Effect of Rigid Basement Shear Walls on Seismic Behaviour of Reinforced Concrete Structures according to TBEC 2018

Hurmet Kucukgoncu[1]
[1] 0000-0001-5148-8753, Abdullah Gül University, Civil Engineering Department, Kayseri, Türkiye, hurmet.kucukgoncu@agu.edu.tr

Abstract. Some buildings are designed with a basement in the architectural plan for various reasons. Since structures with a basement are directly connected to the soil, the interaction between the structure and the soil must be considered when analysing such structures. Thus, interactions between the structure and soil that significantly affect the structure should be considered in the analysis. Therefore, it is common practice to construct rigid shear walls around basement floors. In this application, the seismic behaviours are decoupled due to the rigidity of the basement walls and the higher flexibility of the superstructure relative to the basement floors. However, since the superstructure and basement floors are components of the same structure, they are structurally interconnected and dynamically interact. In the latest Turkish Building Earthquake Code 2018 (TBEC 2018), the calculation steps for structures designed with rigid basement walls differ, including the earthquake load reduction coefficients. For this reason, the building designed as a dual functional structural system with rigid basement shear walls, and the dual functional building designed without rigid basement shear walls were analysed using the mode superposition method in SAP 2000 software according to the TBEC 2018 provision. Both buildings have the same architectural and floor plan. Seismic properties, including period, frequency, interstory drift, storey displacements, storey shear forces, and base shear forces, obtained for both buildings were compared. As a result of the comparisons, rigid shear wall basements contributed positively to both the usable architectural space and seismic performance of the building.

Keywords: Mode superposition method, Rigid basement shear wall, Seismic behaviour, TBEC 2018

1 Introduction

Numerous reinforced concrete buildings feature basements for functional purposes like parking, machinery, storage, or shelter in Türkiye. Basement floors are surrounded by rigid shear walls for architectural and structural reasons, such as retaining the soil around the designed basement floors. Due to the rigid shear walls added to the basement floor, the strength, rigidity and seismic behaviour of the basement floors and the relatively more flexible superstructure are different from each other [1]. For this reason, although the substructure and superstructure of such buildings interact with each other through connections in earthquake codes, the Load-Bearing System Behaviour Coefficient (R) and the Excess Strength Coefficient (D), which are defined based on ductility, are considered at different values for the superstructure and the more rigid basements. Therefore, the specific design rules and foundational criteria regarding the calculation of structures with rigid shear wall basements are officially prescribed within the Turkish Building Earthquake Code 2018 (TBEC 2018) [2]. According to TBEC 2018 [2], structural analysis of configurations with basements can be conducted via the equivalent lateral seismic force technique or modal superposition methodologies; within this framework, the lower substructure and upper framework are modelled independently prior to their combined

evaluation. In this context, several studies have been conducted on modelling, design, and analysis of buildings with rigid basements [1,3-14]. Previous research on rigid basements shows their direct effects on the seismic behaviour of [4, 5, 8, 13]. Buildings with basements reduced the damage caused by earthquakes [4], and basement walls were shown to reduce roof or top displacements and base shear forces under seismic forces [5, 8, 13]. Furthermore, it was observed that the ductility demand was reduced and the effect of soft storey damage was lower [5]. In terms of load bearing, deformation, and practical usage, designing a basement in high-rise buildings provides significant advantages [13].

Different modelling approaches and seismic codes have been evaluated for structures with basements [1, 3, 9, 11, 14]. While these approaches minimally affected the superstructure's natural vibration period, variations occurred in storey shear forces and relative drift ratios [3]. Some studies performed response spectrum and time history analyses incorporating structure-soil interaction [8, 14], noting that nonlinear dynamic time history analysis factoring soil properties offers the most realistic approach. To model and design structures with rigid basements, previous studies evaluated international or national seismic codes, proposing distinct evaluation techniques, two-stage analyses, or complementary modal methods [1, 9, 11]. The seismic behaviour of high-rise buildings with large basement floors, common podiums, or shared basements with neighbouring buildings was also demonstrated [6, 7, 10]. Experiments and analyses reported that in order to obtain the seismic behaviour envelopes, the structure should be modelled and analysed separately and together with the common podium floors [6], or modelled together with neighbouring buildings [10]. Additionally, a single-tower model featuring partially fixed end restraints was found to overestimate internal forces within the podium floors [7]. Investigating the location and quantity of basement shear walls revealed that seismic wall moments decreased as more rigid basement walls were added [12].

As demonstrated, literature includes various studies evaluating basement-supported structures. Especially with the analysis methods added to TBEC 2018 [2] regarding structures with basements, studies in this direction have gained momentum. Conversely, existing literature predominantly examines the seismic response of deep-basement high-rise structures [3, 6, 10, 13] or relies on outdated seismic codes [1, 4]. Although TBEC 2018 is considered in some research [11], its application on low-to-medium rise buildings remains limited. However, low-to-medium rise buildings with the basements were investigated according to the older seismic codes [4]. This study examines seismic behaviour in a 5-storey building designed per TBEC 2018 [2]. The effects of rigid basement wall on the structural behaviour of a low-rise building, which was commonly found in the building stock located on a dangerous earthquake zone, were investigated after it was designed with rigid basement walls in the study. The differences between models with and without basements are analysed to evaluate the current code requirements for typical multi-storey structures. The mode superposition method was used among the different methods proposed for the analysis of rigid basement shear walls in TBEC 2018 [2]. Consequently, structural response parameters such as period, top displacement, storey shear forces, and interstory drifts were evaluated and compared for buildings with and without rigid basement shear walls.

2 Material and Method

In accordance with the Turkish Building Earthquake Code 2018 [2], this investigation models and analyses two structural systems that are architecturally identical, contrasting a building with rigid basement shear walls against a reference building without them.

2.1 TBEC 2018 Approach

To design structures with rigid basements, TBEC 2018 incorporates linear methods based on a two-stage analysis. Initially, the rigid basement is modelled as massless, whereas the superstructure retains its mass, which is exclusively considered in the first seismic analysis. The

Structural System Behaviour Coefficient, R_{top}, is used for the superstructure's seismic force calculation. During the subsequent stage, the superstructure is assumed massless, while the rigid basement is modelled including its own mass. Consequently, the analysis considers solely the mass of the rigid basement. According to the structural characteristics of the subsystem, seismic forces for the rigid basement are determined utilizing the behaviour coefficient R_{bottom} [2]. Subsequently, vertical and horizontal forces transferred from the superstructure are added to the rigid basement seismic forces calculated in this way.

First, the building base and height of rigid basement shear walls must be determined according to TBEC 2018 [2]. When both criteria (a) and (b) are fully satisfied, the building base is taken at the slab level right above the basement walls. Otherwise, this base level must be shifted down to the top of the foundation [2].

(a) The structural perimeter is enclosed by rigid basement walls on all sides or a minimum of three sides.

(b) In the dominant vibration mode along each orthogonal axis, the natural period computed for the complete structure ($T_{p,all}$) does not exceed 1.1 times the period obtained by neglecting all basement masses ($T_{p,top}$), satisfying the condition ($T_{p,all} \leq 1.1\ T_{p,top}$).

Two different Structural System Behaviour Coefficients (R) and Excess Strength Coefficients (D) are considered for the substructure and superstructure. The Seismic Load Reduction Coefficient (Ra) is calculated using *Equation 1* and *2*, where I is the Building Importance Coefficient, T is the natural period, and T_B is the spectrum corner period:

$$R_a(T)=\frac{R}{I} \qquad T>T_B \qquad (1)$$

$$R_a(T)=D+\left(\frac{R}{I}-D\right)\frac{T}{T_B} \qquad T\leq T_B \qquad (2)$$

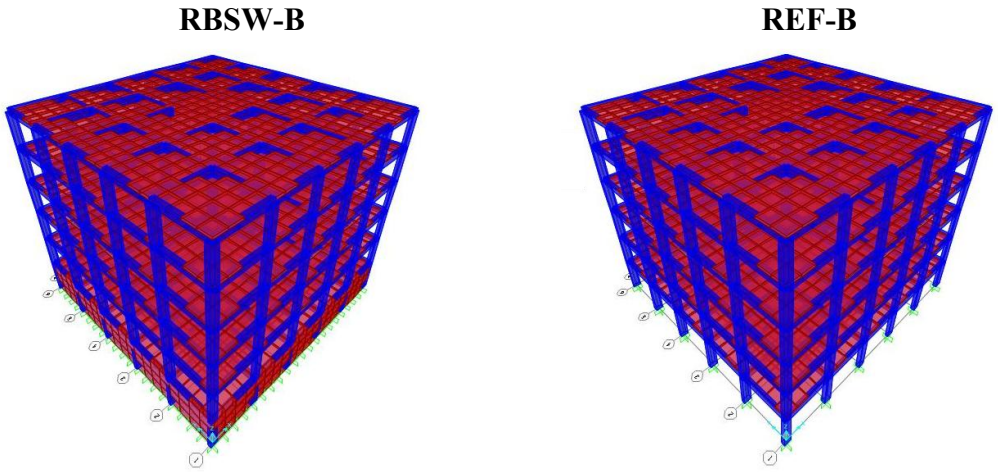
Under these conditions, seismic analysis can employ either the mode superposition method or the equivalent lateral seismic force technique or mode superposition method. Since the mode superposition method is used in this study, its specific steps within the two-loading approach where the upper and lower sections are modelled together as a single system but analysed separately due to stiffness and vibration mode differences are detailed below [2]:

For the first loading scenario, the mode superposition method is applied considering only the superstructure masses. To establish a sufficient number of vibration modes, the effective mass participation ratios corresponding to the superstructure's total mass are evaluated. $(R_a)_{top}$ is calculated using R_{top} and D_{top}. Reduced internal forces are determined for both sections, and the superstructure design is conducted based on these forces for ductile behaviour. To accommodate non-ductile structural actions, the internal forces determined for the superstructure are amplified by D_{top}. These forces are amplified by the second order and equivalent base shear force amplification factors, if necessary [2].

For the second loading scenario, the superstructure is assumed massless, whereas the rigid basement is modelled with its own mass. To establish the number of vibration modes, evaluation relies on the effective mass participation ratios of the basement. $(R_a)_{bottom}$ is calculated by taking $R_{bottom}/I = 2.5$ and $D_{bottom} = 1.5$. To address the ductile performance of sub-grade components, design action values are established by superimposing the second-stage loading responses onto the forces extracted from the lower substructure during the initial loading phase. In the case of non-ductile behaviour, design forces are determined by combining the second loading forces amplified by D_{bottom} with the first loading lower section forces scaled by $0.6D_{top}$ [2].

2.2 Numerical Method

In this study, a building with 1 basement storey and 5 normal storeys was designed and analysed as rigid basement shear walls and without rigid basement shear walls (reference building). Throughout the study, the building with rigid basement shear walls is called RBSW-B and the building without rigid basement shear walls analysed as reference is called REF-B. The structures are identical in terms of both architectural plan, load-bearing system members, dimensions, reinforcement diameters, and amounts. The illustrations of both models are given in *Fig. 1*. The only difference is the rigid shear walls surrounding the basement floor on four sides. The reinforced concrete bearing system of the structure consists of frames and walls surrounding the core on three sides and is a dual functional bearing system. Along each orthogonal axis (x and y), the configuration comprises a total of 6 axes and 5 spans. The length between the axes in both directions is 4m. Both orthogonal plan dimensions of the structure measure 20 m. A uniform thickness of 300 mm is utilized for both the peripheral basement walls and the central core shear walls. A slab thickness of 15 cm is defined, with gravity loads specified as 2.5 kN/m² for dead load, 2.0 kN/m² for live load, and a roof-level snow load of 0.75 kN/m². The concrete class is C30/35, the reinforcement class is S420. The storey height is 2.85m. Since the condition of $T_{p,all} \leq 1.1T_{p,upper}$ given for buildings with rigid basements in TBEC 2018 [2] is met, the total height of the building is considered as 14.25 m. Column dimensions are 300x600 mm^2 and the column longitudinal reinforcement ratio is 0.0183. Beam dimensions are 300x500 mm^2 and the beam longitudinal reinforcement ratio is 0.0071. Dimensions and reinforcement arrangements of column and beam elements are given in *Fig. 2*.



Rigid Basement Shear Wall Building Reference Building

Fig.1. Building with rigid basement shear walls and building without rigid basement shear walls (reference) model.



Longitudinal Rebars: 10Ø20
Transverse Rebars: Ø10/100

Longitudinal Rebars: 5Ø16 (bottom) and 3Ø12 (top)
Transverse Rebars: Ø8/100

Fig. 2. Dimensions of the structural members' elements and reinforcement arrangements.

For the building models, the dimensions of all bearing members were selected by performing preliminary dimensioning calculations to meet the requirements of TBEC 2018 [2] and TS 500-2000 [15]. After the analyses using the SAP 2000-v22 [16], there is an A1 building irregularity in both directions and a B2 irregularity in the y-direction. In addition, the interstory drifts and second-order effects in the structure were also checked, and the necessary conditions were provided. The floor slabs were modelled as rigid diaphragms. To comply with TBEC 2018 [2], effective stiffness modifiers for the reinforced concrete structural components were also integrated into the software. Subsequently, mode superposition method was performed on the structural models in accordance with the TBEC 2018 [2] framework. *Table 1* presents the seismic parameters and response spectrum values of the building bearing system models.

Table 1. Seismic design parameters and response spectrum values.

Parameter and Definition	**Value / Coefficient**
Earthquake Ground Motion Level	DD2
Local Soil Class	ZC
Soil Parameters (T_A&T_B)	T_A = 0.0688 sn, T_B = 0.3439 sn
Seismic Coefficients (SDS&SD1)	SDS = 1.291g, SD1 = 0.444g
Building Classification	BKS = 3, I = 1, DTS = 1, BYS = 6
Bearing System Behaviour Coefficient (R)	R_{upper} = 7, $R_{basement}$ = 2.5
Excess Strength Coefficient (D)	D_{upper} = 2.5, $D_{basement}$ = 1.5
Sae - Elastic Superstructure (g)	Sae(T(x)) = 0.7274 g, Sae(T(y)) = 1.0176 g
Ra - Superstructure	Ra(T(x)) = 7, Ra(T(y)) = 7
SaR - Superstructure (g)	SaR(T(x)) = 0.1039 g, SaR(T(y)) = 0.1454 g
SaR - Basement (g)	$SaR_{basement}$ (T) = 0.2066 g

Assuming the structures are located in Istanbul's Bakırköy district, design spectrum parameters and spectral acceleration coefficients were derived based on this coordinate using data from the AFAD Turkish Earthquake Hazard Maps Interactive Web Application [17]. Spectrum curves were generated following the computation of both the horizontal elastic and reduced design spectral acceleration values. Separate reduced design spectra required for the modal superposition analysis were constructed for both the superstructure and the lower rigid basement section. Thus, the reduced design acceleration spectra obtained for the lower part and superstructure sections of the structure according to TBEC 2018 [2] are given comparatively in *Fig. 3*.

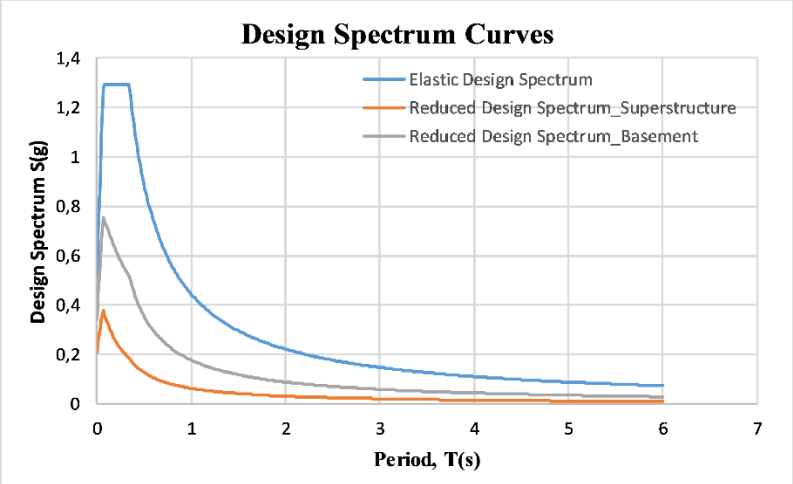


Fig. 3. Design acceleration spectra: elastic and reduced curves.

As mentioned above, both building models were created with the SAP 2000-v22 [16] software according to the mode superposition method principles within TBEC 2018 [2]. First, the first-case earthquake loading of the rigid basement shear wall building was performed. In this case, the modal analysis was performed with the help of the reduced design acceleration spectrum obtained for the superstructure in *Fig. 3*, with the upper section of the building having mass and the lower section having no mass. Then, the second-case earthquake loading was performed with the upper section of the building having mass and the lower section having mass. In this case, modal analysis was performed with the help of the reduced design acceleration spectrum obtained for the lower section in *Fig. 3*. Load combinations on the structure models were created separately for the design issues to be made according to ductile and non-ductile behaviour, considering the loading in both cases.

3 Results and Discussion

To evaluate the structural performance under both seismic directions and loading cases, numerical analysis yielded critical parameters—including period, frequency, top displacement, interstory drift, alongside storey and base shear forces—for both the reference structure and the model with rigid basement shear walls. The results obtained from the rigid basement shear wall building were shown with the name RBSW-B, and the rigid basement shear wall building analysed as the reference was shown with the name REF-B.

3.1 Building Period and Frequency

The modal analyses results, the dominant period and frequency values of both building models are given in *Table 2*. In addition, the period and frequency percentage difference of the rigid basement shear wall building compared to the reference building is also given in *Table 2*. Accordingly, the period value of the rigid basement shear wall building is smaller than the period value of the reference building, while the frequency value is slightly larger. The reason for this is the extra rigidity provided to the building by the rigid basement shear walls.

Table 2. Modal parameters of reference versus rigid basement-walled models.

Models	T(s)	f (1/s)	T%	f%
RBSW-B	0.610	1.638	-	-
REF-B	0.712	1.405	14.326	16.584

3.2 Storey Displacement and Interstory Drift

The top displacements are the maximum drifts obtained from the top storey of each model and are given in *Table 3*. Accordingly, the top displacements of the rigid shear wall basement structures are lower than the reference structure without a rigid shear wall. This difference between the top storey drifts is around 10% for both directions. This effect arises because the rigid basement inclusion significantly increases the overall structural stiffness.

Table 3. Maximum storey drift values of reference versus rigid basement-walled models.

Models	dx_{max} (m)	dy_{max} (m)	dx_{max}%	dy_{max}%
RBSW-B	0.02949	0.02998	-	-
REF-B	0.03296	0.03303	10.536	9.251

Table 4 shows the storey drifts of the lower part and the upper structure for both earthquake directions and the differences in the storey drifts of the rigid shear wall and basement building compared to the reference building. Accordingly, the storey drifts of the rigid shear wall and basement building are smaller than those of the reference building for both directions. While the difference is highest in the basement, this difference decreases as the number of storeys

increases. In particular, while this difference is around 90% in the basement, it decreases to around 10% on the top storey. Thus, the effect of rigid basement walls on storey drifts decreases as the storeys go up.

Table 4. Storey displacements of reference and rigid basement shear wall models.

Storey No	RBSW dx_{max} (m)	RBSW dy_{max} (m)	REF dx_{max} (m)	REF dy_{max} (m)	dx_{max}%	dy_{max}%
5	0.029491	0.029978	0.032964	0.033034	10.53574	9.251075
4	0.024752	0.024151	0.028432	0.027281	12.94316	11.47319
3	0.018903	0.017767	0.022903	0.021029	17.46496	15.51191
2	0.012407	0.01123	0.016774	0.014629	26.03434	23.23467
1	0.002095	0.005059	0.010402	0.008494	79.85964	40.44031
B	0.000346	0.000377	0.004224	0.003191	91.80871	88.18552

Interstory drifts, which express the difference in drifts between consecutive storeys, are given in *Fig. 4* and as can be seen from this graph, the relative storey drifts of the rigid shear wall basement building in the x direction are greater than the reference building. However, the difference in interstory drifts obtained in the y-direction is relatively low. This indicates that the interstory drifts of rigid basement walls increase in parallel with the displacement difference between storeys, especially with the increase in the number of storeys.

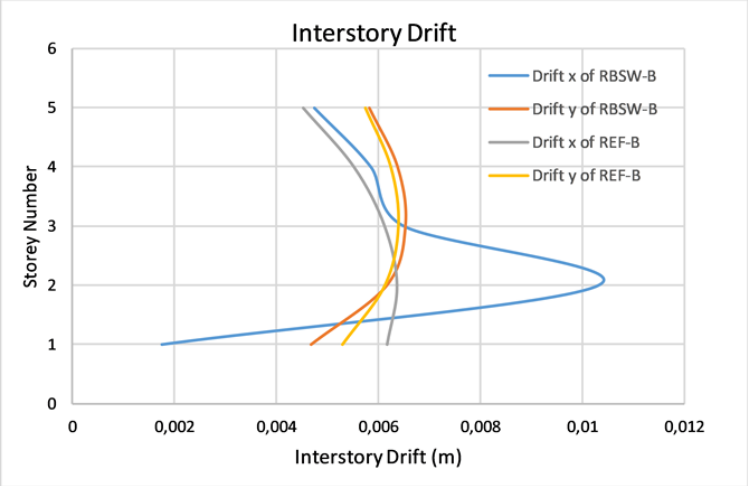


Fig. 4. Interstory drifts of reference and rigid basement shear walls buildings.

3.3 Shear Force

The base shear forces of the basement floor (lower part) for the building with rigid basement walls and the reference building are given in *Table 5*. As seen from *Table 5*, the base shear forces obtained from the building with rigid basement walls for both earthquake directions are smaller than those obtained from the reference building. The recorded deviations are 9% along the x-axis and 2% along the y-axis. By the addition of rigid basement walls to the structure, an average decrease of approximately 5% in the base shear forces was observed.

Table 5. Base shear forces of reference and rigid basement shear wall models.

Models	Vx (kN)	Vy (kN)	Vx%	Vy%
RBSW-B	6686.968	7674.671	-	-
REF-B	7303.719	7856.093	9.223	2.364

The induced superstructure lateral shear forces computed under each orthogonal seismic direction (x and y) for both structural configurations are summarized in *Table 6.* Accordingly, the shear forces acting on the storeys in the structure with rigid basement shear in both x and y directions are smaller than those in the reference building. Along the x-axis, this variance ranges from 4% to 7%, while it spans between 3% and 6% in the y direction. Rigid basement walls reduce the storey shear forces of the superstructure as they increase the rigidity of the structure.

Table 6. Storey shear forces of reference and rigid basement shear wall models.

Storey No	RBSW Vx (kN)	RBSW Vy(kN)	REF Vx (kN)	REF Vy(kN)	Vx%	Vy%
5	2376.278	2894.402	2541.47	3047.299	6.952	5.283
4	3792.884	4341.998	4003.125	4499.447	5.543	3.626
3	4757.928	5213.513	4995.379	5466.092	4.991	4.845
2	5568.364	6147.567	5884.682	6527.167	5.681	6.175
1	6334.26	7190.999	6613.993	7492.877	4.416	4.198

Figure 5 illustrates a graphical representation of the superstructure column shear forces, highlighting the lateral shear responses computed along both orthogonal axes (x and y) for the reference and rigid-basement structures. Accordingly, as the storey numbers increase, the shear forces on the storeys also increase proportionally. However, an increase in the total number of storeys for the rigid-basement configuration led to a more pronounced divergence between the lateral forces computed along both orthogonal axes (x and y). This difference is minimum at the base and maximum at the top storey. Although this difference is very small, it is greater in the reference building than in the building with rigid basement walls. Thus, rigid basement walls have slightly reduced the difference in storey shear forces between storeys.

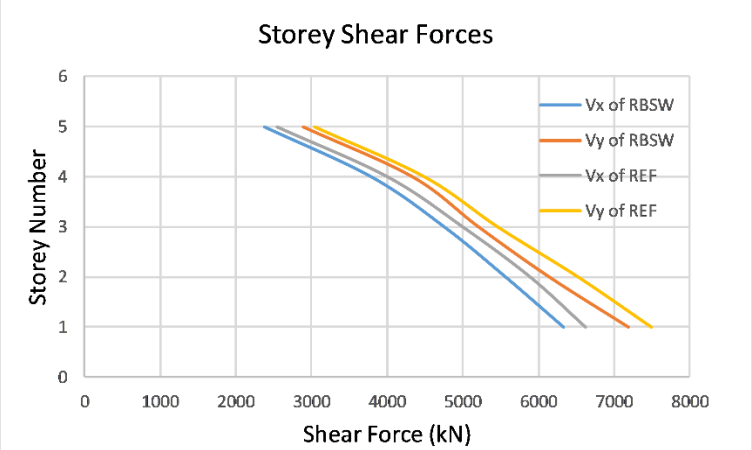


Fig. 5. Storey shear forces corresponding to columns of reference and rigid basement shear walls buildings.

4 Conclusion

In the study, two buildings with 5 normal storeys on a basement floor designed with and without rigid basement walls were analysed using the mode superposition method according to TBEC 2018. Following the computational analysis, critical structural responses—encompassing period, top displacement, interstory drifts, alongside storey and base shear forces—were extracted and evaluated across the investigated building models. In the light of this data, the following results were obtained.

- Adding rigid basement shear walls to the building reduces the period of the building and increases its frequency.
- Rigid shear walls reduce the top displacement of the top storey of the building by approximately 10%.
- The storey drifts of the superstructure have decreased with the addition of rigid basement shear walls to the structure. This amount is 10% on the top storey and approximately 90% on the basement floor.
- Rigid basement walls have reduced the base shear forces acting on the building by approximately 5%.
- Rigid basement walls have reduced the storey shear forces acting on the building storeys by an average of 5%.

As a result, the addition of rigid basement shear walls provided additional rigidity to the building, resulting in positive contributions to the seismic behaviour of the building. Even though this difference remains around 5%-10% in terms of seismic effects, it is important that rigid shear wall basements provide additional usage areas such as storage, parking, machine room, etc. to buildings, while also improving the seismic behaviour of the building. Thus, designing buildings with rigid basement walls according to TBEC 2018 offers various advantages in many aspects.

References

1. Altındal, A., Tanrıverdi, S.: Bodrumlu yapıların deprem hesabında kat ağırlıklarının ve kat sayılarının değişiminin kolon uç momentleri üzerindeki etkisi. Sakarya University Journal of Science 6(2), 172–177 (2002) https://doi.org/10.16984/saufbed.17829.
2. AFAD: Turkey building earthquake code (TBEC 2018): Provisions for the design of buildings under earthquake effects. Disaster and Emergency Management Authority, Ankara, Turkey (In Turkish) (2018).
3. Naeim, F., Tileylioglu, S., Alimoradi, A., Stewart, J.P.: Impact of foundation modeling on the accuracy of response history analysis of a tall building. In: SMIP08 Seminar on Utilization of Strong-Motion Data, pp. 19–56 (2008)
4. Caglar, N., Sert, S., Imbabi, M.S., Serdar, A.H.: The effect of a basement story on the earthquake response of RC buildings constructed on soft surface soil. In: 3rd International Symposium On Innovative Technologies In Engineering And Science, Valencia, Spain (2015)
5. Kumar, M.A., Maheedhar, B.R., Goud, G.J.: Comparative study on analysis and design of G+12 stories building with and without basement walls of two basements. International Journal of Engineering and Techniques 4(2), 240–245 (2018)
6. Zhou, Y., Chen, P., Wang, C., Zhang, L., Lu, L.: Seismic performance evaluation of tall, multitower reinforced concrete buildings with large bottom podiums. Structural Concrete 19(6), 1591–1607 (2018). https://doi.org/10.1002/suco.201700142
7. Tura, C., Orakçal, K.: Earthquake response analysis of multiple towers on a common podium: A representative case study. Technical Journal 30(6), 9647–9673 (2019) https://doi.org/10.18400/tekderg.467371.
8. Alomari, J.A.: Effect of the presence of basements on the vibration period and other seismic responses of RC frames. Engineering, Technology & Applied Science Research 9(5), 4743–4748 (2019) https://doi.org/10.48084/etasr.3005
9. Abediasl, N.: Seismic resistant design of building structures with rigid basement levels. Master's thesis, Institute for Graduate Studies in Science and Engineering, Bogazici University, İstanbul, Türkiye (2019)
10. Jeong, S.Y., Kang, T.H.K., Yoon, J.K., Klemencic, R.: Seismic performance evaluation of a tall building: Practical modeling of surrounding basement structures. Journal of Building Engineering 31, 101420 (2020). https://doi.org/10.1016/j.jobe.2020.101420

11. Özuygur, A.R., Dilsiz, A.: A discussion on the design of buildings with rigid basement according to TBSC 2018. International Journal of Engineering Research and Development 13(1), 243–249 (2021) https://doi.org/10.29137/umagd.807186.
12. Ünsal, İ., Şahan, M.F.: The influence of basement rigid wall design on structural behavior. Kahramanmaras Sutcu Imam University Journal of Engineering Sciences 25(3), 296–312 (2022)
13. Do, T.M.D.: Horizontal displacement of high-rise buildings with and without basement shear walls. Multidisciplinary Science Journal 6(6), 2024093 (2024). https://doi.org/10.31893/multiscience.2024093
14. Verdugo, J., Dávila, D.: Seismic analysis of buildings with basements. In: MATEC Web of Conferences, vol. 396, p. 03004. EDP Sciences (2024). https://doi.org/10.1051/matecconf/202439603004
15. TS 500 (TS500-2000): Requirements for design and construction of reinforced concrete structures. Turkish Standards Institute, Ankara (2000)
16. Computers and Structures, Inc.: SAP2000: Static and dynamic finite element analysis and design of structures (Version 22), Walnut Creek, CA, USA (2020)
17. AFAD: Turkey earthquake hazard maps interactive web application. Disaster and Emergency Management Authority, https://tdth.afad.gov.tr

Author Contribution Statement

- *Conceptualization:* Hurmet Kucukgoncu
- *Methodology:* Hurmet Kucukgoncu
- *Investigation:* Hurmet Kucukgoncu
- *Writing – Original Draft:* Hurmet Kucukgoncu
- *Writing – Review & Editing:* Hurmet Kucukgoncu

Conflict of Interest Statement: The author declares no conflict of interest regarding the publication of this paper.
Funding Acknowledgements: The author received no financial support for the research, authorship, and/or publication of this article.
Data Availability Statement: The data that support the findings of this study are available from the corresponding author upon reasonable request.
Ethical Approval Statement: Not applicable. This study does not involve human participants or animal subjects.

Publication Note

This paper was peer-reviewed, accepted for presentation, and included in the proceedings of the ACE2026 – International Conference on Advances in Civil Engineering, held on 12–14 October 2026 in Trabzon, Türkiye.

This paper may be cited as follows:

Hurmet Kucukgoncu, "The Effect of Rigid Basement Shear Walls on Seismic Behaviour of Reinforced Concrete Structures according to TBEC 2018," in Proceedings of the ACE2026 – International Conference on Advances in Civil Engineering, Trabzon, Türkiye, 12–14 October 2026.

Seismic Performance Assessment of a 100-M-Span Steel Bridge Using Fluid Viscous Dampers

Sadi Özsaraç[1] and Fatih Yılmaz[2]
[1] 0009-0005-6959-2870, Erciyes University, Graduate School of Natural and Applied Sciences, Department of Civil Engineering, Kayseri, Türkiye,
4010530252@erciyes.edu.tr
[2] 0000-0001-6913-5067, Erciyes University, Department of Civil Engineering, Kayseri, Türkiye,
fatihyilmaz@erciyes.edu.tr

Abstract. Railway bridges are critical transportation infrastructure components which demand high structural resilience to maintain safe transit operations under earthquake loading conditions. Given that a significant portion of existing railway bridges were constructed nearly a century ago, assessing and enhancing their seismic capacity has become a critical concern. In this study, the seismic performance of a 100-m-span steel railway bridge was investigated by comparative simulations of two distinct structural states: the unretrofitted baseline configuration and the damped counterpart equipped with longitudinally oriented fluid viscous dampers (FVDs). A three-dimensional (3D) finite element model of the bridge was developed to capture its structural behavior under dynamic loading. The numerical analyses were performed in SAP2000 using a suite of scaled ground-motion records. Within the scope of this study, to evaluate the global structural behavior and identify potential failure mechanisms under seismic demand, the analysis results were assessed comparatively based on key response parameters, including acceleration, displacement, base shear force, and energy dissipation behavior. Results demonstrate that longitudinal FVDs significantly affect energy dissipation by converting seismic energy into heat. Even though middle-span displacements and deck accelerations experience only minor reductions, the FVDs can be shown to operate efficiently within their safe stroke limits without changing the period. As a structural response, total base shear demands were increased due to the added damper reactions transferred to the substructure.

Keywords: Steel Railway Bridge; Seismic Performance; Fluid Viscous Damper; Time History Analysis; Numerical Model;

1 Introduction

Long-span steel railway bridges face three primary structural weaknesses: destructive pounding, deterioration of track alignment, and the formation of a permanent plastic hinge under severe seismic loading. Pounding risk arises from excessive longitudinal displacements at support connections [1]. Dynamic mid-span deflections in railway bridges significantly degrade track alignment, thereby compromising running safety and increasing derailment risks [2]; furthermore, the manifestation of cyclic plastic hinging within the primary steel load-bearing members induces severe residual deformations and permanent structural damage, which further threatens long-term operational integrity [3]. All these situations can be solved using traditional retrofitting methods and damping systems. The traditional retrofitting method is connected to stiffness enhancement. Resorting to the traditional method to mitigate structural problems causes the structure to shift to more unfavorable regions of the acceleration spectrum, thereby further amplifying the seismic inertia forces pulled by the system [4].

However, the integration of supplemental damping devices, specifically fluid viscous dampers (FVDs) in this study, substantially enhances the seismic performance of the bridge without introducing additional stiffness to the structural system [5]. Operating as velocity-

dependent devices, FVDs dissipate seismic energy by converting kinetic energy into thermal energy through fluid orifice flow. Consequently, they mitigate structural response without altering the fundamental dynamic characteristics, such as the natural periods and mode shapes, of the structure [6].

This study aims to evaluate the seismic performance of a 100-m-span steel truss railway bridge using Nonlinear Time-History Analyses in accordance with ASCE 41-13 [7] and TSC-2018 [8] specifications. The dynamic responses of the undamped baseline structure and the retrofitted model with longitudinal fluid viscous dampers (FVDs) are comparatively examined in terms of energy dissipation capacity, mid-span displacement demand, deck acceleration, base shear transfer to the substructure, and component-level plastic hinge formation.

2 Numerical Model

The structural system consists of a 100-m-long, simply supported steel truss bridge. To accurately replicate its geometry, a 3D numerical model was constructed in SAP2000 Finite Element Software [9], featuring custom-built-up cross-sections precisely defined via the integrated Section Designer module. Fig.1. illustrates the 3D model of the structure. The structural steel members were modelled assuming a structural steel grade of S235 with a nominal yield strength *(f_y)* of 235 MPa and an elastic modulus *(E)* of 210 GPa. To accurately capture the post-yield behavior during nonlinear time-history analyses, an isotropic strain-hardening material model with a hardening ratio of 0.02 was implemented. In terms of loading, superimposed dead loads were applied directly onto the longitudinal beams, while the railway traffic live loads were simulated using the standard load model 71 (LM71) governed by the DIN EN 1991-2 provisions [10] (Fig. 2). To capture the nonlinear dynamic response under seismic excitation, lumped plastic hinges were assigned to the structural members in strict accordance with ASCE 41-13 [7]. For the dynamic characterization, a modal analysis utilizing load-dependent Ritz vectors was conducted to ensure maximum modal mass participation.

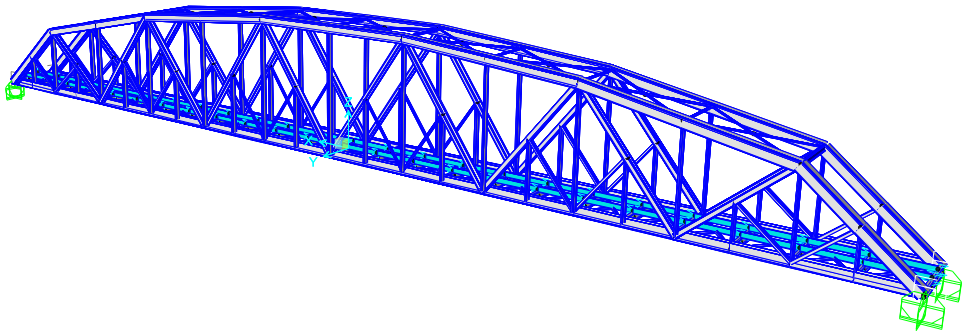


Fig. 1. The 3D 100-M-Span Steel Truss Railway Bridge Model.

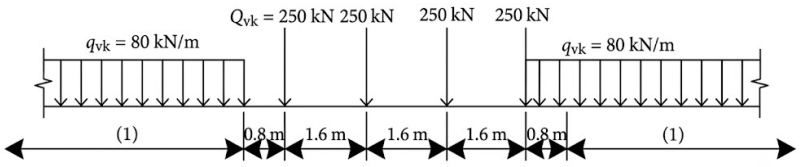


Fig. 2. Load Model 71 according to DIN EN 1991-2 [10].

3 Fluid Viscous Dampers

Nonlinear fluid viscous dampers (FVDs) were integrated into roller support regions of the bridge, while the other side is a pinned support region. In accordance with ASCE 41-13 [7], the damping force generated by the FVDs is governed by equation 1:

$$F = Cv^{\alpha} \quad (1)$$

Where C is the damping coefficient, υ is the piston velocity, and α is the velocity exponent.
Nonlinear fluid viscous dampers (FVDs) were joined to the bridge's roller support regions. To achieve a target viscous damping ratio *(ξ)* of 20% in accordance with ASCE 41-13 [7], the required total damping coefficient was analytically determined using the structural dynamic properties. Utilizing the fundamental period (T = 0.11 s) and the effective modal mass (m = 50.57 tons), the natural circular frequency (ω_n) and the theoretical critical damping coefficient (C_{cr}) were computed as 57.11 rad/s and 5777 kNs/m, respectively. Accounting for the symmetrical deployment of two FVDs at the support, the design damping coefficient per device equated to C= 578 kN(s/m)$^{0.4}$ with a non-linear velocity exponent of α = 0.4. To ensure practical feasibility, the dampers were configured based on the Taylor Devices catalogue model number 17130 [11], which features a peak force capacity of 500 kN and a stroke limit of ±100 mm. Figure 3 depicts the finite element model retrofitted with these longitudinal FVDs.

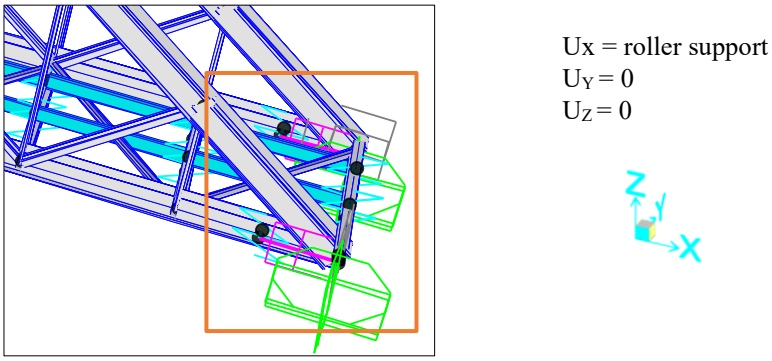


Fig. 3. Three-dimensional (3D) finite element model of the steel truss railway bridge retrofitted with longitudinally oriented FVDs which are purple colored.

4 Selection of the Ground Motion Records

Seismic inputs for the nonlinear time-history analyses were established based on local soil conditions and the Turkish Earthquake Hazard Map published by the Disaster and Emergency Management Authority (AFAD) [12]. Horizontal and vertical response spectra were defined for the DD1 (maximum considered earthquake) and DD2 (design earthquake) seismic hazard levels, which are compatible with the seismic regulations, namely the Guidelines for the Seismic Design of Highway and Railway Bridges [13] and the Turkish Building Code (TSC 2018) [8]. Moreover, seven real earthquake records have been selected from the PEER NGA-WEST2 global database [14] based on parameters such as fault mechanism, fault magnitude, fault distance to the bridge, and soil class, and scaled using the spectral matching method via the SeismoMatch [15] software. Ground motion records are shown in Table 1.

Table 1. Ground Motion Records

Ground Motion	Date	Magnitude (M_w)	Fault Type
RSN 286 (ITALY)	11/23/1980	6.9	Normal
RSN 736 (LOMAP)	10/18/1989	6.93	Reverse
RSN 746 (LOMAP)	10/18/1989	6.93	Reverse
RSN 1206 (CHICHI)	09/20/1999	7.62	Reverse
RSN 4101 (PARKFIELD)	09/28/2004	6.0	Strike Slip
RSN 3747 (CAPEMEND)	04/25/1992	7.01	Reverse
RSN 451 (MORGAN)	04/24/1984	6.19	Strike Slip

In accordance with Guidelines for the Seismic Design of Highway and Railway Bridges [13], spectral matching was confined to the $0.2T_1$ – $1.5T_1$ period interval across all directions

(corresponding to 0.022 s – 0.165 s for the longitudinal direction) to ensure that the natural frequency characteristics of the selected ground motions remained entirely unchanged. The high accelerations emerging beyond this band were intentionally retained to test the FVDs capacities under an extreme upper-bound period elongation scenario (Fig. 4).

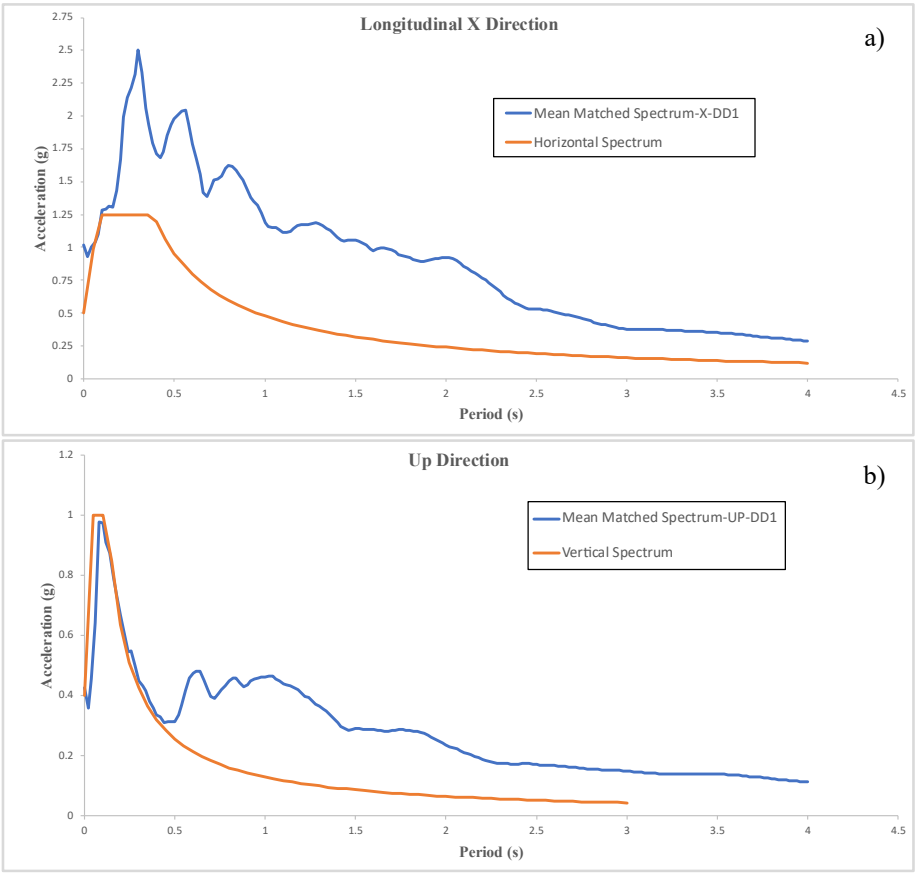


Fig. 4. Comparison of target and mean matched response spectra for DD1 seismic hazard level for (a) longitudinal and (b) vertical direction.

5 Results and Discussion

This section evaluates the seismic performance of the steel truss bridge retrofitted with fluid viscous dampers (FVDs) by analyzing energy dissipation behavior, displacement responses, base shear demands, deck accelerations, and plastic hinging mechanisms under the DD1 and DD2 seismic hazard levels. The comparative numerical results between the undamped and longitudinally damped models demonstrate that the integration of FVDs provides a continuous, stable energy dissipation mechanism that effectively mitigates dynamic responses and localized structural damage. While the extreme initial rigidity of the bridge inherently leads to a minor increase in total base shear due to superimposed velocity-dependent damping forces, the overall structural demand on primary members is substantially reduced, as evidenced by a controlled distribution of plastic hinges. While the analysis of the undamped baseline model revealed that fundamental periods of $T_1 = 0.11$ s in the longitudinal direction and $T_2 = 0.81$ s in the transverse direction, the damped model of the period revealed the same results which are $T_1 = 0.11$ s in the longitudinal direction and $T_2 = 0.81$ s in the transverse direction. This low longitudinal period indicates the extreme inherent rigidity of the structural system.

5.1 Energy Dissipation

The seismic energy-dissipation performance of FVDs is evaluated at the DD1 seismic hazard level. Fig. 5 illustrates the time-history energy components for the governing RSN 1206

earthquake. While the undamped model relies entirely on global structural damping, the retrofitted model with a longitudinal damper exhibits a continuous accumulation of nonlinear viscous damping energy, thereby reducing the demand on primary structural members. This performance is validated by the elliptical force-displacement hysteretic loops in Fig. 6, which indicate a stable energy-dissipation mechanism without stiffness degradation. Finally, Fig.7 shows the energy comparison across seven earthquakes. It appears that FVDs absorb energy prominently.

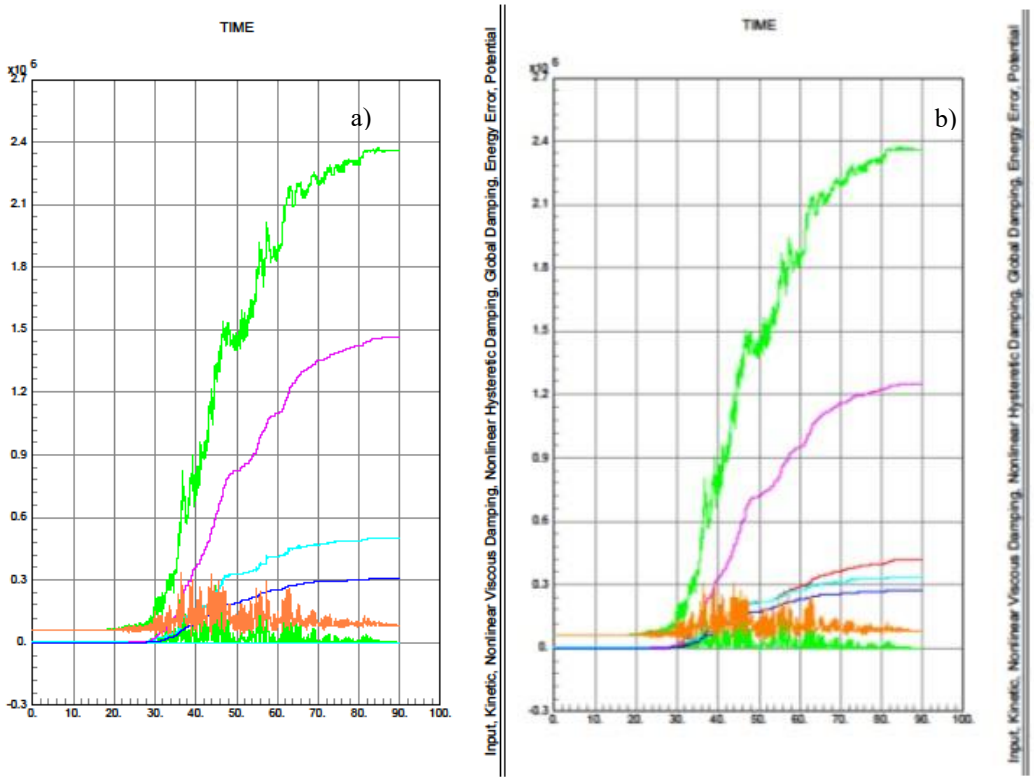


Fig. 5. Time history energy components for the RSN1206 earthquake under the DD1 seismic hazard level: (a) Undamped model and (b) longitudinal damping model.

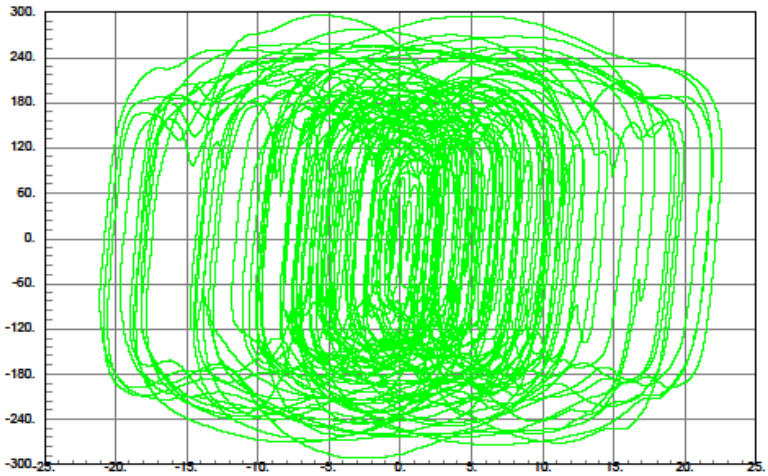


Fig. 6. Force-displacement nonlinear hysteretic behavior of the longitudinal FVDs under the RSN 1206 earthquake in DD1 seismic hazard level.

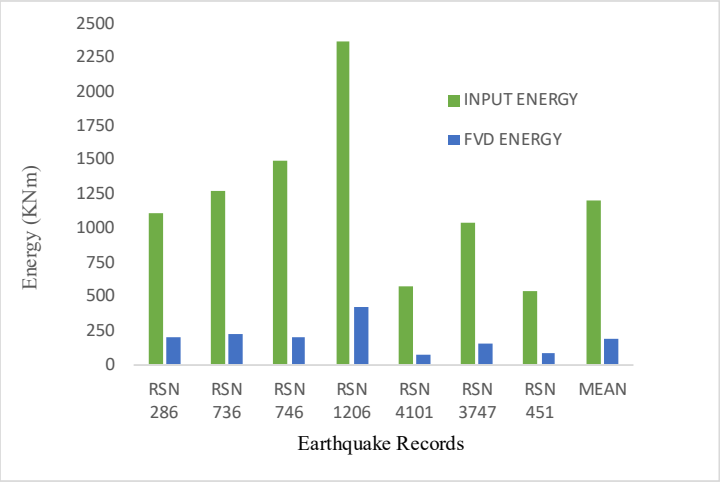


Fig. 7. Comparison of total seismic input energy and energy dissipated by fluid viscous dampers (FVDs) under the DD1 seismic hazard level across seven selected earthquake records.

5.2 Displacements

To evaluate the structural control efficacy of the longitudinal Fluid Viscous Dampers (FVDs), nonlinear time-history analyses were executed under the DD1 seismic hazard level utilizing seven distinct, spectrum-matched ground-motion records. The critical response quantities were monitored at the mid-span bottom-chord joint of the steel truss superstructure, which serves as a benchmark node due to its susceptibility to severe dynamic amplification. Table 2 comprehensively presents the comparative peak translational displacements for both the unretrofitted (undamped) and retrofitted (longitudinal damper) structural configurations. Intriguingly, although the supplemental damping system is physically oriented along the longitudinal axis of the bridge, the most substantial absolute and percentage reductions are manifested in the lateral direction *(U2)*.

Table 2. Peak joint displacements at the mid-span bottom chord node under the DD1 seismic hazard level.

	U1 (mm) (longitudinal direction)		**U2 (mm) (lateral direction)**		**U3 (mm) (vertical direction)**	
Earthquakes	Undamped	Longitudinal Damper	Undamped	Longitudinal Damper	Undamped	Longitudinal Damper
RSN 286	19.2	18.78	137.3	134.23	84.21	82.67
RSN 736	25.88	24.92	140.99	125.57	87.5	87.74
RSN 746	25.85	24.47	134.98	122.33	92.08	90.55
RSN 1206	22.27	21.19	157.86	148.48	91.91	88.89
RSN 4101	17.42	16.55	130.29	118.41	81.09	79.69
RSN 3747	17.03	16.04	127.47	116.1	67.84	65.66
RSN 451	17.17	16.03	106.64	99.54	74.28	71.25

5.3 Base Shear Force

Figure 8 illustrates a comparison of the peak longitudinal base reactions. Due to the high initial rigidity of the bridge structure (T=0.11 s), incorporating longitudinal FVDs inherently elevates the maximum base shear demand by approximately 10% under the DD1 seismic hazard level. According to structural dynamics principles and ASCE 41-13 [7], the total base shear ($Vtotal$) transferred to substructure is the simultaneous combination of the structure's restoring force and the supplemental damping force. This relationship is expressed in equation (2).

$$Vtotal = k_{eff}.D + Cv^{\alpha} \quad (2)$$

Where $keff$ is the effective structural stiffness, D is the displacement, C is the damping coefficient, and V^{α} represents the velocity-dependent term of the FVD.

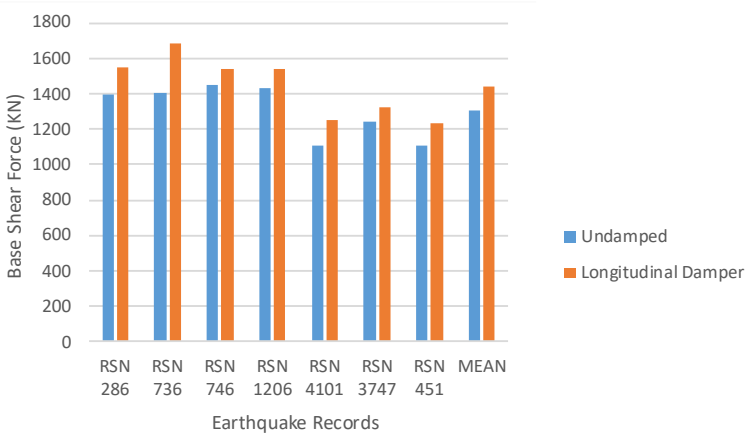


Fig. 8. Comparison of the peak longitudinal base shear forces transferred to the substructure under the DD1 seismic hazard level for seven earthquake records.

In this structural context, the extreme initial stiffness of the superstructure severely restricts longitudinal displacement responses to a scale of mere millimetres, thereby keeping the elastic restoring force vector ($k_{eff}.D$) virtually undiminished. Because the peak velocity-dependent damping forces ($C\upsilon^{\alpha}$) generated by the FVDs operate out of phase with the maximum elastic displacements, their non-linear vector superposition onto a stiff system inherently results in elevated peak concurrent reactions that are transferred directly to the substructure components.

5.4 Deck Accelerations

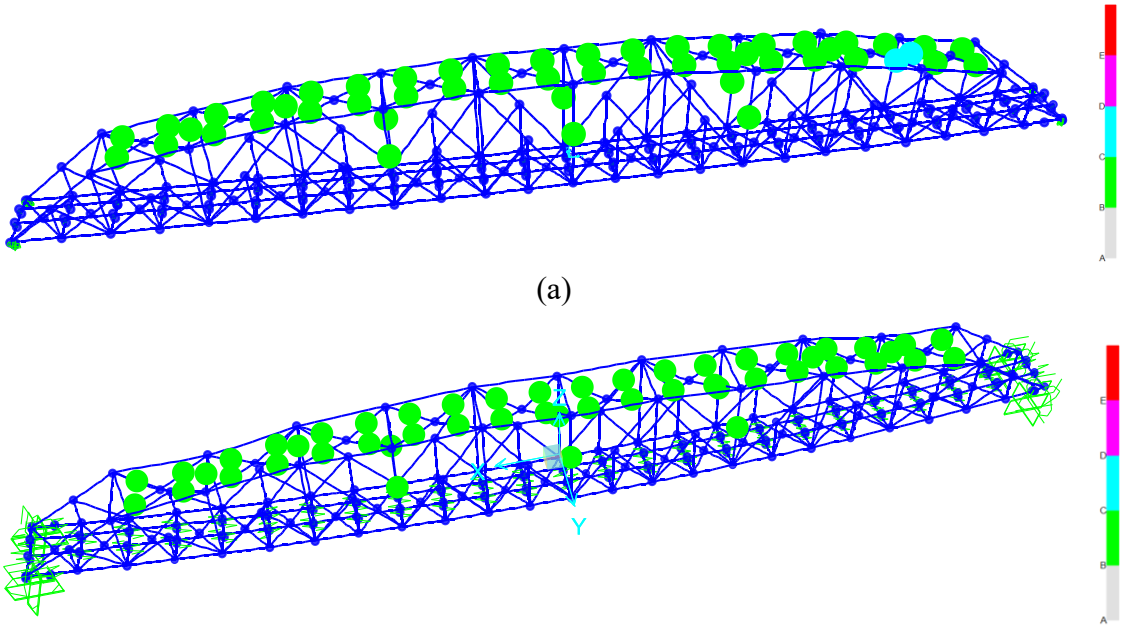
Peak longitudinal deck accelerations were investigated according to DD1 and DD2 seismic hazard levels for seven earthquakes from the middle bottom joint node of the steel bridge. Here is Table 3 showing the longitudinal acceleration values for all earthquakes at the bottom. Across all considered seismic records, the integration of FVDs provided a highly consistent reduction ratio, uniformly decreasing the peak accelerations by approximately 2% under the DD1 seismic hazard level and 3% under the DD2 seismic hazard level because of the high rigidity of the structure.

Table 3. Peak joint accelerations at the middle bottom node under the seismic hazard levels

Earthquakes		**U1 (m/s²) (longitudinal direction)**	
		Undamped	**Longitudinal Damper**
RSN 286	DD1	12.61	12.53
	DD2	5.47	5.43
RSN 736	DD1	10.72	10.23
	DD2	4.95	4.84
RSN 746	DD1	13.16	12.56
	DD2	6.25	5.15
RSN 1206	DD1	12.07	11.58
	DD2	5.27	5.21
RSN 4101	DD1	5.68	5.65
	DD2	3.44	3.49
RSN 3747	DD1	11.84	11.8
	DD2	5.64	5.65
RSN 451	DD1	8.94	8.75
	DD2	4.52	4.47

5.5 Element-Based Plastic Hinging Mechanism

The nonlinear material behavior and local damage states of the steel bridge members are evaluated based on the generalised component force deformation backbone curve (A-B-C-D-E) specified in ASCE 41-13 [7]. In this fundamental framework, point A represents the unloaded origin, B is the effective yield point (onset of plastic deformation), C denotes the ultimate strength, D indicates the residual strength, and E marks the total loss of load-carrying capacity. Fig.8. showed that the distribution of plastic hinges under the governing RSN 1206 earthquake under DD1 seismic hazard level. In the undamped model (Fig.8a), most members, especially on the top, exceed their elastic limit (B). Several local plastic hinges progress deeply into the inelastic region (between B and C), indicating the onset of permanent material deformations. Conversely, the integration of longitudinal FVDs (Fig.8b) visibly mitigates the formation and progression of these plastic hinges.



(a)

(b)

Fig. 8. Plastic hinging mechanism of (a) undamped and (b) longitudinal damper model of the bridge under the RSN 1206 ground motion in DD1 seismic hazard level.

6 Conclusions

This study presented a comprehensive numerical investigation into the seismic retrofitting of a highly rigid, 100-meter-span steel-truss railway bridge utilizing longitudinal fluid viscous dampers (FVDs). The dynamic performance and structural efficacy of this strategy were rigorously evaluated through nonlinear time-history analyses executed under both the DD1 and DD2 seismic hazard levels. Based on the numerical findings, the following conclusions can be drawn:

- Energy Dissipation Efficacy: The integration of the longitudinal dampers successfully altered the global energy balance of the superstructure. Across the seven selected ground-motion records, the FVDs established a highly stable energy-dissipation mechanism, absorbing an average of 16% of the total seismic input energy. Crucially, this supplemental damping capacity was achieved without altering the fundamental natural periods or structural configuration of the bridge.
- Three-Dimensional Kinematic Behavior: Due to the inherently high baseline rigidity of the existing steel truss bridge in the longitudinal direction (T = 0.11 s), boundary

displacements along the operational axis were naturally constrained. Consequently, while the FVDs induced minor displacement reductions in the longitudinal and vertical directions, they yielded a substantial mitigation of approximately 10% in the lateral direction (T = 0.81 s). This cross-directional control highlights a strong multi-directional spatial coupling in the 3D kinematic behavior of the truss deck. Furthermore, the peak damper forces and stroke demands remained safely within the design limits across all seismic loading scenarios.

- Substructure Force Demands: Contrary to typical supplemental damping applications in flexible building structures, incorporating FVDs into this highly rigid system elevated the maximum base shear demand transferred to the foundations by approximately 10%. Because the extreme stiffness of the bridge limits displacement reductions, the primary elastic restoring forces remain fully active. The non-linear vector superposition of the velocity-dependent damping forces onto these undiminished restoring forces inevitably increases the concurrent global foundation demands.
- Acceleration Control and Railway Safety: Due to the low relative velocities associated with the stiff truss configuration, the FVDs provided marginal numerical reductions in the peak accelerations at the mid-span bottom chord node. However, the supplemental damping successfully suppressed transient dynamic amplifications under both the DD1 and DD2 seismic hazard levels. This attenuation provides a crucial upper-bound safety margin necessary to preserve track alignment and prevent train derailment risks.
- Localized Damage Mitigation: Although the high inherent rigidity of the superstructure bounded any drastic variations in the global plastic hinge distribution, the integration of FVDs provided a clear structural benefit. The supplemental energy dissipation effectively alleviated localized material strains, thereby maintaining critical structural members closer to their linear elastic thresholds and preventing severe hysteretic degradation.

Acknowledgements
The authors acknowledge the use of the Gemini AI tool for English-language refinement, while retaining full responsibility for structural analysis, results, and scientific conclusions.

References

1. Jankowski, R.: Earthquake-induced pounding between elevated building segments or bridge spans. Engineering Structures 30(8), 2041–2052 (2008).
2. Xia, H., Han, Y., Zhang, N., Guo, W.: Dynamic analysis of train-bridge system subjected to earthquakes. Earthquake Engineering and Engineering Vibration 5(1), 51–60 (2006).
3. Bruneau, M., Uang, C.M., Sabelli, S.R.: Ductile Design of Steel Structures. 2nd edn. McGraw-Hill Education, New York (2011).
4. Soong, T.T., Spencer, B.F.: Supplemental energy dissipation: state-of-the-art and state-of-the-practice. Engineering Structures 24(3), 243–259 (2002).
5. Chopra, A.K.: Dynamics of Structures: Theory and Applications to Earthquake Engineering. 4th edn. Prentice Hall, New Jersey (2011).
6. Symans, M.D., Charney, F.A., Whittaker, A.S., Constantinou, M.C., Kircher, C.A., Johnson, M.W., McNamara, R.J.: Energy dissipation systems for seismic applications: current practice and recent developments. Journal of Structural Engineering 134(1), 3–21 (2008).
7. American Society of Civil Engineers (ASCE): *Seismic Evaluation and Retrofit of Existing Buildings (ASCE/SEI 41-13).* American Society of Civil Engineers, Reston, VA (2014).

8. Ministry of Environment and Urbanization: Turkish Seismic Code (TSC 2018). Ministry of Environment and Urbanization, Ankara (2018).
9. Computers and Structures, Inc. (CSI): SAP2000 v26: Integrated software for structural analysis and design. Computers and Structures, Inc., Walnut Creek, CA (2024).
10. German Institute for Standardization (DIN): DIN EN 1991-2: Eurocode 1: Actions on structures- Part 2: Traffic loads on bridges. Berlin (2010).
11. Taylor Devices, Inc.: Fluid Viscous Dampers for Seismic and Wind Protection. Taylor Devices, North Tonawanda, NY (2023).
12. AFAD Turkish Earthquake Hazard Map, https://tdth.afad.gov.tr, last accessed 2026/06/30.
13. Ministry of Transport and Infrastructure: Guidelines for the Seismic Design of Highway and Railway Bridges. Ankara (2020).
14. PEER Ground Motion Database, https://ngawest2.berkeley.edu, last accessed 2026/06/30.
15. Seismosoft: *SeismoMatch: A computer program for spectrum matching of earthquake records.* Seismosoft, Pavia, Italy (2024).

Author Contribution Statement

- *Conceptualization:* Fatih Yılmaz, Sadi Özsaraç
- *Methodology:* Sadi Özsaraç
- *Investigation:* Sadi Özsaraç
- *Writing – Original Draft:* Sadi Özsaraç
- *Writing – Review & Editing:* Fatih Yılmaz

List of Abbreviations

- **FVDs** — Fluid Viscous Dampers
- **DD1** — Maximum Considered Earthquake
- **DD2** — Design Earthquake

Note: Following the conference, this Publication Note will be added to each paper; therefore, authors are kindly requested not to remove the note below and to complete the author(s) and paper title information.

Publication Note

This paper was peer-reviewed, accepted for presentation, and included in the proceedings of the ACE2026 – International Conference on Advances in Civil Engineering, held on 12–14 October 2026 in Trabzon, Türkiye.

This paper may be cited as follows:

Ozsarac S., Yılmaz F., "Seismic Performance Assessment of a 100-M-Span Steel Bridge Using Fluid Viscous Dampers", in Proceedings of the ACE2026 – International Conference on Advances in Civil Engineering, Trabzon, Türkiye, 12–14 October 2026.

Effect of Opening Location on GFRP-RC Deep Beam Shear Behavior

Farid Abed [1], Anas Saber[2], Aroob Alateyat[3], Tamer El-Maaddawy[4]
[1] 0000-0002-9202-694X, American University of Sharjah, Civil Engineering Department, Sharjah, UAE, fabed@aus.edu, Corresponding Author
[2] 0009-0006-0444-6730, American University of Sharjah, Civil Engineering Department, Sharjah, UAE, b00083401@alumni.aus.edu
[3] 0000-0002-1670-4307, American University of Sharjah, Civil Engineering Department, Sharjah, UAE, aalateyat@aus.edu
[4] 0000-0003-2734-018X, United Arab Emirates University, Civil and Environmental Engineering Department, Al Ain, UAE, tamer.maaddawy@uaeu.ac.ae

Abstract. The durability of steel-reinforced deep beams can be significantly affected by aggressive environmental conditions, where reinforcement corrosion is a major concern. Fiber-reinforced polymer (FRP) reinforcement offers a corrosion-resistant alternative; however, its brittle behavior and the limited design guidance available for deep beams require further investigation. This study examines the shear behavior of high-strength concrete (HSC) deep beams reinforced with glass fiber-reinforced polymer (GFRP) bars. Three specimens were tested, including a reference beam without an opening and two beams with web openings at different locations, to evaluate the influence of opening presence and position on shear performance. The experimental program included load–deflection measurements, ultimate shear capacity assessment, and full-field strain monitoring using Digital Image Correlation (DIC). The results showed that web openings significantly reduced shear capacity, with strength losses of up to 49% compared to the solid reference beam. Locating the opening away from the primary diagonal load path toward the mid-span region recovered approximately 13% of the lost capacity relative to an opening located closer to the support. Strain measurements and DIC analyses confirmed the observed failure mechanisms and clearly identified the primary and alternative load-transfer paths in beams with openings.

Keywords: GFRP-RC Deep Beams, Web opening, DIC Camera.

1 Introduction

Fiber-reinforced polymer (FRP) reinforcement has emerged as a durable, corrosion-resistant alternative to steel reinforcement, particularly for structures exposed to aggressive environments. However, its application in heavily loaded members such as deep beams remains challenging due to their nonlinear stress distribution and arch-action load-transfer mechanism, which render conventional beam theory inapplicable [1,2]. Despite increasing interest in FRP-reinforced concrete (FRP-RC) structures, the behavior of FRP-RC deep beams is not yet fully understood. Previous studies have shown that the shear capacity of FRP-RC deep beams is strongly influenced by the shear span-to-depth ratio (a/d), with lower values enhancing strength through improved arch action [1,4–6]. While FRP-RC deep beams can achieve shear capacities comparable to or exceeding those of steel-reinforced beams, they generally exhibit more brittle behavior and wider cracking. Shear resistance is governed primarily by concrete strut action, whereas aggregate interlock and dowel action contribute minimally [7]. Increasing FRP web reinforcement has been shown to improve strength and crack control; however, significant size effects remain [7,8].

Research on FRP-RC deep beams with openings, particularly those constructed with high-strength concrete (HSC), remains limited. Existing studies indicate that opening location relative to the primary load path is a key parameter affecting shear strength [9]. Moreover, current design provisions, such as ACI 440.11-22 [3], do not provide specific guidance for their design.

To address these gaps, this study investigates the shear behavior of HSC GFRP-RC deep beams with web openings at different locations. Three beams were tested, including a solid reference beam and two beams with openings positioned away from the primary shear load path. Digital Image Correlation (DIC) was employed alongside conventional instrumentation to monitor strain development and crack propagation, providing insight into the influence of opening location on shear load-transfer mechanisms.

2 Experimental Testing

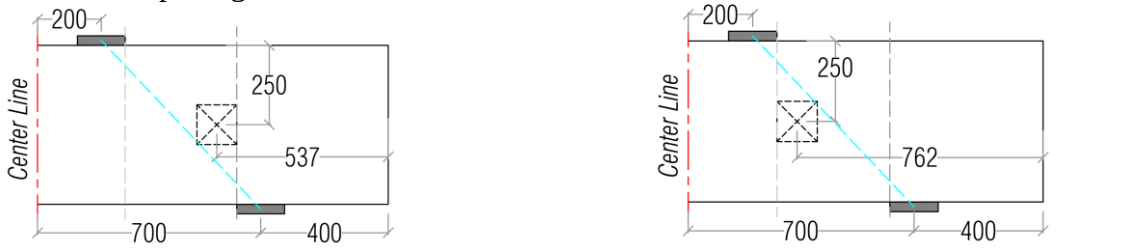
2.1 Materials

The beam specimens were cast using high-strength concrete with a target 28-day compressive strength of 70 MPa. Cylinder tests conducted on the day of beam testing in accordance with ASTM C39/C39M-14 [10] indicated an average compressive strength of 74 MPa.. The GFRP reinforcement, supplied by Unique Fiberglass and Composites and manufactured in accordance with ASTM D8505-23 [11], included 20 mm diameter bottom flexural bars (Ultimate strength (f_u) = 804 MPa, Elastic modulus (E) = 50 GPa), 12 mm diameter top hanger bars (f_u = 860 MPa, E = 48 GPa), and 10 mm diameter bars for longitudinal skin reinforcement and shear stirrups (f_u = 945 MPa, E = 45 GPa).

2.2 Specimens' Details

The experimental program was conducted to investigate the shear behavior of GFRP-RC deep beams, with all specimens designed to promote shear-dominated failure. Flexural design followed ACI 440.1R-22 [3] using a conservative approach to prevent premature flexural failure, while shear capacity was evaluated using the strut-and-tie method in accordance with ACI 318-25 [12], given the absence of specific provisions for deep beams in ACI 440.1R-22 [3].

Three beams were tested: B1-OL1, B2-OL2, and B3-REF. The designation "B" denotes the beam series, "N" denotes the specimen number, "OL1/OL2" Denotes the location of the opening relative to the hypothetical compression strut (left or right), and "REF" the reference beam without openings. Beams B1-OL1 and B2-OL2 contained a 125 × 125 mm web opening at the bottom and top support edges, respectively (*Fig. 1*). Both specimens had identical reinforcement, consisting of six Ø20 mm bottom flexural bars, two Ø12 mm top hanger bars, and web reinforcement comprising 2 Ø10 mm horizontal bars at 86 mm spacing and 2-legged Ø10 mm vertical stirrups at 80 mm spacing. Beam B3-REF was identical to the other specimens but without a web opening.



(a) Opening at edge of bottom support, B1-OL1 (b) Opening at edge of top support, B2-OL2

Fig. 1. Detailed geometry and reinforcement schemes for test specimens.

2.3 Test Setup and Instrumentation

The beam specimens were tested under four-point bending using a Universal Testing Machine (UTM) with a constant shear span of 500 mm ($a/h = 1.0$) to ensure deep beam behavior. Two concentrated loads, spaced 400 mm apart, were applied under displacement control at a rate of 0.015 mm/s, while load, deflection, cracking, and failure data were continuously recorded. Strain development was monitored using electrical resistance strain gauges installed on the longitudinal reinforcement, web reinforcement, and selected concrete locations, while mid-span deflections were measured using an LVDT. In addition, a Digital Image Correlation (DIC) system was employed to capture full-field displacement, strain, and crack propagation using a calibrated high-resolution camera and a speckle-patterned beam surface under controlled lighting conditions.

3 Results and Discussion

3.1 Failure Mode and Cracking Patterns

All specimens exhibited shear-dominated failure governed by diagonal tension cracking. In beams with web openings, cracks initiated at the upper and lower corners of the openings and propagated toward the supports and loading points, forming a distinct diagonal failure plane. These cracks widened rapidly with increasing load until failure. In the reference beam, diagonal cracks formed near the loading and support regions and gradually merged into a main shear crack.

Although all beams failed in a similar diagonal shear mode (*Fig. 2*), the presence and location of openings significantly influenced crack development and shear capacity. Beam B2-OL2 (opening closer to the loading point) exhibited wider cracks at failure than B1-OL1, indicating higher shear resistance. This is attributed to the interaction between the opening and the principal compression strut: openings closer to the support more severely disrupt the load path, reducing shear capacity, while those nearer mid-spans have a lesser effect. Similar trends have been reported in previous studies [13,14].



(a) (b)

Fig. 2. Cracking patterns at failure for the samples: (a) B1-OL1, (b) B2-OL2.

3.2 Load-Deflection Relationship

Fig. 3 shows the load–deflection response of the tested specimens, which exhibited a bilinear behavior consisting of an initial uncracked stiffness followed by a reduced post-cracking stiffness.

Beam B1-OL1 (opening toward the support) showed a 49% reduction in shear capacity and a 30% reduction in deformation capacity compared with the reference beam. Beam B2-OL2 (opening toward the loading point) exhibited lower reductions of 36% in both shear and deformation capacity. Although relocating the opening toward the loading zone reduces its adverse effect on shear resistance, it may increase vulnerability in the flexural region.

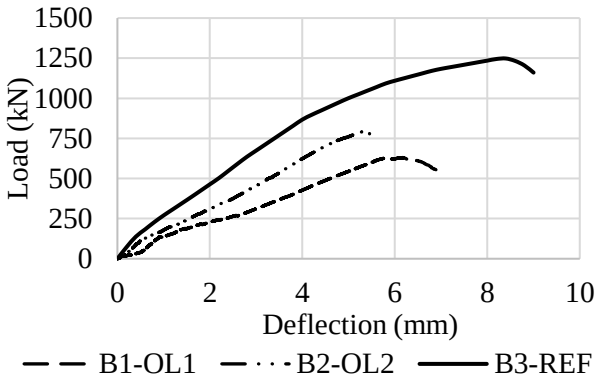
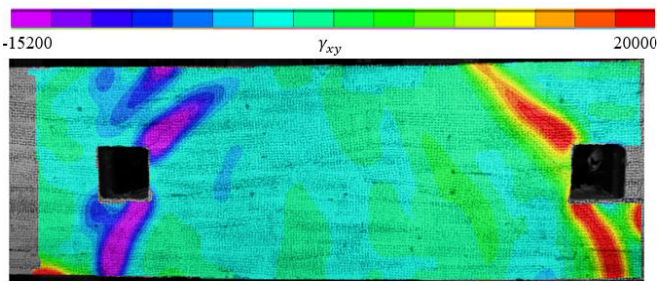


Fig. 3. Load-deflection curves for all tested beams.

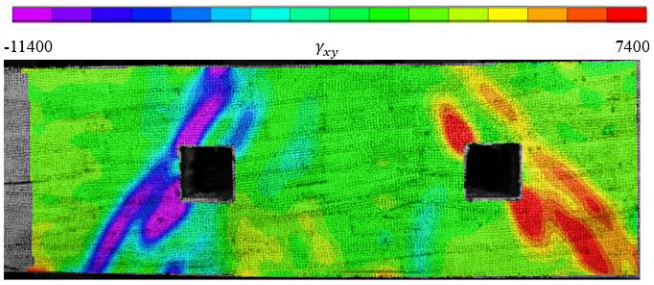
3.3 Strains Development

Strain gauges on the longitudinal bottom GFRP bars recorded high tensile strains, with mid-span values of 2000–3000 με (12–18% of ultimate strain). Similar high strains (up to ~3000 με) were measured near opening corners in longitudinal bars and stirrups due to diagonal crack proximity. In contrast, the top mid-span gauge recorded low to moderate compressive strains (<2000 με), indicating that concrete crushing did not govern failure.

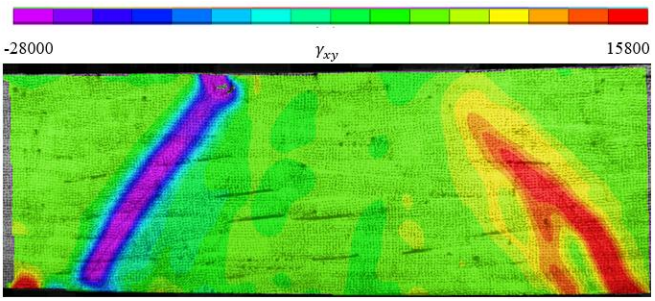
The DIC-based surface strain measurements were calibrated and analyzed to obtain full-field strain contours at peak load. Figure 4 presents the in-plane shear strain (γ_{xy}) distribution, showing localized concentrations along diagonal crack paths, confirming the dominant role of shear action. The strain fields follow the expected diagonal compression strut between the load and support; however, openings significantly affect this load path. In beam B2-OL2 (*Fig. 4(b)*), partial stress redistribution around the opening indicates a less disturbed strut and the formation of alternative load paths. In contrast, beam B1-OL1 (*Fig. 4(a)*) shows a more pronounced interruption of the diagonal strut, resulting in higher strain localization and reduced shear efficiency.



(a) B1-OL1



(b) B2-OL2



(c) B3-REF

Fig. 4. DIC strain contours for the tested beams: (a) B1-OL1, (b) B2-OL2, (c) B3-REF.

4 Conclusions

- The presence of a web opening significantly reduced the shear capacity of the GFRP-RC deep beams, with strength reductions ranging from 36% to 49%, depending on the opening location.
- The influence of opening location was substantial. Relocating the opening away from the primary diagonal load path and toward the mid-span region reduced the loss in shear capacity by approximately 13% compared with an opening located closer to the support. However, this configuration resulted in approximately 6% greater deformation at failure.
- Strain measurements obtained from both conventional strain gauges and DIC were in good agreement and effectively captured the structural response of the tested beams.
- The DIC results provided clear visualization of the principal and alternative load-transfer paths, confirming the observed failure mechanisms in beams containing web openings.

Acknowledgments

This research project was supported by the American University of Sharjah under Grant No. FRG23-C-E04.

References

1. Abed, F., Al-Mimar, M., & Ahmed, S. (2021). Performance of BFRP RC beams using high strength concrete. Composites Part C: Open Access, 4, 100107. https://doi.org/10.1016/j.jcomc.2021.100107.
2. Abed, F., Alhoubi, Y., & Mahaini, Z. (2023). Flexural Performance of UHPC Beams Reinforced with BFRP Bars. Building for the Future: Durable, Sustainable, Resilient, 1395–1402. https://doi.org/10.1007/978-3-031-32519-9_141.
3. ACI Code-440.11-22, *Building code requirements for structural concrete reinforced with GFRP bars and commentary*. Farmington Hills, Michigan: American Concrete Institute, 2022.
4. Alhamad, S., Al Banna, Y., Al Osman, A., Mouthassseeb, J., Abdalla, S., & Abed, F. (2017). Effect of shear span-to-depth ratio on the shear behavior of BFRP-RC deep beams. MATEC Web of Conferences, 120, 1012. https://doi.org/10.1051/matecconf/201712001012.
5. Abed, F., El Refai, A., & Abdalla, S. (2019). Experimental and finite element investigation of the shear performance of BFRP-RC short beams. Structures, 20, 689–701. https://doi.org/10.1016/j.istruc.2019.06.019.
6. Abed, F., El Refai, A., & Abdalla, S. (2019). Experimental and finite element investigation of the shear performance of BFRP-RC short beams. Structures, 20, 689–701. https://doi.org/10.1016/j.istruc.2019.06.019.
7. Peng, F., Cai, Y., Yi, W., & Xue, W. (2023). Shear behavior of two-span continuous concrete deep beams reinforced with GFRP bars. Engineering Structures, 290, 116367. https://doi.org/10.1016/j.engstruct.2023.116367.
8. Jin, L., Song, B., Zhang, J., & Du, X. (2026). Experimental and analytical investigation of the influence of horizontal and vertical web reinforcement on shear failure and size effect in FRP-reinforced concrete deep beams. Engineering Structures, 350, 121938. https://doi.org/10.1016/j.engstruct.2025.121938.
9. Al-Enezi, M. S., Yousef, A. M., & Tahwia, A. M. (2023). Shear capacity of UHPFRC deep beams with web openings. Case Studies in Construction Materials, 18, e02105. https://doi.org/10.1016/j.cscm.2023.e02105.
10. ASTM International Committee C09 on Concrete and Concrete Aggregates, *Standard test method for compressive strength of cylindrical concrete specimens*, 2014.

11. ASTM Committee D30, *Standard Specification for Basalt and Glass Fiber-Reinforced Polymer (FRP) Bars for Concrete Reinforcement (D8505-23)*, West Conshohocken, PA. USA., 2023.
12. American Concrete Institute, *ACI CODE-318-25: Building Code for Structural Concrete — Code Requirements and Commentary*, Farmington Hills, MI, USA., 2025.
13. Guan, H. (2005). Strut-and-tie model of deep beams with web openings - An optimization approach. Structural Engineering and Mechanics, 19(4), 361–379. https://doi.org/10.12989/sem.2005.19.4.361.
14. Yang, K. H., Chung, H. S., & Ashour, A. (2007). Influence of inclined web reinforcement on reinforced concrete deep beams with web openings. https://doi.org/10.14359/18860.

Author Contribution Statement

- *Conceptualization:* Farid Abed
- *Methodology:* Anas Saber, Tamer Maaddawy
- *Investigation:* Aroob Alateyat, Farid Abed
- *Writing – Original Draft:* Aroob Alateyat, Farid Abed
- *Writing – Review & Editing:* Farid Abed, Tamer Maaddawy

List of Abbreviations

- **FRP** — Fiber Reinforced Polymer
- **HSC** — High Strength Concrete
- **GFRP** — Glass Fiber Reinforced Polymer
- **DIC** — Digital Image Correlation
- **UTM** — Universal Testing Machine
- **LVDT**— Linear Variable Displacement Transducer
- **SG** — Strain Gauge
- **FRP-RC** — Fiber Reinforced Polymer-Reinforced Concrete

Publication Note

This paper was peer-reviewed, accepted for presentation, and included in the proceedings of the ACE2026 – International Conference on Advances in Civil Engineering, held on 12–14 October 2026 in Trabzon, Türkiye.

This paper may be cited as follows:

Farid Abed, Anas Saber, Aroob Alateyat, Tamer El-Maaddawy, “Shear Response of GFRP-Reinforced High Strength Concrete Deep Beams with Openings,” in Proceedings of the ACE2026 – International Conference on Advances in Civil Engineering, Trabzon, Türkiye, 12–14 October 2026.

Corner Radius Effect on Confined Strengths of FRP-Wrapped Rectangular Concrete Members

Onur Gedik[1]
[1] 0000-0002-3969-7824, İstanbul Okan University, Civil Engineering Department, İstanbul, Türkiye, onur.gedik@okan.edu.tr

Abstract. FRP strengthening of axial compressive strength in rectangular columns is more complex than in circular columns due to the non-uniform distribution of lateral confinement stresses along the perimeter. The rupture strain values of FRP obtained from coupon tests are significantly reduced in actual specimens, which is commonly attributed to microcracking, differences in loading conditions, and the presence of sharp corners. Failure of the wrapping material typically occurs at the corner regions near mid-height, highlighting the critical influence of corner geometry. To investigate the contribution of corner radius to confined strength, a comprehensive database of FRP-wrapped rectangular concrete specimens was compiled from experimental studies available in the literature. Although rounding the corners of rectangular cross-sections improves the overall structural behavior, the presence of existing longitudinal reinforcement and aspect ratio introduce physical boundary constraints. In this study, the effect of corner radius is evaluated in conjunction with aspect ratio, unconfined compressive strength, and confinement ratios. Furthermore, several existing analytical models and design-oriented expressions are reviewed and compared against experimental results, particularly in terms of minimum corner radius requirements and expected confinement efficiency. The findings aim to provide improved insight into the role of rounded corners in enhancing confinement performance and to support the development of more reliable and practical design recommendations for FRP-strengthened rectangular members.

Keywords: FRP, Compressive Strengthening, Concrete, Corner Radius

1 Introduction

FRP (Fiber Reinforced Polymer) confinement of concrete columns in order to enhance the axial compressive strength is in use for decades. Most of the studies carries out for such structural members were conducted over circular cross-sections, where the majority of the columns in need for retrofitting are rectangular cross-sections. Unlike circular cross-sections, the effectiveness of FRP confinement in rectangular cross-sections remains comparatively lower, mainly due to the non-uniform distribution of lateral confining stresses along the perimeter. These lateral stresses tend to concentrate at the corners, and, particularly in specimens with sharp corners, premature rupture occurs at stress levels significantly lower than those obtained from FRP coupon tests. As a result, the specimens fail before reaching their presumed maximum axial capacities. Since the corner radius represents the transition from a rectangular cross-section toward a circular geometry, it will be investigated as one of the most critical parameters governing the ultimate strength of FRP-confined specimens. After introducing the application of corner radius effect for the overall performance of the specimens defined by guidelines and prediction models, the contribution of the corner radius will also be evaluated with respect to the unconfined concrete strength, the aspect ratio of the section and the confinement ratios.

2 Database

A total of 455 FRP-confined specimens were collected from the literature [1]. All specimens consisted of rectangular concrete sections confined with carbon FRP (CFRP). Approximately 60% of the specimens were square sections. The unconfined concrete strength was categorized into three classes as low-, normal-, and high-strength concrete. Corner radii were divided into four groups with intervals of 10 mm. The confinement ratio ranges were determined based on the minimum threshold values associated with the observed strength enhancement reported in the study by Gedik [1], as well as the lower-bound limits defined by ACI 318 [2]. In addition, the confinement ratios for all specimens were calculated according to the TEC 2018 [3] equations. A summary of the database is presented in Table 1.

Table 1. Database Summary (Specimen Ratios)

		Geometry		f_{co} [MPa]			f_l/f_{co}			r_c [mm]			
		Sq.	Rec.	Low	Med	High	Low	Med	High	(1)	(2)	(3)	(4)
Geo.	Square	0.61	-	0.05	0.36	0.19	0.18	0.19	0.24	0.07	0.11	0.26	0.18
	Rectangle	-	0.39	0.04	0.23	0.12	0.12	0.14	0.13	0.04	0.08	0.22	0.05
f_{co}	$f_{co} \leq 20$	0.05	0.04	0.09	-	-	0.01	0.02	0.06	0.01	0.04	0.01	0.03
	$20 < f_{co} \leq 35$	0.36	0.23	-	0.60	-	0.13	0.19	0.28	0.06	0.09	0.32	0.13
	$f_{co} > 35$	0.19	0.12	-	-	0.31	0.16	0.12	0.04	0.03	0.05	0.15	0.08
$\frac{f_l}{f_{co}}$	$\frac{f_l}{f_{co}} < 0.05$	0.18	0.12	0.01	0.13	0.16	0.30	-	-	0.07	0.06	0.15	0.03
	$0.05 \leq \frac{f_l}{f_{co}} \leq 0.083$	0.19	0.14	0.02	0.19	0.12	-	0.33	-	0.02	0.09	0.14	0.08
	$\frac{f_l}{f_{co}} > 0.083$	0.24	0.13	0.06	0.28	0.04	-	-	0.37	0.01	0.04	0.19	0.13
r_c	< 10 (1)	0.07	0.04	0.01	0.06	0.03	0.07	0.02	0.01	0.10	-	-	-
	$10 < r_c \leq 20$ (2)	0.11	0.08	0.04	0.09	0.05	0.06	0.09	0.04	-	0.18	-	-
	$20 < r_c \leq 30$ (3)	0.26	0.22	0.01	0.32	0.15	0.15	0.14	0.19	-	-	0.48	-
	> 30 (4)	0.18	0.05	0.03	0.13	0.08	0.03	0.08	0.13	-	-	-	0.24

3 Corner Radius Effect in Guideline and Model Expressions

To investigate the contribution of corner radius to the strength enhancement of FRP-confined reinforced concrete members, selected design guidelines and predictive models will be examined. The considered codes and models were chosen based on their demonstrated accuracy in predicting the ultimate strength of FRP-confined rectangular sections [1]. Among the design guidelines, in addition to the Turkish Building Earthquake Code (TEC 2018) [3], which is used to define the strength classes adopted in this study, the provisions of ACI 440.2R-17 [2] and CNR-DT200 R1/2013 [4] will also be evaluated. As predictive models, the formulations proposed by İlki et al. [5], Wu and Wei [6], and Lim and Ozbakkaloglu [7] will be considered, as these models have been shown to provide the most reliable estimates of the maximum axial load capacities of FRP-confined rectangular sections.

3.1 Guidelines

TEC 2018 [3]. The Turkish code incorporates the effect of corner radius into the calculation of lateral confining pressure through a shape factor. The function given in Eq. (1) is a simplified form of the shape factor originally proposed by Restrepo and Vino [8]. However, the influence of varying aspect ratios can only be represented as a secondary effect, even when the maximum possible corner radius is applied. In this formulation, a shape factor equal to 1.0, corresponding to a circular section, is obtained when the corner radius is taken as one-half of the shorter side dimension.

$$\kappa_a = 1 - \frac{(b - 2r_c)^2 + (h - 2r_c)^2}{3bh} \tag{1}$$

For square specimens with no corner rounding, the shape factor is equal to 0.33, implying that approximately 67% of the confinement effectiveness expected for a circular section is lost. Although the Turkish code does not prescribe a minimum corner radius requirement, it specifies that sections with an aspect ratio greater than 2.5 are not considered suitable for this strengthening technique.

ACI 440.2R-17 [2]. ACI 440 imposes an aspect ratio limit of 2.0 and additionally requires that the largest cross-sectional dimension does not exceed 900 mm. Similar to TEC 2018 [3], the shape factor is defined based on the ratio of the effectively confined area, represented by the region enclosed by four parabolic curves, to the total cross-sectional area. However, unlike TEC 2018 [3], the effect of an aspect ratio different from unity is accounted for separately in both the calculation of the effectively confined area and the determination of the shape factor. Furthermore, this shape factor explicitly incorporates the area of the existing longitudinal reinforcement into the calculation. Shape factor can be found in Eq. (2).

$$\kappa_a = \frac{1 - \dfrac{\left[\left(\frac{b}{h}\right)(b - 2r_c)^2 + \left(\frac{h}{b}\right)(h - 2r_c)^2\right]}{3bh} - \rho_g}{1 - \rho_g}\left(\frac{b}{h}\right)^2 \tag{2}$$

Similar to the Turkish code, the American guideline considers the corner radius only as a parameter affecting the calculation of the effectively confined area. Likewise, for an unreinforced square section, the shape factor approaches 1.0 when the corner radius reaches its maximum possible value. Therefore, the main differences between the ACI 440 [2] approach and TEC 2018 [3] arise in the treatment of rectangular sections with aspect ratios other than unity and in cases where the contribution of existing longitudinal reinforcement is taken into account.

CNR-DT200 R1/2013 [4]. The Italian guideline employs a three-component effectiveness coefficient consisting of longitudinal, transverse, and inclined contributions. Among these, the transverse effectiveness coefficient is calculated directly as a function of the cross-sectional geometry. The shape factor adopted for this purpose is identical to that specified in the Turkish code. In addition, the same cross-sectional limitations defined by the American guideline are adopted. The corresponding shape factor formulation is presented in Eq. (3).

$$\kappa_a = 1 - \frac{(b-2r_c)^2 + (h-2r_c)^2}{3bh} \tag{3}$$

Overall, all three design guidelines employ similar shape factor formulations to account for the influence of cross-sectional geometry and corner rounding, and none of them prescribes a minimum corner radius requirement.

3.2 Prediction Models

İlki et al. [5]. In the model proposed by İlki et al., the calculation of the shape factor is refined by accounting for the reduction in cross-sectional area resulting from corner rounding. Apart from this modification, no additional treatment of the corner radius is introduced, and its influence is evaluated in a manner consistent with the approaches adopted in the design guidelines. The corresponding formulation is presented in Equation (4).

$$\kappa_a = 1 - \frac{(b-2r_c)^2 + (h-2r_c)^2}{3bh} - \frac{4r_c^2 - \pi r_c^2}{bh} \tag{4}$$

Wu and Wei [6]. Unlike the other approaches, the model proposed by Wu and Wei incorporates the effects of aspect ratio and corner radius through two separate terms within the lateral confining pressure formulation. The study in which this model was developed was specifically conducted to investigate the influence of aspect ratio on the behavior of FRP-confined rectangular members. The findings demonstrated that, after corner radius, the aspect ratio is the second most influential parameter governing the effectiveness of FRP confinement. The corresponding equation is presented below in Eq. (5).

$$\kappa_a = \left(\frac{2r_c}{b}\right)^{0.72} \left(\frac{h}{b}\right)^{-2.5} \tag{5}$$

According to the study, the confinement effectiveness progressively decreases as the aspect ratio approaches 2.0, eventually becoming negligible for highly elongated rectangular sections. As can be inferred from the form of the shape factor, this model is based on the premise that the effectiveness of FRP confinement is governed more by the geometric characteristics of the cross-section than by the concept of an effectively confined area. Accordingly, the influence of corner radius and aspect ratio is treated as a direct geometric effect on confinement efficiency rather than solely through the estimation of the effectively confined region.

Lim and Ozbakkaloglu [7]. Since the model proposed by Lim and Ozbakkaloglu was developed primarily using data from high-strength concrete specimens, consistent with the authors' earlier studies, its main focus was on the influence of unconfined concrete strength on the ultimate confined strength. Under such conditions, the lateral confining pressure becomes relatively small compared with the existing axial stress, and post-peak softening behavior becomes more pronounced. Consequently, unlike the model of Wu and Wei [6], the proposed formulation does not incorporate only the geometric characteristics of the section into the shape factor; it also accounts for the influence of the unconfined concrete strength. Equation (6) presents only the geometric contribution to the confinement effectiveness factor.

$$\kappa_a = \left(\frac{2r_c}{\sqrt{(h^2+b^2)/2}}\right)^{0.67}\left(\frac{h}{b}\right)^{0.5} \quad (6)$$

Furthermore, the study revealed that the attainable confinement-induced strength enhancement diminishes with increasing unconfined concrete strength, and this phenomenon was explicitly incorporated into the proposed model, unlike in most existing formulations.

4 Investigation of Corner Radius

To evaluate the influence of corner radius while accounting for the most significant size-related parameter, the ratio of corner radius to the cross-sectional perimeter was adopted. The analysis was conducted using the strength enhancement ratio, defined as $\boldsymbol{f_{cc}/f_{co}}$. The strength enhancement values presented in Figure 1 represent the mean values and corresponding standard deviations as shaded area, calculated from all specimens within each group.

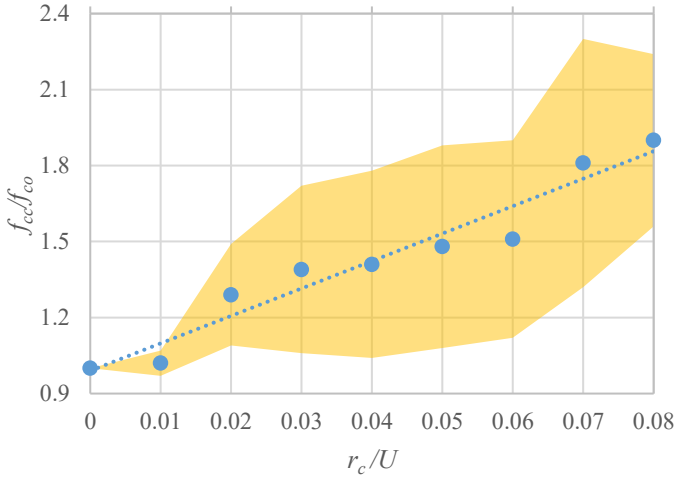


Fig. 1. Effect of corner radius over the enhancement ratio.

As can be observed from the figure, the strength enhancement ratio increases with increasing corner radius ratio. The irregular variation between these two parameters, together with the relatively high standard deviation values, can be attributed to the omission of other influential variables in the analysis. In addition to corner radius, parameters such as unconfined concrete strength, cross-sectional area, aspect ratio, and the ultimate strain capacity of the FRP material are expected to significantly influence the ultimate strength response.

In the following sections, the contribution of corner radius will be further examined with respect to unconfined concrete strength, aspect ratio, and confinement ratio.

4.1 Unconfined Concrete Strength

In order to evaluate the influence of unconfined concrete strength on the contribution of corner radius, a subset consisting of 150 × 150 mm square specimens was analyzed. Within the previously defined strength ranges, the variation of strength enhancement ratios with increasing corner radius is presented in Figure 2.

As seen in Figure 2, while the unconfined strength of specimens increases, the efficiency of the CFRP wraps reduces. Even though the efficiency reduces, with an increase in corner radius, the enhancement also increases. It is more prominent in low strength range while the contribution slows down with the increase in unconfined strength values as concluded in previous studies [9]. It should be kept in mind that the confinement ratios are varying and the given enhancement ratios are just average values.

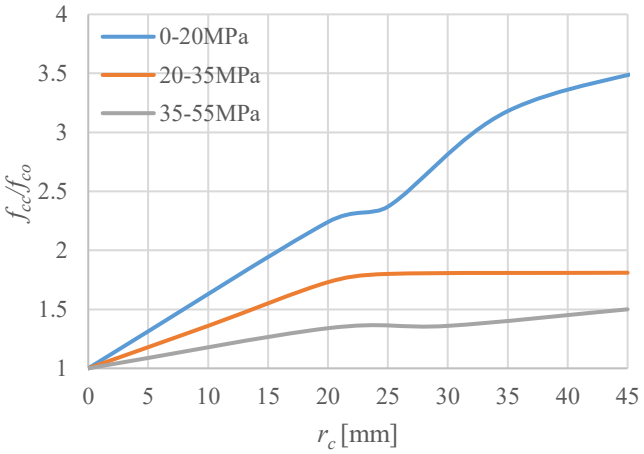


Fig. 2. Effect of corner radius over the enhancement ratio.

4.2 Aspect Ratio

The influence of corner radius was also investigated with respect to the aspect ratio using rectangular specimens with unconfined concrete strengths ranging from 20 to 43MPa. For this purpose, square specimens $(h/b = 1.0)$ and two types of rectangular sections $(h/b = 1.5)$ and $(h/b = 2.0)$ were considered. No restrictions were imposed on the confinement ratio or cross-sectional area, and the corresponding average values are presented in Figure 3.

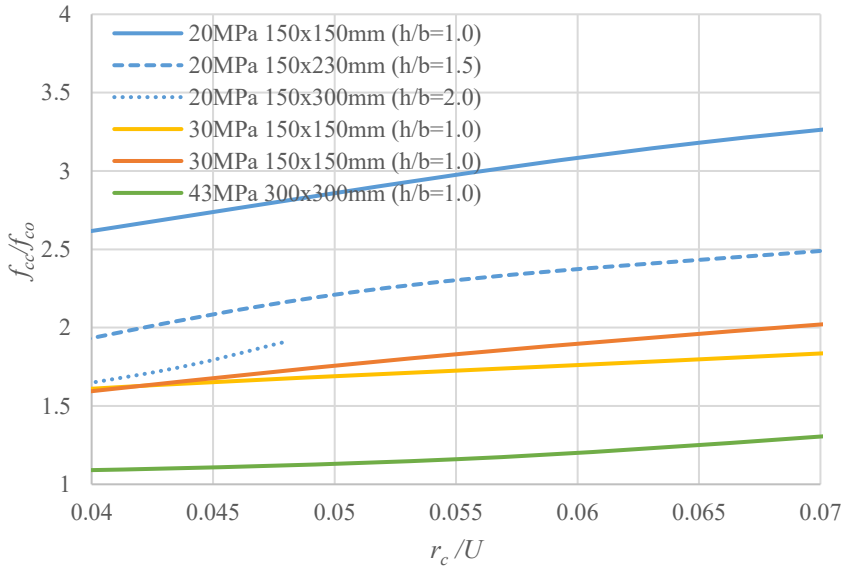


Fig. 3. Effect of aspect ratio over the enhancement ratio.

As shown in Figure 3, although the strength enhancement decreases with increasing aspect ratio for a given unconfined concrete strength, the influence of the corner radius-to-perimeter ratio remains evident. This observation suggests that neither the cross-sectional area nor the aspect ratio significantly affects the effectiveness of the corner radius ratio as a governing parameter for confinement-induced strength enhancement.

4.3 Confinement Ratio

The confinement ratio is defined as the ratio of the lateral confining pressure to the unconfined concrete strength, f_l/f_{co}. The lateral confining pressure was calculated using the expression given in Equation (7), which is based on the formulation adopted in TEC2018, excluding the

effect of the shape factor. This approach was selected as the reference measure of confinement intensity throughout the study.

$$f_l = \frac{E_{frp}\varepsilon_{frp}(b+h)tn}{bh} \tag{7}$$

Figure 4 illustrates the influence of corner radius on typical square specimens subjected to different confinement ratios. As can be observed from the figure, the contribution of corner radius to strength enhancement becomes more pronounced as the confinement ratio increases. In other words, the effect of corner rounding on the ultimate confined strength grows with increasing levels of FRP confinement.

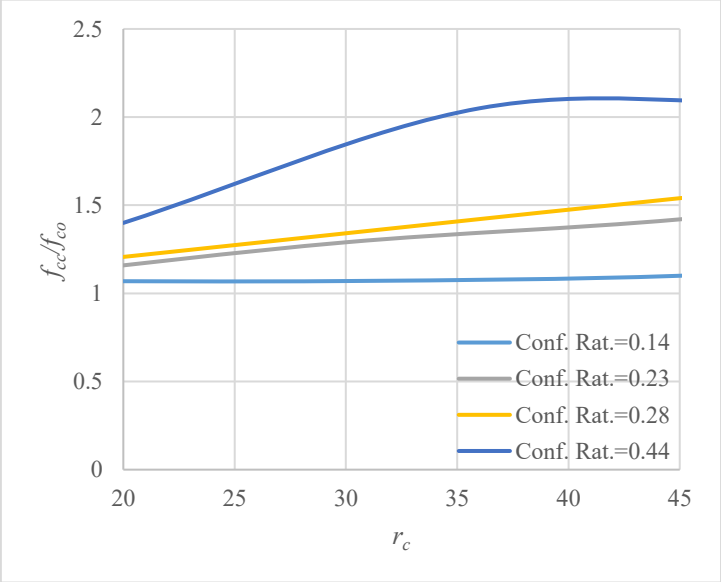


Fig. 4. Effect of corner radius over the enhancement ratio for several confinement ratios.

5 Comparison of Guideline and Model Expressions for Investigated Properties

The representation of corner radius within the shape factors adopted by the selected design guidelines and predictive models was discussed previously. The performance of these formulations in predicting the ultimate confined strength with respect to the investigated parameters was evaluated using the mean and standard deviation of the prediction results, and the findings are summarized in Table 2. In the table, the first value corresponds to the mean prediction ratio, while the second value represents the associated standard deviation. The predictive performance was assessed using the ratio of the predicted confined strength to the experimental confined strength, f_{cc}/f_{co}.

Table 2. Performance of the Expressions for Unconfined Concrete Strength Ranges

	f_{co} $[MPa]$								
	$f_{co} \leq 20$			$20 < f_{co} \leq 35$			$35 < f_{co}$		
r_c $[mm]$	$r_c \leq 15$	$15 < r_c \leq 30$	$30 < r_c$	$r_c \leq 15$	$15 < r_c \leq 30$	$30 < r_c$	$r_c \leq 15$	$15 < r_c \leq 30$	$30 < r_c$
TEC 2018 [3]	0.79/0.13	0.71/0.17	0.55/0.09	0.89/0.13	0.80/0.10	0.73/0.12	1.02/0.11	0.95/0.12	0.82/0.14
ACI 440.2R-17 [2]	0.85/0.17	0.80/0.10	0.66/0.07	0.97/0.14	0.86/0.12	0.84/0.11	1.11/0.11	1.00/0.12	0.94/0.14
CNR-DT200 R1/2013 [4]	0.99/0.16	0.89/0.20	0.70/0.12	1.08/0.15	1.00/0.11	0.93/0.14	1.21/0.13	1.14/0.14	1.02/0.16
İlki et al. [5]	0.93/0.14	0.91/0.19	0.72/0.10	0.99/0.12	0.95/0.09	0.89/0.13	1.10/0.12	1.04/0.13	0.91/0.14
Wu and Wei [6]	0.92/0.15	0.94/0.14	0.83/0.17	0.96/0.14	0.93/0.13	0.92/0.12	1.04/0.12	0.99/0.13	0.90/0.13
Lim and Ozbakkaloglu [7]	0.91/0.14	0.90/0.23	0.81/0.15	0.93/0.12	1.00/0.16	1.00/0.16	0.99/0.10	1.00/0.15	0.94/0.14

As can be seen from Table 2, almost none of the evaluated design equations adequately captures the influence of corner radius when the effect of unconfined concrete strength is considered. Among the examined formulations, only the model proposed by Wu and Wei can be regarded as providing relatively consistent predictions for the low-strength concrete group.

Table 3 summarizes the assessment of aspect ratio in relation to corner radius. The results indicate that the model proposed by İlki et al. [5] provides reliable predictions across all corner radius ranges for specimens with high aspect ratios. In contrast, for sections with $h/b \leq 1.5$, the provisions of the CNR guideline [4] appear to yield more accurate predictions.

Table 3. Performance of the Expressions for Aspect Ratio Ranges

	h/b								
	$h/b = 1.0$			$h/b = 1.5$			$h/b = 2.0$		
r_c [mm]	$r_c \leq 15$	$15 < r_c \leq 30$	$30 < r_c$	$r_c \leq 15$	$15 < r_c \leq 30$	$30 < r_c$	$r_c \leq 15$	$15 < r_c \leq 30$	$30 < r_c$
TEC 2018 [3]	0.92/0.15	0.81/0.15	0.74/0.16	1.02/-	0.83/0.13	0.76/0.08	0.91/0.12	0.86/0.11	0.89/0.12
ACI 440.2R-17 [2]	1.05/0.14	0.96/0.13	0.90/0.16	1.05/-	0.84/0.13	0.76/0.08	0.87/0.12	0.82/0.12	0.84/0.12
CNR-DT200 R1/2013 [4]	1.11/0.17	1.00/0.16	0.93/0.19	1.28/-	1.03/0.15	0.97/0.09	1.10/0.13	1.06/0.13	1.10/0.14
İlki et al. [5]	1.02/0.13	0.94/0.13	0.87/0.16	1.27/-	0.97/0.13	0.94/0.07	1.00/0.12	1.00/0.13	1.03/0.10
Wu and Wei [6]	1.00/0.14	0.98/0.15	0.92/0.15	1.18/-	0.89/0.12	0.89/0.06	0.92/0.11	0.91/0.11	0.94/0.09
Lim and Ozbakkaloglu [7]	0.91/0.11	0.90/0.12	0.90/0.13	1.21/-	0.98/0.14	1.09/0.07	1.02/0.12	1.10/0.18	1.16/0.18

Finally, the evaluation of the influence of corner radius with respect to different confinement ratio ranges is presented in Table 4. For low and medium confinement levels, the model proposed by İlki et al. [5] provides the most accurate predictions. For high confinement ratios, the model developed by Lim and Ozbakkaloglu [7] yields the most accurate estimates, although with slightly higher standard deviation values.

Table 4. Performance of the Expressions for Confinement Ratio Ranges

	f_l/f_{co}								
	$f_l/f_{co} < 0.05$			$0.05 \leq f_l/f_{co} \leq 0.083$			$0.083 < f_l/f_{co}$		
r_c [mm]	$r_c \leq 15$	$15 < r_c \leq 30$	$30 < r_c$	$r_c \leq 15$	$15 < r_c \leq 30$	$30 < r_c$	$r_c \leq 15$	$15 < r_c \leq 30$	$30 < r_c$
TEC 2018 [3]	0.98/0.10	0.94/0.07	0.97/0.06	0.89/0.13	0.87/0.12	0.83/0.14	0.75/0.18	0.73/0.12	0.67/0.12
ACI 440.2R-17 [2]	1.05/0.12	0.97/0.09	1.02/0.08	0.97/0.17	0.93/0.15	0.94/0.15	0.87/0.18	0.85/0.15	0.80/0.14
CNR-DT200 R1/2013 [4]	1.15/0.12	1.10/0.09	1.14/0.06	1.10/0.16	1.07/0.15	1.03/0.18	0.96/0.22	0.93/0.15	0.86/0.15
İlki et al. [5]	1.03/0.11	0.98/0.08	1.00/0.06	1.01/0.15	0.99/0.14	0.92/0.17	0.98/0.18	0.93/0.14	0.85/0.14
Wu and Wei [6]	0.96/0.09	0.92/0.08	0.95/0.06	0.96/0.14	0.93/0.13	0.89/0.14	1.09/0.22	0.98/0.18	0.93/0.15
Lim and Ozbakkaloglu [7]	0.93/0.08	0.91/0.08	0.95/0.04	0.95/0.14	0.98/0.16	0.95/0.17	0.97/0.18	0.98/0.18	0.95/0.17

6 Conclusions

The influence of corner radius, one of the most critical parameters governing the strength enhancement of FRP-confined rectangular sections, was investigated with respect to the other characteristics of the specimens. By evaluating subsets of the database while keeping selected variables constant, it was found that increases in both unconfined concrete strength and confinement ratio enhance the contribution of corner radius to the ultimate strength gain. In contrast, variations in aspect ratio were observed to have little to no influence on the effectiveness of corner radius in improving the ultimate confined strength.

In addition, predictive models for estimating the strength of CFRP-confined concrete columns were evaluated with particular emphasis on the variation of corner radius. The interaction between unconfined concrete strength and corner radius was not consistently captured by any of the investigated models. With respect to aspect ratio, the Italian guideline [4] was found to provide more accurate predictions for square specimens, whereas the model

proposed by İlki et al. [5] yielded the most reliable results for rectangular specimens with an aspect ratio of 2.0.

References

1. Gedik O.: Comparison and enhancement of design procedures for guideline expressions to predict the compressive capacity of FRP-wrapped concrete members. Arabian Journal for Science and Engineering 49, 13559-13576, (2024). 10.1007/s13369-024-08707-1
2. ACI: ACI 440.2R-17 Guide for the design and construction of externally bonded FRP systems for strengthening concrete structures. ACI, MI (2017).
3. T.C. Başbakanlık Afet ve Acil Durum Yönetimi Başkanlığı: Türkiye bina deprem yönetmeliği. TMMOB, Ankara (2018).
4. CNR: CNR-DT 200 R1/2013 Guide for the design and construction of externally bonded FRP systems for strengthening existing structures. CNR (National Research Council), Rome (2013).
5. İlki A., Kumbasar N. and Koc V.: Low strength concrete members externally confined with FRP sheets. Structural Engineering and Mechanics 18(2), (2004). 10.12989/sem.2004.18.2.167
6. Wu Y.-F., Wei Y.-Y.: Effect of cross-sectional aspect ratio on the strength of CFRP-confined rectangular concrete columns. Engineering Structures 32, 32-45 (2010). 10.1016/j.engstruct.2009.08.012
7. Lim J.C., Ozbakkaloglu T.: Design model for FRP-confined normal- and high-strength concrete square and rectangular columns. Magazine of Concrete Research 66(20), (2014). 10.1680/macr.14.00059
8. Restrepol J.I., de Vino B.: Enhancement of the axial load-capacity of reinforced concrete columns by means of fiberglass-epoxy jackets. In: Second International Conference on Advanced Composite Materials in Bridges and Structures, Montreal (1996).
9. Abbasnia R., Hosseinpour F., Rostamian M., Ziaadiny H.: Effect of corner radius on stress-strain behavior of FRP confined prisms under axial cyclic compression. Engineering Structures 40, 529-535 (2012). 10.1016/j.engstruct.2012.03.020

Publication Note

This paper was peer-reviewed, accepted for presentation, and included in the proceedings of the ACE2026 – International Conference on Advances in Civil Engineering, held on 12–14 October 2026 in Trabzon, Türkiye.

This paper may be cited as follows:

Onur Gedik, “Corner Radius Effect on Confined Strengths of FRP-Wrapped Rectangular Concrete Members,” in Proceedings of the ACE2026 – International Conference on Advances in Civil Engineering, Trabzon, Türkiye, 12–14 October 2026.

Automated Equivalent Frame Modelling and Seismic Assessment of URM Buildings Using MATLAB – SAP2000 Integration

Y. Semerdoken[1] and M.A. Erberik[2]
[1]0000-0002-8438-3058, Erzurum Technical University, Civil Engineering Department, Erzurum, Türkiye, yavuz.semerdoken@erzurum.edu.tr
[2]0000-0002-2123-1647, Middle East Technical University, Civil Engineering Department, Ankara, Türkiye, altug@metu.edu.tr

Abstract. The structural modelling and analysis of unreinforced masonry (URM) buildings involves significant challenges due to their inherent complexities. Furthermore, the structural interactions and boundary conditions between different load-bearing components, such as continuous walls, vertical piers, horizontal spandrels and floor diaphragms, are often difficult to define, particularly in walls with irregular openings. To address these analytical difficulties, this study focuses on the Equivalent Frame (EF) method. This is a highly effective, simplified modelling approach that has recently been added to the current version of the Turkish Building Earthquake Code (TBEC-18). This study specifically investigates one of the most sensitive parameters in the EF method: the definition of rigid offsets, which determine the rigid nodes and the effective deformable length of the macro-elements, and evaluates its impact on the global seismic assessment. To achieve this, a comprehensive computational framework is developed using a MATLAB-based algorithm integrated with the SAP2000 Open Application Programming Interface (OAPI). By employing this computational tool, the study evaluates three URM structures impacted by the destructive 1995 Dinar earthquake. The aim is to establish the correlation between the actual physical damage and the analytical outcomes specified in the TBEC-18. Although post-earthquake field evaluations showed that these buildings sustained only limited damage during the 1995 Dinar earthquake, the TBEC-18 categorized them as 'Collapse Performance Level'. This discrepancy indicates that the structural safety limits defined in the code may underestimate the actual seismic capacity of existing URM buildings.

Keywords: URM Buildings, Equivalent Frame Method, Rigid Offsets, Seismic Assessment, Seismic Codes, MATLAB, SAP2000 OAPI.

1 Introduction

The evaluation of the seismic vulnerability of existing masonry buildings continues to be an important issue worldwide. Many of these structures, including those of historical significance, are located in areas with varying levels of seismic risk and tend to show varying degrees of deterioration. Accurately assessing their earthquake risk is essential for identifying the most susceptible structures and determining the most appropriate strengthening procedures. This requires reliable and efficient modeling approaches that can realistically represent their seismic response (Pasticier et al., 2008).

Various modelling approaches for the structural analysis of masonry buildings have been proposed in the literature, each involving a different degree of idealization. As Lourenço (1996) explained, three main strategies can be adopted, depending on the desired accuracy of the model and the required computational efficiency (see Fig. 1). In the detailed micro-modelling approach, the masonry units and the mortar joints are represented separately using continuum elements and the interfaces between them are modelled using discontinuous elements. In the

simplified micro-modelling technique, the masonry units are expanded and the mechanical response of the mortar joints and interfaces is incorporated into the discontinuous elements. By contrast, the macro-modelling approach treats the masonry assemblage as a homogeneous continuum by averaging the properties of the units, the mortar and the interfaces.

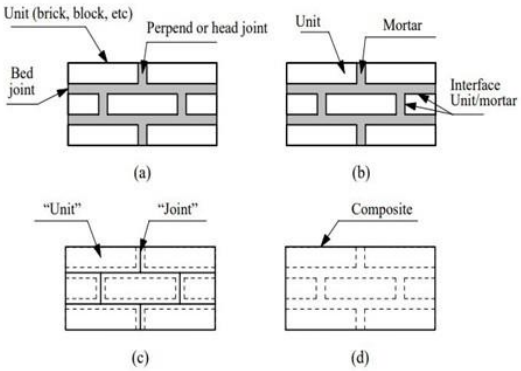


Fig. 1. Illustration of modeling strategies for masonry: a) sample of masonry; b) detailed micro-modeling; c) simplified micro-modeling; d) macro-modeling (Lourenço, 1996)

Among the various modelling approaches available in the literature, this study employs the EF method which is a well-known macro-modelling technique that is both practical and computationally efficient. In this approach, load-bearing masonry walls are represented by one-dimensional elements that simulate the behavior of individual wall segments. The EF model considers the axial, flexural and shear deformability of masonry panels, and rigid connections are employed to link these components (Siano et al., 2017). This method is based on the similarity between masonry buildings and two-dimensional frame systems, resulting in the structure being modelled as a combination of deformable macro-elements (piers and spandrels) and rigid nodes, as shown in Fig. 2.

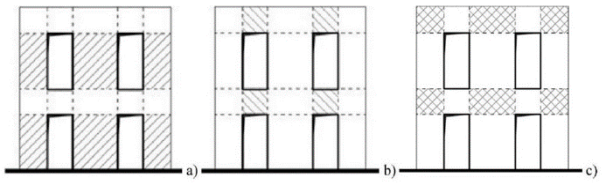


Fig. 2. URM wall idealization according to EF method: a) piers; b) spandrels; c) node panels (Siano et al., 2017)

The accuracy of the EF method is highly sensitive to the geometric definition of its components, specifically the definition of rigid offsets (RO), which dictate the rigid boundary zones and the effective deformable lengths of piers and spandrels. In the literature, various RO models for pier and spandrel members have been proposed (e.g., Dolce, 1991; Augenti, 2006; Moon et al., 2006; Cattari and Lagomarsino, 2009; Lagomarsino et al., 2013; Bracchi et al., 2015; Manzini et al., 2022). Different RO assumptions can drastically alter the lateral stiffness, period, and overall seismic performance evaluation of a masonry structure, leading to significant uncertainties in code-based assessments. Therefore, this study aims to investigate the seismic assessment of URM buildings and to evaluate the conservatism of code-based methodologies given in the TBEC-18 [11]. To achieve this, a comprehensive and fully automated computational framework is developed by integrating a MATLAB-based algorithm [12] with the SAP2000 OAPI [13]. This advanced tool enables the rapid generation of EF models and the automated execution of linear seismic assessments. Using this framework, a comparative analysis is performed on three URM buildings that survived the devastating 1995 Dinar earthquake. By comparing the analytical performance thresholds set out in the TBEC-18 with the actual post-earthquake damage states of these buildings, this study highlights the dramatic contrasts between code-based calculations and physical structural behavior.

2 Automated Methodology: MATLAB – SAP2000 Integration

Despite their conceptual efficiency, manually generating 3D EF models for complex, multi-story URM buildings is a highly challenging, time-consuming and error-prone process. The manual calculation of effective deformable lengths, the assignment of specific material properties, and particularly the precise geometric definition of RO for hundreds of structural members requires immense effort. To overcome these limitations and ensure analytical consistency, this study develops a novel, fully automated MATLAB-based algorithm. The algorithm begins with the preparation of a text-based input file (*.txt), which defines the coordinates of the exterior walls, interior walls, as well as door and window openings, as illustrated in Fig. 3.a. Once this dataset has been imported into the program, a sequential computational workflow is initiated. Firstly, the algorithm generates a three-dimensional visualization of the building's geometry for verification purposes (see Fig. 3.b). Subsequently, the program's integrated selection modules allow the user to dictate specific modelling assumptions by choosing the preferred effective height criterion for the piers and spandrel members (see Fig. 4). In this part, two distinct approaches are adopted for the EF model analysis: the “No RO” method and the “Dolce RO” method. The rationale for selecting these specific methods lies in their regulatory and academic relevance; the “No RO” approach is explicitly defined within the “Regulations Governing the Identification of Risky Buildings” (Riskli Yapıların Tespit Edilmesine İlişkin Esaslar-RYTEİE, 2019) [14], whereas the “Dolce RO” [4] method is one of the most widely cited and utilized approaches in the literature. Additionally, given the limited criteria available for their effective deformability, spandrels are modelled as fully rigid elements throughout this analysis. Finally, the algorithm automatically constructs the complete EF model of the building as shown in Fig. 5.

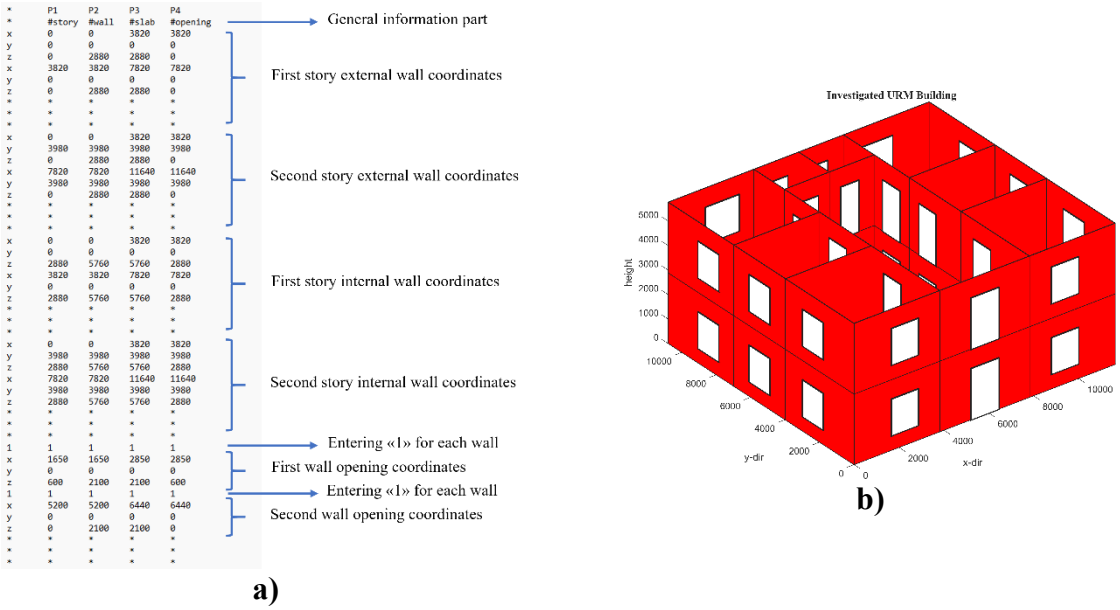
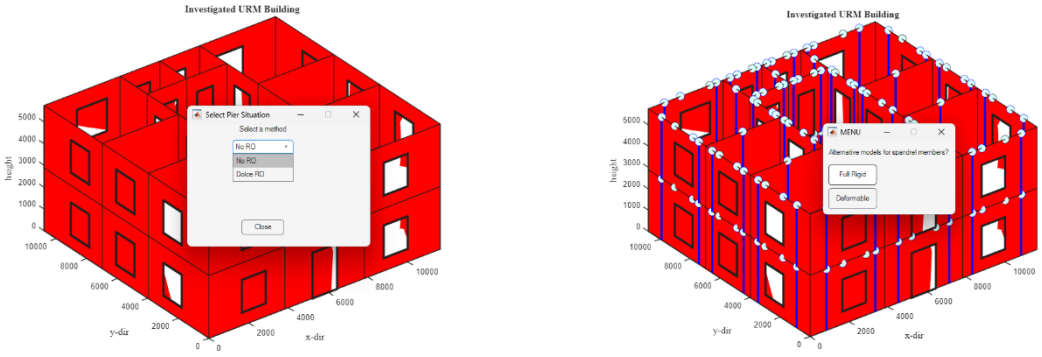
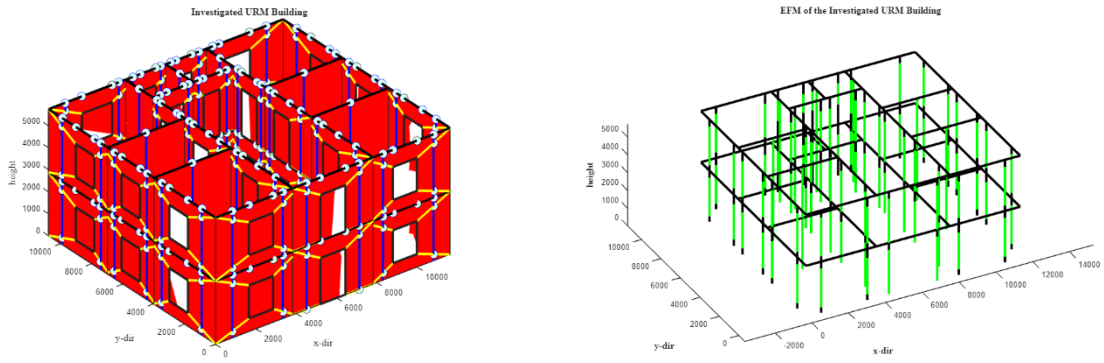


Fig. 3. a) a “txt” file example; b) an example of the 3D model of a URM building created in the developed algorithm



a) b)

Fig. 4. MATLAB-based graphical user interface (GUI) for the selection of macro-element topological parameters.



a) b)

Fig. 5. Automatically generated 3D EF model of a two-story URM building, illustrating the Dolce RO criteria and fully rigid spandrels.

3 Case Studies and Results

In order to compare code-based analytical assessments with physical structural behavior, a linear seismic evaluation is conducted on three existing URM buildings affected by the 1995 Dinar earthquake (see Fig. 6) [15].



a) b) c)

Fig. 6. External views of the existing URM buildings investigated as case studies following the 1995 Dinar earthquake: (a) single-story (B1), (b) two-story(B2), and (c) three-story (B3) buildings

To accurately determine the seismic performance of the buildings under investigation, the first step is to generate representative mathematical models. In TBEC-2018, structural analysis can be performed using either the finite element or equivalent frame approaches. For this study, the computational models are constructed using the EF method (see Fig. 7).

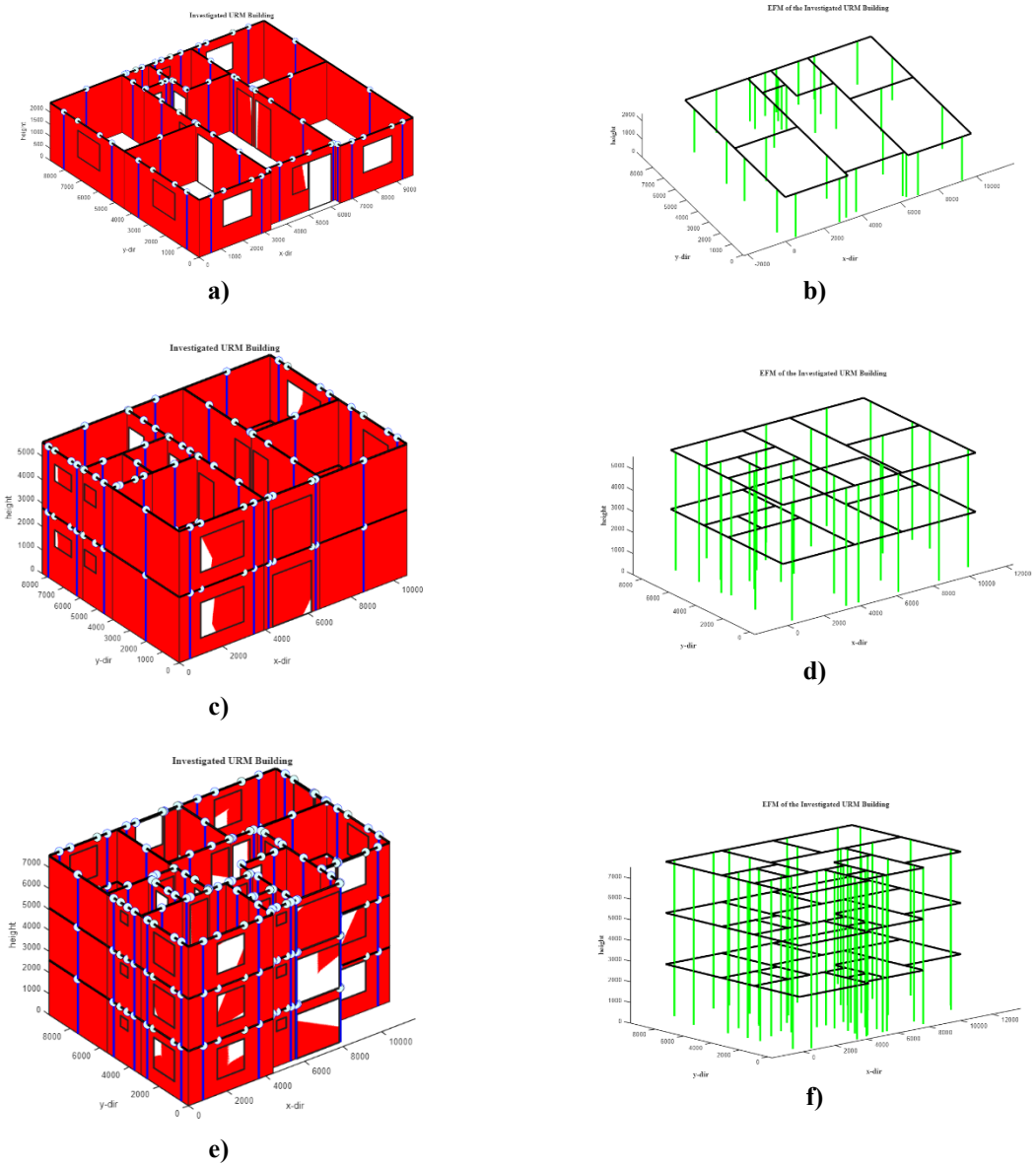


Fig. 7. 3D and EF views of the investigated URM buildings: a) B1; b) B2; c) B3, generated using the No RO criteria and fully rigid spandrels.

After defining the geometric dimensions and material properties, linear structural analyses are performed under the load combinations specified by TBEC-2018 (see Table 1). These analytical combinations are divided into two groups, COMB-A and COMB-B, based on varying gravity load magnitudes and multidirectional seismic actions. Specifically, combinations COMB1 to COMB8 fall within the COMB-A group [$G + Q + 0.2S + E_d^{(H)} + 0.3E_d^{(Z)}$], which considers the maximum vertical seismic effects by scaling the dead load factors to ($1 + 0.3*(2/3*S_{DS})$) and combining 100% of the horizontal seismic action in the principal direction with a 30% contribution from the orthogonal direction. Conversely, COMB9 to COMB16 fall within the COMB-B group [$0.9G + H + E_d^{(H)} – 0.3E_d^{(Z)}$], which employs a reduced gravity load of ($0.9 – 0.3*(2/3*S_{DS})$) to evaluate the structure under minimum vertical load.

The specific seismic demands acting on the structures are derived based on the local soil conditions and seismic hazard parameters obtained directly from the Türkiye Earthquake Hazard Map. For the specific location of the case study buildings (Konak, Dinar district (Latitude:38.078872; Longitude:30.169655)), the seismic parameters are determined corresponding to the seismic intensity level-2 (DD-2), which represents the standard design earthquake with a 10% probability of exceedance in 50 years (a return period of 475 years). Accordingly, the map spectral acceleration coefficients for the short period (S_S), the one-second period (S_1), the design spectral acceleration coefficients for the short period (S_{DS}) and the one-second period (S_{D1}) are obtained as 0.799, 0.188, 0.719, and 0.150 respectively. Furthermore, the peak ground acceleration (PGA) and peak ground velocity (PGV) for the investigated site are determined as 0.334 g and 18.630 cm/s, respectively.

Table 1. Load combinations according to TBEC-18

COMB – A	$G + Q + 0.2S + E_d^{(H)} + 0.3E_d^{(Z)}$
COMB – B	$0.9G + H + E_d^{(H)} - 0.3E_d^{(Z)}$

For the linear seismic assessment, the 'Equivalent Seismic Load Method (ESLM)' procedure specified in TBEC-18 is employed. According to this method, the total equivalent seismic load (i.e., base shear force), V_t, acting on the entire building in the considered earthquake direction is calculated using Eq. 1.

$$V_{tE}^{(X)} = m_t \times S_{aR}(T_p^{(x)}) \geq 0.04 \times m_t \times I \times S_{DS} \times g \quad (1)$$

The mechanical and physical properties of the masonry materials used in the structural models are defined in accordance with the reference values specified in TBEC-2018. Assuming solid clay brick construction, the unit weight of the load-bearing walls is 1.9 t/m³. In line with the code provisions, the characteristic compressive strength of the masonry (f_k) is assigned a value of 9 MPa. Consequently, the modulus of elasticity (E_m) is calculated as 6750 MPa using the specified correlation of $750*f_k$. Additionally, the initial shear strength (f_{v0}) of the walls is assumed to be 0.20 MPa.

In this study, the mathematical models of the investigated buildings are constructed utilizing the developed MATLAB-based algorithm. All geometric and topological parameters required for the EF model are computed in MATLAB and automatically transferred to SAP2000. Following this, the performance levels of the structures are evaluated using linear seismic assessments in the SAP2000 software. According to TBEC-18, the seismic performance of masonry buildings is evaluated based on three distinct criteria:

- the Limited Damage Performance Level (LDPL),
- the Controlled Damage Performance Level (CDPL), and
- the Collapse Performance Level (CPL).

A building is considered to satisfy the LDPL when the seismic shear demand can be resisted by all walls in both orthogonal directions. If, at any story, the walls with insufficient shear capacity account for less than 40% of the total story shear in the loading direction, the building is classified as meeting the CDPL. However, when this ratio exceeds 40%, the structure is classified as CPL (TBEC-18).

The detailed story- and direction-specific collapse ratios for different seismic load combinations are comprehensively presented in Fig. 8. As shown in the figure, the computed collapse ratios exceed the 0.40 limit defined by TBEC-18, regardless of the number of stories (B1, B2 or B3) or the orthogonal loading direction (x or y). While the 'Dolce RO' modelling approach changes the distribution of internal forces, often reducing the collapse ratios for certain combinations compared to the 'No RO' condition, these changes are insufficient to shift the global performance state. While some specific loading scenarios satisfy the CDPL

thresholds (e.g. COMB7 and COMB8 in the Y direction for the B3 building), the governing combinations generally push the structures into the collapse zone. Following the linear analysis procedure defined by TBEC-18, all three investigated buildings are classified under the CPL. The analytical results revealed the underlying critical structural behavior for this classification: while the load-bearing walls in these buildings safely withstood the applied axial compressive forces, they significantly failed to satisfy the required shear stress criteria. Consequently, this widespread inadequacy in shear capacity dictated their global seismic performance state.

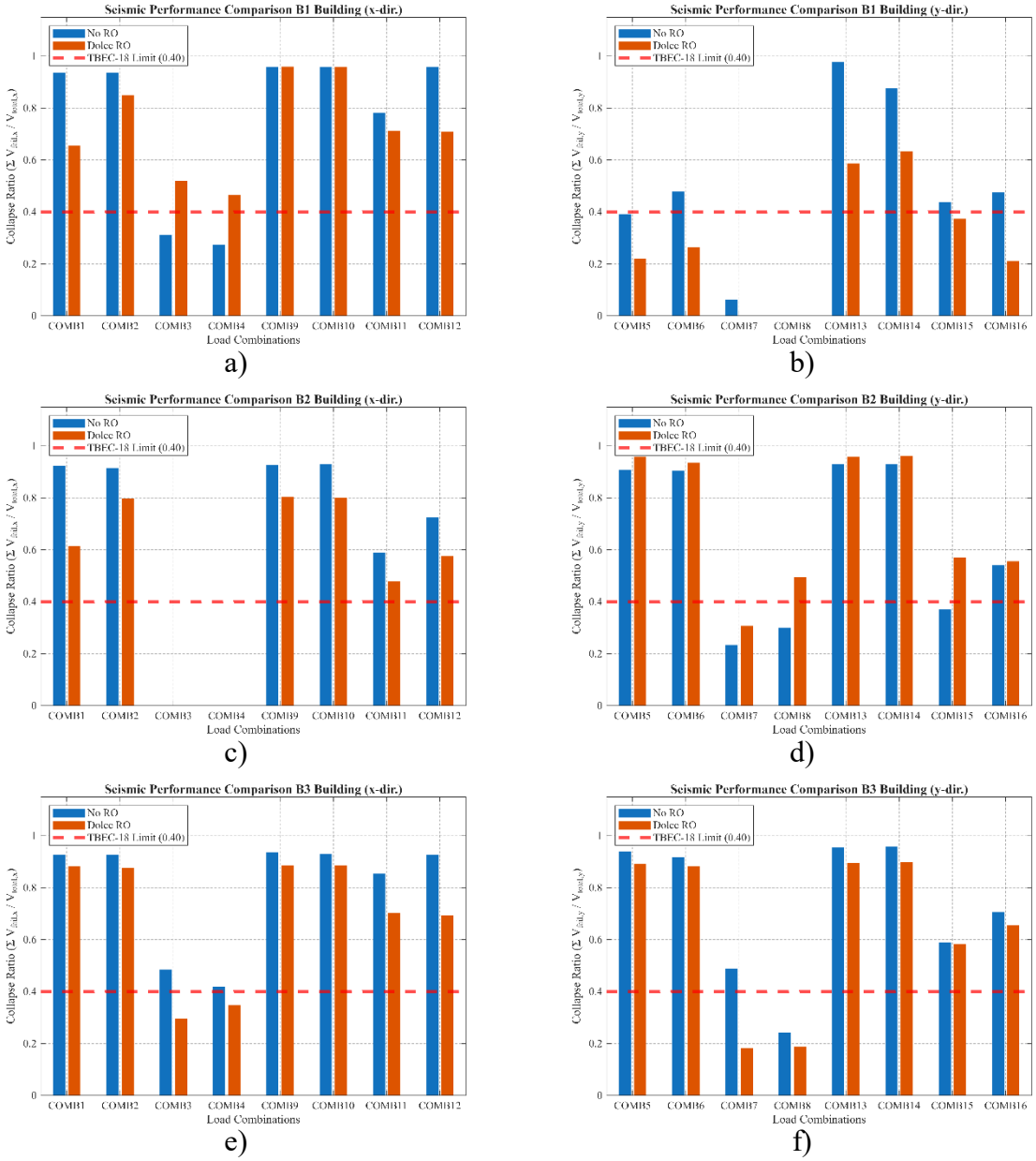


Fig. 8. Comparison of the seismic collapse ratios for different load combinations with "No RO" and "Dolce RO" modeling assumptions for the investigated URM buildings: (a, b) B1, (c, d) B2, and (e, f) B3 in the orthogonal x and y directions, respectively. The red dashed line denotes the critical threshold of 0.40 specified by TBEC-18 for the CPL.

4 Summary and Conclusion

This study investigates the provisions of TBEC-18 regarding the seismic performance assessment of URM buildings, comparing the code-based calculations with observed physical structural behavior. Despite the fact that post-earthquake inspections reported only minor to moderate damage in these buildings after the 1995 Dinar earthquake (Figure 6) (METU-EERC, 1996) [16], linear elastic evaluations performed according to TBEC-18 placed all of them in the CPL state. The clear discrepancy between the buildings' actual structural behavior and the results of the code-based assessment indicates that TBEC-18 may significantly underestimate the seismic capacity of existing URM buildings.

In summary, post-earthquake field observations show that the seismic response of URM buildings is strongly influenced by the intensity of earthquake demand as well as the interaction of major structural characteristics. Among these, building height, wall area ratio, and compliance with code-based plan layout requirements play a decisive role in improving structural performance. Therefore, a reassessment of the limit values specified in TBEC-18 for URM buildings would be appropriate.

References

1. Pasticier, L., Amadio, C., and Fragiacomo, M. Non-linear Seismic Analysis and Vulnerability Evaluation of a Masonry Building by means of the SAP2000 V.10 code. Earthquake Eng. Struct. Dyn. 37, 467-485 (2008).
2. Lourenco, P. Computational Strategies for Masonry Structures. Civil Engineering, Delft University of Technology, PhD Thesis, 220 p (1996).
3. Siano, R., Camata, G., Sepe, V., Spacone, E., Roca, P., and Pela, L. Finite Elements vs. Equivalent-Frame Models for URM Walls' In-Plane Behavior. In: 16th World Conference on Earthquake Engineering, paper no:3264, Santiago, Chile (2017).
4. Dolce, M. Schematizzazione e modellazione degli edifici in muratura soggetti ad azioni sismiche, L'Industria delle Costruzioni, 25, 44-57 (1991).
5. Augenti, N. Seismic Behavior of Irregular Masonry Walls. In: 1st European Conference on Earthquake Engineering and Seismology, paper no:86, Geneva, Switzerland (2006).
6. Moon, F. L., Yi, T., Leon, R. T., and Kahn, L. F. Recommendations for Seismic Evaluation and Retrofit of Low-Rise URM Structures. J. Struct. Eng., 132(5), 663-672 (2006).
7. Cattari and Lagomarsino, 2009.
8. Lagomarsino, S., Penna, A., Galasco, A., and Cattari, S. TREMURI program: an Equivalent Frame Model for the Nonlinear Seismic Analysis of Masonry Buildings. Engineering Structures, 56, 1787-1799 (2013).
9. Bracchi, S., Rota, M., Penna, A., and Magenes, G. Consideration of Modelling Uncertainties in the Seismic Assessment of Masonry Buildings by Equivalent-Frame Approach. Bulletin Earthquake Engineering, 13, 3423-3448 (2015).
10. Manzini, C. F., Ottonelli, D., Abbati, S. D., Marano, C., Cordasco, E. A., Modelling the Seismic Response of a 2-story URM Benchmark Case Study: Comparison among Different Equivalent Frame Models. Bulletin of Earthquake Engineering, 20, 2045-2084 (2022).
11. Turkish Republic Prime Ministry Disaster and Emergency Management Presidency. Turkish Building Earthquake Code. TBEC-18. Ankara, Türkiye (2018).
12. MathWorks. 2023. MATLAB (R2023a). The MathWorks, Inc.
13. SAP2000 v25.3.1. 2025. Structural Analysis Program, Computers and Structures. University of Ave. Berkeley.
14. Riskli Yapıların Tespit Edilmesine İlişkin Esaslar, T.C. Şehircilik ve Çevre Bakanlığı, RYTEİE, Ankara, Türkiye (2019).
15. Erberik, M. A. Generation of fragility curves for Turkish masonry buildings considering in-plane failure modes. Earthquake Engineering & Structural Dynamics, 37(3), 387-405 (2008).
16. METU-EERC. Repair and Rehabilitation Project for Moderately Damaged Masonry Structures after 1995 Dinar Earthquake. Earthquake Engineering Research Center, Civil Engineering Department, METU, Ankara, Türkiye (1996).

Author Contribution Statement

- *Conceptualization:* Yavuz Semerdöken, Murat Altuğ Erberik
- *Methodology:* Yavuz Semerdöken, Murat Altuğ Erberik
- *Investigation:* Yavuz Semerdöken
- *Writing – Original Draft:* Yavuz Semerdöken
- *Writing – Review & Editing:* Murat Altuğ Erberik

Note: Following the conference, this Publication Note will be added to each paper; therefore, authors are kindly requested not to remove the note below and to complete the author(s) and paper title information.

Publication Note

This paper was peer-reviewed, accepted for presentation, and included in the proceedings of the ACE2026 – International Conference on Advances in Civil Engineering, held on 12–14 October 2026 in Trabzon, Türkiye.

This paper may be cited as follows:

Semerdoken, Y., and Erberik, M. A., "Automated Equivalent Frame Modelling and Seismic Assessment of URM Buildings Using MATLAB–SAP2000 Integration," in Proceedings of the ACE2026 – International Conference on Advances in Civil Engineering, Trabzon, Türkiye, 12–14 October 2026.

Mechanical Behavior of Timber Folded Plate Joints: An Experimental Comparison of Adhesive and Mechanical Fasteners

Muhammed Emin Akyürek[1], Cenk Aksoylar[2], Nihan Doğramacı Aksoylar[3], Mehmet Selim Ökten[4], Muhammet Ali İpekçi[5], Haşim Çayır[6]

[1] 0000-0001-9382-0435, Istanbul Sabahattin Zaim University, Department of Architecture, İstanbul, Türkiye, muhammed.akyurek@izu.edu.tr

[2] 0009-0006-5887-7421, Fatih Sultan Mehmet Vakıf University, Department of Civil Engineering, İstanbul, Türkiye, caksoylar@fsm.edu.tr

[3] 0000-0002-4569-5403, Fatih Sultan Mehmet Vakıf University, Department of Civil Engineering, İstanbul, Türkiye, ndogramaci@fsm.edu.tr

[4] 0000-0003-4689-767X, Mimar Sinan Fine Arts University, Deparment of Architecture, İstanbul, Türkiye, selim.okten@msgsu.edu.tr

[5] 0009-0000-9839-6389, Istanbul Sabahattin Zaim University, Department of Construction and Technical Work, İstanbul, Türkiye, muhammed.ipekci@izu.edu.tr

[6] 0000-0001-8131-4703, Fatih Sultan Mehmet Vakıf University, Department of Civil Engineering, İstanbul, Türkiye, hcayir@fsm.edu.tr

Abstract. Cross-Laminated Timber (CLT) combined with folded plate systems offers highly efficient structural solutions, yet their overall performance is heavily dictated by the semi-rigid behavior of their angled joints. This study experimentally investigates the closing-mode bending performance of 90-degree L-type CLT joints to characterize their moment capacity, rotational stiffness, ductility, and progressive failure mechanisms. The experimental program was conducted using a 6-axis Load and Boundary Conditions Box (LBCB) at the FSMVU Structural Laboratory. Three distinct joint configurations were tested: pure structural adhesive (PUR), a mechanical cam-and-dowel system (Maxifix), and an internal steel angle bracket. Results revealed significant variations in load-displacement behavior. The pure adhesive joint exhibited the highest peak load capacity but failed catastrophically with a sudden rupture, characterized by severe wood fiber pull-out and cross-section splitting. The Maxifix system demonstrated moderate peak capacity; however, it provided substantial ductility. The steel pins embedded into the surrounding wood without shearing, allowing the joint to articulate safely like a hinge without total detachment. The steel angle bracket showed unexpected progressive failure, including premature screw shearing and internal wood wedge crushing due to geometric constraints. The findings conclude that while pure adhesives provide high initial stiffness, they lack essential ductility for extreme conditions. Conversely, mechanical systems offer high ductility but lower strength. Future studies will focus on hybrid systems combining structural adhesives with mechanical fasteners. This approach aims to achieve both high strength and post-peak ductility, providing a fail-safe mechanism for modular timber structures while optimizing manufacturing and assembly costs.

Keywords: Timber Folded Plates, Closing-Mode Bending, Progressive Failure, Mechanical Fuse

1 Introduction

Timber folded plate systems are innovative structures with high structural efficiency that, owing to their form-active nature, can span large openings with very slender cross-sections. These structures transform the material's own tectonics into an architectural expression while creating spatial boundaries (Fig. 1). However, the overall stability and performance of these load-bearing systems depend largely on the semi-rigid behavior at the intersection points of the plates.

In such composite systems, Cross-Laminated Timber (CLT) offers a revolutionary solution by acting as a continuous shear wall. In industrial structural applications, CLT panels are generally manufactured and used with a thickness greater than 6 cm and with at least three layers (laminae). However, recent analyses of the structural behavior of form-active timber folded plate systems relax this thickness requirement. Finite Element Analysis (FEA) and optimization studies conducted in a previous work (Akyürek and Köymen, 2026) showed that, thanks to the advantage provided by the form, spans of 10-12 meters can be safely covered with slender CLT plates 30-40 mm thick. Based on this scientific finding, the test specimens in the presented empirical study were standardized to a thickness of 40 mm.



Fig. 1. Architectural concept model of the "Barkat" project, featuring a cross-laminated timber folded plate structure.

In the literature, the potential of timber folded plates was demonstrated by Buri and Weinand (2008) specifically for plywood and CLT; however, particular attention was drawn to the mechanical constraints at acute-angled corner joints ranging between 10° and 80°. The stripping of wood fibers by traditional nailed or screwed connections reduces the structural capacity. Current industrial CLT design guides (KLH, 2012; Swedish Wood, 2019) generally provide solutions for standard right-angle connections, while data on the concealed (internal) use of metal reinforcements in variable-angle forms remain lacking. In studies conducted in Türkiye, Ceylan and Girgin (2019; 2020) investigated the withdrawal resistance of nails and metal angle brackets in CLT wall-floor connections. Ilgın et al. (2021), on the other hand, emphasized the potential of geometric interlocking methods such as dovetail and comb joints in solid timber, but noted that multi-axis CNC requirements limit industrial accessibility. Similarly, although Robeller et al. (2017) demonstrated the rotational stiffness of integrated mechanical joints in double-layered folded plates, the requirement for 5-axis CNC complicates practical application. On the other hand, the withdrawal strength of systems such as Maxifix (cam-and-dowel), a practical and demountable connection hardware in the timber industry, was investigated by Efe et al. (2012), pointing to the alternative potential of these fittings in structural joints.

In the digital design and static (FEA) modeling stages, timber joints are generally idealized mathematically as "fully rigid." In physical reality, however, joints inherently undergo deformation and exhibit a "semi-rigid" character. This critical interface between the rigid assumption in design and the actual mechanical capacity of the connection points makes it

essential to perform empirical mechanical tests in order to verify the structural safety of the system.

In line with this requirement, the 90-degree L-Type bending/closing test (Eckelman, 2003; Kasal et al., 2025), a universal standard in furniture and timber engineering, was applied in the experimental design of the presented study. The experiments were carried out using the 6-axis Load and Boundary Conditions Box (LBCB) at the Structural Laboratory of Fatih Sultan Mehmet Vakıf University (FSMVU). This laboratory's versatile testing capacity and infrastructure have proven their reliability in recent research investigating historic and modern timber joints (Doğramacı Aksoylar et al., 2026).

The main aim of this study is to comparatively investigate the mechanical behavior of concealed mechanical joint techniques (Maxifix, internal steel angle bracket) and integrated methods that are applicable to slender (40 mm) CLT folded plate systems without compromising aesthetics, against a reference specimen using pure structural adhesive (PUR). The original contribution of the study is that it reveals for the first time how these fittings—not previously tested empirically in the literature for acute-angled heavy timber plates—not only facilitate on-site work by aligning the panels during assembly, but also act as a ductile "mechanical fuse" that prevents sudden collapse in the event of brittle rupture of the adhesive under excessive load. It is intended that the resulting data on moment capacity, rotational stiffness, ductility, and progressive failure will provide a new reference set for the literature and pioneer the low-cost, safe construction of modular timber structures.

2 Materials and Methods

The specimen manufacturing processes in this study were carried out at the İZÜ Barkat Timber Construction Workshop, while the mechanical testing stages were conducted under the coordination of the FSMVU Structural Laboratory. Within the scope of the study, three different configurations were designed and tested in order to empirically compare the different joint details of folded plate systems.

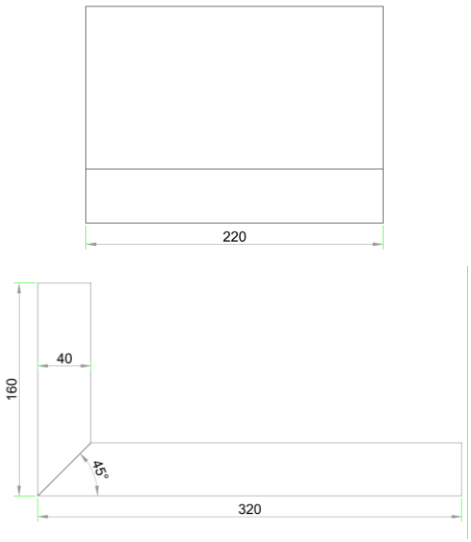
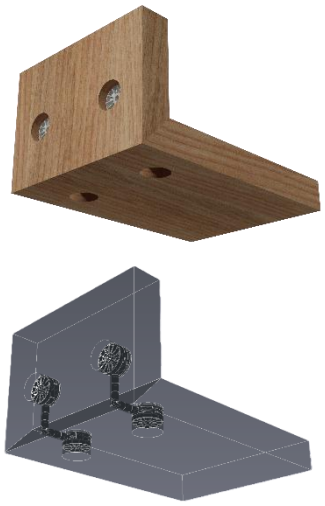
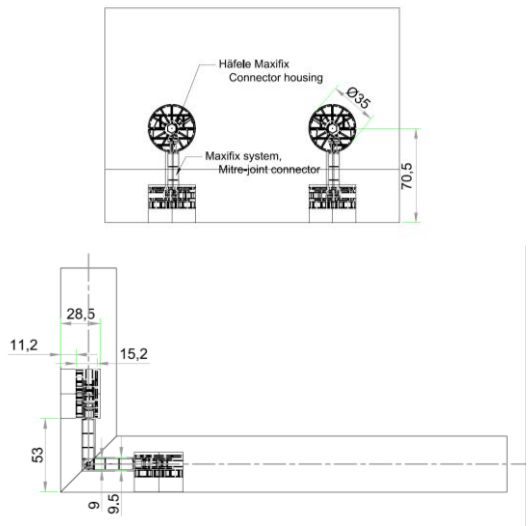
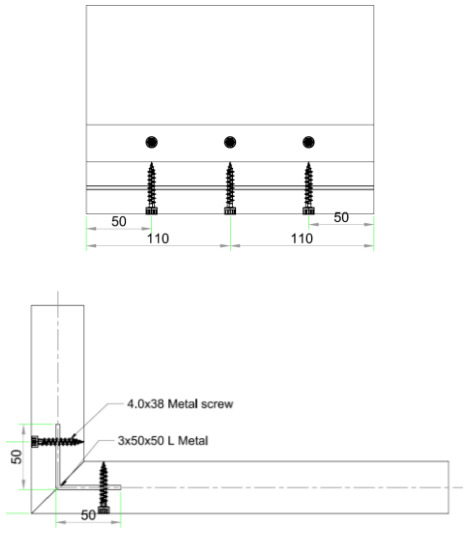
2.1. Specimen Geometry and Joint Types

The specimens used in the experiments were produced from 40 mm thick Cross-Laminated Timber (CLT) panels, predicted by FEA analyses to be capable of spanning 10-12 meter openings in timber folded plate structures. In accordance with the L-type test configuration, the specimens were standardized with a fixed arm of 160 mm, a moving arm 320 mm high, and a width of 220 mm for both arms (Table 1). The cross-sectional faces were cut at a 45° miter angle to maximize moment transfer.

Three different joint types were addressed within the scope of the study:

1. **Adhesive (PUR) Joint:** This is the reference group, in which full surface-to-surface bonding is achieved using only structural polyurethane (PU) adhesive.
2. **Maxifix Connection (Mechanical Cam-and-Dowel):** This is a demountable mechanical system created using 35 mm diameter steel housings positioned 70.5 mm inward from the wood surface and 9 mm diameter articulated connecting dowels. No adhesive was used between the panels.
3. **Angle Bracket (Metal Angle Bracket) Joint:** This is a system in which a continuous steel L-profile measuring 3x50x50 mm placed at the inner corner is anchored with 5x40 mm countersunk-head sheet-metal screws driven in a staggered pattern from the inside outward into the solid part of the CLT. It was designed as a concealed detail in which the external architectural surface is not penetrated. However, due to manufacturing constraints, a 1.5x20x20 mm steel angle bracket and 5x50 mm chipboard screws were used in the experiments, and owing to geometric necessity the screws were oriented into the wood at an angle (diagonally).

Table 1. General views, connection details, and dimensions of the tested joint configurations.

Joint Type	3D Visualization	Technical Details & Dimensions
Pure Adhesive (PUR) Joint		
Mechanical Cam-and-Dowel (Maxifix) Joint		
Metal Angle Bracket Joint		

2.2. Test Setup

The experimental investigation of the L-Type timber joints was carried out using a six degree of freedom Load and Boundary Condition Box (LBCB) at the "Structural Mechanics and Earthquake Research Laboratory" of Fatih Sultan Mehmet Vakif University. To ensure a stable and rigid connection between the loading system and test specimen, a rigid steel reaction wall which is fabricated from steel sections and plates was bolted to the LBCB. The tests system capable of operating under both load-controlled or displacement-controlled loading protocols. A general view of the test setup used in this study is illustrated in *Fig. 2a*.

The test setup was designed based on a recently developed timber connection testing system reported in the literature (Dogramacı Aksoylar et al., 2026). The horizontal member (short arm) of the specimen was rigidly attached to the steel reaction wall using a fixing steel plate (10 x 50 x 320 mm) fastened with two M12 bolts. The displacement was applied to the free end of the vertical member (long arm) through a steel angle. The details of the test setup and applied boundary conditions are presented in *Fig. 2b*.

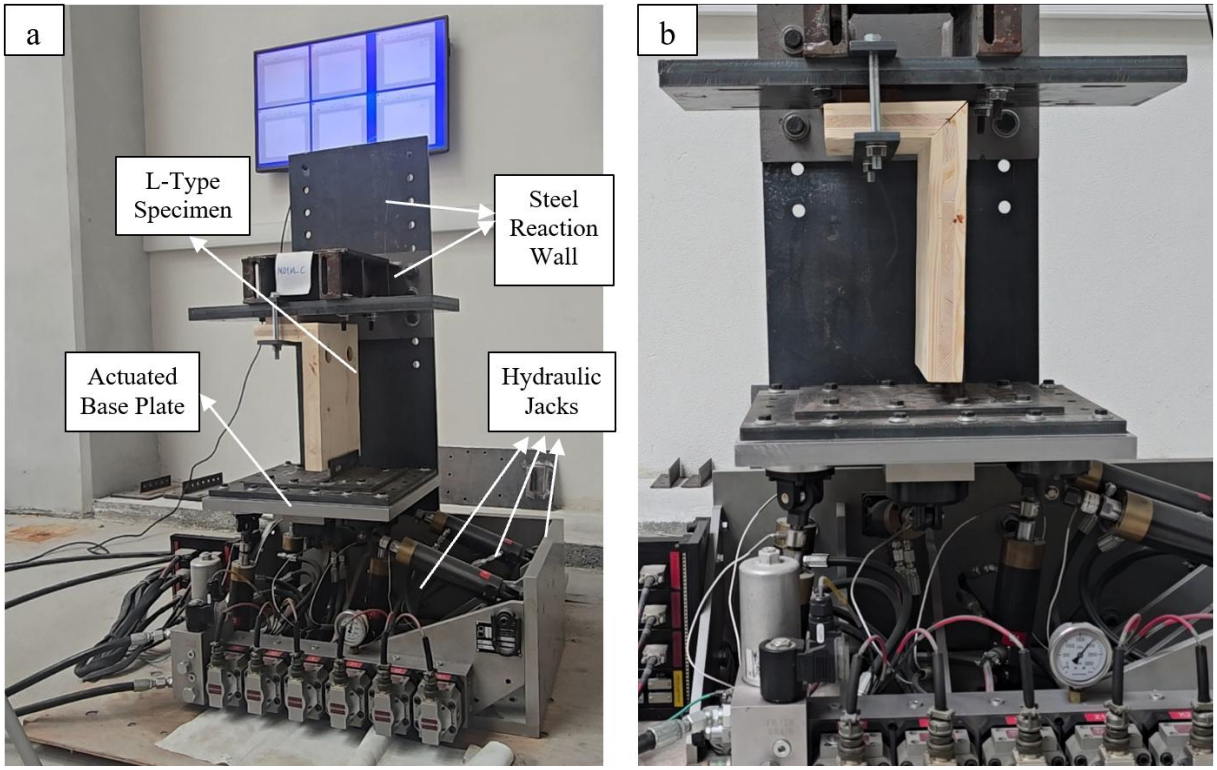


Fig. 2. Test setup a) general view b) applied boundary conditions.

2.3. Loading Protocol

The joint angles of folded plate systems may vary depending on the timber structural configuration. In this study, a standard joint geometry was adopted to enable a reliable and comparable evaluation of their behavior and load carrying capacities. For this purpose, a 90° L-type corner joint which is widely used in timber engineering and furniture studies (Eckelman, 2003; Kasal et al., 2025). was selected. The experiments were conducted in closing configuration in order to investigate the influence of using different fasteners on the mechanical performance of the joints.

The initial closing tests of L-type connections are carried out under monotonic loading to determine their maximum load carrying capacity and yield/ultimate displacements. In these tests, displacement-controlled loading is used and the free end of the vertical member is pushed upward in 1 mm incremental steps until a total displacement of 80 mm is reached. At each step,

the displacement was applied to specimen using moving plate and corresponding reaction force was recorded.

3 Experimental Results and Discussion

The load-carrying capacities and failure modes of corner joints with three different configurations were experimentally investigated. The configurations consisted of joints bonded only with structural polyurethane (PUR) adhesive, internal steel angle bracket, mechanical cam-and-dowel (Maxifix) connector. Their mechanical behavior was compared based on load-carrying capacity, stiffness and failure characteristics. The load – displacement relations obtained from the monotonic closing tests of joints are presented in *Fig. 3*. Table 1 summarizes the maximum lateral load, displacement at maximum load, stiffness evaluated at a displacement of 20 mm and corresponding failure modes of each specimen.

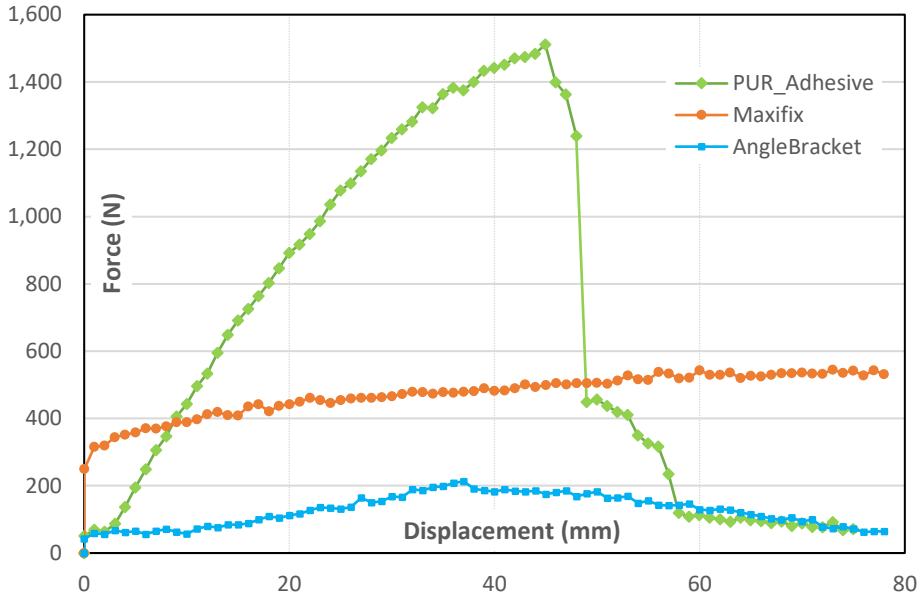


Fig. 3. Load-displacement relationships of L-type timber joints.

The experimental results showed that the type of fastener had a significant influence on the lateral behavior of the L-type joints. The specimen bonded with PUR adhesive exhibited highest lateral load capacity among all test specimens. The connection reached a maximum load of 1510 N at a displacement of 45mm. The load increased almost linearly during the initial loading stage, indicating high stiffness. The stiffness at a displacement of 20mm was 44.6 N/mm showed the high rigidity of bonding joint. After reaching the peak load, a sudden and substantial loss in load capacity occurred, with the resistance rapidly decreasing by approximately 450 N followed by a rapid reduction to nearly zero. This behavior indicates brittle failure mode caused by adhesive debonding at the wood-adhesive interface.

The specimen with the Maxifix connector exhibited a stable and consistent ductile response throughout the test despite its lower lateral load- capacity compared to the PUR adhesive. The load increased continuously without any significant loss, reaching its maximum capacity of 545 N at a displacement of 73 mm which was the largest displacement among all test specimens. At a displacement of 20 mm the stiffness was 22,1 N/mm approximately half of the PUR adhesive joint. At larger displacement levels, minor fluctuations were observed in the load-displacement curve. These fluctuations did not lead to a significant reduction in overall capacity. This indicates that joint with Maxifix connector possessed deformation capability. The connection exhibited stable and ductile response with failure characterized by wood embedment and deformation on the connector components (*Fig. 4*)

Table 2. Summary of experimental results.

Specimen Type	Maximum Load (N)	Disp. at max. load (mm)	Stiffness at 20mm (N/mm)	Failure Modes
Pure (PUR) Adhesive	1510	45	44,6	Brittle Failure Adhesive Debonding
Mechanical Cam and Dowel (Maxifix)	545	73	22,1	Ductile Behavior / Wood embedment
Inner Angle Bracket	213	37	55,9	Gradual Loss / Bending of angle bracket or pull out screws

Among all test specimens, the connection with inner angle bracket exhibited the lowest load-carrying capacity. The maximum lateral load was only 213 N at a displacement of 37 mm. Although this connection showed the highest initial stiffness (55,9 N/mm) its load-carrying capacity remained limited. The load increased almost linearly to the maximum load and then gradually decreased with increasing displacement. Unlike the PUR adhesive joint, no sudden loss was observed after the maximum load. The connection experienced a progressive reduction in load-carrying capacity due to bending of internal angle bracket and/or screw pull out. The observed failure mechanisms of each specimen examined and are presented in *Fig. 4*.

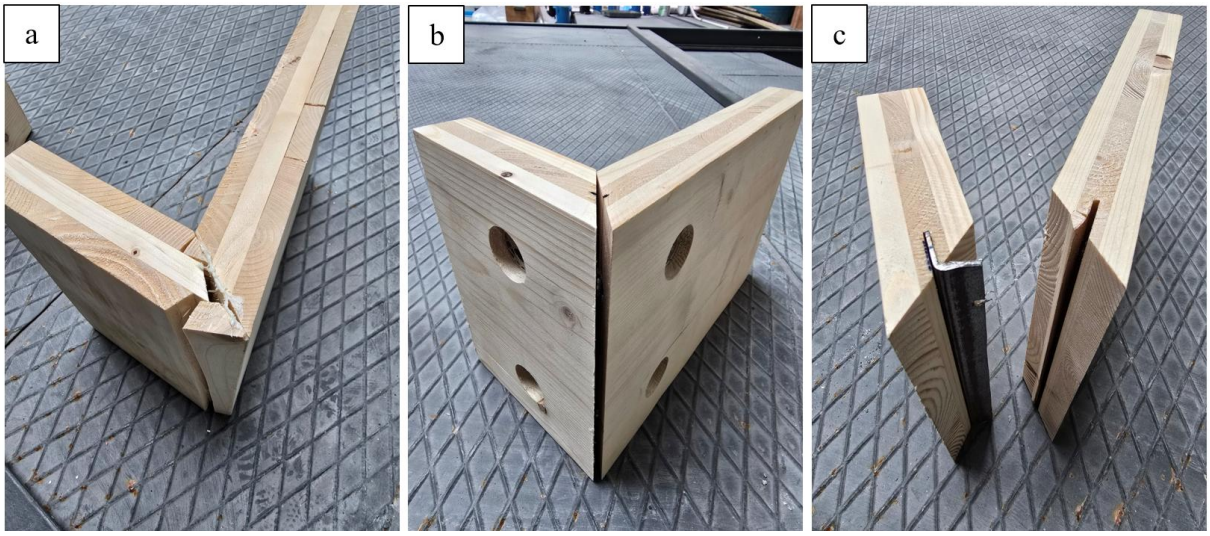


Fig. 4. Failure mechanisms of the three joint configurations at ultimate displacement: (a) Pure adhesive, (b) Maxifix system, (c) Angle bracket.

4 Conclusion

In this study, the bending/closing performance, moment capacity, and failure mechanisms of L-type corner joints configured with 40 mm thick CLT panels for use in timber folded plate systems were investigated empirically. The laboratory tests revealed that the joint types possess opposing but complementary potentials in their structural behavior.

The main conclusions obtained from the study can be summarized as follows:

- **PUR Adhesive Joint:** By offering the highest initial stiffness and moment-carrying capacity, it has the potential to initially meet the "fully rigid" expectation of theoretical

FEA analyses. However, at ultimate failure it exhibited a sudden and brittle fracture with tearing of the wood fibers, demonstrating a major weakness in terms of structural safety under excessive loading.

- **Maxifix Joint:** Although it lagged behind the adhesive systems in peak load capacity, it exhibited outstanding structural ductility thanks to its ability to crush the wood and continue rotating like a hinge.
- **Angle Bracket Joint:** The fitting-size constraints encountered in manufacturing and the resulting mandatory angled screwing caused the screws to tear the steel and strip out prematurely, preventing the system from displaying its full potential. This proved how critical geometry and fitting tolerances are in concealed detail solutions.

In light of these findings, it was concluded that, for the safe construction of large-span, slender modular timber folded plates, neither purely adhesive nor purely mechanical connections would be sufficient on their own. In this case, the ideal structural solution is considered to be "hybrid joint systems" in which the high stiffness of structural adhesive and the deformation capacity of concealed mechanical fittings are combined at the same interface.

In the subsequent stages of the study, different joint scenarios—adhesive, mechanical, and hybrid—will be tested with multiple repetitions in order to seek more comprehensive and definitive findings. In addition, the rotational stiffness and moment capacity data obtained from these studies will be used directly in the calibration of the Finite Element (FEA) model of the project's digital twin. Thus, the hypothesis that, in the event of debonding of the adhesive under extreme loading or environmental fatigue, the internal mechanical fitting will act as a ductile "structural fuse" that saves the structure from sudden collapse will be examined, contributing new findings to the timber engineering literature.

Acknowledgments

This research was partially supported by the Istanbul Sabahattin Zaim University Scientific Research Projects (BAP) Coordination Unit under grant number İZÜ BAP-2025-400-065. The authors gratefully acknowledge the Fatih Sultan Mehmet Vakıf University (FSMVU) Structural Laboratory and the İZÜ Barkat Timber Construction Workshop for providing the testing facilities and infrastructural support during the manufacturing and experimental phases of this study. Furthermore, special thanks are extended to Ali Özben for his valuable support in material procurement.

References

1. Akyürek, M. E., & Köymen, E. (2026). *From parametric design to digital fabrication: Optimizing the Barkat CLT construction system*. In *Proceedings of the 20th Symposium on Digital Design in Architecture (MSTAS 2026)* (pp. 153-164). https://mstas2026.tedu.edu.tr/sites/default/files/inline-files/MSTAS_2026_TEDU.pdf
2. Buri, H. U., & Weinand, Y. (2008). ORIGAMI - Folded plate structures, architecture. *10th World Conference on Timber Engineering*, Miyazaki, Japan.
3. Ceylan, A., & Girgin, Z. C. (2019). Çapraz Lamine Ahşap (CLT) Duvar-Döşeme Birleşiminin Yapısal Davranışının Deneysel İncelenmesi. *Megaron*, 14(4), 521-529. https://doi.org/10.14744/MEGARON.2019.75508
4. Ceylan, A., & Girgin, Z. C. (2020). Comparisons on withdrawal resistance of resin and phosphate coated annular ring nails in CLT specimens. *Construction and Building Materials*, 238, 117742. https://doi.org/10.1016/j.conbuildmat.2019.117742
5. Doğramacı Aksoylar, N., Gürgün, B. N., & Ökten, M. S. (2026). Tarihi Ahşap Çatı Birleşim Davranışının Deneysel İncelenmesi. *Turkish Journal of Civil Engineering* (Basım Aşamasında). https://doi.org/10.18400/tjce.1719905

6. Eckelman, C. A. (2003). *Textbook of product engineering and strength design of furniture*. Purdue University Press.
7. Efe, H., Kasal, A., Çağatay, K., & Kuşkun, T. (2012). Ahşap Boy Birleştirmelerde Farklı Bağlantı Tekniklerinin Çekme Mukavemetlerinin Karşılaştırılması. Kastamonu University Journal of Forestry Faculty, 12(1), 80-89. https://izlik.org/JA28PM75UP
8. Kasal, A., Sayarcan, S., & Kuşkun, T. (2025). Panel mobilya birleştirmeleri için inovatif bağlantı elemanı tasarımı ve performansı. *Mobilya Ve Ahşap Malzeme Araştırmaları Dergisi*, 8(2), 204-219. https://doi.org/10.33725/mamad.1580105
9. KLH. (2012). *Component Catalogue for Cross Laminated Timber Structures*. Teufenbach-Katsch: KLH Massivholz GmbH.
10. Robeller, C., Gamerro, J., & Weinand, Y. (2017). Théâtre Vidy Lausanne - A double-layered timber folded plate structure. *Journal of the International Association for Shell and Spatial Structures*, 58(4), 295-314. https://doi.org/10.20898/j.iass.2017.194.864
11. Swedish Wood. (2019). *The CLT Handbook, CLT structures - facts and planning*. Stockholm: Swedish Forest Industries Federation.

Author Contribution Statement

- *Conceptualization:* Muhammed Emin Akyürek, Mehmet Selim Ökten
- *Methodology:* Cenk Aksoylar, Nihan Doğramacı Aksoylar, Haşim Çayır, Muhammet Ali İpekçi
- *Data Analysis and Visualization:* Muhammed Emin Akyürek, Muhammet Ali İpekçi, Haşim Çayır
- *Writing – Original Draft:* Muhammed Emin Akyürek, Nihan Doğramacı Aksoylar
- *Writing – Review & Editing:* Cenk Aksoylar, Mehmet Selim Ökten

List of Abbreviations

- **CLT** — Cross Laminated Timber
- **FEM** — Finite Element Method
- **LBCB** — Load and Boundary Conditions Box
- **PUR** — Polyurethane Reactive
- **UTM** — Universal Testing Machine

Publication Note

This paper was peer-reviewed, accepted for presentation, and included in the proceedings of the ACE2026 – International Conference on Advances in Civil Engineering, held on 12–14 October 2026 in Trabzon, Türkiye.

This paper may be cited as follows:

Akyürek, M.E., Aksoylar, C., Doğramacı Aksoylar, N., Ökten, M.S., İpekçi, M.A., Çayır, H, "Mechanical Behavior of Timber Folded Plate Joints: An Experimental Comparison of Adhesive and Mechanical Fasteners," in Proceedings of the ACE2026 – International Conference on Advances in Civil Engineering, Trabzon, Türkiye, 12–14 October 2026.

Mapping Research on AI-Enhanced Mechanical Behavior of Laminated Glass: A Scientometric Analysis

E. Dural[1], G.B.O. Öztürk[1]
[1] [0000-0002-5519-2498, 0000-0003-4617-6936], Aydın Adnan Menderes University, Civil Engineering Department, Aydın, Türkiye, ebru.dural@adu.edu.tr, gbozturk@adu.edu.tr

Abstract. This paper presents a scientometric analysis of research on the AI-enhanced mechanical behavior of laminated glass, based on 345 publications retrieved from the Scopus database between 2017 and 2026. Following relevance-based filtering, 74 studies were selected and analysed using keyword co-occurrence mapping and visualisation with VOSviewer. Five thematic clusters were identified: (1) fracture and mechanical behavior of glass materials, (2) mechanical behavior of laminated glass systems, (3) computational modelling of glass structures, (4) data-driven modelling of glass structural behavior, and (5) AI-enabled structural health monitoring. The findings reveal that foundational research on fracture mechanics and laminated glass behavior is well established. However, significant research gaps remain at the interfaces between the thematic clusters. One of the most important gaps is the limited integration of physics-informed neural networks with structural health monitoring frameworks. Another critical gap is the absence of data-driven models linking interlayer viscoelasticity to the structural response of laminated glass systems. These topics represent some of the most strategically significant and underexplored research directions in the field.

Keywords: Laminated Glass, Artificial Intelligence, Machine Learning, Structural Health Monitoring, Mechanical Behavior.

1 Introduction

Laminated glass has become an essential structural material in modern architecture due to its ability to simultaneously satisfy transparency, safety, and mechanical performance requirements. Unlike monolithic glass, laminated glass consists of two or more glass plies bonded by a polymeric interlayer, enabling the fractured glass fragments to remain attached after breakage [6] and thereby reducing the risk of catastrophic failure. This unique post-fracture behavior has promoted its widespread application in façades, roofs, skylights, pedestrian bridges, balustrades, and other load-bearing structural components where both structural integrity and occupant safety are critical.

Despite its increasing utilization, accurately predicting the mechanical behavior of laminated glass remains a challenging task. Its response is governed by highly nonlinear interactions among the glass layers, the viscoelastic interlayer, environmental conditions, loading rate, and fracture mechanisms [10]. The time- and temperature-dependent characteristics of polymer interlayers further complicate numerical modelling and structural analysis [4]. Consequently, conventional analytical formulations and finite element simulations often require substantial computational effort while remaining dependent on simplifying assumptions that may limit predictive accuracy for complex loading scenarios.

Recent advances in artificial intelligence (AI) have introduced new opportunities for addressing these challenges. Machine learning (ML), deep learning (DL), artificial neural networks (ANNs), convolutional neural networks (CNNs), support vector machines (SVMs) [5], and, more recently, physics-informed neural networks (PINNs) have demonstrated considerable potential for predicting structural responses, identifying damage, optimizing

design parameters, and supporting structural health monitoring (SHM). These data-driven approaches are capable of extracting complex nonlinear relationships from experimental and numerical datasets, thereby complementing conventional mechanics-based modelling techniques [8]. As a result, AI has emerged as an increasingly important research direction in the field of laminated glass engineering.

The rapid expansion of publications in this interdisciplinary domain has generated a diverse body of knowledge spanning fracture mechanics, computational modelling, optimization algorithms, structural monitoring, and intelligent prediction systems. However, despite the growing number of studies, current research remains fragmented across multiple disciplines. Existing review articles have primarily focused on either the mechanical behavior of laminated glass or the application of specific AI techniques, without providing a comprehensive overview of the intellectual structure and thematic evolution of this emerging research field. Consequently, researchers lack a systematic understanding of the dominant research themes, collaboration patterns, emerging topics, and future research opportunities.

Scientometric analysis provides a quantitative framework for exploring the development of scientific disciplines by combining bibliographic data with visualization techniques [1]. Unlike conventional narrative reviews, scientometric approaches reveal relationships among publications, keywords, authors, and research themes, enabling the identification of knowledge structures and emerging research frontiers [1]. Among the available visualization tools, VOSviewer has become one of the most widely adopted software packages [3] for constructing bibliometric networks and performing keyword co-occurrence analyses because of its effectiveness in revealing thematic clusters and research trends.

Motivated by these considerations, this study presents a comprehensive scientometric assessment of artificial intelligence applications in the mechanical behavior analysis of laminated glass. Publications indexed in the Scopus database between 2017 and 2026 were systematically screened using predefined inclusion and exclusion criteria, resulting in a final dataset of 74 publications extracted from an initial pool of 345 records. Bibliometric analyses were subsequently performed using VOSviewer to identify publication trends, research hotspots, thematic clusters, and emerging research directions. Particular emphasis is placed on examining how AI techniques have been integrated into laminated glass research and identifying existing knowledge gaps that may guide future investigations.

The findings reveal five major thematic research clusters that characterize the current landscape of AI-assisted laminated glass studies, encompassing fracture mechanics and mechanical performance, laminated glass behavior, computational modelling, data-driven predictive approaches, and AI-enabled structural health monitoring. Furthermore, the analysis highlights several underexplored research areas, including the integration of physics-informed neural networks with structural health monitoring systems, uncertainty-aware predictive modelling, hybrid AI–finite element frameworks, and digital twin technologies for intelligent glass structures. By providing a systematic overview of the existing literature and identifying future research priorities, this study contributes to establishing a clearer roadmap for the continued development of AI-assisted laminated glass engineering.

2 Research Methodology

This study employed a scientometric approach to systematically investigate the development of artificial intelligence (AI) applications in the mechanical behavior analysis of laminated glass. Scientometric analysis enables the quantitative evaluation of scientific literature by identifying publication trends, research hotspots, thematic relationships, and emerging research directions through bibliographic data and network visualization techniques.

Compared with traditional narrative reviews, this approach provides an objective and reproducible framework for revealing the intellectual structure of a research field [1].

2.1 Data Collection

The bibliographic data were collected from the Scopus database, which is one of the largest multidisciplinary citation databases and is widely used for bibliometric and scientometric research because of its comprehensive journal coverage and standardized indexing system [2]. Scopus was selected due to its high-quality metadata, extensive citation information, and compatibility with bibliometric visualization software such as VOSviewer.

The literature search covered publications published between 2017 and 2026, representing the period during which AI-based techniques experienced rapid development and increasing adoption in structural engineering applications [4]. To ensure comprehensive coverage of the relevant literature, a combination of keywords related to laminated glass, artificial intelligence, machine learning, deep learning, computational modelling, structural health monitoring, and mechanical behavior was employed. Boolean operators ("AND", "OR") were used to construct the search strategy and maximize retrieval accuracy.

The initial search identified 345 publications. Subsequently, duplicate records, conference announcements, editorials, notes, and publications unrelated to the mechanical behavior of laminated glass were excluded through a systematic screening process. After applying the predefined inclusion and exclusion criteria and performing a manual relevance assessment, the final dataset consisted of 74 publications, which formed the basis of the subsequent scientometric analyses.

Figure 1 illustrates the overall workflow adopted in this study, including database searching, screening, eligibility assessment, and bibliometric analysis.

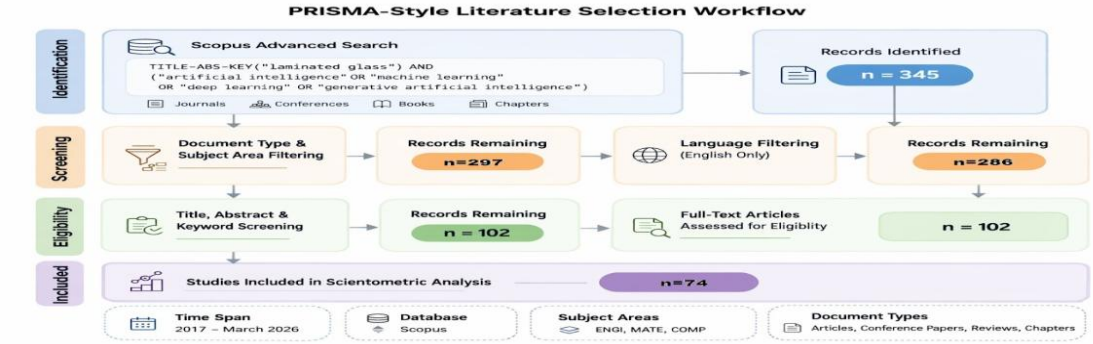


Fig. 1. Research workflow adopted for the scientometric analysis.

2.2 Bibliometric Analysis

The selected publications were analyzed using VOSviewer (version 1.6.x), one of the most widely used software packages for constructing and visualizing bibliometric networks [3]. VOSviewer provides powerful visualization capabilities for examining relationships among publications, keywords, authors, institutions, and countries through network-based mapping techniques.

In this study, keyword co-occurrence analysis was employed to identify the conceptual structure of the research field. Author keywords and index keywords were extracted from the selected publications, and a minimum occurrence threshold was defined to eliminate infrequently used terms that do not significantly contribute to thematic interpretation. Similar keywords with identical or closely related meanings were standardized to improve the consistency of the network structure.

The resulting keyword network was clustered automatically using the association-strength normalization algorithm implemented in VOSviewer [3]. In the generated maps, the size of each node represents the frequency of keyword occurrence, whereas the thickness of the connecting links reflects the strength of the relationships between keywords. Different colors indicate distinct thematic clusters representing major research topics within the field.

2.3 Research Framework

Following the construction of the keyword network, the identified clusters were interpreted qualitatively by examining the dominant keywords within each cluster together with the associated publications. This combined quantitative–qualitative approach enabled a comprehensive interpretation of the intellectual structure of AI-assisted laminated glass research.

The analysis focused on four principal aspects: publication characteristics and temporal research trends; conceptual relationships identified through keyword co-occurrence analysis; thematic research clusters describing the major scientific directions; and emerging research opportunities and knowledge gaps.

The identified research themes were subsequently interpreted in terms of their scientific significance and technological implications for future developments in laminated glass engineering. Particular attention was given to recent advances involving machine learning, deep learning, computational mechanics, structural health monitoring, and hybrid physics-based artificial intelligence approaches [4, 5].

By integrating bibliometric mapping with thematic interpretation, the adopted methodology provides a comprehensive overview of the current state of research while simultaneously identifying promising directions for future investigations. This framework also facilitates a better understanding of how AI techniques have evolved within laminated glass research and highlights emerging interdisciplinary connections between computational intelligence, structural engineering, and materials science.

3 Results and Discussion

3.1 Publication Characteristics and Research Trends

The bibliometric analysis reveals a remarkable increase in research activity concerning the application of artificial intelligence (AI) to the mechanical behavior analysis of laminated glass during the last decade. Following the screening procedure described in Section 2, a total of 74 publications were selected from an initial dataset of 345 records. The analyzed publications demonstrate that AI-assisted laminated glass research has evolved from a niche topic into an emerging interdisciplinary field that integrates structural engineering, materials science, computational mechanics, and data-driven modelling.

The annual publication trend indicates relatively limited research output before 2020, followed by a significant increase after 2021. This growth coincides with the rapid advancement of machine learning algorithms, increased computational capabilities, and broader adoption of intelligent modelling techniques within structural engineering [4]. Recent studies increasingly combine numerical simulations with artificial intelligence to improve prediction accuracy, reduce computational costs, and enhance structural safety assessments [8].

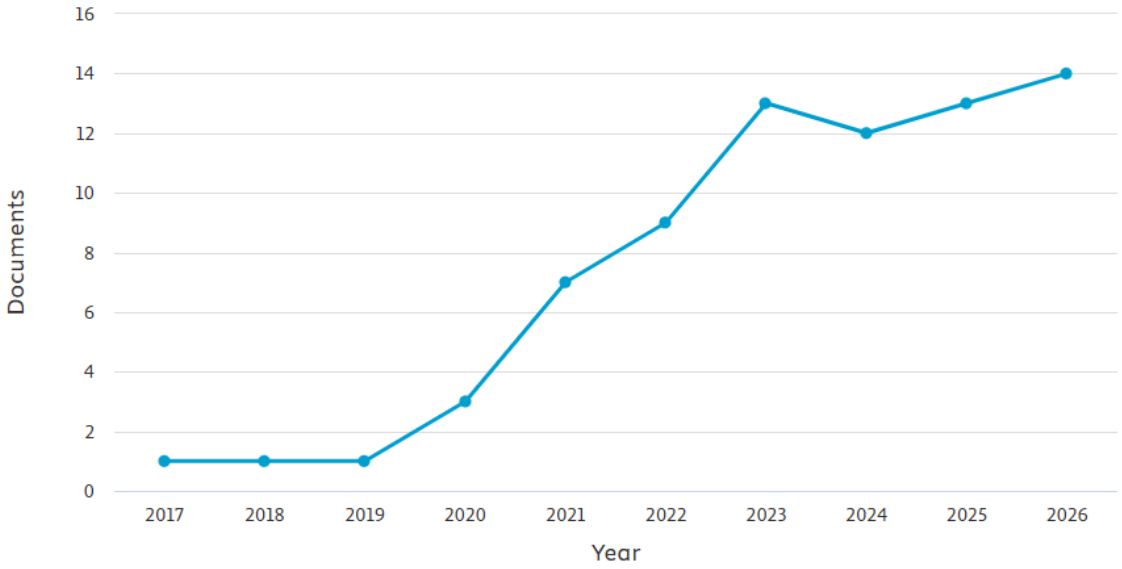


Fig. 2. Annual number of publications on AI-enhanced mechanical behavior of laminated glass, 2017–2026.

The geographical distribution of publications further demonstrates the global expansion of this research area. Significant contributions originate from countries with strong research activities in structural glass engineering and computational mechanics, particularly in Europe and Asia. International collaborations have also become increasingly common, reflecting the multidisciplinary nature of the field and the growing interest in integrating AI with advanced engineering applications.

Overall, the publication characteristics indicate that AI-assisted laminated glass research is currently transitioning from exploratory investigations toward more application-oriented studies involving intelligent structural design, performance prediction, and structural health monitoring.

3.2 Keyword Co-occurrence Network Analysis

To identify the conceptual structure of the research field, a keyword co-occurrence analysis was conducted using VOSviewer [3]. The generated bibliometric network reveals strong interconnections among engineering mechanics, artificial intelligence, computational modelling, and structural monitoring.

The keyword network is dominated by terms such as laminated glass, mechanical behavior, finite element analysis, machine learning, structural health monitoring, optimization, damage detection, and deep learning. The frequent occurrence of these keywords demonstrates that recent studies increasingly emphasize intelligent prediction methods rather than purely analytical or numerical approaches [5].

The visualization also highlights the existence of several densely connected research communities. High-frequency keywords occupy central positions within the network and exhibit strong link strengths, indicating their significant influence on the overall development of the research field. In contrast, recently emerging keywords appear on the periphery of the network, suggesting promising opportunities for future investigations.

The clustering algorithm implemented in VOSviewer identified five major thematic clusters, each representing a distinct yet interconnected research direction. Together, these clusters provide a comprehensive overview of the current scientific landscape of AI-assisted laminated glass engineering.

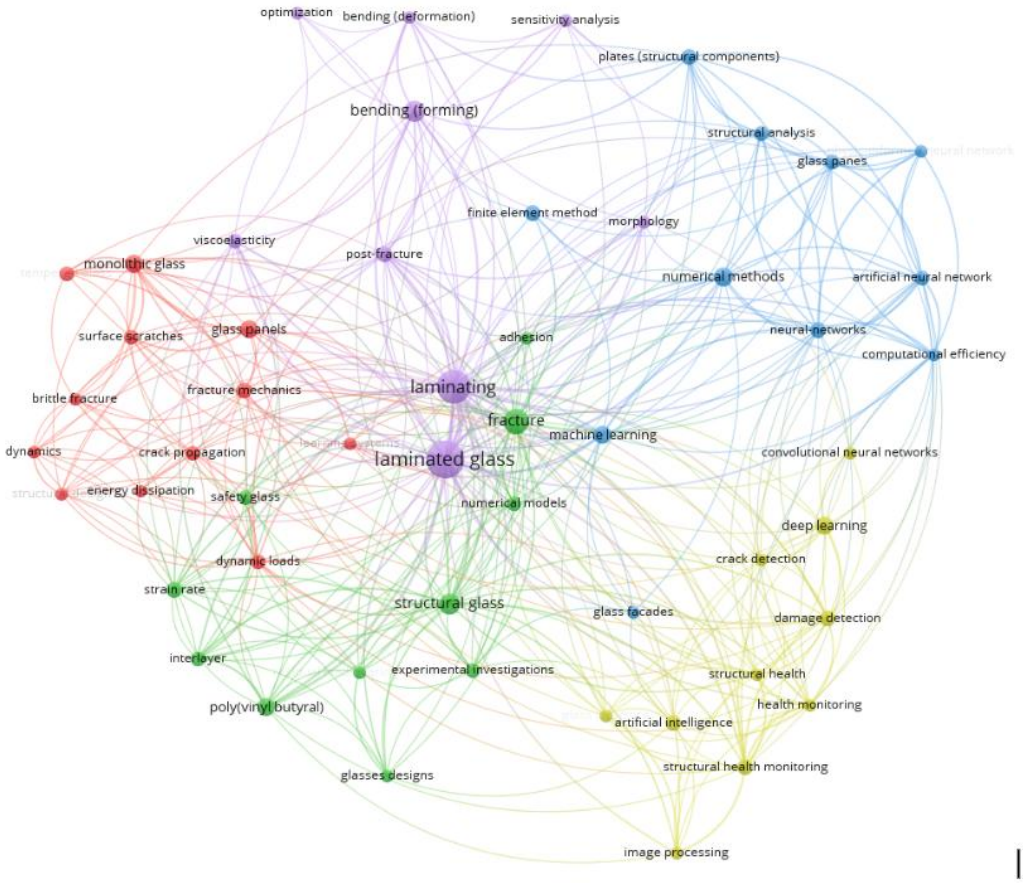


Fig. 3. Keyword co-occurrence network generated using VOSviewer.

3.3 Thematic Cluster Analysis

Figure 4 summarizes the functional role of each thematic cluster within the overall research ecosystem, illustrating how the field progresses from foundational mechanical knowledge toward applied, AI-enabled monitoring solutions.

Cluster	Role	Network position	Impact profile	Maturity
C1 Fracture & Mechanical Behaviour	Knowledge base	Low centrality, high citation impact	High individual paper quality	Established — foundational
C2 Laminated Glass Systems	Network backbone	Highest inter-cluster connectivity	Volume-driven, moderate NC	Mature — high output
C3 Computational Modelling	Method frontier	Newest avg. pub. year of all clusters	Low NC, rapidly growing	Emerging — pre-impact
C4 Data-Driven Modelling	Domain core	Dominant TLS; highest-NC niche (opt.)	Bimodal: dominant + isolated	Active — maturing
C5 AI-Enabled SHM	Applied frontier	High TLS, near-zero NC for newest kws	Citation lag — very recent	Nascent — pre-citation

Fig. 4. Functional roles of the five thematic clusters within the AI-enhanced laminated glass research ecosystem.

Cluster 1 – Fracture Mechanics and Mechanical Performance.
The first cluster primarily focuses on the mechanical response and fracture behavior of laminated glass subjected to various loading conditions. The associated studies investigate crack initiation, crack propagation, impact resistance, blast loading, and post-fracture structural performance [6, 10]. These investigations provide the mechanical foundation upon which intelligent prediction models are subsequently developed.

Although finite element analysis remains the dominant computational tool within this cluster, recent publications increasingly employ machine learning algorithms to predict fracture loads and residual load-carrying capacity [9]. AI models have demonstrated promising capabilities for learning complex nonlinear relationships that are difficult to represent using conventional constitutive formulations.

The evolution of this cluster illustrates the gradual transition from purely mechanics-based analyses toward hybrid computational approaches combining numerical simulations with data-driven prediction techniques.

Cluster 2 – Laminated Glass Behavior and Interlayer Mechanics.

The second thematic cluster concentrates on the influence of polymer interlayers on the structural performance of laminated glass. The viscoelastic characteristics of materials such as polyvinyl butyral (PVB) introduce significant nonlinearities that complicate structural analysis under varying environmental and loading conditions [4].

Numerous studies investigate temperature-dependent behavior, time-dependent deformation, and interlayer stiffness through experimental testing and numerical modeling [10]. More recently, artificial intelligence has been employed to estimate interlayer properties using limited experimental datasets, thereby reducing the need for extensive laboratory testing [7].

Despite these developments, accurately modelling interlayer viscoelasticity remains one of the most challenging problems in laminated glass engineering. This issue represents one of the major knowledge gaps identified through the scientometric analysis.

Cluster 3 – Artificial Intelligence and Computational Modelling.

The third cluster represents the core of AI-based laminated glass research. It encompasses machine learning, artificial neural networks, deep learning, surrogate modelling, and optimization techniques developed to predict mechanical behavior with reduced computational effort [4].

Traditional finite element simulations often require extensive computational resources, particularly for nonlinear dynamic analyses. AI algorithms offer an attractive alternative by rapidly approximating structural responses while maintaining acceptable prediction accuracy [8]. Consequently, recent studies increasingly employ neural networks as surrogate models for finite element analyses.

Emerging research within this cluster also investigates physics-informed neural networks (PINNs), which combine governing physical equations with machine learning algorithms [5]. Although only a limited number of studies currently apply PINNs to laminated glass structures, this approach appears highly promising for improving prediction accuracy while maintaining physical consistency.

Cluster 4 – Data-Driven Prediction and Structural Optimization.

The fourth thematic cluster focuses on intelligent prediction systems developed using data-driven methodologies. These studies primarily utilize machine learning algorithms for estimating structural capacity, optimizing material configurations, and improving engineering decision-making [7].

Optimization techniques supported by artificial intelligence enable engineers to identify efficient laminated glass configurations while satisfying mechanical and safety requirements. Various algorithms have been proposed to optimize glass thickness, interlayer properties, and structural configurations simultaneously [5].

Another emerging research direction involves uncertainty-aware prediction models capable of incorporating experimental variability into engineering design. Such approaches may significantly improve the reliability of AI-assisted structural assessment methods.

Cluster 5 – AI-Enabled Structural Health Monitoring.
The fifth cluster represents one of the fastest-growing research directions identified in the present study. Structural health monitoring (SHM) systems increasingly integrate artificial intelligence with sensor technologies to enable continuous condition assessment of laminated glass structures [5].

Deep learning algorithms, particularly convolutional neural networks, have demonstrated considerable success in automated damage detection, crack identification, and image-based inspection [8]. Combined with vibration monitoring and digital sensing technologies, methods enable early identification of structural deterioration before catastrophic failure occurs.

Nevertheless, the scientometric analysis indicates that relatively few studies have successfully integrated SHM systems with advanced AI frameworks capable of simultaneously considering mechanical behavior, environmental effects, and long-term structural performance. Consequently, this topic represents one of the most promising future research directions.

3.4 Emerging Research Opportunities

The thematic analysis demonstrates that artificial intelligence has become an increasingly important component of laminated glass engineering. However, several significant research gaps remain.

One of the most promising future directions is the integration of physics-informed neural networks with finite element modeling [5]. Such hybrid frameworks have the potential to combine the computational efficiency of machine learning with the physical reliability of mechanics-based simulations.

Another emerging opportunity involves the development of digital twins capable of continuously updating structural models using real-time sensor data. When integrated with AI-assisted structural health monitoring systems, digital twins may enable predictive maintenance strategies for glass structures operating under complex service conditions.

The analysis also highlights the need for explainable artificial intelligence (XAI) methods that improve the transparency and interpretability of machine learning predictions. Since engineering applications require reliable and physically meaningful predictions, improving model interpretability will become increasingly important for practical implementation.

Finally, future investigations should focus on developing unified AI frameworks capable of simultaneously considering fracture mechanics, viscoelastic interlayer behavior, environmental effects, and long-term structural performance. Such multidisciplinary approaches are expected to significantly advance the application of intelligent computational methods in laminated glass engineering.

4 Conclusions

This study presented a comprehensive scientometric analysis of artificial intelligence (AI) applications in the mechanical behavior analysis of laminated glass, providing a systematic overview of the current research landscape and identifying emerging directions for future investigations. Based on a carefully screened dataset of 74 publications retrieved from an initial pool of 345 records indexed in the Scopus database [2], bibliometric mapping and

keyword co-occurrence analyses were performed using VOSviewer [3] to reveal the intellectual structure of this rapidly evolving interdisciplinary research field.

The results demonstrate a clear increase in scientific interest in AI-assisted laminated glass research, particularly after 2021, reflecting the growing adoption of data-driven methods in structural engineering [4]. The bibliometric analysis identified five major thematic research clusters that collectively describe the current state of the field: (i) fracture mechanics and mechanical performance, (ii) laminated glass behavior and interlayer mechanics, (iii) artificial intelligence and computational modelling, (iv) data-driven prediction and structural optimization, and (v) AI-enabled structural health monitoring. These interconnected themes illustrate the transition from conventional mechanics-based analyses toward intelligent computational approaches that combine experimental observations, numerical simulations, and machine learning techniques [5, 6, 8].

The keyword network analysis further indicates that AI has evolved from a supporting computational tool into an integral component of laminated glass research [5]. Machine learning algorithms, artificial neural networks, deep learning techniques, and optimization methods are increasingly being employed to predict structural responses, reduce computational costs, improve design efficiency, and enhance damage assessment [7, 9]. At the same time, finite element modelling remains an essential analytical framework, suggesting that future developments are likely to rely on hybrid methodologies integrating physics-based simulations with data-driven intelligence.

Despite these significant advances, the scientometric analysis revealed several important research gaps. The integration of physics-informed neural networks with structural health monitoring systems remains limited [5], while uncertainty-aware predictive models and digital twin technologies have received comparatively little attention [4]. Furthermore, accurately representing the time-dependent viscoelastic behavior of polymer interlayers within AI-based predictive frameworks continues to be a major scientific challenge. Addressing these limitations will require stronger interdisciplinary collaboration among structural engineers, materials scientists, computational mechanics researchers, and artificial intelligence specialists [10].

Overall, this study provides a quantitative and visual representation of the evolution of AI-assisted laminated glass research while highlighting the principal scientific trends, thematic developments, and future research opportunities. The presented findings may serve as a useful reference for researchers seeking to identify promising research directions and develop more reliable, efficient, and intelligent computational approaches for laminated glass structures. As AI technologies continue to advance, their integration with computational mechanics, structural monitoring, and digital engineering is expected to play an increasingly important role in the design, analysis, and long-term performance assessment of laminated glass systems.

References

1. Donthu, N., Kumar, S., Mukherjee, D., Pandey, N., Lim, W.M.: How to conduct a bibliometric analysis: An overview and guidelines. Journal of Business Research 133, 285-296 (2021). https://doi.org/10.1016/j.jbusres.2021.04.070
2. Pranckute, R.: Web of Science (WoS) and Scopus: The Titans of Bibliographic Information in Today's Academic World. Publications 9(1), 12 (2021). https://doi.org/10.3390/publications9010012
3. van Eck, N.J., Waltman, L.: Software survey: VOSviewer, a computer program for bibliometric mapping. Scientometrics 84(2), 523-538 (2010). https://doi.org/10.1007/s11192-009-0146-3

4. Herrmann, L., Kollmannsberger, S.: Deep learning in computational mechanics: a review. Computational Mechanics 74, 281-331 (2024). https://doi.org/10.1007/s00466-023-02434-4
5. Kraus, M.A., Drass, M. Artificial intelligence for structural glass engineering applications — Overview, case studies and future potentials. Glass Structures & Engineering: 6, 103-139 (2021). https://doi.org/10.1007/s40940-020-00132-8
6. Osnes, K., Holmen, J.K., Grue, T., Børvik, T.: Perforation of laminated glass: An experimental and numerical study. International Journal of Impact Engineering 156, 103922 (2021). https://doi.org/10.1016/j.ijimpeng.2021.103922
7. Ahani, A., Ahani, E.: An overview for materials and design methods used for enhancement of laminated glass. Journal of Building Engineering 95, 110073 (2024).
8. Wang, Y., Oyen, D., Guo, W.G., Mehta, A., Braker Scott, C., Panda, N., Fernandez-Godino, M.G., Srinivasan, G., Yue, X.: StressNet - Deep learning to predict stress with fracture propagation in brittle materials. npj Materials Degradation 5, 6 (2021). https://doi.org/10.1038/s41529-021-00151-y
9. Bohmann, L., Schuster, M., Seel, M., Kraus, M.: Experimental statistical fracture pattern analysis of glass panes with varying pre-stress levels. Glass Structures & Engineering 11, 8 (2026). https://doi.org/10.1007/s40940-026-00320-y
10. Vedrtnam, A., Pawar, S.J.: Laminated glass: Classification, characterization, and future perspectives. Journal of Materials Education 42(1-2), 51-61 (2020).

Author Contribution Statement

- *Conceptualization:* E. Dural, G. B. Öztürk Özeray
- *Methodology:* E. Dural, G. B. Öztürk Özeray
- *Investigation:* E. Dural, G. B. Öztürk Özeray
- *Writing – Original Draft:* E. Dural, G. B. Öztürk Özeray
- *Writing – Review & Editing:* E. Dural, G. B. Öztürk Özeray

List of Abbreviations

- **AI** — Artificial Intelligence
- **ML** — Machine Learning
- **DL** — Deep Learning
- **ANN** — Artificial Neural Network
- **CNN** — Convolutional Neural Network
- **SVM** — Support Vector Machine
- **PINN** — Physics-Informed Neural Network
- **SHM** — Structural Health Monitoring
- **XAI** — Explainable Artificial Intelligence
- **PVB** — Polyvinyl Butyral

The authors declare that they have no known competing financial interests or personal relationships that could have appeared to influence the work reported in this paper.

Publication Note
This paper was peer-reviewed, accepted for presentation, and included in the proceedings of the ACE2026 – International Conference on Advances in Civil Engineering, held on 12–14 October 2026 in Trabzon, Türkiye.

This paper may be cited as follows:
G.B.O. Öztürk, E. Dural, "Mapping Research on AI-Enhanced Mechanical Behavior of Laminated Glass: A Scientometric Analysis," in Proceedings of the ACE2026 – International Conference on Advances in Civil Engineering, Trabzon, Türkiye, 12–14 October 2026.

Comparative Linear and Nonlinear Seismic Analysis of a Historical Masonry Arch Bridge: Dynamic Response and Damage Evolution

Emre ALPASLAN[1] and Muhammed Mustafa ÖZTÜRK[2]
[1] 0000-0002-3715-990X, Ondokuz Mayıs University, Civil Engineering Department, Samsun, Türkiye, emre.alpaslan@omu.edu.tr
[2] 0000-0002-6327-2308, Tokat Gaziosmanpaşa University, Civil Engineering Department, Tokat, Türkiye, mmustafa.ozturk@gop.edu.tr

Abstract. In this study, the seismic behavior of a historic multi-span masonry arch bridge under bidirectional seismic effects was investigated comparatively using linear and non-linear dynamic analysis methods in the time domain. A three-dimensional finite element model of the bridge was created in the ANSYS environment using the SOLID65 element. To represent the non-linear plasticity behavior of the masonry material and the cracking/crushing damage mechanisms, the Drucker–Prager yield criterion and the Willam–Warnke failure criterion were used in combination. The Rayleigh damping approach was adopted for the damping matrix calculation, and acceleration records from the bridge site were scaled and applied simultaneously. The analysis results demonstrated that linear analysis was inadequate for representing the structure's post-elastic behavior and significantly underestimated the seismic demands. In the non-linear analyses, increases in displacements (magnification factors) ranging from 4.29 to 187.86 times, as well as permanent deformations, were observed due to cracking and stiffness loss. Stress distributions revealed that tensile and compressive stress increased markedly in conjunction with non-linear behavior, and that plastic stresses and cracking patterns were concentrated particularly in the arch vaults, arch-wall junction zones, and abutments. The findings demonstrate that non-linear material modeling is essential for the seismic performance assessment of historic masonry arch bridges and for the planning of conservation and reinforcement projects.

Keywords: Historical masonry arch bridges, Nonlinear time-history analysis, Seismic performance assessment, Damage mechanism.

1 Introduction

Historic masonry structures rank among the most valuable elements of humanity's cultural and architectural heritage, and the arch bridges found within these structures have formed critical components of transport networks for centuries. Masonry arch bridges are constructed from stone or brick materials, which, despite their high compressive strength, possess a very low tensile capacity and, by their very nature, exhibit quasi-brittle behavior [1,2]. The behavior of these structures under seismic loads is characterized by extreme complexity and non-linearity due to frictional sliding, micro-cracking, disintegration of the joint mortar, and axial/shear interactions [3].

The safe preservation of historic masonry bridges in earthquake-prone regions for future generations depends on determining their seismic performance and potential damage mechanisms using realistic methods. Linear elastic analysis approaches, which were frequently favored in the past, are inadequate for representing the gradual loss of stiffness that the material undergoes under seismic loads, the redistribution of internal forces following cracking, and permanent deformations [4]. To overcome these limitations, recent research has widely

employed constitutive equations that combine pressure-dependent plasticity with macro-modeling-based fracture criteria.

Whilst the Drucker–Prager (DP) yield criterion is the leading approach for characterizing the yield behavior of earth under hydrostatic pressure [5], the Willam–Warnke (WW) failure criterion has been successfully applied to simulate tensile cracking and compressive crushing mechanisms in the material under three-dimensional stress conditions [6]. The combination of these two constitutive models has become a standard and reliable approach for modeling the non-linear behavior of granular and concrete-like quasi-brittle materials in specialized solid-element formats such as ANSYS SOLID65 [7,8].

In this study, the behavior of a historic masonry arch bridge with four spans under scaled simultaneous horizontal and vertical earthquake acceleration records was investigated using linear and non-linear (DP + WW) time-domain analysis methods. As part of the research, displacement time histories, displacement amplification factors, principal stress concentrations, equivalent plastic stress distributions, and cracking patterns were compared in detail, thereby revealing the decisive role of material non-linearity in the seismic response and damage mechanism of the historic bridge.

2 Nonlinear Constitutive Model

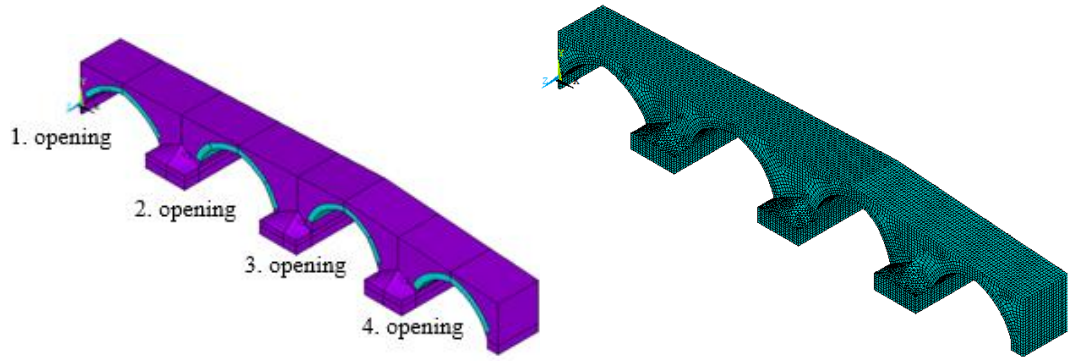
The nonlinear mechanical behavior of masonry is governed by frictional sliding, tensile cracking, and compressive crushing. Owing to its quasi-brittle nature, masonry exhibits high compressive strength but limited tensile capacity, rendering linear-elastic constitutive models inadequate for capturing stiffness degradation and irreversible damage under seismic loading. Therefore, pressure-dependent plasticity models, combined with fracture criteria, are widely employed in nonlinear finite element (FE) analysis of masonry structures [1].

The Drucker–Prager (DP) model is widely adopted because it accounts for the influence of hydrostatic pressure on yielding through material cohesion and internal friction angle, providing a realistic representation of masonry subjected to multiaxial stress states [5]. Since the DP criterion alone cannot simulate tensile cracking and compressive crushing, it is coupled with the five-parameter Willam–Warnke (WW) failure criterion, which predicts crack initiation, crack propagation, and compressive failure under complex loading conditions. Implemented in the ANSYS SOLID65 element, the combined DP–WW formulation has become a well-established approach for nonlinear analysis of historical masonry bridges, enabling realistic simulation of material degradation while maintaining computational efficiency through open- and closed-crack shear transfer coefficients [6–8].

3 Finite Element Model

A three-dimensional FE model of the historical multi-span masonry bridge was developed using ANSYS Mechanical APDL to investigate its seismic response under bidirectional earthquake excitation. As illustrated in Fig. 1, the bridge geometry was discretized using the eight-node SOLID65 element, which can represent both linear elastic behavior and nonlinear material response through tensile cracking and compressive crushing formulations. The arch barrels and side walls were modeled as separate material regions to account for their different mechanical properties, while the bridge foundations were assumed to be fully fixed at the base. The adopted FE discretization comprises 58,066 solid elements and 63,636 nodes, providing sufficient spatial resolution to accurately represent the bridge geometry and capture the structural response during both linear and nonlinear time-history analyses. The mesh density was selected to achieve a reasonable balance between geometric representation and computational efficiency for the transient dynamic analyses. The same FE model, mesh configuration, boundary conditions, and earthquake loading were employed in both the linear and nonlinear analyses to

ensure that any differences in structural response resulted solely from the constitutive material models adopted.



(a) (b)

Fig. 1. FE model of the historical masonry bridge, (a) three-dimensional geometric model and (b) discretized FE mesh.

3.1 Material Properties

The nonlinear constitutive model adopted in this study was defined using a macro-modeling approach, in which the masonry was represented as an equivalent homogeneous continuum. The linear elastic properties, including the elastic modulus, Poisson's ratio, and mass density, were assigned separately for the arch barrel and side walls to account for their different structural characteristics. To simulate the inelastic behavior of masonry under increasing loads, the DP yield criterion was used to model the onset of plasticity, while the WW failure criterion was used to simulate tensile cracking and compressive crushing. This combined constitutive formulation has been widely adopted for nonlinear FE analyses of historical masonry bridges because it realistically represents the frictional–cohesive nature of masonry while maintaining computational efficiency within the SOLID65 element available in ANSYS.

The nonlinear material parameters presented in Table 1 were selected based on published numerical investigations of historical masonry arch bridges. The adopted material properties represent a literature-based constitutive model that has previously been validated for historical masonry bridge analyses [9,10] and are therefore considered appropriate for the nonlinear time-history simulations performed in the present study.

3.2 Selection of Rayleigh Damping Parameters

The seismic response of historical masonry bridges is significantly influenced by energy dissipation mechanisms arising from frictional sliding, microcracking, mortar degradation, and contact interaction between structural components. Since these mechanisms are highly nonlinear and difficult to model explicitly, proportional (Rayleigh) damping is commonly used in both linear and nonlinear finite element (FE) analyses for its computational efficiency and numerical robustness [11,12].

In this study, the damping matrix was defined using the classical Rayleigh formulation, in which the viscous damping matrix is expressed as a linear combination of the global mass and stiffness matrices. A target damping ratio of 5% was adopted, consistent with values commonly reported for unreinforced historical masonry structures when experimental damping data are unavailable [13,14]. Prior to the time-history analyses, a modal analysis was performed to identify the bridge's dynamic characteristics. The first three natural frequencies were 12.781 Hz, 14.471 Hz, and 15.142 Hz, representing the dominant global vibration modes of the structure (Fig. 2).

Table 1. Mechanical properties and nonlinear constitutive parameters adopted for the historical masonry bridge.

Property	**Arch**	**Side Wall**
E (MPa)	3000	2500
ν	0.20	0.20
Density (kg/m³)	1900	1800
Cohesion c (MPa)	0.40	0.35
Friction angle φ	40°	40°
Dilatancy angle ψ	20°	20°
βopen	0.25	0.25
βclosed	0.75	0.75
fc	2.73 MPa	2.50 MPa
ft	0.27 MPa	0.25 MPa

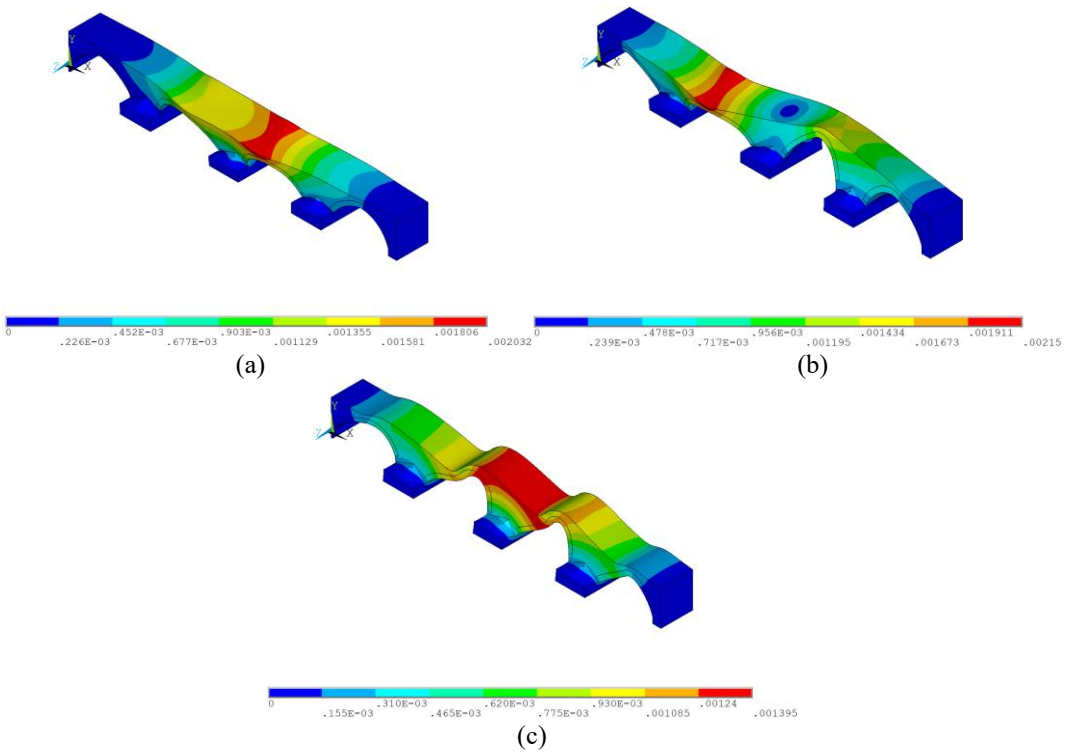


Fig. 2. First three mode shapes of the FE model of the historical masonry bridge: (a) first mode (12.781 Hz), (b) second mode (14.471 Hz), and (c) third mode (15.142 Hz).

The Rayleigh damping coefficients were calibrated using the first and twentieth natural frequencies. Unlike detailed three-dimensional solid models, which generate numerous localized high-frequency modes, the selected frequency range primarily reflects the global dynamic behavior that governs the seismic response. This approach provides a nearly uniform

damping ratio over the dominant vibration modes while avoiding excessive damping of localized deformation modes [15–17].

The same Rayleigh damping coefficients were employed in both the linear and nonlinear time-history analyses to ensure a consistent basis for comparison. In the nonlinear analyses, additional energy dissipation was captured through the Drucker–Prager and Willam–Warnke constitutive models, whereas the Rayleigh damping matrix represented only the viscous component of structural damping. This combined strategy provides a physically realistic and numerically stable representation of the seismic behavior of historical masonry bridges [15,17].

3.3 Selection and Scaling of the Earthquake Ground Motion

The seismic response of the historic masonry bridge was evaluated using the horizontal and vertical components of the Erzincan earthquake record, which were scaled according to the seismic demand specified by the current Turkish seismic design code for the bridge location (Fig. 3). The scaled ground motions were simultaneously applied in the longitudinal (X) and vertical (Z) directions to realistically represent the multidirectional seismic excitation and to capture the influence of vertical ground motion on the nonlinear response of the masonry bridge.

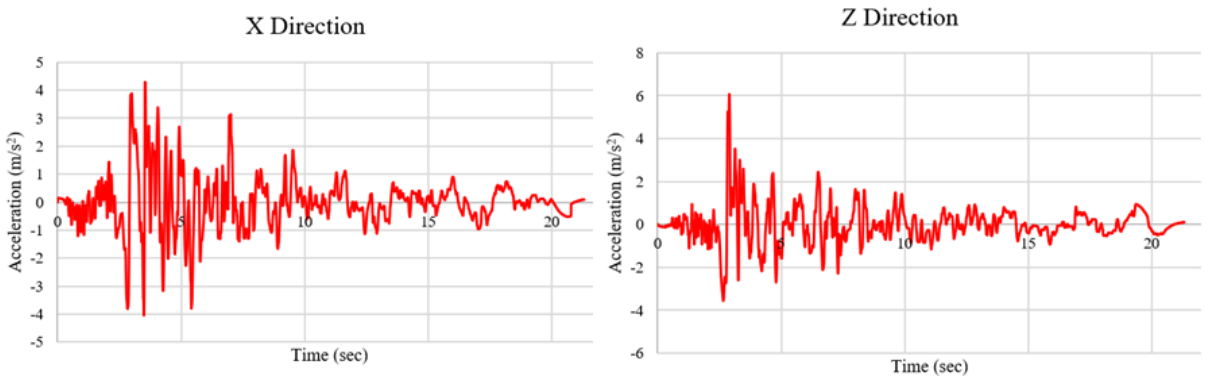


Fig. 3. Scaled horizontal (X) and vertical (Z) acceleration time histories of the Erzincan earthquake record adopted for the bridge site in accordance with the seismic demand specified by the Turkish seismic design code.

4 Results and Discussions

The seismic performance of the historic masonry bridge was evaluated through a comparative assessment of the linear and nonlinear dynamic analyses under the scaled Erzincan earthquake record. The discussion focuses on differences in displacement response, stress distribution, and damage evolution to elucidate the influence of material nonlinearity on the bridge's structural behavior. Together, these results provide a comprehensive understanding of the mechanisms governing the seismic response of historic masonry arch bridges.

4.1 Displacement response

The normalized displacement time histories presented in Fig. 4 highlight the differences between the linear and nonlinear dynamic responses of the historical masonry bridge. Since each displacement record was normalized by its own maximum absolute value, the comparison emphasizes the evolution of the response, oscillation characteristics, phase shifts, and stiffness degradation rather than the displacement magnitude.

The linear analysis exhibits oscillatory responses centered on the initial equilibrium position throughout the earthquake excitation, reflecting the constant-stiffness assumption of linear elasticity. In contrast, the nonlinear analysis follows the linear response during the early stage of the record but undergoes a distinct transition after approximately **5–6 s**, when cracking and

material degradation become significant. Following this transition, the displacement histories exhibit reduced vibration frequencies, noticeable phase shifts, and changes in equilibrium position, indicating progressive stiffness degradation and irreversible structural response.

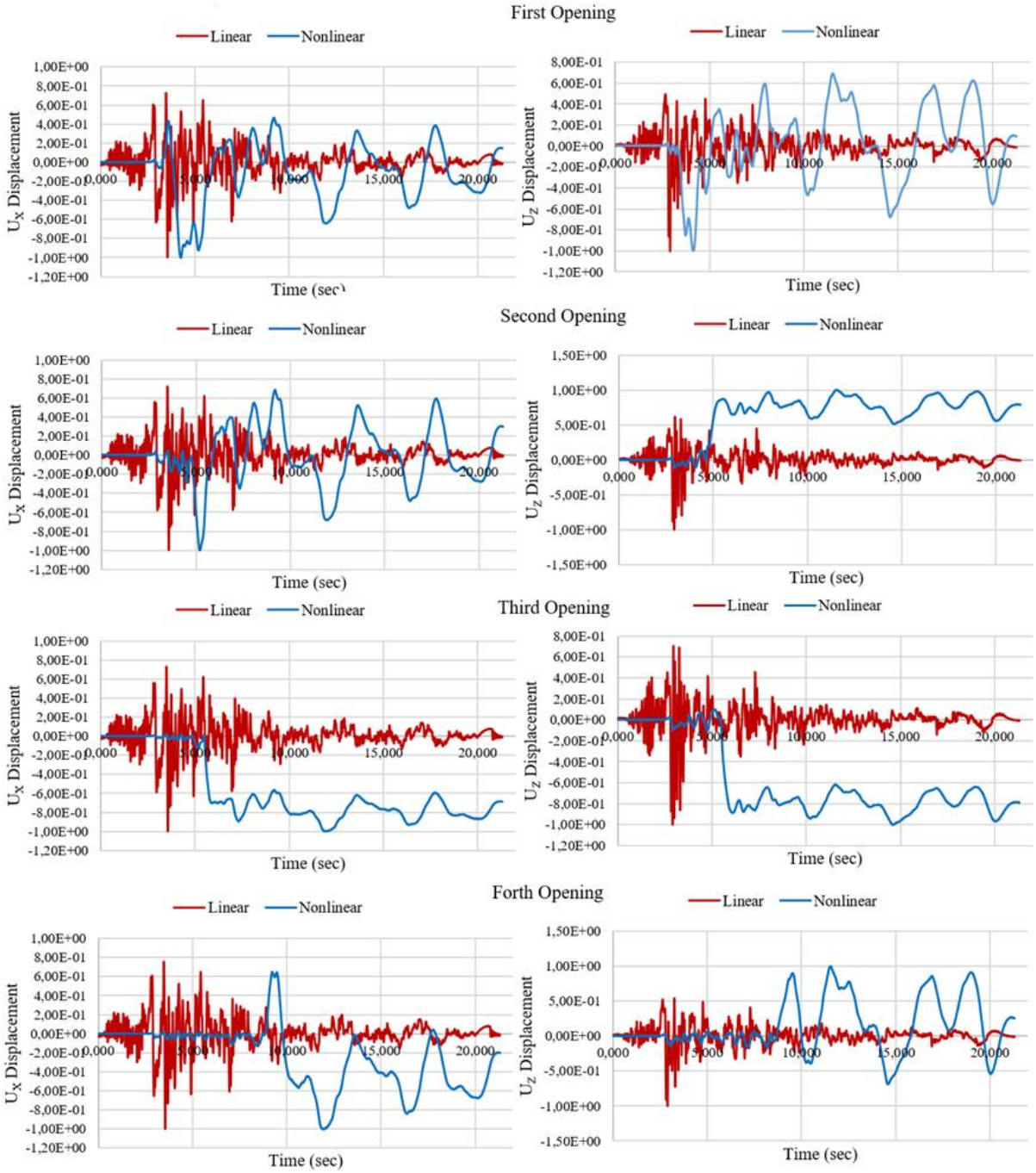


Fig. 4. Comparison of the normalized horizontal (UX) and vertical (UZ) displacement time histories at the first, second, third, and fourth bridge openings obtained from the linear and nonlinear dynamic analyses. Each displacement record was normalized by its maximum absolute displacement to facilitate comparison of temporal response characteristics, oscillation patterns, and nonlinear response evolution independent of displacement magnitude.

The nonlinear behavior varies among the four bridge openings. The first opening shows pronounced low-frequency oscillations after damage initiation, whereas the second opening, particularly in the vertical direction, develops a permanent positive equilibrium shift, indicating

irreversible deformation. In contrast, the third opening exhibits a persistent negative displacement bias, while the fourth opening experiences delayed nonlinear response accompanied by large-amplitude oscillations. These observations demonstrate that nonlinear material degradation and internal force redistribution are spatially non-uniform and strongly influenced by bridge geometry.

The normalized displacement histories should be interpreted together with the displacement amplification factors summarized in Table 2. While the normalized responses illustrate the temporal evolution of stiffness degradation and changes in vibration characteristics, the amplification factors quantify the increase in displacement due to material nonlinearity. The nonlinear analysis produced considerably larger maximum displacements than the linear analysis, with amplification factors ranging from 4.29 to 180.71 in the horizontal direction and 18.40 to 187.86 in the vertical direction. These findings demonstrate that linear dynamic analysis substantially underestimates both the magnitude and temporal evolution of the seismic response, highlighting the necessity of nonlinear dynamic analysis for the reliable seismic assessment of historical masonry arch bridges.

Table 2. Comparison of maximum displacements obtained from linear and nonlinear dynamic analyses.

Openings	Linear U_{xmax} (m)	Nonlinear U_{xmax} (m)	Amplification Factor	Linear U_{zmax} (m)	Nonlinear U_{zmax} (m)	Amplification Factor
1	2.62E-04	4.31E-02	164.51	2.64E-04	4.54E-02	172.28
2	6.92E-04	5.09E-02	73.57	9.86E-04	1.85E-01	187.86
3	7.18E-04	3.08E-03	4.29	1.27E-03	2.33E-02	18.4
4	3.27E-04	5.90E-02	180.71	3.40E-04	5.36E-02	157.856

4.2 Stress Distribution

Fig. 5 compares the distributions of the first (S1) and third (S3) principal stresses obtained from the linear and nonlinear dynamic analyses at the critical response time (t = 11.66 s). Compared with the linear analysis, the nonlinear model exhibits pronounced tensile and compressive stress redistribution, with localized stress concentrations around the arch barrels and pier–arch interfaces, reflecting stiffness degradation and internal force redistribution due to material nonlinearity.

Table 3 summarizes the corresponding principal stress and stress intensity values. The nonlinear analysis produced substantially higher tensile and compressive stress demands together with a significant increase in stress intensity, quantitatively confirming the stress redistribution observed in Fig. 5. These results demonstrate that linear dynamic analysis considerably underestimates the seismic stress demand of the historic masonry bridge.

4.3 Damage Mechanism

Fig. 6 presents the equivalent plastic stress distribution and the corresponding crack pattern at the critical response time (t = 11.66 s), which corresponds to the maximum resultant displacement of the third bridge opening. The equivalent plastic stress contours indicate that nonlinear material yielding is primarily concentrated around the arch barrels, arch–spandrel interfaces, and pier regions, reflecting localized inelastic deformation under seismic loading. The crack pattern exhibits a similar spatial distribution, confirming that damage initiates and propagates predominantly in the same critical zones where elevated plastic stresses develop.

The close agreement between the plastic stress concentration and crack distribution demonstrates that the nonlinear response of the bridge is governed by localized tensile cracking and progressive material degradation rather than uniform stress development. These observations are consistent with the previously discussed displacement response and highlight the importance of nonlinear material modeling for accurately capturing damage evolution in historic masonry arch bridges.

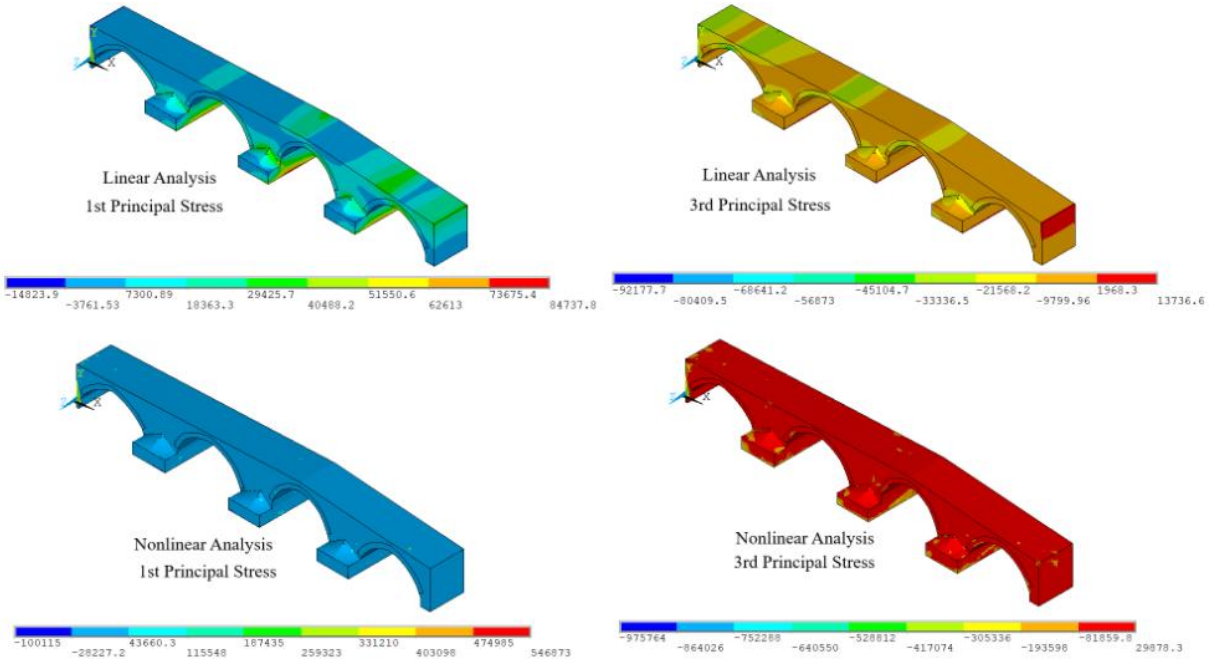


Fig. 5. Comparison of the first and third principal stress distributions obtained from the linear and nonlinear dynamic analyses at the critical response time corresponding to the maximum resultant displacement of the third bridge opening.

Table 3. Comparison of principal stress and stress intensity values at the critical response time.

Analysis	**Max. Principal Stress (MPa)**	**Min. Principal Stress (MPa)**	**Stress İntensity (MPa)**
Linear	0.085	-0.092	0.086
Nonlinear	0.547	-0.976	1.01

5 Conclusions

This study compared the seismic response of a historical four-span masonry arch bridge through linear and nonlinear time-history analyses using a three-dimensional FE model incorporating the Drucker–Prager plasticity model and the Willam–Warnke failure criterion. The results demonstrated that material nonlinearity significantly influences the bridge's dynamic response. Compared with the linear analysis, the nonlinear model predicted larger displacement amplitudes, stiffness degradation, phase shifts, changes in equilibrium, and permanent deformation after crack initiation. The wide range of displacement amplification factors further confirmed that linear analysis substantially underestimates the seismic response of historical masonry bridges.

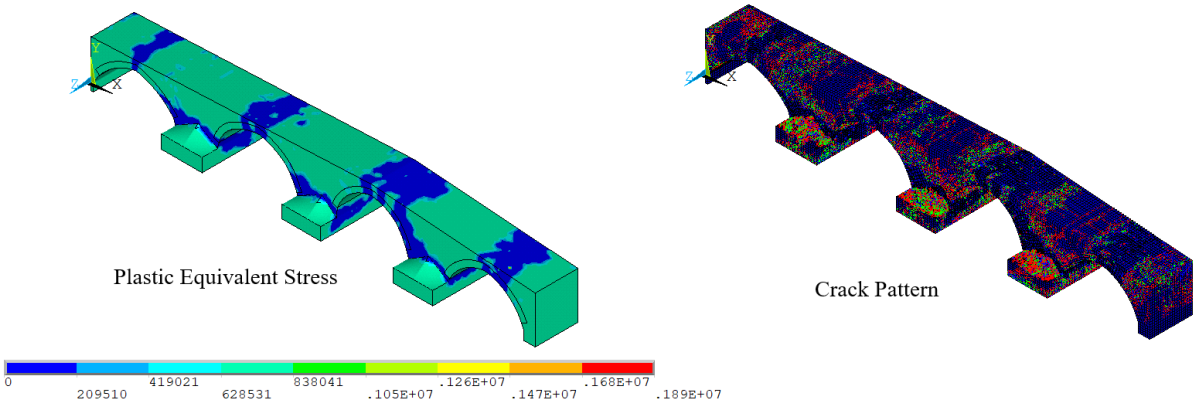


Fig. 6. Equivalent plastic stress and crack pattern obtained from the nonlinear dynamic analysis at the critical response time

The nonlinear analysis also produced considerably higher principal stress and stress intensity, revealing localized stress concentrations that the linear model could not capture. The agreement among the principal stress distributions, equivalent plastic stress, and crack patterns indicated that damage was concentrated primarily around the arch barrels, arch–spandrel interfaces, and pier regions, reflecting progressive material degradation and internal force redistribution under seismic loading.

Overall, the results confirm that nonlinear constitutive modeling is essential for realistic seismic assessment of historical masonry arch bridges. While linear dynamic analysis may be suitable for preliminary evaluation, it cannot adequately represent stiffness degradation, permanent deformation, stress redistribution, or damage evolution. Therefore, nonlinear dynamic analysis provides a more reliable basis for seismic vulnerability assessment and the development of effective conservation and strengthening strategies for historical masonry bridges.

Acknowledgments

The authors would like to express their sincere appreciation to the General Directorate of Highways (KGM), Türkiye, for providing the bridge geometry and the associated technical data, which formed the basis for the FE model developed in this study.

References

1. Lourenço, P. B.: Computational Strategies for Masonry Structures. PhD Thesis, University of Porto, Portugal (1996).
2. Roca, P., Cervera, M., Gariup, G., Pelà, L.: Structural analysis of masonry historical constructions. Classical and advanced approaches. Archives of Computational Methods in Engineering, 17(3), 299-325, Springer (2010).
3. Riveiro, B., Caamaño, J. C., Arias, P., Sanz, E.: Photogrammetric 3D modelling and mechanical analysis of masonry arches: An approach based on a discontinuous model of voussoirs. Automation in Construction, 20(4), 380–388 (2011).
4. Pelà, L., Cervera, M., Roca, P.: Continuum damage model for orthotropic materials: Application to masonry. Computer Methods in Applied Mechanics and Engineering, 200(9-12), 917–930 (2011).
5. Drucker, D. C., Prager, W.: Soil mechanics and plastic analysis for limit design. Quarterly of Applied Mathematics, 10(2), 157–165 (1952).
6. Willam, K. J., Warnke, E. P.: Constitutive model for the triaxial behavior of concrete. In: Proc. Int. Association for Bridge and Structural Engineering (IABSE), vol. 19, pp. 1–30. ISMES, Bergamo (1975).

7. Fanning, P. J., Boothby, T. E.: Three-dimensional modeling and full-scale testing of stone arch bridges. Computers & Structures, 79(29-30), 2645–2662 (2001).
8. Sevim, B., Bayraktar, A., Altunişik, A. C., Atamtürktür, S., Birinci, F.: Assessment of nonlinear seismic performance of a restored historical arch bridge using ambient vibrations. Nonlinear Dynamics, 63(4), 755–770 (2011).
9. Alpaslan, E., Yilmaz, M. F., Şengönül, B. D.: Rating and reliability assessment of a historical masonry arch bridge. Journal of Civil Structural Health Monitoring, 13(4), 1003-1021 (2023).
10. Hejazi, M., Mehdian, A.: Experimental and numerical investigation on masonry arch bridges under uniform and line loads. Structures; 47: 665–80 (2023).
11. Clough, R.W., Penzien, J.: Dynamics of Structures. 2nd edn. McGraw-Hill, New York (1993).
12. Chopra, A.K.: Dynamics of Structures: Theory and Applications to Earthquake Engineering. 5th edn. Pearson, Upper Saddle River (2017).
13. Bayraktar, A., Türker, T., Altunişik, A.C.: Experimental frequencies and damping ratios for historical masonry arch bridges. Construction and Building Materials, 75, 234–241 (2015).
14. Şakalak, E., Sever, A.E., Usta, P.: Investigation of dynamic behavior of a historical masonry arch bridge: A comparative study on solid and shell element models with SAP2000. Konya Journal of Engineering Sciences, 14(1), 497–517 (2026).
15. Hall, J.F.: Problems encountered from the use (or misuse) of Rayleigh damping. Earthquake Engineering & Structural Dynamics, 35(5), 525–545 (2006).
16. Charney, F.A.: Unintended consequences of modeling damping in structures. Journal of Structural Engineering, 134(4), 581–592 (2008).
17. Jehel, P., Léger, P., Ibrahimbegovic, A.: Initial versus tangent stiffness-based Rayleigh damping in inelastic time history seismic analyses. Earthquake Engineering & Structural Dynamics, 43(3), 467–484 (2014).

Author Contribution Statement

- *Conceptualization:* Emre ALPASLAN
- *Methodology:* Emre ALPASLAN, Muhammed Mustafa ÖZTÜRK
- *Investigation:* Emre ALPASLAN, Muhammed Mustafa ÖZTÜRK
- *Writing – Original Draft:* Emre ALPASLAN
- *Writing – Review & Editing:* Muhammed Mustafa ÖZTÜRK

List of Abbreviations

- **FE** — Finite Element
- **DP** — Drucker–Prager
- **WW** — Willam–Warnke

Publication Note

This paper was peer-reviewed, accepted for presentation, and included in the proceedings of the ACE2026 – International Conference on Advances in Civil Engineering, held on 12–14 October 2026 in Trabzon, Türkiye.

This paper may be cited as follows:

Emre ALPASLAN, Muhammed Mustafa ÖZTÜRK, "Comparative Linear and Nonlinear Seismic Analysis of a Historical Masonry Arch Bridge: Dynamic Response and Damage Evolution," in Proceedings of the ACE2026 – International Conference on Advances in Civil Engineering, Trabzon, Türkiye, 12–14 October 2026.

SSI Analysis of a NPP Building for FWN Ground Motion Model

Gizem Çağlar Dal[1] and Kurtuluş Soyluk[2]
[1] 0009-0000-7951-1783, Çankaya University, Civil Engineering Department, Ankara, Türkiye, gcaglar@cankaya.edu.tr
[2] 0000-0002-3039-0332, Gazi University, Civil Engineering Department, Ankara, Türkiye, ksoyluk@gazi.edu.tr

Abstract. In this study, random vibration analysis (RVA) of a nuclear power plant (NPP) structure under seismic loads was performed and its structural behavior was evaluated using the 1995 Kobe earthquake as a data point. A typical NPP structure, used in China, modeled as a three-dimensional system. In this study, RVA were conducted for firm, medium, and soft soil conditions to determine the effects of seismic motions on NPP systems. The study utilized a RVA theory based on the filtered white noise (FWN) ground motion model. The aim was to compare the obtained results for the fixed-base model and the soil-structure interaction (SSI) model. Thus, the effects of different soil types and SSI on the dynamic behavior of the structure are investigated using a RVA. The study concluded that soil type and SSI significantly affect the dynamic behavior of the studied NPP structure compared to the fixed-base assumption.

Keywords: Random vibration analysis (RVA), soil-structure interaction (SSI), filtered white noise (FWN) ground motion model, nuclear power plant (NPP)

1 Introduction

The dynamic behavior of NPP structures under seismic effects has long been assessed primarily using deterministic analysis methods. Deterministic approaches allow the structural response to be easily calculated under well-defined, uncertainty-free loads [1]. However, due to the inherently random nature of earthquake loads, these methods have limitations in accurately reflecting the real seismic behavior. In reality, dynamic effects such as earthquakes are often influenced by multiple vibration sources, and these effects exhibit a random character. Therefore, the use of RVA has become necessary to evaluate the behavior of NPP structures under seismic actions in a more realistic and reliable manner. This requirement becomes even more important, especially in cases where soil conditions play a decisive role in structural response. Particularly in NPP structures built on non-stiff soils, SSI is a critical parameter directly affecting the seismic performance of the structure, and considering the combined behavior of the soil and structure is of great importance for a safe design. In this context, numerous studies in the literature have examined the effects of SSI on the seismic behavior of NPP structures, and highlighting the decisive role of SSI in structural response.

Wang et al. [2] used a finite element model (FEM) with conductive boundaries to investigate the SSI of NPP buildings against vertical seismic effects and examined factors affecting computational accuracy, such as the dimension of the domain and the types of artificial boundaries. Firoj and Maheshwari [3] presented a detailed literature review of finite element method (FEM)-based approaches that consider SSI for NPP founded on alluvial soil. Nguyen et al. [4] investigated the effects of earthquake frequency content and SSI on the seismic behavior of nuclear reactor buildings by performing three-dimensional nonlinear analyses in the time domain. The study showed that both the earthquake frequency content and SSI highly influence how nuclear buildings behave under seismic load. Maheshwari and Firoj [5] presented the studies about SSI analysis in NPP and discussed the key issues. Bahuguna and Firoj [6] investigated the seismic performance of NPP structures constructed on layered sand soil by

considering the nonlinear behavior of both the structure and the soil using a FEM in ABAQUS. Li et al. [7] developed general SSI method based on the geographic information system, which can practically consider topographic irregularities and is suitable for efficient dynamic analyses in the time domain. Li et al. [8] investigated the seismic behavior of base-isolated NPP in layered sites using a nonlinear numerical analysis method and concluded that SSI, soil nonlinearity, and embedment effects have significant influences on the structural response. Wang et al. [9] investigated the effects of site conditions, seismic input, and artificial boundaries on structural response using a 3D FEM for buried NPP structures. Li et al. [10] developed a large-scale computational method for NPP structures using the scaled boundary FEM and conducted SSI analyses considering embedment effects, different foundation shapes and soil conditions.

Unlike previous studies in the literature, this study investigates the SSI behavior of a NPP structure under different ground conditions using RVA based on a FWN model. Within the scope of the analysis, a system modeled with both soil and structure was compared with a fixed-base structure model; SSI effects were evaluated based on stress and displacement results. Thus, the response of the structure under random dynamic loads such as earthquakes was revealed more realistically, and the effect of different ground conditions on the structural response was analyzed. It is predicted that the findings of this study will contribute to the more realistic determination of SSI in NPP structures.

2 Finite Element Model (FEM) of The NPP-Soil System

2.1 NPP Containment Building

A FEM of the NPP structure was created using the ABAQUS program, and numerical analyses were performed. In this study, two separate models of the NPP building were developed: a fixed-base model and a NPP model including the SSI**.** The FEM of the selected NPP containment building is given in Fig. 1.

The NPP containment structure model used in this study represents a typical NPP containment structure commonly used in China, and the geometric features, dimensions, and material parameters of the structure were created based on the data given in Lu X et al. [11] and Sadique MR et al. [12].

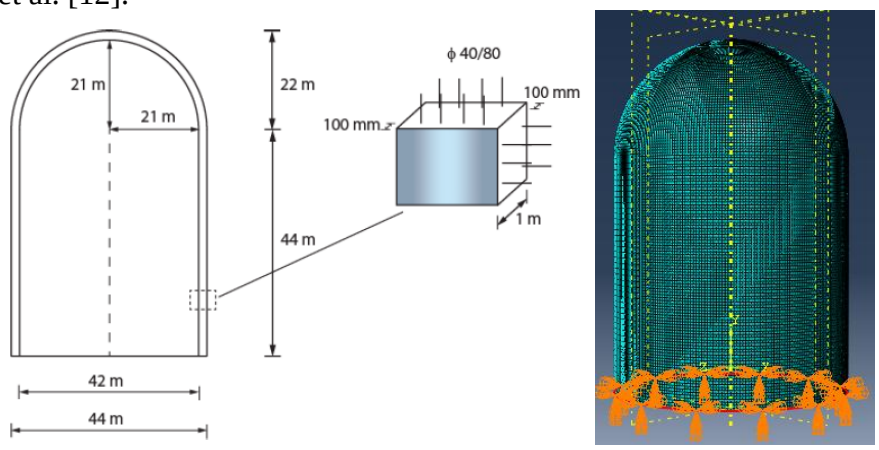


Fig. 1. Cross-sectional view and 3D FEM model of the NPP

For the NPP building B50 class concrete is used, and the concrete damaged plasticity model available in ABAQUS program is used for the concrete. The parameters used in the study were presented by Esfahani et al. [13].

The material properties for reinforcing steel are shown in the Table 1.

Table 1. Material properties for reinforcing steel [14].

Density (kg/m^3)	Young's Modulus (GPa)	Poisson's Ratio	Yield Stress (MPa)	Tensile Stress (MPa)
7850	210	0.3	503.06	603.43

2.2. Soil System

In order to determine the effect of the SSI on the considered NPP containment building, three homogeneous soil conditions are used, namely the firm, medium and soft soil conditions. For the selected soil conditions, standard soil properties obtained from the literature [4] are used (Table 2). In this study, the soil profile is assumed to be a single soil layer located on a rigid half-space. The thickness of the soil profile was assumed to be 30 m. To be able to take into account the nonlinear behavior of the soil medium in the analyses, the Mohr–Coulomb plasticity model included in ABAQUS is considered as the constitutive model.

Table 2. Soil properties [4]

Soil Type	Young`s modulus (MPa)	Poisson`s ratio	Unit weight (kN/m^3)	Damping (%)	Cohesion (MPa)	Friction angle (°)	Dilation angle (°)
Firm	2000	0.30	20	5	0.19	30	15
Medium	500	0.35	19	5	0.05	30	15
Soft	150	0.35	19	5	0.05	30	15

2.3. FE Modeling Of The NPP Containment Building-Soil System

ABAQUS/CAE 6.11 [14] software is used in this study to model the three-dimensional FEM of the NPP containment building-soil system. Considering a direct SSI approach, the NPP containment building, the foundation and the soil are modeled as a single interacting system. Fig. 2 shows the 3D FEM of the SSI.

The FEM of the structure was modeled in ABAQUS using layered shell elements, with a mesh size of 0.7 m x 0.5 m, and S4R type linear quadrilateral shell elements (30964 elements) were used. On the other hand, the soil and foundation are modeled using solid elements. Linear brick elements of type C3D8R (186984 elements) and quadratic brick elements of type C3D20R elements (58996 elements) are used in FE model of the underlying soil and foundation, respectively. The global mesh size of the soil below the foundation is considered as 0.7 m. While the mesh size increases gradually up to 4 m at the side boundaries, it increases from 2 m to 2.8 m along the depth of the soil medium.

As known, to avoid wave reflection from the boundaries, large soil domains can be used as a solution. But, considering the fact that enlarging the soil domain will require much computational work, in this study it is intended to use infinite elements (CIN3D8) at the lateral boundaries available in ABAQUS. Infinite elements provide quiet boundaries to the FEM in dynamic analyses [15]. On the other hand, the radius of the soil is considered as 140 m, more than three times the radius of the foundation. While the interaction between NPP and foundation is modeled with "Shell to Solid Coupling" contact, the interaction between foundation and soil is modeled with "Tie" contact. Fixed boundary conditions are adopted at the bedrock below the soil layer.

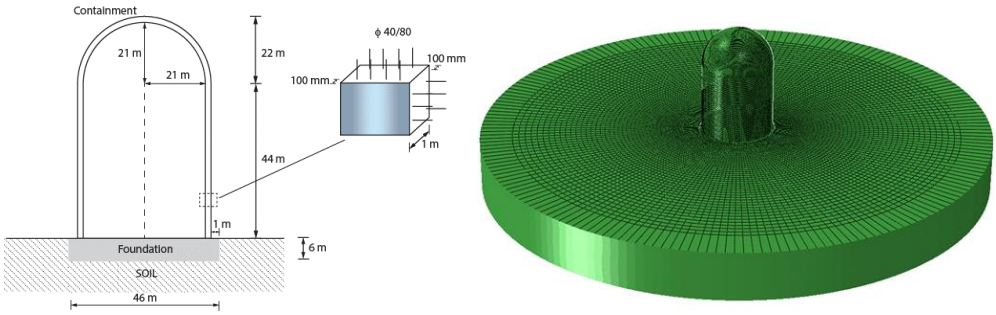


Fig. 2. Cross-sectional view and 3D FEM of the NPP building–soil system

2.4. Modal Characteristics

Eigenvalue analyses are performed to obtain its modal characteristics so that the Rayleigh damping coefficients α and β needed in ABQUS can be determined. The coefficients α and β can be determined as [16]:

$$\alpha = \xi \frac{2w_i w_j}{w_j + w_j} \quad , \quad \beta = \xi \frac{2}{w_j + w_j} \tag{1}$$

In this study, Rayleigh damping coefficients are determined from the dominant modes (w_i and w_j) of the combined soil-structure system and the damping ratios of the soil (ξ_{Soil}) and structure ($\xi_{Structure}$). A similar strategy was used by Bayraktar and Hökelekli [16]. While the dominant modes of the SSI system with firm soil are the 1st (f_1 = 3.1728 Hz) and 25th (f_{25} = 4.8195 Hz) modes, the dominant modes of the SSI system with soft soil are the 1st (f_1 = 0.9027 Hz) and 25th (f_{25} = 0.9509 Hz) modes. Similarly, for the SSI system with medium soil, the dominant modes are the 1st (f_1 = 2.1426 Hz) and 25th (f_{25} = 2.4302 Hz) modes. Thus, the calculated Rayleigh coefficients are given in Table 3.

Table 3. α and β parameters

Soil Type	Mass-proportional coefficient (α)	Stiffness-proportional coefficient (β)
Firm	1.202	0.00199
Medium	0.716	0.00348
Soft	0.291	0.00859

2.5. Earthquake Records

Table 4 contains information regarding the earthquake records used in the analysis. Only far-fault records were considered for this study. Additionally, the $(V_s)_{30}$ value, the most important parameter for determining soil class, was utilized. The $(V_s)_{30}$ value represents the average slip velocity in the first 30 meters, and in this study, soils were classified as soft (0-360 m/s), medium (360-700 m/s), and stiff (larger than 700 m/s).

Table 4. Kobe earthquake records

Earthquake	**Station Name**	**Earthquake Magnitude**	**Fault Distance (km)**	**Soil Class**	**$(V_s)_{30}$ (m/s)**	**PGA (g)**	**PGV (cm/s)**
Kobe	Rincon Hill	6.93	74.14	B	873.10	0.093	11.04

Earthquake	Station Name	Earthquake Magnitude	Fault Distance (km)	Soil Class	$(V_s)_{30}$ (m/s)	PGA (g)	PGV (cm/s)
Loma Prieta	B. Strawberry Canyon	6.93	78.41	C	512.27	0.075	9.68
Kobe	Kakogawa	6.90	22.50	D	312.00	0.324	26.86

3 Random Vibration Analysis

In order to investigate the effects of earthquakes in detail, analyses were carried out using random vibration theory, taking into account the FWN ground motion model. In this study, RVA were performed using the power spectral density (PSD) functions defined for the FWN model. RVA is an analysis method that takes into account uncertainties and random variables. This analysis can help to make design decisions to reduce risks by assessing the effects of random loads to which NPP structures may be subjected to over a period of time. The terms used in this study, such as PSD function, root mean square, etc., are expressed in the following formulations [15]. Abaqus obtains the root mean square (RMS) value by integrating a single-sided PSD across the frequency range.

$$\sigma(x) = \sqrt{R_x(0)} = \sqrt{\int_0^\infty S_x(f)df} \tag{2}$$

where $S_x(f)$ is the PSD function and $R_x(0)$ is the autocorrelation function of a variable.

3.1. Filtered White Noise (FWN) Ground Motion Model

This mathematical model is used to represent ground motions caused by earthquakes. The model filters out white noise in a specific frequency band to produce motions that represent real earthquake behavior. According to Clough and Penzien [18], the PSD function of ground acceleration is in the following form.

$$S_{\ddot{v}_g}(w) = S_0|H_g(w)|^2|H_f(w)|^2 \tag{3}$$

$$|H_g(w)|^2 = \frac{w_g^4+4\xi_g^2w_g^2w^2}{\left(w_g^2-w^2\right)^2+4\xi_g^2w_g^2w^2} \tag{4}$$

$$|H_f(w)|^2 = \frac{w^4}{(w_f^2-w^2)^2+4\xi_f^2w_f^2w^2} \tag{5}$$

Eqs. (4-5) are the frequency response functions of the first and second filters, respectively. These equations represent the dynamic properties of the soil system, the amplitude parameter of the white noise bedrock acceleration is defined as S0. Furthermore, the resonance frequency and damping ratio of the first filter are expressed by the parameters ωg and ξg, respectively, while the resonance frequency and damping ratio of the second filter are expressed by the parameters ωf and ξf. In this study, different homogeneous soil types were evaluated and for filter parameters, the values recommended by Der Kiureghian and Neuenhofer [19] were used as given in Table 5.

Table 5. Power spectral density (PSD) parameters for model soil types

Soil type	w_g (rad/s)	ξ_g	w_f (rad/s)	ξ_f

Firm	15.0	0.6	1.5	0.6
Medium	10.0	0.4	1.0	0.6
Soft	5.0	0.2	0.5	0.6

The S_0 coefficient was calculated for the stochastic analysis of the structures, for which the STOCAL [20] and STOCAL-II [21] computer programs were used. In the first stage, the PSD functions of the seismic motions evaluated in the study were obtained using STOCAL, and in the second stage, the PSD variances corresponding to the FWN ground motion models were calculated using the STOCAL-II program. S_0, is calculated as the ratio of the actual earthquake acceleration variance to the FWN model variance for each ground motion component as follows,

$$S_0=\frac{\sigma^2{}_{\ddot{u}g}}{\int_0^{\infty} H_g(w)^2 H_f(w)^2 dw}=\frac{\sigma^2{}_{\ddot{u}g}}{\Phi} \tag{6}$$

where $\sigma^2{}_{\ddot{u}_g}$ and Φ represent the variances of the actual ground motion acceleration and the FWN model, respectively. After generating the PSD values versus frequency by STOCAL, the variances of the ground motion components are determined by STOCAL-II. For the Kobe earthquake acceleration, the S_0 values were obtained as follows (Table 6).

Table 6. S_0 coefficient values for the Kobe earthquake

Soil Type	S_0 Coefficient Values for the Kobe Earthquake (m^2/s^3)
Firm	4.0843×10^{-5}
Medium	6.6067×10^{-5}
Soft	1.935×10^{-3}

The spectral density functions of FWN ground motion models were obtained for each soil type using the calculated S_0 coefficients.

Mean max values were calculated by considering the RMS of displacement (RU1) and the RMS of velocity (RV1) from the formulations given below [22]. The mean of maximum value can be expressed as follows, here p is the peak factor and σz is the RMS response.

$$\mu = p\sigma_z \tag{7}$$

$$p = \sqrt{(2lnv_eT)} + \frac{0.5772}{\sqrt{(2lnv_eT)}} \tag{8}$$

$$v_e = (1.9\xi^{0.15} - 0.73)v_0 \tag{9}$$

$$v_0 = \frac{1}{\pi}\frac{\sigma_{\dot{z}}}{\sigma_z}=\frac{1}{\pi}\left(\frac{\int_{-\infty}^{\infty} w^2 S_z(w)dw}{\int_{-\infty}^{\infty} S_z(w)dw}\right)^{1/2} \tag{10}$$

In the equation, the parameters ν_e and ν_0 represents reduced mean zero-crossing rate and mean zero-crossing rate respectively. T represents the duration of motion. In addition, ξ, σ_z and $\sigma_{\dot{z}}$ represents the modal damping ratio, standard deviation of the random process and its derivative, respectively. In the analyses, the duration of movement for each earthquake was determined from the recorded data, and a damping ratio of 5% was used as the basis.

4 Results and Discussion

This study investigates the RVA of a NPP structure under seismic loading and explores its effects on the SSI system. Analyses were conducted using random vibration theory, considering the FWN ground motion model. The FWN ground motion model was determined, and the seismic motion in the RVA is expressed as a spectral density function as shown in Fig. 3. A typical NPP structure was selected as an application. A FEM was obtained for the RVA of this structure system under the influence of seismic motion applied in the horizontal direction, and RVA was performed.

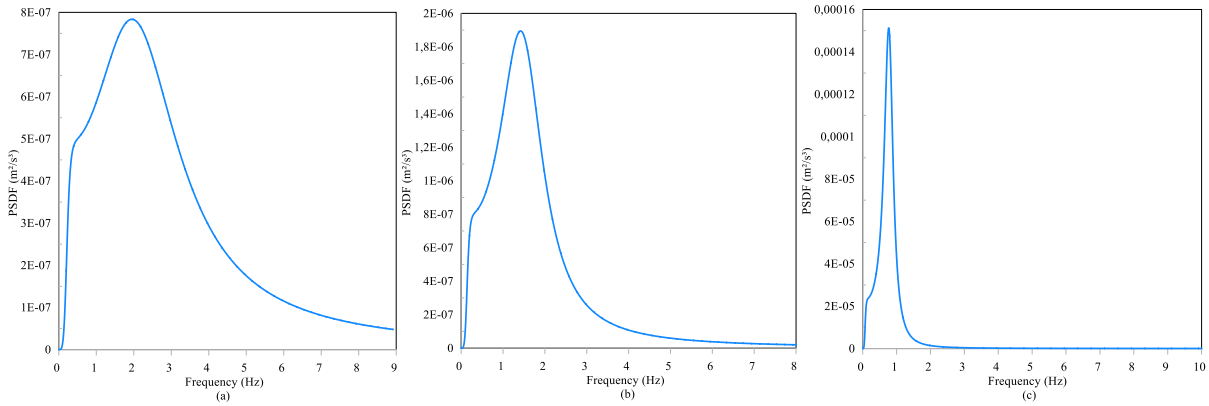


Fig. 3. PSD functions for (a) firm soil, (b) medium soil, (c) soft soil

The PSD functions given in Fig. 3 show that the dynamic behavior of the system changes significantly depending on the soil type. For firm soil, the energy is distributed over a wider frequency range, while as the soil softens, this distribution narrows and the dominant frequency shifts to lower frequency values. In the NPP-soil model, the dominant frequencies are obtained as 3.17 Hz, 2.17 Hz, and 0.90 Hz for firm, medium, and soft soils, respectively, while in the fixed-base model, this value is approximately 4.46 Hz. Especially in soft soil, the energy is concentrated in a narrow frequency band, forming a sharp peak. This variation causes a significant increase in the maximum displacement and stress values in soft soil condition and clearly demonstrates that SSI affects the structural response.

Since the maximum displacement occurs at the top of the structure, the mean maximum displacement value was calculated using Eq. (7) and presented in Table 7. In addition to the displacements, the maximum structural stresses (RMS of stress-RS11) were also compared as shown in Table 7.

Table 7. Mean of max displacement and max stresses in the NPP building

Kobe Eartquake								
	Soil+NPP				Fixed-base model			
Soil Type	**RU1 (m)**	**RV1 (m/s)**	**Mean Max Value (mm)**	**RS11 (N/m²)**	**RU1 (m)**	**RV1 (m/s)**	**Mean Max Value (mm)**	**RS11 (N/m²)**
Firm	4.00E-4	7.80E-3	1.22	5.64E+4	1.03E-4	2.76E-3	0.32	6.73E+3
Medium	1.70E-3	2.21E-2	4.98	1.25E+5	6.75E-5	1.66E-3	0.21	4.20E+3
Soft	1.92E-2	1.38E-1	52.14	5.63E+5	1.65E-4	2.22E-3	0.48	8.15E+3

Fig. 4 shows the displacement variation over the height of the NPP+soil and the fixed-base NPP model.

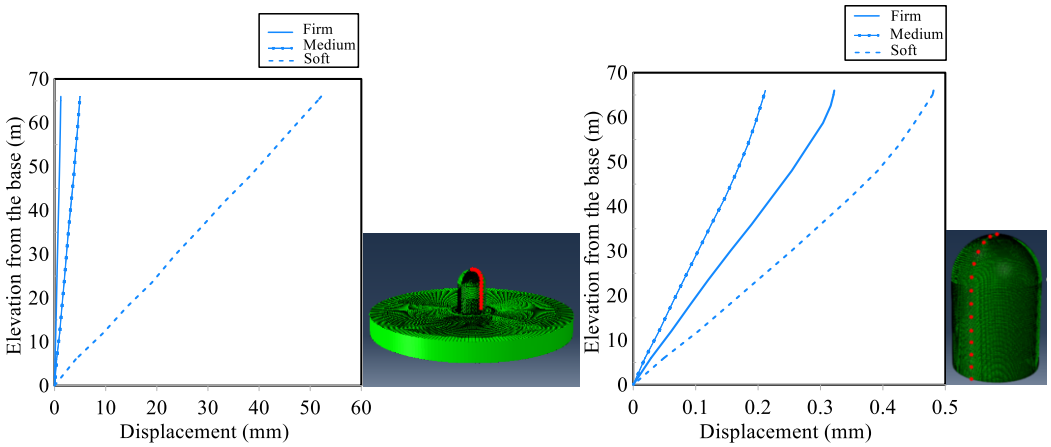


Fig. 4. Elevation–displacement graph for NPP+soil and fixed-base models.

Additionally, the variations of the maximum stresses RS11 in the NPP structure are presented in Fig. 5 and Fig.6.

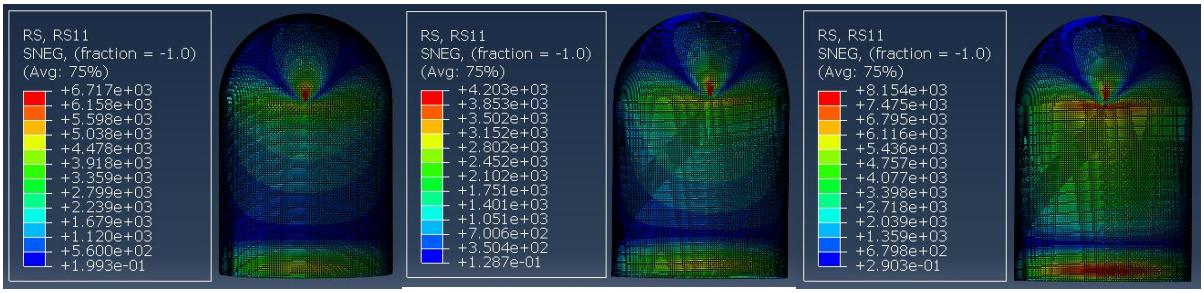


Fig. 5. RS11 stresses for firm, medium, and soft soils respectively (fixed-base model).

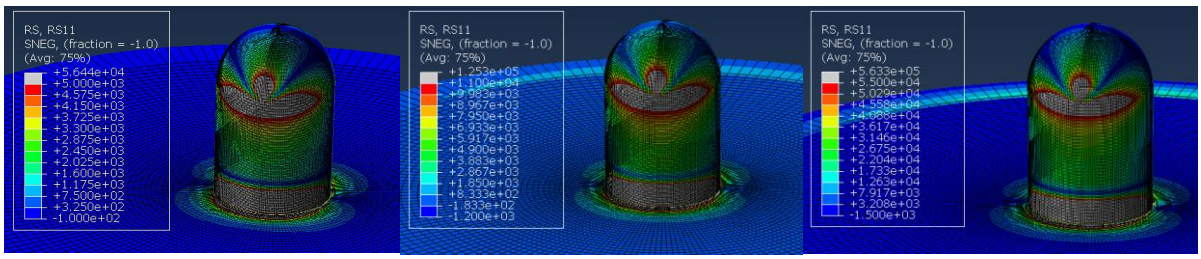


Fig. 6. RS11 stresses for firm, medium, and soft soils respectively (NPP-soil model)

The decisive influence of SSI effect on the seismic behavior can be clearly observed from the obtained results. As expected, the mean of max. displacement and RS11 stresses obtained for the NPP+soil model are larger for all soil types if compared with the fixed-base model. This difference is particularly pronounced in medium and soft soils. It can also be observed that the fixed-base model significantly underestimates displacements and stresses if soil deformation and wave propagation are neglected.

Considering the RVA based on the FWN model, it can be noticed that the soil medium causes an amplification effect in the frequency components, and this effect significantly increases the structural responses. In the NPP+soil model, due to the limited soil rigidity, the natural period of the system extends, and accordingly larger displacement and stress values take place under seismic loads. On the other hand, since the soil is assumed to be infinitely rigid in the fixed-base model, these amplification mechanisms are ignored, and the results are far from representing the actual behavior, especially for weak soil conditions.

5 Conclusions

Neglecting SSI, especially in medium and soft soil conditions, leads to underestimation of the results that may cause significant errors in engineering design. Therefore, using models that incorporate the SSI effect in conjunction with FWN-based RVA is of great importance in obtaining more reliable and realistic design results.

As future studies, it can be suggested that the results obtained using RVA be investigated comparatively with the fixed-base model, with the infinite element approach, and with the modeling by using spring-damper elements in external boundaries. It is believed that such comparisons will contribute to the identification of more realistic modeling approaches by revealing the effect of boundary conditions on the dynamic responses of NPP systems.

References

[1] Soyluk, K.: Stochastic Analysis of Cable-Stayed Bridges. Master's Thesis, Karadeniz Technical University, Institute of Science, Trabzon, Türkiye, 160 pp. (1997).

[2] Wang X, Zhou Q, Zhu K, Shi L, Li X, Wang H.: Analysis of seismic soil-structure interaction for a nuclear power plant (HTR-10). Sci Technol Nucl Install 2017, 1–13 (2017) DOI:10.1155/2017/2358403

[3] Nguyen, D. V., Kim, D., & Nguyen, D. D.: Nonlinear seismic soil-structure interaction analysis of nuclear reactor building considering the effect of earthquake frequency content. Structures, 26, 901–914 (2020). https://doi.org/10.1016/j.istruc.2020.05.013

[4] Firoj, M., & Maheshwari, B. K.: A review on soil-structure interaction for nuclear power plants. In: 16th Symposium on Earthquake Engineering (16SEE), pp. 71. IIT Roorkee, India, (2018).

[5] Maheshwari BK, Firoj M.: A State of Art: Seismic Soil–Structure Interaction for Nuclear Power Plants. In: Sitharam TG, Jakka R, Kolathayar S, (ed.), Latest Developments in Geotechnical Earthquake Engineering and Soil Dynamics, p. 393–409. Springer Transactions in Civil and Environmental Engineering, (2021). https://doi.org/10.1007/978-981-16-1468-2_17

[6] Bahuguna, A., & Firoj, M.: Nonlinear seismic performance of nuclear structure with soil–structure interaction. Iranian Journal of Science and Technology Transactions of Civil Engineering, 46, 2975–2988 (2022). https://doi.org/10.1007/s40996-021-00728-2

[7] Li, J., Zhou, L., Li, S., Lin, G., & Ding, Z.: Soil–structure interaction analysis of nuclear power plant considering three-dimensional surface topographic irregularities based on automatic octree mesh. Engineering Structures, 275, 115161 (2023). https://doi.org/10.1016/j.engstruct.2022.115161

[8] Li, J., Liu, Y., Li, Z., & Lin, G.: Global method for nonlinear seismic analysis of embedded base-isolated nuclear island buildings in layered sites. Structures, 56, 105042 (2023). https://doi.org/10.1016/j.istruc.2023.105042

[9] Wang, X., Zhao, M., Guan, J., Yang, J., Du, X., & Zhao, X.: Site effect on seismic response of buried nuclear power plant structure. Soil Dynamics and Earthquake Engineering, 183, 108759 (2024). https://doi.org/10.1016/j.soildyn.2024.108759

[10] Li, J., Hou, H., Li, Z., & Lin, G.: Efficient approach for ground dynamic impedance function of the large-scale nuclear power plant footing under a layered site considering the embedded effect. Computers and Geotechnics, 178, 106917 (2025). https://doi.org/10.1016/j.compgeo.2024.106917

[11] Lu, X., Lin, K., Cen, S., Xu, Z., Lin, L.: Comparing different fidelity models for the impact analysis of large commercial aircrafts on a containment building. Eng. Fail. Anal. 57, 254–269 (2015). https://doi.org/10.1016/j.engfailanal.2015.08.002

[12] Sadique, M.R., Iqbal, M.A., Bhargava, P.: Nuclear containment structure subjected to commercial and fighter aircraft crash. Nucl. Eng. Des. 260, 30–46 (2013). https://doi.org/10.1016/j.nucengdes.2013.03.009
[13] Esfahani, H.M., Hejazi, F., Vaghei, R., Bin Jaafar, M.S., Karimzade, K.: Simplified damage plasticity model for concrete. Struct. Eng. Int. 27 (1), 68–78 (2017). https://doi.org/10.2749/101686616X1081
[14] Soyluk, K., Sadegh-Azer, H.,: Beyond-Design Basis Analyses of Nuclear Power Plant Structures, (International Post Doctoral Research Fellowship Programme) (2020).
[15] ABAQUS Analysis User's Manual: Version 6.6., https://books.google.com.tr/books?id=gPdPvwEACAAJ, last accessed 2024/04/11.
[16] Chopra AK.: Dynamics of Structures: Theory and Applications to Earthquake Engineering. 3rd edn. Prentice Hall, New Jersey (2007).
[17] Bayraktar A, Hökelekli E.: Influences of earthquake input models on nonlinear seismic performances of minaret-foundation-soil interaction systems. Soil Dynamics and Earthquake Engineering 139,106368 (2020). https://doi.org/10.1016/j.soildyn.2020.106368
[18] Clough RW, Penzien J.: Dynamics of structures. 2rd ed. McGraw- Hill, Singapore (1993).
[19] Der Kiureghian A, Neuenhofer A.: A response spectrum method for multiple-support seismic excitations. Earthquake Engineering Research Center, College of Engineering, University of California, Berkeley, CA, Report No. 66 (1991).
[20] Button MR, Der Kiureghian A, Wilson EL.: STOCAL-User information manual. Earthquake Engineering Research Center, College of Engineering, University of California, Berkeley, CA, Report No. UCB/SEMM-81/2 (1981).
[21] Wung CD, Der Kiureghian A.: STOCAL-II: Computer-assisted learning system for stochastic dynamic analysis of structures. Part I. Theory and development. Report No. UCB/SEMM-89/10, Department of Civil Engineering, University of California, Berkeley, USA (1989).
[22] Lee MC, Penzien J.: Stochastic seismic analysis of nuclear power plant structures and piping systems subjected to multiple support excitations. Report No. UCB/EERC-80/19. Earthquake Engineering Research Center, College of Engineering, University of California, Berkeley, CA (1980).

Author Contribution Statement

- *Conceptualization:* Kurtuluş Soyluk
- *Methodology:* Gizem Çağlar Dal
- *Investigation:* Gizem Çağlar Dal, Kurtuluş Soyluk
- *Writing – Original Draft:* Gizem Çağlar Dal
- *Writing – Review & Editing:* Kurtuluş Soyluk

List of Abbreviations

- **FEM** — Finite Element Method
- **NPP**—Nuclear Power Plant
- **RVA**— Random Vibration Analysis
- **RU1**—Root Mean Square of Displacement
- **RV1**— Root Mean Square of Velocity
- **RMS**— Root Mean Square
- **FWN**—Filtered White Noise
- **SSI** — Soil-Structure Interaction
- **PSD**— Power Spectral Density

Conflict of Interest

The authors declare that they have no conflict of interest.

Publication Note
This paper was peer-reviewed, accepted for presentation, and included in the proceedings of the ACE2026 – International Conference on Advances in Civil Engineering, held on 12–14 October 2026 in Trabzon, Türkiye.

This paper may be cited as follows:
Çağlar Dal, G., Soyluk, K., "SSI Analysis of a NPP Building for FWN Ground Motion Model," in Proceedings of the ACE2026 – International Conference on Advances in Civil Engineering, Trabzon, Türkiye, 12–14 October 2026.

Nonlinear Time History Analysis of a 2.5 MW Onshore Wind Turbine Under Earthquake Loads

Ecmel Eylül Naz Özdoğan[1] and Özgür Özçelik[2]
[1] [0009-0008-3991-4754], Department of Civil Engineering, Dokuz Eylul University, 35160 Izmir, Turkey, ozdogan.ecmeleylulnaz@ogr.deu.edu.tr
[2] [0000-0002-1114-4689], Department of Civil Engineering, Dokuz Eylul University, 35160 Izmir, Turkey, ozgur.ozcelik@deu.edu.tr

Abstract. The use of wind energy has increased rapidly in recent years, making the seismic performance of large wind turbines an important research topic. In this study, nonlinear time-history analyses were performed to investigate the earthquake response of an existing 2.5 MW onshore wind turbine. A detailed finite element model including the tower and blades was developed in OpenSees. The model was defined using appropriate element types, material models, structural idealizations, and boundary conditions for nonlinear dynamic analysis.

Three recorded ground motions were selected for the analyses. Two records had approximately the same peak ground acceleration (PGA) of 0.38g, while the third had a lower PGA of approximately 0.14g. The records with similar PGA values were selected to examine whether nearly identical peak accelerations can produce different structural demands. The lower-PGA record was included to evaluate whether a smaller PGA can still generate a comparable or greater structural response. In addition, all records were scaled by a factor of 15 to provide a common high scale-factor level and clearly expose nonlinear effects such as yielding and residual displacement. This scale factor was used for comparison purposes and does not represent a design earthquake. The structural response was evaluated in terms of tower-top displacement, base shear, base bending moment, and stress demand. The results were compared to assess the relationship between PGA and structural response and to determine the effect of scaling the ground motions by a factor of 15 on the nonlinear behavior of the wind turbine.

Keywords: Wind turbines; nonlinear time history analysis; finite element modeling; earthquake
ground motion

1 Introduction

Wind turbines are tall, flexible structures with a large mass concentration near the top of the tower. Their earthquake response is controlled by the distribution of mass and stiffness, the interaction among the tower, rotor-nacelle assembly, and blades, and the frequency, velocity, and duration characteristics of the input motion. Consequently, peak ground acceleration (PGA), although convenient, may not represent the interaction between a record and the turbine's dominant vibration modes.

The structure investigated in this study is a 2.5 MW onshore wind turbine located at the Wind Power Plant in Urla, İzmir, Türkiye. The turbine consists of a tapered tubular steel tower, a rotor-nacelle assembly, and three blades.

Previous studies have investigated wind-turbine response using time-domain analysis, nonlinear finite element models, and incremental dynamic procedures. Ishihara and Sarwar [1] highlighted higher-mode effects; Nuta et al. [2] and Patil et al. [3] evaluated nonlinear seismic

demand and damage states; and Katsanos et al. [4] emphasized the variability associated with ground-motion selection. This study therefore compares two records with nearly identical PGAs and one lower-PGA record at SF1 and SF15 to determine whether PGA-based ranking reproduces the ranking of tower-top displacement, base shear, base moment, and local material demand.

2 Numerical Modeling of the Wind Turbine

2.1 General Description of the Wind Turbine

The investigated system is a 2.5 MW onshore wind turbine consisting of a tapered tubular steel tower, a rotor-nacelle assembly, and three blades. The tower height is approximately 78 m, the hub height is approximately 90 m, and the rotor diameter is 90 m. The varying tower diameter and wall thickness were defined from the available technical data. At the same time, the rotor-nacelle mass and blade system were included to reproduce the dominant fore-aft and side-side response.

Table 1. Main properties of the investigated wind turbine.

Property	Value
Rated power	2.5 MW
Rotor diameter	90 m
Tower height	78 m
Hub height	90 m
Nacelle mass	91 tons
Rotor mass	55 tons

2.2 Model Generation and Material Properties

The model was generated in STKO, which served as the graphical pre- and post-processing environment for OpenSees [5]. Geometry, elements, materials, fiber sections, boundary conditions, and analysis stages were defined in STKO; the resulting Tcl files were fed into the OpenSees engine. This workflow also enabled verification of connectivity, local axes, section assignments, mode shapes, and nonlinear response quantities.

Blade geometry was reconstructed from technical drawings. Representative sections were assigned along a three-dimensional line-element idealization to retain the variation in blade stiffness and mass without incurring the computational cost of a detailed shell model. The tower and blades were modeled using three-dimensional nonlinear beam-column elements with fiber sections. The tubular steel sections of the tower were discretized into fibers, with all fibers assigned the same S355 steel. Although the tower sections consist of a single material, the fiber-section formulation enables the nonlinear stress-strain distribution across the section and the progressive spread of yielding under combined axial force and bending to be captured. Similar fiber-based modeling approaches have been adopted in previous nonlinear studies of wind-turbine towers [6]. This beam-based idealization is also consistent with wind-turbine models that use simplified rotor-nacelle masses to capture the global response efficiently [7, 8]. The tower fibers were assigned the OpenSees Steel02 material, based on the Giuffré-Menegotto-Pinto model with isotropic strain hardening. This material model was used to represent cyclic yielding, stiffness transition during load reversals, and the local stress-strain response of S355 steel. Representative GFRP properties were used for the blades to reproduce their global stiffness and mass contribution. Geometric nonlinearity was included using a P-Delta transformation.

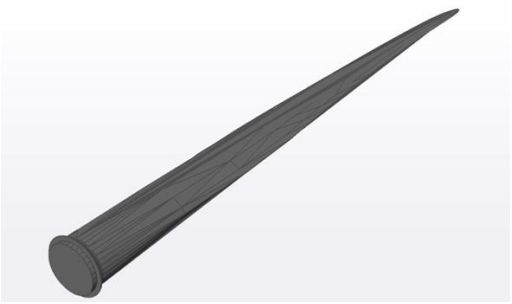
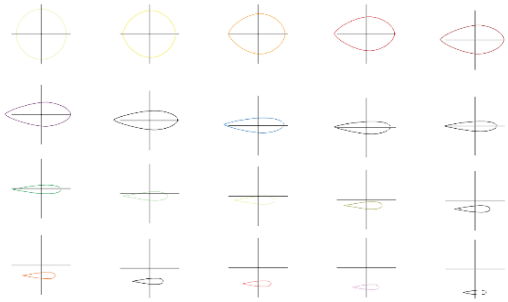
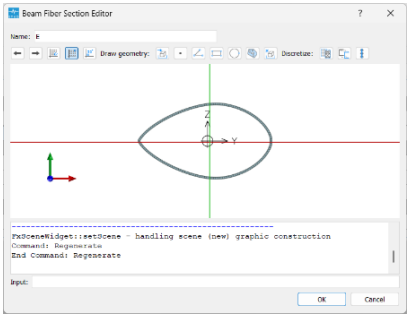


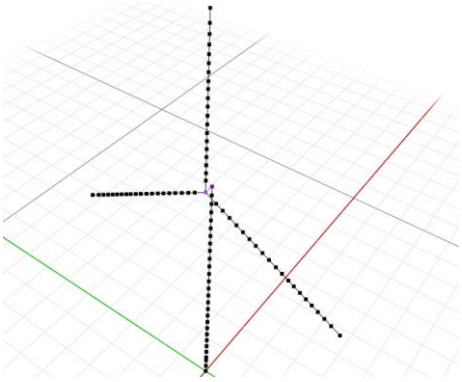
Fig. 1(a). 3D blade geometry

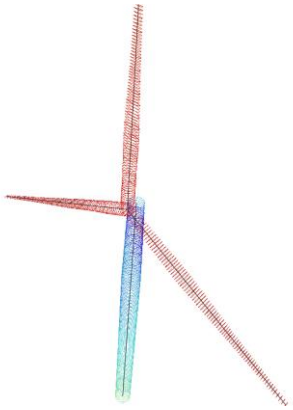




(b) **(c)**

Fig. 1(b). Extracted sections along the blade span. Fig. 1(c). Representative section definitions as beam fiber section





(d) **(e)**

Fig. 1(d). Beam-column element idealization adopted for the wind turbine in the numerical model. (e). Fiber sections assigned to the beam-column elements in the numerical model.

S355 steel fibers represented the tower, whereas representative GFRP properties were assigned to the blades because their principal role was to reproduce global stiffness, mass distribution, and load transfer. The adopted material parameters are summarized in Tables 2 and 3.

Table 2. Mechanical properties of S355 structural steel.

Property	Value
Yield strength	355 MPa
Tensile strength	510-630 MPa
Modulus of elasticity	200 GPa
Shear modulus	81 GPa
Density	7850 kg/m³
Poisson's ratio	0.3

Table 3. Representative mechanical properties used for the GFRP blades.

Property	Value
Yield strength	450 MPa
Modulus of elasticity	38 GPa

The nacelle and the non-blade components of the rotor were represented by lumped masses at the hub-tower connection and linked to the tower and blade roots through rigid links. The mass and weight of the blades were assigned directly to the blade elements, avoiding double counting. This approach preserves the influence of the upper assembly on the natural frequencies and global response without explicitly modeling the drivetrain and hub mechanisms [3, 8]. The blades were assumed to remain stationary, and aero-servo-elastic effects were excluded.

Rayleigh damping was adopted in the nonlinear dynamic analyses. A critical damping ratio of 1% was used for the parked condition considered in all earthquake cases. This value is within the 0.5%-1% range reported for idle turbines and is consistent with the 1% Rayleigh damping used in parked-turbine seismic analysis [3, 7]. The Rayleigh coefficients were calculated from selected modes of the updated numerical model.

2.3 Modal Verification of the Numerical Model

Modal analysis was used to verify the global mass and stiffness distribution. The experimentally identified frequencies were approximately 0.36, 3.00, and 8.35 Hz. These values were obtained from field measurements on the same wind turbine examined in the present study, whose experimental modal characterization was reported in [9], where these frequencies were identified as its dominant global modes. The corresponding fore-aft and side-side frequencies from the OpenSees model are listed in Table 4. Close agreement in the first mode confirms that the model reproduces the dominant global bending response required for the subsequent nonlinear analyses.

Table 4. Updated numerical and experimental modal frequencies of the wind turbine.

Modal results	1st mode fre-	Effective modal mass (%)	2nd mode frequency (Hz)	Effective modal mass (%)	3rd mode frequency (Hz)	Effective modal mass (%)
Experimental	0.36	-	3	-	8.35	-
OpenSees - Fore-Aft	0.36	63.852	2.436	8.4	8.806	0.928
OpenSees - Side-Side	0.359	63.296	2.695	9.49	8.849	1.027

2.4 Boundary Conditions

Foundation flexibility was represented by a three-dimensional zero-length spring element placed between the tower-base node and the ground-side support node. Linear-elastic uniaxial materials were assigned to the six translational and rotational degrees of freedom of the zero-length element. The horizontal translational stiffness was defined as 2.76×10^7 kN/m in both the x and y directions, while the vertical translational stiffness in the z direction was taken as 4.25×10^7 kN/m. The rotational stiffness was defined as 9.60×10^8 kN·m/rad about each of the three global axes. The upper node of the zero-length element was connected to the tower base, whereas the lower node represented the ground-side support. This configuration allowed the flexibility of the foundation-soil system to be incorporated through equivalent translational and rotational springs without explicitly modeling the complete foundation and surrounding soil domain. All spring components were assumed to remain linear elastic throughout the analyses.

The earthquake records were applied using the OpenSees MultipleSupport excitation pattern. For each analysis, the acceleration time history was imposed on the ground-side support node in the selected horizontal direction. Zero acceleration values were added before and after each recorded ground motion. The values added at the beginning allowed the analysis to start from a stationary condition. In contrast, those added at the end allowed the structural response to be evaluated after the ground-motion excitation had ended. The original time increment of each record was retained.

3 Ground-Motion Selection and Analysis Procedure

3.1 Targeted Ground-Motion Selection

The study adopts a focused comparative nonlinear time-history framework rather than a code-based statistical assessment or formal fragility analysis. The selected records are treated as representative case studies because statistically calibrated fragility or incremental dynamic analysis requires a larger record set and multiple intensity levels [10].

The ground-motion records were selected considering the regional seismotectonic characteristics and local soil conditions of the wind turbine site at the Wind Power Plant in Urla, İzmir. The geotechnical investigation conducted at the site reported shear-wave velocities ranging from 600 to 1000 m/s. From the records satisfying these site-related criteria, three ground motions, denoted EQ1, EQ2, and EQ3, were adopted for the focused comparative analyses. EQ1 and EQ2 have nearly identical PGA values of 0.382 g and 0.381 g, respectively, whereas EQ3 has a lower PGA of 0.142 g. This selection directly tests whether PGA alone can rank earthquake severity for a slender, dynamically sensitive wind turbine.

Table 5. Selected ground motions and analysis intensity levels.

Record	Earthquake	Year	Station	Magnitude (Mw)	Rjb (km)	Vs30 (m/s)	PGA at SF1 (g)	PGA at SF15 (g)
EQ1	San Fernando	1971	Lake Hughes #12	6.61	13.99	602.1	0.382	5.73
EQ2	Northridge-01	1994	LA 00	6.69	9.87	706.22	0.381	5.715
EQ3	Taiwan SMART1(45)	1986	SMART1 E02	7.3	51.35	671.52	0.142	2.13

3.2 Analysis Cases and Response Measures

Each ground motion was applied in its original form (SF1) and after amplitude scaling by a factor of 15 (SF15). SF1 characterizes record-to-record variability at the original intensity, whereas SF15 drives the model toward the nonlinear range, allowing response amplification and local yielding to be compared.

The engineering demand parameters were the maximum relative tower-top displacement, base shear and base bending moment, together with the stress-strain response at a common reference fiber located at the tower base. For all three records, this response was extracted from Element 117, Gauss point 0, Fiber 190. Additional tower-wide post-processing was used to identify localized yielding associated with residual deformation.

3.3 Fourier Analysis Procedure

To support the PGA-based comparison, Fourier amplitude spectra were calculated for the three acceleration records. The first fore-aft and side-side modal frequencies obtained from the numerical model were 0.360 Hz (T = 2.778 s) and 0.359 Hz (T = 2.786 s), respectively. The corresponding second-mode frequencies were 2.436 Hz in the fore-aft direction and 2.695 Hz in the side-side direction. These four modal frequencies were superimposed on the Fourier

spectra to compare the frequency content of each record with the fundamental dynamic characteristics of the turbine. Because the two first-mode frequencies are nearly identical, their markers appear very close together on the spectra and together represent the fundamental-frequency range of the structure. Fourier amplitude spectra do not explicitly account for damping, phase characteristics, excitation duration, modal participation, or frequency shifts associated with nonlinear stiffness changes. Therefore, they were used as a qualitative and complementary frequency-domain measure rather than as a standalone predictor of structural demand. Therefore, a high Fourier amplitude near a modal frequency does not necessarily mean that the structure will experience a large nonlinear response. This is especially important at SF15, where nonlinear behavior can change the stiffness and vibration characteristics of the turbine during the earthquake. These changes cannot be captured by the Fourier spectrum of the input ground motion alone.

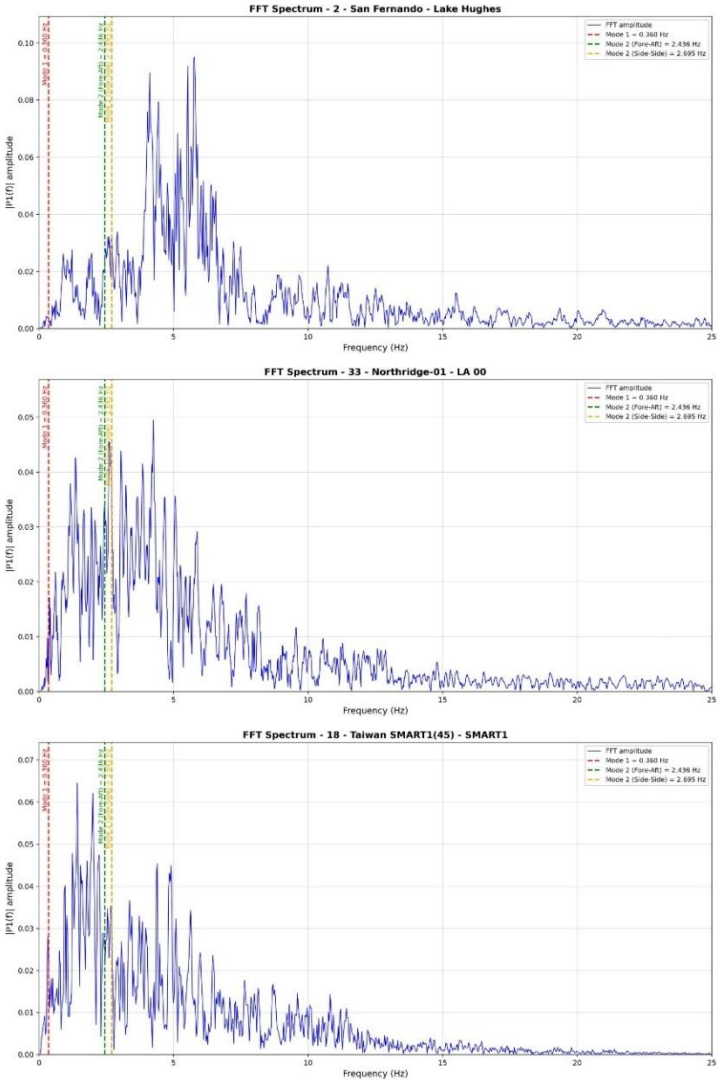


Fig. 2. Fourier amplitude spectra with the first and second structural frequencies superimposed: (a) EQ1-San Fernando, Lake Hughes; (b) EQ2-Northridge-01, LA 00; and (c) EQ3-Taiwan SMART1(45), SMART1.

4 Results and Discussion

4.1 Peak Structural Response

Table 6 summarizes the peak responses from the six nonlinear analyses. At SF1, EQ1 and EQ2 have virtually identical PGA, yet EQ2 produces approximately 57% greater tower-top displacement, 81% greater base shear, and 73% greater base moment than EQ1. The

pronounced differences cannot be explained by PGA amplitude alone and instead reflect record-specific characteristics such as frequency content, duration, and modal participation, consistent with the ground-motion variability documented for wind-turbine seismic assessment [4, 8].

The lower-PGA EQ3 provides a clearer example: despite a PGA of only 0.142g, it produces the largest SF1 tower-top displacement (0.199 m), a larger base moment than EQ1 and a stress demand comparable with EQ2. Thus, ranking the records by PGA does not reproduce the ranking of structural demand, in agreement with earlier observations that nonlinear time-history analysis is needed to capture record-specific amplification of wind-turbine seismic demand that PGA alone cannot predict [2, 3].

Table 6. Peak global response under SF1 and SF15.

Record/scale	PGA (g)	Maximum Relative Displacement (m)	Maximum Base Shear (kN)	Maximum Base Moment (kN.m)
EQ1 / SF1	0.382	0.067	412.542	9,688.715
EQ1 / SF15	5.730	0.530	6,160.000	124,516.442
EQ2 / SF1	0.381	0.105	745.170	16,809.054
EQ2 / SF15	5.715	1.441	8,614.011	182,059.341
EQ3 / SF1	0.142	0.199	341.695	15,937.173
EQ3 / SF15	2.130	2.494	5,129.924	193,178.325

At SF15, EQ2 and EQ1 retain nearly identical scaled PGA values, but EQ2 produces 2.72 times the displacement, 1.40 times the base shear, and 1.46 times the base moment of EQ1. EQ3, although having the lowest scaled PGA, governs tower-top displacement (2.494 m) and base moment (193,178 kN m), whereas EQ2 governs base shear (8,614 kN).

The results indicate that PGA compatibility alone may not be sufficient for selecting ground motions for wind-turbine analysis. Records with similar PGA values produced different structural responses, while records with lower PGA values produced greater demands. Therefore, ground-motion selection should consider spectral characteristics in relation to the dominant structural periods, and multiple response measures should be evaluated concurrently.

4.2 Frequency Content and Response-History Interpretation

Figure 2 shows that EQ1 has relatively low ground motion energy near the first fore-aft and side-side modal frequencies of 0.360 Hz and 0.359 Hz, respectively, whereas EQ2 and EQ3 contain more pronounced energy content in this range. This closer correspondence with the first structural modes is consistent with the larger displacement and base-moment demands produced by EQ2 and EQ3 compared with EQ1. The spectra were also examined near the second fore-aft and side-side modal frequencies of 2.436 Hz and 2.695 Hz, respectively, to assess the possible contribution of higher-mode excitation. In contrast, the dominant frequency content of EQ1 is concentrated mainly around 4-6 Hz, above the first- and second-mode frequencies considered in the comparison, which helps explain its lower displacement response.

The response histories in Fig. 3 are consistent with the peak values reported in Table 6. At SF1, EQ3 produces the largest tower-top displacement, whereas EQ2 produces the largest base shear and base bending moment. This response ordering is also consistent with the FFT comparison, since EQ2 and EQ3 have greater Fourier amplitudes near the first structural frequency than EQ1.

At SF15, EQ3 produces the largest tower-top displacement and base bending moment, whereas EQ2 exhibits a different response characteristic. Following the Northridge-01 excitation, the EQ2-SF15 tower-top displacement continues to oscillate about a shifted equilibrium position,

indicating a persistent residual response. The fiber-level mechanism associated with this displacement offset is examined in Section 4.3.

This contrast shows that peak global demand and residual response need not be governed by the same record. Accordingly, PGA, peak response, and post-earthquake residual deformation should be evaluated as complementary indicators rather than as interchangeable measures [2-4].

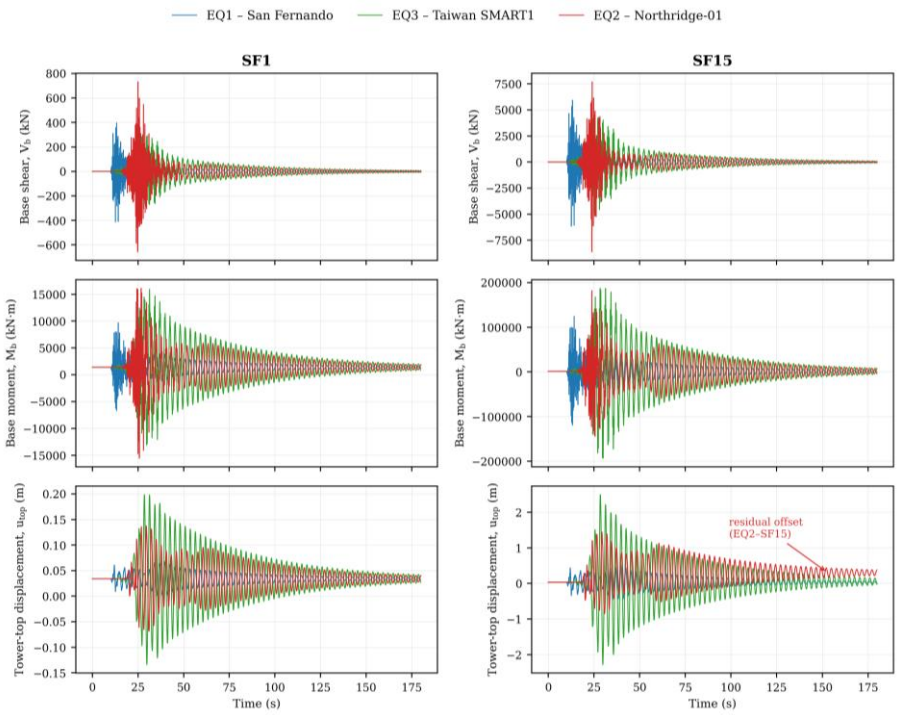


Fig. 3. Comparative SF1 and SF15 time histories of base shear, base bending moment, and tower-top relative displacement for EQ1-San Fernando, EQ2-Northridge-01, and EQ3-Taiwan SMART1. The EQ2-SF15 displacement history exhibits a persistent post-earthquake offset.

4.3 Fiber-Level Response and Residual Deformation at SF15

Table 7 and Figure 4 compare the stress-strain responses obtained from the same tower-base reference fiber (Fiber 190), located within Gauss point 0 of Element 117, for all three SF15 analyses. This common location was selected to provide a consistent basis for comparing the local material demands generated by the three records; it was not assumed to represent the maximum material response over the entire tower. For S355 steel with E = 200 GPa and a nominal yield stress of 355 MPa, the corresponding nominal elastic yield strain is approximately 0.00178.

Table 7. Peak response at the common tower-base fiber under SF15.

Record	Max. stress (MPa)	Max. strain	Response interpretation
EQ1	248.5	0.0012460	Essentially elastic
EQ2	341.0	0.0018807	Limited hysteretic response at base fiber
EQ3	354.7	0.0019245	Most pronounced base-fiber response

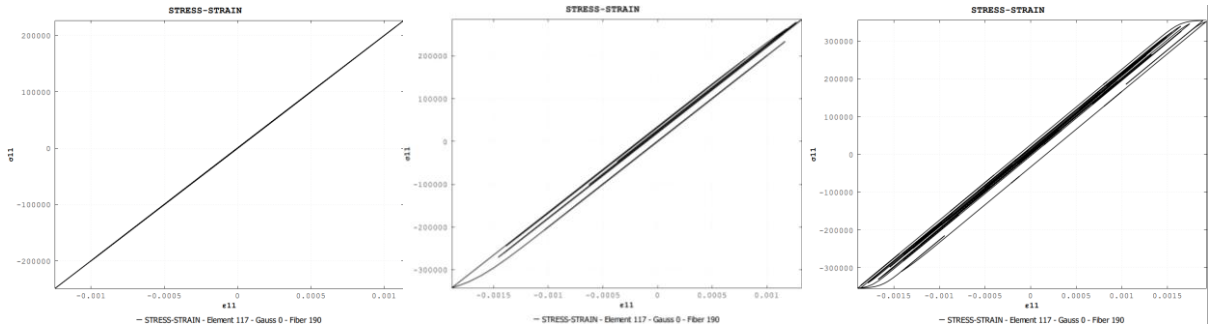


Fig. 4. Stress-strain response at the common tower-base fiber (Fiber 190) located within Gauss point 0 of Element 117, under SF15: (a) EQ1, (b) EQ2 and (c) EQ3.

At the selected tower-base fiber, EQ1 remains elastic, reaching a maximum stress of 248.5 MPa and a strain of 0.001246. EQ2 shows only minor hysteretic behavior. Although EQ3 has a lower PGA, it produces the largest response at this fiber, with a peak stress of 354.7 MPa, a maximum strain of 0.0019245, and the widest hysteresis loop.

However, the base-fiber results do not capture the most critical response along the tower. For EQ2 at SF15, more significant yielding occurs at an upper-tower section corresponding to Element 108, Gauss point 1, Fiber 163. The stress-strain loops at this location indicate repeated yielding and plastic-strain accumulation, as shown in Fig. 5.

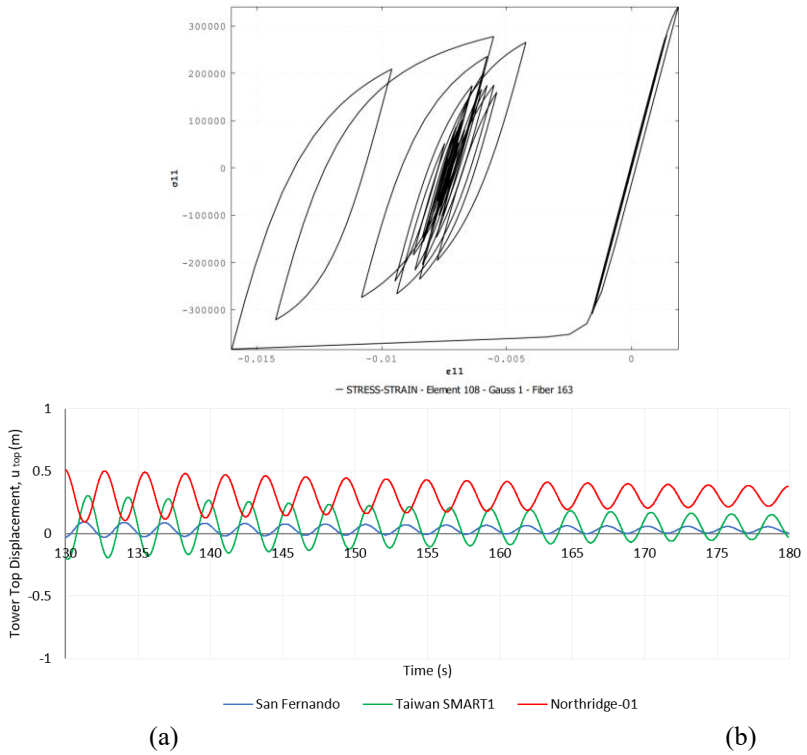


Fig. 5. Localized upper-tower yielding under EQ2-Northridge-01 at SF15 and the corresponding residual tower-top displacement: (a) upper-tower hysteretic response and (b) shifted free-vibration response.

The upper-tower yielding observed in the EQ2-SF15 analysis is consistent with the residual offset in the tower-top displacement response. The two fiber locations represent different aspects of the structural behavior. The base fiber compares the three earthquake records at a common location, while the upper-tower fiber captures the local yielding associated with the residual deformation in EQ2-SF15.

These results describe local fiber-level behavior and should not be interpreted as yielding of the entire tower. Identifying nonlinear response at two different elevations also demonstrates the ability of the fiber-section beam-column model to capture distributed plasticity along the tower, consistent with previous studies on offshore wind-turbine structures [6]. Previous studies have investigated nonlinear seismic response in wind turbines and the effects of ground-motion characteristics and record-to-record variability [2-4]. Other studies have also used fragility analysis to evaluate wind-turbine seismic performance [7,8]. This study adds to the literature by directly comparing two records with nearly identical PGA values and one record with a lower PGA for the same 2.5 MW onshore wind turbine. The results show that similar PGA values do not necessarily produce similar structural demands, and that a record with lower PGA can govern some response measures. They also show that peak displacement, base shear, base moment, and local nonlinear response may be governed by different records. Therefore, wind-turbine seismic assessment should consider both ground-motion characteristics and multiple structural response measures, rather than PGA alone.

5 Conclusions

This study investigated the nonlinear seismic response of an existing 2.5 MW onshore wind turbine using three ground-motion records at SF1 and SF15. The results showed that PGA alone did not consistently represent the relative severity of the structural response. Records with nearly identical PGA values produced different displacement and force demands, while the lower-PGA record governed some response quantities.

The analyses also showed that different response measures may be governed by different records. In particular, the record producing the largest tower-top displacement did not necessarily produce the most pronounced local nonlinear response or residual deformation. These findings indicate that wind-turbine seismic assessment should consider ground-motion characteristics together with multiple global and local response measures rather than relying on PGA alone.

The study was intentionally limited to three records and two intensity levels for a focused comparison. Therefore, the results should be regarded as illustrative rather than statistically generalizable. The analyses were also limited to a single turbine under parked, single-horizontal-direction excitation, and SF15 was used to expose nonlinear behavior rather than to represent a site-specific design earthquake.

Future studies should consider larger ground-motion sets and multiple intensity levels. Incremental dynamic analysis and fragility-based assessment could be used to quantify record-to-record variability and to investigate structure-related intensity measures such as spectral acceleration near the dominant vibration periods.

References

1. Ishihara, T., Sarwar, M.: Numerical and theoretical study on seismic response of wind turbines. In: European Wind Energy Conference and Exhibition, pp. 1-5 (2008).
2. Nuta, E., Christopoulos, C., Packer, J.A.: Methodology for seismic risk assessment for tubular steel wind turbine towers: application to Canadian seismic environment. Can. J. Civ. Eng. 38(3), 293-304 (2011).
3. Patil, A., Jung, S., Kwon, O.S.: Structural performance of a parked wind turbine tower subjected to strong ground motions. Eng. Struct. 120, 92-102 (2016).
4. Katsanos, E.I., Thöns, S., Georgakis, C.T.: Wind turbines and seismic hazard: a state-of-the-art review. Wind Energy 19(11), 2113-2133 (2016).

5. Mazzoni, S., McKenna, F., Scott, M.H., Fenves, G.L., et al.: Open System for Earthquake Engineering Simulation (OpenSees): Command Language Manual. Pacific Earthquake Engineering Research Center, University of California, Berkeley, Berkeley, CA (2006).
6. Tran, T.T., Hussan, M., Kim, D., Nguyen, P.C.: Distributed plasticity approach for the nonlinear structural assessment of offshore wind turbine. Int. J. Nav. Archit. Ocean Eng. 12, 743-754 (2020).
7. Asareh, M.A., Schonberg, W., Volz, J.: Fragility analysis of a 5-MW NREL wind turbine considering aero-elastic and seismic interaction using finite element method. Finite Elem. Anal. Des. 120, 57-67 (2016).
8. Mo, R., Kang, H., Li, M., Zhao, X.: Seismic fragility analysis of monopile offshore wind turbines under different operational conditions. Energies 10(7), 1037 (2017).
9. Özçelik, Ö., Dönmez, C., Günel, S., Eğilmez, O.Ö., Öztürkoğlu, O.: Kurulu rüzgâr türbinleri için yapı sağlığı izleme sisteminin geliştirilmesi; operasyonel ve çevresel faktörlerin kule dinamik özelliklerine etkisinin araştırılması ve çoklu tehlike kırılganlık eğrilerinin otonom hasar tespiti amacıyla kullanılması. TÜBİTAK Project No. 120M218 (1001 Program), Final Report. The Scientific and Technological Research Council of Türkiye (TÜBİTAK), Ankara, Türkiye (2023).
10. Vamvatsikos, D., Cornell, C.A.: Incremental dynamic analysis. Earthq. Eng. Struct. Dyn. 31(3), 491-514 (2002).

Publication Note

This paper was peer-reviewed, accepted for presentation, and included in the proceedings of the ACE2026 – International Conference on Advances in Civil Engineering, held on 12–14 October 2026 in Trabzon, Türkiye.

This paper may be cited as follows:

Ecmel Eylül Naz Özdoğan and Özgür Özçelik, “Nonlinear Time History Analysis of a 2.5 MW Onshore Wind Turbine Under Earthquake Loads” in Proceedings of the ACE2026 – International Conference on Advances in Civil Engineering, Trabzon, Türkiye, 12–14 October 2026.

Application of CatBoost Gradient Boosting for Precise Shear Capacity Assessment of Exterior RC Beam-Column Joints

Selin ESFENDİYAR[1] and Gamze DOĞAN[2]
[1] 0000-0002-7380-5462, PhD Candidate, Konya Technical University, Faculty of Engineering and Natural Sciences, Department of Civil Engineering, Konya, Türkiye, e258122002001@ktun.edu.tr
[2] 0000-0002-0339-8048, Assoc. Prof. Dr., Konya Technical University, Faculty of Engineering and Natural Sciences, Department of Civil Engineering, Konya, Türkiye, gdogan@ktun.edu.tr

Abstract

Accurate prediction of the shear capacity of reinforced concrete (RC) exterior beam-column joints is important for seismic assessment and design. This study investigates the use of CatBoost for predicting exterior joint shear capacity using a database of 270 experimental specimens described by 14 geometric, material, reinforcement, and loading variables. Feature-importance analysis identified column height (h_c), column width (b_c), and beam width (b_b) as the most influential variables, while SHAP analysis showed that h_c, b_b, and b_c had the widest contribution ranges. The results indicate that CatBoost can represent the nonlinear relationships governing exterior joint shear capacity while providing interpretable information on the contribution of key variables. The proposed approach can be considered a complementary data-driven tool for structural engineering assessment and future model-development studies.

Keywords: Exterior Beam-Column Joint, CatBoost, Gradient Boosting, Machine Learning, Shear Capacity, SHAP

1 Introduction

In reinforced concrete (RC) frame systems, the beam-column joints represent critical regions that facilitate force transfer between members under seismic action. In particular, exterior joints are susceptible to high shear stresses and brittle failure mechanisms due to the more limited confinement effect they experience compared to interior joints *(Figure 1)*. Therefore, it is imperative to reliably estimate the shear strength of the joint region to ensure the ductile behavior of the structural system [1-3].

A variety of analytical models and code-based empirical equations have been developed to determine joint shear strength. However, it should be noted that joint behavior is influenced by numerous variables, including column and beam geometry, concrete strength, longitudinal and transverse reinforcement detailing, and axial load. The inherent multivariate and nonlinear characteristics of this phenomenon have led to a significant increase in the utilization of machine learning methodologies in recent years for the purpose of predicting the strength and damage behavior of beam-column joints [4,5].

Research on machine learning is also rapidly increasing in the literature. Karabini et al. [6] and Karampinis et al. [7] employed ensemble learning and SHapley Additive exPlanations (SHAP)-based interpretability approaches to predict damage modes in beam-column joints. Mehta et al. [8] addressed the shear strength and damage modes of exterior joints using machine learning on an extensive experimental database. Kamal and Abd El Ghany [9] evaluated 203 experiments on RC exterior beam-column joints using Random Forest, XGBoost, and neural network-based models, while utilizing SHAP and permutation importance analyses. Shah et al. [10] examined various models using data from 194 experimental joints, employing ten-fold cross-validation and SHAP/PDP analyses. Recent studies have demonstrated that, in addition

to prediction accuracy, the interpretability of model decisions from an engineering perspective is becoming increasingly significant.

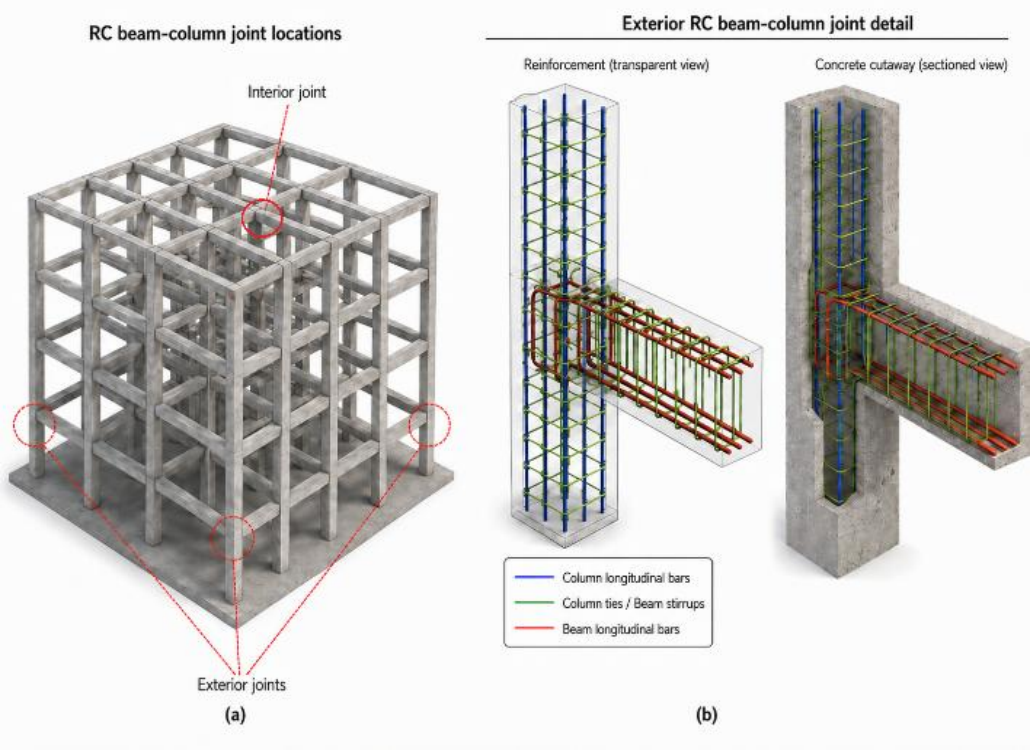


Figure 1. (a) Locations of beam-column joints in an RC frame, (b) 3D reinforcement detailing of an exterior RC beam-column joint.

Contrary to extant literature, this study utilizes the CatBoost regression algorithm, developed as an optimal model for limited datasets, to calculate the shear capacities of beam-column joints. In this context, a database comprising 270 experimental specimens [11] was analyzed using the CatBoost regression model. The performance of the model was evaluated based on success metrics, and the relative influence of parameters affecting shear capacity was examined through feature importance scores and SHAP analysis [13]. The objective of this study is to integrate CatBoost-based prediction with model interpretability within a unified evaluation framework.

2 Methodology and Data Framework

2.1 Data Compilation

The present study employs a database of exterior RC beam-column joints, which was compiled from experimental studies specifically, those utilized by Doğan [11] and published by Parate and Kumar [12]. The database under consideration contains parameters for a total of 270 exterior joint specimens obtained from experimental studies conducted between 1967 and 2016. For each specimen, the joint geometry, material properties, reinforcement layout, and axial load data are presented alongside the experimental shear strength.

The analyses were conducted using a total of 14 input variables and a single target variable. The input variables encompass concrete compressive strength, column and beam cross-sectional dimensions, reinforcement ratios, reinforcement yield strengths, joint region reinforcement areas, and axial load. The target variable is the experimental joint shear strength ($V_{ij,exp}$). Prior to analysis, the data file was examined for numerical validity and the presence

of missing observations; no missing observations were identified. The parameter names, units, and basic statistical values are presented in *Table 1.*

Table 1. Statistical values for Input and output parameters

Parameter		Details	Unit	Min	Max	Median
Input	f_c	Concrete Compressive Strength	MPa	18.00	109.60	37.00
	P_{axial}	Axial Load	kN	-100.00	2156.00	200.00
	h_c	Column Height	mm	140.00	550.00	300.00
	b_c	Column Width	mm	100.00	550.00	250.00
	ρ_{col}	Column Reinforcement Ratio	%	0.26	4.18	1.61
	f_{yc}	Column Reinforcement Yield Strength	MPa	303.00	630.00	467.30
	h_b	Beam Height	mm	150.00	750.00	400.00
	b_b	Beam Width	mm	100.00	600.00	230.00
	ρ_t	Top Reinforcement Ratio (Beam)	%	0.15	2.09	0.98
	ρ_c	Bottom Reinforcement Ratio (Beam)	%	0.15	2.27	1.20
	f_{yb}	Beam Reinforcement Yield Strength	MPa	276.00	710.00	485.00
	A_{sjh}	Horizontal Web Reinforcement Area	mm^2	0.00	2281.00	160.00
	A_{sjv}	Vertical Web Reinforcement Area	mm^2	0.00	3278.00	0.00
	f_{yjv}	Web Reinforcement Yield Strength	MPa	0.00	610.00	458.90
Output	$V_{ij,exp}$	Shear Strength	kN	62.29	1771.80	331.60

2.2 CatBoost Model

CatBoost is a gradient boosting algorithm based on decision trees [13]. In the gradient boosting approach, multiple trees constructed sequentially are used in conjunction rather than a single decision tree. The incorporation of each new tree into the learning process serves to minimize the prediction errors committed by the preceding model. This structural design enables the model to represent non-linear relationships and interactions among input variables.

In this study, the CatBoost regression algorithm architecture, a gradient boosting tree model, was selected to predict the shear strength of exterior beam-column joints in RC buildings. During the implementation process, the experimental dataset was initially loaded into the

system, and data preprocessing steps were initiated. The model was implemented using the Python programming language via the Spyder interface. A total of 14 parameters, as identified in the extant literature, were designated as independent variables (inputs) within the model. These parameters are believed to directly influence joint shear strength. The defined inputs and the target variable, experimental shear strength (Vij,exp), were formatted numerically. The dataset was examined for missing or erroneous observations (NaN), and data consistency was verified. The prepared dataset was divided into two main groups to impartially evaluate the model's generalization capability. The dataset, constituting 80% of the total was designated as the training set to optimize the model's decision tree structures and weights, while the remaining 20% was set aside as the test set to measure performance on data the model had not previously encountered.

In regard to the hyperparameters utilized for the CatBoost regression model, the values of 1,000 for the number of iterations, 0.03 for the learning rate, and 6 for the depth were employed. The RMSE was designated as the loss function, and the model was trained using these parameters. The hyperparameter configuration was set to yield the most optimal prediction. During the training process, the CatBoost model generated predictions by establishing a correlation between the target shear strength and the independent input parameters found in the test set.

The algorithm's prediction accuracy and model performance were evaluated using the Coefficient of Determination (R^2), Root Mean Squared Error (RMSE), and Mean Absolute Error (MAE) metrics. Furthermore, CatBoost feature importance scores were calculated to ascertain which variables the model relied on most during the prediction process and the weight assigned to each variable within the model's decision-making mechanism. Finally, SHapley Additive exPlanations (SHAP) analysis was employed to assess the contribution of the variables, whether increasing or decreasing, to the model's predictions [14]. The algorithm's code flow is presented in *Table 2.*

Table 2. CatBoost model analysis flow.

Algorithm: CatBoost model for RC exterior joints
Require: Experimental dataset D containing 270 specimens, 14 input variables X, and target variable $y = V_{ij,exp}$
Ensure: Predicted shear strengths, performance metrics, feature importance scores, and SHAP values
1: Check numerical consistency of the dataset
2: Remove observations containing missing values
3: Split the dataset into training and test subsets:
Training set: 80% (n = 216) Test set: 20% (n = 54) random_state = 42
4: Initialize CatBoost regression model:
iterations = 1000,
learning_rate = 0.03,
depth = 6,
loss_function = RMSE,
random_seed = 42
5: Train the CatBoost model using the training dataset
6: Predict shear strength values for the test dataset
7: Evaluate model performance using R^2, *RMSE*, and *MAE*
8: Calculate CatBoost feature importance scores
9: Compute SHAP values using the training dataset
10: Generate prediction and interpretation plots
11: Return Predicted values, performance metrics, feature importance scores, and SHAP results

3 Results

3.1 Model Performance

The CatBoost model's prediction performance on the test set was found to be $R^2 = 0.913$, with error metrics RMSE = 107.07 and MAE = 51.35. The R^2 value indicates a strong agreement between experimental results and model predictions. The higher value of the root mean square error (RMSE) relative to the mean absolute error (MAE) indicates the presence of larger discrepancies between the ground truth (i.e., the experimental results) and the predicted values in certain samples.

Figure 2 compares the experimental and predicted shear strength values of RC column-beam joint regions. A considerable proportion of the data points align with the ideal fit line, represented by the equation y = x. The model demonstrates a general adherence to the prevailing trend, particularly at low and medium strength levels. However, a notable concern emerges when examining samples from the high-strength region, where substantial underestimations or overestimations are observed. These deviations are hypothesized to be associated with the limited number of high-shear-strength samples in the test set and the fact that the database was compiled from disparate experimental programs.

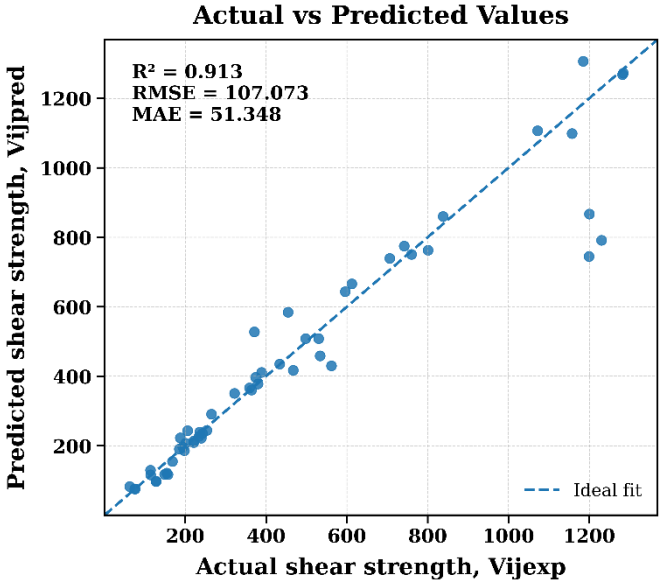


Figure 2. Comparison of experimental and predicted shear strength values.

3.2 Feature Importance and SHAP Analysis

The CatBoost feature importance results are presented in *Figure 3*. The highest importance scores were obtained for the column height (h_c), column width (b_c), and beam width (b_b) variables. These variables are followed by the top beam reinforcement ratio (ρt) and beam height (h_b). The findings suggest that the model places significant reliance on variables delineating the joint geometry when generating predictions. However, it is imperative to acknowledge that feature importance scores are not a direct measure of physical causality. Instead, they reflect the model's predictive behavior based on the existing dataset.

The SHAP summary plot in *Figure 4* illustrates the direction and magnitude of the contributions of the variables in the training set to the predictions. The variables h_c, b_b, and b_c demonstrate wider SHAP distributions in comparison to the remaining parameters. This result aligns with the key geometric parameters that were identified as significant in the feature importance analysis. It has been demonstrated that elevated values of h_c, b_b, and b_c are

predominantly associated with positive SHAP contributions, whereas diminished values are associated with negative contributions. Consequently, the trained CatBoost model has demonstrated a consistent correlation between increased geometric dimensions and enhanced shear strength predictions.

While the axial load variable acting on the column element at the connection zone is considered low in terms of overall importance, it yields high positive SHAP contributions in certain instances. This finding indicates that the effect of axial load does not manifest at the same level across all samples. While SHAP results can facilitate the comprehension of the relationships within the model, they should not be regarded as direct evidence of causality.

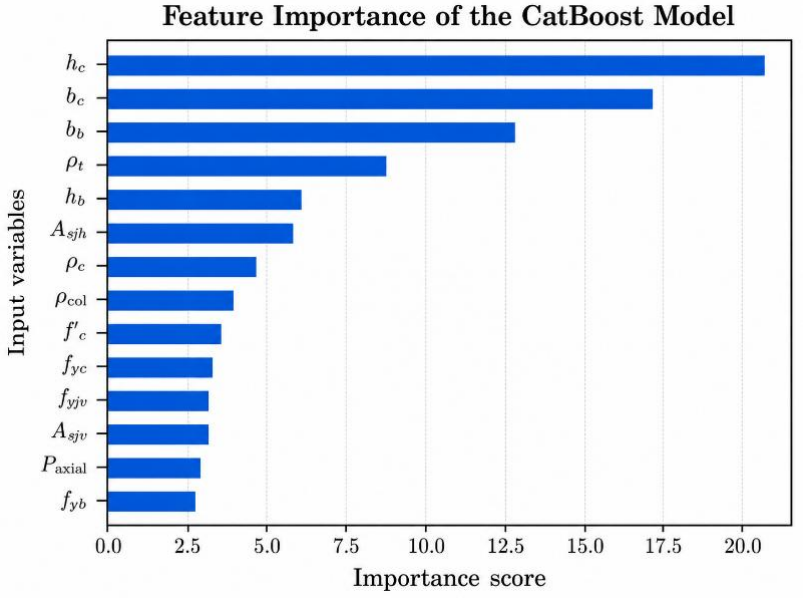


Figure 3. CatBoost model feature importance scores.

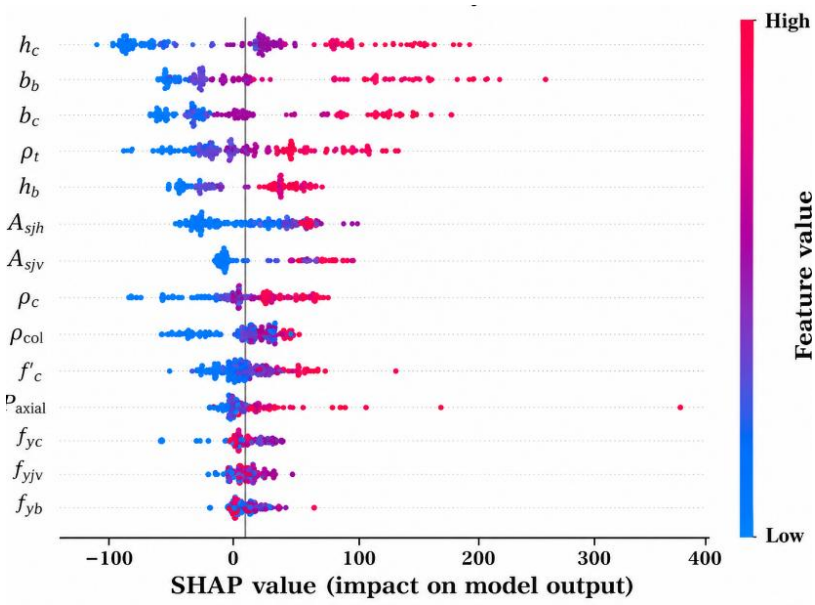


Figure 4. CatBoost model SHAP graph.

4 Conclusion and Discussion

In this study, the shear strength of RC external beam-column joints, which play an essential role in structural systems, was estimated using the CatBoost algorithm. The findings indicate

that the CatBoost algorithm constitutes a viable data-driven approach, capable of representing nonlinear relationships in external joint shear strength.

Feature significance and SHAP analyses have demonstrated that geometric variables such as column height (h_c), column width (b_c), and beam width (b_b) are particularly salient in model predictions. The SHAP analysis indicated that elevated values of these parameters are predominantly correlated with favorable prediction contributions. Consequently, the model can be utilized not only to generate predictions but also to examine the relative effects of variables on model behavior.

In scenarios where ground truth data is scarce, the CatBoost algorithm has demonstrated its efficacy, particularly for small and medium-sized datasets. This is due to its capacity to discern intricate nonlinear relationships and its incorporation of mechanisms that curtail overlearning. The study's findings indicate that CatBoost is a highly suitable and superior option when compared to other machine learning regression algorithms, particularly Boosting models.

Machine learning methods have seen increased utilization in a variety of structural engineering problems, including strength estimation, damage classification, structural performance evaluation, and rapid preliminary assessment. The findings of this study demonstrate that the CatBoost algorithm and explainable artificial intelligence approaches can be used as effective and complementary tools in data-driven evaluation of RC joint behavior. However, in order to more comprehensively demonstrate the generalization capacity of the model, further studies are necessary to consider larger and more balanced databases, different joint geometries, and loading conditions. Furthermore, comparisons with independent experimental validation datasets will contribute to the evaluation of the reliability of the developed approach and its usability in practical engineering applications.

References

1. ACI-ASCE Committee 352. (2002). Recommendations for Design of Beam-Column Connections in Monolithic Reinforced Concrete Structures (ACI 352R-02). American Concrete Institute, Farmington Hills, MI.
2. Hwang, S.J. & Lee, H.J. (1999). Analytical model for predicting shear strengths of exterior reinforced concrete beam-column joints for seismic resistance. ACI Structural Journal, 96(5), 846-857. https://doi.org/10.14359/739
3. Park, S. & Mosalam, K.M. (2012). Parameters for shear strength prediction of exterior beam-column joints without transverse reinforcement. Engineering Structures, 36, 198-209. https://doi.org/10.1016/j.engstruct.2011.11.017
4. Mangalathu, S. & Jeon, J.-S. (2018). Classification of failure mode and prediction of shear strength for reinforced concrete beam-column joints using machine learning techniques. Engineering Structures, 160, 85-94. https://doi.org/10.1016/j.engstruct.2018.01.008
5. Ramavath, S. & Suryawanshi, S.R. (2024). Optimal prediction of shear properties in beam-column joints using machine learning approach. International Journal of Engineering, 37(1), 67-82. https://doi.org/10.5829/ije.2024.37.01a.07
6. Karabini, M., Karampinis, I., Rousakis, T., Iliadis, L. & Karabinis, A. (2024). Machine learning ensemble methodologies for the prediction of the failure mode of reinforced concrete beam-column joints. Information, 15(10), 647. https://doi.org/10.3390/info15100647
7. Karampinis, I., Karabini, M., Rousakis, T., Iliadis, L. & Karabinis, A. (2024). Analytical equations for the prediction of the failure mode of reinforced concrete beam-column joints based on interpretable machine learning and SHAP values. Sensors, 24(24), 7955. https://doi.org/10.3390/s24247955
8. Mehta, V., Jang, S.H. & Chey, M.H. (2026). Predictive framework for shear strength and failure modes of exterior reinforced concrete beam-column joints using machine learning. Structural Concrete, 27(2), 1549-1580. https://doi.org/10.1002/suco.70391

9. Kamal, A.Y. & Abd El Ghany, R. (2026). Explainable machine learning models for predicting shear capacity of exterior reinforced concrete beam-column joints. Discover Civil Engineering, 3, 118. https://doi.org/10.1007/s44290-026-00521-y
10. Shah, Q., Ullah, I., Khoso, W.A. et al. (2026). Interpretable machine learning for predicting reinforced concrete beam column joint shear strength. Discover Civil Engineering, 3, 153. https://doi.org/10.1007/s44290-026-00539-2
11. Dogan, G. (2024). Machine learning-based shear strength prediction of exterior RC beam-column joints. Multiscale and Multidisciplinary Modeling, Experiments and Design, 7, 2319-2341. https://doi.org/10.1007/s41939-023-00338-7
12. Parate, K. & Kumar, R. (2019). Shear strength criteria for design of RC beam-column joints in building codes. Bulletin of Earthquake Engineering, 17, 1407-1493.
13. Prokhorenkova, L., Gusev, G., Vorobev, A., Dorogush, A.V. & Gulin, A. (2018). CatBoost: Unbiased boosting with categorical features. Advances in Neural Information Processing Systems, 31, 6639-6649.
14. Lundberg, S.M. & Lee, S.-I. (2017). A unified approach to interpreting model predictions. Advances in Neural Information Processing Systems, 30, 4765-4774.

Author Contribution Statement

- Conceptualization: Gamze DOĞAN
- Methodology: Gamze DOĞAN
- Software and Visualization: Selin ESFENDİYAR
- Investigation and Formal Analysis: Selin ESFENDİYAR, Gamze DOĞAN
- Writing - Original Draft: Selin ESFENDİYAR, Gamze DOĞAN
- Writing - Review & Editing: Selin ESFENDİYAR, Gamze DOĞAN
- Supervision: Gamze DOĞAN

Note: Following the conference, this Publication Note will be added to each paper; therefore, authors are kindly requested not to remove the note below and to complete the author(s) and paper title information.

Publication Note

This paper was peer-reviewed, accepted for presentation, and included in the proceedings of the ACE2026 – International Conference on Advances in Civil Engineering, held on 12–14 October 2026 in Trabzon, Türkiye.

This paper may be cited as follows:

Esfendiyar, S., Dogan, G., "Application of CatBoost Gradient Boosting for Precise Shear Capacity Assessment of Exterior RC Beam-Column Joints," in Proceedings of the ACE2026 – International Conference on Advances in Civil Engineering, Trabzon, Türkiye, 12–14 October 2026.

Micromechanical Explicit Finite Element Analysis of the Fracture Evolution in Structures under Crack Parallel Stress Condition

Sedat Kömürcü[1] and Ferhun C. Caner[2]
[1] 0000-0003-2981-0755, Istanbul Technical University, Civil Engineering Department, Istanbul, Türkiye, komurcus@itu.edu.tr
[2] 0000-0002-6448-0942, Universitat Politecnica de Catalunya-BarcelonaTECH, Institute of Energy Technologies and Department of Materials Science and Engineering, Barcelona, Spain, ferhun.caner@upc.edu

Abstract. This study presents a micromechanical explicit finite element model to investigate fracture evolution in structures subjected to crack parallel stress (CPS) conditions. Conventional fracture mechanics approaches primarily focus on crack opening mechanisms driven by tensile stresses normal to the crack surface, recent studies have demonstrated that stresses acting parallel to the crack propagation direction may significantly influence fracture energy dissipation and damage evolution in materials. In this context, the present study aims to analyze the effects of crack parallel stresses by modelling the Bažant's Gap Test, which has recently attracted considerable attention in the literature. Achieving this objective as realistically as possible is essential to ensure that the developed framework can serve as a reliable computational reference for future research. In order for the model to be presented in a way that includes micro effects, the developed M7 concrete micromaterial model is used in the ABAQUS software via a subroutine file. The proposed three-dimensional modelling approach incorporates a micromechanical representation of damage initiation and propagation under dynamic loading conditions. The results demonstrate that crack parallel stresses substantially alter the evolution of the fracture process. The findings of this study contribute to the understanding of multiaxial fracture behavior and provide a computational basis for improving predictive fracture models in concrete like materials.

Keywords: Computational modelling; Fracture mechanics; Gap test; Micro-plane model.

1 Introduction

Recent advances in fracture mechanics have focused on understanding the CPS effect, a phenomenon that significantly influences fracture energy, crack propagation, and damage mechanisms across a wide range of materials. The gap test, first formalized by Nguyen et al. [1], has become the benchmark experimental approach for isolating and quantifying CPS effects in quasi-brittle fracture. Subsequent studies by Bažant, Dönmez, and co-workers [2, 3] refined theoretical interpretations through phase-field, peridynamic, and crack-band models, emphasizing the need to revise classical fracture mechanics assumptions. Zhang et al. [4] explored hydraulic and shale fracture behavior under CPS conditions. Brockmann and Salviato [5] demonstrated the broad applicability of CPS based analyses. Collectively, these works establish the CPS effect as a micromechanical mechanism governing energy dissipation, localization, and fracture scaling, highlighting its crucial role in advancing predictive modeling of materials.

In this study, an explicit finite element model of the gap test is developed to investigate the influence of CPS effect on microcrack initiation, propagation, and stress redistribution. An

explicit finite element model of the gap test is developed with the primary objective of systematically investigating the influence of CPS on the fracture behavior of materials. The model explicitly captures microcrack initiation and subsequent propagation, allowing for a detailed examination of how these stresses affect both the growth of microcracks within the fracture process zone. By integrating these features, the proposed approach provides a comprehensive tool for understanding the micromechanical mechanisms governing fracture under multiaxial stress states, offering insights that can inform improved predictive models and design strategies for concrete, composites, and other heterogeneous materials.

2 Gap Test and Microplane Modelling

Bažant, proposed the gap test to address the limitations of traditional methods, providing a theoretical framework and preliminary experimental results that highlight the importance of CPS effect. Schematically representation of Bazant's gap test set-up is shown in Fig. 1 [1]. In this set-up, *a* is crack length, *D* is panel width, *L* is roller span length and *s* is top span length. The scope of this research encompasses developing and validating a numerical model for the gap test, with a critical evaluation of the literature to identify gaps in current understanding. The importance lies in providing a more accurate representation of material behavior under stress, which has significant implications for engineering design and safety. This approach offers several innovative contributions such as scientific quality, innovation potential, methodological contribution and theoretical contribution. The research will refine the theoretical understanding of CPS effects and provide robust numerical data to support Bazant's gap test methodology. The development of a sophisticated finite element model represents a methodological advancement, enabling more precise simulations of material behavior under complex stress conditions.

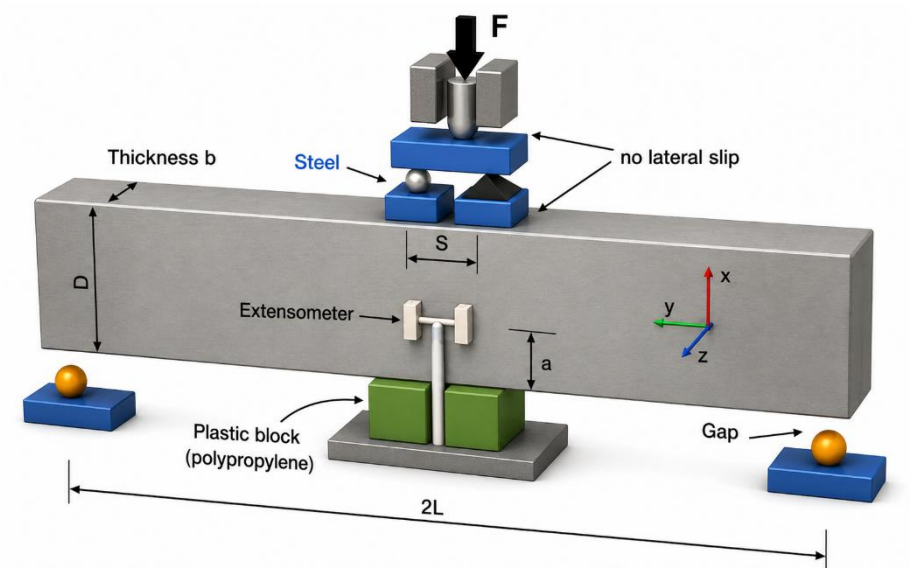


Fig. 1. Bazant's gap test experimental set-up [1].

In micro-plane models, the strain tensor at a given integration point is projected onto micro-planes oriented to encompass all directions in 3-dimensional space. The structural formulation is defined on the micro-plane as a function of the micro-plane strain components, and the resulting micro-plane stress components are integrated to obtain the stress tensor. The micro-plane approach has several key advantages. First, structural equations do not need to be defined in terms of stress and strain tensor invariants or prime values, which, although often becoming overly complex, provide little improvement in model predictions. Instead, they are defined more simply as strain and stress vectors acting on the micro-plane, which naturally reduces

complexity. However, such invariants and prime values can still be used in micro-plane structural relationships if needed. Furthermore, micro-planes oriented to encompass all possible directions in 3-dimensional space represent potential shear planes at material microstructure scales larger than 100 μm. Therefore, the micro-plane approach results in a multifaceted plasticity model where yield surfaces are automatically activated according to kinematic constraints, without the need for complex rules for selective activation of yield surfaces depending on applied stress and strain tensors. The interactions of inelastic deformations in different micro-planes are automatically captured through dependence on parameters such as the triaxial nature of stress. Another advantage is that this structure allows for the capture of fracture and damage with post-peak softening behavior. Since a micro-plane model is, in principle, a multifaceted plasticity model, it should be able to capture the peak effect. This effect is observed when an axially loaded ductile material suddenly bends while the axial load is kept constant. This load path is also called lateral loading with reference to the yield surface. During lateral loading, the material response is much less rigid than the elastic response, which still indicates that inelastic deformation is occurring. This situation cannot be explained by a single yield surface but requires the activation of multiple yield surfaces.

In order for the model to be presented in a way that includes micro effects, the previously developed M7 concrete micromaterial model in [6, 7] is used in the ABAQUS software. This model, having gone through various stages, is quite advanced and is known in the literature as the model that best reflects the behavior of concrete materials. For this model to be used in the software, the material must be introduced to the program correctly. Introducing the material as M7FCONCRETE and using USER MATERIAL is an important step. Also, since the model used includes micro-planes, the DEPVAR value must be entered as 189 to correctly introduce the parameters used in creating the material model to the program. All these steps are necessary adjustments for the M7 material model to work seamlessly with ABAQUS. The M7 micromaterial model is introduced to the program as a Subrotine file. The first analyses in this regard are aimed at determining that the material model works correctly in the program.

3 Results and Validation

Fig. 2 presents the distributions of the minimum principal stress obtained from the gap test analysis at different time steps. At the beginning of loading (t = 0.2 s), the compressive stresses are concentrated within a narrow and localized region along the loading axis. Stress concentration begins to develop at the tip of the existing notch. As the loading progresses (t = 0.4 and 0.6 s), the compressive stress field propagates into the specimen, the stress concentration at the notch tip becomes more pronounced, and higher compressive stresses accumulate around the crack tip. At t = 0.8 s, the compressive stress zone expands laterally around the crack, indicating that the applied load is transferred not only along the loading axis but also through the intact material surrounding the crack. At the final loading stage (t = 1.0 s), the compressive stresses spread over a wider region, resulting in a more uniform stress distribution and the load transfer is redistributed as crack propagation progresses. The symmetric stress distribution observed throughout all time steps confirms that the boundary conditions and contact definitions have been properly implemented. Furthermore, the compressive stresses acting parallel to the crack plane compress the crack faces, delaying crack propagation and consequently increasing the apparent fracture toughness of the material. These results successfully demonstrate the fundamental mechanism of the gap test.

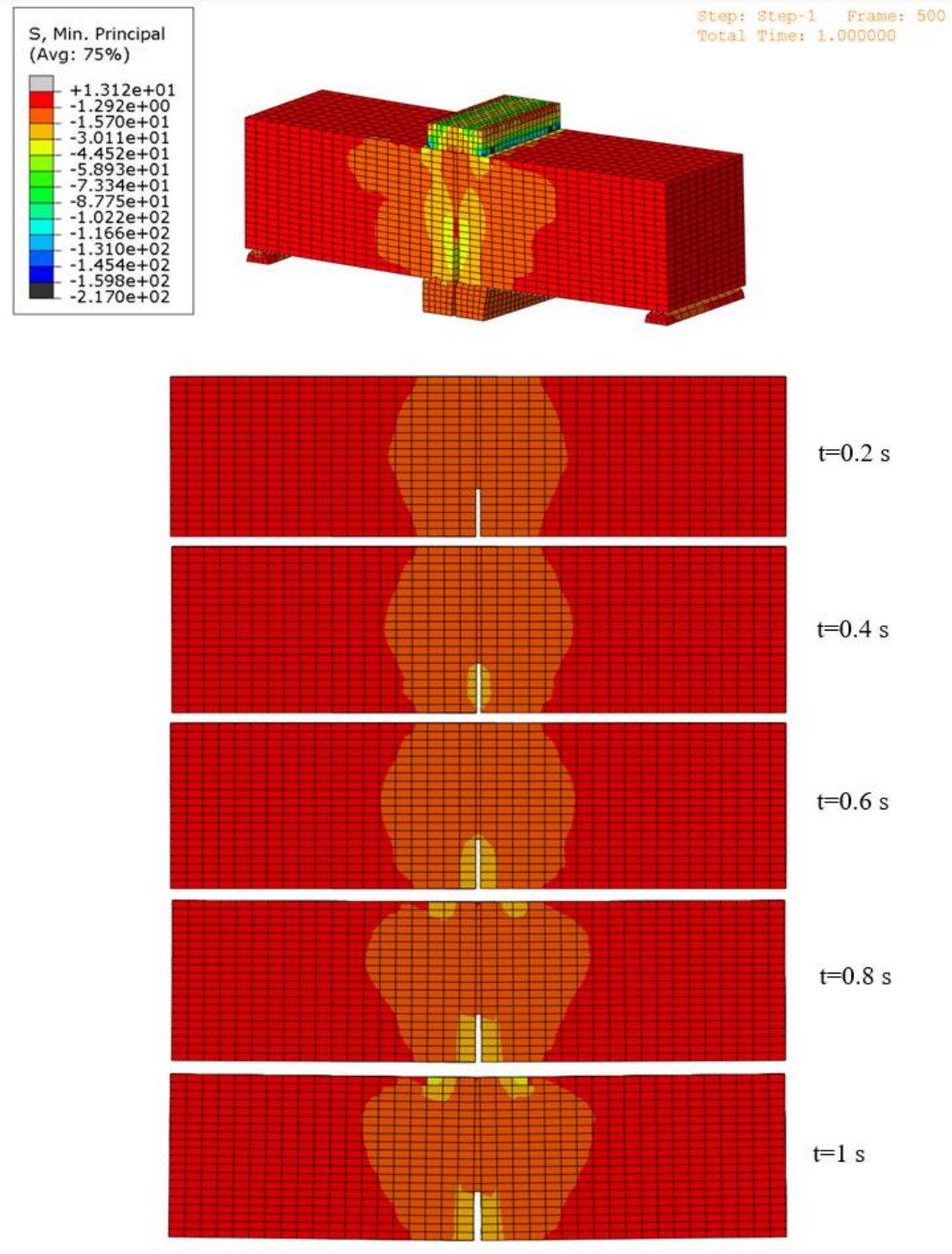


Fig. 2. Minimum principal stress distributions at different time steps of the gap test.

The load displacement curve in Fig. 3 shows that the applied load increases rapidly with displacement during the initial stage in a nonlinear manner. Between approximately 0 and 1 mm of displacement, the specimen exhibits high stiffness and predominantly elastic behavior. As loading continues, the slope of the curve gradually decreases while the load continues to increase, indicating that the specimen is still able to carry the applied load despite the initiation of microcracks within the material. After approximately 4 mm of displacement, several small load drops are observed, representing local damage events and stress redistribution associated with crack propagation. No significant loss of load carrying capacity occurs, and the load continues to increase until reaching approximately 41 kN. This behavior demonstrates that the compressive stresses acting parallel to the crack plane keep the crack faces closed, thereby preserving the load carrying capacity of the specimen.

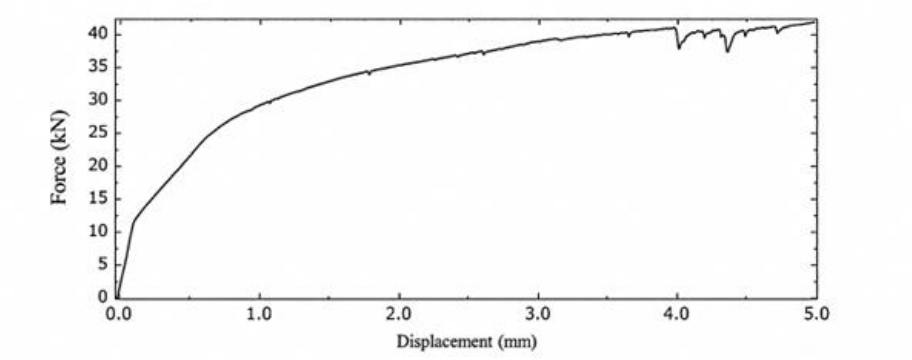


Fig. 3. Force-displacement graph at the end of the analysis.

The load and crack mouth opening displacement curve in Fig. 4 further indicates that crack opening remains relatively limited throughout the analysis. Although the crack mouth opening displacement reaches approximately 0.8 mm, the applied load remains nearly constant. The small oscillations and local load drops observed along the curve correspond to intermittent crack growth and progressive damage evolution at the crack tip. Overall, the combined interpretation of both curves demonstrates that the specimen undergoes a stable and controlled fracture process. The ability to obtain this behavior at advanced levels demonstrates the superiority of the M7 material model used in the model.

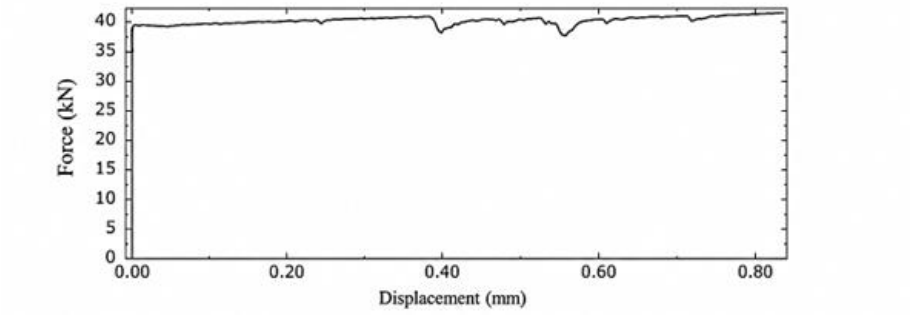


Fig. 4. Force and crack tip opening displacement graph.

4 Conclusion

In this study, the gap test is successfully analyzed by generating a three-dimensional finite element model using the M7 micro-plane damage model. To capture the effects of stresses parallel to the crack, it is necessary to model the fracture as a band in front of the crack and to use a micro-plane that can reproduce oriented microcracks or slips. Furthermore, loading should be applied gradually for accurate gap test results. Explicit dynamic analyses can be performed with the created model. A crack, by its nature, is not a line but a three-dimensional fracture zone. The three-dimensional model created in this study is found to be suitable for investigating real crack behavior. Model parameters can be calibrated for different materials and used in CPS analyses. Thanks to the effective use of the generated finite element models, it is possible to analyze the effects of stresses parallel to the crack, a crucial topic in fracture mechanics, on the fracture mechanisms of structures more accurately.

Acknowledgments
The authors would like to thank the Scientific and Technical Research Council of Turkey (TÜBİTAK) 2219 Program. This study is supported by TÜBİTAK.

References

1. Nguyen, H. T., Pathirage, M., Cusatis, G., & Bažant, Z.P.: Gap Test of Crack-Parallel Stress Effect on Quasibrittle Fracture and Its Consequences. Journal of Applied Mechanics, 87 (2020).
2. Bažant, Z. P., Dönmez, A. A., & Nguyen, H. T.: Précis of gap test results requiring reappraisal of line crack and phase-field models of fracture mechanics, Engineering Structures, 250, 113285, (2022).
3. Dönmez, A. A., Nguyen, H. T., Xu, H., & Bažant, Z. P.: Crack-parallel stress effect on fracture energy of plastic hardening polycrystalline metal identified from gap test scaling. Journal of the Mechanics and Physics of Solids, 173, 105222, (2023).
4. Zhang, M., Zhang, G., Zhu, W., & Zhou, D.: Crack-parallel stress effects on energy dissipation mechanisms across fracture process zone in shale. Theoretical and Applied Fracture Mechanics, 139, 105125, (2025).
5. Brockmann, J., & Salviato, M.: The Gap test - Effects of crack parallel compression on fracture in carbon fiber composites, Composites: Part A, 164, 107252, (2023).
6. Caner, F. C. & Bažant, Z.P.: Microplane Model M7 for Plain Concrete. I: Formulation. Journal of Engineering Mechanics, 139(12), 1714-1723 (2013).
7. Caner, F. C. & Bažant, Z.P.: Microplane Model M7 for Plain Concrete. II: Calibration and Verification. J. Eng. Mech., 139(12), 1724-1735 (2013).

Author Contribution Statement

- *Conceptualization:* Ferhun Caner
- *Methodology:* Ferhun Caner, Sedat Kömürcü
- *Investigation:* Ferhun Caner, Sedat Kömürcü
- *Writing – Original Draft:* Sedat Kömürcü
- *Writing – Review & Editing:* Ferhun Caner

Conflict of interest
The authors declare that they have no conflict of interest.

Funding
This research is supported by Scientific and Technical Research Council of Turkey (TÜBİTAK).

Data availability statement
The authors confirm that the data supporting the findings of this study are available within the article.

Publication Note
This paper was peer-reviewed, accepted for presentation, and included in the proceedings of the ACE2026 – International Conference on Advances in Civil Engineering, held on 12–14 October 2026 in Trabzon, Türkiye.

This paper may be cited as follows:
Sedat Kömürcü and Ferhun C. Caner, "Micromechanical Explicit Finite Element Analysis of the Fracture Evolution in Structures under Crack Parallel Stress Condition," in Proceedings of the ACE2026 – International Conference on Advances in Civil Engineering, Trabzon, Türkiye, 12–14 October 2026.

The Solution of the Optimal Sensor Placement Problem for Planar Truss System

Barbaros ATMACA[1], Hülya PİR[2], Büşra YAKAK VATANDAŞ[3] and Tayfun DEDE[4]
[1] 0000-0003-3336-2756, Karadeniz Technical University, Civil Engineering Department, Trabzon, Türkiye, atmaca@ktu.edu.tr
[2] 0009-0005-4079-0988, Karadeniz Technical University, Civil Engineering Department, Trabzon, Türkiye, hulyaaksy61@gmail.com
[3] 0009-0006-6653-7312, Karadeniz Technical University, Civil Engineering Department, Trabzon, Türkiye, busra.yakak@ktu.edu.tr
[4] 0000-0001-9672-2232, Karadeniz Technical University, Civil Engineering Department, Trabzon, Türkiye, dtayfun@ktu.edu.tr

Abstract. This study presents a comprehensive investigation of the optimal sensor placement (OSP) problem for structural health monitoring (SHM) using a 17-member planar steel truss system. The primary objective is to examine the theoretical basis of OSP and to evaluate the influence of three modal assurance criterion (MAC)-based placement strategies, max-MAC, ave-MAC, and rms-MAC, on sensor configuration outcomes. This work focuses on understanding the behavior of MAC-based objective functions and their role in determining effective sensor locations. The structural model consists of 17 truss elements and 10 nodes arranged in a single plane, with translational degrees of freedom considered in both x and y directions. A MATLAB-based computational framework was developed to perform a complete combinatorial evaluation of all possible sensor configurations for varying sensor numbers. For each configuration, objective function values corresponding to the three MAC-based criteria were calculated, and the configurations minimizing modal correlation were identified as optimal. The results indicate that increasing the number of sensors consistently reduces the off-diagonal terms of the MAC matrix, leading to improved modal independence. While the three criteria generally yield different sensor placement patterns for lower sensor counts, their solutions tend to converge as the number of sensors increases. Furthermore, it is observed that configurations with very few sensors, particularly a single sensor, are insufficient to capture the modal characteristics of the system effectively. The study provides a clear and systematic framework for applying OSP techniques to planar truss systems and highlights the impact of different MAC-based criteria on sensor placement strategies.

Keywords: Optimal sensor placement; Structural health monitoring; Truss system; Modal assurance criterion.

1 Introduction

The construction sector occupies an important place in our lives, and a great variety of structures are continuously being built. However, construction alone is not sufficient; these structures must also be preserved and kept under control. Structural health monitoring (SHM) systems are being used with growing frequency in civil engineering to enable the safety and performance of structures to be monitored [1]. SHM is a method based on the continuous observation of a structure's dynamic behavior through sensors, allowing the early detection of damage caused by external effects such as temperature, earthquakes, traffic loads, and wind. The success of an SHM system depends to a large extent on the number and location of the sensors installed on the structure. Placing sensors at incorrect locations results in erroneous or incomplete data.

When too few sensors are used, data cannot be collected from some critical regions of the structure, problems within the system may go unnoticed for longer, and the early-warning capability of the system is weakened. On the other hand, using more sensors than necessary increases hardware, installation, maintenance, and data-processing costs, while the excessive volume of data generated complicates the processing and analysis procedures and hinders access to meaningful information. For this reason, determining the optimum number of sensors to be used in a structure and their most suitable locations stands out as optimum sensor placement (OSP) problem in the design of SHM systems [2].

Bridge-type structures occupy a particularly important place in OSP literature, given that they are among the most critical components of transportation infrastructure. In these structures, placing sensors in the correct number and at the correct locations plays a decisive role in reliably monitoring the structure's dynamic behavior and in detecting possible damage at an early stage. Accordingly, the literature contains a considerable number of OSP studies addressing different bridge types and scales. Sun and Büyüköztürk applied a discrete artificial bee colony algorithm, combined with a MAC-based objective function, to a 27-element truss bridge [3]. Working on the Nottingham Wilford suspension bridge, Meo and Zumpano compared several placement techniques, including effective independence, driving-point residue, and the eigenvalue vector product [4]. Studying the I-40 Bridge in Albuquerque, New Mexico, Li et al. compared the modal kinetic energy and effective independence methods and established the mathematical relationship between the two approaches [5]. Examining the historic Saint Francesco da Paola bridge in Italy, Quaranta et al. combined finite element modelling with various placement criteria to determine the minimum number of sensors required to represent the structure, verifying their results using the MAC criterion [6]. Chang and Pakzad proposed a framework based on a MAC-derived variance criterion and showed that this method achieved superior performance compared with other approaches on the Northampton Street Bridge and the Golden Gate Bridge [7]. Li et al further emphasized that, due to the limited number of sensors that can be used on suspension bridges, determining the optimal placement is of critical importance, four different placement methods were evaluated using criteria such as the Fisher information matrix, MAC, and condition number [8]. In more recent work, Kaveh et al. compared a Q-learning-based water strider algorithm (QWSA) with other metaheuristic methods on dome-truss structures [9]. Meng et al., for their part, proposed a deep-reinforcement-learning-based algorithm that uses the MAC criterion to evaluate the quality of sensor configurations, and demonstrated that this algorithm achieved more successful results than genetic algorithms and particle swarm optimization on a 10-story frame structure and the Haicang Bridge [10]. Chioccarelli et al. combined effective-independence-based sensor placement with modal analysis methods in ambient vibration tests of an existing bridge, accurately determining the bridge's natural frequencies and mode shapes using a minimal number of accelerometers [11].

Prior research in this area has predominantly emphasized algorithmic performance, leaving the underlying theoretical basis of the OSP problem comparatively underexplored. Rather than deploying an optimization algorithm, this study instead sets out to clarify the basic reasoning behind the OSP problem and to illustrate, through a straightforward example, how different placement criteria influence the outcome. A further goal is to provide the literature with an instructive, easily interpretable reference model that can support future optimization-based research. To this end, a 17-member planar steel truss bridge is adopted as the test structure, and three MAC-derived criteria, max-MAC, ave-MAC, and rms-MAC, are used to guide sensor placement. A MATLAB [12] code exhaustively evaluated every feasible sensor combination, identifying the optimum configuration under each of the three criteria.

2 Structural Model Description

The 17-member planar steel truss bridge is a truss bridge model consisting of 17 bars and 10 nodal points located in the same plane [13]. In this system, the translational degrees of freedom in the x and y directions are taken into account. In the model shown in *Fig. 1*, node 6 is held by a fixed support and therefore does not possess any degree of freedom. Node 10, on the other hand, is fitted with a roller support, so only its degree of freedom in the y-direction is restrained. Overall, the system has a total of 17 degrees of freedom, 9 of which are in the x-direction and 8 of which are in the y-direction. Within the scope of the OSP problem, the three MAC-based functions were employed for this simple system with the aim of identifying the most suitable sensor locations for different numbers of sensors. A program developed in MATLAB was used to obtain the best solution among all possible combinations.

For all elements in the system, the cross-sectional area is A = 10 in², the modulus of elasticity is E = 30×10⁶ lb/in², the mass per unit length is $\bar{m}$ = 0.1 lb·sec²/in², and the element length is L = 60 in.

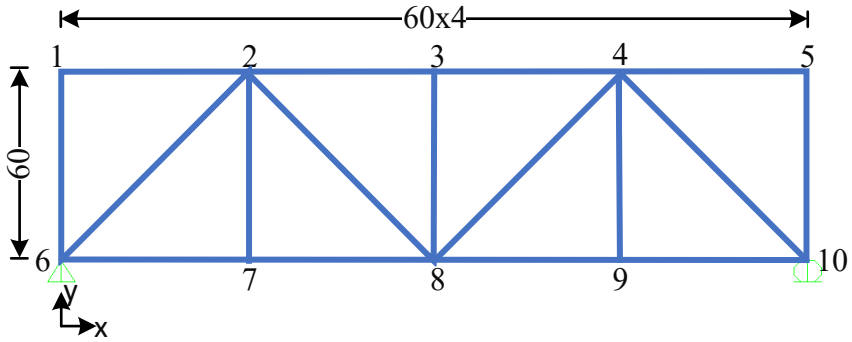


Fig. 1. 17-member planar steel truss bridge.

3 Methodology

To identify the most appropriate degrees of freedom (DOFs) for sensor placement, this study relies on the Modal Assurance Criterion (MAC), a widely used index for quantifying the correspondence between two mode shapes [14]. The MAC value ranges from 0 to 1: values approaching unity indicate that the compared modes are nearly identical, while values close to zero denote modes that are essentially independent of one another. From a sensor-placement standpoint, the underlying goal is to minimize the resemblance among mode shapes so that the selected measurement locations can capture the structure's modal information as distinctly as possible. The MAC between two mode-shape vectors, Φ_i and Φ_j, is defined as

$$MAC_{ij} = \frac{(\Phi_i^T \Phi_j)^2}{(\Phi_i^T \Phi_i)(\Phi_j^T \Phi_j)} \tag{1}$$

where the subscripts i and j denote the corresponding column vectors of the modes being compared.

Three objective functions related to the Modal Assurance Criterion were employed for sensor placement. The first is the max-MAC method, which aims to minimize the maximum similarity between mode shapes by considering the largest value among the off-diagonal elements of the MAC matrix. In this way, the max-MAC method seeks to maximize the independence of the mode-shape vectors throughout the optimization process. The second objective function minimizes the average of all off-diagonal MAC elements, thereby reducing the overall degree of correlation among the mode shapes. The third objective function computes the root-mean-square (rms) of the off-diagonal elements of the MAC matrix. This formulation

is used to quantify the overall level of inter-modal dependence, with a lower rms value indicating greater independence among the modes. Because each formulation weighs modal correlation differently, comparing all three enables the most effective sensor locations to be identified from complementary perspectives. The mathematical formulations of the max-MAC, ave-MAC, and rms-MAC methods are given in Eqs. (2), (3), and (4), respectively.

$$f_a(x) = max\{MAC_{ij}(x)\} \quad i \neq j \tag{2}$$

$$f_b(x) = ave\{MAC_{ij}\} = \frac{1}{mode(mode-1)} \sum_{i=1}^{mode} \sum_{j=1}^{mode} (MAC_{ij}) \quad i \neq j, j \neq i \tag{3}$$

$$f_c(x) = rms\{MAC_{ij}\} = \sqrt{\frac{1}{mode(mode-1)} \sum_{i=1}^{mode} \sum_{j=1}^{mode} (MAC_{ij})^2} \quad i \neq j, j \neq i \tag{4}$$

The primary aim of this study is to demonstrate the underlying theory of the optimum sensor placement problem on a simple structural system. For this purpose, rather than relying on an optimization algorithm, a MATLAB code was developed that exhaustively evaluates all possible sensor combinations for each objective function and identifies the configuration yielding the best value along with its corresponding objective-function result. This exhaustive search procedure was repeated separately for each of the three objective functions: max-MAC, ave-MAC, and rms-MAC. For every objective function, the number of sensors increased incrementally from 1 up to the total number of degrees of freedom of the structure; since the system considered in this study has 17 degrees of freedom, sensor numbers ranging from 1 to 17 were examined. For each sensor count, the optimal sensor configuration and its associated objective-function value were determined according to the criterion being evaluated.

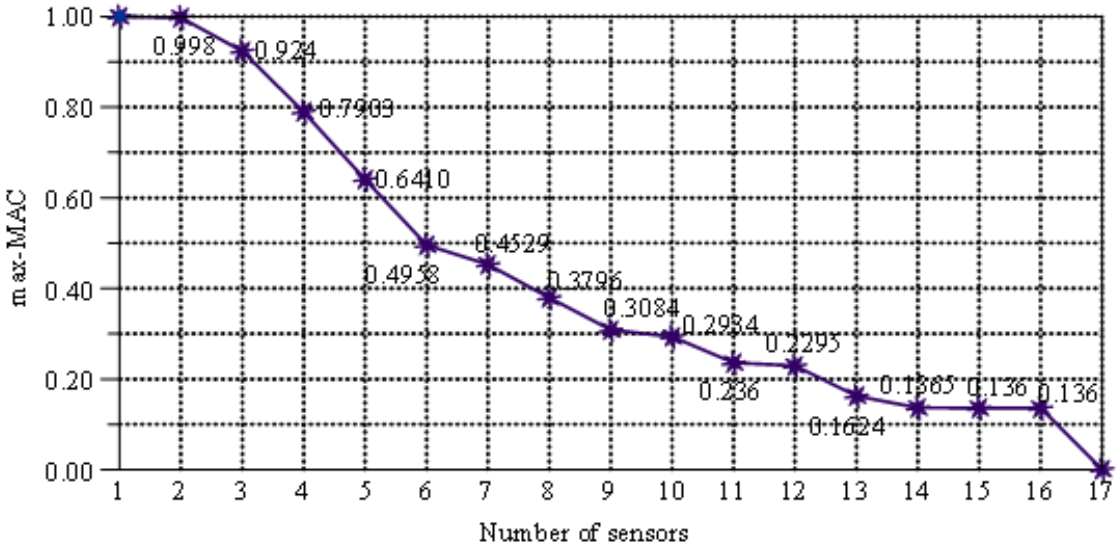
4 Numerical Results

Since the 17-member planar steel truss bridge system possesses 17 degrees of freedom, its modal analysis yields a total of 17 mode shapes; in this study, all of these modes were taken into account without any reduction, so as to fully capture the dynamic behavior of the structure. In this context, the objective function of the max-MAC method defined in Eq. (2), $f_a(x)$, was used to minimize the largest off-diagonal value of the MAC matrix. Analyses performed for different numbers of sensors revealed that the largest off-diagonal value of the MAC matrix decreases as the number of sensors increases. This indicates that a denser distribution of sensors enhances modal independence and improves monitoring capability. The variation in the max-MAC value with respect to different numbers of sensors is presented in *Fig. 2(a)*.

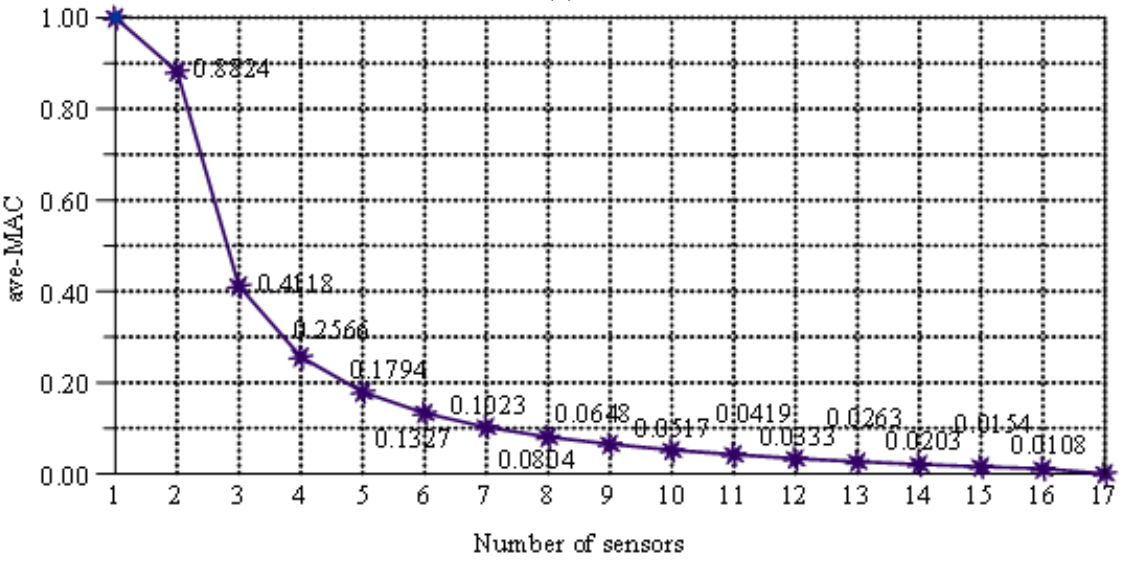
In addition, using the objective function of the ave-MAC method given in Eq. (3), $f_b(x)$, the sensor combinations that minimize the average of the off-diagonal values of the MAC matrix for different numbers of sensors were determined. The analyses showed that the average of the off-diagonal values of the MAC matrix decreases as the number of sensors increases. This finding reveals that modal measurement sensitivity improves as sensor density increases. The variation in the ave-MAC value with respect to different numbers of sensors is shown in *Fig. 2(b)*.

Finally, using the objective function of the rms-MAC method defined in Eq. (4), $f_c(x)$, the sensor combinations that minimize the root-mean-square of the off-diagonal values of the MAC matrix were examined. The analyses demonstrated that the rms-MAC value decreases as the number of sensors increases and that modal independence is markedly improved. The variation in the rms-MAC value with respect to different numbers of sensors is presented in *Fig. 2(c)*. Collectively, these analyses clearly demonstrate the effect of sensor number on modal analysis and the contribution of different MAC-based approaches to sensor placement.

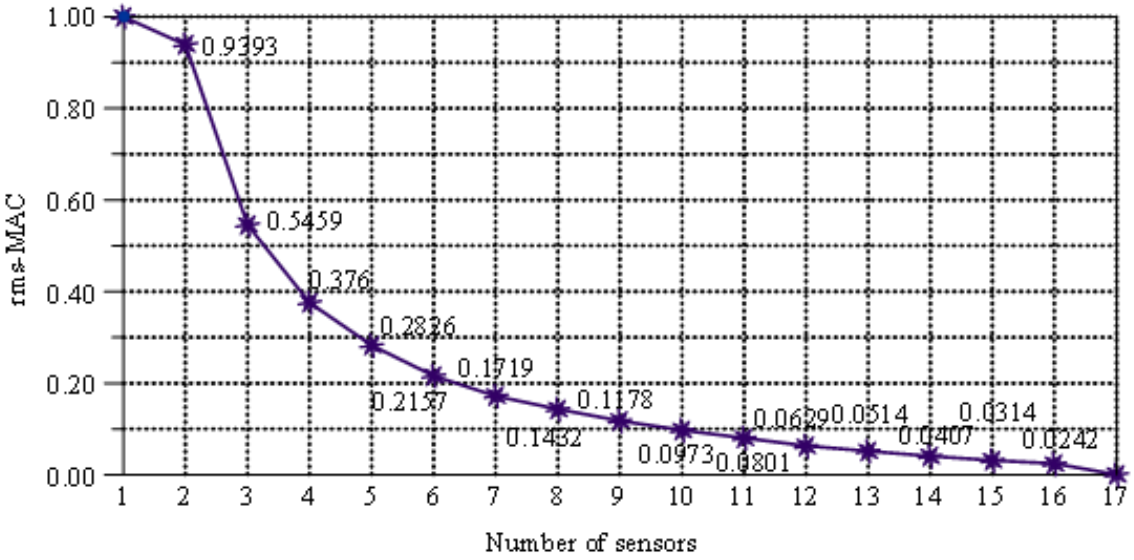
When only a single sensor is placed on the system, 17 different combinations arise, and in every case the largest off-diagonal value of the MAC matrix is equal to 1. This result shows that a single sensor is insufficient to ensure the independence of the mode-shape vectors. It was observed that more meaningful and reliable results can be obtained as the number of sensors is increased. However, once two or more sensors are placed on the system, the number of possible combinations grows substantially, making the identification of the best sensor arrangement a considerably more complex problem.



(a)



(b)



(c)

Fig. 2. Convergence of objective functions at different sensor numbers: (a) max-MAC, (b) ave-MAC, and (c) rms-MAC.

The optimal sensor configurations obtained for all three objective functions, together with their corresponding max-MAC, ave-MAC, and rms-MAC values for each sensor count, are summarized in *Table 1*. These results once again demonstrate that sensor placement plays a critical role in the success of modal monitoring processes in bridge systems, and that different formulations can lead to markedly different optimization outcomes. The overall results presented in *Table 1* show that, as the number of sensors increases, the objective-function value of each method decreases steadily and modal independence improves. In particular, it was observed that as the number of sensors increases, the sensor locations recommended by the max-MAC, ave-MAC, and rms-MAC methods converge to a greater number of common points. This indicates that although method-dependent differences in sensor placement are pronounced at low sensor densities, these differences diminish as sensor density increases. As a representative example, the optimal sensor configurations obtained for a five-sensor arrangement under each of the three criteria are illustrated in *Fig. 3*.

Although the fundamental objective of each method is to increase the linear independence among the mode-shape vectors, the proposed sensor placements were found to vary due to differences in the strategies employed. This finding indicates that the choice of sensor placement method should be made in accordance with the dynamic characteristics of the structure and the intended monitoring objective. Accordingly, the careful selection of sensor placement strategies in SHM systems is of critical importance for obtaining reliable and effective results.

Table 1. Sensor locations of the 17-member planar steel truss bridge system.

Sensor combinations	f_a	f_b	f_c	**Combinations** f_a	**Combinations** f_b	**Combinations** f_c
17-2	0.9980	0.8824	0.9393	2x-8x	1x-1y	1x-1y
17-3	0.9240	0.4118	0.5459	3x-3y-9x	1y-7x-7y	1y-2x-9y
17-4	0.7903	0.2566	0.3760	2x-4x-8x-9x	1y-3y-5x-10x	1y-3y-5x-10x
17-5	0.6410	0.1794	0.2826	1x-2y-3x-7x-8y	1y-3y-5x-7y-9x	1y-2x-3y-8x-9y
17-6	0.4958	0.1327	0.2157	3x-3y-4y-5x-7x-9y	1y-4x-4y-8y-9x-10x	1y-2y-3x-5x-7x-10x
17-7	0.4529	0.1023	0.1719	3x-3y-4y-5x-7x-9y-10x	1y-3x-3y-4x-7y-9y-10x	1x-1y-2y-5x-8y-9x-10x
17-8	0.3796	0.0804	0.1432	1x-4x-4y-5x-5y-8y-9x-10x	1y-3x-3y-4x-7y-9x-9y-10x	1y-2y-3x-3y-5x-7x-7y-10x
17-9	0.3084	0.0648	0.1178	1x-4x-4y-5x-5y-7x-8y-9x-10x	1y-3x-3y-4x-5y-7y-9x-9y-10x	1y-2y-3x-3y-4x-5x-7x-7y-10x
17-10	0.2934	0.0517	0.0973	1x-2x-2y-4x-5x-5y-8x-8y-9x-10x	1x-1y-3y-5x-5y-7x-7y-9x-9y-10x	1x-1y-2y-4x-5x-5y-7x-8y-9x-10x
17-11	0.2360	0.0419	0.0801	2x-2y-3x-3y-4x-4y-5y-7y-8x-9x-10x	1x-1y-3x-3y-5x-5y-7x-7y-9x-9y-10x	1y-2y-3x-3y-4x-4y-5y-7x-7y-9x-10x
17-12	0.2295	0.0333	0.0629	2x-2y-3x-4x-4y-5x-5y-7x-7y-8x-8y-10x	1x-1y-3x-3y-4y-5x-5y-7x-7y-9x-9y-10x	1y-2y-3x-3y-4x-4y-5x-5y-7x-7y-9x-10x
17-13	0.1624	0.0263	0.0514	1x-2x-2y-3x-3y-4x-4y-5x-5y-7x-7y-9x-10x	1x-1y-3x-3y-4y-5x-5y-7x-7y-8y-9x-9y-10x	1y-2x-2y-3x-3y-4x-4y-5x-5y-7x-7y-9x-10x
17-14	0.1365	0.0203	0.0407	1x-2x-2y-3x-3y-4x-4y-5x-5y-7x-8y-9x-9y-10x	1x-1y-2y-3x-3y-4x-5x-5y-7x-7y-8y-9x-9y-10x	1x-1y-2x-2y-3x-4x-4y-5x-5y-7x-7y-8y-9x-10x
17-15	0.1360	0.0154	0.0314	1x-2x-2y-3x-3y-4x-4y-5x-5y-7x-7y-8y-9x-9y-10x	1x-1y-2y-3x-3y-4x-4y-5x-5y-7x-7y-8y-9x-9y-10x	1x-1y-2x-2y-3x-3y-4x-4y-5x-5y-7x-7y-8y-9x-10x
17-16	0.1360	0.0108	0.0242	1x-1y-2x-2y-3x-3y-4x-4y-5x-5y-7x-7y-8y-9x-9y-10x	1x-1y-2y-3x-3y-4x-4y-5x-5y-7x-7y-8x-8y-9x-9y-10x	1x-1y-2x-2y-3x-3y-4x-4y-5x-5y-7x-7y-8x-8y-9x-10x

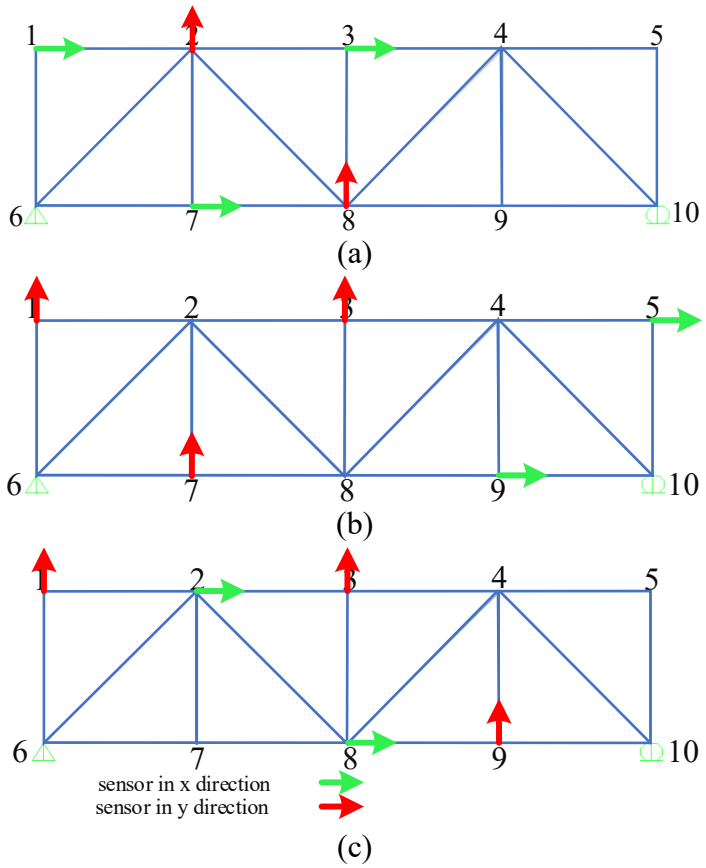


Fig. 3. Optimal sensor configurations obtained for five sensors under (a) max-MAC, (b) ave-MAC, and (c) rms-MAC criteria.

5 Conclusion

This study presents a numerical example developed to explain the working principle of the optimum sensor placement (OSP) problem and to compare how different placement criteria influence the resulting sensor configurations. A 17-member planar steel truss bridge served as the test structure for demonstrating the OSP procedure on a simple, easily interpretable system. Three MAC-derived criteria, max-MAC, ave-MAC, and rms-MAC, were applied to identify the most suitable degrees of freedom for sensor installation. A dedicated MATLAB code exhaustively searched every feasible sensor arrangement for sensor counts between 1 and 17, reporting the best configuration obtained under each criterion.

- A configuration with only one sensor cannot guarantee independence among the mode-shape vectors; consequently, the off-diagonal MAC value remains equal to 1 in every case.
- As additional sensors were introduced, the objective-function value associated with each of the three criteria declined steadily, reflecting a growing degree of linear independence among the mode shapes.
- Although the three criteria typically point to different sensor arrangements when the sensor count is fixed, their recommended locations increasingly overlap once the number of sensors becomes sufficiently large.
- Because max-MAC, ave-MAC, and rms-MAC rely on distinct mathematical formulations, each pursuing linear independence in a different way, the sensor layouts they propose are not identical even though they share the same underlying objective.

References

1. Farrar C.R., Worden K.: An introduction to structural health monitoring, Philos. Trans. R. Soc. A Math. Phys. Eng. Sci. 365, 303–315 (2007).
2. Hassani, S., Dackermann, U.: A Systematic Review of Optimization Algorithms for Structural Health Monitoring and Optimal Sensor Placement. Sensors 23(6), 3293 (2023).
3. Sun, H., Büyüköztürk, O.: Optimal sensor placement in structural health monitoring using discrete optimization. Smart Materials and Structures 24(12), 125034 (2015).
4. Meo, M., Zumpano, G.: On the optimal sensor placement techniques for a bridge structure. Engineering Structures 27(10), 1488-1497 (2005).
5. Li, D.S., Li, H.N., Fritzen, C.P.: The connection between effective independence and modal kinetic energy methods for sensor placement. Journal Of Sound and Vıbratıon 305(1), 945-955 (2007).
6. Quaranta, G., Marano, G. C., Trentadue, F., Monti, G.: Numerical study on the optimal sensor placement for historic swing bridge dynamic monitoring. Structure and Infrastructure Engineering 10(1), 57–68 (2014).
7. Chang, M., Pakzad, S. N.: Optimal sensor placement for modal identification of bridge systems considering number of sensing nodes. Journal of Bridge Engineering 19(6), 04014019 (2014).
8. Li, B., Li, D., Zhao, X., Ou, J.: Optimal sensor placement in health monitoring of suspension bridge. Science China Technological Sciences 55(7), 2039–2047 (2012).
9. Kaveh, A., Eslamlou, A. D., Rahmani, P., Amirsoleimani, P.: Optimal sensor placement in large-scale dome trusses via Q-learning-based water strider algorithm. Structural Control and Health Monitoring 29(7), 1–20 (2022).
10. Meng, X., Zhang, H., Jia, K., Li, H., Huang, Y.: Optimal sensor placement for structural health monitoring based on deep reinforcement learning. Smart Structures and Systems 31(3), 247-257 (2023).
11. Chioccarelli, E., Giunta, D., De Angelis, A., Bilotta, A.: Discussing optimal sensor placement for ambient vibration test of an existing bridge. Engineering Structures 310, 118000 (2024).
12. The MathWorks, Inc., MATLAB (R2023b), (2023).
13. Paz M., Kim Y. H.: Structural Dynamics, Springer Nature Switzerland AG, USA, (2018).
14. Carne T.G., Dohrmann C.F.: A modal test design strategy for model correlation Thomas G. Carne and Clark Ft. Dohrmann Sandia National Laboratories Albuquerque, New Mexico 87185-0557 (1995).

Author Contribution Statement

- *Conceptualization:* Barbaros ATMACA, Tayfun DEDE
- *Methodology:* Barbaros ATMACA, Büşra YAKAK VATANDAŞ
- *Investigation:* Barbaros ATMACA, Hülya Pir, Büşra YAKAK VATANDAŞ
- *Writing – Original Draft:* Hülya Pir, Büşra YAKAK VATANDAŞ
- *Writing – Review & Editing:* Barbaros ATMACA

List of Abbreviations

- **SHM** — Structural Health Monitoring
- **OSP** — Optimal Sensor Placement
- **MAC** — Modal Assurance Criterion
- **DOFs** — Degrees of Freedom
- **max-MAC** — Maximum Modal Assurance Criterion
- **ave-MAC** — Average Modal Assurance Criterion
- **rms-MAC** — Root-Mean-Square Modal Assurance Criterion

Conflict of interest
The authors declare that they have no conflict of interest.

Note: Following the conference, this Publication Note will be added to each paper; therefore, authors are kindly requested not to remove the note below and to complete the author(s) and paper title information.

Publication Note
This paper was peer-reviewed, accepted for presentation, and included in the proceedings of the ACE2026 – International Conference on Advances in Civil Engineering, held on 12–14 October 2026 in Trabzon, Türkiye.

This paper may be cited as follows:
Atmaca B., Pir H., Yakak Vatandas B., Dede T., "The Solution of the Optimal Sensor Placement Problem for Planar Truss System" in Proceedings of the ACE2026 – International Conference on Advances in Civil Engineering, Trabzon, Türkiye, 12–14 October 2026.

A Comparative Study on the Seismic and Environmental Performance of Geopolymer and Conventional Reinforced Concrete Buildings

İffet Gamze Mütevelli Özkan[1] and İhsan Türkel[2]
[1] 0000-0002-0239-4280, Kastamonu University, Civil Engineering Department, Kastamonu, Türkiye, gmutevelli@kastamonu.edu.tr
[2] 0000-0002-6841-0482, Kastamonu University, Civil Engineering Department, Kastamonu, Türkiye, iturkel@kastamonu.edu.tr

Abstract. This study comparatively investigates the seismic and environmental performance of a four-story reinforced concrete structure using conventional concrete and a geopolymer concrete mixture designated GPCM8, both with the same compressive strength. In both models, the story plan, number of stories, structural system arrangement, cross-sectional dimensions, and loading conditions were kept constant; thus, only the effect of the material type on the structural behaviour was evaluated. The seismic performance of the structures was determined using the response spectrum analysis method, in accordance with the Turkish Building Earthquake Code (TBEC 2018). Due to its lower modulus of elasticity, the GPCM8 model exhibited 16.80% longer natural vibration periods, 13.92% lower base shear, and 16.09% greater roof displacement than the C30/37 model. Additionally, there was an approximately 16% increase in interstory drift and story displacements, suggesting greater deformation demands. Nevertheless, GPCM8 reduced carbon emissions by approximately 37.6%. The findings indicate that GPCM8 geopolymer concrete is a sustainable and promising alternative to conventional concrete. Nevertheless, in structural design, the modulus of elasticity and the corresponding displacement demands must be considered in addition to compressive strength. It is determined that GPCM8 concrete can offer adequate seismic performance in reinforced concrete structures when designed appropriately, taking these parameters into consideration.

Keywords: Geopolymer concrete; Seismic performance; Environmental performance; Sustainability

1 Introduction

Concrete's high compressive strength, broad availability, and low production cost make it one of the most popular building materials in the construction sector. However, substantial energy consumption and CO_2 emissions are produced during the manufacture of Portland cement, the primary binder in ordinary concrete. These emissions are caused by the direct release of CO_2 during the calcination of limestone as well as by manufacturing activities such as the processing and transportation of raw materials, the use of fossil fuels to reach high temperatures, and the usage of electricity [1]. In fact, producing one ton of cement is thought to release roughly the same amount of CO_2 into the environment. Reducing the environmental impact of cement-based concrete manufacturing has become a crucial demand for a sustainable construction sector, given that global carbon emissions reached 36.8 billion tons in 2023 and that cement production accounts for about 7–8% of these emissions [2]. Thus, geopolymer concrete (GPC) stands out as a substitute binder system made by reacting industrial byproducts

such as fly ash (FA), blast furnace slag (BFS), and metakaolin, which have high concentrations of silica and alumina, with alkali activators, in place of Portland cement (PC) [3, 4]. This approach reduces the environmental impact of concrete by limiting PC use [5].

The mechanical properties of geopolymer concretes are substantially influenced by the mix design, curing conditions, alkali activator type and concentration, and the ratio of FA and granulated BFS used. The compressive strength and elasticity modulus of GPC containing FA and granulated BFS were experimentally investigated by Bellum et al. (2020) [3]. The results showed that at the same 28-day compressive strength level, the modulus of elasticity of GPC was approximately 15–28% lower compared to PC concrete. Moreover, Nath and Sarker (2017) [6] compared ordinary PC concrete and low-calcium FA-based GPC cured at ambient temperature. They found that the modulus of elasticity of the GPC was approximately 25–30% lower at the same compressive strength level. Similar results were obtained in the experimental study conducted by Liu et al. (2022) [7] on GPC with a triple binder system produced using BFS, FA, and zeolite powder; it was reported that the modulus of elasticity of GPC was 25.8% lower than that of ordinary PC concrete with the same compressive strength. These investigations indicate that GPCs may exhibit a lower modulus of elasticity than conventional concrete (CC), despite attaining comparable compressive strengths. This distinction should be considered when assessing the material's dynamic behaviour and structural rigidity.

Using concretes with different modulus of elasticity at the same compressive strength level can affect seismic behaviour parameters such as stiffness, natural vibration period, base shear force, story displacements, and relative story drift ratios at the structural scale. The literature indicates that changes in concrete stiffness and strength affect the dynamic seismic behaviour of reinforced concrete (RC) frame structures, and that structural stiffness is a determining factor in the natural vibration period and seismic demands [8, 9]. Therefore, for GPC to be considered an alternative to CC, it needs to be examined not only in terms of compressive strength and environmental sustainability but also in terms of seismic performance [10]. Studies on the mechanical properties of GPC and the behaviour of RC elements show that the bending and shear behaviour of GPC beams is generally comparable to that of conventional PC-concrete beams [11, 12].

Regarding column behaviour, several studies have investigated the effects of parameters such as axial load, fiber reinforcement, reinforcement type, and confinement effect on the load-carrying capacity and damage evolution of geopolymer RC columns [13, 14]. In addition, the behaviour of beam-column connections, a critical area under earthquake effects, under reversible cyclic loads has been investigated; in these studies, seismic performance indicators such as load-carrying capacity, stiffness reduction, ductility, energy dissipation, and damage mechanisms have been evaluated [15, 16]. However, a significant portion of current studies remains limited to the material level, individual RC elements, or beam-column connection regions. Although research evaluating the potential of GPC in terms of seismic resistance has accelerated in recent years, it is emphasized that studies conducted at the structural scale are still limited [10, 17].

The limited number of studies comparing RC structures modelled with CC and GPC, both at the same compressive strength level, in terms of natural vibration period, base shear force, story displacements, and relative story drift ratios using regulation-based dynamic analysis methods constitutes a significant gap in the literature. Therefore, GPC needs to be evaluated not only in terms of compressive strength, durability, and sustainability, but also in terms of its effects on structural rigidity and global structural behaviour under seismic influence. This study comparatively investigates the seismic behavior of a four-story regular RC structure designed using CC and GPC with the same compressive strength level. The reference model was created based on C30/37, while the alternative model utilized the experimental material properties of the M8 geopolymer concrete (GPCM8) mix given by Bellum et al. [3]. In both models, the story

plan, story number, structural system arrangement, cross-sectional dimensions, loading conditions, and unit weight were kept the same; thus, the effect of the change in elasticity modulus on the structural behavior was evaluated. In addition, the potential of GPC in terms of environmental sustainability was discussed, as it reduces the use of PC and allows for the utilization of industrial by-products such as FA and BFS.

2 Materials and Methods

This study comparatively investigates the seismic behaviour of a four-story RC structure modelled using CC and GPC with the same compressive strength. To enable comparison solely based on concrete type, the story plan, story height, structural system arrangement, element cross-sections, reinforcement properties, boundary conditions, and loading conditions were kept identical in both structural models. The C30/37 concrete class was employed as the CC. For the GPC model, the cube compressive strength of the M8 mixture, as described in the study by Bellum et al. (2020) [3], was considered and referred to as GPCM8. Furthermore, the environmental impacts of producing both concrete types were comparatively evaluated using CO_2-equivalent emissions.

2.1 Structural Model Characteristics

The structure under investigation is designed as a regular four-story RC frame system in plan. The story height is 3 m, and the total building height is 12 m. The building plan measures 12 m x 12 m, and the load-bearing system consists of RC columns and beams in both directions. Column cross-sections are 40 cm x 40 cm, beam cross-sections are 25 cm x 50 cm, and the slab thickness is 15 cm. Column and beam elements are modelled with bar elements. It is assumed that the floor slabs have sufficient rigidity within their own planes, and rigid diaphragms are defined at the story levels. The column supports at the foundation level are considered fixed. The story plan and 3D view of the building model are shown in Fig. 1. The SAP2000 [18] finite element analysis program was used to create the structural models and perform the analyses.

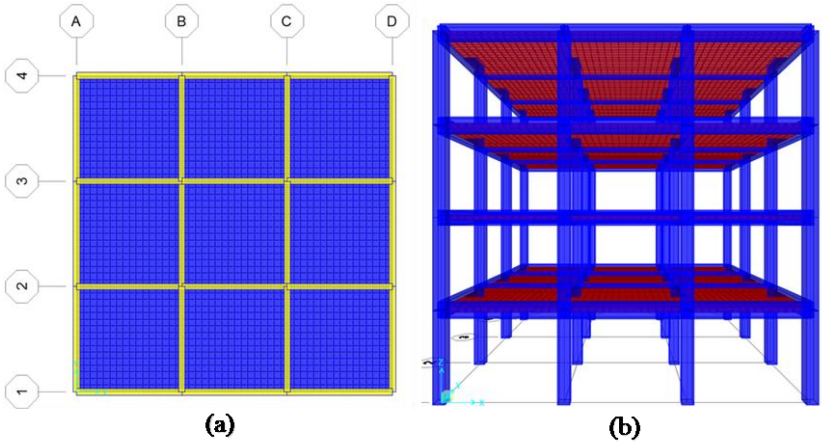


Fig. 1. (a) Story plan and (b) 3D view of the building model.

The behavior of buildings under seismic effects was investigated using the Response Spectrum Analysis (RSA) method, applied in accordance with the provisions of the 2018 Turkish Building Earthquake Code (TBEC 2018) [19].

2.2 Material Properties

In the reference structural model, CC with a characteristic cylinder compressive strength of 30 MPa was used. In the GPC model, the material properties of the M8 mix, experimentally

investigated by Bellum et al. (2020) [3], were used as the basis. The 28-day cube compressive strength of this mix is 38.25 MPa, which is quite close to the characteristic cube compressive strength of 37 MPa defined for the C30/37 concrete class. Therefore, it was assumed that the M8 mix has approximately the same compressive strength as C30/37, and an equivalent cylinder compressive strength of 30 MPa was adopted for the GPC in the structural analysis. Thus, the two concrete types were compared at nominally similar compressive strength levels. For both concrete types, the unit volume mass was accepted as 2392 kg/m³, as reported by Bellum et al. for the M8 mix. The corresponding unit volume weight was calculated to be 23.47 kN/m³, using a gravitational acceleration of 9.81 m/s². Although the compressive strength of the concrete was kept constant in both models, the modulus of elasticity of CC and GPC was defined separately. The modulus of elasticity of CC was calculated using Equation 1 according to ACI318-19 [20], while the modulus of elasticity of GPC was obtained from the results of the reference experimental mixture. Thus, in both structural models, the geometry, loading conditions, and structural weight were held constant, and the concrete types were assumed to have approximately equivalent compressive strength levels. This approach aimed to determine the effect of differences in material properties, primarily the modulus of elasticity, on the structure's natural vibration periods, displacements, and internal force demands.

$$E_c = {w_c}^{1.5} 0.043 \sqrt{f_c'} \quad (1)$$

Here, $E_c$represents the modulus of elasticity of concrete (MPa); w_c represents the unit volume mass of concrete (kg/m³); and f_c' represents the cylinder compressive strength (MPa) used in the design.

The necessary mechanical properties of the concrete materials used are presented in Table 1.

Table 1. Properties of the concrete used in the building model.

Material property	**C30/37**	**GPCM8**
Concrete cylinder compressive strength (MPa)	30	30
Modulus of Elasticity of Concrete (GPa)	27.553	20.196
Unit Weight (kN/m³)	23.47	23.47
Poisson's Ratio	0.20	0.20
Reinforcement Yield Strength (MPa)	420	420
Modulus of Elasticity of Reinforcement (GPa)	200	200

2.3 Load Definition

The dead and live loads acting on the structure were determined by considering the relevant load standards and intended use. Dead loads due to floor finish layers, partition walls, and other non-structural elements were modelled as equivalent uniformly distributed loads. An additional dead load of 2.00 kN/m² and a live load of 2.00 kN/m² were applied to the floor slabs. The weights of the infill and partition walls in the structure were modelled as uniformly distributed loads acting on the beams. A wall load of 6.00 kN/m was applied to the frame beams where the exterior walls are located, and a wall load of 4.00 kN/m was applied to the interior beams where the interior partition walls are located. The same load values and loading arrangement were used in both structural models. The mass source used in the seismic analysis of the analysis model was created as in Equation (2), based on the sum of all dead loads and 30% of the live loads.

$$M = G + 0.30Q \quad (2)$$

Here, G represents the dead loads, while Q represents the live loads. The live-load participation factor of 0.30 used for the mass source was determined based on the structure's intended use

and the provisions of TBEC 2018 [19]. The analysis results from the structural models developed for conventional C30/37 and GPCM8 were evaluated under the G + Q + E load combination, which considers gravity loads and seismic effects simultaneously.

2.4 Definition of Earthquake Effects

The seismic behaviour of the structures was determined using the RSA method in accordance with the TBEC 2018 [19]. The seismic parameters used in the analyses were determined assuming that the buildings are located in Pazarcık district of Kahramanmaraş province and are presented in Table 2.

Table 2. Earthquake parameters.

Parameters	**Assumptions**
Earthquake ground motion level	DD-2
Soil class	ZC
Peak ground acceleration (PGA)	0.477 g
Peak ground velocity (PGV)	32.487 cm/s
Latitude of the region	37.489371°
Longitude of the region	37.229512°

Seismic effects were applied separately along the two orthogonal principal directions of the structure. In the modal analysis, a sufficient number of vibration modes were included to achieve a cumulative effective modal mass participation ratio of at least 95% in each horizontal direction. The Complete Quadratic Combination (CQC) method was used to combine the modal responses. Since the two systems have the same number of spans, the same axis spacing, identical cross-sections, and symmetrical placement of structural elements in the X and Y directions, comparative evaluations were conducted using the global X-direction U1 (UX) responses. The effects of concrete type-dependent variations in the modulus of elasticity on the seismic behaviour of the structure were evaluated by comparing the natural vibration periods, horizontal displacements, interstory drifts, base shear forces, and internal force demands obtained from the response spectrum analyses of the C30/37 and GPCM8 models.

2.5 Environmental Assessment Methodology

The environmental impacts of CC and GPC were compared based on estimated carbon emissions. The assessment was conducted for 1 m^3 of concrete encompassing all processes from raw material extraction and processing through concrete production. The calculations considered the amounts of binder, aggregate, water, and alkali activator. The amount of each concrete component in 1 m^3 of mix was multiplied by the relevant unit emission factor obtained from the literature; the total carbon emission was determined by summing the emission values calculated for all components. The unit emission factors used in the calculations were taken from the study conducted by Tushar et al (2025) [5]. The mix components and component amounts of the geopolymer concrete were determined based on the M8 mix developed by Bellum et al. (2020) [3]. The CC mix was formulated to represent the C30/37 concrete class, with a water/cement ratio of 0.45. This value was chosen based on the maximum water/binder ratio limits specified in ACI 318-19 [20] for certain environmental exposure classes.

In order to keep the effect of aggregate quantity and total unit volume mass constant in the comparison, the unit volume mass of the C30/37 reference concrete was assumed to be equal to the experimentally reported value of 2392 kg/m^3 for the GPCM8 mix. Similarly, the amounts of fine and coarse aggregate in the C30/37 mix were determined as 610 and 1221.5 kg/m^3, respectively, based on the values reported in the M8 mix developed by Bellum et al. Thus, the total aggregate amount became 1831.5 kg/m^3, and the total amount of cement and water to reach

the target unit volume mass was calculated as 560.5 kg/m³. Assuming a water/cement ratio (W/C) of 0.45, the amounts of cement and water were calculated as approximately 386.6 kg/m³ and 174.0 kg/m³, respectively, from Equation (3) and Equation (4). This mixture is a reference mix, not an experimental concrete mix design, intended to consistently determine material quantities in environmental comparisons. Emissions from transportation distances and on-site applications were treated as the same for both concrete types and were excluded from the comparison.

$$W = 0.45C \quad (3)$$

$$C + W = 560.5 \quad (4)$$

3 Results and Discussion

This section comparatively evaluates the modal analysis, RSA, and approximate carbon emission results obtained from four-story reinforced concrete frame models constructed using C30/37 and GPCM8. In both structural models, the plan geometry, load-bearing element cross-sections, reinforcement properties, loads, mass source, boundary conditions, and seismic parameters were held constant. In addition, the compressive strength and unit weight of the two concrete types were assumed to be identical. Therefore, the differences observed in the structural analysis results can primarily be attributed to the variation in the modulus of elasticity between C30/37 and GPCM8.

3.1 Natural Vibration Periods

Modal analysis showed that the first two periods were 0.740105 s for C30/37 and 0.864455 s for GPCM8, while the third periods were 0.619974 s and 0.724141 s, respectively (Table 3).

Table 3. Fundamental periods of the structure.

Models	**T_1 (s)**	**T_2 (s)**	**T_3 (s)**
C30/37	0.740105	0.740105	0.619974
GPCM8	0.864455	0.864455	0.724141
Relative change (%)	+16.80	+16.80	+16.80

The first three natural vibration periods of the GPCM8 model were approximately 16.80% longer than those of the C30/37 model. Since the mass and geometric properties of the structure were kept constant, this increase was primarily attributed to the GPCM8 model's lower lateral stiffness, resulting from the lower modulus of elasticity of GPC. Specifically, the elasticity modulus of GPCM8 was approximately 26.70% lower than that of C30/37, thereby reducing overall structural stiffness and consequently increasing the natural vibration periods. The fact that the first and second mode periods are equal in both models can be explained by the structure having equal spans in the X and Y directions, the same cross-sectional properties, and symmetrical placement of structural elements. This result indicates that the structure exhibits similar dynamic characteristics in the two principal horizontal directions.

3.2 Base Shear and Roof Displacement

The base shear and roof displacement values in the X direction obtained from the response spectrum analysis of the structures are compared in Table 4.

Table 4. Comparison of analysis results in the X direction.

Models	**Base shear (kN)**	**Roof displacement (mm)**
C30/37	490.738	13.415
GPCM8	422.420	15.574
Relative change (%)	−13.92	+16.09

In the C30/37 model, the base shear was calculated to be 490.738 kN, whereas in the GPCM8 model, it was 422.420 kN. Accordingly, the base shear of the GPCM8 model is approximately 13.92% lower than that of the C30/37 model.

The fundamental structural periods of both models are located in the region of decreasing spectral acceleration, between the corner period (TB) of 0.328 s and the long period (TL) of 6.00 s in the design spectrum used. In this region, the spectral acceleration decreases with increasing period. The lower modulus of elasticity of GPCM8 has extended the fundamental structural period, resulting in a lower spectral acceleration ordinate. The decrease in base shear is consistent with this spectral change.

The roof displacement in the C30/37 model was 13.415 mm. In the GPCM8 model, the roof displacement was calculated as 15.574 mm. The roof displacement of the GPCM8 model is approximately 16.09% higher than that of the C30/37 model. This increase can be explained by the GPCM8 model's lower horizontal rigidity and longer natural vibration period.

3.3 Story Displacement and Interstory Drift

Table 5 and Fig. 2 show that, in both structural models, the story displacements increase linearly with height. The largest displacement values were obtained on the fourth story, at 13.415 mm and 15.574 mm for the C30/37 and GPCM8 models, respectively.

Table 5. Story displacement and interstory drift values of the structures in the X direction.

Story	Story Displacement (mm)		Interstory Drift (mm)	
	C30/37	GPCM8	C30/37	GPCM8
1	3.298	3.850	3.298	3.850
2	7.734	8.988	4.436	5.138
3	11.246	13.053	3.512	4.065
4	13.415	15.574	2.169	2.521

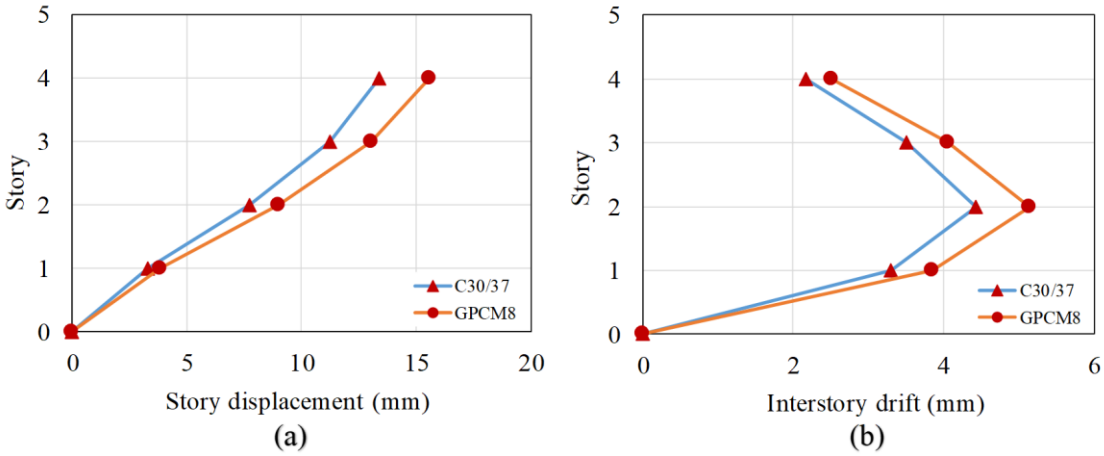


Fig. 2. (a) Story displacement and (b) interstory drift of the structures in the X direction.

The peak displacement of the GPCM8 model is approximately 16.09% higher than that of the C30/37 model. Similarly, the story displacements in the GPCM8 model are approximately 16.07%–16.74% greater than those in the C30/37 model at all stories. Interstory displacements reached their maximum value on the second story in both models; calculated as 4.436 mm and 5,138 mm for the C30/37 and GPCM8 models, respectively. After the second story, interstory displacements decrease with height along the structure. Interstory displacements in the GPCM8 model are approximately 15.75%–16.74% higher than in the C30/37 model across all stories.

These results can be explained by the lower elastic modulus of GPCM8, which leads to reduced horizontal rigidity and greater displacement demands under seismic loading.

3.4 Comparison of Carbon Emissions

A comparison of CO_2-eq emissions for C30/37 and GPCM8 is given in Table x. The total CO_2-eq emissions for the C30/37 and GPCM8 mixtures were calculated to be 365.90 and 228.46 kg CO_2-eq/m³, respectively. Accordingly, the GPCM8 mixture produced approximately 37.6% lower CO_2-eq emissions than the C30/37 concrete.

Table 6. Mix proportions and CO_2-equivalent emissions of concrete mixtures.

Component	**Emission factor (kg CO_2-eq/kg component)**	**C30/37 content (kg/m³)**	**C30/37 emission (kg CO_2-eq/m³)**	**GPCM8 content (kg/m³)**	**GPCM8 emission (kg CO_2-eq/m³)**
Portland cement	0.901	386.6	348.33	-	-
Fly ash	0.0277	-	-	122.10	3.38
GGBS	0.0613	-	-	284.90	17.46
Water	0.0010	174.0	0.17	-	-
Sodium hydroxide (NaOH)	1.8224	-	-	46.51	84.76
Sodium silicate (Na_2SiO_3)	0.9068	-	-	116.29	105.45
Fine aggregate	0.0031	610.0	1.89	610.00	1.89
Coarse aggregate	0.0127	1221.5	15.51	1221.50	15.51
Total CO_2-eq emission		-	365.90	-	228.46

Approximately 95.2% of the total emissions in CC result from Portland cement. While the use of fly ash and GGBS in the GPCM8 mix reduced binder-related emissions, alkali activators were the primary source of emissions. The total emission contribution of sodium silicate and sodium hydroxide was 190.21 kg CO_2-eq/m³, accounting for approximately 83.3% of GPCM8's total emissions. Since the amounts of fine and coarse aggregates were kept the same in both mixes, emissions from aggregates did not affect the comparison result. Therefore, it appears that the emission reduction in GPCM8 is primarily due to the absence of Portland cement, but the high emissions from alkali activators partially offset this advantage.

4 Conclusion

This study compares the seismic behaviour and approximate carbon emissions of four-story reinforced concrete structures modelled using C30/37 and GPCM8, both with the same compressive strength and unit weight.

The approximately 26.70% lower modulus of elasticity of GPCM8 compared with C30/37 resulted in a reduction in structural stiffness and an approximately 16.80% increase in the first three natural vibration periods. Consistent with this increase in the vibration periods, the base shear of the GPCM8 model decreased by 13.92%, while the roof displacement increased by 16.09%.

Story displacements increased progressively with height in both models, while the maximum interstory displacement occurred at the second story. In the GPCM8 model, story displacements were approximately 16.07%–16.74% higher and interstory displacements were 15.75%–16.74% higher compared to the C30/37 model. These results demonstrate that the lower modulus of elasticity of geopolymer concrete increases the structural deformation demands.

In the environmental assessment, the total emissions of C30/37 and GPCM8 were calculated to be 365.90 and 228.46 kg CO_2-eq/m³, respectively. Accordingly, the GPCM8 mixture

produced approximately 37.6% lower carbon emissions than C30/37. However, sodium silicate and sodium hydroxide in the GPCM8 mixture accounted for a significant portion of the total emissions.

In conclusion, GPCM8 represents a promising environmental alternative due to its lower carbon emissions. However, in structural design, not only compressive strength but also the modulus of elasticity and the associated displacement demands should be taken into account. The findings indicate that, when these parameters are properly considered in the design process, GPCM8 has the potential to provide satisfactory seismic performance in reinforced concrete structures.

References

1. Ige, O.E., Von Kallon, D.V., Desai, D.: Carbon emissions mitigation methods for cement industry using a systems dynamics model. Clean Techn Environ Policy. 26, 579–597 (2024). https://doi.org/10.1007/s10098-023-02683-0
2. IEA, C.: Technology roadmap: low-carbon transition in the cement industry. International Energy Agency (IEA), Cement Sustainability Initiative (CSI), (2018).
3. Bellum, R.R., Muniraj, K., Madduru, S.R.C.: Investigation on modulus of elasticity of fly ash-ground granulated blast furnace slag blended geopolymer concrete. Materials Today: Proceedings. 27, 718–723 (2020). https://doi.org/10.1016/j.matpr.2019.11.299
4. Shaikh, F.U.A.: Mechanical and durability properties of fly ash geopolymer concrete containing recycled coarse aggregates. International Journal of Sustainable Built Environment. 5, 277–287 (2016). https://doi.org/10.1016/j.ijsbe.2016.05.009
5. Tushar, Q., Bhuiyan, M.A., Abunada, Z., Lemckert, C., Giustozzi, F.: Carbon Footprint and Uncertainties of Geopolymer Concrete Production: A Comprehensive Life Cycle Assessment (LCA). C. 11, 55 (2025). https://doi.org/10.3390/c11030055
6. Nath, P., Sarker, P.K.: Flexural strength and elastic modulus of ambient-cured blended low-calcium fly ash geopolymer concrete. Construction and Building Materials. 130, 22–31 (2017). https://doi.org/10.1016/j.conbuildmat.2016.11.034
7. Liu, J., Zhao, W., Su, X., Xie, X.: Assessment and prediction of the mechanical properties of ternary geopolymer concrete. Front. Struct. Civ. Eng. 16, 1436–1452 (2022). https://doi.org/10.1007/s11709-022-0889-y
8. Liu, L., Pelecanos, L.: The effects of concrete stiffness and strength on the seismic response of RC frame buildings. In: UKIERI Concrete Congress (2019).
9. Paredes, J., Ramirez, W., Pico, F., Acosta, R., Toapanta, O.G., Mayacela, M.: Impact of Structural Stiffness on Vibration Periods of Concrete Buildings: A Systematic Review. Materials. 18, 2612 (2025). https://doi.org/10.3390/ma18112612
10. Mostofizadeh, S., Tee, K.F.: Review of next-generation earthquake-resistant geopolymer concrete. Discov Mater. 4, 62 (2024). https://doi.org/10.1007/s43939-024-00132-3
11. Ansari, M.A., Shariq, M., Mahdi, F.: Structural behavior of reinforced geopolymer concrete beams–A review. Materials Today: Proceedings. (2023).
12. Lin, Y., Yuan, Y., Wan, S., Ding, B., Yang, C., Zong, Z., Gu, X., Cai, J.: Flexural behaviour of reinforced one-part geopolymer concrete beams. Journal of Building Engineering. 96, 110435 (2024). https://doi.org/10.1016/j.jobe.2024.110435
13. Peng, C., Mao, Y., Li, S., Xing, Y., Du, Y., Shi, C.: Research progress on the structural performance of reinforced geopolymer concrete columns. Journal of Building Engineering. 113805 (2025). https://doi.org/10.1016/j.jobe.2025.113805
14. Farhan, N.A., Sheikh, M.N., Hadi, M.N.: Behaviour of ambient cured steel fibre reinforced geopolymer concrete columns under axial and flexural loads. In: Structures. pp. 184–195. Elsevier (2018). https://doi.org/10.1016/j.istruc.2018.07.001

15. Mao, Y., Du, Y., Hwang, H., Su, J., Hu, X., Liu, Y., Shi, C.: Seismic performance of interior beam-column joints using reinforced slag-based geopolymer concrete. Earthq Engng Struct Dyn. 52, 285–307 (2023). https://doi.org/10.1002/eqe.3760
16. Raj, S.D., Ganesan, N., Abraham, R., Raju, A.: Behavior of geopolymer and conventional concrete beam column joints under reverse cyclic loading. Advances in concrete construction. 4, 161 (2016). https://doi.org/10.12989/acc.2016.4.3.161
17. Noh, G., Shin, M., Yang, K.-H.: Structural Performance of Geopolymer Concrete: Bond, Flexural, Shear, and Axial Strengths. ACI Structural Journal. 122, (2025). https://doi.org/10.14359/51744396
18. SAP2000: CSI Analysis Reference Manual for SAP2000, ETABS, SAFE and CSiBridge, (2021).
19. TBEC 2018: Turkish Building Earthquake Code. Disaster and Emergency Management Presidency, (2018).
20. Committee, A.C.I.: Building code requirements for structural concrete (ACI 318–19) and commentary. Presented at the (2019).

Author Contribution Statement

- *Conceptualization:* İffet Gamze Mütevelli Özkan, İhsan Türkel
- *Methodology:* İffet Gamze Mütevelli Özkan, İhsan Türkel
- *Investigation:* İffet Gamze Mütevelli Özkan, İhsan Türkel
- *Writing – Original Draft:* İffet Gamze Mütevelli Özkan, İhsan Türkel
- *Writing – Review & Editing:* İffet Gamze Mütevelli Özkan

Funding

The authors received no funding for this work.

Conflict of interest

The authors declare no competing interests.

Data Availability

Data are available from the corresponding author upon reasonable request.

Publication Note

This paper was peer-reviewed, accepted for presentation, and included in the proceedings of the ACE2026 – International Conference on Advances in Civil Engineering, held on 12–14 October 2026 in Trabzon, Türkiye.

This paper may be cited as follows:

İffet Gamze MÜTEVELLİ ÖZKAN and İhsan TÜRKEL, "
A Comparative Study on the Seismic and Environmental Performance of Geopolymer and Conventional Reinforced Concrete Buildings" in Proceedings of the ACE2026 – International Conference on Advances in Civil Engineering, Trabzon, Türkiye, 12–14 October 2026.

A Data-Driven Framework for Assessing the Energy Dissipation Characteristics of Reinforced Concrete Columns

Ziya Muderrisoglu[1] and Yaşar Avcı[2]
[1] https://orcid.org/0000-0003-1220-8047, Istanbul Beykent University, Civil Engineering Department, Istanbul, Türkiye, ziyamuderrisoglu@beykent.edu.tr
[2] https://orcid.org/0000-0001-6483-9428, Istanbul Technical University, Earthquake Engineering Program, Istanbul, Türkiye, yasaravci@itu.edu.tr

Abstract. This paper introduces a data-driven framework to assess the energy dissipation characteristics of reinforced concrete columns subjected to cyclic loading. Specifically, total dissipated energy was selected as the target parameter for the assessment method. A comprehensive dataset of flexure-controlled reinforced concrete columns was compiled from open-access sources and used to train and evaluate multiple machine learning models based on key input parameters such as material properties, reinforcement ratios, and deformation-related parameters. Several machine learning algorithms were implemented and compared, including ensemble learning methods such as Extreme Gradient Boosting, Random Forest models, and LightGBM, as well as kernel-based methods and artificial neural networks (i.e., Support Vector Machines, and Multilayer Perceptron). The influence of the selected input features on dissipated energy level was assessed through a model interpretability analysis. Each model performance was evaluated using k-fold cross-validation and commonly-used statistical metrics. Furthermore, an external validation study was performed for the best-performing model to assess the accuracy level. Results show that all models provide satisfactory predictive capability, while ensemble-based approaches generally provided superior accuracy and robustness. As a result, the study demonstrates the potential of machine learning techniques to predict the energy dissipation capacity in reinforced concrete columns, supporting future developments in data-driven, energy-based structural assessment and design methodologies.

Keywords: Data-driven approach; Energy dissipation; Energy-based design.

1 Introduction

The seismic performance of reinforced concrete (RC) columns is mainly governed by their ability to dissipate the input energy via inelastic deformation. Specifically, the energy dissipation capacity of a member is considered as a key performance point, as well as the deformation and strength capacities, in the design/assessment of earthquake resistant structures. In this respect, an accurate quantification of the capacity plays a vital role in understanding the response of a member subjected to cyclic loading and enabling the improvement of performance-based seismic design frameworks. Therefore, studies on the energy dissipation capacity of reinforced concrete members have received considerable attention over the past decades, through studies generally focusing on several key aspects.

Experimental studies have been commonly performed to assess the cyclic behavior and the energy dissipation mechanisms under different loading cases [1-5]. For instance, Park and Eom [1] proposed a nonlinear finite element-based method for predicting the energy dissipated by RC columns subjected to flexural actions. Validation against existing experimental results

confirmed the accuracy of the proposed approach, demonstrating good predictive performance. A non-parametric empirical approach was proposed by Poljanšek et al. [2] to predict the dissipated energy and deformation capacity deterioration. Results demonstrated that axial load, confinement, and longitudinal reinforcement significantly influence the energy dissipation and deformation capacity of reinforced concrete columns. Additionally, numerous analytical and empirical models have been proposed to predict energy dissipation capacity, including a wide range from simplified regression-based formulations to mechanics-based approaches. Among these, Liu et al. [6] developed a two-parameter analytical fatigue-based model that takes into account the dissipated energy and cumulative hysteretic energy under cyclic loading, while Zhang et al. [7] proposed an energy-based hysteretic model for RC columns that is based on cumulative energy dissipation, displacement amplitude, and loading direction. Furthermore, the influence of key parameters (e.g., axial load ratio, concrete strength, confinement, and reinforcement configuration) has been investigated in detail [8-9]. More recently, machine learning-based approaches have arisen as alternative data-driven tools for predicting the energy dissipated by reinforced concrete members, presenting improved accuracy and efficiency compared to traditional models [10-12].

Although previous studies have provided valuable insights into the behavior of RC members during the dissipation process, a comprehensive assessment of the energy dissipation characteristics of RC columns using cumulative energy dissipation capacity remains limited. In particular, most existing approaches rely on simplified empirical formulations, while data-driven techniques such as machine learning have not been fully exploited for this purpose. Furthermore, the relative importance of key design parameters governing energy dissipation capacity has not yet been systematically quantified. Therefore, this study uses machine learning techniques to assess the energy dissipation characteristics of RC columns through cumulative energy dissipation capacity, and to quantify the influence of key design parameters using a large experimental database.

2 Proposed Data-Driven Framework

This proceeding aims to propose a data-driven framework for assessing the energy dissipation characteristics of flexure-controlled reinforced concrete (RC) columns subjected to cyclic loading via the total dissipated energy level. The total dissipated energy capacity of structural members subjected to cyclic loading is quantified by the area inside a force–displacement hysteresis loops. This capacity is typically evaluated through analytical models, experimental testing, or a combination of both. In this study, a machine learning approach is incorporated into a prediction-based analytical framework to predict the total dissipated energy capacity of structural members. Therefore, the framework is based on predicting the total dissipated energy using supervised machine learning models trained on experimentally derived dataset compiled from open-access literature sources. Specifically, the overall workflow of a framework consists of four main phases: i) data collection and preprocessing, ii) selection&definition of model features, iii) development of a model&training, iv) performance evaluation and comparison. A basic representation of the workflow of proposed framework is presented in Fig. 1.

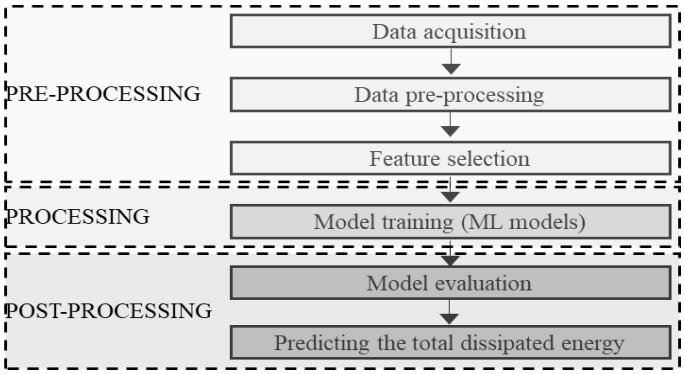


Fig. 1. Schematic representation of the workflow of proposed data-driven framework.

2.1 Data Collection

A comprehensive dataset of 160 flexure-controlled RC column specimens was assembled from open-access experimental studies [13,14]. The dataset consists of column specimens tested under cyclic loading actions to ensure a consistent failure mode classification. The compiled dataset includes fundamental input variables such as material properties (e.g., concrete compressive strength and steel yield strength), geometric properties, reinforcement ratios, and deformation-related parameters.

2.2 Feature Definition and Selection

In this study, total dissipated energy, E_{cd} was implemented as a target variable to represent the energy dissipation capacity of RC columns subjected to cyclic loading. Moreover, the input features were selected based on their relevance to the energy dissipation behavior of RC columns under cyclic loading. Specifically, 7 input features such as the concrete compressive strength, f_c, yield strength of longitudinal rebar, f_{yl}, longitudinal rebar ratio, ρ_l, shear span-to-depth ratio, a/d, volumetric ratio of transverse rebar, ρ_t, equivalent damping ratio, ζ_{eqv}, and peak drift ratio, Δ_{max} were considered during the analyses. A correlation-based analysis was conducted to evaluate the relationship between input features and a target variable [15]. A violin plot representing the normalized distributions of selected features and the target parameter is given in Fig. 2 (e.g., 0 and 1 corresponds to the normalized values where minimum and the maximum value in a range -as given in figure- is considered, respectively). Figure indicates that the parameters exhibit different levels of dispersion, reflecting the diversity of the collected samples. Here, the wide ranges observed for the material and geometric parameters ensure that the machine learning models are trained over a sufficiently diverse design space, improving their ability to capture complex relationships between the input variables and the target response.

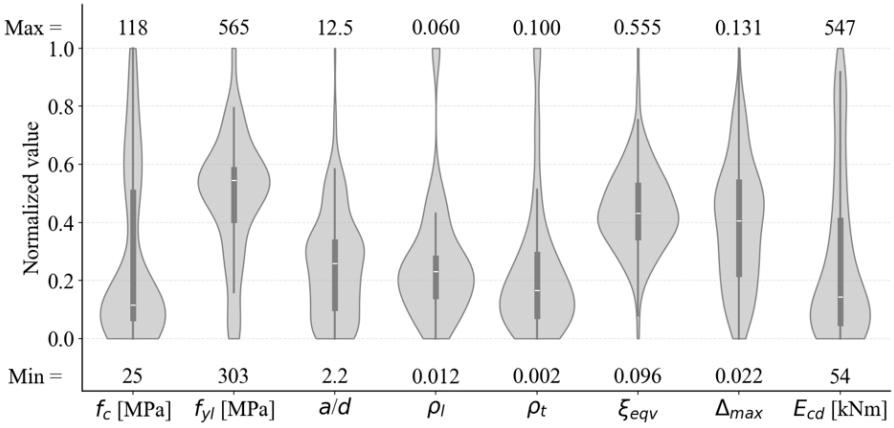


Fig. 2. Distribution characteristics of the dataset variables.

2.3 Development of a Machine Learning Model

Commonly-used supervised machine learning techniques were implemented to construct the relationship between selected input features and total dissipated energy. These models include ensemble learning methods such as *Extreme Gradient Boosting* (*XGBoost*), *Random Forest* (*RF*), and *Light Gradient Boosting Machine* (*LightGBM*), as well as kernel-based methods and artificial neural networks, including *Support Vector Machines* (*SVM*), and *Multilayer Perceptron* (*MLP*).

2.4 Evaluation Methodology

The performance of a model was assessed via K-Fold cross-validation approach [16] to get robustness and reduce bias related to data splitting. Here, the parameter, *K* denotes the number of folds into which the dataset is separated. Following the random partitioning process, cross-validation is performed by taking into account (*K*-1) folds to train and test the remaining fold. Moreover, commonly-used statistical performance metrics were employed to obtain the predictive accuracy, including the normalized root mean square error (*NRMSE*), the mean absolute percentage error (*MAPE*), and the coefficient of determination (R^2). Furthermore, the Pearson correlation coefficient [17], $\rho_{a,p}$ was calculated to quantify the correlation between the actual and predicted energy dissipation capacities, providing additional insight into the consistency of model predictions (Eq. 1).

$$\rho_{FT} = \frac{\sigma_{FT}}{\sigma_F \sigma_T} \tag{1}$$

where σ_{FT} denotes the covariance measure describing the relationship between the feature and target variables, whereas σ_F and σ_T represent the corresponding standard deviations of the feature and target parameters, respectively. Specifically, a comparative analysis allowed identification of the most effective modeling approach for predicting energy dissipation in RC columns.

3 Predicting the Total Dissipated Energy

This section provides preliminary results based on the prediction of total dissipated energy using different machine learning techniques. Specifically, ensemble learning methods (Extreme Gradient Boosting, Random Forest, and LightGBM), Support Vector Machines, and Multilayer Perceptron Networks, are implemented and compared. The predictive performance of each model is evaluated based on the mean values of performance indicators obtained from K-Fold cross-validation. Here, a six-fold cross-validation strategy was employed to evaluate the proposed model. The dataset comprising 160 samples was divided into six subsets. During each iteration, approximately 83% of the data (about 133 samples) were used for training, whereas the remaining 17% (~27 samples) were used for testing. The process was repeated six times, allowing each subset to be utilized as the test set once, and the performance metrics were averaged across all iterations. Furthermore, an external validation process was applied for the best-performing model to assess the accuracy level of a framework.

3.1 Performance Assessment of ML Models within the Proposed Framework

The implementation of the considered machine learning models is carried out within a proposed framework. For each model, a grid search-based optimization procedure is performed over a predefined hyperparameter space to determine the optimal parameter values. The resulting configurations are subsequently used for performance evaluation and comparative analysis. The investigated ranges and the optimal hyperparameter values that resulted in the best cross-validation performance are presented in Table 1. The results demonstrate that the proposed framework, particularly when stayed with ensemble learning methods, achieves high predictive

accuracy for total energy dissipation level, as evidenced by the high R^2 and consistently low NRMSE and MAPE values.

Table 1. Comparative performance assessment of the implemented machine learning models.

Model ID	Hyperparameter			R^2	NRMSE	MAPE
	Name	**Search range**	**Optimal value**			
XGBoost	n_{est}; objective; max_d; r_l	[50,1000]; [reg:logistic,binary:logistic]; [1,20]; [0.001,1.0]	50; reg:logistic; 6; 0.5	0.74	0.37	0.28
LightGBM	n_{est}; objective; max_d; r_l	[50,1000]; [l2]; [1,20]; [0.001,1.0]	1000; l2; 3; 0.02	0.71	0.40	0.34
RF	n_{est}	[10,1000]	100	0.63	0.45	0.39
MLP	solver; alpha; hidden layer sizes; max. iterations	[lbfgs,adam]; [0.0001-0.01]; (100,200)-(400,400); [10-1000]	lbfgs; 0.01; (200,200); 100	0.58	0.46	0.44
SVM	kernel; C; epsilon; gamma	[rbf]; [1,1000]; [0.001,0.2]; [0.01,0.5]	[rbf]; 10; 0.2; 0.5	0.43	0.55	0.61

* n_{est}: number of estimators, max_d: maximum tree depth, r_l: boosting learning rate.

This finding is further validated by evaluating the Pearson correlation coefficient between the predicted and actual energy dissipation capacities, $\rho_{p,a}$ presented in Fig. 3. The results indicate a strong correlation between the predicted and measured values, demonstrating the high predictive accuracy and reliability of the developed models for an ensemble learning method supported framework, XGBoost.

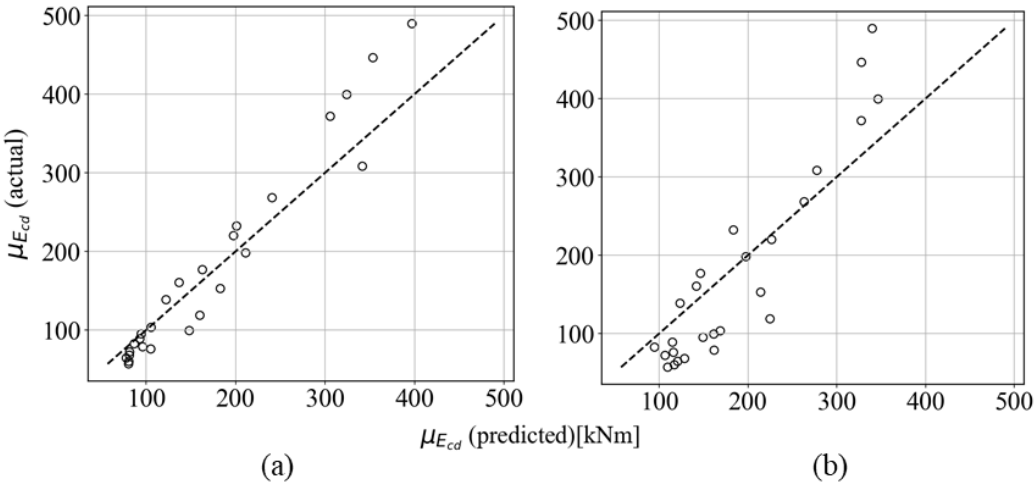


Fig. 3. Predicted versus actual values obtained via: a) XGB ($\rho_{p,a\text{-}XGB}$=0.98), b) SVM ($\rho_{p,a\text{-}SVM}$=0.93) models

3.2 Investigating the Accuracy Level of Predicted Results

Following the assessment of implemented ML techniques via selected performance metrics, the global feature importance and the predictive accuracy of the best-performing model, XGBoost, are further investigated. Specifically, the mean absolute SHAP (Shapley Additive Explanations) [18] of each feature is evaluated. Here, the mean absolute SHAP value quantifies the average contribution magnitude of each input variable to the prediction of target parameter, E_{cd} and higher values indicate stronger influence on the XGBoost-based predictions. Results

indicate that, peak drift ratio and longitudinal steel strength were identified as the most influential parameters, whereas transverse reinforcement ratio exhibited comparatively lower influence (Fig. 4a).

Finally, the developed XGBoost-based model was further evaluated using an independent validation dataset consisting of 15 reinforced concrete columns that were not included during model development. The Pearson correlation coefficient between the predicted and measured values is 0.90, compared with 0.98 obtained during cross-validation (Fig. 4b). The relatively small reduction (~8%) in correlation indicates that the proposed model preserves a strong agreement between predicted and measured responses when applied to unseen specimens. Nevertheless, the validation dataset comprised only 15 specimens. Future validation using a larger and more diverse dataset would enable a more comprehensive assessment of the model's robustness and generalization capability.

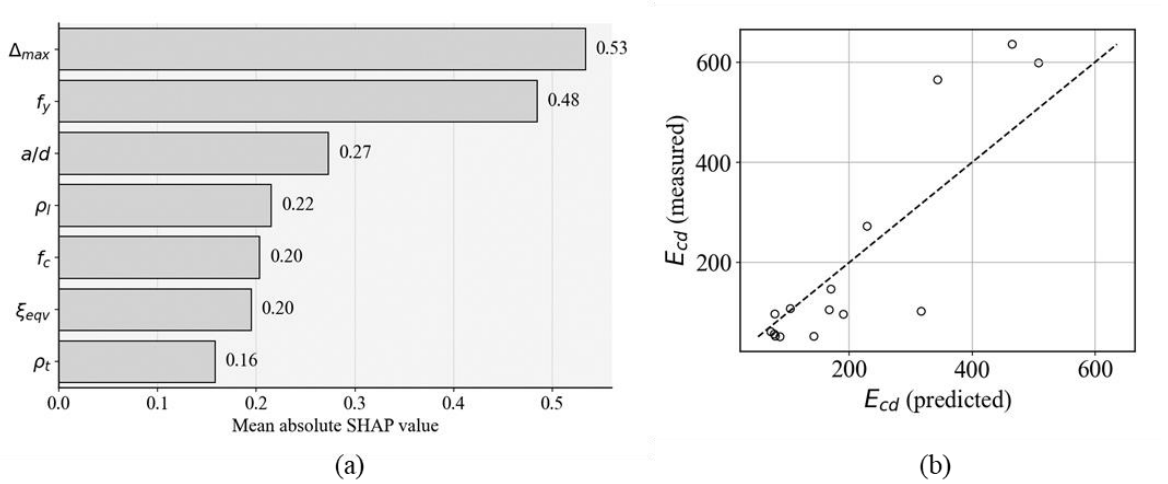


Fig. 4. Results based on post-processing phase: a) SHAP-based global feature importance of the implemented XGBoost model, b) comparison between the predicted and measured dissipated energy for the independent validation dataset.

4 Conclusions

Details of a data-driven framework based on commonly-used machine learning (ML) techniques are presented in this paper. The total dissipated energy, quantified by the area inside the force–displacement hysteresis loops, is adopted as the target parameter to quantitatively evaluate the energy dissipation characteristics of reinforced concrete columns under cyclic loading. Five enhanced ML techniques are implemented to predict this parameter using a comprehensive dataset of 160 specimens. Furthermore, the predictive performance of the best-performing model is investigated. The main findings of this study are summarized as follows:

- All ML-based models showed satisfactory predictive capability, with ensemble-based methods (i.e., XGBoost and LightGBM) providing the best overall accuracy and robustness.
- Following the evaluation of mean absolute SHAP values, it was observed that the peak drift ratio and longitudinal reinforcement strength were the dominant features to be considered in the process, whereas the transverse reinforcement ratio contributed comparatively less to the model predictions within a selected feature set.
- The predictive capability of the best-performing model, XGBoost, was further assessed via an independent validation study. Specifically, 15 reinforced concrete columns that were not included in the model development process were used for validation. The relatively small reduction (approximately 8%) in the correlation coefficient between the model development and validation stages shows that the proposed model keeps a

strong agreement between predicted and experimental responses when applied to independent specimens.

As a summary, it can be concluded that ML-supported data-driven frameworks (e.g., especially with ensemble-based approaches) can be utilized to assess the energy dissipation characteristics of reinforced concrete columns based on different target parameters. Increasing the size and using more diverse dataset would enable a more comprehensive assessment of the implemented model's generalization capability.

References

1. Park, H., & Eom, T.: A simplified method for estimating the amount of energy dissipated by flexure-dominated reinforced concrete members for moderate cyclic deformations. Earthquake Spectra, 22(2), 459–490 (2006). https://doi.org/10.1193/1.2197547.
2. Poljanšek, K., Peruš, I., & Fajfar, P.: Hysteretic energy dissipation capacity and the cyclic to monotonic drift ratio for rectangular RC columns in flexure. Earthquake Engineering & Structural Dynamics, 38(7), 907–928 (2009). https://doi.org/10.1002/eqe.875.
3. Acun, B., & Sucuoğlu, H.: Energy Dissipation Capacity of Reinforced Concrete Columns under Cyclic Displacements. ACI Structural Journal, 109(4), 531–540 (2012). https://doi.org/10.14359/51683872.
4. Xiao, S. Y., Li, J. B., & Mo, Y. L.: Dynamic behaviours of reinforced concrete columns under cyclic loading with variable rates. Advances in Structural Engineering, 23(4), 779-793 (2020). https://doi.org/10.1177/1369433219881753.
5. Aydemir, M. E., Aydemir, C., & Arslan, G.: Experimental study on the energy dissipation and seismic behavior of RC columns due to repeated earthquakes including vertical excitation. Engineering Structures, 293, 116650 (2023). https://doi.org/10.1016/j.engstruct.2023.116650.
6. Liu, Z., Wang, Y., Cao, Z., Chen, Y., & Hu, Y.: Seismic energy dissipation under variable amplitude loading for rectangular RC members in flexure. Earthquake Engineering &Structural Dynamics, 47(4), 831-853 (2018). ttps://doi.org/10.1002/eqe.2993.
7. Zhang, G., Sun, B., & Bai, W.: Hysteretic model for RC columns based on effective hysteretic energy dissipation with positive and negative directions. Buildings, 13(5), 1140 (2023). https://doi.org/10.3390/buildings13051140.
8. Muderrisoglu, Z., Dindar, A. A., Bozer, A., Özkaynak, H., Güllü, A., Güngör, B., ..., & Hasanoğlu, S.: A quantitative investigation on the effects of flexure-dominated reinforced concrete column characteristics on the dissipated energy. Turkish Journal of Civil Engineering, *35*(2), 87-102 (2023). https://doi.org/10.18400/tjce.1272125.
9. Yıldızel, S. A., Özkılıç, Y. O., Bahrami, A., Aksoylu, C., Başaran, B., Hakamy, A., & Arslan, M. H.: Experimental investigation and analytical prediction of flexural behaviour of reinforced concrete beams with steel fibres extracted from waste tyres. Case Studies in Construction Materials, 19, e02227 (2023). https://doi.org/10.1016/j.cscm.2023.e02227.
10. Lee, C. S., Park, Y., & Jeon, J. S.: Model parameter prediction of lumped plasticity model for nonlinear simulation of circular reinforced concrete columns. Engineering Structures, *245*, 112820 (2021). https://doi.org/10.1016/j.engstruct.2021.112820.
11. Topaloglu, B., Kaya, G. T., Sutcu, F., & Deger, Z. T.: Machine learning-based estimation of energy dissipation capacity of RC shear walls. In Structures, 45, 343-352 (2022). https://doi.org/10.1016/j.istruc.2022.08.114.
12. Yaghoubi, S. T., Deger, Z. T., Taskin, G., & Sutcu, F.: Machine learning-based predictive models for equivalent damping ratio of RC shear walls. Bulletin of Earthquake Engineering, 21(1), 293-318 (2023). https://doi.org/10.1007/s10518-022-01533-6.

13. Ghannoum, W., Sivaramakrishnan, B., Pujol, S., Catlin, A. C., Wang, Y., Yoosuf, N., & Fernando, S.: NEES: ACI 369 Circular column database (2015a). https://doi.org/10.4231/D39Z90B9T
14. Ghannoum, W., Sivaramakrishnan, B., Pujol, S., Catlin, A. C., Wang, Y., Yoosuf, N., & Fernando, S.: NEES: ACI 369 Rectangular column database (2015b). https://doi.org/10.4231/D36688J50.
15. Muderrisoglu, Z.: Total Dissipated Energy Prediction for Flexure-Dominated Reinforced Concrete Columns via Extreme Gradient Boosting. Afyon Kocatepe Üniversitesi Fen Ve Mühendislik Bilimleri Dergisi, *25*(3), 604-612 (2025). https://doi.org/10.35414/akufemubid.1541763.
16. Anguita, D., Ghelardoni, L., Ghio, A., Oneto, L., & Ridella, S.: The 'K' in K-fold Cross Validation. *ESANN*, 102, 441-446 (2012).
17. Pearson, K.: Notes on the history of correlation. Biometrika, *13*(1), pp.25-45 (1920). https:/doi.org/10.2307/2331722.
18. Lundberg, S. M., & Lee, S. I.: A unified approach to interpreting model predictions. Advances in neural information processing systems, 30 (2017).

Author Contribution Statement

- *Conceptualization:* Ziya Muderrisoglu, Yaşar Avcı
- *Methodology:* Ziya Muderrisoglu, Yaşar Avcı
- *Investigation:* Ziya Muderrisoglu, Yaşar Avcı
- *Writing – Original Draft:* Ziya Muderrisoglu
- *Writing – Review & Editing:* Yaşar Avcı

Publication Note

This paper was peer-reviewed, accepted for presentation, and included in the proceedings of the ACE2026 – International Conference on Advances in Civil Engineering, held on 12–14 October 2026 in Trabzon, Türkiye.

This paper may be cited as follows:

Müderrisoğlu, Z., and Avcı, Y., "A Data-Driven Framework for Assessing the Energy Dissipation Characteristics of Reinforced Concrete Columns," in Proceedings of the ACE2026 – International Conference on Advances in Civil Engineering, Trabzon, Türkiye, 12–14 October 2026.

Structural Performance of Reinforced Concrete Frames with Lightweight Steel Wall Panels

Hussien Alkasim SOALIH [1], Fatih CEBİR [2], Serhat DEMİR[3], Metin HÜSEM[4] and Ramazan LİVAOĞLU[5]

[1] 0000-0002-2194-7362, Department of Civil Engineering, School of Civil and Hydraulic Engineering, Institute of Technology, University of Gondar, Gondar, Ethiopia, halkasim@gmail.com

[2] 0009-0009-8581-4372, Karadeniz Technical University, Civil Engineering Department, Trabzon, Türkiye, fatihcebir@ktu.edu.tr

[3] 0000-0002-3542-0908, Karadeniz Technical University, Civil Engineering Department, Trabzon, Türkiye, s.demir@ktu.edu.tr

[4] 0000-0002-6084-2192, Karadeniz Technical University, Civil Engineering Department, Trabzon, Türkiye, mhusem@ktu.edu.tr

[5] 0000-0001-8484-6027, Bursa Uludag University, Civil Engineering Department, Bursa, Türkiye, rliva@uludag.edu.tr

Abstract. This study investigates the effect of prefabricated lightweight steel wall panel systems designed as an alternative to traditional masonry infill walls to enhance the seismic performance of reinforced concrete frames. Conventional brick infill walls significantly increase seismic mass to the structure and cause substantial environmental post-earthquake waste. In contrast, the proposed lightweight steel panel systems are considerably lighter than traditional infill walls that offer a sustainable and innovative solution with fully recyclable nature. Within the scope of the research, a comprehensive experimental program was conducted on a total of four specimens, including a reference frame, brick infilled frame, and frames with lightweight steel wall panels, under constant axial load and quasi-static cyclic lateral loading. The results demonstrate that the integration of lightweight steel walls significantly increases frame strength, exhibits stable cyclic behavior, and provides a ductile structural response. Unlike traditional masonry infills, lightweight steel walls provide a controllable seismic behavior by preventing sudden and brittle failures occurring at low drift levels. Consequently, it has been determined that lightweight steel walls are an eco-friendly infill solution that minimizes structural weight, limits brittle damage mechanisms, and can be safely implemented in seismically prone regions.

Keywords: Lightweight steel wall, Reinforced concrete, Cyclic loading

1 Introduction

In current design practice, infill walls are generally considered non-structural elements and are only taken into account as dead loads in structural analyses. However, these elements significantly influence the lateral stiffness and seismic response of reinforced concrete frames [1,2]. Due to their low cost and widespread availability, masonry infill walls are commonly used in construction. Although they contribute to the elastic behavior of structures by providing initial stiffness at low drift levels, their brittle nature results in sudden strength degradation, cracking, and eventual collapse under increasing deformation demands [3,4]. Consequently, the behavior of masonry infill walls cannot be effectively controlled during seismic events. Furthermore, their additional mass increases the seismic demands acting on the structure. This situation not only poses risks to life safety but also leads to significant economic losses due to high repair costs and post earthquake debris generation.

From an environmental perspective, brick production contributes substantially to global carbon emissions, while the recycling of brick debris generated after earthquakes remains highly limited due to logistical and energy-related constraints [5–7]. The tens of millions of tons of debris generated during the 2023 Kahramanmaraş earthquakes clearly highlighted the need for more sustainable alternative systems.

Prefabricated lightweight steel wall panels have emerged as a promising solution due to their high strength-to-weight ratio, rapid installation, and 100% recyclability. Existing studies have primarily focused on the individual behavior of these panels and the effects of parameters such as sheathing type, fastening systems, and panel configurations on their cyclic performance. In addition, their interaction with steel framing systems has also been investigated [8–11]. However, their influence on the behavior of reinforced concrete frames remains largely unknown.

In this study, the effects of prefabricated lightweight steel wall panels and conventional masonry infill walls on the behavior of reinforced concrete frames were experimentally investigated through a comparative approach. The results demonstrate that lightweight steel wall panels provide a more ductile and environmentally sustainable alternative for structures subjected to seismic loading.

2 Experimental Studies

2.1 Material Properties

The average compressive strength of the concrete used in the production of the reinforced concrete frames was 30.15 MPa, while the yield and ultimate tensile strengths of the reinforcing bars were 431 MPa and 545 MPa, respectively. For the lightweight steel wall panel system, cold-formed steel (CFS) profiles of S235JR grade were selected, with yield and ultimate tensile strengths of 247 MPa and 313 MPa, respectively. For the masonry infill wall, perforated clay bricks measuring 135 × 190 × 190 mm with a characteristic compressive strength of 5.7 MPa and ready-mixed medium-strength mortar with a compressive strength of 15.2 MPa were used [12].

2.2 Test Specimens

Fig. 1 illustrates the infill configurations of the four single-story, single-bay reinforced concrete (RC) frame specimens. The specimen designated as Ref represents the bare frame used as the reference specimen (*Fig. 1a*), while the specimen labeled BRK represents the frame infilled with a brick masonry wall (*Fig. 1b*). The specimens denoted as CFS-Br-Stf and CFS-PL are frames infilled with lightweight steel wall panels of different configurations (*Figs. 1c and 1d*). In both wall systems, the primary framing consists of horizontal and vertical cold-formed steel (CFS) C-section profiles with a thickness of 1.5 mm. In addition, the CFS-Br-Stf system includes C-section diagonal bracing members, whereas the CFS-PL system incorporates 1.5 mm thick steel sheathing. The CFS profiles have a flange width of 50 mm and different web depths: 135 mm for vertical members, 130 mm for horizontal members, and 125 mm for diagonal members. The CFS profiles were assembled using self-drilling screws in accordance with previous studies [9,10]. The wall panels were anchored to the reinforced concrete frame using concrete nails. The geometric and reinforcement details of the reinforced concrete frames are presented in *Fig. 2.*



Fig. 1. Test Specimens

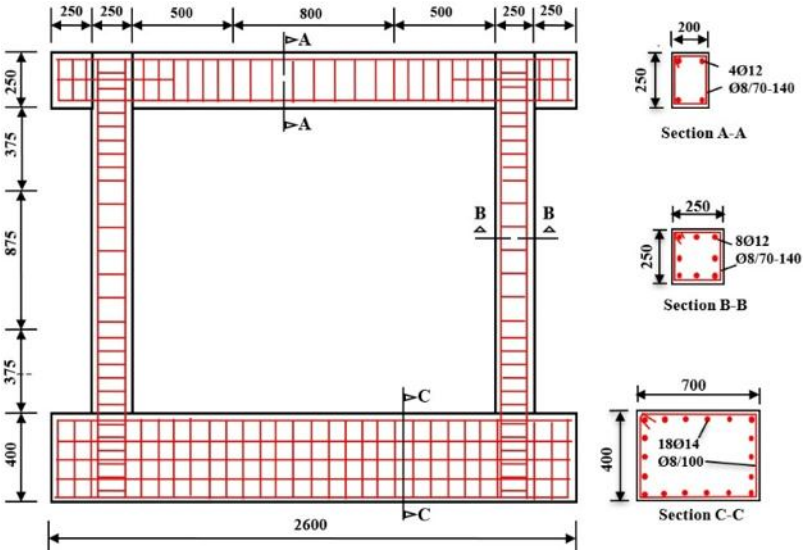


Fig. 2. Reinforced Concrete Frame Details

2.3 Test Setup, Instrumentation, and Loading Protocol

A schematic view of the test setup is presented in *Fig. 3*. Throughout the experiments, a constant axial load corresponding to 10% of the axial load capacity of the columns was applied. During the lateral loading stage, a displacement-controlled quasi-static cyclic loading protocol was

adopted in accordance with [13]. The loading sequence was initiated at a minimum interstory drift ratio of 0.15%, at which damage initiation was expected, and the displacement amplitudes were subsequently increased by 40% at each drift level. The first displacement amplitude was repeated six times, whereas all subsequent amplitudes were repeated twice. Throughout the tests, lateral load data were recorded using a load cell, while displacement measurements were simultaneously obtained through linear potentiometric displacement transducers.

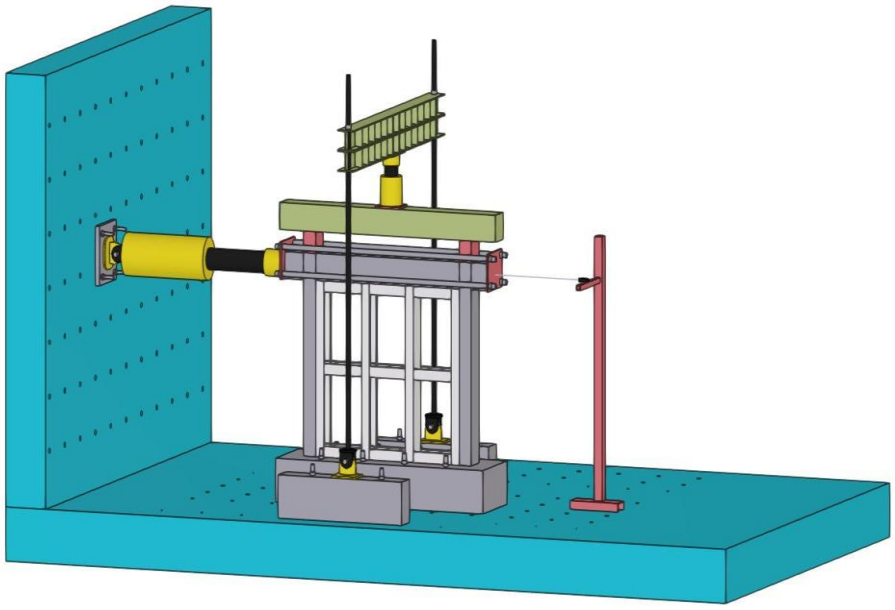


Fig. 3. Experimental Setup

3 Results and Discussion

The damage patterns observed in the test specimens are presented in *Fig. 4*, while the envelope curves, energy dissipation capacities, and stiffness degradation diagrams obtained from the cyclic loading tests are shown in *Fig. 5*. The experimental results reveal significant differences in the structural performance of the specimens.

The reference specimen (Ref) reached a peak lateral load of approximately 132 kN at a drift ratio of 2.21%. Damage progressed in the form of flexural cracks within the column confinement regions and shear cracks at the beam–column joints. In contrast, the masonry infilled specimen (BRK) exhibited a high initial stiffness, reaching approximately 251 kN nearly twice the capacity of the Ref specimen at very low drift levels of 0.29–0.41%. However, a sudden loss of capacity occurred at later stages due to crushing of the masonry wall and its separation from the surrounding frame.

The proposed lightweight steel panel systems exhibited a considerably more stable and consistent response compared to the BRK specimen. The CFS-Br-Stf specimen provided an average increase in lateral load capacity of 51% relative to the Ref specimen at a drift ratio of 2.21%. The energy dissipation was achieved through the progressive failure of screw connections and local/global buckling of the compression diagonals. The steel-sheet-sheathed panel system (CFS-PL) demonstrated the highest performance among all specimens, reaching a maximum lateral load of approximately 305 kN at a drift ratio of 1.13%. Local buckling was observed in both the steel sheathing and the longitudinal framing members. Furthermore, the shear failure of most anchorage screws at a drift ratio of 3% indicated a high degree of interaction between the panel and the reinforced concrete frame.

The total energy dissipated by the Ref, CFS-Br-Stf, BRK, and CFS-PL specimens was approximately 24 kJ, 33 kJ, 35 kJ, and 45 kJ, respectively. While the masonry infill wall

dissipated most of its energy at low drift levels, the lightweight steel panel systems primarily dissipated energy during the intermediate and large displacement stages.



Fig. 4. Damage Patterns of the Test Specimens

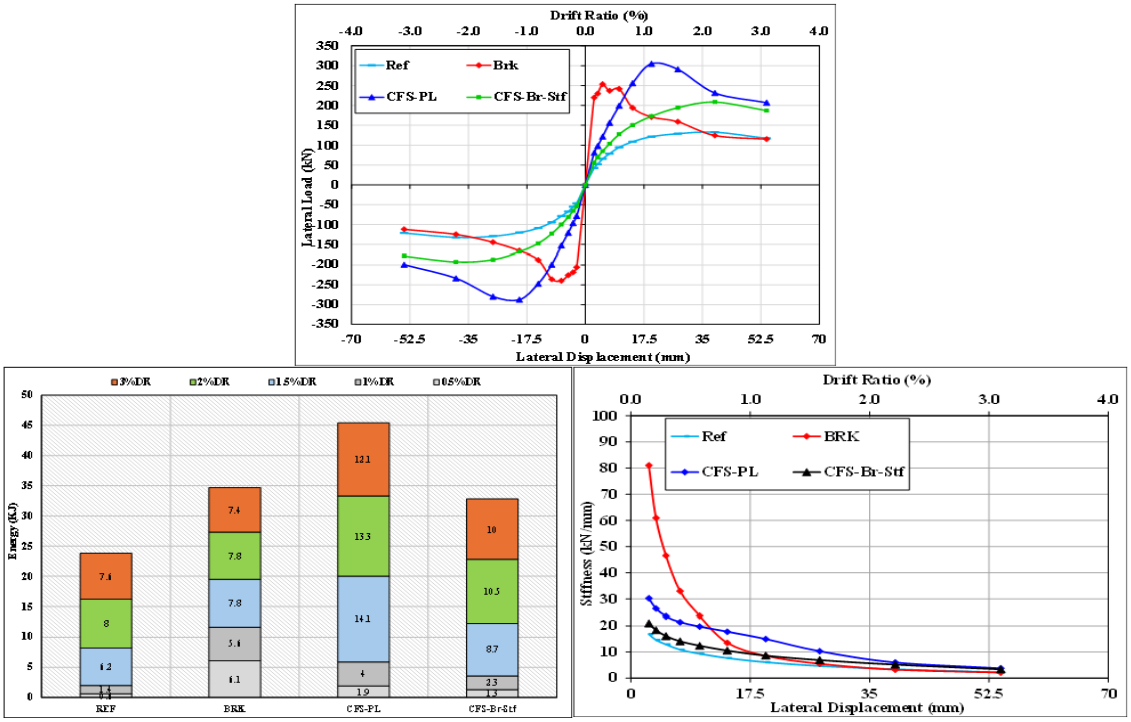


Fig. 5. Experimental Results

4 Conclusions

The results of this study demonstrated that the integration of lightweight steel wall panels significantly enhanced the strength of the reinforced concrete frame, provided a stable cyclic response, and promoted a ductile structural behavior. In contrast, although the masonry infill wall substantially increased the initial stiffness of the frame, the sudden and brittle failures observed at very low drift levels revealed that the seismic response of conventional masonry infills is unstable and difficult to control.

Overall, lightweight steel wall panels represent an environmentally friendly wall solution that minimizes structural weight while preventing brittle failure mechanisms within the wall system. The proposed approach demonstrates that by enabling the framing components commonly used in dry-wall construction systems to actively participate in load resistance, the seismic performance of reinforced concrete structures can be significantly improved.

Acknowledgments

This study was supported by the Scientific and Technological Research Council of Türkiye (TÜBİTAK) under Project No. 124M606.

References

1. Milijaš, A., Marinković, M., Butenweg, C., Klinkel, S.: Experimental results of reinforced concrete frames with masonry infills with and without openings under combined quasi-static in-plane and out-of-plane seismic loading. Bulletin of Earthquake Engineering 21, 3537–3579 (2023). https://doi.org/10.1007/s10518-023-01664-4
2. Zhai, C., Kong, J., Wang, X., Chen, Z.: Experimental and finite element analytical investigation of seismic behavior of full-scale masonry infilled RC frames. Journal of Earthquake Engineering 20, 1171–1198 (2016). https://doi.org/10.1080/13632469.2016.1138171
3. Penava, D., Sarhosis, V., Kožar, I., Guljaš, I.: Contribution of RC columns and masonry wall to the shear resistance of masonry infilled RC frames containing different in size window and door openings. Engineering Structures 172, 105–130 (2018). https://doi.org/10.1016/j.engstruct.2018.06.007
4. Furtado, A., Arêde, A., Rodrigues, H., Varum, H.: The role of the openings in the out-of-plane behaviour of masonry infill walls. Engineering Structures 244, 112793 (2021). https://doi.org/10.1016/j.engstruct.2021.112793
5. Fořt, J., Černý, R.: Transition to circular economy in the construction industry: Environmental aspects of waste brick recycling scenarios. Waste Management 118, 510–520 (2020). https://doi.org/10.1016/j.wasman.2020.09.004
6. Horckmans, L., Nielsen, P., Dierckx, P., Ducastel, A.: Recycling of refractory bricks used in basic steelmaking: A review. Resources, Conservation and Recycling 140, 297–304 (2019). https://doi.org/10.1016/j.resconrec.2018.09.025
7. Pacheco-Torgal, F., Ding, Y., Colangelo, F., Tuladhar, R., Koutamanis, A.: Advances in Construction and Demolition Waste Recycling. Elsevier (2020). https://doi.org/10.1016/C2018-0-05197-X
8. Selvaraj, S., Madhavan, M.: Investigation on sheathing-fastener connection failures in cold-formed steel wall panels. Structures 20, 176–188 (2019). https://doi.org/10.1016/j.istruc.2019.03.007
9. Pehlivan, B.M., Baran, E., Topkaya, C., Isik, Y.T.: Investigation of CFS shear walls with two-sided sheathing and dense fastener layout. Thin-Walled Structures 180, 109832 (2022). https://doi.org/10.1016/j.tws.2022.109832
10. Yilmaz, F., Mojtabaei, S.M., Hajirasouliha, I., Becque, J.: Behaviour and performance of OSB-sheathed cold-formed steel stud wall panels under combined vertical and seismic

loading. Thin-Walled Structures 183, 110419 (2023). https://doi.org/10.1016/j.tws.2022.110419
11. Wang, J., Zhou, T., Wu, H., Guan, Y., Zhang, L.: Cyclic performance of steel frame fabricated with cold-formed steel composite wall structure. Engineering Structures 270, 114892 (2022). https://doi.org/10.1016/j.engstruct.2022.114892
12. Kaushik, H.B., Rai, D.C., Jain, S.K.: Stress-strain characteristics of clay brick masonry under uniaxial compression. Journal of Materials in Civil Engineering 19, 728–739 (2007). https://doi.org/10.1061/(ASCE)0899-1561(2007)19:9(728)
13. FEMA 461: Interim Testing Protocols for Determining the Seismic Performance Characteristics of Structural and Nonstructural Components. Federal Emergency Management Agency (2007). https://www.atcouncil.org/pdfs/FEMA461.pdf, last accessed 2024/11/07.

Author Contribution Statement

- *Conceptualization:* Hussien Alkasim Soalih, Serhat Demir, Ramazan Livaoğlu
- *Methodology:* Hussien Alkasim Soalih, Serhat Demir, Fatih Cebir,
- *Investigation:* Hussien Alkasim Soalih, Fatih Cebir, Serhat Demir, Metin Hüsem
- Writing – Original Draft: Hussien Alkasim Soalih, Serhat Demir
- Writing – Review & Editing: Hussien Alkasim Soalih, Serhat Demir

Publication Note

This paper was peer-reviewed, accepted for presentation, and included in the proceedings of the ACE2026 – International Conference on Advances in Civil Engineering, held on 12–14 October 2026 in Trabzon, Türkiye.

This paper may be cited as follows:

Hussien Alkasim SOALIH, Fatih CEBİR, Serhat DEMİR, Metin HÜSEM and Ramazan LİVAOĞLU, “Structural Performance of Reinforced Concrete Frames with Lightweight Steel Wall Panels” in Proceedings of the ACE2026 – International Conference on Advances in Civil Engineering, Trabzon, Türkiye, 12–14 October 2026.

Monitoring the Transformation of Residential Typology from Building Permit Data in Trabzon (2010–2025)

Abdullah BOSTANCI[1] and Sina ATABEY[2]
[1] 0000-0002-5306-9795, Department of Construction, Vocational School, Avrasya University, Trabzon, Türkiye, abdullah.bostanci@avrasya.edu.tr
[2] 0009-0000-2514-8499, Department of Civil Engineering, Faculty of Engineering and Natural Sciences, Avrasya University, Trabzon, Türkiye, sina.atabey@avrasya.edu.tr

Abstract. Building permits are widely regarded as one of the most reliable leading indicators of the future urban environment, since the decision to permit a structure precedes its construction and reflects demographic pressure, investor expectations, regulatory cycles, and local planning policy. This study reveals the transformation of residential typology in Trabzon over 2010–2025 using such data. Trabzon is selected because its constrained coastal-mountainous geography, sustained tourism investment, and recent multi-storey development make its building stock particularly sensitive to typological change. Open data published by the Turkish Statistical Institute (TurkStat) under the Classification of Types of Constructions (CC), at provincial level and annual frequency, were used. Permits are disaggregated at the three-digit CC level, and the yearly share of each subcategory in total permits is computed. Trend significance is tested with the Mann-Kendall test and Sen's slope estimator, while structural breaks are examined with the Pettitt test. Robustness is checked under sensitivity scenarios excluding the two non-comparable boundary years — the anomalously compiled 2010 and the scope-expanded 2025 — while the 6 February 2023 Kahramanmaraş earthquake is weighed in interpreting late-period dynamics. Contrary to the national apartmentation trend, the findings indicate a statistically significant rise in the share of one-dwelling permits and a corresponding decline in the share of multi-dwelling buildings, with a common structural break around 2018; hotel permits trend significantly upward, consistent with a tourism-investment cycle. The study provides a province-specific empirical baseline for Trabzon and a transferable, data-driven methodology to support evidence-based decisions on densification, parking provision, and social-facility allocation.

Keywords: Building permit; Residential typology; Time series analysis.

1 Introduction

Building permits are among the most widely used leading indicators of the future built environment: the administrative decision to authorise a structure precedes its physical completion, so permit records register demographic pressure, investor expectations, regulatory cycles and planning policy well before these forces become visible in the standing stock [1], and the time-series analysis of archived permit data is an established means of tracking shifts in the size, value and type of authorised construction [2]. What a permit series reveals, however, depends on the level at which it is read. Aggregate counts capture the volume of anticipated construction and move largely with the macroeconomic and credit cycle, but they are silent about its composition; it is the disaggregated, typology-level series — the relative weight of single-dwelling, multi-dwelling and non-residential categories — that exposes structural

transformation in how a settlement is being built, and a surge of multi-unit permits that outpaces population or employment growth can be an early signal of looming oversupply [3].

In the Turkish context this indicator is tightly coupled to the financing environment: analyses of 2005–2015 monthly data report that sectoral-credit and building-permit series are cointegrated, with causality running from credit to permits [4]. The dominant mode of residential production over the same decades has been "apartmentation" — the progressive replacement of low-rise dwellings by multi-storey apartment blocks — which the Turkish housing literature treats as a defining feature of the urbanisation process [5]; against this national baseline, a provincial series that moves in the opposite direction is analytically significant. Interpreting such a series nonetheless demands methodological care, because TurkStat periodically revises the concept, scope and method of its statistics and maintains a register of the resulting series breaks [6].

Trabzon offers a particularly instructive setting in which to examine these dynamics. Its constrained coastal-mountainous geography limits the supply of developable central land, while sustained tourism investment subjects the building stock to simultaneous and partly opposing pressures. Remote-sensing studies of the province document pronounced urban-fringe expansion, with development pushed outward from the saturated centre [7]; the broader coastal-Turkey literature attributes much recent land-use change to tourism and residential development [8]; and comparable Black Sea cases link migration-driven sprawl to measurable land-use/land-cover change [9]. These spatial accounts strongly suggest that the typological composition of Trabzon's permits should be changing, but they neither quantify the shift in typology shares nor identify when it occurred.

This study addresses that gap by reconstructing the transformation of residential typology in Trabzon over 2010–2025 directly from permit data. Open TurkStat data under the Classification of Types of Constructions (CC) are disaggregated to the three-digit level at provincial scale and annual frequency, and the yearly share of each subcategory in the relevant reference total is computed; working with shares rather than raw counts isolates compositional change from the underlying volume cycle. Trend significance is assessed with the non-parametric Mann-Kendall test together with Sen's slope estimator, and structural breaks are located with the Pettitt test. Because the two boundary years — the anomalously compiled 2010 and the scope-expanded 2025 — could distort the series, every result is re-examined under sensitivity scenarios that successively exclude them, and only findings that remain significant across all scenarios are reported as robust; the 6 February 2023 Kahramanmaraş earthquake, interior to the series, is weighed in interpretation.

Contrary to the national apartmentation narrative, the analysis reveals a robust reversal at the provincial scale: within residential permits the share of one-dwelling buildings rises significantly while the share of multi-dwelling buildings declines, both with a common structural break around 2018, and hotel permits exhibit a significant upward trend consistent with a tourism-investment cycle. Stable across every sensitivity scenario, these results provide a province-specific empirical baseline and a transferable, data-driven monitoring methodology for evidence-based planning on densification, parking provision and social-facility allocation.

2 Materials and Methods

2.1 Study area and data

The study area is the province of Trabzon (TurkStat code 61) on the eastern Black Sea coast of Türkiye, where a narrow coastal plain backed by a steep mountainous hinterland sharply constrains the supply of developable central land. The empirical basis is the open Building Permit Statistics published by the Turkish Statistical Institute (TurkStat) under the

Classification of Types of Constructions (CC), retrieved at provincial level and annual frequency for the sixteen years from 2010 to 2025. The unit of observation is the number of buildings for which a building permit was issued in a given year; floor area and dwelling counts are not used, so the series measures the count and composition of authorised structures rather than their physical size. Figure 1 situates the province in this physical setting and illustrates the outward, fringe-ward expansion of its built-up area between 2000 and 2025.

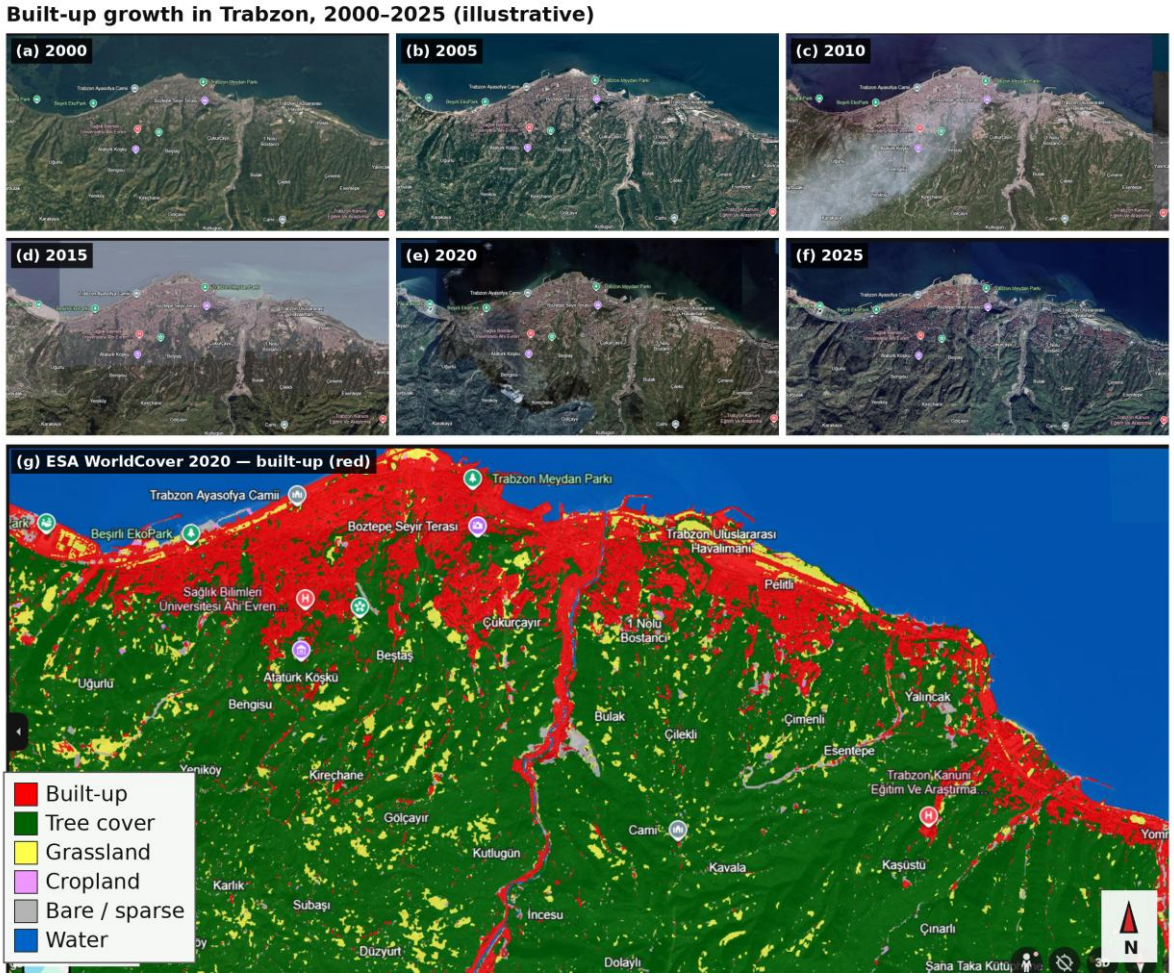


Fig. 1. Built-up growth in central Trabzon and its southern fringe, 2000–2025. Panels (a)–(f) are Google Earth historical imagery (acquisition years as labelled; 2025 = 31 Oct 2025); panel (g) is ESA WorldCover 2020 land cover, with built-up areas in red, over a slightly wider extent reaching Yomra. The figure is qualitative: frames are not co-registered and scales are approximate. Sources: Google Earth (© Google; Maxar/CNES/Airbus); ESA WorldCover 2020 v100 (© ESA; contains modified Copernicus Sentinel data), Zanaga et al. [10].

Permits are disaggregated to the three-digit CC level. Within the residential class (CC 11) three subcategories are distinguished — one-dwelling buildings (111), two-or-more-dwelling buildings (112) and residences for communities (113) — while the non-residential class (CC 12) is resolved into hotels and similar buildings (121), office buildings (122), wholesale and retail trade buildings (123), traffic and communication buildings (124), industrial buildings and warehouses (125), public-entertainment, education, hospital or institutional-care buildings (126) and other non-residential buildings (127). Together with the residential, non-residential and overall totals, this yields thirteen raw count series spanning the study period; these categories and the share series derived from them are listed in Table 1.

Table 1. Building permit categories analysed at the three-digit CC level and the seven share series derived from them. Within-residential shares use residential permits (CC 11) as denominator; sectoral shares use all permits (CC 1).

CC code	Building category	Derived share series
1	All buildings (total)	(reference total)
11	Residential buildings	Residential % of total
111	One-dwelling buildings	One-dwelling % of residential
112	Two-or-more-dwelling buildings	Multi-dwelling % of residential
113	Residences for communities	Communal % of residential
12	Non-residential buildings	Non-residential % of total
121	Hotels and similar buildings	Hotels % of total
122	Office buildings	–
123	Wholesale and retail trade buildings	–
124	Traffic and communication buildings	–
125	Industrial buildings and warehouses	Industrial % of total
126	Public-entertainment, education and health buildings	–
127	Other non-residential buildings	–

Two features of the data require caution and motivate the robustness checks reported below. First, the 2010 figures are anomalously high across almost all categories, consistent with a different compilation basis in that year, so the opening observation is treated as potentially non-comparable. Second, from the second quarter of 2025 the statistics were expanded beyond municipal authorities to incorporate permits issued by other bodies—special provincial administrations, organised-industrial-zone directorates, free-zone authorities and the like—so the closing observation may not be fully comparable with the municipally based earlier years. The 6 February 2023 Kahramanmaraş earthquake, which reshaped construction demand nationally, falls within the interior of the series and is taken into account when the late-period dynamics are interpreted. The full set of annual permit counts analysed is openly available from TurkStat [6].

2.2 Permit typology shares

Raw permit counts conflate two distinct signals: the overall volume of anticipated construction, which moves with the macroeconomic and credit cycle, and the typological composition of that construction, which is the object of this study. To separate composition from volume, each category is expressed as an annual share of an appropriate reference total, following standard compositional-data practice [11]. For category i in year t the share is

$$share_{i,t} = (n_{i,t} / N_t) \times 100 \tag{1}$$

where $n_{i,t}$ is the number of permitted buildings in category i and N_t the corresponding reference total. Two reference bases are used. The internal composition of residential construction is captured by expressing the one-dwelling, multi-dwelling and communal subcategories as percentages of residential permits (CC 11), while the sectoral composition of construction is captured by expressing residential, non-residential, hotel and industrial permits as percentages of all permits (CC 1). This procedure produces seven derived share series, analysed alongside the thirteen count series and plotted in Figure 2. In panel (a), the communal series is interrupted at 2017, when no communal-residence permits were recorded – a missing observation, not a structural break.

2.3 Trend and change-point detection

Because annual permit series of sixteen points are short, non-normal and unlikely to satisfy parametric assumptions, trends and breaks are assessed with non-parametric procedures established in the environmental time-series literature. The presence and direction of a monotonic trend are tested with the Mann-Kendall test [12,13], which is based on the signs of all pairwise differences within a series and yields the statistic S, a standardised normal variate Z, a two-sided p-value and Kendall's τ as a scale-free measure of association; a trend is reported as significant at $p < 0.05$.

The magnitude of any trend is estimated with Sen's slope [14], the median of the slopes formed by all data pairs, which provides a robust estimate of change per year in the units of the series (percentage points per year for the share series). A single structural break in the mean is located with the Pettitt test [15], a rank-based change-point procedure that identifies the most probable break year together with its significance; where a break is detected, the associated level shift is illustrated by fitting linear trends to the pre- and post-break sub-periods. All tests were computed in Python, using the *pymannkendall* package (original test) for the Mann-Kendall and Sen procedures and the *pyhomogeneity* package for the Pettitt test.

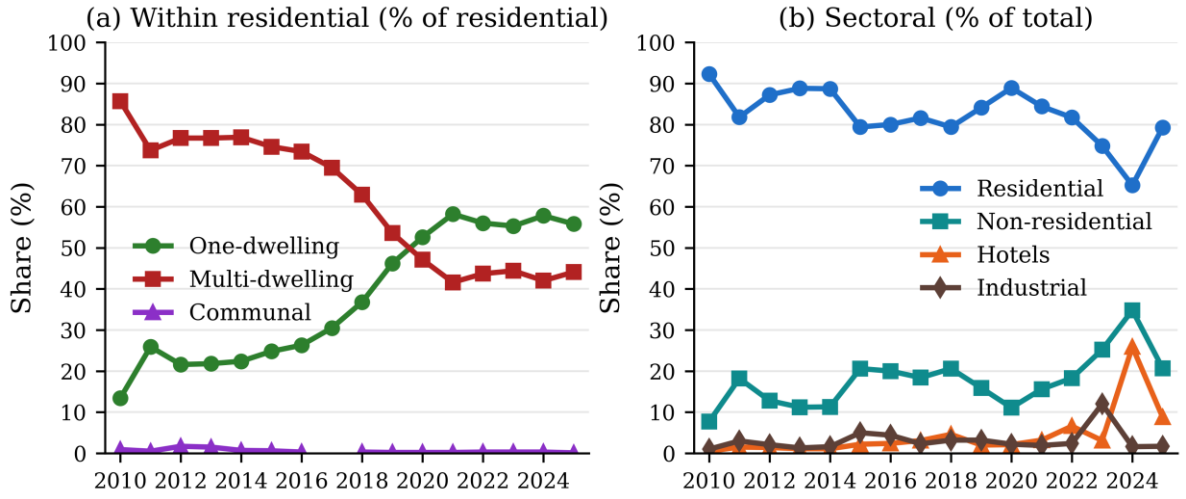


Fig. 2. Derived permit-share series for Trabzon, 2010–2025. (a) one-dwelling, multi-dwelling and communal buildings as percentages of residential permits (CC 11); (b) residential, non-residential, hotel and industrial buildings as percentages of all permits (CC 1). Series are shown without trend fitting; the statistical analysis is reported in Section 3.

2.4 Sensitivity analysis

To ensure that the reported trends and breaks are not artefacts of the two non-comparable boundary years, every test is repeated under three nested scenarios. Scenario S0 uses the full series (2010–2025); S1 excludes the anomalous opening year (2011–2025); and S2 excludes both boundary years (2011–2024), thereby removing the 2025 scope expansion as well. A finding is reported as robust only when it remains statistically significant, with a consistent sign, across all three scenarios; results that lose significance once a boundary year is removed are reported as fragile and are not over-interpreted.

3 Results

3.1 Trends and structural breaks

Table 2 reports the Mann-Kendall, Sen and Pettitt results for the seven share series over the full period (S0). Three of them show strong, highly significant trends. The one-dwelling share of

residential permits rises steeply ($Z = +4.37$, $p < 0.001$) at a Sen slope of +3.13 percentage points per year, while the multi-dwelling share falls almost symmetrically ($Z = -4.10$, $p < 0.001$; -3.08 pp/yr). Both are dated by the Pettitt test to a common change-point in 2018 ($p < 0.001$), so that within little more than a decade the composition of residential permits is effectively inverted: multi-dwelling buildings fall from about 86% of residential permits in 2010 to roughly 44% in 2025, and one-dwelling buildings rise from about 13% to 56% over the same span (Figs. 3 and 4).

The hotel share of all permits also trends significantly upward ($Z = +3.65$, $p < 0.001$; +0.39 pp/yr), with a Pettitt break in 2016 ($p = 0.003$) and a pronounced 2024 spike of 314 permits, by far the largest annual count in the series. The communal-residence share declines ($Z = -3.27$, $p = 0.001$; Pettitt break 2016) but from a very low base and with negligible magnitude (Sen slope ≈ -0.05 pp/yr), so it carries little substantive weight. By contrast, the residential and non-residential shares of total permits show only a weak full-period signal ($Z = -2.21$ and +2.21 respectively, $p = 0.027$) with no significant Pettitt break ($p \approx 0.06$), and the industrial share shows no trend at all ($Z = +0.41$, $p = 0.685$).

Table 2. Trend and change-point results for the share series over the full period (S0, 2010–2025). Z and p are the Mann-Kendall standardised statistic and two-sided p-value; Sen is the Theil–Sen slope in percentage points per year. The Pettitt break year is reported only where the test is significant ($p < 0.05$); – otherwise.

Share series	n	Trend	Z	p	Sen (pp/yr)	Pettitt p	Break
One-dwelling % of residential	16	increasing	+4.37	<0.001	+3.13	<0.001	2018
Multi-dwelling % of residential	16	decreasing	-4.10	<0.001	-3.08	<0.001	2018
Communal % of residential	15	decreasing	-3.27	0.001	-0.05	<0.001	2016
Residential % of total	16	decreasing	-2.21	0.027	-0.79	0.063	–
Non-residential % of total	16	increasing	+2.21	0.027	+0.79	0.061	–
Hotels % of total	16	increasing	+3.65	<0.001	+0.39	0.003	2016
Industrial % of total	16	no trend	+0.41	0.685	+0.03	0.202	–

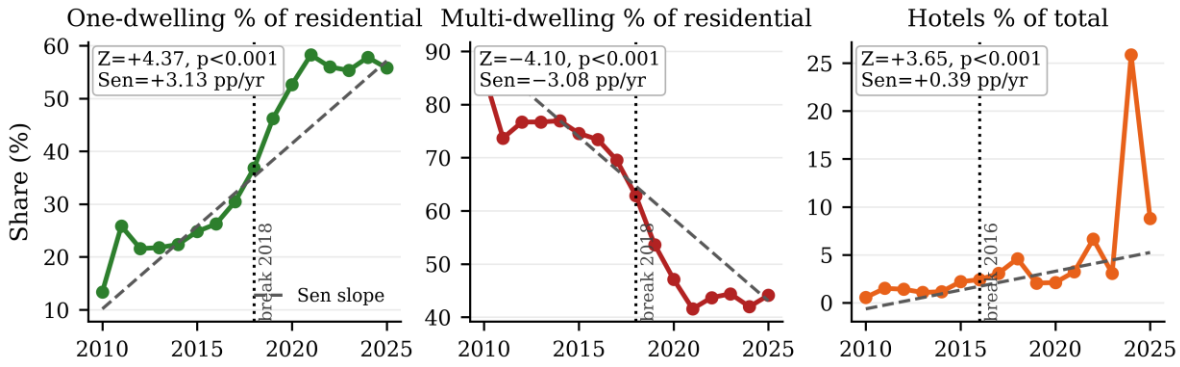


Fig. 3. The three statistically robust share series with Theil–Sen trend lines (dashed) and Pettitt change-points (dotted vertical lines). Mann-Kendall Z, two-sided p and the Sen slope (percentage points per year) are annotated in each panel. The 2024 value in the hotel panel corresponds to the 314-permit spike.

3.2 Robustness across scenarios

To separate genuine structure from artefacts of the two non-comparable boundary years, every test was repeated under scenarios S0, S1 and S2 (Table 3 and Fig. 5). The three headline findings are robust: the one-dwelling increase, the multi-dwelling decrease and the hotel increase remain significant at $p < 0.01$ in every scenario, keep their sign and magnitude, and retain the same break years (2018, 2018 and 2016).

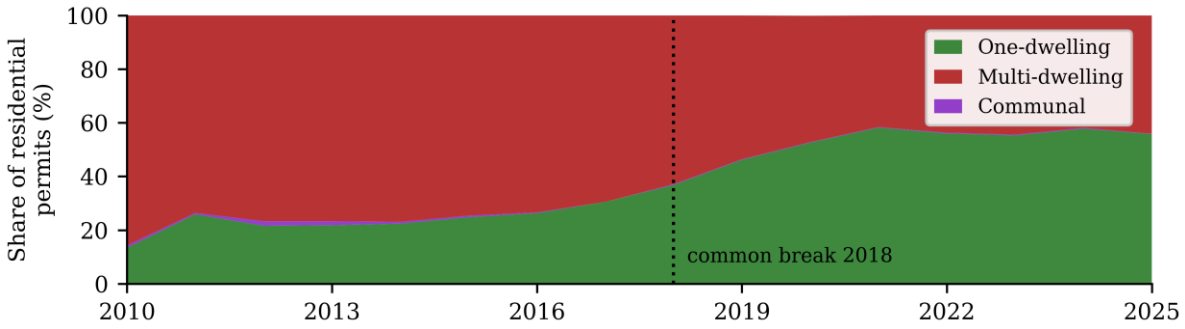


Fig. 4. Residential permit composition as a 100% stacked area, 2010–2025: one-dwelling, multi-dwelling and communal buildings as shares of residential permits. The crossover of the one-dwelling and multi-dwelling bands around the common 2018 break (dotted line) is the headline transition.

Table 3. Sensitivity of the Mann-Kendall trend test across scenarios (two-sided p-values). S0 = 2010–2025; S1 = 2011–2025 (excluding the anomalous 2010); S2 = 2011–2024 (excluding 2010 and 2025). A finding is robust when significant ($p < 0.05$) with consistent sign in all three scenarios.

Share series	p (S0)	p (S1)	p (S2)	Assessment
One-dwelling % of residential	<0.001	<0.001	<0.001	Robust (increase)
Multi-dwelling % of residential	<0.001	<0.001	<0.001	Robust (decrease)
Communal % of residential	0.001	0.002	0.009	Robust (decrease, small)
Residential % of total	0.027	0.093	0.189	Fragile
Non-residential % of total	0.027	0.093	0.189	Fragile
Hotels % of total	<0.001	0.001	0.003	Robust (increase)
Industrial % of total	0.685	0.843	0.913	No trend

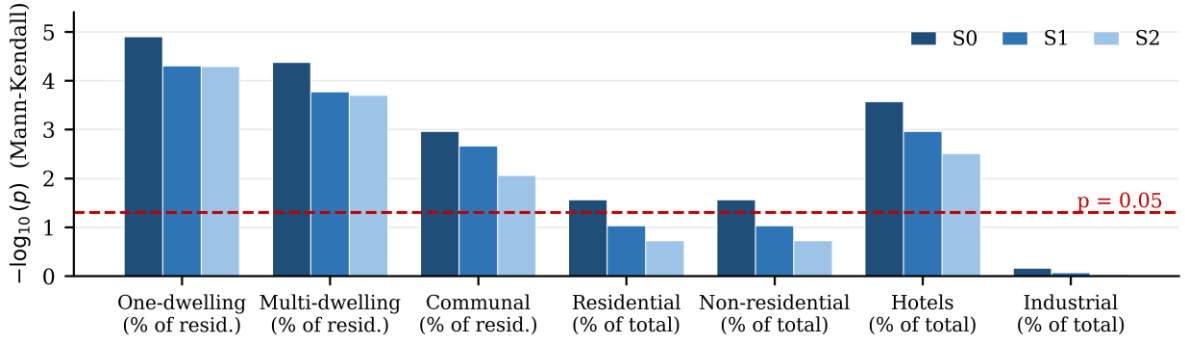


Fig. 5. Robustness of the Mann-Kendall trend across scenarios, shown as $-\log_{10}(p)$ for each share series under S0, S1 and S2. Bars above the dashed line ($p = 0.05$) are significant. The one-dwelling, multi-dwelling and hotel signals clear the threshold in every scenario, whereas the residential and non-residential signals fall below it once 2010 is excluded.

The residential-versus-non-residential shift is significant only when 2010 is retained (S0: $p = 0.027$; S1: $p = 0.093$; S2: $p = 0.189$), with no significant Pettitt break; it is reported as fragile — an artefact of the unusually multi-dwelling-heavy 2010 observation.

4 Discussion

4.1 A regional reversal of apartmentation

The central result of this study is a robust inversion of residential permit composition in Trabzon between 2010 and 2025. The one-dwelling share rises by roughly three percentage points per year and the multi-dwelling share falls at almost the same rate, both pivoting around a common 2018 change-point and surviving removal of the two non-comparable boundary years. At face value this runs counter to the apartmentation narrative that the Turkish housing literature treats

as the defining feature of the country's urbanisation [5]: Trabzon is not de-densifying in absolute terms, but at the margin the balance of new permits has shifted decisively toward lower-density forms. Table 4 summarises how each finding relates to the literature.

Table 4. Synthesis of the robust and fragile findings against the literature. Citation numbers refer to the reference list.

Finding	Key statistics	Literature link	Interpretation
One-dwelling share rises (within residential)	$Z = +4.37$, $p < 0.001$; Sen +3.13 pp/yr; break 2018; robust in S0–S2	Fringe and peri-urban expansion [7], [9]; counter to apartmentation [5]	Regional reversal of the apartmentation norm; satellite-corroborated
Multi-dwelling share falls (within residential)	$Z = -4.10$, $p < 0.001$; Sen −3.08 pp/yr; break 2018; robust in S0–S2	Credit-to-permit causality [4]; post-2017 financing tightening	Symmetric counterpart; 2018 break tied to the credit shock and central saturation
Hotel share rises (of total)	$Z = +3.65$, $p < 0.001$; Sen +0.39 pp/yr; break 2016; 2024 spike (314); robust	Tourism-driven coastal land-use change [8]	Tourism-investment cycle; 2024 spike flagged for scrutiny
Residential vs non-residential shift	Significant in S0 only ($p = 0.027$); non-significant in S1 and S2	TurkStat series-break guidance [6]	Fragile; not interpreted – a 2010 boundary-year artefact

Two independent lines of evidence make this reversal interpretable. First, it is spatially corroborated: remote-sensing studies document peri-urban expansion pushed outward from a topographically confined centre [7, 9], and the built-up sequence in Fig. 1 concentrates along the coastal fringe and lower slopes, where detached and low-rise construction is feasible. Second, the timing is economically interpretable: credit-to-permit causality is documented for Türkiye [4], and the 2018 change-point coincides with the post-2017 tightening of the credit and currency environment, which weighed most on the capital-intensive multi-dwelling segment; the reversal is thus plausibly the joint product of a binding land constraint and a financing shock to large-scale apartment production.

4.2 Tourism dynamics and the limits of the sectoral signal

The second robust finding – an upward trend in the hotel share with a 2016 change-point – aligns with the coastal-Turkey literature attributing much recent land-use change to tourism pressure along the shoreline [8]. The 2024 spike of 314 hotel permits warrants scrutiny; whether it reflects a genuine investment wave, a reporting effect or the 2025 scope change cannot be resolved from the aggregate series.

Equally important is what the analysis declines to claim: as Section 3.2 shows, the residential-versus-non-residential shift is fragile — an artefact of the anomalous 2010 boundary year, consistent with the series breaks TurkStat documents [6] — and is therefore reported as inconclusive.

4.3 Contribution, implications and limitations

Methodologically, the contribution is not the tests themselves – standard in environmental time-series analysis – but their transfer to provincial permit typology shares and the attached robustness protocol. Permit-based monitoring has been pursued elsewhere [2], but typically on counts or valuations; three-digit CC shares instead isolate the compositional transition that count-based monitoring would miss.

For local authorities this is a reproducible early-warning signal: a sustained move toward one-dwelling permits implies lower density, greater per-capita infrastructure demand and more dispersed social-facility need, and the methodology tracks such shifts annually from open data.

Several limitations bound these conclusions. The data are provincial: variation between the constrained centre and expanding districts is not resolved; the unit is the permitted building, not floor area or dwelling count, so building-type change need not map one-to-one onto housing supply; the short series (sixteen points) limits statistical power and restricts Pettitt to a single change-point; and the 2010 anomaly and the 2025 scope expansion remain uncertainties that the sensitivity analysis mitigates but cannot remove, and together they define the agenda for follow-up work.

5 Conclusions

Analysing sixteen years of TurkStat building-permit data for Trabzon with the Mann-Kendall, Sen and Pettitt tests, this study finds a statistically robust reversal of residential permit composition: the one-dwelling share rises and the multi-dwelling share falls, both breaking around 2018, while the hotel share trends upward from a 2016 break. The results are stable across every sensitivity scenario, run counter to the national apartmentation norm, are consistent with satellite evidence of outward, fringe-ward and tourism-linked growth, and pivot on breaks that predate the February 2023 Kahramanmaraş earthquake.

The study contributes a province-specific baseline for Trabzon and a transferable, open-data methodology for monitoring typological change in the building stock, supporting evidence-based planning on densification, parking and social facilities. Extending it to district-level, spatially explicit data enriched with land-cover and terrain information is the natural next step.

Acknowledgments

The authors thank TurkStat for the openly published Building Permit Statistics; all data are accessible at https://data.tuik.gov.tr. Generative AI (Claude, Anthropic) was used under the authors' supervision for language editing, formatting and figure preparation; the authors take full responsibility for the content. This research received no external funding, and the authors declare no conflict of interest.

References

1. OECD: Composite Leading Indicators (CLI). OECD, Paris. https://www.oecd.org/en/data/datasets/oecd-composite-leading-indicators-clis.html, last accessed 2026/07/17.
2. Cortes, G., LaPoint, C.: Housing is the financial cycle: evidence from 100 years of local building permits. SSRN Working Paper (2024). https://ssrn.com/abstract=4855353
3. Glaeser, E.L., Gyourko, J., Saiz, A.: Housing supply and housing bubbles. Journal of Urban Economics 64(2), 198–217 (2008). https://doi.org/10.1016/j.jue.2008.07.007
4. Dücan, E., Güğerçin, U.: Çeşitlendirme stratejisi örneği olarak Türkiye'de konut yatırımları ve sektörel krediler ilişkisi. Bolu Abant İzzet Baysal Üniversitesi Sosyal Bilimler Enstitüsü Dergisi 16(4), 93–110 (2016). https://doi.org/10.11616/basbed.vi.455407
5. Balamir, M.: Türkiye'de "Apartkent"lerin oluşumu: mülkiyet ilişkilerinin dönüşümüne dayalı kentleşme. In: Sey, Y. (ed.) Tarihten Günümüze Anadolu'da Konut ve Yerleşme, pp. 335–344. Tarih Vakfı, İstanbul (1996).
6. Turkish Statistical Institute (TurkStat): Building permit statistics — metadata and series-break register. https://data.tuik.gov.tr/Kategori/GetKategori?p=Insaat-ve-Konut-116, last accessed 2026/07/17.
7. Sancar, C., Turan, S.O., Kadıoğulları, A.İ.: Land use-cover change processes in urban fringe areas: Trabzon case study, Turkey. Scientific Research and Essays 4(12), 1454–1462 (2009).
8. Güneroğlu, N., Güneroğlu, A., Dihkan, M., et al.: Determining anthropogenic pressure on the Southern Black Sea blue flag beaches. Journal of Coastal Conservation 28(3), 55 (2024). https://doi.org/10.1007/s11852-024-01057-y

9. Ustaoglu, E., Aydınoglu, A.C.: Regional variations of land-use development and land-use/cover change dynamics: a case study of Turkey. Remote Sensing 11(7), 885 (2019). https://doi.org/10.3390/rs11070885
10. Zanaga, D., Van De Kerchove, R., De Keersmaecker, W., et al.: ESA WorldCover 10 m 2020 v100. Zenodo (2021). https://doi.org/10.5281/zenodo.5571936
11. Aitchison, J.: The statistical analysis of compositional data. Journal of the Royal Statistical Society: Series B (Methodological) 44(2), 139–160 (1982). https://doi.org/10.1111/j.2517-6161.1982.tb01195.x
12. Mann, H.B.: Nonparametric tests against trend. Econometrica 13(3), 245–259 (1945). https://doi.org/10.2307/1907187
13. Kendall, M.G.: Rank Correlation Methods, 4th edn. Charles Griffin, London (1975).
14. Sen, P.K.: Estimates of the regression coefficient based on Kendall's tau. Journal of the American Statistical Association 63(324), 1379–1389 (1968). https://doi.org/10.1080/01621459.1968.10480934
15. Pettitt, A.N.: A non-parametric approach to the change-point problem. Journal of the Royal Statistical Society: Series C (Applied Statistics) 28(2), 126–135 (1979). https://doi.org/10.2307/2346729

Author Contribution Statement

- *Conceptualization:* Abdullah Bostancı
- *Methodology:* Abdullah Bostancı, Sina Atabey
- *Investigation:* Abdullah Bostancı, Sina Atabey
- *Writing – Original Draft:* Abdullah Bostancı
- *Writing – Review & Editing:* Sina Atabey

List of Abbreviations

- **CC** — Classification of Types of Constructions
- **MK** — Mann-Kendall (trend test)
- **TurkStat** — Turkish Statistical Institute
- **pp/yr** — percentage points per year
- **S0–S2** — sensitivity scenarios (full series; excluding 2010; excluding 2010 and 2025)

Note: Following the conference, this Publication Note will be added to each paper; therefore, authors are kindly requested not to remove the note below and to complete the author(s) and paper title information.

Publication Note

This paper was peer-reviewed, accepted for presentation, and included in the proceedings of the ACE2026 – International Conference on Advances in Civil Engineering, held on 12–14 October 2026 in Trabzon, Türkiye.

This paper may be cited as follows:

Bostancı A., Atabey S., "Monitoring the Transformation of Residential Typology from Building Permit Data in Trabzon (2010–2025)," in Proceedings of the ACE2026 – International Conference on Advances in Civil Engineering, Trabzon, Türkiye, 12–14 October 2026.

Design Considerations for Concrete Structures Under Fire Exposure

Furkan Varinlioglu[1], Huseyin Okan Anadut[2], Fuat Koksal[3]

[1] 0009-0004-0177-0514, Yozgat Bozok University, Civil Engineering Department, Yozgat, Türkiye, furkan.varinlioglu@bozok.edu.tr
[2] 0000-0002-9185-2174, Yozgat Bozok University, Civil Engineering Department, Yozgat, Türkiye, okan.anadut@bozok.edu.tr
[3] 0000-0002-3436-1694, Yozgat Bozok University, Civil Engineering Department, Yozgat, Türkiye, fuat.koksal@bozok.edu.tr

Abstract. Fire is a loading effect that is often not explicitly considered in the analysis and design of engineering structures. Reinforced concrete structures exposed to fire are at significant risk in terms of their mechanical, physical, and durability properties depending on the temperature level and duration of fire exposure. Therefore, understanding the behavior of concrete under elevated temperatures is of great importance for evaluating the fire resistance of reinforced concrete structures. This study presents a literature-based review of the design principles for reinforced concrete structures subjected to fire exposure. Experimental and analytical studies conducted to date have been comparatively evaluated, and the effects of elevated temperatures on concrete behavior as well as the residual load-carrying capacity after fire exposure have been examined in detail. In addition, the influences of critical parameters such as aggregate type, moisture content, water-to-cement ratio, concrete cover thickness, and fiber reinforcement on fire performance have been investigated. The reviewed studies indicate that elevated temperatures lead to severe deterioration in the microstructural and mechanical properties of concrete due to dehydration, thermal incompatibility, pore pressure development, and progressive cracking mechanisms. Nevertheless, it has been determined that appropriate material selection and fire-resistant design approaches can significantly improve the thermal stability and post-fire performance of reinforced concrete structures. The findings of this review contribute to a better understanding of fire-induced concrete deterioration and provide a useful guide for the design of safer and more durable reinforced concrete structures under fire conditions.

Keywords: Fire exposure; Concrete structures; Fire-resistant design; Mechanical properties;

1 İntroduction

Fire is one of the most significant factors affecting the structural integrity, safety, and service life of concrete structures. Unlike conventional design actions—such as dead, live, wind, snow, and seismic loads—that threaten the intended performance of concrete structures primarily through mechanical effects, fire causes substantial changes in many properties of concrete, particularly its mechanical properties, owing to elevated temperatures [1–4]. Concrete has traditionally been regarded as a fire-resistant construction material because of its low thermal conductivity and non-combustible nature [5]. However, prolonged exposure to elevated temperatures causes deterioration in concrete, resulting in reductions in stiffness, strength, modulus of elasticity, durability, and load-bearing capacity [6]. Therefore, understanding the behaviour of concrete under fire exposure and designing fire-resistant concrete have become important considerations in structural engineering.

The behaviour of concrete under fire exposure is more complex than that of many other construction materials. This complexity arises from the heterogeneous nature of concrete, which consists of cement paste, aggregates, pores, and moisture, each responding differently to

increasing temperatures. As the temperature rises, concrete undergoes interrelated physical, chemical, and mechanical transformations, including the evaporation of internal moisture, dehydration of cement hydration products, thermal incompatibility between the aggregate and cement paste, and the formation of microcracks. These transformations increase the permeability and degree of damage in concrete while adversely affecting its mechanical properties, particularly its compressive strength, modulus of elasticity, and stiffness [5].

Over the past decade, numerous studies have investigated the behaviour of concrete under fire exposure using experimental, analytical, and numerical approaches. Although these studies have contributed significantly to understanding the fundamental mechanisms responsible for fire-induced deterioration in concrete, the available findings have generally focused on isolated material-level responses or a limited number of parameters. Comparative assessments of the effects of critical parameters—such as aggregate type, moisture content, water-to-cement ratio, fibre reinforcement, and concrete cover thickness—based on combined experimental and analytical findings remain limited. Therefore, a comprehensive literature-based investigation is needed to evaluate the influence of these parameters on the fire performance of concrete from a holistic perspective and to provide a valuable reference for structural engineering practice and future research.

2 Behavior of Concrete Under Fire Exposure

Concrete exposed to fire undergoes a series of interrelated processes that alter its properties and critically affect its structural performance. As the temperature increases, its behaviour is governed by physicochemical changes in the aggregate and cement paste, thermal incompatibility arising from differences in the thermal expansion of these constituents, moisture migration, and changes in the pore structure. These phenomena collectively lead to the progressive deterioration of the concrete microstructure. Therefore, the behaviour of concrete under fire exposure cannot be attributed to a single deterioration mechanism [5]. Instead, it results from the combined effects of multiple interacting processes that occur simultaneously as the temperature rises. The severity of these processes is influenced by both the characteristics of the concrete mixture and the prevailing environmental conditions. This complex interaction makes it difficult to accurately predict the performance of concrete under fire exposure.

One of the most significant responses of concrete to elevated temperatures is the evaporation of free water and the gradual release of chemically bound water from cement hydration products. As the temperature continues to rise, dehydration of the cement matrix, differential thermal expansion between the aggregate and cement paste, and the build-up of internal vapour pressure promote the formation and propagation of microcracks within the concrete. Once the temperature reaches critical levels, explosive spalling may occur, directly exposing the reinforcing steel in reinforced concrete members to fire and thereby dramatically accelerating structural deterioration. Overall, these transformations alter the internal structure of concrete and significantly affect its mechanical performance both during and after fire exposure [7–9].

The deterioration of concrete at the microstructural level is directly reflected in its mechanical behaviour. Numerous experimental and numerical studies have reported that increasing temperature leads to reductions in the compressive strength, tensile strength, modulus of elasticity, stiffness, and residual load-bearing capacity of concrete. However, the extent of this deterioration depends not only on the maximum temperature attained but also on the heating rate, duration of thermal exposure, cooling conditions, moisture content, aggregate characteristics, and mixture proportions. Consequently, concrete specimens exposed to similar temperatures may exhibit markedly different performance depending on their material composition and structural configuration.

Although fire-induced deterioration mechanisms have been extensively investigated in the literature, the fire resistance of concrete results from the interaction of several material- and design-related parameters acting simultaneously. Therefore, understanding both the individual and combined effects of these parameters is essential for accurately assessing fire-induced damage and improving the thermal stability of reinforced concrete structures. Accordingly, the following section examines the effects of aggregate type, moisture content, water-to-cement ratio, concrete cover thickness, and fibre reinforcement, which are among the parameters most frequently investigated in the literature.

3 Evaluation of the Parameters Affecting the Fire Performance of Concrete

3.1 Aggregate Type

The type of aggregate used in concrete production is one of the most important parameters influencing the fire performance of concrete. This is primarily because aggregates constitute approximately 60–75% of the total volume of concrete and largely govern its mechanical and thermal behaviour at critical temperatures. During fire exposure, the heat-transfer characteristics, thermal expansion, and moisture-related behaviour of aggregates influence crack development and the stability of the interfacial transition zone (ITZ). All these factors also affect the residual mechanical properties of concrete after cooling. Although recent studies examining the influence of aggregate type have traditionally focused on the distinction between commonly used siliceous and calcareous aggregates, the findings indicate that fire performance is governed not merely by the selection of a particular aggregate type but also by its mineralogical composition, crystallinity, pore structure, thermophysical properties, and interaction with the cementitious matrix. Consequently, selecting suitable aggregates for fire-resistant concrete design requires a comprehensive understanding of both the intrinsic thermal properties of the aggregates and their compatibility with the cementitious matrix during heating.

Conventionally used calcareous aggregates have generally been considered more suitable than siliceous aggregates for concrete exposed to elevated temperatures because of their relatively lower thermal expansion and lower susceptibility to quartz-related phase transformations at intermediate temperatures [6]. Nevertheless, comparative findings indicate that a simple classification into calcareous and siliceous aggregates is insufficient. In particular, another study reported that quartzite aggregates remained relatively stable despite the α-to-β quartz transformation, whereas moisture-sensitive, low-permeability flint particles experienced substantial internal damage and caused extensive cracking in the surrounding concrete.

Furthermore, the relative performance of the aggregates varied with the quality of the cementitious matrix. Concrete containing calcareous aggregates exhibited more favourable performance when used with a normal-strength matrix, whereas quartzite aggregate concrete demonstrated better residual behaviour when incorporated into a denser, high-performance matrix. At even higher temperatures, the advantage of calcareous aggregates observed at intermediate temperatures may diminish because calcination and the subsequent hydration of calcium oxide after cooling can trigger delayed deterioration. These findings demonstrate that aggregate performance depends on both the temperature level and matrix characteristics and, therefore, cannot be reliably predicted solely on the basis of broad mineralogical classifications [10].

Aggregate mineralogy strongly influences the thermal behaviour of aggregates. Previous studies have shown that the behaviour of concrete at elevated temperatures is governed by the relationship between the mineral composition of the aggregate and its microstructural characteristics. Aggregates with similar mineralogical compositions may exhibit different fire performance depending on their crystallinity, permeability, pore structure, and moisture condition. This indicates that the mechanisms governing fire-induced damage extend beyond

mineral composition and are closely associated with moisture transport and aggregate–cement paste interactions during heating [10,11]. Furthermore, thermal incompatibility between the aggregate and cement paste, arising from differences in their thermal expansion, promotes microcrack formation within the interfacial transition zone. In contrast, calcareous and lightweight aggregates may limit such damage because of their greater thermal compatibility with the cementitious matrix. Microstructural observations have demonstrated that improved thermal compatibility preserves the integrity of the interfacial transition zone and thereby enhances the residual strength of concrete [1,2,11].

Recent studies have demonstrated that lightweight aggregates can improve the fire performance of concrete through mechanisms that differ from those associated with normal-weight aggregates. Their relatively high porosity, low thermal conductivity, and ability to alleviate the build-up of internal vapour pressure reduce temperature gradients and thermally induced stresses. Consequently, concrete containing lightweight aggregates generally exhibits greater residual strength and a lower risk of spalling. However, these advantages should be evaluated in conjunction with the potential reduction in the mechanical strength of lightweight concrete at ambient temperature. Indeed, a higher residual strength ratio does not necessarily correspond to a higher absolute strength after fire exposure [1,2,6].

3.2 Moisture Content

Moisture content is a critical parameter governing the fire performance of concrete because it simultaneously influences heat transfer, the development of pore pressure, crack formation, and spalling behaviour. During the initial stages of heating, moisture can temporarily slow the temperature increase by absorbing thermal energy. However, as the temperature rises, the resulting water vapour may be unable to migrate through the pore network, leading to a build-up of pore pressure. The combined effects of this pressure, thermally induced stresses, and the progressive reduction in the tensile strength of concrete may eventually exceed the material's resistance, thereby causing cracking and spalling. Therefore, the influence of moisture cannot be evaluated independently of permeability, pore connectivity, matrix density, heating rate, and cross-sectional dimensions [7–9]. This interaction also links moisture-related behaviour to the aggregate-related mechanisms discussed in Section 3.1, since aggregate porosity, interfacial characteristics, and thermophysical properties influence both moisture transport and thermally induced cracking [1,10,11].

The influence of moisture varies considerably with temperature. At moderate temperatures, internal moisture may provide temporary thermal buffering through latent heat absorption and may support ongoing hydration or pozzolanic reactions. Previous studies have reported either limited strength loss or an increase in strength at approximately 200 °C in specimens with high moisture contents, whereas drier mixtures exhibited earlier deterioration due to dehydration. However, this beneficial effect disappeared as the temperature increased. At approximately 400 °C, the decomposition of hydration products, pore coarsening, thermal incompatibility, and cracking within the interfacial transition zone became dominant. At 600 °C, a higher moisture content generally resulted in lower residual strength and more severe physical damage [7–9]. Therefore, moisture should not be regarded as either entirely beneficial or entirely detrimental to the fire performance of concrete.

In one of the studies reviewed, fully saturated normal-strength concrete did not exhibit spalling, whereas saturated high-strength concrete experienced significant spalling and a sudden loss of strength between 400 and 600 °C [7]. Similarly, another study reported that larger high-strength concrete specimens suffered severe damage under moist and saturated conditions, whereas dry specimens maintained their integrity more effectively [9]. These findings were attributed to the connected pore network of normal-strength concrete, which facilitates the continuous transport and release of water vapour, and to the dense and less

interconnected pore structure of high-strength concrete, which restricts vapour migration and pressure dissipation. This observation provides a direct link to the influence of the water-to-cement ratio discussed in Section 3.3. Although a low water-to-cement ratio improves strength and durability at ambient temperature, the resulting dense microstructure may increase susceptibility to fire-induced spalling when sufficient internal moisture is present.

Because water is generally distributed heterogeneously within concrete, total moisture content alone cannot fully explain its fire performance. Studies have shown that partial drying primarily removes moisture from the outer layers of concrete, while the inner regions remain relatively moist, thereby creating steep surface-to-core moisture gradients. Furthermore, larger specimens experienced more severe damage at 600 °C because water vapour had to travel a greater distance to reach the surface, resulting in moisture becoming trapped within the inner regions [9]. Direct pore-pressure measurements revealed that the maximum pressure did not occur at the heated surface but at an intermediate depth, where inward vapour migration and condensation created a moisture-clogged zone. In mixtures that exhibited spalling, peak pore pressures of approximately 3.29–6.03 MPa were recorded at a depth of 30 mm [8]. These results demonstrate that cross-sectional geometry, drying depth, and internal moisture distribution are at least as important as the average moisture content in determining the fire performance of concrete.

The studies reviewed demonstrate that the influence of moisture cannot be evaluated independently of the internal composition of concrete, because vapour transport is governed by aggregate characteristics and matrix permeability. One study reported that concrete containing siliceous–calcareous aggregates rich in flint developed significantly more internal cracking than concrete produced with calcareous or quartzite aggregates. This behaviour was attributed to the lower permeability and greater moisture sensitivity of the flint particles, which promoted localised vapour accumulation and internal damage as the temperature increased [10]. Moreover, another study demonstrated that temperature distribution within concrete depends not only on the thermal conductivity of the aggregates but also on moisture redistribution and the latent heat associated with water evaporation. This finding confirms that the thermal properties of aggregates alone cannot fully explain the fire performance of concrete [11]. By contrast, more favourable behaviour has been observed in lightweight aggregate concrete [1]. Lightweight aggregates have been shown to improve thermal compatibility between the aggregate and cement paste, while other studies have reported less extensive cracking, lower thermal conductivity, and better residual mechanical properties than those observed in concrete containing conventional aggregates [2,6]. Although these studies did not directly measure pore pressure, their findings suggest that, provided they are not fully saturated, porous lightweight aggregates may offer additional internal space for accommodating water vapour and redistributing stresses, thereby reducing thermally induced damage.

3.3 W/C Ratio

The water-to-cement ratio plays a decisive role in the fire performance of concrete by governing its initial strength, porosity, permeability, degree of hydration, and the quality of the interfacial transition zone.

The studies reviewed generally indicate that concrete with a lower water-to-cement ratio retains a higher absolute compressive strength after heating. In one study, reducing the water-to-cement ratio decreased the apparent porosity at ambient temperature and significantly increased both the initial and residual compressive strengths [12]. Another study similarly reported higher residual mechanical capacities for mixtures with lower water-to-cement ratios, although the mixture designs also differed in terms of cement content and initial strength [3].

The studies reviewed indicate that the influence of the water-to-cement ratio varies with temperature. Temporary increases in strength have been observed at approximately 200–300

°C, although the magnitude of these increases differed among studies because of variations in initial moisture content, pre-drying conditions, cement content, aggregate type, and heating method. Above 300 °C, C–S–H dehydration, portlandite decomposition, pore coarsening, and thermally induced microcracking become increasingly dominant. Under these conditions, concrete with a high water-to-cement ratio generally deteriorates more rapidly because its weaker and more porous interfacial transition zone facilitates crack propagation [3,12]. Another study observed similar low-temperature strength fluctuations in hardened cement paste without aggregates, confirming that these changes arise directly from the characteristics of the cementitious matrix rather than solely from aggregate-related mechanisms [13]. However, previous studies have also demonstrated that modifications to the cementitious matrix can alter the relative performance of aggregates at elevated temperatures. Therefore, the effects of aggregate type and water-to-cement ratio should be considered together. Aggregate type governs heat transfer, thermal expansion, and aggregate–matrix incompatibility, whereas the water-to-cement ratio influences matrix quality, permeability, and the integrity of the interfacial transition zone ([3], [10–12]).

The influence of a low water-to-cement ratio at elevated temperatures varies according to the mechanical property under consideration. Concrete with a lower water-to-cement ratio has been observed to retain higher residual compressive strength and fracture energy. By contrast, unstable fracture toughness decreased similarly at elevated temperatures across all mixture types. This finding indicates that a dense cementitious matrix may delay crack initiation and propagation but cannot prevent the widespread thermal damage that ultimately leads to unstable cracking at high temperatures [12]. Furthermore, the dense, low-permeability microstructure produced by a low water-to-cement ratio may increase pore pressure, particularly under moist conditions, thereby increasing the severity of spalling [7–9]. Consequently, although a low water-to-cement ratio may be advantageous under controlled heating or relatively dry conditions, it can increase susceptibility to spalling when rapid heating and high internal moisture levels occur simultaneously.

3.4 Concrete Cover Thickness

Concrete cover enhances the fire resistance of reinforced concrete members by delaying heat transfer to the reinforcing steel and the relatively less-damaged concrete core. However, the studies reviewed indicate that this protective effect is not uniform under all conditions and that increasing the concrete cover thickness does not necessarily result in a proportional increase in residual load-bearing capacity.

An experimental study directly compared concrete cover thicknesses of 20 and 30 mm and found that, particularly at low and moderate temperatures, the thicker cover provided better protection for both concrete integrity and the tensile properties of the reinforcement by extending the heat-transfer path between the exposed surface and the reinforcing steel [14]. Similarly, another study investigated recycled-aggregate reinforced concrete columns with cover thicknesses of 30, 40, and 50 mm. Increasing the cover thickness reduced the temperatures within the concrete core and reinforcement, thereby improving the axial load-bearing capacity. However, the magnitude of this improvement became progressively less pronounced as the cover thickness increased [15]. These findings suggest that concrete cover acts primarily as a thermal barrier during the initial stages of heat exposure. By contrast, another study reported that concrete cover thicknesses ranging from 20 to 50 mm had no statistically significant effect on the post-fire yield and tensile strengths of embedded reinforcing bars exposed to the ISO 834 standard fire curve [16]. This apparent discrepancy can largely be explained by the different response variables considered in the respective studies. Kigha et al. (2015) evaluated reinforcing bars isolated from the surrounding concrete after cooling, whereas Chen et al. (2020) and Khiyon et al. (2019) investigated the performance of composite

reinforced concrete members, in which a thicker cover primarily reduced reinforcement heating and deterioration of the inner concrete rather than directly altering the residual properties of the cooled reinforcing steel. A comparison of these studies clearly demonstrates that the protective role of concrete cover may depend on the duration of thermal exposure and the depth reached by the thermally damaged zone. Chen et al. (2020) observed that prolonged heating at 600 °C significantly reduced the benefit provided by a thicker concrete cover compared with short-term heating, as thermal damage penetrated deeper into the cross-section. Similarly, another study examining conventional and self-compacting concrete beams subjected to different fire durations and cooling regimes showed that the influence of cover thickness depended on the concrete type, heating duration, and cooling method [17]. Water-cooled beams experienced greater strength losses than air-cooled specimens because rapid cooling induced thermal shock and additional cracking. This deterioration was particularly severe in higher-strength self-compacting concrete and was attributed to its denser pore structure, lower permeability, and greater susceptibility to vapour-pressure-induced damage. These findings indicate that increasing the concrete cover thickness may not necessarily improve fire performance when the outer concrete layer is susceptible to thermal cracking or spalling.

3.5 Fibre Reinforcement

Fibre reinforcement can improve the fire performance of concrete through two distinct mechanisms. Steel and glass fibres, which have relatively high melting temperatures, primarily preserve mechanical integrity by bridging thermally induced cracks. By contrast, polymeric fibres with low melting temperatures, such as polypropylene and polyethylene fibres, are incorporated to mitigate pore-pressure-induced spalling by melting during heating and facilitating vapour transport. However, the studies reviewed indicate that fibre effectiveness depends not only on fibre type and dosage but also on melting behaviour, geometry, matrix permeability, initial moisture content, and the continuity of the channels formed within the concrete during heating [8,18,19].

A previous study investigated the physical, mechanical, and microstructural properties of self-compacting concrete mixtures containing different types of fibres—polypropylene, glass, and steel—at elevated temperatures while maintaining the same base mixture composition [18]. The results demonstrated that steel fibres had a pronounced effect on preserving the structural integrity and mechanical properties of concrete. Because steel fibres retained their crack-bridging capacity as the temperature increased, they provided the highest residual compressive and tensile strengths, whereas glass fibres produced more moderate improvements. By contrast, polypropylene fibres exhibited behaviour that differed from that of the other fibre types. At ambient temperature, polypropylene fibres provided only a limited improvement in tensile behaviour compared with the unreinforced specimens, while their residual compressive and tensile strengths generally remained lower as the temperature increased. This outcome was attributed to the melting of polypropylene fibres at approximately 150–170 °C. As the temperature increased further, the fibres largely disappeared from the matrix and left additional voids, thereby reducing the residual mechanical properties of the concrete. Nevertheless, this finding does not imply that polypropylene fibres are ineffective under fire exposure. Their primary function is not to preserve post-fire strength but to melt and form pathways that facilitate vapour release, thereby reducing the risk of explosive spalling. Because the specimens in the study were pre-dried at 105 °C, most of the free moisture was removed before heating. Consequently, the results primarily reflect the influence of fibre melting on the residual mechanical properties rather than the ability of polypropylene fibres to prevent explosive spalling.

A previous study demonstrated that fibre melting does not necessarily provide effective vapour-pressure relief. The study investigated dense, high-strength engineered cementitious

composites containing polyethylene fibres under five different moisture conditions [8]. Severe explosive spalling occurred in specimens with high moisture contents because of the accumulation of internal pore pressure.

Another study compared the thermal and mechanical behaviour of conventional concrete with that of ultra-high-performance fibre-reinforced concrete containing steel microfibres under elevated temperatures [19]. The results showed that increasing the steel-fibre dosage enhanced the initial tensile and flexural properties of the ultra-high-performance fibre-reinforced concrete and improved crack control; however, it did not eliminate the susceptibility of the dense matrix to fire-induced damage. Although a higher fibre dosage contributed to better preservation of concrete integrity, explosive spalling continued to occur at elevated temperatures, and the residual compressive strength decreased markedly at temperatures above approximately 500 °C.

4 Discussion and Conclusions

This section provides a comparative evaluation of the key parameters affecting the fire performance of concrete, as discussed in the preceding section. It further examines the implications of the damage mechanisms governing concrete behaviour at elevated temperatures for fire-resistant concrete design.

The studies reviewed demonstrate that the fire performance of concrete cannot be explained by any single material- or design-related parameter. Aggregate type, moisture content, water-to-cement ratio, concrete cover thickness, and fibre reinforcement influence concrete behaviour through different mechanisms. Because an improvement in one parameter may simultaneously affect another damage mechanism, these parameters must be evaluated in terms of their combined and interacting effects.

Aggregate mineralogy and structure govern phase transformations and thermal expansion at elevated temperatures, whereas aggregate porosity and moisture-retention capacity influence internal vapour transport. Nevertheless, the findings indicate that classifying aggregates solely according to type is insufficient for predicting or improving the fire performance of concrete. A particular aggregate may exhibit satisfactory performance within one cementitious matrix yet promote more extensive internal cracking in another matrix with a different water-to-cement ratio or moisture content. Therefore, the thermal compatibility between the aggregate and cement paste, the integrity of the interfacial transition zone, moisture condition, and matrix permeability should be evaluated collectively. The studies reviewed further demonstrate that not only average moisture content but also drying depth, surface-to-core moisture gradients, and pore-pressure development play significant roles in the behaviour of concrete at elevated temperatures. From a design perspective, the findings indicate that fire-resistant concrete cannot be achieved solely by targeting high initial strength or low permeability. An appropriate mixture design should establish a balance among adequate mechanical strength, thermal compatibility, and controlled vapour-transport capacity. The aggregate should be thermally and mechanically compatible with the cementitious matrix; the water-to-cement ratio should provide the required strength without producing an excessively impermeable microstructure; and fibre type and dosage should be selected according to whether the primary objective is crack control or pore-pressure relief. In this context, hybrid fibre systems combining steel and polymeric fibres may be employed to preserve mechanical performance while simultaneously facilitating vapour release. Further experimental research should therefore investigate the effectiveness of such hybrid fibre systems under fire exposure. A major limitation of the existing literature is that these parameters have generally been investigated independently and that many studies have been conducted using small-scale, unloaded, and pre-dried specimens. Future research should examine their combined effects under more representative conditions, including realistic

moisture states, structural loading, large-scale members, different fire-exposure durations, and various cooling regimes.

References

1. Yoon, M., Kim, G., Choe, G.C., Lee, Y., Lee, T.: Effect of coarse aggregate type and loading level on the high temperature properties of concrete. *Construction and Building Materials* 78, 26–33 (2015). https://doi.org/10.1016/j.conbuildmat.2014.12.096
2. Ozturk, A.B., Turan, A.I., Kumbasaroglu, A., Yalciner, H., Ayaz, Y.: The effect of elevated temperature on the mechanical properties of concrete produced with raw perlite aggregate. *Journal of Building Engineering* 118, 115093 (2026). https://doi.org/10.1016/j.jobe.2025.115093
3. Al-Jabri, K.S., Waris, M.B., Al-Saidy, A.H.: Effect of aggregate and water to cement ratio on concrete properties at elevated temperature. *Fire and Materials* 40(7), 913–925 (2016). https://doi.org/10.1002/fam.2351
4. Moradi, M.S., Tavana, M.H., Habibi, M.R., Amiri, M.: Effect of water to cement ratio on mechanical properties of FRC subjected to elevated temperatures: Experimental and soft computing approaches. *Heliyon* 10, e39513 (2024). https://doi.org/10.1016/j.heliyon.2024.e39513
5. Denoël, J.-F.: *Fire Safety and Concrete Structures*. FEBELCEM—Federation of the Belgian Cement Industry, Brussels (2007).
6. Abdullah, A.H., Mohammed, S.D.: Effect of lightweight expanded clay aggregate as partial replacement of coarse aggregate on the mechanical properties of fire-exposed concrete. *Journal of the Mechanical Behavior of Materials* 32, 20220299 (2023). https://doi.org/10.1515/jmbm-2022-0299
7. Kirchhof, L.D., Lima, R.C.A., Santos Neto, A.B.S., Quispe, A.C., Silva Filho, L.C.P.: Effect of moisture content on the behavior of high strength concrete at high temperatures. *Matéria* 25(1), e-12573 (2020). https://doi.org/10.1590/S1517-707620200001.0898
8. Yu, J., Zhang, Z.: Role of moisture content in governing elevated-temperature spalling of high-strength engineered cementitious composites. *Construction and Building Materials* 528, 146542 (2026). https://doi.org/10.1016/j.conbuildmat.2026.146542
9. Abbas, H., Abadel, A., Alaskar, A., Almusallam, T., Al-Salloum, Y.: Effects of moisture on properties of concrete exposed to elevated temperature. *Arabian Journal for Science and Engineering* 50, 1477–1492 (2025). https://doi.org/10.1007/s13369-024-09012-7
10. Xing, Z., Beaucour, A.-L., Hebert, R., Noumowe, A., Ledesert, B.: Influence of the nature of aggregates on the behaviour of concrete subjected to elevated temperature. *Cement and Concrete Research* 41, 392–402 (2011). https://doi.org/10.1016/j.cemconres.2011.01.005
11. Xing, Z., Beaucour, A.-L., Hebert, R., Noumowe, A., Ledesert, B.: Aggregate's influence on thermophysical concrete properties at elevated temperature. *Construction and Building Materials* 95, 18–28 (2015). https://doi.org/10.1016/j.conbuildmat.2015.07.060
12. Hlavička, V.: The effect of the water-cement ratio on the residual fracture mechanical properties of concrete after heat loading. *Journal of Thermal Analysis and Calorimetry* (2026). https://doi.org/10.1007/s10973-026-15801-z
13. Fehérvári, S.: The effect of elevated temperature on ordinary Portland cements. *Periodica Polytechnica Civil Engineering* 67(1), 224–231 (2023). https://doi.org/10.3311/PPci.20519
14. Khiyon, M.I., Kadir, M.A.A., Mohd Sam, A.R., Hasanah, N., Mohamed, R.N., Yussof, M.M., Mohamad Zukri, S.N.N., Nurizaty, Z.: The effect of concrete cover thickness subjected to elevated temperatures. *IOP Conference Series: Materials Science and Engineering* 620, 012054 (2019). https://doi.org/10.1088/1757-899X/620/1/012054

15. Chen, Z., Liang, Y., Mo, L., Ban, M.: Residual properties and axial bearing capacity of steel reinforced recycled aggregate concrete column exposed to elevated temperatures. *Frontiers in Materials* 7, 187 (2020). https://doi.org/10.3389/fmats.2020.00187
16. Kigha, F., Sadeeq, J.A., Abejide, O.S.: Effects of temperature levels and concrete cover thickness on residual strength characteristics of fire exposed reinforced concrete beams. *Nigerian Journal of Technology* 34(3), 429–437 (2015). https://doi.org/10.4314/njt.v34i3.1
17. Anand, N., Andrushia, A.D., Mathews, M.E., Kiran, T., Chandramohan, D.L., Carmichael, M.J.: Effect of cover thickness on flexural behaviour of conventional and self compacting concrete beams subjected to elevated temperature. *Materials Today: Proceedings* 60, 173–180 (2022). https://doi.org/10.1016/j.matpr.2021.12.294
18. Boğa, A.R., Karakurt, C., Şenol, A.F.: The effect of elevated temperature on the properties of SCC's produced with different types of fibers. *Construction and Building Materials* 340, 127803 (2022). https://doi.org/10.1016/j.conbuildmat.2022.127803
19. Dehghani Ashkezari, G., Razmara, M.: Thermal and mechanical evaluation of ultra-high performance fiber-reinforced concrete and conventional concrete subjected to high temperatures. Journal of Building Engineering 32, 101621 (2020). https://doi.org/10.1016/j.jobe.2020.101621

Author Contribution Statement

- *Conceptualization:* Furkan Varinlioglu, Huseyin Okan Anadut, Fuat Koksal
- *Methodology:* Furkan Varinlioglu
- *Investigation:* Furkan Varinlioglu
- *Writing – Original Draft:* Furkan Varinlioglu
- *Writing – Review & Editing:* Furkan Varinlioglu, Huseyin Okan Anadut, Fuat Koksal

Funding

This research received no specific grant from any funding agency in the public, commercial, or not-for-profit sectors.

Conflict of Interest

The authors declare that there is no conflict of interest regarding the publication of this paper.

Data Availability Statement

No new data were generated in this study. All information evaluated in this review was obtained from the published studies cited in the reference list.

Publication Note

This paper was peer-reviewed, accepted for presentation, and included in the proceedings of the ACE2026 – International Conference on Advances in Civil Engineering, held on 12–14 October 2026 in Trabzon, Türkiye.

This paper may be cited as follows:

Varinlioglu, F., Anadut, H.O., and Koksal, F., "Design Considerations for Concrete Structures Under Fire Exposure" in Proceedings of the ACE2026 – International Conference on Advances in Civil Engineering, Trabzon, Türkiye, 12–14 October 2026.

Effect of Structural Steel Profile Geometry on the Cyclic Behavior of SRC Columns: A Numerical Investigation

Halit Erdem Çolakoğlu[1]
[1] 0000-0002-4498-3569, Giresun University, Keşap Vocational School, Department of Construction, Giresun, Türkiye, erdem.colakoglu@giresun.edu.tr

Abstract. Steel-reinforced concrete (SRC) columns are composite structural members created by embedding structural steel sections into concrete, offering higher ductility and energy dissipation capacity compared to conventional reinforced concrete columns. While the geometric shape of the steel section embedded within the cross-section is a key parameter affecting the cyclic behavior of SRC columns, there are limited studies in the literature that evaluate this effect independently of the amount of steel and cross-sectional properties. In this study, the behavior of 300×300 mm SRC columns containing structural steel sections with box, H, and plus (+) cross-sections—whose cross-sectional areas and moments of inertia were kept similar—under cyclic lateral loading was numerically investigated using the Abaqus finite element program. Concrete was modeled using the Concrete Damaged Plasticity (CDP) model, while the reinforcing steel and structural steel were modeled using multilinear material models derived from experimental stress-strain curves. Cyclic horizontal displacements with gradually increasing amplitude, in accordance with the FEMA 461 protocol, were applied to the columns. The results showed that the model with the plus (+) cross-section achieved significantly higher horizontal load-carrying, displacement, and energy dissipation capacities compared to the other two geometries; while the box and H-section profiles exhibited similar behavior, the H-section profile exhausted its capacity at a lower displacement level. In contrast, no significant difference was observed among the three profile geometries examined in terms of the secant stiffness-displacement ratio. The findings reveal that, in SRC column design, structural steel profile geometry is a critical design parameter that determines ductility and energy dissipation performance, particularly during the advanced deformation stage, while it has only a secondary effect on global stiffness behavior.

Keywords: SRC column, energy dissipation capacity, cyclic loading, steel profile shape.

1 Introduction

Steel-reinforced concrete (SRC) columns are composite load-bearing members in which structural steel sections work in conjunction with reinforcement within a reinforced concrete cross-section. The combined use of concrete and steel can provide higher load-carrying capacity, ductility, and energy dissipation potential compared to reinforced concrete columns; the concrete cover also contributes to protecting the structural steel against fire effects and local buckling. Due to these characteristics, SRC columns have become an important alternative composite structural system, particularly in buildings subjected to both high vertical loads and seismic effects [1, 2, 3, 4].

Experimental and numerical studies on the seismic behavior of SRC columns have revealed the effects of numerous parameters—such as the axial load ratio, steel ratio, cross-sectional shape, transverse reinforcement, concrete confinement conditions, slenderness, shear span, and

concrete strength—on cyclic behavior. In particular, the reduction in horizontal load capacity, strength, and stiffness under cyclic loading, as well as displacement/ductility capacity and energy dissipation capacity, are used as key indicators in evaluating the seismic performance of SRC columns. However, it has been reported that the literature on the seismic behavior of SRC columns remains more limited compared to that for reinforced concrete and steel members, and there is a need to increase experimental data, particularly regarding nonlinear modeling and performance evaluation [5].

The geometry of the steel section within the cross-section is one of the key variables that can influence the behavior of SRC columns. Section geometry can affect not only the distribution of the steel within the cross-section but also the contact and interaction conditions between the steel and concrete, the way the concrete core is enclosed, and the development of nonlinear deformations. Indeed, the cyclic behavior of SRC columns using I-shaped, H-shaped, and cross-section/special-shaped steel profiles has been investigated in the literature; it has been shown that the profile shape can influence performance indicators such as load-carrying capacity, ductility, reduction in stiffness, and energy dissipation [6].

In particular, studies conducted on cross-shaped steel sections indicate that the geometry of steel sections should not be considered merely as a cross-sectional property in the seismic behavior of SRC columns. An experimental study conducted by Mostafa et al. demonstrated that the horizontal load capacity, displacement, and ductility behavior of SRC columns with different steel section configurations vary [7]. Similarly, experimental and numerical studies examining the cyclic behavior of SRC columns with T- and L-shaped steel sections have reported that section geometry and the associated asymmetric confinement conditions influence damage mechanisms and seismic performance [8].

However, a significant portion of existing studies also alter the steel content, cross-sectional area, confinement conditions, or other geometric variables while modifying the profile geometry. Consequently, it is not always possible to distinguish whether the observed performance differences stem directly from the profile geometry or from changes in steel content and cross-sectional properties. A comprehensive literature review on SRC columns has also noted that studies have largely focused on traditional and simple steel profile arrangements, while research on different profile configurations has been more limited [1]. This situation makes the question of how different geometric arrangements of profiles with similar steel quantities and similar cross-sectional inertia properties affect the cyclic performance of SRC columns particularly important. From an engineering perspective, this question is directly related to design optimization: Could selecting a different profile geometry while using the same amount of structural steel alter not only the column's elastic stiffness but also its advanced displacement capacity and the energy it can dissipate during an earthquake? The answer to this question is important for evaluating whether profile selection based solely on steel area, strength, or moment of inertia is sufficient.

In this study, to answer this research question, the behavior of SRC columns with three different structural steel profile geometries—whose cross-sectional areas and moments of inertia were kept similar—under cyclic lateral loading was investigated using the finite element method. In the models created using box, H, and plus (+) section profiles, the concrete, reinforcement, column geometry, axial load level, and loading conditions were kept constant; thus, the steel profile geometry was highlighted as the key variable for comparison. The models were compared in terms of lateral load–displacement behavior, secant stiffness reduction, and cumulative energy dissipation capacity.

The primary objective of this study is to determine which performance indicators are most significantly influenced by different profile geometries—which have similar steel content and inertia properties—in the cyclic behavior of SRC columns. In this context, the study aims to evaluate the effect of profile geometry on global stiffness separately from its effects on

advanced deformation, strength retention, and energy dissipation capacity. It is intended that the results obtained will contribute to the evaluation of structural steel profile selection for SRC columns not only based on cross-sectional area and elastic section properties but also in terms of nonlinear deformation and energy dissipation performance.

2 Numerical Model

2.1 Column Geometry, Reinforcement Arrangement, and Structural Steel Profiles

The SRC column models under investigation were designed with a 300×300 mm square cross-section and a total height of 2,950 mm. The 500-mm-long regions at the top and bottom ends of the column are support/loading head (rigid end) regions, where closely spaced Ø8/50 transverse reinforcement (stirrups) was used. In the 1,950-mm-long middle section of the column, Ø8/100 spaced transverse reinforcement was applied. Eight Ø18 ribbed reinforcing bars were used as longitudinal reinforcement in all cross-sections, and the concrete cover thickness was assumed to be 25 mm. The column geometry, reinforcement arrangement, and the placement of reinforcement and steel profiles in the A-A cross-section are shown in Figure 1.

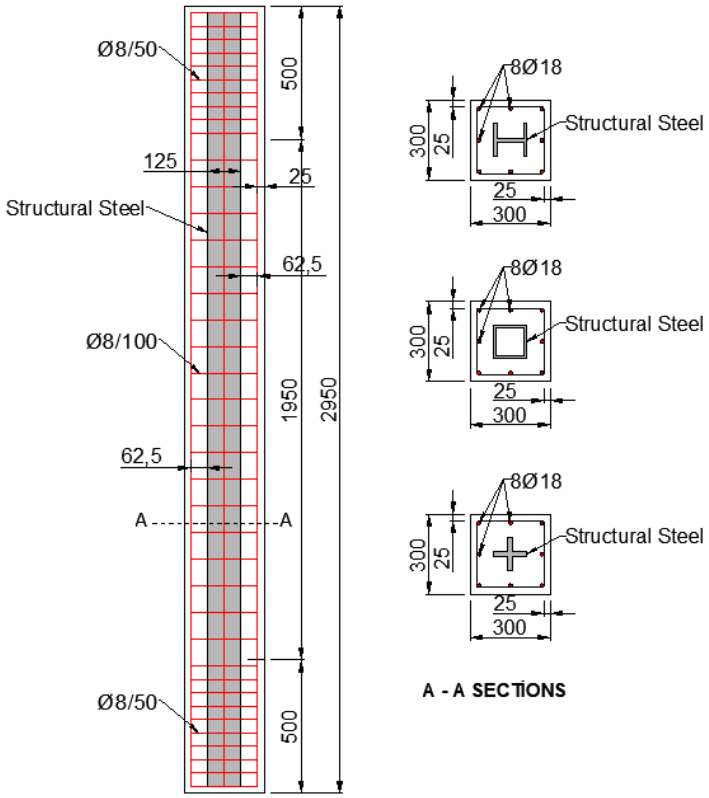


Fig. 1. Column geometry, reinforcement arrangement, and steel profile placement in the A-A cross-sections

Structural steel profiles with different geometries were placed at the center of the cross-section, such that they would fit within a 125×125 mm envelope area in all models: (i) an H-section profile, (ii) a box (square-section) profile, and (iii) a plus (+)-section profile. The outer envelope dimensions of all three profiles were set to 125×125 mm, and the web thicknesses were adjusted so that the cross-sectional areas (approximately 4540–4600 mm²) and, consequently, the moments of inertia would be similar. For the H-section profile, the flange thickness is 13 mm, the web thickness is 13 mm, and the net web height is 99 mm; for the box-section profile, the web thickness is 10 mm (internal opening 105×105 mm); and for the plus-section profile, the leg thickness is 20 mm. The cross-sectional dimensions of the profiles are shown in Figure 2.

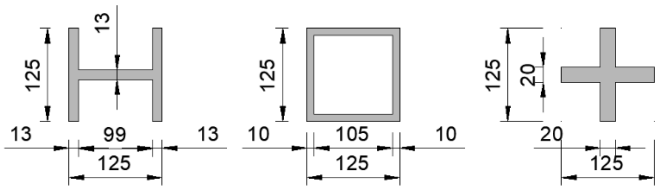


Fig. 2. H, box sections, and plus (+) sections: cross-sectional dimensions of structural steel sections (mm)

2.2 Material Models and Mechanical Properties

Concrete with a compressive strength of 30 MPa was used in all SRC column models considered in this study, and the stress–strain relationships for the concrete under compression and tension are shown in Figure 3.

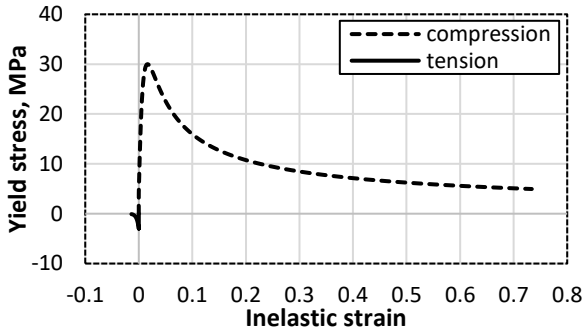


Fig. 3. The stress–inelastic strain relationship for concrete

The reduction in stiffness resulting from cracking and crushing in concrete under cyclic lateral loads was simulated in ABAQUS using stiffness reduction parameters (Figure 4).

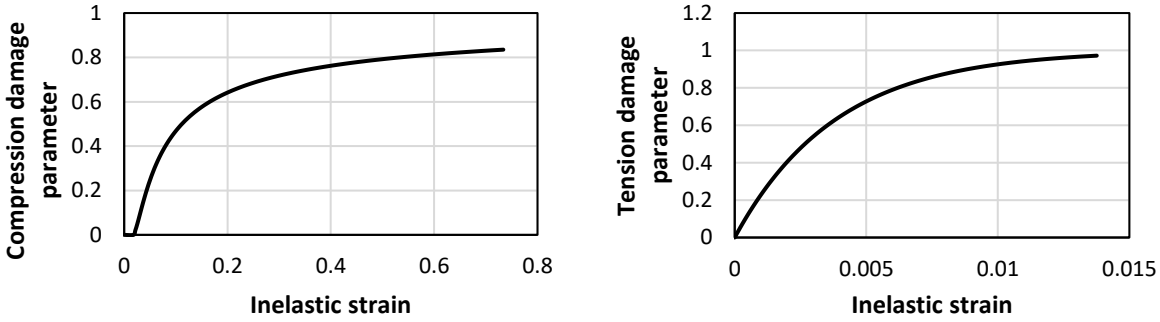


Fig. 4. Stiffness reduction parameters for concrete under compression and tension

The stress-strain behavior of the reinforcing steel and structural steel sections was modeled using a multilinear plasticity model based on the experimental axial tensile curves shown in Figure 5.

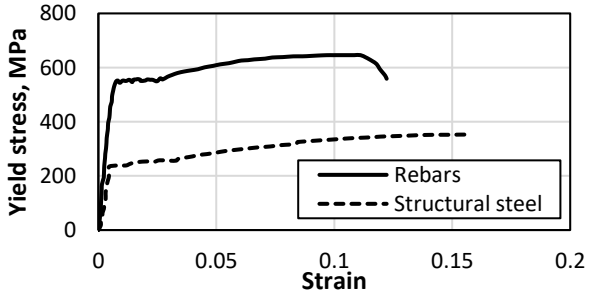


Fig. 5. The stress–strain relationship of reinforcing steel and structural steel

The values for the modulus of elasticity and Poisson's ratio for concrete, reinforcing bars, and structural steel are given in Table 1.

Table 1. Mechanical properties of materials

Materials	Elastic Modulus, E (MPa)	Poisson ratio, ν	Yield stress (MPa)	Tension stress (MPa)
Concrete	26366	0.18	-	-
Rebars	200000	0.30	552	645
Structural steel	200000	0.30	252	350

The concrete material was modeled in Abaqus using the Concrete Damaged Plasticity (CDP) model. Accordingly, the CDP plasticity parameters used in the finite element model are shown in Table 2.

Table 2. CDP plasticity parameters

Dilation angle, ψ	Eccentricity, e	f_{b0}/f_{c0}	K	Viscosity
37°	0.1	1.16	0.667	0.001

2.3 Finite Element Modeling

The column models were created in the Abaqus finite element software. Concrete and structural steel sections were modeled using the C3D8R element, an 8-node, reduced-integration 3D solid element; while longitudinal and transverse reinforcements were modeled using the T3D2 element, a 2-node 3D truss/link element. The reinforcement was defined as embedded within the concrete member using an "embedded region" constraint. The structural steel was simulated in accordance with the friction-based connection interaction model, using a friction coefficient of 0.6 and surface-to-surface interaction (Figure 6). The lower end of the column was fixed in all degrees of freedom; a constant axial compression load was first applied to the upper end, followed by a displacement-controlled cyclic horizontal displacement (Figure 6).

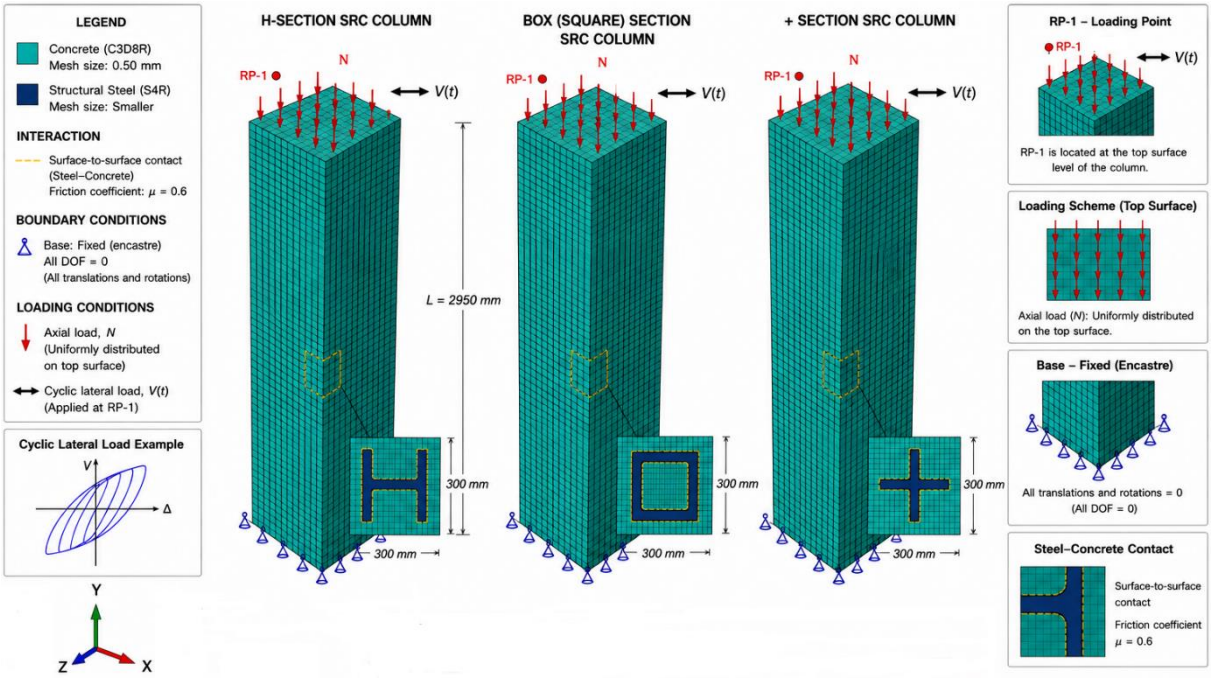


Fig. 6. Finite element models of SRC column members, boundary and loading conditions

2.4 Loading Protocol

In all analyses, a cyclic lateral displacement was applied from the RP-1 point—located at the same level as the column top—to the column top, with displacement control and a gradually increasing amplitude, in accordance with the FEMA 461 loading protocol. In the loading protocol shown in Figure 7, the amplitude was increased at each loading stage, starting with a low-amplitude cycle that would cause the first crack to form in the SRC column. Loading was continued up to the final stage, corresponding to a horizontal displacement ratio of ±12.5%. The same loading protocol and the same axial load level were applied to all three models (SRC_box, SRC_H, SRC_+) to isolate the effect of the cross-sectional steel profile shape.

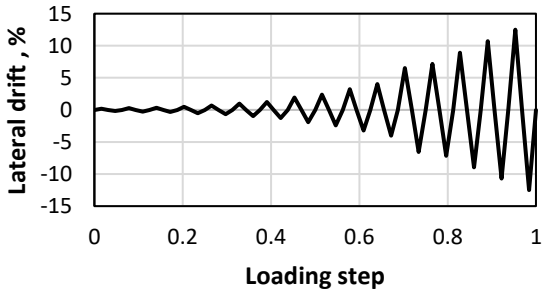


Fig. 7. Circular lateral loading protocol prepared in accordance with FEMA 461

3 Findings and Discussing

The relationships between the lateral load–lateral displacement ratio, stiffness–lateral displacement ratio, and energy dissipation capacity–lateral displacement ratio—obtained from cyclic analyses of SRC column models containing box, H-shaped, and plus (+)-shaped structural steel sections—are presented in a comparative manner in Figures 8–10.

3.1 Lateral Load–Lateral Drift Relationship

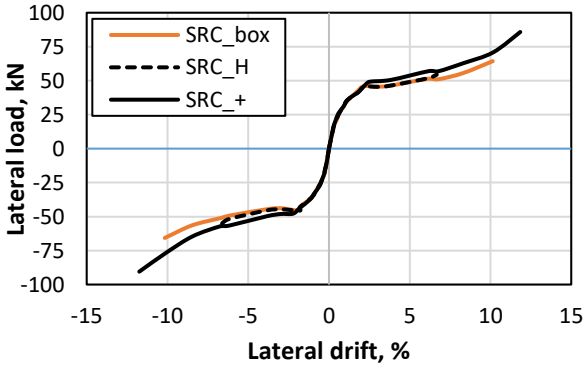


Fig 8. Horizontal load–horizontal displacement ratio envelope curves for the SRC_box, SRC_H, and SRC_+ models

Figure 8 compares the horizontal load–horizontal displacement ratio envelope curves for the SRC_box, SRC_H, and SRC_+ models. The results indicate that the geometric shape of the structural steel section has a significant effect on the horizontal load-carrying capacity and deformation capacity of SRC columns at high displacement levels. In particular, the SRC_+ model, which incorporates a plus (+) cross-section, achieved higher horizontal load levels in both positive and negative loading directions compared to the other two models.

The SRC_+ model maintained its load-carrying capacity up to a lateral displacement ratio of approximately 12% and reached a maximum horizontal load value of approximately 85–90

kN at this level. In contrast, the maximum horizontal load capacities of the SRC_box and SRC_H models remained in the range of approximately 60–65 kN. Thus, although the cross-sectional areas and moments of inertia of the steel sections were kept similar, it is evident that the profile geometry can result in a significant difference in horizontal load-carrying capacity. This result indicates that not only the amount of structural steel used but also its distribution within the cross-section and the manner of its interaction with the concrete may play a significant role in the behavior of composite columns.

While it is noteworthy that the maximum horizontal load capacities of the SRC_box and SRC_H models are similar, it is evident that these two models differ significantly in terms of their deformation capacity. While the SRC_H model exhausted its capacity at a horizontal displacement ratio of approximately 6–7% and was excluded from the analysis, the SRC_box model maintained its load-carrying capacity up to a displacement ratio of approximately 10%. Therefore, although the I-beam and box profiles reached similar horizontal load levels, it can be said that they did not demonstrate equivalent performance in terms of cyclic deformation capacity. This situation demonstrates that profile geometry must be evaluated not only in terms of maximum strength but also in terms of the ability to maintain that strength through advanced deformation levels.

The fact that the SRC_+ model exhibits higher strength and displacement capacity compared to the other two models can be attributed to the geometry of the plus-section profile—which radiates in four directions from the section center—ensuring a more balanced distribution of steel within the composite section. This geometry may have contributed to a more balanced interaction between the steel profile and the surrounding concrete in different directions and to the preservation of composite behavior for a longer duration at advanced displacement levels. The fact that this geometric effect becomes more pronounced during stages where deformations increase under cyclic loading can be considered a possible mechanism explaining the SRC_+ model's ability to maintain its load-carrying capacity up to a 12% displacement level.

3.2 Relationship Between Stiffness and Lateral Drift Relationship

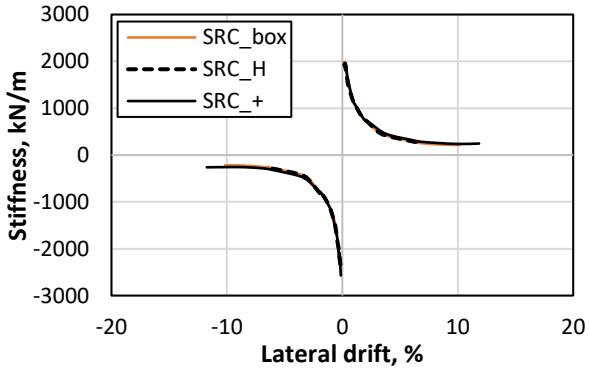


Fig 9. Stiffness–lateral drift relationships for the SRC_box, SRC_H, and SRC_+ models

Figure 9 compares the secant stiffness–lateral displacement ratio relationships for the SRC_box, SRC_H, and SRC_+ models. Secant stiffness was evaluated based on the slope between the load and displacement values for each cyclic displacement level and was used to determine the change in the column's stiffness under cyclic loading. This approach allows for the evaluation of the effects of concrete cracking, material nonlinearity, and damage accumulation on cross-sectional behavior under cyclic loading.

One of the key findings of the study is that the secant stiffness–displacement ratio curves for SRC columns with different structural steel profile geometries are quite similar. Since the cross-sectional areas and moments of inertia of box, H, and plus (+) section profiles are kept close to

one another, it is observed that the profile geometry does not result in a significant difference in secant stiffness. This result suggests that, among the parameters examined, the global section stiffness is controlled more by the overall mechanical properties of the composite section—formed by the concrete, reinforcement, and structural steel—rather than by the geometric shape of the profile itself.

In other words, while all three models may exhibit a similar overall decrease in stiffness during cyclic loading, the level of deformation up to which this stiffness—along with the load-carrying capacity—can be maintained varies depending on the profile geometry. This indicates that the seismic performance of SRC columns should not be evaluated solely based on stiffness loss. Despite similar trends in the reduction of secant stiffness, the differences observed in horizontal load capacity, maximum displacement capacity, and energy dissipation capacity indicate that profile geometry plays a more pronounced role in behavior, particularly during advanced stages of damage and deformation.

The fact that the secant stiffness–displacement relationships are similar for the three models is consistent with the fact that all models were examined under the same conditions in this study in terms of concrete, reinforcement, column geometry, axial load level, and loading protocol. Since the primary variable distinguishing the models is the cross-sectional geometry of the structural steel profile, the fact that the effect of profile geometry on global secant stiffness remains limited—while differences in load-carrying capacity and energy dissipation behavior emerge at advanced displacement levels—suggests that profile geometry may have a greater influence on composite interaction during stages where damage progresses further.

In particular, the fact that the secant stiffness curve of the SRC_H model does not diverge significantly from that of the other models, even though the SRC_H model is excluded from the analysis at a lower displacement level, provides an important insight. This result demonstrates that the secant stiffness of an SRC column at a specific deformation level does not, on its own, represent the element's strength and deformation capacity beyond that deformation level. Therefore, in the evaluation of cyclic behavior, secant stiffness must be considered in conjunction with horizontal load, displacement capacity, and energy dissipation capacity.

In general, under the parameters and loading conditions examined in this study, it was observed that the effect of structural steel profile geometry on the secant stiffness–horizontal displacement relationship of SRC columns is limited. Three different profile geometries, for which the cross-sectional area and moment of inertia were kept similar, exhibited similar trends in secant stiffness reduction. In contrast, significant differences emerged in the horizontal load-carrying capacity, maximum displacement capacity, and cumulative energy dissipation capacity.

3.3 Relationship Between Energy Dissipation Capacity and Lateral Drift

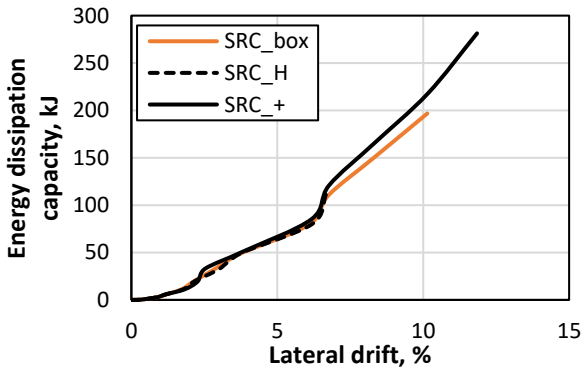


Fig 10. Cumulative energy dissipation capacity–lateral displacement ratio relationships for the SRC_box, SRC_H, and SRC_+ models

Figure 10 compares the energy dissipation capacity–horizontal displacement ratio relationships for the SRC_box, SRC_H, and SRC_+ models. Energy dissipation capacity was evaluated based on the cumulative sum of the areas formed by the load–displacement curves over the course of cycles during cyclic loading. This parameter is important not only for assessing the models' horizontal load-carrying capacity at a specific displacement level but also for evaluating the extent to which externally applied energy can be dissipated throughout the loading process.

Examining Figure 10, it can be seen that as the horizontal displacement ratio increases, there is a continuous increase in the energy dissipation capacity of all models. The primary reason for this is that, as the displacement level increases under cyclic loading, the area enclosed by the load–displacement curve grows with each loading cycle, leading to an increase in cumulative energy consumption. However, it is observed that the differences in energy dissipation among the models become particularly pronounced at higher displacement levels.

While the SRC_+ model achieved the highest energy dissipation capacity at approximately 280 kJ, the SRC_box model remained at approximately 210 kJ, and the SRC_H model at approximately 115 kJ. Accordingly, the energy dissipation capacity of the SRC_+ model is approximately 33% higher than that of the SRC_box model and approximately 59% higher than that of the SRC_H model. The energy dissipation capacity of the SRC_box model is also approximately 45% higher than that of the SRC_H model. These results demonstrate that the geometry of the structural steel profile has a significant effect on the energy dissipation capacity of SRC columns under cyclic loading.

This ranking of energy dissipation capacity is consistent with the horizontal load–displacement behavior shown in Figure 8. The SRC_+ model not only reached higher horizontal load levels but also maintained its behavior up to a displacement ratio of approximately 12%. While the SRC_box model maintained its capacity up to a displacement ratio of approximately 10%, the SRC_H model failed the analysis at a displacement ratio of approximately 6–7%. Therefore, it is understood that high energy dissipation capacity does not stem solely from high maximum horizontal load capacity but is also related to the element's ability to continue bearing loads at higher levels of deformation. In other words, the simultaneous preservation of strength and deformation capacity directly contributes to an increase in cumulative energy dissipation capacity.

From this perspective, it can be said that the effect of the profile geometry becomes more pronounced, particularly during the advanced deformation stage. Models with similar secant stiffnesses at low displacement levels exhibited different horizontal load-carrying and energy-dissipation capacities as the displacement level increased. This behavior suggests that the steel profile geometry, in conjunction with the concrete core and reinforcement, may influence the behavior of the composite section during the advanced deformation stage. However, since the current analysis results do not directly identify which components account for the difference in energy dissipation capacity, the contributions of mechanisms such as concrete damage, plasticization of the steel section, or interactions at the concrete–steel interface cannot be definitively distinguished within the scope of this study.

The fact that the SRC_+ model achieves the highest energy dissipation capacity should be evaluated in conjunction with its higher horizontal load-carrying capacity and higher displacement capacity. The geometric arrangement of the plus (+) cross-section profile, by altering the steel distribution within the composite section and the interaction conditions with the concrete, may have contributed to the load-carrying capacity being maintained for a longer period at advanced displacement levels. However, to verify this interpretation, it is necessary to further examine the profile stresses, plastic deformations, concrete damage variables, and the contact behavior at the concrete–steel interface.

It is also noteworthy that the SRC_H model achieved the lowest energy dissipation capacity, at approximately 115 kJ. Because this model was excluded from the analysis at a lower displacement level, it was able to dissipate energy within a more limited deformation range throughout the cyclic loading. Consequently, the low cumulative energy dissipation capacity obtained for the H-profile is related not only to the profile's low load capacity at a specific displacement level but also to its inability to reach higher displacement levels.

The results show that, among the three profiles examined, the SRC_+ model exhibited the most advantageous behavior in terms of overall cyclic performance, the SRC_box model ranked second, and the SRC_H model demonstrated more limited performance, particularly in terms of forward displacement and energy dissipation capacity. However, it should be noted that this ranking applies only to the concrete strength, steel profile properties, axial load level, cross-sectional geometry, and loading protocol used in this study; the effect of profile geometry must be reevaluated under different design and loading conditions.

4 Conclusions

In this study, the effect of three different structural steel profile geometries—with similar cross-sectional areas and moments of inertia—on the cyclic behavior of SRC columns was investigated numerically. The findings reveal that the effect of profile geometry cannot be explained solely by the elastic properties of the cross-section and becomes more pronounced, particularly during the advanced deformation stage. The main conclusions drawn from the study are summarized below.

The geometry of the steel profile affects the advanced deformation capacity of SRC columns more than their global secant stiffness. The fact that significant differences arise in the models' horizontal load-carrying, displacement, and energy-damping performance—despite similar trends in secant stiffness—points to the role of profile geometry in the composite section, particularly during the nonlinear behavior phase.

Similar amounts of steel and similar moments of inertia do not result in similar cyclic performance. This finding indicates that selecting profiles for SRC columns based solely on cross-sectional parameters—such as steel area or moment of inertia—may not be sufficient. The geometric distribution of steel within the cross-section should be considered as an independent design variable in terms of advanced deformation capacity and energy dissipation performance.

From an engineering design perspective, the selection of profiles for SRC columns—where high deformation is expected, particularly under seismic loads—should not be based solely on the approach of increasing the maximum horizontal load. Maintaining horizontal load capacity at high displacement levels and energy dissipation capacity should also be part of the design decision. In this regard, the behavior exhibited by the plus (+) section profile among the profile geometries examined in this study suggests the potential to optimize profile geometry performance without increasing the amount of steel. However, this conclusion is limited by the scope of the current numerical model and should not be interpreted as a direct design recommendation.

A key limitation of this study is that the effect of the profile geometry was examined only within the context of a single column geometry, material properties, axial load level, and cyclic loading protocol. Therefore, it should be noted that the performance rankings obtained may vary under different design conditions.

In future studies, parametric analyses should be conducted for different axial load ratios, concrete strengths, and steel section sizes and geometries; furthermore, concrete damage, steel plasticity, and the interaction at the concrete–steel interface should be examined in detail. In particular, multivariate studies supported by experimental work can contribute to translating the

effect of profile geometry on the ductility and energy dissipation capacity of SRC columns into generalizable design parameters.

References

[1] Mostafa, M. M., Wu, T., Liu, X., & Fu, B. (2019). The composite steel reinforced concrete column under axial and seismic loads: a review. International Journal of Steel Structures, 19(6), 1969-1987.

[2] Gautham, A. S. D. R., & Sahoo, D. R. (2021). Behavior of steel-reinforced composite concrete columns under combined axial and lateral cyclic loading. Journal of Building Engineering, 39, 102305.

[3] Liu, J., Cheng, R., Wang, Y., Hu, C., Xu, X., & Liu, Y. (2026). Cyclic loading test on seismic shear behavior of CFST column to USCC beam joints with T-shaped interior diaphragms. Engineering Structures, 348, 121752.

[4] Wang, Q., Shi, Q., & Tian, H. (2016). Experimental study on shear capacity of SRC joints with different arrangement and sizes of cross-shaped steel in column. Steel and Composite Structures, 21(2), 267-287.

[5] Hassan, W. M., & Farag, M. (2021). Seismic performance of steel-reinforced concrete composite columns in existing and modern construction. Soil Dynamics and Earthquake Engineering, 151, 106945.

[6] Fang, L., Zhang, B., Jin, G. F., Li, K. W., & Wang, Z. L. (2015). Seismic behavior of concrete-encased steel cross-shaped columns. Journal of constructional steel research, 109, 24-33.

[7] Mostafa, M. M., Chen, S., Wu, T., Liu, X., & Liu, Y. (2022). Experimental seismic analysis of new types of steel-reinforced lightweight concrete columns with cross-shaped steel section. Journal of Building Engineering, 60, 105202.

[8] Liu, X., Zeng, L., Xiao, Y., Liu, Y., Zhang, H., & Cao, Y. (2022). Experimental and Numerical Investigation on the Cyclic Behavior of SRC Columns considering Unsymmetrical Confinement Effect. KSCE Journal of Civil Engineering, 26(4), 1880-1893.

Publication Note

This paper was peer-reviewed, accepted for presentation, and included in the proceedings of the ACE2026 – International Conference on Advances in Civil Engineering, held on 12–14 October 2026 in Trabzon, Türkiye.

This paper may be cited as follows:

Colakoglu, HE., "Effect of Structural Steel Profile Geometry on the Cyclic Behavior of SRC Columns: A Numerical Investigation" in Proceedings of the ACE2026 – International Conference on Advances in Civil Engineering, Trabzon, Türkiye, 12–14 October 2026.

Performance-Based Optimization of Buckling-Restrained Braces for RC Structures Using Nonlinear Response History Analysis

Clifford Phiri[1,*] and Çağlayan Hızal[2]
[1] Graduate School of Natural and Applied Sciences, Ege University, 35040 İzmir, Türkiye
[2] Department of Civil Engineering, Ege University, 35040 İzmir, Türkiye
* Corresponding author: Clifford Phiri, 91240000679@ogrenci.ege.edu.tr
ORCID (C. Phiri): 0009-0003-0317-0275

Abstract. Buildings damaged in the 2023 Kahramanmaraş earthquakes exposed persistent vulnerabilities of the Turkish reinforced concrete (RC) stock, notably soft stories and brittle column failures. Buckling-restrained braces (BRBs) offer a low-intrusion retrofit, but their optimal number and placement are hard to determine. This study couples the NSGA-II genetic algorithm with nonlinear response history analysis (NRHA) in OpenSeesPy to optimize BRB retrofits of five 10-story, 4-bay RC archetypes representing the pre-2000 stock (C16 concrete, S220 plain bars): a baseline frame, a pilotis frame, a gravity-consistent uniform pilotis (A4) with constant 400×400 mm columns, a geometric setback and a mid-height weak story, all assessed under a seven-record suite scaled to the TBDY 2018 DD-2 spectrum. A drift-based objective proves inadequate: it reduced drift yet increased collapse-level column hinges. A member-level damage index built from TBDY 2018 sec.15.3.2 hinge damage-zone classification and sec.7.5.2 joint shear checks is therefore adopted, and the knee point of a five-seed pooled Pareto front is taken as the optimal design. The central result is that seismic benefit is not confined to code-flagged irregularity: A4 is formally regular under TBDY 2018 Table 3.6 (max η_{ki} = 1.571 against the 2.0 threshold) yet its optimized retrofit removes collapse-level column damage entirely. An ablation shows that only the pairing of braces and column confinement produces the recovery. Two mechanisms limit the retrofit elsewhere: BRB diagonals amplify adjacent-column axial demands by up to 2.07 times and introduce column tension up to 503 kN, and joint shear demand-capacity ratios change by at most 3.0% between the bare and optimal states (1.31-1.37 in A1, A2, A3; 0.77-0.79 in A0, A4), being set by the 300×300 mm joints, not by brace placement. Optimally placed BRBs must therefore be paired with column confinement and joint strengthening.

Keywords: Buckling-Restrained Braces (BRBs); Genetic Algorithm; Nonlinear Response History Analysis; Multi-Objective Optimization; TBDY 2018.

1 Introduction

The February 6, 2023 Kahramanmaraş earthquake sequence caused heavy damage to, or the collapse of, a large number of reinforced concrete buildings, with soft or weak stories, insufficient transverse reinforcement, poor concrete quality and beam-column joint failures repeatedly identified among the governing deficiencies [1]. Field surveys in Malatya [2] and Hatay [3] document plain reinforcing bars and concrete strengths below 10 MPa [2], and strong beam-weak column behaviour and joint-shear failures concentrated in the older buildings [3]. These observations renewed attention on the seismic rehabilitation of the pre-2000 Turkish building stock, for which conventional interventions such as added shear walls or systematic column jacketing restore lateral capacity but impose large stiffness increases, foundation demands and severe architectural restrictions.

Buckling-restrained braces offer a less intrusive alternative. By encasing a yielding steel core in a mortar-filled restraining tube, the brace yields symmetrically in tension and compression without global buckling, producing full and stable hysteresis loops [4, 5]. Acting as replaceable structural fuses, BRBs concentrate inelastic deformation in the core while shielding the gravity system. Their component behaviour and frame-level demands are well

documented for steel construction [6, 7], where it is also established that brace yielding, rather than elastic load combinations, governs the axial demands delivered to the columns of braced bays [8, 9]. Applications to existing RC frames have demonstrated the feasibility of BRB retrofits, and Di Sarno and Manfredi, Sutcu et al. and Almeida et al. all stress that the force and stiffness delivered to the existing members must be controlled carefully [10-12].

Determining the optimal number and placement of BRBs in a deficient RC frame is a difficult combinatorial problem. Heuristic placement can relocate drift concentrations, overload the columns and joints at the brace connections, and transfer large forces to elements that were never designed for them. Formal optimization requires an objective function that reflects the failure modes the retrofit is intended to prevent, and an analysis engine rigorous enough to expose them.

Retrofit studies conventionally select case-study frames by their code-recognized irregularity, on the implicit assumption that a code trigger is what identifies a frame as a candidate for bracing. The contribution of this study is to test that assumption directly. Alongside four archetypes that span the irregularity types of TBDY 2018 [13] Table 3.6, a fifth archetype (A4) is included that is geometrically a pilotis, that is, a taller and open ground story, but is detailed with gravity-consistent, constant 400×400 mm columns over the full height. It is formally regular: neither the B1 strength check nor the B2 stiffness check is triggered. It is therefore a full, standalone fifth archetype and a design-sensitivity case, not a fourth irregularity type and not a variant of A1, and the question it answers is whether measurable seismic benefit from optimally placed BRBs requires a code-recognized trigger at all.

2 Methodology

2.1 Archetype frames and numerical modelling

Five 10-story, 4-bay plane RC frames are studied (Fig. 1, Table 1). A0 is the baseline control frame. A1 introduces a pilotis: a 4.5 m open ground story with 300×300 mm columns against 400×400 mm above, giving a strength ratio η_{ci} = 0.562 and triggering the B1 check. A4 retains the 4.5 m ground story but keeps 400×400 mm columns throughout, so the section schedule follows the gravity demand rather than creating an artificial weak story; it satisfies both B1 and B2 (Table 2). A2 introduces a geometric setback in which stories 7-10 narrow to two bays, and A3 a mid-height weak story with 300×300 mm columns at story 5 only. Materials deliberately represent the pre-2000 stock: C16 concrete and S220 plain bars throughout, with as-built transverse reinforcement of 2-leg D8 hoops at 200 mm.

All frames are modelled in OpenSeesPy [14]. Beams and columns are force-based elements with fibre plastic-hinge regions at both ends and an elastic interior, with hinge length Lp = 0.5h per TBDY sec.5.4.1. Core and cover concrete follow Concrete02 with the Mander et al. [15] confined and unconfined envelopes; reinforcing steel and the BRB core use Steel02 (Giuffre-Menegotto-Pinto). BRBs are corotational truss elements with a 3,000 mm² LYP235 core (fy = 235 MPa, post-yield ratio b = 0.02, yield force Py = 705 kN); the symmetric tension-compression yielding of the restrained core justifies a uniaxial truss representation. Expected material strengths are taken as the characteristic values per the Chapter 15 existing-building assessment assumption with a knowledge factor of 1.0. Rayleigh damping of 5% is anchored at the first two modes. In the retrofitted models, columns are simultaneously upgraded to seismic hoops (4-leg D10 at 100 mm), representing a confinement retrofit installed together with the braces; this doubles the collapse-limit concrete strain of sec.5.8.1 (adopted for existing buildings by sec.15.7.1.3) while leaving shear strength essentially unchanged. The two interventions are separated by the ablation of Section 3.5. Although the plane-frame analysis loads a single critical direction, the physical retrofit is intended to be

installed bidirectionally, with the optimized brace positions and identical member sizes mirrored in the orthogonal direction. That extension is not verified by the present model.

Table 1. Archetype geometry and code classification.

Archetype	Stories	H (m)	Geometry	Lower columns	Upper columns	Table 3.6 verdict
A0 — Baseline	10	30.0	Baseline control frame	400×400 8-D20	400×400 8-D20	B2
A1 — B1 Pilotis	10	31.5	Pilotis, 4.5 m open ground story	300×300 8-D16	400×400 8-D20	B1
A4 — Uniform Pilotis	10	31.5	Pilotis geometry, gravity-consistent sections	400×400 8-D20	400×400 8-D20	Regular
A2 — Geometric Setback	10	30.0	Geometric setback, stories 7-10 at two bays	400×400 8-D20	300×300 8-D16	B2
A3 — B1 Mid-Notch	10	30.0	Mid-height weak story at story 5	400×400 8-D20	400×400 8-D20 (story 5: 300×300 8-D16)	B1+B2

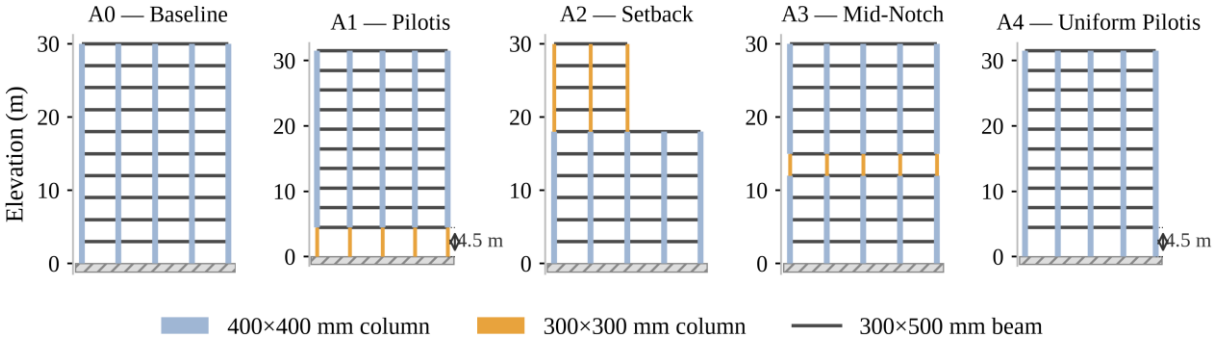


Fig. 1. Bare-frame elevations of the five archetypes, drawn to scale.

2.2 Seismic hazard and ground motions

The site is Bornova, İzmir (38.46 N, 27.22 E), soil class ZD, evaluated at the TBDY 2018 DD-2 hazard level (475-year return period; SDS = 1.148 g, SD1 = 0.542 g), the reference hazard for the Controlled Damage performance objective of existing buildings. Seven records are used: Kocaeli 1999, Düzce 1999, Erzincan 1992, Northridge 1994, El Centro 1940, Kobe 1995 and Chi-Chi 1999 (trimmed to its D5-D95 significant duration). Each is amplitude-scaled so that its mean spectral acceleration over $[0.2T_1, 1.5T_1]$ matches the DD-2 target over the same band. Scale factors are recomputed whenever the fundamental period changes, so bare and retrofitted models are each scaled consistently with the code procedure; Section 3.6 removes this scaling difference as a confound. The three Turkish records form a screening suite used inside the GA loop; all seven form the validation suite, and every quotable value below comes from the validation pass.

2.3 Irregularity classification

The B1 strength and B2 stiffness checks of TBDY 2018 Table 3.6 were computed from the elastic model rather than assumed from the geometry under a code lateral load pattern (Table 2). B1 flags a story whose effective shear area ratio η_{ci} falls below 0.80; B2 flags a stiffness ratio η_{ki} above 2.0. Because η_{ki} depends on the assumed load pattern, every check was repeated under both an inverted-triangular and a uniform pattern; the maximum difference in η_{ki} across all five archetypes is 0.122 and no verdict changes, so the verdicts do not depend on the load pattern. B1 is triggered by A1 and A3. B2 is triggered by A0, A2 and A3; A1 and A4 do not trigger B2. A4 triggers neither, with a maximum η_{ki} of 1.571 against the 2.0 threshold. It is the code-compliant geometry whose retrofit response Section 3.4 examines.

Table 2. TBDY 2018 Table 3.6 checks, both lateral load patterns.

Archetype	B1?	min η_{ci}	B2? (tri)	max η_{ki} (tri)	critical story	max η_{ki} (uniform)	$\lvert\Delta\rvert$
A0 — Baseline	False	1.000	True	2.905	2	2.799	0.105
A1 — B1 Pilotis	True	0.562	False	1.470	8	1.591	0.122
A4 — Uniform Pilotis	False	1.000	False	1.571	2	1.595	0.024
A2 — Geometric Setback	False	1.000	True	2.916	2	2.805	0.111
A3 — B1 Mid-Notch	True	0.562	True	2.910	2	2.805	0.105

2.4 Member-level performance evaluation

Performance is assessed at the member level per TBDY 2018. Envelope section demands from the record suite are classified against the sec.15.7.1 strain limits (sec.5.8.1) into the sec.15.3.2 Limited, Controlled, Significant (IH) and Collapse (G) damage zones; the counts of column hinge ends in the IH and G zones, col_IH and col_G, summarize brittle column damage. Beam-column joint shear is checked per sec.7.5.2: the demand follows Eq. 7.11 with 1.25 fyk overstrength on the beam bars and the column shear taken as the minimum of the values above and below the joint, while the capacity follows Eqs. 7.12-7.13 as $V_n = \gamma \cdot b_j \cdot h \cdot \sqrt{f_{ck}}$ with the characteristic strength under the root and $\gamma = 1.0$. The confined classification of sec.7.5.1 requires beams framing into all four faces of the joint, each covering at least three quarters of the column width, a property of the surrounding beams and not of the column hoops. The plane frame has no transverse beams, so $\gamma = 1.0$ follows for every joint; this is an implication of the two-dimensional idealization, and physical joints may qualify as confined once transverse framing is present. The resulting capacities are $1.0 \times 400 \times 400 \times \sqrt{16} = 640.0$ kN for the 400×400 mm columns framed by a 300 mm beam and 360.0 kN for the 300×300 mm columns. Joints are modelled as rigid, with no joint-panel or shear-spring element, so this is a post-processing check: the beam-bar term of Eq. 7.11 is fixed by the section, and the check measures the frames' pre-existing joint deficiency, not additional shear delivered by the braces. Transient non-convergence is interpreted as numerical collapse and treated as the worst outcome rather than as missing data.

2.5 Optimization framework

Each candidate retrofit is encoded as a 20-bit chromosome in which every bit activates one symmetric pair of BRB diagonals (a bay on the left half of the frame and its mirrored right-half counterpart in the same story), enforcing plan symmetry and reducing the search space to 2^{20} configurations. NSGA-II [16], implemented in DEAP [17] with the selNSGA2 selection operator and tournament-DCD mating selection, evolves a population of 20 individuals for 20 generations with two-point crossover (probability 0.70) and per-bit flip mutation (bit probability 1/20, individual probability 0.20). Fitness is evaluated on the three-record screening suite inside the loop and the resulting Pareto set is re-evaluated under the full seven-record suite.

A population of 20 over 20 generations samples 400 designs from a space of about 1.05 million, so the search is deliberately budget-limited by the cost of embedding full NRHA in the fitness function. Stochastic robustness is therefore addressed by repetition rather than by population size: the entire optimization is run independently with five seeds (7, 21, 42, 99, 1337), the five Pareto sets are pooled, the non-dominated subset of the pool is extracted, and the knee point of that pooled front is reported as the optimal design of the archetype. Designs with zero braces are excluded from knee candidacy, since a null retrofit is not a design.

The first objective is the column damage index of Eq. (1); the second is the number of installed braces, f_2, as the cost proxy:

$$f_1 = n_{IH} + 10\, n_G + 999\, \delta_{nc} + \Sigma_j\, 500\, \max(0,\, DCR_j - 1) \quad (1)$$

where n_{IH} and n_G are the column hinge ends in the sec.15.3.2 Significant Damage and Collapse zones, δ_{nc} equals 1 if any record fails to converge, and DCR_j is the sec.7.5.2 demand-capacity ratio of joint j. The weights encode the code damage hierarchy: one

collapsed column end outweighs ten significantly damaged ones; non-convergence can never be dominated by a converging design; and a single joint 20% over capacity costs the equivalent of ten collapsed column ends. Beams are deliberately excluded, since beam yielding is the intended ductile mechanism.

3 Results and Discussion

3.1 Bare-frame baseline

Table 3 summarizes the pre-retrofit NRHA under the seven-record suite. All five bare frames reach the Collapse performance level under TBDY sec.15.8 and none approaches the Controlled Damage target, so the need for retrofit is established in quantitative terms for the regular and the irregular geometries alike. The three archetypes with 300×300 mm sections additionally enter the assessment with beam-column joints already over the sec.7.5.2 shear capacity.

Table 3. Bare-frame NRHA baseline (seven-record envelope).

Archetype	T_1 (s)	Env. IDR (%)	col_IH	col_G	Max joint DCR	#DCR ≥ 1	Converged
A0 — Baseline	1.616	3.78	0	5	0.766	0	Yes
A1 — B1 Pilotis	1.992	3.48	0	5	1.356	3	No
A4 — Uniform Pilotis	1.755	4.03	0	5	0.771	0	Yes
A2 — Geometric Setback	1.375	3.74	0	8	1.360	4	Yes
A3 — B1 Mid-Notch	1.657	4.19	3	11	1.324	3	No

3.2 Inadequacy of a drift-based objective

The first optimization round minimized the envelope peak inter-story drift ratio, the most common objective in the retrofit-optimization literature. It succeeded on its own terms and failed as engineering: drift decreased, yet sec.15.3.2 hinge-zone inspection revealed more collapse-level column ends in three of the four archetypes then studied. Drift is a story-level metric that cannot distinguish ductile beam yielding from brittle column failure, and an optimizer given a blind metric exploits its blindness. A co-location analysis identified the mechanism: 25-60% of the newly collapsed column ends shared a node directly with a brace, and every new collapse occurred in the story immediately above a braced story. This was the first appearance of the force-couple mechanism quantified in Section 3.6, and the damage index of Eq. (1) was adopted in response.

3.3 Optimal designs and verification

Figure 2 shows the pooled Pareto fronts with their knee points and Fig. 3 the corresponding brace placements. Table 4 reports the seven-record verification of each knee-point design against its bare baseline. Collapse-level column damage falls for A0 — Baseline, A1 — B1 Pilotis, A4 — Uniform Pilotis and A3 — B1 Mid-Notch, and rises for A2 — Geometric Setback. A2 needs an explicit note because the two suites disagree: on the three-record screening suite used in the optimization the knee-point design appears to help (collapse-zone column ends fall from 5 to 2), but under the seven-record validation the count rises from 8 to 11. The screening-stage gain does not survive validation, so A2 is reported as the one archetype where the retrofit does not help; the reason is visible in the objective decomposition, where the joint-shear penalty, which brace layout changes only marginally, dominates the knee-point score.

Table 4. Seven-record verification of the knee-point designs against the bare frames.

Archetype	#BRB	T_1,opt (s)	Env. IDR (%)	col_IH	col_G (bare → opt)	Max joint DCR	Converged
A0 — Baseline	18	0.558	0.96	0	5 → 0	0.789	Yes
A1 — B1 Pilotis	4	1.549	3.66	1	5 → 2	1.374	Yes
A4 — Uniform Pilotis	18	0.583	1.13	2	5 → 0	0.789	Yes
A2 — Geometric Setback	2	1.300	4.80	1	8 → 11	1.358	Yes
A3 — B1 Mid-Notch	6	1.546	3.71	0	11 → 5	1.314	Yes

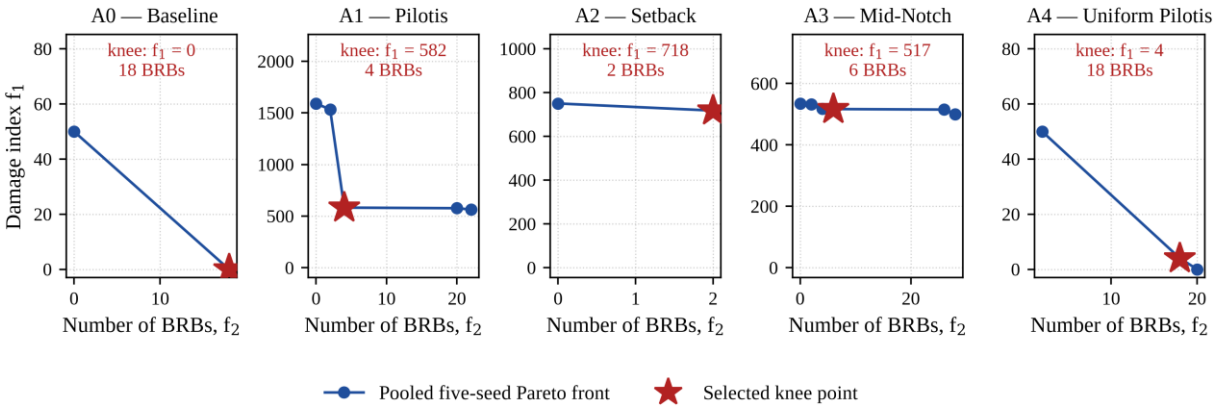


Fig. 2. Pooled five-seed Pareto fronts with the selected knee points.

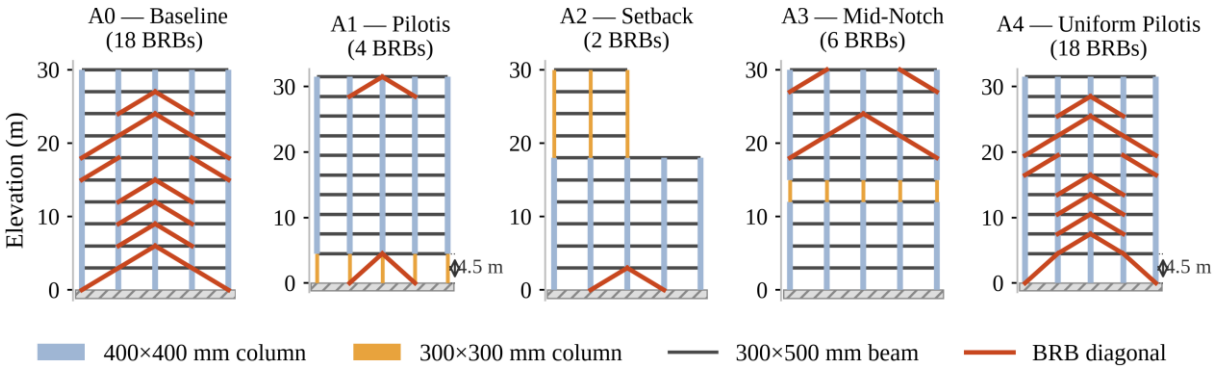


Fig. 3. Knee-point optimal BRB placements.

3.4 Seismic benefit without a code trigger: the A4 case

A4 — Uniform Pilotis is the archetype a code-based screening would not select. Its columns are constant 400×400 mm over the full height, its section schedule follows the gravity demand, and both Table 3.6 checks are negative, with a maximum η_{ki} of 1.571 against the 2.0 threshold. Its only departure from A0 is the taller ground story, which is an architectural fact rather than a detailing deficiency. Nevertheless the bare frame reaches Collapse under the record suite with 5 collapse-zone column ends and an envelope drift of 4.03%, and its optimized retrofit reduces these to 0 and 1.13% respectively, with all joints below the sec.7.5.2 capacity in both states (max DCR 0.771 bare, 0.789 optimal). Under the common-period diagnostic of Section 3.6, which removes the scaling difference between the bare and retrofitted models, its drift falls from 4.03% to 1.16%.

The implication is not that TBDY Table 3.6 is deficient, since its checks flag the strength and stiffness discontinuities they are written to flag, but that the absence of a trigger is not evidence that a frame will not benefit from bracing. A geometrically sound, gravity-consistent pilotis whose columns are nowhere weaker than the story above still concentrates deformation demand in a tall ground story, and an optimally placed BRB layout still removes that concentration. Retrofit prioritisation schemes that use code irregularity as an inclusion criterion will therefore systematically overlook frames of this kind.

3.5 Separating the braces from the confinement upgrade

Because the retrofitted models carry both BRBs and upgraded column hoops, an ablation over the two interventions is required before either can be credited (Table 5). Four conditions are analysed per archetype: as-built bare, braces with as-built hoops, confinement upgrade alone, and both together. The two interventions work together rather than add up, and the effect differs by archetype. For A0 — Baseline, braces alone leave the collapse-zone count unchanged (col_G 5 → 5) and the confinement upgrade alone likewise (5 → 5), while the pair together eliminates collapse damage entirely (5 → 0). For A4 — Uniform Pilotis a single

intervention is worse than ineffective: braces alone make the frame worse (5 → 7) and confinement alone leaves it unchanged (5 → 5), yet the pair again eliminates collapse damage (5 → 0). For A2 — Geometric Setback the pair improves but does not resolve the frame on the screening suite, reducing col_G from 5 to 2 (not confirmed by the seven-record validation, Section 3.3). The mechanism is the one Table 5 is built to show: braces redistribute deformation demand away from the critical story, and the doubled sec.5.8.1 collapse-limit strain is what allows the remaining hinge demand to be classified below the collapse threshold.

Table 5. Ablation over braces and column confinement (screening suite; nc = non-convergent).

Archetype	Bare, as-built	BRBs only	Confinement only	BRBs + confinement
A0 — Baseline	0/5	0/5	0/5	0/0
A1 — B1 Pilotis	0/5 (nc)	1/2 (nc)	0/5 (nc)	0/2
A4 — Uniform Pilotis	0/5	1/7	0/5	4/0
A2 — Geometric Setback	0/5	3/5	0/5	1/2
A3 — B1 Mid-Notch	1/8 (nc)	2/3 (nc)	1/7	0/5

3.6 The BRB-column axial force couple

A braced story resists lateral load like a story of a vertical truss: the diagonal force P delivers a horizontal component P cos θ as story shear and injects a vertical component P sin θ into the columns at the brace end nodes. Under cyclic loading the columns bounding a braced bay therefore carry an alternating axial couple superimposed on gravity, accumulating over the height of a braced stack exactly as overturning demands accumulate in shear-wall boundary elements. The mechanism is well established for steel BRBFs [6, 8, 9] and directly controls in RC retrofit design procedures [10-12]. Its magnitude here is severe relative to the existing members: at core yield each brace injects approximately 363 kN vertically (472 kN in the 4.5 m pilotis story), about 63% of the entire gravity axial load of a base column.

The extracted column axial envelopes confirm the mechanism empirically (Table 6, Fig. 4). Columns are classified as BRB-adjacent when they share a node with a brace. Where braces are few and concentrated the adjacent columns carry up to 2.07 times (A2 — Geometric Setback) the axial peaks of the remaining columns, and the largest single column force is of the order of the brace yield force itself. Where the optimizer disperses braces over many columns the per-column amplification dilutes toward unity, so dispersion is itself a mitigation of the couple (A3, with a ratio below one, carries less axial load in its adjacent columns than in the others). The tension side is equally real: the optimized designs pull columns to as much as 503 kN net tension, a demand the bare frames never see and a governing anchorage and lap-splice check for plain S220 bars.

Table 6. Column axial envelopes of the optimal designs (seven-record envelope).

Archetype	BRB-adjacent cols	Mean |N| adj. (kN)	Mean |N| other (kN)	Amplification	Max |N| any col (kN)	Max tension (kN)
A0 — Baseline	34	605.8	450.4	×1.35	1380.4	503.0
A1 — B1 Pilotis	9	346.7	332.1	×1.04	793.7	0.0
A4 — Uniform Pilotis	34	583.9	453.9	×1.29	1216.9	488.7
A2 — Geometric Setback	4	552.6	266.9	×2.07	632.1	174.2
A3 — B1 Mid-Notch	16	167.1	392.1	×0.43	603.3	0.0

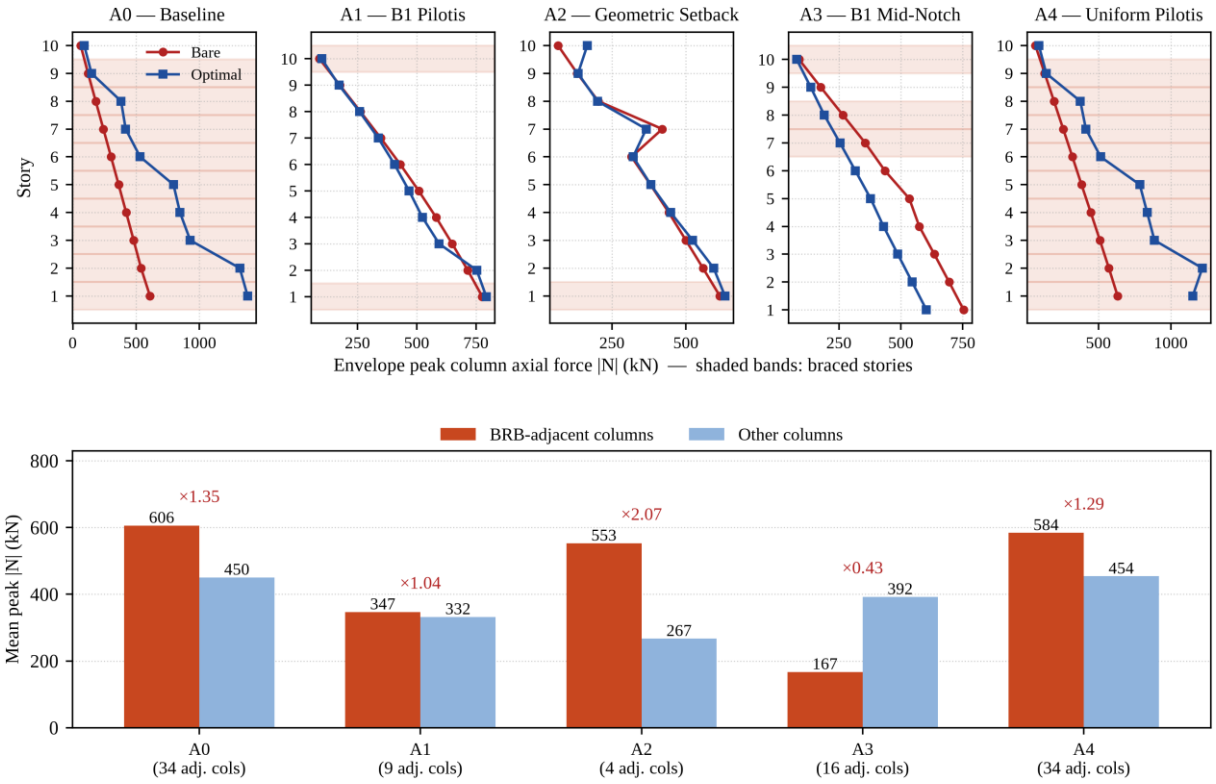


Fig. 4. Column axial force envelopes and the BRB-adjacent versus other column comparison.

Because adding braces shortens the period and therefore raises the record scale factors, each optimal design was additionally re-analysed with records scaled to the bare-frame period (Table 7). This confound does not change the conclusions: the archetypes whose drift improves under own-period scaling improve under common-period scaling as well, and the joint deficiencies exist already in the bare frames at bare-frame scaling.

Table 7. Common-period diagnostic (both models at the bare T_1).

Archetype	Reference T_1 (s)	Bare IDR (%)	Optimal IDR (%)	Δ (%)
A0 — Baseline	1.624	3.51	1.17	-2.34
A1 — B1 Pilotis	2.003	3.16	3.32	0.17
A4 — Uniform Pilotis	1.764	4.03	1.16	-2.87
A2 — Geometric Setback	1.381	2.41	2.96	0.55
A3 — B1 Mid-Notch	1.666	3.76	3.64	-0.12

3.7 Beam-column joint shear

Comparing the sec.7.5.2 joint fields of the bare and retrofitted frames answers whether braces relieve or aggravate joint shear: they are essentially neutral. The peak demand-capacity ratio changes by +3.0%, +1.3%, +2.3%, -0.2% and -0.8% for A0, A1, A4, A2 and A3 respectively (Table 8), and the count of over-capacity joints is identical in the bare and optimal state of every archetype. The ratio is set mainly by the shear area of the 300×300 mm column joints rather than by brace placement: the three archetypes containing them exceed capacity in both states (1.31-1.37), the two with constant 400×400 mm columns stay below it (0.77-0.79). The changes are small and of mixed sign because the beam-bar term of Eq. 7.11 is fixed by the section: only the column shear subtracted from it varies with the brace layout. Joint deficiency is therefore a pre-existing, retrofit-independent brittle failure mode: joints over capacity in the bare frame require local strengthening, such as jacketing, regardless of the brace layout, exactly as the dominance of the joint penalty in the objective already signals to the optimizer. Applied as a hard constraint (DCR ≤ 1), the check would leave no feasible design in A1, A2 and A3 (lowest Pareto peak 1.31-1.36) and would never bind in A0 and A4 (0.76-0.81); at an interior 300×300 mm joint it needs a column shear of at least 158 kN, against the roughly 13-

45 kN implied by the analyses (back-calculated from the DCRs). BRBs alone are therefore not sufficient in these frames: joint strengthening must be designed together with the braces.

Table 8. Joint shear comparison, bare versus optimal.

Archetype	Max DCR bare	#DCR ≥ 1 bare	Max DCR optimal	#DCR ≥ 1 optimal	Change (%)	Net effect
A0 — Baseline	0.766	0	0.789	0	+3.0	higher
A1 — B1 Pilotis	1.356	3	1.374	3	+1.3	higher
A4 — Uniform Pilotis	0.771	0	0.789	0	+2.3	higher
A2 — Geometric Setback	1.360	4	1.358	4	-0.2	neutral
A3 — B1 Mid-Notch	1.324	3	1.314	3	-0.8	lower

4 Conclusions

A multi-objective GA-NRHA framework was applied to the BRB retrofit of five 10-story RC archetypes representative of the pre-2000 Turkish stock, with member-level performance evaluated strictly per TBDY 2018. The principal conclusions are as follows.

First, seismic benefit from optimally placed BRBs does not require a code-recognized irregularity. The gravity-consistent pilotis A4 satisfies both TBDY Table 3.6 checks (max η_{ki} = 1.571) yet its bare frame reaches Collapse and its optimized retrofit removes collapse-level column damage. Code irregularity is a valid screening flag but not a necessary condition for retrofit candidacy.

Second, drift alone is not a valid retrofit-optimization objective: minimizing inter-story drift reduced drift while increasing collapse-level column hinges, because a story-level metric cannot separate ductile beam yielding from brittle column failure. A member-level damage index assembled from sec.15.3.2 hinge classification and sec.7.5.2 joint checks gives the optimizer a signal aligned with the code damage hierarchy.

Third, braces and column confinement act in synergy, not in sum. For A0 neither intervention alone changes the collapse-zone count (5 → 5) while the pair eliminates it (5 → 0); for A4 braces alone are harmful (5 → 7) and confinement alone neutral (5 → 5), yet the pair eliminates collapse damage; for A2 the pair reduces col_G from 5 to 2 on the screening suite, a gain the seven-record validation does not confirm. Braces redistribute the deformation demand and the doubled collapse-limit strain absorbs what remains.

Fourth, BRB diagonals impose a large cyclic axial force couple on adjacent columns, amplifying their axial envelopes by up to 2.07 times and introducing net column tension of up to 503 kN; dispersed placements measurably dilute this effect. Fifth, beam-column joint shear deficiency is essentially insensitive to brace placement: the peak DCR changes by at most 3.0% between the bare and optimal states (1.31-1.37 in A1, A2 and A3; 0.77-0.79 in A0 and A4) and the number of over-capacity joints is unchanged, since it is governed by the 300×300 mm column joint geometry under the γ = 1.0 unconfined classification (640.0 kN exterior joint capacity for 400×400 mm columns, 360.0 kN for 300×300 mm).

The results therefore define a three-part rehabilitation strategy in which BRBs provide global drift control, column confinement and local strengthening at brace connections carry the force couple including its tension side, and joint jacketing addresses the joints that exceed capacity before any brace is installed. Extension of the framework to member sizing, with the core area as a design variable, and to three-dimensional models is ongoing work.

Acknowledgments

This study was conducted within the first author's M.Sc. thesis research at the Graduate School of Natural and Applied Sciences, Ege University. The nonlinear response history analyses were performed on the TRUBA high-performance computing resources of TÜBİTAK ULAKBİM.

References

1. Altunışık, A.C., Arslan, M.E., Kahya, V., et al.: Field observations and damage evaluation in reinforced concrete buildings after the February 6th, 2023, Kahramanmaraş-Türkiye earthquakes. Journal of Earthquake and Tsunami 17(6), 2350024 (2023).

2. Erbaş, Y., Mercimek, Ö., Anıl, Ö., Çelik, A., Akkaya, S.T., Kocaman, İ., Gürbüz, M.: Design deficiencies, failure modes and recommendations for strengthening in reinforced concrete structures exposed to the February 6, 2023 Kahramanmaraş earthquakes (Mw 7.7 and Mw 7.6). Natural Hazards 121(3), 3153-3194 (2025).

3. Doğan, T.P., Kalkan, H., Aldemir, Ö., Ayhan, M., Böcek, M., Anıl, Ö.: Investigation of RC structure damages after February 6, 2023, Kahramanmaraş earthquake in the Hatay region. Bulletin of Earthquake Engineering 22(10), 5201-5229 (2024).

4. Watanabe, A., Hitomi, Y., Saeki, E., Wada, A., Fujimoto, M.: Properties of brace encased in buckling-restraining concrete and steel tube. In: Proc. 9th WCEE, vol. IV, pp. 719-724. Tokyo-Kyoto (1988).

5. Black, C.J., Makris, N., Aiken, I.D.: Component testing, seismic evaluation and characterization of buckling-restrained braces. Journal of Structural Engineering 130(6), 880-894 (2004).

6. Sabelli, R., Mahin, S., Chang, C.: Seismic demands on steel braced frame buildings with buckling-restrained braces. Engineering Structures 25(5), 655-666 (2003).

7. Fahnestock, L.A., Sause, R., Ricles, J.M.: Seismic response and performance of buckling-restrained braced frames. Journal of Structural Engineering 133(9), 1195-1204 (2007).

8. Richards, P.W.: Seismic column demands in ductile braced frames. Journal of Structural Engineering 135(1), 33-41 (2009).

9. López, W.A., Sabelli, R.: Seismic Design of Buckling-Restrained Braced Frames. Steel Tips, Structural Steel Educational Council, Moraga, CA (2004).

10. Di Sarno, L., Manfredi, G.: Seismic retrofitting with buckling restrained braces: application to an existing non-ductile RC framed building. Soil Dynamics and Earthquake Engineering 30(11), 1279-1297 (2010).

11. Sutcu, F., Takeuchi, T., Matsui, R.: Seismic retrofit design method for RC buildings using buckling-restrained braces and steel frames. Journal of Constructional Steel Research 101, 304-313 (2014).

12. Almeida, A., Ferreira, R., Proença, J.M., Gago, A.S.: Seismic retrofit of RC building structures with buckling restrained braces. Engineering Structures 130, 14-22 (2017).

13. AFAD: Türkiye Bina Deprem Yönetmeliği (TBDY 2018). Disaster and Emergency Management Presidency, Ankara (2018).

14. Zhu, M., McKenna, F., Scott, M.H.: OpenSeesPy: Python library for the OpenSees finite element framework. SoftwareX 7, 6-11 (2018).

15. Mander, J.B., Priestley, M.J.N., Park, R.: Theoretical stress-strain model for confined concrete. Journal of Structural Engineering 114(8), 1804-1826 (1988).

16. Deb, K., Pratap, A., Agarwal, S., Meyarivan, T.: A fast and elitist multiobjective genetic algorithm: NSGA-II. IEEE Transactions on Evolutionary Computation 6(2), 182-197 (2002).

17. Fortin, F.-A., De Rainville, F.-M., Gardner, M.-A., Parizeau, M., Gagné, C.: DEAP: evolutionary algorithms made easy. Journal of Machine Learning Research 13, 2171-2175 (2012).

Author Contribution Statement

Conceptualization: Clifford Phiri, Çağlayan Hızal; Methodology: Clifford Phiri, Çağlayan Hızal; Software and investigation: Clifford Phiri; Writing, original draft: Clifford Phiri; Writing, review and editing; supervision: Çağlayan Hızal.

List of Abbreviations

BRB — Buckling-Restrained Brace; **BRBF** — Buckling-Restrained Braced Frame; **DCR** — Demand-Capacity Ratio; **DD-2** — TBDY 2018 design earthquake level (475-year return period); **GA** — Genetic Algorithm; **IDR** — Inter-Story Drift Ratio; **IH** — Significant Damage (İleri Hasar) damage zone, TBDY sec.15.3.2; **G** — Collapse (Göçme) damage zone, TBDY sec.15.3.2; **LYP** — Low-Yield-Point steel; **NRHA** — Nonlinear Response History Analysis; **NSGA-II** — Non-dominated Sorting Genetic Algorithm II; **RC** — Reinforced Concrete; **TBDY** — Türkiye Bina Deprem Yönetmeliği (Turkish Building Earthquake Code, 2018).

Publication Note

This paper was peer-reviewed, accepted for presentation, and included in the proceedings of the ACE2026 — International Conference on Advances in Civil Engineering, held on 12–14 October 2026 in Trabzon, Türkiye.

This paper may be cited as follows:

Phiri C., Hızal C., "Performance-Based Optimization of Buckling-Restrained Braces for RC Structures Using Nonlinear Response History Analysis," in Proceedings of the ACE2026 — International Conference on Advances in Civil Engineering, Trabzon, Türkiye, 12–14 October 2026.

Numerical Prediction of the Seismic Behavior of Steel Plate Reinforced Concrete Squat Shear Walls: A Python-Based Parametric Study

Mustafa Ozdemir[1] and Muslum Kilinc[2]

[1] 0009-0004-9922-4254, Erciyes University, Civil Engineering Department, Kayseri, Türkiye, mustafa_ozdemr@hotmail.com

[2] 0000-0002-8837-3922, Erciyes University, Civil Engineering Department, Kayseri, Türkiye, kilinc@erciyes.edu.tr

Abstract. Squat shear walls constructed from reinforced concrete (RC) with aspect ratios below 1.0 are susceptible to brittle diagonal shear failure under seismic loading. To predict the seismic response of steel plate-reinforced concrete (SPRC) squat walls and to isolate the effects of web reinforcement and centrally embedded S235 steel plates, a nonlinear finite element framework was developed in Python using OpenSeesPy. The analysis employed multi-layer ShellMITC4 elements incorporating a plastic-damage concrete model, smeared reinforcement layers, and J2-plasticity plate layers, all subjected to boundary conditions replicating a quasi-static test setup. Four wall configurations measuring 400×1000×125 mm were examined: plain concrete, plate-only, conventional RC, and SPRC. The unreinforced wall failed by brittle shear at a drift of 0.09%, while all reinforced and composite configurations achieved a drift of 2%. A parametric study of plate thickness (1–10 mm) demonstrated that capacity increased by 1.8 to 5.3 times relative to the RC reference, with diminishing returns as plate thickness increased. For equivalent steel content (approximately 3.15 kg), the embedded plate configuration exhibited 47% greater capacity than conventional rebar. The embedded plate also mitigated mesh-dependent strain localization observed in the RC model, functioning as a physical regularizer. Independent verification was conducted using a nonlinear SAP2000 model for both plain concrete and RC walls. Elastic stiffness values agreed within 10%, and the SAP2000 pushover analysis of the RC wall yielded a peak capacity within the ACI analytical range and exhibited post-peak softening, consistent with the upper-bound response from OpenSeesPy. The reported capacities correspond to the full-composite upper bound. Perforated-plate (perfobond) detailing is proposed as a potential experimental bonding solution. The developed framework provides a pre-experimental design tool for optimizing composite strengthening of squat walls.

Keywords: Squat Shear Wall; Steel Plate Reinforced Concrete; OpenSeesPy; Layered Shell; Seismic Ductility

1 Introduction

Reinforced concrete (RC) squat shear walls with shear span ratios below 1.0 function as primary elements for resisting lateral loads in basement storeys, industrial facilities, and retaining structures. Experimental studies demonstrate that the behaviour of these walls is governed by the shear span ratio. As the ratio decreases, shear strength increases, while deformation capacity and energy dissipation decrease significantly. Failure is more likely to occur through brittle diagonal compression mechanisms [1]. Such brittle shear failure limits the overall ductility of the structure, which necessitates the implementation of composite strengthening methods.

Steel plate reinforced concrete (SPRC) walls, which incorporate steel plates within conventional reinforced concrete (RC) walls, have emerged as an effective composite system, particularly for high-rise buildings in seismically active regions [2, 3]. Cyclic testing of

embedded steel plate–high strength concrete composite walls has demonstrated significantly enhanced load-bearing capacity, deformation ability, and energy dissipation compared to conventional RC walls, provided that the steel ratio and axial load ratio remain within recommended limits [4]. In China, hysteretic models of SPRC walls developed using OpenSees have been validated against experimental results and utilized for parametric design studies, reflecting the widespread application of this system in super-tall buildings [4]. The SPRC concept has also been extended to coupling beams, where the quantity of embedded steel strongly influences strength, while excessive longitudinal reinforcement reduces ductility [5].

Another category of systems positions the steel plate outside or adjacent to the concrete. Examples include composite steel plate shear walls with reinforced concrete (RC) face panels [6], steel plate shear walls with boundary frames [7], dual-plate walls with infilled concrete channels [8], precast fiber-reinforced concrete panel systems [9], single-side concrete-encased plates [10], prefabricated end-plate connections [11], and partially connected infill plates [12]. In these configurations, the concrete restrains the plate from buckling, promoting shear yielding rather than elastic buckling. Advanced smeared-crack formulations, such as the Disturbed Stress Field Model, have been applied to composite wall elements and have demonstrated the ability to reproduce capacity, ductility, and failure sequence [13]. Additionally, three-dimensional continuum models using ANSYS and ABAQUS have quantified the effects of reinforcement ratio, concrete strength, and plate properties on cyclic response [14, 15]. A numerical comparison of four different systems indicated that the wall with a single plate embedded within the concrete core exhibited the best overall seismic performance, absorbing approximately twice the energy of conventional RC and external-plate systems [15].

Reliable composite action is essential for the performance of these systems. Interface solutions identified in the literature include headed studs and tie bars [2, 16], rubber-coated uplift-restrained studs designed to soften the interface and protect the concrete [17], and shear connectors for thin embedded plates [16]. Retrofitting alternatives, such as steel wire mesh combined with polymer mortar, have also demonstrated effectiveness for shear-deficient walls [18].

Although extensive research exists, systematic numerical studies that (i) isolate the individual effects of web reinforcement and embedded plates within the same squat-wall configuration, and (ii) investigate the influence of plate thickness per unit of steel, remain limited. To address this gap, the present study employs an open-source, Python-based OpenSeesPy framework as the initial phase of an integrated numerical and experimental program. The objectives are to: (1) develop and validate a nonlinear multi-layer shell model of a squat wall under boundary conditions consistent with experimental tests; (2) compare four configurations (plain concrete, plate-only, reinforced concrete (RC), and steel plate reinforced concrete (SPRC)) under monotonic pushover loading; (3) conduct a parametric study on embedded plate thickness (ranging from 1 to 10 mm); and (4) evaluate steel efficiency while maintaining constant steel mass. The numerical results are independently verified using a separate nonlinear SAP2000 model and closed-form analytical approximations.

2 Numerical Modeling Methodology

2.1 Geometry, Boundary Conditions, and Loading

The reference wall measures 400 mm in height, 1000 mm in length, and 125 mm in thickness, resulting in an aspect ratio ($\lambda = H/L$) of 0.40. This configuration classifies the specimen as a short wall where shear is the dominant structural action. The wall is discretized using four-node ShellMITC4 multi-layer shell elements. Boundary conditions replicate those of the intended quasi-static test setup (Fig. 1a): the base is fully fixed to represent an anchored foundation

block, while out-of-plane translations and drilling rotations are restrained to simulate lateral bracing. A stiff steel loading beam (HEB200), modeled with elastic beam-column elements, distributes the load along the top of the wall. Loading is applied in two stages. Initially, a constant axial force of 250 kN is imposed at two actuator positions (125 kN at L/4 and 3L/4). Subsequently, a monotonic lateral pushover is performed under displacement control, with increments of 0.02 mm, until a top displacement of 8 mm (corresponding to a 2% drift) is achieved.

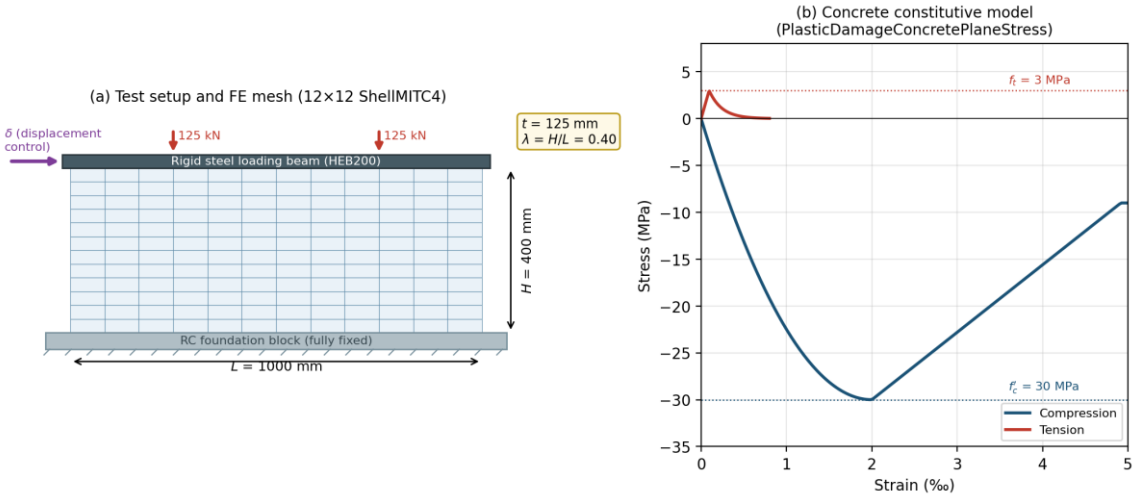


Fig. 1. (a) Test-consistent finite element model and boundary conditions; (b) uniaxial response of the concrete constitutive model.

2.2 Materials and Layered Shell Section

Grade C30 concrete is characterized using a plane-stress plastic-damage model, with a compressive strength (fc′) of 30 MPa and a tensile strength (ft) of 3 MPa. This material is converted into a shell element through a plate-from-plane-stress wrapper, as illustrated in Fig. 1b. The web reinforcement comprises a double layer of Ø8/200 bars in both directions, with a reinforcement ratio (ρ) of 0.40% per direction, utilizing B420C steel with a yield strength (fy) of 420 MPa. These reinforcements are represented by smeared rebar layers exhibiting Steel02 uniaxial material behavior. The embedded S235 plate, possessing a yield strength (fy) of 235 MPa and an ultimate strength (fu) of 360 MPa, is modeled using J2 (von Mises) plasticity, which is appropriate due to the tensile-compressive symmetry of steel. In the initial set of simulations, this model was intentionally excluded for the concrete, as it does not capture cracking behavior. The SPRC section consists of nine layers (see Fig. 2): cover concrete, horizontal and vertical rebar layers, core concrete separated by the centrally embedded plate, and a symmetric mirror sequence. Full composite action between the plate and the concrete is assumed; therefore, the resulting capacities represent theoretical upper bounds [13].

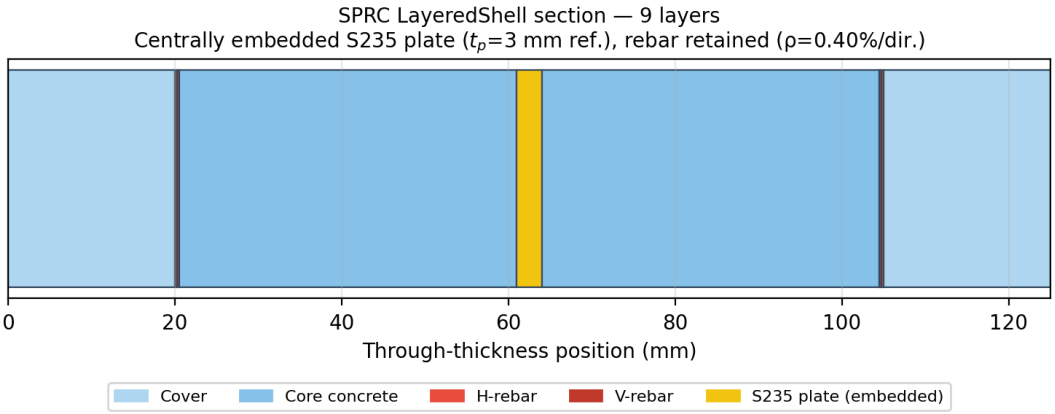


Fig. 2. Nine-layer SPRC layered-shell section with centrally embedded S235 plate (rebar layers exaggerated for visibility).

Model parameters are summarized in Table 1.

Table 1. Principal model parameters.

Parameter	Value	Parameter	Value
Wall H × L × t (mm)	400×1000×125	Rebar (both dir.)	Ø8/200, double curtain
Aspect ratio λ	0.40	Rebar ratio ρ (per dir.)	0.40%
Concrete	C30 (fc′=30, ft=3 MPa)	Rebar steel	B420C (fy=420 MPa)
Ec (MPa)	32 000	Plate steel	S235 (fy=235, fu=360 MPa)
Axial load	2×125 kN (constant)	Plate thickness tp	1 / 3 / 5 / 10 mm
Lateral loading	Displ. control, 0.02 mm	Element / section	ShellMITC4 / layered shell

3 Model Verification

3.1 Mesh Convergence and Failure Mechanism of the Plain Wall

Mesh refinement was conducted on the unreinforced wall, with mesh sizes ranging from 4×4 to 16×16 (see Fig. 3). For the 12×12 and 16×16 meshes, the peak load capacity converged between 634 and 672 kN, which aligns with the analytical upper bound of 0.2fc′Acv = 750 kN. The finer meshes exhibited a sudden loss of equilibrium at a top displacement of approximately 0.25 to 0.34 mm (corresponding to a drift of 0.06 to 0.09 percent), indicating brittle diagonal shear failure of plain concrete rather than a numerical artifact. Consequently, the 12×12 mesh (element size 83×33 mm) was selected as the reference mesh for subsequent analyses.

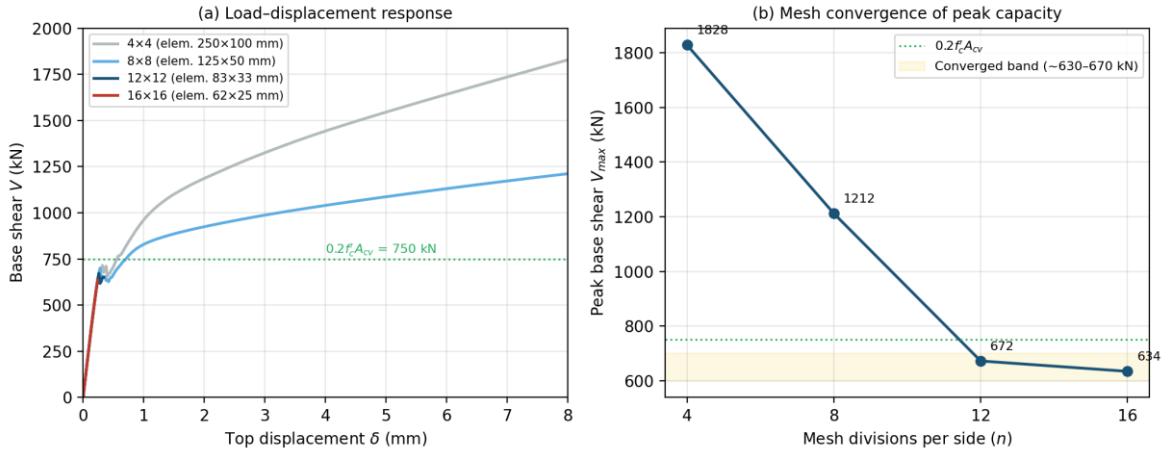


Fig. 3. Mesh convergence of the unreinforced wall: (a) load–displacement response; (b) peak capacity versus mesh density.

3.2 Cross-Platform Verification with SAP2000

To validate the framework, the simple and reinforced concrete (RC) walls were reconstructed in SAP2000 v24 using layered-shell sections with identical geometry, mesh, and material definitions as previously described. This included a user-defined nonlinear C30 stress–strain curve and smeared reinforcement layers with an equivalent thickness of 0.2513 mm per curtain in each direction. A nonlinear gravity stage was implemented to transfer the initial stress state into a displacement-controlled pushover, following the OpenSeesPy protocol.

Within the elastic range, the initial lateral stiffness agreed within 10% across the platforms (see Table 2), confirming the accuracy of the geometry, boundary conditions, and elastic material properties. Following the onset of cracking, the two platforms provided complementary information (Fig. 4 and Table 3). For the plain wall, both models predicted a brittle response terminating below a top displacement of 0.35 mm, corresponding to a drift of less than 0.1%. The SAP2000 solution ceased due to a null-step limit at a load of 189 kN, whereas the OpenSeesPy plastic-damage model redistributed forces up to the diagonal-strut limit at 672 kN. For the reinforced concrete (RC) wall, the SAP2000 pushover reached a maximum load of 404 kN at a displacement of 3.7 mm and exhibited post-peak softening, resulting in approximately a 71% strength loss at 8 mm. In contrast, the OpenSeesPy RC response increased to 2023 kN without any softening. Closed-form estimates indicated that the RC shear capacity ranged between the ACI nominal value ($V_n \approx 326$ kN) and the code upper limit ($0.83\sqrt{f'_c}A_{cv} \approx 568$ kN). The peak load from the SAP2000 RC model fell within the analytically predicted range and included the descending branch characteristic of shear-controlled squat walls. The OpenSeesPy value represented an upper bound consistent with the full-composite, perfect-bond idealization and the absence of compression softening in the current concrete model. Notably, the SAP2000 RC curve displayed a local dip at 0.09 mm, which corresponds to the displacement at which the plain wall fails. Subsequently, the reinforcement bridged the crack and the curve recovered. The RC response thus incorporated the plain-wall response as its initial segment, providing an internally consistent check between the two separate SAP2000 models.

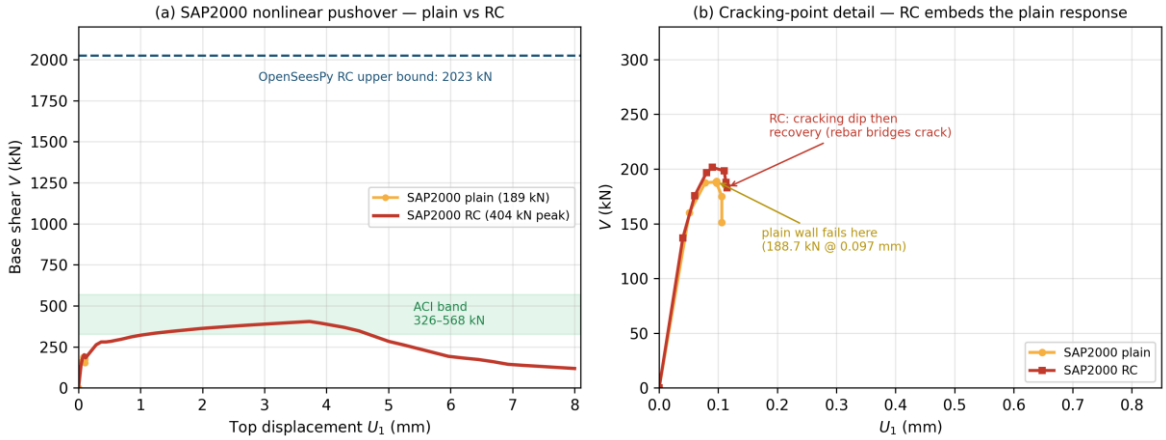


Fig. 4. Independent SAP2000 nonlinear verification: (a) plain and RC pushover curves relative to the OpenSeesPy RC upper bound and the ACI analytical band; (b) cracking-point detail showing that the RC response embeds the plain-wall response.

Table 2. Cross-platform verification of elastic lateral stiffness.

Model	Mesh	K0 (kN/mm)	Difference
SAP2000 v24, linear shell	4×4	3132	—
OpenSeesPy, J2 (pre-cracking)	4×4	2885	7.9%
OpenSeesPy, plastic-damage	4×4	2879	8.1%
OpenSeesPy, plastic-damage	12×12	2826	9.8%

Table 3. Cross-platform nonlinear pushover comparison (plain and RC walls).

Quantity	SAP2000	OpenSeesPy	Analytical (ACI)
Plain wall, peak V (kN)	189	672	0.2fc′Acv = 750
Plain wall, failure	Brittle, <0.11 mm	Brittle, 0.34 mm	Diagonal shear
RC wall, peak V (kN)	404 @ 3.7 mm	2023 (no peak)	Vn = 326–568
RC wall, post-peak	−71% at 8 mm	Not captured	Softening expected
RC/plain capacity ratio	2.14×	3.0×	Same trend

This comparison both reinforces confidence in the model and highlights its limitations. Constitutive uncertainty is greatest for the unreinforced wall and decreases as reinforcement is introduced. Therefore, the quantitative capacities for OpenSeesPy presented below should be considered as complete upper bounds. In contrast, the primary results are the qualitative conclusions, specifically the brittle-to-ductile transition and the relative contributions of the rebar and the plate.

4 Results and Discussion

4.1 Contribution of Reinforcement and Embedded Plate

Four configurations were evaluated using the reference mesh with a plate thickness of 3 mm: (1) plain concrete, (2) concrete with a plate, (3) conventional reinforced concrete, and (4) SPRC, as illustrated in Fig. 5 and detailed in Table 4. The initial stiffness values differ by less than 8%, indicating that both the reinforcement and the plate are largely inactive prior to cracking. Significant changes occur in the post-cracking phase. The plain wall fails by brittle shear at a drift of 0.09%, whereas the walls with the plate, reinforced concrete, and SPRC remain intact up to a drift of 2%. The 3 mm plate alone provides an additional 4957 kN compared to the plain wall, which is 3.7 times the contribution of the rebar (1351 kN). The capacity of the SPRC (6153 kN) is less than the sum of the individual contributions (6980 kN), suggesting that both the plate and the rebar partially fulfill the same crack-bridging function. This behavior aligns with experimental findings that the embedded plate serves as the primary component for carrying lateral loads, while the surrounding concrete secures it in place [2, 3, 15].

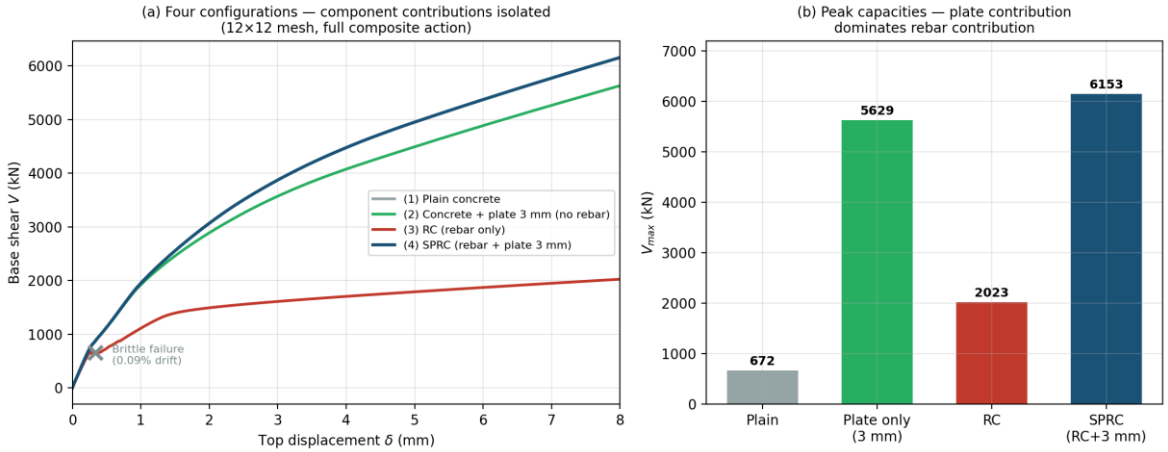


Fig. 5. Four-configuration comparison (12×12 mesh, full composite action): (a) load–displacement curves; (b) peak capacities.

Table 4. Four-configuration results (12×12 mesh; plate tp = 3 mm where present).

Configuration	Vmax (kN)	K0 (kN/mm)	Behavior
(1) Plain concrete	672	2826	Brittle shear, 0.09% drift
(2) Concrete + plate (no rebar)	5629	3059	Ductile, ≥ 2% drift
(3) RC (ρ = 0.40%/dir.)	2023	2826	Ductile, ≥ 2% drift
(4) SPRC (rebar + plate)	6153	3049	Ductile, ≥ 2% drift

4.2 Parametric Study on Plate Thickness

The SPRC configuration was evaluated for embedded plate thicknesses of 1, 3, 5, and 10 mm (see Fig. 6 and Table 5). Structural capacity increased consistently with plate thickness, ranging from 1.8 times that of the RC reference at 1 mm to 5.3 times at 10 mm. However, the marginal gains diminished: the first millimetre of plate resulted in an increase of 1698 kN, while each additional millimetre between 5 and 10 mm contributed only 546 kN. Initial stiffness increased modestly by 3% to 25%, consistent with the limited elastic contribution of the plate to the gross section. All thicknesses exhibited a ductile response up to a drift of 2%. This trend of diminishing returns supports experimental recommendations to maintain the steel ratio in embedded-plate composite walls within an optimal range [4].

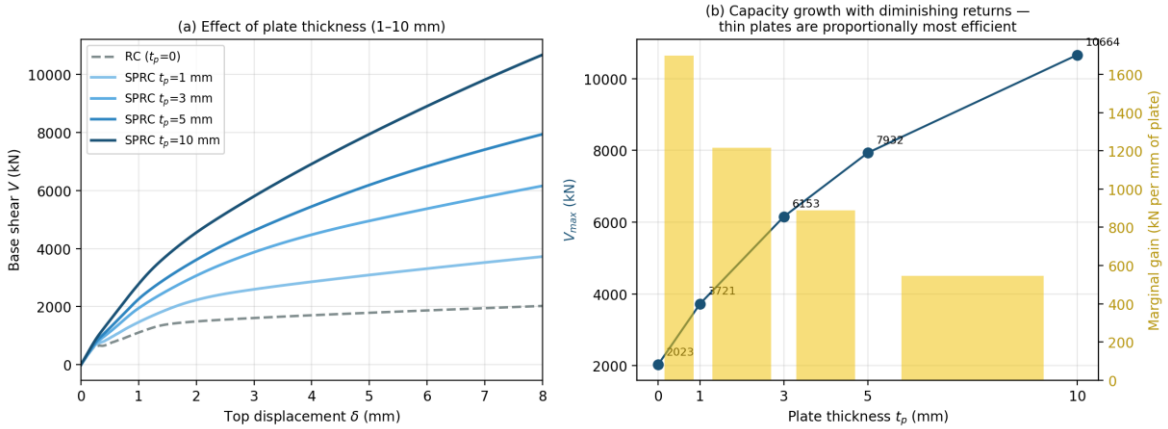


Fig. 6. Effect of embedded plate thickness: (a) load–displacement curves; (b) capacity growth and marginal gain per mm of plate.

Table 5. Parametric results and steel quantities (12×12 mesh).

tp (mm)	Plate steel (kg)	Vmax (kN)	K0 (kN/mm)	Vmax/VRC
0 (RC)	0	2023	2826	1.00
1	3.14	3721	2902	1.84
3	9.42	6153	3049	3.04
5	15.70	7932	3192	3.92
10	31.40	10664	3534	5.27

4.3 Steel Efficiency at Equal Steel Mass

The double-curtain constructed with an Ø8/200 mesh and the 1 mm plate contain nearly identical amounts of steel (3.16 kg and 3.14 kg, respectively), enabling a direct comparison based on steel mass (see Fig. 7). When utilized as an embedded plate, this steel quantity provides a maximum capacity of 2973 kN, whereas its use as rebar results in a capacity of 2023 kN, representing a 47 percent increase. Regarding performance, both configurations exhibit a higher capacity per unit mass of steel compared to a plain wall: the plate configuration achieves 733 kN/kg, while the rebar achieves 428 kN/kg. This enhancement arises because the plate resists in-plane tension and shear in all directions, while the bars resist loads only along their axes. These values assume full composite action; however, actual efficiency will depend on the interface details addressed in the following section.

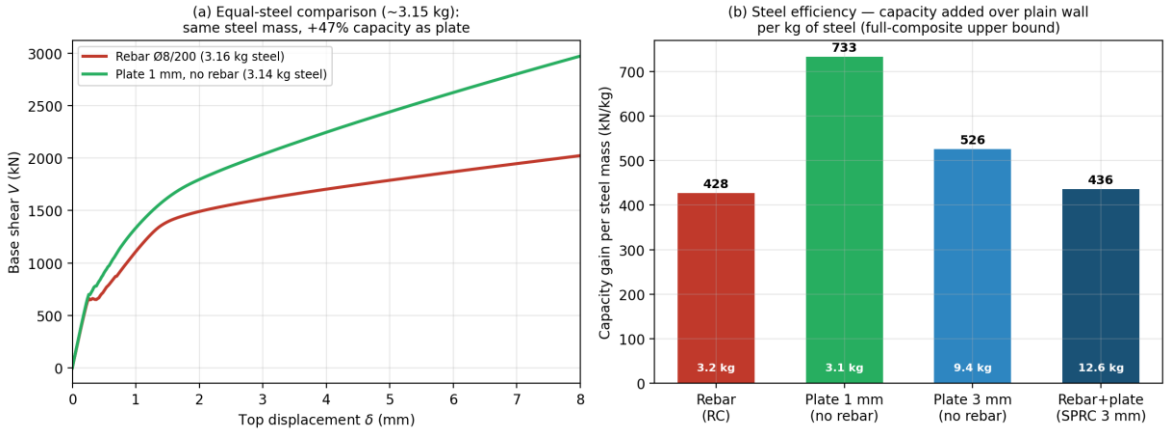


Fig. 7. Steel efficiency: (a) equal-steel comparison (≈3.15 kg); (b) capacity gain over the plain wall per kg of steel.

4.4 Numerical Observations and Practical Considerations

Mesh objectivity. The reinforced concrete (RC) model exhibited typical mesh dependence associated with non-regularized strain-softening, as structural capacity decreased continuously with mesh refinement and premature failure occurred in the finest mesh due to localization within a single element band. The embedded plate approach addressed this issue, with the SPRC meshes converging smoothly (6048–6989 kN, representing a 1.7% change between the two finest meshes). This convergence was achieved because the continuous plate spans cracks across the entire structure, thereby preventing strain localization (Fig. 8). Crack-band (fracture-energy) regularization of concrete softening is planned for the next stage to achieve mesh-objective RC results [13]. The SAP2000 RC model, which simulates post-peak softening within the analytical band, will serve as an independent reference for this calibration.

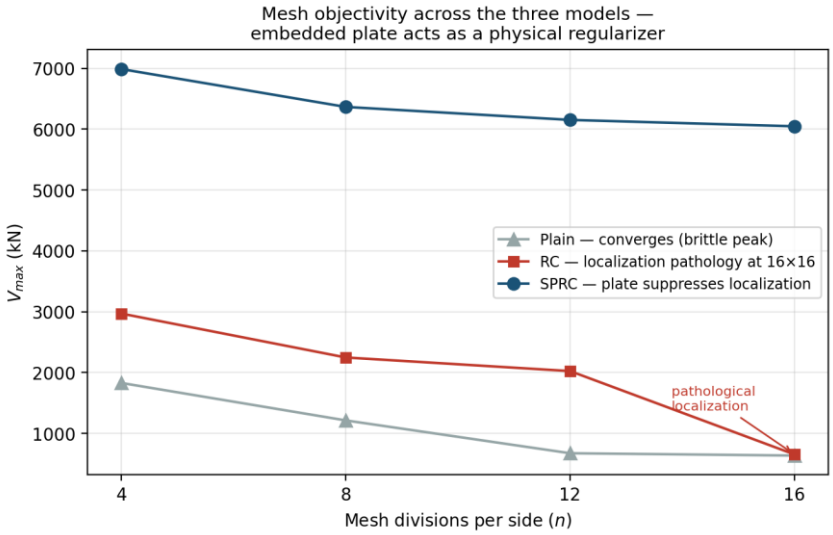


Fig. 8. Mesh behavior of the three models: the embedded plate suppresses the localization observed in the RC model.

Bond and perforated-plate detailing. The assumption of full composite action establishes an upper bound, as interfacial slippage and plate buckling are recognized limitations of the perfect bond approach [13]. During the experimental phase, the use of a perforated embedded plate is proposed. Concrete dowels passing through the perforations, along with optional transverse bars, create a mechanical interlock analogous to that of perfobond (PBL) connectors. The shear resistance in this system arises from the combined effects of interface bonding, concrete-dowel action, and the contribution of transverse bars [16]. In this context, the resulting reduction in net section area can be represented by an effective plate thickness. Alternative solutions that reduce the interface, such as rubber-coated studs [17] and retrofit techniques for existing walls [18], offer additional options tailored to specific applications.

5 Conclusions

A Python-based framework employing multi-layer shell elements was developed and evaluated to predict the seismic behavior of squat steel plate reinforced concrete (SPRC) walls. Validation was performed using a nonlinear SAP2000 model and closed-form analytical calculations. For the configuration studied ($\lambda = 0.40$, C30 concrete, S235 plates, and full composite action), several findings were established. The unreinforced squat wall exhibited brittle diagonal shear failure at a drift of 0.09%, with a capacity of approximately 670 kN, confirming its vulnerability and the necessity for composite strengthening. Conventional web reinforcement and centrally embedded steel plates transformed this brittle response into a ductile one, sustained up to a drift of 2%. The steel plate was identified as the primary contributor; a 3 mm plate increased capacity by 3.7 times compared to the minimum web reinforcement specified in the code. Increasing plate thickness resulted in a consistent rise in capacity (from 1.8 to 5.3 times the reinforced concrete reference as plate thickness increased from 1 to 10 mm), although incremental gains diminished, indicating that thinner plates are proportionally more efficient. With equal steel content, the embedded plate configuration achieved 47% greater capacity than conventional rebar (733 kN/kg versus 428 kN/kg). The embedded plate also served as a physical regularizer, mitigating mesh-dependent strain localization. Cross-platform comparisons revealed that constitutive uncertainty was highest for the unreinforced wall and decreased with reinforcement. The pushover curve from the SAP2000 reinforced concrete model peaked within the ACI band and demonstrated realistic post-peak softening, while the OpenSeesPy response provided a consistent upper bound. The reported capacities represent theoretical upper limits.

Ongoing research addresses fracture-energy regularization, cyclic loading with energy dissipation, interface modeling of perforated plates, and experimental validation using scaled specimens.

Acknowledgments

This study was conducted within the scope of the first author's M.Sc. research at Erciyes University under the supervision of the second author.

References

1. Wei, F., Chen, H., Xie, Y.: Experimental study on seismic behavior of reinforced concrete shear walls with low shear span ratio. Journal of Building Engineering 45, 103602 (2022). https://doi.org/10.1016/j.jobe.2021.103602
2. Gan, C.J., Lu, X.L., Wang, W.: Seismic behavior of steel plate reinforced concrete shear walls. In: Proceedings of the 14th World Conference on Earthquake Engineering, Beijing, China, 12–17 October 2008.
3. Xiao, C., Zhu, A., Li, J., Li, Y.: Experimental study on seismic performance of embedded steel plate-HSC composite shear walls. Journal of Building Engineering 34, 101909 (2021). https://doi.org/10.1016/j.jobe.2020.101909
4. Wang, B., Jiang, H., Lu, X.: Seismic performance of steel plate reinforced concrete shear wall and its application in China Mainland. Journal of Constructional Steel Research 131, 132–143 (2017). https://doi.org/10.1016/j.jcsr.2017.01.003
5. Hou, W., Lin, G., Chen, B., Guo, Z.: Cyclic behavior and analysis of steel plate reinforced concrete coupling beams with a span-to-depth ratio of 2.5. Soil Dynamics and Earthquake Engineering 148, 106817 (2021). https://doi.org/10.1016/j.soildyn.2021.106817
6. Astaneh-Asl, A., Zhao, Q.: Seismic Behavior and Design of Composite Steel Plate Shear Walls. Technical Information & Product Service, Structural Steel Educational Council, Moraga, CA (2002).
7. Bruneau, M., Berman, J.W., Lopez-Garcia, D., Vian, D.: A review of steel plate shear wall design requirements and research. Engineering Journal (AISC) 44(1), 27–34 (2007).
8. Zhang, W., Wang, K., Chen, Y., Ding, Y.: Experimental study on the seismic behaviour of composite shear walls with stiffened steel plates and infilled concrete. Thin-Walled Structures 144, 106279 (2019). https://doi.org/10.1016/j.tws.2019.106279
9. Ayazi, A., Shafaei, S.: Steel–concrete composite shear walls using precast high performance fiber reinforced concrete panels. The Structural Design of Tall and Special Buildings 28(12), e1628 (2019). https://doi.org/10.1002/tal.1628
10. Qi, Y., Gu, Q., Wang, H.: Study on the shear mechanism and resistance of single-side concrete-encased composite plate shear wall. Thin-Walled Structures 180, 109876 (2022). https://doi.org/10.1016/j.tws.2022.109876
11. Yu, J.-G., Feng, X.-T., Hao, J.-P., Gao, X.: Experimental study of composite steel plate shear wall with flush end-plate connection. International Journal of Steel Structures 20(1), 136–150 (2020). https://doi.org/10.1007/s13296-019-00275-7
12. Yang, Y., Mu, Z., Zhu, B.: Study on shear strength of partially connected steel plate shear wall. Metals 12(7), 1060 (2022). https://doi.org/10.3390/met12071060
13. Vecchio, F.J., McQuade, I.: Towards improved modeling of steel-concrete composite wall elements. Nuclear Engineering and Design 241(8), 2929–2942 (2011). https://doi.org/10.1016/j.nucengdes.2011.05.023
14. Najm, H.M., Ibrahim, A.M., Sabri, M.M., Hassan, A., Morkhade, S., Mashaan, N.S., Eldirderi, M.M.A., Khedher, K.M.: Modelling of cyclic load behaviour of smart composite

steel-concrete shear wall using finite element analysis. Buildings 12(6), 850 (2022). https://doi.org/10.3390/buildings12060850
15. Labibzadeh, M., Salehnia, A., Hossain, K.M.A., Jing, D.-H.: Performance of composite shear walls subjected to in-plane cyclic loading – a numerical parametric study. Periodica Polytechnica Civil Engineering 65(4), 1134–1152 (2021). https://doi.org/10.3311/PPci.16944
16. Kruszewski, D., Zaghi, A.E.: Load transfer between thin steel plates and ultra-high performance concrete through different types of shear connectors. Engineering Structures 227, 111450 (2021). https://doi.org/10.1016/j.engstruct.2020.111450
17. Feng, X., Yu, J., Shen, J.: Seismic behavior of composite steel plate shear walls with rubber-coated uplift-restrained studs. Journal of Constructional Steel Research 182, 106683 (2021). https://doi.org/10.1016/j.jcsr.2021.106683
18. Xie, X., Guo, Z., Basha, S.H., Huang, Q.: A novel shear strengthening of existing RC shear walls using steel wire mesh and polymer mortar. Buildings 12(2), 219 (2022). https://doi.org/10.3390/buildings12020219

Author Contribution Statement

– *Conceptualization:* Muslum Kilinc, Mustafa Ozdemir
– *Methodology:* Mustafa Ozdemir
– *Investigation:* Mustafa Ozdemir
– *Writing – Original Draft:* Mustafa Ozdemir
– *Writing – Review & Editing:* Muslum Kilinc

List of Abbreviations

– **RC** — Reinforced Concrete
– **SPRC** — Steel Plate Reinforced Concrete
– **FE** — Finite Element
– **PBL** — Perfobond Leiste (perforated-plate shear connector)

Funding

This work was supported by Erciyes University under the Scientific Research Project (BAP Project ID: 16176). The authors gratefully acknowledge this support.

Publication Note
This paper was peer-reviewed, accepted for presentation, and included in the proceedings of the ACE2026 – International Conference on Advances in Civil Engineering, held on 12–14 October 2026 in Trabzon, Türkiye.

This paper may be cited as follows:
Ozdemir, M., and Kilinc., M, "Numerical Prediction of the Seismic Behavior of Steel Plate Reinforced Concrete Squat Shear Walls: A Python-Based Parametric Study," in Proceedings of the ACE2026 – International Conference on Advances in Civil Engineering, Trabzon, Türkiye, 12–14 October 2026.

Recent Progress in Geopolymer-Based Applications for Bridge Structures: From Material Feasibility to Deployment Readiness

Oğuzhan Çetindemir[1]
[1] 0000-0002-1018-4515, İstanbul Okan University, Department of Motor Vehicles and Transportation Technologies, İstanbul, Türkiye, oguzhan.cetindemir@okan.edu.tr

Abstract. A 2025 review of geopolymer concrete (GPC) in bridge engineering documented a growing portfolio of field applications but also identified limited full-scale evidence, insufficient long-term structural data, and gaps in standardization. This paper provides a focused update on post-review and near-contemporaneous developments published during 2025 through 8 August 2026 and evaluates how the research frontier has shifted toward deployment readiness. Recent studies now include full-scale precast and prestressed alkali-activated concrete (AAC) members, nine-month testing of composite prestressed girders, bridge-deck repair interface models, performance-based chloride testing, fatigue synthesis, anchorage formulations, high-strength engineered geopolymer composites, and embedded ultrasonic monitoring of full-scale prestressed AAC bridge-deck components. The most consequential finding is that demonstrating adequate short-term compressive strength is no longer the sole deployment challenge. Time-dependent deformation, prestress loss, bond and interface deterioration, limit-state-specific design-model accuracy, exposure-specific durability qualification, and production reliability have become increasingly decisive. The new evidence supports a transition from material feasibility toward component-level verification and monitored pilot deployment, but does not yet demonstrate routine use in conventional highway bridges. A deployment-oriented research agenda is therefore proposed, prioritizing long-term prestressed behavior, coupled fatigue-durability testing, code calibration, field monitoring, and performance-based qualification.

Keywords: Bridges; geopolymer concrete; alkali-activated concrete; prestressed concrete; durability; structural health monitoring; deployment readiness.

1 Introduction

Geopolymer concrete (GPC) and related alkali-activated binders have been investigated for bridge applications because they can combine lower Portland-cement demand with favorable mechanical and durability characteristics. The 2025 review by Çetindemir [1] synthesized bridge applications reported up to 2024, including precast panels, bridge decks, prestressed girders, pedestrian and cycle bridges, repair mortars, and circular-bridge concepts. That review also showed that practical implementation remained modest relative to the volume of material-level research. The principal barriers were not simply compressive strength, but the limited amount of long-term field evidence, uncertainty in creep and shrinkage, incomplete code coverage, durability-test compatibility, construction-scale reproducibility, and the absence of mature monitoring and acceptance procedures.

The literature published after that review indicates a notable change in emphasis. Although mixture-dependent strength development and production-scale quality control remain relevant, recent work increasingly addresses the structural, durability, monitoring, and design uncertainties that govern whether bridge owners and designers can deploy AAC/GPC with acceptable risk. Full-scale prestressed members have been produced and tested; time-dependent flexural response has been measured over months; interface constitutive models have been

developed for bridge-deck strengthening; chloride testing has moved toward a RILEM performance-based recommendation; and embedded sensing has been demonstrated on full-scale prestressed AAC bridge elements [2-7]. These developments represent a shift from proof-of-concept research toward deployment-enabling engineering evidence.

Terminology requires care. “Alkali-activated concrete” (AAC) and “alkali-activated materials” (AAMs) are broader categories than geopolymer concrete in the strict chemical sense, and calcium-rich slag systems are not necessarily geopolymers. However, the bridge-related literature published in 2025-2026 increasingly adopts AAC/AAMs terminology. Excluding these studies would omit some of the most relevant new evidence on prestressing, time-dependent response, durability qualification, and monitoring. Accordingly, this paper preserves the terminology used by each source while using “geopolymer-based” as a broad bridge-engineering descriptor when discussing the research field as a whole.

The objective of this paper is therefore not to repeat the bridge case histories already compiled in [1], but to determine what has materially changed since that review. The paper focuses on five questions: whether structural scale has increased; whether time-dependent behavior is being quantified at member level; whether repair and durability assessment are becoming design-oriented; whether standardization is progressing; and whether monitoring can reduce uncertainty during early field deployment. Based on these developments, a concise research agenda for bridge engineering is proposed.

2 Scope and approach

This study is a focused narrative update rather than a new systematic review. Post-review and near-contemporaneous publications appearing during 2025 through 8 August 2026 were screened for direct bridge relevance or for a clear deployment-enabling contribution that was not incorporated into the evidence base of [1]. Priority was given to peer-reviewed journal articles, RILEM outputs, and publisher-verifiable records addressing structural-scale behavior, bridge-deck repair, bond and anchorage, chloride transport, fatigue, high-performance composites, and structural monitoring.

The scope intentionally excludes general mixture-optimization studies that do not materially change bridge design or deployment decisions. Earlier field applications remain important background, but they are referenced through the 2025 review [1] rather than reproduced. The resulting update is therefore organized around engineering readiness rather than chronology alone. Table 1 summarizes the principal post-review developments considered in the synthesis.

Table 1. Main post-review developments relevant to bridge deployment readiness.

Research direction	Representative evidence	Main advance	Readiness and remaining limitation
Prestressed members	Qian et al. [2]; Magnuson et al. [3]	Time-dependent composite-girder testing and full-scale precast/prestressed production	Full-scale feasibility demonstrated; time-dependent prestress, bond and serviceability require longer validation.
Full-scale component SHM / pilot-deployment readiness	Cheng et al. [4]	Embedded ultrasonic indicators validated on prestressed AAC beams and a slab	Full-scale component validation achieved; field thresholds and environmental compensation remain unresolved.
Deck repair interfaces	Li et al. [5]; Zhao et al. [6]	Bond-strength relations, bond-slip behavior, and crack-evolution assessment	Design-oriented bond models emerging; cyclic and environmental interface durability remains uncertain.
Durability qualification	Castel et al. [7]	RILEM 10 V RCPT recommendation validated against bulk diffusion testing	AAC-specific chloride classification available; corrosion thresholds and service-life transfer still require validation.
Fatigue and cyclic demand	Melo et al. [8]	Consolidation of formulation, frequency, fiber, and environmental effects	Evidence base expanding, but standardized S–N/design relationships remain unavailable.
Anchorage and structural design	Rúa-Patiño et al. [9]	Microstructure-informed extension of anchorage mechanics	Mechanistic design framework emerging; calibration range remains too narrow for code use.
High-performance and standardization	Xu et al. [10]; Ye and Dehn [11]; Kar et al. [12]	HS-EGC synthesis and RILEM consolidation/interlaboratory evidence	Reproducibility improving; scale-up, long-term behavior and cost remain barriers.

3 Recent progress toward deployment

3.1 Prestressed members and time-dependent structural response

The clearest advance is the increased attention to prestressed AAC at realistic member scale. Qian et al. [2] investigated composite girders comprising a precast prestressed AAC inverted-T girder and a cast-in-situ AAC topping. Compared with the 28-day reference specimen, the specimen tested at approximately nine months exhibited a 44% lower cracking load. Moreover, the 0.2 mm crack-width criterion was reached at load levels of 160 and 180 kN for the two nine-month specimens, compared with 220 kN for the 28-day specimen. The authors attributed the reduced cracking resistance primarily to pronounced prestress losses associated with ongoing shrinkage and creep, while the larger crack widths may also reflect deterioration of bond between AAC and the prestressing strands.

The time-dependent effects also influenced failure mechanisms and analytical predictions. The nine-month specimen subjected only to self-weight developed anchorage failure, whereas the specimen subjected to additional sustained loading exhibited concrete crushing in the topping, indicating flexural failure. The authors further inferred a possible reduction in strand–AAC bond with time. Analytical models that neglected restrained shrinkage and creep between the precast girder and cast-in-situ topping underestimated prestress loss and consequently overestimated cracking resistance; agreement improved when the restraint level was incorporated. These findings indicate that 28-day structural testing alone is insufficient for

qualification of the AAC system investigated and that time-dependent prestress, bond, restraint, cracking, and anchorage behavior require explicit consideration in structural design [2].

Magnuson et al. [3] provide a complementary production-scale perspective. Full-scale prestressed AAC beams were successfully fabricated using existing precast-plant technology, but transferability of conventional design equations depended on the limit state. Measured flexural capacity was approximately 10% greater than the ACI 318-19 prediction, whereas two of three shear specimens developed capacities approximately 2–4% below the corresponding predictions, making the conventional shear calculation slightly unconservative for those specimens. Production was also sensitive to fresh-state control: unplanned addition of water to improve workability reduced compressive strength by as much as 33%. Although the AAC compressive strength at transfer was only 20.1 MPa, below the specified 24.1 MPa, no strand slip or end cracking was observed during prestress transfer [3]. These results show that deployment requires both limit-state-specific code calibration and controlled production protocols rather than a generic assumption that conventional concrete provisions transfer uniformly to AAC.

3.2 Bridge-deck repair and rehabilitation interfaces

Repair and rehabilitation may offer a lower-risk adoption pathway than complete replacement of conventional bridge concrete. Li et al. [5] investigated GPC for bridge-deck strengthening and showed that substrate treatment governed interface performance: direct-shear bond strength increased from approximately 3.05 MPa for untreated concrete to 3.90 MPa for grooved and 4.55 MPa for roughened surfaces. Hooked steel fibers provided additional mechanical interlocking, but their effectiveness depended strongly on adequate substrate roughness. The study also developed a bond-strength expression and bilinear bond-slip model, moving the evidence toward structural analysis rather than isolated interface tests [5].

Zhao et al. [6] provide an important counterpoint to strength-based optimization. Increasing red-mud content improved compressive and interfacial bond strength, but high red-mud contents reduced flexural strength and increased brittle behavior. Together, these studies show that bridge-repair qualification should consider fracture behavior, compatibility, cyclic degradation, thermal and moisture effects, and long-term bond retention rather than maximizing short-term bond or compressive strength alone [5, 6].

3.3 Durability qualification and standardization

One of the most consequential standardization advances is the RILEM TC 283-CAM recommendation for chloride transport [7]. Because the conventional 60 V ASTM C1202 procedure can cause excessive heating in AAC, the recommendation adopts a 10 V rapid chloride permeability test (RCPT) validated against ASTM C1556 bulk diffusion tests. It proposes three permeability classes: ≤200 C as low, 200–600 C as medium, and >600 C as high. Low-permeability AAC was considered suitable for severe chloride exposure, including tidal conditions, subject to the important assumption that its corrosion-initiation chloride threshold is comparable to that of conventional concrete. Medium-permeability mixtures require additional diffusion-based verification for severe exposure, while high-permeability mixtures cannot be qualified for reinforced chloride environments from the 10 V test alone.

The 2026 RILEM state-of-the-art report [11] and interlaboratory work on fiber-reinforced Ground Granulated Blast-Furnace Slag (GGBFS)-based AAC [12] further indicate that the standardization problem is shifting from absence of evidence toward conversion of experimental knowledge into transferable design provisions, performance classes, and acceptance criteria.

3.4 Fatigue, anchorage, and high-performance composites

Traffic loading makes fatigue a central bridge-specific issue. Melo et al. [8] identified only 33 relevant AAC fatigue studies, of which 83.3% concerned flexural fatigue, 13.3% compressive fatigue, and 3.3% punching shear. Test configurations, loading frequencies, environmental conditions, and mixture formulations remain heterogeneous, and one-third of the studies did not apply statistical analysis despite the intrinsic scatter of fatigue data. Although several studies reported favorable AAC behavior, superiority over Portland-cement concrete cannot be generalized; one reinforced-beam study reported delayed crack initiation but approximately 15% lower fatigue life. Accordingly, the current literature is insufficient to establish transferable AAC-specific S–N relationships or bridge fatigue resistance factors.

At the reinforcement level, Rúa-Patiño et al. [9] proposed a microstructure-informed extension of classical anchorage mechanics in which gel density and interfacial porosity are linked to bond response; gel chemistry explained approximately 93% of the observed variation in 28-day anchorage stiffness within the investigated program. However, calibration was limited to a single Class-F fly-ash AAC system, one bar diameter, two cover depths, and quasi-static loading. Its significance is therefore methodological rather than code-ready: it demonstrates how binder chemistry may eventually be translated into structural design parameters, while broader validation remains necessary for development length, splitting, confinement, sustained loading, and fatigue.

High-strength engineered geopolymer composites (HS-EGC) expand the material design space, but remain at an earlier deployment stage. Xu et al. [10] screened approximately 2500 records yet identified only 44 studies satisfying their strict HS-EGC criteria, despite reported compressive strengths reaching approximately 180 MPa in optimized systems. For bridge engineering, their most credible near-term role is therefore selective use in thin overlays, joints, closure regions, or localized strengthening where tensile ductility and crack control provide disproportionate benefit. Long-term shrinkage, scale-up, activator impacts, fiber cost, and structural validation remain barriers to broader application.

3.5 Structural health monitoring (SHM) as an enabling technology

Cheng et al. [4] validated embedded piezoelectric ultrasonic indicators through full-scale laboratory tests on two prestressed AAC beams and a slab assembled from three beams, providing a basis for subsequent pilot-bridge monitoring. Within the controlled tests, a waveform-coherency coefficient of approximately 0.85 was associated with serviceability-limit-state crack initiation and a relative wave-velocity ratio of approximately 0.90 with more advanced damage; however, these values are material-, geometry-, and loading-specific rather than universal thresholds [4].

The significance of this work lies not only in the sensing technique but in using SHM as part of the qualification strategy for an emerging bridge material. Field interpretation nevertheless remains unresolved because ultrasonic indicators may respond simultaneously to traffic-induced stress, crack opening and closure, creep, shrinkage, temperature, environmental variation, and sensor drift. Project-specific calibration, adaptive baselines, and multi-sensor cross-validation are therefore required before laboratory indicators can function as quantitative bridge-management thresholds.

4 What has changed since the 2025 review?

Compared with the evidence synthesized in the 2025 review [1], the principal advance is not a sudden increase in completed GPC/AAC bridges but a shift in the quality of deployment-enabling evidence. Structural-scale testing now includes prestressed beams, composite girders, and bridge-deck assemblies [2-4]; time-dependent prestress, creep, shrinkage, restraint and strand bond are being addressed as coupled structural problems [2]; bridge-repair research is

progressing toward interface constitutive models [5, 6]; durability assessment now includes an AAC-specific performance-based chloride procedure [7]; and SHM has emerged as an enabling tool for pilot-deployment readiness [4]. Collectively, these developments shift the dominant question from basic material feasibility toward reliability across production, serviceability, durability, monitoring, and code verification. Fig. 1 conceptually summarizes this transition from material feasibility to deployment readiness. The final two stages in Fig. 1 represent the forward deployment pathway rather than the current state; the available evidence is concentrated primarily on component verification, qualification, and preparation for monitored pilot deployment.

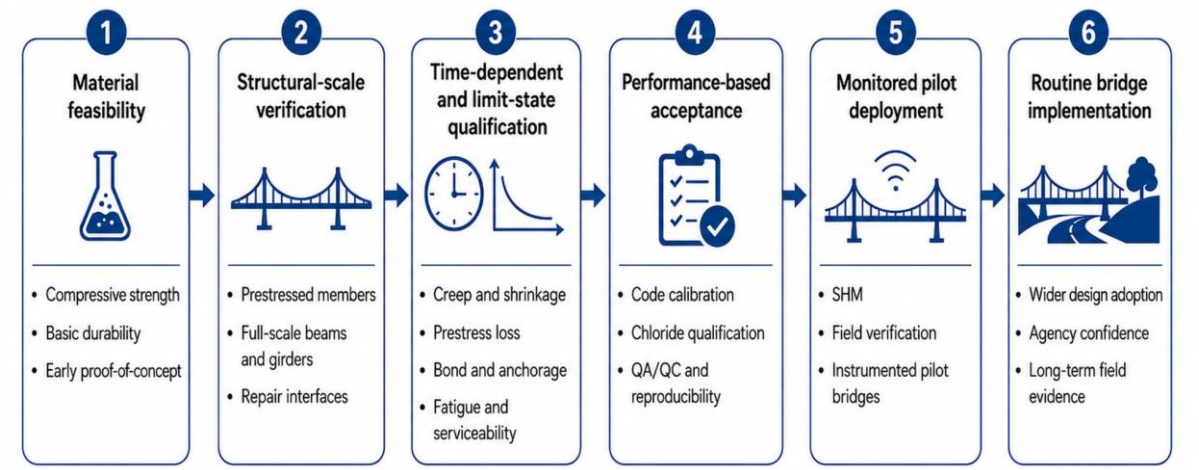


Fig. 1. Evolution of geopolymer-based bridge research from material feasibility to deployment readiness.

Despite this progress, the evidence remains insufficient to support routine deployment in primary highway bridge structures. The recent studies are concentrated in a limited number of material systems and research groups; long-term observations are measured in months or a few years rather than decades; fatigue and environmental effects are rarely coupled; and code calibration remains incomplete. The current stage is best described as preparation for monitored pilot deployment and design-method maturation rather than widespread commercialization for primary highway bridge structures.

5 Priority research needs for bridge engineering

The first priority is long-term prestressed behavior. Multi-year tests are needed to quantify creep, shrinkage, relaxation interaction, strand bond, transfer length, camber, deflection, cracking, and anchorage performance under sustained loading, with particular attention to the large reduction in cracking resistance and altered failure modes observed in [2]. The influence of precast-to-cast-in-situ restraint identified in [2] should be extended to realistic composite deck and girder details, temperature gradients, differential drying, and staged construction.

The second priority is coupled fatigue-durability testing. The current fatigue database is too heterogeneous to define bridge-specific S–N relationships reliably [8]. Bridge decks and girders experience repeated traffic loading while simultaneously being exposed to chlorides, wet-dry cycles, freeze-thaw action, temperature variation, and in some regions deicing salts. Separate fatigue and durability tests cannot fully represent these interactions. A useful bridge-oriented program should measure stiffness degradation, crack growth, residual strength, chloride transport, reinforcement corrosion, and bond deterioration under combined cyclic and environmental exposure. The fatigue synthesis in [8] provides a basis for defining the variables that require standardization.

The third priority is code calibration and performance-based qualification. The 10 V RCPT recommendation [7] is an important model because it adapts the test method to the binder rather than forcing AAC into an unsuitable Ordinary Portland Cement (OPC)-based procedure. Similar efforts are needed for elastic modulus, creep and shrinkage, tensile strength, shear, anchorage, prestress loss, crack-width control, and fatigue. The different flexural and shear prediction trends observed in [3] demonstrate that conventional code equations should be evaluated separately by material family and limit state, with model bias and uncertainty quantified explicitly.

The fourth priority is field-scale verification with transparent monitoring data. Pilot bridges should be instrumented before opening to traffic, with baseline measurements and documented material characterization. Monitoring should capture deformation, strain, temperature, cracking, and where appropriate ultrasonic or acoustic indicators [4, 13, 14]. The work in [4] demonstrates a technically credible starting point. Open or at least well-documented datasets would allow independent validation and accelerate confidence among bridge authorities. Field interpretation should include environmental compensation and adaptive baseline updating rather than direct transfer of laboratory SHM thresholds [4].

Finally, deployment studies should integrate constructability and sustainability. A bridge material is not low-carbon in practice if it depends on impractical curing, highly variable precursors, excessive activator transport, difficult quality control, or premature repair. Future assessments should therefore link structural performance to mixture variability, batching scale, curing demand, local precursor availability, service life, maintenance, and end-of-life scenarios. High-performance geopolymer composites may be most effective when used selectively in components where their properties produce a measurable reduction in material quantity or maintenance demand rather than through indiscriminate full-volume substitution [10].

6 Conclusions

The 2025–2026 evidence confirms measurable progress from material feasibility toward deployment-oriented bridge engineering. Full-scale prestressed AAC members can be produced using conventional precast infrastructure, but structural design transfer is limit-state dependent: available testing found conventional flexural predictions conservative while some shear predictions were slightly unconservative. More importantly, nine-month testing of prestressed composite girders revealed a 44% reduction in cracking load relative to the 28-day reference, increased crack widths, substantial prestress loss, bond deterioration, and age-dependent anchorage behavior. These results establish time-dependent serviceability, bond, and restraint as primary design issues rather than secondary material effects.

Parallel progress has occurred in deployment-enabling technologies. GPC repair studies now provide quantitative interface and bond-slip models; RILEM has introduced an AAC-specific chloride-permeability classification; fatigue research has expanded but remains too heterogeneous for transferable bridge design relationships; and full-scale laboratory bridge components have demonstrated embedded ultrasonic indicators intended for pilot-bridge monitoring. Anchorage and HS-EGC research further indicate movement toward material-specific structural design, although both remain insufficiently validated for routine code application.

Accordingly, short-term compressive strength should no longer be treated as the sole qualification criterion for geopolymer-based bridge materials. The near-term pathway is selective deployment in controlled precast applications, rehabilitation systems, high-value localized components, and monitored pilot bridges, accompanied by long-term prestress and bond characterization, coupled fatigue-durability testing, limit-state-specific code calibration, performance-based durability qualification, and transparent field monitoring. Current evidence supports design-method maturation and preparation for monitored pilot deployment, but not yet

routine substitution of AAC/GPC for conventional concrete in primary highway bridge structures.

References

1. Çetindemir, O.: Geopolymer-based applications for bridge structures: A review. Structural Concrete 26, 2998–3052 (2025). https://doi.org/10.1002/suco.70087
2. Qian, Z., Zhang, S., Ye, G., Matthys, S., Luković, M.: Time-dependent flexural behaviour of prestressed alkali-activated concrete (AAC) girder with cast-in-situ AAC topping. Construction and Building Materials 484, 141615 (2025). https://doi.org/10.1016/j.conbuildmat.2025.141615
3. Magnuson, G.P., Christiansen, M.U., Dymond, B.Z.: Design and performance of precast, prestressed concrete beams made with fly-ash-based alkali-activated concrete. PCI Journal 70, 35–51 (2025). https://doi.org/10.15554/pcij70.4-02
4. Cheng, H., Zhang, S., Qian, Z., Ye, G., Yang, Y.: Evaluating cracking behaviours in precast prestressed alkali-activated concrete (AAC) bridge decks using ultrasonics-based damage indicators. Engineering Structures 360, 122675 (2026). https://doi.org/10.1016/j.engstruct.2026.122675
5. Li, X., Sun, Q., Li, J., Liu, Y., Sun, H., Zhang, C.: Experimental study on the shear performance of the bonding interface between geopolymer concrete and cement concrete. Journal of Building Engineering 103, 112193 (2025). https://doi.org/10.1016/j.jobe.2025.112193
6. Zhao, X., Jiang, J., Ou, X., Chen, M., Wei, D., Cai, X., Song, W., Yu, P.: Interfacial study of steel slag-red mud-based geopolymer concrete with cement concrete substrates: bond strength and crack evolution. Journal of Building Engineering 113, 114083 (2025). https://doi.org/10.1016/j.jobe.2025.114083
7. Castel, A., Nguyen, Q.D., Law, D., Kim, T., Samson, G., Cyr, M., Provis, J.L., Li, W.: Recommendation of RILEM TC 283-CAM: performance-based assessment of alkali-activated concrete durability using the 10 V rapid chloride permeability test. Materials and Structures 58, 219 (2025). https://doi.org/10.1617/s11527-025-02738-2
8. Melo, A.R., Souza, M.L., Gomes, J.E., Gomes, L.S., Sousa, A.I., Babadopulos, L.F.: Fatigue behavior of alkali-activated concrete linked to microstructural characteristics: a comprehensive review. Journal of Building Engineering 113, 114148 (2025). https://doi.org/10.1016/j.jobe.2025.114148
9. Rúa-Patiño, R., Hoyos-Montilla, A.A., Tobón, J.I.: Microstructural η: chemical–mechanical bridge for anchorage design in alkali–activated concretes. Materials and Structures 59, 170 (2026). https://doi.org/10.1617/s11527-026-02963-3
10. Xu, L.-Y., Lao, J.-C., Shi, D.-D., Cai, J., Xie, T.-Y., Huang, B.-T.: Recent advances in High-Strength Engineered Geopolymer Composites (HS-EGC): Bridging sustainable construction and resilient infrastructure. Cement and Concrete Composites 165, 106307 (2025). https://doi.org/10.1016/j.cemconcomp.2025.106307
11. Ye, G., Dehn, F.: Mechanical Properties of Alkali-Activated Materials: State-of-the-Art Report of the RILEM Technical Committee 294-MPA. Springer Nature: Cham, Switzerland (2026). https://doi.org/10.1007/978-3-032-07116-3
12. Kar, A., Chottemada, P.G., Hanžič, L., Kalyana Rama, J., Kara De Maeijer, P., Nematollahi, B., Ramagiri, K.K., Rossi, L., Šajna, A., Zhang, S., Zhang, M., Ye, G., Dehn, F.: RILEM TC 294-MPA: interlaboratory study of the mechanical properties of fiber-reinforced ground granulated blast furnace slag-based alkali-activated concrete. Materials and Structures 58, 230 (2025). https://doi.org/10.1617/s11527-025-02757-z
13. Karakostas, C., Quaranta, G., Chatzi, E., Zülfikar, A.C., Çetindemir, O., De Roeck, G., Döhler, M., Limongelli, M.P., Lombaert, G., Apaydın, N.M.: Seismic assessment of bridges

through structural health monitoring: a state-of-the-art review. Bulletin of Earthquake Engineering 22, 1309–1357 (2024). https://doi.org/10.1007/s10518-023-01819-3
14. Memisoglu Apaydin, N., Zulfikar, A.C., Cetindemir, O.: Structural health monitoring systems of long-span bridges in Turkey and lessons learned from experienced extreme events. Journal of Civil Structural Health Monitoring 12, 1375–1412 (2022). https://doi.org/10.1007/s13349-022-00551-x

Author Contribution Statement

- *Conceptualization:* Oğuzhan Çetindemir
- *Methodology:* Oğuzhan Çetindemir
- *Investigation:* Oğuzhan Çetindemir
- *Writing – Original Draft:* Oğuzhan Çetindemir
- *Writing – Review & Editing:* Oğuzhan Çetindemir

List of Abbreviations

- **AAC** — Alkali-Activated Concrete
- **AAMs** — Alkali-Activated Materials
- **GGBFS** — Ground Granulated Blast-Furnace Slag
- **GPC** — Geopolymer Concrete
- **HS-EGC** — High-Strength Engineered Geopolymer Composite
- **OPC** — Ordinary Portland Cement
- **RCPT** — Rapid Chloride Permeability Test
- **SHM** — Structural Health Monitoring

Conflict of Interest

The author declares no conflict of interest.

Data Availability

No new experimental or field data were generated in this study. The evidence synthesized in the paper is available in the cited publications.

Publication Note

This paper was peer-reviewed, accepted for presentation, and included in the proceedings of the ACE2026 – International Conference on Advances in Civil Engineering, held on 12–14 October 2026 in Trabzon, Türkiye.

This paper may be cited as follows:

Çetindemir O., "Recent Progress in Geopolymer-Based Applications for Bridge Structures: From Material Feasibility to Deployment Readiness," in Proceedings of the ACE2026 – International Conference on Advances in Civil Engineering, Trabzon, Türkiye, 12–14 October 2026.

Bridge Damage during the 2023 Kahramanmaraş Earthquake Sequence: Failure Mechanisms and Seismic Risk-Reduction Strategies

Oğuzhan Çetindemir[1]
[1] 0000-0002-1018-4515, İstanbul Okan University, Department of Motor Vehicles and Transportation Technologies, İstanbul, Türkiye, oguzhan.cetindemir@okan.edu.tr

Abstract. The 6 February 2023 Kahramanmaraş earthquake sequence produced a rare regional dataset for evaluating the seismic resilience of highway bridges under intense shaking, near-fault effects, and widespread ground failure. This study presents a document-based forensic synthesis of observed bridge damage and translates the observations into a mechanism-based risk-reduction framework. Reconnaissance groups collectively visited 140 bridges, with performance ranging from no damage to total collapse. Recurring damage included abutment cracking and translation, shear-key failure, bearing displacement or dislodgement, girder distress, pier plastic hinging and residual drift, and damage to decks and carried utilities. Representative cases from Hatay, including the Demirköprü, Karasu, Hatay Stadium, D817, Bekir Karabacak, and Utku Acun Street bridges, show that structural damage was frequently coupled with liquefaction, lateral spreading, riverbank instability, approach settlement, and abutment movement. The central finding is that many severe outcomes resulted from a system-level failure chain rather than from one deficient component. Accordingly, the paper proposes an integrated mitigation strategy combining liquefaction and lateral-spreading screening, foundation and abutment strengthening, unseating prevention, displacement-capable bearings and expansion joints, ductile and replaceable shear keys, pier retrofit, appropriately designed isolation or damping devices, fragility-based network prioritization, and structural health monitoring (SHM). The framework is intended to support retrofit decisions for existing bridge inventories in Türkiye and comparable high-seismicity regions.

Keywords: Kahramanmaraş earthquakes; bridge damage; liquefaction; lateral spreading; seismic retrofit; bridge resilience.

1 Introduction

Bridges are not only individual structural assets; after a major earthquake they become part of the emergency-response system. Loss of a bridge can isolate communities, delay rescue and medical access, interrupt utility corridors, and force traffic onto longer or less reliable routes. This system role is why bridge seismic design cannot be judged solely by collapse prevention. The relevant performance objectives also include controlled damage, rapid inspection, continued or quickly recoverable functionality, and network redundancy. These objectives are consistent with the broader resilience concepts of robustness, redundancy, resourcefulness, and rapidity [1].

The 6 February 2023 Kahramanmaraş earthquake sequence provides an unusually important case history. Bas et al. [2] compiled observations from multiple reconnaissance groups that collectively visited 140 bridges; the reported damage spectrum extended from no damage to total collapse. The most common component-level observations included abutment cracking and shifting, failure of pier-cap shear blocks, bearing-pad movement or dislodgement, girder cracking and loss of prestress, plastic hinging and residual drift of piers, and distress to deck

surfaces, handrails, and carried utilities. These observations resemble failure modes documented after earlier destructive earthquakes, including the 1994 Northridge [3] and 2010 Maule [4] events, but the 2023 sequence is particularly instructive because structural demands were repeatedly combined with liquefaction, lateral spreading, approach settlement, and riverbank instability.

The geotechnical contribution is evident in the bridge-specific case histories. Demirköprü Bridge experienced liquefaction-induced failure of its pile foundation and retaining system [5], while the Karasu Bridge approaches developed mapped lateral spreading exceeding 1.5 m and settlements of approximately 0.40-0.55 m [6]. Regional liquefaction reconnaissance further documented extensive soil ejecta and ground deformation, including severe liquefaction-related damage near Demirköprü Bridge [7]. Detailed GEER surveys of four concrete bridges in Antakya recorded large deck translations, abutment rotations, pile cracking and spalling, shear-key damage, retaining-wall failures, and slope movements adjacent to river crossings [8].

The principal engineering question therefore extends beyond documenting what failed: which interventions could have interrupted the observed failure chains, and how should limited retrofit resources be prioritized? Seismic fragility research has established probabilistic methods for linking ground-motion intensity, component demand, damage state, and system performance [9-14]. Retrofit studies show that relative displacement, unseating potential, and isolation performance can be modified substantially through targeted devices and component upgrades [14-16]. Soil-pile-structure interaction (SPSI) research likewise demonstrates that foundation response and kinematic soil demands must be represented explicitly when bridge behavior depends on deforming ground [17].

This work critically synthesizes the 2023 bridge observations with these established seismic assessment and retrofit concepts. Its contribution is a mechanism-to-intervention framework that links the observed damage to practical risk-reduction measures at the ground, foundation, abutment, bearing, superstructure, pier, and network levels.

2 Evidence Base and Analytical Framework

2.1 Selection and use of sources

The evidence base comprises 20 references selected to balance event-specific observations with established studies on bridge seismic performance, fragility, retrofit, SPSI, resilience, and structural health monitoring (SHM). Priority was given to (i) peer-reviewed studies and reconnaissance reports directly addressing the 2023 earthquake sequence and (ii) widely cited foundational studies providing the analytical and mitigation basis for interpreting the observed damage. The seven event-specific sources [2, 5-8, 18, 19] provide the observed evidence; the remaining sources [1, 3, 4, 9-17, 20] provide the analytical and mitigation basis used to interpret that evidence. Table 1 summarizes these evidence classes, their primary roles in the present study, and the corresponding references.

Table 1. Evidence classes used in the mechanism-based synthesis.

Evidence class	Primary role in this study	References
Regional bridge reconnaissance	Regional damage spectrum and recurring component failure modes	[2, 8]
Liquefaction-related bridge case histories	Ground deformation, abutment/foundation response, and serviceability loss	[5-7]
Monitored bridge and expansion-joint performance	Observed dynamic response, joint/device demand, and monitoring value	[18, 19]
Empirical and analytical fragility	Component/system vulnerability and retrofit prioritization	[3, 9-13]

Evidence class	Primary role in this study	References
Retrofit, SPSI, and historical bridge evidence	Restraining, isolation, foundation interaction, and transferable failure lessons	[4, 15-17]
Resilience and SHM	Network-level objectives and rapid post-event decision support	[1, 20]

2.2 Failure-chain interpretation

For each case, the observed damage is interpreted through six linked stages: hazard and ground deformation; foundation/abutment response; component response; substructure response; system-level failure; and operational consequence. A corresponding intervention is then assigned to the earliest feasible point in the failure chain. This is important because strengthening a downstream component can simply transfer demand elsewhere. For example, a stronger shear key does not solve liquefaction-induced abutment translation, and a high-capacity bearing does not eliminate unseating risk if seat width and residual ground displacement are inadequate. The proposed measures should therefore be understood as coordinated design checks rather than isolated products. The resulting system-level failure chain and the corresponding intervention points are schematically illustrated in Fig. 1.

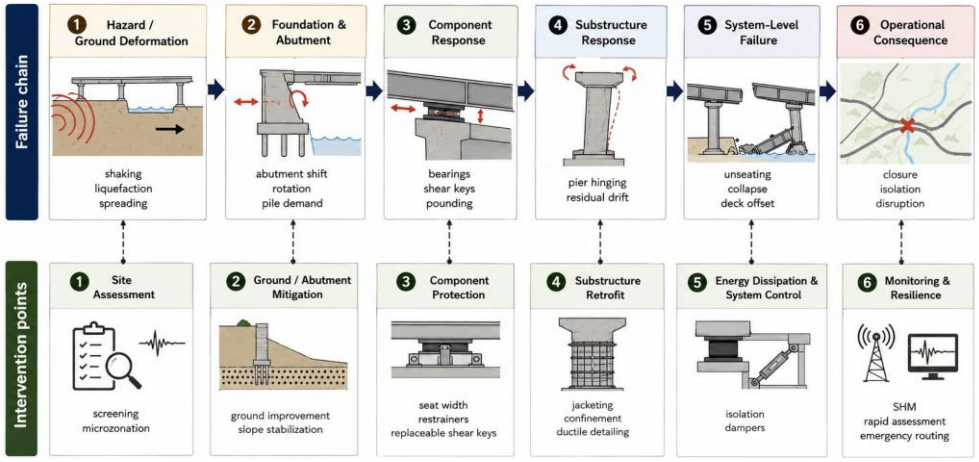


Fig. 1. Conceptual system-level failure chain for earthquake-induced bridge damage and corresponding intervention points.

3 Observed Bridge Damage and Dominant Failure Mechanisms

3.1 Regional pattern

Regional observations show recurring damage to bearings, shear blocks, abutments, deck interfaces, girders, and piers [2], consistent with system-fragility studies showing that multiple components can jointly control bridge vulnerability [12, 13]. Even without collapse, failure of bearings, joints, shear keys, approaches, or utility crossings could control functionality. At river crossings, structural and geotechnical response were inseparable: liquefaction, slope movement, and permanent ground displacement imposed kinematic demands and residual offsets on abutments and piles, as illustrated by Demirköprü, Karasu, and the GEER Antakya surveys [5-8].

3.2 Representative case histories

Representative bridge case histories were examined to identify how site-specific geotechnical conditions and structural vulnerabilities interacted during the earthquake sequence. Table 2 summarizes representative bridge cases illustrating interactions between site-specific ground deformation, support movement, and structural vulnerability, with damage ranging from localized distress to partial span collapse.

Table 2. Representative bridge observations from the 2023 Kahramanmaraş earthquake sequence, dominant interpreted mechanisms, and operational implications.

Bridge / location	Key observed damage	Dominant mechanism	Operational implication / source
Demirköprü Bridge, Hatay	Severe bridge damage associated with liquefaction; pile-foundation and retaining-system failure documented.	Liquefaction-induced permanent ground deformation and foundation/abutment demand.	Loss of operability / severe damage [5, 7].
Karasu Bridge, Hatay	Lateral spreading >1.5 m; mapped approach settlements about 0.40-0.55 m.	Liquefaction of silty sands; lateral spreading and differential settlement at approaches.	Major deformation threatening approach/bridge functionality [6].
Hatay Stadium Bridge	Deck transverse offsets about 17-21 cm at east abutment; south deck translation about 59-63 cm at west; shear-key and girder damage; local slope failure.	Pounding/sliding combined with approach settlement and riverbank instability.	Heavily damaged and closed to regular traffic during reconnaissance [8].
D817 Bridge, Antakya	Abutment/deck compression and separation; pile cracking/spalling; abutment tilt; riverbank offsets locally up to about 0.8 m.	Bank/slope movement imposed abutment rotation and pile kinematic demand, with deck pounding.	Remained open, but with distributed structural/geotechnical damage [8].
Bekir Karabacak Bridge	South deck uplift about 0.37 m; pavement compression up to about 0.50 m; deck cracking; all four wingwall/retaining-wall corners failed.	Large relative longitudinal deformation and retaining-fill/abutment system failure.	Only the north twin bridge remained open during reconnaissance [8].
Utku Acun Street Bridge	Approach-deck gaps about 0.10-0.16 m; north deck shifted about 0.17 m; girder cracking, shear-key damage, bearing relative movement.	Lateral movement toward river plus abutment rotation and deck/bearing displacement.	Open to traffic despite localized damage [8].
Old bridge south of Hatay Hospital	Three easternmost deck spans collapsed; local bank slumping was observed nearby.	Local collapse associated with severe support/ground movement environment; detailed causal attribution requires bridge-specific investigation.	Partial span collapse [8].

3.3 System-level interpretation

Across the cases, ground movement altered foundation or abutment geometry, generating relative displacement at deck supports and demand on bearings, shear keys, girders, and piers. Consequently, post-earthquake functionality was often governed by displacement compatibility rather than member strength alone [3, 4, 11-13].

Monitoring of the Nissibi, Ağın, and Kömürhan bridges further demonstrated the value of recorded response for rapid condition assessment [18], while expansion-joint observations confirmed that special devices remain vulnerable when displacement capacity is incompatible with near-fault and permanent-deformation demands [19].

4 How Could the Observed Damage Have Been Reduced?

The principal damage mechanisms identified from the 2023 observations and the corresponding risk-reduction measures are schematically summarized in Fig. 2. The figure emphasizes that seismic mitigation should address the bridge as a coupled ground–foundation–substructure–superstructure system rather than as a collection of isolated components.

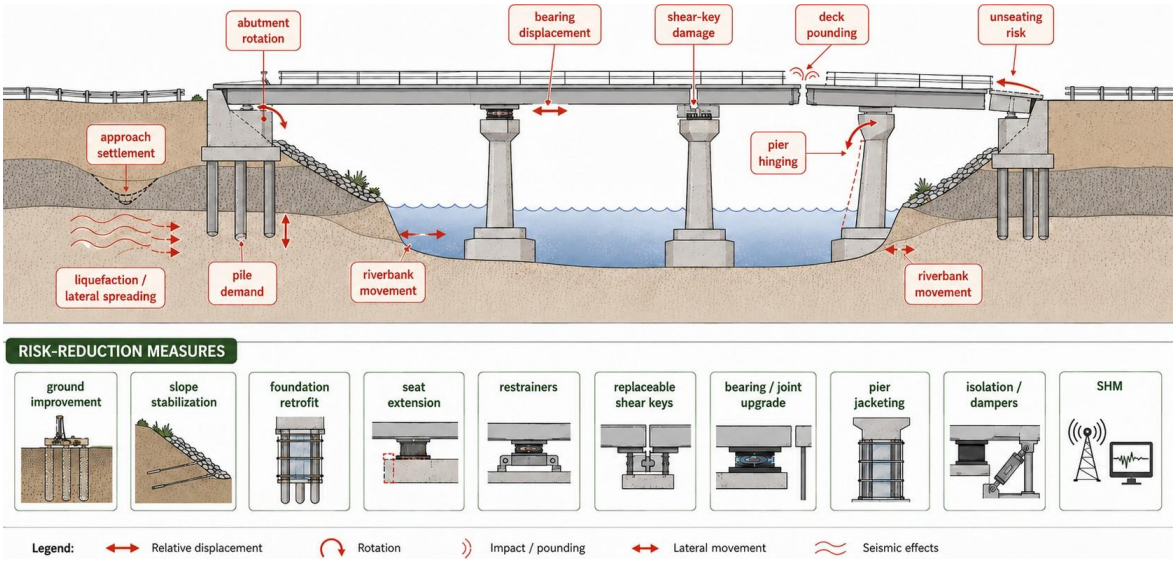


Fig. 2. Major bridge damage mechanisms identified from the 2023 Kahramanmaraş earthquake observations and corresponding seismic risk-reduction measures.

4.1 Geotechnical screening, ground improvement, and foundation design

The highest-priority intervention for river crossings on young alluvium is to quantify permanent ground-deformation demand before selecting a structural retrofit. The Demirköprü and Karasu cases [5-7] show that liquefaction and lateral spreading can generate displacement demands far larger than those implied by inertial analysis alone. A screening program should therefore identify saturated loose or medium-dense granular layers, susceptible silty mixtures, free faces, riverbanks, approach fills, retaining systems, and evidence of historical or current lateral movement. Where screening indicates significant risk, bridge-specific investigations should evaluate liquefaction triggering, post-liquefaction strength, lateral-spreading displacement, settlement, and the kinematic loading imposed on piles and abutments.

Mitigation can then be selected at the source or at the structure. Source-oriented measures include densification, drainage, deep mixing, stone columns or other ground-improvement systems where constructability and environmental constraints permit; slope stabilization and retaining-system strengthening may be equally important near channels. Structural measures include piles and pile groups designed for combined inertial and kinematic actions, adequate ductility where yielding is permitted, and abutment details capable of accommodating predicted permanent ground displacement without brittle loss of support. The dynamic soil-pile-structure experiments of Boulanger et al. [17] underscore the need to represent nonlinear soil response and pile-soil interaction explicitly. For existing bridges, the key principle is not to "strengthen the pier first," but to determine whether the ground and foundation will impose the controlling deformation.

4.2 Unseating prevention, bearings, shear keys, and expansion joints

Several 2023 cases were dominated by large relative deck-to-support movements [2, 8, 19]. The first line of defense should therefore be a positive unseating-prevention system: sufficient seat width, seat extensions where necessary, longitudinal and transverse restrainers, and details that maintain a viable load path after bearing displacement. Restrainer systems can substantially reduce relative movement; superelastic shape-memory-alloy (SMA) restrainers, for example, were shown by DesRoches and Delemont [15] to provide large recoverable deformation capacity in simply supported bridge retrofit applications. The specific restrainer type should be chosen from demand, durability, inspection, and replaceability requirements rather than from device novelty.

Bearings, shear keys, and expansion joints should be designed as a compatible system. Shear keys can act as sacrificial, replaceable fuses, but their protected components and post-yield load path must be explicitly defined. Bearing travel, uplift resistance where relevant, keeper geometry, and joint opening/closing capacity should be checked against bidirectional displacement histories and residual offsets, not only peak force demand. The Hatay Stadium and Utku Acun observations [8] illustrate the consequences of large transverse translation and shear-key/bearing movement, while Bayraktar et al. [19] demonstrate that near-fault pulse and permanent-deformation effects can produce severe joint and device demands. A practical retrofit therefore combines seat capacity, restraining, replaceable fuses, and sufficient joint/bearing travel rather than relying on one component.

4.3 Pier ductility and capacity-protected load paths

Pier plastic hinging and residual drift were among the regional damage modes reported by Bas et al. [2]. Where assessment identifies deficient confinement, inadequate lap-splice behavior, low shear margin, or poor displacement capacity, column retrofit should target stable cyclic ductility and an intentional hierarchy of strength. The objective is to prevent brittle shear or connection failure while allowing controlled flexural response in inspectable regions. Fragility-based retrofit studies [9, 14] are useful because they quantify whether a proposed intervention actually reduces bridge-system failure probability rather than merely increasing the capacity of one member. Particular attention is required when stronger piers or shear keys may transfer larger forces into foundations, caps, or bearings.

4.4 Isolation and damping under near-fault displacement demand

Seismic isolation can reduce force demand and fragility when the isolation system is properly selected and proportioned. Zhang and Huo [16] showed that isolation effectiveness and optimal properties can be evaluated directly through fragility functions. However, the 2023 sequence cautions against treating isolation or damping as a universal solution. Near-fault velocity pulses, large displacement demand, pounding, and permanent tectonic or ground offsets can govern performance [19]. Isolation bearings and dampers should therefore be checked for maximum and residual displacement, stroke, velocity, stability, temperature and aging effects, uplift or rotation where applicable, and the consequences of exceeding design travel. Supplemental damping is most effective when it is embedded within a displacement-compatible system that also provides adequate seats, joints, and restrainers.

4.5 Structural health monitoring and rapid post-earthquake assessment

A resilient bridge network must support fast decisions after shaking stops. Permanent monitoring cannot replace inspection, but it can identify changes in vibration characteristics, unusually large displacements, residual offsets, bearing/joint demand, or cable response and thereby prioritize field resources. The SHM framework summarized by Farrar and Worden [20] provides the general basis for data-driven condition assessment, while the 2023 monitored cable-stayed bridge study [18] demonstrates its direct value during a real earthquake sequence. For strategically important bridges, a minimum instrumentation package can include strong-motion accelerometers, displacement or joint sensors at selected supports, and environmental measurements needed to distinguish earthquake-induced changes from normal variability.

The most useful output is not a large volume of raw data but a pre-agreed decision protocol. Thresholds should be tied to inspection actions: immediate closure, restricted use, priority inspection, or continued operation subject to verification. Post-event measurements should also update analytical models and fragility estimates. In this way, monitoring becomes part of emergency management rather than a stand-alone research system. Based on the preceding observations and mitigation considerations, Table 3 synthesizes the principal vulnerabilities,

recommended intervention sequences, performance objectives, and supporting evidence into a mechanism-to-intervention framework.

Table 3. Mechanism-to-intervention matrix proposed from the 2023 observations.

Observed vulnerability	Preferred intervention sequence	Primary performance objective	Evidence
Liquefaction / lateral spreading	Screen site → quantify permanent deformation → improve ground or stabilize slope → design/retrofit piles and abutments for kinematic demand	Prevent loss of support and excessive residual deformation	[5-8, 17]
Short seats / unseating risk	Increase seat width → add longitudinal/transverse restrainers → verify residual support after bearing movement	Maintain gravity load path after large relative displacement	[2, 4, 15]
Bearing / shear-key damage	Define fuse hierarchy → provide replaceable shear keys/keepers → verify bearing travel and uplift/rotation demand	Control damage location and preserve inspectable/repairable support	[2, 8, 12-14, 19]
Expansion-joint pounding / opening	Displacement-based joint design → compatible bearings/restrainers → check near-fault pulse and residual offset	Maintain deck continuity and post-event serviceability	[8, 16, 19]
Pier hinging / residual drift	Assess ductility and shear → retrofit deficient regions → capacity-protect caps/foundations/bearings	Avoid brittle failure and excessive residual drift	[2, 9, 14]
Critical-route uncertainty after event	Install targeted SHM → define alarm/inspection thresholds → update fragility and emergency routing	Reduce closure uncertainty and inspection time	[2, 18, 20]

5 Proposed Risk-Reduction Framework for Bridge Networks in Türkiye

5.1 Screening and prioritization

A network-scale retrofit program should begin with consequences as well as fragility. Bridges carrying emergency routes, providing the only access across a river or valley, or supporting utilities should receive higher priority because their loss produces disproportionate system consequences [1]. Within that critical set, vulnerability screening should flag bridges with liquefiable foundations, riverbank free faces, large or skewed deck discontinuities, short seats, older or deteriorated bearings, unrestrained simply supported spans, deficient pier detailing, and high near-fault displacement demand. Component-based fragility methods [9-14] can then rank the probability of reaching operationally relevant damage states rather than relying only on qualitative condition scores.

5.2 A practical three-tier intervention hierarchy

For limited budgets, the recommended sequence is three-tiered. Tier 1 addresses collapse and access-loss mechanisms with high consequence: liquefaction/lateral-spreading hazards, inadequate seat width, missing restrainers, unstable abutment or retaining systems, and critical foundation deficiencies. Tier 2 targets repairability and downtime through bearing/joint replacement, ductile and replaceable shear keys, pier ductility upgrades, and protection of carried utilities. Tier 3 enhances rapid recovery through optimized isolation or damping where justified, strategic monitoring, digital bridge inventories, pre-defined inspection thresholds, and fragility-informed emergency routing. The tiers are cumulative; a sophisticated monitoring system should not substitute for a known unseating or foundation vulnerability.

This hierarchy also clarifies what “damage reduction” means. The objective is not necessarily to eliminate every crack or replaceable-device failure during an extreme event. A resilient design may deliberately concentrate damage in accessible fuses while preserving

foundation stability, gravity support, deck continuity, and emergency functionality. Fragility analysis is valuable precisely because it can compare alternative retrofit packages in terms of the probability of exceeding these system-level performance states [9, 13, 14]. The proposed three-tier intervention hierarchy and its progression from collapse prevention to rapid recovery are summarized in Fig. 3.

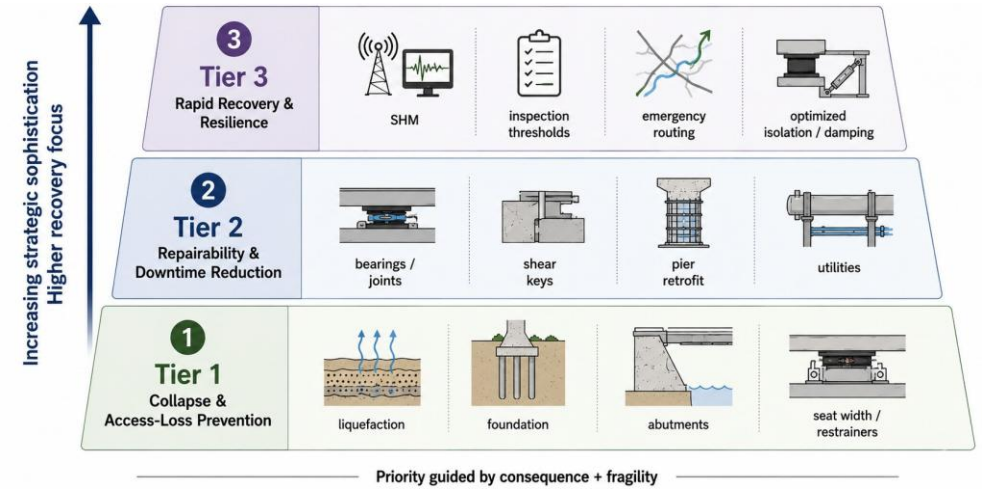


Fig. 3. Proposed three-tier hierarchy for seismic risk reduction and retrofit prioritization of bridge networks.

6 Conclusions

The 2023 Kahramanmaraş earthquake sequence showed that bridge performance was governed by coupled structural and geotechnical mechanisms. Across 140 bridges visited during post-earthquake reconnaissance, the damage spectrum ranged from no damage to total collapse, with recurring distress at abutments, shear blocks, bearings, girders, piers, decks, and utilities. Detailed Hatay case histories further showed that liquefaction, lateral spreading, approach settlement, riverbank instability, and retaining-system movement can initiate or amplify structural damage.

The most important risk-reduction lesson is therefore system compatibility. Ground, piles, abutments, bearings, shear keys, joints, decks, and piers must be checked as one displacement-sensitive load path. The highest-value interventions are: (1) site-specific liquefaction and permanent-ground-deformation assessment; (2) foundation and abutment measures that tolerate or reduce kinematic demand; (3) positive unseating prevention through seat capacity and restrainers; (4) bearings, shear keys, and joints designed as compatible and preferably replaceable components; (5) ductile, capacity-protected pier response; and (6) isolation or damping devices proportioned for near-fault displacement and residual offset rather than force reduction alone.

At network level, fragility-based prioritization and SHM can reduce both physical risk and post-event decision time. The proposed mechanism-to-intervention matrix should be treated as a screening framework: each bridge still requires site-specific geotechnical characterization, structural analysis, detailing review, and constructability assessment. The 2023 evidence nevertheless indicates that many severe consequences could be reduced by intervening earlier in the failure chain, before ground movement or support displacement is allowed to propagate into loss of deck support and network functionality.

References

1. Bruneau, M., Chang, S.E., Eguchi, R.T., Lee, G.C., O'Rourke, T.D., Reinhorn, A.M., Shinozuka, M., Tierney, K., Wallace, W.A., Von Winterfeldt, D.: A framework to

quantitatively assess and enhance the seismic resilience of communities. Earthquake spectra 19, 733–752 (2003). https://doi.org/10.1193/1.1623497
2. Bas, S., Hunt, J., Gencturk, B., Jampole, E., Sonmezer, Y.B., Chancellor, B., Bassal, P., Celiker, M., Apaydin, N., Sezen, H.: Seismic performance and damage assessment of bridges during the 2023 Kahramanmaras, Türkiye earthquakes (M w= 7.8, M w= 7.6). Earthquake Spectra 40, 2339–2363 (2024). https://doi.org/10.1177/87552930241262043
3. Basöz, N.I., Kiremidjian, A.S., King, S.A., Law, K.H.: 2. Statistical Analysis of Bridge Damage Data from the 1994 Northridge, CA, Earthquake. Earthquake spectra 15, 25–54 (1999). https://doi.org/10.1193/1.1586027
4. Kawashima, K., Unjoh, S., Hoshikuma, J.-I., Kosa, K.: Damage of bridges due to the 2010 Maule, Chile, earthquake. Journal of Earthquake Engineering 15, 1036–1068 (2011). https://doi.org/10.1080/13632469.2011.575531
5. Ocak, S., Cetin, K.O.: Liquefaction-Induced failure of Demirköprü Bridge pile foundation and retaining system following the February 6 Kahramanmaraş earthquake sequence. Journal of Earthquake Engineering 29, 3505–3519 (2025). https://doi.org/10.1080/13632469.2024.2390096
6. Ozkaynak, M.I., Cetin, K.O.: The performance of Karasu Bridge following the February 6, 2023 Kahramanmaras-Turkiye earthquake sequence. Engineering Geology 335, 107512 (2024). https://doi.org/10.1016/j.enggeo.2024.107512
7. Cetin, K.O., Soylemez, B., Guzel, H., Cakir, E.: Soil liquefaction sites following the February 6, 2023, Kahramanmaraş-Türkiye earthquake sequence. Bulletin of Earthquake Engineering 23, 921–944 (2025). https://doi.org/10.1007/s10518-024-01875-3
8. Moug, D., Bassal, P., Bray, J., Cetin, K., Kendir, S., Sahin, A., Cakir, E., Soylemez, B., Ocak, S.: February 6, 2023 Türkiye earthquakes: GEER phase 3 team report on selected geotechnical engineering effects. Geotechnical Extreme Events Reconnaissance (GEER) Association, Report No. GEER-082-S1 (2023). https://doi.org/10.18118/G6F379
9. Muntasir Billah, A., Shahria Alam, M.: Seismic fragility assessment of highway bridges: a state-of-the-art review. Structure and infrastructure engineering 11, 804–832 (2015). https://doi.org/10.1080/15732479.2014.912243
10. Shinozuka, M., Feng, M.Q., Lee, J., Naganuma, T.: Statistical analysis of fragility curves. Journal of engineering mechanics 126, 1224–1231 (2000). https://doi.org/10.1061/(ASCE)0733-9399(2000)126:12(1224)
11. Choi, E., DesRoches, R., Nielson, B.: Seismic fragility of typical bridges in moderate seismic zones. Engineering structures 26, 187–199 (2004). https://doi.org/10.1016/j.engstruct.2003.09.006
12. Nielson, B.G., DesRoches, R.: Seismic fragility methodology for highway bridges using a component level approach. Earthquake engineering & structural dynamics 36, 823–839 (2007). https://doi.org/10.1002/eqe.655
13. Nielson, B.G., DesRoches, R.: Analytical seismic fragility curves for typical bridges in the central and southeastern United States. Earthquake spectra 23, 615–633 (2007). https://doi.org/10.1193/1.2756815
14. Padgett, J.E., DesRoches, R.: Methodology for the development of analytical fragility curves for retrofitted bridges. Earthquake Engineering & Structural Dynamics 37, 1157–1174 (2008). https://doi.org/10.1002/eqe.801
15. DesRoches, R., Delemont, M.: Seismic retrofit of simply supported bridges using shape memory alloys. Engineering structures 24, 325–332 (2002). https://doi.org/10.1016/S0141-0296(01)00098-0
16. Zhang, J., Huo, Y.: Evaluating effectiveness and optimum design of isolation devices for highway bridges using the fragility function method. Engineering Structures 31, 1648–1660 (2009). https://doi.org/10.1016/j.engstruct.2009.02.017

17. Boulanger, R.W., Curras, C.J., Kutter, B.L., Wilson, D.W., Abghari, A.: Seismic soil-pile-structure interaction experiments and analyses. Journal of geotechnical and geoenvironmental engineering 125, 750–759 (1999). https://doi.org/10.1061/(ASCE)1090-0241(1999)125:9(750)
18. Bayraktar, A., Akköse, M., Taş, Y., Ventura, C.E., Yang, T.Y.: Monitored seismic performance assessment of cable-stayed bridges during the 2023 Kahramanmaraş earthquakes (M7. 7 and M7. 6). Journal of Civil Structural Health Monitoring 14, 1667–1685 (2024). https://doi.org/10.1007/s13349-024-00807-8
19. Bayraktar, A., Taş, Y., Akköse, M., Hökelekli, E., Ventura, C.E., Yang, T.Y.: Seismic performance of bridge expansion joints with and without viscous dampers during the 6 February 2023 Kahramanmaraş earthquakes. Buildings 14, 2538 (2024). https://doi.org/10.3390/buildings14082538
20. Farrar, C.R., Worden, K.: An introduction to structural health monitoring. New trends in vibration based structural health monitoring 1–17 (2010). https://doi.org/10.1007/978-3-7091-0399-9_1

Author Contribution Statement

- *Conceptualization:* Oğuzhan Çetindemir
- *Methodology:* Oğuzhan Çetindemir
- *Investigation:* Oğuzhan Çetindemir
- *Writing – Original Draft:* Oğuzhan Çetindemir
- *Writing – Review & Editing:* Oğuzhan Çetindemir

Conflict of Interest

The author declares no conflict of interest.

Data Availability

No new experimental or field data were generated in this study. The evidence synthesized in the paper is available in the cited publications and reconnaissance report.

List of Abbreviations

GEER - Geotechnical Extreme Events Reconnaissance
SHM - Structural Health Monitoring
SMA - Shape-memory-alloy
SPSI - Soil-pile-structure Interaction

Publication Note

This paper was peer-reviewed, accepted for presentation, and included in the proceedings of the ACE2026 – International Conference on Advances in Civil Engineering, held on 12–14 October 2026 in Trabzon, Türkiye.

This paper may be cited as follows:

Çetindemir O., "Bridge Damage during the 2023 Kahramanmaraş Earthquake Sequence: Failure Mechanisms and Seismic Risk-Reduction Strategies," in Proceedings of the ACE2026 – International Conference on Advances in Civil Engineering, Trabzon, Türkiye, 12–14 October 2026.

Performance of Metaheuristic Algorithms in Cost Optimization of Precast Segmental Circular Tunnel Linings

Semiha Hayrioğlu[1] and Hasan Tahsin Öztürk[2]
[1] 0000-0002-0770-4321, Karadeniz Technical University, Graduate School of Natural and Applied Science, Department of Civil Engineering, Trabzon, Türkiye
semihahayrioglu@gmail.com
[2] 0000-0001-8479-9451, Karadeniz Technical University, Department of Civil Engineering, Trabzon, Türkiye
htozturk@ktu.edu.tr

Abstract. This study evaluates the performance of twenty contemporary metaheuristic algorithms in the minimum cost optimization of precast reinforced concrete segmental tunnel linings. The optimization model aims to minimize costs by determining the optimal joint locations, lining thickness, and principal reinforcement amount across a six-segment lining system. The problem is formulated using twelve discrete design variables, with design viability governed by eight structural and geometric constraints. Structural analyses are conducted employing a computationally efficient analytical method tailored for optimization processes. The research investigates the impacts of geometry and soil quality on the optimal design by systematically varying the tunnel radius (2.5 to 4.5 m) and the subgrade reaction coefficient of the surrounding soil (5,000 to 20,000 kN/m³). To ensure a rigorous and fair comparison, the algorithmic simulations are assessed using standard statistical metrics alongside non-parametric Friedman and Wilcoxon tests. Furthermore, stability analyses are executed for the top three competitive algorithms. The findings indicate that the vertical displacement limit at the tunnel crown acts as the primary active constraint dictating the design, particularly under weak soil conditions. Furthermore, concrete expenses constitute a significantly larger share of the total cost compared to reinforcement expenses. Through rigorous statistical and stability analyses, the Cuckoo Search (CS) and Stochastic Fractal Search (SFS) algorithms are identified as the most robust and highest-performing methods. Consequently, these algorithms are highly recommended as effective computational tools for similar structural optimization problems in the literature.

Keywords: Optimization; Segmental Tunnel Lining; Cost; Metaheuristic Search Algorithms

1 Introduction

Escalating costs and limited resources necessitate that modern engineering projects satisfy strength and safety criteria at a minimum cost. In solving complex, non-linear optimization problems, heuristic algorithms are frequently preferred due to the implementation flexibility they provide. In Türkiye, the length of highway tunnels constructed over the past two decades has reached 753 km, and metro lines, which predominantly consist of circular precast concrete segmental linings, have reached 231 km. This rapid expansion indicates that optimization-oriented designs in such high-budget projects play a critical role in the national economy.

The literature encompasses various studies on the analytical modeling of segmental tunnel linings [1–6], the impact of the number of segments on structural behavior [7], machine learning-based prediction models [8], and the optimization of specific parameters using heuristic algorithms [9–11]. However, there is a lack of comprehensive research that simultaneously optimizes joint locations, lining thickness, and reinforcement quantities to

directly minimize lining costs. The primary reason for this gap is that the high computational cost associated with structural analyses significantly restricts iterative optimization processes.

Aiming to address this deficiency, the present study establishes a suitable foundation for the optimization process by employing an analytical structural analysis method [5] that features low computational complexity and proven accuracy. The main objective of this research is to determine the optimal design variables that minimize lining costs under various subgrade reaction coefficients and tunnel diameters, utilizing twenty different metaheuristic algorithms widely adopted in the literature. Algorithm performances are evaluated using non-parametric Friedman [12] and Wilcoxon [13] tests in accordance with standard experimental procedures, and stability analyses are conducted for the competitive algorithms. The paper is structured as follows: problem definition, discussion of the simulation findings, and presentation of the obtained results.

2 Problem Definition

In this section, an optimization problem related to the design of a segmented tunnel lining has been formulated. In this problem, the objective function consists of the cost per unit length of the tunnel lining. This objective function is given in Eq. 1.

$$min\ f(x) = V_c C_c + W_s C_s \tag{1}$$

Here, V_c represents the volume per unit length of the tunnel lining, C_c represents the unit cost of concrete, W_s represents the weight of reinforcement used per unit length of the tunnel lining, and C_s represents the unit cost of reinforcement. The optimization problem involves a total of 12 design variables, which are shown in Fig. 1.

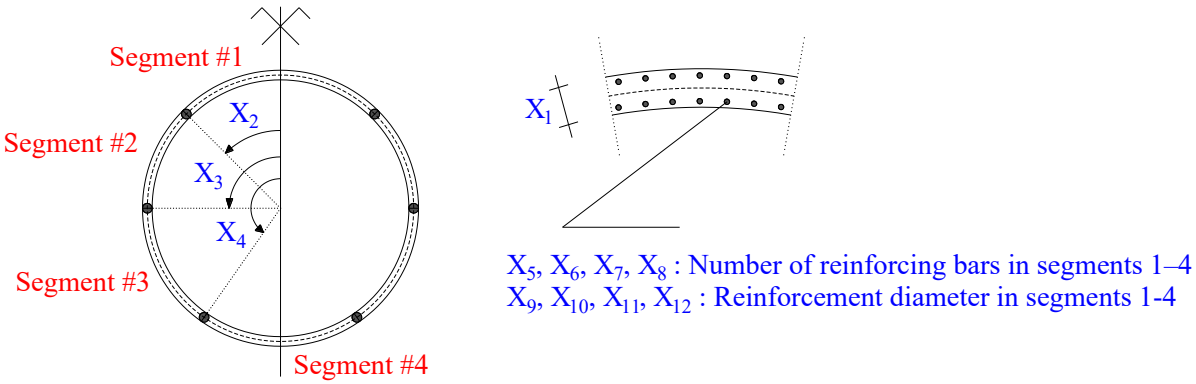


Fig. 1. Design variables of the problem.

While searching for the lowest-cost design during the optimization process, various constraints must be defined to ensure that the designs meet the necessary limit states in terms of strength and durability. The constraints presented here have been formulated in accordance with the conditions set forth in published international guidelines on segmental tunnel linings [14,15]. The first of these constraints involves verifying the moment-carrying capacity of the segment cross-sections. Since the segment cross-sections are subjected to combined bending effects, the condition $M_r \geq M_d$ is checked for the moment-carrying capacities calculated from the interaction diagrams created for the cross-sections, assuming $N_r = N_d$ in the cross-section under consideration. The normalized constraint in Eq. 2 was used for this check.

$$g_1(x) = \frac{M_d}{M_r} - 1 \leq 0 \tag{2}$$

For each member cross-section, the condition $V_r \geq V_d$ must be verified to ensure that the shear force-carrying capacity is met. Here, the shear force-carrying capacity (V_r) of the cross-section

is considered to be the shear force carried by the concrete in the member cross-section. The normalized constraint in Eq. 3 below is used for the shear force control.

$$g_2\,(x) = \frac{V_d}{V_r} - 1 \leq 0 \tag{3}$$

An analytical method with relatively low computational complexity was chosen to determine the design section effects (Nd, Md, Vd) in tunnel segments [5]. In this method, the force method is used for the structural analysis of a segmentally lined circular tunnel. In the relevant reference, the authors demonstrated the accuracy of the proposed method by comparing the internal forces obtained using this method with findings from model tests. In the method, the loading condition shown in Fig. 2 was established by taking into account the effects of soil and hydrostatic pressures on the tunnel. The guidelines of the International Tunneling Association [14] were used in the calculation of these loads.

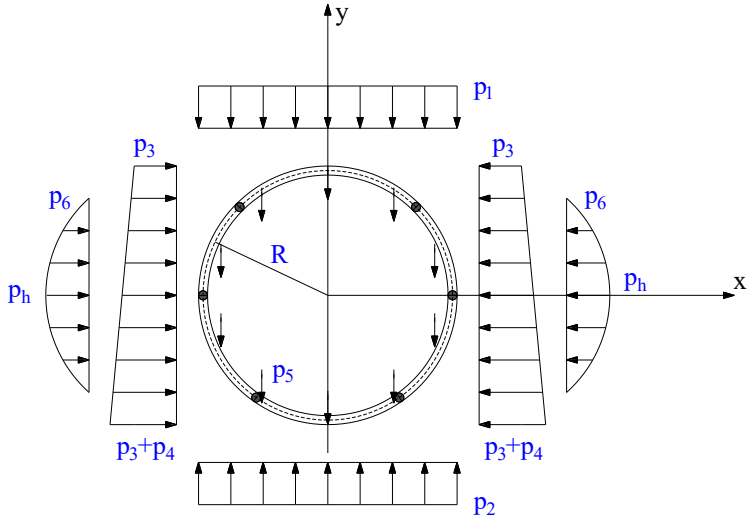


Fig. 2. Load condition considered for the tunnel [5].

The load combination given in Eq. 4 is used to determine the design section effects.

$$1{,}25(w + WA_p\,) + 1{,}35\,(EH + EV) + 1{,}5\,ES \tag{4}$$

Here, w represents the self-weight, WA_p represents groundwater pressure, EH represents horizontal soil pressure, EV represents vertical soil pressure, and ES represents surcharge load. The horizontal soil reaction, denoted by p6 in the loading condition shown in Fig. 2, is calculated using Eq. 5 based on the tunnel's horizontal displacement and the coefficient of soil reaction.

$$\mathrm{p_6} = \mathrm{p_h}(1 - 2\cos^2\varphi) \quad \rightarrow \quad \mathrm{p_h} = \mathrm{K_s} \cdot \Delta_\mathrm{h} \tag{5}$$

Here, p_h represents the soil resistance developing along the tunnel's centerline, φ is the angle measured vertically around the tunnel, K_s is the coefficient of soil reaction, and Δ_h is the horizontal displacement along the tunnel's centerline. For more detailed information on the calculation of cross-sectional effects, see references [5,16].

Another condition that must be monitored during the optimization process is the control of tunnel displacements. Regarding displacement limits, the literature recommends that the maximum displacement at the tunnel roof ($\Delta_{v,max}$) be 15 mm and the maximum displacement at the wall ($\Delta_{h,max}$) be 35 mm [17]. The normalized constraints in Eq. 6–7 were used for these checks.

$$g_3\,(x) = \Delta_v/\Delta_{v,max}\; - 1 \leq 0 \tag{6}$$

$$g_4\,(x) = \Delta_h/\Delta_{h,max}\; - 1 \le 0 \tag{7}$$

In addition, the reinforcement ratio limits in the designed cross-sections (segments) are also checked. In the design, the reinforcement ratio limits were set at ρ_{min} = 0.002 and ρ_{max} = 0.035 [18]. Let ρ denote the reinforcement ratio in the cross-section; for these checks, the normalized constraints in Eq. 8–9 were used.

$$g_5\,(x) = \frac{\rho_{min}}{\rho} - 1 \le 0 \tag{8}$$

$$g_6\,(x) = \frac{\rho}{\rho_{max}}\; - 1 \le 0 \tag{9}$$

The reinforcement spacing to be used in cross-sections must be a maximum (s_{max}) of 150 mm [18] and a minimum (s_{min}) of 25 mm [19]. These checks are performed using the following normalized constraints.

$$g_7\,(x) = \frac{s_{min}}{s} - 1 \le 0 \tag{10}$$

$$g_8\,(x) = \frac{s}{s_{max}} - 1 \le 0 \tag{11}$$

The design variables for circular tunnel design were shown in Figure 1. The lower and upper limits of the 12 design variables to be used in this study are presented in Table 1. To evaluate the optimal design for different tunnel diameters and coefficient of soil reaction a problem set consisting of the 9 problems listed in Table 2 was created.

The design parameters kept constant across all problem sets are presented in Table 3 below. The unit costs presented in Table 3 are taken from the 2026 construction and installation unit prices of the Ministry of Environment, Urbanization, and Climate Change of the Republic of Türkiye.

Table 1. Design variables for applications: lower and upper limits, increments

Design Variables	Lower Bound	Upper Bound	Increment
X_1	0,15 m	1 m	0,01
X_2	1°	60 °	1°
X_3	1°	60 °	1°
X_4	1°	59 °	1°
X_5	#1	#50	#1
X_6	#1	#50	#1
X_7	#1	#50	#1
X_8	#1	#50	#1
X_9	{10 12 14 16 18 20 22 24} mm		
X_{10}	{10 12 14 16 18 20 22 24} mm		
X_{11}	{10 12 14 16 18 20 22 24} mm		
X_{12}	{10 12 14 16 18 20 22 24} mm		

Table 2. Problem sets prepared for the evaluation of the optimal design for different tunnel diameters and coefficient of soil reaction

Problem Number	P1	P2	P3	P4	P5	P6	P7	P8	P9
Tunnel Radius	2,5 m	2,5 m	2,5 m	3,5 m	3,5 m	3,5 m	4,5 m	4,5 m	4,5 m
Subgrade Coefficient (kN/m^3)	5000	10000	20000	5000	10000	20000	5000	10000	20000

3 Results and Discussions

In this study, 20 meta-heuristic algorithms were used to investigate the optimal designs of segmented tunnel linings. These algorithms, listed in alphabetical order, as follows: Artificial Bee Colony (ABC), Big Bang–Big Crunch (BBBC), Child Drawing Development Optimization (CDDO), Coyote Optimization (COA), Cuckoo Search (CS), Differential Evolution (DE), Flower Pollination (FPA), Genetic Algorithm (GA), Gaining-Sharing Knowledge-Based (GSK), Grey Wolf Optimizer (GWO), Harmony Search (HS), JAYA, Particle Swarm Optimization (PSO), Simulated Annealing (SA), Stochastic Fractal Search (SFS), Snake Optimizer (SO), Symbiotic Organisms Search (SOS), Teaching Learning Based Optimization (TLBO), Transit Search (TS), and Whale Optimization (WOA). It is clear that performance comparisons of these algorithms will be influenced by their parameter settings. Therefore, to ensure a fair comparison, the parameter settings recommended by the developers of the meta-heuristic algorithms were used. Other conditions considered to objectively compare the search performance of the algorithms used are listed below.

- The maximum number of function evaluations (maxFEs) was used as the algorithm's termination criterion, and maxFEs was set to 10,000xD. Here, D represents the number of design variables.
- For each problem, 25 independent simulations were performed using each algorithm.
- All experimental studies were conducted in a laboratory equipped with an Intel® Core™ i5-144000F CPU @ 2.50 GHz Intel® X64 processor and 16 GB of RAM, using MATLAB R2026a.

Table 3. Design parameters to be kept constant across all problem sets

Design Parameter	Value	Unit
Relative stiffness ratio of the joint	0,1	-
Embedded depth	30	m
Concrete Grade	C30	-
Steel Grade	B420C	-
Young's modulus	35000	MPa
Segment width	1000	mm
Net concrete cover	50	mm
Soil horizontal pressure coefficient	0,50	-
Overcharge load	30	kN/m^2
Unit cost of steel (B420C)	44681.18	₺/ton
Unit cost of concrete (C30)	3836.85	₺/m3

3.1 Investigation of the Optimal Solution

In this subsection, the best solutions obtained by the algorithms used in this study for the nine problems formulated for the optimal design of segmented tunnel linings are investigated. The best solutions obtained are presented in Table 4.

Table 4 summarizes the best solution values obtained for a problem set (P1–P9) consisting of nine different problems with varying tunnel diameters and coefficient of soil reaction, along with the design variables derived for these solutions. Upon analyzing the table, it is observed that in all problems, the total concrete cost accounts for a much larger share of the budget compared to the total steel cost. In problems P1, P4, and P7, which represent weak soil conditions with a coefficient of soil reaction of 5000 kN/m^3, the vertical displacements at the tunnel crown reached 14.99 mm, 14.95 mm, and 14.89 mm, respectively. This demonstrates that the 15 mm displacement limit is an active and design-constraining factor in scenarios with low soil quality. As the tunnel radius increases from 2.5 meters to 4.5 meters, it was found that both the amount of reinforcement used and the segment thicknesses increase significantly, thereby notably driving up the total cost.

Table 4. Details of the best solutions obtained

	P1	P2	P3	P4	P5	P6	P7	P8	P9
Seg. thickness (mm)	260	280	300	440	470	510	670	710	780
1. joint angle (°)	28	35	30	32	30	33	32	26	35
2. joint angle (°)	112	120	119	109	120	119	112	116	112
3. joint angle (°)	150	155	158	144	153	150	145	146	142
Reinforcement in Seg. 1	6 Ø 10	6 Ø 10	6 Ø 10	8 Ø 12	6 Ø 10	7 Ø 10	8 Ø 14	10 Ø 10	10 Ø 10
Reinforcement in Seg. 2	6 Ø 10	6 Ø 10	6 Ø 10	6 Ø 10	6 Ø 10	7 Ø 10	9 Ø 10	10 Ø 10	10 Ø 10
Reinforcement in Seg. 3	6 Ø 10	6 Ø 10	6 Ø 10	6 Ø 10	6 Ø 10	7 Ø 10	6 Ø 12	10 Ø 10	10 Ø 10
Reinforcement in Seg. 4	6 Ø 10	6 Ø 10	6 Ø 10	10 Ø 12	6 Ø 10	7 Ø 10	19 Ø 10	11 Ø 10	10 Ø 10
Vertical Disp. (mm)	14.99	9.49	6.68	14.95	10.99	6.85	14.89	11.38	7.06
Horizontal Disp. (mm)	8.2	4.64	3.17	8.66	5.51	3.5	8.24	5.99	3.87
Total Steel Cost (₺)	5192.6	5192.6	5192.6	10494.1	7269.7	8481.3	18796.2	15872.1	15577.8
Total Concrete Cost (₺)	14904.2	16050.7	17197.2	35311.5	37719.1	40929.2	69132.6	73259.9	80482.7
Total Cost (₺)	20096.8	21243.3	22389.8	45805.6	44988.7	49410.5	87928.8	89132.0	96060.5

3.2 Identification of Competitive Algorithms

For each problem in the problem set, the Friedman scores of the competing algorithms were calculated using the Friedman test [12], taking into account the obtained solutions. Based on these scores, the top three algorithms for each problem were identified as competing algorithms. The Friedman scores of the algorithms for each problem are presented in Table 5.

In this table, the green, blue, and orange colors in each problem's column represent the first, second, and third algorithms, respectively. According to this explanation, 12 of the 20 algorithms used in the experimental studies ranked among the top three for at least one problem, thereby qualifying as competing algorithms. An examination of the average Friedman scores in the table reveals that the CS algorithm is the most successful among the twenty algorithms.

A Wilcoxon signed-rank test was conducted to evaluate the relative performance of the CS algorithm, which was the most successful algorithm based on the Friedman mean score, compared to other competing algorithms. The results of this analysis are presented in Table 6.

Upon analyzing Table 6, it is evident that for problems P1, P2, P4, P5, P8, and P9, the CS algorithm achieved a statistically significant advantage over the vast majority of other algorithms. In particular, for problem P9, the CS algorithm outperformed 18 of its 19 competitors statistically, demonstrating its most dominant performance. The only problem in which the CS algorithm statistically performed worse than its competitors was P7. In this problem, the FPA and GSK algorithms produced better solutions than the CS algorithm. This indicates that, within the solution space created by the combination of a large tunnel diameter (4.5 m) and poor soil quality, the search strategies of FPA and GSK performed more consistently. In the P3 and P6 problems, where the coefficient of soil reaction is high, the CS algorithm showed statistically similar performance to 10 different algorithms and was able to outperform only 9 of them.

Table 5. Friedman scores of algorithms for the problems investigated

Algorithm	Friedman Score									
	P1	P2	P3	P4	P5	P6	P7	P8	P9	Mean Score
CS	5.04	4.84	7.46	3.70	5.20	6.90	5.42	4.06	4.12	5.19
SFS	5.38	4.84	7.46	3.60	6.08	6.90	4.76	3.98	4.60	5.29
FPA	5.04	6.26	7.46	4.86	5.38	6.90	3.82	6.36	5.72	5.76
GSK	5.42	5.48	7.74	3.26	6.32	7.68	3.54	7.26	9.00	6.19
COA	5.60	5.14	7.46	6.32	5.48	6.90	6.88	5.88	6.70	6.26
JAYA	6.10	7.76	7.46	6.94	6.62	6.90	8.42	7.00	6.62	7.09
SOS	7.04	6.56	7.78	6.36	10.32	7.18	5.60	7.68	6.10	7.18
ABC	6.22	5.40	7.78	9.76	4.78	7.62	7.54	5.50	10.46	7.23
PSO	8.66	10.52	10.24	8.48	7.28	7.18	7.54	7.54	10.54	8.66
GWO	8.68	10.92	7.80	9.28	8.92	6.90	8.74	11.04	7.56	8.87
TLBO	9.84	11.54	10.12	7.52	10.74	9.22	8.74	9.62	8.68	9.56
HS	11.84	8.56	7.46	14.70	11.48	7.22	14.72	12.12	6.64	10.53
TS	12.56	10.36	7.46	12.66	10.58	8.80	12.16	10.24	11.22	10.67
DE	13.36	12.00	9.38	15.12	10.26	9.88	15.36	11.32	9.26	11.77
SO	14.34	14.62	12.62	10.58	13.90	16.06	10.20	12.82	14.38	13.28
WOA	14.10	13.62	12.42	17.44	16.32	17.66	18.16	17.60	17.68	16.11
GA	16.24	15.90	15.60	17.58	16.52	15.86	17.32	16.36	16.28	16.41
BBBC	16.98	17.82	18.70	15.12	16.42	16.88	14.64	16.14	17.28	16.66
SA	17.60	17.90	17.72	16.72	17.44	17.36	16.44	17.48	17.16	17.31
CDDO	19.96	19.96	19.88	20.00	19.96	20.00	20.00	20.00	20.00	19.97

Table 6. Wilcoxon test results of algorithms for the problems investigated

Algorithm vs CS	Wilcoxon Test Comparison (Loss / Tie / Win)								
	P1	P2	P3	P4	P5	P6	P7	P8	P9
ABC	0/0/1	0/1/0	0/1/0	0/0/1	0/1/0	0/1/0	0/0/1	0/1/0	0/0/1
BBBC	0/0/1	0/0/1	0/0/1	0/0/1	0/0/1	0/0/1	0/0/1	0/0/1	0/0/1
CDDO	0/0/1	0/0/1	0/0/1	0/0/1	0/0/1	0/0/1	0/0/1	0/0/1	0/0/1
COA	0/1/0	0/1/0	0/1/0	0/0/1	0/1/0	0/1/0	0/1/0	0/0/1	0/0/1
DE	0/0/1	0/0/1	0/0/1	0/0/1	0/0/1	0/0/1	0/0/1	0/0/1	0/0/1
FPA	0/1/0	0/0/1	0/1/0	0/1/0	0/1/0	0/1/0	1/0/0	0/0/1	0/0/1
GA	0/0/1	0/0/1	0/0/1	0/0/1	0/0/1	0/0/1	0/0/1	0/0/1	0/0/1
GSK	0/1/0	0/1/0	0/1/0	0/1/0	0/1/0	0/1/0	1/0/0	0/0/1	0/0/1
GWO	0/0/1	0/0/1	0/1/0	0/0/1	0/0/1	0/1/0	0/0/1	0/0/1	0/0/1
HS	0/0/1	0/0/1	0/1/0	0/0/1	0/0/1	0/1/0	0/0/1	0/0/1	0/0/1
JAYA	0/0/1	0/0/1	0/1/0	0/0/1	0/1/0	0/1/0	0/0/1	0/1/0	0/0/1
PSO	0/0/1	0/0/1	0/0/1	0/0/1	0/0/1	0/1/0	0/1/0	0/0/1	0/0/1
SA	0/0/1	0/0/1	0/0/1	0/0/1	0/0/1	0/0/1	0/0/1	0/0/1	0/0/1
SFS	0/1/0	0/1/0	0/1/0	0/1/0	0/1/0	0/1/0	0/1/0	0/1/0	0/1/0
SO	0/0/1	0/0/1	0/0/1	0/0/1	0/0/1	0/0/1	0/0/1	0/0/1	0/0/1
SOS	0/0/1	0/0/1	0/1/0	0/0/1	0/0/1	0/1/0	0/1/0	0/0/1	0/0/1
TLBO	0/0/1	0/0/1	0/0/1	0/0/1	0/0/1	0/0/1	0/0/1	0/0/1	0/0/1
TS	0/0/1	0/0/1	0/1/0	0/0/1	0/0/1	0/0/1	0/0/1	0/0/1	0/0/1
WOA	0/0/1	0/0/1	0/0/1	0/0/1	0/0/1	0/0/1	0/0/1	0/0/1	0/0/1
∑	0/4/15	0/4/15	0/10/9	0/3/16	0/6/13	0/10/9	2/4/13	0/3/16	0/1/18

3.3 Algorithm Stability Analysis

The purpose of the stability analysis conducted in this subsection is to examine the stability of the competing algorithms identified for specific problems and the time required to obtain these solutions. This allows for a comparison of algorithms that exhibit statistically similar performance in finding optimal solutions in terms of success rates, and facilitates the selection of the most effective algorithm for optimizing the problems [20]. To this end, the stability of 12 competitive algorithms was analyzed for all problems. The success rates obtained from the analysis are presented in Table 7. The last column of Table 7 shows the average success rates of the algorithms.

Table 7. Stability analysis results of competing algorithms for the problems investigated

	Success Rate (%)									
Algorithm	P1	P2	P3	P4	P5	P6	P7	P8	P9	Mean SR
CS	100	100	100	20	100	100	8	52	100	76
SFS	100	100	100	40	76	100	4	16	92	70
FPA	88	100	100	8	84	100	4	4	84	64
JAYA	88	100	100	4	64	100	4	12	92	63
COA	96	100	100	4	100	100	0	4	44	61
GSK	100	100	100	4	96	96	4	0	44	60
ABC	84	92	100	0	96	84	0	0	4	51
GWO	60	100	100	0	24	100	0	4	52	49
SOS	60	100	92	8	40	96	0	8	20	47
HS	24	100	100	0	20	96	0	0	76	46
PSO	44	80	84	0	60	88	0	4	4	40
TS	0	100	100	0	12	76	0	0	20	34

An examination of the mean success rate (Mean SR) data in Table 7 reveals that the Cuckoo Search (CS) algorithm achieved a success rate of 76%, while the Stochastic Fractal Search (SFS) algorithm achieved a success rate of 70% both of which are quite high. These rates demonstrate that these algorithms possess a strong global search capability even in a challenging engineering problem with many variables and constraints, such as fragmented tunnel lining. It is noteworthy that the CS and SFS algorithms achieved a 100% success rate in problems P1, P2, P3, P6, and P9. This indicates that these algorithms provide robustness in finding the optimal design across various combinations of soil types and tunnel diameters and can achieve the same successful outcome in all independent simulations.

In summary, the stability analysis in Table 7 documents that the Cuckoo Search (CS) and SFS algorithms are stable and highly successful analytical tools capable of replacing traditional trial and error methods in structural optimization processes.

4 Conclusion

Within the scope of this study, the performance of twenty different state-of-the-art meta-heuristic algorithms was evaluated for the optimization of precast reinforced concrete segmental tunnel linings at minimum cost. In the developed optimization model, lining thickness, optimal joint locations, and primary reinforcement quantities were defined as design variables, and the structural and geometric adequacy of the system was verified using eight different constraints. As a result of analyses conducted on nine different problem sets (P1–P9), generated by systematically varying the tunnel radius and coefficient of soil reaction, the following key findings were obtained:

- In all design configurations, it was found that concrete costs account for a much larger share of the total cost compared to steel (reinforcement) costs. In problems P1, P4, and P7, which represent weak soil conditions with a coefficient of soil reaction of 5000 kN/m^3, the vertical displacement values at the tunnel crown reached the limit value of 15 mm (14.99 mm, 14.95 mm, and 14.89 mm, respectively). This demonstrates that, in scenarios with low soil quality, the vertical displacement limit is the primary active constraint guiding the design. As the tunnel radius increased (from 2.5 meters to 4.5 meters), it was observed that the amounts of reinforcement and segment thicknesses increased significantly to accommodate the rising internal forces, thereby markedly raising the system cost.
- The search performance of meta-heuristic algorithms was compared using non-parametric Friedman and Wilcoxon tests, in addition to standard statistical data. Considering the average Friedman scores, the Cuckoo Search (CS) algorithm emerged as the most successful among the other nineteen algorithms in the pool. Wilcoxon analyses also confirmed that the CS algorithm achieved a statistically significant advantage over the vast majority of other algorithms in problems P1, P2, P4, P5, P8, and P9. When stability analyses were evaluated, the CS algorithm emerged as the most stable method with an average success rate of 76%, followed by Stochastic Fractal Search (SFS) with a success rate of 70%.

In summary, the findings demonstrate that the meta-heuristic algorithms evaluated, particularly Cuckoo Search (CS) and Stochastic Fractal Search (SFS) are reliable and effective tools specifically for the problems addressed in this study. These algorithms have the potential to generate safe and economically viable optimization solutions in tunnel engineering and are recommended for similar structural problems in the literature.

References

1. C. Shi, Z. Wang, C. Gong, J. Liu, Z. Peng, C. Cao, Prediction of the additional structural response of segmental tunnel linings induced by asymmetric jack thrusts, Tunnelling and Underground Space Technology 124 (2022). https://doi.org/10.1016/j.tust.2022.104471.
2. Z. Xiaohui, Z. Shunhua, D. Honggui, W. Peixin, W. Jingtong, Semi–analytical solution for ultimate bearing capacity of straight–jointed segmental tunnel lining, Tunnelling and Underground Space Technology 138 (2023). https://doi.org/10.1016/j.tust.2023.105160.
3. W.M. Huang, J.C. Wang, Z.X. Yang, R.Q. Xu, Analytical model for segmental tunnel lining with nonlinear joints, Tunnelling and Underground Space Technology 114 (2021). https://doi.org/10.1016/j.tust.2021.103994.
4. J.C. Wang, W.M. Huang, R.Q. Xu, Z.X. Yang, R.Q. Xu, Analytical Solution for Segmental-Tunnel Lining Incorporating Interaction between Adjacent Rings, J. Eng. Mech. 146 (2020). https://doi.org/10.1061/(asce)em.1943-7889.0001799.
5. K.M. Lee, X.Y. Hou, X.W. Ge, Y. Tang, An analytical solution for a jointed shield-driven tunnel lining, Int. J. Numer. Anal. Methods Geomech. 25 (2001) 365–390. https://doi.org/10.1002/nag.134.
6. G. Meschke, G.E. Neu, A. Marwan, Robust segmental lining design – Potentials of advanced numerical simulations for the design of TBM driven tunnels, Geomechanik Und Tunnelbau 12 (2019) 484–490. https://doi.org/10.1002/geot.201900032.
7. A. Majdi, H. Ajamzadeh, S. Nadimi, Optimization of the Number of Segments per Ring and Its Effects on Segmental Tunnel Lining Behavior- Case Study: Line 4 Tehran Subway, in: 51st U.S. Rock Mechanics/Geomechanics Symposium, San Francisco, 2017.
8. A. Rastbood, Y. Gholipour, A. Majdi, Finite Element Based Response Surface Methodology to Optimize Segmental Tunnel Lining, Engineering, Technology & Applied Science Research 7 (2017) 1504–1514. https://doi.org/10.48084/etasr.1045.

9. A. Caratelli, A. Meda, Z. Rinaldi, S. Spagnuolo, G. Maddaluno, Optimization of GFRP reinforcement in precast segments for metro tunnel lining, Compos. Struct. 181 (2017) 336–346. https://doi.org/10.1016/j.compstruct.2017.08.083.
10. G.E. Neu, P. Edler, S. Freitag, V. Gudžulić, G. Meschke, Reliability based optimization of steel-fibre segmental tunnel linings subjected to thrust jack loadings, Eng. Struct. 254 (2022) 113752. https://doi.org/10.1016/j.engstruct.2021.113752.
11. C. Proksch-Weilguni, H. Wolfger, J. Kollegger, Optimized reinforcement in longitudinal joints of segmental tunnel linings, Geomechanics and Tunnelling 14 (2021) 390–399. https://doi.org/10.1002/geot.202000046.
12. M. Friedman, A Comparison of Alternative Tests of Significance for the Problem of m Rankings, The Annals of Mathematical Statistics 11 (1940) 88–92.
13. F. Wilcoxon, Individual Comparisons by Ranking Methods, Biometrics Bulletin 1 (1945) 80–83. https://doi.org/10.2307/3001968.
14. ITA Working Group 2, Guidelines for the Design of Segmental Tunnel Linings, France, 2019.
15. I.T.A. Working Group No. 2, Guidelines for the design of shield tunnel lining, Tunnelling and Underground Space Technology 15 (2000) 303–331. https://doi.org/10.1016/S0886-7798(00)00058-4.
16. H.T. Ozturk, Tüneller ve Tasarım İlkeleri, Master Thesis, Karadeniz Technical University, 2007.
17. Austrian Society for Concrete and Construction Technology, Concrete Segmental Lining Systems, Wien, 2011. http://www.concrete-austria.com.
18. ITA-AITES, Recommendations for the design, production and installation of segmental rings, 2013. www.daub-ita.de.
19. ACI 318, Building Code Requiremnets for Structural Concrete, 2019.
20. H.T. Öztürk, H.T. Kahraman, Metaheuristic search algorithms in frequency constrained truss problems: Four improved evolutionary algorithms, optimal solutions and stability analysis, Appl. Soft Comput. 171 (2025) 112854. https://doi.org/10.1016/j.asoc.2025.112854.

Author Contribution Statement

- *Conceptualization:* Hasan Tahsin Öztürk
- *Methodology:* Hasan Tahsin Öztürk
- *Investigation:* Semiha Hayrioğlu, Hasan Tahsin Öztürk
- *Writing – Original Draft:* Semiha Hayrioğlu
- *Writing – Review & Editing:* Hasan Tahsin Öztürk

Publication Note

This paper was peer-reviewed, accepted for presentation, and included in the proceedings of the ACE2026 – International Conference on Advances in Civil Engineering, held on 12–14 October 2026 in Trabzon, Türkiye.

This paper may be cited as follows:

Semiha Hayrioğlu, Hasan Tahsin Öztürk, "Performance of Metaheuristic Algorithms in Cost Optimization of Precast Segmental Circular Tunnel Linings," in Proceedings of the ACE2026 – International Conference on Advances in Civil Engineering, Trabzon, Türkiye, 12–14 October 2026.

Vision-Based Unsupervised Anomaly Detection and Regional Damage-Sensitive Mapping of Masonry Minarets: Laboratory Validation and Field Demonstration

Tunahan Aslan[1], Kemal Hacıefendioğlu[2], Ali Motamedi[3], Cemile Duman[4]
[1] 0009-0008-6303-1425, Karadeniz Technical University, Civil Engineering Department, Trabzon, Türkiye, hann80@outlook.com
[2] 0000-0002-5791-8053, Karadeniz Technical University, Civil Engineering Department, Trabzon, Türkiye, kemalhaciefendioglu@ktu.edu.tr
[3]0009-0005-3454-2304, Karadeniz Technical University, Civil Engineering Department, Trabzon, Türkiye, ali.motamedi00@yahoo.com
[4]0000-0001-8190-7082, Gazi University, Graduate School of Natural and Applied Sciences, Ankara, Türkiye, cemile.duman@gazi.edu.tr

Abstract. Historical masonry minarets are slender heritage structures for which repeated sensor installation and direct access to critical regions can be difficult. This study presents a multi-camera vision-based approach for non-contact anomaly detection and regional damage-sensitive assessment of masonry minarets. Structural displacements are obtained by tracking selected surface regions using the Pyramidal Lucas–Kanade optical-flow algorithm and converting the resulting pixel motions into physical units. A one-dimensional convolutional autoencoder trained exclusively on healthy-reference measurements is then used to calculate reconstruction-error-based anomaly scores, while relation-based analysis provides spatial inspection-priority information. The approach is first validated using a laboratory masonry minaret model subjected to controlled shaking-table excitations. Camera-derived dominant frequencies showed close agreement with accelerometer measurements, with differences below 2.1%. Following the excitations, the identified modal frequencies decreased by approximately 13.9–17.9%, visible cracking developed mainly in the shaft and transition regions, and reconstruction errors increased markedly toward the advanced damage state. The method is subsequently demonstrated on İskenderpaşa Mosque Minaret in Trabzon, where persistent anomaly exceedances were accompanied by higher regional inspection priorities around the balcony and transition zones. Visible cracking observed in these regions provided qualitative support for the spatial assessment. The results demonstrate the potential of vision-derived displacement measurements and healthy-reference anomaly analysis for non-contact monitoring and targeted inspection of masonry minarets.

Keywords: onry minarets; Vision-based monitoring; Structural health monitoring; Unsupervised anomaly detection; Convolutional autoencoder.

1 Introduction

Historical masonry structures require effective monitoring strategies to support their preservation and structural assessment. Masonry minarets are particularly vulnerable because of their slender geometry, high aspect ratio, and exposure to seismic and environmental actions [1–3]. Damage may develop through cracking, joint separation, material degradation, or stiffness loss, some of which may not be readily identified by visual inspection alone. Periodic monitoring can therefore help detect changes in structural behavior and guide detailed inspection. Conventional structural health monitoring (SHM) commonly relies on contact

sensors such as accelerometers, displacement transducers, and strain gauges [4–6]. Although accurate, their use in historical and tall structures may be limited by installation, cabling, accessibility, maintenance, and conservation requirements. Vision-based techniques offer a non-contact alternative by tracking structural motion remotely and providing displacement time histories suitable for dynamic and damage-sensitive assessment [7–9].

A key challenge is interpreting these measurements because labeled data representing different damage states are generally unavailable for historical structures. Unsupervised learning addresses this limitation by establishing a baseline from assumed healthy measurements. Autoencoders trained on healthy-reference data typically produce low reconstruction errors for baseline-like responses, while structural changes may increase these errors [10–11]. Such errors should be interpreted as indicators of deviation from reference behavior rather than direct measures of physical damage.

Recent studies have also demonstrated the potential of vision-based and data-driven approaches for the structural assessment of masonry minarets [12,13]. This study presents a vision-based framework combining non-contact displacement measurement, healthy-reference reconstruction-error analysis, and regional damage-sensitive mapping. The methodology is first validated on a laboratory masonry minaret subjected to controlled shaking-table excitations, with camera-derived dynamic responses compared against accelerometer measurements. It is then demonstrated on İskenderpaşa Mosque Minaret as a representative field application, where reconstruction-error trends and relation-based regional mapping are used to identify persistent deviations and prioritize regions for inspection.

2 Vision-Based Monitoring and Anomaly Assessment

2.1 Multi-Camera Vision-Based Measurement

The proposed monitoring system uses four synchronized high-speed monochrome CoaXPress cameras for non-contact displacement measurement: two VICTOREM 16B276MCX cameras (1456×1088 pixels at 276 fps) and two VICTOREM 32B216MCX cameras (2064×1544 pixels at 216 fps). All cameras have a 3.45×3.45 μm² pixel size and 75 mm C-mount lenses. Video acquisition was performed using an IO Industries DVR Express Core 2 unit and controlled through CoreView software, enabling simultaneous monitoring of different structural elevations. Structural motion was extracted from the recorded image sequences using the Pyramidal Lucas–Kanade optical-flow algorithm. For each camera, predefined target regions were selected on the structural surface and tracked frame by frame. The resulting pixel trajectories were converted into physical displacement histories using a scale factor obtained from a known reference length within the measurement plane. The conversion can be expressed as

$$s = \frac{L_{\mathrm{ref}}}{L_{\mathrm{px}}}, \qquad d_{\mathrm{phys}} = s\, d_{\mathrm{px}} \tag{1}$$

where (L_{ref}) is the known physical reference length, (L_{px}) is its corresponding length in pixels, and (d_{px}) and (d_{phys}) denote the measured displacement in pixel and physical units, respectively. The resulting multi-point displacement histories formed the input for dynamic-response evaluation and data-driven anomaly assessment. For the laboratory validation, the displacement records were additionally analyzed in the frequency domain and compared with

accelerometer measurements.

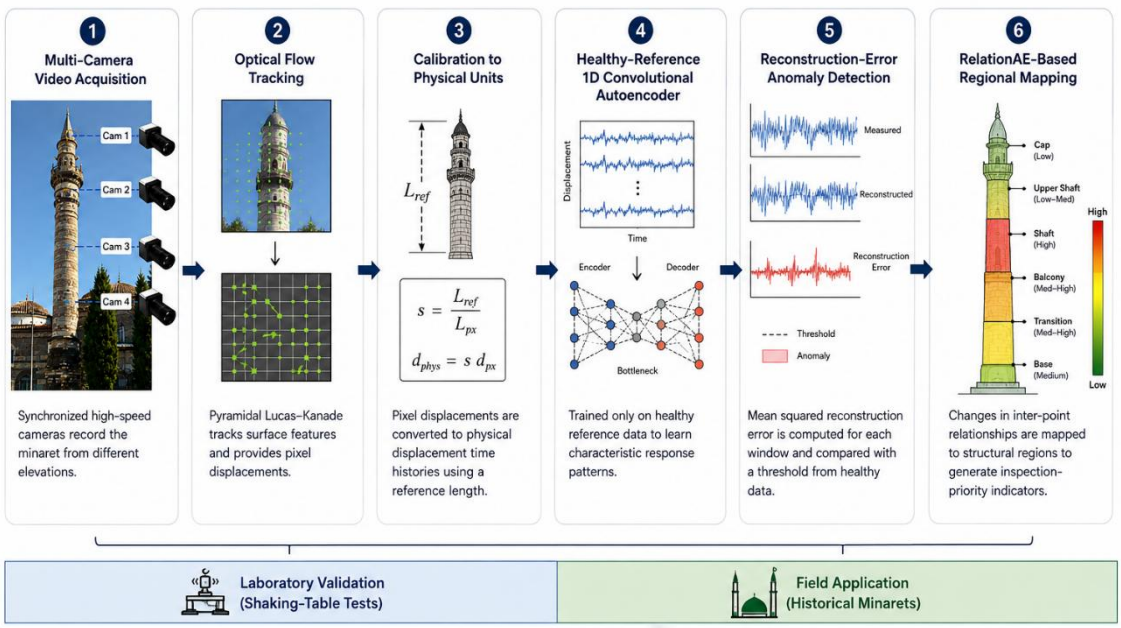


Fig. 1. Overview of the proposed multi-camera vision-based monitoring and unsupervised anomaly assessment framework.

2.2 Reconstruction-Error and Regional Anomaly Assessment

An unsupervised one-dimensional convolutional autoencoder (1D CAE) was used to identify deviations from the healthy-reference response. The multi-channel displacement records were divided into normalized temporal windows, and the model was trained exclusively on healthy data. The encoder compressed each window into a latent representation, while the decoder reconstructed the input. The deviation between the measured and reconstructed responses was quantified using the mean squared reconstruction error:

$$\left[RE_i = \frac{1}{WC}\sum_{c=1}^{C}\sum_{t=1}^{W}\left(x_{i,c,t} - \hat{x}_{i,c,t}\right)^2\right] \tag{2}$$

where W is the window length, C is the number of measurement channels, $x_{i,c,t}$ is the normalized measured response, and $\hat{x}_{i,c,t}$ is the reconstructed response. Four displacement channels were used. The anomaly threshold was derived solely from the healthy training-error distribution, and threshold exceedances were interpreted as deviations from the learned reference behavior rather than direct measures of physical damage. To provide spatial interpretation, a relation-based autoencoder (RelationAE) was additionally applied to healthy-reference relationships between monitored-point pairs. Pair-specific anomaly scores were mapped to predefined structural regions to generate relative inspection-priority maps. Thus, reconstruction error identifies when the response departs from the healthy baseline, whereas RelationAE indicates where the strongest deviations are concentrated.

3 3 Laboratory Validation

3.1 Laboratory Model and Shaking-Table Testing

The proposed approach was first evaluated on a laboratory masonry minaret model constructed in the Structural Health Monitoring Laboratory of Karadeniz Technical University. The model,

representing the main structural regions of a typical masonry minaret, was built using clinker bricks and hydraulic lime-based mortar and installed on a uniaxial shaking table. Four cameras positioned approximately 4.5 m from the model were used for simultaneous displacement measurements, while six accelerometers at three elevations provided reference data for validation. Before excitation, the undamaged model was monitored for 20 days using 2-min synchronized video recordings to establish the healthy-reference dataset. The minaret was then subjected to sinusoidal excitations of 10, 20, and 30 mm at 1 Hz for five cycles. Visible cracking developed during the final 30-mm excitation, mainly along masonry interfaces in the shaft and transition-zone regions, providing physical evidence of structural change for comparison with the anomaly indicators.



Fig. 2. Laboratory validation setup: (a) masonry minaret model and multi-camera measurement configuration, (b) shaking-table installation, and (c) representative cracking observed after the final excitation.

3.2 Dynamic Validation and Reconstruction-Error Response

The reliability of the vision-based displacement measurements was first assessed through frequency-domain comparison with accelerometer records. In the healthy condition, the first dominant frequency was identified as 9.364 Hz from the accelerometers and 9.322 Hz from the camera response, corresponding to a difference of 0.45%. The second dominant frequency was 47.536 and 47.131 Hz, respectively, with a difference of 0.85%. After the shaking-table tests, the corresponding frequencies were 7.692 and 7.755 Hz for the first mode and 39.750 and 40.577 Hz for the second mode, with differences remaining below 2.1%. Compared with the healthy state, the modal frequencies decreased by approximately 13.9–17.9%, confirming that the vision-based system captured the principal dynamic changes of the model. The four-channel displacement data were then evaluated using the reconstruction-error-based anomaly framework. The 1D CAE was trained only on healthy-reference windows, and the anomaly threshold was derived exclusively from the training reconstruction-error distribution.

As shown in Fig. 3, anomaly scores remained generally low and stable during the training and test periods. In Damage 1, reconstruction-error variability increased and threshold exceedances became more frequent. In Damage 2, the anomaly scores increased markedly and remained above the healthy-reference threshold for extended periods, indicating a progressively stronger departure from the learned healthy behavior.

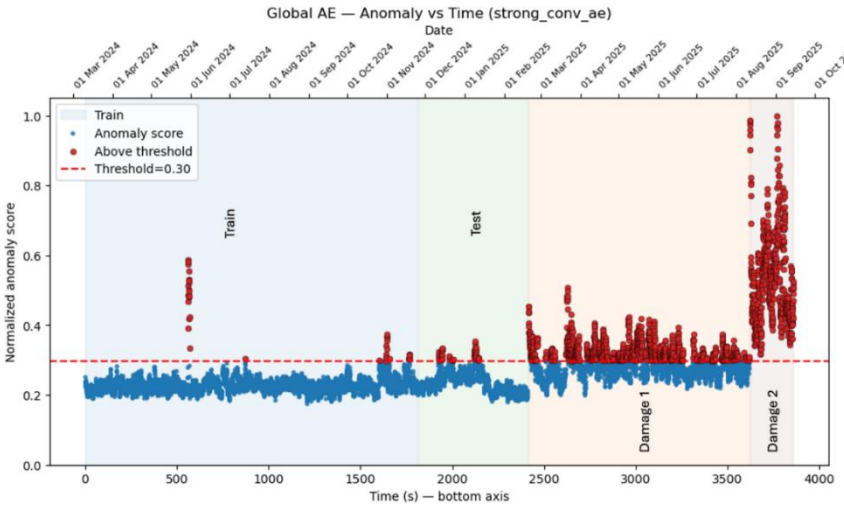


Fig. 3. Normalized reconstruction-error-based anomaly scores of the laboratory minaret model for the training, test, Damage 1, and Damage 2 measurement periods.

The discrimination capability of the reconstruction-error scores was also examined retrospectively using receiver operating characteristic and precision–recall analyses. Under the controlled laboratory conditions, the model achieved an ROC–AUC of 0.916 and an average precision of 0.856. These values support the observed separation between the healthy-reference and damaged-state responses; however, they represent classification performance under controlled experimental conditions rather than a quantitative measure of physical damage severity.

3.3 Regional Damage-Sensitive Assessment

The RelationAE analysis was used to investigate whether the experimentally induced structural changes also altered the relationships between responses measured at different locations. Pairwise anomaly scores remained generally stable during the training and test periods, while intermittent deviations emerged in Damage 1. In Damage 2, pronounced and sustained threshold exceedances occurred across all evaluated measurement-point pairs. The Point 2–Point 4 relationship exhibited the largest deviation, while Point 1–Point 4 and Point 2–Point 3 also showed substantial changes. To obtain a spatially interpretable representation, the pairwise anomaly contributions were mapped to the corresponding structural regions. The resulting inspection-priority map is presented in Fig. 4. The upper shaft was identified as the highest-priority region. The balcony, lower shaft, and transition zone were classified as medium-priority regions, whereas the base and cap were assigned low priority. The high priority attributed to the upper shaft was consistent with the visible cracking observed in the shaft region after the shaking-table tests. The transition zone, where additional cracking was also observed, received a medium-priority classification, indicating that the relation-based assessment captured a notable response change in this region, although at a lower level than in the upper shaft.

The spatial distribution should nevertheless be interpreted with caution because the resulting regional scores depend on the number and location of the monitored points, the relationships represented by each point pair, and the assignment of these measurements to predefined structural regions. Accordingly, the map should be considered a relative damage-sensitive inspection-priority indicator rather than a direct or complete representation of the physical crack distribution. Overall, the laboratory results provided complementary evidence at different assessment levels. The modal-frequency reductions indicated a global change in dynamic behavior, the reconstruction-error analysis identified the temporal progression of deviations

from the healthy reference, and the RelationAE assessment provided a regional interpretation of the detected changes.

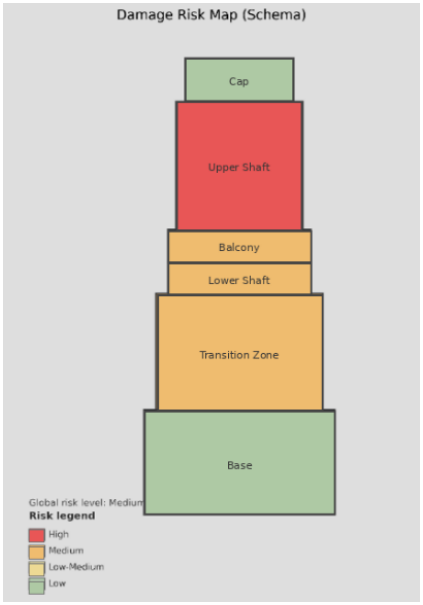


Fig. 4. RelationAE-based regional inspection-priority map of the laboratory minaret model.

4 Field Application: İskenderpaşa Mosque Minaret

4.1 Field Monitoring and Reconstruction-Error Assessment

Following the laboratory validation, the vision-based monitoring framework was applied to eight historical masonry minarets in Trabzon under different structural and environmental conditions. Because each structure had a different geometry, camera configuration, visibility condition, and surrounding environment, the displacement responses were evaluated relative to structure-specific reference measurements rather than using a common threshold. Among the monitored structures, İskenderpaşa Mosque Minaret exhibited the most persistent reconstruction-error exceedances and was therefore selected as the representative field case for detailed regional assessment. İskenderpaşa Mosque Minaret was monitored at approximately monthly intervals. Its courtyard provided a suitable location for repeatable installation of the multi-camera system despite the surrounding urban environment. Four target regions distributed along different elevations of the minaret were monitored using the same vision-based measurement system described in Section 2. Natural masonry features and clearly identifiable surface details were used as tracking targets, while the camera geometry was documented to improve repeatability between successive monitoring campaigns.

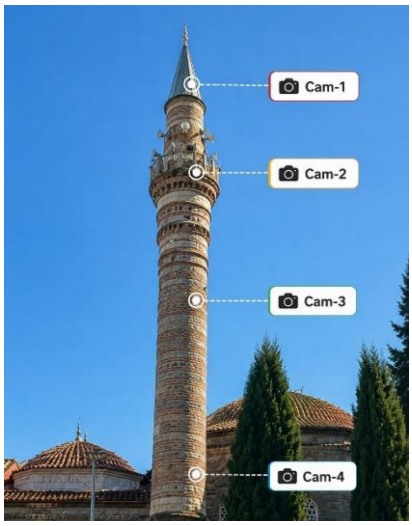


Fig. 5. İskenderpaşa Mosque Minaret and the selected camera-based monitoring regions.

The measured displacement histories were processed using the same healthy-reference anomaly framework employed in the laboratory study. A 1D CAE was trained using the reference portion of the field measurements, and reconstruction errors obtained from subsequent monitoring windows were compared with the threshold derived exclusively from the training-error distribution. As shown in Fig. 6, İskenderpaşa Mosque Minaret exhibited a more pronounced anomaly pattern than the other monitored structures. A substantial proportion of the test windows exceeded the training-calibrated threshold, and the exceedances were relatively dense and persistent throughout the evaluated monitoring period. Although individual threshold exceedances cannot independently be interpreted as evidence of physical damage, their persistence indicated a systematic departure from the response patterns represented by the reference measurements and justified a more detailed local assessment.

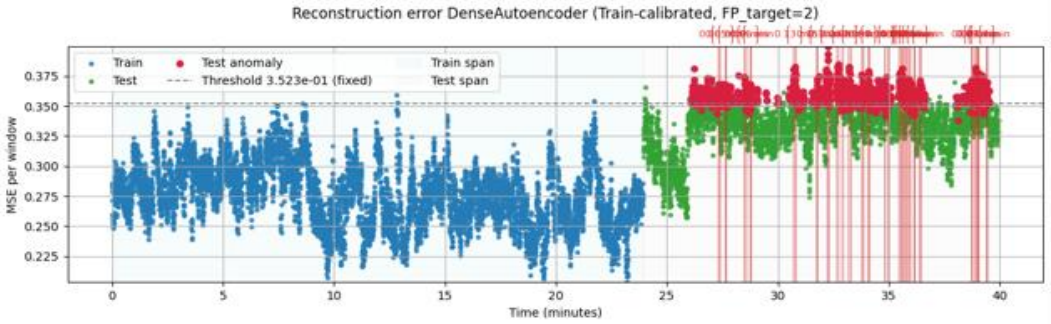


Fig. 6. Reconstruction-error-based anomaly assessment of İskenderpaşa Mosque Minaret.

4.2 Regional Anomaly Mapping and Visual Corroboration

A RelationAE-based analysis was subsequently performed to investigate whether the detected field anomalies were associated with particular relationships between the monitored regions. The anomaly pattern was distributed across several sensor pairs rather than being concentrated in a single relationship. The S1–S4 pair showed the largest number of anomalous segments, followed by S2–S4 and S1–S2, while the remaining sensor combinations also exhibited threshold exceedances. The sensor-level anomaly contributions were then mapped onto the structural regions of the minaret to provide a spatial interpretation of the detected deviations. The resulting regional inspection-priority map identified the balcony and transition zones as the highest-priority regions. The lower shaft and base were classified as medium priority, while the upper shaft showed a low-to-medium priority level and the cap remained in the low-priority

category. The distribution indicates that the detected deviations were more strongly associated with the middle and lower monitored regions than with the upper part of the minaret.

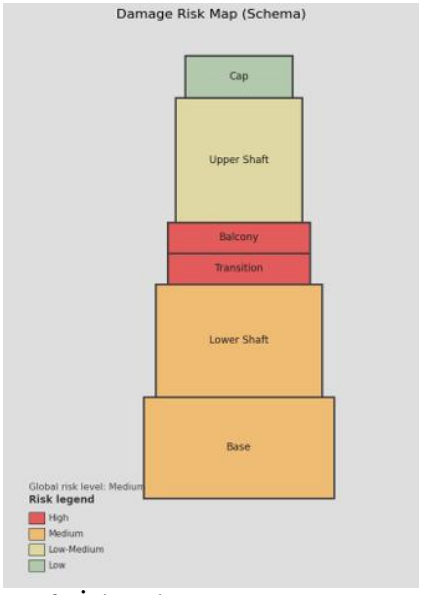


Fig. 7. Regional assessment of İskenderpaşa Mosque Minaret: (a) RelationAE-based inspection-priority map and

5 Discussion

The laboratory and field applications demonstrate the complementary roles of vision-based displacement measurement, reconstruction-error analysis, and relation-based regional assessment. In the laboratory tests, the close agreement between camera- and accelerometer-derived dominant frequencies confirmed the reliability of the optical-flow measurements. Following the shaking-table excitations, modal frequencies decreased by approximately 13.9–17.9%, accompanied by visible cracking in the shaft and transition regions. Reconstruction-error analysis captured the progression from stable healthy and test responses to more frequent exceedances in Damage 1 and persistent anomalies in Damage 2. RelationAE further provided spatial information, identifying the upper shaft as the highest-priority region; the balcony, lower shaft, and transition zone as medium priority; and the base and cap as low priority. The field application demonstrated the extension of the framework to a full-scale historical structure under more variable environmental and operational conditions. İskenderpaşa Mosque Minaret exhibited the most persistent reconstruction-error exceedances among the monitored structures, while RelationAE concentrated the highest inspection priorities around the balcony and transition regions. These findings indicate that frequency-based assessment, reconstruction error, and regional mapping provide complementary global, temporal, and spatial indicators of structural change.

The proposed framework should be interpreted as an inspection-support tool rather than a direct damage-quantification method. Anomaly scores indicate deviations from learned reference behavior but do not directly quantify physical damage severity. Their interpretation may also be affected by camera motion, illumination, viewing geometry, environmental variability, tracking uncertainty, and measurement-point distribution. Therefore, persistent anomalies and regional maps should be evaluated together with repeated monitoring, visual inspection, and complementary structural assessment.

6 Conclusions

This study presented a multi-camera vision-based framework for non-contact anomaly detection and regional damage-sensitive assessment of masonry minarets. The method combines Pyramidal Lucas–Kanade optical-flow displacement measurements with healthy-reference 1D CAE reconstruction error and RelationAE-based regional interpretation. Laboratory validation showed close agreement between camera- and accelerometer-derived dominant frequencies, while the 13.9–17.9% frequency reductions and visible cracking after shaking-table excitation confirmed structural change. Reconstruction-error scores progressively increased from the healthy and test periods to Damage 1 and Damage 2. The framework was also demonstrated on İskenderpaşa Mosque Minaret, where persistent reconstruction-error exceedances indicated deviation from the reference response and RelationAE identified the balcony and transition as the highest-priority regions.

Overall, the approach provides a minimally invasive tool for detecting structural-response changes and supporting inspection prioritization. The anomaly indicators should not be interpreted as direct measures of physical damage and should be evaluated together with repeated monitoring, visual inspection, and complementary non-destructive assessment. Future work should consider longer monitoring periods, environmental variability, and denser multi-view measurements.

Acknowledgments
The authors gratefully acknowledge the support provided by the Directorate General of Foundations of Türkiye and the Trabzon Regional Directorate of Foundations. This study was supported by the TÜBİTAK 1001 – Scientific and Technological Research Projects Support Program within the project entitled “Video Camera-Based Structural Health Monitoring of Historical Masonry Minarets and Development of a Long-Term Decision-Making Model Based on Deep Learning Method” (Project No. 222M140).

References

1. P. Usta, “Assessment of seismic behavior of historic masonry minarets in Antalya, Turkey,” *Case Studies in Construction Materials*, vol. 15, p. e00665, 2021, doi: 10.1016/j.cscm.2021.e00665.
2. E. Durgut, M. Ispir, and A. Ilki, “Seismic fragility curves of a historical brick masonry minaret,” *Earthquake Spectra*, vol. 41, no. 5, pp. 3499–3525, 2025, doi: 10.1177/87552930251342827.
3. B. Erdil, M. Tapan, I. Akkaya, and F. Korkut, “Effects of structural parameters on seismic behaviour of historical masonry minaret,” *Periodica Polytechnica Civil Engineering*, vol. 62, no. 1, pp. 148–161, 2018, doi: 10.3311/PPci.10687.
4. M. Rossi and D. A. Bournas, “Structural health monitoring and management of cultural heritage structures: A state-of-the-art review,” *Applied Sciences*, vol. 13, no. 11, p. 6450, 2023, doi: 10.3390/app13116450.
5. C. R. Farrar and K. Worden, “An introduction to structural health monitoring,” *Philosophical Transactions of the Royal Society A: Mathematical, Physical and Engineering Sciences*, vol. 365, no. 1851, pp. 303–315, 2007, doi: 10.1098/rsta.2006.1928.
6. J. M. W. Brownjohn, “Structural health monitoring of civil infrastructure,” *Philosophical Transactions of the Royal Society A: Mathematical, Physical and Engineering Sciences*, vol. 365, no. 1851, pp. 589–622, 2007, doi: 10.1098/rsta.2006.1925.
7. D. Feng and M. Q. Feng, “Vision-based multipoint displacement measurement for structural health monitoring,” *Structural Control and Health Monitoring*, vol. 23, no. 5, pp. 876–890, 2016, doi: 10.1002/stc.1819.

8. Y. Xu and J. M. W. Brownjohn, “Review of machine-vision based methodologies for displacement measurement in civil structures,” *Journal of Civil Structural Health Monitoring*, vol. 8, no. 1, pp. 91–110, 2018, doi: 10.1007/s13349-017-0261-4.
9. H. Yoon, H. Elanwar, H. Choi, M. Golparvar-Fard, and B. F. Spencer Jr., “Target-free approach for vision-based structural system identification using consumer-grade cameras,” *Structural Control and Health Monitoring*, vol. 23, no. 12, pp. 1405–1416, 2016, doi: 10.1002/stc.1850.
10. M. Azimi, A. D. Eslamlou, and G. Pekcan, “Data-driven structural health monitoring and damage detection through deep learning: State-of-the-art review,” *Sensors*, vol. 20, no. 10, p. 2778, 2020, doi: 10.3390/s20102778.
11. J. Mao, H. Wang, and B. F. Spencer Jr., “Toward data anomaly detection for automated structural health monitoring: Exploiting generative adversarial nets and autoencoders,” *Structural Health Monitoring*, vol. 20, no. 4, pp. 1609–1626, 2021, doi: 10.1177/1475921720924601.
12. K. Hacıefendioğlu, V. Kahya, T. Aslan, C. Duman, H. B. Başağa, F. Y. Okur, et al., “Anomaly detection in masonry minarets through hybrid video-based deep learning methodologies,” *International Journal of Architectural Heritage*, vol. 20, no. 2, pp. 178–206, 2026, doi: 10.1080/15583058.2025.2524764.
13. K. Hacıefendioğlu, V. Kahya, M. G. Limongelli, E. Temur, K. Özgan, T. Aslan, et al., “A vision-based unsupervised framework for structural damage localization in masonry minarets using slope-informed convolutional autoencoders,” *Engineering Structures*, vol. 361, p. 122861, 2026, doi: 10.1016/j.engstruct.2026.122861.

Author Contribution Statement

- *Conceptualization:* Tunahan Aslan, Kemal Hacıefendioğlu
- *Methodology:* Tunahan Aslan, Kemal Hacıefendioğlu
- *Investigation:* Tunahan Aslan, Kemal Hacıefendioğlu
- *Writing – Original Draft:* Tunahan Aslan, Kemal Hacıefendioğlu, Ali Motamedi, Cemile Duman
- *Writing – Review & Editing:* Tunahan Aslan, Kemal Hacıefendioğlu

List of Abbreviations

- **SHM** —Structural Health Monitoring
- **CAE** — Convolutional Auto Encoder
- **AE** — Auto Encoder

Publication Note

This paper was peer-reviewed, accepted for presentation, and included in the proceedings of the ACE2026 – International Conference on Advances in Civil Engineering, held on 12–14 October 2026 in Trabzon, Türkiye.

This paper may be cited as follows:

Tunahan Aslan, Kemal Hacıefendioğlu, Ali Motamedi, Cemile Duman, “Vision-Based Unsupervised Anomaly Detection and Regional Damage-Sensitive Mapping of Masonry Minarets: Laboratory Validation and Field Demonstration” in Proceedings of the ACE2026 – International Conference on Advances in Civil Engineering, Trabzon, Türkiye, 12–14 October 2026.

Architecture and Implementation of an AI- and ROS 2-Based Quadrupedal Platform for Post-Earthquake Crack Inspection

Ali MOTAMEDI[1] and Kemal HACIEFENDİOĞLU[2]
[1] 0009-0005-3454-2304, Karadeniz Technical University, Civil Engineering Department, Trabzon, Türkiye, ali.motamedi00@yahoo.com
[2] 0000-0002-5791-8053, Karadeniz Technical University, Civil Engineering Department, Trabzon, Türkiye, kemalhaciefendioglu@ktu.edu.tr

Abstract. Post-earthquake visual inspection is time-sensitive, yet unstable components, debris, and restricted access may expose engineers to avoidable risk. This paper presents the architecture, implementation, and controlled experimental assessment of a human-supervised quadrupedal platform for preliminary crack-related inspection. The system combines a Unitree Go2 EDU robot, an Intel RealSense D435i RGB-D camera, a Unitree 4D LiDAR L1, external computing hardware, YOLOv8x crack-candidate detection, aligned-depth distance association, and ROS 2 communication. Annotated images, cropped candidate regions, approximate camera-to-target distances, system states, and control-related messages are integrated within an operator-supervised workflow. The platform was evaluated in a controlled indoor course containing eight prepared crack models using four fixed camera-pitch configurations. The −15°, 0°, +15°, and +30° configurations produced observed coverage of 1/8, 3/8, 7/8, and 7/8 targets, respectively, indicating a strong practical influence of camera viewpoint on crack-candidate visibility. These observations represent scenario-level system evaluation rather than statistical detector validation. The platform is intended as an inspection-support tool and does not determine crack geometry, structural severity, or building safety.

Keywords: Post-earthquake inspection; quadrupedal robot; structural crack detection; RGB-D sensing; ROS 2; YOLOv8x

1 Introduction

Post-earthquake assessment requires the rapid documentation of visible damage while preserving the engineering judgement needed to distinguish superficial cracking from potentially significant distress. Established safety procedures place trained personnel at the centre of occupancy and intervention decisions [1–3]. Applying these procedures, however, may require entry into buildings affected by unstable finishes, falling hazards, damaged stairs, debris, poor lighting, and uncertain floor conditions. Robotic inspection is therefore most defensible as a means of collecting preliminary evidence before, or alongside, direct professional assessment rather than as an automated substitute for it.

Mobile robotic systems can extend visual access and improve the traceability of inspection records, although their usefulness depends on mobility, sensing quality, communication, and operator control [4]. Quadrupedal platforms are relevant to built environments because legged locomotion can negotiate thresholds and irregular surfaces that may constrain conventional wheeled bases. Field studies with legged robots have demonstrated inspection in industrial and sewer environments, while also identifying practical limits associated with payload, power, sensing geometry, and environmental variability [5, 6]. These constraints are particularly important after earthquakes, when irregular access or an unsuitable viewpoint may result in a missed or ambiguous observation.

Computer vision provides a complementary means of screening inspection imagery. Convolutional approaches have been developed for crack detection and the recognition of multiple visual damage types in civil infrastructure [7–9]. One-stage object detectors provide bounding-box outputs that can be incorporated into mobile sensing workflows [10, 11], whereas segmentation methods produce richer pixel-level representations [12, 13]. Neither output removes the need for scale, calibration, contextual evidence, and engineering interpretation. A crack-related visual indication must therefore be connected to sensing context, evidence storage, and a controllable robotic platform.

ROS 2 provides the middleware needed to connect distributed sensing, perception, robot-state, and operator-facing processes [14, 15]. Related work has also demonstrated real-time structural crack inspection using a quadrupedal robotic platform [16]. In the present system, ROS 2 connects RGB-D sensing, crack-candidate detection, aligned-depth distance context, environmental sensing, evidence recording, platform communication, and human supervision.

The contribution of this work is the implementation and controlled system-level assessment of a human-supervised quadrupedal inspection platform integrating RGB-D sensing, deep-learning crack-candidate detection, approximate distance association, ROS 2 communication, environmental sensing, evidence recording, and operator control. The integrated workflow is evaluated using prepared crack targets under four camera-pitch configurations to examine the practical influence of viewpoint on observed detection coverage. The study does not claim structural diagnosis, crack-severity classification, exact crack measurement, complete three-dimensional localisation, certified safety operation, or unrestricted autonomous building inspection.

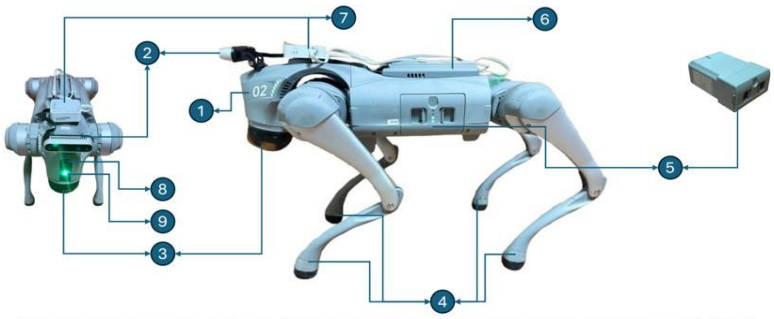
2 System Design and Architecture

2.1 Quadrupedal robotic platform

The mobile base is a Unitree Go2 EDU quadrupedal robot [17], which serves as the carrier for the inspection sensors and provides mobility for collecting visual and spatial evidence. Its legged configuration is relevant to built environments where thresholds and surface irregularities may constrain conventional wheeled platforms. Robot-state and command-related communication are separated from the perception layer so that crack-candidate processing remains independent of structural interpretation while the operator retains supervisory control.

2.2 Sensor and computing configuration

The platform carries a front-mounted Intel RealSense D435i for RGB-D inspection sensing and a Unitree 4D LiDAR L1 for surrounding-geometry information. RGB images from the D435i support crack-candidate detection, while aligned depth provides approximate distance context. An Orin NX 8 GB expansion module is installed on the robot; however, during the reported implementation, YOLOv8x inference and the principal ROS 2 monitoring processes were executed on an external Lenovo L340 equipped with an Intel Core i7 processor, 16 GB RAM, and an NVIDIA GTX 1650 GPU.



1.	Unitree GO2 EDU
2.	Intel RealSense D435i Depth Camera
3.	Unitree 4D LiDAR L1
4.	Leg and Knee
5.	High-Capacity Battery
6.	Expansion Dock Orin NX 8GB
7.	Wireless Communication Modem (Wi-Fi / LTE / 5G)
8.	Front Illumination Lamp
9.	Front-View Camera

Fig. 1. Hardware configuration of the Unitree Go2 EDU inspection platform, including the RealSense D435i, Unitree 4D LiDAR L1, and Orin NX 8 GB expansion module.

Table 1. System components and their implementation roles.

Component	**Function**	**Data or communication role**
Unitree Go2 EDU	Mobile sensor carrier	Robot state and command-related communication
Intel RealSense D435i	RGB-D inspection sensing	RGB images and aligned-depth images
Unitree 4D LiDAR L1	Environmental sensing	Surrounding-geometry data for operator awareness
Expansion Dock Orin NX 8 GB module	Robot-mounted expansion computing	Installed hardware; not documented as the YOLO inference device
Lenovo L340 with GTX 1650	External processing computer	YOLOv8x inference, ROS 2 processes, monitoring, and logging
ROS 2 and Go2 SDK	Middleware and robot interface	Sensor, state, log, and control-related message exchange

2.3 ROS 2 communication architecture

ROS 2 forms the communication backbone between the robot interface, sensing processes, perception node, monitoring tools, and control-related messages. Robot data exchange uses WebRTC-based communication and the go2_ros2_sdk framework, including its go2_robot_sdk package [18]. The driver exposes robot state and sensor information to ROS 2 and accepts command-related messages. Unitree SDK Python provides high-level control access when direct operator intervention or perception-related behaviour is required.

The RealSense interface publishes colour and aligned-depth images. A single-frame RGB queue replaces an older waiting frame when a newer image arrives, thereby limiting the accumulation of stale imagery. The latest aligned-depth frame is retained separately and queried when the crack-processing node produces a candidate region. This division keeps semantic processing in the RGB branch and uses depth selectively for geometric context.

The perception node publishes annotated evidence and damage-related messages, while the operator interface presents module states and logs. The topics /yolo/stop_trigger and /yolo/stop_state communicate perception-related stop conditions to other processes. These messages are software communication mechanisms, not certified safety functions. Figure 2 summarises the sensing, perception, communication, evidence, and supervision paths.

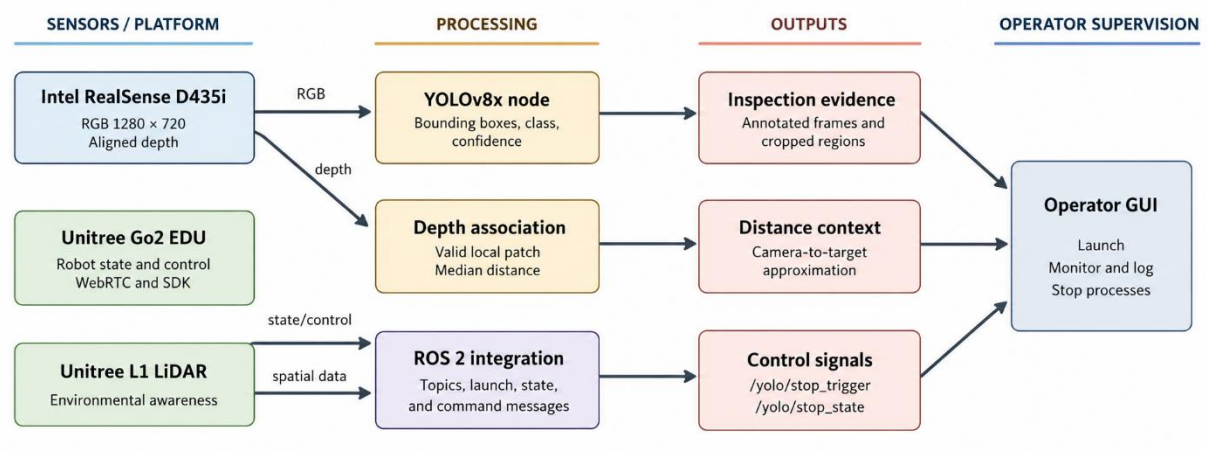


Fig. 2. ROS 2-based data flow for crack-candidate detection, aligned-depth association, evidence generation, control signals, and operator supervision.

3 Crack-Inspection Methodology

3.1 RGB image acquisition and YOLOv8x processing

The visual-processing module uses the Ultralytics YOLOv8x object-detection architecture, initialised from pretrained yolov8x.pt weights with Ultralytics version 8.2.92 [19]. The model was adapted to a single class, crack, using labelled crack images and bounding-box annotations from the SurfaceCrackDetection dataset on Roboflow Universe [20]. The present paper focuses on system architecture and implementation; dataset statistics and model-development outcomes are therefore outside its scope.

The RealSense colour stream is configured at 1280 × 720 pixels and 30 frames/s. Incoming frames are converted into the representation expected by the YOLO node, after which configurable confidence filtering and non-maximum suppression remove unsuitable or overlapping candidate boxes. For each retained candidate, the node records the bounding-box coordinates, class identifier, confidence value, and annotated RGB image. A cropped image of the candidate region may also be generated for later review.

The term crack candidate is used deliberately throughout this paper. A bounding box directs attention to an image region but does not provide a segmentation mask or determine crack length, width, orientation, physical depth, mechanism, or structural significance.

3.2 RGB-depth alignment

The RealSense interface aligns the depth image to the RGB image so that a pixel coordinate produced by the visual detector can be queried in the corresponding depth frame. RGB and depth remain separate data products: the RGB image supplies the appearance information used by YOLOv8x, whereas the aligned-depth image supplies local range information. The

architecture retains the latest depth frame and associates it with a candidate only when the required aligned data are available.

Alignment supports pixel-level correspondence between the two streams, but correspondence alone does not establish a calibrated position in the robot or building coordinate system. Such a transformation would require camera intrinsics, camera-to-robot extrinsics, time synchronisation, and appropriate coordinate-frame transformations.

3.3 Local median-depth association

Depth association begins at the centre pixel of the detected bounding box. Because a single depth sample can be invalid near edges, reflective regions, or occlusion boundaries, the implementation extracts a local patch around that centre. Values outside the accepted depth limits are removed, and the median of the remaining samples is converted to metres when the depth image is represented in millimetres:

$$d = median\{D(u,v) \mid d_{min} < D(u,v) < d_{max}\} \quad (1)$$

Here, $D(u, v)$ is the aligned-depth value at image coordinate (u, v), and $d$min and $d$max define the accepted depth interval. The resulting quantity is an approximate camera-to-target distance associated with the candidate region. Median filtering limits the influence of isolated invalid samples, but it does not provide exact crack depth, crack width, three-dimensional crack localisation, structural severity, or a calibrated structural measurement.

3.4 Evidence recording and damage-related messages

The perception process combines visual and distance information within a common evidence record. Annotated frames retain the bounding box and confidence value in the surrounding scene, while candidate crops and the available approximate distance can be saved for subsequent review. The node also publishes /yolo/stop_trigger and /yolo/stop_state messages to communicate configured crack-candidate conditions to downstream processes. These outputs support operator supervision and evidence review rather than structural or safety decisions.

4 Operator Interface and System Workflow

The graphical user interface provides a common entry point for launching and monitoring the robot interface, camera, perception, and supporting ROS 2 processes. Module states and textual logs allow the operator to identify active processes, communication faults, missing sensor data, and node termination without changing applications. Visual evidence and perception-related information are presented together with the relevant system state to support traceable inspection review.

The operator can stop individual process groups or terminate active processes when intervention is required. Perception-related stop messages provide an additional software mechanism for holding robot activity when a candidate region requires attention. Because visual candidates and local depth values do not independently establish structural significance, the operator remains responsible for reviewing the evidence and deciding how the platform should proceed.

5 Experimental Test Course and Procedure

The integrated robotic workflow was evaluated in a controlled indoor inspection course using eight prepared visual crack models positioned at different heights. The targets were used as repeatable crack-related visual features rather than representations of the full variability or structural significance of earthquake-induced cracking. Models 1–8 were positioned at heights of 90, 50, 100, 45, 90, 70, 30, and 90 cm from the ground, respectively. Their distribution provided targets across different portions of the robot-mounted camera's vertical field of view.

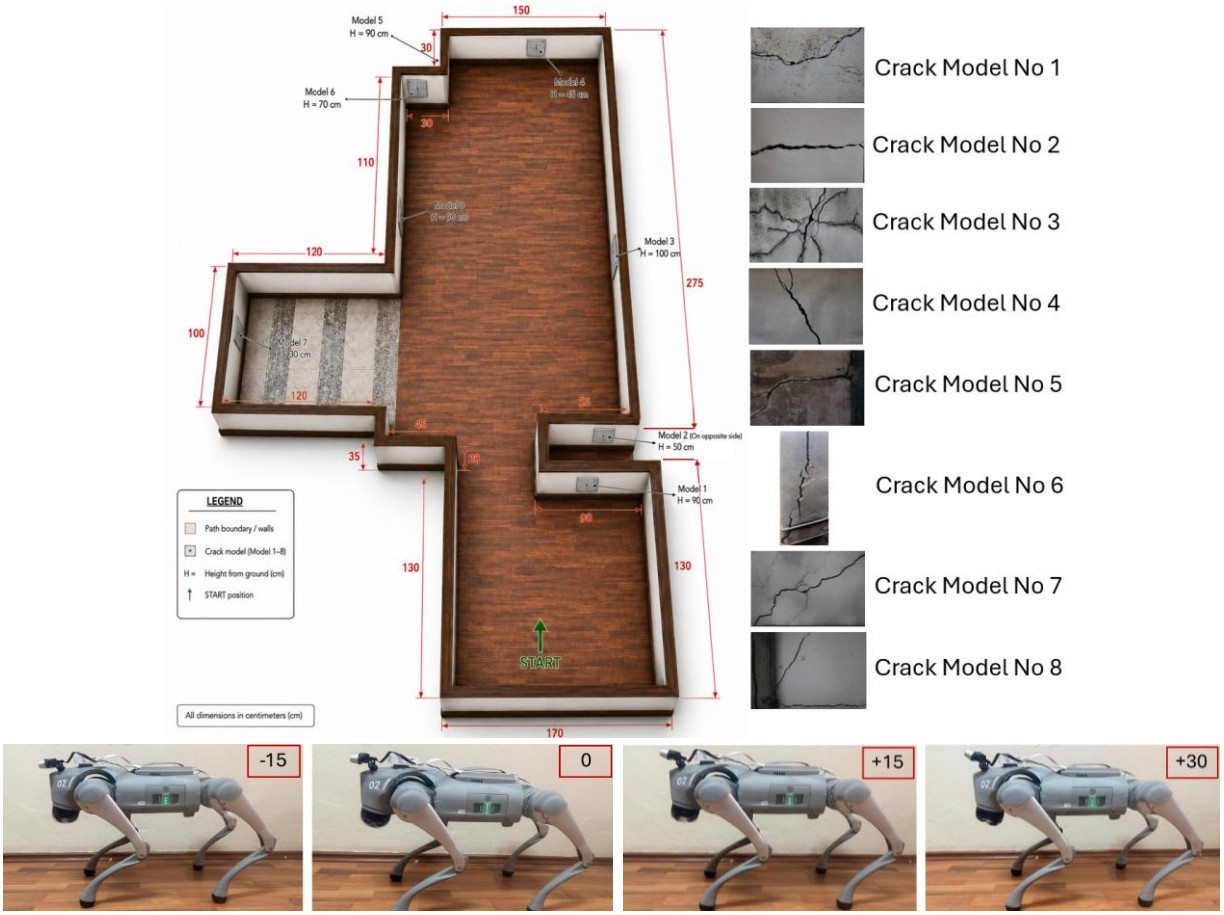


Fig. 3. Controlled indoor inspection test course used for the integrated robotic experiments.

Four experimental scenarios were defined by changing the fixed pitch of the Intel RealSense D435i while maintaining the same inspection course and prepared targets. Scenario 1 used −15°, Scenario 2 used 0°, Scenario 3 used +15°, and Scenario 4 used +30°. Each configuration was represented by one documented integrated run. The scenarios were intended to examine how camera orientation and the viewpoints produced during robotic inspection affected crack-candidate visibility. Consequently, the runs are treated as controlled scenario observations rather than repeated statistical trials or detector-validation measurements.

6 Experimental Results and Discussion

The observed detection coverage varied substantially among the four camera-pitch configurations. At −15°, only Model 7 was observed, corresponding to 1 of the 8 prepared targets. At 0°, Models 2, 4, and 7 were observed, increasing coverage to 3 of 8. The +15° configuration produced substantially broader coverage, with Models 2, 3, 4, 5, 6, 7, and 8 observed and only Model 1 missed. The +30° configuration also produced 7-of-8 coverage, detecting Models 1, 2, 3, 4, 5, 6, and 8 while Model 7 was not observed.

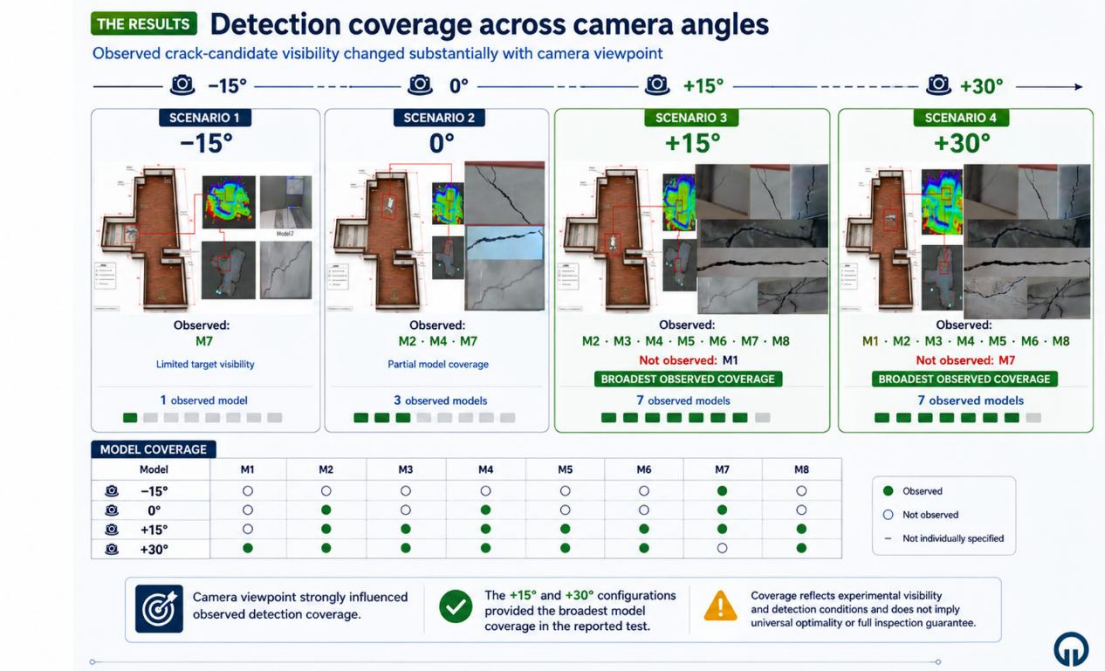


Fig. 4. Detection coverage across the four tested camera-pitch configurations, showing representative scenario outputs and the observed model coverage for the prepared crack targets.

The results indicate that the downward −15° configuration favoured the lowest target, Model 7 at 30 cm, but provided limited useful visibility of higher targets. The horizontal configuration remained biased toward lower-to-medium targets under the achieved viewpoints. Both positive-pitch configurations produced the broadest observed coverage. The +15° configuration retained visibility of the 30 cm target while also detecting Model 3 at 100 cm, whereas +30° favoured medium and higher targets but did not observe the lowest model. No single tested camera pitch independently produced observations of all eight targets.

These findings should not be interpreted as evidence of a universally optimal camera angle. Crack-candidate visibility in the integrated robotic workflow depended on the interaction of camera pitch, field of view, target height, standoff distance, robot pose, surface approach geometry, target scale, and image quality. In addition, each camera configuration was represented by only one documented integrated run, and the experiments used prepared visual crack models in a controlled indoor environment. The results therefore demonstrate scenario-based system behaviour and the practical importance of viewpoint selection rather than statistical repeatability, structural-damage classification, or field performance in earthquake-damaged buildings.

7 Experimental Results and Discussion

This paper presented the architecture, implementation, and controlled experimental assessment of a human-supervised quadrupedal platform for post-earthquake crack inspection. The system integrates a Unitree Go2 EDU, RealSense D435i RGB-D sensing, Unitree 4D LiDAR L1 environmental sensing, external computing, YOLOv8x crack-candidate processing, local median-depth association, ROS 2 communication, evidence recording, and operator supervision. Controlled inspection-course observations showed that camera viewpoint had a strong practical influence on crack-candidate coverage. The −15°, 0°, +15°, and +30° configurations produced observed coverage of 1/8, 3/8, 7/8, and 7/8 prepared targets, respectively, while the two positive-pitch configurations missed different targets. The findings show that useful robotic inspection depends on the interaction between perception and achieved

viewpoint rather than on visual detection alone. The platform remains an inspection-support system and does not determine crack geometry, structural severity, structural condition, or building safety. Further assessment should include repeated trials, calibrated spatial association, more diverse damage conditions, and representative field environments.

Acknowledgments

Funding: This research was funded by Karadeniz Technical University Scientific Research Projects Coordination Unit, with support and funding from Research Grant No: FBA-2024-11049, Focused Research Universities Support Program Project (BAP13).

References

1. Applied Technology Council, Procedures for Postearthquake Safety Evaluation of Buildings (ATC-20). Applied Technology Council, 1989.
2. Federal Emergency Management Agency, Rapid Visual Screening of Buildings for Potential Seismic Hazards: A Handbook, 3rd ed., FEMA P-154. Federal Emergency Management Agency, 2015.
3. American Society of Civil Engineers, Seismic Evaluation and Retrofit of Existing Buildings (ASCE/SEI 41-17). American Society of Civil Engineers, 2017.
4. R. Almadhoun, T. Taha, L. Seneviratne, J. Dias, and G. Cai, "A survey on inspecting structures using robotic systems," International Journal of Advanced Robotic Systems, vol. 13, no. 6, pp. 1–18, 2016. https://doi.org/10.1177/1729881416663664.
5. C. Gehring, P. Fankhauser, L. Isler, R. Diethelm, S. Bachmann, M. Potz, L. Gerstenberg, and M. Hutter, "ANYmal in the field: Solving industrial inspection of an offshore HVDC platform with a quadrupedal robot," in Field and Service Robotics, pp. 247–260. Springer, 2021. https://doi.org/10.1007/978-981-15-9460-1_18.
6. H. Kolvenbach, D. Wisth, R. Buchanan, G. Valsecchi, R. Grandia, M. Fallon, and M. Hutter, "Towards autonomous inspection of concrete deterioration in sewers with legged robots," Journal of Field Robotics, vol. 37, no. 8, pp. 1314–1327, 2020. https://doi.org/10.1002/rob.21964.
7. Y.-J. Cha, W. Choi, and O. Büyüköztürk, "Deep learning-based crack damage detection using convolutional neural networks," Computer-Aided Civil and Infrastructure Engineering, vol. 32, no. 5, pp. 361–378, 2017. https://doi.org/10.1111/mice.12263.
8. Y.-J. Cha, W. Choi, G. Suh, S. Mahmoudkhani, and O. Büyüköztürk, "Autonomous structural visual inspection using region-based deep learning for detecting multiple damage types," Computer-Aided Civil and Infrastructure Engineering, vol. 33, no. 9, pp. 731–747, 2018. https://doi.org/10.1111/mice.12334.
9. S. Dorafshan, R. J. Thomas, and M. Maguire, "Comparison of deep convolutional neural networks and edge detectors for image-based crack detection in concrete," Construction and Building Materials, vol. 186, pp. 1031–1045, 2018. https://doi.org/10.1016/j.conbuildmat.2018.08.011.
10. J. Redmon, S. Divvala, R. Girshick, and A. Farhadi, "You only look once: Unified, real-time object detection," in 2016 IEEE Conference on Computer Vision and Pattern Recognition, pp. 779–788, 2016. https://doi.org/10.1109/CVPR.2016.91.
11. Q. Qiu and D. Lau, "Real-time detection of cracks in tiled sidewalks using a YOLO-based method applied to unmanned aerial vehicle images," Automation in Construction, vol. 147, 104745, 2023. https://doi.org/10.1016/j.autcon.2023.104745.
12. C. V. Dung and L. D. Anh, "Autonomous concrete crack detection using deep fully convolutional neural network," Automation in Construction, vol. 99, pp. 52–58, 2019. https://doi.org/10.1016/j.autcon.2018.11.028.

13. X. Yang, H. Li, Y. Yu, X. Luo, T. Huang, and X. Yang, "Automatic pixel-level crack detection and measurement using fully convolutional network," Computer-Aided Civil and Infrastructure Engineering, vol. 33, no. 12, pp. 1090–1109, 2018. https://doi.org/10.1111/mice.12412.
14. S. Macenski, T. Foote, T. Gerkey, B. Lalancette, and W. Woodall, "Robot Operating System 2: Design, architecture, and uses in the wild," Science Robotics, vol. 7, no. 66, eabm6074, 2022. https://doi.org/10.1126/scirobotics.abm6074.
15. Y. Maruyama, S. Kato, and T. Azumi, "Exploring the performance of ROS2," in Proceedings of the 13th International Conference on Embedded Software, pp. 1–10, 2016. https://doi.org/10.1145/2968478.2968502.
16. K. Hacıefendioğlu, V. Kahya, A. Motamedi, and A. Bostan, "Real-time post-earthquake structural crack segmentation using a quadrupedal robotic inspection platform," Applied Sciences, vol. 16, no. 14, 6922, 2026. https://doi.org/10.3390/app16146922.
17. Unitree Robotics, "Unitree Go2." https://www.unitree.com/go2/, accessed July 13, 2026.
18. N. Abizov, "go2_ros2_sdk, including the go2_robot_sdk ROS 2 package." https://github.com/abizovnuralem/go2_ros2_sdk/tree/81681928f035d85ef7f30c3a0e67666d408ae89f, accessed July 13, 2026.
19. G. Jocher, J. Qiu, and A. Chaurasia, "Ultralytics YOLO, version 8.2.92." https://github.com/ultralytics/ultralytics/releases/tag/v8.2.92, accessed July 13, 2026.
20. Crack Detection, "SurfaceCrackDetection Dataset," Roboflow Universe, CC BY 4.0. https://universe.roboflow.com/crack-detection/surfacecrackdetection, accessed July 13, 2026.

Author Contribution Statement

- *Conceptualization:* Ali MOTAMEDI and Kemal HACIEFENDİOĞLU
- *Methodology:* Ali MOTAMEDI and Kemal HACIEFENDİOĞLU
- *Investigation:* Ali MOTAMEDI
- *Software:* Ali MOTAMEDI
- *Supervision:* Kemal HACIEFENDİOĞLU
- *Writing – Original Draft:* Ali MOTAMEDI
- *Writing – Review and Editing:* Ali MOTAMEDI and Kemal HACIEFENDİOĞLU

List of Abbreviations

- **AI** — Artificial Intelligence
- **GPU** — Graphics Processing Unit
- **GUI** — Graphical User Interface
- **LiDAR** — Light Detection and Ranging
- **RGB-D** — Red, Green, Blue and Depth
- **ROS 2** — Robot Operating System 2
- **SDK** — Software Development Kit
- **YOLO** — You Only Look Once

Declarations

Compliance with ethical standards

Conflicts of interest: The authors declare that they have no conflict of interest.

Data availability: No new dataset was generated as part of this study. The publicly available image dataset used for model adaptation is identified in Reference [20].

Publication Note
This paper was peer-reviewed, accepted for presentation, and included in the proceedings of the ACE2026 – International Conference on Advances in Civil Engineering, held on 12–14 October 2026 in Trabzon, Türkiye.

This paper may be cited as follows:
Ali MOTAMEDI and Kemal HACIEFENDİOĞLU, "Architecture and Implementation of an AI- and ROS 2-Based Quadrupedal Platform for Post-Earthquake Crack Inspection," in Proceedings of the ACE2026 – International Conference on Advances in Civil Engineering, Trabzon, Türkiye, 12–14 October 2026.

Seismic Retrofit of Slender Observation Platforms: An Optimized Tuned Mass Damper Approach

Maziar Fahimi Farzam[1], Adnan Kiral[2] and Zeliha Tonyali[3]
[1] 0000-0001-9635-8186, Department of Structural Engineering, University of Maragheh, Maragheh, Iran, m.farzam@maragheh.ac.ir
[2] 0000-0002-4534-3686, Recep Tayyip Erdogan University, Faculty of Engineering and Architecture, Department of Civil Engineering, Rize, 53100, Türkiye, adnan.kiral@erdogan.edu.tr
[3] 0000-0002-6637-7949, Recep Tayyip Erdogan University, Faculty of Engineering and Architecture, Department of Civil Engineering, Rize, 53100, Türkiye, zeliha.tonyali@erdogan.edu.tr

Abstract. In recent years, glass-bottomed observation platforms built along cliff edges have become prominent architectural landmarks for tourism. Despite their aesthetic appeal, ensuring the seismic safety of these structures poses a major engineering challenge. Their massive viewing decks, coupled with highly flexible steel supports and low natural damping, amplify their sensitivity to seismic ground motions. In this study, the optimization and seismic performance evaluation of a steel observation platform using a Tuned Mass Damper (TMD) as a passive control strategy are investigated. To design an efficient control system, the optimal parameters of the damper (including damping ratio, and tuning frequency) were determined considering the objective function of minimizing the peak displacement response of the structure. Following the development of the 3D structural model, its seismic response was evaluated under 4 benchmark earthquake records using time-history analyses. The performance evaluation indices in this research include the reduction of Peak and Root Mean Square (RMS) values for both displacement and acceleration responses. The analysis results indicate that the optimized tuned mass damper exhibited excellent performance in mitigating seismic responses under all investigated records. Implementing this control system not only leads to a significant reduction in displacement and acceleration demands in the main structure but also improves the deformation distribution in the deck. These findings demonstrate that utilizing optimized TMD systems serves as an efficient and practical methodology for enhancing the seismic performance of slender steel observation platforms.

Keywords: Glass observation platform; Tuned mass damper (TMD); Optimization; Seismic performance evaluation.

1 Introduction

The twenty-first century has witnessed a remarkable transformation in the philosophy of tourism-oriented structural engineering [1, 2]. Observation platforms, once regarded as simple viewpoints for appreciating natural landscapes, have evolved into internationally recognized architectural landmarks that symbolize technological innovation, engineering excellence, and regional identity [3]. Enabled by rapid advances in structural steel, laminated glass technology, digital fabrication, and computational mechanics, modern glass observation platforms are becoming increasingly slender, transparent, and architecturally ambitious. Their dramatic cantilevered forms, often extending beyond steep cliffs or mountainous terrain, provide visitors with the extraordinary sensation of walking in mid-air while maintaining uninterrupted panoramic views [4-6].

Among countries actively investing in such landmark infrastructure, Türkiye has emerged as one of the world's most dynamic tourism destinations. Beyond its exceptional cultural

heritage and natural landscapes, recent years have witnessed substantial investments in panoramic viewing terraces, glass observation decks, skywalks, and other iconic tourism-oriented structures located in mountainous and coastal regions [5].

This architectural evolution reflects a broader trend in structural engineering toward maximizing structural efficiency while minimizing visual obstruction. Similar developments have historically transformed the design philosophy of long-span bridges, where advances in structural analysis enabled engineers to move beyond purely strength-based designs toward significantly more slender and elegant structural systems while maintaining satisfactory safety and serviceability [7-10]. Observation platforms follow the same philosophy. Unlike conventional buildings, whose structural members are generally hidden within architectural finishes, the supporting system of an observation platform remains continuously exposed to public view.

From a structural engineering perspective, glass observation platforms constitute a unique class of flexible cantilevered structures. Their structural systems typically consist of a relatively massive viewing deck supported by slender steel trusses possessing low inherent damping and limited lateral stiffness. Such configurations produce dynamic characteristics that differ substantially from those of conventional buildings. The combination of concentrated deck mass, significant cantilever action, geometric irregularity, and relatively small structural damping increases their susceptibility to earthquakes, strong wind events, and pedestrian-induced vibrations [3, 9-11].

Mitigating structural vibrations has remained one of the central research topics in structural dynamics for more than a century [12-14]. Since Frahm first introduced the concept of an auxiliary oscillating mass in 1909, passive vibration control systems have continuously evolved through the pioneering contributions of Lanchester and Den Hartog into the classical Tuned Mass Damper (TMD), which remains one of the simplest, most reliable, and most widely implemented structural control devices [15, 16]. Owing to its mechanical simplicity, robustness, and independence from external power sources, the TMD has been successfully employed in numerous skyscrapers, communication towers, long-span bridges, stadium roofs, offshore platforms, and industrial facilities subjected to dynamic loading. Nevertheless, the overwhelming majority of these investigations have focused on conventional buildings and bridge structures, while applications to cantilevered tourist observation platforms remain remarkably scarce [17].

Interestingly, vibration control devices themselves have also become part of modern architectural expression [18]. One of the best-known examples is the 660-ton TMD installed in the Taipei 101, which, unlike conventional practice, was intentionally left visible to visitors rather than concealed within the structure. Such a philosophy is particularly relevant for modern observation platforms, where engineering innovation increasingly forms part of the attraction itself [17].

Despite the growing number of observation platforms constructed worldwide, research on their seismic vibration control remains extremely limited. Existing studies have primarily addressed architectural design, visitor perception, tourism development, structural safety assessment, and pedestrian serviceability, whereas the application of optimized passive vibration control systems has received little attention. Furthermore, because observation platforms differ fundamentally from conventional buildings through their dominant cantilever action, localized flexibility, concentrated deck mass, and unique performance requirements, design methodologies developed for ordinary structures cannot be directly generalized without careful verification [5].

Motivated by these observations, this study investigates the seismic retrofit of a slender steel observation platform using an optimally designed Tuned Mass Damper. A detailed three-dimensional finite element model is developed, and the optimal TMD parameters—including

frequency ratio, and damping ratio—are determined through numerical optimization. The seismic performance of the controlled structure is subsequently evaluated using linear time-history analyses under four representative earthquake records [19].

2. Materials and Methods

The Oylat Glass Observation Platform (GOP) recently constructed as a tourism landmark, located in Hilmiye Village, İnegöl district, Bursa Province, in northwestern Türkiye, was selected as the numerical case study. *Fig.* 1 (left) illustrates the general configuration of the investigated observation platform together with the proposed location of the Tuned Mass Damper (TMD). A detailed three-dimensional finite element model of the observation platform was developed using the commercial finite-element software SAP2000 v26 [20], as shown in *Fig.* 1 (right). The structural members were modeled using three-dimensional frame elements capable of accurately representing both flexural and axial deformation characteristics. The self-weight of all structural components, permanent gravity loads associated with the glass flooring system, and other dead loads were incorporated according to the original design specifications.

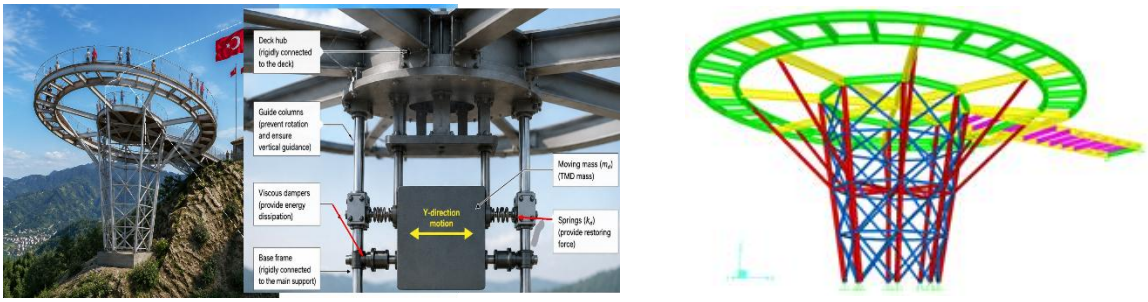


Fig. 1. The Oylat GOP and the position of TMD attached under the deck center joint (left), 3D model of the GOP (right)

The structure consists of a circular cantilevered viewing deck supported by a conical three-dimensional steel truss system anchored directly to the rock foundation. Owing to its lightweight steel configuration, long cantilever span, and relatively low inherent damping, the platform exhibits pronounced flexibility, making it potentially vulnerable to dynamic excitations induced by earthquakes and other transient loading conditions.

The supporting foundation was assumed to be rigidly connected to the underlying rock formation, resulting in fixed boundary conditions at the base of the supporting steel tower. Geometric properties, member connectivity, and material characteristics were adopted directly from the original structural design model provided by the project engineers.

The supporting foundation was assumed to be rigidly connected to the underlying rock formation, resulting in fixed boundary conditions at the base of the supporting steel tower. Geometric properties, member connectivity, and material characteristics were adopted directly from the original structural design model provided by the project engineers.

To improve the dynamic performance of the structure, an optimally tuned passive vibration control device was incorporated into the numerical model. The proposed TMD was installed near the central node of the upper deck support system, where modal participation and structural deformation indicated the highest control effectiveness. Within SAP2000, the TMD was represented by an auxiliary concentrated mass connected to the main structure through linear spring and viscous dashpot elements, enabling simultaneous simulation of inertia, stiffness, and energy dissipation mechanisms.

The TMD was designed according to the classical passive vibration control concept using a fixed auxiliary mass of 5 tons, corresponding to approximately 5% of the effective mass of the

GOP. Since the auxiliary mass was predefined, the optimization problem involved only two design variables, namely the frequency ratio and the damping ratio of the TMD. These parameters were optimized through an iterative numerical procedure coupled with linear time-history analyses in SAP2000. The objective function was defined as the minimization of the maximum deck displacement under the El Centro earthquake record. After obtaining the optimum nondimensional parameters, the corresponding spring stiffness and viscous damping coefficient were calculated and assigned to the numerical model for subsequent seismic performance evaluation.

The seismic performance of the uncontrolled and TMD-controlled observation platform was evaluated using linear time-history analyses under four benchmark earthquake records. To investigate the influence of different seismic characteristics, two far-field earthquakes (El Centro 1940 and Hachinohe 1968) together with two pulse-like near-fault earthquakes (Northridge 1994 and Kobe 1995) were selected. These benchmark records have been widely employed in previous structural control studies, allowing meaningful comparison with existing literature. The benchmark earthquake ground motions adopted in this study are illustrated in *Fig. 2*.

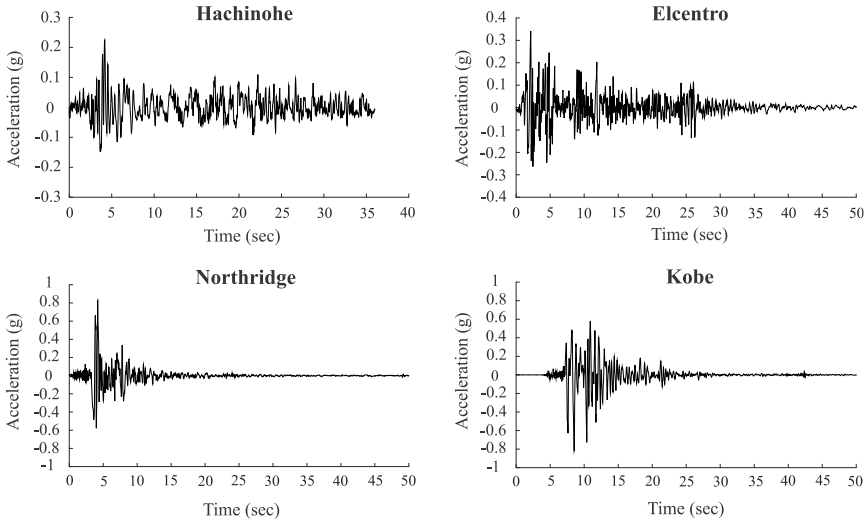


Fig. 2. Time history of benchmark ground motions

Each benchmark earthquake record was applied simultaneously along the two horizontal global directions (U1 and U2) of the three-dimensional structural model by assigning the same single-component ground motion to both directions. The dynamic analyses were carried out using Nonlinear Direct Integration Time History Analysis in SAP2000 with the Hilber–Hughes–Taylor (HHT) integration algorithm and an output time step of 0.01 s. Geometric nonlinearity was neglected, and a proportional damping model corresponding to an inherent structural damping ratio of 0.5% was adopted to represent the low intrinsic damping of the lightweight steel observation platform. Throughout the analyses, relative deck displacements were used to evaluate the effectiveness of the TMD, whereas absolute deck accelerations were employed to assess vibration comfort and seismic acceleration demands.

The effectiveness of the proposed vibration control strategy was assessed by comparing the seismic responses of the uncontrolled and controlled structural models. Two complementary response indices were adopted. The first group consists of conventional peak responses, including the maximum deck displacement and peak acceleration, which represent the maximum structural demand during earthquake excitation and are commonly employed in performance-based seismic design. The second group comprises the Root Mean Square (RMS) values of displacement and acceleration responses. Unlike peak responses, RMS indices

characterize the overall intensity of structural vibrations throughout the entire duration of the earthquake and therefore provide a more comprehensive assessment of the sustained dynamic response. Since observation platforms are continuously occupied by visitors, RMS responses are particularly relevant because they better reflect vibration serviceability, occupant comfort, and the overall effectiveness of the passive control system in suppressing structural vibrations during seismic excitation.

3. Optimum Design of Tuned Mass Damper

A preliminary modal analysis was performed to identify the dominant dynamic characteristics of the uncontrolled observation platform prior to the TMD design. The first vibration mode is primarily torsional, with a natural period of 1.28 s (0.78 Hz) and a rotational modal participation ratio of 82.3% about the vertical axis. Since the objective of the present study is to mitigate the lateral vibration of the observation deck rather than its torsional response, the TMD was tuned to the third vibration mode, which governs the translational response in the global Y-direction. This mode has a natural period of 0.55 s, corresponding to a natural frequency of 1.83 Hz, and exhibits a translational modal participation ratio of approximately 77.3% in the Y-direction. It should be noted that the observation platform is connected to the surrounding terrain through a relatively stiff access walkway aligned with the global X-direction. This structural configuration considerably increases the lateral stiffness of the system in the X-direction, resulting in relatively small translational responses and lower modal participation in that direction. Consequently, the global Y-direction governs the lateral dynamic behavior of the platform and was therefore selected as the target mode for TMD tuning.

If the (ω_d) and (ω_s) represents damper frequency and structural frequency, the frequency and damping ratios could be defined by Eq. (1). These parameters are considered as TMD free parameters, and the optimum values of these parameters are determined such that the structural response is minimized.

$$f = \frac{\omega_d}{\omega_s},\ \zeta_d = \frac{c_d}{2m_d\omega_d} \tag{1}$$

In Eq. (1), the frequency ratio (f) is defined as the auxiliary mass frequency to main mass frequency, and the damping ratio (ζ_d) is defined for the damper with the ratio of its damping to the critical damping. In the latter equation, c_d and m_d are the damping and the mass of damper, respectively.

General steps of the TMD optimum parameters calculation for this equivalent structure are as follows:

1. A frequency analysis is performed and natural frequencies, and modal shapes are realized.
2. Dynamical properties of the first mode (mass, stiffness and damping) are determined, and an equivalent SDOF structure is constructed.
3. Optimization algorithm is employed to find the TMD optimum parameters. In this procedure, the minimization of the maximum deck center displacement is selected as the objective function, and the frequency and damping ratios are applied as the design variables.
4. For the optimum design, a 5-ton TMD (corresponding to approximately 5.4% of the platform mass) was obtained with an optimum frequency ratio of f = 0.95 and an optimum damping ratio of ζ_d = 0.027. The uncontrolled platform exhibits a first natural frequency of 1.83 Hz, resulting in an optimum TMD frequency of 1.74 Hz. The corresponding spring stiffness and viscous damping coefficient were calculated as approximately 600 kN/m and 3000 N·s/m, respectively, and subsequently assigned to the numerical model.

4. Seismic Performance of Optimum TMD

The seismic performance of the optimized TMD was evaluated through linear time-history analyses under four benchmark earthquake records, including two far-field motions (El Centro and Hachinohe) and two near-fault motions (Kobe and Northridge). The dynamic responses were assessed in terms of deck-center displacement, deck-center acceleration, and TMD stroke histories. Both peak and root-mean-square (RMS) response indices were considered to evaluate not only the maximum structural demand but also the overall vibration energy throughout the excitation duration.

Fig. 3 compares the displacement time histories of the uncontrolled and TMD-controlled platform. For all earthquake records, the optimized TMD effectively suppresses the vibration amplitude immediately after the onset of strong shaking and accelerates the decay of free vibration after the principal excitation. Although the effectiveness varies depending on the frequency content and duration of each earthquake, the controlled responses consistently remain below those of the uncontrolled structure. The most pronounced improvement is observed under the El Centro earthquake, where the peak deck displacement decreases by approximately 38%. The Kobe record also exhibits a substantial reduction of about 34%, while reductions of approximately 21% and 17% are obtained for the Hachinohe and Northridge records, respectively. These results demonstrate that the optimized TMD remains effective under both pulse-like near-fault and conventional far-field ground motions despite their significantly different dynamic characteristics.

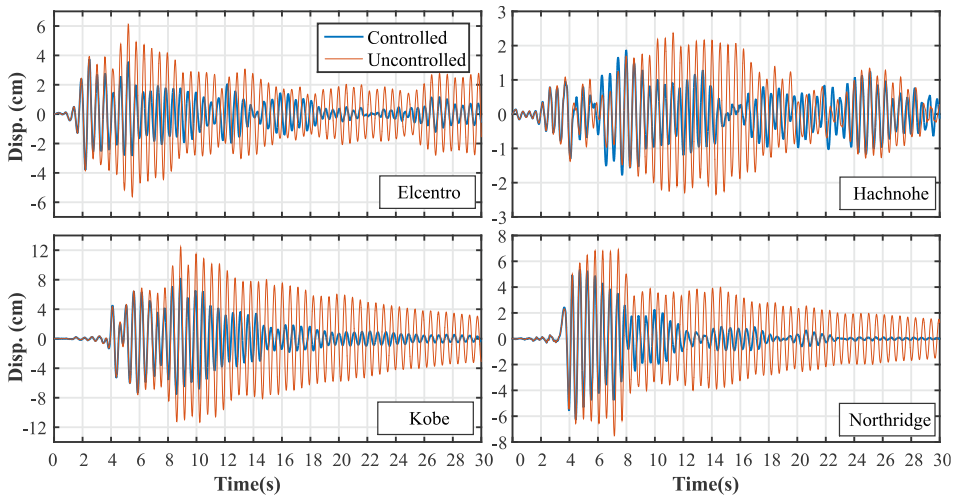


Fig. 3. Deck center displacement history of uncontrolled and controlled platform under four different earthquake.

The acceleration responses shown in *Fig.* 4 exhibit similar trends. Since acceleration is directly associated with occupant comfort and serviceability of observation platforms, its mitigation is particularly important for tourism-oriented structures. The optimized TMD substantially reduces the acceleration amplitudes during the strong-motion phase while also shortening the vibration decay period. Again, the highest improvement is achieved under the Kobe earthquake, where the peak acceleration decreases by approximately 34%, whereas reductions of about 25%, 16%, and 18% are obtained for El Centro, Hachinohe, and Northridge, respectively. These observations confirm that the TMD efficiently dissipates the seismic input energy over a broad range of excitation characteristics.

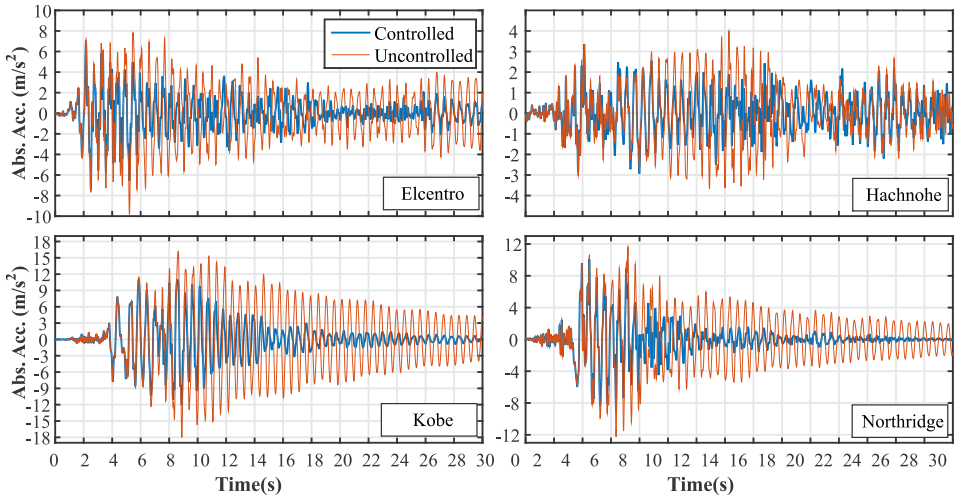


Fig. 4. Deck center Acceleration history of uncontrolled and controlled platform under four different earthquake.

A more comprehensive comparison is presented in Tables 1 and 2. Besides the reduction in maximum responses, the RMS values reveal an even more significant improvement. The RMS displacement decreases by approximately 49%, 35%, 51%, and 44% for El Centro, Hachinohe, Kobe, and Northridge earthquakes, respectively. Likewise, the RMS acceleration is reduced by approximately 43%, 30%, 47%, and 40%, respectively. The consistently larger reductions in RMS responses compared with peak responses indicate that the TMD not only limits the maximum structural demand but also dissipates vibration energy efficiently throughout the entire earthquake duration. This finding is particularly important because RMS represents the cumulative dynamic response of the structure and therefore better reflects vibration mitigation performance, fatigue-related demands, and post-earthquake serviceability than peak values alone.

Table 1. The maximum uncontrolled vs controlled responses at the deck level for different earthquakes

Response	Structure	Far field Earthquakes		Near Field Earthquakes	
		Elcentro	Hachinohe	Kobe	Northridge
Max Disp. (cm)	Uncontrolled	6.11	2.37	12.44	7.52
	Controlled	3.79	1.87	8.16	6.26
Reduction Max Disp. (%)		**37.93**	21.11	34.35	**16.78**
Max Acc. (m/s^2)	Uncontrolled	9.83	3.99	18.04	12.26
	Controlled	7.44	3.36	12.06	10.08
Reduction Max Acc. (%)		24.26	**15.8**	**33.16**	17.77

Table 2. The RMS of uncontrolled vs controlled responses at the deck level for different earthquakes

Response	Structure	Far field Earthquakes		Near Field Earthquakes	
		Elcentro	Hachinohe	Kobe	Northridge
RMS Disp. (cm)	Uncontrolled	1.96	0.93	4.46	2.41
	Controlled	1.00	0.60	2.23	1.35
Reduction RMS Disp. (%)		49.16	**35.21**	**50.12**	44.18
RMS Acc. (m/s^2)	Uncontrolled	2.71	1.34	6.00	3.29
	Controlled	1.56	0.95	3.18	1.95
Reduction RMS Acc. (%)		42.42	**28.89**	**46.91**	40.64

Another interesting observation is that the earthquake producing the largest peak reduction is not necessarily associated with the highest RMS reduction, suggesting a trade-off between instantaneous peak suppression and long-term energy dissipation. Consequently, evaluating only maximum responses may not provide a complete picture of control effectiveness. Simultaneous consideration of both peak and RMS indices offers a more comprehensive assessment of the overall seismic performance of passive control systems.

The displacement histories of the TMD mass relative to the deck are illustrated in *Fig.* 5. As expected, the largest TMD stroke occurs in the dominant vibration direction (Y-direction), while considerably smaller relative motions develop along the orthogonal direction. The maximum stroke reaches approximately ±50 cm under the Kobe record, whereas significantly smaller values are observed for the remaining earthquakes. More importantly, the displacement histories remain smooth without abrupt impacts or unstable oscillations, indicating that the selected tuning frequency and damping ratio enable stable energy exchange between the main structure and the auxiliary mass. The maximum relative displacement obtained in this study may serve as a preliminary design parameter for sizing the available TMD travel and clearance in future practical implementations.

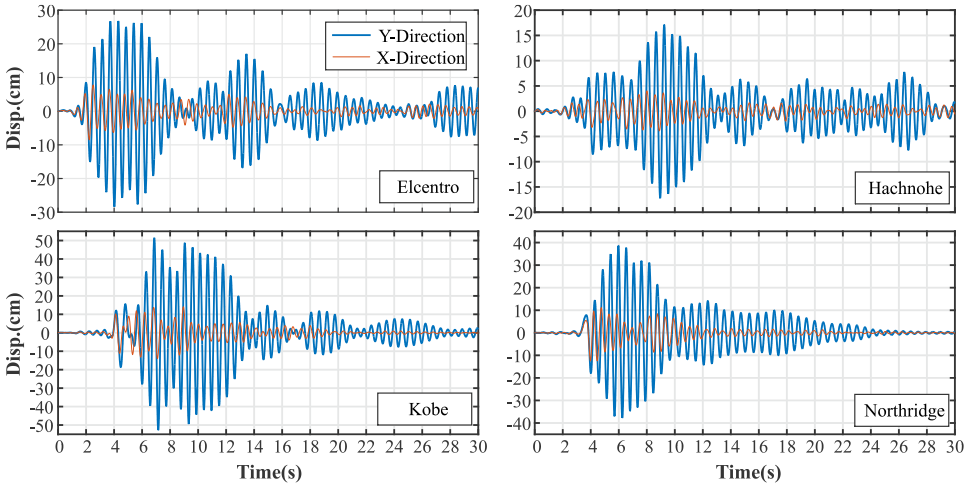


Fig. 5. TMD stroke history in X and Y-direction under four different earthquake.

Overall, the numerical results demonstrate that the optimized TMD provides a reliable passive vibration control solution for slender observation platforms subjected to different seismic scenarios. Besides reducing peak structural demands, the considerable reduction in RMS responses indicates a substantial improvement in global vibration mitigation efficiency, making the proposed system particularly attractive for landmark tourist structures where both structural safety and visitor comfort are of primary importance.

5. Conclusion

This study presented the seismic performance evaluation of a slender steel observation platform equipped with an optimized tuned mass damper (TMD). The TMD parameters were optimized by minimizing the peak deck displacement, and the effectiveness of the proposed passive control strategy was assessed through linear time-history analyses under two far-field and two near-fault earthquake records.

The numerical results demonstrated that the optimized TMD effectively mitigates both displacement and acceleration responses for all investigated earthquakes. Peak deck displacement and acceleration were reduced by up to approximately 38% and 34%, respectively, while the RMS responses exhibited even greater reductions, reaching approximately 51% for displacement and 47% for acceleration. These results indicate that the

proposed TMD effectively suppresses both the peak and sustained dynamic responses of the observation platform throughout the earthquake duration.

The results also highlight that the vibration mitigation performance is highly sensitive to the tuning frequency of the TMD. Therefore, careful optimization of the frequency ratio, which directly governs the equivalent stiffness of the damper, is essential for achieving efficient seismic response reduction.

The computed TMD stroke histories remained stable under all considered earthquake records, providing useful information for the preliminary sizing of the TMD travel during the conceptual design stage.

Overall, the proposed optimized TMD provides an efficient, practical, and economical passive vibration control solution for slender observation platforms. The presented methodology can be readily extended to other lightweight landmark structures, including panoramic viewing decks, skywalks, elevated pedestrian platforms, and similar flexible steel systems where structural safety and visitor comfort are both critical design objectives.

References

1. Deriu, D., *Skywalking in the city: Glass platforms and the architecture of vertigo.* Emotion, Space and Society, 2018. **28**: p. 94-103.
2. Leiper, N. and S.Y. Park, *Skyscrapers' influence on cities' roles as tourist destinations.* Current Issues in Tourism, 2010. **13**(4): p. 333-349.
3. Çakır, M., & Tekin, Y. (2025). A Spatial and Experiential Assessment of the Kirazlıdere Glass Observation Deck: Urban Integration and User Perception. *GSI Journals Serie A: Advancements in Tourism Recreation and Sports Sciences*, ***8***(2), 677-697.
4. Tank, Y.R. and G.R. Vesmawala, *Serviceability assessment of lively skywalk footbridge under dynamic loadings of human motions in the vadodara metropolitan area.* Asian Journal of Civil Engineering, 2025. **26**(2): p. 617-634.
5. Ergün, M., B. Tayfur, and E. Güneş, *Structural condition assessment of the Bamsı Beyrek observation terrace in Bayburt, Türkiye, on autonomous updated FEMs.* Bulletin of Earthquake Engineering, 2026. *24*(6), 4317-4347.
6. Bedon, C. and S. Mattei, *Remote facial expression and heart rate measurements to assess human reactions in glass structures.* Advances in Civil Engineering, 2021. **2021**(1), 1978111
7. Zhang, M., et al., *Vortex-induced vibration control of bridge decks using energy dissipative devices: A review of recent developments.* Advances in Wind Engineering, 2025. **2**(3).
8. Li, Y., et al., *Effects of bridge deck gratings on the aerostatic responses of a long-span pedestrian suspension bridge with a SDBG.* Advances in Structural Engineering, 2026. **29**(3): p. 614-631.
9. Li, Y., et al., *Human-induced vertical vibration of a glass suspension footbridge: experimental study and numerical analysis.* Structure and Infrastructure Engineering, 2025. **21**(4): p. 656-674.
10. Gong, M., et al., *Glass Suspension Footbridge: Human-Induced Vibration, Serviceability Evaluation, and Vibration Mitigation.* Journal of Bridge Engineering, 2021. **26**(11).
11. Bedon, C., M. Fasan, and S. Noè, *Body Motion Sensor Analysis of Human-Induced Dynamic Load Factor (DLF) for Normal Walks on Slender Transparent Floors.* Journal of Sensor and Actuator Networks, 2022. **11**(4).
12. Kiral, A., Z. Tonyali, and S. Elias, *Optimizing seismic performance of base-isolated buildings with mass and stiffness variations under near and far fault ground motions.* Structures, 2025. **76**.

13. Kiral, A. and Z. Tonyali, *The effect of LRB stiffness changes with and without supplemental viscous dampers on seismic responses of an experimentally verified mdof building.* Sigma Journal of Engineering and Natural Sciences, 2025. **43**(1): p. 301-315.
14. Ergun, M., et al., *Resilience-oriented seismic retrofit of heritage masonry minarets using hybrid base isolation and supplemental damping.* Structures, 2026. **83**.
15. Farzam, M.F. and A. Kaveh, *Optimum Design of Tuned Mass Dampers Using Colliding Bodies Optimization in Frequency Domain.* Iranian Journal of Science and Technology, Transactions of Civil Engineering, 2019: p. 1-16.
16. Kaveh, A., M. Fahimi Farzam, and H. Hojat Jalali, *Statistical seismic performance assessment of tuned mass damper inerter.* Structural Control and Health Monitoring, 2020. **27**(10).
17. Elias, S. and V. Matsagar, *Research developments in vibration control of structures using passive tuned mass dampers.* Annual Reviews in Control, 2017. **44**: p. 129-156.
18. Scaramozzino, D., G. Lacidogna, and A. Carpinteri, *New trends towards enhanced structural efficiency and aesthetic potential in tall buildings: The case of diagrids.* Applied Sciences (Switzerland), 2020. **10**(11).
19. Kaveh, A., et al., *Robust optimum design of a tuned mass damper inerter.* Acta Mechanica, 2020. **231**(9): p. 3871-3896.
20. Computers and Structures, Inc. (CSI). SAP2000 *Integrated Software for Structural and Earthquake Engineering*, Version 26. Berkeley, CA, USA; 2024.

Author Contribution Statement

- *Conceptualization:* Maziar Fahimi Farzam, Adnan Kiral, Zeliha Tonyali
- *Methodology:* Maziar Fahimi Farzam, Adnan Kiral, Zeliha Tonyali
- *Investigation:* Maziar Fahimi Farzam, Adnan Kiral, Zeliha Tonyali
- *Writing – Original Draft:* Maziar Fahimi Farzam
- *Writing – Review & Editing:* Maziar Fahimi Farzam, Adnan Kiral, Zeliha Tonyali

Publication Note

This paper was peer-reviewed, accepted for presentation, and included in the proceedings of the ACE2026 – International Conference on Advances in Civil Engineering, held on 12–14 October 2026 in Trabzon, Türkiye.

This paper may be cited as follows:

Maziar Fahimi Farzam, Adnan Kiral and Zeliha Tonyali, "Seismic Retrofit of Slender Observation Platforms: An Optimized Tuned Mass Damper Approach," in Proceedings of the ACE2026 – International Conference on Advances in Civil Engineering, Trabzon, Türkiye, 12–14 October 2026.

Investigation of Thermal Stresses in Composite Structural Elements Using the Photoelasticity Method: Mechanical Modeling and Preliminary Validation Study

Omer Canbey Cucemen[1] and Osman Bulut[2]
[1] 0000-0001-8718-1833, Istanbul Technical University, Civil Engineering Department, Istanbul, Türkiye, cucemen@itu.edu.tr
[2] 0000-0001-8200-1119, Istanbul Technical University, Civil Engineering Department, Istanbul, Türkiye, buluto@itu.edu.tr

Abstract. In modern structural engineering, composite materials are widely used, but varying coefficients of thermal expansion (CTE) among components generate complex internal stresses under high temperature differences. These thermal stresses can lead to interfacial stress concentrations, microcracks, and delamination. While these mechanisms are extensively studied using numerical methods in the literature, there remains a significant need for experimental validation under complex boundary conditions. The primary objective of this study is to experimentally investigate thermal stresses in composite systems using the photoelasticity method. Before advancing to multi-component tests, this preliminary study aims to simulate targeted thermal behavior using the mechanical modeling principle and validate the obtained photoelastic data.

In the experimental phase, the stress-freezing technique was employed. A specifically designed specimen was heated to its viscoelastic temperature, subjected to a mechanical tensile load to reflect uniform thermal deformations, and then cooled to room temperature under a controlled regime to freeze the deformations.

The pre-strained components obtained from this specimen were subsequently bonded to initially unloaded components containing a geometric discontinuity. A second thermal cycle was then applied to release the frozen deformations and generate a self-equilibrated stress field resulting from the strain incompatibility between the bonded components. Stress measurements were subsequently performed at designated points using a polariscope. To verify the optical results, both experimental stages were modeled using ABAQUS finite element analysis, while analytical solutions based on the wedge problem and an axisymmetric thermoelastic model were employed for the corresponding stages.

The experimental optical data, numerical finite element analysis, and analytical solutions demonstrated a reasonable agreement, following the expected stress attenuation trend. This convergence indicates that the stress-freezing technique can be used to simulate thermal stress behaviors in composites. Overall, this validated experimental approach provides a basis for analyzing more complex composite models in subsequent research stages.

Keywords: Photoelasticity; Thermal stress; Composite materials; Mechanical modeling

1 Introduction

The design of contemporary load-bearing systems extends beyond mere mechanical strength and capacity; thermomechanical stability under environmental variations is an equally critical criterion [1]. While composite materials offer substantial advantages such as high strength-to-

weight ratios and corrosion resistance—making them ideal for civil infrastructure and aerospace applications—their heterogeneous nature presents unique challenges. When exposed to significant thermal gradients, the mismatch in the coefficients of thermal expansion (CTE) among different constituents induces unbalanced internal forces [2, 3]. Such thermal mismatches are known to cause cracking in the concrete surrounding FRP reinforcement [1], pose pressurized thermal shock (PTS) threats in nuclear facilities [2], and affect the mechanical response of composite laminates under repeated impact loading [5].

In the current literature, the assessment of these complex thermal interactions heavily relies on computational and analytical frameworks. Extensive research has been dedicated to estimating thermal loads in steel-concrete girders, predicting the thermal buckling of functionally graded (FGM) plates, and solving 1D and 3D heat conduction problems in multilayered shells [3, 6-11]. Analytical formulations have also been established for axisymmetric configurations, including elastic matrices reinforced with fiber rods and cylinders exhibiting radially dependent properties [8, 9]. Concurrently, numerical simulations have been utilized to evaluate the stress fields in multi-bolt aircraft hybrid panels subjected to extreme thermal environments [14].

Although numerical and analytical models provide useful information on thermomechanical behavior, verifying these theoretical predictions through physical experiments is essential, especially for structures with intricate interfaces and varying boundary conditions [3, 4]. Optical techniques, particularly photoelasticity, address this gap by exploiting the birefringence of certain transparent polymers to capture full-field stress distributions [15]. Digital photoelasticity has been successfully implemented to quantify strain intensity factors near inclusions, assess stress concentrations around stiffeners, and observe thermal stress fields in graded materials [4, 12, 13]. Such optical measurements are crucial for calibrating finite element models and correcting assumptions related to boundary constraints.

Based on this need, the current study presents an experimental methodology to simulate temperature-induced stresses in composite structures via the "mechanical modeling" concept, utilizing the stress-freezing technique. Rather than applying direct thermal gradients, a specially manufactured variable cross-section polymer specimen was utilized. The process involved heating the material in a temperature-controlled oven at a rate of 7°C/h until it reached its viscoelastic state (155°C). A predefined mechanical tensile load was then introduced to mimic the targeted thermal expansion. By systematically cooling the specimen back to ambient conditions while maintaining the load, the induced deformations were permanently locked into the molecular structure. The stress-frozen specimen was then sectioned into radial components, which were bonded to initially unloaded components containing a geometric discontinuity. During a second thermal cycle, the recovery tendency of the pre-strained components was restrained by the bonded components, thereby generating a self-equilibrated stress field that mechanically represents thermally induced strain incompatibility. The radial stress fields acquired from polariscope readings were subsequently correlated with a corresponding ABAQUS finite element model and Timoshenko's analytical solutions for a wedge subjected to a concentrated load [16]. The strong correlation between the optical, numerical, and theoretical findings confirms the reliability of the stress freezing procedure, thereby providing an experimental basis for the future analysis of multi-phase composite geometries.

2 Experimental Methodology

2.1 Photoelastic Material Characterization

Initially, the material for fabricating the experimental specimens was determined. Epoxy resin was selected for this purpose due to its high light transmittance and known stress-optic coefficient.

Since the subsequent mechanical modeling stages require both the critical temperature at which the material exhibits linear elastic behavior and its modulus of elasticity at this specific temperature, corresponding tests were conducted to evaluate these properties.

To determine the critical temperature and the thermomechanical behavior of the selected epoxy resin, test specimens were manufactured and subjected to a single-cantilever bending test using a DMA Q800 (Dynamic Mechanical Analyzer). This test facilitated the precise determination of the glass transition and critical temperature values. This identified critical temperature represents the exact thermal state required to successfully freeze the induced deformations and stresses within the material.

As observed in Figure 1, the critical temperature was determined to be 155°C by considering the region where the values stabilize. Tensile test specimens were fabricated from the selected epoxy resin, heated to 155°C in the DMA, and subjected to tensile testing at this elevated temperature. The results of these tests facilitated the determination of the modulus of elasticity and the overall mechanical behavior of the epoxy resin at the specified thermal state. An examination of the resulting plot in Figure 1 confirms that the material explicitly exhibits linear elastic behavior at this temperature.

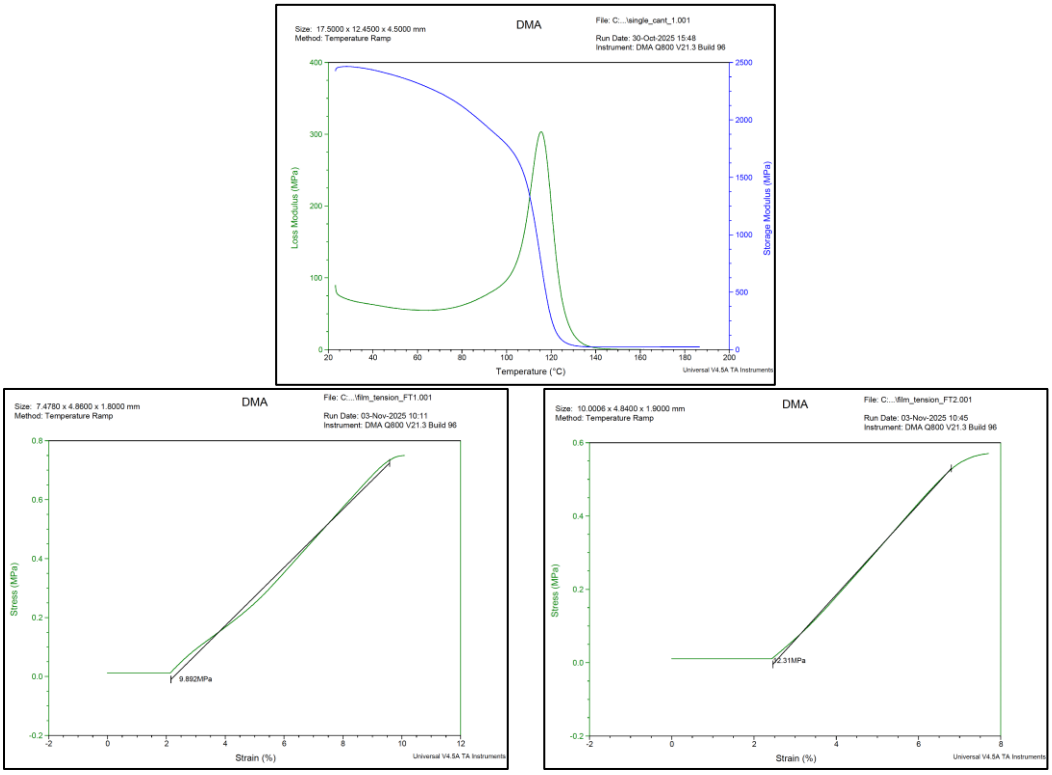


Fig. 1. Epoxy Resin Flexural Test Results and Tensile Test Results

2.2 Mechanical Simulation of Thermal Strain

Following the characterization of the material's mechanical properties, the experimental procedure advanced to the fabrication of the specimen required to simulate the thermal induced deformations via mechanical loading. In this phase, a tensile test specimen featuring a variable cross-section was designed to generate radial stresses. A CNC machine was utilized to achieve high dimensional accuracy and precision during the fabrication process. The resulting tensile specimen is depicted in Figure 2.



Fig. 2. CNC Cutting and Tensile Test Specimen

The specimen was heated in a controlled manner to the previously determined critical temperature so that the radial stresses and strains induced in the specimen could be permanently retained using the stress-freezing technique. To obtain a temperature distribution as uniform as possible within the specimen and to minimize undesirable residual stresses that could arise during heating, the temperature was increased at a rate of approximately 7°C/h until 155°C was reached. The specimen was held at this temperature for approximately two hours to ensure that the entire cross-section reached the target temperature. This temperature corresponds to the viscoelastic state of the epoxy resin suitable for the stress-freezing process, as determined from the DMA tests.

Following thermal equilibration, an axial tensile load was applied to the specimen. Owing to the variable cross-section geometry, the applied axial load generated a radially varying stress and strain field in the body region of the specimen. Thus, without directly applying a thermal gradient, a radial strain distribution intended to represent the target thermal expansion behavior was mechanically generated. The strain state obtained under loading was subsequently used as the initial strain state in the bonded model prepared in the following stage.

While the applied load was maintained, the specimen was subjected to a controlled cooling program, and the temperature was reduced to room temperature at approximately 4°C/h. Cooling under load enabled the strains generated at the elevated temperature to be frozen within the specimen. As a result, the stress field produced by mechanical loading and representing the targeted thermal strain state was retained in the specimen even after the external load was removed.

Before and after the stress-freezing process, the specimen was examined under a polariscope. The isochromatic fringe pattern observed after loading clearly demonstrates the stress field generated by mechanical loading in the variable cross-section region in Figure 3. The resulting stress distribution was also related to the analytical solution based on the wedge problem, which was used to evaluate the theoretical behavior of the variable cross-section specimen.

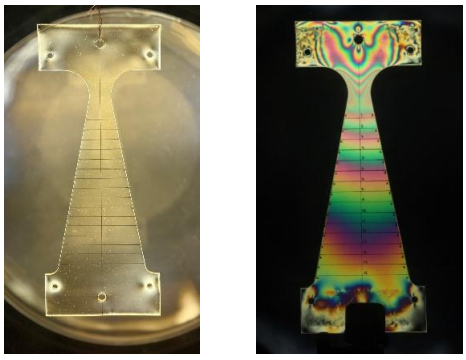


Fig. 3. Photoelastic fringe patterns of the variable cross-section specimen before and after stress-freezing

2.3 Preparation of the Bonded Composite Model

After completion of the stress-freezing process, photoelastic readings were taken at selected points on the specimen using a polarizing microscope. Subsequently, radial strips were cut from the variable cross-section specimen by CNC machining in order to transfer the mechanically generated and frozen strains into a bonded model. Thus, each strip retained the frozen strain state corresponding to the radial position it occupied during mechanical loading.

A second group of specimens with the same geometric characteristics but without prior mechanical loading was prepared to correspond to the pre-strained strips obtained above. Geometric discontinuities were also introduced into these specimens to investigate local stress concentrations. By bonding the stress-frozen strips to their initially unloaded counterparts, a composite experimental model consisting of two components with different initial strain states was obtained.

An epoxy-based adhesive was used for the bonding process. The adhesive and hardener were heated to approximately 55–60°C and mixed at a ratio of 1.5 g hardener per 10 g epoxy resin. The prepared mixture was applied to the contact surfaces, and the specimens were mechanically clamped to prevent gaps at the interface. Additional weights were placed on the specimens to limit relative sliding between the components during bonding. The bonded specimens were first kept at room temperature for 48 h and were then placed in an oven at 50°C for 24 h to complete the bonding process.

After bonding was completed, the composite specimen was subjected to a second thermal cycle. The model was again heated in a controlled manner to the critical temperature of 155°C and held at this temperature for approximately one hour. Upon reaching the critical temperature, the frozen stresses in the strips that had been pre-strained during the first mechanical loading and stress-freezing stage began to relax. The tendency of the pre-strained strips to recover their free deformation state was restrained by the initially unloaded component to which they had been bonded. As a result of this strain incompatibility, internal force transfer occurred between the two components, generating a self-equilibrated stress field in the composite model without the application of an external mechanical load. This procedure mechanically simulates the thermal stress mechanism that develops when components with different thermal expansion behavior restrain one another during a temperature change.

After completion of the second thermal cycle and cooling of the specimen back to room temperature, the bonded model was examined under a polariscope. The stress field produced by the strain incompatibility between the pre-strained and initially unloaded components was observed through the development of isochromatic fringes. In particular, the increase in fringe density around the geometric discontinuity, as shown in Figure 4, clearly indicated a local stress concentration in this region.

To quantify the stress values, measurements were performed using a polarizing microscope at selected distances from the geometric discontinuity and in regions where the stress distribution became more regular. The experimental values obtained were subsequently compared with the finite element analysis and analytical solution results.

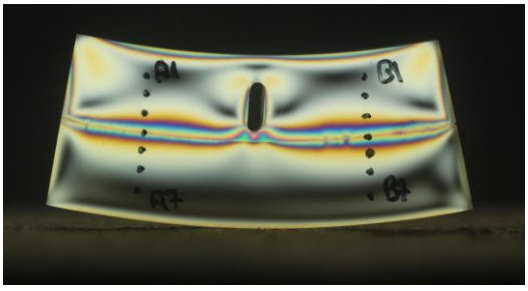


Fig. 4. Stress distribution developed in the bonded model after the second thermal cycle

3 Analytical Model

A two-stage analytical approach was adopted to theoretically evaluate the stress and strain distributions generated at different stages of the experimental study. In the first stage, the behavior of the variable cross-section specimen produced for mechanical modeling was examined under tensile loading; in the second stage, the self-equilibrated stress distribution arising after bonding the stress-frozen and initially unloaded components was evaluated analytically. Thus, both the generation of the initial strain state and its transformation into stresses within the bonded model due to strain incompatibility were considered separately.

The variable cross-section specimen used for mechanical modeling was designed so that the applied axial tensile load produced a radially varying stress and strain distribution in the body region. The behavior of this specimen under mechanical loading was evaluated using the classical wedge problem in elasticity under a concentrated load. This solution established the relationship between the applied tensile force and the radial stresses generated at different radial positions of the specimen. The radial stress equation used is expressed as follows:

$$\sigma_r = -\frac{P\cos\theta}{r\left(\alpha + \frac{\sin(2\alpha)}{2}\right)} \tag{1}$$

Using this equation, the radial stresses and corresponding strain values at different radial positions were determined. Accordingly, the initial strain distribution carried by the radial strips after stress-freezing was theoretically defined, providing an analytical reference for evaluating the photoelastic results obtained during the mechanical modeling stage.

To determine the self-equilibrated stresses developed in the bonded experimental model, the system was idealized as an axisymmetric annular section. The inner and outer radii were denoted by a and b, respectively, while the radius c represented the boundary between regions having different initial strain states (Figure 5). The problem was considered under plane-stress conditions, and all mechanical quantities were assumed to depend only on the radial coordinate. The mechanically generated initial strain incompatibility was represented in the analytical model by an equivalent radially varying temperature effect, T(r).

In the region $a \le r \le c$, the equivalent temperature effect was taken as zero, whereas T=T(r) was defined for $c \le r \le b$. Since the inner and outer surfaces were traction-free, the boundary conditions were applied as $\sigma_r(a)=0$ and $\sigma_r(b)=0$.

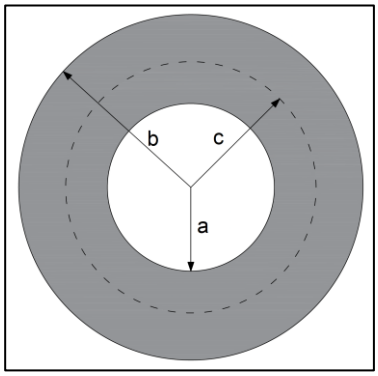


Fig. 5. Problem definition

Before substituting the obtained constants into the displacement expression, the integral terms were represented by symbols to simplify the subsequent expressions. The first integral extends

from the inner radius a to an arbitrary radius r, whereas the second extends from radius c to the outer radius b and also appears in the previously obtained constants.

$$\int_a^r (\alpha T) r dr = I \quad , \quad \int_c^b (\alpha T) r dr = \bar{I} \tag{2}$$

Substitution of these expressions into the displacement and stress relations yields the final equations.

$$\sigma_r = -\frac{E}{r^2}(I) + \frac{E(\bar{I})}{b^2 - a^2}\left(1 - \frac{a^2}{r^2}\right) = \frac{E}{r^2}\left(-(I) + \frac{(\bar{I})}{b^2 - a^2}\left(r^2 - a^2\right)\right) \tag{3}$$

$$\sigma_\theta = \frac{E}{r^2}\left((I) - \alpha T r^2 + (\bar{I})\left(\frac{r^2 + a^2}{b^2 - a^2}\right)\right) \tag{4}$$

The analytical results obtained in this manner were directly compared with the photoelastic measurements on the bonded specimen and the finite element analysis results.

4 Finite Element Analysis

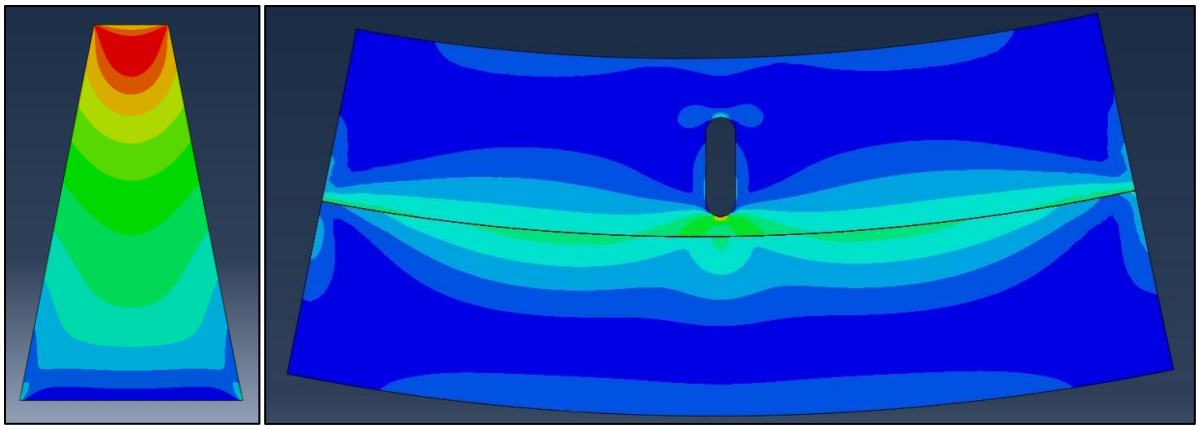
To numerically evaluate the results obtained from the experimental and analytical studies, two separate models were developed in ABAQUS. The first model represented the variable cross-section specimen used in the mechanical modeling stage, whereas the second represented the final experimental specimen obtained by bonding the stress-frozen and initially unloaded components. Thus, both stages of the experimental procedure were investigated numerically.

The first finite element model was developed to determine the behavior of the variable cross-section tensile specimen under mechanical loading. The model was defined using a two-dimensional planar shell representation consistent with the experimental specimen geometry, and the mechanical loading conditions applied in the experiment were transferred to the model. The radial stress and strain distributions obtained from this analysis were compared with the analytical solution based on the wedge problem and the photoelastic experimental results, thereby providing a numerical validation of the mechanical modeling stage.

The second finite element model was created to represent the bonded composite specimen. As in the experimental model, the pre-strained component and the initially unloaded component were modeled as separate geometries, and their contacting surfaces were connected using a tie constraint. The initial strain values to be applied to the pre-strained component were obtained from the analytical relations used in the first stage and introduced into the model accordingly. In this way, the strain incompatibility generated experimentally by the stress-freezing technique was represented numerically.

In both models, the mechanical properties of the epoxy resin at the critical temperature of 155°C were used. The elastic modulus and Poisson's ratio were defined in the model based on the values determined from the material characterization tests. The mechanical behavior of the material at this temperature had therefore been established experimentally.

In the finite element mesh of the bonded specimen, local mesh refinement was employed to capture the high stress gradients around the geometric discontinuity more accurately. An element size of approximately 0.5 mm was used in regions away from the discontinuity, while the element size was gradually reduced to approximately 0.1 mm toward the discontinuity. Following the analysis, the stress values corresponding to the photoelastic measurement locations were extracted and compared with the experimental results (Figure 6).



(a) (b)

Fig. 6. Finite element models used in the numerical analysis: (a) variable cross-section specimen for the mechanical loading stage, (b) bonded two-component model

5 Results and Discussion

After completion of the experimental study, stress values at the selected measurement points on the bonded specimen were obtained using the photoelastic method and compared with the ABAQUS finite element and analytical model results. Measurements were taken at different distances on both sides of the geometric discontinuity, and the stress distribution was observed to increase markedly as the discontinuity was approached. The highest experimental stress differences occurred around the geometric discontinuity, whereas the stress values gradually decreased in regions farther away.

Comparison of the experimental and finite element results, as shown in Figure 7, indicated that the stress distributions were particularly close in regions away from the discontinuity. For example, the experimental and ABAQUS results exhibited similar values at measurement points on the negative side, whereas the discrepancy between the two methods increased as the geometric discontinuity was approached. These differences are considered to arise from the high stress gradient near the discontinuity, the sensitivity of the photoelastic measurements to the exact measurement location, and geometric differences between the experimental specimen and the idealized numerical model.

The analytical solution provides a reference particularly for evaluating the overall behavior of the stress distribution and its variation along the radial direction. However, because the analytical model is based on axisymmetry and idealized geometric assumptions, it is not expected to represent local stress concentrations around the geometric discontinuity with the same level of detail as the experimental and finite element models. Nevertheless, the combined evaluation of the experimental, analytical, and numerical approaches indicates that the proposed mechanical modeling method can be used to experimentally investigate self-equilibrated stresses arising from thermally induced strain incompatibility.

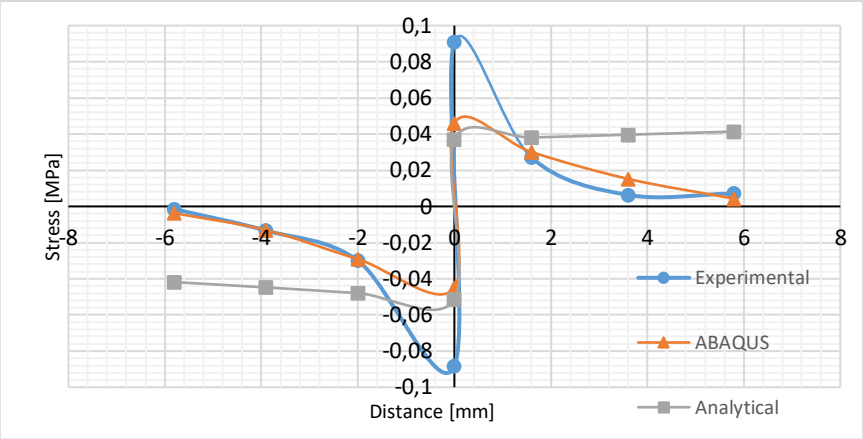


Fig. 7. Comparison of experimental, finite element and analytical stress distributions.

6 Conclusion

In this study, a two-stage mechanical modeling approach was implemented to investigate, using photoelasticity, strain incompatibilities and the associated self-equilibrated stresses that may develop in composite elements due to temperature differences. In the first stage, the target radial strain distribution was generated by applying a mechanical load to a variable cross-section specimen and was permanently retained within the specimen using the stress-freezing technique. In the second stage, pre-strained components obtained from this specimen were bonded to initially unloaded components, and a second thermal cycle generated self-equilibrated stresses resulting from the strain incompatibility between the two components.

Photoelastic measurements revealed a pronounced stress concentration around the geometric discontinuity. Comparison of the experimental results with the finite element analysis showed similar stress distributions particularly in regions away from the discontinuity, whereas more pronounced differences were observed in regions of local stress concentration. The analytical solutions enabled the two stages of the experimental procedure to be evaluated theoretically and the overall stress distribution to be interpreted. The results indicate that the combined use of mechanical modeling and stress-freezing provides a feasible approach for experimentally modeling stresses arising from thermal incompatibility.

References

1. Abdalla, H.: Concrete cover requirements for FRP reinforced members in hot climates. Composite Structures 73(1), 61–69 (2006). doi: 10.1016/j.compstruct.2005.01.033.
2. Qian, G., Niffenegger, M., Karanki, D.R.: Procedures, methods and computer codes for the probabilistic assessment of reactor pressure vessels subjected to pressurized thermal shocks. Nuclear Engineering and Design *258*, 35–50 (2013). doi: 10.1016/j.nucengdes.2013.01.030.
3. Wang, R., Peng, K., Peng, C., Wang, C.: Thermal load models for the static design of steel-concrete composite girders. arXiv preprint arXiv:2212.05746 (2022). doi: 10.48550/arXiv.2212.05746.
4. Baytak, T., Bulut, O.: Thermal stress in functionally graded plates with a gradation of the coefficient of thermal expansion only. Experimental Mechanics 62(4), 655–666 (2022). doi: 10.1007/s11340-021-00818-2.
5. Amaro, A.M., Reis, P.N.B., Neto, M.A.: Experimental study of temperature effects on composite laminates subjected to multi-impacts. Composites Part B: Engineering 98, 23–29 (2016). doi: 10.1016/j.compositesb.2016.05.021.
6. Brischetto, S., Torre, R.: Thermo-elastic analysis of multilayered plates and shells based on 1D and 3D heat conduction problems. Composite Structures 206, 326–353 (2018). doi: 10.1016/j.compstruct.2018.08.042.

7. Rajput, M.S., Kiran, R., Pathak, H.: Thermo-mechanical crack growth investigation in foam core graphite epoxy laminated sandwich structure using phase field method. Advanced Theory and Simulations 8(10), e00679 (2025). doi: 10.1002/adts.202500679.
8. Gulyaev, V.I., Mozgovyi, V.V., Shevchuk, L.V., Bilobryts'ka, O.I.: On thermomechanical effects in elastic media with reinforcing rods (fibers). Strength of Materials 54*(*2), 199–209 (2022). doi: 10.1007/s11223-022-00392-5.
9. Tokovyy, Y., Chyzh, A., Ma, C.-C.: An analytical solution to the axisymmetric thermoelasticity problem for a cylinder with arbitrarily varying thermomechanical properties. *Acta Mechanica* 230, 1469–1485 (2019). doi: 10.1007/s00707-017-2012-3.
10. Swaminathan, K., Sangeetha, D.M.: Thermal analysis of FGM plates – A critical review of various modeling techniques and solution methods. Composite Structures 160, 43–60 (2017). doi: 10.1016/j.compstruct.2016.10.047.
11. Trabelsi, S., Frikha, A., Zghal, S., Dammak, F.: A modified FSDT-based four nodes finite shell element for thermal buckling analysis of functionally graded plates and cylindrical shells. Engineering Structures 178, 444–459 (2019). doi: 10.1016/j.engstruct.2018.10.047
12. Noselli, G., Dal Corso, F., Bigoni, D.: The stress intensity near a stiffener disclosed by photoelasticity. International Journal of Fracture 166, 91–103 (2010). doi: 10.1007/s10704-010-9502-9.
13. Jobin, T.M., Khaderi, S.N., Ramji, M.: Experimental evaluation of the strain intensity factor at the inclusion tip using digital photoelasticity. *Optics and Lasers in Engineering* **126**, 105855 (2020). doi: 10.1016/j.optlaseng.2019.105855.
14. Zhang, J., Zheng, J., Zeng, J., Yang, G., Tong, M.: Thermal and mechanical stress analysis in aircraft hybrid panels with multi-bolt joints. Materials 17(8), 1872 (2024). doi: 10.3390/ma17081872.
15. Chen, L., Zhang, M., Li, D., Li, Y.: Visualization and quantification of the stress distribution on epoxy resin through photoelasticity and infrared radiation techniques. AIP Advances 12(1), 015312 (2022). doi: 10.1063/5.0074643.
16. Timoshenko, S.P., Goodier, J.N.: Theory of Elasticity. 2nd edn. McGraw-Hill, New York (1951).

Author Contribution Statement

- *Conceptualization:* Ömer Canbey Cücemen, Osman Bulut
- *Methodology:* Ömer Canbey Cücemen, Osman Bulut
- *Investigation:* Ömer Canbey Cücemen, Osman Bulut
- *Writing – Original Draft:* Ömer Canbey Cücemen
- *Writing – Review & Editing:* Ömer Canbey Cücemen, Osman Bulut

Publication Note

This paper was peer-reviewed, accepted for presentation, and included in the proceedings of the ACE2026 – International Conference on Advances in Civil Engineering, held on 12–14 October 2026 in Trabzon, Türkiye.

This paper may be cited as follows:

Cucemen, O.C., Bulut, O., "Investigation of Thermal Stresses in Composite Structural Elements Using the Photoelasticity Method: Mechanical Modeling and Preliminary Validation Study," in Proceedings of the ACE2026 – International Conference on Advances in Civil Engineering, Trabzon, Türkiye, 12–14 October 2026.

Effect of Material Degradation on Structural Performance: A Pushover-Based Assessment

Berna İstegün[1] & Erkan Çelebi[2] & Julia Eberl[3] and Alexander Stark [4]

[1] 0000-0001-8906-119X, Sakarya University, Department of Civil Engineering, Türkiye
bernaistegun@sakarya.edu.tr
[2] 0000-0002-3526-7384, Sakarya University, Department of Civil Engineering, Türkiye
ecelebi@sakarya.edu.tr
[3] 0000-0002-0031-5833, Karlsruhe Institute of Technology, Institute of Concrete Structures and Building Materials, Germany
julia.eberl@kit.edu
[4] 0000-0001-6380-5146, Karlsruhe Institute of Technology, Institute of Concrete Structures and Building Materials, Germany
alexander.stark@kit.edu

Abstract. This study investigates the influence of material properties on the seismic performance of RC frame structures through nonlinear static (pushover) analysis and provides a mechanical interpretation of construction-period-dependent material assessment adopted in rapid seismic screening methodologies. A five-story RC frame building is selected as the structural model. The C25–S500 material combination is adopted as the reference model representing the best material conditions. To investigate the influence of material degradation, additional models are developed using C20–S420, C15–S220, and C10–S220 material combinations. The C20–S420 model represents typical contemporary construction practice, whereas the C15–S220 and C10–S220 models represent the material characteristics commonly associated with aging Turkish RC building stock. All models possess identical geometry, member dimensions, loading conditions, and structural configuration. Nonlinear static analyses are performed in SAP2000 using the default ASCE 41-13 plastic hinge definitions. Structural performance is evaluated under four earthquake hazard levels (DD1–DD4) in terms of lateral load capacity, yielding behavior, target displacement, and nonlinear deformation characteristics.
The observed progressive reduction in structural capacity provides analytical support for construction-period-dependent material scoring, where building age represents the cumulative effects of historical construction practice, material quality, reinforcement characteristics, structural detailing, and long-term deterioration. Although the numerical models primarily represent the characteristics of the Turkish RC building stock, the proposed engineering interpretation is equally applicable to countries such as Germany, where construction period reflects the historical evolution of structural standards, ductility requirements, and seismic design philosophy rather than concrete strength alone. The findings contribute to a better understanding of the seismic behavior of aging RC buildings and provide an analytical basis for rapid seismic prioritization, performance-based assessment, and retrofit decision-making of existing building inventories.
Keywords: Material Degradation, Seismic Performance, Pushover Analysis, Target Displacement, Low-Strength Concrete, Existing RC Building Stock

1 Introduction

The seismic assessment of existing reinforced concrete (RC) buildings has become an increasingly important challenge in earthquake engineering due to the large number of aging structures that were constructed before the implementation of modern seismic design provisions. In many countries, these buildings constitute a significant portion of the existing building stock and may exhibit deficiencies related to material quality, reinforcement detailing, structural configuration, and long-term deterioration. Since detailed nonlinear evaluation of every existing building is practically infeasible, reliable methods for rapid seismic assessment and prioritization have become essential for effective seismic risk mitigation. Türkiye represents one of the most critical examples of this problem. Rapid urbanization during the second half of the twentieth century resulted in an extensive RC building stock constructed with varying levels of engineering supervision and quality control. Istanbul alone contains approximately 1.16 million buildings, nearly 70% of which were constructed before the 1999 Marmara earthquakes, while approximately 800.000 buildings were built before 2000 [1, 2]. Assessing such a large inventory using detailed nonlinear analyses is unrealistic because of the required time, cost, and engineering effort. Consequently, efficient rapid assessment methodologies are indispensable for identifying buildings that require detailed investigation. Numerous field investigations have demonstrated that the material properties of the Turkish RC building stock are strongly related to the construction period. Based on core tests performed on representative substandard buildings in Istanbul, Aydoğdu et al. [2] reported an average in-situ concrete compressive strength of approximately 14.6 MPa and identified the coexistence of S220 plain reinforcement and S420 deformed reinforcement within the investigated buildings. Similarly, Özmen et al. [3] represented buildings designed according to the 1975 Turkish Seismic Code using concrete strengths of 10 and 16 MPa, whereas buildings designed according to the 1998 code were represented using concrete strengths of 16 and 25 MPa. Their nonlinear analyses demonstrated that buildings designed according to newer seismic provisions possess considerably higher lateral strength and deformation capacity, while inadequate concrete quality and transverse reinforcement detailing may reduce structural ductility by approximately 50% at the Life Safety performance level and by as much as 58% at the Collapse Prevention level. These findings indicate that, for the Turkish RC building stock, construction period serves as a practical engineering indicator of expected material quality, reinforcement characteristics, construction practice, and overall seismic performance. Recent numerical studies have further emphasized the importance of material properties and detailing in the seismic performance assessment of existing RC buildings. Özmen and İnel [4] investigated 48 nonlinear models representing Turkish residential RC buildings designed according to the 1975 and 1998 seismic codes by considering different concrete strengths and lateral reinforcement detailing conditions. Their results demonstrated that seismic damage rates are strongly influenced by concrete strength, transverse reinforcement detailing, and the applicable seismic design code, with the influence of these parameters becoming increasingly pronounced at higher performance levels and under greater nonlinear displacement demands. Işık et al. [5] investigated the influence of different structural and seismic parameters on the target displacement of reinforced concrete buildings. Their results showed that concrete strength is one of the parameters affecting the seismic displacement demand of RC structures.

The aging of the building stock is also an important issue in Germany, although the characteristics of the existing RC inventory differ from those in Türkiye. National housing statistics indicate that approximately two-thirds of the residential buildings located in the federal states associated with Germany's comparatively more seismically active regions including Baden-Wuerttemberg and North Rhine-Westphalia were constructed before 1980 [6].

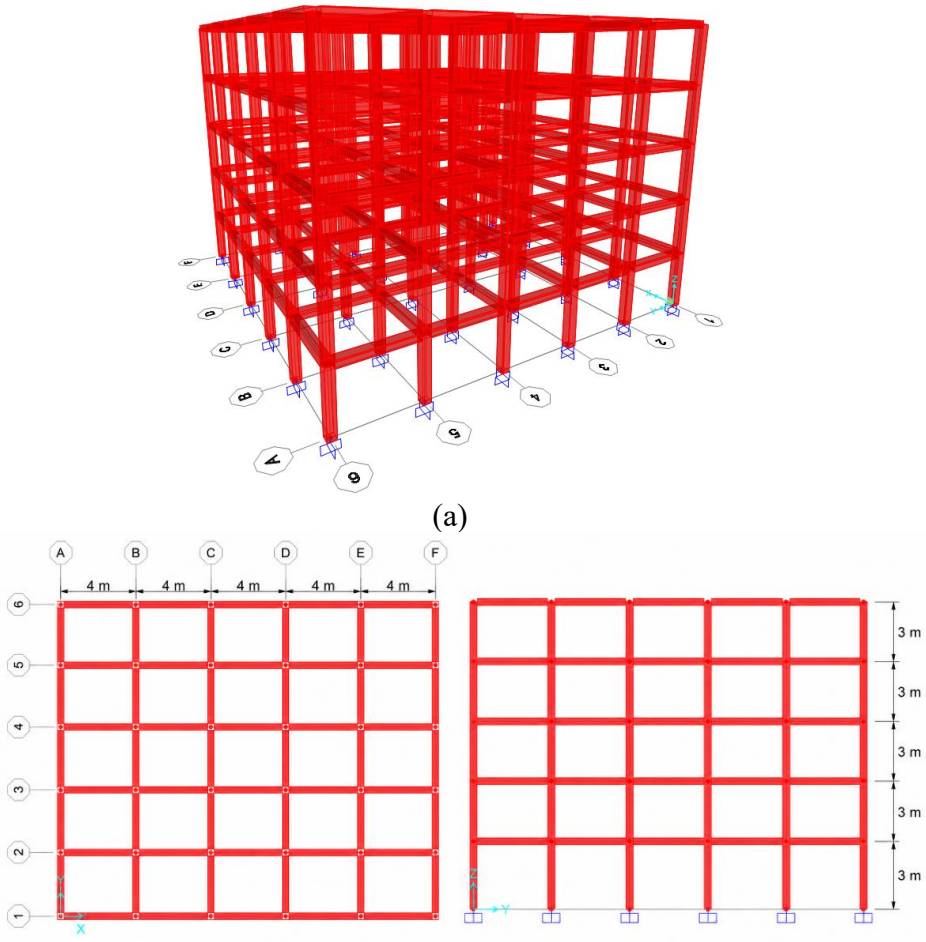
Although Germany is characterized by a substantially lower overall seismic hazard than Türkiye, the coexistence of aging building inventories and regions of relatively elevated seismicity highlights the importance of systematic assessment and prioritization. Unlike the Turkish building stock, where construction period is closely associated with significant differences in concrete quality and reinforcement characteristics, the evolution of construction practice in Germany is primarily reflected by successive improvements in structural standards, seismic design philosophy, and detailing requirements. Early versions of DIN 4149 [7] mainly provided general recommendations regarding structural configuration, bracing, foundations, and overall structural layout. Later revisions progressively introduced explicit requirements concerning structural regularity, ductility, reinforcement detailing, and limitations on simplified seismic design. The introduction of DIN 4149:2005 established minimum concrete strength requirements for ductile seismic design, while Eurocode 8 [8] subsequently incorporated capacity design principles together with ductility classes (DCL, DCM, and DCH), defining comprehensive rules for material properties, reinforcement detailing, and energy dissipation capacity. Consequently, in Germany, construction period should be interpreted not merely as an indicator of concrete strength, but as a proxy for the historical evolution of structural design philosophy, detailing practice, and expected seismic reliability. Despite these national differences, construction period remains one of the most effective parameters for rapid seismic prioritization because it reflects the expected structural quality associated with the corresponding design era. Within the rapid earthquake risk assessment methodology previously developed by the authors, this concept is incorporated through the Damage and Material Degradation category, which combines indicators related to concrete quality, deterioration, cracking, corrosion, reinforcement exposure, inappropriate repairs, and remaining service life. Accordingly, the construction period dependent coefficients assigned to this category represent the expected influence of historical construction practice, material characteristics, and long-term deterioration on structural vulnerability rather than simply the chronological age of a building. Among available analytical techniques, nonlinear static (pushover) analysis provides an efficient means of quantifying the mechanical consequences of material degradation. By evaluating lateral load capacity, yielding behavior, target displacement, and nonlinear deformation characteristics, pushover analysis enables the direct assessment of how progressive variations in concrete compressive strength and reinforcing steel yield strength influence the global seismic response of RC structures under different seismic demand levels. Such analytical evidence also provides a mechanical basis for interpreting material-related vulnerability indicators adopted in rapid seismic assessment procedures.

In the present study, four structural models of a representative five-story Turkish RC frame building are developed. The models have identical geometry, member dimensions, loading conditions, and structural configuration but differ in concrete compressive strength and reinforcing steel yield strength. The model with a concrete compressive strength of 25 MPa and reinforcing steel yield strength of 500 MPa (C25–S500) is adopted as the reference model, representing the best material conditions. The C20–S420 model represents typical contemporary construction practice in Türkiye, whereas the C15–S220 and C10–S220 models represent the material characteristics commonly associated with the older Turkish RC building stock. Consequently, the observed differences in structural response originate exclusively from variations in material properties. Nonlinear static analyses are performed for four decreasing seismic hazard levels (DD1, DD2, DD3 and DD4), allowing the combined influence of progressive material degradation and increasing seismic demand on structural performance to be systematically evaluated.

The primary objective of this study is to quantify the influence of concrete compressive strength and reinforcing steel yield strength on the nonlinear seismic performance of RC frame structures. Particular attention is given to the variation of lateral load capacity, yielding behavior, target displacement, and deformation capacity as both the material quality and seismic demand change. While the numerical models were developed to represent the Turkish RC building stock, the engineering interpretation presented in this study can also be extended to countries such as Germany, where construction period reflects the historical evolution of seismic design philosophy, structural standards, and ductility provisions. Consequently, the findings provide not only insight into the seismic behavior of aging RC buildings but also a mechanical interpretation of the material-related vulnerability concept adopted in rapid seismic assessment methodologies, thereby supporting the engineering rationale behind construction-period-dependent prioritization of existing building stocks.

2 Numerical Modeling

A five-story reinforced concrete (RC) moment-resisting frame building representative of conventional Turkish construction practice was used as the benchmark structure in this study. The building has a square floor plan measuring 20 × 20 m, corresponding to a footprint area of 400 m². Both principal directions consist of five equal bays with a span length of 4.0 m, while the interstory height is 3.0 m, resulting in an overall structural height of 15 m (Fig. 1).



(a) (b) (c)

Fig. 1. Reference reinforced concrete building adopted in the numerical study: (a) three-dimensional view, (b) plan view, and (c) elevation view.

The structural members were modeled using 40 × 40 cm square columns and 40 × 35 cm rectangular beams. Columns were reinforced with 12Ø20 longitudinal bars and Ø10 transverse reinforcement spaced at 100 mm, whereas the beams contained 4Ø16 top and 3Ø16 bottom longitudinal reinforcement. A uniformly distributed gravity load of 10 kN/m² (G + nQ) was assigned to all floors. The structure was assumed to be located in Pazarcık on ZE soil conditions and evaluated under the DD1-DD4 earthquake levels specified by the Turkish Seismic Code. The nonlinear model was developed in SAP2000 using the default ASCE 41-13 [9] plastic hinge definitions. Since predefined hinge properties were employed, the transverse reinforcement detailing was not explicitly incorporated into the hinge formulation. In addition, the effective stiffness reduction factors recommended by ASCE 41-13 were assigned to all structural members. Flexural and shear stiffness modifiers of 0.7 and 0.4 were used for columns, while the corresponding values for beams were taken as 0.3 and 0.4, respectively.

To examine the influence of material degradation, four different material combinations were analyzed: C25–S500, C20–S420, C15–S220, and C10–S220. The C25–S500 model, representing improved material quality, was adopted as the reference model, whereas the C20–S420 model represents material properties commonly used in modern Turkish reinforced concrete buildings. The C15–S220 and C10–S220 models were introduced to simulate older reinforced concrete buildings constructed before 1975, when lower concrete strengths and plain reinforcing bars were widely used in Turkish construction practice. Throughout the analyses, all geometric characteristics, reinforcement detailing, boundary conditions, loading conditions, and modeling assumptions were kept unchanged. Consequently, the differences observed in the structural response can be attributed solely to variations in material properties.

3 Nonlinear Analysis Procedure and Results

Nonlinear static analyses were carried out in SAP2000 using a displacement-controlled pushover procedure. The lateral load distribution was defined according to the first vibration mode, which was verified through modal analysis to be predominantly translational without significant torsional participation. Owing to the regular and symmetric layout of the building, together with identical geometric characteristics in the two principal directions, comparable structural responses were expected in both the X and Y directions. Consequently, the nonlinear analyses were performed in a single principal direction, which was considered sufficient to represent the global seismic behavior of the structure. To evaluate the influence of material degradation, the same analytical procedure was applied to four material configurations (C25–S500, C20–S420, C15–S220, and C10–S220) while preserving the structural geometry, support conditions, and loading scheme. Before the pushover analyses, gravity loads corresponding to G + nQ = 10 kN/m² were assigned to the structure. Cracked-section behavior was represented by adopting the effective stiffness reduction factors recommended in ASCE 41-13. Beam nonlinearity was modeled using the default ASCE 41-13 flexural hinge properties implemented in SAP2000, whereas the column response was determined based on the corresponding material properties assigned to each model. The seismic demand was represented by elastic design response spectra defined in the Turkish Seismic Code for the DD1, DD2, DD3, and DD4 earthquake levels. The structural performance was subsequently assessed using the FEMA 440 [10] performance evaluation procedure, from which the performance point and the corresponding target displacement were obtained for each material model. Figure 2 presents the pushover curves obtained from the nonlinear analyses of the four investigated structural models.

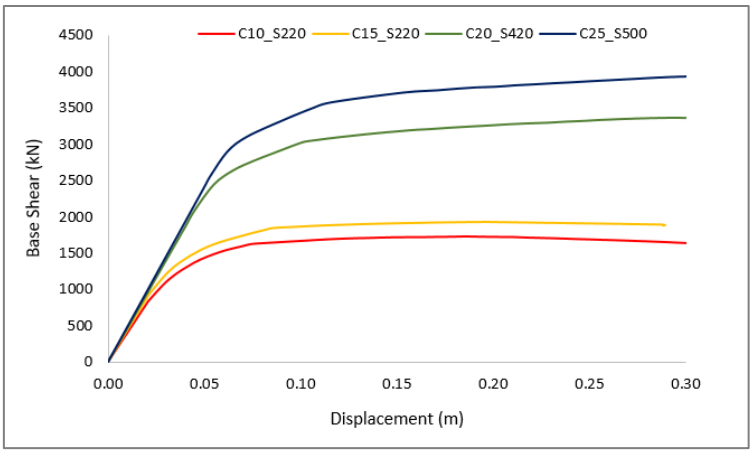


Fig. 2. Nonlinear pushover capacity curves for the models.

Table 1 summarizes the peak base shear capacities and corresponding target displacements obtained at the performance point for all material models under the four earthquake intensity levels. N.A. denotes "Not Available" and indicates cases in which a performance point could not be obtained for the corresponding earthquake intensity level; therefore, the associated base shear and target displacement values could not be determined.

Table 1. Base shear capacity and performance-point displacement of the models under different earthquake intensity levels.

Model	Earthquake Level	Base Shear (kN)	Target Displacement (m)
C25-S500	DD1	3783.00	0.408
	DD2	3810.00	0.210
	DD3	3174.00	0.078
	DD4	2650.64	0.055
C20-S420	DD1	3350.00	0.270
	DD2	3234.72	0.181
	DD3	2731.54	0.072
	DD4	2212.40	0.048
C15-S220	DD1	N.A.	N.A.
	DD2	1923.88	0.216
	DD3	1628.53	0.056
	DD4	1304.42	0.034
C10-S220	DD1	N.A.	N.A.
	DD2	1531.84	0.373
	DD3	1672.80	0.099
	DD4	1508.42	0.057

As expected, the reference model (C25–S500) consistently exhibited the highest base shear capacity, while a progressive reduction in concrete and reinforcing steel strengths resulted in a systematic decrease in lateral load-carrying capacity. The influence of material degradation became particularly evident at the DD2 earthquake level, where the base shear capacity decreased from 3810 kN for the C25–S500 model to 1531.84 kN for the C10–S220 model,

corresponding to an approximately 60% reduction in lateral strength. In contrast, the target displacement showed an opposite trend, increasing from 0.210 m to 0.373 m as the material properties deteriorated. This indicates that weaker material properties not only reduce the strength capacity of the structure but also lead to larger deformation demands. Under the most severe earthquake level (DD1), the C15–S220 and C10–S220 models failed to reach a performance point, indicating that their lateral capacities were insufficient to satisfy the seismic demand. At the lower earthquake intensity levels (DD3 and DD4), the target displacement did not follow a monotonic trend, with the C15–S220 model exhibiting smaller target displacements than the reference model despite its considerably lower strength. This behavior suggests that the performance-point displacement is governed by the interaction between the structural capacity curve and the seismic demand spectrum rather than by material strength alone. Therefore, target displacement should always be interpreted together with the corresponding lateral load capacity when evaluating the seismic performance of structures with degraded material properties.

Table 2. Relative variation in base shear capacity and target displacement with respect to the reference model (C25–S500).

Material Model	Earthquake Level	V (kN)	ΔV (%)	D (m)	ΔD (%)
C25–S500	DD1	3783.000	—	0.408	—
C20–S420		3350.000	−11.4	0.270	−33.8
C15–S220		N.A.	N.A.	N.A.	N.A.
C10–S220		N.A.	N.A.	N.A.	N.A.
C25–S500	DD2	3810.000	—	0.210	—
C20–S420		3234.720	−15.1	0.181	−13.8
C15–S220		1923.880	−49.5	0.216	+2.9
C10–S220		1531.842	−59.8	0.373	+77.6
C25–S500	DD3	3174.000	—	0.078	—
C20–S420		2731.542	−13.9	0.072	−7.7
C15–S220		1628.533	−48.7	0.056	−28.2
C10–S220		1672.797	−47.3	0.099	+26.9
C25–S500	DD4	2650.640	—	0.055	—
C20–S420		2212.400	−16.5	0.048	−12.7
C15–S220		1304.420	−50.8	0.034	−38.2
C10–S220		1508.420	−43.1	0.057	+3.6

To provide a clearer comparison of the influence of material degradation on structural performance, the results were normalized with respect to the reference model (C25–S500) at each earthquake intensity level (Table 2). For each material model, the corresponding base shear capacity and target displacement at the performance point were compared with those of the reference model, and the relative percentage changes were calculated. This approach enables the influence of material degradation to be evaluated independently for each earthquake level and facilitates a direct comparison of the variations in strength and deformation capacity among the investigated material models.

As presented in Table 2, the C25–S500 model consistently achieved the highest base shear capacity under all earthquake intensity levels. Under the DD1 earthquake, the C15–S220 and C10–S220 models were unable to reach the performance point, indicating that their lateral resistance was insufficient to satisfy the highest seismic demand. For the remaining earthquake levels, the C20–S420 model exhibited a relatively moderate reduction in base shear capacity, ranging from 11.4% to 16.5%, whereas the reductions became much more significant for the

C15–S220 (48.7–50.8%) and C10–S220 (43.1–59.8%) models. In terms of target displacement, the C10–S220 model exhibited the most unfavorable response, reaching an increase of 77.6% under the DD2 earthquake level. However, unlike the base shear capacity, the target displacement did not vary monotonically with decreasing material strength. For example, the C15–S220 model exhibited lower target displacements than the reference model under the DD3 (−28.2%) and DD4 (−38.2%) earthquake levels. To further investigate the influence of material degradation on structural damage, the distribution of plastic hinge states was evaluated at the performance point corresponding to the DD2 earthquake level. At the corresponding performance point of each model, the hinge state of every beam and column was extracted from the nonlinear pushover analysis and classified according to the ASCE 41-13 performance limits as Immediate Occupancy (A–IO), Life Safety (IO–LS), and beyond Collapse Prevention (CP). The total number of hinges within each performance range, together with their corresponding percentages, was subsequently determined to quantify the distribution of structural damage and to evaluate the influence of material degradation on the seismic performance of the investigated models.

Table 3. Distribution of plastic hinge performance states at the performance point under the DD2 design earthquake.

Model	A–IO	IO–LS	>CP	A–IO (%)	IO–LS (%)	>CP (%)
C10–S220	637	136	187	66.4	14.2	19.5
C15–S220	724	236	0	75.4	24.6	0.0
C20–S420	744	216	0	77.5	22.5	0.0
C25–S500	756	204	0	78.8	21.3	0.0

Table 3 presents the distribution of plastic hinge states at the performance point for the DD2 earthquake level. As the material strength increased, the proportion of hinges remaining within the A–IO range increased from 66.4% for the C10–S220 model to 78.8% for the C25–S500 model, indicating an improvement in the overall structural performance. Conversely, the percentage of hinges within the IO–LS range remained relatively stable, varying between 14.2% and 24.6%. The most significant difference was observed in the collapse-level hinge distribution. While no hinges exceeded the Collapse Prevention (CP) limit in the C15–S220, C20–S420, and C25–S500 models, the C10–S220 model developed 187 hinges (19.5%) beyond the CP state. This result indicates that the combination of low concrete and reinforcement strength leads to a substantial increase in severe damage, whereas moderate improvements in material properties are sufficient to prevent collapse-level hinge formation under the DD2 earthquake demand. Figure 3 shows the distribution of plastic hinge performance states at the performance point under the DD2 earthquake level for the investigated material models. A clear reduction in both the extent and severity of plastic hinge formation is observed as the material properties improve from C10–S220 to C25–S500. The C10–S220 model exhibits the most extensive nonlinear response, with numerous hinges progressing to advanced damage states, whereas the C25–S500 model shows a more favorable hinge distribution, with damage remaining comparatively limited.

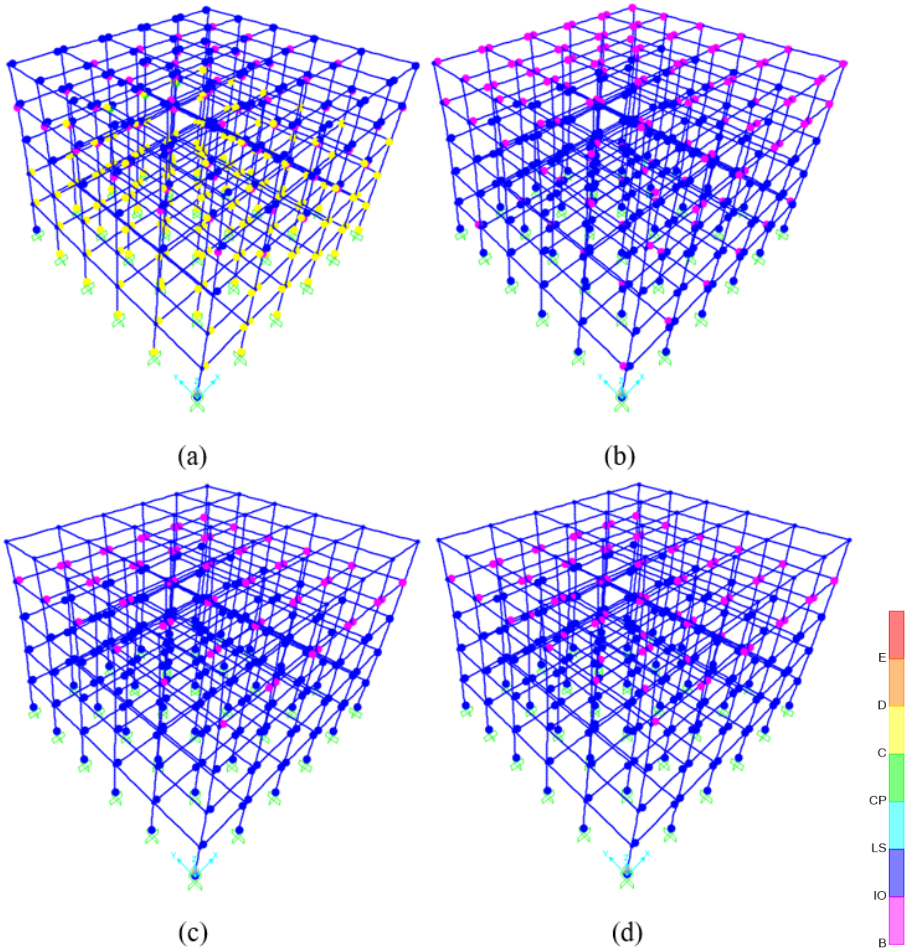


Fig. 3. Distribution of plastic hinge performance states at the DD2 performance point: (a) C10–S220, (b) C15–S220, (c) C20–S420, and (d) C25–S500.

3.1 Material Performance Index (MPI)

Although the base shear capacity and plastic hinge distribution provide valuable information regarding the seismic performance of the investigated material models, these parameters describe different aspects of structural behavior and are generally evaluated separately. To provide a single quantitative measure of the influence of material degradation, a new Material Performance Index (MPI) is proposed (Eq.1). The proposed index combines the normalized lateral load-carrying capacity with the proportion of hinges remaining below the Collapse Prevention (CP) limit, thereby incorporating both the global structural response and the extent of severe local damage into a single performance indicator. Higher MPI values indicate better seismic performance, whereas lower values reflect a greater deterioration in structural capacity and damage resistance.

$$MPI = \frac{1}{2}\left[\frac{V_{Model}}{V_{Ref}} + \left(1 - \frac{N_{>CP}}{N_{total}}\right)\right] \text{(Eq. 1)}$$

Where V_{Model} is the base shear capacity of the investigated material model at the performance point, V_{Ref} is the base shear capacity of the reference model (C25–S500), $N_{>CP}$ is the number of plastic hinges exceeding the Collapse Prevention (CP) limit, and N_{total} is the total number of plastic hinges in the structure. The first term represents the normalized lateral load-carrying capacity, while the second term reflects the proportion of hinges that remain below the CP limit. Consequently, the proposed MPI provides a combined measure of global structural strength and

local damage severity. As presented in Table 4, the proposed MPI successfully captures the influence of material degradation on the overall seismic performance of the investigated structures. The reference model (C25–S500) achieved an MPI value of 1.000, representing the highest structural performance. A moderate reduction in material strength (C20–S420) resulted in a relatively small decrease in MPI to 0.925, indicating that the structure maintained a high level of seismic performance. In contrast, the C15–S220 model exhibited a significant reduction in MPI (0.752), primarily due to its substantially lower base shear capacity.

Table 4. Material Performance Index (MPI) values for the investigated material models at the DD2 earthquake level.

Model	V_{Model}/V_{Ref}	$1-\frac{N_{>CP}}{N_{total}}$	**MPI**
C10–S220	0.402	0.805	0.604
C15–S220	0.505	1	0.752
C20–S420	0.849	1	0.925
C25–S500	1	1	1

The lowest MPI value (0.604) was obtained for the C10–S220 model, reflecting not only the considerable loss of lateral load-carrying capacity but also the occurrence of plastic hinges beyond the Collapse Prevention (CP) limit. These results demonstrate that the proposed MPI effectively combines global structural capacity and local damage characteristics into a single performance indicator, providing a straightforward quantitative measure of the adverse effects of material degradation on seismic behavior.

4 Conclusions

The nonlinear analyses demonstrated that reductions in concrete compressive strength and reinforcing-steel yield strength substantially impair the seismic performance of reinforced concrete frame structures. At the DD2 earthquake level, the base shear capacity decreased by approximately 60% from the C25–S500 reference model to the C10–S220 model, while the C10–S220 model also developed 19.5% of its plastic hinges beyond the Collapse Prevention limit. In addition, the C15–S220 and C10–S220 models were unable to reach a performance point under the DD1 demand. These results show that very low material strength affects both the global lateral resistance and the severity of local structural damage.

The proposed Material Performance Index provides a mechanical basis for calibrating material-related penalty factors used in rapid seismic screening methodologies. For the Turkish building stock, where concrete strengths of approximately 10–15 MPa are frequently encountered in older reinforced concrete buildings, the obtained MPI values support penalty factors of about 20–25% for C15 concrete and about 40% for C10 concrete. When Schmidt hammer measurements indicate an in-situ concrete strength below approximately 10 MPa, a penalty factor in the range of 40–50% may be considered for preliminary screening. These findings may serve as a basis for calibrating penalty factors in rapid seismic screening methodologies, allowing poor concrete quality to be more explicitly reflected in building prioritization.

For Germany, concrete quality is generally not the dominant source of seismic vulnerability; however, material-related penalty factors may still be appropriate for older reinforced concrete buildings. For buildings constructed before approximately 1980, particularly those with concrete strengths in the C15–C20 range, penalty factors of up to about 20% may be considered as a preliminary estimate, reflecting not only lower material properties but also the limitations

of earlier seismic provisions and detailing practices. Therefore, the proposed index offers a practical framework for defining country-specific penalty factors and for improving the consistency of rapid seismic prioritization in both Türkiye and Germany.

Acknowledgments
The authors gratefully acknowledge the support of the Karlsruhe Institute of Technology (KIT) under the University of Excellence – The Research University in the Helmholtz Association / Living the Change program. This study was conducted within the framework of the research fellowship awarded to Prof. Dr. Erkan Çelebi and the collaborative research project hosted by Prof. Dr.-Ing. Alexander Stark at the Institute of Concrete Structures and Building Materials, KIT. The support and research environment provided by KIT are sincerely appreciated.

References

1. Istanbul Metropolitan Municipality (IMM): Istanbul Earthquake Mobilization Plan, https://depremzemin.ibb.istanbul/en/istanbul-earthquake-mobilization-plan, last accessed 2026/07/18.
2. Aydogdu, H.H., Demir, C., Kahraman, T., Ilki, A.: Evaluation of rapid seismic safety assessment methods on a substandard reinforced concrete building stock in Istanbul. Structures 56, 104962 (2023).
3. Ozmen, H.B., Inel, M., Şenel, Ş.M.: Strength and Deformation Properties of Existing Turkish Building Stock. In: Seventh National Conference on Earthquake Engineering, Istanbul, Turkey, 30 May–3 June 2011.
4. Ozmen, H.B., Inel, M.: Effect of Concrete Strength and Detailing Properties on Seismic Damage for RC Structures. Research & Design 1(1), 1–11 (2024).
5. Işık, E., Hadzima-Nyarko, M., Bilgin, H., Ademović, N., Büyüksaraç, A., Harirchian, E., Bulajić, B., Ozmen, H.B., Aghakouchaki Hosseini, S.E.: A Comparative Study of the Effects of Earthquakes in Different Countries on Target Displacement in Mid-Rise Regular RC Structures. Applied Sciences 12(23), 12495 (2022).
6. Statistikportal.de: Wohngebäude nach Baujahr. https://www.statistikportal.de/de/wohngebaeude-nach-baujahr, last accessed 2026/07/18.
7. Deutsches Institut für Normung (DIN): DIN 4149:2005-04 – Buildings in German Earthquake Areas – Design Loads, Analysis and Structural Design of Buildings. Beuth Verlag, Berlin (2005).
8. CEN (European Committee for Standardization): EN 1998-1:2004 Eurocode 8 – Design of Structures for Earthquake Resistance – Part 1: General Rules, Seismic Actions and Rules for Buildings. Brussels (2004).
9. ASCE: Seismic Evaluation and Retrofit of Existing Buildings (ASCE/SEI 41-13). American Society of Civil Engineers, Reston, VA (2013).
10. FEMA: Improvement of Nonlinear Static Seismic Analysis Procedures (FEMA 440). Federal Emergency Management Agency, Washington, DC (2005).

Author Contribution Statement

- *Conceptualization: Erkan Çelebi, Alexander Stark*
- *Methodology: Berna İstegün, Erkan Çelebi, Julia Eberl, Alexander Stark*
- *Investigation: Berna İstegün, Erkan Çelebi, Julia Eberl, Alexander Stark*
- *Writing – Original Draft: Berna İstegün, Erkan Çelebi*
- *Writing – Review & Editing: Berna İstegün, Erkan Çelebi, Julia Eberl, Alexander Stark*

Note: Following the conference, this Publication Note will be added to each paper; therefore, authors are kindly requested not to remove the note below and to complete the author(s) and paper title information.

Publication Note

This paper was peer-reviewed, accepted for presentation, and included in the proceedings of the ACE2026 – International Conference on Advances in Civil Engineering, held on 12–14 October 2026 in Trabzon, Türkiye.

This paper may be cited as follows:

Istegün B., Celebi E., Eberl J., Stark A., "Effect of Material Degradation on Structural Performance: A Pushover-Based Assessment," in Proceedings of the ACE2026 – International Conference on Advances in Civil Engineering, Trabzon, Türkiye, 12–14 October 2026.

Multi-Modal Seismic Response of RC Buildings with Combined Soft-Story and Torsional Irregularities: A Performance-Based Perspective for Rapid Assessment

Berna İstegün[1] & Erkan Çelebi[2] & Julia Eberl[3] and Alexander Stark [4]

[1] 0000-0001-8906-119X, Sakarya University, Department of Civil Engineering, Türkiye
bernaistegun@sakarya.edu.tr
[2] 0000-0002-3526-7384, Sakarya University, Department of Civil Engineering, Türkiye
ecelebi@sakarya.edu.tr
[3] 0000-0002-0031-5833, Karlsruhe Institute of Technology, Institute of Concrete Structures and Building Materials, Germany
julia.eberl@kit.edu
[4] 0000-0001-6380-5146, Karlsruhe Institute of Technology, Institute of Concrete Structures and Building Materials, Germany
alexander.stark@kit.edu

Abstract. The seismic performance of existing reinforced concrete (RC) buildings is strongly influenced by structural irregularities. Rapid Seismic Screening (RSS) methods are therefore widely used to prioritize large building inventories for detailed assessment and retrofit planning. In these methodologies, severe vertical and plan irregularities are typically penalized through substantial score reductions. However, irregularities are generally evaluated independently, and the quantitative validation of such penalty mechanisms against nonlinear structural performance remains limited. This may lead to unconservative prioritization outcomes, particularly when multiple unfavorable mechanisms coexist and interact under seismic loading.

This study presents a numerical investigation of five-story RC buildings exhibiting torsional irregularity and the combined presence of torsional and soft-story irregularities. The parametric analysis employs systematically modified structural models in which selected mass- and stiffness-related characteristics are varied while the principal member properties and material characteristics are maintained. A key methodological feature is the implementation of Incremental Response Spectrum Analysis (IRSA), a multi-modal nonlinear analysis procedure, which enables higher-mode participation and torsional response mechanisms to be explicitly considered. The nonlinear response of the structural models is evaluated through global pushover curves, together with base shear response, target displacements, and structural performance states under the design earthquake.

Comparative evaluation of the capacity curves is performed to quantify the reduction in lateral load-carrying capacity associated with the introduced irregularities. Capacity reduction ratios are subsequently examined in relation to the penalty scores assigned to structural irregularities in rapid seismic assessment methodologies. The results indicate that the combined presence of torsional and soft-story irregularities produces a substantially greater reduction in structural capacity than torsional irregularity alone. The study provides a performance-based perspective for interpreting irregularity penalty scores and contributes to

establishing a stronger methodological connection between nonlinear structural performance and rapid seismic vulnerability assessment.

Keywords: Rapid Seismic Screening, Nonlinear Capacity Assessment, Soft-Story and Torsional Interaction, Incremental Response Spectrum Analysis.

1 Introduction

Structural irregularities are among the major factors influencing the seismic response of reinforced concrete (RC) buildings. Although structural regularity provides a convenient basis for seismic analysis and design, actual buildings frequently exhibit variations in mass, stiffness, strength, geometry, or the arrangement of lateral-load-resisting elements. Seismic codes generally classify these features as either plan or vertical irregularities; however, this distinction does not imply that the two occur independently. De Stefano and Pintucchi [1] emphasized that real buildings may exhibit combinations of plan and vertical irregularities, although the two categories have traditionally also been treated separately in much of the research literature.

Among plan irregularities, torsional irregularity is particularly important because asymmetric distributions of mass, stiffness, or strength can produce rotational response in addition to the translational motion of the floor system. Consequently, lateral deformation and seismic demand may become non-uniform across the plan. The torsional response of multistory buildings is influenced not only by the magnitude of eccentricity but also by the distribution of stiffness and strength and by the dynamic characteristics of the structural system. Bhasker and Menon [2] further demonstrated that different measures used to characterize torsional irregularity do not necessarily maintain the same relationship with structural demand throughout the elastic and inelastic response ranges. This highlights the importance of evaluating torsional behavior within the nonlinear structural response rather than relying exclusively on an initial measure of eccentricity or irregularity.

The complexity of irregular structural response has also motivated the development of nonlinear procedures capable of accounting for modal contributions beyond the fundamental translational mode. Chopra and Goel [3] proposed the Modal Pushover Analysis (MPA) procedure to estimate seismic demands by independently evaluating modal responses and subsequently combining their contributions. The procedure was later extended to unsymmetric-plan buildings [4]. For vertically irregular structures, Chintanapakdee and Chopra [5] compared modal pushover predictions with nonlinear response-history analyses for frames containing stiffness, strength, and combined irregularities, demonstrating the relevance of higher-mode contributions in the evaluation of such structural configurations.

An alternative multi-mode formulation was introduced by Aydınoğlu [6] through the Incremental Response Spectrum Analysis (IRSA) procedure. IRSA was developed as a theoretically based multi-mode pushover approach in which response spectrum analysis is applied incrementally throughout the nonlinear response, allowing modal displacement increments and corresponding structural response quantities to be evaluated at successive analysis steps. The procedure is not restricted to two-dimensional response and can be applied to three-dimensional structural systems while incorporating multiple vibration modes and P-delta effects. Aydınoğlu [7] subsequently demonstrated the procedure on a three-dimensional building model with artificial mass eccentricity, where multiple modes were considered to represent coupled lateral–torsional response. This formulation provides the methodological basis for the incremental multi-modal nonlinear analysis adopted in the present study.

Vertical stiffness irregularity represents another important source of unfavorable seismic behavior. A soft story may develop when the lateral stiffness of one story is substantially lower than that of adjacent stories, resulting in concentration of deformation and nonlinear demand at that level. Dya and Oretaa [8] investigated soft-story RC buildings using pushover analysis and introduced different irregularity levels by increasing the first-story height while maintaining the remaining structural configuration. Their results showed that increasing soft-story severity progressively concentrated structural damage at the irregular story. This modeling concept is particularly relevant to existing buildings in which increased ground-story height can produce a pronounced reduction in lateral stiffness.

The seismic response may become more unfavorable when vertical stiffness irregularity coexists with asymmetry in plan. Ouazir et al. [9] investigated torsionally unbalanced structures with a soft first story and demonstrated that coupling between the two response mechanisms can substantially influence displacement demand, particularly on the flexible side of the structure. Earlier work by Goh and Pan [10] similarly examined the torsional response of nonductile structures with a soft first story and identified significant displacement amplification associated with the coupled response. More recently, Satheesh et al. [11] investigated the effect of in-plan eccentricity on vertically stiffness-irregular buildings and found that eccentricity can amplify the unfavorable response associated with stiffness irregularity, particularly when the irregular story is located in the lower portion of the building. Their findings led them to emphasize the importance of considering in-plan eccentricity when evaluating buildings containing vertical stiffness irregularities.

The importance of interaction between different irregularity mechanisms has also been examined for other combinations of structural irregularities. Sadashiva et al. [12] investigated the seismic response of structures with coupled vertical stiffness–strength irregularities, providing additional evidence on the response of buildings containing more than one form of vertical irregularity. Hareen and Mohan [13] subsequently examined the torsional response of ductile RC buildings with soft first stories using nonlinear static and bidirectional nonlinear dynamic analyses. Their results showed that damage to bottom-story columns can reduce both lateral and torsional stiffness and amplify the torsional response at the irregular story. In the investigated buildings, this amplification resulted in larger displacements and more severe damage at the flexible side. Collectively, these studies demonstrate that the simultaneous presence of different irregularity mechanisms warrants explicit consideration when evaluating seismic response.

Such findings are particularly relevant to rapid seismic screening (RSS), where structural irregularities are incorporated as indicators of potential seismic vulnerability. FEMA P-154 [14], for example, provides a rapid visual screening procedure for identifying and prioritizing potentially hazardous buildings using basic structural scores and score modifiers associated with building characteristics and seismic deficiencies. The technical basis underlying the screening procedure and its scoring methodology is documented in FEMA P-155 [15]. Rapid assessment procedures are intended to prioritize large building inventories for subsequent detailed evaluation rather than to reproduce the results of comprehensive nonlinear analysis. A direct example of linking nonlinear structural response to such a screening parameter was presented by Dya and Oretaa [8]. Rather than treating soft-story irregularity solely as a binary condition, they used pushover-derived vulnerability measures to develop score modifiers corresponding to different levels of soft-story severity. Their approach demonstrates that nonlinear structural response can provide a quantitative basis for interpreting and refining irregularity-related parameters used in preliminary seismic assessment.

However, an important distinction exists between the available literature on structural response and that on rapid seismic screening. Previous studies have provided substantial evidence that torsional irregularity and soft-story irregularity can interact and amplify nonlinear seismic response [9–11,13], but their primary objective has generally been to characterize structural behavior rather than to examine how this deterioration should be represented in rapid screening. Conversely, the use of nonlinear response to derive or interpret screening score modifiers has been demonstrated for an individual irregularity such as the soft story [8]. Thus, although the nonlinear consequences of combined torsional and soft-story irregularities have been investigated, the translation of these consequences into the interpretation of irregularity-related penalties in rapid seismic screening has received comparatively limited attention.

The present study addresses this gap by quantitatively examining the performance deterioration associated with torsional irregularity and its coexistence with a soft-story configuration. Five-story RC buildings are investigated using two complementary mechanisms for producing torsional response: mass eccentricity in moment-resisting frame models and stiffness eccentricity introduced through the location of an RC core wall in wall-frame models. The nonlinear response is evaluated using an incremental multi-modal analysis procedure, with particular emphasis on modal characteristics, pushover response, base shear and displacement at the DD-2 target point, structural damage distribution, and secant stiffness. By comparing torsion-only and combined torsional–soft-story configurations, the study quantifies the associated reductions in lateral resistance and secant stiffness and subsequently interprets these reductions from the perspective of irregularity-related penalty mechanisms used in rapid seismic screening.

2 Numerical Modeling

A five-story reinforced concrete (RC) moment-resisting frame building representative of conventional Turkish construction practice was adopted as the reference structure in this study. The building has a square floor plan measuring 20 × 20 m, corresponding to a footprint area of 400 m². Both principal directions consist of five equal bays with a span length of 4.0 m. The reference model has a uniform story height of 3.0 m, resulting in a total structural height of 15 m (Fig. 1). Reinforced concrete slabs with a uniform thickness of 110 mm were assigned at every floor level and were assumed to act as rigid diaphragms.

To investigate the influence of structural irregularities on the global seismic behavior, five finite element models were developed while maintaining the same basic frame dimensions, material properties, and total gravity loading. The models differ in terms of plan irregularity, vertical irregularity, and the presence and location of a structural wall core.

The Reference (R0) model represents a regular RC moment-resisting frame without any intentional irregularity. The second model, designated IR1_T, incorporates a plan mass irregularity. Four slab panels located at the upper-right corner of the floor plan were removed from every story (Fig. 1). To preserve the total seismic mass of the building, the gravity loads associated with the removed slab panels were redistributed to the slab located at the lower-left corner of the plan. Consequently, the total building mass remained unchanged while the center of mass shifted, producing a pronounced torsional irregularity.

The third model, IR2_TS, includes the same plan mass irregularity as the IR1_T model together with a soft-story configuration. The ground-story height was increased from 3.0 m to 5.0 m, whereas all upper stories retained a height of 3.0 m.

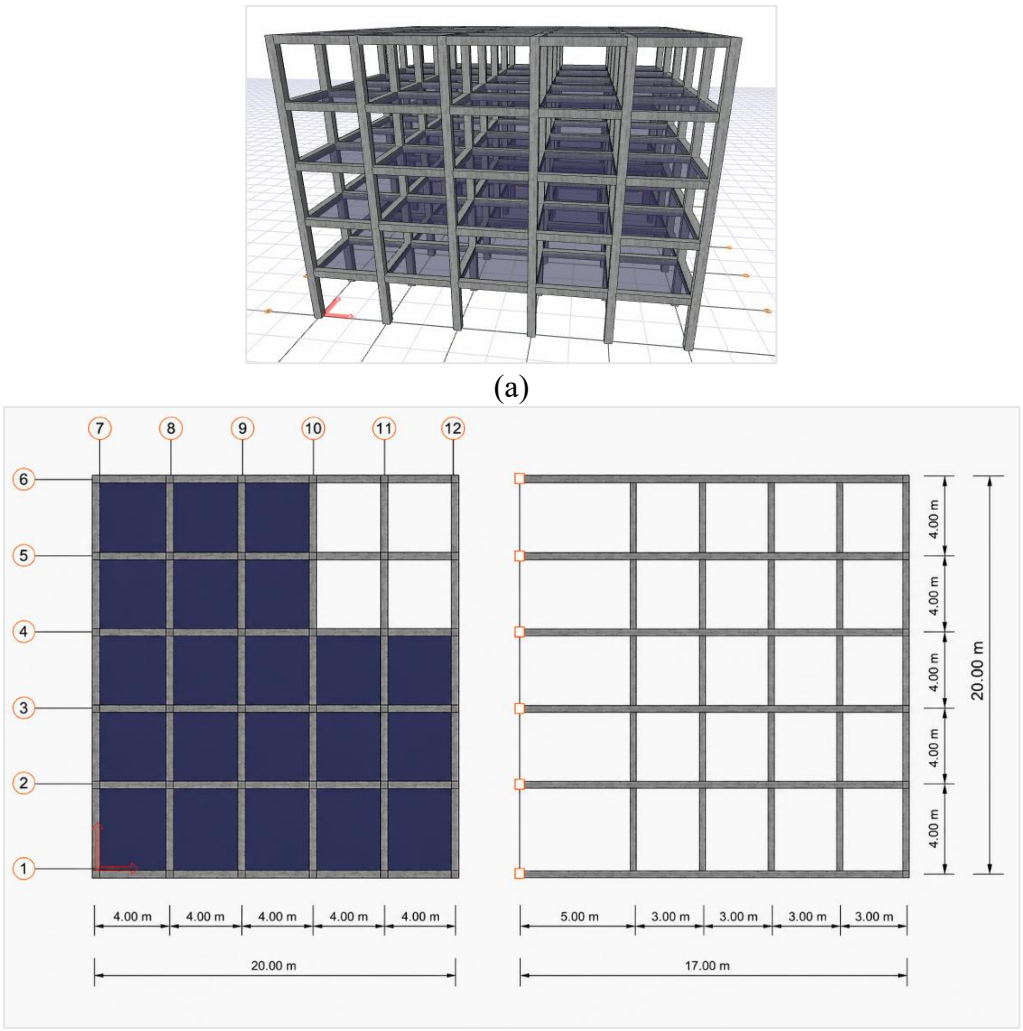
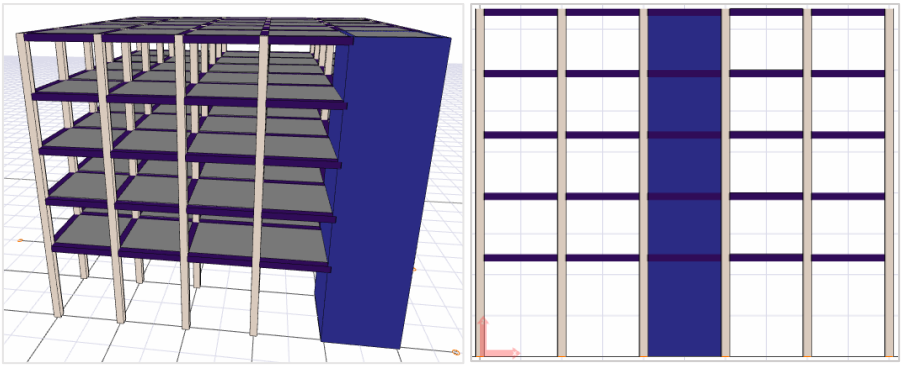


Fig. 1. Geometrical configuration of the frame models: (a) 3D view of the reference model (R0), (b) plan view of the IR1_T model, and (c) elevation view of the IR2_TS model.

The fourth model, IR3_EW, represents a wall-frame structural system. In addition to the 5.0 m ground-story height adopted in the IR2_TS model, a reinforced concrete core wall was introduced at the upper-right corner of the floor plan. Unlike IR1_T and IR2_TS, the floor slabs remained continuous throughout the building. The eccentric location of the core wall produces an asymmetric distribution of lateral stiffness and was adopted to investigate torsional response associated with stiffness eccentricity.

The fifth model, IR4_CW, has the same structural configuration, story heights, member properties, and core wall geometry as IR3_EW, but the reinforced concrete core wall was positioned at the center of the floor plan. The centrally located core provides a more balanced distribution of lateral stiffness compared with IR3_EW. Therefore, comparison of IR3_EW and IR4_CW allows the influence of core-wall location and the resulting stiffness eccentricity on the torsional response to be investigated while maintaining the same soft-story configuration (Fig. 2).



(a) (b)

Fig. 2. Geometrical configuration of the wall-frame models: (a) 3D view of the eccentrically located core wall model (IR3_EW), and (b) elevation view of the centrally located core wall model (IR4_CW).

The beams have rectangular cross-sections of 400 × 350 mm and were reinforced with 4Ø16 top and 3Ø16 bottom longitudinal bars, together with 2Ø10/100 mm transverse reinforcement. The columns have square cross-sections of 400 × 400 mm and were reinforced with 12Ø20 longitudinal bars and Ø10/100 mm transverse reinforcement. The same reinforcement configuration was maintained throughout the building height. The reinforced concrete core walls in IR3_EW and IR4_CW had dimensions of 250 × 4300 mm and were designed to satisfy the minimum reinforcement requirements in accordance with the Turkish Building Earthquake Code [16]. A uniformly distributed gravity load of 10 kN/m² (G + nQ) was assigned to all floors. C20 concrete and S420 reinforcing steel were used in all structural models. Nonlinear analyses were performed using ideCAD Structural, where the nonlinear behavior of reinforced concrete members was represented using concentrated plasticity models.

3 Nonlinear Analysis Procedure and Results

Nonlinear seismic analyses were carried out using the Incremental Response Spectrum Analysis (IRSA) method implemented in ideCAD Structural. The method provides a multi-modal nonlinear analysis framework in which the response spectrum is incorporated directly into the incremental analysis procedure. Rather than representing the seismic demand by a single invariant lateral load pattern, the structural response is determined by considering the contributions of multiple vibration modes throughout the nonlinear analysis. This feature is particularly important for irregular structures, where higher-mode effects and coupling between translational and torsional response may become significant. During the analysis, the structural state is updated as yielding and plastic hinge formation progress. The modal properties corresponding to the current stiffness state are recalculated, and the response contributions associated with the considered vibration modes are determined and combined at each stage. Consequently, changes in the dynamic characteristics of the structure resulting from stiffness degradation are reflected in the subsequent response increments. The procedure therefore provides an adaptive representation of nonlinear seismic response while retaining the response-spectrum-based formulation of modal analysis [6,7].

The use of IRSA is particularly suitable for the present study because torsional response constitutes a principal component of the investigated irregularities. In the frame models, translational–torsional coupling is induced by the asymmetric mass distribution, whereas in the wall-frame models it is influenced by the location of the structural wall core and the corresponding stiffness distribution. By simultaneously accounting for multiple modes, the adopted procedure enables these coupled response mechanisms to be represented within the

nonlinear analysis. The method also generates modal capacity curves in modal pseudo-acceleration–modal displacement coordinates for the contributing modes, while the global base shear–displacement response was adopted herein for comparison of the five structural models. Prior to the evaluation of the nonlinear response, the modal characteristics of the five structural models were examined to identify the influence of the introduced irregularities on their dynamic behavior. Table 1 summarizes the first three natural periods of the five structural models obtained from modal analysis.

Table 1. First three natural periods of the structural models.

Model	Structural configuration	T_1 (s)	T_2 (s)	T_3 (s)
R0	Regular frame	0.8885	0.8885	0.7906
IR1_T	Mass-eccentric frame	0.9046	0.8800	0.7486
IR2_TS	Mass-eccentric frame + soft story	1.1603	1.1276	0.9561
IR3_EW	Eccentric-core wall-frame + soft story	0.7886	0.4693	0.3121
IR4_CW	Central-core wall-frame + soft story	0.5442	0.4558	0.4558

As shown in Table 1, R0 and IR1_T exhibit very similar natural periods. This was an intended feature of the model configuration, as the torsional response in IR1_T was introduced by modifying the spatial distribution of mass while leaving the stiffness properties of the frame members unchanged. Thus, the close modal periods of R0 and IR1_T indicate that torsional effects were introduced without a substantial alteration of the overall translational dynamic characteristics. In IR2_TS, however, increasing the ground-story height from 3.0 to 5.0 m led to a clear increase in the natural periods, reflecting the reduction in lateral stiffness associated with the soft-story configuration. For the wall-frame models, identical member properties and core-wall dimensions were maintained, with only the location of the core being changed. Nevertheless, IR3_EW and IR4_CW exhibited noticeably different modal periods. Relocating the core from the center to the corner alters the spatial distribution of stiffness relative to the mass center and introduces stronger translational–torsional coupling. Therefore, although the sectional stiffness properties of the structural members remain unchanged, the global dynamic characteristics of the system are modified, resulting in different modal periods. Examination of the modal response indicated that the introduced irregularities modify the torsional characteristics of the structural response. While the first two modes of R0 are predominantly translational and the third mode is essentially torsional, the mass eccentricity introduced in IR1_T leads to coupled translational–torsional response. A similar modal pattern is retained in IR2_TS, accompanied by longer periods due to the soft-story configuration. For the wall-frame models, the centrally located core in IR4_CW results in a clearer separation between torsional and translational modes, whereas relocating the core to the corner in IR3_EW produces stronger translational–torsional coupling. These modal characteristics support the use of a multi-modal nonlinear analysis procedure for evaluating the capacity of the irregular models considered herein. Figure 3 compares the nonlinear pushover responses of the R0, IR1_T, and IR2_TS frame models. The curves presented are shown up to the target displacement determined for the DD-2 seismic demand. The capacity curve of IR1_T remains relatively close to that of the regular R0 model, although a moderate reduction in lateral load-carrying capacity is observed as a result of the introduced mass-induced torsional irregularity. This behavior is consistent with the model configuration, in which torsional response was introduced without modifying the stiffness properties of the frame members. In contrast, IR2_TS exhibits a substantially lower capacity curve over the entire displacement range. The additional soft-story irregularity, introduced by increasing the ground-story height, reduces both the lateral stiffness and the base shear attained at the DD-2 target point. The comparison therefore indicates that torsional irregularity alone produces a relatively limited reduction in global lateral capacity, whereas the

coexistence of torsional and soft-story irregularities results in a markedly greater deterioration of the nonlinear response.

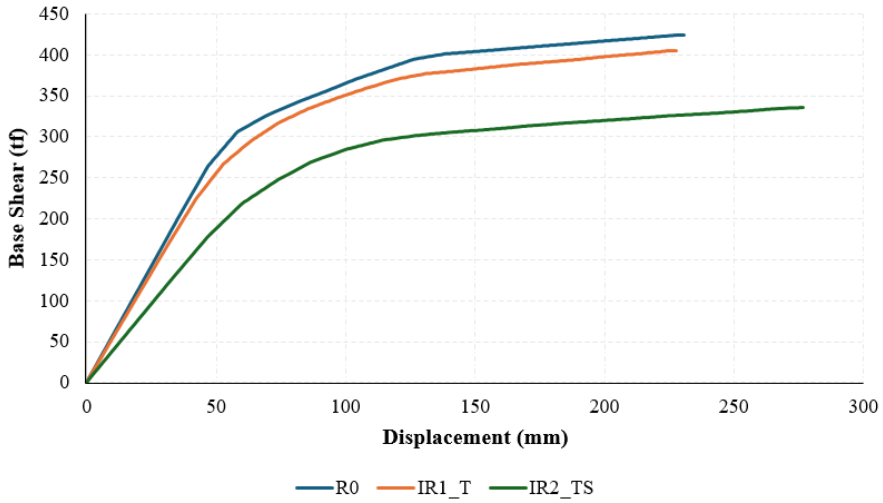


Fig. 3. Comparison of nonlinear pushover curves for the frame models.

Figure 4 compares the nonlinear pushover responses of the two wall-frame models.

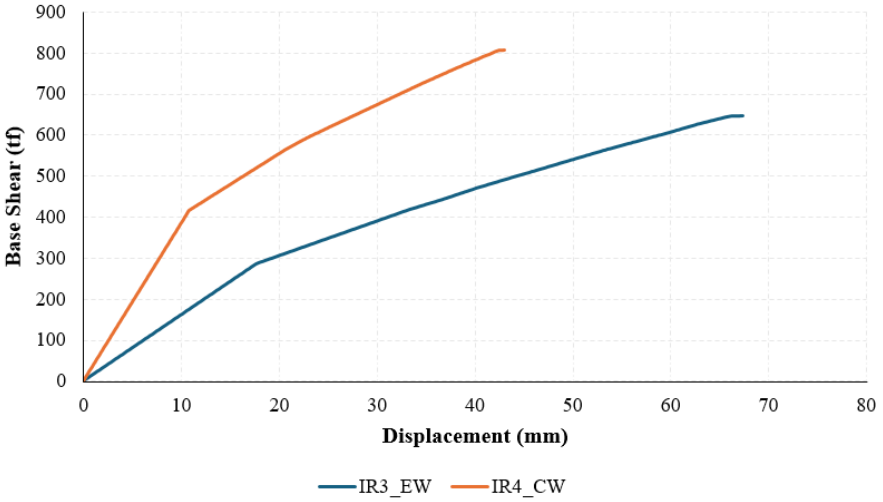


Fig. 4. Comparison of nonlinear pushover curves for the wall-frame models.

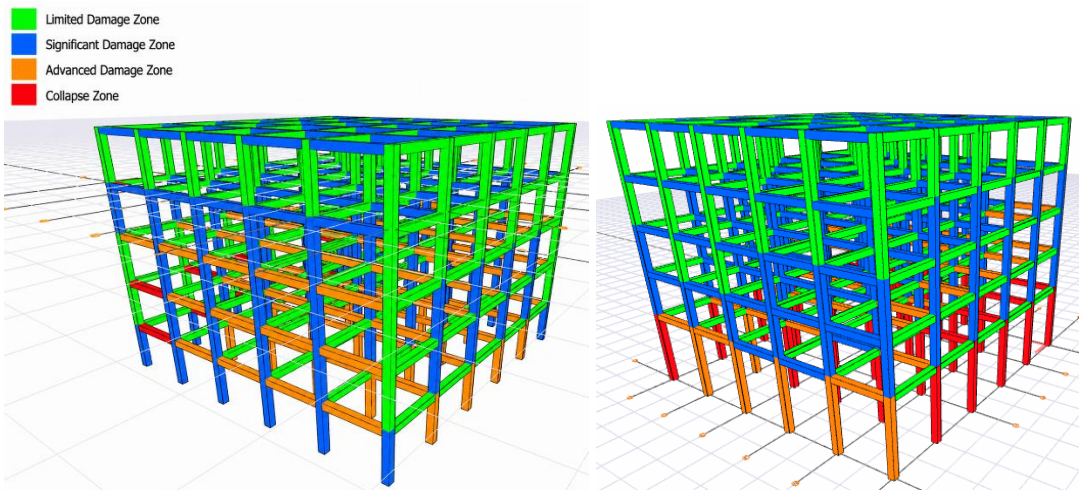
Although the wall-frame models exhibit higher absolute lateral capacities than the reference frame due to the presence of the RC core, the comparison between IR3_EW and IR4_CW provides a complementary evaluation of the influence of torsional response. Both wall-frame models have the same soft-story configuration and identical core-wall properties; however, the eccentric core location in IR3_EW produces stronger translational–torsional coupling and a lower lateral capacity than IR4_CW. Under the DD-2 earthquake demand, IR4_CW achieved the Limited Damage performance level, whereas all other models were classified at the Controlled Damage level. More importantly, the more pronounced capacity reduction observed in IR2_TS compared with IR1_T highlights the adverse response associated with the coexistence of torsional and soft-story irregularities. This interaction is particularly relevant to rapid seismic screening methodologies, where the simultaneous presence of these irregularities may require greater consideration than their independent evaluation alone.

Table 2. Relative variation in base shear at the DD-2 target point for the investigated model comparisons.

Comparison	Baseline capacity (tf)	Compared-model capacity (tf)	Capacity reduction (%)
R0 → IR1_T	424.261	404.467	**4.67**
IR1_T → IR2_TS	404.467	335.558	**17.04**
R0 → IR2_TS	424.261	335.558	**20.91**
IR4_CW → IR3_EW	808.498	647.220	**19.95**

Table 2 quantifies the capacity reductions associated with the investigated irregularity scenarios. The introduction of mass-induced torsional irregularity alone reduced the base shear capacity by only 4.67% relative to the regular reference model. When the soft-story condition was added to the torsionally irregular frame, an additional capacity reduction of 17.04% was observed, resulting in an overall reduction of 20.91% relative to R0. A comparable sensitivity to torsional response was observed in the wall-frame systems. Although both models contained the same soft-story configuration, relocating the core from the center to the plan corner resulted in a 19.95% reduction in base shear at the DD-2 target point. This comparison demonstrates that, within an already vertically irregular system, the spatial distribution of lateral stiffness and the associated torsional coupling can substantially influence the nonlinear response.

The software provides member damage distributions for the different analysis cases considered in the performance assessment. To illustrate the development and spatial distribution of nonlinear damage, the G+0.3Q+E_x analysis case was selected, representing the structural response under gravity loads combined with the seismic action in the positive X direction. Figure 5 compares the resulting damage distributions of the regular reference model (R0) and the model with combined torsional and soft-story irregularities (IR2_TS). While damage in R0 is more distributed over the structural system, IR2_TS exhibits a pronounced concentration of severe damage in the ground-story columns. Several columns in this story reach the advanced damage and collapse zones, indicating localization of the nonlinear response at the elongated ground story. This observation is consistent with the lower lateral response obtained for IR2_TS and demonstrates the pronounced localization of nonlinear damage associated with its combined irregular configuration.



(a) (b)

Fig. 5. Comparison of member damage distributions under the G+0.3Q+E_x performance analysis: (a) R0 and (b) IR2_TS.

The pushover results indicate that the influence of structural irregularities is reflected not only in the lateral load-carrying capacity but also in the force–deformation response of the structural system. Therefore, in addition to the base shear attained at the DD-2 target point, the corresponding secant stiffness was evaluated to provide a complementary measure of the response. The secant stiffness, K_{sec}, was calculated as V_{DD2}/Δ_{DD2}, where V_{DD2} and Δ_{DD2} denote the base shear and displacement at the DD-2 target point, respectively. The resulting values and their percentage reductions are summarized in Table 3.

Table 3. Comparison of lateral capacity and secant stiffness at the DD-2 target point.

Model	V_{DD2} (tf)	Δ_{DD2} (mm)	Ksec (tf/mm)	Capacity reduction (%)	Secant stiffness reduction (%)
R0	424.261	230.770	1.838	–	–
IR1_T	404.467	227.550	1.778	**4.67**	**3.29**
IR2_TS	335.558	276.660	1.213	**20.91**	**34.03**
IR3_EW	647.220	67.390	9.604	**19.95**	**48.92**
IR4_CW	808.498	43.000	18.802	–	–

For the frame models, reductions were calculated relative to R0, whereas IR4_CW was adopted as the baseline for the wall-frame comparison. Torsional irregularity alone in IR1_T resulted in relatively small reductions of 4.67% in lateral capacity and 3.29% in secant stiffness. In contrast, IR2_TS, in which torsional and soft-story irregularities coexist, exhibited reductions of 20.91% and 34.03%, respectively. The wall-frame comparison shows a similar sensitivity to torsional response, with IR3_EW exhibiting 19.95% lower lateral capacity and 48.92% lower secant stiffness than IR4_CW. Overall, the results demonstrate that the combined irregular configuration is associated with deterioration in both lateral resistance and force–deformation response, with substantially larger reductions observed for IR2_TS than for the torsion-only frame model. This distinction is particularly relevant to rapid seismic screening, where the simultaneous presence of torsional and soft-story irregularities may warrant greater attention than torsional irregularity alone.

4 Conclusions

This study investigated the nonlinear seismic response of five-story RC buildings with different configurations of torsional and soft-story irregularities using a multi-modal nonlinear analysis procedure. The results demonstrate that the influence of structural irregularities becomes particularly significant when unfavorable plan and vertical configurations coexist.

For the frame systems, introducing mass-induced torsional irregularity alone produced relatively limited changes in the global response. Compared with the regular R0 model, IR1_T exhibited a 4.67% reduction in lateral capacity and a 3.29% reduction in secant stiffness at the DD-2 target point. In contrast, when the torsional irregularity was accompanied by the soft-story configuration in IR2_TS, the reductions increased to 20.91% in lateral capacity and 34.03% in secant stiffness. The damage distribution further supported this trend, showing a pronounced concentration of severe nonlinear damage in the ground-story columns of IR2_TS. The wall-frame models provided a complementary assessment of torsional response associated with stiffness eccentricity. Relocating the core wall from the center to the plan corner resulted in a 19.95% reduction in lateral capacity and a 48.92% reduction in secant stiffness. In addition, the centrally located core model, IR4_CW, achieved the Limited Damage performance level

under DD-2 demand, whereas the remaining models were classified at the Controlled Damage level. These findings demonstrate that the spatial distribution of lateral stiffness can substantially influence both the dynamic characteristics and nonlinear force–deformation response, even when the structural member and wall properties remain unchanged.

The results also highlight the importance of multi-modal analysis in structures with significant torsional response. Although single-mode analyses were also performed, their detailed results were omitted due to space limitations. For IR2_TS, the single-mode analysis underestimated the displacement response by approximately 47.6% compared with the multi-modal IRSA result. This substantial difference indicates that neglecting higher-mode and torsional contributions may lead to a significant underestimation of seismic displacement demand.

Overall, the results show that evaluating torsional irregularity independently may not fully represent the severity of the structural response when it coexists with a soft-story configuration. While torsional irregularity alone resulted in comparatively small reductions in the investigated frame system, the combined irregular configuration was associated with substantially greater losses in both lateral resistance and secant stiffness, together with increased localization of structural damage. From a rapid seismic screening perspective, these findings suggest that buildings exhibiting both torsional and soft-story irregularities should receive particular attention and that their simultaneous occurrence may warrant a more severe assessment than that implied by considering each irregularity independently. Further studies involving a broader range of building geometries and irregularity levels are required before quantitative modifications to existing rapid-screening penalty schemes can be proposed.

References

1. De Stefano, M., Pintucchi, B. (2008). A review of research on seismic behaviour of irregular building structures since 2002. Bulletin of Earthquake Engineering, 6(2), 285–308. https://doi.org/10.1007/s10518-007-9052-3.
2. Bhasker, R., Menon, A. (2020). Torsional irregularity indices for the seismic demand assessment of RC moment resisting frame buildings. Structures, 26, 888–900. https://doi.org/10.1016/j.istruc.2020.05.018.
3. Chopra, A. K., Goel, R. K. (2002). A modal pushover analysis procedure for estimating seismic demands for buildings. Earthquake Engineering & Structural Dynamics, 31(3), 561–582. https://doi.org/10.1002/eqe.144.
4. Chopra, A. K., Goel, R. K. (2004). A modal pushover analysis procedure to estimate seismic demands for unsymmetric-plan buildings. Earthquake Engineering & Structural Dynamics, 33(8), 903–927. https://doi.org/10.1002/eqe.380.
5. Chintanapakdee, C., Chopra, A. K. (2004). Seismic response of vertically irregular frames: Response history and modal pushover analyses. Journal of Structural Engineering, 130(8), 1177–1185. https://doi.org/10.1061/(ASCE)0733-9445(2004)130:8(1177).
6. Aydınoğlu, M. N. (2003). An incremental response spectrum analysis procedure based on inelastic spectral displacements for multi-mode seismic performance evaluation. Bulletin of Earthquake Engineering, 1(1), 3–36. https://doi.org/10.1023/A:1024853326383.
7. Aydınoğlu, M. N. (2004). Incremental Response Spectrum Analysis (IRSA) procedure for multi-mode pushover including P-delta effects. Proceedings of the 13th World Conference on Earthquake Engineering, Vancouver, B.C., Canada, August 1–6, 2004, Paper No. 1440.

8. Dya, A. F. C., Oretaa, A. W. C. (2015). Seismic vulnerability assessment of soft story irregular buildings using pushover analysis. Procedia Engineering, 125, 925–932. https://doi.org/10.1016/j.proeng.2015.11.103.
9. Ouazir, M., Kassoul, A., Ouazir, A., Achour, B. (2018). Inelastic seismic response of torsionally unbalanced structures with soft first story. Asian Journal of Civil Engineering, 19, 571–581. https://doi.org/10.1007/s42107-018-0043-2.
10. Goh, K. S., Pan, T.C. (2015). Torsional response of nonductile structures with soft-first-storey. Earthquake Engineering & Structural Dynamics, 44(1), 1–21. https://doi.org/10.1002/eqe.2452.
11. Satheesh, A. J., Jayalekshmi, B. R., Venkataramana, K. (2020). Effect of in-plan eccentricity on vertically stiffness irregular buildings under earthquake loading. Soil Dynamics and Earthquake Engineering, 137, 106251. https://doi.org/10.1016/j.soildyn.2020.106251.
12. Sadashiva, V. K., MacRae, G. A., Deam, B. L. (2012). Seismic response of structures with coupled vertical stiffness–strength irregularities. Earthquake Engineering & Structural Dynamics, 41(1), 119–138. https://doi.org/10.1002/eqe.1121.
13. Hareen, C. H. B. V., Mohan, S. C. (2021). Evaluation of seismic torsional response of ductile RC buildings with soft first story. Structures, 29, 1640–1654. https://doi.org/10.1016/j.istruc.2020.12.031.
14. Federal Emergency Management Agency (FEMA). (2015). Rapid Visual Screening of Buildings for Potential Seismic Hazards: A Handbook, Third Edition. FEMA P-154. Washington, DC: Federal Emergency Management Agency.
15. Federal Emergency Management Agency (FEMA). (2015). Rapid Visual Screening of Buildings for Potential Seismic Hazards: Supporting Documentation, Third Edition. FEMA P-155. Washington, DC: Federal Emergency Management Agency.
16. TBEC (2018): Turkish Building Earthquake Code. Disaster and Emergency Management Authority (AFAD), Ankara, Türkiye.

Author Contribution Statement

- *Conceptualization: Erkan Çelebi, Alexander Stark*
- *Methodology: Berna İstegün, Erkan Çelebi, Julia Eberl, Alexander Stark*
- *Investigation: Berna İstegün, Erkan Çelebi, Julia Eberl, Alexander Stark*
- *Writing – Original Draft: Berna İstegün, Erkan Çelebi*
- *Writing – Review & Editing: Berna İstegün, Erkan Çelebi, Julia Eberl, Alexander Stark*

Publication Note

This paper was peer-reviewed, accepted for presentation, and included in the proceedings of the ACE2026 – International Conference on Advances in Civil Engineering, held on 12–14 October 2026 in Trabzon, Türkiye.

This paper may be cited as follows:

Istegun, B., Celebi, E., Eberl, J., Stark, A., "Multi-Modal Seismic Response of RC Buildings with Combined Soft-Story and Torsional Irregularities: A Performance-Based Perspective for Rapid Assessment," in Proceedings of the ACE2026 – International Conference on Advances in Civil Engineering, Trabzon, Türkiye, 12–14 October 2026.

Analytical Timber Spaced-Column P-M Interaction Diagram

Rabia Izol[1] and Ahmet Turer[2]
[1] 0000-0002-7568-3817, Istanbul Technical University, Civil Engineering Department, Istanbul, Türkiye, rizol@itu.edu.tr
[2] 0000-0002-2214-1387, Middle East Technical University, Civil Engineering Department, Ankara, Türkiye, aturer@metu.edu.tr

Abstract. International codes do not allow the application of bending moment along with axial compression on timber spaced columns except for minor dead-load-related moments. This study attempts to derive an interaction relationship between axial load and bending moment on spaced (built-up) columns using gussets. The capacity is determined using Finite Element Modeling (FEM), especially for slender spaced columns. The approach considers a) buckling (local or global) stability of the whole column and b) compressive strength of members considering allowable stresses. Two lengths of 3 m and 5.8 m were selected for the FEM models, and buckling loads were obtained to determine three-dimensional P-M diagrams. An attempt was made to fit equations to the obtained P-M curves. Although the study is purely numerical, it highlights important missing aspects of spaced-column design and should be supported with experimental studies in the future. The results of this work might help to improve international timber design codes. Significant efforts are underway to enhance the utilization of structural timber in construction, while an international race to construct taller timber high-rise buildings is gathering momentum. Several countries, including Canada, USA, and New Zealand, as well as European countries, have established wood research centers to foster a sustainable construction industry and promote the widespread use of structural wood. The extensive application of timber in both regular and high-rise buildings may require the adoption of spaced-column designs capable of accommodating bending moments.

Keywords: Mass Timber, Spaced-Column, P-M Diagram

1 Introduction

Structural wood is a sustainable material, and timber buildings are efficient while also contributing to carbon sequestration by capturing and storing CO_2 from the atmosphere. Although timber houses constitute about 1.5% of the building stock in Turkiye, their use and importance are gradually increasing both locally and throughout Europe and Asia. One of the underrated structural elements is the spaced column, which is not commonly used in light-frame and post-and-beam construction.

Timber Columns can be used in two different cross-sections: solid (Fig. 1.a) and built-up cross-section columns (Fig. 1.b-d2). The built-up cross-section columns are used in 3 different patterns: mechanically jointed columns (Fig. 1.b), spaced columns (with gussets (Fig. 1.c1) and packs (Fig. 1.c2)), and lattice columns (N-type (Fig. 1.d1) and V-type (Fig. 1.d2)). Mechanically jointed columns consist of bringing n number of shafts of the same size, side by side and connecting them with fasteners (bolts, nails, etc.) or adhesives. Elements of spaced columns are comprised of placing gussets or packs between shafts of the same size and

connecting them with fasteners such as bolts, nails, etc. A lattice column's elements are generally formed by combining two struts with diagonal and horizontal wooden elements by means of fasteners such as bolts, nails, etc.

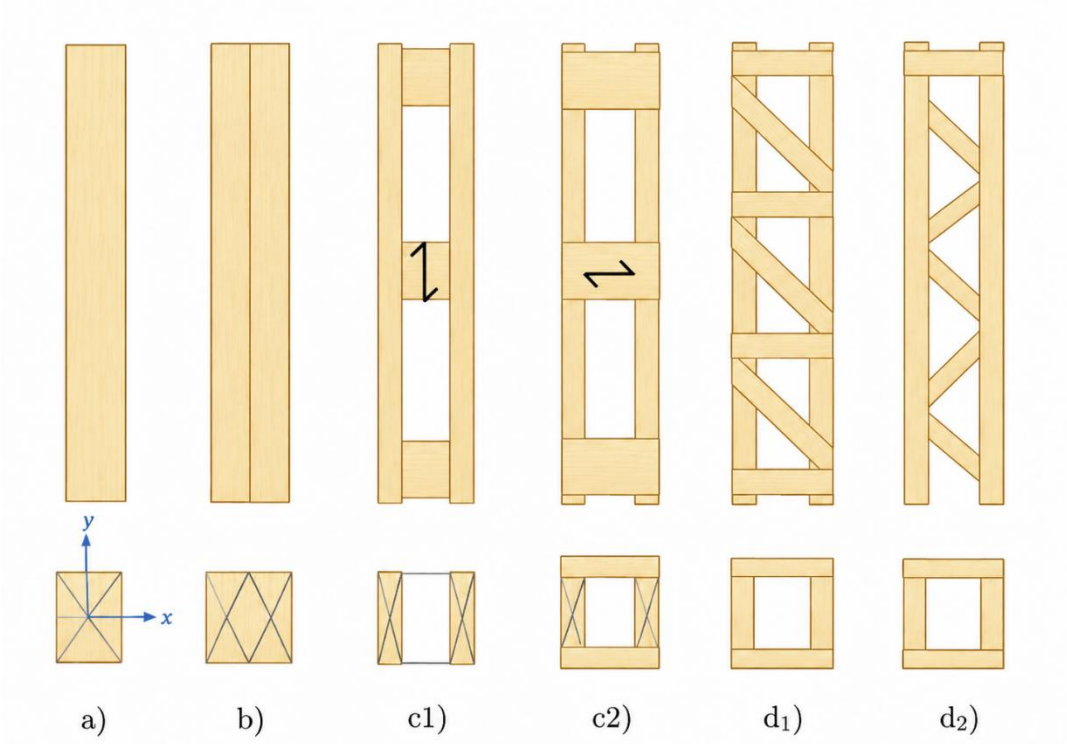


Fig. 1. Types of timber columns: a) Solid column, b) Mechanically jointed column, c_1) Spaced column with gussets, c_2) Spaced column with packs, d) Lattice column, d_1) N type, d_2) V type

Since long, single piece large-sized solid timber columns are difficult to obtain, spaced columns are generally preferred for supporting high ceilings. Additionally, solid columns may present problems such as shrinkage during drying and increased material costs. Therefore, there is a need for a better and more fundamental understanding of the behavior of built-up cross-section timber columns and for the development of appropriate design formulas [1]. International codes do not allow for bending moments in the design of spaced columns; however, all columns may experience bending moments, and special, impractical pinned connections may be required to almost fully eliminate them. Additional problems such as shrinkage and deformation (e.g., cupping, bowing, and twisting) may also be reduced by using built-up members [2]. Consequently, the current practice of designing spaced columns considering only axial loads represents a major limitation, which is addressed in this study.

The derivation of the interaction between axial load and bending moment on spaced (built-up) columns using gussets is attempted using analytical methods. The capacity calculations based on Finite Element Modeling (FEM) are conducted using SAP2000 software [3]. Gussets are assumed to be rigidly connected using glue; nailed or screwed connections may introduce additional flexibility and load capacity results may be overestimated. Especially slender spaced columns are used in the study, due to the fact that linear analysis software can only conduct elastic buckling, and plastic buckling for shorter columns has to be backed up by laboratory testing using actual physical models. The approach followed in this study considers a) buckling (local or global) stability of the whole column and b) compressive strength of members considering allowable stresses. Mainly two different lengths of 3m (10 feet) and 5.8m (19.3 feet) are used for the same cross section that was produced by two 50mm × 100mm (2 by 4)

members with gussets at every 0.7m (2.3 feet) apart along the length. Three-dimensional (3D) P-M diagrams and generalized equations to fit 2D P-M curves were obtained.

2 Previous Works

There are some previous studies to obtain P-M diagrams of timber columns. Van Dyer (1976) [4] experimentally investigated the strength of timber columns under axial compressive load in his PhD thesis; however, his work included only concentric load (he emphasized that eccentric loading should also be examined). Van Dyer and Malhotra (1985) [1] carried out both experimental and theoretical studies to obtained strength of spaced columns for the purpose of i) to verify pre-developed theoretical information, ii) to compare efficiency of spaced columns with different types (i.e., first within themselves and then against solid and mechanically connected columns, iii) to investigate the effect of number of blocks on the strength of columns. They pointed out that the axial strength of columns changed depending on the number of elements, member sizes, and number of blocks. Jumaat (1991) [2] conducted both numerical and experimental studies for the purpose of determining the buckling strength of columns in his study. He tested 89 columns with mechanically nailed joints and spaced columns that are under axial load effect. He did not consider any bending moment effect though. Van Dyer (1992) [5] presented a rational procedure in order to obtain the strength of spaced columns. He tested 40 spaced columns with gussets and observed a good correlation between the experimental results and theoretical predictions. Again, bending moment effects have not been taken into account. Van Dyer and Masih (1993) [6] investigated the effectiveness of mechanically jointed column elements and their contribution to strength for different sizes and different eccentric loads. A total of 216 compression tests were conducted for 72 columns. The load capacities of 'mechanically jointed columns' in pure axial and eccentrically loadings conditions were compared against each other. In that study, spaced columns have not tested. Śliwka (2017) [7] tested spaced columns with gussets that were made using different materials such as lumber, plywood, chipboard, and fiberboard. Based on the theory presented by Timoshenko and Gere, the author derived various formulas describing the column critical force, slenderness ratio, shear force applied to the column, and the maximum shear force capacity of a column; however, bending moment effects, again, have not been taken into account.

Spaced columns have been used in the construction industry for many years. Although they are relatively easy to construct, their analysis is complex due to the numerous factors affecting their strength and structural behavior. In addition, columns may be subjected to eccentric loading due to various factors. The strength of eccentrically loaded spaced columns is primarily governed by the combined effects of axial force and bending moment. Therefore, bending moments should be taken into account under eccentric loading conditions. A review of previous studies indicates that mechanically jointed columns have been investigated under eccentric loading; however, studies on spaced columns have generally been limited to concentric axial loading.

3 Material Properties, Geometric Dimensions and Finite Element Model of Timber Elements

For the analysis of spaced columns under eccentric loading, the cross-sectional dimensions of the shafts were selected as 50 × 100 mm (2 × 4 in.), while the gusset dimensions were adopted as 50 × 200 mm, since 25 mm-thick gussets themselves exhibited local buckling, in a way considering highly rigid gussets. Buckling analyses were performed for column heights of 3 m and 5.8 m. The clear horizontal spacing between the shafts was taken as 150 mm, while the clear vertical spacing between the gussets was taken as 500 mm.

The shafts were modeled using frame elements, whereas the gussets were modeled using shell elements. The shafts and gussets were connected by rigid links simulating a glued rigid connection (Fig. 2). A total of five gussets, including those at the top and bottom ends, were modeled to connect the two shafts in the 3m model and 9 gussets were used in the 5.8m model. The horizontal translations of the columns in both the x- and y-directions were restrained at the top and bottom ends. The vertical translation at the base was also restrained to represent an idealized pinned support condition. Torsional instability of the columns was prevented by assigning rotational restraints about the vertical axis at both the top and bottom joints.

The shafts and gussets were assigned the same material properties, with an elastic modulus of 11 GPa, a Poisson's ratio of 0.3, and a unit weight of 4.28 kN/m³. The rigid links connecting the shafts and gussets were modeled as 100 mm-diameter steel rods with an elastic modulus of 210 GPa and zero mass. The Poisson's ratio of wood has been reported to vary in the longitudinal, tangential, and radial directions for both low- and high-density wood species, ranging from 0.18 to 0.43. Therefore, a value of 0.3 was adopted as an approximate average. The use of Poisson's ratios of 0.25 and 0.35 had no significant effect on the buckling results (less than 0.1‰).

The spaced columns were modeled using the SAP2000 finite element analysis program based on the selected dimensions and material properties. Linear buckling analyses were performed using the buckling analysis option available in the program. Since SAP2000 does not provide a practical option for plastic buckling analysis, relatively long columns were considered to ensure that buckling occurred within the elastic range. The columns were subjected to loads with different eccentricities ranging from 0.1 m to 184 m. The eccentricity was increased geometrically by a factor of 1.6 at each step, resulting in a total of 17 loading cases.

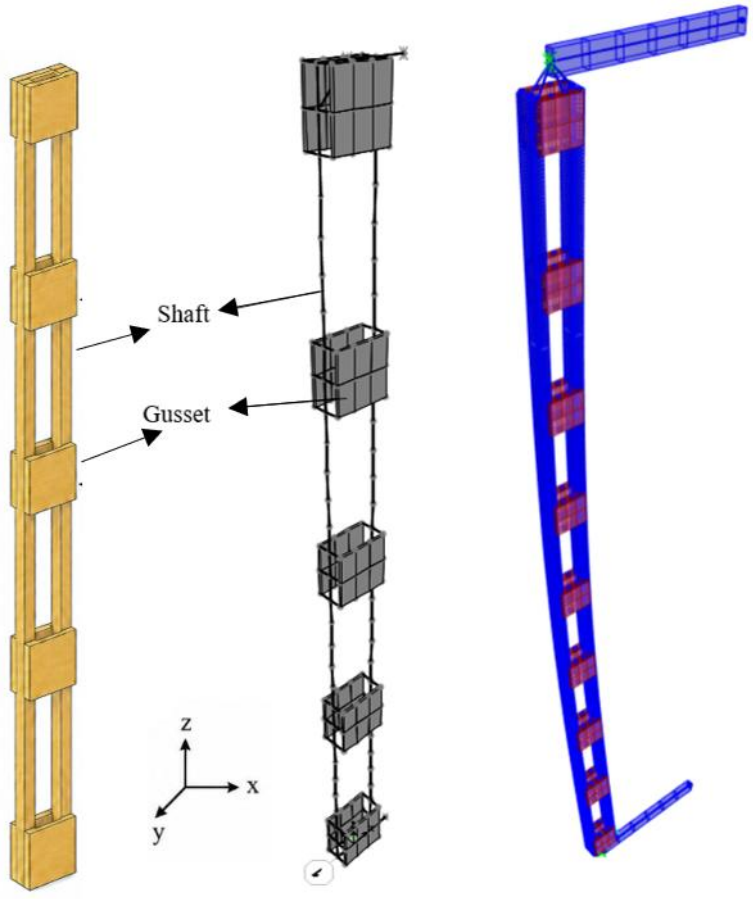


Fig. 2. Solid and SAP2000 model of the spaced column with gussets

A large number of data points was required to construct the P–M interaction diagram. If the eccentricity had been increased at constant intervals, the resulting data points would have been concentrated in the moment-dominated region of the interaction diagram. In theory, reaching the point where P = 0 on the horizontal axis requires an infinitely large eccentricity, which cannot be achieved in practice. For this reason, very large eccentricities with geometric increments were considered. At low eccentricities, the axial force P is dominant, whereas at high eccentricities, the bending moment M becomes dominant (Fig. 3). Based on the analysis results, the axial load–moment interaction diagrams (P–M diagrams) were obtained analytically.

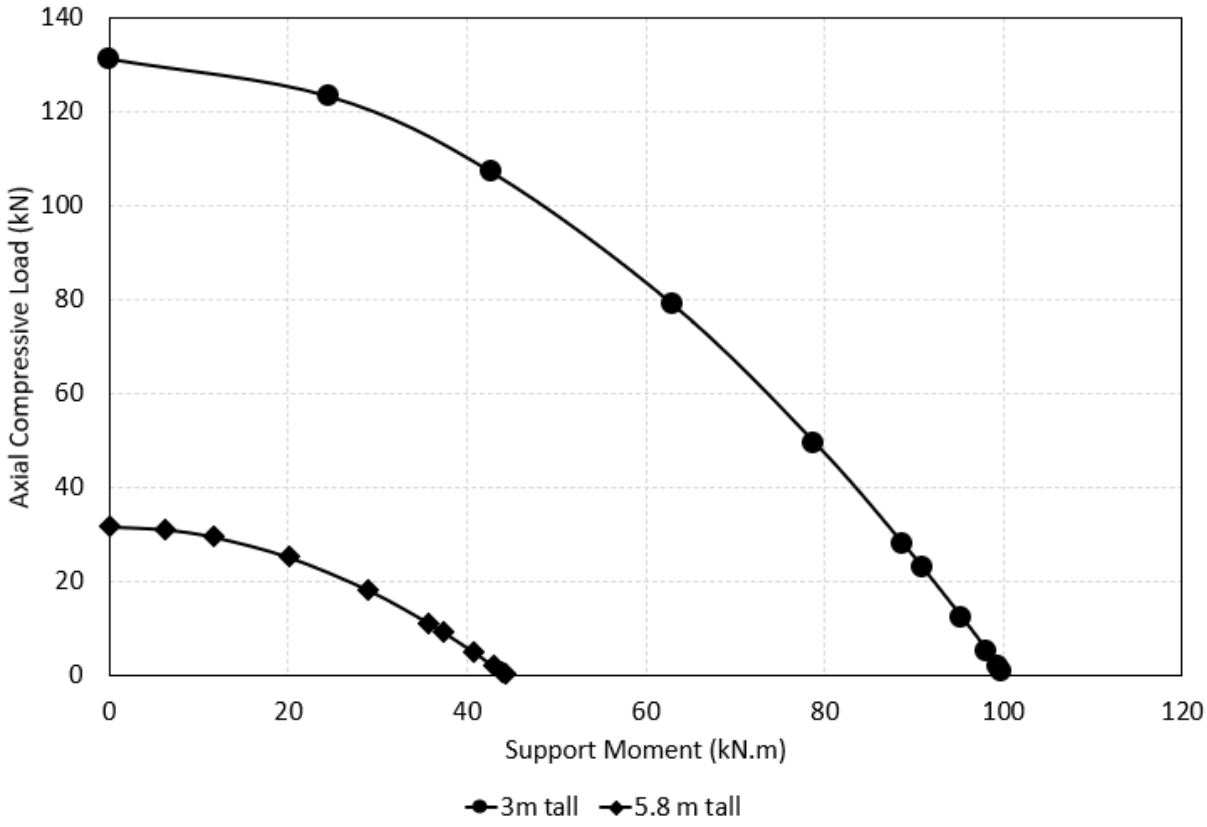
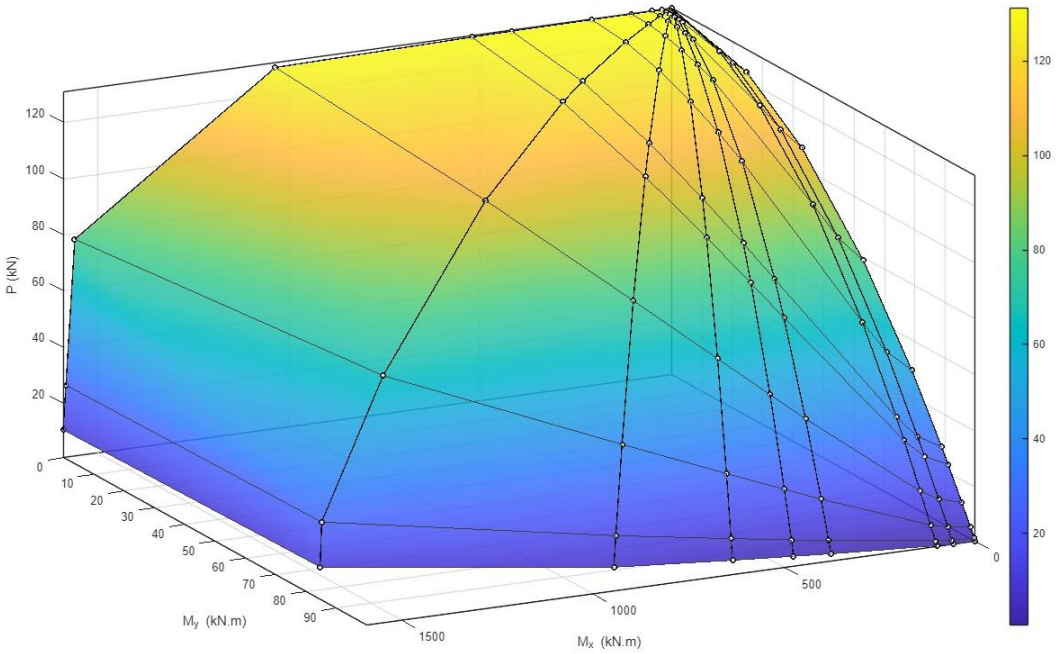
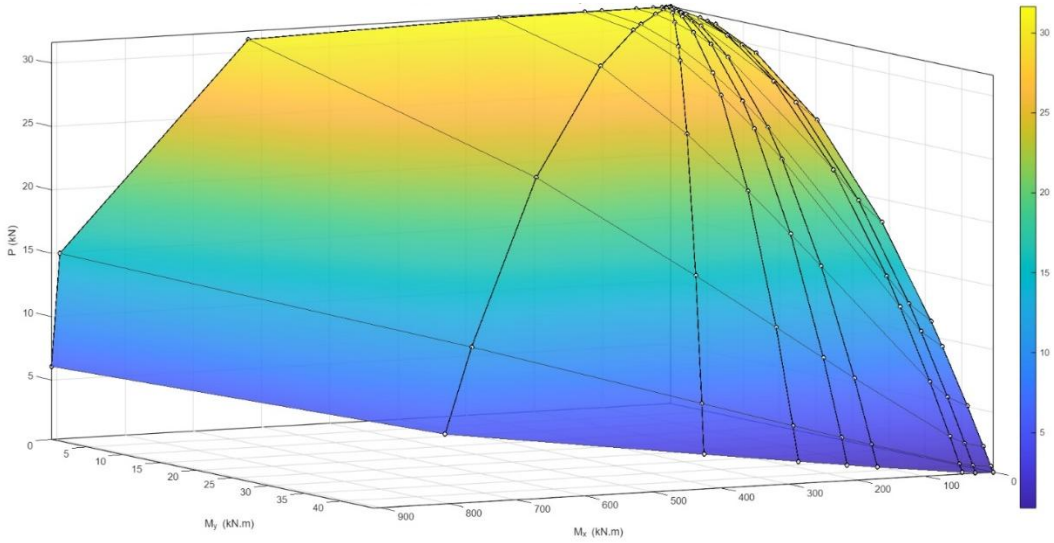


Fig. 3. P-M diagrams of 3m and 5.8m tall spaced columns

An attempt was also made to construct a three-dimensional P–M interaction diagram by developing an OAPI code in Matlab to control SAP2000 externally and perform numerous buckling analyses. The direction of the bending moment was varied from 0° to 90° in 15° or less increments, together with its magnitude. At a rotation of 90°, the P–M interaction diagram corresponds to bending about the weak axis. The results indicated that the buckling capacity increased significantly for bending about the weak axis, which is counterintuitive (Fig. 4). This trend became more pronounced as the eccentricity increased. For the 3 m column, for example, the critical buckling load increased from 78.8 kN at 0° to 131.1 kN at 90° for an eccentricity of 0.8 m, while at an eccentricity of 3.2 m, the corresponding values were 27.8 kN and 130.8 kN, respectively. A similar directional dependence was also observed for the longer column, indicating a strong influence of the bending direction on the buckling response of the spaced columns.



(a)



(b)

Fig. 4. 3D P–Mx–My interaction diagrams for the spaced columns: (a) 3 m column; (b) 5.8 m column.

The effect of gusset thickness on the buckling capacity of the spaced column was also investigated by comparing models with 10 mm and 50 mm thick gussets (Fig. 5). A noticeable increase in capacity was observed as the gusset thickness increased. For a nearly concentric loading condition with an eccentricity of 0.01 m, the critical axial load increased from 116.2 kN for the 10 mm gusset to 131.1 kN for the 50 mm gusset, corresponding to an increase of approximately 12.8% for the 3m long spaced column (Fig. 5). This result indicates that gusset stiffness has a significant influence on the buckling behavior of spaced columns, likely due to the enhanced interaction and restraint provided between the individual shafts.

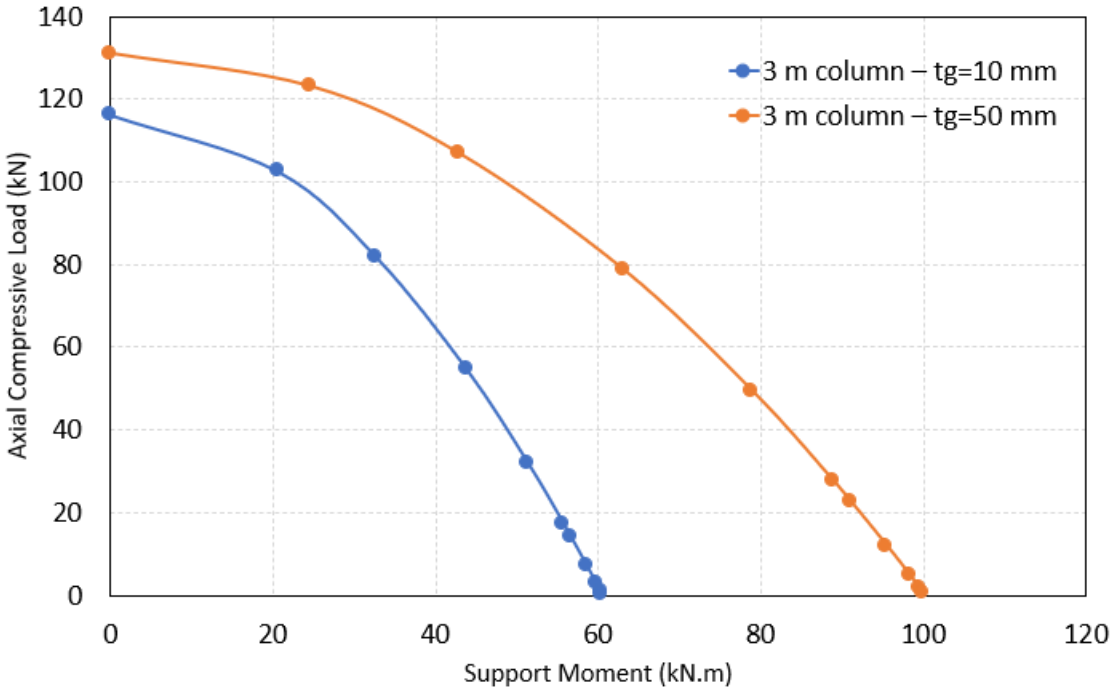


Fig. 5. Effect of gusset thickness (t_g) on the P–M interaction behavior of the 3 m spaced column

4 Discussions and Conclusions

Buckling analyses were conducted for two different column lengths using a two-shaft spaced column composed of 50 × 100 mm timber members with 200 mm distance between shaft centers. The results were used to construct linear-elastic eigenvalue-buckling P–M envelopes for the spaced columns. Local buckling of the gussets was suppressed by increasing their thickness to 50 mm, and the gussets were rigidly connected to the shafts. To assess whether flexural instability would precede compression failure in the compression-dominated region, the Eurocode 5 procedure for concentrically loaded spaced columns was applied. For the 3 m column, the effective slenderness ratios (λ_{eff}) were calculated as 88.8 and 201 for buckling about the strong and weak axes, respectively. The corresponding relative compression slenderness ratios, calculated as $\lambda_{rel,i}=(\lambda_{eff,i} / \pi) * (f_{c,0,k} / E_{0.05})^{(0.5)}$, were 1.5 and 3.4 in the strong axes. These values correspond to ideal Euler critical stresses of approximately $0.44*f_{c,0,k}$ and $0.086*f_{c,0,k}$, respectively; i.e., instability (buckling) occurs before the material reaches half of its characteristic compressive strength. However, SAP2000 based P-M interaction diagrams indicated that the bending moments to cause buckling are extremely high generating bending stresses well beyond material bending strength. This initial contradiction is actually a verification of stability being insensitive to bending action. When the shafts are bent in their weak axis, the buckling was not affected since parallel shafts rigidly connected to each other using gussets generated a stable condition for shafts; they did not go through buckling similar to a standard beam, since the compression generated by bending could not buckle sideways.

Defining the transition to elastic buckling by $\sigma_{Elastic}= 0.5f_{c,0,k}$ gives $\lambda_{rel,crit}=1.414$ as we consider elastic buckling to be $1/(\lambda_{rel,crit})^2=0.5$. Since the minimum relative compression slenderness obtained in the study was 1.5, the compression-dominated buckling modes of both

the 3 m and 5.8 m columns were considered to lie on the elastic-buckling side of the adopted transition criterion. As the bending stresses climb up to 50-100 kN.m on M_y and 900-1500 kN.m on M_x, the bending stresses are beyond any reasonable material capacity (Fig. 4). This is an indication of spaced column being insensitive to the bending moment even for 5.8 m tall case.

Various curve-fitting analyses in the M_y vs P case (Fig. 3) when M_x=0 indicated that a second-order polynomial provided the best fit, with $R^2 = 1$. Assuming a zero slope at M = 0, the interaction curve can be expressed in the form $P=B-AM^2$ (Fig 6). The axial load capacity at M = 0 is denoted by P_0, while the bending moment capacity at P=0 is denoted by M_0. Substituting these boundary conditions gives

$$P = P_0 - \frac{P_0}{M_0^2} M^2 \tag{1}$$

which can be rearranged as

$$P = P_0 \left(1 - \frac{M^2}{M_0^2}\right) \tag{2}$$

and finally expressed in normalized form as in Equation 3.

$$\frac{P}{P_0} + \left(\frac{M}{M_0}\right)^2 = 1 \tag{3}$$

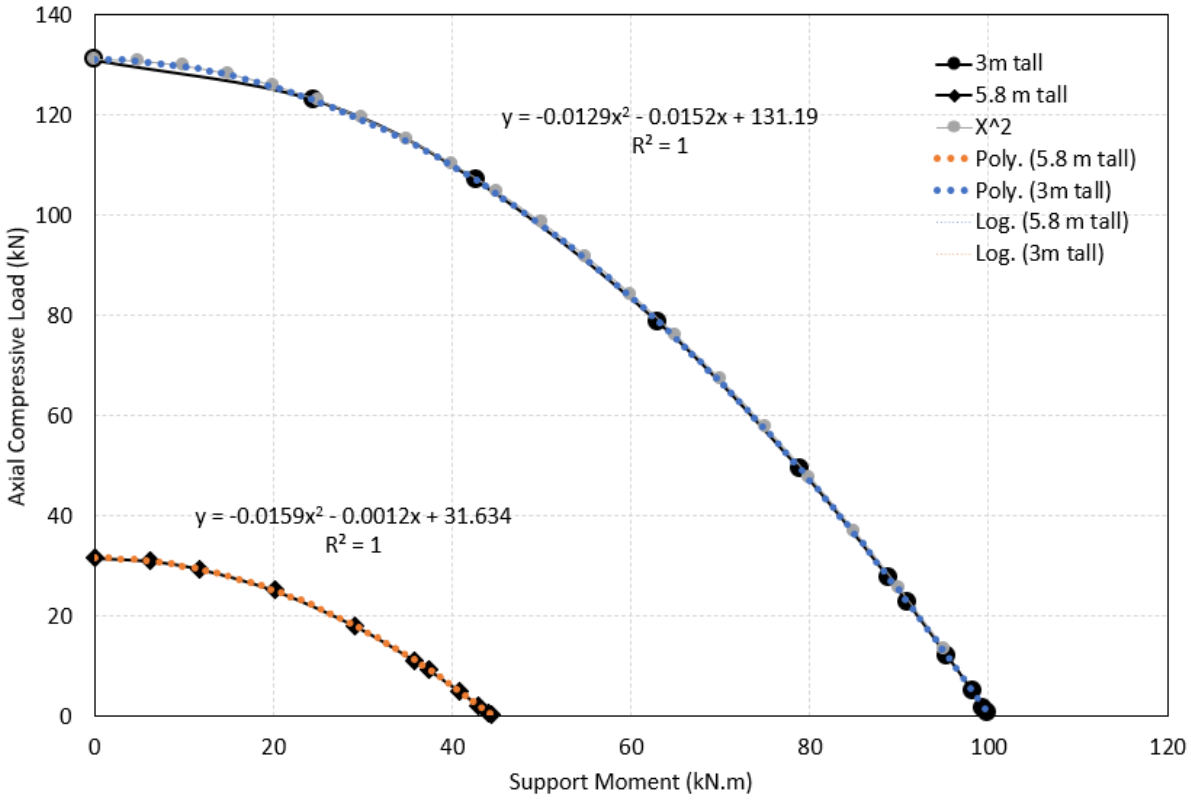


Fig. 6. 2D P-M diagrams of 3m and 5.8m tall spaced columns with curve fit

Even if end moments quickly exceed material capacities indicating insensitivity between buckling load and end moments, a generalized Eq. (3) would be useful for defining the relationship between the axial load, P, and bending moment, M, acting on a extremely slender spaced timber column; where, P_o is the uniaxial buckling strength and M_o is the bending strength including lateral torsional buckling. The selected 50x100 mm shafts orientation did not

buckle in the weak axis because of bending moment. The proposed interaction relationship can be established if the concentric buckling load and the corresponding moment capacity are known. These values can be readily obtained from the FEM of the spaced column by applying a concentric axial load and equal and opposite end moments, respectively. Once these two values, P_0 and M_0, are determined, the P-M interaction curve can be constructed using Eq. (3). It should be noted that both end moments are the same and moment is constant along the column (shear is zero); additional analyses are necessary if the moment is changing and additional shear's effect on the gussets. Nevertheless, constant bending moment is deemed as the upper limit for buckling, and unequal or opposite sign end moments would make the buckling less critical. Selected 3m and 5.8m columns had small contribution to buckling although they are slender and expected to go through elastic buckling. If the column moment is not constant, the moment effect is expected to be even smaller on the buckling. The buckling moments are generating stresses beyond material capacity.

The results obtained from the three-dimensional P-M interaction diagram indicate that bending about the weak axis governs is actually stronger regarding moment and axial load buckling interaction. The moment direction causing compression in one of the shafts also very large although more critical than the other direction as a single shaft can buckle easier. The buckling capacity of the selected spaced columns are primarily governed by the axial load causing buckling about the weak axis. An additional bending moment around the strong axis results in only a minor reduction in the buckling load, since the three-dimensional interaction surface is nearly flat in this direction. Therefore, buckling and stress capacities should be considered simultaneously, similar to the considerations associated with Euler buckling, for which the elastic buckling assumption becomes invalid at high stress levels.

The authors also conclude that the current study had surprising results, although (a) the present study is based solely on linear finite element analysis, and experimental testing is required to validate the numerical results and (b) the results are limited to linear elastic buckling. As the spaced column enters the plastic buckling range, the interaction curve is expected to approach a more linear relationship.

Acknowledgments
Authors acknowledge TUBITAK 222M270 project for setting the basis for this additional analytical study.

References

1. Van Dyer, D.B., Malhotra, S.K.: Strength of spaced timber columns. Canadian Journal of Civil Engineering 12 (1985).
2. Jumaat, M.Z.: Analysis of built-up timber columns using matrix progression method. Journal of Structural Engineering 117, 1911–1928 (1991).
3. Computers and Structures, Inc.: SAP2000, Integrated Software for Structural Analysis and Design. Computers and Structures, Inc., Berkeley, California, USA
4. Van Dyer, D.B.: Strength of built-up timber columns. Ph.D. Thesis, Technical University of Nova Scotia, Halifax, N.S. (1976).
5. Van Dyer, D.B.: Strength of battened timber columns. Transactions of the ASAE 35(1), 311 (1992).
6. Van Dyer, D.B., Abdul Masih: Strength and efficiency of eccentrically loaded layered timber columns. Journal of Structural Engineering 119(5), 1662–1668 (1993).
7. Śliwka, K.: A static analysis of two-shaft columns spaced by gussets. Journal of Wood Science 63, 236–247 (2017).

Author Contribution Statement

- *Conceptualization:* Ahmet Turer, Rabia Izol
- *Methodology:* Ahmet Turer, Rabia Izol
- *Investigation:* Ahmet Turer, Rabia Izol
- *Writing – Original Draft:* Rabia Izol, Ahmet Turer
- *Writing – Review & Editing:* Ahmet Turer, Rabia Izol

Conflict of Interest

The authors declare that they have no conflict of interest.

Note: Following the conference, this Publication Note will be added to each paper; therefore, authors are kindly requested not to remove the note below and to complete the author(s) and paper title information.

Publication Note

This paper was peer-reviewed, accepted for presentation, and included in the proceedings of the ACE2026 – International Conference on Advances in Civil Engineering, held on 12–14 October 2026 in Trabzon, Türkiye.

This paper may be cited as follows:

Izol R., Turer A., "Analytical Timber Spaced-Column P-M Interaction Diagram," in Proceedings of the ACE2026 – International Conference on Advances in Civil Engineering, Trabzon, Türkiye, 12–14 October 2026.

Performance Comparison of Fiber-Based and Lumped Plasticity Models in Nonlinear Time-History Analysis of RC Frames

Siamak Aghaei[1], Mehmet Ada[2], Yusuf Ayvaz[1]

[1] https://orcid.org/0000-0002-5796-9280, Yildiz Technical University, Civil Engineering Department, Istanbul, Türkiye,
smkaghaei@gmail.com
[2] https://orcid.org/0000-0002-7099-590X, Usak University, Civil Engineering Department, Usak, Türkiye,
mehmet.ada@usak.edu.tr
[1] https://orcid.org/0000-0003-3174-4494, Yildiz Technical University, Civil Engineering Department, Istanbul, Türkiye,
yayvaz@yildiz.edu.tr

Abstract. Seismic evaluation of reinforced concrete buildings requires numerical models capable of capturing nonlinear behavior, strength degradation, and large deformations. This study compares two nonlinear modeling approaches: fiber-based distributed plasticity and lumped plasticity for 3D reinforced concrete frames. A five-story three-dimensional flexural frame was modeled in OpenSees. The lumped plasticity model employed the modified Ibarra–Krawinkler (ModIMK) formulation, with post-peak parameters estimated using Haselton's empirical relationships. Model performance was assessed through nonlinear static and time-history analyses. Both models predicted similar peak base shear and story drift demands. At the section level, however, the fiber model maintained its moment over a wider curvature range. When code-based damage limits were checked, a portion of the fiber locations exceeded the Controlled Damage and Collapse Prevention strain limits, whereas no hinge in the lumped plasticity model exceeded its rotation limits. Overall, the calibrated lumped plasticity model reproduced the base shear and story drift demands of the fiber model and may serve as a practical alternative, although the damage assessment depends on the modeling approach and the criteria used.

Keywords: Distributed Plasticity; Lumped Plasticity; Nonlinear Time-History Analysis; OpenSees; Reinforced Concrete Frames.

1 Introduction

Performance-based earthquake engineering requires numerical models that can capture the nonlinear and post-peak response of reinforced concrete (RC) members. Two widely used approaches are distributed plasticity and concentrated plasticity [1–3]. Distributed plasticity models discretize the cross-section into fibers representing confined concrete, unconfined concrete, and reinforcing steel, allowing inelasticity to spread along the member length according to the material response of the constituent fibers. Concentrated plasticity models instead lump the inelastic response into nonlinear rotational springs at the member ends, with the spring behavior defined by a calibrated moment-rotation backbone, such as the Ibarra-Medina-Krawinkler (IMK) deterioration model [3]. The backbone parameters are commonly estimated using the empirical relationships proposed by Haselton et al. [2], which were derived from a large database of column tests. Comparisons of concentrated and distributed plasticity models in terms of seismic fragility have also been reported [9]. This study compares fiber-based and lumped-plasticity models for the same five-story, 3D RC moment-resisting frame and evaluates their predicted performance according to TBEC 2018 [4].

2 Numerical Modeling

Both models were implemented in OpenSeesPy [5] for the same five-story, 3D RC moment-resisting frame. The frame has three 6.0 m bays in the X direction and three 5.0 m bays in the Y direction, with a uniform story height of 3.0 m. At each story, the frame consists of four interior columns (C1) and twelve exterior/corner columns (C2). The beams are classified into two section types based on story level: B1 for stories 1-4, and B2 for story 5. The concrete compressive strength (fc) is 39 MPa, and the longitudinal reinforcing steel yield strength (fy_L) is 504 MPa for all members.

2.1 Fiber Model

Columns and beams are modeled as force-based beam-column elements with Gauss–Radau plastic-hinge integration (*HingeRadau*), with the plastic hinge length taken as $Lp = 0.5h$ in accordance with TBEC 2018 Section 5.3.1.2, where h is the section depth in the direction of bending. Each cross-section is discretized into confined core fibers, unconfined cover fibers, and discrete longitudinal reinforcing bar fibers. Concrete is modeled with *Concrete02* [6], with the confined-concrete parameters including peak stress, strain, and ultimate strain, derived from the Mander confinement model [7]. Longitudinal reinforcing steel is modeled using *Steel02* (*Giuffre-Menegotto-Pinto*) [8] with strain-hardening ratio of 1%.

2.2 Lumped Plasticity Model

In the lumped-plasticity model, beam-column members are modeled using an elastic beam-column element with zero-length rotational springs at both ends. The springs use the *ModIMKPeakOriented* material, and the backbone parameters $\mathrm{K_e}, \mathrm{M_c}, \theta_\mathrm{P}, \theta_\mathrm{pc}, \mathrm{and}\, \lambda$ are calculated using the empirical equations of Haselton et al. [2]. The yield moment (M_y) is determined separately from the moment–curvature analysis of the corresponding fiber section using the yield criterion specified in Section 5.3.1.5(b) of TBEC 2018. This yield moment is used in both models, whereas the other backbone parameters for the lumped-plasticity model are determined using the Haselton et al. [2] relationships. As shown in Fig. 1a, a zero-length element is placed at each member end to represent the nonlinear rotational response, while the remaining degrees of freedom are constrained. These elements are connected to an elastic beam-column element with a modified-stiffness section. Fig. 1b shows the resulting idealized backbone for the first-story interior column (C1, (P=1941.5) kN), based on the trilinear moment–chord rotation relationship of Haselton et al. [2].

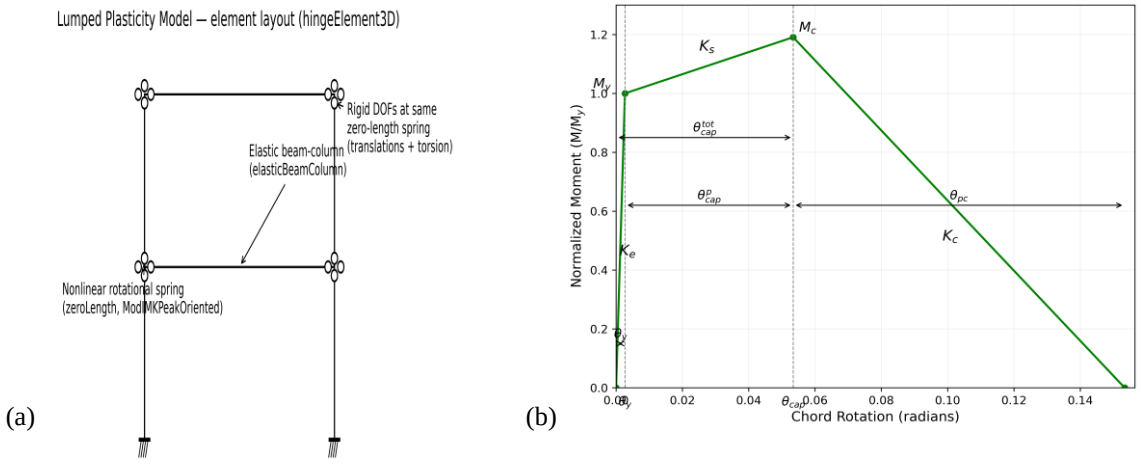


Fig. 1. Lumped plasticity model element layout (a) and idealized trilinear backbone for the first-story interior column (C1) (b).

2.3 Performance Levels

TBEC 2018 Section 5.8.1 defines strain limits for reinforced-concrete members of new buildings at three performance levels: Limited Damage (LD), Controlled Damage (CD) and Collapse Prevention (CP). For the fiber model, the limiting compressive strain for confined concrete at the CP level is calculated with TBEC 2018 Eq. (5.4a), which is given here as Eq. (1):

$$\varepsilon_c^{CP} = 0.0035 + 0.04\sqrt{\omega_{we}} \leq 0.018 \quad (1)$$

where ω_{we} is the effective confinement mechanical volumetric ratio. The corresponding tensile-strain limit for reinforcing steel $\varepsilon_s^{CP} = 0.4\,\varepsilon_{su}$ is taken from TBEC 2018 Eq. (5.5), where ε_{su} is the strain corresponding to the tensile strength of the reinforcing steel. At the CD level, limiting strains are taken as 75% of the CP limits (Eq. 5.7a). At the LD level, the limiting strains are $\varepsilon_c^{LD} = 0.0025$ and $\varepsilon_s^{LD} = 0.0075$, and no plastic-hinge rotation is permitted ($\theta_p^{(LD)} = 0$). For the lumped plasticity model, TBEC 2018 Section 5.8(b) specifies that the LD criterion for models using the effective-stiffness formulation of Section 5.4.5.2 is that no plastic hinge may form ($\theta_p = 0$); the CD and CP plastic-rotation capacities are obtained from an independent moment-curvature analysis pushed to the same strain limits, via TBEC Eq. 5.6, given here as Eq. (2):

$$\theta_{p(CP)} = \left(\frac{2}{3}\right)\left[(\varphi_u - \varphi_y)L_p\left(1 - \frac{0.5L_p}{L_s}\right) + 4.5\varphi_u d_b\right] \quad (2)$$

with $\theta_p^{CD} = 0.75 \times \theta_p^{CP}$ *(Eq. 5.7b).* The LD criterion differs fundamentally between the two models: for the fiber model it is a strain threshold reached during the actual pushover response, whereas for the lumped plasticity model it is, by definition, the onset of any inelastic rotation.

3 Case-Study Building

The case-study building is a five-story, symmetric 3D reinforced-concrete moment-resisting frame with three 6.0 m bays in the X direction and three 5.0 m bays in the Y direction, corresponding to overall plan dimensions of 18.0 m × 15.0 m. The story height and slab thickness are 3.0 m and 0.20 m, respectively. The dead and live loads are 7.26 and 2.00 kN/m², while the exterior and interior wall line loads are 10.50 and 6.25 kN/m, respectively. The mean concrete compressive strength is 39 MPa, with an elastic modulus of 34.3 GPa, whereas the reinforcing steel has a mean yield strength of 504 MPa, an elastic modulus of 200.1 GPa, and a strain-hardening ratio of 1%. The column and beam section properties and material definitions adopted in both models are summarized in Table 1.

Table 1. Column and beam cross-section properties (B = width, H = depth).

Section	B (mm)	H (mm)	Cover (mm)	Bottom bars	Top bars	Side bars	Stirrups
C1	700	700	50	4Ø25	4Ø25	2Ø25	5L10 @ 100
C2	600	600	50	5Ø20	5Ø20	3Ø20	4L10 @ 100
B1	400	500	50	2Ø25	4Ø25	–	2L10 @ 100
B2	400	500	50	2Ø25	3Ø25	–	2L10 @ 100

The confined concrete properties were calculated using the Mander model [7]. The values obtained for C1 were ($f_{cc} = 54.0$) MPa and ($\varepsilon_{ccu} = 0.0179$). For C2, the corresponding values were 53.8 MPa and 0.0175. For B1, ($f_{cc} = 46.1$)MPa and ($\varepsilon_{ccu} = 0.0170$), while for B2 they were 45.9 MPa and 0.0171.

Before applying the lateral loads, the gravity-load results of the two models were compared. The total vertical reaction at the base was calculated for the ($G + 0.3Q$) load combination. The reaction was 20864.26 kN in both models. Therefore, the gravity loads and mass assignment resulted in the same total vertical response in the two models. The first three modes were calculated for the SAP2000 model and the three OpenSees models. The periods and mode

directions are given in Table 2. The mode direction was determined from the eigenvector components in X, Y, and RZ. The results are close for the four models. In all models, the first mode is in the X direction, the second mode is in the Y direction, and the third mode is mainly torsional. The mode shapes are shown in Fig. 2.

Table 2. Modal periods

Mode	Lumped Plasticity	Fiber (HingeRadau)	Elastic (OpenSees)	SAP2000 (Elastic)
1	0.705	0.588	0.581	0.604
2	0.67	0.554	0.546	0.574
3	0.658	0.549	0.543	0.523

4 Analysis and Results

4.1 Static Pushover Analysis

A displacement-controlled pushover analysis was performed in both the X and Y directions using the first-mode eigenvector and story masses to define the lateral load pattern. The resulting capacity curves are shown in Fig. 3, with the LD, CD, and CP performance points defined by TBEC 2018. The corresponding values are summarized in Table 3.

In the X direction, the two models give similar peak base shear values. The fiber model reaches 4979.3 kN, while the lumped-plasticity model reaches 4742.5 kN, giving a difference

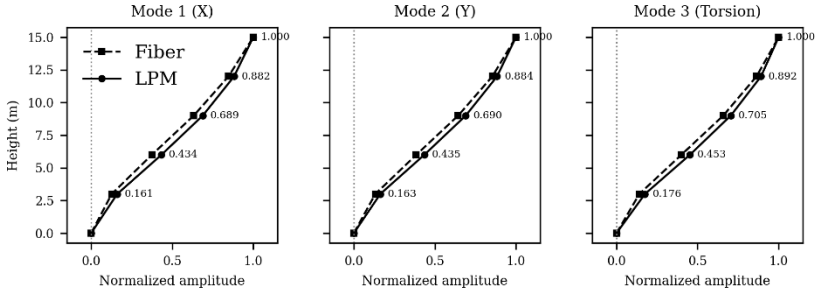


Fig. 2. First three mode shapes (X, Y, torsional) for the fiber and lumped plasticity models.

of about 5%. This relatively close agreement is expected because the same yield moment M_y, obtained from the fiber-section analysis, is used in both models. The curves, however, differ after yielding because K_e, M_c, θ_P, and θ_{PC} in the lumped-plasticity model are obtained from the Haselton et al. [2] equations rather than directly from the fiber response.

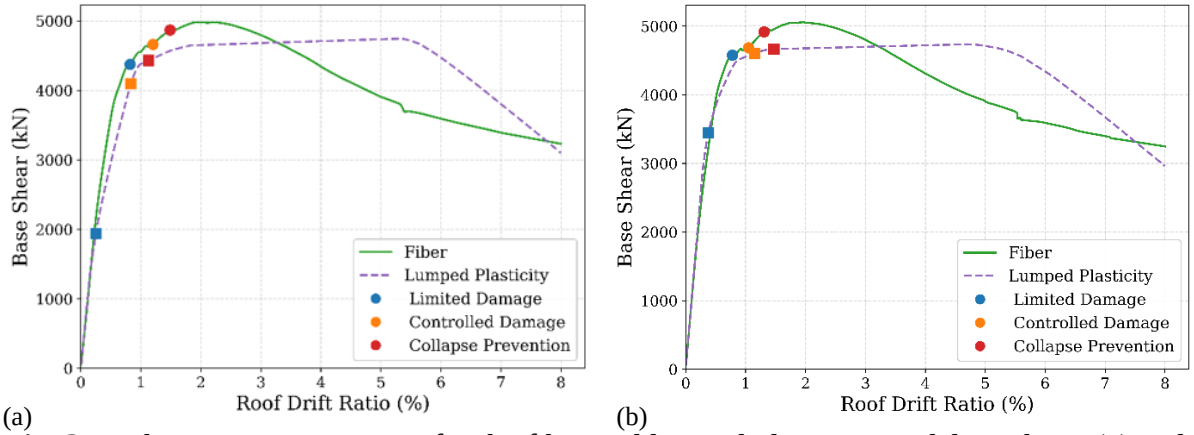


Fig. 3. Pushover capacity curves for the fiber and lumped plasticity models in the X (a) and Y (b) direction, with TBEC 2018 LD/CD/CP performance points.

Table 3. TBEC 2018 performance points and peak base shear (V_{max}) for both models, X and Y directions.

Direction	Level	Fiber model			Lumped plasticity model		
		Δ_{roof} (cm)	Drift (%)	V (kN)	Δ_{roof} (cm)	Drift (%)	V (kN)
X	LD	12.3	0.82	4372.1	3.8	0.25	1942.9
	CD	18	1.2	4659.6	12.5	0.83	4023.2
	CP	22.3	1.49	4866.6	16.9	1.13	4420.3
	Vmax	29	1.93	4979.3	79.9	5.33	4742.5
Y	LD	11.7	0.78	4576.6	5.7	0.38	3447.7
	CD	15.7	1.05	4684	17.2	1.15	4603.5
	CP	19.6	1.31	4916.9	22.1	1.47	4665.1
	Vmax	29.4	1.96	5056.6	70.4	4.69	4735.6

4.2 Moment-Curvature Comparison

Moment–curvature analyses were also carried out for two first-story columns to compare the post-yield response of the two models. The first was the interior column C1, subjected to an axial load of P=1941.5 kN. The second was the exterior column C2, subjected to an axial load of P=1277.9 kN, representing the maximum axial load among the first-story C2 columns. The lumped-plasticity response was obtained from the *ModIMKPeakOriented* backbone, while the fiber-section analysis was continued to large curvature. The results are shown in Fig. 4. The difference between the two models becomes more noticeable after the capping point. The capping curvatures of the lumped-plasticity model are 0.153 1/m for C1 and 0.145 1/m for C2. After capping, the fiber model keeps almost the same moment over a larger curvature range, whereas the lumped-plasticity model decreases according to the Haselton post-capping branch. The plastic rotation capacities are also different. The values from TBEC Eq. (5.6) are 0.00815 rad for C1 and 0.00994 rad for C2, while the Haselton backbone gives 0.0507 rad and 0.0467 rad, respectively. At large curvature, a small decrease in moment is observed in the fiber model when the confined-concrete strain reaches ε_{ccu}, at 0.139 1/m for C1 and 0.160 1/m for C2.

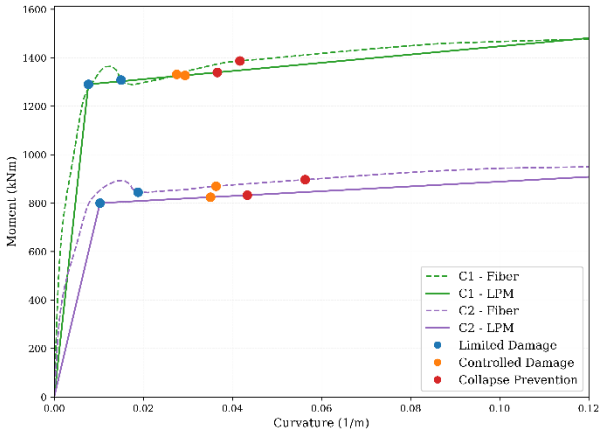


Fig. 4. Moment-curvature response of the first-story interior (C1) and exterior (C2) columns.

4.3 Dynamic Analysis and Fragility Curves

Nonlinear time-history analyses (NTHA) were carried out using ground-motion records from the PEER NGA-West2 database. Twenty-two records were initially considered from the FEMA P695 [10] far-field set, and 21 records were finally used after applying the scaling and convergence criteria. The records were scaled to the DD-2 target spectrum based on the AFAD seismic hazard map of Türkiye. The response spectra and selected records are given in Table

A1 and Fig. A2 in the Appendix. Both horizontal components of each record were applied to the fiber and lumped-plasticity models. For each analysis, the maximum interstory drift ratio, (D), was obtained and related to the spectral acceleration at the fundamental period, S_{aT_1}. A log-linear regression was used for the 21 records [11]:

$$\ln(D) = a + b \ln[Sa(T1)] \quad (3)$$

The dispersion, σ, was calculated as the standard deviation of the regression residuals. The resulting PSDMs for the two models are shown in Fig. 5. For the fiber model, the fitted PSDM is given by:

$$ln(D) = -4.458 + 0.565\, ln[Sa(T1 = 0.588\, s)]$$

with $\beta D = 0.327$. For the lumped plasticity model, the corresponding relationship is

$$\ln(D) = -4.406 + 0.664 \ln[Sa(T1 = 0.705\, s)]$$

with $\beta D = 0.215$.

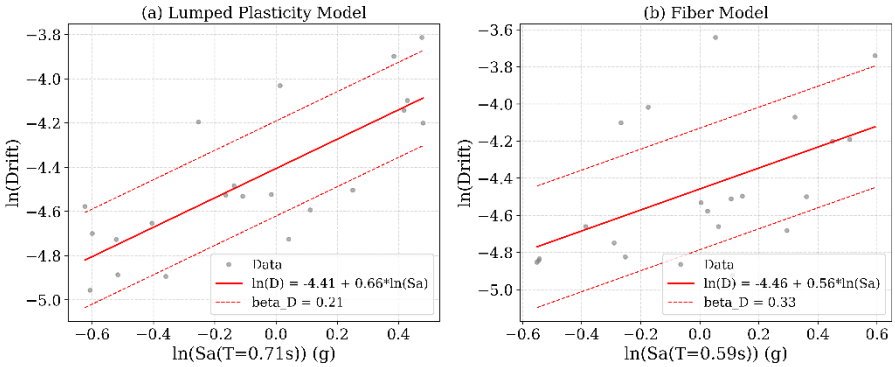


Fig. 5. Probabilistic seismic demand models (PSDM) for the lumped plasticity model (a) and fiber model (b).

Fig. 6a compares the peak drift demands from the 21 ground motions. The logarithmic residuals between the LPM and fiber results remain close to zero, with no clear trend as (Sa) increases.

The residual regression is given by $\ln(Residual) = -0.002 + 0.019\, ln(Sa)$, with $\sigma = 0.112$. The residuals are close to zero, with a small slope and low dispersion, and the two models give similar drift demands for the individual records. The fragility curves for the LD, CD and CP levels (Fig. 6b) were obtained from the fitted PSDMs using the corresponding drift capacities given in Table 3. The median $Sa_{(T1)}$ was obtained by inverting the PSDM at each drift capacity, and the dispersion was taken as β_D. The resulting median Sa values and dispersions are reported in Table 4. The LPM-LD median is not tabulated because it falls below the range of spectral accelerations covered by the selected ground motions, so the plotted LPM-LD curve is an extrapolation of the PSDM. The fragility curves differ even though the drift demands are similar, partly because the performance limits used for the two models are different.

Table 4. Median Sa(T1) (g) and logarithmic dispersion of the fragility curves.

Level	**Lumped plasticity model (LPM)**		**Fiber model**	
	Median Sa (g)	Dispersion	Median Sa (g)	Dispersion
LD	-	0.215	0.543	0.327
CD	0.563	0.215	1.065	0.327
CP	0.888	0.215	1.557	0.327

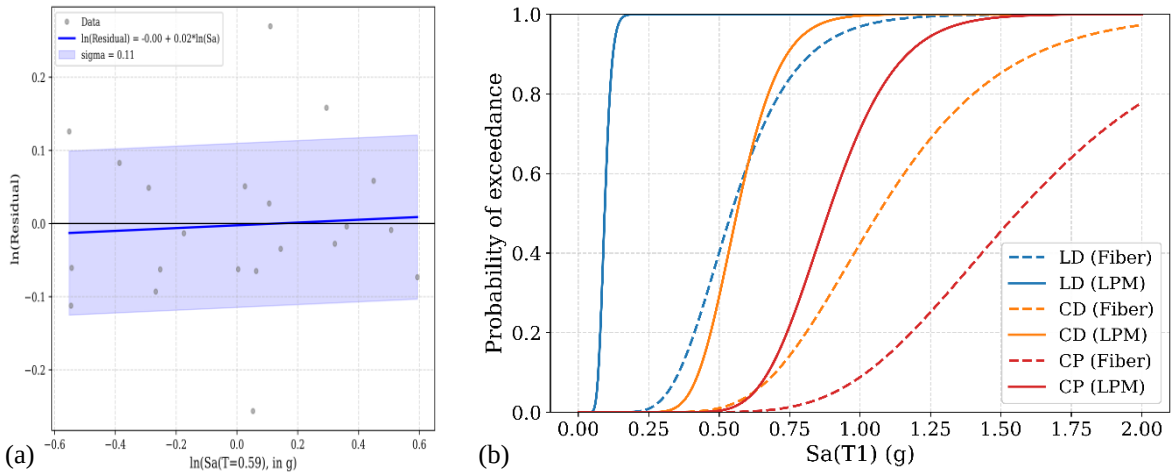


Fig. 6. Comparison of the LPM and fiber models: logarithmic residuals of peak drift demands for the 21 ground motions (a) and fragility curves for the LD, CD and CP performance levels (b).

The median spectral accelerations at the CD and CP levels are lower for the lumped plasticity model than for the fiber model. At the CD level, the median $Sa_{(T1)}$ is 0.563 g for the LPM and 1.065 g for the fiber model. At the CP level, the corresponding values are 0.888 g and 1.557 g. The dispersion is also lower for the LPM (βD = 0.215) than for the fiber model (βD = 0.327). The LD level is considered separately because the two models use different criteria. The effective story drift was checked according to TBEC 2018 Eq. (4.34a), given here as Eq. (4). For the building without a flexible joint between the infill walls and the frame, the limiting value is 0.008. The λ factor is the ratio of the DD-3 to DD-2 spectral ordinates. Since the periods of both models fall within the constant-velocity range for the two hazard levels, the same value, λ = 0.445, is used for both models, and the condition becomes:

$$\lambda \frac{\delta_{i,\max}^{(X)}}{h_i} \leq 0.008\kappa \qquad (4)$$

The maximum mean story drift ratios from the 21 ground motions were used to calculate the effective drift ratios in the X and Y directions. Both models satisfy the 0.008 limit in the X and Y directions after applying the DD-3/DD-2 factor. The values are given in Table 5. The effective drift ratios range from 0.421% to 0.505%, which are below the 0.8% limit. The mean story-drift profiles of the two models are similar in both directions. The maximum drift occurs at the second or third story rather than at the roof. The drift profiles for the 21 ground motions and their mean values are shown in Fig. 7.

The individual ground motions show some variation in the story-drift profiles, with a few records exceeding 2%; however, the mean profiles are similar for both models in each direction. According to TBEC 2018 Section 5.7.4, the mean maximum demands were compared with the corresponding performance-level capacities. For the fiber model, demands at 2696 beam and

Table 5. Maximum and effective interstory drift ratios in the X and Y directions

Model / Direction	Maximum drift (%)	Effective drift, κλΔ/h (%)	Limit
Fiber, X	0.971	0.432	PASS
LPM, X	0.947	0.421	PASS
Fiber, Y	1.135	0.505	PASS
LPM, Y	1.122	0.499	PASS

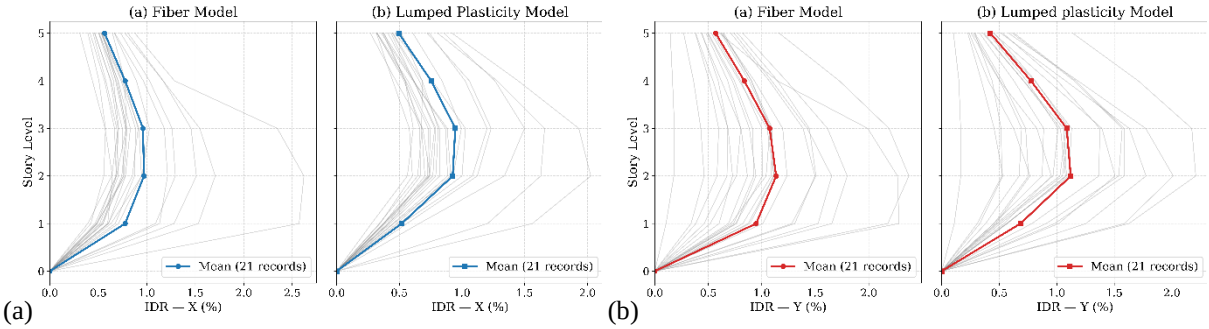


Fig. 7. Story-drift profiles for all 21 records and their mean: fiber model (a) and lumped plasticity model (b); X-direction (left) and Y-direction (right).

column fiber locations were evaluated against the strain limits in TBEC 2018 Eqs. (5.4a)-(5.5) with 692 (25.7%), 314 (11.6%), and 221 (8.2%) exceeding the LD, CD, and CP limits, respectively. For the lumped-plasticity model, 166 of 560 hinge DOFs (29.6%) exceeded the LD limit, while no CD or CP exceedances were observed.

The two models show similar LD exceedance rates (25.7% for the fiber and 29.6% for the LPM). CD and CP exceedances occur only in the fiber model (11.6% and 8.2%), while the LPM remains within these limits, with maximum demand-to-capacity ratios of 0.52 and 0.39, respectively. This difference partly reflects the use of fiber strains in the fiber model and hinge rotations in the LPM (Fig. 8).

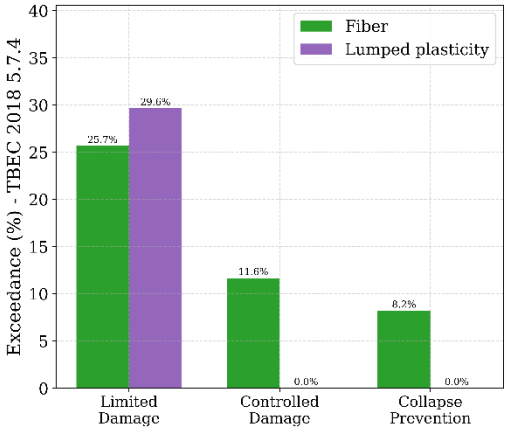


Fig. 8. Mean-demand exceedance rates for the fiber and lumped-plasticity models.

5 Conclusions

The static pushover results show that the fiber and lumped-plasticity models provide similar overall responses. The peak base shear differs by about 5%, while the capacity curves follow similar trends. The difference in the first-mode period is mainly attributed to the effective secant stiffness used in the lumped-plasticity model. The most noticeable difference is at the LD level, where the two models are evaluated using different acceptance criteria. The nonlinear time-history analyses of 21 ground motions yield similar findings. The residual sigma is 0.112, with no clear trend in the residuals as the intensity increases. Both models satisfy the story-drift requirements and show similar LD exceedance rates. CD and CP exceedances occur only in the fiber model, which also has higher fragility medians. Because the two models use different damage criteria (strain limits in the fiber model, rotation limits in the lumped model), these differences partly reflect the criteria and not only the modeling approach. For this frame, the calibrated lumped-plasticity model reproduces the base shear and drift demands of the fiber

model, whereas the damage assessment depends on the modeling approach and the criteria used. The fiber model, in turn, provides a more direct representation of local nonlinear behavior.

References

1. Bruschi, E., Calvi, P.M., Quaglini, V.: Concentrated plasticity modelling of RC frames in time-history analyses. Engineering Structures. 243, 112716 (2021). https://doi.org/10.1016/j.engstruct.2021.112716.
2. Haselton, C.B., Deierlein, G.G.: Assessing Seismic Collapse Safety of Modern Reinforced Concrete Moment-Frame Buildings. PEER Report 2007/08, Pacific Earthquake Engineering Research Center, University of California, Berkeley (2008).
3. Ibarra, L.F., Medina, R.A., Krawinkler, H.: Hysteretic models that incorporate strength and stiffness deterioration. Earthquake Eng. Struct. Dyn. 34, 1489–1511 (2005). https://doi.org/10.1002/eqe.495.
4. Disaster and Emergency Management Presidency of Turkey, "Turkish Building Earthquake Code: Specifications for design of buildings under earthquake effects," Ankara, Turkey, 2018.
5. McKenna, F.: OpenSees: A Framework for Earthquake Engineering Simulation. Comput. Sci. Eng. 13, 58–66 (2011). https://doi.org/10.1109/MCSE.2011.66.
6. Kent, D.C., Park, R. (1971). Flexural Members with Confined Concrete. J. Struct. Div., ASCE, 97(7), 1969-1990. DOI: 10.1061/JSDEAG.0002957.
7. Mander, J.B., Priestley, M.J.N., Park, R.: Theoretical Stress-Strain Model for Confined Concrete. J. Struct. Eng. 114, 1804–1826 (1988). https://doi.org/10.1061/(ASCE)0733-9445(1988)114:8(1804).
8. Menegotto, M., Pinto, P.E. (1973). Method of analysis of cyclically loaded RC plane frames. Preliminary Report IABSE, vol. 13.
9. Rodrigues, I.D., Cavalcante, G.H.F., Pereira, E.M.V., Vieira Júnior, L.C.M., Liel, A., Siqueira, G.H.: Seismic fragility assessment of a RC frame considering concentrated and distributed plasticity modelling. Rev. IBRACON Estrut. Mater. 17, e17105 (2024). https://doi.org/10.1590/s1983-41952024000100005.
10. FEMA (2009), "Quantification of Building Seismic Performance Factors," FEMA P695, Applied Technology Council for FEMA, Washington, D.C., USA, 2009.
11. Freddi, F., Padgett, J.E., Dall'Asta, A.: Probabilistic seismic demand modeling of local level response parameters of an RC frame. Bull Earthquake Eng. 15, 1–23 (2017). https://doi.org/10.1007/s10518-016-9948-x.

Author Contribution Statement

- *Conceptualization:* SA, MA, YA
- *Methodology:* SA, MA, YA
- *Investigation:* SA, MA, YA
- *Writing – Original Draft:* SA, MA, YA
- *Writing – Review & Editing:* SA, MA, YA

List of Abbreviations

- TBEC 2018 — Turkish Building Earthquake Code (2018)
- LPM — Lumped Plasticity Model
- LD — Limited Damage (SH in TBEC 2018)
- CD — Controlled Damage (KH in TBEC 2018)
- CP — Collapse Prevention (GO in TBEC 2018)
- PSDM — Probabilistic Seismic Demand Model

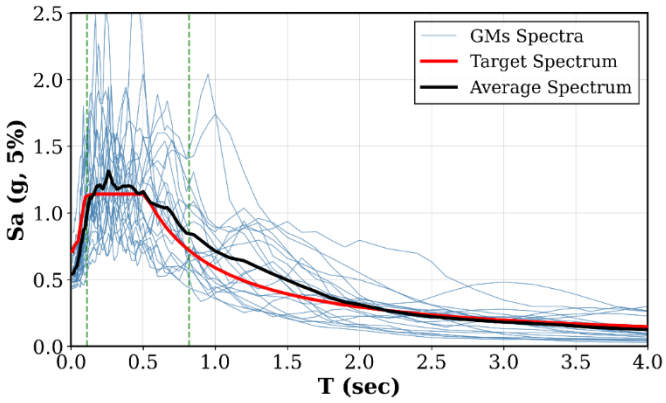
The authors declare no conflict of interest.

Appendices

Appendix A. Additional Data

A1. Ground motion records used in the nonlinear time-history analyses.

RSN	Earthquake Event	Year	Station	Mag.	Rjb (km)	Vs30 (m/s)	Scale Factor
68	San Fernando	1971	LA - Hollywood Stor FF	6.61	22.77	316.46	2.0478
125	Friuli, Italy-01	1976	Tolmezzo	6.5	14.97	505.23	1.4676
169	Imperial Valley-06	1979	Delta	6.53	22.03	242.05	1.3777
174	Imperial Valley-06	1979	El Centro Array #11	6.53	12.56	196.25	1.1871
459	Morgan Hill	1984	Gilroy Array #6	6.19	9.85	663.31	1.5453
728	Superstition Hills-02	1987	Westmorland Fire Sta	6.54	13.03	193.67	1.7803
752	Loma Prieta	1989	Capitola	6.93	8.65	288.62	0.8791
825	Cape Mendocino	1992	Cape Mendocino	7.01	0	567.78	0.4764
828	Cape Mendocino	1992	Petrolia	7.01	0	422.17	0.7902
1111	Kobe, Japan	1995	Nishi-Akashi	6.9	7.08	609	1.0215
1116	Kobe, Japan	1995	Shin-Osaka	6.9	19.14	256	1.8664
1148	Kocaeli, Turkey	1999	Arcelik	7.51	10.56	523	3.175
1158	Kocaeli, Turkey	1999	Duzce	7.51	13.6	281.86	1.1942
1201	Chi-Chi, Taiwan	1999	CHY034	7.62	14.82	378.75	1.547
1204	Chi-Chi, Taiwan	1999	CHY039	7.62	31.87	201.21	3.7202
1485	Chi-Chi, Taiwan	1999	TCU045	7.62	26	704.64	1.0356
1602	Duzce, Turkey	1999	Bolu	7.14	12.02	293.57	0.6566
1611	Duzce, Turkey	1999	Lamont 1058	7.14	0.21	529.18	4.7259
1633	Manjil, Iran	1990	Abbar	7.37	12.55	723.95	0.8155
1787	Hector Mine	1999	Hector	7.13	10.35	726	1.423
3548	Loma Prieta	1989	L G - Lexington Dam	6.93	3.22	1070.34	1.0751



A2. Scaling of ground motion records to the target spectrum

Publication Note
This paper was peer-reviewed, accepted for presentation, and included in the proceedings of the ACE2026 – International Conference on Advances in Civil Engineering, held on 12–14 October 2026 in Trabzon, Türkiye.

This paper may be cited as follows:
Aghaei S., Ada M., Ayvaz Y., "Performance Comparison of Fiber-Based and Lumped Plasticity Models in Nonlinear Time-History Analysis of RC Frames," in Proceedings of the ACE2026 – International Conference on Advances in Civil Engineering, Trabzon, Türkiye, 12–14 October 2026.

Parametric Analysis of Load-Carrying Capacity and Reinforcement Optimization in Slab-on-Grade Foundations

Mehmet Sefa Orak
0000-0002-5783-479X, Department of Civil Engineering, Maltepe University, Istanbul, Türkiye, sefaorak@maltepe.edu.tr

Abstract. In an industrial setting, a concrete slab-on-grade (SOG) is an essential structural element for handling the uniform, linear, and point live loads one might expect. The bearing capacity of this type of foundation is not a simple matter; it is a function of several interacting variables, from the subgrade reaction modulus to where the load is applied, as well as the flexural strength of the concrete and its reinforcement. With that in mind, this study assessed how these slabs perform under a range of design conditions in terms of thickness, behavior, and load-bearing ability. A group of unreinforced concrete, rebar mesh, and steel fiber-reinforced concrete (SFRC) were tested, pitting analytical Westergaard closed-form solutions against shell finite element models in SAP2000. The results show just how much of an impact a stiff subgrade can have. Take a 100 kPa storage load, for example: moving from a soft clay subgrade (7 MN/m³ modulus of elasticity) to crushed rock (45 MN/m³) allows for a 44.4 percent drop in slab thickness, from 360 mm down to 200 mm. A step up in concrete grade from C25/30 to C40/50 will see another 20.0 to 21.4 percent reduction. Then the question is where the load is placed. Interior loading is of little concern when compared with the stress concentrations at the edges and corners of the structure, which carry a 35 and 72.2 percent penalty, respectively. To help determine the impact of soil improvement, reinforcement, and slab size, an iso-thickness response map is presented to define the relevant decision boundaries.

Keywords: Slab-on-Grade, Load-Carrying Capacity, Subgrade Reaction Modulus, SAP2000 Shell FEA, Reinforcement Optimization.

1 Introduction

The concrete ground slab, or Slab-on-Grade (SOG), is still the structural foundation of choice in modern construction. One finds this to be the case in all manner of present-day operations, from manufacturing and logistics to port terminals. It is not to be confused with a suspended slab on beams and columns; the SOG is something quite different in nature. As a ground-supported element, it has an ongoing and selective relationship with the soil continuum, which is never still. What determines its load-bearing capacity and overall performance is the way the subgrade support stiffness, the demands placed upon the facility, and the flexural rigidity of the concrete itself come into play [1, 2].

In practice, the subgrade support is typically defined by Winkler's linear spring model, with the subgrade reaction modulus k (in MN/m3 or kN/m3) as the descriptor. This is the linear assumption put forward in most concrete design standards such as TR34 [2], ACI 360R-10 [3] and EN 1992-1-1 [4]. Yet at the outset of a design, proper subgrade site preparation often gets short shrift. A failure to account for the true stiffness of the subgrade will result in an unnecessarily thick slab being specified, with all the attendant costs in materials, embodied carbon and construction that entails.

The classical analytical solutions for ground slabs are due to the pioneering efforts of Westergaard [1], who put together closed-form formulations for loading at the interior, edge and corner from Kirchhoff thin-plate theory on a Winkler foundation. For a preliminary figure, these equations are handy, but they make some heavy idealizations, not least of which are infinite slab dimensions and uncracked elastic behavior with no shear deformation. Where greater accuracy is needed to deal with finite geometries, non-uniform subgrade, or the pressure patch of a forklift wheel, advanced numerical modeling is called for. Advanced numerical modeling using Mindlin-Reissner thick-shell theory [5] in SAP2000 [6] is called for. Finite element re-evaluations of Westergaard formulations were provided by Ioannides et al. [7], and airport pavement wheel load extensions were detailed by Guo and Marsey [8].

There is much to be said for the use of Steel Fiber Reinforced Concrete (SFRC) in industrial floor construction as a workable substitute for conventional steel mesh. By introducing discrete fibers, one can improve joint stability and energy absorption without sacrificing the residual flexural strength ($f_{R,1k}$, $f_{R,3k}$) that remains after cracking. These gains have been shown to allow for a thinner slab [9, 10], a point the fib Model Code [11] backs up. One would think the literature would have more to offer on the subject, with parametric studies tying SFRC performance and subgrade reaction modulus to the concrete grade and load position under a range of industrial scenarios; but for the time being, those are not to be found.

With that in mind, this work has three objectives. It sets out to assess the sensitivity of the load capacity and necessary slab thickness (h) to the subgrade reaction modulus and the strength of the concrete. It also aims to quantify the stress-concentration penalties for loads placed at the corner, edge, or interior. Finally, it puts Westergaard's closed-form predictions to the test against 3D Mindlin-Reissner shell FEA in SAP2000 [6]. The intent is to produce an iso-thickness design response map with decision boundaries useful to the practicing engineer.

2 Methodology

2.1 Analytical Formulation (Westergaard Plate Theory)

The design of a slab-on-grade foundation has its theoretical basis in Westergaard's differential equation. This equation is used to represent an elastic plate on an isotropic Winkler subgrade [1]. In this context, the radius of relative stiffness, l (mm), is the variable that exerts the most control. It is what defines the elastic flexural radius of influence:

$$l = \sqrt[4]{\frac{E \cdot h^3}{12 \cdot (1-\nu^2) \cdot k}} \tag{1}$$

where E is the concrete elastic modulus (MPa), h is the slab thickness (mm), ν is Poisson's ratio ($\nu = 0.20$ for concrete), and k is the subgrade reaction modulus (N/mm^3). Under an interior uniformly distributed storage load q (kPa) over a footprint radius a, the maximum flexural bending moment M_{int} (kN·m/m) and corresponding tensile stress σ_{int} (MPa) are given by:

$$M_{\text{int}} = 0.169 \cdot q \cdot l^2, \sigma_{\text{int}} = \frac{6 \cdot M_{\text{int}}}{h^2} \tag{2}$$

For concentrated point or wheel axle loads P (kN) acting over an equivalent circular contact area of radius b, the interior (σ_{int}), free edge (σ_{edge}), and free corner (σ_{corner}) tensile stresses are expressed as:

$$\sigma_{\text{int}} = \frac{3 \cdot P \cdot (1+\nu)}{2 \cdot \pi \cdot h^2} \cdot \left[\ln\left(\frac{l}{b}\right) + 0.615\right] \tag{3}$$

$$\sigma_{\text{edge}} = \frac{0.572 \cdot P}{h^2} \cdot \left[3 \cdot (1+\nu) \cdot \log_{10}\left(\frac{l}{b}\right) + 0.359\right] \tag{4}$$

$$\sigma_{\text{corner}} = \frac{3 \cdot P}{h^2} \cdot \left[1 - \left(\frac{b \cdot \sqrt{2}}{l}\right)^{0.6}\right] \tag{5}$$

Design compliance requires that the maximum tensile stress σ_{max} does not exceed the design flexural tensile strength of concrete $f_{ctd,fl}$, incorporating Eurocode 2 (EN 1992-1-1 Eq. 3.23) size-effect factor [4]:

$$f_{ctd,fl} = \frac{f_{ctk,0.05}}{\gamma_c} \cdot \left[1 + \sqrt{\frac{200}{h}}\right] \leq 2.0 \cdot f_{ctd} \tag{6}$$

The structural safety factor (SF) is evaluated as:

$$SF = \frac{f_{ctd,fl}}{\sigma_{max}} \geq 1.0 \tag{7}$$

2.2 Finite Element Model (SAP2000)

The analytical formulations for the test under complex load footprints were developed by means of 3D numerical models in SAP2000 [6]. These were built on 4-node Mindlin-Reissner shell elements of the Shell-Thick type [5]; the theory's ability to handle transverse shear deformation makes it well suited for the precision required with thick ground slabs having a small span-to-thickness ratio [5].

To characterize the subgrade interaction, a two-dimensional area spring mesh with linear Winkler stiffness (k_z = k) is used for each unit of area. The springs were assigned non-linear behavior so as to admit compression but rule out any false tensile reaction from the ground. As for the 12 m by 12 m slab, it was modeled in 0.25 m square shell elements; this degree of refinement was found to be sufficient after convergence tests indicated stress variations of under 0.5%.

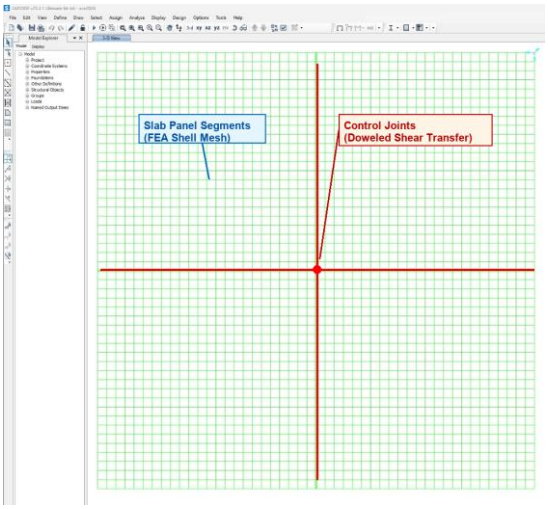


Fig. 1. SAP2000 shell finite element model setup showing slab meshing, area springs, and load application grid.

2.3 Parametric Matrix Description

A comprehensive matrix demonstrating several unique evaluation cases was constructed across five major parameters, as summarized in Table 1.

Table 1. Summary of parametric analysis variables.

Parameter	Investigated Range / Classes	Design Purpose
Subgrade Reaction Modulus k	7, 15, 20, 30, 45 MN/m^3	Evaluate soil stiffness impact
Concrete Strength Class	C25/30, C30/37, C35/45, C40/50	Quantify concrete material effect
Storage Uniform Load q	12, 25, 50, 75, 100, 125, 150, 175, 200 kPa	Industrial storage load range
Forklift Axle Load P	4t (20kN), 8t (40kN), 12t (60kN), 16t (90kN)	Concentrated wheel pressure
Load Position	Interior, Free Edge, Free Corner	Stress concentration penalty

3 Results and Discussion

3.1 Benchmarking Westergaard Analytical vs. SAP2000 FEA Models

Table 2 and Fig. 2 offer a side-by-side view of the maximum flexural tensile stresses, with the Westergaard closed-form analytical figures set against what the SAP2000 3D shell finite element models have to show. The case in point is a C35/45 concrete slab of 350 mm thickness under a uniform q = 100 kPa load, where one will note the subgrade stiffness is not uniform.

Table 2. Westergaard analytical versus SAP2000 FEA flexural tensile stress comparison (C35/45, h = 350 mm, q = 100 kPa).

k (MN/m³)	Soil Type	l (mm)	Westergaard σ (MPa)	SAP2000 FEA σ (MPa)	Divergence (%)
7	Soft Clay	2022	2.41	2.49	+3.3%
15	Medium Clay	1672	1.94	2.00	+3.1%
20	Stiff Clay	1556	1.78	1.83	+2.8%
30	Dense Sand	1406	1.66	1.70	+2.4%
45	Crushed Rock	1270	1.58	1.63	+3.2%

Table 3 compares flexural tensile capacity formulations, size-effect provisions, design strengths, and structural safety implications between ACI 360R-10 and Eurocode 2 (EN 1992-1-1) for C30/37 concrete.

Table 3. Flexural tensile capacity: ACI 360R-10 vs. Eurocode 2 (C30/37 concrete).

Criterion	ACI 360R-10	Eurocode 2 (EN 1992-1-1)	Design Impact
Governing Formula	$f_r = 0.373 \cdot \sqrt{f_c'}$ [MPa]	$f_{ctm} = 0.30 \cdot f_{ck}^{(2/3)}$; $f_{ctd,fl} = (1.6 - h/1000) \cdot f_{ctm} / \gamma_M$	EC2 includes depth size effect
Design Strength	2.05 MPa	2.41 MPa ($\gamma_M = 1.5$)	EC2 ~17% higher for C30/37
Unfactored Strength	2.05 MPa	3.62 MPa (h = 350 mm, factor = 1.25)	EC2 size factor benefits thinner slabs
Size Effect	Neglected	$(1.6 - h/1000) >= 1.0$	Thinner slabs stronger per EC2
Conservatism	Higher (10–15% more concrete)	Realistic (scale-adjusted)	ACI yields thicker sections

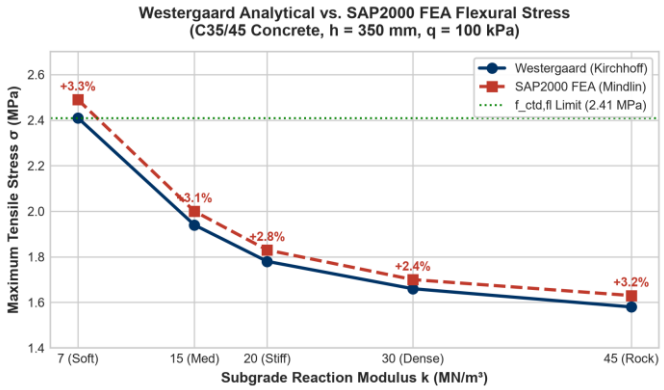


Fig. 2. Comparison of Westergaard analytical model predictions versus SAP2000 FEA flexural stresses across subgrade stiffnesses (C35/45, h = 350 mm, q = 100 kPa).

The FEA results agree well with Westergaard analytical predictions, with maximum divergence ranging from +2.4% to +3.3%. The slightly higher stresses in FEA stem from

transverse shear deformation captured by Mindlin shell theory, which classical Kirchhoff thin-plate formulations neglect.

3.2 Subgrade Stiffness Impact on Required Slab Thickness

As can be seen in Fig. 3, the subgrade reaction modulus k and the slab thickness h are linked for C35/45 concrete when subjected to a q = 100 kPa load. With a soft subgrade of k = 7 MN/m3, one would need a 360 mm thickness. But if the subgrade is made stiffer at k = 15 MN/m3, that requirement comes down to 290 mm, a 19.4% reduction. A more substantial gain is possible with a crushed aggregate subbase (k = 45 MN/m3), where the necessary thickness is only 200 mm, for an overall saving of 44.4%.

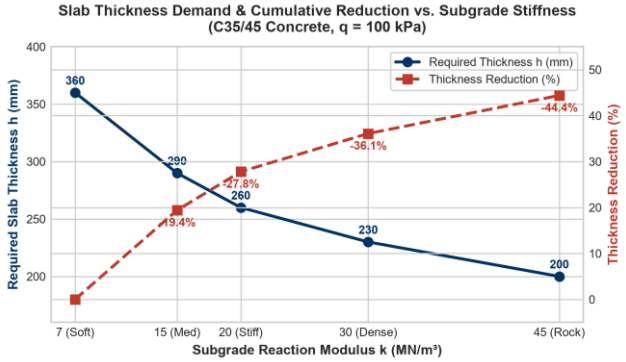


Fig. 3. Slab thickness demand h (mm) and cumulative percentage reduction vs. subgrade reaction modulus k (MN/m^3) for C35/45 concrete under q = 100 kPa uniform load.

3.3 Stress Concentration Penalties and Load Positioning Sensitivity

Fig. 4 presents required slab thickness curves for interior, free-edge, and free-corner load positions under q = 100 kPa. Free-edge loading imposes a 35.0% thickness penalty (h increases from 360 mm to 490 mm for k = 7 MN/m3), while free-corner loading imposes a 72.2% thickness penalty (h increases to 620 mm).

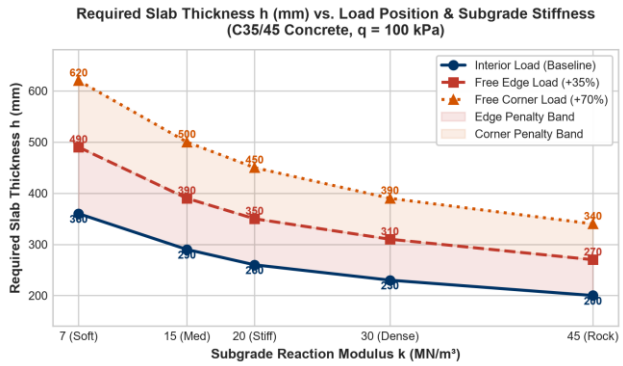


Fig. 4. Multi-series thickness response curves h (mm) vs. subgrade reaction k for three loading positions (interior/free edge / free corner) with shaded penalty bands (C35/45, q = 100 kPa).

3.4 Concrete Strength Class Sensitivity

A comparison of the slab thicknesses called for in four concrete strength grades, C25/30 through C40/50, is provided in Fig. 5. On a soft subgrade (k = 7 MN/m3), moving to a higher grade of concrete in the range of C40/50 as opposed to C25/30 will see the necessary thickness drop by 21.4 per cent, from 420 mm down to 330 mm. The figures are similar for a stiff subgrade (k = 20 MN/m3), where an upgrade in strength yields a 20.0 percent reduction in thickness, going from 300 mm to 240 mm.

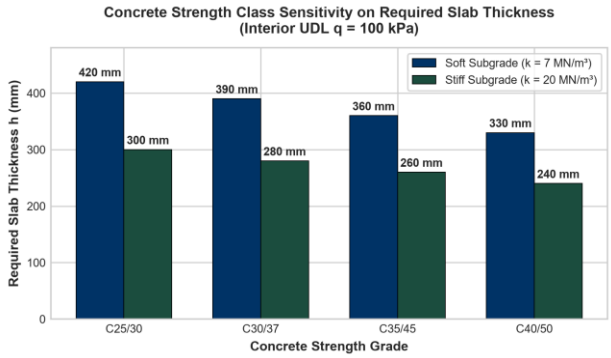


Fig. 5. Concrete strength class sensitivity on required slab thickness h (mm) for soft (k = 7 MN/m^3) and stiff (k = 20 MN/m^3) subgrades under q = 100 kPa storage load.

3.5 Iso-Thickness Design Response Map & Decision Boundaries

To synthesize the 540 parametric scenarios into a practical engineering tool, Fig. 6 presents an Iso-Thickness Design Response Map mapping required slab thickness h as a function of subgrade reaction modulus k and storage load q for C35/45 concrete.

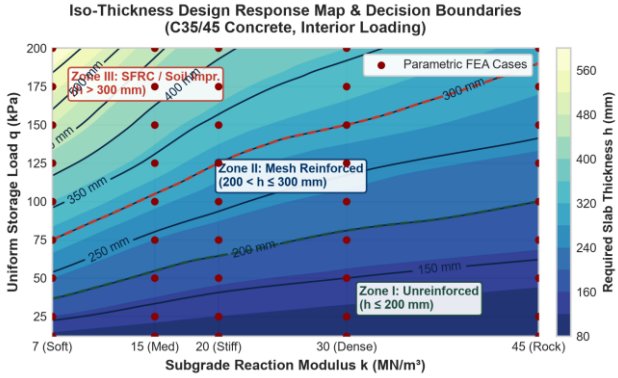


Fig. 6. Iso-thickness design response map h (mm) vs. subgrade reaction k (MN/m^3) and uniform load q (kPa) (C35/45, interior loading) with annotated structural decision boundaries (Zones I, II, and III).

The response map delineates three separate structural decision zones.

Zone I (h ≤ 200 mm) is for unreinforced or lightly meshed concrete slabs of the kind one would find in commercial or light industrial settings; here k is at least 30 MN/m3 and q does not exceed 75 kPa.

Where h is between 200 and 300 mm, Zone II calls for double rebar mesh reinforcement, a specification well suited to heavy manufacturing floors and standard logistics warehouses.

Finally, for any slab over 300 mm in thickness, Zone III employs Steel Fiber Reinforced Concrete (SFRC, 30-45 kg/m3) along with subgrade soil stabilization so as to keep the slab thickness from becoming uneconomical.

3.6 Heavy Forklift Loading and SAP2000 FEA Stress Contours

Fig. 7 and Fig. 8 illustrate the SAP2000 3D FEA load application and resulting principal flexural tensile stress contours (S_{11}) under a 16-ton heavy forklift axle load (90 kN per dual-wheel patch, 360 kPa pressure).

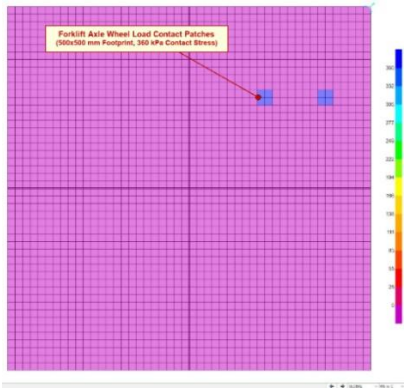


Fig. 7. SAP2000 FEA load setup interface showing localized patch pressure distribution for 16-ton heavy forklift axle loading.

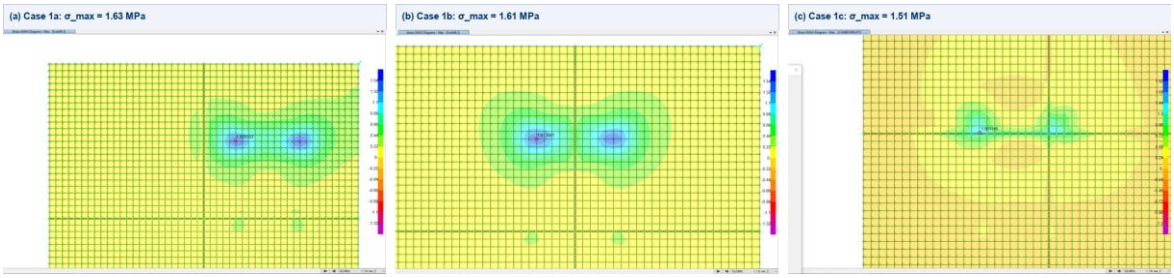


Fig. 8. SAP2000 FEA flexural tensile stress contour output S_{max} (MPa) displaying peak stress concentrations under forklift dual-wheel loading.

For C30/37 concrete, maximum tensile stress reaches 1.63 MPa (close to $f_{ctd,fl}$ = 2.05 MPa limit). Upgrading to C40/50 concrete reduces peak tensile stress to 1.45 MPa, providing a robust safety margin against fatigue cracking.

4 Conclusions

In this research, a thorough parametric optimization was carried out on industrial concrete slab-on-grade foundations for a range of design configurations. To put Westergaard's analytical equations to the test, they were benchmarked with 3D Mindlin shell finite element work in SAP2000; the results left no room for doubt as to their validity. The closed-form solutions from Westergaard are in close accord with the three-dimensional analysis, showing a stress deviation of no more than +2.4 to +3.3 percent at most.

What the study brings to light is that one cannot optimize slab thickness without considering how well the subgrade soil has been prepared. Take the subgrade reaction modulus as an example: moving it up from 7 to 45 MN/m³ will see the necessary slab thickness drop by as much as 44.4 percent, from 360 mm down to 200 mm. Then there is the matter of load placement and its effect on stress concentration. Free-edge or free-corner loading demands a 35.0 and 72.2 percent increase in thickness over what is needed for interior loading, making the use of edge dowel bars and thickened edge beams compulsory. Even with the subgrade held constant, a step up in concrete strength to C40/50 from C25/30 will cut the required thickness by between 20.0 and 21.4 percent.

For the structural engineer in the conceptual phase of a foundation design, an Iso-Thickness Design Response Map is a handy visual aid. It is intended to allow for the quick determination of the right concrete grade and slab thickness, as well as the best approach to reinforcement and overall optimization.

References

1. Westergaard, H.M.: Stresses in concrete pavements computed by theoretical analysis. Public Roads 7(2), 25–35 (1926).
2. Concrete Society: TR34 Concrete Industrial Ground Floors - A Guide to Design and Construction. 4th edn. Concrete Society, Technical Report No. 34, Camberley (2016).
3. ACI Committee 360: Design of Slabs-on-Ground. ACI 360R-10, American Concrete Institute, Farmington Hills (2010).
4. CEN: EN 1992-1-1 Eurocode 2: Design of concrete structures - Part 1-1: General rules and rules for buildings. European Committee for Standardization, Brussels (2004).
5. Mindlin, R.D.: Influence of rotatory inertia and shear on flexural motions of isotropic, elastic plates. ASME Journal of Applied Mechanics 18(1), 31-38 (1951).
6. Computers and Structures Inc. (CSI): SAP2000 Integrated Software for Structural Analysis and Design, Version 25, Computers and Structures Inc., Berkeley, California (2022).
7. Ioannides, A.M., Thompson, M.R., Barenberg, E.J.: Westergaard solutions reconsidered. Transportation Research Record 1043, 16–23 (1985).
8. Guo, H.H., Marsey, W.B.: Theoretical manual for airport pavement design and evaluation. Federal Aviation Administration, Report DOT/FAA/AR-02/78, Washington, D.C. (2002).
9. Barros, J.A.O., Figueiras, J.A.: Flexural behavior of steel fiber-reinforced concrete slabs-on-ground. ASCE Journal of Materials in Civil Engineering 11(3), 225–235 (1999).
10. Roesler, J.R., Altoubat, S.A., Rieder, K.A., Lange, D.A.: Effect of synthetic fibers on structural behavior of concrete slabs-on-ground. ACI Materials Journal 103(1), 3–10 (2006).
11. fib Bulletin 56: Model Code 2010 - First Complete Draft, Volume 2—International Federation for Structural Concrete (fib), Lausanne (2010).

Author Contribution Statement

Conceptualization, Methodology, Investigation, Writing – Original Draft, Writing – Review & Editing: Mehmet Sefa Orak

List of Abbreviations

SOG — Slab-on-Grade
FEA — Finite Element Analysis
SFRC — Steel Fiber Reinforced Concrete
UDL — Uniformly Distributed Load
ACI — American Concrete Institute
EN — Eurocode (European Standard)

Publication Note

This paper was peer-reviewed, accepted for presentation, and included in the proceedings of the ACE2026 – 16th International Congress on Advances in Civil Engineering, held on 12–14 October 2026 in Trabzon, Türkiye.

This paper may be cited as follows:

Orak M.S., "Parametric Analysis of Load-Carrying Capacity and Reinforcement Optimization in Slab-on-Grade Foundations," in Proceedings of the ACE2026 – 16th International Congress on Advances in Civil Engineering, Trabzon, Türkiye, 12–14 October 2026.

Free Vibration Response of Homogeneous Porous Beams with Edge Cracks Using Finite Element Method

Serhan Koç[1], Muhittin Turan[2], Gökhan Adıyaman[3], and Volkan Kahya[4]
[1] 0000-0003-4792-2179, Karadeniz Technical University, Civil Engineering Department (Faculty of Engineering), Trabzon, Türkiye, serhan.koc@ktu.edu.tr
[2] 0000-0002-5703-0580, Karadeniz Technical University, Civil Engineering Department (Of Faculty of Technology), Trabzon, Türkiye, m.turan@ktu.edu.tr
[3] 0000-0002-3076-4090, Karadeniz Technical University, Civil Engineering Department (Faculty of Engineering), Trabzon, Türkiye, gadiyaman@ktu.edu.tr
[4] 0000-0003-1392-4483, Karadeniz Technical University, Civil Engineering Department (Faculty of Engineering), Trabzon, Türkiye, volkan@ktu.edu.tr

Abstract. In this study, the free vibration behavior of homogeneous porous beams with edge cracks is investigated using the finite element method (FEM) based on the higher-order shear deformation theory (HSDT). Beams with rectangular cross-sections are considered, and the material properties are assumed to be homogeneous and isotropic. Three different porosity distribution patterns are considered across the beam cross-section, and their influence on the dynamic response is examined comparatively. The crack is modeled as a geometric open crack located on the upper surface of the beam, where material is removed over a finite element width. It is assumed that the crack affects only the stiffness matrix of the finite element model, while the mass matrix remains unchanged. Analyses are performed under three different boundary conditions, simply supported (S-S), clamped-clamped (C-C), and clamped-free (C-F). The effects of porosity ratio, crack depth ratio, and crack location on the natural frequencies of the beam are examined through parametric studies. When crack depth, porosity ratio, different boundary conditions, and crack positions are examined, they are found to affect the natural frequency. The numerical results are validated against the literature, and different parametric results are presented.

Keywords: Free vibration, porosity, finite element method, higher-order shear deformation theory, boundary conditions.

1 Introduction

Functionally graded materials (FGMs) offer exceptional durability, thermal resistance, and structural efficiency by blending distinct constituents, such as metals and ceramics, across a continuous gradient. This smooth transition reduces internal stress concentrations. Incorporating internal void networks and porous structures into these materials reduces weight while introducing valuable energy-absorption, acoustic, and thermal performance capabilities. However, internal pores simultaneously alter both mass and stiffness, meaning that the dynamic response depends heavily on both total porosity and its cross-sectional distribution.

Cracks, which represent a critical factor governing the dynamic behavior of beams, predominantly originate from fatigue degradation, manufacturing defects, or excessive mechanical loading. Even stable cracks induce localized stiffness degradation, consequently perturbing the fundamental natural frequencies and mode shapes. In this regard, the quantitative evaluation of these modal shifts constitutes a fundamental prerequisite for robust vibration-based damage identification and structural health monitoring (SHM) frameworks.

The free vibration analysis of porous and functionally graded beams has been extensively investigated over the years [1-4]. Early analytical studies established a foundational framework for graded beam dynamics [5], while subsequent finite element methods accelerated this progress by expanding into sandwich and multi-layered configurations [6,7]. These studies confirm that the porosity ratio and its distribution govern the balance between mass and stiffness; however, they frequently couple porosity with material gradation [4], making their

individual effects difficult to isolate. In this study, a homogeneous isotropic base material is employed, and solely the porosity distribution and crack parameters are varied.

The modeling of cracked beams commonly relies on local flexibility matrices, rotational spring analogies, or direct cross-sectional reductions, where the resulting frequency shifts are governed by the crack depth and its relative position with respect to the mode shapes [8,9]. Furthermore, higher-order shear deformation theories eliminate the need for a shear correction factor, thereby yielding superior accuracy, particularly in the dynamic analysis of deep (short) beams [10].

Comprehensive studies simultaneously addressing cracking and porosity remain limited, particularly across extensive combinations of crack depths, locations, porosity patterns, and boundary conditions [11,12]. This conference paper utilizes a three-node, 12-degree-of-freedom higher-order finite element model to address this gap. Three distinct porosity patterns (G-1, G-2, G-3) and three boundary conditions (S-S, C-C, C-F) are investigated. The crack is incorporated directly into the element stiffness matrix as a localized geometric reduction. Following validation through mesh sensitivity analyses and benchmark literature data, the model comprehensively demonstrates how the porosity ratio, crack depth, and crack location collectively influence the fundamental natural frequency.

2 Theoretical Formulation

2.1 Physical Model and Material Properties

The physical beam model considered in this work is illustrated in Fig. 1. The beam has a length of L and a rectangular cross-section of width b and height h. A single open edge crack of depth a is located along the top surface at a distance L_c from the left support, and the figure also shows the resulting uncracked and cracked cross-sections. In the finite element formulation, the crack is modeled within a single element by reducing the local cross-sectional height from h to $h - a$.

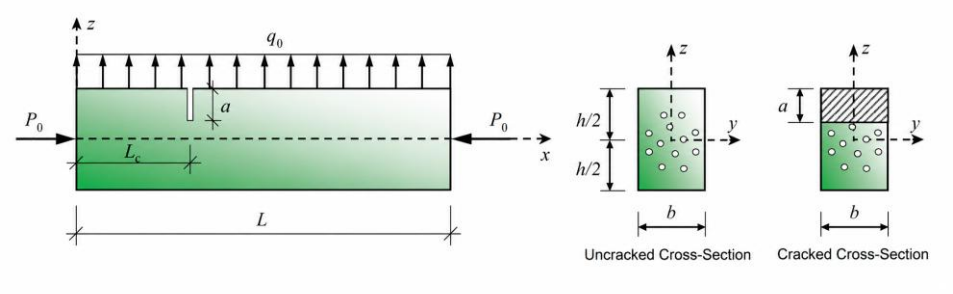


Fig. 1. Beam geometry with uncracked and cracked cross-sections (L, L_c, a, b, h); P_0, q_0 not applied in the free vibration analysis

Material gradation terms from the general 2D-FGM model are omitted here to focus on a homogeneous base structure. Setting the gradation exponents to zero leaves a fully ceramic base matrix, where the effective properties of the porous material simplify to [13]

$$P(z) = P_c - \frac{e(z)}{2}(P_c + P_m), \qquad P = E, \rho, \tag{1}$$

with P_c and P_m representing ceramic and metal constituents used for porosity correction. The metal property P_m is retained exclusively within this correction term, ensuring that $P(z) \to P_c$ as $e \to 0$ to maintain a homogeneous ceramic base material. The effective Young's modulus and mass density are expressed as

$$E(z) = E_c - \frac{e(z)}{2}(E_c + E_m), \qquad \rho(z) = \rho_c - \frac{e(z)}{2}(\rho_c + \rho_m) \tag{2}$$

Assuming a constant Poisson's ratio of 0.30 across constituents, the shear modulus is evaluated directly via

$$G(z) = \frac{E(z)}{2(1+\nu)}, \qquad \nu = 0.30 \tag{3}$$

The geometric and material parameters used in the free vibration analysis are listed in Table 1.

Table 1. Geometric and material parameters of the beam

Parameter	Symbol	Value
Beam length	L	1 m
Beam width	b	0.05 m
Beam height	h	0.05 m
Ceramic Young's modulus	E_c	380 GPa
Metal Young's modulus	E_m	70 GPa
Ceramic density	ρ_c	3960 kg/m³
Metal density	ρ_m	2702 kg/m³
Poisson's ratio	$\nu_c = \nu_m$	0.30

Three distinct porosity distributions (G-1, G-2, and G-3) are examined across the beam thickness, as depicted in Fig. 2. Following Turan [4], these profiles are defined as

$$e_{\text{G-1}}(z) = e, \qquad e_{\text{G-2}}(z) = e\left(1 - \frac{2|z|}{h}\right), \qquad e_{\text{G-3}}(z) = e\left(\frac{2|z|}{h}\right), \tag{4}$$

where e represents the maximum porosity ratio and $e(z)$ defines its variation through the beam thickness.

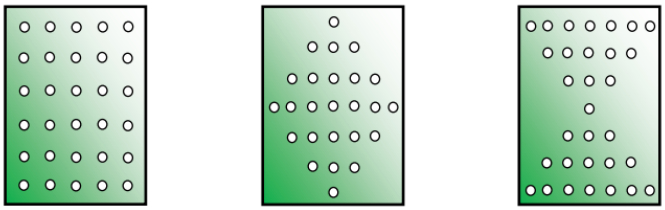


Fig. 2. Porosity distribution patterns (G-1, G-2, G-3)

In these models, G-1 represents a uniform distribution across the beam thickness, G-2 concentrates the highest porosity near the mid-plane and decreases toward the top and bottom surfaces, and G-3 exhibits the lowest porosity at the mid-plane with peak values at the outer surfaces. For the cracked element, only the stiffness matrix is modified to incorporate the reduced cross-section while the mass matrix remains unchanged [13]. Because the crack removes material over a very narrow axial span, its influence on global inertia is negligible compared to its localized effect on bending stiffness.

2.2 Mathematical Formulation

Based on the third-order shear deformation theory, the axial and transverse displacement field is expressed as [14]

$$u(x,z,t) = u_0(x,t) - z\,w_{0,x}(x,t) + \left(z - \frac{4z^3}{3h^2}\right)\phi_0(x,t), \qquad w(x,z,t) = w_0(x,t) \tag{5}$$

The corresponding normal and shear strains are defined as

$$\begin{aligned} \varepsilon_{xx} &= \frac{du_0}{dx} - z\frac{d^2w_0}{dx^2} + \left(z - \frac{4z^3}{3h^2}\right)\frac{d\phi_0}{dx}, \\ \gamma_{xz} &= \frac{dw_0}{dx} - \frac{dw_0}{dx} + \left(1 - \frac{4z^2}{h^2}\right)\phi_0 = \left(1 - \frac{4z^2}{h^2}\right)\phi_0 \end{aligned} \tag{6}$$

Constitutive relations for normal and transverse shear stresses follow linear elasticity:

$$\sigma_{xx} = E(z)\varepsilon_{xx}, \qquad \tau_{xz} = G(z)\gamma_{xz} \tag{7}$$

Strain energies for uncracked and cracked elements are evaluated separately as [13]

$$U_{\text{uncracked}} = \frac{1}{2}\int_0^{L_e}\int_{-b/2}^{b/2}\int_{-h/2}^{h/2}(\sigma_{xx}\varepsilon_{xx} + \tau_{xz}\gamma_{xz})\, dz\, dy\, dx,$$
$$U_{\text{cracked}} = \frac{1}{2}\int_0^{L_e}\int_{-b/2}^{b/2}\int_{-h/2}^{h/2-a}(\sigma_{xx}\varepsilon_{xx} + \tau_{xz}\gamma_{xz})\, dz\, dy\, dx \quad (8)$$

In Eq. (8), the presence of the crack is accounted for by adjusting the upper bound of the thickness integration from $h/2$ to $h/2 - a$. In contrast, the kinetic energy is calculated across the full cross-section for all elements:

$$T = \frac{1}{2}\int_0^{L_e}\int_{-b/2}^{b/2}\int_{-h/2}^{h/2}\rho\,(z)(\dot{u}^2 + \dot{w}^2)dz\, dy\, dx \quad (9)$$

In the absence of external forces, the system Lagrangian for free vibration analysis reduces to

$$\Pi = T - U \quad (10)$$

2.3 Finite Element Solution

The formulation employs a three-node higher-order beam element of length L_e with 12 degrees of freedom, as shown in Fig. 3. The element nodal displacement vector is defined as

$$\mathbf{u} = \{u_1\ u_2\ u_3\ w_1\ w_2\ w_3\ \phi_1\ \phi_2\ \phi_3\ w_{,x1}\ w_{,x2}\ w_{,x3}\}^T \quad (11)$$

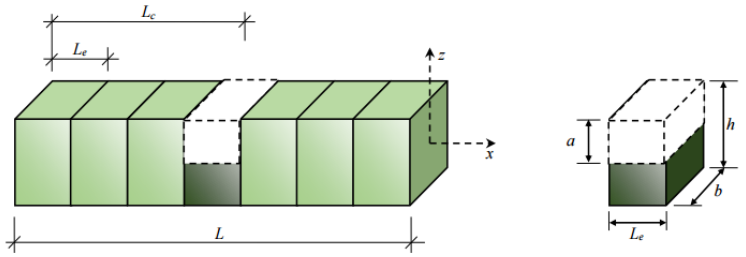


Fig. 3. Finite element discretization with localized crack

Interpolation of the generalized displacement fields across the element domain is performed using appropriate shape functions:

$$u_0(x) = \sum_{i=1}^{3}\psi_{1i}\,(x)u_i,$$
$$w_0(x) = \sum_{i=1}^{3}\psi_{2i}\,(x)w_i + \sum_{i=1}^{3}\psi_{3i}\,(x)w_{,xi}, \quad (12)$$
$$\phi_0(x) = \sum_{i=1}^{3}\psi_{1i}\,(x)\phi_i$$

Here, ψ_{1i}, ψ_{2i}, and ψ_{3i} denote the higher-order interpolation functions of the element, illustrated in Fig. 4.

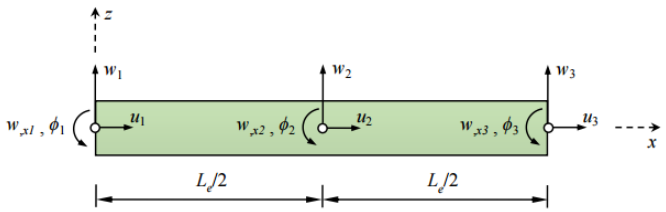


Fig. 4. Higher-order finite element

Applying the Lagrange equations,

$$\frac{d}{dt}\left(\frac{\partial \Pi}{\partial \dot{q}_i}\right) - \frac{\partial \Pi}{\partial q_i} = 0, \quad (13)$$

gives the element equation of motion

$$\mathbf{m}\ddot{\mathbf{u}} + \mathbf{k}_e\mathbf{u} = \mathbf{0} \quad (14)$$

After assembly, the free vibration equation of the beam becomes

$$\mathbf{M}\ddot{\mathbf{X}} + \mathbf{K}_e\mathbf{X} = \mathbf{0} \tag{15}$$

Introducing the harmonic solution $\mathbf{X} = \mathbf{U}e^{i\omega t}$ gives

$$(\mathbf{K}_e - \omega^2\mathbf{M})\mathbf{U} = \mathbf{0} \tag{16}$$

Here, ω is the angular natural frequency in rad/s. The natural frequency reported in Hz is obtained from

$$f = \frac{\omega}{2\pi} \tag{17}$$

All frequencies reported in the following sections are given in Hz.

The kinematic boundary conditions corresponding to the three boundary conditions considered in this study (simply supported, clamped-clamped, and clamped-free) are given in Table 2.

Table 2. Kinematic boundary conditions for each support type

Support Type	x = 0	x = L
Simply supported (S-S)	u = 0, w = 0	w = 0
Clamped-clamped (C-C)	u = 0, w = 0, φ = 0, w,x = 0	u = 0, w = 0, φ = 0, w,x = 0
Clamped-free (C-F)	u = 0, w = 0, φ = 0, w,x = 0	Free (no constraints)

3 Numerical Results and Discussion

In this section, the numerical results demonstrating the accuracy and effectiveness of the developed finite element model are presented and discussed in detail. All parameters used in the analyses are kept constant, and the effects of porosity, crack location and depth, material gradation exponents, and boundary conditions on structural behavior are examined comparatively. Throughout the study, the beam length is taken as $L = 1$ m, and the cross-sectional dimensions are $b = h = 0.05$ m. The elastic moduli of the metal and ceramic phases are assumed to be $E_m = 70$ GPa and $E_c = 380$ GPa, respectively, while the corresponding densities are $\rho_m = 2702$ kg/m^3 and $\rho_c = 3960$ kg/m^3. The Poisson's ratio is taken as constant, $\nu = 0.3$.

3.1 Mesh Convergence and Discretization

Because the geometric crack is assigned to a single finite element, changing the number of elements modifies not only the discretization but also the axial extent over which the cross-section is reduced. The following analysis should therefore be interpreted as a mesh-sensitivity study for the adopted crack representation rather than as a conventional mesh-convergence test for an unchanged crack geometry. A G-1 porous beam with $e = 0.1$ is analyzed using $N = 10$, 20, 50, 100, and 200 elements for the S-S, C-C, and C-F boundary conditions. The crack is placed at $L_c/L = 0.25$ and two crack depth ratios, $a/h = 0.2$ and $a/h = 0.4$, are considered.

The results are summarized in Table 3. For the shallower crack the predicted frequency is almost independent of the mesh, the largest change between $N = 10$ and $N = 200$ being 0.56%. The deeper crack is more sensitive, as expected for a geometric crack model in which a coarse mesh spreads the reduced cross-section over a relatively large portion of the beam: the corresponding changes reach 1.82% for S-S and 2.95% for C-F. In all cases the results stabilize rapidly, and the difference between $N = 100$ and $N = 200$ never exceeds 0.03%. Accordingly, $N = 200$ is adopted consistently in all subsequent validation and parametric analyses, so that the crack always extends over an axial length of $L_e = L/N$ and the numerical comparisons reported below are performed with the same crack representation. For reference, the fundamental frequencies of the corresponding uncracked beams at $N = 200$ are 224.1507, 501.7247, and 80.0306 Hz for the S-S, C-C, and C-F cases, respectively.

Table 3. Mesh convergence of the fundamental frequency (Hz) (G-1, $e = 0.1$, $L_c/L = 0.25$)

N	S-S		C-C		C-F	
	a/h = 0.2	**a/h = 0.4**	**a/h = 0.2**	**a/h = 0.4**	**a/h = 0.2**	**a/h = 0.4**
10	222.7072	216.7859	501.7153	500.6306	79.1439	75.6495
20	223.4871	220.7600	501.7815	501.6104	79.4971	77.3703
50	223.4456	220.7620	501.6517	501.3097	79.5960	77.9724
100	223.4660	220.8627	501.6558	501.3902	79.5861	77.9302
200	223.4545	220.8109	501.6432	501.3451	79.5897	77.9501

3.2 Validation Against Literature for the Homogeneous Case

After selecting the element number, the finite element formulation is validated for a homogeneous, isotropic reference beam against published experimental and numerical results for cracked beams [15,16]. This validation step isolates the implementation of the beam kinematics, crack representation, and boundary conditions before the effects of porosity are examined.

Table 4 compares the first two natural frequencies obtained from the present model with experimental, FEFM, and FEM results reported by Kam and Lee, Lee and Chung, and Long et al. [15-17]. Three crack locations ($L_c = 80$, 140, and 200 mm) and two crack depths ($a = 2$ and 6 mm) are considered. The first-mode predictions are consistently close to the reference values for both crack depths. Somewhat larger differences occur in the second mode, which is more sensitive to the local representation of the crack and to differences between the underlying modeling approaches. Overall, the comparison confirms that the present element reproduces the principal frequency trends associated with crack depth and location.

Table 4. Comparison of the natural frequencies of cracked and uncracked homogeneous beams with literature

L_c (mm)	Methods	a = 2 mm		a = 6 mm	
		1st mode (Hz)	**2nd mode (Hz)**	**1st mode (Hz)**	**2nd mode (Hz)**
80	Present	184.1274	1132.2377	181.4436	1130.2022
	Experiment	184.00	1160.00	174.70	1155.30
	FEFM	184.00	1159.80	177.10	1154.70
	FEM	184.20	1159.30	175.30	1153.90
140	Present	184.3198	1130.3569	183.3440	1111.7244
	Experiment	184.70	1153.10	181.20	1092.90
	FEFM	184.70	1153.20	181.80	1102.90
	FEM	184.70	1153.10	181.40	1091.10
200	Present	184.4062	1128.1253	184.2156	1117.0354
	Experiment	185.00	1155.00	184.30	1106.30
	FEFM	185.00	1155.00	184.40	1114.80
	FEM	185.00	1154.90	184.30	1106.20
Uncracked beam (a = 0 mm)					
	Present	184.4271	1132.4670		
	Experiment	185.20	1160.60		
	FEFM	185.10	1160.40		
	FEM	185.10	1159.90		

In cracked configurations, where the natural frequencies are significantly influenced by crack location (L_c) and depth (a), a decline in both the first and second mode frequencies is observed as the depth increases. This behavior stems from the loss of beam stiffness induced by the crack, which consequently weakens the overall vibration characteristics of the system. These results,

summarized in Table 4, exhibit high agreement with numerical and experimental findings from the literature.

3.3 Parametric Study

Following model validation, a parametric study evaluated how porosity ratio, crack depth, and crack location influence the S-S, C-C, and C-F boundary conditions.

Fig. 5 illustrates the fundamental frequency of the uncracked beam across varying porosity ratios (e). For patterns G-1 and G-2, the natural frequency steadily rises with increasing porosity because material density decreases faster than elastic modulus, effectively boosting the overall stiffness-to-mass ratio. Pattern G-3 shows a slight frequency reduction as porosity grows. Since porosity in G-3 concentrates near the outer surfaces where contribution to bending stiffness is most critical, the loss of structural stiffness outweighs the reduction in mass.

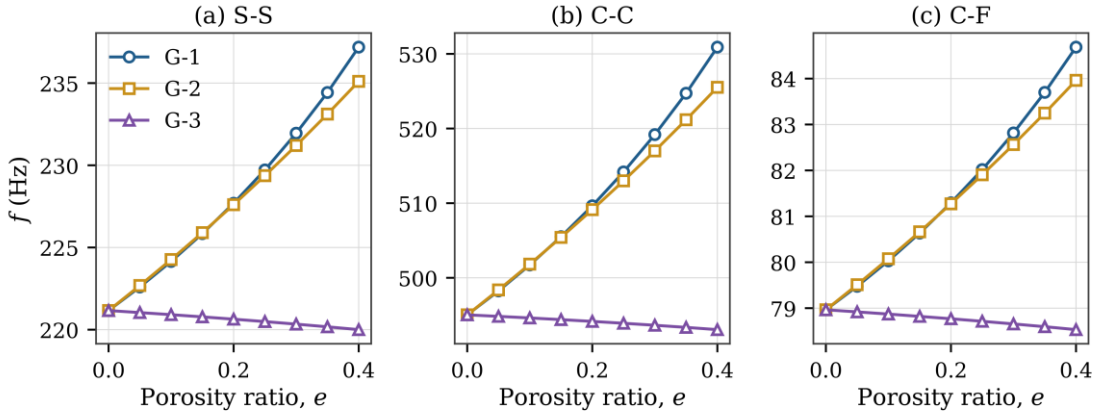
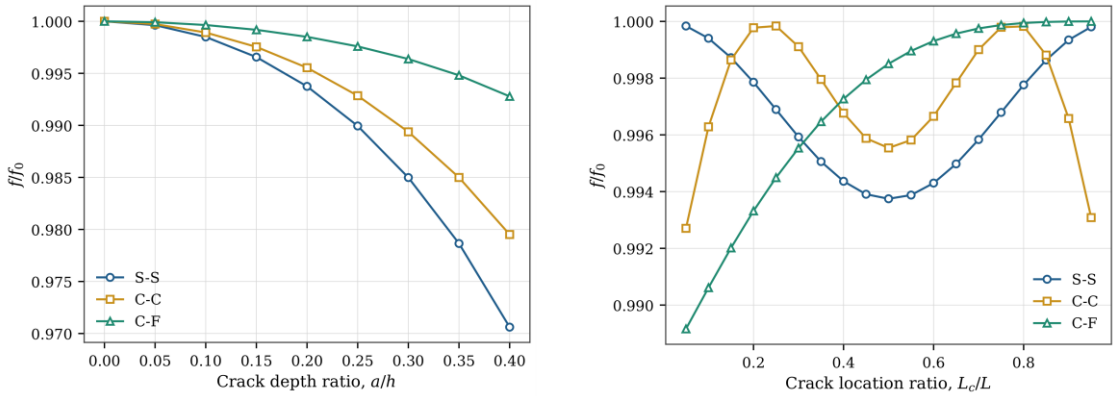


Fig. 5. Effect of porosity ratio and pattern on the fundamental frequency, (a) S-S, (b) C-C, (c) C-F

In the following analyses, the fundamental frequency of the cracked beam (f) is normalized by f_0, representing the uncracked state with matching porosity and boundary conditions.

As observed in Fig. 6(a), a pronounced decrease occurs in the normalized frequency (f/f_0) as the crack depth ratio (a/h) increases. At $a/h = 0.4$, the maximum frequency reduction is observed in the S-S boundary condition, followed by C-C, and the least reduction occurs in the C-F boundary condition. This difference in sensitivity directly depends on the local curvature distribution. A crack located at the mid-span coincides with the region of highest modal curvature under the S-S boundary condition. Conversely, because the mid-span curvature is lowest in the C-F boundary condition, the resulting impact is also minimized.

Fig. 6(b) presents the effect of the crack location ratio (L_c/L) on the normalized frequency. The frequency reduction trend directly mirrors the fundamental mode shape of the beam across all investigated cases. The highest sensitivity to the crack is observed at the S-S boundary condition, followed by C-F, whereas for the C-C boundary condition, it is seen both near the clamped support regions and at the mid-span. Peak frequency drops coincide with locations where maximum bending moments develop, while the ratios approach unity again where the modal curvature vanishes. Because the normalized frequency is calculated by referencing f_0, the curves corresponding to distinct porosity patterns nearly overlap at low porosity ratios.



(a) crack depth ratio, $L_c/L = 0.5$ (b) crack location ratio, $a/h = 0.2$

Fig. 6. Variation of normalized frequency with (a) crack depth and (b) crack location for $e = 0.1$ (G-1)

Table 5. Effect of porosity parameter (e) and distribution pattern on the cracked beam (a/h = 0.4)

e	S-S			C-C			C-F		
	G-1	**G-2**	**G-3**	**G-1**	**G-2**	**G-3**	**G-1**	**G-2**	**G-3**
0.0	2.94	2.94	2.94	2.05	2.05	2.05	0.72	0.72	0.72
0.1	2.94	2.99	2.89	2.05	2.08	2.02	0.72	0.73	0.71
0.2	2.94	3.04	2.84	2.05	2.11	1.98	0.72	0.75	0.70
0.3	2.94	3.09	2.78	2.05	2.15	1.95	0.72	0.76	0.68
0.4	2.94	3.15	2.72	2.05	2.18	1.91	0.72	0.78	0.67

The frequency variation depends directly on the porosity distribution type. For G-1, the frequency drop remains unchanged because uniform porosity degrades each layer uniformly. For G-2, porosity is concentrated at the mid-plane, leading the crack to remove material from the stiffer outer layers and increasing the stiffness reduction at higher porosity ratios. In contrast, for G-3, porosity concentrates near the outer surfaces, resulting in a lower frequency decrease. The same trend is observed for all boundary conditions.

4 Conclusions

The proposed model demonstrates strong agreement with benchmark results from the literature. The porosity distribution type plays a key role in the fundamental frequency behavior, where higher porosity increases the natural frequency for G-1 and G-2 but decreases it for G-3. With increasing crack depth, the most pronounced frequency drop is observed under the S-S boundary condition, followed by C-C, while C-F exhibits the smallest reduction. The extent of frequency loss is directly governed by the porosity pattern: it remains unchanged for G-1, increases for G-2 due to the loss of stiffer outer material, and decreases for G-3. Future studies may extend the present finite element formulation to cover multiple cracks, breathing-crack behavior, and higher vibration modes.

Acknowledgments

The authors would like to acknowledge the financial support provided by the Scientific and Technological Research Council of Türkiye (TÜBİTAK) under Project No. 125M090. Their support is gratefully appreciated.

References

1. Li, X.-F., Wang, B.-L., Han, J.-C.: A higher-order theory for static and dynamic analyses of functionally graded beams. Arch. Appl. Mech. **80**(10), 1197–1212 (2010). doi: https://doi.org/10.1007/s00419-010-0435-6

2. Thai, H.-T., Vo, T.P.: Bending and free vibration of functionally graded beams using various higher-order shear deformation beam theories. Int. J. Mech. Sci. **62**(1), 57–66 (2012). doi: https://doi.org/10.1016/j.ijmecsci.2012.05.014
3. Adiyaman, G.: Free vibration analysis of a porous 2D functionally graded beam using a high-order shear deformation theory. J. Vib. Eng. Technol. **12**, 2499–2516 (2024). doi: https://doi.org/10.1007/s42417-023-00996-4
4. Turan, M.: Mixed series solution for vibration and stability of porous bi-directional functionally graded beams. Arch. Appl. Mech. **94**(6), 1785–1806 (2024). doi: https://doi.org/10.1007/s00419-024-02611-8
5. Aydogdu, M., Taskin, V.: Free vibration analysis of functionally graded beams with simply supported edges. Mater. Des. **28**(5), 1651–1656 (2007). doi: https://doi.org/10.1016/j.matdes.2006.02.007
6. Kahya, V., Turan, M.: Finite element model for vibration and buckling of functionally graded beams based on the first-order shear deformation theory. Compos. Part B Eng. **109**, 108–115 (2017). doi: https://doi.org/10.1016/j.compositesb.2016.10.039
7. Kahya, V., Turan, M.: Vibration and stability analysis of functionally graded sandwich beams by a multi-layer finite element. Compos. Part B Eng. **146**, 198–212 (2018). doi: https://doi.org/10.1016/j.compositesb.2018.04.011
8. Christides, S., Barr, A.D.S.: One-dimensional theory of cracked Bernoulli–Euler beams. Int. J. Mech. Sci. **26**(11), 639–648 (1984). doi: https://doi.org/10.1016/0020-7403(84)90017-1
9. Rizos, P.F., Aspragathos, N., Dimarogonas, A.D.: Identification of crack location and magnitude in a cantilever beam from the vibration modes. J. Sound Vib. **138**(3), 381–388 (1990). doi: https://doi.org/10.1016/0022-460X(90)90593-O
10. Reddy, J.N.: A simple higher-order theory for laminated composite plates. J. Appl. Mech. **51**(4), 745–752 (1984). doi: https://doi.org/10.1115/1.3167719
11. Saimi, A., Bensaid, I., Fellah, A.: Effect of crack presence on the dynamic and buckling responses of bidirectional functionally graded beams based on quasi-3D beam model and differential quadrature finite element method. Arch. Appl. Mech. **93**(8), 3131–3151 (2023). doi: https://doi.org/10.1007/s00419-023-02429-w
12. Dahmane, M., Benadouda, M., Bennai, R., Saimi, A., Atmane, H.A.: Effect of crack on the dynamic response of bidirectional porous functionally graded beams on an elastic foundation based on finite element method. Acta Mech. **235**(6), 3849–3860 (2024). doi: https://doi.org/10.1007/s00707-024-03906-1
13. Karamanlı, A., Vo, T.P.: Bending, vibration, buckling analysis of bi-directional FG porous microbeams with a variable material length scale parameter. Appl. Math. Model. **91**, 723–748 (2021). doi: https://doi.org/10.1016/j.apm.2020.09.058
14. Reddy, J.N.: Analysis of functionally graded plates. Int. J. Numer. Methods Eng. **47**(1–3), 663–684 (2000). doi: https://doi.org/10.1002/(SICI)1097-0207(20000110/30)47:1/3<663::AID-NME787>3.0.CO;2-8
15. Kam, T.Y., Lee, T.Y.: Detection of cracks in structures using modal test data. Eng. Fract. Mech. **42**(2), 381–387 (1992). doi: https://doi.org/10.1016/0013-7944(92)90227-6
16. Lee, Y.-S., Chung, M.-J.: A study on crack detection using eigenfrequency test data. Comput. Struct. **77**(3), 327–342 (2000). doi: https://doi.org/10.1016/S0045-7949(99)00194-7
17. Long, H., Liu, Y., Huang, C., Wu, W., Li, Z.: Modelling a cracked beam structure using the finite element displacement method. Shock Vib. **2019**, 7302057 (2019). doi: https://doi.org/10.1155/2019/7302057

Author Contribution Statement

Conceptualization: Muhittin Turan, Gökhan Adıyaman.
Methodology: Muhittin Turan, Volkan Kahya.
Investigation: Serhan Koç.

Writing – Original Draft: Serhan Koç.
Writing – Review & Editing: Gökhan Adıyaman, Volkan Kahya.
Supervision: Muhittin Turan, Gökhan Adıyaman, Volkan Kahya.

Biography

Res. Asst. Serhan Koç — Division of Mechanics, Dept. of Civil Engineering, Faculty of Engineering, Karadeniz Technical University. Research focus: mechanical behavior of composite materials and numerical modeling.

Assoc. Prof. Dr. Muhittin Turan — Division of Mechanics, Dept. of Civil Engineering, Of Faculty of Technology, Karadeniz Technical University. Research focus: structural mechanics and strength of materials.

Assoc. Prof. Dr. Gökhan Adıyaman — Division of Mechanics, Dept. of Civil Engineering, Faculty of Engineering, Karadeniz Technical University. Research focus: solid mechanics and computational engineering.

Prof. Dr. Volkan Kahya — Division of Mechanics, Dept. of Civil Engineering, Faculty of Engineering, Karadeniz Technical University. Research focus: fracture mechanics and structural dynamics.

Publication Note

This paper was peer-reviewed, accepted for presentation, and included in the proceedings of the ACE2026 – International Conference on Advances in Civil Engineering, held on 12–14 October 2026 in Trabzon, Türkiye.

This paper may be cited as follows:

Koc S., Turan M., Adıyaman G., Kahya V., "Free Vibration Response of Homogeneous Porous Beams with Edge Cracks Using Finite Element Method," in Proceedings of the ACE2026 – International Conference on Advances in Civil Engineering, Trabzon, Türkiye, 12–14 October 2026.

A Modified Beam-End Test Method for Bond Behavior of Reinforced Concrete Elements

Ahmet Akif Akcora[1]*, Serhan Sensoy[2], Ozgur Eren[3]

[1]Department of Civil Engineering, Eastern Mediterranean University, Famagusta, North Cyprus
*Corresponding Author E-mail: ahmet.akcora@emu.edu.tr
[2]Department of Civil Engineering, Eastern Mediterranean University, Famagusta, North Cyprus
[3]Department of Civil Engineering, Eastern Mediterranean University, Famagusta, North Cyprus

Abstract. The bond interaction between concrete and reinforcing steel is a critical parameter affecting the structural performance and load transfer mechanism of reinforced concrete elements. Among the major durability problems affecting reinforced concrete structures, reinforcement corrosion significantly influences bond behavior by weakening the interaction between steel and concrete.
Therefore, the bond mechanism has been extensively investigated in previous studies.

Various experimental methods have been developed to investigate bond performance. Among these, the Pull-Out test is widely preferred due to its simplicity and ease of application. However, previous studies have shown that bond strength values obtained from Pull-Out tests may overestimate actual bond performance because the stress distribution differs from real structural conditions. Furthermore, accelerated corrosion testing of specimens subjected to tensile bond evaluation presents several practical and experimental challenges.

In this study, a Modified Beam-End Test methodology was investigated to obtain a more representative assessment of steel–concrete bond behavior. The proposed experimental setup addresses several limitations associated with conventional Pull-Out testing. The modified specimen geometry and loading configuration provide a more realistic representation of the stress transfer mechanism between reinforcement and concrete. Furthermore, the geometry of the test specimen is particularly advantageous for accelerated corrosion testing, enabling a more practical and efficient implementation of the experimental procedure.

The proposed methodology is expected to provide a practical and reliable alternative for future experimental studies investigating bond degradation in corrosion-damaged reinforced concrete structures. The effectiveness of the Beam-End Test methodology is evaluated by comparison with previous studies

Keywords: Reinforcement Corrosion, Bond Strength, Modified Beam-End Test.

1 Introduction

Reinforced concrete (RC) structures rely on the bond between reinforcing steel and concrete to ensure effective stress transfer, composite action, crack control, and adequate anchorage. The integrity of this bond is therefore essential for the structural performance and serviceability of RC members.

Corrosion of reinforcing steel can significantly alter the bond response of reinforced concrete members. As steel deteriorates, the products formed at the bar surface expand against the surrounding concrete, initiating local tensile stresses and eventually causing cover cracking. Continued deterioration weakens the restraint around the bar and damages the steel–concrete contact zone, leading to reduced bond resistance and anchorage performance [1–3]. Bond behavior is also governed by several geometric and material variables, including concrete quality, cover depth, reinforcement size, bonded length, transverse confinement, and the extent of corrosion [3,4].

Among the available experimental methods, the Pull-Out Test is widely used because of its simple specimen preparation and testing procedure. However, the compressive confinement generated around the reinforcement during testing produces a stress state that differs from that occurring in actual RC members and may result in comparatively high bond strength values [5,6]. Beam-End Tests provide a more representative stress transfer mechanism, although their specimen preparation and loading arrangements are generally more complex [6–8].

The evaluation of corrosion-induced bond deterioration introduces additional experimental challenges. In conventional Pull-Out specimens, accelerated corrosion may be affected by non-uniform current distribution, electrolyte leakage, and localized corrosion, which can reduce the consistency of the corrosion process [9,10]. Therefore, a test configuration that combines representative bond conditions with practical accelerated corrosion application is required.

In this study, a Modified Beam-End Test (MBE) methodology is proposed for evaluating the bond behavior of corroded reinforcement. The proposed configuration aims to maintain a representative bond stress transfer mechanism while simplifying specimen preparation and accelerated corrosion application. Its performance is experimentally evaluated at different corrosion levels and compared with findings reported in previous studies.

2 Limitations of Conventional Bond Test Methods

2.1 Pull-Out Test

The Pull-Out Test is widely used to characterize steel–concrete bond due to its simple specimen preparation and testing procedure. In this method, tensile force is applied to a reinforcing bar embedded over a defined length, while bar slip is measured to obtain the bond–slip response [11]. However, the loading condition differs from that experienced by reinforcement in structural members. As illustrated in Fig. 1, the reaction acting on the concrete introduces compressive stresses around the bonded region, providing additional confinement [12]. This may suppress splitting cracks and lead to higher bond strengths than those developed under less confined structural conditions [13].

This effect is particularly relevant in corrosion studies, where deterioration of the concrete cover progressively reduces confinement. The confinement inherent in the Pull-Out configuration may therefore influence the measured bond degradation. In addition, its geometry can complicate accelerated corrosion procedures through difficulties in controlling electrolyte exposure, electrical isolation, and localized corrosion [14].

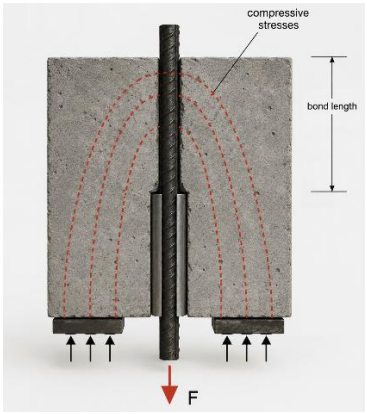


Fig. 1. Conventional Pull-Out Test configuration and associated stress transfer mechanism.

2.2 Beam and Beam-End Test

Beam-type bond tests provide an alternative approach that more closely represents the stress conditions occurring in reinforced concrete members. Unlike the Pull-Out Test, the tensile force in the reinforcement and the compressive reaction are separated, reducing the artificial confinement around the bonded region. Consequently, the resulting stress transfer mechanism and failure behavior are generally more representative of reinforcement anchored within structural members.

The Beam-End Test provides a more compact configuration while maintaining the principal advantages of beam-type testing. In this arrangement, the reinforcing bar is pulled in tension, whereas the supporting reaction is introduced into the concrete at a location separated from the active bond zone [15].

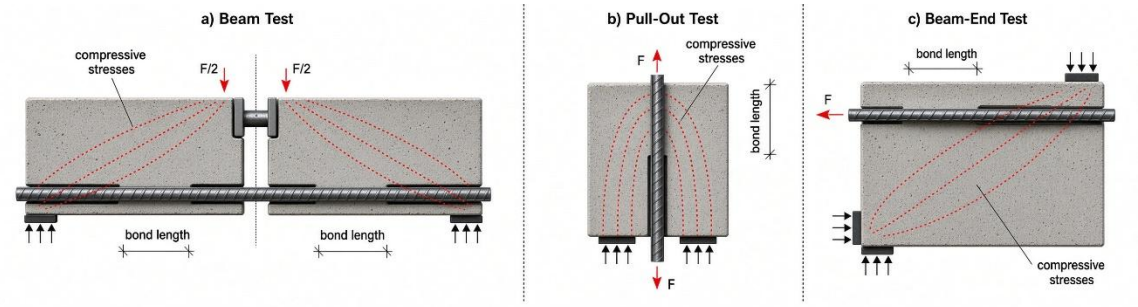


Fig. 2. Comparison of the load-transfer mechanisms in Pull-Out and Beam-End Tests.

However, conventional Beam and Beam-End Tests generally require more complicated specimen preparation and loading arrangements than Pull-Out Tests. These difficulties become more significant when accelerated corrosion is incorporated, as the specimen must simultaneously provide appropriate mechanical boundary conditions and controlled access to the reinforcement for corrosion exposure.

Therefore, conventional bond testing methods involve a trade-off between experimental simplicity and structural representativeness. While the Pull-Out Test offers practical advantages, Beam and Beam-End Tests provide a more realistic stress transfer mechanism but introduce greater experimental complexity. These considerations motivated the adoption of the Modified Beam-End approach examined in this study.

3 Development of the Modified Beam-End Test

In reinforced concrete members, tensile forces in the reinforcement are transferred to the surrounding concrete through bond along the anchorage region. The interaction between the bar ribs and concrete generates both longitudinal and radial forces. The longitudinal component transfers force along the reinforcement, whereas the radial component acts outward from the bar and can promote splitting of the concrete when confinement is inadequate.

The Modified Beam-End (MBE) configuration was developed to represent this mechanism under controlled experimental conditions. Tensile load is applied directly to the reinforcing bar, and unbonded zones are used to restrict stress transfer to a predefined bond region. This arrangement enables the measured bond stress and slip to be associated with the selected anchorage zone while allowing bond-induced cracking to develop around the reinforcement, as schematically presented in Fig. 3.

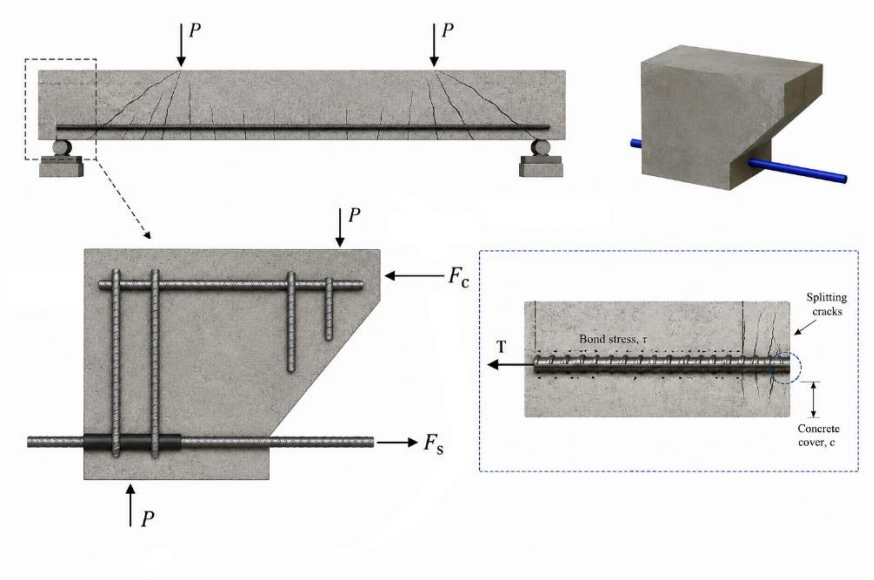


Fig. 3. Schematic representation of reinforcement–concrete interaction in the MBE configuration.

The proposed geometry is also suitable for accelerated corrosion studies. The accessible and defined bond region facilitates controlled corrosion exposure while allowing corrosion-induced expansion and cracking to develop around the reinforcement. Consequently, corrosion and its subsequent influence on bond behavior can be investigated within the same test region.

4 Experimental Program

An experimental program was conducted to evaluate the applicability of the proposed Modified Beam-End Test for investigating steel–concrete bond behavior under uncorroded and corroded conditions. For this purpose, control specimens and specimens subjected to accelerated corrosion were prepared with identical geometric and material properties. Two nominally identical specimens were tested for each condition to evaluate the consistency of the experimental response.

4.1 4.1. Materials and Specimens

Ready-mixed concrete with a target strength class of C25/30 was employed throughout the experimental program to maintain consistent material conditions among the MBE specimens. Concrete strength was evaluated using cube samples produced from the same concrete batches as the test specimens. The cube tests compressive strengths of 32.7 and 36.7 MPa.

Deformed steel reinforcement with a diameter of 14 mm was used as the main tensile reinforcement. As shown in the Fig. 3,the effective bonded length was limited to 78 mm, while PVC pipes were placed around the remaining portion of the bar to prevent bond transfer outside the intended test region. Additional reinforcement was provided within the specimen to prevent undesirable failure mechanisms and to maintain the intended load-transfer mechanism.

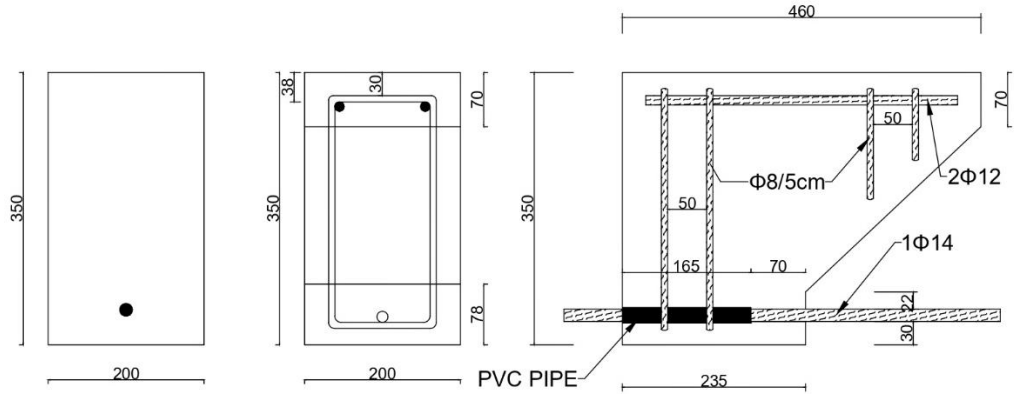


Fig. 3. Geometry and reinforcement arrangement of the Modified Beam-End specimen.

The distance between the reinforcement and the nearest concrete surface was maintained at 30 mm for the entire specimen series. The experimental matrix included five specimens representing uncorroded, low-corrosion, and moderate-corrosion conditions. Two replicate specimens were tested under the control and moderate corrosion conditions, while one specimen was evaluated at the low corrosion level. The measured corrosion rates ranged from 1.13% for the low-corrosion specimen to approximately 3% for the moderately corroded specimens. The specimen identification, corrosion condition, concrete cover, and corresponding corrosion rates are summarized in Table 1.

Table 1. Details and experimental parameters of the test specimens.

Specimen	Condition	Concrete Cover	Corrosion Rate
C_0-C_3^1	Control	30mm	%0
C_0-C_3^2	Control	30mm	%0
C_L-C_3	Low Corrosion	30mm	%1.13
C_M-C_3	Moderate Corrosion	30mm	%2.95

4.2 Accelerated Corrosion and Bond Testing Procedure

Accelerated corrosion was applied to the specimens using the impressed-current technique. The reinforcing bars were connected as anodes, while metallic plates placed in the electrolyte solution served as cathodes. The specimens were connected in parallel to a DC power supply, and the electrical current passing through each specimen was monitored throughout the corrosion process. The general configuration of the accelerated corrosion system is shown in Fig. 6. The accumulated current over the exposure period was used to estimate the theoretical corrosion level according to Faraday's law.

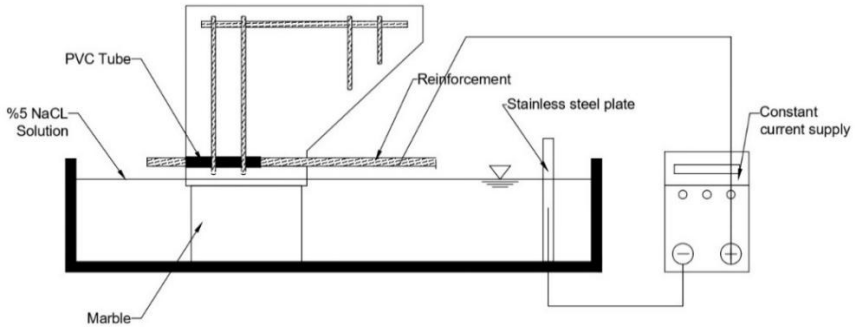


Fig. 6. Accelerated corrosion setup used for the Modified Beam-End specimens.

After completion of the corrosion stage, bond tests were performed with the MBE loading arrangement shown in Figure 7. A hydraulic system pulled the reinforcing bar while the specimen was restrained through the reaction frame. The applied force was quantified by load cells positioned along the load-transfer path. Bar slip was determined from LVDT readings referenced to the concrete body. All sensor outputs were collected by a TDS-303 data acquisition unit, providing synchronized measurements throughout the loading sequence and allowing the bond stress–slip response to be established.



Fig. 7. Modified Beam-End Test setup and instrumentation.

5 Results and Discussion

The experimental results were evaluated in terms of bond strength, bond stress–slip response, and observed failure behavior. The results obtained from the control and corroded Modified Beam-End (MBE) specimens are summarized in Table 2. The experimental results indicate that the bond response was strongly influenced by the level of reinforcement corrosion.

Table 2. Table 2. Summary of bond test results for the MBE specimens.

Specimen	Maximum Force (kN)	Bond Strength (MPa)	Corrosion Rate
C_0-C_3^1	19.33	6.28	%0
C_0-C_3^2	22.83	7.41	%0
C_L-C_3	24.66	8.01	%1.13
C_M-C_3	10.33	3.35	%2.99

The two uncorroded specimens developed bond strengths of 6.28 and 7.41 MPa, giving an average value of 6.85 MPa. This average was used as the reference for assessing the effect of corrosion. At a corrosion rate of 1.13%, specimen C_L-C_3 reached the highest bond strength of 8.01 MPa, approximately 17% above the control average. This increase may be associated with the early expansion of corrosion products at the steel–concrete interface, which can temporarily improve radial pressure and mechanical interaction between the reinforcement and concrete. A different response was observed for C_M-C_3 at a corrosion rate of 2.99%. Its bond strength decreased to 3.35 MPa, representing approximately 51% loss relative to the control average. This reduction suggests that progressive corrosion increasingly disrupts the bond zone through interface degradation and damage within the concrete surrounding the reinforcement.

Fig. 8 presents the variation in bond strength observed with increasing reinforcement corrosion. An initial increase is observed at the low corrosion level, followed by a marked decrease at approximately 3% corrosion. Within the scope of the available test data, bond performance showed a non-linear response to increasing corrosion.

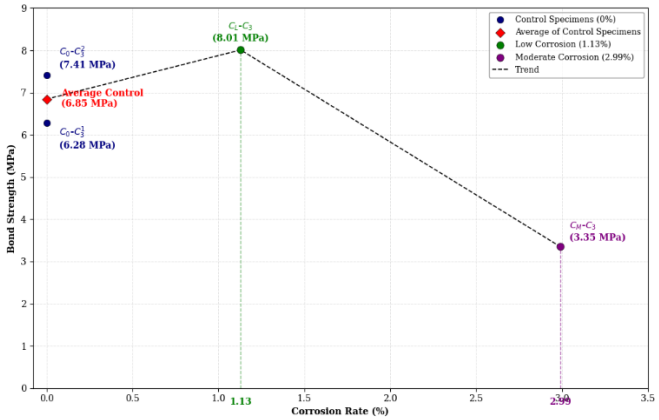


Fig. 8. Effect of reinforcement corrosion rate on bond strength of the Modified Beam-End specimens.

The corresponding bond stress–slip curves are presented in Fig. 9. The control specimens provide the baseline response, whereas C_L-C_3 develops a higher peak bond stress. In contrast, C_M-C_3 shows a considerable loss of bond resistance, demonstrating the deterioration of the bond response with increasing corrosion.

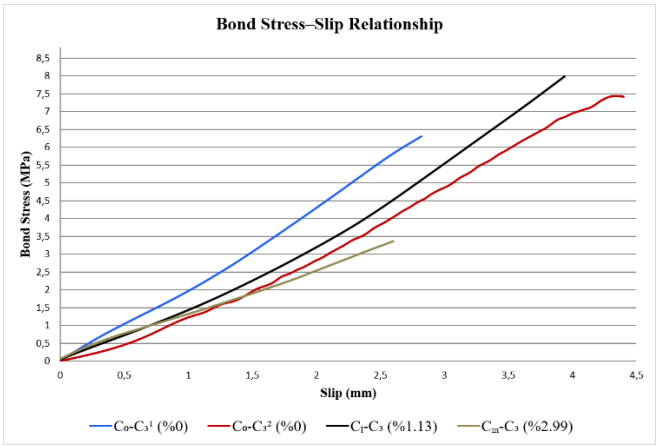


Fig. 9 . Bond stress–slip relationships of the control, low-corrosion, and moderate-corrosion Modified Beam-End specimens.

Overall, the MBE results captured two distinct stages of corrosion-related bond behavior: a limited increase in bond capacity at the early corrosion stage and a substantial reduction as corrosion approached 3%. The proposed test configuration therefore shows potential for assessing changes in steel–concrete bond behavior caused by reinforcement corrosion. Nevertheless, additional specimens and corrosion levels are required before a generalized relationship between corrosion and bond strength can be established.

5.1 Comparison with Previous Studies

The present MBE results were compared with previous studies based on Pull-Out and Beam Test configurations, as summarized in Table 3. Although differences in concrete strength, cover thickness, corrosion level, and specimen geometry should be considered, the comparison provides useful insight into the influence of the test method on measured bond strength.

The Pull-Out results reported by Yalciner et al. [2] show considerably higher bond strengths than those obtained from the present MBE specimens. For example, the uncorroded Pull-Out specimens with a 30 mm concrete cover reached bond strengths of 13.26 and 21.20 MPa, whereas the average value obtained from the MBE control specimens was 6.85 MPa. Relatively high bond strengths were also reported for the corroded Pull-Out specimens. This difference may be partly associated with the additional compressive confinement generated around the bonded region in the Pull-Out configuration, which can restrict splitting and increase the measured bond resistance. In comparison, the Beam Test results reported by Hongwei et al. [16] were closer to the range obtained from the MBE specimens. Despite differences in concrete cover and corrosion level, both beam-type configurations showed lower bond strengths than the Pull-Out results presented in Table 3. Overall, these comparisons support the importance of test configuration when evaluating bond performance and suggest that the proposed MBE method provides a less confined bond response than conventional Pull-Out testing.

Table 2. Comparison of bond strength results obtained from different test methods.

Study	Test Method	Concrete Cover (mm)	Concrete Strength (MPa)	Corrosion Level (%)	Bond Strength (MPa)
Present study	MBE	30	34,7*	0	6.85*
Present study	MBE	30	34,7*	1.13	8.01
Present study	MBE	30	34,7*	2.95	1.89
Yalciner et al. [2]	Pull-Out	30	51	0	21.20*
Yalciner et al. [2]	Pull-Out	30	23	0	13.26*
Yalciner et al. [2]	Pull-Out	30	51	1.7	14.00
Yalciner et al. [2]	Pull-Out	30	23	3.45	9.6
L. Hongwei et al.[16]	Beam Test	40	30	0	8.59
L. Hongwei et al. [16]	Beam Test	40	30	4.52	6.20

*Average of specimens

6 Conclusions

The experimental investigation demonstrated the potential of the Modified Beam-End (MBE) approach for assessing the effect of reinforcement corrosion on steel–concrete bond. The main findings are summarized below:

- The proposed MBE configuration provided a practical approach for obtaining bond stress–slip behavior while allowing accelerated corrosion to be applied within the intended bond region.
- For the reference specimens, the mean bond strength was 6.85 MPa. With 1.13% reinforcement corrosion, the measured value reached 8.01 MPa, suggesting that slight corrosion can temporarily improve bond resistance.
- When corrosion reached 2.99%, bond strength fell to 3.35 MPa. This corresponds to a loss of approximately 51% relative to the reference condition and indicates a clear deterioration in bond performance as corrosion progresses.
- Comparison with previous studies indicates that conventional Pull-Out tests generally produce higher bond strengths, which may be associated with the additional confinement generated by their loading configuration.
- Overall, the MBE method offers a promising alternative for studying corrosion-related bond deterioration under a more representative load-transfer mechanism. However, further tests covering a wider range of corrosion levels are required to confirm the observed trends.

References

1. Almusallam, A. A., Al-Gahtani, A. S., Aziz, A. R., & Rasheeduzzafar.: “Effect of reinforcement corrosion on bond strength.” Construction and Building Materials, 10(2), 123–129 (1996).
2. Yalçıner, H., Eren, Ö., & Şensoy, S..: “An experimental study on the bond strength between reinforcement bars and concrete as a function of concrete cover, strength and corrosion level.” Cement and Concrete Research, 42(5), 643–655 (2012).
3. Wang, X. & Liu, X.: “Modelling effects of corrosion on cover cracking and bond in reinforced concrete.” Magazine of Concrete Research, 56(4), 191–199 (2004).
4. Yalçıner, H., & Marar, K.: “Experimental Study on the Bond Strength of Different Geometries of Corroded and Uncorroded Reinforcement Bars.” Journal of Materials in Civil Engineering, 29(7) (2017).
5. Baktheer, A., Spartali, H., Hegger, J., & Chudoba, R.: High-cycle fatigue of bond in reinforced high-strength concrete under push-in loading characterized using the modified beam-end test. Cement and Concrete Composites, 118, 103978 (2021).
6. Zhou, K. P., Yi, W. J., Hwang, H. J., & Zhou, Y.: “Influence of bond test methods on the bond performance between reinforcing bars and concrete.” Structures, 54, 1299–1311 (2023).
7. Bošnjak, J., Sharma, A., & Öttl, C.: “Modified beam-end test setup to study the bond behavior of reinforcement in concrete after fire.” Materials and Structures, 51, 13 (2018).
8. Metelli, G., Cairns, J., & Plizzari, G.: “A new fib Model Code proposal for a beam-end type bond test.” Structural Concrete, 24(4), 4446–4463 (2023).
9. Fu, C., Fang, D., Ye, H., Huang, L., & Wang, J.: “Bond degradation of non-uniformly corroded steel rebars in concrete.” Engineering Structures, 226, 111392 (2021).
10. Wu, J., Guo, L., Jin, L., & Du, X.: “Experimental Investigation of the Bond Performance between Nonuniformly Corroded Reinforcing Bar and Concrete.” Journal of Materials in Civil Engineering, 34(12) (2022).

11. RILEM, RC6: Bond Test for Reinforcement Steel – Pull-Out Test; ACI Committee 408, Bond and Development of Straight Reinforcing Bars in Tension, ACI 408R-03, 2003
12. Anaëlle Torre-Casanova, Ludovic Jason, Luc Davenne, Xavier Pinelli.: Confinement effects on the steel- concrete bond strength and pull-out failure. Engineering Fracture Mechanics, 97, pp.92–104 (2013).
13. Tepfers, R., A Theory of Bond Applied to Overlapped Tensile Reinforcement Splices for Deformed Bars, Chalmers University of Technology, 1973; ACI Committee 408 (2003).
14. Lundgren, K., "Modelling the Effect of Corrosion on Bond in Reinforced Concrete", Magazine of Concrete Research, 2002; Fang, C., Lundgren, K., Chen, L. and Zhu, C., "Corrosion Influence on Bond in Reinforced Concrete", Cement and Concrete Research (2004).
15. ASTM A944/A944M-22, Standard Test Method for Comparing Bond Strength of Steel Reinforcing Bars to Concrete Using Beam-End Specimens, ASTM International (2022).
16. Lin, H., & Zhao, Y.: Effects of confinements on the bond strength between concrete and corroded steel bars. Construction and Building Materials, 118, 127-138 (2016).

Author Contribution Statement

- *Conceptualization:* Ahmet Akif Akcora, Serhan Sensoy, Ozgur Eren.
- *Methodology:* Ahmet Akif Akcora.
- *Investigation:* Ahmet Akif Akcora.
- *Writing – Original Draft:* Ahmet Akif Akcora.
- *Writing – Review & Editing:* Ahmet Akif Akcora, Serhan Sensoy, Ozgur Eren.

Publication Note

This paper was peer-reviewed, accepted for presentation, and included in the proceedings of the ACE2026 – International Conference on Advances in Civil Engineering, held on 12–14 October 2026 in Trabzon, Türkiye.

This paper may be cited as follows:

Akcora A.A., Sensoy S., Eren O., "A Modified Beam-End Test Method for Bond Behavior of Reinforced Concrete Elements," in Proceedings of the ACE2026 – International Conference on Advances in Civil Engineering, Trabzon, Türkiye, 12–14 October 2026.

Evaluation of Acceleration, Velocity, and Displacement Response Spectra of the February 6, 2023 Kahramanmaraş Earthquakes in the Hatay Region Considering Local Site Classes

Merve ARLI SÖNMEZ[1] and Ali KOÇAK[2]
[1] 0009-0004-0518-3528, Yildiz Technical University, Graduate School of Science and Engineering, Civil Engineering Master's Program, Istanbul, Türkiye, merve.sonmez1@std.yildiz.edu.tr
[2] 0000-0002-5874-2715, Yildiz Technical University, Civil Engineering Department, Istanbul, Türkiye, akocak@yildiz.edu.tr

Abstract. The February 6, 2023 Kahramanmaraş earthquake sequence caused severe ground-motion demands in southern Türkiye, particularly in Hatay, where extensive structural damage was observed. This study evaluates acceleration, pseudo-spectral velocity, and spectral displacement response spectra of selected strong motion records obtained from AFAD stations in the Hatay region during the Pazarcık main shock. Thirteen stations and two horizontal components for each station were considered, resulting in 26 horizontal acceleration records. Five-percent-damped response spectra were calculated in MATLAB using the Newmark-β average acceleration method over a period range of 0.01–8.00 s. The horizontal components were evaluated separately and then combined to obtain resultant spectra. The mean resultant spectra were compared with DD-2 elastic design spectra generated according to the Turkish Building Earthquake Code 2018 for different local site classes, while the mean acceleration spectrum was also compared with DD-1 spectra. The results show significant period-dependent demands. The mean resultant pseudo-spectral acceleration reached approximately 1.9 g at about 0.5–0.7 s, while the mean pseudo-spectral velocity and spectral displacement reached about 380–390 cm/s and 320–325 cm, respectively. The spectra exceeded DD-2 design demands over a broad period range and approached or exceeded some DD-1 spectra in certain intervals. These findings indicate that PGA alone is insufficient for interpreting seismic demand in Hatay; velocity- and displacement-related demands should also be considered.

Keywords: Kahramanmaraş earthquakes; response spectra; Hatay region; local site class; spectral demand.

1 Introduction

On February 6, 2023, two major earthquakes occurred in southeastern Türkiye within approximately nine hours. The Pazarcık earthquake occurred at 04:17 local time with a moment magnitude of Mw 7.7, followed by the Elbistan earthquake at 13:24 local time with a moment magnitude of Mw 7.6. The earthquake sequence affected a wide region, including Kahramanmaraş, Hatay, Adıyaman, Gaziantep, Malatya, Osmaniye, and surrounding provinces, and caused extensive structural damage and significant loss of life [1,2].

Hatay was among the most severely affected regions. In addition to the intensity of the recorded ground motions, local geological and geotechnical conditions played an important role in the spatial variation of damage. Previous studies indicate that Antakya and İskenderun are largely underlain by Quaternary alluvial deposits consisting of clayey, sandy, silty, and gravelly

materials. Such local site conditions may significantly influence the amplitude, frequency content, and duration of ground motion, particularly in soft soil deposits [3].

The evaluation of earthquake demand only in terms of peak ground acceleration may not be sufficient to explain structural response. Ground motions with similar peak acceleration values may produce different demands depending on their frequency content, duration, velocity demand, displacement demand, and spectral characteristics. Therefore, spectral acceleration, pseudo-spectral velocity, and spectral displacement should be considered together, as they provide complementary information on force-related, velocity-related, and displacement-related seismic demands. Several post-earthquake studies reported that response spectra obtained from strong ground motion records during the Kahramanmaraş earthquakes exceeded the elastic design spectrum values of the Turkish Building Earthquake Code 2018 in certain locations and period ranges [4,5]. Recent site-response studies also emphasized that local site effects and site amplification may significantly influence the spectral characteristics of ground motions in the affected regions [6]. These findings highlight the need for a detailed spectral evaluation of recorded ground motions, especially in heavily affected regions such as Hatay.

This study evaluates acceleration, pseudo-spectral velocity, and spectral displacement response spectra of selected strong ground motion records obtained from AFAD stations in the Hatay region during the Pazarcık main shock. Thirteen stations and both horizontal components of each record are considered. The 5%-damped response spectra are computed in MATLAB using the Newmark-β average acceleration method and compared with TBDY 2018 elastic design spectra for different local site classes [7]. The main objective is to investigate how spectral demand in Hatay varies with period range and local site class, and to provide a preliminary basis for future seismic demand and performance-based assessments of reinforced concrete buildings affected by the 2023 earthquake sequence.

2 Strong Ground Motion Records Used in the Study

The strong ground motion records used in this study were obtained from the Turkish Strong Ground Motion Database operated by AFAD [1]. The record selection was limited to stations located in the Hatay region during the February 6, 2023 Pazarcık earthquake. The availability of two horizontal components, time-step suitability, and regional representativeness were considered in the selection process.

A total of 13 AFAD stations located in Antakya, Belen, Dörtyol, Hassa, and Kırıkhan districts and their surroundings were selected. For each station, the north-south and east-west horizontal components were evaluated separately, resulting in 26 horizontal acceleration records. The vertical components were not used in the response spectrum calculations, but their PGA values are listed in Table 1 for completeness.

The PGA values are given in cm/s², and the records were converted to m/s² before the numerical analyses. The VS30 values listed in Table 1 range from 271 m/s at station 3139 to 688 m/s at station 3137, indicating different near-surface stiffness conditions within the selected Hatay dataset.

The selected dataset includes stations with different source-to-site distances and local geological conditions within the Hatay region, allowing the evaluation of period-dependent acceleration, velocity, and displacement demands. The records were not modified by spectral matching or amplitude scaling; only unit conversion and basic preprocessing were applied to preserve their original spectral characteristics.

Table 1. Selected strong ground motion records used in the study.

No	Event	Station Code	Location	PGA-NS (cm/s²)	PGA-EW (cm/s²)	PGA-UD (cm/s²)	Rrup (km)	VS30 (m/s)
1	Pazarcık	3115	Hatay / Belen	286.72	241.50	214.81	38.53	424
2	Pazarcık	3123	Hatay / Antakya	655.57	593.94	867.58	72.58	469
3	Pazarcık	3124	Hatay / Antakya	572.63	638.32	578.08	69.66	283
4	Pazarcık	3134	Hatay / Dörtyol	246.11	203.91	141.51	16.71	374
5	Pazarcık	3137	Hatay / Hassa	428.37	670.17	448.37	18.44	688
6	Pazarcık	3138	Hatay / Hassa	888.73	746.66	1296.27	9.70	619
7	Pazarcık	3139	Hatay / Kırıkhan	577.13	504.82	378.62	28.54	271
8	Pazarcık	3141	Hatay / Antakya	961.12	868.82	722.66	54.20	338
9	Pazarcık	3142	Hatay / Kırıkhan	651.69	739.29	456.90	38.09	538
10	Pazarcık	3143	Hatay / Hassa	381.09	351.38	412.11	8.10	444
11	Pazarcık	3144	Hatay / Hassa	611.27	763.36	451.61	12.36	485
12	Pazarcık	3145	Hatay / Kırıkhan	591.88	692.29	609.73	21.68	533
13	Pazarcık	3146	Hatay / Belen	483.85	346.93	341.39	41.57	560

The spatial distribution of the selected stations is shown in Figure 1. The map values correspond to the maximum horizontal peak ground acceleration, PGAmax,h, calculated from the two horizontal components of each record. To relate the station distribution to the observed damage concentration, the Antakya district was highlighted on the map. Reported district-level damage figures indicate 6,369 collapsed, 3,734 emergency-demolition, and 21,830 heavily damaged buildings in Antakya, corresponding to 31,933 severely damaged buildings and approximately 35.9% of the severe-damage building count reported for Hatay province [9]. An official district list also documents heavily damaged buildings scheduled for demolition [10]. This information was included only as district-level damage context and was not used to establish a direct building-level damage correlation.

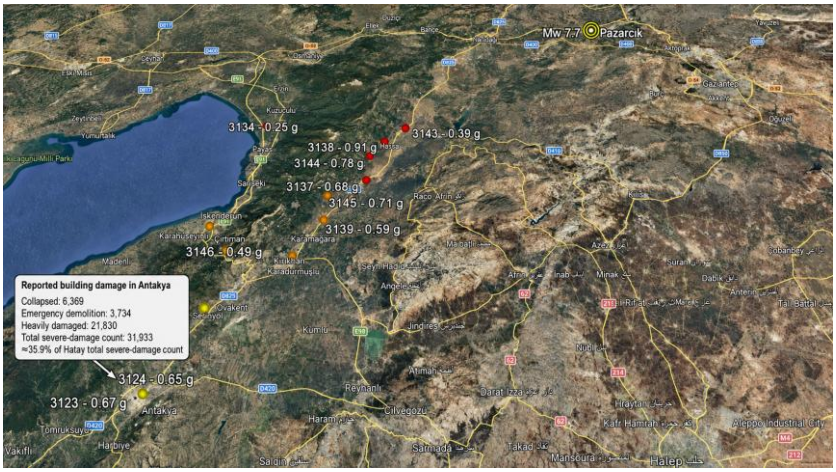


Fig. 1. Selected strong-motion stations, PGA values, and Antakya damage context. Base map: Google Earth. Strong ground motion data: AFAD Turkish Strong Ground Motion Database [1].

3 Methodology

The selected acceleration records were processed to compute 5%-damped response spectra and to compare the obtained spectra with code-based elastic design spectra for different local site classes. The north-south and east-west horizontal components were evaluated separately. The records, originally given in cm/s², were converted to m/s², and the mean value of each acceleration record was removed to reduce possible baseline offset effects. The response spectra were computed in MATLAB using the Newmark-β average acceleration method [8]. A damping ratio of 5% and a period range of 0.01–8.00 s were used. For each oscillator period, the maximum relative displacement response was obtained and used to calculate spectral displacement, pseudo-spectral velocity, and pseudo-spectral acceleration as follows:

$$S_d(T) = \max |u(t)|, \quad S_v(T) = \omega\, S_d(T), \quad S_a(T) = \omega^2\, S_d(T) \tag{1}$$

where $\omega = 2\pi/T$ is the circular frequency. The spectral acceleration values were expressed in terms of g, while pseudo-spectral velocity and spectral displacement were expressed in cm/s and cm, respectively.

For each station, a resultant spectrum was calculated from the two horizontal components as:

$$S_R(T) = \sqrt{[S_N(T)^2 + S_E(T)^2]} \tag{2}$$

The SRSS combination was applied to the spectral ordinates of the two horizontal components at each oscillator period. Since pseudo-spectral velocity and pseudo-spectral acceleration are derived from spectral displacement by multiplication with ω and ω² at the same period, the SRSS operation is mathematically consistent for Sd, Sv, and Sa. The resulting spectrum represents a component-wise resultant spectrum and should not be interpreted as a time-domain vector resultant or as a RotD50-type orientation-independent spectrum.

The mean resultant spectra were compared with elastic design spectra generated according to the Turkish Building Earthquake Code 2018 [7]. The mean ± one standard deviation range was also calculated at each oscillator period to represent record-to-record dispersion.

4 Design Spectra for Different Local Site Classes

Elastic design spectra were generated according to the Turkish Building Earthquake Code 2018 to evaluate the influence of local site class on spectral demand [7]. The reference spectral acceleration parameters were obtained for the selected location in the Hatay region, and the corresponding design parameters were calculated for local site classes ZA, ZB, ZC, ZD, and ZE. Both DD-1 and DD-2 earthquake ground motion levels were considered. DD-1 represents the maximum considered earthquake level, whereas DD-2 represents the design earthquake level. The short-period and 1.0-s spectral acceleration parameters, SDS and SD1, were calculated using the corresponding local site coefficients. The design spectra were computed over the same period range as the recorded spectra and used for direct comparison with the mean resultant spectra. Table 2 presents the parameters used to construct the elastic design spectra.

Table 2. TBDY 2018 design spectral acceleration parameters for different local site classes.

Level	Site class	SS	S1	Fs	F1	SDS	SD1

DD-1	ZA	2.067	0.560	0.800	0.800	1.654	0.448
DD-1	ZB	2.067	0.560	0.900	0.800	1.860	0.448
DD-1	ZC	2.067	0.560	1.200	1.440	2.480	0.806
DD-1	ZD	2.067	0.560	1.000	1.740	2.067	0.974
DD-1	ZE	2.067	0.560	0.800	2.080	1.654	1.165
DD-2	ZA	1.026	0.268	0.800	0.800	0.821	0.214
DD-2	ZB	1.026	0.268	0.900	0.800	0.923	0.214
DD-2	ZC	1.026	0.268	1.200	1.500	1.231	0.402
DD-2	ZD	1.026	0.268	1.090	2.064	1.118	0.553
DD-2	ZE	1.026	0.268	1.079	2.960	1.107	0.793

As shown in Table 2, the design spectral parameters vary depending on the local site class. In general, the short-period range is mainly controlled by S_{DS}, whereas medium- and long-period demands are more influenced by S_{D1}. Therefore, the recorded ground motions were evaluated not only in terms of spectral acceleration, but also in terms of pseudo-spectral velocity and spectral displacement.

5 Spectral Demand Evaluation

The calculated response spectra were evaluated in terms of pseudo-spectral acceleration, pseudo-spectral velocity, and spectral displacement to investigate the period-dependent seismic demand of the selected Hatay records. The individual resultant spectra were examined together with the mean resultant spectra and compared with TBDY 2018 elastic design spectra for different local site classes.

5.1 Evaluation of Resultant Response Spectra

Figures 2–4 present the individual resultant spectra, the mean spectrum, and the mean ± one standard deviation range, which illustrates the record-to-record dispersion of the selected Hatay ground motions.

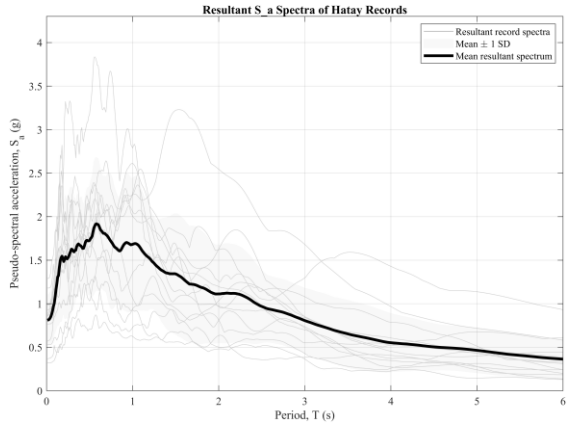


Fig. 2. Resultant S_a spectra with mean ± 1 SD.

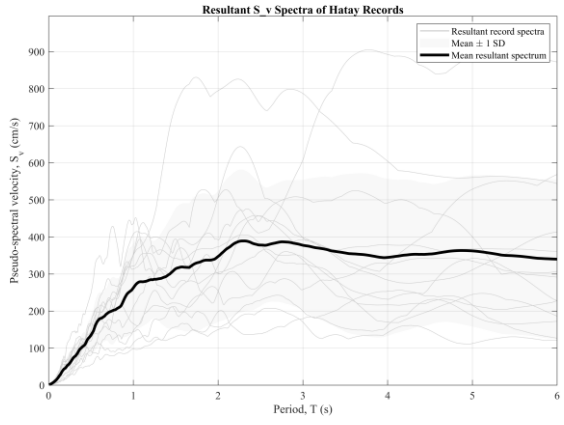


Fig. 3. Resultant Sv spectra with mean ± 1 SD.

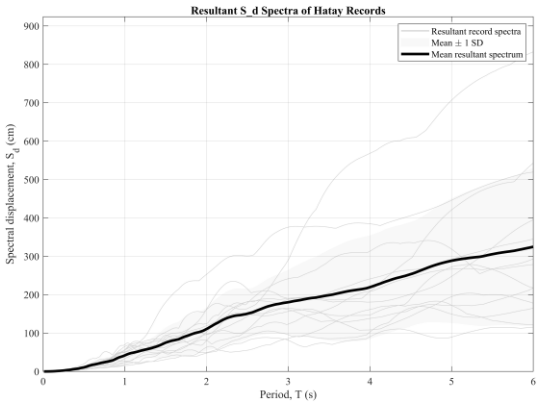


Fig. 4. Resultant Sd spectra with mean ± 1 SD.

Figure 2 shows the resultant pseudo-spectral acceleration spectra of the selected Hatay records together with the mean spectrum and the mean ± one standard deviation band. The mean Sa spectrum reaches approximately 1.9 g at about T = 0.5–0.7 s, while some individual records exceed 3.0 g in the short- and medium-period ranges. This period range is significant because it may correspond to the fundamental periods of mid-rise reinforced concrete buildings, depending on their height, stiffness, and structural configuration. Previous evaluations of earthquake-damaged buildings in Türkiye associated similar period ranges with multi-story reinforced concrete structures, while field observations after the February 6, 2023 earthquakes showed severe damage particularly in multi-story buildings in heavily affected areas [2,5]. Therefore, the high Sa demand in this range may be interpreted as an indicator of force-related demand on the reinforced concrete building stock in the Hatay region.

Figure 3 presents the resultant pseudo-spectral velocity spectra of the selected records. The mean Sv spectrum reaches approximately 380–390 cm/s around T = 2.2–2.8 s, with considerable record-to-record dispersion in the medium-period range. These high Sv values indicate that the selected records may impose significant velocity-sensitive and cyclic-deformation-related demands on reinforced concrete buildings. Repeated inelastic cycles may contribute to damage accumulation, stiffness degradation, and residual drift; therefore, the seismic demand should not be interpreted only as force-related, but also as velocity-sensitive and deformation-related.

Figure 4 presents the resultant spectral displacement spectra of the selected records. The mean Sd spectrum increases with period and reaches approximately 320–325 cm at T = 6 s, while some individual records produce much larger displacement demands at longer periods. The increasing width of the mean ± one standard deviation band also indicates considerable record-to-record variability in the long-period range. Large spectral displacement demand is directly related to deformation-sensitive structural response. In reinforced concrete buildings, increased displacement demand may lead to larger interstory drift ratios, stiffness degradation, concentration of deformation in weaker stories, and second-order P-Δ effects, particularly in buildings with vertical irregularities, insufficient lateral stiffness, or limited deformation capacity.

Overall, Figures 2–4 show that the selected Hatay records produced significant acceleration, velocity, and displacement demands over different period ranges. Therefore, the seismic demand in the Hatay region should not be evaluated only in terms of PGA. The combined assessment of Sa, Sv, and Sd provides a more comprehensive interpretation of the ground-motion characteristics.

Figure 5 provides a schematic interpretation of the structural mechanisms associated with different spectral demand ranges. Short-period acceleration demand may be related to force-controlled brittle damage mechanisms, while long-period displacement demand may be associated with drift-sensitive mechanisms such as soft-story response and P-Δ effects.

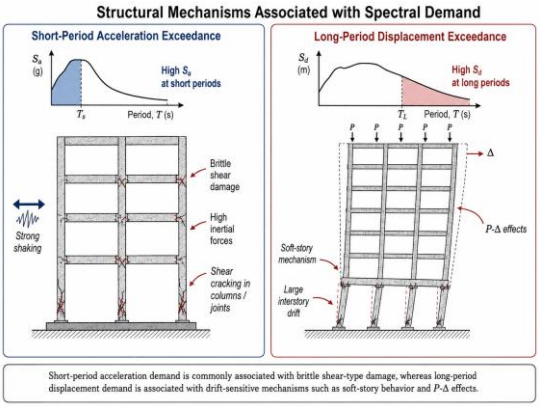


Fig. 5. Schematic illustration of spectral-demand-related damage mechanisms.

5.2 Comparison with TBDY 2018 DD-2 Design Spectra

Figures 6–8 compare the mean resultant Sa, Sv, and Sd spectra with the TBDY 2018 DD-2 spectra for different local site classes.

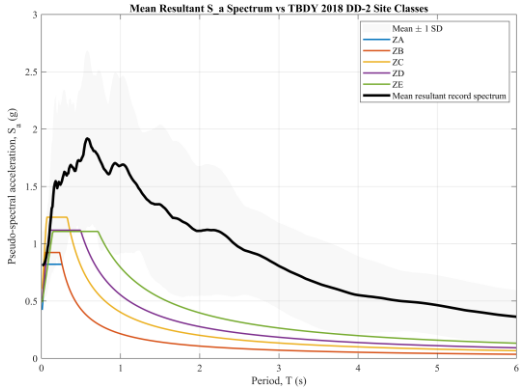


Fig. 6. Mean Sa and TBDY 2018 DD-2 spectra.

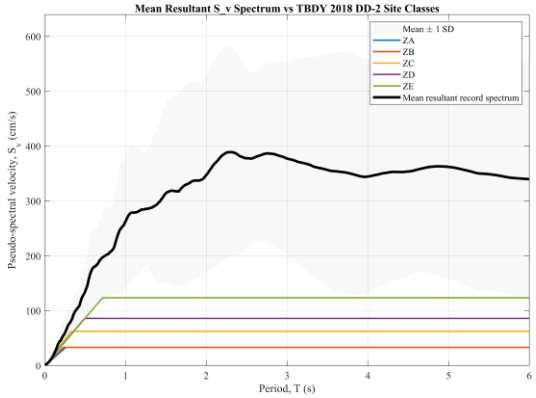


Fig. 7. Mean Sv and TBDY 2018 DD-2 spectra.

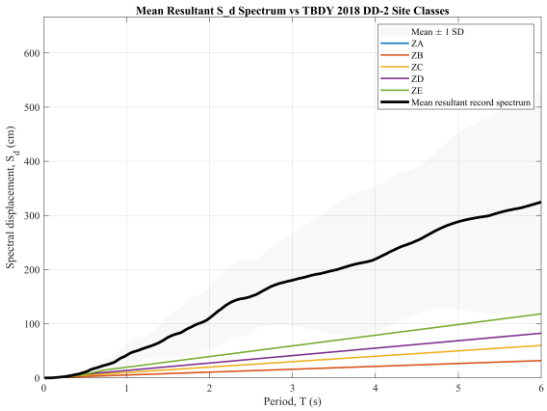


Fig. 8. Mean Sd and TBDY 2018 DD-2 spectra.

Figure 6 shows the mean resultant pseudo-spectral acceleration spectrum and its mean ± one standard deviation band with the TBDY 2018 DD-2 elastic design spectra for different local site classes. The mean recorded spectrum exceeds the DD-2 spectra over a broad period range, particularly in the short- and medium-period ranges where it remains above the code-based spectra for all considered local site classes. This indicates that the selected Hatay records produced acceleration demands higher than the design earthquake level represented by DD-2 spectra. The peak of the mean Sa spectrum occurs around T = 0.5–0.7 s, corresponding to the period range of many mid-rise reinforced concrete buildings depending on their stiffness, height, and structural configuration. Therefore, the high Sa demand in this range may be associated with significant force-related demand on the regional building stock.

However, the acceleration spectrum alone does not fully represent the destructive potential of the selected ground motions. Therefore, the Sa comparison in Figure 6 should be interpreted together with the Sv and Sd comparisons in Figures 7 and 8.

Figure 7 shows the mean resultant pseudo-spectral velocity spectrum with the TBDY 2018 DD-2 pseudo-spectral velocity spectra. The recorded Sv demand remains considerably higher than the code-based spectra over a wide period range for all local site classes, with the difference becoming especially pronounced in the intermediate- and long-period ranges. The high Sv demand is one of the important findings of this study. Pseudo-spectral velocity is not a direct measure of input energy; however, it is commonly used as an indicator of velocity-sensitive structural response and cyclic deformation demand. Large Sv values may therefore be associated with damage accumulation, stiffness degradation, residual drift potential, and increased ductility demand in reinforced concrete buildings.

Although PGV and pseudo-spectral velocity are not identical parameters, both highlight the importance of velocity-related demand in interpreting strong ground motion effects. Previous evaluations of the Kahramanmaraş earthquake sequence also emphasized the role of high PGV values, pulse-like velocity histories, and near-field ground-motion characteristics [13]. In this study, the mean resultant Sv spectrum reaches approximately 380–390 cm/s in the medium-period range, indicating substantial velocity-related demand that may be critical for medium- and longer-period reinforced concrete buildings.

Figure 8 presents the comparison of the mean resultant spectral displacement spectrum with the TBDY 2018 DD-2 spectral displacement spectra. The recorded Sd demand exceeds the code-based spectra for all considered local site classes, especially at medium and long periods, and the difference increases with period. This finding shows that the selected Hatay records produced considerable displacement-related demand in addition to high acceleration and velocity demands. Large Sd values are directly related to deformation-sensitive structural response and may lead to larger interstory drift ratios, concentration of deformation in weaker stories, stiffness degradation, residual drift, and second-order P-Δ effects in reinforced concrete buildings. The displacement-related interpretation is especially important for flexible and longer-period buildings. As the period increases, the response becomes less acceleration-sensitive and more influenced by velocity and displacement demand. This is consistent with the tripartite representation of response spectra, in which short-period response is mainly acceleration-sensitive, intermediate-period response is velocity-sensitive, and long-period response is displacement-sensitive [13].

Overall, the DD-2 comparisons indicate that the selected Hatay records produced spectral demands exceeding the design-level code spectra in terms of acceleration, velocity, and

displacement. The mean ± one standard deviation bands also show considerable record-to-record dispersion, indicating that individual records may impose substantially higher demands over specific period ranges. These results confirm that the seismic demand in the Hatay region cannot be explained by PGA or Sa alone; Sv and Sd should also be considered to capture velocity-sensitive and deformation-related demands, particularly in the medium- and long-period ranges. It should be emphasized that the mean resultant spectrum represents the average response of the selected Hatay records and is not a site-class-specific mean spectrum. The ZA–ZE comparisons were used as a parametric code-based reference to evaluate the influence of local site class on spectral shape. A fully site-consistent comparison would require site-class-based record grouping and station-specific site response analyses, which are beyond the scope of this study.

5.3 Comparison with TBDY 2018 DD-1 Design Spectra

Figure 9 compares the mean resultant pseudo-spectral acceleration spectrum with the TBDY 2018 DD-1 elastic design spectra. The comparison was included to evaluate whether the recorded acceleration demand approaches the maximum considered earthquake level. The mean recorded spectrum is generally lower than the upper DD-1 spectra in the short-period range; however, it approaches or exceeds some DD-1 site-class spectra in certain medium- and long-period intervals. This indicates that the selected Hatay records produced demands clearly above the DD-2 design level and locally comparable to the DD-1 level in some period ranges. The mean ± one standard deviation band also shows considerable dispersion, indicating that individual records may impose demands substantially higher than the mean response. The DD-1 comparison supports the need for a period-dependent interpretation of seismic demand. While acceleration demand is critical at shorter periods, longer-period response should also be interpreted together with velocity- and displacement-related quantities as part of a broader Sa–Sv–Sd assessment.

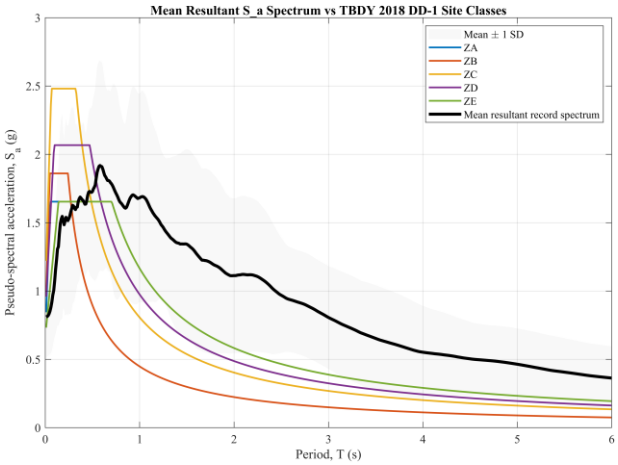


Fig. 9. Mean Sa and TBDY 2018 DD-1 spectra.

5.4 Case-Based Interpretation: Rönesans Residence

To provide an engineering interpretation of the calculated spectral demands, the Rönesans Residence in Antakya was considered as a representative collapsed reinforced concrete building case discussed in previous research [11]. The building complex was located in Ekinci Mahallesi, Antakya, and consisted of A1, A2, and A3 blocks separated by expansion joints. According to the available technical information, the A blocks had two basement stories, a

ground story, and 12 normal stories, with a total height of approximately 44 m from the foundation level. The structural system was reported as a reinforced concrete wall-frame system with C30 concrete and S420 reinforcing steel [12].

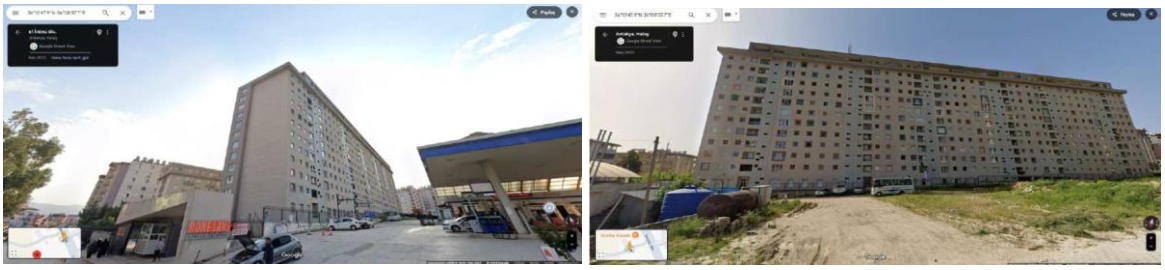


Fig. 10. Pre-earthquake Google Maps view of the Rönesans Residence, reproduced from [12].

The modal analysis results reported for the A blocks indicate first-mode periods of 2.1681 s, 2.2188 s, and 2.0036 s for A1, A2, and A3, respectively [12]. These periods were used to relate the calculated regional response spectra to the dynamic characteristics of an actual collapsed reinforced concrete building case in Antakya. It should also be noted that the reported modal periods correspond to linear elastic model properties and were used only as reference periods for spectral interpretation. Possible period elongation, stiffness degradation, and changes in effective damping during nonlinear response were not simulated in this study. The mean spectral ordinates corresponding to these first-mode periods were obtained by linear interpolation from the calculated mean resultant spectra, as summarized in Table 3.

Table 3. Fundamental periods of the Rönesans A-blocks and mean resultant spectral demands.

Block	Structural Condition	T_1 (s)	T_2 (s)	Mean $S_a(T_1)$ (g)	Mean $S_v(T_1)$ (cm/s)	Mean $S_d(T_1)$ (cm)
A1	Collapsed	2.1681	1.7802	1.12	379	131
A2	Collapsed	2.2188	1.7574	1.11	385	136
A3	Collapsed	2.0036	1.6840	1.11	348	111

Note: Spectral demands were obtained by linear interpolation from the calculated mean resultant spectra at the first-mode periods.

The interpolated values indicate that the first-mode periods of the Rönesans Residence A blocks correspond to mean pseudo-spectral acceleration values of approximately 1.11–1.12 g, mean pseudo-spectral velocity values of approximately 348–385 cm/s, and mean spectral displacement values of approximately 111–136 cm. These values show that the case-study building periods fall within a range where velocity- and displacement-related demands remain significant. To visually support this case-based interpretation, the fundamental periods of the Rönesans Residence A blocks were also marked on the mean resultant S_a, S_v, and S_d spectra, as shown in Figure 11. Previous research on the Rönesans Residence and similar post-2000 reinforced concrete buildings described this failure type as an uprooting collapse mechanism and emphasized that such collapses may occur when several adverse conditions act together, including high velocity demand, flexible load-bearing systems, improper structural member configuration, and high height-to-width ratio [11]. In the present study, the high S_v and S_d demands observed near the Rönesans A-block period range are therefore consistent with the need to evaluate not only acceleration-related demand, but also velocity- and displacement-related demand when interpreting the seismic performance of flexible reinforced concrete

buildings. This case-based interpretation does not aim to establish a direct collapse causality for the Rönesans Residence. Such a conclusion would require building-specific nonlinear analyses, detailed as-built information, construction quality assessment, soil-structure interaction evaluation, and complete damage observations. However, the spectral ordinates corresponding to the fundamental period range of the Rönesans Residence A blocks provide a practical connection between the regional spectral demand results of this study and an actual collapsed reinforced concrete building case in the Hatay region.

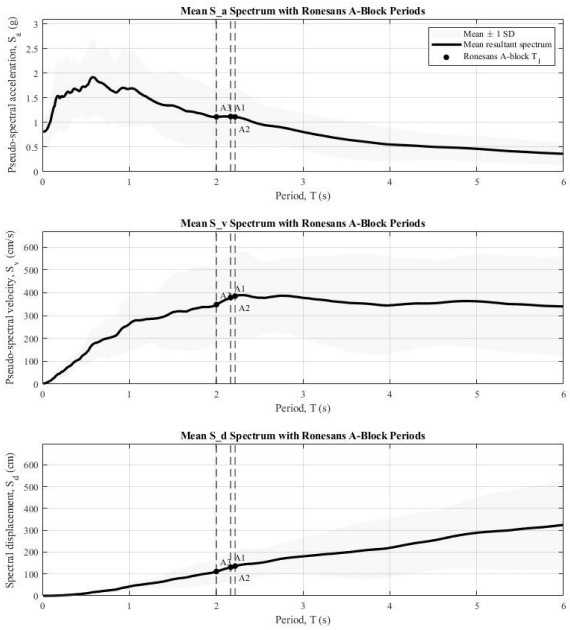


Figure 11. Rönesans Residence A-block periods marked on the mean resultant Sa, Sv, and Sd spectra.

5.5 Engineering Implications of Velocity- and Displacement-Related Demands

The results indicate that the selected Hatay records cannot be interpreted only through acceleration-related parameters. The Sv and Sd spectra show significant velocity-sensitive and deformation-related demands, including cyclic deformation, drift concentration, residual drift, and second-order P-Δ effects. This interpretation is consistent with the Rönesans Residence case; however, it does not establish direct collapse causality. The comparison with TBDY 2018 spectra should therefore be regarded as a code-based reference rather than a substitute for detailed site response or nonlinear structural performance analysis. Future studies should include station-specific geotechnical data, site response analyses, and nonlinear evaluations of representative reinforced concrete buildings.

6 Conclusions

In this study, acceleration, pseudo-spectral velocity, and spectral displacement response spectra were evaluated for selected strong ground motion records obtained from the Hatay region during the February 6, 2023 Pazarcık earthquake. Thirteen AFAD stations and both horizontal components of each record were considered, and the calculated spectra were compared with TBDY 2018 elastic design spectra for different local site classes. The following conclusions can be drawn from the study:

· The selected Hatay records produced significant spectral demands over a wide period range. The mean resultant pseudo-spectral acceleration spectrum reached approximately 1.9 g in the medium-period range, while some individual records produced considerably higher demands. This indicates that the ground-motion demand in the region was highly variable and dependent on station location and period range.

· The seismic demand was not limited to acceleration-related effects. The pseudo-spectral velocity and spectral displacement spectra remained high in the medium- and long-period ranges, indicating considerable velocity-sensitive and deformation-related demands. Therefore, velocity- and displacement-related spectral quantities should be evaluated together with acceleration-based parameters.

· The comparison with TBDY 2018 design spectra showed that the selected Hatay records produced demands clearly above the DD-2 design level over a broad period range and locally comparable to the DD-1 level in some intervals. This exceedance was observed not only in the acceleration spectrum but also in the velocity and displacement spectra.

· The comparison of different local site classes showed that soil-dependent design parameters significantly affect the spectral shape. While SDS mainly controls the short-period acceleration demand, SD1 becomes more influential in the medium- and long-period velocity and displacement demands. Therefore, local site effects should be considered together with Sa, Sv, and Sd when evaluating seismic demand.

· The case-based interpretation using the Rönesans Residence indicates that the fundamental period range of a collapsed reinforced concrete building in Antakya coincides with the period range where high velocity- and displacement-related demands were observed. However, since the present study is based on selected strong motion records and code-based local site class comparisons, future studies should include station-specific geotechnical data, detailed site response analyses, near-field ground motion characteristics, and nonlinear structural performance evaluations of reinforced concrete buildings in the Hatay region.

References

1. Disaster and Emergency Management Presidency (AFAD): Turkish Strong Ground Motion Database (TADAS), https://tadas.afad.gov.tr, last accessed 2026/08/09.
2. Turkish Chamber of Civil Engineers (TMMOB-IMO): Observation and Evaluation Report on Structural Damages Caused by the February 6, 2023 Kahramanmaraş Earthquakes. Publication No: İMO/23/03, Ankara (2023).
3. İlhan, O., Indır, O., Muratoğlu, G., İçen, A., Albayrak, K., Sandıkkaya, M.A., Askan, A., Arduino, P., Taciroğlu, E.: Local site effects at the selected stations affected by the February 6 2023 Türkiye Earthquake Sequences. Soil Dynamics and Earthquake Engineering 178, 108454 (2024). https://doi.org/10.1016/j.soildyn.2024.108454.
4. Gürbüz, T., Cengiz, A.: Structural damages during the February 06, 2023 Kahramanmaraş Earthquakes in Turkey. Soil Dynamics and Earthquake Engineering 191, 109214 (2025). https://doi.org/10.1016/j.soildyn.2025.109214.
5. Avşar, Ö.: Pazarcık (Kahramanmaraş) Mw 7.7 ve Elbistan (Kahramanmaraş) Mw 7.6 Depremlerinde Hatay ve Çevresinde Hasar Gören Binaların İncelenmesi ve Hasar Nedenlerinin Araştırılması İçin Saha Verilerinin Toplanması. Eskişehir Technical University, Türkiye (2023).

6. İlhan, O., Zulfikar, A.C., Taskiran, T., Eroglu, K.N., Okuyan Akcan, S., Ugurlu, H.A.: The Observed and Simulated Site Effects at the Selected Regions Influenced by 2023 Turkey Earthquake Sequences: A Preliminary Evaluation. Journal of Earthquake Engineering 29(16), 3283–3302 (2025). https://doi.org/10.1080/13632469.2024.2336197.
7. Disaster and Emergency Management Presidency (AFAD): Turkish Building Earthquake Code 2018. Ankara, Türkiye (2018).
8. Newmark, N.M.: A method of computation for structural dynamics. Journal of the Engineering Mechanics Division, ASCE 85(EM3), 67–94 (1959).
9. Anadolu Agency: Depremlerin vurduğu Hatay'da en ağır yıkım Antakya'da. Anadolu Ajansı, 8 April 2023. https://www.aa.com.tr/tr/asrin-felaketi/depremlerin-vurdugu-hatayda-en-agir-yikim-antakyada/2866977, last accessed 2026/08/15.
10. Governorship of Hatay: Çevre, Şehircilik ve İklim Değişikliği İl Müdürlüğü ağır hasarlı yapı listesi. Hatay, Türkiye (2023). https://www.hatay.gov.tr/cevre-sehircilik-ve-iklim-degisikligi-il-mudurlugu-agir-hasarli-yapi-listesi, last accessed 2026/08/15.
11. Smyrou, E., Vuran, E., Bal, I.E.: Uprooting collapse mechanism of RC structures in earthquakes. Engineering Failure Analysis 182, 110105 (2025). https://doi.org/10.1016/j.engfailanal.2025.110105.
12. İstanbul Technical University: Technical Report on the Evaluation of Building Performance Analyses Prepared for the Building Located at 2329 Parcel, Ekinci Mahallesi, Antakya, Hatay [in Turkish]. İstanbul, Türkiye (2024).
13. Beyen, K.: 6 Şubat 2023 Kahramanmaraş Depremlerinin Yıkıcı Karakteristiği [Destructive Characteristics of the February 6, 2023 Kahramanmaraş Earthquakes, in Turkish]. Turkish Chamber of Civil Engineers, Istanbul Branch, Publication No: İMO/25/03, İstanbul, Türkiye (May 2025). ISBN: 978-605-01-1675-5.

Author Contribution Statement

Conceptualization and methodology: Merve Arlı Sönmez and Ali Koçak. Investigation, data curation, software, formal analysis, and writing – original draft: Merve Arlı Sönmez. Writing – review & editing and supervision: Ali Koçak.

List of Abbreviations

AFAD: Disaster and Emergency Management Presidency of Türkiye; TADAS: Turkish Strong Ground Motion Database; TBDY: Turkish Building Earthquake Code; DD: earthquake ground motion level; PGA: peak ground acceleration; PGV: peak ground velocity; Sa: pseudo-spectral acceleration; Sv: pseudo-spectral velocity; Sd: spectral displacement.

Publication Note

This paper was peer-reviewed, accepted for presentation, and included in the proceedings of the ACE2026 – International Conference on Advances in Civil Engineering, held on 12–14 October 2026 in Trabzon, Türkiye.

This paper may be cited as follows:

Arlı Sönmez, M., Koçak, A.: "Evaluation of Acceleration, Velocity, and Displacement Response Spectra of the February 6, 2023 Kahramanmaraş Earthquakes in the Hatay Region Considering Local Site Classes." In: Proceedings of the ACE2026 – International Conference on Advances in Civil Engineering, Trabzon, Türkiye, 12–14 October 2026.

Experimental study of cold-formed steel stud's cyclic axial response

Hiba MEDDAH[1*], Nouredine BOURAHLA[2], Hakim BECHTOULA[1] and Hassan AKNOUCHE[1]

[1] National Center of Applied Research in Earthquake Engineering (CGS), Algiers, Algeria
2 LGSDS Laboratory, Civil Engineering Department, National Polytechnic School, Algiers, Algeria
* https://orcid.org/0000-0002-3130-9655 h.meddah@cgs-dz.org

Abstract. This study summarizes the results of an experimental program conducted at the Laboratory of the National Centre for Applied Research in Earthquake Engineering (CGS)-ALGERIA, which examined the cyclic axial behavior of cold-formed steel studs. Three distinct specimen lengths (L = 2000 mm, L/2 = 1000 mm and L/4 = 500 mm) were used to determine specific buckling modes, such as local, distortional or global buckling. There were four specimens in each group. Each group underwent two cyclic axial loading tests, as well as two monotonic axial concentric loading tests (one compression and one tension). The cyclic loading protocol was modelled on FEMA 461, and the initial displacement was derived from the monotonic testing. The results showed that the slenderest specimens are more susceptible to localized geometric imperfections in the edge stiffeners due to their deformation capacity and behavior. As height decreases, the interaction between local buckling and global flexural buckling also decreases. These results provide valuable empirical evidence to inform the design of seismic codes, particularly with regard to predicting failure mechanisms and energy dissipation in thin-walled members. This study provides practicing engineers with a rational basis for optimizing stud slenderness ratios and stiffener detailing in earthquake-resistant, cold-formed steel framing, by quantifying instability modes under cyclic loads. It also provides researchers with a validated experimental benchmark for creating more accurate numerical models that capture interactive buckling under severe loading histories.

Keywords: Cold-formed steel column, Axial loading, Hysteretic load-deformation behavior, Buckling.

1 Introduction

Cold-formed steel (CFS) sections are becoming increasingly common in modern construction, particularly in low and medium-rise commercial, industrial and residential buildings. They have several advantages over hot-rolled steel sections, including a higher strength-to-weight ratio, faster fabrication, higher recycling rates and lower carbon emissions. However, the thin walls of CFS sections make them prone to instability, including local and global buckling modes [1, 2, 5, 7]. These buckling interactions become much more complex under seismic loading conditions, so a thorough understanding of the cyclic axial behavior of the CFS structural members is required. Understanding the hysteretic behavior and energy dissipation capacity of these sections is essential for performance-based seismic design.

Unlike hot-rolled steel sections, CFS members exhibit complex buckling interactions that can significantly influence their deformation and failure modes under cyclic loading [5,7]. Cold-formed steel lipped channel sections are commonly used as studs in shear wall panel systems. They are prone to three main types of buckling modes: local buckling (local instability of the flange or web), distortional buckling (distortion of flange and lip relative to web), and

global buckling -flexural or flexural-torsional buckle of the entire member [1,7]. The combination of these buckling behaviors has been recognized as a key factor in determining the ultimate strength and post-buckling behavior of a CFS member [7,9].

Recent investigations have indicated that the slenderness of CFS studs has a considerable influence on the buckling behavior of CFS studs [1, 10,11]. Thin sections with larger web-height-to-thickness ratios are more susceptible to local geometric imperfections, particularly in the edge stiffener regions [1]. Moreover, the interaction between local and global buckling modes depends strongly on the member length, with shorter specimens exhibiting less interaction between local and global buckling [1,7,11]. The cyclic axial behavior of bare CFS studs has been studied and several researches has been done on the monotonic axial behavior of CFS columns [6,8,9,10,11,12,13].

Although substantial progress has been made in understanding the behavior of CFS under monotonic loading [6, 9, 14], there is limited experimental data available on the cyclic axial behavior of bare CFS studs, particularly in relation to the effect of specimen length on the interaction of buckling modes under reversed cyclic loading. Most of the existing cyclic studies have concentrated on sheathed wall panels [3,4] or beam-column members under combined loading [8], which has left a gap in understanding the fundamental cyclic axial behavior of bare studs.

This work intends to fill this gap by an experimental investigation of the behavior of cold-formed steel studs under cyclic axial loading. The specific objectives are:

1.To identify the influence of specimen length on the activation of local, distortional, and global buckling modes under cyclic axial loading;

2.To characterize the deformation capacity and failure mechanisms of CFS studs with varying slenderness ratios;

3.To investigate the interaction between local and global buckling modes as a function of member height.

Three different specimen lengths (L=2000mm, L/2=1000mm, and L/4=500mm) were selected to capture distinct buckling modes. Each group comprised four specimens, subjected to monotonic compression, monotonic tension, and two cyclic axial loading. The cyclic loading protocol was adapted from FEMA 461, with initial displacement amplitudes derived from monotonic test results.

2 Experimental program

2.1 Specimen's dimensions and materials properties

Twelve cold-formed steel section specimens were used in the experiment. As illustrated in Fig.1, the cross-section used for each specimen is 600s200-68, which was chosen from the standard sizes listed in the Structural Stud Manufacturers Association (SSMA) catalog [15].

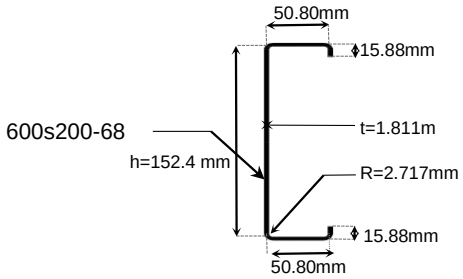


Fig. 1. Cross-section geometry 600-S200-68

Tensile tests were performed in accordance with the ASTM A370-12a 2012 criteria to determine the basic mechanical properties of the CFS utilized in the test specimens, as illustrated in Fig.2. The yield strength and ultimate tensile strength had average values of 281.62 MPa and 311.22 MPa, respectively. The elasticity modulus was assumed to be 203400 MPa in accordance with AISI S100-2012 [16].

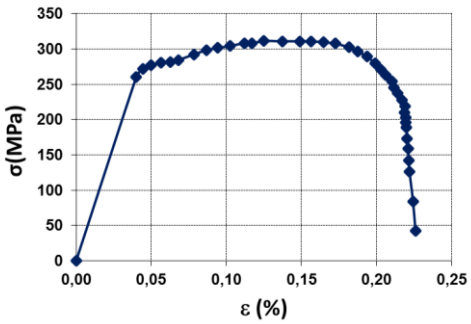


Fig. 2. Stress-strain relationship for CFS (Tensile test) [2].

The specimen's Length was varied to isolate each buckling limit state (global buckling, local buckling, and distortional buckling), Three different lengths were considered (L=2000mm, 1/2L=1000mm and 1/4L=500mm). The test program includes two specimens subjected to monotonic axial displacement (compression and tension) and two specimens subjected to quasi-static cyclic axial displacement per specimen length.

The representative load-deformation envelope and the ultimate displacement were estimated using the monotonic tests. Cyclic experiments were conducted. to ascertain the hysteretic energy dissipation and axial hysteretic response, Specimen's nomenclature is summarized in Table 1. As implemented in the real field, boundary conditions were taken to be fixed-fixed.

Table 1. Specimen's dimensions and nomenclature

Length (mm)	**Specimens**	**Test**	**Loading rate (mm/s)**
L= 2000 mm	LWOWM	Monotonic compression	0.02
	LWOWMT	Monotonic Tension	0.02
	LWOWC1	Cyclic 1	0.5
	LWOWC2	Cyclic2	0.5
1/2L= 1000 mm	1/2LWOWM	Monotonic compression	0.02
	1/2LWOWMT	Monotonic Tension	0.02
	1/2LWOWC1	Cyclic 1	0.5
	1/2LWOWC2	Cyclic2	0.5
1/4L= 1000 mm	1/4LWOWM	Monotonic compression	0.02
	1/4LWOWMT	Monotonic Tension	0.02
	1/4LWOWC1	Cyclic 1	0.5
	1/4LWOWC2	Cyclic2	0.5

2.2 Test setup and instrumentation

A loading frame was used to test the studs vertically at the National Center of Applied Research in Earthquake Engineering Laboratory (CGS)-Algeria, as shown in Fig.3(a). To transfer axial load, end plates were attached to both ends of the specimens. All out-of-plane displacements were prohibited by lateral braces.

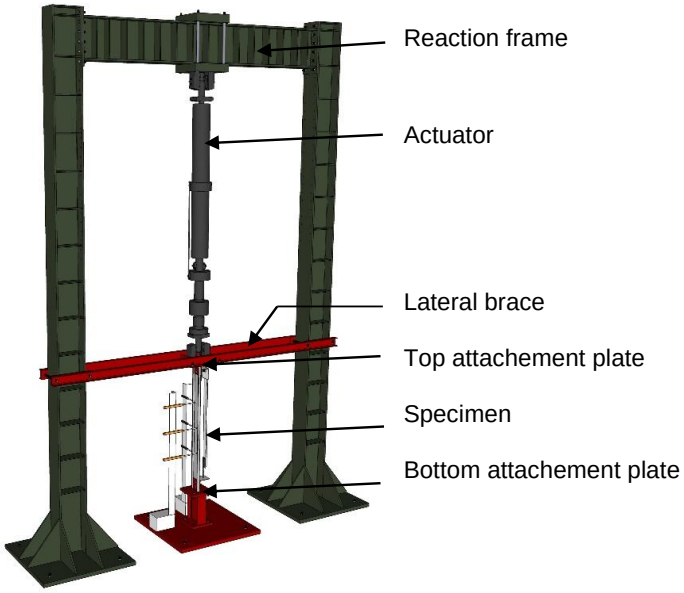


Fig. 3. Test setup.

2.3 Loading protocol

During the monotonic tests, an increasing displacement-controlled load was supplied at a rate of 0.02 mm/s until the specimen failed in tension or compression.

The approach for quasi-static cyclic loading was adapted from FEMA461. This procedure is suited for hysteretic testing, also known as racking testing, which quantifies all damage states that require the development of fragility functions [17].

Iterative cycles with increasing deformation amplitudes constitute the FEMA reversed cyclic protocol. Each amplitude consists of two cycles. The beginning amplitude is δ_0, and the final projected amplitude is δ_m. δ_i is the amplitude of the cycles as they grow in magnitude. δ_m is defined as the displacement observed when the post-peak resistance is reduced to 80% of the ultimate resistance, and it is estimated from the monotonic test. The protocol consists of six modest-amplitude δ_0=0.018 δ_m initiation cycles. The amplitude δ_{i+1} of the step i+1 (not of each cycle, since each step has two cycles) is given by the equation δ_{i+1}=1.4 δ_i where δ_i is the amplitude of the preceding step. Fig.4. shows the reversed cyclic loading history applied during the tests [17].

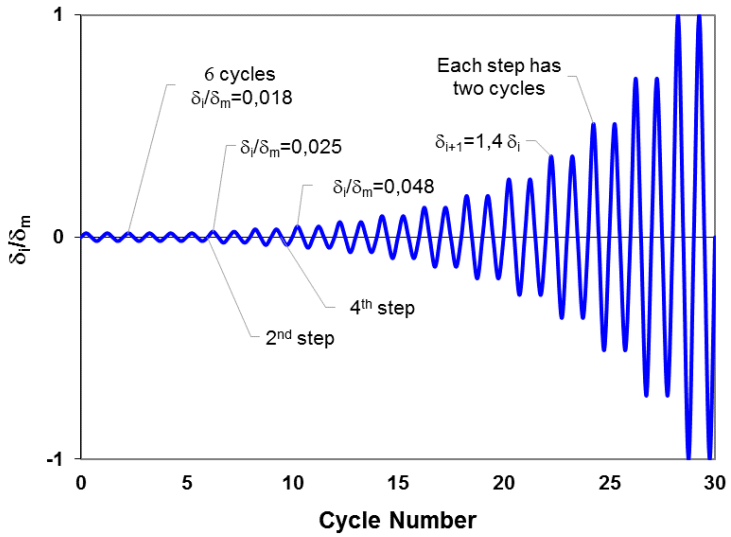


Fig. 4. Loading path [17].

3 Experimental program

3.1 Monotonic response

The LWOW specimens exhibited a monotonic response with flexural buckling of the weak axis first, followed by a few waves of local buckling when the maximum compressive load was attained (see Fig.5a). Following that, the compressive strength and stability of the LWOWs gradually declined upon unloading, with compressive damage accumulating in the mid-height (see Fig.5b).

From here on, "compression" is represented by positive displacement and "tension" by negative displacement.



(a) LWOWM- maximum compressive load (b) LWOWM-End test

Fig. 5. Deformed shape-Monotonic test-LWOW specimens

The 1/2LWOW specimens had a monotonic reaction, with many waves of local buckling occurring across the entire height of the web. This happened when the maximum compressive load was met, as illustrated in Fig.6a. The web of the part near the top end of the flanges suffered significant damage. However, as seen in Fig.6b, web deformations were more obvious than flange openings.



(a) 1/2LWOWM- maximum compressive load (b) 1/2LWOWM-End test

Fig. 6. Deformed shape-Monotonic test-1/2LWOW specimens

The 1/4LWOW specimens' monotonic response was marked by web buckling, with buckling waves occurring before reaching the maximum compressive load. After reaching the maximum load, one of the waves got stuck in mid-height, resulting in damage accumulating at this point

(see Fig.7). As indicated in Fig.8, compressive strength and unloading stiffness declined rapidly.



(a) 1/4LWOWM- maximum compressive load (b) 1/4LWOWM-End test

Fig. 7. Deformed shape-Monotonic test-1/4LWOW specimens

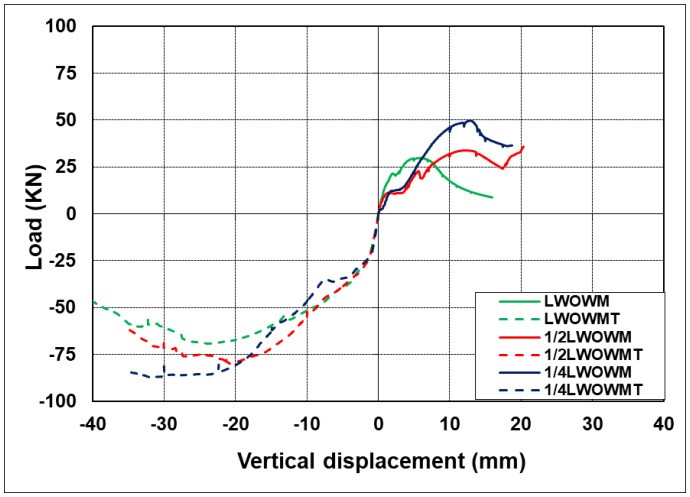


Fig. 8. Monotonic behavior

The monotonic tensile response of the specimens exhibited modest linearity in their monotonic tensile response up to 30% of the maximum tensile load, which corresponds to the onset of plastic deformation in the web, followed by nonlinearity corresponding to deformation propagating around the cross-section.

3.2 Cyclic response

Based on general test results, all specimens showed global buckling deformation about the minor axis, which interacted with local buckling.

Once the maximum compressive load was attained, the compressive strength declined faster due to the accumulation of local damage. Figs 9,10 and 11 show the deformations.

Fig.9 displays the more slender LWOW specimens, where the local-global interaction is more evident. Furthermore, it was discovered that the slendernest specimens had a capacity and deformation behavior that was more susceptible to localized geometric imperfections in the edge stiffeners. As the height reduces, there is less interaction between local buckling and global flexural buckling.

The cyclic response of the LWOW specimens was represented by buckling about the minor axis, as well as edge stiffener opening, flange bending, and section tearing at mid-height (Fig 9).



Fig. 9. Deformed shape-Cyclic test-LWOW specimens

The cyclic response of the 1/2LWOW specimens was marked by flexural buckling around the weak axis, with the flanges bending at mid-height. As well, inelastic buckling caused by warping occurred near the supports as damage accumulated at the upper end's bent flanges, which was the final failure mode, as illustrated in Fig.10.



Fig. 10. Deformed shape-Cyclic test-1/2LWOW specimens

Fig.11 indicates the cyclic response of the 1/4LWOW specimens, which included buckling along the weak axis and warping of the web and flanges at mid-height.

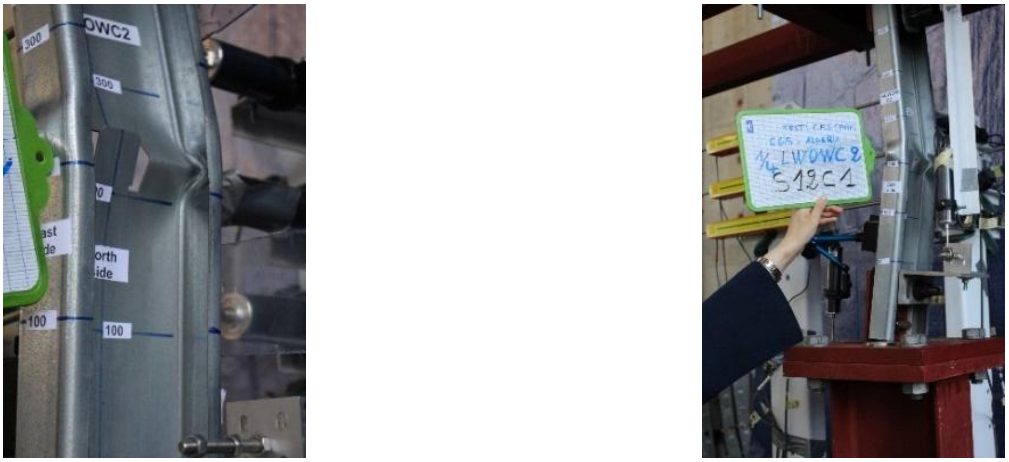


Fig. 11. Deformed shape-Cyclic test-LWOW specimens

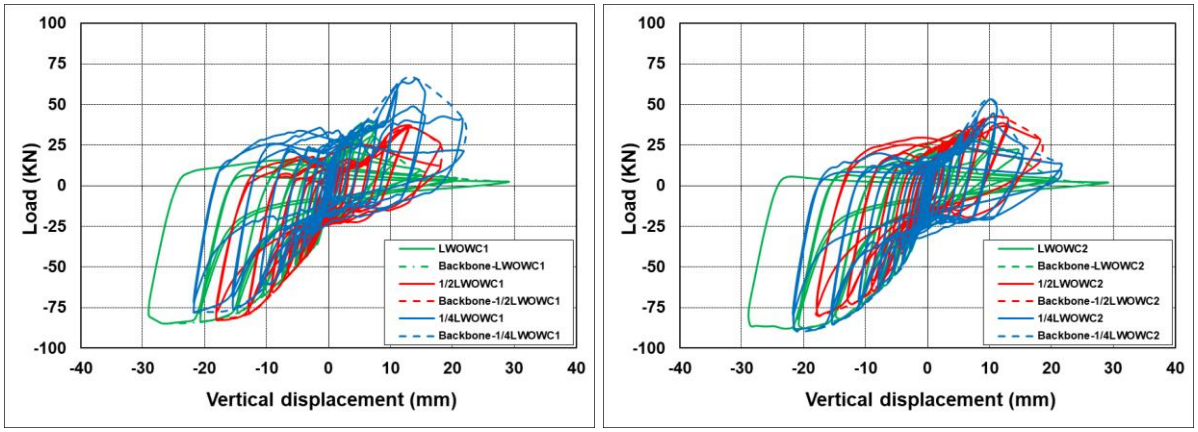


Fig. 12. Cyclic behavior

3.3 Hysteretic energy dissipation

By determining the area enclosed by a single-cycle hysteresis loop, the specimen's hysteretic energy dissipation can be determined.

Fig. 13 displays the energy dissipation time history. The findings demonstrated that, for low cycle numbers, the energy dissipation of the slendernest specimens is the most significant, and it rapidly increased for the highest number of cycles.

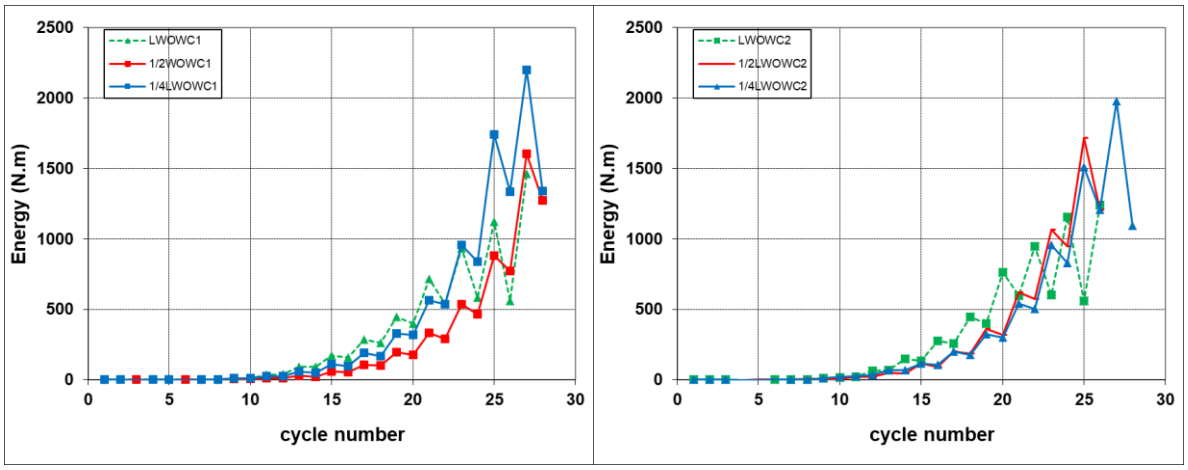


Fig. 13. Hysteretic energy dissipated

4 Conclusion

A parametric experimental investigation was conducted on cold-formed steel specimens of various heights to determine the effect of height on cyclic axial behavior and energy dissipation capacity, based on twelve monotonic and cyclic tests.

Under monotonic loading, the LWOW specimens failed in a combination of buckling and local warping, with damage accumulating at mid-height by the end of the test. Cyclic loading also caused opening of the edge stiffeners, bending of the flanges and tearing of the section at mid-height

The monotonic response of the 1/2LWOW specimens was highlighted by multiple waves of local buckling throughout the whole height, as well as considerable damage to the section's web

toward the top end. This was related to the deformation of the mid-height flanges, which was the ultimate failure mode under cyclic loads.

The 1/4LWOW specimens were distinguished by a combination of buckling and local warping of the web and flanges, with damage accumulating at mid-height by the end of the test under monotonic and cyclic loads.

It has been noticed that the slenderest specimens have a higher deformation capacity and are more sensitive to local geometric imperfections in the edge stiffeners. As the height decreases, the interaction between local and global flexural buckling becomes less pronounced.

Acknowledgments
The technical support of the National Center of Applied Research on Earthquake Engineering (CGS) for carrying this research is greatly acknowledged. As well as many thanks for the financially support by Frame-metal and Blida University.

References

1. H.Meddah, N.Bourahla, H.Bechtoula, H.Aknouche: Experimental Investigation on Axial Response of Composite Wood - Cold-Formed - Steel Fixed Ended Studs. Inżynieria Mineralna 2(2). (2025). https://doi.org/10.29227/IM-2025-02-02-050
2. H.Meddah, N.Bourahla, H.Bechtoula, H.Aknouche, A.Nour: Cyclic axial Response of composite wood-cold-formed steel stud: experimental and numerical investigation. International Journal of Steel Structures 22, 1126-1146. (2022). https://doi.org/10.1007/s13296-022-00624-z
3. F.Yilmaz, J.Becque, S.M.Mojtabaei, I. Hajirasouliha: Capacity and Behavior of Sheathed Cold-Formed Steel Stud Walls under Outward Flexural Loading. Journal of Structural Engineering, 151(1). (2024). https://doi.org/10.1061/JSENDH.STENG-13802
4. S. Ariana, K. D. Peterman: Experimental hysteretic response of cold-formed steel fastened connections sheathed with fiber-cement boards with varied edge distance. Engineering Structures 303, 117510. (2024). https://doi.org/10.1016/j.engstruct.2024.117510
5. Y. Yılmaz, S. Demir, F. Öztürk: Buckling behavior of cold-formed steel lipped channel beam-column members under monotonic and cyclic loadings. Structural Engineering and Mechanics 90(5), 435–446. (2024). https://doi.org/10.12989/sem.2024.90.5.435
6. S. Mishra, C. McNally, A. M. Wrzesien, D. P. McCrum: Experimental axial-compressive behaviour of bare cold-formed-steel studs with semirigid-track and ideal-hinged boundary-conditions. Journal of Constructional Steel Research 216, 108422. (2024). https://doi.org/10.1016/j.jcsr.2024.108600
7. G. Y. Matsubara, E. M. Batista: Local-distortional-global buckling interaction of steel cold-formed columns. Thin-Walled Structures 206, 113735. (2025). https://doi.org/10.1016/j.tws.2025.113735
8. F. Öztürk, Y. Yılmaz, S. Demir, F. Öztürk: Experimental and Numerical Investigation of the Cyclic Behaviors of Cold-Formed Steel Beam-Columns Under Axial Force and Uniaxial/Biaxial Bending. Journal of Earthquake Engineering 29(3), 636–668. (2025). https://doi.org/10.1080/13632469.2024.2435501
9. S. Mishra, D. P. McCrum: Prediction of axial-compressive behaviour of bare cold-formed steel studs through a new stud-to-track contact modeling approach. Engineering Structures 318, 118757. (2024). https://doi.org/10.1016/j.engstruct.2024.118757
10. D. A. Padilla-Llano: A Framework for Cyclic Simulation of Thin-Walled Cold-Formed Steel Members in Structural Systems. PhD thesis, Virginia Polytechnic Institute (2015). http://hdl.handle.net/10919/52904

11. D. Padilla-Llano, C. D. Moen, M. R. Eatherton: Cyclic axial response and energy dissipation of cold-formed steel framing members. Thin-Walled Structures 78, 95–107. (2014). https://doi.org/10.1016/j.tws.2013.12.011
12. D. C. Fratamico, S. Torabian, X. Zhao, K. J. R. Rasmussen, B. W. Schafer: Experiments on the global buckling and collapse of built-up cold-formed steel columns. Journal of Constructional Steel Research 144, 65–80. (2018). https://doi.org/10.1016/j.jcsr.2018.01.007
13. D. C. Fratamico, S. Torabian, X. Zhao, K. J. R. Rasmussen, B. W. Schafer: Experimental study on the composite action in sheathed and bare built-up cold-formed steel columns. Thin-Walled Structures 127, 290–305. (2018). https://doi.org/10.1016/j.tws.2018.02.002
14. K. J. R. Rasmussen, M. Khezri, H. Zhang, B. W. Schafer: Recent Research on Built-Up Cold-Formed Steel Structures. Lecture Notes in Civil Engineering 504, 11–24. (2024). https://doi.org/10.1016/j.tws.2025.113546
15. Steel Stud Manufacturers Association (SSMA): Product technical information. ICBO Evaluation Service Evaluation Report No. 4943-P. (2011). https://ssma.com/
16. American Iron and Steel Institute (AISI), North American specification for the design of cold-formed steel structural members, AISI S100, Washington, D.C., USA. (2012).
17. Federal Emergency Management Agency (FEMA): Interim Testing Protocols for Determining the Seismic Performance Characteristics of Structural and Nonstructural Components. Report No. FEMA 461, Washington, D.C., USA. (2007). atcouncil.org

Author Contribution Statement

- *Conceptualization:* H.MEDDAH, N.BOURAHLA
- *Methodology:* H.MEDDAH, H.BECHTOULA
- *Investigation:* H. MEDDAH, N. BOURAHLA, H. BECHTOULA,H. AKNOUCHE
- *Writing – Original Draft:* H.MEDDAH
- *Writing – Review & Editing:* N.BOURAHLA, H.BECHTOULA

Publication Note

This paper was peer-reviewed, accepted for presentation, and included in the proceedings of the ACE2026 – International Conference on Advances in Civil Engineering, held on 12–14 October 2026 in Trabzon, Türkiye.

This paper may be cited as follows:

Hiba MEDDAH, Nouredine BOURAHLA, Hakim BECHTOULA and Hassan AKNOUCHE, “Experimental study of cold-formed steel stud’s cyclic axial response,” in Proceedings of the ACE2026 – International Conference on Advances in Civil Engineering, Trabzon, Türkiye, 12–14 October 2026.

Optimal Sizing and Post-Tensioning Force Design of Cable-Stayed Footbridges via the Rao-2 Algorithm

Chiraz FAZZAA[1], Barbaros ATMACA[2], Büşra YAKAK VATANDAŞ[3] and Şevket ATEŞ[4]
[1] 0009-0001-1050-3221, Karadeniz Technical University, Civil Engineering Department, Trabzon, Türkiye, chirazfazzaa@gmail.com
[2] 0000-0003-3336-2756, Karadeniz Technical University, Civil Engineering Department, Trabzon, Türkiye, atmaca@ktu.edu.tr
[3] 0009-0006-6653-7312, Karadeniz Technical University, Civil Engineering Department, Trabzon, Türkiye, busra.yakak@ktu.edu.tr
[4] 0000-0001-9229-6256, Karadeniz Technical University, Civil Engineering Department, Trabzon, Türkiye, sates@ktu.edu.tr

Abstract. The continuous expansion of contemporary urban infrastructure necessitates the design of highly resilient and material-efficient cable-stayed footbridge (CSFB) structures. In this paper, an optimization framework is established by coupling the metaphor-free Rao-2 metaheuristic algorithm with finite element modeling via MATLAB and the SAP2000 OAPI environment. The central aim is to achieve a lightweight cable arrangement alongside appropriate PTF distributions while strictly satisfying all allowable stress and displacement limits under varied static and dynamic loading scenarios. Demonstrated on a numerical model of a twin-pylon steel CSFB with a modified fan cable arrangement, the proposed approach achieved a significant stay-cable weight reduction of nearly two-thirds while fully preserving structural integrity. Consequently, the results highlight the efficacy and practical applicability of the Rao-2 algorithm for multi-variable optimization in cable-stayed pedestrian bridges.

Keywords: Cable-stayed footbridge; Stay-cable optimization; Post-tensioning force; Cable cross-sectional area; SAP2000 OAPI; Rao-2 algorithm.

1 Introduction

Cable-stayed bridges have become one of the most effective and visually appealing structural solutions for medium- to long-span projects, relying on a self-anchored system in which inclined stay cables transfer deck loads directly to the pylons and thereby enable slender, elegant bridge forms whose global performance and serviceability are fundamentally governed by the intensity and allocation of prestressing loads applied to the stay cables. Consequently, determining the ideal initial prestressing forces represents a vital phase in both bridge design and erection. These forces are essential to establishing a viable equilibrium state wherein the completed bridge matches its intended profile under permanent dead loading, minimizes girder and pylon bending moments, and ensures a balanced stress distribution within safe deflection thresholds. Nevertheless, identifying such optimal forces is exceptionally challenging due to system nonlinearities, high dimensional complexity, and strong structural component coupling.

As modern bridge layouts often feature scores or even hundreds of individual cables, the resulting design space expands substantially, making conventional trial-and-error techniques and manual iterative calculations impractical and excessively labor-intensive. To overcome this difficulty, five main categories of methods have been introduced. The trial-and-error method, the most conventional and instinctive approach, relies primarily on the engineer's experience and skill, manually adjusting cable forces through repeated structural analyses until a satisfactory, though not necessarily optimal, solution is reached, and is widely recognized as time-consuming, costly, and almost impossible to apply to large and complex bridges. The zero-

displacement method of Wang et al. [1] identifies the cable tensions that return the deck and pylons to their specified design geometry under permanent dead load, minimizing vertical deck drop and horizontal pylon displacement while accounting for important nonlinearities such as cable sag and large-displacement (P-Delta) effects, although it proves computationally intensive and thus less effective for modern long-span bridges. The force equilibrium method of Chen et al. [2] instead concentrates on the internal force state, computing initial cable tensions that produce a predefined distribution of bending moments along the deck girder, an approach proclaimed easier and more powerful for practical design, particularly of prestressed concrete bridges, but one that usually assumes linear elastic, force-based equilibrium and may not account for the considerable geometric nonlinearities that develop during construction and service. The unit load method of Janjic et al. [3] offers a more complete framework that employs influence matrices to relate small variations in cable forces to variations in internal forces and displacements, enabling the structured incorporation of construction sequence, nonlinear geometric behavior, and time-dependent effects such as concrete creep, shrinkage, and steel relaxation, though it may not always yield a perfectly balanced and optimal distribution of cable forces and girder bending moments for super long-span bridges. Finally, optimization methods, as formulated by Boyd and Vandenberghe [4], systematically select the best possible solution by minimizing or maximizing an objective function while satisfying all equality and inequality constraints, allowing engineers to express design, control, and resource-allocation problems as mathematical programs and thereby find solutions with the best performance, least cost, or maximum reliability within specified limits.

Within an optimization-oriented approach, this study addresses the concurrent sizing and prestress force determination of stay cables by coupling the Rao-2 metaheuristic algorithm with MATLAB [5] and the SAP2000 [6] Open Application Programming Interface (OAPI). The primary objective is to achieve a lightweight cable system subject to stress and displacement boundaries under multiple static and dynamic load combinations. Through this strategy, the study seeks to characterize load-sharing mechanisms among structural components and clearly identify the dominant constraints—specifically differentiating between stress-governed and displacement-controlled bridge responses.

2 Structural Model Description of the bridge

The selected case study shown in *Fig. 1* is a double-pylon, modified fan-type cable configuration steel footbridge [7], chosen to investigate the application of the Rao-2 optimization algorithm in determining the optimal cable forces and cable dimensions. The footbridge, adopted from [7], spans a total of 61.30 m, with a 32.70 m central section supported by two 12.95 m steel pylons of hollow rectangular section, each carrying a modified fan-type arrangement of 14 stay cables per pylon connected to the deck. With a deck width of 4.20 m, the hybrid system integrates longitudinal and transverse steel I-shaped beams with a 12 cm concrete slab and lateral steel bracing, while the stay cables attach to the girder at mean intervals of 4.0785 m. Following the parameters established in [7], *Table 1* presents the material and geometrical properties: 28 stay elements made of nine-strand Grade 270 tendons are configured in a modified fan layout and divided into seven symmetrical groups (A_1–A_7), carrying initial prestressing force levels between −0.0001 and −0.0014. Because its structural stiffness is disregarded during computational modeling, the 12 cm concrete deck slab functions exclusively as applied dead load.

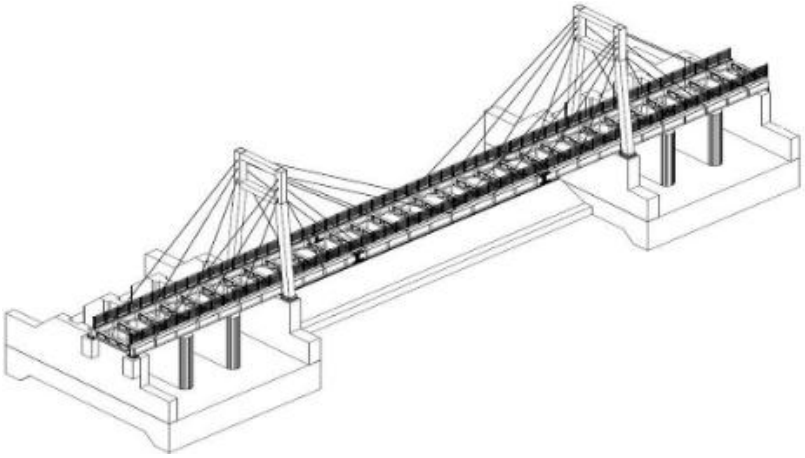


Fig. 1. Selected footbridge elevation [7].

Table 1. Stay-cable properties.

Property	Description	Value / Specification
Cable type	-	9-strand Grade270 low-relaxation prestressing steel
Ultimate tensile strength	f_{pu}	1862 MPa
Allowable stress	σ_{all}	1395 MPa (0.75 ×f_{pu})
Strand cross-sectional area	A_{strand}	140 mm²
Total cross-sectional area per cable	A_{total}	1260 mm²
Number of cables	-	28
Cable groups	-	A_1, A_2, A_3, A_4, A_5, A_6, A_7
Young's modulus	E	195 GPa
Post-tensioning strain	ε	–0.0001 to –0.0014

3 Load Combinations

Throughout this study, the load types considered in the structural analysis are identified by standard notation. Self-weight of the structural and non-structural members is captured by the dead load G, whereas the pedestrian live load Q is applied as a uniformly distributed load representing foot traffic across the deck. Wind action is treated in both principal directions, with *Wx* and *Wy* denoting the wind pressure acting along the longitudinal and transverse axes, respectively. Cable pre-stress is simulated by introducing the post-tensioning force (PTF) P as an initial strain, and seismic effects are likewise accounted for in both directions, with Ex and Ey representing earthquake excitation in the longitudinal and transverse directions, respectively. In accordance with the loading strategy defined by [7] for this bridge geometry, 14 load cases were implemented, consisting of eight static combinations (Comb1–Comb8) alongside six earthquake combinations (Comb9–Comb14); the detailed load categories and sign arrangements are detailed in *Table 2.*

Table 2. Load-combination sign patterns.

Load Combinations	Load zone on deck				Pylon-1		Pylon-2		Earthquake		Load Patterns
	1	2	3	4	W_x	W_y	W_x	W_y	U_x	U_y	
Comb1	+	+	+	+	+	+	+	+			$1.35G+1.5Q+0.9W_y+0.3W_x+P$
Comb2	+	+	+	+	+	+	+	+			$1.35G+1.5Q+0.3W_y+0.9W_x+P$
Comb3	+	-	+	-	-	+	+	+			$1.35G+1.5Q+0.9W_y+0.3W_x+P$
Comb4	+	-	+	-	-	+	+	+			$1.35G+1.5Q+0.3W_y+0.9W_x+P$
Comb5	-	+	+	-	+	+	+	+			$1.35G+1.5Q+0.9W_y+0.3W_x+P$
Comb6	-	+	+	-	+	+	+	+			$1.35G+1.5Q+0.3W_y+0.9W_x+P$
Comb7	+	-	-	+	-	+	+	+			$1.35G+1.5Q+0.9W_y+0.3W_x+P$
Comb8	+	-	-	+	-	+	+	+			$1.35G+1.5Q+0.3W_y+0.9W_x+P$
Comb9	+	+	+	+					+	+	$G+Q+0.3E_X+E_Y+P$
Comb10	+	+	+	+					+	+	$G+Q+E_X+0.3E_Y+P$
Comb11	+	+	+	+					+	-	$G+Q+0.3E_X+E_Y+P$
Comb12	+	+	+	+					-	+	$G+Q+E_X+0.3E_Y+P$
Comb13	+	+	+	+					-	-	$G+Q+0.3E_X+E_Y+P$
Comb14	+	+	+	+					-	-	$G+Q+E_X+0.3E_Y+P$

4 Methodology

A twin-pylon, modified fan-type steel cable-stayed footbridge (CSFB) was selected as the numerical model for the optimization study. The stay cables represent the main design variables of the optimization problem. Their cross-sectional areas and PTFs were simultaneously optimized to minimize the total cable weight while satisfying the required structural performance criteria. The optimization was performed by coupling the Rao-2 optimization algorithm with the finite element analysis software SAP2000 through its Open Application Programming Interface (OAPI). MATLAB was used as the main programming environment to control the optimization procedure and communicate with the SAP2000 model.

The main objective of the optimization was to minimize the total weight of the stay cables, expressed as:

$$W_{min} = \sum_{i=1}^{n_{sc}} \rho \, L_i \, A_i \tag{1}$$

Here W is the objective function defining the total weight of the cable system, ρ indicates the material density, L_i signifies the length of the i-th stay cable, A_i denotes its respective cross-sectional area, while n_{sc} represents the total number of stay cables in the bridge model.

In addition to minimizing cable weight, the optimized design was required to satisfy cable stress, deck displacement, and pylon displacement constraints. The constraint functions were defined as:

$$\mathrm{g}_i = \frac{\sigma_i}{\sigma_u} - 1 \leq 0 \; \mathrm{i} = 1, \ldots, nsc \tag{2}$$

$$\mathrm{g}_i = \frac{\delta_j}{\delta_{u-deck}} - 1 \leq 0 \; \mathrm{j} = 1, \ldots, npd \tag{3}$$

$$\mathrm{g}_k = \frac{\delta_k}{\delta_{u-pylon}} - 1 \leq 0 \; \mathrm{k} = 1, \ldots, npp \tag{4}$$

$$\text{If } \mathrm{g} > 0 \; \mathrm{c} = \mathrm{g} \text{ else } \mathrm{c} = 0 \tag{5}$$

In these expressions, σ_i and σ_u denote the computed axial stress and allowable stress limit for the cables, respectively, with nsc indicating the total number of stay cables. The terms npd and npp represent the number of nodes on the slab and towers, δ_j and δ_{u-deck} correspond to the computed and allowable vertical displacements of the deck, and δ_k and $\delta_{u-pylon}$ denote the computed and allowable horizontal displacements of the tower. When a constraint is satisfied,

the corresponding penalty parameter remains zero; otherwise, a non-zero violation value is assigned. The cumulative penalty value (C) for the entire optimization system is then determined via the following relation.

$$C = \sum_{i\,1}^{nsc} c_i \; + \sum_{j\,1}^{npd} c_j + \sum_{k=1}^{mpp} c_k \tag{6}$$

The Rao-2 algorithm is a simple, metaphor-free population-based optimization technique designed to solve complex optimization problems with a limited number of algorithm-specific parameters [8]. It improves candidate solutions by utilizing information from the best and worst solutions while also considering a randomly selected solution within the population.
The Rao-2 algorithm was employed to optimize the cross-sectional areas and PTFs of the stay cables. During each iteration, the candidate solutions are updated using the best and worst solutions of the current population, together with a randomly selected solution. Two random numbers, (r_1) and (r_2), within the range [0,1] are used in the updating process. In this study, a population size of 30 and a maximum of 1000 iterations were considered. The updated design variables were evaluated through SAP2000 using the MATLAB–OAPI interface, and the optimization continued until the maximum number of iterations was reached. The Rao-2 update equation is given as follows:

$$X'_{j,k,i}=X_{j,k,i} + r_{1,j,i}\left(X_{j,best,i} - X_{j,worst.i}\right) + r_{2.j.i}\left(\left|X_{j,k,i} or\ X_{j,l,i}\right| - \left|X_{j,l,i} or\ X_{j,k,i}\right|\right) \tag{7}$$

where is $X_{j,k,i}$ the value of the (j)-th design variable of the (k)-th solution at iteration (i), ($X_{j,best,i}$) and ($X_{j,worst.i}\}$) represent the corresponding variables of the best and worst solutions, respectively, and ($X_{j,l,i}$) denotes a randomly selected solution. The “or” terms are determined according to the objective-function values of the current and randomly selected solutions.

5 Numerical Results

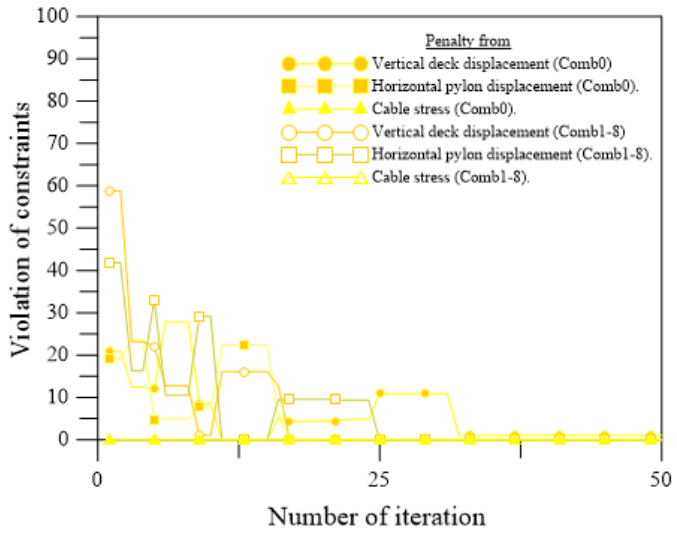
To assess the effectiveness of the developed optimization framework, a single independent execution of the Rao-2 algorithm was carried out based on the established problem parameters. The optimization was performed to determine whether the algorithm could obtain a feasible design while satisfying the prescribed stress and displacement constraints. The evolution of constraint violations throughout the optimization process is presented in *Fig. 2(a)*.

As shown in *Fig. 2(a),* the initial design contains several constraint violations, with the most significant violations associated with the displacement responses of the deck and pylons. In particular, the vertical deck displacement under Comb1–8 represents one of the dominant violations at the beginning of the optimization, while violations in the horizontal pylon displacement are also observed. In contrast, the cable stress violation remains very small compared with the displacement-related penalties. As optimization progresses, the constraint violations generally decrease as the cable cross-sectional areas and PTFs are continuously updated by the Rao-2 algorithm. Some fluctuations can be observed during the intermediate iterations, reflecting the search process of the algorithm. The remaining displacement violations are gradually reduced, and all constraint-violation curves eventually converge to zero. This indicates that the final optimized design satisfies the required stress and displacement limits for the considered load combinations. Overall, the results demonstrate that the optimization process was primarily governed by the deck and pylon displacement constraints, whereas the cable stress constraint was comparatively less critical.

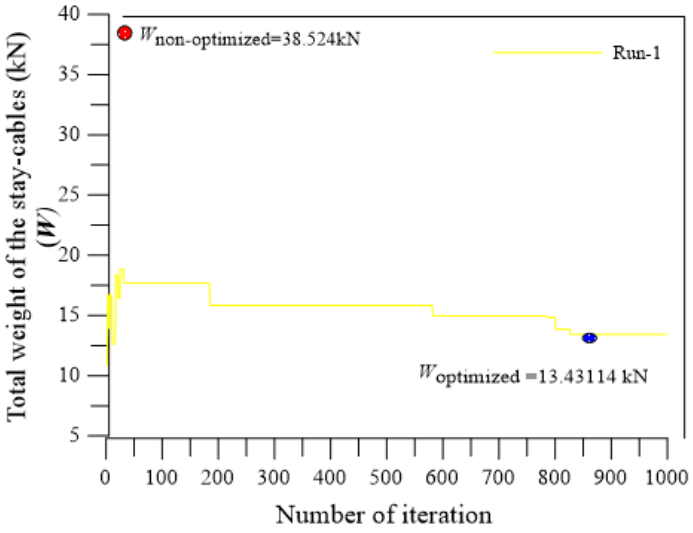
One independent optimization run was conducted using the Rao-2 algorithm to evaluate the optimization performance and determine the final optimized weight of the stay-cable system. *Fig. 2(b)* presents the variation of the total weight of the stay-cables with the number of

iterations. The initial unoptimized design had a total stay-cable weight of approximately 38.524 kN. During the initial iterations, the total cable weight showed some fluctuations as the algorithm searched for more efficient combinations of cable cross-sectional areas and PTFs. The objective function then gradually stabilized as the optimization progressed, indicating convergence toward an optimum solution. The final optimized stay-cable weight was 13.43114 kN at the 828th iteration, after which no significant improvement was observed. Compared with the initial design, this represents a substantial reduction in the total stay-cable weight while satisfying the imposed structural constraints. Overall, the convergence history demonstrates the ability of the Rao-2 algorithm to efficiently reduce cable weight and obtain a stable optimized solution.

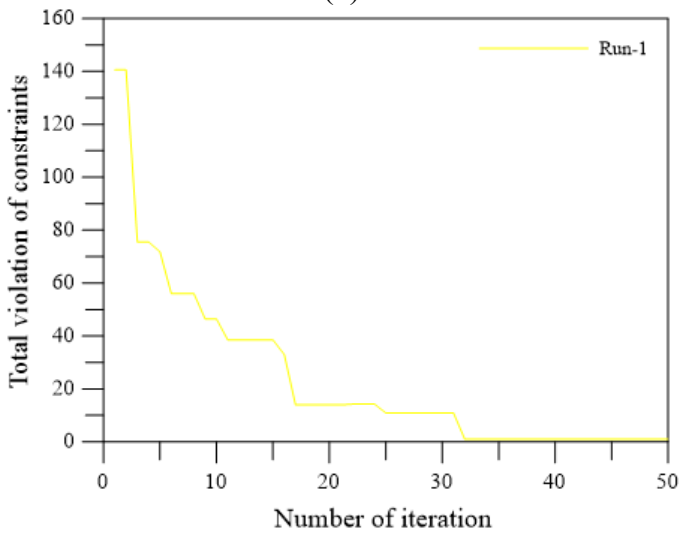
Fig. 2(c) illustrates the variation of the total constraint violation with the number of iterations for Run-1. At the beginning of the optimization process, the total constraint violation is approximately 140, indicating that the initial design does not satisfy the imposed structural constraints. As the number of iterations increases, the total violation decreases progressively, although several small fluctuations can be observed during the early and intermediate stages of the optimization. These changes reflect the adjustment of the cable cross-sectional areas and PTFs as the Rao-2 algorithm searches for a feasible solution. The total constraint violation continues to decrease throughout the optimization process and reaches zero at approximately the 34th iteration. A zero value indicates that all imposed stress and displacement constraints are satisfied. After reaching zero, the constraint violation remains at zero, confirming that the optimized solution remains within the required constraint limits. Overall, the convergence history demonstrates that the Rao-2 algorithm successfully guided the initial infeasible design toward a feasible solution within a relatively small number of iterations.



(a)



(b)

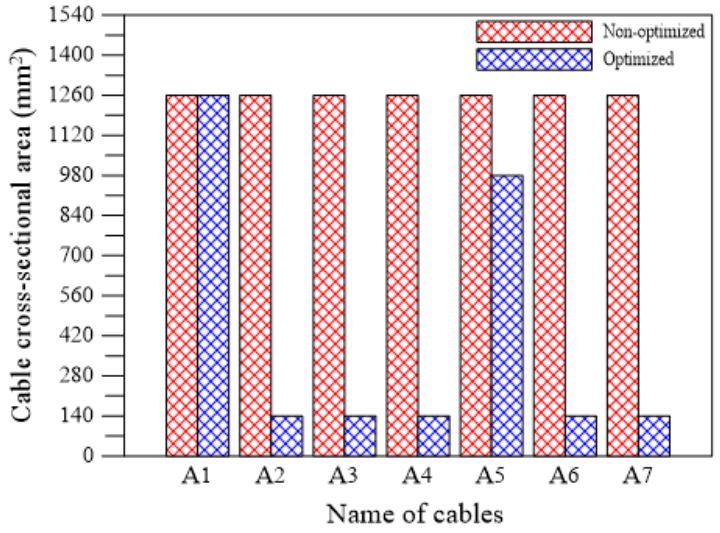


(c)

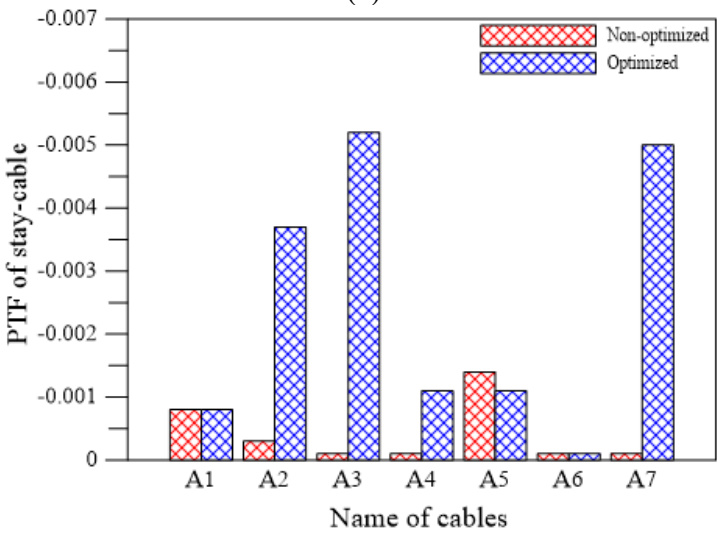
Fig. 2. Convergence of the Rao-2 optimization process: (a) individual constraint violation curves, (b) stay-cable weight across iterations, and (c) total violation of constraints.

Fig. 3(a) compares the cross-sectional areas of the stay-cable groups before and after optimization using the Rao-2 algorithm. In the non-optimized design, all cable groups have an identical cross-sectional area of 1260 mm², indicating a uniform initial cable configuration. Following optimization, the cable areas are redistributed according to the structural requirements of each cable group. The cross-sectional area of A1 remains relatively close to its initial value, decreasing slightly to approximately 1120 mm², while the areas of A2, A3, A4, A6, and A7 are significantly reduced to approximately 140 mm². In contrast, A5 retains a considerably larger cross-sectional area of approximately 980 mm², indicating that this cable group requires greater capacity to satisfy the structural constraints. This non-uniform distribution demonstrates that the Rao-2 algorithm effectively identifies cable groups where material can be reduced while maintaining sufficient capacity in the more critical cable groups. Overall, the optimized configuration results in a substantially more efficient distribution of cable material compared with the initial uniform design, contributing to the reduction in the total stay-cable weight from 38.524 kN to 13.43114 kN, corresponding to an overall reduction of approximately 65.14%.

Fig. 3(b) compares the PTFs applied to the stay-cable groups before and after optimization using the Rao-2 algorithm. The non-optimized configuration shows a relatively limited and uneven distribution of PTF among the cable groups. Following optimization, the PTF values are redistributed considerably between the different cable groups rather than being modified uniformly. The optimized solution maintains a similar PTF for A1, while noticeable increases in the magnitude of PTF are observed for A2, A3, A4, and A7. In contrast, A5 shows a slight reduction in the magnitude of the applied PTF, while A6 remains approximately zero. This redistribution indicates that the optimization process adjusts the prestressing forces according to the structural response of each cable group. The optimized PTF distribution works together with the optimized cable cross-sectional areas to satisfy the imposed displacement and stress constraints while reducing the overall cable weight. Therefore, the results demonstrate that the Rao-2 algorithm does not simply minimize the cable size but simultaneously determines a more suitable distribution of prestressing forces among the stay-cables.



(a)



(b)

Fig. 3. Comparison between non-optimized and Rao-2 optimized stay-cable parameters: (a) cable cross-sectional area, and (b) cable PTF.

6 Conclusion

This study presents a numerical optimization framework for determining the optimum cross-sectional areas and post-tensioning forces (PTFs) of stay-cables in a cable-stayed footbridge

(CSFB). The Rao-2 algorithm was integrated with MATLAB and SAP2000 through the OAPI interface to minimize the total stay-cable weight while satisfying the prescribed stress and displacement constraints. A twin-pylon, modified fan-type steel CSFB was used as the numerical model to demonstrate the applicability of the proposed optimization approach. Based on the results obtained, the following conclusions can be drawn:

- The Rao-2 optimization reduced the total stay-cable weight from 38.524 kN to 13.43114 kN, corresponding to an overall reduction of approximately 65.14% while satisfying the imposed structural constraints.
- The optimized cable cross-sectional areas were redistributed according to the structural requirements of each cable group, resulting in a more efficient allocation of cable material compared with the initial uniform configuration.
- The optimization process successfully determined suitable PTF for the individual stay-cables, contributing to the satisfaction of the required displacement and stress limits.
- The convergence results indicate that deck and pylon displacement constraints were more critical than cable stress constraints, while all imposed constraints were ultimately satisfied by the optimized design.

References

1. Wang, P. H., Tseng, T. C., Yang, C. G.: Initial Shape of Cable-Stayed Bridges. Computers and Structures 46, 1095–1106 (1993).
2. Chen, D. W., Au, F. T.: Determination of Initial Cable Forces in Prestressed Concrete Cable-Stayed Bridges for Given Design Deck Profiles Using the Force Equilibrium Method. Computers and Structures 74, 1–9 (2000).
3. Janjic, D., Pircher, M., Pircher, H.: The unit load method – some recent applications. In: Proceedings of the Third International Conference on Advances in Steel Structures (ICASS '02), vol 2, pp. 831–837. Elsevier, Hong Kong (2002).
4. Boyd, S., Vandenberghe, L.: Convex Optimization. Cambridge University Press, Cambridge (2004).
5. The MathWorks, Inc., MATLAB version R2023b, (2023).
6. Computers and Structures, Inc.: SAP2000 User Manual (2016).
7. Atmaca, B.: Size and post-tensioning cable force optimization of cable-stayed footbridge. Structures 33, 2036–2049 (2021).
8. Rao, R. V.: Rao algorithms: Three metaphor-less simple algorithms for solving optimization problems. International Journal of Industrial Engineering Computations 11, 107–130 (2020).

Author Contribution Statement

- *Conceptualization:* Barbaros ATMACA, Tayfun DEDE
- *Methodology:* Barbaros ATMACA, Chiraz FAZZAA
- *Investigation:* Barbaros ATMACA, Chiraz FAZZAA, Büşra YAKAK VATANDAŞ
- *Writing – Original Draft:* Chiraz fazzaa,
- *Writing – Review & Editing:* Barbaros ATMACA

List of Abbreviations

- **PTF** — Post tensioning Force
- **OAPI** — Open Application Programming Interface
- **CSFB** — Cable-Stayed Footbridge

Conflict of interest

The authors declare that they have no conflict of interest.

Publication Note

This paper was peer-reviewed, accepted for presentation, and included in the proceedings of the ACE2026 – International Conference on Advances in Civil Engineering, held on 12–14 October 2026 in Trabzon, Türkiye.

This paper may be cited as follows:

Fazzaa C., Atmaca B., Yakak Vatandas B., Ates S., "Optimal Sizing and Post-Tensioning Force Design of Cable-Stayed Footbridges via the Rao-2 Algorithm" in Proceedings of the ACE2026 – International Conference on Advances in Civil Engineering, Trabzon, Türkiye, 12–14 October 2026.

Optimum Redesign of a Real-World Large-Span Steel Truss Roof in One Overnight Run

Dr. Hasan Eser[1] and Prof. Dr. Oğuzhan Hasançebi[2]
[1] 0000-0001-8527-020X, Middle East Technical University, Civil Engineering Department, Ankara, Türkiye, heser@metu.edu.tr
[2] 0000-0002-5501-1079, Middle East Technical University, Civil Engineering Department, Ankara, Türkiye, oguzhan@metu.edu.tr

Abstract. This study presents a comparative assessment of the original and optimum designs of a real-world large-span steel truss roof system in terms of cost efficiency and compliance with key design constraints, including demand-to-capacity (D/C) ratios and maximum displacements. The truss system has plan dimensions of 94.25 m × 64.00 m, corresponding to a total covered area of 6032 m². Structural weight was adopted as a cost proxy, and both designs were evaluated on the same basis (i.e., identical code provisions, loading, load combinations, member grouping, and section catalog) so that they differ only in the sizing decision. The optimization was carried out using a recently developed, design-driven technique called the Capacity Controlled Search (CCS) algorithm. To mitigate run-to-run variability, 15 independent runs were performed, each capped at 500 structural analyses. The minimum-weight feasible design across all runs was selected as the optimum solution and yielded a structural weight reduction of 16.4% relative to the original engineering-office design. Notably, the heaviest design across all runs was still 11.9% lighter than the original, so that a single overnight run (10 h 33 min on a notebook PC) is sufficient in a design-office setting. Beyond direct material savings, this weight reduction translates into lower fabrication, transportation, and erection costs, as well as a reduced environmental footprint. These findings illustrate that design-driven optimization can be integrated into real engineering workflows, offering a practical and computationally affordable pathway to cost-efficient, sustainable structural design.

Keywords: Large-Span Steel Truss Roof System, Structural Design Optimization, Design-Driven Optimization, Real-World Structures, Sustainable Structural Design

1 Introduction

In modern civil engineering practice, large-span steel truss roof systems are frequently preferred for covering wide, column-free spaces such as those in sports arenas, shopping malls, and industrial facilities. They are also unusually favorable targets for optimization: they comprise hundreds of members, are highly redundant, are priced by tonnage, and are assembled from a limited number of repeated member groups, so that an improvement obtained for one group propagates across the entire roof. These structures are typically designed via iterative, trial-and-error procedures driven by engineering judgment, with member sizes selected from a discrete catalog of commercially available sections. Since designers can manually explore only a fraction of a vast design space, the resulting structures are often over-designed, leading to unnecessarily inflated material costs, which in turn cascade into higher fabrication, transportation, and erection costs, as well as a larger overall environmental footprint.

A systematic search of the design space to identify economically optimal solutions can be automated via structural optimization. Early optimization methods (e.g., mathematical programming, optimality criteria) relied on gradient information to determine search directions

[1–3]. These approaches, however, are largely impractical for real-world steel design problems characterized by discrete cross-sectional variables and nonlinear, non-convex constraints. Consequently, metaheuristic algorithms have gained significant research interest [4]. While metaheuristics can easily handle discrete variables without requiring gradient calculations, thousands of structural analyses are typically required before converging to a high-quality feasible design due to their stochastic nature. Moreover, multiple independent runs must be performed before any reported design can be trusted. This computational cost becomes especially prohibitive in practical applications, where even a single analysis can be computationally expensive owing to large models, numerous load combinations, and the nonlinear procedures increasingly required by modern codes [5].

This computational burden was largely overcome with the development of design-driven (guided) optimization methods [6–9]. These algorithms substantially accelerate the search process by leveraging structural response information obtained in previous iterations. The present study employs one such method: the Capacity Controlled Search (CCS) algorithm [10]. CCS is deliberately adopted here for its algorithmic simplicity, robustness, and fast convergence, which make it well suited to practical project schedules. CCS uses maximum demand-to-capacity (D/C) ratios to rapidly direct the search toward lighter yet highly utilized designs, while employing probabilistic rules to manage global displacement constraints and to retreat from infeasible regions.

Despite these algorithmic advances, the adoption of optimization in professional practice remains limited. One reason is that academic research is dominated by simplified or idealized benchmark structures on which algorithms are compared against one another rather than against an actual design produced by an engineering office. Applications to real structures do exist [4, 11], but they remain few relative to the benchmark literature, and differ in structural type, design code, and comparison basis. Therefore, the savings margin available within any given typology cannot yet be regarded as established; what is needed, then, is not a further demonstration that optimization is feasible on a real structure, but the accumulation of same-basis, code-compliant comparisons across practical typologies, each reported together with the analysis budget it consumed. The remaining barriers to adopting optimization in practice are largely non-technical: limited familiarity with advanced techniques, the misconception that heavier structures are inherently safer, and an underappreciation of optimization's broader benefits among stakeholders [11].

This study presents a comparative assessment of a real-world large-span steel truss roof system covering 6032 m² (94.25 m × 64.00 m). The original engineering-office design was compared against a minimum-weight code-compliant design generated by the CCS algorithm under identical code provisions, loading, load combinations, member grouping, and section catalog, so that the two designs differ only in the sizing decision. Through this comparison, this study ultimately aims to (1) quantify the material savings achievable through optimization relative to a conventional design-office solution for the given typology; and (2) demonstrate the practical viability of design-driven optimization for real-world engineering applications in terms of computational cost and time.

The rest of this paper is organized as follows. Section 2 outlines the mathematical formulation of the structural optimization problem. Section 3 provides a brief summary of the CCS algorithm. Section 4 presents the real-world large-span truss roof system, detailing the comparative analysis between the original engineering-office design and the optimum design. Finally, Section 5 summarizes the conclusions drawn from this study.

2 Optimum Design Problem Formulation

In steel design, member sections are selected from a predefined pool of standard profiles. These available sections are ordered from the smallest to the largest and assigned index numbers

accordingly. Since using too many different section types is generally undesirable from a fabrication and erection standpoint, structural members are usually grouped, and all members within the same group are assigned the same section. Based on this approach, the discrete sizing optimization problem for a steel structure can be formulated as follows:

$$\mathbf{I^T} = \left[I_1, I_2, \dots, I_{N_g}\right] \tag{1}$$

$$W = \sum_{i=1}^{N_g} \gamma_i A_i \sum_{j=1}^{N_{m,i}} L_{j,i} \tag{2}$$

$$g_k \leq 0, \quad k = 1, 2, \dots, N_c \tag{3}$$

where $\mathbf{I}$ is the vector of section indices assigned to the N_g member groups; γ_i and A_i are the unit weight and cross-sectional area of group i, respectively; $N_{m,i}$ is the number of members in group i; $L_{j,i}$ is the length of member j in group i; g_k is the $k-th$ normalized design constraint; and N_c is the total number of constraints.

A design is considered feasible only if it satisfies the relevant code requirements. In this study, the strength and serviceability constraints are defined according to the Turkish Structural Steel Design Specification [12]. The following constraints are considered.

For doubly and singly symmetric members under combined axial force and bending moment:

$$\left(\frac{P_r}{P_c}\right)_j \geq 0.2, \qquad g_1 = \left(\frac{P_r}{P_c}\right)_j + \frac{8}{9}\left(\frac{M_{rx}}{M_{cx}} + \frac{M_{ry}}{M_{cy}}\right)_j - 1.0 \leq 0 \tag{4}$$

$$\left(\frac{P_r}{P_c}\right)_j < 0.2, \qquad g_1 = \left(\frac{P_r}{2P_c}\right)_j + \left(\frac{M_{rx}}{M_{cx}} + \frac{M_{ry}}{M_{cy}}\right)_j - 1.0 \leq 0 \tag{5}$$

For members subjected to shear force:

$$g_2 = \left(\frac{V_r}{V_c}\right)_j - 1 \leq 0 \tag{6}$$

For tubular and box-section members subjected to the combined effects of torsion, shear, bending, and axial force:

$$\left(\frac{T_r}{T_c}\right)_j \geq 0.2, g_3 = \left(\frac{P_r}{P_c} + \frac{M_{rx}}{M_{cx}} + \frac{M_{ry}}{M_{cy}}\right)_j + \left(\frac{V_{\mathrm{rx}}}{V_{\mathrm{cx}}} + \frac{V_{\mathrm{ry}}}{V_{\mathrm{cy}}} + \frac{T_r}{T_c}\right)_j^2 - 1 \leq 0 \tag{7}$$

Here, g_1, g_2, and g_3 denote the strength constraints for members under axial force and bending, shear, and combined axial force-bending-shear-torsion effects, respectively. P_r, M_{rx}, M_{ry}, V_{rx}, V_{ry}, and T_r represent the required axial force, bending moments, shear forces about the x- and y-axes, and torsional moment, respectively. P_c, M_{cx}, M_{cy}, V_{cx}, V_{cy}, and T_c are the corresponding available strengths defined by the design code. The x and y subscripts refer to the major and minor axes.

For large-span steel roof systems, serviceability requirements are also important. Therefore, the displacement constraint for the roof trusses is defined as:

$$g_4 = \frac{\Delta_i^{max}}{\Delta_i^a} - 1 \leq 0 \tag{8}$$

Here, Δ_i^{max} is the maximum displacement of truss i under the governing load combinations, and Δ_i^a is the allowable displacement limit.

In this study, an exterior penalty function approach [13] is used to handle constraint violations. Designs violating one or more constraints (i.e., infeasible designs) are penalized through the following expression:

$$\phi = W[1 + Penalty(\mathbf{I})] = W\left[1 + r_o\left(\sum_{k=1}^{N_c} \max(0, g_k)\right)\right] \tag{9}$$

where ϕ is the penalized objective function, g_{k} is the $k-th$ normalized constraint, N_c is the total number of constraints, and r_o is the penalty coefficient, taken as 1.0 in this study. At the end of the optimization process, the lightest feasible design obtained during the search is selected as the optimum solution.

3 Optimization Algorithm

The optimization was performed using CCS algorithm [10], a design-driven optimization method that uses maximum D/C ratios to quickly guide the search toward near-optimal solutions. The search process is initialized with the largest available sections for each member group. The penalized weight and the group-wise maximum D/C ratios are then evaluated. Next, a candidate design is generated by perturbing member groups, where modification likelihoods and adaptive step sizes are determined based on corresponding D/C ratios. Similarly, displacement constraints are handled with D/C ratio-based probabilistic rules to retreat from infeasible regions. Candidate solutions are first screened using a pre-analysis objective function, and only promising designs undergo full structural analysis. A candidate replaces the current elite design only if it yields a lower objective function value. In case of a prescribed number of non-improving iterations, a stagnation escape period (SEP) is activated. During SEP, limited uphill moves are temporarily allowed to escape from a local optimum. The search is terminated when a stopping criterion is satisfied. Full details regarding the implementation steps of the CCS algorithm are provided in Eser and Hasançebi [10].

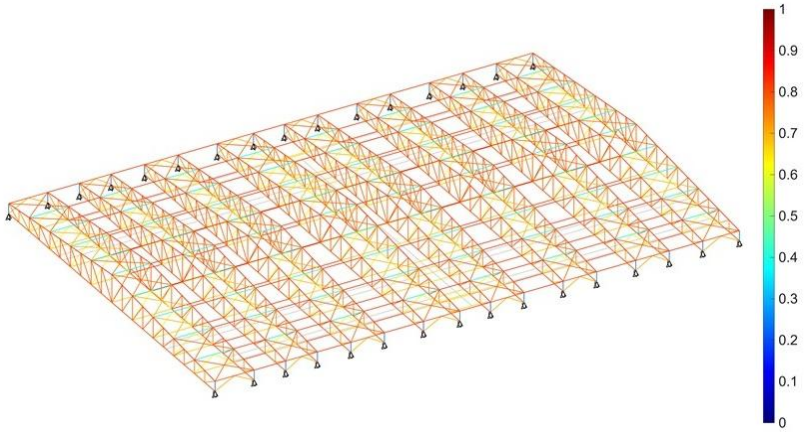
4 Real-World Design Case: 1941-Member Large-Span Steel Truss Roof System

In this study, a large-span steel truss roof consisting of 1941 steel truss members is optimized (Fig. 1). The roof has plan dimensions of 94.25 m × 64.00 m, and the maximum truss depth is 5 m. In line with the problem formulation of the original design, the members are divided into 17 sizing groups and assigned sections from two distinct S355 profile lists: H-sections and CHS (tube) sections. In the design, 121 load combinations are considered, including 115 for strength checks and 6 for deflection control, with the maximum vertical truss displacement limited to L/300 (21.3 cm). The analysis and design of the structure were performed on SAP2000 [14], whereas the optimization algorithm was coded to run in MATLAB [15].

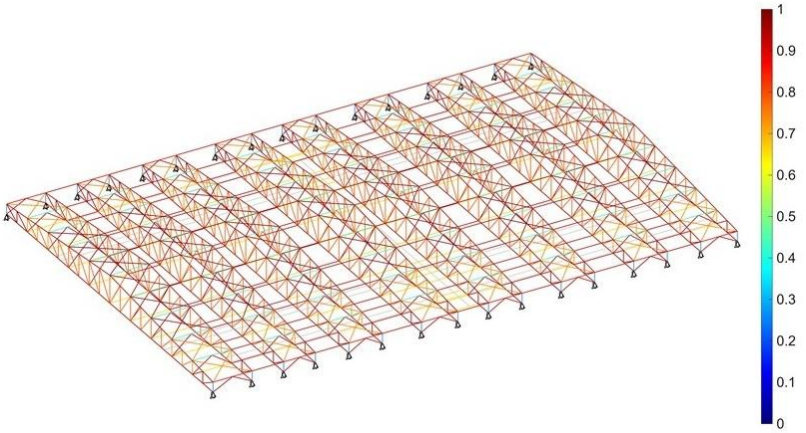
To mitigate run-to-run variability, 15 independent runs were executed, each capped at 500 structural analyses, and the minimum-weight feasible design obtained across all runs was adopted as the optimum. All runs terminated feasible, with design weights ranging from 296.41 t to 308.47 t. The optimum design weighs 296.41 t, resulting in a reduction of 48.62 t (16.4%) relative to the original design, which weighs 345.03 t. These designs are tabulated in Table 1. The group-based D/C ratios in Fig. 1 reveal that the members are utilized more efficiently in the optimum design than in the original design. Both designs satisfy the deflection limit, the

maximum vertical displacement increasing from 13.4 cm to 15.6 cm (73% of the allowable value), which indicates that the optimum design is governed by strength rather than serviceability.

Regarding computational cost, the best run was initialized with the largest available cross-sections and located optimum design at 273rd analysis, after 5 h 45 min of computation on a notebook PC with an Intel i7-12700H processor and 32 GB DDR5-4800 RAM; the run then continued to the cap of 500 analyses, requiring 10 h 33 min in total. Since even the heaviest of the 15 designs remains 11.9% lighter than the original engineering-office design, a single run would suffice in a design-office setting, placing the computational demand at one overnight job for a structure of this size.



(a) Original Design



(b) Optimum Design

Fig. 1. Group-based D/C ratios of original and optimum designs for 1941-member truss roof system

5 Conclusion

In this study, a real-world large-span steel truss roof system with a total covered area of 6032 m² was designed for minimum weight using the Capacity Controlled Search algorithm. The results show that a 16.4% (48.62 t) reduction in structural weight relative to the original engineering-office design can be achieved while satisfying all design constraints. A lighter structure translates into lower material, fabrication, transportation, and erection costs as well as a reduced environmental footprint, thus promoting sustainable construction. Since the heaviest design across 15 independent runs is 11.9% lighter than the original design, even a single overnight run (10 h 33 min on a notebook PC) is sufficient in a design-office setting. Therefore,

design-driven optimization is practically suitable for integration into real-world engineering workflows.

Table 1. Original and optimum designs for 1941-member truss roof system

#	Groups	Original Design	Optimum Design
1	BOTTOM_CHORD	HE240B	HE260A
2	TOP_CHORD	HE360B	HE300B
3	UPRIGHTS_SUPPORT	HE240B	HE260A
4	WEB_MEMBERS1	CHS 165,1x4,0	CHS 165,1x4,0
5	WEB_MEMBERS2	CHS 165,1x4,0	CHS 165,1x4,0
6	WEB_MEMBERS3	CHS 273,0x6,0	CHS 244,5x5,0
7	CROSS_BRIDGING1	CHS 101,6x3,0	CHS 88,9x3,0
8	CROSS_BRIDGING2	CHS 101,6x3,0	CHS 101,6x3,0
9	CROSS_BRIDGING3	CHS 165,1x4,0	CHS 159,0x3,0
10	HORIZONTAL_BRIDGING1	CHS 114,3x3,0	CHS 114,3x3,0
11	HORIZONTAL_BRIDGING2	CHS 114,3x3,0	CHS 114,3x3,0
12	HORIZONTAL_BRIDGING3	CHS 177,8x4,0	CHS 165,1x4,0
13	HORIZONTAL_BRIDGING4	CHS 139,7x3,0	CHS 133,0x3,0
14	HORIZONTAL_BRACES1	CHS 177,8x4,0	CHS 165,1x4,0
15	HORIZONTAL_BRACES2	CHS 219,1x4,0	CHS 193.7x4.0
16	HORIZONTAL_BRACES3	CHS 244,5x5,0	CHS 244,5x5,0
17	CATWALK	HE160A	HE160A
Design Weight (t)		345.03	296.41
Savings (t)		48.62	
Savings (%)		16.4	

Acknowledgments
Authors would like to thank the engineering office for providing the SAP2000 structural model of the original design.

Conflict of Interest
The authors declare that they have no known competing financial interests or personal relationships that could have appeared to influence the work reported in this paper.

References
1. Erbatur, F., Al-Hussainy, M. M. Optimum Design of Frames. Computers & Structures, 45, 887-91, 1992. https://doi.org/10.1016/0045-7949(92)90047-4
2. Tabak E. I., Wright, P. M. Optimality Criteria Method for Building Frames. Journal of Structural Division, ASCE, 107, 1327–1342, 1981. https://doi.org/10.1061/JSDEAG.0005735
3. Saka, M. P. Optimum Design of Steel Frames with Stability Constraints. Computers & Structures, 41, 1365-1377, 1991. https://doi.org/10.1016/0045-7949(91)90274-P
4. Saka, M. P., Hasançebi, O., Eser, H., Geem, Z. W. Historical Evolution of Structural Optimization Techniques for Steel Skeletal Structures Including Industrial Design Applications. Engineering Optimization, 57(1), 69-129, 2025. https://doi.org/10.1080/0305215X.2024.2390130
5. Zakian, P., Kaveh, A. Seismic Design Optimization of Engineering Structures: A Comprehensive Review. Acta Mechanica, 234, 1305–1330, 2023. https://doi.org/10.1007/s00707-022-03470-6
6. Elvin A, Walls R, Cromberge D. Optimising Structures Using the Principle of Virtual Work.

Journal of the South African Institution of Civil Engineering, 51(2), 11–9, 2009.
7. Walls R, Elvin A. Optimizing Structures Subject to Multiple Deflection Constraints and Load Cases Using the Principle Of Virtual Work. Journal of Structural Engineering, 136(11), 1444–52, 2010. https://doi.org/10.1061/(ASCE)ST.1943-541X.0000246
8. Flager, F., Soremekun, G., Adya, A., Shea, K., Haymaker, J., Fischer, M. Fully Constrained Design: A General and Scalable Method for Discrete Member Sizing Optimization of Steel Truss Structures. Computers & Structures, 140, 55-65, 2014. https://doi.org/10.1016/j.compstruc.2014.05.002
9. Azad, S. K., Hasançebi, O. Computationally Efficient Discrete Sizing of Steel Frames via Guided Stochastic Search Heuristic. Computers & Structures, 156, 12-28, 2015. https://doi.org/10.1016/j.compstruc.2015.04.009
10. Eser, H., Hasançebi, O. Capacity Controlled Search: A New and Efficient Design-Driven Method for Discrete Size Optimization of Steel Frames. Computers & Structures, 275, 106937, 2023. https://doi.org/10.1016/j.compstruc.2022.106937
11. Eser, H., Hasançebi, O. Ülkemiz Mühendislik Uygulamalarında Çelik Çatı Sistemlerinin Optimum Tasarımına Dair İnceleme [A Study on the Optimum Design of Steel Roof Systems in Turkish Engineering Practice]. Turkish Journal of Civil Engineering, 36(3), 39-57, 2025. https://doi.org/10.18400/tjce.1543461
12. T. C. Çevre, Şehircilik ve İklim Değişikliği Bakanlığı. Çelik Yapıların Tasarım, Hesap ve Yapımına Dair Esaslar, 2018.
13. Coello, C. A. C. Theoretical and Numerical Constraint-Handling Techniques Used with Evolutionary Algorithms: A Survey of The State of the Art. Computer Methods in Applied Mechanics and Engineering, 191(11-12), 1245-1287, 2002. https://doi.org/10.1016/S0045-7825(01)00323-1
14. Computers and Structures Inc. SAP2000 version: 21.0.2. Berkeley, California, 2019.
15. MathWorks Inc. MATLAB version: 9.14.0 (R2023a), Natick, Massachusetts, 2023.

Author Contribution Statement

- *Conceptualization:* Dr. Hasan Eser, Prof. Dr. Oğuzhan Hasançebi
- *Methodology:* Dr. Hasan Eser, Prof. Dr. Oğuzhan Hasançebi
- *Investigation:* Dr. Hasan Eser
- *Writing – Original Draft:* Dr. Hasan Eser
- *Writing – Review & Editing:* Prof. Dr. Oğuzhan Hasançebi

List of Abbreviations

- **CCS** — Capacity Controlled Search
- **D/C** — Demand-to-Capacity
- **SEP** — Stagnation Escape Period

Publication Note

This paper was peer-reviewed, accepted for presentation, and included in the proceedings of the ACE2026 – International Conference on Advances in Civil Engineering, held on 12–14 October 2026 in Trabzon, Türkiye.

This paper may be cited as follows:

Eser, H. & Hasançebi, O., "Optimum Redesign of a Real-World Large-Span Steel Truss Roof in One Overnight Run," in Proceedings of the ACE2026 – International Conference on Advances in Civil Engineering, Trabzon, Türkiye, 12–14 October 2026.

Progressive Collapse of Reinforced Concrete Buildings with Ground-Floor Slab Discontinuity: Effectiveness of the Tie Force Method and the Role of Column Orientation

Alaaddin ALJUNEED[1], Temel TÜRKER[1]

1 Department of Civil Engineering, Karadeniz Technical University, 61080 Trabzon, Türkiye
aljuneed@ktu.edu.tr · temelturker@ktu.edu.tr

Abstract. Diaphragm discontinuity is treated by current seismic codes purely as an in-plane force-transfer problem, and the indirect tie force (TF) design route of UFC 4-023-03 presumes that internal ties run uninterrupted across the floor and that peripheral ties form a closed ring. A large slab opening violates that premise geometrically, yet no provision addresses it. This study examines, through 60 nonlinear dynamic column-removal analyses in LS-DYNA, how a ground-floor slab opening of constant area but varying position affects progressive collapse response, and whether the TF method remains effective when the diaphragm is interrupted. A three-storey 4×3-bay reinforced concrete frame-slab building is used as the regular reference; three opening layouts of equal area (corner, central and full-row) are generated, and all four buildings are then redesigned according to UFC 4-023-03, giving four matched pairs that differ only in tie reinforcement. The numerical model reproduces the full-scale corner-column removal test of Adam et al. (2020) with 0.0% error in peak and +5.6% in residual displacement. Peak displacements range from 15.1 to 30.0 mm and chord rotations remain below 40% of the UFC acceptance limit, placing the entire response in the flexural regime: compressive arch action is not even reached. The effect of the discontinuity varies between −0.9% and +37.8% depending on the scenario, governed by whether the opening interrupts the alternate load path at the position of the removed column rather than by its area. Tie reinforcement reduces peak displacement by 7.5–8.7%, but the measured rotations are only 1.6–3.1% of the 0.20 rad on which the method relies; three independent observations show the gain to be a flexural stiffness effect rather than the intended catenary action. Tied buildings with openings do not reach the performance of the untied regular building. Finally, column orientation emerges as an independent governing parameter: two long-edge columns carrying loads within 0.3% of each other produce peak displacements 41% apart depending on which axis the remaining bridging supports bend about.

Keywords: Progressive collapse; Diaphragm discontinuity; Tie force method; Alternate path method; Nonlinear dynamic analysis; LS-DYNA

1. Introduction

Progressive collapse is the propagation of an initial local failure from element to element until a portion of the structure — or the whole of it — is lost, and the final damage is disproportionate to the triggering event (Starossek, 2014). Since the Ronan Point and Alfred P. Murrah Federal Building failures, design guidance has converged on two complementary routes. The indirect route prescribes minimum continuity, ductility and redundancy through tie forces, without requiring any removal analysis. The direct route, the Alternate Path (AP) method, removes a load-bearing element and verifies that the remaining structure can bridge over the resulting gap. GSA (2016) and UFC 4-023-03 (DoD, 2016) are the two documents most widely used for both, and their application to reinforced concrete framed buildings has been examined in detail by Helmy et al. (2012).

The tie force (TF) method of UFC 4-023-03 rests on a specific mechanical premise: that under a column loss the floor system develops tensile membrane and catenary action, and that the tie reinforcement is able to sustain its design force at a rotation of 0.20 rad (McKay et al., 2012). Equally important, and more often overlooked, is a geometric premise: internal ties must run uninterrupted from one edge of the floor to the other, and peripheral ties must close a continuous

ring around it. A large opening in the floor slab — an atrium, a stairwell and lift core, a double-height void — breaks both continuities at the ground floor, precisely where the consequences of a column loss are most severe.

Current codes do not address this. Diaphragm discontinuity is classified as an irregularity only in relation to seismic in-plane force transfer: TBDY-2018 defines type A2 irregularity when the total opening area exceeds one third of the gross floor area, and ASCE 7-16 sets the corresponding limit at one half. Both are area-ratio criteria, and neither carries any requirement for the case of vertical element loss. Whether an area ratio is an adequate descriptor of progressive collapse vulnerability has not been tested.

The importance of modelling the slab itself is now well established. Pang et al. (2021), Cheng et al. (2024) and Mohieldin et al. (2026) all show that frame-only models substantially misrepresent the alternate load path, because the slab supplies both flexural continuity and, at large displacement, tensile membrane action. Yu and Tan (2013) quantified the displacement thresholds at which the successive resisting mechanisms are mobilised, and their results remain the standard reference for deciding which regime a given response belongs to. Studies of irregular buildings (Yavari et al., 2019; Azim et al., 2020) have concentrated on plan and vertical irregularity rather than on diaphragm openings, and where openings are considered the opening area rather than its position is the variable.

This study addresses that gap. Three slab opening layouts of identical area but different position are compared against a regular reference building, each with and without UFC tie reinforcement, under GSA-compliant column removal scenarios. The objectives are to quantify (i) how strongly the position of an equal-area opening governs the response, (ii) whether the TF method remains effective, and through which mechanism it actually works, when the diaphragm is interrupted, and (iii) an effect that emerged during the analyses and proved larger than expected — the orientation of the rectangular columns that support the bridging frame.

2. Numerical modelling

2.1. Solution scheme and material models

All analyses were carried out in LS-DYNA using the explicit central-difference solver. Concrete was represented by *MAT_CSCM_CONCRETE (MAT 159), a continuous surface cap model developed and calibrated for impulsive loading (Murray, 2007), with f'c = 30 MPa, ρ = 2380 kg/m³, maximum aggregate size 19 mm, strain-rate effects active (IRATE = 1), element erosion at ERODE = 1.05 and a maximum compressive strain of 0.08. Reinforcement was modelled with *MAT_PIECEWISE_LINEAR_PLASTICITY (MAT 24) with fy = 420 MPa, E = 200 GPa, ν = 0.3, failure strain 0.12 and Cowper–Symonds rate parameters C = 40 s^{-1} and p = 5. Reinforcement was represented by beam elements coupled to the concrete solid mesh through *CONSTRAINED_LAGRANGE_IN_SOLID, which permits an independent mesh for the bars while enforcing displacement compatibility. The mesh size was 100 mm in plane and 50 mm through the slab thickness.

The analysis followed the sequence prescribed by GSA (2016). Gravity loads under the combination wF = 1.2(D + Sw) + 0.5L were applied from zero in at least ten increments until full static equilibrium was reached. The target column was then removed with *LOAD_REMOVE_PART over a period shorter than one tenth of the vertical vibration period of the bays above it, so that the removal is effectively instantaneous. The dynamic response was followed for 1.5 s, approximately ten oscillation cycles, so that both the peak and the settled position could be read from the same record.

2.2. Validation

The model was validated against the full-scale sudden corner-column removal test reported by Adam et al. (2020), which remains one of the few experiments performed on a complete real-scale reinforced concrete building rather than a subassemblage (Yu and Tan, 2013; Qian and

Li, 2015) or an isolated flat-plate specimen (Peng et al., 2017). The comparison is given in Table 1. The peak vertical displacement is reproduced exactly; the residual value is 5.6% larger than measured, a deviation attributable to the incomplete representation of post-cycle stiffness recovery in concrete and well within the range normally accepted for this class of problem.

Table 1. Validation against the full-scale corner-column removal test of Adam et al. (2020).

	Peak vertical displacement (mm)	**Residual vertical displacement (mm)**
Test (Adam et al., 2020)	48.1	42.8
Present numerical model	48.1	45.2
Deviation	**0.0%**	**+5.6%**

2.3. Building models and removal scenarios

The reference building is a three-storey reinforced concrete frame-slab structure with 4×3 bays of 4.8 m and a storey height of 3.2 m, designed to TBDY-2018. The slab is 150 mm thick, beams are 300×500 mm and all columns are 300×600 mm with 12Ø14 longitudinal bars and Ø8/8/10/13 ties. Superimposed dead load is 2.0 kN/m² and live load 2.5 kN/m²; cladding load is 11.0 kN/m on exterior beams and 7.0 kN/m on interior beams. The rectangular columns are placed in a checkerboard pattern, with each column rotated 90° relative to its neighbours — a common arrangement in practice, and one whose consequences are examined in Section 3.3.

Three ground-floor opening layouts were generated from this reference, each removing four bay panels, i.e. approximately one third of the floor area: a corner opening (P2), a central opening (P3) and a full-row opening extending along the whole A–B band (P4). Each of the four buildings was then redesigned according to the UFC 4-023-03 tie force method, producing a second group (P5–P8) in which geometry, materials, loading and analysis settings are identical and the only difference is the tie reinforcement. The eight models therefore form four matched pairs, so that any observed difference within a pair can be attributed to the ties alone.

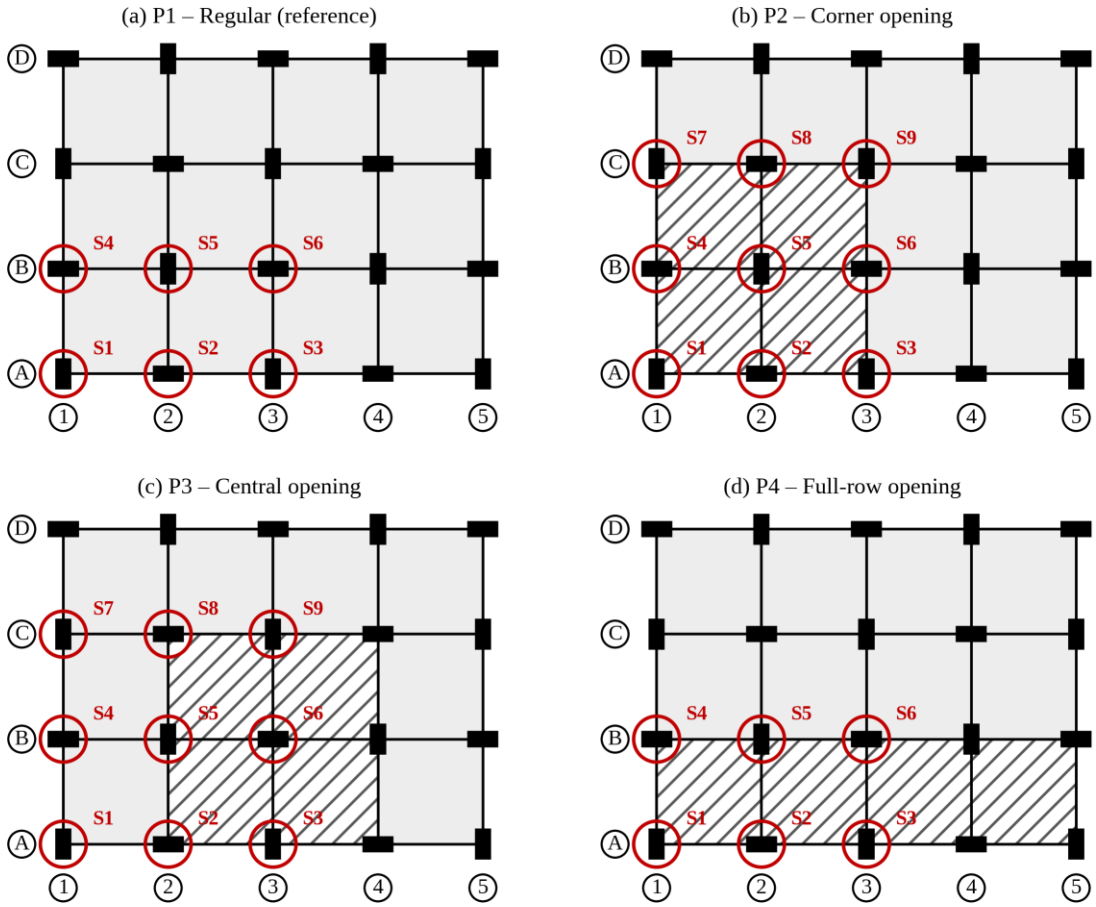


Fig. 1. Ground-floor layouts and column removal scenarios. Hatching marks the slab opening; the 300×600 mm columns are drawn to scale to show the checkerboard orientation.

Column removal scenarios follow GSA (2016), which requires the corner, long-edge, short-edge and interior positions to be examined. The scenarios S1–S9 correspond to columns A1, A2, A3, B1, B2, B3, C1, C2 and C3 (Figure 1). In the regular buildings P1 and P5, axes B and C are mirror images including column orientation, so scenarios S1–S6 represent all distinct positions. In the full-row models P4 and P8 the opening lies in the A–B band, this symmetry does not hold, and the C-axis scenarios were excluded as being remote from the opening. In the corner and central models the opening destroys both symmetries and all nine scenarios were analysed. In total 60 nonlinear dynamic analyses were performed. So that the four slab layouts are always compared on identical ground, every cross-comparison reported below is made on the common S1–S6 basis.

2.4. Tie force design

Required tie strengths were computed from the UFC 4-023-03 expressions with wF = 8.15 kN/m² and a span of 4.8 m; reinforcement areas follow from As = F / (φ · 1.25 · fy) with φ = 0.75. The results are summarised in Table 2. Internal ties were spaced at not more than 0.2L and anchored into the peripheral ties, and the peripheral ties were placed within a 1.0 m edge strip. The vertical tie requirement was satisfied by making half of the existing column longitudinal reinforcement continuous through the joints.

Table 2. Required tie forces and reinforcement according to UFC 4-023-03.

Tie type	Expression	Required force	Required As	Provided
Internal tie (both directions)	Fi = 3wF L	117.4 kN/m	2.98 cm²/m	2Ø14/m
Peripheral tie – exterior	Fp = 6wF L + 3Wc,e	287.8 kN	7.31 cm²	5Ø14
Peripheral tie – interior	Fp = 6wF L + 3Wc,i	273.4 kN	6.94 cm²	5Ø14
Vertical tie (per column)	Fv (one storey)	304.4 kN	7.73 cm²	6Ø14 cont.

2.5. Numerical reliability checks

Because the explicit scheme does not enforce energy conservation, every analysis was checked after the fact against the energy database. The hourglass energy remained below 0.9% of the internal energy and the kinetic energy below 0.4% of it during the gravity stage, confirming that the preload phase is quasi-static. The internal energy immediately before removal was identical to within 0.3% across all scenarios of a given building and 7% lower in the models with openings, consistent with the four missing slab panels. Total base reactions were 12,838–12,886 kN for the regular buildings and 11,938–12,070 kN for those with openings. In every analysis the reaction at the removed column fell to zero, and the sum of the reaction changes at the remaining columns recovered 99.7% of the removed load, confirming the redistribution calculations.

3. Results and discussion

3.1. Displacement level and the resisting regime

Peak vertical displacements at the node above the removed column are given in Table 3 for all eight buildings. They range from 15.1 mm (P5, A3 removal) to 30.0 mm (P4, A2 removal). Chord rotations were evaluated as $\theta = \Delta/L$ with L = 4800 mm. Because the mid-span stirrup spacing of 200 mm exceeds d/3 = 150 mm, the beams were conservatively classified as non-conforming, for which UFC 4-023-03 permits $\theta_{lim} = 0.0157$ rad. The computed rotations lie between 0.0031 and 0.0063 rad, the largest being 40% of the limit. No collapse mechanism formed in any model.

Table 3. Peak vertical displacement (mm) above the removed column, and maximum chord rotation for each building.

Scenario	Column	Position	P1	P2	P3	P4	P5	P6	P7	P8
S1	A1	Corner	22.9	29.0	23.7	29.2	20.8	26.0	20.8	26.0
S2	A2	Long edge	23.0	27.8	26.1	30.0	21.2	25.6	23.3	27.4
S3	A3	Long edge	16.3	17.5	22.4	19.9	15.1	16.2	20.7	18.4
S4	B1	Short edge	21.9	26.2	24.0	22.2	19.8	23.6	21.4	20.4
S5	B2	Interior	18.0	19.7	19.6	17.8	17.0	18.9	18.5	16.8
S6	B3	Interior	16.1	16.9	16.5	17.2	15.2	15.7	15.7	16.2
Mean	–	–	**19.7**	**22.8**	**22.1**	**22.7**	**18.2**	**21.0**	**20.1**	**20.9**
θmax, rad	–	–	**0.0048**	**0.0060**	**0.0054**	**0.0063**	**0.0044**	**0.0053**	**0.0049**	**0.0057**
θmax/θlim	–	–	**31%**	**38%**	**35%**	**40%**	**28%**	**34%**	**31%**	**36%**

This displacement level determines how every other result must be read. Yu and Tan (2013) located compressive arch action capacity at 0.18–0.46 times the beam depth, the onset of catenary action at approximately one beam depth and catenary capacity beyond two beam depths. For the 500 mm beams used here these thresholds correspond to 90–230 mm, 500 mm and 1000 mm respectively. The largest displacement obtained in the whole series, 30.0 mm, is one third of the lower bound for compressive arch action and 3% of the catenary threshold. The

alternate load path in these buildings is therefore established entirely in the flexural (Vierendeel) regime: compressive arch action is not even reached, and neither catenary action nor tensile membrane action of the slab is mobilised.

Two conclusions follow. First, for this class of building — regularly framed, three storeys, designed to a modern seismic code, with the slab modelled in three dimensions — the loss of a single column produces limited local damage rather than collapse, and the acceptance criterion is met with a wide margin. Second, and consequently, an assessment reduced to pass/fail conveys very little. The differences produced by the discontinuity all lie inside that margin, so they can only be seen through relative performance.

3.2. Position dependence of the discontinuity

Although the three opening layouts have identical area, the increase in peak displacement relative to the regular building varies from −0.9% to +37.8% depending on the scenario (Figure 2). What governs is not the area of the opening but the position of the removed column and whether the opening interrupts the alternate load path at that particular position.

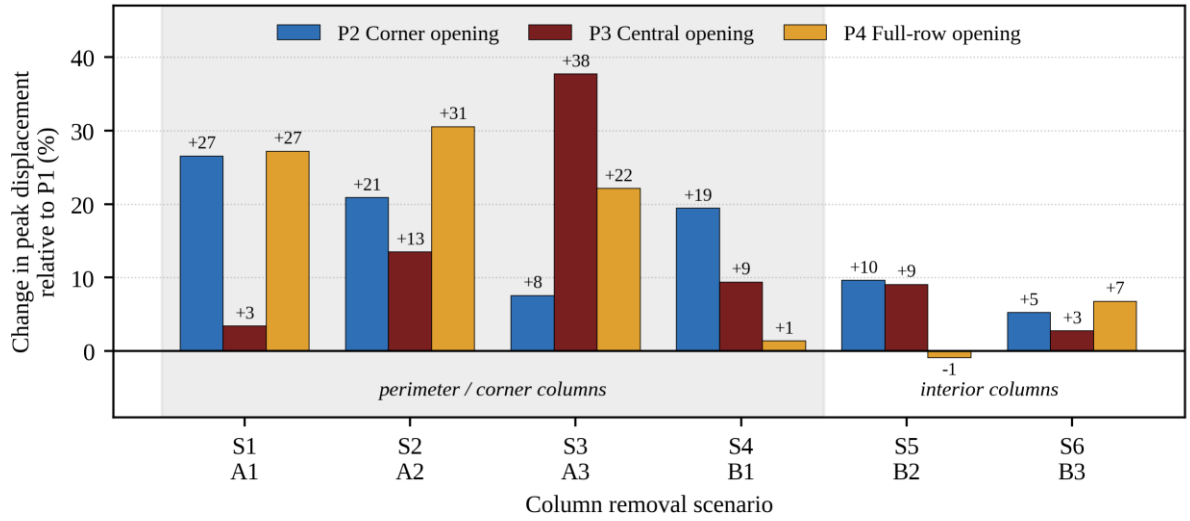


Fig. 2. Change in peak vertical displacement relative to the regular building P1, by scenario.

The full-row model illustrates this most clearly. Removing A2 raises the peak displacement from 23.0 mm to 30.0 mm (+30.5%), whereas removing B2 lowers it from 18.0 mm to 17.8 mm (−0.9%). Both columns sit on the boundary of the same opening, whose geometry, area and position are identical in the two cases. The difference is that A2 is a perimeter column: with the slab removed on one side and the building edge on the other, the alternate load path is reduced to the axis-A frame alone. B2 is an interior column; the A–B band is missing but the B–C band is intact, and four-way beam continuity is preserved. Averaged over the three layouts, perimeter scenarios show increases of +15.9% to +20.3% and interior scenarios of +2.9% to +7.4%. When the removed column is one bay away from the opening, the effect falls to the limit of measurability.

The discontinuity also makes the building sensitive to which column is lost. The spread between the most and least severe scenario within a single building is 40–43% for the regular models but reaches 48–75% for those with openings. A building with an opening is therefore not merely weaker on average; its worst case is further from its average, which is the more important property for a hazard whose location cannot be predicted.

This has a direct bearing on how irregularity limits are drawn. The opening ratio studied here sits at the TBDY-2018 type A2 threshold and below the ASCE 7-16 limit, so these buildings would not be classified as irregular under ASCE 7. Yet three layouts of identical area behave very differently from one another. An area-ratio criterion cannot distinguish between them, because the quantity that matters is whether the internal and peripheral tie paths are severed, not how much slab is missing.

3.3. The effect of column orientation

The clearest opportunity to isolate this effect is provided by two adjacent scenarios on the long edge. Columns A2 and A3 are of the same position type — perimeter, long edge — and in the regular building they carry practically the same load, 587 and 589 kN, a difference of 0.3%. Their removal nevertheless produces markedly different responses: 23.0 mm for A2 against 16.3 mm for A3, a difference of 41% (Figure 3). Repeating the comparison in the tied regular building P5 gives 40%. Since load, position type and slab layout are identical, the difference can only be attributed to column orientation.

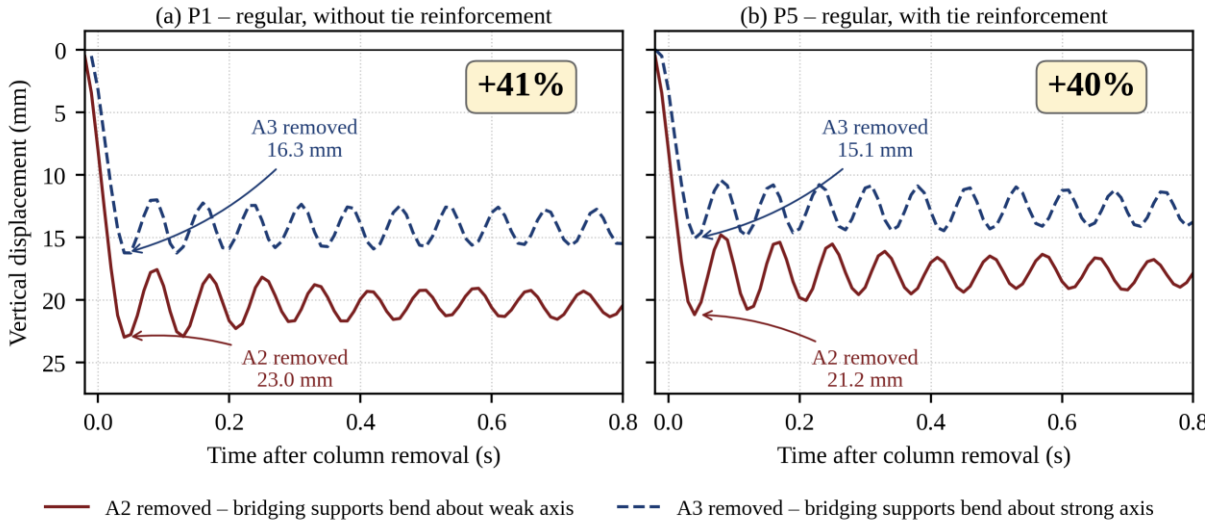


Fig. 3. Displacement histories for the removal of two long-edge columns carrying loads within 0.3% of one another, in the regular building without (a) and with (b) tie reinforcement.

The mechanism is the checkerboard arrangement. When A2 is lost, the bridging frame spans between A1 and A3, whose 300 mm dimension is parallel to the span, so both supports bend about their weak axis. When A3 is lost, the supports are A2 and A4, whose 600 mm dimension is parallel to the span. The same comparison between the interior columns B2 and B3 gives only 12%, because an interior loss develops bridging in two directions at once and the orientation of any single support matters much less.

The practical consequence is that identifying the critical removal scenario from position type and axial load alone — which is what the code scenario lists effectively do — can be wrong by 40% in a building of entirely ordinary layout. Where rectangular columns are placed in alternating orientation, the scenario set should include the perimeter column whose neighbours bend about their weak axis.

3.4. Effectiveness and actual mechanism of the tie force method

Tie reinforcement reduced the peak displacement in all four pairs, by 7.5% to 8.7% on average (Figure 4). Taken at face value this confirms the method. The difficulty is that the rotations at which it was achieved are 1.6–3.1% of the 0.20 rad on which the method is founded. At that

level the tie reinforcement is working at a very small fraction of its tensile capacity, and the improvement cannot be the catenary contribution the method intends to provide.

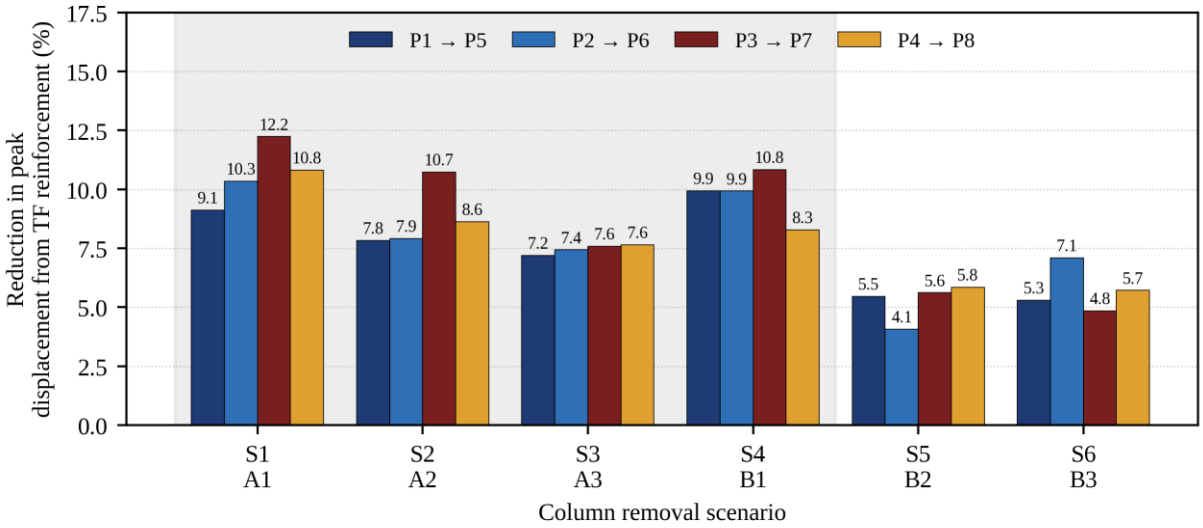


Fig. 4. Reduction in peak vertical displacement produced by UFC 4-023-03 tie reinforcement, by scenario and slab layout. Shaded band: perimeter and corner scenarios (mean 9.2%); unshaded: interior scenarios (mean 5.5%).

Three independent observations identify the mechanism as flexural instead. First, the reduction in the mean displacement at the end of the analysis (10.5–11.6%) is 1.34 to 1.47 times the reduction in the peak. The ties do not merely damp the first excursion; they raise the position at which the structure settles, which is the signature of a permanent stiffness gain rather than a transient dynamic effect. Second, the reduction at perimeter and corner scenarios (9.2%) is 1.68 times that at interior scenarios (5.5%). This follows directly from the ties lying in the top reinforcement plane of the slab, where they raise the hogging capacity and the cracked-section stiffness over the supports — the governing component of the load path precisely when the subsystem cantilevers, as it does at a perimeter or corner loss. Third, adding ties makes the redistribution more local, not less: the share taken by adjacent columns rises while that of remote columns is unchanged. A tensile chain would be expected to carry load across the opening to more distant frames; the observed trend is the opposite.

The consequences for discontinuous diaphragms are direct. Buildings with openings that have been tied according to UFC 4-023-03 do not reach the performance of the untied regular building: their mean peak displacement is 20.1–21.0 mm against 19.7 mm for P1. The penalty imposed by the discontinuity is barely changed by tying — it is +12.6% to +14.8% in the untied group and +11.2% to +14.5% in the tied group. Most tellingly, at the opening-boundary scenarios S1 and S2, which are the critical ones, no tied model with an opening falls below the untied regular reference. The tie force method reduces the loss caused by the discontinuity but does not remove it, and the assumption that it implicitly covers diaphragm discontinuity fails exactly where it matters most.

One consequence is favourable. Because the redistribution stays local, adding ties to an existing building does not require capacity re-checks on remote columns: no column in any analysis exceeded a load amplification factor of 1.56.

3.5. Load redistribution

The load released by the removed column is taken up almost entirely in its immediate neighbourhood. Adjacent columns absorb 118–142% of it — the figure exceeds unity because some columns in the ring unload — while columns three bays away or further change by only 4–7%. The distribution among the adjacent columns follows connection continuity rather than distance. When A2 is removed, the interior column B2, continuous in four directions, takes 70% of the released load, whereas the corner column A1, connected by only two beams, takes 18%. Across all scenarios, four-way continuous interior columns take 40–70% and perimeter or corner columns 14–19%.

4. Conclusions

1. Under single column loss, all eight buildings satisfied the UFC 4-023-03 acceptance criterion with a wide margin: peak displacements of 15.1–30.0 mm and chord rotations below 40% of the limit. The alternate load path formed entirely in the flexural regime; compressive arch action was not reached and catenary action was never mobilised.

2. A ground-floor slab opening of approximately one third of the floor area changes the peak displacement by −0.9% to +37.8% depending on the scenario. What governs is the position of the removed column and whether the opening severs the alternate load path there, not the area of the opening. Perimeter scenarios show mean increases of +15.9% to +20.3% against +2.9% to +7.4% for interior ones.

3. The discontinuity also widens the scatter between scenarios, from 40–43% in the regular buildings to 48–75% in those with openings, so that the worst case moves further from the average.

4. Because three layouts of identical area behave very differently, an irregularity classification based on the opening area ratio is not a sufficient indicator of progressive collapse vulnerability. The criterion should be whether the internal and peripheral tie paths are interrupted.

5. UFC 4-023-03 tie reinforcement reduced the peak displacement by 7.5–8.7%. However, the measured rotations reached only 1.6–3.1% of the 0.20 rad on which the method relies, and three independent observations — the larger reduction in the settled position, the 1.68-fold concentration of the benefit at perimeter and corner scenarios, and the increased locality of redistribution — show that the gain comes from added flexural stiffness, not from the intended catenary mechanism.

6. Tied buildings with openings did not reach the performance of the untied regular building, and the discontinuity penalty was essentially unchanged by tying. At the critical opening-boundary scenarios no tied model fell below the untied regular reference. For discontinuous diaphragms the tie force method should not be relied upon alone; the scenarios at the opening boundary warrant direct Alternate Path analysis.

7. Column orientation is an independent governing parameter. Two long-edge columns carrying loads within 0.3% of each other produced peak displacements 41% apart, according to whether the remaining bridging supports bend about their weak or strong axis. The effect falls to 12% for interior columns, where bridging develops in two directions. Scenario selection based on position type and axial load alone can therefore miss the critical case.

8. Load redistribution is strongly local: adjacent columns take 118–142% of the released load and remote columns 4–7%. The share follows connection continuity — 40–70% for four-way

continuous interior columns against 14–19% for perimeter and corner columns — and no column exceeded a load amplification of 1.56.

The results are limited to vertical-load response under single column loss; soil–structure interaction, infill contribution, multi-column loss (Parisi and Scalvenzi, 2020) and the initiating event itself were outside the scope. Because the response never approached the rotation at which the tie force method is meant to operate, the performance of that method in the catenary regime remains untested here and is the natural subject of a pushdown study on the critical scenarios.

REFERENCES

1. Adam, J.M., Buitrago, M., Bertolesi, E., Sagaseta, J., Moragues, J.J., 2020. Dynamic performance of a real-scale reinforced concrete building test under a corner-column failure scenario. Engineering Structures 210, 110414.
2. ASCE, 2017. Minimum Design Loads and Associated Criteria for Buildings and Other Structures (ASCE/SEI 7-16). American Society of Civil Engineers, Reston, VA.
3. Azim, I., Yang, J., Bhatta, S., Wang, F., Liu, Q.F., 2020. Factors influencing the progressive collapse resistance of RC frame structures. Journal of Building Engineering 27, 100986.
4. Cheng, X., Zhang, Y., Liu, Y., Wei, H., 2024. Experimental and numerical study on progressive collapse of miniature reinforced concrete flat slabs under column removal scenario using LS-DYNA. Engineering Structures 309, 117985.
5. DoD, 2016. Design of Buildings to Resist Progressive Collapse (UFC 4-023-03). U.S. Department of Defense, Washington, D.C.
6. GSA, 2016. Alternate Path Analysis and Design Guidelines for Progressive Collapse Resistance. General Services Administration, Washington, D.C.
7. Helmy, H., Salem, H., Mourad, S., 2012. Progressive collapse assessment of framed reinforced concrete structures according to UFC guidelines for alternative path method. Engineering Structures 42, 127–141.
8. McKay, A., Marchand, K., Diaz, M., 2012. Alternate path method in progressive collapse analysis: Variation of dynamic and non-linear load increase factors. Practice Periodical on Structural Design and Construction ASCE 17(4), 152–160.
9. Mohieldin, O., Jadallah, M., Cicos, C., Mehdi, F., Sağıroğlu, S., Doğangün, A., 2026. Evaluating progressive collapse in multi-story buildings: Influence of slabs and building height. Advances in Structural Engineering 29(8), 1606–1628.
10. Murray, Y.D., 2007. User's Manual for LS-DYNA Concrete Material Model 159. Report FHWA-HRT-05-062, Federal Highway Administration, USA.
11. Pang, B., Wang, F., Yang, J., Nyunn, S., Azim, I., 2021. Performance of slabs in reinforced concrete structures to resist progressive collapse. Structures 33, 4843–4856.
12. Parisi, F., Scalvenzi, M., 2020. Progressive collapse assessment of gravity-load designed European RC buildings under multi-column loss scenarios. Engineering Structures 209, 110001.
13. Peng, Z.H., Orton, S.L., Liu, J.R., Tian, Y., 2017. Experimental study of dynamic progressive collapse in flat-plate buildings subjected to interior column removal. Journal of Structural Engineering ASCE 143(9), 04017125.
14. Qian, K., Li, B., 2015. Progressive collapse resistance of RC beam–column subassemblages with different span-to-depth ratios. Journal of Structural Engineering ASCE 141(7), 04014170.
15. Starossek, U., 2014. Progressive Collapse of Structures, 2nd ed. ICE Publishing, London.
16. TBDY, 2018. Türkiye Bina Deprem Yönetmeliği (Turkish Building Earthquake Code). Disaster and Emergency Management Presidency (AFAD), Ankara.
17. Yavari, H., Ghobadi, M., Yakhchalian, M., 2019. Progressive collapse potential of different types of irregular buildings. Heliyon 5(2), e01137.
18. Yu, J., Tan, K.H., 2013. Structural behavior of RC beam–column subassemblages under a middle column removal scenario. Journal of Structural Engineering ASCE 139(2), 233–250.

Note: Following the conference, this Publication Note will be added to each paper; therefore, authors are kindly requested not to remove the note below and to complete the author(s) and paper title information.

Publication Note

This paper was peer-reviewed, accepted for presentation, and included in the proceedings of the ACE2026 – International Conference on Advances in Civil Engineering, held on 12–14 October 2026 in Trabzon, Türkiye.

This paper may be cited as follows:

Author(s), "Title of the Paper," in Proceedings of the ACE2026 – International Conference on Advances in Civil Engineering, Trabzon, Türkiye, 12–14 October 2026.

Toward Unified Machine Learning Models for Reinforced Concrete Columns and Shear Walls: Digital Twin Framework and Preliminary Validation

Şevket ATEŞ

0000-0001-9229-6256, Karadeniz Technical University, Civil Engineering Department, Trabzon, Türkiye.
sates@ktu.edu.tr

Abstract. Rapid and reliable prediction of the nonlinear behavior of reinforced concrete elements is critical in performance-based earthquake engineering. This study develops a digital twin-based framework for machine-learning prediction of the initial stiffness, yield displacement and post-yield stiffness ratio of reinforced concrete columns and shear walls. The methodology comprises numerical model calibration in OpenSeesPy, synthetic data generation by Latin Hypercube Sampling, and a comparison of column-specific, wall-specific and unified models. The column model was calibrated on two real specimens from the PEER Structural Performance Database. For a specimen whose properties are precisely documented, the base shear capacity was predicted with a 2.9 % error; for a specimen with unverified properties, the deviation was 53.9 %. A sensitivity analysis then back-calculated the section size that reproduces the measured capacity, illustrating a diagnostic use of the digital twin: a physically plausible back-calculated value implicates a single misestimated parameter. Calibration of the wall model against experimental wall tests remains for future work. The synthetic data pipeline was verified at small scale (N = 25 per element type; 24/25 column and 25/25 wall runs converged; mean $R^2 > 0.95$). The study establishes the framework required to quantify the accuracy-practicality trade-off between component-specific and unified surrogate models in future work.

Keywords: Digital twin, Machine learning, Reinforced concrete, Seismic behavior, OpenSeesPy.

1 Introduction

Performance-based earthquake engineering requires an accurate characterization of the nonlinear behavior of structural elements. The conventional method for determining the stiffness, yield strength and deformation capacity of reinforced concrete (RC) columns and shear walls is finite-element-based pushover analysis. These analyses, however, impose a significant computational burden when large building inventories or many design alternatives must be evaluated, since each element and building configuration requires separate modeling and analysis.

Combining the digital twin concept with machine learning (ML) has recently emerged as a promising route around this bottleneck. Bárkányi et al. examined the role of surrogate models in digital twin applications and showed that such models can substantially reduce the computational cost of complex physical systems [1].

Kuria and Kegyes-Brassai developed a Random Forest-based digital twin framework using pushover curves from two hundred layered-shell models and reported coefficients of determination of 0.996, 0.995 and 0.925 for the initial stiffness, yield displacement and post-yield stiffness ratio of RC shear walls [2]. Angarita et al. predicted the pushover curves of low-rise RC frame buildings with ML models at a fraction of the computation time of nonlinear OpenSeesPy analyses [3]. At the element scale, Huang et al. proposed an XGBoost-based model for the shear strength of flexure-shear type columns [4], and Kaveh and Amiri developed a physics-informed, region-specific approach for the seismic demand of RC frames [5].

Although these studies demonstrate high accuracy and significant computational gains, the majority address a single element type. Whether a generalized architecture spanning different element types is feasible — and what accuracy is sacrificed for that generality — has not been sufficiently addressed. This study therefore proposes a digital twin-ML approach covering both RC columns and shear walls, and presents (i) parametric synthetic data generation calibrated in OpenSeesPy, (ii) a comparison of component-specific and unified models, and (iii) practical recommendations for digital twin architecture design derived from pilot calibrations on real experimental data.

2 Methodology

The proposed methodology follows a hybrid approach combining experimental data with parametric numerical modeling in OpenSeesPy. The workflow consists of five steps (Fig. 1): data collection, numerical model calibration, synthetic data generation, feature extraction, and ML model training with comparative evaluation.

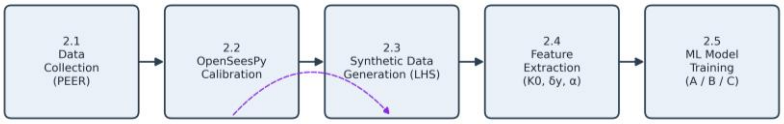


Fig. 1. Workflow of the proposed digital twin–machine learning methodology.

2.1 Data Collection

Column behavior is taken from the PEER Structural Performance Database [6], which covers rectangular- and spiral-reinforced column tests. Experimental wall data will be compiled from a separate wall test database in the next stage of the study. For every specimen the geometry, material strengths, reinforcement ratios, axial load level and the complete measured force-displacement history are compiled.

2.2 Numerical Model Calibration

Columns are modeled with fiber-section **forceBeamColumn** elements using the Concrete02 and Steel02 material models (Fig. 2). Shear walls are modeled with the MVLEM (Multiple-Vertical-Line-Element Model) formulation (Fig. 3), which keeps the computational cost low enough for the large parametric sweeps required in Section 2.3.

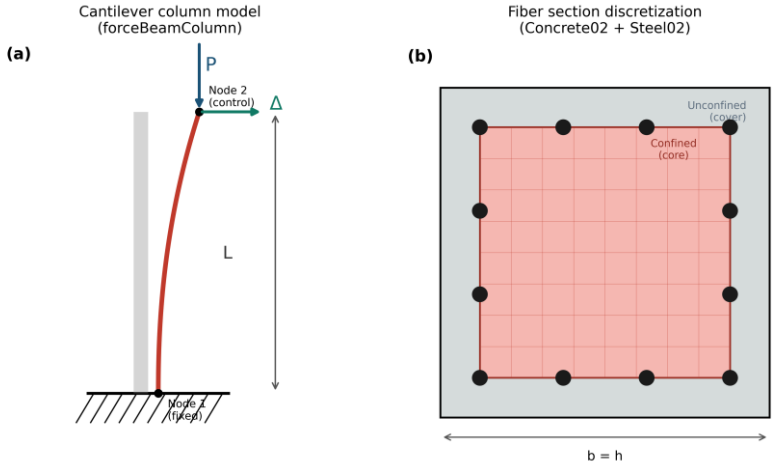


Fig. 2. RC column model: (a) cantilever elevation and (b) fiber section discretization.

```
ops.section('Fiber', sec_tag, '-GJ', GJ)
ops.patch('rect', mat_conf, n_fibers_core, n_fibers_core,
          -core_half_b, -core_half_h, core_half_b, core_half_h)
ops.layer('straight', mat_steel, n_bars_x, bar_area,
          -core_half_b, core_half_h, core_half_b, core_half_h)
```

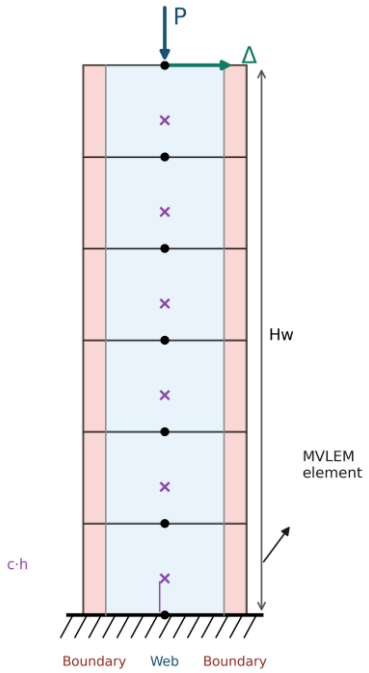


Fig. 3. Shear wall MVLEM model

```
ops.element('MVLEM', ele_tag, 0.0, i+1, i+2, m_fibers, c,
    '-thick', *thick, '-width', *widths, '-rho', *rho,
    '-matConcrete', *mat_concrete_tags,
    '-matSteel', *mat_steel_tags, '-matShear', mat_shear_tag)
```

A common analysis driver applies a constant axial load followed by displacement-controlled lateral loading. Adaptive step-size control combined with alternative solver algorithms (**Newton, ModifiedNewton, KrylovNewton, NewtonLineSearch, Broyden**) substantially reduced convergence difficulties in the softening region of the force-based column formulation.

2.3 Synthetic Data Generation

A separate parameter space was defined for each element type (Table 1) and sampled by Latin Hypercube Sampling [7], which limits clustering in a multi-dimensional space and thereby represents parameter interactions better than random sampling. The column section depth range (200–500 mm) was chosen to cover approximately 80 % of the rectangular-reinforced columns in the PEER Structural Performance Database, whose mean depth is 319 mm [6].

```
sampler = qmc.LatinHypercube(d=len(names), seed=seed)
unit = sampler.random(n=n_samples)
scaled = qmc.scale(unit, bounds[:, 0], bounds[:, 1])
```

Table 1. Parameter ranges used for Latin Hypercube Sampling.

Element	Parameter	Range
Column	b = h	200–500 mm
	L/b	2.5–6.0
	Bar diameter	16–32 mm
	fc / fy	20–40 / 350–500 MPa
	Axial load ratio	0.05–0.35
Wall	Hw	1.5–4.0 m
	Hw/Lw	1.2–3.0
	tw	100–250 mm
	ρv (web / boundary)	0.15–0.50 / 1.0–3.0 %
	fc / fy	20–40 / 350–500 MPa
	Axial load ratio	0.02–0.15

2.4 Feature Extraction

The pushover curve from each run is reduced to a bilinear idealization defined by the initial stiffness K0, the yield displacement δy and the post-yield stiffness α, fitted by least squares. The peak base shear Vmax is recorded separately as a validation quantity.

```
def _bilinear_model(d, K0, dy, alpha):
    Vy = K0 * dy
    return np.where(d <= dy, K0*d, Vy + alpha*(d - dy))
```

2.5 Model Training and Comparison Strategy

Three models will be trained on the resulting feature-target dataset: Model A (column-specific), Model B (wall-specific) and Model C (unified, with element type as a categorical feature). Performance will be evaluated with Random Forest and XGBoost under nested cross-validation, reported through R^2, MAE, RMSE and 95 % confidence intervals. Comparing Model C to Models A and B quantifies the accuracy cost of a single generalized architecture.

3 Preliminary Implementation and Interim Findings

3.1 Pilot Calibration of Column Models

Two shear-critical column specimens with different levels of input verification were used: Sezen and Moehle Specimen 1 [8], whose geometry and material properties are precisely documented, and Wight and Sozen Specimen WS033AE [9], modeled with approximate values because the source report could not be accessed directly. Although both specimens are archived

in the same database, they originate from independent experimental programs. The complete measured histories (2384 and 349 points, respectively) were obtained and the positive envelope curves extracted.

For the Sezen specimen the model predicted V_{max} with a 2.9 % error against the reported value of 303 kN. A known deviation appeared in the yield displacement (6.7 mm against 13.9 mm estimated with the method of [10]), because the fiber formulation represents neither bar slip nor shear deformation; these components can account for a substantial share of the total drift in shear-critical columns [11, 12]. For the Wight and Sozen specimen the model underestimated the measured V_{max} of 98.8 kN by 53.9 % (the database summary table lists 94 kN for this specimen). Fig. 4 compares both models against their experimental envelopes.

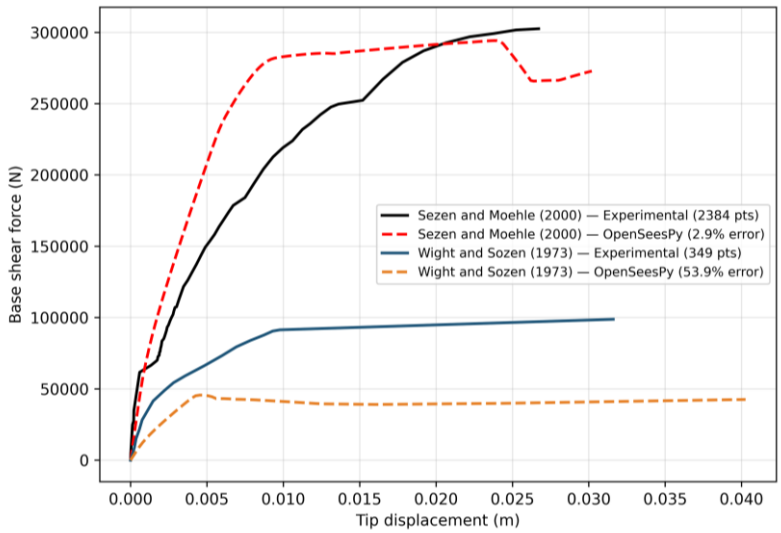


Fig. 4. OpenSeesPy pushover curves compared with the measured envelope curves for Sezen and Moehle Specimen 1 [8] and Wight and Sozen Specimen WS033AE [9].

3.2 Status of the Shear Wall Model

An initial wall pilot based on the file labeled Thomsen and Wallace 1994, A1 has been withdrawn. Inspection of the PEER Structural Performance Database showed that this specimen (Test 200, peak shear 44 kN) belongs to the rectangular-reinforced column dataset rather than to a wall test, so a comparison with a slender-wall MVLEM model is not meaningful. Consequently, the MVLEM wall formulation has so far been exercised only in the synthetic runs of Section 3.4, and its calibration against genuine experimental wall tests is deferred to future work.

3.3 Sensitivity Analysis and Calibration Guidance

The two column pilots show a consistent pattern (Table 2): the error is small where the inputs are documented and large where they are assumed. This section uses the digital twin in reverse — as a diagnostic tool — by sweeping the most uncertain input and back-calculating the value that reproduces the measured capacity.

Table 2. Effect of input verification level on the accuracy of the predicted base shear capacity.

Specimen	Input verification	Vmax error
Sezen and Moehle [8]	Precise literature values	+2.9 %
Wight and Sozen [9]	Approximate, unverified	−53.9 %

For the Wight and Sozen specimen, all parameters except the section size were held fixed and b = h was swept from 140 to 225 mm (Fig. 5). Reproducing the measured capacity requires a section of approximately 222 mm, 46 % larger than assumed. Because this value remains physically plausible, the deviation can plausibly be attributed to a single misestimated parameter that can be settled by consulting the source report.

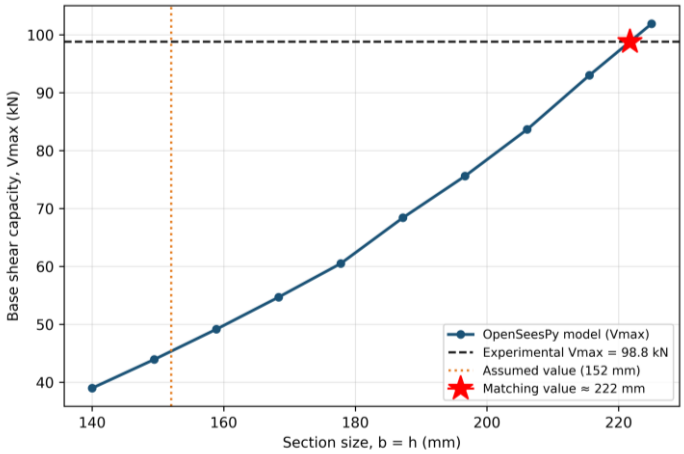


Fig. 5. Sensitivity of Vmax to section size for the Wight and Sozen specimen [9]

The Wight and Sozen sweep suggests a reusable calibration guide. First, when a model deviates from measurement, sweep the single most uncertain input. Second, if the back-calculated value is physically plausible, treat it as evidence of one misestimated parameter and verify that quantity at its source. Third, if the back-calculated value is implausible, conclude that the deviation arises from the combined effect of several parameters and move to a multi-parameter verification; this branch has not yet been demonstrated on a real specimen and will be tested once verified specimen data are available. The framework is thus usable in the reverse direction, from behavior to input, as well as the forward direction.

3.4 Pilot Synthetic Data Generation

The sampling pipeline of Section 2.3 was run at small scale, N = 25 per element type, over the ranges in Table 1. All 25 wall runs and 24 of the 25 column runs converged (the single failure was a short, thick column, L/b ≈ 2.5, in the softening range), and the bilinear fit quality reached a mean R^2 above 0.95 for both element types (Table 3), indicating that the pipeline is ready to be executed at the scale of thousands of runs required for model training.

Table 3. Summary of the pilot Latin Hypercube sampling run.

Criterion	Column (N = 25)	Wall (N = 25)
Successful convergence	24/25	25/25
Mean R^2 (bilinear fit)	0.959	0.963
R^2 range	0.712–0.999	0.730–0.998
Vmax range	78–571 kN	91–1072 kN

4 Conclusions and Future Work

A digital twin-machine learning framework for predicting the seismic behavior of RC columns and shear walls has been presented, and its calibration, feature extraction and synthetic

data generation components have been implemented; the column components were verified on two real specimens together with a small-scale sampling study. The pilot with documented input properties reproduced the measured shear capacity to within 2.9 %, whereas the pilot with assumed properties deviated by 53.9 %. A sensitivity analysis converted this deviation into diagnostic information by back-calculating the section size that reproduces the measurement, and yielded a three-step calibration guide. The wall formulation has so far been verified only on synthetic runs.

Future work will (i) verify the geometry and material properties of the Wight and Sozen column specimen at its primary source, (ii) calibrate the wall model against experimental wall tests from a dedicated wall database, (iii) convert the back-calculation logic into an automated calibration module, (iv) expand the sampling run to thousands of cases, (v) train and compare the component-specific and unified models, and (vi) translate the outcome into practical recommendations for digital twin architecture design.

Acknowledgments

The author gratefully acknowledges the financial support provided by the Scientific Research Projects Coordination Unit of Karadeniz Technical University under Project No. FAY-2024-11226.

References

1. Barkanyi, A., Chovan, T., Németh, S., Abonyi, J.: Modelling for digital twins – potential role of surrogate models. Processes 9(3), 476 (2021). https://doi.org/10.3390/pr9030476
2. Kuria, K.K., Kegyes-Brassai, O.: Digital twin-based machine learning framework for predicting nonlinear seismic response of reinforced concrete shear walls using analytical data. Scientific Reports 16, 3081 (2026). https://doi.org/10.1038/s41598-025-32626-2
3. Angarita, C., Montes, C., Arroyo, O.: Machine learning-based approach for predicting pushover curves of low-rise reinforced concrete frame buildings. Structures 70, 107694 (2024). https://doi.org/10.1016/j.istruc.2024.107694
4. Huang, T., Wan, C., Liu, T., Miao, C.: A data-driven prediction method for shear bearing capacity of flexural-shear type RC column based on PCC-XGB-SHAP. Case Studies in Construction Materials 22, e04712 (2025). https://doi.org/10.1016/j.cscm.2025.e04712
5. Kaveh, A., Amiri, A.: Efficient and interpretable seismic demands prediction for RC frames: a physics-informed, region-specific approach. Asian Journal of Civil Engineering 27, 1011–1031 (2026). https://doi.org/10.1007/s42107-025-01546-x
6. Berry, M., Parrish, M., Eberhard, M.: PEER Structural Performance Database User's Manual, Version 1.2. Pacific Earthquake Engineering Research Center, University of California, Berkeley (2004).
7. McKay, M.D., Beckman, R.J., Conover, W.J.: A comparison of three methods for selecting values of input variables in the analysis of output from a computer code. Technometrics 21(2), 239–245 (1979). https://doi.org/10.1080/00401706.1979.10489755
8. Sezen, H., Moehle, J.P.: Shear strength model for lightly reinforced concrete columns. Journal of Structural Engineering 130(11), 1692–1703 (2004). https://doi.org/10.1061/(ASCE)0733-9445(2004)130:11(1692)
9. Wight, J.K., Sozen, M.A.: Shear Strength Decay in Reinforced Concrete Columns Subjected to Large Deflection Reversals. Structural Research Series No. 403, University of Illinois, Urbana-Champaign (1973).
10. Berry, M.P., Eberhard, M.O.: Performance Models for Flexural Damage in Reinforced Concrete Columns. PEER Report 2003/18, Pacific Earthquake Engineering Research Center, University of California, Berkeley (2003).

11. Sezen, H.: Seismic Behavior and Modeling of Reinforced Concrete Building Columns. PhD thesis, University of California, Berkeley (2002).
12. Elwood, K.J.: Shake Table Tests and Analytical Studies on the Gravity Load Collapse of Reinforced Concrete Frames. PhD thesis, University of California, Berkeley (2002).

Author Contribution Statement

- *Conceptualization:* Şevket Ateş
- *Methodology:* Şevket Ateş
- *Software:* Şevket Ateş
- *Investigation:* Şevket Ateş
- *Writing – Original Draft:* Şevket Ateş
- *Writing – Review & Editing:* Şevket Ateş

List of Abbreviations

- **RC** – Reinforced Concrete
- **ML** – Machine Learning
- **PEER** – Pacific Earthquake Engineering Research Center
- **MVLEM** – Multiple-Vertical-Line-Element Model
- **LHS** – Latin Hypercube Sampling
- **RF** – Random Forest
- **XGBoost** – Extreme Gradient Boosting
- **MAE** – Mean Absolute Error
- **RMSE** – Root Mean Square Error
- $\mathbf{R^2}$ – Coefficient of Determination
- $\mathbf{V_{max}}$ – Maximum Base Shear Capacity
- $\mathbf{K_o}$ – Initial Stiffness
- $\boldsymbol{\delta_y}$ – Yield Displacement
- $\boldsymbol{\alpha}$ – Post-Yield Stiffness Ratio
- $\mathbf{A_g}$ – Gross Cross-Sectional Area

Publication Note

This paper was peer-reviewed, accepted for presentation, and included in the proceedings of the ACE2026 – International Conference on Advances in Civil Engineering, held on 12–14 October 2026 in Trabzon, Türkiye.

This paper may be cited as follows:

Ates S., “Toward Unified Machine Learning Models for Reinforced Concrete Columns and Shear Walls: Digital Twin Framework and Preliminary Validation,” in Proceedings of the ACE2026 – International Conference on Advances in Civil Engineering, Trabzon, Türkiye, 12–14 October 2026.

Three-Dimensional Elasticity-Based Buckling Analysis of Functionally Graded Sandwich Plates on Kerr Foundation Using State-Space Differential Quadrature Method

Sebahat Şimşek[1] and Magd Abdel Wahab[2]
[1] ORCID: 0000-0001-5941-031X, Karadeniz Technical University, Civil Engineering Department, Trabzon, Türkiye
sebahatkaraca@ktu.edu.tr
[2] ORCID: 0000-0002-3610-865X, Ghent University, Faculty of Engineering and Architecture, Soete Laboratory, Ghent, Belgium
Magd.AbdelWahab@UGent.be

Abstract. This study presents a three-dimensional elasticity-based state-space differential quadrature formulation for the buckling analysis of functionally graded sandwich (FGS) plates resting on a full three-parameter Kerr elastic foundation. The plate is modeled directly within three-dimensional elasticity, while the in-plane derivatives are discretized using the differential quadrature method and the through-thickness equations are written in state-space form. The resulting equations are assembled by a scaled Global Matrix Method. The formulation is first assessed against available buckling solutions for unsupported and elastically supported FGS plates. A concise parametric study is then carried out for a simply supported Type A plate under uniaxial compression to examine the independent effects of the upper spring stiffness, lower spring stiffness, and intermediate shear-layer stiffness of the Kerr model. The results show that all three foundation components increase the critical buckling load within the investigated ranges, with the upper spring stiffness producing the most pronounced variation. The proposed formulation provides a three-dimensional framework for evaluating the stability response of FGS plates supported by a full Kerr foundation.

Keywords: Functionally graded sandwich plate; buckling; three-dimensional elasticity; Kerr foundation; differential quadrature method; state-space method.

1 Introduction

Functionally graded sandwich (FGS) plates combine the structural efficiency of sandwich construction with a continuous variation of material properties through the thickness. This gradual material distribution can reduce abrupt interfacial property changes while allowing the stiffness distribution to be tailored for structural requirements. Buckling under in-plane compression is an important design consideration for such plates because the critical load is influenced by material gradation, layer arrangement, plate geometry, and support conditions. Various reduced-order formulations, including first-order, higher-order, and quasi-three-dimensional plate theories, have therefore been developed for the stability analysis of FGS plates [1-3].

Although reduced-order plate theories provide computationally efficient models, their accuracy depends on the assumed through-thickness kinematics. Three-dimensional elasticity formulations avoid a predefined displacement variation and retain transverse normal and shear effects directly in the governing equations. State-space approaches are particularly suitable for layered and functionally graded structures because the variation of the field variables through the thickness can be treated explicitly. Alibeigloo and Alizadeh [4] combined the state-space method with the differential quadrature method (DQM) for three-dimensional analyses of FGS plates, providing a useful basis for extending the formulation to stability problems.

The interaction between a plate and an elastic supporting medium can also modify its buckling response. Most available buckling studies on FGS sandwich plates have considered Winkler or Pasternak foundations [5-8]. The Kerr model provides a more general representation by introducing an intermediate shear layer between upper and lower spring layers [9,10]. The three foundation stiffness components can therefore be specified independently. While Kerr-type foundations have been considered in vibration studies of functionally graded plates, their use in three-dimensional buckling analyses of FGS plates remains comparatively limited.

In this study, a three-dimensional elasticity-based state-space differential quadrature method (SSDQM) formulation is employed to investigate the buckling behavior of FGS plates resting on a full Kerr elastic foundation. The upper spring stiffness, lower spring stiffness, and intermediate shear-layer stiffness are retained as independent foundation parameters. The numerical model is first checked against available buckling solutions, after which the individual influence of the Kerr foundation parameters on the critical buckling load is examined for a representative simply supported Type A FGS plate under uniaxial compression.

2 Theoretical Formulation

2.1 FGS plate and material model

A rectangular Type A FGS plate with length a, width b, and total thickness h, resting on a full Kerr elastic foundation, is considered as shown in Fig. 1. The plate consists of two functionally graded face sheets and a homogeneous ceramic core, with perfect bonding assumed at the layer interfaces. The material variation in the face sheets is described by a power-law distribution. For the ceramic volume fraction,

$$V_c(z) = \begin{cases} \left(\frac{z-z_0}{z_1-z_0}\right)^p, & z_0 \le z \le z_1 \\ 1, & z_1 \le z \le z_2 \\ \left(\frac{z_3-z}{z_3-z_2}\right)^p, & z_2 \le z \le z_3 \end{cases} \tag{1}$$

where p is the power-law index.

The effective Young's modulus is obtained from the rule of mixtures as

$$E(z) = E_m + (E_c - E_m)V_c(z) \tag{2}$$

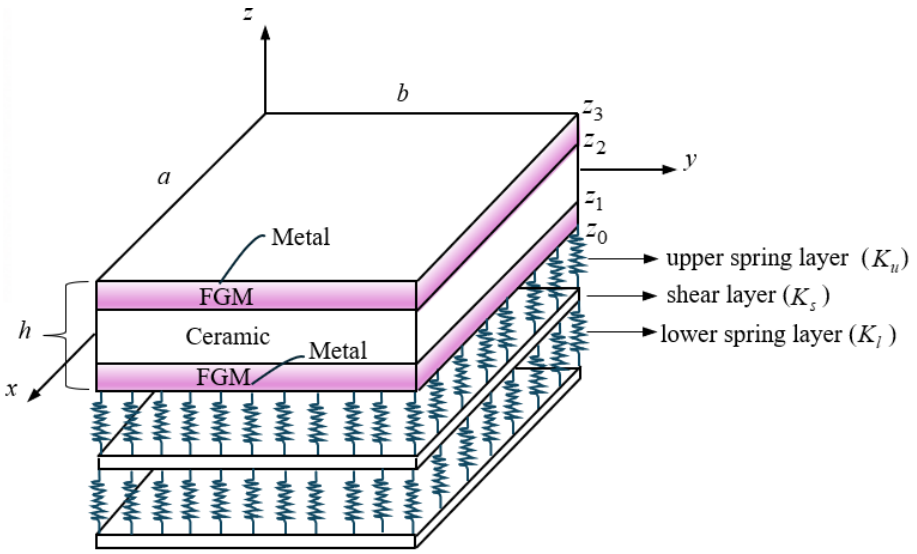


Fig. 1. Geometry and material configuration of the Type A functionally graded sandwich plate resting on a full Kerr elastic foundation.

where the subscripts m and c denote the metal and ceramic constituents, respectively. Poisson's ratio is assumed to remain constant through the thickness.

2.2 Three-dimensional buckling formulation and Kerr foundation

The stability problem is formulated within three-dimensional linear elasticity without introducing a predefined through-thickness displacement field. The displacement components are denoted by u, v, and w, and the constitutive relation is written in compact form as

$$\boldsymbol{\sigma} = \mathbf{C}(z)\boldsymbol{\varepsilon} \tag{3}$$

For the present study, uniform uniaxial compression is applied in the x-direction,

$$N_x = -\lambda, \qquad N_y = N_{xy} = 0 \tag{4}$$

where λ is the buckling load parameter. The corresponding initial in-plane stresses are included in the linearized three-dimensional equilibrium equations. The transverse equilibrium equation can be expressed as

$$\tau_{xz,x} + \tau_{yz,y} + \sigma_{z,z} + \sigma_x^0 w_{,xx} + \sigma_y^0 w_{,yy} = 0 \tag{5}$$

The full Kerr foundation consists of an upper spring layer with stiffness K_u, a lower spring layer with stiffness K_l, and an intermediate shear layer with stiffness K_s [9,10]. Introducing w_f as the displacement of the intermediate layer, the foundation reaction is

$$q_f = K_u\left(w - w_f\right) \tag{6}$$

while the equilibrium of the intermediate layer is written as

$$K_u\left(w - w_f\right) = K_l w_f - K_s\left(\frac{\partial^2 w_f}{\partial x^2} + \frac{\partial^2 w_f}{\partial y^2}\right) \tag{7}$$

At the plate-foundation interface, the transverse normal stress is balanced by the foundation reaction, while the transverse shear tractions vanish.

2.3 State-space differential quadrature solution

The displacement components and transverse stresses are selected as the state variables. For the *r*-th layer,

$$\mathbf{S}^{(r)} = [U \quad V \quad W \quad \sigma_z \quad \tau_{xz} \quad \tau_{yz}]^T, \qquad r = 1,2,3 \tag{8}$$

where *r* denotes the layer number and the governing equations are transformed into the first-order state-space form

$$\frac{d\mathbf{S}^{(r)}}{dz} = \mathbf{A}^{(r)}(z,\lambda)\mathbf{S}^{(r)}, \qquad r = 1,2,3 \tag{9}$$

Perfect bonding is imposed by enforcing the continuity of all state variables across the layer interfaces. The in-plane derivatives are discretized by DQM using Chebyshev-Gauss-Lobatto grid points [4]. The simply supported boundary conditions, surface conditions, interface continuity equations, and discretized Kerr-foundation equations are assembled simultaneously

using the scaled Global Matrix Method (GMM). The resulting homogeneous system is written as

$$\mathbf{G}(\lambda)\mathbf{d} = \mathbf{0} \tag{10}$$

where $\boldsymbol{G}(\lambda)$ is the parameter-dependent global matrix and $\mathbf{d}$ collects the layer-boundary state vectors and the discrete foundation variables. A non-trivial solution exists when

$$det[\,\boldsymbol{G}(\lambda)] = 0 \tag{11}$$

The smallest positive value of λ satisfying Eq. (11) is taken as the critical buckling parameter λ_{cr}. For reporting the numerical results, the critical buckling load and the Kerr foundation stiffness parameters are expressed in nondimensional form as

$$\overline{N}_{cr} = \frac{N_{cr}a^2}{100E_0h^3} \tag{12}$$

$$\overline{K}_u = \frac{k_u h}{E_0}, \overline{K}_l = \frac{k_l h}{E_0}, \overline{K}_s = \frac{k_s}{E_0 h} \tag{13}$$

where E_0 = 1 GPa is the reference Young's modulus used for nondimensionalization, h is the total plate thickness, and k_u, k_l, and k_s denote the dimensional upper spring, lower spring, and intermediate shear-layer stiffness parameters, respectively.

3 Numerical Results

3.1 Validation

The present formulation is first validated for a simply supported (SSSS) Type A FGS plate without an elastic foundation. To keep the comparison concise, the 2-1-2 thickness scheme is selected, and the dimensionless critical buckling loads are compared with the hyperbolic shear deformation theory (HSDT), sinusoidal shear deformation theory (SSDT), third-order shear deformation theory (TSDT), and first-order shear deformation theory (FSDT) solutions available in the literature for several power-law indices under uniaxial compression.

Good agreement is obtained over the considered range of the power-law index. The present 3D SSDQM results follow the same variation as the reference solutions, and the maximum relative difference between the present results and the reference solutions listed in Table 1 remains below approximately 0.8%. To further assess the implementation of the elastic-foundation terms, a second validation is performed for the same Type A FGS configuration resting on a Pasternak foundation.

Table 1. Comparison of dimensionless critical buckling loads for the SSSS Type A FGS plate with the 2-1-2 thickness scheme under uniaxial compression.

Method	p **= 0**	p **= 1**	p **= 5**	p **= 10**
HSDT, El Meiche et al. [2]	13.0055	5.8394	3.0414	2.7450
SSDT, Zenkour [1]	13.0061	5.8412	3.0441	2.7484
TSDT, Zenkour [1]	13.0050	5.8401	3.0426	2.7463
FSDT, Zenkour [1]	13.0045	5.8138	3.0225	2.7263
Present 3D SSDQM	**13.0391**	**5.8591**	**3.0383**	**2.7308**

Table 2. Representative validation of the dimensionless critical buckling load for the Type A FGS plate with the 2-1-2 thickness scheme (p = 2) on a Pasternak foundation under uniaxial compression.

Method	$K_w = K_s = 0$	$K_w = K_s = 10$	$K_w = K_s = 100$
Akavcı [11]	2.8455	5.6690	31.0244
Van and Hieu [8]	2.9113	5.8178	32.1766
Present 3D SSDQM	**2.8823**	**5.7463**	**31.2998**

Table 2 compares the present results with the solutions of Akavcı [11] and Van and Hieu [8] for three foundation-stiffness levels. The present predictions remain between the two reference solutions throughout the range investigated and show good agreement with both sets of results. These comparisons support the accuracy of the three-dimensional buckling formulation and the implementation of the elastic-foundation terms before application to the full Kerr model.

3.2 Effect of Kerr foundation parameters

The effects of the three Kerr foundation parameters are examined separately for a simply supported Type A FGS plate with the 2-1-2 thickness scheme and (p = 2) under uniaxial compression. In each analysis, one foundation parameter is varied while the remaining parameters are kept at their reference values. This procedure allows the individual sensitivity of the critical buckling load to each component of the Kerr foundation to be evaluated.

Fig. 2 shows a monotonic and nonlinear increase in the dimensionless critical buckling load with increasing upper spring stiffness. As $\bar{K}_u$ increases from 0.01 to 100, $\bar{N}_{cr}$ rises from approximately 2.9789 to 5.7382. The increase becomes particularly pronounced over the intermediate stiffness range, whereas the curve progressively flattens at larger values of $\bar{K}_u$.This trend indicates that the critical buckling load becomes less sensitive to further increases in the upper spring stiffness once the foundation response is sufficiently stiff.

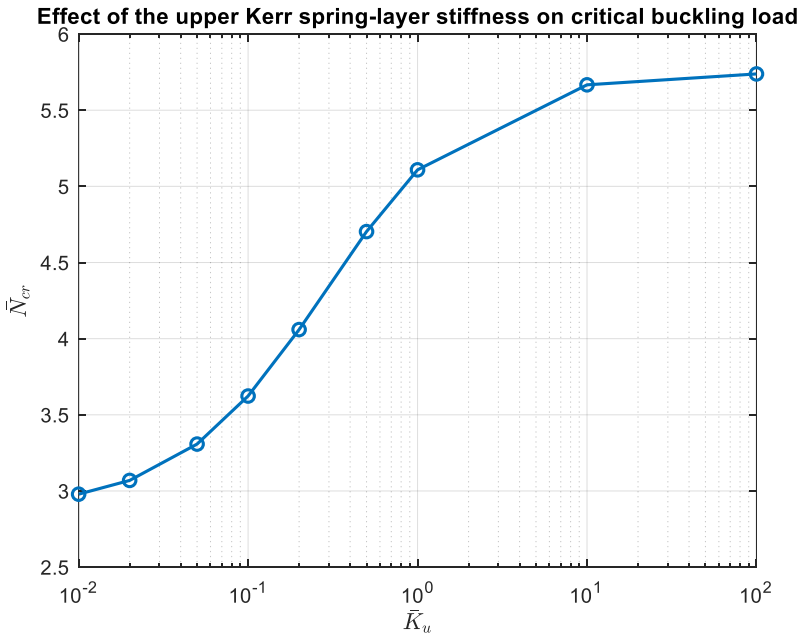


Fig. 2. Effect of the upper Kerr spring-layer stiffness on the dimensionless critical buckling load.

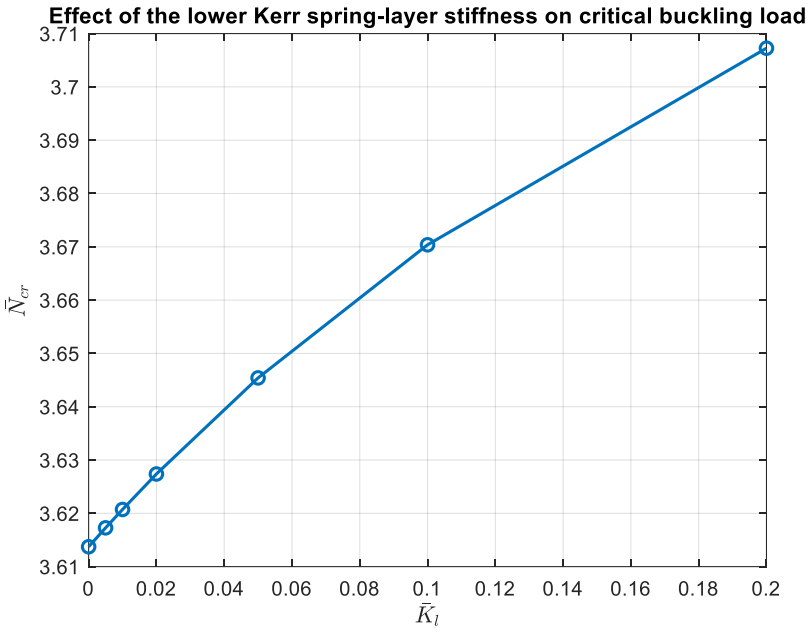


Fig. 3. Effect of the lower Kerr spring-layer stiffness on the dimensionless critical buckling load.

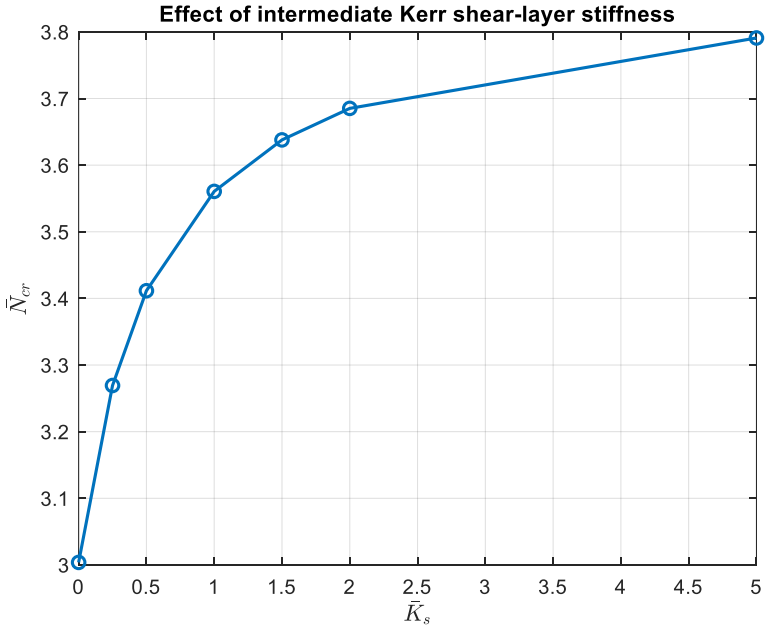


Fig. 4. Effect of the intermediate Kerr shear-layer stiffness on the dimensionless critical buckling load.

Fig. 3 illustrates the effect of the lower spring stiffness on the stability response. The dimensionless critical buckling load increases monotonically from approximately 3.6137 to 3.7073 as $\bar{K}_l$ varies from 0 to 0.2. Compared with the variation observed for the upper spring layer, the change is relatively small, indicating a lower sensitivity of the critical buckling load to $\bar{K}_l$ for the reference configuration considered. The response is also nearly linear over the investigated interval.

As shown in Fig. 4, increasing the intermediate shear-layer stiffness also enhances the buckling resistance. The dimensionless critical buckling load increases from approximately 3.0038 to 3.7909 as $\bar{K}_s$ varies from 0 to 5. The response is relatively steep at low stiffness levels

and gradually becomes flatter as $\overline{K}_s$ increases, indicating diminishing increments in the critical load at higher shear-layer stiffnesses. Thus, the intermediate shear layer has a clear stabilizing effect, although its influence becomes progressively less pronounced as the layer becomes stiffer.

Taken together, Figs. 2–4 show that the three Kerr parameters influence the buckling response with different sensitivities. Within the nondimensional parameter ranges considered, the upper spring stiffness produces the largest variation in the critical buckling load, the shear-layer stiffness has an intermediate effect, and the lower spring stiffness produces the smallest change. This comparison is specific to the adopted reference configuration and parameter ranges.

4 Conclusions

A three-dimensional elasticity-based state-space differential quadrature formulation was employed to investigate the buckling behavior of functionally graded sandwich plates resting on a full Kerr elastic foundation. The formulation showed good agreement with available reference solutions for both unsupported and Pasternak-supported FGS plates, supporting the accuracy of the buckling formulation and the implementation of the elastic-foundation terms. For the representative Type A plate considered, increasing each Kerr foundation parameter increased the dimensionless critical buckling load within the investigated ranges. The upper spring stiffness $\overline{K}_u$ produced the most pronounced variation, with the response becoming less sensitive at higher stiffness levels. The intermediate shear-layer stiffness $\overline{K}_s$ also provided a clear stabilizing effect with diminishing increments as its stiffness increased, whereas the lower spring stiffness $\overline{K}_l$ produced a comparatively smaller change. These findings show that the individual components of the full Kerr foundation influence the stability response with different sensitivities and highlight the importance of retaining the three foundation parameters independently.

Acknowledgments

This study was supported by the Scientific Research Projects Coordination Unit of Karadeniz Technical University within the scope of BAP05 Project No. 17329.

References

1. Zenkour, A.M.: A comprehensive analysis of functionally graded sandwich plates: Part 2-Buckling and free vibration. International Journal of Solids and Structures 42, 5243-5258 (2005). DOI: 10.1016/j.ijsolstr.2005.02.016.
2. El Meiche, N., Tounsi, A., Ziane, N., Mechab, I., Adda Bedia, E.A.: A new hyperbolic shear deformation theory for buckling and vibration of functionally graded sandwich plate. International Journal of Mechanical Sciences 53, 237-247 (2011). DOI: 10.1016/j.ijmecsci.2011.01.004.
3. Neves, A.M.A., Ferreira, A.J.M., Carrera, E., Cinefra, M., Roque, C.M.C., Jorge, R.M.N., Soares, C.M.M.: Static, free vibration and buckling analysis of isotropic and sandwich functionally graded plates using a quasi-3D higher-order shear deformation theory and a meshless technique. Composites Part B: Engineering 44, 657-674 (2013). DOI: 10.1016/j.compositesb.2012.01.089.
4. Alibeigloo, A., Alizadeh, M.: Static and free vibration analyses of functionally graded sandwich plates using state space differential quadrature method. European Journal of Mechanics-A/Solids 54, 252-266 (2015). DOI: 10.1016/j.euromechsol.2015.06.011.
5. Kiani, Y., Bagherizadeh, E., Eslami, M.R.: Thermal and mechanical buckling of sandwich plates with FGM face sheets resting on the Pasternak elastic foundation. Proceedings of the

Institution of Mechanical Engineers, Part C: Journal of Mechanical Engineering Science 226, 32-41 (2012). DOI: 10.1177/0954406211413657.
6. Yaghoobi, H., Yaghoobi, P.: Buckling analysis of sandwich plates with FGM face sheets resting on elastic foundation with various boundary conditions: An analytical approach. Meccanica 48, 2019-2035 (2013). DOI: 10.1007/s11012-013-9720-0.
7. Sobhy, M.: Buckling and free vibration of exponentially graded sandwich plates resting on elastic foundations under various boundary conditions. Composite Structures 99, 76-87 (2013). DOI: 10.1016/j.compstruct.2012.11.018.
8. Van, V.T., Hieu, N.V.: Buckling analysis of functionally graded sandwich plates resting on Pasternak foundation using a novel refined quasi-3D third-order shear deformation theory. Journal of Science and Technology in Civil Engineering 16(1), 68-79 (2022). DOI: 10.31814/stce.huce(nuce)2022-16(1)-06.
9. Kerr, A.D.: A study of a new foundation model. Acta Mechanica 1, 135-147 (1965). DOI: 10.1007/BF01174308.
10. Jones, R., Xenophontos, J.: On the Vlasov and Kerr foundation models. Acta Mechanica 25, 45-49 (1976). DOI: 10.1007/BF01176928.
11. Akavcı, S.S.: Mechanical behavior of functionally graded sandwich plates on elastic foundation. Composites Part B: Engineering 96, 136-152 (2016). DOI: 10.1016/j.compositesb.2016.04.035.

Author Contribution Statement

- *Conceptualization:* Sebahat Şimşek
- *Methodology:* Sebahat Şimşek
- *Investigation:* Sebahat Şimşek
- *Writing – Original Draft:* Sebahat Şimşek
- *Writing – Review & Editing:* Sebahat Şimşek, Magd Abdel Wahab

Publication Note

This paper was peer-reviewed, accepted for presentation, and included in the proceedings of the ACE2026 – International Conference on Advances in Civil Engineering, held on 12–14 October 2026 in Trabzon, Türkiye.

This paper may be cited as follows:

Şimşek, S., and Abdel Wahab, M., "Three-Dimensional Elasticity-Based Buckling Analysis of Functionally Graded Sandwich Plates on Kerr Foundation Using State-Space Differential Quadrature Method," in Proceedings of the ACE2026 – International Conference on Advances in Civil Engineering, Trabzon, Türkiye, 12–14 October 2026.

CHAPTER 2

Construction Materials

37 papers

Role of Nano Silica Dispersion Methods in the Mechanical and Physical Performance of High-Performance Concrete

Irem Bagca[1] and Kutalmış Recep Akça[2]
[1] 0000-0002-0881-9307, Sakarya University of Applied Sciences, Faculty of Technology, Civil Engineering Department, Sakarya, Türkiye, irembagca@subu.edu.tr
[2] 0000-0002-6155-8521, Sakarya University of Applied Sciences, Faculty of Technology, Civil Engineering Department, Sakarya, Türkiye, akca@subu.edu.tr

Abstract. The use of nano silica (NS) in high-performance concrete has increased considerably in recent years due to its filler effect and high pozzolanic reactivity. However, agglomeration of nano-sized particles may limit the expected performance improvement. Therefore, the dispersion method of nano silica is an important parameter affecting concrete performance. In this study, the effects of different nano silica mixing methods on the mechanical and physical properties of fly ash-based high-performance concrete mixtures were investigated. Within the scope of the study, concrete series containing nano silica and fly ash were evaluated. In the reference mixtures, nano silica was directly incorporated into the dry binder before concrete production. The same mixtures were also produced by mechanically dispersing nano silica in the mixing water together with the superplasticizer prior to mixing. In addition, the same concrete series were also produced using ultrasonic dispersion to enable a comparative evaluation of the three nano-silica dispersion methods. The experimental program includes compressive strength tests, flexural strength tests, unit weight and slump flow measurements. Results indicated that mechanically dispersed nano silica provided higher compressive strength compared to the dry-mixing method under similar workability conditions. The obtained findings indicate that the dispersion quality of nano silica may have a significant effect on the mechanical and physical performance of high-performance concrete.

Keywords: dispersion method; nano silica; high performance concrete; ultrasonic dispersion.

1 Introduction

High-performance and reactive powder concrete matrix systems represent innovative cementitious composites engineered to exhibit exceptional mechanical strength and superior durability characteristics. To further optimize the efficiency of these high-performance materials, the incorporation of nanoparticles—most notably nano-silica (NS)—has attracted profound scientific interest due to its extremely fine particle size and massive specific surface area. Nanomaterials fundamentally enhance the cementitious matrix through physical and chemical pathways; while they act as ultra-fine pore fillers that structurally occupy nano scale voids to enhance particle packing density, they also exhibit high pozzolanic reactivity that accelerates cement hydration and promotes the formation of supplementary calcium silicate hydrate (C-S-H) gels [1,2]. This collaborative mechanism significantly densifies the microstructure, refines the pore distribution and improves the overall interfacial transition zone (ITZ) [3].

Due to their exceptionally high specific surface area, NS particles exhibit a strong tendency to agglomerate in cementitious systems. This agglomeration hinders the homogeneous

distribution of NS, critically affecting both the mechanical properties and workability of the concrete matrix. A significant portion of the contradictory results regarding NS application in the literature can be attributed to inadequate dispersion [4-5]. Proper dispersion is essential to maximize the positive effects of nanoparticles and minimize their drawbacks, which is crucial for developing high-performance composite materials [6].

To achieve effective dispersion, various physical and chemical methods have been explored, including high-speed mechanical mixing, ultrasonication, and the use of dispersion agents like superplasticizers. Mechanical and ultrasonic methods aim to separate particles through high shear forces and cavitation, respectively. While ultrasonication is highly effective in breaking down agglomerates through cavitation and enhancing hydration, prolonged exposure to high-frequency sound waves can generate excessive heat within the aqueous medium. This intensive acoustic energy can alter the structural and morphological properties of the nanoparticles [6]. Alternatively, chemical modification using polycarboxylate-based superplasticizers (PCE) provides physical or steric hindrance on the NS surface, significantly improving particle distribution and preventing rapid re-agglomeration in the cement pore solution [5].

Previous studies have highlighted that dispersion efficiency directly depends not only on the NS dosage but also on the mixing sequence, form of NS and the type of dispersion technique applied. In high performance concrete (HPC) formulations, where supplementary cementitious materials like fly ash are utilized, the interaction between nanoparticles and the binder matrix becomes even more critical. Incorporating dry NS powder directly into the mix often leads to poor dispersion and subsequent performance reductions [7-8]. Conversely, pre-dispersing NS in an aqueous solution with a superplasticizer has been proven to optimize the matrix microstructure and enhance early age properties [9-10].

To address these challenges, this study investigates the effects of different nano-silica mixing methodologies on the mechanical and physical properties of fly ash-based high-performance concrete mixtures. Within the scope of the experimental program, concrete series containing a fixed 2% NS replacement were evaluated. The investigation primarily compares a reference dry-mixing approach, in which nano silica was directly incorporated into the dry constituents, with mechanical pre-dispersion of nano silica in the mixing water containing the superplasticizer. Additionally, ultrasonic dispersion method was included in the experimental matrix for comparative analysis. The performance of the mixtures was comprehensively evaluated through slump flow, unit weight, compressive strengths, and flexural strength tests. Based on findings, this paper delineates how dispersion quality fundamentally dictates the physical and mechanical efficiency of NS-modified high-performance composites.

2 Materials and Methods

2.1 Materials

Ordinary Portland cement (CEM I 42.5 R) conforming to TS EN 197-1 [11] was used as the primary binder material. Class F fly ash (FA) was incorporated as a supplementary cementitious material at a replacement level of 10% by weight of cement. Nano silica (NS) (Fig. 1), consisting of amorphous silicon dioxide (SiO_2) nanoparticles with a particle size ranging from 15 to 35 nm, was utilized as a mineral additive due to its high pozzolanic activity and filler effect.



Fig. 1. Nano silica (NS) used in this study.

A polycarboxylate ether-based superplasticizer was employed to maintain adequate workability at a low water-to-binder ratio. Fine aggregate consisted of quartz powder (0-100 μm) and two silica sand fractions (100-300 μm and 300-700 μm) with different particle size distributions selected according to an optimized particle packing design. As steel fiber reinforcement, recycled steel fibers (Fig. 2) recovered from end-of-life tires were used in all mixtures. The fibers had an average length of approximately 13 mm and were incorporated to improve the mechanical performance of the concrete matrix. Potable tap water was used for mixing and curing.



Fig. 2. Recycled steel fibers (RSF).

2.2 Mixture Proportions

The concrete mixtures investigated in this study were derived from a previously developed high-performance concrete mixture [12]. A constant water-to-binder ratio of 0.25 was adopted for all series. Fly ash and nano-silica contents were fixed at 10% and 2% of the binder, respectively. While recycled steel fibers were incorporated at a constant dosage of 2.0 vol.%, throughout the study.

To isolate the effect of the nano-silica dispersion technique, all mixture parameters, including binder composition, aggregate content, fiber dosage, and curing conditions, were kept constant. The detailed mixture proportions are presented in Table 1.

Table 1. Mix proportions normalized by cement mass (cement=1.0).

Cement	Water	Superplast.	Quartz Powder	Silica Sand (100–300 μm)	Silica Sand (300–700 μm)	FA	NS	Recycled Steel Fiber (RSF)
1.0	0.284	0.045	0.247	0.238	0.366	0.114	0.023	2% (by total volume)

2.3 Nano-Silica Dispersion Procedures

Three different nano-silica incorporation techniques were evaluated. In the dry-mixed mixture (DM), NS powder was directly added to the dry constituents and mixed together prior to water addition. This method represents the simplest and most commonly applied incorporation technique in practice.

In the mechanically dispersed mixture (MD), NS was first dispersed in the mixing water containing the superplasticizer using a high-speed mechanical mixer before being introduced into the concrete mixture. This procedure was intended to improve particle distribution and reduce agglomeration.

In the ultrasonically dispersed mixture (UD), NS was dispersed in a water–superplasticizer solution using a probe-type ultrasonic processor for 30 min before being incorporated into the concrete mixture.

2.4 Specimen Preparation and Curing

All mixtures were produced using a laboratory mortar mixer following a standardized mixing sequence. Depending on the dispersion method, nano-silica was either directly incorporated into the dry constituents prior to mixing, mechanically dispersed in the mixing water containing the superplasticizer, or ultrasonically dispersed in the same solution before concrete production. Fresh concrete properties were evaluated immediately after mixing through slump-flow measurements.

Subsequently, 50×50×50 mm cubic specimens and 40×40×160 mm prism specimens were cast into steel molds and manually compacted by rodding under laboratory conditions for compressive and flexural strength testing, respectively.

After approximately 24 h, the specimens were demolded and cured in lime-saturated water at 20±2 °C in accordance with EN 12390-2 [13] until the designated testing ages of 28 days. Identical curing conditions were maintained for all mixtures to ensure that any observed differences in performance could be attributed solely to the nano-silica dispersion method.

2.5 Test Methods

The influence of the NS dispersion technique on the fresh, physical, and mechanical properties of high performance concrete was evaluated through slump-flow, bulk density, compressive strength, and flexural strength tests.

Slump-flow measurements were conducted in accordance with ASTM C1611/C1611M-21 [14] to assess the workability of fresh concrete mixtures. The bulk density of hardened concrete specimens was determined following EN 12390-7 [15]. Compressive strength tests were performed on 50×50×50 mm cube specimens following the loading procedure specified in ASTM C109/C109M-20B [16]. Flexural strength tests were performed at 28 days using 40×40×160 mm prism specimens following the procedures specified in ASTM C348-14 [17].

The obtained results were used to evaluate the effectiveness of the different NS dispersion methods and their influence on the physical and mechanical performance of fly ash-based high-performance concrete.

3 Result and Discussion

3.1 Workability

Fig. 3 presents the slump-flow results of the concrete mixtures prepared using different nano-silica dispersion methods. Both the dry-mixed (DM) and ultrasonically dispersed (UD) mixtures showed a slump flow of 34 cm, while the mechanically dispersed mixture (MD) exhibited a slump flow of 31 cm.

Although the MD mixture exhibited a slightly lower slump-flow value, all mixtures provided adequate workability for high-performance concrete production. The reduced flowability of the MD mixture may be attributed to the more uniform dispersion of nano-silica particles, which increases their effective surface area and consequently the water demand of the mixture. In contrast, the relatively higher slump-flow values observed for the DM mixture may be associated with particle agglomeration, which decreases the effective surface area of nano-silica and limits its interaction with the mixing water. The identical slump-flow values obtained for the DM and UD mixtures indicate that, under the conditions investigated, ultrasonic dispersion did not produce a noticeable change in the workability of the fresh concrete.

Since all mixtures exhibited relatively similar workability, any differences observed in the subsequent mechanical properties are likely to be associated with the effectiveness of the nano-silica dispersion rather than with variations in fresh concrete consistency.

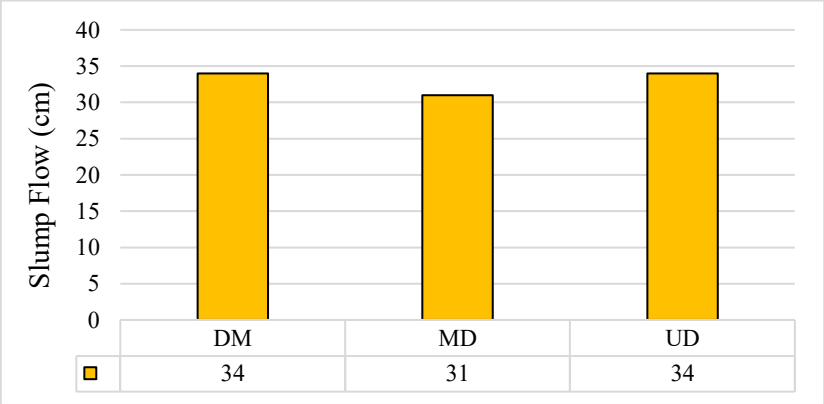


Fig. 3. Slump-flow results of the concrete mixtures.

3.2 Bulk Density

Fig. 4 presents the bulk density results of the concrete mixtures prepared using different NS dispersion methods. The average unit weights of the DM, MD and UD mixtures were 2.26, 2.29 and 2.33 kg/dm³, respectively. Among the investigated mixtures, the UD mixture exhibited the highest unit weight, whereas the DM mixture showed the lowest value.

The relatively lower unit weight of the DM mixture may be attributed to the agglomeration of nano-silica particles, which reduces their filler efficiency by causing them to behave as larger clusters rather than uniformly dispersed nanoparticles. Consequently, particle packing becomes less efficient, leading to the formation of locally less dense regions within the cementitious matrix. In contrast, the higher unit weights obtained for the MD and UD mixtures suggest that improved nano-silica dispersion promoted more efficient particle packing and a denser internal structure.

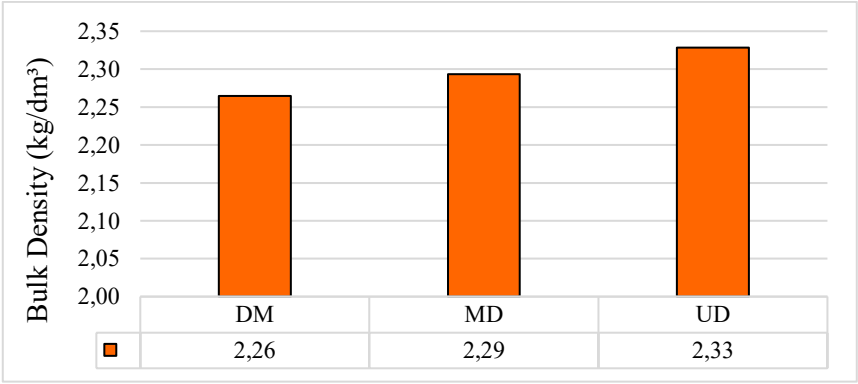


Fig. 4. Bulk density results of the concrete mixtures.

3.3 Compressive Strength

Fig. 5 presents the compressive strength results of the concrete mixtures prepared using different nano-silica dispersion methods. The average 28-day compressive strengths of the 50 × 50 × 50 mm cube specimens were 76.96 MPa, 112.73 MPa and 94.01 MPa for the DM, MD, and UD mixtures, respectively. Among the investigated mixtures, the MD mixture exhibited the highest compressive strength, whereas the DM mixture produced the lowest 28-day compressive strength. Compared with the dry mixing method, mechanical dispersion increased the 28-day compressive strength by approximately 46%, demonstrating the significant influence of nano-silica dispersion method on the mechanical performance of high-performance concrete.

The superior performance of the MD mixture may be attributed to the more effective dispersion of nano-silica particles within the cementitious matrix. A more homogeneous distribution of nano-silica increases its effective reactive surface area, enhancing both the filler effect and the pozzolanic reaction. In contrast, direct incorporation of nano-silica in dry form may promote particle agglomeration, reducing its efficiency and limiting its contribution to strength development. Similar observations have been reported by Elkady et al. [9] and Du et al. [10], who demonstrated that pre-dispersion of nano-silica is more effective than direct dry incorporation.

Following the flexural strength test, compressive strength tests were also carried out on the prism halves (40 × 40 × 40 mm). The average compressive strengths of the DM, MD and UD mixtures were 107.19 MPa, 125.84 MPa and 125.72 MPa, respectively. Similar to previous studies [18-19], the compressive strengths obtained from the prism halves were higher than those measured on the 50 × 50 × 50 mm cube specimens, which can be attributed to the specimen size effect [20]. Since the surface layer constitutes a larger proportion of the total cross-sectional area in smaller specimens, its beneficial influence on mechanical performance becomes more pronounced. In addition, according to Weibull's statistical size effect theory, smaller specimens have a lower probability of containing critical flaws, leading to higher measured compressive strengths [12]. Accordingly, the compressive strengths of the 40 × 40 × 40 mm specimens were approximately 12% to 39% higher than those of the 50 × 50 × 50 mm cube specimens, confirming the influence of specimen size on the measured strength values. The MD and UD mixtures exhibited nearly identical compressive strengths, while the DM mixture again produced considerably lower strength. These findings indicate that both mechanical and ultrasonic dispersion methods were similarly effective in improving the compressive performance of the investigated high-performance concrete. In contrast, direct dry incorporation of nano-silica resulted in consistently lower compressive strength, highlighting the importance of achieving adequate nano-silica dispersion.

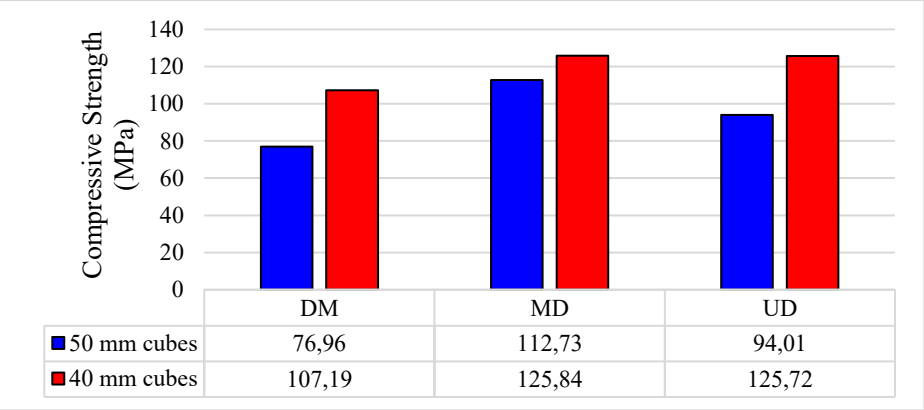


Fig. 5. Compressive strength results of the concrete mixtures.

3.4 Flexural Strength

Fig. 6 presents the flexural strength results of the concrete mixtures prepared using different nano-silica dispersion methods. The average flexural strengths of the DM, MD and UD mixtures were 18.58 MPa, 19.95 MPa and 15.17 MPa, respectively. Accordingly, the MD mixture exhibited the highest flexural strength, followed by the DM mixture, while the UD mixture produced the lowest value. Furthermore, the flexural strength of the MD mixture was approximately 7.4% higher than that of the reference dry-mixed (DM) mixture.

The differences in flexural strength may be associated not only with the dispersion of nano-silica but also with the distribution and orientation of recycled steel fibers within the specimens. While improved nano-silica dispersion is expected to enhance matrix densification, flexural performance of fiber-reinforced concrete is governed largely by the effectiveness of fiber bridging across the crack plane. Examination of the fractured cross-sections (Fig. 7) revealed that the MD and DM mixtures contained a higher concentration of fibers near the tensile region, whereas the UD mixture exhibited a more uniform fiber distribution throughout the cross-section. Since flexural cracks initiate from the tensile face, the higher local fiber concentration in this region likely enhanced crack-bridging capacity, delayed crack propagation, and resulted in higher flexural strengths for the MD and DM mixtures. This observation also explains why the UD mixture, despite exhibiting considerably higher compressive strength than the DM mixture, produced the lowest flexural strength among the investigated mixtures.

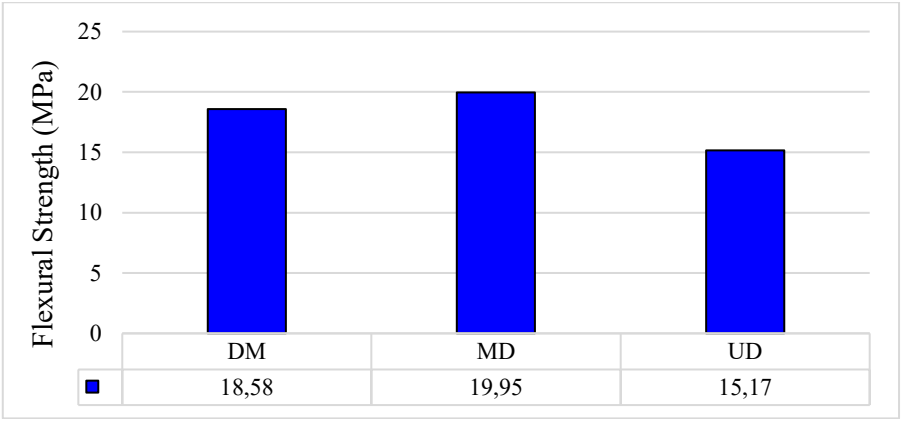


Fig. 6. Flexural strength results of the concrete mixtures.

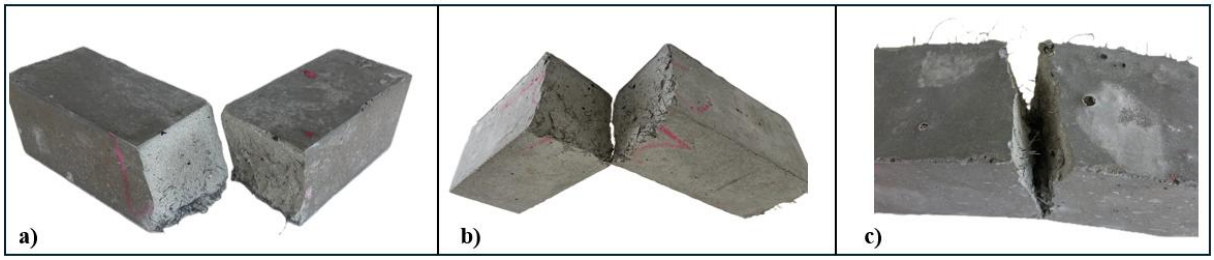


Fig. 7. Representative fracture surfaces after flexural testing: (a) DM, (b) MD, and (c) UD.

4 Conclusions

This study investigated the influence of different nano-silica dispersion methods on the fresh, physical, and mechanical properties of fly ash-based high-performance concrete. Based on the experimental findings, the following conclusions can be drawn:

- The nano-silica dispersion method had only a limited influence on the workability of the mixtures, as all concretes exhibited comparable slump-flow values.

- Improved nano-silica dispersion enhanced the compactness of the concrete matrix. Accordingly, the ultrasonically dispersed mixture exhibited the highest bulk density, whereas the dry-mixed mixture produced the lowest value.
- Mechanical dispersion produced the highest 28-day compressive strength in the 50 mm cube specimens and increased compressive strength by up to approximately 46% compared with direct dry mixing. Although the mechanically and ultrasonically dispersed mixtures exhibited nearly identical compressive strengths in the 40 mm cube specimens, both methods clearly outperformed the dry-mixing approach. These findings demonstrate that selecting an appropriate nano-silica dispersion technique can improve compressive strength by up to 46%, emphasizing the importance of proper nano-silica dispersion for enhancing the performance of high-performance concrete.
- The highest flexural strength was obtained in the mechanically dispersed mixture, while the ultrasonically dispersed mixture exhibited the lowest flexural strength. This behavior was associated with differences in the distribution of recycled steel fibers within the specimens, with the MD and DM mixtures exhibiting a higher concentration of fibers near the tensile region than the UD mixture.

Overall, the results demonstrate that the nano-silica dispersion technique is a key parameter governing the performance of high-performance concrete. Among the investigated methods, mechanical dispersion provided the most balanced overall performance, combining the highest compressive and flexural strengths with satisfactory physical properties. Although ultrasonic dispersion produced comparable compressive strength in the 40 mm specimens and the highest bulk density, these improvements did not translate into a clear overall performance advantage considering its additional processing time and specialized equipment requirements. Therefore, mechanical dispersion can be considered a more practical and efficient technique for incorporating nano-silica into high-performance concrete, while direct dry incorporation proved to be the least effective approach. Further microstructural investigations are recommended to better explain the relationship between nano-silica dispersion, fiber distribution, and the resulting mechanical behavior.

Acknowledgments

The authors gratefully acknowledge the financial support provided by the Scientific Research Projects Coordination Unit (BAP) of Sakarya University of Applied Sciences under Project No. 338-2025. The authors also gratefully acknowledge Prof. Keziban Atacan for her valuable support and for providing access to the ultrasonic dispersion equipment and laboratory facilities used for the nano-silica dispersion process.

References

1. Rong, Z., Sun, W., Xiao, H., Jiang, G. Effects of nano-SiO_2 particles on the mechanical and microstructural properties of ultra-high performance cementitious composites. Cement and Concrete Composites 56, 25–31 (2015). https://doi.org/10.1016/j.cemconcomp.2014.11.001
2. Singh, L. P., Ali, D., Tyagi, I., Sharma, U., Singh, R., Hou, P. Durability studies of nano-engineered fly ash concrete. Construction and Building Materials 194, 205–215 (2019). https://doi.org/10.1016/j.conbuildmat.2018.11.022
3. Ghafari, E., Costa, H., Júlio, E. Critical review on eco-efficient ultra high performance concrete enhanced with nano-materials. Construction and Building Materials 101, 201–208 (2015). https://doi.org/10.1016/j.conbuildmat.2015.10.066
4. Ahmed, R., Niyazi, M., Kockal, U. Nanoparticles used as an ingredient in different types of concrete. SN Applied Sciences 3, 1–17 (2021). https://doi.org/10.1007/s42452-021-04461-3

5. Gu, Y., Ran, Q., Shu, X., Yu, C., Chang, H., Liu, J. Synthesis of nano-SiO_2 PCE core-shell nanoparticles and its effect on cement hydration at early age. Construction and Building Materials 114, 673–680 (2016). https://doi.org/10.1016/j.conbuildmat.2016.03.093
6. Verma, P., Shukla, S., Pal, P. Potential application of nano-silica in concrete pavement: A bibliographic analysis and comprehensive review. Materials Today Sustainability 29, 101079 (2025).
7. Ghafari, E., Costa, H., Júlio, E., Portugal, A., Durães, L. The effect of nanosilica addition on flowability, strength and transport properties of ultra high performance concrete. Materials & Design 59, 1–9 (2014). https://doi.org/10.1016/j.matdes.2014.02.051
8. Haruehansapong, S., Pulngern, T., Chucheepsakul, S. Effect of the particle size of nanosilica on the compressive strength and the optimum replacement content of cement mortar containing nano-SiO_2. Construction and Building Materials 50, 471–477 (2014). https://doi.org/10.1016/j.conbuildmat.2013.10.002
9. Elkady, H., Serag, M. I., Elfeky, M. S. Effect of nano silica de-agglomeration and methods of adding superplasticizer on the compressive strength and workability of nano silica concrete. Civil and Environmental Research 3(2), 21–34 (2013).
10. Du, H., Du, S., Liu, X. Durability performances of concrete with nano-silica. Construction and Building Materials 73, 705–712 (2014). https://doi.org/10.1016/j.conbuildmat.2014.10.014
11. EN 197-1:2011. Cement – Part 1: Composition, Specifications and Conformity Criteria for Common Cements. European Committee for Standardization (CEN), Brussels, Belgium (2011).
12. Akça, K. R., İpek, M. Effect of different fiber combinations and optimisation of an ultra-high performance concrete (UHPC) mix applicable in structural elements. Construction and Building Materials 315, 125777 (2022). https://doi.org/10.1016/j.conbuildmat.2021.125777
13. EN 12390-2. Testing Hardened Concrete—Part 2: Making and Curing Specimens for Strength Tests. European Committee for Standardization, Brussels, Belgium (2009).
14. ASTM C1611/C1611M-21. Standard Test Method for Slump Flow of Self-Consolidating Concrete. ASTM International, West Conshohocken, PA, USA (2021).
15. EN 12390-7:2009. Testing Hardened Concrete—Part 7: Density of Hardened Concrete. European Committee for Standardization, Brussels, Belgium (2009).
16. ASTM C109/C109M-20. Standard Test Method for Compressive Strength of Hydraulic Cement Mortars (Using 2-in. or [50 mm] Cube Specimens). ASTM International, West Conshohocken, PA, USA (2020). https://doi.org/10.1520/C0109_C0109M-20B
17. ASTM C348-14. Standard Test Method for Flexural Strength of Hydraulic-Cement Mortars. ASTM International, West Conshohocken, PA, USA (2014).
18. Rawat, S., Zhang, Y. X., Lee, C. K. Effect of specimen size and shape on the compressive performance of high strength engineered cementitious composites at elevated temperatures. Innovative Infrastructure Solutions 9(8), 317 (2024). https://doi.org/10.1007/s41062-024-01628-w
19. Nalon, G. H., Martins, R. O. G., Alvarenga, R. D. C. S. S. A., Lima, G. E. S. D., Pedroti, L. G., Santos, W. J. D. Effect of specimens' shape and size on the determination of compressive strength and deformability of cement-lime mortars. Materials Research 20(Suppl. 2), 819–825 (2018). https://doi.org/10.1590/1980-5373-MR-2016-1006
20. Fládr, J., Bílý, P. Specimen size effect on compressive and flexural strength of high-strength fibre-reinforced concrete containing coarse aggregate. Composites Part B: Engineering 138, 77–86 (2018). https://doi.org/10.1016/j.compositesb.2017.11.032

Author Contribution Statement

- *Conceptualization:* Kutalmış Recep Akça
- *Methodology:* Kutalmış Recep Akça, Irem Bagca
- *Investigation:* Irem Bagca
- *Writing – Original Draft:* Irem Bagca
- *Writing – Review & Editing:* Kutalmış Recep Akça, Irem Bagca

List of Abbreviations

- **NS** — Nano Silica
- **HPC** — High-Performance Concrete
- **FA** — Fly Ash
- **PCE** — Polycarboxylate Ether
- **ITZ** — Interfacial Transition Zone
- **C-S-H** — Calcium Silicate Hydrate
- **MD** — Mechanically Dispersed
- **DM** — Dry-Mixed
- **UD** — Ultrasonically Dispersed
- **RSF** — Recycled Steel Fiber

Publication Note

This paper was peer-reviewed, accepted for presentation, and included in the proceedings of the ACE2026 – International Conference on Advances in Civil Engineering, held on 12–14 October 2026 in Trabzon, Türkiye.

This paper may be cited as follows:

Irem Bagca and Kutalmış Recep Akça, "Role of Nano Silica Dispersion Methods in the Mechanical and Physical Performance of High-Performance Concrete," in Proceedings of the ACE2026 – International Conference on Advances in Civil Engineering, Trabzon, Türkiye, 12–14 October 2026.

Performance-Based Comparison of Fly Ash and Recycled Glass Powder in Low-Carbon Concrete: A Carbon Reduction Efficiency Approach

Ebru Dural[1,2,*], Gulmira Adzhygulova[2], Gulnara Karadeniz[3], Mehmet Karadeniz[4]

[1] 0000-0002-5519-2498, Department of Civil Engineering, Aydin Adnan Menderes University, Aydin, Türkiye, ebru.dural@adu.edu.tr
[2] 0009-0009-5917-7111, Department of Technical Programs, Kyrgyz-Turkish Manas University, Bishkek, Kyrgyzstan, gulmira.acigulova@manas.edu.kg
[3] 0000-0002-8409-7027, Department of Economics and Administration Programs, Kyrgyz-Turkish Manas University, Bishkek, Kyrgyzstan, gulnara.karadeniz@manas.edu.kg
[4] 0000-0001-5162-4698, Department of Electric and Electronics Engineering, Kyrgyz-Turkish Manas University, Bishkek, Kyrgyzstan, mehmet.karadeniz@manas.edu.kg
* Corresponding Author: ebru.dural@adu.edu.tr

Abstract. This study presents a performance-based comparison of fly ash (FA) and recycled glass powder (GP) as partial cement replacements in concrete, evaluated under identical mixture design conditions. Concrete mixtures were prepared with replacement levels of 10%, 20%, and 30% by weight of cement, at a constant water-to-cement ratio of 0.60 and without chemical admixtures. Mechanical performance was assessed through 28-day compressive strength, while environmental impact was evaluated through embodied carbon calculations covering the cradle-to-gate, construction, and end-of-life stages. A novel Carbon Reduction Efficiency (CRE) index was introduced to quantify the trade-off between carbon savings and strength loss, complemented by a Carbon–Performance Quadrant framework. Results show that FA mixtures achieved a more favorable balance between carbon reduction and mechanical performance than GP mixtures: FA-30 reduced embodied carbon by 26.7% while limiting the strength loss to 9.3%, whereas GP-30 achieved a comparable 24.0% carbon reduction at the cost of an 18.9% strength loss. FA-20 emerged as the most balanced replacement level, reducing embodied carbon by 17.8% while maintaining a strength loss of only 5.2%. The findings provide practical guidance for selecting supplementary cementitious materials in low-to-medium strength applications such as pavements, mass concrete, and leveling layers.

Keywords: Fly ash; Recycled glass powder; Carbon reduction efficiency; Compressive strength; Low-carbon concrete.

1 Introduction

Cement manufacturing contributes substantially to the carbon budget, accounting for roughly 7-8% of the man-made CO2 emissions [1]. Due to the immense volumes of concrete produced globally, even slight reductions in cement usage can yield cumulative savings. For this reason, partial replacement of cement with industrial byproducts has become a common approach. Two of the most used alternatives are fly ash (FA) and glass powder (GP).

The primary mechanism of FA is the pozzolanic reaction, in which it interacts with calcium hydroxide produced during cement hydration. This reaction forms additional C-S-H gel, densifying the pore structure and improving long-term durability. However, as a result of this relatively slow mechanism, more FA may reduce early-age strength [3]. The mechanism of glass powder is similar when it is ground fine enough to become reactive. In general, it has a

positive effect on strength and permeability at replacement levels of about 10–20%, but any further increase causes a decrease in these properties [4]. Studies on the environmental effects of concrete mixes containing FA and GP, prepared under the same conditions and applied at the same substitution ratios, are limited in the literature. Few studies have compared FA–GP blends [5, 6]; however, controlled comparative studies in practical engineering metrics like CO_2 per unit of strength remain scarce.

This paper aims to fill that gap. FA and GP were tested at replacement levels of 10%, 20%, and 30% under identical conditions (w/c = 0.60, no admixtures), reflecting the low-to-medium strength concretes used in pavements, mass fills, and leveling layers. Beyond simply reporting carbon and strength values side by side, we propose a Carbon Reduction Efficiency (CRE) metric–defined as the amount of carbon saved per unit of strength sacrificed–and present the results using a Carbon–Performance Quadrant. This visualization is intended to clearly identify which replacement level is practically advantageous.

2 Materials and Methods

A total of seven different mixtures were made: a control mixture of only Portland cement, and three FA and three GP mixtures with cement substitution amounts of 10%, 20%, and 30% by weight. No chemical admixtures were used, while the water-to-cement ratio was kept at 0.60 for all mixes. This way, any discrepancies that may be noted will be due solely to the difference in the replacement material used, not to other changes in the mix design. The maximum size of aggregates did not exceed 20 mm. All mix proportioning details are listed in Table 1.

Table 1. Concrete mixture proportions.

Mix Code	Cement (kg)	Additive	Additive (kg)	Water (L)	Sand (kg)	Aggregate (kg)
Control	350	–	0	210	708	1085
FA-10	315	Fly ash	35	210	708	1085
FA-20	280	Fly ash	70	210	708	1085
FA-30	245	Fly ash	105	210	708	1085
GP-10	315	Glass powder	35	210	708	1085
GP-20	280	Glass powder	70	210	708	1085
GP-30	245	Glass powder	105	210	708	1085

The fly ash used was a low-calcium type per EN 450-1 [7] ($SiO_2 + Al_2O_3 + Fe_2O_3 > 70\%$), and the glass powder was ground soda-lime glass waste, composed primarily of silica ($SiO_2 \approx 69.4\%$) along with Na_2O and CaO. Five cubes were cast per mixture — 35 in total – and tested at 28 days following TS EN 12390-3 [8]. Embodied carbon was calculated by multiplying each material's mass by its emission factor, using the ICE database for cement, fly ash, and aggregate, and a Tier-1 IPCC estimate for the glass powder [9, 10]. Additionally, a flat 28.0 kg CO_2/m^3 was added for transport, construction, and end-of-life, based on assumptions of a 100 km haul, 5 kWh/m^3 of construction energy, and a 70% recycling rate [11] – constant for all mixtures, as these stages are independent of the cement replacement level.

To obtain a relatinship between the environmental and mechanical sides of the picture, we defined a Carbon Reduction Efficiency (CRE) index:

$$CRE = \Delta EC / \Delta fc = (ECcontrol - ECmix) / (fc,control - fc,mix) \quad (1)$$

Here, ΔEC and Δfc represent the reductions in embodied carbon (kg CO_2/m^3) and 28-day compressive strength (MPa), respectively, relative to the control mixture. A higher CRE indicates greater carbon savings per unit of strength loss (per MPa). A Carbon–Performance Quadrant was also constructed, with the control mixture (27.0 MPa, 362.47 kg CO_2/m^3) as the origin, where the x-axis represents strength and the y-axis represents total embodied carbon – providing a visual assessment of which mixtures fall within a favorable zone.

3 Results and Discussion

The 28-day compressive strength of the control mixture was 27.0 MPa. As the replacement levels increased, FA exhibited a gradual reduction in compressive strength. The compressive strength was 26.8, 25.6, and 24.5 MPa at replacement levels 10%, 20%, and 30%, respectively. On the other hand, a more pronounced reduction was observed in compressive strength of GP mixtures. The corresponding compressive strengths were 26.2, 23.4, and 21.9 MPa at replacement levels of 10%, 20%, and 30%, respectively. This indicates that the compressive strength of GP-30 was approximately 19% lower than that of the control mixture. The compressive strength of each mixture remained within the 21.9-27.0 MPa band. This is typical for low-to-medium-strength concrete at the given water-to-cement ratio (Fig. 1). The one-way ANOVA confirmed statistically significant differences among the seven mixtures ($F(6,28)= 43.95$, $p< 0.01$, $\eta^2= 0.904$).Tukey's HSD post-hoc test indicated that FA and GP separated significantly from each other at replacement levels above 10%.

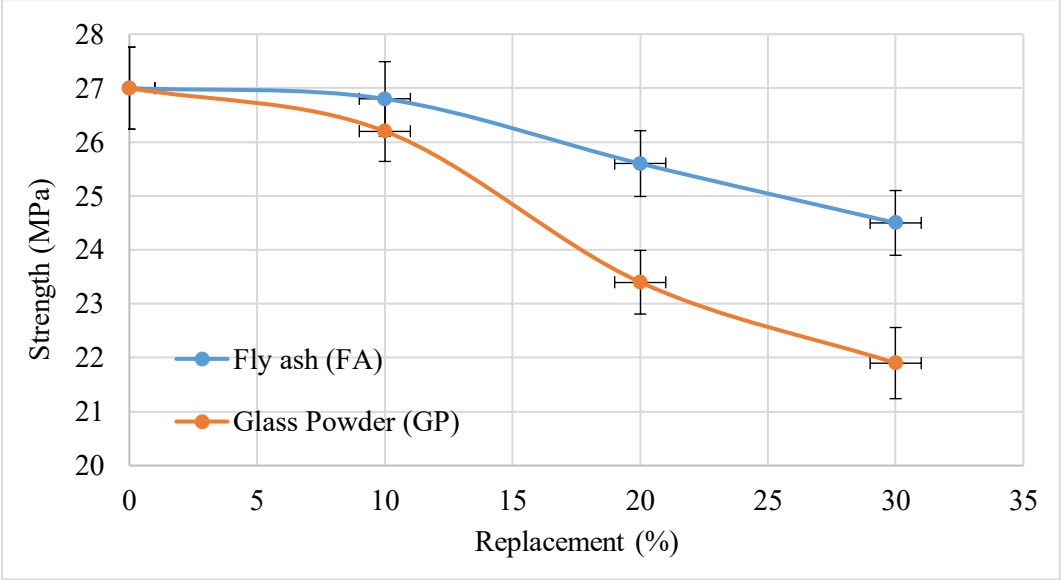


Fig. 1. 28-day compressive strength of FA and GP mixtures (error bars show standard deviation).

To assess embodied carbon and carbon intensity, the analysis incorporated the transportation, construction, and end-of-life stages. The control mixture exhibited the highest overall carbon footprint, amounting to 362.47 kg CO_2/m^3. For both replacement materials, embodied carbon decreased as the replacement level increased. FA-30 achieved a 26.7% reduction (265.66 kg CO_2/m^3), while GP-30 followed closely with a 24.0% reduction (275.32 kg CO_2/m^3). However, embodied carbon values alone are insufficient for the evaluation of the environmental performance of the mixtures. The carbon intensity (CI) was calculated by normalizing the embodied carbon with respect to compressive strength (CI = EC/fc). FA replacement mixtures

showed steady improvement, decreasing from 12.32 kg CO_2/MPa at FA-10 to 10.84 kg CO_2/MPa at FA-30 — a 19.2% improvement over the control's 13.42 kg CO_2/MPa. In contrast, the GP replacement mixtures remained relatively unchanged, ranging from 12.57 to 13.01 kg CO_2/MPa across the series. This indicates that the carbon savings due to reduced cement content are largely offset by the accompanying strength losses (Table 2).

Table 2. Embodied carbon (EC), 28-day compressive strength (fc), and carbon intensity (CI) of all mixtures.

Mix Code	EC (kg CO2/m3)	fc (MPa)	CI (kg CO2/m3/MPa)	CO2 Reduction (%)
Control	362.47	27.0	13.42	–
FA-10	330.20	26.8	12.32	8.9
FA-20	297.93	25.6	11.64	17.8
FA-30	265.66	24.5	10.84	26.7
GP-10	333.42	26.2	12.73	8.0
GP-20	304.37	23.4	13.01	16.0
GP-30	275.32	21.9	12.57	24.0

The Carbon Reduction Efficiency (CRE) index, which represents the relationship between mechanical performance and environmental benefit, was calculated as the ratio of embodied carbon reduction to compressive strength reduction relative to the control mixture (CRE = ΔEC / Δfc). Table 3 and Fig. 2 clearly demonstrate that FA provided greater carbon reduction per unit of strength lost (CRE) than GP at every comparable replacement level. FA-20 achieved a CRE of 46.1 kg CO_2/MPa with a strength loss of only 5.2%, whereas GP-20 achieved a CRE of only 16.1 kg CO_2/MPa with a considerably higher strength loss of 13.3%.The CRE value of FA-10 (161.4 kg CO_2/MPa*)* appears unusually high; however, this is largely an artifact of the minimal 0.2 MPa strength reduction — dividing by a near-zero value inflates the ratio. Therefore, this figure should be interpreted alongside CI rather than on its own.

Table 3. Carbon Reduction Efficiency (CRE) index of FA and GP mixtures.

Mix	ΔEC (kg CO2/m3)	Δfc (MPa)	Strength Loss (%)	CRE (kg CO2/MPa)
FA-10	32.3	0.2	0.7	161.4
FA-20	64.5	1.4	5.2	46.1
FA-30	96.8	2.5	9.3	38.7
GP-10	29.1	0.8	3.0	36.3
GP-20	58.1	3.6	13.3	16.1
GP-30	87.2	5.1	18.9	17.1

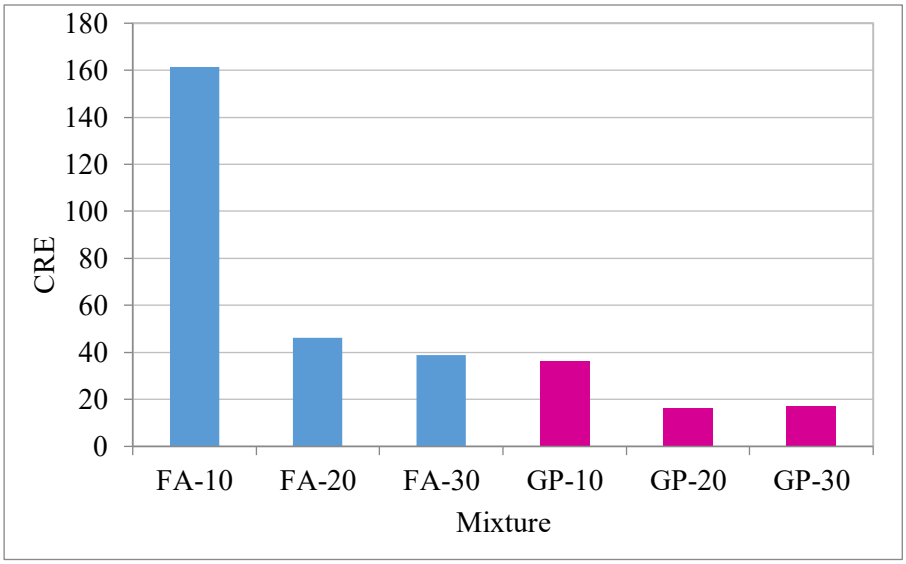


Fig. 2. Carbon Reduction Efficiency (CRE) index for FA (blue) and GP (pink) mixtures.

To evaluate the trade-off between carbon footprint and mechanical performance, a carbon–performance quadrant analysis was carried out. In this framework, the control mixture served as the reference point. The plot was divided into four quadrants, which represent the strength and carbon performance of each mixture relative to the control. Fig. 3 presents the carbon–performance quadrant analysis results. As shown in Fig. 3, none of the mixtures were positioned in Zone I, which is due to the strength reduction inherently associated with cement replacement. Instead, all mixtures were positioned in Zone II (lower carbon, lower strength). Among the mixtures, FA-20 and FA-30 were located closest to the Zone I boundary, offering 17.8% and 26.7% carbon savings alongside modest strength losses of 5.2% and 9.3%, respectively. GP-20 and GP-30 were located further from that boundary – similar carbon savings, but with higher strength losses, indicating a more limited applicable range for glass powder once replacement exceeds 10%.

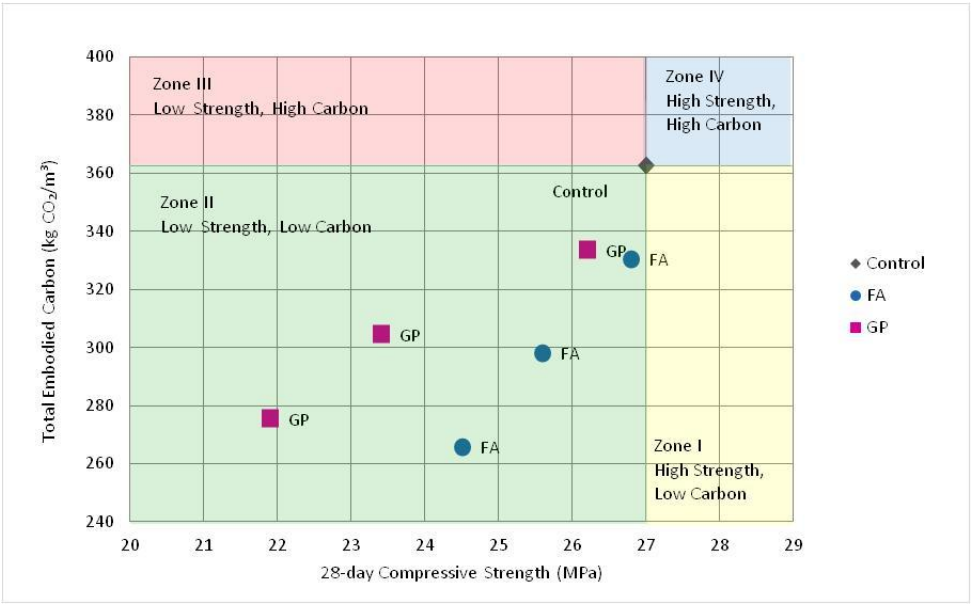


Fig. 3. Carbon–Performance Quadrant Analysis of FA and GP concrete mixtures.

The combined evaluation using the CRE index and the carbon–performance quadrant identified FA-20 as the most balanced mixture, achieving a 17.8% reduction in embodied

carbon with only a 5.2% reduction in compressive strength. If reducing embodied carbon is prioritized over maximizing compressive strength, FA-30 may also be considered, although its slower long-term strength development should be taken into account. By comparison, glass powder appeared to be competitive only up to a replacement level of approximately 10%, beyond which the strength penalty outweighed the environmental benefit.

4 Conclusions

In this study, FA and GP were investigated as partial cement replacements at replacement levels of 10%, 20%, and 30%. The concrete mixtures were produced without chemical admixtures and at a constant water-to-cement ratio of 0.60 to enable a direct comparison of the effects of the two supplementary cementitious materials on mechanical and environmental performance. The mixture containing 30% fly ash demonstrated the highest environmental efficiency, with a carbon intensity of 10.84 kg CO_2/MPa, corresponding to a 19.2% reduction compared with the control. For recycled glass powder, the 20% replacement level offered the most balanced performance, while higher replacement ratios led to more pronounced strength losses. This study provides a direct comparison of FA and GP under identical mixture conditions using performance-normalized environmental indicators. The results indicate that, under the tested conditions, fly ash exhibits a better combination of carbon emission reduction and mechanical strength than recycled glass powder. These conclusions rest on 28-day results from a single mix design; therefore longer-term testing and a broader set of durability measures would be a natural next step.

Acknowledgments
This research was funded by the Kyrgyz Turkish Manas University Department of Scientific Research Council, grant number KTMU-BAP-2024.FB.27. The authors thank Medcem Global for providing the fly ash used in this study.

References

1. Strunge, T., Küng, L., Sunny, N., Shah, N., Renforth, P., Van der Spek, M.: Finding least-cost net-zero CO2 strategies for the European cement industry using geospatial techno-economic modelling. RSC Sustain. 10, 3054–3076 (2024).
2. Nayak, D.K., Abhilash, P.P., Singh, R., Kumar, R., Kumar, V.: Fly ash for sustainable construction: A review of fly ash concrete and its beneficial use case studies. Clean. Mater. 6, 100143 (2022).
3. Fraay, A.L.A., Bijen, J.M., de Haan, Y.M.: The reaction of fly ash in concrete: a critical examination. Cem. Concr. Res. 19, 235–246 (1989).
4. Jiang, Y., Ling, T.C., Mo, K.H., Shi, C.: A critical review of waste glass powder—multiple roles of utilization in cement-based materials and construction products. J. Environ. Manag. 242, 440–449 (2019).
5. Su, Q., Liang, X., Xu, J.: Multi-scale regulation of mechanical properties and micro-damage evolution in green concrete activated by glass powder–fly ash composite system. Constr. Build. Mater. 492, 143051 (2025).
6. Yusuf, M.O., Al-Sodani, K.A.A., Adewumi, A.A., Abdulkareem, M., Alateah, A.H.: Strength and microstructural characteristics of fly ash-waste glass powder ternary blended concrete. Materials 18, 4483 (2025).
7. EN 450-1: Fly Ash for Concrete—Definition, Specifications and Conformity Criteria. European Committee for Standardization, Brussels (2012).
8. TS EN 12390-3: Testing Hardened Concrete—Part 3: Compressive Strength of Test Specimens. Turkish Standards Institution, Ankara (2019).

9. Hammond, G., Jones, C.: The Inventory of Carbon and Energy (ICE). University of Bath, Bath (2011).
10. Intergovernmental Panel on Climate Change (IPCC): 2006 IPCC Guidelines for National Greenhouse Gas Inventories. IGES, Hayama (2006).
11. European Parliament, Council of the European Union: Directive 2008/98/EC on Waste. Off. J. Eur. Union L 312, 3–30 (2008).
12. Cohen, J.: Statistical Power Analysis for the Behavioral Sciences. 2nd edn. Lawrence Erlbaum Associates, Hillsdale, NJ (1988).
13. Habert, G., Arribe, D., Dehove, T., Espinasse, L., Le Roy, R.: Reducing environmental impact by increasing the strength of concrete: quantification of the improvement to concrete bridges. J. Clean. Prod. 35, 250–262 (2012).
14. Damineli, B.L., Kemeid, F.M., Aguiar, P.S., John, V.M.: Measuring the eco-efficiency of cement use. Cem. Concr. Compos. 32, 555–562 (2010).
15. Etxeberria, M.: Evaluation of eco-efficient concretes produced with fly ash and uncarbonated recycled aggregates. Materials 14, 7499 (2021).

Author Contribution Statement

- *Conceptualization:* E. Dural, G. Karadeniz
- *Methodology:* E. Dural, G. Adzhygulova, G. Karadeniz
- *Investigation:* E. Dural, G. Adzhygulova, M. Karadeniz, G. Karadeniz
- *Writing – Original Draft:* E. Dural, G. Karadeniz
- *Writing – Review & Editing:* E. Dural, G. Adzhygulova, G. Karadeniz

List of Abbreviations

- **FA** — Fly Ash
- **GP** — Glass Powder
- **SCM** — Supplementary Cementitious Material
- **EC** — Embodied Carbon
- **CI** — Carbon Intensity
- **CRE** — Carbon Reduction Efficiency
- **w/c** — Water-to-Cement Ratio
- **ANOVA** — Analysis of Variance

Publication Note

This paper was peer-reviewed, accepted for presentation, and included in the proceedings of the ACE2026 – International Conference on Advances in Civil Engineering, held on 12–14 October 2026 in Trabzon, Türkiye.

This paper may be cited as follows:

Dural, E., Adzhygulova, G., Karadeniz, G., Karadeniz, M., "Performance-Based Comparison of Fly Ash and Recycled Glass Powder in Low-Carbon Concrete: A Carbon Reduction Efficiency Approach," in Proceedings of the ACE2026 – International Conference on Advances in Civil Engineering, Trabzon, Türkiye, 12–14 October 2026.

Life Cycle Assessment of Reinforced Concrete Structures using Pozzolanic Materials

Ali Danandeh Mehr[1], Emirhan Yener[2] and Kaan Beyazkılıç[2]
[1] 0000-0003-2769-106X, Antalya Bilim University, Civil Engineering Department, Antalya, Türkiye, ali.danandeh@antalya.edu.tr
[2] Antalya Bilim University, Civil Engineering Department, Antalya, Türkiye, emirhan.yener@std.antalya.edu.tr; kaan.beyazkilic@std.antalya.edu.tr

Abstract. Sustainability goals and stricter environmental protection requirements now guide a wide range of experts, from materials scientists to architects, to find practical ways to incorporate byproducts and waste materials into concrete construction. The urgent focus on climate change has led researchers to investigate materials like polymers and pozzolans as additives, offering ecological solutions to reduce heavy cement use and lower carbon emissions from concrete structures. This study explores the effects of supplementary cementitious materials, specifically fly ash, ground granulated blast-furnace slag, and silica fume, on delaying chloride-induced corrosion initiation and influencing service-life outcomes under Mediterranean marine chloride conditions. Life-365 is employed to conduct a comparative service-life assessment using a realistic dynamic diffusion approach, combined with a multi-category life cycle assessment framework to facilitate interpretation beyond a single climate indicator. The analysis has been adapted to the conditions of the Antalya coastal region, considering seasonal temperature fluctuations to reflect sensitivity to chloride flow. The results, quantified through service life level indicators, indicated that at 50 mm cover, replacing 40% of cement with a pozzolan mix containing 10% silica fume, 15% slag, and 15% fly ash offers the greatest carbon reduction, although multi-category results reveal significant environmental trade-offs regarding toxicity. Additionally, increasing concrete cover from 30 mm to 50 mm consistently prolongs the predicted time to corrosion initiation and extends overall service life across all mixtures, with the degree of improvement heavily depending on binder composition.

Keywords: Life cycle; fly ash; slag; silica fume.

1 Introduction

Concrete remains indispensable to buildings and infrastructure; however, long-term performance is frequently determined by durability rather than strength, particularly in chloride-laden coastal environments. From a sustainability standpoint, durability is not only a technical requirement but also a life-cycle driver because interventions add up over time, cumulatively increasing material use, energy consumption, and associated environmental burdens. Consequently, service-life differences can alter sustainability conclusions even when initial environmental impacts appear similar. Recent literature on cement and concrete decarbonization emphasizes that sustainability outcomes depend on broader system choices and transparent modeling assumptions [1]. Country-specific life cycle assessment (LCA) studies indicate that decarbonization is possible by aligning energy systems and technologies with local conditions and inventory assumptions [2]. Recent sustainability-oriented studies state that environmental conclusions for cement and concrete are highly sensitive to methodological

choices and system framing. Reviews of current practice highlight that differences in functional unit selection, boundary definition, and scenario assumptions can lead to substantially different comparative outcomes, even when the same material system is evaluated [3-4]. Scenario-based LCA of concrete production at the building scale, different datasets indicate that embodied-carbon values can vary significantly across datasets, highlighting the need for consistent boundaries and careful comparability [5].

Carbon assessments can also be affected by the long-term uptake of CO_2 by cement-based materials through carbonation, which complicates net emission assessments and highlights the need for consistent methodological treatment [6]. These findings suggest that sustainability should be evaluated together with durability. If supplementary cementitious materials (SCM) mixtures delay the commencement of corrosion, fewer repairs are needed, which reduces the total environmental burden over the service life. Experimental microstructural evidence supports the plausibility of pore refinement and durability improvements in Portland cement systems partially replaced by fly ash, slag, and silica fume [7]. Systems incorporating both coal fly ash and Ground Granulated Blast Furnace Slag (GGBFS) have been investigated for chloride diffusion behaviour and are relevant to strategies aimed at reducing chloride ingress in reinforced concrete [8]. Multiscale modelling for fly ash concretes suggests that mixture-dependent microstructural features can be combined with effective chloride diffusion predictions [9]. Long-term aged slag and fly ash concretes have been evaluated using data-driven methods linking mixture characteristics to durability indicators, reinforcing that performance evolves with age and mixture properties [10].

Existing research on SCMs generally focuses on their individual effects on concrete durability or isolated embodied carbon metrics. However, this study distinguishes itself by bridging the critical gap between long-term service-life prediction and a comprehensive environmental impact assessment. The primary novelty of this research lies in its multi-dimensional approach. First, it directly couples chloride-induced corrosion initiation modeling, performed via Life-365 (v2.2.3), with a multi-category LCA framework. This expands the environmental evaluation beyond the standard Global Warming Potential (GWP) to include ozone layer depletion, human carcinogenicity, and ecological toxicity. Second, this study explicitly investigates the synergistic interaction between material composition—varying dosages of fly ash, slag, and silica fume—and geometric protection by comparing structural elements (beams and slabs) under different concrete cover depths (30 mm and 50 mm). Finally, to ensure regional accuracy and practical relevance, the service-life modeling incorporates site-specific monthly temperature profiles from Antalya, Türkiye, capturing the dynamic nature of chloride diffusion under realistic coastal Mediterranean conditions. By integrating these elements, this study provides a holistic, durability-informed sustainability perspective, demonstrating how long-term maintenance reductions drive the true environmental performance of reinforced concrete

2 Materials and Methods

Six distinct concrete mix designs with different weight percentages of slag, fly ash, and silica fume, along with a base design without admixtures, were formulated to study these pozzolans as partial cement substitutes. The life-365 model was used to evaluate the service life and life cycle of the concrete produced. These materials, the mix design, and the model's principles are explained in the following sections.

2.1 Pozzolons

SCMs refine concrete microstructure and boost durability by reducing permeability through the pozzolanic reaction, in which reactive silica/alumina from SCMs combines with portlandite to form additional C–S–H, densifying the pore structure and limiting aggressive-agent transport

[11]. Fly ash generates extra cementitious compounds that lower cost and carbon footprint, while ultrafine silica fume from alloy production acts as both a pozzolan and microfiller, physically densifying the matrix, raising strength and bond, and aiding waste management.

In Turkey, blended cements already hold a substantial market share (40.7 % of strength classes 32.5 and above in 2017), and ready-mix practice routinely incorporates SCMs (average fly ash 38.2 kg/m³, blast-furnace slag 2.3 kg/m³), confirming their practicality for chloride-exposed coastal infrastructure. Local Mediterranean supply chains further support this: silica fume is produced in Antalya, ground granulated blast-furnace slag is available from İSDEMİR in İskenderun, and fly ash can be sourced from regional plants such as Yatağan and Tunçbilek, making high-SCM mixes feasible for Antalya's coastal construction.

In the present study, six concrete mixes (scenarios) were prepared and tested to obtain the optimal mix design, as detailed in Table 1.

Table 1. Concrete mix designs (Type I cement) weight values

Scenario	Amount (Kg)	Cement (kg)	Fly Ash (kg)	Slag (kg)	Silica Fume (kg)
1	400	380	10	10	0
2	400	360	20	20	0
3	400	350	20	20	10
4	400	340	20	20	20
5	400	300	40	40	20
6	400	240	60	60	40

The control design (baseline mix) consisted of approximately 400 kg/m³ cement, 900 kg/m³ sand, 1000 kg/m³ coarse aggregate (5-10 mm), and 160 kg/m³ drinking water resulting in a water-cement ratio of 0.42 and a density of 2460 kg/m³. All mixtures were defined in Life-365 with w/cm = 0.42. Mix #1 consisted of 2.5% Class F fly ash, 2.5% slag, and 0% silica fume. Mix #2 increased Class F fly ash and slag to 5.0% each while keeping silica fume at 0%. Mix #3 retained 5.0% Class F fly ash and 5.0% slag and added 2.5% silica fume. Mix #4 kept Class F fly ash and slag at 5.0% and increased silica fume to 5.0%. Mix #5 increased Class F fly ash and slag to 10.0% each and used 5.0% silica fume. Mix #6 used the highest SCMs contents, with 15.0% Class F fly ash, 15.0% slag, and 10.0% silica fume. Ordinary Portland cement constituted the remaining binder fraction in each mixture. This structured progression enables interpretation of durability trends as SCMs dosage increases while preserving comparability by holding other mixture parameters constant. In all scenarios, we kept the total volume of pozzolans lower than the Portland cement content in concrete mixtures to guarantee enough calcium hydroxide (CH) for the pozzolanic reaction, sufficient early strength, good workability, and compliance with performance standards as suggested in the relevant literature [7,12].

2.2 Servis Life Prediction and LCA

In this study, chloride-induced corrosion initiation is estimated by modelling ingress as diffusion-controlled transport via a closed-form solution of Fick's second law, yielding chloride concentration as a function of time and depth. To capture Mediterranean coastal seasonality, a dynamic diffusion process is used in place of annual averages: the diffusion coefficient varies with time and temperature within a two-dimensional equation solved by the Crank–Nicolson method. Surface-chloride boundary conditions are strengthened to reflect Antalya's high-salinity marine environment, recognising that this concentration—driven by coastline proximity and elevated temperatures—is the dominant durability parameter [3]. Deterministic surface-chloride calculations and probabilistic service-life estimates then employ an aging factor, activation energy, and reference values of 28 days and 293°K [14].

Table 2. A comparison of the varying results for the diffusion coefficient with the ageing factor

Mixture	D28 (m^2/sec)	Aging Exponent (m)	Chloride Threshold (Ct, %wt. conc.)	Energy Activation (U)
Mix 1	8.8716E-12	0.23	0.050	35000J/mol
Mix 2	8.8716E-12	0.27	0.050	35000J/mol
Mix 3	5.8729E-12	0.27	0.050	35000J/mol
Mix 4	3.8878E-12	0.27	0.050	35000J/mol
Mix 5	3.8878E-12	0.34	0.050	35000J/mol
Mix 6	1.7038E-12	0.41	0.050	35000J/mol

The model of deterioration shown in Fig. 1 consists of two distinct phases: chloride penetration, followed by a period of corrosion leading to unacceptable damage. Life-365 provides an option to estimate surface chloride and apparent diffusion parameters from chloride profile measurements consistent with ASTM C1556, enabling calibration when laboratory or field data are available. The framework further represents service life as initiation time plus a propagation period (See Figure 1) and can generate repair schedules and life-cycle cost calculations based on intervention timing and user-defined repair strategies. While corrosion propagation in real-world structures is highly dependent on binder composition, concrete resistivity, cracking, and moisture state, Life-365's mathematical framework is primarily designed to calculate the initiation phase via Fickian diffusion. Therefore, a constant propagation period of 6 years was adopted for all scenarios. This standardized assumption intentionally isolates the comparative effects of SCMs on chloride ingress and initiation time, rather than attempting to provide an absolute, definitive prediction of structural failure. Following this, we calculate the Service Life Level (SLL) through the ratio of lifelong of each sample mixture (tri) to the service lifelong of baseline sample (trb) for six designs listed in Table 2.

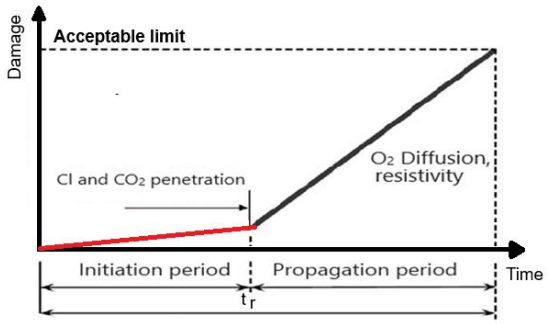


Fig. 1. Components of Concrete Service Life Calculation

2.3 Service-Life Evaluation for Reinforced Concrete

In addition to the general durability interpretation for reinforced concrete elements, a dedicated evaluation was performed for reinforced concrete beams and slabs to explicitly investigate the interaction between mixture composition and cover depth under chloride exposure. Beams and slabs were selected because they represent a common structural element in buildings and are often more sensitive to cover depth variations due to reinforcement placement and bending-induced cracking tendencies. All the scenarios were evaluated under a consistent modelling framework.

As illustrated in Fig. 2, the beam geometry was defined as a prismatic member with a length of 1.0 m and an overall depth of 250 mm; beam width was not treated as a governing parameter for the comparisons reported here because the analysis targets corrosion initiation at

reinforcement depth. The water-to-cementitious materials ratio was held constant at w/cm = 0.42 for all mixtures to isolate the effect of SCMs incorporation. Two concrete cover depths were considered in the beam analysis: 30 mm (3 cm), representing conventional practice, and 50 mm (5 cm), representing an enhanced durability design scenario. All other exposure-related parameters were held constant across scenarios, and a repeating monthly temperature profile representative of a coastal Mediterranean climate was applied over the analysis horizon. To broaden the structural interpretation of the study, the service-life analysis was also extended to reinforced concrete slabs model under the same environmental and mixture assumptions.

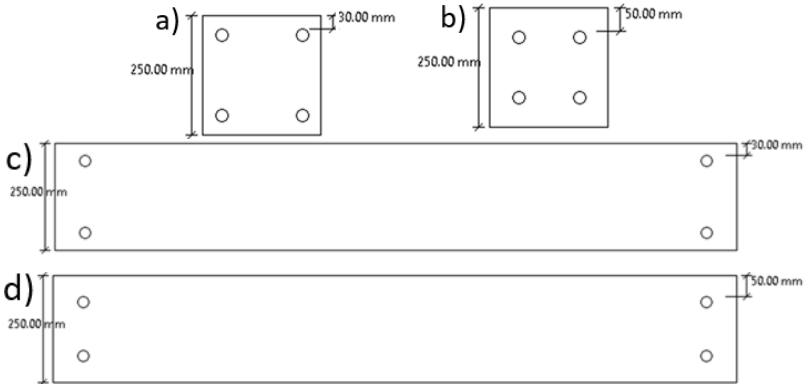


Fig. 2. Dimensions of the experimental reinforced concrete beam (a and b) and slab (c and d)

For the slab analysis, the element type was defined in Life-365 as a slab/wall member. The slab thickness was taken as 250 mm, the reference area was 1 m², and the corresponding concrete volume was 0.20 m³. Similar to beam scenarios, two reinforcement depths, corresponding to concrete covers of 30 mm and 50 mm, were considered. The same six SCM-containing mixtures used in the beam analysis were adopted for the slab scenarios, and the same Antalya monthly temperature profile and w/cm ratio of 0.42 were maintained throughout. In this way, the slab analysis was incorporated to determine whether the durability trends observed in beams would remain valid for another common reinforced concrete member under identical exposure and binder conditions.

3 Results

The results indicate a systematic increase in predicted corrosion initiation time as SCM content increases, with a strongly non-linear response at higher SCM dosages. At 30 mm cover, SCM do not significantly increase service life. However, higher SCM contents, especially in Mix #6 (i.e., 15% fly ash + 15% slag + 10% silica fume), clearly extend the initiation time. At 50 mm cover, the influence of mixture composition became substantially more pronounced, indicating a strong interaction between geometric protection and mixture quality under diffusion-controlled chloride ingress. Similar mixture-dependent effects on chloride diffusion behaviour have been discussed for fly ash and slag blended systems [8] and in long-term evaluations of aged SCM concretes [10]. From a sustainability perspective, these beam results reinforce the importance of durability-oriented design for structural elements subjected to chloride exposure, because delaying corrosion initiation reduces the likelihood and frequency of repair interventions that contribute additional material and energy burdens over the service life.

The results of this study are interpreted from a durability-informed sustainability perspective, where predicted corrosion initiation times and intervention schedules are considered key drivers of long-term environmental burdens, rather than focusing solely on initial embodied impacts. Contemporary cement and concrete literature increasingly emphasize that sustainability outcomes depend on system-level choices, regional context, and methodological boundaries rather than on single material substitutions [1,2,5]. These findings underline the importance of situating mixture-level durability improvements within a broader sustainability framing.

The modelling results indicate that increasing SCM incorporation, particularly in ternary systems combining fly ash, slag, and silica fume, can systematically delay chloride-induced corrosion initiation. The beam results illustrate this clearly through the large initiation-time shift from Mix 1 to Mix 6 at both cover depths and the particularly strong increase observed when higher SCM dosages are paired with increased cover. In the long term, these delays become directly relevant to sustainability because repair and maintenance interventions introduce additional material and energy demands.

Infrastructure-focused sustainability literature emphasizes that maintenance cycles can dominate cumulative environmental burdens when service life is limited, especially for chloride-exposed structures [15,16]. Within this framework, the increase in durability, achieved by SCM-rich mixtures represents a path to sustainability, supported not only by the initial reduction in cement content but also, by a decrease in the frequency of interventions. A critical implication of this interpretation is that sustainability assessment based on a single indicator may be insufficient. Scenario-based LCAs show that strategies reducing climate impacts can change other environmental categories depending on inventory assumptions and boundaries [5].

Fig. 3 presents the environmental input profile used in Life-365, including the historical monthly temperature derived from observational data for Antalya, Türkiye. In addition, the chloride exposure boundary condition was defined using a time-dependent surface chloride build-up assumption where the surface chloride level increases over the initial years and then reaches a plateau at a regional maximum value. This seasonal and time-dependent exposure representation was adopted to reflect the sensitivity of chloride transport and corrosion initiation to temperature and long-term chloride accumulation under coastal Mediterranean conditions.

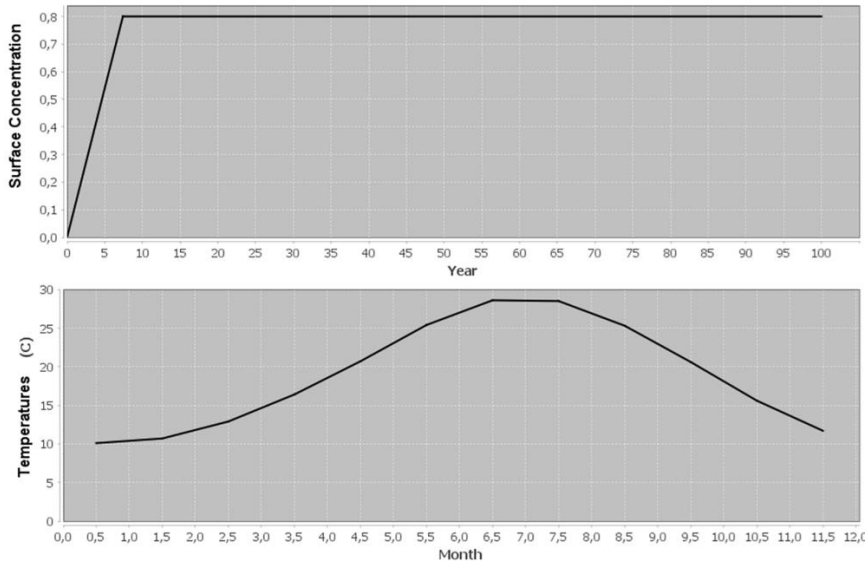


Fig. 3. Graph of changes in ion concentration and average monthly ambient temperature of concrete

To evaluate the combined influence of mixture composition and cover depth under the same exposure framework, seven binder configurations were defined at a constant w/cm ratio of 0.42: a base mix with no SCM replacement (Class F fly ash = 0%, slag = 0%, silica fume = 0%), and six SCM-containing mixtures (Mix #1–Mix #6) as specified in the Life-365 software. Under the Antalya temperature profile, the base mix provides a reference for cover-depth sensitivity: at 30 mm cover, the predicted initiation time was 2.2 years with a total service life of 8.2 years, whereas at 50 mm cover the initiation time increased to 4.5 years and total service life to 10.5 years. The same cover effect was observed across SCM mixtures, but the magnitude depended strongly on SCM dosage. At 30 mm cover, predicted total service life increased from 8.4 years

(Mix 1) to 19.5 years (Mix 6), while at 50 mm cover total service life increased from 10.8 years (Mix 1) to 53.3 years (Mix 6).The other mixtures values at 30 mm cover, total service life values were 8.5 (Mix 2), 9.2 (Mix 3), 10.3 (Mix 4), and 11.1 years (Mix 5), whereas at 50 mm cover these increased to 11.4, 13.4, 16.4, and 19.5 years, respectively. Because the propagation period was kept constant (6.0 years), the observed differences in total service life were driven primarily by changes in predicted corrosion initiation time. Overall, the results demonstrate a clear interaction: increasing cover depth consistently delays initiation for all mixtures, and increasing SCM dosage further amplifies this delay—especially at higher replacement levels—indicating that geometric protection (cover) and mixture quality act synergistically in diffusion-controlled chloride ingress.

A parallel set of service-life predictions was also obtained for reinforced concrete slabs in order to compare member-level durability behavior under the same chloride exposure conditions. Similar to the beam results, the slab predictions showed that both increasing cover depth and increasing SCM content led to longer corrosion initiation times and longer total service life. For the slab scenarios with 30 mm cover, the predicted corrosion initiation times were 3.2, 3.4, 4.4, 5.7, 6.8, and 18.2 years for Mix #1 through Mix #6, respectively. With a constant propagation period of 6.0 years, the corresponding total service life values became 9.2, 9.4, 10.4, 11.7, 12.8, and 24.2 years. When the cover depth was increased to 50 mm, the predicted initiation times increased to 6.4, 6.9, 9.6, 13.4, 17.8, and 63.7 years, while the corresponding total service life values increased to 12.4, 12.9, 15.6, 19.4, 23.8, and 69.7 years, respectively.

These slab results confirm the same overall pattern observed in the beam analysis. Increasing the concrete cover from 30 mm to 50 mm consistently improved both the predicted corrosion initiation time and the total service life for all mixtures. In addition, the improvement became more pronounced as the SCM replacement level increased, with Mix 6 again providing the strongest durability performance among the evaluated alternatives.

When the beam and slab results are considered together, the same durability ranking among mixtures is preserved in both member types, even though the absolute service-life values differ. This indicates that the beneficial influence of SCM incorporation is not limited to a single structural element definition but can also be observed in slab scenarios under the same exposure and temperature assumptions. In both member types, the combined effect of higher SCM replacement and greater concrete cover produced the most favorable durability outcomes, showing that mixture design and geometric protection should be evaluated together rather than separately.

The results of the environmental assessment for the mixtures are summarized in Table 3. For each mix and cover depth, Table 3 reports the selected LCA indicators (GWP, ODP, carcinogenicity, and ecological toxicity) expressed per cubic meter of concrete, together with the corresponding percentage changes relative to the Base mix at the same cover depth. This structure enables direct comparison of mixture effects at fixed cover (e.g., Base vs Mix 6 at 30 mm) and cover effects at fixed mixture, supporting a durability-informed sustainability interpretation in which longer predicted service life is linked to reduced maintenance-driven burdens across multiple impact categories.

When the 3 cm cover depth is considered, the increase in total service life between successive mixture designs is relatively limited for low-SCM mixtures. Compared to the base mixture, Mix #1 shows only a marginal increase of approximately 1.02 times, followed by a further 1.01 times increase from Mix 1 to Mix 2. A noticeable improvement appears when moving from Mix 2 to Mix 3, with an increase of about 1.08 times, and continues from Mix 3 to Mix 4 with 1.12 times increase. The transition from Mix 4 to Mix 5 yields a moderate gain of approximately 1.08 times, whereas a pronounced jump is observed between Mix 5 and Mix 6, where total service life increases by about 1.76 times.

At the 5 cm cover depth, a similar trend is observed but with generally stronger gains between mixture designs. The increase from the base mixture to Mix 1 is approximately 1.03×, followed by a 1.06× increase from Mix 1 to Mix 2. A clearer improvement occurs between Mix 2 and Mix 3, corresponding to a 1.18× increase, and this effect becomes more noticeable from Mix 3 to Mix 4 with an increase of about 1.22×. The transition from Mix 4 to Mix 5 results in a further 1.19× increase, while the largest improvement again occurs between Mix 5 and Mix 6, where total service life increases by approximately 2.73×. These results indicate that incremental increases in SCM content produce limited service-life gains at low replacement levels, whereas significantly larger improvements happen once higher SCM dosages are combined with increased cover depth.

Environmental impacts were quantified using the standardized life-cycle inventory and characterization models embedded within the Alternative Case Scenario (ACS) Calculation tool provided by the American Concrete Institute (ACI). The GWP was quantified in kg CO_2-eq/m³, representing aggregated greenhouse gas emissions relative to carbon dioxide. Human carcinogenicity (CTUh/m³) was generated by the ACS tool's default characterization framework to represent potential human health risks, respectively. Ozone layer depletion was quantified in kg CFC-11-eq/m³, expressing the relative contribution of ozone-depleting substances to stratospheric ozone loss. Ecological toxicity was expressed in comparative toxic units for ecosystems (CTUe/m³), representing potential impacts of emissions on freshwater ecosystems through fate–exposure–effect modelling. By relying on the ACS tool's internal database for material processing and default supply-chain logistics, the environmental contribution of each mixture can be compared under a standardized framework

Transport can be incorporated in the inventory using a mass–distance activity approach (ton-kilometre), computed as the product of delivered mass for each constituent and an assumed hauling distance. Including transport is justified because life-cycle conclusions are sensitive to inventory definition and scenario choices; methodological reviews emphasize that boundary and scenario assumptions can materially affect comparative outcomes [3,4]. Scenario-based regional cement LCAs indicate that non-climate categories can become hotspots depending on background conditions such as grid mix and process characteristics [2]. For long-term analysis, transport linked to intervention activities may accumulate and become non-trivial when maintenance frequency is high, consistent with the observation that maintenance cycles can dominate cumulative burdens when service life is limited [15,16]. Therefore, transport was treated explicitly in the inventory rather than assumed to be negligible.

In practical terms, these metrics allow material-related emissions to be translated into comparable impact values; for example, cement production contributes to GWP primarily through CO_2 emissions from clinker production, while trace emissions associated with fuel combustion and raw material processing contribute to carcinogenicity and ecological toxicity indicators. By assigning characterization factors to inventory flows, the environmental contribution of each mixture can be expressed in terms of kilograms of carbon dioxide equivalent per cubic meter, comparative toxic unit for humans per cubic meter (CTUh/m³), kilograms of trichlorofluoromethane per cubic meter (kgCFC-11-eq/m³), and comparative toxic unit for ecosystems per cubic meter CTUe/m³, Megajoules per cubic meter ,enabling direct comparison of mixtures with different SCM contents under a durability-informed service-life framework. LCA was conducted using the ACS Calculation tool provided by the American Concrete Institute (ACI). This tool standardizes the environmental impacts of concrete mixtures across multiple categories. For each mix and cover depth, Table 3 reports the used LCA indicators expressed per cubic meter of concrete.

Table 3. Environmental impacts attained for the baseline (400kg cement) and mixing scenarios

Impact	Unit	Baseline	Mix #1	Mix #2	Mix #3	Mix #4	Mix #5	Mix #6
Global Warming	$kgCO_2/m^3$	368.309	355.602	342.895	339.172	335.449	310.035	277.174
Carcinogenicity	$CTUh/m^3$	5.22E-06	5.20E-06	5.18E-06	5.52E-06	5.87E-06	5.83E-06	6.48E-06
Ozone Layer Depletion	$KgCFC-11/m^3$	1.59E-05	1.53E-05	1.48E-05	1.48E-05	1.49E-05	1.38E-05	1.28E-05
Ecological Toxicity	$CTUe/m^3$	606.350	601.106	595.862	626.870	657.878	647.390	698.918
Fossil Fuel	MJ/m^3	145.713	110.439	122.632	133.520	134.173	134.825	140.269

The comparative LCA results in Table 3 point out different environmental performances across different impact categories between the mixtures. Increasing SCM content strongly improves climate conditions, but environmental impacts can vary.

In terms of GWP, Mix #6 provides the highest advantage, and achieves a 25% reduction in carbon emissions compared to Baseline. In addition, Mix #5 and #6 show the lowest Ozone Layer Depletion, making high-SCM systems significantly effective for climate conditions.

On the other hand, high-SCM mixtures offer certain drawbacks in terms of toxicity. While Mix #6 minimizes carbon emission, it exhibits the highest human carcinogenicity and ecological toxicity. In contrast, Mix #2 offers the most balanced profile and provides the lowest carcinogenic potential and optimal ecosystem protection. Additionally, about Fossil Fuel consumption, Mix #1 is the most efficient, as higher SCM dosages slightly increase energy demand due to material processing and logistics.

In summary, while Mix #6 is the ideal choice for carbon-reduction targets, the multi-category LCA reveals an inherent environmental trade-off. B As no normalization has been carried out across categories, it is not possible to determine with certainty which is objectively the ‘best’ mixture. However, Mix #2 presents an alternative compromise scenario that limits carcinogenic potential while still providing moderate durability benefits.

3.1 Comparative Discussion of Beam and Slab Behaviors

When the beam and slab results are considered together, the same overall durability ranking among mixtures is preserved in both member types, even though the absolute service-life values differ. In both beams and slabs, increasing SCM content led to longer corrosion initiation times and longer total service life, and this improvement became more pronounced when the concrete cover was increased from 30 mm to 50 mm. This indicates that the beneficial influence of SCM incorporation is not limited to a single structural element definition but remains consistent across both member types under the same exposure and temperature assumptions.

A comparison relative to the Base mix further clarifies this trend. For beams at 30 mm cover, the corrosion initiation time increased from 2.2 years for the Base mix to 13.5 years for Mix 6, corresponding to an increase of approximately 6.1 times, while the total service life increased from 8.2 to 19.5 years, representing an increase of about 138%. At 50 mm cover, the same comparison shows an even stronger improvement: the initiation time increased from 4.5 years to 47.3 years, or approximately 10.5 times, while the total service life increased from 10.5 to 53.3 years, corresponding to an increase of about 408%. These results indicate that, for beams, the improvement associated with higher SCM replacement becomes substantially more significant at higher cover depth.

A similar pattern was observed for slabs, but with even larger absolute gains. At 30 mm cover, the slab initiation time increased from 2.9 years for the Base mix to 18.2 years for Mix

#6, corresponding to an increase of approximately 6.3 times, while the total service life increased from 8.9 to 24.2 years, representing an increase of about 172%. At 50 mm cover, the initiation time increased from 5.8 years to 63.7 years, which corresponds to approximately 11.0 times the Base value, while the total service life increased from 11.8 to 69.7 years, representing an increase of about 491%. Like the beam results, these slab results show that the influence of SCM incorporation becomes much more pronounced at higher replacement levels and at greater cover depth.

Another important observation is that the relative gains at low SCM dosages remained limited in both member types, whereas much larger improvements were obtained at the higher replacement levels, particularly in Mix #5 and Mix #6. This suggests that minor SCM additions provide only modest durability benefits relative to the Base mix, while higher combined dosages of fly ash, slag, and silica fume produce a much stronger resistance to chloride ingress. Therefore, the results do not simply indicate that SCM use is beneficial in general; rather, they show that the magnitude of the benefit depends strongly on replacement level and becomes especially significant when combined with increased concrete cover.

Within the present model setup, the slab cases yielded longer initiation times and longer total service lives than the corresponding beam cases at the same depth and mixture level. However, this difference should be interpreted as a model-based comparison within the adopted member definitions rather than as a universal practical ranking for all structural conditions. The more important finding is that the same material trend is preserved in both element types: higher SCM replacement and greater cover depth consistently produced the most favorable durability outcomes. This supports the interpretation that mixture design and geometric protection should be evaluated together rather than separately in durability-oriented reinforced concrete design.

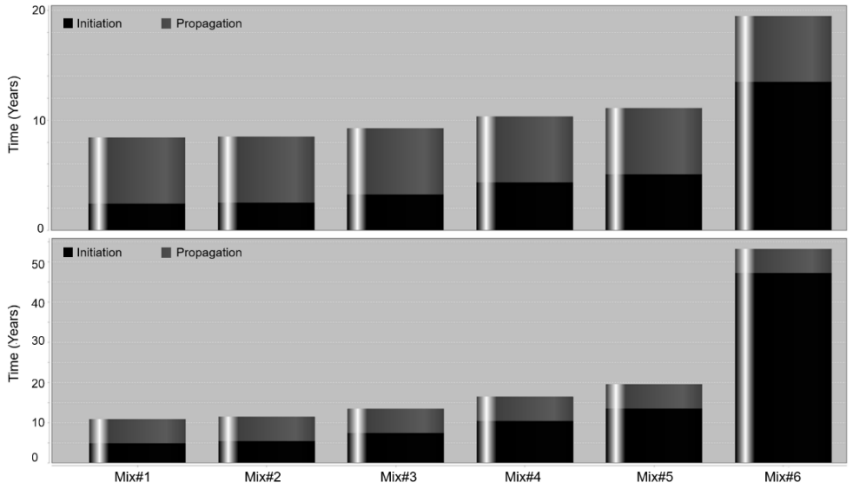


Fig. 4. Service life of the concrete produced with different designs compared to the service life of the base concrete when cover is 3 cm (top panel) and 5 cm (bottom panel)

To explicitly quantify these durability improvements, the SLL indicators were evaluated for each scenario. For the 30 mm cover depth, the results are as follows: SLL values of 1.02, 1.04, 1.12, 1.26, 1.35, and 2.38 for Mix #1 through Mix #6, respectively. For the 50 mm cover depth, the SLL values demonstrate more increase, recorded as 1.03, 1.09, 1.28, 1.56, 1.86, and a notable peak of 5.08 for Mix #6. These SLL indicators clearly illustrate that while lower SCM replacement levels provide low benefits, the relationship between high pozzolanic content and increased concrete cover depth results in a considerable enhancement in structural durability.

4 Conclusion

This study shows that SCMs critically enhance the durability of chloride-exposed reinforced concrete and thereby improve long-term sustainability by reducing maintenance demand. Beam

and slab modelling demonstrated that raising cover depth from 30 mm to 50 mm increased both corrosion-initiation time and total service life for every mixture, with the magnitude of the gain strongly dependent on binder composition; higher SCM dosages further prolonged initiation, so that the fixed 6-year propagation period left differences in overall service life driven almost entirely by initiation-time changes. Comparative results confirmed that elevated combined fly-ash, slag and silica-fume contents consistently delayed chloride-induced corrosion onset, establishing mixture design and adequate cover as complementary controls on diffusion-driven deterioration. Under the dynamic Mediterranean diffusion model these gains were quantified by SLL indicators that peaked at 5.08 for the highest-SCM mixture. When coupled with multi-category LCA, the extended service life reduces repair interventions and the associated material and energy burdens across global-warming potential, ozone depletion and ecological toxicity; yet trade-offs remain, with the highest-SCM design maximizing carbon reduction while moderate substitution yields a more balanced human-health toxicity profile. Collectively the findings support a durability-oriented sustainability strategy in which service-life extension is recognized as a primary mechanism for lowering cumulative environmental impacts.

References

1. Chaulagain, A., Lama, P., Adhikari, A., Mandal, S., & Uprety, B. (2025). Comparative life cycle assessment of decarbonization pathways for cement production in Nepal. Energy Conversion and Management: X, 28, 101284.
2. Wolde, M. G., Khatiwada, D., Bekele, G., & Palm, B. (2024). A life cycle assessment of clinker and cement production in Ethiopia. Cleaner Environmental Systems, 13, 100180.
3. Habibi, A., Tavakoli, H., Esmaeili, A., & Golzary, A. (2023). Comparative life cycle assessment (LCA) of concrete mixtures: A critical review. European Journal of Environmental and Civil Engineering, 27(3), 1285–1303.
4. Olsson, J. A., Miller, S. A., & Kneifel, J. D. (2024). A review of current practice for life cycle assessment of cement and concrete. Resources, Conservation & Recycling. 206, 107619.
5. Anderson, J., & Moncaster, A. (2020). Embodied carbon of concrete in buildings, Part 1: Analysis of published EPD. Buildings and Cities, 1(1), 198–217.
6. Wu, S., Shao, Z., Andrew, R. M., Niu, L., Liu, Z., Bing, L., Wang, J., & Xi, F. (2024). Global CO_2 uptake by cement materials accounts 1930–2023. Scientific Data.
7. Nedunuri, S. S. S. A., Sertse, S. G., & Muhammad, S. (2020). Microstructural study of Portland cement partially replaced with fly ash, ground granulated blast furnace slag and silica fume as determined by pozzolanic activity. Construction and Building Materials, 238, 117561.
8. Sanjuan, M. A., Rivera, R. A., Martin, D. A., & Estevez, E. (2022). Chloride diffusion in concrete made with coal fly ash ternary and ground granulated blast-furnace slag Portland cements. Materials, 15(24), 8914.
9. Liu, J., Wang, Y., & colleagues. (2022). Predicting the chloride diffusion in concrete incorporating fly ash by a multi-scale model. Journal of Cleaner Production. 330, 129767.
10. Yoon, Y.-S., Kwon, S.-J., Kim, K.-C., Kim, Y., Koh, K.-T., Choi, W.-Y., & Lim, K.-M. (2023). Evaluation of durability performance for chloride ingress considering long-term aged GGBFS and FA concrete and analysis of the relationship between concrete mixture characteristic and passed charge using machine learning algorithm. Materials, 16, 7459.
11. Federal Highway Administration. (2016). Supplementary cementitious materials: Best practices for concrete pavements (FHWA-HIF-16-001). U.S. Department of Transportation.
12. Wang, H., Liu, X., & Zhang, Z. (2023). Pozzolanic activity evaluation methods of solid waste: A review. Journal of Cleaner Production, 402, 136783.

13. Shakouri, M., & Trejo, D. (2017). A time-variant model of surface chloride build-up for improved service life predictions. Cement and Concrete Composites, 84, 99–110.
14. Shoaei, S., Shoaei, A., & Danandeh Mehr, A. (2025). Service life prediction and life cycle assessment of pozzolanic concretes. Journal of Civil and Environmental Engineering, 54(117), 29-36.
15. Milic, I., & Bleiziffer, J. (2024). Life cycle assessment of the sustainability of bridges: Methodology, literature review and knowledge gaps. Frontiers in Built Environment, 10, 1410798.
16. Hadizadeh-Bazaz, M., Navarro, I. J., & Yepes, V. (2023). Life cycle assessment of a coastal concrete bridge aided by non-destructive damage detection methods. Journal of Marine Science and Engineering.

Author Contribution Statement

- *Conceptualization:* Ali Danandeh Mehr
- *Methodology:* Ali Danandeh Mehr, Emithan Yener, Kaan Beyazkılıç
- *Investigation:* Ali Danandeh Mehr, Emithan Yener, Kaan Beyazkılıç
- *Writing – Original Draft:* Emithan Yener, Kaan Beyazkılıç
- *Writing – Review & Editing:* Ali Danandeh Mehr

List of Abbreviations

- **SCM** — Supplementary Cementitious Materials
- **SLL** — Service Life Level

Publication Note

This paper was peer-reviewed, accepted for presentation, and included in the proceedings of the ACE2026 – International Conference on Advances in Civil Engineering, held on 12–14 October 2026 in Trabzon, Türkiye.

This paper may be cited as follows:

Mehr A.D., Yener E., Beyazkılıç K.,"Life Cycle Assessment of Reinforced Concrete Structures using Pozzolanic Materials," in Proceedings of the ACE2026 – International Conference on Advances in Civil Engineering, Trabzon, Türkiye, 12–14 October 2026.

Evaluation of ImageJ-Based Image Processing Workflows for Aggregate Particle Size Distribution Analysis of Hardened Concrete Sections

Pınar Yıldırım[1*]

[1*] *Civil Engineering Department, Istanbul Aydin University, Florya Campus, Istanbul, Turkey*
pinaryildirim@aydin.edu.tr https://orcid.org/0000-0002-8336-1826

Abstract.

The traditional sieve analysis method has long been used to determine aggregate particle size distribution, which plays a crucial role in the mechanical and durability properties of concrete. However, the inability to apply the traditional sieve analysis method to hardened concrete, particularly in post-earthquake debris assessments, has prompted researchers to explore alternative approaches. In this context, image processing-based analysis methods have gained considerable attention in recent years.

This study proposes an image-based particle analysis method for the characterization of aggregate particles by systematically comparing different preprocessing workflows in ImageJ. The effects of different thresholding, binarization (black-white), particle separation, analysis settings on particle size distribution results were evaluated. The results demonstrated that preprocessing settings have a significant influence on the determination of particle size distribution. Therefore, accurate analysis settings are crucial for obtaining reliable, repeatable, and traceable results. Finally, the aggregate granulometry curve obtained with different preprocessing settings was compared with experimental results obtained from the conventional sieve analysis method. It is believed that this study will contribute to the creation of a standard application procedure for image-based aggregate particle size analysis in the future, and has the potential to provide rapid and reliable results, especially in the evaluation of post-earthquake debris.

Keywords: *Image processing, particle size distribution, ImageJ, thresholding, binarization*

1. Introduction

Aggregate particle size distribution has a significant effect on the strength and durability properties of concrete [1] [2] [3] [4]. In addition, particle size is quite important in geotechnical studies related to the soil [5] [6]. Traditionally, sieve analysis methods are used to determine the particle size distribution of aggregate and soil samples. However, the time-consuming nature and practical limitations associated with applying this method in large-scale infrastructure projects, areas without laboratory facilities, and construction site environments requiring rapid decision-making, as well as its inability to be used in examinations of hardened concrete, etc., have led researchers to seek alternative methods. In this field, image processing techniques have emerged as a significant alternative [7]. These techniques enable the determination of the particle size distribution in hardened concrete, as well as to visualize and quantify the macro and micro voids in the concrete [8]. Some disadvantages of the methods used to determine cavity structure are leading researchers to this field. The inadequacy of traditional porosity assay results in determining closed voids and capillary voids, the inability

to determine the macro void structure due to the small sample size in devices such as SEM, and the disruption of capillary and micro void structures by the pressure applied in pressure porosimetry experiments are among the disadvantages. For this reason, imaging techniques that provide both practical and realistic results have begun to be proposed. In this field, void structure can be revealed from images obtained with artificial intelligence-based imaging models [9] and devices such as versatile modular polarized microscopes [10].

Image processing techniques for particle size analysis generally rely on determining particle areas from the image captured and calculating the ratio of these area values [11]. These analyses can be performed on samples taken from a mixed aggregate or soil sample pile. In these studies, results obtained through imaging are usually compared with sieve analysis test results to verify the method [12] [13].

The nature of the applied image analyses varies depending on the imaging purpose. In addition to determining the size distribution of macroparticles [14], it is also possible to perform microanalyses that allow for the separation of fine aggregates, cement and mineral additives from each other with image analyses [8]. While macro analyses can be performed with high-resolution camera images, micro analyses generally require microscopic imaging techniques such as SEM, TOM, and BSE [15] [16]. However, given the difficulty in accessing these advanced imaging methods, the extra time required to obtain and evaluate results, and the high costs when mass use is necessary, research continues into developing different techniques for microimaging [17].

This study focuses on estimating aggregate particle size distribution through imaging of cross-sections taken from hardened concrete samples. Although studies on the use of imaging techniques for this purpose have been frequently conducted in recent years, information regarding the necessary settings in analysis programs is quite limited. However, establishing standardized procedures is crucial for situations where it is not possible to verify imaging results by comparing them with experimental results. For this purpose, this study evaluates the preprocessing steps for ImageJ software and offers suggestions for accurately determining particle size distribution. This study systematically compares different preprocessing workflows for determining aggregate granulometry from hardened concrete sections using ImageJ, verifies these workflows through experimental sieve analysis, and discusses the suitability of different workflows for different particle size ranges. Due to its open access feature, this program was chosen for evaluation in post-earthquake debris assessments, particularly in environments lacking laboratory facilities such as construction sites, as it provides quick and easy access for users. In the analysis program, the effects of different thresholding, binary (black-white) conversion, particle separation, etc., analysis settings on particle size distribution results were comparatively examined. The data obtained showed that the analysis settings have a significant effect on the results. Therefore, it is considered important to standardize the analysis settings in order to obtain reliable, repeatable, and traceable results.

2. Materials and Methods

For the study, cylindrical specimens with a diameter of 100 mm and a length of 200 mm were prepared in accordance with the TS EN 12350-1 [18] standard. The particle size distribution of the aggregates used in the manufacture of the specimens is presented in Figure 1. The top and bottom surfaces of the samples, which were cured for 7 days, were smoothed by grinding with a grinding machine, and then each sample was cut into three pieces using a cutting device (Figure 2). The sample surfaces were wetted before imaging to increase the visibility of the aggregate particles. Then, the sample surfaces were imaged using the experimental setup shown

in Figure 3. Particle analysis was performed using image of the central surfaces, as this would more accurately represent the aggregate distribution.

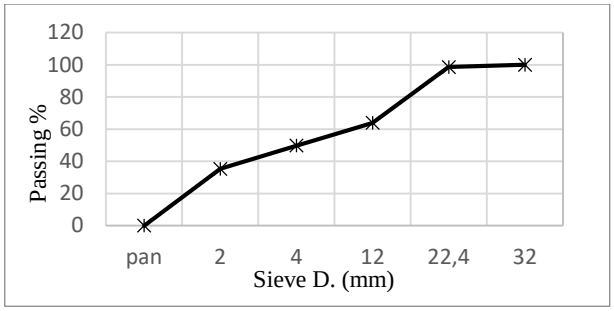


Figure 1. Aggregate sieve analysis results used in sample production.



Figure 2. Preparation of hardened concrete samples.

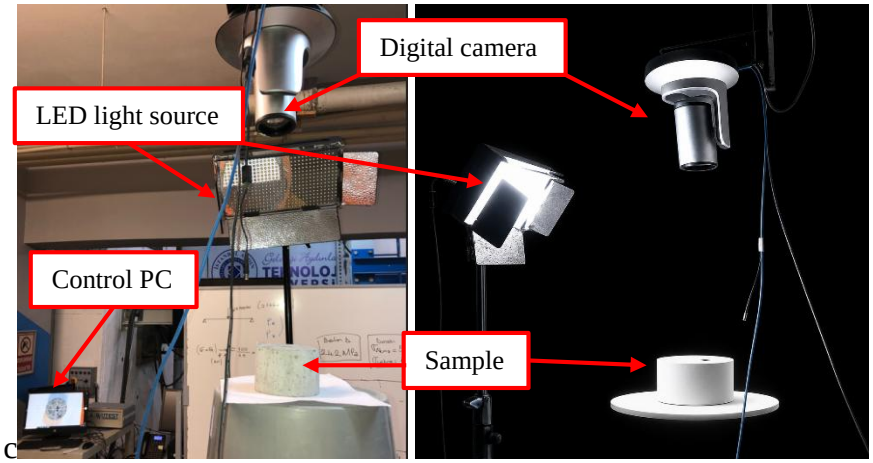


Figure 3. Viewing setup.

After the imaging process was completed, the analysis procedures were carried out. First, the images were converted to 8-bit and scaled using the built-in scale bar to achieve a sample diameter of 100 mm (Figure 4). To investigate the effect of preprocessing operations on the characterization of aggregate particles, ten different image processing workflows presented in Table 1 were evaluated. As can be seen in Table 1, binary (black-and-white) image generation, filling voids on the particles (Fill Holes), separating combined particles (Watershed), and edge erosion (Erode) options were applied in different combinations as preprocessing. The analysis ranges were determined by considering the sieve diameters used in the concrete. Since the analysis was performed considering the areas of the particles, the areas corresponding to two consecutive sieve diameters was entered into the analysis menu, and the total area of the particles remaining between these areas, the number of particles, and the average particle area were calculated. Since the calculated area values are the areas of the particles remaining on the

sieve, the cumulative areas passing through each sieve were also calculated as a percentage, and granulometry curves were obtained for each analysis.

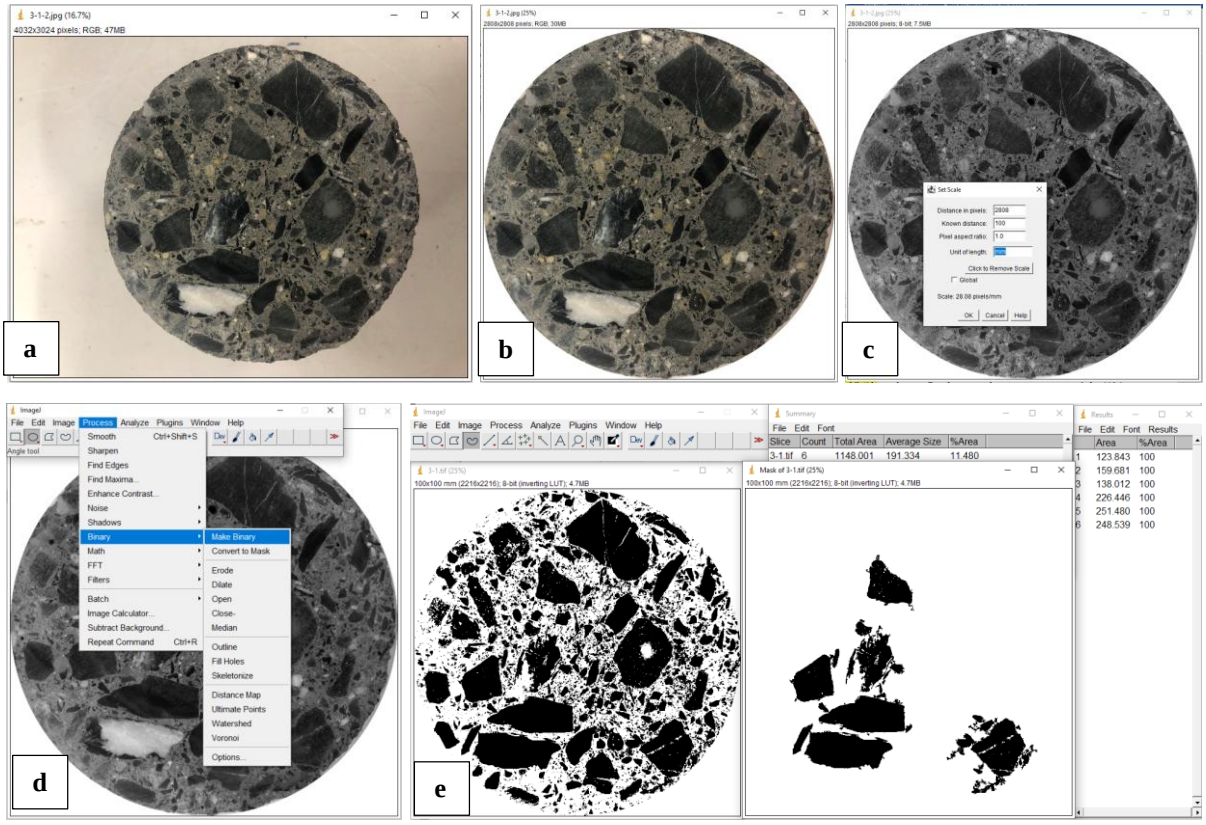


Figure 4. Analysis process steps: a) Original image b) Cropping process c) Conversion to 8-bit and scaling to 100 mm d) Binary (black and white) conversion and preprocessing selection e) Analysis

Table 1. Ten different preprocessing steps applied.

Method No	Image Processing Workflow	Description
M-1	Binary	Binary image generation only
M-3	Binary → Fill Holes	Filling internal holes within particles
M-7	Binary → Fill Holes → Watershed	Hole filling followed by particle separation
M-8	Binary → Erode → Watershed	Edge erosion followed by particle separation
M-9	Binary → Erode → Fill Holes → Watershed	Erosion, hole filling, and particle separation
M-10	Binary → Erode → Fill Holes	Erosion followed by hole filling
M-11	Binary → Fill Holes → Erode	Hole filling followed by erosion
M-12	Binary → Fill Holes → Erode → Watershed	Hole filling, erosion, and particle separation
M-13	Binary → Erode	Binary image with erosion
M-14	Binary → Watershed	Binary image with particle separation

3. Findings and Discussion

This study aimed to establish a standardized preprocessing method for determining aggregate granulometry using imaging techniques on hardened concrete surfaces in Image-J program. Nine images from three samples divided into three parts were used. Each image was analyzed using ten different methods presented in Table 1. The percentage values passing through each sieve were determined from the area values obtained from the images, and the average and standard deviation values for each sieve size were calculated and presented in Table 2. Mean

Absolute Error (MAE) and Root Mean Square Error (RMSE) values were also added to the table to determine which pretreatment step yielded the closest result to the experimental granulometry. Since 100% of the particles passed through the 32 mm sieve in all analyses, they were not included in the MAE and RMSE calculations. The results are also presented graphically in Figure 5. According to these results, considering all sieve diameters, it can be said that the analysis performed according to the M-7 method, which has the lowest MAE and RMSE values, gave the closest result to the experimental sieve analysis. This is followed by M-8, M-9, and M-12, respectively. It is noteworthy that particle separation preprocessing was applied in all of these methods. In addition, the lower MAE values calculated in the M-7 and M-8 methods show that in cases where fine and coarse aggregates need to be evaluated together, results closer to experimental data are obtained in methods where both void filling and edge erosion preprocessing are not used.

Table 2. Comparison of image processing workflows based on average passing percentage (± standard deviation), MAE and RMSE.

Passing Percentage (%) (Average / Standard deviation)												
Sieve D. (mm)	32		22,4		12		4		2		MAE[2]	RMSE[3]
M-1	100,0	0,0	87,1	9,5	56,0	4,9	30,2	4,4	15,6	2,2	14,7	15,5
M-3	100,0	0,0	87,0	9,7	55,5	5 5	29,7	4,7	14,9	2,7	15,2	16,0
M-7	100,0	0,0	95,9	5,8	75,4	7,0	43,6	3,9	23,1	3,4	8,1	9,0
M-8	100,0	0,0	98,1	5,5	86,9	10,0	61,3	6,4	32,0	6,7	9,6	13,0
M-9	100,0	0,0	96,5	6,6	75,6	8,6	39,2	3,5	19,4	2,9	10,1	11,3
M-10	100,0	0,0	94,2	11,1	58,6	6,6	29,3	4,8	13,1	2,2	13,1	15,5
M-11	100,0	0,0	91,6	10,4	55,4	6,0	29,0	5,8	12,2	2,2	14,8	16,5
M-12	100,0	0,0	96,5	6,5	73,7	6,7	37,7	3,8	17,9	2,5	10,4	11,7
M-13	100,0	0,0	95,1	10,3	61,0	6,2	29,6	5,6	13,2	2,4	12,2	15,2
M-14	100,0	0,0	98,4	4,5	89,4	9,1	66,2	5,4	37,3	6,9	11,0	15,2
E.A.[1]	100,0		98,6		63,9		49,8		35,3			

[1] Experimental sieve analysis results, [2] MAE: Mean Absolute Error, [3] RMSE: Root Mean Square Error

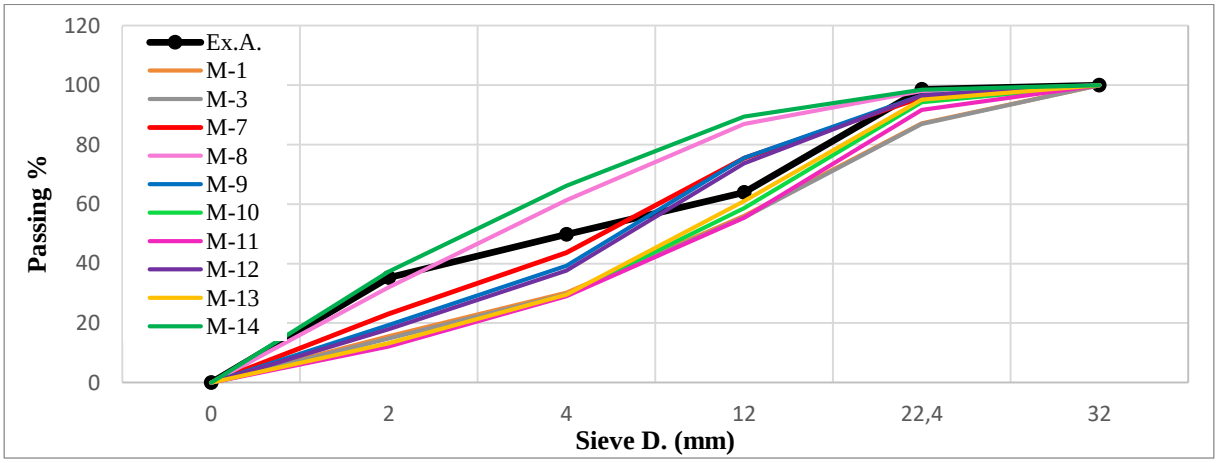


Figure 5. Comparison of image-based particle analysis and experimental sieve analysis

Particle images obtained from analyses performed on the same image for each method presented in Table 1 are shown in Figure 6 for a sample. Here, particle images obtained from analyses performed on the same sample image for the range of 113.1-394.08 mm^2 (12-22.4 mm) are shown. The images were found to be important in revealing the effect of pre-analysis settings on particle number and size. For example, when only binary (black-and-white) image generation (Figure 6.a), binary and Fill Holes (Figure 6.b) are applied to this image, an increase

in the number of particles and therefore an increase in the scanned area is observed. Similarly, there are significant differences between the results obtained when Fill Holes is applied first and then Watershed is applied (Figure 6.c) and the images obtained when Erode is applied first and then Watershed is applied (Figure 6.d). Similar differences are observed for all methods. It is particularly noteworthy that in the image where only particle Watershed preprocessing is applied after binary generation, there are no particle images at all for this mesh size (Figure 6.j). These differences, presented as an example in Figure 6, are observed for all imaging processes.

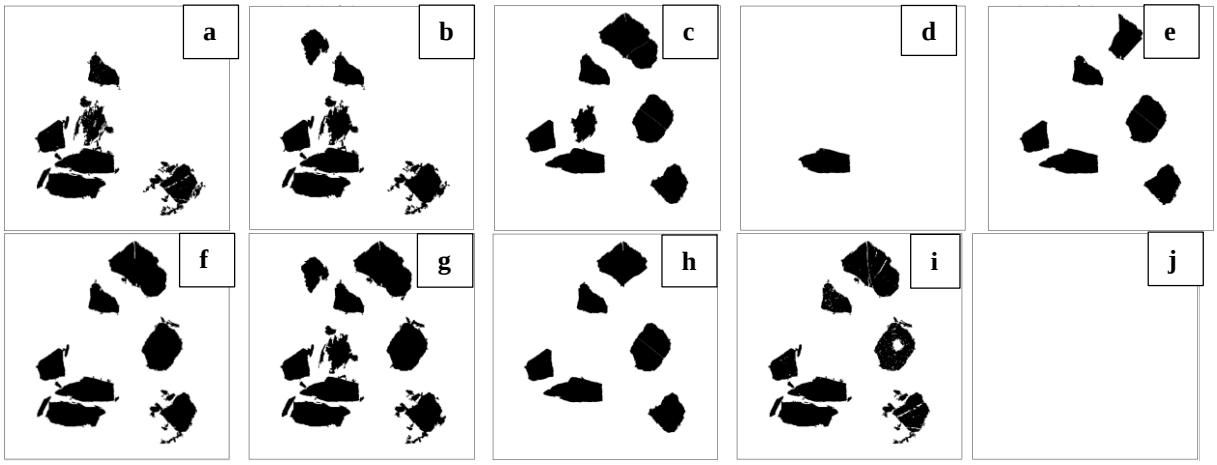


Figure 6. Particle images obtained from analyses performed on a sample for the range of 113.1-394.08 mm^2 as an example: a) M-1, b) M-3, c) M-7, d) M-8, e) M-9, f) M-10, g) M-11, h) M-12, i) M-13, j) M-14

Considering the differences presented in Figure 6 and examining Figure 5, it is seen that different pretreatment steps are effective in predicting the fine and coarse aggregate particle size distribution. To numerically evaluate this situation, the analyses performed for sieve openings between 0-4 mm and 4-32 mm were considered separately, and MAE and RMSE were calculated. The evaluation results are presented in Table 3 and Figure 7. As can be seen, Method-8 provides the closest results to the experimental result for fine aggregates. This is followed by Method-7 and Method-14 with the same MAE values. It is observed that "Watershed" was applied in the pretreatment steps in these three methods, which have the lowest MAE values. This finding emphasizes the importance of particle separation in the visualization of fine aggregates. Separating particles that are in contact with each other has resulted in more successful fine aggregate visualization. In Method 8, the voids on the aggregate particles were first closed using "Fill Holes," then the particle edges were abraded with "Erode," and finally, the particles were completely separated using "Watershed," resulting in a successful outcome for fine aggregates. For coarse aggregates, the closest result to the experimental grain distribution was obtained from Method-13, followed by Methods-10 and 12. Looking at the preprocessing settings, it is seen that "Erode" was applied to the images in all three methods. In Method-13, which yielded the best result for coarse aggregates, only "Erode" was applied after converting the image to binary (black-and-white). This preprocessing setting abraded the particle edges by approximately 1 pixel, resulting in the separation of aggregate grains. Applying "Fill Holes" after "Erode" to the image caused the spaces between closely spaced particles to refill, thus slightly increasing the MAE. The subsequent "Watershed" preprocessing setting is thought to have a negative effect because it caused some aggregate grains, which are actually single pieces, to be separated and displayed as different grains due to color differences in their natural structure.

These results are also significant in that they highlight the importance of the preprocessing sequence. For example, Methods 10 and 11 demonstrate a significant effect of the "Erode-Fill Holes" application sequence on the results. In Method 10, "Erode" was applied first, followed by the "Fill Holes" setting. In Method 11, "Fill Holes" was applied first, followed by "Erode". This resulted in a significant difference when considering sieve openings in the 4-32 mm range. In Method 11, applying Fill Holes first caused two separate aggregate particles located close together to be perceived as a single aggregate particle, and the subsequent Erode application eroded the edges of this combined aggregate.

Table 3. Comparison of image processing workflows based on MAE and RMSE for fine and coarse aggregate fractions.

Fine aggregate (0–4 mm)			Coarse aggregate (4–32 mm)		
Method No	MAE[1]	RMSE[2]	Method No	MAE[1]	RMSE[2]
M-1	19,6	19,6	M-1	9,7	9,9
M-3	20,3	20,3	M-3	10,0	10,2
M-7	9,2	9,6	M-7	7,1	8,3
M-8	7,4	8,5	M-8	11,8	16,3
M-9	13,3	13,5	M-9	6,9	8,4
M-10	21,4	21,4	M-10	4,8	4,9
M-11	21,9	22,0	M-11	7,7	7,8
M-12	14,8	15,0	M-12	6,0	7,1
M-13	21,2	21,2	M-13	3,2	3,2
M-14	9,2	11,6	M-14	12,9	18,0

[1] MAE: Mean Absolute Error, [2] RMSE: Root Mean Square Error

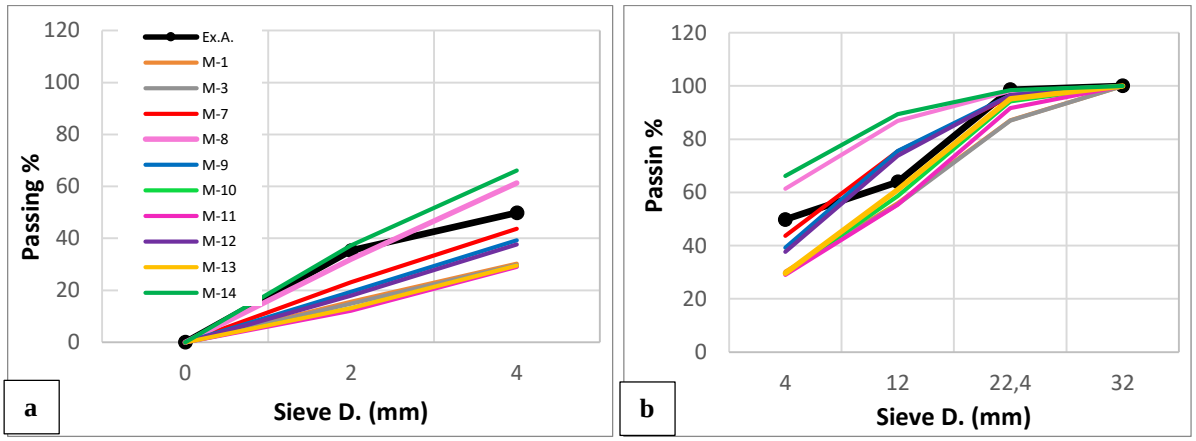


Figure 7. Comparison of image-based and experimental cumulative passing curves for a) fine aggregate (0–4 mm) and b) coarse aggregate (4–32 mm).

4. Results

This study focuses on predicting aggregate particle size distribution through imaging of cross-sections taken from hardened concrete samples. For this purpose, preprocessing steps in ImageJ software were evaluated, and suggestions for accurately predicting particle size distribution were made. A systematic comparison of different preprocessing workflows, their validation through experimental sieve analysis, and the suitability of different workflows for different particle size ranges were discussed. The results obtained are presented below.

- When comparing the analysis results after 10 different preprocessing steps, it was determined that the image processing order has a significant effect on aggregate particle

size distribution, and that an appropriate preprocessing workflow should be selected to obtain reliable image analysis results.

- The method (Method-7) that applied the Binary → Fill Holes → Watershed preprocessing steps in sequence, using all sieve diameters used in concrete samples for general particle size distribution, provided the lowest MAE and RMSE values and the best agreement with the experimental sieve analysis results.
- Analysis results have shown that applying separate preprocessing steps for coarse and fine aggregates in particle size evaluations allows for obtaining results closer to experimental results. For the fine aggregate fraction (0–4 mm), the M-8 method, which uses Binary → Erode → Watershed, showed the best performance with 7.4% MAE and 8.5% RMSE. In contrast, for the coarse aggregate fraction (4–32 mm), the M-13 method, which uses Binary → Erode, produced the lowest MAE and RMSE values with 3.2% MAE and 3.2% RMSE.
- When comparing experimental results with methods that yielded lower MAE and RMSE values, the "Watershed" preprocessing step stood out in fine aggregate preprocessing, while the "Erode" preprocessing step stood out in coarse aggregate preprocessing.

The proposed methodology offers a practical and low-cost alternative for estimating aggregate size distribution in hardened concrete. The proposed method has the potential to support future image analysis applications, while highlighting the importance of pre-processing steps in analyses.

Acknowledgments

The author would like to express her sincere gratitude to İstanbul Aydın University and Prof. Dr. Cem Aydemir for his continuous support throughout this study. The author also gratefully acknowledges Boğaziçi Beton Zeytinburnu Akin Production Plant and Mr. Erol Kaya for providing the concrete specimens used in this research. Special thanks are extended to the laboratory technical staff of İstanbul Aydın University, Ms. Nurgün Temizer and Mr. Necmi Ömerustaoğlu, for their valuable assistance with the cutting and grinding of the concrete specimens.

Finally, the author would like to express her deepest gratitude to Prof. Dr. Savaş Erdem for introducing the image analysis approach that formed the foundation of this study.

Referances

[1] M. S. Meddah, S. Zitouni ve S. Belâabes, «Effect of content and particle size distribution of coarse aggregate on the compressive strength of concrete,» *Construction and Building Materials,* cilt 24, no. 4, pp. 505-512, 2010.

[2] S. Subash, L. Parida ve S. Moharana, «Study on the Impact of Aggregate Size Gradation on Concrete: Mechanical, Durability and Microstructure Study,» *International Journal of Concrete Structures and Materials,* cilt 19, no. 114, 2025.

[3] J. Pan, W. Wang, J. Wang, Y. Bai ve J. Wang, «Influence of coarse aggregate size on deterioration of concrete affected by alkali-aggregate reaction,» *Construction and Building Materials,* cilt 329, p. 127228, 2022.

[4] G. A. Mohammed ve S. A. A. Al-Mashhadi, «Effect of Maximum Aggregate Size on the Strength of Normal and High Strength Concrete,» *Civil Engineering Journal,* cilt 6, no. 6, 2020.

[5] X. Liu, . D. Zou, J. Liu, C. Zhou ve B. Zheng, «Experimental study to evaluate the effect of particle size on the small strain shear modulus of coarse-grained soils,» *Measurement,* cilt 163, p. 107954, 2020.

[6] Y. Wang , K. Li, J. Li ve S. Tang, «Influence of Soil Particle Size on the Engineering Properties and Microstructure of a Red Clay,» *Applied Sciences,* cilt 11, no. 10887, 2021.

[7] J. Han, K. Wang, X. Wang ve P. J. Monteiro, «2D image analysis method for evaluating coarse aggregate characteristic and distribution in concrete,» *Construction and Building Materials,* cilt 127, pp. 30-42, 2016.

[8] M. Pourebrahimi, V. Şahhosseini ve A. . A. Ramezanianpour, «Innovative sieve simulation and microstructure image analysis techniques for estimation of aggregate size distribution in hardened concrete,» *Construction and Building Materials,* cilt 384, p. 131456, 2023.

[9] S. Zhou , W. Sheng, Z. Wang, W. Yao, H. Huang , Y. Wei ve R. Li, «Quick image analysis of concrete pore structure based on deep learning,» *Construction and Building Materials,* cilt 208, pp. 144-157, 2019.

[10] P. Yıldırım, S. Erdem ve M. Uysal, «Development of sustainable and thermally activated nano cementitious composites containing graphene oxide and phase change materials: Tensile, pore structure and microstructural evaluation,» *Sustainable Chemistry and Pharmacy,* cilt 51, no. 102393, 2026.

[11] M. Ozen ve M. Guler, «Assessment of optimum threshold and particle shape parameter for the image analysis of aggregate size distribution of concrete sections,» *Optics and Lasers in Engineering,* cilt 53, pp. 122-132, 2014.

[12] P. Yıldırım, «Application of Fractal Analysis in Civil Engineering: Aggregate Size Distribution, Surface Damage Detection, and Crack Propagation Monitoring,» *Journal of Building Pathology and Rehabilitation,* 2026.

[13] R. Hassan, K. C. Onyelowe ve A. A. Zamel, «Image processing and neural network technique for size characterization of gravel particles,» natureportfolio, 2024.

[14] M. Ullah, J. Mir, S. S. Husain, M. L. U. R. Shahid ve A. Afaq, «Concrete forensic analysis using deep learning-based coarse aggregate segmentation,» *Automation in Construction*, cilt 162, p. 105372, 2024.

[15] F. Radica, A. Casarin, G. Iezzi, M. Brava, J. Brito, A. Galderisi, G. Brando, M. Nazzari ve P. Scarlato, «Cement vs aggregates and textures of aggregates in a mortar: Comparative image analysis methods and analytical protocols,» *Construction and Building Materials*, cilt 453, p. 139033, 2024.

[16] H. S. Wong ve N. R. Buenfeld, «Determining the water–cement ratio, cement content, water content and degree of hydration of hardened cement paste: Method development and validation on paste samples,» *Cement and Concrete Research*, cilt 39, no. 10, pp. 957-965, 2009.

[17] S. S. Bangaru, C. Wang, X. Zhou ve M. Hassan, «Scanning electron microscopy (SEM) image segmentation for microstructure analysis of concrete using U-net convolutional neural network,» *Automation in Construction*, cilt 144, no. 104602, 2022.

[18] «TS EN 12350-1,» Turkish Standards Institute, Ankara, 2019.

Publication Note

This paper was peer-reviewed, accepted for presentation, and included in the proceedings of the ACE2026 – International Conference on Advances in Civil Engineering, held on 12–14 October 2026 in Trabzon, Türkiye.

This paper may be cited as follows:

Yıldırım P., "Evaluation of ImageJ-Based Image Processing Workflows for Aggregate Particle Size Distribution Analysis of Hardened Concrete Sections," in Proceedings of the ACE2026 – International Conference on Advances in Civil Engineering, Trabzon, Türkiye, 12–14 October 2026.

Effects of Partial Fine Aggregate Replacement with Crumb Rubber on the Mechanical and Durability Properties of Concrete

İsmail Onur Öztürk[1], Arda Ziya[2], Umut Yüksel[3], Beyza Güngör[4], Sidar Nihat Bıçakçı[5]
Hasan Nuri Türkmenoğlu[6], Mesut Küçük[7] and Hakan Nuri Atahan[8]

[1] İstanbul Technical University, Civil Engineering Department, Undergraduate Student, İstanbul, Türkiye, ozturkism20@itu.edu.tr

[2] İstanbul Technical University, Civil Engineering Department, Undergraduate Student, İstanbul, Türkiye, ziya20@itu.edu.tr

[3] İstanbul Technical University, Civil Engineering Department, Undergraduate Student, İstanbul, Türkiye, yukselu21@itu.edu.tr

[4] İstanbul Technical University, Civil Engineering Department, Undergraduate Student, İstanbul, Türkiye, gungorbey21@itu.edu.tr

[5] 0000-0002-1545-0376, İstanbul Technical University, Civil Engineering Department, İstanbul, Türkiye, bicakcis@itu.edu.tr

[6] 0000-0003-4765-8590, İstanbul Technical University, Civil Engineering Department, İstanbul, Türkiye, turkmenogluh@itu.edu.tr

[7] 0000-0002-2073-0671, Erzincan Binali Yıldırım University, Civil Engineering Department, Erzincan, Türkiye, mkucuk@erzincan.edu.tr

[8] 0000-0002-7917-3021, İstanbul Technical University, Civil Engineering Department, İstanbul, Türkiye, atahanh@itu.edu.tr

Abstract. The use of crumb rubber (CR) as a partial replacement for fine aggregate offers a sustainable alternative for recycling end-of-life tires while reducing the consumption of natural resources. However, its influence on concrete properties requires further investigation. This study experimentally evaluates the mechanical, elastic, and durability properties of concrete in which 10%, 20%, 30%, and 40% of the fine aggregate was replaced by CR by volume. Compressive strength (CS), splitting tensile strength (STS), stress–strain behavior, modulus of elasticity (MOE), Poisson's ratio, impact load response, sorptivity, and freeze-thaw resistance were investigated. The results showed that CS and STS decreased progressively with increasing CR replacement ratio. Likewise, the MOE decreased, whereas Poisson's ratio remained essentially unchanged. Despite the reduction in strength, concrete containing 10% CR exhibited a STS comparable to that of the reference (REF) concrete while demonstrating a significantly higher energy absorption capacity under impact loading. Sorptivity tended to decrease at 10% and 20% replacement levels but significantly increased when the replacement ratio reached 30% and 40%. After 50 freeze-thaw cycles, the CS of the REF mixtures decreased by approximately 25%, whereas mixtures containing CR exhibited strength increases ranging from 8% to 14%. Nevertheless, surface scaling was observed in the CR concretes while no noticeable surface deterioration occurred in the REF concrete. These findings indicate that low replacement levels of CR, particularly 10%, can significantly improve impact resistance and enhance freeze-thaw performance while maintaining acceptable mechanical properties.

Keywords: Crumb rubber concrete, Mechanical properties, Elastic properties, Impact resistance, Freeze-thaw resistance.

Introduction

The modern construction industry is under severe environmental pressure due to intensive natural resource consumption and high greenhouse gas emissions. While Portland cement

production is responsible for approximately 5-8% of global CO_2 emissions, mining activities carried out for aggregate procurement also lead to ecosystem destruction [1]. In parallel with this situation, approximately 1 billion waste tires are generated globally each year, and this stock is projected to reach 5 billion units annually by 2030 [2]. The vulcanized, cross-linked polymeric structure of tires makes their biological decomposition in nature difficult [3]. While the uncontrolled storage of waste poses public health and fire risks, its incineration leads to the emission of toxic smoke [1]. To minimize these risks, one of the most robust circular economy approaches is the partial utilization of waste tires in the form of crumb rubber (CR) as a replacement for natural aggregate [1–3].

Rubberized concretes are produced by granulating waste tires and replacing a certain portion of the natural fine aggregate [1,4]. Life cycle assessments reveal that rubber-modified concretes reduce the carbon footprint and dependency on natural aggregate resources [3]. However, the technical challenge created by the use of rubber in concrete is that it leads to mechanical strength losses due to the weak Interfacial Transition Zone (ITZ) formed with the cement matrix, which stems from the low stiffness and hydrophobic nature of rubber [1]. Microstructural analyses conducted by Garcia-Troncoso et al. [5] also confirm this distinct ITZ gap between the rubber particle and the cement matrix. In the literature, surface modification techniques, such as chemical pretreatments with sodium hydroxide (NaOH) [6] or aqua-thermal treatments (ATT) proposed by Sanjaya et al. [7], are applied to mitigate these disadvantages. Furthermore, despite the losses in mechanical strength, as demonstrated in dynamic tests by Xiong et al. [3] and Eltayeb et al. [8], the flexible structure of the rubber additive alleviates stress concentrations at crack tips, thereby imparting a ductile fracture characteristic to the material. At high strain rates, the energy absorption capacity of rubberized aggregate concrete is far superior to that of normal concrete. In seismic performance tests conducted by Chao et al. [9], it was also proven that the energy damping capacity of components containing rubber increases. In terms of durability, analyses carried out by Zhai et al. [6] show that, due to the water-repellent nature of rubber, capillary water absorption pathways are interrupted within the 10-20% band; however, when this critical threshold is exceeded, ITZ vulnerabilities exert negative effects on freeze-thaw resistance. In infrastructure engineering, as emphasized in the study conducted by Zakerzadeh et al., the use of CR in mixtures such as Stone Mastic Asphalt (SMA) offers advantages such as extended service life and crack limitation [2]. Shafabakhsh et al. [10] and Assaggaf et al. [11] also support, through dry methods, that waste tire-derived rubber increases flexibility in asphalt mixtures.

In light of these scientific findings, the primary objective of the present study is to determine the optimum utilization rate by investigating the effects of using CR at various ratios on the mechanical and durability properties of concrete, and to contribute to both existing literature and future research.

2 Materials and Method

A reference (REF) mixture was designed with a 360 kg/m³ cement and a water-to-cement (W/C) ratio of 0.50. The mixtures incorporated CEM II/A-L 42.5 R cement, natural sand, crushed sand, and crushed stone (with a maximum aggregate size of 16 mm), with specific gravities of 3.03, 2.56, 2.74, and 2.70 g/cm³, respectively. The aggregate proportions were adjusted to closely follow the B16 reference grading curve specified in the TS 802 [12]. Subsequently, four different concrete mixtures were designed by replacing the total fine aggregate in the REF mixture with CR, which has a specific gravity of 1.00 g/cm^3, at volumetric replacement ratios of 10%, 20%, 30%, and 40%. The designed concrete mixtures were named as CR10, CR20, CR30, and CR40 based on their fine aggregate replacement percentages. Two different types of CR, namely fine (0.125–1 mm) and coarse (0.5–4 mm), were utilized in the designs. To ensure compatibility with the particle size distribution of the fine aggregates used, the fine and

coarse CRs were blended at a ratio of 40% and 60%, respectively. The mix proportions per cubic meter of the concrete mixtures are presented in Table 1.

The slump test was performed on the fresh concrete in accordance with EN 12350-2 [13]. To achieve the target S2 workability class, a polycarboxylate-based superplasticizer (SP) was utilized. Its dosage relative to the binder content is presented in Table 1. For each mixture, eight 100×100×100 mm cubic specimens, six Φ100×200 mm cylindrical specimens, one 70×70×280 mm prismatic specimen, and three 150×600×35 mm prismatic specimens were cast. The specimens were cured in lime-saturated water at 20±2 °C until reaching a curing age of 28 days.

Table 1. Mix proportions (kg/m^3).

	REF	**CR10**	**CR20**	**CR30**	**CR40**
Cement	360	360	360	360	360
Water	180	180	180	180	180
Natural Sand	307	276	246	215	184
Crushed Sand	657	591	526	460	394
Crushed Stone	865	865	865	865	865
Fine CR	0	14.4	28.8	43.2	57.6
Coarse CR	0	21.6	43.2	64.8	86.3
SP (%)	0.9	0.6	0.5	0.5	0.4

Out of the produced cubic specimens, four were subjected to the compressive strength (CS) test in accordance with the EN 12390-3 [14], while the remaining four specimens were subjected to the freeze-thaw test. For this purpose, specimens were subjected to 50 freeze–thaw cycles after 28 days of standard water curing. Each cycle consisted of 8 hours of freezing at −40°C and 16 hours of immersion in water at +20°C.

A deformation-controlled compression test was performed on four of the cylindrical specimens using lateral and vertical LVDTs to obtain the stress-strain curves. From these curves, the Poisson's ratio and modulus of elasticity were determined. The remaining two cylindrical specimens were cut in half perpendicular to long axis, yielding four Φ100×100 mm specimens for each mixture. The splitting tensile strength (STS) test was conducted on these obtained specimens in accordance with the EN 12390-6 [15]. Meanwhile, the single 70×70×280 mm prismatic specimen was divided into three equal pieces with a cross-sectional area of 70×70 mm², and the sorptivity coefficients of the samples were measured based on the amount of capillary water absorption over a 4-hour period. The weight of the specimens was measured in the dry state (0 min), as well as at 5, 10, 20, 30, 60, 90, 120, 180, and 240 min. The formula used for the sorptivity coefficient (k) is

$$q^2 = k \times t \tag{1}$$

where q=water absorption per unit area; and t=time. The sorptivity coefficient, k, was determined as the slope of the linear relation drawn between q and $\sqrt{t}$.

On the 150×600×35 mm prismatic specimens, impact tests were performed using a spring-actuated universal impact testing device [16], as illustrated in Figure 1. The specimens were supported at two points, and an impact load was applied to their midpoint. In the experiments, the impact load–time relationship, the velocity of the impact trolley at the moment of impact with the specimen, and the post-impact motion–time data were obtained using the DEWE-43A data acquisition device, which has a high data acquisition rate. Using the data recorded during the experiments, the “impact force–time” and “post-impact motion–time” relationships were evaluated.

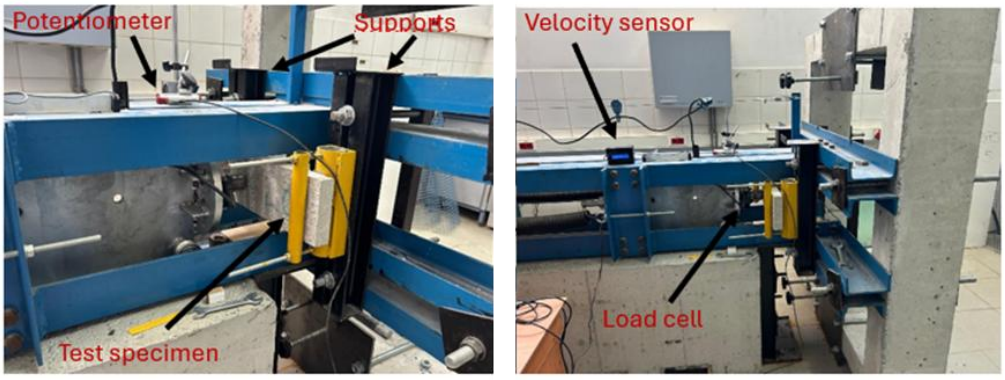


Fig. 1. Impact test device.

3 Results and Discussions

3.1 Strength and Stress-Strain Relations

The CS and STS values were determined as the mean of the results along with their standard deviations. The results are presented as bar charts in Figure 2.

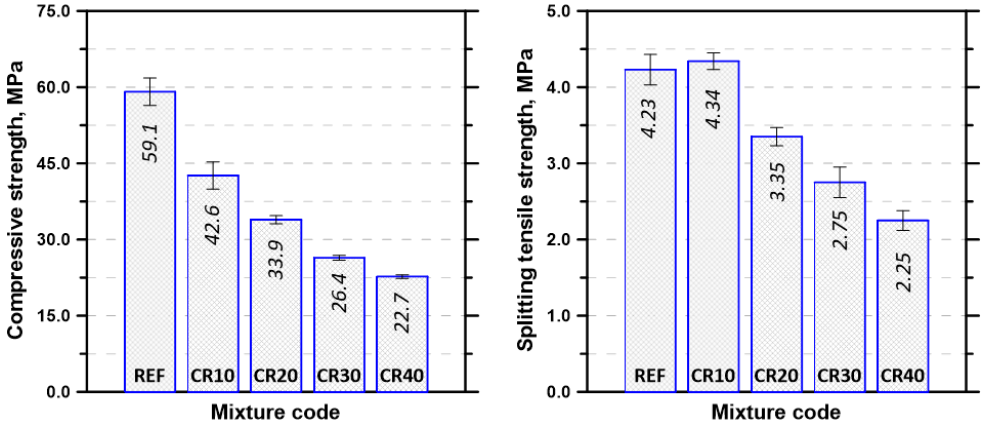


Fig. 2. Bar graph of CS results (*left*), and STS results (*right*). (*Error bars: ±1St.Dev.*)

The CS systematically decreased with the increase in CR replacement. This reduction is attributed to the lower stiffness of CR particles compared to natural aggregates, which creates an elastic incompatibility between the CR and cement matrix [1]. Another reason is that while the cement paste is hydrophilic, CR is hydrophobic. Due to this incongruity, the cement gel cannot bond strongly to the CR surface, resulting in a weak ITZ between them [1,5]. Regarding the STS results, a slight increase was observed at 10% CR replacement compared to the REF mixture, followed by a systematic decrease beyond this replacement level. However, analyzing the STS/CS ratios reveals a value of 0.07 for REF, whereas this ratio revolves around 0.10 for CR-containing mixtures (approximately 50% higher than REF). Due to its rigid structure, concrete exhibits brittle behavior and is highly sensitive to voids or defects, which leads to sudden failure under tensile loads and reduces tensile strength. Conversely, the flexible nature and deformability of CR prevent sudden crack initiation. Furthermore, when a crack reaches a CR particle, the particle acts as a fiber, slowing down crack propagation and dissipating energy by changing the crack path, thereby enhancing the ductility of the concrete.

The stress-strain relationships were obtained using four specimens for each mixture, and a representative behavior from each is shown in Figure 3.

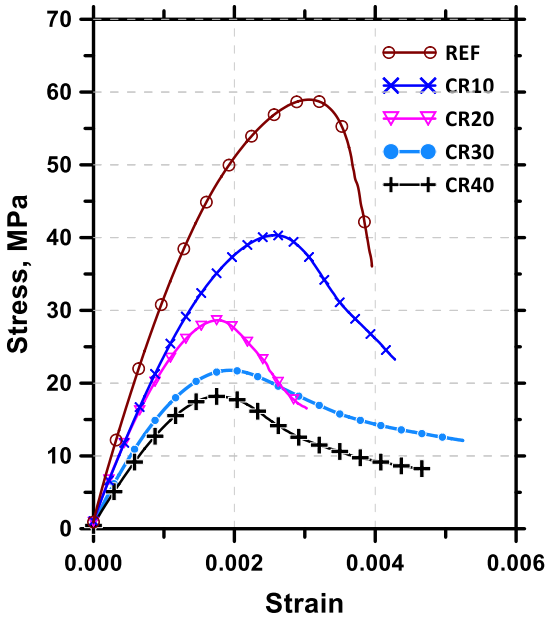


Fig. 3. Representative graphs for stress-strain relations.

As shown in Figure 3, the slope of the descending branch decreased with increasing CR replacement, which is a significant indicator of an enhanced energy absorption capacity. Furthermore, the strain values corresponding to the peak stress significantly decreased with increasing CR replacement. The modulus of elasticity (MOE) and Poisson's ratio, calculated from the stress-strain curves, are presented as bar charts in Figure 4. Similar to the CS results, the MOE decreased as the CR replacement increased, which is attributed to the same factors underlying the reduction in CS. Regarding the Poisson's ratio, on the other hand, the CR replacement caused no significant change, with the ratio calculated at approximately 0.18 for all mixtures.

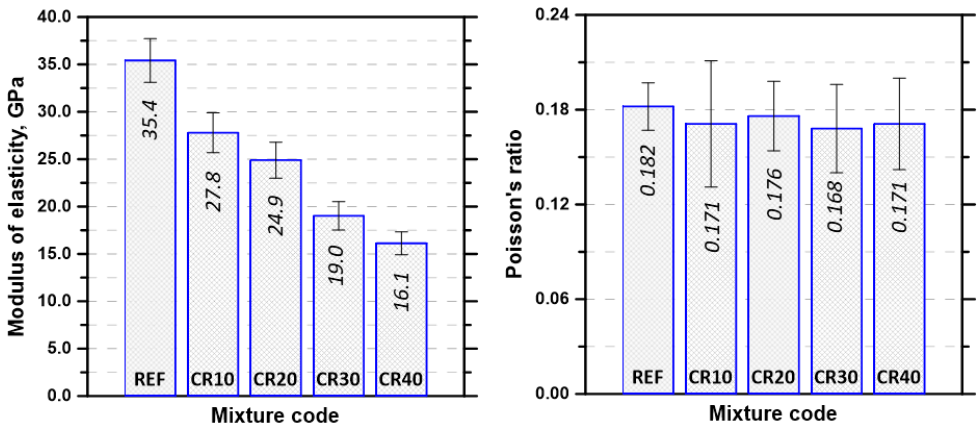


Fig. 4. MOE (*left*) and Poisson's ratio (*right*) results. (*Error bars: ±1St.Dev.*)

3.2 Sorptivity and Freeze-thaw test results

The bar charts of the calculated sorptivity values are presented in Figure 5. Similar to the trends reported by Zhai et al. [6], the sorptivity coefficients exhibited a distinct biphasic behavior with increasing CR content. Within the 10–20% replacement band (CR10 and CR20), the sorptivity values slightly decreased compared to the REF mixture. This reduction is attributed to the hydrophobic nature of the rubber particles, which effectively blocks and interrupts the interconnected capillary pathways. However, once this critical threshold was exceeded, a

significant increment was observed for the CR30 and CR40 mixtures. This sharp upward trend indicates that at higher replacement levels, the defects associated with the weak ITZ and increased micro-porosity dominate the matrix, thereby facilitating water penetration despite the hydrophobic character of the rubber.

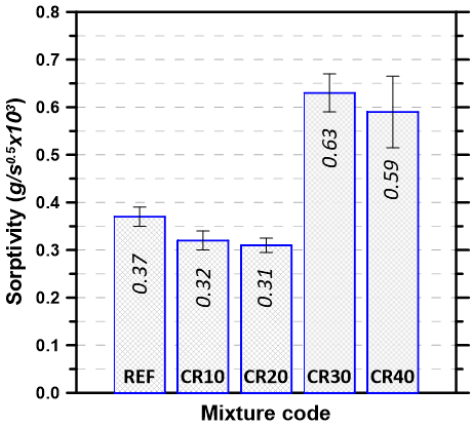


Fig. 5. Sorptivity results. *(Error bars: ±1St.Dev.)*

The freeze–thaw performance of the specimens was evaluated using two approaches: (i) the surface material loss (scaling) from the specimen faces after cycling (*cm³/100 cm²*), and (ii) the CS of the specimens after cycling, which was compared with the 28-day standard cured reference strengths. A photograph showing the surface condition of the specimens after 50 cycles is given in Figure 6. The amount of surface material loss is presented in Figure 7 (*left*), while the variation in CS relative to the 28-day standard cured specimens, as a function of CR replacement ratio, is shown in Figure 7 (*right*).



Fig. 6. Surface views of the specimens after 50 freeze–thaw cycles.

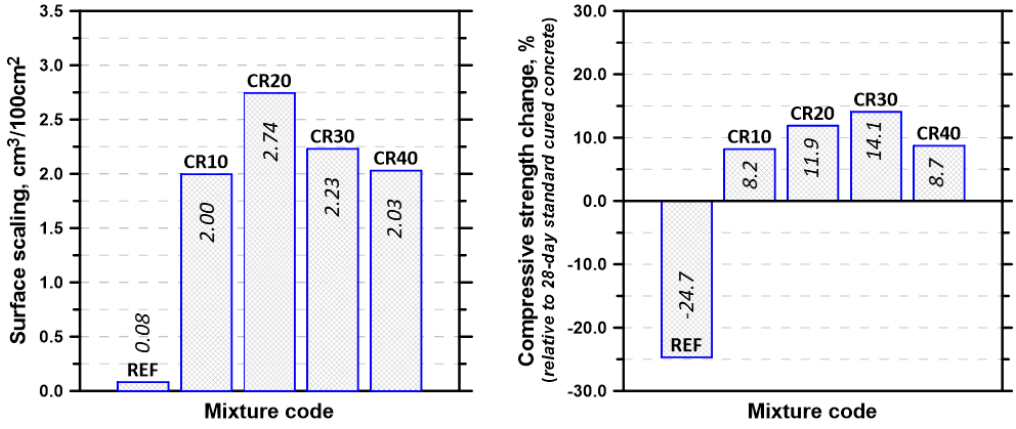


Fig. 7. Surface scaling as a function of CR replacement ratio (*left*), CS variation relative to 28-day standard cured specimens as a function of CR replacement ratio (*right*).

When Figure 6 is examined, no scaling, spalling, or significant surface deterioration was observed on the REF specimens after the freeze–thaw cycles. This visual assessment is also supported by the results presented in Figure 7 (left). Compared to the rubber-containing groups, the REF specimens exhibited negligible surface scaling. In contrast, as shown in Figure 6, noticeable surface scaling was observed in the CR-containing specimens. The most severe volume loss was recorded in the CR20 concrete, reaching 2.74 $cm^3/100\ cm^2$.

As seen in Figure 7 (*right*), an opposite trend to the surface scaling results is observed. After freeze–thaw cycles, the REF specimens exhibited approximately 25% reduction in CS compared to their 28-day standard cured counterparts, whereas all CR-containing mixtures showed strength increases ranging between 8% and 14%. This behavior is attributed to the ability of CR-modified concretes to more effectively dissipate internal stresses developed during freeze–thaw action. Volumetric expansion of pore water during freezing, together with thermal strains induced by an approximately 60°C temperature difference throughout the cycles, generates additional stresses within the cementitious matrix. The elastic nature of CR particles helps absorb part of these stresses, reducing stress concentrations and limiting microstructural damage. In addition, due to their low stiffness and deformable nature, CR particles may act similarly to entrained air voids by providing local relief zones for the expansion of freezing water. This mechanism can reduce hydraulic and crystallization pressures, thereby contributing to improved freeze–thaw resistance. As a result, internal damage induced by freeze–thaw cycles is likely mitigated, and continued hydration may also contribute to the observed strength gain in CR-containing specimens. However, this beneficial effect is not sufficient to prevent surface deterioration.

3.3 Energy Absorption under Impact Force

The force–time graphs obtained under impact are presented in Figure 8 (*left*). These graphs illustrate the maximum force values generated at the moment of impact, the time-dependent variation of the force, and the system's dynamic response. It was assumed that the impact trolley damaged the specimen and that its subsequent partial free motion occurred over a time interval of approximately 0.016 seconds. Data regarding the impact trolley's motion after striking the specimen are presented graphically in Figure 8 (*right*).

The resulting velocity-time graphs provide important information for evaluating the system's kinematic behavior after a collision, its tendency to rebound or continue in the direction of motion, and the mechanism of energy transfer. In this context, the velocity-time curves were analyzed over a time interval of up to 0.016 seconds in order to determine the impact energy absorbed by the specimens until damage occurred. In addition, the change in momentum (I_p) at the moment of impact was obtained by calculating the area under the impact force-time graph up to 0.016 seconds. The velocity (V_r) of the impact vehicle after striking the specimen was calculated using Equation 2, based on the impulse value. Once V_r is determined, the residual kinetic energy of the impact trolley can be calculated. The energy absorbed by the concrete plate specimen (E_{abr}) was calculated by subtracting the impact energy from the rebound energy using Equation 3 [17]. The results presented in Table 2 allow for an evaluation of the specimens' energy absorption capacities (E_{abr}) based on their average values.

$$V_r = V_{impact} - \frac{I_p}{m} \tag{2}$$

$$E_{abr} = E_{impact} - 0{,}5\ x\ m\ x\ V_r^2 \tag{3}$$

Where *m* presents the mass of the impact vehicle. When REF specimens are compared with specimens containing different proportions of rubber, it is evident that the rubber content has an effect on energy dissipation behavior. The energy absorption values of the concrete specimens, calculated based on varying rubber contents, are shown in Figure 9.

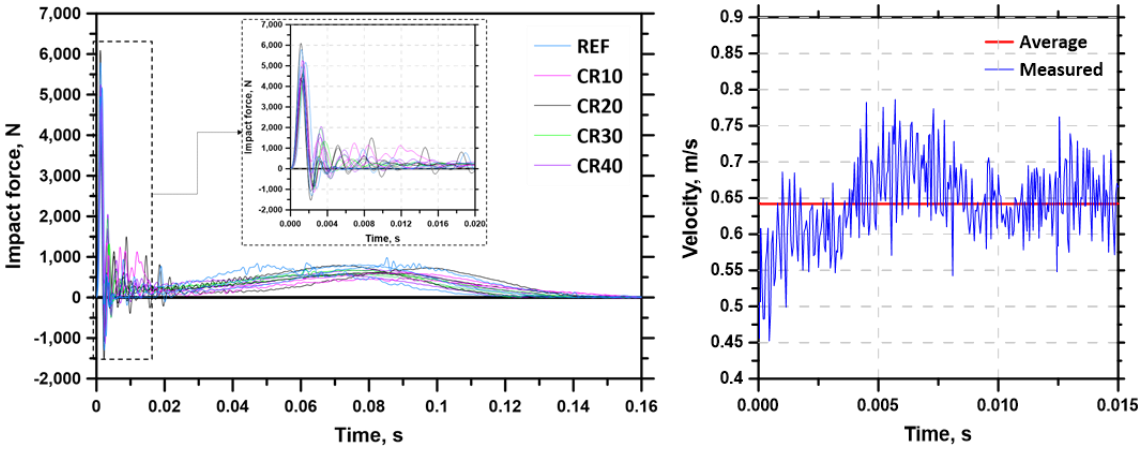


Fig. 8. Impact force-time graphs obtained from the experiments (*left*), and data on the post-impact motion of the impact trolley (*REF specimen*) (*right*).

Table 2. Absorbed energy ($E_{abr\text{-}mean}$, *Joule*)

Sample #	**REF**	**CR10**	**CR20**	**CR30**	**CR40**
1	6.59	4.55	3.73	3.99	4.36
2	3.55	8.07	4.66	5.48	4.74
3	2.97	7.65	6.11	4.66	4.81
Average:	4.37	6.76	4.83	4.71	4.64

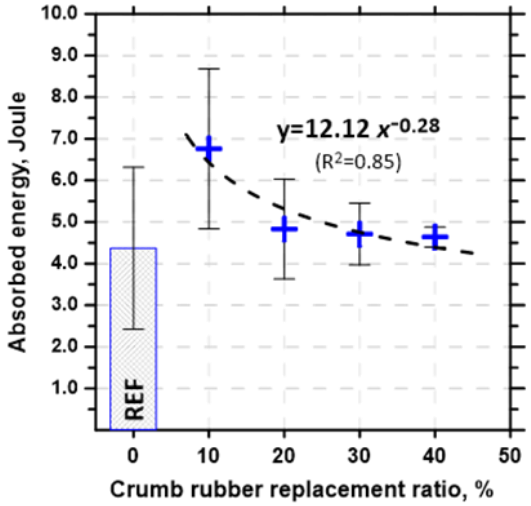


Fig. 9. CR replacement ratio *vs.* absorbed energy. (*Error bars: ±1St.Dev.*)

In Figure 9, it can be observed that the incorporation of CR into concrete increases the amount of absorbed energy under impact loading compared to the REF mixture. The most pronounced improvement was obtained at a 10% CR content. However, when the rubber-containing concretes are evaluated within themselves, the absorbed energy values decrease with increasing rubber content. This behavior can be explained by the significant reductions in compressive and STSs associated with higher rubber replacement ratios. These results indicate that the energy absorption capacity depends not only on the amount of CR but also strongly on the mechanical strength properties of the concrete. Indeed, when the REF concrete and the concrete containing 10% CR, which exhibit similar STSs, are compared, it is clearly seen that even a 10% rubber replacement leads to a significant increase (55%) in absorbed energy relative to the REF mixture.

4 Conclusions

This study experimentally evaluated the feasibility of incorporating CR as a partial volume replacement (10% to 40%) for fine aggregate in concrete, focusing on its mechanical, elastic, and durability properties.

The experimental results demonstrate a progressive reduction in CS, STS, and MOE with increasing CR content, while Poisson's ratio remains virtually unaffected. However, a detailed analysis of the STS/CS ratios reveals that CR-containing mixtures exhibit a ratio of approximately 0.10, nearly 50% higher than the 0.07 recorded for the REF concrete, indicating a significant improvement in relative tensile performance and a transition toward a less brittle failure mode. This enhanced ductility is further substantiated by the stress–strain behavior and the outstanding energy absorption capacity under impact loading, particularly at the 10% CR replacement level, which maintains an STS comparable to the REF concrete.

In terms of durability, the inclusion of CR drastically improves freeze-thaw performance; after 50 cycles, the REF mixture suffered a 25% strength loss while CR concretes exhibited a strength increase of 8% to 14%. However, regarding surface durability, noticeable surface scaling occurred in the CR concretes, whereas the REF concrete showed no significant surface deterioration. Furthermore, sorptivity characteristics are optimized at lower replacement levels (10% and 20%) but degrade significantly at higher contents (30% and 40%).

Overall, the findings conclusively indicate that a low replacement level, specifically 10% CR, represents an optimal threshold.

Acknowledgement

The authors gratefully acknowledge the "LAGEDO" for providing crumb rubber samples.

References

1. N. Hisbani, N. Shafiq, M.A. Shams, S.A. Farhan, M. Zahid, Properties of concrete containing crumb rubber as partial replacement of fine Aggregate—A review, Hybrid Advances 10 (2025). https://doi.org/10.1016/j.hybadv.2025.100481.
2. M. Zakerzadeh, B. Shahbodagh, J. Ng, N. Khalili, The use of waste tyre rubber in Stone Mastic Asphalt mixtures: A critical review, Constr. Build. Mater. 418 (2024). https://doi.org/10.1016/j.conbuildmat.2024.135420.
3. Z. Xiong, Z. Fang, W. Feng, F. Liu, F. Yang, L. Li, Review of dynamic behaviour of rubberised concrete at material and member levels, Journal of Building Engineering 38 (2021). https://doi.org/10.1016/j.jobe.2021.102237.
4. C. Bu, D. Zhu, X. Lu, L. Liu, Y. Sun, L. Yu, T. Xiao, W. Zhang, Modification of Rubberized Concrete: A Review, Buildings 12 (2022). https://doi.org/10.3390/buildings12070999.
5. N. Garcia-Troncoso, S. Acosta-Calderon, J. Flores-Rada, H. Baykara, M.H. Cornejo, A. Riofrio, K. Vargas-Moreno, Effects of Recycled Rubber Particles Incorporated as Partial Sand Replacement on Fresh and Hardened Properties of Cement-Based Concrete: Mechanical, Microstructural and Life Cycle Analyses, Materials 16 (2023). https://doi.org/10.3390/ma16010063.
6. S. Zhai, J. Hu, R. Hai, L. Cui, Y. zhang, L. Yang, J. Zhang, Y. Zhang, L. Liu, Y. Sun, Investigation on the durability performance and mechanism analysis of modified crumb rubber concrete, Constr. Build. Mater. 471 (2025). https://doi.org/10.1016/j.conbuildmat.2025.140746.
7. B.G.V. Sanjaya, S. Venkatesan, J.M.R.S. Appuhamy, W.M.K.R.T.W. Bandara, R.J. Gravina, Enhancing structural integrity and crack resistance of rubberized concrete using aqua-thermally treated rubber aggregates and recycled tire steel fibers for structural applications, Sustainable Materials and Technologies 46 (2025). https://doi.org/10.1016/j.susmat.2025.e01720.

8. E. Eltayeb, X. Ma, Y. Zhuge, J. Xiao, O. Youssf, Dynamic performance of rubberised concrete and its structural applications – An overview, Eng. Struct. 234 (2021). https://doi.org/10.1016/j.engstruct.2021.111990.
9. L. Chao, A. Li, Y. Wang, Y. Deng, Experimental study on seismic performance of crumb rubber aeolian sand concrete columns, Structures 61 (2024). https://doi.org/10.1016/j.istruc.2024.105970.
10. G. Shafabakhsh, M. Sadeghnejad, P. Mahmoudi, R. Ebrahimnia, Sustainable Nano-TiO2 modified asphalt with fine aggregate replacement using rubber powder, Transportation Engineering 20 (2025). https://doi.org/10.1016/j.treng.2025.100332.
11. R.A. Assaggaf, M. Maslehuddin, S.U. Al-Dulaijan, M.A. Al-Osta, M.R. Ali, M. Shameem, Cost-effective treatment of crumb rubber to improve the properties of crumb-rubber concrete, Case Studies in Construction Materials 16 (2022). https://doi.org/10.1016/j.cscm.2022.e00881.
12. Design of concrete mixes, 2016.
13. BSI Standards Publication Testing fresh concrete, 2019.
14. Testing hardened concrete. Part 3, Compressive strength of test specimens, BSI, 2019.
15. B. Standard, Testing hardened concrete Part 6: Tensile splitting strength of test specimens, 2010.
16. M. Kucuk, M. Hejazi, A. Sari, A Novel Spring-Actuated Low-Velocity Impact Testing Setup, Applied System Innovation 7 (2024). https://doi.org/10.3390/asi7060108.
17. H. Erkan, S. Aslan, H. Erol, H.S. Şengel, T. Yilmaz, M.H. Arslan, Ö. Anil, Investigation of the effects of shear reinforcement ratio and opening size on the impact behavior of RC beams produced with geopolymer concrete, Structures 75 (2025). https://doi.org/10.1016/j.istruc.2025.108868.

Author Contribution Statement

- *Conceptualization:* H.N. Atahan, H.N. Türkmenoğlu
- *Methodology:* H.N. Atahan, H.N. Türkmenoğlu, S. N. Bıçakçı, M. Küçük
- *Investigation:* A. Ziya, İ.O. Öztürk, U. Yüksel, B. Güngör, S.N. Bıçakçı, M. Küçük
- *Writing – Original Draft:* All the authors
- *Writing – Review & Editing:* All the authors

List of Abbreviations

- **CS** — Compressive Strength
- **STS** — Splitting Tensile Strength
- **CR** — Crumb Rubber
- **MOE** — Modulus of Elasticity
- **REF** — Reference

Publication Note

This paper was peer-reviewed, accepted for presentation, and included in the proceedings of the ACE2026 – International Conference on Advances in Civil Engineering, held on 12–14 October 2026 in Trabzon, Türkiye.

This paper may be cited as follows:

Öztürk İ. O., Ziya A., Yüksel U., Güngör B., Bıçakçı S. N., Türkmenoğlu H. N., Küçük M., Atahan H. N., "Effects of Partial Fine Aggregate Replacement with Crumb Rubber on the Mechanical and Durability Properties of

Concrete," in Proceedings of the ACE2026 – International Conference on Advances in Civil Engineering, Trabzon, Türkiye, 12–14 October 2026.

Tetraethyl Orthosilicate-Based Fiber-Reinforced Geopolymer Mortars under Comparative Evaluation of Different Curing Methods

Beyza AYGUN[1*], Mucteba UYSAL[2], Turgay COSGUN[3], Turhan BILIR[3]

[1] 0000-0002-1317-9148, Istanbul Okan University, Vocational School, Istanbul, Türkiye, beyza.aygun@okan.edu.tr
[2] 0000-0002-6827-9904 , Yıldız Technical University, Civil Engineering Department, Istanbul, Türkiye, mucteba@yildiz.edu.tr
[3] 0000-0002-5417-9312, Istanbul University-Cerrahpasa, Civil Engineering Department, Istanbul, Türkiye, costur@iuc.edu.tr
[4] 0000-0003-0317-026X, Istanbul University-Cerrahpasa, Civil Engineering Department, Istanbul, Türkiye, tbilir@iuc.edu.tr

Abstract. Tetraethyl orthosilicate (TEOS) is the latest reactive silica source added to the geopolymer matrix, which effectively promotes gel formation, increases the rate of geopolymerization, and improves the pore structure. This research specifically used TEOS as an active component of an innovative alkaline activator to enhance the short- and long-term properties of geopolymer mortars reinforced with fibers. The binder used was either 100% granulated blast furnace slag (GBFS) or a combination of 75% GBFS and 25% Class F fly ash (FA). The activating solution included sodium silicate (57.8%), 8 M sodium hydroxide (28.9%), and TEOS (13.3%). The activator-to-binder (A/B) ratio was 0.7. CF and SF fibers were used at volume fractions of 0.25% and 0.75%, respectively, to assess their impact on geopolymer matrix crack resistance and mechanical performance. Curing was conducted in ambient atmosphere: by conventional thermal treatment at 70°C for 48 h, and by an innovative electrical curing method using electrodes that generate resistive heating within the mortar samples. Compressive, flexural, and splitting tensile strength as well as ultrasonic pulse velocity (UPV) of geopolymer composite specimens were measured at ages of 7 and 28 days. It was established that TEOS significantly enhanced matrix densification and reduced porosity, whereas electrical curing accelerated geopolymerization, resulting in improved early-age strength compared to other curing methods. Moreover, the effect of fibers on tensile strength and crack resistance was positive, especially for higher fiber volume fractions.

Keywords: Geopolymer; Tetraethyl orthosilicate; Electrical curing; Mechanical properties.

1 Introduction

Tetraethyl orthosilicate (TEOS), also called ethyl silicate or tetraethoxysilane, is a silicon-based alkoxide that has attracted significant interest due to its ability to form silica-enriched networks via hydrolytic condensation reactions. In contrast to the mineral additions, which usually serve as inert filler materials, TEOS participates in the formation of siloxane structures, modifies the pore structure, decreases permeability, and increases structural integrity. Hydrolysis of TEOS leads to the transformation of TEOS molecules into silanol groups and to their further condensation into interlinked silica networks, thereby refining the microstructure and stabilizing the material. Due to such features, TEOS is widely used as a consolidant for porous materials and as a precursor in sol–gel technologies. Moreover, hybrid and modified systems

based on TEOS are used to improve the mechanical performance of composite materials, provide corrosion resistance, and address brittleness-related issues such as crack formation. Performance improvements using TEOS have been confirmed in a variety of engineering research studies [1-3]. Johnson and Worrall [4] studied the application of TEOS to seal the pore structures of zeolitic materials and to analyze changes in ion-exchange performance compared with unmodified samples. The authors found that TEOS treatment decreased pore connectivity and increased physical stability. Similar results were obtained by Altube et al. [5] when studying the properties and corrosion resistance of sol-gel coatings prepared by TEOS and deposited on aluminum alloys. Attention was paid to the influence of pH on the hydrolysis process, and it was shown that an electrochemical coating based on TEOS provides better corrosion protection than traditionally dip-coated coatings. Another investigation conducted by Kucuk and Demirkal [6] showed that incorporating TEOS into zirconium phosphate/polyethylene oxide composites prepared using the sol-gel method renders the material thermally stable up to 300°C without losing water retention capability. Bian et al. [7] studied the effect of TEOS on the performance of rubber-modified asphalt and found that it positively influences physical and rheological properties and high-temperature stability. However, a TEOS content that was too high decreased fatigue resistance. Thus, all of the abovementioned studies demonstrated the potential to improve the material's performance using TEOS. Despite the intensive use of TEOS in advanced materials, its application in construction materials remains rather limited. Research on TEOS applications is mainly devoted to performance improvement, surface modification, and pore refinement, rather than to its incorporation into cementitious binders. Barberena-Fernández et al. [8] studied the applicability of TEOS as a component of nano-lime and nano-silica treatments used for Portland cement mortars and found that TEOS contributes to porosity reduction, improves compressive and flexural performance, maintains the surface appearance, and increases water repellence of the materials. In comparison with the large number of research studies on TEOS applications in coating, composite materials, asphalt technology, recycled aggregate, and conventional cement-based materials, only a very few papers on TEOS applications in geopolymer systems exist. A comprehensive literature review showed a lack of research on the interaction between TEOS and a geopolymer binder. Among the existing papers, the contribution of dos Reis et al. [9], who used methylpolysiloxane, methylphenylpolysiloxane, and TEOS in the synthesis of hybrid geopolymer materials prepared from natural kaolin, should be mentioned. While it was shown that the incorporation of silica-based organosilicon compounds is possible, no geopolymer mortars or concretes were produced in the course of this research, so it can be regarded as unrelated to the structural application of geopolymer binders. Also, the role of TEOS as an ingredient in the alkaline activator was not systematically investigated. Therefore, the question of the influence of TEOS on the kinetics of geopolymerization, gel formation, pore refinement, and the mechanical performance of geopolymer mortars remains unclear. In addition to the activator chemistry, curing conditions are another factor influencing the properties of geopolymer materials. Thermal curing is widely used to accelerate dissolution and polycondensation processes. However, the search for alternative curing techniques to make the reaction more efficient and consume less energy continues.

Electrical curing has become a promising technique because it induces internal heating through conductive paths and does not require additional thermal input. However, the interaction between electrically initiated curing and TEOS-modified geopolymer binders remains unknown. There is also a lack of information on the influence of the combination of TEOS-assisted activation and fiber reinforcement on the performance of geopolymer binders. The addition of carbon fibers (CFs) and steel fibers (SFs) may affect crack propagation, stress transfer, conductivity, and curing efficiency; however, no studies have addressed this topic [10, 11].Considering the aforementioned gaps in previous research, the aim of the present study is

to develop TEOS-modified geopolymer mortars activated by a hybrid NaOH+Na_2SiO_3+TEOS system. Special attention will be paid to the assessment of TEOS not as an external surface treatment or additive, but as a part of the alkaline activator. Moreover, carbon and steel fibers will be incorporated to investigate their influence on mechanical behavior under different curing environments. Comparison of ambient, thermal, and electric curing will allow assessing the efficiency of such curing conditions in terms of strength development and matrix densification. Compressive strength, flexural strength, splitting tensile strength, and ultrasonic pulse velocity (UPV) tests will be carried out. Thus, the present research will make a contribution to a limited body of literature on TEOS-assisted geopolymerization and will reveal the influence of activator chemistry, reinforcement, and curing conditions on the performance of high-performance geopolymer mortars. The scope of the study was limited to a geopolymer mortar with a binder composed of 75 wt.% GBFS and 25 wt.% FA activated by an 8 M NaOH+Na_2SiO_3+TEOS system. Mechanical performance was investigated up to 28 days using compressive, flexural, splitting tensile, and UPV tests. Investigations into long-term durability, shrinkage, permeability, and microstructure were outside the scope of this research and may be the subject of future studies.

2 Materials and Methods

2.1 Materials

The geopolymer mortars that have been mixed in the current study have been synthesized by combining aluminosilicate precursors, which have included ground granulated blast furnace slag (GBFS), acquired from Oyak Cement (İstanbul, Türkiye), and class F fly ash (FA), obtained from the Catalagzı Thermal Power Plant (Zonguldak, Türkiye). The mixing ratio included 75 wt.% GBFS and 25 wt.% FA, with natural river sand as the fine aggregate *(Table 1).* Chemical activation was performed by means of the alkaline liquid activator, including an 8 M solution of analytical grade sodium hydroxide pellets (99 % purity, AS Kimya, İstanbul, Türkiye) and commercially available sodium silicate solution (AS Kimya, İstanbul, Türkiye) with approximate silica and soda content of 27.2% and 8.2%, respectively. To facilitate additional silica supply, tetraethyl orthosilicate (TEOS) has been added to the activator mixture. Therefore, the composition of the activator mixture was constituted with approximately 58.7% of sodium silicate solution, 27.0% of sodium hydroxide solution, and 14.3% of TEOS in terms of the total activator weight. TEOS used for experimental work has been the commercial oligomerization-grade tetraethyl orthosilicate (Dynasylan 40®, Degussa-Evonik), with a degree of polymerization of about 4. In order to increase the reactivity of silica and ensure the formation of a more continuous geopolymeric structure, hydrophobic amorphous silica nanoparticles with functionality of 1,1,1-trimethyl-N-(trimethylsilyl)silanamine (Aeroxide LE1®, Degussa-Evonik), with the average particle size of about 14 nm, have been added to the TEOS-containing activator mixture. Nanoparticles have been used to refine the microstructure, improve gel structure, and reduce porosity by increasing matrix density. The mechanical reinforcement of composite materials was achieved by applying different types of fibers, characterized by distinctive geometry and physical properties. Hooked end steel fibers (SF) with a length of 35 mm were used to increase crack-arresting and load-carrying capability after crack formation *(Table 2).* Chopped carbon fibers (CF) (SIGRAFIL®, SGL Carbon, Wiesbaden, Germany) with the same length of 35 mm and density of 1.80 g/cm³ were applied to increase tensile strength and provide stress transfer through the matrix *(Table 3).*

Table 1. Chemical composition of materials.

Material	SiO_2	Al_2O_3	Fe_2O_3	TiO_2	CaO	MgO	K_2O	Na_2O	LOI	MnO
GBFS	40.55	12.83	1.10	0.75	35.58	5.87	0.68	0.79	0.03	-
FA	58.75	25.24	5.76	-	1.46	2.22	-	0.60	0.015	-

Table 2. Physical properties of steel fiber.

Type of Fiber	Length (mm)	Diameter (mm)	Tensile Strength (MPa)	Specific Gravity	Density (g/cm^3)
SF	35	0.17	2100	7.85	1.3

Table 3. Properties of carbon fiber.

Parameters	Unit	C6-47/240-T130
Filament diameter	μm	7
Tensile strength	GPa	4
Elasticity modulus	GPa	240
Elongation	%	1.7
Single-filament resistance	Ω	15

2.2 Optimization of the Alkaline Activation System

Prior to the experimental program, a detailed optimization analysis was conducted to determine the optimal parameter combination required to activate the GBFS-FA geopolymer mortar system. A number of trial mixtures, referred to as B2-B10, were prepared to examine the impact of the activator composition, precursor proportions, mixing procedure, TEOS addition, and curing regime on both fresh-state properties and mechanical performance of mixtures. Initial mixtures were designed using a balanced binder composition, whereas the activator contained a rather low content of NaOH and Na_2SiO_3. TEOS was added to the mixture within the predefined concentration range to assess its effect on reaction rate, gel formation, and microstructure improvement. Initial formulations, designed with an activator/binder mass ratio of 0.45, showed poor workability, and hence the mixture preparation was complicated. To improve the rheological properties, an additional amount of water was added, resulting in an activator/binder ratio of 0.70. Even though this change led to successful specimen preparation, the mechanical properties of the mixtures were still unacceptable. The reason was that the level of activation did not provide a sufficient rate of geopolymerization reaction. Therefore, the chemical composition of the activator was successively varied, especially in B3 and B4 mixtures, due to the increase in the content of NaOH and Na_2SiO_3. As a result, precursor dissolution improved, and the reaction rate increased significantly. During the optimization process, TEOS was not used as an individual additive; instead, its effect was investigated alongside the impact of activator chemistry on the reaction. Further modifications were performed in the series of B5-B8 mixtures due to the variation of activator composition and precursor proportions in order to investigate TEOS behavior in different chemical environments. More significant changes were introduced starting with the B9 series mixtures; however, their mechanical performance proved rather poor, and they were therefore rejected for further investigation. In addition to variations in chemical composition, the effects of different curing regimes were also studied. Elevated-temperature curing was shown to significantly increase the reaction rate and improve strength development at early ages. Hence, some mixtures were cured at approximately 70°C for 48 hours and then stored at room temperature (25 °C). Evaluation of workability, strength development, processability, and curing effect revealed that the system's performance cannot be attributed solely to the use of TEOS. Instead, the most appropriate results were obtained from the combination of optimal values for activator chemistry, precursor composition, mixing procedure, and curing regime. The most balanced mixture, which showed the best results, was the B4 mixture, and it was chosen as the reference system for further investigations *(Table 4).*

Table 4. Preliminary optimization mixtures, processing modifications and compressive strengths.

Mix ID	GBFS (g)	FA (g)	NaOH (g, 8 M)	Na_2CO_3 (g)	Na_2SiO_3 (g)	TEOS (g)	Sand (g)	Key Modification / Observation	Compressive Strength (MPa) (7d)	Compressive Strength (MPa) (28d)
B2	225.0	–	27.0	–	49.5	22.5	562.5	Initial activator-to-binder ratio was 0.45; due to insufficient workability, 50 g of distilled water was added, increasing the ratio to approximately 0.70. No additional water was used in subsequent mixtures because of the low strength obtained.	–	–
B3	225.0	–	35.0	–	65.0	57.5	562.5	Increased activator content compared with B2.	4.88, 6.85 (equipment malfunction); later average: 11.90	13.45
B4	225.0	–	42.5	–	92.5	22.5	562.5	Cured at 70°C for 48 h and subsequently stored under moist conditions at 25°C until testing; TEOS was not added dropwise.	15.00, 17.50	18.43
B5	225.0	–	38.25	4.25	92.5	22.5	562.5	Na_2CO_3 was dissolved in a small amount of water and incorporated into the activator under magnetic stirring.	39.96, 44.12	53.05
B6	225.0	–	41.25	–	82.5	22.5	562.5	Trial mixture prepared with an activator-to-binder ratio of 0.65.	37.91, 45.13	40.24
B7	225.0	–	45.0	–	90.0	22.5	562.5	Mixing continued for 60–90 min until a noticeable viscosity change occurred; sand was added afterward.	26.00, 25.73	21.35
B8	225.0	–	45.0	–	90.0	22.5	562.5	4.5 g nano-SiO_2 was incorporated instead of Na_2CO_3.	24.51, 26.83	19.90
B9	157.5	67.5	45.0	–	90.0	22.5	562.5	GBFS, FA, and sand were first homogenized; TEOS was introduced dropwise while NaOH and Na_2SiO_3 were continuously stirred.	33.20, 35.23	20.43
B10	157.5	67.5	38.25	4.25	92.5	22.5	562.5	TEOS incorporated through controlled dropwise addition.	18.22, 22.88	26.21
B4-2	–	–	–	–	–	–	–	**Repeated B4 formulation for verification purposes.**	**35.45, 36.00**	–

***Note:** The preliminary optimization program was designed to evaluate the influence of activator composition, TEOS incorporation strategy, precursor type, supplementary additives, and curing methodology on strength development. Among the investigated formulations, B5 exhibited the highest 28-day compressive strength (53.05 MPa) within the primary optimization series. The results further demonstrated that controlled TEOS addition, precursor selection, and activator chemistry substantially affected geopolymerization efficiency and mechanical performance.

2.3 Mix Design

All geopolymer mortars tested in this work were prepared according to the optimized mix design developed in the preliminary investigation stage. The geopolymer binder was composed of 75 wt.% GBFS and 25 wt.% FA, while NS was used as the fine aggregate material with the S/B ratio of 2.5. The activator-to-binder (A/B) ratio was set at 0.75. As an alkaline activator, the NaOH+Na_2SiO_3+TEOS solution was utilized with an approximate molar ratio of 2.17:1:0.53, respectively. NaOH concentration was always equal to 8 M in all mixtures. Since the activity of TEOS depends heavily on its hydrolysis and dispersion in the activating solution, special attention was paid to the procedure for its preparation. In contrast to approaches involving pre-hydrolysis, ultrasonic treatment, vacuum-assisted dispersion, or the TEOS nanosilica-assisted hybrid technique, a practical, scalable procedure was employed. The adopted procedure is the same as CU3-TEOS in *Table 5,* except that TEOS is added dropwise to the alkaline solution. To perform the selected method, TEOS was first poured into a plastic cylinder with a diameter of approximately 5 cm and a height of 100 cm, fitted with an outlet valve. Another cylindrical container with a diameter of approximately 15 cm and a height of

100 cm was placed below the upper container and filled with the previously prepared NaOH+Na_2SiO_3 solution. NaOH solutions were prepared 4–5 days in advance and stored under laboratory conditions until use. Then, the NaOH and Na_2SiO_3 solutions were mixed to obtain the alkaline solution. Further, TEOS was dripped from the upper cylinder into the alkaline solution under magnetic stirring for 6–7 h. To avoid any undesirable influence of moisture and CO_2 from the atmosphere, both cylinders were sealed with nylon stretch film during the dripping and stirring procedures. Once the activator solution was prepared, the solid materials were mechanically mixed for approximately 2–3 min. The prepared activator solution was added, and mixing was continued for 4–5 min to achieve better wetting and particle interaction. After that, the mixture was rested for approximately 60–90 min to allow the initiation of reaction processes and the development of the initial geopolymer gel. Fine aggregate was added to the mixture after the maturation period, and final mixing was performed for approximately 2–3 min. The described optimal procedure has been applied to all subsequent mixes to achieve an optimal balance between processability and mechanical characteristics. *Table 6* shows the quantities of ingredients and obtained results of geopolymer mortars containing 0.50 vol.% CF prepared at various reactant-to-binder ratios for the casting volume of 250 cm^3 (two 50 mm cube specimens).

Table 5. TEOS-based geopolymer mortars containing 50 wt.% GBFS and 50 wt.% FA.

Series Code	Distinguishing Feature	Sol–Gel Preparation	Activator System	EtOH/H_2O Ratio	Mixing Method	Additives	Curing Regime	Expected Effect
CU1-TEOS-Ref	Reference TEOS formulation	TEOS + EtOH (60°C, 30 min) + HNO_3 + H_2O	Direct 10 M NaOH activation	1/1	Magnetic stirring	None	80°C for 24 h	Limited reaction development; benchmark mixture
CU3-TEOS-Drip	Controlled dropwise NaOH addition	Same procedure as CU1	8 M NaOH introduced gradually	1/3	Vacuum-assisted and magnetic mixing	None	60°C for 48 h followed by ambient curing	Balanced gel formation and controlled reaction progression
CU5-TEOS-HighSi	High-silica-content formulation	Sol–gel synthesis with 5% Na_2SiO_3 incorporation	10 M NaOH	1/1	Homogenization	Na_2SiO_3	80°C for 24 h	Improved Si/Al balance and network development

Table 6. Mixture proportions and compressive strengths of geopolymer mortars incorporating 0.50 vol.% CF at different A/B ratios (250 cm^3 batch volume).

Component	A/B Ratio = 1.10	A/B Ratio = 0.90	A/B Ratio = 0.75
Binder (g)	130.21	130.21	130.21
GBFS (75 wt.%) (g)	97.66	97.66	97.66
FA (25 wt.%) (g)	32.55	32.55	32.55
Activator (g)	143.23	117.19	97.66
8 M NaOH (27 wt.%) (g)	38.67	31.64	26.37
Na_2SiO_3 (58.7 wt.%) (g)	84.08	68.79	57.32
TEOS (14.3 wt.%) (g)	20.48	16.76	13.96
NS (B/S= 1:2.5) (g)	325.52	325.52	325.52
CF (1.80 g/cm^3, 0.50 vol.%) (g)	2.25	2.25	2.25
Compressive Strength after 48 h of Curing at 70°C (MPa)	14.78	16.12	21.73

***Note:** Among the investigated formulations, the highest compressive strength was achieved at an activator-to-binder ratio of 0.75, reaching 21.73 MPa after 48 h of curing at 70°C. Accordingly, this ratio was selected for all subsequent phases of the experimental program due to its superior mechanical performance.

2.4. Methods

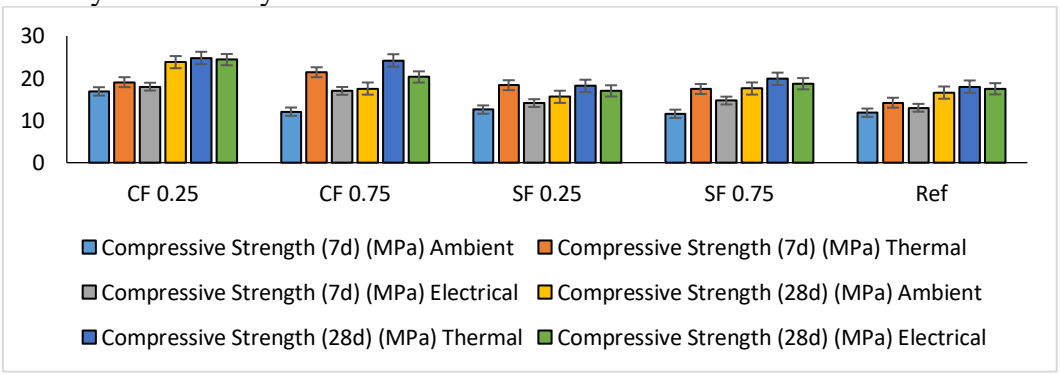
Fresh geopolymer mortars were cast into 40 × 40 × 160 mm steel prism molds and compacted on a vibrating table. After demolding, the specimens were subjected to ambient curing, thermal

curing at 70 °C for 48 h, or electrical curing, and then stored under laboratory conditions until testing at 7 and 28 days. Flexural and compressive strength tests were conducted in accordance with EN 196-1. Flexural strength was first determined by a three-point bending test on 40 × 40 × 160 mm prism specimens, after which the two fractured halves of each prism were immediately used for compressive strength measurements. The reported values represent the average of three specimens for each mixture.

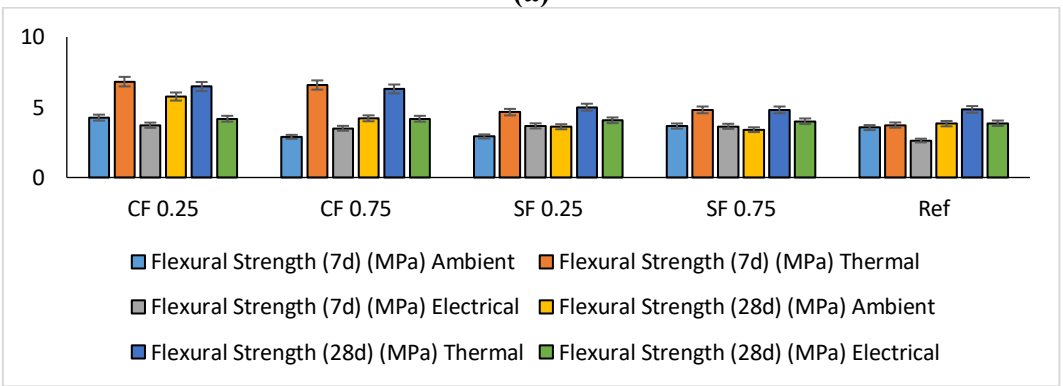
3 Results and Discussions

As shown in *Fig. 1,* the usage of TEOS significantly altered the performance characteristics of GBFS–FA-based geopolymer mortars under all curing conditions. Apart from being a source of silicon, TEOS acted as a structural modifier, leading to densification of the geopolymer gel, pore refinement, and a denser matrix due to enhanced interfacial interactions between the binder and the reinforcing additives. Therefore, mortar mixtures with CFs and SFs outperformed the reference samples in terms of compressive, flexural, and splitting tensile strengths, as well as UPV. Under the influence of alkalinity, the formation of Si–O–Si and Si–O–Al bonds led to a denser microstructure and lower internal discontinuities, resulting in more efficient stress transfer within the geopolymer composite. Thus, the reference sample had compressive strengths of 11.83 MPa, 14.20 MPa, and 13.00 MPa under ambient, thermal, and electrical curing, respectively; however, significantly higher strengths were observed in some TEOS-assisted mixtures. Among them, CF 0.25 could be referred to as one of the most effective samples, since its compressive strengths were 16.88 MPa under ambient curing, 19.07 MPa under thermal curing, and 18.00 MPa under electrical curing, resulting in 42.7%, 34.3%, and 38.5% improvements, respectively, in comparison to the reference specimens. It can be seen that TEOS successfully enhances the reaction leading to the formation of geopolymer products responsible for strength development. This trend is even more visible on day 28, when compressive strengths were 23.81 MPa, 24.80 MPa, and 24.40 MPa for ambient, thermal, and electrical curing, respectively, which was more than 43.5%, 37.8%, and 39.4% greater than the reference value of 16.59 MPa. As can be concluded from the results, the improvement remains significant at later ages, and it is caused by the participation of silica species derived from TEOS in further matrix densification, via filling residual microvoids and the development of the geopolymer network. The same effect was observed in tensile parameters. The splitting tensile strengths of 1.31 MPa, 2.08 MPa, and 1.80 MPa were achieved with CF 0.25 under ambient, thermal, and electrical curing, resulting in improvements of 5.6%, 56.4%, and 38.5%, respectively, compared with the reference value of 1.24 MPa. The fiber–matrix interface strength is increased, enabling better crack bridging and stress redistribution by CFs. Also, UPVs showed that a more homogeneous internal structure developed, as CF 0.25 had UPVs of 2731 m/s under ambient curing, 2830 m/s under thermal curing, and 2582 m/s under electrical curing, all greater than the reference value of 2473 m/s. Moreover, the improvement of the flexural properties was also observed, since CF 0.25 had flexural strengths of 5.76 MPa, 6.47 MPa, and 4.18 MPa, which resulted in the improvements of 50.4%, 33.6%, and 8.3%, respectively, in comparison to the control sample. The further increase in the CF content to 0.75% led to a quite different response, especially regarding the tensile properties. Under ambient curing, a splitting tensile strength of 2.71 MPa, 118% greater than that of the control sample and one of the highest values obtained during the experiment, was achieved. Under thermal and electrical curing, values of 2.45 MPa and 2.36 MPa, representing improvements of 84% and 81.5%, respectively, were observed. However, the improvement in compressive strength in this case was comparatively low, with values of 17.55 MPa, 24.22 MPa, and 20.30 MPa under ambient, thermal, and electrical curing, respectively. This can be explained by the fact that, along with increased crack-arresting efficiency, fiber clustering reduces the mixture's ability to carry compressive loads. The flexural strengths were 4.21 MPa, 6.30 MPa, and 4.18

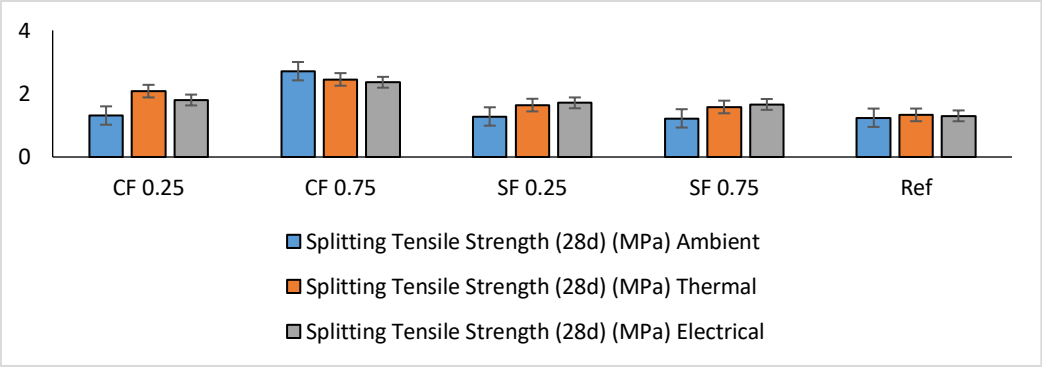
MPa under ambient, thermal, and electrical curing, respectively, while the UPV of 2808 m/s under thermal curing confirmed the efficiency of TEOS-assisted CF reinforcement in improving the internal structure and crack arrest. In turn, SF-containing formulations showed a more balanced relationship between increased stiffness and crack arrest efficiency. So, although the SF 0.25 sample did not exceed the reference sample in compressive resistance under ambient curing and had a value of 15.60 MPa, which was about 6% less than the reference value, its performance under thermal and electrical curing was quite good, since its strengths were 18.18 MPa and 17.00 MPa, respectively. Much more important is the influence of SFs on the tensile parameters, as the splitting tensile strengths of 1.28 MPa, 1.64 MPa, and 1.71 MPa under ambient, thermal, and electrical curing, respectively, were 3%, 23%, and 31.5% higher than the reference value. This trend shows that SFs successfully prevent microcrack coalescence and delay their propagation, thereby improving crack resistance without a dramatic increase in compressive properties. This conclusion is supported by the fact that the UPV of 2658 m/s under thermal curing was more than 1.3% greater than the reference value, showing that the internal structure was relatively dense and continuous. Also, the flexural performance of 5.00 MPa under thermal curing was 3% greater than that of the control sample. The SF 0.75 mixture demonstrated optimal performance under thermal curing, with a compressive strength of 19.86 MPa, an improvement of 10.3% over the control sample. A favorable response was also observed under electrical curing, as it produced a compressive strength of 18.70 MPa and an improvement of 6.8%. Furthermore, the splitting tensile strength of 1.66 MPa under electrical curing was 27.7% greater than the reference value, while the flexural strength of 4.81 MPa under thermal curing was very close to the reference level. Overall, SFs primarily improve crack stability and ductility.



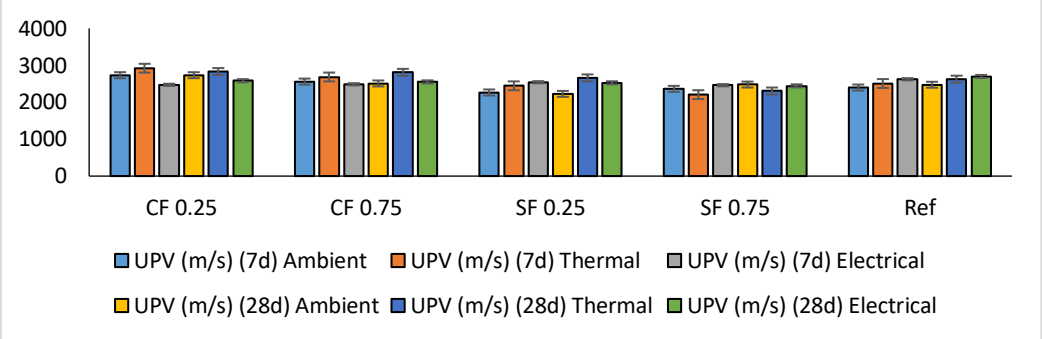
(a)



(b)



(c)



(d)

Fig. 1. Comparison of the mechanical and physical properties of TEOS-modified fiber-reinforced geopolymer mortars under different curing regimes: (a) compressive strength, (b) flexural strength, (c) splitting tensile strength, and (d) UPV at 7 and 28 days.

4 Conclusions

- The optimum A/B ratio was determined as 0.75, yielding a compressive strength of 21.73 MPa after 48 h of curing at 70°C.
- Among the initial optimization mixes, the B5 mix had the highest compressive strength of 28 days, which was 53.05 MPa.
- The highest splitting tensile strength in the experiment was 2.71 MPa in the CF 0.75 mix under ambient conditions, which was an enhancement of about 118% compared to the control sample.
- The maximum flexural strength of 6.47 MPa was exhibited by the CF 0.25 mix under oven curing condition, whereas its enhancement relative to the control sample was about 33.6%.
- The compressive strengths of the SF reinforced geopolymer mortar were found to be 19.86 MPa, and splitting tensile strengths were 1.71 MPa.
- SF-reinforced geopolymer mortars reached compressive strengths up to 19.86 MPa and splitting tensile strengths up to 1.71 MPa, depending on curing condition and fiber dosage.

Acknowledgments

The authors gratefully acknowledge the financial support provided by the Scientific and Technological Research Council of Türkiye (TÜBİTAK) under Project No. 123M470.

References

1. Barberena-Fernández, A.M., Carmona-Quiroga, P.M., Blanco-Varela, M.T.: Interaction of TEOS with cementitious materials: Chemical and physical effects. Cement & Concrete Composites 55, 145–152 (2015).

2. Kou, C., Zhang, M., Kang, A., Chen, Z., Hu, H.: Physical and microstructural properties of recycled concrete aggregates treated by tetraethyl orthosilicate. Construction and Building Materials 344, 128246 (2022).
3. Qiu, P., Sakai, Y., Tamura, Y., Ogiwara, N., Uchida, S.: Direct synthesis of construction material from low-quality sand. Construction and Building Materials 392, 131906 (2023).
4. Johnson, E., Worrall, F.: Chemical pore closure of zeolite A using tetraethyl orthosilicate (TEOS): A potential method for enhancing the use of zeolites as part of a long-term waste immobilization strategy. Journal of Hazardous Materials 108(1–2), 55–65 (2004).
5. Altube, A., Autric, M., Gervasi, C.A., Di Sarli, A.R., Vilche, J.R.: Influence of deposition conditions on the protective behavior of tetraethyl orthosilicate (TEOS) sol–gel films on AA5754 aluminum alloy. Progress in Organic Coatings 73(1), 35–42 (2012).
6. Kucuk, A.Ç., Demirkal, E.: Sol-jel yöntemi ile zirkonyum fosfat ve poli(etilen oksit) temelli polimer kompozit malzeme (ZrP/PEO) sentezi ve karakterizasyonu. Sakarya University Journal of Science 22(2), 748–754 (2018).
7. Bian, G., Qi, L., Liu, J., Wang, X., Xu, X., Wang, Z.: Effects of tetraethyl orthosilicate on rheological behaviors of crumb rubber modified asphalt. Construction and Building Materials 325, 126807 (2022).
8. Barberena-Fernández, A.M., Blanco-Varela, M.T., Carmona-Quiroga, P.M.: Use of nanosilica- or nanolime-additioned TEOS to consolidate cementitious materials in heritage structures: Physical and mechanical properties of mortars. Cement and Concrete Composites 95, 271–276 (2019).
9. dos Reis, G.S., Lima, E.C., Sampaio, C.H., Rodembusch, F.S., Petter, C.O., Cazacliu, B.G., Dotto, G.L., Hidalgo, G.E.N.: Novel kaolin/polysiloxane based organic–inorganic hybrid materials: Sol–gel synthesis, characterization and photocatalytic properties. Journal of Solid State Chemistry 260, 106–116 (2018).
10. Fukumoto, S., Makimoto, K., Ohta, K., Nakamura, T., Matsushima, M., Fujimoto, K.: Change in electrical conductivity of electrically conductive adhesives during curing process. Journal of Materials Science 57(24), 11189–11201 (2022).
11. Krishna, S.R.S., Mishra, J., Meher, S., Das, S.K., Mustakim, S.M., Singh, S.K.: Investigation of the electrical properties of graphene-reinforced geopolymer composites. Materials Proceedings 13(1), 34 (2023).

Author Contribution Statement

Conceptualization: Beyza AYGUN, Mucteba UYSAL, Turgay COSGUN, Turhan BILIR
Methodology: Beyza AYGUN, Mucteba UYSAL, Turgay COSGUN, Turhan BILIR
Investigation: Beyza AYGUN, Mucteba UYSAL, Turgay COSGUN, Turhan BILIR
Writing – Original Draft: Beyza AYGUN
Writing – Review & Editing: Beyza AYGUN

List of Abbreviations

- **CF** — Carbon Fiber
- **FA** — Class F Fly Ash
- **GBFS** — Ground Granulated Blast Furnace Slag
- **NS** — Natural Sand
- **SF** — Steel Fiber
- **TEOS** — Tetraethyl Orthosilicate

Note: Following the conference, this Publication Note will be added to each paper; therefore, authors are kindly requested not to remove the note below and to complete the author(s) and paper title information.

Publication Note

This paper was peer-reviewed, accepted for presentation, and included in the proceedings of the ACE2026 – International Conference on Advances in Civil Engineering, held on 12–14 October 2026 in Trabzon, Türkiye.

This paper may be cited as follows:

Aygun, B., Uysal, M., Cosgun, T., Bilir, T., "Tetraethyl Orthosilicate-Based Fiber-Reinforced Geopolymer Mortars under Comparative Evaluation of Different Curing Methods," in Proceedings of the ACE2026 – International Conference on Advances in Civil Engineering, Trabzon, Türkiye, 12–14 October 2026.

Durability Performance of TEOS-Modified Fiber-Reinforced Geopolymer Mortars under High Temperature Effects

Beyza AYGUN[1*], Mucteba UYSAL[2], Turgay COSGUN[3], Turhan BILIR[3]

[1] 0000-0002-1317-9148, Istanbul Okan University, Vocational School, Istanbul, Türkiye, beyza.aygun@okan.edu.tr
[2] 0000-0002-6827-9904 , Yıldız Technical University, Civil Engineering Department, Istanbul, Türkiye, mucteba@yildiz.edu.tr
[3] 0000-0002-5417-9312, Istanbul University-Cerrahpasa, Civil Engineering Department, Istanbul, Türkiye, costur@iuc.edu.tr
[4] 0000-0003-0317-026X, Istanbul University-Cerrahpasa, Civil Engineering Department, Istanbul, Türkiye, tbilir@iuc.edu.tr

Abstract. Tetraethyl orthosilicate (TEOS) plays a crucial role in geopolymer systems by acting as a highly reactive silica source. It enhances gel connectivity, reduces pore size, and improves microstructural stability. In this study, TEOS-modified fiber-reinforced geopolymer mortars (GMs) were produced using 100% GBFS and a 75:25 GBFS–Class F fly ash (FA) mixture activated with a hybrid alkaline solution composed of sodium silicate (57.8%), sodium hydroxide (28.9%). and TEOS (13.3%), with an activator-to-binder (A/B) ratio of 0.7. Carbon (CF) and steel (SF) were incorporated at volumetric ratios of 0.25% and 0.75%. Based on mechanical performance results obtained at 7 and 28 days, selected mixtures were subjected to durability evaluations, including high-temperature exposure tests (200, 400, 600, and 800 °C). The degradation mechanisms were assessed through changes in residual strengths and ultrasonic pulse velocity (UPV). The findings revealed that TEOS significantly improved thermal stability by enhancing matrix integrity and limiting microcrack formation. Fiber reinforcement played a critical role in bridging cracks and maintaining load-bearing capacity under elevated temperatures, while also substantially reducing surface wear under abrasive conditions. Particularly at higher fiber contents, specimens exhibited lower strength loss and improved resistance to thermal and mechanical degradation. Overall, the combined effect of TEOS modification and fiber reinforcement resulted in geopolymer mortars with superior durability performance. highlighting their strong potential for use in aggressive service environments, this approach presents a highly promising avenue for the development of advanced geopolymer composites.

Keywords: Geopolymer; Tetraethyl orthosilicate; Electrical curing; Durability properties.

1 Introduction

Recently, Tetraethyl orthosilicate (TEOS), also known as tetraethoxysilane/ethyl silicate, has received considerable attention for its high efficiency in improving the microstructural stability and durability of inorganic building materials. The silicon alkoxide having the formula $Si(OC_2H_5)_4$, TEOS, undergoes hydrolysis in contact with moisture, producing silanol (Si–OH) groups that subsequently condense, giving rise to the complex siloxane (Si–O–Si) network. Unlike typical mineral admixtures containing silica, which mostly act as fillers, TEOS participates in chemical reactions, helping to form additional silica structures and refine the pore structure. Thanks to its low viscosity and chemical and thermal stability, TEOS can be easily incorporated into porous matrices and used in aggressive environments that require

durable materials. Therefore, TEOS became one of the key sol–gel precursors and efficient modifiers for advanced cementitious and geopolymeric materials. The efficiency of TEOS has been demonstrated in many engineering applications, including cultural heritage preservation and advanced composite materials. Thus, in stone conservation, TEOS is widely used as a consolidant due to its high penetration and ability to increase cohesion in deteriorated porous materials. Johnson and Worrall [1] have demonstrated that TEOS efficiently seals the zeolite pore structure, reducing pore connectivity and improving resistance to physical deterioration. Likewise, Altube et al. [2] studied TEOS-based sol-gel coatings applied to aluminum alloys and demonstrated that proper control of TEOS hydrolysis results in significantly greater corrosion resistance than traditional coating methods. Furthermore, in another study, Kucuk and Demirkal [3] have produced zirconium phosphate/polyethylene oxide composites from TEOS as a starting material using the sol–gel method, thus obtaining materials with excellent thermal stability up to 300 °C and good water retention properties. Similarly, Bian et al. [4] demonstrated that TEOS improves the rheological and physical properties, as well as the high-temperature stability, of crumb rubber-modified asphalt; however, excessive TEOS reduces fatigue resistance. All these studies demonstrate that TEOS is much more than a silica source – it is a powerful microstructural engineer, improving not only mechanical properties but also durability. In cement-based materials, TEOS has mostly been studied as a surface treatment or consolidant rather than a binder component. For example, Barberena-Fernández et al. [5] demonstrated that combining TEOS with nano-lime or nano-silica significantly decreases porosity while increasing compressive and flexural strengths, water repellency, and surface integrity in Portland cement (PC) mortars.

Geopolymers are among the most promising alternatives to ordinary Portland cement (OPC) due to their much lower carbon emissions, higher chemical resistance, and improved mechanical properties. Geopolymerization does not involve hydration; rather, it involves the dissolution of aluminosilicates in a very alkaline environment, followed by polycondensation, producing three-dimensional aluminosilicate gel networks. GBFS and Class F fly ash (FA) are the most commonly used geopolymer precursors due to complementary chemical composition. GBFS acts as a source of reactive calcium, forming C-(A)-S-H gels that promote rapid strength development, while FA provides aluminosilicates that contribute to N-A-S-H gel formation, thereby providing durability and chemical resistance. Hence, GBFS-FA geopolymer systems provide an optimal balance between early-age strength and durability, enabling the simultaneous use of waste materials. Despite significant progress in geopolymer science and technology over the past two decades, most research has focused on optimizing precursor composition, activator concentration, and curing conditions to improve composite material performance. Relatively few studies have considered the modification of activator chemistry using reactive organosilicon compounds such as TEOS. The number of existing studies on the usage of TEOS in geopolymer compositions has been quite limited so far, and all have been focused on the synthesis of hybrid organic-inorganic materials without considering their application in structural geopolymer mortars. For example, dos Reis et al. [6] synthesized hybrid geopolymeric materials based on kaolinite using TEOS; however, this research did not include structural mortar applications or durability assessment. Thus, the effects of TEOS on the kinetics of geopolymerization, gel network formation, pore refinement, thermal stability and engineering performance should be investigated in more detail. The curing method is another influential parameter that affects the performance of geopolymer-based materials. Ambient, thermal, and water curing have been used to date to facilitate geopolymerization. High-temperature curing can accelerate dissolution and condensation processes, thus facilitating fast strength development and denser microstructure formation. Nonetheless, the traditional oven-curing method involves heat transfer from the surface to the interior of the sample, resulting in a thermal gradient and microcracking due to differential shrinkage.

Recently, electrical curing has been proposed as an alternative to facilitate geopolymerization by generating heat within the sample via Joule heating. This method allows achieving a more uniform temperature distribution, a shorter curing time, lower energy consumption, and improved efficiency of the geopolymerization process. Recent studies by Cai et al. [7], Aygun et al. [8], and Ekmekci [9] have shown that the use of conductive fillers can significantly increase the effectiveness of electrical curing by improving the electrical conductivity of the geopolymer matrix. To achieve both conductivity and increased crack resistance, some conductive reinforcements have recently been introduced into geopolymer-based compositions. Carbon fibers (CFs) possess high tensile strength and excellent electrical conductivity; steel fibers (SFs) can provide crack bridging ability and increased post-cracking toughness. It has been demonstrated that these conductive materials can significantly enhance the efficiency of early-age geopolymerization, mechanical properties, and electrical conductivity. However, there is almost no information on the interactions between these conductive materials and TEOS-modified alkaline activator systems, especially their durability under harsh environmental conditions.

Durability has become one of the key requirements for geopolymer construction materials, as structural elements are exposed to various deteriorating factors, such as high temperatures, wear, freezing-thawing and chemical corrosion, during their lifetime. Among these deteriorating agents, high-temperature exposure plays an important role, as the dehydration of geopolymer gels, thermal incompatibility of matrix components, pore pressure, and microcracking can lead to the loss of structural integrity. Thus, testing the residual properties of geopolymer mortars after high-temperature exposure allows evaluating their applicability for fire-resistant and high-temperature structural applications. A detailed review of the literature demonstrates the important research gap. Despite the great potential of TEOS for microstructure refinement in various materials, the introduction of TEOS into hybrid activator systems for GBFS-FA geopolymer mortars has not yet been studied. In addition, the effects of TEOS modification, conductive reinforcements, and curing methods on the durability parameters, especially thermal stability, have not yet been investigated. Therefore, investigating these effects is needed to develop durable geopolymer-based composites. Thus, this study evaluates the durability performance of TEOS-modified fiber-reinforced geopolymer mortars using the hybrid activator system NaOH + Na_2SiO_3 + TEOS. CFs and SFs have been used as reinforcing materials, and the mixtures optimized for mechanical performance have been tested using the UPV and elevated-temperature exposure at 200, 400, 600, and 800 °C.

2 Materials and Methods

2.1 Materials

Geopolymer mortars in the current research were produced through the synthesis of a blended aluminosilicate precursor system based on granulated blast-furnace slag (GBFS) obtained from Oyak Cement (İstanbul, Turkey) and class F fly ash (FA) from Catalagzı Thermal Power Plant (Zonguldak, Turkey). A precursor mixture in the form of a dry powder was prepared in a composition containing 75 wt.% GBFS and 25 wt.% FA ratios. Natural river sand was used as the fine aggregate material *(Table 1).* Geopolymer synthesis was achieved by chemical activation of aluminosilicate precursors with an aqueous solution of sodium hydroxide pellets (99%, AS Kimya, Istanbul, Turkey) dissolved in distilled water, yielding an 8 M NaOH solution. and a commercial sodium silicate solution (AS Kimya, Istanbul, Turkey) having 27.2% SiO_2 and 8.2% Na_2O. Additionally. tetraethyl orthosilicate (TEOS) was added to the activator mixture to serve as a silica source and to ensure proper reaction conditions for geopolymer synthesis. An activator solution with 58.7% sodium silicate. 27.0% sodium hydroxide and 14.3% TEOS by weight was received. All TEOS applied in the current research was a commercial oligomeric tetraethyl orthosilicate (Dynasylan 40®. Degussa-Evonik) with

an average degree of polymerization of about 4. To enhance the reactivity of silica and to receive a more homogeneous structure. hydrophobic silica nanoparticles modified with 1.1.1-trimethyl-N-(trimethylsilyl)silanamine (Aeroxide LE1®. Degussa-Evonik) were introduced to the TEOS-containing activator mixture. The average particle size of silica nanoparticles was about 14 nm. Several types of fibers were used to provide mechanical reinforcement of geopolymer composite materials. Hooked-end SFs of 35 mm in length were used to enhance the crack arrest capability and load-bearing capacity of composite materials after cracking *(Table 2).* Chopped CFS (SIGRAFIL®. SGL Carbon. Wiesbaden. Germany) of 35 mm in length and density of 1.80 g/cm³ were applied to increase the tensile strength of composite materials and improve stress transfer *(Table 3).*

Table 1. Chemical composition of materials.

Material	SiO_2	Al_2O_3	Fe_2O_3	TiO_2	CaO	MgO	K_2O	Na_2O	LOI	MnO
GBFS	40.55	12.83	1.10	0.75	35.58	5.87	0.68	0.79	0.03	-
FA	58.75	25.24	5.76	-	1.46	2.22	-	0.60	0.015	-

Table 2. Physical properties of steel fiber.

Type of Fiber	Length (mm)	Diameter (mm)	Tensile Strength (MPa)	Specific Gravity	Density (g/cm^3)
SF	35	0.17	2100	7.85	1.3

Table 3. Properties of carbon fiber.

Parameters	Unit	C6-47/240-T130
Filament diameter	μm	7
Tensile strength	GPa	4
Elasticity modulus	GPa	240
Elongation	%	1.7
Single-filament resistance	Ω	15

2.2 Optimization of the Alkaline Activation System

Before performing the experiments, various tests were conducted to optimize the activation scheme for the GBFS-FA geopolymer mortar system. A number of experimental mixes (B2-B14) were produced in order to evaluate the joint influence of the activator chemistry, ratios of precursors, mixing scheme, TEOS addition, and curing on fresh-state properties and mechanical characteristics of mortars. Initially, the mixes were prepared using well-balanced combinations of GBFS and FA. Small amounts of NaOH and Na_2SiO_3 were used as the activation agent in the mixture. TEOS was added in a specified amount to investigate its effects on reaction rate, gel formation, and microstructure. First, the mixes with an activator/binder ratio of approximately 0.45 had poor workability, which prevented specimen preparation and compaction. Additional water was added to achieve an activator/binder ratio of 0.70. This improved the rheological properties but yielded poor engineering properties, suggesting that the activation is insufficient to intensify the geopolymerization process. Next, the activator chemistry was changed gradually by increasing the amounts of NaOH and Na_2SiO_3 in mixes B3 and B4. This improved precursor dissolution and increased reaction rate. At all the optimization steps, TEOS was never investigated independently. Instead, the effect of this additive was evaluated as part of the activator composition, considering its impact on silica supply and its contribution to condensation reactions and network formation. Mixes B5-B8 were developed with the gradual change in the ratios of the activators and precursors to evaluate the effect of TEOS under various conditions of the mixture. More significant changes in the mix composition were introduced in the B9 series; however, they had poor engineering properties and were therefore not considered further. Along with the mix investigation, the effect of curing was investigated. High-temperature curing showed good potential to accelerate

reaction rates and develop strength at early ages. That is why certain mixes were cured at 70°C for 48 hours, then stored at 25°C under laboratory conditions. It was shown that investigating workability, strength development, processability, and curing conditions cannot reveal the effect of TEOS on geopolymer mortars. In turn, optimal results were obtained by optimizing the activator ratio, precursor ratios, mixing, and curing. As a result of the analysis, precursor ratios were identified as optimal and chosen as the reference material for further experiments *(Table 4).*

Table 4. Preliminary optimization mixtures, processing modifications and compressive strengths.

Mix ID	GBFS (g)	FA (g)	NaOH (g, 8 M)	Na_2CO_3 (g)	Na_2SiO_3 (g)	TEOS (g)	Sand (g)	Key Modification / Observation	Compressive Strength (MPa) (7d)	Compressive Strength (MPa) (28d)
B2	225.0	–	27.0	–	49.5	22.5	562.5	Initial activator-to-binder ratio was 0.45; due to insufficient workability, 50 g of distilled water was added, increasing the ratio to approximately 0.70. No additional water was used in subsequent mixtures because of the low strength obtained.	–	–
B3	225.0	–	35.0	–	65.0	57.5	562.5	Increased activator content compared with B2.	4.88, 6.85 (equipment malfunction); later average: 11.90	13.45
B4	225.0	–	42.5	–	92.5	22.5	562.5	Cured at 70°C for 48 h and subsequently stored under moist conditions at 25°C until testing; TEOS was not added dropwise.	15.00, 17.50	18.43
B5	225.0	–	38.25	4.25	92.5	22.5	562.5	Na_2CO_3 was dissolved in a small amount of water and incorporated into the activator under magnetic stirring.	39.96, 44.12	53.05
B6	225.0	–	41.25	–	82.5	22.5	562.5	Trial mixture prepared with an activator-to-binder ratio of 0.65.	37.91, 45.13	40.24
B7	225.0	–	45.0	–	90.0	22.5	562.5	Mixing continued for 60–90 min until a noticeable viscosity change occurred; sand was added afterward.	26.00, 25.73	21.35
B8	225.0	–	45.0	–	90.0	22.5	562.5	4.5 g nano-SiO_2 was incorporated instead of Na_2CO_3.	24.51, 26.83	19.90
B9	157.5	67.5	45.0	–	90.0	22.5	562.5	GBFS, FA, and sand were first homogenized; TEOS was introduced dropwise while NaOH and Na_2SiO_3 were continuously stirred.	33.20, 35.23	20.43
B10	157.5	67.5	38.25	4.25	92.5	22.5	562.5	TEOS incorporated through controlled dropwise addition.	18.22, 22.88	26.21
B4-2	–	–	–	–	–	–	–	**Repeated B4 formulation for verification purposes.**	**35.45, 36.00**	–

***Note:** The preliminary optimization program was designed to evaluate the influence of activator composition, TEOS incorporation strategy, precursor type, supplementary additives, and curing methodology on strength development. Among the investigated formulations, B5 exhibited the highest 28-day compressive strength (53.05 MPa) within the primary optimization series. The results further demonstrated that controlled TEOS addition, precursor selection, and activator chemistry substantially affected geopolymerization efficiency and mechanical performance.

2.3 Mix Design

All geopolymer mortars examined in the current research were fabricated using a recipe optimized during the preliminary tests. In particular, the geopolymer binder consisted of 75 wt.% GBFS and 25 wt.% FA. The fine aggregate (natural sand – NS) was added with S/B = 2.5. Throughout the experimental campaign, the A/B value remained 0.75. As for the alkaline

activator, it consisted of NaOH, Na_2SiO_3, and TEOS in the mass proportions of 2.17:1:0.53, respectively. All examined mortars were fabricated by applying a constant 8 M NaOH solution. As mentioned earlier, the activity of TEOS largely depends on the hydrolysis and dispersion properties of the substance; thus, it was necessary to pay special attention to the preparation procedure of the activator. Some researchers use pre-hydrolyzed TEOS, the ultrasonic method, vacuum dispersion, or TEOS nanosilica hybridization. However, it is worth noting that TEOS was added directly to the solution in the CU3-TEOS method described in *Table 5.* First of all, TEOS was loaded into a vertical cylindrical plastic container with a diameter of 5 cm and a height of 100 cm, equipped with a controlled outlet valve; another vertical cylinder, with a diameter of 15 cm and a height of 100 cm, was placed under the first one and filled with the previously prepared NaOH + Na_2SiO_3 solution. Solutions of NaOH were prepared approximately four to five days before mixing and stored in laboratory conditions. Then the NaOH and Na_2SiO_3 solutions were mixed to prepare an alkaline solution. Afterward, TEOS was transferred from the first cylinder to the second cylinder, with simultaneous magnetic stirring to ensure controlled hydrolysis and proper dispersion of TEOS in the liquid phase. The whole process took 6-7 hours. To avoid possible influence of water vapor and carbon dioxide, both cylinders were wrapped in the nylon stretch film. After preparing the activator, the dry mixing of the solid precursors lasted 2-3 minutes. The modified activator solution was then added, and the mixing was continued for 4-5 minutes. This allowed achieving wetting and the chemical reaction between the particles. Next, the mixture was left for 60-90 minutes to start reactions and form the initial geopolymeric gels. Only after that period was the fine aggregate added, and mixing continued for 2-3 minutes. The procedure described above was used for all subsequent mixes, as it enabled achieving optimal processability and mechanical characteristics. *Table 6* presents the quantities of components and the results of geopolymer mortars with 0.50 vol.% CF fabricated at different R/B ratios, with a casting volume of 250 cm^3. This quantity of material allows the production of two specimens in the shape of 50 mm cubes.

Table 5. TEOS-based geopolymer mortars containing 50 wt.% GBFS and 50 wt.% FA.

Series Code	Distinguishing Feature	Sol–Gel Preparation	Activator System	EtOH/H_2O Ratio	Mixing Method	Additives	Curing Regime	Expected Effect
CU1-TEOS-Ref	Reference TEOS formulation	TEOS + EtOH (60°C, 30 min) + HNO_3 + H_2O	Direct 10 M NaOH activation	1/1	Magnetic stirring	None	80°C for 24 h	Limited reaction development; benchmark mixture
CU3-TEOS-Drip	Controlled dropwise NaOH addition	Same procedure as CU1	8 M NaOH introduced gradually	1/3	Vacuum-assisted and magnetic mixing	None	60°C for 48 h followed by ambient curing	Balanced gel formation and controlled reaction progression
CU5-TEOS-HighSi	High-silica-content formulation	Sol–gel synthesis with 5% Na_2SiO_3 incorporation	10 M NaOH	1/1	Homogenization	Na_2SiO_3	80°C for 24 h	Improved Si/Al balance and network development

Table 6. Mixture proportions and compressive strengths of geopolymer mortars incorporating 0.50 vol.% CF at different A/B ratios (250 cm^3 batch volume).

Component	A/B Ratio = 1.10	A/B Ratio = 0.90	A/B Ratio = 0.75
Binder (g)	130.21	130.21	130.21
GBFS (75 wt.%) (g)	97.66	97.66	97.66
FA (25 wt.%) (g)	32.55	32.55	32.55
Activator (g)	143.23	117.19	97.66
8 M NaOH (27 wt.%) (g)	38.67	31.64	26.37
Na_2SiO_3 (58.7 wt.%) (g)	84.08	68.79	57.32
TEOS (14.3 wt.%) (g)	20.48	16.76	13.96

Component	A/B Ratio = 1.10	A/B Ratio = 0.90	A/B Ratio = 0.75
NS (B/S= 1:2.5) (g)	325.52	325.52	325.52
CF (1.80 g/cm³, 0.50 vol.%) (g)	2.25	2.25	2.25
Compressive Strength after 48 h of Curing at 70°C (MPa)	14.78	16.12	21.73

***Note:** Among the investigated formulations, the highest compressive strength was achieved at an activator-to-binder ratio of 0.75, reaching 21.73 MPa after 48 h of curing at 70°C. Accordingly, this ratio was selected for all subsequent phases of the experimental program due to its superior mechanical performance.

2.4 Methods

Based on the mechanical properties achieved at 7 and 28 days selected geopolymer mortar mixtures have been examined for durability namely resistance to high temperatures. The samples have been heated at 200, 400, 600, and 800 °C using an electrically controllable laboratory furnace. The heating process was performed at a heating rate of 5 °C/min until the required temperature was reached, then the sample was held at that temperature for 2 hours. After this period, the samples have been naturally cooled to room temperature within the same furnace. UPVs have been measured before and after thermal exposure in accordance with ASTM C597 to assess the internal integrity and damage evolution of the geopolymer mortars.

3 Results and Discussions

Figs. 1 and *2* illustrate the compressive strength, flexural strength, and UPV results for Ref, CF 0.25, CF 0.75, SF 0.25, and SF 0.75 mortars after heat treatment. Thermal degradation depended on microstructural degradation, ITZ damage, and the loss of load-transfer capability. Compressive strength was affected by the load-bearing capacity of the structure, while flexural strength was determined by the crack propagation process. UPV showed the structural homogeneity of the material. Heating the specimens to 200 °C did not cause any significant degradation, as prism weight losses did not exceed 1%, indicating that moisture evaporated. CF0.75 retained about 92% of its initial UPV, compared with only 79% for the reference mortar. In addition, CF0.75 retained more than 90% of its initial flexural strength, whereas the reference mortar retained only about 73% of its strength. SF0.75 also maintained more than 80% of its flexural capacity. Regarding compression, SF0.25 exhibited the highest residual strength (>94%), while the reference mortar retained about 89% of its initial strength. These results show that moderate heat treatment promoted further geopolymerization and matrix densification, while fibers were effective in limiting thermally induced microcracking. At 400 °C, dehydration and microcracking prevailed; therefore, UPV and mechanical properties decreased. However, CF0.25 showed the highest UPV, while CF0.75 obtained the highest residual flexural strength. With regard to compression, SF0.25 and SF0.75 preserved about 72-73% of the initial compressive strength, which is better than CF-reinforced mortars and the reference mortar. Carbon fibers positively affected crack bridging and bending resistance in mortars, while steel fibers were better at stress redistribution and preserving load transfer. At 600 °C, irreversible microstructural degradation prevailed due to progressive dehydration, pore-size growth, and loss of matrix cohesion. Consequently, compressive strength, flexural strength, and UPV decreased substantially. However, both types of fibers performed better than the reference mortar, though their effectiveness as reinforcements declined due to a weakened fiber-matrix interface. Nonetheless, SF mixtures showed slightly higher UPV and superior compressive strength compared with CF mixtures. After heat treatment at 800 °C, progressive degradation of the geopolymer matrix was observed in all samples. Extensive dehydration, interfacial debonding, and crack interconnection led to the lowest UPV and mechanical properties. Although fiber reinforcement could not prevent extensive degradation in mortars, SF0.75 exhibited the highest residual flexural and compressive strengths, confirming the superior thermal resistance of steel fiber reinforcements at high temperatures. In general, thermal

degradation began with the beneficial densification of the matrix at 200 °C, progressed to progressive dehydration and cracking at 400-600 °C, and culminated in extensive degradation of the matrix at 800 °C. Carbon fibers were more effective at maintaining flexural strength through crack bridging, while steel fibers provided the best compressive strength retention.

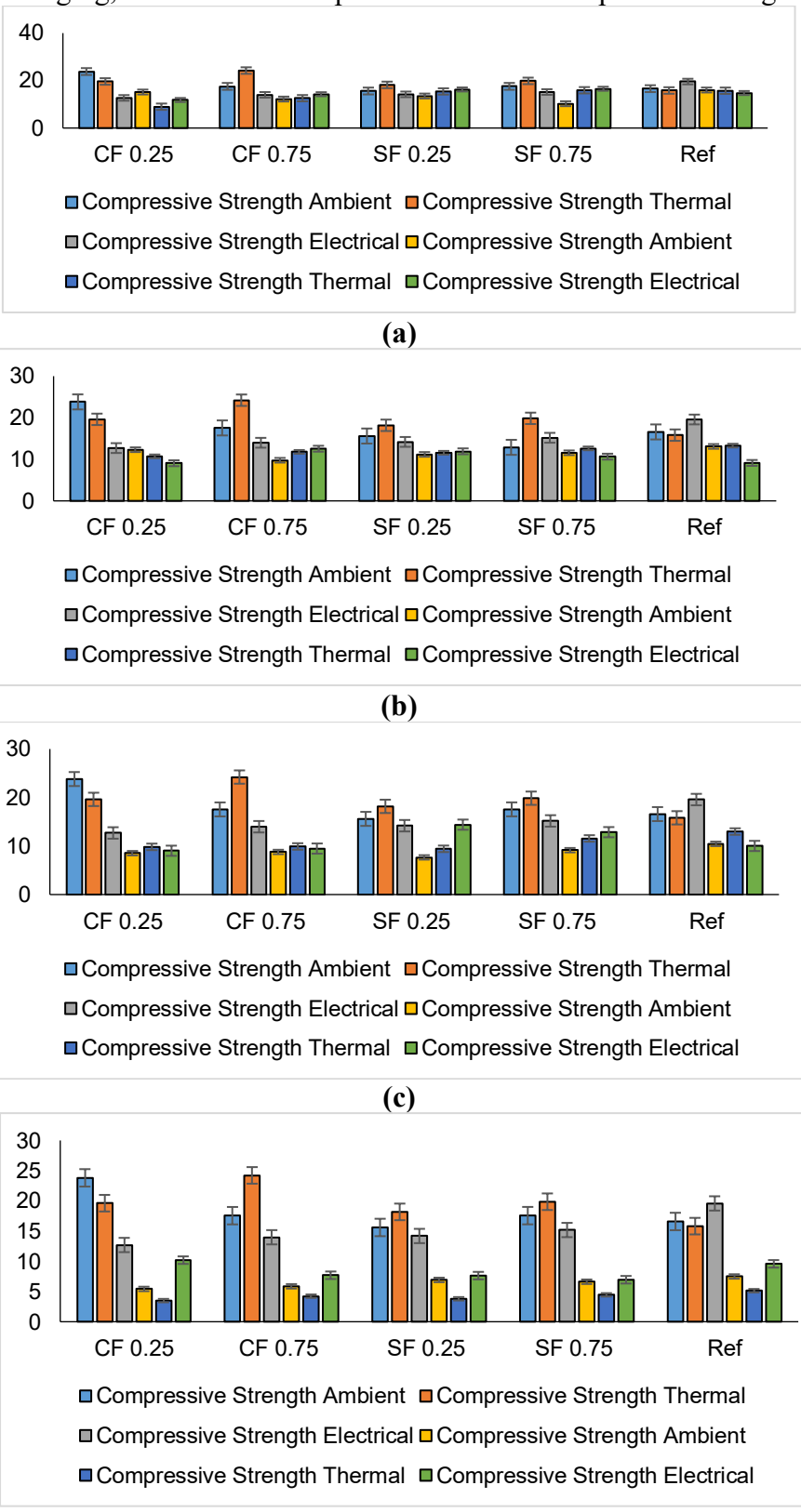
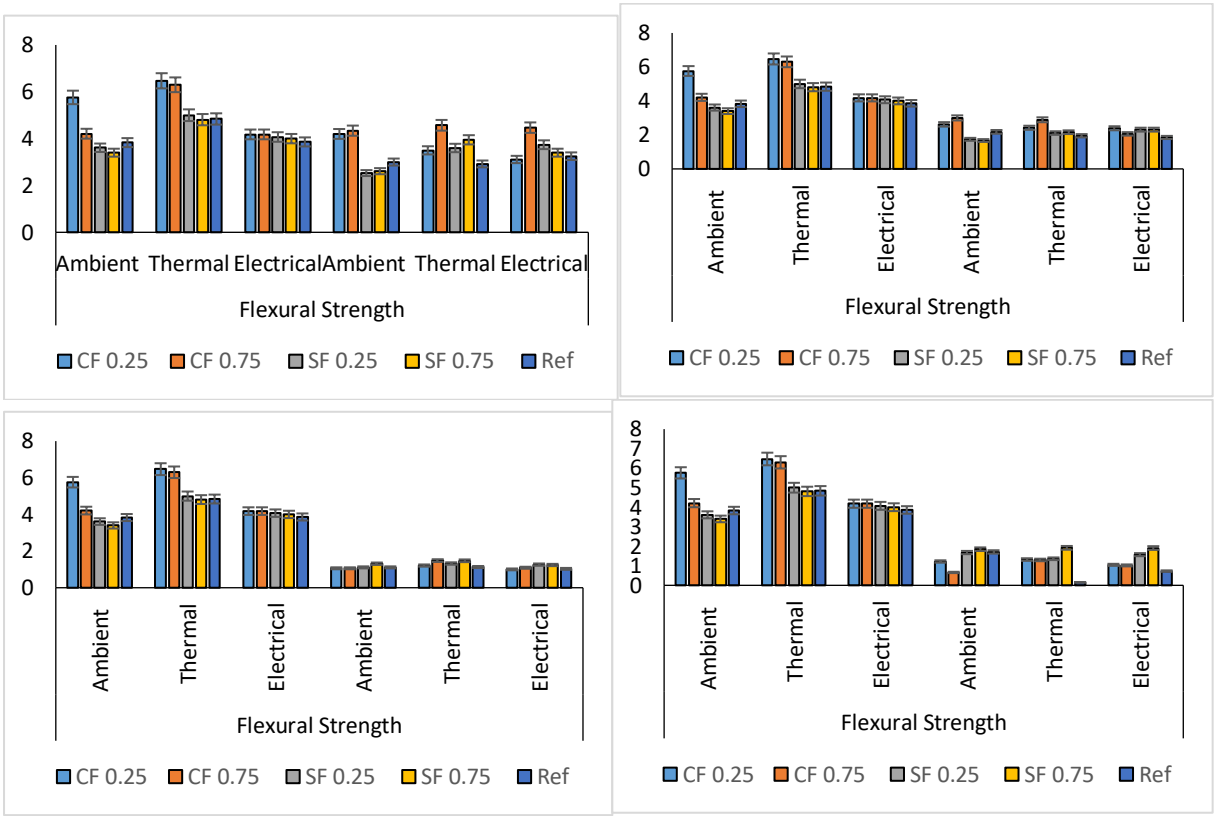


Fig.1. Compressive strength of TEOS-modified fiber-reinforced geopolymer mortars after exposure to elevated temperatures: (a) 200 °C, (b) 400 °C, (c) 600 °C, and (d) 800 °C.



200 °C	UPV (before)			UPV (after)		
	Ambient	Thermal	Electrical	Ambient	Thermal	Electrical
CF 0.25	2232	1938	2131	1939	1686	1790
CF 0.75	2028	2147	2130	1876	1889	2028
SF 0.25	1817	2082	2222	1533	1704	1501
SF 0.75	1771	1835	2029	1528	1639	1876
Ref	2043	2030	2196	1504	1536	1927

(a)

400 °C	UPV (before)			UPV (after)		
	Ambient	Thermal	Electrical	Ambient	Thermal	Electrical
CF 0.25	2127	1981	2060	1331	1315	1411
CF 0.75	2168	2528	2105	1139	1428	1452
SF 0.25	1835	2057	2005	1007	1257	1215
SF 0.75	1884	1767	2141	969	1041	1437
Ref	1942	1959	2099	1299	1187	1117

(b)

600 °C	UPV (before)			UPV (after)		
	Ambient	Thermal	Electrical	Ambient	Thermal	Electrical
CF 0.25	2111	2266	2295	986	1025	1165

(c)

CF 0.75	2590	2417	2308	1221	1190	1030
SF 0.25	1739	1990	1936	950	1055	742
SF 0.75	1706	1736	2073	889	872	967
Ref	1706	1736	2073	889	872	967

UPV (before) UPV (after)

800 °C	Ambient	Thermal	Electrical	Ambient	Thermal	Electrical
CF 0.25	1859	1998	2098	1162	1181	1187
CF 0.75	2286	2162	2189	1260	1223	1268
SF 0.25	1846	2036	2171	1254	1083	1248
SF 0.75	1774	1812	2120	1303	1224	1207
Ref	2020	2031	2151	1266	1242	1196

(d)

Fig. 2. Flexural strength and UPV of TEOS-modified fiber-reinforced geopolymer mortars before and after exposure to elevated temperatures: (a) 200 °C, (b) 400 °C, (c) 600 °C, and (d) 800 °C.

4 Conclusions

- TEOS-modified geopolymer mortars reinforced with fibers demonstrated satisfactory thermal resistance up to 400 °C. However, all samples showed a significant drop in UPV and mechanical properties due to matrix degradation at 600- 800 °C.
- At 200 °C, the highest level of thermal resistance was shown by CF 0.75, maintaining about 92% of the initial UPV value and over 90% of the initial flexural strength, whereas the maximum value of compressive strength after heating was recorded for SF 0.25 (about 94%).
- At 400 °C, the maximum residual flexural strength was recorded in the sample CF 0.75, while SF 0.25 and SF 0.75 managed to preserve about 72-73% of their initial compressive strength, which indicates good compressive resistance of those samples when subjected to moderate heating.
- All samples showed severe damage after being heated up to 800 °C; however, the most stable thermo-mechanical characteristics were demonstrated by SF 0.75, while the reference mixture had the lowest values of internal integrity and mechanical properties.

Acknowledgments

The authors gratefully acknowledge the financial support provided by the Scientific and Technological Research Council of Türkiye (TÜBİTAK) under Project No. 123M470.

References

1. Johnson, E., Worrall, F.: Chemical pore closure of zeolite A using tetraethyl orthosilicate (TEOS): A potential method for enhancing the use of zeolites as part of a long-term waste immobilization strategy. Journal of Hazardous Materials 108(1–2), 55–65 (2004).
2. Altube, A., Autric, M., Gervasi, C.A., Di Sarli, A.R., Vilche, J.R.: Influence of deposition conditions on the protective behavior of tetraethyl orthosilicate (TEOS) sol–gel films on AA5754 aluminum alloy. Progress in Organic Coatings 73(1), 35–42 (2012).
3. Kucuk, A.Ç., Demirkal, E.: Sol-jel yöntemi ile zirkonyum fosfat ve poli(etilen oksit) temelli polimer kompozit malzeme (ZrP/PEO) sentezi ve karakterizasyonu. Sakarya University Journal of Science 22(2), 748–754 (2018).
4. Bian, G., Qi, L., Liu, J., Wang, X., Xu, X., Wang, Z.: Effects of tetraethyl orthosilicate on rheological behaviors of crumb rubber modified asphalt. Construction and Building Materials 325, 126807 (2022).

5. Barberena-Fernández, A.M., Blanco-Varela, M.T., Carmona-Quiroga, P.M.: Use of nanosilica- or nanolime-additioned TEOS to consolidate cementitious materials in heritage structures: Physical and mechanical properties of mortars. Cement and Concrete Composites 95, 271–276 (2019).
6. dos Reis, G.S., Lima, E.C., Sampaio, C.H., Rodembusch, F.S., Petter, C.O., Cazacliu, B.G., Dotto, G.L., Hidalgo, G.E.N.: Novel kaolin/polysiloxane based organic–inorganic hybrid materials: Sol–gel synthesis, characterization and photocatalytic properties. Journal of Solid State Chemistry 260, 106–116 (2018).
7. Cai, J., Li, X., Tan, J., Vandevyvere, B.: Fly ash-based geopolymer with self-heating capacity for accelerated curing. Journal of Cleaner Production 261, 121119 (2020).
8. Aygun, B.F., Uysal, M., Bilir, T., Coşgun, T., Dilbaş, H.: An investigation on physical, mechanical and microstructural properties of electricity-based cured GBFS-FA geopolymer. Construction and Building Materials 458, 139526 (2025).
9. Ekmekci, S., Uysal, M., Aygun, B.: Advancing geopolymer mortars with recycled concrete aggregates through joule heating curing. In: Proceedings of the 4th International Civil Engineering & Architecture Conference, Trabzon, Türkiye, pp. 1339–1344 (2025).

Author Contribution Statement

Conceptualization: Beyza AYGUN, Mucteba UYSAL, Turgay COSGUN, Turhan BILIR
Methodology: Beyza AYGUN, Mucteba UYSAL, Turgay COSGUN, Turhan BILIR
Investigation: Beyza AYGUN, Mucteba UYSAL, Turgay COSGUN, Turhan BILIR
Writing – Original Draft: Beyza AYGUN
Writing – Review & Editing: Beyza AYGUN

List of Abbreviations

- **CF** — Carbon Fiber
- **FA** — Class F Fly Ash
- **GBFS** — Ground Granulated Blast Furnace Slag
- **NS** — Natural Sand
- **SF** — Steel Fiber
- **TEOS** — Tetraethyl Orthosilicate

Note: Following the conference, this Publication Note will be added to each paper; therefore, authors are kindly requested not to remove the note below and to complete the author(s) and paper title information.

Publication Note

This paper was peer-reviewed, accepted for presentation, and included in the proceedings of the ACE2026 – International Conference on Advances in Civil Engineering, held on 12–14 October 2026 in Trabzon, Türkiye.

This paper may be cited as follows:

Aygun, B., Uysal, M., Cosgun, T., Bilir, T., "Durability Performance of TEOS-Modified Fiber-Reinforced Geopolymer Mortars under High Temperature Effects," in Proceedings of the ACE2026 – International Conference on Advances in Civil Engineering, Trabzon, Türkiye, 12–14 October 2026.

Effects of Disinfectant and Oxidizing Agent Exposure on Mechanical and Physical Properties of Concrete

Yılmaz M.[1], Bilici S.[2], Badawi B.[3], Mutlu İ. F.[4], Akbay Arama Z.[5]
[1] 0000-0001-8663-0406, Haliç University, Construction Technology Program, Istanbul, Türkiye, meryemyilmaz@halic.edu.tr
[2]0000-0002-9698-8900, Akçansa Çimento Sanayi ve Ticaret A.Ş., Product Development and Central Laboratory, Istanbul, Türkiye, senem.bilici@akcansa.com.tr
[3] 0000-0002-2716-7818, Istanbul University-Cerrahpaşa, Institute of Graduate Studies, Istanbul, Türkiye, bashar.badawi@ogr.iuc.edu.tr
[4] 0009-0001-3420-1623, Istanbul University - Cerrahpasa, Civil Engineering Department, Istanbul, Türkiye, ibrahimfiratmutlu@ogr.iuc.edu.tr
[5] 0000-0001-8185-7329, Istanbul University - Cerrahpasa, Civil Engineering Department, Istanbul, Türkiye, zakbay@iuc.edu.tr

Abstract. The collapse of structures during seismic events results in concrete debris that may become contaminated with chemical substances during cleanup and disinfection. This study investigated the variations in compressive strength and ultrasonic pulse velocity (UPV) of two concrete strength classes (C16 and C25) exposed to a 2% (v/v) iodine-based disinfectant (pH 4.5) and a 20% (v/v) oxidative chlorine-based disinfectant. Specimens were examined for cumulative periods of up to 118 days, comprising 28 days of initial water curing followed by 28, 56, and 90 days of chemical immersion. Experimental results indicated that neither disinfectant produced a statistically meaningful reduction in compressive strength relative to the reference water-cured specimens within the examined timescale. However, C25 specimens showed a modest downward offset at 118 days, suggesting a potential sensitivity of denser matrices to prolonged chemical interaction. Notably, UPV measurements did not consistently track compressive strength trends. In C16 specimens, chemically exposed groups exhibited markedly higher UPV values than the reference group at 118 days, shifting their quality classification from "Good" to "Excellent" without a corresponding gain in strength. This divergence is attributed to elevated pore saturation and moisture retention rather than matrix densification. The findings indicate that these disinfectants are unlikely to cause acute structural degradation of concrete debris at the tested concentrations. However, the study underscores that UPV alone can yield misleadingly favorable readings, highlighting the need for caution when relying solely on non-destructive testing for post-disaster debris management.

Keywords: concrete deterioration, disinfectant, oxidizing agent, compressive strength, ultrasonic pulse velocity, post-earthquake debris

1 Introduction

Earthquakes cause widespread structural damage in a short period of time, generating large amounts of debris; the composition and volume of this debris vary significantly depending on the nature of the affected building stock. The safe removal, transport, temporary storage, and final disposal of this debris during the post-disaster process is one of the fundamental components of disaster management [1, 2]. However, concrete debris should not be considered merely as physical waste; concrete is a material that can undergo significant changes during its interaction with the service or exposure environment, which can adversely affect its engineering

properties [3, 4]. These changes in the physical and mechanical properties of concrete can be further exacerbated depending on the type of chemical to which it is exposed, the concentration of the solution, and the presence of concurrent environmental effects [5]. Therefore, the behavior of concrete waste in debris management processes must be evaluated not only in terms of heavy equipment and logistics but also in terms of workplace safety and environmental sustainability; because earthquake debris management can pose additional risks to the environment and public health [2, 6]. In this context, the chemicals used for cleaning, hygiene, and disinfection during the collection, temporary storage, transportation, recovery, and final disposal of debris create an exposure environment that could lead to additional changes in the physical and mechanical properties of concrete [5, 7]. This situation highlights the importance of considering concrete debris not merely as solid waste, but also as an engineering material susceptible to chemical effects and potentially exposed to liquid chemical agents [3, 8]. The degradation of concrete due to external environmental conditions, particularly under chemical attack, has long been a well-known problem [9-14]. Studies examining the effects of chemical exposure on concrete properties have shown that the reduction in compressive strength depends on the type of solution to which the concrete is exposed and its composition [15, 16]. Findings indicate that acidic environments are particularly harmful to cement-based materials; in such environments, calcium-containing hydration products dissolve, calcium hydroxide and calcium silicate hydrate phases separate, and this leads to a weakening of the binding matrix [17, 18]. Furthermore, it has been shown that expansion products accumulating over time damage the walls of capillary voids, reduce the calcium hydroxide concentration, and accelerate strength loss due to the degradation of the C-S-H gel [15, 16]. Studies on wastewater and aggressive chemical environments have also revealed that changes in compressive strength are sensitive to the type of solution and pH, with the most pronounced decrease observed under acidic conditions [15, 19]. In this context, it has been observed that studies on the behavior of concrete in aggressive chemical environments have primarily focused on long-term durability issues such as sulfate attack, acid attack, seawater, chloride penetration, and industrial chemicals. However, various disinfectants are widely used after disasters to reduce the risk of infectious diseases and ensure hygienic conditions, suggesting that disinfectants and oxidizing chemicals used in the aftermath of disasters may also trigger similar degradation mechanisms in concrete debris. In particular, iodine-based and chlorine-based disinfectant solutions are frequently used in search-and-rescue operations, the disinfection of debris sites, temporary shelters, and environmental hygiene applications [20]. During this process, concrete debris may be exposed to these chemical solutions through spraying, washing, or prolonged contact. At the same time, these chemicals can penetrate the soil environment and, in post-disaster reconstruction scenarios, may come into direct contact with concrete [21, 22]. The interaction of chemical substances with the cement matrix of concrete can negatively affect the physical and mechanical properties of concrete by causing degradation of hydration products, changes in pore structure, and the formation of microcracks [23]. However, there are few studies in the literature that directly examine the effects of iodine-based or oxidative chlorine-based disinfectant solutions on concrete following an earthquake [24]. Therefore, the experimental evaluation of the effects of these chemicals on the strength and internal structural integrity of different concrete classes aims to address a significant research gap. Non-destructive methods are generally preferred for the rapid and field-applicable assessment of chemically affected concrete. Ultrasonic pulse velocity (UPV) is one of the most common and widely accepted ultrasonic non-destructive testing methods for assessing the internal continuity and quality level of concrete [25-27]. It has been noted that UPV depends on the material properties of the concrete and the presence of discontinuities such as cracks; it yields higher velocity values in high-quality, intact concrete and lower values in concrete containing internal defects. Furthermore, it has been shown that porosity, microcracks, the state of saturation, and other

physical factors significantly influence UPV results [28, 29]. Previous studies indicate that, in most cases, similar trends exist between UPV and compressive strength [30, 31]. In this context, investigating changes in compressive strength and UPV in concrete with different strength classes following exposure to iodine-based and oxidative chlorine-based disinfectant solutions is important for understanding the mechanism of material degradation, ensuring the safe management of concrete debris after a disaster, and facilitating post-disaster reconstruction processes. The fact that water-cured concrete exhibits higher initial values for UPV and compressive strength also allows for a more controlled interpretation of the changes that occur following chemical exposure [32]. Consequently, such an approach can provide a scientific basis for the technical assessment, classification, and management of chemically contaminated concrete debris. Building on this foundation, the present study reports preliminary findings from a laboratory investigation examining how C16 and C25 concrete specimens responded to two disinfectants over cumulative exposure periods of up to 118 days. Two properties were monitored throughout: compressive strength and UPV. The primary objective was to determine whether clinically relevant concentrations of these agents produced measurable changes in either parameter within a post-disaster timescale. A secondary but equally important question was whether compressive strength and UPV tracked each other consistently under these conditions or diverged, a distinction with direct implications for field debris assessment, where UPV is routinely employed to estimate structural integrity without resorting to destructive testing.

2. MATERIALS AND METHODS

2.1 Concrete Mix Design and Specimen Preparation

Two concrete strength classes were produced: C16 and C25, selected to represent the range of structural concrete quality found in the existing building stock of Istanbul's central districts. CEM II A-V 52.5N cement was used for both classes, and all aggregate was sourced from a single batch to eliminate inter-batch variability. Mix proportions are provided in Table 1. Cylindrical specimens measuring 100 mm in diameter and 200 mm in height were cast in moulds, and demoulded at 24 hours. All specimens were then water-cured at 20 ± 2°C for 28 days before any chemical exposure began.

Table 1. Concrete mix proportions for C16 and C25.

Component	Unit	C16	C25
Cement	kg/m³	200	250
Slag	kg/m³	30	40
Water	kg/m³	196	164
Superplasticizer	kg/m³	1.84	3.63
Fine Aggregate (0–4 mm)	kg/m³	834	647
Coarse Aggregate #1 (4–11,2 mm)	kg/m³	489	405
Coarse Aggregate #2 (11,2–22,4 mm)	kg/m³	357	560
Natural Sand	kg/m³	179	294

2.2 Chemical Exposure Conditions

Following the 28-day water curing period, specimens were assigned to one of three exposure groups: reference (continued water immersion), iodine-based disinfectant solution (2% v/v iodine solution, pH 4.5), and oxidative chlorine-based disinfectant solution (20% v/v chlorine solution). All containers were sealed and maintained at 20 ± 2°C. Specimens were retrieved for testing at cumulative ages of 56 days (28 days water cure + 28 days chemical exposure), 84 days (28 + 56 days), and 118 days (28 + 90 days).

2.3 Test Methods

Compressive strength was measured in accordance with TS EN 12390-3 using a servo-controlled testing machine at a loading rate of 0.5 MPa/s. Three specimens per group and age were tested; results are reported as group means. UPV measurements were carried out immediately before destructive testing, following TS EN 12504-4, using a portable device with 54 kHz exponential transducers in direct transmission mode. Transducers were placed at the mid-height of each cylinder on diametrically opposite faces, with coupling gel applied at each contact point. Transit time was recorded in microseconds and converted to pulse velocity using $v = L/t$, where $L = 200$ mm is the specimen diameter.

3. RESULTS AND DISCUSSION

Table 2 summarizes mean compressive strength and UPV results for all groups and testing ages, together with the quality classification at 118 days.

Table 2. Summary of mean compressive strength and UPV results.

Class	Medium	Compressive Strength (MPa)				UPV (m/s)			UPV quality classification *
		28d	56d	84d	118d	56d	84d	118d	(118d)
C16	Reference (Water)	19.1	21.0	22.0	22.6	4246	4175	4219	Good
C16	iodine-based disinfectant	–	21.1	22.4	22.3	4248	4177	4619	Excellent
C16	oxidative chlorine-based disinfectant	–	21.4	23.1	22.3	4264	4204	4574	Excellent
C25	Reference (Water)	32.1	37.3	38.9	41.5	4640	4773	4773	Excellent
C25	iodine-based disinfectant	–	38.2	38.1	40.3	4571	4532	4858	Excellent
C25	oxidative chlorine-based disinfectant	–	37.8	39.2	38.9	4601	4518	4863	Excellent

** UPV quality scale: > 4500 m/s — Excellent; 3500–4500 m/s — Good; 3000–3500 m/s — Medium; < 3000 m/s — Poor [33]*

3.1 Compressive Strength

For C16 specimens, the reference group exhibited a gradual and consistent strength increase over the entire monitoring period, rising from 21.0 MPa at 56 days to 22.6 MPa at 118 days. This trajectory is consistent with the well-documented behaviour of cement-based materials, in which hydration continues beyond the conventional 28-day reference point and may contribute to incremental strength gains over several months, particularly under continuously moist conditions [34]. The iodine-exposed and chlorine-exposed C16 groups followed a broadly similar pattern. These values are comparable to, and in certain cases marginally exceed, those of the reference group, suggesting that neither chemical environment suppressed continued hydration during the observation period. For C25 specimens, reference compressive strength increased from 37.3 MPa at 56 days to 41.5 MPa at 118 days, confirming the ongoing maturation of this higher-strength class. The iodine-exposed group attained 40.3 MPa and the chlorine-exposed group 38.9 MPa at 118 days, both of which are slightly below the reference value. While these differences are modest, the downward offset observed in C25 may reflect the greater sensitivity of denser, lower-porosity matrices to chemical interaction at the pore surface level, a relationship previously noted in studies examining cement paste behaviour under variable pH environments [35,36]. The mildly acidic character of the iodine-based solution (pH 4.5) is broadly consistent with conditions under which calcium hydroxide dissolution and C-S-H destabilisation are initiated in Portland cement pastes, though such mechanisms typically produce measurable strength losses only at lower pH values or over extended periods [17]. The absence of pronounced strength reduction in the present data may therefore reflect the relatively dilute concentration of the iodine solution, the buffering capacity of the concrete matrix, or the comparatively short duration of exposure within 118-day. The strongly alkaline nature of the oxidative chlorine-based solution, by contrast, would not be expected to dissolve calcium hydroxide and may in some cases promote densification of the interfacial transition zone, which could account for the partial maintenance of strength observed in C16 [37]. Taken together, these results indicate that within the post-disaster timescale examined here, neither disinfectant at the concentrations tested produced a statistically discernible deterioration in compressive strength relative to reference specimens. This does not preclude the possibility of latent or progressive degradation at longer exposure durations, a question that the ongoing microstructural characterization is expected to address.

3.2 Ultrasonic Pulse Velocity

UPV measurements at 56, 84, and 118 days are summarized in Table 2 alongside the UPV quality classification assigned at the final testing age. The results exhibit several features that complement and partially diverge from the compressive strength findings. For C16 reference specimens, UPV values ranged between 4175 and 4246 m/s across the monitoring period, placing this group consistently within the "Good" quality band (3500–4500 m/s). In contrast, both chemically exposed C16 groups recorded markedly higher UPV values at 118 days, 4619 m/s for the iodine group and 4574 m/s for the chlorine group, elevating them into the "Excellent" category (>4500 m/s). UPV is sensitive not only to bulk matrix properties but also to the degree of pore saturation and internal moisture content, factors that are known to exert a significant influence on pulse transmission velocity [38]. Specimens maintained in chemical solutions throughout the exposure period may retain a higher degree of internal saturation relative to reference specimens, even where the chemical properties of the solution differ. This moisture effect may account, at least in part, for the elevated UPV values observed in the chemically exposed groups at 118 days, independent of any genuine change in matrix stiffness or density. A similar saturation-driven inflation of UPV has been reported in comparative

studies examining wet versus dry concrete specimens, where differences of several hundred metres per second have been attributed solely to pore moisture content rather than structural changes [39]. For C25 specimens, the reference group maintained UPV values above 4600 m/s throughout, remaining firmly within the "Excellent" band. The iodine and chlorine-exposed groups exhibited modestly lower UPV values at 84 days, 4532 and 4518 m/s respectively, before recovering to 4858 and 4863 m/s at 118 days, exceeding the reference value of 4773 m/s. This non-monotonic pattern is difficult to attribute to a single mechanism and may reflect competing influences: localised pore modification, moisture redistribution, or minor changes in gel density within the C-S-H framework [40, 41]. Overall, UPV measurements in this study demonstrate a trend broadly consistent with, but not precisely tracking, compressive strength. Specifically, the divergence observed in C16, where UPV places exposed specimens in a higher quality class than the reference, while compressive strength values remain comparable, illustrates that the two parameters do not respond identically to chemical exposure.

3.3 Implications for Post-Earthquake Debris Management

The findings outlined in Sections 3.1 and 3.2 entail significant implications for the systematic assessment and management of concrete debris in post-earthquake contexts. First, the data indicate that exposure to iodine-based and oxidative chlorine-based disinfectant solutions at the concentrations examined here did not produce significant reductions in compressive strength or UPV during the 118-day exposure period. From a debris management perspective, this suggests that, under the conditions simulated in this study, the structural load-bearing capacity of concrete fragments would not be substantially compromised by contact with these agents during typical post-disaster operations. This is a practically relevant finding given that disinfectant application is routine in the weeks and months following a major seismic event [42]. Second, and importantly, the results reveal a measurable divergence between compressive strength and UPV responses. In C16 specimens, UPV values in chemically exposed groups exceeded those of the reference group at 118 days, sufficient to shift the UPV quality classification from "Good" to "Excellent", while compressive strength showed no equivalent improvement. This discrepancy underscores a recognised limitation of UPV as a standalone diagnostic tool: the method is sensitive to pore moisture content, saturation state, and other physical factors that do not necessarily correspond to changes in structural capacity [39]. In the context of field debris assessment, where UPV is frequently employed as a rapid proxy for concrete quality, this finding suggests that prolonged contact with aqueous chemical solutions may produce misleadingly elevated velocity readings that overestimate the actual mechanical performance of a specimen. Field practitioners relying exclusively on UPV to classify chemically contaminated debris should therefore exercise caution, and where possible, corroborate non-destructive readings with complementary methods or targeted destructive sampling [43]. Third, the difference in behavior between C16 and C25 under chemical exposure, with C25 showing a modest but consistent compressive strength offset relative to the reference at 118 days, suggests that concrete quality class may modulate susceptibility to chemical interaction. Higher-strength concretes, characterized by lower water-to-cement ratios and finer pore structures, may present a different exposure dynamic than lower-grade materials. Given that the existing building stock in earthquake-prone urban centers such as Istanbul includes a wide range of concrete quality, from pre-standard construction of potentially sub-C16 grade to modern C30 and above, any future classification framework for chemically contaminated debris would need to account for this variability.

4. CONCLUSIONS

This paper reports preliminary findings from a laboratory study examining the effect of 2% iodine-based disinfectant solution and 20% oxidative chlorine-based disinfectant solution exposure on the compressive strength and ultrasonic pulse velocity of C16 and C25 concrete specimens over cumulative periods of up to 118 days. The main observations are as follows:

1. Neither the iodine-based (2% v/v, pH 4.5) nor the oxidative chlorine-based (20% v/v) disinfectant solution produced a statistically meaningful reduction in compressive strength in C16 or C25 specimens over the 118-day exposure period. Reference and exposed groups remained broadly comparable.
2. UPV values in chemically exposed specimens were, in several cases, equal to or higher than those of reference specimens at equivalent testing ages. For C16 groups, this elevated UPV at 118 days was sufficient to shift the quality classification from "Good" to "Excellent," despite the absence of a corresponding improvement in compressive strength.
3. The divergence between UPV and compressive strength responses, most evident in C16, points to the influence of specimen saturation and pore moisture on pulse velocity measurements. UPV alone should not be treated as a reliable indicator of mechanical performance in concrete that has been in prolonged contact with aqueous chemical solutions.
4. C25 specimens exhibited a modest downward offset in compressive strength relative to the reference under both chemical environments at 118 days, suggesting that the influence of chemical exposure may differ between concrete quality classes, with denser matrices potentially more susceptible to surface-level interaction over time.
5. Within the post-disaster timescale examined here, the disinfectant concentrations commonly applied in field operations appear unlikely to produce acute structural degradation of concrete debris. However, the saturation-related distortion of UPV readings has direct implications for debris classification protocols that rely on non-destructive testing alone.

Acknowledgments

This study was supported by the Scientific and Technological Research Council of Türkiye (TÜBİTAK) - UDAP under grant number 124M665 within the scope of the "TÜBİTAK- AFAD 1001-UDAP Joint Call for National Earthquake Research Program" and by the Istanbul University-Cerrahpaşa Scientific Research Projects Unit (IUC BAP) as a PhD Thesis Project under grant number 38685. The authors would like to express their gratitude to TÜBİTAK and IUC BAP for their support.

Additionally, the authors would like to express their gratitude to Akçansa Çimento Sanayi ve Ticaret A.Ş. for their valuable support, technical contributions, and resources provided during the production of all concrete specimens investigated in this project and study.

References

[1] Askarizadeh, L., Karbassi, A.R., Ghalibaf, M.B., Nouri, J.: Management of post-earthquake construction debris in Tehran Metropolitan. International Journal of Environmental Science and Technology 13, 639–648 (2016).
[2] Mavroulis, S., Mavrouli, M., Lekkas, E., Tsakris, A.: Managing Earthquake Debris: Environmental Issues, Health Impacts, and Risk Reduction Measures. Environments 10, 192 (2023).

[3] Glasser, F.P., Marchand, J., Samson, E.: Durability of concrete: Degradation phenomena involving detrimental chemical reactions. Cement and Concrete Research 38(2), 226–246 (2008).
[4] Qu, F., Li, W., Dong, W., Tam, V.W.Y., Yu, T.: Durability performance deterioration of concrete under marine environment from material to structure: A critical review. Journal of Building Engineering 35, 102074 (2020).
[5] Wang, R., Zhang, Q., Li, Y.: Deterioration of concrete under the coupling effects of freeze–thaw cycles and other actions: A review. Construction and Building Materials 319, 126045 (2022).
[6] Bektaş, N., Zhang, J.: Sustainable waste management strategies for earthquake debris: Lessons from the 2008 China and 2023 Türkiye-Syria disasters. International Journal of Disaster Risk Reduction 116, 105153 (2025). https://doi.org/10.1016/j.ijdrr.2024.105153
[7] Shkromada, O., et al.: Defining patterns in the influence exerted by the interrelated biochemical corrosion on concrete building structures under the conditions of a chemical enterprise. Eastern-European Journal of Enterprise Technologies 2(6-110), 52–60 (2021).
[8] Bilgili, L., Çetinkaya, A.Y.: Environmental impact assessment of earthquake-generated construction and demolition waste management: a life cycle perspective in Turkey. Environment Systems and Decisions 44, 424–432 (2024).
[9] Costa, A., Appleton, J.: Case studies of concrete deterioration in a marine environment in Portugal. Cement & Concrete Composites 24(1), 169–179 (2002).
[10] Bangert, F., Grasberger, S., Kuhl, D., Meschke, G.: Environmentally induced deterioration of concrete: physical motivation and numerical modeling. Engineering Fracture Mechanics 70, 891–910 (2003).
[11] Boyd, A. J., & Skalny, J.: Environmental deterioration of concrete. Environmental deterioration of materials, 28, 143-184 (2007).
[12] Breysse, D. (ed.): Non-destructive evaluation of reinforced concrete structures. Woodhead Publishing, Oxford (2010).
[13] Zhao, H., Hu, Y., Tang, Z., Wang, K., Li, Y., Li, W.: Deterioration of concrete under coupled aggressive actions associated with load, temperature and chemical attacks: A comprehensive review. Construction and Building Materials 322, 126466 (2022).
[14] Khan, A. M., Khan, H., Usman, M., Bin Zahid, Z., & Ahmad, J.: Multi-phase forensic characterization of durability failures: a case study on pathological investigation of chemical, physical, and hygrothermal distress in concrete infrastructure. Journal of Structural Integrity and Maintenance, 11(1), 2616863 (2026).
[15] Liu, X., Feng, P., Yu, X., Huang, J.: Decalcification of calcium silicate hydrate (C-S-H) under aggressive solution attack. Construction and Building Materials 342, 127988 (2022).
[16] Abd El Fattah, A.M., Amao, A.O., Riding, K. et al. Durability of Fly Ash and Limestone Concrete Under Combined Sulfate and Chloride Attack. International Journal of Concrete Structures and Materials 20, 16 (2026).
[17] Hilbig, H., Gutberlet, T., & Beddoe, R. E. (2024). Acid attack on hydrated cement: effect of organic acids on the degradation process. Materials and Structures, 57(4), 83.(2024).
[18] Löher, M., Ukrainczyk, N., Bogner, A., Hirsch, A., Dehn, F., Koenders, E.: Reactive transport modeling of acetic acid-induced degradation in portland cement paste. Cement and Concrete Research 187, 107704 (2025).
[19] Dwiriyadhi, M.G., Suwondo, R.: The effect of crystalline technology on concrete as coating to improve its durability. In: IOP Conf. Ser.: Earth Environ. Sci. 1324, 012017 (2024).

[20] Lantagne, D., Wolfe, M., Gallandat, K., Opryszko, M.: Determining the Efficacy, Safety and Suitability of Disinfectants to Prevent Emerging Infectious Disease Transmission. Water 10, 1397 (2018).
[21] Zhang, F., Wei, F., Wu, X., Hu, Z., Li, X., Gao, L.: Study on Concrete Deterioration and Chloride Ion Diffusion Mechanism by Different Aqueous NaCl-MgSO4 Concentrations. Buildings 12, 1843 (2022).
[22] Mei, X., Zhang, Y., Ni, D., Yang, D., Su, T.: Analysis of the ion diffusion mechanism affecting the durability of concrete in saline-alkali soils in Western China. Construction and Building Materials 475, 141213 (2025).
[23] Hasanzadeh, R., Ahmadi, J., Eghbali, M., Samadian, D., Salmanmohajer, H.: Reduction of seismic resiliency of RC structures caused by chloride corrosion for typical school buildings located in hot climates. Structures 34, 4060–4076 (2021).
[24] Lange, S., Isaacs, M., Klinkenberg, M., Read, D., Bosbach, D., Deissmann, G.: Uptake of iodine by cement hydration phases: Implications for radioactive waste disposal. Applied Geochemistry 181, 106301 (2025).
[25] Karaiskos, G., Deraemaeker, A., Aggelis, D.G., Van Hemelrijck, D.: Monitoring of concrete structures using the ultrasonic pulse velocity method. Smart Materials and Structures, 24(11), 113001(2015).
[26] Ndagi, A., Umar, A.A., Hejazi, F., Jaafar, M.S.: Non-destructive assessment of concrete deterioration by ultrasonic pulse velocity: A review. In: IOP Conf. Ser.: Earth Environ. Sci. 357, 012015 (2019).
[27] Liu, D., Gong, C., Tang, Y., Jian, Y., Cao, K., Chen, H.: Evaluation of Corrosion Damage in Sulfate-Attacked Concrete by CT, Ultrasonic Pulse Velocity Testing and AHP Methods. Sensors 22, 3037 (2022).
[28] Gehlot, T., Sankhla, S.S., Gupta, A.: Study of Concrete Quality Assessment of Structural Elements Using Ultrasonic Pulse Velocity Test. IOSR Journal of Mechanical and Civil Engineering 13(5), 22-29 (2016).
[29] Espinosa, A.B., Revilla-Cuesta, V., Skaf, M., Faleschini, F., Ortega-López, V.: Utility of Ultrasonic Pulse Velocity for Estimating the Overall Mechanical Behavior of Recycled Aggregate Self-Compacting Concrete. Applied Sciences 13, 874 (2023).
[30] Ghosh, R., Sagar, S.P., Kumar, A., Gupta, S.K., Kumar, S.: Estimation of geopolymer concrete strength from ultrasonic pulse velocity (UPV) using high power pulser. Journal of Building Engineering 16, 39–44 (2018).
[31] Zárate, D.M., Cárdenas, F., Forero, E.F., Peña, F.O.: Strength of concrete through ultrasonic pulse velocity and uniaxial compressive strength. International Journal of Technology 13, 103–114 (2022).
[32] Hossain, Khandaker M. Anwar. "Influence of extreme curing conditions on compressive strength and pulse velocity of lightweight pumice concrete." Computers and concrete (2014): 437-450.
[33] Citra, Z., Wibowo, P. D., Malinda, Y., Wibisono, A., Apdeni, R., & Herol, H. Testing of concrete structures with non-destructive test method (NDT) using ultrasonic pulse velocity (UPV) at the Building on the Ancol Beach. CIVED, 11(1), 217-225(2024).
[34] Linderoth, O., Wadsö, L., & Jansen, D. Long-term cement hydration studies with isothermal calorimetry. Cement and Concrete Research, 141, 106344 (2021).
[35] Zhang, G., Wu, C., Hou, D., Yang, J., Sun, D., & Zhang, X. Effect of environmental pH values on phase composition and microstructure of Portland cement paste under sulfate attack. Composites Part B: Engineering, 216, 108862 (2021).
[36] Guo, H., Liu, Y., Tai, B., Zhang, Z., & Zhu, Y. Effect of environmental pH value on mechanical properties and microstructure of hardened sulphoaluminate cement paste. Construction and Building Materials, 325, 126848 (2022).

[37] Hemstad, P., Machner, A., & De Weerdt, K. The effect of artificial leaching with HCl on chloride binding in ordinary Portland cement paste. Cement and Concrete Research, 130, 105976 (2020).
[38] Jedidi, M. Evaluation of concrete by non-destructive ultrasonic pulse velocity method. Civil Engineering and Architecture, 10(4), 1623-1630(2022).
[39] Lencis, U., Udris, A., Kara De Maeijer, P., & Korjakins, A. Methodology for determining the correct ultrasonic pulse velocity in concrete. Buildings, 14(3), 720 (2024).
[40] Ortega, J. M., Miro, M., Ibanez-Gosalvez, J., & Tenza-Abril, A. J. Non-destructive evaluation of the effects of exposure environment in mortars using non-linear ultrasonic measurements. Developments in the Built Environment, 14, 100142 (2023).
[41] Lencis, U., Klaucans, R., Udris, A., Korjakins, A., Zhou, X., & Bumanis, G. The Moisture Effect on Ultrasonic, Rebound Hardness and Drilling Resistance Data in Non-Destructive Testing of Concrete. Applied Sciences, 15(22), 11973 (2025).
[42] Krelani, V., Ahmeti, M., & Kryeziu, D. Increased durability of concrete structures under severe conditions using crystalline admixtures. Buildings, 15(3), 352 (2025).
[43] Ahmed, N. S., & Ahmed, A. A. Predicting the Strength of Submerged and Saturated Concrete Structures using Non-Destructive Ultrasonic Pulse Velocity Testing. Engineering, Technology & Applied Science Research, 15(3), 23840-23845 (2025).

Author Contribution Statement

- *Conceptualization:* Z. Akbay Arama, S. Bilici
- *Methodology:* Z. Akbay Arama, M. Yılmaz
- *Investigation:* M. Yılmaz, B. Badawi
- *Writing – Original Draft:* Z. Akbay Arama, S. Bilici
- *Writing – Review & Editing:* S. Bilici, İ. F. Aydın

List of Abbreviations

- **UPV** — Ultrasonic Pulse Velocity
- **C-S-H** — Calcium Silicate Hydrate
- **pH**— Potential of Hydrogen

Publication Note

This paper was peer-reviewed, accepted for presentation, and included in the proceedings of the ACE2026 – International Conference on Advances in Civil Engineering, held on 12–14 October 2026 in Trabzon, Türkiye.

This paper may be cited as follows:

Yılmaz M., Bilici S., Badawi B., Mutlu İ. F., Akbay Arama Z., "Effects of Disinfectant and Oxidizing Agent Exposure on Mechanical and Physical Properties of Concrete" in Proceedings of the ACE2026 – International Conference on Advances in Civil Engineering, Trabzon, Türkiye, 12–14 October 2026.

Use of Kufeki Stone Powder as a Cement and Limestone Replacement in OPC and LC^3 Mortars

Mahmut Cenk SAYIL[1] and Şirin KURBETCİ[2]
[1] 0009-0008-9588-3622, Karadeniz Technical University, Civil Engineering Department, Trabzon, Türkiye, cenksayil@ktu.edu.tr
[2] 0000-0002-2000-571X, Karadeniz Technical University, Civil Engineering Department, Trabzon, Türkiye, skurbetci@ktu.edu.tr

Abstract. The fact that the effects of global warming have become increasingly tangible and that the production of Portland cement contributes significantly to greenhouse gas emissions has led researchers to develop greener alternatives. One approach is using industrial byproducts to replace cement clinker. In this study, effects of kufeki stone powder on mechanical and durability properties and environmental performance of ordinary Portland cement mortars at different replacement ratios (5%, 10% and 15%) were studied. In addition, kufeki stone powder is also used to produce a well-known alternative limestone-calcined clay cement by replacing the limestone with kufeki powder to investigate kufeki powder's applicability to produce even greener cement. Results were compared to ordinary Portland cement and plain limestone-calcined clay cement reference mixtures. Flexural and compressive strength values were determined at the end of 7 and 28 days of standard curing, in addition to investigations of capillary water absorption and elevated temperature resistance when the samples were subjected to 400 ℃ and 800 ℃. In addition, carbon emissions stemming from each mixture design were calculated through carbon emission factors obtained from databases. Results revealed that low replacement levels of kufeki stone powder could maintain or slightly improve the compressive strength of OPC mortars, although capillary water absorption increased with increasing replacement ratio. In LC3 mortars, replacing the limestone fraction with kufeki maintained compressive strength while markedly reducing capillary absorption, and kufeki-containing mixtures also showed promising residual strength performance after exposure to elevated temperatures.

Keywords: Kufeki powder, sustainability, limestone calcined clay cement, LCA

1 Introduction

Production of Portland cement causes a significant portion of anthropogenic carbon emissions, resulting in approximately 8% of total emissions [1, 2]. This is mostly caused by the energy consumed to calcine and grind the clinker. Thus, although Portland cement has great technical properties, producing one ton of Portland cement releases approximately 0.9 ton CO_2 to the atmosphere [3, 4]. This clearly demonstrates the necessity of taking protective measures in cement production industry and developing greener alternatives [2]. A common approach adopted to ensure sustainability in cement production is using supplementary cementitious materials to replace cement clinker at certain ratios, thus reducing the amount of clinker to be used and to prevent emissions arising from clinker usage to some extent. Some common pozzolans include silica fume, fly ash and ground granulated blast furnace slag. However, in recent years, the availability of these has become limited when compared to cement production demand [5, 6]. This has led researchers to seek other alternatives.

Ternary blended systems have been developed where the synergistic effects of more than one pozzolanic material are utilized to decrease emissions further, whilst sourcing pozzolans from different, more abundant resources. One such alternative is limestone calcined clay cement (LC^3), first proposed by Antoni et al. [7]. LC^3 utilizes the synergistic effects between kaolinitic clay and limestone, as aluminates from kaolinitic clay react with carbonates from limestone to form mono and hemicarboaluminate phases, promoting acceptable strength development while allowing for a greater amount of clinker to be replaced. However, even for LC^3, preserving natural resources is of utmost importance, especially for limestone and clay.

At this point, kufeki stone powder stands out. Kufeki is a fossiliterous hollow cryptocrystalline limestone of Upper Miocene age that was extracted from quarries in the present-day Istanbul provinces of Bakırköy, Sefaköy, Halkalı, and Hadımköy-Sazlıbosna. On the other hand, it is reported that the majority of the quarries are not in operation actively [8, 9]. The matrix of Kufeki limestone largely comprises $CaCO_3$ (93–100%) surrounding the mactra, melanopsis, helix and crinoid pieces. There are no rifts, and it can be found in nature in massive amounts and in intact form [9–11]. The possibility of kufeki stone powder being an amorphous material makes it a good candidate when it comes to replacing cement clinker. Moreover, since it resembles limestone in terms of chemical composition, the idea of using kufeki powder to replace limestone powder in LC^3 is worthy of testing since it has potential to further decrease the already lesser carbon emissions caused by LC^3 production, and to contribute to the preservation of limestone resources.

Literature review reveals that, to the authors' knowledge, kufeki stone powder have not been utilized as a cementitious material to produce any kind of cement, including ordinary Portland Cement (OPC) mortars and LC^3. Arıoğlu and Arıoğlu [8] focused on works of Master Architect Sinan and assessed mechanical properties of kufeki limestone as a building block to understand the reasons lying behind Master Architect Sinan's choice of using kufeki limestone, revealing that carbonation effect helped improving mechanical properties such as compressive, tensile and shear strength. Demir and İlki [9] evaluated mechanical performance of multi-leaf masonry walls belonging to the Ottoman era, one of the constituent materials being local kufeki limestone. Umaroğulları and Kartal [12] assessed physical and mechanical properties of kufeki stones sourced from different quarries, and considering cylindrical and spherical pores within the samples, proposed a mathematical model that defines a relationship between porosity and strength. Eyecioğlu et al. [13] prepared polypyrrole and kufeki stone containing composites by mixing at appropriate ratios and then pressed them to form pellets having a diameter of 10 mm and thickness values of 1-2 mm. Dielectric properties were assessed and different machine learning algorithms were adopted to estimate these properties. Similarly, Eyecioğlu [14] prepared similar samples and trained machine learning models to estimate AC conductivity of the samples produced. Angı et al. [15] assessed Bakırköy kufeki stone as a Global Heritage Stone Resource (GHSR) nominee in terms of its historical use, quarry distribution and mineralogical–petrographic, geochemical, and physico-mechanical characteristics.

As is seen, there has not been an attempt to produce a construction material using ground kufeki stone in powder form. To fill this gap in the literature, it was aimed to investigate the applicability of kufeki stone powder to produce cement mortars. Three different replacement ratios were adopted (5, 10 and 15%) to produce OPC mortars. In addition, due to its resemblance to limestone powder, it was also desired to investigate the possibility of using kufeki stone powder instead of limestone to produce LC^3 mortars. Thus, kufeki stone powder was used to fully replace the limestone in a typical LC^3-50 mixture design, being used to replace 15% of the total binder by mass. Flexural and compressive strength values, capillary water absorption and elevated temperature resistance of mortar samples were assessed. In addition, a life cycle assessment (LCA) analysis was performed in order to determine the amount of $CO_{(e)}$

emission per unit compressive strength to make an evaluation about the environmental performances of the resulting mixture designs.

2 Materials and Methodology

2.1 Materials

Commercial CEM-I 42.5 R Portland cement, kufeki stone powder (KP) and metakaolin (MK) were used. Limestone (LS) was obtained from Anadolu Mikronize, and gypsum (G) was obtained from Trabzon Aşkale Cement Factory. Table 1 shows chemical composition of the kufeki stone powder used in this study. According to Mastersizer results, kufeki stone powder used had a d_{50} value of 25.3 μm. Commercial standardized sand was used as fine aggregate.

Table 1. Semi-quantitative elemental analysis of kufeki stone powder

Oxide	Content (%)
Na_2O	0.034
MgO	0.380
Al_2O_3	0.283
SiO_2	0.695
P_2O_5	0.031
SO_3	0.042
Cl	0.012
K_2O	0.041
CaO	59.113
TiO_2	0.040
MnO	0.013
Fe_2O_3	0.288
SrO	0.028
LOI	38.87

2.2 Methodology

As shown in Table 2, kufeki stone powder was utilized to produce OPC mortars at three different replacement ratios (5%, 10%, and 15% by weight). Additionally, one LC3 mortar, coded as KC3 (kufeki-calcined clay cement), was produced by fully replacing the limestone fraction (representing a 15% replacement ratio of the total binder). As a benchmark, a plain OPC mortar and a typical LC^3 mortar were also produced to compare mechanical and durability properties and environmental performance. Binder-to-aggregate ratio was kept as 1:3, while water-to-binder ratio was 0.50 for all mixture designs. To prepare a mortar batch of approximately 0.768 L, a total of 450 g of binder, 1350 g of standardized sand, and 225 g of water were utilized. Consistency values obtained from flow table test and the amount of superplasticizer used are also given in Table 2.

Table 2. Mixture designs

ID	OPC (%)	KP (%)	MK (%)	LS (%)	G (%)	Consistency (cm)	SP (%)
OPC	100	-	-	-	-	17	0.17
LC3	50	-	30	15	5	17	0.40
K5	95	5	-	-	-	16	0.08
K10	90	10	-	-	-	16	0.04
K15	85	15	-	-	-	16	0.02
KC3	50	15	30	-	5	17	0.35

Samples were cured for 7 and 28 days under standard curing conditions. For the determination of flexural strength, in accordance with ASTM C293-16 [16], six 4x4x16 cm prism samples were produced for each mixture design for 7- and 28-days strength determination. Flexural strength was taken as the average of three values. Compressive strength was determined using the broken pieces of the prisms as the average of six values. For capillary water absorption, in accordance with ASTM C1585 [17], three 5 cm cubic samples were produced for each mixture design. For the determination of elevated temperature resistance, six 5 cm cubic samples were produced; half of them were subjected to 400℃ exposure while the rest was subjected to 800℃. Assessment was made based on residual strength.

For the assessment of environmental performance, a life cycle assessment (LCA) analysis was performed. Emissions associated with cement and concrete production stem from raw materials, transportation and production processes [18]. However, in literature, it is stated that emissions arising from the materials itself are the major contributors and emissions due to transportation and production processes are negligible when compared to these. Thus, this study focused on emissions due to raw materials; emissions factors will be multiplied with the amount of materials used [18, 19]:

$$mCO_2 = \sum_{i+1}^{n}(CO_{2i} x M_i) \quad (1)$$

where CO_{2i} is the emission factor ($kgCO_{2(e)}/kg$) and M_i is the mass of the material used per unit volume (kg/m^3). For this, cradle-to-gate carbon emission factors for raw materials were taken from ICE Database v4.1 [20], factors were multiplied with the amounts of the materials used. In order to make a realistic assessment, total carbon emissions caused by each mixture design was divided by that design's 28-days compressive strength value to reveal carbon emissions per unit strength ($kgCO_{2(eq)}/m^3(MPa)$ [19]:

$$mCO_{2-\sigma} = mCO_2/\sigma \quad (2)$$

where σ is the 28-day compressive strength.

3 Results and Discussion

3.1 Flexural and Compressive Strength

Figures 1-2 show 7 and 28 days flexural and compressive strength values under standard curing conditions.

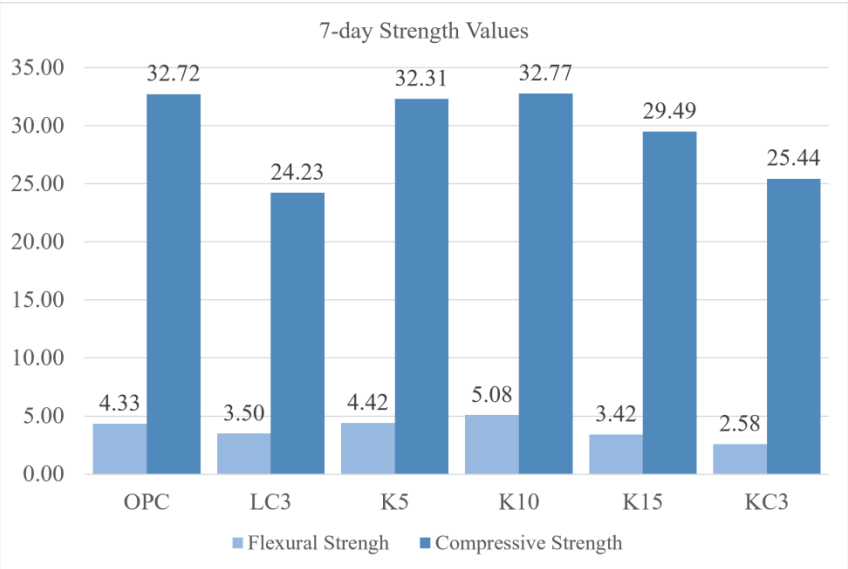


Fig. 1. 7-day strength values

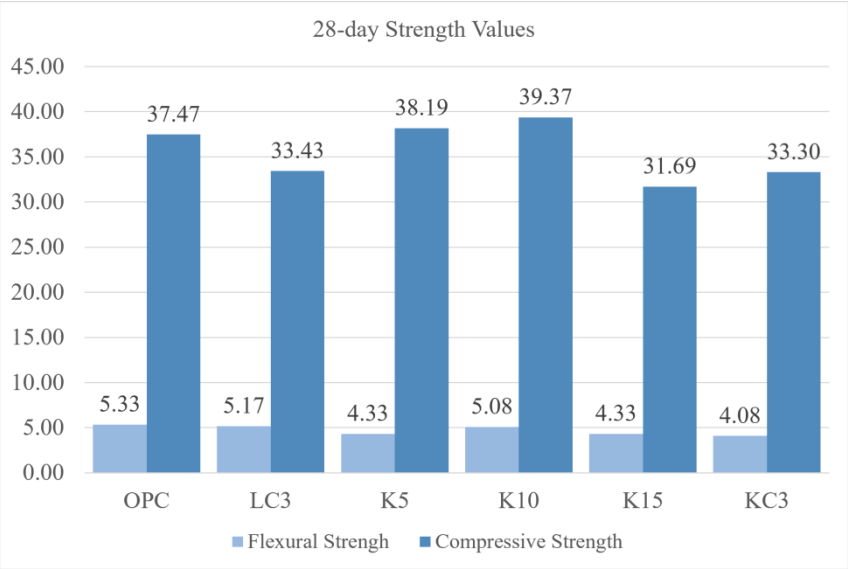


Fig. 2. 28-day strength values

When used to replace CEM-I, kufeki yielded the best results at 10% replacement ratio in terms of compressive strength. While K5 and K10 exhibited 7-day compressive strengths comparable to that of OPC, their 28-day compressive strengths were 1.9% and 5.1% higher, respectively. However, at 15% replacement ratio, 28-day compressive strength was reduced by 15.4%. This might imply the fact that at lower replacement ratios, kufeki stone powder was able to compensate for the dilution effect through filler effect and nucleation; however, at higher replacement ratios dilution effect might become dominant.

When used as a complete replacement for the limestone fraction in LC3, kufeki stone powder increased the 7-day compressive strength by 5.0%, while the 28-day strength remained essentially unchanged, with a reduction of only 0.4% compared with LC3. These results suggest that kufeki stone powder may serve as an alternative carbonate component in LC^3 systems, slightly improving strength development at 7 days without compromising later-age compressive strength.

3.2 Capillary Water Absorption

Figure 3 shows capillary water absorption test results as capillarity coefficients. It is seen that, in OPC-based mixture designs, capillarity coefficients increased by 4.3%, 11.0% and 32.5% for K5, K10 and K15, respectively. Although an increase in capillarity might be viewed as a contradiction despite the preservation or limited increase in compressive strength, such a relationship does not necessarily exist between them. While compressive strength is related to the load-bearing solid matrix, capillary water absorption is controlled primarily by the connectivity of water-permeable pores, the critical pore diameter, and pore tortuosity. Therefore, a low-ratio replacement of the matrix with clay may have led to an increase in interconnected capillary pores or water-permeable internal surfaces without adversely affecting the solid matrix.

When used as a complete replacement for the limestone fraction in LC3, kufeki stone powder decreased capillarity coefficient by 40.3% although 28-day compressive strength remained almost the same. This finding suggests that kufeki stone powder could be an effective carbonate source alternative to limestone for LC^3 matrices while providing advantages in terms of capillary water transportation. On the other hand, since this paper lacks microstructural analyses, this cannot be directly attributed to pozzolanic activity or promotion of

carboaluminate formation. Observed improvement could stem from particle size distribution, morphology, packing density or changes in pore connection structures.

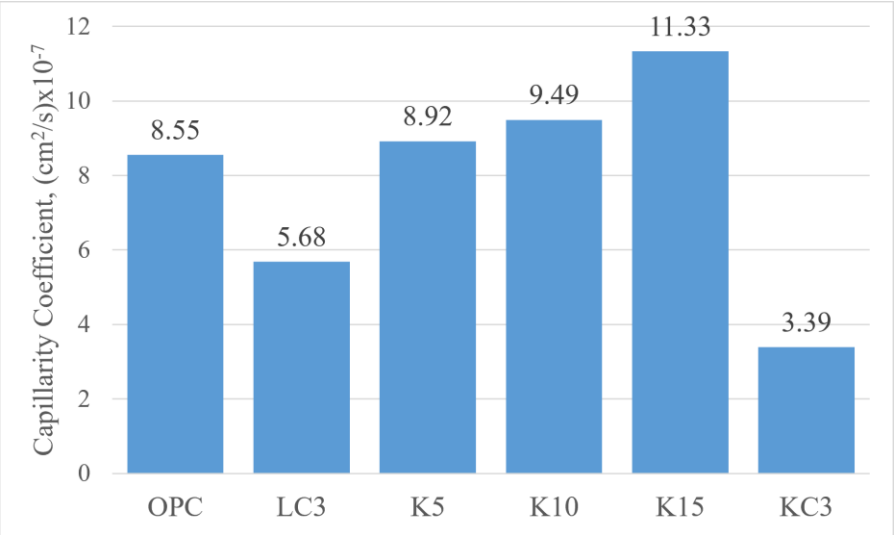


Fig. 3. Capillarity coefficients

3.3 High Temperature Resistance

The residual strengths in percentage are presented in Table 3 for all mix designs and 400℃ and 800℃ heat exposures.

Table 3. Residual strength values (%) after high temperature exposure

ID	400℃	800℃
OPC	67.86	37.90
LC3	100.00	30.63
K5	116.83	28.95
K10	111.07	26.58
K15	129.26	28.57
KC3	109.66	42.92

Exposure to elevated temperatures resulted in markedly different residual compressive strength responses depending on the binder system. At 400 °C, OPC retained only 67.9% of its original compressive strength, whereas K5, K10 and K15 exhibited residual strengths of 116.8%, 111.1% and 129.3%, respectively. Thus, partial replacement of CEM-I with kufeki stone powder appeared to improve strength retention at 400 °C, although no systematic relationship between replacement level and residual strength was observed. The increase above the initial strength may be associated with temperature-induced effects such as further hydration of previously unhydrated particles, moisture removal and temporary changes in the cementitious matrix; however, the underlying mechanism cannot be conclusively identified without further microstructural investigation. At 800 °C, extensive strength loss occurred in all mixtures, and the residual strengths of K5–K15 ranged only between 26.6% and 28.9%, indicating that increasing kufeki content provided no additional benefit at this temperature.

A different trend was observed for the LC3-based mortars. KC3 retained 109.7% and 42.9% of its initial compressive strength after exposure to 400 and 800 °C, respectively, compared with 100.0% and 30.6% for the LC3 reference. These findings suggest that replacing the limestone fraction of LC3 with kufeki stone powder may improve its resistance to elevated

temperatures. Nevertheless, additional mineralogical and microstructural analyses are required to identify the mechanisms responsible for this improvement.

3.4 Life Cycle Assessment (LCA) Analysis

Figure 4 shows LCA analysis results. It is seen that, kufeki stone powder's capability of retaining strength of LC^3 matrix whilst reducing emissions significantly made it possible to obtain the lowest carbon emission per unit strength for KC3 mixture design.

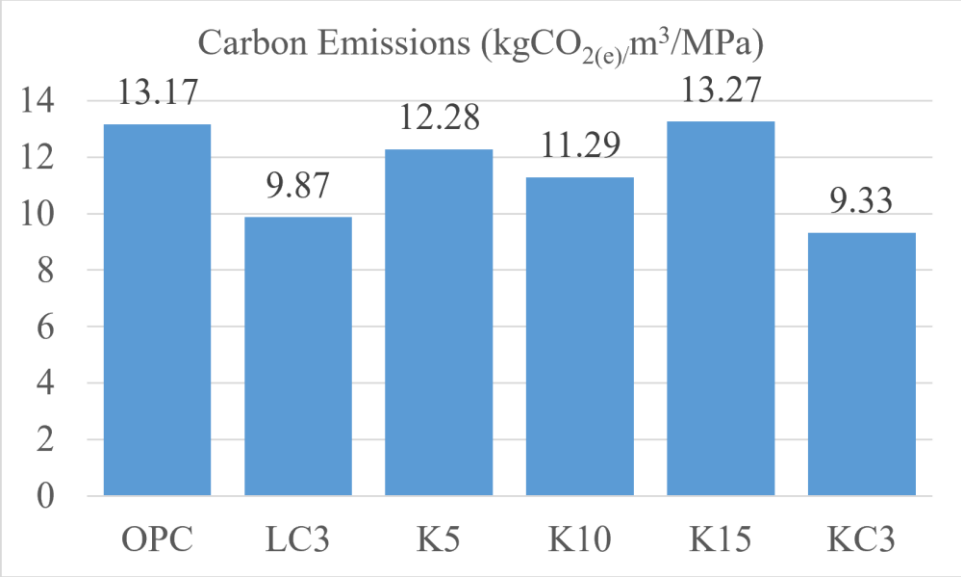


Fig.4. Carbon emissions

4 Conclusion

The main conclusions of this study can be summarized as follows:

- Partial replacement of CEM-I with kufeki stone powder was feasible at low replacement levels. K5 and K10 maintained the 7-day compressive strength of OPC, while their 28-day strengths were 1.9% and 5.1% higher, respectively. However, increasing the replacement ratio to 15% resulted in a 15.4% reduction in 28-day compressive strength.
- Capillary water absorption increased progressively with increasing kufeki content in OPC-based mortars, indicating a possible trade-off between strength preservation and resistance to capillary water transport. In contrast, replacing the limestone fraction of LC3 with kufeki reduced the capillary absorption coefficient by approximately 40% while maintaining comparable 28-day compressive strength.
- Kufeki-containing OPC mortars exhibited residual compressive strengths above 100% after exposure to 400 °C, whereas OPC retained only 67.9% of its initial strength. However, no systematic relationship between kufeki replacement level and residual strength was observed. At 800 °C, substantial strength losses occurred in all mixtures.
- KC3 showed promising thermal performance, retaining 109.7% and 42.9% of its initial compressive strength at 400 and 800 °C, respectively. Overall, the influence of kufeki stone powder appears to depend strongly on the binder system and exposure condition, and further microstructural investigations are required to clarify the underlying mechanisms.
- For K5, K10 and LC3 systems, the use of kufeki stone powder made it possible to decrease equivalent carbon dioxide emissions per unit compressive strength, improving environmental performance.

Future work on the use of kufeki stone powder as a possible supplementary cementitious material for OPC and LC^3 mortars should focus on a broader range of durability properties, and microstructural analyses must be performed in order to fully understand the mechanisms lying behind the obtained improvements or deteriorations in mechanical and durability properties.

Acknowledgments
The authors have no acknowledgments to declare.

References

1. Andrew, R.M.: Global CO_2 emissions from cement production. Earth Syst. Sci. Data. 10, 195–217 (2018). https://doi.org/10.5194/essd-10-195-2018
2. Altuntas, I.O., Ozturk, O., Yildirim, G.: Exploring the viability of low-grade Turkish clays in the development of limestone calcined clay cement (LC3) and mortars. Constr. Build. Mater. 463, 140077 (2025). https://doi.org/10.1016/j.conbuildmat.2025.140077
3. Hasanbeigi, A., Price, L., Lu, H., Lan, W.: Analysis of energy-efficiency opportunities for the cement industry in Shandong Province, China: A case study of 16 cement plants. Energy. 35, 3461–3473 (2010). https://doi.org/10.1016/j.energy.2010.04.046
4. Atasever, M., Erdoğan, S.T.: Characterization of Limestone Calcined Clay Cement Made with Calcium Sulfoaluminate Clinker. International Journal of Civil Engineering. 22, 2407–2419 (2024). https://doi.org/10.1007/s40999-024-01009-5
5. Lothenbach, B., Scrivener, K., Hooton, R.D.: Supplementary cementitious materials. Cem. Concr. Res. 41, 1244–1256 (2011). https://doi.org/10.1016/j.cemconres.2010.12.001
6. Hu, Y., Xiong, L., Yan, Y., Geng, G.: Performance of limestone calcined clay cement (LC3) incorporating low-grade marine clay. Case Studies in Construction Materials. 20, e03283 (2024). https://doi.org/10.1016/j.cscm.2024.e03283
7. Antoni, M., Rossen, J., Martirena, F., Scrivener, K.: Cement substitution by a combination of metakaolin and limestone. Cem. Concr. Res. 42, 1579–1589 (2012). https://doi.org/10.1016/j.cemconres.2012.09.006
8. Arioğlu, N., Arioğlu, E.: Engineering Mystery of Master Architect Sinan's "Kufeki" Shell Limestone. Archit. Sci. Rev. 48, 163–171 (2005). https://doi.org/10.3763/asre.2005.4820
9. Demir, C., Ilki, A.: Characterization of the materials used in the multi-leaf masonry walls of monumental structures in Istanbul, Turkey. Constr. Build. Mater. 64, 398–413 (2014). https://doi.org/10.1016/j.conbuildmat.2014.04.099
10. Arıoğlu, N., Tuğrul, A., Zarif, İ., Girgin, Z., Arıoğlu, E.: Kufeki taşının dayanıklılık analizi: Şehzade Camisi örneği-1. Yapı Dergisi. (1999)
11. Arıoğlu, N., Tuğrul, A., Zarif, H., Girgin, Z., Arıoğul, E.: Kufeki taşının dayanıklılık analizi: Şehzade Camii örneği-II. Yapı Dergisi. (1999)
12. Umaroğulları, G., Kartal, S.: A Model Proposal on Results of Physical and Mechanical Properties of Trakia Region Kufeki Stone Used at Early Period Ottoman Buildings. Mimarlık Bilimleri ve Uygulamaları Dergisi (MBUD). 384–395 (2021). https://doi.org/10.30785/mbud.918698
13. Eyecioglu, Ö., Karabul, Y., Kılıç, M., Güven Özdemir, Z.: Application of Supervised Machine Learning Regression Algorithm to Prediction of Dielectric Properties of PPy/Kufeki Stone Composites for Energy Implementations. Gazi University Journal of Science. 35, 235–254 (2022). https://doi.org/10.35378/gujs.810948
14. Eyecioğlu, Ö.: Machine learning models for estimating the <scp>AC</scp> conductivity mechanism of Edirne Kufeki stone reinforced Polypyrrole composites. J. Appl. Polym. Sci. 139, (2022). https://doi.org/10.1002/app.52194

15. Angı, O.S., Mahmutoğlu, Y., Çiftçi, E., Akyüz, H.S.: Bakırköy Kufeki Stone: A Heritage Stone Nominee with regards to the UNESCO World Heritage Site of Istanbul, Türkiye. Geoheritage. 18, 74 (2026). https://doi.org/10.1007/s12371-026-01293-8
16. ASTM-C293: C293 - 16 Flexural Strength of Concrete (Using Simple Beam With Center-Point Loading). ASTM International. (2025)
17. ASTM C1585: Standard Test Method for Measurement of Rate of Absorption of Water by Hydraulic Cement Concretes. ASTM International. 41, (2020)
18. Yang, K.-H., Jung, Y.-B., Cho, M.-S., Tae, S.-H.: Effect of supplementary cementitious materials on reduction of CO2 emissions from concrete. J. Clean. Prod. 103, 774–783 (2015). https://doi.org/10.1016/j.jclepro.2014.03.018
19. Wang, Y.-S., Oh, S., Ishak, S., Wang, X.-Y., Lim, S.: Recycled glass powder for enhanced sustainability of limestone calcined clay cement (LC3) mixtures: mechanical properties, hydration, and microstructural analysis. Journal of Materials Research and Technology. 27, 4012–4022 (2023). https://doi.org/10.1016/j.jmrt.2023.10.245
20. Jones, C., Hammond, G., Burrow, J., Rouse, J., Zhu, C., Unnad, V., Wickens, K., Relph, T., Seprini, L., Lowe, E.: Embodied Carbon Footprint Database (ICE Database V4.1). , Circular Ecology Ltd, https://circularecology.com/embodied-carbon-footprint-database.html (2025)

Author Contribution Statement

- *Conceptualization:* Mahmut Cenk SAYIL, Şirin KURBETCİ
- *Methodology:* Mahmut Cenk SAYIL, Şirin KURBETCİ
- *Investigation:* Mahmut Cenk SAYIL, Şirin KURBETCİ
- *Writing – Original Draft:* Mahmut Cenk SAYIL
- *Writing – Review & Editing:* Şirin KURBETCİ

List of Abbreviations

- **LCA** — Life Cycle Assessment
- **LC^3** — Limestone Calcined Clay Cement
- **OPC** — Ordinary Portland Cement
- **LOI** — Loss On Ignition
- **KC3** — Kufeki Calcined Clay Cement

Publication Note

This paper was peer-reviewed, accepted for presentation, and included in the proceedings of the ACE2026 – International Conference on Advances in Civil Engineering, held on 12–14 October 2026 in Trabzon, Türkiye.

This paper may be cited as follows:

Sayil, M.C., Kurbetci, S., "Use of Kufeki Stone Powder as a Cement and Limestone Replacement in OPC and LC^3 Mortars," in Proceedings of the ACE2026 – International Conference on Advances in Civil Engineering, Trabzon, Türkiye, 12–14 October 2026.

Mechanical properties of engineered cementitious composites incorporating waste tire rubber

Akbar Mikaeelnezhad[1], Reza Saleh Ahari*[2]
[1] 0009-0002-2577-2245, Department of Civil Engineering, Ta.C., Islamic Azad University, Tabriz, Iran, mikaeelnezhad.akbar@gmail.com
[2] 0000-0003-3471-1727, Department of Civil Engineering, Ta.C., Islamic Azad University, Tabriz, Iran, rsalehahari@iau.ac.ir

Abstract. This study investigates the combined effects of waste tire rubber (WTR) and polypropylene (PP) fiber dosage on the mechanical performance of engineered cementitious composites (ECC), with the aim of promoting waste utilization while maintaining satisfactory engineering properties. WTR replaced natural fine aggregate at levels of 0–40%, while PP fibers were incorporated at volume fractions of 1.0% and 1.5%. Compressive, splitting tensile, and flexural strengths were evaluated at 7 and 28 days. The results showed that increasing WTR content progressively reduced compressive strength, whereas splitting tensile and flexural strengths exhibited non-linear responses, with a noticeable recovery at 20% WTR. Increasing the PP fiber dosage had only a marginal effect on compressive strength but considerably improved tensile and flexural performance. Among the rubber-containing mixtures, the combination of 20% WTR and 1.5% PP fibers provided the most favorable mechanical balance, achieving 28-day compressive, splitting tensile, and flexural strengths of approximately 48.9, 4.59, and 7.50 MPa, respectively. The findings demonstrate that an appropriate combination of WTR and PP fibers can partially offset the mechanical drawbacks associated with rubber incorporation, providing a promising approach for developing resource-efficient ECC while reducing the consumption of natural fine aggregate.

Keywords: Engineered cementitious composites; waste tire rubber; compressive strength; splitting tensile strength; flexural strength

1 Introduction

Engineered Cementitious Composites (ECC) have attracted considerable attention as one of the most advanced cement-based construction materials. First developed by Li et al., ECC is characterized by high tensile ductility, strain-hardening behavior, and multiple microcracking, with tensile strain capacities exceeding 3-5%, providing significantly greater ductility and toughness than conventional concrete [1-4]. Owing to these characteristics, ECC has been widely recognized as a promising material for durable and resilient infrastructure applications.

To improve the sustainability and cost-effectiveness of ECC, increasing attention has been directed toward incorporating recycled and waste-derived materials [5]. Among these, waste tire rubber (WTR) has emerged as an attractive alternative because of its ability to improve deformability, impact resistance, and energy absorption while providing an environmentally sustainable solution for recycling end-of-life tires [6-8]. However, the low stiffness of rubber particles and their weak bond with the cementitious matrix generally reduce the mechanical strength of rubberized cementitious composites [8,9]. Compared with conventional concrete, ECC provides a more compatible matrix for waste tire rubber because its intrinsic strain-hardening behavior better accommodates the deformable nature of rubber particles [10]. Previous studies have shown that rubberized ECC can retain strain-hardening characteristics while improving deformability, impact resistance, and vibration damping [11,12].

Several studies have investigated the incorporation of waste tire rubber in cementitious materials. Sofi [13], Valente et al. [14], Fauzan et al. [15], and Ahmad et al. [16] consistently reported that increasing rubber content generally reduces compressive strength, density, and stiffness, although improvements in crack resistance, abrasion resistance, deformability, and other durability-related properties were observed at moderate replacement levels. Likewise, studies on rubberized ECC have demonstrated that supplementary cementitious materials and fibers can compensate for some of the adverse effects of rubber incorporation while improving rheology, ductility, and durability [17]. Adesina and Das [18] further reported significant improvements in tensile strain and durability despite reductions in compressive strength, whereas Lee et al. [19] demonstrated that ECC produced with locally available materials exhibited superior tensile ductility and compressive strength compared with conventional concrete.

Despite these advances, the combined effects of waste tire rubber and polypropylene (PP) fibers on the mechanical behavior of ECC remain insufficiently understood. Therefore, this study experimentally investigates the mechanical properties of ECC mixtures incorporating PP fibers at dosages of 1.0% and 1.5% together with waste tire rubber as a partial replacement for natural fine aggregate at levels of 10%, 20%, 30%, and 40%.

2 Materials and Methods

2.1 Materials

Type II Portland cement (PC), conforming to ASTM C150 was used as the primary binder. Granulated blast furnace slag (GBFS), with a specific gravity of 2.89, was used as the supplementary cementitious material. The chemical composition and physical properties of both PC and GBFS are presented in Table 1. A polycarboxylate ether-based superplasticizer (SP), commercially identified as Carboxal HF5000, with a specific gravity of 1.10, was used to obtain the desired workability. Natural fine aggregate obtained from the Ghareh-Ghom mine (Marand, East Azerbaijan, Iran) had a maximum particle size of 4.75 mm and a specific gravity of 2.63. WTR, produced from shredded end-of-life automobile tires, was used as a partial replacement for natural fine aggregate. The WTR particles had a size range of 1.18-4.75 mm and a specific gravity of 0.96. Polypropylene fibers, with a specific gravity of 0.91 and an aspect ratio of 863, were used as reinforcement. To ensure uniform dispersion, the fibers were manually separated before mixing. The PP fibers and WTR used in this study are shown in Fig. 1(a) and Fig. 1(b), respectively.

Table 1. Physical and chemical properties of PC and FA

	CaO, (%)	SiO_2, (%)	Al_2O_3, (%)	Fe_2O_3, (%)	MgO, (%)	SO_3, (%)	K_2O, (%)	Na_2O, (%)	TiO, (%)	BaO (%)	FL (%)	Other minor oxides, (%)	LOI, (%)	SG	Blaine, (cm^2/g)
PC	64.4	21.7	5.22	3.74	2.22	1.18	0.58	0.22	0.16	0.11	0.21	0.26	1.34	3.16	3230
GBFS	44.6	29.1	5.43	0.73	5.99	3.21	1.19	0.71	1.25	5.26	0.69	1.84	0.42	2.89	3720

FL: Free lime, LOI: Loss on ignition, SG: Specific gravity



(a) (b)

Fig. 1. Materials used in the study: (a) polypropylene fibers and (b) waste tire rubber

2.2 Mix Proportions and Mixing

As summarized in Table 2, eight ECC mixtures were designed with an approximately constant water-to-binder (w/b) ratio of 0.25. The total binder content was 980.2 kg/m^3 for the mixtures containing 1.0% polypropylene fibers and 975.2 kg/m^3 for those containing 1.5% PP fibers. To enhance environmental sustainability and reduce PC consumption, GGBS was incorporated as a 50% replacement for PC by mass in all mixtures. The experimental variables included two PP fiber volume fractions (1.0% and 1.5%) and five WTR replacement levels (0%, 10%, 20%, 30%, and 40%) as volumetric replacements for natural fine aggregate (FA). The mixtures were prepared using a laboratory-scale mixer following a three-stage mixing procedure to ensure the homogeneous distribution of all constituents, particularly the PP fibers. First, the fine aggregate and one-third of the total mixing water were mixed. Next, the cementitious materials (PC and GBFS) together with another one-third of the mixing water were added and mixed thoroughly. Finally, the PP fibers and WTR particles were gradually incorporated, followed by the remaining mixing water and the superplasticizer, after which mixing continued until a uniform and homogeneous mixture was obtained. After mixing, the fresh ECC mixtures were cast into molds. The specimens were demolded after 24 h and subsequently cured in a water tank maintained at 23 ± 2 °C until the specified testing ages. The mix proportions are summarized in Table 2.

Table 2. Mix proportions of the ECC mixtures (kg/m^3)

Mix ID	PC	GBFS	PP	Water	SP	WTR	FA
PP1	490.1	490.1	8.9	247.5	4.90	0	1113
PP1+T10	490.1	490.1	8.9	247.5	4.90	41.2	1002
PP1+T20	490.1	490.1	8.9	247.5	4.90	82.4	891
PP1+T30	490.1	490.1	8.9	247.5	4.90	123.6	779
PP1+T40	490.1	490.1	8.9	247.5	4.90	164.8	668
PP1.5	487.6	487.6	13.4	246.3	4.88	0	1108
PP1.5+T10	487.6	487.6	13.4	246.3	4.88	41.0	997
PP1.5+T20	487.6	487.6	13.4	246.3	4.88	82.0	886
PP1.5+T30	487.6	487.6	13.4	246.3	4.88	123.6	775
PP1.5+T40	487.6	487.6	13.4	246.3	4.88	164.8	665

2.3 Testing Procedure

The compressive strength test was performed in accordance with ASTM C109 [20] using 100 × 100 × 100 mm cube specimens. The splitting tensile strength test was conducted in accordance

with ASTM C496 [21] on cylinders measuring 100 mm in diameter and 200 mm in height. Flexural strength was determined according to ASTM C78 [22] using prism specimens with dimensions of 100 × 100 × 450 mm. All mechanical tests were conducted after 7 and 28 days of water curing. For each mixture, three specimens were tested for each mechanical property, and the reported results represent the average values. The experimental setups for the compressive, splitting tensile, and flexural strength tests are presented in Figs. 2, 3, and 4, respectively.



Fig. 2. Compressive strength test setup



Fig. 3. Splitting tensile strength test setup



Fig. 4. Flexural strength test setup

3 Results and Discussion

3.1 Compressive Strength

The compressive strength results obtained after 7 and 28 days of curing are presented in Fig. 5, while the influence of WTR replacement on the 28-day compressive strength is illustrated in Fig. 6. As shown in Fig. 5, all mixtures exhibited higher compressive strengths at 28 days than at 7 days, reflecting the continued hydration of the PC-GBFS binder system. Regardless of curing age, replacing natural fine aggregate with WTR progressively reduced the compressive strength, and the reduction became more pronounced with increasing WTR content. In contrast, increasing the PP fiber dosage from 1.0% to 1.5% had only a negligible effect on the control mixtures, increasing the 7-day strength from 44.95 MPa to 45.10 MPa (0.33%) and the 28-day strength from 54.53 MPa to 54.70 MPa (0.31%).

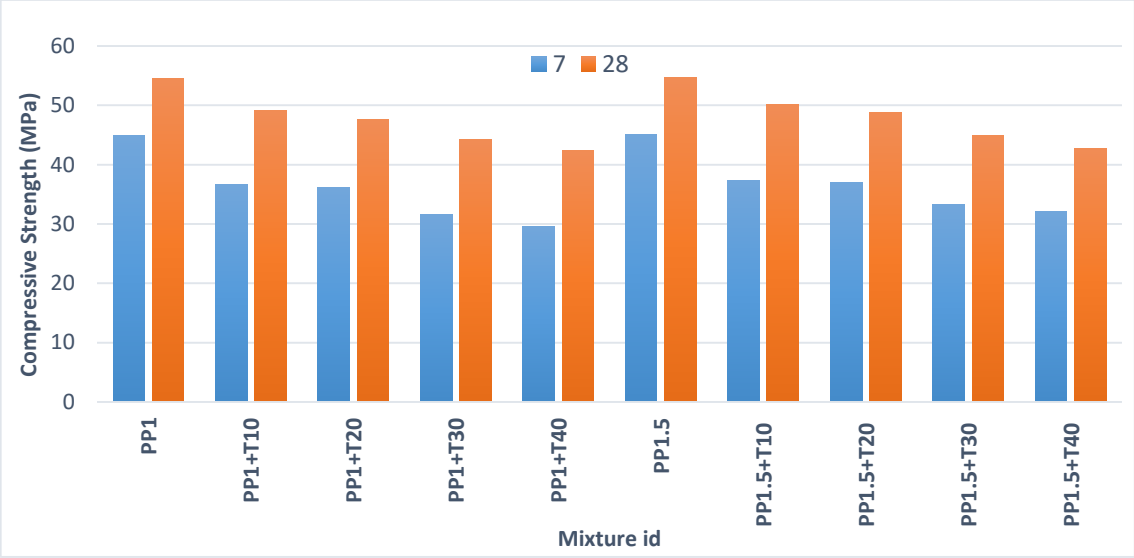


Fig. 5. Compressive strength of ECC specimens at different curing ages.

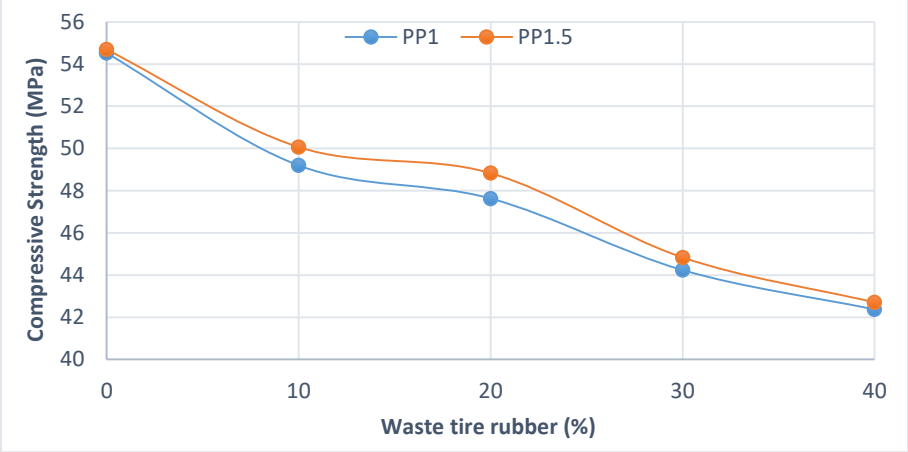


Fig. 6. Compressive strength at 28 days as a function of WTR replacement ratio

The influence of WTR replacement is more clearly observed in Fig. 6. For both fiber dosages, the compressive strength decreased almost linearly as the WTR replacement level increased. The reduction remained relatively moderate up to 20% WTR, whereas a steeper decline occurred between 20% and 40%, indicating that higher rubber contents substantially weaken

the load-carrying capacity of the ECC matrix. At all replacement levels, mixtures reinforced with 1.5% PP fibers exhibited slightly higher compressive strengths than the corresponding 1.0% PP mixtures. For the PP1 mixtures, replacing natural fine aggregate with 10%, 20%, 30%, and 40% WTR reduced the 7-day compressive strength by 18.46%, 19.47%, 29.81%, and 34.37%, respectively, while the corresponding reductions at 28 days were 9.77%, 12.65%, 18.89%, and 22.30%. For the PP1.5 mixtures, the reductions were 17.07%, 18.07%, 26.05%, and 28.71% at 7 days and 8.46%, 10.73%, 18.04%, and 21.94% at 28 days.

The reduction in compressive strength is primarily attributed to the lower stiffness and elastic modulus of WTR compared with natural sand, causing rubber particles to behave as soft inclusions within the cementitious matrix. In addition, the hydrophobic rubber surface results in a weak and porous interfacial transition zone (ITZ), while increased air entrainment further raises the overall porosity of the composite. Similar findings have been reported by Sofi et al. [10] and Valente et al. [11]. Although increasing the PP fiber dosage had little influence on the compressive strength of the control mixtures, it partially compensated for the adverse effect of WTR, particularly at higher replacement levels. At 7 days, the PP1.5 mixtures exhibited compressive strengths 0.33%, 2.05%, 2.07%, 5.71%, and 8.98% higher than the corresponding PP1 mixtures for WTR replacement levels of 0%, 10%, 20%, 30%, and 40%, respectively. The corresponding improvements at 28 days were 0.31%, 1.77%, 2.52%, 1.36%, and 0.78%. Overall, WTR replacement was the dominant parameter governing compressive strength, whereas increasing the PP fiber dosage from 1.0% to 1.5% provided only a modest improvement, particularly at higher WTR contents.

3.2 Splitting Tensile Strength

The splitting tensile strength results obtained after 7 and 28 days are presented in Figs. 7 and 8, respectively. Compared with compressive strength, the tensile behavior of ECC was considerably more sensitive to the PP fiber dosage, whereas the incorporation of WTR produced a non-linear response. As shown in Fig. 7, all mixtures exhibited higher splitting tensile strengths at 28 days than at 7 days because of the continued hydration of the PC-GBFS binder system. Increasing the PP fiber dosage from 1.0% to 1.5% noticeably improved the tensile strength of the control mixtures. The 7-day strength increased from 3.82 MPa to 4.34 MPa (13.6%), while the 28-day strength increased from 4.67 MPa to 5.14 MPa (10%). These results confirm that, unlike compressive strength, the tensile performance of ECC is highly dependent on fiber reinforcement owing to the crack-bridging capability of PP fibers.

The influence of WTR replacement is more clearly illustrated in Fig. 8. For both fiber dosages, the tensile strength decreased when 10% WTR was incorporated, partially recovered at 20% WTR, and then declined again at 30% and 40% WTR. This indicates that an optimum WTR content of approximately 20% exists for tensile performance. For the PP1 mixtures, the 7-day tensile strength decreased by 21.2%, 8.38%, 22.5%, and 26.9% at WTR replacement levels of 10%, 20%, 30%, and 40%, respectively, while the corresponding reductions at 28 days were 17.34%, 5.57%, 19.9%, and 24.4%. A similar trend was observed for the PP1.5 mixtures, where the corresponding reductions at 7 days were 20.74%, 13.13%, 26.04%, and 30.41%, respectively. The temporary recovery observed at 20% WTR is attributed to the elastic nature of the rubber particles, which enhances crack deflection and energy absorption without severely disrupting matrix continuity. However, at higher replacement levels, the low stiffness of WTR together with its weak interfacial bonding with the cementitious matrix leads to stress concentration and premature crack propagation. Similar observations have been reported by Sofi et al. [10] and Valente et al. [11]. For all WTR replacement levels, mixtures reinforced with 1.5% PP fibers consistently exhibited higher tensile strengths than those containing 1.0% PP fibers. At 10%, 20%, 30%, and 40% WTR, increasing the PP fiber dosage improved the 28-

day tensile strength by 7.25%, 4.08%, 6.15%, and 3.97%, respectively. This improvement is attributed to the higher fiber-bridging density, which limits crack opening and delays crack propagation, thereby partially compensating for the weakening effect of WTR.

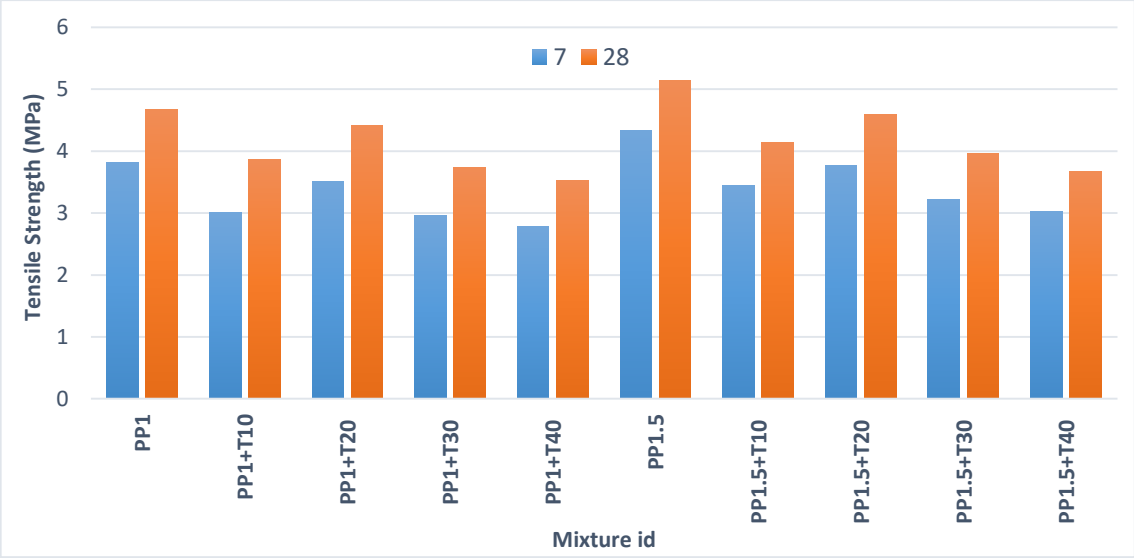


Fig. 7. Splitting tensile strength of ECC specimens at different curing ages

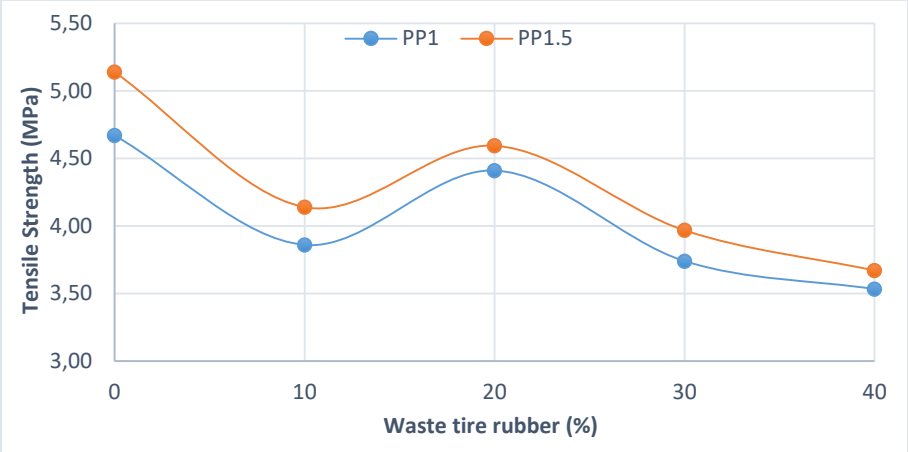


Fig. 8. Splitting tensile strength at 28 days as a function of WTR replacement ratio

3.3 Flexural Strength

The development of flexural strength at 7 and 28 days for the different ECC mixtures is shown in Fig. 9. A clear age-dependent improvement was observed for all mixtures, while the magnitude of flexural strength was governed by both WTR replacement and PP fiber dosage. The WTR-free mixtures exhibited the highest values within each fiber series. At 28 days, increasing the PP fiber content from 1.0% to 1.5% increased the flexural strength from 7.66 to 8.32 MPa, corresponding to an improvement of approximately 8.6%. This enhancement was considerably more pronounced than that observed for compressive strength, reflecting the greater contribution of PP fibers under bending through crack bridging and restriction of crack opening.

The effect of WTR replacement on the 28-day flexural response is presented more clearly in Fig. 10. Unlike the nearly continuous reduction observed in compressive strength, the flexural response followed a non-linear pattern. For the PP1 series, the strength initially decreased from 7.66 MPa to 6.68 MPa at 10% WTR, but subsequently recovered to 7.08 MPa at 20% WTR. A

similar behavior occurred for the PP1.5 series, where the corresponding values were 8.32, 7.23, and 7.50 MPa at 0%, 10%, and 20% WTR, respectively. Further increasing the WTR content to 30% and 40% caused renewed strength reductions in both series. Thus, among the rubber-containing mixtures, 20% WTR consistently provided the most favorable flexural response. The reduction in flexural strength at higher WTR replacement levels can be attributed to the same mechanisms discussed previously for the compressive and splitting tensile strength results. As the WTR content increases, these adverse effects become increasingly dominant, leading to a progressive deterioration in flexural resistance.

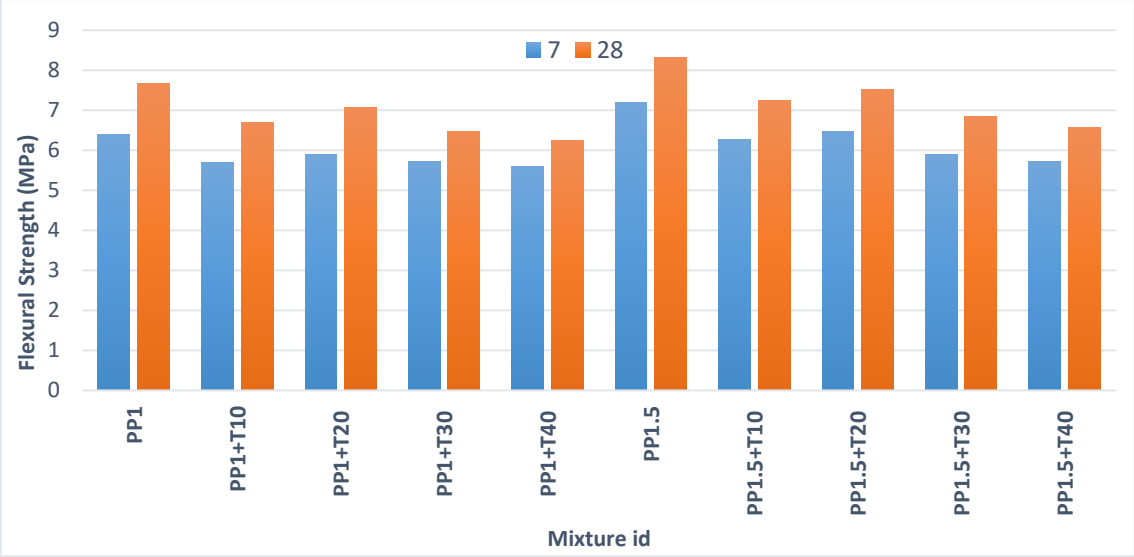


Fig. 9. Flexural strength of ECC specimens at different curing ages.

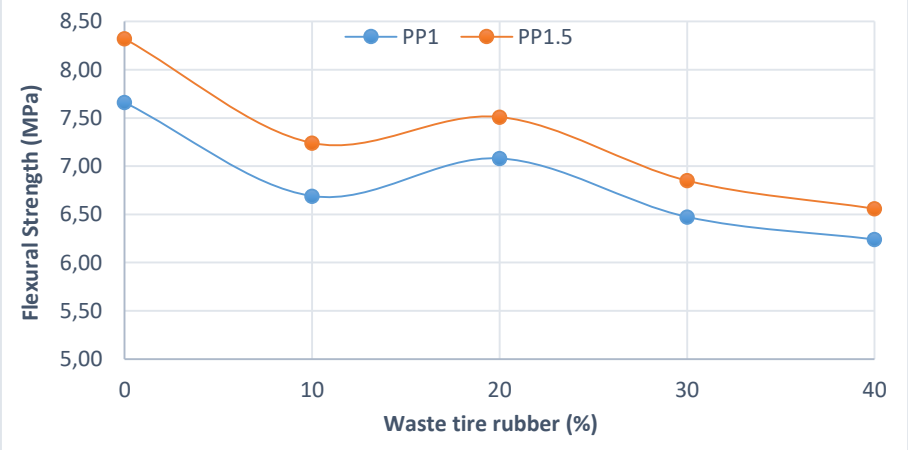


Fig. 10. Flexural strength at 28 days as a function of WTR replacement ratio

Another important feature of Figs. 9 and 10 is the consistently superior flexural performance of the mixtures containing 1.5% PP fibers. Unlike the limited influence of fiber dosage on compressive strength, the higher fiber content provided a noticeable advantage under flexural loading across the entire WTR range. The denser fiber network enhances crack bridging and stress transfer across developing cracks, thereby improving resistance to bending. Nevertheless, this benefit becomes insufficient to fully compensate for the deterioration of the matrix at high WTR contents, particularly at 30% and 40% replacement. From a mechanical-performance perspective, the results indicate that 20% WTR combined with 1.5% PP fibers provides the most favorable configuration among the rubber-containing mixtures investigated. This

combination maintains comparatively high flexural strength while enabling a substantial proportion of natural fine aggregate to be replaced with recycled tire rubber.

4 Conclusions

This study investigated the combined effects of WTR replacement and polypropylene fiber dosage on the mechanical performance of ECC. Based on the experimental results, the following conclusions can be drawn:

- WTR replacement progressively reduced compressive strength, with the greatest reductions occurring at higher replacement levels. At 28 days, incorporating 40% WTR reduced compressive strength by approximately 22%.
- Increasing the PP fiber dosage from 1.0% to 1.5% had only a minor effect on compressive strength but noticeably improved splitting tensile and flexural performance. In the WTR-free mixtures, the corresponding 28-day improvements were approximately 10.0% and 8.6%, respectively.
- Splitting tensile and flexural strengths exhibited a non-linear response to WTR. Following an initial reduction at 10% WTR, both properties partially recovered at 20% WTR, whereas further replacement to 30% and 40% resulted in renewed strength deterioration.
- The higher PP fiber dosage consistently improved tensile and flexural performance in the presence of WTR, indicating that enhanced fiber bridging can partially compensate for the mechanical weakness introduced by rubber particles.
- Among the rubber-containing mixtures, 20% WTR combined with 1.5% PP fibers provided the most favorable mechanical balance, achieving approximately 48.9 MPa compressive strength, 4.59 MPa splitting tensile strength, and 7.50 MPa flexural strength at 28 days.
- The findings demonstrate that an appropriate combination of WTR and PP fibers can enable meaningful replacement of natural fine aggregate while maintaining satisfactory mechanical performance, supporting the development of more resource-efficient ECC mixtures.

References

1. Li, V.C.: From micromechanics to structural engineering. Journal of Structural Mechanics and Earthquake Engineering 10(2), 37-48 (1993).
2. Li, V.C., Wang, S.: Flexural behaviors of glass fiber-reinforced polymer (GFRP) reinforced engineered cementitious composite beams. ACI Materials Journal 99(1), 11-21 (2002).
3. Li, V.C., et al.: Tensile strain-hardening behavior of PVA-ECC. ACI Materials Journal 98(6), 483–492 (2001).
4. Helal, K.A., Tahwia, A.M., Youssf, O.: Behavior of functionally graded concrete beams made of eco-friendly engineered cementitious composites. Innovative Infrastructure Solutions 10, 287 (2025).
5. Mollaei, H., Shaghaghi, T.M., Afshin, H., Ahari, R.S., Mirrezaei, S.S.: Mechanical, rheological, and durability analysis of self-consolidating concretes containing recycled aggregates. Structural Engineering and Mechanics 88(2), 141-157 (2023).
6. Bulut, H.A., Kandil, U.: Mechanical properties of cement-based composites incorporating eco-friendly aggregate of waste rubber. Revista de la Construcción 23(2), 246-270 (2024).
7. Saad, A.G., Sakr, M.A., Khalifa, T.M., Darwish, E.A.: Numerical analysis of rubberized engineered cementitious composite (RECC) RC beams under impact loads. Construction and Building Materials 409, 134162 (2023).

8. Al-Hadeethi, M.I.M., Ecemiş, A.S.: Mechanical behaviour evaluation of scrab tire based rubberized lightweight and normal structural concrete and response at elevated temperatures. Scientific Reports 15, 45570 (2025).
9. Nehdi, M., Khan, A.: Cementitious composites containing recycled tire rubber. Cement, Concrete and Aggregates 23(1), 3-10 (2001).
10. Zhang, Z., Ma, H., Qian, S.: Investigation on properties of ECC incorporating crumb rubber of different sizes. Journal of Advanced Concrete Technology 13(5), 241-251 (2015).
11. Aslani, F., Ma, G.: Normal and high-strength lightweight self-compacting concrete incorporating perlite, scoria, and polystyrene aggregates at elevated temperatures. Journal of Materials in Civil Engineering 30(12), 04018328 (2018).
12. Ismail, M.K., Hassan, A.A.: Performance of full-scale self-consolidating rubberized concrete beams in flexure. ACI Materials Journal 113(2), 207-218 (2016).
13. Sofi, A.: Effect of waste tyre rubber on mechanical and durability properties of concrete: A review. Ain Shams Engineering Journal 9(4), 2691-2700 (2018).
14. Valente, M., Sibai, A.: Rubber/crete: Mechanical properties of scrap to reuse tire-derived rubber in concrete; A review. Journal of Applied Biomaterials & Functional Materials 17(1S), 2280800019835486 (2019).
15. Fauzan, Nur, O.F., Albarqi, K., Melinda, A.P., Al Jauhari, Z.: The effect of waste tyre rubber on mechanical properties of normal concrete and fly ash concrete. International Journal of GEOMATE 20(77), 55-61 (2021).
16. Ahmad, J., Zhou, Z., Majdi, A., Alqurashi, M., Deifalla, A.F.: Overview of concrete performance made with waste rubber tires: A step toward sustainable concrete. Materials 15, 5518 (2022).
17. Al-Fakih, A., Mohammed, B.S., Liew, M.S.: On rubberized engineered cementitious composites (R-ECC): A review of the constituent material. Case Studies in Construction Materials 14, e00536 (2021).
18. Adesina, A., Das, S.: Performance of engineered cementitious composites incorporating crumb rubber as aggregate. Construction and Building Materials 274, 122033 (2021).
19. Lee, S.W., Oh, C.L., Md Zain, M.R.: Mechanical properties of engineered cementitious composites using local ingredients. Journal of Mechanical Engineering 16(2), 145-157 (2019).
20. ASTM International: ASTM C109/C109M: Standard test method for compressive strength of hydraulic cement mortars (using cube specimens). ASTM International, West Conshohocken, PA (2020).
21. ASTM International: ASTM C496/C496M: Standard test method for splitting tensile strength of cylindrical concrete specimens. ASTM International, West Conshohocken, PA (2017).
22. ASTM International: ASTM C78/C78M: Standard test method for flexural strength of concrete (using simple beam with third-point loading). ASTM International, West Conshohocken, PA (2021).

Author Contribution Statement

- *Conceptualization:* Akbar Mikaeelnezhad
- *Methodology:* Reza Saleh Ahari
- *Investigation:* Akbar Mikaeelnezhad, Reza Saleh Ahari
- *Writing – Original Draft:* Akbar Mikaeelnezhad
- *Writing – Review & Editing:* Reza Saleh Ahari

Publication Note
This paper was peer-reviewed, accepted for presentation, and included in the proceedings of the ACE2026 – International Conference on Advances in Civil Engineering, held on 12–14 October 2026 in Trabzon, Türkiye.

This paper may be cited as follows:
Mikaeelnezhad A., Ahari R. S., "Mechanical properties of engineered cementitious composites incorporating waste tire rubber," in Proceedings of the ACE2026– International Conference on Advances in Civil Engineering, Trabzon, Türkiye, 12–14 October 2026.

Effect of zeolite on the mechanical properties of polypropylene fiber-reinforced mortars under different curing temperatures

Mohammad Mahdi Milani[1], Reza Saleh Ahari*[2]
[1] 0009-0009-3892-4368, Department of Civil Engineering, Ta.C., Islamic Azad University, Tabriz, Iran, mm.milani1996@gmail.com
[2] 0000-0003-3471-1727, Department of Civil Engineering, Ta.C., Islamic Azad University, Tabriz, Iran, rsalehahari@iau.ac.ir

Abstract. The use of polypropylene (PP) fibers in cementitious mortars can improve flexural strength and ductility but may reduce compressive strength due to increased porosity and matrix discontinuity. Natural pozzolans such as natural zeolite (NZ) can potentially compensate for this reduction. This study investigates the effects of NZ (5, 10, 15, and 20% cement replacement) and PP fibers (0.1, 0.2, and 0.3%) on the compressive and flexural strengths of mortars cured at -15, 0, 20, and 35 °C for 3, 7, and 28 days. Curing temperature strongly influenced strength development, with -15 °C causing compressive strength losses exceeding 90% relative to 20 °C. Curing at 35 °C accelerated early-age strength development but resulted in an 8-12% reduction in 28-day strength. Although PP fibers alone reduced compressive strength by 10-13%, NZ effectively compensated for this reduction. The optimum performance was obtained with 15% zeolite and 0.3% PP fibers, achieving 25% higher compressive strength and 26% higher flexural strength than the control mixture. The findings highlight the potential of combining NZ and PP fibers to improve mechanical performance under different curing temperatures.

Keywords: Natural zeolite; polypropylene fibers; mechanical properties; curing condition.

1 Introduction

The growing demand for cementitious materials has intensified concerns regarding CO_2 emissions from Portland cement production, making supplementary cementitious materials (SCM) an effective strategy for reducing clinker consumption [1]. Among natural SCMs, natural zeolite (NZ) has attracted attention due to its pozzolanic activity, porous aluminosilicate structure, high specific surface area, and low density, which can improve the hydration and microstructural characteristics of cementitious matrices [2-4]. However, cement-based materials remain inherently brittle, and discrete fibers are commonly incorporated to improve crack control, tensile behavior, ductility, and post-cracking performance [5]. Polypropylene (PP) fibers are particularly attractive because of their low density, corrosion resistance, chemical stability, and cost-effectiveness [6,7], although their performance depends strongly on fiber dosage and the characteristics of the surrounding matrix.

Curing temperature represents another key parameter because it governs the kinetics of cement hydration and pozzolanic reactions and therefore affects the development of the matrix in which the fibers are embedded. Changes in temperature can alter hydration rate, reaction-product formation, interfacial characteristics, and strength evolution [8-10]. This issue is particularly important for zeolite-containing mortars, since the contribution of a pozzolanic material may vary considerably with curing conditions. Consequently, the mechanical response of a mortar containing both NZ and PP fibers cannot necessarily be inferred from studies in which these variables are examined independently. Previous investigations illustrate these individual effects. Alani et al. [11] showed that calcined nano-montmorillonite could modify the strength retention of mortar subjected to elevated temperatures, while Marzouk and Hussein

[12] demonstrated the strong influence of curing temperature and initial moist-curing duration on the strength development of cementitious systems containing silica fume and fly ash. Soriano et al. [13] further reported that pozzolanic additions affected hydration and relative strength development under low-temperature curing. For NZ specifically, Kriptavičius et al. [14] identified a favorable clinoptilolite replacement level of approximately 15% by volume based on flowability, compressive strength, and hydration characteristics. More broadly, SCM incorporation has been shown to significantly modify the fresh and hardened behavior of cement-based materials [15,16].

The role of PP fibers has also been shown to depend strongly on the surrounding matrix and exposure conditions. Richardson reported that increasing PP fiber content could reduce compressive strength and density because of fiber-induced air entrainment [17], whereas Smarzewski [18] demonstrated that PP fibers improved resistance to freeze-thaw deterioration by restricting crack propagation and water ingress. Together, these studies show that neither SCM incorporation nor fiber reinforcement produces a universally beneficial response; their effectiveness depends on dosage, matrix characteristics, and environmental conditions. Despite the extensive literature on natural pozzolans, PP fibers, and temperature-related effects, their combined influence remains insufficiently understood. In particular, limited information is available on how NZ replacement and PP fiber incorporation interact under different curing temperatures to govern the mechanical development of cement mortar. Therefore, the present study investigates the combined effects of NZ as a partial cement replacement, PP fiber dosage, and curing temperature on the mechanical properties of cement mortars. The results are intended to clarify the interaction among these variables and to identify mixture conditions capable of maintaining satisfactory mechanical performance under different curing environments.

2 Experimental and Numerical Methods

2.1 Materials

Type II Portland cement (PC), conforming to ASTM C150, was used as the primary binder, while NZ was incorporated as a supplementary cementitious material. The physical properties and chemical compositions of PC and zeolite are summarized in Table 1. Natural silica sand was used as fine aggregate (FA), with a maximum particle size of 4.75 mm and a saturated surface-dry (SSD) specific gravity of 2.63. A polycarboxylate ether-based high-range water-reducing admixture (HRWR), commercially known as Carboxal HF5000, with a specific gravity of 1.10, was incorporated to achieve the required workability. Polypropylene fibers were used as reinforcement and had a length of 19 mm, a diameter of 22 μm, a specific gravity of 0.91, an aspect ratio (L/d) of approximately 863, and a circular cross-section. Prior to mixing, the PP fibers were manually separated to promote uniform dispersion throughout the mortar and minimize fiber agglomeration.

Table 1. Physical and chemical properties of PC and NZ

	CaO, (%)	SiO_2, (%)	Al_2O_3, (%)	Fe_2O_3, (%)	MgO, (%)	SO_3, (%)	K_2O, (%)	Na_2O, (%)	TiO, (%)	FL (%)	Other minor oxides, (%)	LOI, (%)	SG	Blaine, (cm^2/g)
PC	67.65	9.53	7.8	4.08	4.26	1.18	0.71	0.22	0.16	2.21	0.86	1.34	3.14	3312
NZ	4.20	80.50	6.76	1.59	1.55	0.06	2.11	2.65	0.32	-	0.06	0.2	2.15	4290

FL: Free lime, LOI: Loss on ignition, SG: Specific gravity

2.2 Mix proportions and Specimen Preparation

Eight mortar mixtures were designed with a constant water-to-binder (w/b) ratio of 0.46, as summarized in Table 2. The experimental variables were the PP fiber volume fraction (0.1%, 0.2%, and 0.3%) and the zeolite replacement level (5%, 10%, 15%, and 20% by mass of cement). For mixtures containing both NZ and PP fibers, the fiber content was fixed at 0.3% by volume. A three-stage mixing procedure was adopted to achieve uniform distribution of the constituents. First, the fine aggregate was mixed with one-third of the total mixing water. The binder materials (PC and NZ) were then introduced together with the second third of the water. Finally, the PP fibers were gradually added, followed by the remaining water premixed with the HRWR, and mixing was continued until a homogeneous mortar was obtained. After mixing, the mortar was cast into molds and consolidated using a vibrating table. The specimens were demolded after 24 h and subsequently exposed to four curing temperatures: -15, 0, 20, and 35 °C, using controlled curing environments appropriate for each temperature. Representative specimens under the different curing conditions are shown in Fig. 1.

Table 2. Mix proportions of the mortar specimens (kg/m^3)

Mix ID	Water	PC	NZ	PP	HRWR	FA
Control	230	500	0	0	5	1542
PP 0.1	230	500	0	0.9	5	1540
PP 0.2	230	500	0	1.8	5.7	1537
PP 0.3	230	500	0	2.7	6.2	1532
NZ5 + PP 0.3	230	475	25	2.7	6.2	1523
NZ10 + PP 0.3	230	450	50	2.7	6.4	1513
NZ15 + PP 0.3	230	425	75	2.7	6.5	1504
NZ20 + PP 0.3	230	400	100	2.7	6.6	1492



Fig. 1. Mortar specimens under different curing conditions.

2.3 Mechanical properties

The mechanical performance of the mortar mixtures was evaluated through compressive and flexural strength tests. Compressive strength was determined in accordance with ASTM C109 [19] using 50 mm cubic specimens, while flexural strength was determined in accordance with ASTM C348 [20] using 40×40×160 mm prismatic specimens subjected to three-point bending. The experimental setups for the compressive and flexural strength tests are shown in Figs. 2(a) and 2(b), respectively. For both tests, the reported results represent the average of three specimens. A coefficient of variation (CV) of 4-5% was considered acceptable; tests exceeding this range were repeated to ensure consistency and reliability of the measurements.



(a) (b)

Fig. 2. Mechanical strength test setups: (a) compressive strength and (b) flexural strength

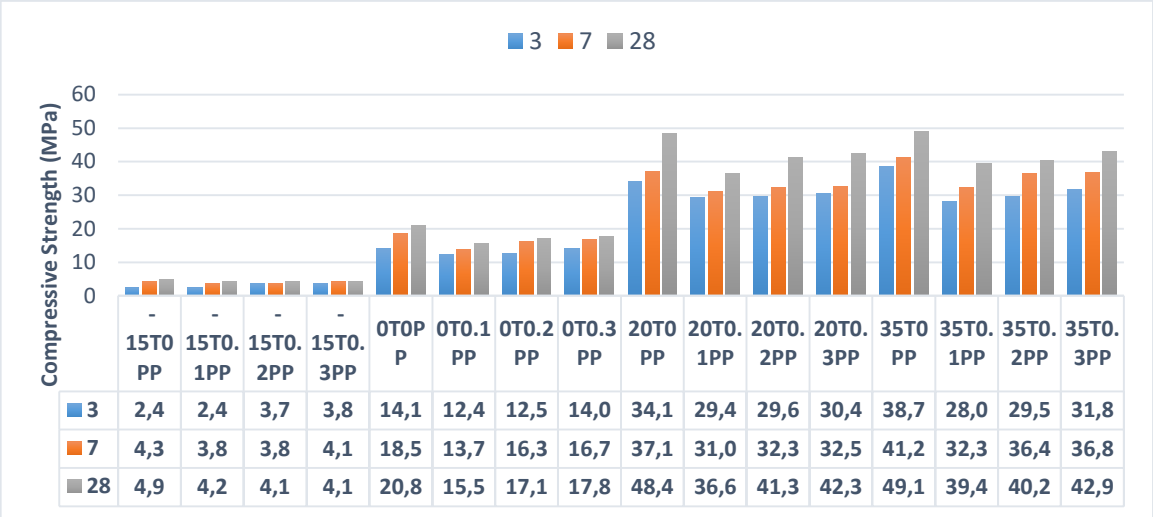
3 Results and Discussion

3.1 Compressive Strength

The compressive strength development of the PP fiber-reinforced mortars at 3, 7, and 28 days under different curing temperatures is presented in Fig. 3, while Fig. 4 illustrates the effect of PP fiber dosage on the 28-day strength. The results demonstrate that curing temperature was the dominant parameter governing strength development. Increasing the temperature from -15 to 35 °C substantially enhanced compressive strength, whereas PP fiber incorporation generally reduced the strength relative to the corresponding unreinforced control.

At -15 °C, all mixtures exhibited limited strength development, with 28-day values ranging from 4.1 to 4.9 MPa. Although the 0.2% and 0.3% PP mixtures showed higher 3-day strengths than the control, this advantage disappeared at later ages. At 0 °C, the 28-day strength decreased from 20.8 MPa for the control to 15.5, 17.1, and 17.8 MPa for the 0.1%, 0.2%, and 0.3% PP mixtures, respectively. A similar response occurred at 20 °C, where the control reached 48.4 MPa compared with 36.6-42.3 MPa for the fiber-reinforced mixtures. At 35 °C, the corresponding values were 49.1 MPa for the control and 39.4, 40.2, and 42.9 MPa for the three PP dosages. Thus, although PP fibers generally reduced compressive strength, increasing their content from 0.1% to 0.3% progressively moderated this reduction.

The reduction associated with PP fibers may be attributed to increased air entrapment, disruption of matrix continuity, and the relatively low stiffness of PP fibers under compressive loading. Similar reductions in compressive strength with PP fiber incorporation were reported by Ibrahim et al. [21]. Conversely, higher curing temperatures promoted matrix development and substantially increased strength, consistent with the temperature-dependent behavior reported by Lu et al. [22]. Overall, Figs. 3 and 4 indicate that curing temperature exerted a substantially greater influence on compressive strength than PP fiber dosage.



	-15T0PP	-15T0.1PP	-15T0.2PP	-15T0.3PP	0T0PP	0T0.1PP	0T0.2PP	0T0.3PP	20T0PP	20T0.1PP	20T0.2PP	20T0.3PP	35T0PP	35T0.1PP	35T0.2PP	35T0.3PP
3	2,4	2,4	3,7	3,8	14,1	12,4	12,5	14,0	34,1	29,4	29,6	30,4	38,7	28,0	29,5	31,8
7	4,3	3,8	3,8	4,1	18,5	13,7	16,3	16,7	37,1	31,0	32,3	32,5	41,2	32,3	36,4	36,8
28	4,9	4,2	4,1	4,1	20,8	15,5	17,1	17,8	48,4	36,6	41,3	42,3	49,1	39,4	40,2	42,9

Fig. 3. Compressive strength development of PP fiber-reinforced mortars under different curing temperatures

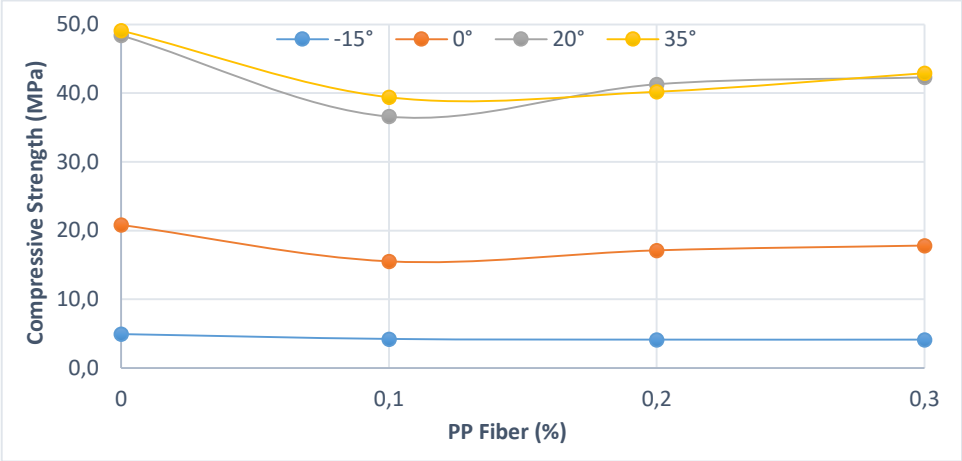
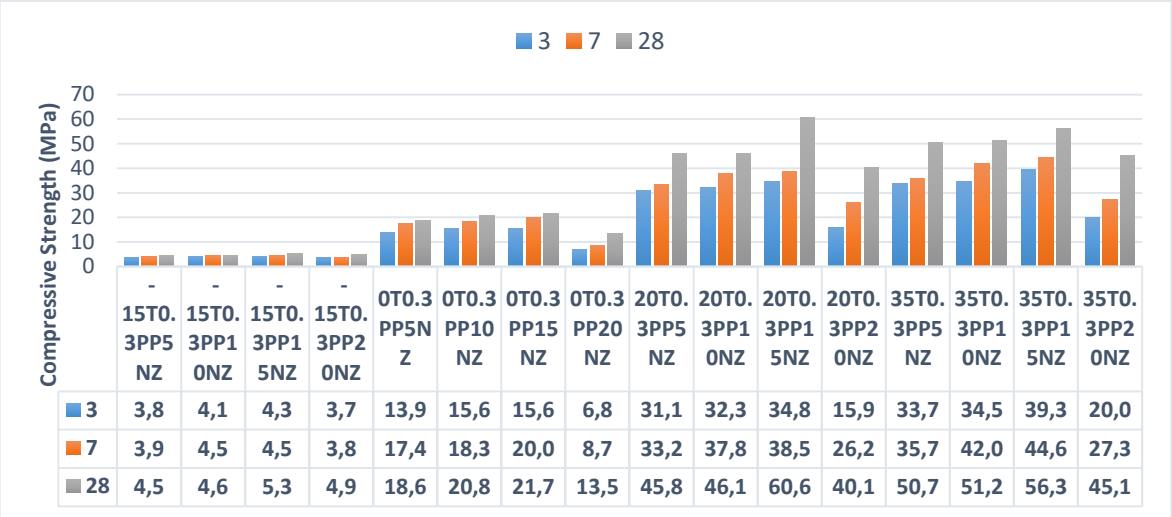


Fig. 4. Effect of PP fiber dosage on 28-day compressive strength under different curing temperatures

The influence of NZ replacement on mortars containing 0.3% PP fiber is presented in Fig. 5, while Fig. 6 shows the corresponding 28-day trends. At -15 °C, NZ content had little influence, with 28-day strengths ranging from 4.1 to 5.3 MPa. At 0 °C, increasing NZ from 0% to 15% increased the 28-day strength from 17.8 to 21.7 MPa, whereas 20% NZ reduced it to 13.5 MPa. The beneficial effect of NZ became considerably more pronounced at 20 °C. The 28-day strength increased from 42.3 MPa without NZ to 45.8, 46.1, and 60.6 MPa at 5%, 10%, and 15% replacement, respectively. Thus, 15% NZ produced a 43.3% improvement, whereas increasing the replacement to 20% reduced the strength to 40.1 MPa. At 35 °C, a similar trend was observed, with strength increasing from 42.9 MPa to 50.7, 51.2, and 56.3 MPa at 5%, 10%, and 15% NZ before decreasing to 45.1 MPa at 20%.

The improvement at moderate NZ contents can be associated with its filler and pozzolanic contributions, whereas excessive replacement may reduce the effective cement content and increase water demand. The favorable performance of mortars incorporating natural zeolite and PP fibers is consistent with the findings of Dabbaghi et al. [3]. Overall, the results reveal a clear interaction between curing temperature and NZ content. Among the investigated combinations, 15% NZ with 0.3% PP fiber provided the highest compressive strength, reaching 60.6 MPa at 28 days under 20 °C curing.



	-15T0.3PP5NZ	-15T0.3PP10NZ	-15T0.3PP15NZ	-15T0.3PP20NZ	0T0.3PP5NZ	0T0.3PP10NZ	0T0.3PP15NZ	0T0.3PP20NZ	20T0.3PP5NZ	20T0.3PP10NZ	20T0.3PP15NZ	20T0.3PP20NZ	35T0.3PP5NZ	35T0.3PP10NZ	35T0.3PP15NZ	35T0.3PP20NZ
3	3,8	4,1	4,3	3,7	13,9	15,6	15,6	6,8	31,1	32,3	34,8	15,9	33,7	34,5	39,3	20,0
7	3,9	4,5	4,5	3,8	17,4	18,3	20,0	8,7	33,2	37,8	38,5	26,2	35,7	42,0	44,6	27,3
28	4,5	4,6	5,3	4,9	18,6	20,8	21,7	13,5	45,8	46,1	60,6	40,1	50,7	51,2	56,3	45,1

Fig. 5. Compressive strength development of NZ-modified PP fiber-reinforced mortars under different curing temperatures

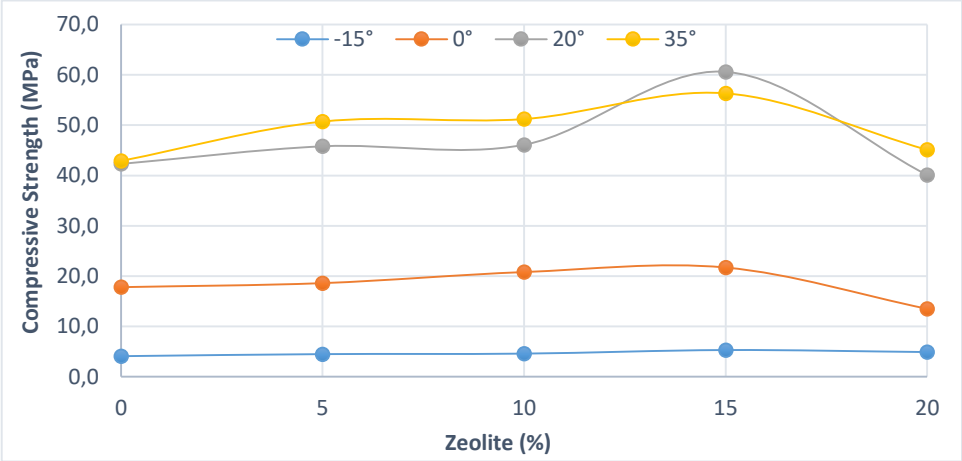
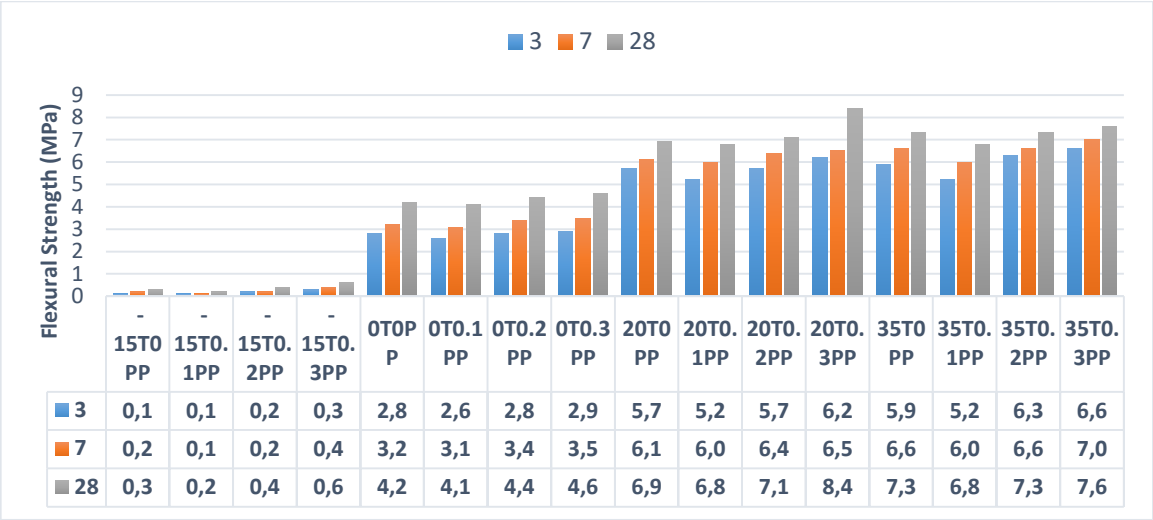


Fig. 6. Effect of NZ replacement level on 28-day compressive strength under different curing temperatures

3.2 Flexural Strength

The flexural strength development of PP fiber-reinforced mortars at 3, 7, and 28 days under different curing temperatures is presented in Fig. 7, while Fig. 8 illustrates the effect of PP fiber dosage on the 28-day strength. Overall, curing temperature strongly influenced flexural strength, while the effect of PP fiber dosage was non-linear and dependent on the curing condition. At -15 °C, flexural strength remained extremely low, with 28-day values ranging from 0.2 to 0.6 MPa, indicating severely restricted matrix development. At 0 °C, the 28-day strength varied from 4.1 to 4.6 MPa for the fiber-reinforced mixtures compared with 4.2 MPa for the control. At higher curing temperatures, the influence of PP fibers became more evident. At 20 °C, the 28-day flexural strengths of the control and mixtures containing 0.1%, 0.2%, and 0.3% PP were 6.9, 6.8, 7.1, and 8.4 MPa, respectively. Thus, 0.3% PP resulted in a 21.7% increase relative to the control. At 35 °C, the corresponding values were 7.3, 6.8, 7.3, and 7.6 MPa, respectively. As further illustrated in Fig. 8, low PP dosages did not necessarily improve flexural strength; however, further increasing the fiber content resulted in strength recovery, with 0.3% PP providing the highest strength at both 20 and 35 °C. The beneficial effect at higher fiber contents can be attributed to enhanced crack bridging, which restricts crack propagation

and increases resistance to flexural failure. Similar beneficial effects of PP fibers on flexural behavior have been reported by Fu et al. [23] and Wei et al. [24].



	-15T0PP	-15T0.1PP	-15T0.2PP	-15T0.3PP	0T0PP	0T0.1PP	0T0.2PP	0T0.3PP	20T0PP	20T0.1PP	20T0.2PP	20T0.3PP	35T0PP	35T0.1PP	35T0.2PP	35T0.3PP
3	0,1	0,1	0,2	0,3	2,8	2,6	2,8	2,9	5,7	5,2	5,7	6,2	5,9	5,2	6,3	6,6
7	0,2	0,1	0,2	0,4	3,2	3,1	3,4	3,5	6,1	6,0	6,4	6,5	6,6	6,0	6,6	7,0
28	0,3	0,2	0,4	0,6	4,2	4,1	4,4	4,6	6,9	6,8	7,1	8,4	7,3	6,8	7,3	7,6

Fig. 7. Flexural strength development of PP fiber-reinforced mortars under different curing temperatures

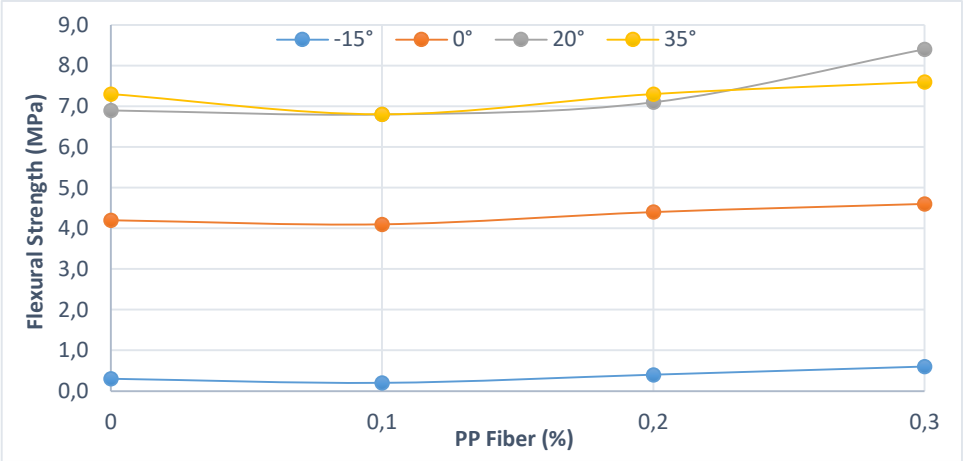
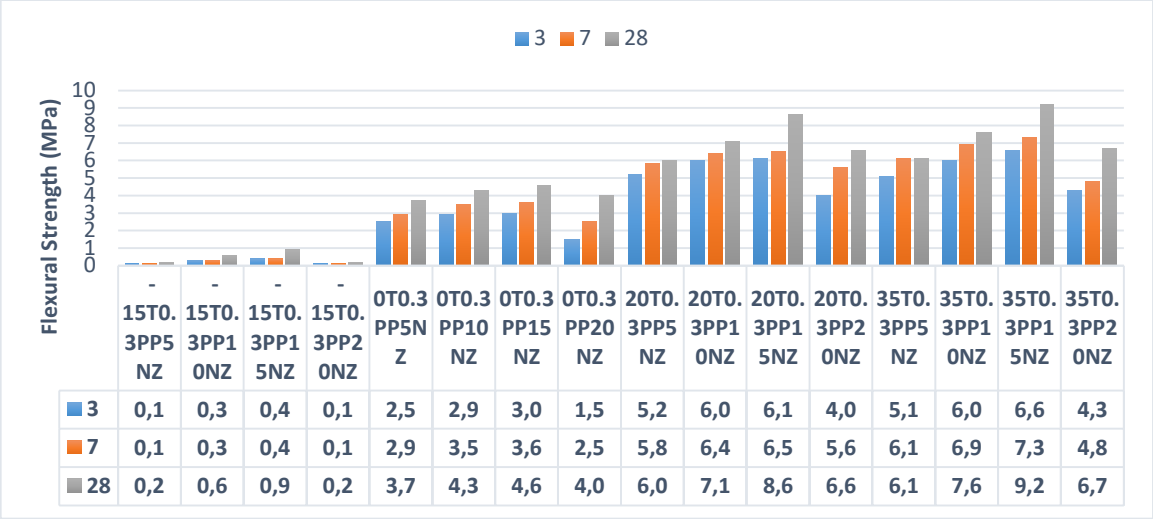


Fig. 8. Effect of PP fiber dosage on the 28-day flexural strength under different curing temperatures

The combined effects of NZ replacement and curing temperature on the flexural strength of mortars containing 0.3% PP fiber are presented in Fig. 9, while the corresponding 28-day trends are shown in Fig. 10. The results reveal a distinctly non-linear response to NZ content. At -15 °C, strength development remained severely restricted; nevertheless, the 15% NZ mixture reached the highest 28-day strength of 0.9 MPa compared with 0.6 MPa for the NZ-free mixture. At 0 °C, the 28-day strengths at 0%, 5%, 10%, 15%, and 20% NZ were 4.6, 3.7, 4.3, 4.6, and 4.0 MPa, respectively, indicating that the contribution of NZ remained limited under low-temperature curing. The influence of NZ became considerably more pronounced at higher temperatures. At 20 °C, the 28-day flexural strength initially decreased from 8.4 MPa without NZ to 6.0 MPa at 5% replacement, followed by an increase to 7.1 and 8.6 MPa at 10% and 15% NZ, respectively. Further increasing the replacement to 20% reduced the strength to 6.6 MPa. A similar trend was observed at 35 °C, where the corresponding strengths were 7.6, 6.1, 7.6, 9.2, and 6.7 MPa. As clearly shown in Fig. 10, 15% NZ represented the optimum replacement level, producing the highest flexural strength at all curing temperatures. The maximum value of 9.2 MPa was obtained at 35 °C, representing an improvement of approximately 21.1% over

the corresponding NZ-free mixture. The favorable performance at 15% NZ may be associated with an effective balance between matrix refinement and fiber matrix interaction, which enhances the crack-bridging efficiency of PP fibers. In contrast, the strength reduction at 20% NZ suggests that excessive cement replacement offsets these beneficial effects through dilution of the cementitious matrix and increased water demand. Overall, the results demonstrate that the flexural response is governed by a coupled interaction among curing temperature, PP fiber dosage, and NZ content. Among the investigated combinations, 0.3% PP fiber with 15% NZ provided the most favorable flexural performance, reaching 9.2 MPa at 28 days under 35 °C curing.



	-15T0.3PP5NZ	-15T0.3PP10NZ	-15T0.3PP15NZ	-15T0.3PP20NZ	0T0.3PP5NZ	0T0.3PP10NZ	0T0.3PP15NZ	0T0.3PP20NZ	20T0.3PP5NZ	20T0.3PP10NZ	20T0.3PP15NZ	20T0.3PP20NZ	35T0.3PP5NZ	35T0.3PP10NZ	35T0.3PP15NZ	35T0.3PP20NZ
3	0,1	0,3	0,4	0,1	2,5	2,9	3,0	1,5	5,2	6,0	6,1	4,0	5,1	6,0	6,6	4,3
7	0,1	0,3	0,4	0,1	2,9	3,5	3,6	2,5	5,8	6,4	6,5	5,6	6,1	6,9	7,3	4,8
28	0,2	0,6	0,9	0,2	3,7	4,3	4,6	4,0	6,0	7,1	8,6	6,6	6,1	7,6	9,2	6,7

Fig. 9. Flexural strength development of NZ-modified PP fiber-reinforced mortars under different curing temperatures

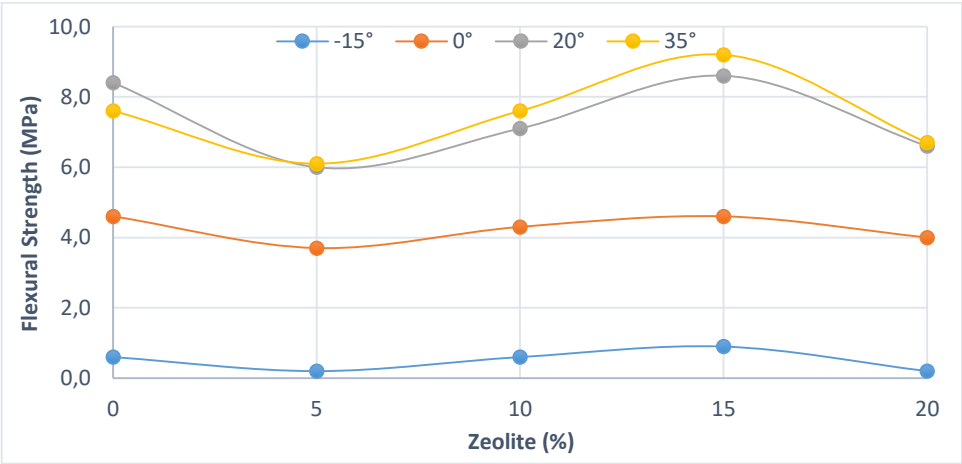


Fig. 10. Effect of NZ replacement level on the 28-day flexural strength under different curing temperatures

4 Conclusion

This study investigated the combined effects of NZ, PP fibers, and curing temperature on the mechanical performance of cement mortars. The following conclusions can be drawn:

- Curing temperature was the dominant factor controlling mechanical performance. Sub-zero curing at -15 °C severely restricted strength development, whereas higher curing temperatures substantially improved both compressive and flexural strengths.
- PP fibers affected compressive and flexural strengths differently. Fiber incorporation generally reduced compressive strength, while 0.3% PP provided the best performance among the fiber-reinforced mixtures and increased the 28-day flexural strength by 21.7% at 20 °C compared with the unreinforced control.
- The effect of NZ was non-linear and temperature-dependent. A replacement level of 15% consistently provided the most favorable response, whereas increasing NZ to 20% generally resulted in strength deterioration.
- The combination of 15% NZ and 0.3% PP fiber was identified as the optimum mixture within the investigated ranges. It achieved the highest 28-day compressive strength of 60.6 MPa at 20 °C, representing a 43.3% improvement over the corresponding NZ-free mixture.
- The same mixture achieved the highest flexural strength of 9.2 MPa at 35 °C, approximately 21.1% higher than its NZ-free counterpart. This demonstrates that the optimum curing temperature is property-dependent, with maximum compressive and flexural strengths occurring at different temperatures.
- Overall, the findings highlight the importance of jointly optimizing NZ content, PP fiber dosage, and curing temperature, rather than considering their effects independently.

References

1. Wongkeo, W., Thongsanitgarn, P., Chaipanich, A.: Compressive strength and drying shrinkage of fly ash-bottom ash-silica fume multi-blended cement mortars. Materials & Design 36, 655–662 (2012).
2. Sedaqatdoost, A., et al.: Effects of zeolite on compressive strength of lightweight concrete. In: 1st National Concrete Industry Conference (2012).
3. Dabbaghi, F., Sadeghi-Nik, A., Libre, N.A., Nasrollahpour, S.: Characterizing fiber reinforced concrete incorporating zeolite and metakaolin as natural pozzolans. Structures 34, 2617–2627 (2021).
4. Ahmadi, B., Shekarchi, M.: Use of natural zeolite as a supplementary cementitious material. Cement and Concrete Composites 32(2), 134–141 (2010).
5. Afridi, B.Z., Shahzada, K., Naqash, M.T.: Mechanical properties of polypropylene fibers mixed cement-sand mortar. Journal of Applied Engineering Science 17(2), 116–125 (2019).
6. Kim, J.H., Qudoos, A., Jakhrani, S.H., Atta-ur-Rehman, Lee, J.B., Kim, S.S., Ryou, J.S.: Mechanical properties and sulfate resistance of high volume fly ash cement mortars with air-cooled slag as fine aggregate and polypropylene fibers. Materials 12(3), 469 (2019).
7. Wang, Y., Chen, S., Xu, Z., Liu, S., Hu, H.: Damage processes of polypropylene fiber reinforced mortar in different fiber content revealed by acoustic emission behavior. Journal of Wuhan University of Technology-Materials Science Edition 33(1), 155–163 (2018).
8. Aqil, M., Bahi, L., Ouadif, L., Belhaj, S., Edderkaoui, R.: The influence of curing temperature, plastic additives and polypropylene fibers on the mechanical behaviour of cementitious materials. E3S Web of Conferences 150, 02012 (2020).
9. Khatib, J.M.: Low temperature curing of metakaolin concrete. Journal of Materials in Civil Engineering 21(8), 362–367 (2009).

10. Huang, D., Wang, Y., Xia, Q., Tian, J., Li, Y., Peng, G.: Effect of curing temperature on microstructure and durability of concrete: A review. Journal of Engineering 2026, 5688760 (2026).
11. Alani, S., Hassan, M., Jaber, A., Ali, I.: Effects of elevated temperatures on strength and microstructure of mortar containing nano-calcined montmorillonite clay. Construction and Building Materials 263, 120895 (2020).
12. Marzouk, H., Hussein, A.: Effect of curing age on high-strength concrete at low temperatures. Journal of Materials in Civil Engineering 7(3), 161–167 (1995).
13. Soriano, L., Monzó, J., Bonilla, M., Tashima, M.M., Payá, J., Borrachero, M.V.: Effect of pozzolans on the hydration process of Portland cement cured at low temperatures. Cement and Concrete Composites 42, 41–48 (2013).
14. Kriptavičius, D., Girskas, G., Skripkiūnas, G.: Influence of natural zeolite on Portland cement hydration processes and properties of hardened cement paste. Ceramics–Silikáty 65(3), 247–254 (2021).
15. Saleh Ahari, R., Erdem, T., Ramyar, K.: Effect of various supplementary cementitious materials on rheological properties of self-consolidating concrete. Construction and Building Materials 75, 89–98 (2015).
16. Kim, H.-K.: Utilization of sieved and ground coal bottom ash powders as a coarse binder in high-strength mortar to improve workability. Construction and Building Materials 91, 57–64 (2015).
17. Richardson, A.E.: Compressive strength of concrete with polypropylene fibre additions. Structural Survey 24(2), 138–153 (2006).
18. Smarzewski, P.: Freeze-thaw resistance and mechanical properties of high-performance self-compacting concrete with polypropylene fibers. Applied Sciences 10(19), 6753 (2020).
19. ASTM International: ASTM C109: Standard test method for compressive strength of hydraulic cement mortars (using cube specimens). ASTM International, West Conshohocken, PA (2009).
20. ASTM International: ASTM C348: Standard test method for flexural strength of hydraulic-cement mortars. ASTM International, West Conshohocken, PA (2008).
21. Ibrahim, Y.A., Hasan, A.H., Maroof, N.R.: Effects of polypropylene fiber content on strength and workability properties of concrete. Polytechnic Journal 9(1), 7–12 (2019).
22. Lu, J., Liu, J., Yang, H., Gao, J., Wan, X., Zhang, J.: Influence of curing temperatures on the performances of fiber-reinforced concrete. Construction and Building Materials 339, 127640 (2022).
23. Fu, Q., Zhang, Z., Xu, W., Zhao, X., Zhang, L., Wang, Y., Niu, D.: Flexural behavior and prediction model of basalt fiber/polypropylene fiber-reinforced concrete. International Journal of Concrete Structures and Materials 16, 31 (2022).
24. Wei, Y., Qin, Y., Chai, J., Xu, C., Zhang, Y., Zhang, X.: Experimental study on compressive and flexural performances of polypropylene fiber-reinforced concrete. Geofluids 2022, 4168918 (2022).

Author Contribution Statement

- *Conceptualization:* Mohammad Mahdi Milani
- *Methodology:* Reza Saleh Ahari
- *Investigation:* Mohammad Mahdi Milani, Reza Saleh Ahari
- *Writing – Original Draft:* Reza Saleh Ahari
- *Writing – Review & Editing:* Reza Saleh Ahari

Publication Note
This paper was peer-reviewed, accepted for presentation, and included in the proceedings of the ACE2026 – International Conference on Advances in Civil Engineering, held on 12–14 October 2026 in Trabzon, Türkiye.

This paper may be cited as follows:
Milani M. M., Ahari R. S., “Effect of zeolite on the mechanical properties of polypropylene fibre-reinforced mortars under different curing temperatures” in Proceedings of the ACE2026 – International Conference on Advances in Civil Engineering, Trabzon, Türkiye, 12–14 October 2026.

Effect of fibre type and content on the interlayer bond strength of fibre-reinforced self-consolidating concrete cast in distinct layers

Meysam Khalilzadeh[1] and Reza Saleh Ahari*[2]
[1] https://orcid.org/0009-0007-0280-8272, Department of Civil Engineering, Ta.C., Islamic Azad University, Tabriz, Iran, khalilzadehmeysam0@gmail.com
[2] https://orcid.org/0000-0003-3471-1727, Department of Civil Engineering, Ta.C., Islamic Azad University, Tabriz, Iran, rsalehahari@iau.ac.ir

Abstract. The multilayer casting of self-consolidating concrete (SCC) may significantly reduce interlayer bond performance, particularly when successive layers are placed after prolonged casting intervals. However, the influence of fiber reinforcement on mitigating this deterioration has not been comprehensively investigated. This study evaluated the effectiveness of glass fibers (GF) and steel fibers (SF), used in mono and hybrid configurations, for improving the residual bond strength (RBS) of multilayer SCC. Fiber dosages of 0.5%, 1.0%, and 1.5% (by volume) were investigated under casting intervals of 0, 40, 80, 120, and 160 min. Interlayer bond performance was assessed using direct shear strength tests. Fiber incorporation substantially enhanced bond retention compared with the control mixture, with the improvement becoming increasingly pronounced as the casting interval increased. Among the mono-fiber mixtures, 1.5% GF achieved an RBS of approximately 51% after a 160 min delay, whereas 1.5% SF exhibited superior performance with an RBS of about 63%, compared with nearly 37% for the control mixture. Increasing the fiber dosage from 0 to 1.5% improved bond strength by approximately 18% and 20% under monolithic casting for GF- and SF-reinforced mixtures, respectively, while the corresponding enhancements increased to about 62% and 105% after 160 min. Hybrid fiber systems exhibited a clear synergistic effect. The optimum performance was obtained with a 30%GF-70%SF hybrid at a total fiber dosage of 1.5%, achieving approximately 158% higher interlayer bond strength than the control and the highest RBS (about 71%) after 160 min. These findings demonstrate that optimized hybrid fiber reinforcement effectively mitigates time-dependent interlayer bond deterioration in multilayer SCC.

Keywords: Self-consolidating concrete; Residual bond strength; Glass fiber; Steel fibers.

1 Introduction

The use of self-consolidating concrete (SCC) has become increasingly common in large concrete elements where construction is carried out through the sequential placement of multiple lifts. Unlike conventionally vibrated concrete, SCC relies entirely on its self-flowing capability, making the quality of the interface between successive layers highly dependent on the condition of the previously placed concrete. As the elapsed time between placements increases, the lower layer gradually loses its fresh characteristics owing to structural buildup and early hydration, which weakens the interaction between adjacent lifts and promotes the formation of cold joints. Consequently, the interlayer region often becomes the weakest part of the composite element, reducing its structural reliability under service loads [1,2].

The quality of the bond developed at the interface is controlled by both material characteristics and casting conditions. Fresh-state rheology governs the ability of the newly placed layer to penetrate and integrate with the underlying concrete, while prolonged delays

between successive placements increase the likelihood of cold joint formation [3,4]. In addition, mixture design parameters such as fiber type and dosage, binder composition, water-to-powder ratio, supplementary cementitious material (SCM) type and dosage, superplasticizers, and viscosity-modifying admixtures directly influence workability, structural buildup, and ultimately the bond performance between successive layers [5,6]. Although considerable attention has been devoted to improving the mechanical properties of fiber-reinforced SCC [7,8], the combined influence of fiber type, fiber content, and casting delay on the interlayer bond behavior of multilayer SCC has not yet been fully clarified. Addressing this knowledge gap is essential for the reliable design and construction of multilayer SCC structures.

Fiber incorporation is widely recognized as an effective approach for enhancing the tensile strength, crack resistance, toughness, and durability of cementitious materials. However, these benefits are generally accompanied by modifications in the fresh-state behavior of SCC. Previous studies have demonstrated that fiber type, geometry, and dosage significantly affect rheological parameters, including yield stress, plastic viscosity, and flowability. In general, increasing the fiber content increases particle interlocking and mixture cohesiveness, resulting in higher resistance to flow and a more pronounced structural build-up of the fresh matrix [8-10]. Recent investigations have further shown that fiber reinforcement influences the thixotropic behavior and structural recovery of cementitious materials. Since structural build-up governs the evolution of the fresh concrete surface during resting periods, it plays a critical role in determining the degree of intermixing between successive concrete layers. A rapid increase in structural build-up before the placement of a new layer may reduce interface cohesion and promote cold-joint formation, whereas excessive fiber contents may further intensify these effects through increased yield stress and cohesiveness [8-10].

Hybrid fiber reinforcement has attracted increasing attention because combining fibers with different mechanical characteristics can provide performance levels that cannot be achieved using a single fiber type alone. Previous studies have shown that different fiber types contribute differently to the fresh and hardened behavior of cementitious composites, making hybrid fiber systems an attractive approach for improving overall performance [7-10]. The complementary actions of these fibers are expected to enhance stress transfer across the interlayer interface and improve bond integrity under delayed casting conditions. Nevertheless, although hybrid fiber systems have been extensively investigated for improving the mechanical performance of cementitious composites, their influence on the interlayer bond behavior of multilayer SCC has received limited attention.

Despite these advances, existing studies have primarily focused on the influence of fibers on rheological properties, workability, and thixotropic behavior, whereas their direct effect on the interlayer bond performance of multilayer SCC has received considerably less attention. In particular, the combined effects of fiber type, fiber dosage, and casting interval on the residual bond strength between successive layers remain insufficiently understood. Therefore, this study experimentally investigates the effectiveness of glass fibers (GF), steel fibers (SF), and hybrid fiber systems in improving the interlayer bond performance of multilayer SCC subjected to different casting intervals. The findings provide practical guidance for optimizing fiber-reinforced SCC mixtures intended for multilayer construction applications.

2 Experimental procedures

2.1 Materials

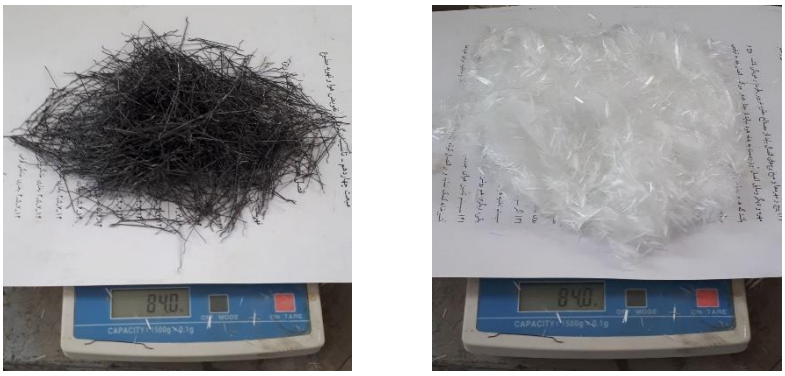
The SCC mixtures in this study were prepared using ordinary Portland cement (PC, Type I-425) conforming to ASTM C150 [11] Type I. A Class F fly ash (FA) was used as a supplementary cementitious material by replacing 20 wt.% of the PC. The physical and

chemical properties of the PC and FA are presented in Table 1. Two types of discontinuous fibers, namely alkali-resistant E-glass fibers (GF) and steel fibers (SF), were used as reinforcing materials. The fibers were incorporated individually and in hybrid combinations at total fiber contents of 0.5%, 1.0%, and 1.5% by mass of the total cementitious materials. For the hybrid mixtures, the total fiber dosage was divided either equally between glass and steel fibers (50% GF-50% SF) or at a ratio of 30% glass fibers and 70% steel fibers. Photographs of the glass and steel fibers are presented in Fig. 1. Natural river aggregates with a maximum particle size of 15 mm for coarse aggregate and 5 mm for fine aggregate were utilized. The bulk specific gravity of the coarse and fine aggregates was 2.62 and 2.59, respectively, with absorption capacities of 2.04% and 3.22%. A polycarboxylate ether-based high-range water-reducing admixture (HRWR), commercially designated as CARBOXAL SRF521, conforming to ASTM C494 Type F [12] and having a specific gravity of 1.08, was employed to obtain the desired workability.

Table 1. Physical and chemical properties of PC and FA

	CaO, (%)	SiO_2, (%)	Al_2O_3, (%)	Fe_2O_3, (%)	MgO, (%)	SO_3, (%)	K_2O, (%)	Na_2O, (%)	TiO, (%)	FL (%)	Other minor oxides, (%)	LOI, (%)	SG	Blaine, (cm^2/g)
PC	67.65	9.53	7.8	4.08	4.26	1.18	0.71	0.22	0.16	2.21	0.73	1.34	3.14	3312
FA	2.6	51.91	34.8	4.18	0.75	0.09	0.61	0.14	2.15	0.69	0.45	1.13	2.23	4037

FL: Free lime, LOI: Loss on ignition, SG: Specific gravity



(a) (b)

Fig. 1. Fibers used in this study: (a) steel fibers (SF) and (b) glass fibers (GF)

2.2 Mix proportions and mixing

Table 2 summarizes the mixture proportions, which consisted of one control SCC mixture without fibers and twelve fiber-reinforced mixtures incorporating different fiber types and dosages. All mixtures were produced with a water-to-binder ratio of 0.36 and a binder content of 500 kg/m^3. The fine-to-total aggregate ratio by mass was maintained at approximately 0.52. For each mixture, the dosage of the HRWR was adjusted to achieve a slump flow of 650 ± 10 mm, ensuring that all fresh concretes satisfied the self-consolidation requirements specified in the EFNARC European Guidelines [13]. Mixing was carried out using a 20 L rotary planetary mixer following a five-step sequence: (i) the aggregates were mixed with 35% of the mixing water for 1 min; (ii) the cementitious materials and 40% of the remaining water were added and mixed for 2 min; (iii) the HRWR, previously diluted in the remaining water, was gradually introduced over 2 min; (iv) the mixture was allowed to rest for 2 min; and (v) the designated fibers were gradually added to the fresh mixture, which was then mixed for an additional 2 min to ensure their uniform dispersion. The temperature during mixing was maintained at 21 ± 2 °C.

Table 2. Mix proportions of SCC mixtures containing different types of fiber (kg/m^3)

Mixture ID	Water	PC	FA	GF	SF	HRWR	Aggregates, (SSD)	
							Fine	Coarse
Control	180	400	100	-	-	4.2	815	762
0.5GF	180	400	100	2.5	-	4.3	812	760
1.0GF	180	400	100	5	-	4.8	809	757
1.5GF	180	400	100	7.5	-	6.5	806	754
0.5SF	180	400	100	-	2.5	4.3	812	758
1.0SF	180	400	100	-	5	4.8	810	756
1.5SF	180	400	100	-	7.5	6.5	808	754
0.5GF50SF50	180	400	100	1.25	1.25	4.3	813	760
1.0GF50SF50	180	400	100	2.5	2.5	4.8	810	758
1.5GF50SF50	180	400	100	3.75	3.75	6.5	808	757
0.5GF30SF70	180	400	100	0.75	1.75	4.3	813	760
1.0GF30SF70	180	400	100	1.5	3.5	7.8	811	757
1.5GF30SF70	180	400	100	2.25	5.25	8.5	808	754

2.3 Evaluation of fresh properties and interlayer bond strength

Fresh-property testing was initiated approximately 11 min after the initial contact between water and the cementitious materials, corresponding to approximately 3 min after completion of the mixing procedure. The slump-flow test was conducted in accordance with the EFNARC European Guidelines [13]. The slump-flow value was determined as the average of two spread diameters measured in perpendicular directions.

Interlayer bond performance was evaluated using the direct shear test. Prismatic specimens of identical dimensions were cast in two successive layers with a horizontal interface. Casting intervals of 0, 40, 80, 120, and 160 min were considered between the placement of the first and second layers. For the 0-min condition, the second layer was placed immediately after the first layer without any intentional casting delay. After curing, the specimens were positioned so that the bond interface was vertically oriented during testing, as illustrated in Fig. 2.

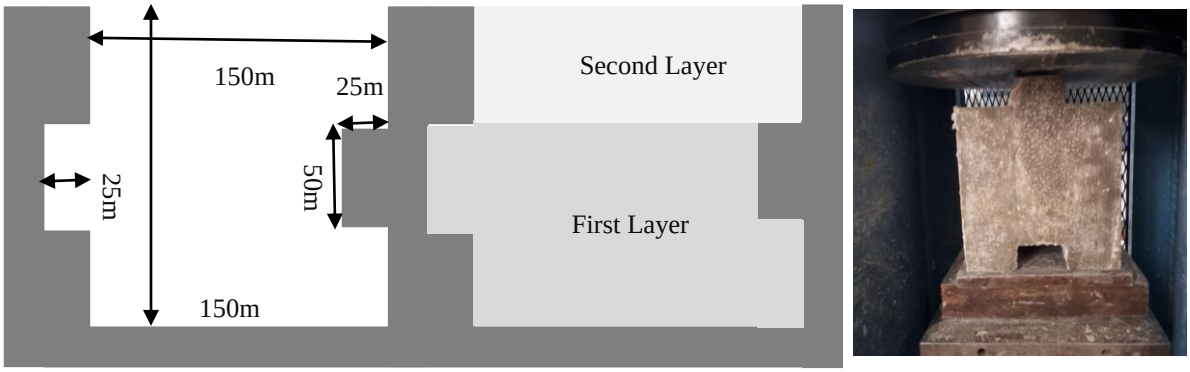


Fig. 2. Direct shear strength mold arrangement and sample under testing

The direct interlayer shear strength, V, was calculated using Eq. (1):

$$V = \frac{P}{2bd} \quad (1)$$

where V is the direct interlayer shear strength (MPa), P is the maximum failure load (N), and b and d are the width and depth of the prism specimen (mm), respectively. The residual bond strength (RBS) was used to quantify the time-dependent reduction in interlayer performance. For each mixture, the bond strength measured at casting intervals of 40, 80, 120, and 160 min

was normalized with respect to the corresponding bond strength obtained at 0 min, according to Eq. (2):

$$\text{RBS (\%)} = \frac{Bond\ strength\ at\ each\ time\ interval}{Bond\ strength\ at\ 0\ min} \times 100 \quad (2)$$

The 0-min condition was used as the reference and therefore corresponded to an RBS of 100%.

3 Results and Discussion

3.1 HRWR demand

The variation in the required HRWR dosage to maintain the target slump flow of 650 ± 10 mm is presented in Fig. 3. As summarized in Table 2, the HRWR demand generally increased with increasing fiber dosage regardless of fiber type. Among the mono-fiber mixtures, the required HRWR dosage increased from 4.2 kg/m^3 for the control mixture to 8.5 kg/m^3 for mixtures containing 1.5% GF or 1.5% SF. A similar trend was observed for the hybrid fiber systems, where most mixtures required progressively higher HRWR dosages as the total fiber content increased. The mixture containing 1.0% total fiber with a 30%GF-70%SF hybrid combination required 7.8 kg/m^3 of HRWR, whereas the corresponding 1.5% hybrid mixture required the highest dosage of 8.5 kg/m^3. Overall, these results indicate that increasing the total fiber content increased the demand for HRWR, although the required dosage was also influenced by the hybrid fiber composition.

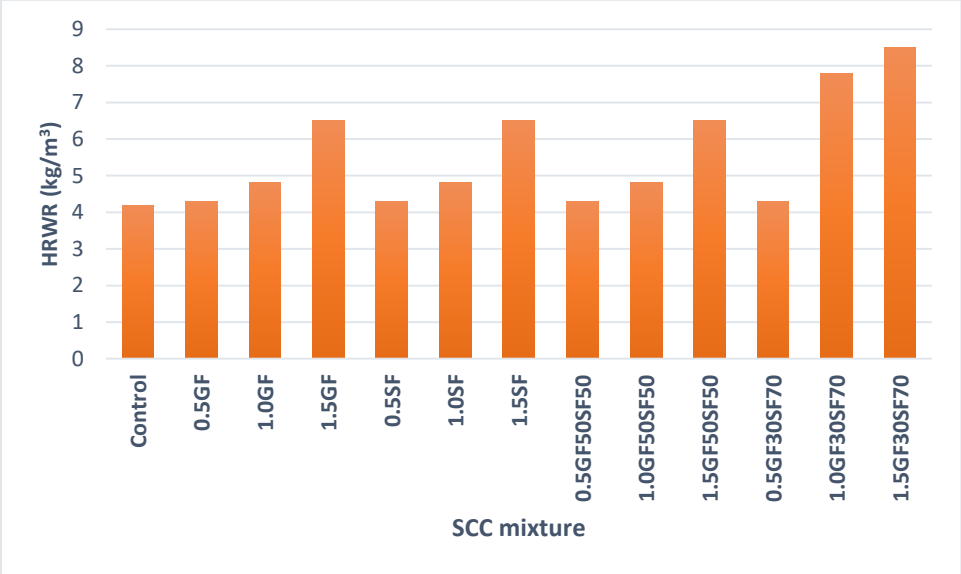


Fig. 3. Variation in the HRWR dosage required to achieve a constant slump flow of 650 ± 10 mm for different SCC mixtures.

The increase in HRWR demand is mainly attributed to the larger specific surface area introduced by the fibers and the intensified fiber-fiber and fiber-aggregate interactions, which restrict the free movement of solid particles and reduce the flowability of fresh SCC. Consequently, additional superplasticizer was required to compensate for the increased internal friction and maintain the self-consolidating characteristics of the mixtures. Similar trends have been reported in previous studies, where increasing fiber dosage resulted in higher yield stress and plastic viscosity, thereby increasing the superplasticizer demand required to achieve the

desired workability [8,10]. Furthermore, previous investigations have shown that once the fiber content exceeds a critical threshold, particle interactions become more pronounced, leading to a significant deterioration in the rheological performance of fiber-reinforced SCC [8].

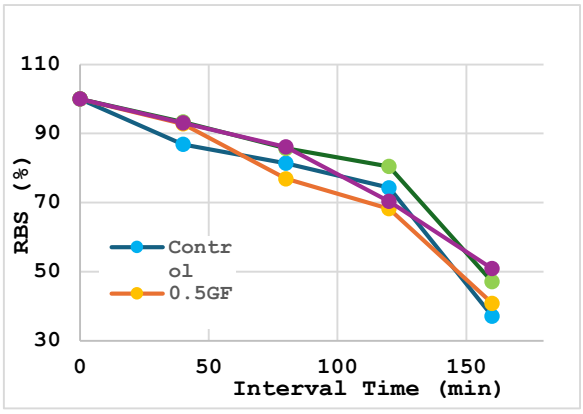
3.2 Effect of interval time on residual bond strength

The influence of casting interval on the residual bond strength of fiber-reinforced SCC mixtures is presented in Fig. 4(a-d). Regardless of fiber type or dosage, increasing the interval time between successive concrete layers resulted in a continuous reduction in RBS, confirming that the progressive structural build-up and early hydration of the previously placed layer significantly weaken the interlayer bond. During the resting period, the fresh SCC gradually loses its ability to remix with the subsequently placed layer, leading to a weaker interface and lower bond strength [1,2]. However, both the magnitude and rate of bond deterioration were strongly affected by the fiber reinforcement system.

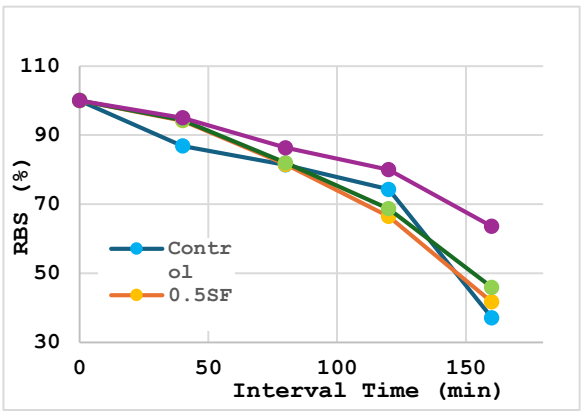
For the GF-reinforced mixtures (Fig. 4(a)), the reduction in RBS was relatively limited during the first 40 min, after which bond deterioration became more pronounced, particularly beyond 120 min. Increasing the GF dosage consistently improved bond retention throughout the investigated interval range. At the longest casting interval, the mixture containing 1.5% GF retained approximately 51% of its initial bond strength, whereas the corresponding value for the control mixture was only about 37%. Although glass fibers reduced the adverse influence of prolonged casting intervals, the improvement remained relatively moderate compared with the other fiber systems.

A similar decreasing trend was observed for the steel fiber-reinforced mixtures (Fig. 4(b)); however, the beneficial effect of fiber incorporation was considerably greater. Increasing the steel fiber dosage progressively improved the residual bond strength, particularly at longer casting intervals. At 160 min, the mixture reinforced with 1.5% SF retained approximately 64% of its original bond strength, representing a substantial improvement over both the control mixture and the corresponding glass fiber mixture. These results indicate that steel fibers become increasingly effective as the interlayer region progressively weakens.

The hybrid fiber systems exhibited the highest resistance to time-dependent bond degradation (Fig. 4(c-d)). Hybrid mixtures containing equal proportions of glass and steel fibers consistently outperformed the mono-fiber mixtures, indicating a beneficial interaction between the two fiber types. A further improvement was achieved by increasing the proportion of steel fibers in the hybrid system. Among all investigated mixtures, the hybrid system incorporating 30% glass fibers and 70% steel fibers at a total fiber content of 1.5% exhibited the highest RBS throughout the investigated interval range and retained approximately 71% of its initial bond strength after 160 min. In comparison, the corresponding value for the equal-ratio hybrid mixture was approximately 66%, while the control mixture retained only about 37% of its initial bond strength.



(a)



(b)

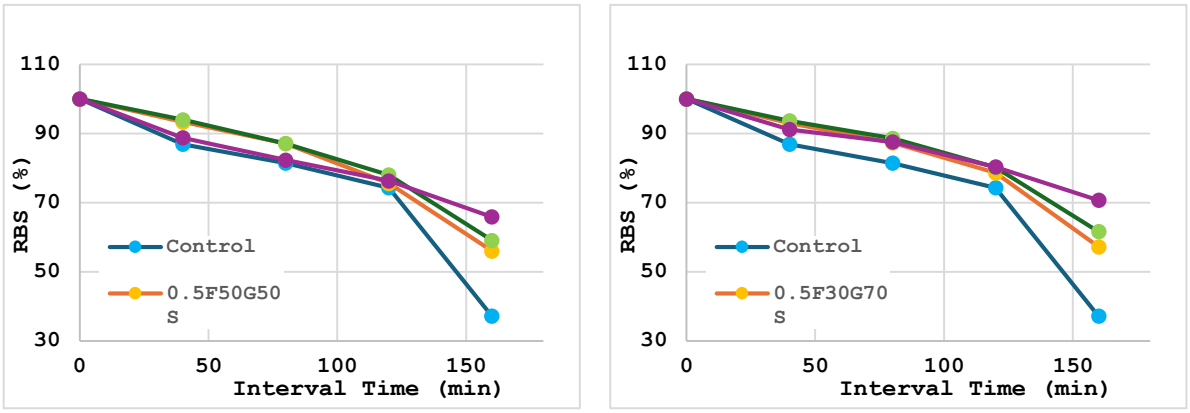


Fig. 4. Effect of casting interval on the RBS of fiber-reinforced SCC mixtures: (a) GF, (b) SF, (c) 50% GF-50% SF, and (d) 30% GF-70% SF.

Overall, the results demonstrate that although increasing the casting interval inevitably leads to interlayer bond deterioration, fiber reinforcement substantially mitigates this adverse effect. Moreover, the beneficial contribution of fibers became increasingly pronounced with increasing casting interval, indicating that fiber bridging across the developing interface plays a progressively more important role as the mechanical continuity between successive concrete layers decreases. Among the investigated reinforcement systems, the hybrid mixture containing 30% glass fibers and 70% steel fibers at a total fiber dosage of 1.5% exhibited the most effective resistance against time-dependent interlayer bond deterioration.

3.3 Effect of fiber dosage on residual bond strength

The influence of fiber dosage on the residual bond strength of SCC mixtures subjected to different casting intervals is presented in Fig. 5(a-d). For all fiber systems, increasing the fiber dosage resulted in higher residual bond strength, although the magnitude of improvement depended strongly on the casting interval. At short placement intervals (0-80 min), increasing the fiber content produced only moderate improvements because the interface remained relatively fresh and sufficient mechanical continuity already existed between successive layers. In contrast, the beneficial effect of fiber incorporation became considerably more pronounced at longer casting intervals, particularly after 160 min, where the interlayer bond had significantly deteriorated.

For the glass fiber mixtures (Fig. 5(a)), increasing the fiber dosage from 0.5% to 1.5% produced a gradual increase in RBS at all casting intervals. The improvement was relatively limited at 0 min, where the normalized bond strength increased from approximately 114% to 118%, but became substantially greater after prolonged delays. At 160 min, increasing the glass fiber content from 0.5% to 1.5% increased the normalized bond strength from approximately 125% to 162%, demonstrating that higher glass fiber contents are more effective in maintaining bond integrity after extended resting periods. A similar but more pronounced trend was observed for the steel fiber mixtures (Fig. 5(b)). Increasing the steel fiber dosage consistently enhanced the residual bond strength at all casting intervals, with the greatest improvement again occurring after 160 min. At this interval, the normalized RBS increased from approximately 126% for the mixture containing 0.5% SF to nearly 206% for the mixture incorporating 1.5% SF, indicating that steel fibers provided more efficient crack bridging and stress transfer across the weakened interface than glass fibers. The hybrid fiber systems exhibited the greatest sensitivity to fiber dosage (Fig. 5(c-d)). For the equal-ratio hybrid mixtures (50% GF-50% SF), increasing the total fiber dosage resulted in a continuous increase in RBS, particularly at the longest casting interval, where the normalized bond strength reached approximately 241% for the mixture containing 1.5% total fibers.

An even greater improvement was obtained by increasing the proportion of steel fibers to 70% (Fig. 5(d)). Under this configuration, the normalized RBS increased from approximately 193% at 0.5% fiber content to nearly 259% at 1.5% fiber content after 160 min, representing the highest bond enhancement among all investigated mixtures.

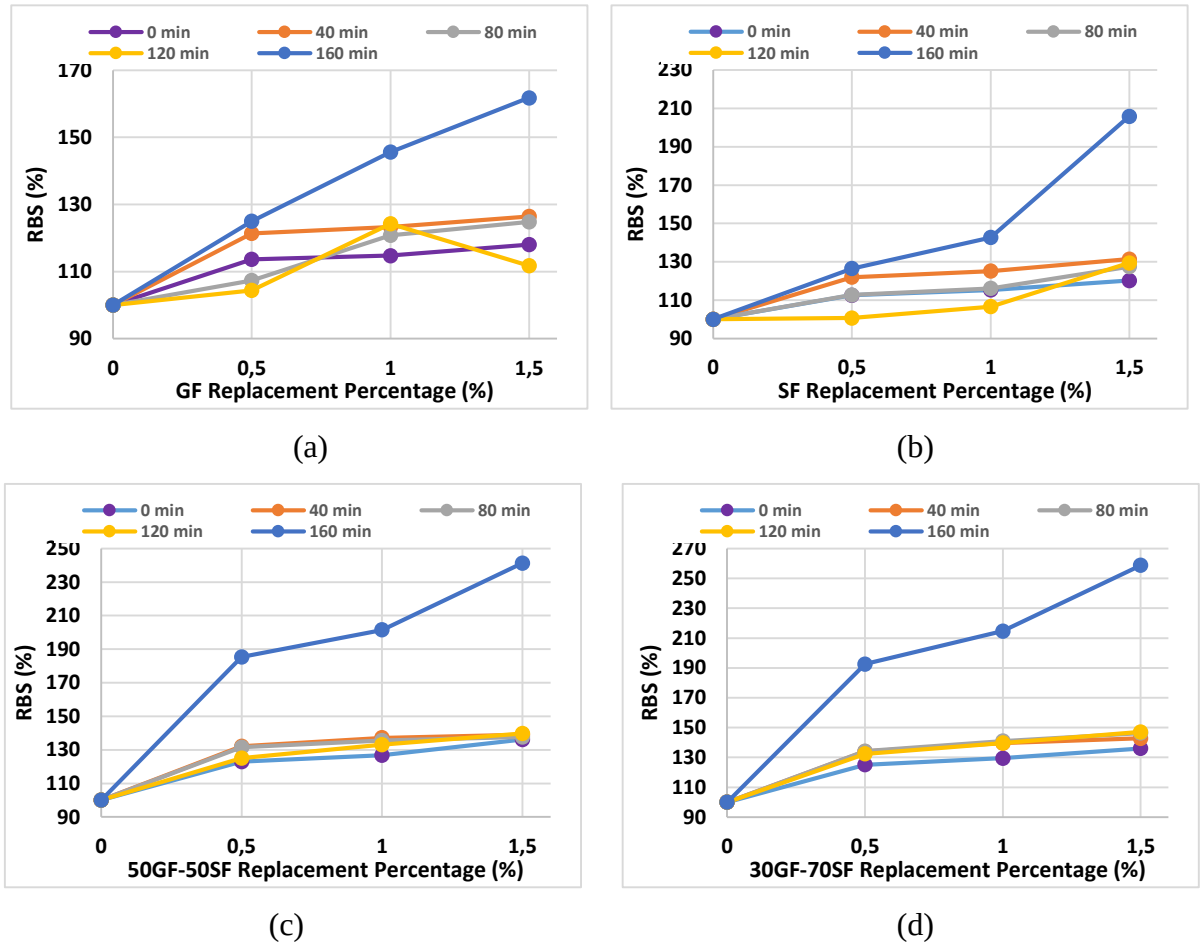


Fig. 5. Influence of fiber dosage on the RBS of SCC mixtures under different casting intervals: (a) GF, (b) SF, (c) 50% GF-50% SF, and (d) 30% GF-70% SF.

These results demonstrate that the effectiveness of fiber dosage depends strongly on the condition of the interlayer interface. When the casting interval was short, increasing the fiber content produced only modest improvements because bond formation was primarily governed by the fresh-state cohesion between adjacent layers. However, as the casting interval increased and the interface progressively weakened, the contribution of fibers became increasingly dominant. Consequently, mixtures incorporating higher fiber dosages, particularly the hybrid system containing 30% glass fibers and 70% steel fibers, exhibited the greatest resistance to interlayer bond deterioration under prolonged casting delays.

4 Conclusions

This study experimentally evaluated the influence of fiber type, fiber dosage, and casting interval on the interlayer bond performance of multilayer SCC using direct shear tests. Based on the obtained results, the following conclusions can be drawn:

- Increasing the fiber dosage increased the demand for HRWR required to maintain the target slump flow of 650 ± 10 mm. This increase was primarily attributed to the greater

specific surface area of the fibers and the intensified fiber-fiber and fiber-aggregate interactions, which reduced the flowability of fresh SCC.

- Increasing the casting interval progressively reduced the RBS of all SCC mixtures owing to the time-dependent structural build-up and reduced intermixing between successive concrete layers. The deterioration became particularly pronounced after 120 min.
- Incorporating fibers effectively mitigated the loss of interlayer bond strength, with the beneficial effect becoming increasingly significant as the casting interval increased.
- Among the mono-fiber systems, steel fibers provided greater improvements in residual bond strength than glass fibers, especially at prolonged casting intervals. At 160 min, mixtures containing 1.5% steel fibers maintained approximately 64% of their initial bond strength, whereas the corresponding value for 1.5% glass fibers was approximately 51%.
- Hybrid fiber reinforcement exhibited a clear synergistic effect. The hybrid system containing equal proportions of glass and steel fibers improved the interlayer bond more effectively than the mono-fiber mixtures, while increasing the steel fiber proportion to 70% produced the highest bond performance.
- The hybrid mixture incorporating 30% glass fibers and 70% steel fibers at a total fiber dosage of 1.5% demonstrated the best overall performance, maintaining approximately 71% of its initial bond strength after a casting interval of 160 min.
- The results demonstrate that optimizing both the fiber dosage and hybrid fiber composition is an effective strategy for reducing time-dependent interlayer bond deterioration in multilayer SCC, thereby improving the reliability of concrete elements constructed using delayed sequential casting.

Acknowledgments

The authors wish to express their sincere appreciation to Çimsa Çimento Sanayi ve Ticaret A.Ş. for its valuable support of this research. The authors also extend their special thanks to Mr. Serhat Sarıkaya, Turkey Sales Manager at Çimsa Çimento Sanayi ve Ticaret A.Ş., for his continuous support, kind cooperation, and valuable assistance throughout the course of this study.

References

1. Megid, W.A., Khayat, K.H.: Bond strength in multilayer casting of self-consolidating concrete. ACI Materials Journal 114(3), 467-476 (2017). https://doi.org/10.14359/51689672
2. Saleh Ahari, R., Bohl, M.D., Erdem, T.K.: Bond strength between successive layers of SCC incorporating various supplementary cementitious materials under different test methods: Thixotropy consequences. Journal of Materials in Civil Engineering 38(9), 04026268 (2026). https://doi.org/10.1061/JMCEE7.MTENG-19878
3. Keita, E., Bessaies-Bey, H., Zuo, W., Belin, P., Roussel, N.: Weak bond strength between successive layers in extrusion-based additive manufacturing: Measurement and physical origin. Cement and Concrete Research 123, 105787 (2019). https://doi.org/10.1016/j.cemconres.2019.105787
4. Brault, A., Lees, J.M.: Wet casting of multiple mix horizontally layered concrete elements. Construction and Building Materials 247, 118514 (2020). https://doi.org/10.1016/j.conbuildmat.2020.118514
5. Ahari, R.S., Erdem, T.K., Ramyar, K.: Thixotropy and structural breakdown properties of self-consolidating concrete containing various supplementary cementitious materials.

Cement and Concrete Composites 59, 26-37 (2015). https://doi.org/10.1016/j.cemconcomp.2015.02.001
6. Ahari, R.S., Erdem, T.K., Ramyar, K.: Effect of various supplementary cementitious materials on rheological properties of self-consolidating concrete. Construction and Building Materials 75, 89-98 (2015). https://doi.org/10.1016/j.conbuildmat.2014.11.027
7. Basser, H., Shaghaghi, T.M., Afshin, H., Ahari, R.S., Mirrezaei, S.S.: An experimental investigation and response surface methodology-based modeling for predicting and optimizing the rheological and mechanical properties of self-compacting concrete containing steel fiber and PET. Construction and Building Materials 315, 125370 (2022). https://doi.org/10.1016/j.conbuildmat.2021.125370
8. Rojo-López, G., González-Fonteboa, B., Martínez-Abella, F., Seara-Paz, S.: Effect of aggregate content and fibre type on the rheological behaviour and structural build-up of fibre reinforced self-compacting concrete using two binder compositions. Construction and Building Materials 442, 137490 (2024). https://doi.org/10.1016/j.conbuildmat.2024.137490
9. Kaya, Y., Biricik, Ö., Bayqra, S.H., Mardani, A.: Rheological properties and thixotropic behavior of cementitious systems containing different fiber types. Arabian Journal for Science and Engineering 49(4), 5203–5223 (2024). https://doi.org/10.1007/s13369-023-08657-6
10. Li, H., Addai-Nimoh, A., Han, S., Khayat, K.H.: Effect of rheology modification on fiber orientation and dispersion in 3D-printed ultra-high-performance concrete. Cement and Concrete Research 206, 108265 (2026). https://doi.org/10.1016/j.cemconres.2026.108265
11. ASTM International.: ASTM C150/C150M-25: Standard Specification for Portland Cement. ASTM International, West Conshohocken, PA (2025). DOI: 10.1520/C0150_C0150M-25.
12. ASTM International.: ASTM C494/C494M-24: Standard Specification for Chemical Admixtures for Concrete. ASTM International, West Conshohocken, PA (2024). DOI: 10.1520/C0494_C0494M-24.
13. EFNARC.: The European Guidelines for Self-Compacting Concrete: Specification, Production and Use. European Federation of National Associations Representing Producers and Applicators of Specialist Building Products for Concrete (EFNARC), Farnham, UK (2005).

Author Contribution Statement

- *Conceptualization:* Meysam Khalilzadeh
- *Methodology:* Reza Saleh Ahari
- *Investigation:* Meysam Khalilzadeh, Reza Saleh Ahari
- *Writing – Original Draft:* Meysam Khalilzadeh
- *Writing – Review & Editing:* Reza Saleh Ahari

Publication Note

This paper was peer-reviewed, accepted for presentation, and included in the proceedings of the ACE2026 – International Conference on Advances in Civil Engineering, held on 12–14 October 2026 in Trabzon, Türkiye.

This paper may be cited as follows:

Khalilzadeh M., Ahari R. S., “Effect of fibre type and content on the interlayer bond strength of fibre-reinforced self-consolidating concrete cast in distinct layers” in Proceedings of the ACE2026 – International Conference on Advances in Civil Engineering, Trabzon, Türkiye, 12–14 October 2026.

Effect of Powder and Colloidal Nano-Silica on the Mechanical and Rheological Properties of Cementitious Composites

Tugba Kuru[1], Hasan Nuri Turkmenoglu[2], Omer Canbey Cucemen[3], Osman Bulut[4]

[1] 0000-0001-7205-3521, Istanbul Technical University, Civil Engineering Department, Istanbul, Türkiye, baytak@itu.edu.tr
[2] 0000-0003-4765-8590, Istanbul Technical University, Civil Engineering Department, Istanbul, Türkiye, turkmenogluh@itu.edu.tr
[3] 0000-0001-8718-1833, Istanbul Technical University, Civil Engineering Department, Istanbul, Türkiye, cucemen@itu.edu.tr
[4] 0000-0001-8200-1119, Istanbul Technical University, Civil Engineering Department, Istanbul, Türkiye, buluto@itu.edu.tr

Abstract. The effectiveness of nano-silica in cementitious composites depends not only on its dosage but also on its physical form and dispersion within the matrix. This study experimentally investigates the effects of powder (pNS) and colloidal nano-silica (cNS) on the workability and mechanical performance of cement mortars. Mixtures containing 0, 1, 1.5, 2, 2.5, and 3% nano-silica by weight of binder were produced under comparable mixture proportions and curing conditions. The pNS was dispersed in mixing water using mechanical stirring followed by ultrasonic homogenization, whereas cNS was directly incorporated by accounting for its water content while maintaining the same water-to-binder ratio. Compressive and flexural strengths were evaluated at 7 and 28 days, together with fresh-state flow measurements. The pNS mixtures generally exhibited improved mechanical performance with increasing dosage, reaching maximum 28-day compressive and flexural strengths of 80.4 and 11.74 MPa, respectively, at 3% pNS. In contrast, cNS exhibited its highest performance at approximately 1%, reaching 68.3 MPa compressive strength and 10.55 MPa flexural strength at 28 days, while higher dosages resulted in reduced strengths. Moreover, cNS mixtures exhibited a lower average flow (160 ± 10 mm) than pNS mixtures (200 ± 10 mm). These findings demonstrate that the physical form and particle characteristics of nano-silica significantly influence both fresh-state and hardened performance and should be considered when determining the optimum nano-silica dosage.

Keywords: Colloidal nano-silica; Powder nano-silica; Slump flow.

1 Introduction

Cement-based materials are the most widely used construction materials owing to their versatility, availability, and relatively low production cost. However, conventional cementitious composites often exhibit limitations in terms of mechanical performance, durability, and fresh-state workability. Consequently, considerable research has focused on the incorporation of nano-scale additives to enhance both the fresh and hardened properties of cement-based materials [1–4].

Among the various nano-materials investigated, nano-silica has received significant attention because of its exceptionally high specific surface area, amorphous structure, and high pozzolanic reactivity. Nano-silica accelerates cement hydration, promotes the formation of additional calcium silicate hydrate (C–S–H) gel, and refines the pore structure through both nucleation and nano-filler effects. These mechanisms have been reported to enhance compressive strength, flexural strength, durability, and the interfacial transition zone (ITZ) in cementitious composites [2–6]. Despite these advantages, the effectiveness of nano-silica depends not only on its dosage but also on its particle size, physical form, and dispersion quality within the cementitious matrix. Due to their high surface energy, nano-sized particles tend to

agglomerate during mixing, which may considerably reduce their beneficial effects. Therefore, several dispersion techniques, including ultrasonic homogenization, have been proposed to improve particle distribution and maximize the effectiveness of nano-silica [5–8].
Commercial nano-silica is generally available in two different forms, namely powder and colloidal suspensions. Although both forms have been individually investigated, direct experimental comparisons under identical mixture proportions and curing conditions remain relatively limited [7–10]. Furthermore, the influence of nano-silica's physical form on both fresh-state workability and mechanical performance has not yet been fully clarified.
Therefore, the present study experimentally investigates the effects of pNS and cNS on the fresh-state and mechanical properties of cement mortar mixtures. pNS was dispersed using a combination of magnetic stirring and ultrasonic homogenization before mixing, whereas cNS mixtures were prepared by maintaining identical mixture proportions and adjusting the effective mixing water according to the suspension's solid content. The findings are expected to contribute to the optimization of nano-silica incorporation in cementitious composites and provide a foundation for future studies on extrusion-based cementitious materials and three-dimensional concrete printing applications.

2 Experimental Program

2.1 Materials

CEM II/A-M(S-L) 42.5 R cement with a specific gravity of 3.11 g/cm³ was used as the primary binder in this study. throughout the experimental program. Natural silica sand with a maximum particle size of 2 mm and a specific gravity of 2.64 g/cm³ was used as the fine aggregate. A modified polycarboxylic ether (PCE)-based high-range water-reducing admixture (Sika ViscoCrete GL 51) was incorporated to obtain the desired workability while maintaining a constant water-to-binder ratio.

pNS with an amorphous structure, a purity greater than 98.5%, and a particle size ranging between 55 and 75 nm was employed in the first stage of the study. Prior to mixing, the pNS was dispersed in mixing water using magnetic stirring followed by ultrasonic homogenization to minimize particle agglomeration and improve particle distribution within the cementitious matrix. In the second stage, cNS, obtained from the same manufacturer as pNS, with a particle size of 8–33 nm and a solid content of 26 wt.%, was utilized to investigate the influence of nano-silica physical form. The amount of colloidal suspension was calculated based on the required solid nano-silica content, and the water introduced by the suspension was deducted from the total mixing water to maintain a constant water-to-binder ratio in all mixtures. Physical properties of the materials are given in Table 1.

Table 1. Physical properties of the materials.

Material	**Specification**
Binder	CEM II/A-M(S-L) 42.5 R, 3.11 g/cm^3
Fine aggregate	Natural Silica Sand (0-2mm), 2.64 g/cm^3*
Superplasticizer	Modified Polycarboxylic ether based, 1.1 g/cm^3*
pNS	55–75 nm, amorphous, 2.4 g/cm^3*
cNS	8–33 nm, amorphous, 26 wt.% solids, 2.4 g/cm^3*

*: Values declared by the manufacturer.

2.2 Mixture Proportions

Two experimental programs were conducted in this study. The first program investigated the influence of pNS, whereas the second focused on cNS. Six different mixtures containing 0, 1, 1.5, 2, 2.5 and 3% nano-silica (by binder weight) were prepared for each experimental program. Nano-silica was added to the mixture directly, in an amount equal to the cement percentage, rather than substituting it.

To ensure a meaningful comparison, identical binder content, sand-to-binder ratio, water-to-binder ratio and superplasticizer dosage were adopted for both pNS and cNS mixtures. The superplasticizer amount is increased with increasing the nano-silica amount to obtain a 200±10 mm flow value for all of the pNS mixtures. After that, the superplasticizer amounts used for pNS mixtures remained the same for the cNS mixtures to prevent the effect of superplasticizer on the mechanical properties. In the colloidal mixtures, only the physical form of nano-silica was altered. The additional water contained in the colloidal suspension was deducted from the mixing water to preserve a constant water-to-binder ratio throughout the study. Mix proportions of the pNS and cNS mixtures are given in Table 2.

Table 2. Mix proportions of pNS and cNS mixtures by binder weight.

	pNS0/ cNS0	**pNS1/ cNS1**	**pNS1.5/ cNS1.5**	**pNS2/ cNS2**	**pNS2.5/ cNS2.5**	**pNS3/ cNS3**
Cement	1					
Sand	1.50					
Water	0.45					
Superplasticizer, %	0.6	0.9	1.0	1.3	1.4	1.6
Nano-silica, %	0	1.0	1.5	2.0	2.5	3.0

2.3 Specimen Preparation and Test Methods

To improve the dispersion of pNS within the cementitious matrix, the nanoparticles were first dispersed in approximately two-thirds of the mixing water containing the required amount of superplasticizer using magnetic stirring, followed by ultrasonic homogenization for 10 min. The remaining mixing water was then mixed with cement before incorporating the nano-silica suspension into the mortar mixture.

After the mixing procedure was completed, a flow table test was performed according to TS EN 1015-3. After determining the flow value, the mortar was mixed at low speed for an additional 30 s and then placed into molds. During the molding process, the mortar was first placed up to half the mold height, and the mold was dropped 60 times on a jolting table. The same procedure was repeated after filling the remaining half of the mold. A total of six prismatic specimens (40 × 40 × 160 mm) were cast in accordance with TS EN 196-1 and demolded after 24 h. Subsequently, the specimens were cured in lime-saturated water until the testing ages of 7 and 28 days. Figure 1 illustrates the preparation procedure of the mortar specimens, including fresh-state flow measurement, casting into prism molds, and curing in a water tank.

For the cNS mixtures, identical mixture proportions, water-to-binder ratio, and superplasticizer dosage were maintained to enable a direct comparison between pNS and cNS. This procedure ensured that any observed differences originated primarily from the physical characteristics of nano-silica rather than variations in mixture composition.

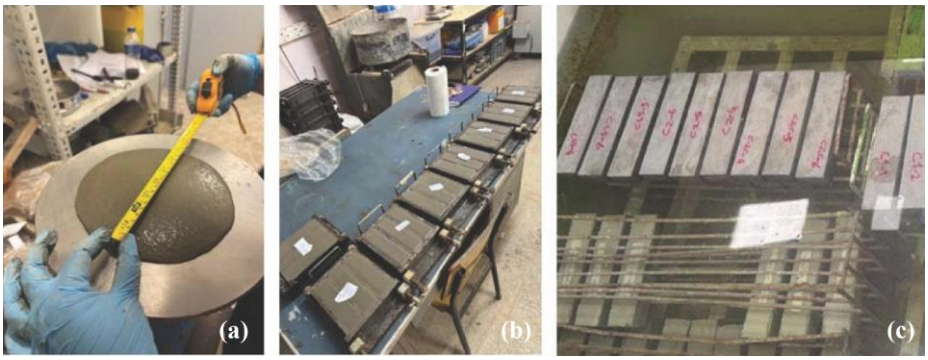


Fig. 1. Preparation of nano-silica mortar mixtures: (a) slump flow measurement, (b) casting of mortar specimens, and (c) water curing of prism specimens.

3 Results and Discussion

3.1 Fresh-State Properties

Figure 2 presents the slump flow results of the pNS and cNS mixtures. For the pNS series, the dosage of the superplasticizer was adjusted to maintain a nearly constant slump flow of approximately 200 ± 10 mm, regardless of the nano-silica dosage. This approach enabled the mechanical performance of the different mixtures to be compared under similar fresh-state workability conditions.

In contrast, the colloidal nano-silica mixtures exhibited an average slump flow of approximately 160 ± 10 mm, although identical mixture proportions, water-to-binder ratio, and superplasticizer dosages were employed. The reduced workability of the cNS mixtures may be associated with their smaller particle size (8–33 nm) and consequently higher specific surface area compared with the powder form (55–75 nm). The higher surface area of finer nano-silica particles can increase water demand and particle interactions within the fresh cementitious matrix, thereby reducing flowability. Similar reductions in workability and changes in the rheological behavior of nano-silica-modified cementitious materials have been reported in previous studies [2,15]. These preliminary findings indicate that the physical form and particle size of nano-silica may significantly influence the fresh-state behavior of cementitious composites even when identical mixture proportions are maintained.

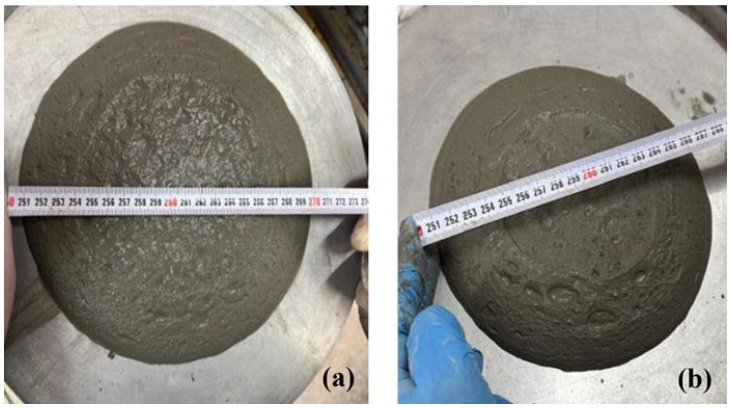


Fig. 2. Slump flow comparison of pNS (a), and cNS (b) mixtures for same mix design.

3.2 Mechanical Properties

Flexural Strength. Prior to compressive strength testing, prism specimens were subjected to three-point bending under displacement control at a loading rate of 0.2 mm/min, as illustrated in Figure 3. The flexural strength results of the pNS and cNS mixtures after 7 and 28 days of curing are presented in Figure 4 and Figure 5.

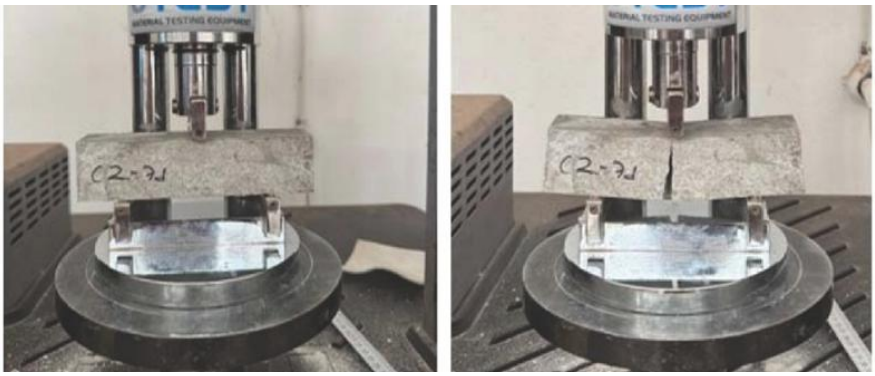


Fig. 3. Flexural test set-up.

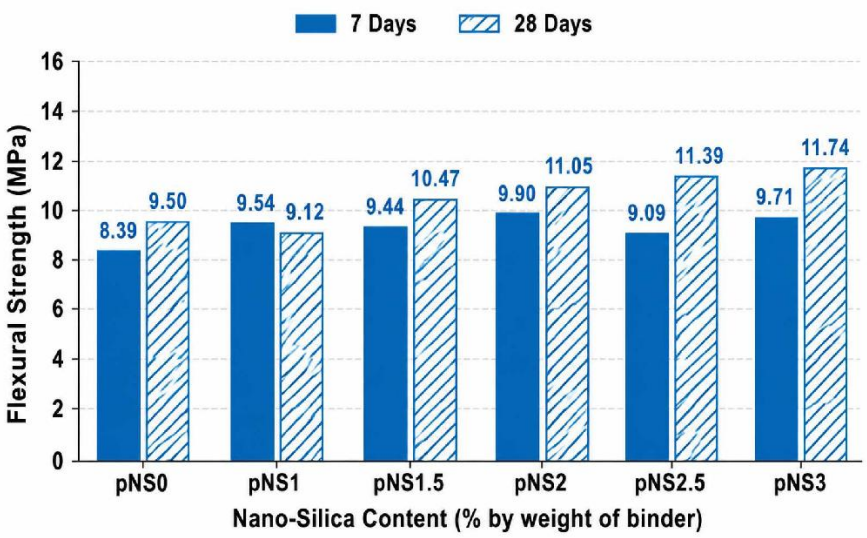


Fig. 4. Flexural strength of pNS mortar mixtures after 7 and 28 days of curing.

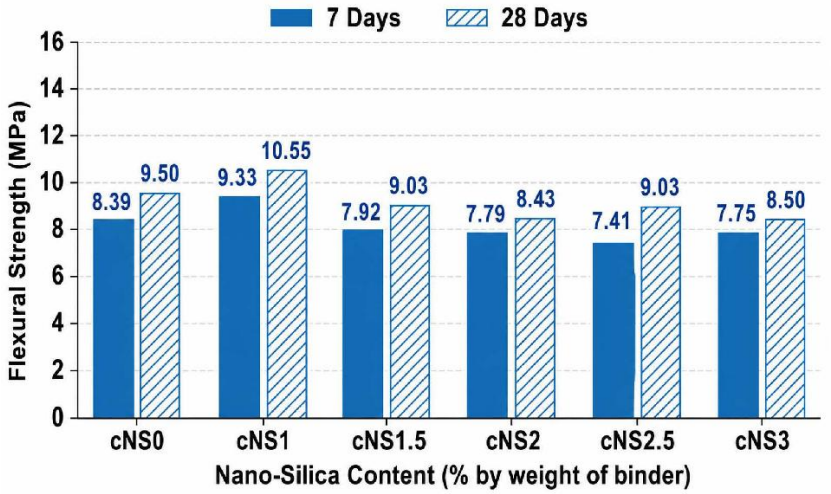


Fig. 5. Flexural strength of cNS mortar mixtures after 7 and 28 days of curing.

For the pNS mixtures, flexural strength generally increased with increasing nano-silica content, particularly after 28 days of curing. The highest flexural strength was obtained for the mixture containing 3% pNS, reaching 11.74 MPa at 28 days. This improvement is consistent with previous studies reporting that nano-silica incorporation can enhance the mechanical

performance of cementitious materials through matrix densification and pore-structurerefinement [2,4].

3.2.1 Compressive Strength

Figures 6-8 present the compressive strength testing and results of the pNS and cNS mixtures after 7 and 28 days of curing, respectively.

The pNS mixtures exhibited a continuous improvement in compressive strength with increasing nano-silica content, particularly after 28 days of curing. Compared with the reference mixture, the beneficial effect of pNS became more pronounced at later curing ages, indicating that the pozzolanic activity and nano-filler effect continued to contribute to cement hydration. Within the investigated dosage range, the highest compressive strength was obtained for the mixture containing 3% pNS, reaching 80.4 MPa after 28 days of curing.

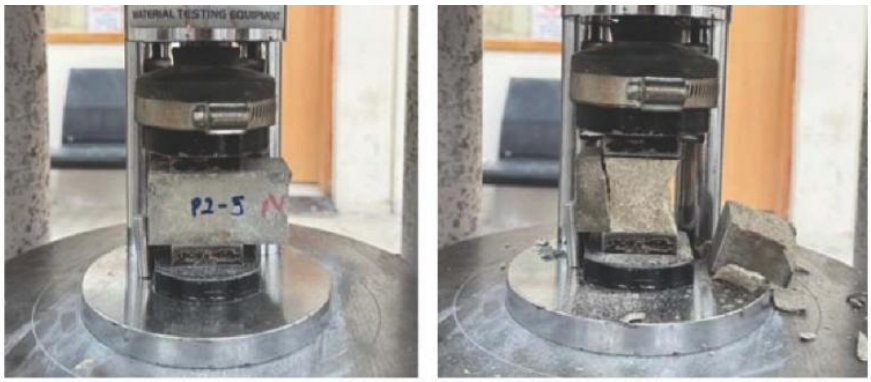


Fig. 6. Compressive test set-up.

In contrast, the cNS mixtures exhibited a different strength development trend. While the incorporation of 1% cNS resulted in the highest compressive strength among the colloidal mixtures (68.3 MPa at 28 days), further increases in nano-silica dosage led to a noticeable reduction in compressive strength. This behavior indicates that the optimum nano-silica dosage depends not only on the replacement level but also on the physical characteristics of the nano-silica employed.

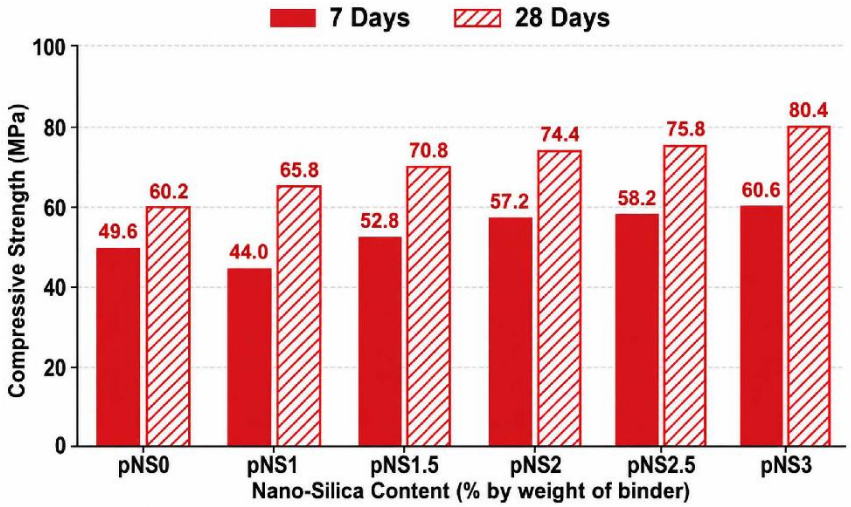


Fig. 7. Compressive strength of pNS mortar mixtures after 7 and 28 days of curing.

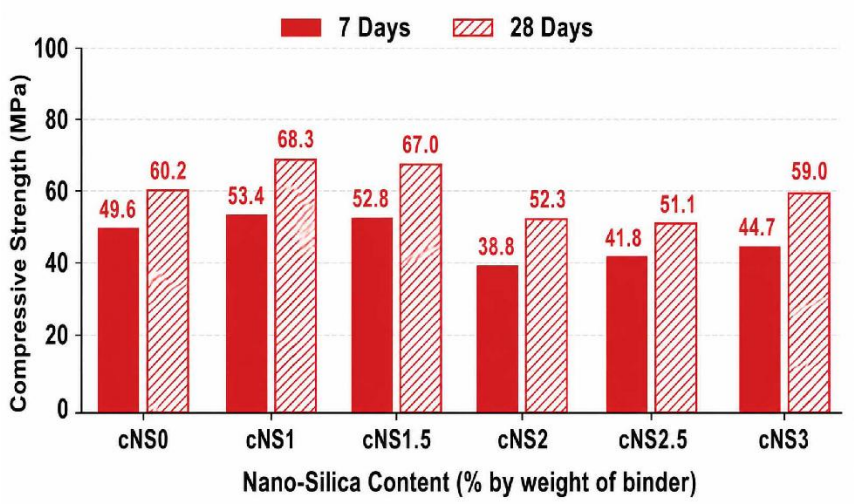


Fig. 8. Compressive strength of cNS mortar mixtures after 7 and 28 days of curing.

Overall, the pNS mixtures demonstrated superior compressive performance at higher nano-silica contents compared with the colloidal mixtures. The different strength development observed between the two nano-silica forms is likely associated with differences in particle size, specific surface area, and their interaction with the cementitious matrix. Detailed microstructural analyses using SEM and XRD will be performed in the subsequent stage of this study to further explain the observed mechanical behavior.

3.3 Comparison of Powder and Colloidal Nano-Silica

The results obtained in this study demonstrate that the physical form of nano-silica plays an important role in determining both the fresh-state and hardened properties of cementitious composites. Although identical mixture proportions, water-to-binder ratio, and superplasticizer dosages were adopted for both experimental series, the two nano-silica forms exhibited noticeably different mechanical responses.

The pNS mixtures showed a progressive improvement in mechanical performance with increasing nano-silica content, particularly at 28 days. The highest 28-day compressive strength was obtained with 3% pNS (80.4 MPa), corresponding to an increase of approximately 33.7% compared with the control mixture (60.2 MPa). The same mixture exhibited an increase of approximately 32.7% from 7 to 28 days. In contrast, the highest compressive strength within the cNS series was obtained with 1% cNS (68.3 MPa at 28 days), representing an improvement of approximately 13.5% over the control. The maximum 28-day compressive strength obtained with pNS was approximately 17.8% higher than the maximum value obtained with cNS.

A similar distinction was observed in flexural performance. The highest 28-day flexural strength of the pNS series was 11.74 MPa at 3% pNS, whereas the highest value for the cNS series was 10.55 MPa at 1% cNS. These results indicate that the optimum dosage and resulting mechanical performance depend on the form and characteristics of the nano-silica.

Furthermore, the cNS mixtures produced a lower average slump flow (160 ± 10 mm) than the pNS mixtures (200 ± 10 mm) despite identical mixture proportions. This difference may be associated with the different physical characteristics of the two nano-silica products, including their particle-size ranges (8–33 nm for cNS and 55–75 nm for pNS), which can influence particle interactions and water demand within the fresh cementitious matrix. Further microstructural investigations are expected to provide additional insight into the mechanisms responsible for the observed differences.

4 Conclusions

The effects of powder and colloidal nano-silica on the fresh-state behavior and mechanical performance of cement mortar mixtures were experimentally investigated. Based on the findings of this study, the following conclusions can be drawn:

- The incorporation of pNS improved both compressive and flexural strengths, particularly after 28 days of curing. The highest mechanical performance was achieved with 3% pNS, reaching 80.4 MPa in compressive strength and 11.74 MPa in flexural strength at 28 days. The 28-day compressive strength was approximately 33.7% higher than that of the control mixture, confirming the beneficial contribution of nano-silica to the mechanical performance of cementitious materials [2,4,11].
- The cNS mixtures exhibited a different mechanical response, with the highest performance generally observed at approximately 1% cNS. At this dosage, the 28-day compressive strength reached 68.3 MPa, corresponding to an increase of approximately 13.5% compared with the control mixture. Higher cNS dosages resulted in reduced mechanical performance, indicating that the optimum nano-silica dosage depends on its physical form and interaction with the cementitious matrix [9,12].
- Comparison of the two nano-silica forms revealed that the maximum 28-day compressive strength obtained with pNS was approximately 17.8% higher than the maximum value obtained with cNS. Similarly, the highest 28-day flexural strengths were 11.74 MPa for pNS and 10.55 MPa for cNS, further demonstrating the different mechanical responses of the two nano-silica forms.
- Despite identical mixture proportions, water-to-binder ratio, and superplasticizer dosage, the cNS mixtures exhibited a lower average slump flow (160 ± 10 mm) than the pNS mixtures (200 ± 10 mm). This difference indicates that the physical characteristics of nano-silica can considerably influence the fresh-state behavior of cementitious composites [3,6,13].
- Overall, pNS exhibited a more consistent improvement in mechanical performance with increasing dosage within the investigated range, whereas cNS showed greater sensitivity to dosage variation. These findings highlight the importance of considering the physical form and characteristics of nano-silica when determining its optimum incorporation level.

Further investigations involving SEM and XRD analyses are underway to better understand the relationship between nano-silica characteristics, hydration products, and the observed mechanical behavior. The optimized mixtures identified in this study will also provide a basis for future investigations involving extrusion-based cementitious materials and three-dimensional concrete printing applications [8,14,15].

Acknowledgments
The authors gratefully acknowledge the financial support provided by the Scientific Research Projects Coordination Unit of Istanbul Technical University (ITU-BAP) under Project No. 46974.

References

1. Zhang, L., Bian, M., Xiao, Z., Wang, X., Han, B.: A comprehensive review of cementitious composites modified with nano silica: Fabrication, microstructures, properties and applications. Construction and Building Materials 409, 133922 (2023).
2. Hamada, H., Shi, J., Yousif, S.T., Al Jawahery, M., Tayeh, B., Jokhio, G.: Use of nano-silica in cement-based materials – A comprehensive review. Journal of Sustainable Cement-Based Materials 12(10), 1286–1306 (2023).
3. Tabish, M., Zaheer, M.M., Baqi, A.: Effect of nano-silica on mechanical, microstructural and durability properties of cement-based materials: A review. Journal of Building Engineering 65, 105676 (2023).
4. AlTawaiha, H., Alhomaidat, F., Eljufout, T.: A Review of the Effect of Nano-Silica on the Mechanical and Durability Properties of Cementitious Composites. Infrastructures 8(9), 132 (2023).
5. Wang, J., Yang, Y., Chu, J., Mo, K.H., Yap, P.-S.: Recent developments in utilization of nano silica in self-compacting concrete: A review. Structural Concrete 24(6), 7524–7548 (2023).
6. Althoey, F., Zaid, O., Martínez-García, R., Alsharari, F., Ahmed, M., Arbili, M.M.: Impact of nano-silica on the hydration, strength, durability, and microstructural properties of concrete: A state-of-the-art review. Case Studies in Construction Materials 18, e01997 (2023).
7. Abdalla, J.A., Hawileh, R.A., Bahurudeen, A., Varghese, J., Kabeer, K.I.S.A., Thomas, B.S.: Influence of synthesized nanomaterials in the strength and durability of cementitious composites. Case Studies in Construction Materials 18, e02197 (2023).
8. Dinesh, A., Yuvaraj, S., Abinaya, S.: Nanopowders as an additive for strength and durability enhancement of cement composite: Review and prospects. Materials Today: Proceedings (2023).
9. Nili, M., Ehsani, A.: Investigating the effect of the cement paste and transition zone on strength development of concrete containing nanosilica and silica fume. Materials & Design 75, 174–183 (2015).
10. Sun, J., Xu, Z., Li, W., Shen, X.: Effect of nano-SiO_2 on the early hydration of alite-sulphoaluminate cement. Nanomaterials 7(5), 102 (2017).
11. Wang, C., Zhang, M., Wang, Q., Dai, J., Luo, T., Pei, W., et al.: Research on the influencing mechanism of nano-silica on concrete performances based on multi-scale experiments and micro-scale numerical simulation. Construction and Building Materials 318, 125873 (2022).
12. Jo, B.W., Kim, C.H., Tae, G.H., Park, J.B.: Characteristics of cement mortar with nano-SiO_2 particles. Construction and Building Materials 21(6), 1351–1355 (2007).
13. Li, H., Xiao, H.G., Yuan, J., Ou, J.: Microstructure of cement mortar with nano-particles. Composites Part B: Engineering 35(2), 185–189 (2004).
14. Qing, Y., Zenan, Z., Deyu, K., Rongshen, C.: Influence of nano-SiO_2 addition on properties of hardened cement paste as compared with silica fume. Construction and Building Materials 21(3), 539–545 (2007).
15. Senff, L., Hotza, D., Lucas, S., Ferreira, V.M., Labrincha, J.A.: Effect of nano-SiO_2 and nano-TiO_2 addition on the rheological behavior and mechanical properties of cement mortars. Materials Science and Engineering A 532, 354–361 (2012).

Author Contribution Statement

- *Conceptualization:* Tuğba Kuru, Osman Bulut
- *Methodology:* Tuğba Kuru, Hasan Nuri Türkmenoğlu
- *Investigation:* Tuğba Kuru, Hasan Nuri Türkmenoğlu, Ömer Canbey Cücemen
- *Writing – Original Draft:* Tuğba Kuru

- *Writing – Review & Editing:* Tuğba Kuru, Hasan Nuri Türkmenoğlu, Ömer Canbey Cücemen, Osman Bulut

List of Abbreviations

- **NS** — Nano-Silica
- **pNS** — Powder Nano-Silica
- **cNS** — ColloidalNano-Silica
- **PCE** — Polycarboxylate Ether (Superplasticizer)
- **C–S–H** — Calcium Silicate Hydrate
- **SEM** — Scanning Electron Microscopy
- **XRD** — X-ray Diffraction

Conflict of Interest

The authors declare that they have no conflict of interest.

Funding

This study was supported by the Scientific Research Projects Coordination Unit of Istanbul Technical University (ITU-BAP Project No: 46974).

Data Availability

The datasets generated and analyzed during the current study are available from the corresponding author upon request.

Note: Following the conference, this Publication Note will be added to each paper; therefore, authors are kindly requested not to remove the note below and to complete the author(s) and paper title information.

Publication Note

This paper was peer-reviewed, accepted for presentation, and included in the proceedings of the ACE2026 – International Conference on Advances in Civil Engineering, held on 12–14 October 2026 in Trabzon, Türkiye.

This paper may be cited as follows:

Kuru T., Turkmenoglu H. N., Cucemen O. C., Bulut O., "Effect of Powder and Colloidal Nano-Silica on the Mechanical and Rheological Properties of Cementitious Composites," in Proceedings of the ACE2026 – International Conference on Advances in Civil Engineering, Trabzon, Türkiye, 12–14 October 2026.

Strength Development under Intermittent Sprinkler Curing: A Comparative Study of Plain and Slag-Blended Concrete

Senem Bilici[1,*], Arif Tufan Salva[2], Muhittin Tarhan[3], Erdal Önkol[4] and Cihan Tayyar Ahı[5]

[1] 0000-0002-9698-8900, Akçansa Cement Industry and Trade Inc., Buyukcekmece, Istanbul, Türkiye, senem.bilici@akcansa.com.tr

[2] 0009-0006-3165-2222, Akçansa Cement Industry and Trade Inc., Buyukcekmece, Istanbul, Türkiye and Boğaziçi University, Civil Engineering Department, 34342 Beşiktaş, Istanbul, Türkiye, arif.salva@akcansa.com.tr

[3] 0009-0001-6755-9699, Akçansa Cement Industry and Trade Inc., Buyukcekmece, Istanbul, Türkiye, muhittin.tarhan@akcansa.com.tr

[4] 0000-0003-1174-1974, Akçansa Cement Industry and Trade Inc., Buyukcekmece, Istanbul, Türkiye, erdal.onkol@akcansa.com.tr

[5] 0009-0008-0131-4411, Akçansa Cement Industry and Trade Inc., Buyukcekmece, Istanbul, Türkiye, cihantayyar.ahi@akcansa.com.tr

[*] Corresponding author

Abstract. The combined influence of curing regime and mold release agent on the strength development of concretes incorporating ground granulated blast-furnace slag (GGBFS) remains insufficiently understood. This study evaluates the compressive and splitting tensile strength of plain and GGBFS-blended concretes belonging to two strength classes (C25/30 and C40/50) under continuous water curing and intermittent sprinkler curing. Two mold release agents, a conventional mineral-oil-based product and a paraffin-containing non-ionic product, were also investigated. The results showed that GGBFS incorporation reduced early-age strength but enhanced later-age strength development, leading to comparable or higher 28-day strengths than the corresponding plain mixtures. The effectiveness of the curing regime depended on both concrete class and binder composition. While intermittent sprinkler curing generally lowered early-age strength, its effect on 28-day performance was limited and, in several slag-containing mixtures, comparable to that of continuous water curing. The type of mold release agent had no systematic influence on either compressive or splitting tensile strength. Overall, binder composition and curing conditions were found to govern strength development to a much greater extent than mold surface treatment. The findings highlight the importance of considering the interaction between binder type and curing practice when optimizing the mechanical performance of plain and slag-blended concretes.

Keywords: Ground granulated blast-furnace slag (GGBFS); curing regime; sprinkler curing; mold release agent; compressive strength; splitting tensile strength.

1 Introduction

Curing is the process of maintaining adequate moisture and temperature conditions in concrete for a sufficient period after casting to allow cement hydration to proceed to the extent required by design. It is well established that inadequate or interrupted curing reduces the degree of hydration and leads to a coarser and more interconnected pore structure, adversely affecting strength, permeability, and durability. Rahal [1] reported reductions of up to 39% in compressive strength for concrete exposed to unfavorable curing conditions compared with laboratory-cured specimens.

The response of concrete to curing conditions depends strongly on binder composition. Ground granulated blast-furnace slag (GGBFS) contributes to hydration through a latent

hydraulic mechanism and generally exhibits slower early-age reactivity than Portland cement. Consequently, the development of mechanical properties in slag-containing systems is highly dependent on sustained moisture availability. Previous studies have shown that insufficient curing may significantly reduce the later-age performance of GGBFS concretes, with the severity of the effect increasing as the slag replacement level increases [2-5].

Another factor that may influence concrete performance is the type of mold release agent applied to the formwork surface. Conventional mineral-oil-based products and non-ionic paraffin-based release agents differ in their wetting characteristics and interfacial behavior. Djelal et al. [6] reported that certain mineral-oil-based formulations may interact with the alkaline pore solution of fresh concrete, whereas non-ionic release agents are generally considered chemically inert and function primarily as physical separation layers. Similarly, Abbas et al. [7] described modern non-ionic emulsion-based release agents as materials designed to improve demolding efficiency and surface quality without participating in cement hydration reactions. Despite these observations, limited information is available regarding their performance under interrupted curing conditions.

Although the individual effects of curing conditions, binder composition, and mold release agent characteristics have been widely investigated, their combined influence on the mechanical performance of concretes with different strength classes remains insufficiently understood. Therefore, the present study evaluates two concrete classes (C25/30 and C40/50), two binder systems (plain Portland cement and GGBFS-blended concrete), two curing regimes (water curing and intermittent sprinkler curing), and two mold release agents (conventional mineral-oil-based and paraffin-containing non-ionic formulations) within a unified experimental program. The study aims to clarify the interaction between binder composition and curing regime while also assessing whether mold release agent type influences the mechanical performance of concretes with different strength classes and binder systems.

2 Materials and Experimental Programme

2.1 Cement and Slag Characterization

A CEM I 42.5 R Portland cement and a ground granulated blast-furnace slag (GGBFS) were used as binder materials. Characterization tests confirmed compliance with TS EN 197-1 and TS EN 15167-1 requirements, respectively. The GGBFS exhibited a higher fineness than the cement. The chemical, physical and mechanical properties of both materials are presented in Table 1.

Table 1. Chemical and physical properties of the CEM I 42.5 R cement and the GGBFS.

Parameter	CEM I 42.5 R	Standard limit	GGBFS	EN 15167-1 limit
SiO_2 (%)	18.69	–	40.93	–
Al_2O_3 (%)	4.92	–	10.84	–
Fe_2O_3 (%)	3.28	–	1.17	–
CaO (%)	62.76	–	36.85	–
MgO (%)	0.97	–	6.73	≤ 18
SO_3 (%)	3.47	≤ 4.0	0.51	≤ 2.5
Cl^- (%)	0.0308	≤ 0.10	0.0209	≤ 0.10
Loss on ignition (%)	4.22	≤ 5.0	0.00	–
Insoluble residue (%)	0.96	≤ 5.0	–	–
$(CaO+MgO+Al_2O_3)/SiO_2$	–	–	1.33	≥ 1.0
Specific gravity (g/cm^3)	3.12	–	2.90	–
Blaine fineness (cm^2/g)	4000	–	4740	–
Initial / final set (min)	117 / 179	≥ 60	143 / 239	–
Soundness, Le Chatelier (mm)	1	≤ 10	1	–
C_3S / C_2S / C_3A / C_4AF (%)	61.1 / 7.6 / 7.5 / 10.0	–	–	–

2.2 Mixture Proportions

Four concrete mixtures, representing two strength classes (C25/30 and C40/50) and two binder systems (plain Portland cement and GGBFS-blended cement), were designed for the experimental programme. To minimize the influence of variables other than binder composition and strength level, the aggregate grading and chemical admixture type were kept constant across the mixtures. The complete mixture proportions are given in Table 2.

Table 2. Mixture proportions (kg/m^3) (P = plain, S = slag-blended).

Constituent (kg/m^3)	C25-P	C25-S	C40-P	C40-S
CEM I 42.5 R	270	210	370	310
GGBFS	0	75	0	75
GGBFS / binder (%)	0	26.3	0	19.5
Water	162	162	155.4	155.4
Superplasticizer	(0.94%)	(0.85%)	(1.0%)	(1.0%)
Fine aggregate (0–4 mm)	469	465	452	448
Coarse aggregate #1 (4–11.2 mm)	455	451	457	453
Coarse aggregate #2 (11.2–22.4 mm)	538	533	499	494
Natural sand	501	496	482	478

2.3 Curing Regimes and Mold Release Agents

After demolding at 24 h, the 100 × 100 × 100 mm cube specimens were subjected to the designated curing regimes and maintained under the respective curing conditions until the relevant testing age. The curing program comprised two methods: continuous water curing at 20 ± 2 °C and intermittent sprinkler curing. Under the intermittent curing regime, specimens were exposed to ambient laboratory conditions and wetted by water spraying for 2 min at 10 min intervals throughout the curing period. Furthermore, to investigate the potential influence of mold release agent characteristics on concrete performance, two commercially available release agents were used during casting: a conventional mineral oil-based mold release agent and a paraffin-containing non-ionic mold release agent.

2.4 Testing Methods

Slump was measured on each fresh batch in accordance with TS EN 12350-2. Compressive strength was determined at 2, 7 and 28 days, and splitting tensile strength at 28 days, each as the mean of three specimens, in accordance with TS EN 12390-3 and TS EN 12390-6, respectively.

3 Results

3.1 Fresh Properties

Slump was maintained at 23.0 ± 1 cm across all sixteen batches, confirming that workability was successfully equalized between the plain and slag-blended mixtures and was not a confounding variable in the strength comparisons that follow. Superplasticizer demand, expressed as a percentage of binder mass, was slightly lower for the slag-blended mixtures than for their plain counterparts within each strength class (0.85% vs 0.94% for the C25 series; 0.96% vs 1.00% for the C40 series), consistent with the smoother particle morphology and higher fineness of the ground slag improving paste rheology at equal or lower free water content.

3.2 Compressive and Splitting Tensile Strength Development

Table 3 presents the full compressive and splitting tensile strength results for the eight mixture/mold-agent combinations under standard (continuous water immersion) curing, and Table 4 the equivalent results under intermittent sprinkler curing.

Table 3. Fresh and hardened properties – standard curing.

Mixture	Mold agent	Slump (cm)	SP (%)	$f_{c,2d}$ (MPa)	$f_{c,7d}$ (MPa)	$f_{c,28d}$ (MPa)	$f_{sp,28d}$ (MPa)
C25-P (plain)	Conventional	22.0	0.94	22.9	28.8	32.8	2.63
C25-P (plain)	Paraffin	22.0	0.94	22.0	29.5	33.3	2.53
C25-S (slag)	Conventional	22.5	0.85	15.2	24.0	35.6	2.73
C25-S (slag)	Paraffin	22.5	0.85	15.7	24.4	36.0	2.73
C40-P (plain)	Conventional	22.5	1.00	38.0	46.5	53.3	3.07
C40-P (plain)	Paraffin	22.5	1.00	37.4	48.7	55.3	3.37
C40-S (slag)	Conventional	23.0	0.96	32.6	45.2	52.8	3.37
C40-S (slag)	Paraffin	23.0	0.96	31.9	46.8	56.4	3.47

Table 4. Fresh and hardened properties – intermittent sprinkler curing.

Mixture	Mold agent	Slump (cm)	SP (%)	$f_{c,2d}$ (MPa)	$f_{c,7d}$ (MPa)	$f_{c,28d}$ (MPa)	$f_{sp,28d}$ (MPa)
C25-P (plain)	Conventional	22.0	0.94	21.0	31.7	36.4	2.43
C25-P (plain)	Paraffin	22.0	0.94	19.2	29.8	34.3	2.63
C25-S (slag)	Conventional	22.5	0.85	14.4	25.1	36.0	2.83
C25-S (slag)	Paraffin	22.5	0.85	15.2	25.6	36.8	2.57
C40-P (plain)	Conventional	22.5	1.00	36.1	48.9	52.4	3.40
C40-P (plain)	Paraffin	22.5	1.00	35.7	46.6	50.7	3.27
C40-S (slag)	Conventional	23.0	0.96	31.9	45.6	57.6	3.70
C40-S (slag)	Paraffin	23.0	0.96	32.0	46.1	58.7	3.33

Regardless of the curing regime, slag replacement led to lower early-age compressive strength, with the reduction being more pronounced in the C25 mixtures than in the C40 mixtures. Under

standard curing, the strength reduction ranged from 28.5% to 33.7% in the C25 mixtures and from 14.0% to 14.8% in the C40 mixtures. Similar reductions were observed under sprinkler curing, corresponding to 20.9–31.4% and 10.3–11.6% for the C25 and C40 series, respectively. At 28 days, the slag mixtures exhibited comparable or higher strengths than the corresponding plain mixtures. Under standard curing, the 28-day compressive strength increased by 8.1–8.5% in the C25 series, whereas the differences in the C40 series remained within ±2%. Under sprinkler curing, the beneficial effect of slag became more pronounced, with strength gains of 4.8–7.3% for the C25 mixtures and 9.9–15.7% for the C40 mixtures relative to their plain counterparts.

The influence of mold release agent type on compressive strength was generally limited. Nevertheless, the paraffin-containing non-ionic release agent tended to provide slightly higher 28-day strengths, particularly in the slag-containing C40 mixtures subjected to sprinkler curing, where the highest compressive strength of the study (58.7 MPa) was achieved. Overall, curing condition and binder composition had a much greater effect on strength development than the mold release agent type.

The 28-day splitting tensile strength results indicate that slag incorporation had a generally positive effect on tensile performance. Under standard curing, tensile strength increased by up to 7.9% and 9.8% in the C25 and C40 series, respectively, while under sprinkler curing the highest improvement reached 8.8% in the C40 mixtures. In contrast, the effect of mold release agent type remained relatively minor, with only small differences observed between the conventional and paraffin-containing non-ionic products.

4 Discussion

The observed strength development confirms the well-established influence of GGBFS on hydration kinetics and microstructural evolution. The slower early-age performance of the slag-containing mixtures can be attributed to the lower clinker content and the delayed hydraulic reactivity of slag compared with ordinary Portland cement [3, 5, 8]. As hydration progresses, the contribution of slag becomes increasingly significant due to the continued formation of secondary C-S-H gel and the refinement of pore structure. This process promotes matrix densification and enhances long-term mechanical performance [4, 9].

The findings further indicate that the effectiveness of GGBFS depends strongly on curing conditions. Previous studies have shown that supplementary cementitious materials require sufficient moisture availability to sustain hydration and achieve their full performance potential [3, 5]. In the present study, the intermittent sprinkler regime appears to have provided adequate moisture for continued hydration. Similar conclusions were reported by Wang et al. [10], who demonstrated that curing regime substantially affects strength development and microstructural quality, and by Guo et al. [11], who observed that moisture-retaining curing systems can effectively support concrete hydration by reducing excessive surface water loss.

Additionally, sprinkler curing did not consistently produce lower later-age strengths than continuous water curing. This suggests that curing efficiency should not be evaluated solely based on the curing method itself but rather in conjunction with binder composition and mixture characteristics. Similar correlations between curing conditions and supplementary cementitious materials have been reported by Sherwani et al. [12] and Ahmad et al. [4].

The influence of mold release agent type was considerably less pronounced than the effects of binder composition and curing regime. Although the paraffin-containing non-ionic release agent occasionally resulted in slightly higher mechanical properties, no systematic trend was observed.

The splitting tensile strength results exhibited trends broadly comparable to those observed for compressive strength. The improvement in tensile performance observed in several slag-containing mixtures may be associated with continued microstructural refinement and

enhancement of the aggregate-paste interfacial transition zone. Comparable findings have been reported by Sang and Khoa [13], Vincent et al. [9], and Ahmad et al. [4], who identified positive relationships between slag hydration, matrix densification, and tensile strength development.

Overall, the present findings indicate that binder composition was the dominant factor governing strength development, followed by curing regime, whereas mold release agent type exerted only a secondary influence. These findings suggest that optimization of binder design and curing practice is more critical to long-term mechanical performance than the selection of the mold release agent.

5 Conclusions

Based on the experimental results obtained from sixteen concrete mixtures incorporating different binder systems, curing regimes, and mold release agents, the following conclusions can be drawn:

1. GGBFS incorporation delayed early-age strength development but contributed positively to later-age mechanical performance. The results confirm that slag-blended concretes can compensate for their initial strength deficit and achieve comparable or superior 28-day compressive and splitting tensile strengths when adequate curing conditions are provided.
2. The effect of curing regime depended on both concrete class and binder type. Intermittent sprinkler curing was generally effective in sustaining the hydration of slag-containing mixtures and produced 28-day strengths comparable to those obtained under continuous water curing. However, its effectiveness was less pronounced for the high-strength plain Portland cement mixtures.
3. The paraffin-containing non-ionic mold release agent did not adversely affect either compressive or splitting tensile strength. The differences between the two mold release agents remained limited throughout the study, indicating that mold release agent type has only a secondary influence on the mechanical performance of concrete compared with binder composition and curing practice.

Overall, the findings highlight the strong interaction between binder composition and curing regime in governing concrete strength development. Continuous water curing remained the most reliable condition for ensuring adequate hydration; however, the sprinkler curing regime investigated in this study also provided satisfactory performance in several mixtures, particularly those containing GGBFS. These results suggest that curing efficiency should be assessed in relation to the characteristics of the concrete system rather than solely on the basis of the curing method employed. Further studies incorporating microstructural characterization techniques and long-term durability assessments are recommended to better understand the interaction between GGBFS hydration and curing conditions governing strength development.

Acknowledgments

The authors would like to thank Samet Top and his team for their support in installing the sprinkler curing system.

References

1. Rahal, K. N. (2016). Effects of improper moist curing on flexural strength of slabs cast under hot weather conditions. Construction and Building Materials, 110, 337–345. https://doi.org/10.1016/j.conbuildmat.2016.02.040
2. Atiş, C. D., & Bilim, C. (2007). Wet and dry cured compressive strength of concrete containing ground granulated blast-furnace slag. Building and Environment, 42(8), 3060–3065. https://doi.org/10.1016/j.buildenv.2006.07.027

3. Yang, H. M., Kwon, S. J., Myung, N. V., Singh, J. K., Lee, H. S., & Mandal, S. (2020). Evaluation of strength development in concrete with ground granulated blast furnace slag using apparent activation energy. Materials, 13(2), 442. https://doi.org/10.3390/ma13020442
4. Ahmad, J., Kontoleon, K. J., Majdi, A., Naqash, M. T., Deifalla, A. F., Ben Kahla, N., Isleem, H. F., & Qaidi, S. M. A. (2022). A comprehensive review on the ground granulated blast furnace slag (GGBS) in concrete production. Sustainability, 14(14), 8783. https://doi.org/10.3390/su14148783
5. Kim, H. S., & Lee, H. S. (2025). Effect of GGBFS content and curing temperature on early-age strength and maturity-based modeling of concrete. Materials, 18(19), 4525. https://doi.org/10.3390/ma18194525
6. Djelal, C., De Caro, P., Libessart, L., Dubois, I., & Pébère, N. (2008). Comprehension of demoulding mechanisms at the formwork/oil/concrete interface. Materials and Structures, 41(3), 571–581. https://doi.org/10.1617/s11527-007-9268-3
7. Abbas, A., Zhang, C., Hussain, S., Tang, Y., Li, Y., Gao, R., & Xu, S. (2023). Preparation of ultrastable oil-in-water emulsion as a robust superwettable and sustainable concrete release agent. Journal of Molecular Liquids, 390, 123043. https://doi.org/10.1016/j.molliq.2023.123043
8. Park, H., Jeong, Y., Jeong, J. H., & Oh, J. E. (2016). Strength development and hydration behavior of self-activation of commercial ground granulated blast-furnace slag mixed with purified water. Materials, 9(3), 185. https://doi.org/10.3390/ma9030185
9. Vincent, J., Natarajan, B., Amaladas, D. D., & Cruze, D. (2023). An evaluation of mechanical properties of nano GGBFS in concrete with statistical validation. Buildings, 13(12), 3060. https://doi.org/10.3390/buildings13123060
10. Wang, L., Wei, W., Zhang, J., Hu, Y., & Zhang, L. (2023). Effect of curing regime on the mechanical properties and durability of steam-cured concrete. Buildings, 13(7), 1697. https://doi.org/10.3390/buildings13071697
11. Guo, G., Zhao, S., Wen, D., Zhang, G., & Liu, L. (2024). Experimental study on the influence of different curing methods on the performance of concrete. Journal of Measurements in Engineering, 13(1), 25–34. https://doi.org/10.21595/jme.2024.24184
12. Sherwani, A. F. H., Younis, K. H., & Arndt, R. W. (2022). Fresh, mechanical, and durability behavior of fly ash-based self-compacted geopolymer concrete: Effect of slag content and various curing conditions. Polymers, 14(15), 3209. https://doi.org/10.3390/polym14153209
13. Sang, N. T., & Khoa, N. T. (2020). Experimental study on effect of ground granulated blast furnace slag of strength and durability of sand concrete. In CIGOS 2019, Innovation for Sustainable Infrastructure (Lecture Notes in Civil Engineering, Vol. 54, pp. 409–416). Springer. https://doi.org/10.1007/978-981-15-0802-8_63

Author Contribution Statement

- *Conceptualization:* Senem Bilici, Muhittin Tarhan, Erdal Önkol, Cihan Tayyar Ahı
- *Methodology:* Senem Bilici, Muhittin Tarhan, Erdal Önkol, Cihan Tayyar Ahı
- *Investigation:* Senem Bilici, Arif Tufan Salva
- *Writing – Original Draft:* Senem Bilici
- *Writing – Review & Editing:* Senem Bilici, Arif Tufan Salva

List of Abbreviations

- **GGBFS** — Ground granulated blast-furnace slag

- **SP** — Superplasticizer
- **C-S-H** — Calcium silicate hydrate
- f_c — Compressive strength
- f_{sp} — Splitting tensile strength

Declarations

Conflict of Interest: The authors declare no conflict of interest.

Data Availability: The data presented in this study are available from the corresponding author upon reasonable request.

Publication Note

This paper was peer-reviewed, accepted for presentation, and included in the proceedings of the ACE2026 – International Conference on Advances in Civil Engineering, held on 12–14 October 2026 in Trabzon, Türkiye.

This paper may be cited as follows:

Bilici S., Salva A. T., Tarhan M., Önkol E., Ahı C. T., "Strength Development under Intermittent Sprinkler Curing: A Comparative Study of Plain and Slag-Blended Concrete," in Proceedings of the ACE2026 – International Conference on Advances in Civil Engineering, Trabzon, Türkiye, 12–14 October 2026.

Moisture Optimization of Roller-Compacted Concrete Pavements Incorporating Recycled Materials

Ola Aljumaili[1], Yunus Emre Demir[2], Yeşim Arslantürk[3], Emine Özdoğru[4], Oğuzhan Şahin[5], Emin Şengün[6]

[1]0009-0003-0967-2241, Ankara Yıldırım Beyazıt University, Civil Engineering Department, Ankara, Türkiye, olaaljumaili340@gmail.com

[2]0009-0003-3832-9194, Ankara Yıldırım Beyazıt University, Civil Engineering Department, Ankara, Türkiye, ynsemredemir292929@gmail.com

[3]0009-0009-5826-4547, Ankara Yıldırım Beyazıt University, Civil Engineering Department, Ankara, Türkiye, yesimarslanturk@aybu.edu.tr

[4]0000-0002-2382-8383, Ankara University, Civil Engineering Department, Ankara, Türkiye, eozdogru@ankara.edu.tr

[5]0000-0003-2104-5761, Ankara University, Civil Engineering Department, Ankara, Türkiye, ohsahin@ankara.edu.tr

[6]0000-0001-7082-0061, Ankara Yıldırım Beyazıt University, Civil Engineering Department, Ankara, Türkiye, esengun@aybu.edu.tr

Abstract. The growing volume of concrete waste, which constitutes a major fraction of construction and demolition (C&D) waste, highlights the need for sustainable reuse in high-value applications. Road construction is a promising pathway, particularly for roller-compacted concrete (RCC), where compaction control is critical for field performance. This study investigated the moisture–density behavior of RCC mixtures incorporating recycled concrete aggregate (RCA) and concrete waste powder (CWP), a finely ground residual fraction generated during RCA processing. Nine mixture designs combining three RCA replacement levels (0%, 50%, and 100%) and three CWP contents (0%, 30%, and 50%) were evaluated at five effective water contents (4.5–8.5%) on a saturated surface-dry (SSD) condition, resulting in 45 mixture conditions. The mixtures were prepared with oven-dry aggregates, and additional water was included to compensate for aggregate absorption. Although the SSD-based optimum moisture content (OMC) remained approximately 6.5%, the total water demand under oven-dry batching increased from 8.4% for RCA0 to 9.7% for RCA50 and 11.2% for RCA100 because of the additional absorption water required by RCA. Increasing RCA content also reduced maximum dry density (MDD) by approximately 5.4% and 10.8% at RCA50 and RCA100, respectively, while the influence of CWP was considerably smaller. VeBe measurements further indicated a stiffer fresh consistency with increasing recycled constituents. From a practical perspective, the results indicate that the conventional RCC OMC can be used as an initial moisture target for RCA-containing mixtures, provided that the additional water required for RCA absorption is added separately. However, because RCA substantially reduces the achievable dry density and may result in a stiffer fresh consistency, field compaction control should be based on mixture-specific MDD values, together with careful monitoring of placement and compaction.

Keywords: Roller-compacted concrete; pavements; recycled concrete aggregate; concrete waste powder; optimum moisture content.

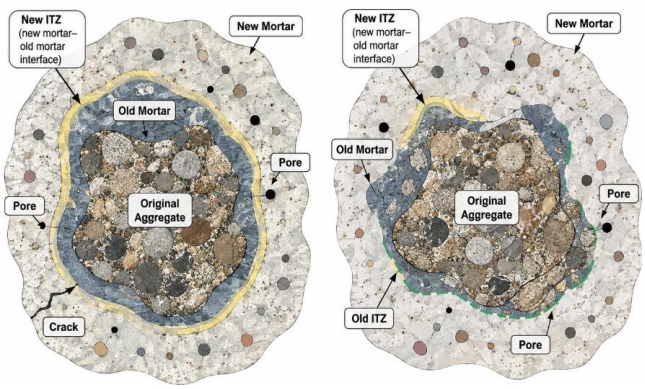
1 Introduction

Roller-compacted concrete (RCC) is a zero-slump concrete placed with paving equipment and compacted by rollers, combining rapid construction with the structural capacity and durability of concrete pavements. Because RCC contains relatively low paste and water contents and relies on external compaction, its performance is highly sensitive to aggregate grading, moisture condition, compactive effort, and curing. The moisture–density relationship is therefore central to RCC mixture design. Insufficient water limits particle rearrangement and results in excessive voids, whereas excess water prevents the formation of a densely packed structure. For a given compaction method and effort, the optimum moisture content (OMC) corresponds to the water content at which the maximum dry density (MDD) is achieved. Since both OMC and MDD are influenced by mixture composition and compaction procedure, they should be considered mixture- and method-specific parameters [1–3].

The use of recycled concrete aggregate (RCA) in RCC provides an opportunity to reduce both the consumption of natural aggregate (NA) and the quantity of concrete waste requiring disposal. Pavement construction is particularly suitable for such large-volume recycling because aggregates constitute the majority of an RCC mixture. However, RCA differs extensively from NA. An RCA particle is generally a composite consisting of the original NA and varying amounts of residual mortar remaining after crushing and processing. This adhered mortar typically has a lower density, greater porosity, higher water absorption, and more microcracking than the original aggregate. Increasing RCA content can therefore reduce the compacted density of RCC while increasing the quantity of water required to achieve adequate particle movement and consolidation. Recent experimental studies on RCA-containing RCC have similarly reported higher moisture demand and lower density as the replacement level increases, although the magnitude of these changes depends on the source and quality of the RCA, its grading, initial moisture state, and processing method [4,5].

The composite structure of RCA creates a more complex interfacial system than NA. As shown in *Fig. 1* (a), when the original aggregate remains covered by adhered mortar, the old ITZ is located between the original aggregate and old mortar, while a new ITZ forms between the old and new mortar. If part of the adhered mortar is removed during processing, the original aggregate becomes locally exposed and an additional new ITZ may form directly between the aggregate and new mortar, as illustrated in *Fig. 1* (b). Thus, several ITZs may coexist within a single RCA particle [6,7]. More importantly for RCC compaction, the porous and microcracked adhered mortar absorbs part of the mixing water and reduces the free water available for particle rearrangement. This effect is particularly significant when oven-dry RCA is used. Therefore, the effective water content expressed on an SSD condition should be distinguished from the total water added under oven-dry conditions, which also includes aggregate absorption. RCA-containing mixtures may consequently exhibit similar SSD-based OMC values but substantially different total water demands, making experimental determination of the moisture–density relationship necessary for each mixture [4-8].

RCA processing also produces a residual fine fraction composed of ground cement paste, mortar, and minor aggregate particles. This material can be reused in RCC as concrete waste powder (CWP). Although its fine particles may improve void filling, its porous nature and high surface area may also affect water demand and compaction. However, limited research has separately examined the effects of RCA and CWP on the OMC and MDD of RCC mixtures over complete moisture–density relationships [9,10].



(a) (b)

Fig. 1. Schematic ITZ configurations in RCA concrete: (a) new ITZ between old and new mortar; (b) additional aggregate–new mortar ITZ after partial removal of adhered mortar. Adapted from [11].

This study therefore investigates the moisture–density behavior of RCC pavement mixtures containing RCA and CWP. Nine mixture designs were formulated by combining RCA replacement levels of 0%, 50%, and 100% with CWP contents of 0%, 30%, and 50% as a partial replacement of Ordinary Portland cement (OPC). For each design, five effective water contents—4.5%, 5.5%, 6.5%, 7.5%, and 8.5%—were evaluated on an SSD condition, resulting in 45 mixture conditions. The mixtures were prepared using oven-dry aggregates, with additional water included to compensate for aggregate absorption. This approach allowed the additional water demand associated with RCA absorption to be distinguished from the effective moisture required for optimum compaction. It also enabled the relative effects of RCA and CWP on OMC and MDD to be evaluated separately.

2 Materials and Moisture–Density Experimental Program

OPC, NA, RCA, and CWP were used in the mixtures. RCA was produced by crushing previously used concrete cubes (*Fig.2*), followed by sieving to obtain the required aggregate gradation. The resulting RCA covered particle sizes from 0.063 to 16 mm. The fine residual fraction generated during RCA processing was further ground to a cement-like powder and used as CWP as a partial replacement of OPC. For volumetric mixture calculations, a particle specific gravity of 2.70 was adopted for CWP.

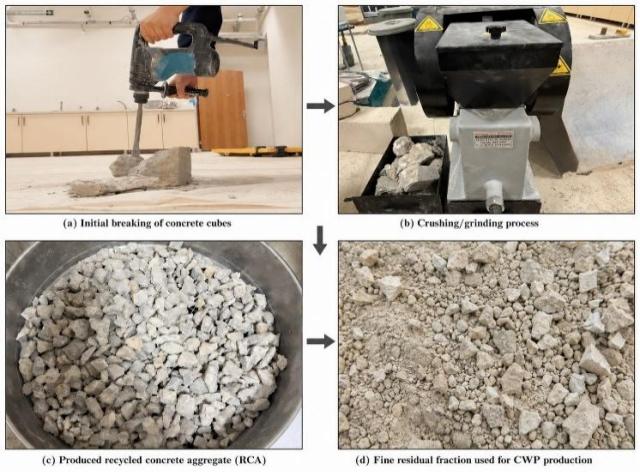


Fig. 2. Production process of RCA and CWP from crushed concrete waste [12].

The main physical properties of the natural and aggregate are summarized in Table 1. Aggregate gradations were selected in accordance with the General Technical Specification for "*Roller-Compacted Concrete Roads"* published by the Turkish Ministry of Environment, Urbanization and Climate Change [13].

Table 1. Physical properties of the RCA and NA used in study [14].

Agg. types	Agg. sieve size	Apparent Particle density (g/cm³)	Oven-Dry Particle Density (g/cm³)	SSD Particle Density (g/cm³)	Water Abs. Capacity (%)
RCA	16–32 mm	2.67	2.41	2.53	2.93
	8–16 mm	2.65	2.37	2.48	4.38
	4–8 mm	2.63	2.33	2.44	5.00
	2–4 mm	2.51	2.08	2.25	8.30
	1–2 mm	2.45	2.02	2.19	8.74
NA	16–32 mm	2.84	2.83	2.83	0.18
	8–16 mm	2.71	2.71	2.72	0.28
	4–8 mm	2.81	2.77	2.78	0.52
	2–4 mm	2.85	2.78	2.81	0.88
	1–2 mm	2.53	2.12	2.28	4.00

Nine RCC mixture designs were developed by combining three RCA replacement levels (0%, 50%, and 100%) with three CWP contents (0%, 30%, and 50%), with CWP replacing OPC by mass. For each mixture design, five effective water contents (4.5%, 5.5%, 6.5%, 7.5%, and 8.5%) were investigated on an SSD condition, resulting in 45 mixture conditions, as summarized in Table 2. The mixtures were prepared using oven-dry aggregates, and additional water was added to account for aggregate absorption. Aggregate quantities were adjusted according to the selected RCA replacement level and water content.

Table 2. Experimental matrix of RCC mixtures.

Mix ID	RCA replacement (%)	CWP replacement (%)	OPC (kg/m³)	CWP (kg/m³)	Effective water content, SSD condition (%)
RCA0-CWP0	0	0	350	0	4.5, 5.5, 6.5, 7.5, 8.5
RCA0-CWP30	0	30	245	105	4.5, 5.5, 6.5, 7.5, 8.5
RCA0-CWP50	0	50	175	175	4.5, 5.5, 6.5, 7.5, 8.5
RCA50-CWP0	50	0	350	0	4.5, 5.5, 6.5, 7.5, 8.5
RCA50-CWP30	50	30	245	105	4.5, 5.5, 6.5, 7.5, 8.5
RCA50-CWP50	50	50	175	175	4.5, 5.5, 6.5, 7.5, 8.5
RCA100-CWP0	100	0	350	0	4.5, 5.5, 6.5, 7.5, 8.5
RCA100-CWP30	100	30	245	105	4.5, 5.5, 6.5, 7.5, 8.5
RCA100-CWP50	100	50	175	175	4.5, 5.5, 6.5, 7.5, 8.5

Note: CWP replacement is expressed as a percentage of total binder mass.

The selected water contents were defined on SSD condition. However, the aggregates were used in the oven-dry (OD) condition during mixture preparation; therefore, additional water corresponding to aggregate absorption was included in the actual batch water. This distinction

was particularly important for RCA because of its considerably higher absorption associated with adhered mortar. The mixtures were compacted using the adopted Proctor procedure, and moisture–density curves were established for each mixture. The SSD-based OMC and corresponding MDD were obtained from these curves. In addition, the total water demand under OD conditions was calculated to evaluate the additional water requirement resulting from RCA absorption.

Moisture–density relationships were determined using the standard Proctor procedure in accordance with ASTM D698. Each RCC mixture was compacted in a 945 cm^3 mold in three equal layers, with 25 blows applied to each layer using the standard Proctor rammer, corresponding to a compactive effort of approximately 600 $kN \cdot m/m^3$. Five effective water contents were evaluated for each mixture on an SSD condition; because the aggregates were batched in the oven-dry condition, additional water was included to account for aggregate absorption. Following compaction, representative samples were oven-dried at 110 °C for 24 h to determine the actual moisture content and dry density. The moisture–density curves were then used to determine the SSD-based OMC and corresponding MDD for each mixture. Vebe consistency was also measured in accordance with ASTM C1170 to characterize the fresh consistency of the RCC mixtures. The Proctor compaction, moisture determination, and Vebe consistency procedures are illustrated in *Fig. 3*.



Fig. 3. Experimental procedures used for moisture–density and consistency evaluation of RCC mixtures [12].

3 Results and Discussion

3.1 Moisture–Density Relationships and OMC

Fig. 4 shows the moisture–density relationships expressed on an SSD condition. Despite substantial changes in RCA and CWP contents, the investigated mixtures exhibited a similar OMC of approximately 6.5%. This indicates that the effective moisture required to achieve optimum compaction remained relatively stable when aggregate absorption was accounted for. Although the position of the density peak changed little, the corresponding MDD decreased

noticeably with increasing RCA content, indicating the lower particle density and porous adhered mortar associated with RCA.

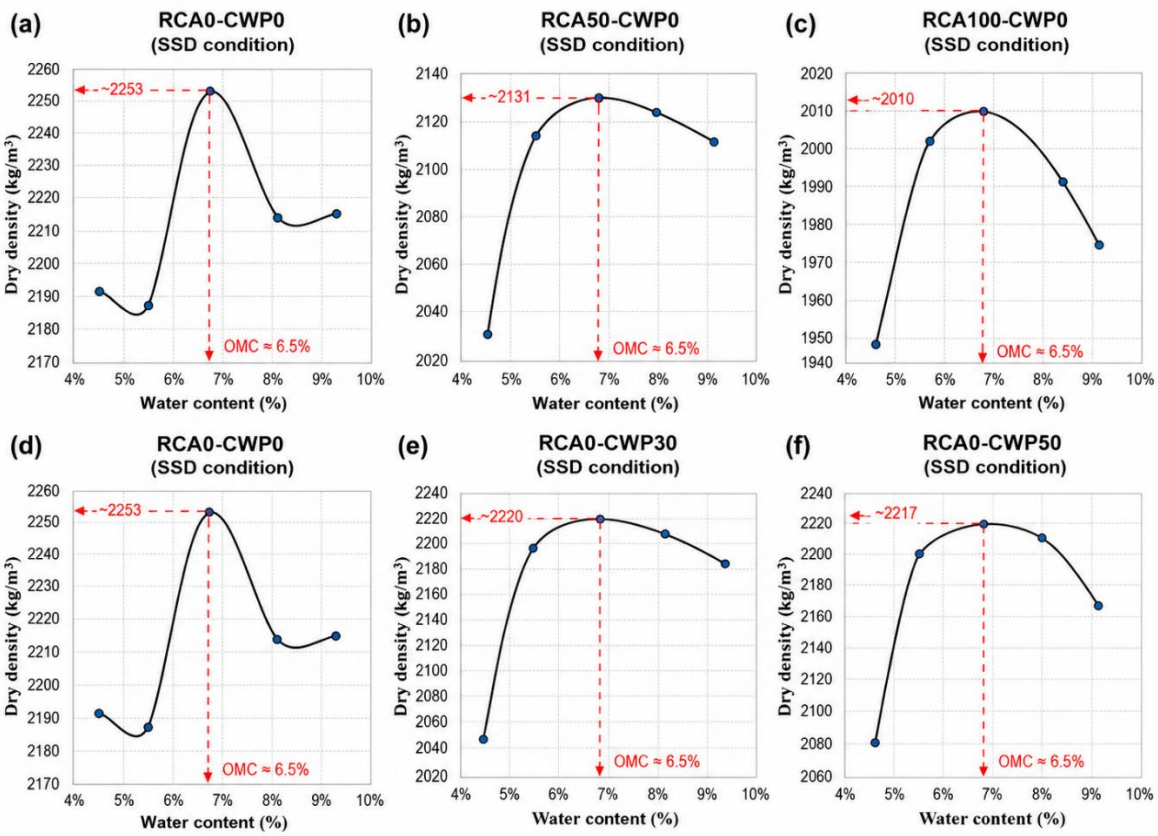


Fig. 4. Moisture–density relationships and SSD-based OMC of RCC mixtures.

A different trend becomes evident when the water content is expressed for mixtures prepared with oven-dry aggregates (*Fig.5*). For the CWP0 series, the total water content corresponding to MDD increased from approximately 8.4% for RCA0 to 9.7% for RCA50 and 11.2% for RCA100. In comparison, changing the CWP content produced considerably smaller shifts in total water demand. For example, at RCA0, the corresponding values remained within approximately 8.4–8.9%. Mixtures containing both RCA and CWP followed the same general pattern, with total water demand governed primarily by the RCA replacement level.

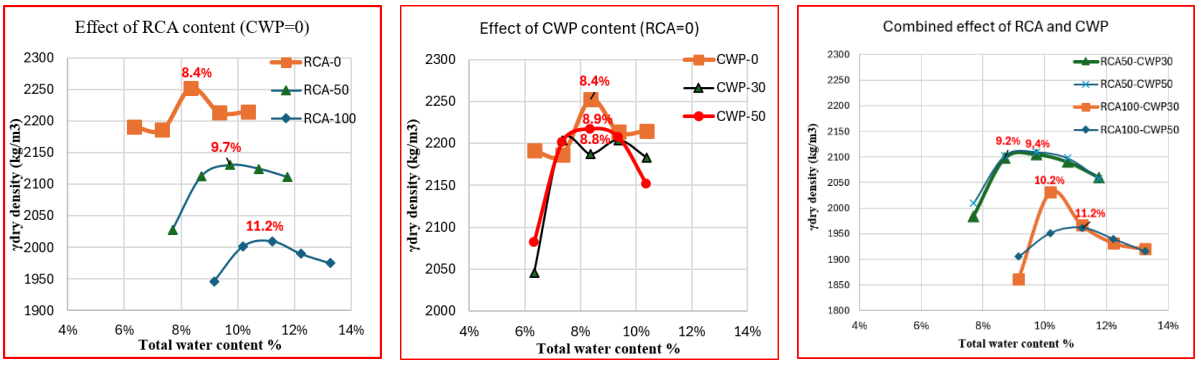


Fig. 5. Total water demand of RCC mixtures under oven-dry conditions.

The comparison between *Fig. 3* and *Fig.4* is particularly important: RCA did not substantially alter the SSD-based OMC, but it markedly increased the total amount of water required when oven-dry aggregates were used. This additional requirement is mainly associated with water

absorbed by the porous adhered mortar in RCA rather than an equivalent increase in the effective moisture needed for compaction. Therefore, SSD-based OMC and total water demand under oven-dry conditions should be clearly distinguished when proportioning RCA-containing RCC mixtures.

Although the mixture constituents affected the magnitude of the achieved dry density, they caused only minor changes in the location of the SSD-based optimum moisture level. This suggests that the primary effect of RCA was not a shift in the effective moisture required for compaction, but an increase in the additional water required to satisfy aggregate absorption when the material was batched in the oven-dry condition.

To complement the moisture–density evaluation, Vebe consistency was measured for three representative mixtures at the SSD-based OMC of approximately 6.5%. The Vebe time increased from 35 s for RCA0-CWP0 to 42 s for RCA0-CWP50 and 47 s for RCA100-CWP0, indicating a progressively stiffer fresh consistency with increasing recycled constituents. Nevertheless, all mixtures remained compactable under the adopted laboratory procedure. From a practical perspective, the higher Vebe times suggest that RCA-containing RCC mixtures may require greater attention to compaction during placement to achieve the target density, even though the SSD-based OMC remained nearly unchanged.

3.2 Effect of RCA and CWP on Maximum Dry Density

Fig.6 summarizes the MDD values of the investigated RCC mixtures. The results show that RCA content had a pronounced effect on MDD. For the mixtures without CWP, MDD decreased from approximately 2253 kg/m^3 for RCA0-CWP0 to 2131 kg/m^3 for RCA50-CWP0 and 2010 kg/m^3 for RCA100-CWP0, corresponding to reductions of approximately 5.4% and 10.8%, respectively. This reduction is consistent with the lower particle density and higher porosity associated with the adhered mortar in RCA. In contrast, the effect of CWP on MDD was considerably smaller. At RCA0, increasing CWP content to 30% and 50% reduced MDD from approximately 2253 to 2220 and 2217 kg/m^3, corresponding to reductions of only 1.5% and 1.6%, respectively. A similarly limited influence of CWP was observed at higher RCA contents. Overall, the results indicate that RCA replacement was the primary factor controlling the reduction in MDD, whereas the influence of CWP was secondary.

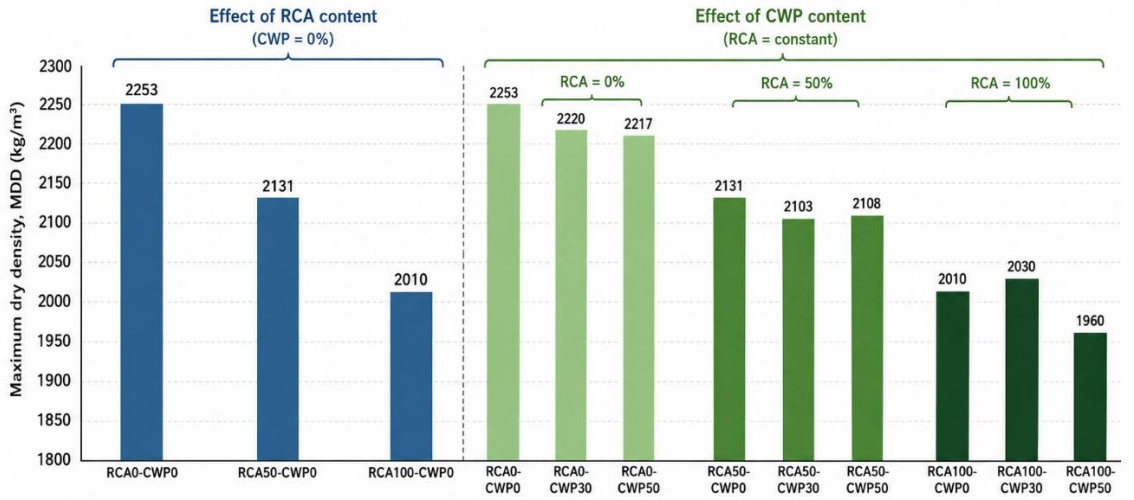


Fig. 6. Effect of RCA and CWP contents on MDD of RCC mixtures

From a practical perspective, the results indicate that the SSD-based OMC of conventional RCC may provide a reasonable initial moisture target for RCA-containing mixtures when aggregate absorption is properly accounted for, since the optimum effective moisture remained close to 6.5% across the investigated mixtures. However, a similar OMC does not imply a similar maximum achievable density or fresh consistency. The MDD decreased substantially with increasing RCA content, indicating that field density acceptance should be based on the mixture-specific laboratory MDD rather than on the reference value of conventional RCC. In addition, the increase in Vebe time with recycled constituents shows that mixtures may become stiffer even at a similar SSD-based OMC, suggesting greater resistance to consolidation and a need for closer compaction control during field placement.

4 Conclusion

The moisture–density behavior of RCC mixtures containing RCA and CWP was evaluated with particular emphasis on distinguishing SSD-based effective moisture from the total water demand of mixtures prepared with oven-dry aggregates. The main conclusions are:

- The SSD-based OMC remained approximately 6.5% across the investigated mixtures, despite substantial changes in RCA and CWP contents. This indicates that the conventional RCC OMC can be used as an initial target for RCA-containing mixtures, provided that the additional water required for RCA absorption is added separately.
- In contrast, the total water demand under oven-dry conditions increased significantly with RCA content, rising from approximately 8.4% for RCA0 to 9.7% for RCA50 and 11.2% for RCA100 in mixtures without CWP. This increase was mainly associated with RCA absorption rather than a corresponding increase in effective compaction moisture.
- RCA had a pronounced effect on MDD. Relative to RCA0-CWP0, MDD decreased by approximately 5.4% at RCA50 and 10.8% at RCA100, whereas the effect of CWP was considerably smaller. Therefore, field density acceptance for RCA-containing RCC should be based on the mixture-specific laboratory MDD rather than the MDD of conventional RCC.
- Similar OMC values did not result in identical fresh consistency. Vebe time increased from 35 s for RCA0-CWP0 to 47 s for RCA100-CWP0, indicating a stiffer consistency with increasing recycled constituents. Thus, RCA-containing RCC may require closer attention to compaction during field placement even when the SSD-based OMC remains nearly unchanged.

Overall, the results show that the principal effect of RCA on RCC mixture design is not a substantial shift in SSD-based OMC, but rather an increase in total water demand, a reduction in achievable dry density, and a stiffer fresh consistency.

Acknowledgments
This study was supported by the Scientific and Technological Research Council of Türkiye (TÜBİTAK) under the 1002-A Short-Term Support Module (Project No. 125M941).

References

1. ACI Committee 327: Guide to Roller-Compacted Concrete Pavements. ACI 327R-14, American Concrete Institute, Farmington Hills, MI (2015).

2. Selvam, M., Singh, S.: Influence of compaction methods on the optimum moisture content and performance of roller-compacted concrete pavements. J. Mater. Civ. Eng. 35(7), 04023176 (2023).
3. Stępień, J., Chomicz-Kowalska, A., Tutaj-Dudała, M., Dudała, M., Maciejewski, K., Ramiączek, P., Iwański, M.M.: Influence of compaction methods on properties of roller-compacted concrete pavement wearing surfaces. Materials 18(3), 492 (2025).
4. Hosseinnezhad, H., Hatungimana, D., Ramyar, K.: Mechanical properties of roller compacted concrete containing recycled concrete aggregate. Revista de la Construcción 20(2), 277–290 (2021). https://doi.org/10.7764/RDLC.20.2.277.
5. Fardin, H.E., Santos, A.G..: Roller compacted concrete with recycled concrete aggregate for paving bases. Sustainability 12(8), 3154 (2020). https://doi.org/10.3390/su12083154
6. Selvam, M., Singh, S., Anjana, A.G.: Enhancing the performance of roller-compacted concrete pavement by synergetic improvement of packing density, lubrication, and moisture state of recycled concrete aggregate. Transp. Res. Rec. 2677(6), 594–608 (2023).
7. Kaabeche, S., Belaoura, M., Kahlouche, R.: The effects of the quality of recycled aggregates on the mechanical properties of roller-compacted concrete. Res. Eng. Struct. Mater. 11(2), 587–605 (2025).
8. Xia, G., Zhao, Y.: Interface parameters of recycled aggregate concrete considering the distribution of old mortar content. Case Stud. Constr. Mater. 20, e03262 (2024).
9. Lu, C., Yu, Q., Wei, J., Niu, Y., Zhang, Y., Lin, C., Chen, P., Shi, C., Yang, P.: Influence of interfacial transition zones and pore structure on the compressive strength of recycled aggregate concrete. Constr. Build. Mater. 456, 139299 (2024).
10. Chen, X., Li, Y., Bai, H., Ma, L.: Utilization of recycled concrete powder in cement composite: Strength, microstructure and hydration characteristics. *J. Renew. Mater.* **9**(12), 2189–2208 (2021). https://doi.org/10.32604/jrm.2021.015394.
11. Rampit, R., Smith, J., Ray, I.: A review of recycled concrete aggregates as a sustainable construction material. In: International Conference on Emerging Trends in Engineering and Technology (IConETech 2020). The University of the West Indies, Faculty of Engineering, Trinidad and Tobago (2020).
12. Aljumili, O.: Performance Assessment of Roller Compacted Concrete Pavements Incorporating Recycled Materials Derived from Construction and Demolition Waste. M.Sc. thesis, Ankara Yıldırım Beyazit University, Ankara, Türkiye (2026).
13. CSIDB, “Silindirle Sıkıştırılmış Beton Yol Genel Teknik Şartnamesi” Ankara, Türkiye, 2020.
14. Aljumaili O, Arslantürk Y, Özdoğru E, Şahin O, Şengün E. Türkiye koşullarında beton atıklarından elde edilen geri dönüşüm agregalarının silindirle sıkıştırılmış beton yol kaplama şartnamesi açısından kullanılabilirliğinin değerlendirilmesi. Pamukkale Üniversitesi Mühendislik Bilimleri Dergisi. 2026; (Advanced Online Publication). https://doi.org/10.65206/pajes.1873481

Author Contribution Statement

- *Conceptualization:* Oğuzhan Şahin, Emin Şengün
- *Methodology:* Ola Aljumaili, Oğuzhan Şahin, Emin Şengün
- *Investigation:* Ola Aljumaili, Yunus Emre Demir, Yeşim Arslantürk, Emine Özdoğru
- *Writing – Original Draft:* Ola Aljumaili, Oğuzhan Şahin, Emin Şengün
- *Writing – Review & Editing:* Ola Aljumaili, Oğuzhan Şahin, Emin Şengün
- *Supervision:* Oğuzhan Şahin, Emin Şengün

List of Abbreviations

- **C&D** — Construction and Demolition

- **CWP** — Concrete Waste Powder
- **MDD** — Maximum Dry Density
- **NA** — Natural Aggregate
- **OD** — Oven-Dry
- **OMC** — Optimum Moisture Content
- **OPC** — Ordinary Portland Cement
- **RCA** — Recycled Concrete Aggregate
- **RCC** — Roller-Compacted Concrete
- **SSD** — Saturated Surface-Dry

Declarations

The authors declare that they have no conflict of interest. The data supporting the findings of this study are available from the corresponding author upon reasonable request.

Publication Note

This paper was peer-reviewed, accepted for presentation, and included in the proceedings of the ACE2026 – International Conference on Advances in Civil Engineering, held on 12–14 October 2026 in Trabzon, Türkiye.

This paper may be cited as follows:

O. Aljumaili, Y. E. Demir, Y. Arslantürk, E. Özdoğru, O. Şahin, and E. Şengün, "Moisture Optimization of Roller-Compacted Concrete Pavement Mixtures Incorporating Recycled Materials," in Proceedings of the ACE2026 – International Conference on Advances in Civil Engineering, Trabzon, Türkiye, 12–14 October 2026.

Technical and Environmental Evaluation of Electric Arc Furnace Slag as Fine Aggregate Replacement in Cement Mortar

Emircan Özçelikci[1], Hussein Abdullahi Ali[2], Mehmet Baran[3]
[1] 0000-0002-6112-9735, Ankara Yıldırım Beyazıt University, Civil Engineering Department, Ankara, Türkiye, eozcelikci@aybu.edu.tr
[2] 0009-0004-8081-6348, Ankara Yıldırım Beyazıt University, Civil Engineering Department, Ankara, Türkiye, husseinaaj2@gmail.com
[3] 0000-0001-6674-7308, Ankara Yıldırım Beyazıt University, Civil Engineering Department, Ankara, Türkiye, mehmet.baran@aybu.edu.tr

Abstract. Electric arc furnace slag (EAFS) is increasingly generated as electric arc furnace-based steel production grows. Its use as an alternative aggregate in cementitious composites may reduce natural aggregate consumption while valorizing an industrial by-product. In this study, EAFS was investigated as a partial fine aggregate replacement in cement mortar. Mortar mixtures were prepared by replacing CEN standard sand with EAFS at 25, 50 and 75%, and their fresh-state behavior and compressive strength development were evaluated. The EAFS exhibited a water absorption capacity of 2.61%, indicating a higher water demand than conventional standard sand. Increasing the EAFS content resulted in a gradual reduction in mortar flow, with the highest replacement level causing approximately 26% lower flow than the reference mixture. This reduction was mainly associated with the rough texture, angular particle shape, and higher absorption capacity of EAFS. At 28 days, the mixture containing 25% EAFS achieved the highest compressive strength as 52.0 MPa, corresponding to about 9% improvement compared with the reference mortar. This improvement was attributed to the rough and angular morphology of EAFS particles, which may enhance mechanical interlocking and paste–aggregate bonding at moderate replacement levels. The 50% replacement level showed comparable strength, whereas 75% replacement led to a strength reduction due to reduced workability and lower effective free water availability. A preliminary life cycle assessment further indicated that EAFS replacement reduced the total global warming potential by up to approximately 6.8%, while 25% replacement provided the best technical–environmental balance.

Keywords: Electric arc furnace slag; fine aggregate replacement; cement mortar; compressive strength; life cycle assessment

1 Introduction

The construction sector consumes large amounts of natural aggregates, particularly fine aggregates used in mortar and concrete production. Continuous extraction of natural sand creates environmental concerns and increases the need for alternative aggregate sources. At the same time, the steel industry generates large quantities of slag, and electric arc furnace slag (EAFS) is becoming increasingly important with the growing share of scrap-based steelmaking. Recent studies have emphasized that EAFS can be considered a potential secondary raw material for concrete and mortar production, supporting resource efficiency and circular construction practices [1,2].

EAFS has several physical characteristics that make it suitable as an alternative aggregate, including high density, angular particle shape, rough surface texture and high mechanical

hardness. These characteristics may improve the aggregate skeleton and paste–aggregate interaction when EAFS is used at suitable replacement levels. However, they may also reduce workability because angular and rough slag particles increase internal friction and may increase water demand. Recent reviews and experimental studies have shown that the effect of steel slag aggregates on mortar and concrete is strongly dependent on slag type, particle size, replacement ratio and mixture design [1–3].

In addition to technical performance, the environmental implication of EAFS use should also be considered. Previous studies have reported that replacing natural aggregates with EAFS can reduce environmental impacts or improve sustainability performance, especially when avoided natural aggregate extraction and reduced slag landfilling are included in the system boundary [2,4]. However, transportation, processing and the dominant contribution of cement may limit the overall reduction in global warming potential. Therefore, a combined evaluation of workability, compressive strength and preliminary environmental performance is needed to identify a balanced replacement level.

In this study, EAFS was evaluated as a partial fine aggregate replacement in cement mortar. CEN standard sand was replaced with EAFS at 25%, 50% and 75% by mass, while a reference mortar without EAFS was also prepared. The fresh behavior was assessed using the flow table test, and compressive strength was measured at 3, 7 and 28 days. In addition, a preliminary cradle-to-gate global warming potential screening was carried out to evaluate the environmental implication of EAFS replacement.

2 Materials and Methodology

2.1 Materials

Ordinary Portland cement, CEN standard sand, tap water and processed electric arc furnace slag (EAFS) were used for the preparation of cement mortar mixtures. The cement was used as the sole binder in all mixtures, while CEN standard sand was used as the reference fine aggregate. EAFS was used as a partial replacement for standard sand. Before mixture preparation, the EAFS was processed as a fine aggregate and its particle size distribution was determined by sieve analysis as shown in Fig. 1. The water absorption capacity of EAFS was measured as 2.61%, indicating a higher absorption potential compared with standard sand. This property was considered important because it may reduce the amount of free mixing water available in the fresh mortar and affect both flowability and strength development.

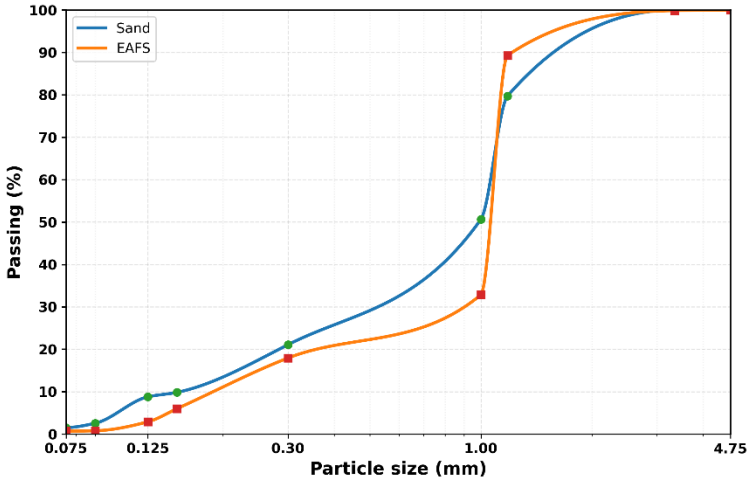


Fig. 1. Particle size distribution of the sand and EAFS

2.2 Mixture Proportions

Four mortar mixtures were prepared with different EAFS replacement levels. The reference mixture contained only CEN standard sand, while the remaining mixtures contained 25%, 50% and 75% EAFS as sand replacement by mass. In all mixtures, the cement content was kept constant at 225 g and the water content was kept constant at 112.5 g, corresponding to a water-to-cement ratio of 0.50. The total fine aggregate content was fixed at 675 g, giving a cement-to-aggregate ratio of 1:3 by mass. The detailed mixture proportions are given in Table 1.

Table 1. Mixture proportions

Mix ID	EAFS replacement (%)	Cement (g)	Water (g)	Standard sand (g)	EAFS (g)
M0	0	225	112.5	675.00	0.00
M25	25	225	112.5	506.25	168.75
M50	50	225	112.5	337.50	337.50
M75	75	225	112.5	168.75	506.25

2.3 Preparation, Curing and Testing

The dry materials were first weighed according to the mixture proportions. Cement, standard sand and/or EAFS were then placed in the mixing bowl and mixed to obtain a uniform dry blend. Water was added gradually, and mixing was continued until a homogeneous mortar was obtained. After mixing, the fresh mortar was used immediately for the flow table test. The remaining mortar was cast into 50 × 50 × 50 mm cube moulds for compressive strength testing. The specimens were compacted to reduce entrapped air and then covered to prevent early moisture loss. After 24 h, the specimens were demoulded and cured in water until the testing ages.

The fresh-state behavior of the mortar mixtures was evaluated using the flow table test in accordance with ASTM C1437. After placing the fresh mortar into the flow mould, the mould was lifted vertically and the flow table was operated according to the standard procedure. The spread diameter of the mortar was measured in two perpendicular directions, and the average value was recorded as the flow diameter. Compressive strength tests were conducted on 50 × 50 × 50 mm mortar cube specimens at 3, 7 and 28 days. Before testing, the specimens were removed from the curing tank and surface-dried. Each specimen was placed centrally in the compression testing machine, and load was applied until failure. The compressive strength was calculated by dividing the maximum failure load by the loaded area of the cube.

2.4 Life cycle assessment

A simplified life cycle assessment (LCA) was carried out to evaluate the global warming potential (GWP) of the mortar mixtures. The assessment was limited to GWP and was conducted with a cradle-to-gate system boundary. The functional unit was defined as 1 m^3 of mortar. The system included the production of cement, standard sand and water, EAFS processing, mixing electricity, transportation of raw materials, and the landfilling of unused EAFS. The environmental data for cement, water, standard sand and transportation were obtained from the Ecoinvent database. Since EAFS was considered as an industrial by-product, no upstream burden from steel production was assigned to it. However, the electricity consumption associated with crushing and size reduction was included for EAFS processing. Transportation distances were assumed as 15 km for cement, 39 km for sand, and 80 km for EAFS. For the landfilling scenario, a transport distance of 50 km was considered.

Multifunctionality related to EAFS utilization was handled by using the M75 mixture as the reference maximum-utilization scenario. Accordingly, for mixtures containing lower amounts of EAFS, the unused EAFS amount relative to M75 was assumed to be sent to landfill and was added to the system inventory. This approach allowed the environmental benefit of increasing EAFS utilization to be reflected in the preliminary GWP comparison.

3 Results and Discussion

3.1 Compressive strength and flow results

The compressive strength and flow results of the mortar mixtures are presented in Fig. 2. The reference mixture (M0) exhibited a flow diameter of 215 mm. With increasing EAFS replacement, the flow values decreased progressively to 195, 178 and 160 mm for M25, M50 and M75, respectively. This corresponds to flow reductions of approximately 9.3%, 17.2% and 25.6% compared with the reference mixture. The decrease in flow can mainly be attributed to the angular shape, rough surface texture and higher water absorption capacity of EAFS particles. Similar reductions in workability have been reported in previous studies where steel slag or EAF slag was used as natural fine aggregate replacement [1,5]. The rough and sharp-edged surface of EAF slag particles increases internal friction within the fresh mortar and reduces the lubricating effect normally provided by rounded or more regular sand particles [5].

The compressive strength results showed that moderate EAFS replacement improved or maintained the mechanical performance of the mortar. At 3 days, M25 achieved the highest strength among the mixtures, with 22.5 MPa compared with 20 MPa for the reference mixture. A similar trend was observed at 7 days, where M25 and M50 reached 32 and 30 MPa, respectively, both slightly higher than the reference mortar. At 28 days, M25 again provided the highest compressive strength, reaching 52 MPa, corresponding to an increase of about 9.1% compared with the reference mixture. The M50 mixture showed a comparable 28-day strength of 48 MPa, while the M75 mixture decreased to 41 MPa. The strength improvement observed at 25% EAFS replacement may be related to the rough and angular morphology of the slag particles, which can enhance mechanical interlocking and improve paste–aggregate bonding. In addition, the high hardness and density of EAFS may contribute to a more resistant aggregate skeleton under compression. Previous studies have similarly reported that EAF slag aggregate can improve compressive strength when used as a partial replacement for natural aggregate [5,6]. However, at high replacement levels, the reduction in workability and the higher absorption capacity of EAFS may reduce the effective free water available in the mixture and make compaction more difficult. This can increase entrapped voids and weaken the matrix, explaining the lower 28-day strength of M75.

Overall, the results indicate that EAFS content has a combined effect on fresh and hardened properties. Increasing EAFS replacement improves the utilization of an industrial by-product but gradually reduces flow. From a mechanical performance point of view, 25% EAFS replacement appears to be the most effective level, providing the highest 28-day compressive strength while maintaining acceptable workability. The 50% replacement level can also be considered feasible because it produced a strength comparable to the reference mixture. In contrast, 75% replacement resulted in a clear loss of workability and lower compressive strength, indicating that high-volume EAFS replacement may require additional mixture optimization, such as pre-wetting or the use of water-reducing admixtures.

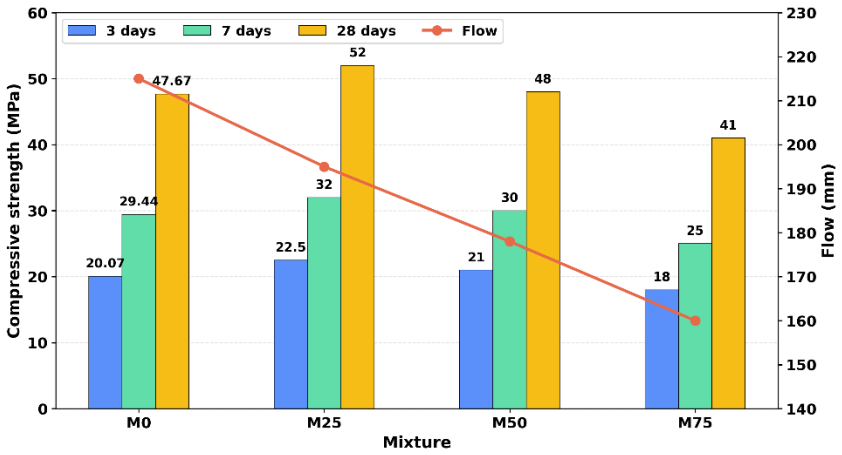


Fig. 2. Compressive strength and flow results of the mixtures

3.2 Life cycle assessment

A preliminary LCA was carried out to evaluate the environmental implication of replacing standard sand with EAFS. The total GWP values of M0, M25, M50 and M75 were calculated as 705.8, 694.0, 682.3 and 658.0 kg CO_2-eq/m³, respectively (Fig. 3.). Compared with the reference mixture, this corresponds to reductions of approximately 1.7%, 3.3% and 6.8% for M25, M50 and M75. The results show that cement was the dominant contributor to total GWP in all mixtures. Since the cement content was kept constant, the overall reduction remained moderate. The environmental benefit of EAFS replacement was mainly associated with the reduction in standard sand consumption and the decrease in the amount of unused EAFS assumed to be sent to landfill [7]. However, this benefit was partly offset by the additional transportation and processing-related emissions associated with EAFS use.

Although M75 provided the lowest total GWP, it also showed the lowest flow and a reduction in 28-day compressive strength. Therefore, the mixture with the lowest environmental impact was not necessarily the best technical option. When mechanical performance and GWP are considered together, M25 appears to be the most balanced mixture, as it reduced the total GWP slightly while providing the highest 28-day compressive strength. M50 also offered a reasonable compromise, with lower GWP than the reference mixture and comparable compressive strength. Overall, the LCA screening indicates that moderate EAFS replacement can improve the resource efficiency of cement mortar without compromising mechanical performance.

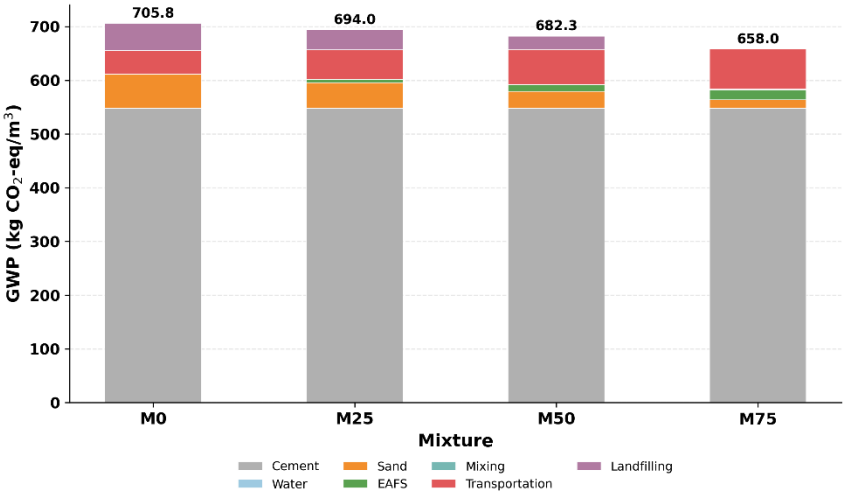


Fig. 3. Life cycle assessment of the mixtures

4 Conclusions

This study investigated the feasibility of using electric arc furnace slag (EAFS) as a partial fine aggregate replacement in cement mortar. Mortar mixtures containing 25%, 50% and 75% EAFS were evaluated in terms of fresh-state behavior, compressive strength development and preliminary GWP performance. The results showed that increasing EAFS content gradually reduced workability, with flow losses of approximately 9.3%, 17.2% and 25.6% for M25, M50 and M75, respectively. However, the 25% replacement level provided the best mechanical performance, increasing the 28-day compressive strength by about 9.1% compared with the reference mortar. The M50 mixture showed comparable strength, whereas M75 resulted in a 14.0% strength reduction. The preliminary GWP screening also indicated environmental benefits, with total GWP reductions of approximately 1.7%, 3.3% and 6.8% for M25, M50 and M75, respectively. Overall, 25% EAFS replacement appears to be the most balanced option, combining improved compressive strength, acceptable workability and a slight reduction in environmental impact.

Acknowledgments

The authors gratefully acknowledge the financial support provided by Ankara Yıldırım Beyazıt University Scientific Research Projects Coordination Unit under the Single-Discipline Basic Research Projects scheme, Project No. 3038. The authors also acknowledge the support of The Scientific and Technological Research Council of Türkiye (TÜBİTAK) through the 3501 Career Development Program, Project No. 226M072.

References

1. Rashad, A. M.: Behavior of steel slag aggregate in mortar and concrete-A comprehensive overview. Journal of building engineering, 53, 104536 (2022).
2. Diotti, A., Cominoli, L., Galvin, A. P., Sorlini, S., & Plizzari, G.: Sustainable recycling of electric arc furnace steel slag as aggregate in concrete: Effects on the environmental and technical performance. Sustainability, 13(2), 521 (2021).
3. Xue, J. C., Wang, W. C., Wu, C. H., Hong, T. J., Chen, T. H., & Huang, C. Y.: Deterioration analysis and expansion behavior prediction of electric arc furnace slag as fine aggregate in mortar. Journal of Building Engineering, 85, 108717 (2024).
4. Kvočka, D., Šušteršič, J., Mauko Pranjić, A., & Mladenović, A.: Mass concrete with EAF steel slag aggregate: workability, strength, temperature rise, and environmental performance. Sustainability, 14(23), 15502 (2022).
5. Coppola, L., Buoso, A., Coffetti, D., Kara, P., & Lorenzi, S.: Electric arc furnace granulated slag for sustainable concrete. Construction and building materials, 123, 115-119 (2016).
6. Monosi, S., Ruello, M. L., & Sani, D.: Electric arc furnace slag as natural aggregate replacement in concrete production. Cement and concrete composites, 66, 66-72 (2016).
7. Evangelista, B. L., Rosado, L. P., & Penteado, C. S. G.: Life cycle assessment of concrete paving blocks using electric arc furnace slag as natural coarse aggregate substitute. Journal of cleaner production, 178, 176-185 (2018).

Author Contribution Statement

- *Conceptualization:* Emircan Özçelikci
- *Methodology:* Emircan Özçelikci
- *Investigation:* Hussein Abdullahi Ali
- *Writing – Original Draft:* Emircan Özçelikci, Hussein Abdullahi Ali
- *Writing – Review & Editing:* Mehmet Baran

List of Abbreviations

- **EAF** — Electric Arc Furnace
- **EAFS** — Electric Arc Furnace Slag
- **LCA** — Life Cycle Assessment
- **GWP** — Global Warming Potential

Declaration of Conflict of Interest

The authors declare that they have no competing financial or non-financial interests that could have influenced the work reported in this paper.

Publication Note

This paper was peer-reviewed, accepted for presentation, and included in the proceedings of the ACE2026 – International Conference on Advances in Civil Engineering, held on 12–14 October 2026 in Trabzon, Türkiye.

This paper may be cited as follows:

Emircan Özçelikci, Hussein Abdullahi Ali, Mehmet Baran, "Technical and Environmental Evaluation of Electric Arc Furnace Slag as Fine Aggregate Replacement in Cement Mortar" in Proceedings of the ACE2026 – International Conference on Advances in Civil Engineering, Trabzon, Türkiye, 12–14 October 2026.

Effect of Activator Type and Dosage on the Mechanical Performance of One-Part Calcined Clay Geopolymer Mortars

Nur Demir[1], Enes Hamidoğlu[2], Ünal Anıl Doğan[3]
[1] 0009-0005-2706-7285, Istanbul Technical University, Civil Engineering Department, Istanbul, Türkiye, demir24@itu.edu.tr
[2] 0009-0005-2180-4619, Istanbul Technical University, Civil Engineering Department, Istanbul, Türkiye, hamidoglu19@itu.edu.tr
[3] 0000-0002-7819-5552, Istanbul Technical University, Civil Engineering Department, Istanbul, Türkiye, doganunal@itu.edu.tr

Abstract. Calcined clays are promising aluminosilicate precursors for low-carbon one-part geopolymer binders, but their performance is strongly controlled by activator chemistry and dosage. This study investigates a low-grade natural clay from the Şile region of Istanbul, Türkiye, as a precursor for one-part geopolymer mortars. The clay is considered waste because its relatively high Fe_2O_3 content makes it unsuitable for ceramic and paper applications. The raw clay was characterized using X-ray fluorescence (XRF) and thermogravimetric analysis (TGA), while X-ray diffraction (XRD) analysis was performed before and after calcination at 700 °C. The calcination temperature of 700 °C was selected based on the Strength Activity Index results obtained at 600, 700, and 800 °C. The calcined clay was activated with six solid activators, sodium hydroxide, potassium hydroxide, sodium silicate, potassium silicate, sodium carbonate, and sodium sulfate, each at activator-to-clay ratios of 15, 30, 45, 60, and 75%. The silicate activators were synthesized from recycled waste glass and the corresponding hydroxides. Mortars were cured at 23±1 °C and 55±5% relative humidity and tested for flexural and compressive strength at 7, 14, and 28 days. Spearman's rank correlation related the 28-day compressive strength to the mix-design and chemical parameters. Silicate activators outperformed the hydroxide, carbonate, and sulfate systems, with sodium silicate giving the highest compressive strength. The correlation analysis linked 28-day strength most closely to alkali availability and the Si/Al and Ca-based ratios.

Keywords: One-Part Geopolymer; Calcined Clay; Mechanical Strength; Alkali Activation.

1 Introduction

Portland cement remains the most widely used construction material because its performance is proven and it is cheap and available, but its production is energy-intensive and generates considerable CO_2, mainly from fuel combustion and the calcination of limestone during clinker manufacture [1]. The cement and concrete sectors are estimated to contribute around 7-8% of global CO_2 emissions [2], and industry roadmaps set steep reduction targets [3], underlining the need for lower-carbon binder systems.

A widely studied route is to replace part of the clinker with supplementary cementitious materials (SCMs) such as ground granulated blast-furnace slag, fly ash, silica fume, and metakaolin, which lower clinker content while preserving or improving performance. However, the supply of conventional SCMs is a growing concern: fly ash will decline as coal plants are phased out, slag depends on the steel industry and may not meet future demand [4], and silica fume is limited by cost and low feasible replacement levels [5]. Attention has therefore shifted toward alternative aluminosilicate resources, especially calcined clays, which are locally

abundant and rich in reactive aluminosilicate phases, and which show potential both as SCMs and as precursors for geopolymer binders [6-9].

Geopolymers form when an aluminosilicate precursor dissolves in a highly alkaline environment and the released Si and Al reorganize through polycondensation into a three-dimensional gel network of N-A-S-H, C-A-S-H, or coexisting phases (Fig. 1). Their performance depends not only on the alkaline activator but also on the precursor's mineralogy, amorphous content, Si/Al ratio, and calcination conditions.

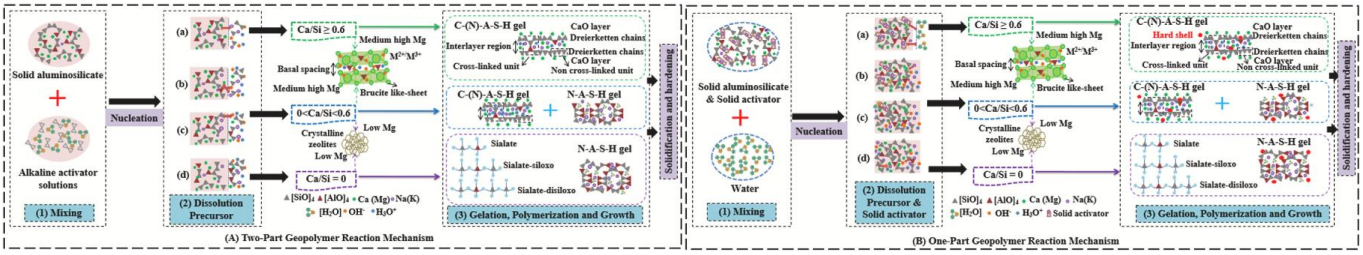


Fig. 1. Schematic illustration of hydration process and reaction mechanism of one-part geopolymer and conventional two-part geopolymer [8]

Geopolymers are produced by two routes. In two-part systems the precursor is mixed with a pre-prepared liquid activator, whereas one-part systems are made by dry-blending the precursor with a solid activator, with reaction beginning only when water is added. This "just-add-water" route is more practical and closer to ordinary cement use, and it avoids preparing, transporting, and handling corrosive alkaline solutions. Its performance, however, depends strongly on the compatibility between precursor and solid activator, since the activator's dissolution rate, setting behavior, and degree of gel formation govern the fresh and hardened properties. Selecting a suitable precursor-activator combination is therefore essential [7-8].

This study investigates a low-grade, iron-rich clay of limited ceramic value as a precursor for one-part geopolymer mortars. The clay was characterized and calcined at 700 °C, then activated with six solid activators at five dosages, and the mortars were evaluated by mechanical testing.

2 Materials and Methods

2.1 Raw Clay, Calcination, and Characterization

The raw material used in this study was a natural clay from the Şile region of Istanbul, Türkiye. The clay is a low-grade material with high iron content. Its iron oxide level produces coloration on firing and excludes it from ceramic and paper use [10]. Iron is a normal constituent of cement, so this is not a barrier to use as a precursor material [11]. The bulk oxide composition was measured by X-ray fluorescence (XRF) and is given in Table 1. The combined SiO_2, Al_2O_3, and Fe_2O_3 content was 84.1 wt.%. This value exceeds the 70 wt.% minimum set by ASTM C618 for Class N pozzolan. The raw clay was dried at 105 °C to a constant dry mass. The dried clay was ground in a ball mill at 70 rpm for 30 min. The specific gravity and the Blaine fineness were 2.77 and 12560 cm²/g, respectively.

Table 1. Chemical composition of raw clay and waste glass determined by XRF (wt.%)

	Na_2O	MgO	Al_2O_3	SiO_2	K_2O	CaO	TiO_2	Fe_2O_3	SO_3	*LOI
Raw Clay	0.10	1.12	22.31	52.49	3.50	0.26	1.34	9.29	0.19	9.11
Waste Glass	8.87	1.51	1.65	72.43	0.53	13.22	0.13	1.08	0.10	0.10

Thermogravimetric analysis (TGA) was carried out under a nitrogen atmosphere at a heating rate of 10 °C/min from room temperature to 950 °C. Fig. 2 shows a minor mass loss below 150 °C attributed to free water. The DTG curve showed a small peak between 200 and 400 °C, which may be related to decomposition of iron oxyhydroxide phases, consistent with the high Fe_2O_3 content of the clay [12]. The main mass loss occurred between 350-650 °C, corresponding to dehydroxylation of the clay minerals [13]. The DTG curve showed a shoulder near 400-450 °C, which might reflect the partially overlapping dehydroxylation of kaolinite and illite in the mixed-mineral clay [14]. The TGA curve stabilized beyond approximately 700 °C, indicating that dehydroxylation was essentially complete by this temperature.

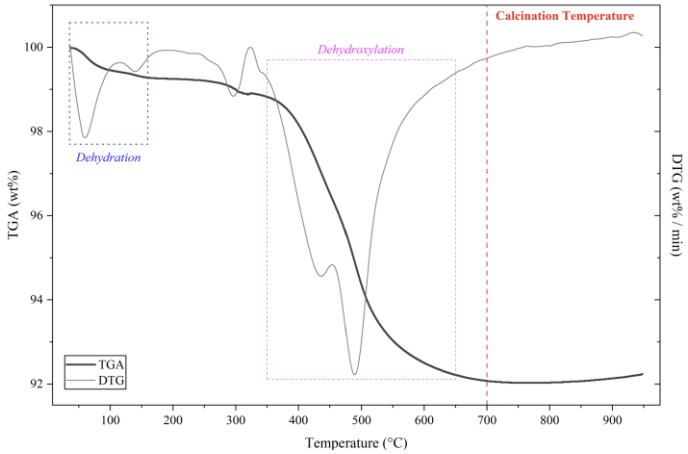


Fig. 2. TGA/DTG curves of the raw clay showing dehydration, dehydroxylation, and the selected calcination temperature of 700 °C.

Based on the TGA results, calcination temperatures at and beyond the completion of dehydroxylation were selected for evaluation. The clay was calcined at 600, 700, and 800 °C and tested as a 20 wt.% cement replacement using the Strength Activity Index (SAI). Calcination at 700 °C gave the highest activity for this clay and was adopted for the present study. The clay was calcined in a preheated muffle furnace at 700 °C for 1 h and then cooled rapidly to room temperature to preserve the disordered, reactive structure.

X-ray diffraction (XRD) was carried out on the raw and the 700 °C clay. Fig. 3 shows the raw clay with reflections of kaolinite, illite, quartz, and feldspar. After calcination at 700 °C, the kaolinite reflection had disappeared. This indicates the breakdown of kaolinite and its conversion to metakaolinite. The quartz and feldspar reflections remained. The change confirmed the formation of a more reactive aluminosilicate.

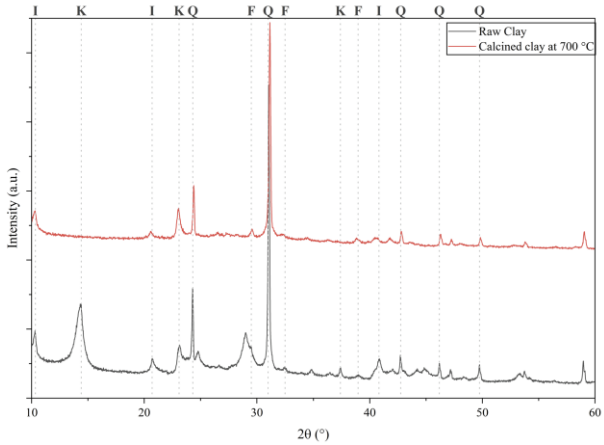


Fig. 3. XRD patterns of raw clay and clay calcined at 700 °C. The calcined clay pattern was vertically shifted for clarity. K: kaolinite; I: illite; Q: quartz; F: feldspar.

The particle size distribution and physical properties of the raw and calcined clay are summarized with the distribution curves in Fig. 4. After calcination, the clay showed a coarser particle size distribution, along with a slight increase in specific gravity and specific surface area.

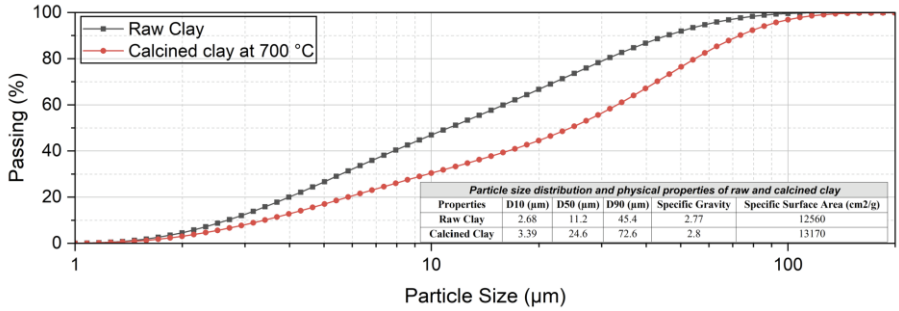


Fig. 4. Particle size distribution of raw and calcined clay determined by laser diffraction

2.2 Activators

Six solid activators were used in this study: sodium hydroxide, potassium hydroxide, sodium carbonate, sodium sulfate, sodium silicate, and potassium silicate. Their chemical formulas and densities are summarized in Table 2. NaOH, KOH, Na_2CO_3, and Na_2SO_4 were obtained commercially as solid reagents.

Table 2. Solid activators used in the study.

Activators	Na_2CO_3	NaOH	KOH	Na_2SO_4	Na_2SiO_3 (Ms*=1)	K_2SiO_3 (Ms*=1)
Code	NC	NH	KH	NSO	NS	KS
Density (g/cm³)	2.54	2.13	2.04	2.66	2.43	2.52

*Ms: silica modulus.

The sodium and potassium silicate activators (Ms = 1, where Ms is the molar SiO_2/M_2O ratio) were synthesized in the laboratory from recycled waste glass, providing a more sustainable alternative to commercial silicate activators. The waste glass was obtained from the Şişecam factory in Istanbul. It was ground in a mill for 5000 revolutions to a specific surface area of 7820 cm²/g. Its bulk oxide composition (XRF) is given in Table 1, and confirmed a high silica content, with SiO_2 as the dominant oxide. Sodium silicate was produced by a hydrothermal synthesis method, reacting the ground glass with NaOH and a small addition of water, heated at 250 °C for 2 h. Potassium silicate was produced by a thermochemical synthesis method, reacting the ground glass with KOH without water addition, heated at 400 °C for 2 h. Both products were obtained as solids and ground to powder for use as activators.

2.3 Mix Design

Natural sand was used as the fine aggregate in all geopolymer mortar mixtures. The specific gravity and fineness modulus of the sand were 2.64 and 2.69, respectively. The sand content was kept constant at 1188 g for all mixtures. The particle size distribution of the sand was determined by sieve analysis in accordance with EN 933-1. The characteristic particle sizes were D_{10} = 0.31 mm, D_{30} = 0.59 mm, and D_{60} = 1.57 mm, corresponding to a coefficient of uniformity (C_u) of 5.06 and a coefficient of curvature (C_c) of 0.72.

Thirty mixtures were prepared, combining the six activators at five activator-to-clay ratios (15, 30, 45, 60, and 75 wt.%). Each mix is identified by its activator code followed by its activator-to-clay ratio (e.g., NS-60). The binder was defined as the combined mass of calcined clay and activator. The water-to-binder ratio (w/b) was adjusted for each mix between 0.50 and 0.65 to maintain workability and is reported for each mix in Table 3. The flow of the fresh mortars was determined using a flow table following ASTM C1437. The flow value was taken

as the average spread diameter of the mortar. Mixture proportions and fresh-state properties are also summarized in Table 3.

Table 3. Mixture proportions and fresh-state properties of calcined clay geopolymer mortars

Mix ID	Clay (g)	Activator (g)	Sand (g)	Water (g)	w/b	Unit weight	Flow
NC-15	429.1	64.4	1188.0	296.1	0.60	2.16	14.2
NC-30	378.1	113.4	1188.0	270.3	0.55	2.14	16.1
NC-45	337.9	152.0	1188.0	269.5	0.55	2.16	-*
NC-60	305.4	183.3	1188.0	268.8	0.55	-	-
NC-75	278.7	209.0	1188.0	268.2	0.55	-	-
NH-15	424.5	63.7	1188.0	292.9	0.60	2.13	13.5
NH-30	352.1	105.6	1188.0	274.7	0.60	2.17	15.5
NH-45	312.8	140.8	1188.0	272.2	0.60	-	-
NH-60	296.3	177.8	1188.0	260.7	0.55	2.18	15.8
NH-75	269.2	201.9	1188.0	259.1	0.55	2.15	18.0
KH-15	423.3	63.5	1188.0	292.1	0.60	2.11	17.5
KH-30	350.4	105.1	1188.0	273.3	0.60	2.11	25.2
KH-45	327.2	147.2	1188.0	261.0	0.55	2.19	26.0
KH-60	293.9	176.3	1188.0	258.6	0.55	2.13	25+
KH-75	266.7	200.0	1188.0	256.7	0.55	2.06	25+
NSO-15	430.2	64.5	1188.0	296.8	0.60	2.11	16.3
NSO-30	379.8	113.9	1188.0	271.5	0.55	2.15	21.0
NSO-45	339.9	153.0	1188.0	271.1	0.55	2.15	18.9
NSO-60	307.6	184.6	1188.0	270.7	0.55	2.16	19.3
NSO-75	281.0	210.7	1188.0	270.4	0.55	2.14	15.0
NS-15	406.3	60.9	1188.0	303.7	0.65	2.15	15.3
NS-30	357.0	107.1	1188.0	278.4	0.60	2.20	16.5
NS-45	318.6	143.4	1188.0	277.2	0.60	-	25+
NS-60	320.5	192.3	1188.0	256.4	0.50	2.22	19.2
NS-75	292.1	219.0	1188.0	255.6	0.50	2.28	19.6
KS-15	406.0	60.9	1188.0	280.1	0.60	2.17	16.3
KS-30	358.2	107.5	1188.0	279.4	0.60	2.18	21.3
KS-45	320.1	144.1	1188.0	278.5	0.60	-	-
KS-60	322.5	193.5	1188.0	258.0	0.50	2.25	23.4
KS-75	277.2	207.9	1188.0	266.8	0.55	2.13	25+

*A hyphen indicates that the value was not determined. Flow values marked as 25+ indicate that the spread exceeded the reported scale.

Mortar specimens were cast in accordance with EN 196-1, using 40 × 40 × 160 mm prismatic molds. Mixing followed a modified EN 196-1 procedure, adapted to the one-part approach used in this study, in which the solid activator was dry-blended with the calcined clay before water and sand were added. Specimens were demolded after a minimum of 24 h, or later if the mortar had not yet hardened sufficiently. All specimens were cured at ambient laboratory temperature 23±1 °C and 55±5 % relative humidity until testing.

2.4 Mechanical Testing and Statistical Analysis

Flexural and compressive strength were determined in accordance with EN 196-1. Prismatic specimens (40 × 40 × 160 mm) were tested in three-point bending at a loading rate of 0.4

mm/min to determine flexural strength. The resulting halves from each specimen were then tested in compression at a loading rate of 1 mm/min. Testing was carried out at 7, 14, and 28 days for each mix.

Statistical analysis was carried out using IBM SPSS Statistics. Spearman's rank correlation was used to assess the strength and direction of the association between the 28-day compressive strength and the mix-design and chemical parameters of the mixtures, with correlations taken as significant at $p < 0.05$.

3 Results

3.1 Compressive Strength

Compressive strength was controlled by the type of activator rather than only by its dosage. The compressive strength of all mixtures at 7 and 28 days are shown in Fig. 5, with the full 7, 14, and 28-day values listed in Table 4.

Table 4. Flexural and Compressive strength of one-part calcined clay geopolymer mortars at 7, 14, and 28 days.

Mix ID	Flexural Strength (MPa)			Compressive Strength (MPa)		
	7-day	14-day	28-day	7-day	14-day	28-day
NC-15	0.27	0.24	0.43	0.65	0.52	0.81
NC-30	-*	-	0.73	0.80	0.81	0.83
NC-45	0.78	0.84	0.93	2.20	2.19	1.46
NC-60	2.76	2.23	1.83	7.52	6.77	4.80
NC-75	4.92	3.90	3.40	11.80	9.20	7.86
NH-15	0.40	0.52	0.55	1.01	1.27	1.35
NH-30	0.99	1.11	1.06	2.85	3.35	3.85
NH-45	0.21	0.18	0.24	0.46	0.61	0.66
NH-60	-	-	-	0.13	0.15	-
NH-75	-	-	-	-	-	-
KH-15	0.15	0.21	0.17	0.20	0.31	0.34
KH-30	0.05	0.09	0.12	0.35	0.08	0.16
KH-45	-	0.07	0.11	0.21	0.35	0.27
KH-60	-	-	0.28	-	-	0.63
KH-75	-	-	0.19	-	-	0.64
NSO-15	-	0.15	0.15	0.29	0.41	0.38
NSO-30	0.27	0.31	0.40	0.74	0.56	0.54
NSO-45	0.32	0.45	0.58	0.74	1.17	1.13
NSO-60	0.57	0.60	0.79	1.85	2.26	2.27
NSO-75	0.56	0.48	0.57	1.98	2.41	2.24
NS-15	0.28	0.40	0.38	0.69	0.73	0.79
NS-30	0.41	0.70	0.66	1.00	1.18	1.31
NS-45	1.85	3.29	3.53	13.19	12.73	14.28
NS-60	4.53	-	4.80	16.09	-	17.16
NS-75	6.74	5.47	6.28	27.13	22.69	18.56
KS-15	0.39	0.35	0.34	1.08	1.12	0.99
KS-30	1.36	1.45	1.64	6.25	6.83	7.81
KS-45	0.74	1.58	0.53	10.06	10.25	10.00
KS-60	0.99	0.91	1.07	5.51	5.43	6.29
KS-75	0.98	0.91	1.17	7.01	6.61	7.30

*A hyphen indicates that the strength value was not available.

In these one-part systems, the silicate activated mortars reached strengths well above the hydroxide and sulfate systems, peaking at 27.13 MPa for sodium silicate (NS-75) at 7 days, whereas no hydroxide or sulfate mix exceeded 3.85 MPa (NH-30) at any age (Table 4). A hydroxide activator raises the pore solution pH and dissolves the aluminosilicate precursor [15], but it contributes no silica of its own, so gel growth depends entirely on silicon released from the clay. A soluble silicate activator instead delivers reactive silicate directly into the pore solution, which enhances the condensation process and introduces additional silicon into the aluminosilicate chain, producing a denser and better-connected gel [16].

With sodium silicate, strength did not climb gradually with dosage. At 15% and 30% the 28-day strength stayed near 1 MPa, then jumped to 14.28 MPa at 45% (Fig. 5). Below this dosage there is too little dissolved silicate to form a continuous gel; above it a connected network forms and strength develops. This is consistent with reports on one-part geopolymers, where an insufficient activator dosage leaves the precursor incompletely dissolved and prevents the formation of an interconnected gel network, so strength remains low until dosage is high enough to build a continuous matrix [17].

Sodium carbonate at 45%, 60%, and 75%, together with sodium silicate at 75%, were strongest at 7 days yet lost strength by 28 days, whereas sodium silicate at 45% and 60% continued to gain with age. This behavior may be associated with over-activation, in which the activator supplies more alkali than the forming gel can bind, so the excess remains mobile in the pore solution rather than incorporated into the network [18]. Visible efflorescence was observed on these specimens, the surface expression of that free alkali migrating and carbonating, and the accompanying leaching increases porosity and destabilizes the gel, lowering strength over time [17-18-19]. Where the alkali is instead more fully consumed into the gel, the mortars densify and strengthen with age. Early-age and long-term strength therefore diverge only once dosage exceeds what the gel can bind, so for sodium silicate the best dosage was not the one with the highest early strength.

Potassium silicate produced the most consistent dosage response of the set: strength rose to a maximum at 45% dosage and held that level, changing little between 7 and 28 days at any dosage. This age stability indicates that its gel forms early and does not continue to restructure, so the binder is essentially complete by the first test age. The choice of alkali cation is known to affect precursor dissolution, gel structure, and aluminum incorporation, with the potassium cation, being larger and of lower charge density, associating more easily with silicate and aluminosilicate in solution [15].

Among the non-silicate activators, sodium carbonate produced the highest strength, its 28-day values rising steadily with dosage from about 0.8 MPa at 15% to 7.86 MPa at 75%. This gradual gain, rather than the sharp threshold seen with sodium silicate, may be related to sodium carbonate being a weaker activator whose lower pore-solution alkalinity slows precursor dissolution [20].

The hydroxide and sulfate activators formed only weak binders. Sodium hydroxide reached its highest 28-day strength of 3.85 MPa at 30% and fell as dosage rose, failing to harden at all at 75%; this might be due to the absence of a silicate source, which leaves the gel silica starved so that adding more alkali does not improve condensation [16]. Potassium hydroxide developed almost no strength, not exceeding 0.35 MPa through 45% and reaching only 0.63 to 0.64 MPa at 60% and 75% by the final test age, where its late strength gain points to slow, incomplete gel formation. Sodium sulfate gave low but stable strengths, staying near 2.2 MPa at its higher dosages. It is a weak activator whose solution is only mildly alkaline, around pH 9 to 10, so it dissolves little of the precursor; its activation also depends largely on reaction with calcium, which a calcined clay contains very little of, leaving little gel to form [21].

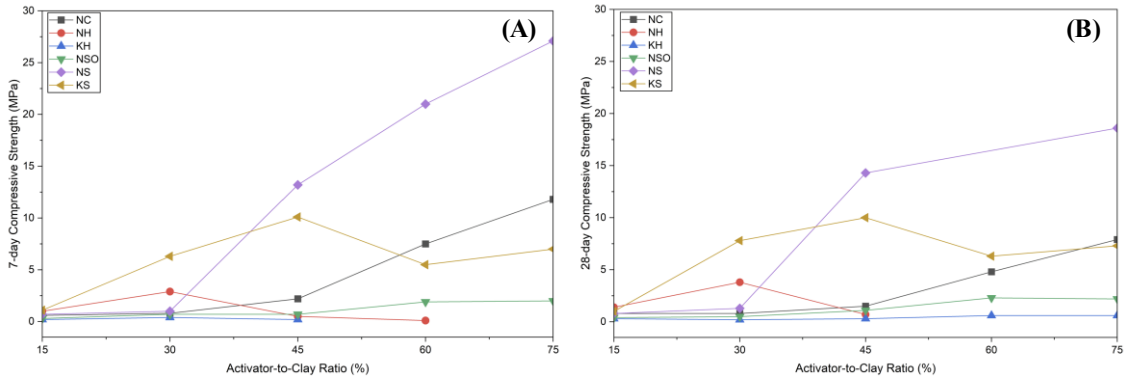


Fig. 5. Compressive strength of the calcined clay geopolymer mortars versus activator-to-clay ratio at (A) 7 days, (B) 28 days.

3.2 Flexural Strength

Flexural strength followed the same pattern as compressive strength. Sodium silicate gave the highest flexural strengths, reaching 6.74 MPa (NS-75) at 7 days, while no hydroxide or sulfate mix exceeded 1.11 MPa (NH-30) at any age (Table 4); the soluble silicate that builds a well-connected gel is also what carries tensile load and resists cracking [16].

Potassium silicate did not follow its compressive trend. At 28 days its compressive strength peaked at 45% (10.0 MPa), yet its flexural strength at that dosage was only 0.53 MPa, one of its lowest. Sodium silicate behaved oppositely: its flexural and compressive strengths increased together, and both peaked at 75% (6.28 and 18.56 MPa at 28 days). Sodium silicate reaching higher flexural strength than potassium silicate is consistent with metakaolin-based geopolymers, where sodium metasilicate has given higher flexural strength than potassium formulations [22].

3.3 Correlation Analysis

Spearman's rank correlation analysis presented in Table 5 showed the 28-day compressive strength was significantly related to several chemical parameters. The strongest positive relationships were found for the Si/Al, Ca/Si and Ca/(Si+Al) ratios, all of which were positively associated with 28-day strength at the same level of correlation. Significant positive correlations were also identified for Na/Al, Na_2O content, and activator ratio. These findings suggest that alkali availability, particularly together with the Si/Al ratio, was closely linked to strength development.

By contrast, clay content was negatively correlated with 28-day compressive strength. Since a higher clay ratio corresponds to a lower activator content, this negative correlation reflects the lower strength observed at higher clay replacement levels. A significant negative correlation was also observed between K_2O and compressive strength. For SiO_2, SO_3, CaO, MgO, S/Al and K/Al, however, the correlations were not statistically significant. Overall, the analysis indicates that Si/Al, the Ca-based molar ratios, Na/Al, Na_2O content and activator ratio were the parameters most closely associated with 28-day compressive strength in the mixtures investigated. These findings are in line with previous studies indicating that strength development in geopolymer binders is strongly influenced by alkali availability, Si/Al balance, and the contribution of Ca-bearing reaction products to the binding matrix [8-9].

Table 5. Spearman correlations of selected parameters with 28-day compressive strength

Parameter	Si/Al	Ca/Si	Ca/(Si+Al)	Na/Al	Na_2O	Activator Ratio	Clay Ratio	K_2O
Spearman's ρ	0.598	0.598	0.598	0.508	0.499	0.473	-0.467	-0.394
p-value	<0.001	<0.001	<0.001	0.007	0.008	0.013	0.014	0.042

4 Conclusions

This study evaluated six solid activators, each at five dosages, for one-part geopolymer mortars made from a low-grade Şile calcined clay. Activator type controlled strength more than dosage. The silicate activators gave by far the highest strengths, because a soluble silicate supplies the reactive silicate that drives gel condensation, whereas the hydroxide, carbonate, and sulfate systems depend on silicon released from the calcined clay alone. Sodium silicate developed strength as a threshold response, remaining weak at low dosage and rising sharply once enough soluble silicate was present, while the highest silicate and carbonate dosages lost strength with age as excess alkali effloresced. Sodium carbonate produced the highest strengths among the non-silicate activators, developing gradually with dosage. Potassium silicate reached high compressive strength but low flexural strength, and the hydroxide and sulfate activators formed only weak binders. Each activator had its own effective dosage window, so no single activator-to-clay ratio suited them all. The statistical analysis supported these trends, with alkali availability and the Si/Al and Ca-based ratios most closely associated with 28-day compressive strength. Overall, sodium silicate was the most effective activator tested, with activator type having a greater influence on one-part geopolymer performance than dosage.

Further work is needed to link these mechanical trends to the binder microstructure, to clarify the compression to flexure gap of the potassium silicate system and the calcium dependent behavior of the sulfate activator, and to assess the long-term durability of the most promising mixes.

Acknowledgments
The authors gratefully acknowledge the financial support provided by the Scientific Research Projects Coordination Unit of Istanbul Technical University under project numbers MYLB-2025-47503 and MYLB-2025-47694.

References

1. Altinkaynak, M., Kabul, A., Kizilkan, Ö.: Exergetic assessment of a rotary kiln for clinker production in cement industry. International Journal of Exergy 16(3), 263 (2015). https://doi.org/10.1504/ijex.2015.068226
2. Kindi, H.A., Abdel-Gawwad, H.A., Meddah, M.S., Jabri, K.A., Mohamedzein, Y.: An overview of the critical influential parameters on the performance of limestone calcined clay cement paste, mortar, and concrete. Construction and Building Materials 444, 137615 (2024). https://doi.org/10.1016/j.conbuildmat.2024.137615
3. CEMBUREAU – The European Cement Association: From ambition to deployment: Our 2050 roadmap. https://www.atic.pt/wp-content/uploads/2024/06/2024.05.21-cembureau-net-zero-roadmap.pdf, last accessed 2026/07/07
4. Chu, D.C., Amar, M., Kleib, J., Benzerzour, M., Betrancourt, D., Abriak, N., Nadah, J.: The pozzolanic activity of sediments treated by the flash calcination method. Waste and Biomass Valorization 13(12), 4963–4982 (2022). https://doi.org/10.1007/s12649-022-01789-8
5. Kang, S., Hong, S., Moon, J.: Performance comparison between densified and undensified silica fume in ultra-high performance fiber-reinforced concrete. Materials 13(17), 3901 (2020). https://doi.org/10.3390/ma13173901
6. Barreto, I.A.R., Da Costa, M.L.: Synthesis of geopolymer with KOH by two kaolinitic clays from the Amazon: Influence of different synthesis parameters on the compressive strength. Materials Chemistry and Physics 287, 126330 (2022). https://doi.org/10.1016/j.matchemphys.2022.126330
7. Peng, M.X., Wang, Z.H., Shen, S.H., Xiao, Q.G., Li, L.J., Tang, Y.C., Hu, L.L.: Alkali fusion of bentonite to synthesize one-part geopolymeric cements cured at elevated temperature by comparison with two-part ones. Construction and Building Materials 130, 103–112 (2016). https://doi.org/10.1016/j.conbuildmat.2016.11.010
8. Ghafoor, M.T., Rakhimova, N., Shi, C.: One part geopolymers: A comprehensive review of advances and key challenges. Journal of Building Engineering 111, 113112 (2025). https://doi.org/10.1016/j.jobe.2025.113112
9. Turan, E., Oltulu, M.: Towards sustainable geopolymers: Utilization of diverse calcined clays as alternative precursors. Construction and Building Materials 484, 141785 (2025). https://doi.org/10.1016/j.conbuildmat.2025.141785

10. Murray, H.H., Kogel, J.E.: Engineered clay products for the paper industry. Applied Clay Science 29(3–4), 199–206 (2005). https://doi.org/10.1016/j.clay.2004.12.005
11. Ye, S., Feng, P., Liu, J.: Dissolution and early hydration of tetracalcium aluminoferrite (C4AF) in water and in aqueous sulfate solutions. Cement and Concrete Research 186, 107676 (2024). https://doi.org/10.1016/j.cemconres.2024.107676
12. Jayathilakage, R., Gunasekara, C., Law, D., Setunge, S., Cwirzen, A.: Mechanochemical-calcination of mixed layer and pure kaolinite/illite clays for use as supplementary cementitious materials: Reactivity and strength. Archives of Civil and Mechanical Engineering (2026). https://doi.org/10.1007/s43452-026-01480-y
13. Cao, Y., Wang, Y., Zhang, Z., Ma, Y., Wang, H.: Recent progress of utilization of activated kaolinitic clay in cementitious construction materials. Composites Part B: Engineering 211, 108636 (2021). https://doi.org/10.1016/j.compositesb.2021.108636
14. Msinjili, N.S., Gluth, G.J.G., Sturm, P., Vogler, N., Kühne, H.-C.: Comparison of calcined illitic clays (brick clays) and low-grade kaolinitic clays as supplementary cementitious materials. Materials and Structures 52(5), 94 (2019). https://doi.org/10.1617/s11527-019-1393-2
15. Duxson, P., Lukey, G.C., Separovic, F., van Deventer, J.S.J.: Effect of alkali cations on aluminum incorporation in geopolymeric gels. Industrial & Engineering Chemistry Research 44(4), 832-839 (2005). https://doi.org/10.1021/ie0494216
16. Nath, P., Sarker, P.K.: Effect of GGBFS on setting, workability and early strength properties of fly ash geopolymer concrete cured in ambient condition. Construction and Building Materials 66, 163-171 (2014). https://doi.org/10.1016/j.conbuildmat.2014.05.080
17. Poojalakshmi, E.S., Nagarajan, P., Sudhakumar, J., Thomas, B.S.: Impact of alkaline activator concentration on mechanical properties and microstructure of a ternary blended one-part geopolymer cement. Scientific Reports 15, 33808 (2025). https://doi.org/10.1038/s41598-025-01610-1
18. Longhi, M.A., Zhang, Z., Walkley, B., Rodríguez, E.D., Kirchheim, A.P.: Strategies for control and mitigation of efflorescence in metakaolin-based geopolymers. Cement and Concrete Research 144, 106431 (2021). https://doi.org/10.1016/j.cemconres.2021.106431
19. Sharmin, S., Sarker, P.K., Biswas, W.K.: Efflorescence behaviour of ternary blended geopolymers containing waste clay brick powder: Performance assessment and microstructural evolution. Construction and Building Materials 532, 146713 (2026). https://doi.org/10.1016/j.conbuildmat.2026.146713
20. G, I., Singh, B., Deshwal, S., Bhattacharyya, S.K.: Effect of sodium carbonate/sodium silicate activator on the rheology, geopolymerization and strength of fly ash/slag geopolymer pastes. Cement and Concrete Composites 97, 226–238 (2019). https://doi.org/10.1016/j.cemconcomp.2018.12.007
21. Gong, M., Shen, A., Wang, Y., Lin, H., He, R.: Alkali and sulfate effects on mechanical properties and microscopic mechanisms of slag and fly ash geopolymers. Scientific Reports 15, 3681 (2025). https://doi.org/10.1038/s41598-025-88194-y
22. Sá Ribeiro, R.A., Sá Ribeiro, M.G., Samuel, D.M., Ozer, A., Numkiatsakul, P., Kriven, W.M.: Metakaolin-based geopolymer matrix formulations for higher strength and thermal stability. Materials and Structures 58, 142 (2025). https://doi.org/10.1617/s11527-025-02670-5

Author Contribution Statement

- *Conceptualization:* Nur Demir, Enes Hamidoğlu, Ünal Anıl Doğan
- *Methodology:* Nur Demir, Enes Hamidoğlu, Ünal Anıl Doğan
- *Investigation:* Nur Demir, Enes Hamidoğlu
- *Writing – Original Draft:* Nur Demir, Enes Hamidoğlu
- *Writing – Review & Editing:* Ünal Anıl Doğan

Publication Note

This paper was peer-reviewed, accepted for presentation, and included in the proceedings of the ACE2026 – International Conference on Advances in Civil Engineering, held on 12–14 October 2026 in Trabzon, Türkiye.

This paper may be cited as follows:

Demir, N., Hamidoglu, E., and Dogan, U. A., "Effect of Activator Type and Dosage on the Mechanical Performance of One-Part Calcined Clay Geopolymer Mortars" in

Proceedings of the ACE2026 – International Conference on Advances in Civil Engineering, Trabzon, Turkiye, 12–14 October 2026.

Mechanical and High-Temperature Performance of Geopolymer Foam Concrete Substituted with Marble Powder and Reinforced with PVA Fibers

Rümeysa Atmaca[1], Damla Nur Çelik[2], Rüya Kılıç Demircan[3], Gökhan Kaplan[4]*
[1]Department of Civil Engineering, Atatürk University, Erzurum, Türkiye
[2] 0000-0001-8356-4263, Department of Civil Engineering, Gazi University, Ankara, Türkiye
[3] 0000-0001-7318-9383, Department of Construction, Sinop University, Sinop, Türkiye
[4] 0000-0001-6067-7337, Department of Civil Engineering, Atatürk University, Erzurum, Türkiye
*Corresponding Author E-mail: gkaplan@atauni.edu.tr

Abstract. This study examined the influence of waste marble powder and polyvinyl alcohol (PVA) fibers on the fresh, physical, mechanical, thermal, and high-temperature properties of blast furnace slag-based geopolymer foam concrete. Nine different mixes were created by replacing marble powder with blast furnace slag at 0%, 20%, and 40% by weight, and adding PVA fibers at 0%, 0.6%, and 1.2% by volume. A standard amount of SLS-based foam, incorporating expanded perlite and activated with sodium metasilicate, was used, and the samples were cured at 75 °C for 24 h. Increasing the marble powder substitution resulted in a larger flow diameter, higher apparent porosity and water absorption, and reduced density and mechanical strength. The addition of PVA fibers reduced workability; however, a fiber content of 0.6% notably enhanced the structural integrity and mechanical strength of foam. The MP0-F0.6 mixture had the lowest apparent porosity of 16.43%, the highest density of 883 kg/m³, and achieved the greatest 28-day compressive and flexural strengths of 6.585 MPa and 0.78 MPa, respectively. The thermal conductivity ranged from 0.143 to 0.229 W/(m·K), with the lowest value observed in the MP40-F1.2 mixture. After high-temperature testing, MP0-F0.6 retained the highest strength, and MP20-F0.6 maintained approximately 61.5% of its original strength at 600 °C. Overall, 0.6% PVA was identified as the optimal fiber content for the best combination of physical, mechanical, and high-temperature properties of the composites.

Keywords: Geopolymer foamed concrete; waste marble powder; PVA fiber; thermal conductivity; high-temperature resistance.

1. Introduction

Rapid population growth and relentless urbanization worldwide have driven the demand for building materials in the construction sector to enormous levels. Currently, ordinary Portland cement (OPC), the most common and basic binder material, is responsible for approximately 8% of global carbon dioxide (CO_2) emissions due to limestone calcination and high fossil fuel consumption during its production [1,2]. In addition, cement production consumes natural resources and energy at extraordinary rates, causing irreversible damage to the ecosystems [3,4]. To promote environmental sustainability in construction and reduce the industry's carbon footprint, there has been an increasing shift towards eco-friendly binders that consume less energy and can replace OPCs. Geopolymer technology, introduced by French scientist Davidovits in the 1970s, has emerged as a leading and revolutionary alternative owing to its amorphous and semi-crystalline inorganic polymeric network [4,5]. Geopolymers are synthesized by reacting aluminosilicate-rich industrial wastes or byproducts, such as blast furnace slag, fly ash, silica fume, and metakaolin, with alkaline activators such as sodium

hydroxide and sodium silicate [6,7]. This polycondensation reaction (geopolymerization) can occur at low temperatures and has the potential to reduce CO_2 emissions by 70% to 80% compared to OPC production [8]. Geopolymer systems derived from blast furnace slag (BFS) can cure rapidly at room temperature owing to their high calcium levels. They develop a dense gel network of C-A-S-H/N-A-S-H, providing excellent early strength and resistance to chemical corrosion [6,9].

Advances in traditional concrete technology have paved the way for the development of geopolymer foam concrete (GFC) to meet the need for lightweight, highly insulating building elements. GFC is an innovative, ultra-lightweight material in which controlled air voids are trapped within its cellular structure using chemical (e.g., hydrogen peroxide) or mechanical foaming agents [10,11]. Geopolymer foam concretes are specialized composites that combine the low dry density (typically 280–1000 kg/m^3), superior thermal insulation, and high acoustic damping capacity of traditional lightweight concretes with the chemical, mechanical, and thermal stability of geopolymers [12]. GFC offers an ideal range of solutions for partition walls, roof insulation panels, sound barriers, and lightweight building elements in sustainable architecture and energy-efficient buildings [13–15]. However, the intentionally high void ratio in the matrix significantly decreases the mechanical strength of the material, including its compressive and flexural capacities. Additionally, the spongy characteristics of the matrix make it more brittle [16,17]. Maintaining the stability of fresh foam without collapse and without loss of load-bearing capacity in the hardened material are the most significant drawbacks of the widespread commercial-scale production of GFCs [3,17].

To address the mechanical limitations of GFC and advance environmental sustainability alongside economic benefits, it is crucial to incorporate industrial waste (solid waste materials) into geopolymer production systems, in addition to using binders or aggregates [8,11]. In this context, recent academic research has focused on the use of waste marble powder (MP) [18]. Worldwide, quarrying and the marble sector produce millions of tons of marble slurry and fine dust each year from cutting and polishing. The mismanagement of such waste causes groundwater contamination, reduces soil permeability, destroys agricultural soil, and poses considerable health problems due to air pollution [15,19]. The use of marble dust as an additive or replacement for some precursors in fly ash geopolymer cement (GFC) matrices solves the problem of environmental waste management and minimizes ecological impact [14,15]. Because of its very small particle size, the main role of the marble powder is as a micro-filler, filling the interparticle voids and resulting in denser foam walls [18]. In addition, because of its high calcium carbonate content, it may promote gel nucleation at an early age [18]. On the other hand, marble powder possesses low reactivity; in larger amounts, it might result in the dilution of aluminosilicate gels, thus preventing the process of geopolymerization and decreasing the amount of the main binder [20]. Determining the optimal waste substitution ratio is essential for balancing fresh workability, such as rheological fluidity, with hardened physical strength [14,19].

However, the problem of matrix is brittle owing to the stress concentration inherent to the mechanical voids and cellular structure. This problem can be addressed by introducing reinforcing fibers into the composite material [21,22]. There are three types of fibers: synthetic, inorganic, and natural. However, Polyvinyl Alcohol (PVA) fibers constitute a unique reinforcing element for alkali-activated geopolymeric systems owing to their high tensile strength, high modulus of elasticity, and high resistance to corrosion in alkali environments [23]. The main feature of PVA fibers is the possibility of creating a reliable chemical bond and a high-friction interface (interfacial transition zone—ITZ) between the fibers and inorganic

matrix owing to the presence of hydroxyl groups on the PVA fiber surface [24]. PVA fibers can prevent crack formation in the matrix, limit matrix movements, and physically stop crack propagation with the help of the fiber bridging mechanism when using a specific volume fraction of fibers (from 0.2% to 1.2%) [21,22]. This avoids sudden brittle fractures in GFC, making the composite more ductile and capable of absorbing deformations [21]. Thus, the compressive, flexural, and splitting tensile strengths of the material increased, whereas its impact toughness improved dramatically [21]. However, owing to the hydrophilic nature of PVA fibers, excessive use can significantly reduce the workability of fresh mortar by absorbing free water. This can result in fiber balling and the formation of additional voids, which ultimately cause mechanical performance issues [23]. Therefore, to optimize the integrity of the foam walls, analyses of the fiber size and volumetric dosage must be performed with extreme precision.

Geopolymer technology clearly demonstrates the extraordinary benefits and opportunities for recovering inorganic industrial wastes. However, there is a significant lack of systematic research in the literature that addresses the synergistic and antagonistic interactions created simultaneously by high substitution rates of waste marble powder (20% and 40%) and various dosages of PVA fiber (0.6% and 1.2%) in slag-based geopolymer foam concrete. The volumetric threshold values at which potential strength reductions caused by the dilution effect of waste marble dust can be offset by the energy-absorbing bridging mechanisms of PVA fibers, and how the material preserves its structural stability under different thermal and mechanical stresses, such as high-temperature shocks up to 600 °C, in a complex cellular system with lightweight aggregates (expanded perlite), have not yet been thoroughly documented. This study aims to determine the optimal mix design for an innovative geopolymer foam concrete that uses blast furnace slag and waste marble powder as binders, expanded perlite as aggregate, and PVA fiber for reinforcement. This study explores how varying marble powder and PVA fiber ratios affect the workability, physical properties such as porosity and water absorption, mechanical strengths such as compressive and flexural strength, and resistance to high temperatures. The aim was to create a sustainable insulation and building material characterized by low carbon emissions, an ultra-lightweight design, high fire resistance, and improved ductility. This approach promotes a circular economy by repurposing industrial marble waste into valuable products.

2. A Subsection Sample

2.1.Raw materials

In this experiment, BFS was used as the primary source of aluminosilicates, with waste marble powder (MP) as its partial replacement. BFS is a waste material known for its glassy phase and large amounts of CaO, SiO_2, Al_2O_3, and MgO, as well as its high reactivity in alkaline media. Alkali activation allows the dissolution of the slag and the formation of binders' reaction products, namely C-(A)-S-H, which helps the foam concrete gain mechanical strength through pore wall reinforcement. MP is a finely divided waste material that primarily contains calcite from the processing of marble blocks. For alkali-activated systems, its role is primarily to fill empty spaces, increase grain packing, and provide nucleation centers to create a more homogeneous matrix and dense pore walls. Higher amounts of MP may have a diluting effect and decrease the volume of the binder gel due to the lower reactive slag content. Therefore, waste marble powder was used to replace BFS at 20% and 40% by weight in this study. The chemical compositions of BFS and MP, determined by XRF, are presented in Table 1, and their mineralogical properties, determined by XRD, are presented in Figure 1.

Table 1. Chemical composition of BFS and MP

	SiO_2	Al_2O_3	Fe_2O_3	CaO	Na_2O	K_2O	MgO	SO_3	LOI
BFS	37.5	10.1	3.5	35.6	0.2	0.6	11.5	0.3	0.6
MP	0.2	0.2	0.1	54.3	0.1	0.2	0.4	0.1	44.3

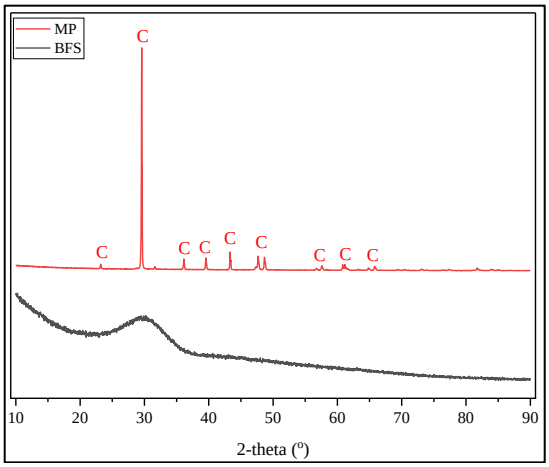


Fig. 1. Mineralogical properties of BFS and MP (C: Calcite)

In this study, expanded perlite with a particle size of 0-4 mm was used as a lightweight aggregate. The bulk density of perlite is 0.22 g/cm³, while the water absorption rate by weight is 147%, owing to its open and interlinked porous nature. The low specific gravity of perlite decreases the volume weight of the composite and improves the lightweight concrete properties of the composite. Simultaneously, the porosity of perlite provides more thermal insulation. The solid alkali activator sodium metasilicate (Na_2SiO_3) was used for the geopolymerization process; its specific gravity was 2.61, and it contained 53% SiO_2 and 46% Na_2O. Sodium lauryl sulfate (SLS), also known as sodium dodecyl sulfate (SDS), served as the foaming surfactant. SLS is a synthetic anionic surfactant with the chemical formula $C_{12}H_{25}NaO_4S$. In this study, 12 mm long polyvinyl alcohol (PVA) fibers were used to improve the crack control and mechanical integrity of geopolymer foam concrete. The technical properties of the PVA fibers are listed in Table 2.

Table 2. Technical properties of PVA fiber

Length (mm)	Diameter (μm)	Density (g/cm^3)	Young's modulus (GPa)	Tensile strength (MPa)	Elongation (%)
12	40	1.3	40	1500	6.5

2.2. Mix design

This study prepared nine different mixtures by varying the replacement level of blast furnace slag with MP at 0%, 20%, and 40% (by mass). PVA fibers were added at concentrations of 0%, 0.6%, and 1.2% (by volume) to the concrete. All mixtures maintained a constant total of 750 kg/m³ for BFS and MP, with water and sodium metasilicate kept constant at 300 and 150 kg/m³, respectively. The PVA fiber amounts of 0.6% and 1.2% by volume corresponded to 7.8 and 15.6 kg/m³, respectively. The expanded perlite content was adjusted to 67.3–70.9 kg/m³ to ensure volumetric balance. The detailed mixture compositions are listed in Table 3.

SLS was used as a foaming agent. The foaming solution was prepared by adding 5% SLS (50 g) to 1 L of water, and the resulting solution was foamed using a mechanical mixer. The wet density of the foam was approximately 120 g/L. To ensure comparability among the mixtures,

the foam quantity was kept constant across all series and added to the fresh mixture at a rate of 30 kg/m³.

Table 3. Mixing ratios and material amounts

Mix ID	Mix ratio (%)		Material amounts (kg/m³)						
	MP	PVA fiber	BFS	MP	Water	Sodium metasilicate	Expanded perlite	PVA fiber	Foam
MP0-F0	0	0	750	0	300	150	70.9	0.0	30
MP20-F0	20		600	150	300	150	70.2	0.0	30
MP40-F0	40		450	300	300	150	69.4	0.0	30
MP0-F0.6	0	0.6	750	0	300	150	70.2	7.8	30
MP20-F0.6	20		600	150	300	150	69.5	7.8	30
MP40-F0.6	40		450	300	300	150	68.4	7.8	30
MP0-F1.2	0	1.2	750	0	300	150	69.3	15.6	30
MP20-F1.2	20		600	150	300	150	68.1	15.6	30
MP40-F1.2	40		450	300	300	150	67.3	15.6	30

2.3. Mixing, Casting and Curing

To prepare the mixtures, BFS, MP, sodium metasilicate, and expanded perlite were mixed until a homogeneous distribution was achieved. Water was then added to the system, and mixing continued until the binder slurry attained a uniform consistency. In mixtures containing PVA fibers, the fibers were added to the mixture in stages to prevent clumping and ensure homogeneous distribution within the matrix.

Pre-prepared SLS-based foam with a wet density of approximately 120 g/L was used at 30 kg/m³ in all mixtures. To protect the pore structure of the foam and minimize air loss, it was added at the final stage of mixing and stirred at a low speed until evenly distributed. The fresh geopolymer foam concrete mixes were then poured into the test molds and smoothed on the surface. These specimens underwent thermal curing at 75 °C for 24h to accelerate geopolymerization. After curing, the specimens were demolded and stored in a laboratory setting until testing.

2.4. Test methods

The workability of the geopolymer foam concrete in its fresh state was determined using a spread-table test conducted in accordance with ASTM C1437, and the results were recorded as the flow diameter (mm). Apparent porosity and oven-dried density tests were conducted on 28-day-old cubic specimens measuring 50 mm × 50 mm × 50 mm. After drying the specimens at 50 °C for 3 days, their dry masses were determined. Subsequently, the masses of the specimens, both on the saturated surface and in water, were measured after they were saturated with water. The apparent porosity was calculated as the ratio of the volume of water-absorbing accessible voids to the total volume of the samples, and the results are expressed as percentages (%). The oven-dried density was calculated by dividing the dry sample mass by the solid volume and expressed in kg/m³.

The water absorption test was conducted on 28-day-old cubic specimens measuring 50 mm × 50 mm × 50 mm. The samples were dried at 50 °C for 3 days to determine their dry mass and then saturated with water. The water absorption rate was calculated as the difference between the saturated and dry masses divided by the dry mass and expressed as a percentage (%). The capillary water absorption test was conducted according to the TS EN 1015-18 standard. Only the bottom surfaces of the dried specimens were brought into contact with water, and the mass

increase at specific time intervals was recorded. The capillary water absorption behavior was determined based on the surface area in contact with water. The capillary water absorption of the specimens was determined after 24h. The physical parameters, such as water absorption, apparent porosity, and oven-dry density, were determined in accordance with the ASTM C642 standards. The thermal conductivity of the specimens was determined in accordance with ASTM C518 for 28-day-old specimens, whose size was 200 mm × 200 mm × 30 mm. Before performing the measurements, the specimens were dried in an oven at 50 $^{\circ}C$ for three days. The measurement was performed using a heat flux meter, and the results were obtained in W/(m.K).

Flexural and compressive strength tests were conducted on the specimens at 7 and 28 days. The flexural strength was measured on prismatic specimens measuring 40 × 40 × 160 mm in accordance with ASTM C348. Compressive strength tests were performed on the broken fragments from the flexural tests, in accordance with ASTM C349. The test results were reported in MPa.

High-temperature tests were performed on 28-day-old cubic specimens measuring 50 mm × 50 mm × 50 mm. The samples were heated in a laboratory muffle furnace at 10 °C/min to temperatures of 200, 400, and 600 °C. After the samples reached the target temperature, they were left to stand for 1 h and then allowed to cool inside the oven. Their masses were recorded before and after heating to assess weight loss, and the compressive strengths were measured post-exposure. The results were analyzed by comparing them with those of samples kept at the reference temperature.

3. Results and Discussions

3.1. Fresh properties

The spreading diameters of the mixtures ranged from 125 to 164 mm (Fig. 2). The spreading diameter of the reference mixture MP0-F0 was 149 mm, while in the fiber-free series, this value reached 156 mm (4.7% increase) and 164 mm (10.1% increase) by increasing the marble powder substitution to 20% and 40%, respectively. The maintenance of a similar increasing trend at both fiber levels indicates that marble powder improves the fluidity of the fresh mixture owing to its lower reactivity and physical effect of reducing friction between particles. The literature also reports that the spreading diameter increases with increasing marble powder content in BFS-marble waste-based alkali-activated systems [25].

In contrast, increasing the PVA fiber content significantly reduced the spreading diameter of the droplets. In the series without marble powder, 0.6% and 1.2% PVA reduced the spreading diameter by 5.4% and 16.1%, respectively, compared with that of the reference. The same trend was observed for the MP20 and MP40 series. This reduction can be explained by the hydrophilic PVA fibers with a high specific surface area retaining mixing water and by interfiber interactions that increase internal friction and limit the paste's free movement. Shah et al. reported that PVA fibers reduced the spreading of single-component alkali-activated mortars, depending on the fiber dosage [26]. Overall, marble powder partially offset the workability loss caused by PVA; however, the PVA fiber ratio was the determining parameter for the fresh-state behavior.

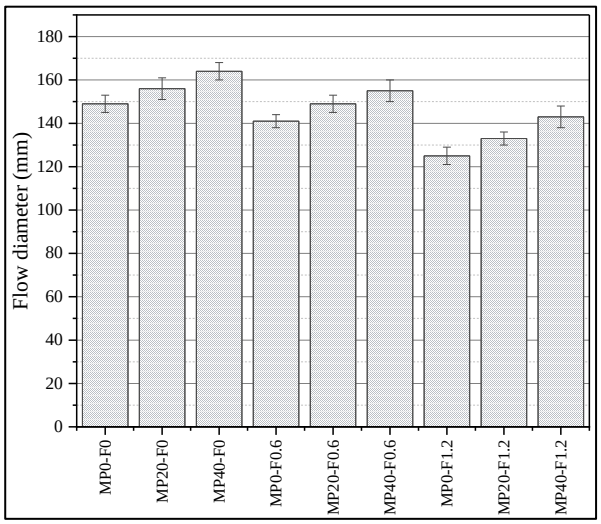


Fig. 2. Flow diameters of geopolymer foams

3.2. Physical Properties

The apparent porosities of the mixtures ranged from 16.43% to 41.43%, and their oven-dry densities ranged from 558 to 883 kg/m³ (Fig. 3). In the fiber-free series, increasing the marble powder ratio to 20% and 40% increased the apparent porosity by 16.7% and 41.8%, respectively, compared with the MP0-F0 reference, and decreased the oven-dry density by 4.7% and 7.4%. This trend can be explained by the dilution effect of the reduced reactivity of BFS at high marble powder ratios, the dominance of the filling effect of the marble powder, and a decrease in the volume of the binder gel that forms the pore walls. It has been reported that low marble powder ratios can improve the pore structure in alkali-activated slag systems; however, porosity and water absorption can increase again at ratios above 20% [18].

The effect of PVA fiber was particularly pronounced at 0.6% PVA fiber content. In the MP0-F0.6 mixture, the apparent porosity decreased by 43.8% to 16.43% compared to that of the reference, while the oven-dry density increased by 34.2% to 883 kg/m³. This suggests that an appropriate fiber ratio increases the cohesion of the fresh mixture, creating more compact pore walls and a less connected open-pore structure. However, increasing the fiber ratio to 1.2% increased the porosity of the same mixture to 25.62%, and the density decreased to 766 kg/m³. The irregular distribution of fibers, agglomeration, and formation of additional voids at the fiber-matrix interface may have contributed to this change at high fiber content. It has been previously reported that PVA fibers can increase pore connections in alkali-activated slag matrices, and that the fiber effect depends on the interface properties [27].

Generally, increasing the marble powder proportion at all fiber levels led to higher porosity and lower density. The lowest density recorded was 558 kg/m³ in MP40-F1.2, whereas the highest porosity was 41.43% in MP40-F0. However, because apparent porosity only measures open, water-accessible voids, a direct inverse correlation with density is not always expected for every mixture [27]. The water absorption values by immersion ranged from 14.56% to 37.65%, and the capillary water absorption values ranged from 11.35–23.46 kg/m² (Fig. 4). Increasing the proportion of marble powder in the fiber-free series negatively affected both properties of the samples. Compared to the reference MP0-F0, immersion and capillary water absorption increased by 32.2% and 12.5% in the MP20-F0 mixture and by 53.4% and 40.7% in the MP40-F0 mixture, respectively. This result can be attributed to the decrease in the amount of reactive BFS with marble powder substitution, weakening of the binder gel continuity, and increase in the associated open pore volume. It has been similarly reported that high proportions of marble

powder in alkali-activated slag systems can increase porosity and water absorption owing to the dilution effect [18].

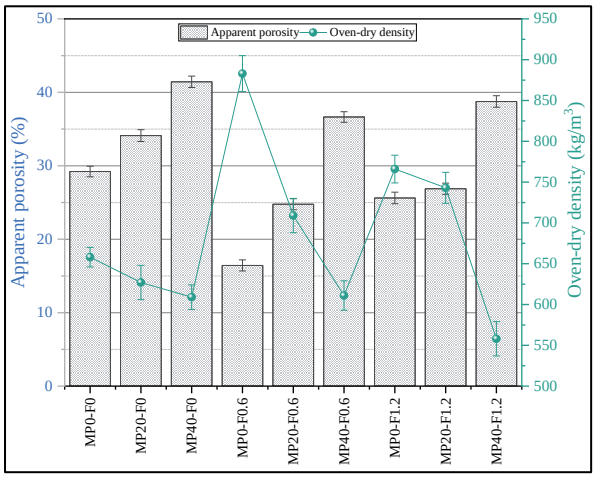


Fig. 3. Apparent porosity and oven-dry density of geopolymer foams

The most significant effect of PVA fibers was observed at a fiber volume ratio of 0.6% and in the MP0-F0.6 blend; immersion and capillary water absorption decreased by 40.7% and 31.9%, respectively, compared with the reference, reaching the lowest values among all the blends. Similarly, in the MP20 series, 0.6% PVA reduced water absorption and capillary water absorption by 31.8% and 10.6%, respectively, compared with those of the fiber-free counterpart. In the MP40 series, the reductions were 17.1% and 10.0%. This improvement can be explained by the appropriate fiber ratio, which enhances blend cohesion and foam stability, tightens pore walls, and limits associated capillary pathways.

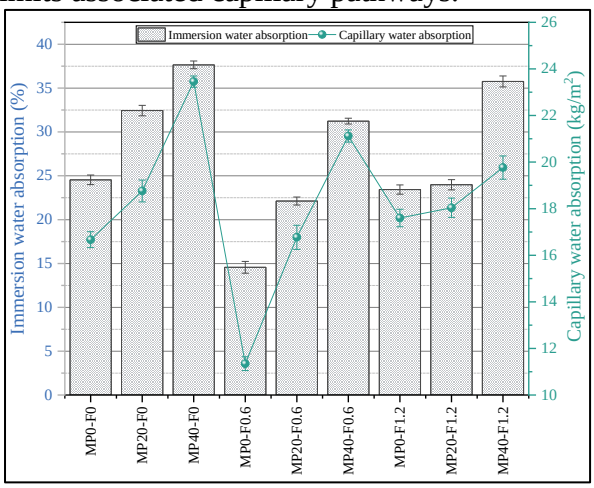


Fig. 4. Immersion and capillary water absorption

Increasing the fiber content to 1.2% did not provide the same level of improvement. In particular, the capillary water absorption of the MP0-F1.2 mixture was 5.6% higher than that of the reference. The decreased workability at high fiber contents, irregular fiber distribution, and connected passage paths formed at the fiber-matrix interfaces may have influenced this behavior. It has also been reported that PVA fibers can increase capillary pore connectivity in alkali-activated slag matrices [27]. In general, the results were consistent with the apparent porosity values, and the best water impermeability performance was obtained with the MP0-F0.6 mixture. In contrast, the worst performance was obtained with the MP40-F0 mixture.

3.3. Thermal performance

The thermal conductivities of the mixtures ranged from 0.143 to 0.229 W/(m·K). In the fiber-free series, adding 20% and 40% marble powder decreased the thermal conductivity by 6.1% and 9.2%, respectively, compared to that of MP0-F0 reference (Fig. 5). This decrease correlates with a reduction in the oven-dry density from 658 kg/m³ to 627 and 609 kg/m³, and an increase in the apparent porosity. The presence of air in the pores, combined with disrupted heat transfer pathways in the solid matrix, enhanced the insulation properties of the marble powder-containing mixtures. The literature also indicates that the thermal conductivity of geopolymer foams is heavily influenced by the pore amount, size, and distribution, as well as the overall density [28,29].

The effect of the PVA fibers was nonlinear. In the MP0-F0.6 mixture, the thermal conductivity increased by 40.5% relative to that of the reference, reaching a maximum of 0.229 W/(m·K). This result can be explained by the fact that 0.6% PVA stabilized the foam structure, reduced the apparent porosity, and increased the density to 883 kg/m³. Increasing the fiber ratio to 1.2% again decreased the density, reducing the thermal conductivity of the MP0-F1.2 mixture to 0.193 W/(m·K). However, the fiber effect is not solely dependent on fiber content; fiber distribution, foam stability, and pore interconnectivity are also important factors.

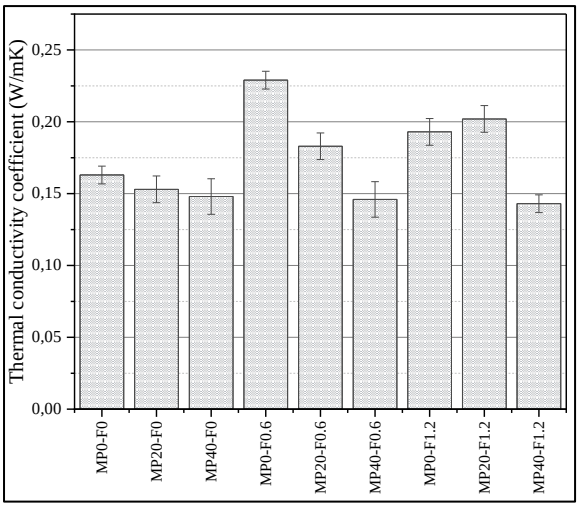


Fig. 5. Thermal performance of geopolymer foams

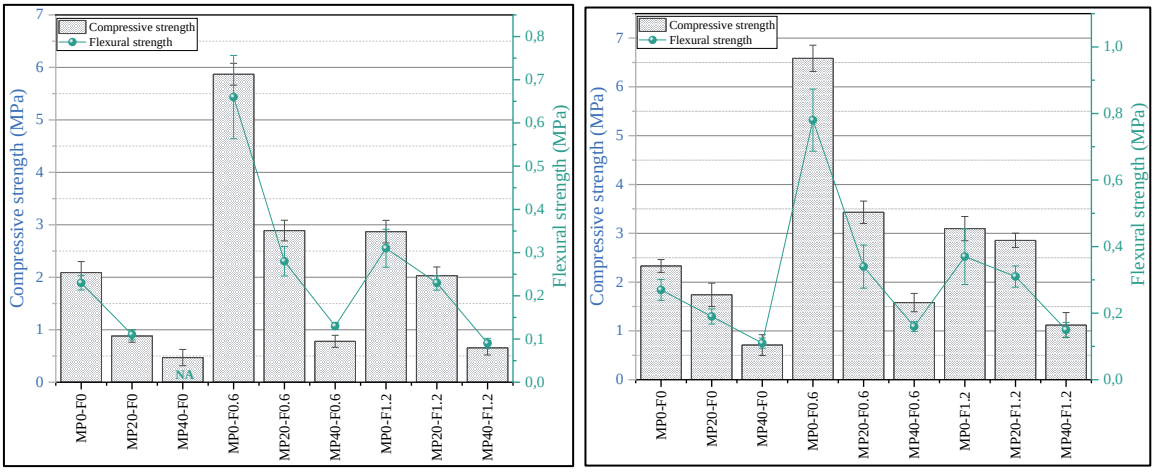
The lowest thermal conductivity, 0.143 W/(m·K), was observed for the MP40-F1.2 mixture. The combined evaluation of the data showed a strong positive correlation between thermal conductivity and oven-dry density and a strong negative correlation with apparent porosity. Therefore, in the system studied, the thermal performance was primarily determined by changes in the density and pore structure created by these components, rather than by the direct effects of PVA or marble powder.

3.4. Mechanical properties

In all mixtures, the 28-day strengths were found to be increased compared to the 7-day values (Fig. 6a). This increase indicates that the alkali activation reactions and binder gel formation continued even after 24h of heat curing at 75 °C. However, while the improvement between 7 and 28 days was more limited in strong and dense mixtures, the proportional increase was higher in mixtures containing marble powder; however, this increase could not compensate for the lower initial strengths. In the fiber-free series, substituting marble powder significantly reduced the mechanical performance. The 28-day compressive and flexural strengths of reference MP0-F0 were 2.33 and 0.27 MPa, respectively (Fig. 6b). In MP20-F0, these values

decreased by 25.3% and 29.6%, respectively, and in MP40-F0, by 69.5% and 59.3%, respectively. This behavior can be explained by the dilution effect from the reduced reactive slag as the marble powder ratio increases, the weakening of binder gel continuity, and the increased porosity observed in previous results. It has been reported that low marble powder ratios can provide a filling effect in alkali-activated slag systems. However, strength decreases at high substitution ratios owing to increased porosity and dilution of the slag [18,30].

The most significant effect of the PVA fibers was observed at a volumetric percentage of 0.6%. The 28-day compressive and flexural strengths of the MP0-F0.6 mixture were 6.585 and 0.78 MPa, respectively, representing increases of approximately 183% and 189% compared with the reference. This improvement is attributed to the 0.6% PVA bridging microcracks and maintaining the integrity of the foam walls, as well as the mixture's lowest apparent porosity and highest density. The literature also reports that PVA fibers can improve the compressive and, in particular, flexural performance of single-component alkali-activated systems [26].



(a) 7 days (b) 28 days

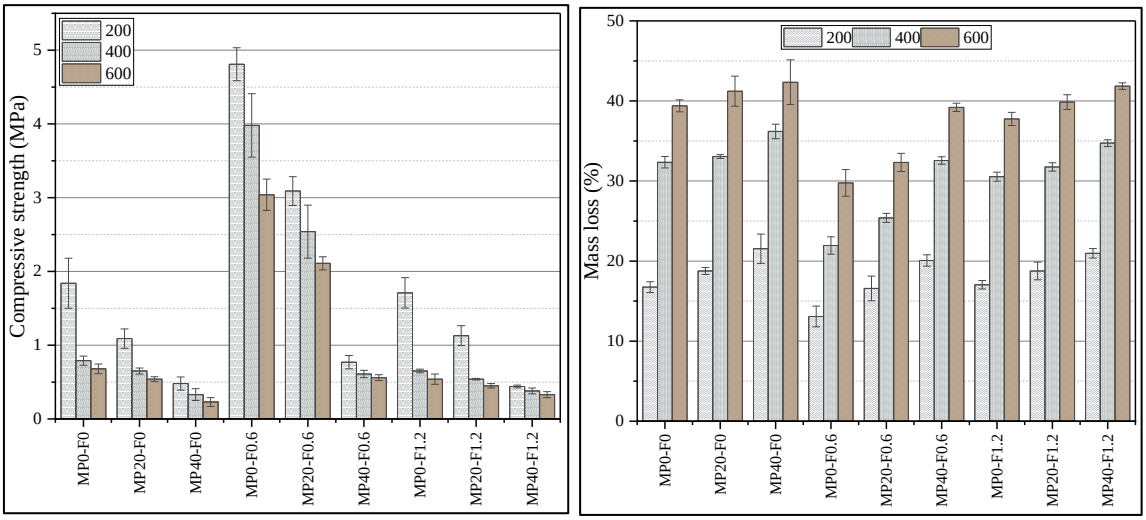
Fig. 6. Mechanical properties of geopolymer foams

Increasing the fiber content to 1.2% increased the strength compared to fiberless mixtures at all marble powder levels; however, it was not as effective as 0.6%-PVA. For example, the 28-day compressive strength of MP0-F1.2 was 3.10 MPa, and its flexural strength was 0.37 MPa. The reduction in flow diameter at high fiber contents, irregular distribution of fibers, and additional voids at the fiber-matrix interface may have limited the fiber-bridging effect. Overall, the highest mechanical performance was obtained with the MP0-F0.6 mixture, and the lowest 28-day performance was obtained with the MP40-F0 mixture. As the 7-day flexural strength of the MP40-F0 mixture could not be determined, this value was not included in the comparison.

3.5. High-temperature resistance

As the temperature increased from 200 to 600 °C, all mixtures showed a gradual decline in compressive strength, along with increasing mass loss (Fig. 7). This trend is attributed to the removal of free and bound water, the dehydration of alkali activation products, and the development of microcracks caused by thermal mismatch. In the series without fibers, a higher marble powder content led to a lower compressive strength. For instance, at 600 °C, the strengths of MP0-F0, MP20-F0, and MP40-F0 were 0.68, 0.54, and 0.23 MPa, respectively. Correspondingly, their mass loss increased from 39.39% to 42.34%. The initial porosity from high marble powder levels and limited BFS weakened the matrix at high temperatures. Additionally, the decomposition of some loosely crystallized carbonate phases at higher temperatures may have contributed to mass loss [31,32]. The most significant positive impact

of PVA fibers was observed at a volume concentration of 0.6 %. The MP0-F0.6 mixture exhibited the highest strengths at 200, 400, and 600 °C, with values of 4.81, 3.98, and 3.04 MPa, respectively. Conversely, the MP20-F0.6 mixture exhibited the greatest strength retention relative to its initial strength, maintaining about 90.1%, 74.1%, and 61.5% at those temperatures. The improved thermal performance is attributed to the more balanced pore structure created by the moderate marble powder and 0.6% PVA, along with its low thermal conductivity and fiber-bridging mechanism, which inhibited thermal damage progression.



(a) Compressive strength (b) Mass loss

Fig. 7. Mechanical and physical properties of geopolymer foams exposed to high temperatures.

Increasing the fiber ratio to 1.2% negatively affected the high-temperature performance of the asphalt mixture. PVA fibers melt or decompose at approximately 220 °C, creating voids and vapor release channels within the matrix. While these channels can reduce the risk of explosive spillage, they lead to the loss of the fiber bridging effect and an increase in porosity [27,33]. Therefore, significant strength losses were observed in mixtures containing 1.2% PVA, particularly after 400 and 600 °C. In general, 0.6% PVA was the optimum fiber ratio in terms of limiting mass loss and maintaining compressive strength, whereas increasing the marble powder content to 40% weakened the high-temperature performance at all fiber contents.

4. Conclusions

This study examined the influence of waste marble powder and PVA fibers on the performance of blast furnace slag-based geopolymer foam concretes. The key findings are summarized as follows:

- The substitution of marble powder increased the flow diameter, whereas the addition of PVA fibers reduced the workability of the mixtures. Marble powder partially compensated for the fluidity loss caused by the addition of fibers.
- Increasing the proportion of marble powder increased the apparent porosity and water absorption, while decreasing the density. The MP0-F0.6 mixture, which contained 0.6% PVA by volume, exhibited the highest density and lowest porosity and water absorption. Increasing the fiber ratio to 1.2% did not yield similar improvements.
- The thermal conductivity coefficients ranged from 0.143 to 0.229 W/(m·K) and were mainly influenced by the density and pore structure. The lowest value was observed for the MP40-F1.2 mixture.

- Although replacing marble powder reduced the mechanical strength, adding 0.6% PVA fiber significantly improved it. The 28-day compressive strength of the MP0-F0.6 mixture was 6.585 MPa, and its flexural strength was 0.78 MPa, which were approximately 183% and 189% higher than those of the reference, respectively.
- As the temperature increased, all the mixtures exhibited a decrease in compressive strength and an increase in mass loss. The MP0-F0.6 mixture exhibited the highest strengths, and MP20-F0.6 retained approximately 61.5% of its initial strength at 600 °C.

The 0.6% PVA fiber ratio was found to be optimal for the physical, mechanical, and high-temperature performance. MP0-F0.6 emerged as the best overall mixture, whereas MP20-F0.6 was ideal for applications requiring both waste utilization and high-temperature resistance.

References

[1] M. Abdellatief, A.E. Hassanien, M. Mortagi, H. Hamouda, Geopolymer foam concrete: A review of pore characteristics, compressive strength, and artificial intelligence in GFC strength simulations, Discov. Concr. Cem. 1 (2025) 4. https://doi.org/10.1007/s44416-025-00003-x.

[2] G.A.M. Metwally, W.E. Elemam, M. Mahdy, M. Ghannam, Metakaolin-based ultra-high-performance geopolymer concrete, role of basalt, glass, granite, and marble waste powders, Innov. Infrastruct. Solut. 10 (2025) 527. https://doi.org/10.1007/s41062-025-02281-7.

[3] F.A. Shilar, M. Shilar, Review: Foam geopolymer synthesis macro- to micro-properties, J Mater Sci 60 (2025) 23176–23226. https://doi.org/10.1007/s10853-025-11707-7.

[4] S. Luhar, D. Nicolaides, I. Luhar, Fire Resistance Behaviour of Geopolymer Concrete: An Overview, Buildings 11 (2021) 82. https://doi.org/10.3390/buildings11030082.

[5] J. Davidovits, Geopolymers: Inorganic polymeric new materials, Journal of Thermal Analysis and Calorimetry 37 (2005) 1633–1656. https://doi.org/10.1007/bf01912193.

[6] Y. Hao, G. Yang, K. Liang, Development of fly ash and slag based high-strength alkali-activated foam concrete, Cement and Concrete Composites 128 (2022) 104447. https://doi.org/10.1016/j.cemconcomp.2022.104447.

[7] J.L. Provis, S.A. Bernal, Geopolymers and Related Alkali-Activated Materials, Annual Review of Materials Research 44 (2014) 299–327. https://doi.org/10.1146/annurev-matsci-070813-113515.

[8] M. Abdellatief, M.A. Elrahman, H. Alanazi, A.A. Abadel, A. Tahwia, A state-of-the-art review on geopolymer foam concrete with solid waste materials: components, characteristics, and microstructure, Innov. Infrastruct. Solut. 8 (2023) 230. https://doi.org/10.1007/s41062-023-01202-w.

[9] C. Karakurt, A.F. Şenol, N.Ç. Demiral, Effects of curing temperatures and waste marble aggregates on the properties of geopolymer mortars produced with industrial by-products and waste baked clay powders, Advanced Powder Technology 36 (2025) 104946. https://doi.org/10.1016/j.apt.2025.104946.

[10] R.M. Novais, Robert.C. Pullar, J.A. Labrincha, Geopolymer foams: An overview of recent advancements, Progress in Materials Science 109 (2020) 100621. https://doi.org/10.1016/j.pmatsci.2019.100621.

[11] A. Siddika, A. Hajimohammadi, V. Sahajwalla, A novel eco-friendly foaming technique for developing sustainable glass foams from the waste glass, Resources, Conservation and Recycling 190 (2023) 106801. https://doi.org/10.1016/j.resconrec.2022.106801.

[12] Z. Zhang, J.L. Provis, A. Reid, H. Wang, Mechanical, thermal insulation, thermal resistance, and acoustic absorption properties of geopolymer foam concrete, Cement and Concrete Composites 62 (2015) 97–105. https://doi.org/10.1016/j.cemconcomp.2015.03.013.

[13] Y.H.M. Amran, N. Farzadnia, A.A. Abang Ali, Properties and applications of foamed concrete; a review, Construction and Building Materials 101 (2015) 990–1005. https://doi.org/10.1016/j.conbuildmat.2015.10.112.

[14] M. Uysal, Y. Aygörmez, O. Canpolat, T. Cosgun, Ö. Faruk Kuranlı, Investigation of using waste marble powder, brick powder, ceramic powder, glass powder, and rice husk ash as eco-friendly aggregate in sustainable red mud-metakaolin based geopolymer composites, Construction and Building Materials 361 (2022) 129718. https://doi.org/10.1016/j.conbuildmat.2022.129718.

[15] A.A. Aliabdo, A.E.M. Abd Elmoaty, E.M. Auda, Re-use of waste marble dust in the production of cement and concrete, Construction and Building Materials 50 (2014) 28–41. https://doi.org/10.1016/j.conbuildmat.2013.09.005.

[16] K. Dhasindrakrishna, S. Ramakrishnan, K. Pasupathy, J. Sanjayan, Collapse of fresh foam concrete: Mechanisms and influencing parameters, Cement and Concrete Composites 122 (2021) 104151. https://doi.org/10.1016/j.cemconcomp.2021.104151.

[17] K. Dhasindrakrishna, K. Pasupathy, S. Ramakrishnan, J. Sanjayan, Progress, current thinking and challenges in geopolymer foam concrete technology, Cement and Concrete Composites 116 (2021) 103886. https://doi.org/10.1016/j.cemconcomp.2020.103886.

[18] A.M. Rashad, M.M. Mokhtar, M.H. El-Nashar, R. Abu-Elwafa Mohamed, Waste marble powder emerges as a promising material choice to enhance the properties of alkali-activated slag cement, Sustainable Chemistry and Pharmacy 43 (2025) 101864. https://doi.org/10.1016/j.scp.2024.101864.

[19] A.İ. Çelik, Mechanical Performance of Geopolymer Concrete Based on Basalt and Marble Powder, Iran J Sci Technol Trans Civ Eng 47 (2023) 2173–2187. https://doi.org/10.1007/s40996-023-01063-4.

[20] J. Dang, X. Tang, J. Xiao, A. Han, Influence of alkaline activator and precursor on the foam characterization and alkali-activated foamed concrete properties, Cement and Concrete Composites 145 (2024) 105341. https://doi.org/10.1016/j.cemconcomp.2023.105341.

[21] P. Zhang, Z. Feng, W. Yuan, S. Hu, P. Yuan, Effect of PVA fiber on properties of geopolymer composites: A comprehensive review, Journal of Materials Research and Technology 29 (2024) 4086–4101. https://doi.org/10.1016/j.jmrt.2024.02.151.

[22] Y. Wu, M. Chen, D. Chen, X. Zhou, J. He, Modification of ultra-high molecular weight polyethylene fiber to improve mechanical properties of foamed concrete, Construction and Building Materials 450 (2024) 138681. https://doi.org/10.1016/j.conbuildmat.2024.138681.

[23] J. Li, A. Hajimohammadi, Y. Yu, B.Y. Lee, T. Kim, Mechanism of PVA Fiber Influence in Foam Concrete: From Macroscopic to Microscopic View, Journal of Materials in Civil Engineering 35 (2023) 04023447. https://doi.org/10.1061/JMCEE7.MTENG-16124.

[24] S. Li, S. Qiu, H. Zheng, H. Yu, Influence of fibers on the multiscale properties of fly ash and slag based geopolymer foam concrete, Construction and Building Materials 515 (2026) 145596. https://doi.org/10.1016/j.conbuildmat.2026.145596.

[25] G.Ç. Ulubeyli, R. Artır, Synthesis and Characterization of an Alkali-Activated Binder from Blast Furnace Slag and Marble Waste, Materials 17 (2024). https://doi.org/10.3390/ma17215248.

[26] S.F.A. Shah, B. Chen, S.Y. Oderji, M. Aminul Haque, M.R. Ahmad, Comparative study on the effect of fiber type and content on the performance of one-part alkali-activated mortar, Construction and Building Materials 243 (2020) 118221. https://doi.org/10.1016/j.conbuildmat.2020.118221.

[27] Z. Abdollahnejad, M. Mastali, M. Falah, K.M. Shaad, T. Luukkonen, M. Illikainen, Durability of the Reinforced One-Part Alkali-Activated Slag Mortars with Different Fibers, Waste Biomass Valor 12 (2021) 487–501. https://doi.org/10.1007/s12649-020-00958-x.

[28] Y. Cui, D. Wang, J. Zhao, D. Li, S. Ng, Y. Rui, Effect of calcium stearate based foam stabilizer on pore characteristics and thermal conductivity of geopolymer foam material, Journal of Building Engineering 20 (2018) 21–29. https://doi.org/10.1016/j.jobe.2018.06.002.

[29] C. Bai, T., Ni, Q., Wang, H. Li, P. Colombo, Porosity, mechanical and insulating properties of geopolymer foams using vegetable oil as the stabilizing agent, Journal of the European Ceramic Society 38 (2018) 799–805. https://doi.org/10.1016/j.jeurceramsoc.2017.09.021.

[30] B. Bodur, M.A.M. İşik, G. Kaplan, O.Y. Bayraktar, Multifunctional Utilization of Marble Wastes in One-Part and Two-Part Geopolymer Production Methods: Applications as Filler and Fine Aggregate, KUJES 11 (2025) 12–20. https://doi.org/10.55385/kastamonujes.1628523.

[31] B. Liu, S. Geng, J. Ye, X. Liu, W. Lin, S. Wu, K. Qian, A preliminary study on waste marble powder-based alkali-activated binders, Construction and Building Materials 378 (2023) 131094. https://doi.org/10.1016/j.conbuildmat.2023.131094.

[32] A. Öz, H. Çil, A. Benli, G. Kaplan, Enhanced mechanical and durability properties of alkali-activated composites through the use waste tire aggregates, brick powder, and marble powder, Journal of Sustainable Cement-Based Materials 15 (2026) 1673–1701. https://doi.org/10.1080/21650373.2026.2612726.

[33] K. Dhasindrakrishna, K. Pasupathy, S. Ramakrishnan, J. Sanjayan, Rheology and elevated temperature performance of geopolymer foam concrete with varying PVA fibre dosage, Materials Letters 328 (2022) 133122. https://doi.org/10.1016/j.matlet.2022.133122.

Publication Note

This paper was peer-reviewed, accepted for presentation, and included in the proceedings of the ACE2026 – International Conference on Advances in Civil Engineering, held on 12–14 October 2026 in Trabzon, Türkiye.

This paper may be cited as follows:

Rümeysa Atmaca, Damla Nur Çelik, Rüya Kılıç Demircan, Gökhan Kaplan, "Mechanical and High-Temperature Performance of Geopolymer Foam Concrete Substituted with Marble Powder and Reinforced with PVA Fibers" in Proceedings of the ACE2026 – International Conference on Advances in Civil Engineering, Trabzon, Türkiye, 12–14 October 2026.

Investigation of the Usability of Hemp Powders in Cementitious Composites

Abdulrezzak Alkan[1], Yunus Gündüz[2*] and Yuşa Şahin[3]
[1] 0000-0001-8920-1535, Yozgat Bozok University, School of Graduate Studies, Yozgat, Türkiye, rezzakalkan@hotmail.com
[2] 0000-0001-9740-0980, Yozgat Bozok University, Civil Engineering Department, Yozgat, Türkiye, yunus.gunduz@bozok.edu.tr
[3] 0000-0002-3586-412X, Yozgat Bozok University, Civil Engineering Department, Yozgat, Türkiye, yusa.sahin@bozok.edu.tr

Abstract. Cement is one of the most widely used materials in the world. In this context, efforts to reduce the carbon footprint in cement production have increased. Pozzolanic materials are actively used in the cement industry for this purpose. However, the frequent use of pozzolanic materials has raised the possibility of their depletion in the coming years. Industrial hemp is one type of bio-based product that has potential as a pozzolanic material. This study investigated the usability of powders obtained from two different hemp plant genders as a supplementary material for cement. The water-to-cement ratio of the cementitious mortars was adjusted to 0.3 and 0.7. Hemp powders were used in the mixture at three different ratios as, 1%, 3%, and 5%. The physical and mechanical properties of the cementitious composites were determined by spreading, unit weight, compressive, and flexural strength tests. It has been observed that as the amount of hemp powder products in cementitious mortars increases, the spread and unit weight values decrease. Similarly, as the amount of hemp powder products increases, the flexural and compressive strength of the mortars decreases. As a result, it has been determined that hemp powders can be used as an aggregate rather than as a binder in cementitious composites.

Keywords: Hemp powder; Cement; Mortar; Mechanical Properties.

1 Introduction

Previous studies have demonstrated the potential use of various waste-derived powders as binders or fillers in cement-based composites. A study [1] investigated the feasibility of incorporating agricultural waste ashes, including rice husk, hazelnut shell, sunflower, and corn ashes, as partial cement replacements at substitution levels of 2–10%. Among the investigated materials, hazelnut ash exhibited a flexural strength of 7 MPa and a compressive strength of 15 MPa, indicating its potential applicability in cement-based construction materials.

Tuyan investigated the production and performance of geopolymer paste, mortar, and concrete using various aluminosilicate materials, including natural pozzolans (zeolite and trass), waste brick powder, Class C fly ash, bottom ash, and Class F fly ash. The effects of alkali activator concentration, water-to-binder ratio, and curing conditions on the mechanical and durability properties of geopolymer mixtures were evaluated. Among the investigated binders, Class F fly ash-based mixtures exhibited the highest compressive strength, whereas zeolite-based mixtures showed the lowest. Binary binder systems incorporating Class F fly ash significantly improved the strength of mixtures containing waste brick powder, bottom ash, trass, or zeolite. In general, geopolymer concretes demonstrated higher bond strength with

reinforcement and lower drying shrinkage than conventional Portland cement concrete. The study also reported that increasing the Na_2O content and reducing the water-to-binder ratio enhanced compressive strength, while the influence of curing temperature and duration varied depending on the aluminosilicate source [2].

Mahmood investigated the use of waste polyvinyl chloride (PVC) fibers as reinforcement in cement mortars and evaluated their effects on fresh and hardened properties. PVC fibers were incorporated at volumetric contents of 0–3%, while silica fume and microsilica were used as partial cement replacements at replacement levels of 0–15%. The results showed that increasing the PVC fiber content reduced workability and fresh density while increasing porosity and water absorption. Although the addition of PVC fibers led to a reduction in compressive strength, higher fiber contents improved the ductility of the mortars by preventing sudden brittle failure. Mixtures containing silica fume exhibited lower water absorption and higher compressive and flexural strengths than both the control and microsilica-modified mixtures, with the highest compressive strength achieved in the mortar containing 15% silica fume without PVC fibers [3].

Malkoç investigated the influence of natural wollastonite as a partial cement replacement on the mechanical and durability properties of high-performance mortar. Wollastonite was incorporated at replacement levels of 3–15% while maintaining a constant water-to-binder ratio. Mechanical properties were evaluated through compressive strength, flexural strength, and ultrasonic pulse velocity tests, whereas durability was assessed using capillary water absorption and gas permeability tests. The results indicated that the incorporation of 3% wollastonite provided the greatest improvement in both strength and durability, while higher replacement levels resulted in a gradual reduction in performance, although 6% replacement still outperformed the control mixture. The enhanced performance was attributed to the needle-like morphology and high elastic modulus of wollastonite, which contributed to improved mechanical behavior and reduced capillary water permeability [4].

Mısır investigated the production of alkali-activated mortar using finely ground ferrochrome slag as the sole binder, eliminating the use of Portland cement. Marble powder (5–15%) and 0.5% glass fibers were incorporated as additives, while a combination of sodium hydroxide and sodium silicate ($NaOH/Na_2SiO_3$ = 1:2) served as the alkali activator at activator-to-binder ratios of 0.35–0.45. The mortars were evaluated for fresh, mechanical, durability, and microstructural properties. The results showed that the combined use of ferrochrome slag, marble powder, and glass fibers produced satisfactory performance, with the highest 28-day compressive strength of 21.09 MPa obtained for the mixture containing 10% marble powder at an activator-to-binder ratio of 0.35. The combined use of sodium hydroxide and sodium silicate was found to effectively enhance the binding performance of the alkali-activated mortar [5].

Bıçakcı investigated the durability performance of self-compacting concrete (SCC) containing limestone powder and fly ash as mineral admixtures. SCC mixtures were produced with constant cement and water contents while the mineral admixture content was varied, and their performance was compared with that of conventional concrete. Fresh properties and a comprehensive range of durability tests, including water absorption, chloride permeability, carbonation, electrical resistivity, freeze–thaw resistance, sulfate resistance, and water permeability, were evaluated. The results showed that increasing the mineral admixture content generally improved the durability of SCC. Fly ash mixtures exhibited superior durability compared with limestone powder mixtures in most tests, except for carbonation resistance.

Overall, SCC mixtures outperformed conventional concrete, demonstrating enhanced durability characteristics, particularly when fly ash was used as the mineral admixture [6].

Gülengül investigated the use of expanded glass as a partial replacement for natural sand in lightweight concrete at replacement levels of 0–20%. The effects of expanded glass on density, compressive strength, dynamic elastic modulus, thermal conductivity, and water absorption were evaluated. The results showed that increasing the expanded glass content reduced the density, compressive strength, elastic modulus, and thermal conductivity of the concrete, while maintaining the characteristics of structural lightweight concrete. The reduction in mechanical properties was attributed to the low density and strength of expanded glass aggregate. Nevertheless, the use of expanded glass provided significant benefits in terms of reducing structural dead load, improving thermal insulation, and promoting the recycling of waste glass, demonstrating its potential as a sustainable lightweight aggregate for concrete production [7].

Özdal investigated the effects of metakaolin, ground granulated blast furnace slag (GGBFS), and nano-sized TiO_2 on the mechanical properties of basalt aggregate concrete. Metakaolin and GGBFS were incorporated individually and in combination, while TiO_2 was used as a nano-filler. Compressive strength, flexural strength, and water absorption tests were conducted to evaluate concrete performance. The results indicated that the individual use of metakaolin or GGBFS provided better mechanical performance than their combined use. Furthermore, the incorporation of nano-TiO_2 enhanced the strength of the concrete, highlighting the potential of nano-materials to improve the performance of high-strength and durable cement-based composites [8].

Within the scope of this study, the use of powders obtained from the root and stalk parts of the hemp plant in cementitious composites was investigated. Hemp stalk and root materials were processed into powder and their potential use as binder or filler materials in cementitious composites was evaluated. In addition, the mechanical properties of the cementitious composites were investigated. Thus, the feasibility of using hemp-based products in cementitious composites in Türkiye was evaluated.

2 Material

CEM I 42.5 R type cement was used in the study. The chemical composition of the cement is presented in Table 1.

Table 1. Chemical composition of the cement.

Chemical composition	%
CaO	61.75
SiO_2	17.01
Al_2O_3	4.8
SO_3	3.75
Fe_2O_3	3.04
MgO	2.53
K_2O	1.23
Na_2O	0.249
LOI	4.86

In this study, crushed limestone sand with a particle size range of 0–5 mm, obtained from a crushed stone plant, was used. The specific gravity and water absorption of the limestone sand

were 2.6 and 1.95%, respectively. Polycarboxylate ether-based, high-range water-reducing/setting-accelerating superplasticizer (MasterGlenium 51) was used as a concrete admixture.

Hemp stalk and hemp root powders were used in mortar production. Within the scope of the study, two different gender of hemp plants, namely female and male plants, were used. Photographs of the hemp gender are presented in Figure 1.

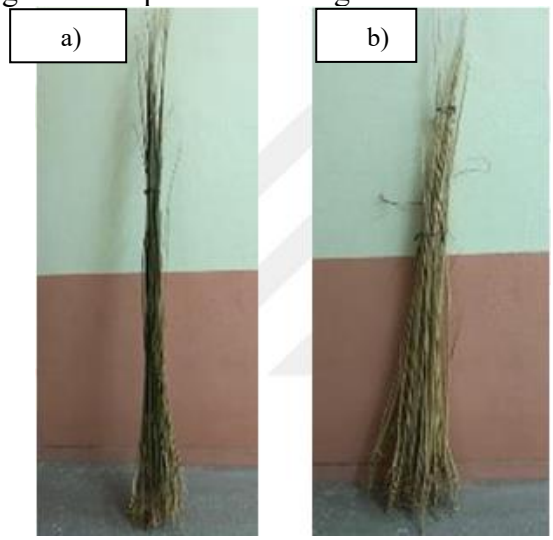


Fig. 1. a) Female hemp b) male hemp

The hemp stalk and hemp root were first cut into small pieces and subsequently ground into powder using a grinding machine. The powdered samples were sieved through a 0.063 mm sieve to obtain a fine particle size for the experimental study. The physical properties of the powdered samples are presented in Table 2.

Table 2. Physical Properties of the Hemp Powder Samples.

Hemp powder	Specific Gravity, kg/m^3	Water Absorption, %
Female root	1.43	242
Female stalk	1.02	225
Male root	1.15	258
Male stalk	0.96	276

Photograph of the hemp powder used in the study are shown in Figure 2.



Fig. 2. Hemp powder

Within the scope of the study, limestone sand mortars with water-to-cement (W/C) ratios of 0.3 and 0.7 were produced by replacing cement with hemp powder products at substitution rates of 1%, 3%, and 5%. The following examples are provided to explain the specimen designation used in the study.

DG3-1: A specimen in which female hemp stalk powder was substituted for cement at a rate of 1% in a mixture with a W/C ratio of 0.3.

EK7-3: A specimen in which male hemp root powder was substituted for cement at a rate of 3% in a mixture with a W/C ratio of 0.7.

The designations and quantities of the materials used in the study are presented in Table 3.

Table 3. Mortar mixture composition.

Specimen Code	Hemp Powder (g)	Cement (g)	Water (g)	Sand (g)	SP (g)
3K	-	450	135	1350	3.5
FR3-1	4.5	445.5			3.5
FR3-3	13.5	436.5			7
FR3-5	22.5	427.5			10
FS3-1	4.5	445.5			3.5
FS3-3	13.5	436.5			7
FS3-5	22.5	427.5			10
MR3-1	4.5	445.5			3.5
MR3-3	13.5	436.5			7
MR3-5	22.5	427.5			10
MS3-1	4.5	445.5			3.5
MS3-3	13.5	436.5			7
MS3-5	22.5	427.5			10
7K	-	450			-
FR7-1	4.5	445.5			-
FR7-3	13.5	436.5			-
FR7-5	22.5	427.5			-
FS7-1	4.5	445.5			-
FS7-3	13.5	436.5			-
FS7-5	22.5	427.5			-
MR7-1	4.5	445.5			-
MR7-3	13.5	436.5			-
MR7-5	22.5	427.5			-
MS7-1	4.5	445.5			-
MS7-3	13.5	436.5			-
MS7-5	22.5	427.5			-

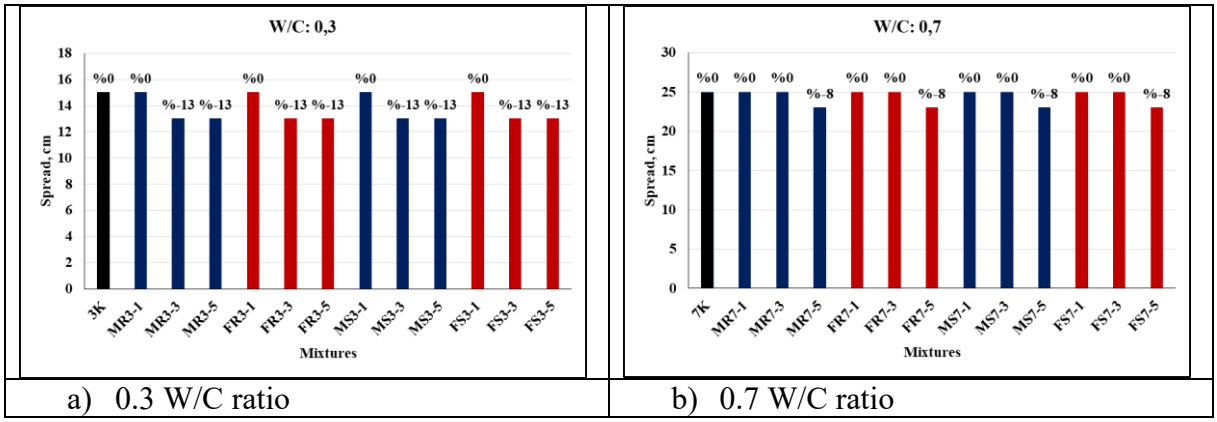
Within the scope of the study, a flow table test in accordance with TS EN 1015-3, a compressive strength test in accordance with TS EN 196-1, and flexural strength tests were

performed. Flexural strength tests were conducted on prismatic specimens with dimensions of 4 × 4 × 16 cm produced. The flexural strength tests were performed at a loading rate of 0.05 kN/s using three specimens from each mixture group. The test result was determined by taking the average of the results obtained from the three specimens.

Compressive strength tests were subsequently performed on the specimens obtained from the flexural strength tests. The compressive strength tests were conducted at a loading rate of 2.4 kN/s using a total of six specimens obtained by splitting the specimens into two pieces after the flexural strength test. The compressive strength was determined by taking the average of the results obtained from the six specimens.

3 Results

The graphs of the flow table test results are presented in Figure 3.



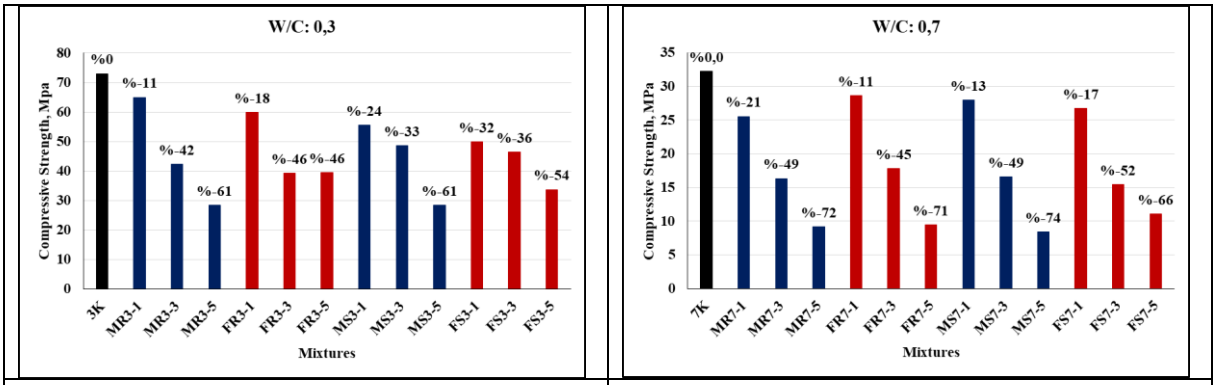
a) 0.3 W/C ratio b) 0.7 W/C ratio

Fig. 3. Spread test results.

For specimens with a W/C ratio of 0.3, the flow values of the mortars decreased as the volume of hemp powder increased. No significant difference was observed between the flow values of the reference specimen and those of the mixtures containing 1% hemp powder by volume. However, as the volume of hemp powder increased, a decrease in the flow values of the mixtures was observed. The results indicated that neither the female nor male hemp powder gender had a significant effect on the flow values. Similarly, no significant effect of hemp root or stalk powders on the flow values was observed. A chemical admixture was used to ensure adequate workability of the mixtures. The differences observed in the flow values are considered to be attributable to the use of the chemical admixture.

For specimens with a W/C ratio of 0.7, the flow values of the mixtures containing 5% hemp powder by volume decreased compared with the reference specimen. However, no change was observed in the flow values of the mixtures containing 1% and 3% hemp powder by volume. The results indicated that neither the female nor male hemp powder gender had a significant effect on the flow values. Similarly, no significant effect of hemp root or stalk powders on the flow values was observed.

The graphs of the compressive strength test results are presented in Figure 4.



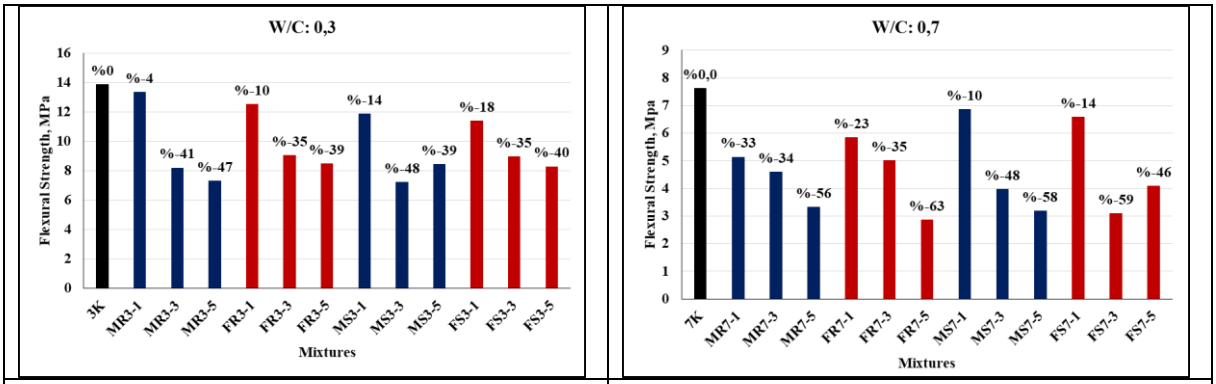
a) 0.3 W/C ratio b) 0.7 W/C ratio

Fig. 4. Compressive strength test results.

For specimens with a W/C ratio of 0.3, the compressive strength values of the mixtures decreased as the volume of hemp powder increased. The compressive strength of the reference specimen was determined to be 73 MPa. The lowest reduction in compressive strength, 11%, was observed for the mixture coded MR3-1. No significant difference was observed between mixtures containing female and male hemp powders in terms of compressive strength. Similarly, neither hemp stalk nor hemp root powders were found to have a significant effect on compressive strength.

For specimens with a W/C ratio of 0.7, a decrease in the compressive strength of the mixtures was observed as the volume of hemp powder increased. The compressive strength of the reference specimen was determined to be 32.2 MPa. The compressive strength values of the hemp powder-containing mixtures were lower than that of the reference specimen. The lowest reduction in compressive strength, 11.2%, was observed for the mixture coded FR7-1. No significant effect of female and male hemp powders on the compressive strength was observed. Similarly, neither hemp stalk nor hemp root powders were found to have a significant effect on compressive strength.

The graphs of the flexural strength test results are presented in Figure 5.



a) 0.3 W/C ratio b) 0.7 W/C ratio

Fig. 5. Flexural strength test results.

For specimens with a W/C ratio of 0.3, the flexural strength values of the mixtures decreased as the volume of hemp powder increased. The flexural strength of the reference specimen was determined to be 13.85 MPa. In the mixtures containing 3% and 5% hemp powder, the flexural strength values decreased significantly compared with the reference specimen. The greatest reduction, 48%, was observed for the mixture coded MS3-3. No significant effect of female and male hemp powder on the flexural strength was observed. Similarly, neither hemp stalk nor hemp root powders were found to have a significant effect on flexural strength.

For specimens with a W/C ratio of 0.7, the flexural strength values of the mixtures decreased as the volume of hemp powder increased. The flexural strength of the reference specimen was determined to be 7.63 MPa. The flexural strength values of the hemp powder-containing mixtures were lower than that of the reference specimen. The greatest reduction, 62.7%, was observed for the mixture coded FR7-5. No significant effect of female and male hemp powders on the flexural strength was observed. Similarly, neither hemp stalk nor hemp root powders were found to have a significant effect on flexural strength.

4 Conclusion

The results obtained from the study are presented below.

As the volume of hemp powder products in the cementitious composites increased, a decrease in the flow values was observed. The greatest reduction in flow value, 13.3%, was observed in the mixtures containing 3% and 5% hemp powder. This decrease is considered to be attributable to the high water absorption capacity of the hemp powder products, which adversely affected the flowability of the mixtures.

As the volume of hemp powder products in the cementitious composites increased, a decrease in compressive strength was observed. The greatest reduction in compressive strength, 74%, was obtained in the mixtures containing 5% hemp powder and having a high W/C ratio.

As the volume of hemp powder products in the cementitious composites increased, a decrease in flexural strength was observed. The greatest reduction in flexural strength, 62.7%, was obtained in the mixtures containing 5% hemp powder and having a high W/C ratio.

In conclusion, the results indicate that hemp powders are not suitable for use as a partial replacement for the binder in cementitious composites. However, hemp powders may be considered for use as a partial replacement for aggregate in future studies. In addition, further research is recommended to determine the long-term performance of cementitious composites containing hemp powder.

Acknowledgments
This study was supported by the Yozgat Bozok University Research Projects Unit under project code 6601a-FBE/20-372.

References

1. Kumaş, H. (2019). Bitkisel Atık Küllerinin Yapı Malzemesi Olarak Kullanılabilirliğinin Araştırılması. Yüksel Lisans Tezi. Tekirdağ Namık Kemal Üniversitesi Fen Bilimleri Enstitüsü. Tekirdağ.
2. Tuyan, M. (2017). Doğal ve Atık Malzemelerle Geopolimer Harç ve Beton Geliştirilmesi. Doktora Tezi, Ege Üniversitesi Fen Bilimleri Enstitüsü, İzmir.

3. Mahmood, R.A. (2020). Plastik Atıkların Harçlarda Lif Olarak Kullanılabilirliğinin Araştırılması. Yüksek Lisans Tezi. Akdeniz Üniversitesi Fen Bilimleri Enstitüsü, Antalya.
4. Malkoç, B. (2020). Doğal Vollastonitin Yüksek Performanslı Harç Üzerine Etkileri. Plastik Atıkların Harçlarda Lif Olarak Kullanılabilirliğinin Araştırılması. Yüksek Lisans Tezi. Niğde Ömer Halisdemir Üniversitesi Fen Bilimleri Enstitüsü, Antalya.
5. Mısır, M. N. (2021). Elazığ Ferrokrom Cürufu İle Alkali Aktive Edilmiş Cam Lifi ve Atık Mermer Tozu Katkılı Harçların Mühendislik Özelliklerinin Belirlenmesi. Yüksek Lisans Tezi. Fırat Üniversitesi Fen Bilimleri Enstitüsü. Elazığ.
6. Bıçakcı, S. N. (2019). İnce Malzeme Oranı ve Cinsinin 10 Mm İri Agregalı Kendiliğinden Yerleşen Betonların Durabilite Özelliklerine Etkisi. Yüksek Lisans Tezi. İstanbul Teknik Üniversitesi Fen Bilimleri Enstitüsü. İstanbul.
7. Gülengül, S. (2019). Genleştirilmiş Camın Hafif Beton Agregası Olarak Değerlendirilmesi. Yüksek Lisans Tezi. Fırat Üniversitesi Fen Bilimleri Enstitüsü. Elazığ.
8. Özdal, V. (2019). Karma Puzolanların Kullanıldığı Yüksek Performanslı Nano Beton Üretimi. Yüksek Lisans Tezi. Düzce Üniversitesi Fen Bilimleri Enstitüsü. Düzce.

Author Contribution Statement

- *Conceptualization:* Abdulrezzak Alkan, Yuşa Şahin
- *Methodology:* Abdulrezzak Alkan, Yuşa Şahin
- *Investigation:* Abdulrezzak Alkan
- *Writing – Original Draft:* Yunus Gündüz
- *Writing – Review & Editing:* Yunus Gündüz, Yuşa Şahin

Conflicts of Interest

The authors declare that there are no conflicts of interest.

Note: Following the conference, this Publication Note will be added to each paper; therefore, authors are kindly requested not to remove the note below and to complete the author(s) and paper title information.

Publication Note

This paper was peer-reviewed, accepted for presentation, and included in the proceedings of the ACE2026 – International Conference on Advances in Civil Engineering, held on 12–14 October 2026 in Trabzon, Türkiye.

This paper may be cited as follows:

Alkan, A., Gündüz, Y., and Şahin, Y., "Investigation of the Usability of Hemp Powders in Cementitious Composites," in Proceedings of the ACE2026 – International Conference on Advances in Civil Engineering, Trabzon, Türkiye, 12–14 October 2026.

Performance assessment of geopolymer mortar using industrial by-product components

Alara Girgin[1] , Mihriban Sarı[2], Kaan Aksoy[3] and Zeynep Başaran Bundur[4]
[1] 0009-0007-4265-5362, Özyeğin University, Civil Engineering Department, İstanbul, Türkiye
alara.girgin@ozu.edu.tr
[2] 0000-0001-6237-6538, Betek Boya ve Kimya Sanayii A.Ş. , Istanbul, Turkey
[3] 0000-0001-6830-5538, Betek Boya ve Kimya Sanayii A.Ş. , Istanbul, Turkey
[4] 0000-0003-1398-4021, Özyeğin University, Civil Engineering Department, İstanbul, Türkiye

Geopolymer concretes have been introduced as promising low-carbon alternatives to Ordinary Portland cement (OPC) due to their comparable mechanical performance and lower carbon dioxide (CO_2) emissions. However, the declining availability of conventional precursors such as fly ash and slag prompted the search for alternative materials. Stone wool kiln ash (SWKA), an industrial residue from mineral wool production, represents a potential alternative precursor due to its chemical similarity to traditional aluminosilicate materials. This study investigates the use of SWKA as a supplementary cementitious material in cement-based mixtures and as a substitute for ground granulated blast-furnace slag (GGBS) in geopolymer systems. Silica fume (SF) with a high content of amorphous silica was included in the mixture designs. Thus, cement was partially replaced with 30% SF, 30% SWKA, and 30% fly ash in cement-based mixtures. Geopolymer-based mixtures are composed of 60-100% GGBS, 0-10% SF, and 10-30% SWKA, and activated with sodium hydroxide (NaOH) at 15% by weight of the binder. Workability, setting time, compressive strength, and flexural strength tests were performed on fresh and hardened samples at 7 and 28 days. X-ray diffraction (XRD) was used to investigate the material characteristics. Results from cement-based mixtures indicated that SWKA exhibited pozzolanic activity. In geopolymer systems, 80% GGBS + 10% SF + 10% SWKA achieved the highest compressive strength (47.4 MPa) in 28 days, 18% higher than the 100% cement control mixture and 25% higher than 100% GGBS. SWKA content above the optimum level adversely affected the strength development.
Keywords: Geopolymer concrete, cement, silica fume, NaOH, stone wool kiln ash

1 Introduction

The continuous increase in CO_2 emissions has led to deteriorating environmental conditions and has significantly contributed to climate change by intensifying the greenhouse effect. Cement production accounts for about 7% of global CO_2 emissions [1], primarily due to clinker manufacturing and the calcination of limestone. Growing cities have led to the estimate that civil and architectural works would double, requiring a 25% increase in ordinary Portland cement (OPC) production by the 2030s [2]. Therefore, researchers have begun investigating sustainable, low-carbon construction materials, and geopolymers have emerged as a promising alternative.

Geopolymers utilize industrial by-products such as GGBS [3-5], silica fume [4-6], and fly ash [3-6], and may provide mechanical performance and durability comparable to that of ordinary cement. They are inorganic aluminosilicate materials from alumina- and silica-rich precursors activated by alkaline activators. Geopolymerization consists of three main stages: dissolution, reorientation, and finally polycondensation. Polycondensation leads to gel

formation (N-A-S-H, C-A-S-H) from dissolved species, resulting in a three-dimensional aluminosilicate network that depends on the precursor composition.

GGBS is one of the most widely used precursors in alkali-activated systems. Its high calcium content promotes the formation of dense reaction products due to its rapid reactivity under alkaline conditions, resulting in early strength development. However, primary steel production is gradually declining, and the increasing demand for GGBS has raised concerns regarding cost and long-term availability [7-8]. Thus, researchers have partially focused on alternative industrial by-products as supplementary materials to replace GGBS and maintain sustainable production in the future.

The large volume of stone wool waste requires proper storage; if stored in open areas, it may pollute the air, groundwater, soil, and plants. Stone wool kiln ash (SWKA) is a silica-rich by-product of stone wool insulation production [9]. Pavlin et al. [10] reported that the pozzolanic reactivity of mineral wool residues depends on their chemical composition, amorphous phase content, particle size distribution, and curing conditions. On the other hand, supplementary silica is used to enhance geopolymerization reactions. Silica fume (SF), a by-product of the production of silicon metal or ferrosilicon alloys, consists of almost amorphous silica. Earlier studies [4-6] reported that the high reactivity and extremely fine particle size of SF result in matrix densification, reduced porosity, and enhanced mechanical properties in alkali-activated binders.

Despite growing interest in alternative aluminosilicate precursors, the feasibility of using SWKA as a partial replacement for GGBS in geopolymer systems has not yet been systematically investigated. This study examines the fresh and mechanical properties of geopolymer-based mortars using GGBS as the primary binder, with SF replacing GGBS and varying levels of SWKA. The incorporation of SWKA was investigated with respect to workability, initial setting, flexural strength, and compressive strength. Geopolymer-based specimens were compared with cementitious mixtures to comprehend the feasibility of using SWKA as an alternative precursor to OPC.

2 Materials and Methods

2.1 Materials

In this study, two binder systems were investigated: OPC (CEM I) based mortars and alkali-activated geopolymer mortars. CEM I 42.5 R was selected for the cement-based mixtures, and GGBS served as the main precursor in geopolymer mixtures**.** SWKA was incorporated at different GGBS replacement levels. SF and SWKA were included as supplementary materials in both cement-based and geopolymer mortars. In addition, Class F fly ash (FA) was introduced as an additional series in the cement-based mixtures. NaOH pearls with 99% purity were used as the alkaline activator. Standard CEN sand conforming to TS EN196 was used as the fine aggregate in all the mixtures. The sand-to-binder ratio was kept constant. A polycarboxylate ether-based superplasticizer, Sika Visco Crete PC-61, was added to selected geopolymer mixtures to improve workability. For simplicity, Portland cement, GGBS, and SWKA will be abbreviated as C, G, and WA in the following mixture designs.

The mineralogical composition of the raw materials was determined by X-ray diffraction analysis and is presented in Figure 1. Fly ash exhibited crystalline phases corresponding to quartz (Q), mullite (M), hematite (H), and magnetite (Mag), as well as an amorphous aluminosilicate phase that contributes to long-term strength through pozzolanic activity. GGBS showed an amorphous hump at 20 $^{\circ}$-35 $^{\circ}$ 2θ, indicating a predominantly glassy structure. Alkaline activation of GGBS indicates high reactivity due to the presence of the amorphous

calcium aluminosilicate phase. The high amorphous content from calcium aluminosilicate indicated a potential for alkali activation. The XRD pattern of silica fume shows a broad, diffuse peak associated with amorphous SiO_2, confirming its amorphous nature. The absence of crystalline phases suggests high silica reactivity, which can promote matrix densification through pozzolanic activity and the filler effect. On the other hand, SWKA exhibited both crystalline and amorphous characteristics of calcium-magnesium aluminosilicate minerals; the main crystalline phases identified were gehlenite (G), akermanite (A), and merwinite (Me). The presence of calcium- and aluminosilicate-bearing phases suggests that SWKA may undergo partial dissolution, releasing Ca, Si, and Al species that actively contribute to alkaline reactions [11-12].

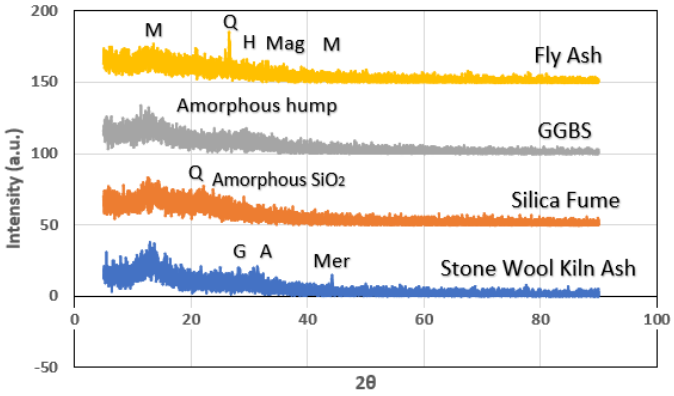


Fig. 1 XRD results of binding materials (M= Mullite, Q= Quartz, H= Hematite, Mag= Magnetite, G= Gehlenite, A= Akermenite, Mer= Merwinite)

2.2 Mix Proportions

Four cement-based mortars were produced: a control OPC mortar, and three mixtures in which 30% of OPC (135 g) was individually replaced by SF, SWKA, and FA, e.g., 70% C + 30% SF, 70%C+30% WA, 70%C+30%FA. The total binder was kept constant at 450 g, with a water-to-binder ratio (*w/b*) of 0.50 and a sand content of 1350 g. Superplasticizer (6 g) was used to improve workability only in 30%SF and 30%SWKA replacements.

For the geopolymer-based mortars, the total binding material was also kept constant at 450 g. GGBS was used as the main precursor and was activated using a 7 M NaOH solution prepared with 67.5 g NaOH and 225 g water, together with 1350 g of sand. GP_100%G, which is composed of 450 g of GGBS, was prepared as a control geopolymer mixture. For the other four mixes (GP_90%G+10%SF, 80%G+10%SF+10%WA, 70%G+10%SF+20%WA, 60%G+10%SF+30%WA), GGBS was progressively replaced by SWKA while keeping the SF content constant at 45 g. The dosage of the superplasticizer varied with the mixture composition. No superplasticizer was added to the control sample. 4.5 g of superplasticizer was used in GP_90%G+10%SF to improve the workability. 10 g of superplasticizer was incorporated into the other three geopolymer mixtures due to declining workability.

Table 1 Cement-based and geopolymer-based mixtures

Mixtures	Binding materials	Portland cement (OPC)	Ground gran. blast furnace slag (GGBS)	Silica fume	Stone wool kiln ash (SWKA)	Fly ash
		C	G	SF	WA	FA
Cement-based mixtures						
70%C+30%SF		315 g		135 g		
70%C+30%WA		315 g			135 g	
70%C+30%FA		315 g				135 g
Geopolymer mixtures						
GP_100%G	450 g		450 g			
GP_90%G+10%SF			405 g	45 g		
GP_80%G+10%SF+10%WA			360 g	45 g	45 g	
GP_70%G+10%SF+20%WA			315 g	45 g	90 g	
GP_60%G+10%SF+30%WA			270 g	45 g	135 g	

2.3 Mixing Procedure

The cement-based mortars were prepared in accordance with ASTM C305. The binding materials were first dry-mixed at low speed (140 rpm) for 30 s. Water was then added, and the mixture was mixed for an additional 30 s at low speed and 30 s at high speed (240 rpm). Afterward, the mixing bowl was taken out and scraped for 90 s. The mortar was then mixed again at a higher speed for 60 s.

The geopolymer-based mortars were first dry mixed at low speed for 30 s. When needed, the superplasticizer was dissolved in the mixing water. NaOH pearls were dissolved in water to ensure complete dissolution before being added to the dry precursor mixture, and the mixture was mixed for 30 s after the addition. Standard CEN sand was gradually added, and the mixture was mixed until a homogeneous mortar was obtained.

2.4 Test Methods

Workability was evaluated using a flow table in accordance with ASTM C1437. The setting behavior was assessed using a Vicat apparatus, and the initial setting time was determined by needle penetration. The tests were conducted at ambient conditions.

Fresh mortar mixtures were cast into molds and compacted to minimize the entrapped air. The specimens were cured at 30 ºC and 50% RH until testing at 7 and 28 days. Mechanical performance was evaluated using compressive strength tests on an electromechanical universal hydraulic testing machine (UTEST Material Testing equipment, Turkey). The flexural strength was determined by a three-point bending test.

3 Results and Discussion

3.1 Workability of designed geopolymer mortars

In the geopolymer-based series, as SWKA content increased, flowability decreased (Figure 2). Replacing GGBS's glassy morphology with SWKA, which has surface roughness and an angular particle shape, ultimately increased internal friction and water demand. SF addition also reduced the availability of free water due to its ultrafine particle size. The flow diameter of the cement-based samples ranged from 16.25 to 18.25 cm. The addition of FA yielded the highest value at 18.25 cm due to its spherical morphology and reduced internal friction [13].

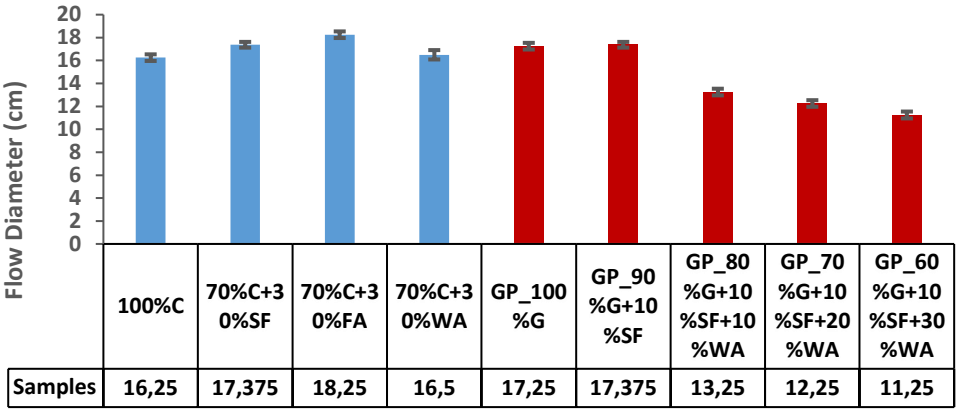


Fig. 2 Workability of mixtures (C=Cement, SF=Silica fume, WA=SWKA,Stone wool kiln ash, G=GGBS)

3.2 Initial setting time of geopolymer binders

The initial setting times of the cement and geopolymer-based pastes are presented in Figure 3. The cement-based pastes had significantly longer set times (470 min to 1425 min) than the geopolymer-based pastes (15 min to 60 min) due to differences in cement hydration and alkali activation. The 70%C+30%SF sample exhibited a longer setting time than the control 100%C. This phenomenon is attributed to the higher quantity of SF than of $Ca(OH)_2$, namely CH or portlandite, which binds to form C-S-H gel. Thus, SF acts as a filler rather than a chemical binder in the early hours. In the geopolymer-based series, there is rapid dissolution of Si-O-Si bonds due to a high-pH activator and the amorphous nature of SF, which has ultrafine particles. This behavior is likely due to SF combining with dissolved calcium and aluminum from the slag, thereby promoting the formation of C-A-S-H and N-A-S-H gels [14]. FA and SWKA prolonged the initial setting due to their relatively lower early-age reactivity compared to Portland cement. Based on XRD analysis, SWKA contains gehlenite, akermanite, and merwinite, whose relatively slow dissolution rates may contribute to delayed early-age reactions. Their slower dissolution may restrict the availability of Ca, Si, and Al at early ages, thereby limiting reaction product formation and delaying the densification of the reaction matrix [12]. In addition, an increasing amount of SWKA extended the initial setting time (27 to 60 min) due to the reduction in the highly reactive, amorphous GGBS.

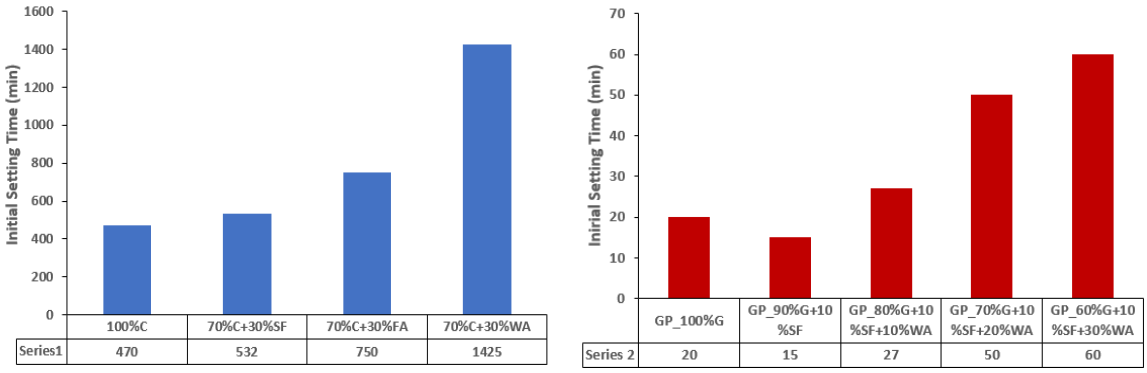
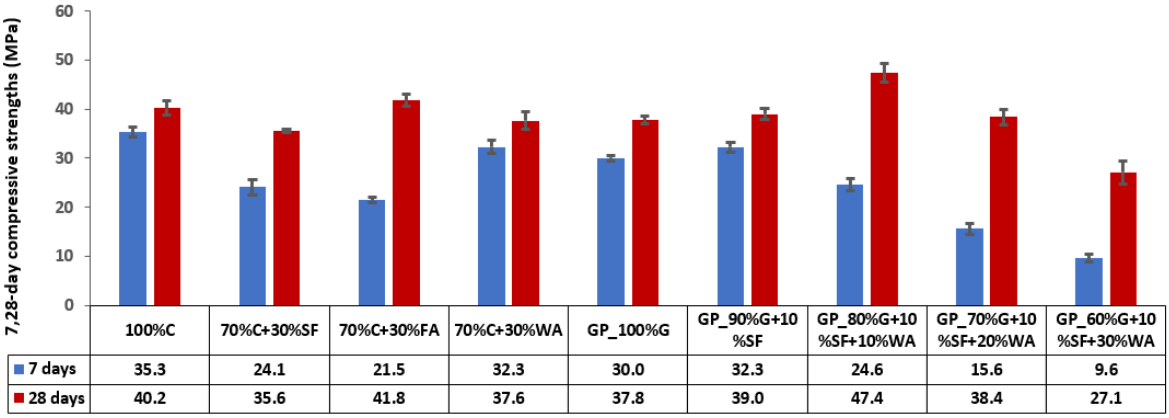


Fig. 3 Initial setting time of (a) cement-based pastes (b) geopolymer-based pastes

3.3 Compressive Strength

The highest 7-day compressive strength among the cement-based series was achieved for the 100%C, reaching 35.3 MPa due to its rapid hydration. The incorporation of supplementary materials reduced the 7-day strengths to 24.1 MPa, 21.5 MPa, and 32.3 MPa for 70%C+30%SF, 70%C+30%FA, and 70%C+30%WA, respectively. The strength reduction in the 30% SF mixture can be attributed to the high replacement level. Several studies [15-16] reported the optimal SF replacement range to be 10-22%. They noted a negative effect of higher replacement levels due to reduced cement content and a lack of CH to bind in the early-age period. Lower workability of the 70%C+30%SF mixture resulted in compaction problems that might have decreased compressive strength as well. These align with Khoso et al. [16], who noted a gradual decline in both strength and workability beyond 10% SF; in their study, the 7-day strength with a 30% SF replacement dropped by 52.9% compared to 100%C. A 30% FA incorporation had the lowest compressive strength (21.5 MPa). FA exhibits slow early-age pozzolanic reactivity and subsequently reacts with CH to form additional C-S-H gel. A higher compressive strength than that of the SF and FA mixtures was achieved with 30% SWKA (32.3 MPa). Early-age compressive strength suggests that SWKA may have enhanced the hydration process through filler and nucleation effects, likely promoting early hydration and improving particle packing.

For geopolymer samples, the highest 7-day compressive strength (32.2 MPa) was achieved with GP_90%G+10%SF. The incorporation of 10% SF slightly increased the compressive strength compared to GP_100%G (30 MPa). The filler effect of SF, due to its ultrafine particles, promoted the formation of a denser matrix. As SWKA replacement levels increased, early-age strengths gradually decreased with 10%SF+10%WA (24.6 MPa), 10%SF+20%WA (15.6 MPa), and 10%SF+30%WA (9.6 MPa). This reduction in strength might have been related to the lower reactivity of SWKA compared with GGBS, resulting in slower aluminosilicate dissolution and thus reduced formation of geopolymer gels. As the replacement levels of SWKA increase, the reduced availability of calcium due to lower GGBS content leads to a less dense microstructure, thereby lowering compressive strength.



	100%C	70%C+30%SF	70%C+30%FA	70%C+30%WA	GP_100%G	GP_90%G+10%SF	GP_80%G+10%SF+10%WA	GP_70%G+10%SF+20%WA	GP_60%G+10%SF+30%WA
7 days	35.3	24.1	21.5	32.3	30.0	32.3	24.6	15.6	9.6
28 days	40.2	35.6	41.8	37.6	37.8	39.0	47.4	38.4	27.1

Fig. 4 7, 28-day compressive strengths in cement-based and geopolymer-based mortar (C=Cement, SF=Silica fume, WA=SWKA, Stone wool kiln ash, G=GGBS)

Regarding the 28-day compressive strength, 30% SF yielded 35.6 MPa, a 47.7% increase. The difference between the 7-day and 28-day might be due to SF not reacting on its own and instead consuming CH from cement hydration to form C-S-H gels. At an early age, a 30% SF mixture may not have fully reacted until sufficient CH had accumulated. The 30% FA mixture, with the lowest strength (21.5 MPa) at 7 days, achieved the highest strength (41.8 MPa) at 28 days, with a 94.4% increment. FA reacts slowly at an early age, and continuous pozzolanic reactions with CH refine the pore structure and create C-S-H gels. 30% SWKA mixture reached

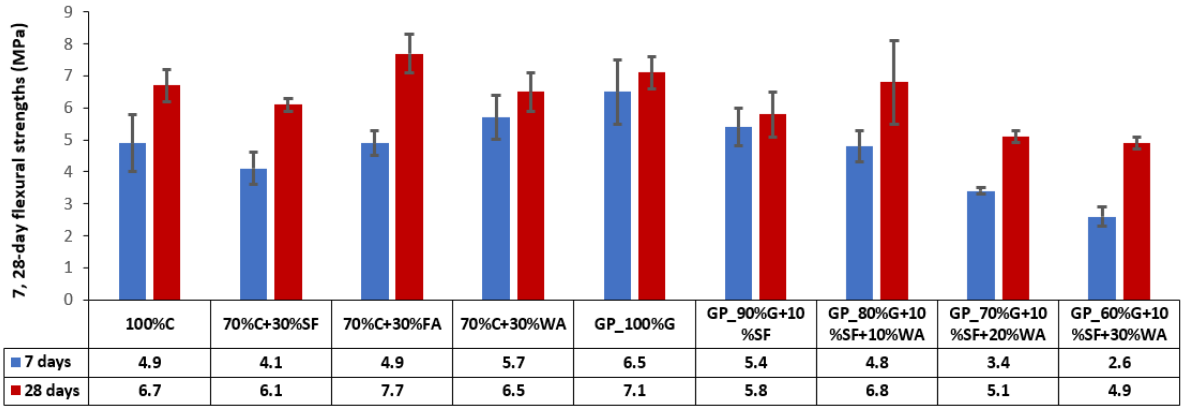
37.6 MPa at 28 days, with only a 16.4% increase after 7 days. The results of 30% SWKA indicate that it is a promising supplementary cementitious material for partial replacement of cement to achieve satisfactory mechanical performance.

The geopolymer-based control sample (GP_100%G) exhibited a 26.0% increase in compressive strength from the 7th day to the 28th day. GP_90%G+10%SF increased strength by 21% (39 MPa) due to ongoing geopolymerization and additional reaction products from the SF content. 80% GGBS with 10% SF and 10% SWKA attained the highest compressive strength (47.4 MPa). An optimized level of SWKA is likely associated with better particle packing while also providing an additional source of aluminosilicates. The effect of SWKA is strongly dependent on its replacement level. 10% SWKA was beneficial to later-age strength; the higher replacement levels could not compensate for the reduction in GGBS content. 20% SWKA reduced strength compared to 10% SWKA; however, the increment in 28-day strength relative to 7-day strength was 146.2%. 30% SWKA showed the highest relative strength gain, increasing from 9.6 to 27.1 MPa (+182.3%) between 7 and 28 days; however, the 28-day strength remained the lowest in comparison to the other geopolymer mixtures. This situation explains further that even though SWKA exhibited considerable later-age strength development, its excessive SWKA replacement limited the overall mechanical performance. Late reaction can also be correlated with phases such as akermanite, gehlenite, and merwinite, which possess high chemical stability and resist early rapid reactions [12], a trend that also correlates with Vicat test results.

3.4 Flexural Strength

For the 7-day early strength in cement-based mortars, the highest flexural strength was observed in 70% C + 30% SWKA at 5.7 MPa, followed by 100% C and 70% C + 30% FA at 4.9 MPa; 30% SF incorporation exhibited the lowest value (4.1 MPa) (Figure 5). 30% SF exceeds the optimum range by reducing the amount of cement available for early hydration. Lower workability and higher water demand due to the surface area of SF also negatively affected early-age flexural strength. 30% FA replacement achieved performance similar to 100% C; incorporating FA did not adversely affect early-age flexural strength, although the FA mixture exhibited better long-term strength due to its pozzolanic reaction. The highest strength (5.7 MPa) was observed in the 30% SWKA sample, exceeding 100%C by 16%. SWKA positively affected the early-age flexural strength in the cement-based series.

In the 7-day geopolymer series, the highest strength (6.5 MPa) was achieved in the 100% G control sample, with a gradual decline in the early strengths of the other mixtures. This phenomenon can be attributed to alkali-activated GGBS reacting rapidly and promoting the formation of calcium-aluminosilicate hydrates (C-A-S-H), thereby making the matrix cohesive and indicating superior performance at early ages. On the contrary, decreasing strength in 90%G+10%SF may be attributed to less calcium content and changes in reaction product chemistry, as silica fume modifies the silicate structures of C-S-H and aluminosilicate gels [17]. SF's fine particles and high specific surface area may increase the demand for alkaline activator liquid, thus reducing the water available to dissolve slag particles at early ages. The mixtures with 10%, 20%, and 30% SWKA undergo a slow alkaline dissolution due to their high crystalline stability. When GGBS is partially replaced by less reactive SWKA, the reduced GGBS may decrease the availability of calcium, aluminum, and silicon ions at early ages [18].



	100%C	70%C+30%SF	70%C+30%FA	70%C+30%WA	GP_100%G	GP_90%G+10 %SF	GP_80%G+10 %SF+10%WA	GP_70%G+10 %SF+20%WA	GP_60%G+10 %SF+30%WA
7 days	4.9	4.1	4.9	5.7	6.5	5.4	4.8	3.4	2.6
28 days	6.7	6.1	7.7	6.5	7.1	5.8	6.8	5.1	4.9

Fig. 5 7, 28-day flexural strengths in cement-based and geopolymer-based mortar

Regarding the 28-day cement-based series, the highest flexural strength (7.7 MPa) was achieved with a 30% FA replacement (a 57.1% increase compared to 7 days). The 30% SWKA mixture reached 6.5 MPa, exceeding the 30% SF mixture (6.1 MPa). At longer durations, hydraulic and pozzolanic reactivity increase its strength. However, compared with the FA mixture, SWKA's increase was moderate over the 28 days.

For the geopolymer-based series, the highest flexural strength (7.1 MPa) was attained in 100%G control samples; however, the strength gain (9.2%) was minimal. The highest flexural increment (50%) was observed in 10%SF+20%WA, following 10%SF+10%WA (41.7%) replacements. These results indicate that both FA and SWKA react mainly at a late age.

4 Conclusions

In this study, SWKA was investigated as an alternative aluminosilicate precursor in cement-based and alkali-activated geopolymers. The effects of replacing GGBS with SWKA in the presence of SF were evaluated for fresh properties, setting behavior, and mechanical performance in cement-based and alkali-activated geopolymers.

- In the cement-based series, 30% FA replacement achieved the highest compressive strength (41.8 MPa) at 28 days, exceeding the 100%C control (40.2 MPa). Pozzolanic reaction and filler effect of fly ash were observed at longer curing durations, which promoted a denser microstructure.
- The 70%C+30%SF sample exhibited a slightly lower compressive strength (35.6 MPa) than 100C, due to reduced workability and increased water demand from ultra-fine silica fume particles.
- An 80% GGBS + 10% SF + 10% SWKA mixture yielded the highest compressive strength (47.4 MPa) at 28 days. Compared to the 100% GGBS control sample, the 25% higher strength indicated a beneficial effect of optimal SWKA incorporation.
- 30% SWKA replacement for the geopolymer series adversely affected the mechanical characteristics. This suggests an excessive amount of SWKA, limiting the available calcium phases from GGBS and gel formation.
- The highest flexural strength (7.1 MPa) was achieved with the 100% GGBS control mixture. 10% SF + 10% SWKA replacement achieved the second-best performance, reaching 6.8 MPa at 28 days.

The results show that SWKA can be incorporated into GGBS-based geopolymers at optimal replacement levels. Using SWKA, this utilization of waste-derived by-products can reduce dependence on OPC while supporting sustainable, low-carbon construction materials. Further durability and microstructural investigations (e.g., SEM, pore-structure analysis) are

recommended to confirm the reaction mechanisms proposed here, based on the XRD and mechanical test results.

ACKNOWLEDGEMENTS

This research was conducted with financial assistance from the Scientific and Technical Research Council (TÜBİTAK) of Turkey, Project: N-UPAG-224N740. The authors would like to thank Dr. Shaghayegh Benam for their valuable assistance and support during the experimental work of this project.

REFERENCES

1. Ige, O.E., Kabeya, M.: Decarbonizing the cement industry: Technological, economic, and policy barriers to CO2 mitigation adoption. Clean Technologies **7**(4), 85 (2025). DOI: 10.3390/cleantechnol7040085.
2. BBC: Climate change: The massive CO2 emitter you may not know about. BBC News, https://www.bbc.com/news/science-environment-46455844, last accessed 2026/08/10.
3. Mohammed, T.O., Ul Haq, A., Harun, M.Z.B., Fanijo, E.O.: Recent advances in fly ash- and slag-based geopolymer cements. Sustainability 17(24), 11167 (2025). DOI: 10.3390/su172411167.
4. Wang, S., Liang, Y., Mo, D., Zhang, C., Xue, J., Song, X., Wang, Y.: Doping silica fume enhances the mechanical strength of slag/fly ash geopolymer paste under frost attack. Minerals 13(7), 925 (2023). DOI: 10.3390/min13070925.
5. Singh, R.P., Vanapalli, K.R., Jadda, K., Mohanty, B.: Durability assessment of fly ash, GGBS, and silica fume-based geopolymer concrete with recycled aggregates against acid and sulfate attack. Journal of Building Engineering 82, 108354 (2024). DOI: 10.1016/j.jobe.2023.108354.
6. Okoye, F.N., Durgaprasad, J., Singh, N.B.: Effect of silica fume on the mechanical properties of fly ash based-geopolymer concrete. Ceramics International 42(2), 3000–3006 (2016). DOI: 10.1016/j.ceramint.2015.10.084.
7. Millward-Hopkins, J., Zwirner, O., Purnell, P., Velis, C.A., Iacovidou, E., Brown, A.: Resource recovery and low carbon transitions: The hidden impacts of substituting cement with imported ‘waste’ materials from coal and steel production. Global Environmental Change 53, 146–156 (2018). DOI: 10.1016/j.gloenvcha.2018.09.003.
8. Whittle, J.W., Rihner, M.C.S., Hafez, H., Eufrasio Espinosa, R.M., Fletcher, D.I., Walkley, B., Koh, L.S.C.: From symbiosis to scarcity: Evaluating disruption associated with decarbonisation to circular waste materials between the UK cement and steel sectors. Resources, Conservation & Recycling 224, 108560 (2026). DOI: 10.1016/j.resconrec.2025.108560.
9. Aydın, T., Başaran Bundur, Z., Aksoy, K., Karabıyık, B., Perin, E., İnce, T., Sarı, M.: Utilization of stone wool kiln ash in cement-based materials. Materials Proceedings 15, 89 (2024). DOI: 10.3390/materproc2023015089.
10. Pavlin, M., Horvat, B., Frankovič, A., Ducman, V.: Mechanical, microstructural and mineralogical evaluation of alkali-activated waste glass and stone wool. Ceramics International 47(11), 15102–15113 (2021). DOI: 10.1016/j.ceramint.2021.02.068.

11. Kriskova, L., Pontikes, Y., Cizer, Ö., Van Balen, K., Jones, P.T., Blanpain, B.: Alkali activation of γ-dicalcium silicate and merwinite. In: Proceedings of the 3rd International Slag Valorisation Symposium, *pp. 323–326. Leuven, Belgium (2013).*
12. Engström, F., Adolfsson, D., Samuelsson, C., Sandström, Å., Björkman, B.: A study of the solubility of pure slag minerals. Minerals Engineering 41, 46–52 (2013). DOI: 10.1016/j.mineng.2012.10.004.
13. Kizilkanat, A.B., Oktay, D., Kabay, N., Tufekci, M.M.: Comparative experimental study of mortars incorporating pumice powder or fly ash. Journal of Materials in Civil Engineering 28(2), 04015119 (2016). DOI: 10.1061/(ASCE)MT.1943-5533.0001407.
14. Du, W., Ni, L., Lv, Y., Zheng, D., Tang, W., Cui, H.: Role of silica fume in the hydration evolution of fly ash-slag-based geopolymers. Construction and Building Materials 451, 138879 (2024). DOI: 10.1016/j.conbuildmat.2024.138879.
15. Uddin, M.A., Bashir, M.T., Khan, A.M., Alsharari, F., Farid, F., Alrowais, R.: Effect of silica fume on compressive strength and water absorption of the Portland cement–silica fume blended mortar. Arabian Journal for Science and Engineering 49(4), 4803–4811 (2024). DOI: 10.1007/s13369-023-08204-x.
16. Khoso, S., Khan, J.S., Ansari, A.A., Khaskheli, Z.H.: Experimental investigation on the properties of cement concrete partially replaced by silica fume and fly ash. Journal of Applied Engineering Science 14(3), 345–350 (2016). DOI: 10.5937/jaes14-11116.
17. Lee, N.K., An, G.H., Koh, K.T., Ryu, G.S.: Improved reactivity of fly ash–slag geopolymer by the addition of silica fume. Advances in Materials Science and Engineering 2016, Article ID 2192053 (2016). DOI: 10.1155/2016/2192053.
18. Mohamed, O.A.: A review of durability and strength characteristics of alkali-activated slag concrete. Materials 12(8), 1198 (2019). DOI: 10.3390/ma12081198.

Author Contribution Statement

- *Conceptualization & Supervision:* Zeynep Başaran Bundur & Kaan Aksoy
- *Methodology:* Zeynep Başaran Bundur, Alara Girgin, Mihriban Sarı
- *Investigation:* Alara Girgin
- *Writing – Original Draft:* Alara Girgin
- *Writing – Review & Editing:* Zeynep Başaran Bundur, Alara Girgin

Note: Following the conference, this Publication Note will be added to each paper; therefore, authors are kindly requested not to remove the note below and to complete the author(s) and paper title information.

Publication Note

This paper was peer-reviewed, accepted for presentation, and included in the proceedings of the ACE2026 – International Conference on Advances in Civil Engineering, held on 12–14 October 2026 in Trabzon, Türkiye.

This paper may be cited as follows:

Girgin A., Sarı M., Aksoy K., Başaran Bundur Z.,
"Performance assessment of geopolymer mortar using industrial by-product components,"
in Proceedings of the ACE2026 – International Conference on Advances in Civil Engineering, Trabzon, Türkiye, 12–14 October 2026.

Use of Recycled Concrete Powders as Supplementary Cementitious Materials in Mortar Mixtures

Kadircan Varan[1], Ünal Anıl Doğan[1], Aleyna Dinçer[1], Ayşegül Koyunlular[1], Beyza Uslu[1], Kağan Sevinç[1], Tarık İlyas Özyurt[1], Tuba Gündoğdu[1], İsmail Gökalp[2]

[1] 0009-0004-9367-7869, Istanbul Technical University, Civil Engineering Department, Istanbul, Türkiye, varank19@itu.edu.tr
[1] 0000-0002-7819-5552, Istanbul Technical University, Civil Engineering Department, Istanbul, Türkiye, doganunal@itu.edu.tr
[1] 0009-0007-7095-1935, Istanbul Technical University, Civil Engineering Department, Istanbul, Türkiye, dincera21@itu.edu.tr
[1] 0009-0008-2870-4567, Istanbul Technical University, Civil Engineering Department, Istanbul, Türkiye, koyunlular20@itu.edu.tr
[1] 0009-0004-1409-0681, Istanbul Technical University, Civil Engineering Department, Istanbul, Türkiye, uslu22@itu.edu.tr
[1] 0009-0008-9241-3625, Istanbul Technical University, Civil Engineering Department, Istanbul, Türkiye, sevinc21@itu.edu.tr
[1] 0009-0005-9694-6435, Istanbul Technical University, Civil Engineering Department, Istanbul, Türkiye, ozyurtt22@itu.edu.tr
[1] 0009-0001-4210-3986, Istanbul Technical University, Civil Engineering Department, Istanbul, Türkiye, gundogdu20@itu.edu.tr
[2] 0009-0000-6661-8928, Akcansa Cement Industry and Trade Inc., Buyukcekmece, Istanbul, Türkiye, ismail.gokalp@akcansa.com.tr

Abstract. This study investigates the use of recycled concrete powders as a cement substitute in mortar. The effect of using fly ash in combination with recycled concrete powders (RCP) in concrete powder mixtures was also examined. Four different RCPs with varying compositions were used in the study; three were prepared in the laboratory, while one was obtained from actual concrete. Crushed sand was incorporated at volumetric ratios of 0% (ARCP), 20% (ARCF20), and 40% (ARCF40) into the laboratory-prepared artificial concrete waste whilst the aggregate content of the actual concrete waste powder (RCF) was unknown. The materials produced in the laboratory were milled after ninety days of curing. For comparison, reference mortar containing CEM I, CEM II mortar, and mixtures with fly ash replacing 20% cement were prepared. The specific gravity and blaine fineness of RCPs varied from 2.3 to 2.57 g/cm³ and from 4300 to 4750 cm²/g, respectively. A total of 12 mixtures were prepared according to ASTM C311. In fresh state, unit weight and flow tests; and in the hardened state, 2, 7, and 28 days compressive and flexural tests were applied. Based on the results, it can be concluded that mixtures containing recycled concrete powder when used alone, increase the water demand, therefore their use in combination with fly ash is appropriate. Compressive strength activity of 20FA, 10ARCF2010FA, 10ARCF4010FA and 10RCF10FA mixtures provided 75% that of the reference mixture and can be used as pozzolan in concrete applications.

Keywords: Recycled concrete powder; cement replacement; strength activity index; alternative cementitious materials.

1 Introduction

The production of Portland cement is closely related to both natural resource consumption and carbon dioxide emissions. Consequently, the use of supplementary cementitious materials (SCMs) or alternative mineral admixtures that can substitute for cement offers the possibility of directly reducing the clinker ratio. The development of cement-based materials has also become an important element for more sustainable cement production. However, the availability of SCMs can vary depending on the source and production processes. This situation increases the need for studies related to the search for SCMs. Construction and demolition waste (CDW) constitutes a potential secondary resource for the cement and construction industries. Concrete waste contains both mineral aggregates and cementitious phases. By processing this waste and incorporating it into cement production, it is possible to produce fine materials containing hydrated cement paste. These fine materials are generally referred to as recycled concrete dust. Studies in the literature have shown the potential for recovering and using fractions containing hydrated cement recovered from demolished concrete [1-4]. The use of such materials is consistent with a circular approach because it involves recovering material from concrete waste and reintroducing it into the production chain [5]

Despite this potential, the behavior of using recycled concrete powder in place of cement is largely dependent on the material's composition and processing history. RCP may contain hydrated cement paste and fine aggregate. Composition dependent differences can affect its physical, chemical and mineralogical properties. This different aggregate content provides the opportunity to provide insight into the effect of the concrete powder source and composition. Previous research has highlighted the importance of determining and characterizing the composition to understand the effect of using recycled concrete powders in cement-based materials on performance [6-8].

The substitution of recycled concrete powders for cement in the mortar phase can affect fresh state and mechanical properties. Recycled concrete powders differ from Portland cement in terms of fineness, specific gravity and surface properties. Therefore, the water demands necessary to achieve a certain workability may vary. Changes in water demands can affect the pore structure and mechanical performance in the hardened state. Furthermore, the reduction in clinker content due to the hydrated phases and aggregate content in the material substituted for Portland cement will cause a decrease in the amount of clinker. Therefore, reductions in strength may occur in mixtures with a high percentage of recycled concrete powder substitution. Due to these effects, it can be said that the performance of recycled concrete powder depends not only on the substitution percentage but also on the properties of the material [8-10]. Fly ash (FA) can be a suitable complementary cementitious material to be considered together with recycled concrete powder.

The aim of this study is to compare the physical, chemical and mineralogical properties of materials and performances of twelve different mortar compositions, including CEM I Portland cement, CEM II limestone cement, a mixture with 20% fly ash replacement for Portland cement, four 20% replacement recycled concrete powder mixtures, four 10% recycled concrete powder and 10% fly ash hybrid mixtures, and finally a 20% recycled concrete powder and 10% fly ash hybrid mixture, as well as four different types of recycled concrete powder, on their fresh and hardened state performance. Furthermore, the strength activity index (SAI) specified in the ASTM C311 (Standard Test Methods for Sampling and Testing Fly Ash or Natural Pozzolans for Use in Portland-Cement Concrete) standard was used as a reference in determining the strength activity of pozzolanic materials substituted for cement. According to this standard, the material(s) replacing 20% of the cement must provide at least 75% of the 28-day strength of the reference Portland cement mixture. In addition, the water demand associated with each type of recycled concrete powder, the effect of the type of recycled concrete powder

on 28 days compressive and flexural strength and the effect of replacing half of the recycled concrete powder with fly ash and replacing it entirely with recycled concrete powder were investigated. The main contribution of the study is to establish a link between hybrid systems containing only recycled concrete powder and those containing both recycled concrete powder and fly ash at a consistent replacement ratio.

2 Materials and Methods

The experiment utilized recycled concrete powder with four different compositions. ARCP represents hydrated cement paste. ARCF20 and ARCF40 contain 20% and 40% crushed sand, respectively. These three materials were produced in a laboratory setting and represent recycled concrete powders with different compositions that can be obtained from real demolition waste through a specific process. RCF was obtained from real concrete waste and represents the powder of demolished concrete obtained from real demolition waste. All four RCPs were selected to compare their effects on mortar performance. In the experiments, CEM I Portland cement was used as the main reference binder material. CEM II was also present in the experimental setup as a different reference. Fly ash was used alone as a 20% substitute in one series, while in other hybrid mixtures, fly ash was used as a 10% substitute alongside the concrete powder to replace cement.

Table 1. Chemical and physical analysis.

Chemical Components (%)	**ARCP**	**ARCF20**	**ARCF40**	**RCF**	**PC**
CaO	53.1	54.3	54.0	17.0	65.9
SiO_2	16.1	12.0	9.1	50.5	21.0
Al_2O_3	3.7	2.5	1.8	9.5	5.2
Fe_2O_3	2.9	2.0	1.3	4.2	3.8
MgO	0.9	0.8	0.7	2.2	0.8
Na_2O	0.2	0.2	0.2	1.8	0.2
K_2O	0.3	0.2	0.2	1.4	0.5
Cr_2O_3	0.1	-	-	-	-
SO_3	3.1	2.1	1.4	0.5	0.4
Mn_2O_3	0.1	-	-	0.1	-
F	0.1	0.1	0.1	0.2	-
P_2O_5	0.2	0.1	0.1	0.1	-
LOI	20.5	26.2	32.1	11.9	2.1
Total	100.7	100.2	100.8	99.0	99.9
Specific Gravity (g/cm^3)	2.30	2.40	2.50	2.57	3.12
Fineness (cm^2/g)	4750	4500	4500	4300	3700

Before mortar production began, the physical, chemical, and mineralogical properties of the recycled concrete powders to be used were determined. Specific gravity and blaine specific

surface area tests were performed for physical characterization. The chemical composition was determined by X-ray fluorescence (XRF) in Table 1. The mineralogical composition was determined by X-ray diffraction (XRD) in Table 2.

Table 2. Mineralogical analysis results with the rietveld method.

Phases (%)	ARCP	ARCF20	ARCF40	RCF
Tobermorit (CSH)	80.4	63.4	51.2	14.3
Portlandit (CH)	15.1	16.7	12.3	-
Calcium Carbonate	3.9	18.8	36.0	20.0
Kuzelite	0.6	0.5	-	-
Ettringite	-	0.5	0.3	0.3
Calcium Carboaluminate	-	0.1	0.1	-
Quartz	-	-	-	33.3
Albite	-	-	-	29.1

The specific gravities of RCPs ranged from 2.30 to 2.57. This value is smaller than the specific gravity of Portland cement used in the experiments. ARCP showed the lowest specific gravity while shows the highest blaine fineness. RCF, on the other hand, showed the highest specific gravity while exhibiting the lowest blaine fineness (Table 1). These values affect the water demand in the mixtures where the materials are used. XRF results clearly show a significant difference between artificial RCPs and RCF. ARCP, ARCF20, and ARCF40 have a CaO content exceeding 50%. This is due to their richness in hydrated cement paste. In contrast, RCF contains a high amount of aggregate based silica sources, resulting in a SiO_2 content exceeding 50%. It yielded a result close to 17% in terms of CaO content. When the loss on ignition values were examined, the reason for the higher number of RCPs containing 20% and 40% crushed sand by volume is the use of limestone-based sand in their composition (Table 1).

XRD with the rietveld method results show that the RCPs have different compositions. ARCP, since it contains only hydrated cement paste, contains 80.4% tobermorite or calcium silicate hydrate (CSH) and 15.1% portlandite according to the XRD Rietveld analysis results. With increasing limestone-based crushed sand content, the CSH ratios decreased to 63.4% and 51.2% in ARCF20 and ARCF40, respectively. Calcium carbonate phase contents, on the other hand, increased from 3.9% to 18.8% and 36% in artificial RCPs. RCF has different mineralogical properties from artificial materials. While the CSH content is limited to 14.3%, it contains quartz and other components. This difference in composition is related to the high aggregate ratio in RCF (Table 2).

The experimental study was designed and tested in accordance with the general approach of ASTM C311 for alternative cement substitutes. Twelve different mortar mixtures were designed with a constant sand content of 1375 grams according to the ASTM C311 standard (Table 3). Reference CEM I, CEM II, 20% substitute, and 10% binary hybrid mixtures were prepared according to the standard with a binder content of 500 grams. Importantly, the water content was not kept constant as required by the standard. Instead, it was adjusted to remain 5 mm below or above the flow value provided by the CEM I potland cement mixture with 242 grams of water in its fresh state. This ASTM C311 SAI approach allows for an assessment of the fresh water requirement of each substituted material. Consequently, differences in mechanical performance are not solely dependent on chemical reaction and substitution ratio but should also be evaluated according to the water/binder (w/b) ratio of the mixture, the

properties of the RCP used in the mixture, and the structure of the binder phase (Table 3). The mixture codes were designed according to the mass percentages of the constituent materials. In the coding system, the numerical value indicates the mass percentage of the corresponding material, while the letters identify the material type. For instance, 100CEMI and 100CEMII mean that these cements are used 100% in these mixtures. In others, they represent the percentage of cement substitution. For example, 10ARCP10FA means that a total of 20% cement is replaced by a hybrid mixture of 10% recycled concrete powder and 10% fly ash.

Table 3. Mix_proportions.

Mixture Code	Cement (g)	Water (g)	Sand (g)	Fly Ash (g)	RCP (g)	W/B
100CEM I	500	242	1375	0	0	0.48
100CEM II	500	252	1375	0	0	0.50
20FA	400	232	1375	100	0	0.58
20ARCP	400	270	1375	0	100	0.68
20ARCF20	400	254	1375	0	100	0.64
20ARCF40	400	265	1375	0	100	0.66
20RCF	400	258	1375	0	100	0.65
10ARCP10FA	400	250	1375	50	50	0.63
10ARCF2010FA	400	250	1375	50	50	0.63
10ARCF4010FA	400	245	1375	50	50	0.61
10RCF10FA	400	240	1375	50	50	0.60
20RCF10FA	350	242	1375	50	100	0.69

The flow diameter and unit weight measurements were taken in the prepared mortars. Flow diameter was done to evaluate the workability obtained after adjusting the water content of the mixture. Unit weight indicated the effect of recycled concrete powder and fly ash on mortar density. The set mortars were subjected to flexural and compressive tests after 2, 7 and 28 days.

3 Findings

All twelve mixtures were produced according to a fixed nominal binder quantity. The water content was adjusted to achieve the target consistency. Therefore, the water/binder (w/b) ratios are related to the binder phase content. Mixtures containing recycled concrete powder generally required more water than the reference mixture (Fig. 1).

The CEM I reference mixture required the lowest water demand. Mixtures containing RCP showed higher water demands. This difference is significant because increased water demand can increase the void ratio in the hardened state and reduce the density of the matrix. Consequently, it can decrease mechanical performance. When comparing the strengths of mixtures containing RCP, not only the percentage of substitution but also the w/b ratio should be considered (Fig. 1).

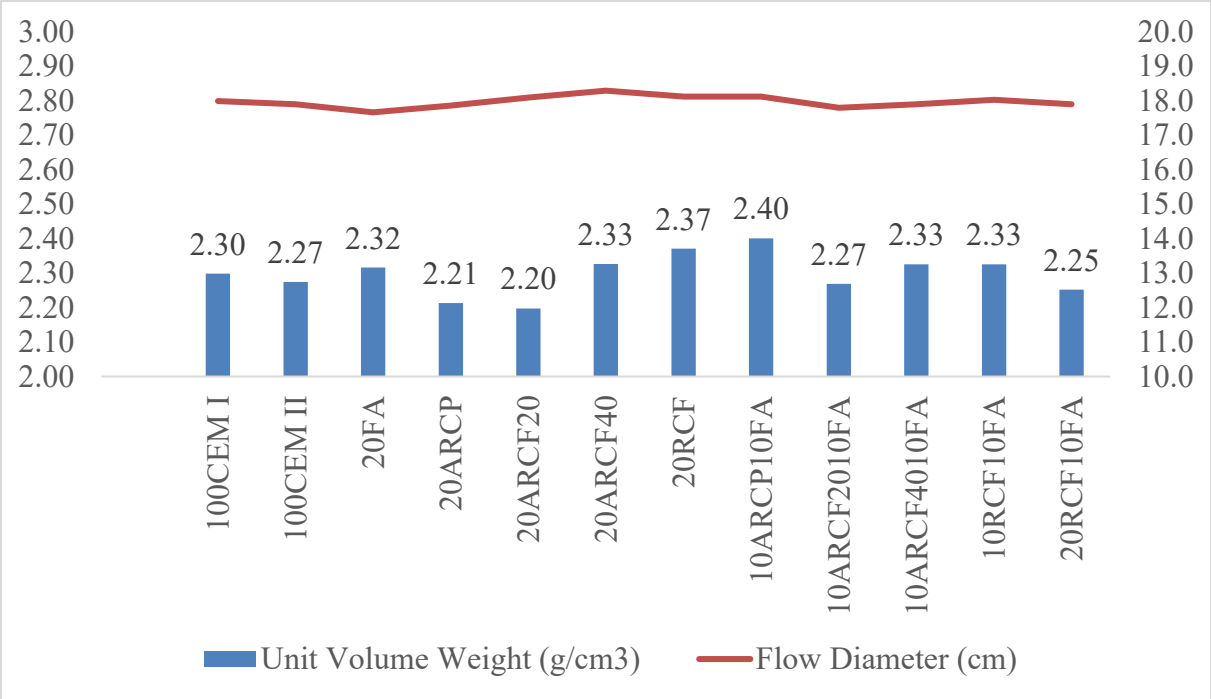


Fig. 1. Unit volume weight and flow diamater results of mixtures.

The reference CEM I mixture of compressive strength reached 31.8 MPa in 2 days, 58.1 MPa in 7 days, and 67.9 MPa after 28 days. The reference CEM II mixture reached 58 MPa in 28 days. The mixture with 20% fly ash substitution showed slower early age development, reaching 24.3 MPa in 2 days, 43.4 MPa in 7 days and 51.2 MPa in 28 days. Mixtures containing only 20% RCP substitution showed lower strength performance compared to the reference. The 20ARCP, 20ARCF20, 20ARCF40, and 20RCF mixtures reached strengths of 40.8 MPa, 45.1 MPa, 44.3 MPa, and 29.3 MPa, respectively. Among the RCP containing mixtures, the 20RCF mixture showed the largest decrease in strength (Fig. 2).

Hybrid mixtures containing fly ash and recycled concrete powder yielded different results. 10ARCP10FA reached 47.2 MPa at 28 days, 10ARCF2010FA 51.7 MPa, 10ARCF4010FA 54.3 MPa, and 10RCF10FA 52.5 MPa. Therefore, hybrid mixtures showed improved strength performance because they also reduced water requirements in the presence of fly ash (Fig. 2).

When flexural strengths were evaluated, the CEM I reference reached 10.2 MPa at 28 days, while the CEM II mixture reached 8.7 MPa. The 20% fly ash mixture reached 8.9 MPa. In systems containing only RCP, 20ARCF20 showed the highest 28-day flexural strength at 8.8 MPa, while 20RCF showed the lowest value at 6.5 MPa. Various RCP types in hybrid mixtures showed different performances. 10ARCF2010FA and 10ARCF4010FA reached values of 8.5 and 8.6 MPa, respectively after 28 days. These results show that the positive effect of hybridization is not limited to compression alone and can also be observed in bending response; however, the hybrid mixtures did not exceed the CEM I reference value after 28 days (Fig. 3).

Strength increases between 7 and 28 days are a significant indicator of pozzolanic behavior. The CEM I reference mixture showed a 16.8% increase, while the CEM II mixture showed a 9.2% increase. The 20% fly ash mixture showed a 18% increase. For mixtures containing only RCP, the increases were 35.2% for 20ARCP, 39.7% for 20ARCF20, 43.5% for 20ARCF40, and decrease were -11.8% for 20RCF. Hybrid mixtures showed increases of 26.4%, 30.9%, 31.0%, and 14.3%, respectively. Particularly noteworthy strength improvements were observed in hybrid ARCF systems. Their final 28 days strengths showed higher compressive and flexural strengths compared to mixtures containing only RCP. This suggests that fly ash containing mixtures provided more favorable strength development (Fig. 2 and Fig. 3).

A direct comparison between systems containing 20% RCP and those containing 10% RCP along with 10% fly ash is one of the most important findings of the experiment. For ARCP, increase was from 40.8 to 47.2 MPa or 6.4MPa, for ARCF20, the corresponding increase was from 45.1 to 51.7 MPa, or 6.6 MPa. For ARCF40, the increase was from 44.3 to 54.3 MPa or 10 MPa. For RCF, the increase was from 29.3 to 52.5 MPa, or 23.2MPa. The amount of improvement in strength with the use of fly ash was least in the RCP type ARCP and best in the RCF because the 20RCF mixture had the lowest 28 days strength among the four different RCP substitutions. Therefore, it can be said that the addition of fly ash appears to be more beneficial in systems with weaker RCF (Fig. 2).

A similar trend was observed in flexural strengths. Hybrid mixtures improved the 28 days flexural strength for ARCP, ARCF40, and RCF compared to their counterparts containing only RCP, while the ARCF20 pair showed only a small difference. It can be said that hybrid systems can improve the overall mechanical performance (Fig. 3).

The results show significant variability depending on the source of the material used in the mixture. Therefore, there are strength differences among four different RCP mixtures substituted with the same 20%. When the characterization results provided for RCPs are evaluated against mechanical results, differences in specific gravity, fineness, chemical composition, and mineralogical structure can affect the water requirement and the contribution of RCPs to the binder phase in mixtures produced with these materials (Fig. 2 and Fig. 3).

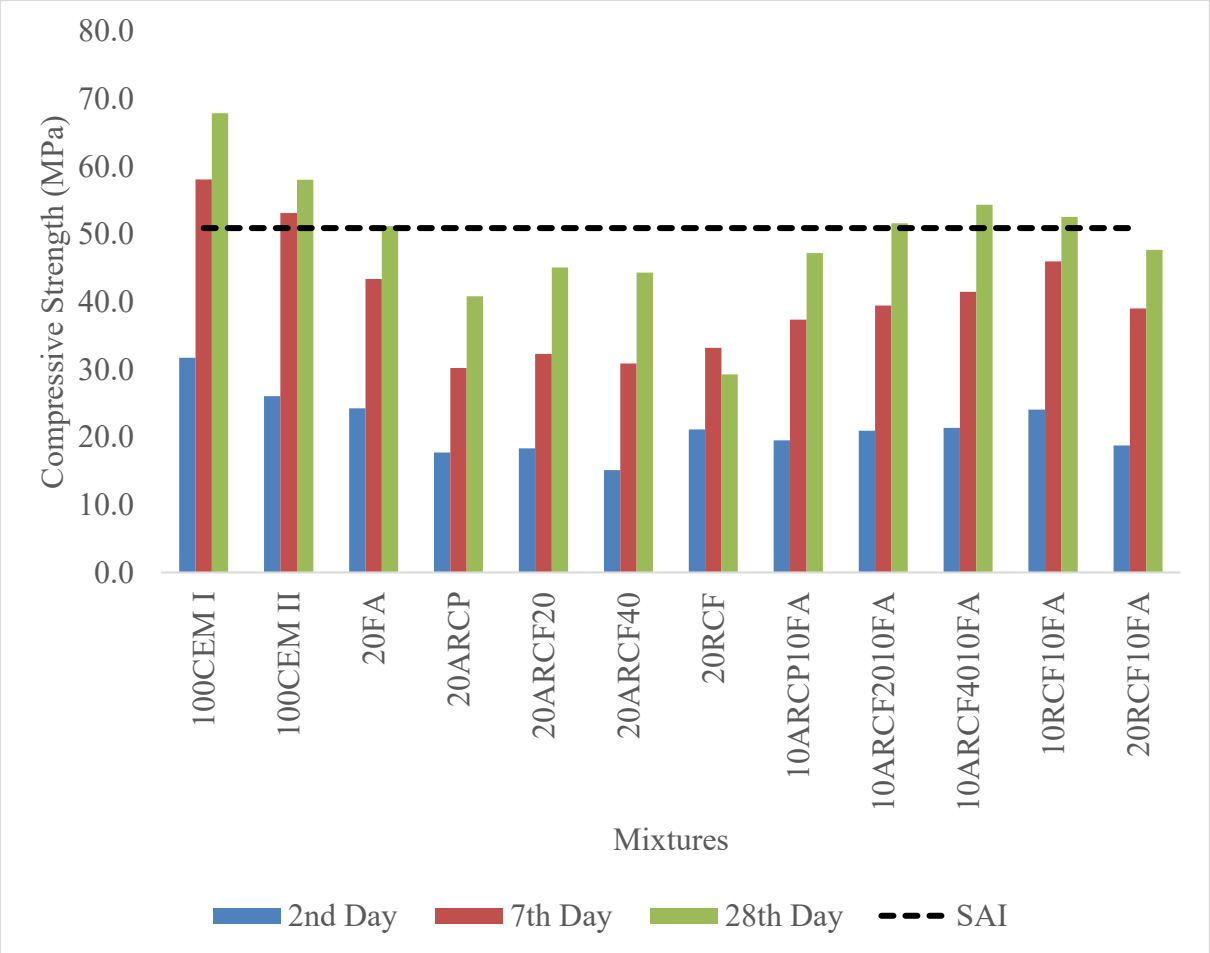


Fig. 2. Compressive strength results.

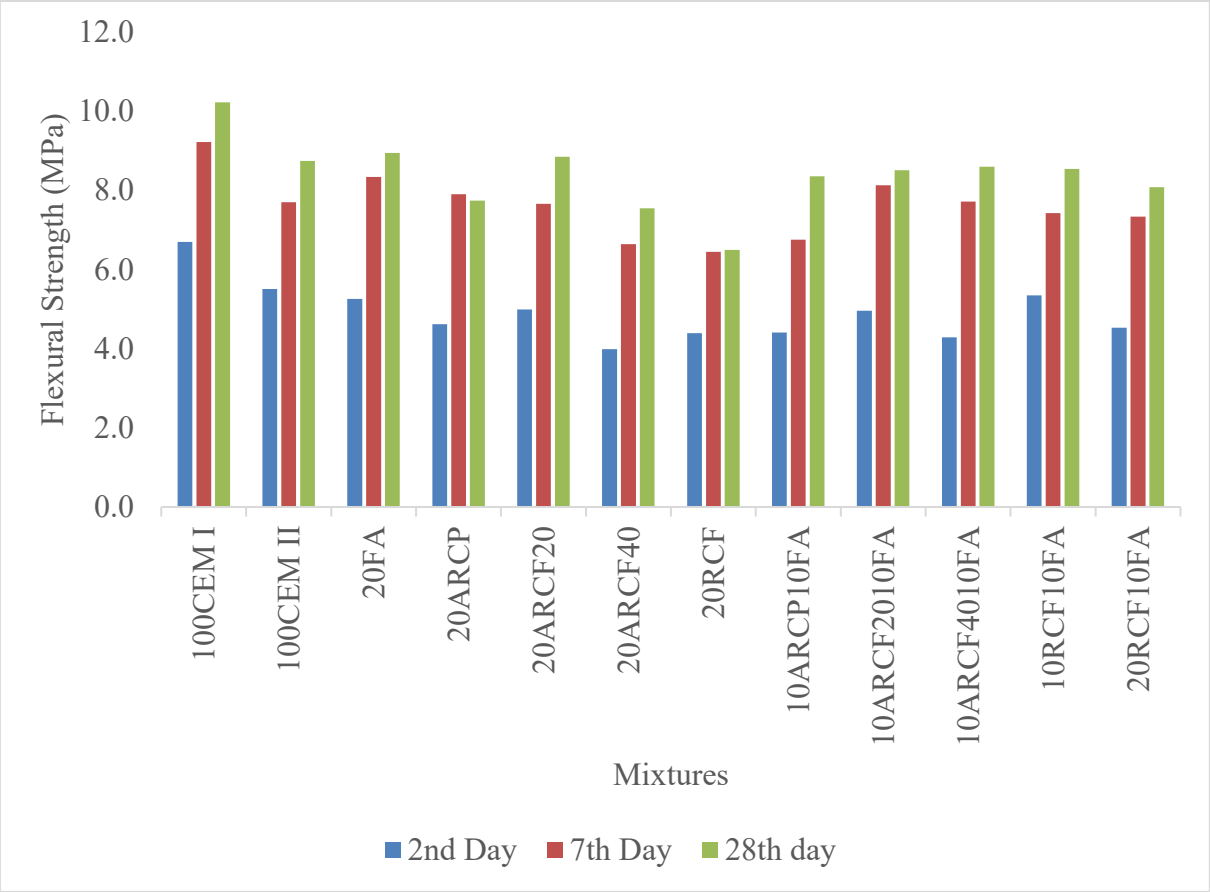


Fig. 3. Flexural strength results.

4 Conclusion

Overall, the results suggest that recycled concrete powder can be used partially in place of cement but its mechanical performance depends significantly on the properties of the recycled concrete powder used and the water demand in the mix. Direct 20% RCP substitution resulted in a significant decrease in 28 days strength. However, hybrid mixes using 10% RCP and 10% FA together provided a more balanced mechanical performance. It can be said that it compensated to some extent for the strength losses that occurred in some mixes using only RCP. The mix that best achieved fly ash recovery was the one using RCP; fly ash recovery was limited in the mix using ARCP. Therefore, based on the results RCP alone should not be considered a supplementary cementitious material. The compressive strength activity of the 20FA, 10ARCF2010FA, 10ARCF4010FA, and 10RCF10FA mixtures provided 75% of the reference mixture and can be used as pozzolans in concrete applications according to the ASTM C311 standard. Optimization within the mix should consider the type of RCP used, the w/b ratio and the use of other materials. Finally, the hybrid RCP-FA combination approach allows for acceptable mechanical performance using recycled materials.

Acknowledgments

All authors contributed to the conception and design of the study. Material preparation, data collection and manuscript writing were performed collaboratively by the authors. All authors reviewed and approved the final manuscript. This study is supported by the Scientific and Technological Research Council of Türkiye (TÜBİTAK) BİDEB 2210 National Graduate Scholarship Programme. Also, the authors gratefully acknowledge the financial support

provided by the Scientific Research Projects Coordination Unit of Istanbul Technical University under project numbers MYLB-2026-48466.

References

[1] Zajac, M., Skocek, J., Skibsted, J., Durdzinski, P., & Ben Haha, M. (2021). CO_2 mineralization of demolished concrete wastes into a supplementary cementitious material – A new CCU approach for the cement industry. *RILEM Technical Letters*, 6, 53–60.
[2] Zhan, B., Poon, C. S., & Shi, C. (2020). Recycled powder from construction and demolition waste: Material characterization and its feasibility in cementitious materials. *Resources, Conservation and Recycling*, 150, 104440.
[3] Li, X., Zhang, J., Wang, T., & Liu, B. (2020). Activation and utilization of recycled cementitious materials from concrete demolition waste. *Journal of Materials in Civil* Engineering, 32(1), 04019349.
[4] Shi, C., & Kan, L. (2022). Use of recycled concrete powders in cement-based materials: A review. *Cement and Concrete Composites*, 125, 104295.
[5] Chen, X., Li, Y., Zhu, Z., & Ma, L. (2022). Evaluation of waste concrete recycled powder (WCRP) on the preparation of low-exothermic cement. *Journal of Building Engineering*, 53, 104511.
[6] Likes, L., Markandeya, A., Haider, M. M., Bollinger, D., McCloy, J. S., & Nassiri, S. (2022). Recycled concrete and brick powders as supplements to Portland cement for more sustainable concrete. *Journal of Cleaner Production*, 364, 13265.
[7] Jiang, Y., Li, B., Liu, S., He, J., & Garcia Hernandez, A. (2022). Role of recycled concrete powder as sand replacement in the properties of cement mortar. *Journal of Cleaner Production*, 371, 133424.
[8] Rocha, J. H. A., & Toledo Filho, R. D. (2023). The utilization of recycled concrete powder as supplementary cementitious material in cement-based materials: A systematic literature review. *Journal of Building Engineering*, 76, 107319.
[9] Xiao, J., et al. (2021). Investigation of using recycled powder from the preparation of recycled aggregate as a supplementary cementitious material. *Construction and Building Materials,* 267, 120976.
[10] Mao, Y., Hu, X., Alengaram, U. J., Chen, W., & Shi, C. (2024). Use of carbonated recycled cement paste powder as a new supplementary cementitious material: A critical review. *Cement and Concrete Composites,* 154, 105783.

Publication Note
This paper was peer-reviewed, accepted for presentation, and included in the proceedings of the ACE2026 – International Conference on Advances in Civil Engineering, held on 12–14 October 2026 in Trabzon, Türkiye.

This paper may be cited as follows:
Varan, K., Doğan, Ü. A., Dinçer, A., Koyunlular, A., Uslu, B., Sevinç, B., Özyurt, T. İ., Gündoğdu, T., and Gökalp, İ., "Use of Recycled Concrete Powders as Supplementary Cementitious Materials in Mortar Mixtures," in Proceedings of the ACE2026 – International Conference on Advances in Civil Engineering, Trabzon, Türkiye, 12–14 October 2026.

Effect of Carbonation Treatment on the Reuse of Concrete Sludge as a Clinker-Reducing Mineral Additive in Cementitious Materials

Kadircan Varan[1], Senem Bilici[2] , İsmail Gökalp[2], Teoman Erenoğlu[2], Büşra Çınar Ernek[2]

[1] 0009-0004-9367-7869, Istanbul Technical University, Civil Engineering Department, Istanbul, Türkiye, varank19@itu.edu.tr
[2] 0000-0002-9698-8900, Akçansa Cement Industry and Trade Inc., Istanbul, Türkiye, senem.bilici@akcansa.com.tr
[2] 0009-0000-6661-8928, Akçansa Cement Industry and Trade Inc., Istanbul, Türkiye, ismail.gokalp@akcansa.com.tr
[2] 0009-0008-8341-1724, Akçansa Cement Industry and Trade Inc., Istanbul, Türkiye, teoman.erenoglu@akcansa.com.tr
[2] 0009-0006-6620-9263, Akçansa Cement Industry and Trade Inc., Istanbul, Türkiye, busra.cinar@akcansa.com.tr

Abstract. Concrete sludge waste generated during the ready-mixed concrete production process contains hydrated cementitious phases and fine aggregate. Due to the heterogeneous content of concrete sludge, its direct reuse in concrete is limited. This study investigated the use of two different types of concrete sludge, obtained directly from the bottom of a pool and processed through a filter press, and obtained through carbonation as a substitute for cement. In the carbonation process, the materials were first moistened by adding water at 25% of their dry mass. The materials were carbonated for an hour in an environment of 75 ºC and 100% CO_2. Physical, chemical and mineralogical properties were determined both before and after carbonation. The sieve residues, blaine fineness, water demand and setting times of the binder phases of mixtures with 6% and 15% cement substitution were examined. The compressive strengths of the produced mortars were determined and their mechanical performance was analyzed. The results indicate that substitution levels such as 6%, are suitable for the evaluation of materials like concrete sludge. However, higher levels of substitution indicate that the mineralogical composition, particle size and carbonation process of the concrete sludge need to be optimized together.

Keywords: Alternative supplementary cementitious materials; CO_2 sequestration and mineralization; recycled materials.

1 Introduction

A large portion of the carbon emissions released in cement production originates from clinker production and fuel. Therefore, reducing the clinker ratio in cement production and developing alternative binder materials remains important. This is the first step towards the cement and concrete industry becoming carbon neutral [1,2]. With the circular economy, not only additives such as fly ash and blast furnace slag but also the use of powders obtained from concrete waste as alternative complementary cementitious materials in cement production has gained importance [3,4].

Concrete sludge, which is formed after washing mixers in ready-mix concrete plants or after the return of unpoured concrete from the construction site, may contain components such as hydrated or partially hydrated cement particles, calcium hydroxide, calcium carbonate, and fine aggregate. Direct storage of this material poses an environmental risk due to both the need for

storage space and the high alkalinity of the material. In contrast, appropriate dewatering, drying, and grinding processes can allow concrete sludge to be pulverized and used as a substitute for cement or fine aggregate. However, the variable internal structure, low reactivity and water-increasing effect of this material may limit its usage rate [3-5].

Carbonation of concrete waste is an approach that allows calcium-containing hydrated phases, which are the hydration products of cement, and calcium silica hydrate to react with CO_2 to form stable calcium carbonate phases. Carbonation efficiency can vary depending on the particle and surface properties, void ratio, water absorption properties, and mineralogical structure of the material [4,6,7]. It can be said that carbonated reclaimed fine materials can accelerate hydration, fill pore structures and contribute to mechanical strength when used up to a certain percentage [5-8]. Carbonation efficiency depends on parameters such as CO_2 concentration, temperature, relative humidity, processing time, particle size, and initial moisture content. Water is required in the medium for the reaction. Excess water in the medium can prevent the gas from penetrating into the particles; low water content can limit the dissolution and penetration of ions [6].

Many studies exist in the literature on the carbonation of recycled concrete powders. However, studies on the use of fine fractions obtained from ready-mixed concrete plants after several processing flows as cement substitutes are limited. Furthermore, there is a lack of research on the carbonation of this material. Therefore, chemical, mineralogical and mechanical investigations related to the carbonation of concrete sludge are important.

The aim of this study was to compare two different types of concrete sludge obtained from the bottom of sedimentation pool (WCS) or filter presses (FCS), in their carbonated and non-carbonated forms (cWCS and cFCS) by substituting 6% and 15% cement in the mortar phase. X-ray fluorescence (XRF) and X-ray diffraction (XRD) analyses were performed to understand the effect of carbonation. Specific gravity, blaine fineness, sieve analysis, water demand, and setting time tests were conducted on the binder phase mixtures in the mortar. The compressive strengths of the produced mortars were evaluated at 1, 2, 7, and 28 days.

2 Materials and Methods

In the experiments, ordinary portland cement (PC) was used as the reference binder. Two different types of concrete sludge were selected. These were wet concrete sludge (WCS) taken from the bottom of the settling pool and concrete sludge (FCS) that passed through the filter press process after the settling pool. The carbonated versions of these concrete sludges were coded as cWCS and cFCS, respectively.

Two different concrete sludges (WCS and FCS) were moistened with water at a rate of 25% of their dry weight prior to carbonation. The moistened materials were then carbonated in a controlled environment with a 100% carbon dioxide (CO_2) concentration and a temperature of 75 °C for one hour. The high CO_2 concentration and temperature enabled the acceleration of the mineralogical transformation in such a short time as one hour.

The main oxide components in PC, WCS, FCS, cWCS, and cFCS samples were determined using X-ray fluorescence spectrometry (XRF) in Table 1. The CaO content of concrete sludges varies between 29.8% and 33.9%. SiO_2 content ranges from 23.3% to 33.2%, and Al_2O_3 content from 6.2% to 7.6% (Table 1). The lower CaO/SiO_2 content of concrete sludges compared to PC does not necessarily mean that these materials will not exhibit PC like hydration behavior. However, the remaining hydrated phases with their fine particles, filling, and nucleating effects can contribute to mechanical performance. After carbonation of the concrete sludges, the ignition loss value of WCS increased from 20.9% to 28% (Table 1). This increase in ignition loss is consistent with the increase in the XRD results (Table 2). The same behavior was observed in the FCS sample. The ignition loss value of FCS also increased from 23.2% to 25.2%

(Table 1). The greater change in ignition loss of WCS suggests that the material has a higher carbonable phase content and is more susceptible to carbonation. The specific gravities of WCS, FCS, cWCS, and cFCS are 2.47, 2.70, 2.40, and 2.60, respectively. Decreases in specific gravities were observed after carbonation of the materials. Therefore, when concrete sludge is substituted for cement, the volume of the binder phase may increase slightly. This increase in volume can cause changes in water demand.

The mineralogical phase structure of the concrete sludges was determined by X-ray diffraction (XRD). XRD analysis revealed the presence of calcite, quartz, alite, portlandite, tobermorite, and silica phases in the materials using the Rietveld method (Table 2). According to XRD results, the dominant phase structure in the concrete sludges is calcite. Calcite, which was 60.1% in WCS, increased to 93.9% in cWCS (Table 2). Furthermore, while portlandite and tobermorite phases were present in WCS, these phases could not be detected in cWCS. This result suggests that carbonation converts portlandite to calcium carbonate and then also degrades tobermorite, converting its calcium content to calcium carbonate. The dissolution and carbonation of calcium-containing hydrated phases are consistent with the mechanisms described in the literature for recycled concrete powders [5-7]. No carbonation effect was observed in the FCS sample as in the WCS sample. The limited increase in calcium carbonate suggests that FCS may have already carbonated before carbonation or that the reactive calcium phases were lower (Table 2).

Table 1. Chemical analysis.

Component (%)	WCS	FCS	cWCS	cFCS	PC
CaO	33.9	29.8	33.7	30.7	65.2
SiO_2	28.0	33.2	23.3	30.0	19.4
Al_2O_3	7.6	6.6	6.5	6.2	5.1
Fe_2O_3	3.9	3.1	3.5	3.3	3.4
MgO	2.3	2.5	1.9	2.3	1.1
Na_2O	0.7	1.1	0.6	1.0	0.2
K_2O	0.8	0.8	0.7	0.8	0.8
SO_3	1.8	0.4	1.6	0.6	2.8
Mn_2O_3	0.1	0.1	0.1	0.1	-
F	0.1	0.1	0.1	0.1	-
P_2O_5	0.1	0.1	0.1	0.1	-
LOI	20.9	23.2	28.0	25.2	2.2
Total	100.2	101.0	100.1	100.3	100.2
Specific Gravity (g/cm^3)	2.47	2.70	2.40	2.60	3.13

Table 2. Mineralogical analysis results with the rietveld method.

Phases (%)	WCS	FCS	cWCS	cFCS
Calcite	60.1	78.7	93.9	79.0
Quartz	6.0	9.8	3.2	8.2
Alite	3.8	1.1	-	-
Portlandite	0.9	1.4	-	-
Tobermorite	26.2	1.1	-	8.7
Silica	2.7	7.5	2.6	3.4

Materials derived from concrete sludge were used in mixtures at 6% and 15% by weight as replacements for portland cement. The reference mixture used 450 grams of PC, 1350 grams of standard sand and 225 grams of water, according to European standards. In the 6% concrete sludge replacement series, 423 grams of PC and 27 grams of substitute material were used; in the 15% concrete sludge replacement series, 382.5 grams of PC and 67.5 grams of substitute material were used. The water/binder (w/b) ratio was kept constant at 0.5 in all mixtures. No additional chemical additives were used in the mixtures (Table 3).

Table 3. Mix proportions of the mortars.

Mixture	PC	FCS	WCS	cFCS	cWCS	Sand	Water
Reference	450	-	-	-	-	1350	225
6FCS	423	27	-	-	-	1350	225
15FCS	382.5	67.5	-	-	-	1350	225
6WCS	423	-	27	-	-	1350	225
15WCS	382.5	-	67.5	-	-	1350	225
6cFCS	423	-	-	27	-	1350	225
15cFCS	382.5	-	-	67.5		1350	225
6cWCS	423	-	-	-	27	1350	225
15cWCS	382.5	-	-	-	67.5	1350	225

The 32, 45, and 90 µm sieve values, blaine specific surface area and specific gravity of the prepared binder phase mixtures containing carbonated and non-carbonated concrete sludges were determined in Table 4. The specific surface areas of the binder mixtures varied between 4500-4550 cm^2/g, but efforts were made to keep them close to each other. In addition, the sieve oversize values increased with increasing carbonated or non-carbonated concrete sludges substitution ratio (Table 4). The standard consistency water demand and setting initial and final times of these binder mixtures were measured. The 1, 2, 7, and 28-day compressive strengths of the mortar samples were measured.

Table 4. Physical properties of the binder phases in the mortar mixtures.

Mixture	32 µm (%)	45 µm (%)	90 µm (%)	Specific Gravity (g/cm^3)	Fineness (cm^2/g)
Reference	22.4	11.1	1.4	3.14	4500
6FCS	24.0	11.9	1.6	3.03	4510
15FCS	30.4	17.0	2.4	3.07	4520
6WCS	23.6	12.4	1.3	3.11	4540
15WCS	31.1	20.1	2.2	3.09	4550
6cFCS	22.5	11.6	1.6	3.03	4510
15cFCS	28.8	16.8	2.6	3.07	4520
6cWCS	23.1	12.7	1.6	3.11	4500
15cWCS	29.4	16.4	2.0	3.09	4510

3 Findings

In the consistency test, water demands varied within a narrow range of 23.8%-25.6% in all mixtures. The 6WCS mixture had the lowest water requirement at 23.8%, while the 15cWCS mixture had the highest at 25.6%. The initial and final setting times of the reference mixture were 129 and 201 minutes, respectively (Fig. 1). The 6WCS mixture showed an earlier setting time compared to the reference mixture, with a setting start time of 116 minutes and a setting final time of 186 minutes. In contrast, the initial setting time of the 6cWCS mixture increased to 160 minutes, and the final setting time increased to 250 minutes. In mixtures using FCS, the 15cFCS mixture showed initial setting time of 195 minutes and final setting time of 283 minutes. The literature does not provide consistent interpretations regarding the behavior of carbonated materials in relation to setting time. Since it will vary depending on the physical, chemical and mineralogical properties of the carbonated material, it may also have positive or negative effects on the hydration mechanism [5,8]. According to this study, it can be said that carbonated materials generally extend the setting time (Fig. 1).

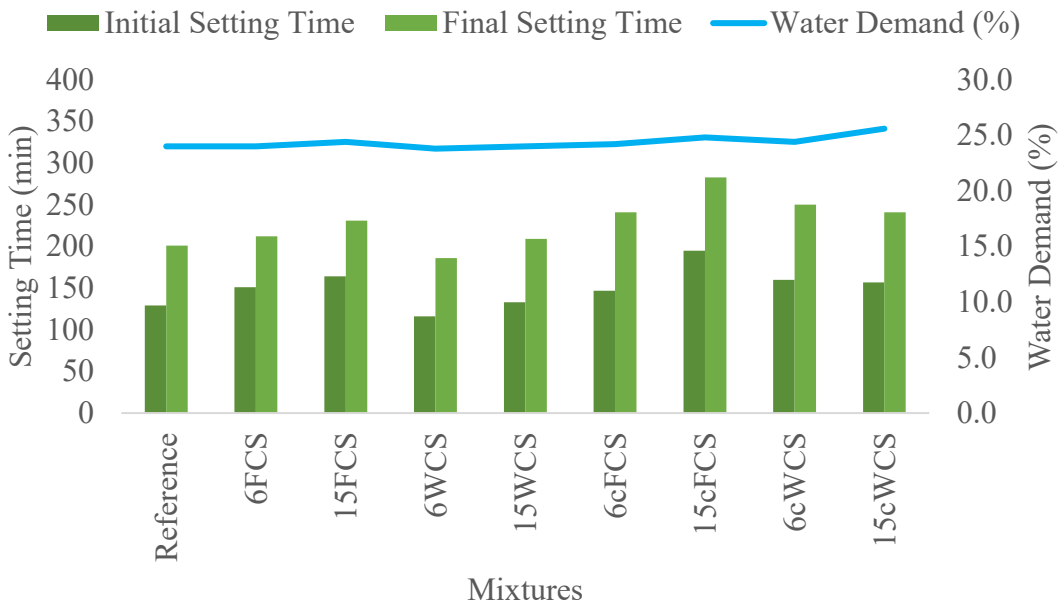


Fig. 1. Setting time results of all mixtures.

The 1, 2, 7, and 28-day strengths of the reference mortar were 21.2, 33.1, 49.2, and 59.2 MPa, respectively in Figure 2. All sludge substituted mixtures performed below the strength of the reference mixture at all days. The main reasons for this are the reduced clinker content and the low early reactivity of the sludge-based material. Despite this, the strength difference decreased in some substituted mixtures at higher ages. The 6FCS mixture exhibited the best performance among the sludge substituted mixtures. 6FCS showed a compressive strength of 48.4 MPa at 7 days and 58.2 MPa at 28 days. These values correspond to approximately 95% of the compressive strength of the reference mixture. The 6cFCS mixture also reached approximately 95% of the reference at 28 days with 56.4 MPa. The 6WCS and 6cWCS mixtures yielded strengths of 53.6 and 54.0 MPa, respectively. These results indicate that a 6% substitution rate was able to maintain mechanical performance. At a 15% substitution rate, a significant loss of strength was observed across all series. The 28-day strengths of the 15FCS, 15WCS, 15cFCS, and 15cWCS mixtures were 45.3, 44.3, 46.8, and 44.9 MPa, respectively. As the substitution

rate increased, the carbonated series showed better improvements compared to the non-carbonated series. cFCS provided 1.5 MPa higher 28-day strength than FCS, while cWCS provided 0.6 MPa higher 28-day strength than WCS. Nevertheless, the improvement in the carbonated mixtures was not sufficient to compensate for the loss of strength (Fig. 2).
The effect of carbonation on strength can vary depending on the material type and the percentage of substitution. Carbonation of FCS at 6% reduced the 28-day strength by 1.8 MPa, while carbonation of WCS increased it by 0.5 MPa. At a 15% substitution level, carbonated mixtures yielded higher strength than non-carbonated mixtures. Based on these results, it can be said that optimum carbonation should not be attributed solely to calcium carbonate formation. Advanced carbonation can reduce reactivity by consuming hydrated phases and improve carbonation nucleation behavior [6-9]. When comparing WCS-cWCS, although the increase in calcite after carbonation was high, the strength gain was limited. In other words, it can be said that the effect on mechanical performance is not limited only to mineralogical change. In conclusion, a linear relationship between CO_2 sequestration capacity and cement substitution performance should not always be expected (Fig. 2).

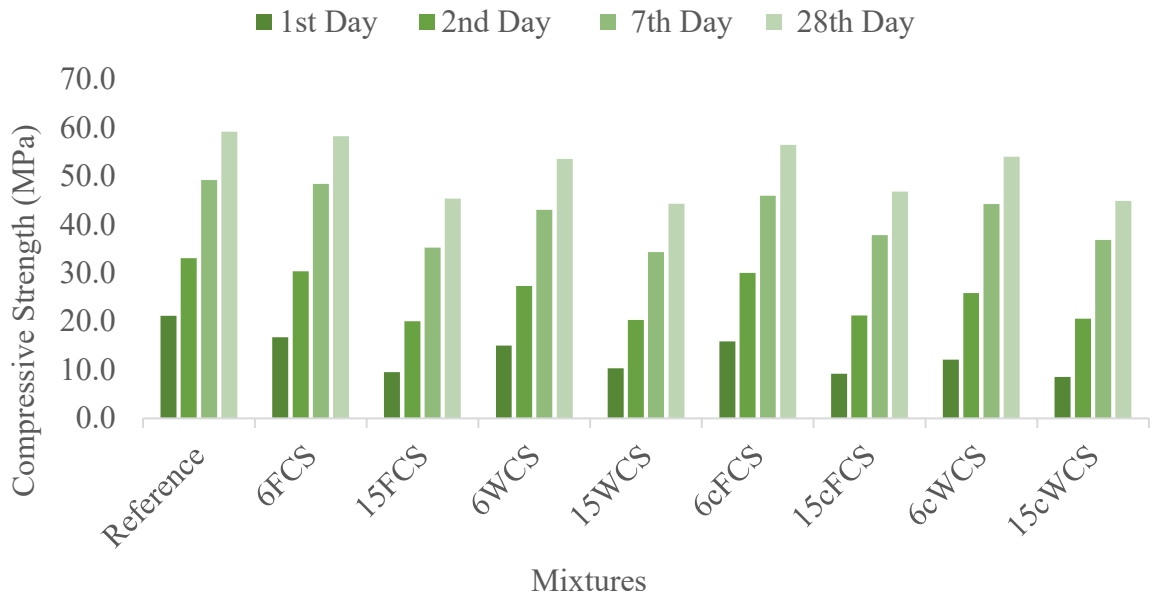


Fig. 2. Compressive strength results of all mixtures.

4 Conclusion

In this study, carbonated derivatives of concrete sludges processed in two different ways (WCS and FCS) were investigated under conditions of 100% CO_2 concentration, 75 °C temperature, 25% humidification and 1 hour by substituting 6% and 15% portland cement. The results obtained are:
-Carbonation caused a mineralogical change in WCS, increasing the calcite content from 60.1% to 93.9%. Portlandite and tobermorite structures were not detected.
-Loss on ignition values increased from 20.9% to 28% in WCS and from 23.2% to 25.2% in FCS. This behavior indicates calcium carbonate formation.
-Water demands varied between 23.8% and 25.6%, and the setting times of carbonated materials were generally longer.
-6FCS mixture gave the best compressive strength result in concrete sludge substitute mixtures.

-Increasing the substitution ratio to 15% resulted in a loss of strength in all series. In mixtures containing carbonated materials, an increase in strength was observed but it did not reach the strength of the reference mixture.
-The results indicate that using 6% concrete sludge is a promising study in terms of recovery and sustainability. For higher concrete sludge substitution ratios, particle size distribution, degree of carbonation, reactivity, and other factors should be considered together.

Acknowledgments
All authors contributed to the conception and design of the study. Material preparation, data collection, analysis, and manuscript writing were performed collaboratively by the authors. All authors reviewed and approved the final manuscript. This study is supported by the Scientific and Technological Research Council of Türkiye (TÜBİTAK) BİDEB 2210 National Graduate Scholarship Programme. Also, the authors gratefully acknowledge the financial support provided by the Scientific Research Projects Coordination Unit of Istanbul Technical University under project numbers MYLB-2026-48466.

References

[1] Scrivener, K. L., John, V. M., Gartner, E. M. (2018). Eco-efficient cements: Potential, economically viable solutions for a low-CO_2 cement-based materials industry. *Cement and Concrete Research*, 114, 2-26.
[2] CEMBUREAU (2020). Cementing the European Green Deal: Reaching Climate Neutrality along the Cement and Concrete Value Chain by 2050. Brussels.
[3] Zhang, T., Chen, M., Wang, Y., Zhang, M. (2023). Roles of carbonated recycled fines and aggregates in hydration, microstructure and mechanical properties of concrete: A critical review. *Cement and Concrete Composites*, 138, 104987.
[4] Bergmans, J., Kamyab, H. K., Ghosh, D., Van Mierloo, P., Carens, H., Nielsen, P. (2024). Carbonation of recycled concrete aggregates for new concrete and concrete fines to make cement-free hollow blocks. *Sustainability*, 16, 3494.
[5] Zhang, J., Zhang, L., Xu, B., Yuan, J. (2023). Influences of carbonated recycled concrete fines on cement hydration. *Buildings*, 13, 926.
[6] Gholizadeh-Vayghan, A., Snellings, R. (2022). Beneficiation of recycled concrete fines through accelerated carbonation. *Materials and Structures*, 55, 214.
[7] Zajac, M., Skibsted, J., Skocek, J., Durdzinski, P., Bullerjahn, F., Ben Haha, M. (2020). Phase assemblage and microstructure of cement paste subjected to enforced carbonation. *Cement and Concrete Research*, 130, 105990.
[8] Fang, Y., Chang, J. (2015). Microstructure changes of waste hydrated cement paste induced by accelerated carbonation. *Construction and Building Materials*, 76, 360-365.
[9] Shi, C., Li, Y., Zhang, J., Li, W., Chong, L., Xie, Z. (2016). Performance enhancement of recycled concrete aggregate: A review. *Journal of Cleaner Production*, 112, 466-472.
[10] Fernández Bertos, M., Simons, S. J. R., Hills, C. D., Carey, P. J. (2004). A review of accelerated carbonation technology in the treatment of cement-based materials and sequestration of CO_2. *Journal of Hazardous Materials*, 112, 193-205.

Publication Note
This paper was peer-reviewed, accepted for presentation, and included in the proceedings of the ACE2026 – International Conference on Advances in Civil Engineering, held on 12–14 October 2026 in Trabzon, Türkiye.

This paper may be cited as follows:
Varan, K., Bilici, S., Gökalp İ., Erenoğlu, T., Çınar Ernek, B., "Effect of Carbonation Treatment on the Reuse of Concrete Sludge as a Clinker-Reducing Mineral Additive in Cementitious Materials," in Proceedings of the ACE2026 – International Conference on Advances in Civil Engineering, Trabzon, Türkiye, 12–14 October 2026.

Early-age strength development in slag-fly ash geopolymers: effect of varying ohmic heating curing durations

Mazem Yılmaz[1] and Mucteba Uysal[2]
[1] 0000-0003-3616-9396, Istanbul Aydin University, Civil Engineering Department, Istanbul, Türkiye, mazembalaban@aydin.edu.tr
[2] 0000-0002-6827-9904, Yildiz Technical University, Civil Engineering Department, Istanbul, Türkiye, mucteba@yildiz.edu.tr

Abstract. In this study the effects of ohmic heating curing duration on the physical and mechanical properties of slag-fly ash-based geopolymers were investigated. Specimens were subjected to electrical curing under constant voltage for 3, 6, 12, and 24 hours, and the development of UPV, compressive strength, and flexural strength was evaluated. In addition, the 3-day strength values of specimens cured for 24 hours were compared with those cured at room temperature in terms of setting time, unit weight, porosity, and water absorption. The results show that increasing the ohmic heating duration accelerates geopolymerization kinetics, shortens the setting time, and significantly enhances early-age mechanical strength. In addition, ohmic heating curing method reduced the final setting time by 82% compared with ambient curing condition and under ohmic heating curing while the geopolymer achieved a compressive strength of 24.63 MPa after only 3 hours. Furthermore, the effects of different ohmic heating durations on strength development were clearly identified, providing valuable insights for optimizing the curing period. Overall, the results demonstrate that ohmic heating curing is an effective and practical method for achieving rapid strength gain and process optimization in geopolimer production.

Keywords: Ohmic heating curing; early-age strength; geopolymer; potassium activator.

1 Introduction

Due to sustainability-oriented approaches, research on geopolymer materials has increased significantly. Geopolymers are amorphous binder materials formed by the activation of aluminosilicate-based raw materials, such as ground granulated blast furnace slag (GGBS) and fly ash (FA), using potassium-based, sodium-based, or combined hydroxide-silicate alkaline solutions [1]. In geopolymer systems, thermal curing is generally required to achieve high early-age strength [2] [3]. FA with low calcium content exhibit slow strength development at ambient temperature. The curing method plays a decisive role in determining the physical and mechanical properties of geopolymer systems in the hardened state [4]. Various curing techniques can be applied to these materials, including ambient curing, thermal curing, steam curing, and ohmic heating [5].

Ohmic heating is a rapid curing technique based on the application of alternating current (AC) to the specimens and has emerged as a more environmentally friendly alternative compared to conventional dry steam curing methods [6]. Also referred to as electrical curing, this method converts electrical energy directly into thermal energy by passing an electric current through a medium with limited electrical conductivity [7]. As a result, the specimen is heated volumetrically and uniformly, significantly reducing the temperature gradient between the interior and the surface [8]. Consequently, crack formation caused by thermal gradients is more limited compared to other thermal curing methods. Moreover, curing techniques involving

external heating, such as autoclaving or steam curing, are difficult to implement under construction site conditions, whereas the application of AC to fresh concrete through ohmic heating enables early-age strength development in situ. In addition, ohmic heating significantly shortens the setting time by accelerating the early-age reaction kinetics [9]. This approach may help overcome major barriers to the widespread use of geopolymer materials. Kovtun et al. [10] reported that the 28-day compressive strength of alkali-activated FA concrete produced using electrical curing reached 48.5 MPa, whereas the same mixture cured under ambient conditions exhibited a compressive strength of only 10.9 MPa. Aygun et al. [11] reported that, in GGBS-FA-based geopolymers, replacing 80 °C thermal curing with electrical curing resulted in an increase in compressive strength of up to %148.

In this study, the effect of ohmic heating curing on the early-age mechanical and physical properties of GGBS-FA-based geopolymer mortars activated with potassium-based activators was investigated. Within this scope, the strength development of geopolymer mortars up to 3 days was examined. In addition, the setting times of specimens produced under ambient and ohmic curing conditions were compared, and their unit weight, porosity, and water absorption values at the age of 3 days were determined in accordance with ASTM C642 standard.

2 Materials and Experimental Methods

Ground granulated blast furnace slag (GGBS) and fly ash (FA), whose chemical composition are given in Table 1, were used as cementitious materials. Natural sand with a particle size range of 0-5 mm was selected as the fine aggregate. Potassium hydroxide (KOH) with molarity of 12 M and potassium silicate (K_2SiO_3) were used as alkaline activators.

Table 1. The chemical composition of the binders (%).

	SiO_3	Al_2O_3	Fe_2O_3	TiO_2	CaO	MgO	K_2O	Na_2O	SO_3	LOI
S	40.80	12.82	1.13	0.77	34.56	6.57	0.63	0.81	0.22	0.03
FA	59.67	25.22	4.61	-	0.47	2.27	1.36	0.61	0.55	0.013

GGBS and FA were used as binders as a 1:1 ratio by weight. The binder-to-sand ratio was 1:2.5, the activator-to-binder ratio was 0.60, and the KOH-to-K_2SiO_3 ratio was 1:2. The specimen preparation was carried out in the following stages. First, the dry materials were mixed for 2 minutes to ensure homogeneity. The alkaline activators were mixed for 2 minutes after which they added to the dry mixture. The resulting mixture was then mixed for an additional 2 minutes. The freshly prepared geopolymer mortar was cast into prismatic molds with dimension of 40 x 40 x 160 mm^3 in two layers, and each layer was compacted using a vibration table. The prepared specimens were then subjected to the curing conditions specified in Table 2.

Table 2. Curing conditions.

Curing Type	**Curing conditions**	**Curing procedure**
Ambient curing	22±1 °C and %65 relative humidity	After casting, the specimens were kept in the molds for 24 h and then demolded.
Ohmic heating	Constant 25±1 V voltage	Immediately after casting, the specimens were subjected to electric curing at the specified voltage for 3, 6, 12, or 24 h, and then demolded.

Under ohmic heating conditions, copper plates were attached to the 40 x 40 mm cross-sectional faces of the wooden molds (40 x 40 x 160 mm), and a constant voltage applied to the specimens

through these plates using and AC power supply. The variation of the current and specimen temperature as a function of time during 24 h of ohmic heating is presented in Fig. 1.

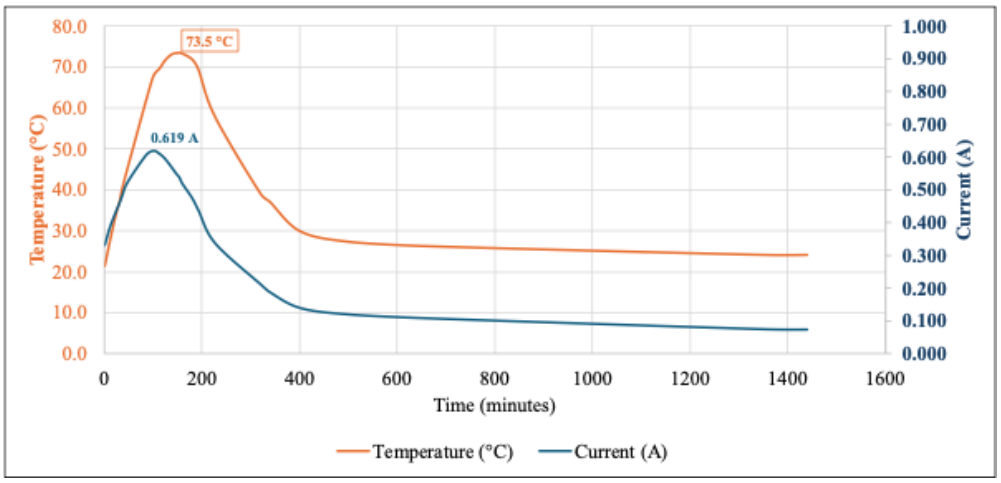


Fig. 1. Variation of current and specimen temperature as a function of time during 24 h of ohmic heating.

To evaluate the strength development of specimens subjected to ohmic heating curing, ultrasonic pulse velocity (UPV) measurements, as well as compressive and flexural strength test, were conducted at curing ages of 3, 6, 12, and 24 hours, and at 3 days, in accordance with TS EN 196-1. The specimens were exposed to ohmic heating curing for a maximum duration of 24 hours. Specimens tested at 3 days were stored under ambient conditions after first day. For comparison, specimens cured under ambient conditions were also tested for UPV, flexural and compressive strength at 1 and 3 days, the results were compared with those of the ohmic heating cured specimens. In addition, setting times were measured for both curing methods. Furthermore, the bulk density, water absorption, and porosity of the 3-day-old specimens were determined using the wire basket method.

3 Result and Discussion

3.1 Setting Time

The setting time result are presented in Table 3, and it is observed that ohmic heating has a pronounced shortening effect on the setting time. While specimens cured under ambient conditions completed their setting in approximately 245 minutes, the final setting time of the specimens subjected to ohmic curing was reduced to about 45 minutes, indicating an acceleration of the setting process by approximately 82%.

Table 3. Setting time results.

Curing condition	Initial setting time (min)	Final setting time (min)
Ambient curing	200	245
Ohmic heating curing	35	45

3.2 Unit Weight, Porosity, and Water Absorption Results

The results presented in Table 4 indicate that ambient curing and ohmic curing have limited effects on the unit weight, porosity, and water absorption properties of the specimens. While

the unit weight of the specimens cured under ambient conditions was determined to be 2.06 g/cm³, a slight decrease to 2.04 g/cm³ was observed for the specimens subjected to ohmic curing. An examination of the porosity values reveals that the porosity of the ohmic curing specimens was slightly higher (15.5%) compared to that of the ambient curing specimens (14.9%). Similarly, the water absorption ratio of the ohmic curing specimens was measured as 7.54%, showing a marginal increase relative to the ambient-cured specimens (7.13%). These increases suggest that the rapid reaction development induced by ohmic heating at early ages may lead to the formation of a relatively more open pore structure, particularly during the initial stages.

Table 4. Setting time results.

Curing type	Unit weight (%)	Porosity (%)	Water absorption (%)
Ambient curing	2.06	14.9	7.13
Ohmic curing	2.04	15.5	7.54

3.3 Compressive Strength, Flexural Strength and UPV

The results presented in Fig. 2 and Fig. 3 clearly demonstrate that ohmic heating curing significantly accelerates early-age compressive strength development. Specimens subjected to ohmic curing achieved a compressive strength of 24.63 MPa after only 3 hours, which increased to 31.43 MPa after 12 hours, corresponding to an increase of approximately 27.6%. The rate of strength gain was notably high during the first 12 hours, after which the rate of increase gradually decreased. This rapid early strength development can be attributed to the homogeneous internal temperature rise induced by ohmic heating, which accelerates reaction kinetics within the binder system. The internally generated ohmic heating enhances ion mobility and promotes faster formation of the binding gel phase, leading to early matrix densification. As the reactions progress and the availability of reactive phases decreases, the strength gain rate diminishes at later ages. In contrast, specimens cured under ambient conditions exhibited a compressive strength of 8.10 MPa at 1 day, which is approximately 74.3% lower than that of the ohmic-cured specimens (31.48 MPa). Although the compressive strength under ambient curing increased by 116.3% from 1 to 3 days, reaching 17.52 MPa, this value still corresponded to only 44.9% of the strength achieved with ohmic curing. These findings indicate that ohmic heating curing provides a substantially more effective approach for enhancing early-age compressive strength compared to ambient curing.

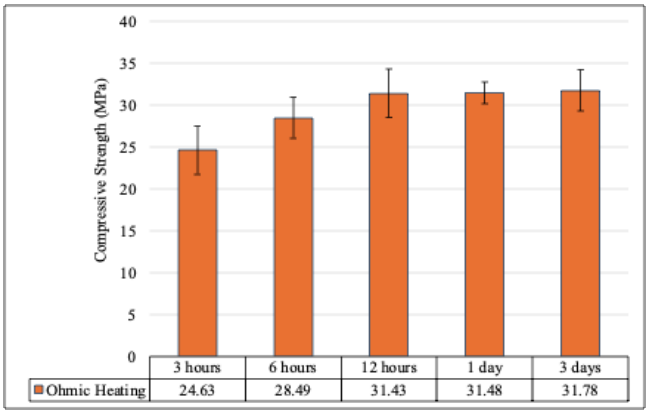


Fig. 2. Compressive strength development of the specimens during the first 3 days under ohmic curing.

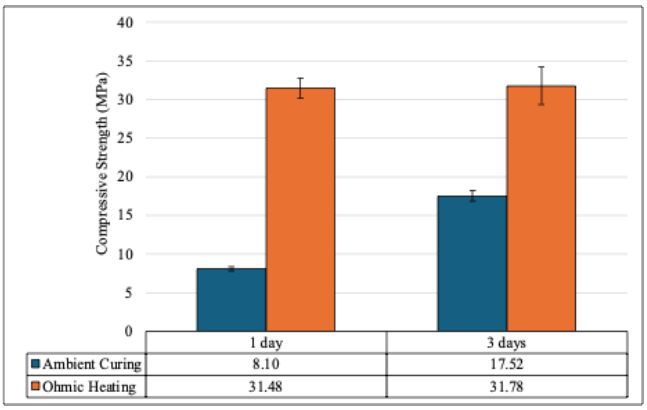


Fig. 3. Compressive strength results under ambient and ohmic curing.

The development of flexural strength under ohmic heating curing during the first 3 days is presented in Fig. 4, while the comparative results with ambient curing are given in Fig. 5. The findings clearly indicate that the application of ohmic heating significantly accelerates the development of early-age flexural strength. For the specimens subjected to ohmic curing, the flexural strength reached 4.706 MPa after only 3 hours and increased to 6.189 MPa at 1 day, corresponding to an increase of approximately 31.5%. In contrast, the specimens cured under ambient conditions exhibited a flexural strength of only 2.160 MPa at 1 day, which is considerably lower than that of the ohmic-cured specimens.

After 3 days of curing, the flexural strength values reached 3.769 MPa and 6.275 MPa for the ambient-cured and ohmic-cured specimens, respectively. Despite the gradual strength gain observed under ambient curing, the flexural strength achieved at 3 days remained lower than that obtained with ohmic curing. These results demonstrate that ohmic heating curing promotes a faster development of the microstructure at early ages, leading to a pronounced improvement in flexural strength.

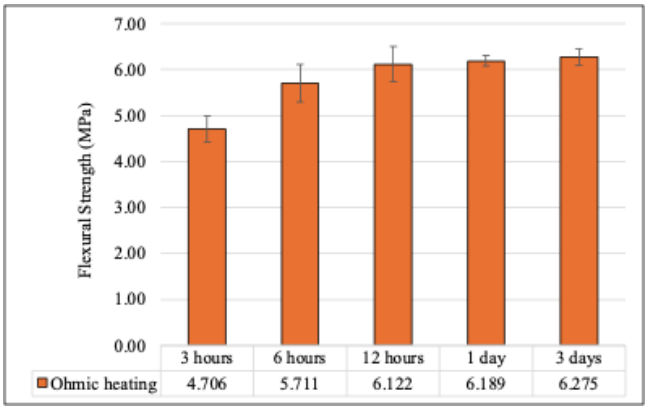


Fig. 4. Flexural strength development of the specimens during the first 3 days under ohmic curing.

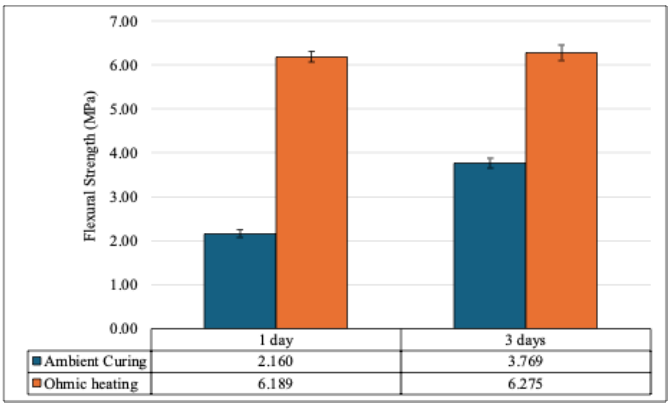


Fig. 5. Flexural strength results under ambient and ohmic curing.

UPV is non-destructive testing method used to evaluate internal voids, cracks, and discontinuities in concrete. An increase in ultrasonic wave velocity generally indicates improved homogeneity, and overall quality of the concrete. The development of UPV under ohmic heating curing during the first 3 days is presented in Fig. 6, while the comparative result with ambient curing is provided in Table 5. The result show that the UPV value of the specimens subjected to ohmic heating reached 3226 m/s after only 3 hours and increased by approximately 12.2% to 3618 m/s at. 3 days. In contrast, the UPV value of the specimens cured under ambient conditions was measured as 3504 m/s at 3 days. These findings are consistent with the compressive strength results and suggest that ohmic heating curing contributed to a more compact matrix structure, which was reflected in the higher early-age UPV values.

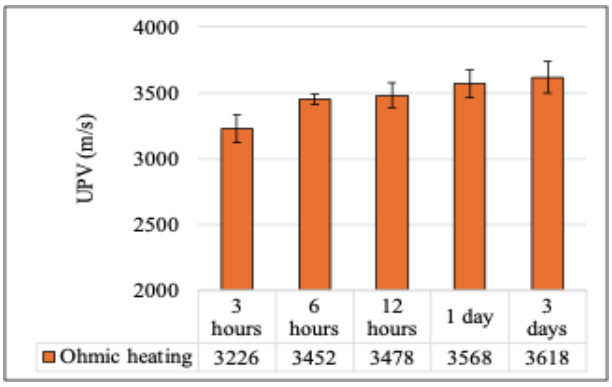


Fig. 6. UPV development of the specimens during the first 3 days under ohmic curing.

Table 5. UPV results.

Curing condition	**UPV (m/s)**	
	1 day	**3 days**
Ambient curing	3319	3504
Ohmic curing	3568	3618

4 Conclusion

The main conclusion obtained from this study are presented below.

- Ohmic heating resulted in an approximately 82% shorter final setting time compared to ambient curing.
- Ohmic heating curing achieved a compressive strength of 24.63 MPa after only 3 hours.

- Ambient-cured specimens exhibited a 44.9% lower compressive strength (17.52 MPa) lower than the 3-day compressive strength of those subjected to ohmic curing (31.78 MPa).
- Ambient-cured specimens exhibited a 39.9% lower flexural strength (3.769 MPa) lower than the 3-day flexural strength of those subjected to ohmic curing (6.275 MPa).
- Ambient curing and ohmic curing have limited effects on the unit weight, porosity, and water absorption properties of the specimens.

Acknowledgments
The authors used ChatGPT (OpenAI) for translation and language editing. The authors reviewed and revised all AI-assisted text and take full responsibility for the final content.

References

1. Davidovits, Joseph.: Geopolymer : chemistry and applications. Institut Géopolymère (2020).
2. Ding, Y., Dai, J.-G., Shi, C.-J.: Mechanical properties of alkali-activated concrete: A state-of-the-art review. Constr. Build. Mater. 127, 68–79 (2016). https://doi.org/10.1016/j.conbuildmat.2016.09.121.
3. Cheah, C.B., Samsudin, M.H., Ramli, M., Part, W.K., Tan, L.E.: The use of high calcium wood ash in the preparation of Ground Granulated Blast Furnace Slag and Pulverized Fly Ash geopolymers: A complete microstructural and mechanical characterization. J. Clean. Prod. 156, 114–123 (2017). https://doi.org/10.1016/j.jclepro.2017.04.026.
4. Chuewangkam, N., Payakaniti, P., Chindaprasirt, P., Pinitsoontorn, S.: Ohmic heating as an effective path to rapidly cure and strengthen alkali activated material. Constr. Build. Mater. 322, 126425 (2022). https://doi.org/10.1016/j.conbuildmat.2022.126425.
5. Nodehi, M., Ozbakkaloglu, T., Gholampour, A., Mohammed, T., Shi, X.: The effect of curing regimes on physico-mechanical, microstructural and durability properties of alkali-activated materials: A review. Constr. Build. Mater. 321, 126335 (2022). https://doi.org/10.1016/j.conbuildmat.2022.126335.
6. Wang, J., Ren, X., Cai, Y., Xiang, Y., Abdullahi Umar, H., Li, Y., Xiao, Q., Long, G.: Effect of direct electric curing on the mechanical properties, hydration process, and environmental benefits of cement-steel slag composite. Constr. Build. Mater. 406, 133382 (2023). https://doi.org/10.1016/j.conbuildmat.2023.133382.
7. Anvari, A., Azimi Yancheshme, A., Kekre, K.M., Ronen, A.: State-of-the-art methods for overcoming temperature polarization in membrane distillation process: A review. J. Memb. Sci. 616, 118413 (2020). https://doi.org/10.1016/j.memsci.2020.118413.
8. Wang, J., Long, G., Xiang, Y., Dong, R., Tang, Z., Xiao, Q., Yang, Z., Ma, K.: Influence of rapid curing methods on concrete microstructure and properties: A review. Case Studies in Construction Materials. 17, e01600 (2022). https://doi.org/10.1016/j.cscm.2022.e01600.
9. Uygunoğlu, T., Hocaoğlu, İ.: Effect of electrical curing application on setting time of concrete with different stress intensity. Constr. Build. Mater. 162, 298–305 (2018). https://doi.org/10.1016/j.conbuildmat.2017.12.036.
10. Kovtun, M., Ziolkowski, M., Shekhovtsova, J., Kearsley, E.: Direct electric curing of alkali-activated fly ash concretes: a tool for wider utilization of fly ashes. J. Clean. Prod. 133, 220–227 (2016). https://doi.org/10.1016/j.jclepro.2016.05.098.
11. Aygun, B.F., Uysal, M., Bilir, T., Çoşgun, T., Dilbas, H.: An investigation on physical, mechanical and microstructural properties of electricity-based cured GBFS-FA geopolymer. Constr. Build. Mater. 458, 139526 (2025). https://doi.org/10.1016/j.conbuildmat.2024.139526.

Author Contribution Statement

- *Conceptualization:* Mazem Yılmaz
- *Methodology:* Mazem Yılmaz, Mucteba Uysal
- *Investigation:* Mazem Yılmaz, Mucteba Uysal
- *Writing – Original Draft:* Mazem Yılmaz
- *Writing – Review & Editing:* Mazem Yılmaz, Mucteba Uysal

List of Abbreviations

- **GGBS** — Ground Granulated Blast Furnace Slag
- **FA** — Fly Ash
- **AC** — Alternating Current
- **UPV** — Ultrasonic Pulse Velocity

Publication Note

This paper was peer-reviewed, accepted for presentation, and included in the proceedings of the ACE2026 – International Conference on Advances in Civil Engineering, held on 12–14 October 2026 in Trabzon, Türkiye.

This paper may be cited as follows:

Mazem Yılmaz and Mucteba Uysal, "Early-age strength development in slag-fly ash geopolymers: effect of varying ohmic heating curing durations," in Proceedings of the ACE2026 – International Conference on Advances in Civil Engineering, Trabzon, Türkiye, 12–14 October 2026.

Effects of Reactive Magnesia in Portland Cements Including Fly Ash and GGBFS for Different Curing Regimes in Short Term

M. Kemal Ardoğa[1], İ. Özgür Yaman[2] and Mustafa Tokyay[3]
[1] 0000-0002-3132-0192, Hacettepe University, Civil Engineering Department, Ankara, Türkiye, mkardoga@gmail.com
[2] 0000-0001-6489-6852, Middle East Technical University, Civil Engineering Department, Ankara, Türkiye, ioyaman@metu.edu.tr
[3] 0000-0002-2454-6759, Middle East Technical University, Civil Engineering Department, Ankara, Türkiye mtokyay@metu.edu.tr

Abstract. One of the most popular methods for reducing the carbon footprint of cement-based materials is to incorporate mineral admixtures capable of carbonation, such as reactive magnesia, into the systems. However, studies on their use in construction materials are very limited. In this research, two distinct magnesia sources—magnesite and dolomite—were calcined at different temperatures and exposure times in laboratory conditions to produce magnesias with varying reactivities. Their reactivities were compared using the citric acid reactivity test, the corrected hydration conversion ratio and the change in mass during calcination. Based on the results, the most reactive magnesia was selected and added to Portland cement containing fly ash and GGBFS, at 15% and 30% of the total powder content by mass. The specimens were exposed to three different CO_2 concentrations: 0.04% (for 28 days), 20% (for 2 days), and 50% (for 2 days) under similar temperature and humidity conditions. Their mechanical performance on the 1st, 3rd, 7th, and 28th days was compared. The most reactive magnesia samples were obtained from calcining dolomite at 800 °C for 3 hours and from magnesite at 600 °C for 2 hours. The mortars containing reactive magnesia showed low strength regardless of the curing regime. However, the presence of reactive magnesia modified the strength gain in CO_2 curing regimes.

Keywords: Carbonation; Reactive magnesia; Curing; Portland cement.

1 Introduction

Nowadays, in order to reduce the carbon footprint of cement-based construction materials, a very common method is to incorporate mineral admixtures, which can be inert or have hydraulic and/or pozzolanic properties, into Portland cement clinker [1]. Few of them, however, can enhance mechanical properties by binding the CO_2 in the air to their structure. In other words, they have the ability to react with CO_2 in air and form carbonates, increasing strength by carbonation [2]. One of the most popular admixtures for enhancing strength of cementitious composite with such a mechanism is reactive magnesia.

The reactive magnesia is generally obtained through a calcination process of magnesium carbonates, which leads to the decomposition of the carbonate structure and removal of the CO_2 [2, 3]. The calcination temperature causes microstructure modifications and differences in the reactivity of the magnesia produced [2, 4, 5]. Therefore, the magnesias obtained are usually divided into groups according to their calcination temperature and, hence, their reactivity [3, 4, 6, 7, 8]. These, from the highest to the lowest reactivity, can be classified as reactive, dead-burned and fused magnesia. It is determined that the reactivity of the reactive magnesia produced at low temperatures such as 600 °C, is higher than that of the dead-burned magnesia obtained from the calcination at high temperatures such as 1500 °C since the latter has a denser crystalline structure than the former. On the other hand, the magnesia reactivity

depends not only on calcination temperature but also other factors such as residence (exposure) time and impurities [4, 7].

The magnesium carbonate, present as an impurity of limestone in raw meal of Portland cement clinker is burned at temperatures of about 1500 °C where the clinker is produced in rotary kilns of cement plants. Due to its exposure to these temperatures, its structure decomposes, forming dead-burned magnesia. Since its reactivity rate is lower than that of the Portland cement, the reactions of magnesia take place later than those of the Portland cement. Since the volume of the hydration products is higher, expansion cracks develop and they undermine the mechanical performance of the whole system [9]. As a result of this, standards regarding the specification of Portland cement, limit the maximum amount of magnesia present in the clinker to 5% or 6%, by weight [10, 11]. Unlike dead-burned magnesia, the reactive magnesia does not cause to crack due to expansion in the matrix. The reactions of reactive magnesia occur at the same time as or before the hydration of the Portland cement, so the hydration/carbonation products requiring higher space to form, do not lead to the expansion cracks in the fresh state of Portland cement fraction [2]. This allows reactive magnesia to be used safely in Portland cement systems [2].

Blends of Portland cement and reactive magnesia are defined as reactive magnesia cements [6]. In order to avoid undesirable consequences, it is important to determine the reactivity of magnesia before its use in the cement since that it can create unintentionally expansions or not is depending on its reactivity [4, 9]. To measure its reactivity, methods such as the citric acid coloration time or the magnesia hydration conversion ratio tests have been proposed by researchers [2, 8, 9, 12].

The reactive magnesia cements are reported to reduce the overall CO_2 emissions due to not only a reduction in the amount of Portland cement clinker but also its ability to absorb CO_2 in air to its structure [2]. In addition, it is considered that if stack gas of a typical cement plant is used for the curing environment of the reactive magnesia-incorporated cementitious composites, the overall emissions can be reduced further [5, 13, 14].

The largest mineral reserve of Türkiye is dolomite, the volume of which is estimated to be 15.8 billion tons [15]. Turkish magnesite production in 2016 reached 3.2 million tons, which positioned Türkiye as the world's leading magnesite producer after China [16 ,17]. It is therefore important to find possible ways to utilize them in cement industry in regarding to proposing a solution to reduce CO_2 emissions resulted from cement plants. Incorporating the reactive magnesias produced from two different Turkish magnesium carbonate sources into Portland-composite cements can both decrease the overall carbon footprint for the production and increase the mechanical performance of the end products through their ability to be carbonated.

In the literature, numerous studies were conducted on the microstructure, mechanical performance and durability of reactive magnesia cements, preferring not producing by calcining magnesium carbonates to obtain reactive magnesia, but utilizing commercially-available MgO having almost no impurity, as the reactive magnesia [2, 8]. However, in this study, the reactive magnesia was selected among the magnesias produced by calcining two different magnesium carbonate sources with different burning regimes under laboratory conditions. This paper aims to achieve the following: (1) to obtain reactive magnesia, by calcining naturally obtained magnesium carbonate sources, namely dolomite and magnesite, mined in Türkiye, under different burning regimes and determine the most reactive one with respect to its reactivity; (2) to investigate its mechanical performance in different CO_2 levels for Portland-composite cements in the short term; (3) for reactive magnesia cements, to assess the suitability of the mineral admixtures, namely fly ash and ground granulated blast furnace slag frequently used for producing Portland-composite cements. In this study, naturally-obtained sources, namely dolomite and magnesite, were burned under different burning

regimes and the obtained magnesias were compared by means of the change in mass during calcination, the corrected hydration conversion ratio and the citric acid coloration time. After determining the most reactive magnesia sample, it was included to Portland-fly ash and Portland-slag cements at 15% and 30% by mass of total binder. The mortars based on these cements were exposed to different CO_2 curing regimes. The effect of reactive magnesia on the compressive strength was determined under low-, medium- and high-level CO_2 curing regimes and compared with the control samples.

2 Materials and Methodology

2.1 Materials

As the magnesium carbonate sources to produce reactive magnesias, dolomite (D) and magnesite (M) were obtained from Antalya and Kütahya regions of Türkiye, in crushed form, respectively. After grinding them using a laboratory – scale ball mill, their chemical properties were determined as shown in Table 1. Fig. **1** shows the XRD profile of the magnesium carbonate sources used.

Table 1. Chemical analysis results and physical properties.

		Dolomite (D)	**Magnesite (M)**	**Portland Cement (P)**	**Fly Ash (F)**	**Ground granulated blast furnace slag (S)**
Oxide Analyses (%)	LOI	46.1	49.5	4.8	-	-
	CaO	33.1	0.9	60.1	3.7	38.2
	MgO	18.5	43.3	1.7	1.4	5.7
	SiO_2	0.3	0.7	18.9	55.6	37.8
	Fe_2O_3	0.2	0.5	2.7	9.1	0.8
	Al_2O_3	0.1	0.1	4.0	23.1	12.9
	SO_3	0.1	0.03	5.7	0.5	1.3
Physical Properties	Density (g/cm^3)	2.83	2.95	3.07	2.24	2.85
	Fineness (cm^2/g)	~4000	~4000	~4000	~2850	~4800

The Portland-composite cements were produced by incorporating the mineral admixtures to Portland cement (P). As the main binder, the Portland cement (P) used in this study and obtained from Baştaş Cement Factory, was classified CEM I 42.5 R according to TS EN 197-1. The mineral admixtures used were F-type fly ash (F) from Sugözü Thermal Power Plant and ground granulated blast furnace slag (S) from İskenderun Demir Çelik A.Ş. Their oxide composition and XRD profiles are depicted in Table 1 and Fig. **2**, respectively.

2.2 Methodology

The magnesium carbonate sources, namely magnesite and dolomite, were burned under different burning regimes based on TGA results. Various preliminary tests were applied to the magnesias produced to determine the most reactive magnesia sample. The selection considered not only the reactivity of the magnesia, but also the required temperature and exposure time to produce it for environmental considerations. Using the selected reactive magnesia and three curing regimes having different CO_2 levels, mortars were produced to investigate their compressive strength performance.

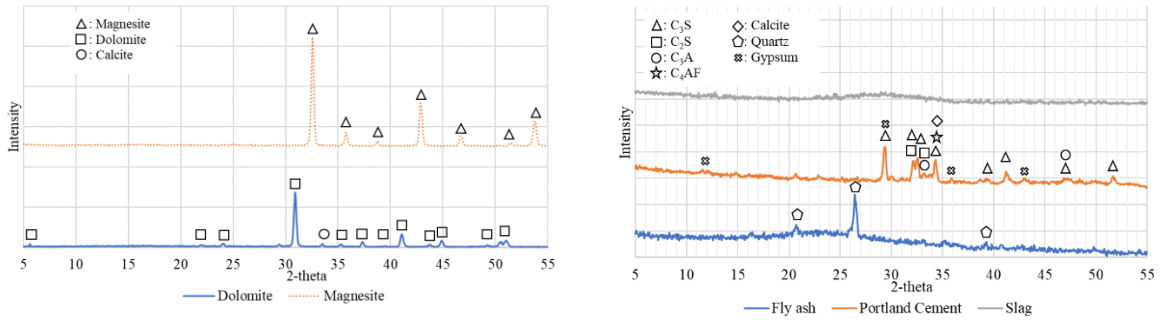


Fig. 1. XRD profiles of the materials utilized.

The calcination process was applied by a furnace and the rate of interior temperature increase was kept constant at about 100 °C/hour. The material was allowed to cool down in the furnace after burning. The magnesias were subjected to various preliminary tests proposed in the literature [8] in order to determine their reactivity:

Citric acid coloration time: This was defined as the required time for 1 g calcined magnesium carbonate sample in 200 mL of 0.0175 M citric acid solution containing a phenolphthalein indicator to change the color of the solution from white to pink during being stirred at a constant rate of 600 rpm. After 30 minutes (1800 seconds), the experiment was terminated for the samples not showing any color change. This method is based on the procedure proposed by Zhu et al. [12].

Change in mass during calcination: The oven-dried magnesium carbonate source, the weight of which was already recorded, was exposed to the burning regime and the mass decrease due to the removal of its CO_2, occurred in the specimen was measured. Even if the loss cannot give any insight into the crystallinity or reactivity, showed whether the temperature was sufficient to calcine the material completely, or not.

Corrected magnesia hydration conversion ratio: A 2 g of dried magnesia sample was mixed with 100 g of distilled water, and in the following day, the solution was filtered to obtain particles in solution with a vacuum pump. The change of mass in dry condition (w_1) shows the mass of water reacted with magnesia to form magnesium hydroxide. Based on stoichiometric calculations and chemical reaction, the magnesia hydration conversion ratio can be written in Eqn. 1. However, due to impurities present in magnesium carbonate sources (which can not be calcined), a factor indicating the purity of the sample (Mass ratio of MgO in calcined sample) should be introduced as presented in Eqn. 2. This method is based on the procedure proposed by Zhu et al. [12].

$$X\,(\%) = \frac{40.30(w_1 - 2)}{18.02 w_0} \cdot 100 \qquad \textbf{Eqn. 1}$$

$$X_{corrected}\,(\%) = X\,(\%) \cdot \frac{1}{\text{Mass ratio of MgO in calcined sample}} \qquad \textbf{Eqn. 2}$$

According to the experimental findings, the most reactive magnesia (RM) was mixed with P, S and F to produce reactive magnesia cements according to the mixture proportions stated in Table 2. The amount of the pozzolanic mineral admixtures (S and F) was adjusted to be 30% of the Portland cement fraction, representing CEM II/B-S and CEM II/B-V types, frequently produced in Türkiye. The amount of reactive magnesia was set relative to the total weight of the Portland cement and mineral admixtures at 15% and 30%. The content of the calcareous sand was fixed at 2.75 times the total binder content (P + S + F + RM) to produce mortars. The mixing process for the mortars was carried out in accordance with ASTM C 109. The reactive magnesia and mineral admixtures were added to the portland cement at the very beginning. The water content of the mortars was adjusted based on mass loss during the calcination process, the details of which are explained in subsequent sections.

Table 2. Mix proportions of reactive magnesia cements.

Reactive Magnesia Cements	Portland Cement (%)	Ground Granulated Blast Furnace Slag (%)	Fly Ash (%)	Reactive Magnesia (%)
	P	**S**	**F**	**RM**
C	100	0	0	0
CS	77.0	23.0	0	0
CF	77.0	0	23.0	0
15CM	87.0	0	0	13.0
15CMS	67.0	20.0	0	13.0
15CMF	67.0	0	13.0	13.0
30CM	77.0	0	0	23.0
30CMS	59.3	17.7	0	23.0
30CMF	59.3	0	17.7	23.0

It was determined that three CO_2 curing regimes would be applied to the specimens in a carbonation chamber. For these, the CO_2 levels were determined to be 0.04% (low level – ambient), 20% (medium level) and 50% (high level). These concentration levels represented the ambient conditions, typical stack gas obtained from a cement factory and CO_2 enriched stack gas of a cement factory, respectively [13, 14]. The curing relative humidity (RH) and temperature were kept constant at 90% and 25 °C, respectively for all curing regimes. To see the effect of CO_2 curing regimes in the short term, the mortars were cured in three regimes having different CO_2 concentrations for just two days. In labelling the specimens, the number represents the amount of reactive magnesia. The suffixes after the name are put to indicate the curing regime. The specimens marked with '-', '+' and '++' were cured in the low-, medium- and high-level CO_2 curing regimes, respectively. In the 2nd day, all samples cured in medium- and high-level CO_2 regimes were moved to low-level CO_2 regime.

5 cm-cubic molds were filled with the mortars and immediately after casting, the materials were moved to curing regime. For 1st-, 3rd-, 7th- and 28th- day compressive strength, at least 3 specimens were failed according to the standard ASTM C109.

The thermogravimetric analyses were performed with Perkin Elmer Pyris 1 TGA Instrument. The temperature range was arranged 35 – 1050 °C and the burning rate was adjusted to be 20 °C/min. The XRD profiles were obtained with BTX III Benchtop XRD Analyzer having 5–55 2-theta XRD range. The curing of the specimens was performed in a carbonation chamber, capable of controlling CO_2 concentration, temperature and humidity.

3 Results and Discussion

The higher loss on ignition results seen in Table 1 showed the content of CO_2 removed from the carbonates present in dolomite and magnesite due to ignition process. All the CO_2 was resulted from the calcination of the carbonates present in the sources during burning. The contents of the magnesium carbonates are about 39% and 90% in dolomite and magnesite, respectively. As the amount of the calcium carbonate present in dolomite is 59%, its amount in magnesite is negligible. In order to get a clue about their calcination temperatures, the thermogravimetric analyses conducted to the magnesite and dolomite were investigated and their results (Fig. **2**) showed that the maximum mass losses occurred at the temperatures slightly higher than 600 °C and 750 °C, respectively. In addition, the ultimate mass losses of the dolomite and magnesite were determined to be approximately 52% and 48%, respectively. Considering that the mass losses were resulted from the decomposition of carbonates, these results are consistent with the CO_2 content shown in their chemical analysis results.

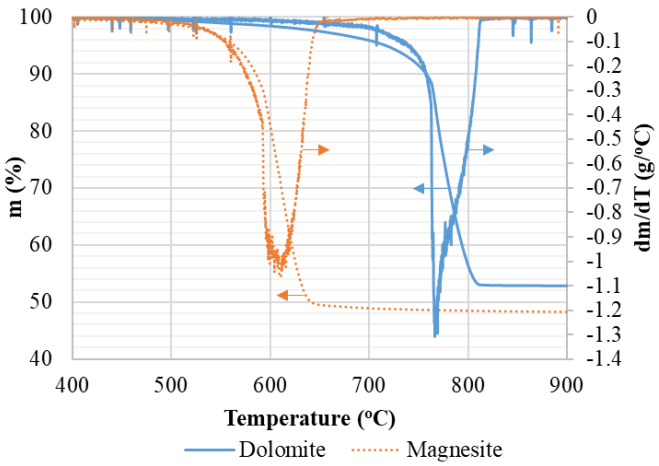


Fig. 2. The TGA results for the magnesium carbonate sources.

Based on the results of the thermogravimetric analyses, the oven-dried magnesite and dolomite were calcined with the maximum temperatures varying from 500 °C to 800 °C with the intervals of 100 °C. The residence times were ranged from 60 minutes to 180 minutes with the periods of 30 minutes. The specimens obtained were named according to their burning regimes and the former and latter numbers represented the burning temperatures in °C and residence time in minutes, respectively, in the names of the reactive magnesia candidates. The first letter, 'D' or 'M' stood for the magnesium carbonate source type, dolomite and magnesite, respectively.

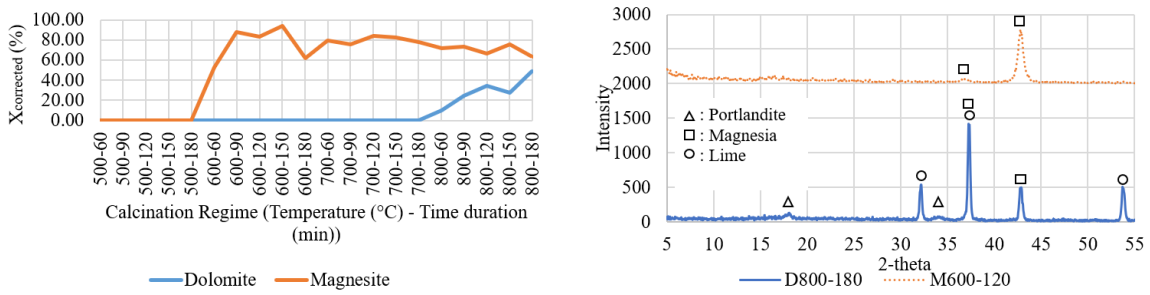
The results of the preliminary experiments to determine the reactivity of the magnesias produced are shown in Table 3 and Fig. **3**(a). The mass changes during calcination did not change significantly until the temperature 800 °C and 600 °C, for dolomite and magnesite, respectively. This shows that the calcination started at about these temperatures. The higher calcination temperature of dolomite than that of magnesite was undoubtfully resulted from the higher calcium carbonate content of the dolomite. The citric acid coloration time determined also supported these findings. The coloration times measured for the magnesia produced at below these temperatures were so long (higher than 1800 s) that these magnesias could be assumed to be unreactive. When considering hydration conversion ratios, the samples produced from magnesite in the calcination temperature of 600 °C had the highest reactivity. However, for the samples produced from dolomite in higher temperatures of 700°C showed a slight reactivity. The samples yielding lower citric acid coloration time had higher conversion ratio, indicating the higher reactivity of magnesia with water. It is clear that the increase in temperature resulted in the decrease of the coloration time, and correspondingly, increase in the reactivity. Considering the results, for the most reactive magnesia should be chosen among the magnesia candidates burned at temperatures of 800 and 600 °C for the magnesite and dolomite, respectively. In addition, for these, best results were obtained at the exposure times of 180 and 120 minutes. The results show the production of the ‘D800-180’ magnesia was more energy-intensity process than that of the ‘M600-120’ magnesia. To obtain a more ‘green’ reactive magnesia produced with lower CO_2 emission, the source should not be burned at higher temperatures (The higher the calcination temperature, the more energy consumed and the higher the CO_2 emission due to burning process).

Table 3. Results of preliminary experiments.

Magnesia	Mass change during	Citric acid coloration	Magnesia	Mass change during	Citric acid coloration

	calcination (%)	time (s)		calcination (%)	time (s)
D500-60	0.71	> 1800	**M500-60**	9.20	> 1800
D500-90	1.23	> 1800	**M500-90**	3.97	> 1800
D500-120	1.28	> 1800	**M500-120**	4.33	> 1800
D500-150	1.33	> 1800	**M500-150**	6.39	> 1800
D500-180	1.44	> 1800	**M500-180**	10.58	> 1800
D600-60	2.89	> 1800	**M600-60**	31.68	154
D600-90	1.92	> 1800	**M600-90**	49.31	40
D600-120	2.31	> 1800	**M600-120**	51.15	26
D600-150	2.32	> 1800	**M600-150**	49.91	32
D600-180	3.99	> 1800	**M600-180**	37.68	90
D700-60	5.48	> 1800	**M700-60**	50.06	30
D700-90	5.17	> 1800	**M700-90**	49.94	31
D700-120	6.36	> 1800	**M700-120**	50.11	29
D700-150	6.42	> 1800	**M700-150**	50.35	33
D700-180	7.46	> 1800	**M700-180**	50.41	34
D800-60	41.37	18	**M800-60**	50.42	31
D800-90	30.43	26	**M800-90**	50.42	28
D800-120	34.37	18	**M800-120**	50.51	32
D800-150	37.89	20	**M800-150**	50.94	33
D800-180	46.50	10	**M800-180**	50.95	32

The reactive magnesias were investigated with their XRD profiles as shown Fig. **3**(b). It was determined that since the 'D800-180' magnesia had free lime, the probability of occurrence of soundness problem due to its presence was higher. So, for oncoming experiments, as the reactive magnesia (RM), the 'M600-120' magnesia was preferred to use to produce cement mortars, instead of the 'D800-180' magnesia.



(a) (b)

Fig. 3. (a) $X_{corrected}$ results for magnesias produced. **(b)** XRD results for M600-120 and D800-180.

For preparation of mortars, the mix design stated for ordinary Portland cement in ASTM C 109 standards, was based; however, it was seen that RM reacted with water in the very first minutes vigorously, resulting higher amount of heat evolved. Since it caused loss of consistency, extra water was added to the mixtures to compensate the loss of water. Therefore, the total water content was calculated by Eqn. 3:

$$w_t = 0.484\,x(RM + P + F + S) + 0.43\,x\,RM \qquad \textbf{Eqn. 3}$$

where, 0.484 is the water / cement ratio specified in ASTM C 109 standard. The water content to hydrate 1 g of reactive magnesia with no impurities can be calculated by the molar

masses of the chemical compounds in following the chemical reaction, $MgO + H_2O \rightarrow Mg(OH)_2$. Accordingly, the content of the water consumed in that reaction is just the proportion of the molar mass of water (18) to the molar mass of magnesia (40), which is 0.45 g (=18/40). However, the M600-120 cannot be obtained purely due to the impurity present. Assuming that magnesite lost its all CO_2 during calcination, approximately 95 % of the material is MgO. Therefore, it can be concluded that 1 g of RM (with its impurities) reacted with 0.43 (=0.45 x 0.95) g of water.

The compressive strength results can be seen in Fig. **4**. It is obvious that F and S were effective in contributing especially early and late age, respectively. This was due to the higher pozzolanic effect of F and latent hydraulic properties of S [1]. The RM in cements decreased the strength because of M – S – H gels or brucite produced from its hydration reaction (It was stated that the CO_2 concentration in ambient conditions was not sufficiently high to yield carbonation products of the RM [2]). It was reported that since the RM hydration products had higher porosity and lower binding property than the hydration products of P [2, 6, 8]. It is recognized that the 2d- CO_2 curing regime modified the effect of mineral admixtures on the strength. The F caused the formation of C – S – H gels because of the pozzolanic reaction of SiO_2 with portlandite produced from hydration of P [1]. The CO_2 in medium- and high-level curing regimes led to the consumption of portlandite to from calcite (having lower binding properties than C – S – H gels) [18]. This can reduce the effect of F. The strength contribution of slag was dependent on the pH of the pore solution. According literature, the activation of slag was possible only in higher alkaline solutions, and because of higher CO_2, the portlandite, mainly responsible for high pH, was consumed by possible carbonation reactions [1, 18]. When considering 15CM in different curing regimes, it is obvious that the higher CO_2 concentration led to a slight decrease in strength. However, among all the specimens 30CM, the highest strength was obtained for medium-level CO_2 curing regime. High-level curing regime caused a lower strength even than the low-level one. Although the strength obtained for the specimen 30CM+ (~23 MPa) was slightly lower than the specimen 15CM+ (~24 MPa), it can be concluded that 30% RM addition is the most appropriate one considering the reduction in the amount of P. In addition, it was seen that the decreases in strengths due to addition of RM differed for different curing regimes. Therefore, the 28^{th} day-strength reductions for reactive magnesia cement mortars with respect to the cement mortars containing none cured in the same curing regime were calculated. Fig. **4**(d) shows the results for all curing regimes. As expected, the cement mortars containing 30% RM showed higher strength reductions than the ones containing 15% due possibly to the dilution effect for all curing regimes. On the other hand, for medium-level curing regime, the strength reduction had a tendency to decrease. This was due to the reaction of CO_2 with the RM incorporated to cement mortars. As a result, the carbonation products formed partially compensate the strength reduction detected. However, in high-level curing regime, it was seen that the decrease in strength to increase unlike medium-level CO_2 curing regime. Initially, the carbonation started at the surfaces of the specimens and it was considered that the carbonation products have lower permeability for gas ingress into specimen. So, the impermeable shell formed, as a result of the carbonation of P as well as RM, at the surface prevented further carbonation reactions and strength gain for the interior sections of the specimens [18]. Thus, it can be concluded that for reactive magnesia cements, the concentration of CO_2 was a crucial parameter and it was important to find out optimum CO_2 concentration for RM to be carbonated effectively.

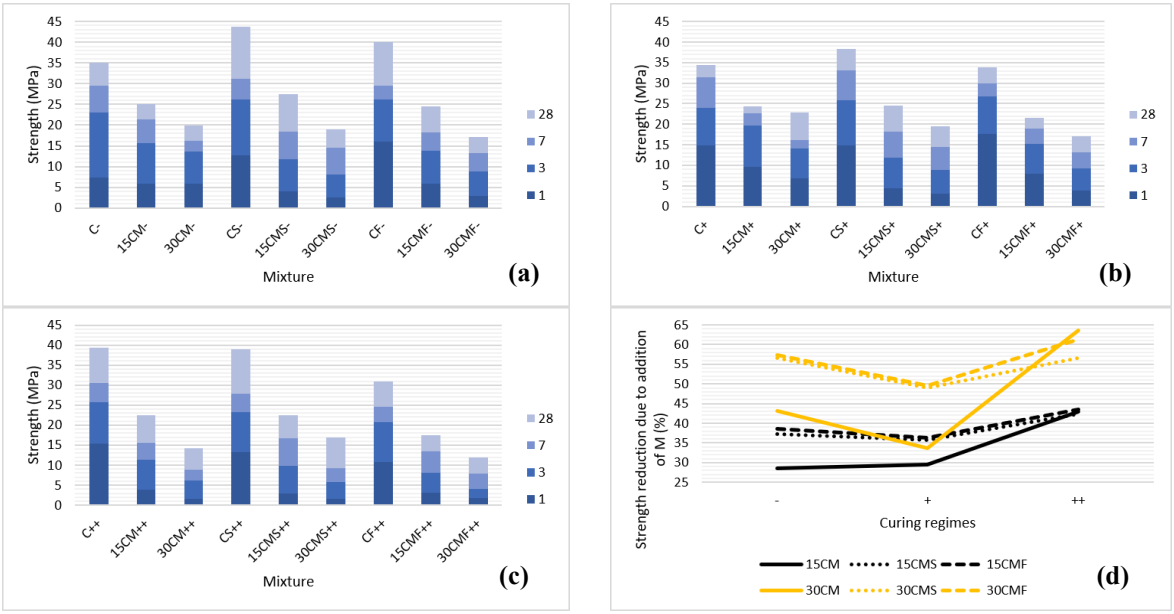


Fig. 4. (a, b, c) Compressive strength results for the specimens cured in low-, medium- and high-level CO_2 regimes. **(d)** Strength reduction due to addition of reactive magnesia.

4 Conclusion

In this study, the following conclusions were reached:

- It was possible to produce reactive magnesias by calcining magnesite and dolomite at the temperatures of 600°C and 800°C, respectively. However, since calcined dolomite had free lime and its calcination temperature was higher, the reactive magnesia obtained from magnesite was selected to produce reactive magnesia cements with Portland cements.
- At low-level CO_2 curing regime, it was seen that the increase in reactive magnesia of the cements caused strength to be lower, because of the dilution effect. The hydration products of the reactive magnesia fraction could not contribute the strength sufficiently.
- It was concluded that the CO_2 concentration was a key parameter for the carbonation of reactive magnesia. The strength decrease at medium-level CO_2 regime due to the addition of reactive magnesia was not so high as that observed in the high-level one. This was resulted from the impermeable carbonate barrier, preventing CO_2 ingress and hence the carbonation further at high-level CO_2 regime. In medium-level CO_2 regime, the concentration was not so high for this type of shell formation. However, the carbonation products compensated the decrease.
- The effect CO_2 level differed on the reactions of fly ash and GGFBS. Since the CO_2 reacted with the portlandite present in pore solution, CO_2 effect was much more pronounced. The activation of GGFBS was directly related with the pH of the pore solution, and in the case of medium- or high-level CO_2 curing regimes, the pH was lowered. But, this effect was detected to be limited due to latent hydraulic properties of GGFBS. In addition, the portlandite necessary for the pozzolanic reaction of fly ash was consumed by CO_2, its effects were limited in medium- and high-CO_2 curing regimes.

References

1. Tokyay, M. Cement and Concrete Mineral Admixtures. 1st edn. CRS Press. (2016).
2. Walling, S.A.; Provis, J. L. Magnesia-Based Cements: A Journey of 150 Years, and Cements for the Future? Chemical Reviews 116 4170-4204 (2016).
3. Shand, M. The Chemistry and Technology of Magnesia. Wiley-Interscience (2006).
4. Jin F.; Al-Tabbaa, A. Characterisation of Different Commercial Reactive Magnesia. Advances in Cement Research 26(2). 101-113 (2014).

5. Unluer, C.; Ruan S. Comparative Life Cycle Assessment of Reactive MgO and Portland Cement Production. Journal of Cleaner Production 137. 258-273 (2016).
6. Al-Tabbaa. Reactive Magnesia Cements. In Eco-Efficient Concrete (Pacheco-Torgal F, Jalali S, Labrincha J and John VM (eds)) Elsevier. (2013).
7. Bassioni, G.; Farid, R.; Mohammed, M.; Hammouda, R. M.; Kühn, F. E. Effect of Different Parameters on Caustic Magnesia Hydration and Magnesium Hydroxide Rheology: A Review. Materials Advances 2. 6519-6531 (2021).
8. Josè, N.; Ahmed, H.; Miguel, B.; Luis E.; Jorge, B. Magnesia (MgO) Production and Characterization, and Its Influence on the Performance of Cementitious Materials: A Review. Materials 13. 4752 – 4783 (2020).
9. Liwu, M.; Min D.; Mingshu T. Effect of Calcination Temperature on the Microstructure, Activity and Expansion of Mgo-type Expansive Additive used in Cement-based Materials. Key Engineering Materials 400 – 402. 169 – 174 (2008).
10. ASTM C150 - Standard Specification for Portland Cement. ASTM International, West Conshohocken, PA, USA. (2020).
11. EN 197-1 Cement - Part 1: Composition, specifications and conformity criteria for common cements. European Standards. (2011).
12. Zhu, J.; Ye, N. Liu, J. Yang, J. Evaluation on Hydration Reactivity of Reactive Magnesium Oxide Prepared by Calcining Magnesite at Lower Temperatures. Industrial & Engineering Chemistry Research 52. 6430 – 6437 (2013).
13. Schakel, W.; Hung, C. R.; Tokheim, L.; Stromman, A. H.; Worrel, E. Ramirez, A. Impact of fuel selection on the environmental performance of postcombustion calcium looping applied to a cement plant. Applied Energy 210. 75 – 87 (2018).
14. Wang, S.; Hang X. Sustainable Cement Production with Improved Energy Efficiency and Emerging CO2 Mitigation. Advances in Chemical Engineering and Science 2. 123 – 128 (2012).
15. Anadolu Ajansı. Turkey's Possible Mineral Reserves Around 2.5 Trillion Usd. https://www.aa.com.tr/en/archive/turkeys-possible-mineral-reserves-around-25-trillion-usd/425575. last accessed 2026/07/19.
16. Hastorun, S. The Mineral Industry of Turkey. USGS. 2022.
17. Euromines. The European Magnesite / Magnesia Industry: Enabler in the Transition to A-low Carbon Economy. European Association of Mining Industries. (2020).
18. Savija, B.; Lukovic, M. Carbonation of cement paste: Understanding, challenges and opportunities. Construction and Building Materials 117. 285 – 301 (2016).

Author Contribution Statement

- *Conceptualization, methodology:* Mustafa Tokyay
- *Investigation, writing – original draft:* M. Kemal Ardoğa
- *Writing – review & editing:* İ. Özgür Yaman

Publication Note

This paper was peer-reviewed, accepted for presentation, and included in the proceedings of the ACE2026 – International Conference on Advances in Civil Engineering, held on 12–14 October 2026 in Trabzon, Türkiye.

This paper may be cited as follows:

Ardoğa, M. Kemal; Yaman, İ. Özgür; Tokyay, Mustafa, "Effects of Reactive Magnesia in Portland Cements Including Fly Ash and GGBFS for Different Curing Regimes in Short Term," in Proceedings of the ACE2026 – International Conference on Advances in Civil Engineering, Trabzon, Türkiye, 12–14 October 2026.

The Usability of Metakaolins Produced from Kaolinitic Raw Materials in Green Cement Production

Kadircan Varan[1], Fatma Zehra Toker[2], İsmail Gökalp[3], Teoman Erenoğlu[4], Pınar Uysal Tüten[5], Yıldız Yıldırım[6], Hasan Ahmet Uzunoğlu[7], Hasan Ergin[8]

[1] 0009-0004-9367-7869, Akcansa Cement Industry and Trade Inc., Buyukcekmece, Istanbul, Türkiye, kadircan.varan@akcansa.com.tr
[2] 0009-0009-2822-7112, Istanbul Technical University, Department of Mining Engineering, Istanbul, Türkiye, tokerf16@itu.edu.tr
[3] 0009-0000-6661-8928, Akcansa Cement Industry and Trade Inc., Buyukcekmece, Istanbul, Türkiye, ismail.gokalp@akcansa.com.tr
[4] 0009-0008-8341-1724, Akcansa Cement Industry and Trade Inc., Buyukcekmece, Istanbul, Türkiye, teoman.erenoglu@akcansa.com.tr
[5] 0009-0002-0758-5913, Akcansa Cement Industry and Trade Inc., Ezine, Canakkale, Türkiye, pinar.uysaltuten@akcansa.com.tr
[6] Kaleseramik, Canakkale Kalebodur Ceramic Industry Joint Stock Company, Türkiye, yildizyildirim@kale.com.tr
[7] Kalemaden Raw Materials Industries Inc., Can, Canakkale, Türkiye ahmetuzunoglu@kale.com.tr
[8] 0000-0001-6692-7456, Istanbul Technical University, Department of Mining Engineering, Istanbul, Türkiye, hergin@itu.edu.tr

Abstract. A large portion of carbon emissions in cement production originates from clinker production. Therefore, reducing the clinker ratio is a cornerstone of carbon neutrality strategies for the cement and ready-mixed concrete sectors, both in the short and long term. In this study, eight different clays with varying chemical and mineralogical properties were calcined and their pozzolanic properties were measured. The characterization of the eight different calcined clays was determined using XRF and XRD. The samples were calcined in a static kiln for 120 minutes at the particle size of less than 3 mm. The pozzolanic activity of the calcined products was determined using the Chapelle test. The mixtures were substituted into Portland cement at 20, 25 and 30% alone, or in combination of limestone at 10, 12.5, and 15%. The chemical composition, specific gravity, fineness, specific surface area, sulfate content, setting time, water requirements, and compressive strength of the produced cement mixtures were investigated. The amorphous phase ratios of the clays ranged from 16 to 50%. In general, limestone-free mixtures containing 20-25% metakaolin showed good performance in terms of strength. In mixtures containing limestone, low limestone ratios were effective. However, as the proportion of calcined clay in the mixtures increased, the water requirement increased and generally shortened the setting time. The findings showed that low-carbon, environmentally friendly cements can be produced when appropriate clay selection, degree of calcination, sulfate balance, and limestone ratio are ensured.

Keywords: Green cement; metakaolin; clinker substitute; pozzolanic activity.

1 Introduction

The cement industry is responsible for approximately 8% of global carbon dioxide emissions. A large portion of these emissions occur during the clinker production phase of cement manufacturing. A significant portion of the emissions in clinker originates from the calcination of limestone and fuels. Therefore, issues such as alternative fuels, raw material carbon capture

and storage, energy efficiency, and alternative pozzolanic materials are becoming increasingly important in cement production [1,2].
By-products such as fly ash and ground blast furnace slag have been used as clinker reducers in cement for many years. It is predicted that the use of these products will decrease over the years due to the green transformation in the energy and iron and steel sectors [2-4]. Calcined clay, being a widely available raw material worldwide, requiring a lower calcination time and temperature compared to clinker production, and exhibiting pozzolanic activity after firing, has significant potential as an alternative pozzolanic raw material [5].
In kaolinite containing clays, after undergoing dehydroxylation during heat treatment and losing a significant amount of water, they transform into amorphous and reactive metakaolin. If the calcination temperature is insufficient, the amorphous phase may not form; if heated excessively, it may sinter, causing the resulting amorphous structure to revert back to a crystalline structure. The pozzolanic reactivity formed after calcination depends not only on the chemical composition of the clay but also on the degree of crystallization, grain size, and mineralogical structure [3-6]. When metakaolin is substituted for cement in a specific portion of the matrix, it reacts with calcium hydroxide, a hydration product of cement, to form a CASH structure. When limestone is also added, the reactive phase in metakaolin combines with limestone to form carboaluminate. Carboaluminate can improve the pore structure in the matrix and compensate for the strength loss in mixtures with low clinker content [4-7].
Studies in the literature mention that water requirements increase and workability decreases with increasing metakaolin content. However, it can be said that when used up to a certain ratio, it improves strength and resistance to external influences [8]. Therefore, in the substitution of metakaolin, it is not only the pozzolanic activity of the material that should be used, but also the fineness, chemical properties, specific surface area of the material to be substituted for cement, and its performance in conjunction with the chemical additives to be used should be considered [9-10]. The aim of this study is to compare the fresh state and strength performance of kaolinitic clays obtained from different regions, either directly as a replacement for cement or in combination with limestone, after calcination.

2 Materials and Methods

2.1 Raw Materials and Metakaolin Production

Eight different clay samples obtained from various sources were used in this study. The chemical composition using XRF (Table 1). Mineralogical analysis of the samples were determined using XRD testing (Table 2). The samples were calcined in a static electric furnace for 120 minutes each, to a particle size of less than 3 mm. Calcination temperatures were determined using the TGA test method applied to the clays. The appropriate calcination temperature was determined by identifying the dehydroxylation range of the clay from the TGA results. Clays K1 and K2 were calcined at 800°C, clays K3, K4 and K5 at 850°C, and clays K6, K7 and K8 at 900°C.

Table 1. Chemical analysis.

Sample Code	LOI (%)	SiO_2 (%)	Al_2O_3 (%)	TiO_2 (%)	Fe_2O_3 (%)	CaO (%)	MgO (%)	Na_2O (%)	K_2O (%)	P_2O_5 (%)	SO_3 (%)
K-1	2.6	71.3	23.1	0.4	0.8	0.1	0.1	0.1	1.1	0.2	1.0
K-2	1.1	71.7	24.3	0.5	1.7	0.1	0.1	0.1	0.2	0.2	0.1
K-3	0.5	72.1	24.4	0.5	1.8	0.1	0.1	0.1	0.2	0.2	0.1
K-4	1.2	69.6	26.9	0.4	0.7	0.1	0.1	0.1	0.6	0.2	0.4
K-5	1.5	77.7	16.9	0.6	2.1	0.1	0.0	0.1	0.3	0.3	0.3
K-6	0.8	68.2	22.3	1.3	4.0	0.2	0.3	0.4	2.2	0.3	0.1
K-7	0.7	66.6	22.6	1.2	5.1	0.2	0.2	0.8	2.2	0.3	0.2
K-8	0.9	77.4	15.3	0.8	4.1	0.2	0.2	0.2	0.4	0.2	0.3

Table 2. Mineralogical analysis with the rietveld method.

Sample Code	Mineral Phases - XRD
K-1	75.66% Low Quartz + 0.31% Anatase + 24.03% Amorphous Phase
K-2	32.83% Low Quartz + 29.13% Cristobalite + 38.04% Amorphous Phase
K-3	31.76% Low Quartz + 24.27% Cristobalite + 43.53% Amorphous Phase + 0.44% Hematite
K-4	62.85% Low Quartz + 37.15% Amorphous Phase
K-5	82.48% Low Quartz + 0.38% Anatase + 0.63% Hematite + 0.22% Cristobalite + 16.30% Amorphous Phase
K-6	34.08% Low Quartz + 1.97% Proto.Hematite + 17.19% Muscovıte + 6.86% Sanidine + 39.90% Amorphous Phase
K-7	45.59% Low Quartz + 2.31% Hematite + 9.30% Muscovıte 2M1 + 42.80% Amorphous Phase
K-8	45.20% Low Quartz + 1.42% Hematite + 1.36% Mica + 52.01% Amorphous Phase

2.2 Pozzolanic Activity and Cement Mixtures Activators

The pozzolanic activity of calcined clays obtained from eight different sources was measured using the Chapelle method (Table 3). The results are presented as mg $Ca(OH)_2$/g. The substitution rates of calcined clays for cement were 20, 25, and 30%. In addition, series with 10, 12.5, and 15% limestone were prepared. Accordingly, the non-limestone series contain 70-80% clinker, while the limestone systems contain 55-70% clinker.

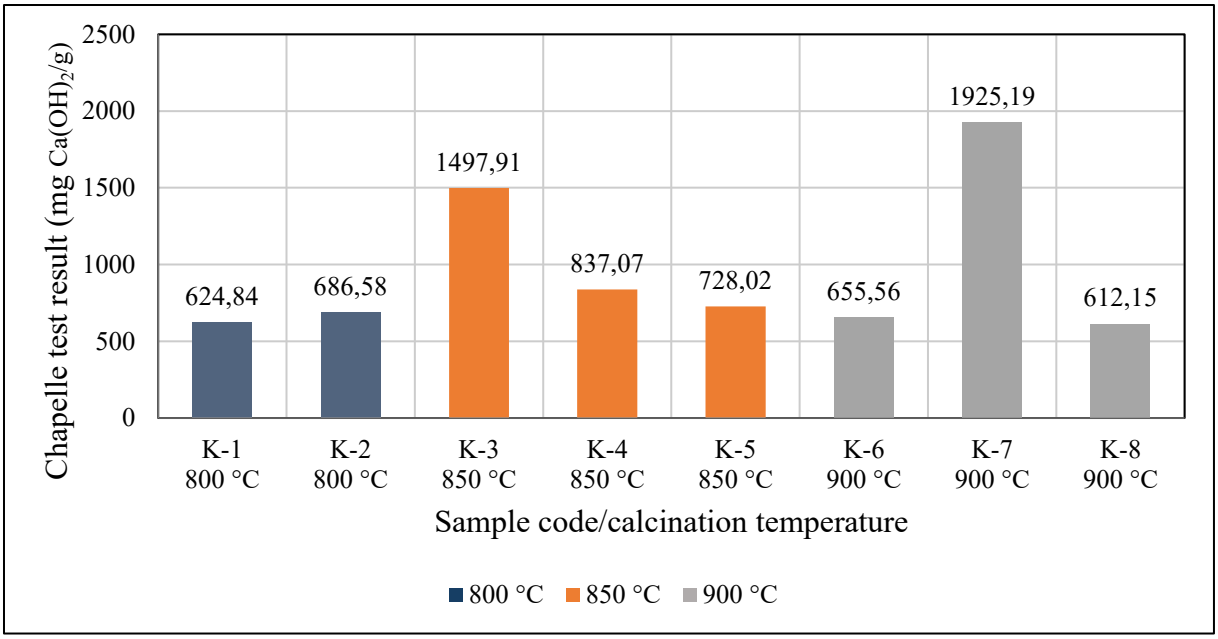


Fig. 1. Pozzolanic properties results.

2.3 Mix Design

The chemical composition, SO_3 content, sieve analysis, Blaine specific surface area, water requirements, setting initial and final times, and compressive strengths of the prepared binder mixtures were determined. The results were compared with a standard Portland cement reference.

The mixtures contain cement, metakaolin, limestone, sand and water according to their composition. Each mixture is produced according to EN 197-1, and the binder phase of the mixtures contains 450 g of binder phase, 1350 g of sand, and 225 g of water. The water/binder ratio of all mixtures is 0.5 and is kept constant (Table 3).

Table 3. Mix proportions.

Mix (x = 1 to 8)	Cement (g)	Metakaolin (g)	Limestone (g)
K-x/1	360.0	90.0	-
K-x/2	337.5	112.5	-
K-x/3	315.0	135.0	-
K-x/4	315.0	90.0	45
K-x/5	281.25	112.5	56.25
K-x/6	247.5	135.0	67.5

3 Findings

The Blaine specific surface areas of the series ranged from 3750-7150 cm^2/g, with an average of 5400 cm^2/g. The average percentage above a 45 µm sieve was 6.2%. When the metakaolin ratios in the mixtures were high, the Blaine value also increased. However, while a positive relationship with strength was expected due to the filler effect when this value increased, fineness alone could not be established as an indicator of its effect on strength.

Water demands generally ranged between 28.6 and 31.0% in the K1-K5 series. In the K6-K8 series, it ranged between 31.6 and 32.0%. In the scenario where the metakaolin ratio increased from 20 to 30%, the water demand increased by an average of 1.5-2.5%. The lowest water demand values were observed in mixtures using 20% metakaolin and 10% limestone

powder. The highest water demand was observed in mixtures combining 30% metakaolin and 15% limestone powder.

The SiO_2 content of the calcined clays ranges from 66.6-77.4%, and the Al_2O_3 content from 15.3-26.9%. The highest Al_2O_3 content was found in clay K4, and the highest SiO_2 content in clay K5. The higher Fe_2O_3 values in clay samples K6, K7, and K8 compared to other samples necessitate further evaluation of these materials in terms of color and chemical equilibrium with the clinker. In addition, the total SiO_2, Al_2O_3, and Fe_2O_3 ratios of all samples are suitable according to the required chemical composition properties of pozzolanic materials. No consistent trend was found between the amorphous phase content and the Chapelle test values. For example, K8 has the highest amorphous phase ratio, but its Chapelle value of 612.2 mg/g places it in the lower ranks of the clay group. K7 clay, with an amorphous phase ratio of 41.8%, gave the highest activity value of 1925.2 mg/g. K3 clay showed the highest pozzolanic activity with a value of 1497.9 mg/g. K1, K2, K6, and K8 clays exhibited results around 700 mg/g. Chapelle results alone cannot provide insight into the performance of the cement matrix. Besides pozzolanic activity, the filling effect needs to be evaluated the particle size of the material, and the sulfate balance formed by the system.

SO_3 content was approximately 2.8-3.0% in batches without limestone and around 2.6% in batches with limestone. As the proportion of limestone and calcined clay increases, the amount of clinker decreases. Therefore, since the sulfate/aluminate ratio in the system also changes, the optimum gypsum requirements of mixtures containing limestone and calcined clay may be compared to the reference Portland cement.

In mixtures containing limestone powder, strength generally performed worse than in mixture series containing only 20-25% metakaolin. The best balance was given by mixtures containing 25% metakaolin and 12.5% limestone. According to studies in the literature, it is emphasized that reactive aluminates in calcined clay form monocarboaluminates together with the clays, and this resulting phase binds the aluminate, increasing the volume and structural density of the hydration products [4-7]. For this synergy to occur, the purity and fineness of the reactive alumina limestone in metakaolin must be controlled.

Setting generally started between 150-190 minutes and setting ended between 230-260 minutes. The use of metakaolin shortened the setting time by 15-25 minutes. Limestone addition reduced the setting time in some batches, while in others it had no noticeable effect.
The 28-day compressive strength results for all K1, K2, K3, K4, and K5 series exceeded the reference mixture's strength of 59.2 MPa. The K1 series yielded approximately 61-62 MPa, the K2 and K5 series approximately 62-63 MPa, the K4 series approximately 63-64 MPa, and the K3 series approximately 64-65 MPa. The K6 series yielded approximately 58-59 MPa, and the K8 series approximately 59-60 MPa, yielding results equal to or exceeding the reference mixture. Based on these results, it can be said that mixtures containing 20-25% metakaolin alone produce results superior to the reference due to pozzolanic reaction and filler effect (Figure 2).It is expected that K3, which gives the highest chapelle test result, will provide the highest strength. However, the fact that metakaolins with lower pozzolanic reactivity, such as K1, K2, and K8, perform better than the reference mixture demonstrates that this is not solely related to their free lime consumption capacity. The fact that K7 has a very high chapelle value but is limited in cement performance is consistent with and supports this connection. Variables such as the high iron content, particle size distribution, or sulfate ratio of K7 may be the reasons why it does not fully reflect its pozzolanic activity in the mortar strength (Figure 2).

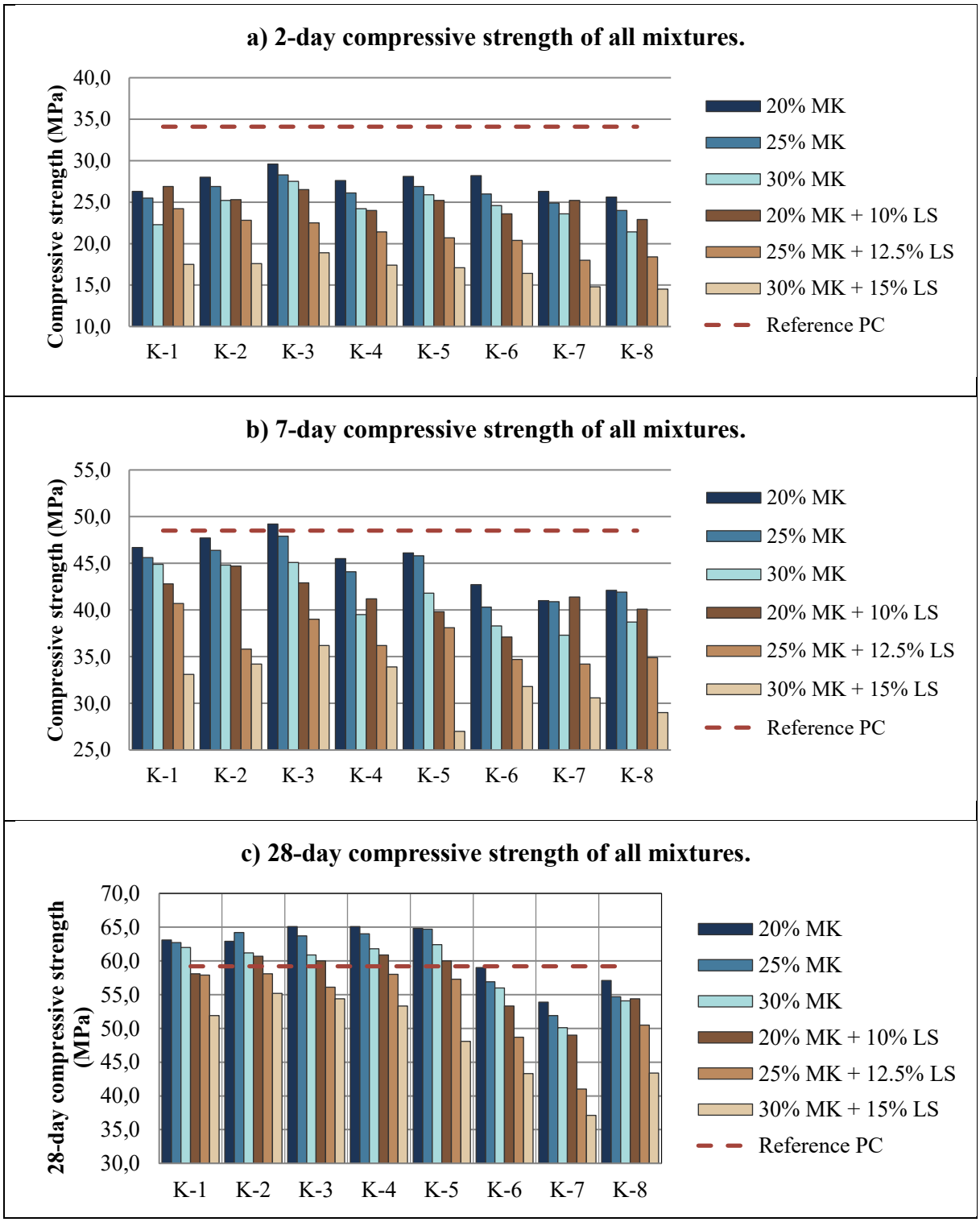


Fig. 2. Compressive strength of all mixtures.

4 Conclusion

Metakaolins, obtained by calcining kaolin-containing raw materials coded K1 to K8 at 800-900°C for 120 minutes, showed variations according to the phase structures formed after calcination. Amorphous phase ratios ranged from 16-52%, and Chapelle activity values ranged from 612-1925 mg $Ca(OH)_2$/g. Raw material selection and calcination conditions were influential in determining metakaolin quality. Metakaolins K3 and K7 yielded the highest pozzolanic activity values. However, the effect on cement strength performance does not

directly correlate with pozzolanic activity performance. Pozzolanic activity is related to phase structure, particle properties, sulfate ratios, and other components of the mixture.

In the experiments, it can be concluded that all series between K1-K5 exceeded the reference mixture values. K3 was the series that gave the best value with 65 MPa. In general, limestone-free mixtures containing 20-25% metakaolin have yielded the most stable strength performance. In low-clinker mixtures with limestone, a content of 20% metakaolin and 12.5% limestone can be considered feasible (Figure 2). Increasing the metakaolin ratio increases the water requirement but it can also shorten the setting time. Optimizing the SO_3 levels with component properties is an important aspect.

In conclusion, kaolinitic clays can enable the production of green cement containing calcined clay by achieving a controlled particle size distribution and calcination parameters.

Acknowledgments

All authors contributed to the conception and design of the study. Material preparation, data collection, analysis, and manuscript writing were performed collaboratively by the authors. All authors reviewed and approved the final manuscript. This research was carried out under the comprehensive project supported by the Scientific and Technological Research Council of Turkey (TÜBİTAK), 1832-Green Transformation in Industry Program (Project No. 3248046).

References

[1] Scrivener, K. L., John, V. M., Gartner, E. M. (2018). Eco-efficient cements: Potential, economically viable solutions for a low-CO_2 cement-based materials industry. *Cement and Concrete Research*, 114, 2-26.

[2] CEMBUREAU (2020). Cementing the European Green Deal: Reaching Climate Neutrality along the Cement and Concrete Value Chain by 2050. Brussels.

[3] Fernandez, R., Martirena, F., Scrivener, K. L. (2011). The origin of the pozzolanic activity of calcined clay minerals: A comparison between kaolinite, illite and montmorillonite. *Cement and Concrete Research*, 41, 113-122.

[4] Antoni, M., Rossen, J., Martirena, F., Scrivener, K. (2012). Cement substitution by a combination of metakaolin and limestone. *Cement and Concrete Research*, 42, 1579-1589.

[5] Ghazy, M.F., Maaty, E.S., Elaty, M.A., Alrwashdeh, A.A. (2025). A comprehensive review of limestone calcined clay cement (LC3): Environmental and properties benefits, challenges, opportunities, and future directions. *Results in Engineering.*

[6] Tironi, A., Trezza, M. A., Irassar, E. F., Scian, A. N. (2012). Thermal treatment of kaolin: effect on the pozzolanic activity. *Procedia Materials Science.*

[7] Tang, J. et al. (2024). The synergistic effect of calcined coal-series kaolinite and limestone on the hydration of Portland cement. *Material*s, 17, 4512.

[8] Chen, J. J., Li, Q. H., Ng, P. L., Li, L. G., Kwan, A. K. H. (2020). Cement equivalence of metakaolin for workability, cohesiveness, strength and sorptivity of concrete. *Materials*, 13, 1646.

[9] Fu Q., Liu Y., Niu D., (2026). Hydration characteristics and microstructure of limestone calcined clay cement. *Journal of Building Engineering.*

[10] Hosen, K., Chen, B. (2025). Limestone calcined clay cement (LC3): A review of materials, properties, production and environmental impact. *Journal of Building Engineering.*

Publication Note
This paper was peer-reviewed, accepted for presentation, and included in the proceedings of the ACE2026 – International Conference on Advances in Civil Engineering, held on 12–14 October 2026 in Trabzon, Türkiye.

This paper may be cited as follows:
Varan, K., Ergin, H., Toker, F.Z., Gökalp, İ., Erenoğlu, T., Uysal Tüten, P., Yıldırım, Y., Uzunoğlu, H.A., "The Usability of Metakaolins Produced from Kaolinitic Raw Materials in Green Cement Production," in Proceedings of the ACE2026 – International Conference on Advances in Civil Engineering, Trabzon, Türkiye, 12–14 October 2026.

Neural Network-Driven Forecasting of Concrete Compressive Strength

Mehmet Nadir[1] and Mehmet Sefa Orak[2]
[1] Ninova Mühendislik, Istanbul, Türkiye, mehmet@ninovamuhendislik.com
[2] 0000-0002-5783-479X, Department of Civil Engineering, Maltepe University, Istanbul, Türkiye, sefaorak@maltepe.edu.tr

Abstract. One cannot have a design of any merit that will stand up to quality control without a precise estimate of the concrete's compressive strength. Nor can one optimize materials in a sustainable fashion without it. The problem with conventional methods, whether they be empirical correlations or the physical testing of cylinders, is that they are resource intensive and do not cope well with the intricate chemistry of today's multi-component binders. Our solution is a robust feedforward artificial neural network (ANN). We have evaluated the ANN's predictive capacity against 1,030 experimental records for eight design parameters; the proposed ANN significantly outperforms XGBoost, Random Forest, Support Vector Regression, and Multiple Linear Regression, while achieving performance highly competitive with the top-performing CatBoost model. Over the whole of the multi-age dataset the model yields an R^2 of 0.9280 and an RMSE of 4.4500 MPa; for the 28-day subset these come in at 0.8250 and 4.9100 MPa respectively, comparable to the 0.8303 R^2 from the CatBoost model. An examination of the correlation and parametric sensitivity shows that cement content and curing age are the primary drivers of strength, while water content is the principal limiting factor. In short, the ANN is a computational, non-destructive means of appraising strength which makes for a simpler mix design and obviates the need for excessive physical trial batches, thereby reducing the infrastructure's embodied carbon.

Keywords: Concrete Compressive Strength, Artificial Neural Networks, CatBoost, Machine Learning, Mix Design Optimization, Predictive Modeling.

1 Introduction

It is hardly necessary to make the case for concrete as the foundation of modern civil engineering. Our essential infrastructure is built on it, from a highway bridge to the underpinnings of a commercial high-rise or any heavy industry. The safety and structural integrity of such systems are only as good as the uniaxial compressive strength of the concrete employed. To be sure of quality one must have cylinders or cubes of concrete cast and allowed to cure in a moist environment for 28 days before subjecting them to mechanical testing [1, 2]. While a 28-day figure will satisfy the design code, there is a logistical and scheduling cost to waiting four weeks on the lab numbers at the site of construction [3].

Portland cement, water, and mineral aggregate are no longer the only ingredients one will find in the field. High-performance concretes of the present day are of a different order of sophistication, with chemical superplasticizers and industrial SCMs in the form of fly ash or GGBFS being employed [4, 5]. A multi-component binder is the outcome, its non-linear hydration

kinetics a product of both pozzolanic and hydraulic reactions; a complexity defying the standard linear or polynomial regression [3, 6]. Machine learning is an appealing solution in this respect as it can extract the physical and chemical patterns from the empirical data [4–6]. For tabular regression, there is room for ensemble methods such as CatBoost or XGBoost, but when it comes to mapping the continuous non-linearities and high-dimensional feature interactions at hand, deep feedforward Artificial Neural Networks (ANNs) are more fitting [1, 7–9].

An experimental dataset of 1,030 records of concrete mixtures has been the basis for a rigorous evaluation of the feedforward artificial neural network in our work. To see how it stacks up, the proposed architecture is pitted against five top machine learning algorithms [10, 11]; testing has been carried out under both 28-day fixed and multi-age curing conditions. The aim is to provide a computational framework with real heft to the engineer, something robust and practical that will allow a swift assessment of mix performance and do away with the necessity of too many laboratory batch trials. In this way, we can further the cause of sustainable concrete production.

2 Dataset Description and Exploratory Data Analysis

2.1 Concrete Mixture Dataset

The 1,030 laboratory concrete mixture records that form the basis of this study were taken from the empirical data of some of the more highly regarded experimental testing programs [1]. Together, they constitute a dataset with eight continuous inputs, namely the cement content, blast furnace slag and fly ash, water, superplasticizer, coarse and fine aggregate, as well as curing age. One also has the uniaxial compressive strength (measured in megapascals). Of the total, 425 have been set aside to assess how the model performs in accordance with standard design code; these are all specimens cured for 28 days. Prior to training, we normalized the input features in order to be free of any bias arising from scale and to ensure a uniform convergence of the gradient descent across the various parameter ranges.

2.2 Exploratory Data Analysis and Feature Correlations

To determine the material mechanisms in play, we have put the two dataset partitions through an assessment of their Pearson correlation coefficients. The 1,030 samples in their entirety reveal cement content to be most positively correlated with compressive strength ($r = +0.50$), a result one would anticipate given that reactive binder is readily available for the formation of hydration products.

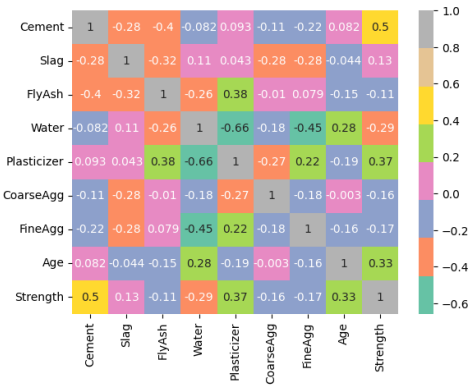


Fig. 1. Pearson correlation matrix for full concrete dataset (N = 1030) across 8 input variables and compressive strength.

Curing age has exhibited a positive trend (r = +0.33), indicative of the microstructure's increased density over time. One can attribute the superplasticizer dosage to a correlation of r = +0.37 as well, given its role in dispersing the cement grains and reducing the need for water. Then there is the water content, which, in accordance with Abrams' law on the water-to-cement ratio, is negatively correlated in a significant way (r = -0.29).

When one looks at the 28-day fixed-curing subset, the influence of mix proportions is much more pronounced. The cement content registers a positive correlation coefficient of r = +0.67 while that of the water content is a negative r = -0.40. These are results that bear out what the water-to-binder ratio will allow in terms of compressive strength, curing time being a given.

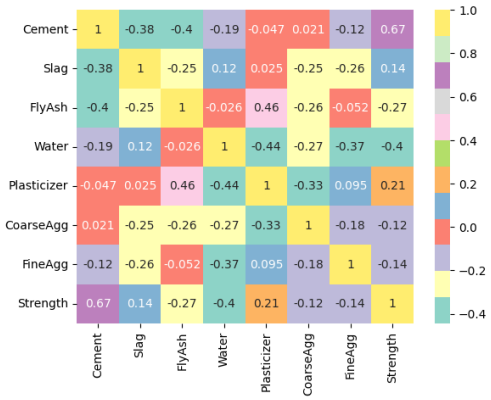


Fig. 2. Pearson correlation matrix for 28-day concrete dataset (N = 425) with fixed curing age.

3 Methodology

3.1 Neural Network Model Architecture

The present study employs a multi-layer feedforward ANN. In the way the network is designed, one finds an input layer of eight neurons and a linear output made up of a single neuron with a number of dense hidden layers in between, all running on ReLU activation functions. We have opted for Adam stochastic gradient optimization as it is both numerically stable and does not tax computational resources. To prevent any overfitting [5], a dropout regularization of 0.15 is in place.

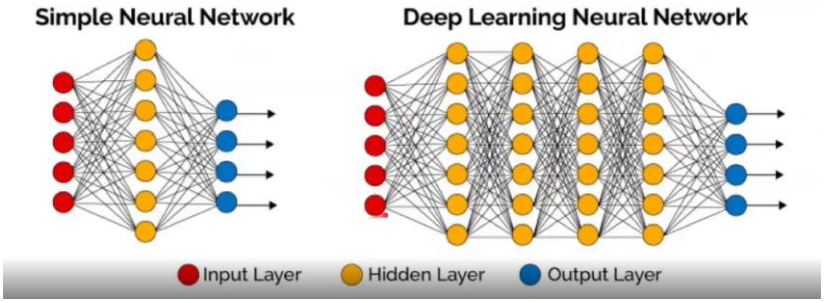


Fig. 3. Workflow of the proposed neural network concrete strength prediction framework.

3.2 Benchmark Machine Learning Models

To gauge the predictive power of the artificial neural network (ANN) we have put forward, it was pitted against a selection of AI paradigms that are well established in the field. Five machine

learning algorithms were trained to this end with an 80/20 train-test split [12–15]. The models are: CatBoost (Categorical Boosting), a gradient boosting framework which relies on symmetric and oblivious decision trees to stave off prediction shift [12]; XGBoost, or Extreme Gradient Boosting, for its scalability as a tree booster and by virtue of its regularized loss objectives and second-order Taylor expansion [13]; and Random Forest (RF), an ensemble bagging technique that randomizes feature subspace sampling to assemble de-correlated decision trees [14]. For non-linear applications, we made use of Support Vector Regression (SVR), a kernel method of structural risk minimization apt for the mapping of features to high-dimensional hyperspaces [4, 5]. As a parametric baseline to judge first-order linear relationships, Multiple Linear Regression (MLR) was also applied.

4 Evaluation Metrics

Model predictive accuracy was evaluated using four standard statistical metrics: Coefficient of Determination (R^2), Mean Absolute Error (MAE), Mean Squared Error (MSE), and Root Mean Squared Error (RMSE).

$$R^2 = 1 - \frac{\sum_{i=1}^{n} \left(y_i - \hat{y}_i\right)^2}{\sum_{i=1}^{n} (y_i - \bar{y})^2} \tag{1}$$

$$\text{MAE} = \frac{1}{n} \sum_{i=1}^{n} \left| y_i - \hat{y}_i \right| \tag{2}$$

$$\text{MSE} = \frac{1}{n} \sum_{i=1}^{n} \left(y_i - \hat{y}_i\right)^2 \tag{3}$$

$$\text{RMSE} = \sqrt{\frac{1}{n} \sum_{i=1}^{n} \left(y_i - \hat{y}_i\right)^2} \tag{4}$$

The variables are defined as follows: y_i represents the measured experimental compressive strength in MPa, $\hat{y}_i$ denotes the compressive strength predicted by the model (MPa), $\bar{y}$ is the mean of the measured experimental values across the dataset, and n is the total number of test samples in the evaluation.

5 Results and Discussion

5.1 Machine Learning Model Performance Benchmarking

An account of how the various models have performed is given in Table 1, which covers the metrics for the entire dataset (N = 1030) as well as the 28-day subset (N = 425).

Table 1. Machine learning model performance comparison for the full dataset (N = 1030) and 28-day concrete strength forecasting (N = 425).

Model Algorithm	Full Dataset R^2	Full Dataset RMSE (MPa)	28-Day Subset R^2	28-Day Subset RMSE (MPa)
CatBoost (Best ML)	**0.9367**	**4.3018**	**0.8303**	**4.8351**
XGBoost Ensemble	0.9245	4.6820	0.8120	5.0210
Random Forest (RF)	0.9110	5.1200	0.7980	5.2400
Proposed Feedforward ANN	0.9280	4.4500	0.8250	4.9100
Support Vector Reg. (SVR)	0.8420	6.8900	0.7150	6.4500
Multiple Linear Reg. (MLR)	0.6120	10.4200	0.5410	8.1200

One need only refer to Table 1 to see the linear baseline significantly outperformed by the non-linear ensemble boosting and neural network algorithms. In a way CatBoost is the machine learning standard here: for the full dataset it has an R^2 of 0.9367 and an RMSE of 4.3018 MPa, while on the 28-day subset the corresponding values are 0.8303 and 4.8351 MPa. Then there is the feedforward ANN we have put forward, its predictive precision is no less impressive. Over all the data it yields a coefficient of determination of 0.9280 with an RMSE of 4.4500 MPa; for the 28-day portion one finds an R^2 of 0.8250 and an RMSE of 4.9100 MPa. They are numbers that speak to the model's capacity to make sense of what multi-component hydration kinetics can throw at it.

```
=== Regression Model Comparison ===
```

	Model	R2	RMSE
0	CatBoost	0.936737	16.301778
1	XGBoost	0.923075	19.822068
2	HistGradientBoosting	0.912152	22.636847
3	Gradient Boosting	0.882089	30.383423
4	Random Forest	0.876230	31.893268
5	Extra Tree	0.839407	41.381799
6	MLP	0.825028	45.086939
7	Decision Tree	0.804260	50.438604
8	AdaBoost	0.762543	61.188118
9	KNN	0.679777	82.515386
10	BayesianRidge	0.627697	95.935483
11	Linear	0.627542	95.975484
12	KernelRidge	0.626012	96.369511
13	Ridge	0.625534	96.492884
14	SGD	0.620092	97.895158
15	SVR	0.605662	101.613487
16	Huber	0.586939	106.437904
17	NuSVR	0.581872	107.743684
18	OMP	0.251831	192.788897
19	Lasso	0.188441	209.123526
20	ElasticNet	0.055112	243.479822
21	RANSAC	-0.611062	415.140191

Fig. 4. Comparison of machine learning model performances (R^2 and RMSE) for full concrete dataset (N = 1030).

```
=== Regression Model Comparison ===
```

	Model	R2	RMSE
0	CatBoost	0.830343	48.351802
1	HistGradientBoosting	0.824562	49.999345
2	Random Forest	0.823097	50.416957
3	XGBoost	0.815377	52.617008
4	Gradient Boosting	0.814603	52.837699
5	Extra Tree	0.754897	69.853683
6	MLP	0.742526	73.379593
7	BayesianRidge	0.736543	75.084664
8	Linear	0.735574	75.360755
9	SGD	0.731883	76.412622
10	Huber	0.731728	76.456782
11	KernelRidge	0.730927	76.685063
12	Ridge	0.728446	77.392277
13	Decision Tree	0.726302	78.003232
14	AdaBoost	0.723772	78.724392
15	KNN	0.721350	79.414482
16	RANSAC	0.677122	92.019535
17	OMP	0.508327	140.125618
18	SVR	0.486301	146.403007
19	NuSVR	0.427708	163.101713
20	Lasso	0.361080	182.090533
21	ElasticNet	0.066844	265.947041

Fig. 5. Comparison of machine learning model performances (R^2 and RMSE) for 28-day concrete dataset (N = 425).

5.2 Neural Network Model Validation and Predictive Capability

The data are presented in Figs. 1 to 6 in the form of exploratory correlation heatmaps and some scatter plots that set the predicted compressive strengths up against what was measured, as well as for a comparative benchmarking of the models' metrics. There is no question from the R^2 figures that the non-linear dynamics at play among the cementitious binders, water and chemical

admixtures have been readily handled by the multi-layer neural network. As for the mechanics, large aggregate volumes do not unduly sway the weight updates thanks to feature normalization. The model also holds its own with test data it has never seen before; overfitting is precluded by the use of dropout regularization.

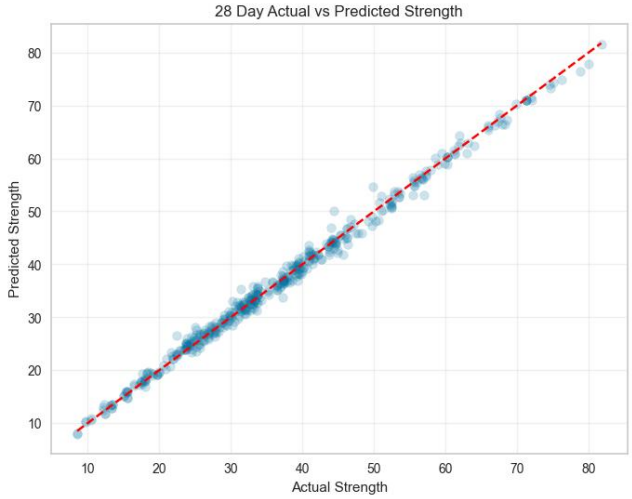


Fig. 6. Actual versus predicted compressive strength values (MPa) using the proposed neural network model.

6 Practical Engineering Applications

The computational framework of this work is of no small practical value in the design of structural engineering and for operating ready-mix concrete batch plants [16]. There are three principal uses to which it can be put.

To begin with, it puts an expedited method of mix formulation at the disposal of the design engineer; in seconds, dozens of binder combinations can be evaluated so that recourse to physical trial batches when a project is first being designed is largely unnecessary [16].

Then there is the matter of sustainable material optimization. The framework lends itself to a proper appraisal of high replacement levels in the form of industrial by-products such as slag or fly ash, thereby reducing the amount of Portland cement called for and bringing down embodied carbon emissions in some cases by 30% [6, 16–18].

As for quality assurance at the plant, ready-mix suppliers may make use of the predictive algorithms in their control software. A case in point is the projection of 28-day strength prior to shipping, which not only precludes the possibility of non-compliance but also ensures that waste is kept to an absolute minimum.

7 Conclusions

To forecast the compressive strength of concrete we put together a neural network framework; after its methodical construction it was validated on experimental data of various ages. The results are:

• A CatBoost ensemble proved to be very accurate on the whole of the data, with an R^2 of 0.9367 and RMSE of 4.3018 MPa. Our feedforward ANN was not far behind, producing R^2 values of 0.9280 (full set) and 0.8250 (28-day subset), the latter entailing an RMSE of 4.9100 MPa against 4.4500 for the former. Such performance is well beyond the capabilities of classical linear models.

• Compressive strength is positively driven above all by the age of curing and the amount of cement; water content is the principal limiting factor.

• There is a need to exercise close control of the water-to-binder ratio, as 28-day curing renders the compressive strength more susceptible to variations in binder proportions.

• We have employed dropout regularization (0.15) and feature normalization to guard against overfitting and see that the model generalizes to test mixtures it has not been exposed to.

• In the end, the proposed architecture is an effective means of non-destructive computation. It offers a way to streamline the proportioning of concrete mixes and do away with some of the laboratory trial batching, which is conducive to sustainable construction practices.

References

1. Yeh, I.C.: Modeling of strength of high-performance concrete using artificial neural networks. Cement and Concrete Research 28(12), 1797–1808 (1998).

2. Abrams, D.A.: Design of Concrete Mixtures. Structural Materials Research Laboratory, Lewis Institute, Bulletin 1, Chicago (1918).

3. Neville, A.M.: Properties of Concrete, 5th edn. Pearson Education, London (2011).

4. Asteris, P.G., et al.: Predicting concrete compressive strength using hybrid ensembling of surrogate machine learning models. Cement and Concrete Research 145, 106449 (2021).

5. Chou, J.S., Pham, A.D.: Enhanced artificial intelligence for ensemble approach to predicting high-performance concrete compressive strength. Construction and Building Materials 49, 554–563 (2013).

6. Naderpour, H., Rafiean, A.H., Fakharian, P.: Compressive strength prediction of environmentally friendly concrete using artificial neural networks. Journal of Building Engineering 16, 213–219 (2018).

7. Chopra, P., Sharma, R.K., Kumar, M.: Prediction of compressive strength of concrete using artificial neural network and genetic programming. Advances in Materials Science and Engineering 2016, Article ID 7648467 (2016).

8. Ni, H.-G., Wang, J.-Z.: Prediction of compressive strength of concrete by neural networks. Cement and Concrete Research 30(8), 1245–1250 (2000).

9. Golafshani, E.M., Behnood, A., Arashpour, M.: Predicting the compressive strength of normal and high-performance concretes using ANN and ANFIS hybridized with grey wolf optimizer. Construction and Building Materials 232, 117266 (2020).

10. Khademi, F., Akbari, M., Jamal, S., Nikoo, M.: Multiple linear regression, artificial neural network, and fuzzy logic prediction of 28-day compressive strength of concrete. Frontiers of Structural and Civil Engineering 11(1), 90–99 (2017).

11. Nguyen, H., Vu, T.-A., Vo, T.P., Thai, H.-T.: Efficient machine learning models for prediction of concrete strengths. Construction and Building Materials 266, 120950 (2021).

12. Prokhorenkova, L., Gusev, G., Vorobev, A., Dorogush, A.V., Gulin, A.: CatBoost: unbiased boosting with categorical features. Advances in Neural Information Processing Systems (NeurIPS) 31, 6639–6648 (2018).

13. Chen, T., Guestrin, C.: XGBoost: A scalable tree boosting system. In: Proceedings of the 22nd ACM SIGKDD International Conference on Knowledge Discovery and Data Mining (KDD), pp. 785–794 (2016).

14. Breiman, L.: Random forests. Machine Learning 45(1), 5–32 (2001).

15. Feng, D.-C., Liu, Z.-T., Wang, X.-D., Chen, Y., Chang, J.-Q., Wei, D.-F., Jiang, Z.-M.: Machine learning-based compressive strength prediction for concrete: an adaptive boosting approach. Construction and Building Materials 230, 117000 (2020).

16. Duan, Z.H., Kou, S.C., Poon, C.S.: Prediction of compressive strength of recycled aggregate concrete using artificial neural networks. Construction and Building Materials 40, 1200–1208 (2013).

17. Ulucan, M., Gunduzalp, E., Yıldırım, G., Alatas, B., Alyamaç, K.: Optimizing sustainable concrete compressive strength prediction: a new particle swarm optimization-based metaheuristic approach to neural network modeling for circular economy and disaster resilience. Structural Concrete 26, 1226–1244 (2024).

18. Sharma, U., Gupta, N., Verma, M.: Prediction of the compressive strength of Flyash and GGBS incorporated geopolymer concrete using artificial neural network. Asian Journal of Civil Engineering 24(8), 2837–2850 (2023).

Author Contribution Statement

- *Conceptualization:* Mehmet Nadir, Mehmet Sefa Orak
- *Methodology:* Mehmet Nadir, Mehmet Sefa Orak
- *Investigation:* Mehmet Nadir, Mehmet Sefa Orak
- *Writing – Review & Editing:* Mehmet Nadir, Mehmet Sefa Orak

Publication Note

This paper was peer-reviewed, accepted for presentation, and included in the proceedings of the ACE2026 – 16th International Congress on Advances in Civil Engineering, held on 12–14 October 2026 in Trabzon, Türkiye.

This paper may be cited as follows:

Mehmet Nadir, Mehmet Sefa Orak, “Neural Network-Driven Forecasting of Concrete Compressive Strength,” in Proceedings of the ACE2026 – 16th International Congress on Advances in Civil Engineering, Trabzon, Türkiye, 12–14 October 2026.

Mechanical Properties of Cements Produced with Construction and Demolition Waste in Accordance with TS EN 197-6

Yasemen Polat[1],*, Özer Sevim[1], M. Kemal Ardoğa[2], Mustafa Şahmaran[2]

1 Corresponding Author * ORCID: 0009-0008-6663-4248 and ORCID:0000-0001-8535-2344 , Civil Engineering Department, Kırıkkale University, Kırıkkale, Türkiye

2 Department of Civil Engineering, Building Materials Division, Hacettepe University, Ankara, Türkiye

Corresponding author: polatyasemen@gmail.com

Abstract. The construction sector is one of the largest producers of solid waste globally, and the sustainable management of construction and demolition waste (CDW) has become a critical environmental and engineering challenge. This study investigated the mechanical and physical properties of cements produced by adding recycled concrete fines (RCF) to ordinary Portland cement at replacement ratios of 20% and 30%, by mass, in compliance with the TS EN 197-6 standard for low-clinker cements. The primary objective was to evaluate whether Konya-based RCF could meet the mechanical performance limits defined by TS EN 197-6, thereby offering a viable pathway to reduce clinker consumption and associated CO_2 emissions. The experimental work included compressive and flexural strength testing at standard curing ages under both air-curing and water-curing conditions, together with chemical, physical and durability characterization of the RCF-incorporated cement blends. It was found that curing regime strongly governed whether Konya-sourced concrete fines could be used to produce a Portland-recycled-fines cement satisfying the TS EN 197-6 strength requirements: under water curing, 20% replacement meets the 32.5 strength class threshold at 28 days, whereas under air curing neither replacement ratio met these limits.

Keywords: Construction and demolition waste, recycled concrete fines, TS EN 197-6, supplementary cementitious materials, compressive strength.

1 Introduction

In the 21st century, the construction industry faces two simultaneous global challenges: cement production, one of the principal drivers of the climate crisis owing to its highly energy- and raw-material-intensive manufacturing process [1], and the inevitable increase in construction and demolition waste (CDW) [2]. The clinkerization process in Portland cement production, based on the high-temperature calcination of calcium carbonate, releases substantial amounts of carbon dioxide; cement production is responsible for approximately 7–8% of global CO_2 emissions [1, 3]. It is reported that global annual cement production exceeds 4 billion tons, making the reduction of the environmental impact associated with clinker production critically important for global sustainability targets [1]. In order to reduce the clinker amount, one of the most common approaches is to substitute cement with reliable mineral admixtures. While fly ash, ground granulated blast furnace slag and natural pozzolans have been used for decades, recycled concrete fines (RCF), which can be obtained from the concrete fraction of construction and demolition waste (CDW), have recently emerged as a potential mineral component for low-clinker cement production. The TS EN 197-6 standard,

which entered into force in 2023, has introduced new low-clinker cement classes (CEM II/A-M, CEM II/B-M and CEM II/C-M) that allow the use of RCF which can be obtained from CDWs, in combination with other mineral components [4].

The CDW constitutes approximately 30–37% of total waste generation in European Union countries, making it one of the largest waste streams [2], of which concrete-based waste accounts for approximately 70–80% [5]. In Türkiye, approximately 20 million tons of CDW are generated annually as a result of the destruction of old buildings within the scope of urban renewal projects [6]. The increasing generation of CDW, and hence as a huge part of this, RCF highlight the need for effective recycling and recovery strategies, particularly for concrete-derived fractions that may be suitable for use in cement-based materials.

Although it is reported that in most cases, concrete-based CDW utilized as an ingredient of concrete acts as an inert material, fine grinding and appropriate activation can enable it to exhibit pozzolanic reactivity owing to its SiO_2, CaO and Al_2O_3 phases [7]. However, the performance of concrete waste as a mineral admixture is dependent on numerous variables including the type and quantity of cement in the parent structure, aggregate mineralogy, water/binder ratio, curing regime and the environmental exposure history of the parent structure prior to demolition (e.g., carbonation, weathering) [8, 9]. Curing condition in particular is known to strongly influence the degree of hydration in blended cement systems, since supplementary cementitious materials with limited early reactivity depend on sustained moisture availability to develop later-age strength [10, 11].

Most studies in the literature examine concrete waste utilization on the basis of a single, controlled waste source and a single curing regime; a systematic treatment addressing both source diversity and curing sensitivity remains a clear gap. This paper presents the mechanical performance of the mortar having TS EN 197-6-compliant cements produced by incorporating recycled concrete fines (RCF) obtained from construction and demolition waste collected in Konya, Türkiye at 20% and 30% replacement ratios by mass, under both water-curing and air-curing conditions after conformity tests. The primary objective is to characterize the chemical, physical and mineralogical properties of Konya-based RCF and to evaluate whether the resulting cement blends meet the mechanical performance limits defined by TS EN 197-6 under each curing regime, thereby assessing the utilization of this specific waste source as a pathway to reduce clinker consumption and associated CO_2 emissions.

2 Materials and Methodology

2.1 Materials

The recycled concrete fines (RCF) were obtained from the construction and demolition waste (CDW) of the Eski Sanayi industrial zone of Konya, Türkiye. About 100 kg waste material was obtained from the site with appropriate sampling methods. The waste brought to the laboratory was first crushed using a jaw crusher to reduce oversized fragments, and oven-dried at 105 °C for 24 hours to remove residual moisture. Following drying, the material was ground in a laboratory-type ball mill (internal drum dimensions 30.5 × 30.5 cm with approximately 22 L of volume) operated at a constant speed of 70 rpm; the ball charge was determined on the basis of the standard Bond mill configuration [12]. The grinding duration for the Konya sample was set at 30 minutes to achieve a similar fineness to that of the reference cement. The resulting fine powder was mechanically homogenized and stored in airtight containers to prevent moisture uptake prior to any testing.

The CEM I 42.5 R Portland cement supplied by Baştaş Çimento Sanayi A.Ş., was used as the reference binder. CEN standard reference sand, compliant with TS EN 196-1 and produced by Limak Trakya Cement factory, was used as fine aggregate in the mortar mixtures.

2.2 Mix Design

Table 1 presents the mortar mix proportions used in the study. The replacement ratios of 20% and 30% were selected within the compositional limits defined by TS EN 197-6 for recycled concrete fines (RCF) as a main constituent. Under this standard, RCF (designated as "F") can be incorporated as the sole non-clinker main constituent in Portland-recycled-fines cements, with the CEM II/A-F class allowing 6–20% RCF and the CEM II/B-F class allowing 21–35% RCF by mass. Accordingly, the 20% replacement level corresponds to the upper compositional limit of the CEM II/A-F class, while the 30% replacement level falls within the compositional range of the CEM II/B-F class. Since both replacement levels were obtained using RCF alone, without a second non-clinker constituent, the experimental matrix was designed to evaluate the mechanical and durability performance of RCF-containing Portland cements at replacement levels representing both CEM II/A-F (20%) and CEM II/B-F (30%) compositions. For each mixture, two specimen series were cast from the same batch and subjected to two different curing regimes until the relevant test age: (i) water curing, in which specimens were immersed in a water tank at 20 ± 1 °C in accordance with TS EN 196-1, representing an idealized, continuously moist condition; and (ii) air curing, in which specimens were demolded after 24 hours and thereafter stored in laboratory ambient air at 20 ± 2 °C without further water contact, representing a field-representative condition in which continued hydration relies solely on moisture retained within the specimen. In addition, cement paste specimens were prepared in accordance with TS EN 196-3 for setting time and soundness tests.

Table 1. Mortar mix proportions.

Mixture	Cement (g)	RCF (g)	Sand (g)	Water (g)
Control	450	0	1350	225
Konya 20%	360	90	1350	225
Konya 30%	315	135	1350	225

2.3 Methodology

Mixing of the mortar specimens was carried out in accordance with TS EN 196-1 using a standard mortar mixer. All mixtures were prepared with the same total water/binder ratio for comparing the workability and performance of mixtures containing different proportions of RCF. The specimens were cast into 40 × 40 × 160 mm prismatic steel molds, compacted with a vibrating table, covered with stretch film and stored at 20 ± 2 °C in curing room to minimize moisture loss for 24 hours before demolding. Then each specimen series was assigned to either the water-curing or the air-curing regime described above until the relevant test age. In addition, the durability specimens (28-day water-cured) were also prepared with the same procedure. The following experimental program was applied to the Konya RCF and the resulting cement systems:

Chemical and mineralogical characterization: The oxide composition was determined with X-ray fluorescence (XRF). The methylene blue (MB) value in accordance with TS EN 933-9 and total organic carbon (TOC) content in accordance with TS EN 13639 were found, also.

Physical characterization: The RCF developed was investigated via density (according to ASTM C 188) as well as laser diffraction particle size analysis.

Fresh-state properties: Consistency (flow) in accordance with ASTM C 1437 was determined for each mixture. Standard consistency, setting time (Vicat apparatus) and soundness (Le Chatelier method) tests were conducted in accordance with TS EN 196-3.

Mechanical properties: The flexural and compressive 2nd, 7th and 28th day-strengths of the mortars were determined in accordance with TS EN 196-1. The pozzolanic activity index (PAI) determined on a separate, water-cured mixture series prepared at 25% replacement, calculated as the ratio of the compressive strength of the RCF-substituted mortar to that of the control mortar at the same curing age, expressed as a percentage.

Durability properties (evaluated on water-cured specimens): Combined sulfate/acid resistance was evaluated by immersing 28-day water-cured specimens in a 1% H2SO4 solution and in water (reference) and determining flexural and compressive strength at 28, 56 and 90 days. To determine water permeability of the mortars, rapid chloride ion permeability test, was performed in accordance with ASTM C1202 on 50 × 100 mm cylindrical specimens water cured for 28 days, by applying 60 V DC for 6 hours and measuring the total charge passed (Coulombs). Freeze-thaw resistance was evaluated in accordance with TS EN 12390-9 by applying one freeze-thaw cycle per day and measuring mass loss and remaining flexural/compressive strength at 30, 56 and 76 cycles. The accelerated carbonation resistance was determined in a carbonation chamber, the interior CO2 concentration of which was adjusted at 1% with 80% relative humidity and 20 °C. The carbonation depth was detected using a 1% phenolphthalein indicator solution and remaining flexural/compressive strength determined after exposure.

3 Results and Discussion

3.1.Chemical Characterization

Table 2 presents the oxide composition of Konya-sourced RCF, as determined by XRF analysis, in comparison with the reference cement.

Table 2. Oxide composition of Konya RCF and reference cement (XRF).

Oxide	Konya RCF (%)	Cement (%)
SiO_2	8.0	15.2
Al_2O_3	1.1	4.2
Fe_2O_3	2.4	4.0
CaO	51.9	61.6
MgO	0.3	1.2
SO_3	0.7	3.8
K_2O	0.6	0.96
CO_2	35.0	8.0

The Konya RCF exhibits a markedly low SiO_2 content (8.0%) relative to the reference cement (15.2%), while its CaO content (51.9%) is comparatively close to that of the reference cement (61.6%). This combination indicates that carbonate-based (limestone-derived) components are likely dominant in the aggregate/paste fraction of the parent concrete, rather than a silica-rich composition typically associated with pronounced pozzolanic reactivity [13, 14]. This interpretation is further supported by the material's high CO_2 content, recorded at approximately 35.0%. On the basis of the low SiO2 and high CaO and CO_2 contents, the Konya RCF is expected to behave predominantly as a filler-type addition rather than as a strongly reactive pozzolanic material.

Table 3 summarizes the compliance of Konya RCF with relevant chemical limits defined in TS EN 197-6. The chloride content of the Konya RCF was 0.0715% and the Cl^- limit is stated to be 0.1%; The sulfate content (SO_3) of the Konya RCF was 0.27%, which is substantially below the 2.0% limit specified for recycled concrete fines in TS EN 197-6, confirming compliance with the sulfate requirement. The methylene blue value was 0.50 g/kg (equivalent

to 0.05 g/100 g), which is well below the 1.20 g/100 g limit specified in TS EN 197-6, indicating a low content of clay and clay-like harmful fines. The total organic carbon content (TOC) was 0.76%, which complies with the 0.80% upper limit specified in TS EN 197-6.

Table 3. Chemical compliance of Konya RCF.

Parameter	Konya RCF	Limit	Compliance
Cl^- content	0.0715%	≤ 0.10% (TS EN 197-6)	Compliant
SO_3 content	0.27%	≤ 2.00% (TS EN 197-6)	Compliant
Methylene blue (MB)	0.05 g/100 g	≤ 1.20 g/100 g (TS EN 197-6)	Compliant
TOC	0.76%	≤ 0.80% (TS EN 197-6)	Compliant

3.2.Physical Characterization

Fig.1 presents the particle size distribution curve obtained by laser diffraction (Mastersizer 2000) for the Konya RCF in comparison with the reference cement. The Konya RCF displays a substantially coarser particle size distribution than the reference cement when assessed by laser diffraction. The distribution span (4.041 vs. 2.571) and uniformity coefficient (1.31 vs. 0.801) of the Konya RCF further confirm a wider and more heterogeneous particle size distribution than that of the reference cement.

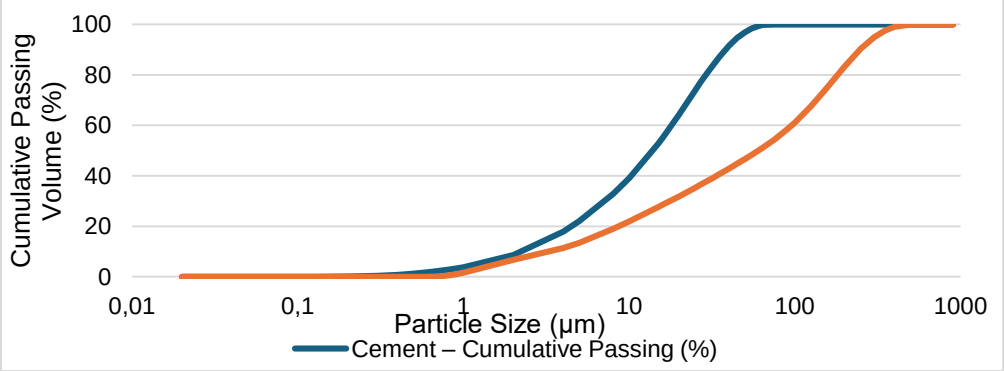


Fig. 1. Particle size distribution.

3.3.Fresh-State Properties

Table 4 presents the flow (consistency) results obtained on the paste mixtures. The control mixture exhibited a flow value of 17.5 cm. The Konya 20% mixture showed a slightly reduced flow (16.25 cm) relative to the control, consistent with the increased water demand typically associated with the finer fraction and angular morphology of the ground recycled aggregate, whereas the Konya 30% mixture exceeded the control (17.75 cm). This recovery — and, at the 30% replacement level, exceedance — of flow relative to the control may be attributed to a "ball-bearing" effect of the coarser, more rounded RCF particles present at the higher replacement level, which can locally improve particle mobility within the fresh mixture, together with a proportional reduction in the fine paste fraction as the replacement level increases.

Table 4. Flow (consistency) results.

Mixture	Control	Konya 20%	Konya %30
Flow (cm)	17.5	16.25	17.75

Table 5. Setting time and soundness results.

Mixture	w/c	Initial set (min)	Final set (min)	Soundness (mm)
Control	0.33	165	225	1
Konya 20%	0.32	165	270	1
Konya 30%	0.31	180	285	1

The water/cement (w/c) ratios reported in Table 5 correspond to the water demand required to achieve standard consistency for each paste mixture, determined in accordance with TS EN 196-3, and are therefore independent of the fixed water/binder ratio used in the mortar mix design (Table 1). The initial and final setting times of the RCF-substituted paste mixtures were both extended relative to the control (165 min / 225 min): the Konya 20% mixture recorded 165 min / 270 min, and the Konya 30% mixture recorded 180 min / 285 min. This extension is consistent with the dilution of clinker content, which slows the early-age hydration reactions responsible for paste stiffening [10]. The Le Chatelier expansion (soundness) values for both the Konya 20% and Konya 30% mixtures remained at 1 mm, well below the 10 mm limit set in TS EN 197-1 and retained in TS EN 197-6, confirming that Konya RCF incorporation does not compromise the volumetric stability of the cement paste at either replacement level.

3.4.Mechanical Properties

Tables 6 and 7 present the flexural and compressive strength results, respectively, obtained for the control and Konya-RCF mortar mixtures under both the air-curing series (tested at 2, 7 and 28 days) and the water-curing series (tested at 2, 7 and 28 days for flexural strength and at 2, 7 and 28 days for compressive strength).

As expected, strength increased with curing age within each series, and water-cured specimens consistently outperformed their air-cured counterparts for every mixture and every property. The effect of curing regime is most evident in 28-day compressive strength: for the control mixture, air curing yielded 43.3 MPa versus 50.9 MPa under water curing — a reduction of approximately 15% attributable to curing regime alone — confirming that, even for an unblended reference cement, the absence of continuous moist curing measurably limits attainable strength [15]. Notably, the air-cured control mixture continued to gain compressive strength between 7 days (35.8 MPa) and 28 days (43.3 MPa), whereas the air-cured Konya 20% series showed the same strength over the same interval (27.4 MPa at both 7 and 28 days), which is consistent with limited continued hydration once moisture within the RCF-substituted specimen is depleted, combined with possible drying-shrinkage-related microcracking under uncontrolled ambient conditions, rather than with genuine further strength development [16, 17]. For the Konya-RCF mixtures, the curing-regime effect compounds the dilution effect already observed under water curing. At 28 days, air-cured compressive strength decreased from 43.3 MPa (control) to 27.4 MPa (Konya 20%, −37%) and to 22.4 MPa (Konya 30%, −48%), exceeding the reductions observed under water curing (−32% and −40%, respectively, relative to the water-cured control) and indicating that the adverse effect of RCF replacement on strength is amplified under air-curing conditions. Flexural strength followed a similar pattern, with the air-cured Konya 30% mixture showing a particularly low 2-day value (1.7 MPa) relative to the control (4.4 MPa), suggesting that early-age flexural capacity is especially sensitive to the combination of high replacement ratio and unfavorable (air) curing.

Table 6. Flexural strength under air curing and water curing (MPa).

Mixture	Air 2 d	Air 7 d	Air 28 d	Water 2 d	Water 7 d	Water 28 d
Control	4.4	5.0	6.0	4.9	6.7	8.1
Konya 20%	3.4	4.1	4.1	3.8	6.3	7.3
Konya 30%	1.7	4.3	4.3	3.0	6.4	6.5

Table 7. Compressive strength under air curing and water curing (MPa).

Mixture	Air 2 d	Air 7 d	Air 28 d	Water 2 d	Water 7 d	Water 28 d
Control	24.8	35.8	43.3	22.1	41.8	50.9
Konya 20%	18.3	27.4	27.4	14.8	29.7	34.4
Konya 30%	13.7	21.2	22.4	11.1	25.9	30.6

TS EN 197-6 classifies RCF-containing cements according to the strength classes defined in EN 197-1, of which the lowest, 32.5, requires a minimum 28-day compressive strength of 32.5 MPa. Under water curing, the Konya 20% mixture (34.4 MPa) satisfies this minimum requirement, whereas the Konya 30% mixture (30.6 MPa) falls just below it. Under air curing, however, neither Konya mixture reaches the 32.5 MPa threshold: the Konya 20% mixture attains only 27.4 MPa and the Konya 30% mixture only 22.4 MPa at 28 days, whereas the air-cured control mixture (43.3 MPa) comfortably exceeds this threshold — confirming that the failure to meet the strength class under air curing is attributable specifically to RCF incorporation rather than to the curing regime itself. This finding substantially refines the answer to the central question posed in the abstract of this study — whether RCF-based supplementary cementitious materials can meet the mechanical performance thresholds defined by TS EN 197-6. For the Konya-sourced material, meeting this threshold is achievable, but only at the lower (20%) replacement ratio and only under adequately moist (water) curing; under field-representative air curing, the tested Konya-RCF blends do not reach the minimum strength class at either replacement ratio within the 28-day period examined. This underlines that, in practical applications, curing management is at least as decisive as replacement ratio in determining whether an RCF-based cement meets TS EN 197-6 requirements.

Pozzolanic activity index (PAI) results obtained for the (water-cured) Konya RCF at a 25% replacement ratio were determined to be 66%, 73% and 66% at 2, 7 and 28 days, respectively — all remaining below the 75% threshold generally accepted as indicative of adequate pozzolanic activity. This can show that the effect of RCF as a pozzolanic material was very limited. This is consistent with its lower SiO_2 content and its coarser particle size. This supports the characterization of Konya RCF as behaving predominantly as a filler-type, rather than strongly pozzolanic, addition — a behavior that is particularly disadvantaged when continuous moisture for late-age pozzolanic reaction is not guaranteed, as under air curing.

3.5.Durability Properties

Table 8 summarizes the durability performance of the (water-cured) Konya-RCF mortar mixtures under sulfate/acid exposure (1% H_2SO_4 solution, 90 days), rapid chloride permeability testing, freeze-thaw cycling (F-T) (76 cycles) and accelerated carbonation exposure.

Table 8. Summary of durability performance water-cured series.

Mixture	Sulfate strength loss, 90 d (%)	RCPT (C) / Class	Freeze-thaw mass loss, 76 cyc. (%)	Residual compressive strength, 76 cyc. (F-T) (MPa)	Carbonation compressive strength (MPa)
Control	12.91	3466 / Medium	0.43	45.7	43.6
Konya 20%	14.90	4601 / High	0.57	32.6	31.0
Konya 30%	23.49	5582 / High	0.51	27.2	29.1

Under sulfuric acid exposure, the compressive strength loss of the control mixture reached 12.91% after 90 days. The Konya 20% mixture exhibited a comparable strength loss of 14.90% at 90 days, indicating a favorable sulfate/acid resistance at this replacement level, potentially attributable to a buffering effect of the calcite-rich RCF, which may act partly as an inert filler that densifies the pore structure while limiting the proportion of reactive aluminate phases susceptible to expansive sulfate-related reaction products [18]. In contrast, the Konya 30% mixture exhibited a substantially higher strength loss, reaching 23.49% at 90 days, indicating that the buffering capacity observed at 20% replacement is insufficient to offset the effects of increased porosity and binder dilution at the higher replacement ratio.

The rapid chloride permeability test (RCPT) results, expressed as total charge passed (Coulombs) in accordance with ASTM C1202, classified the control mixture as exhibiting "Medium" permeability (3466 C). Both Konya-RCF mixtures were classified as exhibiting "High" permeability, with values of 4601 C (20% replacement) and 5582 C (30% replacement) — the latter representing a further increase relative to the 20% mixture. This result indicates that the coarse particle structure and limited pozzolanic reactivity of Konya RCF result increased pore connectivity and permeability [19], an effect that intensifies with increasing replacement ratio.

Under freeze-thaw cycling, mass loss after 76 cycles remained of a broadly similar order across all mixtures (control: 0.43%; Konya 20%: 0.57%; Konya 30%: 0.51%), with residual compressive strength (Table 9) decreasing from 45.7 MPa (control) to 32.6 MPa (Konya 20%) and 27.2 MPa (Konya 30%) at 76 cycles — values broadly proportional to the corresponding unexposed 28-day water-cured strengths.

Following accelerated carbonation exposure, the residual compressive strength of the Konya 20% and Konya 30% mixtures (31.0 MPa and 29.1 MPa, respectively) remained broadly consistent with their corresponding unexposed 28-day water-cured compressive strength values (34.4 MPa and 30.6 MPa), indicating that carbonation exposure under the tested conditions did not cause strength decrements further.

4 Conclusions

Based on the experimental characterization and testing of construction and demolition waste-derived recycled concrete fines (RCF) sourced from Konya, Türkiye, under both water-curing and air-curing regimes, the following conclusions can be drawn:

1. The chemical composition of Konya RCF is characterized by a low SiO_2 content and a high CaO/CO_2 content, indicating a carbonate (limestone)-dominated composition rather than a silica-rich composition typically associated with strong pozzolanic reactivity. Chloride, sulfate, methylene blue and total organic carbon values all remain within the limits defined by TS EN 197-6, confirming the chemical suitability of the material for use as a mineral admixture.

2. Incorporation of Konya RCF extends setting time and slightly alters flow behavior relative to the control mixture, but soundness remains well within the limits defined by TS EN 197-1/197-6 at both 20% and 30% replacement ratios.

3. Curing regime has a decisive effect on mechanical performance. Under water curing, the 28-day compressive strength of the Konya 20% mixture (34.4 MPa) satisfies the minimum requirement of the 32.5 strength class defined in TS EN 197-6, whereas the Konya 30% mixture (30.6 MPa) does not. Under air curing, any mixture reaches this threshold, even though the air-cured control mixture (43.3 MPa) comfortably exceeds it — indicating that the failure to meet TS EN 197-6 mechanical requirements under air curing is driven specifically by RCF incorporation, and that adequate moist curing remains essential for Konya-sourced RCF cement to meet these requirements.

4. The pozzolanic activity index of Konya RCF (66-73% across 2-28 days at 25% replacement, water-cured) remains below the 75% threshold generally accepted for adequately pozzolanic materials, consistent with a predominantly filler-type behavior that is particularly disadvantaged under curing regimes offering limited sustained moisture.

5. Durability results (water-cured specimens) indicate acceptable sulfate/acid resistance at 20% replacement, comparable to the control mixture, but substantially reduced resistance at 30% replacement. Freeze-thaw mass loss after 76 cycles remained low and broadly similar across all mixtures (0.43–0.57%), without a clear trend with replacement ratio. Chloride permeability is classified as “High” at both replacement levels, with permeability increasing with replacement ratio.

6. Taken together, these findings indicate that it is possible to utilize Konya-sourced concrete fines for the production of a TS EN 197-6-compliant Portland-recycled-fines cement from a strength perspective, provided that (i) the replacement ratio is limited to approximately 20% and (ii) adequate moist curing is ensured; a 30% replacement ratio, and air-curing conditions at either replacement ratio, are not recommended for this specific waste source without additional activation (e.g. mechanical, chemical, or nano-suspension activation) or curing control measures.

7. These results, obtained for a single waste source, underline the importance of source-specific characterization of construction and demolition waste and of realistic curing assessment prior to its use as a mineral admixture, and support the broader conclusion that the safe replacement ratio for recycled concrete fines in TS EN 197-6-compliant cements is materially dependent on both the mineralogical and physical properties of the parent waste source and the curing conditions expected in service.

5 References

1. IEA (International Energy Agency). (2023). Cement – Tracking Report. Paris.

2. Eurostat. (2022). Waste statistics – construction and demolition waste. Luxembourg: Publications Office of the European Union.

3. GCCA (Global Cement and Concrete Association). (2022). GCCA in Numbers 2022.

4. TS EN 197-6 (2023). Cement – Part 6: Cement with recycled construction and demolition materials. Turkish Standards Institution, Ankara.

5. European Commission. (2016). EU Construction and Demolition Waste Management Protocol. Brussels.

6. Yılmaz, T., Erçıkdı, B., & Deveci, H. (2018). Utilisation of construction and demolition waste as cemented paste backfill material for underground mine openings. Journal of Environmental Management, 222, 250–259. https://doi.org/10.1016/j.jenvman.2018.05.075

7. Sousa, L. N., Zepper, J. C. O., Schollbach, K., & Brouwers, H. J. H. (2024). Improving the reactivity of industrial recycled concrete fines: Exploring mechanical and hydrothermal activation. Construction and Building Materials, 442, 137594.

8. Rocha, J. H. A., & Toledo Filho, R. D. (2023). The utilization of recycled concrete powder as supplementary cementitious material in cement-based materials: A systematic literature review. Journal of Building Engineering, 76, 107319.

9. Pani, L., Francesconi, L., Rombi, J., Mistretta, F., Sassu, M., & Stochino, F. (2020). Effect of parent concrete on the performance of recycled aggregate concrete. Sustainability, 12(22), 9399.

10. Scrivener, K. L., John, V. M., & Gartner, E. M. (2018). Eco-efficient cements: Potential economically viable solutions for a low-CO_2 cement-based materials industry. Cement and Concrete Research, 114, 2–26.

11. López Gayarre, F., López-Colina Pérez, C., Serrano López, M. A., & Domingo Cabo, A. (2014). The effect of curing conditions on the compressive strength of recycled aggregate concrete. Construction and Building Materials, 53, 260–266.

12. Bond, F. C., & Maxson, W. L. (1943). Standard grindability tests and calculations. Transactions of the American Institute of Mining and Metallurgical Engineers, 153, 362–372.

13. Kou, S. C., & Poon, C. S. (2015). Effect of the quality of parent concrete on the properties of high performance recycled aggregate concrete. Construction and Building Materials, 77, 501–508.

14. Xiao, J., Li, W., Fan, Y., & Huang, X. (2012). An overview of study on recycled aggregate concrete in China (1996–2011). Construction and Building Materials, 31, 364–383.

15. Mehta, P. K., & Monteiro, P. J. M. (2014). Concrete: Microstructure, Properties, and Materials (4th ed.). McGraw-Hill Education.

16. Bentz, D. P., & Snyder, K. A. (1999). Protected paste volume in ultra-high performance cementitious pastes using internal curing. Cement and Concrete Research, 29(11), 1863–1867. https://doi.org/10.1016/S0008-8846(99)00178-5

17. Silva, R. V., de Brito, J., & Dhir, R. K. (2015). Establishing a relationship between cured concrete properties and recycled aggregate characteristics. Construction and Building Materials, 91, 281–298. https://doi.org/10.1016/j.conbuildmat.2015.05.029

18. Zhu, P., Chen, W., Yan, X., He, Z., Liu, H., Ma, T., Qiao, S., & Zhao, X. (2024). Improving sulfate resistance of 100% recycled coarse aggregate concrete by simultaneous application of limestone powder and EDTA-2Na. Construction and Building Materials, 418, 135390.

19. Zhang, H., Zhang, C., He, B., Yi, S., & Tang, L. (2024). Recycling fine powder collected from construction and demolition wastes as partial alternatives to cement. Journal of Building Engineering, 71, 106507.

20. TS EN 196-1 (2016). Methods of testing cement – Part 1: Determination of strength. Turkish Standards Institution, Ankara.

21. TS EN 196-3 (2017). Methods of testing cement – Part 3: Determination of setting times and soundness. Turkish Standards Institution, Ankara.

22. TS EN 197-1 (2012). Cement – Part 1: Composition, specifications and conformity criteria for common cements. Turkish Standards Institution, Ankara.

Publication Note

This paper was peer-reviewed, accepted for presentation, and included in the proceedings of the ACE2026 – International Conference on Advances in Civil Engineering, held on 12–14 October 2026 in Trabzon, Türkiye.

This paper may be cited as follows:

Polat Y., Sevim Ö., Ardoğa M. K., Şahmaran M., "Mechanical Properties of Cements Produced with Construction and Demolition Waste from Konya in Accordance with TS EN 197-6," in Proceedings of the ACE2026 – International Conference on Advances in Civil Engineering, Trabzon, Türkiye, 12–14 October 2026.

Fresh-State Performance and Printability of Brick Powder-Based 3D Printable Concrete with GGBFS and Fly Ash

Muhammed Çeçen[1*], Derya Kurt[2], Yeşim Tarhan[3], İsmail Hakkı Tarhan[4]
[1]0009-0006-4206-7360, *Department of Civil Engineering, Institute of Graduate Studies, Tokat Gaziosmanpaşa University, Tokat, 60150, Türkiye*
[2]0009-0002-2754-9688, *Department of Civil Engineering, Institute of Graduate Studies, Tokat Gaziosmanpaşa University, Tokat, 60150, Türkiye*
[3]0000-0002-3901-9070, *Technical Sciences Vocational School, Ardahan University, Ardahan, 75000, Türkiye*
[4]0000-0002-5161-3718, *Department of Civil Engineering, Faculty ofEngineering and Architecture, Tokat Gaziosmanpaşa University, Tokat, 60150, Türkiye*
*Corresponding Author E-mail: curtigiy@hotmail.com

Abstract. The fresh-state behavior of cementitious mixtures is a critical factor in 3D concrete printing, as printable materials must provide adequate workability, continuous extrusion, and buildability after deposition. The use of brick powder as a fine aggregate component provides a sustainability-oriented approach by valorizing ceramic-based construction waste and reducing the demand for conventional fine aggregates. Nevertheless, the fresh-state performance of brick powder-based printable mixtures requires further evaluation, as fine aggregate characteristics directly affect flow behavior, extrusion continuity, and buildability. Therefore, this study investigates the effects of ground granulated blast furnace slag (GGBFS) and fly ash (FA), used as supplementary cementitious materials (SCMs), on the fresh-state performance and printability of 3D printable concrete produced with brick powder fine aggregate. The mixtures were composed of CEM I 42.5 R cement, sand, brick powder fractions, calcined kaolin, polypropylene fibers, viscosity-modifying admixture, superplasticizer, and water. Four mixtures were prepared: a reference mixture and three modified mixtures incorporating GGBFS, FA, or their combined use at a total replacement level of 30% by mass of binder, corresponding to 30% GGBFS, 30% FA, and 15% GGBFS + 15% FA, respectively. The mixtures were evaluated by unit weight, flow table, extrudability, and buildability tests. The results showed that all mixtures exhibited acceptable fresh-state behavior for 3D concrete printing under the adopted laboratory-scale conditions. The combined GGBFS-FA mixture showed the lowest spread diameter of 11.5 cm, indicating a more stable consistency and lower tendency to flow. In terms of working time, the mixture containing 30% GGBFS provided the longest workable period (126 min), while the 30% FA mixture exhibited the shortest period (86 min); however, this duration still indicates an adequate processing window. The buildability results also indicated that the tested mixtures maintained their layer stability, with measured settlement values remaining in a narrow range. These findings suggest that GGBFS and FA can be used to modify the fresh-state behavior of 3D printable concrete with brick powder fine aggregate. Further optimization of SCM replacement ratios and admixture dosage may contribute to developing mixtures with a better balance between workability, extrudability, and buildability.

Keywords: 3D Printable Concrete; Brick Powder Fine Aggregate; Fresh-State Properties; Printability

1 Introduction

Three-dimensional concrete printing (3DCP) offers an alternative to conventional concrete construction by enabling automated, digitally controlled, and largely formwork-free production. In conventional concrete construction, formwork may account for approximately 50-75% of the total execution time and 35-54% of the cost of concrete structures [1]. By reducing the dependence on formwork and automating material placement, 3DCP can provide shorter construction times, lower labor requirements, reduced material waste, and greater geometric freedom. Reported estimates indicate potential reductions of approximately 30-60% in construction waste, 50-80% in labor costs, and 50-70% in production time compared with conventional construction methods [2]. However, improving the sustainability of 3DCP requires not only advances in the production process but also careful consideration of the materials used in printable mixtures. The cement industry is responsible for approximately 7-8% of global greenhouse-gas emissions [3], while construction and demolition waste constitutes a substantial share of the global solid-waste stream [4]. Therefore, reducing Portland cement consumption and incorporating industrial and construction-derived materials into printable mixtures are important strategies for improving the environmental performance of 3DCP.

Achieving these potential benefits strongly depends on the fresh-state performance of the cementitious material. Unlike conventional concrete, a 3D-printable mixture must satisfy several successive and sometimes competing requirements during pumping, extrusion, deposition, and layer-by-layer construction [5,6]. The material must remain sufficiently workable for transport, be extruded continuously without segregation or blockage, retain its geometry after leaving the nozzle, and develop sufficient early structural stability to support subsequent layers. Extrudability and buildability are therefore closely related to workability and open time [7]. From a rheological perspective, adequate flow during pumping and extrusion must be balanced with sufficient yield stress and rapid structural build-up after deposition to maintain layer geometry and prevent collapse [8,9]. Experimental studies have likewise shown that unit weight, flow behavior, extrudability, buildability, open time, and rheological parameters should be considered together when evaluating a printable cementitious mixture [10]. A recent review further emphasizes that flowability, buildability, extrudability, pumpability, and open time are fundamental fresh-state criteria and that all mixture constituents can influence the rheological response of 3D-printable cementitious composites [11].

The aggregate phase can significantly influence this fresh-state balance. Brick-derived fine particles generally differ from natural sand in porosity, water absorption, angularity, and surface roughness. These characteristics can modify the amount of free water available in the mixture, interparticle friction, flowability, and consistency retention; the magnitude of the effect depends on particle size, replacement level, moisture condition, and additional-water management [12]. In 3D-printable concrete, recycled brick aggregate has been shown to require additional water because of its relatively high porosity and absorption, demonstrating the importance of accounting for aggregate characteristics when designing printable mixtures [13]. More recent work has also shown that fine recycled aggregates derived from brick and concrete can be incorporated into cement-based mixtures intended for extrusion, although workability, shape retention, and stability still require careful optimization [14]. Thus, the use of brick powder as fine aggregate provides a promising route for valorizing construction waste and reducing the consumption of conventional natural fine aggregates, while making fresh-state control particularly important.

Binder composition is equally important in controlling fresh-state behavior. Ground granulated blast furnace slag (GGBFS) and fly ash (FA) are widely used supplementary cementitious materials (SCMs), but their influence on 3DCP is not limited to hardened properties. Binder type, particle characteristics, fineness, and interactions with water and

chemical admixtures can alter yield stress, viscosity, structural build-up, consistency retention, and overall printability [15]. Experimental investigations specifically examining FA and GGBFS in cement-based 3D-printing materials have reported measurable changes in fluidity, rheological properties, setting behavior, extrudability, and buildability as their contents are varied [16]. Similarly, 3D-printable concrete mixtures containing different FA and GGBFS replacement levels have been successfully extruded and evaluated through buildability testing, confirming that both the type and dosage of the SCM influence printing performance [17]. Printable cementitious systems containing GGBS have also been assessed through actual printing trials together with density, static yield stress, and time-dependent structural build-up measurements, illustrating the value of evaluating fresh-state behavior under the specific material and process conditions used for printing [18].

Although brick-derived fine aggregates, GGBFS, and FA have each been investigated in 3DCP, comparatively limited information is available on their combined use in the same Portland-cement-based printable system. In particular, the individual and combined effects of GGBFS and FA on the fresh-state behavior of 3D-printable concrete incorporating brick powder as fine aggregate require further evaluation. Therefore, this study comparatively investigates a reference mixture and mixtures containing GGBFS, FA, and their combined use. Unit weight, flow-table spread, workable time, extrudability, and buildability were evaluated to determine how these supplementary cementitious materials influence the balance between flowability, extrusion stability, and shape retention in 3D-printable concrete incorporating brick powder as fine aggregate.

2. Materials and Method

2.1 Materials

Portland cement (CEM I 42.5 R), supplied by the ADOÇİM Tokat plant, was used as the primary binder. Ground granulated blast furnace slag (GGBFS), obtained from the OYAK Cement Bolu plant, and Class C fly ash (FA), supplied by the İSKEN Energy Thermal Power Plant in Hatay, were used as supplementary cementitious materials for partial cement replacement. The aggregate phase consisted of 0.5–1.5 mm quartz sand supplied by Aydınlar Madencilik (İzmir) and recycled brick particles with size fractions of 1–2 mm and 0–1 mm. To improve the printability of the mixtures, BMT-brand calcium sulfate hemihydrate ($CaSO_4 \cdot 0.5H_2O$) was used as a viscosity-modifying component and was included in the total binder content. Calcined kaolin clay, 6 mm polypropylene fibers, and a polycarboxylate-based superplasticizer (Sika ViscoCrete ACE 450 TR) were also incorporated into the mixtures. Potable tap water supplied by Tokat Gaziosmanpaşa University was used as the mixing water.

2.2 Mix designs

Four different mixtures were prepared while keeping the total binder content and water-to-binder ratio constant. The reference mixture contained Portland cement and calcium sulfate hemihydrate, whereas in the other three mixtures Portland cement was partially replaced by 30% GGBFS, 30% FA, and a combination of 15% GGBFS + 15% FA, respectively. The total binder content was fixed at 500 g, including calcium sulfate hemihydrate at 20% of the total binder mass, while the water-to-binder ratio was maintained at 0.66. Superplasticizer and calcined kaolin were added at 1.3% and 5% of the total binder mass, respectively. The polypropylene fiber content was kept constant at 0.2% by volume of the total mixture for all mixtures. The mixture proportions are presented in Table 1.

Table 1. Proportions of 3D Printable Concrete Mixtures (Unit: g)

Mixture	Cement	Wt.	VMA	Clay	FA	GGBFS	Fiber	SP	Sand %20	BP 1-2mm %20	BP 0-1mm %60
Control	400	330	100	25	-	-	1.82	6.5	250	250	750
G30	250	330	100	25	-	150	1.82	6.5	250	250	750
F30	250	330	100	25	150	-	1.82	6.5	250	250	750
G15-F15	250	330	100	25	75	75	1.82	6.5	250	250	750

2.3 Specimen preparation procedure

The mixtures were prepared according to a fixed mixing sequence. First, the dry constituents, including cement, GGBFS, FA, aggregates, polypropylene fibers, calcined kaolin, and calcium sulfate hemihydrate, were mixed at low speed (62.5 rpm) for 2 min. Then, 200 g of water was added, and mixing was continued at the same speed for another 2 min. Subsequently, the remaining 130 g of water and 6.5 g of superplasticizer were added, followed by 1 min of low-speed mixing. Finally, the mixture was mixed at a higher speed of 125 rpm for 2 min to obtain a homogeneous mixture.

The prepared mixtures were subjected to fresh density, extrudability, buildability, flow-table spread, and workable-time tests.

3. Results and Discussion

To evaluate the fresh-state properties and printability of the mixtures, fresh density was determined in accordance with TS EN 12350-6, and the results are presented in Table 2.

Table 2. Density of the Concrete Mixtures

Mixture	Mass (g)	Volume (cm^3)	Density (g/cm^3)
Control	383.35	174	2.20
G30	369.25	174	2.12
F30	387.10	174	2.23
G15F15	390.39	174	2.24

The fresh densities of the mixtures were relatively close to one another, ranging from approximately 2.12 to 2.24 g/cm^3, as presented in Table 2. G15F15 exhibited the highest fresh density, whereas G30 showed the lowest value. The relatively small differences among the mixtures may be associated with variations in the density and fineness of the constituent materials.

Since a full-scale 3D concrete printer was not available during the experimental program, extrudability was evaluated using a mortar injection pump equipped with a nozzle. The mixtures were assessed in terms of their ability to be extruded continuously and homogeneously, while the width and thickness of the extruded filaments were measured to evaluate dimensional stability and shape retention. Buildability was evaluated by depositing successive layers and monitoring their ability to retain their geometry under the load of the overlying layer. The consistency and spread diameter of the mixtures were determined using the flow-table method in accordance with EN 1015-3, which specifies the determination of fresh-mortar consistency by flow value. Workable time was determined in accordance with EN 1015-9, which covers the determination of the workable life of fresh mortar, by monitoring the time required for the flow value to decrease by 30 mm from its initial value.

During the extrudability tests performed using the mortar injection pump, all mixtures were discharged continuously and homogeneously through the nozzle. The measured filament widths and thicknesses showed only small deviations, indicating satisfactory extrusion stability and shape retention under the adopted test conditions. The extrudability results are presented in Table 3 and Fig. 1.

Table 3. Extrudability Test Results

Samples	Extrudability Measurements		
	Thickness	**Width**	**Observation**
REF	1.6 cm	5.75 cm	Printable
G30	1.6 cm	5.70 cm	Printable
F30	1.7 cm	5.70 cm	Printable
G15F15	1.7 cm	5.8 cm	Printable

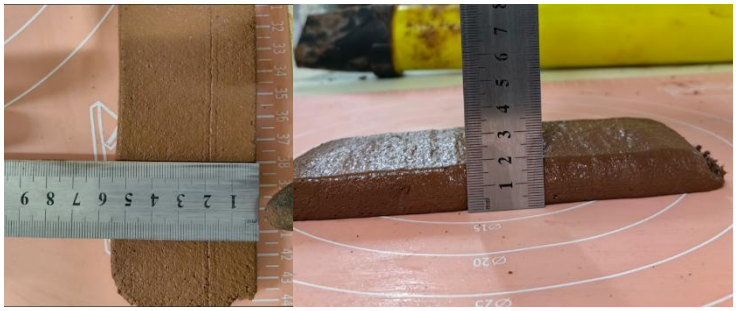


Fig. 1. Extrudability Test

Table 4. Buildability Test Results (ThicknessValues)

Samples	Thickness1 (cm)	Thickness2 (cm)	Thickness3 (cm)	Avg. Thickness(cm)
REF	1.6	1.6	1.6	1.60
G30	1.6	1.6	1.6	1.60
F30	1.7	1.7	1.7	1.70
G15F15	1.6	1.6	1.6	1.60

Buildability was evaluated by examining the ability of successive layers to be deposited while maintaining their geometry. As shown in Table 4, the layer thicknesses of all mixtures remained stable under the self-weight of the deposited layers, with thickness values ranging from 1.6 to

1.7 cm. These results indicate that the mixtures containing recycled brick aggregate exhibited adequate load-bearing capacity and shape retention for the adopted layer-by-layer deposition conditions.



Fig. 2. Buildability Test

In the flow-table test, the G15F15 mixture exhibited the lowest average spread diameter, at 11.5 cm, indicating lower flow tendency and greater fresh-state shape stability. This behavior may be advantageous for maintaining layer geometry during 3D printing. The spread diameters of all mixtures were within the range considered suitable for printable cementitious mixtures, and the results are presented in Table 5.

Table 5. Flow Table Spread Diameters of the Mixtures (cm)

Sample	Average Spread Diameter (cm)
REF	13.25
G30	12.9
F30	12.85
G15F15	11.5



Fig. 3. Flow Table Test

To determine the workable time (open time), the flow-table test was repeated at 15 min intervals, and the elapsed time until the spread diameter decreased by 3 cm from its initial value was recorded as the workable time. G30 exhibited the longest workable time, reaching 126 min, whereas F30 showed the shortest value at 86 min. The G15F15 mixture provided a workable time of 102 min, relatively close to that of the reference mixture, indicating that the combined use of GGBFS and FA maintained an adequate processing window. Overall, GGBFS tended to

extend the workable time, while FA shortened it under the investigated conditions. The results are presented in Table 6.

Table 6. Workable Time of the Mixtures (Time Corresponding to a 3 cm Reduction in Spread Diameter, min)

Reduction in Spread Diameter	REF (min)	G30 (min)	F30 (min)	G15F15 (min)
1 cm	39	42	29	34
2 cm	78	84	58	68
3 cm	117	126	86	102

3. Conclusion

This study investigated the effects of ground granulated blast furnace slag (GGBFS) and fly ash (FA) on the fresh-state properties and printability of 3D-printable concrete incorporating brick powder as fine aggregate. All mixtures exhibited continuous extrusion and adequate layer stability under the adopted laboratory-scale printing conditions, indicating that the incorporation of these supplementary cementitious materials did not prevent satisfactory printability.

Among the mixtures, G15F15 exhibited the lowest flow-table spread of 11.5 cm, indicating greater resistance to flow and improved shape retention after deposition. In terms of workable time, G30 provided the longest processing window at 126 min, whereas F30 showed the shortest workable time at 86 min. The G15F15 mixture maintained an intermediate workable time of 102 min, providing a favorable balance between consistency retention and processing duration. These results demonstrate that GGBFS and FA influence fresh-state behavior differently and that their combined use can provide a suitable balance between flowability, extrusion stability, shape retention, and workable time.

The results also indicate that brick powder can be incorporated as a fine aggregate component together with GGBFS and FA without compromising the fresh-state requirements evaluated in this study. Thus, the combined use of brick-derived construction waste and supplementary cementitious materials offers a promising approach for reducing the consumption of Portland cement and natural fine aggregate in 3D-printable cementitious mixtures.

The present investigation was limited to laboratory-scale extrusion and two-layer deposition because of equipment and operational constraints. Future studies should therefore evaluate the mixtures using a larger number of printed layers and automated printing systems to verify their buildability under more demanding conditions. Further investigations should also quantify the effects of GGBFS and FA through rheological measurements, including yield stress, viscosity, and structural build-up, and examine the influence of viscosity-modifying admixture and superplasticizer dosage on the printing window. In addition, interlayer bond strength, long-term mechanical performance, durability, and resistance to thermal and chemical exposure should be investigated to support the development of optimized mixtures for larger-scale 3D concrete printing applications.

References

1. Kaszyńska, M., Skibicki, S., Hoffmann, M.: 3D concrete printing for sustainable construction. Energies 13(23), 6351 (2020). https://doi.org/10.3390/en13236351

2. Girskas, G., Kligys, M.: 3D concrete printing review: Equipment, materials, mix design, and properties. Buildings 15(12), 2049 (2025). https://doi.org/10.3390/buildings15122049
3. Kumar, S., Gangotra, A., Barnard, M.: Towards a net zero cement: Strategic policies and systems thinking for a low-carbon future. Current Sustainable/Renewable Energy Reports 12, 5 (2025). https://doi.org/10.1007/s40518-025-00253-0
4. Ginga, C.P., Ongpeng, J.M.C., Daly, M.K.M.: Circular economy on construction and demolition waste: A literature review on material recovery and production. Materials 13(13), 2970 (2020). https://doi.org/10.3390/ma13132970
5. Buswell, R.A., Leal de Silva, W.R., Jones, S.Z., Dirrenberger, J.: 3D printing using concrete extrusion: A roadmap for research. Cement and Concrete Research 112, 37-49 (2018). https://doi.org/10.1016/j.cemconres.2018.05.006
6. Mechtcherine, V., Bos, F.P., Perrot, A., Leal da Silva, W.R., Nerella, V.N., Fataei, S., Wolfs, R.J.M., Sonebi, M., Roussel, N.: Extrusion-based additive manufacturing with cement-based materials - Production steps, processes, and their underlying physics: A review. Cement and Concrete Research 132, 106037 (2020). https://doi.org/10.1016/j.cemconres.2020.106037
7. Le, T.T., Austin, S.A., Lim, S., Buswell, R.A., Gibb, A.G.F., Thorpe, T.: Mix design and fresh properties for high-performance printing concrete. Materials and Structures 45(8), 1221-1232 (2012). https://doi.org/10.1617/s11527-012-9828-z
8. Roussel, N.: Rheological requirements for printable concretes. Cement and Concrete Research 112, 76-85 (2018). https://doi.org/10.1016/j.cemconres.2018.04.005
9. Perrot, A., Rangeard, D., Pierre, A.: Structural built-up of cement-based materials used for 3D-printing extrusion techniques. Materials and Structures 49, 1213-1220 (2016). https://doi.org/10.1617/s11527-015-0571-0
10. Tarhan, Y., Şahin, R.: Fresh and rheological performances of air-entrained 3D printable mortars. Materials 14(9), 2409 (2021). https://doi.org/10.3390/ma14092409
11. Rahman, M., Rawat, S., Yang, R.C., Mahil, A., Zhang, Y.X.: A comprehensive review on fresh and rheological properties of 3D printable cementitious composites. Journal of Building Engineering 91, 109719 (2024). https://doi.org/10.1016/j.jobe.2024.109719
12. Dang, J., Zhao, J., Hu, W., Du, Z., Gao, D.: Properties of mortar with waste clay bricks as fine aggregate. Construction and Building Materials 166, 898-907 (2018). https://doi.org/10.1016/j.conbuildmat.2018.01.109
13. Christen, H., van Zijl, G., de Villiers, W.: The incorporation of recycled brick aggregate in 3D printed concrete. Cleaner Materials 4, 100090 (2022). https://doi.org/10.1016/j.clema.2022.100090
14. Pepe, M., Lombardi, R., Lima, C., Paolillo, B., Martinelli, E.: Experimental evidence on the possible use of fine concrete and brick recycled aggregates for 3D printed cement-based mixtures. Materials 18(3), 583 (2025). https://doi.org/10.3390/ma18030583
15. Tarhan, Y., Tarhan, İ.H., Şahin, R.: Comprehensive review of binder matrices in 3D printing construction: Rheological perspectives. Buildings 15(1), 75 (2025). https://doi.org/10.3390/buildings15010075

16. Xu, Z., Zhang, D., Li, H., Sun, X., Zhao, K., Wang, Y.: Effect of FA and GGBFS on compressive strength, rheology, and printing properties of cement-based 3D printing material. Construction and Building Materials 339, 127685 (2022). https://doi.org/10.1016/j.conbuildmat.2022.127685
17. Tseng, K.-C., Chi, M., Yeih, W., Huang, R.: Influence of slag/fly ash as partial cement replacement on printability and mechanical properties of 3D-printed concrete. Applied Sciences 15(7), 3933 (2025). https://doi.org/10.3390/app15073933
18. Tarhan, İ.H., Tarhan, Y.: Nonlinear in-plane response of 3D-printed concrete walls with varied infill patterns: Experimental mix design and numerical structural assessment. Challenge Journal of Structural Mechanics 11(3), 160-173 (2025). https://doi.org/10.20528/cjsmec.2025.03.005

Author Contribution Statement

- *Conceptualization:* Muhammed Çeçen, Derya Kurt, İsmail Hakkı Tarhan, Yeşim Tarhan
- *Methodology:* Muhammed Çeçen, Derya Kurt, İsmail Hakkı Tarhan, Yeşim Tarhan
- *Investigation:* Muhammed Çeçen, Derya Kurt, İsmail Hakkı Tarhan, Yeşim Tarhan
- *Writing - Original Draft:* Muhammed Çeçen, Derya Kurt
- *Writing - Review & Editing:* Muhammed Çeçen, Derya Kurt, İsmail Hakkı Tarhan, Yeşim Tarhan

List of Abbreviations

- 3DCP - Three-Dimensional Concrete Printing
- GGBFS - Ground Granulated Blast Furnace Slag
- FA - Fly Ash
- BP - Brick Powder
- SCM - Supplementary Cementitious Material
- VMA - Viscosity-Modifying Admixture
- SP – Superplasticizer
- REF - Reference Mixture
- G30 - Mixture containing 30% GGBFS
- F30 - Mixture containing 30% FA
- G15F15 - Mixture containing 15% GGBFS and 15% FA

Note: Following the conference, this Publication Note will be added to each paper; therefore, authors are kindly requested not to remove the note below and to complete the author(s) and paper title information.

Publication Note

This paper was peer-reviewed, accepted for presentation, and included in the proceedings of the ACE2026 – International Conference on Advances in Civil Engineering, held on 12–14 October 2026 in Trabzon, Türkiye.

This paper may be cited as follows:

Cecen, M., Kurt, D., Tarhan, Y., Tarhan, I.H., "Fresh-State Performance and Printability of Brick Powder-Based 3D Printable Concrete with GGBFS and Fly Ash," in Proceedings of the ACE2026 – International Conference on Advances in Civil Engineering, Trabzon, Türkiye, 12–14 October 2026.

Effect of Supplementary Cementitious Materials on Hemp Fiber-Reinforced Structural Lightweight Concrete with Pumice Aggregate

Mehmet Kara[1] and Zehra Canan Girgin[2]
[1] 0000-0003-2077-3855, Yıldız Technical University, Faculty of Architecture, Structural Technologies Research Group, İstanbul, Türkiye, mehmet.kara@yildiz.edu.tr
[2] 0000-0003-1985-448X, Yıldız Technical University, Faculty of Architecture, Structural Technologies Research Group, İstanbul, Türkiye, zcgirgin@yildiz.edu.tr

Abstract. Structural lightweight aggregate concrete (LWAC) offers advantages to reduce structural dead loads; however, like conventional concrete, its inherently brittle behavior requires reinforcement to enhance flexural performance. The use of natural fibers as a renewable resource may improve the mechanical response of LWAC. This potential benefit, however, should be evaluated by taking their durability in the alkaline cementitious environment into consideration. This study investigates the mechanical performance of hemp fiber reinforced structural lightweight concrete (HSLWC) incorporating volcanic pumice aggregate (VPA, 2-10 mm) and supplementary cementitious materials (SCMs). Metakaolin (MK), Class F fly ash (FA), and their combination constituted 20% of the total binder content. Binder content was 350 kg/m³ for the reference (C) and MK mixtures, and 400 kg/m³ for the FA and MK+FA mixtures, with a constant water-to-binder ratio (*w/b*) of 0.40. The 100% cement reference was fiber-free, all SCM-containing mixtures contained 1% hemp fiber. Compressive strength was determined at 7 and 28 days, water absorption was measured, and flexural strengths were assessed through three-point bending tests. In addition, 28-day prism specimens were immersed in water at 50 ± 2 °C for seven days to evaluate the effect of accelerated aging. The MK mixture achieved the highest compressive strength and binder efficiency with a total binder content of 350 kg/m³. At a binder content of 400 kg/m³, MK+FA produced higher performance than FA. Water absorption remained within a narrow range of 3.1–4.1% despite the use of 50% VPA by volume. Maximum flexural load increased after accelerated aging, and MK+FA series maintained the highest load before and after aging. Overall, the combined MK+FA system yielded the best balance among compressive strength, flexural performance, water absorption, and sorptivity.

Keywords: Structural lightweight concrete; Hemp fiber; Pumice aggregate; Metakaolin; Class F fly ash; Accelerated water aging.

1 Introduction

Structural lightweight aggregate concrete (LWAC) has a lower unit weight than normal-weight concrete to reduce structural dead loads. This reduction can lead to smaller demands on structural members and foundations and, owing to the mass-dependent nature of earthquake-induced forces, lower seismic actions. Among the lightweight aggregates used in structural LWAC, pumice is a volcanic based natural aggregate that enables the production of concrete with reduced density.

Like conventional concrete, LWAC is inherently brittle; steel or polypropylene fibers were reported to improve its flexural and post-cracking performance, including toughness and energy absorption ([1] [2]). Currently, natural fibers are increasingly investigated as renewable reinforcement materials for cementitious composites. Hemp fibers were previously reported to improve the flexural behavior and energy absorption capacity of concrete [3]. In pumice based

lightweight concrete, hemp fibers have been recently reported to enhance deformation capacity depending on the composition of the cementitious matrix [4]. However, the long-term performance of cellulosic fibers in cementitious matrices remains a critical durability consideration. The alkaline environment of hydrated cement can induce the degradation of lignin and hemicellulose through the penetration of hydration products into the fiber structure, thus leading to fiber mineralization. These mechanisms increase fiber brittleness and consequently impair the long-term reinforcing performance of cellulosic fibers [5].

Supplementary cementitious materials (SCMs) can mitigate the degradation of cellulosic fibers when used as partial replacements for Portland cement. Reductions in $Ca(OH)_2$ content and stabilization of the matrix alkalinity have been identified as mechanisms to enhance durability [6]. Metakaolin can also reduce fiber degradation under accelerated aging conditions [5]. In cellulosic fiber reinforced mortars, its use yielded a marked reduction in capillary absorption [7]. In addition to metakaolin, Class F fly ash was investigated both individually and in combination with other SCMs to mitigate the degradation of cellulosic fiber–cement composites [6].

Accelerated aging procedures provide a means to observe variations in the mechanical performance of fiber reinforced cementitious composites over relatively short experimental periods. Hot-water immersion, a well-established accelerated-aging technique for glass-fiber-reinforced cement composites [8], allows changes under short-term exposure to be related to long-term mechanical behavior.

To the authors' knowledge, only one previous study has combined VPA with hemp fibers to mitigate fiber degradation through SCMs [4]. Against this limited background, the present study focuses on HSLWC incorporating VPA and modified with metakaolin (MK), Class F fly ash (FA), or their combination as partial cement replacements. Compressive strength, water absorption, and sorptivity were determined, while flexural load capacity was assessed before and after accelerated water aging.

2 Materials and Methods

2.1 Materials and Mix Proportions

CEM II/A-S 42.5 R cement was used in all mixtures. Metakaolin (MK) and Class F fly ash (FA) were incorporated as SCMs at a total SCM-to-binder ratio of 20%, comprising 20% MK, 20% FA, or a combination of 10% MK and 10% FA. A fiber-free 100% cement mixture was also designed as the reference mixture (C). The total binder content was 350 kg/m³ for the C and MK mixtures and 400 kg/m³ for the FA and MK+FA mixtures. A constant water-to-binder ratio (*w/b*) of 0.40 was used for all the mixtures. The slump was measured as 16 cm for the reference mixture and ranged from 7 to 10 cm for the fiber reinforced mixtures. The photographs of hemp fiber and VPA as well as production stage are presented in Fig.1. The detailed mix proportions were given in *Table 1.*



Fig.1 Hemp fibers, pumice aggregates, slump test during mixture stage

Volcanic pumice (Nevsehir, 2-10 mm) was used as lightweight aggregate (LWA), constituting 50% of the total aggregate volume. Its bulk density in oven-dry condition is 690 kg/m^3, and the 24-hour water absorption value is 18%. The pumice aggregate was pre-saturated with water prior to mixing. Natural sand and limestone powder were used as normal-weight aggregates.

Hemp fibers with 30 mm length (V_f=1%) were added to MK, FA, and MK+FA mixtures. The fibers were also pre-saturated with water, and excess surface water was removed with a towel before they were added to the mixture.

Table 1. Mix proportions of concrete mixtures

Constituent (kg/m³)	**C**	**MK**	**FA**	**MK+FA**
Cement (C)	350	280	320	320
Metakaolin (MK)	-	70	-	40
Fly ash (FA)	-	-	80	40
Total binder (b)	350	350	400	400
Water (w)	140	126	160	160
Natural sand	558	586	525	527
Limestone powder	375	394	353	354
Pumice LWA	450	474	424	425
Hemp fiber	-	15	15	15
Superplasticizer	1.75	3.15	6.0	6.0
Fresh density	1848	1866	1880	1875

2.2 Preparation of Specimens and Test Setup

After mixing, the fresh concrete was cast into 100 × 100 × 100 mm cube specimens for compressive strength tests at 7 and 28 days and 40 × 40 × 160 mm prism specimens for three-point bending tests at 28 days. The specimens were maintained under ambient laboratory conditions until the specified test ages, without external water curing. The water-storage and gradual-release capacity of the pre-saturated pumice aggregates provided internal curing, thereby eliminating the need for water curing.

Three-point bending tests were performed using a span length of 120 mm. The specimens were loaded at a displacement rate of 0.3 mm/min, and the maximum load was recorded during each test to evaluate their flexural response.

A separate set of prism specimens was subjected to accelerated water aging after 28 days of curing. The specimens were fully immersed in water maintained at 50 ± 2 °C for seven days. Then the maximum loads of the aged specimens were compared with those of the 28-day specimens to evaluate the effect of accelerated water aging on flexural load capacity.

3 Results and Discussion

3.1 Compressive Strength Tests

Compressive strength increased from 7 days to 28 days for all specimens (*Table 2* and Fig.2), with relative increases of 9.5% for C, 22.9% for MK, 53.4% for FA, and 34.5% for MK+FA. The C mixture (V_f=0%) produced the highest compressive strength at both ages, reaching 35.5 MPa at 28 days, followed by MK and MK+FA with 33.3 and 31.2 MPa, respectively. FA had the lowest strength at 7 and 28 days but the greatest relative gain (53.4%) with curing time.

Since the *w/b* ratio was kept constant at 0.40 for all mixtures, the strength differences are primarily attributed to binder composition, total binder content, and fiber incorporation.

Table 2. Compressive strength results

Mixtures	7 Days (MPa)	28 Days (MPa)	Increase (%)
C (0%)	32.4	35.5	9.5
MK (1%)	27.1	33.3	22.9
FA (1%)	16.3	25.0	53.4
MK + FA (1%)	23.2	31.2	34.5

In the first comparison group, C and MK mixtures had the same total binder content of 350 kg/m³, while only MK contained 1% hemp fiber. 28-day strength of MK specimens was only 6.2% lower than that of fiber-free C mixture. A more direct assessment of binder composition is possible for FA and MK+FA mixtures, which had the same binder content of 400 kg/m³ and hemp-fiber volume (1%). The partial replacement of the 20% FA content with MK increased the compressive strength from 16.3 to 23.2 MPa at 7 days and from 25.0 to 31.2 MPa at 28 days. Overall, under the same *w/b* ratio, binder content, and hemp-fiber volume, partial replacement of FA with MK substantially improved compressive strength.

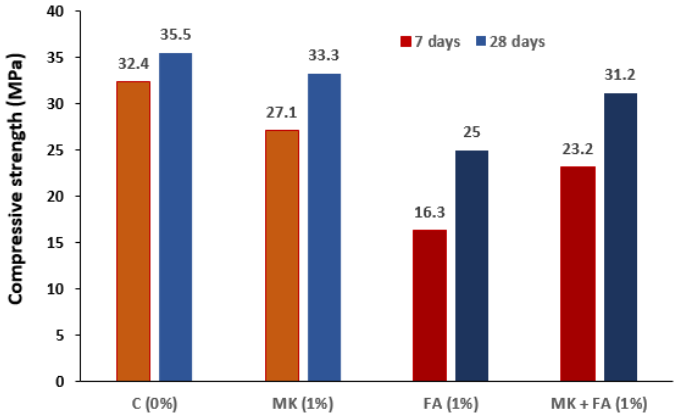


Fig. 2. Compressive strength development of the mixtures at 7 and 28 days.

The variations among the mixtures cannot be attributed solely to the type of supplementary cementitious material. Metakaolin has relatively high pozzolanic activity, particularly at early ages, whereas the effect of Class F fly ash may become more pronounced at later ages. In order to consider the different binder contents of the mixtures, compressive strength was evaluated per unit binder content, namely binder efficiency, as presented in Fig. 3. The C series attained the highest binder efficiency, closely followed by MK. Among 1% hemp fiber-reinforced mixtures, MK ranked first in efficiency despite its lower total binder content. At 28 days, the binder efficiency of MK reached 0.095 MPa.m^3/kg compared with 0.078 MPa.m^3/kg for MK+FA and 0.063 MPa.m^3/kg for FA, further highlighting the beneficial role of MK in the cementitious matrix.

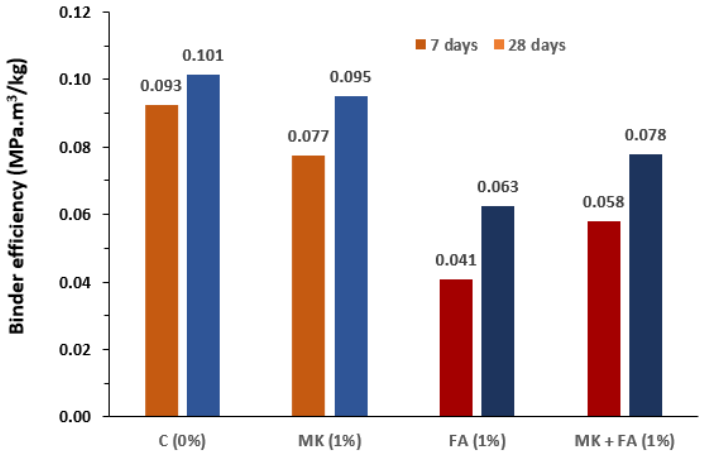


Fig. 3. 7- and 28-day binder efficiency of four mixtures

3.2 Flexural Behaviour and Accelerated Aging

The 28-day flexural behavior of the mixtures was evaluated based on the maximum load recorded during the three-point bending tests. The effect of accelerated water aging was addressed by comparing the results before and after aging, as summarized in *Table 3*. Before aging, MK+FA produced the highest load (2244 N), followed by MK (2040 N) and FA (1795 N). After aging, the values increased to 2428, 2342, and 2153 N, respectively, corresponding to increments of 8.2%, 14.8%, 19.9%. Although FA produced the largest relative increase, MK+FA maintained the highest load both before and after aging.

Table 3. Maximum flexural loads before and after accelerated water aging

Mixtures	28-day (N)	After aging (N)	Change (%)
MK	2040	2342	+14.8
FA	1795	2153	+19.9
MK + FA	2244	2428	+8.2



Examination of the fracture surfaces after aging revealed clear differences in fiber–matrix interaction. In the MK mixture (Fig. 4a), fewer pulled-out fibers were visible, consistent with a denser and more rigid ITZ. This may be attributed to the pozzolanic reaction of MK, which consumes CH and promotes the formation of additional C-S-H/C-A-S-H, thereby strengthening the fiber–matrix interface while reducing the alkaline environment around the fibers. Previous studies have reported that MK reduces pore-solution alkalinity and CH content, limiting fiber mineralization and improving the integrity of the fiber–matrix interface under accelerated exposure conditions [5]. In contrast, numerous exposed fibers were observed in the FA specimen (Fig. 4b), reflecting greater fiber pull-out, although its flexural load was lower than those of MK and MK+FA. More pulled-out fibers were observed in MK+FA than in MK (Fig. 4c), while this mixture also attained the highest flexural load after aging, pointing to a favorable balance between fiber–matrix adherence and pull-out resistance. Moreover, the increase in flexural load after aging may also reflect further strengthening of the cementitious matrix during hot-water exposure rather than changes in fiber behavior alone.



(a) (b) (c)

Fig. 4 View from aged specimens

3.3 Water Absorption and Sorptivity

Since all mixtures were produced at the same *w/b* ratio of 0.40, the observed differences can be considered mainly in relation to binder composition, total binder content, and the presence of hemp fibers (*Table 3*). The C, MK, and MK+FA mixtures had nearly identical water absorption values of 3.1–3.2%, while FA showed a slightly higher value of 4.1%. In the preliminary experiments, by using normal-weight aggregates and 350 kg/m^3 cement, water absorption was determined as 1.5%. Although the porous pumice aggregate constituted 50% of the total aggregate volume and had higher water uptake, water absorption remained within a narrow range of 3.1-4.1%. This is particularly noteworthy considering the differences in total binder content (350 and 400 kg/m^3), binder composition, and the incorporation of 1% hemp fiber.

Capillary water absorption (ASTM 1585-20), commonly used as an indirect indicator of pore connectivity and durability-related transport performance, was evaluated at 4 h in the linear region and at 72 hour in the later nonlinear region (*Table 4* and Fig. 5). Although the C mixture was fiber-free and the MK mixture contained 1% hemp fiber, MK specimens had substantially lower capillary water absorption. This suggests that the pore-refining effect of MK compensated for the water affinity of the hemp fibers and restricted the connectivity of capillary pores. The combined MK+FA mixture yielded the greatest resistance to capillary water transport, with values of 0.00 and 0.30 kg/m^2 at 4 and 72 h, respectively. FA showed the highest total water absorption (4.1%) but considerably lower capillary uptake than C. Moreover, despite the approximately 18% 24-h water absorption of the pumice aggregate, the relatively low water and capillary absorption values may also be associated with its internal-curing effect. The gradual release of stored water from the pumice can promote further hydration in the surrounding cementitious matrix and a denser aggregate–matrix ITZ. This common effect may partly explain why even the C mixture, without pozzolanic replacement, exhibited relatively low water and capillary absorption.

Table 4. Water absorption results of the mixtures

Mixtures	Total binder (kg/m^3)	Water absorption (%)	Capillary water absorption (kg/m^2)	
			4 hours	72 hours
C (0%)	350	3.1	0.6	1.57
MK (1%)	350	3.2	0.23	0.69
FA (1%)	400	4.1	0.20	0.90
MK + FA (1%)	400	3.2	0.00	0.30

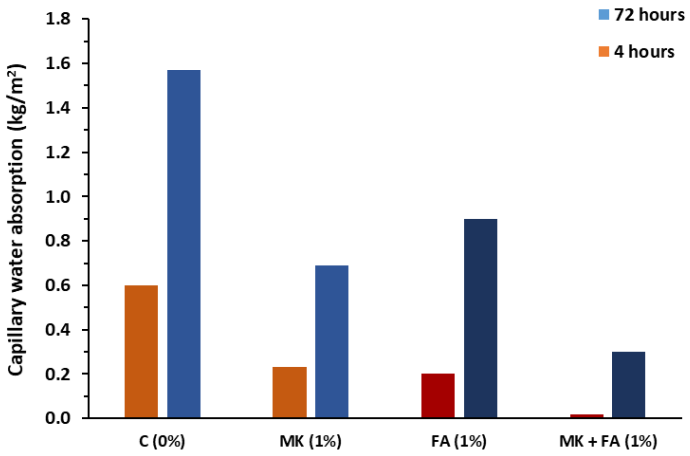


Fig. 5. Cumulative capillary water absorption values of four mixtures

4 Conclusions

The mechanical performance of hemp fiber reinforced structural lightweight concrete containing pumice aggregate was investigated using binder systems modified with metakaolin (MK), Class F fly ash (FA), and their combination. Based on the experimental results, the following conclusions were drawn:

- Among the hemp fiber reinforced mixtures, MK achieved the highest compressive strength and binder efficiency, despite its lower total binder content. Its 28-day compressive strength was only 6.2% below that of the fiber-free C mixture.
- At the same binder content, *w/b* ratio, and fiber content, partial replacement of FA with MK markedly improved performance. MK+FA increased the 28-day compressive strength from 25.0 to 31.2 MPa and provided the highest flexural load among the fiber-reinforced mixtures.
- Water absorption remained within 3.1–4.1%, although pumice constituted 50% of the total aggregate volume and had a 24-h water absorption of 18%. The low absorption of the C mixture and the further reductions in capillary uptake with MK and MK+FA indicate contributions from both pumice internal curing and SCM-induced pore refinement.
- Accelerated hot-water exposure did not reduce the maximum flexural load of any fiber reinforced mixture; instead, increases of 8.2–19.9% were observed. MK+FA maintained the highest load before and after aging, while its fracture surface indicated a favorable balance between fiber–matrix adherence and pull-out resistance.

Acknowledgments

The experiments in this study were carried out in R&D Dept. of NUH Beton Inc. Material, employer and equipment support of the firm to this experimental research are greatly appreciated. The authors would like to thank to Soylu Group providing pumice aggregate and Kaolin EAD providing metakaolin as well. The first author was supported by TÜBİTAK, Directorate of Science Fellowships and Grant Programmes (BİDEB), under the 2211-National Graduate Scholarship Programme.

References

[1] N. A. Libre, M. Shekarchi, M. Mahoutian, and P. Soroushian, "Mechanical properties of hybrid fiber reinforced lightweight aggregate concrete made with natural pumice," *Constr. Build. Mater.*, vol. 25, no. 5, pp. 2458–2464, May 2011, doi: 10.1016/j.conbuildmat.2010.11.058.

[2] K. I. Christidis, E. G. Badogiannis, and C. Mintzoli, "Flexural behaviour of pumice lightweight concrete reinforced with end-hooked steel fibres," *Structures*, vol. 33, pp. 3835–3847, Oct. 2021, doi: 10.1016/j.istruc.2021.06.090.

[3] Z. Li, L. Wang, and X. Wang, "Compressive and Flexural Properties of Hemp Fiber Reinforced Concrete," 2004.

[4] H. M. Tuncer and Z. C. Girgin, "Hemp fiber reinforced lightweight concrete (HRLWC) with coarse pumice aggregate and mitigation of degradation," *Materials and Structures/Materiaux et Constructions*, vol. 56, no. 3, Apr. 2023, doi: 10.1617/s11527-023-02142-8.

[5] J. Wei and C. Meyer, "Degradation mechanisms of natural fiber in the matrix of cement composites," *Cem. Concr. Res.*, vol. 73, pp. 1–16, 2015, doi: 10.1016/j.cemconres.2015.02.019.

[6] B. J. Mohr, J. J. Biernacki, and K. E. Kurtis, "Supplementary cementitious materials for mitigating degradation of kraft pulp fiber-cement composites," *Cem. Concr. Res.*, vol. 37, no. 11, pp. 1531–1543, Nov. 2007, doi: 10.1016/j.cemconres.2007.08.001.

[7] R. M. De Gutiérrez, L. N. Díaz, and S. Delvasto, "Effect of pozzolans on the performance of fiber-reinforced mortars," in *Cement and Concrete Composites*, May 2005, pp. 593–598. doi: 10.1016/j.cemconcomp.2004.09.010.

[8] K. L. Litherland, D. R. Oakley, and B. A. Proctor, "The Use of Accelerated Ageing Procedures to Predict The Long Term Strength of GRC Composites," *Cem. Concr. Res.*, vol. 11, pp. 455–466, 1981.

Author Contribution Statement

- *Conceptualization:* Zehra Canan Girgin
- *Methodology:* Zehra Canan Girgin
- *Investigation:* Mehmet Kara, Zehra Canan Girgin
- *Writing – Original Draft:* Mehmet Kara
- *Writing – Review & Editing:* Mehmet Kara, Zehra Canan Girgin

List of Abbreviations

- **LWAC —** Lightweight Aggregate Concrete
- **LWA —** Lightweight Aggregate
- **VPA —** Volcanic Pumice Aggregate
- **SCM —** Supplementary Cementitious Material
- **MK —** Metakaolin
- **FA** — Class F Fly Ash
- **C** — Reference Mixture
- **w/b** — Water-to-Binder Ratio

Publication Note

This paper was peer-reviewed, accepted for presentation, and included in the proceedings of the ACE2026 – International Conference on Advances in Civil Engineering, held on 12–14 October 2026 in Trabzon, Türkiye.

This paper may be cited as follows:

Mehmet Kara and Zehra Canan Girgin, "Effect of Supplementary Cementitious Materials on Hemp Fiber-Reinforced Structural Lightweight Concrete with Pumice Aggregate," in Proceedings of the ACE2026 – International Conference on Advances in Civil Engineering, Trabzon, Türkiye, 12–14 October 2026.

Influence of GGBFS and Fly Ash on the Mechanical Performance of 3D Printable Concrete Incorporating Brick Powder as Fine Aggregate

Derya Kurt[1*], Muhammed Çeçen[2], İsmail Hakkı Tarhan[3], Yeşim Tarhan[4]
[1]0009-0002-2754-9688, *Department of Civil Engineering, Institute of Graduate Studies, Tokat Gaziosmanpaşa University, Tokat, 60150, Türkiye*
[2]0009-0006-4206-7360, *Department of Civil Engineering, Institute of Graduate Studies, Tokat Gaziosmanpaşa University, Tokat, 60150, Türkiye*
[3]0000-0002-5161-3718, *Department of Civil Engineering, Faculty of Engineering and Architecture, Tokat Gaziosmanpaşa University, Tokat, 60150, Türkiye*
[4] 0000-0002-3901-9070, *Technical Sciences Vocational School, Ardahan University, Ardahan, 75000, Türkiye*
*Corresponding Author E-mail: deryakurt476@gmail.com

Abstract. The design of cementitious mixtures for 3D concrete printing (3DCP) requires a careful balance between printability, mechanical performance, and sustainability. The use of brick powder as an alternative fine aggregate introduces a sustainable aggregate phase into printable mixtures; however, the hardened-state response of such systems depends strongly on binder composition and still requires further evaluation. In this context, the incorporation of ground granulated blast furnace slag (GGBFS) and fly ash (FA) as supplementary cementitious materials (SCMs) offers a potential route for tailoring the strength development of 3D printable concrete while improving the sustainability profile of cement-based composites. This study investigates the effects of GGBFS and FA on the mechanical performance of 3D printable concrete in which brick powder was used as a fine aggregate component. The experimental program included a reference mixture and three modified mixtures incorporating GGBFS, FA, or their combined use at a total replacement level of 30% by mass of binder, corresponding to 30% GGBFS, 30% FA, and 15% GGBFS + 15% FA, respectively. Compressive and flexural strength tests were conducted on standard specimens at 7, 14, and 28 days of curing. The results showed that the incorporation of GGBFS and FA generally reduced early-age strength compared with the reference mixture, mainly due to their slower hydration and pozzolanic reaction mechanisms. However, this trend changed at 28 days, when all SCM-incorporated mixtures reached higher strength values than the reference mixture. Among them, the combined GGBFS-FA mixture, incorporating 15% GGBFS and 15% FA by mass of binder, showed the best mechanical performance, reaching a 28-day compressive strength of 41.48 MPa and a flexural strength of 8.91 MPa. These results indicate that using GGBFS and FA together can enhance the hardened-state performance of 3D printable concrete with brick powder fine aggregate and suggest that further optimization of replacement ratios may lead to more effective and sustainable mixture designs.

Keywords: 3DCP; Clay Brick Powder Fine Aggregate; GGBFS; Fly Ash; Compressive and Flexural Strength

1 Introduction

Extrusion-based three-dimensional concrete printing (3DCP) is a formwork-free manufacturing method in which a cement-based mixture is deposited layer by layer along toolpaths derived from a digital model. Although pumpability, extrudability, and buildability are essential prerequisites for successful printing, the post-hardening mechanical performance of the printed element is also a key factor determining its suitability for engineering applications [1,2]. The layer-by-layer production process, curing conditions, and mixture composition can influence compressive and flexural strengths as well as orientation-dependent mechanical behavior. Tarhan and Şahin [3] showed that air-entraining admixture dosage, curing method, and specimen orientation significantly affect the physicomechanical properties and microstructure of 3D-printed concrete. Similarly, Tarhan et al. [4] investigated the compressive, flexural, and splitting tensile behavior of sustainable 3D-printed composites and demonstrated that material composition and reinforcement can substantially influence hardened-state performance. Therefore, the design of 3DCP mixtures should consider not only printability but also the systematic evaluation of strength development with curing age.

The use of predominantly fine aggregates together with relatively high binder contents in 3DCP mixtures makes the environmental performance of the technology particularly sensitive to material selection [5]. In this context, recycling fired-clay-based construction and demolition waste through crushing and grinding is valuable both for reintegrating waste into the circular economy and for reducing the consumption of natural raw materials [6]. Waste brick can be used either as a partial cement replacement or as recycled fine aggregate. When used as fine aggregate, its porous and angular particle structure, relatively high water absorption, and differences in the aggregate–paste interface may influence the strength of the hardened composite differently from natural sand. The magnitude of these effects depends on particle size, replacement level, moisture condition, and water management within the mixture [6,7].

In addition to the characteristics of brick-derived fine aggregate, binder composition plays an important role in strength development. Ground granulated blast-furnace slag (GGBFS) is a latent hydraulic material, whereas fly ash (FA) primarily exhibits pozzolanic behavior. Partial replacement of Portland cement with these supplementary cementitious materials can alter hydration kinetics, hydration products, and pore structure, thereby affecting both early- and later-age strength development [8,9]. The relatively slow reactions of these mineral additions may limit early-age strength, whereas secondary reactions at later ages can contribute to matrix densification and improved mechanical performance. In the context of 3DCP, Tarhan and Tarhan [10] experimentally determined the compressive and flexural strengths of a printable cementitious mixture containing GGBFS and directly incorporated these properties into the nonlinear structural assessment of 3D-printed walls. This approach highlights that hardened-state testing provides essential data not only for material characterization but also for evaluating structural performance. Studies on the use of GGBFS and FA as partial cement replacements in 3DCP mixtures have likewise reported that both the type and replacement level of these materials can significantly influence mechanical strength development [11].

Previous studies have investigated brick-derived materials in 3DCP for different purposes. Recycled brick aggregate has been used as a replacement for natural aggregate [12]; replacement levels of up to 100% have been examined using fine recycled aggregates derived from brick and concrete [13]; brick powder has been incorporated together with GGBFS as part of the binder/powder fraction [14]; and it has also been used to replace conventional fine aggregate in fiber-reinforced 3DCP mixtures [15]. In the present study, the individual and combined effects of GGBFS and FA on 3D-printable concrete incorporating brick powder as fine aggregate were comparatively investigated through compressive and flexural strength tests conducted at 7, 14, and 28 days.

2 Material and Method

2.1 Material

Portland cement (CEM I 42.5 R) was used as the primary binder in this study. Ground granulated blast furnace slag (GGBFS), exhibiting latent hydraulic properties, and Class C fly ash (FA), exhibiting pozzolanic properties, were used as supplementary cementitious materials to partially replace cement. The aggregate phase consisted of 0.5–1.5 mm natural sand and brick powder (BP) with particle size ranges of 1–2 mm and 0–1 mm. A viscosity-modifying admixture (VMA), calcined kaolin, polypropylene fibers, and a superplasticizer (SP) were used to improve the printability performance of the mixtures. Potable tap water was used as the mixing water.

2.2 Mixture designs

Four different mixtures were prepared while keeping the total binder content and water-to-binder ratio constant. The binder phase of the reference mixture consisted solely of Portland cement. To investigate the effects of the mineral additions, three modified mixtures were designed: G30, in which 30% of the binder was replaced with GGBFS; F30, in which 30% was replaced with FA; and G15–F15, in which 15% GGBFS and 15% FA were used, corresponding to a total replacement level of 30%. Thus, the individual and combined effects of GGBFS and FA on the mechanical properties of 3D-printable concrete incorporating brick powder (BP) were comparatively evaluated. The mixture proportions are presented in Table 1.

Table 1. Proportions of 3D Printable Concrete Mixtures (Unit: g)

Mixture	Cement	Wt.	VMA	Clay	FA	GGBFS	Fiber	SP	Sand %20	BP 1-2mm %20	BP 0-1mm %60
Control	400	330	100	25	-	-	1.82	6.5	250	250	750
G30	250	330	100	25	-	150	1.82	6.5	250	250	750
F30	250	330	100	25	150	-	1.82	6.5	250	250	750
G15-F15	250	330	100	25	75	75	1.82	6.5	250	250	750

For each mixture and curing age (7, 14, and 28 days), three replicate specimens produced and were stored under controlled laboratory conditions at 20 ± 2 °C and 95 ± 5% relative humidity until testing.

Flexural and compressive strength tests were conducted at the end of each curing period. Flexural strength was determined on 40 × 40 × 160 mm prismatic specimens in accordance with TS EN 1015-11, using a loading rate of 0.05 kN/s. Following the flexural test, the fractured prisms were divided into two halves and were used for compressive strength testing. The compressive tests were then performed at a loading rate of 0.5 kN/s in accordance with TS EN 1015-11. This procedure enabled both flexural and compressive strengths to be determined sequentially from the same original specimens. The results for each mixture and curing age were evaluated based on the corresponding mean values.

3 Results and Discussion

3.1 Flexural Strength

The flexural strength results showed a clear age-dependent effect of GGBFS and FA incorporation (Table 2 and Fig.1). At 7 days, the reference mixture exhibited the highest flexural strength of 4.15 MPa, while G30, F30, and G15F15 reached 3.52, 3.43, and 3.39 MPa, respectively. Thus, all SCM-containing mixtures showed lower early-age flexural strength than the reference, with reductions of approximately 15–18%. This behavior is consistent with the relatively slower early-age contribution of GGBFS and FA compared with Portland cement.

Table 2. Flexural strength results of concrete mixtures (MPa)

Mixtures	7 Days	14 Days	28 Days
Control	4.15	5.80	6.59
G30	3.52	5.77	7.24
F30	3.43	6.14	7.12
G15-F15	3.39	5.89	8.91

By 14 days, the differences between the mixtures had substantially decreased. F30 reached the highest flexural strength of 6.14 MPa, approximately 6% higher than the reference value of 5.80 MPa, while G30 and G15F15 exhibited comparable strengths of 5.77 and 5.89 MPa, respectively. This convergence indicates that the contribution of the supplementary cementitious materials became more pronounced as curing progressed.

A more distinct improvement was observed at 28 days, when all SCM-containing mixtures exceeded the reference mixture. The flexural strengths of G30 and F30 increased to 7.24 and 7.12 MPa, corresponding to improvements of approximately 10% and 8%, respectively, over the reference value of 6.59 MPa. The highest strength was obtained for G15F15, reaching 8.91 MPa, approximately 35% higher than the reference mixture. Moreover, the flexural strength of G15F15 increased from 3.39 MPa at 7 days to 8.91 MPa at 28 days, representing a substantially greater strength development than that observed for the reference mixture. These results suggest that the combined use of GGBFS and FA provides a particularly beneficial effect on later-age flexural performance in 3D-printable concrete incorporating brick powder as fine aggregate.

The representative failures in Figs. 2 also show a consistent flexural failure pattern. In both the reference and G15F15 specimens, a dominant crack developed within the central bending region of the prism, without an apparent premature failure near the supports. The G15F15 specimen exhibited a clearly developed central crack at failure while sustaining the highest measured flexural strength. Overall, the experimental results indicate that although partial cement replacement with GGBFS and FA may reduce early-age flexural performance, their contribution becomes increasingly significant with curing time, with the combined GGBFS-FA mixture providing the most pronounced improvement at 28 days.

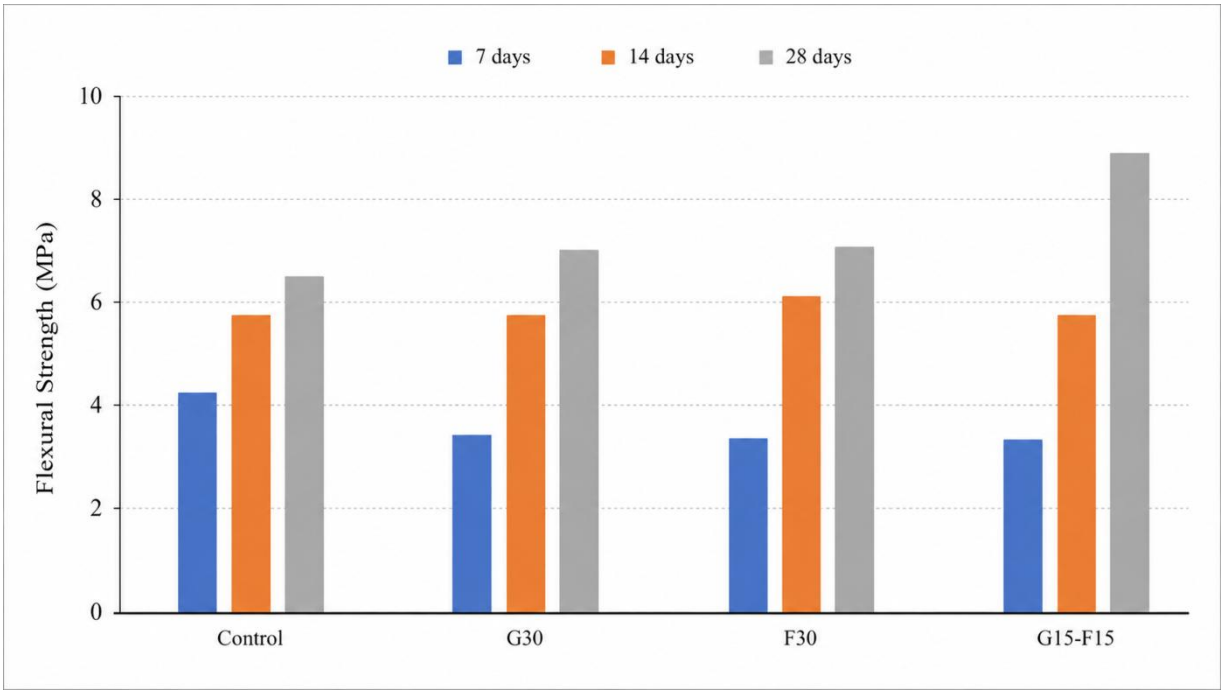


Fig. 1. Flexural strength development of the mixtures at 7, 14, and 28 days



Fig. 2. Typical Flexural Failure Patterns of the Reference and G15F15 Specimens

3.2. Compressive Strength

The compressive strength results are summarized in Table 3 and illustrated in Fig. 3. At 7 days, the reference mixture exhibited the highest strength of 17.33 MPa, while G30, F30, and G15F15 reached 11.51, 12.57, and 12.73 MPa, respectively. These values correspond to early-age reductions of approximately 34%, 27%, and 27% relative to the reference mixture, indicating that partial replacement of Portland cement with GGBFS and FA delayed early strength development.

By 14 days, the differences among the mixtures had narrowed considerably. F30 reached the highest compressive strength of 24.30 MPa, approximately 12% above the reference value of 21.66 MPa, whereas G30 and G15F15 exhibited strengths of 19.31 and 21.31 MPa, respectively.

A clear change in performance was observed at 28 days, as shown in Fig. 3. All SCM-containing mixtures exceeded the reference strength of 27.10 MPa. G30 and F30 reached 31.32 and 29.41 MPa, corresponding to increases of approximately 16% and 9%, respectively. The

most pronounced improvement was obtained with G15F15, which achieved 41.48 MPa, approximately 53% higher than the reference mixture. Its strength increased from 12.73 MPa at 7 days to 41.48 MPa at 28 days, indicating a markedly greater later-age strength development than that of the reference mixture.

Table 3. Compressive strength results of concrete mixtures (MPa)

Mixture	7 Days	14 Days	28 Days
Control	17.33	21.66	27.10
G30	11.51	19.31	31.32
F30	12.57	24.30	29.41
G15-F15	12.73	21.31	41.48

Overall, the results indicate that GGBFS and FA were less effective at early ages but contributed increasingly to compressive strength as curing progressed. The combined use of 15% GGBFS and 15% FA produced the highest 28-day strength, suggesting a beneficial complementary effect between the latent hydraulic contribution of GGBFS and the pozzolanic contribution of FA.

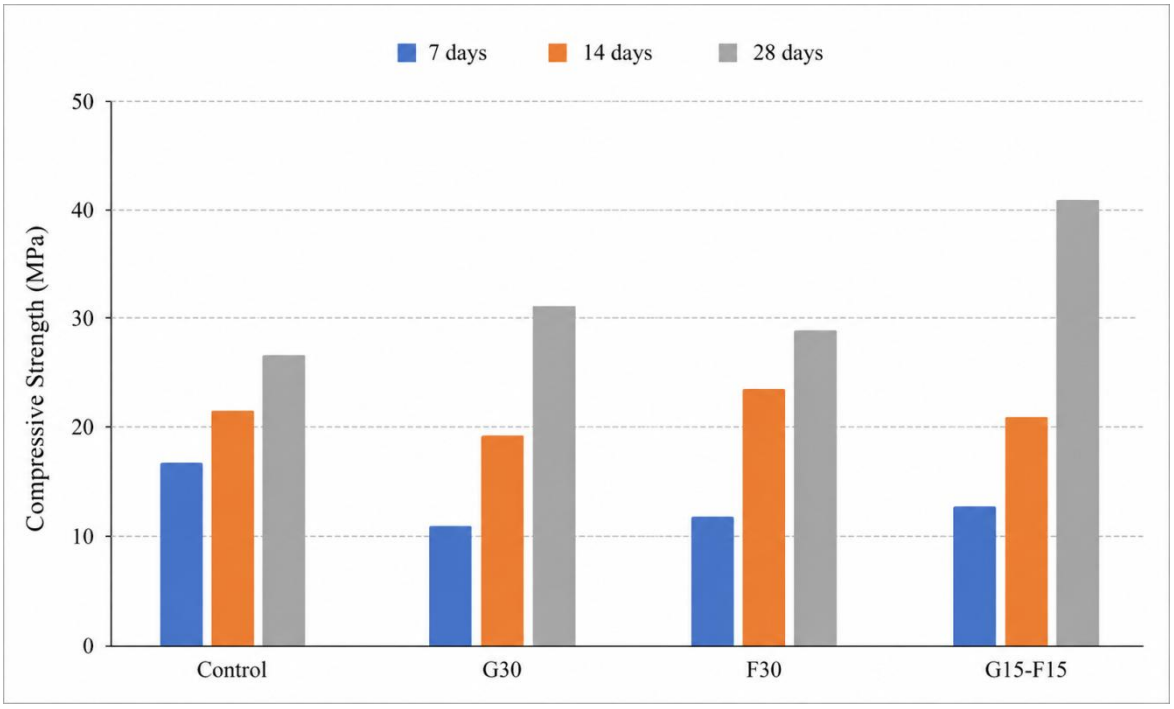


Fig. 3. Compressive Strength Development of the Mixtures at 7, 14, and 28 Days

4 Conclusion

This study experimentally investigated the effects of ground granulated blast furnace slag (GGBFS) and fly ash (FA) on the mechanical performance of 3D-printable concrete incorporating brick powder as fine aggregate. The results showed that the mixtures containing GGBFS and FA exhibited lower early-age compressive and flexural strengths than the reference mixture. This behavior can be attributed to the slower early-age reaction rates of GGBFS and

FA compared with Portland cement, indicating that the typical early-strength reduction associated with these supplementary cementitious materials also occurs in brick-powder-based 3D-printable concrete.

At 28 days, however, the performance of the SCM-containing mixtures improved markedly. In particular, the G15F15 mixture outperformed the reference mixture in both compressive and flexural strength, demonstrating that the combined use of GGBFS and FA can provide a more effective binder system for later-age strength development. These findings show that, despite the reduction in Portland cement content, appropriate combinations of supplementary cementitious materials can maintain and even improve the mechanical performance of 3D-printable concrete incorporating brick powder.

Future studies should investigate the longer-term strength development of the G15F15 mixture and compare a wider range of replacement levels to identify more effective binder compositions. Additional investigations involving microstructural characterization, interlayer bond behavior, and durability performance would also provide a more comprehensive understanding of the behavior of these mixtures under different production scales and service conditions.

References

1. Buswell, R.A., Leal de Silva, W.R., Jones, S.Z., Dirrenberger, J.: 3D printing using concrete extrusion: A roadmap for research. Cement and Concrete Research 112, 37–49 (2018). https://doi.org/10.1016/j.cemconres.2018.05.006
2. Mechtcherine, V., Bos, F.P., Perrot, A., Leal da Silva, W.R., Nerella, V.N., Fataei, S., Wolfs, R.J.M., Sonebi, M., Roussel, N.: Extrusion-based additive manufacturing with cement-based materials—Production steps, processes, and their underlying physics: A review. Cement and Concrete Research 132, 106037 (2020). https://doi.org/10.1016/j.cemconres.2020.106037
3. Tarhan, Y., Şahin, R.: The physicomechanical behavior and microstructure of air-entrained 3D printable concrete. Journal of Materials in Civil Engineering 36(1), 04023489 (2024). https://doi.org/10.1061/JMCEE7.MTENG-16224
4. Tarhan, Y., Tarhan, İ.H., Jacquet, Y., Perrot, A.: Mechanical behaviour of 3D printed and textile-reinforced eco-friendly composites. Journal of Sustainable Cement-Based Materials 14(3), 477–495 (2025). https://doi.org/10.1080/21650373.2024.2396420
5. Bhattacherjee, S., Basavaraj, A.S., Rahul, A.V., Santhanam, M., Gettu, R., Panda, B., Schlangen, E., Chen, Y., Copuroglu, O., Ma, G., Wang, L., Beigh, M.A.B., Mechtcherine, V.: Sustainable materials for 3D concrete printing. Cement and Concrete Composites 122, 104156 (2021). https://doi.org/10.1016/j.cemconcomp.2021.104156
6. He, Z., Shen, A., Wu, H., Wang, W., Wang, L., Yao, C., Wu, J.: Research progress on recycled clay brick waste as an alternative to cement for sustainable construction materials. Construction and Building Materials 274, 122113 (2021). https://doi.org/10.1016/j.conbuildmat.2020.122113
7. Dang, J., Zhao, J., Hu, W., Du, Z., Gao, D.: Properties of mortar with waste clay bricks as fine aggregate. Construction and Building Materials 166, 898–907 (2018). https://doi.org/10.1016/j.conbuildmat.2018.01.109
8. Lothenbach, B., Scrivener, K., Hooton, R.D.: Supplementary cementitious materials. Cement and Concrete Research 41(12), 1244–1256 (2011). https://doi.org/10.1016/j.cemconres.2010.12.001

9. Juenger, M.C.G., Siddique, R.: Recent advances in understanding the role of supplementary cementitious materials in concrete. Cement and Concrete Research 78, 71–80 (2015). https://doi.org/10.1016/j.cemconres.2015.03.018
10. Tarhan, İ.H., Tarhan, Y.: Nonlinear in-plane response of 3D-printed concrete walls with varied infill patterns: Experimental mix design and numerical structural assessment. Challenge Journal of Structural Mechanics 11(3), 160–173 (2025). https://doi.org/10.20528/cjsmec.2025.03.005
11. Tseng, K.-C., Chi, M., Yeih, W., Huang, R.: Influence of slag/fly ash as partial cement replacement on printability and mechanical properties of 3D-printed concrete. Applied Sciences 15(7), 3933 (2025). https://doi.org/10.3390/app15073933
12. Christen, H., van Zijl, G., de Villiers, W.: The incorporation of recycled brick aggregate in 3D printed concrete. Cleaner Materials 4, 100090 (2022). https://doi.org/10.1016/j.clema.2022.100090
13. Pepe, M., Lombardi, R., Lima, C., Paolillo, B., Martinelli, E.: Experimental evidence on the possible use of fine concrete and brick recycled aggregates for 3D printed cement-based mixtures. Materials 18(3), 583 (2025). https://doi.org/10.3390/ma18030583
14. Zhao, Y., Gao, Y., Chen, G., Li, S., Singh, A., Luo, X., Liu, C., Gao, J., Du, H.: Development of low-carbon materials from GGBS and clay brick powder for 3D concrete printing. Construction and Building Materials 383, 131232 (2023). https://doi.org/10.1016/j.conbuildmat.2023.131232
15. Huang, B., Ge, Y., Wang, X., Wang, Y., Wang, J., Song, C., Zhu, J., Amaechi, C.V., Sun, J.: Recycled ceramic brick powder utilization in fiber reinforced 3D printing concrete: An eco-friendly substitute to conventional fine aggregates. Journal of Building Engineering 98, 111441 (2024). https://doi.org/10.1016/j.jobe.2024.111441

Author Contribution Statement

- *Conceptualization*: Derya Kurt, Muhammed Çeçen, İsmail Hakkı Tarhan, Yeşim Tarhan
- *Methodology*: Derya Kurt, Muhammed Çeçen, İsmail Hakkı Tarhan, Yeşim Tarhan
- *Investigation*: Derya Kurt, Muhammed Çeçen, İsmail Hakkı Tarhan, Yeşim Tarhan
- *Writing – Original Draft*: Derya Kurt, Muhammed Çeçen
- *Writing – Review & Editing*: Derya Kurt, Muhammed Çeçen, İsmail Hakkı Tarhan, Yeşim Tarhan

List of Abbreviations

- **3DCP** -Three-Dimensional Concrete Printing
- **GGBFS** - Ground Granulated Blast Furnace Slag
- **FA** - Fly Ash
- **BP** - Brick Powder
- **SCM** - Supplementary Cementitious Material
- **VMA** - Viscosity-Modifying Admixture
- **REF** - Reference Mixture

- **G30** - Mixture with 30% GGBFS replacement
- **F30** - Mixture with 30% FA replacement
- **G15F15** - Mixture with 15% GGBFS and 15% FA replacement

Note: Following the conference, this Publication Note will be added to each paper; therefore, authors are kindly requested not to remove the note below and to complete the author(s) and paper title information.

Publication Note

This paper was peer-reviewed, accepted for presentation, and included in the proceedings of the ACE2026 – International Conference on Advances in Civil Engineering, held on 12–14 October 2026 in Trabzon, Türkiye.

This paper may be cited as follows:

Kurt, D., Cecen, M., Tarhan, I.H., Tarhan, Y., "Influence of GGBFS and Fly Ash on the Mechanical Performance of 3D Printable Concrete Incorporating Brick Powder as Fine Aggregate," in Proceedings of the ACE2026 – International Conference on Advances in Civil Engineering, Trabzon, Türkiye, 12–14 October 2026.

Engineering Sustainable Magnesium Oxalate Cements Using Olivine as a Substitute for Dead-Burned Magnesia

Buse Öztürk[1], Sinan T. Erdoğan[2]
[1] 0009-0007-5140-4266, Middle East Technical University, Department of Civil Engineering, Ankara, Türkiye, buse.ozturk@metu.edu.tr
[2] 0000-0003-0769-1249, Middle East Technical University, Department of Civil Engineering, Ankara, Türkiye, sinante@metu.edu.tr

Abstract. The production of Portland cement is responsible for the emission of high amounts of carbon dioxide (CO_2) due to the decomposition of limestone and the fuel consumed in the rotary kiln. Low-carbon alternatives to portland cement are actively sought. Magnesium oxalate cement (MgOx) is one such alternative binder proposed in recent years. It is obtained through an acid-base neutralization reaction between a basic powder such as dead burnt MgO (DBM) and oxalic acid ($H_2C_2O_4$) or an oxalic acid salt; its main reaction product is glushinskite ($MgC_2O_4.2H_2O$), a hydrated magnesium oxalate. Even though the use of oxalates made from captured CO_2 can decrease the carbon footprint of MgOx, the chemical and fuel-related carbon emissions of DBM make it difficult for the final product to reach carbon neutrality. Also, despite its high early strength, MgOx sets rapidly and liberates a large amount of heat. The present study investigated the use of olivine, a magnesium-iron silicate mineral, to partially or fully replace DBM, rendering MgOx carbon neutral or negative. Various chemical, mechanical, and mineralogical properties of MgOx made with olivine were examined, using X-ray diffraction, pH, setting time and strength. Replacement of DBM with olivine moderates the exothermic reaction of MgOx systems, leading to slower setting. Olivine is shown to dissolve and contribute magnesium ions to the binder. However, the rate and total amount of dissolution is limited. Compressive strength is retained up to ~60 % replacement, beyond which it sharply decreases.

Keywords: magnesium oxalate, clay, olivine, carbon dioxide.

1 Introduction

Portland cement (PC), the ubiquitous construction binder, is used in very large amounts, annual production surpassing 4×10^9 t [1]. Portland cement production not only requires tremendous amounts of energy and raw materials (clay and limestone), but is also responsible for high carbon emission, related with the burning of fuel in the kiln and the decarbonation of carbonate minerals in limestone. These negative environmental impacts have led to a search for alternatives to PC [2]. Various calcium-based and other alternatives have been proposed, each with its own advantages and disadvantages [3,4,5]. Limestone calcined clay cement, geopolymers, and calcium sulfoaluminate cement are notable examples. Binders based on calcium use limestone as an inexpensive raw material and suffer drawbacks similar to PC. The use of pozzolans or supplementary cementitious materials can only partially curb the associated carbon emissions. Some other binders without calcium suffer from low room-temperature reactivity and slow mechanical property development. Attempts to achieve carbon neutrality have also been made by capturing carbon into minerals such as calcite, by carbonating natural or artificial powders, such as wollastonite, various slags, and even recycled concrete fines,

under controlled temperature and relative humidity conditions [6]. However, this approach is more suitable for precast works as small blocks with predetermined shapes are obtained.

Magnesium oxalate cement (MgOx) is a binder recently proposed as an alternative to PC [7,8,9]. It is made by reacting dead-burned magnesia (DBM) with salts of oxalic acid and water (Eqs. 1-3)

$$MgO + 2H^{+} \rightarrow Mg^{2+} + H_2O \quad (1)$$

$$Mg^{2+} + HC_2O_4^{-} + 2H_2O \rightarrow MgC_2O_4.2H_2O + H^{+} \quad (2)$$

$$Mg^{2+} + C_2O_4^{2-} + 2H_2O \rightarrow MgC_2O_4.2H_2O \quad (3)$$

Oxalic acid ($H_2C_2O_4$) can be made from captured CO_2 via electrochemical reduction or other processes [10,11]. Hence, it can be carbon-negative if renewable energy is used for its production. This can balance the carbon footprint of magnesium oxide, obtained economically by decarbonating magnesium carbonate. Figure 1 shows the production scheme for MgOx.

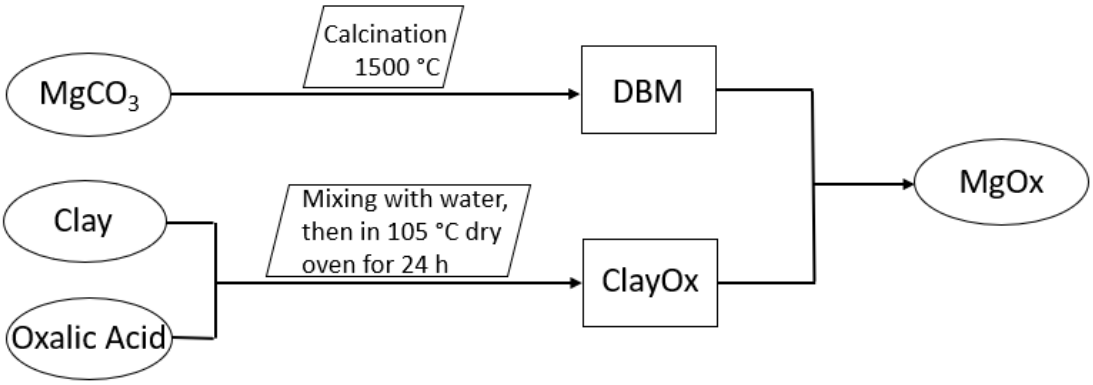


Fig. 1. The production of MgOx (adapted from [12]).

The reaction between light-burned (~600 °C) MgO and oxalic acid is quite exothermic and rapid, leading to a significant rise in the mixture temperature and limiting the size of a feasible mixture. Cracking and the formation of large pores can't be prevented. Hence, two measures are taken. First, oxalic acid is pre-reacted with a suitable base to obtain an acidic oxalate salt. This slightly increases the initial pH of the acidic solution. Next, light-burned MgO replaced with MgO dead-burned at 1400-1500 °C. This reduces the specific surface area and reactivity of MgO. Both of these steps are similar to what is used in magnesium phosphate cement (MPC) production, which uses DBM and an acid salt of phosphoric acid, such as KH_2PO_4.

The reaction in Eqn. 1 is an acid-base reaction which leads to the formation of glushinskite ($MgC_2O_4.2H_2O$), and a near-neutral ultimate paste pH. MgOx differs from other magnesium cements like oxychloride or oxysulfate cements. Owing to the acid-base reaction, MgOx sets rapidly and can gain medium-to-high early strength. Setting time, heat evolution and the development of mechanical properties can be controlled by controlling mixture proportions. Using a high DBM / oxalic acid salt ratio increases the carbon footprint but often benefits property development. A lower ratio decreases the carbon footprint but increases cost. Using an unreactive filler or secondary materials to replace DBM and/or the oxalate salt can decrease both cost and carbon footprint but decrease the total amount of reaction and ultimate strength, beyond a certain replacement ratio. Among those materials used to partially replace DBM and the oxalate salt are ground granulated blast furnace slag and copper slag, which can form new reaction products like calcium or iron oxalates, and silica fume, which does not form any new crystalline reaction products but can alter properties physically [13, 14]. This study investigated

the use of olivine as yet another substitute for DBM. Olivine is a nesosilicate (orthosilicate) mineral represented by the chemical formula $(Mg,Fe)_2SiO_4$. A primary constituent of mafic and ultramafic igneous rocks such as basalt, gabbro, and peridotite, it dominates the composition of Earth's upper mantle, and forms a continuous solid-solution series between the magnesium-rich end-member forsterite (Mg_2SiO_4) and the iron-rich end-member fayalite (Fe_2SiO_4). Given its vast natural abundance, olivine is a potentially viable and sustainable alternative source of magnesium ions without an associated high carbon footprint like DBM [15].

2 Materials and Methods

2.1 Materials

The magnesia (MgO) used was obtained as a light-pink powder. Its rapid neutralization of acetic acid indicated high reactivity in an acid-base system and that it was likely obtained by light burning. This powder was calcined in the laboratory at 1500 °C to obtain dead-burned magnesia (DBM). DBM was ground until 95 % passed a 150 µm sieve. A montmorillonitic clay was obtained from Votorantim Cimentos, Hasanoğlan. The chemical compositions of these materials, determined using x-ray fluorescence spectrometry, and their densities are provided in Table 1.

Table 1. Oxide analysis of the materials used (mass %) [16, 17]

Oxide	MgO	DBM	Clay
SiO_2	10.04	11.02	61.5
Fe_2O3	0.64	0.75	8.6
Al_2O3	0.06	0.08	14.3
MgO	87.3	86.1	2.6
CaO	1.87	1.92	3.7
NiO	0.13	0.14	-
K_2O	-	-	1.6
Na_2O	-	-	0.3
TiO_2	-	-	1.1
SO_3	-	-	0.1
Density	3.10	3.48	2.62

The particular olivine used in this study is magnesium-rich, comprised mostly of forsterite as shown in Fig. 2.

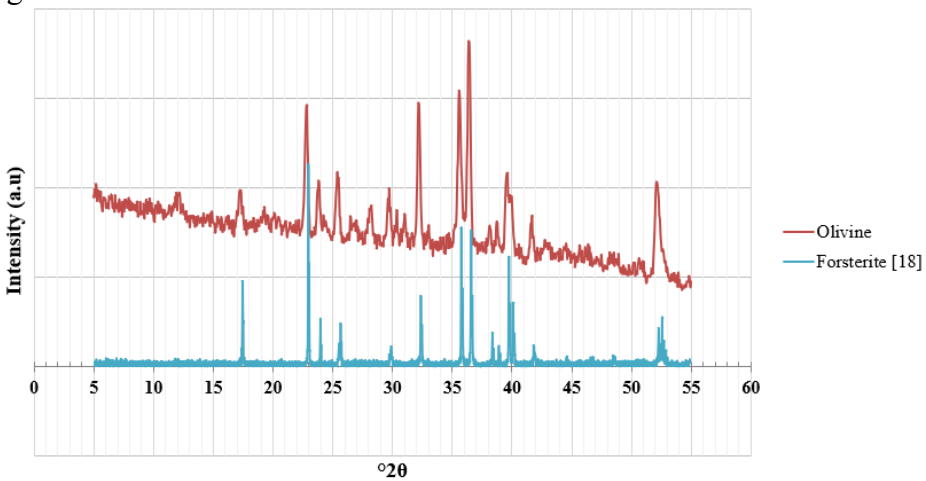


Fig. 2. X-ray diffractograms of the olivine used and forsterite.

2.2 Methods

The clay was ground and mixed with oxalic acid dihydrate and water, at a mass ratio of 1:1:1. The paste obtained was allowed to react in a 105 °C oven for 24 h. The reacted material was further ground in a ball mill to a powder to obtain the component, ClayOx, to react with DBM. ClayOx is the acidic oxalate salt mentioned in Section 1. It contains some free oxalic acid as well as some oxalate salts like iron oxalate, formed between oxalic acid and the clay. Olivine, received as a coarse sand-sized granular material, was ground into a fine powder.

Paste and mortar mixtures were prepared. DBM was gradually replaced with ground olivine as shown in Table 2.

Table 2. Mixture proportions used for sample preparation (by mass)

Mixture	DBM	Olivine	ClayOx	Water	Sand
5D_0O	5	0	5	2.6	22 (mortar samples)
4D_1O	4	1			
3D_2O	3	2			
2D_3O	2	3			
1D_4O	1	4			
0D_5O	0	5			

X-ray diffraction (XRD), pH measurements, and setting time tests were performed on the paste samples. Compressive strength was measured on 10-d-old mortar samples with a sand-to-powder ratio of 2.2. As acid-base cement Silica sand in the 0.2-2 mm size range, conforming to EN 196-1 [19], was used.

3 Results and Discussion

3.1 Chemical and Mineralogical Evolution

Fig. 3 shows the XRD patterns obtained for the paste samples. The main peaks observed correspond to glushinskite (18.4, 28.2 °2θ), periclase (42.9, 36.9 °2θ). Glushinskite is formed by the reaction between Mg^{2+} and $C_2O_4^{2-}$, hence is expected. Periclase is MgO and is therefore associated with unreacted DBM. Naturally, the periclase peak becomes less prominent as the DBM/Olivine ratio decreases and no periclase is observed in 0D_5O.

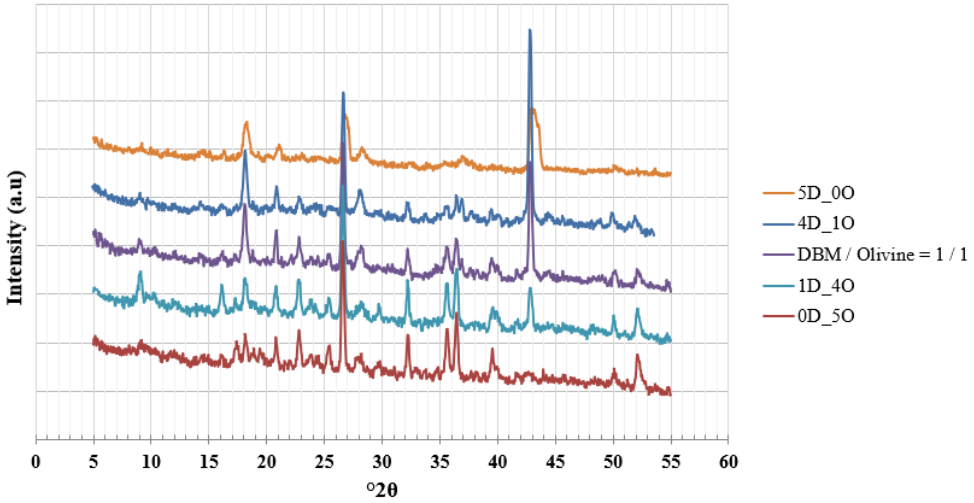


Fig. 3. X-ray diffractograms of the paste samples.

The most intense glushinskite peak is observed for pastes with intermediate DBM/Olivine. The amount of ClayOx is fixed for all pastes. DBM is in excess at very high DBM/ClayOx ratios, hence at high DBM/Olivine ratios. There is not enough dissolved magnesium available for reaction at very low DBM/ClayOx ratios, hence at low DBM/Olivine ratios. The paste containing only ground olivine shows a low-intensity peak for glushinskite, indicating some magnesium has dissolved from olivine and reacted. Fig. 4 shows the pH development of the paste samples.

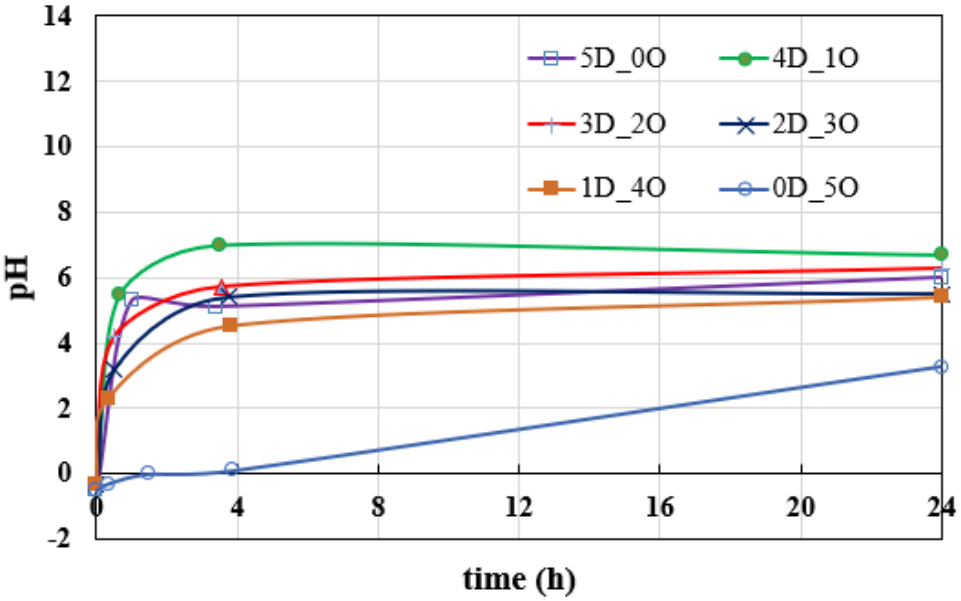


Fig. 4. pH development of the paste samples.

MgOx is an acid-base cement. As such, the initial pH of the paste is dominated by the acidity of ClayOx dissolved in water. This value was measured to be between -0.5 and 0 for all pastes; however, such low pH values measured with glass electrodes carry significant uncertainty. Furthermore, this range falls outside the calibration region of the pH meter. Subsequently, pH rises due to neutralization reactions between oxalate species and magnesium ions. An increase is noticeable for pastes containing DBM, as early as 10-20 min, even before setting. The paste without any DBM, 0D_5O does not show a meaningful rise in pH in the first few hours suggesting that the olivine does not dissolve considerably. After 24 h, all pastes with DBM reach pH values of ~ 5.5-7.0. A neutral or slightly basic pH is expected for a well-performing MgOx, due to the nature of the neutralization reaction and some DBM always remaining unreacted. 0D_5O does reach pH~3.25 indicating some reactions have taken place and partially neutralized the initially acidic solution. Fig. 5 gives the final setting times of the paste samples.

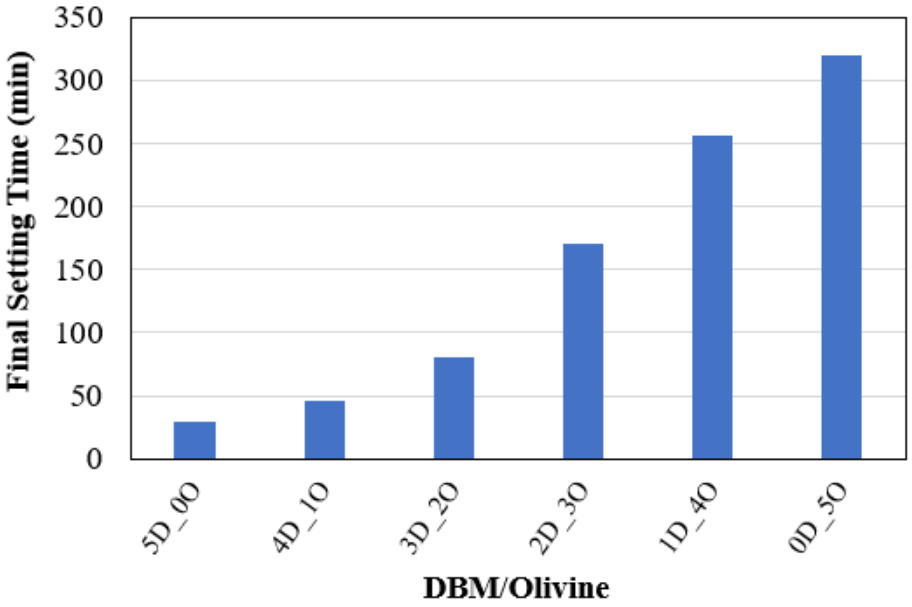


Fig. 5. Final setting times of the pastes.

The mixtures evolve considerable heat and show an initial stiffening upon combining ClayOx with water. However, continued mixing yields a workable paste. Pastes with higher DBM/Olivine ratios set faster, as DBM dissolves much faster than olivine (Fig. 4) and provides magnesium ions for the main glushinskite-forming reaction. The final setting time of 5D_0O is ~0.5 h. In contrast, 0D_5O sets only after several hours.

3.2 Development of Compressive Strength

The compressive strengths of mortar samples are given in Fig. 6.

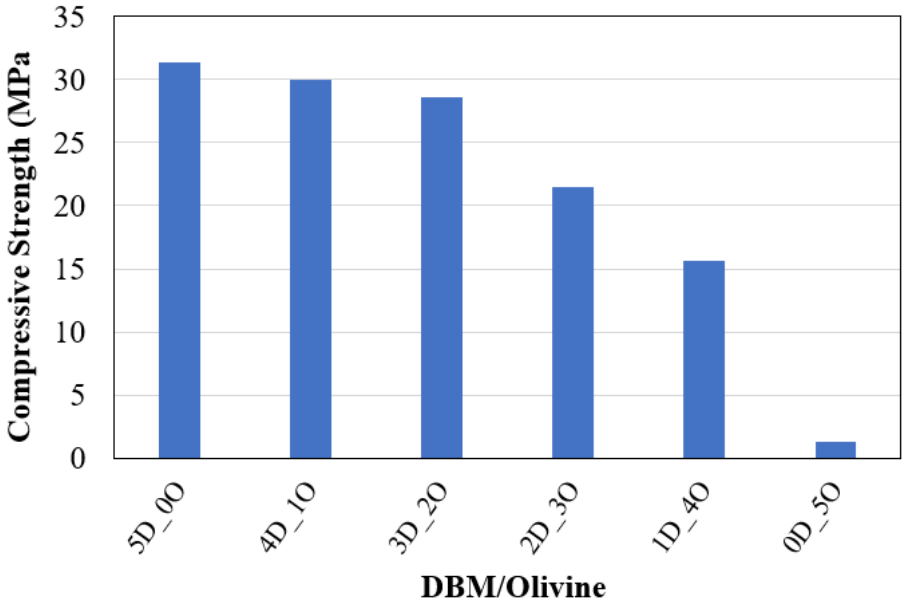


Fig. 6. Compressive strength of mortars.

The replacement of DBM with olivine appears to decrease the strength of mortars, slightly at low ratios but greatly at higher ratios. Mortar samples containing only ground olivine develop minimal strength, indicating that the amount of glushinskite formed (as observed in Fig. 2) is

not sufficient to create a rigid network. A replacement level of 40-60 % is achievable without significantly compromising mechanical properties. This is similar to results reported on the replacement of DBM with silica fume [13], indicating that, despite containing high levels of magnesium and silicon, olivine is not able to dissolve significantly. Thermal or chemical pre-treatment of olivine to reduce its crystallinity and increase its rate of dissolution in the acidic solution of ClayOx and water appears to be necessary to achieve useful mechanical properties at high DBM replacement ratios.

4 Conclusions

The effect of replacing dead-burned magnesia with ground olivine in MgOx mixtures was investigated. The following conclusions were reached:

- Some glushinskite is detected in XRD patterns of pastes without any DBM, suggesting ground olivine partly dissolves in acidic oxalate solutions to provide magnesium ions, despite being a crystalline silicate.
- The amount of dissolved magnesium from olivine is not sufficient to produce significant amounts of glushinskite hence the compressive strength of mixtures with low DBM/Olivine ratios remain low. Nevertheless, mortars with 60 % olivine and 40 % DBM gain > 20 MPa compressive strength.
- The pH of all pastes containing olivine and DBM reach near-neutral values, indicating significant reaction. The pH of the paste containing only olivine remains acidic after 24 h, suggesting the dissolution of olivine is slow and limited.
- Mixtures made with the particular ClayOx used in this study provide long setting times compared with many previous MgOx examples.
- Olivine shows potential as an alternative magnesium source, to obtain MgOx with lower carbon footprints.

References

1. Bărbulescu, A., Hosen, K. Cement Industry Pollution and Its Impact on the Environment and Population Health: A Review. Toxics 13(7), 587 (2025). https://doi.org/10.3390/toxics13070587
2. Barcelo, L., Kline, J., Walenta, G., Gartner, E., Cement and carbon emissions. Materials and Structures 47, 1055-1065 (2024). https://doi.org/10.1617/s11527-013-0114-5.
3. Canbek, O., Shakouri, S., Erdoğan, S.T. Laboratory production of calcium sulfoaluminate cements with high industrial waste content. Cement and Concrete Composites 106, 103475 (2020). https://doi.org/10.1016/j.cemconcomp.2019.103475
4. Scrivener, K., Martirena, F., Bishnoi, S., Maity, S. Calcined clay limestone cements (LC3). Cement and Concrete Research 114, 49-56 (2018). https://doi.org/10.1016/j.cemconres.2017.08.017
5. Davidovits, J. Geopolymer chemistry and applications, Third ed., Institut Géopolymère, St. Quentin, France (2008).
6. Huijgen W. J. J., Witkamp G.-J., Comans R. N. J. Mechanisms of aqueous wollastonite carbonation as a possible CO2 sequestration process. Chem. Eng. Sci. 61(13), 4242-4251 (2006). https://doi.org/10.1016/j.ces.2006.01.048.
7. Erdoğan, S.T. Oxalate acid-base cements as a means of carbon storage. American Geophysical Union Fall Meeting, New Orleans, Dec. 11-15 (2017).
8. Erdoğan, S.T. Magnesium oxalate cements for carbon reuse. American Geophysical Union Fall Meeting 2019, San Francisco, Dec. 11-15 (2019).

9. Erdoğan, S.T., Bilginer, B.A., Canbek, O. Preparation and characterization of magnesium oxalate cement. Engrxiv preprint (2022).
10. Keith, D.W., Holmes, G., St. Angelo, D., Heidel, K. A process for capturing CO2 from the atmosphere. Joule 2, 1573-1594 (2018). https://doi.org/10.1016/j.joule.2018.05.006
11. Schuler, E., Demetriou, M., Shiju, N.R., Gruter, G.J.M. Towards Sustainable Oxalic Acid from CO2 and Biomass, Chem Sus Chem 14, 3636-3664 (2021). https://doi.org/10.1002/cssc.202101272
12. Abdulaal, L., Atasever, M., Erdoğan, S.T. Düşük Karbonlu Yeni Bir Yapısal Bağlayıcı Geliştirilmesi: Magnezyum Oksalat Çimentosu. In Proceedings: 11th National Concrete Conference, pp. 237-244. Turkish Chamber of Civil Engineers, Erzurum (2025).
13. Bilginer, B.A., Erdoğan, S.T. Enhancing magnesium oxalate cements with copper slag and silica fume. Constr. Build. Mater., 452, 138999 (2024) 10.1016/j.conbuildmat.2024.138999
14. Bilginer, B.A. Development of a Sustainable Construction Binder: Oxalate Cements, PhD Thesis, Middle East Technical University, Ankara (2024).
15. Kelemen, P.B., Matter, J., Streit, E.E., Rudge, J.F., Curry, W.B., Blusztajn, J. Rates and mechanisms of mineral carbonation in peridotite: natural processes and recipes for enhanced, in situ CO 2 capture and storage. Annu Rev Earth Planet Sci 39 (1) (2011). (https://doi.org/10.1146/annurev-earth-092010-152509
16. Bilmez, S.B., Erdoğan, S.T. Improving the Sustainability of Magnesium Oxalate Cements Using Clay and Calcium Sulfoaluminate Clinker. J. Mater. Civ. Eng. 37(3), (2024) https://doi.org/10.1061/JMCEE7.MTENG-18860
17. Atasever, M., Erdoğan, S.T. Effects of clay type and component fineness on the hydration and properties of limestone calcined clay cement. Mater. Struct. 57 (8) (2024). https://doi.org/10.1617/s11527-024-02461-4
18. Lafuente, B., Downs, R. T., Yang, H., Stone, N. The power of databases: The RRUFF project. In Highlights in Mineralogical Crystallography. Walter de Gruyter GmbH. [RRUFF ID: R040018]. (2015). https://www.rruff.net/amcsd/, last accessed 2026/18/08.
19. European Committee for Standardization. (2016). Methods of testing cement — Part 1: Determination of strength (EN 196-1) (2016). Brussels.

Author Contribution Statement

- *Conceptualization:* S.T. Erdoğan
- *Methodology:* S.T. Erdoğan
- *Investigation:* B. Öztürk, S.T. Erdoğan
- *Writing – Original Draft:* S.T. Erdoğan
- *Writing – Review & Editing:* B. Öztürk, S.T. Erdoğan

Publication Note

This paper was peer-reviewed, accepted for presentation, and included in the proceedings of the ACE2026 – International Conference on Advances in Civil Engineering, held on 12–14 October 2026 in Trabzon, Türkiye.

This paper may be cited as follows:

Öztürk, B., and Erdoğan, S. T., "Engineering Sustainable Magnesium Oxalate Cements Using Olivine as a Substitute for Dead-Burned Magnesia," in Proceedings of the ACE2026 – International Conference on Advances in Civil Engineering, Trabzon, Türkiye, 12–14 October 2026.

Determination Of The Fracture Energy Of Natural Stone From The Cappadocia Region

Harun Yahya SÜNDÜ[1], Ayşe ERDÖLEN[2], Nabi YÜZER[3]
[1] orcidID 0009-0003-0456-1649, Department of Civil Engineering, Ege University, Bornova, Izmir, Turkey harun.yahya.sundu@ege.edu.tr
[2] orcidID 0000-0002-1576-0198, Department of Civil Engineering, Yıldız Technical University, Davutpaşa Campus, Esenler, Istanbul, Turkey
erdolen@yildiz.edu.tr
[3] orcidID 0000-0003-0269-0140, Department of Civil Engineering, Yıldız Technical University, Davutpaşa Campus, Esenler, Istanbul, Turkey
nyuzer@yildiz.edu.tr

Abstract. The rock structures and fairy chimneys in Cappadocia, a UNESCO World Heritage site, consist of low-strength, highly porous volcanic tuffs with high water absorption capacity. These characteristics make the rock structures vulnerable to physical, chemical, and hydro-mechanical deterioration, causing existing microcracks to propagate into macrocracks over time. To evaluate the effectiveness of consolidation treatments applied to these natural stones, this study proposes a fracture mechanics-based approach. In the literature, material performance is typically assessed via uniaxial compressive strengths. However, this approach inadequately represents heterogeneous materials containing discontinuities, which induce crack-tip stress concentrations and cause premature failure. Therefore, performance must incorporate specimen geometry, notch length, and crack propagation behavior. Consequently, this study adopts a fracture mechanics evaluation, linking loading stresses to fracture toughness rather than yield strength. To assess the fracture toughness of volcanic tuff, three-point bend testing (3PB) was executed. Prismatic specimens measuring 30 × 60 × 280 mm were prepared with notch depths ranging from 3 to 30 mm at 3 mm intervals. Throughout the experimental process, applied forces and crack mouth opening displacement (CMOD) values were acquired concurrently. The load–CMOD data were modeled using polynomial regression, and the derivatives of the regression functions were used to calculate the fracture energy of the specimens. This testing methodology provides a practical means to assess how notch depth impacts the fracture behavior of volcanic tuff, while simultaneously serving as a mechanics-based framework to measure consolidation efficiency. The obtained results demonstrated satisfactory performance of the proposed approach for fracture evaluation.

Keywords: Volcanic Tuff, Fracture Energy, CMOD, Three-Point Bending Test

1 Introduction

Volcanic tuffs are rocks formed as a product of the compaction and cementation of pyroclastic materials to varying degrees; they have high porosity and mechanical properties that can vary widely. Prominent throughout Cappadocia, ignimbritic tuffs have traditionally supported architectural masonry, rock-cut complexes, underground cities, and cultural artifacts. However, prolonged exposure to mechanical, chemical, hydro-mechanical, and environmental effects leads to material deterioration, crack initiation, and a reduction in mechanical strength. Previous studies [1,2] have characterized Cappadocian tuffs as rocks with low unit weight, high porosity, and relatively low mechanical strength. These characteristics highlight the need to investigate and evaluate the propagation behavior of pre-existing cracks and natural discontinuities within the tuff.

Fracture toughness is an important mechanical parameter in evaluating the engineering behavior of rocks. It is defined as the resistance exhibited against the propagation of an existing

crack within the material. Incorporating this property allows for a more realistic representation of rock performance across various engineering domains, such as tunneling, slope stability analysis, natural stone extraction, underground infrastructure design, and dimension stone processing. In brittle geological formations such as volcanic tuffs, the Linear Elastic Fracture Mechanics (LEFM) approach is commonly used to analyze crack formation and propagation; this approach provides a quantitative basis for evaluating fracture toughness and crack propagation under external loads [3,4].

Evaluating Mode I fracture toughness (K_{IC}) in rocks relies on LEFM theory. To this end, researchers widely utilize techniques such as single edge notched bend (SENB) testing, semi-circular bending (SCB), along with disk- and rod-based geometries such as cracked chevron notched Brazilian disc (CCNBD), chevron bend (CB), and short rod (SR). Earlier studies have demonstrated that measured fracture toughness depends significantly on specimen geometry, notch length, and loading configuration [5,6].

Several studies have investigated the physical, mechanical, and durability aspects of the Cappadocia Region tuffs [1,2,9]. Examples of fracture mechanics studies on volcanic tuffs include investigations conducted on the Ogino tuffs in Japan [7] and Mode I fracture toughness studies on Nevada tuff [10]. It has been established through these works that recorded fracture toughness values for tuffs exhibit substantial variation based on porosity, specimen dimensions, and crack configuration. Nevertheless, based on the available literature, the K_{IC} of Cappadocia Region tuffs has not yet been evaluated using standardized fracture mechanics testing methods.

In the present study, the K_{IC} value of volcanic tuff specimens collected from the Cappadocia Region was experimentally evaluated following the ASTM E399 (American Society for Testing and Materials) procedure. The findings are expected to contribute to addressing the existing gap in the literature regarding the fracture behavior of Cappadocia Region tuffs.

2 Materials and Methods

2.1 Materials

Volcanic tuff specimens evaluated in this work were collected from the Cappadocia region as part of a TÜBİTAK-funded project [9]. The natural stone, locally referred to as “Dağ Taşı” and classified as Weak Rock (R2) by the International Society for Rock Mechanics (ISRM), is characterized by the physical and mechanical properties listed in Tables 1 and 2 [9].

Table 1. Mechanical properties of the volcanic tuff [9].

Specimen Name / Classification	Uniaxial Compressive Strength (MPa)	Poisson's Ratio	Elastic Modulus (MPa)
Dağ Taşı/ R2	6,5	0.25	700

Table 2. Physical properties of the local stone [9].

Specimen Name / Classification	Specific Gravity (g/cm³)	Porosity (%)	Water Absorption by Volume (%)	Water Absorption by Mass (%)	Bulk Density (g/cm³)	Compacity (%)
Dağ Taşı/ R2	2.4	41.6	40.8	40.8	1.4	58.4

2.2 Methods

Specimen Preparation. Test samples were fabricated from original volcanic tuff obtained from the Cappadocia Region in accordance with the ASTM E399 standard. A total of ten prismatic SENB specimens with dimensions of 30 × 60 × 280 mm were fabricated. The notch lengths varied from 3 mm to 30 mm in 3 mm increments (3, 6, 9, …, 30 mm), with each specimen corresponding to a distinct notch length. An overview of the prepared test specimens is presented in Figure 1.



Fig. 1. SENB specimens with notch lengths ranging from 3 mm to 30 mm in 3 mm increments.

Verification of Specimen Geometry. Prior to testing, the geometry of all SENB specimens was checked against the criteria specified in ASTM E399. The notation adopted in this study defines "B" as the specimen width, "W" as the specimen height, "a" as the notch length, and "S" as the support span. The dimensional requirements recommended by ASTM E399 for SENB specimens are given in Equations (1) – (3). The specimen dimensions were evaluated based on these criteria, and all prepared specimens were confirmed to satisfy the geometric requirements specified in the standard.

$$B = 0.5W \tag{1}$$

$$0.45 \leq \frac{\mathrm{a}}{\mathrm{W}} \leq 0.55 \tag{2}$$

$$\mathrm{S} = 4\mathrm{W} \tag{3}$$

Experimental Procedure. Ten notched SENB specimens were tested on a three-point bending (3PB) test machine. Once the specimens were symmetrically positioned on the supports, loading was initiated at the span center, and the load was monotonically increased until specimen failure. The SENB configuration and the actual experimental apparatus used in this research are depicted in Figure 2.

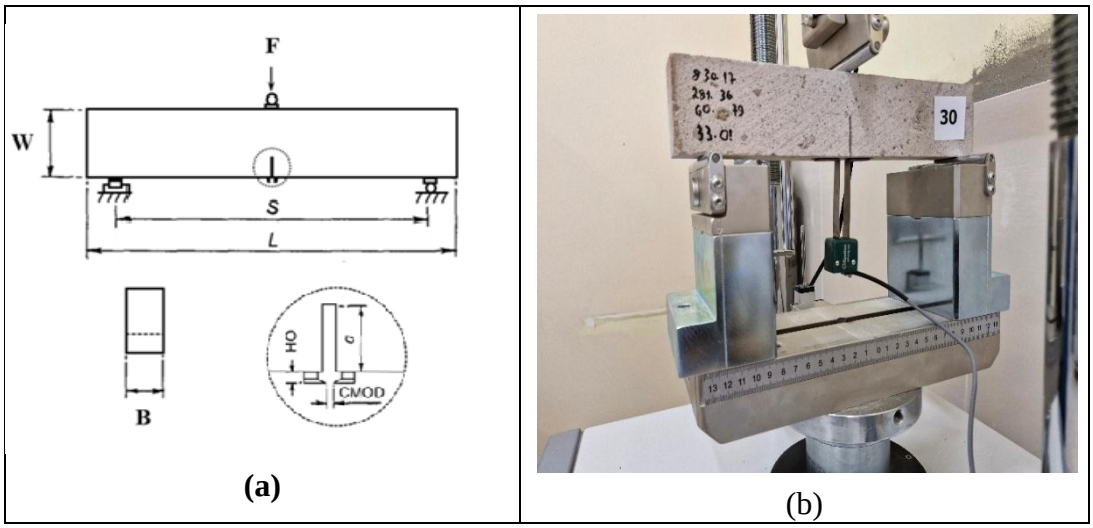


Fig. 2. SENB Setup: **(a)** Schematic model **(b)** physical configuration for CMOD measurement.

To determine the Crack Mouth Opening Displacement (CMOD) during testing, metallic knife edges were fixed onto either side of the crack mouth, serving as mounting points for the clip gauge. Throughout the experiments, a data acquisition system continuously logged both the CMOD data and the corresponding applied force. Figure 3 illustrates the experimental setup, including the specimen-mounted knife edges and the CMOD measuring unit.

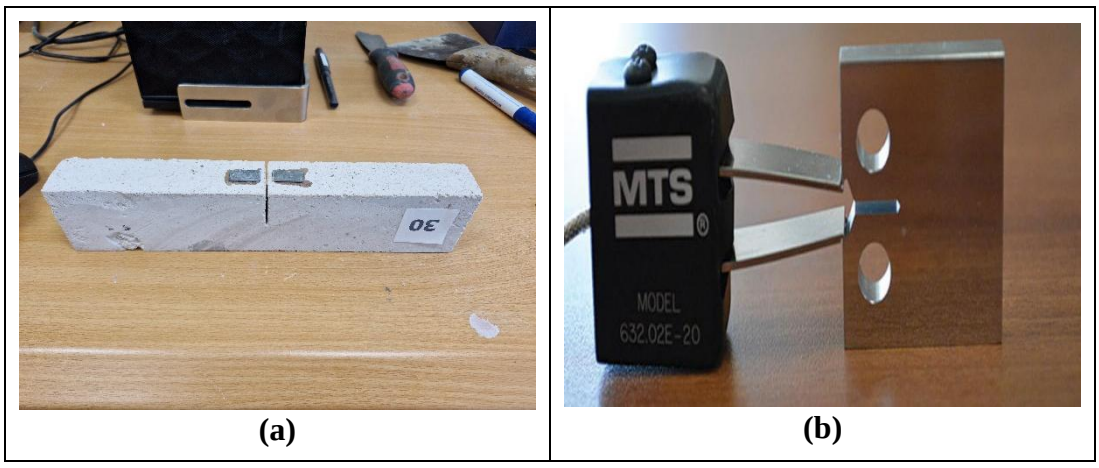


Fig. 3. (a) Knife edges mounted on the specimen **(b)** CMOD measurement system.

Fracture Toughness Calculation. Fourth-order polynomial curves were fitted to the load–CMOD data obtained from each SENB specimen. The compliance values for each specimen were calculated from the linear elastic portion of the fitted curves corresponding to **20%–70%** of the maximum load. Subsequently, the relationship between compliance and notch length was modeled using a fourth-order polynomial based on the compliance values obtained from specimens with different notch lengths. Consequently, the rate of change in compliance with respect to notch length, (dC/da), was determined from the compliance–notch length relationship.

As a core parameter in fracture mechanics, the critical energy release rate (G_{IC}) quantifies the energy dissipated per unit area of newly created crack surface during crack propagation. In this study, $G_{IC}$was calculated using the compliance method according to Equation (4). Finally, K_{IC} was determined from the relationship between the critical energy release rate and the plane strain condition for linear elastic materials using Equation (5). Here, "**F**" denotes the applied

load, "**C**" the compliance, "**a**" the notch length, "**E**" the elastic modulus, and "$\boldsymbol{\nu}$" Poisson's ratio.

$$G_{IC} = \frac{F^2}{2B}\frac{dC}{da} \tag{4}$$

$$K_{IC} = \sqrt{\frac{EG_{IC}}{1-\vartheta^2}} \tag{5}$$

3 Results and Discussion

As a result of the 3PB tests, Load–CMOD curves were obtained for ten SENB specimens with notch depths from 3 mm to 30 mm. Given the consistent mechanical response across all samples, representative curves for 15 mm and 30 mm notch lengths appear in Figs. 4 and 5. An analysis of the curves revealed that linear elastic behavior predominated during the initial loading phase, and deviations from this behavior occurred as the load approached the maximum. After the maximum load was reached, a decrease in the specimens' load-bearing capacity was observed due to crack propagation.

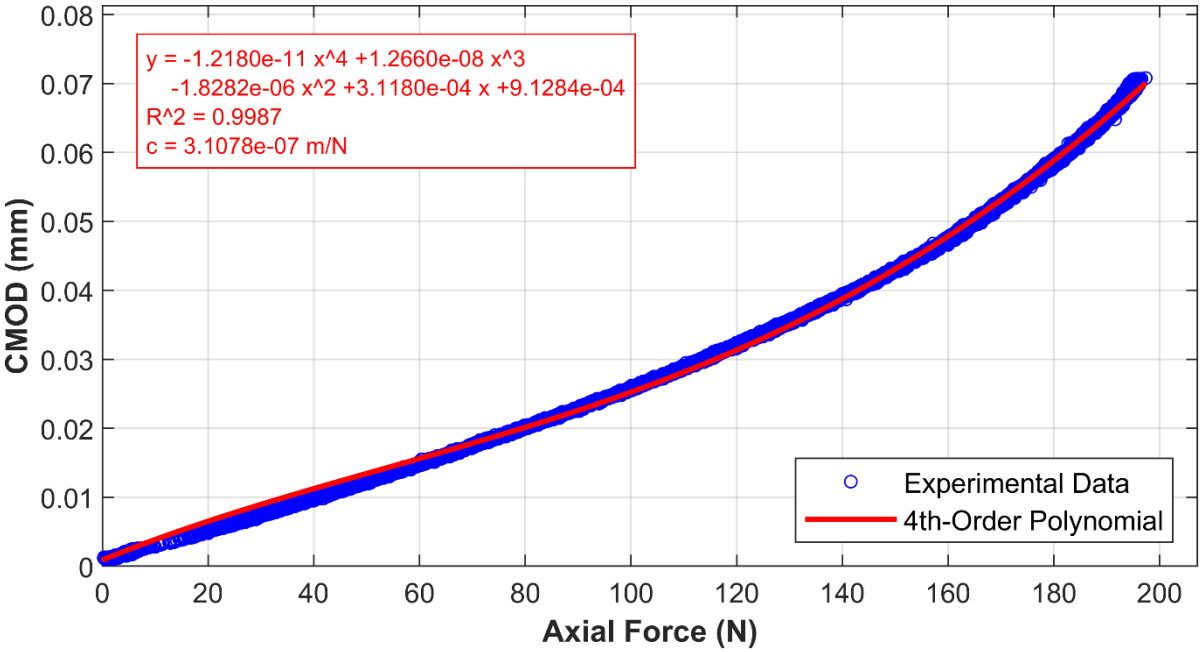


Fig. 4. 4th-Order Polynomial CMOD-Load Curve for 15 mm Notched Specimen

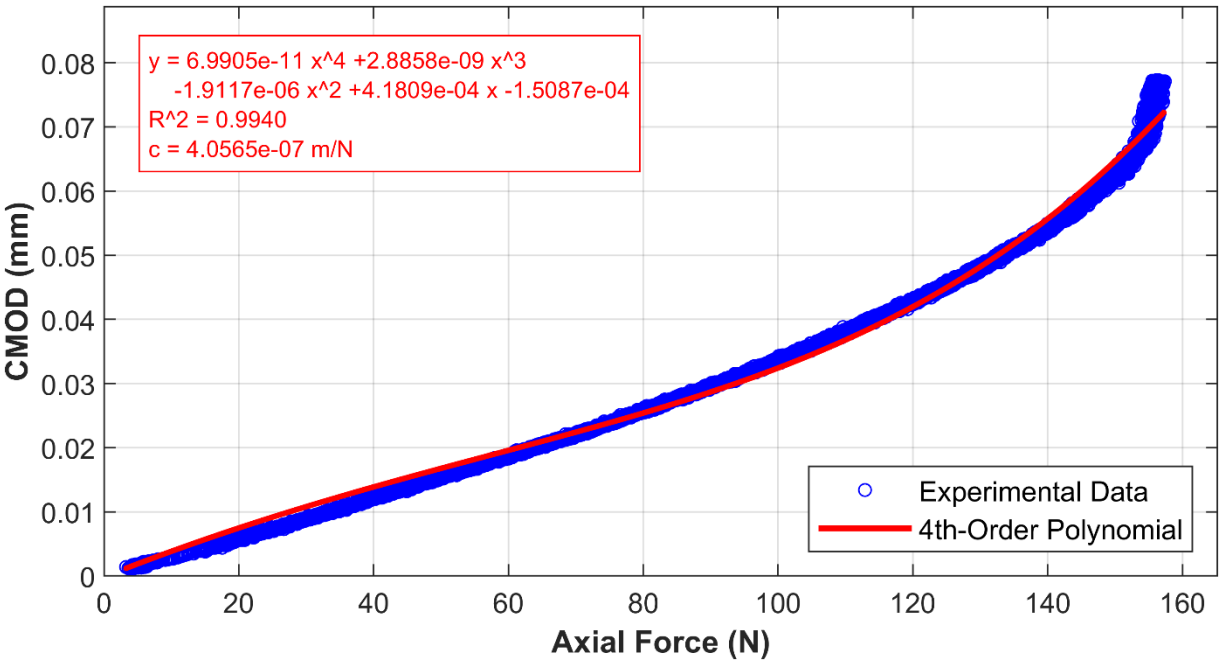


Fig. 5. 4th-Order Polynomial CMOD-Load Curve for 30 mm Notched Specimen

The relationship between compliance and notch length for specimens with different notch lengths is presented in Figure 6. A fourth-order polynomial regression was fitted to the experimental data, yielding a coefficient of determination of $R^2 = 0.81$. This result indicates that the fourth-order polynomial provides an adequate representation of the compliance–notch length relationship.

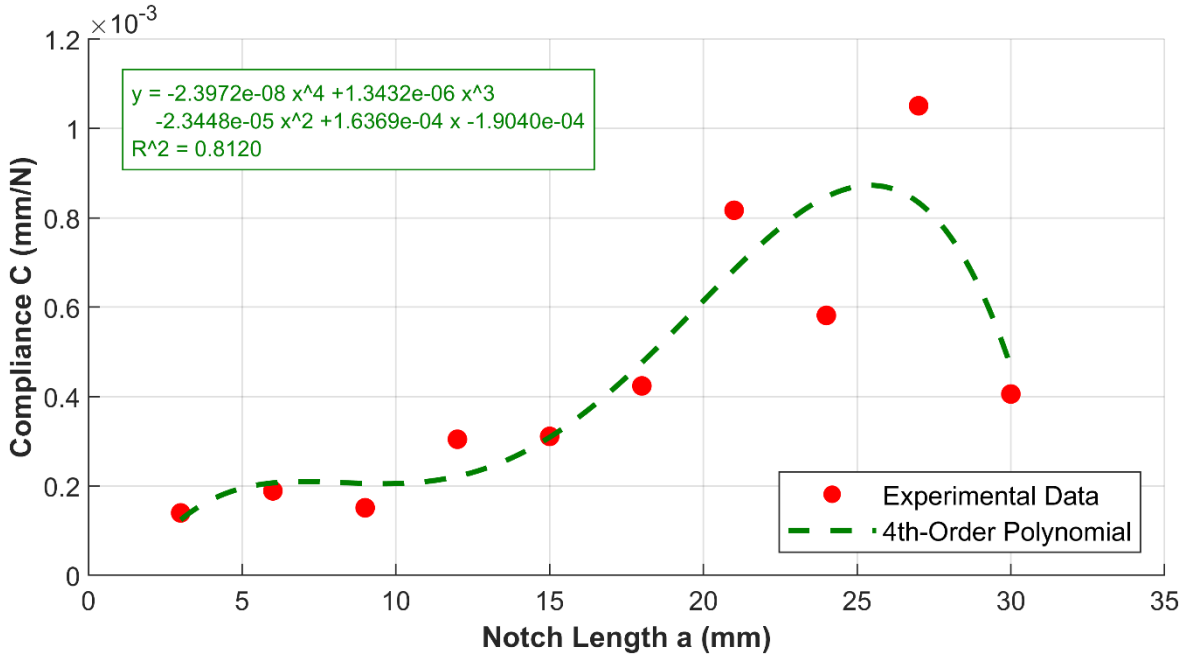


Fig. 6. Relationship between notch length and compliance with the fitted fourth-order polynomial.

Based on the computational approach detailed in the Methodology section, a peak load of 157.38 N recorded for the 30 mm notched sample yielded $K_{IC} = 0.2517$ MPa$\sqrt{\text{m}}$ for Cappadocia tuff.

For the Cappadocia tuff samples, K_{IC} was measured via the ASTM E399 compliance calibration approach. This parameter represents the material's resistance against crack extension within LEFM theory. These findings provide foundational reference values for future research on the failure response of Cappadocia tuffs, with the complete experimental dataset summarized in Table 3.

Table 3. Experimental data and derived fracture parameters

Parameter	**Value**
Rock type	Cappadocia volcanic tuff
Test standard	ASTM E399
Specimen type	SENB (Single Edge Notched Bend)
Number of specimens	10
Specimen dimensions (B × W × L)	30 × 60 × 280 mm
Support span (S)	240 mm
Initial notch length range	3 – 30 mm
Notch length increment	3 mm
(a/W) ratio	0.50
(S/W) ratio	4.00
Loading configuration	Three-point bending
Linear elastic region	20–70% of the maximum load
Maximum load (30 mm notch length)	157.38N
Compliance–notch length equation	$\boldsymbol{C(a) = -2.3972 \times 10^{-8}a^4 + 1.3432 \times 10^{-6}a^3 - 2.3448 \times 10^{-5}a^2 + 1.6369 \times 10^{-4}a - 1.9040 \times 10^{-4}}$
Polynomial order	4
Coefficient of determination, R^2	**0.81**
Calculated G_{IC}	**84.8397 N/m**
Calculated K_{IC}	**0.252 MPa√m**

4 Conclusions

In this study, K_{IC} and G_{IC} of volcanic tuff obtained from the Cappadocia Region were experimentally determined based on the ASTM E399 standard, yielding the following key insights:

The 3PB tests executed on ASTM E399-compliant SENB specimens enabled a reliable characterization of the fracture behavior of the volcanic tuff.

The load–CMOD curves obtained from the SENB tests exhibited predominantly linear elastic behavior during the initial loading stage, followed by a reduction in load-carrying capacity due to crack propagation after the maximum load was reached. This response is characteristic of the brittle fracture behavior of volcanic tuff.

The relationship between compliance and notch length was successfully modeled using a fourth-order polynomial. The resulting model yielded a coefficient of determination of $R^2 = 0.81$, demonstrating that the proposed method can be applied with satisfactory accuracy.

Based on ASTM E399 compliance calibration, K_{IC} for Cappadocia tuff was determined as 0.2517 MPa$\sqrt{\text{m}}$.This result reflects a low capacity to resist crack growth, implying that substantial void spaces and internal structural flaws heavily govern the material's cracking response.

The obtained fracture toughness value provides a fundamental material parameter for engineering analyses supporting the restoration, conservation of rock-carved structures, and consolidation of Cappadocia tuff.

The experimental approach and compliance-based calculation method proposed in this study offer a practical methodology for determining the fracture parameters of other low-strength, porous natural stones with similar characteristics.

The data obtained in this study are expected to serve as reference data for evaluating the fracture behavior of specimens consolidated with grout materials within the scope of the TÜBİTAK 1001 research project.

It is recommended that future studies investigate the fracture behavior more comprehensively by considering the effects of different loading rates, moisture contents, material anisotropy, specimen geometries, and specimens consolidated using grout materials.

Acknowledgments
This work was supported by “The Scientific and Technological Research Council of Türkiye” (TÜBİTAK) under Project No. 224M225, titled *"Experimental, Numerical and Uncertainty Analysis of the Effect of Grout Material Used in the Repair of Rock Carvings and Natural Formations in Cappadocia Region on the Structure.*

References
1. Topal, T., Doyuran, V.: Engineering geological properties and durability assessment of the Cappadocian tuff. Engineering Geology **47**(1–2), 175–187 (1997). https://doi.org/10.1016/S0013-7952(97)00017-3
2. Topal, T., Doyuran, V.: Analyses of deterioration of the Cappadocian tuff, Turkey. Environmental Geology **34**(1), 5–20 (1998). https://doi.org/10.1007/s002540050252
3. Atkinson, B.K. (ed.): Fracture Mechanics of Rock. Academic Press, London (1987). https://doi.org/10.1016/C2009-0-21691-6
4. Hoek, E., Martin, C.D.: Fracture initiation and propagation in intact rock – A review. Journal of Rock Mechanics and Geotechnical Engineering **6**(4), 287–300 (2014). https://doi.org/10.1016/j.jrmge.2014.06.001
5. Tutluoğlu, L., Batan, C., Aliha, M.R.M.: Tensile mode fracture toughness experiments on andesite rock using disc and semi-disc bend geometries with varying loading spans. Theoretical and Applied Fracture Mechanics **119**, 103325 (2022). https://doi.org/10.1016/j.tafmec.2022.103325
6. Yang, H., Krause, M., Renner, J.: Determination of fracture toughness of Mode I fractures from three-point bending tests at elevated confining pressures. Rock Mechanics and Rock Engineering **54**, 6071–6088 (2021). https://doi.org/10.1007/s00603-021-02432-z

7. Kobayashi, R., Matsuki, K., Otsuka, N.: Size effect in the fracture toughness of Ogino tuff. Engineering Fracture Mechanics **25**(5–6), 777–782 (1986). https://doi.org/10.1016/0148-9062(86)91662-1
8. ASTM International: ASTM E399-22. Standard Test Method for Linear-Elastic Plane-Strain Fracture Toughness of Metallic Materials. ASTM International, West Conshohocken, PA (2022). https://doi.org/10.1520/E0399-22
9. Yüzer, N.: "Kapadokya Bölgesi Volkanik Tüfünün Alkaliler ile Aktive Edilerek Tarihi Yığma Yapılarda Kullanılabilirliğinin Araştırılması", TÜBİTAK Project No. 118M321, Final Report (2021).
10. Weisinger, R., Costin, L.S., Lutz, T.J.: KIc and J-resistance-curve measurements on Nevada tuff. Experimental Mechanics 20(2), 68–74 (1980). https://doi.org/10.1007/BF02321037

Author Contribution Statement

- *Conceptualization:* Harun Yahya SÜNDÜ
- *Methodology:* Harun Yahya SÜNDÜ, Ayşe ERDÖLEN, Nabi YÜZER
- *Investigation:* Harun Yahya SÜNDÜ, Ayşe ERDÖLEN, Nabi YÜZER
- *Writing – Original Draft:* Harun Yahya SÜNDÜ
- *Writing – Review & Editing:* Ayşe ERDÖLEN, Nabi YÜZER

List of Abbreviations

- **ASTM** American Society for Testing and Materials
- **CB** Chevron Bend
- **CCNBD** Cracked Chevron Notched Brazilian Disc
- **CMOD** Crack Mouth Opening Displacement
- **ISRM** International Society for Rock Mechanics
- **LEFM** Linear Elastic Fracture Mechanics
- **SCB** Semi- Circular Bend
- **SENB** Single Edge Notched Bend
- **SR** Short Rod
- **UNESCO** United Nations Educational, Scientific and Cultural Organization
- **TÜBİTAK** The Scientific and Technological Research Council of Türkiye

Publication Note
This paper was peer-reviewed, accepted for presentation, and included in the proceedings of the ACE2026 – International Conference on Advances in Civil Engineering, held on 12–14 October 2026 in Trabzon, Türkiye.

This paper may be cited as follows:
Harun Yahya SÜNDÜ, Ayşe ERDÖLEN, Nabi YÜZER, "Determination Of The Fracture Energy Of Natural Stone From The Cappadocia Region" in Proceedings of the ACE2026 – International Conference on Advances in Civil Engineering, Trabzon, Türkiye, 12–14 October 2026.

Assessment of the Combined Effect of Plastic Aggregate and Silica Fume on Concrete

Safa NAYIR[1*],Yılmaz YILMAZ[2], Doğukan ŞAHİNER, Memduh NAS[3], Vahiddin Alperen BAKİ, Şakir ERDOĞDU

[1] 0000-0001-7876-8763, Karadeniz Technical University, Civil Engineering Department, Trabzon, Türkiye, safanayir@ktu.edu.tr
[2] 0009-0008-2871-6357, Karadeniz Technical University, Civil Engineering Department, Trabzon, Türkiye, yilmazyilmaz@ktu.edu.tr
[3] 0009-0009-2426-0978, Karadeniz Technical University, Civil Engineering Department, Trabzon, Türkiye, @ktu.edu.tr
[4] 0000-0001-6978-2811, Karadeniz Technical University, Civil Engineering Department, Trabzon, Türkiye, memduhnas@ktu.edu.tr
[5] 0009-0007-8905-1013, Karadeniz Technical University, Civil Engineering Department, Trabzon, Türkiye, valperenbaki@ktu.edu.tr
[6] 0000-0002-3440-7189, Karadeniz Technical University, Civil Engineering Department, Trabzon, Türkiye, shake@ktu.edu.tr

Abstract. Plastic materials have been widely used in many sectors for over a century due to their advantages such as low density, ease of production, and design flexibility. However, the negative environmental impacts of plastic waste generated at the end of their lifespan have become an increasingly significant problem. In this scope, the utilization of plastic waste as aggregate in concrete production stands out as a sustainable alternative in terms of both waste reuse and the reduction of natural resource consumption. However, plastic aggregates can cause negative effects on some performance characteristics in concrete, and the use of additional supplementary materials may be necessary to mitigate these effects. In this study, the combined effect of plastic waste (PA) and silica fume (SF) on the fresh-state (workability and density) performance of concrete was experimentally evaluated. %20 and %40 plastic aggregate ratios have been determined to be critical threshold values in terms of workability. As the PA content increased, the unit weight of the mixtures tended to decrease. Similarly, an increase in the SF replacement ratio generally resulted in a decrease in unit weight. The effect of PA on reducing unit weight was considerably more pronounced than that of SF.

Keywords: Plastic aggregate; silica fume; concrete; performance; combined effect

1 Introduction

Plastics are widely used in many different sectors due to their numerous advantageous properties such as low density, low cost, abrasion resistance, insulating properties, and ease of production and design [1-2]. These types of plastics include polyester, polyethylene, polycarbonate, high-density polyethylene, polyvinyl chloride (PVC), low-density/linear low-density polyethylene, polylactic acid, polypropylene, and polystyrene, and these materials are widely used in many different fields. According to OECD data, global plastic consumption was 460 Mt in 2019 and is expected to reach 1.23 Mt in 2060. This high volume of plastic use, coupled with misuse and inadequate waste management practices, is currently causing significant pollution and various environmental problems [3-4]. To reduce environmental

problems and contribute to sustainability in the construction sector, various studies are being conducted on the use of plastic waste in the construction industry. In this scope, numerous studies have investigated the use of plastic materials in mortars and concrete. In concrete production, plastic materials are generally used to replace fine or coarse aggregates in certain proportions, or different types of plastic aggregates are used in combination [5-7].

The use of plastic materials in mortar and concrete can improve some properties while negatively impacting others. Therefore, to mitigate the disadvantages of using PA, it may be necessary to use supplementary cementitious materials (SCMs) with plastic aggregates. Various SCMs such as silica fume, nano-silica, fly ash, slag, etc., are used to improve the strength and durability of concrete. It is stated that mechanical properties are improved to a certain extent depending on factors such as the type and dosage of the cement used, but more comprehensive research is still needed [8].

A study on the effects of electronic waste plastic and silica fume on the mechanical properties and thermal performance of concrete indicates that plastic fine aggregate degrades the mechanical properties of concrete but improves its thermal properties, while silica fume mitigates the negative effects caused by plastic fine aggregate [9]. In another study, the combined use of SCMs and waste plastic fibers was proposed as a sustainable approach. It was stated that the combined use of SCMs and RPFs improved both fresh and hardened concrete properties. Furthermore, it was indicated that the addition of SCMs increased the tensile and adhesion strength in mixtures containing RPFs, and that the combined use of SCMs and RPFs provided additional gains in overall performance [10].

In this study, the combined effects of plastic waste (PA) and silica fume (SF) on the fresh properties of concrete were experimentally investigated. Workability and unit weight were evaluated using data obtained from 45 concrete mixtures. For comparison purposes, mixtures without SF and PA were also produced as reference mixtures.

2 Materials and Methods

2.1 Materials

In the experimental study, three types of aggregates were used: coarse aggregate (4-16 mm), fine aggregate (0-5 mm), and sand (0-2 mm). The aggregate mixing ratios were determined as 55%, 33%, and 12% respectively to meet the conditions specified in the TS 802 [4]. standard (a total of 55% coarse and 45% fine aggregates). Silica fume was obtained from a private company. The water/cement ratio in the mixtures was selected as 0.55. SF and superplasticizer, acquired from private company and cement (CEM II/A-L 42.5R) obtained from the Aşkale Plant (Trabzon, Türkiye). In this study, a total of 45 different concrete mixtures were designed and produced by substituting fine aggregate with PVC at volumetric percentages of 0%, 5%, 10%, 15%, 20%, 25%, 30%, 35%, and 40%; and cement with silica fume at weight percentages of 0%, 2.5%, 5%, 7.5%, and 10%. Chemical composition of materials used in experimental study is shown in Table 1.

Table 1. Chemical composition of materials.

Material	SiO_2	Al_2O_3	Fe_2O_3	TiO_2	CaO	MgO	K_2O	Na_2O	LOI	MnO
Cement	11.9	3.15	3.61	0.33	65.6	1.56	0.93	0.20	0.03	0.05
SF	74.9	0.32	0.74	-	0.05	11.11	2.22	1.42	0.015	0.05

When the PVC substitution rate was increased to 45% and 50%, the desired homogeneity and consistency could not be achieved due to a significant decrease in workability, increased void formation, and problems in the setting process during the production of the mixtures. As these negative effects could not be overcome even with the use of plasticizer admixtures, it was

concluded that mixtures containing 45% and 50% PVC could not be produced with suitable properties, and these percentages were not included in the study. Figure 1 shows concrete samples containing 45% PVC and 2.5% SF. The sample surfaces appear quite rough and heterogeneous. This can be attributed to the weaker adhesion between the cement paste and natural aggregates due to the high PVC aggregate content. Furthermore, it was observed that increasing the PVC content made compaction more difficult and resulted in significant voids in the samples. Therefore, workability and compaction problems are evident at high PVC ratios.



Fig. 1. Concrete samples of 2.5SF-45 PVC mixture.

2.2 Mix Design

The experimental study was designed to produce a total of 55 batches, but some batches could not be produced due to a lack of uniformity. Therefore, it was not possible to produce concrete samples at these ratios and consequently, to conduct the relevant experiments. Excluding non-uniform mixtures, a total of 45 productions were carried out.

2.3. Methods

Unit weight determination was carried out on 7.1 cm cube and 10×20 cm cylindrical samples, based on the method specified in the TS EN 12350-6 [11]. standard. Slump tests were applied to each concrete mixture to determine its workability, and measurements were taken in accordance with the TS EN 12390-2 [12] standard. For compressive strength determination, 10 cm cube samples were used, and the tests were conducted according to the TS EN 12390-3 [13] standard. Compressive strength tests were performed on three samples for each mixture at 7, 14, and 28 days of curing age, and the arithmetic mean of the measured values was accepted as the compressive strength of the respective mixture. The loading rate was kept constant at 0.6 MPa/s in all compressive strength tests.

3 Results and Discussions

Observations of the fresh concrete properties within the experimental study indicated that plastic aggregate replacement ratios of 20% and 40% (as a replacement for fine aggregate) represented two critical threshold levels in terms of workability.

Table 2. Mix designs produced in the experimental study.

Code	Cement	SF	Coarse Aggregate	Fine Aggregate	Sand	PVC
0SF-REF	350	0	1027.50	616.50	224.18	0.000
0SF-5PVC	350			585.67	212.97	22.814
0SF-10PVC	350			554.85	201.76	45.628
0SF-15PVC	350			524.02	190.55	68.442
0SF-20PVC	350			493.20	179.34	91.255
0SF-25PVC	350			462.37	168.14	114.069
0SF-30PVC	350			431.55	156.93	136.883
0SF-35PVC	350			400.72	145.72	159.697
0SF-40PVC	350			369.90	134.51	182.511
2.5SF-REF	341,25	8.75	1025.78	615.47	223.81	0,00
2.5SF-5PVC	341,25			584.69	212.26	22.75
2.5SF-10PVC	341,25			583.72	201.43	45.55
2.5SF-15PVC	341,25			523.15	190.24	68.33
2.5SF-20PVC	341,25			492.37	179.05	91.10
2.5SF-25PVC	341,25			461.60	167.85	110.68
2.5SF-30PVC	341,25			430.83	156.66	136.65
2.5SF-35PVC	341,25			400.05	145.47	159.43
2.5SF-40PVC	341,25			369.28	134.28	182.21
5SF-REF	332,5	17.5	1024.06	614.44	223.43	0.000
5SF-5PVC	332,5			583.72	212.26	22.738
5SF-10PVC	332,5			552.99	201.09	45.475
5SF-15PVC	332,5			522.27	189.92	68.213
5SF-20PVC	332,5			491.55	178.75	90.950
5SF-25PVC	332,5			460.83	167.57	113.688
5SF-30PVC	332,5			430.11	156.40	136.426
5SF-35PVC	332,5			399.38	145.23	159.163
5SF-40PVC	332,5			368.66	134.06	181.901
5SF-45PVC	332,5			337.94	122.89	204.639
5SF-50PVC	332,5			307.22	111.72	227.376
7.5SF-REF	323,5	26.25	1022.47	613.48	223.08	0,000
7.5SF-5PVC	323,5			582.81	211.93	22.702
7.5SF-10PVC	323,5			552.13	200.78	45.404
7.5SF-15PVC	323,5			521.46	189.62	68.107
7.5SF-20PVC	323,5			490.79	178.47	90.809
7.5SF-25PVC	323,5			460.11	167.31	113.511
7.5SF-30PVC	323,5			429.44	156.16	136.213
7.5SF-35PVC	323,5			398.76	145.00	158.916
7.5SF-40PVC	323,5			368.09	133.85	181.618
10SF-REF	315	35	1020.63	612.38	222.68	0.000
10SF-5PVC	315			581.76	211.55	22.661
10SF-10PVC	315			551.14	200.41	45.323
10SF-15PVC	315			520.52	189.28	67.984
10SF-20PVC	315			489.90	178.15	90.645
10SF-25PVC	315			459.28	167.01	113.307
10SF-30PVC	315			428.66	155.88	135.968
10SF-35PVC	315			398.05	144.74	158.630
10SF-40PVC	315			367.43	133.61	181.291

As the plastic aggregate content increased, the slump values of the fresh mixtures tended to decrease. This reduction can be attributed to the irregular shape of the plastic particles and the presence of sharp edges on some particles, which may increase interparticle friction [14]. The

slump values and amounts of chemical admixture used for the concrete mixtures are presented in Table 3.

Table 3. Relationship between slump-quantity of chemical admixture

Mixes	Slump	Amount of additive (g)	Mixes	Slump	Amount of additive (g)
0SF-REF	9.5	0	5SF- 25 PVC	5	88
0SF-5 PVC	9	5	5SF-30 PVC	5	94
0SF-10 PVC	10	37	5SF-35 PVC	5	121
0SF-15 PVC	9	41	5SF-40 PVC	5	103.5
0SF-20 PVC	8	84	7.5SF-REF	9	12.5
0SF- 25 PVC	8	107	7.5SF-5 PVC	5.5	32
0SF-30 PVC	10	120	7.5SF-10 PVC	8.5	72.5
0SF-35 PVC	8	60.5	7.5SF-15 PVC	8	72
0SF-40 PVC	6	102	7.5SF-20 PVC	6	75
2.5SF-REF	8.5	0	7.5SF- 25 PVC	5	81
2.5SF-5 PVC	7.5	30	7.5SF-30 PVC	6	94.5
2.5SF-10 PVC	7.5	47	7.5SF-35 PVC	5	100
2.5SF-15 PVC	8.5	59	7.5SF-40 PVC	5	94.5
2.5SF-20 PVC	8	72	10SF-REF	7	32
2.5SF- 25 PVC	7.5	86.5	10SF-5 PVC	7	27.5
2.5SF-30 PVC	6.5	104	10SF-10 PVC	5.5	39.5
2.5SF-35 PVC	6	100.5	10SF-15 PVC	6	59.5
2.5SF-40 PVC	5	144.5	10SF-20 PVC	5	67
5SF-REF	8	5	10SF- 25 PVC	5	82,5
5SF-5 PVC	7	23,5	10SF-30 PVC	5	87
5SF-10 PVC	6.5	37	10SF-35 PVC	6	114.5
5SF-15 PVC	6	61	10SF-40 PVC	5	156
5SF-20 PVC	7.5	80	*First and second codes indicate SF and PA.		

Since the target consistency class was S2, chemical admixture was used in some mixtures to achieve the desired consistency, whereas no admixture was required for several mixtures. Overall, the slump values of all mixtures ranged between 5 and 10 cm. The reference mixtures represent those containing neither silica fume nor plastic aggregate. As the SF replacement ratio increased, the consistency values tended to decrease, which can be attributed to the considerably higher fineness of SF compared with cement. The reference mixtures without SF and those containing 2.5% SF, both without PVC aggregate, satisfied the target S2 consistency; therefore, no chemical admixture was required. For the other reference mixtures containing SF, only a limited amount of chemical admixture was required.

Similarly, an increase in the PVC replacement ratio generally resulted in a decrease in slump values. Accordingly, the amount of chemical admixture required tended to increase. However, despite keeping the other mixture parameters constant, the amount of chemical admixture did not increase consistently with increasing PVC replacement ratio in all cases. For example, approximately 121 g of chemical admixture was used in the mixture coded 5SF-35 PVC, whereas this amount decreased to approximately 103.5 g in the 0SF-40 PVC mixture, despite the PVC replacement ratio increasing to 40%. This observation suggests that variations in the required amount of chemical admixture may be associated with differences in the slump values of the mixtures.

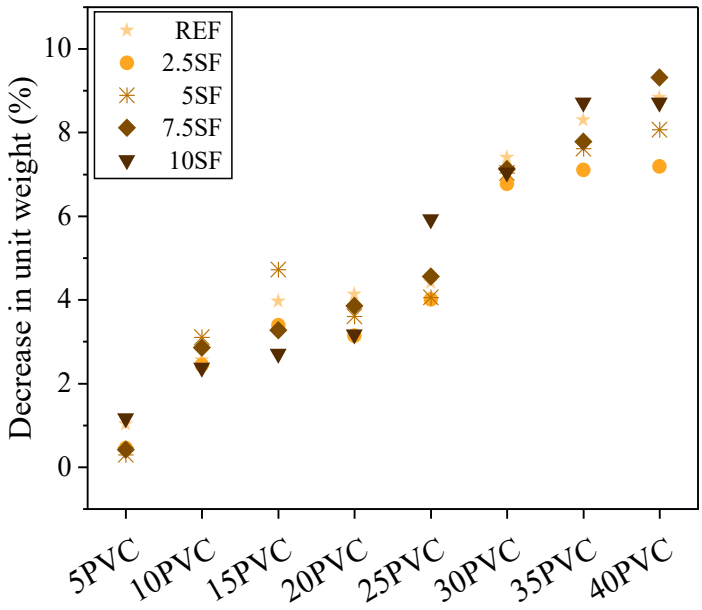


Fig. 2. Percentage reduction in unit weight for mixtures.

Figure 2 shows the percentage decrease in unit weight for the mixtures compared to the reference concrete. As the PA content increased, the unit weight of the mixtures generally tended to decrease. This reduction can be attributed to the lower specific gravity of the plastic aggregate used as a replacement for fine aggregate. Although a decrease in unit weight was expected with increasing PVC content in mixtures with consecutive PVC replacement ratios, slight increases in unit weight were also observed in some mixtures. These variations may be attributed to differences occurring during mixture preparation and placement into the molds. Similarly, an increase in the silica fume replacement ratio generally resulted in a decrease in unit weight, which can be explained by the lower specific gravity of silica fume compared with cement. Overall, increasing PA and SF contents resulted in a decrease in unit weight compared with the reference mixtures. The effect of PA on reducing unit weight was considerably more pronounced than that of SF.

A previous study investigating the use of waste plastic in concrete reported a significant reduction in unit weight with the incorporation of PA. The density of the plastic aggregate was reported to be approximately 70% lower than that of sand [15]. In this study, the density of the PA was approximately 45% lower than that of sand. In addition, the density of silica fume was approximately 25% lower than that of cement.

4 Conclusions

The main findings obtained within the scope of the experimental study are summarized below.

- %20 and %40 plastic aggregate ratios have been determined to be critical threshold values in terms of workability.
- Increasing the PVC replacement ratio generally reduced slump values and increased the required amount of chemical admixture. However, in some cases, the decrease in chemical admixture requirement with increasing PVC content was attributed to variations in slump values.

- As the PA content increased, the unit weight of the mixtures tended to decrease. Similarly, an increase in the silica fume replacement ratio generally resulted in a decrease in unit weight.
- The effect of PA on reducing unit weight was considerably more pronounced than that of SF.

Acknowledgments
The authors gratefully acknowledge the financial support provided by the Scientific and Technological Research Council of Türkiye (TÜBİTAK) under Project No. 125M839.

References

1. Wang, W., Themelis, N. J., Sun, K., Bourtsalas, A. C., Huang, Q., Zhang, Y., Wu, Z.: Current influence of China's ban on plastic waste imports. Waste Disposal & Sustainable Energy 1(1), 67–78 (2019).
2. PlasticsEurope, E.: Plastics – the Facts 2013. An Analysis of European Latest Plastics Production, Demand and Waste Data (2013).
3. OECD: Global Plastics Outlook: Economic Drivers, Environmental Impacts and Policy Options. OECD (2022).
4. Zulkernain, N. H., Gani, P., Chuan, N. C., Uvarajan, T.: Utilisation of plastic waste as aggregate in construction materials: A review. Construction and Building Materials 296, 123669 (2021).
5. Rao, J., Hagare, D., Tao, Z.: Upcycling Mixed Plastic Waste as a Replacement for Natural Aggregate in Concrete: A Critical Review. Journal of Building Engineering, 114037 (2025).
6. Hamada, H. M., Al-Attar, A., Abed, F., Beddu, S., Humada, A. M., Majdi, A., ... Thomas, B. S.: Enhancing sustainability in concrete construction: A comprehensive review of plastic waste as an aggregate material. Sustainable Materials and Technologies 40, e00877 (2024).
7. Mohammed, N. S., Hamza, B. A., Al-Shareef, N. A. H., Hussein, H. H.: Structural behavior of reinforced concrete slabs containing fine waste aggregates of polyvinyl chloride. Buildings 11(1), 26 (2021).
8. Nasir, A., Butt, F., Ahmad, F.: Enhanced mechanical and axial resilience of recycled plastic aggregate concrete reinforced with silica fume and fibers. Innovative Infrastructure Solutions 10(1), 4 (2025).
9. Ali, K., Qureshi, M. I., Saleem, S., Khan, S. U.: Effect of waste electronic plastic and silica fume on mechanical properties and thermal performance of concrete. Construction and Building Materials 285, 122952 (2021).
10. Dong, C., Zhang, Q., Chen, C., Jiang, T., Guo, Z., Liu, Y., Lin, S.: Fresh and hardened properties of recycled plastic fiber reinforced self-compacting concrete made with recycled concrete aggregate and fly ash, slag, silica fume. Journal of Building Engineering 62, 105384 (2022).
11. TS 802: Design of Concrete Mixes. Turkish Standards Institute, Ankara (2016).
12. TS EN 12350-6: Testing Fresh Concrete – Part 6: Density. Turkish Standards Institute, Ankara (2010).
13. TS EN 12350-2: Testing Fresh Concrete – Part 2: Slump Test. Turkish Standards Institute, Ankara (2019).
14. TS EN 12390-3: Testing Hardened Concrete – Part 3: Compressive Strength of Test Specimens. Turkish Standards Institute, Ankara (2019).
15. Rai, B., Rushad, S. T., Kr, B., Duggal, S. K.: Study of waste plastic mix concrete with plasticizer. International Scholarly Research Notices 2012(1), 469272 (2012).

Author Contribution Statement

Conceptualization: Safa NAYIR, Yılmaz YILMAZ, Doğukan ŞAHİNER, Şakir ERDOĞDU
Methodology: Safa NAYIR, Yılmaz YILMAZ, Doğukan ŞAHİNER, Vahiddin Alperen BAKİ
Investigation: Safa NAYIR, Yılmaz YILMAZ, Doğukan ŞAHİNER, Memduh NAS
Writing – Original Draft: Safa NAYIR, Yılmaz YILMAZ
Writing – Review & Editing: Safa NAYIR, Yılmaz YILMAZ

List of Abbreviations

- **PA** — Plastic Aggregate
- **SF** — Silica Fume
- **SCM** — Supplementary Cementitious Materials
- **PVC** — Polyvinyl Chloride

Note: Following the conference, this Publication Note will be added to each paper; therefore, authors are kindly requested not to remove the note below and to complete the author(s) and paper title information.

Publication Note

This paper was peer-reviewed, accepted for presentation, and included in the proceedings of the ACE2026 – International Conference on Advances in Civil Engineering, held on 12–14 October 2026 in Trabzon, Türkiye.

This paper may be cited as follows:

Nayır, S., Yılmaz, Y., Şahiner, D., Nas, M., Baki, V. A., Erdoğdu, Ş., "Assessment of the Combined Effect of Plastic Aggregate and Silica Fume on Concrete," in Proceedings of the ACE2026 – International Conference on Advances in Civil Engineering, Trabzon, Türkiye, 12–14 October 2026.

Flexural Performance of Overlap Configurations for Textile-Reinforced Cementitious Composites

Bedirhan Enes Kelek[1] and Esat Selim Kocaman[2]
[1] 0009-0005-4294-1479, Bogazici University, Department of Civil Engineering, Istanbul, Türkiye, bedirhan.kelek@bogazici.edu.tr
[2] 0009-0002-2934-5574, Bogazici University, Department of Civil Engineering, Istanbul, Türkiye, esatselim.kocaman@bogazici.edu.tr

Abstract. Textile reinforcements offer new possibilities to realize novel thin-section concrete structures due to their structural slenderness, mechanical performance, and durability benefits. When applied in construction, however, a significant challenge emerges due to the limited roll dimensions of commercial textiles. This dictates that the structure needs to be reinforced using multiple textile mesh segments, making the overlapping of these segments essential for adequate stress transfer and structural integrity. In this study, this critical aspect of textile-reinforced cementitious composites was investigated. Textile-reinforced mortars with varying overlap configurations were tested under three-point bending to determine their flexural strength and pseudo-ductility characteristics. Three overlap connection approaches were evaluated, and their effects on structural performance in relation to two different overlap lengths were revealed. The results show that when sufficient overlap length and anchorage are present, clamping the textile reinforcements detrimentally affects both flexural strength and overall toughness in the pseudo-ductility regime. Conversely, for configurations with limited overlap length and insufficient anchorage, the clamps were able to connect the textile segments, providing significant pseudo-ductility for the cementitious composites. However, due to the disruption of matrix continuity, a notable loss in flexural strength was detected for all clamped configurations. Overall, this study enhances the understanding of this critical design consideration, potentially leading to efficient practices that reduce material use while avoiding detrimental connection approaches.

Keywords: Textile-reinforced cementitious composites; reinforcement overlapping; flexural behavior; pseudo-ductility.

1 Introduction

Textile reinforcements have emerged as a promising solution for thin-section concrete shell structures. They are innovative reinforcement alternatives composed of high-strength fibers such as carbon, glass, or basalt fibers arranged in a mesh grid structure. As they are non-metallic, textile-reinforced concrete (TRC) does not need thick concrete cover, which significantly reduces the required structural thickness. They also exhibit high mechanical performance, making them well-suited for the reinforcement of thin sections [1-3]. As they are inherently corrosion-resistant, textile reinforcements provide a longer service life, which is particularly important for structural safety [4]. By enabling thinner and more lightweight

structures, TRC systems can offer significant design freedom, sustainability benefits, and more practical on-site handling compared to traditional materials [5-8].

In practice, the textile reinforcements used in construction are typically provided in roll form with a predetermined roll width by the manufacturers. This essentially means that large structures cannot be reinforced with a single continuous reinforcement layer, and several reinforcement segments must be used for full reinforcement of the structure. For structural integrity, these segments need to be sufficiently overlapped along their intersection to ensure adequate stress transfer between them [8-9]. Proper stress transfer is critical to carry and resist stresses through the reinforcement within the concrete; otherwise, these regions can become vulnerable weak spots for failure, compromising the overall structural integrity of the thin-section cementitious composite. Thus, reinforcement overlapping becomes an important aspect in the design of textile reinforcements, and applying a proper textile connection methodology is critical to attain sufficient structural integrity along these regions.

In this study, we focus on this aspect and investigate the mechanical performance of various textile overlap configurations embedded in textile-reinforced mortars. The primary objective is to evaluate how different overlap connection approaches and overlap lengths influence flexural strength and pseudo-ductility using a three-point bending testing scheme. We demonstrate the effectiveness of these connection approaches in relation to different overlap lengths to provide valuable guidelines for the effective treatment of this critical design aspect.

2 Experimental Methodology

2.1 Materials

In this study, we used textile-reinforced mortars for the overlap configuration investigation. The cementitious matrix was composed of Portland cement, natural sand, tap water, and superplasticizer (SP). The mixture composition is provided in Table 1.

Table 1. Mixture composition.

Material	Mass/Binder
CEM I	1
Natural Sand	1.5
Water	0.45
Superplasticizer	0.0055

For the reinforcements, we used an alkali-resistant (AR) glass fiber textile mesh, which consisted of periodically arranged glass fiber rovings in two orthogonal directions with an epoxy coating. The individual fiber strands had an approximate width of 3 mm and a thickness of 0.3 mm. The textile mesh had square openings of 10 mm in both directions, which allowed the mortar to pass through during casting. This provided sufficient bonding between the textile reinforcements and the cementitious matrix after curing. The reinforcement stiffness and tensile strength are 78 GPa and 1.7 GPa in both weft and warp directions, respectively.

Following standard three-point bending testing procedures for mortar prisms, specimens were cast with a length, width, and thickness of 160 mm, 40 mm, and 40 mm, respectively (see Fig. 1). The textile reinforcements were placed 5 mm above the bottom surface in the tensile region. After casting, specimens were cured in water for 7 days. For each configuration, 3 specimens were prepared and tested. A schematic of the overlap specimens is provided in Fig.

1. In these overlap specimens, two textile segments extend from each side of the specimen along the longitudinal direction such that they overlap at the center of the specimen.

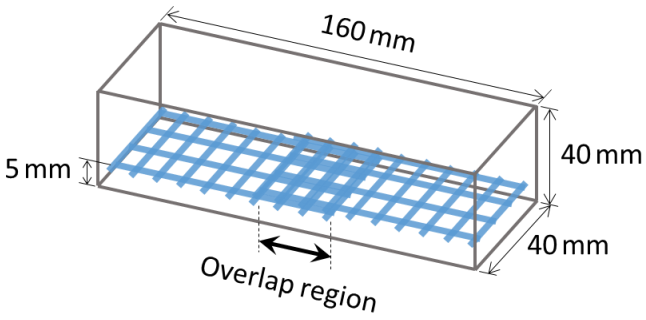


Fig. 1. Specimen dimensions and textile placement.

In this study, 5 different overlap configurations were developed and tested for their flexural behavior. Fig. 2 presents the textile meshes with different overlap approaches, and Table 2 provides the configuration names together with their descriptions. In these configurations, the overlap region was varied based on two parameters: overlap mesh opening number and connection method. For the first parameter, we investigated configurations with overlap lengths corresponding to 1 and 3 mesh openings (equivalent to 1 cm and 3 cm, respectively). For the connection methods, we used 3 different approaches for the overlap regions:

1) Plain overlapping of the two textile segments at the center section. Here, the two textile segments were essentially bonded via the thin cementitious matrix between the layers along the overlap region.
2) We stitched the two textile segments using a thin copper wire with a diameter of approximately 0.25 mm (see Fig. 2a).
3) In addition to plain overlapping, we clamped the two textile segments using plastic clamps along the overlap region as shown in Figs. 2b and 2c.

For the specimens with a 1-mesh opening overlap, we investigated two configurations. Plain overlapping was not tested here as it was not expected to exhibit pseudo-ductility after major crack formation along the center due to the limited anchorage length. We focused on the clamping and wire stitching approaches in configurations 1M-LC and 1M-W, respectively. For the 3-mesh opening overlap, we investigated plain overlapping and clamping approaches in configurations 3M-NC, 3M-LC, and 3M-2CC. Wire stitching was not investigated for the 3-mesh series because it was unable to provide sufficient connection and ductility in the 1M-W specimens, as discussed later in the results section. Instead, we focused on two different clamping configurations: in 3M-LC, 2 clamps were introduced at the center of the specimen (see Fig. 2b); in 3M-2CC, two clamps were introduced along diagonal directions positioned near the ends of the overlap region away from the center (see Fig. 2c).

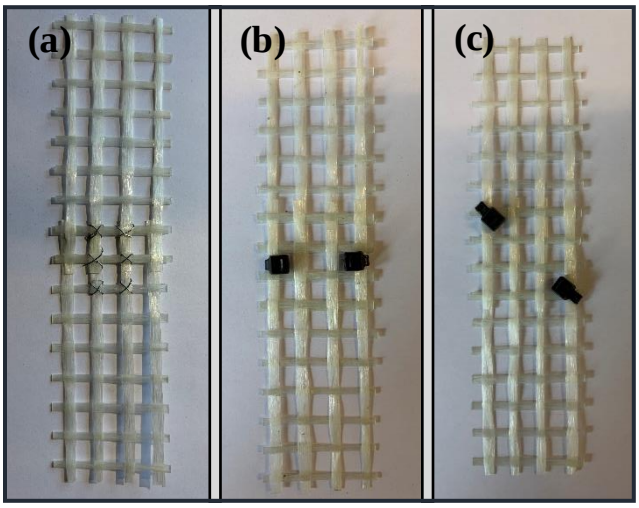


Fig. 2. Illustration of the overlap approaches; **(a)** wire stitching (named W), **(b)** clamping along the longitudinal direction (named LC), **(c)** clamping along the diagonal direction at two locations (named 2CC).

Table 2. Specimen configurations.

Name	Configuration Description
Ref	Reference specimen with a single continuous textile mesh
1M-LC	Overlap region with 1 mesh opening clamped along the longitudinal direction
1M-W	Overlap region with 1 mesh opening stitched using a copper wire along the overlap region
3M-NC	Overlap region with 3 mesh openings without any clamps
3M-LC	Overlap region with 3 mesh openings clamped along the longitudinal direction
3M-2CC	Overlap region with 3 mesh openings clamped at 2 diagonal locations away from the center

2.2 Testing

The specimens with various overlap configurations were tested using a three-point bending scheme to determine their flexural strength and detect if they exhibit pseudo-ductility after matrix rupture. As flexural loading in thin-section panels can be critical, we selected this testing scheme to apply concentrated loading directly along the overlap regions, causing severe flexural deformations. This provided a conservative benchmark for evaluating overlap performance under severe loading conditions.

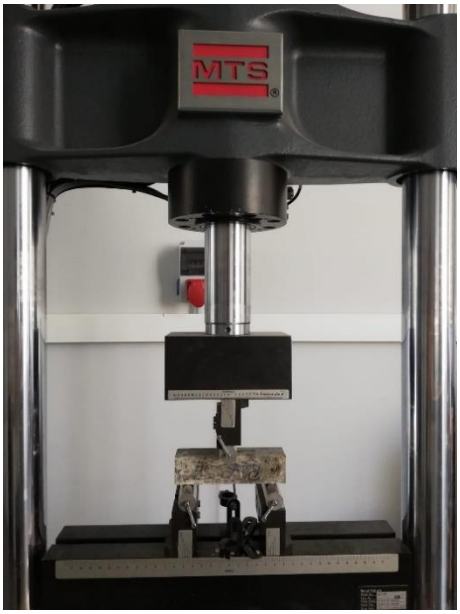


Fig. 3. The 3-point bending test experimental setup.

An MTS closed-loop universal testing machine was used for the flexural tests (see Fig. 3). Testing was conducted in load-controlled mode with a rate of 50 N/s and span length of 100 mm following EN 1015-11. The nominal stress and strain corresponding to the measured force and displacement of the specimens were calculated using the following equations [10]:

$$\sigma = \frac{3FL}{2bd^2}, \tag{1}$$

$$\varepsilon = \frac{6Dd}{L^2}, \text{ and} \tag{2}$$

where L is the span length, b is the width of the beam, d is the thickness of the beam, F is the flexural load, D is the maximum deflection of the center of the beam, σ and ε are the nominal stress and strain at the center of the bottom tensile surface, respectively.

Using these formulations, flexural strengths and nominal strains along the pseudo-ductility regime of the specimens were determined. The flexural strength (modulus of rupture) was determined based on the load corresponding to major matrix crack formation along the center. Matrix rupture was subsequently followed either by a significant drop in stress or by a pseudo-ductility regime depending on the specimen configuration.

3 Results and Discussion

The flexural strength results of the configurations are provided in Fig. 4. The configuration 3M-NC with plain overlapping and no clamps showed the highest flexural strength. The results indicate that using clamps and wires for overlap connection reduces the strength. This can be attributed to the fact that they cause localized stress concentrations leading to early rupture of the cementitious mortar. For the wire stitching approach, this reduction was limited; however, for clamped configurations, strength was significantly reduced. Because the plastic clamps occupied much larger volume than the thin wires, they disrupted matrix continuity significantly, causing higher stress concentrations that led to lower flexural strength. Furthermore, when comparing the clamped configurations, 3M-2CC showed higher flexural strength than 3M-LC.

When the clamps were placed away from the center and the concentrated load, as in 3M-2CC, stress concentrations were less severe, leading to higher flexural strength.

In this study, we also compared the pseudo-ductility behavior of the configurations. Fig. 5 presents the results of the configurations that exhibited pseudo-ductility. The remaining configurations, Ref and 1M-W, did not exhibit ductility after the peak rupture stress. For the reference specimens (Ref) with continuous reinforcement without an overlap, the single layer reinforcement ratio was not sufficient to sustain the cracking load, resulting in immediate tensile rupture of the mesh. For configuration 1M-W, although there was double reinforcement at the center due to the overlap, there was a sudden load drop and premature failure because the anchorage length was insufficient, causing the textile to pull out immediately upon matrix rupture. The wire stitching was not able to provide sufficient connection between the two textile segments to prevent slippage.

The potential of wire stitching needs further study to reach a definitive conclusion on its effectiveness. The stitching methodology can be further investigated in future studies with alternative techniques for more effective connection and enhanced overlap performance.

Among the configurations exhibiting pseudo-ductility, the 3M-NC configuration with plain overlapping and no clamps showed the best overall toughness (see Fig. 5). Due to a casting defect, one specimen was excluded for 3M-NC, and data for the remaining two specimens are presented in Fig. 5. Compared to configuration 1M-W, the embedment length of this configuration with 3 mesh openings was able to provide sufficient anchorage, which introduced post-cracking pseudo-ductility after peak load. The double reinforcement with adequate embedment length at the center ensured sufficient resistance for post-cracking hardening. Because there were no clamps, flexural strength was much higher, which also contributed to higher toughness in the ductility regime.

When we compare configuration 3M-NC with clamped configuration 3M-LC, the results demonstrate the adverse effect of additional clamps due to localized stress concentration. Here, the clamps did not improve the pseudo-ductility regime; in fact, the hardening observed in 3M-NC was replaced by post-cracking softening in 3M-LC at high deformation levels (corresponding to a nominal strain of 0.1), leading to significantly lower overall toughness, as observed in Fig. 5.

On the other hand, the 1M-LC results show that clamping was able to introduce an effective mechanical connection between the textile segments, leading to significant pseudo-ductility with post-cracking softening for the cementitious composite. This was not the case for 1M-W, where the wire stitches failed to hold the textile segments together. This indicates that when the overlap length is below the critical length for sufficient anchorage, clamps can have a positive effect by providing a physical connection and introducing pseudo-ductility to the system. For reduced reinforcement material use, the overall toughness of short-overlap specimens can be significantly increased via this induced pseudo-ductility.

Furthermore, when comparing the clamped configurations with 3 mesh openings, 3M-2CC exhibited higher overall toughness than 3M-LC. With reduced stress concentrations due to positioning the clamps away from the center and the concentrated load, higher overall toughness was attained along the pseudo-ductility regime.

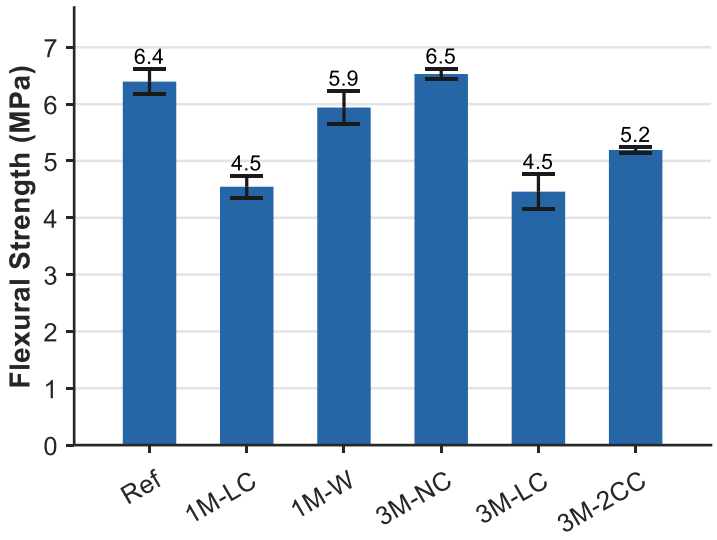


Fig. 4. Flexural strength results for various overlap configurations with standard deviation error bars and mean strengths.

The adverse effect of mechanical clamping on flexural performance warrants careful consideration. While clamping mechanisms are intended to enhance the overlap and maintain continuity, the results indicate that they act as stress concentrators and degrade flexural strength and overall toughness when sufficient bond length already exists. Clamps became beneficial only when the overlap length was insufficient to provide adequate anchorage for pseudo-ductility, as seen in the 1M-LC results. In contrast, configuration 3M-NC, which relied entirely on the cementitious matrix to transfer stresses across the overlap, attained the highest flexural strength and toughness. This indicates that a continuous, undisturbed matrix-to-fiber bond in the overlap region is more effective than mechanically forced connections such as clamping. However, this comes at the cost of using more reinforcement material for the overlap region.

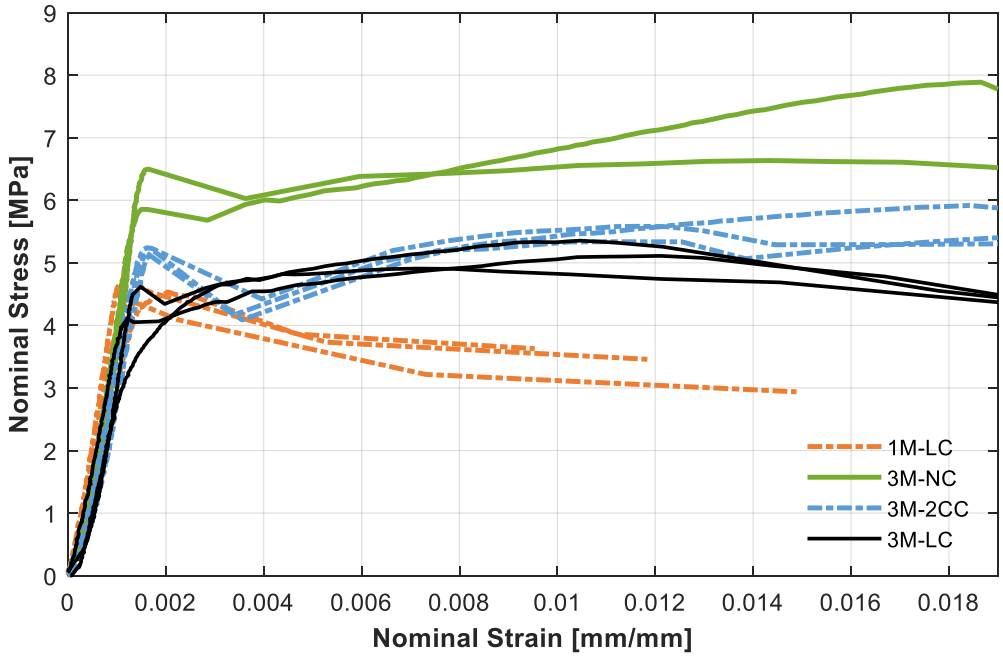


Fig. 5. Nominal stress-strain curves of configurations exhibiting significant ductility due to reinforcement pull-out.

Furthermore, for a comprehensive understanding of these connection approaches and how their influence depends on overlap length, future research can focus on size effects by testing these configurations in larger-scale, thin-section structural elements to determine their global flexural and pseudo-ductile performance.

4 Conclusion

The structural slenderness and high mechanical performance of thin-section textile-reinforced cementitious composites offer new avenues for novel construction applications. However, their effective utilization in real-life structures requires studies on critical design aspects such as reinforcement overlapping. Due to practical reasons such as the limited roll width of reinforcements, different textile segments must be carefully overlapped to ensure structural integrity. To enhance understanding of this critical design aspect, this study investigated textile-reinforced mortars with different overlap configurations and determined their flexural behavior using 3-point bending tests. Based on the findings, the following are concluded:

- The overlap configuration 3M-NC (with no clamps, relying entirely on the cementitious matrix to transfer stresses across the discontinuity with sufficient overlap length) exhibited the best performance, showing the highest flexural strength and overall toughness with pseudo-ductile post-cracking hardening.

- Using plastic clamps along overlap regions significantly reduces flexural strength by creating localized stress concentrations and disrupting matrix continuity; for overlap regions with sufficient bond length, clamping also significantly lowers overall toughness.

- The wire stitching applied in this work did not provide sufficient connection to induce pseudo-ductility in the 1M-W configuration. However, these specimens showed first-crack flexural strength close to the reference case because the thin wire caused minimal matrix disruption compared to plastic clamps. Alternative stitching approaches can be investigated in the future to improve connection efficiency to induce pseudo-ductility.

- When the overlap length is short and anchorage is insufficient, clamping is able to introduce sufficient mechanical connection and pseudo-ductility (exhibiting post-cracking softening), as observed in configuration 1M-LC (compared to abrupt failure in 1M-W). However, when overlap length is already sufficient, clamping has an adverse effect (3M-LC), lowering flexural strength and post-cracking toughness compared to specimens with no clamps (3M-NC).

Optimizing overlap configurations is critical for improving the structural integrity and mechanical performance of thin-section textile-reinforced cementitious composites. This study provides key considerations and guidelines for the effective design of overlap regions, enabling efficient material use and avoiding disadvantageous connection approaches.

Acknowledgments

The authors greatly acknowledge the support from the companies Fibrobeton, Çimsa and Sika Group.

References

1. Rawat P., Liu S., Guo S., Rahman M.Z., Yang T., Bai X., Yao Y., Mobasher B., Zhu D.: A state-of-the-art review on mechanical performance characterization and modelling of high-performance textile reinforced concretes. Constr. Build. Mater. 347, 128521 (2022).
2. Friese D., Scheurer M. Hahn, L., Gries T., Cherif C.: Textile reinforcement structures for concrete construction applications—a review. J. Compos. Mater. 56(26), 4041–4064 (2022).
3. Hegger J., Will N., Bruckermann O., Voss S.: Load–bearing behaviour and simulation of textile reinforced concrete. Mater. Struct. 39(8), 765–776 (2006).
4. Spelter A., Bergmann S., Bielak J., Hegger J.: Long-term durability of carbon-reinforced concrete: an overview and experimental investigations. Applied Sciences 9(8), 1651 (2019).
5. Kalthoff M., Bosbach S., Backes J.G., Cruz C.M., Classen M., Traverso M., Raupach M., Matschei T.: Fabrication of lightweight, carbon textile reinforced concrete components with internally nested lattice structure using 2-layer extrusion by LabMorTex. Constr. Build. Mater. 395, 132334 (2023).
6. Holschemacher K.: Application of textile reinforced concrete in precast concrete industry. In: IOP Conference Series: Materials Science and Engineering 753(4), p. 042086. IOP Publishing (2020).
7. Kelek B.E., Henzel T., Bhat S., Maraşlı M., Kohen B., Kocaman E.S., Gries T., Özyurt N.: Investigation and experimentation of thermoplastic-coated textile reinforcement shaping on curved surfaces. In: D'Erme C., Paglia C., Giner Cordero E. (eds.) Proceedings of the RILEM Spring Convention and Conference 2025, pp. 47–56. Springer Nature Switzerland, Cham (2026)
8. Orlowsky J., Beßling M., Kryzhanovskyi V.: Prospects for the use of textile-reinforced concrete in buildings and structures maintenance. Buildings 13(1), 189 (2023).
9. Azzam A., Richter M.: Investigation of stress transfer behavior in textile reinforced concrete with application to reinforcement overlapping and development lengths. In: 6th Colloquium on Textile Reinforced Structures (CTRS6), pp. 103-116. TU Dresden, Germany (2011).
10. Yu J., Chen Y., Leung C.K.: Mechanical performance of Strain-Hardening Cementitious Composites (SHCC) with hybrid polyvinyl alcohol and steel fibers. Compos. Struct. 226, 111198 (2019).

Author Contribution Statement

- *Conceptualization:* BE Kelek, ES Kocaman
- *Methodology:* BE Kelek, ES Kocaman
- *Investigation:* BE Kelek, ES Kocaman
- *Writing – Original Draft:* BE Kelek
- *Writing – Review & Editing:* ES Kocaman

Publication Note

This paper was peer-reviewed, accepted for presentation, and included in the proceedings of the ACE2026 – International Conference on Advances in Civil Engineering, held on 12–14 October 2026 in Trabzon, Türkiye.

This paper may be cited as follows:

Kelek B.E., Kocaman ES., "Flexural Performance of Overlap Configurations for Textile-Reinforced Cementitious Composites," in Proceedings of the ACE2026 – International Conference on Advances in Civil Engineering, Trabzon, Türkiye, 12–14 October 2026.

Clinker Reduction in Portland Limestone Cement through the Incorporation of Mechanochemically Activated Natural Pozzolans

Amal Chakir[1], Vahiddin Alperen Baki[2], Memduh Nas[3], Yilmaz Yilmaz[4], Safa Nayır[5], Muhammad Ahmad[6], Fatma Ayvaz[7], Murathan Bulut[8], Ayten Çaputcu[9]

[1]*0009-0005-2067-4090, Karadeniz Technical University, Civil Engineering Department, Trabzon, Türkiye, achakir168@gmail.com*

[2] *0009-0007-8905-1013, Karadeniz Technical University, Civil Engineering Department, Trabzon, Türkiye, valperenbaki@ktu.edu.tr*

[3] *0000-0001-6978-2811, Karadeniz Technical University, Civil Engineering Department, Trabzon, Türkiye, memduhnas@ktu.edu.tr*

[4] *0009-0008-2871-6357, Karadeniz Technical University, Civil Engineering Department, Trabzon, Türkiye, yilmazyilmaz@ktu.edu.tr*

[5] *0000-0001-7876-8763, Karadeniz Technical University, Civil Engineering Department, Trabzon, Türkiye, safanayir@ktu.edu.tr*

[6] *0009-0004-9302-6804, Karadeniz Technical University, Civil Engineering Department, Trabzon, Türkiye, 449923@ogr.ktu.edu.tr*

[7] *0009-0006-0746-2031, Karadeniz Technical University, Civil Engineering Department, Trabzon, Türkiye, 450915@ogr.ktu.edu.tr*

[8]*Karadeniz Technical University, Civil Engineering Department, Trabzon, Türkiye, 450880@ogr.ktu.edu.tr*

[9]*Cimsa Cimento Sanayi A. S., Toroslar Mah. Tekke Cad., Yenitaskent, Mersin 33013, Turkey a.caputcu@cimsa.com.tr*

Abstract. This study demonstrates that mechanochemical activation (MCA) can be used as an effective methodology to significantly enhances the reactivity of pyrophyllite, enabling its potential use as a supplementary cementitious material (SCM) for partial replacement of CEM II cement and the development of clinker-reduced binders. The R^3 bound water content increased from 1.22% to 10.05% (approximately 724%), after intense milling, corroborating with delamination and amorphilisation observed in the XRD results. These changes also contributed to improved

mechanical performance, increasing compressive strength from 32.92 MPa for untreated pyrophyllite to 48.79 MPa for activated pyrophyllite, exceeding the CEM II-based PCC reference strength of 41.83 MPa by approximately 16.6%. Overall, MCA enhances pyrophyllite reactivity, which is not possible by using traditional methods, and its potential to replace PCC.

Keywords: SCMs; Pyrophyllite; MCA; R^3 test; Natural pozzolans.

1. Introduction

Replacing a portion of Portland cement with supplementary cementitious materials (SCMs) is one of the most effective approaches to reducing the carbon footprint of the cement and concrete industries [1]. The cement industry is globally responsible for approximately 8–9% of anthropogenic CO_2 emissions [2]. The use of supplementary cementitious materials such as fly ash (FA), ground granulated blast-furnace slag (GGBFS), silica fume, and limestone as partial replacements for cement has long been one of the key strategies for reducing the environmental impacts of the cement and concrete industries [1].

However, the current production of FA and GGBFS is insufficient to meet the increasing global demand for cement. At the same time, the availability of these materials is expected to decline further with the phase-out of coal use and the transition of the steel industry toward more sustainable practices [3], [4]. Therefore, it is necessary to expand the boundaries of this field by developing new SCMs from sustainable sources [5]. Due to their potential to significantly reduce energy consumption and CO_2 emissions, natural pozzolans have increasingly been used in recent years as alternative supplementary materials to Portland cement in the production of Portland pozzolanic cement and concrete [6].

However, one of the major challenges limiting the widespread use of these materials is the low pozzolanic reactivity of natural pozzolans. Previous studies clearly demonstrate this limitation. Replacing 20% of cement with untreated natural pozzolan reduces the 28-day compressive strength by approximately 6.9%, from 68.5 MPa to 63.8 MPa [7]. At higher replacement levels, such as 36% and 56%, even greater reductions in 90-day compressive strength of 18.3% and 42.5%, respectively, have been reported [8]. Furthermore, the 28-day Pozzolanic Activity Index (PAI) values of natural pozzolans such as trachyte and rhyolite are only 89% and 87%, respectively. Rhyolite, however, fails to meet the accepted threshold of 80% for the 90-day PAI [9].

The primary reason for this low reactivity is the mineralogical structure of these materials. Although these materials contain high amounts of silicon dioxide (SiO_2) and aluminium oxide (Al_2O_3), these oxides are predominantly present within stable crystalline structures [9], [10]. Consequently, they react slowly with calcium hydroxide and cannot generate sufficient amounts of strength-contributing C-S-H phases. Furthermore, conventional fine grinding is often insufficient to significantly enhance their reactivity [10]. A large proportion of natural pozzolans do not exhibit a dehydroxylation peak because their crystal structures contain neither hydroxyl groups nor chemically bound water. Therefore, conventional thermal activation methods based on dehydroxylation are ineffective in enhancing the reactivity of these materials

[11]. Recent studies have demonstrated that mechanochemical activation (MCA) has significant potential.

In one study, pumice, perlite, and raw meal were subjected to mechanochemical activation. Following activation, the chemically bound water content and strength activity index were found to be 7.5% and 106% for pumice, 7.07% and 98% for perlite, and 3.40% and 71.05% for raw meal, respectively [12]. Furthermore, pyrophyllite has attracted interest because of its high SiO_2 and Al_2O_3 contents and its potential as a supplementary cementitious material. However, the ordered crystal structure of untreated pyrophyllite can limit the dissolution and the pozzolanic contribution of pyrophyllite. Erdemoğlu et al. [13] showed that mechanical activation dramatically alters pyrophyllite structure and enhances its chemical response. Terzić et al. [14] also showed that the mechanochemical activation state of pyrophyllite is strongly determined by the milling conditions, and that selection of the appropriate activation regime is important. These results demonstrate that mechanochemical activation can significantly enhance the pozzolanic reactivity of these materials. These results demonstrate that mechanochemical activation can significantly enhance the pozzolanic reactivity of these materials. In the MCA process, high-energy milling disrupts crystalline structures, induces structural disorder, and increases the dissolution of reactive Si and Al species.

Although MCA has shown promising results for clay minerals, its systematic application to a pyrophyllite remains insufficiently investigated. In addition, Limestone Calcined Clay Cement (LC^3) systems have successfully reduced clinker content through the use of highly reactive calcined clays. Nevertheless, CEM II–SCM (supplementary cementitious material) systems with compositions similar to Limestone Calcined Clay Cement (LC3) binders have been investigated only to a limited extent in Türkiye, despite the increasing adoption of CEM II cements as part of decarbonisation strategies in the cement and concrete sector and the widespread availability of locally sourced supplementary cementitious materials (SCMs).

The use of commercially available CEM II cements in combination with locally sourced SCMs offers the potential to achieve clinker replacement levels comparable to those of LC3 systems while maintaining similar mechanical and durability performance. Accordingly, the primary objective of this study is to investigate the feasibility of developing LC3-like low-clinker binder systems using commercially available CEM II cements and locally sourced SCMs, thereby providing a practical, scalable, and readily implementable solution for the Turkish cement industry.

2. Materials and Methods

This study systematically assessed the effect of mechanochemical activation (MCA) on the pozzolanic reactivity of pyrophyllite and investigated the changes induced in its crystal structure. First, the pozzolanic reactivity of untreated and MCA-treated pyrophyllite was evaluated using the R³ bound-water test to identify the most effective activation condition. The structural and chemical changes induced by MCA were subsequently investigated using X-ray diffraction (XRD), and their relationship with the bound water test results was assessed. Finally, the pyrophyllite exhibiting the highest bound-water content was evaluated at a 20% cement replacement level through compressive strength testing.

2.1 Materials

The pyrophyllite used in this study were collected as a powder shape from Cimsa Cement, in Turkey. CEM II 42.5 R type Portland composite cement (PCC), containing 8 wt.% pumice, 5 wt.% gypsum, 4 wt.% limestone and 4 wt.% fly ash, from Cimsa Cement was used for preparing the blended cement pastes and mortars. The chemical composition of the raw materials was determined via X-ray fluorescence analysis using the fused beads method (Figure 1). The loss on ignition (LOI) was evaluated by heating for 2 h at 1050 °C.

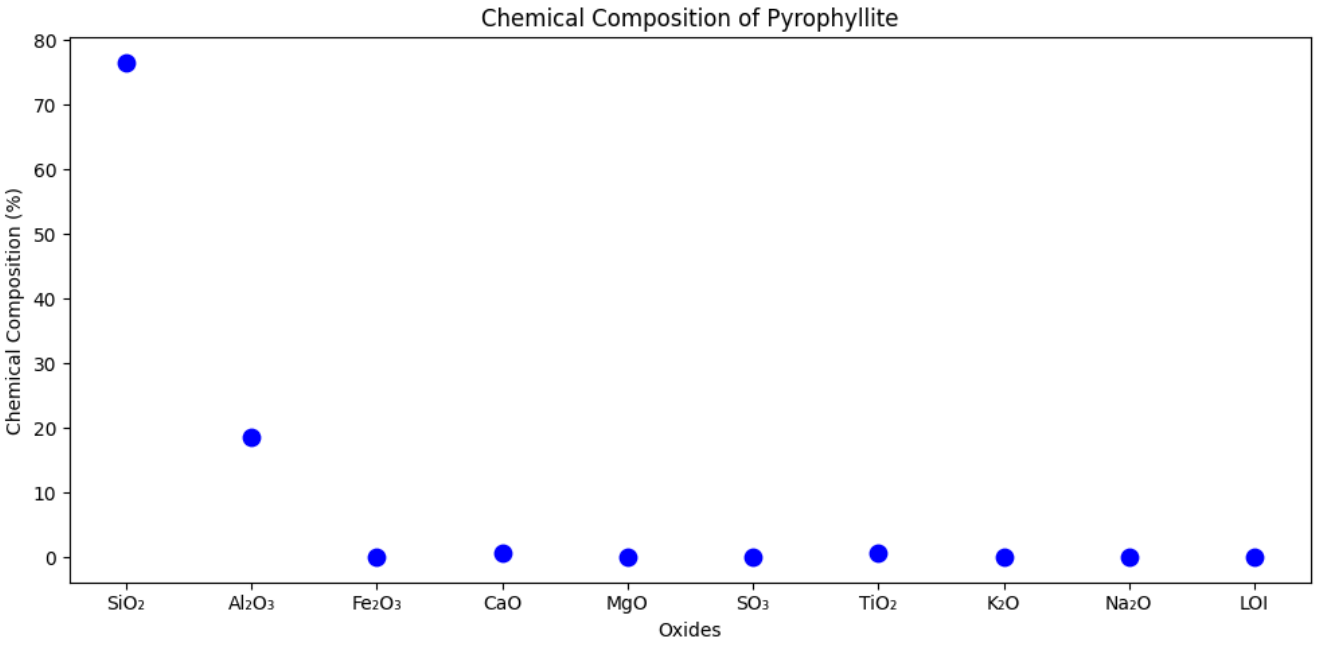


Figure 1. Chemical composition of PCC and natural pyrophyllite determined by XRF (wt.%).

Calcium hydroxide [$Ca(OH)_2$], calcium carbonate ($CaCO_3$), potassium hydroxide (KOH), and potassium sulfate (K_2SO_4) from Sigma Aldrich were used for the R³ reactivity test and standardized sand was used for mortar preparation.

2.2. MCA parameters

The activated samples were produced under different combinations of ball-to-powder ratio (BPR), rotational speed, and milling time in order to evaluate the influence of activation conditions on pyrophyllite reactivity. The activation conditions are expressed as (5–10–20)–(300–400–500)–(20–40–60), where the first number represents the ball-to-powder charge ratio, the second stands for the milling speed (rpm), and the third represents the milling time (min), as shown in Table 1.

Table 1. R³ bound-water content of untreated and mechanochemically activated pyrophyllite samples.

Sample	Activation condition
P1	Untreated
P2	10-300-20
P3	10-400-20
P4	20-500-60
P5	05-500-60
P6	10-500-60
P7	10-500-40
P8	10-500-20

2.3 R³ Bound Water Test

The pozzolanic reactivity of untreated and mechanochemically activated pyrophyllite was evaluated using the Rapid, Relevant and Reliable (R^3) bound-water test. Pyrophyllite was subjected to seven combinations of ball-to-powder ratio (BPR), rotational speed, and milling time. Untreated pyrophyllite (P8/SAF) was used as the reference. For the R^3 mixtures, pyrophyllite was combined with calcium hydroxide [$Ca(OH)_2$] and calcium carbonate ($CaCO_3$) using an SCM:$Ca(OH)_2$ mass ratio of 1:3 and an SCM:$CaCO_3$ ratio of 2:1. The alkaline solution was prepared using 4 g of KOH and 20 g of K_2SO_4 per litre of water. The prepared mixtures were cured at 40 °C, after which chemically bound water was determined. All activation conditions were evaluated to identify the treatment providing the highest pozzolanic reactivity.

2.4 X-ray Diffraction (XRD) Analysis

The crystal structures of the untreated and mechanochemically activated pyrophyllite were determined by the Rigaku-SmartLab X-ray diffractometer using Cu-Kα radiation with a wavelength of 1.5408 Å. The tests were conducted with a step size of 0.02° and a counting time of 3 s/step, from 5° to`` 60° (2θ).

2.5 Mortar Preparation for Compressive Strength Test

Blended cement pastes (20% pyrophyllite + 80%PCC) and mortars were prepared using differently mechanochemically activated and untreated pyrophyllite. Reference samples were prepared with 100 % PCC. The pastes were prepared using a high shear overhead mixer. The paste samples were cured in sealed plastic containers at room temperature (20 ± 2 °C) for 28 days. The mortar samples were produced using BS EN 196-1 standard [15] with a binder to sand ratio of 1:3, and cast using 40 mm × 40 mm × 40 mm moulds.



Figure 2. Mortar specimens prepared for compressive-strength testing.

Following curing, the mortar specimens were subjected to compressive-strength testing to evaluate the mechanical performance of untreated and mechanochemically activated pyrophyllite [12]. The compressive strength of the mortar cubes was evaluated at 28 days of curing.

3. Results and Discussion

3.1 R³ test

R³ bound-water content of MCA pyrophyllite and its untreated counterpart are summarized in Figure 3. Results demonstrate that mechanochemical activation leads to significant increase on the R³ bound-water content of pyrophyllite. The untreated reference sample (P1) showed lowest bound-water content with 1.22%, assigned the lowest pozzolanic reactivity. The bound-water content increased to 3.27% for P2 and 4.85% for P3, and for P8 it reached 3.50% for different milling speed, which can be related with increasing milling speed results in increasing activation efficiency due to further delamination and amorphization. As for charging ratio, highest bound water was observed for P6, which was 10.05%, which also corroborated with amorphization as shown in Figure 3. As for milling time, extended milling leads to improve bound water content, which can be related with further amorphization.

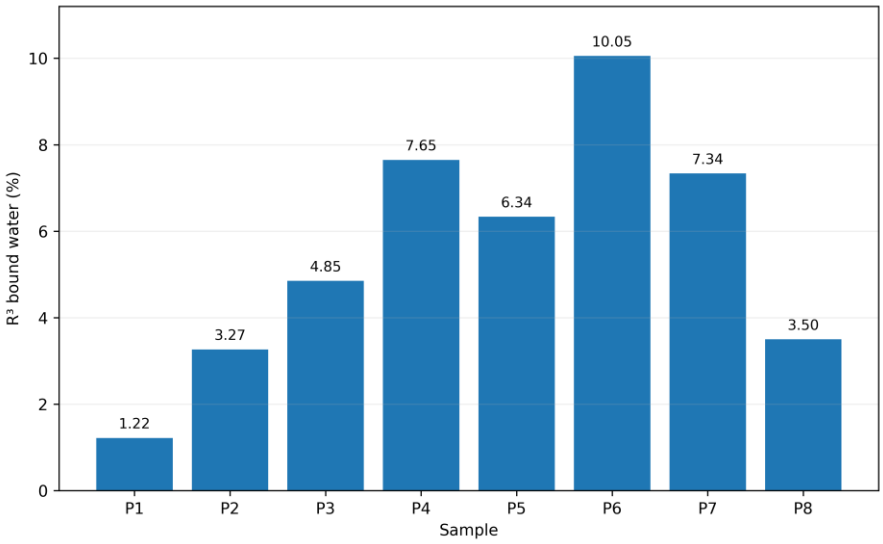


Figure 3. R³ bound-water content of untreated and mechanochemically activated pyrophyllite samples.

These findings is also corroborated with reported literature, where MCA enhances pozzolanic reactivity through particle refinement and progressive disruption of the original mineral structure, increasing structural disorder and availability of reactive sites. Tole et al. [16] also showed that intense mechanochemical activation of natural clay minerals enhances pozzolanic activity through structural disruption and increased amorphization. Another study conducted by Baki et al. [10] showed that high-energy milling can significantly improve the reactivity of aluminosilicate minerals through particle-size reduction and physicochemical modification. Particularly for pyrophyllite, Erdemoğlu et al. [13] reported that mechanical activation changes the mineral structure and increases its chemical responsiveness. The non-monotonic R³ response that we have observed here shows that the effect of activation is more about the milling intensity, structural disorder, and particle agglomeration than about the increase in treatment severity [17].

3.2 XRD

The mineralogy and gel structure of un-treated and mechanochemically activated pyrophyllite minerals were characterized using the XRD, as shown in 3, where XRD pattern of un-treated pyrophyllite indicates the presence of mainly pyrophyllite (Powder diffraction file, PDF# 79-1570) and a small amount of diaspore (PDF# 26-0911) and quartz (PDF# 79-1910 and 79-1911). The results show that the mechanochemical process was able to effectively delaminate and amorphized the crystal structure of the un-treated pyrophyllite after 60 minutes of activation, as indicated by the significant reduction of the pyrophyllite. Similar crystal structure evolution was also observed in literature for pyrophyllite minerals. The trace dickite and Kyanite phases were also completely disappeared after intense milling but the quartz phase still remained after mechanochemical activation, consistent with reported literature.

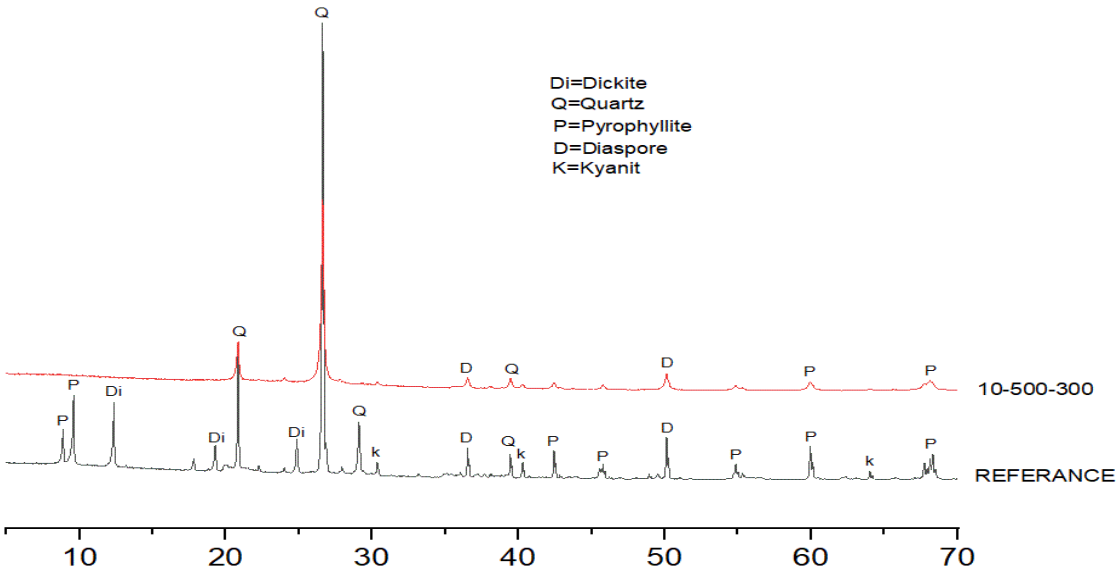


Figure 4. XRD patterns of untreated and mechanochemically activated pyrophyllite samples over the 4-80° 2θ range.

The observed structural modifications are consistent with the increase in R^3 reactivity and with the mechanical response of the selected activated material. Sengul et al. [18] showed that mechanical activation of pyrophyllite produces substantial structural modification and facilitates subsequent chemical attack. Ababneh et al. [19] showed that mechanochemical treatment changes the structural characteristics of pyrophyllite, confirming the sensitivity of this mineral to intensive milling. Tole et al. [20] showed for natural clay minerals that the reduction of crystalline order and the development of structural disorder are associated with enhanced pozzolanic activity. Baki et al. [11] likewise showed that mechanochemical activation can increase the reactivity of aluminosilicate minerals through combined structural and surface modifications. In the present study, the simultaneous XRD modification and increase in R^3 bound water for P6 support the interpretation that milling-induced structural disorder contributed to the enhanced reactivity of activated pyrophyllite [21].

3.3 Compressive strength

To evaluate the effect of mechanochemical activation on pyrophyllite reactivity, compressive strength tests were conducted using the reference Portland cement paste (PCC), untreated pyrophyllite, and mechanochemically activated (MCA) pyrophyllite exhibiting the highest bound water content. The results are summarized in Table 2 and compared graphically in Figure 5.

Table 2. Compressive strength of reference and pyrophyllite-containing mortar mixtures.

Binder system	Strength (MPa)
100% PCC	41,8
20% untreated pyrophyllite	32.92
20% MCA pyrophyllite (selected optimum)	48.79

The mechanochemically activated pyrophyllite system achieved a compressive strength of 48.79 MPa, representing a 48.2% increase compared with untreated pyrophyllite (32.92 MPa). This improvement is attributed to enhanced pozzolanic reactivity following intensive milling. The strength development is consistent with the increased R^3 reactivity and the greater amorphization observed by XRD, suggesting that mechanochemical activation increased the availability of reactive phases and enhanced their contribution to strength development [22].

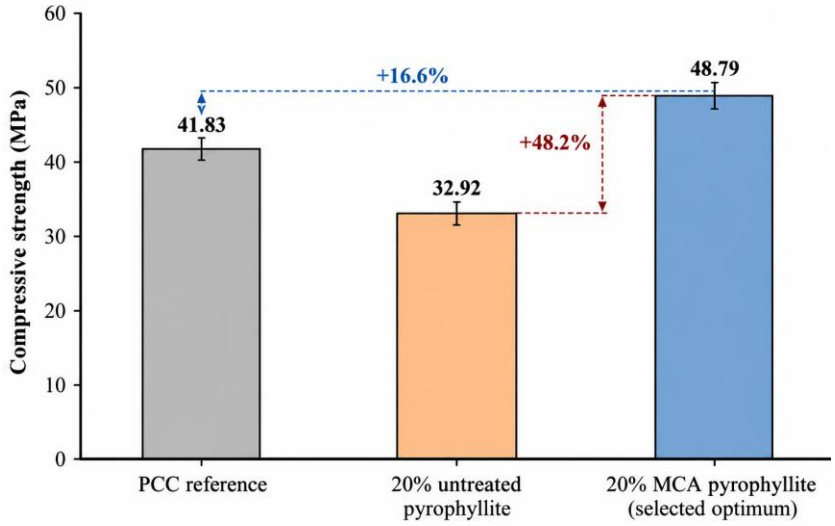


Figure 5. Compressive strength of untreated-pyrophyllite mortar and selected mechanochemically activated pyrophyllite mortar.

Similar finding were also observed in literature, where Terzić et al. [14] showed that the degree of mechanochemical activation of pyrophyllite is closely related to processing conditions and can be used to predict its suitability for cement-binder applications. Amroun et al. [23] showed that mechanochemically activated SCMs can provide improved mechanical performance in cement pastes and mortars when activation sufficiently increases their reactivity. Xu et al. [24] also showed that mechanical activation modifies the pozzolanic response of SCM systems and can enhance their

contribution to strength development. In the present study, the increase in R^3 bound water from 1.22% to 10.05% was accompanied by an increase in compressive strength from 32.92 to 48.79 MPa. The XRD changes observed for P6 provide structural evidence supporting this behavior. These complementary results indicate that the improved strength is associated with milling-induced structural modification, enhanced chemical reactivity and a greater contribution of activated pyrophyllite to hydration and matrix densification [12].

4. Conclusions

This study demonstrates that mechanochemical activation (MCA) can be used as a effective methodology to significantly enhances the reactivity of pyrophyllite, enabling its potential use as a supplementary cementitious material (SCM) for partial replacement of CEM II cement and the development of clinker-reduced binders. The R^3 bound water content increased from 1.22% to 10.05% (approximately 724%), after intense milling, corroborating with delamination and amorphilisation observed in the XRD results. These changes also contributed to improved mechanical performance, increasing compressive strength from 32.92 MPa for untreated pyrophyllite to 48.79 MPa for activated pyrophyllite, exceeding the CEM II-based PCC reference strength of 41.83 MPa by approximately 16.6%. Overall, MCA enhances pyrophyllite reactivity, which is not possible by using traditional methods, and its potential to replace PCC.

References

[1] G. Habert *vd.*, "Environmental impacts and decarbonization strategies in the cement and concrete industries", *Nat Rev Earth Environ*, c. 1, sy. 11, ss. 559-573, Kas. 2020, doi: 10.1038/s43017-020-0093-3.

[2] P. J. M. Monteiro, S. A. Miller, ve A. Horvath, "Towards sustainable concrete", *Nature Mater*, c. 16, sy. 7, ss. 698-699, Tem. 2017, doi: 10.1038/nmat4930.

[3] D. Londono-Zuluaga *vd.*, "Report of RILEM TC 267-TRM phase 3: validation of the R3 reactivity test across a wide range of materials", *Mater Struct*, c. 55, sy. 5, s. 142, May. 2022, doi: 10.1617/s11527-022-01947-3.

[4] K. L. Scrivener, V. M. John, ve E. M. Gartner, "Eco-efficient cements: Potential economically viable solutions for a low-CO2 cement-based materials industry", *Cement and Concrete Research*, c. 114, ss. 2-26, Ara. 2018, doi: 10.1016/j.cemconres.2018.03.015.

[5] V. A. Baki, X. Ke, A. Heath, J. Calabria-Holley, C. Terzi, ve M. Sirin, "The impact of mechanochemical activation on the physicochemical properties and pozzolanic reactivity of kaolinite, muscovite and montmorillonite", *Cement and Concrete Research*, c. 162, s. 106962, Ara. 2022, doi: 10.1016/j.cemconres.2022.106962.

[6] M. S. Felix, R. U. H. Zamora, M. A. A. Rubio, C. C. Gallardo, ve J. M. H. Ramirez, "Sustainable Low-Carbon Cement: Performance Enhancement with Calcined Natural Pozzolans Through Compressive Strength, Porosity, and Microstructural Analysis", *Materials*, c. 18, sy. 8, s. 1776, Oca. 2025, doi: 10.3390/ma18081776.

[7] Y. Derrouiche, D. Achoura, J. Saliba, ve F. Cassagnabère, "Natural pozzolan as a sustainable cement replacement in high-performance concrete: Effects on mechanical properties, durability, and microstructural development", *Scientific African*, c. 27, s. e02574, Mar. 2025, doi: 10.1016/j.sciaf.2025.e02574.

[8] H. Affan, L. Fehr, G. Al-Massri, F. Alassaad, A. Yaghi, ve H. Ghanem, "Strength, Transport Properties, and Life Cycle Impacts of Mortar Containing German Natural Pozzolan.", *Infrastructures*, c. 11, sy. 2, s. 67, Şub. 2026, doi: 10.3390/infrastructures11020067.

[9] V. Baki, S. Nayır, Ş. Erdoğdu, ve I. Ustabaş, "Determination of the Pozzolanic Activities of Trachyte and Rhyolite and Comparison of the Test Methods Implemented", *International Journal of Civil Engineering*, c. 18, ss. 1053-1066, 2020, doi: 10.1007/s40999-020-00516-5.

[10] V. Baki, S. Nay, Ş. Erdoğdu, ve I. Ustabaş, "Pozzolanic properties of trachyte and rhyolite andtheir effects on alkali-silica reaction", c. 11, 2021, doi: 10.12989/acc.2021.11.4.299.

[11] V. A. Baki, X. Ke, A. Heath, J. Calabria-Holley, ve C. Terzi, "Improving the pozzolanic reactivity of clay, marl and obsidian through mechanochemical or thermal activation", *Mater Struct*, c. 57, sy. 1, s. 9, Ara. 2023, doi: 10.1617/s11527-023-02280-z.
[12] S. Nayır, "Improving Reactivity of Pumice, Perlite and Farin by Mechanochemical Activation", *Materials*, c. 19, sy. 9, s. 1702, Oca. 2026, doi: 10.3390/ma19091702.
[13] M. Erdemoğlu, M. Birinci, T. Uysal, E. Porgalı Tüzer, ve T. S. Barry, "Mechanical activation of pyrophyllite ore for aluminum extraction by acidic leaching", *J Mater Sci*, c. 53, sy. 19, ss. 13801-13812, Eki. 2018, doi: 10.1007/s10853-018-2606-8.
[14] A. Terzić *vd.*, "Prediction model based on artificial neural network for pyrophyllite mechano-chemical activation as an integral step in production of cement binders", *Construction and Building Materials*, c. 258, s. 119721, Eki. 2020, doi: 10.1016/j.conbuildmat.2020.119721.
[15] I. Galobardes, R. P. Salvador, S. H. P. Cavalaro, A. Figueiredo, ve C. I. Goodier, "Adaptation of the standard EN 196-1 for mortar with accelerator", *Construction and Building Materials*, c. 127, ss. 125-136, Kas. 2016, doi: 10.1016/j.conbuildmat.2016.09.147.
[16] I. Tole, A. Kothari, M. Rajczakowska, ve A. Cwirzen, "Mechanochemical activation of recycled concrete fines to produce supplementary cementitious materials", *Construction and Building Materials*, c. 520, s. 146017, Nis. 2026, doi: 10.1016/j.conbuildmat.2026.146017.
[17] P. de Azevedo Basto, V. Estolano de Lima, ve A. de Melo Neto, "Capability of R3 test to evaluate pozzolanicity of ground raw and calcined sugarcane bagasse ashes", *Materials Today: Proceedings*, Nis. 2023, doi: 10.1016/j.matpr.2023.04.048.
[18] O. Sengul, S. Azizi, F. Karaosmanoglu, ve M. A. Tasdemir, "Effect of expanded perlite on the mechanical properties and thermal conductivity of lightweight concrete", *Energy and Buildings*, c. 43, sy. 2, ss. 671-676, Şub. 2011, doi: 10.1016/j.enbuild.2010.11.008.
[19] A. N. Ababneh, E. H. Al-Thiab, ve B. H. Al-shorman, "Early strength development in cement mortars containing high proportions of Jordanian natural Pozzolan", *Results in Engineering*, c. 27, s. 105868, Eyl. 2025, doi: 10.1016/j.rineng.2025.105868.
[20] Y. Yan, H. Liu, W. Liu, Z. Li, Y. Zhang, ve G. Ma, "Functional concrete based on expanded perlite - A review", *Journal of Building Engineering*, c. 120, s. 115520, Şub. 2026, doi: 10.1016/j.jobe.2026.115520.
[21] D. Meng, J. N. Yankwa Djobo, I. P. Segura, R. C. Kaze, C. Kuenzel, ve N. Ranjbar, "Clay activation: A review", *Materials Today*, c. 92, ss. 519-551, Oca. 2026, doi: 10.1016/j.mattod.2025.11.024.
[22] M. Frías, A. Alujas, A. Moreno-Reyes, J. A. Ibañez, M. V. Paredes, ve I. Vegas, "Advances in understanding R3 chemical reactivity in various traditional and emerging pozzolans: Chemical, mineralogical and calorimetric dimensions", *Construction and Building Materials*, c. 457, s. 139474, Ara. 2024, doi: 10.1016/j.conbuildmat.2024.139474.
[23] S. Amroun, A. Iyer, ve P. Suraneni, "Performance of mechanochemically activated supplementary cementitious materials in cement pastes and mortars", *Mater Struct*, c. 59, sy. 7, s. 326, Ağu. 2026, doi: 10.1617/s11527-026-03220-3.
[24] X. Xu, F. Wang, X. Gu, ve Y. Zhao, "Mechanism of Different Mechanically Activated Procedures on the Pozzolanic Reactivity of Binary Supplementary Cementitious Materials", *Minerals*, c. 12, sy. 11, s. 1365, Kas. 2022, doi: 10.3390/min12111365.

List of Abbreviations

Abbreviation	**Definition**
SCM	Supplementary Cementitious Material
MCA	Mechanochemical Activation
PCC	Portland Composite Cement
R^3	Rapid, Relevant and Reliable reactivity test
XRD	X-ray Diffraction
BPR	Ball-to-Powder Ratio

SAF	Untreated/reference pyrophyllite
KOH	Potassium Hydroxide
K_2SO_4	Potassium Sulfate
$Ca(OH)_2$	Calcium Hydroxide
$CaCO_3$	Calcium Carbonate
MPa	Megapascal

Publication Note

This paper was peer-reviewed, accepted for presentation, and included in the proceedings of the ACE2026 – International Conference on Advances in Civil Engineering, held on 12–14 October 2026 in Trabzon, Türkiye.

This paper may be cited as follows:

Chakir, A., Baki, V. A., Nas, M., Yılmaz, Y., Nayır, S., Ahmad, M., Ayvaz, F., Bulut, M., Çaputcu, A., "Clinker Reduction in Portland Limestone Cement through the Incorporation of Mechanochemically Activated Natural Pozzolans," in Proceedings of the ACE2026 – International Conference on Advances in Civil Engineering, Trabzon, Türkiye, 12–14 October 2026.

Dry Ice-Driven Mechanochemical Carbonation for Enhanced CO_2 Capture and Reactivity of Bottom Ash

Muhammad Ahmad[1],Vahiddin Alperen Baki[2], Memduh Nas[3], Yilmaz Yilmaz[4], Safa Nayır[5], Amal Chakir[6], Fatma Ayvaz[7], Murathan Bulut[8], Ayten Çaputcu[9]

[1] 0009-0004-9302-6804, Karadeniz Technical University, Civil Engineering Department, Trabzon, Türkiye, 449923@ogr.ktu.edu.tr

[2] 0009-0007-8905-1013, Karadeniz Technical University, Civil Engineering Department, Trabzon, Türkiye, valperenbaki@ktu.edu.tr

[3] 0000-0001-6978-2811, Karadeniz Technical University, Civil Engineering Department, Trabzon, Türkiye, memduhnas@ktu.edu.tr

[4] 0009-0008-2871-6357, Karadeniz Technical University, Civil Engineering Department, Trabzon, Türkiye, yilmazyilmaz@ktu.edu.tr

[5] 0000-0001-7876-8763, Karadeniz Technical University, Civil Engineering Department, Trabzon, Türkiye, safanayir@ktu.edu.tr

[6]0009-0005-2067-4090, Karadeniz Technical University, Civil Engineering Department, Trabzon, Türkiye, achakir168@gmail.com

[7] 0009-0006-0746-2031, Karadeniz Technical University, Civil Engineering Department, Trabzon, Türkiye, 450915@ogr.ktu.edu.tr

[8] Karadeniz Technical University, Civil Engineering Department, Trabzon, Türkiye, 450880@ogr.ktu.edu.tr

[9]Cimsa Cimento Sanayi A. S., Toroslar Mah. Tekke Cad., Yenitaskent, Mersin 33013, Turkey a.caputcu@cimsa.com.tr

Abstract. Due to the worldwide expansion of Waste-to-energy plants, the management of municipal solid waste (MSW) incineration bottom ash (IBA) presents a significant global environmental challenge. IBA, due to its low pozzolanic reactivity, high porosity, the potential leaching of heavy metals, and the presence of metallic aluminum, limits its use as a construction material. Current stabilization methods, including thermal treatment, stabilization/solidification (S/S), chemical treatment, and conventional carbonation, are respectively energy-intensive, volume-increasing, dangerous to handle, time-consuming, and do little to enhance the material's pozzolanic activity. In this study, innovative methods such as Mechanochemical Activation (MCA) and Mechanochemical Carbonation (MCC) were designed to transform IBA into a suitable replacement binder for cement. Initially, MCA was utilized to enhance the pozzolanic reactivity of the IBA structure, increase its specific surface area, and form unique physicochemical properties. Secondly, Mechanochemical Carbonation was also performed to maximize CO_2 sequestration and solidify the structure, encapsulating both heavy metal ions and metallic aluminum. This research thoroughly examines the effects of MCA and MCC on IBA by evaluating chemical and bond structure changes using XRD and TGA analysis. Moreover, the influence of MCC and MCA on pozzolanic

characteristics will be investigated using the R3 bound water test. Based on the R3 bound water test, activated bottom ash with the highest bound water will be used to determine the compressive strength values of mortar by replacing 30% of the cement with treated IBA.

Keywords: MSW incineration bottom ash, Mechanochemical activation, Mechanochemical carbonation, R³ test

1 Introduction

In recent years, Municipal Solid Waste (MSW) has drastically grown due to the worldwide population rise and urbanization. It is now created at a rate of 2 billion tonnes per year, with projections estimating that this value would rise to 3.40 billion tonnes by 2050 (Kaza, Yao, Bhada-Tata, & Van Woerden, 2018; Valavanidis, 2023). It is estimated that 33% of MSW is not being treated in an ecologically acceptable way, frequently ending up in open landfills or being directly burnt, resulting in air, water, and land pollution and considerably contributing to greenhouse gas emissions. (Koliyabandara et al., 2024; Sharma & Jain, 2020). Traditional landfilling is becoming insufficient to handle the growing waste volume, and it also carries significant environmental risks such as methane emissions and leachate formation. (Nanda & Berruti, 2021). From an economic perspective, landfill costs are steadily rising, especially in European countries. In the United Kingdom, the standard landfill tax will increase to £130.75 per ton by April 2026, making alternative waste management methods necessary. (Government, 2025 ; Wang et al., 2023).

In this regard, waste-to-energy (WtE) incineration facilities play a crucial role in sustainable waste management by burning MSW at temperatures between 700 and 1000°C, reducing waste volume by 80–95% and mass by 70–80 % (Khan et al., 2022; Xuan, Tang, & Poon, 2018). The recovered thermal energy is utilized to generate electricity from renewable resources, lessening reliance on traditional fossil fuels. (Kaur, Bharti, & Sharma, 2023; Lombardi & Castaldi, 2024).

Despite the waste-reducing benefits of WtE incineration plants, the process generates three main types of solid residues: boiler fly ash, air pollution control (APC) residues, and incineration bottom ash (IBA) (He & Kasina, 2023; Nguyen et al., 2023). Among these residues, IBA is the most abundant byproduct, accounting for roughly 80-90 percent of the total residues produced (Govindan & Kumar, 2025; Wehrung et al., 2025). Considering that about 0.2-0.3 tons of IBA is generated per ton of waste incinerated, Istanbul's facility alone produces approximately 525,000 tons of IBA annually. Therefore, the sustainability of WtE technology largely depends on the safe and efficient management of this ash.

IBA is a highly heterogeneous, porous, and granular substance mostly made up of slag, glass, ceramics, ferrous and nonferrous metals, and unburnt organic compounds (Magnuson et al., 2023). The fine IBA fraction, particularly particles below 2 mm, contains more heavy metals and metallic aluminum than the coarser fraction, limiting its direct use as a construction material. Fine IBA particles have naturally high porosity and water absorption capacity (averaging around 9.7%), requiring more water when combined with cement, affecting workability and hydration products, resulting in a slowdown of the hydration process (Lynn, Obe, & Ghataora, 2016; Tang, Xuan, Poon, & Tsang, 2019). A further disadvantage of using bottom ash is the presence of metallic aluminum (Al) in IBA, which combines with water and hydroxyl ions in cement's highly alkaline environment, releasing hydrogen gas. This reaction causes expansion, swelling, and internal cracking in the mortar or concrete during setting,

severely damaging the structural integrity of the material (Chen et al., 2024; Saffarzadeh, Arumugam, & Shimaoka, 2016).

To address these problems, researchers have developed various pre-treatment methods. Previous research has demonstrated that natural weathering over a period of 90 days reduced the leaching of hazardous heavy metals by stabilizing the IBA pH and reducing the solubility of metal hydroxides (Chimenos et al., 2000). On the contrary, washing is effective at removing soluble chlorides and sulfates but is insufficient for heavy metal immobilization and generates wastewater that requires further treatment (Sun & Yi, 2020). Thermal treatment can oxidize metallic Al and remove organic residues, but it is energy-intensive and may cause particle sintering, reducing reactivity (Chai et al., 2025).

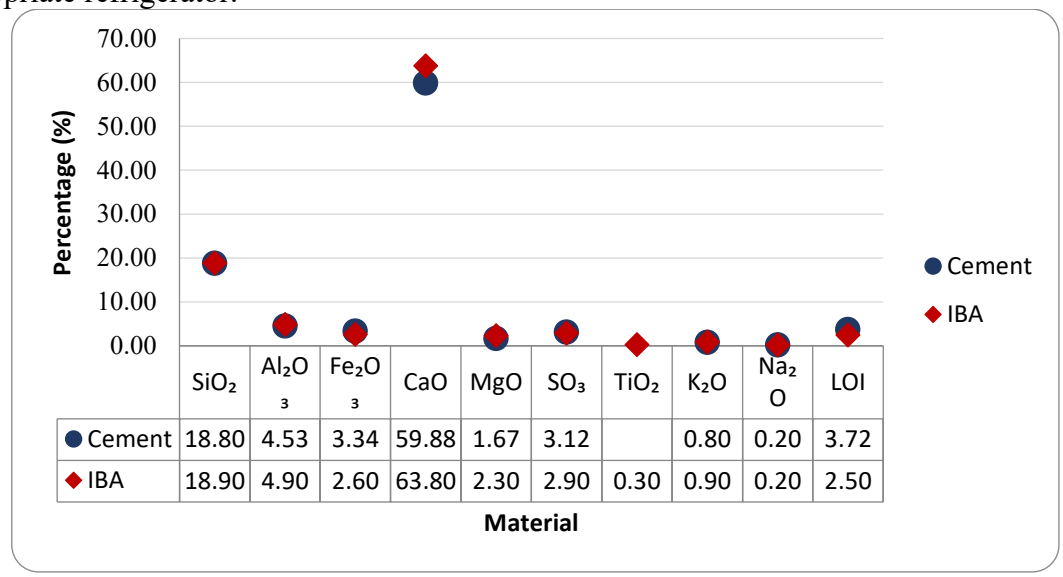
One of the most effective ways to improve the properties of IBA is using accelerated dry carbonation. In this process, IBA is exposed to CO_2 gas under controlled conditions to convert calcium oxide and hydroxide into calcium carbonate ($CaCO_3$). The carbonate minerals formed can physically encapsulate heavy metals and consume free lime, reducing expansion potential. CO_2 uptake ranging from 3% to 14% by weight through dry carbonation, with fine-grained IBA showing higher uptake capacity compared to coarse fractions, has also been reported (Sun, Xu, & Yi, 2024). Research indicates that carbonation generally reduces the leaching of Pb, Zn, and Cu, but results for Cr and Cd are contradictory; some studies report decreased leachability, while others report increases (Sun et al., 2024). Importantly, dry carbonation is primarily a stabilization technique; while it reduces environmental risk, it shows limited effects on the pozzolanic reactivity of the IBA or increases its value as a cement additive. Using treated IBA in concrete, even at replacement rates up to 20%, leads to a noticeable decrease in compressive strength, which has also been reported in a study (Low Shi Li, 2025). However, in accelerated carbonation, an increase in 10-20% compressive strength has been observed, with a 15% replacement of cement(Fan, Cai, Wang, & Liu, 2025). While accelerated carbonation has shown improvement in strength at lower replacement levels, more effective treatment methods are necessary to fully unlock the potential of IBA as a high-performance cement replacement.

On the contrary, MCA has been shown to significantly increase the pozzolanic reactivity of bottom ash (BA). It is observed that combining MCA with diethanol isopropanolamine (DEIPA) increased hydration and induced pozzolanic reactions, resulting in a strength gain of over 20% at 25% BA replacement(Kang, Yang, Kim, Lim, & Moon, 2024). The ball milling combined with $Ca(OH)_2$ treatment enhances early hydration and produces a compact matrix, outperforming milling alone, as reported in a study(Zhu et al., 2026). These findings clearly support using MCA to release the latent reactivity of bottom ash as a high-performance SCM.
While existing approaches generally focus on stabilizing the waste, there is a lack of an integrated method that simultaneously activates the material's pozzolanic reactivity to improve its performance, reliably immobilizes a broad spectrum of heavy metals, and maximizes CO_2 uptake. To address these limitations, two separate treatment methods with varying parameters are explored. The first is Mechanochemical Activation (MCA), where, with the help of a high-energy ball mill, the crystalline structure of IBA particles will be amorphized, producing unique physicochemical properties and creating new reactive surfaces. Secondly, mechanochemical carbonation (MCC) will be performed, where the material will be exposed to CO_2 under controlled moisture conditions. Unlike dry carbonation, the wet environment increases the solubility of CO_2, accelerating reaction kinetics and promoting the formation of a denser carbonate network. The calcium carbonate ($CaCO_3$) phases formed will fill the porous structure of IBA, densifying the microstructure and physically and chemically encapsulating heavy metals, ensuring environmental safety. This process also directly contributes to carbon capture and utilization (CCU) technology, transforming waste material into a carbon sink.

2 Materials and Methods

2.1 Materials

In the experimental study, IBA was collected from the Istanbul waste-to-energy facility in both fine and coarse fractions, but only the fine fraction was used for further research. The chemical composition of Fine IBA was determined using XRF and is shown in Table 1. XRF data show a significant amount of silica, calcium, alumina, and iron oxide, which is comparable to cement raw material and shows the basic chemical composition to function as a supplementary cementitious material. A cement of type CEM II/B-M (P-L) 42.5 R was used and obtained from the Çimsa Plant (Mersin, Turkey), and the XRF results are given in Table 1. For Mechanochemical Carbonation, dry ice as a source of CO2 was obtained and stored in an appropriate refrigerator.



	SiO_2	Al_2O_3	Fe_2O_3	CaO	MgO	SO_3	TiO_2	K_2O	Na_2O	LOI
Cement	18.80	4.53	3.34	59.88	1.67	3.12		0.80	0.20	3.72
IBA	18.90	4.90	2.60	63.80	2.30	2.90	0.30	0.90	0.20	2.50

Figure 1. Chemical composition of materials

2.2 Mix Design

The experimental investigation was planned to develop a total of seven MCA mixes with varying charge ratios, speeds (rpm), and times. A total of 13 MCC mixes were created with different charge ratios, speeds, times, water/material ratios, and dry ice.

2.3. Methods

The methodology for the study was separated into five major sections. The first stage was the process of treating IBA with MCA and MCC procedures in a Retsch PM 100 planetary ball mill equipped with a 125 mL jar. Also, as a reference treatment procedure, an accelerated carbonation test on untreated IBA was performed in a controlled-environment carbonation chamber. The chamber maintained a constant temperature of 23°C, relative humidity of 65%, and CO_2 concentration of 20% (v/v) throughout the process. In the second stage, an X-ray diffraction (XRD) test was performed to identify crystalline phases and assess the degree of amorphization and carbonation caused by MCA and MCC. Thermogravimetric analysis (TGA) was also performed to evaluate CO_2 uptake by measuring mass loss during carbonate decomposition. Following this, the pozzolanic reactivity of treated IBA samples was evaluated using the R^3 test (rapid, relevant, and reliable) according to ASTM C1897. Finally, utilizing the

R3 test data, the best-performing MCA-treated and MCC-treated IBA samples will be chosen to determine the compressive strength of mortar containing 30% treated IBA.

3 Results and Discussions

3.1 Pozzolanic Reactivity:

Table 1

Mix	Bound Water (%)
Untreated IBA	2.79
MCA-10-500-60	11.56
MCC-18-500-10-D5-W150	9.62

The R3 results in Table 2 indicate that untreated IBA had very low pozzolanic reactivity, with a bound water content of 2.79 percent. However, the MCC-treated IBA showed an increase in water bounding of 11.56%, indicating a significant increase in reactivity due to amorphization of the crystalline structures and physicochemical alterations. The MCC-treated IBA samples had a water content of 9.62%, which showed that the combined action of carbonate formation and particle refinement increased reactivity. The lower reactivity of MCC compared to MCA was due to the formation of a dense carbonate layer, which limits access to some reactive sites.

3.2 Compressive Strength Results:

The compressive strength of the reference mortar sample was 41.83 MPa; however, when 20% of the cement is substituted with untreated IBA, the compressive strength lowers to 23.18 MPa, representing a 44.57% reduction. While the MCC-treated IBA showed a compressive strength of 21.35 MPa, it decreased further and was 7.8% lower than the untreated IBA mix. The decrease in compressive strength values was caused by increasing the reactivity of metallic aluminum by exposing fresh surfaces, resulting in increased formation of hydrogen gas. This produces hydrogen gas, resulting in swelling and microcracking in the mix, as seen in the figure.

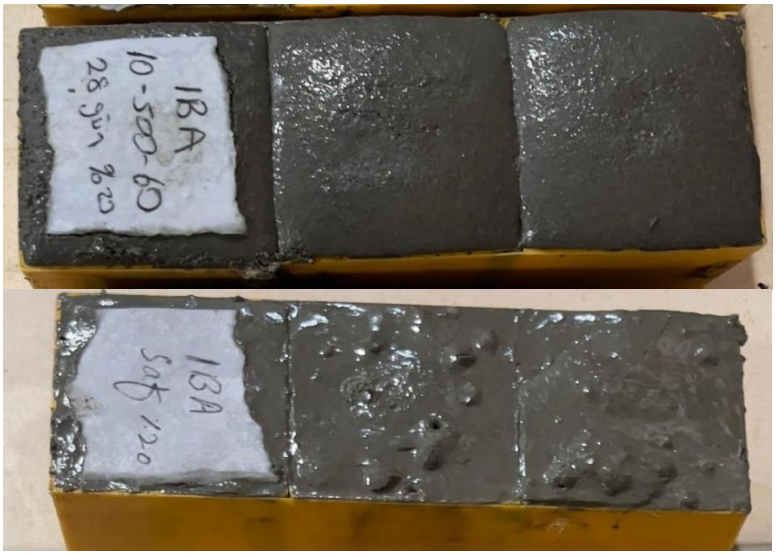


Figure 2. Untreated and MCC-treated IBA mortar Mix.

In contrast, the MCC sample demonstrated an increase in compressive strength values when compared to the mortar mix replaced with 30% IBA in cement. The MCC mix with a charge ratio of 18, milling speed of 500 rpm, dry ice as a CO2 source of 5g, and water content of 150

g for a period of 10 minutes showed a compressive strength of 22.35 MPa, which was higher than both the untreated and MCA-treated mixes. MCC not only densifies the microstructure by creating CaCO3, but it also passivates the metallic aluminum by encapsulating it in carbonate mixes. These dual advantages of the MCC mix decreased the possibility of hydrogen gas formation while also boosting the density and strength of the mix.

Table 2. Mix designs produced in the experimental study.

Mix	Compressive Strength-28 days (MPa)	Relative to Reference
Reference	41.83	-
Untreated IBA (20%)	23.18	-44.57
MCA-10-500-60	21.35	-7.8
Untreated IBA (30%)	21.48	-48.64
MCC-18-500-10-D5-W150*	22.35	+4.05 (w.r.t. untreated)

**18 (Charge ratio), 500 (Rpm), 10 (minutes), D5 (5g dry ice), W150 (150g water)*

3.3 XRD Analysis:

The mineralogical composition of IBA samples was determined using XRD, and the results are displayed in Figure X. The principal crystalline phases discovered are quartz (Q), calcite (C), albite (A), and dolomite. The XRD results of untreated IBA show portlandite (CH) and hydrocaluminate (HC), which are mainly calcium hydroxide and a layered mineral. However, considerable changes were observed in MCC-treated IBA, where the CH and HC peaks totally disappeared while the calcite peaks increased in size, due to carbonation.

$Ca(OH)2 + CO2 \rightarrow CaCO3 + H2O$ ……(1)

The physical influence of the "Mechano" part of the MCC can be seen, particularly between 20 and 35 2 theta, where the curve seems bumpier, indicating amorphous content. This is because high-energy milling broke down the perfect crystalline structures, allowing Co2 to enter and react. For example, the albite crystal peak between 26 and 28 2 theta vanishes completely. This is because albite is a soft mineral, and high-energy milling destroys the crystal structure.

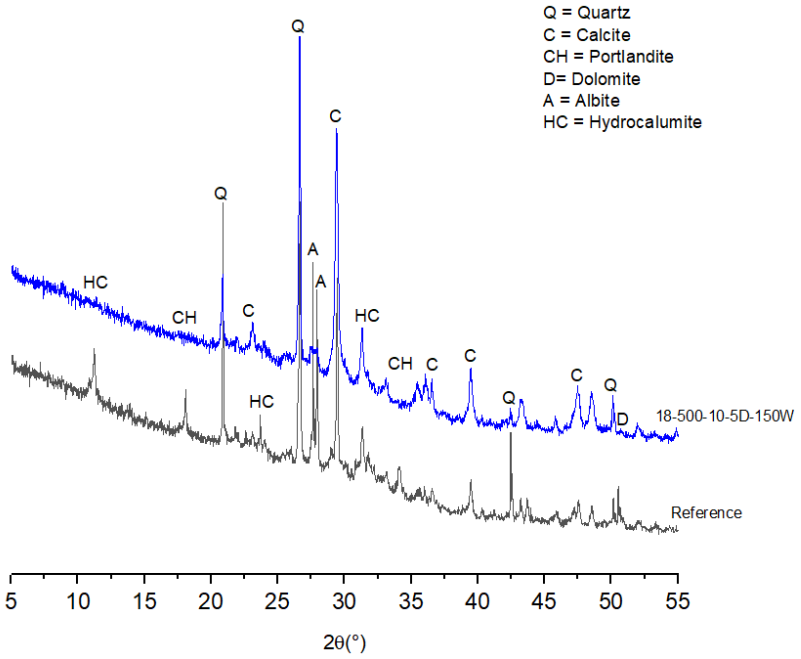


Figure 3. XRD Results of raw and MCC-treated IBA.

Figure 2 shows the XRD patterns for raw IBA and MCA-activated IBA samples of 10-500-60. Clear peaks of Quartz (Q), A (Albite), Calcite (C), and Portlandite (CH) can be observed. Significant shifts can be noticed between 15 and 35 C (°), where the amorphization increased significantly. Furthermore, peaks for portlandite and hydrocalumite completely disappear in MCA-activated samples, implying that the hydrated phases are more susceptible to MCA and are totally transformed into amorphous structures. Following this, the Quartz peak at 26.6 2θ (°) is still evident due to its great hardness and resistance to amorphization. The smaller quartz peaks and albite have either broadened or gone completely into the amorphous background, indicating a loss in crystalline structures and partial structural breakdown**.**

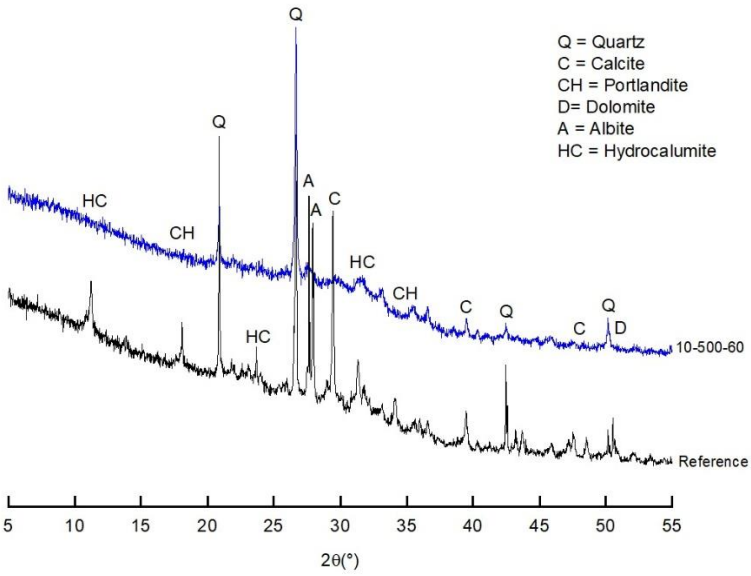


Figure 4. XRD Results of raw and MCA-treated IBA.

3.4 Thermogravimetric Analysis (TGA):

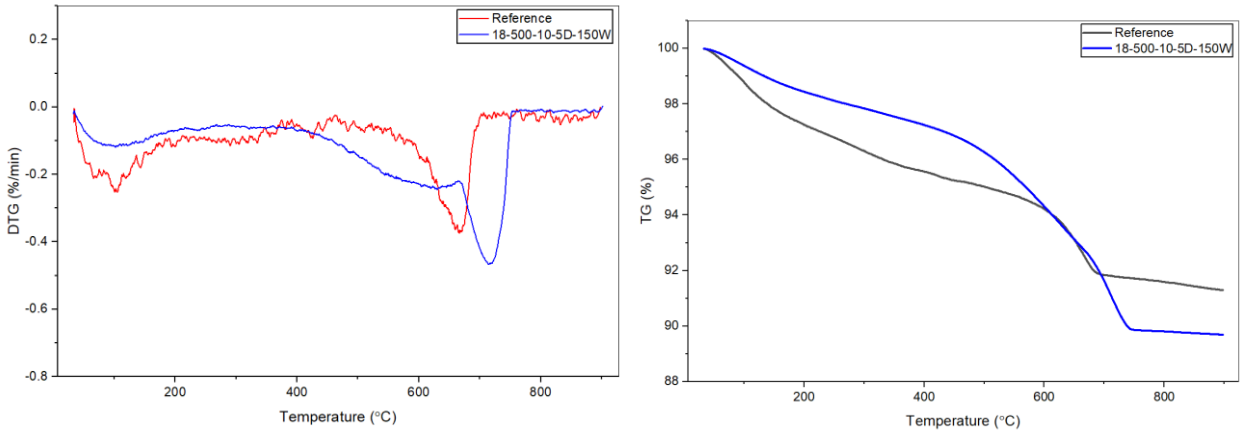


Figure 5. TGA Results of raw and MCC-treated IBA.

Figure 4 shows the thermogravimetric (TG) and derivative thermogravimetric (DTG) profiles of raw IBA and MCC-treated IBA (18-500-10-5D-150W). The DTG curve for raw IBA between 0 and 200 °C reveals a minor peak indicating free moisture evaporation. While the MCC-treated IBA had a much lower peak between 0 and 200 °C, this indicates that the high energy-intensive milling generated sufficient heat to evaporate the water in the IBA. A significant difference between raw and MCC-treated IBA was observed between 600 and 750

°C. First, a peak shifted from approximately 660-680 °C to approximately 700-720 °C from raw to MCC-treated IBA, and second, the MCC-treated IBA's peak became much stronger, showing -0.47%/min while the raw peak shows -0.37%/min. These significant alterations in MCC-treated samples are due to the enhanced reactivity of Ca-bearing phases, which favors the production of $CaCO_3$. As a result, the carbonated IBA exhibits a high DTG peak, which is due to the thermal breakdown of $CaCO_3$ with the emission of CO_2. The TG graphs also show that the carbonated IBA has a sharper TG drop and substantially higher mass loss, particularly at high temperatures, with an 18.5% increase relative to the raw sample. The CO_2 absorption of raw and carbonated IBA was determined from the carbonated-associated mass loss in the TG curve, which was 34.36 and 74.816 g CO_2 per kg IBA, respectively, with a percentage increase of 117.63%.

Table 3. Comparison of CO_2 Uptake (Dry Carbonation vs. MCC treated Samples)

Treatment Method	Processing Time	CO_2 Uptake (g CO_2 / kg IBA)	Relative Efficiency
Dry Carbonation (Reference)	7 days	36	1 x (Baseline)
MCA-10-500-60	10 minutes	74.8	~2× higher

Compared to the dry carbonation results, which exhibit a maximum of 36.0 g/kg after 7 days, the MCC-treated IBA displays a significantly higher carbon capture capacity, showing 74.8 g/kg. This Co2 uptake occurs in under 10 minutes, which is approximately twice the amount of C2 acquired by dry carbonation over a full week.

4 Conclusions

The main findings obtained within the scope of the experimental study are summarized below.

- The R3 water-bound test confirmed an increase in pozzolanic reactivity in both MCC and MCA-treated samples, with MCA exhibiting the highest reactivity due to amorphization and particle refining.
- MCA-treated samples showed a higher water bounding percentage, but lower compressive strength compared to MCC samples due to increased metallic aluminum reactivity. Unlike untreated and MCA-treated mixes, MCC-treated samples perform better overall due to metallic aluminum passivation and microstructural densification.
- MCC treatments caused a dense carbonate network, as proven by XRD and TGA graphs. Additionally, XRD data revealed amorphization of crystalline material due to MCA.

Acknowledgments
The authors gratefully acknowledge the financial support provided by the Scientific.

References
Author Contribution Statement
Conceptualization:
Methodology:
Investigation:

Writing –
Writing –

List of Abbreviations

- **MCA** — Mechanochemical Activation
- **MCC** — Mechanochemical Carbonation
- **IBA** — Incineration Bottom Ash
- **SCM**— Supplementary Cementitious Material

Note:….

Publication Note

This paper was peer-reviewed, accepted for presentation, and included in the proceedings of the ACE2026 – International Conference on Advances in Civil Engineering, held on 12–14 October 2026 in Trabzon, Türkiye.

This paper may be cited as follows:

Ahmad, M., Baki, V. A., Nas, M., Yılmaz, Y., Nayır, S., Chakir, A., Ayvaz, F., Bulut, M., Çaputcu, A., "Dry Ice-Driven Mechanochemical Carbonation for Enhanced CO_2 Capture and Reactivity of Bottom Ash," in Proceedings of the ACE2026 – International Conference on Advances in Civil Engineering, Trabzon, Türkiye, 12–14 October 2026.

Increasing the Reactivity of Natural Pozzolans in Cementitious Systems

Sevgi Özen
0000-0002-5699-3000, Recep Tayyip Erdoğan University, Geological Engineering Department, Rize, Türkiye, sevgi.ozen@erdogan.edu.tr

Abstract. Clinker production at high temperatures (approximately 1430ºC) for cement manufacturing is associated with substantial CO_2 emissions, which requires the development of alternative binder cement systems. In this context, extensive scientific research has focused on blended cements incorporating natural pozzolans as supplementary cementitious materials, due to their widespread availability in nature. Although natural pozzolans contribute to sufficient long-term mechanical development and durability with pozzolanic reactions, their low early-age strength development often limits their replacement levels for cementitious systems. In order to overcome this limitation many activation techniques have been investigated to enhance the reactivity of pozzolanic materials. Among these, calcination is one of the most effective techniques. Calcination significantly improves the chemical reactivity of pozzolans by increasing their amorphous phase content and modifying their mineralogical structure, thus promoting more efficient pozzolanic reactions. As a result, higher replacement levels can be made without decreasing mechanical performance and durability. In this regard, the use of calcined pozzolans in blended cements is considered a promising strategy for reducing clinker content and associated carbon emissions, while maintaining performance characteristics. Furthermore, this approach supports current sustainability goals in the cement industry by enabling the development of low-carbon cement systems.

Keywords: Pozzolan; Calcination; Blended cement; CO_2 emissions.

1 Introduction

Cement production is associated with substantial carbon emissions. Although blended cements provide an effective approach to reducing these emissions, the limited availability of conventional supplementary cementitious materials, such as fly ash and blast-furnace slag, has increased the need for alternative natural pozzolanic resources. In this context, natural pozzolans, zeolites or clay minerals, which are widely available in Türkiye, represent a promising alternative source of natural raw materials. In recent years, limestone calcined clay cement (LC3) has emerged as a low-carbon cement system capable of reducing the clinker content to approximately 50% while achieving mechanical performance comparable to that of conventional cement. Owing to its high clinker replacement level, LC3 can reduce associated CO_2 emissions by up to approximately 30%. In Türkiye, particularly in western Anatolia, the utilization of widely available clay deposits is therefore of considerable importance, both for reducing carbon emissions and for promoting the value-added use of domestic clay resources.

The literature indicates that LC3 cements can significantly reduce carbon emissions and therefore represent a promising alternative to conventional Portland cement [1]. Nevertheless, several challenges associated with the incorporation of calcined clays into cementitious systems have been reported, including increased water demand, reduced workability, and, under certain conditions, lower early-age strength. For instance, Scrivener et al. (2019) reported that the high

specific surface area of calcined clay minerals adversely affects the workability of LC3 systems, thereby increasing the demand for chemical admixtures to achieve a comparable level of flowability [2]. Furthermore, the mineralogical, chemical, and physical characteristics of natural clay resources can vary considerably depending on their geological origin. Such variations directly influence the optimum calcination temperature and, consequently, the reactivity and mechanical performance of calcined clays obtained from different sources. Previous studies have demonstrated that the performance of LC3 cements is strongly governed by several clay-related parameters, including clay content, mineralogical composition, specific surface area, particle size and morphology, as well as the calcination conditions applied.

Similar considerations also apply to natural zeolites. Although the use of natural zeolites in construction materials dates back many years, they have not yet achieved widespread acceptance as commercially established supplementary cementitious materials. One of the major factors limiting their broader utilization in cementitious systems is their relatively low early-age strength development. As the clinker content of cement is reduced and replaced by a natural pozzolan, such as natural zeolite, the dilution of the highly reactive clinker phases, combined with the relatively slow pozzolanic reaction of natural zeolite at early ages, may result in insufficient early-age strength development. Although numerous studies have attempted to overcome this limitation through different activation and modification approaches, the development of cementitious systems containing high proportions of natural zeolite remains challenging. In particular, cement products incorporating natural zeolite at replacement levels as high as approximately 50% have not yet become widely available on the commercial market. Therefore, enhancing the early-age reactivity and mechanical performance of natural zeolite is essential for enabling its use at substantially higher clinker replacement levels and for developing low-carbon cementitious systems with performance comparable to conventional Portland cement.

To overcome these challenges and improve the performance of cementitious systems containing natural pozzolans, various activation methods have been investigated to enhance their pozzolanic reactivity. These methods mainly include mechanical, chemical, and thermal activation techniques, which aim to modify the physical, chemical, and mineralogical characteristics of natural pozzolans.

2 Activation Methods

2.1 Mechanical Activation

Mechanical activation is one of the commonly applied methods for enhancing the pozzolanic reactivity of natural pozzolans. This technique is generally based on intensive grinding, which reduces particle size and increases the specific surface area of the pozzolanic material, thereby providing a larger reactive surface for interaction with hydration products in cementitious systems [3]. In addition to particle size reduction, prolonged or high-energy grinding may induce structural disorder and physicochemical changes in mineral phases, which can further enhance their reactivity. Consequently, mechanical activation can accelerate pozzolanic reactions and improve the contribution of natural pozzolans to strength development, particularly when their initial reactivity is relatively low [4]. Korkmaz and Kayıran (2022) demonstrated that mechanical activation significantly influenced the performance of high-volume natural pozzolanic cements, with grinding conditions playing an important role in the resulting pozzolanic activity and mechanical properties [5]. Similarly, recent studies on natural volcanic materials have shown that mechanical activation can enhance their pozzolanic activity and improve their suitability as supplementary cementitious materials [6]. However, the effectiveness of mechanical activation depends strongly on the mineralogical and physical characteristics of the pozzolan as well as the grinding conditions. Moreover, excessive grinding

may increase energy consumption without providing a proportional improvement in performance. Therefore, optimization of grinding time, particle size distribution, and specific surface area is essential for achieving an appropriate balance between enhanced pozzolanic reactivity and the energy demand associated with mechanical activation.

2.2 Chemical Activation

Chemical activation is another approach used to enhance the reactivity of natural pozzolans and to overcome their relatively slow reaction kinetics at early ages. In this method, chemical activators are introduced into the cementitious system to accelerate the dissolution of reactive silica and alumina species and promote the formation of hydration products. Various compounds, particularly alkali and salt-based activators, have been investigated for this purpose. Shi and Day (2001), for example, investigated the chemical activation of a natural pozzolan using Na_2SO_4 and $CaCl_2$ and compared its effectiveness with mechanical and thermal activation methods [7]. Their results showed that chemical activation considerably accelerated the pozzolanic reaction and improved early-age strength development, although the effectiveness strongly depended on the type and dosage of the activator. The enhancement in reactivity is generally associated with changes in the chemical environment of the pore solution, which can facilitate the dissolution of reactive Si and Al species from the pozzolan and accelerate their subsequent reactions with available calcium species. Accordingly, chemical activation can provide an effective strategy for improving the performance of cementitious systems containing relatively high amounts of low-reactivity pozzolanic materials. However, the selection and dosage of chemical activators must be carefully optimized, since their effectiveness depends on the chemical and mineralogical characteristics of the pozzolan, while excessive addition may adversely affect hydration, setting behavior, durability, or the overall environmental benefits of clinker replacement. Therefore, chemical activation should be designed specifically according to the characteristics of the natural pozzolan and the targeted performance of the cementitious system.

2.3 Thermal Activation

Among the activation methods used to enhance the pozzolanic reactivity of natural pozzolans, thermal activation has received considerable attention due to its ability to directly modify the mineralogical and structural characteristics of the material. Unlike mechanical activation, which primarily modifies the physical characteristics of pozzolans, or chemical activation, which promotes their reaction through the addition of external activators, thermal activation can induce fundamental changes in the crystalline structure of natural pozzolans. When exposed to an appropriate temperature range, thermally induced structural transformations may decrease crystallinity and increase the availability of reactive silica and alumina species, thereby enhancing their participation in pozzolanic reactions. The effectiveness of this process, however, strongly depends on the mineralogical composition of the raw material and the applied calcination conditions, particularly temperature and duration. Therefore, understanding and controlling the structural transformations occurring during calcination is essential for converting relatively low-reactivity natural pozzolans into more reactive supplementary cementitious materials.

One of the key characteristics that should be modified to improve the suitability of natural pozzolans for cement production is their long-range ordered crystalline structure. Due to this structural arrangement, the silica- and alumina-bearing phases present in natural pozzolans may require a relatively long period to dissolve and subsequently participate in pozzolanic reactions. This relatively slow reaction kinetics can contribute to limited strength development at early ages. Therefore, enhancing the early-age reactivity of natural pozzolans requires modification of their crystalline structure into a more disordered and reactive state. Calcination is one of the

most effective approaches for inducing such structural transformations. Through appropriate calcination, the degree of structural order can be reduced and the availability of reactive aluminosilicate species can be increased, thereby accelerating pozzolanic reactions and potentially mitigating the low early-age strength associated with the use of untreated natural pozzolans.

The use of calcined natural pozzolans is also recognized within the EN 197-1 cement classification framework, in which the designation “Q” refers to natural calcined pozzolans used as cement constituents, including in composite cement systems such as CEM V. Several studies have investigated the thermal activation of natural pozzolans and demonstrated that appropriate calcination can significantly modify their mineralogical characteristics and enhance their pozzolanic performance [8-9]. Accordingly, calcination represents a promising strategy for improving the reactivity of natural pozzolans and facilitating their use at higher replacement levels in low-clinker cementitious systems.

3 Results

The reviewed literature demonstrates that the relatively low early-age reactivity of natural pozzolans can be improved through mechanical, chemical, and thermal activation. Mechanical activation mainly enhances reactivity by reducing particle size and increasing the available surface area, whereas chemical activation accelerates the dissolution of reactive silica and alumina species by modifying the chemical environment of the system. However, the effectiveness of these methods strongly depends on the mineralogical and physical characteristics of the natural pozzolan as well as the applied activation conditions. Therefore, optimization of the activation process is essential for improving pozzolanic reactivity and enabling higher clinker replacement levels without compromising cement performance. Chemical activation, on the other hand, modifies the reaction environment and can accelerate the dissolution of reactive silica and alumina species. The addition of suitable chemical activators can therefore promote pozzolanic reactions and improve early-age performance. However, the effectiveness of chemical activation is highly dependent on the type and dosage of the activator and the mineralogical and chemical composition of the pozzolan. Among these approaches, thermal activation by calcination is particularly promising because it can directly modify the crystalline structure of natural pozzolans. Appropriate calcination can decrease structural order and increase the availability of reactive aluminosilicate species, thereby accelerating pozzolanic reactions and improving their contribution to strength development. Furthermore, an optimum calcination condition should be determined for each natural pozzolan to maximize its reactivity and facilitate its use as a supplementary cementitious material in low-clinker cement systems.

4 Conclutions

- Mechanical, chemical, and thermal activation methods can enhance the pozzolanic reactivity of natural pozzolans and contribute to overcoming their relatively low early-age reactivity.
- The effectiveness of activation strongly depends on the mineralogical, chemical, and physical characteristics of the natural pozzolan. Therefore, activation conditions should be optimized according to the specific raw material.
- Thermal activation through calcination is particularly promising because it can modify the crystalline structure of natural pozzolans and increase the availability of reactive aluminosilicate species. However, an optimum calcination temperature and duration should be determined for each pozzolan.

- The effective activation of locally available natural pozzolans can enable higher clinker replacement levels, thereby reducing clinker consumption and associated CO_2 emissions and contributing to the development of more sustainable low-carbon cement systems.

References

1. Dhandapani, Y., Sakthivel, T., Santhanam, M., Gettu, R., Pillai, R.G.: Mechanical properties and durability performance of concretes with Limestone Calcined Clay Cement (LC3). Cement and Concrete Research 107, 136–151 (2018).
2. Scrivener, K., Avet, F., Maraghechi, H., Zunino, F., Ston, J., Hanpongpun, W., Favier, A.: Impacting factors and properties of limestone calcined clay cements (LC3). Green Materials 7(1), 3–14 (2018).
3. Shi, C.: An overview on the activation of reactivity of natural pozzolans. Canadian Journal of Civil Engineering 28(5), 778–786 (2001).
4. Pourghahramani, P., Azami, M.A.: Mechanical activation of natural acidic igneous rocks for use in cement. International Journal of Mineral Processing 134, 128–134 (2015).
5. Korkmaz, A.V., Kayıran, H.F.: Investigation of mechanical activation effect on high-volume natural pozzolanic cements. Open Chemistry 20 (2022).
6. Tang, H., Xu, L., Xue, K., Tian, J., Yang, J., Wang, D., et al.: Effect of mechanical activation on hydration properties of natural volcanic rock towards partially replacing cement in composite cementitious materials. Journal of Building Engineering (2024).
7. Shi, C., Day, R.L.: Comparison of different methods for enhancing reactivity of pozzolans. Cement and Concrete Research 31(5), 813–818 (2001).
8. Habert, G., Choupay, N., Montel, J.M., Guillaume, D., Escadeillas, G.: Effects of the secondary minerals of the natural pozzolans on their pozzolanic activity. Cement and Concrete Research 38(7), 963–975 (2008).
9. Küçükyıldırım, E., Uzal, B.: Characteristics of calcined natural zeolites for use in high-performance pozzolan blended cements. Construction and Building Materials (2014).

Author Contribution Statement

- *Writing – Original Draft:* Sevgi Özen
- *Writing – Review & Editing:* Sevgi Özen

Note: Following the conference, this Publication Note will be added to each paper; therefore, authors are kindly requested not to remove the note below and to complete the author(s) and paper title information.

Publication Note

This paper was peer-reviewed, accepted for presentation, and included in the proceedings of the ACE2026 – International Conference on Advances in Civil Engineering, held on 12–14 October 2026 in Trabzon, Türkiye.

This paper may be cited as follows:

Özen, S., "Increasing the Reactivity of Natural Pozzolans in Cementitious Systems," in Proceedings of the ACE2026 – International Conference on Advances in Civil Engineering, Trabzon, Türkiye, 12–14 October 2026.

CHAPTER 3

Geotechnics

14 papers

3D Numerical Analysis for the Hydraulic Performance of Contemporary Weep Holes in Retaining Structures

Burak ÖZÇÖREKÇİ [1] Mustafa HATİPOĞLU [2]
0009-0000-2219-8730, Istanbul Technical University, Civil Engineering Department, İstanbul, Türkiye, ozcorekci17@itu.edu.tr
0000-0001-6381-4309, Istanbul Technical University, Civil Engineering Department, İstanbul, Türkiye, hatipoglu1@itu.edu.tr

Abstract. One of the most common problems encountered in retaining structures is excessive deformation or more severe cases, structural failure due to inadequate drainage conditions. Such issues not only cause economic losses but can also lead to injuries and fatal accidents. Therefore, to improve the performance of existing retaining structures and alleviate these problems, engineering solutions must be developed to safely drain water accumulated behind the structure. In this context, drainage holes known as “weep holes” are created in the retaining structure to prevent the buildup of hydrostatic water pressures. However, the backfill material behind these holes and walls often lacks adequate filtering properties in practical applications, leading to the transport of fine particles. Additionally, due to external factors, the drainage holes might become clogged over time and cease to function, preventing the retaining structure from consistently providing the expected drainage performance. In this study, a contemporary weep hole model was created that can demonstrate active performance for a much longer period than the traditional solutions for solving inadequate drainage conditions in retaining structures, and a comparison was made between the two.

Within the scope of this study, wall models were created using the PLAXIS 3D software. In addition to the traditional weep hole model, a contemporary weep hole that increases total surface area for the drainage of water by penetrating the soil inside the wall was used. The drainage performance of truncated square pyramid (contemporary weep hole model) and traditional weep holes with varying diameters of 5, 10, and 15 cm were examined with finite element modelling analysis of the flow conditions. Since the models were intended solely to examine the drainage of the water behind the wall, the stresses caused by water and the soil were ignored, and only the permeability effects were examined by assigning different permeability coefficients to differentiate the soils. Furthermore, the effect of various rainfall intensities on the drainage volume were also investigated within the models. Since drainage in low-permeability soils is controlled by the soil’s permeability, the effect of rainfall intensity was not examined. However, because drainage occurs rapidly in high-permeability soil conditions, the effects of rainfall intensity were also examined.

Keywords: Weep Holes, Geotextiles, Drainage Performance, Retaining Walls

1 Introduction

The strength and service life of many structures depend on the effective removal of water from above-ground and below-ground structural elements. Exposure of building materials to water causes degradation of their engineering properties and performance loss over time. The failure to provide the material parameters specified or calculated during the design phase is among the most significant consequences of these effects. For this reason, the proper design of drainage systems is of critical importance in all structural designs. Inadequate drainage practices are one of the most common causes of poor performance observed in retaining structures. If this issue is not dealt with using the necessary engineering approach, problems that directly reduce the life of the structure and require costly remediation solutions are inevitable. One of the methods commonly used to improve drainage performance in retaining structures is the application of weep holes (drains) that reduce hydrostatic pressure by providing controlled water discharge along the wall surface. Saturation of the backfill material, however, can cause a significant increase in active lateral earth pressures behind the retaining structure. For these reasons, a new generation weep hole type was modeled that penetrates the backfill behind the retaining wall and has a larger surface area than a conventional one. The performance differences between these two types were compared using numerical analyses.

2 Model Design

The model dimensions consist of a wall 1 meter high and wide, with a depth of 1 meter extending backward. The weep hole was placed 20 cm above the lower elevation of the simulated box shaped wall backfill (**Fig.1.**). The study aimed to examine the effect of varying drainage diameters by testing weep holes with diameters of 5, 10, and 15 cm. The dimensions and schematic of varying weep holes are given **Fig.2.** and **Table 1.** The effect of permeability was examined using different types of soil in the backfill, and the impact of varying rainfall intensities (5 mm/hour, 10 mm/hour, and 20 mm/hour) on drainage performance were analyzed.

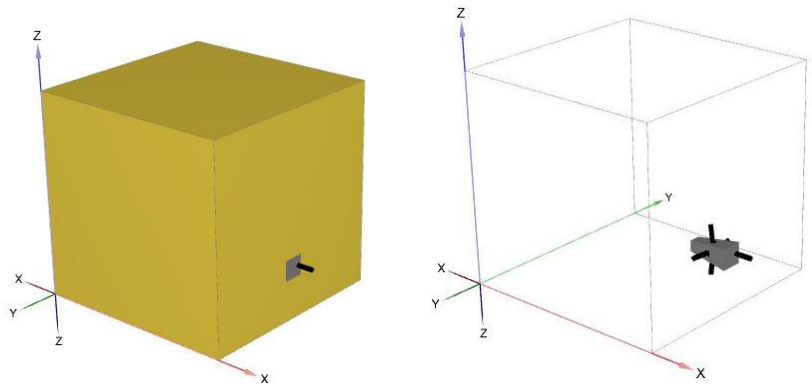


Fig. 1. Model View

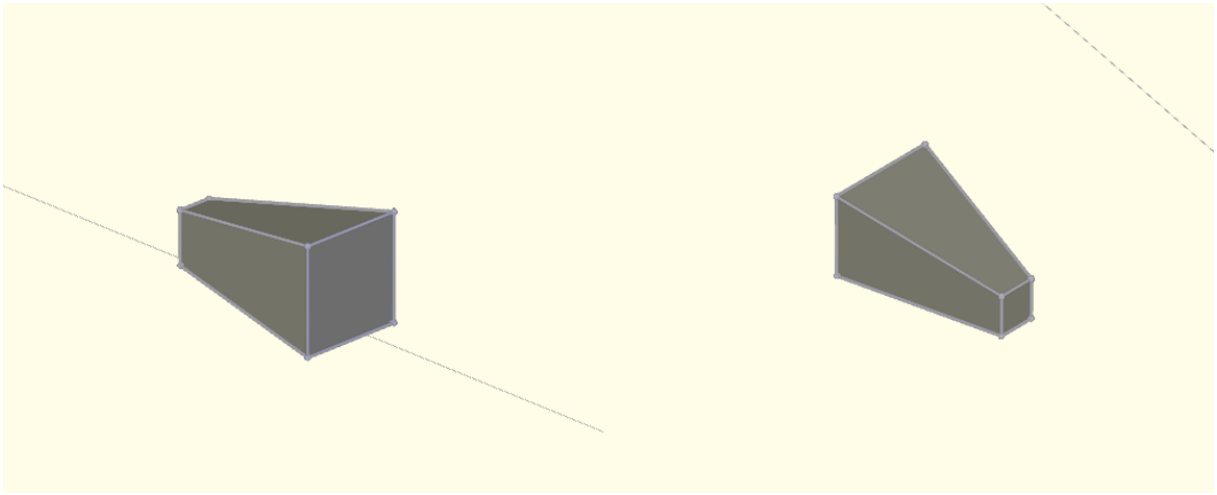


Figure 2. Truncated Square Pyramid Weep Hole View

Table 1. Weep Hole Dimensions

Diameter (cm)	Front Face (cm)	Back Face (cm)	Length (cm)
Q5	5	2.5	8
Q10	10	5	17
Q15	15	7.5	25

Four different soil types were considered in order to evaluate how flow behavior varies depending on the fill material used. The study examined sand–gravel, silty sand, silty clay, and graywack based fill materials, which are widely preferred in the field due to their ease of application. The permeability coefficients for these soils were taken as 1×10^{-2} cm/s, 5×10^{-5} cm/s, 1×10^{-8} cm/s, and 1×10^{-6} cm/s, respectively, in accordance with the literature and engineering standards [3].

The permeability value specified for the gravel material was selected based on the assumption that, following excavation and placement, the material will break down and take on the characteristics of a fine-grained fraction, rather than on its behavior in the natural rock environment. In other words, it was assumed that the hydraulic behavior of the graywack material used as fill is controlled primarily by the properties of the fine-grained matrix rather than by the properties of the intact rock.

In the analyses, a rainfall intensity of 5 mm/hour, representing average conditions, was used as the rainfall input; the relevant reference values are provided in **Table 2**. In the modeling, all boundaries except for the weep holes were assumed to be impermeable, and rainfall effects were defined only from the top surface of the system. The primary objective of this approach is to evaluate the drainage behavior within the system solely based on the performance of the weep holes. In addition, the experimental scenarios developed to examine the effect of rainfall intensity on system behavior were reanalyzed for rainfall conditions of 10 mm/hour and 20 mm/hour, and the results were presented in a comparative manner in the report.

As part of the numerical analysis studies, drainage performance was observed based on hydrostatic pressure data behind a fictitious wall with different soil types, by continuously applying different rainfall intensities to the model over a 30 day period. For highly permeable material (sand-gravel), rainfall was applied directly to the dry soil model. In models with materials of lower permeability, the rainfall could not reach the weep hole level from the top of the model within 30 days; therefore, the material was assumed to be fully saturated to prevent the model solution times from becoming excessively long. The groundwater level was set at the upper part of the soil elevation in the model and left to drain freely without applying rainfall.

Therefore, while the effects of rainfall intensity and weep hole diameter variation were examined in the highly permeable sand-gravel material, the effect of diameter variation was examined in the remaining soil models with relatively lower permeability. In addition, to evaluate the time-dependent effects of the drainage process in low-permeability soil models, models of silty sand, graywack and silty clay were allowed to settle under free drainage conditions for 10, 20, and 30 days, respectively; the hydrostatic pressure distributions and changes behind the wall were examined at the end of each period.

Table 2. Rainfall Intensity Classification [5]

Hourly Rainfall Intensity (mm/hour)	Intensity Class
<4	Light to Moderate Rain
4-10	Heavy Rain
10-50	Heavy Shower
>50	Violent Shower

3 Results and Evaluations

Numerical analyses were performed, and the results presented in **Table 3** and **Figure 3** were obtained. When the graph is evaluated as a whole, it is observed that the truncated square pyramid shaped weep hole type demonstrates more successful drainage performance behind the wall compared to the conventional weep hole across the time range under all experimental conditions. The results indicate that the truncated square pyramid shaped (New Generation) weep hole exhibits more controlled and stable performance under different diameters and rainfall intensities.

Table 3. Properties of Analysis

Analysis No.	Diameter (cm)	Soil Type	Rainfall Intensity (mm/hour)	Duration (Day)
1	5	Sand–Gravel	5	30
2	5	Sand–Gravel	10	30
3	5	Sand–Gravel	20	30
4	10	Sand–Gravel	5	30
5	10	Sand–Gravel	10	30
6	10	Sand–Gravel	20	30
7	15	Sand–Gravel	5	30
8	15	Sand–Gravel	10	30
9	15	Sand–Gravel	20	30
10	5	Silty Sand	-	30
11	10	Silty Sand	-	30
12	15	Silty Sand	-	30
13	5	Silty Clay	-	30
14	10	Silty Clay	-	30
15	15	Silty Clay	-	30
16	5	Graywack	-	30
17	10	Graywack	-	30
18	15	Graywack	-	30

In particular, for sand-gravel material, it is observed that the difference between the new type and the conventional type weep hole increases significantly as rainfall intensity rises. For example, when rainfall intensity for a 5 cm diameter increased from 5 mm/h to 20 mm/h, the hydrostatic pressure ratio behind the wall decreased from 80% to 59%. A similar trend was observed for diameters of 10 cm and 15 cm. This suggests that as rainfall intensity increases, performance loss becomes more pronounced in the conventional type weep holes, whereas the new type weep holes exhibit more stable behavior.

The results for the graywack material reveal a notable effect of diameter increase on system behavior. As the diameter increases, the advantages of the new system become more noticeable. In particular, it was observed that at a diameter of 15 cm, the hydrostatic pressure behind the wall in the new system decreased by 50% compared to the standard system, demonstrating more effective performance.

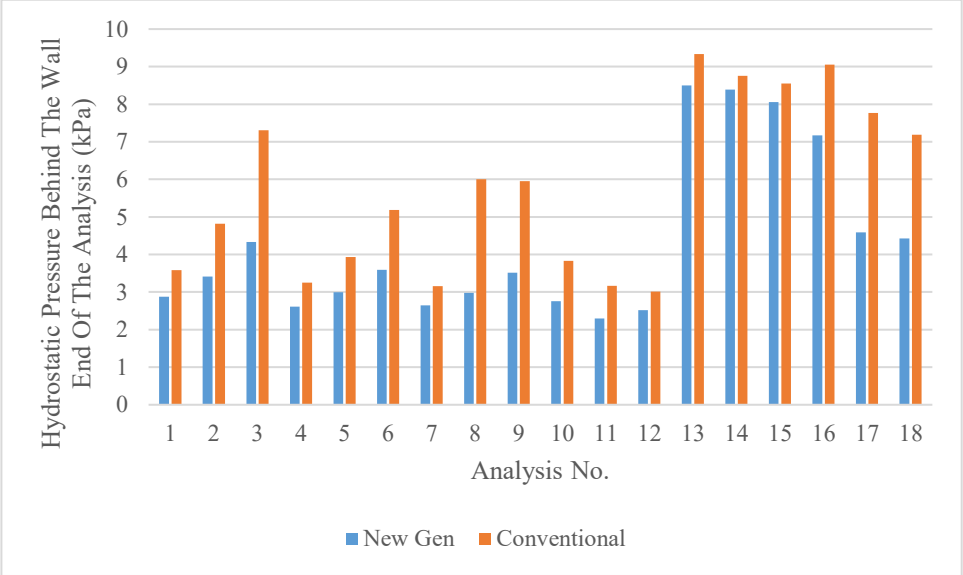


Fig. 3. Comparison of Conventional and New Generation Weep Hole Results

In contrast, it is observed that the two systems yield very similar results in the silty clay material with the lowest permeability. The fact that hydrostatic pressure ratios vary within the range of 90–96% indicates that both systems exhibit similar behavior under these conditions. This suggests that system performance depends not only on the type of weep hole but also on rainfall intensity and soil type. Overall, it was concluded that the new system offers superior performance, particularly under high rainfall intensity.

To enable a comparison of the same parameters across all soil types, the models were analyzed under free drainage conditions, without taking the effect of rainfall intensity into account. To more effectively evaluate drainage behavior based on the permeability characteristics of the soils, the analysis periods were set at 1, 10, 20, and 30 days for the sand-gravel, silty sand, graywack and silty clay models respectively, in descending order of permeability. Analyses were conducted for two different types of weep holes for each soil model, and the hydrostatic pressures behind the wall obtained at the end of the analysis periods were compared. Using the results obtained, the effects of changes in weep hole type and diameter on drainage performance were evaluated. The analysis parameters and results for each soil type are presented in **Table 4** and **Figure 4**.

Table 5 shows the pore water pressure ratio for the new generation weep hole compared to the conventional weep hole for each soil type at different diameters. For example, in the new generation 5 cm diameter weep hole model on sand-gravel material, the ratio of the pore water pressure behind the wall to the water pressure behind the wall obtained in the conventional

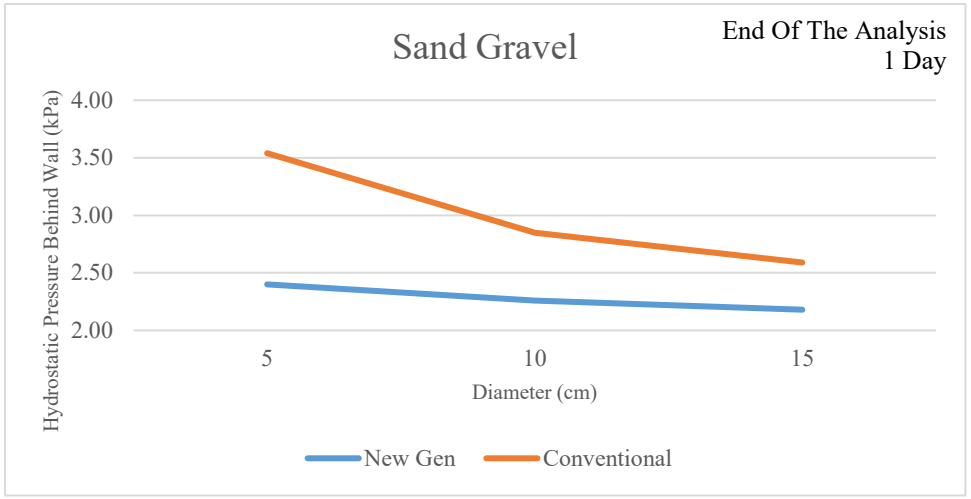
weep hole model is 0.678. In other words, the obtained pore water pressure in the new generation weep hole model is lower than conventional one.

Table 4. Properties of Analysis Models

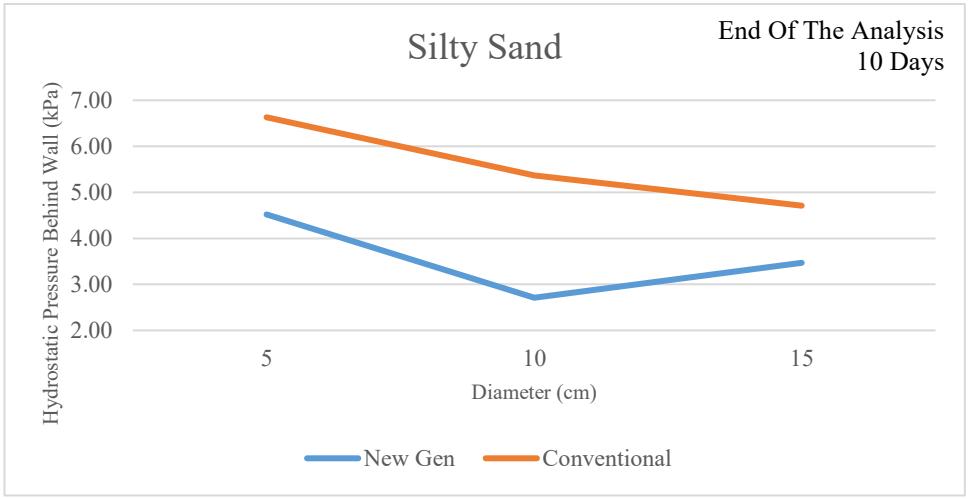
Diameter (cm)	Soil Type	Weep Hole Type	Pore Water Pressure (kPa)	Duration (Day)
5	Sand–Gravel	New Gen	2.40	1
10	Sand–Gravel	New Gen	2.26	1
15	Sand–Gravel	New Gen	2.18	1
5	Sand–Gravel	Conventional	3.54	1
10	Sand–Gravel	Conventional	2.85	1
15	Sand–Gravel	Conventional	2.59	1
5	Silty Clay	New Gen	8.50	30
10	Silty Clay	New Gen	8.39	30
15	Silty Clay	New Gen	8.05	30
5	Silty Clay	Conventional	9.34	30
10	Silty Clay	Conventional	8.75	30
15	Silty Clay	Conventional	8.55	30
5	Graywack	New Gen	7.40	20
10	Graywack	New Gen	4.55	20
15	Graywack	New Gen	4.43	20
5	Graywack	Conventional	9.08	20
10	Graywack	Conventional	6.89	20
15	Graywack	Conventional	7.43	20
5	Silty Sand	New Gen	4.52	10
10	Silty Sand	New Gen	2.71	10
15	Silty Sand	New Gen	3.47	10
5	Silty Sand	Conventional	6.63	10
10	Silty Sand	Conventional	5.37	10
15	Silty Sand	Conventional	4.71	10

Table 5. Porewater Pressure Ratio New Gen Weep Hole Against Conventional One

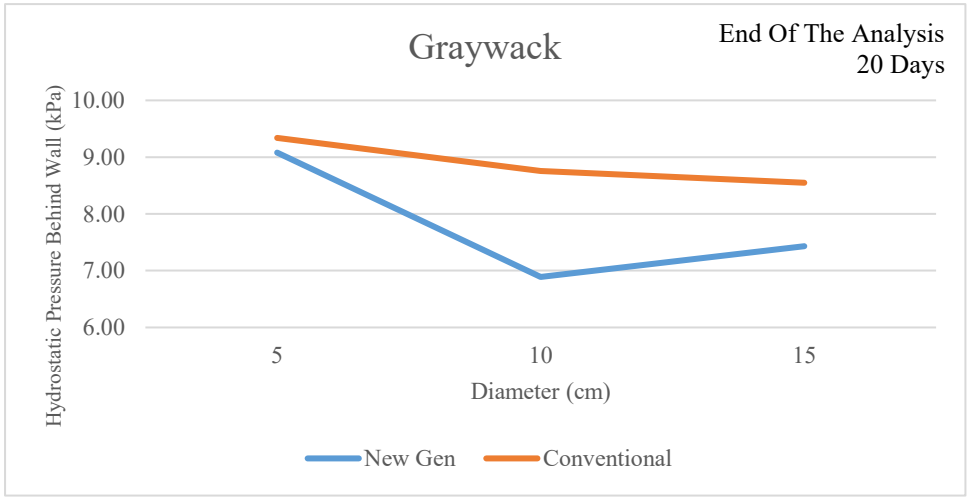
	Weep Hole Diameter (cm)		
Soil Type	**5**	**10**	**15**
Sand–Gravel	0.678	0.793	0.842
Silty Clay	0.910	0.959	0.942
Graywack	0.815	0.661	0.596
Silty Sand	0.682	0.505	0.737



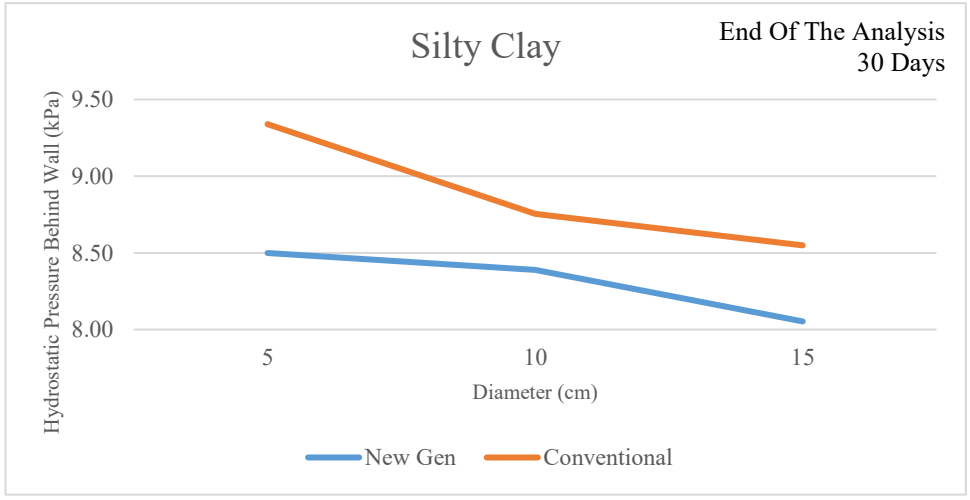
(a)



(b)



(c)



(d)

Figure 4. Comparison of Conventional and New Generation Weep Hole Results, (a. Sand Gravel, b. Silty Sand, c. Graywack, d. Silty Clay)

In sand-gravel soil with high permeability, it is observed that as the weep hole diameter increases, the hydrostatic pressure values behind the wall decrease in both systems. In the new gen weep holes, the hydrostatic pressure value, calculated as 2.40 kPa for a 5 cm diameter, drops to 2.18 kPa for a 15 cm diameter; in the conventional weep holes, the same values were obtained as 3.54 kPa and 2.59 kPa, respectively. The results show that drainage performance in highly permeable soils is significantly affected by the weep hole diameter and that the new generation system provides more effective drainage by producing lower hydrostatic pressure values across all diameters. However, it is observed that the performance difference between the two systems decreases as the diameter increases.

In the silty sand model, increasing the weep hole diameter from 5 cm to 10 cm in both systems resulted in significant reductions in hydrostatic pressure values. However, in the new generation system, the value of 2.71 kPa obtained at a 10 cm diameter rise to 3.47 kPa at a 15 cm diameter. Similarly, while the downward trend continued in the conventional system, the increase in performance was observed to gradually decrease. This indicates that drainage performance depends not only on the weep hole cross-sectional area but is also influenced by the flow regime within the soil and the geometric characteristics of the drainage zone. Under the conditions examined, it was determined that the 10 cm diameter weep hole in the new generation system provided the lowest hydrostatic pressure value.

The effect of changes in weep hole diameter on drainage performance was observed more clearly on the graywack. In the new generation weep holes, the hydrostatic pressure value was 7.40 kPa at a 5 cm diameter, while it decreased to 4.55 kPa at a 10 cm diameter and to 4.43 kPa at a 15 cm diameter. In the conventional system, the values obtained were 9.08 kPa, 6.89 kPa, and 7.43 kPa, respectively. In particular, it was observed that the new generation generated hydrostatic pressure approximately 40% lower than the conventional system at a 15 cm diameter. The results show that the drainage efficiency of the new gen system becomes more pronounced in soils with medium permeability and that it can provide greater benefits than an increase in diameter.

In the silty clay model, the effect of an increase in the weep hole diameter on hydrostatic pressure was more limited compared to other soil types. In the new generation system, hydrostatic pressure values decreased from 8.50 kPa to 8.05 kPa, while in the conventional system, they decreased from 9.34 kPa to 8.55 kPa. Due to low permeability, the movement of water within the soil is restricted, and drainage performance is largely controlled by the soil's hydraulic conductivity. Therefore, while increasing the weep hole diameter provides a certain improvement in drainage capacity, its effect on system performance remains limited.

When all soil types are considered together, it is observed that the new generation weep holes produces lower hydrostatic pressure values compared to the conventional weep holes across all diameters and soil conditions examined. The advantage provided by the system varies depending on soil permeability and becomes particularly pronounced in soils with moderate permeability, such as graywack and silty sand. In contrast, in low-permeability soils such as silty clay, where drainage performance is largely controlled by soil properties, the effect of the diameter of weep hole and type is more limited. These results demonstrate that focusing solely on increasing the diameter in weep hole design is insufficient; rather, soil properties and weep hole geometry must be evaluated together.

4 References

1. Look, B: Handbook of Geotechnical Investigation and Design Tables. Taylor & Francis e-Library (2007)

2. World Meteorological Organization Website, https://community.wmo.int/site/knowledge-hub/programmes-and-initiatives/aviation/aviation-hazards-precipitation, last accessed 2026/06/05

Publication Note

This paper was peer-reviewed, accepted for presentation, and included in the proceedings of the ACE2026 – International Conference on Advances in Civil Engineering, held on 12–14 October 2026 in Trabzon, Türkiye.

This paper may be cited as follows:

Burak ÖZÇÖREKÇİ, Mustafa HATİPOĞLU , "3D Numerical Analysis for The Hydraulic Performance of Contemporary Weep Holes in Retaining Structures" in Proceedings of the ACE2026 – International Conference on Advances in Civil Engineering, Trabzon, Türkiye, 12–14 October 2026.

Response-Based Sensitivity Analysis of Barcelona Basic Model Parameters for Pile Heave in Expansive Ankara Clay

Sefa Yıldırım[1] and Erdal Çokça[2]
[1] https://orcid.org/0000-0002-9906-2978, Middle East Technical University, Department of Civil Engineering, Ankara, Türkiye, sefa.yildirim@metu.edu.tr, tsefayildirim@gmail.com
[2] https://orcid.org/0000-0001-8367-2539, Middle East Technical University, Department of Civil Engineering, Ankara, Türkiye, ecokca@metu.edu.tr

Abstract. Expansive clays are commonly encountered in semi-arid regions where seasonal moisture variations alter matric suction and induce swelling–shrinkage behavior. Because their mechanical response is strongly suction-dependent, conventional constitutive models that neglect unsaturated soil behavior may not adequately represent field conditions. The Barcelona Basic Model (BBM) incorporates suction effects into stress–strain behavior and is widely used for unsaturated expansive soils; however, its calibration generally requires extensive laboratory testing, which limits its routine engineering application. This study evaluates the sensitivity of BBM parameters on the predicted upward movement of a single pile embedded in expansive Çubuk–Ankara clay using numerical analyses performed in RS2 finite element software. The reference BBM parameter set was obtained from soil water retention curve measurements together with saturated and unsaturated mechanical tests. Sensitivity analyses were conducted for $\lambda(0)$, κ, r, β, p_c, k, and M by varying each parameter individually while keeping the remaining parameters constant. The pile response was evaluated using normalized pile movement, u_p/L_e, where L_e is the embedded pile length in clay. The results show that κ, representing the slope of the unloading–reloading line, is the most influential parameter controlling pile movement, followed by $\lambda(0)$, the slope of the virgin compression line. The parameters r and M also produced noticeable effects, whereas p_c, β, and k had comparatively limited influence. These findings indicate that BBM calibration for pile-heave simulations should prioritize parameters controlling stiffness and compressibility.

Keywords: Expansive clay; Barcelona Basic Model; unsaturated soil mechanics; pile heave; finite element analysis

1 Introduction

Expansive clays are problematic geomaterials because their volume-change behavior is governed by variations in water content and matric suction. In semi-arid regions, seasonal wetting and drying cycles may lead to repeated swelling and shrinkage, which can cause ground heave, differential movement, and distress in lightly loaded structures [1,2]. The response of foundations constructed in such soils is therefore not controlled only by conventional strength and stiffness parameters, but also by the hydraulic state of the soil and its suction-dependent deformation behavior [3, 4].

Pile foundations are commonly used in expansive clay deposits to transfer structural loads below the active zone [5,6], where seasonal moisture changes are expected to be less significant [7]. However, the portion of the pile located within the active zone may be subjected to upward shaft forces during wetting [8-10]. The final pile response depends on the swelling potential of the clay, the depth of the active zone, the pile-soil interface behavior, the anchorage length below the active zone, and the deformation characteristics of the surrounding unsaturated soil

[8,9]. For this reason, realistic numerical modelling of pile behavior in expansive clays requires a constitutive framework that can account for suction-dependent stress–strain response [3,11-13]. The conceptual mechanism of swelling-induced pile movement considered in this study is illustrated in Fig. 1. During wetting, suction decreases and the expansive clay in the active zone swells, producing upward shaft forces and pile movement, while the lower embedded portion provides resistance through shaft interaction.

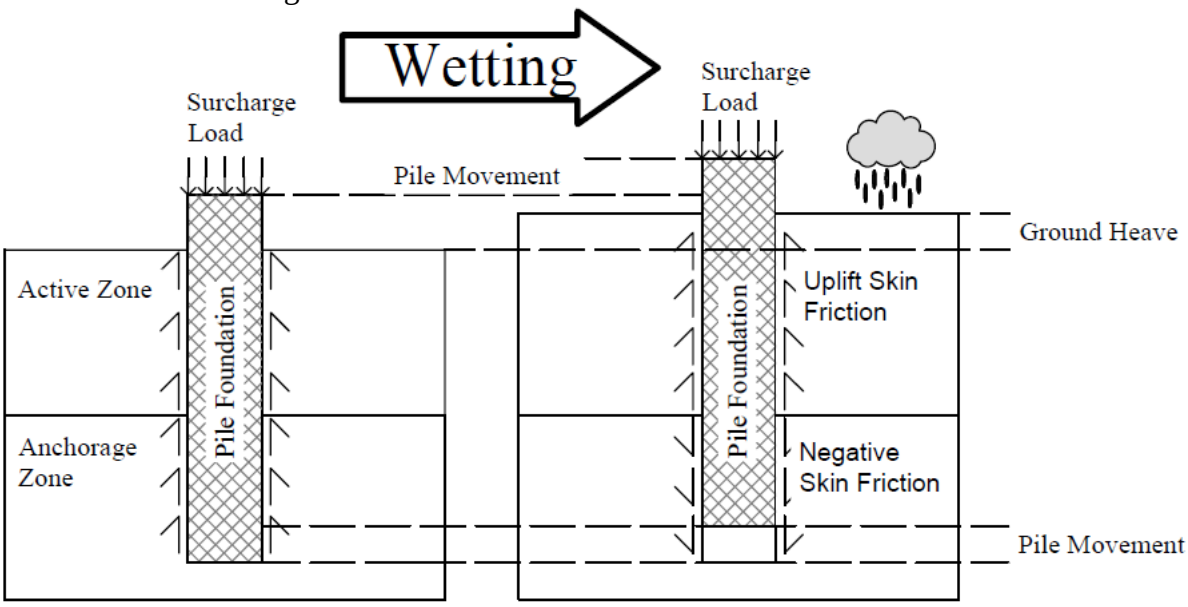


Fig. 1. Conceptual representation of swelling-induced pile movement in expansive clay during wetting [4-6, 9].

The Barcelona Basic Model (BBM) is one of the most widely used constitutive models for unsaturated soils because it incorporates matric suction as an independent stress-state variable. The model provides a theoretical framework for representing suction-dependent stiffness, yielding, and volumetric behavior [11-16]. Despite this advantage, the practical application of the BBM remains challenging because its parameters are not always easy to determine. A complete calibration procedure may require soil water retention curve measurements, saturated and unsaturated consolidation tests, triaxial tests, and suction-controlled testing [3,17,18]. These requirements can make the use of the model time-consuming and experimentally demanding in routine geotechnical practice [11,13,16].

For engineering applications, it is therefore important not only to calibrate BBM parameters, but also to understand which parameters most strongly affect the numerical prediction of the problem of interest. A parameter that has a strong influence on pile movement should be determined with greater care, whereas parameters with limited influence on the same response may be treated with a lower calibration priority. However, the importance of individual BBM parameters may depend on the type of analysis considered. For example, the parameters controlling pile heave may not necessarily be the same as those governing shear strength, post-yield behavior, or failure mechanisms.

This study investigates the sensitivity of selected BBM parameters on the predicted upward movement of a single pile embedded in expansive Çubuk–Ankara clay. The analyses were performed using an axisymmetric finite element model in RS2. The reference BBM parameter set was obtained from previous laboratory-based calibration work involving soil water retention behavior, saturated and unsaturated mechanical tests, and swelling-related characterization of the expansive Ankara clay [4,19]. In the sensitivity analyses, the parameters $\lambda(0)$, κ, r, β, p_c, k, and M were varied individually while the remaining parameters were kept constant.

The main objective of this study is to identify the relative influence of these BBM parameters on swelling-induced pile movement and to establish a practical calibration priority for this specific numerical problem. The scope of the study is limited to the upward displacement response of a single pile under the investigated modelling conditions. Therefore, the sensitivity ranking presented in this paper should not be interpreted as a general ranking for all BBM applications, particularly for analyses focused on shear strength, failure, or large-strain post-yield behavior.

2 Materials and Methods

2.1 Study Material and Reference Data

The analyses were performed for expansive Ankara clay, which is a highly plastic natural clay exhibiting significant suction-dependent volume-change behavior. The experimental database used for defining the reference numerical model included index property tests, mineralogical characterization, swelling tests, soil water retention curve measurements, saturated and unsaturated consolidation tests, triaxial compression tests, concrete–clay interface shear tests, and laboratory-scale single pile tests [4].

The clay was previously identified as an expansive soil containing smectitic and illitic clay minerals together with non-clay minerals such as quartz and calcite. This mineralogical composition, combined with the high plasticity of the soil, indicates a strong potential for swelling upon wetting [19]. Therefore, the Barcelona Basic Model (BBM) was selected to represent the suction-dependent mechanical response of the clay in the numerical analyses.

2.2 Reference BBM Parameter Set

The reference BBM parameter set was established from laboratory test results obtained on the same clay. The saturated compression parameters $\lambda(0)$ and κ were derived from one-dimensional consolidation behavior. Suction-dependent compressibility parameters were evaluated using unsaturated consolidation results, while the critical state parameter M was defined based on triaxial compression tests. The soil water retention curve was used to relate water content and matric suction during the calibration process.

The experimental basis used for determining each BBM parameter and the reference BBM parameters adopted in the numerical model are given in Table 1. This parameter set represents the baseline condition against which the sensitivity analyses were evaluated.

Table 1. Reference BBM parameters used in the numerical analyses [4].

Parameters	Description	Experimental basis	Reference value
$\lambda(0)$	Slope of the virgin compression line at zero suction	Saturated 1-D consolidation test	0.084
κ	Slope of the unloading–reloading line	Saturated 1-D consolidation test	0.0198
r	Parameter controlling suction-dependent compressibility	Unsaturated 1-D consolidation tests and SWRC	0.8909
β	Parameter controlling suction-dependent stiffness variation	Unsaturated 1-D consolidation tests and SWRC	0.0011
p_c	Reference pressure parameter	1-D consolidation and LC curve calibration	7.9

k	Parameter related to suction-induced cohesion increase	Unsaturated triaxial and SWRC	0.56
M	Critical state stress ratio	Saturated CD triaxial	0.67

2.3 Numerical model

The numerical analyses were carried out using RS2 finite element software. An axisymmetric model was adopted to represent the laboratory-scale single pile system. The clay domain was modelled using the BBM, while the concrete pile was represented as a linear elastic material. The pile–soil interaction was simulated using interface elements along the pile shaft, with interface properties defined from concrete–clay direct shear test results [20].

The boundary conditions were selected to represent the laboratory model configuration. The bottom boundary was restrained in both horizontal and vertical directions, whereas the outer vertical boundary was restrained horizontally and allowed to move vertically. The top surface was kept free to allow swelling-induced deformation. The axis of symmetry was restrained in the horizontal direction.

The wetting condition was represented through suction change in the expansive clay based on the soil water retention behavior. The reference analysis was first performed using the calibrated BBM parameter set. The upward vertical displacement of the pile obtained from this reference model was then used as the baseline response for the sensitivity analyses.

2.4 Sensitivity analysis procedure

The sensitivity analyses were conducted to evaluate the influence of selected BBM parameters on the predicted upward movement of the single pile. The investigated parameters were $\lambda(0)$, κ, r, β, p_c, k, and M. A one at a time sensitivity approach was used. In each analysis, only one parameter was varied, while all other parameters were kept constant at their reference values.

The response parameter used for comparison was the upward vertical displacement of the pile. Therefore, the sensitivity ranking presented in this study is specific to swelling-induced pile movement. It does not represent a general BBM sensitivity ranking for all possible geotechnical problems. For analyses governed by shear strength, bearing capacity, or post-yield failure mechanisms, a different parameter ranking may be obtained.

The influence of each parameter was assessed by comparing the calculated pile displacement with the reference model response. Parameters causing larger changes in upward pile movement were interpreted as having higher calibration priority for BBM based pile-heave simulations in expansive clays.

3 Results and Discussion

3.1 Normalized Pile Movement Response

The sensitivity analyses were evaluated using the upward movement of the pile as the response variable. In order to express the displacement in a dimensionless engineering form, the calculated pile movement was normalized by the embedded pile length in the clay. The embedded pile length was 50 mm; therefore, the normalized pile movement was calculated as:

$$\frac{u_p}{L_e}(\%) = \frac{u_p}{50} \times 100 \quad (1)$$

where u_p is the upward movement of the pile and L_e is the embedded pile length. This normalization allows the magnitude of pile movement to be interpreted relative to the pile length embedded in the expansive clay, rather than comparing the BBM parameters directly on the basis of their numerical ranges.

The variations of normalized pile movement with the investigated BBM parameters are shown in Fig. 2. The corresponding range of normalized pile movement for each parameter is summarized in Table 2 and Fig. 3. The results indicate that the calculated pile movement is most sensitive to the parameters controlling the compressibility and stiffness response of the clay.

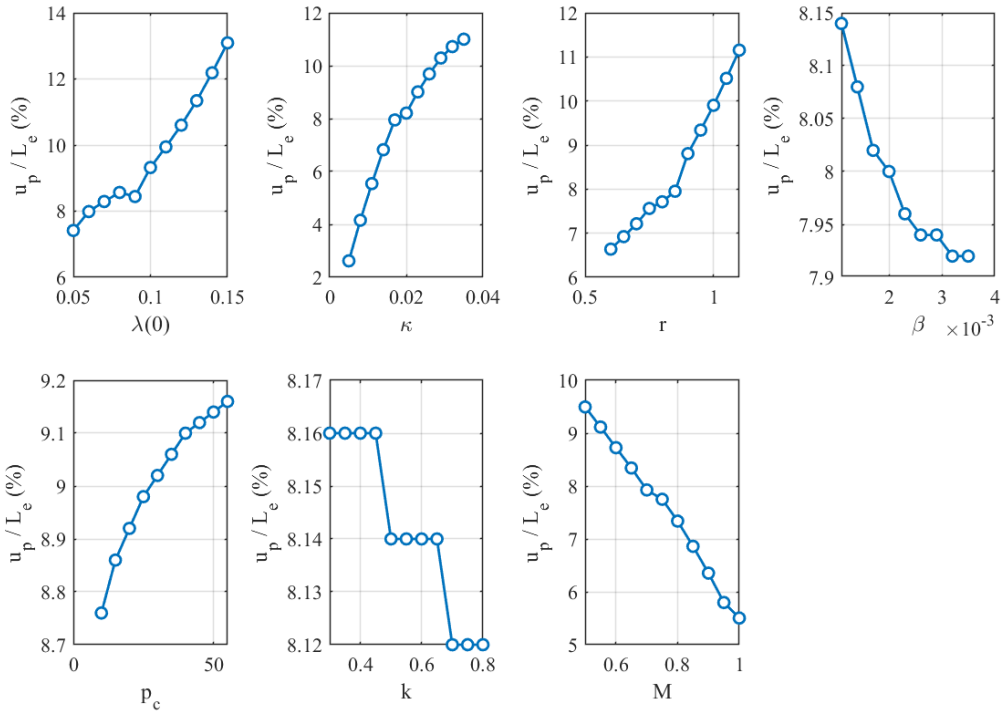


Fig. 2. Variation of normalized pile movement with BBM parameters.

Table 2. Range of normalized pile movement obtained from the BBM parameter sensitivity analyses.

Parameters	**Investigated range**	**Normalized pile movement range, (u_p/Le) (%)**	**Range, (Δu_p/Le) (%)**	**Relative effect**
κ	0.005–0.035	2.62–11.00	8.38	Highest
λ(0)	0.050–0.150	7.42–13.09	5.68	Very high
r	0.600–1.100	6.64–11.15	4.52	High
M	0.500–1.000	5.50–9.50	4.00	High
p_c	10–55	8.76–9.16	0.40	Low
β	0.0011–0.0035	7.92–8.14	0.22	Very low
k	0.300–0.800	8.12–8.16	0.04	Negligible

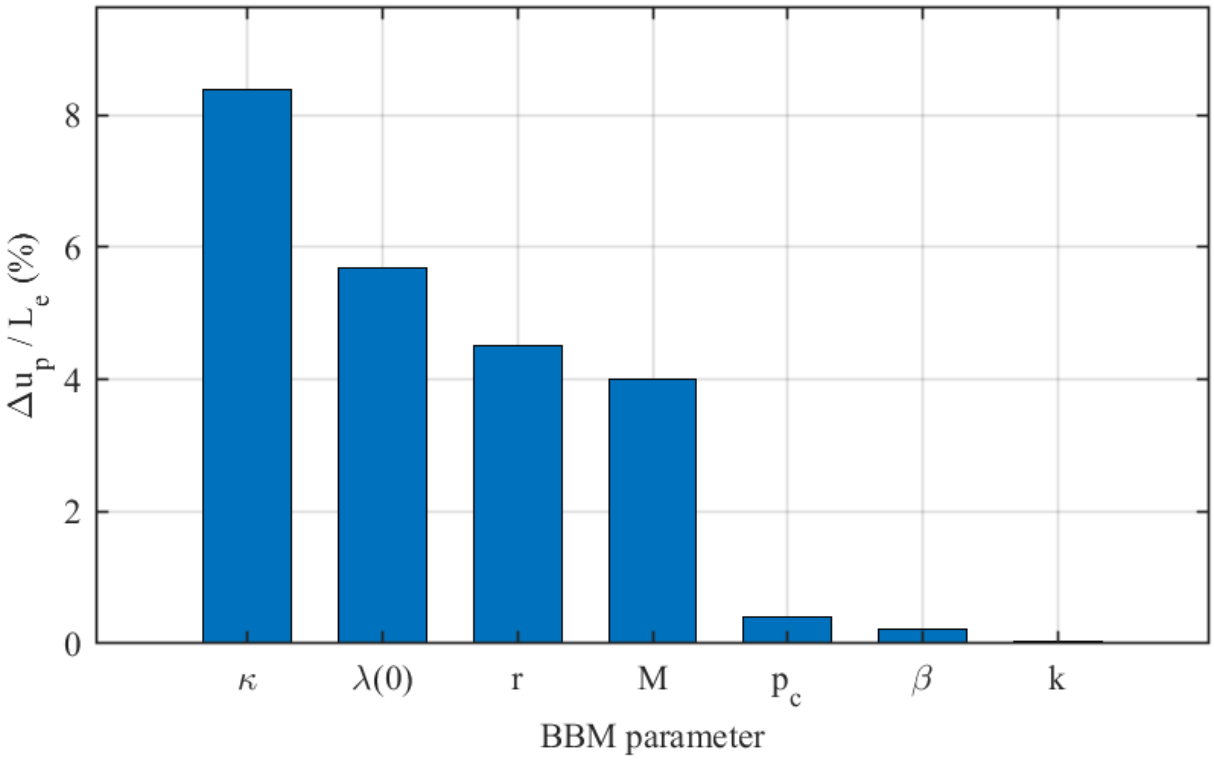


Fig. 3. Sensitivity ranking of BBM parameters based on the range of normalized pile movement.

3.2 Effect of κ and λ(0)

The parameter κ produced the largest variation in normalized pile movement within the investigated parameter range. As κ increased from 0.005 to 0.035, the normalized pile movement increased from 2.62% to 11.00% of the embedded pile length. This corresponds to a total normalized movement range of 8.38%, which was the highest among all parameters examined. Since κ represents the slope of the unloading–reloading line, this result indicates that the elastic volumetric stiffness of the clay has a major influence on the swelling-induced pile displacement.

The parameter λ(0) was the second most influential parameter. The normalized pile movement increased from 7.42% to 13.09% as λ(0) varied between 0.050 and 0.150, giving a total normalized movement range of 5.68%. This parameter defines the slope of the virgin compression line at zero suction and controls the compressibility of the soil skeleton. The strong influence of λ(0) is consistent with the displacement-controlled nature of the problem, since pile heave is governed primarily by the volumetric deformation of the surrounding expansive clay.

The results therefore show that the BBM parameters governing compression and unloading–reloading behavior are the dominant parameters for predicting upward pile movement. For this reason, κ and λ(0) should be treated as primary calibration parameters in BBM-based pile-heave simulations.

3.3 Effect of r and M

The parameter r also had a considerable effect on the calculated pile movement. The normalized pile movement increased from 6.64% to 11.15% as r increased from 0.600 to 1.100, corresponding to a normalized movement range of 4.52%. Since r controls the suction-dependent evolution of compressibility in the BBM formulation, its influence on pile movement is expected in a wetting-induced swelling problem. Although its effect was lower than those of κ and λ(0), r remained an important parameter for the predicted pile response.

The critical state parameter (M) showed a decreasing trend with increasing parameter value. The normalized pile movement decreased from 9.50% to 5.50% as M increased from 0.500 to 1.000, giving a total normalized range of 4.00%. This indicates that M has a noticeable influence on the pile movement response, although the investigated problem is mainly governed by swelling-induced deformation rather than shear failure. Therefore, M should not be considered negligible for the present analysis. However, its role may become even more significant in problems involving bearing capacity, shaft resistance failure, or large post-yield deformation.

3.4 Effect of p_c, β and k

The parameters p_c, β, and k produced comparatively small changes in normalized pile movement within the investigated ranges. The normalized pile movement increased only from 8.76% to 9.16% as pc varied from 10 to 55, corresponding to a movement range of 0.40%. This indicates that pc had a limited effect on the predicted pile heave for the selected modelling conditions.

The influence of β was even smaller. As β increased from 0.0011 to 0.0035, the normalized pile movement slightly decreased from 8.14% to 7.92%, giving a total range of only 0.22%. The parameter k showed an almost negligible effect, with normalized pile movement varying only between 8.12% and 8.16%. These results suggest that uncertainty in p_c, β, and k has a much lower influence on pile movement than uncertainty in κ, λ(0), r, and M for the present pile-heave simulation.

3.5 Overall sensitivity ranking and calibration priority

The sensitivity results were compared using the range of normalized pile movement, u_p/Le, where u_p is the calculated upward pile movement and Le is the embedded pile length in clay. The response curves in Fig. 2 show that the pile movement is mainly affected by κ, λ(0), r, and M, while the variations caused by p_c, β, and k are relatively small. The same trend is more clearly observed in Fig. 3, where the normalized movement ranges are compared directly.

Based on this ranking, κ produced the largest change in pile movement, followed by λ(0), r, and M. This indicates that the parameters controlling volumetric stiffness, compressibility, suction-dependent compressibility, and critical state response have the greatest influence on the predicted pile-heave behavior under the investigated conditions. In contrast, p_c, β, and k had limited influence on the selected response variable.

These results suggest that BBM calibration for swelling-induced pile movement should prioritize κ and λ(0), followed by r and M. However, this priority is specific to the upward displacement of a single pile embedded in expansive clay. For analyses focused on shear strength, bearing capacity, or post-yield deformation, the relative importance of the BBM parameters may be different.

4 Conclusions

This study evaluated the sensitivity of selected Barcelona Basic Model (BBM) parameters on the predicted upward movement of a single pile embedded in Ankara expansive clay. The sensitivity analyses were performed using an axisymmetric finite element model in RS2, and the pile response was evaluated in terms of normalized pile movement, (u_p/L_e), where (L_e) is the embedded pile length in clay.

The following conclusions can be drawn from the analyses:

1. The predicted pile movement was most sensitive to κ, which controls the unloading–reloading stiffness of the soil. Within the investigated range, κ produced the largest variation in normalized pile movement.

2. The parameter $\lambda(0)$, representing the slope of the virgin compression line, was the second most influential parameter. This confirms that the compressibility characteristics of expansive clay have a major effect on swelling-induced pile heave.
3. The parameters r and M also produced noticeable changes in the predicted pile movement. Therefore, these parameters should not be neglected when calibrating the BBM for pile-heave simulations.
4. The effects of p_c, β, and k were comparatively limited within the investigated parameter ranges. Their influence on the selected response variable was much smaller than that of κ, $\lambda(0)$, r, and M.
5. The results indicate that BBM calibration for swelling-induced pile movement should prioritize the parameters controlling volumetric stiffness and compressibility. However, the sensitivity ranking obtained in this study is specific to upward pile displacement. A different ranking may be obtained for analyses focused on shear strength, bearing capacity, or post-yield failure behavior.

Acknowledgments
The authors acknowledge the laboratory and computational facilities of the Department of Civil Engineering at Middle East Technical University, where the experimental database used in this study was generated.

Funding
This research received no external funding.

Conflict of Interest
The authors declare no conflict of interest.

References
1. Chen, F.H.: Foundations on Expansive Soils. 2nd edn. Elsevier, New York (1988).
2. Nelson, J.D., Miller, D.J.: Expansive Soils: Problems and Practice in Foundation and Pavement Engineering. John Wiley & Sons, New York (1992).
3. Fredlund, D.G., Rahardjo, H.: Soil Mechanics for Unsaturated Soils. John Wiley & Sons, New York (1993).
4. Yıldırım, S.: Numerical and experimental analysis of single pile foundation behavior in expansive Ankara clay. Doctoral dissertation, Middle East Technical University, Ankara, Türkiye (2025).
5. Nelson, J.D., Chao, K.C., Overton, D.D., Nelson, E.J.: Foundation Engineering for Expansive Soils. John Wiley & Sons, Hoboken (2015). doi: 10.1002/9781118996096
6. Yıldırım, S., Çokça, E.: Experimental and numerical analysis of single pile foundation behavior in expansive Ankara clay. International Journal of Geotechnical Engineering, in press (2026). doi: 10.1080/19386362.2026.2710998
7. Yıldırım, S., Çokça, E.: Assessment of climatic moisture regime of expansive Çubuk clay using the Thornthwaite Moisture Index. In: 7th International Eurasian Conference on Science, Engineering and Technology (EurasianSciEnTech 2026), pp. 587–592. EurasianSciEnTech, 24–26 June 2026 (2026).
8. Liu, Y., Vanapalli, S.K.: Load-displacement analysis of a single pile in an unsaturated expansive soil. Computers and Geotechnics 106, 83–98 (2019). doi: 10.1016/j.compgeo.2018.10.007
9. Wu, X., Vanapalli, S.K.: Three-dimensional modeling of the mechanical behavior of a single pile in unsaturated expansive soils during infiltration. Computers and Geotechnics 145, 104696 (2022). doi: 10.1016/j.compgeo.2022.104696

10. Soundara, B., Robinson, R.G.: Hyperbolic model to evaluate uplift force on pile in expansive soils. KSCE Journal of Civil Engineering 21(3), 746–751 (2017). doi: 10.1007/s12205-016-1001-8
11. Alonso, E.E., Gens, A., Josa, A.: A constitutive model for partially saturated soils. Géotechnique 40(3), 405–430 (1990). doi: 10.1680/geot.1990.40.3.405
12. Gens, A., Alonso, E.E.: A framework for the behaviour of unsaturated expansive clays. Canadian Geotechnical Journal 29(6), 1013–1032 (1992). doi: 10.1139/t92-120
13. Alonso, E.E., Vaunat, J., Gens, A.: Modelling the mechanical behaviour of expansive clays. Engineering Geology 54(1–2), 173–183 (1999). doi: 10.1016/S0013-7952(99)00079-4
14. Wheeler, S.J., Sivakumar, V.: An elasto-plastic critical state framework for unsaturated soil. Géotechnique 45(1), 35–53 (1995). doi: 10.1680/geot.1995.45.1.35
15. Cui, Y.J., Delage, P.: Yielding and plastic behaviour of an unsaturated compacted silt. Géotechnique 46(2), 291–311 (1996). doi: 10.1680/geot.1996.46.2.291
16. Sheng, D., Fredlund, D.G., Gens, A.: A new modelling approach for unsaturated soils using independent stress variables. Canadian Geotechnical Journal 45(4), 511–534 (2008). doi: 10.1139/T07-112
17. van Genuchten, M.T.: A closed-form equation for predicting the hydraulic conductivity of unsaturated soils. Soil Science Society of America Journal 44(5), 892–898 (1980). doi: 10.2136/sssaj1980.03615995004400050002x
18. Kenanoğlu, M.B., Toker, N.K.: Calibration of Barcelona Basic Model Parameters for Unsaturated Soils: A Practical Framework for Constant Suction Deviatoric Loading. International Journal of Geomechanics 25(9), 04025195 (2025). doi: 10.1061/ijgnai.gmeng-10032
19. Yıldırım, S., Çokça, E.: Reliability of multi-method mineralogical identification in expansive soils. Gazi University Journal of Science 39(3), in press (2026). https://doi.org/10.35378/gujs.1912448
20. Yıldırım, S., Çokça, E.: Determination of the adhesion factor in expansive Ankara-Çubuk clay. In: 9th International Conference on Applied Engineering and Natural Sciences, Konya, Türkiye (2026).

Author Contribution Statement

- *Conceptualization:* Sefa Yıldırım, Erdal Çokça
- *Methodology:* Sefa Yıldırım, Erdal Çokça
- *Investigation:* Sefa Yıldırım
- *Numerical Analysis:* Sefa Yıldırım
- *Writing – Original Draft:* Sefa Yıldırım
- *Writing – Review & Editing:* Erdal Çokça
- *Supervision:* Erdal Çokça

List of Abbreviations

- **BBM** — Barcelona Basic Model
- **FEM** — Finite Element Method
- **SWRC** — Soil Water Retention Curve

Publication Note
This paper was peer-reviewed, accepted for presentation, and included in the proceedings of the ACE2026 – International Conference on Advances in Civil Engineering, held on 12–14 October 2026 in Trabzon, Türkiye.

This paper may be cited as follows:
Yıldırım S., Çokça E., "Response-Based Sensitivity Analysis of Barcelona Basic Model Parameters for Pile Heave in Expansive Ankara Clay," in Proceedings of the ACE2026 – International Conference on Advances in Civil Engineering, Trabzon, Türkiye, 12–14 October 2026.

Osterberg Cell (O-Cell) Load Testing for Deep Foundation Capacity Assessment: Principles, Instrumentation, and Case Studies

Hasan Altawil[1] and Özcan Tan[2]

[1] ORCID: 0000-0002-1234-5678, Islamic University of Gaza, Department of Civil Engineering, Gaza/Palestine, dr.htawil@gmail.com

[2] Deceased. Prof. Dr. Özcan Tan made substantial scientific contributions to the conception, supervision, and development of this work prior to his passing; Konya Technical University, Department of Civil Engineering, Konya, Turkey.

Abstract. Accurate determination of pile bearing capacity is critical for deep foundation design in large-scale infrastructure. Conventional static load testing presents significant limitations for high-capacity piles exceeding 10–20 MN, requiring complex reaction systems and large workspaces. The Osterberg Cell (O-Cell) bidirectional load testing method offers a superior alternative by embedding a hydraulic jack within the pile itself, creating a self-reacting system that eliminates external reaction infrastructure. This study presents a comprehensive review of O-Cell methodology, including working principles, instrumentation systems (Linear Vibrating Wire Displacement Transducers, telltale extensometers, strain gauges, pressure gauges, and automated data loggers), and loading protocols. The method automatically separates skin friction from end-bearing resistance with direct measurements at multiple levels. Two field case studies demonstrate practical applications: (1) the Anadolu Highway Viaduct in Turkey, where O-Cell testing verified a 1.85 m diameter rock-socketed pile at twice the design load with only 0.3% normalized settlement, and (2) the Flame Towers Project in Baku, where a 1.2 m diameter, 36 m deep bored pile yielded an equivalent top-down capacity of 15.4 MN. Key advantages include high loading capacity (up to 320 MN, world record), no external reaction systems, automatic component separation, pile reuse after grouting, minimal workspace requirements, and enhanced safety. The O-Cell method is particularly advantageous for test loads exceeding 10 MN and has been applied in over 900 projects across 32 countries.

Keywords: Osterberg Cell; Bidirectional Load Testing; Pile Bearing Capacity; Deep Foundations; Skin Friction; End Bearing.

1 Introduction

The design of deep foundations represents one of the most complex challenges in geotechnical engineering, particularly in large-scale projects where structural loads far exceed the capacity of shallow foundation systems [1]. In such cases, bored piles (drilled shafts) are employed to transfer superstructure loads to deeper, more competent soil or rock strata. The reliable determination of pile bearing capacity is therefore of paramount importance for ensuring structural safety, optimizing foundation design, and achieving economic efficiency.

Pile bearing capacity can be estimated through theoretical and empirical analytical methods, dynamic testing approaches, and full-scale static load testing. Among these, static load testing remains the most reliable and direct method, as it replicates actual field loading conditions at prototype scale. However, conventional top-down static load testing presents significant practical and economic constraints, particularly when high-capacity piles with test loads in the range of 10–20 MN or greater are involved [2]. The construction of appropriate reaction

systems (anchor piles, ground anchors, or kentledge platforms) demands considerable workspace, time, material resources, and introduces non-trivial safety hazards.

The Osterberg Cell (O-Cell) bidirectional load testing method, developed by Dr. Jorj O. Osterberg of Northwestern University and introduced to the construction industry in 1991, represents a paradigm shift in pile load testing technology [3]. By embedding a hydraulic jack within the pile itself, the O-Cell method exploits the pile's own resistance components as a self-reacting system, thereby circumventing the need for external reaction infrastructure. Since its introduction, the method has been applied in over 900 projects across 32 countries by 2009, with test loads reaching a world record of 320 MN in 2010.

This paper presents a systematic review of O-Cell testing principles, instrumentation, test execution methodology, comparison with conventional methods, and analysis of two significant field case studies conducted in Turkey and Azerbaijan.

2 Background: Deep Foundations and Pile Load Testing

2.1 Deep Foundation Systems

Piles are structural members of timber, concrete, or steel that transfer superstructure loads to deeper soil or rock strata through a combination of shaft friction and end bearing. They are employed when shallow foundations cannot provide adequate bearing capacity, when excessive settlements are anticipated, or when uplift, lateral, or moment loads must be resisted. Pile types are classified by material (timber, steel, reinforced concrete, composite), installation method (driven, bored/cast-in-place, CFA, screw), and load transfer mechanism (friction, end-bearing, combined).

The total axial capacity of a pile is expressed as:

$$Q_f = Q_b + Q_s = q_b.A_b + f_s.A_s \quad (1)$$

where Q_f is the ultimate bearing capacity, Q_b is the end-bearing resistance, Q_s is the total shaft friction resistance, q_b is the unit end-bearing stress, f_s is the unit skin friction stress, A_b is the pile tip cross-sectional area, and A_s is the pile shaft surface area.

2.2 Conventional Pile Load Testing Methods

Static pile load tests are conducted using one of three principal loading configurations: axial compression (ASTM D1143), axial tension/uplift (ASTM D3689), and lateral loading (ASTM D3966) [4]. In axial compression testing, load is applied to the pile head via a hydraulic jack reacting against either a loaded platform (kentledge), anchor piles, or ground anchors, and pile head settlement is measured at specified load increments. Loading procedures include Slow Maintained Load (SML), Quick Maintained Load (QML), Constant Rate of Penetration (CRP), and Cyclic (Swedish) methods.

While these methods are well-established, their application to high-capacity large-diameter bored piles is severely constrained by the size and cost of the required reaction systems. For a 100 cm diameter test pile, ASTM D1143 requires anchor pile clear spacing of five pile diameters or minimum 2.0 m, resulting in workspace requirements of approximately 150 m² or greater. At test loads exceeding 10–20 MN, reaction system construction becomes a primary engineering challenge and cost driver.

3 The Osterberg Cell Method

3.1 Concept and Operating Principle

The Osterberg Cell (O-Cell) is a sacrificial, calibrated, hydraulic flat jack device embedded at or near the base of a bored pile during reinforcement cage assembly. When hydraulically pressurized after pile concreting and curing, the O-Cell expands bidirectionally: the upward reaction load mobilizes shaft friction along the pile segment above the cell, while the equal and

opposite downward reaction load mobilizes shaft friction and end-bearing capacity in the pile segment below the cell [5].

This self-reacting mechanism means that the pile itself serves as both the loading mechanism and the reaction system, eliminating the need for external reaction infrastructure. The O-Cell independently separates and quantifies the two primary resistance components of pile capacity, skin friction and end bearing, which cannot be directly distinguished in conventional top-down testing without supplementary instrumentation.

The O-Cell load value is determined by correlating the applied hydraulic pressure with the cell's load calibration curves provided by the manufacturer. The working principle satisfies the equilibrium condition:

$$P = F \text{ (skin friction above)} = Q \text{ (end bearing + skin friction below)} \quad (2)$$

3.2 Historical Development and Global Adoption

The O-Cell concept was developed and patented by Dr. Jorj O. Osterberg and introduced commercially through LOADTEST Inc. in 1991. The method gained rapid acceptance due to its technical advantages in high-capacity testing scenarios. Key milestones include [6]:

1991: Commercial introduction of O-Cell testing (LOADTEST)
2005: World record test load of 279 MN, Korea
2009: Over 900 O-Cell tests completed in 32 countries
2010: New world record of 320 MN, Missouri–Illinois Bridge (3.35 m diameter piers)
2011: LOADTEST reports over 2,000 test applications, with annual growth of 300–400 tests

Standard O-Cell dimensions and nominal capacities in common use are summarized in Table 1.

Table 1. Standard O-Cell Dimensions and Nominal Capacities (LOADTEST, 1991)

Nominal Diameter (mm)	Nominal Capacity (MN)
230	1.8
330	3.6
540	8.9
660	16.0
870	27.0

4 Instrumentation System

The O-Cell test relies on a comprehensive instrumentation package, all components of which are factory-calibrated and delivered with calibration certificates. The principal instruments are as follows:

4.1 Telltale Rod and Casing Extensometers

Two pairs of telltale rod-and-casing extensometers are installed: one pair extending from the O-Cell upper plate to the pile top (measuring compression of the upper pile segment), and a second pair extending from the O-Cell lower plate to the pile top (measuring compression and tip movement of the lower pile segment). Measurements are rounded to the nearest 0.01 mm.

4.2 Linear Vibrating Wire Displacement Transducers (LVWDT)

Three or four LVWDT units are placed between the upper and lower O-Cell bearing plates at 120° angular spacing to directly and continuously measure O-Cell expansion. Additional LVWDTs attached to telltale rods at the pile head measure upward pile movement relative to an independent reference beam.

4.3 Vibrating Wire Strain Gauges (VWSG)

Multiple strain gauge levels are installed along the pile shaft above and below the O-Cell to determine the distribution of mobilized unit skin friction with depth. Gauges are installed in diametrically opposed pairs at each instrumented level.

4.4 Bourdon Pressure Gauge and Pressure Transducer

A calibrated high-capacity Bourdon gauge measures hydraulic pressure in the pump supply line, while a high-resolution calibrated pressure transducer measures return line pressure for reference confirmation. These readings are used to calculate the applied O-Cell load via the manufacturer's calibration curves.

4.5 Automated Data Logger

All LVDTs, LVWDTs, and VWSGs are connected via multiplexers to an automated data logger interfaced with a laptop computer, enabling simultaneous readings at 0.5-minute intervals throughout the test. The data logger also records temperature readings at each instrumented level for thermal correction purposes.

5 Test Execution Methodology

5.1 Pile Preparation and O-Cell Assembly

Prior to pile installation, the O-Cell assembly (comprising the hydraulic jack, upper and lower bearing plates, LVWDTs, telltale casings, hydraulic supply lines, and strain gauge cables) is welded to the reinforcement cage at the predetermined depth. Temporary support welds maintain assembly integrity during lifting and installation. The cage is lowered into the borehole, verified for verticality (maximum deviation 1/50), and the O-Cell orientation is confirmed perpendicular to the pile axis (tolerance 1/100). Tremie concrete placement proceeds from the bottom up, with concrete strength verified through cube specimens tested at 7, 10, and 21 days.

5.2 Loading Protocol

Testing commences after the pile concrete achieves the minimum specified compressive strength (typically at 10 days). The standard loading program comprises [7]:

Loading phase: 12 equal load increments to maximum test load or O-Cell capacity

Hold criterion at each increment: Minimum 30 minutes OR until creep rate falls below 0.05 mm per 10 minutes (maximum hold time: 3 hours)

Unloading phase: 4 equal decrements with approximately 10-minute holds each

Zero load hold: Minimum 1 hour observation after full unloading

The test is terminated upon reaching the predetermined test load, the O-Cell maximum travel distance (150 mm), or the ultimate capacity of either the upper or lower pile segment.

5.3 Data Interpretation

The equivalent top-down load-settlement curve is constructed by combining the upward and downward displacement measurements from the O-Cell test, accounting for elastic pile compression and pile self-weight. If skin friction failure precedes end-bearing failure, a nominal static load can be applied at the pile top to continue testing for end-bearing capacity. After test completion, the O-Cell cavity is grouted, and the pile can be incorporated into the permanent foundation system.

6 Comparison with Conventional Methods

Table 2 presents a systematic comparison of the O-Cell method with conventional static load testing and dynamic load testing approaches.

Table 2. Comparison of Pile Testing Methods

Parameter	Conventional Static	O-Cell Bidirectional	Dynamic Testing
Maximum Test Load	~20 MN	>320 MN	Moderate
Workspace Required	Large (~150 m²)	Minimal	Small
Separate Components	No	Yes (automatic)	Indirect
Pile Reuse After Test	Possible	Yes (after grouting)	Yes

6.1 Key Advantages of O-Cell Testing

High loading capacity: Routinely achieves 27 MN per single O-Cell; multiple O-Cells enable loads exceeding 220 MN

No reaction system: Eliminates anchor piles, kentledge, and reaction frames

Automatic separation of skin friction and end-bearing components

Rock socket friction assessment: Direct loading of socket zone through targeted O-Cell placement

Pile reuse: Post-test grouting restores structural continuity

Reduced working load stress: Only half the test load acts on any pile cross-section

Minimal workspace: Applicable in confined environments, under structures, and offshore

Enhanced safety: No surface-level high-energy loading systems

6.2 Limitations

Test pile must be pre-designated before construction

Maximum applicable load limited by the lesser of upper skin friction or lower skin friction plus end bearing

Interpretation of results requires specialized expertise

Pile cap zone cannot be directly tested

7 Case Studies

7.1 Case Study 1: Anadolu Highway Viaduct (Gümüşova–Gerede, Turkey)

Project Context:

The Anadolu Highway V4 viaduct required verification of pile capacity in completely weathered meta-diorite rock.

Pile and Test Parameters:

Pile diameter: 1.85 m

Pile length: 12 m (embedded length in rock: 5.40 m)

Rock formation: Completely weathered meta-diorite

Test load achieved: 1,600 tons (2× design load)

Results:

At maximum test load, maximum pile settlement was 5.25 mm, equivalent to a normalized settlement of 0.3% of pile diameter, indicating that the entire axial load was carried by unit skin friction without mobilization of end-bearing failure. Back-analysis yielded an ultimate unit skin friction of $\tau_k = 0.524$ MPa, consistent with competent weathered rock socket performance.

Significance:

This case demonstrates the O-Cell method's capability to directly load a rock-socketed pile at twice the design load, achieving clear verification of capacity with minimal displacement, a result that would have required a very large and costly reaction system with conventional testing.

7.2 Case Study 2: Flame Towers Project, Baku, Azerbaijan

Project Context:

The Flame Towers Project in Baku comprises three high-rise towers with basement parking and retail levels. Given the high seismicity, wind loads, and complex soil profile at the site, piled raft foundations were adopted for each tower, with the Hotel Tower designed on 1.20 m diameter, 34.0 m deep bored piles with an allowable design load of Q_all = 1,150 tonnes.

Test Pile TP1 Configuration:

Nominal diameter: 1,200 mm

Total pile length: 36.0 m

O-Cell location: 11.90 m above pile base

O-Cell size: 2 × 405 mm diameter units, calibrated to 6.3 MN each

Test Execution and Results:

Testing was conducted on 23 October 2008 following preload cycling. The first six load increments yielded coherent and consistent data up to an O-Cell load of 5.71 MN (at 31.03 MPa pressure). At this load level, displacements above and below the O-Cell were 2.5 mm (upward) and 1.2 mm (downward), respectively. Equivalent top-down analysis demonstrated that the O-Cell load of 5.71 MN corresponds to an equivalent conventional top-down load of approximately 15.4 MN. Extrapolated settlement predictions indicated 9.2 mm at working load (11.0 MN) and 13.5 mm at 1.5× working load (16.5 MN), confirming satisfactory pile performance within design limits.

8 Conclusions

This study has presented a comprehensive technical review of the Osterberg Cell (O-Cell) bidirectional pile load testing method and its application in geotechnical engineering practice. The following principal conclusions are drawn:

The O-Cell method provides a reliable, accurate, and self-contained system for determining pile bearing capacity through bidirectional internal loading, automatically separating skin friction from end-bearing resistance without requiring external reaction infrastructure [8].

At test loads exceeding 10 MN, the O-Cell method demonstrates clear cost, safety, and logistical advantages over conventional top-down static load testing, with demonstrated capability up to 320 MN.

The comprehensive instrumentation package, comprising LVWDTs, telltale extensometers, vibrating wire strain gauges, pressure gauges, and automated data loggers, enables high-precision, multi-parameter characterization of pile behavior throughout the test.

Case Study 1 (Anadolu Highway Viaduct) confirmed successful capacity verification at twice the design load for a rock-socketed pile, with an ultimate unit skin friction of τ_k = 0.524 MPa and negligible pile settlement (0.3% D).

Case Study 2 (Flame Towers, Baku) demonstrated the method's effectiveness in a multi-layered soil profile, yielding an equivalent top-down capacity of 15.4 MN from an O-Cell load of 5.71 MN, and providing reliable settlement predictions within acceptable design limits.

Post-test grouting of the O-Cell cavity restores full structural integrity, enabling the test pile to be incorporated into the permanent foundation system, representing an additional economic advantage.

The O-Cell method has established itself as the preferred approach for high-capacity pile load testing worldwide and is expected to continue expanding its application in complex geotechnical environments, offshore foundations, and mega-infrastructure projects.

Acknowledgments

The author wishes to express his deepest gratitude and respect to the late Prof. Dr. Özcan Tan, whose scientific guidance, mentorship, and invaluable contributions laid the foundation for this work. Prof. Tan supervised the research during its development and provided essential

academic insight before his passing. His dedication to geotechnical engineering and his lasting influence on this study are gratefully acknowledged and respectfully remembered.

References

1. ASTM D1143/D1143M-21, Standard test methods for deep foundations under static axial compressive load. American Society for Testing and Materials, Philadelphia (2021).
2. England, M., Review of methods of analysis of test results from bi-directional pile tests. In: Proceedings of the 4th International Conference on Deep Foundation Practice, Singapore (2003).
3. Osterberg, J.O., New simplified method for load testing drilled shafts. Foundation Drilling, ADSC (1984).
4. ASTM D3689/D3689M-21, Standard test methods for deep foundations under static axial uplift load. American Society for Testing and Materials, Philadelphia (2021).
5. Osterberg, J.O., New device for load testing driven piles and drilled shafts separates friction and end bearing. In: Proceedings of the International Conference on Piling and Deep Foundations, London, pp. 421–427 (1989).
6. Fugro–LOADTEST Inc., Bi-directional Osterberg cell load testing, technical brochure. Fugro Group (2012).
7. Dinç, H. "Osterberg hücresi ile kazık taşıma kapasitesinin belirlenmesi. İstanbul Teknik Üniversitesi (İTÜ), Fen Bilimleri Enstitüsü (Istanbul Technical University, Graduate School of Science, Engineering and Technology), (2010).
8. Schmertmann, J.H. and Hayes, J.A., The Osterberg cell and bored pile testing, a symbiosis. In: Proceedings of the 3rd International Geotechnical Engineering Conference, Cairo, pp. 139–166 (1997).

Author Contribution Statement

- *Conceptualization: Hasan Altawil*
- *Methodology: Hasan Altawil*
- *Investigation: Hasan Altawil*
- *Writing – Original Draft: Hasan Altawil*
- *Writing – Review & Editing*
- *Supervision: Özcan Tan*

List of Abbreviations

- **SML** — Maintained Load,
- **QML** — Quick Maintained Load,
- **CRP** — Constant Rate of Penetration,
- **O-Cell** — Osterberg Cell
- **LVWDT** — Linear Vibrating Wire Displacement Transducers
- **VWSG** — Vibrating Wire Strain Gauges

Publication Note

This paper was peer-reviewed, accepted for presentation, and included in the proceedings of the ACE2026 – International Conference on Advances in Civil Engineering, held on 12–14 October 2026 in Trabzon, Türkiye.

This paper may be cited as follows:

Altawil, H., Tan, O., "Osterberg Cell (O-Cell) Load Testing for Deep Foundation Capacity Assessment: Principles, Instrumentation, and Case Studies," in Proceedings of

the ACE2026 – International Conference on Advances in Civil Engineering, Trabzon, Türkiye, 12–14 October 2026.

Investigation of the Geotechnical Properties of Sandy Soils Stabilized with Granular Shingle Waste

Inci Develioglu[1] and Rumeysa Bulut[2]
[1] 0000-0001-6594-8095, Izmir Katip Celebi University, Civil Engineering Department, Izmir, Türkiye, inci.ertam@ikcu.edu.tr
[2] 0009-0000-0896-3723, Izmir Katip Celebi University, Civil Engineering Department, Izmir, Türkiye, rumeysabulut643@gmail.com

Abstract. This study investigates the potential use of granular shingle waste (GSW) as an alternative additive for improving the geotechnical properties of sandy soils. The waste material consists of mineral-based granular particles collected as a by-product during shingle production. Crushed sand was mixed with varying percentages of GSW, and laboratory tests were conducted to evaluate the changes in the engineering behavior of the mixtures. The experimental program includes grain size distribution analysis, specific gravity tests, liquid limit tests, standard Proctor compaction tests and direct shear tests. The influence of different GSW contents on the physical and mechanical properties of the sandy soil was assessed through comparisons of grain distribution, classification, liquid limit, maximum dry unit weight, optimum moisture content and shear strength parameters. Preliminary observations indicate that the inclusion of GSW alters the particle size distribution of the sand and may enhance shear strength characteristics depending on the additive ratio. Test results showed that the liquid limit decreased from 24.9 to 22.0, while specific gravity increased from 2.68 to 2.74 with increasing GSW. The maximum dry unit weight increased from 17.4 kN/m³ to a peak of 18.1 kN/m³ at 10% GSW, beyond which it decreased slightly to 17.3 kN/m³ at 20%, while the optimum moisture content increased steadily from 10.7% to 11.9%. Direct shear tests revealed a substantial increase in the internal friction angle, from 31.5° to 49.9°, accompanied by a decrease in cohesion from 17.8 kPa to 4.6 kPa, indicating a shift toward friction-controlled shear behavior at higher additive contents.

Keywords: Geotechnical index properties; Sandy soil; Shingle waste; Soil improvement

1 Introduction

Due to rapidly increasing population and urbanization, the necessity of constructing structures on and/or within soils that lack the engineering properties suitable for civil engineering applications is becoming an increasingly common issue. Cohesionless and loosely structured sandy soils are often unsuitable for direct use in many engineering projects due to problems such as low bearing capacity, insufficient shear strength, and excessive permeability. Binding materials such as cement, lime, or fly ash have traditionally been used to improve the engineering performance of such soils; however, the production processes of these materials are associated with high energy consumption and carbon emissions. For this reason, the investigation of alternative additive materials that are both economically and environmentally sustainable for soil improvement applications constitutes one of the current and significant research areas in geotechnical engineering [1–3].

In this context, the reuse of various industrial and domestic waste materials for soil improvement purposes has attracted considerable interest in recent years. The use of waste materials as soil additives reduces the consumption of natural resources while also providing

an environmental benefit by decreasing the volume of waste accumulating in landfills. It has been reported that traditional materials such as cement and lime are increasingly being replaced by waste materials such as stone slurry waste, coffee grounds, rice husk ash, crushed waste concrete and glass, natural fibers, sawdust, and waste tires, and that an appropriate amount of waste additive reduces the compressibility of the soil while increasing its maximum dry unit weight (MDU) and shear strength, thereby contributing to soil strengthening. The use of waste materials as additives is regarded as both an economically and ecologically beneficial soil improvement method, as it eliminates material costs and helps mitigate the waste disposal problem, which is often costly and problematic [4].

The literature contains numerous experimental studies supporting this approach. In one such study, plastic waste particles obtained from discarded plastic water bottles were mixed into sandy soil at various proportions (0, 0.5, 0.75, and 1.0% by weight), and direct shear and California bearing ratio (CBR) tests were conducted; it was determined that the addition of plastic waste particles improved the shear strength of the sandy soil due to the increased friction between the soil particles and the plastic waste [5].

The use of waste tires is another method frequently investigated in geotechnical engineering. In a study conducted in Algeria, rubber granules were mixed into sand from the Chlef River at proportions of 5, 10, 15, 20, and 30% by weight, and direct shear tests were performed at various relative density values; it was observed that the rubber granule content increased the shear strength properties of the sand-rubber granule mixtures. [6].

In a study investigating the effect of glass waste on the shear strength of sandy soils, crushed waste glass was mixed into sand at three different sizes and four different percentage ratios, and direct shear tests were performed. The results showed that the addition of crushed waste glass reduced the optimum moisture content (OMC) but had little to no effect on the MDU of the sand. It was reported that the addition of crushed waste glass increased the shear strength of the engineering sand at all ratios, that the highest shear strength was observed at a 5% sand-glass waste mixture across all glass sizes, and that the primary increase occurred in the internal friction angle of the sand [7]. In another study supporting this finding, natural sand was progressively replaced with fine-grained crushed waste glass, and the results revealed that the MDU increased and the OMC decreased; cohesion rose from 0 kPa to 5.7 kPa, while the internal friction angle increased from 41.5° to 44.4° [8].

In a study in which cement kiln dust was used in layers to increase the bearing capacity of sandy soil, factors such as cement kiln dust layer thickness, number of layers, and layer position were evaluated, and a method was proposed in which the optimum cement kiln dust layer position was determined through direct shear testing [9]. Furthermore, in a recent study in which a geopolymer material produced from paper sludge ash was used for the stabilization of loose and poorly graded sands, the effects of curing time, alkali solution concentration and type, and the addition of different paper sludge ash ratios on the strength improvement of the stabilized sandy soil were investigated [10].

When these studies are evaluated as a whole, a wide variety of waste materials, including plastic, rubber, glass, industrial ash, and construction-demolition waste, have the potential to improve the physical and mechanical properties of sandy and other soil types. However, based on the comprehensive literature review conducted, no study has been found in which GSW, a mineral-based granular material generated during roofing (shingle) production, has been used to improve the geotechnical properties of soils. This points both to a significant research gap regarding the utilization of this waste material in geotechnical engineering and to the original contribution of the present study.

GSW has mostly been addressed in literature within the context of shingle (asphalt roofing material) production and recycling processes, in application areas other than soil improvement. Shingle granules are small, mineral-coated particles produced from crushed stone or mineral

blends and coated with ceramic pigments, which cover the surface of asphalt roofing materials; they function to protect the asphalt layer from ultraviolet radiation, thereby extending the service life of the roofing, providing fire resistance, and increasing surface traction during walking. In a study noting that the direct use of recycled asphalt shingle waste as fill material is limited due to its high compressibility, the potential use of recycled asphalt shingle as structural fill material in highway embankments or behind retaining walls was evaluated, and it was stated that, owing to its high compressibility, recycled asphalt shingle was instead selected as a granular additive to improve the mechanical properties of bottom ash and foundry slag. The same study also reported that approximately 11 million tons of asphalt roofing waste are generated annually in the United States, the majority of which is already being utilized by incorporation into hot mix asphalt. The use of shingle waste in the road construction sector is generally widespread as well; it is known that asphalt shingle recycling involves converting shingles into an additive for hot mix asphalt or into cold patches for filling road cracks and potholes. In addition, there are studies evaluating roofing granules as a fine aggregate substitute in concrete and tile production; in these studies, various waste materials such as rubber ash, sawdust, seashells, crumb rubber, pistachio shells, fly ash sand, stone dust, and copper slag have been partially used in place of fine aggregate in roofing tile mortar [11–13].

This study investigates the potential use of GSW, a by-product generated during roofing (shingle) production with a mineral-based granular structure, as an alternative additive material for improving the geotechnical and shear strength properties of sandy soils. Within this scope, clean sand was mixed with GSW at different proportions (5, 10, 15, and 20%), and a comprehensive experimental program was carried out to determine the changes in the engineering behavior of the mixtures, consisting of grain size distribution analysis, specific gravity tests, liquid limit tests, standard Proctor compaction tests, and direct shear tests. The effect of different shingle waste proportions on the soil's grain size distribution, classification, liquid limit, MDU, OMC, and shear strength parameters was comparatively evaluated. This study is expected to contribute to sustainable waste management by reducing the disposal of this industrial waste in landfills, as well as to introduce into the literature the usage potential of a waste material that has not previously been evaluated in geotechnical engineering.

2 Materials and Methods

In this study, crushed sand was used as the base soil material. Crushed sand is a commercially available material that is widely preferred in fills and concrete production. The crushed sand used in the study was obtained from a commercial source, and the geotechnical and mechanical properties of the material were determined prior to the start of testing. The characterization results obtained are presented in the following sections. The physical appearance of the crushed sand is shown in Figure 1a. The GSW used as the additive material in this study was obtained directly from a facility engaged in shingle production. The material was collected from the by-product waste accumulating beneath the production lines and was used without any pretreatment. Although GSW has a mineral-based granular structure, information regarding its grain size, specific gravity, and other physical properties is presented in detail in the experimental results section. The physical appearance of GSW is shown in Figure 1b.

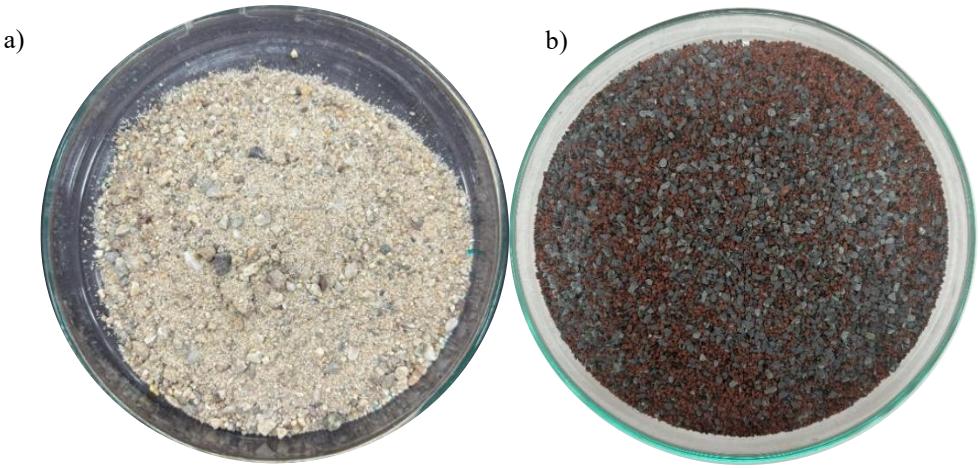


Fig. 1. Physical appearance of a) crushed sand, b) granular shingle waste.

Within the scope of the experimental program, crushed sand was mixed with GSW at proportions of 0, 5, 10, 15, and 20% of the total mixture weight. The 0% specimen was considered the reference soil, while the other proportions were determined to systematically evaluate the effect of increasing additive content on soil behavior. Dry sieve analysis tests were performed to determine the grain size distribution of the sand soil, the GSW, and mixtures based on the ASTM D6913 standard [14]. The specific gravity values of the sand soil, the GSW, and mixtures were determined using the pycnometer method in accordance with the ASTM D854 standard [15]. The liquid limit test using the cone penetration method was performed to evaluate the plasticity of the sand soil and mixtures. The test was conducted based on the BS 1377-2 standard [16]. Standard Proctor tests were performed to determine the compaction properties of the sand, the GSW, and mixtures. The tests were conducted in accordance with the ASTM D698 standard [17]. Direct shear tests were performed to determine the shear strength parameters of the sand, the GSW, and mixtures. The tests were conducted based on the ASTM D3080 standard using a 60 mm × 60 mm shear box [18]. Specimens for each mixture proportion were prepared at the MDU and OMC values obtained from the standard Proctor test. The tests were performed under three different normal stresses of 49, 98, and 196 kPa, with the shear rate kept constant at 0.5 mm/min in all tests. The mixing ratios and sample abbreviations used in the experiments are listed in Table 1.

Table 1. The mixing ratios and sample abbreviations.

Abbreviation	GSW Ratio (%)
S-0SW	0
S-5SW	5
S-10SW	10
S-15SW	15
S-20SW	20

3 Experimental Results

The particle size distribution curves for the addition of GSW at different proportions are shown in Figure 2. It is observed that the general character of the curves is preserved with the addition of GSW; however, the coarse grain fraction increases progressively with increasing additive content. This change has resulted in a limited shift of the particle size distribution curves toward

the coarser grain direction, while no significant difference has occurred in the granulometric properties of the mixtures at the additive proportions examined.

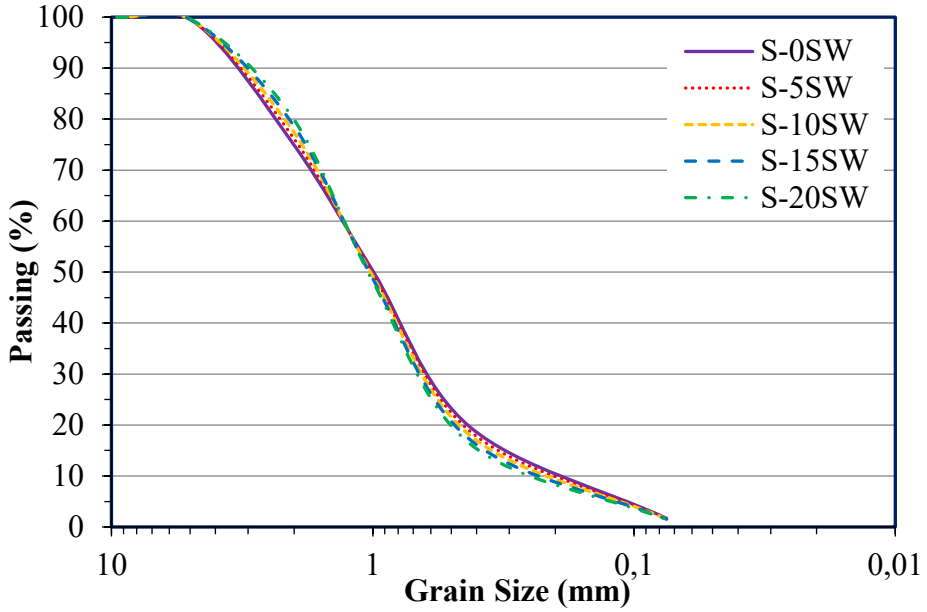


Fig. 2. Grain size distribution curves of sand - GSW mixtures.

Figure 3 shows the effect of the addition of GSW at different proportions on the liquid limit and specific gravity values of the soil. A consistent decrease in liquid limit values occurred with increasing GSW content. The liquid limit value, determined as 24.9 for the sand, was found to be 23.9, 23.4, 23.3, and 22.0 with the addition of 5, 10, 15, and 20% GSW, respectively. At the highest additive proportion, the liquid limit value decreased by approximately 11.6% compared to the initial specimen. This decrease can be attributed to the reduced water retention tendency of the mixture due to the non-plastic nature of the GSW. When the specific gravity results are examined, a consistent upward trend was observed in parallel with the increase in GSW content. The specific gravity, determined as 2.68 for the unamended specimen, reached 2.74 with the addition of 20% GSW, while values of 2.70, 2.71, and 2.72 were obtained at the intermediate additive proportions, respectively.

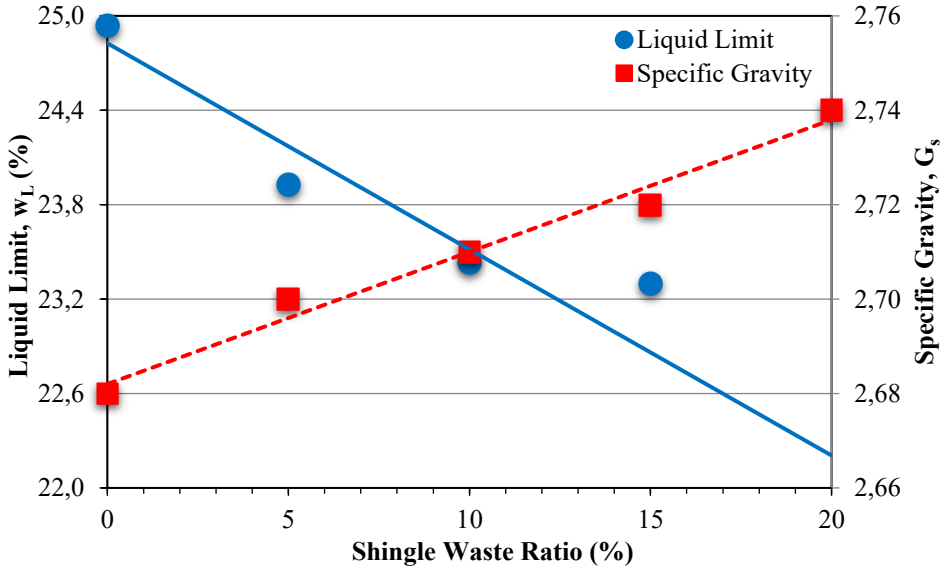


Fig. 3. Variation of liquid limit and specific gravity with GSW content.

The effect of the addition of GSW at different proportions on the MDU and OMC is presented in Figure 4. The test results reveal that the MDU first increases and then tends to decrease with increasing GSW content. The MDU, determined as 17.4 kN/m³ for the natural soil, reached its highest level of 18.1 kN/m³ with the addition of 10% GSW. However, when the additive proportion was increased beyond 10%, a limited decrease occurred in the MDU values, and the MDU was determined as 17.3 kN/m³ in the mixture containing 20% GSW. The findings obtained indicate that, in terms of MDU, a GSW content of approximately 10% provides the optimum compaction properties. When the OMC results are examined, a continuously increasing trend was observed depending on the increase in GSW content. The OMC, determined as 10.7% for the natural soil, increased to 11.9% with the addition of 20% GSW. This increase in OMC indicates that the mixture requires a higher water content to reach optimum compaction conditions in order to attain the MDU.

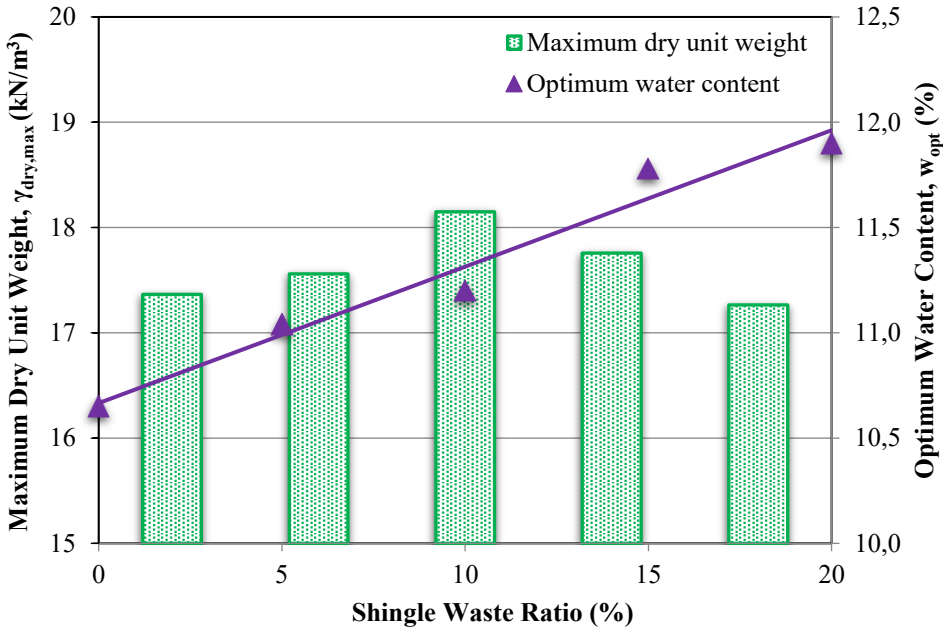


Fig. 4. Effect of GSW content on maximum dry unit weight and optimum moisture content.

Figure 5 presents the effect of the addition of GSW at different proportions on the internal friction angle (ϕ) and cohesion (c). The test results show that significant changes occur in the shear strength parameters with increasing GSW content. The internal friction angle, determined as 31.5° for the natural soil, increased continuously with the increase in GSW content and reached its highest value of 49.9° at 20% GSW content. The results obtained indicate that the addition of GSW significantly increases the frictional resistance of the soil. In contrast, a consistent decreasing trend was observed in cohesion values with increasing GSW. The cohesion, determined as 17.8 kPa for the natural soil, decreased to 4.6 kPa at 20% GSW. This decrease in cohesion can be attributed to the reduction of the binding effect between fine particles caused by the GSW. In contrast, the pronounced increase in the internal friction angle reveals that the shear strength behavior of the mixture increasingly exhibits friction-controlled behavior.

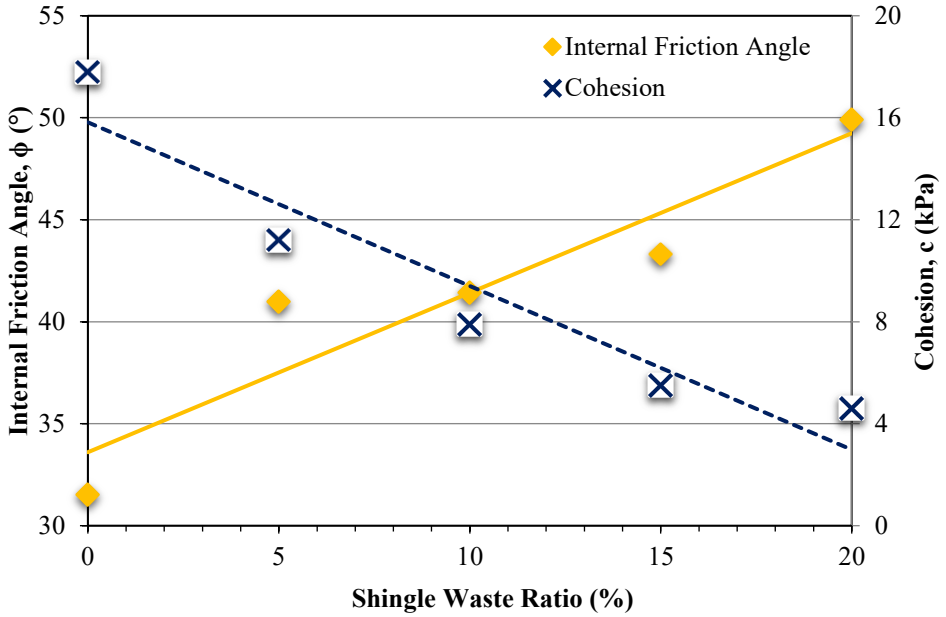


Fig. 5. Variation of cohesion and internal friction angle with GSW content.

4 Discussion

The addition of GSW resulted in noticeable changes in both the physical and mechanical properties of the sand soil. Although no major change was observed in the particle size distribution curves, the coarse grain fraction was found to increase progressively with increasing GSW content. While this did not significantly alter the overall granulometric character of the soil, it contributed to a reorganization of the grain skeleton and a change in the contact conditions between particles. The decrease observed in liquid limit values can be attributed to the non-plastic nature of the GSW. With the addition of GSW, the proportion of granular material in the mixture increased, thereby reducing the influence of fine particles and limiting the consistency change of the soil in the presence of water. In contrast, the increase in specific gravity values can be explained by the fact that GSW has a higher particle density than natural sand. Considered together, these findings suggest that the addition of GSW altered the physical properties of the mixture, contributing to the formation of a denser grain structure and reducing the soil's sensitivity to water. The results obtained from the compaction tests indicate that the changes occurring in the physical properties are directly reflected in the compaction behavior. At low additive proportions, the granular shingle particles filled the voids between sand grains more effectively, resulting in a more regular grain arrangement and contributing to an increase in MDU. However, as the additive proportion increased, the excess amount of GSW partially disrupted the regularity of grain arrangement, causing a limited decrease in MDU. On the other hand, the continuous increase in OMC indicates that the altered grain skeleton requires more water to reach the optimum compaction level. These results indicate that an addition of approximately 10% shingle waste represents the most favorable proportion in terms of compaction. The direct shear test results show that the addition of GSW has a significant effect on the shear strength of the soil. The pronounced increase observed in the internal friction angle can be attributed to the more effective mechanical interlocking developing between the granular shingle particles and the sand grains, along with an increase in inter-particle frictional resistance. In contrast, the decrease occurring in cohesion values can be explained by the granular additive reducing the binding effect between fine particles. This indicates that as the GSW content increases, the contribution of cohesion to the shear strength of the soil diminishes, while inter-particle friction becomes more decisive. Consequently, the addition of GSW increased the shear strength of the soil and contributed to behavior characterized by higher

frictional resistance. Overall, the addition of GSW altered the physical properties of the sand soil and positively affected its compaction and shear strength behavior. In particular, the improvements obtained up to an additive proportion of approximately 10% indicate that GSW can enhance engineering performance when used in an optimum amount. However, the limited changes observed in some properties at higher additive proportions reveal that determining the optimum additive proportion is important for soil improvement applications [19–20].

5 Conclusions

This study investigated the potential use of GSW, a mineral-based by-product generated during roofing (shingle) production, as an alternative additive material for improving the geotechnical properties of sandy soils. Crushed sand was mixed with GSW at proportions of 0, 5, 10, 15, and 20% by weight, and the effects of these mixtures were evaluated through a comprehensive experimental program comprising grain size distribution analysis, specific gravity, liquid limit, standard Proctor compaction, and direct shear tests. Based on the experimental findings, the following conclusions can be drawn:

- The addition of GSW did not substantially alter the overall character of the particle size distribution curves; however, the coarse grain fraction increased progressively with increasing additive content, indicating a limited shift toward coarser gradation and a reorganization of the grain skeleton.
- Liquid limit values decreased consistently with increasing GSW content, from 24.9 for the unamended soil to 22.0 at 20% GSW content, an effect attributed to the non-plastic nature of the additive and the corresponding reduction in the influence of fine particles.
- Specific gravity values increased steadily with increasing GSW relative to natural sand.
- Compaction behavior was found to be sensitive to additive content: the MDU increased from 17.4 kN/m³ to a peak of 18.1 kN/m³ at 10% GSW content, before decreasing slightly to 17.3 kN/m³ at 20% GSW content. The OMC increased continuously with additive content, from 10.7% to 11.9%, indicating that the modified grain skeleton required more water to achieve optimum compaction. These results identify approximately 10% GSW as the most favorable proportion in terms of compaction characteristics.
- Direct shear test results demonstrated a marked improvement in shear strength with increasing GSW. The internal friction angle increased substantially, from 31.5° for the natural soil to 49.9° at 20% GSW content, attributable to enhanced mechanical interlocking and inter-particle friction between the angular shingle particles and sand grains. In contrast, cohesion decreased from 17.8 kPa to 4.6 kPa over the same range, reflecting the reduced binding effect between fine particles as the proportion of granular additive increased. These trends indicate a progressive shift toward friction-controlled shear behavior with increasing GSW content.
- Overall, the incorporation of GSW was found to improve the compaction and shear strength characteristics of sandy soil, particularly at additive proportions up to approximately 10%, beyond which some properties exhibited limited or reversing trends. This underscores the importance of identifying an optimum additive proportion for practical soil improvement applications.

The findings of this study demonstrate, for the first time, the technical feasibility of utilizing GSW as a soil-improvement additive, thereby introducing a previously unexplored waste material into the geotechnical engineering literature. Beyond its technical merits, this approach offers a sustainable pathway for the reuse of an industrial by-product that is otherwise directed to landfill disposal, contributing to both waste minimization and resource efficiency. Future research is recommended to further investigate the long-term durability, environmental

leaching behavior, and field-scale applicability of shingle-waste-stabilized sandy soils, as well as their performance under cyclic and dynamic loading conditions.

Acknowledgments
The authors would like to thank BTM Company for kindly providing the granular shingle waste material used in this study.

Conflict of Interest
The authors declare that they have no known competing financial interests or personal relationships that could have appeared to influence the work reported in this paper.

Funding
This study was supported by the Scientific and Technological Research Council of Turkey (TÜBİTAK) under the 2224-B Grant Program.

References

1. Fatehi, H., Ong, D.E.L., Yu, J., Chang, I.: Biopolymers as Green Binders for Soil Improvement in Geotechnical Applications: A Review. Geosciences 11(7), 291 (2021).
2. Fattahi, S.M., Zamani, S., Imani, M., Heydari, A.: Sustainable stabilization of sandy soil using alkali-activated construction waste binders. Scientific Reports 16, 12012 (2026).
3. Ayeldeen, M.K., Negm, A.M., El Sawwaf, M.A.: Evaluating the physical characteristics of biopolymer/soil mixtures. Arabian Journal of Geosciences 9, 371 (2016).
4. Devi, K., Chhachhia, A., Kumar, A.: Soil Improvement Using Waste Materials: A Review. Journal of Building Material Science 2(1), 11–22 (2020).
5. Farah, R.E., Nalbantoglu, Z.: Performance of plastic waste for soil improvement. SN Applied Sciences 1, 1340 (2019).
6. Kaushik, M.K., Kumar, A., Bansal, A.: Drainage performance of different sizes tire chips used alone and mixed with natural aggregates as leachate drainage layer material. Geotechnical and Geological Engineering 34, 167–191 (2016).
7. Attom, M., Khan, Z., Al Lozi, N., Eltayeb, A.: Geo-environmental solution of using crushed glass waste to improve shear strength properties of sandy soil. In: International Conference on Environmental Geotechnology, Recycled Waste Materials and Sustainable Engineering, pp. 67–75. Springer Nature Singapore, Singapore (2022).
8. Islam, S., Alam, M.J.B., Islam, J., Chowdhury, A.S., Hasnat, N., Rafe, M.T.A., Al Jubair, S.A.: Partial replacement of sand with glass waste for geotechnical applications. In: 7th International Conference on Civil Engineering for Sustainable Development (ICCESD 2024), pp. 1–8. Bangladesh (2024).
9. Fakhraldin, M.K., Abdulabbas, Z.H.: Increasing shear strength parameters of sandy soil by lining CKD. International Journal of Current Engineering and Technology 7(2), 421–425 (2017).
10. Hayder, M.R., Ziari, H., Shaban, A.M.: Strength and microstructural characteristics of sand soils stabilized with paper sludge Ash-based geopolymer. Scientific Reports 15, 8752 (2025).
11. Supar, K., Rani, F.A.A., Mazlan, N.L., Musa, M.K.: Partial replacement of fine aggregate using waste materials in concrete as roof tile: a review. In: GCoMSE 2021, IOP Conf. Ser.: Mater. Sci. Eng., vol. 1200, 012008 (2021).
12. Pasetto, M., Haider, S., Pasquini, E.: Circular economy for transport infrastructure: an overview of the sustainable use of recycled asphalt shingles in asphalt mixtures. Applied Sciences 14(10145), 1–15 (2024).

13. Abbas, A., Kumar, A., Nehdi, M.L.: Recycling roof shingle with added value: critical analysis of characteristics, practices, challenges, and future research directions. Innovative Infrastructure Solutions 11(63), 1–26 (2026).
14. ASTM International: ASTM D6913/D6913M-17: Standard Test Methods for Particle-Size Distribution (Gradation) of Soils Using Sieve Analysis. ASTM International, West Conshohocken (2017).
15. ASTM International: ASTM D854-14: Standard Test Methods for Specific Gravity of Soil Solids by Water Pycnometer. ASTM International, West Conshohocken (2014).
16. British Standards Institution: BS 1377-2:1990: Methods of Test for Soils for Civil Engineering Purposes—Part 2: Classification Tests. BSI, London (1990).
17. ASTM International: ASTM D698-12e2: Standard Test Methods for Laboratory Compaction Characteristics of Soil Using Standard Effort (12,400 ft-lbf/ft³ (600 kN-m/m³)). ASTM International, West Conshohocken (2012).
18. ASTM International: ASTM D3080/D3080M-11: Standard Test Method for Direct Shear Test of Soils Under Consolidated Drained Conditions. ASTM International, West Conshohocken (2011).
19. Anvari, S.M., Shooshpasha, I., Soleimani Kutanaei, S.: Effect of granulated rubber on shear strength of fine-grained sand. Journal of Rock Mechanics and Geotechnical Engineering 9, 936–944 (2017).
20. Islam, S., Islam, J., Alam, M.J.B., Chowdhury, A.S., Hasnat, N.: Partial replacement of sand by fine-grained crushed waste glass along with fly ash stabilization for geotechnical applications in pavement. Heliyon 10, e38754 (2024).

Author Contribution Statement

- *Conceptualization:* Inci Develioglu, Rumeysa Bulut
- *Methodology:* Inci Develioglu, Rumeysa Bulut
- *Investigation:* Inci Develioglu, Rumeysa Bulut
- *Writing – Original Draft:* Inci Develioglu, Rumeysa Bulut
- *Writing – Review & Editing:* Inci Develioglu, Rumeysa Bulut

List of Abbreviations

- **ASTM** — American Society for Testing and Materials
- **BS** — British Standards
- **CBR** — California Bearing Capacity
- **GSW** — Granular Shingle Waste
- **MDU** — Maximum Dry Unit Weight
- **OMC** — Optimum Moisture Content

Publication Note

This paper was peer-reviewed, accepted for presentation, and included in the proceedings of the ACE2026 – International Conference on Advances in Civil Engineering, held on 12–14 October 2026 in Trabzon, Türkiye.

This paper may be cited as follows:

Inci Develioglu and Rumeysa Bulut, "Investigation of the Geotechnical Properties of Sandy Soils Stabilized with Granular Shingle Waste," in Proceedings of the ACE2026 – International Conference on Advances in Civil Engineering, Trabzon, Türkiye, 12–14 October 2026.

Experimental Comparison of Seismic Behavior in Fixed-Base and Soil–Structure Interaction Systems Using Shaking Table Tests

Olguhan Şevket KARAHASAN[1] and Zekai ANGIN[2]
[1] 0000-0001-7096-7282, Karadeniz Technical University, Civil Engineering Department, Trabzon, Türkiye, olguhan@ktu.edu.tr
[2] 0000-0002-6981-6396, Karadeniz Technical University, Civil Engineering Department, Trabzon, Türkiye, angin@ktu.edu.tr

Abstract. Soil–structure interaction (SSI) plays a critical role in determining the seismic response of structures. However, conventional structural design approaches often idealize the foundation system as fixed, neglecting the influence of soil flexibility. This study presents an experimental investigation aimed at comparatively evaluating the seismic behavior of a fixed-base structural model and a system incorporating soil–structure interaction. The experimental program was conducted using a uniaxial shaking table and a soil container made of plexiglass, specifically designed to simulate SSI conditions. The scaled structural model was tested under two different boundary conditions: (i) a fixed-base configuration, in which the structure was rigidly attached to the shaking table, and (ii) an SSI configuration, in which the structure was embedded within a granular soil. Acceleration data were recorded using accelerometers installed at different story levels of the structure. Following data processing and filtering procedures, displacement responses were obtained through numerical integration. Based on the experimental results, response parameters such as acceleration and displacement amplitudes, as well as dynamic characteristics, were evaluated. The findings indicate that the fixed-base assumption may lead to significant discrepancies in estimating both acceleration and displacement demands when compared to the SSI model. Furthermore, variations in natural frequency and damping ratio were observed due to energy dissipation mechanisms within the soil. These results highlight the importance of incorporating soil–structure interaction effects in the seismic performance assessment of structures, particularly those founded on granular soils. The study aims to contribute to the development of more realistic modeling approaches for seismic analysis.

Keywords: Soil–structure interaction; Shaking table; Plexiglass; Seismic behavior

1 Introduction

The seismic performance of civil engineering structures is governed not only by the characteristics of the structural system but also by the interaction between the structure, its foundation, and the supporting soil. During earthquake excitation, soil deformability modifies the dynamic properties of the coupled soil–foundation–structure system by altering its stiffness, damping capacity, and vibration characteristics. Consequently, the conventional fixed-base assumption, which is widely adopted in structural design and analysis, may not accurately represent the actual seismic response of structures founded on deformable soils (Wolf 1985; Kramer 1996; Mylonakis and Gazetas 2000).

Over the past several decades, soil–structure interaction (SSI) has become one of the most extensively investigated topics in earthquake engineering. Previous analytical and numerical studies have demonstrated that SSI may significantly influence natural frequencies, modal damping ratios, acceleration demands, displacement responses, and foundation settlements

depending on the relative stiffness of the soil and structure, foundation conditions, and earthquake characteristics (Stewart et al. 1999; Mylonakis and Gazetas 2000; Kausel 2010). In particular, the flexibility of the supporting soil may either amplify or reduce structural demands, indicating that neglecting SSI may lead to inaccurate estimation of seismic performance.

Although advances in computational methods have considerably improved the capability of finite element and finite difference analyses to simulate coupled soil–structure systems, the nonlinear behavior of soils and the complexity of wave propagation mechanisms continue to present significant challenges. Therefore, experimental investigations remain essential for understanding the actual dynamic behavior of soil–structure systems and for validating numerical simulation techniques. Among available experimental approaches, shaking table testing provides one of the most effective methods for reproducing earthquake loading under controlled laboratory conditions while simultaneously capturing the coupled response of the soil and the superstructure (Gajan et al. 2005; Rayhani and El Naggar 2008; Pitilakis et al. 2014).

Recent experimental studies have consistently reported that soil flexibility alters the distribution of structural acceleration and displacement demands, modifies modal characteristics, and affects the dynamic amplification mechanism throughout the structural height (Pitilakis et al. 2014; Tabatabaiefar et al. 2014; Liu et al. 2020). Nevertheless, relatively few experimental investigations have directly compared the seismic responses of identical structural models tested under both fixed-base and soil–structure interaction conditions using the same structural configuration, instrumentation layout, and earthquake excitation. Such comparative studies provide a more reliable assessment of the influence of soil flexibility by eliminating uncertainties associated with variations in structural properties and experimental conditions.

In this context, the present study experimentally evaluates the dynamic behavior of a scaled structural model under both fixed-base and soil–structure interaction conditions using a uniaxial shaking table. Initially, the dynamic characteristics of the fixed-base model were identified through experimental modal analysis using the Enhanced Frequency Domain Decomposition (EFDD) and Stochastic Subspace Identification (St-SSI) techniques. Subsequently, shaking table tests were carried out using the east–west component of the 1992 Erzincan earthquake record as the input ground motion. The structural responses were evaluated in terms of acceleration and displacement time histories, and the influence of soil flexibility on the seismic behavior of the structural system was investigated. The experimental results provide a valuable benchmark for validating numerical SSI models and contribute to a better understanding of the dynamic behavior of soil–foundation–structure systems subjected to earthquake loading.

1.1 Experimental Modal Characterization and Seismic Response of the Fixed-Base Structural Model

The reference dynamic behavior of the structural model was established through shaking table tests performed under fixed-base boundary conditions. The experimental setup consisted of a uniaxial shaking table, the structural model, and the data acquisition and measurement system. To simulate fixed-base conditions, the structural model was rigidly connected to the shaking table through threaded rod connections anchored to the base plate, thereby ensuring a stable and high-stiffness boundary condition throughout the tests. To characterize the dynamic properties of the structure and monitor its seismic response, accelerometers were installed at the top, middle, and bottom story levels (Fig. 1). Experimental modal identification was carried out using the Enhanced Frequency Domain Decomposition (EFDD) and Stochastic Subspace Identification (St-SSI) methods. The identified natural frequencies and modal damping ratios are summarized in Table 1, while the first two mode shapes obtained from the modal analyses are presented in Fig. 2. The mode shapes identified by both modal identification techniques

exhibit a high degree of agreement, demonstrating the consistency of the experimental modal analysis. Furthermore, owing to the square plan geometry of the structural model, the first two natural frequencies were found to be very close to each other. As presented in Table 1, the natural frequencies and damping ratios obtained from the EFDD and St-SSI methods are in excellent agreement, confirming the reliability and robustness of the experimental modal identification procedure. Following the identification of the dynamic characteristics of the structural model under fixed-base boundary conditions, its seismic response was investigated through shaking table tests. For this purpose, the east–west component of the ground motion recorded during the 1992 Erzincan earthquake was adopted as the input excitation. The acceleration time histories obtained under earthquake excitation are presented in Fig. 3. A consistent increase in acceleration amplitudes from the bottom story to the top story was observed under earthquake excitation. Under the 50% scaled Erzincan earthquake excitation, the measured acceleration responses remained relatively limited. These findings indicate that seismic demands were progressively amplified along the height of the structure, resulting in the largest acceleration responses at the upper stories. The displacement time histories corresponding to the east–west component of the 1992 Erzincan earthquake are presented in Fig. 4. The displacement time histories presented in Fig. 4 indicate that the displacement amplitudes consistently increase from the bottom story to the top story under the 50% scaled Erzincan earthquake excitation. In addition, the peak displacement responses at the upper stories occur with a noticeable time lag relative to those at the lower stories. This behavior can be attributed to the phase difference associated with the dynamic response of the structure and the propagation of structural vibrations along its height.

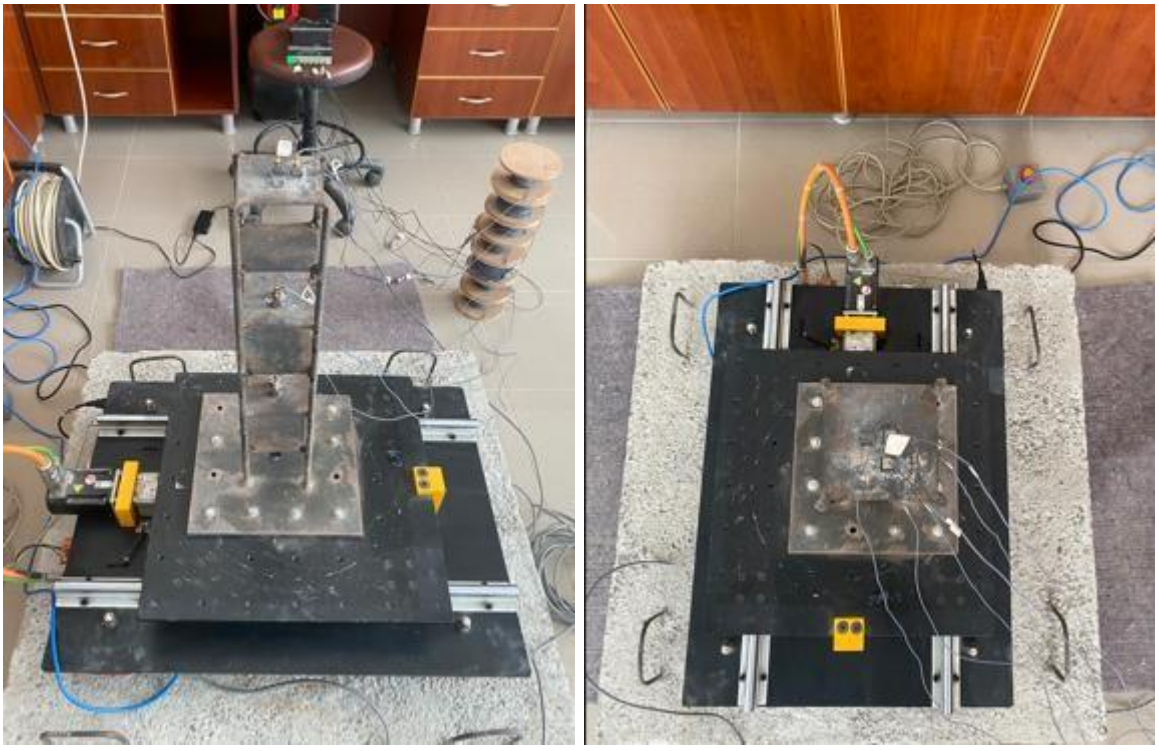


Fig. 1. Experimental setup of the shaking table test for the fixed-base structural model

Table 1. Natural frequencies and modal damping ratios identified using the EFDD and SSI methods.

Mode No.	Natural Frequency (Hz)		Modal Damping Ratio (%)	
	EFDD	St-SSI	EFDD	St-SSI
1	26.097	26.134	0.925	0.862
2	26.819	26.885	0.967	0.912

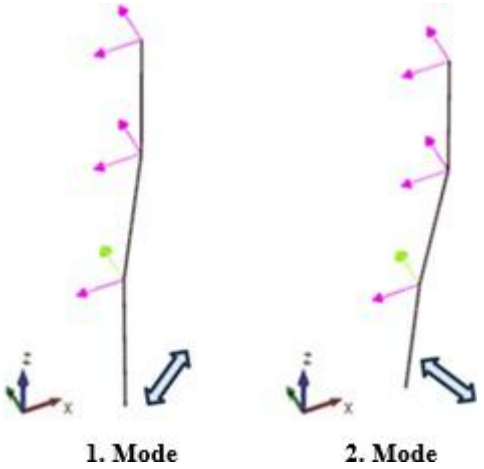


Fig. 2. Mode shapes identified using the EFDD and St-SSI methods

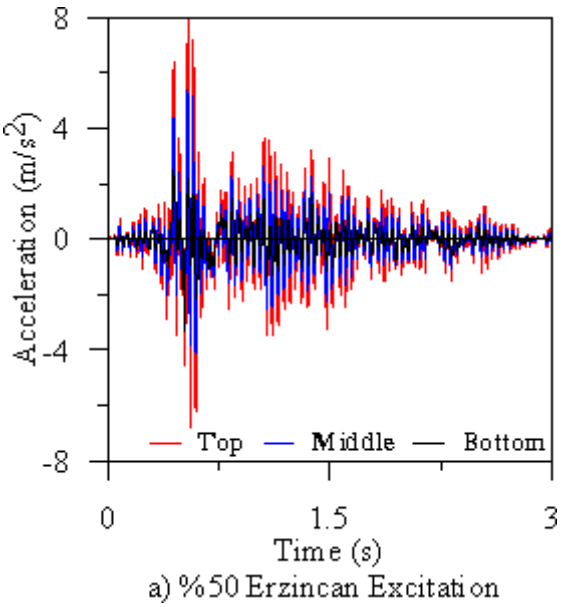
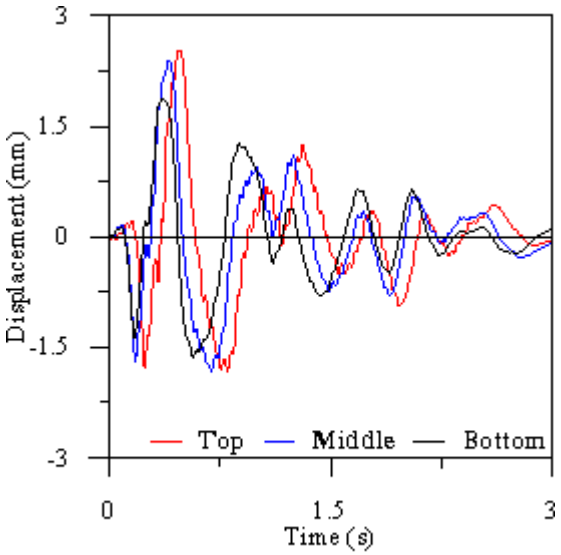


Fig. 3. Acceleration time histories obtained under the Erzincan earthquake excitation



a) %50 Erzincan Excitation

Fig. 4. Displacement time histories obtained under the Erzincan earthquake excitation

1.2 Shaking Table Tests of the Soil–Structure Interaction Model

Following the completion of the fixed-base experiments, the shaking table test setup was reconfigured to investigate soil–structure interaction (SSI). For this purpose, the plexiglass soil container was rigidly attached to the shaking table using threaded rod connections. The soil container was filled with sand to a height of 30 cm, and test were conducted at a relative density of 20%. To capture the dynamic response of the structural model, accelerometers were installed at the top, middle, and bottom stories in both horizontal directions, following the same sensor configuration adopted in the fixed-base experiments. In addition, an extra accelerometer was mounted at the top story in the vertical direction to monitor the vertical settlements induced by seismic loading. The experimental setup developed for the SSI tests, together with representative photographs of the shaking table experiments, is presented in Fig. 5.

Figure 6 presents the acceleration time histories obtained at a relative density of 20% under the 50% scaled earthquake excitation. The results demonstrate a consistent increase in acceleration amplitudes from the bottom story to the top story in both horizontal directions. In the X direction, the measured peak accelerations were 0.644, 0.972, and 1.332 m/s² at the bottom, middle, and top stories, respectively, corresponding to increases of 50.93% between the bottom and middle stories and 37.04% between the middle and top stories. A similar trend was observed in the Y direction, where the recorded accelerations were 0.258, 0.438, and 0.708 m/s², yielding increases of 69.77% and 61.64% between successive story levels. In the vertical direction, the acceleration recorded at the top story was 0.105 m/s². These results indicate that seismic acceleration demands progressively amplify along the structural height, reaching their maximum values at the upper stories. The observed response is indicative of a pronounced dynamic amplification mechanism within the soil–structure system.

Figure 7 presents the displacement time histories obtained at a relative density of 20% under the 50% scaled earthquake excitation. The maximum displacements measured in the X direction were 1.619, 1.611, and 1.445 mm at the top, middle, and bottom stories, respectively. In the Y direction, the corresponding displacement values were 0.044, −0.052, and 0.024 mm, while a vertical displacement of 0.099 mm was recorded at the top story.

The results indicate that the displacement response in the X direction generally increased with structural height, reflecting greater seismic demand at the upper stories. The difference between the top and middle stories was relatively small (0.5%), whereas the displacement increased by 11.5% between the middle and bottom stories. In contrast, the displacement

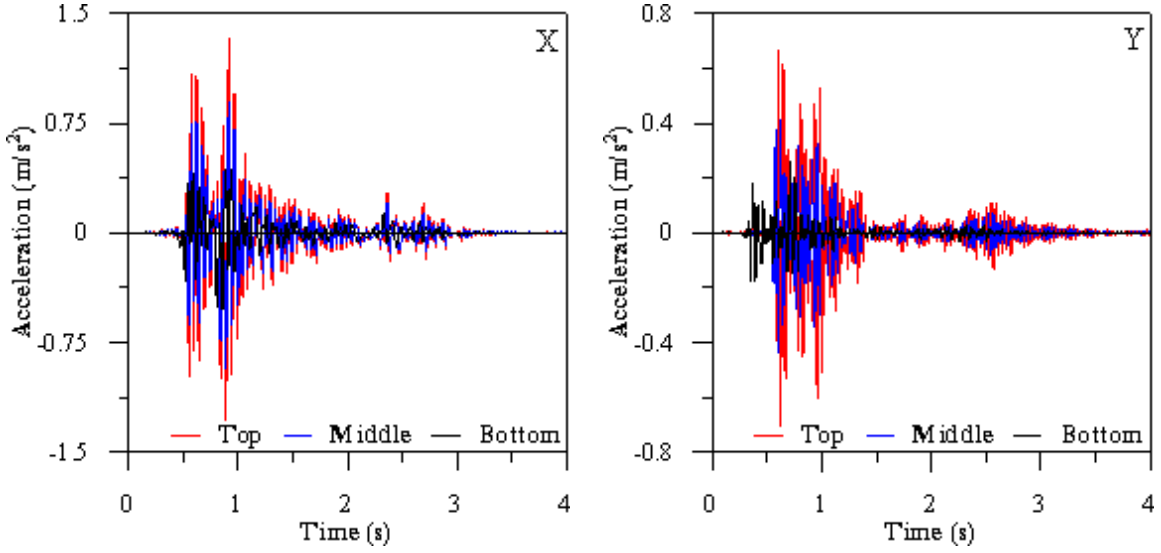
response in the Y direction remained considerably smaller and exhibited a less uniform distribution. This behavior is primarily attributed to the fact that the earthquake excitation was applied in the X direction, causing the structural response to be dominated by motion along this axis. The displacement differences between the top and middle stories and between the middle and bottom stories in the Y direction were calculated as 15.4% and 116.7%, respectively.

Table 2. Natural frequencies and modal damping ratios identified using the EFDD and St-SSI methods.

Test Case	Before Earthquake Excitation				After Earthquake Excitation			
	f_1 (Hz)	f_2 (Hz)	ξ_1 (%)	ξ_2 (%)	f_1 (Hz)	f_2 (Hz)	ξ_1 (%)	ξ_2 (%)
D_r20-Erz50	18.54	20.64	2.465	1.336	17.92	20.53	4.040	1.459



Fig. 5. Experimental setup of the soil–structure interaction (SSI) model for shaking table tests



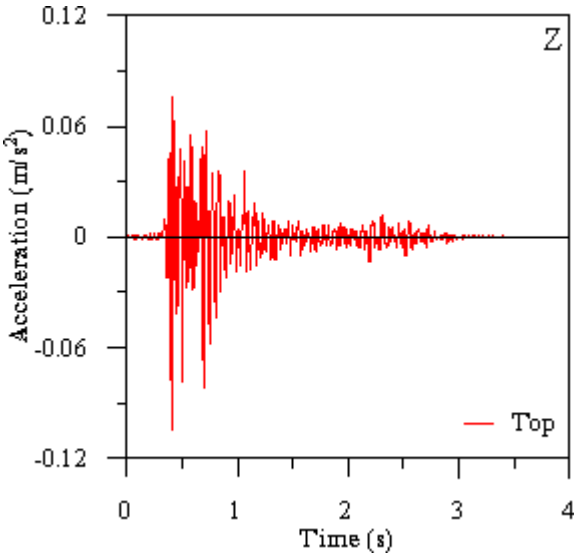


Fig. 6. Acceleration time histories at 20% relative density under the 50% scaled earthquake excitation

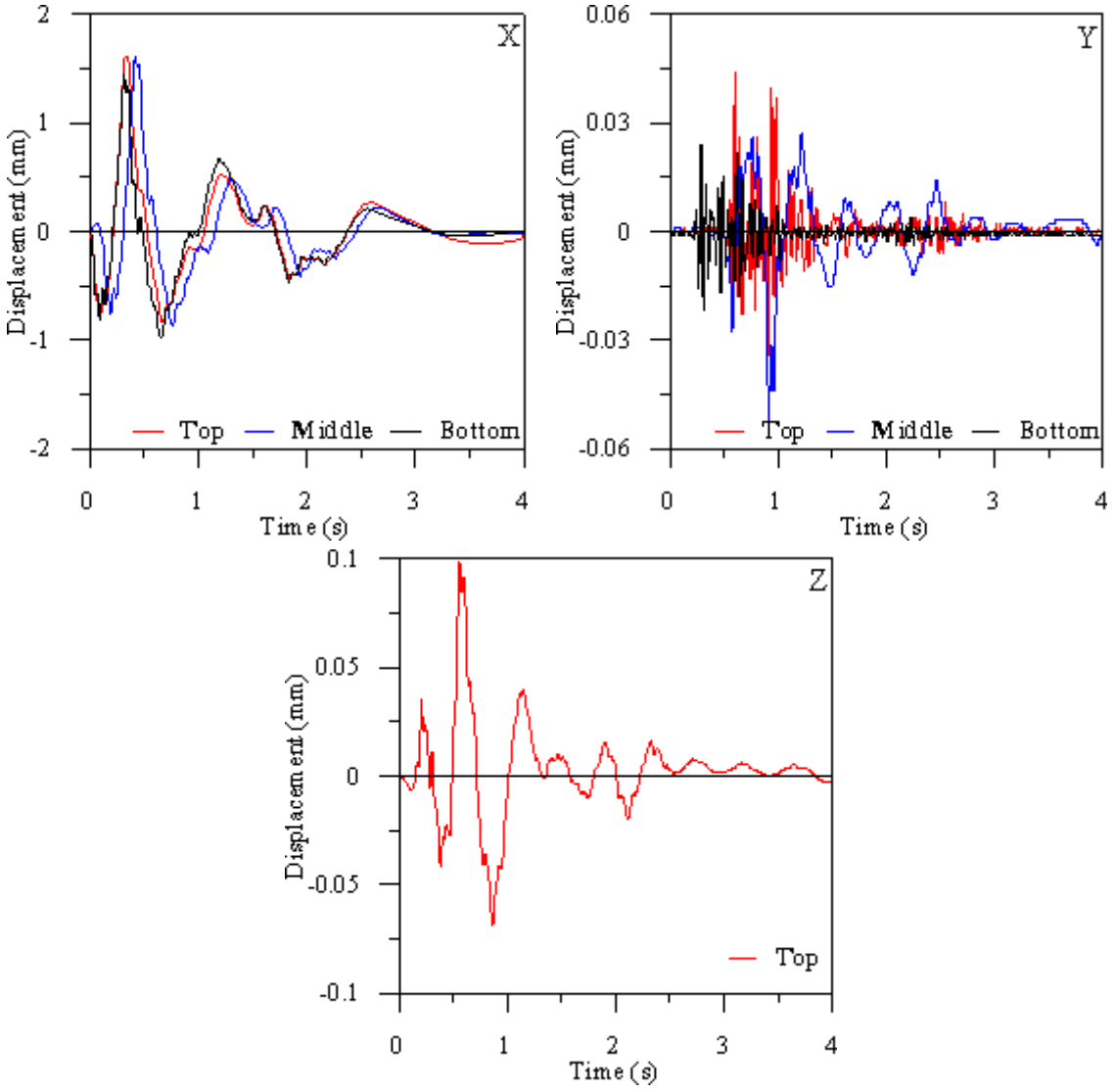


Fig. 7. Displacement time histories at 20% relative density under the 50% scaled earthquake excitation

2 Conclusion

This study experimentally investigated the dynamic characteristics and seismic behavior of a scaled structural model under both fixed-base and soil–structure interaction (SSI) conditions using shaking table tests. The experimental modal analysis demonstrated excellent agreement between the Enhanced Frequency Domain Decomposition (EFDD) and Stochastic Subspace Identification (St-SSI) methods in terms of the identified natural frequencies, modal damping ratios, and mode shapes, confirming the reliability of the adopted modal identification procedure. The shaking table experiments revealed that both acceleration and displacement responses increased progressively from the bottom story to the top story, indicating a pronounced dynamic amplification mechanism along the structural height. Under soil conditions with a relative density of 20%, a similar response trend was observed; however, the presence of the supporting soil modified the distribution of seismic demands throughout the structural system. Furthermore, the structural response was found to be predominantly governed by the direction of the applied earthquake excitation, resulting in considerably larger responses in the loading direction than in the transverse direction. Overall, the experimental findings demonstrate that soil flexibility significantly influences the dynamic behavior of the coupled soil–foundation–structure system and should therefore be considered in realistic seismic performance assessments. The experimental data obtained in this study provide a reliable benchmark for the calibration and validation of numerical soil–structure interaction models and contribute to a better understanding of the seismic behavior of soil–foundation–structure systems subjected to earthquake loading.

References

1. Wolf, J.P.: Dynamic Soil–Structure Interaction. Prentice-Hall, Englewood Cliffs (1985).
2. Kramer, S.L.: Geotechnical Earthquake Engineering. Prentice Hall, Upper Saddle River (1996).
3. Stewart, J.P., Fenves, G.L., Seed, R.B.: Seismic soil–structure interaction in buildings. Journal of Geotechnical and Geoenvironmental Engineering 125(1), 26–37 (1999).
4. Mylonakis, G., Gazetas, G.: Seismic soil–structure interaction: Beneficial or detrimental? Journal of Earthquake Engineering 4(3), 277–301 (2000).
5. Gajan, S., Kutter, B.L., Phalen, J.D., Hutchinson, T.C., Martin, G.R.: Centrifuge modeling of load–deformation behavior of rocking shallow foundations. Soil Dynamics and Earthquake Engineering 25(7), 773–783 (2005).
6. Rayhani, M.T., El Naggar, M.H.: Numerical modeling of seismic response of rigid foundation on soft soil. International Journal of Geomechanics 8(6), 336–346 (2008).
7. Kausel, E.: Early history of soil–structure interaction. Soil Dynamics and Earthquake Engineering 30(9), 822–832 (2010).
8. Pitilakis, K., Crowley, H., Kaynia, A.M. (eds.): SYNER-G: Typology Definition and Fragility Functions for Physical Elements at Seismic Risk. Springer, Dordrecht (2014).
9. Tabatabaiefar, H.R., Fatahi, B., Samali, B.: Lateral seismic response of building frames considering soil–structure interaction effects. Structural Engineering and Mechanics 45(3), 311–321 (2013).
10. Liu, S., Li, P., Zhang, W., Lu, Z.: Experimental study and numerical simulation on dynamic soil–structure interaction under earthquake excitations. Soil Dynamics and Earthquake Engineering 138, 106333 (2020).

Author Contribution Statement

- *Conceptualization:* Olguhan Şevket KARAHASAN, Zekai ANGIN
- *Methodology:* Olguhan Şevket KARAHASAN, Zekai ANGIN
- *Investigation:* Olguhan Şevket KARAHASAN
- *Writing – Original Draft:* Olguhan Şevket KARAHASAN
- *Writing – Review & Editing:* Olguhan Şevket KARAHASAN, Zekai ANGIN

List of Abbreviations

- **EFDD** — Enhanced Frequency Domain Decomposition
- **EMA** — Experimental Modal Analysis
- **SSI** — Soil–Structure Interaction
- **St-SSI** — Stochastic Subspace Identification

Publication Note

This paper was peer-reviewed, accepted for presentation, and included in the proceedings of the ACE2026 – International Conference on Advances in Civil Engineering, held on 12–14 October 2026 in Trabzon, Türkiye.

This paper may be cited as follows:

Karahasan, O.Ş., Angın, Z, "Experimental Comparison of Seismic Behavior in Fixed-Base and Soil–Structure Interaction Systems Using Shaking Table Tests," in Proceedings of the ACE2026 – International Conference on Advances in Civil Engineering, Trabzon, Türkiye, 12–14 October 2026.

Investigation of Consolidation and Swelling Behavior of Fiber-Reinforced Clays

Ehsan Etminan[1,*], Kaveh Dehghanian[2], Beste Koçak Dinç[3], Beste Seyla Göçkün[4] and Alperhan Kapucu[5]

[1] 0000-0003-1490-4011, Işık University, Department of Civil Engineering, Şile, Istanbul, Türkiye, ehsan.etminan@isikun.edu.tr (*Corresponding author)

[2] 0000-0002-6372-4984, İstanbul Aydın University, Department of Civil Engineering, Florya, Istanbul, Türkiye, kavehdehghanian@aydin.edu.tr

[3] 0000-0003-4178-1213, İstanbul Aydın University, Department of Civil Engineering, Florya, Istanbul, Türkiye, bestekocak@aydin.edu.tr

[4] 0000-0002-6524-4052, Işık University, Department of Civil Engineering, Şile, Istanbul, Türkiye, beste.gockun@isikun.edu.tr

[5] 0009-0007-2724-9753, Işık University, Department of Civil Engineering, Şile, Istanbul, Türkiye, kapucualperhan@gmail.com

Abstract. In this study, the effects of polypropylene (PP) and copolymer (CP) fiber inclusions on the consolidation and swelling behavior of low (CL) and high (CH) plasticity clay soils were investigated. Within this scope, one-dimensional oedometer tests were conducted on specimens prepared by adding PP and CP fibers to both soil types at 0.25%, 0.50%, and 0.75% by dry weight. Based on the obtained stress–void ratio (e–log σ′) curves, the free swell percentage, compression index (Cc), recompression index (Cr), and coefficient of consolidation (cv) of the mixtures were determined. The findings indicate that the fiber type and inclusion ratio significantly affect the volumetric behavior of the soils. Fiber inclusion systematically reduced the free swell percentage, with reductions of up to 42% in the CH soil at 0.75% PP content and up to 44% in the CL soil at 0.75% CP content. The compression and recompression indices decreased moderately with increasing fiber content, while the coefficient of consolidation increased, indicating a faster dissipation of excess pore water pressures in the reinforced mixtures. The study comparatively demonstrates the extent to which fiber inclusion controls swelling—particularly in high plasticity clays—and how it modifies the compressibility characteristics. The results suggest that PP and CP fibers can be used as a sustainable and effective stabilization method for improving problematic clays in geotechnical engineering applications.

Keywords: Low plasticity clay, High plasticity clay, Oedometer test, Consolidation, Swelling, Fiber

1 Introduction

Expansive and compressible clayey soils are among the most problematic geomaterials encountered in transportation infrastructure, shallow foundations, and earth structures. Seasonal moisture fluctuations in such soils cause repeated swelling and shrinkage cycles, whereas long-term loading leads to excessive consolidation settlements; both mechanisms are responsible for severe distress in pavements and lightly loaded structures [1, 2]. In conventional practice, weak subgrade soils are excavated and replaced with granular fill; however, excavation, hauling, and material costs make this approach economically and environmentally unattractive, and in-situ improvement of the existing soil is generally the most cost-effective alternative [1].

A wide range of stabilization techniques has been proposed for problematic clays, including chemical additives, compaction control, prewetting, surcharge loading, and reinforcement with geosynthetics [2, 3]. In recent years, the inclusion of randomly distributed discrete fibers has

attracted particular attention because it is simple to apply, does not require curing, does not alter the soil chemistry, and mobilizes tensile resistance isotropically within the soil mass [3, 4]. Previous investigations have shown that discrete polymeric fibers increase the tensile and shear strength of clays [4], restrain crack development [4], and reduce the swelling potential of expansive soils [5–7]. Al-Akhras et al. [6] reported that both the swell percentage and the swelling pressure of a clayey soil decreased significantly as the fiber content increased, while Phanikumar and Singla [7] observed that fiber reinforcement reduced both the heave and the compression index of an expansive clay. Similar improvements in the swell–consolidation response of expansive soils reinforced with polypropylene fibers were reported by Puppala and Musenda [3], Viswanadham et al. [5], and Malekzadeh and Bilsel [8]. Fibers have also been combined with cementitious and pozzolanic additives such as cement and lime, where they mitigate the brittleness introduced by chemical stabilization [9, 10].

Although the strength behavior of fiber-reinforced clays has been studied extensively [4, 9, 11, 12], comparatively fewer studies have addressed the one-dimensional consolidation and swelling response of clays reinforced with different fiber types, and the influence of fiber content on the consolidation parameters (Cc, Cr, cv) is not yet fully clarified. In a previous study by the authors [13], the compaction, unconfined compression, California Bearing Ratio (CBR), and cyclic triaxial behavior of the same CH and CL soils reinforced with polypropylene (PP), copolymer (CP), and virgin homopolymer polypropylene fibers was investigated, and it was shown that fiber inclusion improves both the static strength and the cyclic softening resistance of the mixtures. The present study extends that experimental program to the volumetric behavior of the same soil–fiber combinations. One-dimensional oedometer tests were performed on CH and CL soils reinforced with PP and CP fibers at contents of 0.25%, 0.50%, and 0.75% by dry weight, and the free swell percentage, compression index, recompression index, and coefficient of consolidation of each mixture were evaluated and compared with the available literature.

2 Materials

2.1 Soils

Two natural clayey soils were used in the experimental program, identical to those employed in the companion study [13]. According to the Unified Soil Classification System (ASTM D2487) [14], Soil-I is classified as a high plasticity clay (CH) and Soil-II as a low plasticity clay (CL). Atterberg limit tests indicate that Soil-I has considerably higher plasticity than Soil-II, and hydrometer analyses show that Soil-I also has a higher clay fraction. The index properties of both soils are summarized in Table 1.

Table 1. Index and compaction properties of the soils tested [13].

Property	Soil-I	Soil-II
Liquid limit, LL (%)	78	41
Plastic limit, PL (%)	28	23
Plasticity index, PI (%)	50	18
Gravel (%)	0	0
Sand (%)	3	2
Silt (%)	27	53
Clay (%)	70	45
Optimum water content (%)	27	26

Property	Soil-I	Soil-II
Maximum dry unit weight (kN/m^3)	15.04	15.32
USCS class	CH	CL

2.2 Fibers

Two types of commercially available synthetic fibers were used: fibrillated polypropylene (PP) fibers and monofilament copolymer (CP) fibers. These fibers are primarily marketed for the reinforcement of concrete in accordance with ASTM C1116 [15], where they are used to control plastic and settlement shrinkage cracking. Both fibers exhibit excellent acid and alkali resistance and a specific gravity of 0.91. Prior to mixing, the fibers were cut to a uniform length of 6 cm, consistent with the companion study [13]. The physical properties of the fibers are given in Table 2.

Table 2. Physical properties of the fibers used in the experimental program [13].

Property	PP	CP
Color	White	Gray
Form	Fibrillated fiber	Monofilament fiber
Acid/alkali resistance	Excellent	Excellent
Specific gravity	0.91	0.91
Tensile strength (MPa)	570	758
Length used in tests (cm)	6	6

3 Experimental Program and Testing Procedure

The experimental program was carried out at the Soil Mechanics Laboratories of Işık University and İstanbul Aydın University. Each soil was oven-dried, pulverized, and mixed with PP or CP fibers at contents of 0%, 0.25%, 0.50%, and 0.75% by dry weight of soil. The fibers were added gradually during dry mixing to obtain a uniform, random distribution and to avoid balling of the fibers, after which the required amount of water was added. In total, fourteen mixtures (two plain soils and twelve soil–fiber combinations) were prepared. All specimens were compacted at the maximum dry unit weight and optimum water content obtained from standard Proctor tests (ASTM D698) [16] on the corresponding mixtures.

One-dimensional consolidation tests were performed in fixed-ring oedometers in accordance with ASTM D2435 [17] on specimens 50 mm in diameter and 20 mm in height. Following assembly, the specimens were inundated under a seating pressure of 7 kPa and allowed to swell freely until the swell deformation stabilized; the free swell percentage was computed as the ratio of the swell deformation to the initial specimen height, following the one-dimensional swell procedure of ASTM D4546 [18]. The specimens were subsequently loaded incrementally to 25, 50, 100, 200, 400, and 800 kPa, with each increment maintained for 24 h, and then unloaded in steps back to 25 kPa. Dial gauge readings were recorded at standard time intervals during each increment. The compression index (Cc) was determined from the slope of the virgin portion of the e–log σ′ curve, the recompression index (Cr) from the unloading branch, and the coefficient of consolidation (cv) using Casagrande's logarithm-of-time fitting method for the 100–200 kPa increment.

4 Results and Discussion

4.1 Stress–Void Ratio Response

Representative e–log σ′ curves for the plain and fiber-reinforced CH and CL soils are presented in Fig. 1 and Fig. 2, respectively. For both soils, the addition of fibers shifts the virgin compression line to a flatter slope and reduces the rebound upon unloading, indicating that the fiber network restrains both the compression of the soil skeleton and its elastic recovery. This behavior is consistent with the observations of Phanikumar and Singla [7] and Estabragh et al. [11], who attributed the reduced compressibility of fiber-reinforced clays to the mobilization of tensile stresses along the fiber–clay interfaces, which carry part of the applied load and restrict the rearrangement of clay particles.

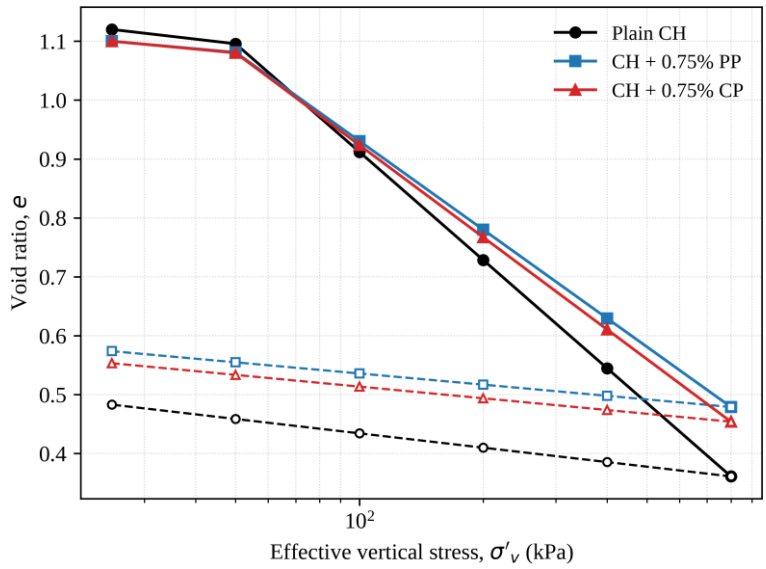


Fig. 1. e–log σ′ curves for plain and fiber-reinforced CH soil (solid lines: loading; dashed lines: unloading).

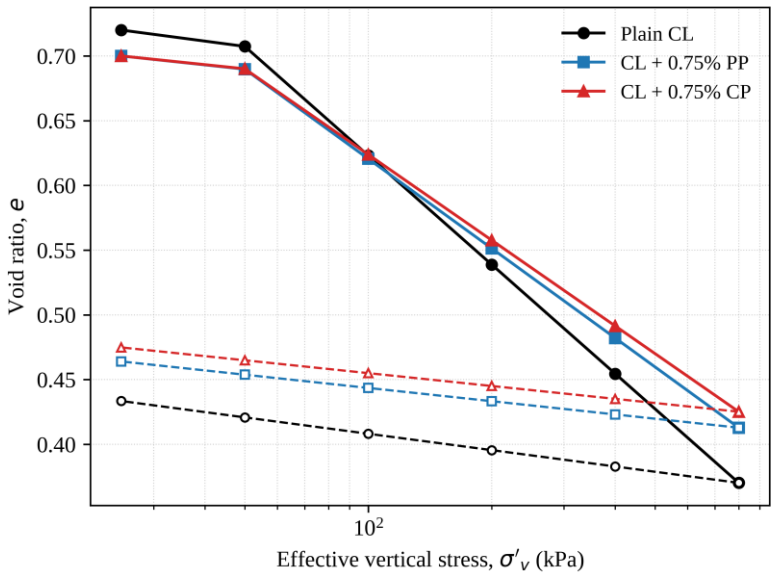


Fig. 2. e–log σ′ curves for plain and fiber-reinforced CL soil (solid lines: loading; dashed lines: unloading).

4.2 Swelling Behavior

The free swell percentages measured upon inundation are listed in Tables 3 and 4 and plotted against fiber content in Fig. 3. The plain CH soil exhibited a free swell of 10.6%, more than twice that of the plain CL soil (4.3%), consistent with its higher plasticity index and clay fraction. The inclusion of both fiber types reduced the swell percentage monotonically over the range of contents investigated. For the CH soil, the free swell decreased to 6.1% at 0.75% PP content (a 42% reduction) and to 6.8% at 0.75% CP content (a 36% reduction). For the CL soil, the corresponding values were 2.8% for PP (35% reduction) and 2.4% for CP (44% reduction).

The reduction in swelling can be attributed to two complementary mechanisms reported in the literature. First, the fibers replace part of the active clay mass, slightly reducing the total swelling potential per unit volume. Second, and more importantly, as the clay minerals hydrate and tend to expand, tensile stresses are mobilized along the fiber–soil interfaces; the randomly oriented fiber network therefore acts as a three-dimensional internal restraint against heave [5–7]. It is noteworthy that the fibrillated PP fibers were somewhat more effective in the high plasticity CH soil, whereas the monofilament CP fibers produced the largest swell reduction in the CL soil. A similar dependence of the optimum fiber type on soil plasticity was observed in the strength results of the companion study [13], where the highest CBR improvement of the CL soil was obtained with 0.75% CP fiber. The fibrillated structure of the PP fibers provides a larger effective interface area, which appears to be mobilized more efficiently by the stronger swelling drive of the CH soil, while the stiffer monofilament CP fibers interact more effectively with the siltier CL matrix.

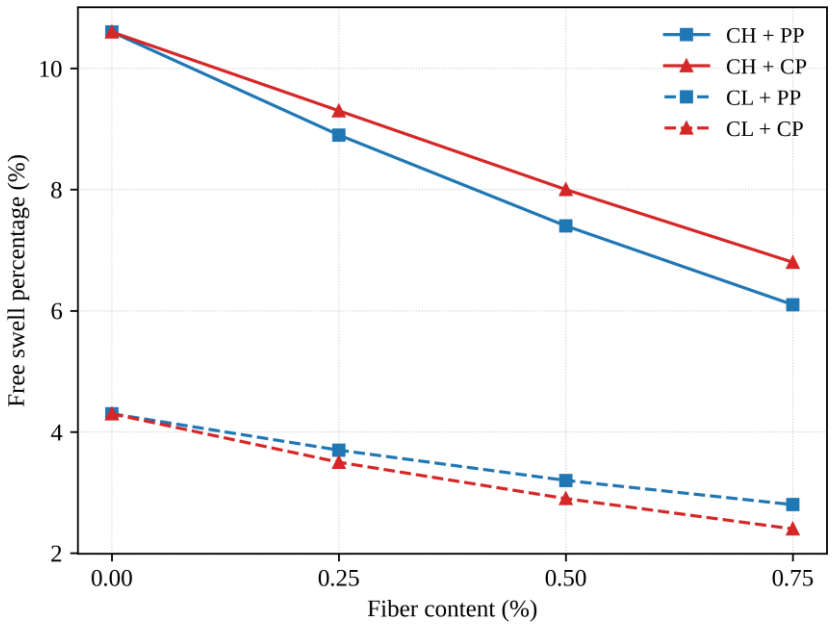


Fig. 3. Variation of free swell percentage with fiber content for CH and CL soils.

4.3 Compressibility and Consolidation Parameters

The consolidation parameters obtained for all fourteen mixtures are summarized in Table 3 for the CH soil and Table 4 for the CL soil. The compression index of the plain CH soil (C_c = 0.61) agrees closely with the empirical correlation $C_c = 0.009(LL - 10)$ proposed by Terzaghi and Peck [19], which yields 0.61 for LL = 78; the plain CL value (C_c = 0.28) is likewise consistent

with the correlation. With increasing fiber content, Cc decreased gradually to 0.50 (PP) and 0.52 (CP) for the CH soil and to 0.23 (PP) and 0.22 (CP) for the CL soil at 0.75% content, corresponding to reductions of about 15–21%. The recompression index followed the same trend, decreasing by roughly 20% at the highest fiber content. These reductions are of the same order as those reported by Phanikumar and Singla [7] for polypropylene fiber-reinforced expansive clays and by Estabragh et al. [11] for fiber–clay composites, and they imply proportionally smaller primary consolidation settlements of reinforced subgrades under embankment and pavement loading.

Table 3. Results of oedometer tests for the CH soil.

No	Mixture	Free swell (%)	C_c	C_r	c_v ($\times 10^{-4}$ cm^2/s)
1	Plain soil (CH)	10.5	0.63	0.084	0.43
2	99.75% CH + 0.25% PP	8.8	0.58	0.075	0.56
3	99.50% CH + 0.50% PP	7.3	0.55	0.069	0.64
4	99.25% CH + 0.75% PP	6.2	0.52	0.063	0.73
5	99.75% CH + 0.25% CP	9.1	0.59	0.073	0.51
6	99.50% CH + 0.50% CP	8.1	0.54	0.069	0.59
7	99.25% CH + 0.75% CP	6.7	0.51	0.063	0.68

Table 4. Results of oedometer tests for the CL soil.

No	Mixture	Free swell (%)	C_c	C_r	c_v ($\times 10^{-4}$ cm^2/s)
1	Plain soil (CL)	4.2	0.27	0.043	0.83
2	99.75% CL + 0.25% PP	3.6	0.26	0.037	1.04
3	99.50% CL + 0.50% PP	3.1	0.24	0.035	1.13
4	99.25% CL + 0.75% PP	2.8	0.23	0.034	1.28
5	99.75% CL + 0.25% CP	3.4	0.25	0.039	1.05
6	99.50% CL + 0.50% CP	2.8	0.23	0.037	1.23
7	99.25% CL + 0.75% CP	2.3	0.22	0.034	1.38

The coefficient of consolidation increased consistently with fiber content for both soils, as shown in Fig. 4. For the CH soil, c_v increased from 0.40×10^{-4} cm^2/s for the plain soil to 0.71×10^{-4} cm^2/s at 0.75% PP content (a 78% increase), while for the CL soil it increased from 0.85×10^{-4} to 1.35×10^{-4} cm^2/s at 0.75% CP content (a 59% increase). Two mechanisms contribute to this acceleration of consolidation. First, the fiber–clay interfaces provide preferential drainage paths that locally increase the permeability of the composite; second, the reduction in volume compressibility (m_v) directly increases c_v, since c_v is proportional to the ratio of permeability to volume compressibility. Comparable increases in the rate of consolidation of fiber-reinforced clays were reported by Malekzadeh and Bilsel [8] and Estabragh et al. [11]. From a practical standpoint, a higher c_v implies that primary settlements of fiber-reinforced subgrades are completed in a shorter time, which is advantageous for staged construction of highway embankments.

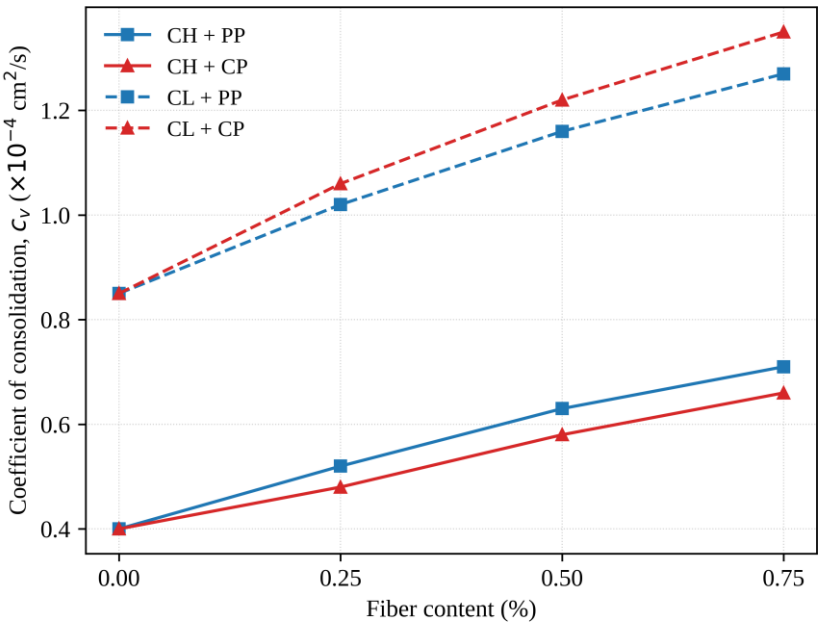


Fig. 4. Variation of the coefficient of consolidation with fiber content for CH and CL soils.

5 Conclusions

This study investigated the one-dimensional consolidation and swelling behavior of high (CH) and low (CL) plasticity clays reinforced with fibrillated polypropylene (PP) and monofilament copolymer (CP) fibers at contents of 0.25%, 0.50%, and 0.75% by dry weight. Based on the results of the oedometer tests, the following conclusions can be drawn:

(1) Fiber inclusion systematically reduced the free swell percentage of both clays over the entire range of contents investigated. The largest reductions were obtained at 0.75% fiber content, reaching 42% for the CH soil with PP fibers and 44% for the CL soil with CP fibers. Fiber reinforcement is therefore an effective means of controlling heave in expansive clay subgrades, particularly in high plasticity soils.

(2) The compression index and recompression index of both soils decreased moderately (by about 15–21%) with increasing fiber content, indicating that the randomly distributed fiber network restrains the compression of the soil skeleton and reduces expected primary consolidation settlements.

(3) The coefficient of consolidation increased by up to 78% for the CH soil and 59% for the CL soil at 0.75% fiber content, implying a faster dissipation of excess pore water pressures and shorter consolidation times for reinforced subgrades.

(4) The fibrillated PP fibers were more effective in the high plasticity CH soil, whereas the monofilament CP fibers gave the best performance in the CL soil, in agreement with the strength results of the companion study on the same soils.

Within the range investigated, the swelling and compressibility parameters improved continuously up to 0.75% fiber content, and no optimum content could be identified from the swelling aspect. In future work, the experimental program should therefore be extended to other fiber percentages (e.g., 1.0%, 1.25%, and intermediate contents) in order to determine the optimum fiber content from the swelling point of view, and the mixtures should also be combined with alternative additives such as fly ash and lime to develop stronger and more volumetrically stable soil combinations.

Acknowledgments

The authors would like to thank the technical staff of the Soil Mechanics Laboratories of Işık University and İstanbul Aydın University for their assistance during the experimental program.

References

1. Şenol, A., Bin-Shafique, M.S., Edil, T.B., Benson, C.H.: Use of Class C fly ash for the stabilization of soft subgrade. ARI The Bulletin of the Istanbul Technical University 53, 89–95 (2003).
2. Sridharan, A., Gurtug, Y.: Swelling behaviour of compacted fine-grained soils. Engineering Geology 72(1–2), 9–18 (2004). https://doi.org/10.1016/S0013-7952(03)00161-3
3. Puppala, A.J., Musenda, C.: Effects of fiber reinforcement on strength and volume change in expansive soils. Transportation Research Record 1736(1), 134–140 (2000). https://doi.org/10.3141/1736-17
4. Ziegler, S., Leshchinsky, D., Ling, H.I., Perry, E.B.: Effect of short polymeric fibers on crack development in clays. Soils and Foundations 38(1), 247–253 (1998). https://doi.org/10.3208/sandf.38.247
5. Viswanadham, B.V.S., Phanikumar, B.R., Mukherjee, R.V.: Swelling behaviour of a geofiber-reinforced expansive soil. Geotextiles and Geomembranes 27(1), 73–76 (2009). https://doi.org/10.1016/j.geotexmem.2008.06.002
6. Al-Akhras, N.M., Attom, M.F., Al-Akhras, K.M., Malkawi, A.I.H.: Influence of fibers on swelling properties of clayey soil. Geosynthetics International 15(4), 304–309 (2008). https://doi.org/10.1680/gein.2008.15.4.304
7. Phanikumar, B.R., Singla, R.: Swell-consolidation characteristics of fibre-reinforced expansive soils. Soils and Foundations 56(1), 138–143 (2016). https://doi.org/10.1016/j.sandf.2016.01.011
8. Malekzadeh, M., Bilsel, H.: Effect of polypropylene fiber on mechanical behaviour of expansive soils. Electronic Journal of Geotechnical Engineering 17(A), 55–63 (2012).
9. Tang, C., Shi, B., Gao, W., Chen, F., Cai, Y.: Strength and mechanical behavior of short polypropylene fiber reinforced and cement stabilized clayey soil. Geotextiles and Geomembranes 25(3), 194–202 (2007). https://doi.org/10.1016/j.geotexmem.2006.11.002
10. Cai, Y., Shi, B., Ng, C.W.W., Tang, C.: Effect of polypropylene fibre and lime admixture on engineering properties of clayey soil. Engineering Geology 87(3–4), 230–240 (2006). https://doi.org/10.1016/j.enggeo.2006.07.007
11. Estabragh, A.R., Bordbar, A.T., Javadi, A.A.: Mechanical behavior of a clay soil reinforced with nylon fibers. Geotechnical and Geological Engineering 29(5), 899–908 (2011). https://doi.org/10.1007/s10706-011-9427-8
12. Mirzababaei, M., Miraftab, M., Mohamed, M., McMahon, P.: Unconfined compression strength of reinforced clays with carpet waste fibers. Journal of Geotechnical and Geoenvironmental Engineering 139(3), 483–493 (2013). https://doi.org/10.1061/(ASCE)GT.1943-5606.0000792
13. Etminan, E., Dehghanian, K., Göçkün, B.S., Koçak Dinç, B.: Influence of adding fibers on engineering properties of clayey soils. In: Proceedings of the 9th Geotechnical Symposium, Istanbul, Türkiye (2023). https://doi.org/10.5505/2023geoteknik.SS-38
14. ASTM D2487: Standard practice for classification of soils for engineering purposes (Unified Soil Classification System). ASTM International, West Conshohocken (2017).
15. ASTM C1116/C1116M: Standard specification for fiber-reinforced concrete. ASTM International, West Conshohocken (2015).
16. ASTM D698: Standard test methods for laboratory compaction characteristics of soil using standard effort. ASTM International, West Conshohocken (2021).
17. ASTM D2435/D2435M: Standard test methods for one-dimensional consolidation properties of soils using incremental loading. ASTM International, West Conshohocken (2020).

18. ASTM D4546: Standard test methods for one-dimensional swell or collapse of soils. ASTM International, West Conshohocken (2021).
19. Terzaghi, K., Peck, R.B., Mesri, G.: Soil Mechanics in Engineering Practice. 3rd edn. John Wiley & Sons, New York (1996).

Author Contribution Statement

– *Conceptualization:* Ehsan Etminan, Kaveh Dehghanian
– *Methodology:* Ehsan Etminan, Kaveh Dehghanian, Beste Koçak Dinç
– *Investigation:* Beste Koçak Dinç, Beste Seyla Göçkün, Alperhan Kapucu
– *Writing – Original Draft:* Ehsan Etminan, Beste Seyla Göçkün
– *Writing – Review & Editing:* Kaveh Dehghanian, Beste Koçak Dinç

List of Abbreviations

– **CH** — High plasticity clay
– **CL** — Low plasticity clay
– **PP** — Polypropylene fiber
– **CP** — Copolymer fiber
– **CBR** — California Bearing Ratio
– **USCS** — Unified Soil Classification System

Publication Note
This paper was peer-reviewed, accepted for presentation, and included in the proceedings of the ACE2026 – International Conference on Advances in Civil Engineering, held on 12–14 October 2026 in Trabzon, Türkiye.

This paper may be cited as follows:
Etminan, E., Dehghanian, K., Kocak Dinc, B., Gockun, B.S., Kapucu, A., "Investigation of Consolidation and Swelling Behavior of Fiber-Reinforced Clays," in Proceedings of the ACE2026 – International Conference on Advances in Civil Engineering, Trabzon, Türkiye, 12–14 October 2026.

3D lithology and soil modeling in urban areas: the case of Fatih District

İzel Yıldız Sertgöz[1], İbrahim Fırat Mutlu[2], Meryem Yılmaz[3], Zülal Akbay Arama[4]
[1] 0009-0008-4237-2159, Istanbul University-Cerrahpaşa, Institute of Graduate Studies, Istanbul, Türkiye, izelyildiz@ogr.iuc.edu.tr
[2] 0009-0001-3420-1623, Istanbul University - Cerrahpasa, Civil Engineering Department, Istanbul, Türkiye, ibrahimfiratmutlu@ogr.iuc.edu.tr
[3] 0000-0001-8663-0406, Haliç University, Construction Technology Program, Istanbul, Türkiye, meryemyilmaz@halic.edu.tr
[4] 0000-0001-8185-7329 Istanbul University - Cerrahpasa, Civil Engineering Department, Istanbul, Türkiye, zakbay@iuc.edu.tr

Abstract. Three-dimensional (3D) soil modeling significantly supports decision-making processes-particularly in geotechnical engineering, urban planning, infrastructure, transportation, and mining engineering projects-by accurately depicting the spatial variation of the subsurface environment. Traditional two-dimensional geological maps and cross-sections cannot adequately represent the continuity of soil stratification or the complex subsurface structure. In particular, conducting new soil investigations in city centers with dense development and archaeological preservation areas is often limited by technical and legal constraints. In this study, a 3D soil model was created using Netcad NetPro/Mine software based on existing borehole data from the Karagümrük neighborhood in the Fatih district of Istanbul, an area subject to similar constraints. Within the scope of the model, lithological units and the groundwater level were evaluated in a shared database to develop a digital subsurface information system. The model enables a reduction in the need for new drilling, the effective use of existing data in areas where drilling is not possible, and rapid access to subsurface conditions. It is anticipated that this study will provide a data infrastructure serving as a decision support system for municipalities and engineering applications.

Keywords: 3D soil modeling, Netcad NetPro/Mine, drilling data, underground information system, Fatih.

1 Introduction

3D soil modeling is one of the fundamental components of modern engineering applications, enabling the numerical representation of the stratigraphic and geological characteristics of the subsurface environment. With the advancement of geographic information systems, digital modeling techniques, and improved data acquisition methodologies, soil data obtained from various sources can be integrated into a single platform, allowing for the high-accuracy modeling of subsurface structures. These models not only enable the 3D visualization of soil layers but also allow for the assessment of the spatial distribution of lithological continuity, groundwater levels, and other geotechnical parameters [1-3]. Today, 3D soil models are effectively used in many fields, including foundation design, tunnel and subway projects, infrastructure investments, urban renewal projects, disaster risk analyses, groundwater management, and mine site analyses. However, conducting new soil investigations in historic city centers is often limited due to dense development, confined work areas, existing infrastructure lines, and archaeological preservation requirements [2, 4]. For this reason, the integrated evaluation of borehole data collected in previous years and their conversion into three-dimensional digital models is of great importance. In this context, the approach of

establishing an integrated city-scale borehole database and generating 3D models has been addressed in only a few independent studies in the literature. In Chennai, India, approximately 175 boreholes from various sources were compiled to create a GIS-based 3D model [1], in Rome, over 800 boreholes were referenced to develop a 3D subsurface model [2], and in Thessaloniki, a database containing over 600 boreholes was used for decision support [5]. The Historic Peninsula of Istanbul is an area where conducting traditional soil investigations is quite challenging due to dense development, narrow transportation corridors, protected cultural heritage sites, and its status as an archaeological site. Furthermore, drilling operations conducted at various depths pose a risk of damaging historic structures and face significant time and cost constraints due to legal permitting processes and archaeological restrictions. For this reason, geotechnical-based 3D modeling approaches-which reduce the need for drilling and can provide continuous data over large areas-are of great importance in determining the region's soil structure. The numerous boreholes drilled at various times throughout the district, when integrated using appropriate methods, form a comprehensive data source representing the region's subsurface structure [6]. In this study, existing drilling data for the Fatih district were converted into a 3D soil model using Netcad NetPro/Mine software; an integrated subsurface information system was created by digitally modeling lithological units and the groundwater level. The developed model is intended to help reduce the need for new drilling, enable the effective use of existing data in areas where drilling is not possible, and allow municipalities and engineering firms to access subsurface information quickly and reliably. Additionally, the data infrastructure created is intended to serve as a foundation for future geotechnical analyses, infrastructure projects, and city-scale digital subsurface information systems.

2 Material and Method

The study area encompasses the Karagümrük neighborhood in the Fatih district, located within the boundaries of Istanbul's Historic Peninsula (Fig. 1). The Karagümrük neighborhood is bordered by Edirnekapı and Topkapı to the north, the Molla Gürani and İskenderpaşa neighborhoods to the east, the Aksaray area to the south, and Silivrikapı and neighborhoods near the city walls to the west. The area has a high population density due to its location along the transportation corridors of the Historic Peninsula.



Fig. 1. The Karagümrük neighborhood in the Fatih district, located within the boundaries of Istanbul's Historic Peninsula

The Karagümrük neighborhood is one of the oldest settlements on Istanbul's Historic Peninsula; due to its dense stock of historic buildings, registered cultural assets, narrow street layout, and archaeological protection status, it is one of the areas where conducting new geotechnical drilling studies is particularly challenging [7, 8]. The urban form of the Historic Peninsula bears layered traces from the Roman, Byzantine, Ottoman, and Republican periods; therefore,

subsurface modeling must also account for a multi-period and heterogeneous subsurface structure [7]. The Karagümrük neighborhood is one of the residential areas with high conservation priority due to its location adjacent to the Theodosius Walls and the numerous registered cultural assets and historic structures in its vicinity. The area is surrounded by historic structures such as the Kariye (Chora) Church, the Tekfur Palace, the Mihrimah Sultan Mosque, and Edirnekapı. Soil investigation surveys and drilling studies to be conducted as part of legal regulations aimed at preserving the mosques, dervish lodges, fountains, cemeteries, and registered examples of civil architecture located in the neighborhood and its immediate surroundings are subject to the approval processes of the relevant preservation boards. Furthermore, due to the existing building density, utility lines, and transportation constraints, drilling is technically impossible at many locations [9]. While this situation limits direct investigation of the subsurface environment, it necessitates an integrated evaluation of drilling data collected in previous years for various purposes. A 3D soil model developed within this framework combines existing drilling data on a single digital platform, enabling reliable predictions of lithological continuity and subsurface conditions in areas where drilling is not possible. Thus, the model contributes to the preservation of historic structures while also serving as an effective decision-support system that reduces the need for new drilling for municipalities, engineering firms, and conservation efforts. For these reasons, as part of this study, a large database has been compiled based on existing geotechnical drilling data obtained from engineering surveys previously conducted by public institutions and private firms. The drilling database includes drilling coordinates, soil elevations, lithological descriptions, stratigraphic boundaries, groundwater levels, and drilling depths, as well as the mechanical properties (stiffness and strength) of the soils. Prior to the 3D modeling process, all drilling records from 2018 to 2026 were reviewed, standardized, and transferred to a common digital database. The first stage of the data transfer process involved the systematic organization of drilling data in Microsoft Excel. In this context, three separate datasets were prepared, each of which was specifically configured for use in the Netcad NetPro/Mine software. The first dataset, the drilling file, contains the X, Y, and Z coordinates for each borehole, along with the total drilling depths (Fig. 2). This file is essential for defining the spatial distribution of the boreholes within the study area and for properly aligning the model with the reference coordinate system. The second dataset, the angle file, contains the initial depth, inclination values, and azimuth information for the boreholes (Fig. 3). This information provides the geometric input necessary to accurately model the borehole axis in three-dimensional space, particularly for inclined or deviated boreholes.

	A	B	C	D	E
1	borehole	depth	y	x	z
2	SK-1	20	4541763	410954	-4.12
3	SK-2	20	4541792	410915.3	-3.5

Fig. 2. A dataset containing the X, Y, and Z coordinates and total drilling depths for each borehole

	A	B	C	D
1	Sondaj No	Derinlik	Eğim(Dip)	Doğrultu(Azimuth)
2	SK-1	20	-90	0
3	SK-2	20	-90	0

Fig. 3. Dataset containing information on the initial depth, inclination values, and direction (azimuth) of boreholes

The third dataset, the lithology file, contains the start and end depths, interval thicknesses, and corresponding soil types (e.g., fill, clay, sand, claystone) for the lithological units identified along each borehole (Fig. 4). This file serves as a critical component for the thematic

classification of lithological units, the creation of surfaces, and the construction of the volume model.

	A	B	C	D
1	SK-NO	BAŞLANGIÇ	BİTİŞ	LİTOLOJİ
2	SK-1	0	3	Dolgu
3	SK-1	3	20	Kiltaşı
4	SK-2	0	3.5	Dolgu
5	SK-2	3.5	20	Kiltaşı

Fig. 4. Lithology dataset

These three data tables (Fig. 2, Fig. 3, Fig. 4) ensured the comprehensive preparation of the spatial, geometric, and lithological information required for the Netcad NetPro/Mine platform to fully process the modeling procedures. The digitization of the data has significantly facilitated the management and analysis of geotechnical data. As a result, data mining and statistical analyses can be performed on large datasets, making it possible to examine the spatial distribution and correlations of soil properties. Specifically, for the Karagümrük neighborhood, 3D modeling studies were conducted for the antic fill, clay, and sand units' dominant in the field using 41 lithological data points (Fig. 5).

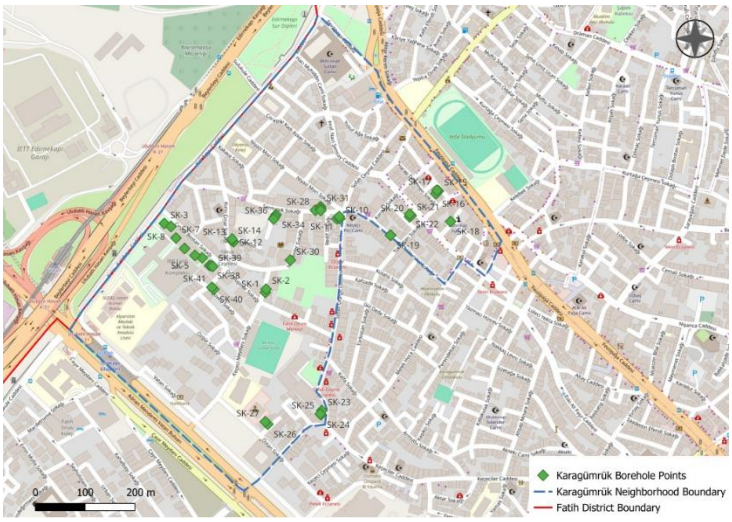


Fig. 5. Soil investigation data points

The 3D subsurface model was developed using Netcad NetPro/Mine software. Once data import was complete, the boreholes were displayed in 3D on the Netcad NetPro/Mine screen. At this stage, the software generated each borehole axis based on its location, inclination, and azimuth, thereby enabling the identification of lithological intervals in terms of both vertical and horizontal continuity. The use of thematic colors to represent these intervals enabled a rapid and analytical assessment of lithological differences and the distribution of strata on a borehole-by-borehole basis. This visualization stage serves as a crucial intermediate step for accurately defining the lithological boundaries required for surface modeling and for conducting correlation analyses between boreholes.

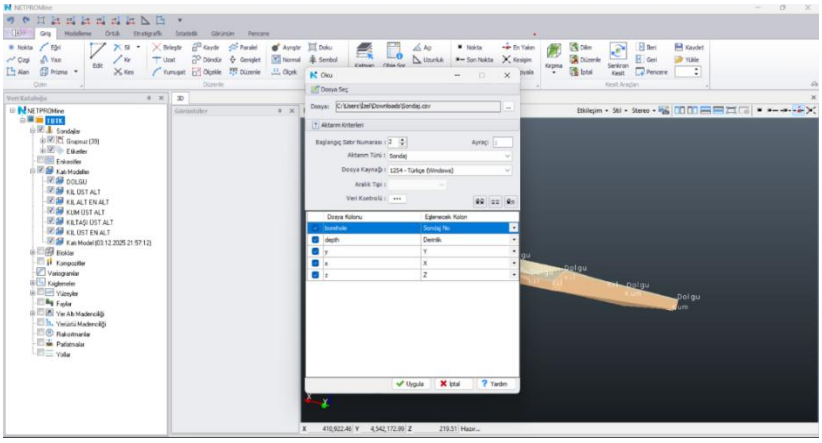


Fig. 6. Visualization of boreholes in a three-dimensional environment

The datasets prepared in Microsoft Excel were loaded into the Netcad NetPro/Mine software in sequence during the second step of the modeling process. First, by importing the borehole file into the system, the software identified the spatial distribution of the boreholes within the study area and established a geometric framework on a three-dimensional coordinate system. Subsequently, upon loading the angle file, Netcad NetPro/Mine calculated the spatial orientation of each borehole, thereby accurately representing the geometric configuration of the borehole axes. With the introduction of the lithology file into the system, the software identified the lithological boundaries for each borehole interval; these boundaries were then visualized using thematic colors and patterns. This made it possible to evaluate the continuity and variation characteristics of lithological units across boreholes. In this context, Fig. 2.6 presents the definition of borehole locations and lithology, while Fig. 2.7 presents the definition of groundwater characteristics and measurement points.

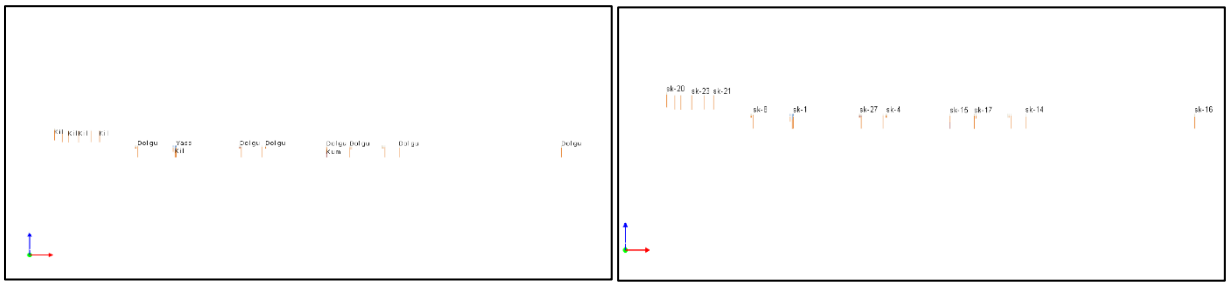


Fig. 2.6: Drilling locations and lithological description

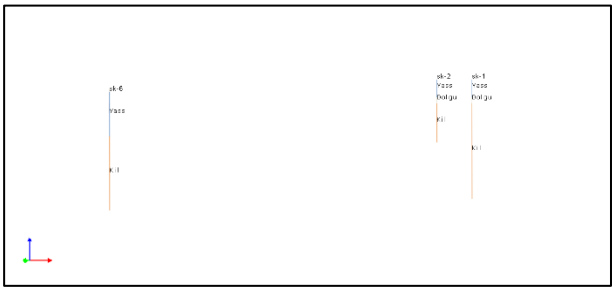


Fig. 2.7: Groundwater monitoring stations

Following the delineation of drilling data in a three-dimensional environment, upper and lower boundary surfaces were created for the lithological units identified in the study area. The Netcad NetPro/Mine software performed surface interpolations for each unit, using the start and end depths of the lithological intervals as references. Within the scope of this study, surface models were generated for three main lithological units (antic fill, sand, clay) and groundwater. The relevant units are presented in Fig.s 2.7-2.14. These surfaces define the spatial continuity of lithological boundaries across the study area and enable the interpretation of horizontal and vertical variations in geological strata.

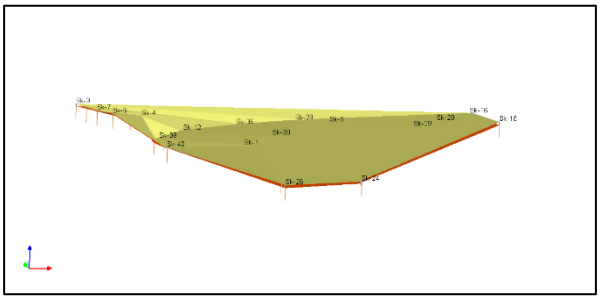


Fig. 2.8: Surface model of the fill unit

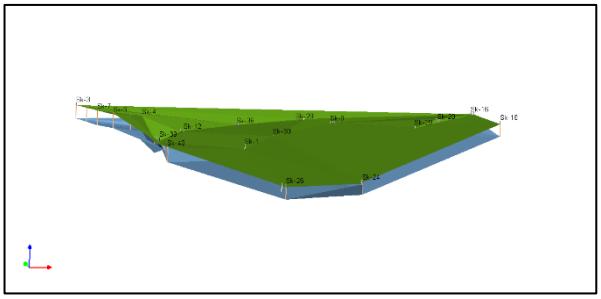


Fig. 2.9: Surface model of the clay unit

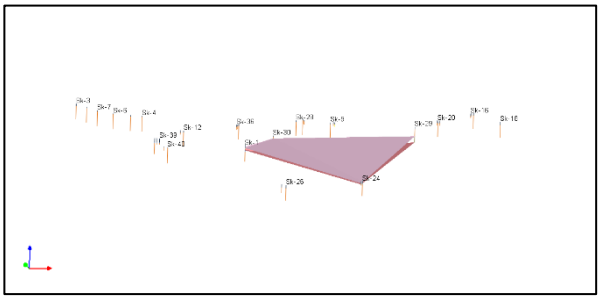


Fig. 2.10: Surface model of the sand unit

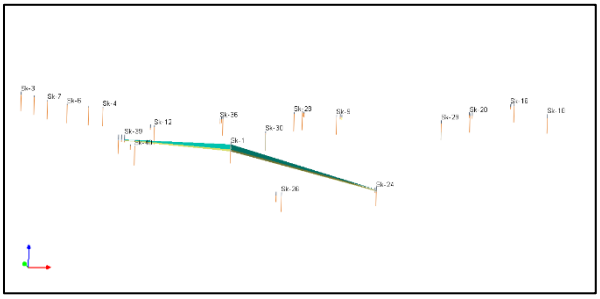


Fig. 2.11: A surface model showing groundwater

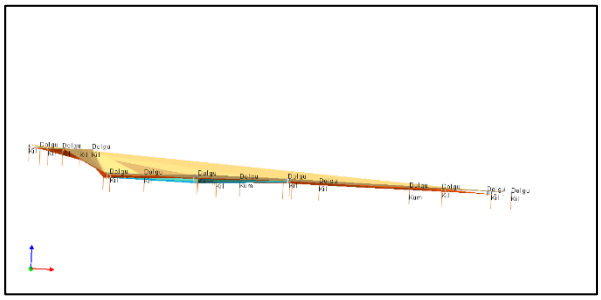


Fig. 2.12: Surface model of the fill unit and groundwater

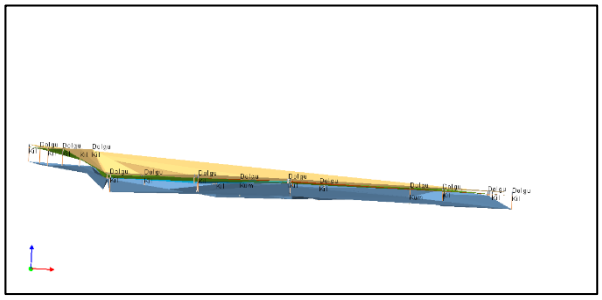


Fig. 2.13: Surface model of groundwater using fill and clay units

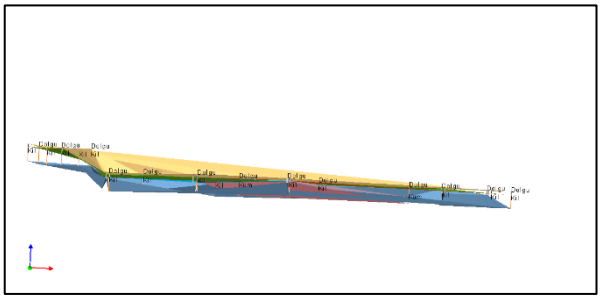


Fig. 2.14: Top view of the surface model of groundwater, showing the fill, clay, and sand units

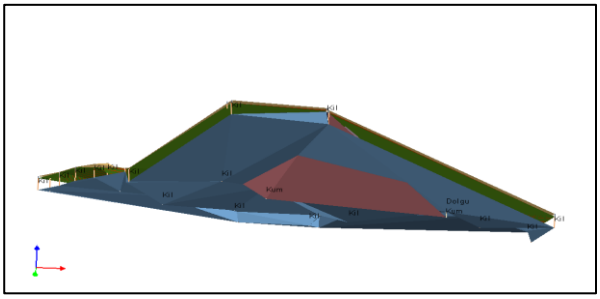


Fig. 2.15: A bottom view of the surface model of groundwater using fill, clay, and sand units

Following the creation of surface models, the lithological units were defined volumetrically. Netcad NetPro/Mine generated three-dimensional solid models for each lithological unit by closing surface pairs. Thus, the volumetric distribution of the fill, clay, and sand units, as well as the layer representing groundwater, within the study area was represented by precise geometric boundaries. Solid models play a fundamental role in geotechnical evaluations because they provide a realistic volumetric representation of soil units, both visually and analytically. Within the scope of this study, solid models were generated for three primary lithological units, and the resulting models are presented in Fig.s 2.15–2.22.

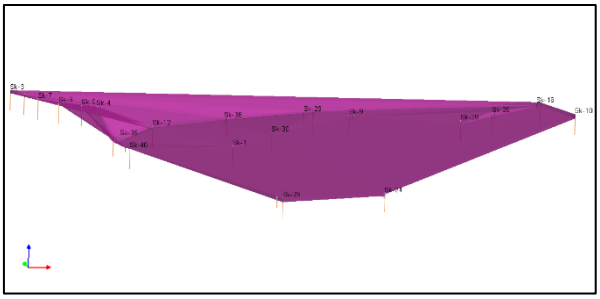


Fig. 2.15: Solid model of the filling unit

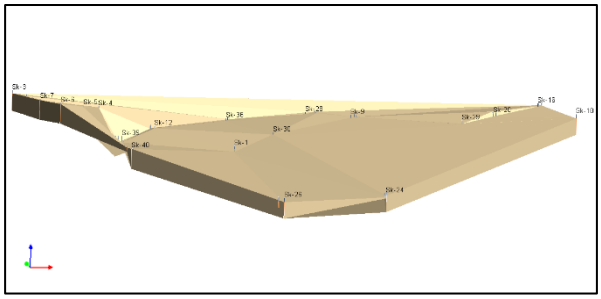


Fig. 2.16: Solid model of the clay unit

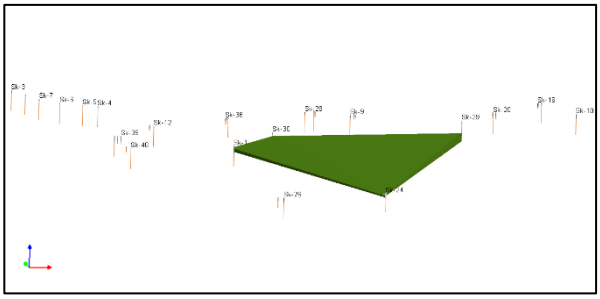


Fig. 2.17: Solid model of the sand unit

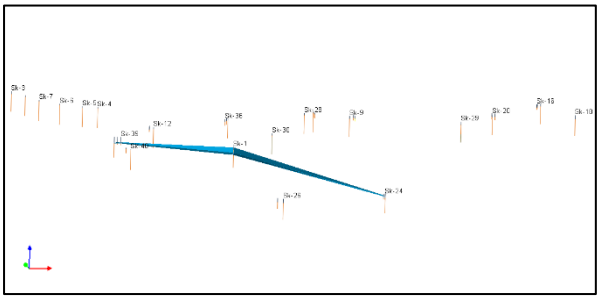


Fig. 2.18: A solid-state model of groundwater

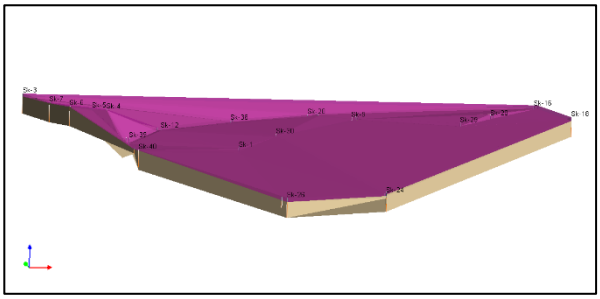


Fig. 2.19: Solid model of the fill and clay unit

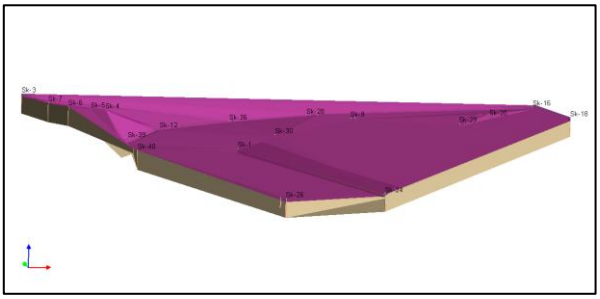


Fig. 2.20: Solid model of the fill, clay, and sand unit

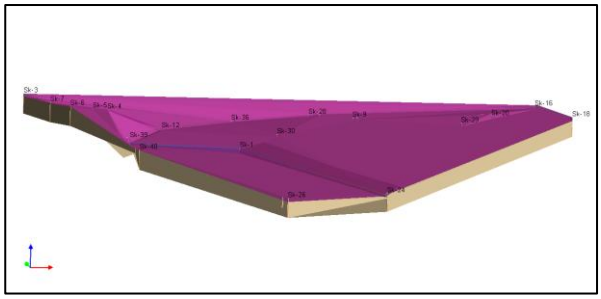


Fig. 2.21: Top view of a solid model representing fill, clay, sand, and groundwater

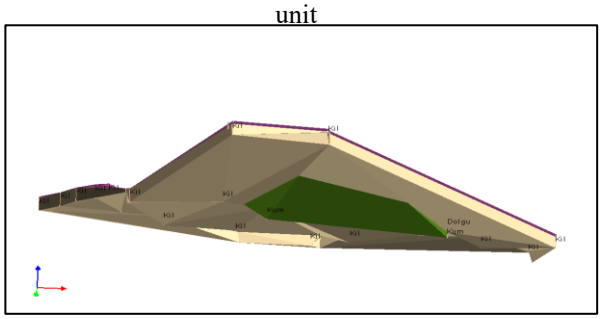


Fig. 2.22: Bottom view of a solid model representing fill, clay, sand, and groundwater

The final stage of the modeling process consisted of block modeling. In this stage, lithological layer models were divided into isometric blocks at a specific resolution; each block was linked to the relevant surface and solid models and classified according to the lithological unit to which it belonged. Thanks to Netcad NetPro/Mine's block modeling module, a structured, numerical, and three-dimensional data structure for the study area was obtained. This block model made a significant contribution to the numerical representation of the spatial distribution of lithological characteristics within the scope of the study. Visualizations of the block modeling work conducted in this context are presented in Fig.s 2.23–2.30.

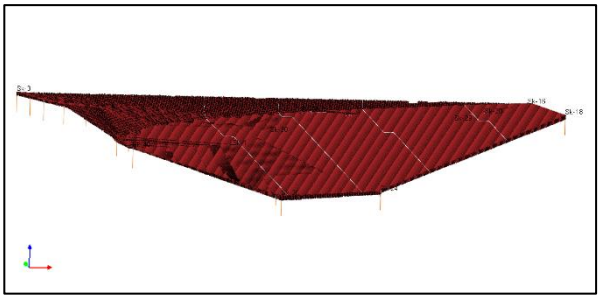


Fig. 2.23: Block model of the filling unit



Fig. 2.24: Block model of a clay unit

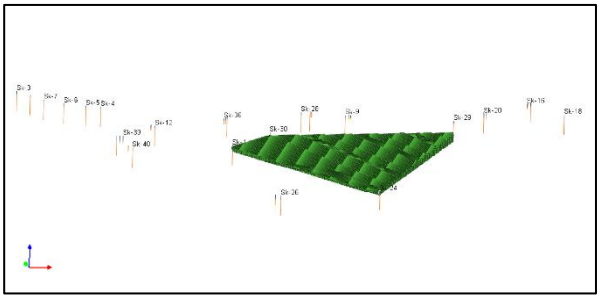


Fig. 2.25: Block model of the sand unit

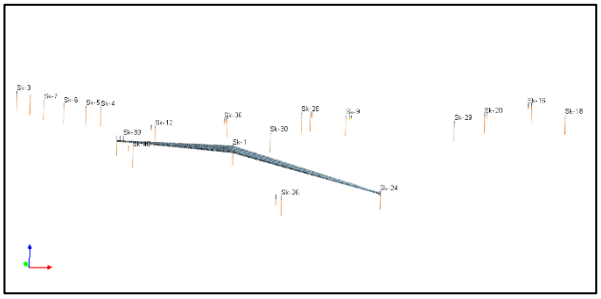


Fig. 2.26: Block model of groundwater



Fig. 2.27: Block model of the fill and clay unit

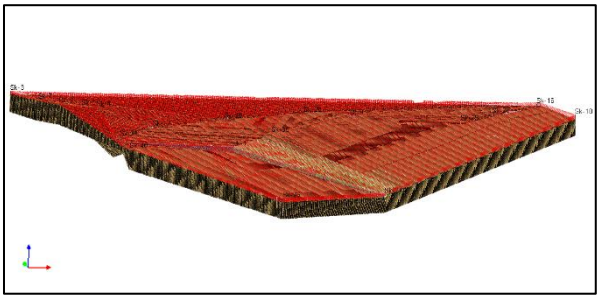


Fig. 2.28: A block consisting of fill, clay, and sand model

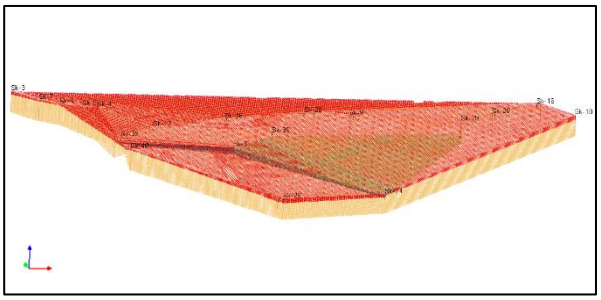


Fig. 2.29: Top view of a block model of groundwater, showing fill, clay, and sand units

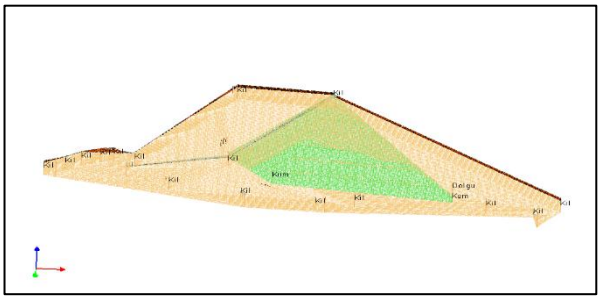


Fig. 2.30: Bottom view of the block model of groundwater, showing the fill, clay, and sand units

As a result of this comprehensive process, the three-dimensional structure of the fill, clay, and sand units in the study area was modeled with high accuracy; lithological boundaries were defined using surface and volume models; and the spatial distribution of soil units was numerically characterized through block modeling. This integrated modeling approach provided by the Netcad NetPro/Mine software has provided a scientific foundation for both the evaluation of field data and the creation of datasets to be used in advanced analyses.

3 Findings

As part of this study, data obtained from geotechnical borings conducted by various institutions in the Karagümrük neighborhood between 2018 and 2026 were consolidated into a single database, and a 3D soil model was successfully created using Netcad NetPro/Mine software. During the modeling process, borehole coordinates, lithological information, stratigraphic boundaries, and other geotechnical data were digitized, thereby enabling a three-dimensional visualization of the study area's subsurface structure. The model clearly reveals the spatial distributions, thickness variations, and interrelationships of the artificial fill, clay, and sand units commonly found in the study area. In particular, it was determined that the surface fill exhibits significant variations in thickness throughout the study area, which is attributed to the Historical Peninsula's long history of settlement, urban development activities, and anthropogenic filling processes. It was also determined that the clay and sand units underlying the fill layer generally exhibit continuity, although variations in thickness and elevation were observed in some areas between boreholes. The lithological surface models and volume models created in the Netcad NetPro/Mine environment have revealed not only the vertical variation of soil units but also their horizontal continuity. Compared to traditional two-dimensional geological cross-sections, the developed three-dimensional model has enabled a more accurate interpretation of the spatial relationships between lithological boundaries. Through the block modeling phase, the lithological units of the study area were represented as a regular grid of numerical cells, thereby creating an integrated subsurface data infrastructure that can be used in engineering analyses. One of the study's most significant findings is that it demonstrates how reliable subsurface data can be generated using existing borehole data in areas where new drilling is not possible due to dense historic development and archaeological preservation requirements. In areas with a high density of historic structures, such as the Karagümrük neighborhood, the ability to conduct new drilling is significantly limited by conservation board permits, existing development, utility lines, and narrow access corridors. Therefore, the three-dimensional model developed reduces the need for new drilling and enables the most effective evaluation of existing data. Through the digital subsurface information system that has been developed, drilling records, lithological units, and other subsurface data can be evaluated together on a single platform, allowing subsurface conditions at any desired location to be visualized quickly. This serves as a crucial decision-support tool, particularly for engineering projects involving foundation design, infrastructure projects, restoration work, urban renewal initiatives, disaster management, and risk analyses of mining sites.

4 Results

In this study, a three-dimensional soil model was created for the Karagümrük neighborhood, located within the boundaries of the Historic Peninsula of Istanbul, using existing geotechnical drilling data within the Netcad NetPro/Mine software environment. The main findings of the study are summarized below.

- Boring data collected by different institutions at various times have been successfully integrated by standardizing them in a common database.

- The three-dimensional spatial distributions, lithological continuities, and volumetric properties of artificial fill, clay, and sand units have been numerically modeled.
- The interpretation of the subsurface structure compared to traditional two-dimensional geological cross-sections.
- It has been demonstrated that reliable subsurface models can be created using existing drilling data in areas where new drilling is not feasible due to dense historical development, archaeological sites, and existing infrastructure.
- The developed model serves as a digital subsurface information system that can be used by municipalities, engineering firms, and public institutions, contributing to a reduction in the need for new drilling and accelerating engineering decision-making processes.

Consequently, the approach developed is not limited to the Karagümrük neighborhood alone but can also be applied to other historic city centers where sufficient drilling data is available. Through this 3D modeling strategy implemented under the TÜBİTAK UDAP 1001 project, it has become possible to develop city-scale digital subsurface information systems by integrating groundwater levels, SPT-N values, shear wave velocity (V_s), permeability, geotechnical parameters, and laboratory test results into the model. Consequently, a comprehensive decision-support system has been established that can be utilized in engineering applications such as earthquake-focused microzoning studies, foundation design, infrastructure planning, restoration projects, and disaster risk management.

Acknowledgments

This study was supported by the Scientific and Technological Research Council of Türkiye (TÜBİTAK) - UDAP under grant number 124M665 within the scope of the "TÜBİTAK- AFAD 1001-UDAP Joint Call for National Earthquake Research Program" and by the Istanbul University-Cerrahpaşa Scientific Research Projects Unit (IUC BAP) as a PhD Thesis Project under grant number 38685. The authors would like to express their gratitude to TÜBİTAK and IUC BAP for their support.

We would also like to extend our sincere thanks to geologicl engineer Cemal Reşit Pehlivanoğlu from YİKOB, AK Zemin, Netcad/Netpromine software team for their valuable contributions and support to the project.

References

1. Divya Priya, B., & Dodagoudar, G. R.: An integrated geotechnical database and GIS for 3D subsurface modelling: Application to Chennai City, India. Applied Geomatics, 10(1), 47–64 (2018).
2. Silvestri, D., Bordoni, P., Famiani, D., Marra, F., Rosa, C., & Salvini, R.: Predict part 2: Building a Geo-Database and a 3D subsurface model for the historical center of Rome. Annals of Geophysics, 68(6) (2025).
3. Ozdemir, A. C. O., & Tore, Y.: An innovative implicit modeling technique to 3D deposit modeling: a case study of the chromite mine. *Journal of Sustainable Mining*, *25*(1), 109-119(2026).
4. Soriano-Cuesta, C., Romero-Hernández, R., Mascort-Albea, E. J., Kada, M., Fuls, A., & Jaramillo-Morilla, A.: Evaluation of open geotechnical knowledge in urban environments for 3D Modelling of the City of Seville (Spain). *Remote Sensing*, *16*(1), 141(2023). https://doi.org/10.3390/rs16010141

5. Kokkala, A., & Marinos, V.: An engineering geological database for managing, planning and protecting intelligent cities: The case of Thessaloniki city in Northern Greece. Engineering Geology, 301, 106617 (2022). https://doi.org/10.1016/j.enggeo.2022.106617
6. Yıldız Sertgöz, İ.: Üç boyutlu zemin haritaları kullanımı ile makine öğrenmesi tekniklerine dayalı geoteknik parametre tahmini. Yüksek Lisans Tezi, İstanbul University-Cerrahpaşa Institute of Graduate Studies, İstanbul (2025).
7. Sarihan, E.: Historical city evaluation in the context of morphological theories (istanbul, last ottoman period). *Architecture and Engineering*, *6*(1), 64-72 (2021).
8. Durhan, S., & Ozguven, Y.: Breaking the duality: The Historical Peninsula of Istanbul as an open-air museum. Journal of Cultural Heritage, 14S, e182-e188, (2013).
9. Kambek, E.: World Heritage of Istanbul from Perspective of Vernacular Architecture. Актуальные проблемы теории и истории искусства, (14), 796-807(2024).

Publication Note

This paper was peer-reviewed, accepted for presentation, and included in the proceedings of the ACE2026 – International Conference on Advances in Civil Engineering, held on 12–14 October 2026 in Trabzon, Türkiye.

This paper may be cited as follows:

İzel Yıldız Sertgöz, İbrahim Fatih Mutlu, Meryem Yılmaz, Zülal Akbay Arama “3D lithology and soil modeling in urban areas: the case of Fatih District,” in Proceedings of the ACE2026 – International Conference on Advances in Civil Engineering, Trabzon, Türkiye, 12–14 October 2026.

A Web-Based Tool for Energy-Corrected SPT Evaluation of Soil Liquefaction Potential

Oguz K. Sivri[1] and Mustafa Tolun[2]
[1] 0009-0002-6732-3421, Adana Alparslan Turkes Science and Technology University, Civil Engineering Department, 01250, Adana, Türkiye, oguzkaansivri@gmail.com
[2] 0000-0002-2073-8796, Adana Alparslan Turkes Science and Technology University, Civil Engineering Department, 01250, Adana, Türkiye, mtolun@atu.edu.tr

Abstract. Soil liquefaction is one of the most crucial geotechnical hazards that affects the performance of foundations and structures under seismic loading. Standard Penetration Test (SPT)-based simplified procedures, as adopted in the Turkish Building Earthquake Code, remain widely used in engineering practice for evaluating liquefaction triggering potential due to their practicality and compatibility with routine site investigation data. Despite the availability of established methodologies and previously developed computational tools, their accessibility, usability, and dissemination to designers remain limited, often due to licensing constraints and restricted availability. This study presents the development of a web-based tool designed to perform energy-corrected SPT-based liquefaction assessment in a transparent and user-friendly environment. For the consideration of liquefaction potential, the computational framework is based on established simplified procedures, including SPT energy corrections, overburden stress normalisation, fines content adjustment, calculation of liquefaction resistance and earthquake-induced cyclic shear stress, and evaluation of the factor of safety against liquefaction. This tool allows users to input both seismic parameters (e.g., earthquake magnitude, short-period spectral acceleration) and layer-dependent soil properties (e.g., unit weight of soil, SPT-N values, and fine contents) that enables the analysis of single-layered and stratified soil profiles. The primary output provides an assessment of whether each soil layer within the profile satisfies the recommended factor of safety against liquefaction, with results presented in both graphical and tabular formats. The developed tool provides an accessible and practical platform for performing SPT-based liquefaction assessments without requiring specialised commercial software.

Keywords: Soil liquefaction, Standard penetration test, Energy correction, Cyclic resistance ratio, Earthquake-induced demand.

1 Introduction

Soil liquefaction is a major geotechnical concern in earthquake-prone regions due to its potentially severe effects on structures and infrastructures [1]. Loose, saturated cohesionless soils generally tend to densify under loading. During seismic loading induced by an earthquake, however, the essentially undrained response prevents the corresponding volume reduction, causing excess pore water pressure to progressively accumulate within the soil [2]. As excess pore water pressure continues to accumulate, the effective stress carried by the soil skeleton progressively decreases and may eventually approach zero, resulting in a state of liquefaction. The associated loss of shear strength and stiffness can cause substantial ground deformation and adversely affect the seismic performance of foundations, buildings, embankments, tunnels, bridges, and other infrastructures [3]. Consequently, extensive research has led to the development of various methods for evaluating earthquake-induced liquefaction potential,

which can broadly be classified as stress, strain, and energy-based approaches [1]. Among these methods, stress-based procedures have gained widespread acceptance in engineering practice, particularly those employing in-situ test data from the Standard Penetration Test (SPT) or Cone Penetration Test (CPT). The stress-based approach, originally introduced within the simplified procedure by Seed and Idriss [2], evaluates liquefaction triggering by comparing the cyclic stress induced by earthquake loading with the cyclic resistance of the soil.

In this study, a web-based tool was developed to implement the stress-based liquefaction assessment procedure specified in the Turkish Building Earthquake Code (TBEC) [4]. The application utilizes Standard Penetration Test (SPT) data, commonly obtained during routine site investigations, together with the relevant properties of the corresponding soil layers. The developed application provides a freely accessible and user-friendly platform for evaluating the liquefaction potential of both single-layered and stratified soil profiles.

2 Methodology

This paper presents a freely accessible web-based tool named GEOLIQA (Geotechnical Liquefaction Analysis) [5], developed to implement the stress-based liquefaction assessment procedure specified in the Turkish Building Earthquake Code. By integrating routinely available SPT data with the required soil and seismic parameters, GEOLIQA aims to facilitate the practical assessment of liquefaction triggering for layered soil profiles. Although the implementation of established liquefaction procedures in computational tools is not a new concept [6], GEOLIQA is intended to provide an openly accessible alternative that requires no commercial software or licensing [7]. More importantly, the platform has been developed with a flexible structure that allows additional liquefaction assessment methods and functionalities to be incorporated in future versions.

The computational procedure implemented in GEOLIQA begins with the definition of the soil profile and seismic input parameters. For each soil layer, the user provides the raw SPT N-value, saturated and unsaturated unit weights, soil type, and fines content, together with the required SPT correction factors such as C_N, C_R, C_S, C_B, and C_E. The groundwater table is defined for the soil profile, while the short-period design spectral acceleration (S_{DS}) and earthquake moment magnitude (M_w) are specified as seismic input parameters (Fig.1). The S_{DS} value should be determined specifically for the site, considering the local soil class and the selected earthquake ground-motion level, using the Türkiye Earthquake Hazard Maps Interactive Web Application provided by AFAD [8].

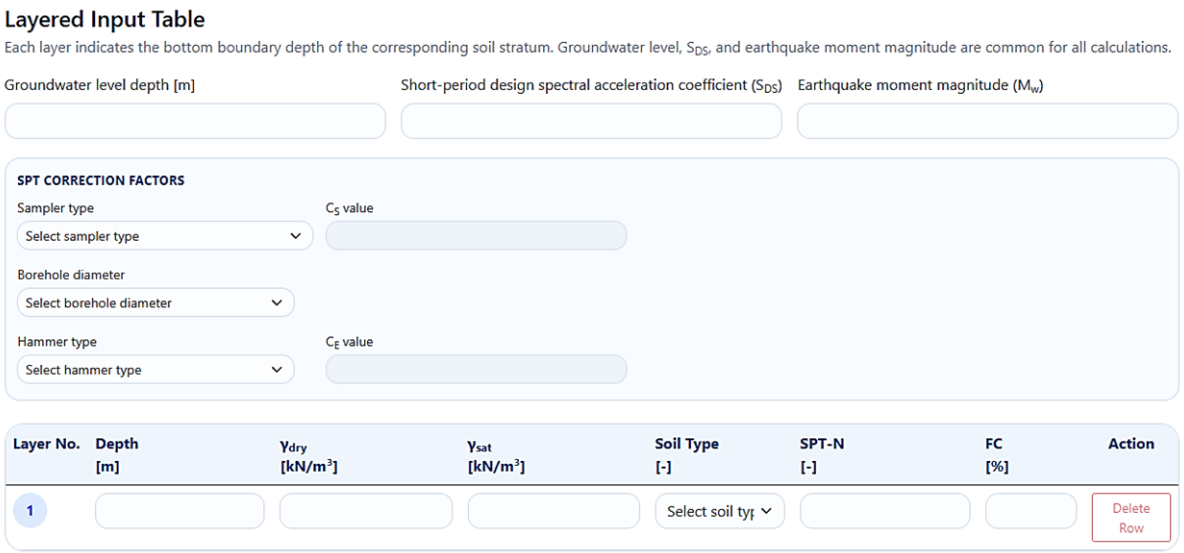


Fig. 1. GEOLIQA interface for defining input parameters and layered soil profiles.

Following the definition of the soil profile and input parameters, GEOLIQA performs the liquefaction assessment for each soil layer. The computational procedure includes correction of the measured SPT blow counts, calculation of total and effective stresses, evaluation of liquefaction resistance and earthquake-induced cyclic demand, and determination of the corresponding factor of safety. The main calculation steps and equations implemented in GEOLIQA in accordance with TBEC are summarized in Table 1.

Table 1. Computational steps and equations implemented in GEOLIQA for SPT-based liquefaction assessment.

Stages/Purposes	Equations/Procedures
Corrected SPT blow count: Correction of measured SPT blow count for field conditions and overburden stress.	$N_{1,60} = NC_N C_E C_B C_R C_S$
Total vertical stress: Determination of total vertical stress at the corresponding depth.	$\sigma_{v0} = \sum \gamma_i h_i$
Pore-water pressure: Determination of hydrostatic pore-water pressure below the groundwater table.	$U = \gamma_w (z - z_w)$
Effective vertical stress: Determination of effective overburden stress at the corresponding depth.	$\sigma'_{v0} = \sigma_{v0} - u$
Fines-corrected SPT blow count: Adjustment of $N_{1,60}$ according to fines content.	$N_{1,60f} = \alpha + \beta N_{1,60}$
Cyclic resistance ratio: Determination of $CRR_{M7.5}$ from the fines-corrected SPT value.	$CRR_{M7.5} = f(N_{1,60f})$
Magnitude correction factor: Adjustment of cyclic resistance according to earthquake magnitude.	$C_M = 10^{2.24}/M_w^{2.56}$
Liquefaction resistance: Determination of cyclic shear resistance of the soil.	$\tau_R = CRR_{M7.5} C_M \sigma'_{v0}$
Earthquake-induced demand: Determination of cyclic shear stress induced by earthquake loading.	$\tau_{earthq} = 0.65\sigma_{v0}(0.4S_{DS})r_d$
Factor of safety: Comparison of liquefaction resistance with earthquake-induced demand.	$FS = \tau_R/\tau_{earthq}$

Based on the calculated factor of safety (FS), GEOLIQA evaluates the liquefaction condition of each soil layer using predefined threshold values. Although a factor of safety higher than unity theoretically indicates that liquefaction triggering is not expected, factors of safety ranging from 1.1 to 1.3 are generally considered appropriate for building sites, with the selected value depending on the importance of the structure and the potential for ground displacement [9–11]. Accordingly, GEOLIQA adopts FS=1.1 as the minimum safety threshold while FS=1.3 is used as the upper threshold to provide a more conservative assessment. In summary, soil layers with FS<1.1 are classified as having high liquefaction potential, those with 1.1≤FS<1.3 are identified as being in a critical condition, while those with FS≥1.3 are classified as having low liquefaction potential.

3 Verification and Application

For verification of GEOLIQA, an example of previously published liquefaction analysis was selected from the literature as a reference case [6]. The input parameters reported in the reference study were introduced into GEOLIQA without modification, and the corresponding analysis was performed under the same conditions. The reference soil profile consists of ten layers extending to a depth of 15 m with a 1.5 m interval, with a groundwater table located at 4 m below the ground surface. The seismic input parameters were M_w=7.5, and S_{DS}=1.14, while the local soil class was defined as ZD. The SPT correction factors were taken as C_B=1.0,

C_E=1.2, and C_S=1.0. Layer-specific SPT-N values, unit weights, and fines contents were adopted directly from the reference study and entered GEOLIQA.

After the definition of the input parameters, the analysis was performed using GEOLIQA. The resulting total and effective vertical stresses and pore-water pressures are presented as depth-dependent profiles, together with the measured SPT-N values, as presented in Fig. 2. The groundwater table is also indicated to facilitate interpretation of the results.

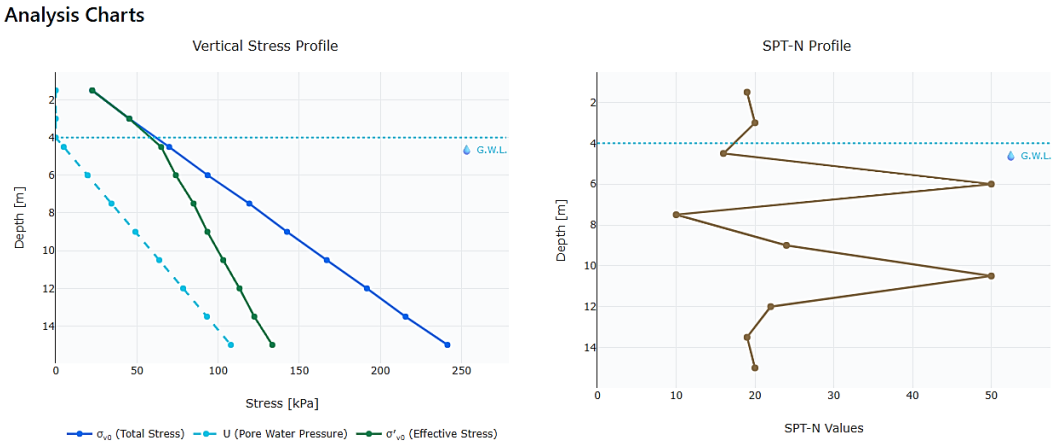


Fig. 2. Vertical stress and SPT-N profiles generated by GEOLIQA.

In addition to the graphical outputs, GEOLIQA provides a detailed layer-by-layer summary of the analysis results, as shown in Fig. 3. The table reports the numerical values of the input, intermediate, and final parameters involved in the calculation procedure, allowing users to directly examine each stage of the liquefaction assessment. This transparent presentation enables the calculated SPT corrections, stress components, liquefaction resistance and demand, and the resulting factor of safety to be readily traced for each soil layer.

Layer No. [-]	Depth [m]	Soil Type [-]	Layer interval [m]	σ_{v0} [kPa]	U [kPa]	σ'_{v0} [kPa]	r_d [-]	C_N [-]	C_R [-]	C_S [-]	C_B [-]	C_E [-]	$N_{1,60}$ [-]	α [-]	β [-]	$N_{1,60f}$ [-]	$CRR_{M7.5}$ [-]	C_M [-]	τ_{demand} [kPa]	τ_R [kPa]	FS [-]	Evaluation [-]
1	1.50	SP	0.00 - 1.50	22.50	0.00	22.50	-	-	-	-	-	-	-	-	-	-	-	-	-	-	-	Liquefaction Not Expected
2	3.00	SP	1.50 - 3.00	45.30	0.00	45.30	-	-	-	-	-	-	-	-	-	-	-	-	-	-	-	Liquefaction Not Expected
3	4.50	SP	3.00 - 4.50	69.90	4.91	65.00	0.97	1.21	0.85	1.00	1.00	1.20	19.80	0.00	1.00	19.80	0.21	1.00	20.01	13.83	0.69	High Liquefaction Potential
4	6.00	SP	4.50 - 6.00	93.60	19.62	73.98	-	1.14	0.95	1.00	1.00	1.20	64.81	-	-	-	-	-	-	-	-	Liquefaction Not Expected
5	7.50	SP	6.00 - 7.50	119.25	34.34	84.92	0.94	1.06	0.95	1.00	1.00	1.20	12.10	3.93	1.09	17.15	0.18	1.00	33.32	15.49	0.46	High Liquefaction Potential
6	9.00	SP	7.50 - 9.00	142.50	49.05	93.45	0.93	1.01	0.95	1.00	1.00	1.20	27.68	0.03	1.00	27.84	0.36	1.00	39.33	34.01	0.86	High Liquefaction Potential
7	10.50	SP	9.00 - 10.50	166.95	63.77	103.19	-	0.96	1.00	1.00	1.00	1.20	57.77	-	-	-	-	-	-	-	-	Liquefaction Not Expected
8	12.00	SP	10.50 - 12.00	191.70	78.48	113.22	0.85	0.92	1.00	1.00	1.00	1.20	24.27	4.29	1.12	31.34	0.60	1.00	48.50	68.37	1.41	Low Liquefaction Potential
9	13.50	SP	12.00 - 13.50	215.55	93.20	122.36	0.81	0.88	1.00	1.00	1.00	1.20	20.16	0.12	1.01	20.45	0.22	1.00	51.98	27.04	0.52	High Liquefaction Potential
10	15.00	SP	13.50 - 15.00	241.35	107.91	133.44	0.77	0.85	1.00	1.00	1.00	1.20	20.32	4.39	1.12	27.20	0.34	1.00	55.33	45.88	0.83	High Liquefaction Potential

Fig. 3. Detailed layer-by-layer analysis results generated by GEOLIQA.

For a more concise interpretation of the results, GEOLIQA also provides a summary table presenting the earthquake-induced demand (τ_{demand}), liquefaction resistance (τ_R), factor of safety (FS), and the corresponding liquefaction assessment for each soil layer (Fig. 4). This summary allows users to readily identify the layers that are potentially susceptible to liquefaction without examining the complete set of intermediate calculation parameters.

Brief Results Summary

Depth [m]	Soil Type [-]	τ_{demand} [kPa]	τ_R [kPa]	FS [-]	Evaluation [-]
1.50	SP	-	-	-	Liquefaction Not Expected
3.00	SP	-	-	-	Liquefaction Not Expected
4.50	SP	20.01	13.83	0.69	High Liquefaction Potential
6.00	SP	-	-	-	Liquefaction Not Expected
7.50	SP	33.32	15.49	0.46	High Liquefaction Potential
9.00	SP	39.33	34.01	0.86	High Liquefaction Potential
10.50	SP	-	-	-	Liquefaction Not Expected
12.00	SP	48.50	68.37	1.41	Low Liquefaction Potential
13.50	SP	51.98	27.04	0.52	High Liquefaction Potential
15.00	SP	55.33	45.88	0.83	High Liquefaction Potential

Fig. 4. Summary of layer-based liquefaction assessment generated by GEOLIQA.

Finally, GEOLIQA provides a graphical layer-based assessment of the investigated soil profile, as shown in Fig. 5. The visualization combines the soil profile with the distribution of factor of safety (FS), indicating the position of each layer relative to the predefined assessment thresholds, and a direct comparison between earthquake-induced demand and liquefaction resistance. This integrated representation enables potentially susceptible layers to be readily identified and provides a comprehensive interpretation of the liquefaction response throughout the soil profile.

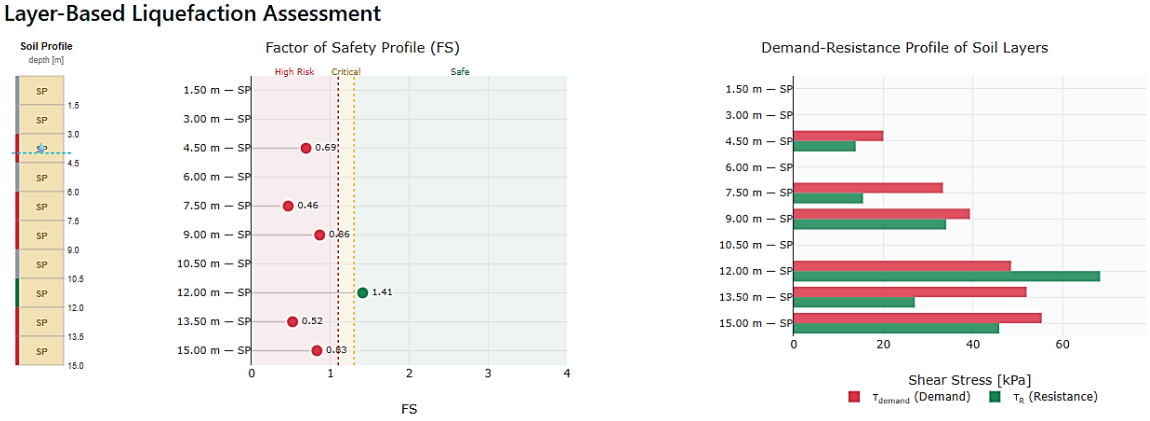


Fig. 5. Graphical layer-based liquefaction assessment generated by GEOLIQA.

It should be noted that GEOLIQA performs the liquefaction triggering assessment only for soil layers satisfying the applicability criteria specified in TBEC [4]. Accordingly, the assessment is applied to potentially liquefiable soils located below the groundwater table and within the upper 20 m of the soil profile, provided that the corrected SPT blow count ($N_{1,60}$) is less than 30 blows/30 cm. Potentially liquefiable soils are defined in TBEC as sand, gravelly sand, silty clayey sand, non-plastic silt, and silt–sand mixtures below the groundwater table. For layers that do not satisfy these criteria, GEOLIQA does not proceed with the liquefaction triggering calculations and reports the result as “Liquefaction Not Expected.”

4 Summary and Conclusions

This study presented GEOLIQA, a freely accessible web-based application developed for SPT-based liquefaction assessment in accordance with the procedure specified in the Turkish Building Earthquake Code (TBEC). The application integrates the required SPT corrections, stress calculations, liquefaction resistance and earthquake-induced demand calculations, and factor of safety assessment within a single computational environment.

The computational implementation was verified using a previously published liquefaction assessment example, in which the same soil profile and seismic input parameters were reproduced in GEOLIQA. The results obtained by GEOLIQA were consistent with the corresponding values reported in the reference study, confirming the correct implementation of the adopted calculation procedure. In addition to the numerical calculations, GEOLIQA provides detailed layer-by-layer results, concise liquefaction classifications, and graphical representations of the factor of safety and demand–resistance relationship throughout the soil profile.

The principal contribution of GEOLIQA is therefore not the introduction of a new liquefaction assessment methodology, but the implementation of an established code-based procedure in a transparent, freely accessible, and user-friendly web environment. By allowing the intermediate and final calculation parameters to be directly investigated, this web-based tool can facilitate both routine engineering assessment and educational use. Furthermore, its web-based structure provides a platform that can be continuously updated and extended as assessment procedures and regulatory requirements evolve.

Declaration of competing interest

The authors declare that there are no known competing financial interests or personal relationships in this paper.

References

1. Arslan E., Bol E., Özocak A., Ecemiş N., Sert, S.: Advances in soil liquefaction prediction: a review of pore pressure generation models. Open Geosciences, 18(1): 20250956, 1-40 (2026). https://doi.org/10.1515/geo-2025-0956
2. Seed H. B., Idriss, I. M.: Simplified procedure for evaluating soil liquefaction potential. Journal of the Soil Mechanics and Foundations Division, 97(9), 1249-1273 (1971). https://doi.org/10.1061/JSFEAQ.000166
3. Önalp A., Özocak A., Bol E., Sert S., Arslan E.: An investigation into dynamic behaviour of reconstituted and undisturbed fine-grained soil during triaxial and simple shear. Bulletin of Earthquake Engineering, 22, 5599–5618 (2024). https://doi.org/10.1007/s10518-024-01980-3
4. AFAD. Turkish Building Earthquake Code (Türkiye Bina Deprem Yönetmeliği). Disaster and Emergency Management Authority, Ankara, Türkiye (2018).
5. GEOLIQA (Geotechnical Liquefaction Analysis) Homepage, https://geoliqa.com/, last accessed 2026/08/15.
6. Dingil M., Keseroglu B., Turedi Y., Ornek M.: TBDY 2018'e göre sıvılaşma potansiyeli analizi için bir geoteknik web uygulamasının geliştirilmesi. Dicle University Journal of Engineering, 16(2), 511-520 (2025). https://doi.org/10.24012/dumf.1653529
7. Rocscience Inc. Settle3, 3D Settlement and Consolidation Analysis Software, Toronto, Canada (2026).
8. Türkiye Earthquake Hazard Maps Interactive Web Application, Disaster and Emergency Management Presidency (AFAD), https://tdth.afad.gov.tr/, last accessed 2026/08/15.

9. Building Seismic Safety Council (BSSC). NEHRP Recommended Seismic Provisions for New Buildings and Other Structures. FEMA P-750, Federal Emergency Management Agency, Washington, DC, USA (2009).
10. Upadhyaya S., Maurer B. W., Green R. A., Rodriguez-Marek A.: Selecting the optimal factor of safety or probability of liquefaction triggering for engineering projects based on misprediction costs. Journal of Geotechnical and Geoenvironmental Engineering, 147(6): 04021026, 1-10 (2021). https://doi.org/10.1061/(ASCE)GT.1943-5606.0002511
11. Nevada Earthquake Safety Council. Guidelines for Evaluating Liquefaction Hazards in Nevada. Nevada Bureau of Mines and Geology, Reno, Nevada, USA (2020).

Author Contribution Statement

- *Conceptualization:* Mustafa Tolun
- *Methodology:* Oguz K. Sivri, Mustafa Tolun
- *Investigation:* Oguz K. Sivri
- *Writing – Original Draft:* Mustafa Tolun
- *Writing – Review & Editing:* Mustafa Tolun

List of Abbreviations

- **TBEC** — Turkish Building Earthquake Code
- **SPT** — Standard Penetration Test
- **CPT** — Cone Penetration Test
- **GEOLIQA** — Geotechnical Liquefaction Analysis
- **AFAD** — Disaster and Emergency Management Presidency
- **FS** — Factor of Safety

Note: Following the conference, this Publication Note will be added to each paper; therefore, authors are kindly requested not to remove the note below and to complete the author(s) and paper title information.

Publication Note

This paper was peer-reviewed, accepted for presentation, and included in the proceedings of the ACE2026 – International Conference on Advances in Civil Engineering, held on 12–14 October 2026 in Trabzon, Türkiye.

This paper may be cited as follows:

Sivri O. K., Tolun M., "A Web-Based Tool for Energy-Corrected SPT Evaluation of Soil Liquefaction Potential" in Proceedings of the ACE2026 – International Conference on Advances in Civil Engineering, Trabzon, Türkiye, 12–14 October 2026.

Effect of EPS Geofoam on Soil Arching and Deflection Behavior of Small-Diameter Buried HDPE Pipes under High Fill Conditions

Perihan Biçer[1],* , Sercan Bozkurt[1], Havvanur Kılıç[2]

[1] 0000-0002-4966-4719, Department of Civil Engineering, Çorlu Engineering Faculty, Tekirdağ Namık Kemal University, Tekirdağ, Türkiye, pbicer@nku.edu.tr

[1] 0000-0002-1003-4445, Department of Civil Engineering, Çorlu Engineering Faculty, Tekirdağ Namık Kemal University, Tekirdağ, Türkiye, sercan.bozkurtt@gmail.com

[2] 0000-0001-9455-1687, Department of Civil Engineering, Faculty of Civil Engineering, Yıldız Technical University, İstanbul, Türkiye, kilic@yildiz.edu.tr

*Corresponding Author E-mail: pbicer@nku.edu.tr

Abstract. The behavior of buried flexible pipes under high fill loading depends on pipe stiffness, backfill properties, and soil–pipe interaction. This study numerically investigates the effect of EPS geofoam on the soil arching and deformation behavior of HDPE pipes with inner diameters of 0.60 m and 0.30 m. A PLAXIS 2D modelling approach calibrated using field measurements from the Deep Burial Project was used. The pipes, defined as HDPE-0.60 and HDPE-0.30, were analyzed under a 30 m fill height. Crushed stone, sand, and clay backfills were considered together with two different EPS geofoam configurations, namely EPS placed above the pipe crown and EPS placed around the pipe. The results were compared with the reference case without EPS. The comparison showed that the use of EPS geofoam increased positive soil arching and generally reduced the stresses transferred to the pipes. For the 0.60 m diameter pipe, at H/D ≈ 48, the vertical arching factor ranged from about 0.20 to 0.30 for granular backfills in the EPS models. For the 0.30 m diameter pipe, at H/D ≈ 96, the lowest vertical arching factor values for granular backfills decreased to approximately 0.15. The model in which the pipe was surrounded by EPS generally produced lower horizontal arching factors, whereas the model with EPS placed above the pipe crown provided vertical deflection ratios closer to zero in several cases. Overall, the results indicate that EPS geofoam configuration and backfill material type affect both stress redistribution and deformation behavior of small-diameter HDPE pipes under high fill conditions.

Keywords: EPS Geofoam; Small-Diameter HDPE Pipe; Soil Arching; High Fill Height

1 Introduction

The behavior of buried flexible pipes cannot be explained solely by the mechanical properties of the pipe material; it is the combined result of pipe stiffness, backfill properties, construction conditions, and soil–structure interaction developing around the pipe. In the calculation of vertical loads transferred to buried pipes, the weight of the soil prism above the pipe and the shear stresses mobilized between this prism and the adjacent soil zones are considered as the main components. This interaction produces soil arching depending on the relative settlement differences around the pipe and causes the load transferred to the pipe to differ from the direct weight of the overlying fill [1, 2]. In flexible pipes, deformation of the pipe section under

vertical loading may cause the soil prism above the pipe to settle more than the adjacent soil zones. In this case, positive soil arching develops; part of the overburden load is transferred to the adjacent soil zones, and the vertical stress acting at the pipe crown may become lower than the geostatic stress [3, 4].

In recent years, HDPE pipes have been widely used in buried infrastructure systems because of their light weight, corrosion resistance, and ease of installation. However, the flexible nature of these pipes makes pipe–soil interaction more important in design. The behavior of HDPE pipes under soil loading has been investigated by different researchers through field measurements, laboratory tests, and numerical analyses, and it has been shown that pipe stiffness, backfill properties, and compaction conditions can play important roles in pipe response [3, 4]. Studies on small-diameter corrugated HDPE pipes have shown that construction effects arising from the layer-by-layer placement and compaction of backfill significantly influence pipe deformation and the earth pressures developing around the pipe. These studies have demonstrated that pipe behavior cannot be explained solely by pipe diameter and pipe stiffness, but should be evaluated together with parameters such as the modulus of the sidefill soil, the degree and method of compaction, trench geometry, and the thickness and unit weight of the soil cover [5–7].

Under high-fill conditions, the earth loads acting on buried pipes increase, and the distribution of vertical and horizontal stresses around the pipe becomes an important design consideration. One method used to reduce these loads is the compressible inclusion approach, commonly referred to as the induced trench or imperfect ditch method. In this method, deformation of a compressible material placed above the pipe crown increases the relative settlement between the soil prism over the pipe and the adjacent soil zones. This increased relative settlement mobilizes shear stresses along the vertical boundaries of the soil prism and promotes positive soil arching, thereby transferring part of the overburden load to the adjacent soil and reducing the vertical load reaching the pipe [4, 8, 9]. EPS geofoam is one of the compressible materials used for this purpose because of its low stiffness and controlled compressible behavior. Previous experimental and numerical studies have shown that EPS geofoam panels can reduce vertical earth pressures acting on buried pipes and modify the horizontal–vertical stress distribution around the pipe [8, 9].

Studies conducted specifically on HDPE pipes have shown that the use of EPS geofoam not only reduces vertical stress but also affects pipe deformation by changing the pipe–soil interaction mechanism. Kılıç and Akınay [4] conducted full-scale laboratory tests on a 300-mm nominal-diameter corrugated HDPE pipe and reported that an EPS panel placed above the pipe crown significantly reduced the vertical stress at the pipe crown, the horizontal stress at the pipe springline, and pipe deflections. Akyelken and Kılıç [10] investigated buried HDPE pipes with EPS geofoam using PLAXIS 2D analyses supported by experimental measurements and showed that EPS geofoam configurations can reduce the vertical and horizontal stresses around buried HDPE pipes. Kılıç et al. [11] also investigated the effects of EPS geofoam configurations on the stress and deformation response of large-diameter thermoplastic pipes under high-fill conditions. In the present study, the investigation is focused on small-diameter HDPE pipes subjected to very high H/D ratios, considering different backfill materials and EPS geofoam configurations.

The numerical modelling approach used in this study was based on field data obtained from the Deep Burial Project, which was conducted to investigate the behavior of buried thermoplastic pipes under high-fill conditions [12]. Using the calibrated PLAXIS 2D modelling approach, small-diameter HDPE pipes with inner diameters of 0.60 m and 0.30 m were analyzed parametrically under a 30 m high fill.

2 Numerical Model and Analysis Program

In the field experiments conducted within the scope of the Deep Burial Project, large-diameter PVC and HDPE pipes were investigated under high fill loads. In these experiments, the vertical stresses acting at the pipe crown, the horizontal stresses acting at the pipe springline, and the horizontal and vertical pipe deflections were measured. These field test conditions were modelled in PLAXIS 2D, and the modelling approach was calibrated by comparing the stress and deflection results obtained from the numerical analyses with the field measurements [11-13].

A two-dimensional plane-strain approach was adopted in the numerical analyses. A medium-density finite-element mesh consisting of 15-node triangular elements was used, and the construction sequence was simulated using staged construction. The lateral boundaries were restrained in the horizontal direction while vertical displacement was allowed, whereas the bottom boundary was fixed in both the horizontal and vertical directions.

Following the calibration stage, parametric analyses were performed for small-diameter HDPE pipes that were not directly included in the field test program. In this study, two HDPE pipes with inner diameters of 0.60 m and 0.30 m were considered, and these pipes are referred to as HDPE-0.60 and HDPE-0.30, respectively. Therefore, the analyses should be considered as calibrated-model-based parametric numerical analyses rather than direct field validation for these specific pipe diameters. The properties of the small-diameter HDPE pipes used in the parametric analyses are given in Table 1. The pipe parameters were taken from the values reported by Bozkurt (2021) [13].

The HDPE pipes were modelled using the tunnel option in PLAXIS 2D, and their behaviour was considered elastic.

Table 1. Properties of the small-diameter HDPE pipes used in the parametric analyses.

Pipe code	Inner diameter, D (m)	Pipe stiffness (kN/m/m)	Moment of inertia, I (m^4/m)	Axial stiffness, EA (kN/m)	Flexural rigidity, EI (kNm^2/m)
HDPE-0.60	0.60	215	1.77×10^{-6}	7500	0.922
HDPE-0.30	0.30	378	4.886×10^{-7}	7032.41	0.1906

Note: The Poisson's ratio of both HDPE pipes was taken as $\nu = 0.46$.

The 30 m embankment fill was constructed in 30 stages by adding 1 m-thick fill layers. Three different backfill materials were considered: crushed stone, sand, and clay. The backfill soils were represented using the Hardening Soil (HS) model. These materials were selected to examine the influence of backfill stiffness and strength properties on stress redistribution, soil arching, and pipe deformation response. The backfill parameters used in the analyses are summarized in Table 2.

EPS geofoam with a nominal density of 15 kg/m³ (EPS15) was used as the compressible inclusion in the analyses. The EPS15 response was represented using a piecewise linear elastic formulation based on the uniaxial compression test data reported in the underlying numerical modelling study [11, 13]. An interface strength reduction factor of R_{inter}=0.67 was used for the pipe–backfill interface, whereas R_{inter}=1.00 was adopted for the pipe–EPS and EPS–backfill interfaces [13]. After the pipe and backfill properties were defined, three numerical model cases were considered to evaluate the effect of EPS geofoam configuration. The reference model represents the case without EPS geofoam.

Table 2. Material properties of the backfill soils used in the numerical analyses.

	Crushed stone	Sand	Clay
Natural unit weight, γ_n (kN/m^3)	22	17.70	20.4
Reference secant stiffness, E_{50}^{ref} (kN/m^2)	180000	9500	5210
Reference tangent oedometric stiffness, E_{oed}^{ref} (kN/m^2)	180000	9500	5210
Reference unloading-reloading stiffness, E_{ur}^{ref} (kN/m^2)	54000	28500	15630
Cohesion, c (kN/m^2)	-	-	34.5
Friction angle, φ (°)	40	37	15
Dilatancy angle, ψ (°)	5	7	-
Power for stress-level dependency, m (-)	0.8	0.5	0.5

In Model 1, EPS geofoam was placed above the pipe crown. In Model 2, EPS geofoam was placed around the pipe. These configurations were used to investigate how the location of the compressible inclusion affects stress redistribution, soil arching, and pipe deformation under high-fill loading [11, 13], as shown in Fig. 1.

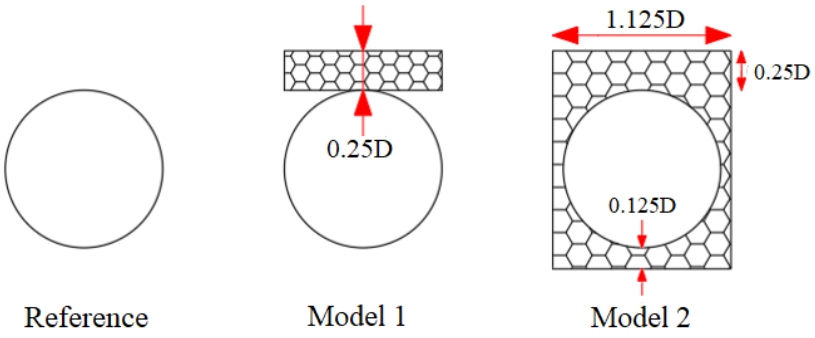


Fig. 1. Numerical model configurations used in the high-fill analyses: reference model, Model 1 with EPS geofoam above the pipe crown, and Model 2 with EPS geofoam around the pipe.

The stress redistribution around the pipe was evaluated using the vertical arching factor (VAF) and horizontal arching factor (HAF), defined as

$$VAF = \frac{W_e}{PL} = \frac{2N_{sp}}{P_L} \quad (1)$$

$$HAF = \frac{W_h}{PL} = \frac{N_c + N_i}{P_L} \quad (2)$$

where W_e and W_h are the total vertical and horizontal loads, respectively; P_L is the prism load; N_{SP} is the soil stress at the pipe springline; and N_c and N_i are the soil stresses at the pipe crown and invert, respectively [11].

The horizontal and vertical pipe deflection ratios were calculated as (Δx/D) x 100 and (Δy/D) x 100, respectively, where Δx and Δy are the changes in the horizontal and vertical pipe diameters and D is the initial inner diameter. Positive values indicate an increase in the corresponding diameter, whereas negative values indicate a decrease.

The results were evaluated in terms of H/D, where H is the embankment fill height and D is the inner pipe diameter.

3 Results and Discussion

The numerical results were evaluated by comparing the reference model with the EPS geofoam configurations for each pipe diameter and backfill material. The vertical arching factor and horizontal arching factor were used to assess the stress redistribution around the pipe, whereas the horizontal and vertical deflection ratios were used to evaluate the pipe deformation response. The results are presented separately for the HDPE-0.60 and HDPE-0.30 pipes in order to examine the influence of pipe diameter and H/D ratio under the same 30 m fill height.

Since the two pipes also have different pipe stiffnesses, the differences between their responses reflect the combined influence of pipe diameter, H/D ratio, and pipe stiffness rather than the isolated effect of H/D.

3.1 Effect of EPS Geofoam on Arching and Deflection Behavior

The variation of vertical and horizontal arching factors with H/D ratio for the HDPE-0.60 pipe is shown in Fig. 2.

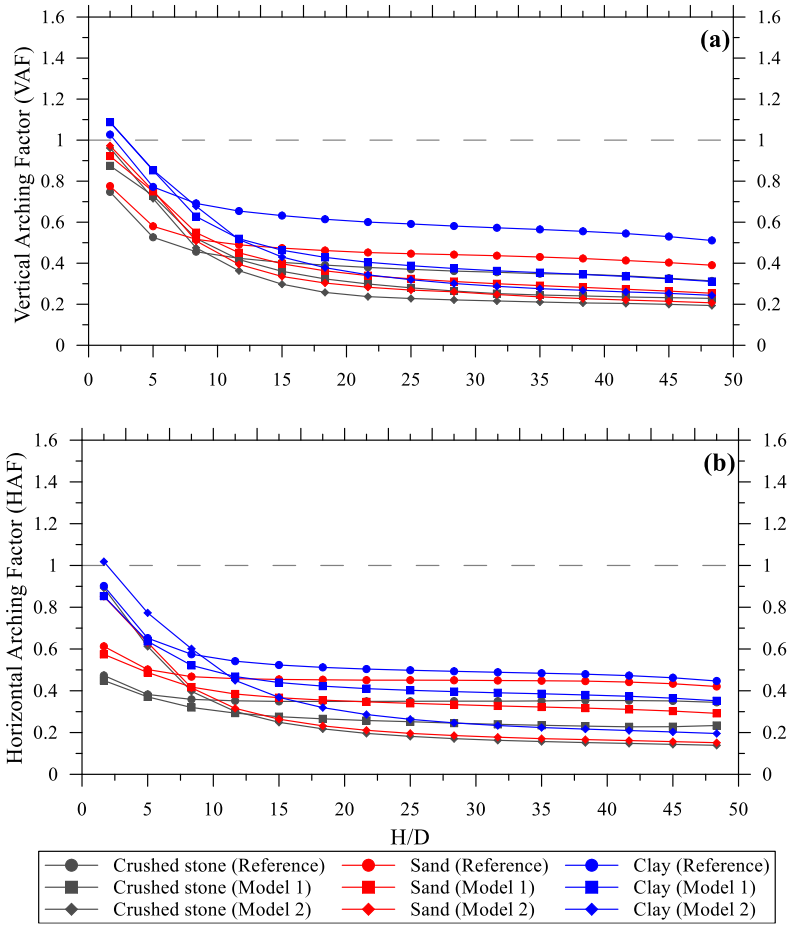


Fig. 2. Variation of arching factors for the HDPE-0.60 pipe under different backfill materials and EPS geofoam configurations: (a) vertical arching factor; (b) horizontal arching factor.

In Fig. 2(a), the vertical arching factor decreases with increasing H/D ratio for all backfill materials and model cases. The decrease is more pronounced at lower H/D values, whereas the curves show a flatter trend at higher H/D values. At the same H/D values, the vertical arching factors for the clay backfill generally remain the highest. Lower vertical arching factors are obtained for the crushed stone and sand backfills. Except at the lowest H/D values, the EPS models generally show lower vertical arching factors than the reference case.

Fig. 2(b) also shows a decreasing trend in the horizontal arching factor with increasing H/D ratio. The horizontal arching factors for the clay backfill generally remain higher than those for the crushed stone and sand backfills. When the EPS configurations are compared, Model 2, in which EPS is placed around the pipe, gives lower horizontal arching factors than Model 1 and the reference model in most cases.

The variation of horizontal and vertical deflection ratios for the HDPE-0.60 pipe is presented in Fig. 3. In Fig. 3(a), the horizontal deflection ratio increases with increasing H/D ratio in the reference cases. Among the reference cases, the highest horizontal deflection ratios are obtained for the clay backfill, followed by sand and crushed stone.

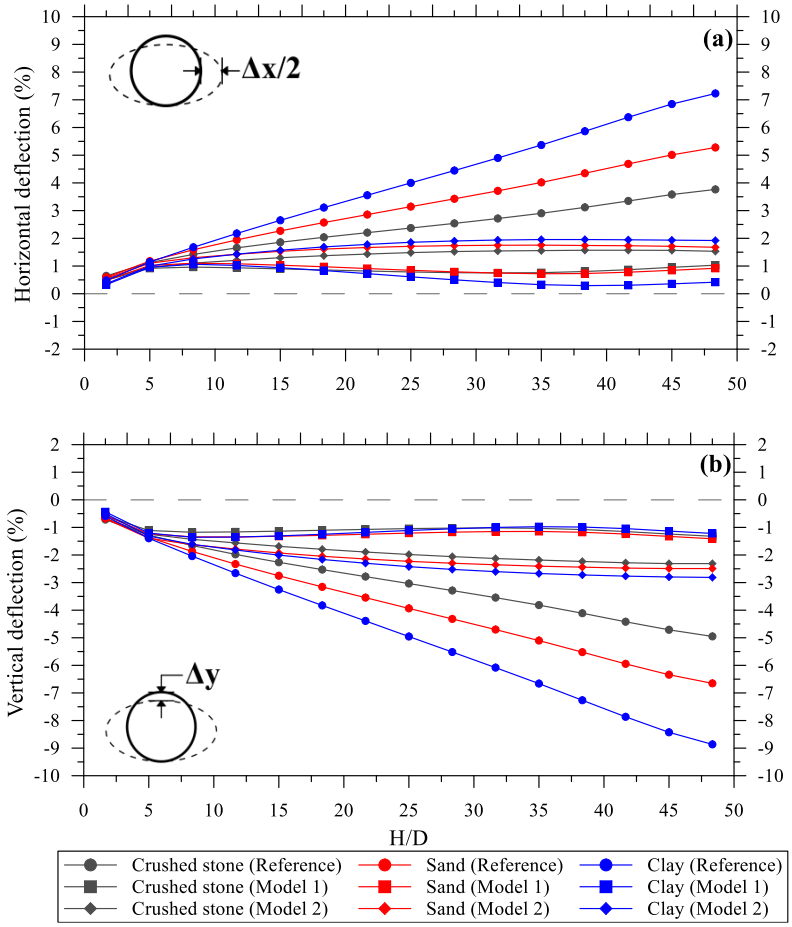


Fig. 3. Variation of pipe deflection ratios for the HDPE-0.60 pipe under different backfill materials and EPS geofoam configurations: (a) horizontal deflection ratio; (b) vertical deflection ratio.

In the EPS models, the horizontal deflection ratios are generally lower than those of the reference cases. Model 1 generally gives the lowest horizontal deflection ratios, whereas the values obtained with Model 2 remain higher than those of Model 1 but generally lower than the reference cases.

Fig. 3(b) shows that the vertical deflection ratios become more negative with increasing H/D ratio in the reference cases. The largest vertical deflection magnitudes are obtained for the clay backfill, followed by sand and crushed stone. Compared with the reference cases, the EPS models reduce the magnitude of vertical deflection for all backfill materials. This reduction is more pronounced for sand and clay backfills. Among the EPS configurations, Model 1 generally gives vertical deflection ratios closer to zero than Model 2.

The variation of vertical and horizontal arching factors with H/D ratio for the HDPE-0.30 pipe is shown in Fig. 4. Since the same 30 m fill height was applied to the smaller pipe diameter, the HDPE-0.30 pipe reached higher H/D values than the HDPE-0.60 pipe.

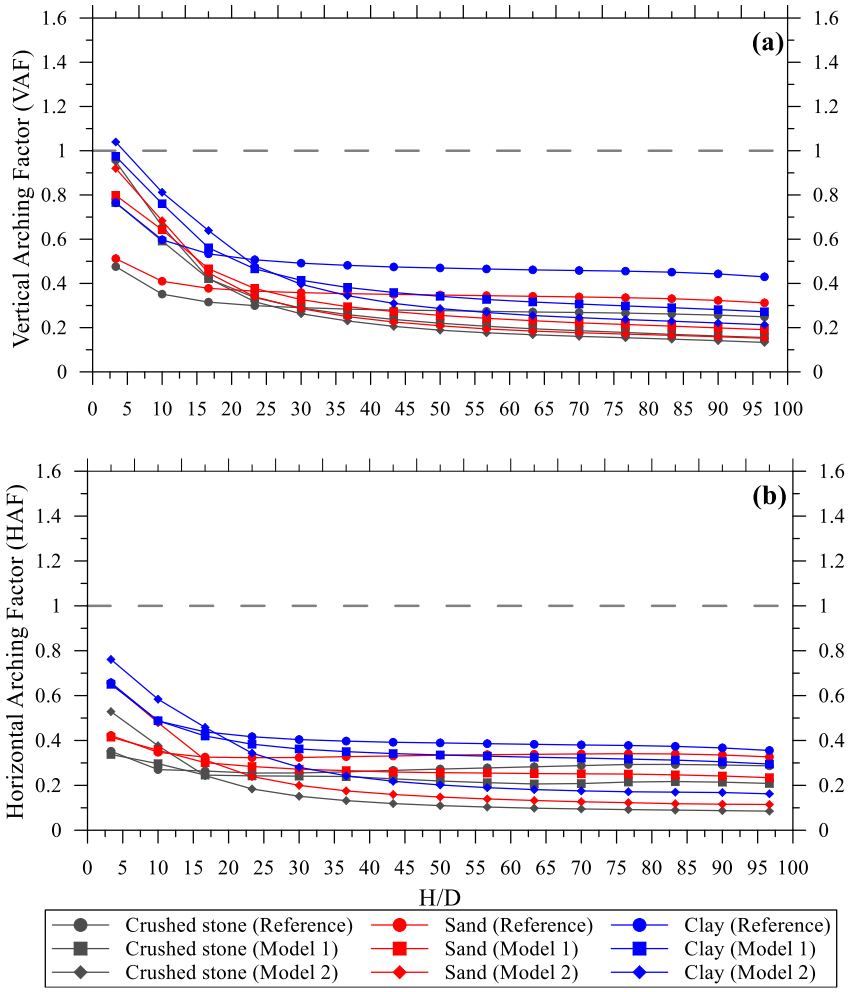


Fig. 4. Variation of arching factors for the HDPE-0.30 pipe under different backfill materials and EPS geofoam configurations: (a) vertical arching factor; (b) horizontal arching factor.

In Fig. 4(a), the vertical arching factor decreases with increasing H/D ratio for all backfill materials and model cases. The decrease is more pronounced at lower H/D values, whereas the curves become flatter at higher H/D values. At the same H/D values, the vertical arching factors for the clay backfill generally remain the highest. The crushed stone backfill generally gives the lowest vertical arching factors, while the sand backfill shows intermediate values. At higher H/D values, the EPS models generally give lower vertical arching factors than the reference case. Fig. 4(b) shows that the horizontal arching factor also decreases with increasing H/D ratio. Similar to the vertical arching factor, the decrease is more rapid at lower H/D values and becomes limited at higher H/D values. The horizontal arching factors for the clay backfill generally remain higher than those for the crushed stone and sand backfills. When the EPS configurations are compared, Model 2, in which EPS is placed around the pipe, generally gives the lowest horizontal arching factors. Model 1 also generally gives lower values than the reference case, but the reduction is generally smaller than that obtained in Model 2.

The variation of horizontal and vertical deflection ratios for the HDPE-0.30 pipe is presented in Fig. 5. In Fig. 5(a), the horizontal deflection ratio increases with increasing H/D ratio in the

reference cases. Among the reference cases, the highest horizontal deflection ratios are obtained for the clay backfill, followed by sand and crushed stone.

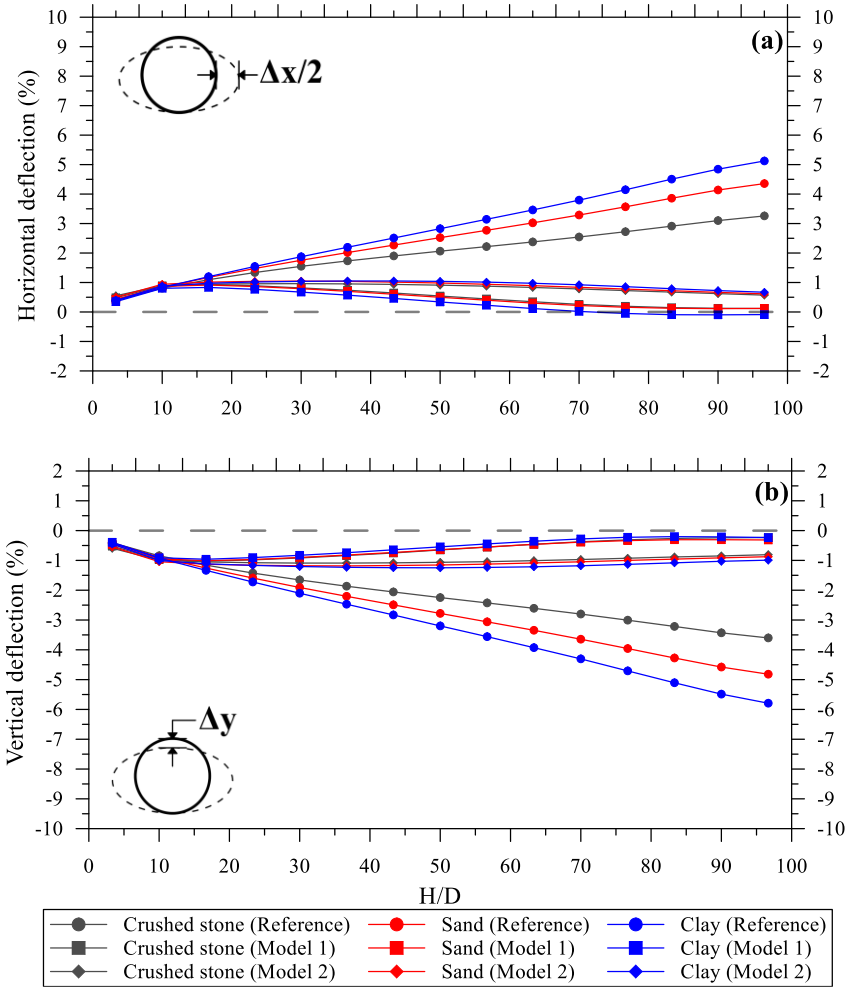


Fig. 5. Variation of pipe deflection ratios for the HDPE-0.30 pipe under different backfill materials and EPS geofoam configurations: (a) horizontal deflection ratio; (b) vertical deflection ratio.

In the EPS models, the horizontal deflection ratios are generally lower than those of the reference cases, with the differences becoming more pronounced as H/D increases. Model 1 generally gives the lowest horizontal deflection ratios and, at higher H/D values, values close to zero or slightly negative.

Fig. 5(b) shows that the vertical deflection ratios become more negative with increasing H/D ratio in the reference cases. The largest vertical deflection magnitudes are obtained for the clay backfill, followed by sand and crushed stone. Compared with the reference cases, the EPS models reduce the magnitude of vertical deflection for all backfill materials. This reduction is more evident at higher H/D values. Among the EPS configurations, Model 1 generally gives vertical deflection ratios closer to zero than Model 2.

3.2 Overall Evaluation of the Results

When the results for the HDPE-0.60 and HDPE-0.30 pipes are evaluated together, the models with EPS generally give lower arching factors than the reference cases. This trend is consistent with previous studies reporting that EPS geofoam, when used as a compressible inclusion, can reduce earth pressures acting on buried pipes by promoting positive soil arching [4, 9]. Similar

reductions in vertical and horizontal stresses around HDPE pipes with EPS geofoam were also reported by Kılıç and Akınay [4] and Akyelken and Kılıç [10].

The results also show that the backfill material affects both the arching factors and the deflection ratios. In the reference cases, clay backfill generally produced higher arching factors and larger horizontal and vertical deflection magnitudes than crushed stone and sand. In the EPS cases, the differences among the backfill materials were generally reduced and depended on the EPS configuration. This observation is in agreement with previous studies showing that pipe response is influenced by the stiffness and compaction characteristics of the surrounding soil, as well as by pipe diameter and pipe stiffness [5–7].

The comparison of EPS configurations indicates that stress reduction and deformation response do not always follow the same trend. Model 2, in which EPS is placed around the pipe, generally gives lower horizontal arching factors, whereas Model 1 provides vertical deflection ratios closer to zero in several cases. In Model 2, the compressible EPS zone along the sides of the pipe allows greater stress redistribution around the springline; compression of this lateral EPS zone contributes to the reduction in horizontal stresses acting on the pipe [11]. Therefore, EPS geofoam configuration should be evaluated by considering both stress redistribution and pipe deformation response.

4 Conclusions

This study investigated the effects of EPS geofoam configuration and backfill material type on the soil arching and deformation behavior of small-diameter buried HDPE pipes under a 30 m high fill. The analyses were performed using a PLAXIS 2D modelling approach calibrated based on field measurements from the Deep Burial Project. The following conclusions can be drawn:

The models with EPS geofoam generally produced lower vertical arching factors than the reference model. This trend was observed for both HDPE-0.60 and HDPE-0.30 pipes. Lower vertical arching factors were generally obtained with crushed stone and sand backfills than with clay backfill. In both pipe diameters, clay backfill generally resulted in higher arching factors than the granular backfills. EPS geofoam configuration affected the horizontal arching factor. Model 2, in which EPS surrounded the pipe, generally resulted in lower horizontal arching factors than Model 1 and the reference model.

The deflection results did not always follow the same trend as the arching factors. Although Model 2 generally produced the lowest horizontal arching factors, Model 1 generally resulted in smaller horizontal and vertical deflection magnitudes. Under the same 30 m fill height, the HDPE-0.30 pipe reached higher H/D values than the HDPE-0.60 pipe and generally exhibited a more pronounced soil-arching response. However, the differences between the two pipe sizes indicate that pipe diameter, H/D ratio, and pipe stiffness should be considered together. Overall, the results indicate that EPS geofoam configuration and backfill material type should be evaluated together when assessing stress redistribution and deformation behavior of small-diameter HDPE pipes under high-fill conditions.

References

1. Marston, A., Anderson, A.O.: The theory of loads on pipes in ditches and tests of cement and clay drain tile and sewer pipe. Bulletin No. 31, Iowa Engineering Experiment Station, Iowa State College of Agriculture and Mechanic Arts, Ames, Iowa (1913).
2. Moser, A.P., Folkman, S.: Buried Pipe Design. 3rd edn. McGraw-Hill, New York (2008).

3. Kang, J.S., Han, T.H., Kang, Y.J., Yoo, C.H.: Short-term and long-term behaviors of buried corrugated high-density polyethylene (HDPE) pipes. Composites Part B: Engineering 40(5), 404–412 (2009). doi:10.1016/j.compositesb.2009.01.006
4. Kılıç, H., Akınay, E.: Effects of using EPS geofoam as compressible inclusion on HDPE pipe behavior. Journal of Pipeline Systems Engineering and Practice 10(2), 04019006 (2019). doi:10.1061/(ASCE)PS.1949-1204.0000368
5. Wang, F., Du, Y.J., Zhou, M., Zhang, Y.J.: Experimental study of the effects produced by a backfilling process on full-scale buried corrugated HDPE pipes in fine-grained soils. Journal of Pipeline Systems Engineering and Practice 7(1), 05015001 (2016). doi:10.1061/(ASCE)PS.1949-1204.0000208
6. Zhou, M., Du, Y.J., Wang, F., Liu, M.D.: Performance of buried HDPE pipes – Part I: Peaking deflection during initial backfilling process. Geosynthetics International 24(4), 383–395 (2017). doi:10.1680/jgein.17.00009
7. Zhou, M., Wang, F., Du, Y.J., Liu, M.D.: Performance of buried HDPE pipes – Part II: Total deflection of the pipe. Geosynthetics International 24(4), 396–407 (2017). doi:10.1680/jgein.17.00010
8. Kim, H., Choi, B., Kim, J.: Reduction of earth pressure on buried pipes by EPS geofoam inclusions. Geotechnical Testing Journal 33(4), 304–313 (2010). doi:10.1520/GTJ102315
9. Witthoeft, A.F., Kim, H.: Numerical investigation of earth pressure reduction on buried pipes using EPS geofoam compressible inclusions. Geosynthetics International 23(4), 287–300 (2016). doi:10.1680/jgein.15.00054
10. Akyelken, F.A., Kılıç, H.: Experimental and numerical analyses of buried HDPE pipe with using EPS geofoam. KSCE Journal of Civil Engineering 26(9), 3968–3977 (2022). doi:10.1007/s12205-022-1541-z
11. Kılıç, H., Biçer, P., Bozkurt, S.: A Numerical Investigation of Induced and Embedded Trench Installations for Large-Diameter Thermoplastic Pipes under High Fill Stresses. Applied Sciences 13(5), 3040 (2023). doi:10.3390/app13053040
12. Sargand, S.M., Hazen, G.A., Masada, T., Schehl, D.J., Moran, A., Altarawneh, B.: Field verification of structural performance of thermoplastic pipe under deep backfill conditions. Report No. FHWA/OH-2002/023, Ohio Department of Transportation, Columbus, Ohio (2002).
13. Bozkurt, S.: Gömülü Esnek Borular Üzerine Etkiyen Gerilmelerin Sıkışabilir Malzeme Kullanılarak Azaltılması. Master's thesis, Tekirdağ Namık Kemal University, Tekirdağ, Türkiye (2021).

Author Contribution Statement

Conceptualization: H.K.; Methodology: H.K., P.B.; Investigation: S.B.; Formal Analysis: S.B.; Writing – Original Draft: P.B.; Writing – Review & Editing: P.B., H.K.

Funding: This research received no external funding.

Conflict of Interest: The authors declare no conflict of interest.

Publication Note

This paper was peer-reviewed, accepted for presentation, and included in the proceedings of the ACE2026 – International Conference on Advances in Civil Engineering, held on 12–14 October 2026 in Trabzon, Türkiye.

This paper may be cited as follows:

Biçer P., Bozkurt S., Kılıç H., "Effect of EPS Geofoam on Soil Arching and Deflection Behavior of Small-Diameter Buried HDPE Pipes under High Fill Conditions," in Proceedings of the ACE2026 – International Conference on Advances in Civil Engineering, Trabzon, Türkiye, 12–14 October 2026.

Dynamic Soil Characterization of Alluvial Deposits in Gölbaşı (Adıyaman) Following the 6 February 2023 Kahramanmaraş Earthquakes

Muhammed Emin Aytekin[1], İhsan Yılmaz[2], Eray Birinci[3], Erhan Tekin[4], Eren Pamuk[5], Kemal Önder Çetin[6], Nihat Sinan Işık[7], Seyhan Fırat[8]

[1,2,3] Department of Civil Engineering, Graduate School of Natural and Applied Sciences, Faculty of Technology, Gazi University, 06560 Yenimahalle, Ankara, Türkiye, m.eminaytekin87@gmail.com, ihsnylmz343@gmail.com, birincieray@gmail.com

[4] Department of Civil Engineering, Faculty of Engineering, Gazi University, 06570 Yenimahalle, Ankara, Türkiye, etekin@gazi.edu.tr

[5] Department of Earth Sciences Engineering, Institute of Earthquake Technology, Erzincan Binali Yıldırım University, Yalnızbağ Yerleşkesi, 24002 Erzincan, Türkiye

[6] Department of Civil Engineering, Faculty of Engineering, Middle East Technical University, 06800 Çankaya, Ankara, Türkiye, eren.pamuk@erzincan.edu.tr

[7,8] Department of Civil Engineering, Faculty of Technology, Gazi University, 06560 Yenimahalle, Ankara, Türkiye, nihatsinan@gazi.edu.tr, sfirat@gazi.edu.tr

Abstract. The 6 February 2023 Kahramanmaraş earthquake sequence caused extensive ground deformation and liquefaction-related damage in Gölbaşı, Adıyaman, emphasizing the influence of local soil conditions on seismic ground response. This study integrates physical and index soil properties, borehole observations, and Multichannel Analysis of Surface Waves (MASW) and Refraction Microtremor (ReMi) measurements to characterize the earthquake-affected deposits. The investigation program comprised ten investigation pits (AÇ-1–AÇ-10) and seven geotechnical boreholes (SK-1–SK-7). Active MASW and ReMi measurements were conducted at the ten AÇ locations, where soil samples were also obtained for physical and index testing, while the SK boreholes provided soil-profile information with depth, Standard Penetration Test (SPT-N) data, soil samples, and groundwater observations. The physical and index characterization presented herein is based on the currently available laboratory test results, as the broader laboratory testing program is ongoing. Based on these available data, USCS classifications show marked spatial variability: AÇ-1, AÇ-4, AÇ-5, and AÇ-7 are dominated by low-plasticity clay (CL), AÇ-2 and AÇ-3 by poorly graded sand (SP), and AÇ-8 and AÇ-9 by well-graded sand (SW), while AÇ-10 contains a predominantly sandy soil with approximately 13% fines. Plasticity index (PI) ranges from 9.1% to 25.6% among the fines-rich AÇ deposits, while relative density (Dr) ranges from approximately 27% to 91% among the granular samples. Measured SPT-N values in the SK boreholes range from 2 to 37, indicating pronounced spatial and depth-dependent variability in penetration resistance across the investigated deposits**.** Groundwater depths vary from 0.7 to 5.5 m. Inversion of the combined MASW- and ReMi-derived dispersion curves yielded V_{s30} values ranging from 159.9 to 210.2 m/s across the ten AÇ locations, with the lowest value at AÇ-7 and the highest at AÇ-8. The complete V_s–depth profiles exhibited pronounced vertical stiffness variations that are not fully represented by V_{s30} alone. The integrated results indicate that field-scale stiffness reflects the combined influence of soil type, plasticity, density state, penetration resistance, groundwater conditions, and vertical stratigraphy, providing a comprehensive basis for seismic site characterization of the Gölbaşı basin.

Keywords: Gölbaşı; Kahramanmaraş earthquakes; MASW; ReMi; USCS; physical soil properties; shear-wave velocity; V_{s30}

1. INTRODUCTION

The 6 February 2023 Kahramanmaraş earthquake sequence caused widespread structural damage and severe ground deformations across southeastern Türkiye. Gölbaşı district of Adıyaman was particularly affected, with post-earthquake investigations documenting sand boils, lateral spreading, settlement, ground cracking, foundation distress, and building tilting

associated with liquefaction-induced ground deformation [1–3]. In the alluvial portion of Gölbaşı, settlements locally reached approximately 40 cm [2]. The location of the study area, the epicenters of the earthquake sequence, and representative earthquake-induced damage are presented in Fig. 1.

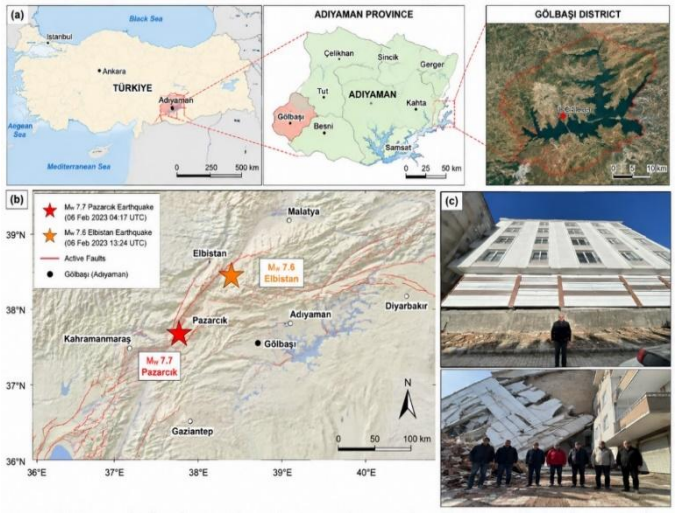


Figure 1. *Location of the Gölbaşı study area and representative earthquake-induced ground and structural damage observed following the 6 February 2023 Kahramanmaraş earthquake sequence.*

The severity of these ground failures is closely related to the geological and geotechnical setting of the Gölbaşı basin. The settlement area is underlain by heterogeneous Quaternary alluvial and marsh deposits comprising gravel, sand, silt, and clay, with locally organic-rich fine-grained sediments near Lake Gölbaşı. Groundwater is also shallow, locally approaching the ground surface [2]. Post-earthquake investigations attributed much of the observed ground failure to liquefaction and cyclic softening and emphasized the influence of local soil conditions on the spatial distribution of damage [3]. Liquefaction-susceptible sandy–silty layers and earthquake-induced strength degradation have also been associated with movements toward Lake Gölbaşı [4].

The earthquake-affected soils exhibit considerable physical variability and cannot be represented solely by clean sands. Fine-containing sands, silts, and low-plasticity clayey soils have also been identified among liquefied or ejected materials [5]. Consequently, grain-size distribution, fines content, natural water content, Atterberg limits, specific gravity, and density state are important for characterizing the heterogeneous deposits and interpreting their geotechnical response.

Geophysical investigations similarly indicate pronounced lateral and vertical variations in the stiffness structure of the Gölbaşı basin, with relatively low shear-wave velocities (V_s) particularly near Lake Gölbaşı [6]. These observations emphasize the importance of evaluating the complete V_s –depth structure rather than relying exclusively on an averaged parameter such as $V_{s\,30}$. Surface-wave methods provide an effective approach for such characterization. Active-source Multichannel Analysis of Surface Waves (MASW) utilizes Rayleigh-wave dispersion to evaluate the 1D shear-wave velocity (V_s) structure with depth [7], whereas Refraction Microtremor (ReMi) utilizes ambient vibrations and extends the investigation toward lower frequencies and longer wavelengths [8]. Their combined use can therefore provide broader dispersion-frequency coverage and improved constraints on one-dimensional V_s profiles.

However, geophysical measurements alone do not fully describe the composition and physical state of heterogeneous deposits, while laboratory index properties obtained from discrete samples cannot provide continuous field-scale stiffness information. Integrating physical soil properties, borehole observations, and surface-wave measurements therefore provides a more comprehensive basis for interpreting the heterogeneous subsurface conditions of Gölbaşı. Despite extensive post-earthquake reconnaissance and recent geotechnical and geophysical investigations, integrated characterization combining spatially distributed MASW–ReMi measurements with physical and index properties remains comparatively limited.

Accordingly, this study integrates geophysical and geotechnical data to characterize the earthquake-affected deposits of Gölbaşı. The investigation program comprised ten investigation pits (AÇ-1–AÇ-10) and seven geotechnical boreholes (SK-1–SK-7). Active MASW and passive ReMi measurements were conducted at the ten AÇ locations to obtain dispersion characteristics, one-dimensional V_s profiles, and V_{s30} values. Soil samples obtained from the AÇ pits and selected depths within the SK boreholes were used for physical and index characterization. Laboratory characterization included grain-size distribution, natural water content, Atterberg limits, specific gravity (Gs), and, for selected granular samples, limiting void ratios and relative density (Dr). SPT-N data and groundwater observations from the SK boreholes were additionally used to characterize depth-dependent subsurface conditions. The combined dataset is used to evaluate spatial and vertical variations in soil composition, physical state, and field-scale stiffness and to provide a basis for subsequent seismic site characterization of the Gölbaşı basin.

2. MATERIALS AND METHODS

2.1. Study Area and Investigation Program

The investigation program was designed to characterize the spatial and vertical variability of the earthquake-affected deposits in the Gölbaşı basin using integrated geotechnical and geophysical data. It comprised ten investigation pits (AÇ-1–AÇ-10), where MASW and ReMi measurements were conducted and soil samples were obtained, and seven geotechnical boreholes (SK-1–SK-7), which provided stratigraphic information, SPT-N data, soil samples, and groundwater observations (Fig. 2).



***Figure 2**. Distribution of the investigation locations in Gölbaşı, showing the AÇ-1–AÇ-10 investigation pits, where MASW–ReMi measurements were conducted, and the SK-1–SK-7 geotechnical boreholes.*

Groundwater depths at SK-1–SK-7 were 2.7, 2.2, 2.7, 1.2, 5.5, 0.7, and 0.8 m below ground surface, respectively, indicating spatially variable but generally shallow groundwater conditions. Measured SPT-N values across the seven boreholes ranged from 2 to 37, indicating considerable spatial and depth-dependent variability in penetration resistance. The lowest SPT-N value (N = 2) was recorded at SK-5 at a depth of 12.00–12.45 m, whereas the highest value (N = 37) was obtained at SK-6 at 19.50–19.95 m. These observations were evaluated together with the borehole stratigraphy and physical soil properties.

2.2. Geotechnical and Physical Soil Characterization

Laboratory testing of samples from the AÇ locations and selected SK borehole depths included natural water content (w), grain-size distribution, fines content, liquid limit (LL), plastic limit (PL), plasticity index (PI), and specific gravity (Gs). For selected granular samples, maximum and minimum void ratios (e_{max} and e_{min}), current void ratio (e), and relative density (Dr) were also evaluated. Grain-size distribution, natural water content, Atterberg limits, and specific gravity were determined in accordance with the applicable ASTM procedures [9–13],

while soils were classified according to the Unified Soil Classification System (USCS) [14]. For selected granular samples, maximum and minimum index densities and relative density were determined in accordance with ASTM D4253 and ASTM D4254 [15,16]. The plasticity index and relative density were calculated as:

$$PI = LL - PL \quad (1)$$

and

$$Dr = [(e_{max} - e)/(e_{max} - e_{min})] \times 100 \quad (2)$$

where LL and PL are the liquid and plastic limits, respectively, and e is the current void ratio. The laboratory results were interpreted together with borehole stratigraphy and SPT-N values to characterize variations in soil type, plasticity, and density or consistency with depth. Detailed physical and index results are provided in Appendix A.

2.3. MASW and ReMi Measurements

Surface-wave measurements were conducted at AÇ-1–AÇ-10 using MASW and ReMi techniques. Active-source MASW method uses Rayleigh-wave dispersion to estimate shear-wave velocity (V_s) with depth [7], whereas ReMi utilizes ambient seismic vibrations and provides complementary lower-frequency and longer-wavelength information to obtain deeper V_s structure [8].

For the MASW surveys, an impact source and a linear multichannel array equipped with 4.5 Hz vertical geophones were deployed, using geophone intervals ranging between 1 and 3 m with source offsets from 4 to 12 m. In contrast, passive surface wave (ReMi) measurements were collected using geophone spacings of 3 to 5 m to record ambient noise without a controlled source; at least eight 30-s records were acquired at each station for dispersion analysis. Representative MASW data acquisition and processing steps are illustrated in Fig. 3

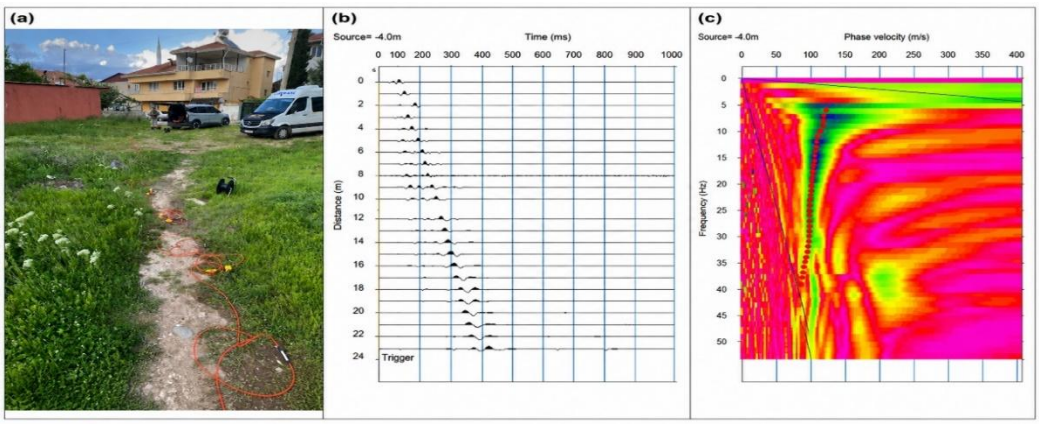


Figure 3. Representative MASW measurements at AÇ-4: (a) field acquisition configuration, (b) recorded multichannel shot gather, and (c) dispersion spectrum with the selected Rayleigh-wave dispersion curve.

2.4. Dispersion Analysis and V_s Profiling

Raw seismic records were initially transformed into the frequency–phase velocity (f–c) domain using distinct wavefield transformation techniques: the phase-shift method was applied to the active-source MASW shot gathers, whereas the τ–p transformation followed by Fourier transform was implemented for the passive ReMi ambient noise records. Fundamental-mode

Rayleigh-wave dispersion trends were subsequently identified and picked from the resulting energy spectra [7,8].

To resolve both near-surface details and deeper strata, high-frequency MASW data and low-frequency ReMi data were merged into a single broadband dispersion curve. A one-dimensional (1D) layered earth inversion was then conducted using the iterative Levenberg–Marquardt damped least-squares algorithm. This inversion scheme successfully resolved high-resolution 1D shear-wave velocity (V_s) profiles at AÇ-1–AÇ-10 [7,17].

The average shear-wave velocity of the uppermost 30 m (V_{s30}) was calculated as follows:

$$V_{s30} = 30/\Sigma(h_i/V_{si}) \quad (3)$$

where h_i and V_{si} are the thickness and shear-wave velocity of the ith layer, respectively, over a total depth of 30 m. V_{s30} values were interpreted together with the complete V_s–depth profiles, and site conditions were evaluated, where applicable, with reference to TBDY 2018 [18].

Finally, the MASW–ReMi-derived V_s profiles were evaluated together with grain-size distribution, fines content, Atterberg limits, water content, Gs, density-state parameters, SPT-N, and groundwater observations. Because laboratory samples represent discrete intervals whereas surface-wave inversion represents larger subsurface volumes, direct point-to-point equivalence was not assumed; instead, the datasets were integrated to assess relationships among soil composition, stratigraphy, physical state, groundwater conditions, and field-scale stiffness.

3. RESULTS AND DISCUSSION

3.1. Physical, Index, and Subsurface Characteristics of the Investigation Locations

The physical, index, and field investigation results demonstrate substantial lateral and vertical variability across the Gölbaşı deposits. The available dataset includes grain-size distribution, fines content, natural water content (w), liquid limit (LL), plastic limit (PL), plasticity index (PI), specific gravity (Gs), and, for selected granular soils, limiting void ratios and relative density (Dr). These results were interpreted together with SPT-N, stratigraphy, and groundwater observations from the SK boreholes. Representative samples and field sampling procedures are shown in Fig. 4.



(a) AC 10 (b) AC 2 (c) AC 6

Figure 4. *Representative field investigation procedures at the AÇ locations in the Gölbaşı study area: (a) disturbed soil sampling at AÇ-10, (b) measurement of the sampling depth at AÇ-2, and (c) measurement of the groundwater level at AÇ-6.*

Based on the USCS criteria [14], the investigated materials range from fines-dominated low-plasticity clayey soils to predominantly granular SP and SW soils. AÇ-1 contained 71.2% fines with LL = 45.6%, PI = 25.6%, w = 17.1%, and Gs = 2.60 and was classified as CL. The adjacent SK-1 similarly comprises predominantly fine-grained clayey and sandy-clayey layers, with generally low shallow SPT-N values and groundwater at 2.7 m. AÇ-4 also contained a high fines fraction (69.7%) but exhibited substantially lower plasticity (LL = 29.9%, PI = 9.1%) and was classified as CL. The adjacent SK-2 is predominantly fine-grained but contains a coarser interval where SPT-N reaches 22; groundwater occurs at 2.2 m. These results demonstrate that similar fines contents may be associated with considerably different plasticity characteristics.

AÇ-5, AÇ-6, and AÇ-7 are also fines-dominated low-plasticity clayey soils. AÇ-5 contains 51.3% fines and PI = 17.7%, whereas AÇ-6 contains approximately 61.84% fines with PI = 15.58%. AÇ-7 contains 54.0% fines and PI = 15.5%. AÇ-5 is adjacent to SK-4, where predominantly clayey and sandy-clayey deposits exhibit shallow SPT-N values of approximately 6–8 and groundwater at 1.2 m. AÇ-6 is adjacent to SK-6, which comprises clayey to sandy-clayey soils with SPT-N increasing from approximately 5–9 near the surface to 37 at greater depth; groundwater occurs at only 0.7 m. AÇ-7 is adjacent to SK-5, which contains clayey, sandy-clayey, and locally organic-bearing soils. SK-5 is characterized by particularly low SPT-N values of approximately 2–7 over several intervals, locally high water contents reaching approximately 68%, and a deeper groundwater level of 5.5 m.

The predominantly granular AÇ locations exhibit substantial variations in density state. AÇ-2 is classified predominantly as SP, with Dr decreasing from 63.71% at 1.50 m to 27.00% at 2.00 m. Its adjacent SK-3 contains shallow gravelly-sandy materials before transitioning to predominantly finer-grained soils below approximately 6 m; groundwater occurs at 2.7 m. AÇ-3 is also predominantly SP and exhibits a relatively dense state, with Dr = 74.95% at approximately 1.60 m.

AÇ-8 and AÇ-9 are predominantly SW and show pronounced variations in density state. AÇ-8 exhibits Dr values of 91.0% and 69.26% at 1.50 and 2.00 m, respectively, representing some of the densest investigated granular conditions. At AÇ-9, the 1.90-m sample contains approximately 10.50% fines, while Dr decreases from approximately 85% at 1.50 m to approximately 28% at 1.90 m. AÇ-10 shows depth-dependent variation in fines content, increasing from approximately 4.46% at 1.50 m to 12.98% at 1.90 m, while the corresponding Dr values are approximately 62% and 54%, respectively. These results demonstrate substantial spatial and vertical variability in packing state even among the predominantly granular deposits.

SK-7 provides additional subsurface information outside the paired AÇ–SK locations and contains predominantly fine-grained to sandy-clayey materials. Groundwater was encountered at approximately 0.8 m, further demonstrating the shallow and spatially variable groundwater conditions across the study area.

The measured SPT-N values across the seven boreholes ranged from 2 to 37, indicating considerable spatial and vertical variability in penetration resistance. Relatively low values were encountered in several shallow to intermediate-depth clayey and sandy–clayey intervals. The lowest measured value (N = 2) occurred in SK-5 at 12.00–12.45 m, whereas the highest

value (N = 37) was recorded in SK-6 at 19.50–19.95 m. In several boreholes, penetration resistance generally increased at greater depths, although the profiles remained heterogeneous rather than exhibiting a uniform depth-dependent trend.

Laboratory characterization of selected SPT samples further demonstrates the vertical variability within the SK boreholes (Table A2). The tested SPT samples exhibit substantial variations in grain-size distribution, natural water content, and plasticity, with predominantly granular materials containing variable fines contents and locally plastic fines. These results complement the depth-dependent SPT-N and borehole observations and further demonstrate that the subsurface conditions cannot be represented by a single soil type.

Overall, the paired AÇ–SK results demonstrate that shallow soil classification alone does not represent the complete subsurface sequence. The investigated deposits exhibit substantial variations in soil type, plasticity, density state, SPT resistance, groundwater conditions, and vertical stratigraphy. Among the granular AÇ samples, Dr ranges from approximately 27% to 91%, while groundwater across SK-1–SK-7 ranges from 0.7 to 5.5 m. Detailed grain-size distribution, natural water content, PI, and USCS classification results for the AÇ samples are presented in Table A1(a), while Gs and density-state parameters are given in Table A1(b). Grain-size distribution, natural water content, PI, and USCS classification results for selected SPT samples from the SK boreholes are presented in Table A2 in Appendix A.

3.2. MASW–ReMi Dispersion and Inversion Results

The MASW and ReMi measurements at AÇ-1–AÇ-10 exhibited complementary dispersion characteristics. MASW primarily constrained the higher-frequency response, whereas ReMi extended the usable information toward lower frequencies and longer wavelengths. Their combination therefore provided broader dispersion-frequency coverage for inversion. Representative MASW and ReMi dispersion curves and the resulting V_s–depth profile at AÇ-4 are presented in Fig. 5.

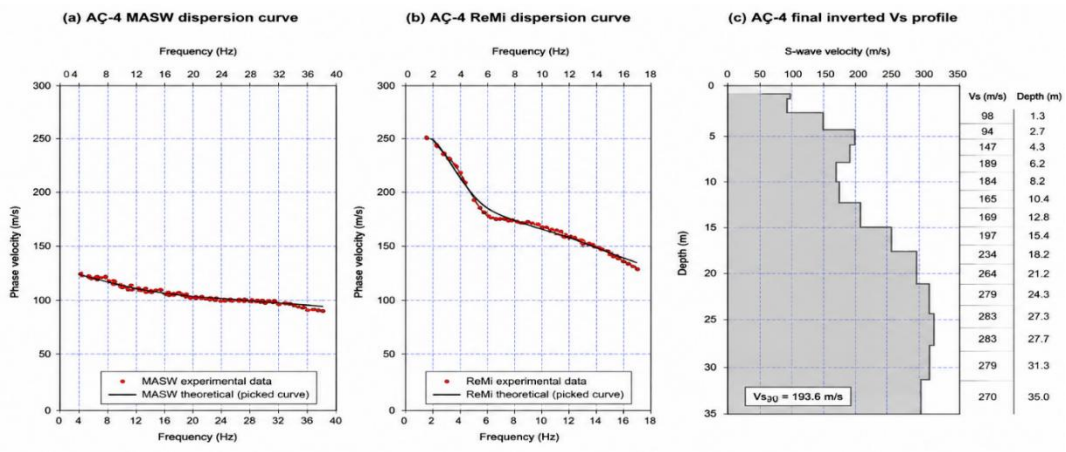


Figure 5. Representative surface-wave analysis at AÇ-4: (a) MASW dispersion curve, (b) ReMi dispersion curve, and (c) final inverted shear-wave velocity (Vs) profile obtained from the combined MASW–ReMi analysis.

Across the ten locations, final RMS misfits ranged from approximately 2.43 to 4.74 m/s (average 3.28 m/s), corresponding to normalized misfits of approximately 1.16–2.81% (average 1.64%). At AÇ-4, the RMS misfit decreased from 12.55 m/s (7.91%) for the initial model to 3.01 m/s (1.58%) for the final solution, indicating a satisfactory fit between the measured and

theoretical dispersion responses. The resulting profile exhibits distinct vertical velocity contrasts, including a shallow velocity reversal followed by a general increase in V_s at greater depths, and yields V_{s30} = 193.6 m/s.

The broad variability observed in the V_s profiles is consistent with the heterogeneous subsurface conditions identified from the nearby boreholes. Measured SPT-N values ranging from 2 to 37, together with alternating clayey, sandy, and mixed soil layers, indicate substantial spatial and depth-dependent variations in soil composition and penetration resistance. These borehole observations are consistent with the vertical stiffness variations revealed by the MASW–ReMi profiles and, together with the differences among investigation locations, highlight the heterogeneous nature of the Gölbaşı deposits. Because the AÇ and SK locations are not spatially coincident in all cases, these observations are interpreted as complementary evidence of subsurface heterogeneity rather than as a direct correlation between SPT-N and V_s.

3.3. V_s Profiles and V_{s30} Distribution

The inverted V_s profiles reveal pronounced lateral and vertical variability across AÇ-1–AÇ-10, including shallow low-velocity zones, velocity contrasts, and local velocity reversals (Fig. 6). V_{s30} ranges from 159.9 to 210.2 m/s. The values are 159.9 m/s at AÇ-7, 163.6 m/s at AÇ-10, 169.0 m/s at AÇ-3, 171.0 m/s at AÇ-6, 171.8 m/s at AÇ-1, 176.4 m/s at AÇ-5, 191.7 m/s at AÇ-9, 193.6 m/s at AÇ-4, 196.6 m/s at AÇ-2, and 210.2 m/s at AÇ-8.

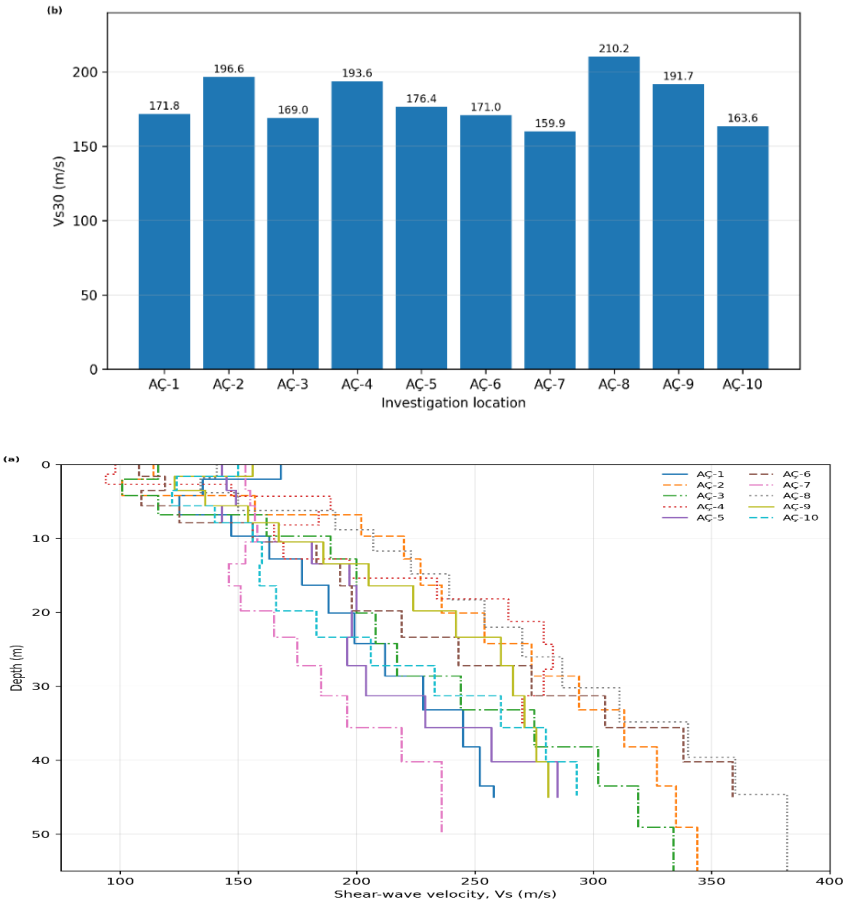


Fig. 6. Comparison of shear-wave velocity characteristics at the ten investigation locations: (a) inverted Vs–depth profiles obtained from the combined MASW–ReMi analyses and (b) corresponding Vs30 values.

Despite the relatively limited V_{s30} range, the complete V_s –depth profiles exhibit substantially greater vertical variability, indicating that V_{s30} alone may mask important differences in shallow stiffness and layer configuration.

3.4. Integrated Interpretation of Physical and Geophysical Characteristics

The integrated dataset indicates that spatial variability in V_s occurs within deposits characterized by variations in grain-size distribution, fines content, plasticity, density state, groundwater conditions, and stratigraphy, rather than being attributable to a single index parameter.

Among the granular locations, AÇ-8 exhibits Dr = 91.0% and 69.26% at 1.50 and 2.00 m, respectively, and the highest V_{s30} (210.2 m/s). AÇ-2 also has a relatively high V_{s30} (196.6 m/s), although Dr decreases from 63.71% at 1.50 m to 27.00% at 2.00 m. Similarly, at AÇ-9, Dr decreases from approximately 85% at 1.50 m to approximately 28% at 1.90 m, while the available gradation results indicate a predominantly granular SW soil with approximately 10.50% fines in the investigated sample; its V_{s30} is 191.7 m/s. In contrast, AÇ-10 contains approximately 12.98% fines, intermediate Dr values of approximately 62% and 54%, and a lower V_{s30} of 163.6 m/s. These comparisons demonstrate that V_{s30} represents the integrated stiffness of the upper 30 m rather than the density state of individual shallow layers.

The fines-rich locations show a similar complexity. AÇ-1 and AÇ-4 contain comparable fines contents of 71.2% and 69.7%, respectively, but differ markedly in PI (25.6% and 9.1%) and V_{s30} (171.8 and 193.6 m/s). Likewise, AÇ-5, AÇ-6, and AÇ-7 contain 51.3%, 61.84%, and 54.0% fines, respectively, with PI values of 17.7%, 15.58%, and 15.5% and V_{s30} values of 176.4, 171.0, and 159.9 m/s, respectively. Thus, fines content alone cannot explain the observed stiffness variations.

The borehole data provide further insight into the spatial and vertical heterogeneity identified by the surface-wave measurements. Across SK-1–SK-7, measured SPT-N values range from 2 to 37, indicating substantial variations in penetration resistance with location and depth. AÇ-7, which has the lowest V_{s30} (159.9 m/s), is located near SK-5, where low SPT-N values, reaching N = 2 at 12.00–12.45 m, together with locally high water contents and organic-bearing soils, indicate relatively soft subsurface conditions. In contrast, AÇ-2 (V_{s30} = 196.6 m/s) is located near SK-3, which contains relatively coarse gravelly-sandy materials within the profile, while AÇ-4 (V_{s30} = 193.6 m/s) is located near predominantly fine-grained SK-2, where SPT-N values locally reach 22. Groundwater conditions also vary considerably across the boreholes, with depths ranging from 0.7 to 5.5 m below ground surface and particularly shallow groundwater encountered at SK-4, SK-6, and SK-7. These observations are considered complementary evidence of subsurface heterogeneity rather than direct point-to-point correlations between SPT-N and V_s, because the AÇ and SK investigation locations are not spatially coincident.

Overall, the laboratory, borehole, and surface-wave datasets provide complementary descriptions of soil composition, physical state, penetration resistance, groundwater conditions, and field-scale stiffness. Their combined interpretation demonstrates pronounced spatial and depth-dependent heterogeneity across the investigated deposits. The results indicate that the MASW–ReMi-derived V_s structure should be interpreted together with physical and index properties, SPT-N measurements, groundwater conditions, and subsurface stratigraphy rather than as the response of a single homogeneous soil type. Detailed physical and index results are provided in Appendix A.

4. CONCLUSIONS

This study integrated laboratory physical and index testing, borehole and SPT observations, groundwater measurements, and combined MASW–ReMi analyses to characterize the earthquake-affected deposits of Gölbaşı, Adıyaman. The results demonstrate pronounced lateral and vertical heterogeneity in soil composition, density state, groundwater conditions, penetration resistance, and field-scale stiffness.

The investigated materials range from fines-dominated low-plasticity clayey soils to predominantly granular sandy deposits. Among the granular AÇ samples, relative density (Dr) varies from approximately 27% to 91%, while the SK boreholes reveal alternating fine- and coarse-grained layers and locally organic-bearing soils. Measured SPT-N values range from 2 to 37 across the seven boreholes, demonstrating substantial spatial and depth-dependent variability in penetration resistance. Groundwater depths range from approximately 0.7 to 5.5 m below ground surface.

Combined MASW–ReMi analyses provided V_s –depth profiles at ten locations, with V_{s30} ranging from 159.9 m/s at AÇ-7 to 210.2 m/s at AÇ-8. The complete profiles exhibit greater vertical variability than indicated by V_{s30} alone, including shallow low-velocity zones, velocity contrasts, and local velocity reversals.

The integrated results indicate that field-scale stiffness cannot be attributed to a single soil property. AÇ-8, with Dr values of approximately 91% and 69%, exhibits the highest V_{s30} (210.2 m/s), whereas AÇ-1 and AÇ-4 have similar fines contents (71.2% and 69.7%) but markedly different PI values (25.6% and 9.1%) and V_{s30} values (171.8 and 193.6 m/s). Furthermore, the lowest V_{s30} at AÇ-7 is consistent with the nearby SK-5 profile, where low SPT-N values, including a minimum measured value of N = 2, together with high-water-content and locally organic-bearing intervals indicate relatively soft subsurface conditions. These observations demonstrate the combined influence of soil composition, plasticity, density state, penetration resistance, groundwater conditions, and vertical stratigraphy on the measured V_s structure.

Overall, integrating the currently available physical and index properties with borehole stratigraphy, SPT-N measurements, groundwater observations, and MASW–ReMi-derived V_s profiles provides a more representative characterization of the heterogeneous Gölbaşı deposits than any individual dataset alone. Because the AÇ and SK investigation locations are not spatially coincident in all cases, the geotechnical and geophysical observations are interpreted as complementary evidence of subsurface heterogeneity rather than as direct point-to-point correlations between SPT-N and V_s. The integrated dataset provides a basis for subsequent seismic site characterization and site-response analyses aimed at evaluating the influence of local soil conditions on earthquake ground response in the Gölbaşı basin.

Acknowledgments

This study is supported by the Scientific and Technological Research Council of Türkiye (TÜBİTAK) under the 1001 Scientific and Technological Research Projects Funding Program (Project No. 125M457) and by Gazi University Scientific Research Projects Coordination Unit (BAP) (Project No. PDP-11242). The authors gratefully acknowledge the financial support provided by both institutions.

References

1. Moss, R.E.S., Altunel, E., Bassal, P., Bray, J.D., Buckreis, T.E., Cetin, K.O., Clahan, K., Duman, E., Frost, D., Hashash, Y., Koehler, R.D., Kozaci, O., Lozano, J.M., Macedo, J., Moug, D., Nichols, E., Pehlivan, M., Pretell, R., Stewart, J.P., Ulmer, K.J., Yildirim, C.: Geotechnical and geological reconnaissance observations of the 6 February 2023 Türkiye earthquakes. *Earthquake Spectra* 41(1), 219–248 (2025).

2. Öztürk Kardoğan, P.S.: Assessment of earthquake-induced settlements and liquefaction triggered by the 6 February 2023 Kahramanmaraş earthquakes in Gölbaşı (Adıyaman) and İskenderun (Hatay). Geomatics, Natural Hazards and Risk 17(1), 2650129 (2026).
3. Cetin, K.O., Moug, D., Soylemez, B., Ayhan, B.U., Zarzour, M., Suhaily, A., Akil, B., Unutmaz, B., Firat, S., Tekin, E., Çakır, E., Frost, D., Macedo, J., Bray, J., Moss, R., Bassal, P., Gurbuz, A., Işık, N.S., Akin, M., Duman, E.: Ground failures and foundation performances in Adıyaman–Gölbaşı following the 6 February 2023 Kahramanmaraş–Türkiye Earthquake Sequence. Earthquake Spectra 41, 249–289 (2025).
4. Karray, M., Karakan, E., Sezer, A., Chiaradonna, A., Gul, T.O., Kıncal, C., Monaco, P., Lanzo, G.: Role of soil type in geotechnical damage observed in Gölbaşı during the 2023 Türkiye earthquake sequence. Acta Geotechnica, 1–32 (2026).
5. Cetin, K.O., Soylemez, B., Guzel, H., Çakır, E.: Soil liquefaction sites following the February 6, 2023, Kahramanmaraş-Türkiye earthquake sequence. Bulletin of Earthquake Engineering 23, 921–944 (2025).
6. Pamuk, E., Fırat, S., Büyüksaraç, A., Çetin, K.Ö., Bektaş, Ö., Işık, N.S., Sarıtepe, H.E.: Three dimensional shear wave velocity (V_s) structure and dynamic soil properties of Adıyaman-Gölbaşı basin using HVSR and SPAC methods. Soil Dynamics and Earthquake Engineering 200, 109744 (2026).
7. Park, C.B., Miller, R.D., Xia, J.: Multichannel analysis of surface waves. *Geophysics* **64**(3), 800–808 (1999).
8. Louie, J.N.: Faster, better: Shear-wave velocity to 100 meters depth from refraction microtremor arrays. *Bulletin of the Seismological Society of America* **91**(2), 347–364 (2001).
9. ASTM International.: ASTM D6913/D6913M-17(2025), Standard Test Methods for Particle-Size Distribution (Gradation) of Soils Using Sieve Analysis. ASTM International, West Conshohocken, PA (2025).
10. ASTM International.: ASTM D7928-21e1, Standard Test Method for Particle-Size Distribution (Gradation) of Fine-Grained Soils Using the Sedimentation (Hydrometer) Analysis. ASTM International, West Conshohocken, PA (2021).
11. ASTM International.: ASTM D2216-19, Standard Test Methods for Laboratory Determination of Water (Moisture) Content of Soil and Rock by Mass. ASTM International, West Conshohocken, PA (2019).
12. ASTM International.: ASTM D4318-17e1, Standard Test Methods for Liquid Limit, Plastic Limit, and Plasticity Index of Soils. ASTM International, West Conshohocken, PA (2017).
13. ASTM International.: ASTM D854-23, Standard Test Methods for Specific Gravity of Soil Solids by the Water Displacement Method. ASTM International, West Conshohocken, PA (2023).
14. ASTM International.: ASTM D2487-17(2025), Standard Practice for Classification of Soils for Engineering Purposes (Unified Soil Classification System). ASTM International, West Conshohocken, PA (2025).
15. ASTM International.: ASTM D4253-16e1, Standard Test Methods for Maximum Index Density and Unit Weight of Soils Using a Vibratory Table. ASTM International, West Conshohocken, PA (2016).
16. ASTM International.: ASTM D4254-16, Standard Test Methods for Minimum Index Density and Unit Weight of Soils and Calculation of Relative Density. ASTM International, West Conshohocken, PA (2016).
17. Xia, J., Miller, R.D., Park, C.B.: Estimation of near-surface shear-wave velocity by inversion of Rayleigh waves. *Geophysics* **64**(3), 691–700 (1999).
18. Disaster and Emergency Management Presidency (AFAD).: *Türkiye Building Earthquake Code (TBDY 2018).* AFAD, Ankara (2018).

Author Contribution Statement

- *Conceptualization:* Seyhan Fırat, Eren Pamuk
- *Methodology:* Seyhan Fırat, Eren Pamuk, Erhan Tekin
- *Investigation:* Muhammed Emin Aytekin, İhsan Yılmaz, Eray Birinci, Eren Pamuk
- *Writing – Original Draft:* Muhammed Emin Aytekin, Eren Pamuk
- *Writing – Review & Editing:* Seyhan Fırat, Eren Pamuk, Kemal Önder Çetin, Nihat Sinan Işık, Erhan Tekin

List of Abbreviations

· **AÇ** — Investigation Pit
· **ASTM** — ASTM International
· **Dr** — Relative Density
· **Gs** — Specific Gravity of Soil Solids
· **GWL** — Groundwater Level
· **LL** — Liquid Limit
· **MASW** — Multichannel Analysis of Surface Waves
· **PI** — Plasticity Index

· **PL** — Plastic Limit
· **ReMi** — Refraction Microtremor
· **RMS** — Root Mean Square
· **SK** — Geotechnical Borehole
· **SPT** — Standard Penetration Test
· **TBDY** — Turkish Building Earthquake Code
· **USCS** — Unified Soil Classification System
· V_S — Shear-Wave Velocity
· V_{s30} — Time-Averaged Shear-Wave Velocity in the Upper 30 m

Appendices
Appendix A.

Physical and Index Properties of the Investigated Soils

This appendix presents the detailed physical and index properties of the investigated soils. Tables A1(a) and A1(b) summarize the laboratory results for samples obtained from the AÇ investigation pits, while Table A2 presents the grain-size distribution, natural water content, plasticity, and USCS classification of selected SPT samples from the SK boreholes.

Table A1(a). Grain-size distribution, plasticity index, and USCS classification of the AÇ samples

Location	Depth (m)	Gravel (%)	Sand (%)	Fines (%)	PI (%)	USCS
AÇ-1	1.60	2.1	26.7	71.2	25.6	CL
AÇ-2	0.10–0.90	11.54	84.89	3.57	NP	SP
AÇ-2	0.90–1.50	37.35	61.62	1.02	NP	SP
AÇ-2	1.50–2.70	9.36	90.20	0.44	NP	SP
AÇ-3	0–1.90	31.82	67.30	0.88	NP	SP
AÇ-3	1.60*	19.91	78.72	1.37	NP	SP
AÇ-3	1.90–2.80	13.13	86.38	0.49	NP	SP
AÇ-4	1.60	0.3	30.0	69.7	9.1	CL
AÇ-5	0.80	9.3	39.4	51.3	17.7	CL
AÇ-6	1.50	**3.48**	**34.68**	**61.84**	15.58	CL
AÇ-7	2.90	4.3	41.8	54.0	15.5	CL
AÇ-8	1.50–2.00	26.15	70.34	3.51	NP	SW
AÇ-9	1.90	3.35	86.15	10.50	–	SW
AÇ-10	1.50	3.52	92.02	4.46	NP	–
AÇ-10	1.90	3.66	83.36	12.98	–	–

Table A1(b). Specific gravity and density-state parameters of the AÇ samples.

Location	Depth (m)	Gs	emax	emin	e	Dr (%)
AÇ-1	1.60	2.60	—	—	—	—
AÇ-2	1.50	2.5686	1.1250	0.7524	0.8876	63.71
AÇ-2	2.00	2.6620	1.3262	0.8202	1.1896	27.00
AÇ-3	1.60	2.6649	1.3032	0.9095	1.0081	74.95
AÇ-4	1.60	—	—	—	—	—
AÇ-5	0.80	2.78	—	—	—	—
AÇ-6	1.50	2.5573	0.8775	0.6637	—	—
AÇ-7	2.90	2.77	—	—	—	—
AÇ-8	1.50	2.6065	1.0429	0.6912	0.7229	91.00
AÇ-8	2.00	2.6023	1.3537	0.8622	1.0132	69.26
AÇ-9	1.50	2.5770	1.3514	0.9791	1.035	85
AÇ-9	1.90	2.6148	1.2929	0.8917	1.181	28
AÇ-10	1.50	2.6666	1.2664	0.9055	1.043	62
AÇ-10	1.90	2.5865	1.3237	0.7633	1.021	54

Table A2. Grain-size distribution, natural water content, plasticity, and USCS classification of selected SPT samples from the SK boreholes.

Borehole	SPT Sample	Depth (m)	Gravel (%)	Sand (%)	Fines (%)	w (%)	PI (%)	USCS
SK-1	SPT-2	3.00–3.45	10.25	78.52	11.23	32.31	15.14	SP/SW-SM*
SK-1	SPT-7	10.50–10.95	13.15	83.20	3.66	27.41	24.78	SP
SK-1	SPT-10	15.00–15.45	2.31	91.07	6.62	28.66	17.84	SP-SC
SK-2	SPT-5	9.00–9.45	5.29	87.91	6.80	27.04	25.96	SP-SC
SK-2	SPT-9	15.00–15.45	5.45	88.44	6.11	25.48	23.00	SW-SC
SK-2	SPT-12	19.50–19.95	8.91	86.01	5.09	19.64	25.48	SW-SC
SK-3	SPT-4	6.50–6.95	0.00	94.20	5.80	29.91	30.97	SP-SM
SK-3	SPT-9	13.50–13.95	4.09	91.76	4.15	26.08	22.70	SP
SK-3	SPT-12	18.00–18.45	1.08	91.09	7.83	28.28	—	SP-SM/SP-SC**
SK-4	SPT-2	3.50–3.95	3.28	92.95	3.77	30.00	15.47	SP
SK-4	SPT-5	7.50–7.95	8.71	83.35	7.93	29.89	16.15	SP-SM
SK-4	SPT-9	13.50–13.95	3.11	93.02	3.87	29.15	25.35	SP
SK-5	SPT-5	7.50–7.95	0.00	96.26	3.74	42.03	—	SP
SK-5	SPT-10	15.00–15.45	2.11	86.79	11.10	40.64	24.29	SP/SW-SC*
SK-5	SPT-12	18.00–18.45	9.57	86.76	3.67	48.12	36.00	SP
SK-7	SPT-8	12.00–12.45	9.31	84.74	5.96	21.00	—	SP-SM/SP-SC**
SK-7	SPT-11	16.50–16.95	6.55	87.02	6.43	26.00	17.23	SP-SM

* The SP/SW distinction could not be conclusively determined from the available gradation data; therefore, the classification is reported as SP/SW-SM or SP/SW-SC, as applicable.
** The SM/SC distinction could not be conclusively determined because plasticity data for the fines fraction were unavailable.

Note: Following the conference, this Publication Note will be added to each paper; therefore, authors are kindly requested not to remove the note below and to complete the author(s) and paper title information.

Publication Note

This paper was peer-reviewed, accepted for presentation, and included in the proceedings of the ACE2026 – International Conference on Advances in Civil Engineering, held on 12–14 October 2026 in Trabzon, Türkiye.

This paper may be cited as follows:

Muhammed Emin Aytekin, İhsan Yılmaz, Eray Birinci, Erhan Tekin, Eren Pamuk, Kemal Önder Çetin, Nihat Sinan Işık, Seyhan Fırat, "Dynamic Soil Characterization of Alluvial Deposits in Gölbaşı (Adıyaman) Following the 6 February 2023 Kahramanmaraş Earthquakes," in Proceedings of the ACE2026 – International Conference on Advances in Civil Engineering, Trabzon, Türkiye, 12–14 October 2026.

Numerical Investigation of Active Earth Pressure on a Cantilever Retaining Wall with a Shear Key in Cohesive-Frictional Backfill

Dina Aqra[1] and Erol Şadoğlu[2]
[1] 0000-0002-5638-6171, Karadeniz Technical University, Civil Engineering Department, Trabzon, Türkiye, dina-aqra@hotmail.com
[2] 0000-0003-3757-5126, Karadeniz Technical University, Civil Engineering Department, Trabzon, Türkiye, esadoglu@ktu.edu.tr

Abstract. Classical Rankine and Coulomb theories often fail to accurately represent stress distributions and failure mechanisms in cantilever retaining walls with cohesive-frictional backfills. To address this limitation, the present study investigates the geotechnical effect of adding a base shear key to this type of wall. A full-scale model of a 5.0 m high cantilever wall was developed in PLAXIS 2D, assuming a hardening soil Model for the backfill. A full-scale model of a 5.0 m high cantilever wall was developed in PLAXIS 2D, assuming a hardening soil Model for the backfill. A parametric analysis was then conducted to evaluate the influence of shear key's vertical height ($H_{shear\ key}$ ranging from 1 m to 1.5 m, corresponding to 0.2H to 0.3H) and its horizontal width ($B_{shear\ key}$ ranging from 0.5 m to 2.5 m). These configurations were tested under cohesive-frictional backfill with 10 kPa cohesion, an internal friction angle (ϕ= 30°) and unit weight (γ= 18 kN/m^3). Active limit states were triggered by applying incremental prescribed structural displacements. Finite element results show that the shear key effect that slip surfaces behind the wall and the earth pressure distribution. Furthermore, the geometry of the key has a meaningful influence on both total active thrust (Pa) and the shape of non-linear lateral pressure profile.

Keywords: Cantilever wall; Shear key; Cohesive-frictional backfill; Active earth pressure.

1 Introduction

Calculations related to lateral earth pressure problems have been carried out since the early 18th century. However, it was only several decades later that Coulomb [1] conducted the first major study of earth pressures, taking into account a rigid mass of soil sliding upon a shear surface. One of the methods that emerged from this study, known as Coulomb (1776), is still widely used today. Decades later, Rankine [2] proposed an alternative stress-field approach, and both methods remain widely used today for determining basic lateral earth pressures. Building upon these foundational theories to address more complex conditions, Shukla et al. [3] investigated an analytical expression for calculating the total active force on retaining walls for c-ϕ soil backfills, incorporating both horizontal and vertical seismic coefficients. Comparative analysis with earlier expressions reveals consistent trends in force variation. It's observed that the inclination of critical failure surfaces decreases with higher seismic coefficient values. The total active force rises with increasing horizontal seismic coefficient, while it decreases with escalating vertical seismic coefficient values, except for extreme horizontal values. Additionally, design charts are provided for practical estimation of total active force considering various seismic coefficients, cohesion, and angle of shearing resistance. Overall, this study enhances understanding and practical application of seismic considerations in retaining wall design [3].

For a c–ϕ backfill, the active pressure coefficient and pressure distribution depend on more than the effective friction angle. Analytical work has shown that cohesion, wall friction, wall

adhesion, unit weight, depth, and arching can influence active pressure behind a wall [4]. Tu and Jia [4] pointed out the shortcomings of traditional theories through an analysis of the active earth pressure, particularly in cohesive-frictional (c-ϕ) backfills. This was made possible through the inclusion of the effect of soil arching and continuous rotation of principal stress, proving through analytical means that the true lateral earth pressure is inherently non-linear in nature. It was additionally stressed that the cohesive nature of the soil is an essential factor in minimizing the active pressure of the soil towards the retaining wall.

The finite-element analyses indicate that active pressure is not mobilized at a certain displacement along the wall height. Mobilization depends on the behavior of the soil and the wall distortions at various depths. Also, it was found in the same study that a nonlinear soil model is better than an elastic-perfectly plastic soil model in order to avoid numerical instabilities in the analysis of soil-wall interaction [5].

This is especially relevant for cantilever retaining walls, where the stem of the wall is less restrained at the bottom and less stiff at the top. Thus, the rigid wall assumption may affect not only the magnitude but also the depth of active pressure [5, 6].

Pressure and wall friction were determined with the help of instrumented panels and load cells over the stem and base plate of a T-shaped wall. Wall friction was found on the vertical wall and upper surface of the base plate even with a horizontal surface of backfill. Wall friction interfered with the principal stress lines for a distance about equal to the wall height, and the test results were different from Coulomb, Terzaghi, and Peck solutions [7].

FE model should incorporate the proper law of friction and adhesion for stem-soil and base-soil contact instead of full bonding because, otherwise, there would be an error in the determination of pressure and sliding resistance [7].

Studies on calculations of soil pressure behind retaining walls has improved significantly over time, in addition to more advanced numerical and analytical modeling that considers arching action in cohesive-frictional backfills. Recent studies conducted by Sarfaraz et al. [8] was emphasis nonlinear stress distribution in sloped walls under static sliding conditions [8]. In another study, finite element method using PLAXIS 2D suggest that cohesion (c) lowers the area of failure zones by up to 40% and controls the shear strain to remain less than 8.5%, unlike the 20% in the case of cohesionless soil. Furthermore, the geometry of the failure surfaces is largely dependent on the heel width ratio (b/H) value [9].

An FE analysis of a 5.4 m flexible cantilever retaining wall with cohesive backfill under static and seismic loads mentions a reduction of up to 50% in seismic active pressure and 52% in total seismic thrust due to the presence of cohesion, along with a lowering of the location of the thrust load application point. However, the same study mentioned that some seismic code methods for estimating seismic active pressure were largely underestimated [10].

Despite these developments in modeling cohesive backfills, the exact geotechnical implications of introducing a shear key in the design of cantilever retaining walls are poorly investigated. In order to solve this problem, the current investigation aims at investigating the impact of the shear key geometry on the resultant active thrust force and non-linear distribution of lateral pressure on the cohesive-frictional backfills.

In the current investigation, an analytical approach will be introduced to estimate the active earth pressure of cohesive-frictional backfill supported by a cantilever retaining wall incorporating a shear key. In order to examine the effect of wall shear key geometry, a parametric matrix containing 9 cases was considered. The 2D finite element analyses were conducted through the PLAXIS 2D software to simulate the mobilization of the active earth pressure behind a cantilever retaining wall supporting a cohesive-frictional soil having a height of 5.0 m.

2 Numerical Modeling Procedure

A series of two-dimensional finite element simulations was conducted using PLAXIS 2D to investigate the mobilization of active earth pressure behind a cantilever retaining wall. The retaining structure supports a 5.0 m high backfill (H = 5.0 m).

To study the effects of wall shear key geometry a parametric matrix consisting of 9 numerical cases was developed (Table 1). Three different shear key's width ratios and three shear key's height were considered:

Table 1. Matrix of Parametric Study.

Case No	Shear key width ratio (β)	Shear key height ratio (α)
1	0.1	0.1
2		0.2
3		0.3
4	0.3	0.1
5		0.2
6		0.3
7	0.5	0.1
8		0.2
9		0.3

The soil backfill has been modeled as cohesive-frictional soil with constant effective cohesion (c) value of 10.0 kPa, an friction angle (ϕ) of 30.0 and °, and a unit weight of 18 kN/m^3. The Hardening Soil (HS) constitutive model [11] has been chosen to include nonlinear stress-dependent behavior, hysteresis effect, and shear hardening of the soil. This material model allows a physically correct description of behavior of the soil's cohesive strength as well as stress dependent stiffness. In particular, reference secant stiffness obtained from drained triaxial tests (E_{50ref}), and reference tangent stiffness obtained under primary loading condition in oedometer test (E_{oedref}) have been assigned as 25.0 MPa. Moreover, reference unloading/reloading stiffness (E_{urref}) is assigned as 75.0 MPa, which avoids strain overestimation during unloading cycles. Also, there is an inclusion of interface strength reduction factor (R_{inter}) of 0.50 to simulate interaction between the retaining structure and the soil.

The cantilever retaining wall along with its base slab and shear key were assumed to be a continuous solid element. In order to simulate the mechanical properties of the concrete material, a Linear Elastic material model was used. This is a common practice for soil-structure interaction numerical analyses because the stiffness of the concrete wall is much greater than that of the backfill and since the main interest of the study is soil yielding processes and not the structural failure of the wall. The concrete material was assumed to be non-porous drainage type material with the unit weight (γ) of 24.0 kN/m^3. The elastic stiffness parameters included the following: Young's modulus (E) of 30 GPa and Poisson's ratio (ν) of 0.20.

The stress-dependence index m for stiffness was selected as 0.60. Also, the "Tension Cut-off" option was enabled with zero tensile strength (0.0 kN/m^2), in order to allow development

of the tensile crack depth (z_c) in view of the physically impossible sustained tensile stress at the upper fill interface.

Staged construction analysis procedure was used for the numerical modeling:

1. **Initial Stage & Excavation:** Activation of the retaining wall and soil-structure interaction interfaces followed by excavation of the soil mass ahead of the wall to create an initial at-rest stress condition.
2. **Translation Mode (Stages 3 to 19):** Application of a horizontal displacement of the wall to induce active limit state of equilibrium. This was achieved through application of an increase in horizontal displacement by 0.001H (0.005 m) in each stage with a maximum of 0.017 (0.085 m).

Vertical Control Section was specified 5 cm behind the retaining wall stem and shear key in order to obtain lateral stress distribution. Active earth pressure condition is assumed to be mobilized when there is no appreciable change in lateral forces with each increment of displacement (approximately 1%).

3 Results and Discussion

3.1 Mobilization of Active Earth Pressure

The relation between the normalized wall displacement (Δx/H) and the total lateral thrust is presented in Fig. 1. In all nine different cases investigated, it can be seen that the transition from the initial state (Δx/H = 0) to the fully active state is demonstrated in Fig. 1. The absolute value of the lateral force experiences a significant decrease at the early stage of the wall displacement. The curves level off at the moment when the change of lateral force becomes negligible, thus reaching the fully mobilized active limit state. As one can see in Fig. 1, this stage is reached at the normalized wall displacement of approximately 0.007 to 0.008, beyond which the curves remain relatively flat.

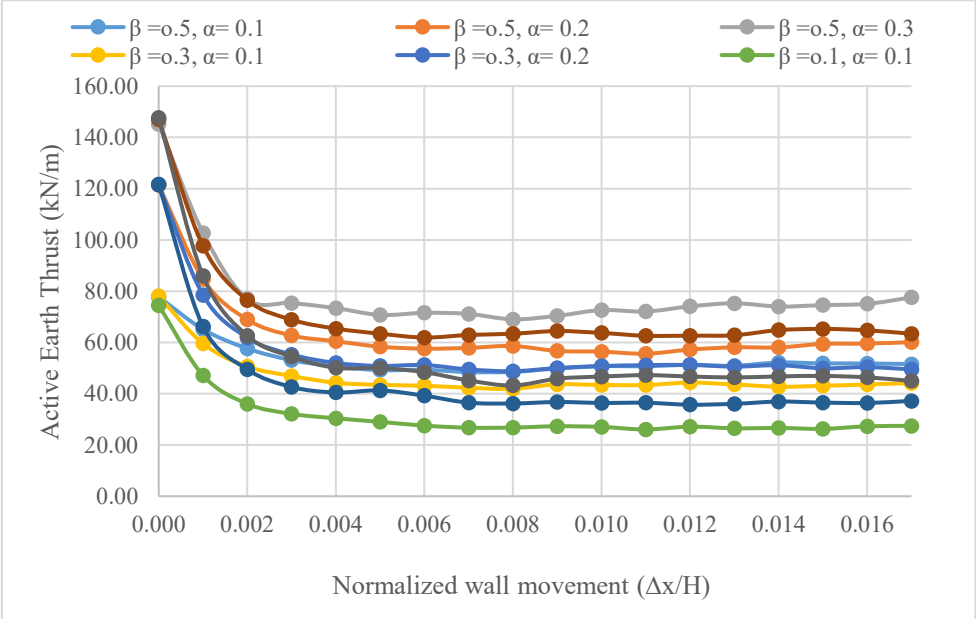


Fig. 1. Variation of active earth thrust with normalized wall movement for different base shear key configurations.

According to the literature data, the active limit state can usually be achieved with a much smaller displacement in conventional walls. Numerical analysis done by Sarfaraz et al. [8] shows that the horizontal earth pressure decreases with the movement of the wall and attains constant values at the active wall movement of about 0.0007 times the wall height. This result

is also consistent with the results of the previous numerical analysis performed by Matsuzawa and Hazarika [12], who showed that active wall movement is equal to ($\Delta x/H$) = 0.0005 to 0.001 for vertical walls.

It should be noted that in the current investigation, the active state is attained at a much larger displacement of $\Delta x/H \approx 0.007$ to 0.008. The considerable delay in active pressure mobilization can be explained by the effect of the presence of the shear key, which is a rigid element of the retaining structure. The shear key becomes a kind of anchor that essentially affects the kinematic behavior of the system, thus replacing the simple and shallow planar failure mechanism with the more complex and deep-seated composite failure mechanism. Therefore, much larger displacement of the wall is required to fully stretch the soil mass and activate the shear strength on the corresponding deep-seated slip surfaces.

3.2 Effect of Shear Key Geometry on Active Earth Thrust

It is apparent from Fig. 1 that the geometry of the shear key has an essential impact on the value of the mobilized lateral earth thrust. From the results of the finite element analysis of the structure, at the fully active state ($\Delta x/H = 0.008$), it can be seen that the relative height ($\alpha = H_{key}/H$) and the relative width ($\beta = b_{key}/H$) modify the active force. An increase in the vertical extent of the shear key leads to an increase in the value of the active force. With the constant width of the key $\beta = 0.5$, the active force increases from 48.52 kN/m at $\alpha = 0.1$, to 58.62 kN/m at $\alpha = 0.2$, and attains 69.02 kN/m at $\alpha = 0.3$. The reason is the increased vertical depth of the sliding soil wedge with the extended shear key, leading to higher geostatic stresses along the slip plane.

Additionally, an increase in the horizontal extent of the shear key β shows an analogous influence on the active force. Comparing the cases with the same relative height of the key $\alpha = 0.3$, the active lateral force increases from 43.20 kN/m for $\beta = 0.1$, to 63.40 kN/m for $\beta = 0.3$, and achieves its maximum value of 69.02 kN/m for $\beta = 0.5$. In general, the minimal active thrust (26.79 kN/m) corresponds to the smallest structural attachment ($\alpha = 0.1$, $\beta = 0.1$). The wider basis of the shear key activates a bigger volume of the cohesive-frictional backfill. Thus, the mechanical contact with this soil wedge moves the slip surface farther from the wall stem.

This is consistent with very recent and sophisticated numerical studies related to the effect of base geometry on soil kinematics. As classical limit equilibrium analysis assumes a simple failure plane, neglecting any structural feature, the above findings support the complexity of such an interaction. For example, Ayman et al. [9] showed that changing the base geometry of a cantilever wall, in particular the heel length at the back, significantly affects the failure process, leading to the choice between the 'short heel' and 'long heel' modes and hence the volume of mobilization of the cohesive backfill. Similarly, the current study clearly indicates that the width and depth of the base shear key have a similar effect as they affect the main slip plane, shifting it outward and increasing the lateral driving thrust. Such local change in the active earth pressure is confirmed by the research of El Yamouni et al. [10], who noted that the boundary conditions and cohesive-frictional interactions result in highly nonlinear earth pressures that classical theories do not properly account for.

3.3 Failure Mechanisms and Plastic Points Analysis

In the analysis of finite element analyses through the use of Hardening Soil (HS) model, it becomes necessary to determine the plastic points in space to understand the yielding and failure characteristics of the backfill. The stresses in PLAXIS 2D models are described using certain plastic point criteria as follows:

Hardening points: are the stresses at which the material first comes to the HS model shear yield surface. Prior to this point, the material response is mainly elastic. However, the HS model has non-linear stress dependent stiffness.

Cap points: Yielding zones under primary volumetric compression.

Failure points: are those zones that have attained the stress state on the Mohr-Coulomb failure envelope and thus active shear slip zones.

Tension cut-off points: Those zones which the stress state is greater than the tensile limit of the cohesive-frictional material resulting to formation of cracks close to the ground surface.

It was essential to evaluate the plastic points distributions both at the mobilized active state (Ax/H=0.008) and after active state (ΔX/H =0.011).

A detailed analysis of the failure angles also shows clear differences from classical geotechnical theory. According to conventional limit equilibrium and Rankine theories, the slip angle (θ) is expected to equal the theoretically predicted value of the active failure angle 45+ϕ/2 (60° for ϕ=30°). Nevertheless, the computed angles are always less than the theoretically predicted values. The explanation of such an inconsistency is that due to the existence of the soil cohesion (c=10 kPa), and the presence of the base shear key, the actual stress path is different from that assumed for the ideal Rankine wedge formation.

Furthermore, the study of the developed failure zones and tension cut-off surfaces indicates that the width (β) and height (α) of the shear key exert considerable effect on the behavior of the system. The increase in the width of the shear key leads to the fact that instead of passing linearly up to the vertical wall stem, the left failure plane (Ψ) runs into an area of tension, failing to continue once it intersects the tension cracks that develop due to the induced tension at the top level. Also, the primary slip surface (θ) is hindered due to the presence of large areas of tension controlled by cohesion of the soil.

Table 2. Measured slip surface angles (Ψ and θ) at active (Δx/H = 0.008) and post-active (Δx/H = 0.011) stages.

		phase 10 (0.008H)		phase 13 (0.011H)	
β	α	Ψ	θ	Ψ	θ
0.5	0.3	65	55	65	50
	o.2	62	55	55	60
	0.1	58	50	50	60
0.3	0.3	70	50	58	55
	o.2	65	55	55	52
	0.1	60	50	55	52
0.1	0.3	65	60	55	50
	o.2	65	50	50	65
	0.1	58	50	57	50

The analysis of failure angles shown in Table 2 gives more insight into the kinematics of the backfill. In accordance with Rankine and Coulomb's theory, the active failure angle is theoretically predicted to be constant and equal to 45° + ϕ/2 (60° for ϕ = 30°). Nevertheless, as can be seen from FEM simulation results, this theoretical prediction is not met due to the significant deviation, which increases with the increasing dimensions of the shear key (α, β).

The Fig. 2 and Fig. 3 present the plastic point distributions acquired from the finite element analysis at the active and after active limit states (Δx / H = 0.008 and Δx / H = 0.011 respectively). An obvious sign of the shear failure surfaces progression can be observed when comparing these two limit states.

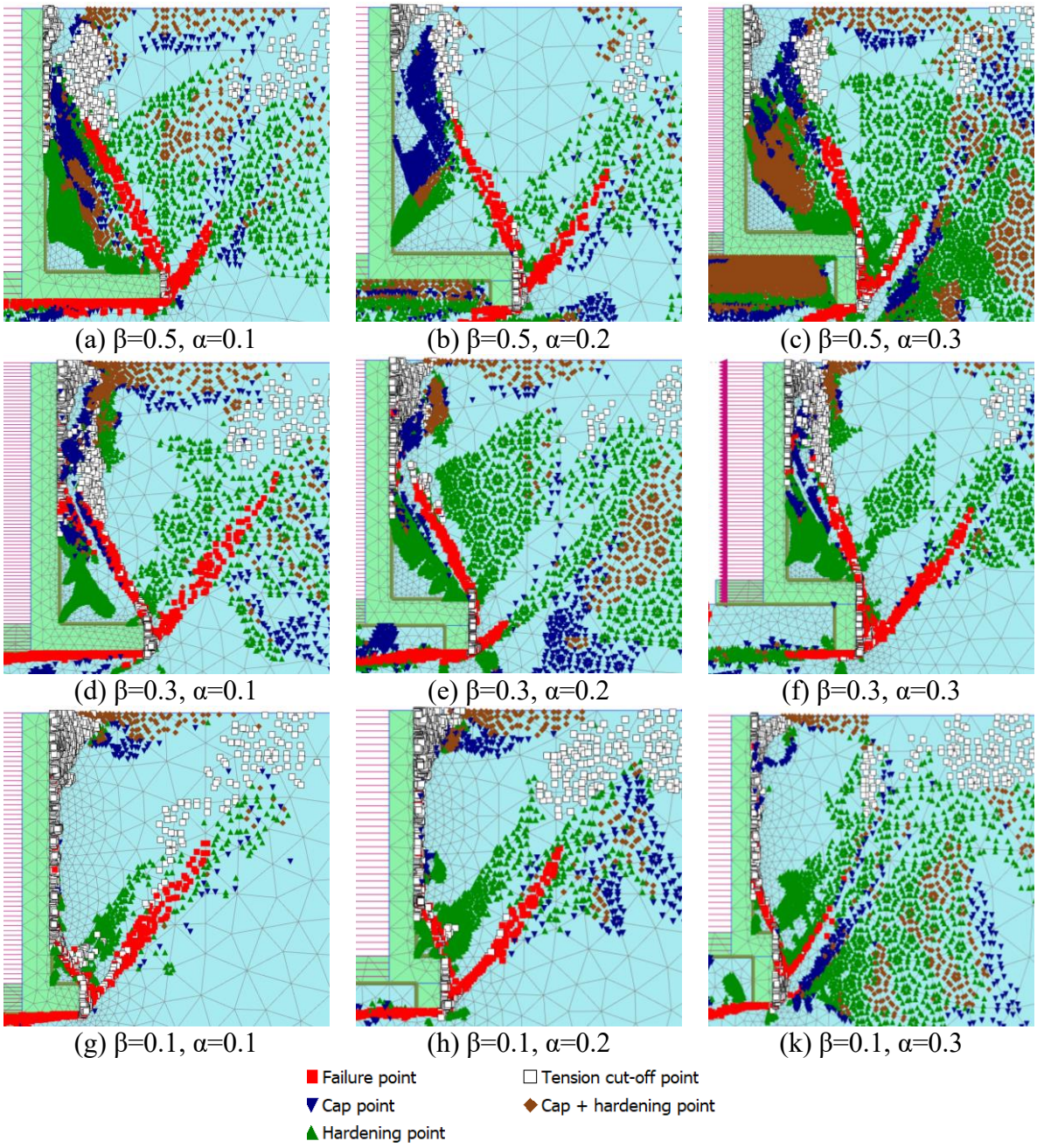


Fig. 2. Plastic point distribution illustrating failure surfaces and tension zones across various α and β configurations at Δx/H = 0.008 wall movement.

In the case of the fully active regime (Phase 10, Δx/H = 0.008), the upper angle of slip (Ψ) generally ranges between 58° to 70°, whereas the lower angle of slip (θ) generally fluctuates between 50° to 55° (sometimes even 60°). As the wall motion proceeds to the post-active regime (Phase 13, Δx/H = 0.011), a certain kind of kinematic change takes place: the upper angle of slip (Ψ) gets reduced (between 50° and 58°), and so does the lower angle of slip (θ).

This shows that the presence of the base shear key does not allow for the development of a single consistent rigid-plastic wedge. The soil mass develops yielding in stages, which means that the presence of cohesion (c = 10kPa) and tensile cut-off zones does not allow the slip surfaces to adhere to analytical formulas.

Upon careful observation of the right-hand failure surface (θ), there appears to be a clear dependence of the slip surface on the width of the shear key (β) and displacement progressions. For instance, in the case where β = 0.5, which represents the widest base key scenario, the right-hand failure surface does not extend up to the wall stem at any ratio of wall height tested (α) in both active and post-active states. In this case, therefore, we can conclude that a wide enough shear key effectively separates the lower failure zone such that the shear is mobilized deep into the backfill. On the other hand, for an intermediate width of β= 0.3, the slip surface does not reach the wall up to Δx/H= 0.008, but gradually reaches and intersects the wall as displacement progresses to the post-active state (Δx/H= 0.011).

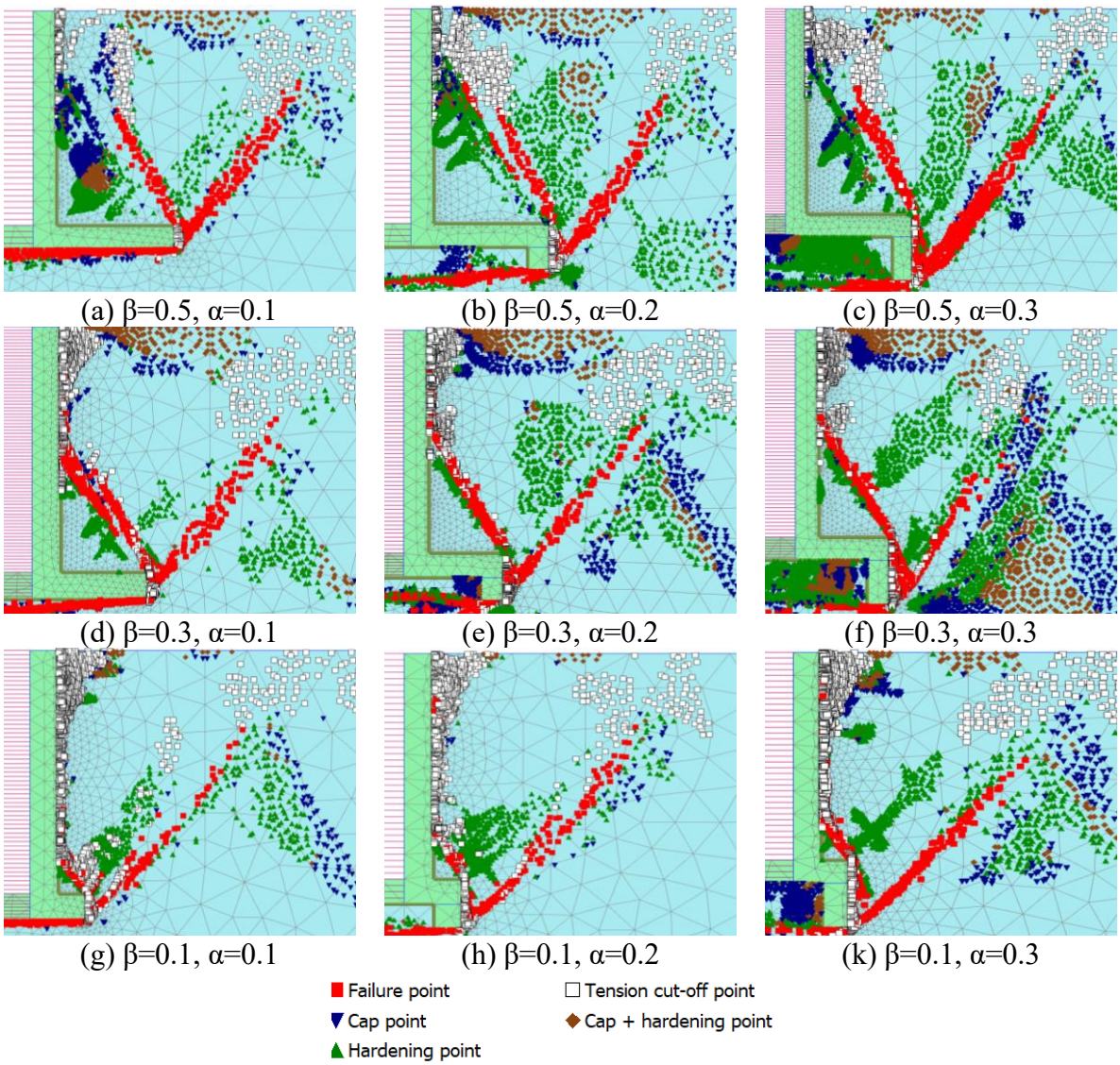


Fig. 3. Plastic point distribution illustrating failure surfaces and tension zones across various α and β configurations at Δx/H = 0.011 wall movement.

4 Conclusion

This study numerically investigated the effect of the shear key on the active lateral earth pressure exerted on cantilever retaining walls supporting cohesive-frictional backfill (c = 10 kPa, ϕ = 30°). Using PLAXIS 2D and the Hardening Soil constitutive model, nine different shear-key geometries have been studied at various displacement stages. The main findings of this analysis are as follows:

• Active Limit State Mobilization: The active limit state is increasingly mobilized by the movement of the wall in the direction of displacement. From the finite element analysis, it can be observed that a lateral displacement of $\Delta x/H$ equal to 0.007 to 0.008 is necessary to mobilize the shear resistance of the cohesive-frictional backfill.

• Effect of Shear Key Geometry: The active lateral force is largely dependent on the two factors: the relative height (α) and relative width (β) of the shear key. An increase in the relative height of the shear key (α) is known to lead to an increase in the active earth thrust. At a constant width ratio ($\beta = 0.5$), when α changes from 0.1 to 0.3, the active force increased from 48.52 kN/m to 69.02 kN/m. An increase in the relative width of the shear key (β) also greatly enhances the lateral thrust. At a constant relative height ratio of $\alpha = 0.1$, when β changes from 0.1 to 0.5, the active force increases from 26.79 kN/m to 48.52 kN/m.

• Failure Mechanisms & Plastic Points: The failure mechanisms and the locations of plastic points, when examined in terms of the plastic points and the failure angles (Ψ and θ), show that the presence of cohesion and the shear key leads to noticeable departures from the classical Rankine and Coulomb theories ($45 + \phi/2$), thereby producing non-linear pressure distributions and areas where tension is cut off which in turn limit the slip surfaces.

References

1. Coulomb, C. A.: Essai sur une application des règles de maximis et minimis à quelques problèmes de statique, relatifs à l'architecture. Mémoires de Mathématique et de Physique 7, 343–382 (1776).
2. Rankine, W. J. M.: On the stability of loose earth. Philosophical Transactions of the Royal Society of London 147, 9–27 (1857).
3. Shukla, S. K., Gupta, S. K., Sivakugan, N.: Active earth pressure on retaining wall for c-ϕ soil backfill under seismic loading condition. Journal of Geotechnical and Geoenvironmental Engineering 135(5), 690–696 (2009).
4. Tu, B., Jia, J.: Active earth pressure from c-φ soil backfill. Proceedings of the Institution of Civil Engineers - Geotechnical Engineering 167(6), 548-559 (2014). https://doi.org/10.1680/GENG.12.00008
5. Elchiti, I., Saad, G., Najjar, S., Nasreddine, N.: Investigation of active soil pressures on retaining walls using finite element analyses. In: Geotechnical Frontiers 2017, pp. 153-162. American Society of Civil Engineers (2017). https://doi.org/10.1061/9780784480458.016
6. Bruner, R. F., Bartoskewitz, R. E.: Cantilever retaining wall design. Research Report 236-2F, Texas Transportation Institute, Texas A&M University System (1992).
7. Fukuoka, M., Yoshida, Y.: Researches on earth pressure about cantilever wall with cohesive soil as backfill. International Journal of Rock Mechanics and Mining Sciences & Geomechanics Abstracts 16(2), 52-53 (1975).
8. Sarfaraz, H., Khosravi, M. H., Pipatpongsa, T.: Theoretical and Numerical Analysis of Cohesive-Frictional Backfill against Battered Retaining Wall under Active Translation Mode. International Journal of Geomechanics 23(6), (2023). https://doi.org/10.1061/IJGNAI.GMENG-8392
9. Ayman, G., El Khannoussi, F., El Yamouni, B., Khamlichi, A.: Analysis of seismic dynamic thrust for cantilever retaining walls as affected by sloped backfill and surcharge: from finite element modeling to simplified sliding surface geometry. Journal of Engineering and Applied Science 72(160), (2025). https://doi.org/10.1186/s44147-025-00746-1
10. El Yamouni, B., El Khannoussi, F., Khamlichi, A.: Numerical Investigation of Seismic Behaviour for a Flexible Cantilever Retaining Wall with Cohesive Backfill. International Journal of Engineering Research in Africa 69, 125–142 (2024). https://doi.org/10.4028/p-Z3wyLG

11. Schanz, T., Vermeer, P. A., Bonnier, P. G.: The hardening soil model: Formulation and verification. In: Beyond 2000 in computational geotechnics, pp. 281–296. Routledge, London (1999).
12. Matsuzawa, H., Hazarika, H.: Analyses of active earth pressure against rigid retaining wall subjected to different modes of movement. Soils and Foundations 36(3), 51–65 (1996).

Author Contribution Statement

- *Conceptualization:* Dina Aqra, Erol Şadoğlu
- *Methodology:* Dina Aqra, Erol Şadoğlu
- *Investigation:* Dina Aqra, Erol Şadoğlu
- *Writing – Original Draft:* Dina Aqra
- *Writing – Review & Editing:* Dina Aqra

List of Abbreviations

- **FE** — Finite Element
- **FEM** — Finite Element Method
- **HS** — Hardening Soil

Note: Following the conference, this Publication Note will be added to each paper; therefore, authors are kindly requested not to remove the note below and to complete the author(s) and paper title information.

Publication Note

This paper was peer-reviewed, accepted for presentation, and included in the proceedings of the ACE2026 – International Conference on Advances in Civil Engineering, held on 12–14 October 2026 in Trabzon, Türkiye.

This paper may be cited as follows:

Aqra, D., Şadoğlu, E., "Numerical Investigation of Active Earth Pressure on a Cantilever Retaining Wall with a Shear Key in Cohesive-Frictional Backfill," in Proceedings of the ACE2026 – International Conference on Advances in Civil Engineering, Trabzon, Türkiye, 12–14 October 2026.

A Discrete Element Modeling of the Vibration of a Horizontal Granular Deposit Harmonically Excited at the Base

Mouloud MANSOURI[1] and Said DERBANE[2]
[1] orcid:0000-0002-4179-7488, Civil Engineering Research Laboratory of Setif (LRGCS), Department of Civil Engineering, Ferhat Abbas Setif1 University, Setif 19000, Algeria.
mansouri.mouloud@univ-setif.dz
[2] orcid:0009-0003-7773-5806, Department of Civil and Hydraulic Engineering, Faculty of Science and Technology, University of Jijel 18000, Algeria
derbane_said@yahoo.fr

Abstract. The transmission and amplification of motion from bedrock to the free soil surface are commonly analyzed using continuum models, such as viscoelastic or hysteretically damped elastic models. However, the discontinuous nature of granular soils makes their response more complex, particularly under large-amplitude vibrations. This study investigates vertical shear-wave propagation in a granular soil deposit using a 2D discrete element model subjected to harmonic base excitation. The analysis focuses on surface motion amplification and its dependence on excitation frequency. The results show that the Dynamic Amplification Factor (*DAF*) increases with frequency, reaches a resonance peak, and then decreases, similarly to an elastic system. However, the resonance frequency is lower than the fundamental frequency obtained from small-amplitude vibrations, with the difference increasing with excitation amplitude. This shift is attributed primarily to strain-dependent shear-modulus degradation in the granular deposit.

Keywords: Sand deposit, Macromechanical behavior, Discrete Element Method, Wave Propagation.

1 Introduction

The propagation of seismic waves from the bedrock to the ground surface is strongly influenced by the mechanical properties of the traversed soil layers. In particular, soil stiffness and damping govern the transmission and amplification of seismic motion. These phenomena are commonly analyzed within the framework of continuum mechanics using constitutive models such as viscoelastic or hysteretic elastic models, which generally provide satisfactory predictions for cohesive soils. However, the discontinuous nature of granular materials makes their dynamic response, especially under large-amplitude vibrations, more complex and difficult to capture using continuum models. In this context, the discrete element method (DEM) offers a valuable framework for investigating the underlying micromechanical mechanisms governing wave propagation and motion amplification in granular soil deposits.

DEM has been widely used to study wave propagation in granular media. Previous studies have examined the effects of contact stiffness, fabric anisotropy, force chains, particle properties, and saturation on wave velocity, attenuation, and dynamic response [1–6]. These investigations have demonstrated that wave propagation is strongly controlled by the contact network and the evolving granular microstructure. Experimental studies have also confirmed the ability of DEM to reproduce wave velocities and dynamic characteristics observed in granular soils [4].

The present study investigates the dynamic behavior of a non-cohesive granular deposit subjected to horizontal harmonic base excitation using a two-dimensional DEM model. Particular attention is devoted to free-surface motion amplification and its dependence on

excitation frequency and amplitude. The macroscopic response of the deposit under large deformations and near-resonance conditions is also analyzed.

1 Discrete element modeling

The discrete element method (DEM), originally proposed by Cundall [7], models granular materials as assemblies of rigid particles interacting through contact laws. The macroscopic response arises from the collective motion of individual particles governed by Newton's laws of motion. Because of their simplicity and the savings in calculation time they involve, circular element shapes are still the most widely used. The motion of each grain is governed by Newton's second law, expressed through the equations of dynamic equilibrium for translational and rotational motion. These equations account for the grain weight, contact forces, and, when applicable, other forces specific to the problem being modeled. Contact forces are decomposed into a normal component and a tangential component. In this work, the normal contact force between two grains is calculated using a viscoelastic model based on their overlap and relative normal velocity, with prescribed normal stiffness k_n and viscous damping constant v_n. The tangential contact force is computed using a viscoelastic model in series with a friction slider, characterized by a tangential stiffness k_s, a viscous damping coefficient v_s and an inter-particle friction coefficient μ_d. Particle velocities and displacements are obtained by integrating the accelerations from the equations of motion. Because contact forces depend on particle positions and velocities, the solution is computed incrementally using successive approximations to ensure consistency between particle positions, velocities, and contact forces at each time step. The time step must be selected such that the evolution of each contact during particle motion is accurately resolved. To account for the damping of natural particle rolling, a rolling resistance torque is introduced by applying the normal contact force with an eccentricity, whose magnitude controls the resistance [8]:. It should be emphasized finally that quantitative agreement with physical experiments requires careful calibration of the model parameters; however, for the present phenomenological study, they are selected primarily to reduce computational cost while preserving physically realistic behavior.

2 Analytical solution of wave propagation in a viscoelastic deposit

Assuming that the granular deposit behaves as a damped elastic continuum, the propagation of a horizontal harmonic displacement (u), along the vertical direction, (z), is governed by the following equation [9]:

$$\frac{1}{c^2}\frac{\partial^2 u}{\partial t^2} = \frac{\partial^2 u}{\partial z^2} + \frac{2\xi}{\omega}\frac{\partial^3 u}{\partial t \partial z^2} \tag{1}$$

In which, c is wave propagation velocity, ξ is the hysteretic damping ratio and ω is the circular frequency of the movement. The analytical solution to this equation, for a deposit overlaying a bedrock subjected to a horizontal harmonic oscillation, is given in [17] as follows:

$$\begin{aligned}\frac{A.u(z,t)}{u_0} = &\cosh(ph)\cos(qh)\cosh(pz)\cos(qz)\sin(\omega t)\\ &+\sinh(ph)\sin(qh)\sinh(pz)\sin(qz)\sin(\omega t)\\ &+\cosh(ph)\cos(qh)\sinh(pz)\sin(qz)\cos(\omega t)\\ &-\sinh(ph)\sin(qh)\cosh(pz)\cos(qz)\cos(\omega t)\end{aligned} \tag{2}$$

In which h is the deposit's thickness and z is the vertical coordinate (depth). A, p and q are calculated from equations : $A = cosh^2(ph) - sin^2(qh)$, $(ph)^2 + (qh)^2 = \frac{(\pi^2/4)(\omega^2/\omega_1^2)}{1+4\xi^2}$ and $(ph)(qh) = \xi\frac{(\pi^2/4)(\omega^2/\omega_1^2)}{1+4\xi^2}$.

The fundamental frequency of the deposit being the first resonance frequency for very low damping, it is given by:

$$\omega_1 = \frac{\pi c}{2h} \tag{3}$$

This analytical solution shows that the displacement profile, representing the variation of displacement with depth at a given instant, depends on the excitation frequency. As illustrative examples, Fig. 3 presents the displacement profiles of a deposit subjected to harmonic base excitation with amplitude u_0 for two frequency ratios $\omega/\omega_1 = 0.42$ and $\omega/\omega_1 = 1.12$. In both cases, the hysteretic damping ratio is set to $\xi = 8\%$.

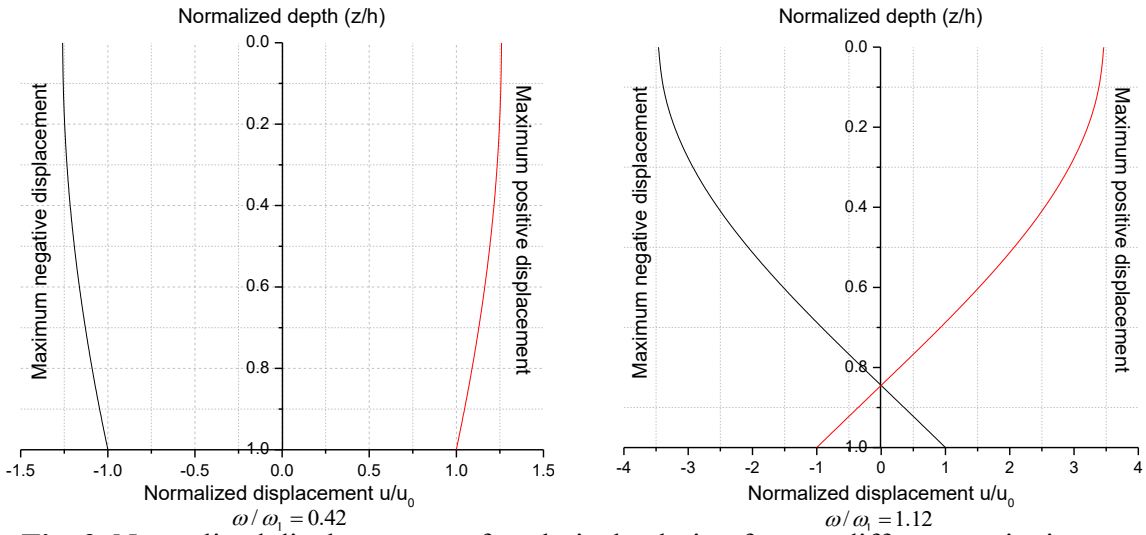


Fig. 2. Normalized displacements of analytical solution for two different excitation frequencies.

Figure 2 shows that when the excitation frequency is lower than the fundamental frequency, the displacement profile resembles the first natural mode shape. As the excitation frequency exceeds the fundamental frequency, the second mode shape emerges, characterized by a nodal point (zero displacement) that moves upward with increasing frequency. Upon reaching the second natural frequency, the third mode shape develops, and the same pattern is repeated for higher modes. In this study, we define the dynamic amplification factor at the top (i.e. the free surface) as $DAF = \frac{u_s}{u_0}$, where u_s and u_0 are the displacement amplitudes at the free surface and at the base respectively. Using the displacement solution (eq. 2), the *DAF* is plotted in figure 3 in terms of the frequency ratio (ω/ω_1) ranging from 0 to 1.12 and for hysteretic damping ratios of 5%, 10% and 15%.

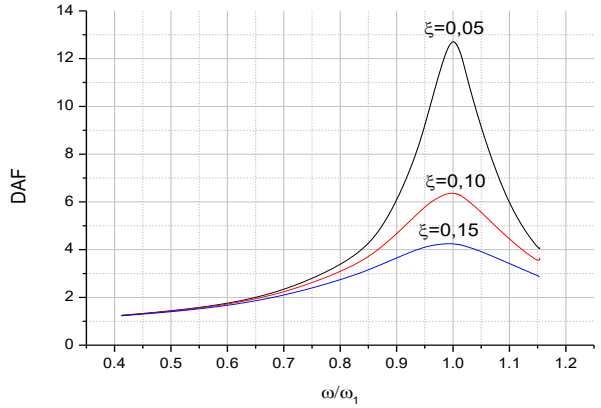


Fig. 3. Dynamic Amplification Factor at the deposit's free surface (*DAF*) in terms of the frequency ratio (ω/ω_1), for hysteretic damping ratios: 5%, 10% and 15%.

This figure shows the typical evolution of the *DAF* with increasing excitation frequency. The *DAF* rises from 1 at low frequencies to a maximum at the first resonance, then decreases. At resonance, its maximum value is inversely proportional to the damping ratio and can be approximated for low damping by $DAF_{max} \approx \frac{2}{\pi\xi}$ [9]. It is worth noting that for common damping ratios, the resonance occurs at frequencies very close to the fundamental frequency.

3 Details of the numerical model to simulate the wave propagation

In the present work, the vertical propagation of a shear wave in a sand deposit is investigated using a 2D discrete element model implemented in C++. A dense deposit is first generated by pluviation under gravity on a horizontal rigid plateau representing the bedrock, with periodic boundaries applied horizontally. After stabilization, the grain positions are stored as reference positions. The deposit is then subjected to horizontal vibration through the bedrock, while its upper surface remains free. To ensure effective motion transmission, the lowest grains are bonded to the bedrock so that they undergo the same imposed displacement. In order to describe the response, the deposit is divided into a number of layers for which the average grain displacements are monitored during the excitation. The deposit width (period) is set to $2m$, resulting in a height of approximately $0.5m$. Figure 3 shows the pluviated sand deposit, its boundary conditions, the bonded grain chain ("excitation chain"), and the subdivision into control layers.

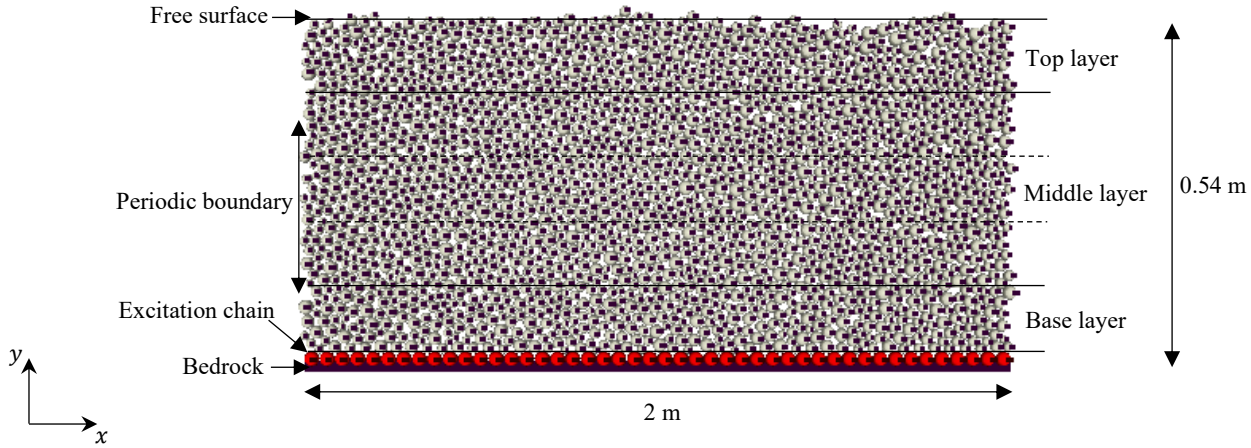


Fig. 4. Illustration of the sand deposit's model, boundary conditions and subdivision into a number of monitoring layers.

The used excitation is harmonic, with prescribed amplitude (u_0) and frequency (ω). To minimize transient effects, the excitation is applied in three stages following [4]: gradual increase to the target amplitude, steady-state oscillation at constant amplitude, and gradual decrease to zero. The durations of these stages are set to $4.5s$, $6s$ and $1.5s$ respectively, allowing transient effects to decay during the steady-state phase. The properties of the grains as well as the micromechanical parameters used in the computation of the intergranular contact forces are presented in Table 1.

Table 1. Model parameters.

Parameters	Value
Number of Grains	5000
Grains radii r_i	$1.00\text{x}10^{-3}$ *to* $2.00\text{x}10^{-3}m$
Density G_s	$2600\ kg/m^3$
Normal intergranular stiffness k_n	$1.2\ \text{x}10^6 N/m$
Shear intergranular stiffness k_s	$9.6\text{x}10^5 N/m$
Intergranular friction coefficient μ	0.5

The results discussed below are mainly obtained during this phase. The deposit is divided into 10 control layers, and the recorded displacements are the averages over all grains belonging to each layer.

4 Simulations, results and discussions

4.1 Displacement time history and movement amplification from base to the surface

In this simulation, the parameters of the exciting displacement in the steady state stage are set to $u_0 = 4x10^{-4}m$ and $\omega = 25\,rad/s$. Figure 4 shows the displacement time history at the bedrock (Fig. 5a) and at the top layer of the deposit (Fig. 5b).

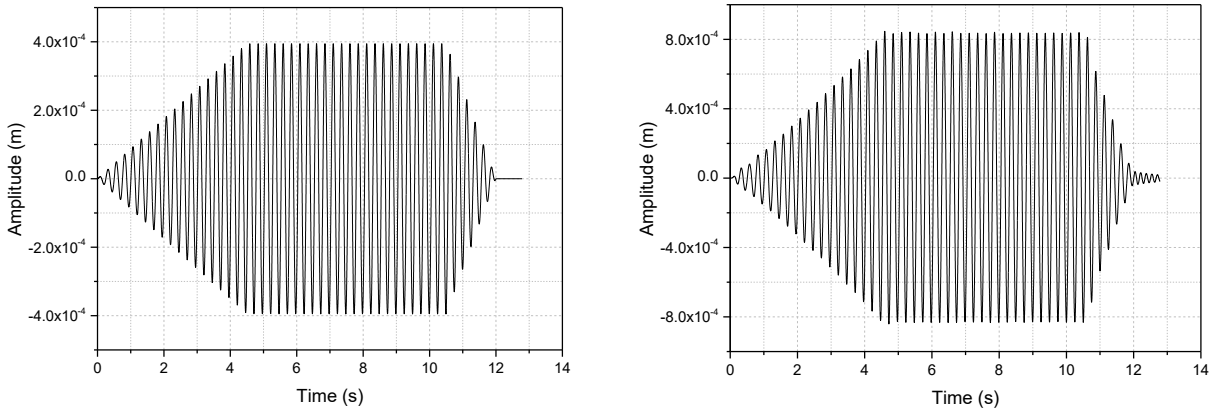
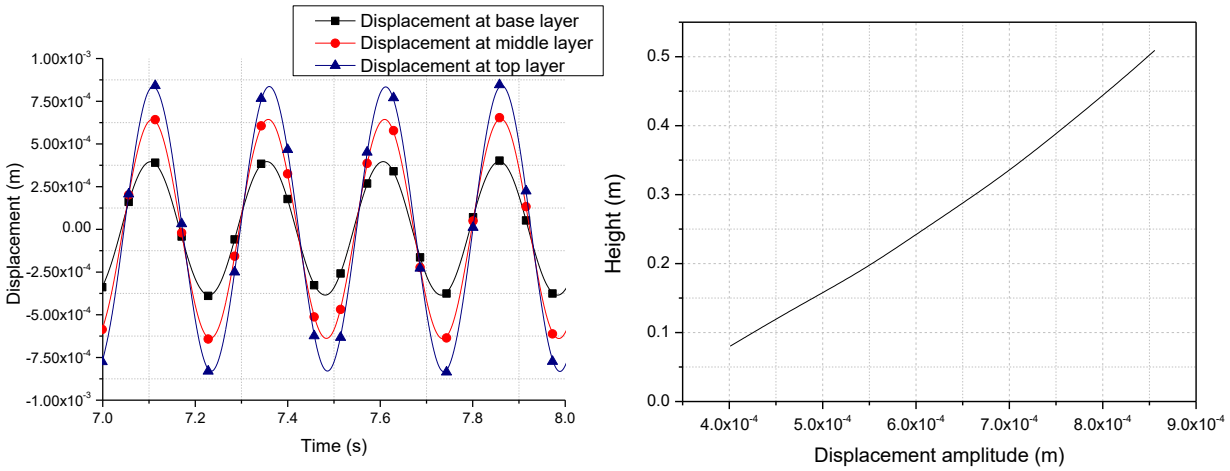


Fig. 5. Displacement time history, left : at the bedrock (excitation), right : at the top layer of the deposit.

The figures illustrate the different motion phases at the bedrock and top layer, representing the deposit surface. In the steady-state phase, the surface amplitude remains nearly constant, indicating that transient effects have decayed. Comparing Figs. 5a and 5b, the imposed bedrock displacement of $0.4mm$ is amplified to approximately $0.85mm$ at the surface. After excitation ends ($t = 12s$), the deposit undergoes free, damped elastic oscillations (Fig. 5b).

Figures 6a and 6b illustrate the movement amplification within the deposit. Fig. 6a shows a part of the steady-state response $(7s \leq t \leq 8s)$ at the base, middle, and top layers, while Fig. 6b presents the vibration amplitude as a function of layer height above the bedrock. These figures show that displacement amplification increases from the base to the surface. Figure 6b also reveals a first-mode vibration profile, indicating that the excitation frequency is below the first resonance frequency of the deposit.



(a) (b)

Fig. 6. (a) Displacement time history for steady state oscillation at three different depths. (b) Displacement amplitude vs. the layer's height during steady state oscillation.

4.2 Fundamental frequency of the deposit

The fundamental frequency of the deposit is defined as the frequency of free elastic vibration corresponding to the first mode shape. To ensure elastic behavior, the vibration must remain at very low amplitude, since granular soils generally exhibit nonlinear elastoplastic behavior, with the deformation modulus degrading as strain increases. Accordingly, this study focuses on the free vibration occurring after the end of the excitation. The excitation parameters used here are a steady-state amplitude of $u_0 = 4 \times 10^{-4} m$ and an angular frequency of $25 rad/s$. Figure 8 presents a zoom of the time history of displacements corresponding to the free vibration phase (after end of excitation) at different depths of the deposit.

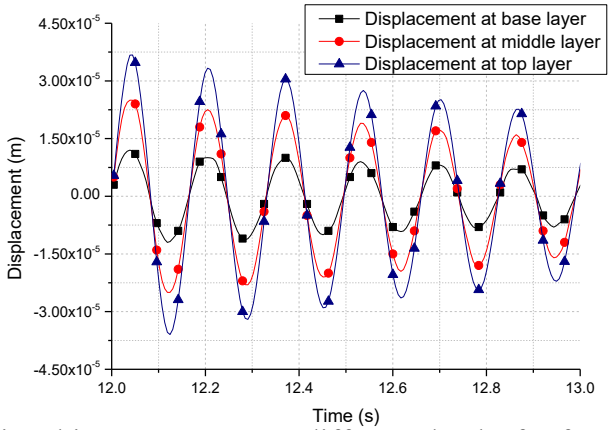
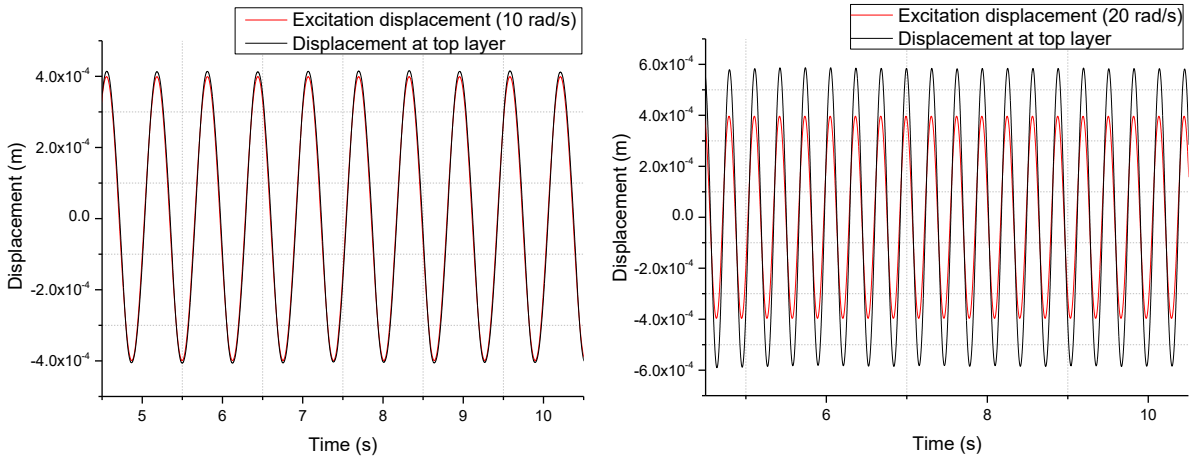


Fig. 8. Zoom of time history response at different depths for free vibration phase.

This figure shows that the displacements are harmonic and without phase offset for the different depths, which corresponds to the oscillation shape of the fundamental mode. The fundamental period can be estimated from the displacement plot, it is about $T = 0.166\, s$. Hence, the fundamental frequency is $\omega_1 = \frac{2\pi}{T} = 37.82\, rad/s$.

4.3 Influence of the excitation frequency on the response of the deposit

In order to show the excitation frequency effect on the deposit's response, several simulations are performed for frequencies ranging from 10 to 40 *rad/s*, while the excitation amplitude is set to $u_0 = 4x10^{-4} m$. Figure 9 shows the time history of displacements during the steady state excitation stage at the bedrock and at the top layer of the deposit for frequencies of 10 and 20 *rad/s*.



(a) (b)

Fig. 9. Steady state displacements time history at the bedrock and at the top layer of the deposit for excitation frequencies: (a) 10 *rad/s*, (b) 20 *rad/s* ($u_0 = 4x10^{-4} m$).

It can be noted that for the frequency of 10 *rad/s*, there is no movement amplification at the top layer, thus the deposit exhibits a behaviour of a rigid body that follows the bedrock's displacement. However, for the frequency of 20 *rad/s*, the movement is amplified at the top layer, indeed in this case the inertial forces become more significant, which causes the deformation of the deposit.

Figure 10 shows the displacement time history of the top layer throughout the excitation. For clarity, only the responses at 20, 30, 32, and 35 rad/s are presented, as they capture the main evolution of the behavior. Increasing the frequency from 20 to 30 rad/s increases the motion amplification, with the top-layer amplitude rising from 0.6 to approximately 1.6 mm. At 32 and 35 rad/s, the top layer exhibits irreversible grain sliding, attributed to strong amplification and the lack of confinement at the deposit surface. Sliding begins when the vibration amplitude becomes sufficiently large, near the onset of the steady-state stage, after which the layer oscillates around a progressively changing equilibrium position. The slight decrease in amplitude over time may result from deposit densification due to significant grain rearrangement, which reduces its deformability.For frequencies associated with top-layer sliding, the steady-state phase is defined as the short interval immediately following the amplitude ramp-up (after 4.5 s), highlighted by the red windows in Fig. 10. This interval is shortened to capture the response before significant densification occurs. To account for any shift from the initial position, the displacement amplitude is calculated as half the difference between the maximum and minimum displacement peaks over the selected interval.

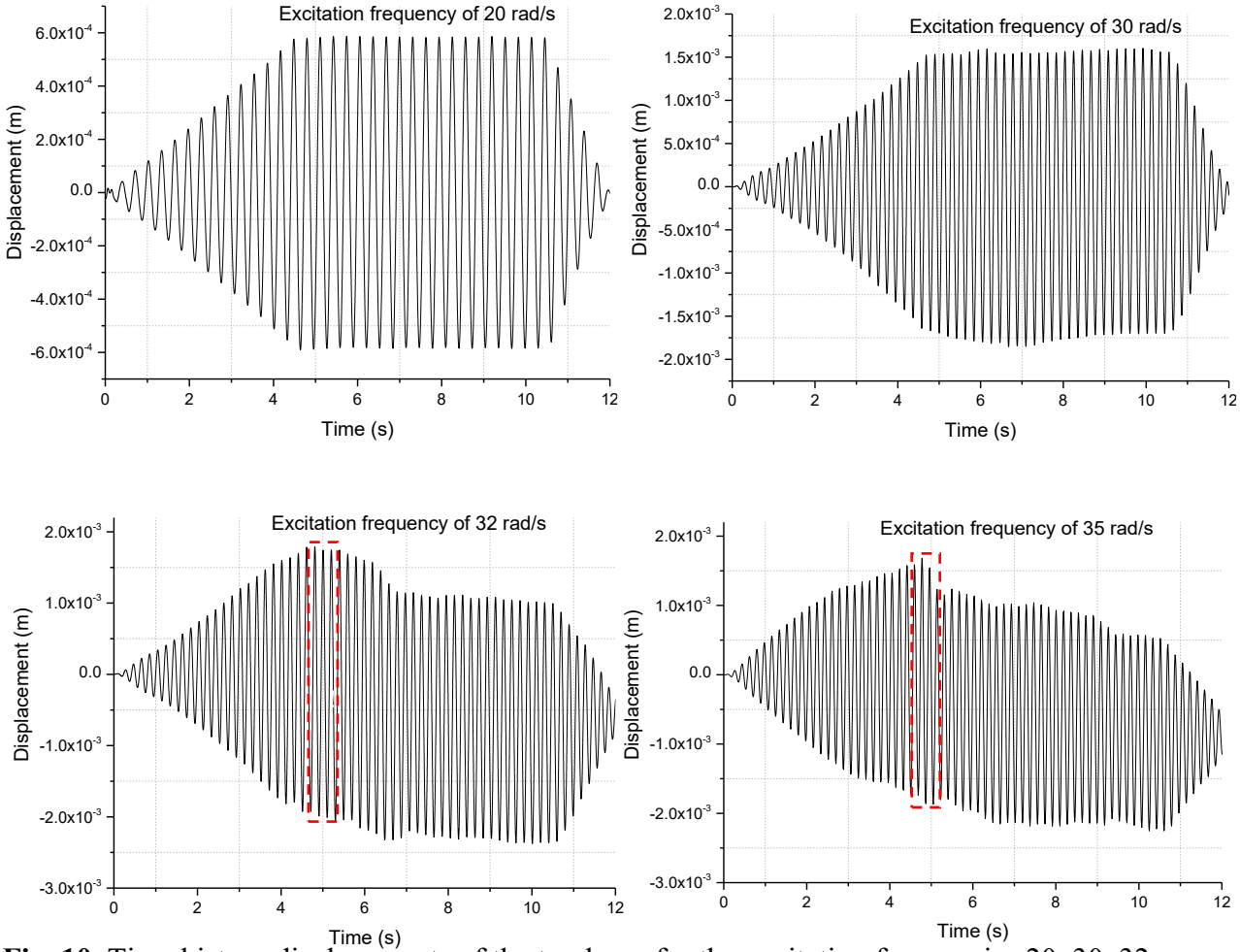
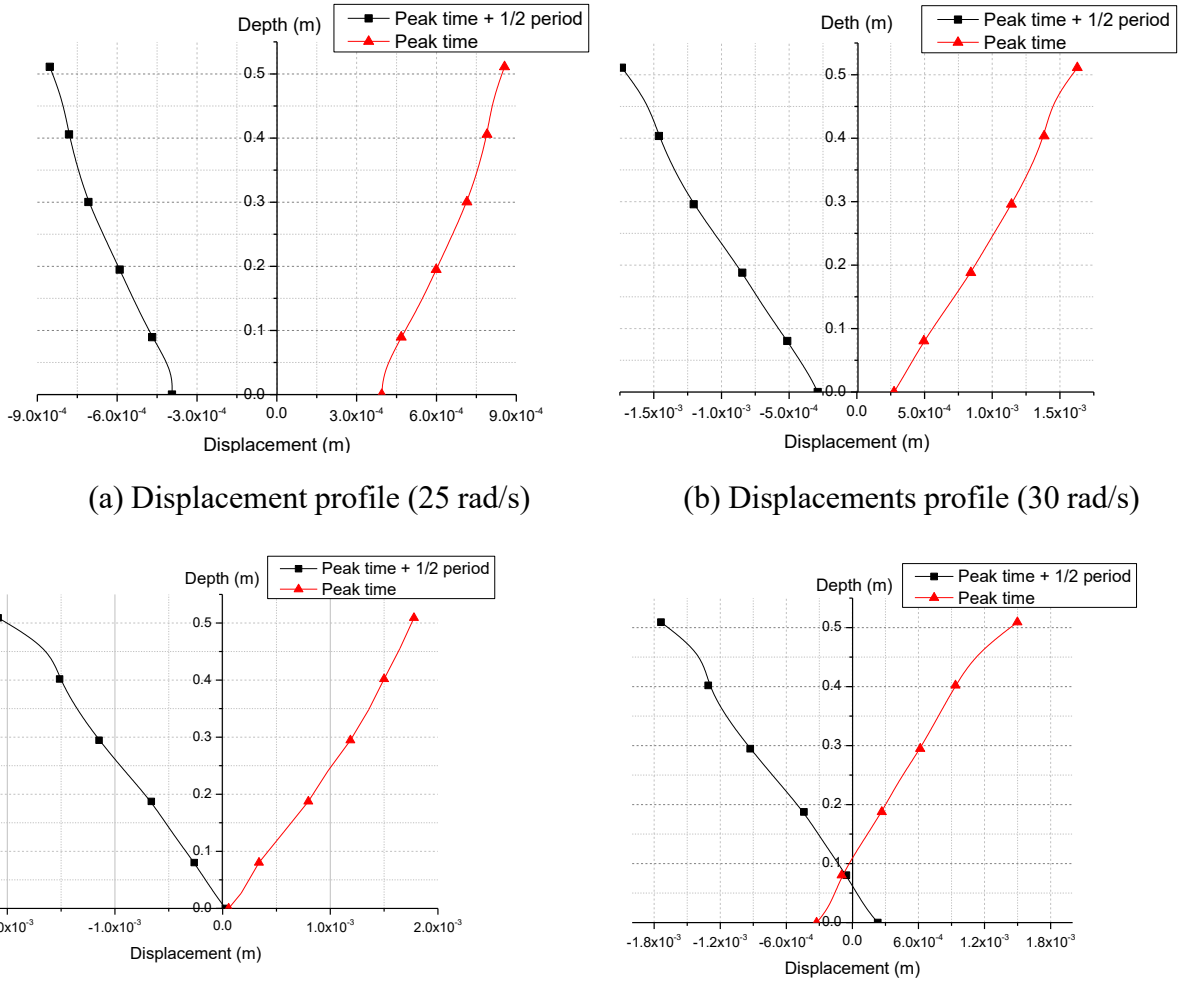


Fig. 10. Time history displacements of the top layer for the excitation frequencies 20, 30, 32 and 35 *rad/s*. Excitation amplitude $u_0 = 4x10^{-4}m$.

Figure 11 presents the displacement profiles (deposit deformation shapes) at the positive and subsequent negative displacement peaks during steady-state vibration. It can be noted that for frequencies up to 30 *rad/s*, the displacement profiles exhibit the first-mode shape. At 32 *rad/s*, a zero-displacement node appears at the base and rises at 35 *rad/s*, indicating that the first resonance is reached and exceeded. Thus, for the considered excitation amplitude ($u_0 = 4x10^{-4}m$), the first resonance frequency is approximately 32 *rad/s*.



(a) Displacement profile (25 rad/s)

(b) Displacements profile (30 rad/s)

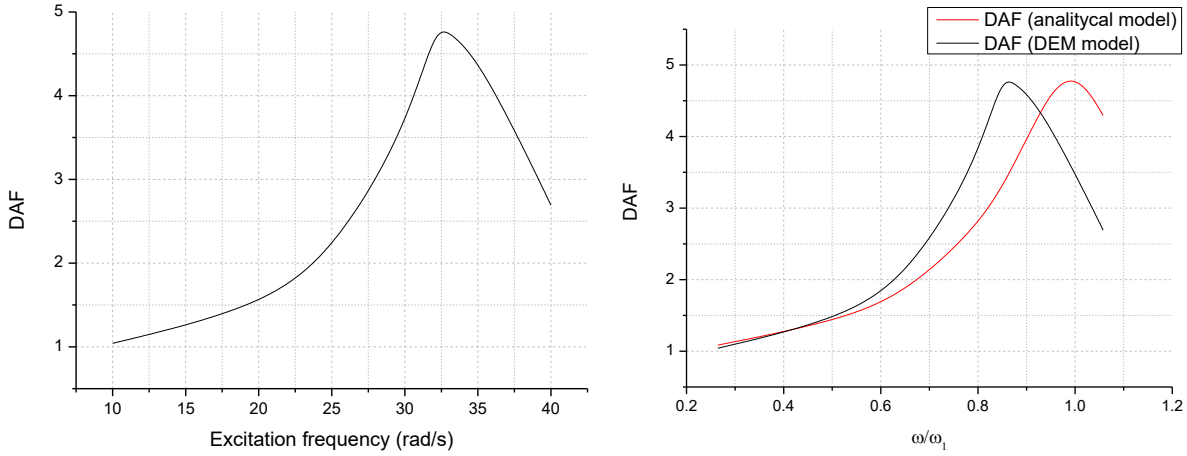
(c) Displacement profile (32 rad/s)

(d) Displacement profile (35 rad/s)

Fig. 11. Displacements profiles for different excitation frequencies. Excitation amplitude $u_0 = 4x10^{-4}m$.

We define in the following the dynamic amplification factor (*DAF*) at the top layer in the steady state vibration phase as: $DAF = \frac{u_s}{u_0}$, where u_s denotes the displacement amplitude at the top layer (surface layer) and u_0 is the displacement amplitude at the bedrock (excitation). In order to show the evolution of the amplification with frequency, the *DAF* is represented in Fig. 12a in terms of the excitation frequency. This figure shows a *DAF* evolution similar to that of an elastic deposit subjected to harmonic base excitation: it increases with frequency up to resonance, then decreases. The resonance frequency being approximately 32 rad/s, is in good agreement with the displacement profiles in Fig. 11. For comparison with the analytical solution, Figure 12b shows the frequency-dependent *DAF* obtained numerically and analytically. The analytical solution uses the numerical deposit parameters, $h = 0.54\ m$ and $\omega_1 = 37.82\ rad/s$, with the damping ratio adjusted to match the numerical resonance peak

($DAF_{max} = 4.75$). From the equation $DAF_{max} \approx \frac{2}{\pi\xi}$, this gives $\xi = 13.4\%$. In this figure, the excitation frequencies are normalized by the model's fundamental frequency. The numerical and analytical *DAF*s show very similar trends, although the numerical resonance frequency is about 13% lower, mainly due to shear-modulus degradation associated with increased shear strains near resonance.



(a) (b)

Fig. 12. Dynamic Amplification Factor vs. excitation frequency for excitation amplitude $u_0 = 4x10^{-4}m$, (a) *DAF* obtained from numerical modelling, (b) *DAF* comparison between numerical modelling and analytical solution.

To assess the influence of strain level on shear-modulus degradation, the analysis is repeated with an excitation amplitude of $4x10^{-6}m$, following the same procedure as for amplitude $4x10^{-4}m$. Therefore, the applied acceleration is reduced by a factor of 100, resulting in lower strains. No sliding of the surface layer is observed, and the motion remains harmonic and regular throughout the deposit. The displacement profiles indicate an increased resonance frequency of approximately 37.5 rad/s. The *DAF* evolution with excitation frequency is presented (Fig. 13), as in Figure 12b.

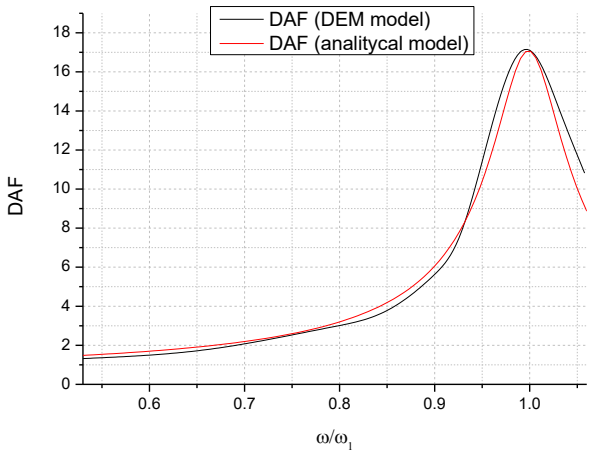


Fig. 13. Dynamic Amplification Factor vs. excitation frequency for excitation amplitude $u_0 = 4x10^{-6}m$, *DAF* obtained from numerical modelling and analytical solution.

This figure shows that the resonance frequency is very close to the fundamental frequency estimated in Section 5.2 ($\omega_1 = 37.82\ rad/s$). Moreover, the maximum dynamic amplification factor increases significantly ($DAF_{max} = 17.08$), corresponding to a damping ratio of approximately 3.73% in the viscoelastic model. These results confirm the well-established

concept in soil dynamics that increasing strain levels lead to shear-modulus degradation and increased damping.

5 Conclusion

This work presented a 2D discrete element analysis of shear-wave propagation in a sand deposit subjected to harmonic base excitation. The model incorporates viscoelastic contact forces, friction, and rolling resistance, with a free surface and periodic lateral boundaries. The simulations qualitatively reproduced key features of deposit vibration, including the displacement profiles and large motions near resonance. Quantitatively, the fundamental frequency was first determined from low-amplitude free vibrations. The frequency-response analysis showed that the Dynamic Amplification Factor (*DAF*) increases from unity at low frequencies, reaches a maximum at resonance, and then decreases. The resonance frequency was found to be close to the fundamental frequency at low excitation amplitudes but decreased as the amplitude increased. This shift is mainly attributed to shear-modulus degradation associated with increasing shear strains.

References

1. J. F. Peters, M. Muthuswamy (2005), Characterization of force chains in granular material, Phys. Rev. E 72, 041307. https://doi.org/10.1103/PhysRevE.72.041307
2. Natasha Zamani, Usama El Shamy (2011), Analysis of wave propagation in dry granular soils using DEM simulations. Acta Geotechnica (2011) 6:167–182. https://doi.org/10.1007/s11440-011-0142-7
3. Z. Ning, A. Khoubani, T.M. Evans (2015), Shear wave propagation in granular assemblies, Computers and Geotechnics 69 (2015) 615–626. https://doi.org/10.1016/j.compgeo.2015.07.004
4. J. O'Donovan and al (2016), Micromechanics of seismic wave propagation in granular materials, Granular Matter (2016) 18:56. https://doi.org/10.1007/s10035-015-0599-4
5. Longlong Fu, Shunhua Zhou et all (2023), Characterizing dynamic load propagation in cohesionless granular packing using force chain, Particuology 81 (2023) 135-148. https://doi.org/10.1016/j.partic.2023.01.007.
6. Mingjin Jiang, Akiyoshi Kamura, Motoki Kazama (2022), Numerical study on liquefaction characteristics of granular materials under Rayleigh-wave strain conditions using 3D DEM, soils and Foundations 62 (2022) 101176. https://doi.org/10.1016/j.sandf.2022.101176
7. Cundall PA, Strack ODL (1979) A discrete numerical model for granular assemblies. Géotechnique 29(1):47–65. https://doi.org/10.1680/geot.1979.29.1.47
8. Khellaf, A., Mansouri, M. (2024). Development of the stick-slip friction model for discrete elements modeling. Technology Audit and Production Reserves, 4 (1 (78)), 17–25. https://doi.org/10.15587/2706-5448.2024.310428
9. Verruijt, A. (2009). An introduction to soil dynamics (Vol. 24). Springer Science & Business Media.

Author Contribution Statement

- *Conceptualization:* Mouloud MANSOURI
- *Methodology:* Mouloud MANSOURI
- *Investigation:* Said DERBANE, Mouloud MANSOURI
- *Writing – Original Draft:* Mouloud MANSOURI
- *Writing – Review & Editing:* Mouloud MANSOURI

List of Abbreviations

- **DEM** — Discrete Element Method
- **DAF** — Dynamic Amplification Factor

Publication Note
This paper was peer-reviewed, accepted for presentation, and included in the proceedings of the ACE2026 – International Conference on Advances in Civil Engineering, held on 12–14 October 2026 in Trabzon, Türkiye.

This paper may be cited as follows:
Mouloud MANSOURI and Said DERBANE, "A Discrete Element Modeling of the Vibration of a Horizontal Granular Deposit Harmonically Excited at the Base," in Proceedings of the ACE2026 – International Conference on Advances in Civil Engineering, Trabzon, Türkiye, 12–14 October 2026.

In-Situ Behavior of Massive Twin Pneumatic Caissons During Close-Proximity Simultaneous Sinking: A Case Study

Feyzullah Gulsen[1], Makoto Tone[2], Naoya Watanabe[3] and Hideo Komine[4]

[1] TODA Corporation, Civil Engineering Department, Tokyo, Japan, feyzullah.gulsen@toda.co.jp
[2] TODA Corporation, Civil Engineering Department, Tokyo, Japan, makoto.tone@toda.co.jp
[3] TODA Corporation, Civil Engineering Tokyo Metropolitan Branch, Tokyo, Japan, naoya.watanabe@toda.co.jp
[4] ORCID: 0009-0002-9304-7205, Waseda University, Department of Civil and Environmental Engineering, Tokyo, Japan, hkomine@waseda.jp

Abstract. The increasing frequency of severe urban flooding necessitates the development of large-scale flood-regulation infrastructures. This paper presents a case study on the Johoku Chuo Park Regulation Pond project in Tokyo, which involves the simultaneous sinking of twin massive pneumatic caissons, each 33.4 m in width, 80.3 m in length, and 35.3 m in depth. The primary geotechnical challenge of this operation is the extremely narrow 2.0 m clearance between the structures, which induces highly confined and complex soil-structure interactions. To evaluate these proximity-induced behaviors, a real-time in-situ monitoring system was deployed to analyze peripheral skin friction, lateral wall reactions, and caissons sinking records. Field measurements revealed that strict synchronization successfully limited the maximum elevation difference between the caissons to 528 mm, remaining safely below the 1.0 m structural safety threshold. However, in deeper dense strata, localized skin friction and lateral wall reactions near the cutting edge exceeded standard empirical criteria by over 200% due to shear-induced dilatancy and particle interlocking. Furthermore, the results demonstrated the effectiveness of the physical friction cut in reducing these lateral stresses. Additionally, the integration of unmanned excavation and continuous data-driven posture control ensured a safe and stable sinking process. Ultimately, this study is expected to serve as a definitive technical reference for future massive caisson operations in urban environments.

Keywords: Pneumatic Caissons; Caisson Sinking; Massive Underground Structures; Real-Time Monitoring.

1 Introduction

The pneumatic caisson method (PCM) is a deep foundation technique that uses compressed air in a sealed working chamber to prevent groundwater inflow, enabling dry excavation as the caisson gradually sinks under its own weight. Invented and patented by British engineer Thomas Cochrane in 1830, the method was first deployed by French engineers in 1839 to sink the Granges Shaft at the Chalonnes-sur-Loire coal mines in France [1], [2].

PCM was introduced to Japan in 1899 with diving-type caissons for harbor reclamation at Yokohama Port, followed by its first structural bridge application in 1909 for the Amnokgang (Yalu) River Railway Bridge. Following the 1923 Great Kanto Earthquake, PCM was systematically adopted for Tokyo's urban reconstruction. Starting in 1924 with major Sumida River crossings—such as the Eitai, Kiyosu, Kuramae, and Kototoi bridges —this effort

pioneered subsequent standardization for challenging fluvial foundations across the Kisogawa and Ibigawa rivers in 1926 [3].

Throughout the late 20th and early 21st centuries, Japanese engineers modernized technology to address severe seismicity, complex soil profiles, and strict safety standards, transforming labor-intensive operations into highly automated processes. The efficient mechanization of pneumatic caissons began in 1971 with overhead-traveling caisson excavators during construction of the Hanshin Expressway Minato Bridge. To eliminate the risk of decompression sickness, the industry pioneered unmanned excavation systems. This evolution progressed from pressurized capsules at the Meiko-West Bridge in 1981 to the world's first fully unmanned pneumatic caisson system at the Kuramae Pump Station in 1990 [4].

Over the past three decades, Japan has continuously expanded the scale and depth of caisson capabilities to accommodate complex urban infrastructure [5]. Fig. 1 illustrates notable contemporary achievements in Japanese pneumatic caisson engineering. Prominent examples include the Kamioyamada Emergency Exit Shaft for the Chuo Shinkansen, which represents one of the deepest applications, reaching a sinking depth of approximately 110 m with a base area of around 1,300 m²; the Higashi Ogu Purification Center (Nishi-Nippori Pump Station), which holds the record for the largest pneumatic caisson footprint at 4,837 m², sunk to a depth of 43.9 m; and the Kajigaya Emergency Exit Shaft, successfully constructed to a depth of 79 m under a hyperbaric pressure of 0.73 MPa [6], [7].

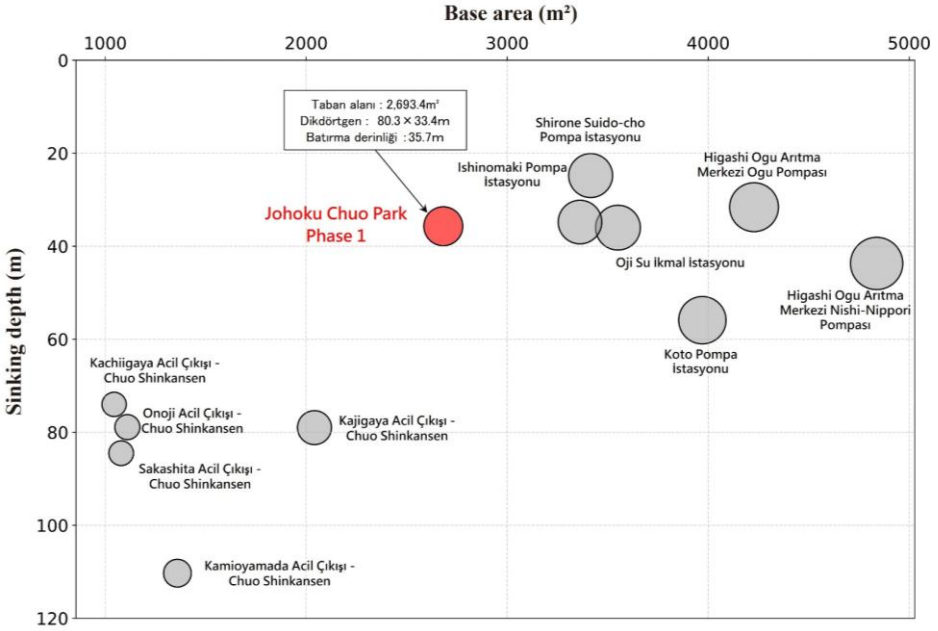


Fig. 1. Base area versus sinking depth of major pneumatic caissons in Japan.

In densely populated regions like Tokyo, severe urban flooding requires large-scale subterranean regulation reservoirs. The PCM has become indispensable for these structures when space constraints prevent conventional open-cut excavations. A prominent example is the Johoku Chuo Park Regulation Pond project. This project involves the simultaneous sinking of twin massive pneumatic caissons. The combined base area of these twin structures is approximately 5,386.8 m², making it the largest pneumatic caisson area in Japan. The primary challenge of this operation is the extremely narrow 2.0 m clearance separating the caissons (Fig. 2). In this context, this paper investigates their sinking behavior using an extensive real-time monitoring network. The study analyzes in situ data on peripheral skin friction, lateral wall reactions, and elevation differences between the caissons. Ultimately, this case study aims to provide a technical reference for future massive caisson sinking operations in confined urban environments.

2 Project Description

The Johoku Chuo Park Regulation Pond is a large-scale subterranean flood mitigation facility along the Shakujii River in Tokyo, designed to withstand intense precipitation events up to 75 mm/h. As shown in Fig. 2, it consists of two adjacent underground structures (Caisson No. 1 and Caisson No. 2) linked by a central connection. Excess river floodwater flows directly into the pond through a dedicated intake structure and is discharged back into the channel once water levels return to normal. The caisson sinking operations commenced from a construction base elevation of A.P. +23.50 m and concluded at a final cutting-edge depth of A.P. −11.8 m. The caisson's top slab will subsequently be covered with a backfill to restore the park surface at a final ground elevation of A.P. +27.0 m.

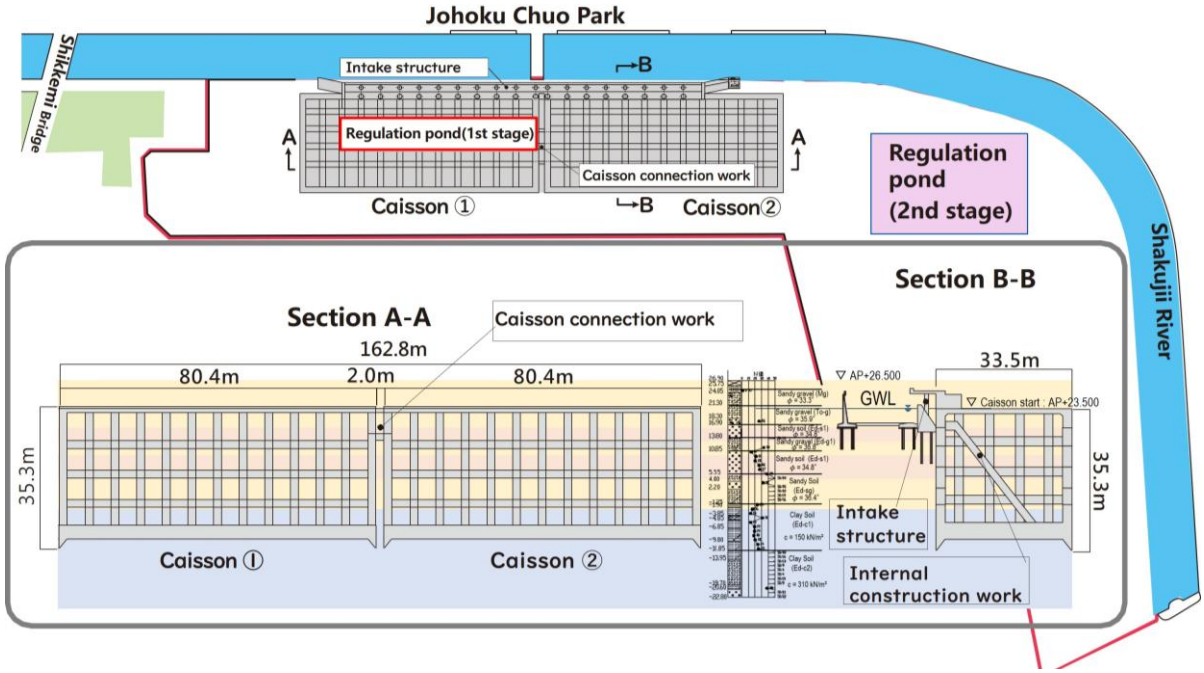


Fig. 2. Plan view and cross-sections of the Johoku Chuo Park Regulation Pond twin caissons.

The primary substructure comprises twin massive pneumatic caissons, each with an excavation base area of 2,693.4 m². Structurally, each rectangular caisson is 33.5 m wide, 80.4 m long, and 35.3 m high. To accommodate massive structural loads, the internal framework is strengthened with a 2.0 m by 2.0 m grid-like arrangement of structural columns and beams. The most critical geotechnical constraint is the extreme proximity of the twin caissons, separated by only 2.0 m. This configuration induces highly confined soil-structure interactions, necessitating strict real-time monitoring and posture control to prevent differential settlement during simultaneous sinking.

2.1 Geotechnical Condition

The project site consists of Late to Early Pleistocene alluvial and diluvial deposits. The natural ground surface elevation is A.P. +26.50 m, and the design groundwater level is A.P. +23.50 m. As shown in Figs. 2 and 6, caisson operations commenced from a construction base elevation of A.P. +23.50 m. The upper profile contains a thin backfill layer (B) and a soft cohesive clay layer (Lc). This soft clay extends down to A.P. +24.05 m and exhibits a low cohesion, c = 11.8 kN/m².

Beneath the surface layer, the stratigraphy transitions into dense granular formations. These include Musashino Gravel (Mg), Tokyo Gravel (To-g), and upper Edogawa Group strata (Ed-

s1, Ed-g1, Ed-sg). These intermediate layers exhibit Standard Penetration Test (SPT) N values ranging from 16 to over 50. Their internal friction angles (ϕ) range between 33.3° and 36.8°.

The bearing layer is the highly consolidated Edogawa silty clay (Ed-c1) with a cohesion of c = 150.0 kN/m². The caisson cutting edges for both caissons were terminated at a depth of A.P. -11.80 m. Directly below this lies the overconsolidated, hard Edogawa Clay (Ed-c2). Starting at A.P. -11.85 m, it has significantly high cohesion of c = 310 kN/m². additionally, an at-rest earth pressure coefficient (K_0) of 0.50 was adopted for all identified strata in structural and lateral stability evaluations.

2.2 Description of the Problem

The primary geotechnical and structural challenge arises when twin caissons sink simultaneously at different depths within a narrow 2.0 m clearance. As illustrated in the geotechnical interaction model in Fig. 3(a), an elevation difference (ΔH) between the leading caisson (No. 1) and trailing caisson (No. 2) causes the ground bearing pressure (Q) beneath the trailing cutting edge to act as a surcharge on the confined soil column. This bearing pressure is defined as $Q = \Sigma(\text{Downward Forces}) - \Sigma(\text{Upward Forces})$. The surcharge transmits an asymmetric horizontal load (P_H) against the leading caisson shaft.

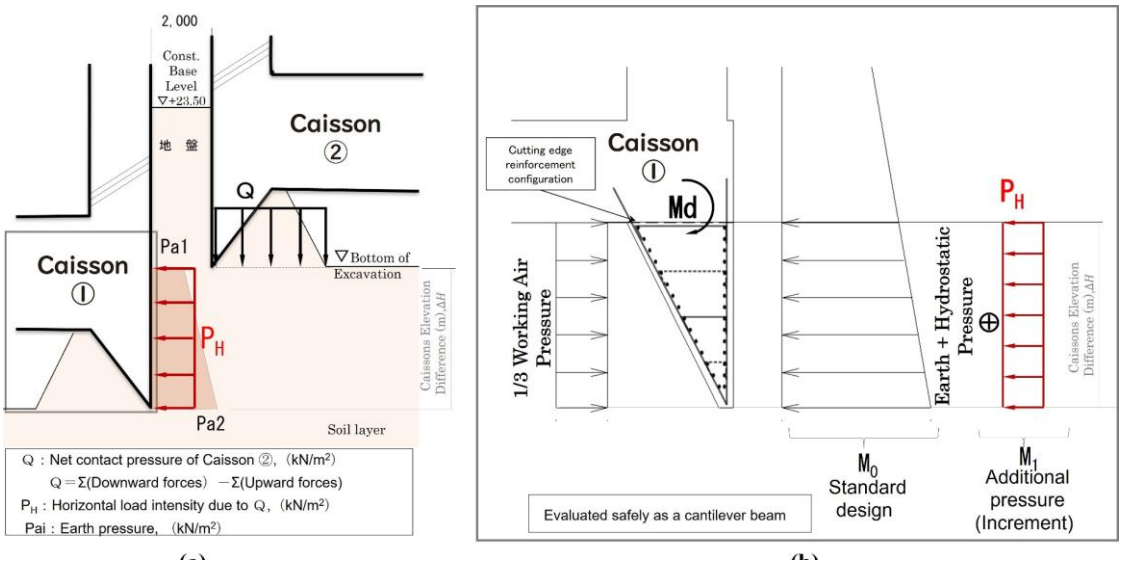


Fig. 3. Proximity-induced stress evaluation: (a) geotechnical interaction model; (b) structural cantilever model.

To evaluate the structural reliability of the reinforced concrete cutting edge under these eccentric forces, a cantilever beam model fixed at the base was used in accordance with the Japan Road Association (JRA) specifications (Fig. 3(b)) [7]. The standards suggest setting the internal air pressure to one-third of its working pressure, acting in the opposite direction to the earth pressure. Under standard conditions, active earth pressure P_a and hydrostatic pressure (P_w) generate a base bending moment (M_0). The additional thrust (P_H) induced by ΔH generates an incremental moment (M_1). To prevent structural cracking or failure, the combined design moment ($\Sigma M = M_0 + M_1$) must maintain tensile stresses in the reinforcement below the short-term allowable limit of 240 N/mm² for SD345 steel.

Analyses were conducted for varying elevation differences (ΔH) between the caissons to establish safe construction tolerances (Fig. 4). The structural limit value was determined as 622.6 kN/m², corresponding to the allowable rebar tensile strength. Calculations demonstrate that maintaining $\Delta H \leq 1.0$ m restricts the maximum horizontal load intensity on the leading caisson to 605 kN/m². Because this value remains safely below the structural limit of 622.6

kN/m², a maximum allowable elevation difference (ΔH) of 1.0 m was established as the primary threshold for construction.

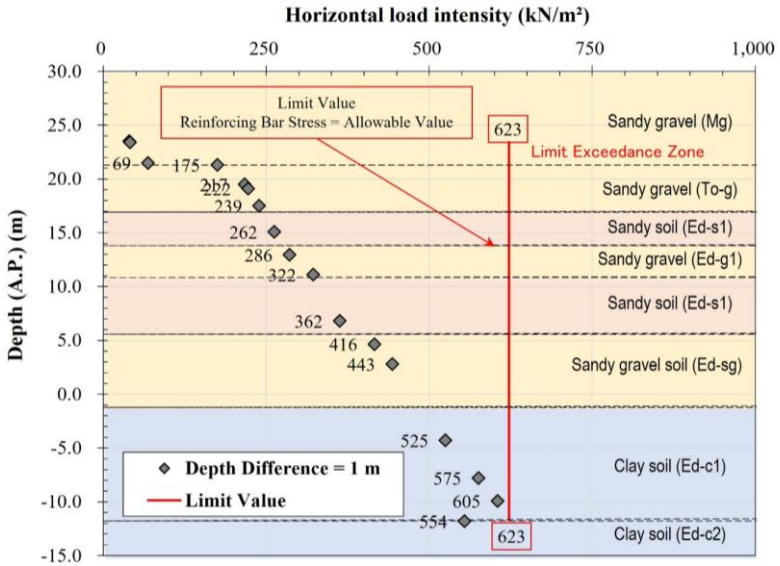


Fig. 4. Horizontal load intensity versus depth for the limit value of 1.0 m elevation difference between caissons.

3 Construction Progress

The sinking of twin caissons commenced on March 18, 2021, with an initial opening phase comprising 644.0 m³ of manual and 5,010.3 m³ of mechanical excavation. Full-capacity mechanized excavation began on June 30, 2021, utilizing 18 unmanned overhead traveling excavators within the pressurized working chamber (Fig. 5), bringing the total excavated volume to 100,731.3 m³ per caisson. Caissons No. 1 and No. 2 reached their final design elevation of A.P. -11.8 m on October 5 and October 6, 2022, respectively. Final working chamber air pressures were recorded at 0.330 MPa for Caisson No. 1 and 0.315 MPa for No. 2.

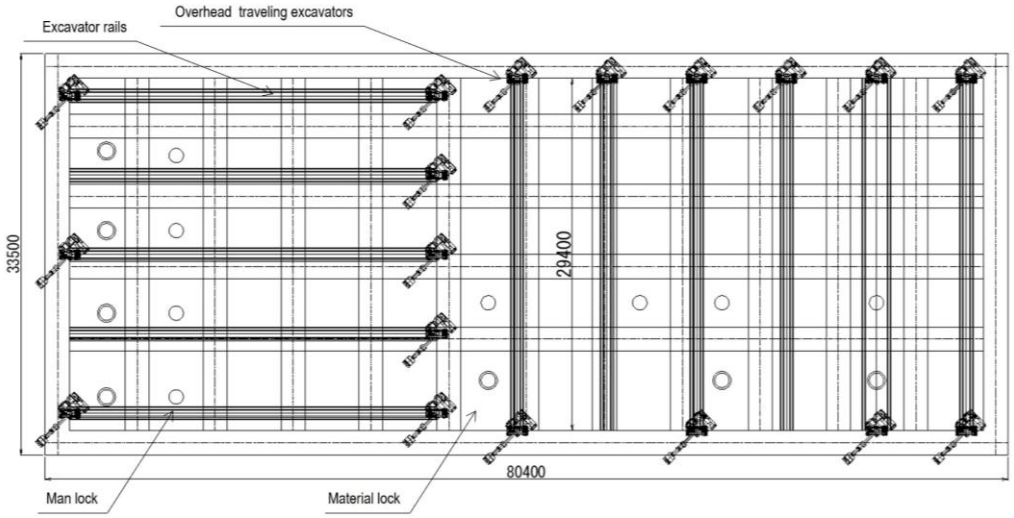


Fig. 5. Layout of unmanned overhead traveling excavators.

To overcome sinking resistance in the dense strata, surcharge water loading was applied from Lot 6 to Lot 9 to increase the downward driving force. Additionally, approximately 402 m³ of bentonite lubricant was injected to reduce peripheral skin friction. Upon completion of the sinking process, 131.5 m³ of contact grouting was injected around the cutting edges to fill peripheral voids and prevent post-construction settlement.

4 Real-Time In-Situ Instrumentation

To evaluate geotechnical forces and ensure structural safety, each caisson was equipped with an array of 58 sensors. As shown in Fig. 6, Lot 1 (1.856 m above the cutting edge) includes 18 vertical reaction gauges, alongside peripheral skin-friction, lateral wall reaction, and pore-water pressure sensors distributed at six horizontal locations. Lot 4 (14.50 m above the cutting edge) has also friction, wall reaction, and pore-water pressure sensors. Lot 7 (26.70 m above the cutting edge) is also instrumented with lateral wall reaction gauges to monitor shallow horizontal pressures. Moreover, laser distance meters and inclinometers continuously tracked the caisson's vertical alignment. This real-time data acquisition enabled immediate operational adjustments, ensuring sinking stability and preventing differential settlement.

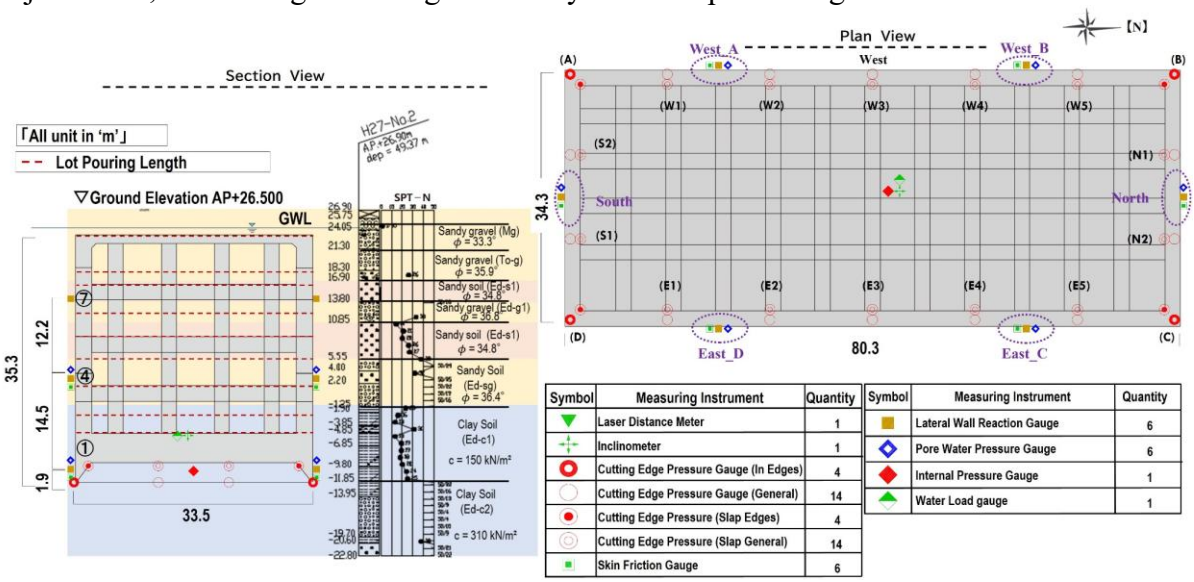


Fig. 6. Instrumentation layout.

5 Measurement Results and Analysis

This section analyzes in-situ data on caisson sinking records, peripheral skin friction, and lateral wall reactions.

5.1 Caisson Sinking Records

Fig. 7 illustrates the sinking progression of the twin caissons. Fig. 7(a) plots the sinking depth over the 21-month construction period against the soil profile. Complementing this, Fig. 7(b) displays the caisson depth on the horizontal axis, the vertical elevation difference on the left vertical axis, and the depth-dependent sinking rates (mm/day) on the right vertical axis. To ensure data accuracy, the sinking rate for each stratum was calculated by averaging the daily depth changes exclusively on active construction days (non-working days were excluded).

The recorded data confirms strict adherence to the pre-established 1.0 m maximum vertical difference criterion. A maximum difference of 528 mm was recorded between the caissons on May 24, 2022, within the dense Ed-sg stratum, successfully preventing structural overstress at the concrete cutting edges. As shown in Fig. 7(b), the sinking rate fluctuated with geotechnical conditions and operational phases. The maximum sinking rate peaked at 136.1 mm/day in the intermediate Ed-s1 sandy layer, while the slowest sinking occurred in the initial Musashino Gravel (Mg), which may have been due to manual excavation and partial equipment usage. Once all 18 overhead excavators became fully operational, progress accelerated. Geotechnically, correlating sinking rates directly to specific soil strata proved difficult. Although the Ed-s1, Ed-g1, and Ed-sg layers have similar internal friction angles (ϕ), their progress behaviors differ significantly, highlighting the critical need for continuous real-time monitoring.

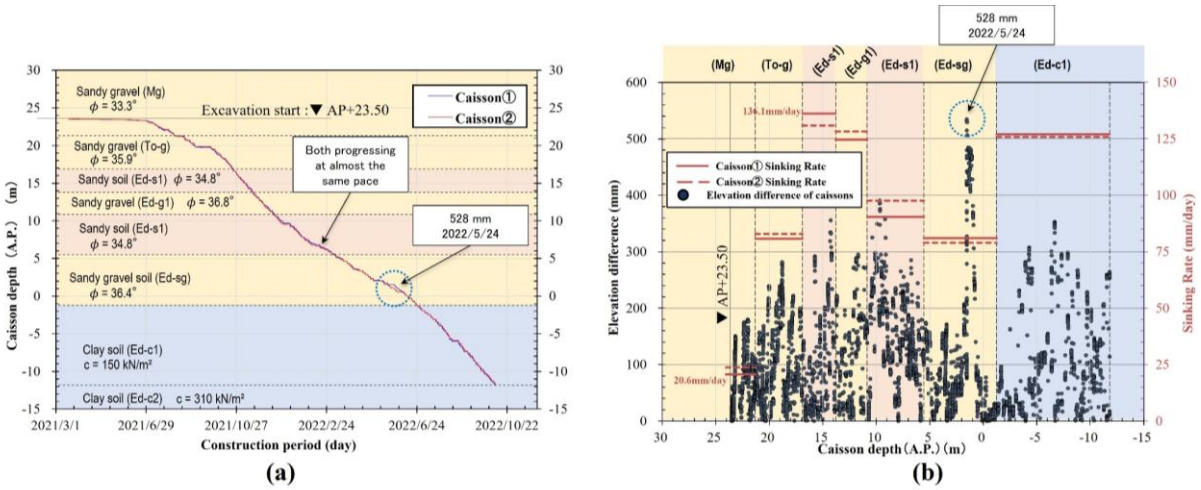
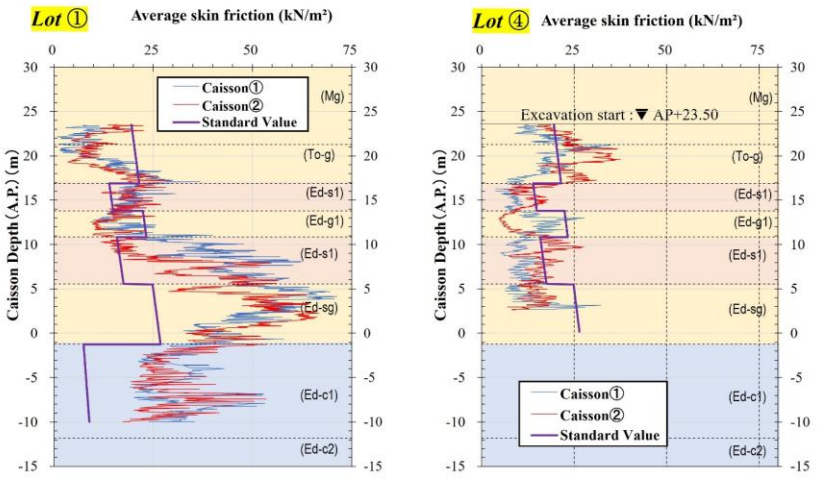


Fig. 7. Caisson sinking records: (a) depth progression over time; (b) caisson elevation difference and sinking rates relative to depth.

5.2 Peripheral Skin Friction Stress

Fig. 8 shows the depth-dependent distribution of average peripheral skin friction at Lots 1 and 4, compared with the Japan Road Association (JRA) standard criteria [7]. In-situ measurements at Lot 1 revealed significant deviations from the suggested standards. While friction in the upper granular layers remained below the standard value, it surged dramatically in the deeper, denser strata, exceeding the JRA empirical criteria by over 200%. This friction spike may be attributed to shear-induced dilatancy of dense sand and gravel particles under high confining pressures. The lateral constraint imposed by the narrow 2.0 m soil column amplifies this volumetric expansion, leading to localized surges in effective normal stresses and particle interlocking.



Average Skin Friction per Layer for Lot 1		
Soil Type	Caisson ①	Caisson ②
Sandy gravel (Mg)	7.14	9.50
Sandy gravel (To-g)	14.40	13.67
Sandy soil (Ed-s1)	19.47	22.63
Sandy gravel (Ed-g1)	19.00	15.95
Sandy soil (Ed-s1)	43.28	31.23
Sandy Soil (Ed-sg)	54.90	51.56
Clay (Ed-c1)	32.33	30.49

Average Skin Friction per Layer for Lot 4		
Soil Type	Caisson ①	Caisson ②
Sandy gravel (Mg)	18.52	22.21
Sandy gravel (To-g)	18.67	27.04
Sandy soil (Ed-s1)	8.86	14.35
Sandy gravel (Ed-g1)	17.56	8.23
Sandy soil (Ed-s1)	10.73	16.15
Sandy Soil (Ed-sg)	10.89	13.27
Clay (Ed-c1)	–	–

Fig. 8. Depth-dependent distribution of average in-situ peripheral skin friction compared with JRA standard values at Lots 1 and Lot 4.

Conversely, skin friction measured at Lot 4 exhibited markedly different behavior. In the upper granular formations, the friction values aligned closely with the standard criteria, likely because the prior sinking of Caisson No. 1 compacted the initially loose soil, increasing the lateral stiffness and normal stresses acting on Caisson No. 2. However, within the deeper layers, friction at Lot 4 was three to four times lower than at Lot 1. This reduction provides clear empirical evidence of the 50 mm friction cut's effectiveness. By creating a physical overcut

void above the cutting edge, the friction cut successfully decoupled the upper concrete shaft from the surrounding soil matrix, reducing mobilized lateral normal stresses.

5.3 Lateral Wall Reactions and Compaction-Induced Stress Amplification

Fig. 9 presents the depth-dependent average lateral reactions at Lots 1, 4, and 7, evaluated against theoretical at-rest ($K_0 = 0.5$, purple line) and active earth pressures (green line). At the upper elevations (Lots 4 and 7), the recorded wall reactions generally remained under these theoretical limits. This data confirms that the physical friction cut successfully maintained lower wall reactions compared to Lot 1. Conversely, Lot 1 measurements near the cutting edge revealed significant stress concentrations. In the deeper Ed-s1 and Ed-sg strata, lateral pressures were approximately 1.5 to 2.0 times higher than standard values. While it might be argued that relatively rapid progress in these strata prevented consistent excavation and increased local deformations, the exact mechanism depends on numerous complex parameters; given these multiple unknowns, a definitive explanation remains elusive and requires further detailed analysis.

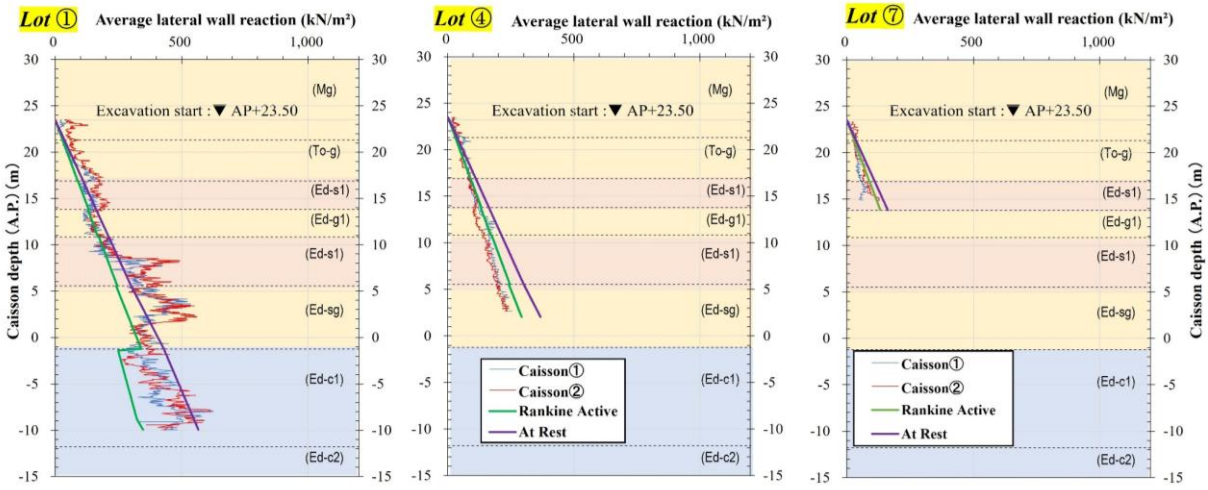


Fig. 9. Depth-dependent distribution of average in-situ lateral wall reactions at Lots 1, 4, and 7, compared with theoretical active and at-rest earth pressures.

Furthermore, comparative analysis revealed a clear "twin-caisson interaction" effect. Across all strata, Caisson No. 2 consistently experienced higher lateral wall reactions than Caisson No. 1. This discrepancy is especially pronounced in the upper granular formations; in the Musashino Gravel (Mg) and Tokyo Gravel (To-g) layers, average reactions for Caisson No. 2 were up to 2.3 times higher. The construction sequence might induce this: Caisson No. 1 was sunk slightly ahead, pre-compacting the loose granular soil confined within the gap. Consequently, Caisson No. 2 penetrated a pre-compacted, significantly stiffer soil matrix, which increased the horizontal normal stresses acting on its shaft.

Fig. 10 shows the spatial distribution of average skin friction and lateral wall reactions for each soil strata. Normalized data reveal an asymmetrical stress distribution, directly governed by twin-caisson interaction. Peak stress concentrations are consistently localized on the adjacent inner boundaries: the North face of Caisson No. 1 and the South face of Caisson No. 2. This stress amplification results from soil confinement and particle interlocking within the clearance gap. Additionally, sinking rates accelerated horizontal soil deformations and shear within this confined zone, inhibiting stress relaxation and further intensifying lateral loads on the adjacent caisson walls.

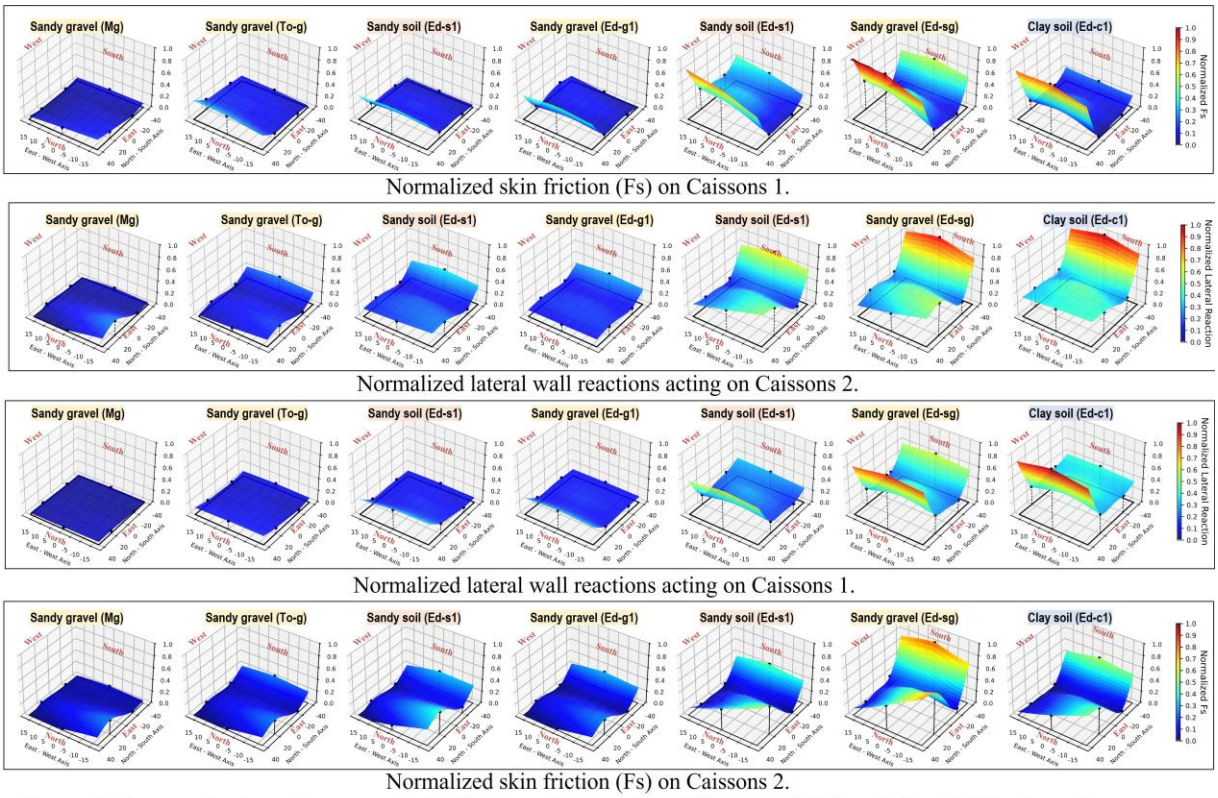


Fig. 10. Normalized skin friction (Fs) and lateral wall reactions act on Caissons 1 and 2 across different soils at Lot 1.

6 Conclusion

The simultaneous sinking of the twin massive pneumatic caissons at Johoku Chuo Park, separated by a narrow 2.0 m clearance, was successfully executed without structural damage. Based on comprehensive in-situ monitoring and geotechnical analyses, the following conclusions are drawn:

- Strict Posture Control: Real-time synchronization effectively limited the maximum depth difference (ΔH) between the twin caissons to 528 mm. This value remained well below the 1.0 m critical design threshold.
- Effectiveness of Friction Reduction: A 50 mm physical friction cut, combined with bentonite lubrication, successfully decoupled the upper concrete shafts from the surrounding soil. This was validated by the in-situ sensors at Lot 4, which recorded skin friction values three to four times lower than those at the cutting edge (Lot 1).
- Proximity-Induced Stress Amplification: In-situ data highlighted stress amplifications within the narrow 2.0 m gap. In deep, dense granular strata, peripheral skin friction and lateral wall reactions at Lot 1 exceeded standard theoretical values by up to 200% due to shear-induced dilatancy and particle interlocking.
- Leading vs. Trailing Caisson Interaction: An interaction effect was recorded based on the sinking sequence. The trailing caisson experienced lateral wall reactions up to 2.3 times higher than the leading caisson in the upper granular layers due to pre-compaction of the soil. Additionally, peak stress concentrations consistently localized on the inner-facing boundaries (the North face of Caisson No. 1 and the South face of Caisson No. 2).

As only standard design formulas proved insufficient to predict complex 3D soil-structure interaction behavior, this study once again highlights the critical importance of integrated real-time in-situ monitoring.

Acknowledgments
The authors wish to express their profound gratitude to the Tokyo Metropolitan Government Bureau of Finance and the engineering execution teams at TODA Corporation and Oriental Shiraishi Corporation for their dedication and technical excellence throughout the Johoku Chuo Park project.

References

1. Cushing, A.G., Sokol, N.K.: History of subaqueous tunneling in New York City. In: Proc., Rapid Excavation and Tunneling Conference (RETC), Society for Mining, Metallurgy, and Exploration (SME), Littleton, CO (2007).
2. West, G.: Innovation and the Rise of the Tunnelling Industry. Cambridge University Press, Cambridge, U.K. (1988).
3. Hirakawa, S.: Historical study of pneumatic caisson method in Japan (Part 2). In: Proc., 7th Annual Conf. on Historical Studies in Civil Engineering, Japan Society of Civil Engineers (JSCE), Tokyo, Japan, pp. 215–220 (1987) (in Japanese).
4. Shiraishi, S.: Unmanned excavation systems in pneumatic caissons. Developments in Geotechnical Engineering, 409–418 (2021). https://doi.org/10.1201/9781003211013-35
5. Gulsen, F., Tone, M.: In-situ monitoring and sinking behavior of a 102 m giant caisson: A case study of the Shirokita open caisson. In: Mitani, Koyama (eds.) Proc., 14th Asian Rock Mechanics Symp. (ARMS14): Rock Mechanics for the Next Generation-Innovations, Sustainability and Resilience, Japanese Society for Rock Mechanics (2026).
6. Japan Pneumatic Caisson Association: Construction records. Japan Pneumatic Caisson Association, https://www.pneumatic.gr.jp/construction/, last accessed 2026/08/10.
7. Japan Road Association: Specifications for Highway Bridges, Part IV: Substructures. Japan Road Association, Tokyo, Japan (2012) (in Japanese).

Author Contribution Statement

- *Conceptualization:* Gulsen, F., Tone, M., and Komine, H.
- *Methodology:* Gulsen, F., Tone, M., and Komine, H.
- *Investigation:* Gulsen, F. and Watanabe, N.
- *Writing – Original Draft:* Gulsen, F.
- *Writing – Review & Editing:* Tone, M., Watanabe, N., and Komine, H.

List of Abbreviations

- **PCM** — Pneumatic Caisson Method
- **A.P.** — Arakawa Peil (Standard Elevation Datum)
- **SPT** — Standard Penetration Test
- **GWL —** Groundwater Level
- **JRA —** Japan Road Association

Publication Note
This paper was peer-reviewed, accepted for presentation, and included in the proceedings of the ACE2026 – International Conference on Advances in Civil Engineering, held on 12–14 October 2026 in Trabzon, Türkiye.

This paper may be cited as follows:
Gulsen F., Tone M., Watanabe N., Komine H., "In-Situ Behavior of Massive Twin Pneumatic Caissons During Close-Proximity Simultaneous Sinking: A Case Study," in Proceedings of the ACE2026 – International Conference on Advances in Civil Engineering, Trabzon, Türkiye, 12–14 October 2026.

Numerical Investigation of Seismic Behavior of Piled Raft Foundation (PRF) and Unconnected Piled Raft Foundation (UPRF) Systems

Burak AKÇAY[1], Osman SİVRİKAYA[1a], Esin ERTÜRK ATMACA[1b], Berk DİKMENOĞLU[1c], Murat GÜNAYDIN[1d], M. Kubilay KELEŞOĞLU[2], Esra Ece BAYAT[3], Fezayil SUNCA[1e], Ertuğrul TACİROĞLU[4], Kemal Önder ÇETİN[5], Ahmet Can ALTUNIŞIK[1f]

[1] 0000-0002-5677-5425, Karadeniz Technical University, Civil Engineering Department, Trabzon, Türkiye, burak.akcay@ktu.edu.tr

[1a] 0000-0001-6513-4526, Karadeniz Technical University, Civil Engineering Department, Trabzon, Türkiye, osivrikaya@ktu.edu.tr

[1b] 0000-0003-4053-0877, Karadeniz Technical University, Civil Engineering Department, Trabzon, Türkiye, esinerturk@ktu.edu.tr

[1c] 0000-0002-9695-441X, Karadeniz Technical University, Civil Engineering Department, Trabzon, Türkiye, berkdikmenoglu@gmail.com

[1d] 0000-0002-8549-2985, Karadeniz Technical University, Civil Engineering Department, Trabzon, Türkiye, muratgunaydin@ktu.edu.tr

[2] 0000-0003-1721-7946, Istanbul Cerrahpasa University, Civil Engineering Department, Istanbul, Türkiye, kelesoglu@iuc.edu.tr

[3] 0000-0002-5774-4911, Istanbul Technical University, Civil Engineering Department, Istanbul, Türkiye, ebayat@itu.edu.tr

[1e] 0000-0003-3033-6237, Karadeniz Technical University, Civil Engineering Department, Trabzon, Türkiye, fezayilsunca@ktu.edu.tr

[4] 0000-0001-9618-1210, University of California, Civil and Environmental Engineering Department, Los Angeles, USA, etacir@ucla.edu

[5] 0000-0003-0540-2247, Middle East Technical University, Civil Engineering Department, Ankara, Türkiye, ocetin@metu.edu.tr

[1f] 0000-0002-2638-2903, Karadeniz Technical University, Civil Engineering Department, Trabzon, Türkiye, ahmetcan@ktu.edu.tr

Abstract. Since a large part of Türkiye is located on active seismic zones, safely assessing the behavior of structures under seismic loads is essential. In addition, increasing population and urbanization make construction on weak or problematic soils inevitable, highlighting the need for safe and cost-effective foundation systems. Piled Raft Foundation (PRF) systems are widely used, particularly for high-rise buildings. However, seismic ground motion is transmitted through the piles and raft to the superstructure, exposing the system to kinematic interaction, while inertial forces generated by the superstructure induce additional stresses in the piles. Due to the rigid pile-raft connection, large shear forces and bending moments may develop, particularly at the pile-raft interface. Therefore, the Unconnected Piled Raft Foundation (UPRF), which eliminates the rigid connection and incorporates a cushion layer between the piles and raft, has emerged as an alternative to conventional PRF systems. The cushion layer limits the transfer of shear forces and moments, reduces pile-raft interaction, and contributes to damping earthquake effects. In this study, 1/10-scale laboratory experiments were analyzed using the finite element method (FEM) with PLAXIS 2D. The UPRF system was compared with a traditional PRF system under seismic loading, and its seismic energy damping performance was evaluated in terms of the soil and piles. Depth-dependent horizontal pile displacements, cross-section forces, and horizontal

accelerations in the soil were determined under dynamic loading to evaluate this performance.

Keywords: Structure-pile-soil interaction, Traditional piled raft foundation, Unconnected piled raft foundation, Numerical analysis

1 Introduction

Turkey is highly vulnerable to earthquakes due to its geographic and geological characteristics, and major earthquakes have caused significant loss of life and property. Although earthquake-resistant structural design is essential for mitigating earthquake-induced losses, ground conditions and soil-structure interaction also play a critical role in determining structural performance. Soil-structure interaction describes the mutual interaction between a structure and the surrounding soil under seismic loading. In weak soil conditions, shallow foundations may be inadequate to safely transfer superstructure loads to the ground, making deep foundation systems a common alternative. Among these, piled raft foundation (PRF) systems are widely employed due to their ability to enhance bearing capacity and reduce total and differential settlements. When piles primarily serve as settlement-reducing elements, the main objective of PRF design is to develop an economical foundation system by effectively mobilizing pile capacity while minimizing the number of piles.

While PRF systems offer numerous advantages under static conditions, one of their major disadvantages under dynamic conditions is the severe stress concentration occurring at the rigid connection between the pile heads and the raft foundation [1]. Under seismic action, complex structure-pile-soil interaction takes place. Seismic waves subject the soil, the soil subjects the piles, the piles subject the raft foundation, and the raft foundation subjects the superstructure to kinematic interaction. The resulting inertial behavior of the superstructure due to this interaction subjects the piles to additional distress. Consequently, the base of the raft foundation is subjected to high shear forces and overturning moments, transferring large lateral forces to the superstructure. Furthermore, as specified in the Turkish Building Seismic Code [2], the analysis of PRF systems using decoupled system approaches is complex and time-consuming, whereas integrated system solutions demand high computational capacity. Numerous studies in the literature have investigated the soil-pile-structure response of PRF systems [3,4,5,6]. To overcome these limitations, an alternative foundation system incorporating a cushion layer between the raft foundation and the piles has been investigated to eliminate the rigid connection and limit the transfer of shear forces and bending moments between the two structural elements. Referred to in the literature as Unconnected Piled Raft Foundation (UPRF) or rigid-pile composite foundation, the cushion material in these systems mitigates piled raft interaction by damping seismic loads [7-12]. Because the cushion layer prevents the direct transfer of superstructure loads to the piles, the unconnected piles act primarily as ground improvement elements rather than pure structural load-bearing elements.

Within the scope of this study, the dynamic response and seismic energy damping efficiency of UPRF systems were numerically investigated as an alternative to traditional piled raft design. Accordingly, 1/10-scale laboratory experiments were analyzed using the finite element method via PLAXIS 2D software. In the study, the dynamic responses of the UPRF system utilizing sand soil with a thickness of 60 mm as a cushion material were comparatively evaluated against the conventional PRF system.

The experimental program to be conducted as part of the Scientific and Technological Research Council of Türkiye (TÜBİTAK) project entitled “Investigation and Development of Design Criteria for the Disconnected Piled Raft Foundation System as an Alternative Approach to Piled Raft Foundation under Earthquake Excitations” (Project No. 224M250) was numerically investigated in this study.

2 Materials and Methods

This section provides a comprehensive overview of the numerical model development process, presenting in detail the modeling steps, the foundation soil and structural material parameters used in the analyses, as well as the definitions and computational settings related to dynamic analyses.

2.1 Modeling of the Soil

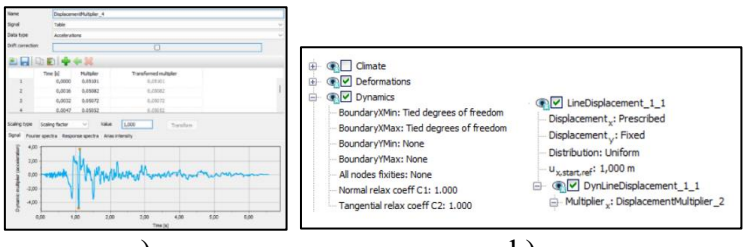
To represent the 1/10-scale laboratory experiments, the defined soil profile consists of two distinct layers with a total thickness of 1.50 m. The upper layer, extending from the surface down to a depth of 0.48 m, was modeled as medium-dense sand, whereas the lower layer, situated in the depth range of 0.48-1.50 m, was modeled as dense sand. The material parameters for both layers were determined based on the results obtained from laboratory tests, along with empirical and semi-empirical relationships widely used in the literature. In the constructed models, the HS Small soil model was selected under drained conditions. In the analyses, the elastic modulus was input into the software in scaled form. The selected parameters are provided in Table 1.

Table 1. Selected soil parameters in PLAXIS 2D

Parameters	Medium-Dense Sand	Dense Sand
Soil Model	HS Small	HS Small
Drainage Type	Drained	Drained
γ (kN/m^3)	14.5	16
e	0.8	0.65
$E_{50}^{ref}=E_{oed}^{ref}$ (kPa)	2500	4750
E_{ur}^{ref} (kPa)	7500	14250
ν	0.3	0.3
power (m)	0.5	0.5
p_{ref}	100	100
G_0^{ref} (kPa)	11000	16600
$\gamma_{0.7}$	0.0006	0.000248
c′	1	1
ϕ'	34	39

2.2 Dynamic Analyses and Numerical Settings

In the PLAXIS 2D dynamic analyses, a scaled acceleration-time record from the 1999 Erzincan earthquake was applied at the base of the soil layer in the horizontal direction (x-axis) using the "Line Displacement" approach. The seismic input is shown in Figure 1a, while the boundary conditions adopted in the numerical model are presented in Figure 1b. Interface elements were defined at the model boundaries to ensure the proper activation of the prescribed boundary conditions during the analyses [13].



a) b)

Fig. 1. PLAXIS 2D numerical model: a) definition of the input motion, b) boundary conditions.

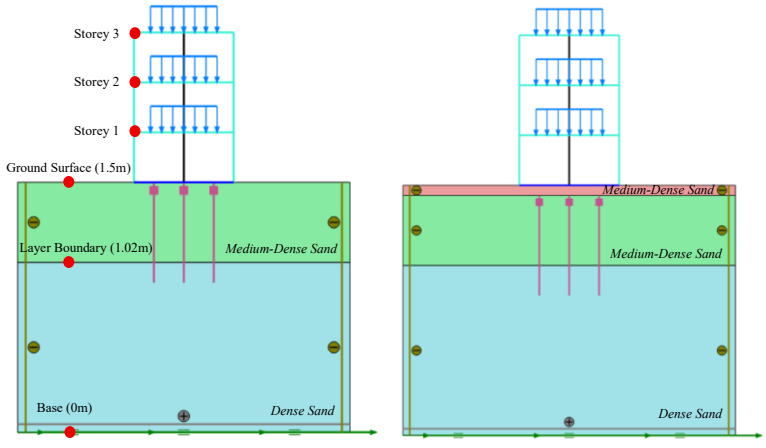
2.3 Modeling of Superstructure and Piles

In the PRF and UPRF models, a two-bay, three-storey superstructure and its supporting piled raft foundation were modeled in PLAXIS 2D. Storey heights and bay widths were 300 mm, with 20x20 mm columns and beams and 600x600x20 mm slabs. The superstructure was supported by a rigid 600x600x60 mm raft foundation. A 3x3 pile group was modeled beneath the raft, with 600 mm long piles spaced 180 mm center-to-center. The raft and piles were represented using "plate" and "embedded beam row" elements, respectively. Steel material properties were adopted for the superstructure and foundation system, with the corresponding parameters given in Table 2. To avoid artificial mass amplification and dynamic response errors caused by the 1 m out-of-plane assumption in PLAXIS 2D plane strain modeling, column unit weight was neglected and the structure mass was assigned to the slabs.

Table 2. Structural element parameters used in numerical modeling.

Plate Element		**Slab**	**Column**	**Raft Foundation**
Unit Weight (w)	[kN/m/m]	1.57	0	4.71
Axial Stiffness (EA)	[kN/m]	$4x10^6$	$133.3x10^3$	$12x10^6$
Bending Stiffness (EI)	[kNm^2/m]	133.3	4.444	3600
Poisson Ration (ν)	-	0.3	0.3	0.3
Thickness (d)	[m]	0.02	0.02	0.06
Embedded Beam Row Element		**Piles**		
Unit Weight (w)	[kN/m^3]	78.5		
$L_{spacing}$	[m]	0.18		
Predefined Cross-section Type	-	Solid Circular Beam		
Diameter	[m]	0.0603		
Young's Modulus (E)	[kN/m^2]	$200x10^6$		
$T_{skin,\ start,\ max}$	[kN/m]	1		
$T_{skin,\ end,\ max}$	[kN/m]	6		
F_{max}	[kN]	8		

In PLAXIS 2D, two cases were modeled: a piled raft foundation system and an unconnected piled raft foundation system. The models created are shown in Figure 3. As part of the dynamic analyses, the horizontal accelerations (a_x) and horizontal displacements (u_x) occurring in the soil during the earthquake duration were evaluated as a function of time. The plotted data were obtained from the measurement points shown in Figure 3.



a) b)

Fig. 3. Scaled model simulations performed in PLAXIS 2D: (a) PRF system, (b) UPRF system

3 Numerical Analysis

In this section, the numerical analysis results for the PRF and UPRF systems are presented in detail. The 1999 Erzincan earthquake was utilized in the dynamic analyses to reveal the system behavior under realistic earthquake conditions.

3.1 PRF System Analysis

According to the analysis results, the maximum displacement in the PRF system under static loading was observed at the center of the raft foundation. The total vertical displacement at this location was 12.33 mm (Figure 4). This value indicates that the pile-raft interaction enables the load to be carried jointly by the piles and the raft, while differential settlements remain limited.

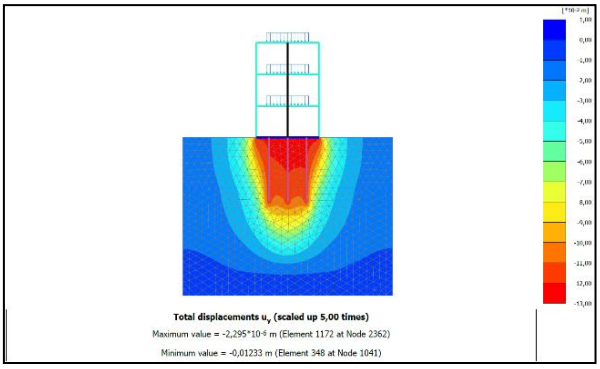


Fig. 4. Vertical displacement (u_y) in the soil in the PRF system under static loading.

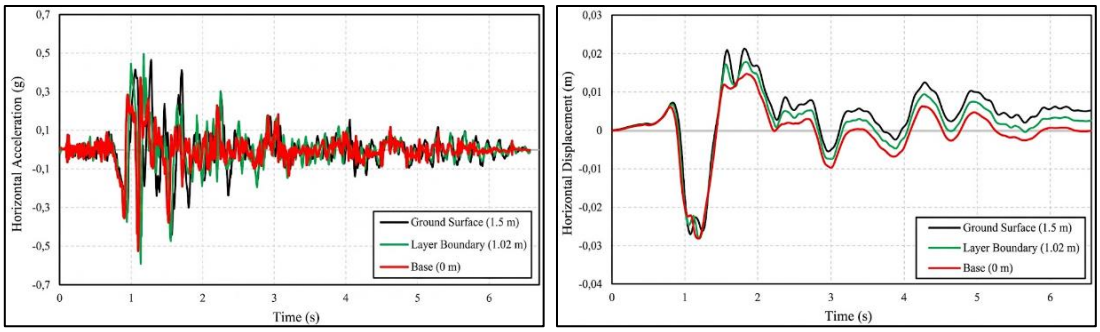
The scaled PRF system model was subjected to a real earthquake input with irregular, multi-component frequency content. Sudden peak values in the acceleration record introduced short-duration, high-amplitude excitations, resulting in irregular displacement time histories with varying amplitudes. Under the Erzincan earthquake excitation, the soil response exhibited a variable time-dependent character (Figure 5).

The maximum horizontal displacement in the soil reached approximately 9.19 mm, while the maximum vertical displacement remained at 22.47 mm (Figure 6). Examination of the soil displacement profiles indicates that horizontal displacements increase toward the ground surface, confirming the presence of the free-surface amplification effect.

The maximum horizontal displacement (u_x) of the piles was 5.34 mm, while the maximum vertical displacement (u_y) was 21.07 mm (Figure 7). The displacement results show that horizontal displacements reach their maximum values near the pile heads and decrease with depth. This indicates that lateral loads from the superstructure primarily induce bending near the pile heads. In contrast, vertical displacements show a more uniform distribution, indicating that the vertical load-carrying capacity of the system is effectively mobilized.

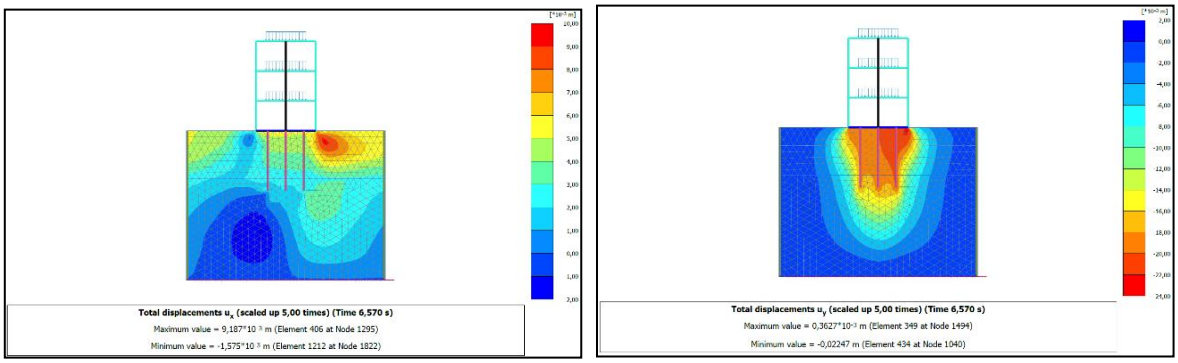
The internal force diagrams show that the maximum shear forces and bending moments occur in the piles located along the outer axes, while the pile along the middle axis is subjected to relatively lower demands due to more symmetric load transfer (Figure 8). Since the lower 12 cm of the piles are embedded in the dense sand layer, a distinct change in slope and increase in the shear force diagram are observed at the layer interface. This indicates that the stiffness contrast between the two layers is reflected in the finite element model. In addition, under the Erzincan earthquake excitation, moment concentration at the pile heads and increasing displacements toward the ground surface are observed.

Overall, the pile heads remained critical zones in the PRF system under the Erzincan earthquake, and the soil-pile-raft interaction was consistently simulated.



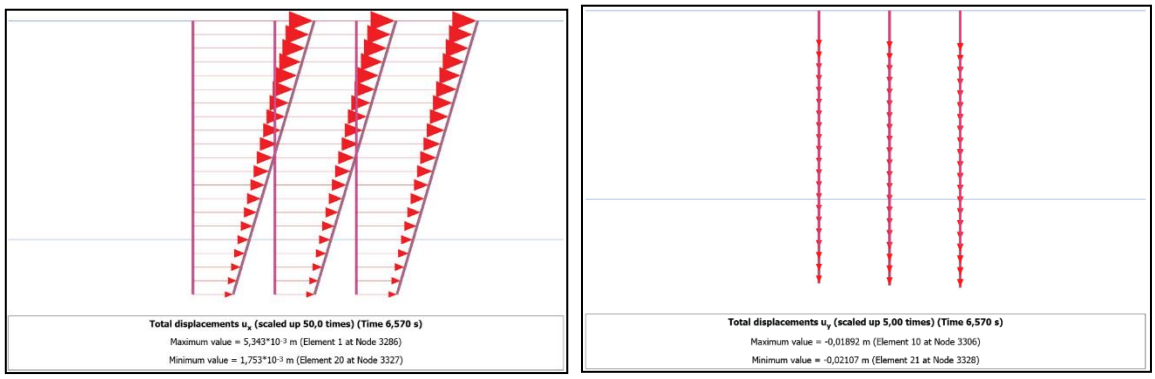
a) b)

Fig. 5. Soil responses in PRF system: (a) acceleration, (b) horizontal displacement time hist.



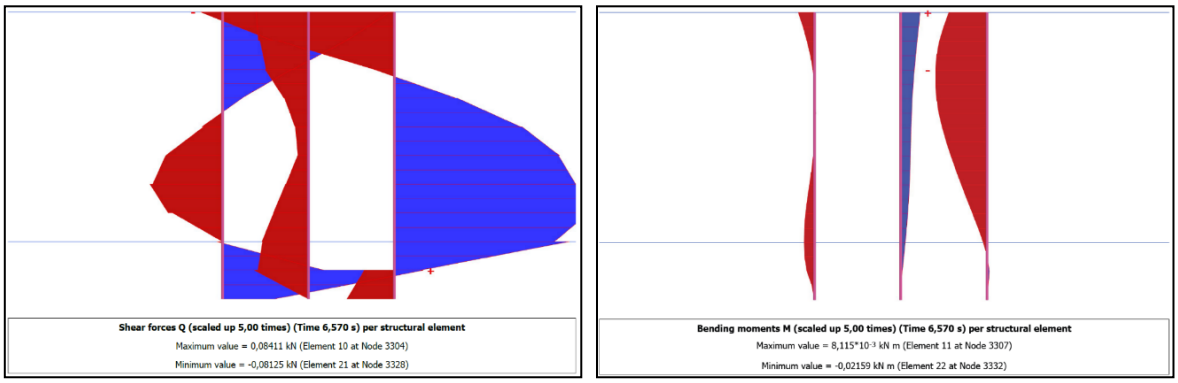
a) b)

Fig. 6. Soil displacements in PRF system: (a) horizontal (u_x), (b) vertical (u_y).



a) b)

Fig. 7. Pile displacements in PRF system: (a) horizontal (u_x), (b) vertical (u_y).



a) b)

Fig. 8. Internal forces in piles for PRF system: (a) shear force (Q), (b) bending moment (M).

3.2 UPRF System Analysis

In experimental studies reported in the literature, cushion layer thicknesses beneath foundations range from 5 mm to 176 mm, depending on the applied scale factors (e.g., 1/10, 1/25, 1/60) [14-19]. In the numerical analyses of the UPRF system, medium-dense sand was selected as the cushion layer material with a thickness of 60 mm. Considering structural safety, serviceability criteria, and scaled model compatibility, this 60 mm thickness aligns well with literature benchmarks and provides an optimal design parameter.

Under static loading, the maximum vertical displacement (u_y) of 21.11 mm was concentrated in the cushion layer directly beneath the center of the raft foundation (Figure 9).

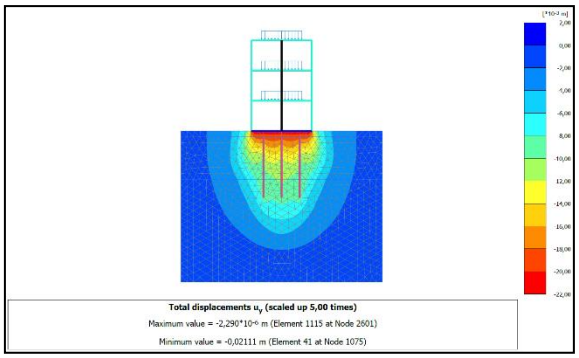
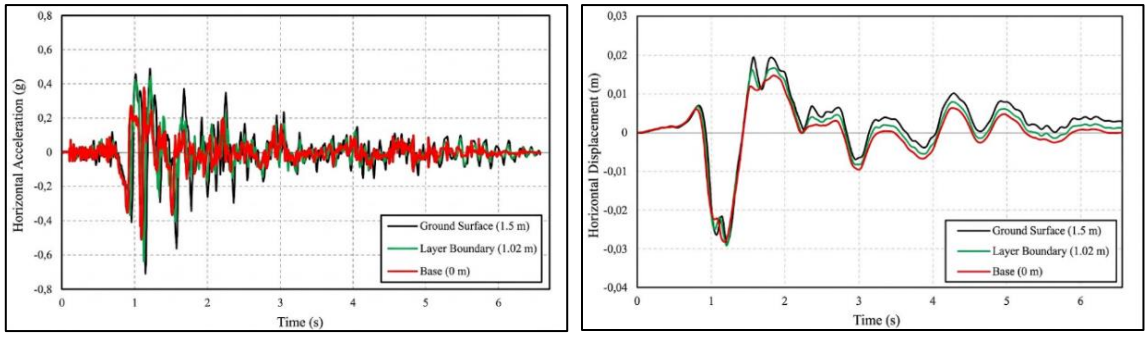


Fig. 9. Vertical displacement (u_y) in the soil in the UPRF system under static loading.

The dynamic analysis results indicate that the system response exhibited an irregular and multi-component character. The sudden peaks observed in the acceleration time histories were accompanied by displacement responses with varying amplitudes in the horizontal displacement time histories (Figure 10). In addition, the frequency content of the input motion was found to be largely preserved throughout the model.

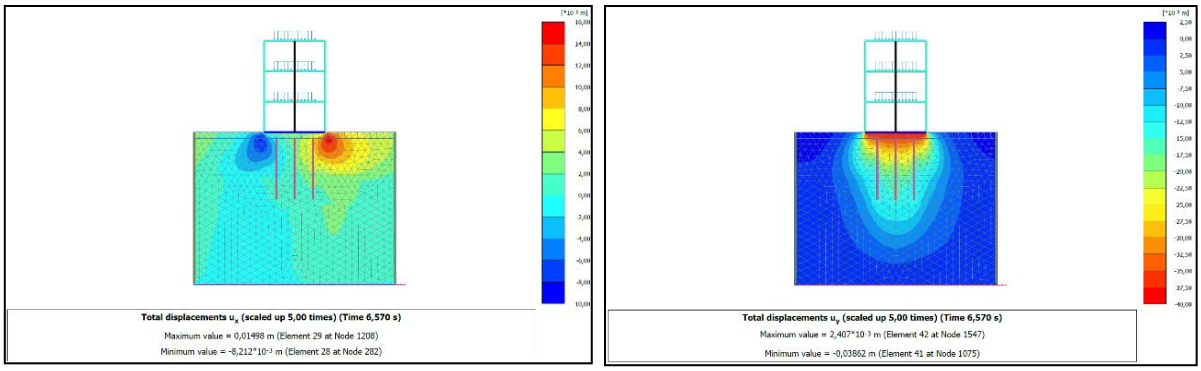
The maximum horizontal displacement in the soil was approximately 14.98 mm, while the maximum vertical displacement was 38.62 mm (Figure 11). Horizontal displacements increased from the base toward the ground surface, indicating that the free-surface amplification effect was also present in the UPRF model.

The maximum horizontal displacement (u_x) of the piles was 8.47 mm, while the maximum vertical displacement (u_y) was 16.37 mm. Horizontal displacements reached their maximum values near the pile heads and decreased with depth (Figure 12). The maximum bending moment and shear force occurred in the piles along the outer axes, while the pile along the middle axis was subjected to relatively lower demands. A distinct change in the shear force diagram was observed at the level where the piles were embedded in the dense sand layer (Figure 13). This indicates that the increase in stiffness at the layer interface was reflected in the model.



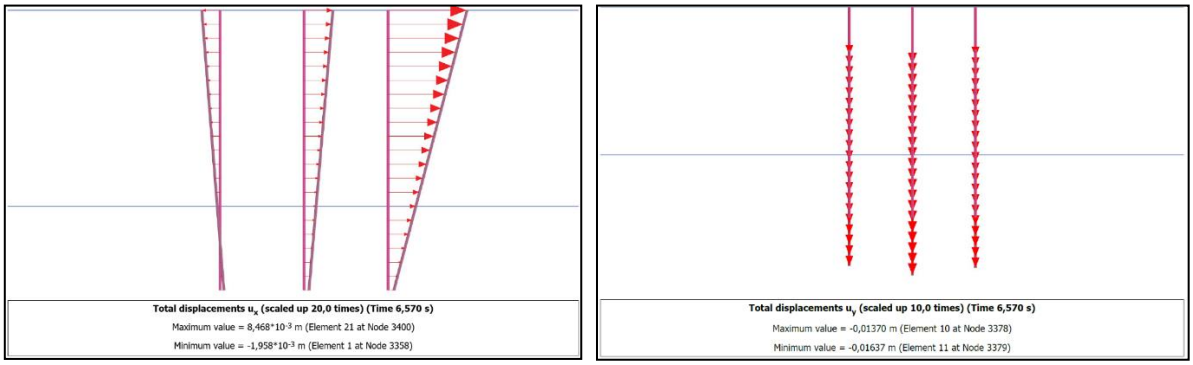
a) b)

Fig. 10. Soil responses in UPRF system: (a) acceleration, (b) horizontal displacement time hist.



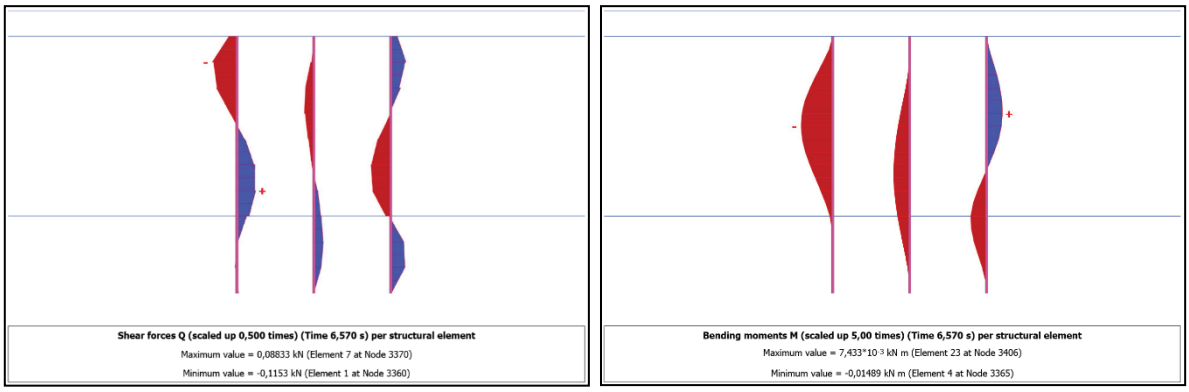
a) b)

Fig. 11. Soil displacements in UPRF system: (a) horizontal (u_x), (b) vertical (u_y).



a) b)

Fig. 12. Pile displacements in UPRF system: (a) horizontal (u_x), (b) vertical (u_y).

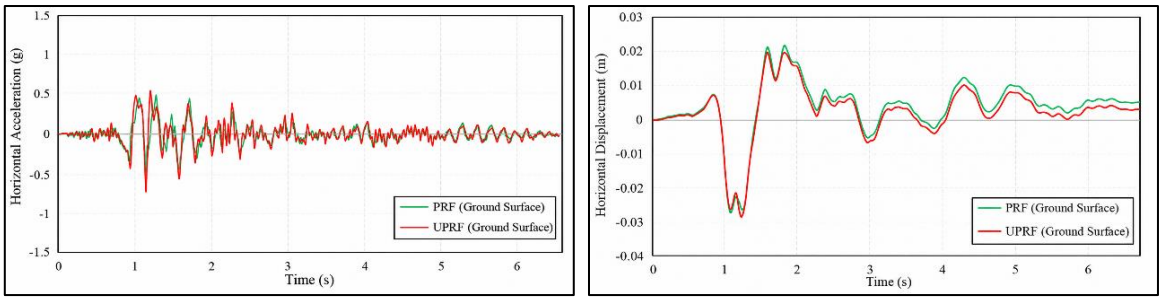


a) b)

Fig. 13. Internal forces in piles for UPRF system: (a)shear force (Q), (b)bending moment (M).

3.3 Comparison of PRF and UPRF systems

The horizontal acceleration values obtained at the center of the raft foundation under the Erzincan earthquake are generally similar for the PRF and UPRF systems; however, the maximum acceleration is higher in the UPRF system. In contrast, the horizontal displacements at the raft foundation level are higher in the PRF system than in the UPRF system. The horizontal accelerations and displacements obtained at the ground surface for the two systems are compared in Figure 14.



a) b)

Fig. 14. Comparison of recorded ground surface responses for the PRF and UPRF systems: (a) horizontal accelerations, (b) horizontal displacements.

Within the scope of this study, the behavior of PRF and UPRF systems under static and dynamic loading conditions was comparatively evaluated, and the obtained data are presented in Tables 3 and 4.

Table 3. Maximum displacements in the soil under static loading for the PRF and UPRF systems.

	Soil	
	$(u_x)_{maks}$ [mm]	$(u_y)_{maks}$ [mm]
PRF	2.72	12.33
UPRF	2.80	21.11

Table 4. Maximum accelerations and displacements of the piles and soil under dynamic loading for PRF and UPRF systems.

	Soil			**Piles**			
	$(a_x)_{max}$ [g]	$(u_x)_{max}$ [mm]	$(u_y)_{max}$ [mm]	$(u_x)_{max}$ [mm]	$(u_y)_{max}$ [mm]	M_{max} [kNm]	M_{max} [kNm]
PRF	0.019	9.19	22.47	5.34	21.07	0.084	0.022
UPRF	0.012	14.98	38.62	8.47	16.37	0.115	0.015

4 Conclusions

The results demonstrate that the overall behavior of the systems should be assessed through a comprehensive evaluation of multiple performance indicators, including pile internal forces, soil and superstructure displacements, and acceleration demands, rather than relying on a single performance metric. Compared with the PRF system, the UPRF system generally exhibited greater vertical deformations. This behavior may be attributed to the reduced overall stiffness of the foundation system resulting from the presence of the cushion layer, which provides a more flexible load-transfer mechanism between the raft and the underlying soil.

The placement of the cushion layer between the raft and the pile group resulted in a more distributed deformation pattern beneath the raft compared with the PRF system. The deformable nature of the cushion layer limited the direct transfer of superstructure loads to the piles, allowing a portion of the load to be carried by the surrounding soil and resulting in a more flexible system response. As shown in Figures 6 and 11, while displacements in the PRF system remained at similar magnitudes along the pile depth, those in the UPRF system were higher, particularly in the upper portions of the piles, and gradually diminished toward the lower levels. However, the reduction in rigid connectivity due to the cushion layer decreased the overall horizontal stiffness of the system, potentially resulting in higher horizontal displacements at

certain excitation amplitudes. In addition, the cushion layer softened abrupt stiffness transitions and contributed to reducing stress concentrations within the soil-pile-raft system.

Evaluation of pile displacements and internal force distributions indicates that the shear forces and bending moments in the UPRF system are more evenly distributed than those in the PRF system. In particular, the peak bending moments and shear forces in the piles along the outer axes were reduced, resulting in a more homogeneous load distribution. The cushion layer reduces the direct rigid connection between the raft and pile heads, thereby limiting abrupt increases in bending moments at the pile heads. In addition, the variations in shear force observed at the level where the piles are socketed into the dense sand layer exhibit a smoother transition in the UPRF system (Figures 8 and 13).

In conclusion, the 2D finite element analyses showed that the rigid connection between the raft and piles in the PRF system resulted in more direct load transfer, leading to higher bending moments and shear forces, particularly at the pile heads. In contrast, the cushion layer in the UPRF system reduced the overall system stiffness and enabled a more gradual and controlled transfer of vertical loads.

From a dynamic response perspective, the PRF system exhibited a stiffer behavior and effectively limited horizontal displacements, whereas the UPRF system demonstrated a more flexible response. However, the reduced peak values in the internal force distributions of the UPRF system indicate a significant advantage in terms of mitigating pile demands. Overall, while the PRF system exhibited a stiffer response with lower displacements, the UPRF system provided greater deformation capacity while reducing the demands imposed on the piles.

The numerical results obtained in this study will be validated through shaking table model tests to be conducted in the laboratory, and the numerical model will be further developed based on the experimental findings.

It should be noted that evaluating the numerical findings related to the cushion layer under different cushion materials, layer thicknesses, and dynamic inputs is important for establishing the generalizability of the results.

Acknowledgments

This study was supported by the Scientific and Technological Research Council of Türkiye (TÜBİTAK) under Project No. 224M250 and the Scientific Research Projects Coordination Unit of Karadeniz Technical University (KTÜ BAP) under Project No. FYD-2026-17124. The authors gratefully acknowledge the financial support provided by both institutions.

References

1. Yang, J., Lu, Z., Li, P.: Large-scale shaking table test on tall buildings with viscous dampers considering pile-soil-structure interaction. Engineering Structures 220, 110960 (2020). https://doi.org/10.1016/j.engstruct.2020.110960
2. TBSC: Turkish Building Seismic Code. T.C. Çevre ve Şehircilik Bakanlığı, Ankara (2018).
3. Durante, M. G., Sarno, L. D., Mylonakis, G., Taylor, C. A.: Soil-pile-structure interaction: experimental outcomes from shaking table tests. Earthquake Engineering & Structural Dynamics 45(7), 1041–1061 (2015). https://doi.org/10.1002/eqe.2694
4. Wang, X., Ye, A., Shang, Y., Zhou, L.: Shake-table investigation of scoured RC pile-group-supported bridges in liquefiable and nonliquefiable soils. Earthquake Engineering & Structural Dynamics 48(11), 1217-1237 (2019). https://doi.org/10.1002/eqe.3186
5. Ko, Y., Li, Y.: Response of a scale-model pile group for a jacket foundation of an offshore wind turbine in liquefiable ground during shaking table tests. Earthquake Engineering & Structural Dynamics 49(15), 1682-1701 (2020). https://doi.org/10.1002/eqe.3323

6. Xu, C., Dou, P., Du, X., El Naggar, M. H., Miyajima, M., Chen, S.: Seismic performance of pile group-structure system in liquefiable and non-liquefiable soil from large-scale shake table tests. Soil Dynamics and Earthquake Engineering 138, 106299 (2020). https://doi.org/10.1016/j.soildyn.2020.106299
7. Liu, D., Zheng, G., Liu, J., Li, J.: Experimental study to reduce differential settlements of raft of composite foundation with rigid piles. Chinese Journal of Geotechnical Engineering 29(4), 517-523 (2007).
8. Guo, Z., Wang, Z., Yang, Z.: Field study of reactions of rigid pile composite foundation for high-rise building. Rock and Soil Mechanics 30(1), 163-168 (2009).
9. Tao, J., Liang, S., Gong, W., Wu, C.: Study on bearing behavior of composite foundation with rigid pile for high-rise buildings. Journal of Southeast University (Natural Science Edition) 39, 238-245 (2009).
10. Zheng, G., Zhou, H.: State-of-the-art review of ultimate bearing capacity and stability of composite foundations. Journal of Tianjin University (Science and Technology) 53(7), 661-673 (2020).
11. Zhao, Y., Gong, W., Ling, X., Li, P., Wang, Z., Fan, H.: Model test on the vibration reduction characteristics of a composite foundation with gravel cushion under different seismic wave amplitudes. Shock and Vibration 2021(1), 6696031 (2021). https://doi.org/10.1155/2021/6696031
12. Yin, Z., Sun, H., Jing, L., Dong, R.: Geotechnical seismic isolation system based on rubber-sand mixtures for rural residence buildings: shaking table test. Materials 15(21), 7724 (2022). https://doi.org/10.3390/ma15217724
13. PLAXIS Materials Manual: PLAXIS 2D-Material models manual. Bentley Systems, Exton, PA, USA (2022).
14. Azizkandi, A. S., Aghamolaei, M., Hasanaklou, S. H.: Evaluation of dynamic response of connected and non-connected piled raft systems using shaking table tests. Soil Dynamics and Earthquake Engineering 139, 106366 (2020). https://doi.org/10.1016/j.soildyn.2020.106366
15. Malekkhani, M. J., Bazaz, J. B.: An analytical model to study the behavior of non-connected piled rafts with granular cushion subjected to vertical load. International Journal of Civil Engineering 19, 941-956 (2021). https://doi.org/10.1007/s40999-021-00611-1
16. Zhao, Y., Gong, W., Ling, X., Li, P., Wang, Z., Fan, H.: Model Test on the Vibration Reduction Characteristics of a Composite Foundation with Gravel Cushion under Different Seismic Wave Amplitudes. Shock and Vibration 2021(1), 6696031 (2021). https://doi.org/10.1155/2021/6696031
17. Yang, Y., Cheng, Y. P., Gong, W., Fan, H., Dai, G.: Effect of cushion types on the seismic response of structure with disconnected pile raft foundation. Structures 48, 1333-1345 (2023). https://doi.org/10.1016/j.istruc.2022.12.099
18. Li, Z., El Naggar, M. H., Dai, G., Liu, H., Luan, Y., Gong, W.: Seismic isolation effect of unconnected piles-caisson foundation: large-scale shake table tests. Soil Dynamics and Earthquake Engineering 176, 108304 (2024). https://doi.org/10.1016/j.soildyn.2023.108304
19. Ranjbar, E. G., Hosseininia, E. S.: Seismic performance of rubber-sand mixture as a geotechnical seismic isolation system using shaking table test. Soil Dynamics and Earthquake Engineering 177, 108395 (2024). https://doi.org/10.1016/j.soildyn.2023.108395

Author Contribution Statement

- *Conceptualization:* Osman SİVRİKAYA
- *Methodology:* Author name
- *Investigation:* Author name 1, Author name 2
- *Writing – Original Draft:* Author name
- *Writing – Review & Editing:* Author name

Burak AKÇAY, Esin ERTÜRK ATMACA, Berk DİKMENOĞLU, Murat GÜNAYDIN,
M. Kubilay KELEŞOĞLU, Esra Ece BAYAT, Fezayil SUNCA,
Ertuğrul TACİROĞLU, Kemal Önder ÇETİN, Ahmet Can ALTUNIŞIK

List of Abbreviations

- **FEM** — Finite Element Method
- **TBSC** — Turkish Building Seismic Code
- **TÜBİTAK** — Scientific and Technological Research Council of Türkiye
- **PRF** — Pile Raft Foundation
- **UPRF** — Unconnected Pile Raft Foundation

Appendices

Appendix A. Numerical Model Validation

This appendix provides detailed validation plots of the numerical model used in the study.

Appendix B. Additional Tables

Tables B1–B3 contain extended parameter lists not included in the main text.

Appendix C. Survey Questionnaire

A full version of the questionnaire used for data collection is provided here.

Authors should also declare any conflict of interest, acknowledge funding sources when applicable, and provide data availability or ethical approval statements if required. Optional additions such as a graphical abstract, highlights, a nomenclature list, software/code availability notes, study limitations, or future work descriptions may be included depending on the nature of the research.

Publication Note

This paper was peer-reviewed, accepted for presentation, and included in the proceedings of the ACE2026 – International Conference on Advances in Civil Engineering, held on 12–14 October 2026 in Trabzon, Türkiye.

This paper may be cited as follows:

Akçay, B., Sivrikaya, O., Ertürk Atmaca, E., Dikmenoğlu, B., Günaydın, M., Keleşoğlu, M. K., Bayat, E. E., Sunca, F., Taciroğlu, E., Çetin, K. Ö., Altunışık, A. C., "Numerical Investigation of Seismic Behavior of Piled Raft Foundation (PRF) and Unconnected Piled Raft Foundation (UPRF) Systems" in Proceedings of the ACE2026 – International Conference on Advances in Civil Engineering, Trabzon, Türkiye, 12–14 October 2026.

CHAPTER 4

Hydraulics

18 papers

Development of an Artificial Intelligence-Based Water Consumption Forecasting Model for İzmir Province

Ergun Uzlu[1]
[1] 0000-0002-2394-179X, Karadeniz Technical University, Civil Engineering Department, Trabzon, Türkiye, ergunuzlu@ktu.edu.tr

Abstract. Accurate forecasting of future water demand is of critical importance for the sustainable management of water resources. Reliable water consumption projections can help prevent water scarcity and promote the efficient use of available resources. In this study, an artificial intelligence-based forecasting model was developed to predict future water consumption in İzmir, one of the major metropolitan cities of Türkiye. The forecasting framework was established using an Artificial Neural Network (ANN) approach, while the network parameters were optimized through the Teaching–Learning-Based Optimization (TLBO) algorithm. TLBO is a population-based optimization technique known for its strong search and optimization capabilities. The proposed model was developed using population and gross domestic product (GDP) data. Data covering the period from 2004 to 2023 were utilized in the study. The dataset for the years 2004–2019 was used for model training, whereas the data from 2020–2023 were employed for model testing. Model performance was evaluated using average relative error (RE), mean absolute error (MAE), mean square error (MSE), and root mean square error (RMSE) criteria. The results demonstrated that the ANN–TLBO model was capable of predicting water consumption in İzmir with a high degree of accuracy. Therefore, the proposed model can serve as a valuable decision-support tool for planners and policymakers involved in water resources management and long-term water supply planning.

Keywords: Water demand forecasting; ANN; TLBO; İzmir.

1 Introduction

Accurate forecasting of future water demand is one of the fundamental requirements for the planning of drinking water supply systems, distribution networks, and water resources management strategies. İzmir, the third-largest city in Türkiye, is a major metropolitan area characterized by intensive economic, commercial, tourism, and industrial activities. Owing to its well-developed transportation infrastructure, industrial zones, educational institutions, and quality of life, the city has experienced continuous population growth over recent decades. The steady increase in population and accelerated urbanization has led to a substantial rise in domestic water demand. Therefore, accurately predicting future water consumption in İzmir is of critical importance for the planning of new water resources, the improvement of existing infrastructure, and the development of sustainable water management policies.

Among the various approaches employed in water demand forecasting studies based on time-series analysis, Artificial Neural Networks (ANNs) have emerged as one of the most widely used techniques. Numerous studies conducted across different countries and at various spatial scales have demonstrated the superior predictive capability of ANN models for water consumption forecasting. Zhao and Chen [1] developed an ANN model using population and several socioeconomic indicators to predict urban water demand in Beijing, China, and reported satisfactory forecasting performance. Similarly, Tang et al. [2] and Tian and Xue [3] developed ANN-based models for Hubei and Guangdong Provinces in China, respectively,

and concluded that these models could reliably estimate water consumption and be effectively applied in different regions. Studies conducted in Türkiye have yielded similar findings. Altunkaynak and Nigussie [4] utilized ANNs to model water consumption in Istanbul and reported that the approach provided effective results. Uzlu [5] developed a hybrid model integrating ANN and the Rao optimization algorithm to generate water consumption projections for Istanbul. In this model, gross domestic product (GDP) and population data were used as input variables, while water consumption constituted the model output. Likewise, Uzlu and Dede [6] proposed a hybrid ANN–Jaya model based on GDP and population data to forecast annual water demand in Ankara. The hybrid models developed by Uzlu [5] and Uzlu and Dede [6] successfully predicted water demand in Istanbul and Ankara, respectively. Finally, these studies demonstrate that ANNs are powerful tools capable of providing highly accurate water demand forecasts and producing reliable projections, particularly for large metropolitan areas characterized by rapid population growth and dynamic water demand patterns.

The primary objective of the present study is to develop a hybrid model integrating ANNs and the Teaching–Learning-Based Optimization (TLBO) algorithm to forecast water consumption in İzmir, the third-largest city in Türkiye. Population and GDP data were employed as input variables, whereas water consumption values constituted the model output. The dataset used for model development covers the period from 2004 to 2020. One of the main motivations behind this study is the lack of previous research specifically focused on forecasting annual water demand in İzmir. Another important motivation is that the capability of the ANN–TLBO technique for water demand modeling has not been investigated previously. It is anticipated that the water demand projections generated using the proposed models will provide valuable support to decision-makers by facilitating more efficient management and planning of existing water resources.

2 Materials and Methods

2.1 Development of the Water Demand Forecasting Model

In the present study, an ANN approach was employed to model the annual water demand of İzmir. As illustrated in Figure 1, a three-layer feed-forward neural network architecture consisting of an input layer, a hidden layer, and an output layer was adopted. The number of neurons in the hidden layer was selected as 5 and 10 in order to evaluate the effect of network complexity on model performance. Hyperbolic tangent sigmoid and linear transfer functions were utilized as the activation functions for the hidden and output layers, respectively. GDP and population data were used as input variables, whereas annual water consumption data constituted the model output.

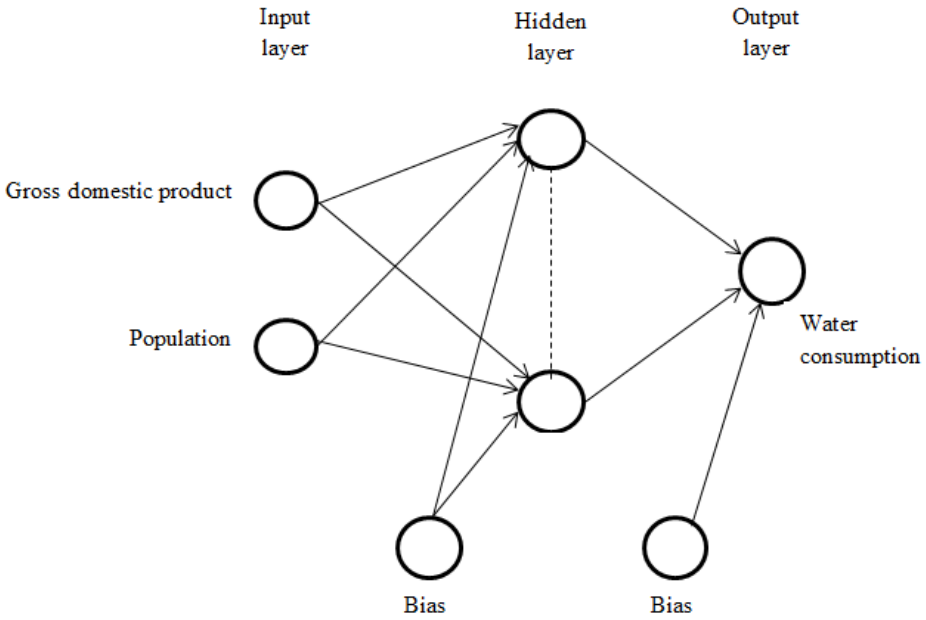


Fig. 1. Proposed ANN model for water demand prediction.

The weights of the ANN models were optimized using the TLBO algorithm. During the training process, the Mean Squared Error (MSE) was adopted as the objective function. The TLBO algorithm iteratively updates the network parameters with the aim of minimizing the MSE value and improving the predictive capability of the model. By integrating TLBO with ANN, the optimization process seeks to identify the optimal set of network weights and biases that yield the highest forecasting accuracy. To evaluate the predictive performance of the trained models, several statistical performance indicators were calculated, including the average relative error (RE), root mean square error (RMSE), and mean absolute error (MAE). These metrics were employed to assess the agreement between the observed and predicted water consumption values and to compare the performance of the developed forecasting models.

$$MSE = \frac{1}{n}\sum_{k=1}^{n}\left(y_k - o_k\right)^2 \tag{1}$$

$$average\ RE = \frac{\sum_{i=1}^{n}\left(\frac{y_k - o_k}{y_k}\right)}{n} \times 100 \tag{2}$$

$$RMSE = \left[\frac{1}{n}\sum_{i=1}^{n}\left(y_k - o_k\right)^2\right]^{1/2} \tag{3}$$

$$MAE = \frac{1}{n}\sum_{i=1}^{n}\left|(y_k - o_k)\right| \tag{4}$$

In the above equations, o_k ve y_k represent the predicted and observed values, respectively, while n denotes the total number of data samples. During the development of the ANN models, the number of runs, maximum number of iterations, and target objective function value were set to 10, 500, 8×10^{-8}, respectively. For the TLBO algorithm, the population size was specified as 50. In addition, the search interval for optimizing the ANN weights was defined within the range of [-1,1].

2.2 TLBO Algorithm

TLBO algorithm is a population-based metaheuristic optimization technique developed by Rao and inspired by the teaching–learning process that occurs in a classroom environment [7]. In the algorithm, each individual represents a candidate solution, while the best-performing individual in the population is designated as the teacher. The remaining individuals, referred to as learners, attempt to improve their knowledge and performance through interactions with the teacher and with one another. The TLBO algorithm consists of two main phases: the teacher phase and the learner phase**.** During the teacher phase, the teacher attempts to increase the overall knowledge level of the class by moving learners toward better solutions. In the learner phase, individuals interact with other learners in the population and update their solutions based on the knowledge gained through these interactions. In both phases, newly generated solutions are accepted only if they improve the value of the objective function, thereby enhancing the overall quality of the population. The optimization process is repeated iteratively until a predefined stopping criterion is satisfied, with the objective of identifying the optimal or near-optimal solution to the problem. One of the major advantages of TLBO is its simplicity, as it requires only a limited number of control parameters, primarily the population size and the maximum number of iterations. This characteristic facilitates its implementation and has contributed to its widespread application in a variety of optimization problems in recent years.

2.3 Data

In this study, GDP and population were selected as the independent variables for forecasting the future water demand of İzmir. GDP and population data were obtained from the Turkish Statistical Institute (TURKSTAT) [8, 9], while water consumption data were acquired from the İzmir Metropolitan Municipality [10]. The dataset covers the period from 2004 to 2020. Figure 2 shows the changes in dependent and independent variables between 2004 and 2020. The data collected between 2004 and 2016 were used for model development and training, whereas the data from 2017 to 2020 were reserved for model testing. This division enabled an independent assessment of the predictive performance and generalization capability of the developed ANN–TLBO models.

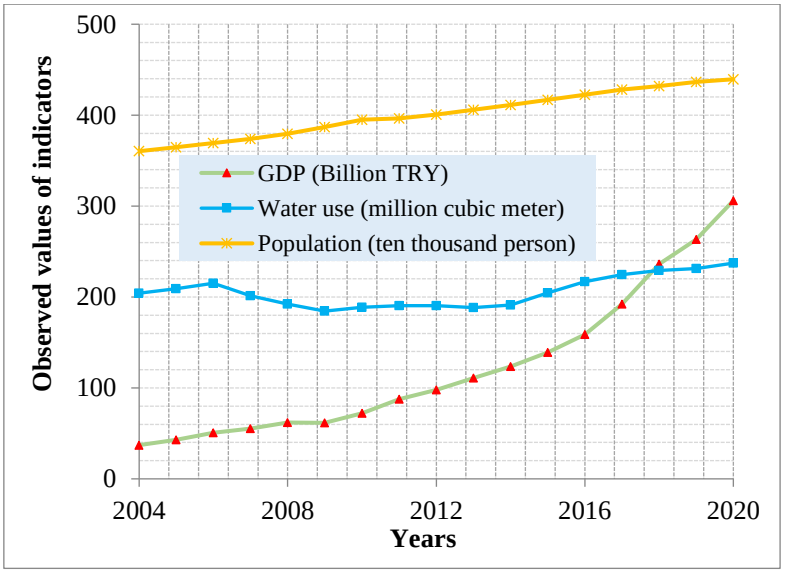


Fig. 2. Variations in dependent and independent variables [8, 9, 10].

2.4 Study Area

İzmir is located in the Aegean Region of western Türkiye and is situated at approximately 38.42° N latitude and 27.14° E longitude. As the third-largest city in the country, İzmir plays a significant role in the national economy due to its strategic port facilities and its well-developed industrial, commercial, tourism, and service sectors. The population of İzmir exceeds 4.5 million, making it one of the major metropolitan areas in Türkiye that continues to experience steady population growth driven by ongoing migration and urban expansion [9]. Consequently, the demand for potable and domestic water has increased substantially over time.

The drinking water demand of İzmir is primarily supplied by several reservoirs, including Tahtalı, Balçova, Gördes, Güzelhisar, Ürkmez, and Alaçatı Kutlu Aktaş dams [10]. Figure 3 illustrates the geographical location of İzmir and the locations of the principal reservoirs used for the city's drinking water supply. These water resources play a critical role in meeting the domestic and municipal water requirements of the population residing in different parts of the metropolitan area. Considering the combined impacts of population growth, urbanization, and climate change, the sustainable management of existing water resources has become increasingly important.

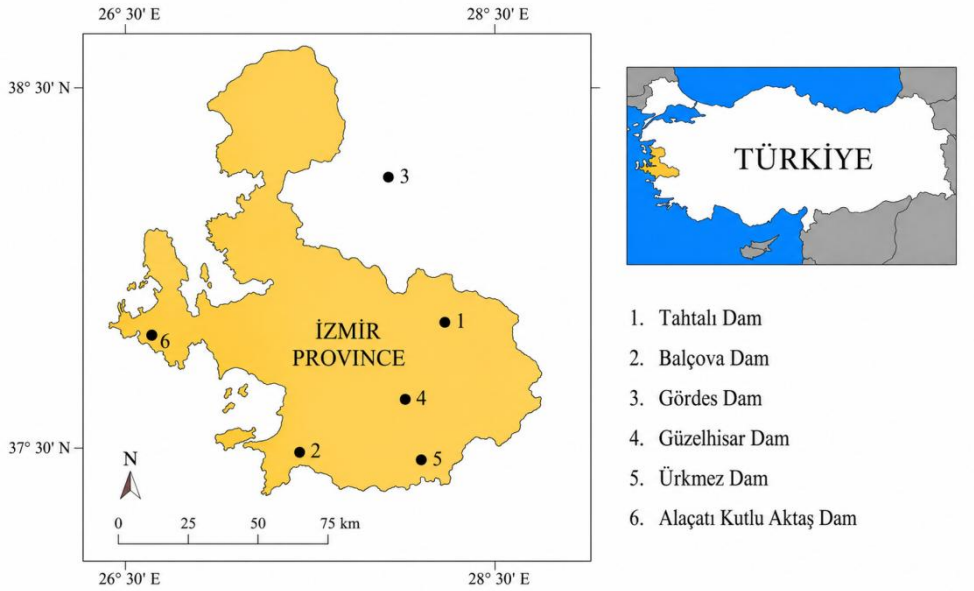


Fig. 3. Location of the İzmir and her water resources.

3 Results and Discussion

In this study, a three-layer ANN architecture, as shown in Figure 1, was selected. The two neurons in the input layer represent GDP and population data. The neuron in the output layer represents water consumption. The TLBO algorithm was preferred for the optimization of the ANN weights. The number of neurons in the hidden layer was selected as 5 and 10, considering the experience gained from previous studies [5, 6]. The training and testing error values obtained for the developed models are presented in Table 1. In addition, comparisons of the values predicted by the developed models with the observed data for the training and testing datasets are presented in Figures 4 and 5, respectively.

Table 1. Error values for the proposed ANN-TLBO models.

ANN architecture	Training set	Testing set		
	MSE (m^6)	RMSE (m^3)	MAE (m^3)	Average RE(%)
2-5-1	55.129	8.463	6.962	3.028
2-10-1	28.503	3.012	2.689	1.167

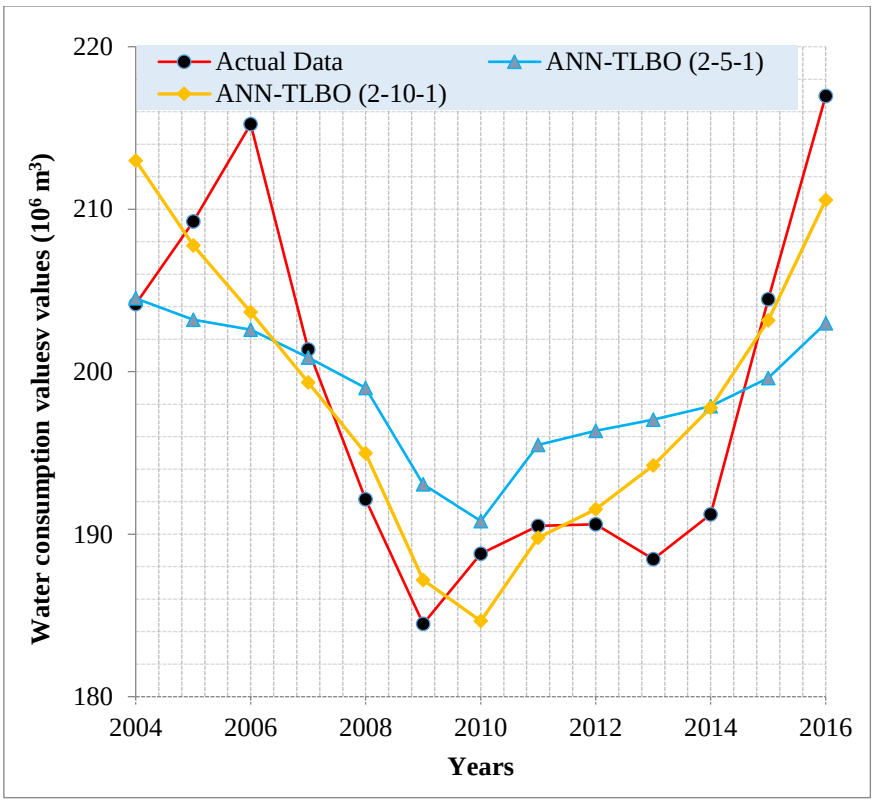


Fig. 4. Performances of the ANN-TLBO (2-5-1) and ANN-TLBO (2-10-1) for the training set.

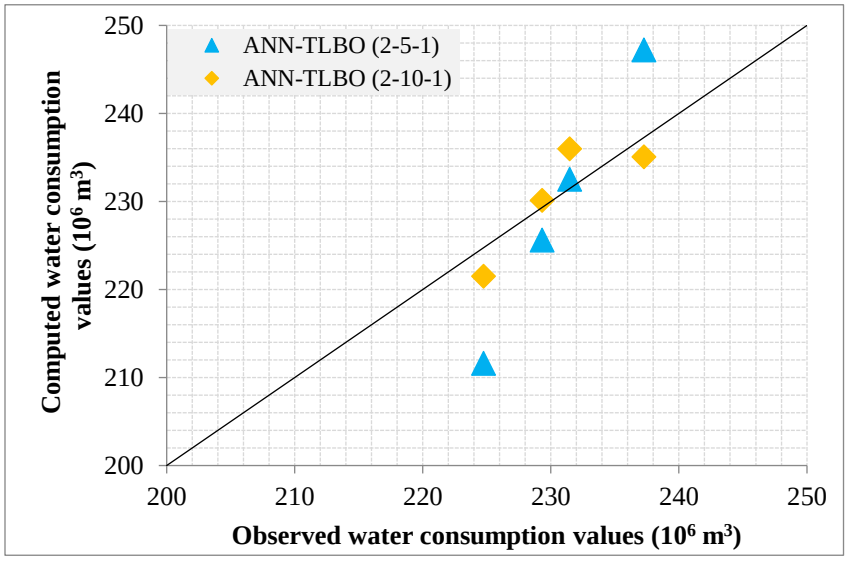


Fig. 5. Performances of the ANN-TLBO (2-5-1) and ANN-TLBO (2-10-1) for the test data.

Examination of Figures 4 and 5 reveals that the ANN–TLBO (2–10–1) model produced predictions that were closer to the observed data than those generated by the ANN–TLBO (2–5–1) model. Similarly, according to the error values presented in Table 1, the best-performing model was the ANN–TLBO (2–10–1) model with 10 neurons in the hidden layer. For the ANN–TLBO (2–10–1) model, the MSE value for the training dataset was 28.503 m^6, while the RMSE, MAE, and mean RE values for the testing dataset were calculated as 3.012 m^3, 2.689 m^3, and 1.167%, respectively. Uzlu [5] reported RMSE, MAE, and mean RE values of 17.649 m^6, 14.197 m^3, and 1.715%, respectively, for the testing dataset of the ANN–Rao model developed to forecast water consumption in Istanbul. In addition, Uzlu and Dede [6] calculated RMSE, MAE, and mean RE values of 8.787 m^6, 7.036 m^3, and 1.475%, respectively, for the testing dataset of the ANN–Jaya model developed to forecast water consumption in Ankara. The error values obtained in the present study are lower than those reported by Uzlu [5] and Uzlu and Dede [6]. Therefore, the performance of the model proposed in this study can be considered satisfactory, and the associated prediction errors are within acceptable limits.

4 Conclusion

Reliable forecasting of water consumption for İzmir is of great importance for the planning of drinking water supply systems, the effective allocation of infrastructure investments, and the sustainable management of water resources. In this study, the water consumption of İzmir was successfully modeled using the ANN–TLBO (2–10–1) model developed based on GDP and population data. As a result of the performance evaluation, the mean RE value for the testing dataset was found to be 1.167%. This result indicates that the proposed model has a high level of forecasting accuracy. The findings demonstrate that the combined use of ANNs and the TLBO algorithm constitutes an effective approach for water demand forecasting. Therefore, the developed model can be considered a reliable tool for predicting the future water demand of İzmir. Furthermore, it is anticipated that water demand projections generated using the proposed model will provide valuable support for decision-makers in the planning and management of water resources, thereby contributing to more efficient and sustainable water resource utilization.

Acknowledgments

The author would like to thank the anonymous reviewers and organizing committee for their constructive comments.

References

1. Zhao Y., Chen, X.J.: Prediction model on urban residential water based on resilient bp learning algorithm. Applied Mechanics and Materials 543, 4086–4089 (2014).
2. Tang Z.Q., Liu G., Xu W.N., Xia Z.Y., Xiao H.: Water demand forecasting in Hubei province with BP neural network model. Advanced Materials Research 599, 701–704 (2012).
3. Tian T., Xue H.: Prediction of annual water consumption in Guangdong Province based on Bayesian neural network. In IOP Conference Series: Earth and Environmental Science 69:012032 (2017).
4. Altunkaynak A., Nigussie T.A.: Monthly water consumption prediction using season algorithm and wavelet transform–based models. Journal of Water Resources Planning and Management 143(6), 04017011 (2017).
5. Uzlu E.: Modeling and forecasting of water demand in the city of İstanbul using artificial neural networks optimized with rao algorithms. Arabian Journal for Science and Engineering 49(10), 13477–13490 (2024).

6. Uzlu E., Dede T. Development of hybrid models to forecast water demand in the city of Ankara. Soft Computing 29(17), 5401-5414 (2025).
7. Uzlu E., Kankal M., Akpınar A., Dede T.: Estimates of energy consumption in Turkey using neural networks with the teaching–learning-based optimization algorithm. Energy 75, 295-303 (2014).
8. Turkish Statistical Institute (TURKSTAT). (2024) https://data.tuik.gov.tr/Bulten/Index?p=Gross-Domestic-Product-by-Provinces-2021-45619&dil=2, 01.06.2026.
9. Turkish Statistical Institue (TURKSTAT). (2024). https://data.tuik.gov.tr/Bulten/Index?p=The-Results-of-Address-Based-Population-Registration-System-2021-45500&dil=2, 01.06.2026.
10. İzmir Metropolitan Municipality Water Works and Canalization Administration (IZSU). "2020-2024 Strategic plan" https://izsu.gov.tr/dokumanlar/stratejik-planlar, 01.06.2026.

Author Contribution Statement

There is only one author. Conceptualization, methodology, investigation and writing processes ware performed by Ergun Uzlu

List of Abbreviations

- **ANN** — Artificial neural network
- **TLBO** — Teaching learning based algorithm
- **TURKSAT** — Turkish statistical institue
- **GDP** — Gross domestic product
- **RE** — Relative error
- **RMSE** — Root mean square error
- **MSE** — Mean square error
- **MAE** — Mean absolute error

Publication Note

This paper was peer-reviewed, accepted for presentation, and included in the proceedings of the ACE2026 – International Conference on Advances in Civil Engineering, held on 12–14 October 2026 in Trabzon, Türkiye.

This paper may be cited as follows:

Ergun UZLU, "Development of an Artificial Intelligence-Based Water Consumption Forecasting Model for İzmir Province," in Proceedings of the ACE2026 – International Conference on Advances in Civil Engineering, Trabzon, Türkiye, 12–14 October 2026.

Assessing Agricultural Water Allocation in Türkiye: A Multi-Level Stakeholder Assessment Based on the EU Water Allocation Framework

Elif ERDEM[1] and Elcin KENTEL ERDOGAN[2]
[1] 0009-0004-6599-3952, Middle East Technical University, Department of Earth System Sciences, Ankara, Türkiye, elif.erdem@metu.edu.tr
[2] 0000-0002-7477-0345, Middle East Technical University, Department of Civil Engineering, Ankara, Türkiye, ekentel@metu.edu.tr

Abstract.
Increasing water scarcity and climate-induced droughts pose significant challenges for water allocation systems, particularly in countries like Türkiye where irrigated agriculture accounts for a large share of water use. Ensuring adaptive and resource-aligned water allocation is therefore a critical policy challenge. This study evaluates agricultural water allocation practices in Türkiye through a stakeholder-based assessment. The survey was developed based on the European Union policy document *The Implementation of Water Allocation in the EU* [1], drawing on its key challenges and good practices. Survey questions were structured around four dimensions covering legal and policy frameworks, resource-aligned allocation, intersectoral coordination and reallocation, and compliance. The survey was conducted with 50 participants representing independent experts, managerial actors, and technical staff. Respondents were also classified according to governance level as central or local actors. Responses were analysed using a threshold-based dominance approach, classifying each question as "Yes-dominant", "No-dominant", or "Don't Know (DK)-dominant" within each stakeholder group. The results indicate that the fundamental legal and institutional components of the allocation system are largely in place, particularly regarding permitting procedures, resource monitoring, and formal compliance mechanisms. However, important implementation challenges persist, especially in intersectoral coordination, adaptive water allocation, and the operational use of decision-support systems. Overall, the findings suggest that while Türkiye's water allocation system is structurally defined, its capacity to adapt allocation decisions under drought conditions remains limited. Observed inconsistencies across governance levels further suggest that this adaptive capacity is unevenly distributed across the system, potentially constraining implementation effectiveness.
Keywords: Water Allocation; Agriculture; Drought; Stakeholder Assessment.

1 Introduction

Türkiye faces increasing challenges related to water scarcity and drought. Agriculture accounts for approximately 77% of total water use in the country and plays a critical role in food production and rural development [2]. At the same time, agriculture is highly vulnerable to drought, as water shortages can cause yield fluctuations, reduce agricultural output, and affect farmers' livelihoods, particularly in semi-arid regions of the country [3]. Climate change is expected to put additional pressure on already limited water resources by increasing the frequency and severity of drought events. Various regions of Türkiye have been identified as particularly vulnerable to drought, while the Mediterranean basin is considered a climate change hotspot with predicted decreases in rainfall and increases in extreme temperatures [4,5].

Under these conditions, sustainable water allocation has become an essential component of water governance. Water allocation policies play a crucial role in determining how limited water resources are distributed among competing users and sectors. Effective allocation systems are expected not only to ensure efficient resource use but also to support environmental sustainability, economic development, and resilience to climate variability [6]. However, increasing water scarcity and drought conditions place growing pressure on existing allocation arrangements, creating challenges related to implementation, coordination, monitoring, and adaptability.

In recent years, the European Union has devoted increasing attention to water allocation as a policy instrument for addressing water scarcity and drought. A key contribution in this area is the report Implementation of Water Allocation in the EU (hereafter referred to as the EU Water Allocation Report), prepared under the Common Implementation Strategy (CIS) on Water Scarcity and Droughts [1]. The report identifies key implementation challenges and good practice principles related to legal frameworks, allocation practices, cross-sectoral coordination, and compliance mechanisms, providing a structured basis for evaluating water allocation systems.

Türkiye has established a broad legal and institutional framework for water allocation, supported by permitting systems, basin planning instruments, monitoring mechanisms, and sectoral coordination processes. Agricultural water allocation is inherently a governance process requiring coordination among multiple institutions operating at different administrative levels. The implementation of agricultural water allocation involves multiple actors with different mandates and responsibilities, including planning, regulation, implementation, monitoring, and water use. Ensuring effective coordination among these actors is essential for translating legal and policy frameworks into consistent allocation practices, particularly under increasing water scarcity and drought conditions.

Against this background, this study uses a stakeholder-based survey to assess agricultural water allocation governance in Türkiye, drawing on the policy assessment logic of the EU Water Allocation Report. Based on the perspectives of actors involved in different stages of the allocation process, the analysis examines perceived strengths, implementation challenges, and areas of institutional uncertainty across four dimensions of water allocation governance. In doing so, the study aims to provide a structured assessment of how existing allocation arrangements are perceived across governance levels and stakeholder groups, and to identify priority areas for improving agricultural water allocation under increasing water scarcity and drought conditions.

2 Methodology

2.1 Conceptual Framework

Drawing on the challenge areas and good-practice principles identified in the EU Water Allocation Report, this study developed a survey instrument tailored to the institutional context of Türkiye, with a specific focus on agricultural water allocation. This focus reflects both the dominant share of agriculture in national water use and the fact that allocation pressures under drought are most acutely experienced in irrigated agriculture. Accordingly, the analytical framework was applied with a sector-specific focus on agricultural water allocation.

In line with this framework, the survey was structured around four analytical dimensions:

1. A supportive legal and policy framework for agricultural water allocation
2. Alignment of water allocation decisions with available water resources including consideration of surface–groundwater interactions and basin-scale water balance;
3. Intersectoral harmonisation and sustainable management of water allocations, with a focus on coordination mechanisms and reallocation practices;

4. Compliance with allocation decisions, including monitoring, enforcement, and sanction mechanisms.

The overall analytical framework adopted in this study is illustrated in Fig. 1.

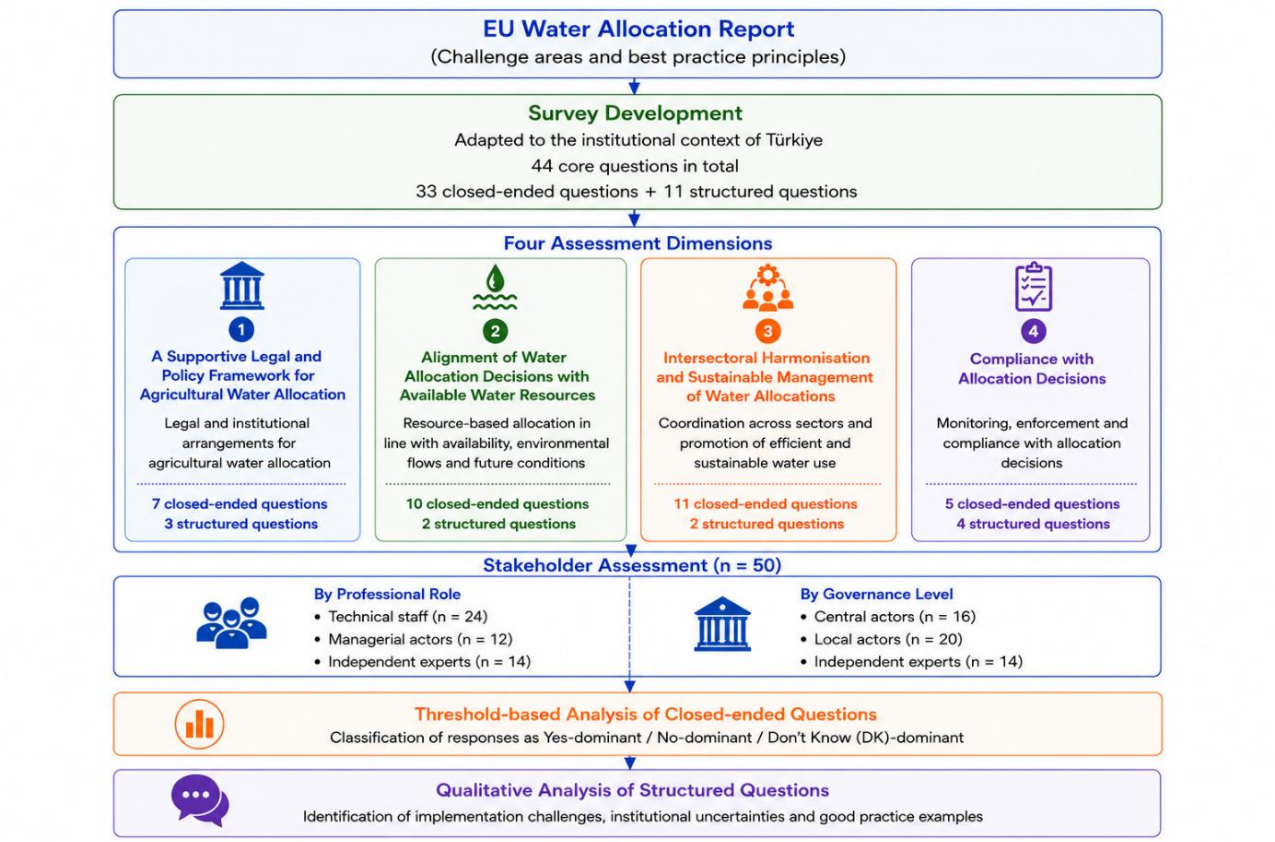


Fig. 1. Conceptual and methodological framework of the study

2.2 Survey Design and Structure

The survey was implemented using Google Forms and administered in Turkish to ensure accessibility and clarity for respondents. The survey questions are provided in Appendix A. The survey consisted of 44 core questions, including 33 closed-ended questions and 11 structured and qualitative questions, allowing respondents to elaborate on specific challenges and examples of good practice. Ethical approval for the survey was obtained from the Middle East Technical University Human Research Ethics Committee (Protocol No. 0522-ODTÜİAEK-2025) prior to data collection.

Survey responses were analysed using a threshold-based interpretive framework. A response category was considered dominant when it accounted for more than 50% of responses within the relevant stakeholder group. Accordingly, each question was classified as Yes-dominant, No-dominant, or Don't Know (DK)-dominant based on the prevailing response pattern.

The survey questions were deliberately formulated as positively framed statements reflecting good practices in water allocation governance. Within this framework, Yes-dominant responses were interpreted as indicating the presence or effective functioning of a governance mechanism or practice. No-dominant responses were interpreted as evidence of implementation gaps, institutional weaknesses, or barriers to effective water allocation management. Rather than being treated as missing data, DK-dominant responses were analysed as indicators of institutional uncertainty, fragmented knowledge, limited information flows, or weak visibility of governance processes across administrative levels.

In addition to the closed-ended questions, optional structured qualitative questions were included to capture contextual information, practical experiences, and stakeholder perspectives that could not be fully reflected through predefined response categories. These qualitative responses were used to support the interpretation of quantitative findings, provide illustrative examples of implementation challenges and good practices, and identify recurring themes related to coordination, enforcement, adaptive management, and stakeholder engagement.

2.3 Stakeholder Groups

As illustrated in Fig. 1, the survey targeted stakeholders involved in different stages of agricultural water allocation planning, implementation, regulation, and monitoring in Türkiye. A total of 50 respondents participated in the survey and were classified according to both professional role and governance level.

Respondents were grouped into three professional categories: technical staff, managerial actors, and independent experts. The independent expert category included academics and other respondents with relevant expertise in water resources management and policy but without direct involvement in institutional decision-making or implementation. Respondents were also classified as central actors, local actors, or other stakeholders. Comparisons across governance levels focused primarily on central and local actors to examine differences in perceptions across administrative scales and institutional responsibilities.

3 Results

Fig. 2 provides an overview of the dominant response patterns identified across all closed-ended survey questions. The following sections discuss these patterns by assessment dimension, supported by qualitative evidence obtained from the open-ended responses.

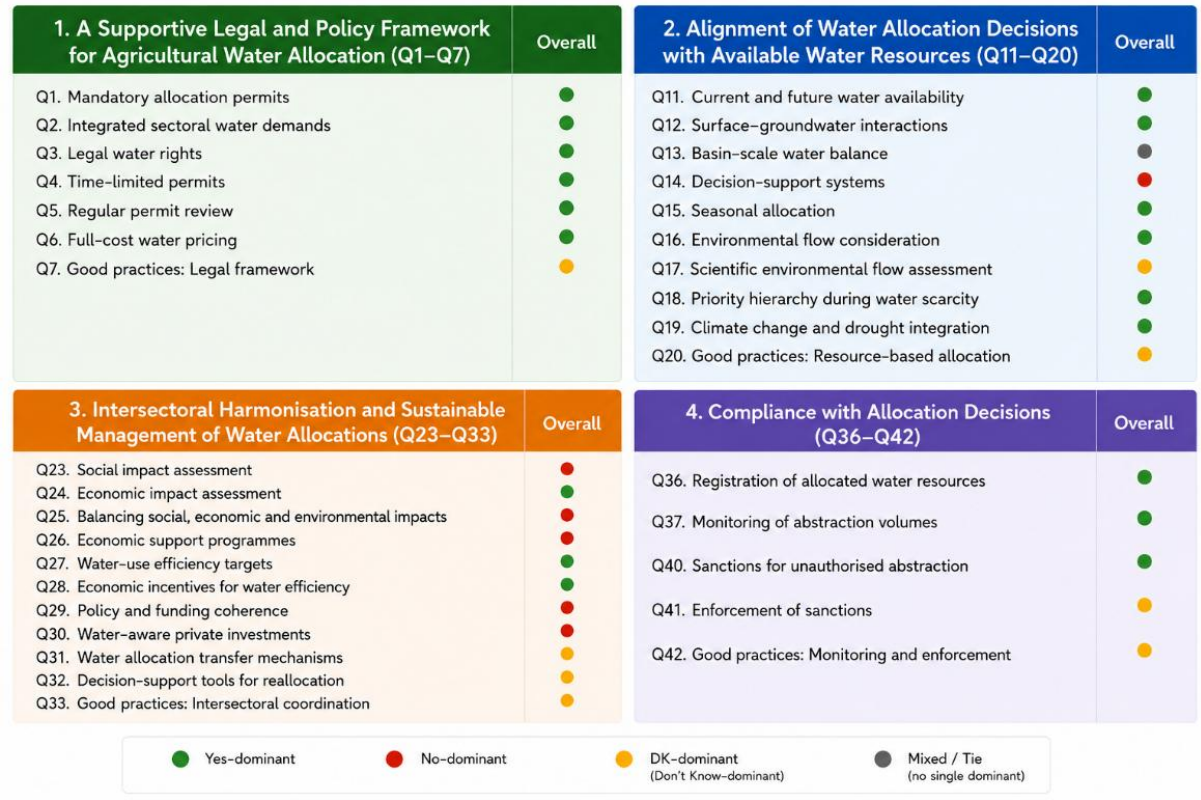


Fig. 2. Summary of Responses to the 33 Closed-Ended Questions Across the Four Assessment Dimensions. Responses to the 11 structured questions are not shown and are discussed separately in the qualitative analysis

3.1 A Supportive Legal and Policy Framework

Positive response patterns were observed for questions concerning the existence of allocation permits, the consideration of sectoral water demands, the legal definition of water ownership and use rights, the existence of time-bound allocation permits, the regular review of allocation permits, and water pricing policies. However, qualitative responses (from the structured open-ended questions) indicate that these arrangements are often implemented through context-specific practices rather than uniformly applied procedures. Permit requirements were described as applying mainly to specific user groups, permit reviews as largely event-driven, and pricing as not fully reflecting supply, environmental, and depreciation costs.

The prevailing DK response was observed for questions regarding examples of good practice within the existing legal and policy framework, suggesting limited visibility and recognition of successful practices across institutions. These findings suggest that compiling and making good practice examples publicly accessible could strengthen knowledge sharing, enhance transparency, and support more consistent implementation across governance levels.

3.2 Alignment of Water Allocation Decisions with Available Water Resources

Positive response patterns were observed for questions concerning the consideration of current and future water availability, surface water–groundwater interactions, seasonal allocation practices, environmental flow requirements, predefined priority mechanisms during water scarcity, and the integration of climate change and drought considerations into allocation decisions. These findings suggest that the key principles of adaptive water allocation are generally recognised within existing allocation practices. This pattern is also broadly consistent with the wider planning context in Türkiye, where basin-scale drought management plans and sectoral water allocation plans constitute important planning instruments for addressing water scarcity and drought-related pressures [7].

The only prevailing No response was associated with the use of decision-support systems. Although qualitative responses acknowledged the availability of modelling approaches and technical assessment tools, respondents frequently indicated that these are not yet routinely integrated into operational allocation decisions. Recent policy developments nevertheless suggest that this may be an area of ongoing institutional improvement. Directorate General of Water Management (GDWM) has initiated work on a Drought Forecasting and Early Warning System, indicating an emerging effort to strengthen the analytical and anticipatory basis of drought and water management in Türkiye [8]. Participants also highlighted challenges related to data availability, monitoring capacity, groundwater management, and institutional coordination, which were perceived to limit the practical application of adaptive water allocation approaches.

The question regarding basin-scale water balance analyses exhibited no dominant response pattern, indicating divergent perceptions among respondents regarding their implementation. This should not be interpreted as the absence of basin-scale analytical work, as hydrological and hydrogeological assessments are included in the General Directorate of State Hydraulic Works' (DSI) river basin master plans [9]. However, it remains unclear to what extent these analyses are systematically incorporated into allocation decisions and day-to-day practice.

In addition, DK-dominant responses were observed for questions concerning the scientific determination of environmental flow requirements and the identification of good practices related to matching allocations with available water resources. These findings suggest that although adaptive water allocation principles are widely recognised, their practical implementation and visibility remain uneven across institutions.

3.3 Intersectoral Harmonisation and Sustainable Management

Positive response patterns were observed for questions concerning the consideration of economic impacts in allocation decisions, the existence of efficiency-oriented rules within the allocation system, and the use of economic instruments to promote efficient water use. These findings suggest that economic considerations and water-use efficiency objectives are formally incorporated into the allocation framework. In practice, such considerations may be reflected through irrigation pricing arrangements, support for irrigation modernization and water-saving technologies, and broader policy efforts aimed at improving water-use efficiency in agriculture. However, the extent to which these instruments systematically shape allocation decisions in practice remains less clear from the survey findings.

However, prevailing No responses were observed regarding the consideration of social impacts, the availability of sufficient knowledge and awareness to balance social, economic, and environmental objectives during reallocation processes, the existence of allocation-specific support mechanisms, the alignment of allocation policies with other sectoral policies, and the compatibility of new private sector investments with available water resources. Taken together, these findings suggest that while economic considerations appear to be more visibly embedded in allocation practice, the social and environmental dimensions of allocation remain comparatively weak, which may also limit alignment with environmental and social safeguard expectations in future water-related investment processes. Qualitative responses frequently highlighted fragmented institutional responsibilities, weak inter-institutional coordination, operational constraints, and inconsistencies between policy objectives and implementation practices.

The DK-dominant questions were associated with mechanisms for transferring water allocation rights, the use of decision-support tools during reallocation processes, and examples of good practice in cross-sectoral coordination. These findings indicate limited awareness and visibility of reallocation mechanisms and coordination practices.

3.4 Compliance with Allocation Decisions

Positive response patterns were observed for questions concerning the registration of allocated water sources, the monitoring of allocation holders' abstraction volumes, and the existence of sanctions for unauthorized use or exceedance of allocated volumes. These findings suggest that the basic monitoring and enforcement framework is formally established. Qualitative responses further indicated that monitoring responsibilities are shared among multiple institutions, with DSI and its regional directorates perceived as the primary authorities responsible for monitoring activities. Several respondents nevertheless pointed to weak coordination among institutions, while others emphasised shortcomings in measurement infrastructure, data verification, and field inspection. These comments suggest that the involvement of multiple actors may complicate implementation and weaken the consistency of monitoring and enforcement practices across basins.

DK-dominant responses were observed regarding the effective enforcement of sanctions and the identification of good practices in monitoring and enforcement. Qualitative responses highlighted challenges related to institutional fragmentation, insufficient monitoring infrastructure, limited field inspection capacity, weak data verification mechanisms, and regional disparities in implementation. Respondents also noted that social and political pressures may influence the consistent application of sanctions, particularly in cases involving unauthorized abstractions and illegal wells.

3.5 Differences Across Stakeholder Groups

Although the overall assessment identified the dominant response patterns presented in Fig. 2, additional differences emerged across stakeholder groups. Managerial actors generally

provided more positive assessments of existing governance arrangements, particularly regarding legal and institutional provisions, whereas independent experts more frequently identified implementation gaps and institutional weaknesses. Technical staff exhibited more heterogeneous response patterns, with relatively positive assessments of allocation practices but greater variation across governance-related issues.

Comparisons across governance levels further indicated that central actors tended to report more positive assessments regarding formal governance arrangements and existing allocation practices, while local actors more frequently expressed uncertainty on implementation-oriented issues, particularly those related to environmental flow assessment, basin-scale water balance, decision-support systems, monitoring practices, and good practice examples. In several of these questions, uncertainty among local actors was accompanied by mixed or negative response patterns, suggesting differences not only in awareness but also in the perceived maturity of implementation across administrative levels. These differences suggest that perceptions of agricultural water allocation governance vary according to institutional role and administrative level.

4 Discussion and Conclusions

The findings indicate that Türkiye has established the principal legal and institutional foundations for agricultural water allocation. While positive response patterns dominated the legal framework, allocation practices, and compliance dimensions, weaker patterns emerged for intersectoral coordination, reallocation processes, and the operational implementation of adaptive allocation measures. Overall, the results suggest that the principal challenges are not associated with the existence of governance arrangements, but rather with their implementation, coordination, and operational application.

An important finding of this study is the relatively high number of DK-dominant responses, particularly regarding reallocation mechanisms, cross-sectoral coordination, environmental flow assessment, and examples of good practice. Depending on the issue considered, these patterns may indicate either limited institutional visibility and uneven awareness across organisations, or the absence and limited operationalisation of certain governance mechanisms. This was particularly evident for reallocation-related questions, where uncertainty was often accompanied by negative response patterns across stakeholder groups. These findings suggest that both the development of governance mechanisms and the communication of existing practices require further attention.

Although this study is based on stakeholder perceptions rather than direct measurements of allocation performance, it provides a systematic governance-oriented assessment of agricultural water allocation in Türkiye. The proposed assessment framework may support future policy development by identifying priority areas for strengthening implementation, coordination, and adaptive governance, while also providing a practical basis for periodically evaluating agricultural water allocation governance.

Based on these findings, several priority areas may be highlighted for strengthening agricultural water allocation governance in Türkiye:

- Document and disseminate good practices on allocation, drought response, monitoring, and environmental flow implementation.
- Strengthen cross-institutional learning and capacity building on basin-scale water balance, environmental flows, and adaptive allocation approaches.
- Operationalise reallocation and coordination mechanisms during periods of water scarcity and intersectoral competition.
- Reinforce the environmental and social dimensions of allocation, which remain less visible than economic and administrative considerations, including in contexts where

water-related investments are expected to align with environmental and social safeguard requirements.

Future research could complement stakeholder-based assessments with basin-scale case studies, hydrological modelling, and performance-based indicators to provide a more comprehensive evaluation of agricultural water allocation systems.

Acknowledgments

The authors would like to thank all survey participants for their valuable contributions and insights. Their experience and perspectives provided an important basis for the analysis presented in this study.

References

1. Rouillard, J., Schmidt, G.: *Implementation of Water Allocation in the EU.* Developed under the Framework Contract "Water for the Green Deal" – Implementation and Development of the EU Water and Marine Policies (09020200/2022/869340/SFRA/ENV.C.1). European Commission, Brussels (2023).
2. Ministry of Agriculture and Forestry (MoAF): *Water Efficiency Strategy Document and Action Plan (2023–2033).* Ministry of Agriculture and Forestry, Ankara (2023).
3. OECD: Building the Resilience of Turkey's Agricultural Sector to Droughts. OECD Food, Agriculture and Fisheries Papers No. 167, OECD Publishing, Paris (2021).
4. Baltaci, H., Alyagut, Y., Silva, A., Gomes, H.: Spatiotemporal characteristics and atmospheric drivers of meteorological droughts in Türkiye. *Atmospheric Research* (2025).
5. Mesta, B., Sasaki, H., Nakaegawa, T., Kentel, E.: Changes in precipitation climatology for the Eastern Mediterranean using CORDEX RCMs, NHRCM and MRI-AGCM. *Atmospheric Research* 272**,** 106140 (2022). https://doi.org/10.1016/j.atmosres.2022.106140
6. UNESCO: *United Nations World Water Development Report 2024: Water for Prosperity and Peace.* UNESCO Publishing, Paris (2024).
7. General Directorate of Water Management (GDWM), *Planlar*, https://www.tarimorman.gov.tr/SYGM/Sayfalar/Detay.aspx?SayfaId=146, last accessed 2026/07/09.
8. General Directorate of Water Management (GDWM), *Kuraklıkla Mücadele*, https://www.tarimorman.gov.tr/SYGM/Belgeler/Neler%20Yap%C4%B1yoruz/kurakl%C4%B1kla%20m%C3%BCcadele.pdf, last accessed 2026/07/09.
9. World Bank, General Directorate of State Hydraulic Works (DSI): *Environmental and Social Systems Assessment: Türkiye Water Efficiency and Climate Resilience for Results*. World Bank, Washington, DC (2026).

Author Contribution Statement

- *Conceptualization:* Elif Erdem
- *Methodology:* Elçin Kentel Erdoğan, Elif Erdem
- *Investigation:* Elif Erdem
- *Writing – Original Draft:* Elif Erdem
- *Writing – Review & Editing:* Elçin Kentel Erdoğan

Appendices

Appendix A. Survey Questions

The survey consisted of dimension-specific closed-ended and structured questions organized under four assessment dimensions.

Assessment Dimension	Questions
A Supportive Legal and Policy Framework	• Is an allocation permit mandatory for all water users? • At which spatial scale are the studies conducted when allocation decisions are made? (Administrative boundaries (province/district/village) / Water source scale (river reach/lake/well group) / Basin scale / I don't know) • Are the water demands of different sectors considered in an integrated manner during the allocation process? • Are ownership of water resources and authority over access and use clearly defined in legal terms? • Are allocation permits issued for a limited duration? • Are allocation permits reviewed on a regular basis? • Do pricing policies applied in water allocation reflect the full cost of supply?
Alignment of Water Allocation Decisions with Available Water Resources	• Are allocations determined by taking into account the current availability of water resources and projected future changes? • Are surface water–groundwater interactions considered when allocating water resources? • Are water allocation decisions based on basin-scale water balance analyses? • Are decision-support systems used when determining water allocations? • Are allocations defined with seasonal variations in allocated volumes? • Are environmental flow requirements taken into account during water allocation? • Are environmental flow requirements determined using scientific methods? • Is there a predefined plan or hierarchy that identifies priority sectors in the event of water scarcity? • Are climate change and drought considerations incorporated into allocation decisions?
Intersectoral Harmonisation and Sustainable Management	• Are the social impacts on local communities taken into account in water allocation decisions? • Are economic impacts included in the assessment of water allocation decisions? • Do you think there is sufficient knowledge and awareness to balance social, economic, and environmental impacts when reallocating water resources among different uses? • Are support programmes implemented to mitigate potential negative economic impacts arising from allocation processes? • Does the allocation system include defined targets or rules aimed at promoting more efficient water use? • Does the allocation system include economic instruments to incentivise efficient water use?

	• Are allocation priorities and policies aligned with other public sectoral policies and funding mechanisms? • Are new private sector investments planned in alignment with water resource availability? • Are there mechanisms that allow the transfer of water allocation rights to another user? • Are decision-support tools used during the reallocation process?
Compliance with Allocation Decisions	• Are all water resources subject to allocation permits fully registered? • Are the abstraction volumes of allocation holders regularly monitored by the allocating authority? • Which institution is responsible for monitoring the abstraction volumes of allocation holders? • Which technologies and methods are used to monitor the abstraction volumes of allocation holders? • Are sanctions in place in cases of unauthorised use or abstraction exceeding allocated volumes? • Are these sanctions effectively enforced in practice?

The following three questions were asked for each of the four assessment dimensions:

- What are the main implementation challenges encountered in this dimension? *(Legal basis / Institutional arrangements / Operational challenges / Regional disparities / Other problems (please explain) / I don't know / No problems are encountered)*
- At which stage do these challenges most frequently occur? *(Planning / Decision-making / Implementation / Monitoring and evaluation / Other / Don't know)*
- Are there any examples of good practice related to this dimension?

The findings reflect stakeholder perceptions and reported practices rather than direct measurements of hydrological performance or allocation outcomes. In addition, the study adopts an expert-based diagnostic approach and does not aim to provide statistically representative results. The results should therefore be interpreted as complementary to quantitative and field-based analysis.

Note: Following the conference, this Publication Note will be added to each paper; therefore, authors are kindly requested not to remove the note below and to complete the author(s) and paper title information.

Publication Note

This paper was peer-reviewed, accepted for presentation, and included in the proceedings of the ACE2026 – International Conference on Advances in Civil Engineering, held on 12–14 October 2026 in Trabzon, Türkiye.

This paper may be cited as follows:

Erdem E., Kentel Erdogan E., "Assessing Agricultural Water Allocation in Türkiye: A Multi-Level Stakeholder Assessment Based on the EU Water Allocation Framework", in Proceedings of the ACE2026 – International Conference on Advances in Civil Engineering, Trabzon, Türkiye, 12–14 October 2026.

Investigating the effect of channel slope on flow characteristics in open channel experiments

Arife Günay[1] , Tuğçe Anılan[2] and Attila Dedeoğlu[3]
[1] 0000-0002-3116-0408, Karadeniz Technical University, Civil Engineering Department, Trabzon, Türkiye, arifegunay@ktu.edu.tr
[2] 0000-0001-9571-4695, Karadeniz Technical University, Civil Engineering Department, Trabzon, Türkiye, tugcekoc@ktu.edu.tr
[3] 0009-0004-0577-4037, Karadeniz Technical University, Civil Engineering Department, Trabzon, Türkiye, 433919@ogr.ktu.edu.tr

Abstract. Open channel experiments are widely used to investigate many hydraulic problems. In open channel experiments, prototype models are generally created using the Froude scale, and parameters such as water depth, velocity, discharge, and surface profiles can be measured or observed in these models. The established models also allow the investigation of the effects of different parameters. Among these parameters, channel slope has a direct and significant impact on the solution of the problem. However, in many studies in the literature, the effect of slope could not be investigated due to the constant slope of the channel. In this study, the general hydraulic properties of flow (such as Froude numbers and critical depth) and the water surface profile were investigated in an open channel with variable slopes of % 0.5, % 1.0 and % 2.0. In all three experiments, the same discharge was maintained. Thus, the effect of the slope parameter on the flow was examined. In this experimental setup, discharge was measured with an electromagnetic flowmeter, and depths were measured with ultrasonic depth gauges. Experimental results showed that the slope of the channel is one of the primary parameters determining the geometric and hydraulic characterization of the water surface profile. The obtained data demonstrate that variations in slope lead to highly sensitive variations in profile depth and flow regime.

Keywords: Open channel experiments; slope of the channel; open channel flow characteristics

1 Introduction

Many problems in hydraulic engineering relate to open-channel flows. Open-channel systems are used in the experimental solutions to these problems. In these open-channel experiments, the Froude scale is used to model the design project discharge, the dimensions of the structure, the catchment area and the slope. Scaling is a powerful tool in the design of physical models and can be used to ensure that the results of the analysis are like those of a prototype [1]. The Froude number is widely used to characterize dynamic similarity in hydraulics [2-4]. Examples of such problems include issues concerning dam design, discharge coefficients for different types of weirs, the determination of water surface profiles, and sediment transport. As examples of such studies, Kırkgöz and Ardıçlıoğlu [5] investigated velocity profiles, whilst Basak and Alauddin [6] examined pressure losses and velocity profiles occurring during subcritical flow via step-wise widening in rigid-bottomed channels. Emiroğlu, Ağaccioğlu and Kaya [7] conducted research on a sharp-crested rectangular side weir in a straight channel, whilst Emiroğlu and Kaya [8] investigated trapezoidal labyrinth side weirs, and Bilhan et al. [9] on circular labyrinth weirs, and Azimi and Shabanlou [10] on the effect of the Froude number on the flow field in the supercritical flow regime along a weir in a U-shaped channel. Furthermore,

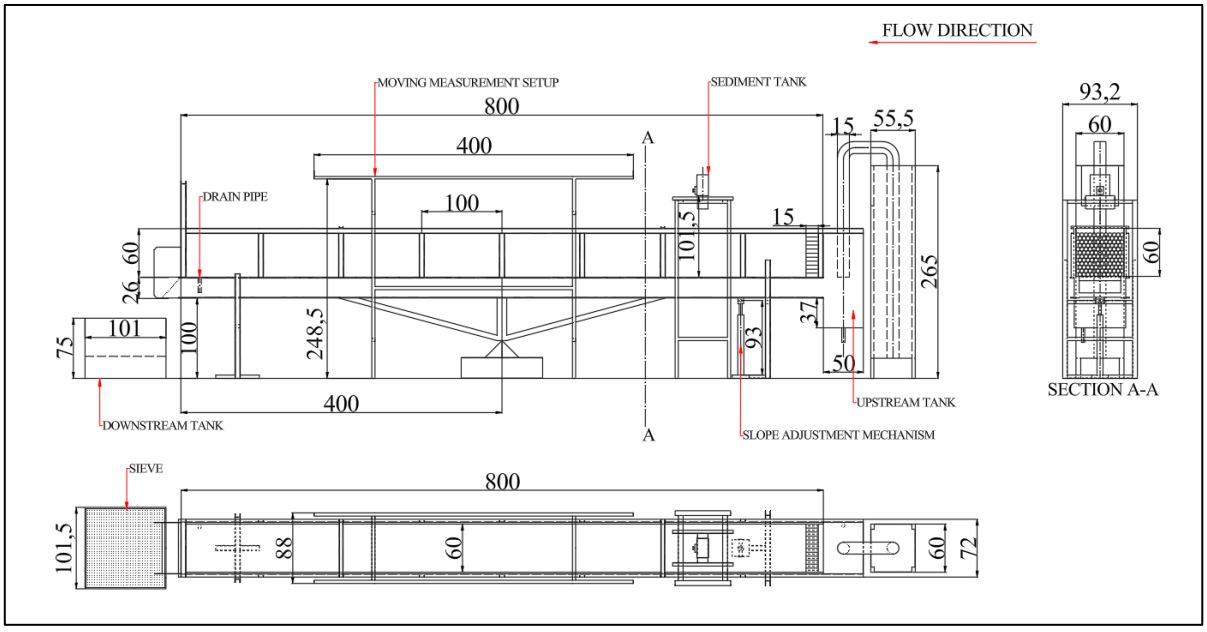
Asnaashari et al. [11] investigated subcritical flow along a transition from rectangular to trapezoidal channels, whilst Al-Hashimi et al. [12], Jiang et al. [13], Muhsun et al. [14], Imanian et al. [15] and Nourani et al. [16] carried out experimental studies on broad-crested weirs to investigate the effects of various hydraulic parameters on flow characteristics and discharge coefficients. In addition, Simsek et al. [17] carried out experimental studies on the characteristics of hydraulic jump at high Froude numbers. Schalko et al. [18] can be cited as an example of studies related to inclined bar screens, while Anılan et al. [19] and Emiroğlu et al. [20] can be cited as examples of studies involving open channel experiments in open check dams.

In most of these studies the channel slope is assumed to be constant due to laboratory constraints. Consequently, in many problems, the effect of the slope parameter which is one of the key factors in many problems is neglected. In this study, however, the effect of the slope parameter on the water surface profile is discussed using a channel setup where the slope varies between 0 and 10%.

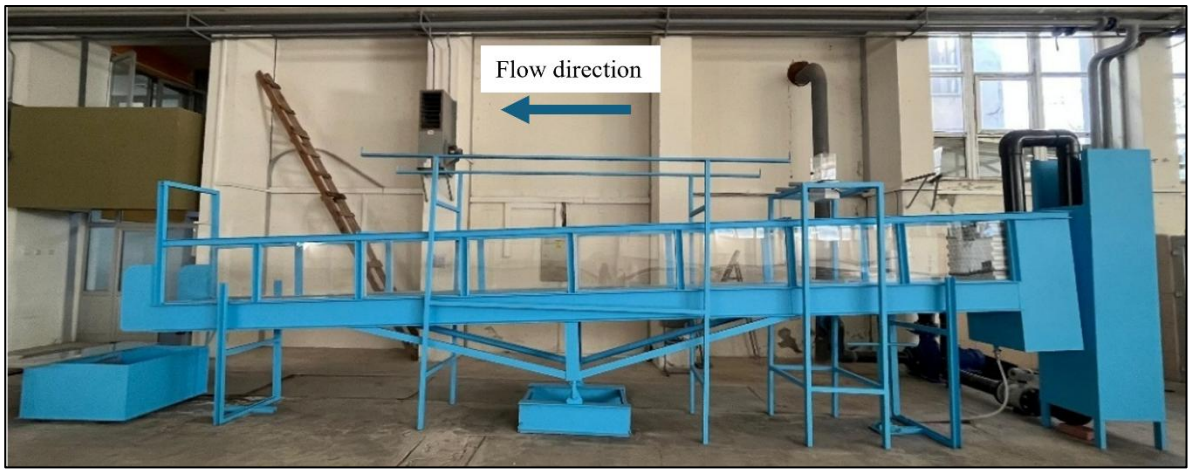
2 Material and Methods

2.1 Physical Methods

The experiments were carried out at the Hydraulics Laboratory of Karadeniz Technical University in Türkiye. The open channel, which has a rectangular cross-section, is 8.00 m long, 0.60 m high, 0.60 m wide and has an adjustable bed slope. Water is supplied to the open channel system from the laboratory's water circulation system, which consists of two water tanks, via a pump with a power of 11 kW and a maximum flow capacity of 90 L/s. The open flume system also incorporates a movable measurement rig. Four depth measurement sensors have been installed in this system to measure water depths (y). Thanks to these depth sensors, the y-value was continuously measured and recorded at four different points throughout the experiment. The positions of the sensors can be adjusted to the desired points using the rig mounted on the flume. An electromagnetic flowmeter (EMDE.CM.0150) was used to measure and adjust the flow rate supplied to the system. The flowmeter operates within a measurement range of 19.08–636.10 m³/h with an accuracy of ±0.5%. The open channel system is shown in Fig. 1.



(a)



(b)

Fig. 1. a) Profile design of the test channel (AutoCAD drawing), b) Manufacturing view.

2.2 Data and Equations Used

The experiments were carried out with a constant discharge of 36.5 m³/h in an open-channel system, for slope (j) values of 0.5 %, 1.0 % and 2.0 %. The critical depth (y_c), one of the key parameters used to determine the flow regime and type, was calculated using the Froude number. For the calculation of uniform water depths at different slopes—another key parameter, Equation (1) was used, obtained by substituting the channel-specific values into Manning's equation. The flow type was determined using the measured water depths and the calculated parameters.

$$0.01014 = \left[\frac{(2y+0.6)}{\left(\frac{2y}{100^{1.5}}+\frac{0.6}{71^{1.5}}\right)}\right]^{2/3} \times \left(\frac{0.6y}{0.6+2y}\right)^{2/3} \times j^{1/2} \times (0.6y) \quad (1)$$

3 Results

In the open channel, under steady-flow conditions and for three different slopes, depths were measured at intervals of 0.5 meters along the channel. In all experiments, fluctuations were observed in the first meter due to inlet turbulence, whilst in the final meter, changes in the water level were observed due to the 5 mm threshold located at the channel outlet. For these reasons, depth measurements were not taken at the end of the channel. The uniform water depths calculated for channel slopes of 0.5 %, 1 % and 2 % were 3.370 cm, 2.724 cm and 2.200 cm respectively, whilst the critical water depth was calculated as 3.076 cm. Table 1 presents the water depths formed in the channel at different slopes values, whilst Fig. 2 shows a graphical representation of these water depths.

Table 1. Water depths in different slopes.

Location (m)	Water depths (cm)		
	0.5%	1.0%	2.0%
0.5	1.915	1.274	0.961
1.0	2.355	1.617	1.120
1.5	2.375	1.699	1.259
2.0	2.629	1.660	1.330
2.5	2.881	1.630	1.050
3.0	2.900	1.607	1.286
3.5	2.912	1.612	1.288
4.0	3.018	1.670	1.138
4.5	3.307	1.742	1.225
5.0	3.377	1.730	1.246
5.5	3.412	1.710	0.862
6.0	3.444	1.870	1.254
6.5	3.472	1.895	1.276
7.0	3.544	1.610	1.325
7.5	3.737	1.320	0.456

As can be seen from Fig. 2, as the channel's slope increases, water levels decrease; however, when each slope is examined individually, depths increase progressively along the length of the channel. A decrease is observed in some of the depth measurements; these decreases may be due to measurement errors. When the slope is 0.5%, a comparison of the calculated depths shows that the uniform water depth exceeds the critical depth; therefore, the flow is in the subcritical regime. However, an examination of the depths obtained from the experiment reveals that the water depth at the point where the flow begins is below the critical depth; consequently, the flow in the channel begins as type M3. The flow continued as an M3-type flow up to a range of 4 – 4.5 m, and within this range, it exhibited a hydraulic jump. By undergoing a hydraulic jump, the flow passed through the uniform water level in the 4.5 – 5 m range and, as the water depth increased, reached above the uniform water level, forming an M1-type flow along the remainder of the channel. When the channel slope is 1%, the uniform water depth is below the critical depth, so the flow is in supercritical regime. As the water depths formed along the channel are less than the uniform water depth, the flow is of type S3 along the channel. As the flow is of type S3, water depths along the channel should increase. However, as can be seen, there are slight decreases at certain points. These decreases may be measurement-related, and it has been observed that the measurements obtained fall within a relative error limit of 2.3%. When the channel slope further increased to 2%, the water depths decreased even further. As the uniform water depth once again fell below the critical depth, flow developed under supercritical conditions. Upon examination of the water depths, it was observed that, similarly to the case where the slope was 1%, the flow along the channel consisted solely of type S3. As the flow is of the S3 type when the slope is 2%, the water depth should have increased; the reductions in water depth observed are due to measurement errors. When the flow in the channel was examined for different slopes, it was observed that whilst a subcritical flow regime formed in the channel when the slope was 0.5 %, the system transitioned to a supercritical flow regime as the slope increased. When the rates of increase in water depth in the channel were examined within the range of 1.5 - 6.5 m to ensure they were not affected by changes at the channel's inlet and outlet it was calculated that the water depth increased by 46.19 % at a slope of 0.5 %, by 11.54 % at a slope of 1 %, and by 1.35 % at a slope of 2 %.

Upon examination of the calculated values, it was observed that as the slope increased, the rate of increase in water depth decreased.

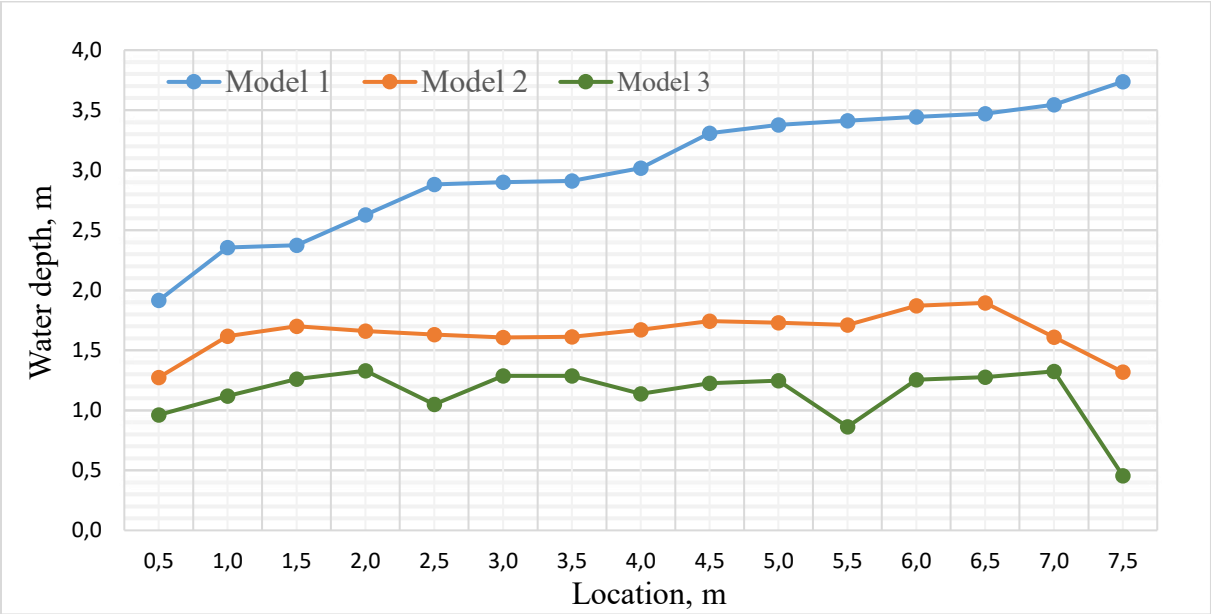


Fig. 2. Water depth values per 50 cm and graphical representation of the water profile.

4 Conclusion

In many problems encountered in open-channel flow, the slope parameter is one of the key parameters that significantly influences the solution. In this study, the effect of the slope parameter was investigated in a rectangular channel 8 metres long with a cross-section of 60 × 60 centimeters. Experiments were carried out under three different conditions: a constant flow rate of 36.5 m^3/h, with channel slopes of 0.5%, 1% and 2%. The effect of a change in channel slope on the flow was observed by examining the flow type and changes in water depth. The results obtained from the experiments are as follows:

- As the channel slope increases, the water depths in the flow decrease, and the rate of this decrease gradually diminishes as the slope increases.
- As the channel slope increases, the rate of increase in water depths along the channel decreases.
- When the channel slope is 0.5%, a river regime is established in the channel, whilst a supercritical regime is established when the slope is set to 1%. It can therefore be concluded that the critical slope value for the channel lies within the range of 0.5–1%.
- When the channel slope is 0.5%, a subcritical regime forms, creating an M3 type in the initial sections of the channel. With the progressively increasing depth, a hydraulic jump occurred in the 4–5 meter range, forming an M1 type.
- Due to the flow types formed in the channel, water depth consistently increases along the length of the channel.

Acknowledgments

This work was supported by Office of Scientific Research Projects of Karadeniz Technical University. Project number: FAY-2024-11226.

5 References

1. Zhou, G. G., Hu, H. S., Song, D., Zhao, T., Chen, X. Q., 2019. “Experimental study on the regulation function of slit dam against debris flows.” Landslides, 16, 75-90. https://doi.org/10.1007/s10346-018-1065-2
2. Heller, V., 2011. “Scale effects in physical hydraulic engineering models.” J Hydraul Res 49(3): 293-306. https://doi.org/10.1080/00221686.2011.578914
3. Iverson, RM. 2015. “Scaling and design of landslide and debris-flow experiments.” Geomorphology 244:9–20.
4. Yuan, D., Liu, J., You, Y., Zhang, G., Wang, D., Lin, Z., 2019. “Experimental study on the performance characteristics of viscous debris flows with a grid-type dam for debris flow hazards mitigation.” Bulletin of Engineering Geology and the Environment, 78, 5763-5774. https://doi.org/10.1007/s10064-019-01524-z
5. Kirkgöz, M. S., & Ardiçlioğlu, M. (1997). Velocity profiles of developing and developed open channel flow. Journal of hydraulic engineering, 123(12), 1099-1105.
6. Basak, B. C., & Alauddin, M. (2010). Efficiency of an expansive transition in an open channel subcritical flow (Doctoral dissertation, DUET Journal).
7. Emiroglu, M. E., Agaccioglu, H., & Kaya, N. (2011). Discharging capacity of rectangular side weirs in straight open channels. Flow Measurement and Instrumentation, 22(4), 319-330.
8. Emiroglu, M. E., & Kaya, N. (2011). Discharge coefficient for trapezoidal labyrinth side weir in subcritical flow. Water resources management, 25(3), 1037-1058.
9. Bilhan, O., Aydin, M. C., Emiroglu, M. E., & Miller, C. J. (2018). Experimental and CFD analysis of circular labyrinth weirs. Journal of Irrigation and Drainage Engineering, 144(6), 04018007.
10. Azimi, H., & Shabanlou, S. (2019). The effect of Froude number on flow field of U-shaped channel along a side weir in supercritical flow regime. Computational Mathematics and Modeling, 30(3), 254-266.
11. Asnaashari, A., Akhtari, A. A., Dehghani, A. A., & Bonakdari, H. (2016). Experimental and numerical investigation of the flow field in the gradual transition of rectangular to trapezoidal open channels. Engineering Applications of Computational Fluid Mechanics, 10(1), 272-282.
12. Al-Hashimi, S. A., Madhloom, H. M., & Nahi, T. N. (2017). Experimental and numerical simulation of flow over broad crested weir and stepped weir using different turbulence models. Journal of Engineering and Sustainable Development, 21(2), 28-45.
13. Jiang, L., Diao, M., Sun, H., & Ren, Y. (2018). Numerical modeling of flow over a rectangular broad-crested weir with a sloped upstream face. Water, 10(11), 1663.
14. Muhsun, S. S., Al-Madhhachi, A. S. T., & Al-Sharify, Z. T. (2020). Prediction and CFD simulation of the flow over a curved crump weir under different longitudinal slopes. International Journal of Civil Engineering, 18(9), 1067-1076.
15. Imanian, H., Mohammadian, A., & Hoshyar, P. (2021). Experimental and numerical study of flow over a broad-crested weir under different hydraulic head ratios. Flow measurement and Instrumentation, 80, 102004.
16. Nourani, B., Arvanaghi, H., & Salmasi, F. (2021). Effects of different configurations of sloping crests and upstream and downstream ramps on the discharge coefficient for broad-crested weirs. Journal of Hydrology, 603, 126940.
17. Simsek, O., Akoz, M. S., & Oksal, N. G. S. (2023). Experimental analysis of hydraulic jump at high froude numbers. Sādhanā, 48(2), 47.
18. Schalko, I., & Weitbrecht, V. (2022). Wood blockage and sediment transport at inclined bar screens. Journal of Hydraulic Research, 60(1), 164-172.

19. Anılan, T., & Akçalı, E. (2023). Fast clogging problem of open check dams and a new type suggestion: curved footed type open check dam. Journal of Mountain Science, 20(5), 1201-1219.
20. Emiroglu, M. E., Ikinciogullari, E., Yalcin, E. E., & Gul, E. (2025). Investigation of the flow characteristics of slit check dams using novel models. Applied Water Science, 15(1), 14.

Author Contribution Statement

- *Conceptualization:* Arife Günay
- *Methodology:* Arife Günay, Tuğçe Anılan
- *Investigation:* Arife Günay, Attila Dedeoğlu, Tuğçe Anılan
- *Writing – Original Draft:* Arife Günay, Attila Dedeoğlu
- *Writing – Review & Editing:* Tuğçe Anılan

Declaration of Competing Interest

The authors declare that they have no known competing financial interests or personal relationships that could have appeared to influence the work reported in this paper.

Note: Following the conference, this Publication Note will be added to each paper; therefore, authors are kindly requested not to remove the note below and to complete the author(s) and paper title information.

Publication Note

This paper was peer-reviewed, accepted for presentation, and included in the proceedings of the ACE2026 – International Conference on Advances in Civil Engineering, held on 12–14 October 2026 in Trabzon, Türkiye.

This paper may be cited as follows:

Author(s)

Günay A., Anılan T., Dedeoğlu A., " Investigating the effect of channel slope on flow characteristics in open channel experiments," in Proceedings of the ACE2026 – International Conference on Advances in Civil Engineering, Trabzon, Türkiye, 12–14 October 2026.

Numerical Modeling of Cavitation Damage in Spillway Using Finite Volume Method

Yasin YATAGANBABA[1], Mehmet SORGUN [1, *]
[1] 0009-0005-0285-897X, Izmir Katip Celebi University, Department of Civil Engineering, Izmir, Türkiye, yasin.ybaba@gmail.com
[1, *] 0000-0003-2323-2499, Izmir Katip Celebi University, Department of Civil Engineering, Izmir, Türkiye, mehmetsorgun@gmail.com

Abstract. Spillway structures in high-head dams are subject to severe cavitation risks due to high-velocity flow regimes and localized low-pressure gradients. Aeration via specialized devices remains the primary strategy to mitigate potential damage. However, predicting air-water interaction at prototype scales presents challenges due to physical modeling limitations in capturing complex flow dynamics. This research proposes a numerical framework to investigate cavitation development and the aeration performance using the Finite Volume Method (FVM) within the ANSYS Fluent software. The numerical model is validated against the experimental benchmarks of Aydin et al. [1], addressing scale effects encountered in laboratory models. The study focuses on a comparative assessment of the predictive accuracy of various turbulence models, specifically evaluating the Standard k-ε, RNG k-ε and SST k-ω approaches within a multiphase Volume of Fluid (VOF) environment. By analyzing critical hydraulic parameters such as pressure distributions, velocity profiles and air concentration levels along the spillway chute, the research aims to identify vulnerable zones susceptible to cavitation inception. The numerical results demonstrate a strong correlation with experimental data, with the RNG k-ε model providing the highest predictive precision for the cavitation index, yielding an Average Absolute Error (AAE) of 0.3165 and an Average Absolute Percentage Error (AAPE) of 21.67%. Furthermore, the interaction between turbulent boundary layer development and aeration efficiency is examined to characterize the protective cushion effect on the spillway surface. The investigation extends to evaluating the stability of the air-water mixture and its role in energy dissipation, providing a multi-dimensional perspective on flow behavior.

Keywords: Spillway Aerator; Cavitation Index; Computational Fluid Dynamics; Finite Volume Method.

1 Introduction

In high-head dams, water flows at very high speeds over the spillways. This high velocity causes the pressure on the concrete surface to drop significantly. If the pressure drops below the vapor pressure of water, vapor bubbles begin to form. When these bubbles travel downstream and burst, they create a strong impact that damages the concrete. This phenomenon is called cavitation. To prevent this damage, the most effective method is to introduce air into the water flow. Special structures called aerators are used to do this. The aerator lifts the water jet off the ground, creating a cavity underneath it. This allows air to mix with the water. The air mixture acts like a cushion and protects the spillway surface from the impact of bursting bubbles. Designing these aerators correctly is very important for dam safety. However, physical tests can sometimes be inaccurate because small-scale models do not behave exactly like real dams. Therefore, CFD simulations are widely used to analyze these flows. In this study, we investigate if a numerical model can reasonably estimate the risk of cavitation. This estimation is performed using various turbulence models to assess their impact on the predicted results.

In order to address these numerical challenges and establish a reliable predictive baseline, numerous investigations have been documented in the literature. Aydin et al. [1] investigated the two-phase flow dynamics and air entrainment rates of a high-head dam spillway aerator using prototype-scaled numerical models to evaluate cavitation mitigation performance. Fadaei-Kermani et al. [2] implemented a numerical approach to detect potential zones of cavitation damage along dam spillways by evaluating critical hydrodynamic parameters. Fadaei Kermani et al. [3] proposed an alternative predictive framework utilizing the fuzzy k-nearest neighbor algorithm to evaluate both the location and intensity levels of cavitation damage along dam spillways. Samadi-Boroujeni et al. [4] conducted a combined physical and numerical study using the VOF framework and RNG k- ε turbulence model within ANSYS Fluent to investigate the specific effects of bed roughness height on the cavitation index along chute spillways. Yusuf and Micovic [5] presented a prototype-scale case study combined with a calibrated numerical model to analyze concrete erosion patterns and evaluate structural mitigation options for spillway steps experiencing cavitation damage. Shayanseresht and Manafpour [6] utilized ANSYS Fluent and the VOF method to perform a comparative assessment of five distinct turbulence models, demonstrating that the RNG k- ε approach provides superior accuracy in predicting flow depth, jet velocity, and cavity characteristics over chute spillway aerators. Almawla et al. [7] implemented ANSYS Fluent and the VOF method combined with the Realizable k- ε turbulence model to simulate free-surface flow patterns over a dam spillway, validating the numerical results against a small-scale physical hydraulic model to predict potential zones of cavitation damage under varying discharges. Wang et al. [8] investigated the subpressure and backwater behavior of chute aerators under varying atmospheric pressures, highlighting how reductions in ambient pressure significantly affect air intake velocity and cavity dimensions. Mozaffari et al. [9] combined a 3D CFD numerical framework with an artificial intelligence model called Gene Expression Programming (GEP) to predict flow discharge over an ogee spillway, noting that the RNG turbulence model achieved the highest compatibility with experimental data among the evaluated formulations. Foroudi and Barati [10] performed a physical experimental study using a 1:50 scale model to analyze the variations in the cavitation index across an ogee spillway by considering different sidewall convergence angles and unit flow rates. Varçın et al. [11] developed a three-dimensional ANSYS Fluent model using the two-phase VOF method and k-ε turbulence formulation to analyze spillway hydraulics, while simultaneously introducing an OpenCV-Python image processing code to track flow velocity and depth. Salmasi and Abraham [12] conducted a comparative numerical analysis using the RNG k- ε turbulence model and multiphase mixture method to evaluate the hydraulic properties and cavitation index values of stepped and smooth spillway configurations. Gadge and Patil [13] conducted numerical studies on a high-head orifice spillway to assess cavitation mitigation performance, demonstrating how aerators protect the chute surface by modifying parameters such as pressure, velocity, air concentration, and jet length under critical gate openings. Safiloo et al. [14] performed a numerical evaluation of various chute spillway aerator configurations using the RNG k-ε turbulence model and multiphase mixture method, indicating that combining bottom and side-wall ramps increases the cavitation index by approximately 55% compared to using a bottom ramp alone. Bagherzadeh et al. [15] utilized 3D two-phase flow simulations within FLOW-3D integrated with a support vector machine (SVM) model to predict the specific locations and intensity levels of cavitation damage along an ogee spillway based on key hydrodynamic parameters. Aydin and Kaplan [16] utilized computational fluid dynamics (CFD) to evaluate the performance of the Ilısu Dam spillway aerators, comparing the initial 1982 design with the revised 2010 geometry to analyze cavitation protection efficiency across different flow conditions. Kökpınar and Göğüş [17] presented an extensive experimental analysis to investigate air-entrainment mechanisms and pressure fluctuations over spillway aerators, evaluating the effects of flow

conditions and different ramp designs under varying bed slopes. Jothiprakash et al. [18] developed a three-dimensional two-phase numerical model using FLUENT to investigate the flow field, pressure distribution, and air entrainment characteristics of an aerator on a deep-seated orifice spillway, validating the results with a 1:25 scale physical model. Arami-Fadafan et al. [19] performed a regression analysis based on experimental data to evaluate bottom air concentration transport downstream of aerators, deriving an empirical equation linked to water jet length to predict aeration rates along the chute. Kumcu and Uçar [20] performed a comparative study using results obtained from a 1:70-scaled physical model and computational fluid dynamics (CFD) simulations to investigate the hydraulic characteristics, velocity patterns, and pressure distributions of a dam spillway.

2 Aim of the Study

This study aims to investigate the cavitation behaviour of a spillway aerator using Computational Fluid Dynamics (CFD). Unlike the reference study by Aydın et al. [1], which utilized Flow-3D with a detailed multiphase model, the present work employs ANSYS Fluent with a two-phase air–water formulation. The main objective is to examine the influence of mesh resolution and turbulence model selection on the calculated cavitation index at various locations along the spillway. For this purpose, a mesh independence study is first performed, followed by a systematic comparison of three commonly used turbulence models: Standard k–ε, RNG k–ε and SST k–ω. The numerical results are subsequently compared with experimental data of Aydin et al., [1] in order to assess the capability of the Fluent two-phase model to predict cavitation risk in spillway aerators.

3 Theory

In this study, the Reynolds-Averaged Navier-Stokes (RANS) equations are solved using the Finite Volume Method (FVM). Since the flow over the spillway involves air-water interaction, the Volume of Fluid (VOF) method is employed to track the free surface.

3.1 Governing Equations (VOF Method)

The VOF model treats the two phases (air and water) as a single continuum. The properties appearing in the transport equations are weighted averages based on the volume fraction (α) Density and Viscosity: The density (ρ) and viscosity (μ) in each computational cell are calculated as:

$$\rho = \alpha_w \rho_w + (1 - \alpha_w)\rho_a \tag{1}$$

$$\mu = \alpha_w \mu_w + (1 - \alpha_w)\mu_a \tag{2}$$

Where:

- α_w: Volume fraction of water$(0 \leq \alpha \leq 1)$
- ρ_w, ρ_a: Density of water and air(kg/m^3)
- μ_w, μ_a: Dynamic viscosity of water and air$(kg/m \cdot s)$

Continuity and Momentum Equation: To ensure mass conservation for the mixture:

$$\frac{\partial}{\partial t}(\rho u) + \nabla \cdot (\rho u u) = -\nabla p + \nabla \cdot [\mu(\nabla u + \nabla u^T)] + \rho g \tag{3}$$

$$\frac{\partial \rho}{\partial t} + \nabla \cdot (\rho \mathbf{u}) = 0 \tag{4}$$

Where:

- u: Velocity vector(m/s)
- p: Staticp ressure(Pa)
- g: Gravitational acceleration(m/s^2)

Volume Fraction Transport Equation: To track the interface between air and water, the transport equation for the volume fraction is solved:

$$\frac{\partial \alpha_w}{\partial t} + \nabla \cdot (\alpha_w u) = 0 \tag{5}$$

Cavitation Index (σ): The potential for cavitation risk is evaluated using the cavitation index, defined as:

$$\sigma = \frac{p - p_v}{\frac{1}{2}\rho V^2} \tag{6}$$

Where:

- p_v: Vapor pressure of water(Pa)
- V: Flow velocity(m/s)

3.2 Turbulence Models

To close the RANS equations, three different turbulence models were applied to predict the Reynolds stresses.

3.2.1 Standard k−ε Model. This model solves two transport equations for turbulent kinetic energy (k) and dissipation rate (ε).

$$\frac{\partial(\rho k)}{\partial t} + \nabla \cdot (\rho k u) = \nabla \cdot \left[\left(\mu + \frac{\mu_t}{\sigma_k}\right)\nabla k\right] + G_k - \rho\varepsilon \tag{7}$$

$$\frac{\partial(\rho \varepsilon)}{\partial t} + \nabla \cdot (\rho \varepsilon u) = \nabla \cdot \left[\left(\mu + \frac{\mu_t}{\sigma_\varepsilon}\right)\nabla \varepsilon\right] + C_{1\varepsilon}\frac{\varepsilon}{k}G_k - C_{2\varepsilon}\rho\frac{\varepsilon^2}{k} \tag{8}$$

3.2.2 RNG k−ε Model. The RNG model includes an additional term Rε in the ε equation to improve accuracy for rapidly strained flows and swirling flows.

$$\frac{\partial(\rho \varepsilon)}{\partial t} + \nabla \cdot (\rho \varepsilon u) = \nabla \cdot \left[\left(\mu + \frac{\mu_t}{\sigma_\varepsilon}\right)\nabla \varepsilon\right] + C_{1\varepsilon}\frac{\varepsilon}{k}G_k - C_{2\varepsilon}\rho\frac{\varepsilon^2}{k} - R_\varepsilon \tag{9}$$

Where:

- Rε: Additional term responsible for the superior performance of RNG in high-curvature flows (like spillway aerators).

3.2.3 SST k–ω Model. The Shear Stress Transport (SST) model combines the k–ω formulation in the near-wall region and the k−ε formulation in the free stream.

Turbulent Kinetic Energy (k):

$$\frac{\partial(\rho k)}{\partial t} + \nabla \cdot (\rho k u) = \nabla \cdot [(\mu + \sigma_k \mu_t)\nabla k] + G_k - \beta^* \rho k \omega \tag{10}$$

Specific Dissipation Rate (ω):

$$\frac{\partial(\rho \omega)}{\partial t} + \nabla \cdot (\rho \omega u) = \nabla \cdot [(\mu + \sigma_\omega \mu_t)\nabla \omega] + \alpha\frac{\omega}{k}G_k - \beta\rho\omega^2 + D_\omega \tag{11}$$

Where:

- ω: Specific dissipation rate(s

- D_ω: Cross-diffusion term (blending function) that triggers the switch between models.

4 Numerical Model

A three-dimensional (3D) two-phase CFD model was developed in ANSYS Fluent to simulate the flow over the spillway. The numerical model aims to investigate how mesh density and turbulence model selection affect the cavitation index along the spillway chute for the discharge Q = 5223 m^3/s.

4.1 Computational Domain and Boundary Conditions

- **Inlet:** An open channel inlet boundary condition was applied at the upstream boundary. The design discharge specified as Q = 5223 m^3/s, along with the corresponding upstream reservoir water level of 417.15m obtained from the discharge-water level. The water volume fraction was set to 1.0
- **Outlet:** A pressure outlet boundary condition was applied at the downstream boundary. The tailwater level of 331.00m, corresponding to the design discharge was prescribed as the outlet boundary conditions.
- **Free Surface:** The top boundary was kept open to the atmosphere, allowing air exchange in the two-phase model.
- **Walls (No-Slip):** The chute floor, aerator ramp and side surfaces were treated as stationary no-slip walls. Wall roughness was neglected.

4.2 Mesh Generation

The flow domain was discretised using a fine grid. A total of 15 mesh levels were created by gradually reducing the cell and face size. The number of cells ranged from approximately 4.1×10^5 to 5.8×10^6 for the best selection (Fig. 1.) For each mesh level, simulations were first carried out with the RNG k–ε turbulence model. The cavitation index σ were recorded and compared between successive meshes. As the mesh was refined, the changes in σ became progressively smaller. For cell counts above approximately 4.4×10^6, the differences in σ were negligible. Therefore, the fine mesh with about 4447179 cells (fine grid) was adopted as the reference mesh for the turbulence model comparison.

4.3 Turbulence Modeling

Following the mesh independence study, the simulations were performed on the selected mesh using ANSYS Fluent. To determine the most accurate approach for this flow type, three different turbulence models were tested: Standard k–ε, RNG k–ε and SST k–ω. The results obtained from these models were then compared to see which one best predicts the cavitation index.

5 Results and Discussion

Numerical analyses were conducted on the spillway geometry to evaluate grid sensitivity and assess the accuracy of different turbulence models. The grid independence study, spanning mesh sizes from approximately 4.1 x 10^5 to 5.8 x 10^6 cells, revealed that the cavitation index exhibited significant fluctuations in fine grids but achieved convergence beyond 4.4 million cells for the Fluent solver. Consequently, these refined mesh configurations were adopted for the final simulations. Upon comparing the predictive performance of the three turbulence models, it was observed that the solvers exhibited different optimal behaviors; the RNG k–ε model yielded the most accurate results for Fluent with Average Percentage Errors (APE) of 21.67%. Table 1 presents a detailed comparison of the predicted cavitation index values from the three turbulence models against the experimental data at various points. Table 2 compares the predictions of the optimal RNG k-ε model with the numerical results obtained by Aydin et

al. [1] using Flow-3D. The comprehensive statistical performance metrics, including I_ , AAE, AAPE and RMSE for the evaluated models are summarized in Table 3. Furthermore, Table 4 provides a direct statistical comparison between the developed CFD model (RNG k–ε) and the reference numerical study by Aydin et al. [1].

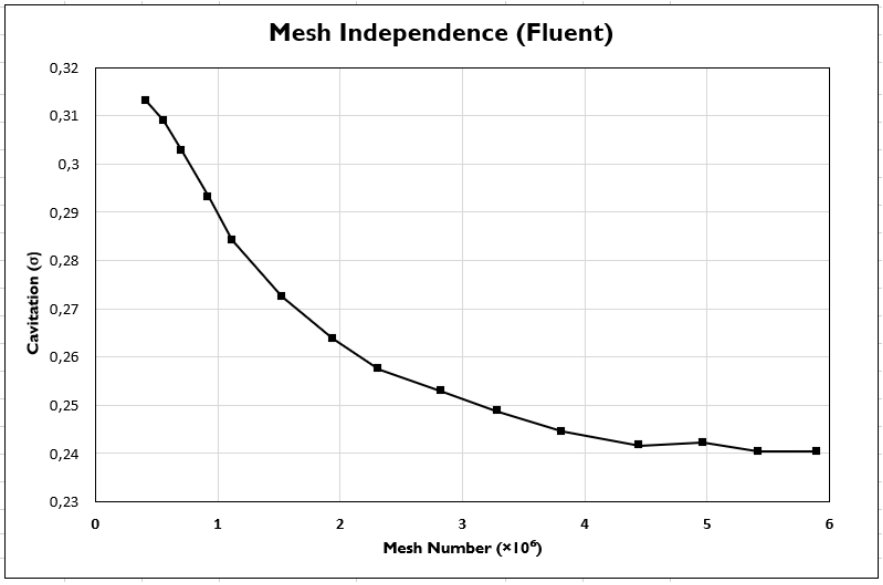


Fig. 1. Mesh Independence

Table 1. Turbulence Model Comparison with experimental cavitation index (σ)

Point	Exp.(σ)	RNG k–ε	k–ω SST	Standard k–ε
1	9.74	12.1244	12.4265	12.6387
2	3.35	4.172	4.1931	4.2029
3	2.03	2.5352	2.6109	2.6211
4	1.51	1.8778	1.9046	1.9142
5	1.07	1.3326	1.3394	1.3557
6	0.97	1.2071	1.2123	1.2285
7	0.74	0.8351	0.8468	0.8507
8	0.49	0.6135	0.6186	0.6245
9	0.21	0.2613	0.2661	0.2667
10	0.19	0.2369	0.2419	0.2425
11	0.23	0.2356	0.2382	0.2416
12	0.15	0.1496	0.1548	0.1589
13	0.05	0.0496	0.052	0.0534
14	0.09	0.0493	0.0517	0.0531
15	0.10	0.0492	0.0514	0.0528
16	0.04	0.0396	0.0409	0.0421

Table 2. Comparison of the optimal turbulence model (RNG k−ε) with Aydin et al. [1].

Point	Exp.(σ)	Aydin et al. (Flow 3D)	RNG k–ε
1	9.74	2.64	12.1244
2	3.35	2.80	4.172
3	2.03	1.83	2.5352
4	1.51	1.38	1.8778
5	1.07	1.04	1.3326
6	0.97	0.79	1.2071
7	0.74	0.67	0.8351
8	0.49	0.51	0.6135
9	0.21	0.33	0.2613
10	0.19	0.30	0.2369
11	0.23	0.23	0.2356
12	0.15	0.21	0.1496
13	0.05	0.13	0.0496
14	0.09	0.12	0.0493
15	0.10	0.12	0.0492
16	0.04	0.10	0.0396

Table 3. R-Square, Average Absolute Error (AAE), Average Absolute Percentage Error (AAPE) and Root Mean Square Error (RMSE) Values of evaluated numerical models.

	R^2	AAE	AAPE	RMSE
RNG k–ε	0.9216	0.3165	21.67	0.6572
k–ω SST	0.9025	0.3458	23.03	0.7327
Standard k–ε	0.8884	0.3641	24.05	0.7839

Table 4. R-Square, Average Absolute Error (AAE), Average Absolute Percentage Error (AAPE) and Root Mean Square Error (RMSE) values of the developed CFD model (RNG k–ε) and the reference study.

	R^2	AAE	AAPE	RMSE
Aydin et al. [1] Flow-3D	0.4227	0.5475	41.32	1.7827
CFD model (RNG k–ε)	0.9216	0.3165	21.67	0.6572

6 Conclusion

- In this study, three widely used turbulence models (RNG k–ε, SST k–ω and Standard k–ε) were evaluated to predict the cavitation index along the spillway.
- The RNG k–ε model provided the highest predictive accuracy among the evaluated configurations (based on RNG k–ε= 21.67%, SST k–ω= 23.03% and Standard k-ε=24.05% AAPE values, respectively).
- Since the RNG k–ε model yielded the most accurate results, it was adopted in the developed Computational Fluid Dynamics (CFD) model.
- The developed CFD model showed a closer agreement with experimental data compared to the reference Flow-3D study by Aydin et al. [1] (based on Flow-3D= 41.32% AAPE value).

References

1. Aydin M.C., Isik E., Ulu A.E.: Numerical modeling of spillway aerators in high-head dams. Applied Water Science 10(42), 1–9 (2020). https://doi.org/10.1007/s13201-019-1126-2

2. Fadaei-Kermani E., Barani G.A., Ghaeini-Hessaroeyeh M.: Numerical Detection of Cavitation Damage on Dam Spillway. Civil Engineering Journal 2(9), 438-447 (2016), https://doi.org/10.28991/cej-2016-00000051

3. Fadaei Kermani E., Barani G.A., Ghaeini Hessaroeyeh M.: Cavitation Damage Prediction on Dam Spillways using Fuzzy-KNN Modeling. Journal of Applied Fluid Mechanics 11(2), 323–329 (2018). https://doi.org/10.29252/jafm.11.02.28356

4. Samadi-Boroujeni H., Abbasi S., Altaee A., Fattahi-Nafchi R.: Numerical and Physical Modeling of the Effect of Roughness Height on Cavitation Index in Chute Spillways. International Journal of Civil Engineering 18(5), 539–550 (2020). https://doi.org/10.1007/s40999-019-00479-2

5. Yusuf F., Micovic Z.: Prototype-Scale Investigation of Spillway Cavitation Damage and Numerical Modeling of Mitigation Options. Journal of Hydraulic Engineering 145(12), 05019003 (2019). https://doi.org/10.1061/(ASCE)HY.1943-7900.0001671

6. Shayanseresht S., Manafpour M.: A Comparative Assessment of Various Turbulence Models Applied for Simulation of Air-Water Flow Over Chute Spillway. Periodica Polytechnica Civil Engineering 65(4), 1200–1212 (2021). https://doi.org/10.3311/PPci.18036

7. Almawla A.S., Kamel A.H., Lateef A.M.: Modelling of Flow Patterns over Spillway with CFD (Case Study: Haditha Dam in Iraq). International Journal of Design & Nature and Ecodynamics 16(4), 373–385 (2021). https://doi.org/10.18280/ijdne.160404

8. Wang Y., Deng J., Wei W.: Investigation on the Cavity Backwater of Chute Aerators under Various Atmospheric Pressures. Water 14(9), 1513 (2022). https://doi.org/10.3390/w14091513

9. Mozaffari S., Amini E., Mehdipour H., Neshat M.: Flow Discharge Prediction Study Using a CFD-Based Numerical Model and Gene Expression Programming. Water 14(4), 650 (2022). https://doi.org/10.3390/w14040650

10. Foroudi A., Barati R.: Experimental study of cavitation index in an ogee spillway by considering convergence angle of sidewalls. Water Supply 22(6), 5729–5741 (2022). https://doi.org/10.2166/ws.2022.228

11. Varçın H., Üneş F., Gemici E., Zelenakova M.: Development of a Three-Dimensional CFD Model and OpenCV Code by Comparing with Experimental Data for Spillway Model Studies. Water 15(4), 756 (2023). https://doi.org/10.3390/w15040756

12. Salmasi F., Abraham J.: Hydraulic characteristics of flow over stepped and chute spillways (case study: Zirdan Dam). Water Supply 23(2), 851–866 (2023). https://doi.org/10.2166/ws.2023.011

13. Gadge P.P., Patil R.G.: Performance evaluation of high head orifice spillway – a case study. Journal of Applied Water Engineering and Research 13(2), 142–153 (2025). https://doi.org/10.1080/23249676.2024.2446327

14. Safiloo F., Salmasi F., Arvanaghi H., Abbaspour A., Abraham J.: Investigating flow characteristics in different types of chute spillway aerators. ISH Journal of Hydraulic Engineering 31(4), 686–706 (2025). https://doi.org/10.1080/09715010.2025.2515486

15. Bagherzadeh S., Ghaeini-Hessaroeyeh M., Fadaei-Kermani E.: Prediction of cavitation damage using SVM model based on air–water two-phase flow over dam spillway. Applied Water Science 15(70), 1–11 (2025). https://doi.org/10.1007/s13201-025-02406-4

16. Aydin M.C., Kaplan C.: Ilısu Barajı Dolusavak Havalandırıcısı Performans Analizi. Omer Halisdemir University Journal of Engineering Sciences 8(2), 902–911 (2019). https://doi.org/10.28948/ngumuh.598248

17. Kökpınar M.A., Göğüş M.: High-speed jet flows over spillway aerators. Canadian Journal of Civil Engineering 29(6), 885–898 (2002). https://doi.org/10.1139/l02-088

18. Jothiprakash V., Bhosekar V.V., Deolalikar P.B.: Flow characteristics of orifice spillway aerator: numerical model studies. ISH Journal of Hydraulic Engineering 21(2), 216–230 (2015). http://dx.doi.org/10.1080/09715010.2015.1007093

19. Fadafan M., Moghaddam A., Barati R.: Reduce Spillways Cavitation Damages through Accurate Prediction of Bottom Air Concentration (2018). https://www.researchgate.net/publication/327791818

20. Kumcu Ş.F., Uçar M.: Effect of Experimental and Mathematical Modeling of Spillway on Dam Safety (2018). https://doi.org/10.1007/978-3-319-94589-7_29

Author Contribution Statement

- *Conceptualization:* Yataganbaba Y., Sorgun M.
- *Methodology:* Yataganbaba Y., Sorgun M.
- *Investigation:* Yataganbaba Y., Sorgun M.
- *Writing – Original Draft:* Yataganbaba Y., Sorgun M.
- *Writing – Review & Editing:* Yataganbaba Y., Sorgun M.

List of Abbreviations

- **FVM** — Finite Volume Method
- **CFD** — Computational Fluid Dynamics
- **VOF** — Volume of Fluid
- **RANS** — Reynold-Averaged Navier-Stokes
- **RNG** — Renormalization Group
- **SST**— Shear Stress Transport
- **AAE** — Average Absolute Error
- **AAPE** — Average Absolute Percentage Error
- **RMSE** — Root Mean Square Error

Publication Note

This paper was peer-reviewed, accepted for presentation, and included in the proceedings of the ACE2026 – International Conference on Advances in Civil Engineering, held on 12–14 October 2026 in Trabzon, Türkiye.

This paper may be cited as follows:

Yataganbaba, Y., and Sorgun, M., "Numerical Modeling of Cavitation Damage in Spillway Using Finite Volume Method," in Proceedings of the ACE2026 – International Conference on Advances in Civil Engineering, Trabzon, Türkiye, 12–14 October 2026.

Is Türkiye Drying? Regional and Seasonal Drought Trends from High-Resolution SPEI

Ahmet Faruk İpek[1] and Ercan Kahya[2]
[1] 0000-0003-4208-4188, Istanbul Technical University, Civil Engineering Department, İstanbul, Türkiye, ipekah20@itu.edu.tr
[2] 0000-0001-9455-6664, Istanbul Technical University, Civil Engineering Department, İstanbul, Türkiye, kahyae@itu.edu.tr

Abstract. Long-term drought variability across Türkiye has become increasingly important under intensifying climate pressures in the Eastern Mediterranean. In this study, the spatial and seasonal distribution of drought trends across Türkiye was analyzed using a high-resolution Standardized Precipitation Evapotranspiration Index (SPEI) dataset covering the 1981–2022 period, with trends assessed using the Modified Mann–Kendall (M-MK) test. The results reveal a spatially heterogeneous pattern with clear seasonal variability rather than a widespread, homogeneous drying trend. Significant drying remained limited throughout the year, ranging from about 2.3% in November to 4.6% in December. In contrast, significant wetting consistently covered larger areas, ranging from about 5.3% in December to 11.9% in March. The most persistent drying signal was detected throughout the year in Southeastern Anatolia (GAP region) and the Upper Euphrates Basin of Eastern Anatolia, whereas the western and central Black Sea hinterland, Thrace, and northern Central Anatolia consistently exhibited wetting trends. These findings demonstrate that drought trends in Türkiye are characterized by pronounced regional and seasonal contrasts rather than a uniform nationwide drying pattern. The persistent drying observed in the GAP region has important implications for agricultural water management and irrigation planning.

Keywords: Drought; Trend; Standardized Precipitation Evapotranspiration Index (SPEI); Modified Mann–Kendall (M-MK) trend test; Türkiye

1 Introduction

The Mediterranean Basin is recognized as one of the regions most vulnerable to the impacts of climate change, with substantial reductions in winter precipitation projected [1]. Therefore, reliable identification of drought trends is essential for water resources management and agricultural planning in Türkiye, which is influenced by Mediterranean, continental, and semi-arid climate regimes. The Standardized Precipitation Evapotranspiration Index (SPEI), one of the most widely used indices for drought assessment, accounts for both precipitation and potential evapotranspiration, thereby incorporating the influence of temperature on drought conditions. In addition, its ability to be calculated at multiple temporal scales provides a significant advantage for drought analysis and monitoring [2]. Previous studies in Türkiye have reported increasing drought trends, particularly in the central and southeastern regions of the country [3].

In this study, drought trends across Türkiye were analyzed at a monthly scale using the Modified Mann–Kendall (MMK) test and a gridded SPEI dataset with an approximate spatial resolution of 5 km covering the period 1981–2022. This approach enables the assessment of drought trends at both monthly and high spatial resolution. The main objectives of the study were to (i) quantify the spatial distribution of statistically significant drying and wetting trends

across Türkiye, (ii) determine the monthly variability of these trends, and (iii) identify regions exhibiting persistent drought signals throughout the annual cycle.

2 Materials and Methods

2.1 Study Area and Data

Türkiye is located in the eastern Mediterranean and is characterized by the coexistence of Mediterranean, continental, and semi-arid climate regimes. Covering an area of approximately 780,000 km² with a mean elevation of 1,130 m, the country exhibits pronounced topographic and climatic diversity [4]. These characteristics make Türkiye particularly sensitive to drought variability.

This study used the CHIRPS–GLEAM subset of the high-resolution global Standardized Precipitation Evapotranspiration Index (SPEI) dataset developed under the Hydro-JULES project [5]. The dataset provides monthly SPEI values for the 1981–2022 period at an approximate spatial resolution of 5 km. To characterize long-term moisture deficits and hydrological drought conditions, the 12-month Standardized Precipitation Evapotranspiration Index (SPEI-12) was used in the analysis. Small data gaps over water bodies were interpolated for visualization purposes only; all analyses were based on the original data.

2.2 Standardized Precipitation Evapotranspiration Index (SPEI)

The Standardized Precipitation Evapotranspiration Index (SPEI), one of the most widely used indices for drought assessment, is based on the standardization of the climatic water balance calculated as the difference between precipitation and potential evapotranspiration (PET) [2]. By accounting for atmospheric evaporative demand in addition to precipitation, SPEI differs from precipitation-based drought indices and provides a more suitable framework for drought assessment under a warming climate [6]. Owing to its multi-temporal nature, SPEI can be calculated over different accumulation periods.

In this study, the 12-month accumulation timescale (SPEI-12) was used to characterize long-term drought conditions. Negative SPEI values indicate dry conditions, whereas positive values indicate wet conditions. A detailed description of the SPEI calculation procedure is available in the literature [2].

2.3 Modified Mann–Kendall (M-MK) Trend Test

Trend analysis was performed using the Modified Mann–Kendall (MMK) test proposed by Hamed and Rao [7], which corrects the variance of the Mann–Kendall test statistic to reduce the over-detection of significant trends in the presence of serial correlation. The analysis was conducted independently for each grid cell by separating the SPEI-12 time series into individual calendar months and applying a separate MMK test to each month. This approach minimizes the influence of the seasonal cycle and enables the long-term trend for each calendar month to be evaluated independently. Trend direction and statistical significance were determined using the standardized test statistic (z), with grid cells having an absolute z-value greater than 1.96 considered significant at the 95% confidence level. Positive z-values indicate wetting trends, whereas negative z-values indicate drying trends.

3 Results

The areal summary of the pixel-based Modified Mann–Kendall (MMK) analysis performed for each calendar month during the 1981–2022 period is presented in Table 1, while the spatial distribution of statistically significant trends is shown in Figure 1. Areal percentages were calculated relative to the total area with valid data for each month. Overall, the results reveal a spatially and seasonally heterogeneous pattern rather than a uniform drying trend across Türkiye. Areas exhibiting statistically significant drying ($z < -1.96$) remained limited

throughout the year, ranging from 2.3% of the study area in November to 4.6% in December. In contrast, statistically significant wetting ($z > +1.96$) consistently covered larger areas, varying from 5.3% in December to 11.9% in March. Accordingly, the area exhibiting significant wetting exceeded that affected by significant drying in every month of the year.

The seasonal distribution of the trends exhibited clear variability. Wetting reached its greatest spatial extent during late winter and early spring, accounting for 11.3% of the study area in February and 11.9% in March, before declining to 5.5–6.3% during summer and autumn. Drying reached its maximum spatial extent in December (4.6%), followed by April (3.9%). December also recorded the smallest extent of significant wetting (5.3%), making it the month in which the spatial extents of drying and wetting were most similar.

From a spatial perspective, the most notable finding was the persistence of drying in specific regions. Statistically significant drying was detected throughout the year in Southeastern Anatolia (the GAP region) and the Upper Euphrates section of Eastern Anatolia. A secondary drying cluster repeatedly occurred in the northeastern interior, while in December the drying pattern expanded across a larger portion of Eastern Anatolia. In contrast, wetting trends were concentrated primarily in the hinterland of the western and central Black Sea region, as well as in Thrace, northern Central Anatolia, and the vicinity of Artvin in northeastern Türkiye. No statistically significant trends were detected across most of the Aegean and Mediterranean coastal zones or over large parts of Central Anatolia throughout the study period.

These spatial patterns are consistent with previous studies identifying Southeastern Anatolia as a major drought hotspot [3, 8] and northern Türkiye as a region exhibiting relatively wetter conditions [3].

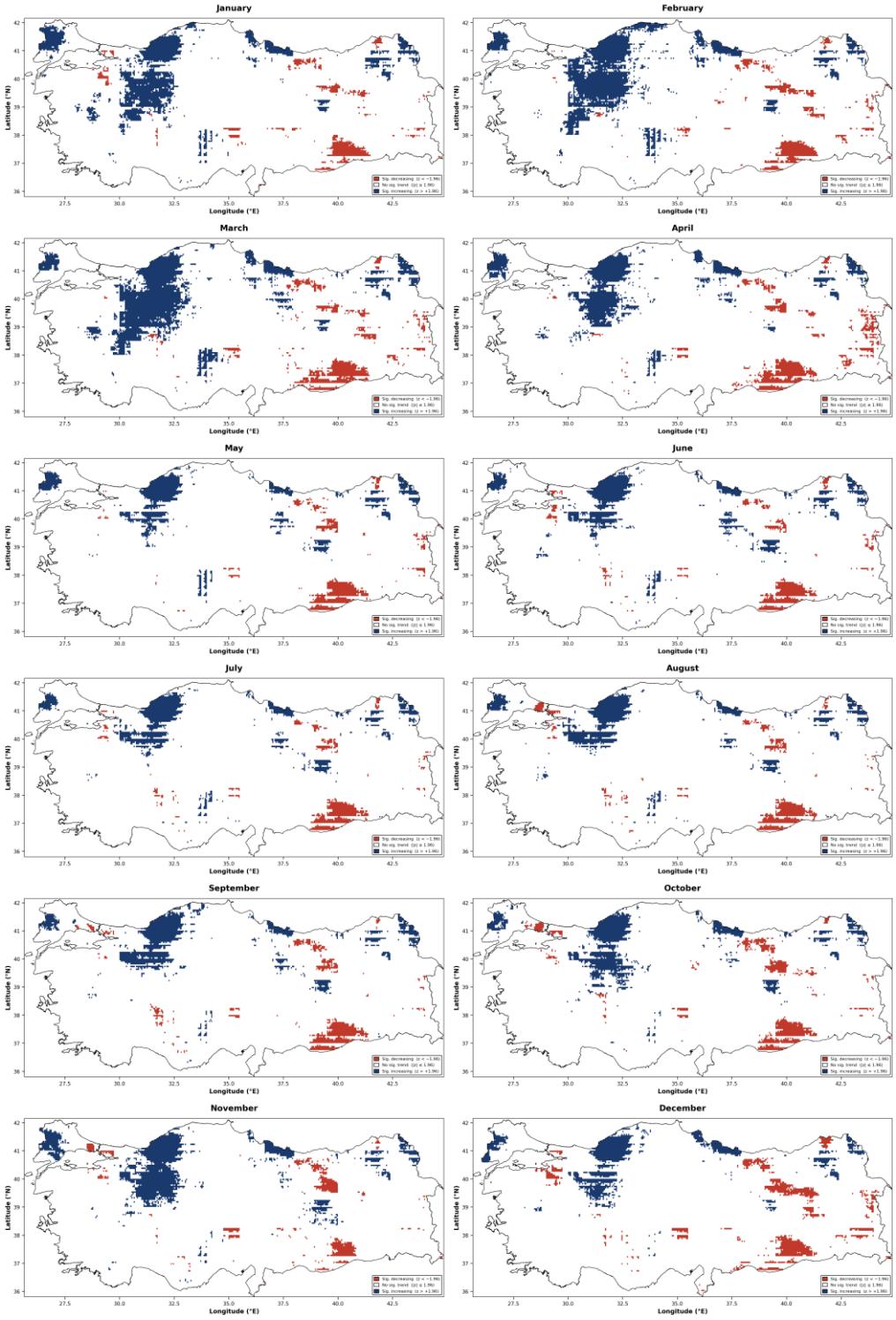


Figure 1. Monthly M-MK trend maps of SPEI-12 (January–December). Red: significant drying; blue: significant wetting; white: non-significant.

Table 1. Areal extent of significant drying and wetting trends from the monthly M-MK analysis

Month	Sig. drying (%)	Sig. wetting (%)
January	2.73	9.33
February	3.14	11.25
March	3.77	11.90
April	3.95	7.65
May	2.76	5.56
June	2.72	6.10
July	2.52	5.62
August	2.66	5.79
September	2.79	6.18
October	3.32	6.33
November	2.33	8.13
December	4.60	5.29

4 Conclusion

This study investigated monthly drought trends across Türkiye for the 1981–2022 period using the Modified Mann–Kendall (M-MK) test applied to a high-resolution gridded SPEI-12 dataset. The use of a high-resolution gridded dataset enabled a detailed assessment of regional drought patterns. The results showed that statistically significant drying remained limited throughout the year, affecting approximately 2.3–4.6% of the study area, whereas significant wetting consistently covered larger areas, ranging from 5.3% to 11.9% of the study area. Persistent drying was detected throughout the year in the GAP region of Southeastern Anatolia and the Upper Euphrates Basin, while recurrent wetting was observed in the western and central Black Sea hinterland, Thrace, and northern Central Anatolia. Overall, the findings indicate that drought trends in Türkiye are characterized by pronounced regional and seasonal variability rather than a uniform nationwide drying pattern. These findings highlight the importance of regional-scale drought assessment for water resources management and agricultural planning, particularly in drought-prone regions. Future studies incorporating multiple SPEI accumulation timescales together with large-scale climate teleconnection indices may provide further insight into the mechanisms driving these regional drought patterns.

Acknowledgments

The authors gratefully acknowledge the Centre for Environmental Data Analysis (CEDA) and the Hydro-JULES project for providing free access to the SPEI dataset used in this study.

References

1. Tuel, A., Eltahir, E.A.B.: Why is the Mediterranean a climate change hot spot? J. Climate 33(14), 5829–5843 (2020). https://doi.org/10.1175/JCLI-D-19-0910.1

2. Vicente-Serrano, S.M., Beguería, S., López-Moreno, J.I.: A multiscalar drought index sensitive to global warming: the standardized precipitation evapotranspiration index. J. Climate 23(7), 1696–1718 (2010). https://doi.org/10.1175/2009JCLI2909.1

3. Serkendiz, H., Tatlı, H., Kılıç, A., Çetin, M., Sungur, A.: Analysis of drought intensity, frequency and trends using the SPEI in Turkey. Theor. Appl. Climatol. 155(4), 2997–3012 (2024). https://doi.org/10.1007/s00704-023-04772-y

4. Türkeş, M.: Climate and drought in Turkey. In: Harmancioglu, N.B., Altinbilek, D. (eds.) Water Resources of Turkey. World Water Resources, vol. 2, pp. 85–125. Springer, Cham (2020). https://doi.org/10.1007/978-3-030-11729-0_4

5. Gebrechorkos, S., Peng, J., Dyer, E., Miralles, D.G., Vicente-Serrano, S.M., Funk, C., Beck, H., Asfaw, D., Singer, M., Dadson, S.: Hydro-JULES: Global high-resolution drought datasets from 1981–2022 – Amendment to CHIRPS_GLEAM subset. NERC EDS Centre for Environmental Data Analysis (2024). https://catalogue.ceda.ac.uk/uuid/e652f0109f21401680bc3c0ac834a96e
6. İpek, A., Kahya, E.: Integrating spatio-probabilistic mapping and remote sensing for comprehensive drought risk assessment. Model. Earth Syst. Environ. 12, 43 (2026). https://doi.org/10.1007/s40808-025-02696-2
7. Hamed, K.H., Rao, A.R.: A modified Mann–Kendall trend test for autocorrelated data. J. Hydrol. 204(1–4), 182–196 (1998). https://doi.org/10.1016/S0022-1694(97)00125-X
8. Gumus, V., Simsek, O., Avsaroglu, Y., Agun, B.: Spatio-temporal trend analysis of drought in the GAP region, Turkey. Nat. Hazards 109(2), 1759–1776 (2021). https://doi.org/10.1007/s11069-021-04897-1

Author Contribution Statement

- *Conceptualization:* A.F. İpek, E. Kahya.
- *Methodology:* A.F. İpek.
- *Investigation:* A.F. İpek.
- *Writing – Original Draft:* A.F. İpek.
- *Writing – Review & Editing:* E. Kahya.

List of Abbreviations

- **SPEI** — Standardized Precipitation Evapotranspiration Index
- **M-MK** — Modified Mann–Kendall Trend Test
- **PET** — Potential Evapotranspiration
- **GAP** — Southeastern Anatolia Project
- **CHIRPS** — Climate Hazards Group InfraRed Precipitation with Station data
- **GLEAM** — Global Land Evaporation Amsterdam Model

Funding
This research received no external funding.

Conflict of Interest
The author declares no conflict of interest.

Data Availability
The dataset supporting the findings of this study is publicly accessible. The high-resolution SPEI dataset used in this study is openly available from the Centre for Environmental Data Analysis (CEDA) at https://catalogue.ceda.ac.uk/uuid/e652f0109f21401680bc3c0ac834a96e.

Ethical Approval
Not applicable.

Publication Note
This paper was peer-reviewed, accepted for presentation, and included in the proceedings of the ACE2026 – International Conference on Advances in Civil Engineering, held on 12–14 October 2026 in Trabzon, Türkiye.

This paper may be cited as follows:
Ahmet Faruk İpek, Ercan Kahya, "Is Türkiye Drying? Regional and Seasonal Drought Trends from High-Resolution SPEI," in Proceedings of the ACE2026 – International Conference on Advances in Civil Engineering, Trabzon, Türkiye, 12–14 October 2026.

Investigation of Uncertainties in 2D Dam Break Simulations by Monte Carlo Simulations

Muhammed Furkan Kart[1] and Ali Ercan[2,*]

[1] 0009-0008-6114-4346, Middle East Technical University, Civil Engineering Department, Ankara, Türkiye, fkart@metu.edu.tr
[2] 0000-0003-1052-4302, Middle East Technical University, Civil Engineering Department, Ankara, Türkiye, ercanali@metu.edu.tr (* corresponding author)

Abstract. Manning's roughness coefficient is a key input in two-dimensional (2D) dam-break flood modelling, yet it cannot be measured directly and is estimated from terrain classification. Deterministic models assign a single fixed value, which does not reflect this estimation uncertainty and can produce overconfident predictions. A Monte Carlo framework is applied to dam-break modelling with GeoClaw, a 2D nonlinear shallow-water solver with adaptive mesh refinement. The 1959 Malpasset dam failure, documented by post-event police high-water marks, is used as the test case. Two roughness configurations (a spatially uniform random coefficient and a region-wise variable field over thirteen sub-regions) and two priors (uniform and log-normal) are combined into four cases, each with fifty Latin-Hypercube realizations. Maximum water-surface elevation, depth and arrival time are extracted at the surveyed points and valley gauges, and a probabilistic inundation map is built from each ensemble. Results show that the inundation footprint is geometry-limited and nearly insensitive to roughness, whereas local depths, peak elevations and especially the wave arrival time are sensitive, the arrival spread growing from seconds near the dam to minutes downstream, broadly consistent with documented field records. The region-wise variable field gives a small improvement in coverage (24–29%) and median error, and the uniform prior outperforms the log-normal one. The framework thus quantifies how roughness uncertainty propagates into the predicted flood and identifies the modelling choices that most affect the depth and timing estimates.

Keywords: Malpasset dam break; Monte Carlo simulation; Manning roughness uncertainty.

1 Introduction

Dam-break floods are among the most destructive hydraulic hazards, and their reliable simulation is essential for hazard assessment, risk mitigation, and emergency planning. Two-dimensional (2D) solvers of the nonlinear shallow-water equations (NSWE) are now routine tools for reproducing a dam-break wave over complex terrain [1, 2, 3]. The predictive quality of such models depends not only on the numerical scheme and the terrain but also on the bottom friction, which is commonly expressed by Manning's roughness coefficient n.

Unlike geometric parameters, Manning's n cannot be measured directly and instead is estimated from land-cover characteristics, and engineering tables which introduce unavoidable uncertainty. Deterministic practice assigns a single roughness n and produces a single flood prediction, hiding parameter uncertainty and conveying a false sense of confidence in the predicted water levels, flood extent, and arrival time. A probabilistic treatment, in which n is

described by a distribution rather than a point value, enables this uncertainty to be explicitly propagated through the numerical model.

Monte Carlo (MC) simulation provides a general framework for such uncertainty propagation by repeatedly sampling the roughness field from a prescribed prior distribution, executing the numerical model for each realization, and statistically analyzing the resulting ensemble. Although roughness-induced uncertainty has been widely investigated for riverine flood modelling using generalized likelihood uncertainty estimation (GLUE) and MC approaches [4-6], similar studies for 2D dam-break simulations remain limited. Existing investigations are generally validated against simulated or mapped inundation extents rather than independent field observations [7]. Moreover, two further modelling choices have been rarely examined together: (i) representing Manning's roughness as either a single domain-wide random variable or a spatially variable field, and (ii) which prior distribution is assigned to the coefficient [7]. This study addresses both issues using a well-established benchmark while directly validating the uncertainty predictions against independent field observations.

The 1959 Malpasset dam failure serves as the benchmark case because it provides a unique set of independent observations, including maximum water levels surveyed at seventeen field locations and recorded failure times of three electrical transformers, which constrain flood-wave arrival times [8-10]. A GeoClaw-based Monte Carlo framework is developed in which Manning's roughness is sampled using Latin Hypercube Sampling under two spatial representations and two prior distributions, resulting in four experimental cases with fifty realizations each. The objectives of this study are to: (i) quantify the propagation of Manning's roughness uncertainty into predicted inundation extent, water depth, and water-surface elevation; (ii) evaluate the influence of roughness representation and prior distribution on prediction uncertainty; (iii) assess the capability of the simulated uncertainty bounds to capture the independent field observations; and (iv) characterize how the uncertainty in the wave arrival time develops along the valley.

2 Study Area and Observational Data

The Malpasset arch dam, located on the Reyran River about 12 km upstream of Fréjus in south-eastern France, failed on the night of 2 December 1959 and released roughly 42 million m^3 of water into the narrow Reyran valley [11, 12]. The flood wave travelled down the valley and reached the Fréjus plain and the Mediterranean Sea in about twenty minutes, causing more than four hundred fatalities [13]. The event has become a standard benchmark for 2D dam-break solvers because of the combination of complex topography, a strongly bending valley, and a documented set of observations [9, 14].

The computational domain used here spans approximately 17.3 km in the along-valley direction and 9.3 km across, covering the reservoir, the Reyran valley, the Fréjus plain, and the coastal outlet. Figure 1 shows the domain topography together with the dam axis, the seventeen police high-water marks (P1–P17) that provide the field validation data, the nine physical-model gauges (G6–G14), and the three electrical transformers (A–C). While the high-water marks and gauges record the peak water level, the three transformers record the wave timing: short-circuited in turn by the arriving flood, their logged power-failure times give observed wave-arrival times of about 100, 1240 and 1420 s [8, 11]. The observed maximum water-surface elevations decrease monotonically along the valley, from about 88 m near the dam (P2) to about 14 m in the downstream reach (P17), reflecting the progressive attenuation and spreading of the wave.

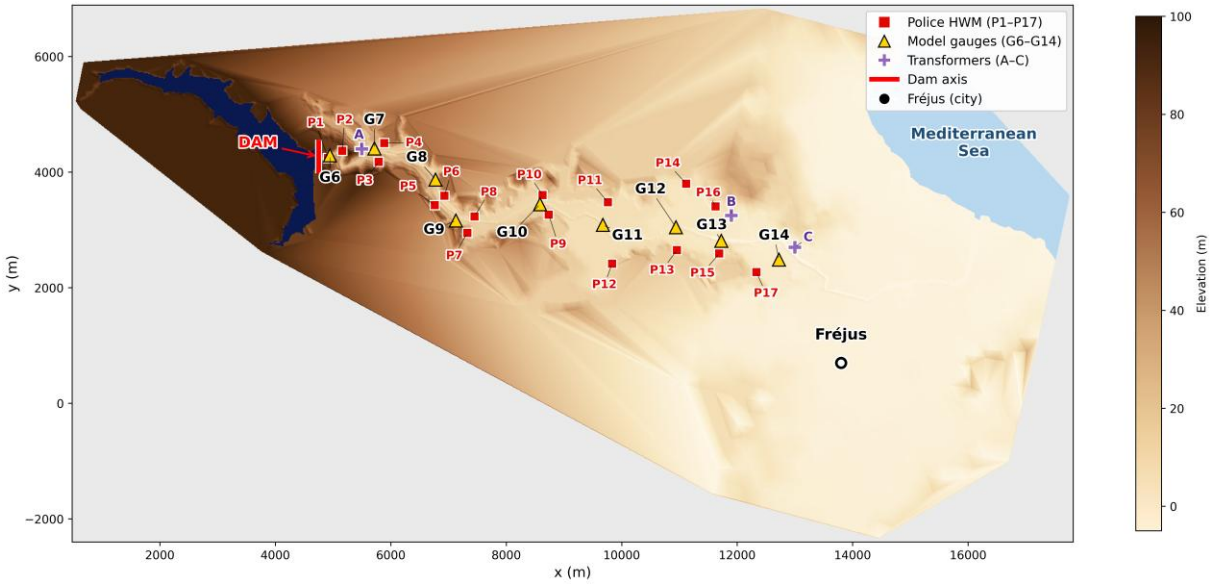


Fig. 1. Malpasset study area: topography, dam axis, police high-water marks (P1–P17), physical-model gauges (G6–G14) and transformers (A–C).

The valley gauges originate from an undistorted 1:400 laboratory model of the flooded reach, built by the Laboratoire National d'Hydraulique (LNH) of Électricité de France (EDF) in 1964, on which peak water levels were recorded at fourteen gauges (S1–S14) [9, 10]. The five reservoir gauges (S1–S5) were unavailable, leaving the nine downstream stations S6–S14 (labelled G6–G14 here), later distributed to the CADAM participants with the digitized topography [8, 11].

Only the seventeen police high-water marks are used as the validation reference in this study. Numerical gauges at the G6–G14 locations are still recorded and are used to examine the simulated flow dynamics (Section 4.5), but they are excluded from all validation metrics, because the 1:400 scaled model was built with a single, spatially uniform roughness by construction [8, 10]; comparing spatially variable roughness configurations against a uniform-roughness laboratory benchmark would be methodologically inconsistent. The field high-water marks, by contrast, are independent observations of the real event.

3 Methodology

The flood is simulated with GeoClaw, an open-source solver of the 2D nonlinear shallow-water equations built on the Clawpack finite-volume framework with block-structured adaptive mesh refinement (AMR) [1, 2, 15]. GeoClaw uses a well-balanced, wave-propagation Riemann solver with robust wetting-and-drying treatment, which makes it suitable for dam-break flows over irregular, initially dry terrain [9]. A high-resolution flux limiter is applied to control numerical oscillations [1]. Three levels of adaptive refinement are used, concentrating resolution on the moving wave front and reaching a finest cell size of about 12.6 m in the valley. Bottom friction is imposed through the Manning formulation, and the roughness field is the uncertain input sampled in the Monte Carlo experiment.

The reservoir is initialized hydrostatically and released instantaneously at t = 0, and each realization is integrated for 4000 s, long enough for the maximum water levels to be established at all validation points. Peak water-surface elevation and depth are recorded on a fixed 20 m grid with the solver's maximum-monitoring (fgmax) capability, and water-depth time series are stored at the surveyed points and the valley gauges (G6–G14) to characterize the flow dynamics and arrival time.

Uncertainty in Manning's n is propagated by Monte Carlo simulation, combining two spatial representations of the roughness field and two priors into the four cases of Table 1. The constant-n cases share one random coefficient over the domain; the variable-n cases partition the flooded envelope into sub-regions with an independent coefficient each. Two priors are tested: a uniform distribution (the standard non-informative choice) and a log-normal distribution (physically motivated for strictly positive parameters and increasingly used in flood modelling).

Table 1. Monte Carlo experimental design.

Case	Roughness field	Prior distribution	Sampled dimensions	Number of samples
1A	Constant	Uniform	1	50
1B	Constant	Log-normal	1	50
2A	Variable	Uniform	13	50
2B	Variable	Log-normal	13	50

In all cases the samples are generated by Latin Hypercube Sampling, which stratifies each marginal and covers the parameter space more efficiently than independent random sampling [16]. The roughness bounds and the number of realizations were guided by a preliminary sensitivity analysis against published values for the site. The uniform prior spans n in [0.020, 0.060], a physically defensible range for the mixed vegetated, rocky and built terrain of the valley; the log-normal prior is centred on the widely used nominal value n = 0.033 [8, 9, 10] with a coefficient of variation of 0.20. The adequacy of fifty realizations was verified for every case by tracking the 5th, 50th and 95th percentiles of the P-RMSE distribution against the cumulative sample size; in each case the median and the 5th–95th range stabilize well before N = 50, in both the one- and thirteen-dimensional configurations.

For the variable-n cases the domain is divided by a 5 × 4 grid clipped to the flooded envelope, yielding thirteen active sub-regions in which the coefficient is sampled independently; the remaining, always-dry or permanently wet cells retain a fixed baseline value. This regular grid is a deliberately simple, geometry-based proxy for spatial heterogeneity rather than a land-cover-derived roughness field; it keeps the sampled dimension modest (thirteen) while letting the roughness differ between reaches, which is sufficient for the present purpose of contrasting a variable field with a single domain-wide value.

Model performance is quantified against the seventeen police high-water marks, whose observed maxima were digitized from the published comparison figures of [9, 10]. For each realization the simulated maximum water-surface elevation is interpolated to every observation point using an inverse-distance weighting of the four nearest fgmax cells, and the point root-mean-square error (P-RMSE) between simulated and observed elevations is computed. The ensemble of P-RMSE values characterizes the accuracy distribution of each case. In addition, the observation coverage is defined as the number of the seventeen field points whose observed elevation falls within the min-max envelope of the ensemble at that point; it measures how well the simulated uncertainty bounds bracket reality. The wave timing is checked separately against the three documented transformer failure times (Section 2). Finally, a probabilistic inundation map is built by counting, for each grid cell, the fraction of realizations in which the depth exceeds a given threshold.

4 Results

The accuracy across the four cases, the water-surface and inundation results, the probabilistic maps, and the flow dynamics and arrival times are presented in turn.

4.1 Accuracy Across Cases

Table 2 summarizes the P-RMSE distribution of the four cases. The median P-RMSE ranges from 3.73 m (Case 2A) to 3.96–3.97 m (Cases 1B and 2B), and the best individual realization reaches 3.23 m, obtained in the constant-n case 1A at the upper end of the roughness range (n ≈ 0.060). This best value is reached without any site-specific calibration, purely as the most favourable draw of the friction prior. Across the constant-n ensemble the P-RMSE is strongly and negatively correlated with the sampled roughness (correlation about −0.97): higher friction reduces the peak elevations and improves the fit at the field points, indicating that in the present configuration the fit improves towards roughness values above the nominal 0.033 (Fig. 2). Because the correlation is monotonic, the best fit is pushed to the upper bound of the prior; since n = 0.060 already represents the upper end of the physically plausible range for this mixed vegetated, rocky and built terrain, the roughness is effectively exhausted at its ceiling, and the residual error cannot be removed by admissible friction alone.

Table 2. P-RMSE distribution and observation coverage for the four cases.

Case	P-RMSE min (m)	P-RMSE median (m)	P-RMSE max (m)	Coverage
1A	3.23	3.78	4.19	4/17 (24%)
1B	3.48	3.97	4.19	4/17 (24%)
2A	3.26	3.73	4.15	5/17 (29%)
2B	3.45	3.96	4.20	5/17 (29%)

Two systematic effects are visible. First, the variable-n cases give a small but consistent improvement over their constant-n counterparts: the median P-RMSE decreases from 3.78 m to 3.73 m and the coverage rises from four to five of the seventeen points. Second, for both spatial representations the uniform prior outperforms the log-normal one by about 0.2 m in median error, because the log-normal samples concentrate near the nominal 0.033 value, which is sub-optimal for this configuration. These error levels are of the same order as earlier deterministic studies of the benchmark: the finite-element (TELEMAC-2D), finite-volume and multi-code CADAM results [8, 9, 10, 11, 17, 18] report their agreement graphically rather than as a single value, and re-evaluating their digitized curves with the present seventeen-point P-RMSE gives about 3.0 m. A strict cross-code ranking is deliberately avoided, however: differences in scheme, mesh, topography and boundary treatment mean that two codes need not reach the same field error even under identical roughness. The analysis is therefore framed as an internal comparison of the four cases, with the solver, mesh and topography held fixed and only the roughness representation and prior varied.

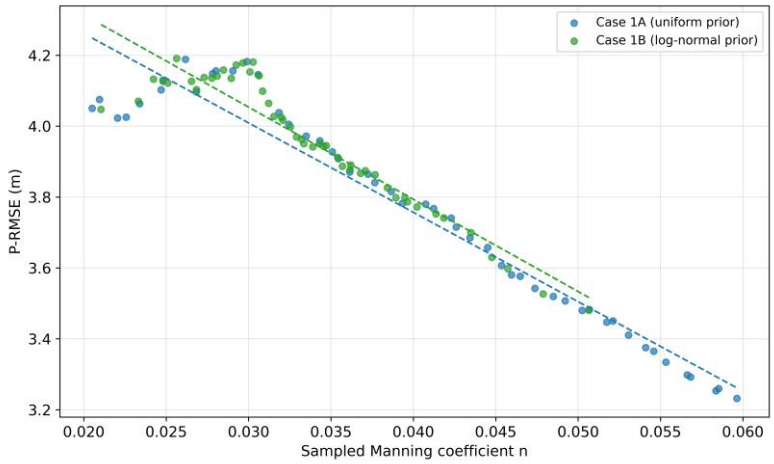


Fig. 2. P-RMSE versus sampled Manning coefficient, constant-n cases (r = −0.97 for Case 1A).

4.2 Water-Surface Elevation

Figure 3 compares the simulated and observed maximum water-surface elevations at the seventeen survey points. The ensemble medians closely reproduce the observed attenuation of the flood wave along the valley, yielding a correlation coefficient of approximately 0.98 and a mean bias of only −0.3 m, indicating excellent agreement with no systematic over- or underestimation. The uncertainty bands, represented by the ensemble minimum and maximum values, are relatively narrow, spanning approximately 2 m at most survey locations and becoming negligible in the downstream reaches where the flow is largely insensitive to Manning's roughness. Consequently, only a limited number of observations fall within the simulated uncertainty envelopes (Table 2). The implications of this limited spread are discussed in Section 5.

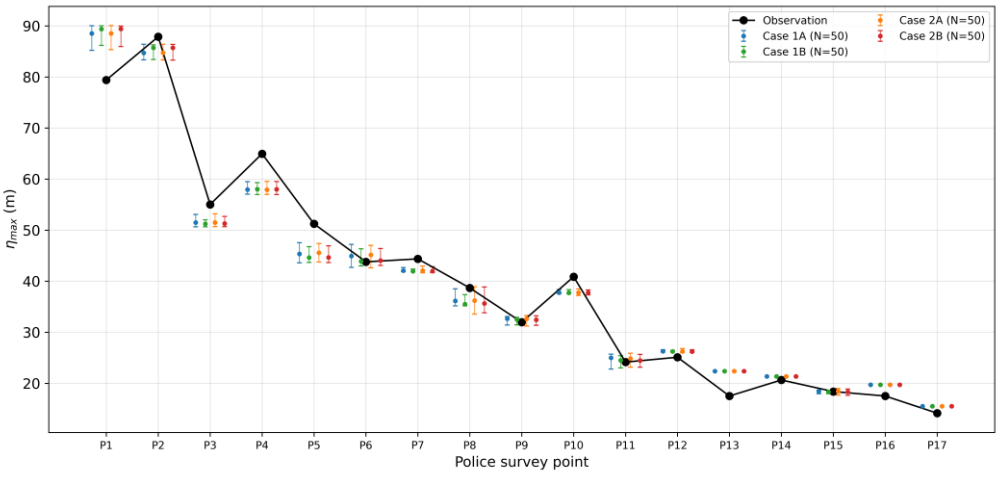


Fig. 3. Maximum water-surface elevation at the survey points: ensemble medians and min-max bands versus field data.

4.3 Inundation Footprint

The mean inundated area at four depth thresholds (h > 0.05, 1, 2 and 5 m) is essentially the same for all four cases, at about 28, 21, 13 and 6 km² respectively, with the four cases differing by at most 1.3 km² at any threshold. The inundation extent is thus geometry-limited: the large release volume fills the Reyran valley and the Fréjus plain to a geometric envelope that is set by the terrain rather than by the roughness. Manning's n modulates the dynamics of the flow (depths, arrival times, and peak elevations) but not the overall area reached by the water.

4.4 Probabilistic Inundation and Uncertainty Maps

The full ensemble is summarized spatially in Figure 4 for the best-performing case (2A). The first two panels show the probability that the local depth exceeds 1 m and 5 m: the valley thalweg and the Fréjus plain are inundated with near-certainty, while the probability decays sharply toward the lateral margins of the flooded envelope, where the wet or dry state depends on the sampled roughness. The third panel maps the ensemble standard deviation of the maximum water-surface elevation, highlighting the margins of the flood and the reaches around the valley bends as the zones of largest predictive uncertainty. Together these maps translate the parameter uncertainty into a spatially explicit hazard product that a single deterministic run cannot provide.

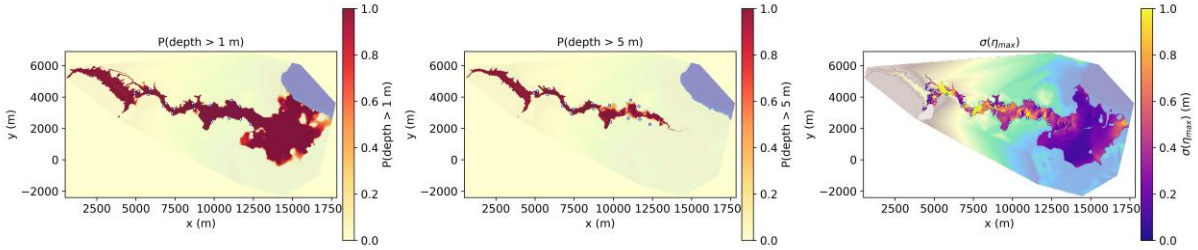


Fig. 4. Ensemble summary for Case 2A: probability of the maximum depth exceeding 1 m (left) and 5 m (centre), and the ensemble standard deviation of the maximum water-surface elevation (right).

4.5 Flow Dynamics and Arrival Time

To examine how the roughness uncertainty propagates into the transient flow, water-depth time series were extracted at four gauge locations spanning the valley from the dam to the downstream reach (G6, G9, G12 and G14 in Fig. 1). As stated in Section 2, these positions are not validation targets. Figure 5 shows the ensemble median and min-max band of the flow depth at these gauges for Case 1A. The peak depth decreases strongly downstream, from about 40 m just below the dam (G6) to about 5 m near the coast (G14), consistent with the attenuation of the wave. The spread of the wave arrival time, by contrast, grows steadily along the valley: the arrival is essentially deterministic near the dam (a spread of only a few seconds across the fifty realizations at G6) but widens to about 130 s at G9, roughly 520 s at G12 and about 800 s (some thirteen minutes) at G14. Thus, although Manning's roughness has almost no effect on the flood extent, it exerts a strong control on the timing of the wave in the downstream reach, where arrival-time uncertainty is largest and most relevant for evacuation planning.

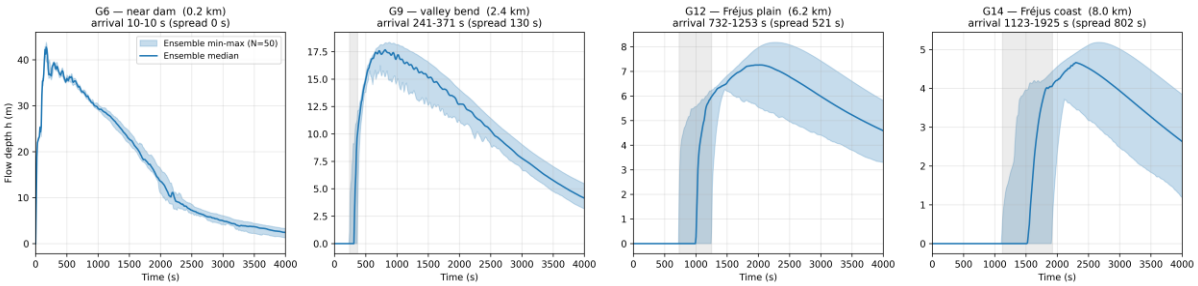


Fig. 5. Ensemble flow-depth time histories at gauges G6, G9, G12 and G14 (Case 1A); grey shading marks the arrival-time spread.

4.6 Comparison with Observed Arrival Times

The simulated arrival times can be compared with the three documented transformer failure times introduced in Section 2 (about 100, 1240 and 1420 s at A, B and C). For Case 1A the two downstream failures fall within the ensemble arrival band, and the near-dam site is reproduced on the same time scale, consistent both with the timing recovered in the deterministic prototype and with the published estimates for this benchmark [10]. This provides an independent, field-based check on the model timing that complements the water-level validation of the previous sections.

5 Discussion

The experiments give a consistent picture of how roughness uncertainty propagates in a 2D dam-break simulation. The inundation footprint is controlled by valley geometry and the release volume and is almost insensitive to Manning's n, whereas the local depths, arrival times and peak elevations are sensitive. For hazard mapping this means that in a terrain-confined valley such as this one the flood extent can be mapped robustly even under substantial roughness uncertainty, but the depth and level estimates that drive structural loading and evacuation timing require the uncertainty to be carried explicitly. The time-history analysis (Fig. 5) sharpens this point: the wave arrival time is almost deterministic near the dam but its ensemble spread grows to about 800 s downstream, so roughness uncertainty translates into a large arrival-time spread precisely in the populated downstream reach where that timing matters most.

Allowing the roughness to vary between sub-regions gives only a marginal gain over a single coefficient (about 0.05 m in median P-RMSE and one extra captured point) because the geometry-limited footprint leaves the additional degrees of freedom acting mainly on local depths. This insensitivity is terrain-regime-dependent: on wider floodplains a distributed roughness has altered the inundated area by about 9% [7], whereas the confined, steep Reyran gorge is terrain-controlled. The uniform prior outperforms the log-normal one, although this partly confounds the prior shape with its range, since the uniform prior also samples the higher n (up to 0.060) where the fit is best; the nominal 0.033 around which the log-normal concentrates is simply sub-optimal in the present configuration.

The ensemble medians reproduce the observed along-valley attenuation closely and without systematic bias, so the central predictions are accurate. The bands from roughness alone are narrow, however, and the coverage in Table 2 should be read as a lower bound obtained from a single uncertainty source. The remaining spread reflects factors not varied here: the reservoir and breach assumptions, the terrain, bathymetry and sea level, the numerical thresholds, the intrinsic uncertainty of the historical high-water marks [19], and the depth-averaged shallow-water approximation in the strongly three-dimensional bends of the valley [14]. This is an expected property of single-source quantification rather than a shortcoming of the model, consistent with the general finding that neglecting structural model uncertainty underestimates the upper tail of flood hazard [20]; the arrival-time check of Section 4.6, which broadly reproduces the transformer records, indicates that the flood is not mis-timed.

The study is deliberately scoped to a single historical event, one solver, and one uncertain input; extending the framework to multiple uncertain inputs and additional dam-break cases is left for future work.

6 Conclusions

A Monte Carlo framework was developed to propagate Manning's roughness uncertainty through GeoClaw simulations of the 1959 Malpasset dam-break event. Four uncertainty scenarios, combining constant and spatially variable roughness representations with uniform and log-normal prior distributions, were evaluated using fifty Latin Hypercube realizations each. The main conclusions are:

- The inundation extent is primarily controlled by valley geometry and exhibits little sensitivity to Manning's roughness, whereas local water depths, peak water levels, and especially wave arrival times are strongly influenced by roughness uncertainty.
- The uncertainty in the wave arrival time grows strongly downstream, from a few seconds near the dam to about 800 s in the downstream reaches, so that roughness uncertainty affects the timing most in the reaches where evacuation planning matters the most.

- A spatially variable roughness field gives a small but consistent improvement over a single domain-wide coefficient, both in median error (3.78 m to 3.73 m) and in observation coverage (24–29%).
- The uniform prior consistently outperforms the log-normal prior, because it also samples the higher roughness values that fit best in the present configuration rather than concentrating on the nominal n = 0.033.
- The ensemble medians closely reproduce the observed maximum water levels, whereas the uncertainty bounds generated from Manning's roughness alone remain relatively narrow. This indicates that roughness is one of the contributors to the overall predictive uncertainty and that additional sources, including terrain uncertainty, breach characteristics, and model structural uncertainty, should be incorporated to fully represent the observed variability.

Acknowledgments

The authors thank the Department of Civil Engineering at Middle East Technical University for computational support. No specific funding was received for this work. The data supporting the findings of this study are available from the authors on request. The authors declare no conflict of interest.

References

1. LeVeque, R.J.: Finite Volume Methods for Hyperbolic Problems. Cambridge University Press, Cambridge (2002). https://doi.org/10.1017/CBO9780511791253
2. LeVeque, R.J., George, D.L., Berger, M.J.: Tsunami modelling with adaptively refined finite volume methods. Acta Numerica 20, 211–289 (2011).
3. Haltas, I., Elci, S., Tayfur, G.: Numerical simulation of flood wave propagation in two-dimensions in densely populated urban areas due to dam break. Water Resources Management 30(15), 5699–5721 (2016). https://doi.org/10.1007/s11269-016-1344-4
4. Beven, K., Binley, A.: The future of distributed models: model calibration and uncertainty prediction. Hydrological Processes 6(3), 279–298 (1992). https://doi.org/10.1002/hyp.3360060305
5. Aronica, G., Bates, P.D., Horritt, M.S.: Assessing the uncertainty in distributed model predictions using observed binary pattern information within GLUE. Hydrological Processes 16(10), 2001–2016 (2002). https://doi.org/10.1002/hyp.398
6. Papaioannou, G., Vasiliades, L., Loukas, A., Aronica, G.T.: Probabilistic flood inundation mapping at ungauged streams due to roughness coefficient uncertainty in hydraulic modelling. Advances in Geosciences 44, 23–34 (2017). https://doi.org/10.5194/adgeo-44-23-2017
7. Almeida, I., Santos, H., de Vasconcelos Costa, O., Graciano, V.: Uncertainty reduction in flood areas by probabilistic analyses of land use/cover in models of two-dimensional hydrodynamic model of dam-break. Stochastic Environmental Research and Risk Assessment 38(4), 1335–1350 (2024). https://doi.org/10.1007/s00477-023-02635-6
8. Hervouet, J.-M., Petitjean, A.: Malpasset dam-break revisited with two-dimensional computations. Journal of Hydraulic Research 37(6), 777–788 (1999).
9. George, D.L.: Adaptive finite volume methods with well-balanced Riemann solvers for modeling floods in rugged terrain: application to the Malpasset dam-break flood (France, 1959). International Journal for Numerical Methods in Fluids 66(8), 1000–1018 (2011).

10. Valiani, A., Caleffi, V., Zanni, A.: Case study: Malpasset dam-break simulation using a two-dimensional finite volume method. Journal of Hydraulic Engineering 128(5), 460–472 (2002).
11. Goutal, N.: The Malpasset dam failure: an overview and test case definition. In: Proceedings of the 4th CADAM Meeting, Zaragoza, Spain (1999).
12. Duffaut, P.: The traps behind the failure of Malpasset arch dam, France, in 1959. Journal of Rock Mechanics and Geotechnical Engineering 5(5), 335–341 (2013).
13. Boudou, M., Moatty, A., Lang, M.: Analysis of major flood events: collapse of the Malpasset Dam, December 1959. In: Vinet, F. (ed.) Floods, vol. 1, pp. 3–19. ISTE Press, Elsevier (2017).
14. Biscarini, C., Di Francesco, S., Ridolfi, E., Manciola, P.: On the simulation of floods in a narrow bending valley: the Malpasset dam break case study. Water 8(11), 545 (2016). https://doi.org/10.3390/w8110545
15. Brodtkorb, A.R., Saetra, M.L., Altinakar, M.: Efficient shallow water simulations on GPUs: implementation, visualization, verification, and validation. Computers & Fluids 55, 1–12 (2012).
16. McKay, M.D., Beckman, R.J., Conover, W.J.: A comparison of three methods for selecting values of input variables in the analysis of output from a computer code. Technometrics 21(2), 239–245 (1979).
17. Alcrudo, F., Gil, E.: The Malpasset dam break case study. In: Proceedings of the CADAM Meeting, Zaragoza, Spain (1999).
18. Soares-Frazao, S., Zech, Y.: 2D and 1D modelling of the Malpasset dam-break test case. In: Proceedings of the CADAM Meeting, Zaragoza, Spain (1999).
19. Koenig, T.A., Bruce, J.L., O'Connor, J.E., et al.: Identifying and preserving high-water mark data. U.S. Geological Survey Techniques and Methods, book 3, chap. A24 (2016).
20. Wong, T.E., Klufas, A., Srikrishnan, V., Keller, K.: Neglecting model structural uncertainty underestimates upper tails of flood hazard. Environmental Research Letters 13(7), 074019 (2018). https://doi.org/10.1088/1748-9326/aacb3d

Author Contribution Statement

- Conceptualization and Methodology: Ali Ercan, Muhammed Furkan Kart
- Software, Simulations, Investigation and Formal Analysis: Muhammed Furkan Kart
- Writing – Original Draft: Muhammed Furkan Kart; Review & Editing: Ali Ercan
- Supervision: Ali Ercan

Publication Note

This paper was peer-reviewed, accepted for presentation, and included in the proceedings of the ACE2026 – International Conference on Advances in Civil Engineering, held on 12–14 October 2026 in Trabzon, Türkiye.

This paper may be cited as follows:

M. Furkan Kart and Ali Ercan, “Investigation of Uncertainties in 2D Dam Break Simulations by Monte Carlo Simulations,” in Proceedings of the ACE2026 – International Conference on Advances in Civil Engineering, Trabzon, Türkiye, 12–14 October 2026.

Comparison of Climate Model Performances of the Same Institutes using Hydrological Model Outputs: A Case Study with CMIP5 GCM, CMIP6 GCM, and CMIP5 RCM over Göksu Basin

Murat Yegin[1], O. Burak Akgun[2] and Elcin Kentel[3]
[1] orcidID, Middle East Technical University, Civil Engineering Department, Ankara, Türkiye, myegin@metu.edu.tr
[2] orcidID, Middle East Technical University, Civil Engineering Department, Ankara, Türkiye, akgunb@metu.edu.tr
[3] orcidID, Middle East Technical University, Civil Engineering Department, Ankara, Türkiye, ekentel@metu.edu.tr

Abstract. Climate models (CMs) developed by different institutes are widely used to assess flood risks; however, their projections differ because of variations in model structure, spatial resolution, and emission scenarios. These differences propagate through hydrological models and introduce uncertainty into streamflow simulations. This study evaluates the consistency of CMs developed by the same research institutes using Global Climate Models (GCMs) from the Coupled Model Intercomparison Project (CMIP) 5 and CMIP6, as well as Regional Climate Models (RCMs) from CORDEX. A total of 42 CMs from 10 institutes are assessed. Daily streamflow is simulated using a HEC-HMS model developed for the Göksu Basin (E17A014 Stream Gage) for 1970–1986, a period selected due to data availability and the construction of major dams after 1986. Model performance is evaluated by comparing simulated and observed flow duration curves through exceedance probabilities.

Results show substantial variability even among models developed by the same institute. For GCMs, differences between observed and simulated discharges exceed 71% for high-flow quantiles (0.002) and 121% for median-flow quantiles (0.5). For RCMs, these discrepancies increase to approximately 600% and 149%, respectively. Although RCMs provide higher spatial resolution, some produce substantially poorer quantile estimates, with errors reaching approximately 185% relative to observations, compared with more robust GCM estimates. These findings demonstrate that models produced by the same institute can yield markedly different hydrological projections and that higher spatial resolution does not necessarily improve streamflow simulations. Overall, the results highlight the importance of adopting a multi-model approach to obtain a more comprehensive and reliable assessment of flood risk under climate change.

Keywords: Climate Models; Hydrological Model; Exceedance Probability; Peak Discharge

1 Introduction

The assessment of flood risk has become increasingly important due to the growing impacts of climate change on the frequency and intensity of extreme hydrological events. Reliable evaluation of future flood hazards is therefore essential for effective water resources management, infrastructure design, and the development of climate adaptation strategies. Climate models developed by numerous research institutions provide projections of future

meteorological variables, such as precipitation and temperature, which serve as key inputs for hydrological modeling and flood risk assessments. However, these models differ in their structure, parameterizations, spatial resolution, and representation of physical processes, leading to considerable variability in their projections. Consequently, selecting appropriate climate models for hydrological applications remains a significant challenge. Furthermore, many research institutions produce multiple climate models with different configurations and assumptions, resulting in additional variability even among models developed by the same institute. Evaluating the consistency and performance of these models is therefore critical for understanding the uncertainties associated with climate projections and improving the reliability of flood risk assessments under changing climate conditions.

Various types of climate model datasets have been widely used to investigate the impacts of climate change on hydrological and meteorological variables. Among the most commonly employed datasets are the Coupled Model Intercomparison Project Phase 5 (CMIP5) Global Climate Models (GCMs) [1–5], CMIP6 GCMs [6–9], and CMIP5-driven Regional Climate Models (RCMs) produced within the Coordinated Regional Climate Downscaling Experiment (CORDEX) framework [10–13]. These datasets have been extensively applied to evaluate projected changes in meteorological variables such as precipitation (2,6,7,10) and temperature (1,6), which are directly available from climate model outputs. In contrast, studies assessing the impacts of climate change on streamflow remain relatively limited (6,13). This is primarily because streamflow is not a direct output of climate models and must instead be simulated using hydrological models driven by climate model projections. The development, calibration, and validation of hydrological models require extensive hydrological and meteorological data, as well as considerable computational effort and time. Consequently, comprehensive evaluations of streamflow responses to different climate model datasets are less common than studies focusing solely on precipitation and temperature projections.

Despite the widespread application of climate model datasets in hydrological impact assessments, limited attention has been given to the consistency of climate models developed by the same research institute and the implications of their differences for streamflow simulations. Therefore, this study aims to evaluate the performance and consistency of climate models produced by the same institutes using GCMs from CMIP5 and CMIP6 and RCMs from the CORDEX initiative. A total of 42 climate models from 10 research institutes are assessed. Daily streamflow is simulated using a calibrated HEC-HMS model for the Göksu Basin, and model performance is evaluated by comparing simulated and observed flow duration curves across different exceedance probabilities. By systematically comparing climate models developed within the same institution, this study provides insights into the variability of hydrological projections attributable to model selection and examines whether higher-resolution regional climate models consistently provide improved streamflow simulations. The findings are expected to contribute to more informed climate model selection and to support more reliable flood risk assessments under changing climate conditions.

2 Study Area and Data

A hydrological model is developed for the E17A014 Stream Gage (SG) located on the Göksu River, which is approximately 271 km long. The basin area is approximately 10,300 km^2, and hydrological simulations are performed using the HEC-HMS developed by the U.S. Army Corps of Engineers. Five meteorological stations are used in the hydrological model (Fig. 1).



Fig. 1. Study area

The GCMs (Table 1*)* and the RCMs (Table 2*)* are given below. The same color in the tables represents models developed by the same institution.

Table 1. GCMs used in the study

Family	Model	Modeling Institution	Country	Horizontal Resolution Lon × Lat, °
CMIP6 GCM	MPI-ESM1-2-HR	Max Planck Institute for Meteorology (MPI)	Germany	0.94 × 0.94
CMIP6 GCM	MPI-ESM1-2-LR	MPI	Germany	1.875 × 1.87
CMIP5 GCM	MPI-ESM-LR	MPI	Germany	1.875 × 1.87
CMIP5 GCM	MPI-ESM-MR	MPI	Germany	1.875 × 1.87
CMIP5 GCM	MRI-CGCM3	Meteorological Research Institute (MRI)	Japan	1.125 × 1.12
CMIP6 GCM	MRI-ESM2-0	MRI	Japan	1.125 × 1.12
CMIP5 GCM	NorESM1-M	Norwegian Climate Centre (NCC)	Norway	2.5 × 1.89
CMIP6 GCM	NorESM2-LM	NCC	Norway	2.5 × 1.89
CMIP5 GCM	EC-EARTH	EC-Earth Consortium	Europe	1.125 × 1.12
CMIP5 GCM	CanESM2	Canadian Centre for Climate Modelling and Analysis (CCCMA)	Canada	2.81 × 2.79
CMIP6 GCM	CanESM5	CCCMA	Canada	2.81 × 2.79
CMIP5 GCM	HadGEM2-CC	Met Office Hadley Centre (MOHC)	United Kingdom	1.875 × 1.25

CMIP5 GCM	HadGEM2-ES	MOHC	United Kingdom	1.875 × 1.25
CMIP5 GCM	CMCC-CESM	Euro-Mediterranean Center on Climate Change (CMCC)	Italy	3.75 × 3.75
CMIP5 GCM	CMCC-CMS	CMCC	Italy	1.875 × 1.87
CMIP6 GCM	CMCC-CM2-SR5	CMCC	Italy	1.25 × 0.94
CMIP6 GCM	CMCC-ESM2	CMCC	Italy	1.25 × 0.94
CMIP5 GCM	MIROC-ESM	JAMSTEC / University of Tokyo / NIES	Japan	2.81 × 2.79
CMIP5 GCM	MIROC-ESM-CHEM	JAMSTEC / University of Tokyo / NIES	Japan	2.81 × 2.79
CMIP5 GCM	MIROC5	University of Tokyo / NIES / JAMSTEC	Japan	1.41 × 1.40
CMIP6 GCM	MIROC6	MIROC Consortium	Japan	1.41 × 1.40
CMIP5 GCM	CNRM-CM5	Centre National de Recherches Météorologiques (CNRM)/Centre Européen de Recherche et Formation Avancée en Calcul Scientifique (CERFACS)	France	1.41 × 1.40
CMIP5 GCM	IPSL-CM5A-LR	Institut Pierre-Simon Laplace (IPSL)	France	3.75 × 1.89
CMIP5 GCM	IPSL-CM5A-MR	IPSL	France	2.5 × 1.27
CMIP5 GCM	IPSL-CM5B-LR	IPSL	France	3.75 × 1.89

Table 2. RCMs used in the study

Driving GCM	**Regional Climate Model (RCM)**	**Modeling Institution**	**Country**	**Horizontal Resolution Lon × Lat, °**
MPI-ESM-LR	CCLM4-8-17	Climate Limited-area Modelling Community (CLM-Community)	Germany	0.11 × 0.11
MPI-ESM-LR	REMO2009 (r1i1p1)	Helmholtz Centre Hereon	Germany	0.11 × 0.11
MPI-ESM-LR	REMO2009 (r2i1p1)	Helmholtz Centre Hereon	Germany	0.11 × 0.11
NorESM1-M	HIRHAM5	Danish Meteorological Institute (DMI)	Denmark	0.11 × 0.11
EC-EARTH	HIRHAM5	DMI	Denmark	0.11 × 0.11
EC-EARTH	CCLM4-8-17	CLM-Community	Germany	0.11 × 0.11
EC-EARTH	RACMO22E	Royal Netherlands Meteorological Institute (KNMI)	Netherlands	0.11 × 0.11
EC-EARTH	RCA4	Swedish Meteorological and Hydrological Institute (SMHI)	Sweden	0.11 × 0.11

IPSL-CM5A-MR	WRF331F	IPSL / WRF consortium	France	0.11 × 0.11
IPSL-CM5A-MR	WRF381P	IPSL / WRF consortium	France	0.11 × 0.11
IPSL-CM5A-MR	RCA4	SMHI	Sweden	0.11 × 0.11
HadGEM2-ES	CCLM4-8-17	CLM-Community	Germany	0.11 × 0.11
HadGEM2-ES	RACMO22E	KNMI	Netherlands	0.11 × 0.11
HadGEM2-ES	RCA4	SMHI	Sweden	0.11 × 0.11
CNRM-CM5	CCLM4-8-17	CLM-Community	Germany	0.11 × 0.11
CNRM-CM5	ALADIN63	Météo-France / CNRM	France	0.11 × 0.11
CNRM-CM5	RCA4	SMHI	Sweden	0.11 × 0.11

3 Methods

In this study, precipitation and temperature datasets obtained from the climate models (Table 1 and Table 2) are used as inputs to a hydrological model developed in HEC-HMS. The model is calibrated and validated using observed precipitation and temperature records from five meteorological stations (Fig. 1). To eliminate the influence of human interventions, the hydrological model is developed for a historical period preceding the construction of the first major hydraulic structure in the basin. The calibrated model is then run with the climate model datasets to simulate daily discharge values. Subsequently, discharge values corresponding to selected exceedance probabilities are extracted from the simulated and observed streamflow series to construct flow duration curves (FDCs). The resulting FDCs are then compared with the observed record, while climate models developed by the same modeling institution are evaluated collectively to investigate similarities and differences in their hydrological performance.

4 Results

Discharge values corresponding to selected exceedance probabilities are provided in Table 3. The comparison of FDC values demonstrates considerable variability among the climate models in reproducing the observed discharge characteristics. The largest discrepancies occur at low exceedance probabilities (0.002–0.02), corresponding to extreme high-flow conditions, whereas the differences gradually decrease toward medium-flow conditions (0.2–0.5). This pattern indicates that simulating extreme discharge remains substantially more challenging than reproducing average flow conditions, highlighting the importance of carefully selecting climate model inputs for flood-related hydrological assessments.

Among the GCMs, several simulations consistently overestimate discharges throughout the FDC. MPI-ESM1-2-HR produces the largest discharge values, exceeding the observed discharge by approximately 71% at the 0.002 exceedance probability. Similarly, CMCC-CMS, IPSL-CM5B-LR, MPI-ESM-MR, MRI-ESM2-0, MRI-CGCM3, HadGEM2-CC, and HadGEM2-ES exhibit substantial positive biases, particularly for high-flow events. These models generally preserve the shape of the observed FDC but shift the entire curve upward, indicating a systematic tendency to generate excessive discharge rather than isolated errors during extreme events.

Conversely, several RCM simulations substantially underestimate discharge across the entire flow regime. IPSL-CM5A-MR RCA4 and HadGEM2-ES RCA4, produce the lowest discharge values among all simulations and considerably underestimate observed high flows. Although these simulations reproduce the overall shape of the FDC, they consistently underestimate

discharge magnitude, suggesting that precipitation inputs or runoff generation are systematically reduced during the downscaling process.

A comparison among different generations developed by the same institution reveals that newer climate models do not necessarily outperform their predecessors. The MPI family provides a clear example of this behavior. While MPI-ESM-LR moderately overestimates observed discharge, both MPI-ESM1-2-LR and MPI-ESM1-2-HR generate considerably larger discharge values, with the high-resolution version exhibiting the largest positive bias. Likewise, MPI-ESM-MR also produces substantially larger discharges than MPI-ESM-LR. These results indicate that increased model resolution or updated model physics do not automatically translate into improved hydrological performance.

The MRI models exhibit considerably more consistent behavior. MRI-CGCM3 and MRI-ESM2-0 produce similar FDCs, with MRI-ESM2-0 generating only slightly higher discharge values throughout the flow regime. Similarly, NorESM1-M and NorESM2-LM show only minor differences, indicating that successive model generations preserve similar hydrological characteristics. However, the downscaled NorESM1-M HIRHAM5 simulation substantially reduces discharge, illustrating the significant influence of RCMs.

The EC-EARTH simulations further demonstrate the importance of regional downscaling. The parent EC-EARTH model moderately overestimates discharge, whereas HIRHAM5, RACMO22E, and RCA4 substantially reduce discharge and produce relatively similar FDCs. In contrast, CCLM4-8-17 maintains considerably larger discharge values than the other regional models. Similar behavior is observed within the IPSL family, where the driving GCMs exhibit moderate to large overestimations, while different RCMs produce markedly different discharge characteristics. WRF381p increases discharge relative to the parent model, RCA4 produces one of the strongest underestimations. These findings indicate that the choice of RCM may introduce uncertainties comparable to those associated with the selection of the driving GCM.

The Canadian Earth System Models exhibit relatively stable behavior across generations. CanESM2 and CanESM5 produce very similar FDCs, with only modest differences in high- and medium-flow conditions, suggesting consistent model development between CMIP5 and CMIP6. Likewise, the MIROC family demonstrates relatively stable performance. MIROC-ESM and MIROC-ESM-CHEM generate nearly identical discharge values, while MIROC6 consistently reduces the positive bias observed in MIROC5, indicating a moderate improvement in reproducing observed discharge characteristics.

The HadGEM and CNRM families illustrate the considerable influence of RCMs. Both HadGEM2-CC and HadGEM2-ES substantially overestimate discharge, whereas the RACMO22E and particularly RCA4 downscaled simulations considerably reduce these biases. A similar pattern is observed for CNRM-CM5, where RCA4 produces one of the closest agreements with observations, while ALADIN63 substantially increases discharge. These comparisons demonstrate that regional downscaling can either amplify or reduce the biases inherited from the driving GCM, depending on the selected RCM.

Overall, the comparisons reveal that differences among RCMs frequently exceed those between successive generations of GCMs. Models developed by the same institution often exhibit markedly different hydrological behavior after regional downscaling, emphasizing that RCM selection represents a major source of uncertainty in climate impact assessments. Furthermore, no individual model consistently reproduces the observed FDC across all exceedance probabilities. Some models better represent extreme flows, whereas others more accurately reproduce medium-flow conditions, supporting the use of multi-model approaches rather than reliance on a single climate model for hydrological impact studies.

Table 3. Discharge Values Corresponding to Selected Exceedance Probabilities

	Exceedance Probability						
	0.002	0.01	0.02	0.04	0.1	0.2	0.5
MPI-ESM-LR CCLM4-8-17	646.5	475.4	423.0	376.6	285.8	183.1	91.2
MPI-ESM-LR REMO2009 (r1i1p1)	1033.7	578.2	474.7	386.6	288.4	218.5	115.4
MPI-ESM-LR REMO2009 (r2i1p1)	1032.9	678.6	527.2	420.0	313.4	249.9	142.8
MPI-ESM1-2-HR	1271.4	698.5	514.2	386.9	287.3	236.1	130.7
MPI-ESM1-2-LR	740	503.5	395.1	323.2	249	204.4	114.6
MPI-ESM-LR	547.1	391.1	330.4	277.4	221.2	188.3	92.6
MPI-ESM-MR	1052.7	802.7	661.7	543.4	400.1	297.8	162.9
MRI-CGCM3	791.8	570.2	457.3	359.3	264.5	218.8	132.5
MRI-ESM2-0	861.9	573.3	474.4	378.7	288.7	238	132.6
NorESM1-M	351.9	289.8	265.9	242.5	209.3	174.5	100.4
NorESM2-LM	393.5	312.3	283	254.2	210.4	179.2	101.2
NorESM1-M HIRHAM5	318.3	246.7	227.7	212.3	182.3	125.4	78.1
EC-EARTH	463.2	404.7	368.6	319.1	254.4	205.2	110.1
EC-EARTH HIRHAM5	367.4	275.6	256.3	232.1	190.9	135.3	77.2
EC-EARTH CCLM4-8-17	607	463.5	405.1	345.5	252.5	163	82.9
EC-EARTH RACMO22E	349.4	297.7	269.3	240.1	188.8	136.2	75
EC-EARTH RCA4	320	260.7	240.1	219.1	176.9	134.2	77.2
IPSL-CM5A-LR	372.2	296.9	273.8	241	205.4	174.4	94.2
IPSL-CM5B-LR	1157.7	707.1	517.8	397.6	277.3	218.5	130.7
IPSL-CM5A-MR	476	355.4	307.2	267.2	222.8	182.6	97.2
IPSL-CM5A-MR WRF331F	611.1	463.1	396.6	299.2	224.5	182.9	92
IPSL-CM5A-MR WRF381P	667.6	537.9	450.0	370.8	276.0	195.0	98.1
IPSL-CM5A-MR RCA4	260.4	228.7	216.4	201.6	160.4	117.4	74.9
CanESM2	343.3	264	244.9	223.3	196.7	156.9	87.7
CanESM5	327.8	275	247.7	229.6	201.2	163.6	99.2
HadGEM2-CC	898.6	525.3	445.3	379.1	306	250.8	152.9
HadGEM2-ES	764.7	470.5	405.7	355.2	286.5	240.8	141.7

HadGEM2-ES CCLM4-8-17	601.8	509.8	439.7	363.8	276	179.6	93.6
HadGEM2-ES RACMO22E	451.9	360.9	321.5	279	196.7	150.7	86.3
HadGEM2-ES RCA4	292.1	251.9	232.8	217.4	180.1	134.7	78.9
CMCC-CESM	389.0	287.3	250.4	216.3	187.4	155.7	93.6
CMCC-CMS	1200.4	645.4	511.6	376.6	273.6	218.8	122
CMCC-CM2-SR5	418.6	315.7	279.3	247.6	211.5	177.1	99.7
CMCC-ESM2	609.3	384.5	325.2	280.3	228.5	193.1	110.2
MIROC-ESM	369.2	304.8	277	252.8	216.6	175.7	90.6
MIROC-ESM-CHEM	372.2	314.4	289	265	220.1	177.8	93.1
MIROC5	672.9	449.8	380.8	325.5	259.1	221.9	135
MIROC6	608.3	421.2	350.3	298.3	238.2	205.1	124.1
CNRM-CM5	559.3	358.3	315.7	284.4	249.2	212.1	135.5
CNRM-CM5 CCLM4-8-17	673.1	463.9	408.9	349.5	268	194.6	101.5
CNRM-CM5 ALADIN63	870.9	615.2	513.3	424.7	316.6	222	129
CNRM-CM5 RCA4	295.1	249.8	236.2	215.1	177.8	136.6	78.8
Observed	**743**	**497**	**418**	**345**	**257**	**178**	**73.8**

5 Conclusion

This study compared the ability of a wide range of CMIP5, CMIP6, and dynamically downscaled climate models to reproduce the observed FDC across different exceedance probabilities. The results demonstrate substantial variability among the simulations, particularly for extreme high-flow conditions, where model uncertainties are considerably larger than those observed for medium-flow conditions.

Most climate models preserve the general shape of the observed FDC but differ substantially in discharge magnitude. Several GCMs, including MPI-ESM1-2-HR, CMCC-CMS, IPSL-CM5B-LR, and HadGEM2-CC, systematically overestimate discharge throughout the flow regime, whereas several RCM simulations, particularly those driven by CCLM4-8-17, and RCA4 configurations, tend to underestimate discharge. These results indicate that model bias is generally systematic rather than restricted to a particular portion of the FDC.

Comparisons among climate models developed by the same institution show that newer model generations do not consistently provide better agreement with observations. In several model families, including MPI and MRI, updates in model generation or spatial resolution resulted in only limited improvements or even larger deviations from observed discharge. Conversely, the CanESM and MIROC families exhibit relatively consistent behavior between CMIP5 and CMIP6 generations, suggesting greater stability in hydrological performance.

The analyses also demonstrate that the selection of the RCM can substantially modify the hydrological response simulated by the driving GCM. In several model families, including EC-EARTH, HadGEM, IPSL, and CNRM, differences introduced by regional downscaling are comparable to or greater than those between different GCM generations. Consequently, uncertainty associated with RCMs should receive equal consideration when selecting climate model inputs for hydrological impact assessments.

Overall, the findings indicate that no single climate model consistently reproduces observed discharge characteristics across the entire FDC. Therefore, relying on an individual model may introduce substantial uncertainty into climate change impact studies. Multi-model ensemble approaches remain the most robust strategy for representing climate uncertainty and improving the reliability of future hydrological projections, particularly for flood-related applications where accurate representation of high-flow conditions is essential.

References

1. Su, F., Duan, X., Chen, D., Hao, Z., & Cuo, L.: Evaluation of the Global Climate Models in the CMIP5 over the Tibetan Plateau. Journal of Climate, 26(10), 3187-3208. https://doi.org/10.1175/JCLI-D-12-00321.1 (2013).
2. Hengade, N., Eldho, T. I., & Ghosh, S.: Climate change impact assessment of a river basin using CMIP5 climate models and the VIC hydrological model. Hydrological Sciences Journal, 63(4), 596–614. https://doi.org/10.1080/02626667.2018.1441531 (2018).
3. Javadinejad, S., Hannah, D., Ostad-Ali-Askari, K. et al.: The Impact of Future Climate Change and Human Activities on Hydro-climatological Drought, Analysis and Projections: Using CMIP5 Climate Model Simulations. Water Conserv Sci Eng 4, 71–88. https://doi.org/10.1007/s41101-019-00069-2 (2019).
4. Guo, Y., Xu, Y. P., Yu, X., Xie, J., Chen, H., & Si, Y.: Impacts of GCM credibility on hydropower production robustness under climate change: CMIP5 vs CMIP6. Journal of Hydrology, 618. https://doi.org/10.1016/j.jhydrol.2023.129233 (2023)
5. Ma, D., Bai, Z., Xu, Y. P., Gu, H., & Gao, C.: Assessing streamflow and sediment responses to future climate change over the Upper Mekong River Basin: A comparison between CMIP5 and CMIP6 models. Journal of Hydrology: Regional Studies, 52. https://doi.org/10.1016/j.ejrh.2024.101685 (2024).
6. Xiang, Y., Wang, Y., Chen, Y., & Zhang, Q.: Impact of Climate Change on the Hydrological Regime of the Yarkant River Basin, China: An Assessment Using Three SSP Scenarios of CMIP6 GCMs. Remote Sensing, 14(1), 115. https://doi.org/10.3390/rs14010115 (2022).
7. Meresa, H., Tischbein, B. & Mekonnen, T.: Climate change impact on extreme precipitation and peak flood magnitude and frequency: observations from CMIP6 and hydrological models. Nat Hazards 111, 2649–2679. https://doi.org/10.1007/s11069-021-05152-3 (2022).
8. Feyissa, T. A., Demissie, T. A., Saathoff, F., & Gebissa, A.: Evaluation of General Circulation Models CMIP6 Performance and Future Climate Change over the Omo River Basin, Ethiopia. Sustainability, 15(8), 6507. https://doi.org/10.3390/su15086507 (2023).
9. Adhikari, R. K., Yilmaz, A. G., Mainali, B., Dyson, P.: Performance evaluation of CMIP6 models for application to hydrological modelling studies – A case study of Australia. Science of the Total Environment, 945. https://doi.org/10.1016/j.scitotenv.2024.174015 (2024)
10. Alemseged, T. H., Tom, R.: Evaluation of regional climate model simulations of rainfall over the Upper Blue Nile basin. Atmospheric Research, 161–162, 57–64. https://doi.org/10.1016/j.atmosres.2015.03.013 (2015).
11. Yira, Y., Diekkrüger, B., Steup, G., Yaovi Bossa, A.: Impact of climate change on hydrological conditions in a tropical West African catchment using an ensemble of climate simulations. Hydrology and Earth System Sciences, 21(4), 2143–2161. https://doi.org/10.5194/hess-21-2143-2017 (2017).
12. Diez-Sierra, J., Iturbide, M., Fernández, J. et al.: Consistency of the regional response to global warming levels from CMIP5 and CORDEX projections. Clim Dyn 61, 4047–4060. https://doi.org/10.1007/s00382-023-06790-y (2023).
13. Yeğin M.: An agent-based model for flood risk mapping: Integration of urbanization and climate change impacts. Doctoral dissertation, Middle East Technical University (2024).

Author Contribution Statement

- *Conceptualization:* Murat Yegin
- *Methodology:* Murat Yegin, O. Burak Akgun, Elcin Kentel
- *Investigation:* Murat Yegin, O. Burak Akgun
- *Writing – Original Draft:* Murat Yegin
- *Writing – Review & Editing:* Murat Yegin, Elcin Kentel

Competing Interests

The authors declare that they have no conflict of interest.

Publication Note

This paper was peer-reviewed, accepted for presentation, and included in the proceedings of the ACE2026 – International Conference on Advances in Civil Engineering, held on 12–14 October 2026 in Trabzon, Türkiye.

This paper may be cited as follows:

Yegin, M., Akgun O.B., Kentel, E., "Comparison of Climate Model Performances of the Same Institutes using Hydrological Model Outputs: A Case Study with CMIP5 GCM, CMIP6 GCM, and CMIP5 RCM over Göksu Basin," in Proceedings of the ACE2026 – International Conference on Advances in Civil Engineering, Trabzon, Türkiye, 12–14 October 2026.

Prediction of Reservoir Sedimentation by RUSLE Incorporating the Effects of DEM Selection and Spatial Resolution

Yakup Darama[1], Kutay Yilmaz[2], Sarp Toprakkale[3], Meric Yilmaz[4]
[1] 0000-0003-0066-2621, Atılım University, Civil Engineering Department, Ankara, Türkiye, yakup.darama@atilim.edu.tr
[2] 0000-0001-5529-9239, Yaşar University, Civil Engineering Department, İzmir, Türkiye, kutay.yilmaz@yasar.edu.tr
[3] 0000-0003-2989-6528, Middle East Technical University, Civil Engineering Department, Ankara, Türkiye, saber.topraghghaleh@metu.edu.tr
[4] 0000-0001-6921-7687, Atılım University, Civil Engineering Department, Ankara, Türkiye, meric.yilmaz@atilim.edu.tr

Abstract. This study evaluates the effects of DEM selection and spatial resolution on RUSLE-based erosion predictions. Accurate assessment of sedimentation is essential for addressing sediment dynamics that directly influence water quality, aquatic ecosystems, and the stability of infrastructure such as dams and bridges. In this study, the LS factor was derived from Digital Elevation Models (DEMs) obtained from various sources: Shuttle Radar Topography Mission (SRTM) and Advanced Land Observing Satellite (ALOS) at 30m resolution, and TerraSAR-X TanDEM-X DEMs at 12m and 5m resolutions provided by the State Hydraulic Works of Türkiye (DSI). A GIS-based RUSLE method was implemented, incorporating R, K, C, and P factor datasets and validated using measured data. The influence of DEM selection and spatial resolution on erosion predictions was analyzed to assess the sensitivity of RUSLE outputs to differences in topographic input data. The result of RUSLE is validated by using Sediment Yield determined by the reservoir bathymetric survey (SY_{RS}) of Borçka Dam (8.695 t/ha/yr). Sediment Delivery Ratios (SDR) of the reservoir is calculated by using Vanoni (1975) and USDR-SCS (1971) methods to relate RUSLE results with that of reservoir sediment yield. The results showed that, RUSLE soil erosion estimates are in good agreement for several DEM–K combinations for Borçka Dam, even when relatively coarse-resolution input datasets are used. Overall, RUSLE can provide reasonable erosion estimates despite differences in the spatial resolution of the input datasets, provided that the accuracy and consistency of the model inputs are considered collectively.

Keywords: RUSLE, Sediment Yield, Reservoir Sedimentation

1 Introduction

Sediment accumulation poses a significant challenge for reservoirs associated with dams. Various factors, such as the geological characteristics of the river basin, topography, climatic conditions, drainage density, and patterns, along with urban development and forest clearance, collectively contribute to an increased sediment load within the basin. Consequently, the sedimentation process leads to a decrease in the storage capacity of the reservoirs. Although historical data on sediment flow and water levels have been utilized to estimate the sediment storage levels and the economic longevity of dams, inaccuracies persist due to the fluctuating nature of meteorological, hydrological, and anthropogenic factors. This has resulted in reservoirs filling up with sediment faster than initially projected. Particularly during brief, high-intensity flood events, a substantial volume of sediment can be carried into the reservoir, leading

to a rapid reduction in storage capacity and overall lifespan of the dam. As dams play a crucial role in providing water for domestic and agricultural purposes, as well as generating hydroelectric power, the determination of sediment load transported by rivers remains essential for effectively managing sedimentation in dam reservoirs ([1-2]).

Determining the quantity of sediment transported by rivers is essential for the estimation of sediment transport within a watershed. As outlined by Walling [3], there exist three approaches for acquiring sediment yield data: (1) the utilization of continuously recorded discharge data along with their application to a previously established sediment rating curve, (2) the integration of continuously recorded discharge and sediment data, and (3) the utilization of data from reservoir surveys. Among these techniques, the periodic collection of data from reservoir surveys is viewed as a more reliable indicator of long-term sediment yield in a given basin ([1], [4-5]). In a research endeavor by Munthali et al [6], employing Geographic Information System (GIS) and the PanEuropean Soil Erosion Risk Assessment model, the scholars sought to ascertain the hydrological potential for sediment, pinpoint regions characterized by significant sediment generation within the Songwe River watershed, and evaluate the probability of sediment accumulation in a proposed reservoir.

In recent years, advances in remote sensing, Geographic Information Systems (GIS), and hydrological modeling have provided valuable tools for studying sediment transport in river systems. Integrating field observations with these technological advancements allows for a more comprehensive assessment of sediment dynamics, which is essential for developing effective management strategies. The Revised Universal Soil Loss Equation (RUSLE) is a widely used method for estimating soil erosion and sediment yield, offering valuable insights into sediment transport processes and sediment delivery ratio (SDR) estimation.

The primary objective of this study is to investigate how DEM selection and spatial resolution influence LS-factor calculation and subsequent RUSLE-based soil erosion estimates in the Çoruh River Basin. The resulting erosion estimates are further evaluated against sediment yield derived from bathymetric survey of the Borçka reservoir. Furthermore, it is aimed to present the spatial distribution of annual soil loss within the Çoruh River Basin for further studies.

2 Study Area and Data

The Çoruh River, a significant waterway in Türkiye renowned for its hydroelectric potential, has seen the construction of multiple dams along its main course to harness this energy resource. However, unlike its energy-producing capacity, the river itself presents challenges due to its supercritical flow regime and sediment-carrying capacity, which is particularly problematic for dam reservoirs. While studies have focused on sedimentation within reservoirs on a micro-scale basis, basin-wide sediment analysis remains unexplored.

Assessing sediment transport at a basin level is pivotal for determining the effective capacity of hydroelectric dams. Unconventionally, dams in the Çoruh River Basin were built downstream to upstream, driven partly by trans boundary nature of the basin. This sequencing commenced with the Muratlı Dam in 2005, followed by the Borçka Dam in 2008, the Deriner Dam in 2012, and others.

The initial sedimentation of Muratlı Dam reservoir began in 2005, followed by Borçka Dam reservoir in 2008, filling their dead volumes more rapidly than anticipated. Bathymetric survey conducted in 2017 for the Borçka Dam revealed significant reduction in its dead volumes, by 28% over a span of 10 years. Further mitigating sedimentation, a cascade of dams, including Deriner, Artvin, Yusufeli, Arkun, Güllübağ, and Laleli, regulated the river's flow, reducing sediment accumulation to some extent. Nonetheless, runoff from precipitation in the basin's high-erosion environment continues to contribute to sedimentation. To quantify sediment yield, bathymetric map from Borçka Dam is analyzed. Fig. 1 illustrates the study area.

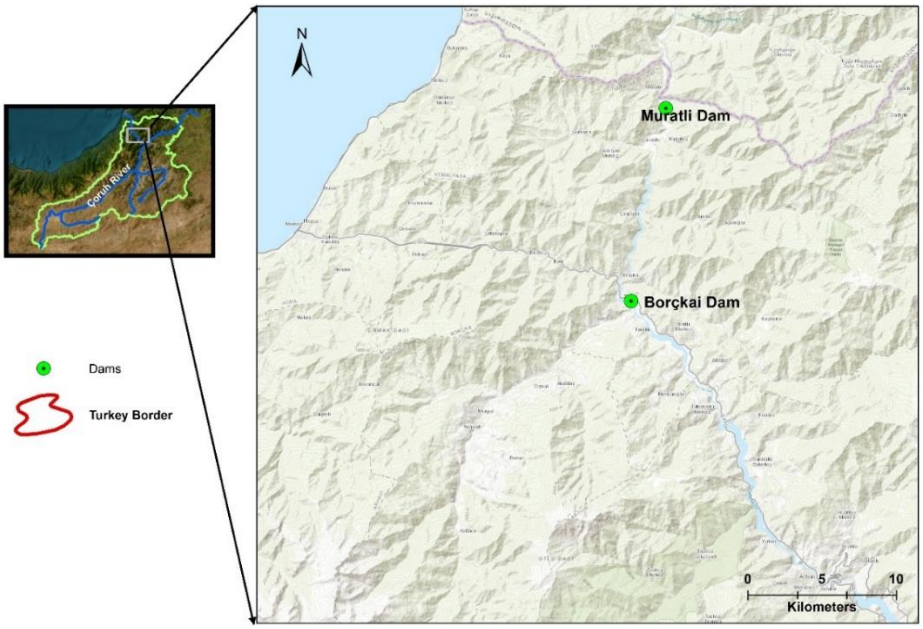


Fig. 1. Study area and location of Borçka Dam.

3 Erosion Prediction By RUSLE

Erosion occurs as a natural phenomenon driven by both wind and water forces. Research from the State Planning Organization (DPT) of Türkiye in 2001 shows that water and rainfall are responsible for 99% of erosion within the country, with wind playing a minor role in the remaining 1%. In order to determine erosion resulting from the rainfall and surface runoff process, the Revised Universal Soil Loss Equation (RUSLE), was used. The RUSLE method, in particular, integrates various key variables contributing to erosion dynamics, including rainfall erosivity (R), soil erodibility (K), topographical attributes like slope length (L) and steepness (S), as well as considerations for crop management (C) and support practices (P). Expressed as an equation, the RUSLE model embodies the relationship as in Eq. (1):

$$A = R \times K \times LS \times C \times P \tag{1}$$

Here, 'A' signifies the annual soil loss (t/ha/yr), 'R' represents the rainfall-runoff erosivity factor (in MJ/mm/ha/h/yr), 'K' denotes the soil erosion sensitivity factor, 'L' corresponds to the slope length factor, 'S' embodies the slope steepness factor, while 'C' and 'P' encapsulate the cover management and support practices factors respectively. Fig. 2 illustrates the flow chart of data needed for a RUSLE model.

3.1 Rainfall Erosivity

The rainfall erosivity factor (R) in the RUSLE equation is considered within the rainfall-runoff interactions framework and is a key determinant influencing soil erosion mechanisms. This factor, denoted as R, is characterized as the product of kinetic energy and the peak 30-minute intensity, serving as an indicator of the erosive potential inherent in rainfall events.

There are numerous methods in the literature to calculate the R factor. In this study, The R factor map is obtained from the European Soil Data Centre (ESDAC) ([7-9]). The map was prepared in 2017 and at resolutions of 30 arc-sec (~1 km at the Equator). Fig. 3 illustrates the R factor for the Çoruh basin.

As illustrated in Fig. 2, the rainfall erosivity (R-Factor) values in the Çoruh River Basin show notable regional variation. The northern portion of the basin, especially the regions with steep slopes and significant precipitation, has the greatest R-Factor values (surpassing 4000 MJ

mm/ha/h/yr) whereas, the southern and central regions of the basin exhibit much lower R-Factor values; the lowest (257 MJ mm/ha/h/yr) indicating comparatively lesser rainfall erosivity.

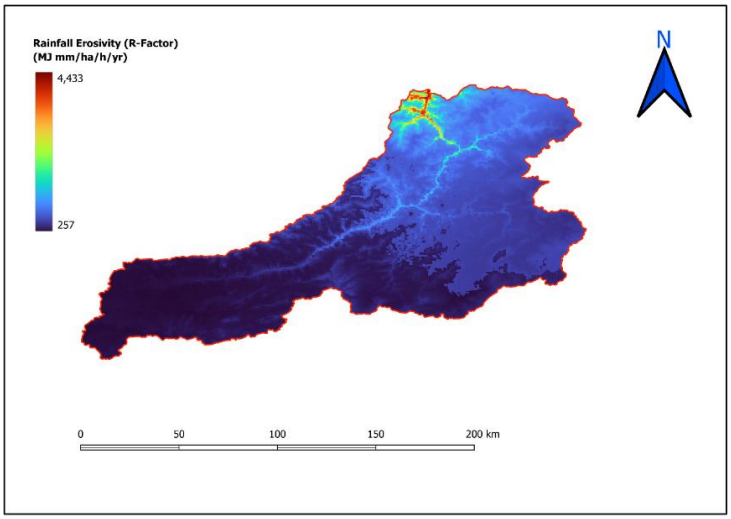


Fig. 2. Rainfall erosivity (R Factor) of Çoruh basin.

3.2 Cover Management Factor (C Factor)

The coverage factor spans from 0 (complete soil coverage) to 1 (no soil coverage). The C factor signifies the impact of soil-disturbing practices, vegetation, crop rotation, productivity level, soil covering, and sub-surface biomass on soil erosion. Natural vegetation primarily contributes to mitigating water erosion [10].

To calculate the C factor, first, a Land Cover map is needed. This map is provided by Copernicus Corine 2018 Land Cover data with 100 m resolution [11]. For each land cover type, C factor values are collected from literature and set to obtain the C factor map ([12-14]. C factor map for the Çoruh basin is provided in Fig. 3 shows the changes of land cover in the Çoruh River Basin, therefore affecting the area's erosion vulnerability. With their lowest C values (0–0.05), densely vegetated areas, whereas places with higher C values (0.1–1.0) mostly agricultural land or barren areas, the northern and middle regions of the basin have lower C values because of better vegetative cover, but the southern and western sections often have higher values, suggesting more exposed terrain.

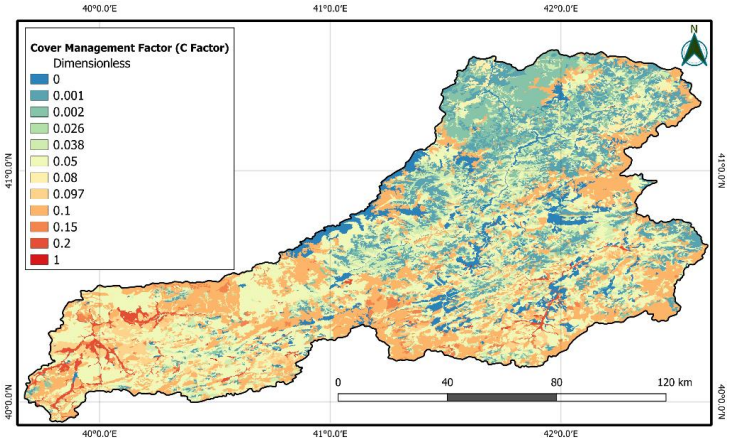


Fig. 3. Cover management factor (C Factor) of Çoruh basin

3.3 Support Practices Factor (P Factor)

The P factor represents the ratio of soil loss under a specific support practice to soil loss under conventional up and down slope tillage. Typically, the conservation practice factor adjusts the

estimation made by the Revised Universal Soil Loss Equation (RUSLE) to account for management and tillage practices that safeguard the soil from erosion.

To provide a P factor map, first, a slope map of the study area with categorized percent units is provided (Fig. 4) using the DEM map. In this study, the P factor map was created using land use/land cover data and support factors. The P values are collected from literature for different land cover and slope values ([13],[15]) were used for the Çoruh river basin and the P Factor map, created using these values was created as shown in Fig. 7. In general, higher P values are assigned to areas lacking conservation practices, such as steep agricultural lands, rangelands, and bare soil, where erosion risk is greater.

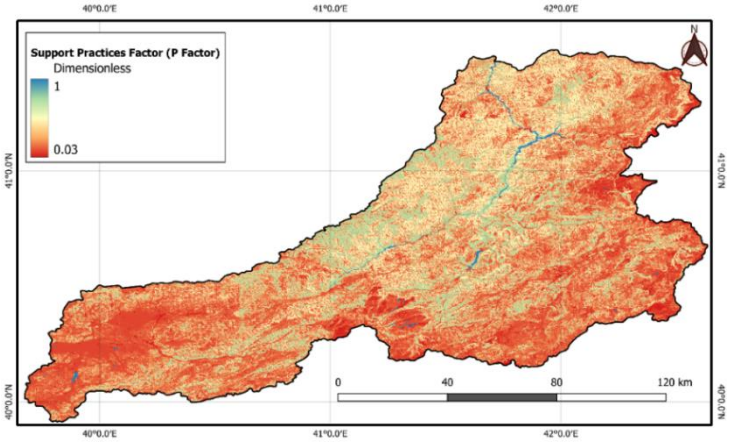


Fig. 4. Support practices factor (P Factor) of the Çoruh basin.

3.4 Soil Erodibility (K Factor)

The soil erodibility factor (K) pertains to how a particular soil and its profile respond over time to the erosive forces caused by rainfall and runoff. It reflects the rate at which soil is lost per unit of rainfall erosion for a given soil type. In the RUSLE model, Wischmeier's method is employed to assess the K factor of a soil type [15]. This method encompasses various soil properties such as particle size (silt, clay, and sand), organic matter content, soil structure, and permeability. The K factor map is provided by the European Soil Data Centre (ESDAC) ([7-9]). Fig. 8 illustrates the soil erodibility map for the Çoruh River Basin.

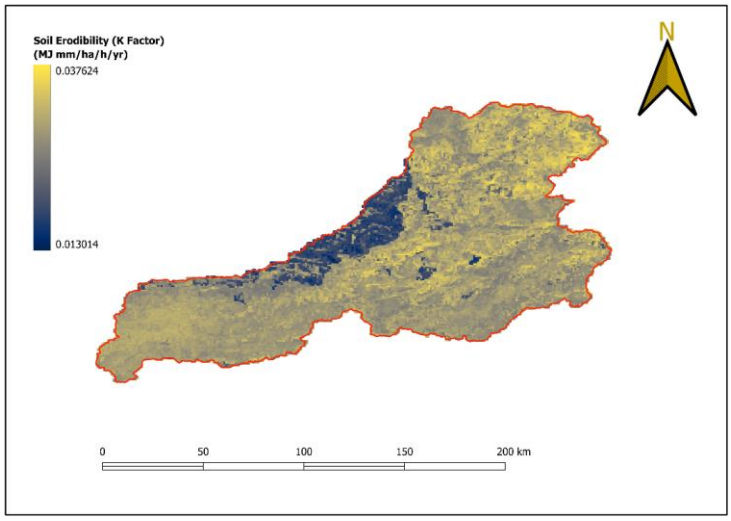


Fig. 5. Soil erodibility (K Factor) of Çoruh basin.

The K Factor values, of the Çoruh River Basin as shown in Fig. 8. The analysis of this figure shows that the K values in the northwestern part are rather high, meaning soils are more prone to erosion The center of the basin reveals moderate K values, meaning mixed soil were here with varying resistance to erosion. On the contrary, the eastern and southeastern areas supply lower K values, meaning these are more stable soils entailing lower susceptibility to detachment by rainfall and runoff.

To enhance the spatial accuracy of the study, the K factor was also calculated using high-resolution soil data based on the EPIC (Erosion-Productivity Impact Calculator) model [16]. Unlike the Wischmeier method [15], which requires soil structure and permeability codes that are often unavailable in high-resolution spatial datasets, the EPIC model estimates K utilizing only organic carbon content and soil particle size distribution (sand, silt, and clay). This approach allowed the integration of finer-scale soil grids to capture local variations in erodibility that coarser data sets might miss.

3.5 Slope Length and Steepness Factor (LS Factor)

The L and S factors within the RUSLE framework represent how topography influences erosion. Research has confirmed that increases in both slope length and steepness lead to higher overland flow and, consequently, increased erosion. Furthermore, it has been noted that changes in slope steepness have a greater impact on gross soil loss compared to changes in slope length. Therefore, topography, especially when the ground slope exceeds a critical angle, emerges as a significant factor in soil loss, primarily because it governs the rate of surface runoff.

The combined LS factor for the Çoruh basin was provided from a Digital Elevation Model (DEM) obtained from three different sources, Shuttle Radar Topography Mission (SRTM) with 30m resolution (SRTM 30m), Advanced Land Observing Satellite (ALOS) with 30m resolution (ALOS 30m), and TerraSAR-X, TanDEM-X satellite provided by State Hydraulic Works (DSI) with 12- and 5-meters resolutions (DSI 12m and DSI 5m). These DEMs differ not only in spatial resolution but also in data source and acquisition characteristics; therefore, the analysis reflects the combined influence of DEM selection and spatial resolution on LS-factor estimation. LS factor was calculated by using Moore & Burch method [17]. Moore and Burch [17] developed an LS factor estimation method using DEM for complex terrain, based on unit stream theory, requiring flow accumulation and slope data. In this study, the previously mentioned DEM data was processed in QGIS to calculate the LS factor. The LS factor was calculated using Eq. (2), which incorporates flow accumulation, and slope steepness.

$$LS = \frac{(FlowAccumulation \times CellSize)^{0.4}}{22.13} \times \frac{(\sin slope)^{1.3}}{0.0896} \quad (2)$$

Here, flow accumulation represents the accumulated upslope contributing area for a given cell, LS denotes the combined slope length and steepness factor, cell size indicates the size of the grid cell (30, 12, and 5 meters in this study), and sin(slope) represents the sine of the slope degree value. The LS factor values across the study area calculated for four different DEM data using the method of Moore and Burch [17] is shown in Fig. 6.

Fig. 6 shows the LS factor's geographical distribution in the Çoruh River Basin, which was obtained from four distinct DEMs (SRTM 30m, ALOS 30m, DSI 12m, and DSI 5m). Because of the steeper slopes and longer slope lengths seen in mountainous areas, the maps constantly display higher LS values there, whereas the western and eastern parts display lower values. The influence of DEM selection and spatial resolution on LS-factor estimation is demonstrated by the fact that higher resolution DEMs (DSI 12m and DSI 5m) show more detailed fluctuations and generally higher LS values when compared to lower resolution DEMs (SRTM 30m and ALOS 30m). The Moore and Burch method [17], which considers flow accumulation, offers a more realistic representation, especially in complex areas. Thus, the Moore and Burch method

is generally preferred for RUSLE, particularly with high-resolution DEMs, for more accurate erosion assessments.

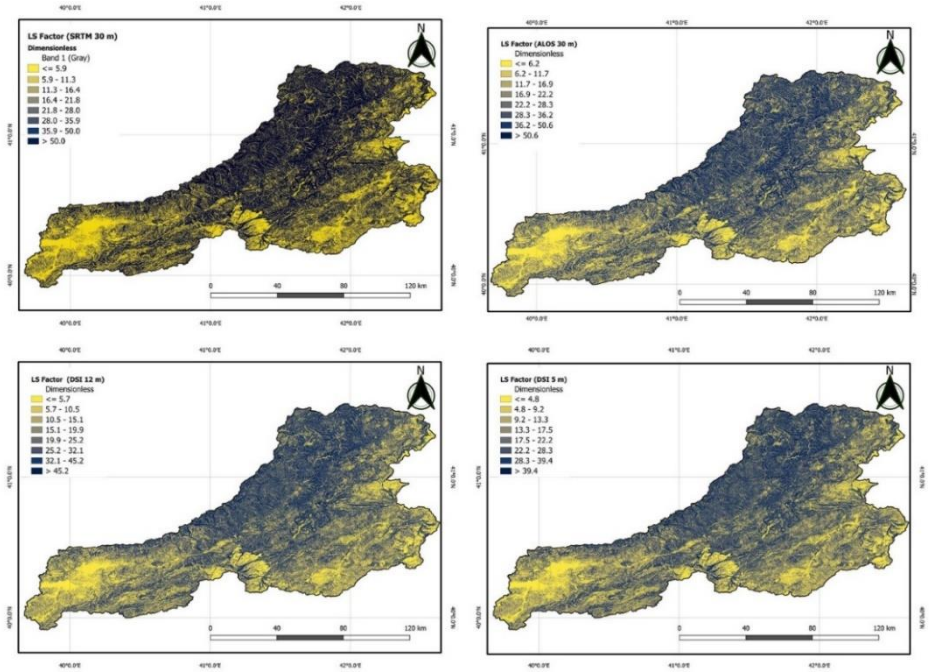


Fig. 6. LS Factor maps of Çoruh River Basin

3.6 Average Annual Soil Loss

The data layers (maps) extracted for the K, LS, R, C, and P factors of the RUSLE model were combined using Eq. (1) within the raster calculator tool of QGIS. This integration aimed to assess, evaluate, and produce maps depicting soil erosion risk and severity for the Çoruh basin. As a result of analyzing, arranging, and making calculations the data obtained from open sources, the spatial distribution and amounts of erosion in the Çoruh basin were obtained by applying the RUSLE method in the GIS environment and are presented in Fig. 7. Understanding the spatial variation of soil erosion, the complex challenges posed by sediment transport could be addressed in the Çoruh River Basin in further studies.

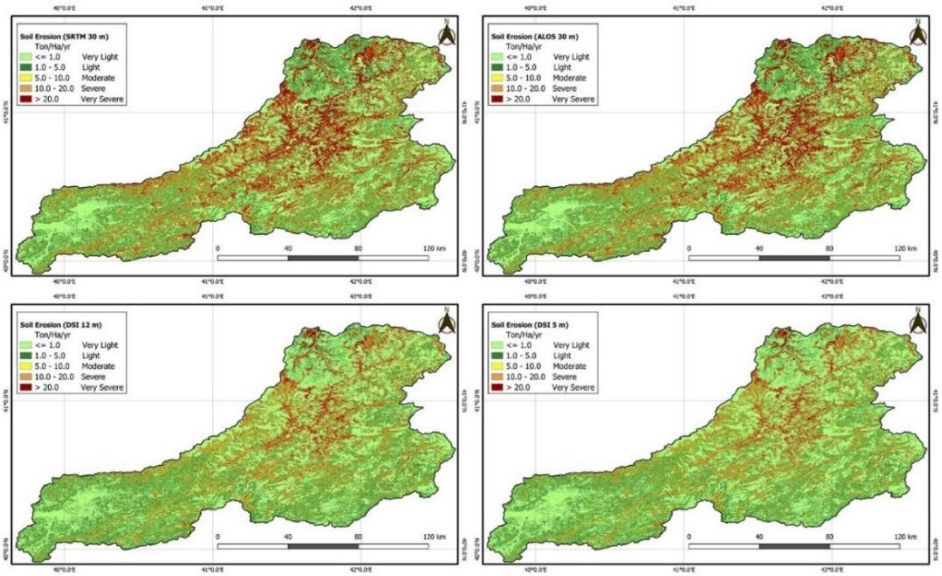


Fig. 7. Average annual soil loss of Çoruh basin.

Accordingly, the average annual soil loss of the basin is shown in Table 1. The total erosion in t/yr for entire basin is also shown in Table 1 for all calculated soil loss on four different resolution DEM, considering all RUSLE parameters.

Table 1. Average annual soil loss (t/ha/yr) and total erosion (t/yr) of Çoruh basin.

	SRTM 30m	ALOS 30m	DSI 12m	DSI 5m
Average annual soil loss (t/ha/yr)	8.76	9.12	8.45	7.47
Total erosion (t/yr)	17,691,220	18,432,007	17,078,041	15,098,590

4 Reservoir Sediment Yield (SY) Calculation

Sediment yield (SY) refers to the amount of sediment transported from a watershed by runoff and delivered to a stream over time. It can also be thought of as the total amount of sediment entering a reservoir at the downstream end of the watershed. SY can be estimated by reservoir surveys or stream sediment measurement programs. However, reservoir surveys are generally considered to be the more reliable method for long-term sediment yield [18].

In this study, sediment yield for the catchment area of Borçka Dam reservoir was calculated using reservoir survey. SY can be calculated with Eq. (3) with reservoir survey ([1-2]).

$$SY_{RS} = \frac{SV\,\gamma_s}{TE\,A} \times 100 \tag{3}$$

Where SY_{RS} is the sediment yield calculated by reservoir survey (t/yr/km²), SV is the annual sediment accumulation rate (m³/yr), γ_s is the unit weight of sediment in the reservoir (t/m³), TE is the sediment retention efficiency of the reservoir (%), and A is the catchment area (km^2).

In this study, the sedimentation process was analyzed using survey conducted for Borçka reservoir in 2017. The sediment accumulation information of the reservoir area of the dam obtained from State Hydraulic Works (DSI) is presented in Table 2.

Table 2. Reservoir area sediment accumulation for Borçka Dam

Years in Op.	Area (ha)	Projected Volume (hm^3)	Volume at Year of Survey (hm^3)	Difference (hm^3)	Annual Avg. Sediment Amount (hm^3)	Design Dead Storage Volume (hm^3)	Dead Storage Volume at Survey (hm^3)	Dead Storage Difference (hm^3)	Annual Avg. Sediment in Dead Storage (hm^3)
9	1014	418.98	323.9	95.08	10.56	268.2	194.69	73.51	8.168

Accordingly, during the 9-year period in which Borçka Dam was in operation, a total of 95.08 hm^3 of sediment accumulated in the reservoir area and formed dead volume. SV was obtained as 10.56 hm^3 for Borçka Dam from DSI data, and the average of the values obtained by taking sediment samples from ground stations in the region was taken for density. Accordingly, the unit weight of the sediment in the reservoir was determined as 1.3 tons/m^3. The sediment trap efficiency (TE) of the reservoir is defined as the ratio of the amount of sediment accumulated in the reservoir against the total sediment input.

One of the most widely used methods for this calculation is the curve developed by Brune [19]. Brune's model assumes that TE depends on the ratio of reservoir capacity (V_{res}) and annual mean inflow (Q_{inflow}) as in Eq. (4).

$$TE = f\left(\frac{V_{res}}{Q_{inflow}}\right) \quad (4)$$

For V_{res}/Q_{inflow} = 418.98/5660=0.074 in sediment trap efficiency calculation (annual average flow of Borçka Dam is 5660 hm³), TE is taken as 82% from Brune's median curve. Accordingly, reservoir sediment yield is SY_{RS} = 8.695 t/ha/yr as shown in Table 3.

Table 3. Reservoir area sediment yield of Borçka Dam

Catchment area, A (km²)	Annual sediment accumulation rate, SV (m³/yr) × 10⁶	Unit weight of sediment in the reservoir, γ_s (t/m³)	Sediment retention efficiency of the reservoir, TE (%)	Reservoir sediment yield, SY_{RS}	
				(t/yr/km²)	(t/yr/ha)
19,255	10.56	1.3	82	869.46	8.695

5 Validation of RUSLE Results by Reservoir Sedimentation

Since RUSLE calculation depends on several variables and data quality, its validation is crucial. To achieve this goal, reservoir sediment yield calculations are considered for validation. The Borçka Dam deposits 8.695 t/ha/yr sediment in the reservoir considering the reservoir survey. To relate RUSLE results with reservoir sediment yield, it's required to calculate sediment delivery ratio (SDR). In literature, several methods are presented for determining SDR which are closely related to basin characteristics. In Türkiye, DSI prefer either USDA-SCS equation (Eq. (5)) or equation proposed by Vanoni [20] (Eq. (6)) due to the similar basins characteristics that are considered in the methods.

$$SDR = 0.51(A)^{-0.11} \quad (5)$$

$$SDR = 0.42(A)^{-0.125} \quad (6)$$

The watershed of Borçka Dam is generated in GIS environment and presented in Fig. 8. The SDR values were calculated using the USDA-SCS and Vanoni equations. Due to the varying watershed area and considering the contribution of each watershed to erosion, the SDR prediction of both equations is close to each other so that the average of SDR values is taken into consideration. Therefore, SDR is determined as 0.26 for Borçka Dam.

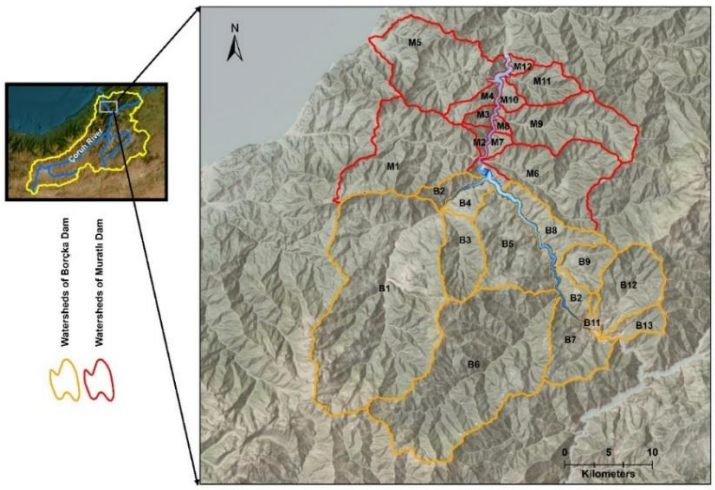


Fig. 8. Watersheds of Borçka Dam (yellow lines).

After having determined the SDR values of the reservoir, reservoir sediment yield is calculated by considering the RUSLE results which are given in Table 4.

Table 4. Sediment Yield (SY_{RS}) for Borçka Dam and RUSLE results

	Reservoir Sediment Yield Considering RUSLE and SDR (t/ha/yr)				
	SRTM 30m	**ALOS 30m**	**DSI 12m**	**DSI 5m**	**SY_{RS}**
K is obtained from ESDAC	8.34	**8.84**	7.71	7.16	8.695
K is obtained by EPIC model	9.33	9.89	**8.78**	8.09	

6 Results and Discussion

Even though the uncertainties and sensitivity resulting from determination of its parameter (R, K, C, LS, P) and due to its empirical formulation, the RUSLE equation is still one of the most used models for estimating long-term soil erosion rates.

Since the DEM is a basic data set in RUSLE, its resolution directly affects the computation of the LS factor, which considers the impacts of slope length and steepness on erosion processes. Erosion estimates were calculated in this study using four DEMs with different spatial resolutions: SRTM 30m, ALOS 30m, DSI 12m, and DSI 5m. Since the DEM is a fundamental input to the calculation of the LS factor, both DEM selection and spatial resolution can influence erosion estimates. The findings demonstrated the model's sensitivity to DEM selection by revealing insignificant variations in the projections of total soil loss as shown in Table 4. In general, also earlier studies showed that erosion estimates from coarser-resolution DEMs (like SRTM 30m) were higher than those from finer-resolution DEMs (like DSI 5m) due to lower-resolution DEMs have tendency to smooth out terrain characteristics which could lead to an overestimation of LS factor and in turn, erosion rates, however, this case was not seen in this study. This may be the topographic characteristics of the catchment of the Borçka Dam.

C and P factors were derived at relatively high spatial resolutions (100m), allowing these parameters to better reflect local land-cover, management, and conservation conditions. In contrast, the R and K factors derived from ESDAC are based on globally produced datasets and therefore have substantially coarser spatial resolutions, generally expressed at the kilometer scale. Moreover, the K factor was additionally estimated using the EPIC model at a higher spatial resolution to investigate the influence of data resolution on the RUSLE results. It should be noted that for the RUSLE calculations, the lowest-resolution results were not differed from the results of the higher-resolution. The results indicate that both DEM selection and spatial resolution did not substantially affect RUSLE-based erosion. It was determined from this study that the results obtained for the Borçka Reservoir indicated that erosion estimates derived from both higher and lower resolution DEMs were consistent with the observed reservoir sediment yield data.

Overall, the results suggest that RUSLE can provide reasonable erosion estimates despite differences in the spatial resolution of the input datasets, provided that the accuracy and consistency of the model inputs are considered collectively.

Acknowledgments

We would like to express our sincere gratitude to the General Directorate of State Hydraulic Works (DSİ) for generously providing the data used in this study, particularly regarding the Çoruh River Basin. We also gratefully acknowledge the financial support provided by The Scientific and Technological Research Council of Türkiye (TÜBİTAK) under project number 121Y456, funded through the TÜBİTAK 1001 Scientific and Technological Research Projects

Support Program. Their support has been instrumental in the successful completion of this research.

References

1. Kokpinar, M. A., Altan-Sakarya, A. B., Kumcu, S. Y., & Gogus, M.: Assessment of sediment yield estimations for large watershed areas: a case study for the Seyhan, Demirköprü and Hirfanlı reservoirs in Turkey. Hydrological Sciences Journal, 60(12), 2189–2203 (2015)
2. Darama Y., Selek Z., Selek B., M.A. Akgul, M. Dagdeviren.: Determination of Sediment Deposition in Hasanlar Dam using Bathymetric and Remote Sensing Studies, Natural Hazards, DOI: 10.1007/s11069-019-03635-y (2019)
3. Walling, D. E.: Measuring sediment yield from river basins. In Soil erosion research methods (pp. 39–80). Routledge (1994)
4. Morris, G. L., & Fan, J. :Reservoir Sedimentation Handbook. New York: McGraw-Hill. (1997)
5. Verstraeten, G., & Poesen, J.: Using sediment deposits in small ponds to quantify sediment yield from small catchments: Possibilities and limitations. Earth Surface Processes and Landforms, 27, 1425–1439. https://doi.org/10.1002/esp.439 (2002)
6. Munthali, K. G., Irvine, B. J., & Murayama, Y.: Reservoir sedimentation and flood control: using a geographical information system to estimate sediment yield of the Songwe river watershed in Malawi. Sustainability, 3(1), 254–269 (2011)
7. European Commission, J.R.C. European Soil Data Centre (ESDAC). Esdac.Jrc.Ec.Europa.Eu. (n.d.)
8. Panagos, P., Van Liedekerke, M., Jones, A., & Montanarella, L.: European Soil Data Centre: Response to European policy support and public data requirements. Land Use Policy, 29(2), 329–338. (2012)
9. Panagos, P., Van Liedekerke, M., Borrelli, P., Köninger, J., Ballabio, C., Orgiazzi, A., Lugato, E., Liakos, L., Hervas, J., & Jones, A.: European Soil Data Centre 2.0: Soil data and knowledge in support of the EU policies. European Journal of Soil Science, 73(6), e13315. (2022)
10. Kheir, R. B., Abdallah, C., & Khawlie, M.: Assessing soil erosion in Mediterranean karst landscapes of Lebanon using remote sensing and GIS. Engineering Geology, 99(3–4), 239–254. (2008)
11. EEA Geospatial Data Catalogue. (n.d.). CORINE Land Cover 2018. Https://Doi.Org/10.2909/960998c1-1870-4e82-8051-6485205ebbac. Last Accessed 2026/04/01
12. Chen, P., Feng, Z., Chen, S., Khan, T. U., & Mannan, A.: Assessment of Soil Loss from Land Use/Land Cover Change and Disasters in The Longmen Shan Mountains, China. Applied Ecology and Environmental Research, 17. https://doi.org/10.15666/aeer/1705_1123311247 (2019)
13. Panagos, P., Borrelli, P., Meusburger, K., Alewell, C., Lugato, E., & Montanarella, L.: Estimating the soil erosion cover-management factor at the European scale. Land Use Policy, 48, 38–50. https://doi.org/https://doi.org/10.1016/j.landusepol.2015.05.021(2015)
14. Rozos, D., Skilodimou, H., Loupasakis, C., & Bathrellos, G.: Application of the revised universal soil loss equation model on landslide prevention. An example from N. Euboea (Evia) Island, Greece. Environmental Earth Sciences, 70. https://doi.org/10.1007/s12665-013-2390-3 (2013)
15. Wischmeier, W. H., & Smith, D. D.: Predicting rainfall erosion losses: a guide to conservation planning (Issue 537). Department of Agriculture, Science and Education Administration. (1978)

16. Williams, J.R.: The EPIC Model. In: Singh, V.P., Ed., Computer Models of Watershed Hydrology, Chapter 25, Water Resources Publications, Highlands Ranch (1995)
17. Moore, I. D., & Burch, G. J.: Physical basis of the length-slope factor in the universal soil loss equation. Soil Science Society of America Journal, 50(5), 1294–1298. (1986)
18. Morris, G. L., & Fan, J.: Reservoir Sedimentation Handbook. New York: McGraw-Hill. (1997)
19. Brune, G.M.: Trap efficiency of reservoirs. Eos, Transactions American Geophysical Union 34(3), 407-418. (1953)
20. Vanoni, V.A.: Sedimentation Engineering Practice. American Society of Civil Engineers, Manuals and Reports on Engineering Practice, No. 54, 745 p. (1975)

Author Contribution Statement

- *Conceptualization:* Yakup Darama, Sarp Toprakkale
- *Methodology:* Yakup Darama, Sarp Toprakkale, Kutay Yilmaz
- *Supervision:* Yakup Darama, Meric Yilmaz
- *Writing – Original Draft:*, Sarp Toprakkale, Yakup Darama, Kutay Yılmaz
- *Writing – Review & Editing:* Yakup Darama, Kutay Yilmaz, Meric Yilmaz

Publication Note

This paper was peer-reviewed, accepted for presentation, and included in the proceedings of the ACE2026 – International Conference on Advances in Civil Engineering, held on 12–14 October 2026 in Trabzon, Türkiye.

This paper may be cited as follows:

Darama, Y., Yilmaz, K., Toprakkale, S., and Yilmaz, M., "Prediction of Reservoir Sedimentation by RUSLE Incorporating the Effects of DEM Selection and Spatial Resolution," in Proceedings of the ACE2026 – International Conference on Advances in Civil Engineering, Trabzon, Türkiye, 12–14 October 2026.

Economic Feasibility Of Rainwater Harvesting Systems In Trabzon, Türkiye: A Water Balance And Cost–Benefit Analysis

Osman Tuğrul BAKİ[1]
[1] 0000-0001-8694-0543, Karadeniz Technical University, Civil Engineering Department, Trabzon, Türkiye, tbaki@ktu.edu.tr

Abstract. Rainwater harvesting and recycling systems (RHRS) offer a promising means of reducing municipal water demand in regions facing increasing water stress. This study presents a daily water balance model combined with a cost-benefit analysis to evaluate the economic feasibility of residential RHRS in Trabzon, Türkiye, one of the country's highest-precipitation provinces, receiving an annual average of 870 mm. Using nine years of daily rainfall data (2014–2022) from the Turkish State Meteorological Service and real Turkish market installation costs, tank sizes of 1–20 m^3 are evaluated across four water price scenarios (0.69–1.50 $/$m^3$). Results reveal a systemic oversizing effect: tanks larger than 5 m^3 yield no additional water savings, making 1–3 m^3 configurations consistently optimal. The break-even water price threshold for these small tanks is 0.71–0.76 $/$m^3$, only 3–10% above the current local tariff, indicating that near-term economic viability is imminent, with the 2 m^3 configuration already nearly at parity under current 2026 pricing. The findings offer an evidence-based framework for infrastructure planning and incentive policy design.

Keywords: rainwater harvesting; water balance model; cost–benefit analysis; Trabzon; economic feasibility; oversizing effect.

1 Introduction

Freshwater scarcity is increasingly recognised as one of the most critical infrastructure challenges of the 21st century. In Türkiye, per capita renewable water availability has declined to below 1,400 m^3/year, approaching the internationally defined water stress threshold [1]. Rapid urbanisation, population growth, and the compounding effects of climate change are projected to intensify this pressure, particularly in regions where precipitation is irregular or declining [2].

Rainwater harvesting and recycling systems (RHRS), which collect rooftop runoff for non-potable uses such as toilet flushing, garden irrigation, and fire suppression, offer a technically straightforward means of reducing dependence on centralised water supply networks. The international literature on RHRS is substantial and spans hydrological performance, tank sizing optimisation, and life-cycle economics. Ghisi et al. [3] demonstrated that even modest tank capacities can achieve meaningful potable water substitution in southeastern Brazil, while Imteaz et al. [4] and Khastagir & Jayasuriya [5] developed optimisation frameworks showing that water savings from RHRS follow strongly diminishing returns beyond a threshold tank size, a pattern closely related to what this study terms the oversizing effect. Roebuck et al. [6] extended this analysis to whole-life costing in the United Kingdom, finding that economic viability depends heavily on local water tariffs and installation costs rather than harvesting potential alone. Ward et al. [7] further showed, through monitored performance data from a large United Kingdom building, that real-world savings often diverge from theoretical estimates, underscoring the value of empirically calibrated, site-specific models such as the one developed here. A recent comprehensive review by Campisano et al. [8] confirms that despite decades of RHRS research, robust economic assessments grounded in local hydroclimatic and

market data remain the exception rather than the rule internationally, and are especially scarce for the Eastern Mediterranean and Black Sea climate regions.

Within Türkiye specifically, most existing rainwater harvesting studies remain limited to single-site case assessments, such as Ertop et al.'s [9] evaluation of harvesting potential in Antalya, and have generally relied on generalised climatic averages rather than long-term daily precipitation records, and have not incorporated real market installation costs or region-specific tariff structures. Trabzon presents a compelling case study to address this gap: with a long-term annual rainfall averaging 870 mm, it ranks among Türkiye's wettest provincial capitals. However, the economic viability of RHRS in high-precipitation settings is not self-evident. High rainfall may paradoxically reduce system efficiency if tank capacity is over-specified relative to demand, a phenomenon this study identifies as the oversizing effect.

This paper addresses three research questions: (1) What is the water-saving potential of residential RHRS in Trabzon under observed daily rainfall patterns? (2) What tank size minimises capital investment while maximising cost-effectiveness? (3) At what water price do these systems become economically viable, and how does this relate to current and projected tariffs?

2 Material and Methods

2.1 Study Area and Data

Daily precipitation records for Trabzon (Station No. 17249; 41.00°N, 39.72°E; elevation 39 m a.s.l.) covering the period 2014–2022 were obtained from the Turkish State Meteorological Service. The dataset comprises 3,272 daily observations with zero missing values; standard quality control procedures (range checks and temporal consistency checks) were applied prior to analysis. Annual summary statistics are presented in Table 1.

Table 1. Annual precipitation statistics for Trabzon station, 2014–2022.

Year	Annual (mm)	Max Daily (mm)	Min Daily (mm)	Mean Daily (mm)	Peak Months
2014	915.0	82.4	0.0	2.39	Jan & Oct
2015	1,007.6	55.2	0.0	2.76	Nov & Dec
2016	1,044.6	67.8	0.0	2.86	Oct & Nov
2017	804.4	61.3	0.0	2.20	Jan & Sep
2018	928.2	72.1	0.0	2.54	Nov & Dec
2019	745.0	58.4	0.0	2.04	Sep & Oct
2020	839.4	64.9	0.0	2.30	Oct & Nov
2021	792.6	59.7	0.0	2.17	Jan & Oct
2022	759.6	53.1	0.0	2.08	Sep & Nov
Mean	870.7	63.9	0.0	2.38	—

Note: Peak months identified as those with the highest mean monthly accumulation in each year.

The data reveal substantial interannual variability, with annual totals ranging from 745 mm (2019) to 1,045 mm (2016), a 40% difference. October and November consistently emerge as the wettest months, collectively accounting for approximately 35% of annual precipitation. The

observed daily maximum of 82.4 mm confirms the presence of intense convective events characteristic of the eastern Black Sea climate regime.

2.2 Methodology

A daily water balance model simulates tank storage behaviour over the full observation period, with the tank assumed empty at the start of the simulation and any inflow exceeding available capacity treated as overflow (lost) rather than stored. On days when stored volume is insufficient to meet demand, the shortfall is assumed to be met by the municipal supply. Harvestable runoff on each day is computed as (m^3):

$$Q = \frac{(P-F)xAxC}{1000} \quad (1)$$

where P is daily rainfall (mm), F is the first-flush loss (2.0 mm), A is rooftop catchment area (150 m^2), and C is the runoff coefficient (0.85). Dividing by 1000 converts the result from litres to cubic metres, consistent with the units used for tank capacity and water pricing throughout this study. Tank storage is updated daily subject to the capacity constraint, and a constant daily non-potable demand of 0.1 m^3 is withdrawn from available storage.

Economic feasibility is assessed using Net Present Value (NPV) over a 20-year horizon at a 5% real discount rate, assumed to reflect typical financing conditions for residential infrastructure investment in Türkiye. Water tariffs are held constant in real terms within each scenario, and reported prices reflect water charges only; wastewater fees, which are billed separately alongside water charges in Turkish municipal tariffs, are excluded (see Discussion for the implications of this simplification). Annual monetary savings equal annual water savings (m^3) multiplied by the prevailing water tariff ($/$m^3$). Installation costs are drawn from Turkish market surveys conducted in 2024 and are treated as $-indexed given the dollar-denominated cost structure of system components, ranging from $64 (1 m^3) to $638 (20 m^3), with $15/year for maintenance. Four price scenarios are evaluated: S1 = 0.69 $/$m^3$ (current Trabzon Tier-1 residential water tariff, [10]); S2 = 0.75 $/$m^3$; S3 = 0.87 $/$m^3$ (current Istanbul Tier-1 residential water tariff, [11]); S4 = 1.50 $/$m^3$ (medium-term projection). ₺-denominated tariffs were converted to $ at an exchange rate of 48 ₺/$. S3 is included not as a literal Istanbul deployment scenario, but as a proxy for the tariff level Trabzon may reach if regional convergence with higher-tariff metropolitan markets continues, consistent with observed trends in Turkish municipal water pricing. Break-even threshold prices (the tariff at which NPV equals zero) are derived analytically for each tank size.

3 Results

Table 2 presents the cost-benefit analysis across all tank sizes and price scenarios. Configurations identified as optimal (★) deliver the highest cost-efficiency under viable economic scenarios.

Table 2. Cost–benefit results by tank size and water price scenario

Tank (m^3)	Install. ($)	Annual Saving (m^3)	Coverage (%)	S1 NPV ($) 0.69$/m	S2 NPV ($) 0.75$/m^3	S3 NPV ($) 0.87$/m^3	S4 NPV ($) 1.50$/m^3
1 ★	64	26.5	72.5	-23	-3	+36	+244
2 ★	96	32.2	88.1	-6	+18	+66	+319
3 ★	128	34.1	93.5	-22	+4	+55	+323

Tank (m^3)	Install. ($)	Annual Saving (m^3)	Coverage (%)	S1 NPV ($) 0.69$/m	S2 NPV ($) 0.75$/m^3	S3 NPV ($) 0.87$/m^3	S4 NPV ($) 1.50$/m^3
5	191	35.9	98.3	-69	-42	+11	+293
8	298	36.2	99.2	-174	-147	-92	+192
10	362	36.2	99.2	-238	-211	-156	+128
15	511	36.2	99.2	-387	-360	-305	-21
20	638	36.2	99.2	-514	-487	-432	-148

★ = *optimal configurations.*

Two patterns are immediately apparent. First, annual water savings plateau at 36.2 m^3/year for tanks of 5 m^3 and above, confirming the oversizing effect: beyond this threshold, additional storage capacity does not translate into additional savings because daily demand (36.5 m^3/year at 0.1 m^3/day) is fully met on virtually every rainy day. The 1–3 m^3 range captures 72–94% of maximum achievable savings at a fraction of the cost.

Second, under the current Trabzon tariff (S1 = 0.69 \$/m^3), no configuration yields a positive NPV, though the 1–3 m^3 range comes close, with the 2 m^3 tank reaching -\$6. Under S2, the 2 m^3 tank turns marginally positive at +\$18. Under S3 (0.87 \$/m^3, the price level currently charged in Istanbul), 1–3 m^3 tanks generate NPVs of +\$36 to +\$66, with the 2 m^3 option now delivering the highest return. Under S4, all tanks up to 5 m^3 produce meaningful positive returns, with the 3 m^3 option delivering the highest NPV at +\$323.

Table 3 shows that 1–3 m^3 tanks reach break-even at water prices of 0.71–0.76 \$/m^3, only 3–10% above the current Trabzon tariff, with the 2 m^3 configuration standing just 2.9% below its break-even threshold. Given that Turkish municipal water tariffs have historically increased at rates well above general inflation, this near-parity suggests that economic viability for small-tank RHRS in Trabzon may already be within reach, rather than requiring a multi-year horizon.

Table 3. Break-even water price thresholds by tank size and feasibility assessment.

Tank (m^3)	**Install. ($)**	**Annual Saving (m^3)**	**Threshold (\$/m^3)**	**Feasibility Assessment**
1	64	26.5	0.76 ✓	Achievable imminently
2	96	32.2	0.71 ✓	Nearly at parity today
3	128	34.1	0.74 ✓	Achievable imminently
5	191	35.9	0.84	Achievable near-term
8	298	36.2	1.07	Requires subsidy
10	362	36.2	1.22	Requires subsidy
15	511	36.2	1.55	Not recommended
20	638	36.2	1.83	Not recommended

4 Discussion

The oversizing effect documented here carries a clear practical message: in high-precipitation settings such as Trabzon, specifying larger tanks to maximise harvested volume is economically counterproductive. A 1 m^3 tank recovers 72.5% of maximum possible savings at $64, whereas a 10 m^3 tank recovers 99.2% of savings at a cost nearly six times higher ($362). For residential construction standards, promoting small and affordable systems is therefore more cost-effective than incentivising large-capacity installations. This finding is broadly consistent with Roebuck et al.'s [6] whole-life costing analysis in the United Kingdom, which similarly found that RHRS economic viability is driven primarily by local tariff levels rather than by maximising harvested volume.

The proximity of the break-even threshold to the current tariff is a significant finding for Turkish infrastructure policy. A modest 30% installation subsidy reduces the break-even threshold to 0.63–0.65 \$/m^3 for 2–3 m^3 tanks, bringing them below the current Trabzon tariff (0.69 \$/m^3) and rendering these configurations immediately viable; the 1 m^3 tank's subsidized threshold (0.70 \$/m^3) sits almost exactly at parity with current pricing. Alternatively, the introduction of block tariff structures that penalise high-volume consumption, such as İSKİ's tiered residential pricing already applied in Istanbul, could accelerate adoption without direct fiscal expenditure.

The study has several limitations worth acknowledging. The 150 m^2 roof and 0.1 m^3/day demand are representative residential assumptions; commercial rooftops and higher demand scenarios would improve system economics. The analysis also assumes constant real water prices within each scenario, whereas actual tariff trajectories are uncertain. The runoff coefficient and first-flush allowance, while representative of typical residential roofing, were not varied parametrically; a formal sensitivity analysis would clarify the robustness of the reported thresholds to these assumptions. The tariff figures used in this study reflect water charges only; wastewater fees, which are typically billed alongside water charges in Turkish municipal tariffs, were excluded from the analysis. Since RHRS reduces potable water withdrawal but does not necessarily reduce wastewater discharge proportionally, incorporating wastewater tariffs would likely increase the effective avoided cost per cubic metre, making the reported break-even thresholds conservative. Water quality treatment and system maintenance costs beyond the assumed $15/year were also not modelled in detail. Future work should extend this framework to multiple climatic zones across Türkiye to map regional variation in both harvesting potential and economic viability.

5 Conclusions

This study evaluated the economic feasibility of residential RHRS in Trabzon using a calibrated daily water balance model and real Turkish market costs. Three principal conclusions emerge:

(1) Oversizing effect: for a 150 m^2 rooftop with 0.1 m^3/day non-potable demand, tanks larger than 3–5 m^3 provide no additional water savings, making small tanks the rational choice in Trabzon's high-rainfall setting.

(2) Near-term threshold: 1–3 m^3 tanks break even at water prices of 0.71–0.76 \$/m^3, only 3–10% above the current local tariff, with the 2 m^3 configuration standing just 2.9% below its break-even threshold, indicating that economic viability is imminent rather than a distant, multi-year prospect.

(3) Policy implication: a 30% installation subsidy would bring 2–3 m^3 RHRS below the current Trabzon tariff (break-even thresholds of 0.63–0.65 \$/m^3 versus a current tariff of 0.69 \$/m^3), making them economically viable immediately, while the 1 m^3 configuration would sit at approximate parity; this offers a low-cost, low-risk policy lever for municipal authorities to accelerate adoption ahead of further tariff increases.

These findings provide an evidence-based foundation for integrating decentralised water management into residential construction practice and urban water policy in Türkiye's Black Sea region.

Acknowledgments

The authors acknowledge the Turkish State Meteorological Service (MGM) for providing precipitation data.

References

1. DSİ.: Toprak Su Kaynakları. DSİ Yayınları, Ankara (2022).
2. Öztürk, A., Çolak, M.S.: A quantitative and qualitative assessment of Turkey's water resources potential. Journal of Agricultural Sciences 30(1), 1–34 (2024).
3. Ghisi, E., Bressan, D.L., Martini, M.: Rainwater tank capacity and potential for potable water savings by using rainwater in the residential sector of southeastern Brazil. Building and Environment 42(4), 1654–1666 (2007).
4. Imteaz, M.A., Shanableh, A., Rahman, A., Ahsan, A.: Optimisation of rainwater tank design from large roofs: A case study in Melbourne, Australia. Resources, Conservation and Recycling 55(11), 1022–1029 (2011).
5. Khastagir, A., Jayasuriya, N.: Optimal sizing of rain water tanks for domestic water conservation. Journal of Hydrology 381(3–4), 181–188 (2010).
6. Roebuck, R.M., Oltean-Dumbrava, C., Tait, S.: Whole life cost performance of domestic rainwater harvesting systems in the United Kingdom. Water and Environment Journal 25(3), 355–365 (2011).
7. Ward, S., Memon, F.A., Butler, D.: Performance of a large building rainwater harvesting system. Water Research 46(16), 5127–5134 (2012).
8. Campisano, A., Butler, D., Ward, S., Burns, M.J., Friedler, E., DeBusk, K., Fisher-Jeffes, L.N., Ghisi, E., Rahman, A., Furumai, H., Han, M.: Urban rainwater harvesting systems: Research, implementation and future perspectives. Water Research 115, 195–209 (2017).
9. Ertop, H., Kocięcka, J., Atilgan, A., Liberacki, D., Niemiec, M., Rolbiecki, R.: The importance of rainwater harvesting and its usage possibilities: Antalya example (Turkey). Water 15(12), 2194 (2023).
10. TİSKİ: TİSKİ Tarife Cetveli 2026, https://www.tiski.gov.tr/uploads/dokuman/eb64a5b9-d942-4be2-b440-fa8720008afb.pdf, last accessed 2026/08/13.
11. İSKİ: Su Birim Fiyatları, İstanbul Su ve Kanalizasyon İdaresi, https://iski.istanbul/abone-hizmetleri/abone-rehberi/su-birim-fiyatlari, last accessed 2026/08/13.

Author Contribution Statement

- *Conceptualization:* Osman Tuğrul BAKİ
- *Methodology:* Osman Tuğrul BAKİ
- *Investigation:* Osman Tuğrul BAKİ
- *Writing – Original Draft:* Osman Tuğrul BAKİ
- *Writing – Review & Editing:* Osman Tuğrul BAKİ

List of Abbreviations

- **NPV** — Net Present Value
- **RHRS** — Rainwater harvesting and recycling systems
- **DSİ** — General Directorate of State Hydraulics Works

Note: Following the conference, this Publication Note will be added to each paper; therefore, authors are kindly requested not to remove the note below and to complete the author(s) and paper title information.

Publication Note

This paper was peer-reviewed, accepted for presentation, and included in the proceedings of the ACE2026 – International Conference on Advances in Civil Engineering, held on 12–14 October 2026 in Trabzon, Türkiye.

This paper may be cited as follows:

Baki O. T., "Economic Feasibility of Rainwater Harvesting Systems in Trabzon, Türkiye: a Water Balance and Cost–Benefit Analysis," in Proceedings of the ACE2026 – International Conference on Advances in Civil Engineering, Trabzon, Türkiye, 12–14 October 2026.

Prediction of Jet Length in Spillways Using Advanced Machine Learning Algorithms

Pelin İlker[1], Ziya Cem Öztürk[2] and Mehmet Sorgun[3]
[1] 0000-0001-7933-4772, Izmir Katip Celebi University, Civil Engineering Department, Izmir, Türkiye, pelin.ilker@ikc.edu.tr
[2] Izmir Katip Celebi University, Civil Engineering Department, Izmir, Türkiye, ziyacem.ozturk@hotmail.com
[3] 0000-0003-2323-2499, Izmir Katip Celebi University, Civil Engineering Department, Izmir, Türkiye, mehmet.sorgun@ikc.edu.tr

Abstract. Prediction of jet length is essential for the hydraulic design of high-speed spillway aerators, since jet development influences cavity formation, reattachment location, air entrainment, and cavitation protection. This study investigates the use of machine learning algorithms for estimating jet length in spillway aerator flows. Four models, namely Gaussian Process Regression, Adaptive Neuro-Fuzzy Inference System, Polynomial Regression, and Regression Tree Ensembles, were developed using dimensionless hydraulic and geometric input parameters. The Froude number, geometric slope parameter, relative aerator geometry, and combined aerator angle-area ratio were used as input variables, while dimensionless jet length was selected as the output. Model performances were assessed using R^2, RMSE, MAE, and AAPE. The results indicated that ANFIS achieved the best overall performance, with an R^2 of 0.98878, RMSE of 0.72459, MAE of 0.44154, and AAPE of 4.3459%. GPR also provided highly accurate predictions, with an R^2 of 0.98579 and AAPE of 4.6784%. Polynomial Regression and Regression Tree Ensembles exhibited lower prediction accuracy. The findings suggest that ANFIS and GPR can successfully represent the nonlinear relationship between hydraulic and geometric parameters and dimensionless jet length. Therefore, these models can be considered useful alternatives to conventional empirical methods for predicting jet length in spillway aerator flows.

Keywords: High-speed spillway aerator; Jet length; Machine learning algorithms

1 Introduction

Spillways are essential hydraulic structures used to safely convey excess water from reservoirs during flood events. In high-head spillways, the flow may reach very high velocities, increasing the risk of cavitation and subsequent damage to the chute surface. Aeration is one of the most effective methods used to reduce cavitation damage in high-speed spillway flows. By introducing air into the lower region of the flow, spillway aerators increase the air concentration near the chute surface and provide protection against cavitation [1].

A spillway aerator generally consists of a deflector, offset, groove, or a combination of these elements. As the flow passes over the aerator, it separates from the chute surface and forms a free jet before reattaching to the downstream surface. An air cavity develops beneath the jet, allowing atmospheric air to enter the flow. Rutschmann and Hager [2] investigated the air entrainment mechanism of spillway aerators and showed that aerator performance is governed by both hydraulic conditions and aerator geometry. Among the main characteristics of this flow, jet length represents the distance between the flow separation and reattachment points and is closely associated with cavity development and air entrainment. The hydraulic characteristics of jets formed by spillway aerators have subsequently been investigated through several experimental studies. Kökpınar and Göğüş [3] examined high-speed jet flows over spillway

aerators and investigated the effects of hydraulic and geometric parameters on jet length, cavity subpressure, and air entrainment. Pfister and Hager [4] conducted systematic experiments on chute aerators and proposed an explicit relationship for jet length based on approach-flow conditions, aerator geometry, and chute bottom angle. Their results also showed the importance of jet length in describing the different flow regions downstream of an aerator. These investigations indicate that jet length results from the combined effects of several hydraulic and geometric parameters and therefore requires reliable prediction methods for aerator design.

Besides experimental and empirical approaches, numerical methods have also been used to investigate the complex air–water flow occurring around spillway aerators. Tokyay and Kurt [5] applied the Volume of Fluid (VOF) method together with the k−ε turbulence model to simulate flow over a bottom-aerated ramp and step structure. Their numerical analyses focused particularly on air entrainment and the jet length between the separation and reattachment points and considered parameters such as Froude number, discharge, aerator arrangement, and ramp geometry. Shayanseresht and Manafpour [6] compared different turbulence models for air–water flow over a chute aerator and reported that the RNG k−ε model provided jet-length predictions close to experimental measurements. He et al. [7] further investigated three-dimensional aerated deflector-generated jets and evaluated the effects of numerical and physical parameters on the predicted aeration characteristics. Their results demonstrated that numerical approaches can successfully reproduce important characteristics of aerated jets, while also showing the sensitivity of predictions to parameters such as wall roughness and multiphase-flow modelling assumptions.

In recent years, data-driven and soft-computing methods have provided another approach for modelling complex hydraulic processes. These techniques are particularly useful when the relationship between the governing variables and the desired output is nonlinear and difficult to represent using a single empirical expression. Their application has therefore expanded to different aeration and air–water flow problems. Li et al. [8], for example, used embedded multi-gene genetic programming to estimate the air demand of spillway aerators. Kumar et al. [9] investigated soft-computing approaches for predicting the oxygen transfer performance of plunging hollow jets, whereas Puri et al. [10] evaluated different soft-computing techniques for predicting aeration effectiveness based on jet geometry and hydraulic parameters. These studies demonstrate the potential of data-driven approaches for representing complex interactions among hydraulic and geometric variables. Machine learning has also been directly applied to the prediction of air entrainment. Alazmi and Al-Anzi [11] evaluated different machine-learning algorithms for predicting air entrainment rates in a confined plunging liquid jet system. Their results showed that machine-learning models could successfully represent the nonlinear relationship between experimental hydrodynamic parameters and air entrainment. More importantly for spillway aerators, Hekmat et al. [12] applied ANFIS and hybrid ANFIS models combined with different metaheuristic optimization algorithms to estimate aerator design parameters, including dimensionless jet length. This study demonstrated that neuro-fuzzy and optimization-based data-driven approaches can provide high prediction accuracy for spillway aerator parameters. Although previous studies have demonstrated the capability of soft-computing techniques for aeration-related problems and the potential of ANFIS-based approaches for predicting spillway aerator parameters, the predictive performance of different classes of machine-learning algorithms may vary depending on the experimental database, input parameters, and modelling approach. A comparison of algorithms with substantially different learning structures using the same dataset can therefore provide useful information on their ability to represent the nonlinear relationship between hydraulic conditions, aerator geometry, and jet length.

In the present study, experimental data originally reported by Demiröz [13] are used to develop data-driven models for the prediction of jet length in spillway aerator flows. Four

different approaches, namely Gaussian Process Regression (GPR), Adaptive Neuro-Fuzzy Inference System (ANFIS), Polynomial Regression (PR), and Regression Tree Ensembles (RTE), are comparatively evaluated. The Froude number, geometric slope parameter, relative aerator geometry, and combined aerator angle- area ratio are used as dimensionless input parameters, while dimensionless jet length is selected as the output. Model performances are evaluated using the coefficient of determination (R^2), root mean square error (RMSE), mean absolute error (MAE), and average absolute percentage error (AAPE). The comparative assessment aims to identify the model that provides the most accurate prediction of dimensionless jet length under the investigated conditions and to evaluate the applicability of different data-driven approaches as predictive tools for spillway aerator design.

2 Materials and Methods

2.1 Dimensional Analysis and Input Parameters

The experimental data used in this study were obtained from the spillway aerator experiments conducted by Demiröz [13]. In these experiments, the lower nappe length was measured under different hydraulic and geometric conditions. For the present analysis, the jet length was expressed in dimensionless form by normalizing the lower nappe length with the flow depth. The dimensionless jet length, denoted by L_{jet} , was defined as

$$L_{jet} = \frac{L_n}{h} \tag{1}$$

where L_n is the lower nappe length and h is the flow depth.

The dimensionless jet length is influenced by the hydraulic characteristics of the approaching flow and the geometry of the spillway aerator. Accordingly, the general functional relationship can be expressed as

$$L_{jet} = f(V, g, h, \alpha, \theta, T_r, H_s, A_a, A_w) \tag{2}$$

where V is the approach flow velocity and g is the gravitational acceleration, α is the chute-related geometric parameter, θ is the aerator angle, T_r is the ramp height, H_s is the step height, A_a is the aerator opening area, and A_w is the water-flow area.

Using dimensional analysis, the hydraulic and geometric variables were represented by four dimensionless parameters. The first parameter was the Froude number, which represents the relative effects of inertial and gravitational forces:

$$\pi_1 = Fr = \frac{V}{\sqrt{gh}} \tag{3}$$

The second parameter represents the effect of the chute-related geometry:

$$\pi_2 = 1 + \alpha \tag{4}$$

The third parameter represents the aerator geometry relative to the flow depth:

$$\pi_3 = \frac{T_r + H_s}{h} \tag{5}$$

and the fourth parameter combines the effects of the aerator angle and area ratio:

$$\pi_4 = (1 + tan\theta)\frac{A_a}{A_w} \tag{6}$$

Accordingly, the dimensionless jet length can be expressed in terms of these four dimensionless parameters as

$$L_{jet} = f\left(Fr, 1 + \alpha, \frac{T_r + H_s}{h}, (1 + tan\theta)\frac{A_a}{A_w}\right) \tag{7}$$

The four dimensionless parameters π_1, π_2, π_3 and π_4 were used as the input variables for the machine learning models, while L_{jet} was used as the target output. The same input-output structure was used for all models to allow their prediction performances to be compared under identical conditions.

2.2 Machine Learning Models

2.2.1 Gaussian Process Regression (GPR)

Gaussian Process Regression (GPR) is a non-parametric probabilistic regression method used to model nonlinear relationships between input and output variables. In GPR, the response is assumed to follow a Gaussian process defined by a mean function and a covariance function. The covariance function, also referred to as the kernel function, determines the relationship between data points and controls the smoothness of the predicted response.

For a set of input variables x, the regression function can be expressed as

$$f(x) \sim GP\big(m(x), k(x, x')\big) \tag{8}$$

where $m(x)$ is the mean function and , $k(x, x')$ is the covariance function. The theoretical background of Gaussian process regression is given in Rasmussen and Williams [14].

In the present study, GPR was used to predict the dimensionless jet length from the four dimensionless input parameters defined in Section 2.1. A squared exponential kernel function was used, and the input variables were standardized before model training. These settings were applied directly in the MATLAB GPR model. The squared exponential covariance function can be written as

$$k(x, x') = \sigma_f^2 exp\left[-\frac{\|x-x'\|^2}{2l^2}\right] \tag{9}$$

where σ_f^2 is the signal variance and l is the characteristic length scale.

2.2.2 Adaptive Neuro-Fuzzy Inference System (ANFIS)

The Adaptive Neuro-Fuzzy Inference System (ANFIS) combines the learning capability of artificial neural networks with the rule-based structure of fuzzy inference systems. ANFIS establishes nonlinear relationships between input and output variables through fuzzy membership functions and a set of if–then rules. The parameters of the fuzzy inference system are adjusted during the training process to minimize the prediction error.

For a first-order Sugeno fuzzy model, a typical rule can be expressed as

$$Rule\ i\text{:}\ If\ x_1\ is\ A_{i1}, \dots, x_n\ is\ A_{in},\ \ then\ f_i = p_{i1}x_1\ \cdots + p_{in}x_n + r_i \tag{10}$$

where A_{ij} represents the fuzzy set associated with the jth input, and p_{ij} and r_i are consequent parameters.

In the present study, the initial fuzzy inference system was generated using the subtractive clustering method. A cluster influence range of 0.6 was adopted, and the ANFIS model was trained for 100 epochs. The four dimensionless parameters defined in Section 2.1 were used as inputs, while L_{jet} was used as the target output.

2.2.3 Polynomial Regression (PR)

Polynomial Regression (PR) extends conventional linear regression by including polynomial and interaction terms of the input variables, allowing nonlinear relationships between the predictors and the target variable to be represented. For the four input variables considered in this study, a second-order polynomial model was used and can be expressed in the general form

$$L_{jet} = \beta_0 + \sum_{i=1}^{4} \beta_i x_i + \sum_{i=1}^{4} \beta_{ii} x_i^2 + \sum_{i<j} \beta_{ij} x_i\, x_j + \varepsilon \tag{11}$$

Where x_i represents the dimensionless input variables, β_0 is the intercept, β_i , β_{ii} , and β_{ij} are the regression coefficients for the linear, quadratic, and interaction terms, respectively, and ε is the residual error.

In the present study, the PR model included the four linear terms, their corresponding quadratic terms, and all pairwise interactions between the input variables. Accordingly, the model was developed using Fr, $1+\alpha$, $\frac{T_r+H_s}{h}$ and $(1+tan\theta)\frac{A_a}{A_w}$ as predictors of L_{jet}. This model structure corresponds directly to the second-order polynomial formulation implemented in MATLAB.

2.2.4 Regression Tree Ensembles (RTE)

Regression Tree Ensembles (RTE) combine the predictions of multiple regression trees to improve predictive performance and reduce the sensitivity associated with a single decision

tree. In the bagging approach, individual regression trees are trained on different bootstrap samples of the training dataset, and their predictions are combined to obtain the final output. The ensemble prediction can be expressed as

$$\hat{L}_{jet} = \frac{1}{M}\sum_{m=1}^{M} f_m(x) \tag{12}$$

Where M is the total number of regression trees, $f_m(x)$ is the prediction obtained from the m th tree, and $\hat{L}_{jet}$ is the predicted dimensionless jet length.

In the present study, the RTE model was developed using the bagging method with 200 regression trees. The minimum leaf size of each tree was set to 2. The four dimensionless parameters defined in Section 2.1 were used as predictor variables, while L_{jet} was used as the target output. These model settings correspond to those implemented in MATLAB.

2.3 Model Development and Performance Evaluation

The dataset consisted of 177 observations, including the four dimensionless input parameters defined in Section 2.1 and L_{jet} as the target output. A random holdout procedure was used to divide the dataset into training and testing subsets. A fixed random seed was applied to ensure reproducibility. 20% of the observations were used for model training, while the remaining 80% were used for model testing. The same data partition was applied to all four machine learning models to provide a common basis for performance comparison.

The predictive performances of the models were evaluated using the coefficient of determination (R^2), root mean square error (RMSE), mean absolute error (MAE), and average absolute percentage error (AAPE). These statistical measures were calculated as

$$R^2 = 1 - \frac{\left\{\sum_{i=1}^{N}\left(L_{jet,i} - \hat{L}_{jet,i}\right)^2\right\}}{\left\{\sum_{i=1}^{N}\left(L_{jet,i} - \bar{L}_{jet}\right)^2\right\}} \tag{13}$$

$$RMSE = \sqrt{\left\{\frac{1}{N}\sum_{i=1}^{N}\left(L_{jet,i} - \hat{L}_{jet,i}\right)^2\right\}} \tag{14}$$

$$MAE = \frac{1}{N}\sum_{i=1}^{N}\left|L_{jet,i} - \hat{L}_{jet,i}\right| \tag{15}$$

$$AAPE = \frac{100}{N}\sum_{i=1}^{N}\left|\frac{L_{jet,i} - \hat{L}_{jet,i}}{L_{jet,i}}\right| \tag{16}$$

3. Results and Discussion

The prediction performances of the GPR, Polynomial Regression, Regression Tree Ensembles, and ANFIS models were evaluated using R^2 , RMSE, MAE, and AAPE. The obtained performance metrics are presented in Table 1.

As shown in Table 1, ANFIS and GPR provided considerably better prediction performance than Polynomial Regression and RTE. ANFIS achieved the highest value (0.98878) and the lowest RMSE (0.72459) and AAPE (4.3459%), indicating close agreement between the experimental and predicted L_{jet} values. GPR showed a similarly high predictive performance, with an R^2 of 0.98579 and an AAPE of 4.6784%. GPR produced a slightly lower MAE (0.44086) than ANFIS (0.44154).

Polynomial Regression showed lower predictive performance, with an R^2 of 0.74873 and an AAPE of 10.234%. This result indicates that the second-order polynomial formulation was less successful in representing the relationship between the hydraulic and geometric input parameters and L_{jet}. RTE provided a higher R^2 value (0.86479) than Polynomial Regression; however, it produced the highest AAPE (22.595%) and MAE (1.8546) among the investigated models.

Table 1. Performance comparison of the machine learning models for prediction.

Model	R^2	**RMSE**	**MAE**	**AAPE (%)**
GPR	0.98579	0.81537	0.44086	4.6784
Polynomial Regression	0.74873	3.4291	1.1962	10.2340
Regression Tree Ensembles	0.86479	2.5154	1.8546	22.5950
ANFIS	0.98878	0.72459	0.44154	4.3459

The considerably better performance of ANFIS and GPR suggests that the relationship between the selected dimensionless parameters and jet length is strongly nonlinear. ANFIS can represent such relationships through its fuzzy rule-based structure, whereas GPR provides a flexible nonlinear mapping through its kernel-based formulation. In contrast, the predefined mathematical structure of the second-order Polynomial Regression model restricts its ability to represent more complex interactions between the input parameters. The RTE model captured part of the nonlinear behavior but showed larger prediction errors than ANFIS and GPR.

The comparison between the experimental and predicted L_{jet} values obtained using the GPR model is presented in Figure 1. Most of the predicted values are located close to the perfect agreement line, with relatively small deviations over the investigated range. This close agreement is also reflected in the statistical performance of the model, with an R^2 of 0.98579, RMSE of 0.81537, MAE of 0.44086, and AAPE of 4.6784%. These results indicate that GPR effectively represents the relationship between the selected dimensionless hydraulic and geometric parameters and L_{jet}.

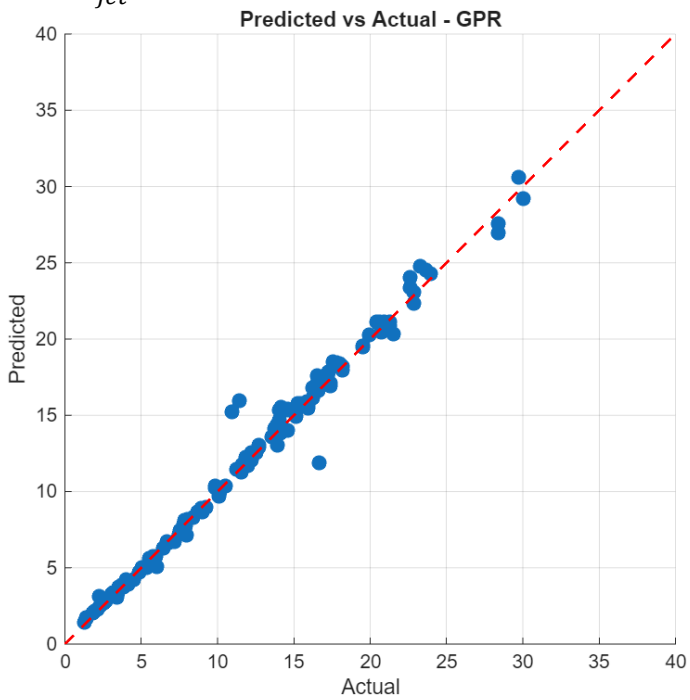


Fig. 1. Actual and predicted jet length values for the GPR model

Figure 2 presents the experimental and predicted L_{jet} values obtained using Polynomial Regression. Compared with GPR, the predicted values show greater scatter around the perfect agreement line. The model yielded an R^2 of 0.74873, RMSE of 3.4291, MAE of 1.1962, and AAPE of 10.234%. The lower prediction accuracy indicates that the second-order polynomial formulation was less effective in representing the relationship between the selected input parameters and L_{jet}.

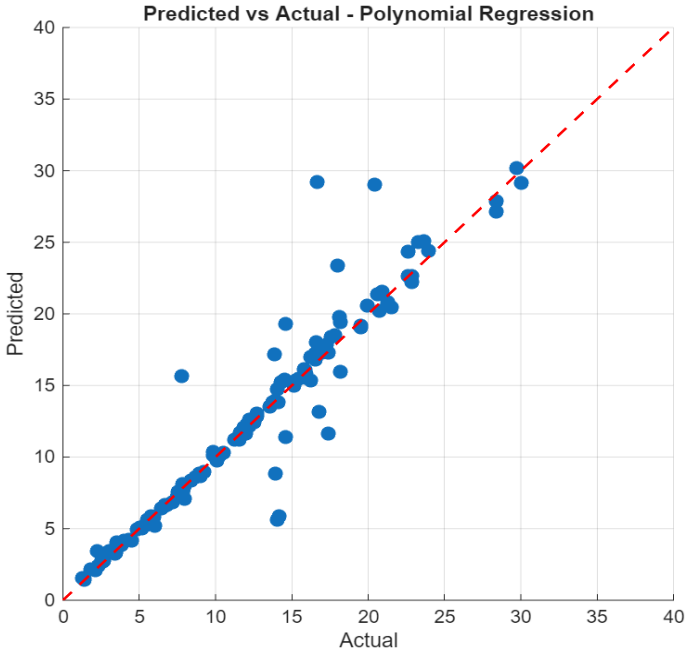


Fig. 2. Actual and predicted jet length values for the Polynomial Regression model.

The prediction results of the RTE model are shown in Figure 3. The model achieved an R^2 of 0.86479, which was higher than that obtained using Polynomial Regression. However, greater deviations between the experimental and predicted values are observed, particularly at larger L_{jet} values, where the model tends to underestimate the experimental values. This behavior is also reflected in the RMSE, MAE, and AAPE values of 2.5154, 1.8546, and 22.595%, respectively. Therefore, although RTE captured part of the nonlinear relationship between the input parameters and L_{jet} , its prediction errors were considerably higher than those obtained using GPR and ANFIS.

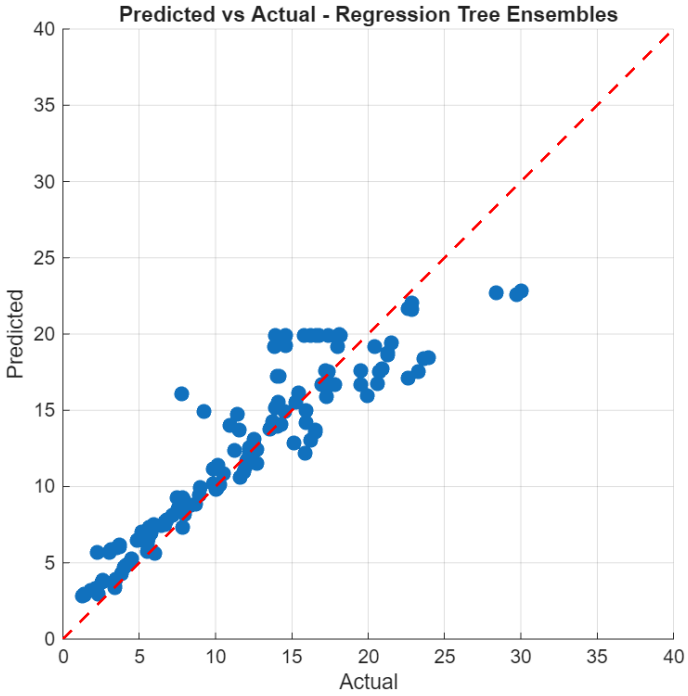


Fig. 3. Actual and predicted jet length values for the Regression Tree Ensembles model.

Figure 4 shows the experimental and predicted L_{jet} values obtained using ANFIS. The predicted values are closely distributed around the perfect agreement line, indicating good agreement with the experimental values. ANFIS achieved the highest R^2(0.98878) and the lowest RMSE (0.72459) and AAPE (4.3459%) among the investigated models. Its MAE of 0.44154 was also

very close to the lowest value obtained using GPR (0.44086). These results show that ANFIS provided the best overall prediction performance, while GPR produced similarly accurate predictions.

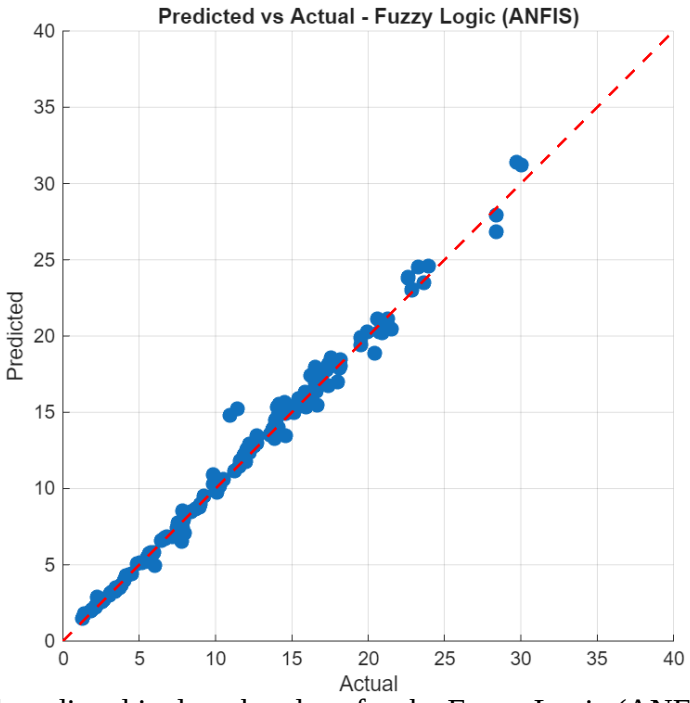


Fig. 4. Actual and predicted jet length values for the Fuzzy Logic (ANFIS) model.

The superior performance of nonlinear data-driven models observed in the present study is in agreement with previous applications of soft computing techniques to aeration-related hydraulic problems. Hekmat et al. [12] investigated hybrid ANFIS models for predicting important spillway aerator design parameters, including the dimensionless jet length. Their best-performing ANFIS-DE model predicted the dimensionless jet length with an R^2 of 0.963, demonstrating the ability of ANFIS-based approaches to represent the complex interactions between hydraulic and geometric parameters. In the present study, the conventional ANFIS model achieved an R^2 of 0.98878 and an AAPE of 4.3459%, further indicating the suitability of neuro-fuzzy modelling for jet length prediction. However, direct comparison of the numerical performance metrics should be made with caution because the datasets, input parameters, and model configurations differ between the studies.

Data-driven approaches have also shown promising performance for other spillway aerator parameters. Li et al. [8] developed an embedded multi-gene genetic programming model for predicting aerator air demand and obtained a coefficient of determination of 0.95. Their model improved prediction accuracy compared with the investigated empirical relationships, showing the potential of data-driven methods for representing complex aerator-flow relationships. Similar observations have been reported for other jet aeration problems. Puri et al. [10] compared several soft computing techniques, including Gaussian Process, Random Forest, Support Vector Machine, and Artificial Neural Network models, for predicting jet aeration efficiency. Their results showed that nonlinear machine learning approaches could successfully represent the effects of hydraulic and geometric variables on aeration performance.

From a hydraulic perspective, the importance of considering both flow conditions and aerator geometry is also supported by earlier experimental investigations. Kökpınar and Göğüş [3] showed that high-speed jet behavior over spillway aerators is influenced by aerator geometry and flow conditions and developed empirical relationships for dimensionless jet length and other aeration parameters. The present results extend this approach by using dimensionless hydraulic and geometric parameters as inputs to machine learning models rather than

prescribing a single empirical functional form. The considerably better performance of ANFIS and GPR compared with Polynomial Regression suggests that flexible nonlinear models are more capable of representing the interactions among these parameters within the investigated dataset. Nevertheless, the developed models are data-driven and their predictive capability should be considered within the range of hydraulic and geometric conditions represented in the experimental database. Further studies using additional experimental datasets and different aerator configurations would be useful to examine the generalization capability of the models.

4. Conclusions

In this study, the applicability of four machine learning approaches, namely Gaussian Process Regression (GPR), Adaptive Neuro-Fuzzy Inference System (ANFIS), Polynomial Regression (PR), and Regression Tree Ensembles (RTE), was investigated for the prediction of dimensionless jet length in spillway aerator flows. Four dimensionless parameters representing the hydraulic and geometric characteristics of the flow and aerator were used as model inputs, while L_{jet} was selected as the target output.

The results showed clear differences among the predictive performances of the investigated models. ANFIS provided the best overall performance, with an R^2 of 0.98878, RMSE of 0.72459, and AAPE of 4.3459%. GPR also showed high prediction accuracy, achieving an R^2 of 0.98579 and an AAPE of 4.6784%. In comparison, PR and RTE produced lower prediction performances, particularly in terms of prediction errors. The better performances of ANFIS and GPR indicate that these models are more capable of representing the nonlinear relationship between the selected dimensionless hydraulic and geometric parameters and jet length.

The findings demonstrate the potential of data-driven approaches for estimating jet length in spillway aerator flows and support previous studies reporting successful applications of ANFIS-based methods to aerator design parameters. However, the developed models were evaluated using a specific experimental database, and their predictive capability should therefore be considered within the range of hydraulic and geometric conditions represented by the available data. Further studies using additional experimental datasets and different aerator configurations would be useful for evaluating the generalization capability of the developed models.

Acknowledgments

The participation in this scientific event was supported by the Scientific and Technological Research Council of Türkiye (TÜBİTAK) under the 2224-B Domestic Scientific Event Participation Support Program (2026/2), Application No. 1919B022604841.

References

1. Falvey, H.T.: *Cavitation in Chutes and Spillways*. Engineering Monograph No. 42, U.S. Department of the Interior, Bureau of Reclamation, Denver, Colorado (1990).
2. Rutschmann, P., Hager, W.H.: Air entrainment by spillway aerators. *Journal of Hydraulic Engineering* 116(6), 765–782 (1990).
3. Kökpınar, M.A., Göğüş, M.: High-speed jet flows over spillway aerators. *Canadian Journal of Civil Engineering* 29(6), 885–898 (2002).
4. Pfister, M., Hager, W.H.: Chute aerators. II: Hydraulic design. *Journal of Hydraulic Engineering* 136(6), 360–367 (2010).
5. Tokyay, T., Kurt, C.: Application of VOF and k–ε turbulence model in simulation of flow over a bottom aerated ramp and step structure. *Water SA* 45(2), 278–287 (2019).
6. Shayanseresht, S., Manafpour, M.: A comparative assessment of various turbulence models applied for simulation of air-water flow over chute spillway. *Periodica Polytechnica Civil Engineering* 65(4), 1200–1212 (2021).
7. He, J., Yin, J., He, H., Ren, P., Zhang, S., Du, Z.: Evaluation and sensitivity analysis of three-dimensional numerical simulation for aerated deflector-generated jets in spillways. *Water Supply* 23(1), 114–128 (2023).

8. Li, S., Yang, J., Liu, W.: Estimation of aerator air demand by an embedded multi-gene genetic programming. *Journal of Hydroinformatics* 23(5), 1000–1013 (2021).
9. Kumar, M., Tiwari, N.K., Ranjan, S.: Soft computing based predictive modelling of oxygen transfer performance of plunging hollow jets. *ISH Journal of Hydraulic Engineering* 28(sup1), 223–233 (2022).
10. Puri, D., Kumar, R., Sihag, P., Thakur, A., Perveen, S., Alfaisal, F.M., Lee, D.: Analytical investigation of the impact of jet geometry on aeration effectiveness using soft computing techniques. *ACS Omega* 8(35), 31811–31825 (2023).
11. Alazmi, A., Al-Anzi, B.S.: Assessment of machine learning algorithms for predicting air entrainment rates in a confined plunging liquid jet reactor. *Sustainability* 15(18), 13802 (2023).
12. Hekmat, M., Sarkardeh, H., Jabbari, E., Samadi, M.: Application of a hybrid ANFIS with metaheuristic algorithms to estimate the aeration design parameters. *Water Supply* 23(6), 2249–2266 (2023).
13. Demiröz, E.: *Dolusavakların boşaltım kanallarındaki büyük hızlı akımlar için kullanılan havalandırıcıların bazı proje kriterleri*. Türkiye Bilimsel ve Teknik Araştırma Kurumu, Mühendislik Araştırma Grubu, Proje No. 606, Ankara (1985).
14. Rasmussen, C.E., Williams, C.K.I.: *Gaussian Processes for Machine Learning*. MIT Press, Cambridge, Massachusetts (2006).

Author Contribution Statement

- *Conceptualization:* Mehmet Sorgun
- *Methodology:* Mehmet Sorgun, Pelin İlker
- *Investigation:* Pelin İlker, Ziya Cem Öztürk
- *Writing – Original Draft:* Pelin İlker, Ziya Cem Öztürk
- *Writing – Review & Editing:* Pelin İlker, Mehmet Sorgun

List of Abbreviations

- **AAPE —** Average Absolute Percentage Error
- **ANFIS** — Adaptive Neuro-Fuzzy Inference System
- **CFD** — Computational Fluid Dynamics
- **GPR** — Gaussian Process Regression
- **MAE** — Mean Absolute Error
- **ML** — Machine Learning
- **RMSE** — Root Mean Square Error
- **RTE** — Regression Tree Ensembles
- **VOF** — Volume of Fluid

Note: Following the conference, this Publication Note will be added to each paper; therefore, authors are kindly requested not to remove the note below and to complete the author(s) and paper title information.

Publication Note

This paper was peer-reviewed, accepted for presentation, and included in the proceedings of the ACE2026 – International Conference on Advances in Civil Engineering, held on 12–14 October 2026 in Trabzon, Türkiye.

This paper may be cited as follows:

İlker P., Öztürk Z.C., Sorgun M., "Prediction of Jet Length in Spillways Using Advanced Machine Learning Algorithms," in Proceedings of the ACE2026 – International Conference on Advances in Civil Engineering, Trabzon, Türkiye, 12–14 October 2026.

Evaluation of the Performance of Various Machine Learning Methods in Rainfall-Runoff Modeling: A Case Study of the Meriç River

Ceydanur Aydın[1], Nira Nur Demir[1] and Nurcan Öztürk[1]
[1]0009-0002-5845-8367, Karadeniz Technical University, Faculty of Technology, Civil Engineering Department, Trabzon, Türkiye, ceydanur36aydin@gmail.com
[1]0009-0001-5613-0678, Karadeniz Technical University, Faculty of Technology, Civil Engineering Department, Trabzon, Türkiye, nirademir@icloud.com
[1]0000-0002-2907-5941, Karadeniz Technical University, Faculty of Technology, Civil Engineering Department, Trabzon, Türkiye, nurcan@ktu.edu.tr

Abstract. This study aims to examine the performance of various machine learning methods in modeling hydrological processes involving nonlinear relationships and in calculating parameters that directly influence hydrological events. To this end, monthly average flow data measured at Flow Observation Station (FOS) No. D01A003 on the Meriç River in the Meriç-Ergene Basin, along with monthly total precipitation and temperature data measured at İpsala Meteorological Observation Station (MOS) No. 17632, were used to evaluate the performance of LSBoost, Multivariate Adaptive Regression Splines (MARS), Model Tree (M5-tree), and Artificial Neural Networks (ANN) were employed to develop four distinct rainfall-runoff models. In this context, the performance of the models developed separately using each machine learning technique was evaluated based on an NSE of ≥ 0.85, and the best models obtained were ANN and LSBoost models with 0.920 and 0.960, respectively. Final models for all machine learning methods under investigation were created using the determined hyperparameters. Based on the performance metrics, the model demonstrating the highest performance was identified as the best model. In conclusion, given the critical importance of future flow forecasts in the planning, design, and operation phases of hydraulic infrastructure projects, it is anticipated that the models developed in this study will be useful for future watershed planning and will also provide effective solutions for the sizing of flood protection structures, a significant risk in our country.

Keywords: Rainfall-Runoff Modeling; Machine Learning; Model Performance.

1 Introduction

As living beings depend on water, people have sought to understand water and water-related issues throughout history. Accordingly, various scientific disciplines have been developed to harness water and manage water resources. Within the field of hydrology, one of these scientific disciplines, rainfall-runoff models are developed to simulate the process by which rainfall falling within a river basin is converted into runoff. By forecasting future flow based on meteorological parameters (precipitation, temperature, etc.), these models provide insights for the design of water infrastructure, particularly in relation to flood events, determining optimal locations and ensuring the effective use of project budgets. As global water resources continue to dwindle, accurately predicting surface runoff has become increasingly important, necessitating the application of ever more precise methods to model the rainfall-runoff process. However, due to the complex relationship between rainfall and surface runoff, accurately forecasting surface runoff is challenging [1-5].

Many researchers have conducted studies on rainfall-runoff modeling, which is based on identifying the relationship between complex and long time series. A review of research in this field reveals that machine learning methods developed in tandem with advances in computer technology have found widespread application among rainfall-runoff modeling techniques. Artificial neural network models have been successfully applied in literature to identify optimal relationships. In one such study, the goal was to develop a point-source rainfall-runoff model using an optimal artificial neural network (ANN) architecture, based on daily average discharge data from Flow Observation Station No. D22A116 on the Aksu Creek in Giresun Province and daily total precipitation data from Giresun Meteorological Station No. 17034. The performance of the models was evaluated by calculating various metrics. The results of the analyses indicated that, although all ANN architectures produced satisfactory results, the best performance was achieved by the ANN-QN architecture trained using the Quasi-Newton (QN) training algorithm [6].

Another study aimed to perform short-term rainfall-runoff modeling using three years' (2014, 2015, and 2016) of synchronized hourly rainfall and runoff data obtained from the Samoggia River basin in Italy. The researchers compared four basic machine learning methods (ANFIS-PSO, ANFIS-FCM, MARS, and M5Tree) with the Multiple Model Simple Average (MM-SA) ensemble method and the EBA4SUB conceptual event-based hydrological model. Among the machine learning methods, the ANFIS-PSO, ANFIS-FCM, and MARS models exhibited similar accuracy and performed better than the M5Tree model. Furthermore, it was concluded that the machine learning methods generally outperformed the conceptual EBA4SUB model [1].

In a study conducted in the Meric River basin, which is also the subject of this study, the statistical relationships between the river's daily flow data and the daily average temperature and daily total rainfall data were examined. Using the methods employed in the study, correlation coefficients between the variables were first calculated, and linear regression analysis was performed by evaluating these coefficients bidirectionally within a 95% confidence interval. According to the results of the study, it was observed that the relationship between daily average temperatures and daily average river flow in the Meriç River is stronger than the relationship with daily total precipitation [7].

Upon reviewing the rainfall-runoff modeling processes examined in the studies cited in the literature, no study was found that aimed to develop a rainfall-runoff model for the Meriç River basin using machine learning methods. Machine learning methods have distinct advantages over traditional statistical and linear methods in hydrological time series modeling. The most significant advantage of these methods is their ability to capture the complex and nonlinear nature of hydrological processes; simple regression cannot model this complexity. Thanks to these advantages, machine learning models produce better results across all scenarios compared to linear methods, offering higher prediction accuracy by providing lower error rates and higher efficiency coefficients.

In this work, a rainfall-runoff model analysis was conducted for the Meriç River basin to determine the optimal solution, using monthly total precipitation and temperature data. In addition to the machine learning methods most frequently used in the literature, this study applied the LSBoost method which has found less application in precipitation-runoff modeling to the Meriç River. The aim was to contribute to the high-accuracy prediction of future flow in this region and in areas with similar flow characteristics. In developing the models, various advanced machine learning methods including Multivariate Adaptive Regression Splines (MARS), Model Tree (M5-tree), and Artificial Neural Networks (ANN) were used in addition to the LSBoost method, and the method with the highest prediction performance was determined.

The main objective of this study is to develop machine learning-based rainfall-runoff models capable of simulating complex and nonlinear hydrological processes. To this end, models that accurately and efficiently predict discharge using monthly total rainfall and temperature data from the Meriç River basin as input will be developed using LSBoost, MARS, M5-tree, and Artificial Neural Network techniques.

2 Methodology

This study is based on a three-phase research design. These phases are data definition, training of the models, and determination of the model with the best performance.

2.1 Data definition

For the preparation of the datasets, the input data, monthly total precipitation and monthly average temperature, were obtained from the İpsala Meteorological Observation Station (MOS) No. 17632, located at 40°53'21.7"N, 26°23'27.5"E. The flow data used cover the period from 1996 to 2021 and were obtained from Flow Observation Station (FOS) No. D01A003 (Table 1; Fig. 1). To ensure the longest continuous data set, the FOS that was operational and the MOS located near the Meriç River were selected. All MOSs in the study basin are shown on the map in Figure 1, and information on the FOS from which flow data will be obtained is presented in Table 1.

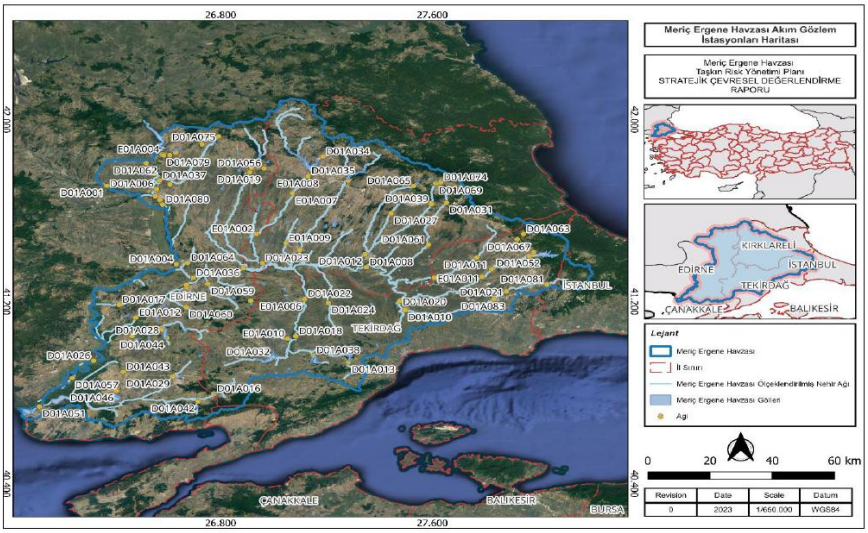


Fig.1. Map of Flow Observation Stations (FOS) in the Meriç-Ergene Basin [8].

Table 1. Flow Observation Station (FOS) used for dataset

Station No	Station Name	Location	Rainfall Area (km²)	Average Elevation (m)	River System
D01A003	Kirişhane	26°34'14" E 41°38'50" N	34990	30	Meriç River

2.2 Development and Training of the Prediction Models

As part of the model development process, four different machine learning approaches will be evaluated. These approaches are presented below.

LSBoost is a regression algorithm based on the gradient-boosted trees method and uses least squares loss. It operates iteratively to improve predictive accuracy by minimizing mean squared errors. In this regard, it is defined as a sequential-correction-based ensemble method that primarily aims for high accuracy by reducing bias. LSBoost stands out for its robust handling

of missing data, scalability on large datasets through histogram-based optimization, and strong capability to model nonlinear, non-monotonic relationships and complex feature interactions. These capabilities enable it to provide accurate and stable hydrological forecasts [9]. Key advantages of the algorithm include its ability to produce consistent and reliable results on both training and test datasets, as well as its low tendency toward overfitting. These characteristics make LSBoost a fast, robust, and computationally efficient method, particularly for prediction and modeling applications in the field of engineering [10]. There are numerous studies in the literature comparing the performance of the LSBoost algorithm with other machine learning methods, such as Support Vector Regression (SVR), Random Forest (RF), and various empirical models. These comparative analyses demonstrate that the LSBoost algorithm exhibits higher prediction accuracy and lower error metrics (RMSE, MAE, etc.), consistently showing superior performance in this regard [11].

MARS is a nonlinear and nonparametric regression method capable of estimating a continuous dependent parameter in high-dimensional data. This method operates through a forward-backward procedure. In the forward step, multiple basis functions are added to the model to overfit the data. These basis functions are based on a spline function that divides the data set into piecewise linear segments. In the backward step, unnecessary basis functions are removed from the model and pruned using a generalized cross-validation criterion. This pruning procedure improves prediction accuracy. MARS falls under the category of regression-based machine learning models and has been successfully used in numerous hydrological applications for decades [1, 12]. MARS is a data-driven technique used to model complex hydrological processes [13]. By automatically optimizing model complexity, the method eliminates the need for additional tuning; and thanks to its feature selection mechanism, it demonstrates superior performance compared to classical linear models in addressing multicollinearity issues [14].

The M5-tree is a machine learning and data mining method frequently used in hydrological modeling. It falls under the category of regression decision trees and aims to estimate the values of numerical variables. Unlike other decision tree algorithms, this algorithm fits a multivariate linear regression model rather than assigning a fixed value to the terminal leaf node. Because of this feature, it is likened to piecewise linear functions. This positions the M5-tree as a multivariate linear model, situated between linear and nonlinear models. The M5-tree uses a hierarchical classification method to partition the dataset into classes. It measures error using the standard deviation of the class values reaching a node and selects the split that maximizes the expected error reduction. This method partitions the nonlinear data space of the input dataset into multiple classes (subspaces), each represented by a simple linear regression. The M5 model has distinct advantages, particularly when compared to complex models. To list a few, the relationships it provides are simpler and more understandable for non-expert users than those of complex nonlinear methods. The training processes are simpler and do not require trial and error, testing, or error evaluation. It is robust in handling incomplete data. Furthermore, thanks to the M5 algorithm's ability to manage non-convergence issues, it does not require the data normalization necessary for models such as ANN. The M5-tree demonstrates satisfactory performance on large datasets and in multidimensional problems, while also being effectively calibrated using a small number of training examples, that is, it is not dependent on the amount of data. In summary, the M5-tree (or M5P) is an efficient tool designed to model complex and multidimensional rainfall-runoff problems by partitioning the data space into manageable subspaces using piecewise linear functions [15–17].

ANN models typically consist of an input layer, one or more hidden layers, and an output layer. The layered feedforward network is the most common and easiest-to-implement architecture. Three-layer feedforward neural networks are widely used for simulation and prediction in engineering problems. Transfer Functions: Sigmoid functions are the most popular transfer functions used to calculate the outputs of nodes. ANN has the ability to learn complex

relationships between input and output data through a training process. During training, the error between the output and the desired value is calculated, and the weights are adjusted using the back-propagation procedure. The Levenberg Marquardt back propagation algorithm is a common technique used in training ANN models. ANN is classified as system-theoretical models or black-box models that rely primarily on precipitation and runoff data, without paying much attention to the details of physical processes. These models have garnered global interest due to their ability to capture the highly nonlinear and complex relationships among hydrological variables. Viewed as a more promising alternative to traditional statistical rainfall-runoff models and conceptual models, ANN is useful in watersheds without hydrometric stations or in areas with limited data [1, 18–20].

2.3 Determination of the Model with the Best Performance

At this stage of the study, final models were generated for each machine learning method for which optimal hyperparameters had been determined, using the entire training and validation datasets. The generated models were tested using a test dataset that had not been used at all during the training and validation phases. Root Mean Square Error (RMSE), Pearson Correlation Coefficient (R), Nash-Sutcliffe Efficiency Coefficient (NSE), Performance Index (PI), and the A10 Index were used to evaluate the performance of the machine learning methods. These metrics were calculated for the test data according to Equations 1–5.

$$RMSE = \left[\frac{1}{n}\sum_{i=1}^{n}(S_i - T_i)^2\right]^{\frac{1}{2}} \tag{1}$$

$$R = \frac{\sum(T_i - \bar{T})(S_i - \bar{S})}{\sqrt{\sum(T_i - \bar{T})^2 \sum(S_i - \bar{S})^2}} \tag{2}$$

$$NSE = 1 - \frac{\sum_{i=1}^{n}(S_i - T_i)^2}{\sum_{i=1}^{n}(S_i - \bar{S})^2} \tag{3}$$

$$\mathrm{PI} = \frac{RRMSE}{1 + r} \tag{4}$$

$$\mathrm{A10} = \frac{M10}{T} \tag{5}$$

In these equations, S_i represents the output value obtained from the current observation stations, $\bar{S}$ represents the average of these values, T_i represents the output value obtained from the model, RRMSE represents the square root of the relative root mean square error, R represents the Pearson correlation coefficient, and n represents the total number of test data points. The root mean square error (RMSE) quantifies the average magnitude of prediction errors, providing information about the absolute deviation between observed and predicted values. The Pearson correlation coefficient (R) evaluates the linear relationship between predictions and observations, with values close to ±1 indicating a strong directional fit. The Nash-Sutcliffe Efficiency Coefficient (NSE) measures the model's relative predictive power compared to the mean of the observed data. An NSE of 1 indicates perfect performance. The Performance Index (PI), a composite metric, combines these measures to provide a holistic assessment of the model's effectiveness. The A10, a useful metric for evaluating the predictive accuracy of regression models within a specific margin of error, enables a more comprehensive assessment of the model's performance when used in conjunction with other performance metrics.

3 Results and Discussions

In this phase of the study, the prediction performance of the developed MARS, M5-tree, LSBoost, and ANN prediction models was analyzed by comparing them. To determine the model with the most effective prediction performance, several performance metrics such as RMSE, R, NSE, PI, and A10 were used. The models were not used during the training and validation phases and were therefore evaluated on test data that the models had not previously seen. The performance metrics obtained from the test data are shown in Table 2. In this table, the ANN model achieved the smallest error value, and based on the condition that NSE ≥ 0.85, both the LSBoost and ANN models demonstrated superior prediction accuracy.

Table 2. Performance metrics obtained from the models for the test dataset.

Models	RMSE	NSE	R	PI	A10
MARS	94.928	0.696	0.894	0.295	0.143
M5-tree	119.859	0.515	0.869	0.378	0.286
LSBoost	48.714	**0.920**	0.975	0.145	0.214
ANN	34.632	**0.960**	0.987	0.103	0.143

Fig. 2 shows scatter plots to determine which of the MARS, M5-tree, LSBoost, and ANN methods used in rainfall-runoff modeling has the most effective prediction performance. As can be seen in Fig. 2, the ANN and LSBoost models exhibit low dispersion, indicating that these two models perform well. This finding is consistent with the data in Table 2.

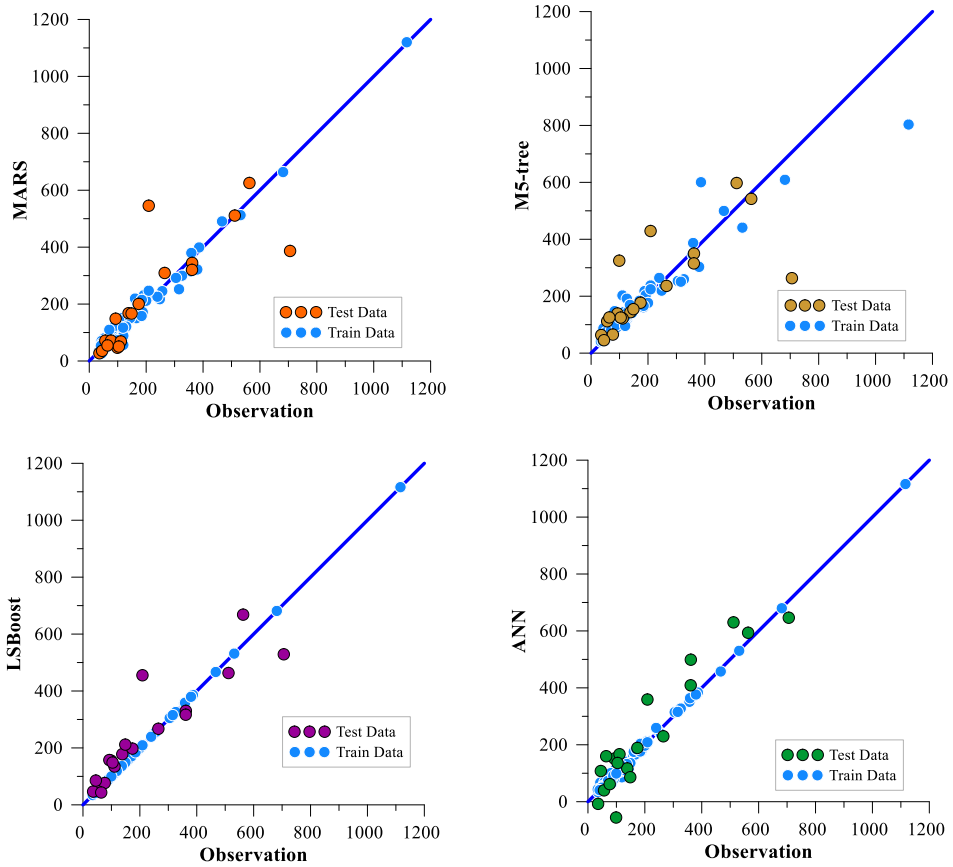


Fig. 2. Scatter graph of observation data with estimated data from the models for the test dataset.

4. Conclusion

In this study, the complex and nonlinear rainfall-runoff relationship in the Meriç River basin was successfully modeled using monthly meteorological and hydrological datasets spanning from 2002 to 2021. Four prominent machine learning techniques, Least-Squares Boosting (LSBoost), Multivariate Adaptive Regression Splines (MARS), Model Tree (M5-tree), and Artificial Neural Networks (ANN), were implemented and compared to predict monthly average river flow at the Kirişhane Flow Observation Station (FOS No. D01A003) based on temperature and precipitation inputs from the İpsala Meteorological Observation Station (MOS No. 17632).

The evaluation of these optimized models on an independent test dataset revealed significant differences in their predictive capabilities. Based on the established performance threshold of NSE ≥ 0.85, both the ANN and LSBoost models demonstrated superior prediction accuracy, exhibiting highly stable performance with minimal dispersion. Among all investigated methods, the ANN model achieved the highest overall performance, yielding the lowest prediction error and the strongest directional fit with an RMSE of 34.632, NSE of 0.960, R of 0.987, PI of 0.103, and A10 of 0.143. The LSBoost model also provided excellent predictive capability, ranking as the second-best model with an RMSE of 48.714, NSE of 0.920, R of 0.975, PI of 0.145, and A10 of 0.214. Conversely, the MARS (NSE of 0.696) and M5-tree (NSE of 0.515) models showed considerably lower performance, indicating limited capacity in fully capturing the complex, non-linear dynamics of the watershed.

The findings of this study confirm that machine learning approaches, particularly ANN and LSBoost, are highly effective tools for simulating complex hydrological processes in the Meriç-Ergene Basin. Given the critical role of accurate streamflow forecasting, the developed models are anticipated to be highly beneficial for future watershed planning, water resource management, and hydraulic infrastructure design. Furthermore, these high-accuracy predictions provide a reliable scientific foundation for optimizing the design and sizing of flood protection structures, which remains a vital necessity in mitigating flood risks in the region.

Acknowledgments

The authors gratefully acknowledge the financial support of the Scientific and Technological Research Council of Türkiye (TÜBİTAK) under the 2209-A University Students Research Projects Support Program [1919B012545379].

References

1. Adnan, R.M., Petroselli, A., Heddam, S., Celso Augusto Guimarães Santos, C.A.G., Kisi, O.: Short term rainfall-runoff modelling using several machine learning methods and a conceptual event-based model. Stochastic Environmental Research and Risk Assessment 35, 597–616 (2020). https://doi.org/10.1007/s00477-020-01910-0.
2. Babacan, H.T., Yüksek, Ö., Saka, F.: Yapay zekâ ve sezgisel regresyon yöntemlerinin yağış-akış modellemesi için performans değerlendirmesi: Aksu Deresi için bir uygulama. Niğde Ömer Halisdemir Üniversitesi Mühendislik Bilimleri Dergisi 11(3), 744-751 (2022).
3. Gümüş, V., Kavşut, M.E., Yenigün, K.: Yağış-Akış İlişkisinin Modellenmesinde YSA Kullanımının Değerlendirilmesi: Orta Fırat Havzası Uygulaması. Bilimde Modern Yöntemler Sempozyumu, pp. 1290-1301 (2010).
4. Seçkin, N., Güven, A., Yurtal, R.: Taşkın Debilerinin Yapay Sinir Ağları ile Modellenmesi: Batı Karadeniz Havzası Örneği. Çukurova Üniversitesi Mhendislik ve Mimarlık Dergisi 25(1-2), 45-57 (2010).
5. Şimşek, O., Çıtakoğlu, H., Gümüş, V., Çetin, S.D.: Applying Machine Learning to Understand Rainfall–Runoff Interactions in the Tigris River Basin of Turkey. Pure and Applied Geophysics 182, 3107–3138 (2025). https://doi.org/10.1007/s00024-025-03749-4.

6. Yüksek, Ö., Babacan, H. T., Saka, F. 2018.: Yağış-Akış Modellemesinde Optimum Yapay Sinir Ağı Yapısının Araştırılması. Türk Hidrolik Dergisi 2(1), 31-37 (2018).
7. İrdem, C.: Meriç Nehri'nde akım-sıcaklık ve akım-yağış arasındaki istatistiksel ilişkilerin günlük veriler üzerinden analizi. Avrasya Beşerî Bilim Araştırmaları Dergisi 4(2), 1–14 (2024).
8. DAI Global, Su-Yapi, Su Pek, Sumodel, Çinar Konsorsiyumu. Meriç-Ergene Havzası Taşkın Risk Yönetim Planı Hazırlanması İçin Teknik Yardım Projesi: Stratejik Çevresel Değerlendirme Raporu Taslağı (Aktivite 4.4 Raporu). Ankara: Tarım ve Orman Bakanlığı, Su Yönetimi Genel Müdürlüğü (2025).
9. Pang, X., Liu, J., Jing, H., Xu, X., Shen, L., Yan, X.: Coupling Hydrological Model With Interpretable Machine Learning for Reliable Streamflow Modeling: Daily Dynamics and Extreme Events. Journal of Flood Risk Management 4, 1-12 (2025). https://doi.org/10.1111/jfr3.70138.
10. Zhang, Y., Xu, X. 2022. "Modulus of elasticity predictions through LSBoost for concrete of normal and high strength". Materials Chemistry and Physics, 283, 126007. https://doi.org/10.1016/j.matchemphys.2022.126007.
11. Akkaş, E., Ünal, B. C., Ersoy, O.: AI-Based Prediction and Optimization of Ammonium Removal Efficiency and Capacity of Natural Zeolites Using LSBoost (XGBoost) for Sustainable Ecosystems. In EGU General Assembly Conference Abstracts (pp. EGU25-809). Vienne, Austria (2025).
12. Friedman, J.H.: Multivariate adaptive regression splines. Ann Stat. 19, 1–67 (1991).
13. Rezaie-Balf, M. ve Zahmatkesh, Z., Kim, S.: Soft Computing Techniques for Rainfall–Runoff Simulation: Local Non–Parametric Paradigm vs. Model Classification Methods. Water Resources Management 31, 3843–3865 (2017). https://doi.org/10.1007/s11269-017-1711-9.
14. Naser, A. H., Badr, A. H., Henedy, S. N., Ostrowski, K. A., Imran, H. "Application of Multivariate Adaptive Regression Splines (MARS) approach in prediction of compressive strength of eco-friendly concrete". Case Studies in Construction Materials, 17, e01262 (2022). https://doi.org/10.1016/j.cscm.2022.e01262.
15. Kumar, S., Pandey, K. K., Ahirwar, A.: Comparison of the performance of SWAT and hybrid M5P tree models in rainfall–runoff simulation. Journal of Water and Health 22(4), 639–651 (2024). https://doi.org/10.2166/wh.2024.022.
16. Molajou, A., Nourani, V., Tajbakhsh, A. D., Variani, H. A., Khosravi, M.: Multi-Step-Ahead Rainfall-Runoff Modeling: Decision Tree-Based Clustering for Hybrid Wavelet Neural- Networks Modeling. Water Resources Management 38, 5195–5214 (2024). https://doi.org/10.1007/s11269-024-03908-7.
17. Nourani, V., Tajbakhsh, A. D., Molajou, A., Gokcekus, H.: Hybrid Wavelet-M5 Model Tree for Rainfall-Runoff Modeling. Journal of Hydrologic Engineering 24(5), 04019012 (2019). https://doi.org/10.1061/(ASCE)HE.1943-5584.0001777.
18. Antar, M. A., Elassiouti, I., Allam, M. N.: Rainfall-runoff modelling using artificial neural networks technique: a Blue Nile catchment case study. Hydrological Processes 20(5), 1201–1216 (2006). https://doi.org/10.1002/hyp.5932.
19. Gholami, V., Sahour, H.: Simulation of rainfall-runoff process using an artificial neural network (ANN) and field plots data. Theoretical and Applied Climatology 147, 87–98 (2021). https://doi.org/10.1007/s00704-021-03817-4.
20. Kumar, S., Roshni, T., Himayoun, D.: A Comparison of Emotional Neural Network (ENN) and Artificial Neural Network (ANN) Approach for Rainfall-Runoff Modelling. Civil Engineering Journal 5(10), 2212-2224 (2019). http://dx.doi.org/10.28991/cej-2019-03091398.

Author Contribution Statement

- *Conceptualization:* Nurcan Öztürk
- *Methodology:* Nurcan Öztürk, Ceydanur Aydın
- *Investigation:* Nurcan Öztürk, Ceydanur Aydın, Nira Nur Demir
- *Writing – Original Draft:* Nurcan Öztürk, Ceydanur Aydın
- *Writing – Review & Editing:* Nurcan Öztürk, Ceydanur Aydın, Nira Nur Demir

List of Abbreviations

- **ML** — Machine Learning
- **A10** — A10 Index
- **ANFIS-FCM** — Adaptive Neuro-Fuzzy Inference System - Fuzzy C-Means
- **ANFIS-PSO** —Adaptive Neuro-Fuzzy Inference System - Particle Swarm Optimization
- **ANN** — Artificial Neural Networks
- **FOS** — Flow Observation Station
- **LSBoost** — Least-Squares Boosting
- **M5-tree** — Model Tree
- **MAE** — Mean Absolute Error
- **MARS** — Multivariate Adaptive Regression Splines
- **MM-SA** — Multiple Model Simple Average
- **MOS** — Meteorological Observation Station
- **NSE** — Nash–Sutcliffe Efficiency Coefficient
- **PI** — Performance Index
- **QN** — Quasi-Newton
- **R** — Pearson Correlation Coefficient
- **RF** — Random Forest
- **RMSE** — Root Mean Square Error
- **RRMSE** — Relative Root Mean Square Error
- **SVR** — Support Vector Regression

Publication Note

This paper was peer-reviewed, accepted for presentation, and included in the proceedings of the ACE2026 – International Conference on Advances in Civil Engineering, held on 12–14 October 2026 in Trabzon, Türkiye.

This paper may be cited as follows:

Ceydanur Aydın, Nira Nur Demir, Nurcan Öztürk "Evaluation of the Performance of Various Machine Learning Methods in Rainfall-Runoff Modeling: A Case Study of the Meriç River," in Proceedings of the ACE2026 – International Conference on Advances in Civil Engineering, Trabzon, Türkiye, 12–14 October 2026.

Modeling the Rainfall-Runoff Interaction Using LSBoost, MARS, M5-tree, and ANN: A Case of Çağlayan Creek

Derya Kılıç[1], Nurcan Öztürk[1] and Hasan Tahsin Öztürk[1]
[1] 0009-0001-0395-9941, Karadeniz Technical University, Faculty of Technology, Civil Engineering Department, Trabzon, Türkiye, deryakilic6540@gmail.com
[1] 0000-0002-2907-5941, Karadeniz Technical University, Faculty of Technology, Civil Engineering Department, Trabzon, Türkiye, nurcan@ktu.edu.tr
[1] 0000-0001-8479-9451, Karadeniz Technical University, Faculty of Technology, Civil Engineering Department, Trabzon, Türkiye, htozturk@ktu.edu.tr

Abstract. Predicting river flows is a highly complex issue, nonlinear and dependent on numerous parameters, making it crucial for watershed and flood management. This study aims to evaluate the performance of various machine learning methods in modeling the rainfall-runoff interaction, a hydrological process involving nonlinear relationships, and in calculating the parameters that directly influence this hydrological phenomenon. Accordingly, using monthly average flow data measured at Flow Observation Station on the Çağlayan Creek and monthly total precipitation and temperature data recorded at Fındıklı Meteorological Observation Station, four distinct rainfall–runoff models were developed through LSBoost, Multivariate Adaptive Regression Spline (MARS), Model Tree (M5-tree), and Artificial Neural Networks (ANN) methods. To this end, the performance of the models created using each machine learning technique was evaluated based on the condition NSE ≥ 0.85, and optimal hyperparameters were determined for the most successful models. Using these hyperparameters, final models were generated for these methods; these models were not used during the training and validation phases and were therefore tested on test data that the models had not previously seen. Performance metrics such as RMSE, Pearson correlation coefficient (R), Nash–Sutcliffe Efficiency Coefficient (NSE), Performance Index (PI), and A10 Index were analyzed for the test data to measure the predictive performance of each model and conduct a comparative evaluation. Given that future flow forecasts play a critical role in the planning, design, and operation of hydraulic structures, this study anticipates that the models to be developed can be effectively utilized in watershed planning efforts.

Keywords: Rainfall-Runoff Modeling; Machine Learning; Performance Metrics.

1 Introduction

Climate change, which has been increasing in Turkey in recent years, is leading to a rise in the frequency and intensity of floods. This increase in flood events is resulting in serious, life-threatening consequences, such as loss of life and property. Floods are the natural disasters that cause the most loss of life and property in our country, second only to earthquakes. Rainfall-runoff modeling plays a vital role in hydrology for flood disaster management and for determining available water quantities in the planning of drinking water, agricultural, and hydroelectric power plants. In recent years, due to water scarcity, the accurate prediction of surface runoff has become a critical issue for hydrologists to conserve available water resources. Rainfall -runoff modeling is one of the most complex problems in hydrological research due to factors such as the constantly variable nature of precipitation regimes, their occurrence over very large areas, the inability to observe them continuously, their susceptibility to varying topographic conditions within a watershed, and the influence of numerous variables [1-5].

A review of research on rainfall-runoff modeling reveals that studies employing machine learning methods have produced more successful results than those based on empirical and physical models [2]. In the study evaluating the use of Artificial Neural Networks (ANN) to model the complex relationship between precipitation and runoff in the Middle Fırat Basin, the researchers examined the relationship between the monthly average discharge data from discharge observation station No. 2122 and the monthly total precipitation data from precipitation observation station No. 17099. The methodological focus of the study was to predict discharge values using the Feedforward Backpropagation Neural Network (FFBNN) method—one of the ANN methods—and to compare these results with those obtained using Multiple Linear Regression (MLR), a more classical method. The study concluded that the FPRNN method, a black-box model, yielded better results than the MLR method in all cases [6].

Another study investigated the accuracy of short-term hourly rainfall-runoff forecasts, which are critical for flood mitigation and the safety of hydraulic structures in the Ilme River basin in Germany. As part of the study, four machine learning methods (Optimally Pruned Overfitting Machine (OPELM), Multivariate Adaptive Regression Splines (MARS), M5 Tree (M5Tree), and the newly developed hybrid MARS-Kmeans) were compared with a conceptual event-based model called EBA4SUB and the Multiple Linear Regression (MLR) method. In analyses conducted using precipitation and runoff data, the hybrid MARS-Kmeans method was found to demonstrate superior performance compared to other ML methods. Event-based comparisons with the conceptual EBA4SUB model, however, showed that all machine learning models provided better accuracy and yielded better results than EBA4SUB [1].

In the study conducted in Mersin on the Lamas (Limonlu) River, researchers compared Artificial Neural Networks (ANN), Support Vector Machines (SVM), and Deep Learning (DL) methods to solve a nonlinear hydrological problem in a study aimed at predicting river flow using monthly average flow data from 1967 to 2020. Upon examining the comparison criteria, it was observed that Deep Learning (DL) was the best method for solving the problem [7].

In Şen (2019)'s study-which aims to determine flood risk under current conditions and various climate change scenarios in the watersheds located within the boundaries of Rize Province (Turkey's rainiest region) and including the Çağlayan Creek, the subject of this study-basin and flood modeling studies were conducted using daily precipitation outputs from the A2 emission scenario, derived from the ECHAM5 global circulation model dynamically downscaled with the RegCM3 regional model. The results of the 100-year flood modeling studies concluded that there is a flood risk for the Çağlayan Creek under the current conditions scenario [8].

Although machine learning-based rainfall-runoff models have been developed in various watersheds in the existing literature, no study has been found that aims to develop a rainfall-runoff model using these machine learning methods in the Çağlayan Creek watershed in Rize, which is the subject of this study. In this study, a rainfall-runoff model was developed to predict future discharge in the Çağlayan Creek watershed using monthly total precipitation and temperature data. This study represents the first application of rainfall-runoff modeling for this watershed and aims to contribute to the high-accuracy prediction of future discharge in this region and in areas with similar flow characteristics. Various advanced machine learning methods, such as LSBoost, Multivariate Adaptive Regression Splines (MARS), Model Tree (M5-tree), and Artificial Neural Networks (ANN), were used in the development of the models to identify the one with the highest prediction performance.

This work is the first to systematically compare various advanced machine learning methods such as LSBoost, Multivariate Adaptive Regression Splines (MARS), Model Tree (M5-tree), and Artificial Neural Networks (ANN) which have not previously been applied to the Çağlayan Creek watershed, in the context of developing a rainfall-runoff model. By determining which

of the machine learning methods used is more accurate, stable, and efficient for predicting future discharge-using appropriate performance metrics-the study will make a significant contribution to researchers and practitioners.

2 Methodology

The Çağlayan Creek, also known as the Abunoğa River or Fındıklı Creek, is a river located in the Fındıklı district of Rize Province that flows into the Black Sea. The river's source is approximately 2600 meters above sea level, and the river is approximately 34.7 km long. The river's channel gradient is 75%. In management plans prepared by the General Directorate of Water Management under the Ministry of Agriculture and Forestry, the coastal streams in the Fındıklı and Arhavi regions, along with valley systems such as the Çağlayan Creek, have been grouped under the Kabısra Creek Sub-Basin (TR22.M5.1) due to their geographical proximity (Fig. 1, Fig. 2). The Çağlayan Creek has its own independent, micro-scale coastal watershed of 174 km² (the Çağlayan Watershed). However, in the official macro-level sub-basin classification, it is classified within the Kabısra group [9].



Fig. 1. Sub-basins of the Eastern Black Sea Basin [9].

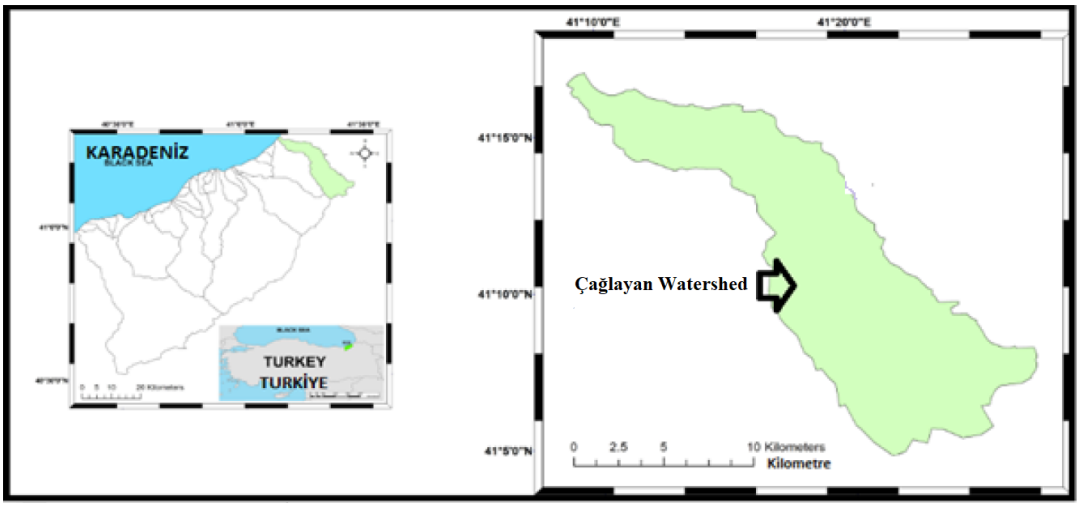


Fig.2. Geographic (locational) representation of the Çağlayan watershed [5].

During the preparation of the datasets, monthly total precipitation and monthly average temperature data were used as input variables. These data will be obtained from the Fındıklı Meteorological Observation Station (MOS) No. 18934, located at coordinates 41°13'44.8"N–41°15'04.8"E. The discharge data to be used in the study cover the years 1992–2021 and were

obtained from the D22A006 Flow Observation Station (FOS) (Table 1). To ensure a continuous and long-term dataset, the FOS, currently active, and the MOS, located near the Çağlayan Creek, were selected. Detailed information concerning FOS from which the flow data was obtained is presented in Table 1.

Table 1. Flow Observation Station (FOS) providing data

Station No	Station Name	Location	Rainfall Area (km²)	Average Elevation (m)	River System
D22A006	Köprübaşı	41°15'3"E 41°15'0"N	156	60	Çağlayan Creek

2.1 Development and Training of the Prediction Models

The four different machine learning methods were applied during the model-building phase to enable comparative analyses. These methods are as follows:

LSBoost (Least-Squares Boosting) is a machine learning algorithm being studied among data-driven models for medium- and long-term flow forecasting. LSBoost is one of the ensemble techniques being evaluated to address the issue of imbalanced datasets that data-driven flow forecasting models face when predicting high flows (floods). It uses a least-squares loss function to weigh the predictions. The LSBoost algorithm proceeds by training models sequentially. Models following the initial model are trained to predict the residual errors of the previous model in the sequence. The prediction at a given training iteration is calculated as the weighted sum of the models trained in previous iterations. Its primary objective is to iteratively train a series of weak learners to minimize the squared error loss [10-12]. Comparative analyses show that the LSBoost algorithm consistently yields higher prediction accuracy and lower error metrics (RMSE, MAE, etc.) [13]. Furthermore, the algorithm stands out for producing stable and reliable results on both training and test datasets and for its low tendency toward overfitting. These characteristics make LSBoost a fast, robust, and computationally efficient method, particularly for prediction problems in engineering applications [14].

MARS (Multivariate Adaptive Regression Splines) is a soft computing model widely used in the field of hydrology. MARS is a nonparametric regression approach introduced by Friedman (1991). It is known as a robust and suitable tool for modeling high-dimensional data. MARS has the capability to examine the effect of each input parameter on the model's output estimate. The model is based on a combination of a series of linear functions known as basic functions. By combining these linear basis functions, a nonlinear model is constructed to determine the functional relationship between the dependent and independent parameters. Input parameters are divided into consecutive segments, and a linear function is defined for each segment; these are referred to as basic functions [1, 15-16].

The M5-tree, a machine learning modeling method in the regression tree category, is based on two steps. The first step is decision tree construction: A decision tree is constructed using a splitting criterion. In the second step, the model tree is designed, the overgrown tree is pruned, and the subtrees are replaced with linear regression functions. The M5-tree uses the binary decision tree concept to split the data, but instead of class labels, it uses linear regression functions that predict continuous numerical attributes at the nodes. The splitting criterion treats the standard deviation of class values reaching a leaf as a measure of error. Standard Deviation Reduction calculates the expected reduction in this error, and M5 selects the split that maximizes the expected error reduction [1]. By combining the intuitiveness of decision trees with the accuracy of linear regression, this hybrid model effectively models piecewise linear and multidimensional relationships by partitioning the data space into homogeneous regions and applying linear regression at each leaf [17]. The M5 Tree is both computationally efficient

and robust against data quality issues in large and complex datasets, and it can successfully model processes at low cost when working with multidimensional numerical variables [18].

Artificial Neural Networks (ANN) are known as systems theory models that aim to capture the relationships between input and output variables in a physical process without considering the underlying physical process itself. An ANN is a highly interconnected network consisting of many simple processing units called neurons, which are modeled after biological neurons in the human brain. ANN typically consists of an input layer, one or more hidden layers, and an output layer. ANN is frequently used by researchers working in the field of hydrology. The ANN technique has proven to be an excellent tool for modeling the complex, dynamic, nonlinear, and piecewise rainfall-runoff process and has demonstrated better performance than traditional modeling techniques. While models developed to simulate the rainfall-runoff process are categorized as empirical, black-box, conceptual, or physically based distributed models, ANN fall under the category of theoretical/black-box models. The primary advantage of ANN is their ability to learn previously unknown relationships between input and output data through a training process, without requiring prior knowledge of watershed characteristics. ANNs are also defined as mathematical structures capable of representing arbitrarily complex nonlinear processes. The most used transfer function for neurons in the hidden layers and the output layer is the sigmoid function; therefore, the network's output range is limited to between zero and one. Consequently, the observed output must be normalized (typically to the range [0.1, 0.9]). In rainfall-runoff modeling, past rainfall (P) and past runoff (Q) amounts are typically used as input variables. Studies have shown that when only past rainfall data are used as input, the models exhibit very low accuracy and low NSE values in hourly runoff forecasting. In contrast, including past flow data as input variables has significantly improved the accuracy of the models [1, 19-20].

2.2 Evaluation of Model Performance and Determination of the Best Model

At this stage, final models were created for each machine learning method with its hyperparameters optimized using the entire training and validation datasets. These models were then evaluated on the test dataset, which was not used at all during the training or validation process. To measure model performance, the following metrics were used: Root Mean Square Error (RMSE), Pearson Correlation Coefficient (R), Nash-Sutcliffe Efficiency Coefficient (NSE), Performance Index (PI), and the A10 Index. These metrics were calculated for the test data based on Equations 1–5.

$$RMSE = \left[\frac{1}{n}\sum_{i=1}^{n}(S_i - T_i)^2\right]^{\frac{1}{2}} \quad (1)$$

$$R = \frac{\sum(T_i - \bar{T})(S_i - \bar{S})}{\sqrt{\sum(T_i - \bar{T})^2 \sum(S_i - \bar{S})^2}} \quad (2)$$

$$NSE = 1 - \frac{\sum_{i=1}^{n}(S_i - T_i)^2}{\sum_{i=1}^{n}(S_i - \bar{S})^2} \quad (3)$$

$$PI = \frac{RRMSE}{1 + r} \quad (4)$$

$$A10 = \frac{M10}{T} \quad (5)$$

In equations (1–4), S_i indicates the output value obtained from the current observation stations, $\bar{S}$ is the average of these values, T_i is the output value obtained from the model,

RRMSE is the square root of the relative root mean square error, r is the Pearson correlation coefficient, and n is the total number of test data points. The root mean square error (RMSE) reflects the average magnitude of prediction errors and provides information about the absolute deviation between observed and predicted values. The Pearson correlation coefficient (R) measures the linear relationship between model predictions and observations; a coefficient approaching ±1 indicates a strong directional fit. The Nash-Sutcliffe Efficiency Coefficient (NSE), on the other hand, evaluates model performance relative to the mean of the observed values; an NSE of 1 indicates that the model has perfect predictive accuracy. The Performance Index (PI), a composite performance metric, evaluates the model's overall effectiveness by combining these metrics into a holistic framework. Also, the A10 index, used to examine the prediction accuracy of regression models within a specific error tolerance range, enables a more comprehensive evaluation of model performance when used alongside other performance metrics. The A10 takes values between 0 and 1; a value closer to 1 indicates that the vast majority of the model's predictions fall within a 10% margin of error relative to the actual values, while a value closer to 0 indicates that only a very small portion of the predictions fall within this range. By using these metrics together, the predictive performance of models is validated in a systematic, detailed, and multifaceted manner, taking into account both the magnitude of error and directional consistency.

3 Results and Discussions

This section presents a comparative analysis of the prediction performances for various models utilized in this study, including the MARS model , M5-tree model, LSBoost model and ANN model. The objective is to identify the models with the most effective prediction performance among those tested.

The evaluation of these models was conducted by examining RMSE, R, NSE, PI and A10 values for training, testing, and all data sets. Table 2 provide these metrics for observed runoff of Çağlayan Creek. In the table, the results that demonstrate the lowest error value and the highest NSE value for test data sets are highlighted in bold.

When evaluating the error and NSE values from the machine learning methods applied in this study, it is evident that for runoff prediction model, the ANN model outperforms other methods in terms of prediction accuracy. Nonetheless, the NSE value for ANN method exceeds 0.85, indicating that the model has a strong correlation with the observation data (Table 2).

Table 2. Performance metrics obtained from MARS, M5-tree, LSBoost and ANN methods for the test dataset.

Models	**RMSE**	**NSE**	**R**	**PI**	**A10**
MARS	2.933	0.566	0.783	0.19	0.17
M5-tree	2.924	0.569	0.844	0.18	0.17
LSBoost	3.328	0.441	0.764	0.22	0.25
ANN	**1.699**	**0.854**	0.927	0.10	0.33

Fig. 3 shows the scatter diagrams for the MARS, M5-tree, LSBoost and ANN methods with respect to runoff prediction model. It can be seen from Fig. 3 that the scattering of the ANN model is the lowest denoting, indicating its best performance. This is also consistent with Table 2.

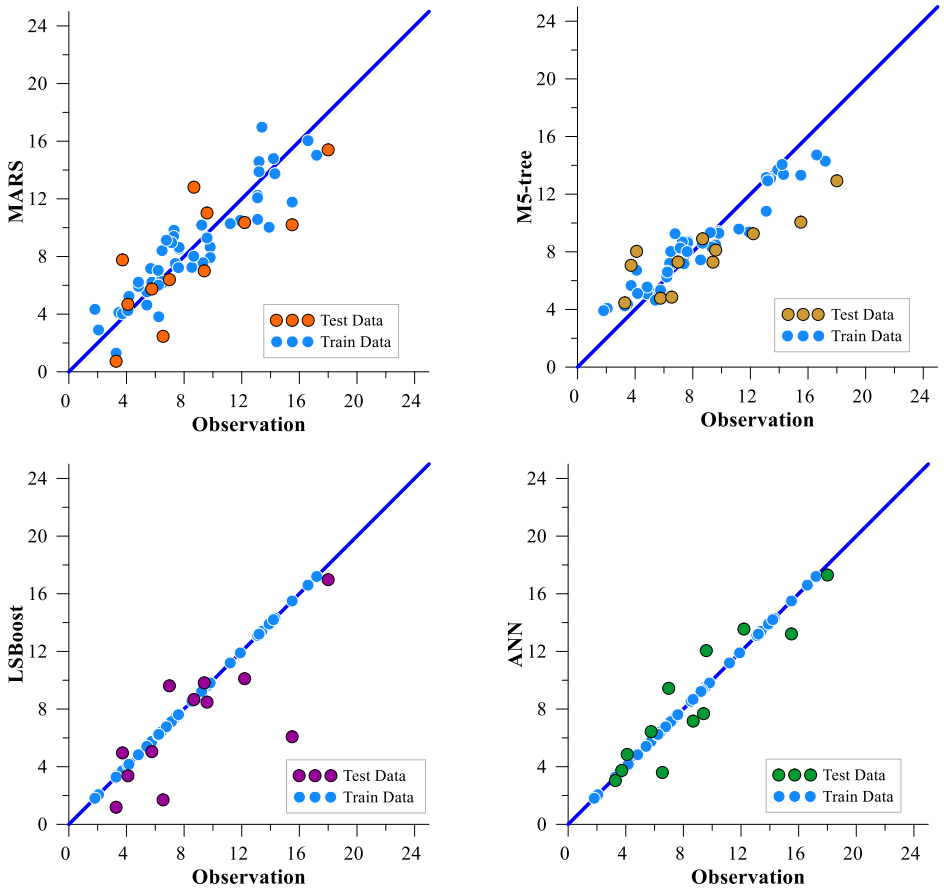


Fig. 3. Scatterplots of observation data with estimated data from MARS, M5-tree, LSBoost and ANN for the test dataset.

4 Conclusion

In this study, the complex and nonlinear rainfall-runoff relationship in the Çağlayan Creek watershed, located in the Fındıklı district of Rize Province, was modeled for the first time using four distinct machine learning methods: Least-Squares Boosting (LSBoost), Multivariate Adaptive Regression Splines (MARS), Model Tree (M5-tree), and Artificial Neural Networks (ANN).

The models were developed using monthly average flow, total precipitation, and average temperature datasets spanning from 1992 to 2021. To assess their generalizability, the performance of each optimized model was evaluated on an independent test dataset that the models had not previously seen during the training and validation phases. Comparing the performance metrics obtained on the test dataset, the Artificial Neural Network (ANN) model demonstrated the highest prediction accuracy, far outperforming the other methods. The ANN model achieved excellent performance with an RMSE of 1.699, NSE of 0.854, R of 0.927, PI of 0.10, and A10 of 0.33, indicating a very strong correlation and robust fit with the observed runoff data. In contrast, the M5-tree (NSE: 0.569) and MARS (NSE: 0.566) models showed moderate predictive performance, while the LSBoost model produced the lowest predictive accuracy with an NSE of 0.441.

As the first application of machine learning-based rainfall-runoff modeling for the Çağlayan Creek watershed, this study provides a crucial tool for high-accuracy future discharge prediction. In a region like Rize, which faces significant flood risks intensified by climate change, these high-performance models can offer invaluable decision support for flood risk management, water resource conservation, and the safe planning, design, and operation of hydraulic structures.

References

1. Adnan, R.M., Petroselli, A., Heddam, S., Celso Augusto Guimarães Santos, C.A.G., Kisi, O.: Comparison of different methodologies for rainfall–runoff modeling: machine learning vs conceptual approach. Natural Hazards 105, 2987–3011 (2021). https://doi.org/10.1007/s11069-020-04438-2.
2. Babacan, H.T., Yüksek, Ö., Saka, F.: Yapay zekâ ve sezgisel regresyon yöntemlerinin yağış-akış modellemesi için performans değerlendirmesi: Aksu Deresi için bir uygulama. Niğde Ömer Halisdemir Üniversitesi Mühendislik Bilimleri Dergisi 11(3), 744-751 (2022).
3. Shah, G., Zaidi, A., Qureshi, A.L., Hussain, S., Aziz, R &T.: Rainfall-runoff modeling using machine learning in the ungauged urban watershed of Quetta Valley, Balochistan (Pakistan). Earth Science Informatics 17, 2661–2677 (2024). https://doi.org/10.1007/s12145-024-01302-w.
4. Wen, X., Feng, Q., Deo, R.C., Wu, M., Yin, Z., Yang, L., Singh, V.P.: Two-phase extreme learning machines integrated with the complete ensemble empirical mode decomposition with adaptive noise algorithm for multi-scale runoff prediction problems. Journal of Hydrology 570, 167–184 (2019). https://doi.org/10.1016/j.jhydrol.2018.12.060.
5. Yüksek, T., Özçelik, A.E., Verep, B.: Çağlayan Havzasının (Fındıklı-Rize) Bazı Hava Karakteristiklerinin Coğrafi Bilgi Sistemleri ile Değerlendirilmesi. Journal of Anatolian Environmental and Animal Sciences 4(3), 532-538 (2019).
6. Gümüş, V., Kavşut, M.E., Yenigün, K.: Yağış-Akış İlişkisinin Modellenmesinde YSA Kullanımının Değerlendirilmesi: Orta Fırat Havzası Uygulaması. Bilimde Modern Yöntemler Sempozyumu, pp. 1290-1301 (2010).
7. Çubukçu, E. A., Demir, V., Sevimli, M. F.: Akım Verilerinin Makine Öğrenmesi Teknikleriyle Tahmin Edilmesi. Gazi Journal of Engineering Sciences 8(2), 257-272 (2022).
8. Şen, O.: İklim ve Hidrolojik Modeller ile Rize'de Bulunan Su Havzalarının Taşkın Risk Tayini. İstanbul Teknik Üniversitesi, Fen Bilimleri Enstitüsü, İstanbul (2019).
9. DAI Global, NFB Mühendislik, SYKE, ACC Konsorsiyumu. Doğu Karadeniz Nehir Havzası Yönetim Planı Stratejik Çevresel Değerlendirme Kapsam Belirleme Raporu (Etkinlik 6.1 Raporu). Ankara: Tarım ve Orman Bakanlığı, Su Yönetimi Genel Müdürlüğü ve Çevre, Şehircilik ve İklim Değişikliği Bakanlığı (2024).
10. Çıtakoğlu, H., Kartal, V., Topcu, E., İkinciogullari, E., Güney, M.: Multiscale drought forecasting via temporal–spectral decomposition and machine learning integration. Theoretical and Applied Climatology 156, 605 (2025). https://doi.org/10.1007/s00704-025-05836-x.
11. Fang, W., Zhou, J.-z., Jia, B.-J., Gu, L., Xu, Z.-x.: Study on the evolution law of performance of mid- to long-term streamflow forecasting based on data-driven models. Sustainable Cities and Society 88, 104277 (2023). https://doi.org/10.1016/j.scs.2022.104277.
12. Snieder, E., Abogadil, K., Khan, U. T.: Resampling and ensemble techniques for improving ANN-based high-flow forecast accuracy. Hydrology and Earth System Sciences 25(5), 2543–2566 (2021). https://doi.org/10.5194/hess-25-2543-2021.
13. Akkaş, E., Ünal, B. C., Ersoy, O.: AI-Based Prediction and Optimization of Ammonium Removal Efficiency and Capacity of Natural Zeolites Using LSBoost (XGBoost) for Sustainable Ecosystems. In EGU General Assembly Conference Abstracts (pp. EGU25-809). Vienne, Austria (2025).
14. Zhang, Y., Xu, X.: Modulus of elasticity predictions through LSBoost for concrete of normal and high strength. Materials Chemistry and Physics 283, 126007 (2022). https://doi.org/10.1016/j.matchemphys.2022.126007.

15. Friedman, J.H.: Multivariate adaptive regression splines. Ann Stat. 19, 1–67 (1991).
16. Vaheddoost, B., Safari, M. J. S., Yilmaz, M. U.: Rainfall-Runoff Simulation in Ungauged Tributary Streams Using Drainage Area Ratio-Based Multivariate Adaptive Regression Spline and Random Forest Hybrid Models. Pure and Applied Geophysics 180, 365–382 (2023). https://doi.org/10.1007/s00024-022-03209-3.
17. Nieto, P. J. G., Gonzalo, E. G., García, L. A. M., Prado, L. Á., Sánchez, A. B.: Predicting the critical superconducting temperature using the random forest, MLP neural network, M5 model tree and multivariate linear regression. Alexandria Engineering Journal 86, 144–156 (2024). https://doi.org/10.1016/j.aej.2023.11.034.
18. Rastgou, M., Liu, S., Wang, J., Li, Y., Xu, J., He, Y., Jiang, Q.: A hybrid approach for optimizing soil greenhouse gas flux predictions: integrating machine learning outputs into hyperparameter-tuned regression trees. Pedosphere, (2025). https://doi.org/10.1016/j.pedsph.2025.10.002.
19. Rajurkar, M. P., Kothyari, U. C., Chaube, U. C.: Artificial neural networks for daily rainfall—runoff modelling. Hydrological Sciences Journal 47(6), 865–877 (2002). https://doi.org/10.1080/02626660209492996.
20. Srinivasulu, S., Jain, A.: A comparative analysis of training methods for artificial neural network rainfall–runoff models. Applied Soft Computing 6(3), 295–306 (2006). https://doi.org/10.1016/j.asoc.2005.02.002.

Author Contribution Statement

- *Conceptualization:* Nurcan Öztürk
- *Methodology:* Nurcan Öztürk
- *Investigation:* Nurcan Öztürk, Derya Kılıç, Hasan Tahsin Öztürk
- *Writing – Original Draft:* Nurcan Öztürk, Derya Kılıç
- *Writing – Review & Editing:* Nurcan Öztürk, Derya Kılıç, Hasan Tahsin Öztürk

List of Abbreviations

- **A10** — A10 Index
- **ANN** — Artificial Neural Networks
- **DL** — Deep Learning
- **FFBNN** — Feedforward Backpropagation Neural Network
- **FOS** — Flow Observation Station
- **LSBoost** — Least-Squares Boosting
- **MAE** — Mean Absolute Error
- **MARS** —Multivariate Adaptive Regression Splines
- **ML** — Machine Learning
- **MLR** — Multiple Linear Regression
- **MOS** — Meteorological Observation Station
- **NSE** — Nash–Sutcliffe Efficiency Coefficient
- **OPELM** — Optimally Pruned Overfitting Machine
- **PI** — Performance Index
- **R** — Pearson Correlation Coefficient
- **RMSE** — Root Mean Square Error
- **RRMSE** — Relative Root Mean Square Error
- **SVM** — Support Vector Machines

Publication Note
This paper was peer-reviewed, accepted for presentation, and included in the proceedings of the ACE2026 – International Conference on Advances in Civil Engineering, held on 12–14 October 2026 in Trabzon, Türkiye.

This paper may be cited as follows:
Derya Kılıç, Nurcan Öztürk, Hasan Tahsin Öztürk "Modeling the Rainfall-Runoff Interaction Using LSBoost, MARS, M5-tree, and ANN: A Case of Çağlayan Creek" in Proceedings of the ACE2026 – International Conference on Advances in Civil Engineering, Trabzon, Türkiye, 12–14 October 2026.

Development of New Software for Feasibility Studies of Hydropower Plants

Onur Kemalli[1], Zafer Bozkuş[2] and T. Kutay Çelebioğlu[3]
[1] 0009-0000-6671-715X, Ministry of Energy and Natural Resources of Turkey, Ankara, Türkiye, e128818@metu.edu.tr
[2] 0000-0001-6863-3531, Department of Civil Engineering, Middle East Technical University, Ankara, Türkiye, bozkus@metu.edu.tr
[3] 0000-0001-8845-4928, Department of Mechanical Engineering, TOBB ETU, Ankara, Türkiye, tkcelebioglu@etu.edu.tr

Abstract. Feasibility studies of hydropower plants include technoeconomic, socioeconomic, and environmental analyses. Technoeconomic analysis involves civil works, electrical works, hydromechanics, and electromechanics. Moreover, socioeconomic analysis encompasses employment, flood control, and relocation of structures. Furthermore, environmental analysis comprises reduction of carbon dioxide, losses in carbon sequestration, and in ecology. This study focuses on the development of new software, called HydroFeasibility, which combines all aspects of feasibility in hydropower investments.

Keywords: Feasibility Software; Hydropower Plant; Cost-Benefit Analysis

1 Introduction

Feasibility studies for hydropower investments are usually conducted via computation of spreadsheet formulas, utilization of equipment characteristics charts, and engineering experience. However, these conventional methods may introduce human error and lead to substantial time loss.

In this study, novel software is developed to assembly the three main pillars of feasibility, which are technoeconomic, socioeconomic, and environmental assessments. The software, called HydroFeasibility, is written in C Sharp (C#) programming language. Its graphical user interphase (GUI) enables convenient implementation of embedded data-driven equations.

2 Digital Tools for Feasibility Studies

There are various software for feasibility studies of hydropower plants. These may vary from custom-programmable digital tools to comprehensive feasibility software with optimization and multiple scenario features.

RETScreen Clean Energy Project Analysis Software by Natural Resources of Canada, for instance, can calculate benefits as power, energy yield, carbon offset revenues, and costs as initial and operational expenses. Korkmaz [1] studied technoeconomic viability of Kadincik-4 HPP in Turkey via RETScreen and founded that the penstock diameters calculated by the software were twenty percent greater than the officially accepted feasibility report. Mutlu [2] assessed feasibility of Niksar HPP in Turkey via RETScreen and identified the software's inadequacy to model sediment conditions and expropriation costs in tunnel/channel excavations. Yuce and Yuce [3] evaluated viability of nine hydropower plants in Turkey. They showed the need to adapt North American hydrological data and adjust cost coefficients/export rates to Turkish settings.

Vilela and Reid [4] used HydroCalculator for evaluation of dam projects in Amazon Basin through economic, social, and environmental aspects. The open-access interactivity with quantitative estimation of net present value, internal rate of return, and greenhouse gas emission

costs were identified as the advantages of HydroCalculator, despite its over simplified financial estimates and deficiency of detailed engineering parameters.

Canales and Beluco [5] modeled a hydropower plant in a hybrid configuration using HOMER. They found that HOMER featured satisfactory optimization of net present cost for hydro, solar, wind and electricity storage hybrid systems, however, with intrinsic requirements of constant head and simplified inflow, it lacked modeling reservoir type hydropower plants.

Bayazit, Bakis, and Koc [6] examined hydropower potential using Geographic Information System (GIS) software in displaying and analyzing river catchment features and employing digital elevation models in detecting sites. Via GIS software, potential locations and their environmental compatibility were identified without acquiring field surveying, while the researchers noted the discrepancies between on-site physical features and digital terrains by GIS database.

Moldoveanu and Popa [7] evaluated the feasibility and design parameters of the Cetateni 2 HPP in Romania via a GIS-based digital tool called VAPIDRO-ASTE. Their work confirmed that while VAPIDRO-ASTE extracted river network, investigated catchment hydrology, and computed the residual potential, it required advanced user proficiency in GIS.

With Super Decisions software, using Multi-Criteria Decision Analysis, Saracoglu [8] scrutinized the investment selection and decision-making problems for small hydropower plants in Turkey. The software allowed the graphical control of hierarchal trees to normalize priorities, with qualitative and quantitative parameters, however, modeling pairwise comparisons observed to be challenging and time-consuming.

As the standard international methods and digital tools lack from excellent alignment with the legislative, financial, and structural feasibility studies in Turkey, development of a localized, custom-built, new feasibility software emerges as a necessity.

3 HydroFeasibility – the Newly Developed Software

In this study, new software, HydroFeasibility was developed for feasibility studies of hydropower plants in Turkey.

The software was coded in C#, in terms of modules and submodules. As a part of .NET environment, WinForms was used as the GUI class library. The computational engine, which was based on object-oriented programming principles, featured an extendible architecture enabling incorporation of additional equations and parameters in the future.

On the GUI, the validity of parameters entered is instantly checked. Progressive exception handling (try-catch blocks and data validation algorithms) was integrated to prevent invalid inputs or undefined results. Upon execution, the application initializes the main window, presenting the user with the menu bar (Fig. 1).

The technoeconomic, socioeconomic, and environmental analysis modules were designed as drop-down menus for benefit and cost calculations. In Technoeconomic Module, cost calculations were further detailed in submodules like Electromechanics, Hydromechanics, Civil Works, and Electrical Works (Fig. 2).

While Socioeconomic Module and Environmental Module encapsulate distinct benefit and cost submodules, Benefit – Cost Module acts as the integration layer, aggregating all system-wide calculations. Results from technoeconomic, socioeconomic, and environmental modules are used to compute benefit to cost ratio of the investment on “present values” basis. The process flow diagram of Benefit – Cost Module is shown in Fig. 3.

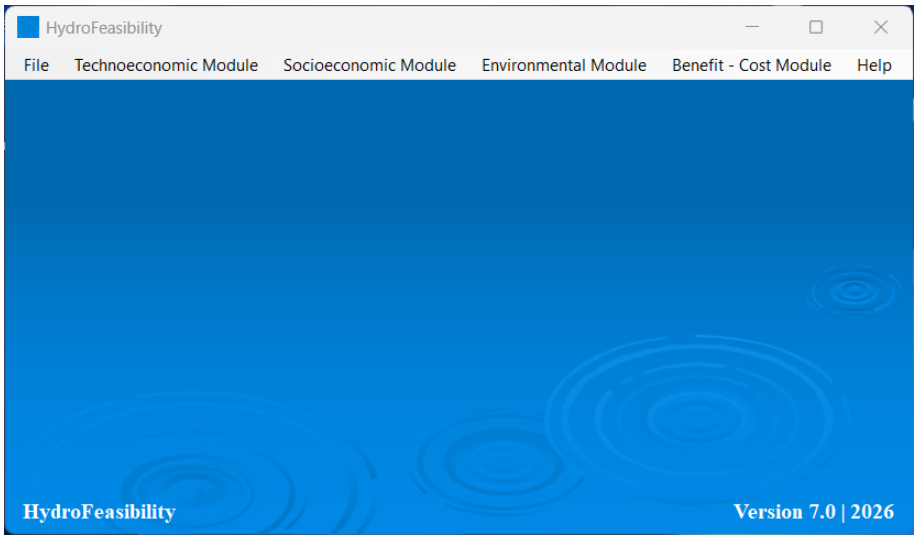


Fig. 1. The main window in HydroFeasibility.

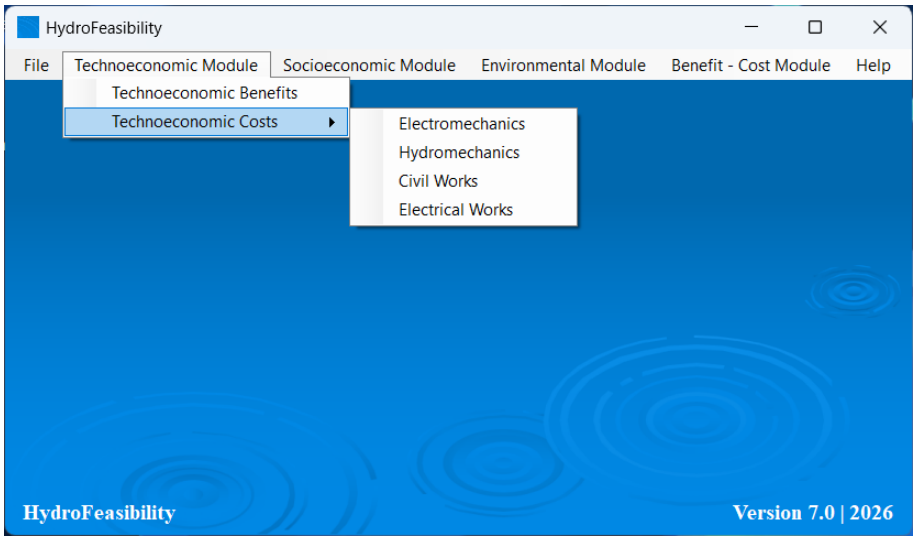


Fig. 2. The Technoeconomic Module in HydroFeasibility.

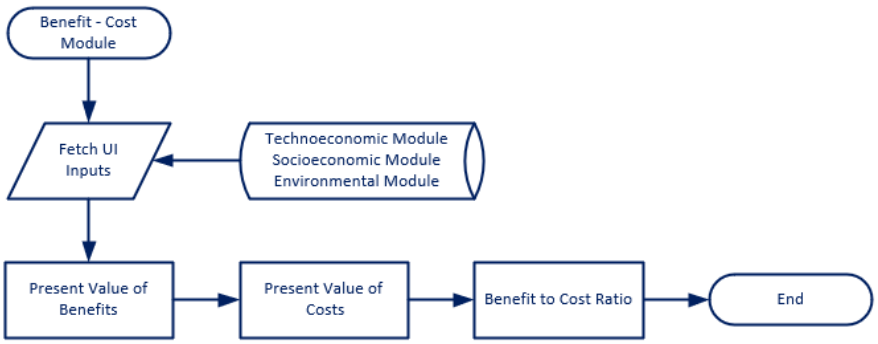


Fig. 3. Process Flow Diagram of Benefit – Cost Module in HydroFeasibility.

4 Case Study – An Application of HydroFeasibility

As an application of the newly developed software, technoeconomic, socioeconomic, and environmental viability of a fictitious hydropower plant is analyzed via HydroFeasibility.

4.1 Technoeconomic Analysis

In this case study, the technoeconomic data for the year 2014 are presented as annual benefits in Table 1, and as initial costs in Table 2.

Table 1. Data for Technoeconomic Annual Benefits.

Item	*Benefit (US $/year)*
Electricity Revenue	4,470,000.00

Table 2. Data for Technoeconomic Initial Costs.

Item	*Cost (US $)*
Civil Works	17,081,900.00
Hydromechanics	2,756,600.00
Electrical Works	352,300.00
Electromechanics	2,936,500.00
Expropriation	599,000.00

The annuities are considered for forty-nine years. The period for construction is taken as two years. The percentage of contingencies, the percentage of feasibility study, project design, engineering, and control are assumed as 15.00 %. The interest rate during construction and the discount rate are adopted as 9.50 %.

Additionally, data for renewal costs of some components are listed in Table 3.

Table 3. Data for Renewal Costs.

Item	*Renewal Cost (US $)*
Concrete Lined Channel	234,920.00
Diversion Structures	4,698.00
Steel Penstock	117,450.00
Power Transmission Line	140,900.00
Powerhouse	196,000.00
Electromechanical Equipment	2,936,500.00
Asphalt Paved Roads	9,278.00
Site Structures	28,190.00
Intake	3,522.00
Weir	14,800.00

Moreover, for operation and maintenance, an annual cost of US $ 70,000.00 is allocated. Similarly, for the project lifespan, miscellaneous annual costs are predicted to be US $ 60,000.00. Then, HydroFeasibility is run for technoeconomic analysis (Fig. 4).

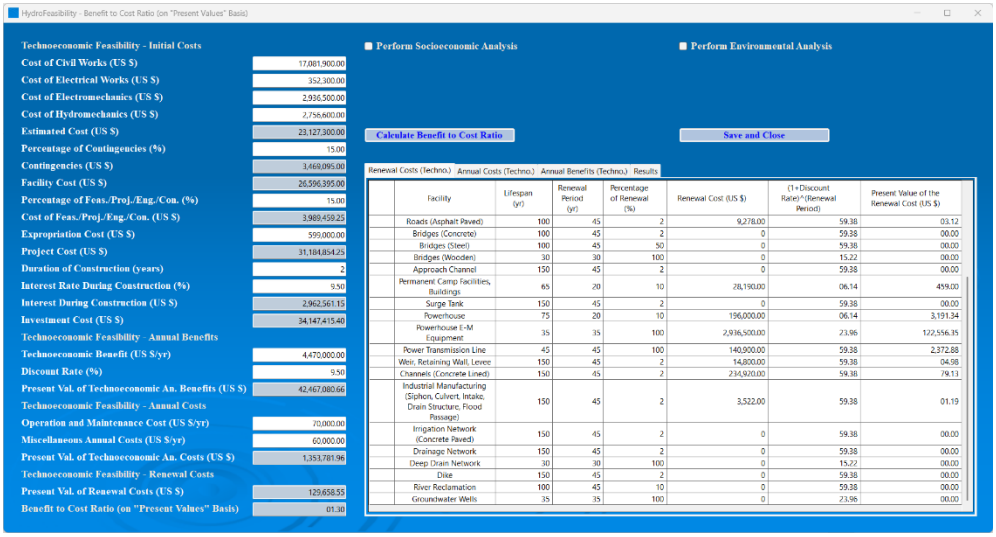


Fig. 4. Technoeconomic Analysis in HydroFeasibility.

The results obtained are shown in Fig. 5, 6, and 7.

Renewal Costs (Techno.) | Annual Costs (Techno.) | Annual Benefits (Techno.) | Results

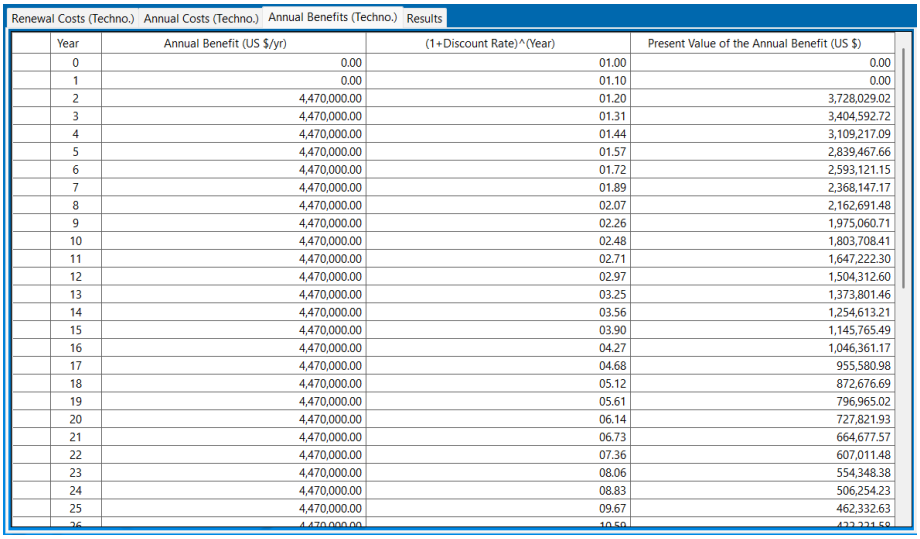
	Facility	Lifespan (yr)	Renewal Period (yr)	Percentage of Renewal (%)	Renewal Cost (US $)	(1+Discount Rate)^(Renewal Period)	Present Value of the Renewal Cost (US $)
	Roads (Asphalt Paved)	100	45	2	9,278.00	59.38	03.12
	Bridges (Concrete)	100	45	2	0	59.38	00.00
	Bridges (Steel)	100	45	50	0	59.38	00.00
	Bridges (Wooden)	30	30	100	0	15.22	00.00
	Approach Channel	150	45	2	0	59.38	00.00
	Permanent Camp Facilities, Buildings	65	20	10	28,190.00	06.14	459.00
	Surge Tank	150	45	2	0	59.38	00.00
	Powerhouse	75	20	10	196,000.00	06.14	3,191.34
	Powerhouse E-M Equipment	35	35	100	2,936,500.00	23.96	122,556.35
	Power Transmission Line	45	45	100	140,900.00	59.38	2,372.88
	Weir, Retaining Wall, Levee	150	45	2	14,800.00	59.38	04.98
	Channels (Concrete Lined)	150	45	2	234,920.00	59.38	79.13
	Industrial Manufacturing (Siphon, Culvert, Intake, Drain Structure, Flood Passage)	150	45	2	3,522.00	59.38	01.19
	Irrigation Network (Concrete Paved)	150	45	2	0	59.38	00.00
	Drainage Network	150	45	2	0	59.38	00.00
	Deep Drain Network	30	30	100	0	15.22	00.00
	Dike	150	45	2	0	59.38	00.00
	River Reclamation	100	45	10	0	59.38	00.00
	Groundwater Wells	35	35	100	0	23.96	00.00

Fig. 5. Calculation of Renewal Costs.

Renewal Costs (Techno.) | Annual Costs (Techno.) | Annual Benefits (Techno.) | Results

	Year	Annual Cost (US $/yr)	(1+Discount Rate)^(Year)	Present Value of the Annual Cost (US $)
	0	0.00	01.00	0.00
	1	130,000.00	01.10	118,721.46
	2	130,000.00	01.20	108,421.43
	3	130,000.00	01.31	99,015.00
	4	130,000.00	01.44	90,424.66
	5	130,000.00	01.57	82,579.60
	6	130,000.00	01.72	75,415.16
	7	130,000.00	01.89	68,872.29
	8	130,000.00	02.07	62,897.07
	9	130,000.00	02.26	57,440.24
	10	130,000.00	02.48	52,456.84
	11	130,000.00	02.71	47,905.79
	12	130,000.00	02.97	43,749.58
	13	130,000.00	03.25	39,953.96
	14	130,000.00	03.56	36,487.63
	15	130,000.00	03.90	33,322.04
	16	130,000.00	04.27	30,431.09
	17	130,000.00	04.68	27,790.95
	18	130,000.00	05.12	25,379.86
	19	130,000.00	05.61	23,177.95
	20	130,000.00	06.14	21,167.08
	21	130,000.00	06.73	19,330.67
	22	130,000.00	07.36	17,653.58
	23	130,000.00	08.06	16,121.99
	24	130,000.00	08.83	14,723.28
	25	130,000.00	09.67	13,445.92
	26	130,000.00	10.59	12,279.27

Fig. 6. Calculation of Annual Costs.



	Year	Annual Benefit (US $/yr)	(1+Discount Rate)^(Year)	Present Value of the Annual Benefit (US $)
	0	0.00	01.00	0.00
	1	0.00	01.10	0.00
	2	4,470,000.00	01.20	3,728,029.02
	3	4,470,000.00	01.31	3,404,592.72
	4	4,470,000.00	01.44	3,109,217.09
	5	4,470,000.00	01.57	2,839,467.66
	6	4,470,000.00	01.72	2,593,121.15
	7	4,470,000.00	01.89	2,368,147.17
	8	4,470,000.00	02.07	2,162,691.48
	9	4,470,000.00	02.26	1,975,060.71
	10	4,470,000.00	02.48	1,803,708.41
	11	4,470,000.00	02.71	1,647,222.30
	12	4,470,000.00	02.97	1,504,312.60
	13	4,470,000.00	03.25	1,373,801.46
	14	4,470,000.00	03.56	1,254,613.21
	15	4,470,000.00	03.90	1,145,765.49
	16	4,470,000.00	04.27	1,046,361.17
	17	4,470,000.00	04.68	955,580.98
	18	4,470,000.00	05.12	872,676.69
	19	4,470,000.00	05.61	796,965.02
	20	4,470,000.00	06.14	727,821.93
	21	4,470,000.00	06.73	664,677.57
	22	4,470,000.00	07.36	607,011.48
	23	4,470,000.00	08.06	554,348.38
	24	4,470,000.00	08.83	506,254.23
	25	4,470,000.00	09.67	462,332.63
	26	4,470,000.00	10.59	422,221.58

Fig. 7. Calculation of Annual Benefits.

Here, Benefit to Cost Ratio (BCR) by the technoeconomic analysis of the project yielded is calculated as 1.30 on present values basis. With BCR greater than or equal to one, the project seems feasible.

4.2 Socioeconomic Analysis

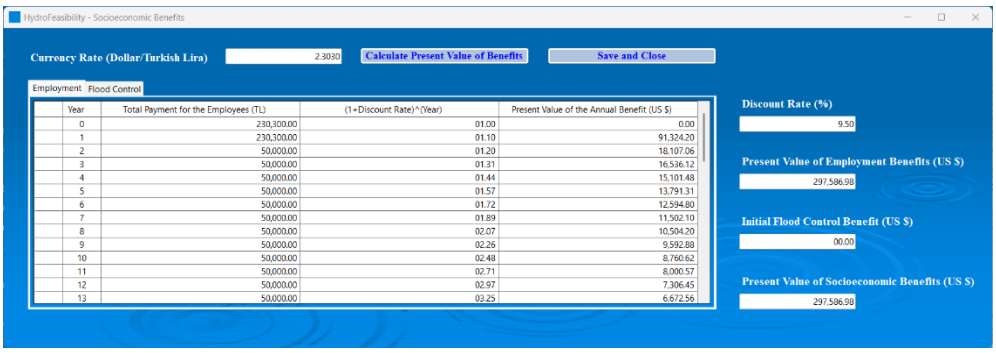
In this case, the socioeconomic benefits involve employment, and the socioeconomic costs includes the relocation of structures.

In the first two years of the project, all the technical staff and security personnel will be on site, however, beginning from the third year, only the operators and the security personnel will remain. The employment benefits are presented in Table 4.

Table 4. Employment Benefits.

Period (years)	*Total Payment for the Employees (₺)*	*Total Payment for the Employees (US $)*
0 – 2	230,300.00	100,000.00
3 – 49	50,000.00	21,710.81

Upon incorporating Socioeconomic Benefits module of HydroFeasibility, the results given in Fig. 8 are found.



	Year	Total Payment for the Employees (TL)	(1+Discount Rate)^(Year)	Present Value of the Annual Benefit (US $)
	0	230,300.00	01.00	0.00
	1	230,300.00	01.10	91,324.20
	2	50,000.00	01.20	18,107.06
	3	50,000.00	01.31	16,536.12
	4	50,000.00	01.44	15,101.48
	5	50,000.00	01.57	13,791.31
	6	50,000.00	01.72	12,594.80
	7	50,000.00	01.89	11,502.10
	8	50,000.00	02.07	10,504.20
	9	50,000.00	02.26	9,592.88
	10	50,000.00	02.48	8,760.62
	11	50,000.00	02.71	8,000.57
	12	50,000.00	02.97	7,306.45
	13	50,000.00	03.25	6,672.56

Fig. 8. Employment Benefits.

For relocation of structures, two types of buildings are taken into consideration (Table 5).

Table 5. Costs for Relocation of Structures.

Structure to Relocate	*Quantity*	*Cost of Relocation (₺)*
Type – 1	1	24,642.10
Type – 2	1	12,896.80

Furthermore, the socioeconomic costs computed by HydroFeasibility are shown in Fig. 9.

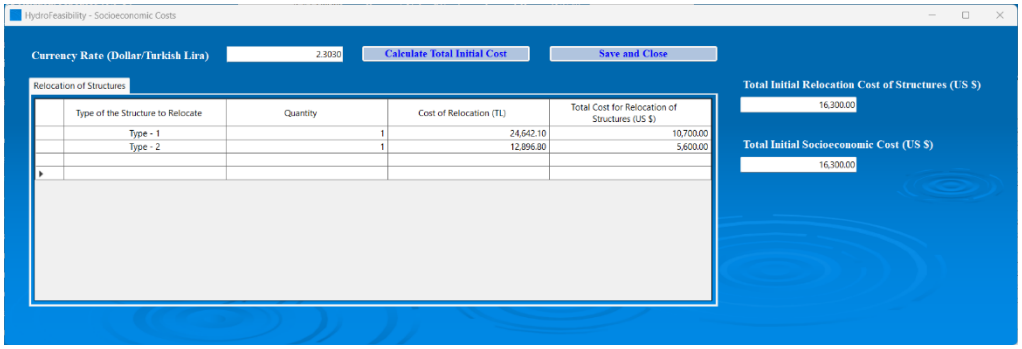


Fig. 9. Costs for Relocation of Structures.

Therefore, after the incorporation of socioeconomic assessment in the feasibility study, the BCR just rose to 1.31 (Fig. 10).

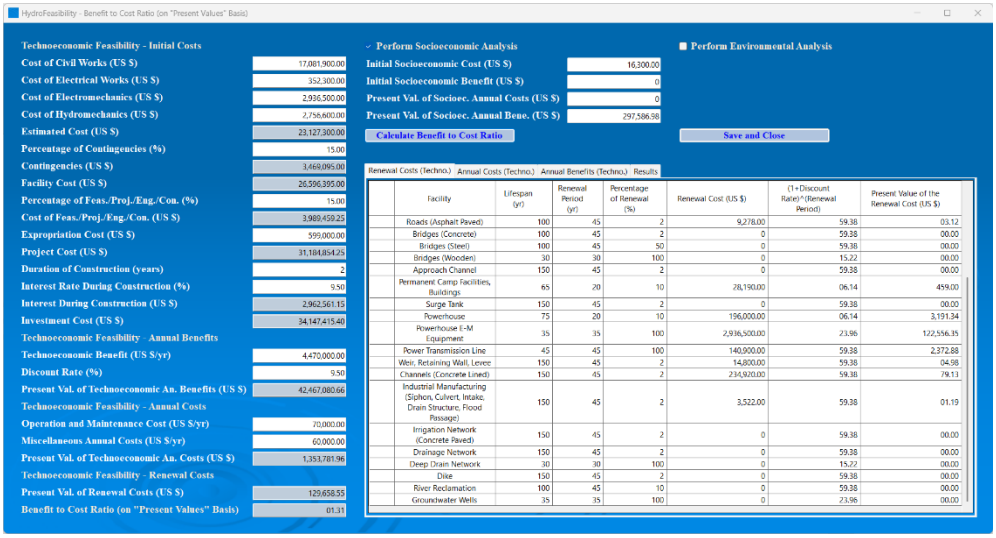


Fig. 10. Technoeconomic and Socioeconomic Assessment.

4.3 Environmental Analysis

Here, the environmental benefits focus on reduction of carbon dioxide with assumption of no harm of the project on vegetation, trees, and crops.

Reduction of carbon dioxide (CO_2) due to hydropower is 45.36 kg per 1 MWh of annual energy [9]. For this case, with energy yield of 30,000.00 MWh/year, CO_2 of 1,360.80 tons/year should be reduced. This reduction is reflected in the Environmental Benefits Module of HydroFeasibility, and the results are illustrated in Fig. 11.

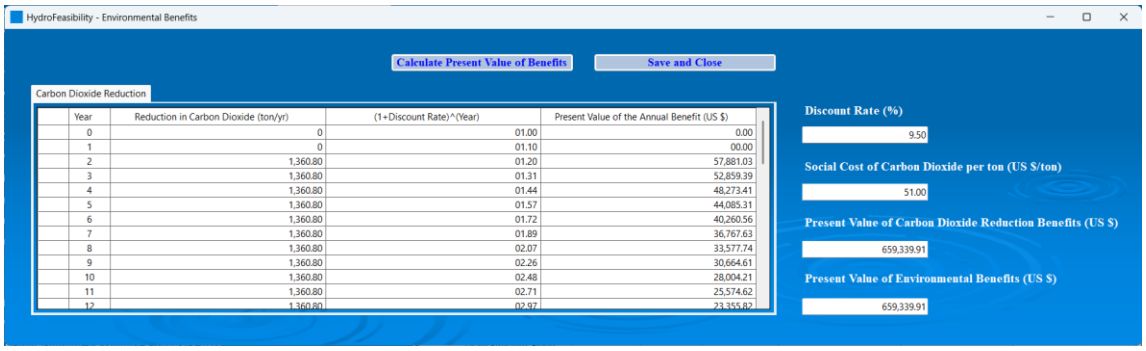


Fig. 11. Environmental Benefits.

After incorporation of environmental assessment, the BCR increased to 1.33 (Fig. 12).

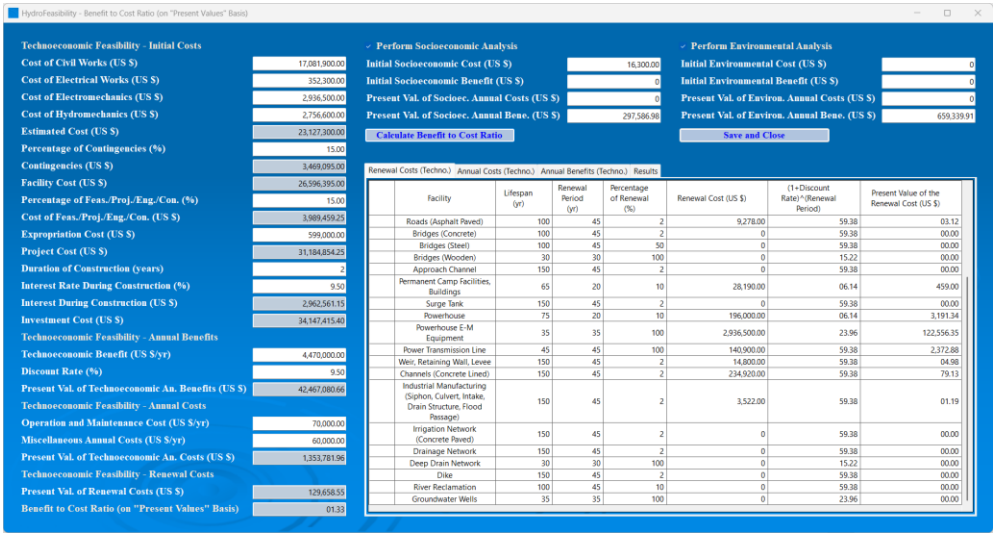


Fig. 12. Technoeconomic, Socioeconomic, and Environmental Assessment.

5 Results and Discussion

In this case study, technoeconomic, socioeconomic, and environmental feasibility of a fictitious hydropower plant with a weir was analyzed.

In technoeconomic analysis, initial costs were costs of civil works, electrical works, electromechanics, hydromechanics, and expropriation. Annual benefits were revenues from electricity generation. Operation and maintenance costs, renewal costs were also considered. BCR calculated for the technoeconomic assessment was 1.30. Since this value was greater than or equal to one, the investment was found to be feasible. Moreover, in socioeconomic analysis, benefits involved employment opportunities, whereas costs comprised relocation of structures. Including the socioeconomic analysis, BCR increased to 1.31. Furthermore, environmental analysis was held with annual benefits of carbon dioxide reduction. Incorporating the environmental aspects, BCR rose to 1.33.

Here, the influences of socioeconomic and environmental parameters on BCR were found to be insignificant. This may be due to small capacity and limited area of the hydropower plant with weir. For a hydropower plant with a dam and substantial reservoir, socioeconomic and/or environmental analyses could have altered the BCR significantly.

6 Conclusion

In this study, the newly developed feasibility software, HydroFeasibility has been presented and used in a comprehensive feasibility analysis of a fictitious hydropower plant with a weir.

The findings highlighted that the progressive inclusion of socio-environmental factors slightly increased the BCR. This exhibited the low-impact characteristics of run-of-river weir plants, compared to facilities with dams and enormous reservoirs.

While the newly developed software, HydroFeasibility, signifies an innovative, localized, multi-dimensional energy planning tool, future versions may require structural updates for adaptation to data transfer attributes and hybrid solutions with electricity storage.

References

1. Korkmaz, O.: A case study on feasibility assessment of small hydropower scheme. Master's thesis, Middle East Technical University, Ankara (2007).
2. Mutlu, R.: Feasibility study of a hydropower project: Case study of Niksar HEPP, Turkey. Master's thesis, Middle East Technical University, Ankara (2010).
3. Yuce, M. I., Yuce, S.: Pre-feasibility assessment of small hydropower projects in Turkey by RETScreen. Journal of the American Water Works Association 108(5), E269–E275 (2016).
4. Vilela, T., Reid, J.: Improving hydropower choices via an online and open access tool. PLoS ONE 12(6), e0179393 (2017).
5. Canales, F. A., Beluco, A.: Modelling a hydropower plant with reservoir with the micropower optimisation model (HOMER). International Journal of Sustainable Energy 36(7), 654–667 (2015).
6. Bayazıt, Y., Bakış, R., Koç, C.: An investigation of small scale hydropower plants using the geographic information system. Renewable and Sustainable Energy Reviews 67, 289–294 (2017).
7. Moldoveanu, A., Popa, B.: Hydropower potential assessment of Prahova river with the informatic tool Vapidro-Aste. Energetica 60(7), 290–295 (2012).
8. Saracoglu, B. O.: An AHP application in the investment selection problem of small hydropower plants in Turkey. International Journal of the Analytic Hierarchy Process 7(2), 215–239 (2015).
9. SmartEnergy Homepage, https://smartenergy.com, last accessed 2025/04/04.

Author Contribution Statement

- *Conceptualization, Methodology, Writing – Original Draft:* Onur Kemalli
- *Writing – Review & Editing:* Zafer Bozkuş, T. Kutay Çelebioğlu

List of Abbreviations

- **BCR** — Benefit to Cost Ratio
- **GIS** — Geographic Information System
- **GUI** — Graphical User Interface
- **HPP** — Hydropower Plant
- **US** — The United States

List of Symbols

- **C#** — C Sharp
- **$** — the US Dollars
- **₺** — Turkish Lira

Conflicts of Interest

The authors declare that they have no known competing financial interests or personal relationships that could have appeared to influence the work reported in this paper.

Publication Note
This paper was peer-reviewed, accepted for presentation, and included in the proceedings of the ACE2026 – International Conference on Advances in Civil Engineering, held on 12–14 October 2026 in Trabzon, Türkiye.

This paper may be cited as follows:
Kemalli, O., Bozkus, Z., Celebioglu, T.K., "Development of New Software for Feasibility Studies of Hydropower Plants," in Proceedings of the ACE2026 – International Conference on Advances in Civil Engineering, Trabzon, Türkiye, 12–14 October 2026.

Experimental and Numerical Investigation of Flow Characteristics and Water Surface Profiles Under a Vertically Moving Cylindrical Gate Using HEC-RAS

Kağan CEBE[1], Yusuf Buğra AKSOY[2], Bilgin Furkan BAYRAK[2] and Aslı ÜLKE KESKİN[3]
[1] 0000-0003-1288-1362, Ondokuz Mayıs University, Civil Engineering Department, Samsun, Türkiye, kagan.cebe@omu.edu.tr
[2] Ondokuz Mayıs University, Civil Engineering Department, Samsun, Türkiye
[3] 0000-0002-9676-8377, Ondokuz Mayıs University, Civil Engineering Department, Samsun, Türkiye, asli.ulke@omu.edu.tr

Abstract. Hydraulic gates are critical structures for regulating discharge and water levels in open channels. Unlike conventional planar sluice or radial gates, vertically moving cylindrical gates exhibit hybrid hydrodynamic behavior by combining linear vertical motion with a streamlined curved boundary. This study experimentally investigated the hydraulic characteristics of flow beneath a vertically moving cylindrical gate (D = 125 mm) in a 5.0 m flume and numerically simulated them using 1D HEC-RAS across three steady discharges (Q = 1.24, 1.49, 1.64 L/s) and gate openings (B = 14, 24, 34 mm). Baseline flume tests established an optimal Manning roughness of n = 0.010 (mean absolute error of 2.91%). In HEC-RAS, default radial gate theoretical exponents render the formulation mathematically identical to the classic sluice gate equation. Conventional planar sluice discharge coefficients (Cu = 0.50 - 0.70) significantly overpredicted upstream headwater depths due to exaggerated contraction assumptions. Calibrating the coefficient to Cu = 0.85 successfully accounted for the streamlined curved surface and reduced vena contracta effects, decreasing mean relative errors to -0.61% for headwater and -1.23% for tailwater depths R2 > 0.999). The findings demonstrate that 1D HEC-RAS sluice formulations accurately replicate cylindrical gate hydrodynamics when calibrated with Cu = 0.85.

Keywords: Open channel flow, HEC-RAS, discharge coefficient, hydraulic modeling, sluice gate

1 Introduction

Hydraulic gates are movable control mechanisms employed in open channels, dams, and river control structures to regulate water levels, control flow, measure discharge, convey specified flow rates, or completely shut off the flow [1-4]. Unlike weirs that discharge flow over their crests, gates generally achieve flow control by forcing the water to pass underneath or through a defined opening. The design of gates requires analysis of complex hydrodynamic forces that vary with the hydraulic head difference between upstream and downstream water levels, the flow regime (free or submerged), and the structural geometry [3, 5].

Based on their geometric forms and operating mechanisms, gates are categorized into types such as sluice, radial (Tainter), miter, sector, and flap. Among these, sluice and radial gates represent the two most widely utilized control structures in hydraulic engineering and water conveyance systems. While sluice gates move along a vertical plane, transferring the hydraulic load to linear guides, radial gates feature circular arc surfaces rotating around a pivot axis, concentrating the hydrodynamic load onto the trunnion pin and thereby minimizing the load on the hoisting mechanism [2, 3, 5]. Sluice gates are commonly used in vertical water control structures due to their structural simplicity, cost-effectiveness, and operational ease. Flow

beneath a sluice gate accelerates through a converging section, displaying orifice-type flow behavior, which results in energy dissipation accompanied by a characteristic water surface profile variation downstream [1, 2]. Consequently, determining the hydraulic behavior under bottom-discharge structures requires accounting for the geometric boundaries and contraction characteristics specific to each gate type [3, 4].

The gate discharge coefficient and the hydraulics of flow beneath gates have been the subject of numerous scientific studies in the literature. Severi, Masoudian [6] experimentally investigated the discharge coefficients, energy losses, and energy variations of vertically moving cylindrical gates. Using PIV measurements on a rising sector gate model, Song, Park [7] investigated flow velocity and turbulence distributions at varying gate openings, demonstrating that larger openings significantly reduce relative turbulence intensity and establishing a functional relationship between maximum mouth velocity and the Froude number for practical operation. Similarly, Abbaszadeh, Daneshfaraz [8] evaluated the effects of sluice gate openings on hydraulic characteristics, demonstrating that smaller openings increase both the contraction and discharge coefficients as well as hydrodynamic forces, while developing accurate non-linear polynomial regression models to predict discharge coefficients and relative energy loss across varying Froude numbers. Regarding downstream flow phenomena and numerical validation, Şimşek, Kösen [9] compared velocity profiles obtained from numerical simulations using ANSYS-Fluent with experimental data for submerged hydraulic jumps at various submergence ratios downstream of a sluice gate. Likewise, Ateş and Yıldız [10] compared experimental measurements of hydraulic jumps formed under a movable vertical gate with numerical results calculated using HEC-RAS (Hydraulic Engineering Center's River Analysis System).

In this study, the hydraulic behavior of flow beneath a vertically moving cylindrical gate was experimentally investigated under various discharge conditions, and the resulting physical data were compared with numerical modeling results from HEC-RAS[11].

2 Materials and Methods

The methodology adopted in this study consists of a three-step framework. In the first step, the channel bed roughness (Manning's n) was determined under baseline (without gate) flow conditions at a constant discharge and bed slope. In the second step, a vertically moving cylindrical gate was installed at the middle of the channel, and headwater and tailwater depths were measured across three distinct discharge rates and three distinct gate openings (14, 24, and 34 mm). In the final step, identical channel and gate geometries were configured in HEC-RAS.

To evaluate the nature of the gate, gate formulations were implemented, discharge coefficients (C_u) were calibrated, and the predictive performance of both approaches was compared against the experimental dataset.

2.1 Governing Equations and Gate Formulations in HEC-RAS

HEC-RAS (Hydrologic Engineering Center's River Analysis System), developed by the U.S. Army Corps of Engineers (USACE), is a public-domain hydraulic modeling software globally recognized as an industry standard in river hydraulics, flood management, and hydraulic structure design. The software is extensively used to simulate steady and unsteady flow regimes in natural river networks and artificial open channels, to perform flood risk assessments, and to evaluate structural hydraulics [12]. The HEC-RAS modeling suite encompasses four primary one-dimensional river analysis components: (1) steady-flow water surface profile calculations, (2) unsteady-flow hydrodynamic simulations (1D and 2D), (3) movable-boundary sediment transport computations, and (4) water quality analysis [11].

HEC-RAS relies on the conservation of mass and momentum, governed by the Saint-Venant equations. For gradually varied 1D unsteady flow, the Saint-Venant continuity and momentum equations are expressed as Equations (1) and (2), respectively:

$$\frac{\partial \mathrm{A}}{\partial \mathrm{t}}+\frac{\partial \mathrm{Q}}{\partial \mathrm{x}}=0 \tag{1}$$

$$\frac{\partial \mathrm{Q}}{\partial \mathrm{t}}+\frac{\partial\left(\frac{Q^2}{A}\right)}{\partial \mathrm{x}}+\mathrm{gA}\frac{\partial \mathrm{H}}{\partial \mathrm{x}}+\mathrm{gA}S_f=0 \tag{2}$$

Where Q is the total discharge, A is the cross-sectional flow area, t is time, x is the distance along the channel, g is the gravitational acceleration, H is the water depth, and S_f is the friction slope. HEC-RAS calculates the friction slope (S_f) using the Manning equation (Equation 3):

$$\mathrm{Q}=\frac{1}{\mathrm{n}}\ \mathrm{AR}^{2/3}\ \mathrm{S}^{1/2} \tag{3}$$

Where n is the Manning roughness coefficient, and R is the hydraulic radius. HEC-RAS solves these one-dimensional governing equations numerically using an implicit finite difference scheme combined with the Newton-Raphson iteration technique [12].

Despite representing a basic and fundamental control structure, the hydraulics of flow beneath gates constitutes a rich and complex topic in fluid mechanics [3, 5]. Flow passing beneath a gate exhibits distinct characteristics depending on the flow regime and is fundamentally categorized into two main regimes: free and submerged flow. The classification of underflow regimes is illustrated in Fig. 1. While the flow passing beneath the gate in the first two diagrams (a and b) represents free flow, the final diagram (c) illustrates submerged flow.

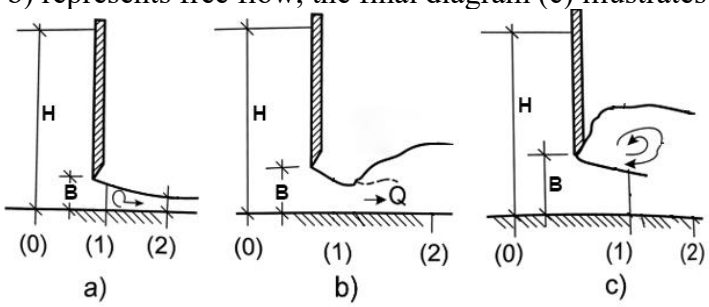


Fig. 1. Flow beneath gates: a) and b) free flow c) submerged flow [2]

In free flow case, the downstream water level has no effect on the high-velocity jet issuing through the gate opening, and the flow beneath the gate discharges freely downstream (Fig 1a & 2b). Based on the channel's hydraulic characteristics, the flow exiting the gate may maintain a supercritical regime or transition to a subcritical state by dissipating energy via a hydraulic jump at a specific distance downstream [2, 5, 13-15].

Sluice Gate Flow Equation

An example sluice gate is presented in Fig. 2.

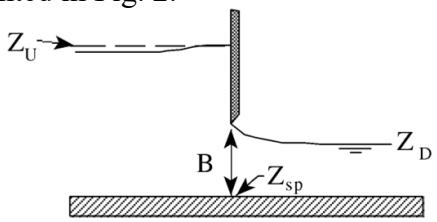


Fig. 2. Sluice gate with broad crested spillway.

In Fig. 2, Z_U is the elevation of the upstream energy grade line (m), Z_D is the elevation of the downstream water surface (m) and Z_{sp} is the elevation of the spillway crest through the gate

(m). The upstream head (H) is the difference of Z_U and Z_D. The equation for a free-flowing sluice gate is as follows [12]:

$$Q = C_u WB\sqrt{2gH} \quad (4)$$

Where, Q is the flow rate (m^3/s), C_u is the unsubmerged discharge coefficient, typically 0.5-0.7, W is the gate width (m), B is the gate opening (m), g is the gravitational acceleration (m/s^2), and H is the upstream head above the spillway crest (Z_U-Z_{sp}). As downstream submergence impairs free flow under the gate, increasing the upstream headwater level for a given flow rate, the program transitions to the following equation [12]:

$$Q = C_u WB\sqrt{2g3H} \quad (5)$$

Flow submergence begins when the tailwater depth to headwater energy ratio over the spillway exceeds 0.67. To bridge free flow and fully submerged regimes, Equation (6) is utilized. This transition ensures a gradual shift toward the fully submerged orifice equation up to a submergence ratio of 0.80.

$$Q = C_s A\sqrt{2gH} \quad (6)$$

Where, Cs is the submerged discharge coefficient (Cs =κ.Cu) The factor κ in this expression always takes a value less than unity and can be derived by formulating the specific force balance between sections (1) and (2) [2]. The default value for the submerged discharge coefficient is 0.8.

Radial Gate Flow Equation

The flow through the gate is considered to be "Free Flow" when the downstream tailwater elevation (Z_D) is not high enough to cause an increase in the upstream headwater elevation for a given flow rate.

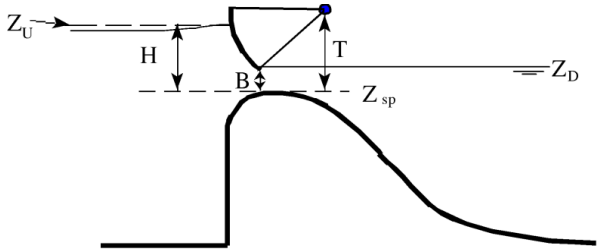


Fig. 3. Typical Radial Gate with an Ogee Spillway Crest [12]

In Fig. 3. Z_U is the elevation of the upstream energy grade line (m), Z_D is the elevation of the downstream water surface (m) and Z_{sp} is the elevation of the spillway crest through the gate (m). The upstream head (H) is the difference of Z_U and Z_D. The equation used for a Radial gate under free flow conditions is as follows [12]:

$$Q = C_u\sqrt{2g}\, WT^{TE}B^{BE}H^{HE} \quad (7)$$

Where, T is the trunnion height (m), TE represents the trunnion exponent, BE is the opening exponent, HE is the head exponent. Upon the onset of downstream submergence, where rising tailwater levels impede free discharge and elevate the required upstream head for a constant flow rate, the formulation transitions to the following expression [12]:

$$Q = C_u\sqrt{2g}\, WT^{TE}B^{BE}(3H)^{HE} \quad (8)$$

Once the ratio of tailwater to upstream energy head over the spillway exceeds 0.67, submergence starts. Equations compute a weighted flow across the transition zone, smoothly shifting the calculation to the fully submerged orifice equation as submergence reaches 0.80. The fully submerged equation is shown in Eq. 6 [12]. When the standard (default) exponents in the interface (TE=0, BE=1 and HE=0.5) are substituted, the equation transforms into the classic orifice/gate flow form where C_s, submerged discharge coefficient is typically 0.8.

2.2 Experimental Setup and Procedure

The TecQuipment H12 – 5 Meter Flow Channel system used in this study (Fig. 4) is an experimental laboratory apparatus designed to investigate the hydraulic characteristics of open-channel flows. The system operates on the principle of continuous closed-loop water recirculation, enabling controlled and precise analysis of various flow conditions. Developed to facilitate the practical observation of open-channel flow theories, the apparatus is widely used in education and research, particularly in hydraulic engineering and fluid mechanics [16].

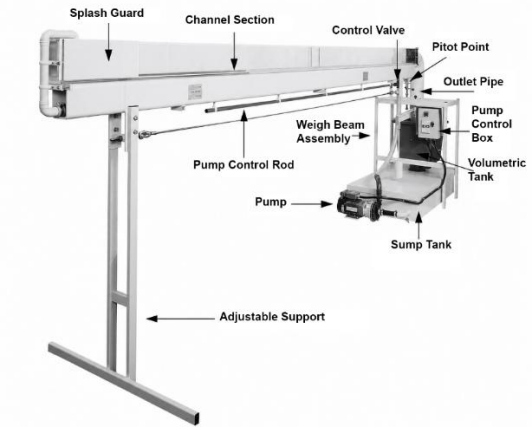


Fig. 4. Tecquipment h12 – 5 Metre Flow Channel

Water from the system's sump tank is delivered to the channel inlet via a centrifugal pump. The flow discharge is regulated by a precision control valve at the inlet section, enabling experiments under various discharge conditions. To promote a more uniform flow pattern along the channel, flow straighteners are employed, thereby mitigating turbulence effects and enhancing measurement accuracy. Additionally, the channel bed slope can be adjusted using an adjustable jacking mechanism, enabling observation of flow behavior across different slope configurations. This feature enables experimental investigation of various flow regimes, including uniform, critical, and supercritical flow [16].

The experiments were conducted using the TecQuipment h12 open-channel flume system, featuring a rectangular cross-section with a length of 5.0 m, a height of 175 mm, a width of 75 mm, and a constant bed slope ($S_o = 0.00506$). Water was supplied via a closed-loop recirculation system powered by a centrifugal pump. The flow discharge (Q) was precisely regulated using an inlet valve and volumetrically verified using the integrated calibration tank combined with time-interval measurements ($\Delta V / \Delta t$).

Prior to installing the gate, baseline experiments were performed in the ungated flume at a constant bed slope ($S_0 = 0.00506$) to determine the channel roughness coefficient. In the second step, a vertically moving cylindrical block (diameter D = 125mm) was installed at the midpoint of the channel (at Station 2.5 m). Headwater and tailwater depths, as well as water surface profiles along the channel, were recorded using point gauges with a measurement precision of ±1mm (Fig. 5).

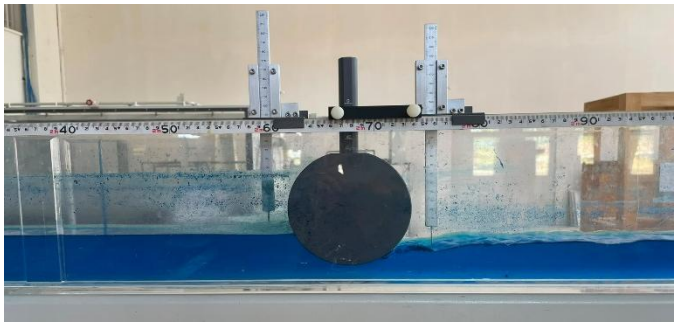


Fig. 5. Experimental setup

2.3 Numerical Modelling and Calibration in HEC-RAS

The un-gated flume model was configured with a length of 5.0 m, a height of 175 mm, a width of 75 mm, and a constant bed slope of S_0 = 0.00506 (Fig. 6-a&c). Cross sections were interpolated at 20 cm intervals along the channel (Fig. 6-b).

In the first phase, the channel bed roughness coefficient (Manning's n) was determined through a combined experimental and numerical calibration process. Baseline physical experiments were initially conducted in the un-gated flume across four distinct discharge rates (Q = 0.69, 1.03, 1.11, and 1.50 L/s), and the corresponding water depths were measured under uniform flow conditions. Subsequently, numerical simulations were executed in HEC-RAS using the same discharge rates with various candidate Manning roughness coefficients (n = 0.010, 0.011, and 0.012). The representative roughness coefficient for the channel was then established by comparing the numerically calculated water depths against the experimentally measured values.

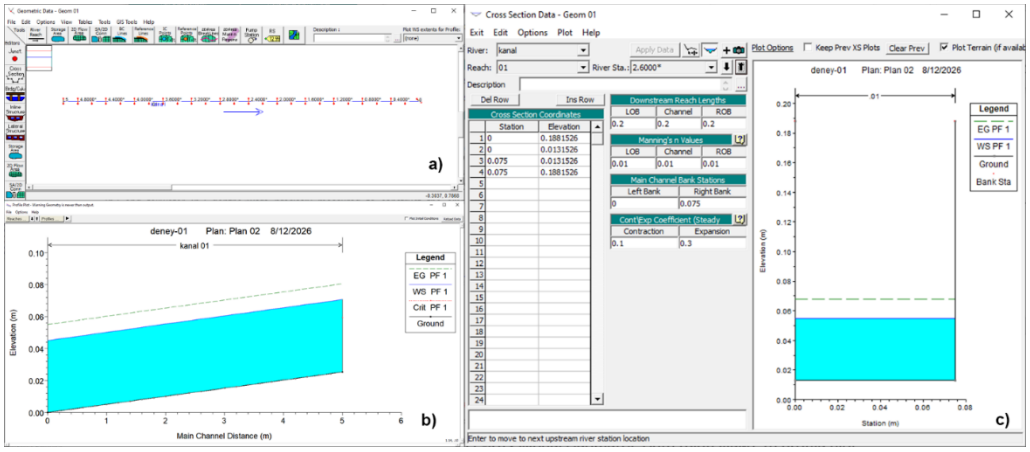


Fig. 6. a) HEC-RAS Model Geometric Data (plan view), b) cross section at 2.60m, c) profile plot

Subsequently, the cylindrical block was incorporated into HEC-RAS as an "Inline Structure" at the channel midpoint (Station 2.5 m; Fig. 7). While HEC-RAS offers standard gate geometries, such as sluice, radial, overflow, and user-defined shapes, the cylindrical obstacle used in this study does not strictly fit any single default category. However, because it combines the vertical movement mechanism of a sluice gate with the circular contact surface of a radial gate, both the sluice and radial-gate formulations can be implemented separately to evaluate their predictive capabilities (Fig. 8).

In HEC-RAS, when default theoretical exponents are adopted for the radial gate configuration, namely, the trunnion exponent (TE = 0), opening exponent (BE = 1), and head exponent (HE = 0.5), the radial formulation mathematically simplifies to the classic sluice gate equation (Eq. 4). Consequently, the numerical simulations were executed using the Sluice Gate methodology. The submerged orifice coefficient (C_s) was retained at its default value of 0.8. Although measured water surface elevations were prescribed at the channel boundaries, HEC-RAS internally computes the upstream energy head based on the specified opening (B) and discharge coefficient (C_u). Standard flat-planar sluice gate guidelines typically recommend C_u values in the range of 0.50 - 0.70. However, this conventional range underestimates the hydraulic efficiency of the curved cylindrical profile, causing the 1D model to significantly overpredict upstream water depths due to exaggerated contraction loss assumptions. To accurately capture the streamlined flow behavior and effectively compensate for the reduced vena contracta effects of the curved cylindrical block, the discharge coefficient was extended

beyond conventional flat-gate limits and systematically evaluated across C_u = 0.70, 0.80, and 0.85.

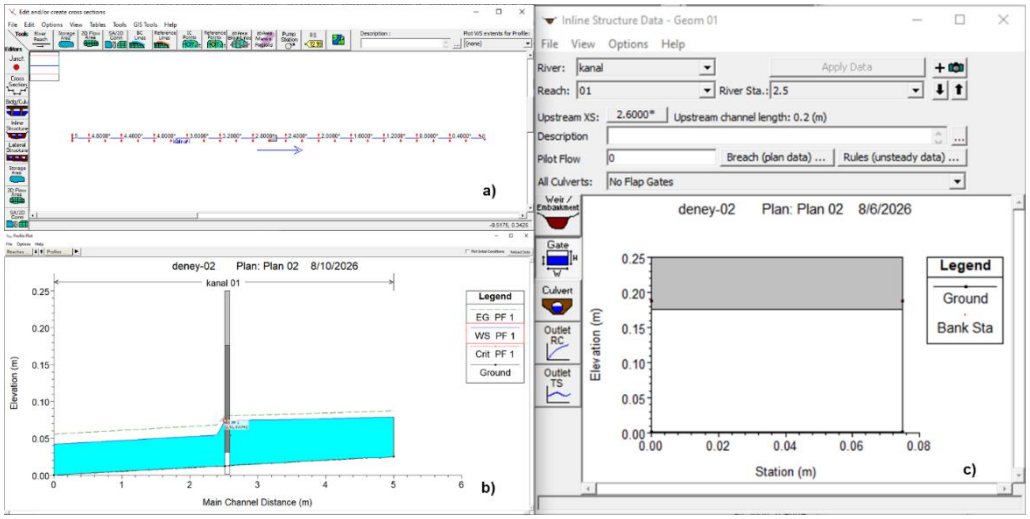


Fig. 7. a) HEC-RAS Model Geometric Data (plan view), b) profile plot and c) Inline structure data window

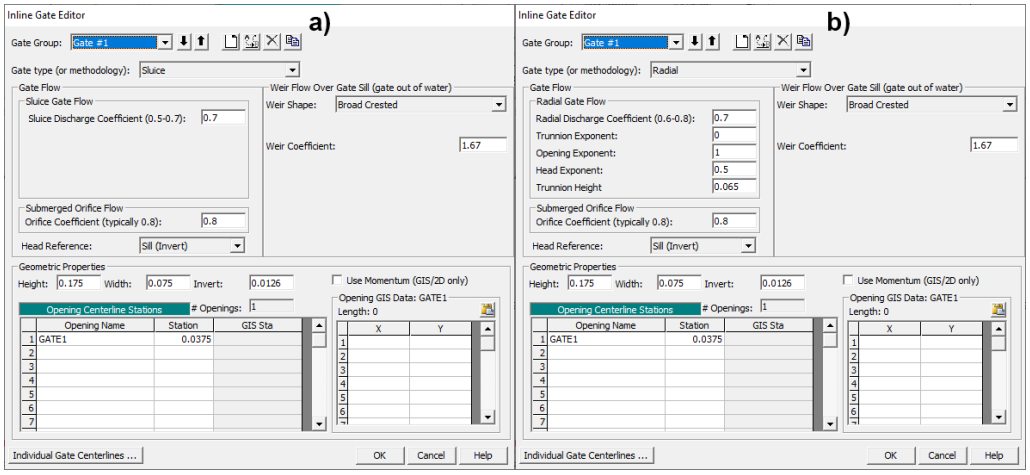


Fig. 8. Comparison of sluice and radial gate editor interfaces in HEC-RAS, a) sluice gate, b) radial gate

The observed discharges (Q1 = 1.64 L/s, Q2 = 1.49 L/s, and Q3 = 1.24 L/s) were prescribed as steady-flow data at the channel inlet. Simulations were executed under mixed flow regime conditions to capture both subcritical and supercritical flow transitions (including hydraulic jumps). The experimentally measured headwater depths and tailwater depths were prescribed as "Known Water Surface Elevations" at the upstream and downstream cross sections, respectively, ensuring that the boundary conditions accurately reflected the physical flume behavior. A total of 27 distinct scenarios were formulated based on discharge, gate opening, and discharge coefficient parameters. Simulation scenarios were named according to the gate type, flow rate, and gate opening configured in the model. The scenario designations based on these parameters are listed in Table 1.

Table 1. Scenario codes, Modeled gate type, discharge, and gate openings

Discharge Coefficient (C_u)	**Discharge (L/s)**	**Gate Openings (mm)**
Cu = 0.70	Q1 = 1.64 L/s	(a): B = 14 mm
Cu = 0.80	Q2 = 1.49 L/s	(b): B = 24 mm
Cu = 0.85	Q3 = 1.24 L/s	(c): B = 34 mm

3 Results and Discussion

3.1 Manning's "n" Calibration Results

Manning roughness calibration results under baseline conditions are shown in Table 2.

Table 2. Manning roughness calibration results under un-gated baseline conditions.

Measured		Calculated			Exact	Relative Error
Discharge Q (L/s)	Depth (mm)	Depth (mm) (n=0.010)	Depth (mm) (n=0.011)	Depth (mm) (n=0.012)	Manning's n (n_{intp})	(n=0.010) (%)
1.50	43	39.48	42.39	45.26	0.0116	8.19%
1.11	32	31.69	33.95	36.17	0.0103	0.97%
1.03	30	29.97	32.09	34.17	0.0100	0.10%
0.69	23	22.45	23.98	25.48	0.0105	2.39%
				Average:	**0.0106**	**2.91%**

As presented in Table 2, the exact interpolated roughness values (n_{intp}) ranged between 0.0100 and 0.0116, yielding a mean Manning coefficient of n_{avg} = 0.0106. Adopting n = 0.010 yielded excellent agreement with experimental depth measurements, with a mean absolute percentage error of only 2.91% and near-perfect predictions for medium-to-low discharges (0.10% error at 1.03 L/s). Consequently, n = 0.010 was selected as the representative bed roughness coefficient for all subsequent gated simulations.

3.2 Water Surface Profile Comparisons Under Various Q and Cu Conditions

To address the overprediction of upstream water depths caused by standard flat-gate assumptions, a systematic sensitivity analysis of the discharge coefficient (C_u) was performed across values of 0.70, 0.80, and 0.85 under different scenarios (Table 3).

Table 3. Measured and HEC-RAS simulated water depths and relative error percentages across different Cu values

Scen.	Discharge (L/s)	Measured			Modelled							
					Cu=0.7		Cu=0.8		Cu=0.85			
		B (mm)	HW (mm)	TW (mm)	HW (mm)	TW (mm)	HW (mm)	TW (mm)	HW (mm)	TW (mm)	HW Err (%)	TW Err (%)
Q1-a	1.64	14	169	43	191.15	41.35	178.55	41.35	168.15	41.35	-0.50%	-3.83%
Q1-b	1.64	24	55	43	82.45	41.85	55.95	41.85	53.45	41.85	-2.81%	-2.67%
Q1-c	1.64	34	55	43	54.85	42.15	56.15	42.15	54.65	42.15	-0.63%	-1.97%
Q2-a	1.49	14	139	38	182.95	37.85	155.95	38.45	137.85	37.85	-0.83%	-0.39%
Q2-b	1.49	24	49	38	67.15	37.95	79.65	38.45	48.95	37.95	-0.10%	-0.12%
Q2-c	1.49	34	49	41	51.45	39.95	68.65	39.45	50.65	39.95	3.37%	-2.55%
Q3-a	1.24	14	96	34	140.95	33.35	107.05	33.35	94.55	33.35	-1.51%	-1.90%
Q3-b	1.24	24	45	34	44.55	34.65	45.75	34.65	44.05	34.65	-2.10%	1.92%
Q3-c	1.24	34	43	36	45.35	36.15	43.15	36.15	42.85	36.15	-0.34%	0.43%
									Average:		**-0.61%**	**-1.23%**

As summarized in Table 3, adopting the conventional sluice gate coefficient (C_u = 0.70) resulted in an overestimation of headwater elevations (HW), as it fails to account for the reduced flow contraction characteristic of cylindrical geometries. Increasing the coefficient to C_u = 0.80 substantially improved the water surface profile agreement. The optimal predictive performance was achieved at C_u = 0.85, yielding near-perfect alignment with physical flume measurements. Under C_u = 0.85, the mean percentage error for upstream headwater (HW) and downstream tailwater (TW) depths was reduced to -0.61% and -1.23%. This demonstrates that

calibrating the discharge coefficient to C_u=0.85 successfully captures the superior hydraulic efficiency and reduced energy head losses of vertically moving cylindrical gates within 1D HEC-RAS formulations.

Fig. 9 illustrates the simulated longitudinal water surface profiles along the 5.0 m flume for the representative discharge Q_2 = 1.49 L/s under three different gate openings (B = 14, 24, and 34 mm) at the calibrated discharge coefficient (C_u = 0.85).

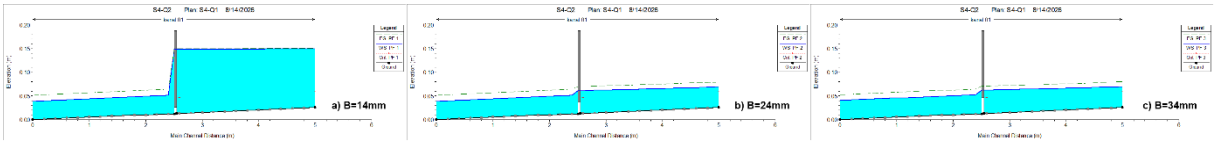


Fig. 9. Profiles for scenarios a) Q2-B=14mm, b) Q2-B=24mm and c) Q2-B=34mm

As observed in Fig 9-a (Scenario Q2-a, B = 14 mm), the constricted gate opening creates a pronounced backwater accumulation upstream (Station 2.5 m to 5.0 m), where the water surface elevates sharply to approximately 137.85 mm. In contrast, downstream of the cylindrical block (Station 0.0 m to 2.5 m), the flow discharges as a supercritical stream before gradually transitioning along the mild slope (S_0 = 0.00506). As the gate opening increases to B = 24 mm (Fig. 9-b) and B = 34 mm (Fig. 9-c), the upstream obstruction is significantly relieved, causing the headwater depth to drop progressively from 137.85 mm to 48.95 mm and 50.65 mm, respectively. This transition highlights that for moderate-to-large gate openings, the cylindrical obstacle exerts minimal choking effects on the channel conveyance capacity, aligning closely with the experimentally recorded water surface profiles.

Fig. 10 illustrates the longitudinal variation of the Froude number (Fr) along the flume for the representative discharge Q2 = 1.49 L/s across three gate openings (B = 14, 24, and 34 mm}$). The abrupt structural transition at the cylindrical inline structure (Station 2.5 m) induces distinct hydrodynamic responses across the channel reaches. For Scenario Q2-a (B = 14 mm, Fig. 10-a), the pronounced upstream backwater accumulation causes a substantial deceleration of flow velocity, resulting in deeply subcritical conditions upstream (Fr = 0.12 - 0.14). As the flow passes beneath the constricted cylindrical opening and discharges downstream (Station 2.4 m to 0.0 m), the velocity accelerates significantly, driving the downstream Froude number up to approximately Fr= 0.83 - 0.85. In contrast, as the gate opening increases to B = 24 mm (Fig. 10-b) and B = 34 mm (Fig. 10-c), the diminished upstream obstruction reduces water depth and accelerates the approach velocity, raising the upstream Froude number to moderate subcritical levels (Fr = 0.60 - 0.68). Across all scenarios, the downstream reach maintains high subcritical to near-critical flow conditions (Fr = 0.82 - 0.85), reflecting stable conveyance behavior under the calibrated Manning roughness (n = 0.010).

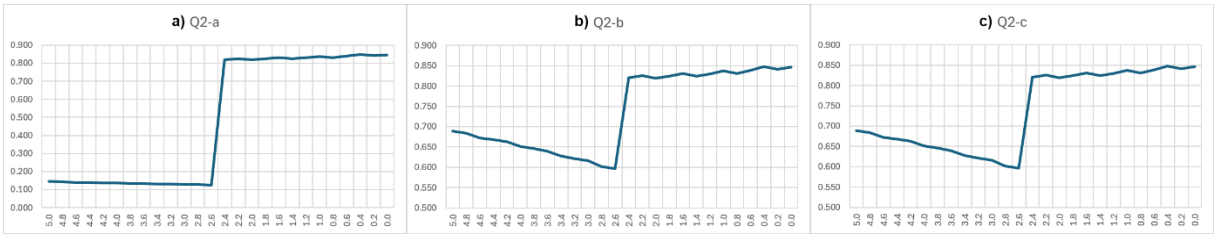


Fig. 10. Froude number distribution along the channel for the scenarios a) Q2-a, b) Q2-b and c) Q2-c

Fig. 11 presents the scatter plots and linear regression relationships between experimentally measured and HEC-RAS simulated water depths for both headwater (HW) and tailwater (TW) across the evaluated discharge coefficients (C_u = 0.70, 0.80 and 0.85). For the upstream

headwater depth (HW, left panel), adopting the standard planar-gate discharge coefficient (C_u = 0.70) resulted in an overestimation slope of y = 1.2334x (R^2 = 0.985). Increasing the coefficient to C_u = 0.80 mitigated this overprediction, improving the regression slope to y = 1.1066x (R^2 = 0.989). The highest degree of correlation and numerical accuracy was achieved at C_u = 0.85, yielding a near-unity slope (y = 0.9928x) and an outstanding determination coefficient (R^2 = 0.999). Conversely, the downstream tailwater depths (TW, right panel) demonstrated consistent, robust agreement across all calibrated coefficients, with regression slopes ranging from y = 0.9853x to y = 0.9869x and determination coefficients exceeding R^2 = 0.999. These regression metrics quantitatively confirm that extending the discharge coefficient to C_u = 0.85 eliminates the artificial upstream head accumulation caused by 1D flat-gate formulations and accurately replicates the physical flow behavior beneath the cylindrical obstacle.

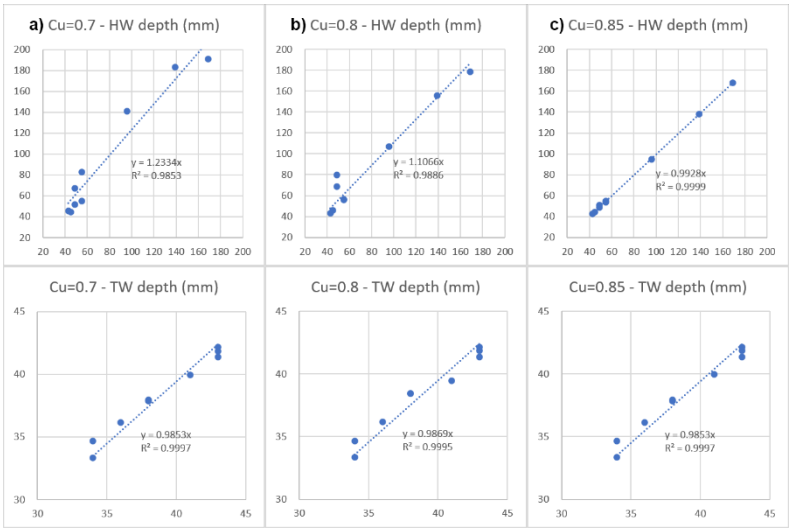


Fig. 11. Scatter plot of measured vs. modelled HW and TW depths a) Cu=0.7, b) Cu=0.8 and c) Cu=0.85

4 Conclusions

In this study, the hydraulic performance and flow characteristics of a vertically moving cylindrical gate were investigated through physical flume experiments and one-dimensional numerical simulations in HEC-RAS. Baseline physical experiments and numerical modeling in the ungated flume demonstrated that a Manning roughness coefficient of n = 0.010 provides excellent agreement with experimental water depths, achieving a mean absolute percentage error of only 2.91%. Under standard theoretical exponents (TE = 0, BE = 1, and HE = 0.5), the HEC-RAS radial gate equation mathematically reduces to the classic planar sluice gate equation. Consequently, adopting the sluice gate methodology in 1D numerical modeling simplifies the computational setup while fully retaining hydraulic validity. Conventional discharge coefficient values recommended for planar sluice gates (Cu = 0.50 - 0.70) significantly overestimate upstream headwater depths (HW) due to exaggerated flow contraction assumptions. Extending the coefficient to Cu = 0.85 successfully captured the streamlined boundary layer and reduced vena contracta effects characteristic of the curved cylindrical surface. At Cu = 0.85, the HEC-RAS model exhibited remarkable agreement with physical measurements across all modeled discharges (Q = 1.24 - 1.64 L/s) and gate openings (B = 14, 24, and 34 mm). The mean relative percentage errors for upstream headwater (HW) and downstream tailwater (TW) were reduced to -0.61% and -1.23%, respectively, with mean absolute errors of less than 1.0 mm and linear correlation coefficients exceeding R^2 = 0.999. The longitudinal Froude number distributions confirmed that the cylindrical obstruction creates

deeply subcritical approach flow upstream (Fr = 0.12 - 0.14) at small openings, which rapidly accelerates to high subcritical and near-critical conditions downstream (Fr = 0.82 - 0.85). Overall, these findings demonstrate that standard 1D HEC-RAS sluice gate formulations can accurately predict the hydraulic behavior of vertically moving cylindrical control structures, provided that the discharge coefficient is calibrated to account for the reduced contraction losses (Cu = 0.85).

References

1. Chow, V.T., *Open channel hydraulics*. 1959: McGraw-Hill, New York.
2. Özbek, T., *Açık Kanal Akımlarının Hidroliği ve Hidrolik Yapılar*. 2009, Ankara: Teknik Yayınevi, Ankara.
3. Erbisti, P.C.F., *Design of Hydraulic Gates*. 2nd ed. 2014: CRC Press, London.
4. Novák, P., et al., *Hydraulic structures*. 2017: CRC Press, London.
5. USBR, *Water Measurement Manual, A Water Resources Technical Publication*. 2021, U.S. Department of the Interior Bureau of Reclamation: Washington D.C.
6. Severi, A., et al., *Experimental investigation on discharge coefficient and energy loss amount changes of a cylindrical weir-gate with vertical movement.* Journal of Civil and Environmental Engineering, 2015. 44(77): p. 65-78.
7. Song, C.G., S.W. Park, and J. Shin, *An Experimental Study of Flow and Turbulence Properties near the Rising Sector Gate Mouth Considering the Gate Opening with a PIV Measuring System.* Water, 2024. 16(20): p. 3004.
8. Abbaszadeh, H., R. Daneshfaraz, and R. Norouzi, *Experimental Analysis of Hydraulic Behavior of Flow through Sluice Gates with Variable Openings.* Turkish Journal of Hydraulic, 2026(2).
9. Şimşek, O., M. Kösen, and V. Gümüş, *Farklı batıklık oranlarına sahip batık hidrolik sıçramanın sayısal modellemesi.* Adıyaman Üniversitesi Mühendislik Bilimleri Dergisi, 2021. 8(15): p. 427-441.
10. Ateş, H. and O. Yıldız, *Kapak Altı Hidrolik Sıçramanın Deneysel ve Sayısal Yöntemlerle İncelenmesi.* Türk Hidrolik Dergisi, 2023. 7(2): p. 1-14.
11. HEC, *HEC-RAS User's Manual*. 2023, US Army Corps of Engineers, Hydrologic Engineering Center.
12. Brunner, G., *HEC-RAS River Analysis System Version 6.0 Beta - Hydraulic Reference Manual.* Hydrologic Engineering Center, Davis, California, US, 2020.
13. Khalili Shayan, H., et al., *Developing discharge-head equation for radial-gated spillways based on physical modeling.* Flow Measurement and Instrumentation, 2024. 100: p. 102692.
14. Shamsi, A. and A.H. Azimi, *Numerical investigations of cylindrical weir-gates with a flow extender.* Flow Measurement and Instrumentation, 2025. 102: p. 102833.
15. Swamee, P.K., *Sluice-Gate Discharge Equations.* Journal of Irrigation and Drainage Engineering, 1992. 118(1): p. 56-60.
16. TecQuipment, *H12 Flow Channel 5 Metre User Manual*. 2008.

Author Contribution Statement

- *Conceptualization:* Kağan CEBE
- *Methodology:* Kağan CEBE
- *Investigation:* Yusuf Buğra AKSOY, Bilgin Furkan BAYRAK
- *Writing – Original Draft:* Kağan CEBE
- *Writing – Review & Editing:* Aslı ÜLKE KESKİN

Publication Note
This paper was peer-reviewed, accepted for presentation, and included in the proceedings of the ACE2026 – International Conference on Advances in Civil Engineering, held on 12–14 October 2026 in Trabzon, Türkiye.

This paper may be cited as follows:
Cebe, K., Aksoy, Y. B., Bayrak, B. F. and Ulke Keskin, A., "Experimental and Numerical Investigation of Flow Characteristics and Water Surface Profiles Under a Vertically Moving Cylindrical Gate Using HEC-RAS," in Proceedings of the ACE2026 – International Conference on Advances in Civil Engineering, Trabzon, Türkiye, 12–14 October 2026.

Spatiotemporal Characteristics of Compound Dry Hot Stress Events in Trabzon Province

Burak Çırağ[1,*] İlteriş Taşkolu[2], Reşat Acar[3], Mahmut Güngör[4]
[1] 0000-0002-7721-5128, Atatürk University, Civil Engineering Department, Erzurum, Türkiye, burak.cirag@atauni.edu.tr
[2] 0000-0002-6230-9148, İstanbul Esenyurt University, Vocational School, İstanbul, Türkiye, ilteristaskolu@esenyurt.edu.tr
[3] 0000-0002-0653-1991, Atatürk University, Civil Engineering Department, Erzurum, Türkiye, racar@atauni.edu.tr
[4] 0000-0001-8019-1430, Pamukkale University, Civil Engineering Department, Denizli, Türkiye, mgungor@pau.edu.tr

Abstract. The frequency and severity of meteorological extremes have increased under climate change conditions. In particular, compound dry hot events caused by the simultaneous occurrence of low precipitation, high temperature, and low relative humidity create significant pressure on hydroclimatic systems. In this study, the spatiotemporal characteristics of compound dry hot stress events were investigated using meteorological stations in Trabzon Province. Monthly precipitation, temperature, and relative humidity data covering the 2012-2025 period were utilized. Compound stress months were identified based on precipitation values below the 25th percentile, temperature values above the 75th percentile, and relative humidity values below the 25th percentile. For the identified compound events, duration, severity, intensity, and peak stress parameters were calculated. In addition, a 90th percentile based rare event frequency analysis was performed to evaluate rare compound event behavior. The SPI-1 benchmark comparison showed that 103 months were jointly detected by both approaches, whereas 46 months were identified only by the compound stress framework. The results indicated that although Trabzon exhibits humid climate characteristics, significant spatial differences exist among the stations in terms of compound stress behavior. Marked differences were observed among the stations in terms of event frequency, duration, severity, and intensity. Higher elevation stations generally exhibited greater compound stress severity and persistence. Rare compound event analysis revealed episodic stress behavior with high severity values at several stations. The findings demonstrate that compound meteorological stress structures may develop even in humid regions and exhibit considerable spatial variability.
Keywords: Compound dry hot events; Meteorological stress; Spatial analysis; SPI; Trabzon.

1 Introduction

Drought is a natural disaster and climate-related phenomenon that can be observed in any region of the world, and the increasing prevalence of both extreme drought and extreme wet conditions in recent years has further heightened the importance of research in this field [1]. In addition, the simultaneous occurrence of drought and high temperature conditions leads to the formation of compound dry-hot events. Such events can have more severe consequences than the effects of a single drought or heatwave and can challenge the adaptability of natural systems [2,3].

The coverage, quality, and record length characteristics of the data sets used in drought studies directly affect the level of uncertainty in drought index predictions [4,5]. Missing or insufficient data can introduce uncertainty in the representation of drought conditions. Preferences for the dry indicator, threshold, and variable combinations used in compound event analyses can also

create differences in the determined event frequency, severity, and spatial pattern [3]. Therefore, the evaluation of atmospheric dryness indicators along with precipitation deficit and high temperature contributes to a more comprehensive definition of compound stress conditions [8].

In the literature, compound dry-hot events have been evaluated using different temporal scales and variable combinations. Bevacqua et al. [2] have demonstrated the decisive effect of mean precipitation trends on the occurrence of future compound hot-dry events using large ensembles of climate models. Hosseinzadehtalaei et al. [3] have shown that the use of different dry indicators has caused significant changes in the projected event probability and uncertainty results. Wang et al. [6] combined daily SZI and STI values using Copula to develop a daily-scale compound dry-hot index and evaluated the method's applicability across seven different climate regions. Yin et al. [7] examined the vegetation vulnerability under compound heat and drought stress using the Vine Copula approach based on SPI and STI. Zhao et al. [8] have demonstrated the importance of the atmospheric dryness component in compound hazard assessment by evaluating high temperature, low relative humidity, and high wind conditions together.

The aim of this study is to determine the spatial and temporal characteristics of compound dry-hot stress events in the province of Trabzon, which has a humid climate and distinct topographic variability, and to compare the obtained results with SPI-1 based drought conditions. In this context, monthly precipitation, temperature, and relative humidity data for the period 2012-2025 from 17 meteorological stations were used. For compound conditions, it was based on the precipitation value being below the 25th percentile and the temperature value being above the 75th percentile [11]. This bivariate definition has been extended by adding the condition that the relative humidity value is below the 25th percentile to represent the effect of atmospheric dryness [8]. The identified events have been examined using duration, severity, intensity, and peak stress metrics. Additionally, rare event characteristics have been evaluated and elevation dependency analysis has been applied. The original contribution of the study is its expansion of the literature framework based on precipitation deficit and high temperature by incorporating low relative humidity, evaluating compound stress conditions through three meteorological variables, and comparing the obtained results with the SPI-1 benchmark.

2 Materials and Methods

2.1 Study Area and Meteorological Dataset

Trabzon is located on the coast of Turkey's Eastern Black Sea Basin, between the latitudes 40°30′-41°30′ north and the longitudes 38°30′-40°30′ east, and has an area of 4,664 km². The province is characterized by mild climate conditions, where summers are not excessively hot and winters are not excessively cold [9]. A total of 17 meteorological stations located throughout Trabzon were included in the study. The data coverage information for the station codes, observation periods, and the precipitation, temperature, and relative humidity data necessary for compound analysis, calculated from records where these data are present in the same month, is presented in Table 1. Station elevation information was obtained from the Turkish State Meteorological Service together with the station metadata.

Table 1. Characteristics and data coverage of the meteorological stations used in the study

Station	Station code	Elevation m	Observation period	Data coverage %
Trabzon Bölge	17037	25	2012-2025	85.7
Trabzon Havalimanı	17038	39	2012-2025	99.4
Çaykara/Uzungöl	17569	1114	2012-2025	100
Akçaabat	17626	3	2012-2025	100
Maçka/Altındere Sümela	17714	1030	2012-2025	100
Of/Fidanlık	17775	6	2012-2025	92.9
Düzköy	18229	622	2012-2025	91.7
Tonya/Kalınçam	18230	1100	2012-2025	94
Beşikdüzü	18231	374	2012-2025	91.7
Hayrat/Pazarönü	18232	395	2012-2025	92.9
Arsin	18233	169	2012-2025	92.9
Dernekpazarı	18570	721	2012-2025	84.5
Köprübaşı/Beşköy	18571	975	2012-2025	84.5
Maçka/Örnekalan Köyü	18572	955	2012-2025	83.9
Çarşıbaşı/Yoroz	18573	370	2012-2025	83.3
Sürmene/Deniz Bilimleri Enstitüsü	18574	5	2012-2025	85.1
Vakfıkebir/Hamzalı Köyü	18575	845	2012-2025	82.7

2.2 Compound Dry Hot Stress Event Identification and Analysis Framework

Compound dry-hot events are generally defined by the occurrence of dry and hot conditions simultaneously or in close periods [10, 12]. In the identification of these events, percentile-based thresholds that take into account regional climate characteristics are also commonly used alongside absolute thresholds [10]. In a study conducted on a monthly scale, the simultaneous occurrence of precipitation values below the 25th percentile and temperature values above the 75th percentile was considered a compound dry-warm event [11].

Based on this literature framework, in the present study, it was deemed necessary for a month to be classified as a compound dry-hot stress month if the precipitation value is below the 25th percentile, the temperature value is above the 75th percentile, and the relative humidity value is below the 25th percentile simultaneously. Threshold values were calculated separately for each meteorological station and calendar month to account for local and seasonal climate variability effects. Because the percentile thresholds were estimated separately for each calendar month, each threshold was based on approximately 10–14 observations per station depending on data availability. Therefore, some uncertainty may arise from the limited sample size used for monthly percentile estimation. By adding the condition of low relative humidity to the analysis, the traditional precipitation-temperature based bivariate definition was expanded, and the effect of atmospheric dryness was also intended to be represented within the compound stress structure [8]. Months with missing records for any variable were excluded from the evaluation.

In the literature, compound dry-hot events are generally evaluated based on different characteristics such as frequency, severity, duration, and magnitude [10]. In this study, consecutive compound stress months have been grouped as a single compound event. Duration shows the number of consecutive compound months that continue throughout an event. Severity

represents the cumulative stress level during the event, intensity represents the average stress level within the event, and peak stress represents the highest stress level reached throughout the event. These characteristics were used not to create a new index but to compare and summarize the structure of the identified events on a station basis.

For each compound month, the normalized monthly stress score was calculated using the dry, hot, and atmospheric dryness components. The dry component was calculated as the difference between the 25th percentile precipitation threshold and the observed precipitation, normalized by the precipitation interquartile range. Hot component was calculated by dividing the excess of the observed temperature value over the 75th percentile threshold by the temperature interquartile range value. The atmospheric dryness component, on the other hand, is obtained by dividing the difference between the 25th percentile relative humidity threshold and the observed relative humidity by the relative humidity interquartile range value. These three components have been defined to produce a positive stress contribution only in the months when compound conditions occur. The monthly stress score has been calculated as the sum of the three component values. Event severity shows the total of monthly stress score values over consecutive compound months. Event intensity has been calculated as the ratio of the event severity value to the duration value. Peak stress, on the other hand, refers to the highest monthly stress score value obtained during the event.

Station-based event frequency is calculated by expressing the ratio of the number of compound months to the number of valid months for the same station as a percentage. The persistence ratio has been evaluated as the ratio of the number of compound events with a duration value of two months or longer to the total number of compound events. These metrics were used to examine the associations between station elevation and compound stress characteristics.

To compare the results obtained with the compound approach with an independent drought indicator that operates solely on precipitation deficit, SPI-1 was calculated using monthly precipitation data. SPI is based on representing precipitation values with a probability distribution and converting the obtained probability values into a standard normal distribution form [13]. Months with an SPI-1 value of -1 or lower are classified as drought months. The comparison of the compound method and SPI-1 was conducted over the common months where valid data was available for both analyses. The months identified by both methods were defined as overlap months, the months identified only by the compound approach as compound only months, and the months identified only by SPI-1 as SPI only months. The agreement rate has been used to show the overall consistency of the months classified in the same way by both approaches.

WMO recommends at least a 30-year continuous monthly precipitation record for reliable SPI estimation [13]. Due to the current study covering the period from 2012 to 2025, the SPI-1 results have been evaluated not as a long-term drought climatology indicator but as an exploratory benchmark providing a comparison with the compound approach. The SPI-1 comparison was recalculated using the same valid station-month records included in the final compound event analysis.

To determine the upper tail stress conditions among compound events, events where at least one of the severity, intensity, or peak stress metrics exceeds its global 90th percentile threshold value have been classified as rare compound events. This threshold has been used not to produce a long-term return period, but to distinguish the structure of upper tail compound stress events within the current observation period. For each station, rare event count, maximum rare severity, dominant season, and empirical recurrence characteristics within the observation period have been evaluated.

To examine the relationships between topographic variability and compound stress behavior, station elevation was compared with event frequency, event count, total severity, mean intensity, persistence ratio, and rare event count. Pearson correlation was used for linear

association and Spearman rank correlation for monotonic association. The obtained correlations only indicate the level of association between the variables and have not been interpreted as a causal relationship.

3 Results and Discussion

3.1 General Characteristics of Compound Dry Hot Stress Events

The distribution of compound dry hot stress conditions across Trabzon has been evaluated based on station-based occurrence and event characteristics. In the examined period of 2012–2025, a total of 149 compound months were identified for 17 meteorological stations. When consecutive compound months are considered under a single event, a total of 141 compound events have been obtained. The values of valid months, compound months, event count, maximum duration, total severity, and mean intensity on a station basis are provided in Table 2.

Table 2. Station based summary of compound dry hot stress characteristics

Station	Valid months	Compound months	Event count	Max duration	Total severity	Mean intensity
Köprübaşı Beşköy	142	17	15	2	34.539	2.066
Vakfıkebir Hamzalı Köyü	139	12	11	2	22.176	1.883
Maçka Örnekalan Köyü	141	12	11	2	27.955	2.274
Dernekpazarı	142	11	8	4	23.493	1.797
Hayrat Pazarönü	156	12	12	1	21.311	1.776
Çaykara Uzungöl	168	12	11	2	16.251	1.353
Maçka Altındere Sümela	168	11	11	1	15.85	1.441
Sürmene Deniz Bilimleri Enstitüsü	143	8	8	1	15.042	1.88
Beşikdüzü	154	8	8	1	12.084	1.51
Trabzon Havalimanı	167	7	7	1	8.322	1.189
Akçaabat	168	7	7	1	5.665	0.809
Düzköy	154	6	6	1	11.613	1.935
Of Fidanlık	156	6	6	1	9.993	1.665
Arsin	156	6	6	1	10.698	1.783
Çarşıbaşı/Yaroz	140	5	5	1	8.606	1.721
Tonya Kalınçam	158	5	5	1	11.756	2.351
Trabzon Bölge	144	4	4	1	4.586	1.146

The results in Table 2 reveal that the compound stress behavior exhibits significant spatial variability throughout Trabzon. Köprübaşı Beşköy has become the station with the highest occurrence value, with 17 compound months and 15 compound events. The same station ranked first in cumulative stress with a total severity of 34.539. In contrast, the Trabzon Bölge has shown the lowest occurrence value with only four compound months and four events.

It is observed that the station ranking varies according to the used stress metric value. The highest mean intensity value was determined to be 2.351 for the Tonya Kalınçam station, while Maçka Örnekalan Köyü with 2.274 and Köprübaşı Beşköy with 2.066 stood out. In terms of maximum duration, Dernekpazarı stands out with a four-month event compared to the other stations. This result shows that the frequency, duration, severity, and intensity values do not

represent the same compound stress characteristic. In the evaluation of compound dry hot events, considering different event characteristics values together is therefore important [10].

3.2 Severe Compound Event Characteristics

To highlight the most significant stress periods within compound events, they have been ranked according to their severity values. The ten events with the highest severity values are presented in Table 3. This assessment allows for the observation of the difference between cumulative stress resulting from long-duration events and short-duration events that produce high intensity and peak stress.

Table 3. Top severe compound dry hot stress events

Rank	Station	Start	End	Duration	Severity	Intensity	Peak stress
1	Dernekpazarı	2014-03	2014-06	4	12.157	3.039	9.061
2	Köprübaşı Beşköy	2014-03	2014-03	1	9.911	9.911	9.911
3	Vakfıkebir Hamzalı Köyü	2014-03	2014-03	1	7.842	7.842	7.842
4	Maçka Örnekalan Köyü	2020-09	2020-10	2	5.872	2.936	5.312
5	Hayrat Pazarönü	2012-11	2012-11	1	5.583	5.583	5.583
6	Arsin	2012-11	2012-11	1	5.172	5.172	5.172
7	Maçka Örnekalan Köyü	2014-02	2014-02	1	5.084	5.084	5.084
8	Tonya Kalınçam	2012-11	2012-11	1	4.887	4.887	4.887
9	Köprübaşı Beşköy	2020-09	2020-10	2	3.956	1.978	2.722
10	Maçka Örnekalan Köyü	2023-10	2023-10	1	3.724	3.724	3.724

The highest event severity during the examined period was determined for the Dernekpazarı station between March 2014 and June 2014. This four-month event reached values of 12.157 severity, 3.039 intensity, and 9.061 peak stress. The single monthly event determined for the Köprübaşı Beşköy station in March 2014 produced a severity of 9.911 and the same value of intensity with peak stress. When these two results are evaluated together, it is observed that the cumulative severity value is dependent not only on the peak stress level but also on the event duration characteristic.

In the March 2014 period, the simultaneous occurrence of high severity values at the Dernekpazarı, Köprübaşı Beşköy, and Vakfıkebir Hamzalı Köyü stations is noteworthy. Similarly, severe compound events were identified at the Maçka Örnekalan Village and Köprübaşı Beşköy stations during the September and October 2020 period. The structure observed during the same periods at different stations may indicate the influence of larger-scale meteorological conditions. However, since atmospheric circulation or synoptic pattern analysis was not conducted in the study, this situation has not been evaluated as a causal relationship.

Among the single-month events, the Köprübaşı Beşköy, Vakfıkebir Hamzalı Köyü, Hayrat Pazarönü, Arsin, and Tonya Kalınçam stations stood out with high intensity values. In contrast, the long duration of the Dernekpazarı event value has been decisive in producing high severity.

Therefore, in the evaluation of severe compound stress, it is more balanced to examine not only the maximum or mean values but also the duration, severity, intensity, and peak stress characteristics together [10].

3.3 Comparison with SPI Based Drought Conditions

The relationship between the stress months determined by the compound framework and the SPI-1 drought conditions based solely on the precipitation variable has been evaluated comparatively. The purpose of this comparison is to reveal the extent to which the two approaches identify the same stress condition together and in which periods they differ. In this context, only common station-month records with valid precipitation, temperature, and relative humidity data for both analyses were considered. The overlap, compound only, SPI only, and overall agreement values for the compound framework and SPI-1 results are presented in Table 4.

Table 4. Simplified comparison between compound method and SPI-1

Metric	Value	Interpretation
Common station month records	2596	Months with valid data for both approaches
Compound months	149	Low precipitation, high temperature and low relative humidity occurred together
SPI-1 drought months	442	Precipitation based drought months
Overlap months	103	Both approaches detected stress
Compound only months	46	Compound stress detected without SPI-1 drought classification
SPI only months	339	Precipitation deficit without simultaneous compound atmospheric stress
Overall agreement %	85.2	General monthly agreement level

As a result of the SPI-1 benchmark analysis, 442 drought months were identified within the common station month records, while the compound framework defined 149 compound months. Both approaches showed a common stress condition for 103 months. Accordingly, approximately 69.1% of the compound months overlap with the SPI-1 drought classification, while 46 months, or about 30.9%, are identified solely by the compound framework.

In 339 out of the 442 months classified as drought by SPI-1, compound conditions did not occur simultaneously. This result stems from the fundamental conceptual difference between the two approaches. While SPI-1 determines drought conditions solely based on precipitation anomaly, the compound framework is based on the simultaneous occurrence of low precipitation, high temperature, and low relative humidity conditions in the same month. Therefore, compound only months should not be interpreted as drought events missed by SPI-1. Similarly, SPI only months are not events missed by the compound framework either. Two methods evaluate different hydroclimatic stress structures.

Overall agreement has been calculated as 85.2%. However, this value should not be considered as a standalone method agreement indicator since it includes both event and non-event classification values together. The joint evaluation of overlap, compound only, and SPI only results is more explanatory. Additionally, SPI-1 has been calculated using precipitation records only from the period 2012–2025. Since the longer observation period condition recommended by the WMO was not met, the SPI-1 results were used not as an indicator of long-term drought climatology but solely for exploratory benchmarking purposes [13].

3.4 Rare Compound Event Characteristics

In order to evaluate the upper tail stress structure among compound events, rare event characteristics have been examined. Severity, intensity, or peak stress metrics values exceeding the global 90th percentile threshold value were classified as rare compound events. A total of 17 rare compound events were identified during the observation period, and these events were observed at nine different stations. The station-based rare event count, maximum rare severity, and dominant season are provided in Table 5.

Table 5. Rare compound event characteristics during the 2012-2025 observation period

Station	Rare events	Max rare severity	Dominant rare season
Köprübaşı Beşköy	4	9.911	Autumn
Dernekpazarı	2	12.157	Spring
Maçka Örnekalan Köyü	3	5.872	Autumn
Vakfıkebir Hamzalı Köyü	1	7.842	Spring
Tonya Kalınçam	2	4.887	Autumn
Hayrat Pazarönü	1	5.583	Autumn
Arsin	1	5.172	Autumn
Sürmene Deniz Bilimleri Enstitüsü	2	3.642	Spring
Of Fidanlık	1	3.035	Autumn

In terms of rare event frequency, Köprübaşı Beşköy ranks first with four events, while Maçka Örnekalan Village ranks second with three events. Two rare events have been identified for the Dernekpazarı, Tonya Kalınçam, and Sürmene Marine Sciences Institute stations. In contrast, one rare event was observed for the Vakfıkebir Hamzalı Köyü, Hayrat Pazarönü, Arsin, and Of Fidanlık stations. In terms of maximum rare severity, Dernekpazarı reached the highest value with 12.157. Although Köprübaşı Beşköy produced more rare events, the maximum rare severity value was determined to be 9.911. This difference shows that the rare event frequency and rare event magnitude values do not represent the same risk characteristic.

When evaluating the seasonal distribution, Autumn was determined to be the dominant season in six out of the nine station values, while Spring was the dominant season in three. The fact that the rare compound stress structure is not limited to Summer can be explained by the relative threshold approach used. Since threshold values are calculated separately for each calendar month, the definition of a month as hot or dry is based on the local distribution characteristics of that month rather than the absolute climate value. Therefore, conditions of high temperature, low precipitation, and low relative humidity according to seasonal norms can also create compound stress during the Spring or Autumn periods.

3.5 Elevation Dependency of Compound Stress Metrics

To evaluate the relationship between Trabzon's distinct topographic variability and compound stress characteristics, associations between station elevation and frequency, event count, total severity, mean intensity, persistence ratio, and rare event count were examined. Linear relationships were evaluated using Pearson correlation, while monotonic relationships were assessed using Spearman rank correlation. The obtained correlation coefficients and significance levels are presented in Table 6.

Table 6. Relationship between elevation and compound stress metrics

Metric	Pearson (r)	Pearson (p)	Spearman (rho)	Spearman (p)	Interpretation
Frequency (%)	0.570	0.017	0.452	0.068	positive linear association with $p<0.05$
Event count	0.551	0.022	0.462	0.062	positive linear association with $p<0.05$
Total severity	0.629	0.007	0.681	0.003	positive association with $p<0.05$
Mean intensity	0.521	0.032	0.458	0.064	positive linear association with $p<0.05$
Persistence ratio	0.604	0.010	0.562	0.019	positive association with $p<0.05$
Rare events	0.366	0.148	0.239	0.355	positive but not significant

Given the exploratory nature of the elevation analysis and the limited number of stations, p values were interpreted without adjustment for multiple comparisons and should therefore be considered exploratory. Positive correlation coefficients were obtained between elevation and all compound stress metrics examined in Table 6. Pearson correlation indicated positive associations with $p<0.05$ for frequency, event count, total severity, mean intensity, and persistence ratio. The strongest linear relationship was observed for total severity with $r=0.629$ and $p=0.007$, followed by persistence ratio with $r=0.604$ and $p=0.010$. Frequency, event count, and mean intensity also showed moderate positive linear associations with elevation.

Spearman rank correlation produced a similar but more selective pattern. Total severity showed the strongest monotonic association with elevation with $rho=0.681$ and $p=0.003$. Persistence ratio was also positively associated with elevation with $rho=0.562$ and $p=0.019$. In contrast, the Spearman relationships for frequency, event count, and mean intensity did not reach the $p<0.05$ level. These differences indicate that some elevation relationships are more evident in their linear structure than in their rank-based pattern.

Rare event count showed positive but statistically non-significant relationships with elevation in both correlation approaches. Overall, the results suggest that higher elevation stations tended to exhibit greater cumulative severity, persistence, and, to some extent, higher compound event occurrence and intensity. Nevertheless, elevation should not be interpreted as an independent causal factor because distance to coast, slope, aspect, local exposure, and atmospheric circulation were not controlled in the present analysis.

4 Conclusion

In this study, compound dry hot stress events were examined for 17 meteorological stations in Trabzon province using precipitation, temperature, and relative humidity data from the period 2012–2025. Compound conditions were defined as the simultaneous occurrence of precipitation values below the 25th percentile, temperature values above the 75th percentile, and relative humidity values below the 25th percentile. A total of 149 compound months and 141 compound events were identified during the examined period. Station-based results have shown that the compound stress characteristics are not homogeneous throughout Trabzon. While Köprübaşı Beşköy stands out in terms of occurrence and total severity, Dernekpazarı has drawn attention with the individual event that has the longest duration and the highest severity value. The highest mean intensity was determined for the Tonya Kalınçam station.

As a result of the benchmark comparison with SPI-1, 103 months were jointly identified by both approaches, while 46 months were defined only by the compound framework. This

difference indicates that the compound approach and the SPI-1 method represent different stress structures. The compound framework takes into account the simultaneous effects of high temperature and low relative humidity conditions alongside the precipitation deficit. However, due to the calculation of SPI-1 results over a 14-year observation period, these results have been evaluated not for the purpose of long-term drought climatology but solely as a comparative benchmark.

A total of 17 rare compound events have been identified within the scope of the rare event analysis. Rare events were predominantly observed during the Autumn and Spring periods, with the highest rare event frequency recorded at the Köprübaşı Beşköy station. Elevation analysis showed positive associations between station elevation and several compound stress characteristics. The most consistent relationships were obtained for total severity and persistence ratio, which showed positive associations with $p<0.05$ in both Pearson and Spearman analyses. Frequency, event count, and mean intensity also showed positive linear associations with elevation, whereas rare event count was not statistically significant. These findings indicate that elevation may contribute to the spatial differentiation of compound stress behavior, although it should not be interpreted as an independent causal mechanism.

The obtained results show that the characteristics of a humid climate do not completely eliminate the formation of compound meteorological stress. The joint evaluation of precipitation, temperature, and atmospheric dryness conditions provides complementary information to the classical precipitation-based drought assessment approach. However, the relatively short observation period and the limited sample size available for calendar-month percentile estimation, together with station-based spatial representation and unexamined atmospheric circulation effects, constitute the main limitations of the study. Studies conducted using longer meteorological records and more detailed spatial data can contribute to a more comprehensive evaluation of the long-term and spatial structure of compound stress behavior characteristics.

Acknowledgments

The authors would like to thank the Turkish State Meteorological Service for providing the meteorological data used in this study.

References

1. Topçu, E., Karaçor, F., Çırağ, B., Taşkolu, İ., Acar, R.: Drought assessment in the northeastern Aras Basin using multi-parameter aggregate drought index and innovative polygon trend analysis. Earth Science Informatics 18(3), 273 (2025). https://doi.org/10.1007/s12145-025-01797-x
2. Bevacqua, E., Zappa, G., Lehner, F., Zscheischler, J.: Precipitation trends determine future occurrences of compound hot-dry events. Nature Climate Change 12, 350–355 (2022). https://doi.org/10.1038/s41558-022-01309-5
3. Hosseinzadehtalaei, P., Termonia, P., Tabari, H.: Projected changes in compound hot-dry events depend on the dry indicator considered. Communications Earth & Environment 5, 220 (2024). https://doi.org/10.1038/s43247-024-01352-4
4. Hoffmann, D., Gallant, A.J., Arblaster, J.M.: Uncertainties in drought from index and data selection. Journal of Geophysical Research: Atmospheres 125(18), e2019JD031946 (2020). https://doi.org/10.1029/2019JD031946
5. Çırağ, B., Bozkurt, C.: Multi-scale drought analysis and machine learning-based completion of missing streamflow data in the Aras Basin. Physics and Chemistry of the Earth, Parts A/B/C, 104410 (2026). https://doi.org/10.1016/j.pce.2026.104410
6. Wang, H., Zhang, G., Zhang, S., Shi, L., Su, X., Song, S., Feng, K., Zhang, T., Fu, X.: Development of a novel daily-scale compound dry and hot index and its application

across seven climatic regions of China. Atmospheric Research 287, 106700 (2023). https://doi.org/10.1016/j.atmosres.2023.106700
7. Yin, H., Bai, F., Wu, H., Yan, M., Zhou, S.: Assessment of vegetation vulnerability in the Haihe River Basin under compound heat and drought stress. Sustainability 16(23), 10489 (2024). https://doi.org/10.3390/su162310489
8. Zhao, H., Zhang, L., Kirkham, M.B., et al.: U.S. winter wheat yield loss attributed to compound hot-dry-windy events. Nature Communications 13, 7233 (2022). https://doi.org/10.1038/s41467-022-34947-6
9. Terzioğlu, Z.Ö., Kankal, M., Yüksek, Ö., Nemli, M.Ö., Akçay, F.: Analysis of the precipitation intensity values of various durations in Trabzon province of Turkey by Şen's innovative trend method. Sigma Journal of Engineering and Natural Sciences 37(1), 241-250 (2019).
10. Feng, S., Wu, X., Hao, Z., Hao, Y., Zhang, X., Hao, F.: A database for characteristics and variations of global compound dry and hot events. Weather and Climate Extremes 30, 100299 (2020). https://doi.org/10.1016/j.wace.2020.100299
11. Meng, Y., Hao, Z., Feng, S., Zhang, X., Hao, F.: Increase in compound dry-warm and wet-warm events under global warming in CMIP6 models. Global and Planetary Change 210, 103773 (2022). https://doi.org/10.1016/j.gloplacha.2022.103773
12. Feng, S., Hao, Z., Zhang, X., Hao, F.: Probabilistic evaluation of the impact of compound dry-hot events on global maize yields. Science of the Total Environment 689, 1228-1234 (2019). https://doi.org/10.1016/j.scitotenv.2019.06.373
13. World Meteorological Organization: Standardized Precipitation Index User Guide. WMO-No. 1090, Geneva (2012).

Author Contribution Statement

- *Conceptualization:* Burak Çırağ
- *Methodology:* Burak Çırağ, İlteriş Taşkolu
- *Investigation:* Burak Çırağ, İlteriş Taşkolu, Reşat Acar
- *Writing – Original Draft:* Burak Çırağ
- *Writing – Review & Editing:* Burak Çırağ, İlteriş Taşkolu, Reşat Acar, Mahmut Güngör

Publication Note

This paper was peer-reviewed, accepted for presentation, and included in the proceedings of the ACE2026 – International Conference on Advances in Civil Engineering, held on 12–14 October 2026 in Trabzon, Türkiye.

This paper may be cited as follows:

Cirag, B., Taskolu, I., Acar, R., Gungor, M., "Spatiotemporal Characteristics of Compound Dry Hot Stress Events in Trabzon Province," in Proceedings of the ACE2026 – International Conference on Advances in Civil Engineering, Trabzon, Türkiye, 12–14 October 2026.

Uncertainty Arising from Effective Rainfall Methods in Agricultural Water Footprint Calculations: A Comparative Analysis at the National Scale

Muhammed Sungur DEMİR[1] and Abdullah MURATOĞLU[2]
[1] 0000-0003-3631-6325, Batman University, Civil Engineering Department, Batman, Türkiye, muhammed.sungur@batman.edu.tr
[2] 0000-0001-8981-5983, Batman University, Civil Engineering Department, Batman, Türkiye, abdullah.muratoglu@batman.edu.tr

Abstract. Accurate partitioning of green and blue water components in agricultural water footprint assessments is critical for water management decisions. Effective rainfall, as a key determinant of this partitioning, directly influences green water contribution estimates and, consequently, freshwater (blue water) demand. In this study, the virtual water content of wheat production in Türkiye was calculated, and the effects of three widely used effective rainfall methods — CROPWAT, USDA-SCS, and Dependable Rain — on the results were comparatively evaluated. The CROPWAT method, which is generally preferred in literature, was adopted as the reference. The green virtual water content of wheat was estimated at 1,282 m³/t using CROPWAT, while USDA-SCS and Dependable Rain yielded 584 m³/t and 566 m³/t, respectively. Both methods produced estimates approximately 54% and 56% lower than CROPWAT, with the national-scale difference reaching 698–716 m³/t. Spatial analyses revealed that deviations increase markedly in regions with limited precipitation, reaching 60–70% around Şanlıurfa under the USDA-SCS approach. The findings demonstrate that effective rainfall method selection constitutes a significant source of uncertainty in agricultural water footprint calculations. Developing locally calibrated approaches that adequately represent Türkiye's diverse hydro-climatic conditions is therefore a priority for improving the reliability of national-scale water footprint analyses.

Keywords: Uncertainty analysis, Effective rainfall approaches, Green water, Türkiye

1 INTRODUCTION

The water footprint (WF) concept quantifies the direct and indirect volumes of water consumed along the production chain of a commodity, thereby providing a holistic assessment of water use that extends beyond conventional water withdrawal measures. Within this framework, water consumption is examined under three principal components: blue water, which denotes irrigation water supplied from surface and groundwater resources; green water, which originates from precipitation and is stored within the crop root zone; and grey water, which represents the associated pollution load. This distinction is particularly critical for agricultural water management, as it enables the irrigation water requirement to be separated from the contribution of precipitation to crop water consumption. The boundary between the blue and green water components is, to a large extent, defined through the concept of effective rainfall (P_{eff}).

According to the FAO definition, effective rainfall refers to the portion of precipitation that contributes to crop production at the location where it falls, without requiring any additional energy input for pumping or conveyance [2]. In practical terms, the concept represents the fraction of rainfall that is temporarily stored in the soil and thus becomes available within the

crop root zone. P_{eff} is therefore a decisive variable in partitioning the blue and green water components in WF assessments, and its accurate estimation is directly critical to the reliability of the resulting calculations.

Direct measurement of P_{eff} under field conditions is nevertheless highly limited, owing to its considerable cost, time and data requirements. Consequently, empirical and semi-empirical approaches are predominantly preferred in practice [5]. Water balance methods, although theoretically more accurate, are impractical for large-scale analyses because they depend on numerous parameters such as evapotranspiration, infiltration, deep percolation and soil hydraulic properties [5]. This situation has led to the widespread use of a variety of effective rainfall estimation methods; however, the structural differences among these methods may generate substantial deviations in net irrigation water requirements and, accordingly, in green WF estimates. Bokke and Shoro [1] demonstrated that irrigation water requirement results vary significantly depending on the method employed. Similarly, Hess [3], in a study conducted at the scale of the United Kingdom, showed that the choice of effective rainfall model considerably affects green WF calculations. Despite this, the vast majority of large-scale water footprint studies in the existing literature adopt the CROPWAT approach directly, without any comparison of methods [3]. This points to the need for a systematic examination of the uncertainty introduced by effective rainfall model selection.

Motivated by this gap, the present study comparatively analyses the influence of the FAO-CROPWAT, USDA-SCS and Dependable Rain methods on wheat agricultural WF calculations at the district scale across Türkiye. Owing to its widespread use in literature, the CROPWAT method is adopted as the reference approach, and the results obtained from the remaining methods are evaluated within this framework. The principal objective of the study is to quantify the uncertainty that effective rainfall model selection introduces into national-scale agricultural water footprint estimates, and to map the spatial pattern of this uncertainty at the district level.

2 MATERIALS AND METHODS

This study was carried out across Türkiye at the district scale and focuses on the green water component of the agricultural WF of wheat, which is the most widely cultivated crop in the country in terms of harvested area.

The analyses were based on meteorological records covering the period 2020–2024, obtained from the Turkish State Meteorological Service upon official request [9]. Precipitation, relative humidity, solar radiation, wind speed, and minimum and maximum air temperature were compiled for each station and used as input to the calculations. Reference evapotranspiration (ET_0) was computed using the FAO Penman–Monteith equation. Wheat yield data for the same period were obtained from the Turkish Statistical Institute [10]. All calculations were performed at the district level, and the resulting values were aggregated to the provincial and national scales for comparative evaluation.

The green virtual water content was computed following the Water Footprint Assessment Manual [4], based on the relationship between crop water use and crop yield (Equation 1). Here, VWC_{green} (m^3/t) denotes the green virtual water content, CWU_{green} (m^3/ha) the green water use of the crop, and Y (t/ha) the crop yield.

$$VWC_{green} = CWU_{green} / Y \quad (1)$$

Crop water use (CWU) represents the total evapotranspiration occurring over the growing period of the crop, whereas CWU_{green} refers to the precipitation-derived fraction of this total consumption (Equation 2).

$$CWU_{green} = 10 \times \sum_{d=1}^{n} ET_{green} \quad (2)$$

Precipitation-derived evapotranspiration (ET_{green}) is determined through the relationship between total crop water requirement (ET_c) and P_{eff} (Equation 3). Accordingly, when soil moisture is sufficient to meet the water requirement of the crop, ET_{green} is taken as equal to the ET_c value of the corresponding time period. Conversely, under conditions of insufficient soil moisture, ET_{green} is constrained by the amount of water available in the root zone.

$$ET_{green} = MİN\left(ET_c, P_{eff}\right) \quad (3)$$

Effective rainfall denotes the portion of precipitation that is stored in the crop root zone and becomes directly available to the plant without any contribution from irrigation. In this study, P_{eff} was computed using different methods and the results were evaluated comparatively. In the CROPWAT method, P_{eff} is calculated through distinct empirical equations depending on whether total monthly precipitation falls below or above a threshold of 250 mm (Equations 4 and 5) [6].

$$P_{eff} = \frac{P\left(125 - 0.2P\right)}{125} \quad \text{if} \quad P \leq 250 \text{ mm} \quad (4)$$

$$P_{eff} = 125 + 0.1P \qquad \text{if} \quad P > 250 \text{ mm} \quad (5)$$

One of the alternative approaches, the USDA-SCS method, is an empirical model developed on the basis of long-term precipitation records from the United States [7]. In this method, the estimation of effective rainfall depends not only on the amount of precipitation but also on the ET_c parameter representing crop water requirement, and it additionally incorporates a storage factor (SF) determined by the usable soil water depletion depth D (mm) (Equations 6 and 7). This dependency indicates that the method may introduce additional uncertainty into the results when applied to climatic regions other than those for which it was developed.

$$P_{eff} = 25.4 \times SF \times \left[\left(0.70917 \times \frac{P}{25.4} \right)^{0.82416} - 0.11556 \right] \times \left(10^{0.02426 \times ET_c}\right) \quad (6)$$

$$SF = 0.531747 + 0.11620D - 0.000089394D^2 + 0.0000002318D^3 \quad (7)$$

The Dependable Rain method is a further empirical approach based on the classification of monthly precipitation according to specified threshold values. In this method, effective rainfall is calculated using two different equations depending on whether monthly precipitation falls below or above a threshold of 70 mm (Equations 8 and 9).

$$P_{eff} = 0.6P - 10 \quad \text{if} \quad P \leq 70 \text{ mm} \quad (8)$$

$$P_{eff} = 0.8P - 24 \text{ if } P>70 \text{ mm} \quad (9)$$

Within this scope, the effects of the effective rainfall values obtained from the CROPWAT, USDA-SCS and Dependable Rain methods on the green water footprint component were analysed comparatively at the district scale across Türkiye.

3 RESULTS AND DISCUSSION

Figure 1 presents the district-scale distribution of the percentage deviation of the effective rainfall values obtained from the USDA-SCS (a) and Dependable Rain (b) methods relative to the CROPWAT method. The results reveal that both empirical methods systematically produce lower effective rainfall values than CROPWAT throughout Türkiye. This pronounced reduction in effective rainfall estimates is directly reflected in the green water footprint results: the green VWC of wheat, determined as 1,282 m³/t on average across Türkiye using the CROPWAT method, decreased to 584 m³/t and 566 m³/t with the USDA-SCS and Dependable Rain methods, respectively, corresponding to reductions of approximately 54% and 56%. These findings are consistent with literature. Mohan et al. [5] reported that the USDA-SCS method tends to underestimate effective rainfall, while Hess (2010) [3] demonstrated that the CROPWAT method yields results relatively closer to those of water balance approaches. Likewise, Muratoğlu et al. [6], in a comparative study based on field data, showed that the CROPWAT method provides more consistent estimates, whereas the USDA-SCS and Dependable Rain methods systematically underestimate effective rainfall.

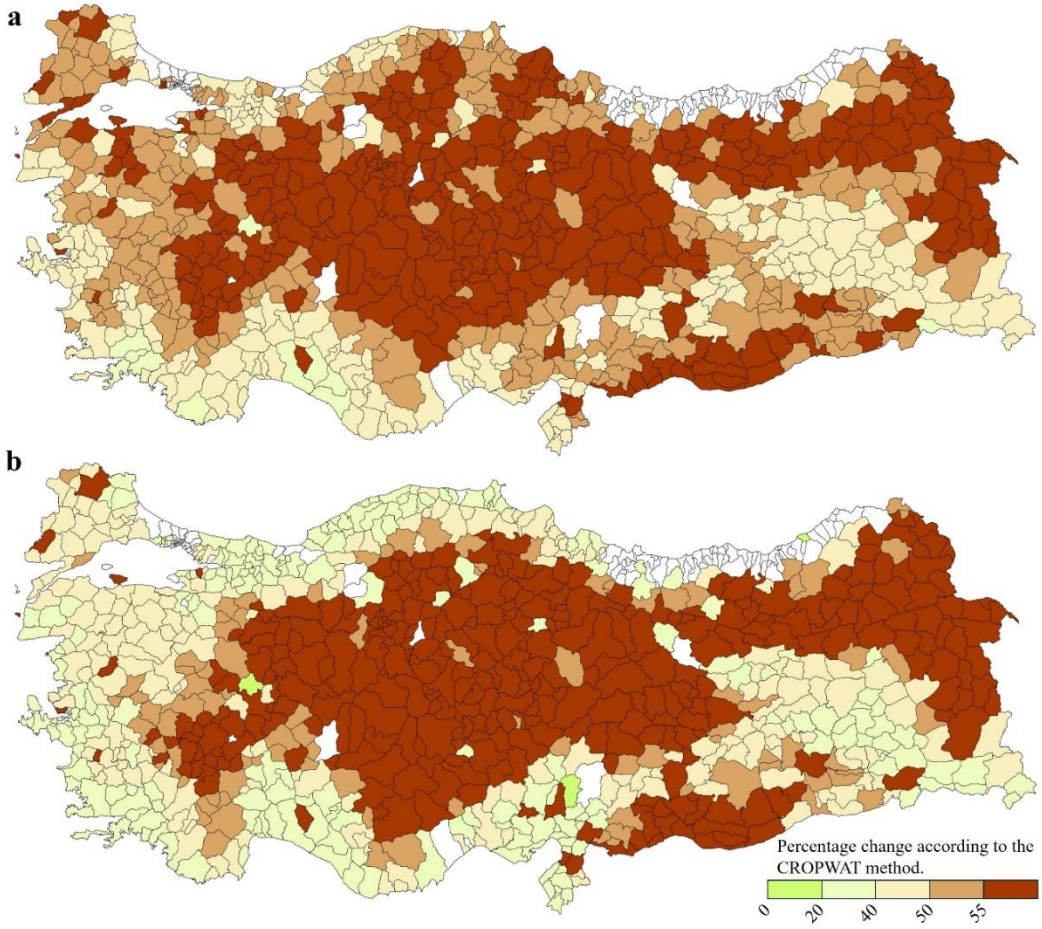


Figure 1. Spatial distribution of the percentage deviations in effective rainfall values obtained from the USDA-SCS (a) and Dependable Rain (b) methods relative to the reference CROPWAT method

An examination of the spatial distribution shows that both alternative methods deviate markedly from the CROPWAT results in Central Anatolia, along the southern border belt and in the north-eastern regions, whereas the deviations remain proportionally more limited in coastal provinces such as Antalya, Muğla and Zonguldak. Where total precipitation is high, as in the coastal areas, the proportional difference between the values produced by the methods diminishes; under the low-precipitation conditions of the interior, however, the influence of the differences between the underlying equations becomes pronounced. In particular, the low-threshold linear relationships employed in the Dependable Rain method suppress effective rainfall dramatically during dry periods, thereby maximising the deviation from CROPWAT. This finding is in agreement with the observations of Saracoglu and Kaynar [8], who emphasised that discrepancies between models may increase in areas characterised by high regional climate variability.

The structural origins of the methods constitute a further important factor explaining the observed deviations. The USDA-SCS method rests on an empirical approach developed using long-term data representative of the climatic conditions of the United States, and it estimates effective rainfall through a function that depends not only on the amount of precipitation but also on crop water requirement (ET_c) (Equations 6–7). This structural characteristic provides the basis for the method to diverge markedly from CROPWAT and to produce inconsistent results, particularly in arid climatic regions with high evaporative demand [7]. The Dependable Rain method, by contrast, has a comparatively simpler parameter structure (Equations 8–9). The fact that all of the methods analysed — including the reference CROPWAT approach — rely on empirical relationships that have not been specifically calibrated for the conditions of Türkiye is the fundamental reason for the pronounced deviations and the methodological uncertainty observed.

At the provincial level, Malatya, Iğdır, Sivas and Şanlıurfa were identified as the provinces exhibiting the largest deviations from CROPWAT for both methods. In these provinces, the deviations between the USDA-SCS and Dependable Rain methods themselves also remain high, indicating that empirical models may diverge substantially from one another under semi-arid geographical conditions. Conversely, it is noteworthy that the two methods display their highest mutual agreement in the province of Ardahan.

Overall, the empirical methods examined can deviate considerably both from one another and from the CROPWAT method taken as the basis for comparison. The sensitivity of effective rainfall — one of the principal inputs of agricultural WF calculations — to method selection points to a significant source of uncertainty and supports the need to develop effective rainfall models calibrated with local data that account for the diverse climatic and topographic conditions of Türkiye.

4 CONCLUSION

This study quantified, at the national scale, the uncertainty that the choice of effective rainfall method introduces into agricultural WF estimates. The USDA-SCS and Dependable Rain methods were found to produce systematically lower effective rainfall values than the reference CROPWAT approach, reducing the green virtual water content of wheat by approximately 54% and 56%, respectively. Rather than being uniformly distributed, these deviations intensified in semi-arid and low-precipitation districts and narrowed along the humid coastal margins, indicating that the choice of method affects not only the magnitude of the estimates but also

their spatial pattern — a consideration of direct relevance where water footprint results are intended to inform basin- or province-level allocation decisions.

The magnitude of these discrepancies is attributable primarily to the fact that none of the methods examined, including CROPWAT, rests on relationships calibrated for the hydro-climatic conditions of Türkiye. Two limitations should be acknowledged in interpreting the results. First, the analysis was confined to a single crop and to the green water component; the propagation of the same uncertainty into blue water and, consequently, into irrigation water requirement estimates remains to be examined. Second, in the absence of measured reference values, the comparison was made relative to CROPWAT rather than against observations, so the reported deviations express inter-method divergence rather than error.

Future work should therefore extend the comparison to the principal irrigated crops and to the blue water component, and should evaluate the examined methods against soil moisture observations or water balance measurements representative of Türkiye's main agro-climatic zones. Such evidence would provide the basis for locally calibrated effective rainfall relationships and, in turn, for more reliable national-scale water footprint assessments.

5 REFERENCES

1. Bokke, A. S., & Shoro, K. E. (2020). Impact of effective rainfall on net irrigation water requirement: The case of Ethiopia. Water Science, 34(1), 155–163. https://doi.org/10.1080/11104929.2020.1749780
2. Dastane, N. G. (1974). Effective rainfall in irrigated agriculture. FAO Irrigation and Drainage Paper No. 25, Food and Agriculture Organization of the United Nations, Rome.
3. Hess, T. (2010). Estimating Green Water Footprints in a Temperate Environment. Water, 2(3), 351–362. https://doi.org/10.3390/w2030351
4. Hoekstra, A. Y., Chapagain, A. K., Aldaya, M. M., & Mekonnen, M. M. (2011). The Water Footprint Assessment Manual: Setting the Global Standard. Earthscan, London, UK.
5. Mohan, S., Simhadrirao, B., & Arumugam, N. (1996). Comparative study of effective rainfall estimation methods for lowland rice. Water Resources Management, 10(1), 35–44. https://doi.org/10.1007/BF00698810
6. Muratoğlu, A., Bilgen, G. K., Angın, I., & Kodal, S. (2023). Performance Analyses of Effective Rainfall Estimation Methods for Accurate Quantification of Agricultural Water Footprint. Water Research. https://doi.org/10.1016/j.watres.2023.120011
7. Patwardhan, A. S., Nieber, J. L., & Johns, E. L. (1990). Effective Rainfall Estimation Methods. Journal of Irrigation and Drainage Engineering, 116(2), 182–193. https://doi.org/10.1061/(ASCE)0733-9437(1990)116:2(182)
8. Saracoglu, F. A., & Kaynar, Y. A. (2025). Assessment of Drought Indices Based on Effective Precipitation: A Case Study from Çanakkale, a Humid Region in Türkiye. Sustainability, 17(22), 10080. https://doi.org/10.3390/su172210080
9. Turkish State Meteorological Service (2025). Daily meteorological observation records for the period 2020–2024. Unpublished dataset provided upon official request. General Directorate of Meteorology
10. Turkish Statistical Institute (2025). Crop production statistics. TurkStat, Ankara, Türkiye. https://biruni.tuik.gov.tr/medas/?kn=92&locale=tr

Author Contribution Statement

- *Conceptualization:* Muhammed Sungur Demir, Abdullah Muratoglu
- *Methodology:* Muhammed Sungur Demir, Abdullah Muratoglu

- *Investigation:* Muhammed Sungur Demir, Abdullah Muratoglu
- *Writing – Original Draft:* Muhammed Sungur Demir
- *Writing – Review & Editing:* Abdullah Muratoglu

Conflict of Interest

The authors declare that they have no known competing financial interests or personal relationships that could have appeared to influence the work reported in this paper.

Publication Note
This paper was peer-reviewed, accepted for presentation, and included in the proceedings of the ACE2026 – International Conference on Advances in Civil Engineering, held on 12–14 October 2026 in Trabzon, Türkiye.

This paper may be cited as follows:
Demir, M. S., & Muratoğlu, A., "Uncertainty Arising from Effective Rainfall Methods in Agricultural Water Footprint Calculations: A Comparative Analysis at the National Scale," in Proceedings of the ACE2026 – International Conference on Advances in Civil Engineering, Trabzon, Türkiye, 12–14 October 2026.

Experimental Investigation of Morphological Equilibrium at a Symmetrical Mobile-Bed River Confluence with a Guiding Wall

Zehra Büyüker[1] and Gökçen Bombar[2]
[1] 0000-0001-9987-0951, İzmir Kâtip Çelebi University, Civil Engineering Department, İzmir, Türkiye, zehra.buyuker@ikc.edu.tr
[2] 0000-0002-8156-6908, İzmir Kâtip Çelebi University, Civil Engineering Department, İzmir, Türkiye, gokcen.bombar@ikc.edu.tr

Abstract. At river confluences, interactions among hydrodynamics, sediment transport, and morpho-dynamics result in changes to bed topography, posing significant risks such as flood, bank erosion, and problems for navigation. Hence, controlling the flow structure and bed morphology in confluence is essential for mitigating or preventing associated risks. This study experimentally investigated the equilibrium bed morphology of a river confluence equipped with a guiding wall designed to prevent the immediate mixing of tributary flows. The experiment was conducted in the large-scale open-channel at the İzmir Kâtip Çelebi University Hydraulics Laboratory, where two symmetrical tributaries merged at a at a 45˚ junction angle into this main channel. Flow was supplied only through the right tributary at a discharge of 15 L/s. The flow depth was adjusted at 5.0 cm over a 21.0 cm sand layer. Bed topography was measured at regular intervals along the cross-section located 5 cm downstream of the guiding wall (x = 105 cm) until equilibrium conditions were reached (t = 167 h). The equilibrium bed morphology was obtained using a Vectrino probe (ADV). According to results, the expected scour at the confluence formed at the tip of the guiding wall. Scour depth increased rapidly during the early stages but gradually slowed as equilibrium was approached. Eroded sediment from the scour hole deposited in the downstream region. With flow supplied only through the right tributary, no significant changes occurred on the left side of the guiding wall or within 30 cm of the left bank, whereas a distinct deposition zone formed along the right bank, extending downstream.

Keywords: Open channel confluence; Sediment transport; Guiding wall; Morphological structure.

1 Introduction

Confluences are locations where two or more open-channels with the equal or different water and sediment discharge rates merge into a single downstream channel, Confluences are rather common features in natural rivers and artificial systems of open-channels [1].

River confluences can display symmetrical or asymmetrical planforms, depending on the angle between the two converging channels and their orientation in relation to the downstream channel (Fig. 1).

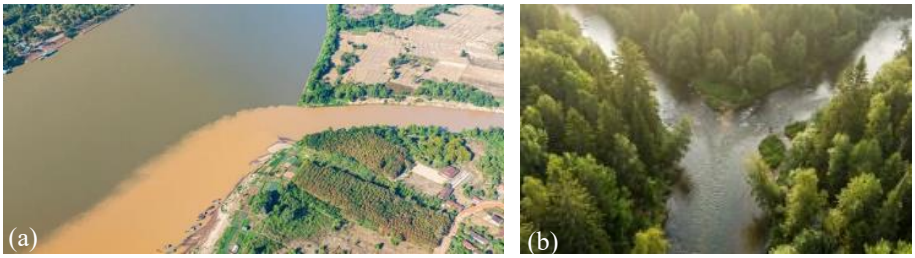


Fig. 1. River confluences: (a) asymmetric; (b) symmetric [2]

At river confluences, hydrodynamic processes and sediment transport mechanisms are strongly interrelated, with each influencing and altering the other. The interaction between flow dynamics within the confluence zone and sediment transport patterns governs the evolution of bed morphology [3-4], while the resulting morphological changes, in turn, affect the local hydrodynamic conditions. Due to these complex and dynamic interactions, river confluences may present significant challenges, including increased risks of flooding, bank erosion, navigation problems, and potential threats to structural safety of bridges or other nearby structures. Given these risks and the widespread occurrence of river confluences, a comprehensive understanding of the flow structure and sediment transport mechanisms in the confluence zone is of significant importance [5].

Therefore, river confluences represent critical environments for both scientific investigations and engineering applications.

In the existent first studies on river confluences, Taylor [6] studied the confluence hydrodynamics of confluent rigid-bed open channels. Advances in measurement techniques and computational technology have substantially improved the understanding of flow structure, sediment transport, and bed evolution at river confluences, leading to a significant increase in experimental and numerical studies since the 1980s. The first comprehensive experimental investigation of mobile-bed river confluences was conducted by Mosley (1976), who examined a small-scale experimental set-up both symmetric and asymmetric confluences under different junction angles, discharge ratios, and sediment supply conditions [7]. The study demonstrated that these parameters strongly influence the development of scour and deposition patterns, showing that increasing sediment supply significantly reduced scour depth in both confluence configurations. Subsequently, Best (1988) investigated sediment transport processes in laboratory and natural river confluences with junction angles ranging from 15° to 105°. The experiments revealed that scour depth increased with increasing junction angle and led to the first conceptual model describing the characteristic bed morphology of mobile-bed river confluences [8].

The conceptual morphological model of natural symmetric and asymmetric mobile-bed river confluences, established on the based on extensive laboratory and field investigations (Fig. 2).

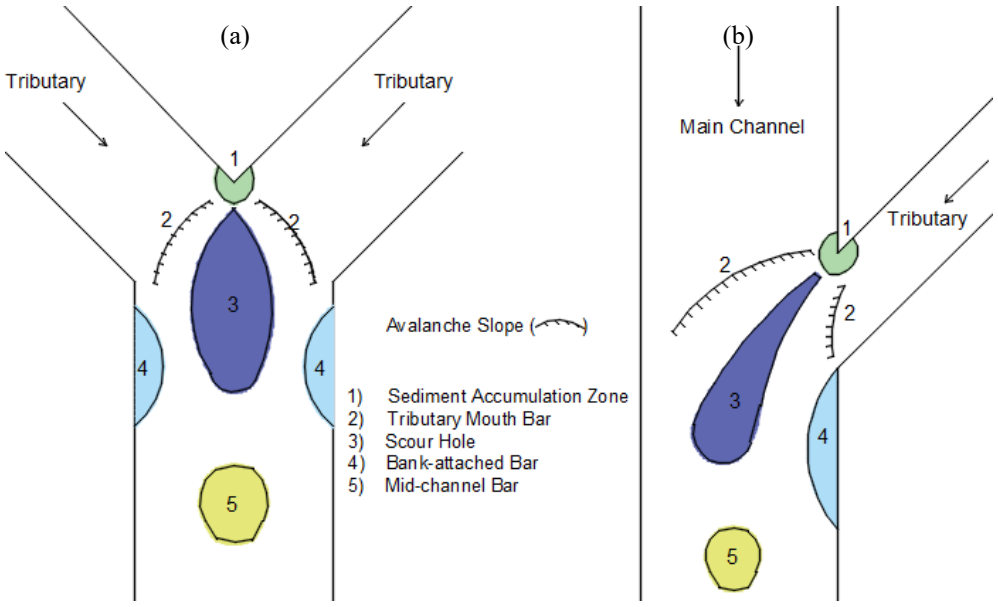


Fig. 2. Bed morphology at open-channel confluences, (a) symmetrical, (b) asymmetrical

The characteristic bed morphology generally consists of all or most of the following features: a sediment accumulation zone (underneath a flow stagnation zone) at the vertex of the junction;

two tributary mouth bars or a main channel bar and a tributary mouth bar (depending on the type of planform); a scour hole (in most cases); one or two bank attached bars (also depending on the type of planform); and a downstream mid channel bar (in some cases) [7,8]. These morphological features are formed as a result of the complex interactions between flow structure and sediment transport processes within river confluences.

Bombar and Cardoso (2020) confirmed that asymmetric mobile-bed confluences are characterized by several distinct morphological features, including scour corridors, tributary mouth bars, and deposition bars [9]. Rhoads and Sukhodolov (2004) demonstrated that sediment eroded from the scour hole is transported and deposited downstream in regions of reduced flow velocity and turbulence intensity [10]. More recently, Öztürk et al. (2022) experimentally investigated the temporal evolution of bed morphology in a symmetric mobile-bed river confluence and reported that both scour holes and deposition zones continued to develop until equilibrium conditions were approached [11].

Numerous experimental and numerical studies have confirmed that scour holes and deposition zones are the dominant morphological features of river confluences. Because excessive scour degrades aquatic habitats, deteriorates water quality, and threatens the stability of hydraulic structures, while excessive sediment deposition reduces channel conveyance capacity and increases flood risk during high-flow events, therefore, controlling the hydro-morpho-dynamic processes occurring at river confluences is of considerable importance for both river engineering applications and sustainable river management. For this purpose, flow-training structures, such as submerged vanes, pile groups, and guiding walls, have been widely employed at river confluences as effective, economical, and low-maintenance measures for modifying the flow pattern and controlling scour and sediment deposition.

The use of river-training structures to control scour and sediment deposition at river confluences has received increasing attention over the past decades. Odgaard and Wang (1991) first demonstrated that submerged vanes could improve navigation by redirecting the flow from the scour region toward downstream deposition zones, thereby reducing scour and enhancing sediment transport [12]. Subsequently, Wuppukondur and Chandra (2015), experimentally investigated the performance of pile groups and submerged vanes in asymmetric river confluences and reported that their geometry and arrangement significantly influenced scour depth, bed morphology, and local scour around the structures [13]. More recently, Ali et al. (2019) numerically evaluated different submerged vane configurations and showed that vane orientation plays a key role in controlling scour and deposition, with vanes installed at 30° providing better performance than those installed at 15° [14].

Despite the extensive research on scour control at river confluences, previous studies have primarily focused on asymmetric confluences. Therefore, there is still limited knowledge regarding the bed morphology of symmetric river confluences incorporating a guiding wall. To address this research gap, the present study experimentally investigates the downstream bed morphology of a large-scale symmetric mobile-bed river confluence, where a guiding wall prevents the converging flows from the two tributaries from merging immediately at the confluence vertex.

2 Experimental Study

The experimental study was conducted in the large-scale open channel located at the Hydraulics Laboratory of İzmir Kâtip Çelebi University.

2.1 Experimental Set-up

The experimental set-up was a large symmetrical confluence which consisted of two rectangular tributary channels merging into an equally rectangular, wider, downstream main channel (see Figure 3 and Figure 4). Both tributaries were 4.9 m long and 1.0 m wide, whereas

the main channel was 6.5 m long and 2.0 m wide, the lateral walls of these channels being 0.9 m high. They were made of smooth concrete, the same as their horizontal bottom. The junction angle between the two tributaries was 90°, and its bisectrix was aligned with the longitudinal axis of the downstream main channel (see Figure 4).

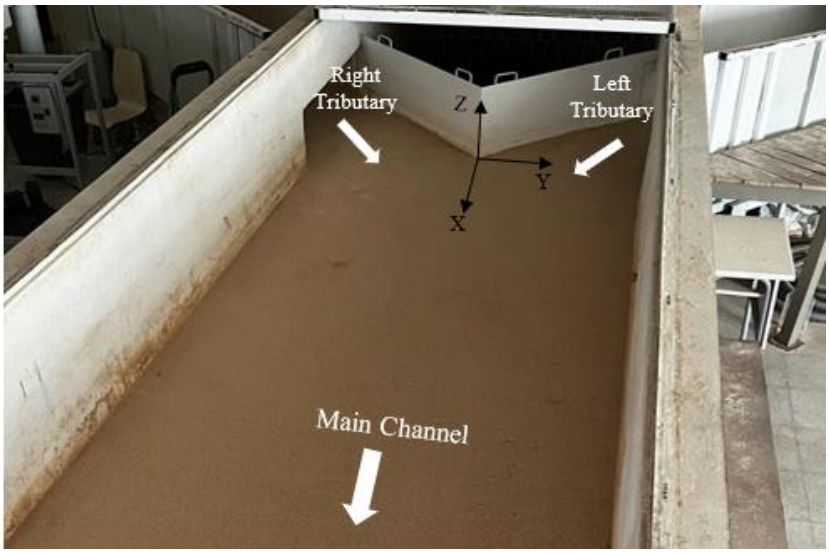


Fig. 3. General view of the experimental set-up

In the area highlighted in yellow in Figure 4, including the main channel and tributary channels, a 20.0 cm thick layer of uniform sand (median diameter, d_{50} = 1.044 mm; geometric standard deviation σ_g=1.16) was added on top of the horizontal concrete bottom. The guiding wall, with dimensions of 100 cm in length, 2 cm in width, and 30 cm in height, was installed in the confluence region to separate the flow and coincided with the longitudinal axis of the main channel. (see Figure 4).

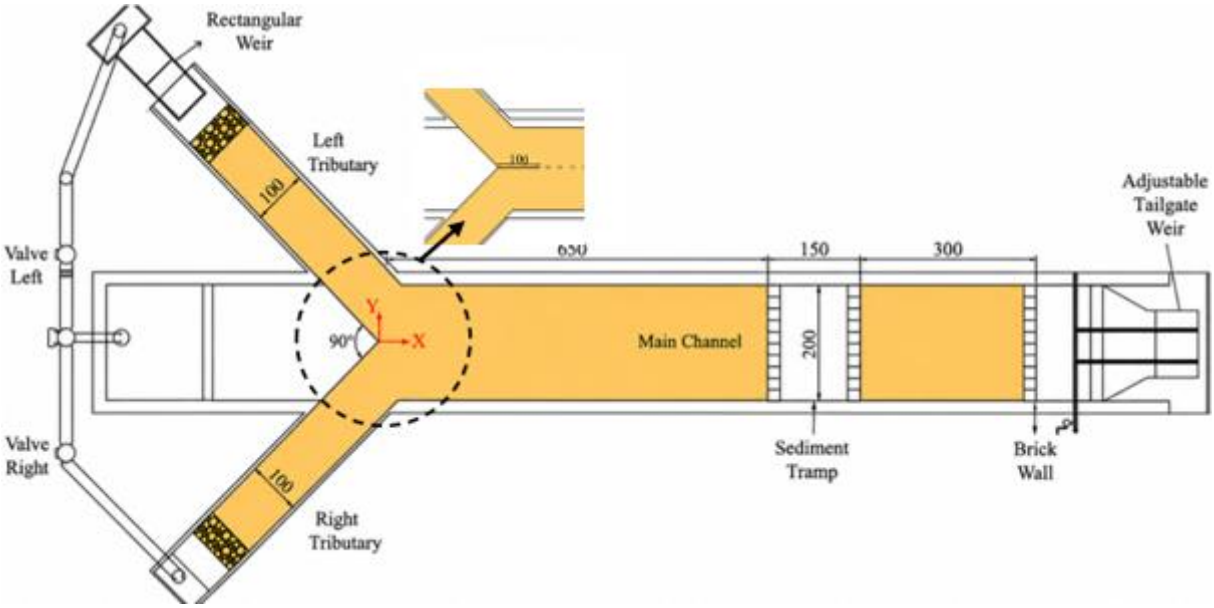


Fig. 4. Plan view of experimental set-up (all units are in cm)

The experimental set-up included a water reservoir placed underneath the laboratory floor. The water was pumped out from there with the help of two centrifugal pumps and circulated in two independent water circuits (one per pump). Each circuit was connected to a different tributary. The circuit of the right tributary was equipped with an electromagnetic flowmeter

used to measure the water discharge (± 0.1 l/s). The discharge in the left tributary was measured using a 0.70 m wide basin weir equipped with a limnimeter. The upstream head over the weir crest (h) was measured as the difference between the water level in the reservoir and the crest elevation, with an accuracy of ±0.1 mm. The discharge coefficient (C_d) of the weir was determined using the empirical equation proposed by Rehbock [15] as given in Eq(1):

$$C_d = 0.602 + 0.83h/P \quad (1)$$

where *P* is the height of weir. The discharge in each circuit was adjusted through one valve per circuit until it reached the predefined value.

The flow depth was controlled by an adjustable tail gate at the downstream end of the experimental setup. It was measured with a limnimeter (± 0.1 mm) and kept constant during the experiment (see Figure 5).

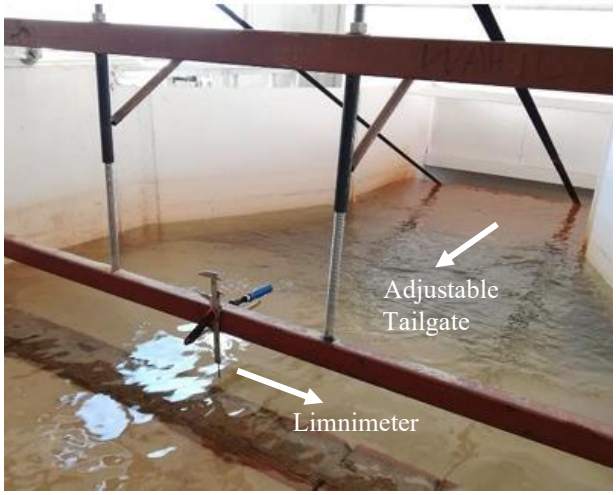


Fig. 5. Adjustable tailgate and limnimeter

The bed morphology was measured using the distance measurement feature of the down-looking Vectrino probe (Figure 6), with a measurement accuracy of 1 mm.



Fig. 6. Downlooking Vectrino probe

2.2 Experimental Procedure

Initially, the 21.0 cm thick sand layer was made perfectly plan with the help of a movable platform. Following the installation of the guiding wall along the longitudinal axis of the main channel, the downstream tailgate was raised and the pump of the right tributary started the pumping a very low discharge rate (2 l/s) to guarantee that the sand bed grains were not entrained. When the flow depth reached 15.0 cm, the discharge was gradually increased to 15.0 l/s by adjusting the valve, ensuring that the sand bed remained undisturbed, while the

discharge in the other tributary was set to zero. Then, the tailgate was gradually lowered until the flow depth reached 5.0 cm above the sand bed, immediately upstream of the downstream water chamber. This instant was considered as the beginning of the experiment (t = 0). Bed topography was measured at specific time intervals along the cross-section located 5 cm downstream of the guiding wall (x = 105 cm), and the measurements continued until no significant morphological changes were observed, indicating equilibrium conditions (t=167 hours). The equilibrium bed morphology was obtained using a Vectrino probe at a grid of points 10 cm apart for x and y directions in the main channel.

3 Experimental Results and Discussion

Bed topography was measured at specific time intervals along the cross-section located 5 cm downstream of the guiding wall (x = 105 cm). Figures 7 and 8 illustrate the time evolution of the scour hole and bed morphology at this cross-section until equilibrium conditions were achieved.

At the beginning of the experiment, a distinct scour hole rapidly developed at the tip of the guiding wall due to the discharge supplied through the right tributary, and it became clearly visible within 50 minutes (Figure 7). The average scour rate was 20.4 mm/h in first 50 min of the experiment, indicating a rapid initial scour development. The incoming flow expanded toward the left side of the main channel after passing the guiding wall.

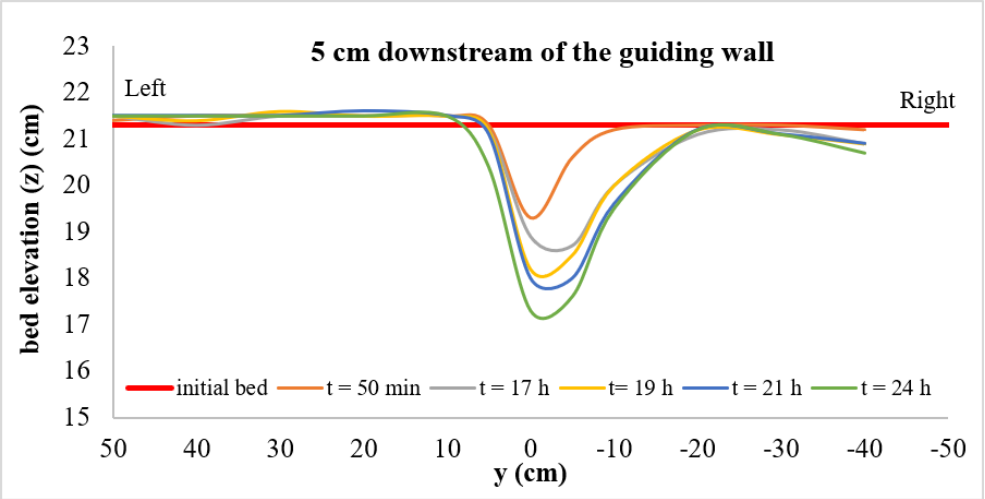


Fig. 7. Early-stage evolution of bed topography during the first 24 h of the experiment

During the initial stage, scour progressed continuously, leading to an increase in both scour depth and scour width. Over the first 24 h, the maximum scour width reached 25.0 cm, while the scour depth increased to 3.7 cm, with an average scour rate of 1.5 mm/h.

The rate of increase in both scour depth and width gradually decreased with time (Figure 8). During the later stages of the experiment, the development of the scour hole became considerably slower, indicating a reduction in the scour rate over time, as also observed by [11]. The bed profiles obtained during the final 55 h showed only a 1.1 cm increase in scour depth.

Over the final 55 h approaching equilibrium conditions, the maximum scour depth increased to 10.9 cm at t = 167 h. The average scour rate between t = 112 h and t = 167 h was only 0.2 mm/h, while no significant variation was observed in the maximum scour width. Although minor variations in the bed profiles continued to occur, these changes remained within an acceptable range for the equilibrium condition and did not significantly modify the overall scour geometry. At the end of the experiment (t = 167 h), the negligible differences between successive bed profiles confirmed that the system had reached a morphological equilibrium condition.

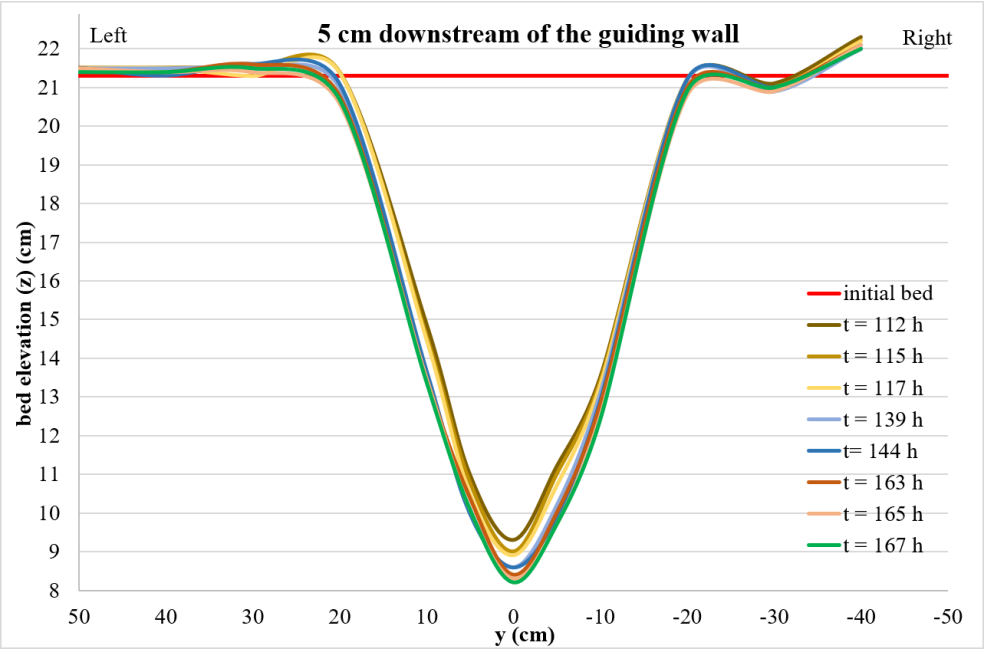


Fig. 8. Evolution of bed topography during the final 55 h approaching equilibrium conditions

The horizontal projection of the confluence bed morphology at equilibrium conditions is given in Figure 9.a, covering the area defined by 0 m ≤ x ≤ 3.5 m and –1 m ≤ y ≤ 1 m. The plan view of the main channel is presented in Figure 9.b.

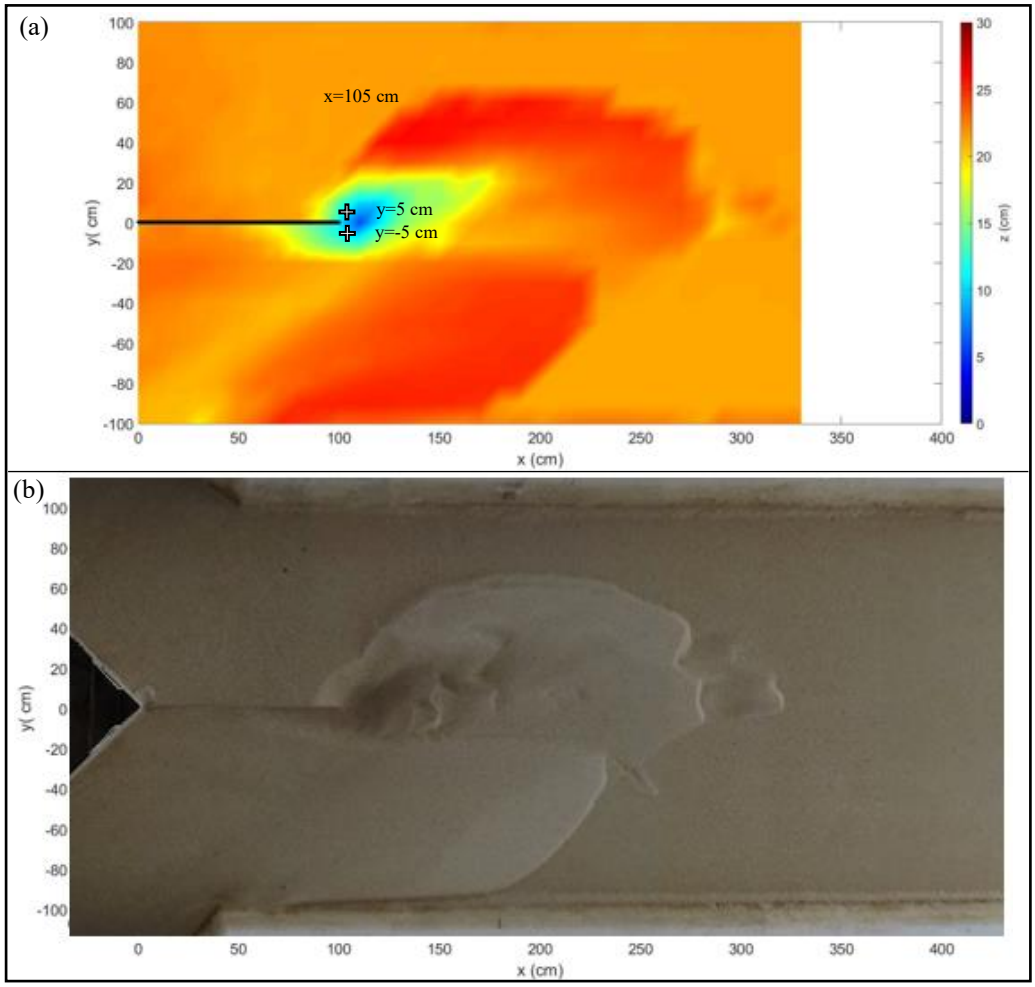


Fig. 9. Bed morphology at equilibrium conditions: (a) bed topography; (b) plan view

The morphological model proposed by [7] and [8] (Figure 2) indicates that a scour hole is formed near the confluence region due to the complex flow interactions. In the present study, the expected scour hole was observed at the tip of the guiding wall instead of the confluence vertex (Figure 9). Eroded sediment from the scour hole was transported downstream and deposited in the downstream region, forming distinct deposition zone. As the discharge was supplied only through the right tributary, no significant bed changes were observed on the left side of the guiding wall or within approximately 30 cm from the left bank. In contrast, a pronounced deposition zone developed along the right bank and extended downstream.

Figure 10 shows the temporal changes in bed elevation at two measurement points located near the tip of the guiding wall. The reduction in bed elevation at the measurement points (x, y) = (105, −5) and (105, 5) reflects the progression of the scour and supports the morphological changes observed in the confluence region. At both locations, the bed elevation remained nearly constant after t = 161 h, suggesting that the scour development had reached a equilibrium condition.

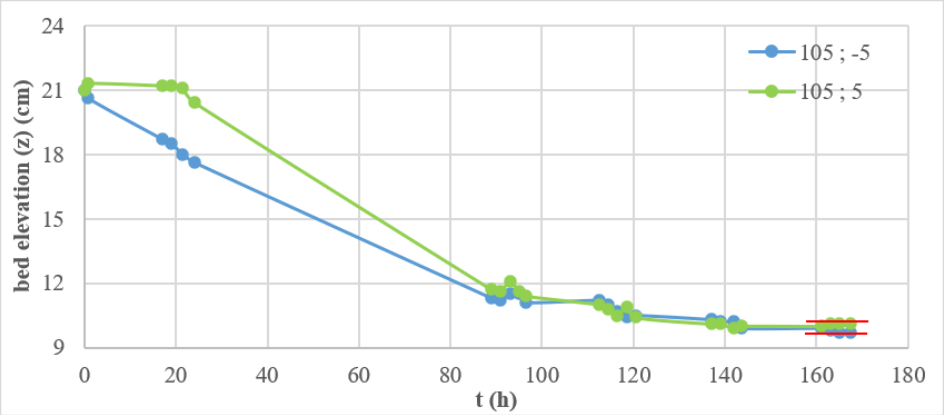


Fig. 10. Temporal changes in bed elevations of the points at x = 105 cm cross-section

4 Conclusions

Controlling the flow structure and bed morphology in river confluences is essential for reducing the potential impacts of associated risks. Therefore, this study aims to investigate the time evaluation and equilibrium bed morphology in a large-scale symmetric mobile-bed river confluence, where the flow and bed morphology are controlled by a guiding wall, in order to address the existing knowledge gap in the literature.

The results showed that the expected scour hole in the confluence region developed at the tip of the guiding wall. The scour depth increased during the early stages of the experiment; however, the rate of scour development gradually decreased as equilibrium conditions were approached. Sediment eroded from the scour hole was transported downstream and deposited in the downstream region. Since the flow was supplied only through the right tributary, no significant bed changes were observed on the left side of the guiding wall or within 30 cm from the left bank. In contrast, a distinct deposition zone developed along the right bank and extended downstream.

Acknowledgments

The authors would like to thank Prof. Dr. António Heleno Cardoso for his valuable contributions to this study who was supported by the TÜBİTAK 2221 Fellowship Program for Visiting Scientists and Scientists on Academic Leave (Sabbatical).

The experiments were conducted using the experimental facility constructed within the scope of the project No. 2016-GAPMÜMF-0020 entitled “Experimental Investigation of Bed Morphological Changes Due to Sediment Load in Symmetric River Confluences.”

This study was supported by the TÜBİTAK 2224-B Domestic Scientific Events Participation Support Program.

References

1. Bombar G., Cardoso A.H.: Effect of the sediment discharge on the equilibrium bed morphology of movable bed open-channel confluences. Geomorphology 367, (2020).
2. River Confluence image archive, Adobe Stock, https://stock.adobe.com/tr/search?k=river+confluence, last accessed 2026/07/22.
3. Joy D.M., Townsend R.D.: Improved flow characteristics at a 90° channel confluence. In: 5th Canadian Hydrotechnical Conference Proceedings, pp. 781–792. Canada (1981).
4. Constantinescu G., Miyawaki S., Rhoads B., Sukhodolov A.: Numerical analysis of the effect of momentum ratio on the dynamics and sediment-entrainment capacity of coherent flow structures at a stream confluence. Journal of Geophysical Research 117(F4028), (2012).
5. Rhoads B.L.: Mean structure of transport-effective flows at an asymmetrical confluence when the main stream is dominant. In: Ashworth P.J., Bennett J.S.J. (eds.) Coherent Flow Structures in Open Channels, pp. 491–517 Wiley, Chichester, UK (1996).
6. Taylor E.H.: Flow characteristics at rectangular open-channel junctions. American Society of Civil Engineers1 70, 119–121 (1944).
7. Mosley M.P.: An experimental study of channel confluences. The Journal of Geology 84(5), 535–562 (1976).
8. Best J.L.: Sediment transport and bed morphology at river channel confluences. Sedimentology 35, 481-498 (1988).
9. Bombar G., Cardoso A.H.: Effect of the sediment discharge on the equilibrium bed morphology of movable bed open-channel confluences. Geomorphology 367, (2020).
10. Rhoads B.L., Sukhodolov A.N.: Spatial and temporal structure of shear-layer turbulence at a stream confluence. Water Resources Research 40, 1–13 (2004).
11. Öztürk B., Büyüker Z., Taşkaya E., Bombar G., Cardoso A.H.: Simetrik akarsu kavşağında zamanın taban morfolojine etkisi, In: 11. Ulusal Hidroloji Kongresi Tam Metin Kitabı, Gaziantep, Türkiye, (2022).
12. Odgaard A.J., Wang Y.: Sediment management with submerged vanes. Journal of Hydraulic Engineering, 117(3), 267 (1991).
13. Wuppukondur A., Chandra V.: An experimental study to control scour at river confluence. AGU Fall Meeting, San Fransisco, 14-16 December 2015.
14. Ali H.L., Yusuf B., Mohammed T.A., Shimizu Y., Ab Razak M.S., Rehan B.M.: Improving the hydro-morpho dynamics of a river confluence by using vanes. Resources 8, (2019).
15. Rehbock T.: Discussion of precise weir measurements by EW Schoder and KB Turner. Transactions of the American Society of Civil Engineers, 93(1), 1143–1162 (1929).

Author Contribution Statement

- *Conceptualization:* Gökçen Bombar
- *Methodology:* Zehra Büyüker, Gökçen Bombar
- *Investigation:* Zehra Büyüker, Gökçen Bombar
- *Writing – Original Draft:* Zehra Büyüker
- *Writing – Review & Editing:* Gökçen Bombar

Conflict of Interest

The authors declare no conflict of interest.

Publication Note
This paper was peer-reviewed, accepted for presentation, and included in the proceedings of the ACE2026 – International Conference on Advances in Civil Engineering, held on 12–14 October 2026 in Trabzon, Türkiye.

This paper may be cited as follows:
Büyüker, Z., and Bombar, G., "Experimental Investigation of Morphological Equilibrium at a Symmetrical Mobile-Bed River Confluence with a Guiding Wall," in Proceedings of the ACE2026 – International Conference on Advances in Civil Engineering, Trabzon, Türkiye, 12–14 October 2026.

A Comparative Assessment of Gravity-Based Block-Type and Conventional Dolphin Systems

Şenol Demirbaş [1,*], Erdal Kesgin [2]

[1] *Department of Coastal Sciences and Engineering, Graduate School, Istanbul Technical University, Istanbul, Türkiye (ORCID: 0009-0001-0432-3291)*

[2] *Department of Civil Engineering, Faculty of Civil Engineering, Istanbul Technical University, Istanbul, Türkiye (ORCID: 0000-0002-9441-5359)*

* *Corresponding author: snldmrbses@gmail.com*

ABSTRACT

Pile-supported dolphins are so widely used at marine terminals that design guidance tends to treat them as the default, and gravity-based options receive little attention when the structural type is chosen. This paper asks what sets the gravity-based block-type dolphin apart from other dolphin types, and when those differences matter. It draws on the design basis and construction records of block-type mooring and breasting dolphins recently completed at an LNG terminal and covers five aspects: load path and structural behaviour, construction method and marine plant, tolerance and execution control practice, foundation and scour interaction, and the connection between precast elements. The block-type dolphin resists actions as a rigid stacked mass, without relying on structural deflection. Its installation avoids the noise of percussive piling, and quality-critical production moves to a precast yard. Execution risk is concentrated in bedding flatness and in placement tolerances that build up layer by layer, and a post-installed dowel-core connection serves as a supplementary provision. For berthing at LAT, one-plane screening of the case-study breasting dolphin gave factors of safety of 6.69 against base sliding and 3.72 against overturning. For berthing at HAT, interlayer screening with a joint friction coefficient of 0.60 gave sliding factors between 2.68 at the uppermost shaft joint and 6.98 at the base slabs. These are demand calculations on disclosed inputs, not code verification. No conclusion on bearing adequacy is drawn. A comparative table of selection criteria is provided to support the choice of dolphin type.

Keywords: *block-type dolphin; dolphin selection; pile-supported dolphin; caisson; gravity-based marine structures; LNG terminal*

1. INTRODUCTION

A dolphin is a freestanding marine structure that takes the berthing impact and mooring line loads of a vessel without the support of a continuous quay. For liquefied natural gas (LNG) the standard arrangement is the open-jetty liquid-bulk terminal, where the berth is made up of a central loading platform flanked by breasting dolphins, which absorb berthing energy through their fender systems, and by mooring dolphins, which anchor the vessel's mooring pattern (Reeve et al., 2018; PIANC, 2002). Since the dolphins, and not a quay wall, form the interface with the vessel, choosing their structural system is one of the first decisions in terminal design and among the most consequential.

Piled dolphins are so common that much of the design literature implicitly takes "dolphin" to mean "piled dolphin". In reality the choice is broader than day-to-day practice would suggest. The gravity family (caissons, cellular sheet-pile cells, and stacked precast blockwork) offers solutions that differ at a fundamental level in behaviour, construction logic, and risk profile (Gaythwaite, 2004; OCDI, 2020; García-Espinel et al., 2015). At the same time, vessels continue to grow in displacement and installed propulsion power, which raises berthing energies, mooring loads, and propeller-induced flows at the seabed, so selecting a structural family whose weaknesses coincide with the governing site conditions now carries greater consequences than before (PIANC, 2015). In terms of method, the paper is a retrospective documentary review of a single case, based on one terminal's disclosed design basis and execution records. Document revisions, signed acceptance records, and measurement distributions are not published here, and statements of achieved compliance are taken from the project records without independent verification.

This paper concentrates on those differences. The full construction procedure is the subject of a companion study from the same research and is not repeated here. Instead, the paper sets out what makes the block-type dolphin distinct and tests these points against the design basis and execution records of dolphins recently

completed at an LNG terminal. It is based on the first author's M.Sc. thesis at Istanbul Technical University; commercial identifiers of the case project are withheld for confidentiality.

2. OVERVIEW OF DOLPHIN STRUCTURAL SYSTEMS

Dolphins are normally grouped by how they resist horizontal actions. Flexible systems, which are either groups of steel, concrete, or timber piles tied by a rigid cap or large-diameter monopiles, deflect under load and dissipate part of the berthing energy through pile bending and soil yielding. Their design is governed by pile structural capacity and by lateral pile–soil interaction (Feygin, 2015; Tomlinson & Woodward, 2015). Rigid systems take the same actions with practically no deflection, mobilizing self-weight, base friction, and footprint geometry, and nearly all of the berthing energy is then taken up by the fender instead of being shared with the structure (Gaythwaite, 2004). Figure 1 compares the two load paths under the fender reaction.

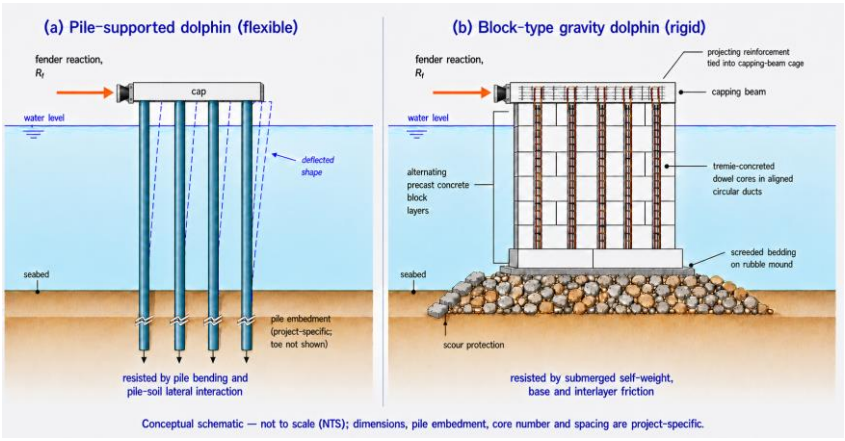


Figure 1. Load paths under the berthing (fender-reaction) action in a pile-supported dolphin and a block-type gravity dolphin. Conceptual schematic, not to scale; dimensions, pile embedment, and the number and spacing of dowel cores are project-specific. Prepared with AI assistance to the authors' specification and technically verified by them; not derived from project documentation or from any project drawing.

Three branches of the rigid family have to be kept apart. A caisson dolphin is a single hollow monolith, cast in a dry dock or casting basin, floated to site, and ballasted down onto a prepared base. A cellular dolphin is a ring of interlocking sheet piles filled with granular material. The block-type dolphin, the subject of this paper, is the modular branch: several large precast units, each of liftable weight, are stacked in layers on a prepared bedding and then connected so that the assembly comes close to acting as one body (OCDI, 2020). The main advantages of the system derive from this modularity, and so do its characteristic risks.

3. DISTINGUISHING FEATURES OF THE BLOCK-TYPE DOLPHIN

3.1. Load path and structural behaviour. A block-type dolphin resists berthing and mooring actions as a rigid body. Sliding is checked at the bedding interface and at each interlayer joint, overturning about the base toe, and bearing under the eccentric base reaction. Because the structure hardly deflects, the fender has to absorb almost all of the energy, so it is usually a compliant, long-stroke unit selected on energy capacity, reaction, hull pressure, and deflection limits, and the governing structural action is the fender reaction, not the berthing energy (PIANC, 2002; British Standards Institution, 2014). In a piled dolphin, the structure itself acts as an energy-absorbing element during the same berthing event. Verification priorities differ as a result. Geotechnical quantities such as friction coefficients, bearing demand, and base contact dominate for the block-type dolphin, and structural ones such as pile section capacity, fatigue, and corrosion allowance for the piled dolphin. Both families need both kinds of check, and what varies is the relative weight. One further feature is specific to blockwork: the interlayer friction available decreases towards the top of the stack, which tends to make the upper joints, and not the base, the critical sliding surfaces. In the case study, interlayer screening for berthing at HAT gave sliding factors from 2.68 at the uppermost shaft joint to 6.98 at the base slabs, against base sliding factors of 6.69 at LAT and 6.33 at HAT.

3.2. Construction method and marine plant. In place of the marine piling spread (piling barge, leader, hydraulic hammer), the block-type dolphin uses a precast yard, a flat-top transport barge, and heavy-lift plant working from a jack-up or spud-stabilized barge. Quality is largely built in onshore under yard conditions,

and offshore work is mostly controlled placement. On the other hand, the offshore operations depend on heavy-lift availability. Without the crane spread, the method cannot proceed. Foundation preparation also becomes a critical control stage. Dredging to formation, placing a 2–20 kg rubble mound, and screeding a 20–40 mm crushed-stone bedding layer to a flatness of ±20 mm over 3 m all take place before any structure is visible. The documented method involves no impact pile driving, which removes the noise source that dominates piled-dolphin construction. However, total underwater noise was not measured for comparison, and how much the difference matters for permitting depends on the site.

3.3. Tolerance and execution control regime. Geometric error in a piled dolphin stays largely with the individual element: a mislocated pile is corrected or accommodated at the cap. In a stacked assembly the errors accumulate, and a non-conforming unit cannot be recovered once another layer has been built over it. The block-type regime therefore rests on survey-verified hold points, running from acceptance of the bedding screed at ±25 mm in level and ±20 mm flatness over 3 m, through base unit placement within ±50 mm in plan and ±25 mm in level, to an assembled face deviation of no more than 50 mm at completion of stacking. It also rests on a strict re-lift rule, under which no unit stays in place with an exceedance carried into the next layer (Project documentation, 2023). Quality control is thus front-loaded and geometric in nature. In piled work it is dominated by driving records and integrity testing.

3.4. Foundation and scour interaction. A gravity dolphin bears directly on the seabed it was built on, whereas a piled dolphin stands on embedment many diameters deep. Scour around the base perimeter of a block-type dolphin can undermine the bedding, change the contact conditions achieved at acceptance, and increase the eccentricity of the base reaction. In a piled structure scour acts differently, reducing lateral soil support and increasing the unsupported pile length (PIANC, 2015). Scour protection is therefore an integral part of the block-type concept and not an add-on. At the case-study dolphins the equilibrium scour depth reported by the project for the native sand, approximately 1.2 m, exceeded the thickness of the bedding works. Protection was differentiated by exposure: a linked-block concrete mattress at least 200 mm thick on the vessel-facing side and, elsewhere, 150–600 kg graded rock at least 1,050 mm thick over geotextile (CIRIA, CUR, & CETMEF, 2007).

3.5. Inter-element connection. Older blockwork relied on friction and shear keys alone. The case-study dolphins add a post-installed dowel-core connection. Vertical ducts of approximately 0.64 to 1.05 m diameter are pre-formed through the layers and aligned during stacking. The ducts are reinforced with duplex stainless steel cages and tremie-concreted after the stack has been surcharged and the project records report that settlement has stabilized, a sequencing rule that keeps incompatible deformations from being locked into the connected system. The dowels are intended to provide a defined shear path across the critical upper joints, tensile continuity into the cast-in-place capping beam, and displacement control between units. They remain a supplementary provision, however. The reported screening takes no credit for them, their capacity calculations are not reproduced, and the in-service degree of composite action was not measured. Even so, the detail sets the modern block-type dolphin apart from loose-stacked blockwork and also from the monolithic caisson, which has no inter-element joints to connect.

4. CASE-STUDY EVIDENCE AND APPLICABILITY RANGE

The two dolphin types at the case-study terminal differ in geometry. Each breasting dolphin has two 0.80 m base slab layers, 8.70 × 11.05 m in plan, and six standard shaft layers 2.50 m high, eight precast layers in all, with the underside of the base slab at −13.80 m CD and a self-weight in air of approximately 40.4 MN. Each mooring dolphin has a single 0.80 m base slab, 9.00 × 11.50 m in plan, and six standard layers 2.30 m high, seven precast layers in all, with the underside at −11.50 m CD and a self-weight of approximately 38.3 MN. The berth is designed for a vessel of approximately 110,000 t displacement approaching at 0.12 m/s, which gives a design berthing energy of approximately 1,050 kN·m and a fender reaction of approximately 2,100 kN; the mooring hook input is 1,500 kN at a line angle of 20°. On these disclosed inputs, one-plane screening gives factors of safety against sliding and overturning of 6.69 and 3.72 for breasting at LAT, 6.33 and 3.52 at HAT, and 8.93 and 4.65 for mooring at HAT. In each of the three reported global base cases the base reaction stays within the middle third. Interlayer screening for berthing at HAT gives sliding factors from 2.68 at the uppermost shaft joint to 6.98 at the base slabs. For reproducibility, the scope of the screening needs to be stated. It is a one-plane rigid-body check. The fender reaction acts at +1.86 m CD, and the 1,500 kN hook load at +5.80 m CD resolves into 1,409.5 kN horizontal and 513.0 kN uplift. Submerged self-weights are 28.1/26.6 MN for the breasting dolphin at LAT/HAT and 25.7 MN for the mooring dolphin at

HAT. The base and joint friction coefficients, 0.50 and 0.60, are assumed values whose source is not reproduced, and no three-dimensional or load-sharing model is implied. Actions are taken from PIANC (2002) and BS 6349-4:2014, the editions referenced in the disclosed case-study inputs (the contractual design-basis register behind these inputs is not reproduced). Current practice is represented by PIANC (2024) and BS 6349-4:2026 (British Standards Institution, 2026). These are illustrative demand calculations and do not constitute code verification. Because neither the allowable bearing pressure nor the geotechnical acceptance basis is reproduced, the computed bearing demands support no conclusion on adequacy (Project documentation, 2023). Table 1 brings the comparative selection criteria together.

Table 1. Selection criteria for pile-supported, caisson, and block-type dolphins. Cellular sheet-pile dolphins (driven construction, with different noise and installation characteristics) are discussed in the text and are not included in the table. Entries are indicative and depend on method, plant, and site conditions (Gaythwaite, 2004; OCDI, 2020; Project documentation, 2023).

Criterion	Pile-supported (flexible)	Caisson (gravity, monolithic)	Block-type (gravity, modular)
Load resistance	Pile bending and pile–soil lateral interaction	Self-weight and base friction of a single monolith	Submerged self-weight, base and interlayer friction; supplementary dowel cores
Deformation behaviour	Flexible; energy partly absorbed by structure deflection	Rigid; berthing energy absorbed by fender	Rigid; berthing energy absorbed by fender
Foundation requirement	Stratum suitable for embedment at depth	Competent stratum at seabed; prepared rubble base	Competent stratum at seabed; rubble mound and screeded bedding
Fabrication / installation	Piles driven in situ (impact or vibratory hammer)	Cast in dry dock or casting basin; floated, towed, ballasted down	Cast at a suitable precast yard (QC, load-out access); barge-hauled; crane-placed in layers
Unit handling	Pile sections; lifts sized to piling plant	Thousands of tonnes (floated, not lifted)	Large precast units (heavy-lift crane)
Underwater noise	Method-dependent; high for impact driving	Low (no driving; floating and ballasting works)	Low (no percussive installation)
Geometric tolerance risk	Per-pile position and rake	Single seating operation	Cumulative, layer-by-layer; survey hold points
Structural joints	Welded / capped connections above water	None below cap (monolithic)	Many interlayer joints; friction plus post-installed dowel cores
Scour vulnerability	Scour reduces lateral soil support; longer free pile length	Moderate–high (bears at seabed)	Moderate–high; protection integral to concept
Typical water depth	Wide range; limited by pile design and plant	Moderate–deep	Shallow–moderate
Repair below water	Project-specific; often difficult offshore	Very difficult	Very difficult

The comparison yields an applicability range and is not meant as a ranking. The block-type concept has its clearest advantage where a competent bearing surface lies at or near the seabed, where underwater noise is restricted, and where heavy-lift plant and precast capacity are already mobilized or can be secured at reasonable cost. Piled dolphins remain the better choice on soft or compressible seabeds where the prepared-bearing assumption breaks down, in water deep enough to push unit weights or placement stability beyond the available plant, and wherever heavy-lift logistics cannot be justified. Where deeper water and an available casting basin favour a floated monolith, caissons become attractive.

5. CONCLUSIONS

The block-type dolphin differs from the rest of the dolphin family in five respects that matter when structural options are being selected. It resists actions as a rigid stacked mass and leaves energy absorption to the fender, so the emphasis of design verification shifts from structural to geotechnical checks; in the reported friction-only screening for berthing at HAT, the lowest interlayer sliding factor was found at the uppermost joint, not at the base. Yard precasting and crane placement take the place of percussive marine piling; the substitution trades underwater noise and driving risk for heavy-lift dependence and demanding foundation preparation.

Execution control is geometric and cumulative and is required from the early stages, by means of survey-verified hold points and a strict re-lift rule. Because the dolphin bears at the seabed, it is sensitive to scour, and protection differentiated by exposure belongs to the structural concept itself. The post-installed dowel-core connection, a supplementary provision, is intended to give a defined load-transfer path into the capping beam; it sets the system apart from loose blockwork and from monolithic caissons without amounting to verified composite continuity. Within its range, the concept is documented as constructible under the disclosed case conditions, and it is an attractive choice where permits restrict underwater noise and logistics favour precasting. The two main research needs that remain open are quantifying the composite contribution of the dowel cores and reproducing the geotechnical acceptance basis needed to turn the reported demands into a verified adequacy statement.

ACKNOWLEDGEMENT

This paper is based on the M.Sc. thesis of the first author, prepared under the supervision of the second author in the Coastal Sciences and Engineering Programme of the Graduate School, Istanbul Technical University. Identifiers specific to the case-study project are withheld for commercial confidentiality. Large language models (ChatGPT, OpenAI; Claude, Anthropic) were used as aids in drafting and language editing. Figure 1 was generated with ChatGPT through its Canva integration, following a technical layout and annotation scheme specified by the authors. All technical content, data, and references come from the first author's M.Sc. thesis and the cited sources. The authors reviewed and verified this material and take full responsibility for the content of the paper.

REFERENCES

British Standards Institution (BSI) (2014). BS 6349-4:2014 Maritime works – Code of practice for design of fendering and mooring systems.

British Standards Institution (BSI) (2026). BS 6349-4:2026 Maritime works – Design of fendering and mooring systems – Code of practice.

CIRIA, CUR, & CETMEF (2007). The rock manual: The use of rock in hydraulic engineering (2nd ed., Publication C683).

Feygin, V. B. (2015). Design of semi-flexible and flexible dolphins with concrete pile caps. Global Journal of Researches in Engineering, 15(E1), 1–22.

García-Espinel, J. D., Alvarez-García-Lubén, R., González-Herrero, J. M., & Castro-Fresno, D. (2015). Glass fiber-reinforced polymer caissons used for construction of mooring dolphins in Puerto del Rosario harbor (Fuerteventura, Canary Islands). Coastal Engineering, 98, 16–25.

Gaythwaite, J. W. (2004). Design of marine facilities for the berthing, mooring, and repair of vessels (2nd ed.). ASCE Press.

Overseas Coastal Area Development Institute (OCDI). (2020). Technical standards and commentaries for port and harbour facilities in Japan.

PIANC. (2002). Guidelines for the design of fender systems: 2002 (Report of Working Group 33).

PIANC. (2015). Guidelines for protecting berthing structures from scour caused by ships (Report No. 180).

PIANC. (2024). Fender guidelines 2024 (MarCom Working Group 211 report).

Project documentation. (2023). Construction documentation for the case-study block-type dolphins [Unpublished project material].

Reeve, D., Chadwick, A., & Fleming, C. (2018). Coastal engineering: Processes, theory and design practice (3rd ed.). CRC Press.

Tomlinson, M. J., & Woodward, J. (2015). Pile design and construction practice (6th ed.). CRC Press.

Publication Note
This paper was peer-reviewed, accepted for presentation, and included in the proceedings of the ACE2026 – International Conference on Advances in Civil Engineering, held on 12–14 October 2026 in Trabzon, Türkiye.

This paper may be cited as follows:
Demirbaş, Ş., Kesgin, E., "A Comparative Assessment of Gravity-Based Block-Type and Conventional Dolphin Systems," in Proceedings of the ACE2026 – International Conference on Advances in Civil Engineering, Trabzon, Türkiye, 12–14 October 2026.

CHAPTER 5

Transportation

28 papers

Determinants of Driver Rejection of Ride Requests in Ride-Hailing Services

Nihat Can Karabulut[1] Mustafa Gursoy[2] Halit Ozen[3]
[1] 0000-0002-4294-0215, Yildiz Technical University, Civil Engineering Department, Istanbul, Türkiye, can.karabulut@std.yildiz.edu.tr
[2] 0000-0002-3782-594, Yildiz Technical University, Civil Engineering Department, Istanbul, Türkiye, gursoy@yildiz.edu.tr
[3] 0000-0003-4031-7283, Istanbul Technical University, Civil Engineering Department, Istanbul, Türkiye, halitozen@itu.edu.tr

Abstract. Ride-hailing research has predominantly represented driver responses as binary accept-reject decisions, offering limited insight into how unsuccessful assignments accumulate for the same passenger request. This study examines sequential rejection exposure at the request level using one month of operational data from Istanbul. The analysis is restricted to 236,384 passenger requests that ultimately achieved a successful driver-passenger match. Rejection counts are strongly overdispersed (variance-to-mean ratio = 2.40) and concentrated at zero (61.3%). Poisson, negative binomial (NB), zero-inflated Poisson (ZIP), and zero-inflated negative binomial (ZINB) specifications were compared; the ZINB model provided the best overall fit according to log-likelihood, AIC, and BIC while closely reproducing the observed zero proportion. Inference is based on robust standard errors clustered at the eventually accepting driver level. In the count component, each additional minute of pickup time and realized travel-time delay relative to free-flow conditions is associated with 15.4% and 4.6% higher conditional rejection counts, respectively, whereas each additional minute of realized trip time is associated with a 2.7% lower count. Evening-peak requests exhibit the largest temporal increase (11.7%). Because operational and driver variables describe the final successful match, estimates are interpreted as conditional associations with preceding rejection exposure, not causal effects on individual rejecting drivers. The findings demonstrate the value of evaluating ride-hailing matching as a request-level sequential process.

Keywords: Ride-hailing; Driver rejection counts; Zero-inflated model.

1 Introduction

Ride-hailing platforms coordinate passenger demand and available drivers through real-time dispatch mechanisms. In a sequential assignment system, however, a successful match is not guaranteed at the first dispatch: the same passenger request may be offered to several drivers before one eventually accepts it. Each unsuccessful assignment keeps the passenger in the matching process and requires the platform to continue searching for another available driver. The operational performance of ride-hailing therefore depends not only on aggregate acceptance rates, but also on how unsuccessful assignments accumulate before a successful match is established [1, 3].

Existing empirical research has predominantly examined driver response at the individual offer level and represented it as a binary accept-reject decision [9-13]. This perspective is appropriate for studying a driver's response to a particular offer, but it does not describe the complete trajectory experienced by a passenger request after an initial rejection. From the request

perspective, the number of preceding rejections is a distinct measure of sequential matching performance because repeated unsuccessful assignments can prolong matching, increase uncertainty, and contribute to cancellation or platform switching [4-6]. This issue is especially relevant in congested and supply-constrained metropolitan markets such as Istanbul.

This study examines the number of preceding driver rejections experienced by passenger requests that ultimately achieve a successful driver-passenger match. The analysis focuses on pickup time, realized trip time, realized travel-time delay relative to a GIS-based free-flow benchmark, temporal request conditions, and characteristics of the eventually accepting driver. Poisson, NB, ZIP, and ZINB specifications are compared, after which the preferred ZINB model is used to characterize variation in sequential rejection exposure. The contribution is a request-level representation of repeated rejection that complements offer-level acceptance research. Because the explanatory variables describe the final successful match rather than the preceding unsuccessful offers, all estimates are interpreted as conditional associations and not as causal effects on individual rejecting drivers.

2 Literature Review

Ride-hailing operations depend on real-time coordination between passenger requests and available drivers. Research on platform operations has consequently examined matching intervals and radii [1], vehicle routing [2], pricing under driver-acceptance uncertainty [3], and adaptive matching mechanisms [7]. These studies show that dispatch performance depends on both the design of the matching system and the willingness of drivers to accept assigned requests.

Driver-side studies commonly formulate the response to an incoming offer as a binary accept-reject outcome [9-13]. This literature demonstrates that acceptance behaviour varies with pickup burdens, trip attributes, expected returns, temporal conditions, and driver heterogeneity. The offer-level formulation is essential for explaining individual decisions, but it does not measure how many unsuccessful assignments the same passenger request accumulates before eventual acceptance.

Repeated rejections also have passenger-facing and platform-level consequences. Continued reassignment can extend the time needed to establish a match and increase uncertainty in service delivery. Unfavourable waiting conditions may contribute to service discontinuation, cancellation, or the use of competing alternatives [4-5], while inefficient matching can reduce effective driver utilization and overall platform performance [6]. Accordingly, the accumulated rejection count provides information that is not contained in a single binary response or an aggregate acceptance rate.

Despite these related research streams, comparatively limited attention has been devoted to sequential rejection exposure as a request-level outcome. The present study addresses this gap by defining the rejection count as the number of unsuccessful driver assignments preceding eventual acceptance and examining how it varies with the operational and temporal characteristics surrounding the final successful match. This framing connects individual dispatch outcomes to the broader matching trajectory while maintaining a clear distinction between request-level associations and the behaviour of the individual drivers responsible for earlier rejections.

3 Data and Variables

This study uses one month of anonymized operational data provided by a ride-hailing platform operating in Istanbul. The raw data include request and acceptance timestamps, driver and passenger locations, realized pickup and trip durations, temporal indicators, and driver characteristics. Requests that remained unmatched or were cancelled before successful acceptance were excluded because the analytical outcome requires an observed endpoint at

eventual acceptance. Records with missing values, inconsistent timestamps, invalid spatial information, or implausible operational values were also removed. The final sample comprises 236,384 successfully matching passenger requests associated with 9,901 active drivers. The results are therefore conditional on eventual successful matching and should not be generalized to unmatched or cancelled requests. Figure 1 summarizes the sequential process considered in the analysis.

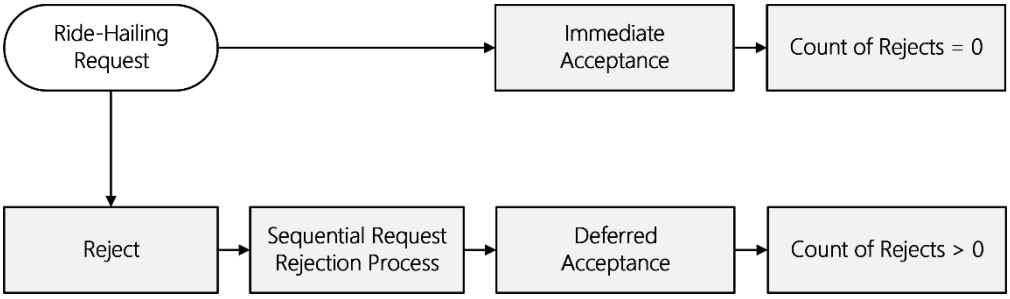


Fig. 1. Conceptual framework of the sequential request rejection process.

The dependent variable, count of rejects, is the number of unsuccessful driver assignments experienced by a passenger request before it is ultimately accepted. A value of zero indicates acceptance at the first dispatch, whereas a positive value indicates one or more preceding rejections before a subsequent driver accepts the request. The measure therefore represents accumulated rejection exposure at the passenger-request level rather than repeated rejection behaviour by a single driver. In the analytical sample, the mean rejection count is 0.90 and the variance is 2.16, yielding a variance-to-mean ratio of 2.40. A total of 144,945 requests (61.3%) has zero preceding rejections, and the distribution is strongly right-skewed (skewness = 1.95), as illustrated in Fig. 2.

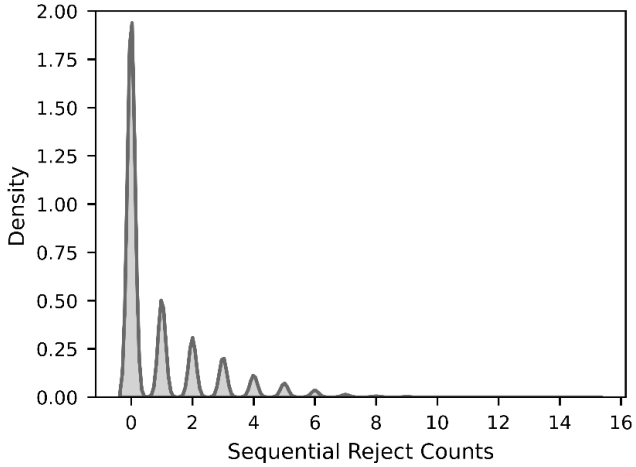


Fig. 2. KDE distributions of dependent variable.

The count component includes pickup time, realized trip time, realized travel-time delay, request day, request-hour category, and driver shift. Driver age and platform experience are included in the zero-inflation component. Pickup time is the elapsed duration between final request acceptance and the arrival of the eventually accepting driver at the passenger's pickup location. Trip time is the realized in-vehicle duration of the final completed trip. Request day distinguishes weekdays from weekends; request hour distinguishes morning peak (7 am-9 am), evening peak (5 pm-7 pm), and non-peak periods; and driver shift distinguishes 2 am-2 pm, 2

pm-2 am, and full-day operation. Driver experience denotes cumulative tenure on the platform rather than general professional driving experience.

GIS-based free-flow benchmarks were constructed by dividing Istanbul into 10,758 regular 500 m x 500 m zones. Trip origins and destinations were assigned to grid cells, and centroid-to-centroid shortest paths were calculated in QGIS using the most recent road-network dataset supplied by Istanbul Metropolitan Municipality. Segment-level free-flow speed values provided with the network were used to derive interzonal free-flow travel times. Intrazonal trips were excluded because centroid-to-centroid network measures are not informative within a single cell; these trips represented only a small share of the original data. Delay is defined as $max(0, T_i^{obs} - T_i^{ff})$, where T_i^{obs} is realized in-vehicle trip time and T_i^{ff} is the corresponding free-flow benchmark. Because delay and trip time are observed after completion of the final successful trip, they characterize the eventual match and are not direct observations of what preceding drivers perceived when evaluating the request.

Driver-specific variables refer to the driver who ultimately accepted the request. Their inclusion in the zero-inflation component captures statistical associations with the additional probability mass at zero and does not identify an 'always-accepting' driver group. Descriptive statistics for the explanatory variables are presented in Tables 1 and 2.

Table 1. Descriptive statistics of independent variables.

Variables	Unit	Min	Mean	Max
Pickup time	min	0.4	2.7	9.0
Trip time	min	3.3	20.6	115.0
Delay	min	0.0	7.6	66.5
Driver age	year	21	43	68
Driver experience	year	0.0	4.0	11

Pickup time ranges from 0.4 to 9.0 min, with a mean of 2.7 min. Realized trip time averages 20.6 min and ranges from 3.3 to 115.0 min. Delay ranges from 0 to 66.5 min, with a mean of 7.6 min. Driver age ranges from 21 to 68 years (mean = 43), while platform experience ranges from 0 to 11 years.

Table 2. Distribution of categorical independent variables.

Variables	Categories	Percentage
Driver shift	2 am – 2 pm	43.6
	2 pm – 2 am	51.4
	Full day	5.0
Request day	Weekday	81.0
	Weekend	19.0
Request hour	Morning peak hours	19.4
	Evening peak hours	15.8
	Non-peak hours	64.8

Regarding driver shift patterns, slightly more than half of the observations correspond to drivers operating between 2 pm and 2 am (51.4%), while 43.6% of drivers work between 2 am and 2 pm. A smaller share of drivers, accounting for 5.0% of the sample, follows a full 24-hour shift schedule. In terms of weekly distribution, most requests occur on weekdays (81.0%), whereas weekend requests represent 19.0% of the sample. The temporal distribution by time of day shows that most requests are observed during off-peak periods, accounting for 64.8% of all requests, followed by morning peak hours from 7 am to 9 am with 19.4% and evening peak hours from 5 pm to 7 pm with 15.8%.

4 Methodology

The rejection count is a non-negative outcome with substantial overdispersion and a pronounced concentration at zero. Because these features alone do not establish the preferred count specification, Poisson, NB, ZIP, and ZINB models were estimated to use the same analytical sample and count-component covariates. The ZIP and ZINB models also used the same zero-inflation covariates. Models were compared using log-likelihood, AIC, BIC, and the predicted zero proportion. The ZINB specification provided the best overall fit and was retained for inference.

The ZINB model represents the observed rejection-count distribution through two statistical components. The zero-inflation component contributes additional probability mass to zero-rejection observations, whereas the negative binomial component models count variation and can also generate zeros. Positive rejection counts arise from the negative binomial component. The zero-inflation component is therefore a statistical representation of excess zeros, not evidence of a behaviourally distinct population of drivers or requests [8].

The probability associated with the zero-inflation component is specified as Equation (1).

$$\pi_i = \frac{\exp(\mathrm{z}_i'\gamma)}{1+\exp(\mathrm{z}_i'\gamma)} \tag{1}$$

where π_i is the zero-inflation probability for request i, z_i is the vector of covariates in the zero-inflation component, and γ is the corresponding parameter vector. The conditional meaning of the negative binomial count component is specified in Eq. (2).

$$\mu_i = \exp(\mathrm{x}_i'\beta) \tag{2}$$

Here, μ_i denotes the expected number of preceding rejections conditional on the count-generating process, x_i is the vector of explanatory variables in the count component, and β is the corresponding parameter vector. Exponentiating β yields an incidence rate ratio (IRR): values above one indicates a positive association with the conditional rejection count, whereas values below one indicates a negative association, holding the remaining variables constant.

The unconditionally expected number of preceding rejections for request i is given by Eq. (3).

$$E(y_i \mid \mathrm{x}_i, \mathrm{z}_i) = (1-\pi_i)\mu_i \tag{3}$$

Accordingly, the overall expected rejection count depends jointly on the additional zero probability and the conditional mean of the negative binomial component. Driver-specific and realized operational variables describe the eventually accepting driver and final successful match; model estimates are therefore interpreted as request-level conditional associations with preceding rejection exposure rather than direct effects on the individual decisions of preceding drivers.

5 Results and Discussion

The Poisson model substantially underpredicted the observed zero proportion (43.6% versus 61.3%) and produced the weakest information criteria. The NB model improved both dispersional fit and zero prediction (60.0%), while the ZIP model predicted 60.9% zeros. The ZINB model achieved the highest log-likelihood (-295,238.0) and the lowest AIC (590,502.0) and BIC (590,636.9), while predicting 60.8% zeros. These diagnostics support the ZINB specification as the preferred overall representation of the rejection-count distribution. Table 3

presents its estimates; statistical inference uses robust standard errors clustered by the eventually accepting driver.

Table 3. Results of zero-inflated negative binomial model.

Variables		**β**	**SE**	**Sig.**	**IRR**
Count model					
Pickup time		0.1434	0.0019	<0.001	1.1542
Trip time		-0.0270	0.0005	<0.001	0.9734
Delay		0.0449	0.0008	<0.001	1.0460
Request day	Weekday	0.0604	0.0086	<0.001	1.0623
	Weekend*				
Request hour	Morning peak hours	0.0600	0.0095	<0.001	1.0618
	Evening peak hours	0.1103	0.0089	<0.001	1.1167
	Non-peak hours*				
Driver shift	2 am – 2 pm	0.0061	0.0269	0.8220	1.0061
	2 pm – 2 am	0.0938	0.0267	<0.001	1.0984
	Full day*				
Constant		0.0255	0.0295	0.3860	
Inflation model					
Driver age		0.0039	0.0015	0.010	
Driver experience		0.0309	0.0047	<0.001	
Constant		-0.7473	0.0745	<0.001	
Wald $\chi^2(8)$		8,386.81		<0.001	
Overdispersion		0.4715	0.0125		
Log-likelihood		-295,238			
AIC		590,502.0			
BIC		590,636.9			

* base category; SE: driver-clustered robust standard error.

Within the negative binomial count component, pickup time has the largest operational association (β = 0.1434; IRR = 1.1542): one additional minute is associated with a 15.4% higher conditional rejection count. Each additional minute of realized delay is associated with a 4.6% increase (β = 0.0449; IRR = 1.0460), whereas each additional minute of realized trip time is associated with a 2.7% decrease (β = -0.0270; IRR = 0.9734). Weekday requests exhibit a 6.2% higher conditional count than weekend requests. Relative to non-peak periods, morning- and evening-peak requests exhibit increases of 6.2% and 11.7%, respectively. The 2 am-2 pm shift does not differ significantly from the full-day reference category, whereas requests eventually accepted by drivers operating the 2 pm-2 am shift are associated with a 9.8% higher conditional count. These patterns show that preceding rejection exposure varies systematically with the operational and temporal conditions surrounding eventual successful matches.

In the zero-inflation component, driver age (β = 0.0039, p = 0.010) and platform experience (β = 0.0309, p < 0.001) are positively associated with the additional probability mass assigned to zero rejection. Because these variables describe the eventually accepting driver, the coefficients do not show that older or more experienced drivers generally reject fewer requests, nor do they identify a persistent 'always-accepting' group. They indicate only that requests eventually matched with older or more experienced drivers receive a greater probability contribution from the model's statistical excess-zero component. The estimated overdispersion parameter (0.4715) further confirms substantial extra-Poisson variation. Operationally, the findings identify pickup-related conditions and evening operating periods as useful targets for dispatch

monitoring, but the request-level data do not reveal the attributes or decision processes of the drivers responsible for earlier rejections.

6 Conclusion

This study reframes repeated driver rejection as a request-level sequential process rather than a collection of isolated binary decisions. Among 236,384 passenger requests that ultimately achieved a successful match, rejection exposure is strongly overdispersed and concentrated at zero, and the ZINB model provides the best fit among the evaluated count specifications. Pickup time is the most pronounced operational correlate, while realized delay and evening-peak conditions are also associated with greater preceding rejection exposure. Longer realized trip times exhibit the opposite pattern.

From a platform perspective, rejection counts provide information beyond aggregate acceptance rates by showing how many unsuccessful assignments a request experiences before eventual acceptance. Improving driver-request proximity, monitoring periods of elevated rejection exposure, and adapting dispatch procedures to pickup-related burdens may help reduce repeated assignment attempts and improve the utilization of available driver supply. These implications should be treated as operational directions for further testing rather than causal effects established by the present observational model.

The findings are subject to important limitations. The data covers one month, one platform, and only requests that ultimately achieved successful matching; unmatched and cancelled requests may contain more severe rejection sequences. Driver age, experience, pickup time, trip time, and delay describe the eventually accepting driver and final completed trip, while the characteristics of preceding rejecting drivers are unavailable. Trip time and delay are also ex-post measures. Future research should combine complete offer-level histories with ex-ante request attributes, unmatched outcomes, richer local supply-demand indicators, and longer multi-platform observation periods.

Acknowledgments

This study was conducted as part of the first author's doctoral research at Yildiz Technical University. This research was supported by the Scientific and Technological Research Council of Türkiye (TUBITAK) under Project No. 225M487, while the first author also received doctoral scholarship support from TUBITAK through the BIDEB 2211 – A Domestic Graduate Scholarship Program.

References

1. Liu Q.: Ding C.: Chen P.: A panel analysis of the effect of the urban environment on the spatiotemporal pattern of taxi demand. Travel Behaviour and Society 18, 29-36 (2020). https://doi.org/10.1016/j.tbs.2019.09.003
2. Yang H.: Qin X.: Ke J.: Ye J.: Optimizing matching time interval and matching radius in on-demand ride-sourcing markets. Transportation Research Part B: Methodological 131, 84-105 (2020). https://doi.org/10.1016/j.trb.2019.11.005
3. Scholl L.: Sabogal-Cardona O.: Oviedo D.: Arellana J.: Cantillo V.: Ojeda-Diaz AJ.: Tech on Wheels: Exploring Microtransit's ICT Perceptions in Latin America and the Caribbean. Transport Policy 176, 103924 (2025). https://doi.org/10.1016/j.tranpol.2025.103924
4. Lotfi S.: Abdelghany K.: Ride matching and vehicle routing for on-demand mobility services. Journal of Heuristics 28(3), 235-258 (2022). https://doi.org/10.1007/s10732-022-09491-7
5. Huang X.: Yilan BU.: Junbei LIU.: Meng M.: Zhang J.: Zhuge C.: A spatial agent-based approach to simulating the ride-hailing system and its environmental impacts. Transport Policy 174, 103848 (2025). https://doi.org/10.1016/j.tranpol.2025.103848

6. Bahrami S.: Nourinejad M.: Nesheli MM.: Yin Y.: Optimal composition of solo and pool services for on-demand ride-hailing. Transportation Research Part E: Logistics and Transportation Review 161, 102680 (2022). https://doi.org/10.1016/j.tre.2022.102680
7. Ricardianto P.: Ikhsan RB.: Suryobuwono AA.: Setiawan EB.: Raharjo EP.: Rahandi R.: Cahyadi D.: What makes consumers attitudinal loyalty on ride-hailing services? An investigation Indonesian consumers' perceived safety in using ride-hailing apps. Journal of Open Innovation: Technology, Market, and Complexity 10(2), 100306 (2024). https://doi.org/10.1016/j.joitmc.2024.100306
8. Bhaduri E.: Goswami AK.: Examining user attitudes towards ride-hailing services–A SEM-MIMIC Ordered Probit approach. Travel Behaviour and Society 30, 41-59 (2023). https://doi.org/10.1016/j.tre.2022.102680
9. Kumar A.: Gupta A.: Parida M.: Chauhan V.: Service quality assessment of ride-sourcing services: A distinction between ride-hailing and ride-sharing services. Transport Policy 127, 61-79 (2022). https://doi.org/10.1016/j.tranpol.2022.08.013
10. Gao J.: Li X.: Wang C.: Huang X.: A pricing mechanism for ride-hailing systems in the presence of driver acceptance uncertainty. IEEE Access 10, 83017-83028 (2022). 10.1109/ACCESS.2022.3196684
11. Lu K.: Shi C.: Why do travelers discontinue using integrated ride-hailing platforms? The role of perceived value and perceived risk. Humanities and Social Sciences Communications 12(1), 1-19 (2025). https://doi.org/10.1057/s41599-025-04683-5
12. Li M.: Jiang G.: Lo HK.: Optimal cancellation penalty for competing ride-sourcing platforms under waiting time uncertainty. Transportation Research Part E: Logistics and Transportation Review 174, 103107 (2023). https://doi.org/10.1016/j.tre.2023.103107
13. Castillo JC.: Knoepfle, D.: Weyl EG.: Matching and pricing in ride hailing: Wild goose chases and how to solve them. Management Science 71(5), 4377-4395 (2025). https://doi.org/10.1287/mnsc.2022.00096
14. Wu H.: Chen Y.: Wang L.: Ma G.: E-ride: An adaptive event-driven windowed matching framework in ridesharing. IEEE Access 10, 43799-43811 (2022). 10.1109/ACCESS.2022.3167033
15. Akram MN.: Amin M.: Afzal N.: Kibria BG.: Kibria–Lukman estimator for the zero inflated negative binomial regression model: theory, simulation and applications. Communications in Statistics-Simulation and Computation 54(5), 1464-1480 (2025). https://doi.org/10.1080/03610918.2023.2286436
16. Fatemi Pour E.: Madnanizdeh SA.: Joshaghani H.: Accept or reject a ride? This is the problem. Journal of Economic Studies 50(7), 1346-1374 (2023). https://doi.org/10.1108/JES-12-2021-0617
17. Lin H.: He Y.: Liu Y.: Gao K.: Qu X.: Deep demand prediction: An enhanced conformer model with cold-start adaptation for origin–destination ride-hailing demand prediction. IEEE Intelligent Transportation Systems Magazine, 16(3), 111-124 (2024). 10.1109/MITS.2023.3309653

Author Contribution Statement

- *Conceptualization:* Nihat Can Karabulut, Halit Ozen
- *Methodology:* Nihat Can Karabulut
- *Investigation:* Nihat Can Karabulut
- *Writing – Original Draft:* Nihat Can Karabulut
- *Writing – Review & Editing:* Mustafa Gursoy, Halit Ozen

List of Abbreviations

- **KDE** — Kernel Density Estimation

- **ZINB** — Zero-Inflated Negative Binomial
- **IRR** — Incidence Rate Ratio
- **SE** — Standard Error

Note: Following the conference, this Publication Note will be added to each paper; therefore, authors are kindly requested not to remove the note below and to complete the author(s) and paper title information.

Publication Note
This paper was peer-reviewed, accepted for presentation, and included in the proceedings of the ACE2026 – International Conference on Advances in Civil Engineering, held on 12–14 October 2026 in Trabzon, Türkiye.

This paper may be cited as follows:
Nihat Can Karabulut, Mustafa Gursoy, Halit Ozen, "Determinants of Driver Rejection of Ride Requests in Ride-Hailing Services," in Proceedings of the ACE2026 – International Conference on Advances in Civil Engineering, Trabzon, Türkiye, 12–14 October 2026.

Urban Air Mobility in Türkiye: Opportunities, Challenges, and Future Perspectives

Selim Dündar[1] and Barış Akdemir[2]
[1] 0000-0003-4433-1998, Istanbul Okan University, Civil Engineering Department, Istanbul, Türkiye, selim.dundar@okan.edu.tr
[2] 0009-0006-8776-301X, Istanbul Okan University, Civil Engineering Department, Istanbul, Türkiye, baris@bnmanagement.com.tr

Abstract. Urban Air Mobility (UAM) has emerged as a significant focus in transportation research, propelled by advancements in electric vertical take-off and landing (eVTOL) aircraft and increasing mobility challenges in metropolitan regions. UAM presents opportunities to reduce urban congestion, enhance emergency medical services, enable air taxi operations, facilitate small-scale logistics, and promote sustainable transport systems. This study analyzes UAM from technical, operational, environmental, social, and regulatory perspectives. The concepts of UAM and Advanced Air Mobility (AAM) are defined, and major eVTOL configurations—including Multicopter, Lift+Cruise, Tiltrotor, and Vectored Thrust—are compared based on speed, range, capacity, energy consumption, and operational suitability. Representative aircraft models such as AirCar, Joby Aviation S4, Eve Air Mobility, and Leonardo AW609 are reviewed to illustrate recent technological developments. The analysis further addresses vertiport infrastructure, site selection, charging requirements, battery safety, airspace integration, environmental impacts, public acceptance, and regulatory preparedness. Special consideration is given to Türkiye, where UAM advancement depends on technological maturity and coordinated progress in infrastructure, airspace management, safety regulation, legal frameworks, cybersecurity, and societal acceptance. The findings suggest that UAM could enhance future urban transportation, but recommend initiating implementation through controlled pilot projects and localized test studies prior to large-scale deployment

Keywords: Urban Air Mobility; eVTOL Aircraft; Vertiport Infrastructure.

1 Introduction

The rapid expansion of cities combined with the steady migration of people into metropolitan areas has been putting growing pressure on urban transportation systems for years. Road networks, in particular, are struggling with a familiar range of persistent issues — heavy traffic congestion, much longer commuting times, rising pollution, safety concerns, and limited access for emergency services and other time-critical needs. These problems are especially pronounced in large cities, where building additional roads or expanding existing ones is rarely feasible due to severe land shortages, extremely high costs, and the practical difficulties created by already dense urban environments.

It is against this challenging background that Urban Air Mobility (UAM) has started to attract serious consideration. While the basic idea of moving people and goods through urban airspace has been around for decades, recent progress in battery systems, electric propulsion, digital control technologies, autonomous systems, and eVTOL aircraft has revived strong interest in the concept. Recent research suggests that enthusiasm for both UAM and the broader Advanced Air Mobility (AAM) field is increasing quickly, largely because eVTOL

aircraft are seen as potentially safer, much quieter, and more economically viable alternatives to conventional helicopter services [1], [2]. UAM is primarily associated with short-distance services within urban and metropolitan areas. Potential applications include urban air taxi operations, airport transfers, emergency medical services, disaster response, tourism, and small-scale cargo or logistics operations. UAM represents not only the introduction of new aircraft technology but also the development of a comprehensive mobility ecosystem that requires integrating vehicles, vertiports, energy systems, airspace management, digital platforms, regulatory frameworks, and user assistance. It calls for the creation of a complete mobility ecosystem that brings together vehicles, vertiports, energy systems, airspace management, digital platforms, regulatory structures, and user support services. Given that eVTOL aircraft are still under development, they are best seen — at least in the short and medium term — as supplementary solutions that can enhance and expand current transportation options rather than fully substitute them [1].

Although Urban Air Mobility offers important opportunities, its implementation also brings a number of infrastructure, operational, environmental, and social challenges. Among these, vertiport planning is particularly important. Vertiports must provide safe areas for take-off and landing, while also supporting passenger processing, charging, maintenance, emergency response, and integration with existing ground transport systems. In addition, operating safely at low altitudes will demand strong communication, navigation, and surveillance capabilities, reliable procedures for traffic separation, well-prepared emergency protocols, and close coordination with today's conventional aviation activities.

Environmental concerns — especially noise pollution and overall life-cycle emissions — as well as social issues such as perceived safety, privacy, affordability, and building public trust, will play a major role in whether UAM gains broad acceptance. Therefore, the rollout of UAM should be treated as a full system-level planning challenge, not just a matter of developing new aircraft technology.

Regulation will play a decisive role in the practical implementation of UAM. UAM brings several new elements into play: different types of aircraft, new ways of using urban airspace at low altitudes, much higher frequency of operations, and safety risks that current aviation rules are not fully equipped to handle. In Türkiye, the present regulatory system is based largely on the Turkish Civil Aviation Law and the rules set by the Directorate General of Civil Aviation (SHGM). However, according to various studies, the country still lacks specific regulations tailored to UAM, detailed rules on safety and environmental protection, and clear instructions on how to integrate low-altitude flights with the existing airspace [3].

In the Turkish context, UAM should be evaluated not only as an aviation-related innovation, but also as a multidisciplinary socio-technical transition. Its implementation requires the coordinated development of vehicle technologies, vertiport infrastructure, energy systems, airspace management, cybersecurity governance, legal responsibility mechanisms, and public acceptance strategies. The use of autonomous or semi-autonomous aerial vehicles in dense urban environments also raises important questions regarding liability, property rights, privacy, software governance, and the distribution of responsibility among operators, manufacturers, infrastructure providers, municipalities, and public authorities [4]. Based on this perspective, the present study provides an integrated assessment of UAM from technical, operational, environmental, social, and regulatory perspectives, with particular attention to its possible future implementation in Türkiye.

2 Conceptual and Methodological Framework

Urban Air Mobility constitutes a novel low-altitude transport system intended for the movement of passengers and freight within metropolitan boundaries. Unlike conventional aviation, which depends on airport infrastructure and extended routes, this model prioritizes

short, high-frequency operations tailored to the demands of densely populated urban settings. AAM represents a broader concept encompassing regional, rural, intercity, and remote-area air transport applications. Accordingly, UAM can be considered an urban subcategory of AAM, with a particular emphasis on congestion mitigation, improved accessibility, reduced travel times, and integration with existing public transport networks [2], [3].

The technological foundation of UAM is closely linked to eVTOL aircraft. These platforms differ from traditional helicopters by utilizing electric propulsion, distributed rotor configurations, lower anticipated noise levels, and the potential for reduced operating and maintenance costs. Performance characteristics vary based on configuration, mission profile, energy system, payload, range, and certification requirements. The literature typically categorizes eVTOL platforms as Multicopter, Lift+Cruise, Tiltrotor, and Vectored Thrust designs. Each configuration presents distinct trade-offs; therefore, aircraft selection should account for speed, range, capacity, energy consumption, safety, noise, infrastructure compatibility, and economic feasibility [5-7].

A structured review-based methodology was employed in this study. Academic literature, regulatory documents, technical reports, and selected aircraft data were analyzed to evaluate UAM across four analytical dimensions. The first dimension is technical and vehicle-related, encompassing eVTOL design, range, speed, capacity, energy consumption, and safety. The second dimension addresses infrastructure and operations, including vertiport planning, charging infrastructure, maintenance, multimodal integration, and low-altitude airspace management. The third dimension considers environmental and social factors, such as emissions, noise, visual impact, privacy, perceived safety, and public acceptance. The fourth dimension focuses on regulatory and Türkiye-specific issues, including legal gaps, Directorate General of Civil Aviation-related concerns, certification requirements, cybersecurity governance, and pilot implementation priorities.

The review incorporates a multidisciplinary perspective, emphasizing that UAM should not be viewed solely as a vehicle-centered aviation innovation. Successful deployment necessitates the involvement of aircraft manufacturers, infrastructure providers, software developers, energy operators, public authorities, municipalities, emergency services, and end users. This approach is particularly pertinent for Türkiye, where UAM-related discussions must address not only technical feasibility but also legal responsibility, product liability, criminal liability, data governance, public acceptance, and institutional readiness [4].

3 eVTOL Configurations and Representative Aircraft Models

The technical feasibility of UAM is intrinsically linked to the development and operational performance of eVTOL aircraft. Unlike conventional fixed-wing aircraft, eVTOLs operate without the need for long runways and enable flexible access to dense urban environments via vertiports or other dedicated landing facilities. eVTOL aircraft encompass multiple technological configurations, each offering specific advantages and limitations in terms of range, speed, payload, energy efficiency, noise, safety, operational reliability, and certification complexity.

Multicopter platforms utilize multiple rotors for vertical take-off, hovering, and flight control. These platforms are mechanically simpler than other eVTOL configurations and are effective during take-off, landing, and low-speed operations. Their simplicity and maneuverability render them suitable for short-distance urban missions, cargo transport, emergency response, and demonstration services. However, the absence of wings limits cruise efficiency, thereby restricting range and endurance and increasing reliance on battery performance and vehicle mass. Research on multirotor aerial vehicles highlights energy storage configuration, propulsion chain sizing, and flight endurance as critical design constraints for this class of aircraft [6], [8].

Lift+Cruise aircraft employ distinct propulsion systems for vertical lift and forward flight. Lift rotors facilitate take-off and landing, while fixed wings and cruise propellers enable efficient horizontal flight. This configuration enhances range and endurance relative to multicopters and is frequently regarded as a balanced solution for urban air taxi services and airport connection routes. However, integrating separate propulsion systems can increase structural weight and design complexity, and the small propellers used for vertical lift may generate additional noise due to elevated blade tip speeds [6], [9].

Tiltrotor and Vectored Thrust configurations deliver higher performance but entail greater complexity. Tiltrotor aircraft feature rotors or propulsion units that rotate during the transition from vertical lift to forward flight, while Vectored Thrust systems utilize propulsion units capable of changing direction to provide both lift and forward thrust. These configurations offer improved cruise efficiency and are suitable for extended UAM or regional air mobility missions. However, they necessitate advanced transition control, redundancy, maintenance protocols, and rigorous certification processes. Recent literature indicates that tiltrotor concepts provide speed and flexibility, multicopters offer simplicity but limited range, and Lift+Cruise designs represent a compromise between endurance and operational flexibility [6], [9].

The variety of eVTOL configurations demonstrates the absence of a dominant aircraft design within the UAM market. Garrow et al. highlight that manufacturers have developed markedly different concepts regarding seating capacity, speed, range, and business models [1]. This lack of convergence is attributable to the novelty of electric propulsion technologies and ongoing uncertainty about commercially viable mission profiles. Some designs prioritize short urban trips, while others are intended for airport shuttles, regional routes, cargo operations, or premium air taxi services. Consequently, UAM planning should align vehicle type with mission profile rather than presuming a universal aircraft solution for all operations.

Representative aircraft models exemplify these technological pathways. AirCar, developed in Türkiye, serves as a short-distance urban aerial mobility concept. The technical data reviewed in this study describe AirCar as a two-passenger vehicle equipped with eight electric motors, a maximum speed of approximately 120 km/h, a range of 50–80 km, and rapid charging capability that achieves 80% charge in 15 minutes. These features render it suitable for short urban operations where turnaround time is critical. However, like other early eVTOL concepts, its scalability depends on certification, operational safety, vertiport availability, charging infrastructure, and public acceptance.

Joby Aviation's S4 exemplifies a more advanced tiltrotor or vectored-thrust design. It accommodates one pilot and four passengers, with a reported cruise speed of approximately 322 km/h, a range of 131–161 km depending on reserve assumptions, and a maximum payload of approximately 450 kg. The aircraft employs six tilting rotors and is frequently cited as one of the more mature eVTOL models for passenger air taxi operations. Its high speed and range render it suitable for short urban trips, metropolitan airport connections, and selected regional missions [6].

Eve Air Mobility, developed by Embraer, exemplifies the Lift+Cruise configuration. This design separates vertical lift and horizontal propulsion and is intended for urban air taxi operations that require a balance of range, capacity, safety, and system simplicity. According to the reviewed material, Eve achieves a cruise speed of approximately 200 km/h, a range of 100 km, and accommodates one pilot plus four passengers, with potential for increased capacity in autonomous operation. Leonardo AW609, a tiltrotor aircraft, differs from fully electric eVTOL models and is positioned between conventional aviation and future advanced air mobility concepts. Although not a direct competitor for urban short-distance eVTOL operations, it serves as a benchmark for tiltrotor performance, certification experience, and the transition from helicopter-like vertical operations to fixed-wing cruise efficiency.

“In summary, eVTOL configurations present distinct trade-offs. Multicopters offer simplicity and are suitable for short missions; Lift+Cruise platforms provide balanced performance; and Tiltrotor or Vectored Thrust systems deliver higher speed and range but entail greater complexity. Table 1 summarizes the operational implications of main eVTOL configurations. For Türkiye, initial UAM deployment will necessitate careful alignment between aircraft type and intended use case. Short urban demonstration routes, airport transfers, emergency medical services, and limited logistics operations may each require specific vehicle configurations, infrastructure designs, operating procedures, and regulatory frameworks.

Table 1. Operational implications of main eVTOL configurations.

Configuration	Operational strengths	Main limitations	Potential early use cases
Multicopter	Mechanical simplicity, hovering capability, maneuverability, flexible take-off and landing.	Limited range and endurance because vertical flight is energy-intensive; sensitive to battery mass.	Short demonstration routes, small cargo, emergency support, controlled urban missions.
Lift+Cruise	More efficient cruise flight through wings; balanced range and operational simplicity.	Separate lift and cruise systems may increase structural weight, complexity, and noise around vertiports.	Airport shuttles, urban air taxi services, hospital connections, medium-distance routes.
Tiltrotor / Vectored Thrust	Higher cruise speed and range; better suitability for metropolitan and regional connections.	Transition control, redundancy, maintenance, and certification are more complex.	Premium air taxi, airport access, regional links, time-critical passenger missions.
Rotorcraft / tiltrotor benchmark	Existing vertical-lift experience, higher payload and range in selected models.	Noise, operating cost, fuel or hybrid architecture, and urban acceptance constraints.	Benchmarking, emergency services, medical transfer, advanced vertical-lift operations.

4 Infrastructure, Airspace, Environmental and Regulatory Requirements

The effective implementation of UAM requires not only mature aircraft but also dedicated ground infrastructure and the safe integration of operations with existing transport and aviation systems. Vertiports represent a critical component of the UAM ecosystem. These facilities extend beyond basic landing and take-off functions to encompass touchdown and lift-off zones, final approach and take-off areas, passenger processing, charging or battery-swap systems, maintenance, emergency response equipment, digital communication infrastructure, and connections to ground transport. Consequently, vertiport planning must be addressed as an integrated challenge involving aviation, urban planning, energy, and transport systems.

Recent literature highlights several key research themes in vertiport development, including location and network planning, capacity and throughput, safety, cost, weather sensitivity, noise, security, and regulatory requirements. Schweiger and Preis demonstrate that the term vertiport has become increasingly prevalent in UAM research, indicating a consensus on the necessity for specialized ground infrastructure [10]. Di Mascio et al. further contend that vertiport design and regulation cannot be directly adapted from conventional airports or heliports, as eVTOL operations involve distinct aircraft characteristics, energy systems, passenger flows, operational frequencies, fire-safety requirements, and urban impacts [11].

The Vertiport location is a critical planning decision. An effective vertiport network must be situated near major demand centers to offer travel-time benefits while also satisfying safety, land-use, structural, environmental, and accessibility requirements. Potential sites

include airport terminals, existing heliports, rooftops of large buildings, parking structures, transport hubs, commercial centers, hospitals, and logistics facilities. The appropriateness of each site depends on factors such as population density, public transport accessibility, road connectivity, structural capacity, emergency access, obstacle clearance, proximity to noise-sensitive areas, and grid connectivity. Therefore, vertiport site selection should employ a multi-criteria framework rather than relying solely on available space.

Energy infrastructure is a fundamental component of vertiport development. As eVTOL vehicles rely on high-capacity batteries or alternative energy systems, vertiports must facilitate rapid charging, battery swapping, energy storage, and grid connectivity. High-frequency operations can result in significant peak electricity demand, particularly in dense urban environments. Accordingly, vertiport design should account for electrical grid capacity, charging schedules, local storage, renewable energy integration, and operational turnaround times. In Türkiye, recent studies indicate that scaling UAM operations will require fast-charging or battery-swap facilities and integration with the energy grid or local storage systems [4].

Safety and emergency management are essential considerations in vertiport planning. eVTOL aircraft utilize energy sources such as lithium-ion batteries or, in some cases, hydrogen systems, which differ from conventional aviation fuels and introduce new requirements for fire safety, maintenance, emergency response, and local safety protocols. Additionally, factors such as downwash and outwash effects, rotor proximity, passenger movement, cybersecurity risks, and automated system failures must be addressed in vertiport design and operation. Updated guidelines on zoning, environmental noise, power infrastructure, and fire safety are necessary before large-scale deployment [4], [11].

Airspace integration constitutes a significant implementation challenge. UAM operations are expected to take place in low-altitude urban airspace, where eVTOL aircraft may interact with helicopters, drones, general aviation, restricted zones, tall structures, and emergency flight operations. Effective UAM deployment requires coordination between traditional Air Traffic Management and Unmanned Aircraft System Traffic Management. Essential requirements include establishing low-altitude corridors, implementing dynamic geofencing, deploying collision-avoidance systems, enabling real-time traffic deconfliction, providing communication and navigation infrastructure, establishing emergency landing procedures, and implementing digital monitoring tools. International initiatives such as Europe's U-Space framework and Japan's AAM roadmap underscore the need for specialized airspace zones and traffic management systems to ensure safe integration [3].

Environmental and social considerations are equally critical in UAM planning. While eVTOL aircraft are anticipated to generate lower local emissions compared to fossil-fuel aircraft during operation, their overall environmental performance is influenced by factors such as the electricity generation mix, battery production, charging infrastructure, vehicle occupancy, operational efficiency, and life-cycle impacts. UAM should not be presumed to be a zero-impact mobility solution. Its sustainability must be assessed based on energy sources, operational patterns, substitution of ground trips, and the environmental costs associated with infrastructure.

Noise remains a significant environmental and social concern. Although eVTOL aircraft are often characterized as quieter than helicopters, frequent low-altitude flights over densely populated urban areas may still cause annoyance, particularly near vertiports, residential neighborhoods, hospitals, schools, and historic districts. UAM planning must therefore incorporate noise-aware route design, strategic selection of vertiport locations, operational time restrictions, and community-sensitive flight procedures. Simulation-based and noise-aware planning methodologies can facilitate more acceptable operations by accounting for fleet size, flight frequency, trajectory design, and community noise constraints [4].

Public acceptance is a fundamental prerequisite, as both users and non-users will be impacted by UAM operations. Factors such as perceived safety, cost, travel time savings, comfort, trust in automation, privacy, and willingness to pay are likely to influence acceptance. Mermertaş and Karakan demonstrate that attitudes toward UAM vary according to socio-economic characteristics, and that willingness to use and pay for UAM services should be assessed prior to implementation [12]. This consideration is particularly relevant for Türkiye, where initial deployments should be accompanied by public engagement and transparent communication regarding safety, cost, and social benefits.

Regulatory readiness is intrinsically connected to safety and public trust. UAM introduces dense low-altitude operations, autonomous or semi-autonomous flight, high-frequency take-off and landing cycles, vertiport-based passenger processing, and digital traffic management. While existing aviation regulations provide a general framework, they do not yet encompass detailed UAM-specific standards for aircraft certification, pilot or operator qualifications, environmental protection, low-altitude corridor management, data privacy, and cybersecurity. Consequently, UAM regulation should address not only aircraft certification but also the broader context of a software-intensive, multi-actor mobility ecosystem [3], [4].

5 Environmental, Social, and Regulatory Considerations

UAM implementation in Türkiye should proceed through a gradual, controlled transition rather than an immediate large-scale deployment. Türkiye possesses favorable conditions, including congested metropolitan areas, expanding domestic technological capacity, established aviation expertise, and diverse potential use cases such as airport access, emergency medical services, disaster response, tourism, and limited logistics. These opportunities must be assessed in conjunction with infrastructure, airspace, regulatory, legal, environmental, and social constraints [3], [4].

The initial priority is to identify realistic pilot use cases. Early deployment should avoid focusing on widespread commercial air taxi services. Instead, limited and high-value applications, including airport-city center connections, medical transport between hospitals, rapid access to disaster zones, and small-scale cargo delivery, should be tested through controlled demonstration corridors. These pilot projects would enable operators and regulators to collect operational data, assess safety risks, test charging infrastructure, evaluate noise impacts, and measure public perception prior to broader deployment.

Major metropolitan areas such as Istanbul, Ankara, and İzmir present strong demand potential but also significant planning challenges. Dense urban structures, restricted airspace, high-rise buildings, limited land availability, and noise-sensitive zones necessitate careful vertiport planning. Potential sites include airport areas, existing heliports, rooftops of structurally suitable buildings, transport hubs, hospitals, and logistics centers. Each location should be evaluated based on safety zones, emergency access, structural capacity, multimodal integration, energy supply, environmental effects, and social acceptance. Recent assessments of Türkiye indicate that vertiports in dense cities require structural reinforcement, noise mitigation, emergency service access, environmental compliance, and integration with metro stations, airports, and bus depots [4].

The second priority is airspace integration. Türkiye currently lacks a dedicated low-altitude corridor system and specific provisions for high-frequency eVTOL operations. SHGM, municipalities, air traffic authorities, emergency institutions, and private operators should collaboratively develop operating zones, low-altitude corridors, geofencing rules, collision-avoidance procedures, real-time traffic management protocols, and emergency response procedures. The absence of UAM-specific operating categories may create uncertainty in certification, liability, and enforcement; therefore, airspace planning must be coordinated with regulatory and legal preparation.

The third priority is establishing a phased regulatory framework. International experience demonstrates that countries preparing for UAM require specific airworthiness standards, pilot and operator certification, vertiport design regulations, public acceptance strategies, and low-altitude traffic management systems. In Türkiye, targeted reforms are necessary for eVTOL certification, operational safety, environmental regulation, cybersecurity, data governance, and urban airspace management. Regulatory sandboxes, controlled test zones, and simulation-based safety assessments can facilitate this transition.

UAM in Türkiye should be conceptualized as a socio-technical mobility transition. Beyond aircraft and infrastructure, deployment will require robust cybersecurity governance, software update management, product liability regulations, data privacy protection, and clear allocation of responsibilities among manufacturers, operators, software developers, infrastructure providers, public authorities, and municipalities. This is essential because autonomous and semi-autonomous aerial vehicles will introduce new questions regarding fault, negligence, foreseeable risk, property rights, neighborhood law, and criminal liability [4]. Türkiye's UAM strategy should commence with controlled pilot projects supported by environmental monitoring, public engagement, safety assessment, and institutional coordination. Suggested pilot implementation priorities for Türkiye is summarized at Table 2.

Table 2. Suggested pilot implementation priorities for Türkiye.

Priority area	Recommended action	Expected contribution
Pilot corridors	Test airport-city, hospital-hospital, disaster logistics, and limited cargo missions before commercial air taxi deployment.	Produces operational data and demonstrates public value in controlled settings.
Vertiports and energy	Evaluate rooftops, heliports, airport areas, hospitals, and transport hubs with charging, storage, and emergency-access requirements.	Links aircraft capability with infrastructure feasibility and multimodal access.
Low-altitude airspace	Define corridors, geofencing, deconfliction, emergency landing rules, and coordination between ATM and UTM functions.	Reduces safety, certification, and enforcement uncertainty.
Governance and acceptance	Use regulatory sandboxes, cybersecurity rules, data-governance procedures, noise monitoring, and public engagement.	Builds institutional readiness, accountability, and social trust.

6 Discussion: Cross-cutting Research Needs

The review suggests that future research on UAM should transition from technology-focused feasibility analyses to integrated planning and governance frameworks. Demand remains a critical uncertainty. UAM will generate significant benefits only if it attracts users from trips with substantial travel-time savings and if access, waiting, boarding, and transfer times do not negate these advantages. Consequently, demand studies should account for total door-to-door travel time, willingness to pay, service reliability, user heterogeneity, and the competitive or complementary roles of metro, rail, bus, taxi, and ride-hailing systems. In Türkiye, such analyses are especially important, as high congestion does not necessarily translate into sufficient willingness to use or pay for aerial mobility services.

A second research priority involves simulation and network design. UAM system performance is determined by the interplay among vertiport locations, fleet size, charging durations, passenger demand, dispatching protocols, airspace limitations, and weather conditions. Simulation tools enable the evaluation of these factors prior to infrastructure investment. For instance, event-based operational simulations and digital-twin methodologies

can assess passenger delays, aircraft utilization, energy consumption, queuing at vertiports, emergency capacity, and noise exposure. These approaches would enable Turkish cities to compare alternative pilot corridors and determine whether proposed vertiport networks can function safely and efficiently under realistic conditions.

Future UAM research in Türkiye should emphasize institutional coordination among aviation authorities, municipalities, transport operators, energy providers, emergency services, technology companies, and legal institutions. Developing a coordinated roadmap is essential to delineate responsibilities for certification, vertiport approval, corridor designation, cyber incident response, environmental monitoring, and public communication.

7 Conclusion

UAM has emerged as a promising mobility concept, driven by eVTOL aircraft, electric propulsion, autonomous systems, digital aviation technologies, and increasing challenges of urban transport. This study demonstrates that UAM could enhance future urban transportation through applications including airport access, emergency medical transport, disaster response, tourism, selected logistics operations, and limited air taxi services. However, UAM should not be evaluated solely as an aircraft technology. It represents a complex mobility ecosystem that requires coordinated development of vehicles, vertiports, energy systems, low-altitude airspace management, safety procedures, regulatory frameworks, and public acceptance.

Different eVTOL configurations offer distinct operational advantages. Therefore, aircraft selection should be aligned with the intended use case, infrastructure capacity, safety standards, and regulatory readiness.

In Türkiye, UAM presents both opportunities and challenges. Metropolitan areas such as Istanbul, Ankara, and İzmir may generate demand for airport access, emergency response, and selected logistics applications, while domestic initiatives suggest emerging technological capacity. However, scalable implementation requires certified vertiport infrastructure, charging and energy systems, dedicated low-altitude corridors, eVTOL-specific standards, operational safety rules, and clearer airspace integration procedures. Existing aviation regulations provide a foundation for conventional aviation but are inadequate for addressing UAM-specific operational, environmental, legal, and cybersecurity concerns.

Therefore, Türkiye should implement a phased approach that includes controlled pilot projects, regulatory sandboxes, public engagement, environmental and noise monitoring, and simulation-based safety assessments. This strategy would enable the testing of technical feasibility while simultaneously developing the institutional, legal, and social readiness necessary for safe, sustainable, and publicly acceptable UAM operations.

Acknowledgments

Grammarly Pro was used to improve grammar and readability. The authors remain responsible for the content, analysis, and conclusions.

References

1. Garrow, L.A., German, B.J., Leonard, C.E.: Urban air mobility: A comprehensive review and comparative analysis with autonomous and electric ground transportation for informing future research. Transportation Research Part C 132, 103377 (2021).
2. Sengupta, R., Bulusu, V., Mballo, C.E., Onat, E.B., Cao, S.A.: Urban air mobility research challenges and opportunities. Annual Review of Control, Robotics, and Autonomous Systems 8, 407–431 (2025).
3. Özmen, A.Z.: Urban Air Mobility (UAM) in Türkiye: Evaluating existing aviation laws and international practices. Süleyman Demirel Üniversitesi Hukuk Fakültesi Dergisi 14(2), 1385–1419 (2024).

4. Dündar, S., Duysak, M., Türker, G.: Urban Air Mobility in Türkiye: Technical feasibility, legal challenges, and societal acceptance in a multidisciplinary framework. In: ITS Istanbul Conference Proceedings (2026).
5. Savaş, Ö.F., Gökşen, Y.: Geleneksel hava taksi ile kentsel hava hareketliliğinin karşılaştırmalı analizi. İzmir Sosyal Bilimler Dergisi 5(1), 21–43 (2023).
6. Tripaldi, F., Vianello, S., Bianchi, N.: Emerging trends in urban air mobility: An extensive review. Energies 18, 1426 (2025).
7. Durak, M.S.: Strategic assessment of eVTOLs for sustainable urban air mobility using the CRITIC-based EDAS method. Journal of Transportation and Logistics 10(1), 193–210 (2025).
8. Chahba, S., Sehab, R., Morel, C., Krebs, G., Akrad, A.: Fast sizing methodology and assessment of energy storage configuration on the flight time of a multirotor aerial vehicle. Aerospace 10, 425 (2023).
9. Xu, J., Guan, C., Wang, Y., Zhuang, J., Gan, W.: A systematic review of urban air mobility development: eVTOL drones' technological challenges and low-altitude policies of Shenzhen. Drones 9, 842 (2025).
10. Schweiger, K., Preis, L.: Urban air mobility: Systematic review of scientific publications and regulations for vertiport design and operations. Drones 6(7), 179 (2022).
11. Di Mascio, P., Del Serrone, G., Moretti, L.: Vertiports: The infrastructure backbone of advanced air mobility - A review. Eng 6(5), 93 (2025).
12. Mermertaş, F., Karakan, H.I.: The future of travel: A study on urban air mobility acceptance. SDÜİİBFD 29(1), 13–24 (2024).

Author Contribution Statement

- *Conceptualization:* Selim Dündar
- *Methodology:* Selim Dündar
- *Investigation:* Selim Dündar, Barış Akdemir
- *Writing – Original Draft:* Selim Dündar, Barış Akdemir
- *Writing – Review & Editing:* Selim Dündar

List of Abbreviations

- **AAM** — Advanced Air Mobility
- **eVTOL** — Electric Vertical Take-Off and Landing
- **SHGM** — Sivil Havacılık Genel Müdürlüğü
- **UAM** — Urban Air Mobility

Publication Note

This paper was peer-reviewed, accepted for presentation, and included in the proceedings of the ACE2026 – International Conference on Advances in Civil Engineering, held on 12–14 October 2026 in Trabzon, Türkiye.

This paper may be cited as follows:

Dündar S., Akdemir B., "Urban Air Mobility in Türkiye: Opportunities, Challenges, and Future Perspectives," in Proceedings of the ACE2026 – International Conference on Advances in Civil Engineering, Trabzon, Türkiye, 12–14 October 2026.

Comparative Analysis of Choice Models and Machine Learning Methods for Synthetic Population-Based Mode Choice Modeling of E-Scooter Users

Selim Dündar[1], Gökçe Yurtseven[2] and Gürkan Günay[3]
[1] 0000-0003-4433-1998, Istanbul Okan University, Civil Engineering Department, Istanbul, Türkiye, selim.dundar@okan.edu.tr
[2] 0009-0005-3060-5697, Istanbul Okan University, Civil Engineering Department, Istanbul, Türkiye, gokyurtseven@stu.okan.edu.tr
[3] 0000-0003-0597-1511, Istanbul Bilgi University, Civil Engineering Department, Istanbul, Türkiye, gurkan.gunay@bilgi.edu.tr

Abstract. Understanding user preferences is a key challenge in transportation planning. Although data mining and big data approaches have advanced considerably, stated-preference surveys remain an effective method for analyzing travel behavior, particularly for future-oriented scenarios and policy alternatives. This study conducted an online Stated Preferences survey to examine the mode-choice behavior of e-scooter users under varying travel-time and cost conditions. Participants evaluated 24 hypothetical scenarios and selected one of four modes: private car, taxi, public transportation, or e-scooter.

The collected data were analyzed using traditional discrete-choice models and four machine-learning methods. Model performance was assessed through accuracy, precision, recall, and F1-score. The results showed that machine-learning methods outperformed traditional choice models, especially in capturing nonlinear relationships and complex interactions among variables.

In the second stage, a synthetic population of 5,000 users was generated from the survey data. Mode choices across the 24 scenarios were estimated using the two best-performing machine-learning methods, Random Forest and Decision Tree, together with the traditional choice model. This enabled comparison not only in terms of classification performance but also in terms of behavioral distributions within the synthetic population.

The findings revealed that models with similar predictive performance can produce different mode-choice distributions in specific scenarios. Therefore, high accuracy alone does not ensure behavioral consistency. The study contributes to the literature by highlighting the importance of considering both prediction accuracy and behavioral plausibility in preference modeling and synthetic population generation.

Keywords: Micromobility; E-scooter users; Machine learning; Behavioral modeling.

1 Introduction

User preferences are a central concern in transportation planning, especially with the introduction of emerging mobility services into established urban transport systems. In densely populated metropolitan areas, rising congestion, limited road capacity, environmental challenges, and evolving mobility needs have promoted the adoption of flexible, short-distance transport alternatives. Shared e-scooters have emerged as a significant element of urban

micromobility because they facilitate first and last kilometer connectivity, complement public transportation, and offer a practical solution for short urban journeys.

The role of e-scooters within urban mobility systems is highly context-dependent. Their adoption is shaped by factors such as travel time, cost, safety perceptions, infrastructure availability, traffic conditions, parking opportunities, trip purpose, and user characteristics. Prior research indicates that e-scooter users differ by socio-demographic attributes, including age, gender, income, education level, and ownership status [1–4]. The transport modes replaced by e-scooter trips also vary by context. Some studies report that e-scooters primarily substitute for walking and public transportation, while others find that they may replace private car, taxi, or ride-hailing trips, depending on local infrastructure, parking, and travel patterns [1, 3–5].

Discrete-choice models have long been employed to analyze mode-choice behavior in transportation planning. Grounded in the principle of utility maximization, these models have been applied to urban and intercity travel, route selection, airport access, freight transport, and emerging mobility services [6–8]. Binary Logit, Multinomial Logit, Nested Logit, and Mixed Logit models establish interpretable relationships between travel attributes and user choices, with Mixed Logit models further accommodating preference heterogeneity [9, 10]. However, the application of these models to e-scooter mode choice remains limited. Existing research has explored e-scooter and e-bike preferences, integration with public transportation, infrastructure selection, and sensitivity to travel time and cost [4, 11–14].

Recent developments in data mining and machine learning have expanded opportunities for modeling travel behavior. Machine-learning techniques can capture nonlinear relationships and complex variable interactions that conventional utility-based models may not fully represent. In the context of e-scooters, prior studies demonstrate that machine-learning approaches are effective for identifying demographic differences, access-related effects, and behavioral patterns in short-distance micromobility choices [15]. Nevertheless, higher predictive accuracy does not guarantee that a model yields behaviorally consistent or policy-relevant outcomes, particularly when applied to scenario-based analyses.

This concern is especially relevant for synthetic population applications. Within the broader transportation modeling literature, synthetic populations and agent-based models have been utilized to represent travel demand, parking demand, shared mobility, and network-level impacts [16–19]. However, the integration of e-scooter mode-choice modeling with synthetic population analysis is still limited. This gap is methodological in nature: models may exhibit comparable classification performance yet produce divergent aggregate mode-choice distributions when applied to larger hypothetical populations.

The present study addresses this methodological gap by comparing traditional discrete-choice models and machine-learning methods for e-scooter mode-choice behavior. An online stated-preference survey was administered in Istanbul to assess user choices under varying travel-time and cost conditions. Participants evaluated 24 hypothetical scenarios designed for a 4 km corridor between Bostancı and Selamiçeşme on Bağdat Avenue, selecting one of four transport modes: private car, taxi, public transportation, or e-scooter. The resulting data were analyzed using both conventional choice modeling and machine-learning techniques, with model performance assessed through accuracy, precision, recall, and F1-score.

In the subsequent stage, a synthetic population of 5,000 users was generated based on the survey data. Mode choices across the 24 scenarios were estimated using the two best-performing machine-learning models, Random Forest (RF) and Decision Tree (DT), alongside the traditional discrete-choice model. This approach enabled a comparison of modeling techniques not only in terms of predictive performance but also regarding the behavioral distributions produced under identical scenario conditions. The study contributes to the literature by demonstrating that prediction accuracy alone is insufficient for model evaluation

and that behavioral plausibility must also be considered in synthetic population-based mode-choice analysis.

2 Survey Design and Data Collection

An online stated-preference (SP) survey was developed to examine mode-choice behavior associated with e-scooter use in Istanbul. The survey sought to determine how users respond to varying combinations of travel time and travel cost when selecting among private car, taxi, public transportation, and e-scooter options. Initially, 512 responses were collected. Given that the study focused exclusively on Istanbul, responses from participants residing outside the city were excluded from the analysis. Following this filtering process, the final sample comprised 461 valid respondents. This sample size was deemed sufficient, as it exceeds the minimum recommended sample size of 384 for heterogeneous populations larger than 500.000 individuals [20].

The questionnaire comprised three main sections. The first section gathered socio-demographic information, including gender, age, education level, income level, driving license ownership, private car ownership, household size, number of cars in the household, and employment status. These variables were incorporated to capture individual heterogeneity in mode-choice behavior and to assess the influence of user characteristics on e-scooter preferences.

The second section addressed respondents' current travel habits and attitudes toward e-scooters. Participants provided information regarding their most frequently used transport mode, primary trip purpose, availability of bicycle lanes within 250 meters of their residence, preferred infrastructure for e-scooter use, willingness to use e-scooters on sidewalks or roads, perceived safety of e-scooters, parking preferences, compliance with traffic regulations, and the main factors influencing their decision to choose or avoid e-scooters. These questions were designed to describe the behavioral and perceptual context underlying the stated-preference choices.

The third section of the survey presented hypothetical mode-choice scenarios. These scenarios were constructed for a 4 km urban trip along Bağdat Avenue, between Bostancı and Selamiçeşme, a dense urban corridor in Istanbul. In each scenario, participants were offered four alternatives: private car, taxi, public transportation, and e-scooter. Each alternative was characterized by two primary attributes: travel time and travel cost. Respondents were instructed to select the mode they would prefer under the specified conditions.

Travel time levels were established based on three traffic conditions: free-flow, unstable, and congested. For private car and taxi, travel times were set at 9, 20, and 30 minutes, respectively. Public transportation travel times were 15, 29, and 45 minutes. As the e-scooter speed was assumed to remain constant regardless of traffic conditions, its travel time was fixed at 16 minutes for the 4 km trip, corresponding to the legal speed limit of 15 km/h.

Travel cost was represented by two levels for each mode, reflecting the base cost and an increased cost level. The increased cost was calculated using the 2023 inflation rate of 65%. For the 4 km trip, the resulting cost levels were 65 TL and 105 TL for private car, 15 TL and 25 TL for public transportation, 75 TL and 125 TL for taxi, and 75 TL and 125 TL for e-scooter. The e-scooter base cost was determined by averaging the prices of three shared e-scooter operators and rounding to 75 TL for clarity in the survey.

A full factorial design would have resulted in 48 scenarios based on the combinations of travel cost levels and traffic conditions. Presenting this number of scenarios to each respondent could have increased response burden and compromised data quality. To address this, a fractional factorial design was implemented to reduce the number of scenarios while maintaining the integrity of the experimental structure. Consequently, the final questionnaire included 24 scenarios. Each of the 461 respondents evaluated 24 scenarios, resulting in a dataset

of 11,064 respondent-scenario observations for subsequent modeling. The properties of the scenarios are given at Table 1.

Table 1. The properties of the scenarios.

		Private Car		Taxi		E-scooter		Public transport	
No	**Scenario**	**Cost**	**Time**	**Cost (TL)**	**Time (min)**	**Cost (TL)**	**Time (min)**	**Cost (TL)**	**Time (min)**
1	1- Free-flow	105	9	125	9	125	16	25	15
2	1- Unstable	105	20	125	20	125	16	25	29
3	1- Congested	105	30	125	30	125	16	25	45
4	2- Free-flow	105	9	125	9	75	16	15	15
5	2- Unstable	105	20	125	20	75	16	15	29
6	2- Congested	105	30	125	30	75	16	15	45
7	3- Free-flow	105	9	75	9	125	16	15	15
8	3- Unstable	105	20	75	20	125	16	15	29
9	3- Congested	105	30	75	30	125	16	15	45
10	4- Free-flow	105	9	75	9	75	16	25	15
11	4- Unstable	105	20	75	20	75	16	25	29
12	4- Congested	105	30	75	30	75	16	25	45
13	5- Free-flow	65	9	125	9	125	16	15	15
14	5- Unstable	65	20	125	20	125	16	15	29
15	5- Congested	65	30	125	30	125	16	15	45
16	6- Free-flow	65	9	125	9	75	16	25	15
17	6- Unstable	65	20	125	20	75	16	25	29
18	6- Congested	65	30	125	30	75	16	25	45
19	7- Free-flow	65	9	75	9	125	16	25	15
20	7- Unstable	65	20	75	20	125	16	25	29
21	7- Congested	65	30	75	30	125	16	25	45
22	8- Free-flow	65	9	75	9	75	16	15	15
23	8- Unstable	65	20	75	20	75	16	15	29
24	8- Congested	65	30	75	30	75	16	15	45

3 Modeling Methodology

A sequential modeling framework was implemented, comprising three primary stages: traditional discrete-choice modeling, machine-learning-based prediction, and synthetic population-based comparison. In the initial stage, discrete-choice models were constructed to estimate respondents' mode choices among private car, taxi, public transportation, and e-scooter alternatives. Discrete-choice models were selected as the starting point because they constitute the conventional framework for mode-choice analysis and offer interpretable utility-based relationships between travel attributes and user choices.

The explanatory variables comprised travel time, travel cost, and selected user-specific characteristics obtained from the survey. Travel time and travel cost were treated as alternative-specific variables, while socio-demographic and attitudinal variables captured preference heterogeneity. Categorical variables were converted into dummy variables prior to model

estimation. Each respondent evaluated 24 stated-preference scenarios, resulting in a modeling dataset with repeated respondent-scenario observations.

The initial discrete-choice models yielded valuable behavioral insights; however, their predictive performance was limited. Both the pooled model and the model for respondents without private car ownership achieved an accuracy of approximately 54%, whereas the model for private car owners attained only 40%. This relatively low performance was primarily due to the dominance of public transportation choices in the dataset and the models' tendency to classify some private car and e-scooter choices as public transportation.

Given the limited predictive performance of the discrete-choice models, supervised machine-learning methods were subsequently evaluated. Four models were developed: an Artificial Neural Network (ANN), a DT, a RF, and a gradient boosting-based classification model (GB). These models were trained using the same survey-based dataset and targeted the selected transportation mode. In contrast to discrete-choice models, machine-learning methods do not require a predefined utility specification and can capture nonlinear relationships, threshold effects, and complex interactions among explanatory variables.

Model performance was assessed using confusion matrices and standard classification metrics, including accuracy, precision, recall, and F1-score. Due to dataset imbalance, both macro and weighted metrics were reported. This distinction was necessary because public transportation and private car constituted the majority classes, while taxi and e-scooter had lower support values. Specifically, the dataset contained 5.186 public transportation observations, 3.663 private car observations, 1.599 e-scooter observations, and 640 taxi observations.

Table 2. Summary of machine-learning model performance.

	Macro				**Weighted**			
	Accuracy	**Precision**	**Recall**	**F1**	**Accuracy**	**Precision**	**Recall**	**F1**
ANN	0,844	0,571	0,509	0,505	0,872	0,717	0,704	0,690
Decision Tree	**0,924**	**0,835**	**0,815**	**0,829**	**0,897**	**0,828**	**0,890**	**0,854**
Random Forest	0,859	0,664	0,553	0,575	0,827	0,701	0,723	0,701
Gradient Boosting	0,833	0,706	0,725	0,698	0,863	0,663	0,524	0,553

The results shown in Table 2 demonstrate that the machine-learning models consistently outperformed the traditional discrete-choice models. Among the evaluated approaches, the Decision Tree model exhibited the strongest overall performance, achieving the highest macro accuracy, macro F1-score, weighted accuracy, and weighted F1-score. The Random Forest model was retained for the synthetic population stage as a benchmark for ensemble-based machine learning. Consequently, Decision Tree and Random Forest were selected as the two machine-learning models for comparison with the discrete-choice model in the subsequent synthetic population analysis.

4 Synthetic Population Generation

Following model development, a synthetic population was constructed to assess the impact of model selection on scenario-based mode-choice outcomes. This stage aimed to extend the analysis beyond observation-level performance metrics by determining whether different models yield consistent aggregate distributions when applied to a larger hypothetical population. A synthetic population of 5.000 users was generated by maintaining the proportional distribution of key characteristics identified in the stated preference (SP) survey, such as socio-demographic variables, travel-related attributes, and e-scooter-related attitudes. Each synthetic user was evaluated across the same 24 scenarios described in Table 1, resulting in 120.000 user-scenario observations. Mode choices were predicted using three models: the

traditional discrete-choice model, Decision Tree, and Random Forest. The discrete-choice model served as an interpretable benchmark, while Decision Tree and Random Forest were selected for their superior machine-learning performance. For each scenario, predicted choices were aggregated to determine the percentage distribution of users selecting private car, taxi, public transportation, or e-scooter. This approach facilitated comparison of the population-level implications of model selection. Although accuracy, precision, recall, and F1-score assess predictive performance, these metrics do not necessarily reflect whether a model produces plausible aggregate mode-choice patterns. Consequently, the synthetic population analysis provided an additional evaluation step to assess behavioral consistency under scenario-based conditions.

5 Results and Discussion

The results were evaluated in two complementary stages. First, the predictive performance of the modeling approaches was assessed using classification metrics. Second, the models were applied to the synthetic population to compare their scenario-based mode-choice distributions. This second stage is significant because models with distinct prediction mechanisms can produce different aggregate behavioral outcomes, even when trained on the same stated-preference dataset.

As shown in Table 2, machine-learning models generally outperformed traditional discrete-choice models in predictive performance. The Decision Tree model demonstrated the strongest overall performance, achieving the highest macro and weighted F1-scores. The Random Forest model also yielded competitive results and was retained as an ensemble-based machine-learning benchmark. In contrast, discrete-choice models exhibited lower predictive accuracy, with the pooled model achieving approximately 54% accuracy. While the discrete-choice model remains valuable as an interpretable benchmark, its limited predictive performance indicates that it may not fully capture nonlinear relationships and interaction effects present in the survey data.

Table 3 presents the mode-choice shares predicted by the Decision Tree, Random Forest, and discrete-choice models for the synthetic population across the 24 stated-preference scenarios. The table enables a direct comparison of how the three modeling approaches respond to changes in travel time and travel cost.

The results indicate substantial differences among the three models. The Decision Tree model produced the most balanced mode-choice distributions across the four alternatives. On average, it predicted 16,2% e-scooter use, 4,8% taxi use, 42,9% public transportation use, and 36,1% private car use across the 24 scenarios. This finding demonstrates that the model distributed choices across alternatives more flexibly and generated non-zero shares for all modes in every scenario. The e-scooter share predicted by the Decision Tree model increased systematically under congested traffic conditions, rising from an average of 3,2% in free-flow conditions to 12,4% in unstable traffic and 33,1% in congested traffic.

The Random Forest model also demonstrated sensitivity to traffic conditions, but it produced more conservative e-scooter shares in free-flow and unstable traffic scenarios. The average e-scooter share was 0,9% in free-flow traffic and 2,3% in unstable traffic, increasing sharply to 30,1% under congested conditions. This pattern suggests that the Random Forest model associated e-scooter preference primarily with situations where e-scooters offered a clear travel-time advantage over motorized modes and public transportation. Regarding overall distribution, Random Forest assigned the highest average share to public transportation, followed by private car, e-scooter, and taxi.

The discrete-choice model produced a more rigid distributional pattern. Across the 24 scenarios, it assigned no taxi share in any scenario and predicted e-scooter use only in four scenarios: Scenarios 6, 12, 18, and 24. These scenarios all represent congested traffic conditions

and feature the lower e-scooter fare of 75 TL. In these cases, e-scooter travel time remains 16 minutes, while private car and taxi travel times increase to 30 minutes and public transportation travel time increases to 45 minutes. Thus, the discrete-choice model predicted e-scooter use only when e-scooters provided both a significant travel-time advantage and a relatively low cost.

Table 3. Scenario-based mode-choice shares predicted by the Decision Tree, Random Forest, and discrete-choice models for the synthetic population.

Scenario	Decision Tree				Random Forest				Multinomial Logit			
	E-scooter	Taxi	Public Transport	Private Car	E-scooter	Taxi	Public Transport	Private Car	E-scooter	Taxi	Public Transport	Private Car
1	1,69	1,50	60,37	36,44	0,26	1,86	77,16	20,72	0,00	0,00	92,64	7,36
2	16,05	0,26	47,05	36,64	1,33	1,17	63,63	33,87	0,00	0,00	84,74	15,26
3	34,59	9,64	34,44	21,32	36,11	1,31	53,11	9,48	0,00	0,00	70,50	29,50
4	5,53	1,57	60,00	32,90	0,97	0,87	78,41	19,75	0,00	0,00	92,78	7,22
5	21,07	0,33	46,68	31,92	4,76	0,00	69,65	25,59	0,00	0,00	91,44	8,56
6	37,95	7,82	34,61	19,61	42,11	1,08	47,66	9,15	43,02	0,00	34,28	22,70
7	1,91	10,04	51,82	36,23	2,03	0,38	78,49	19,10	0,00	0,00	92,78	7,22
8	5,39	8,80	50,40	35,41	3,06	0,14	65,73	31,07	0,00	0,00	91,44	8,56
9	30,66	13,33	36,62	19,39	19,96	5,53	65,28	9,23	0,00	0,00	71,22	28,78
10	5,31	10,90	51,49	32,30	0,45	2,05	77,12	20,38	0,00	0,00	92,64	7,36
11	7,95	9,83	49,90	32,32	2,93	1,52	68,80	26,75	0,00	0,00	84,74	15,26
12	35,26	9,73	36,21	18,80	43,30	3,80	46,04	6,87	43,02	0,00	33,72	23,26
13	1,58	1,54	51,63	45,25	0,75	1,14	51,12	46,99	0,00	0,00	80,16	19,84
14	17,14	0,08	38,35	44,43	1,54	0,40	39,88	58,18	0,00	0,00	71,22	28,78
15	30,05	5,66	34,21	30,07	15,97	0,32	48,45	35,27	0,00	0,00	46,44	53,56
16	2,83	2,47	49,93	44,77	0,84	1,32	47,05	50,79	0,00	0,00	74,52	25,48
17	17,55	1,18	36,48	44,79	1,75	0,76	39,44	58,05	0,00	0,00	70,12	29,88
18	33,41	4,19	33,55	28,84	35,09	0,60	41,31	23,00	33,92	0,00	19,36	46,72
19	1,43	1,70	38,84	58,03	0,67	1,49	39,26	58,58	0,00	0,00	74,52	25,48
20	4,43	0,24	37,28	58,05	1,19	0,89	36,82	61,10	0,00	0,00	70,12	29,88
21	30,17	7,35	35,16	27,32	16,03	0,98	52,45	30,54	0,00	0,00	37,52	62,48
22	5,16	1,70	40,34	52,80	0,87	1,58	48,22	49,33	0,00	0,00	80,16	19,84
23	9,34	0,24	38,78	51,64	1,93	0,82	40,86	56,39	0,00	0,00	71,22	28,78
24	32,29	4,86	35,08	27,77	31,88	1,48	49,33	17,31	33,92	0,00	25,60	40,48

These findings indicate that the discrete-choice model produced a threshold-like behavioral response. In congested scenarios with an e-scooter fare of 125 TL, the model assigned no e-scooter share, despite the travel-time advantage. Similarly, in free-flow and moderate traffic scenarios, the model did not predict e-scooter use because the time advantage was either absent or limited. The variation among the four e-scooter-positive scenarios also demonstrates the effect of private car cost. In Scenarios 6 and 12, where private car cost was 105 TL, the predicted

e-scooter share was 43,02%. In Scenarios 18 and 24, where private car cost decreased to 65 TL, the e-scooter share declined to 33,92%. This suggests that lower private car cost reduces the relative attractiveness of e-scooters, even under congested traffic conditions.

Another notable finding relates to public transportation. The discrete-choice model assigned a high average share to public transportation, approximately 68,9%, particularly under free-flow and unstable traffic conditions where e-scooter use was not predicted. In contrast, the Decision Tree and Random Forest models generated more varied distributions and permitted e-scooter shares to increase incrementally as travel conditions deteriorated.

The comparison further demonstrates that high predictive performance does not necessarily result in identical population-level behavioral outputs. Both the Decision Tree and Random Forest models outperformed the discrete-choice model in classification performance, yet they produced different scenario-based distributions. The Decision Tree model generated higher e-scooter shares across a broader range of scenarios, including some free-flow and unstable traffic cases. In contrast, the Random Forest model was more restrictive, concentrating e-scooter demand primarily in congested scenarios. This difference indicates that even machine-learning models with strong predictive performance may yield distinct behavioral interpretations when applied to a synthetic population.

The results demonstrate that model selection significantly affects scenario-based transportation analysis. The discrete-choice model provided a more interpretable but less flexible representation of e-scooter preferences, while the Decision Tree and Random Forest models produced more responsive aggregate distributions. These findings indicate that, for synthetic population applications and policy-oriented scenario analysis, behavioral plausibility and aggregate distributional effects should be evaluated alongside accuracy and F1-score.

From a policy perspective, the results indicate that e-scooters become competitive primarily when urban traffic conditions deteriorate and their cost remains sufficiently low. Congested scenarios with low e-scooter fares produced the highest e-scooter shares across all models. This finding suggests that e-scooters may serve as an effective alternative for short urban trips under congested conditions, but their competitiveness is highly sensitive to pricing. If e-scooter fares approach or exceed taxi-like cost levels, their modal share may remain limited, even when they offer travel-time advantages. Consequently, pricing strategies, infrastructure provision, and integration with public transportation should be considered collectively when evaluating the future role of e-scooters in urban mobility systems.

6 Conclusion

This study compares traditional discrete-choice models and machine-learning methods for predicting e-scooter-related mode choice using stated preference (SP) survey data from Istanbul. The analysis further examines whether these models yield consistent behavioral distributions when applied to a synthetic population of 5.000 users across 24 scenarios. Results indicate that while discrete-choice models offer valuable behavioral interpretation, their predictive performance is limited. In contrast, machine-learning methods, particularly Decision Tree and Random Forest, demonstrate stronger classification performance and more effectively capture nonlinear relationships in the survey data. However, analysis of the synthetic population reveals that predictive performance alone is insufficient for comprehensive model evaluation. Despite being trained on the same dataset, the models generate different aggregate mode-choice distributions under identical scenario conditions. The discrete-choice model produces a more rigid pattern, predicting e-scooter use primarily in congested scenarios with low e-scooter fares. Conversely, the Decision Tree and Random Forest models yield more flexible distributions and capture gradual shifts in e-scooter preference across varying travel-time and cost conditions. These findings underscore the importance of considering behavioral plausibility and aggregate consistency alongside accuracy, precision, recall, and F1-score. From a policy perspective, the

results indicate that e-scooters become more competitive as congestion increases and fares remain relatively low. Consequently, pricing strategies, infrastructure provision, and integration with public transportation should be jointly evaluated when planning e-scooter systems. Overall, this study advances synthetic population-based mode-choice modeling by demonstrating that model selection can directly influence scenario-based interpretations of micromobility demand.

Acknowledgments
This study was conducted as part of The Scientific and Technological Research Council of Türkiye (TÜBİTAK) 1001 Research Project, numbered 123M063, titled "Determining the Effects of Electric Scooters on Istanbul's Traffic and Environment, and Identifying the Optimal Operating Environment, Conditions, and Regulations," led by Selim Dündar with Gürkan Günay as a researcher and Gökçe Yurtseven as a scholar. The authors express their gratitude to TÜBİTAK for their support. Grammarly Pro was used to improve grammar and readability. The authors remain responsible for the content, analysis, and conclusions.

References

1. Laa, B., Leth, U.: Survey of E-Scooter Users in Vienna: Who They Are and How They Ride. Journal of Transport Geography 89, 102874 (2020).
2. Christoforou, Z., Gioldasis, C., de Bortoli, A., Seidowsky, R.: Who Is Using E-Scooters and How? Evidence from Paris. Transportation Research Part D: Transport and Environment 92, 102708 (2021).
3. Kopplin, C.S., Brand, B.M., Reichenberger, Y.: Consumer Acceptance of Shared E-Scooters for Urban and Short-Distance Mobility. Transportation Research Part D: Transport and Environment 91, 102680 (2021).
4. Reck, D.J., Haitao, H., Guidon, S., Axhausen, K.W.: Explaining Shared Micromobility Usage, Competition and Mode Choice by Modelling Empirical Data from Zurich, Switzerland. Transportation Research Part C: Emerging Technologies 124, 102947 (2021).
5. Şengül, B., Mostofi, H.: Impacts of E-Micromobility on the Sustainability of Urban Transportation—A Systematic Review. Applied Sciences 11(13), 5851 (2021).
6. Ben-Akiva, M., Lerman, S.: Discrete Choice Analysis: Theory and Application to Travel Demand. MIT Press, Cambridge (1985).
7. Prato, C.G.: Route Choice Modeling: Past, Present and Future Research Directions. Journal of Choice Modelling 2(1), 65–100 (2009).
8. Gökaşar, I., Günay, G.: Mode Choice Behavior Modeling of Ground Access to Airports: A Case Study in Istanbul, Turkey. Journal of Air Transport Management 59, 1–7 (2017).
9. McFadden, D., Train, K.: Mixed MNL Models for Discrete Response. Journal of Applied Econometrics 15, 447–470 (2000).
10. Hensher, D.A., Greene, W.H.: The Mixed Logit Model: The State of Practice. Transportation 30(2), 133–176 (2003).
11. Zuniga-Garcia, N., Ruiz Juri, N., Perrine, K.A., Machemehl, R.B.: E-scooters in Urban Infrastructure: Understanding Sidewalk, Bike Lane, and Roadway Usage from Trajectory Data. Case Studies on Transport Policy 9(3), 983–994 (2021).
12. Zuniga-Garcia, N., Tec, M., Scott, J.G., Machemehl, R.B.: Evaluation of E-Scooters as Transit Last-Mile Solution. Transportation Research Part C: Emerging Technologies 139, 103660 (2022).
13. Psarrou Kalakoni, A.M., Christoforou, Z., Gioldasis, C.: The Ambivalent Relationship of E-Scooters and Public Transport: Evidence from France. Transport Policy 159, 215–229 (2024).

14. Esztergár-Kiss, D., Tordai, D., Lopez Lizarraga, J.C.: Assessment of Travel Behavior Related to E-Scooters Using a Stated Preference Experiment. Transportation Research Part A: Policy and Practice 166, 389–405 (2022).
15. Cao, Z., Zhang, X., Chua, K., Yu, H., Zhao, J.: E-Scooter Sharing to Serve Short-Distance Transit Trips: A Singapore Case. Transportation Research Part A: Policy and Practice 147, 177–196 (2021).
16. Guo, L., Huang, S., Sadek, A.W.: A Novel Agent-Based Transportation Model of a University Campus with Application to Quantifying the Environmental Cost of Parking Search. Transportation Research Part A: Policy and Practice 50, 86–104 (2013).
17. Auld, J., Mohammadian, A.: Framework for the Development of the Agent-Based Dynamic Activity Planning and Travel Scheduling (ADAPTS) Model. Transportation Letters: The International Journal of Transportation Research 1(3), 245–255 (2013).
18. Gurumurthy, K.M., de Souza, F., Enam, A., Auld, J.: Integrating Supply and Demand Perspectives for a Large-Scale Simulation of Shared Autonomous Vehicles. Transportation Research Record: Journal of the Transportation Research Board 2674(7), 181–192 (2020).
19. Tzouras, P.G., Mitropoulos, L., Stavropoulo, E., Antoniou, E., Koliou, K., Karolemeas, C., Karaloulis, A., Mirtopoulos, K., Tarousi, M., Vlahogianni, E.I., Kepaptsoglou, K.: Agent-Based Models for Simulating E-Scooter Sharing Services: A Review and a Qualitative Assessment. International Journal of Transportation Science and Technology 12(1), 71–85 (2023).
20. Meyer, J.T.: Fundamental Research Statistics for the Behavioural Sciences. Holt, Rinehart and Winston, New York (1979).

Author Contribution Statement

- *Conceptualization:* Selim Dündar, Gürkan Günay
- *Methodology:* Selim Dündar, Gürkan Günay
- *Investigation:* Selim Dündar, Gürkan Günay, Gökçe Yurtseven
- *Writing – Original Draft:* Selim Dündar
- *Writing – Review & Editing:* Selim Dündar, Gürkan Günay

List of Abbreviations

- **ANN** – Artificial Neural Networks
- **DT** — Decision Tree
- **GB** — Gradient Boosting
- **RF** — Random Forest
- **SP** — Stated Prefence

Publication Note

This paper was peer-reviewed, accepted for presentation, and included in the proceedings of the ACE2026 – International Conference on Advances in Civil Engineering, held on 12–14 October 2026 in Trabzon, Türkiye.

This paper may be cited as follows:

Dündar S., Yurtseven G., Günay G., "Comparative Analysis of Choice Models and Machine Learning Methods for Synthetic Population-Based Mode Choice Modeling of E-Scooter Users," in Proceedings of the ACE2026 – International Conference on Advances in Civil Engineering, Trabzon, Türkiye, 12–14 October 2026.

Modeling and Prediction of Traffic Delay in Closely Spaced Roundabouts

Nurdan AKBAŞ[1], Ruti POLİTİ[2], Serhan TANYEL [3]
[1] 0009-0004-0309-3190, Dokuz Eylül University Faculty Of Engineering, Department of Civil Engineering, Main Campus Adatepe Mah. Dogus Cad. No: 207 / 35390 Buca-İzmir, Türkiye, nurdan_akbs@icloud.com
[2] 0000-0001-7851-2506, Department of Civil Engineering, İzmir University of Economics Faculty of Engineering, Sakarya Caddesi, No:156 35330 Balçova – İzmir, Türkiye, ruti.politi@ieu.edu.tr
[3] 0000-0001-8549-9442, Dokuz Eylül University Faculty Of Engineering, Department of Civil Engineering, Main Campus Adatepe Mah. Dogus Cad. No: 207 / 35390 Buca-İzmir, Türkiye, serhan.tanyel@deu.edu.tr

Abstract. Traffic performance in urban areas can be influenced by the proximity of closely spaced roundabouts and the distance between them. This study investigates the influence of geometric and traffic characteristics on approach-level delays in two closely spaced unsignalized roundabouts. A dataset comprising queue length, delay, and geometric characteristics such as entry width, circulating width, roundabout radius, and the distance between intersections for all turning movements across eight approaches (A-H) was analyzed. Preliminary analysis indicated a nonlinear, quadratic relationship between a combined performance index and degree of saturation, varying by approach. To capture this variability, piecewise regression models were applied approach-by-approach, allowing different functional forms. This method enables good estimation of delay and identification of threshold values where performance deteriorates. Results show that the proposed spillback index-based approach, combined with piecewise modeling, provides a predictive capability across varying flow conditions and approach geometries. The approach-specific models highlight the sensitivity of delay to spillback index. This framework can support traffic engineers in optimizing roundabout spacing and predicting performance under mixed demand scenarios

Keywords:. roundabouts; traffic engineering; delay prediction; piecewise regression

1 Introduction

Closely spaced roundabouts are commonly found in urban networks, where limited space and high traffic demand require careful design and operation [1]. The intermediate distance between adjacent roundabouts can influence traffic behavior, affecting queue formation, delay, and overall performance at each approach [2]. Understanding these effects is essential for accurate delay prediction and effective traffic management.

Previous studies have examined roundabout performance using empirical models, simulation, and analytical approaches [3,4]. Standard guidelines, such as the Highway Capacity Manual (HCM) [5] and tools as SIDRA Intersection, provide methods to estimate approach delays and capacity [6]. However, most existing models focus on isolated roundabouts and do not explicitly address interactions in closely spaced configurations.

This study aims to investigate approach-level delay characteristics in two closely spaced unsignalized roundabouts. A combined performance index was developed to represent geometric and traffic conditions, and its relationship with the flow-to-capacity ratio, degree of saturation was analyzed. Quadratic and piecewise regression models were applied to capture nonlinearities and saturation effects, providing a framework for predicting delays under varying

traffic conditions. The approach-specific analysis highlights how proximity between roundabouts affects performance and identifies thresholds where congestion sharply increases.

2. Data and Study Area

This study focuses on two closely spaced unsignalized roundabouts located in an urban network. Each roundabout has four approaches (A-D for the first, E-H for the second), with turning movements including right, through, and left. Traffic data were analyzed using SIDRA Intersection (version 6.1), which provides detailed operational measures for intersection analysis [3]. Simulation outputs for each scenario were compiled into a structured dataset. The intermediate spacing (L), ranging from 50 m to 250 m, was varied to assess its impact on key performance indicators such as queue length (QL_x) and delay. Shorter spacings can lead to stronger interactions and potential queue spillback, while larger spacings allow more independent operation. The dataset includes approach-level performance measures for all scenarios representing varying traffic demand and operating conditions.

Traffic and geometric parameters were varied within realistic ranges to represent diverse operating conditions. Circulating flow (Q_c) ranged from 200 to 1200 veh/h, while the central island radius (R_i) varied between 10 and 50 m. The number of circulating lanes (n_c) and entry lanes (n_e) ranged from 1 to 3 and 1 to 2, respectively. Circulating width (W_c) and entry width (W_e) were set between 5–12 m and 5–8 m. For each approach, 100 scenarios were performed.

The queue length variable (QL_x) represents the queue formed within the intermediate link between the two roundabouts. It corresponds to the downstream queue at Roundabout 1 (QL_C) for approach C and the upstream queue at Roundabout 2 (QL_E) for approach E. This definition captures the interaction effects of closely spaced roundabouts on intermediate link queue formation.

In addition, a performance index was computed for each approach combining the queue length and spacing between the roundabouts. This index is named spillback index (SI) used as an explanatory variable to model delay (d), capturing both demand intensity and approach capacity, which can be seen in Equation (1).

$$SI = \frac{QL_X}{L} \tag{1}$$

Scenario variations enable the assessment of how traffic demand and geometric features affect queue formation and delay in the intermediate link. The eight approaches were grouped based on their spatial relation to the link: Group 1 (D-F) direct entries, Group 2 (C-E) downstream to upstream approaches, Group 3 (B-H) side entries, and Group 4 (A-G) outer approaches. This classification captures localized interactions between the two roundabouts, which is illustrated in Fig. 1.

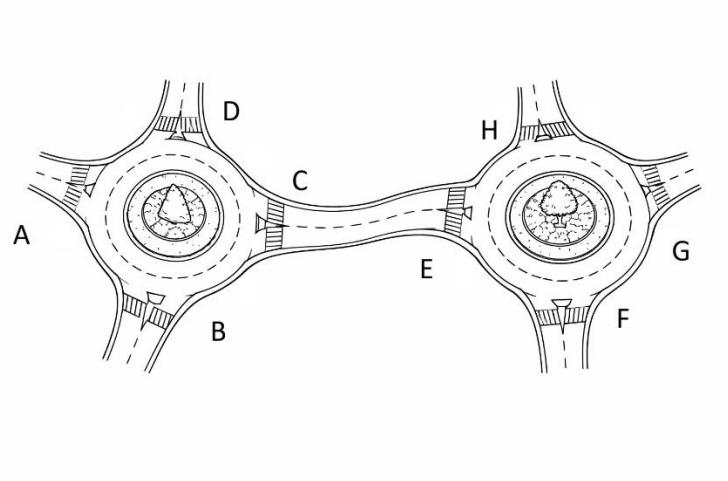


Fig. 1 Closely spaced roundabout system.

3. Methodology

3.1 Spillback index – degree of saturation relationship

Initial analysis revealed a quadratic relationship between the spillback index and X for each approach. This relationship differs across approaches, reflecting local geometry and traffic characteristics. The general form is given in Equation (2).

$$\mathrm{X} = \alpha \cdot (SI)^2 + \beta \cdot (SI) + \gamma \tag{2}$$

where coefficients (α, β, γ) are approach specific.

3.2 Piecewise regression

To capture nonlinearities for high saturation levels (> 1), a piecewise regression was applied. Piecewise regression divides the system of a predictor variable into intervals using breakpoints [7]. For each interval, a separate linear regression model is fitted [8]. The model can be expressed for delay prediction in Equation (3) as:X

$$d = \begin{cases} \beta_2^{(1)} X^2 + \beta_1^{(1)} X + \beta_0^{(1)} & X \le Threshold \\ \beta_0^{(2)} e^{\left[\beta_1^{(2)} X + \beta_2^{(2)} Q_c + \beta_3^{(2)} W_c + \beta_4^{(2)} n_c + \beta_5^{(2)} SI\right]} & X > Threshold \end{cases} \tag{3}$$

This approach allows separate modeling of moderate and oversaturated conditions, improving predictive accuracy. The first model of the model is fitted with 2nd order polynomial, and the second model is represented by log-linear (exponential) model. $\beta_0^{(1)}$ represents the intercept of the first model and β_n^m represents the coefficients. The number of models is m and the number of is shown by n.

4. Results and Discussion

4.1 Spillback Index-degree of saturation relationship

As shown in Fig. 2, the relationship between the spillback index (SI) and the degree of saturation (X) is nonlinear. A 2nd-degree polynomial regression was fitted to the data for all approaches. The regression equation and R^2 value indicate a good fit, capturing the general trend of increasing saturation with higher SI values. This fitted relationship is used for approach-specific prediction of delays in the closely spaced roundabouts studied.

SI values correlate strongly with degree of saturation and indirectly with delays, confirming their ability as a predictive variable. Approach-specific variations reveal that approaches closer to the adjacent roundabout are more sensitive to changes in X. Results indicate that intermediate spacing between roundabouts significantly influences delay, particularly for oversaturated approaches. The regression coefficients can be seen in Table 1.

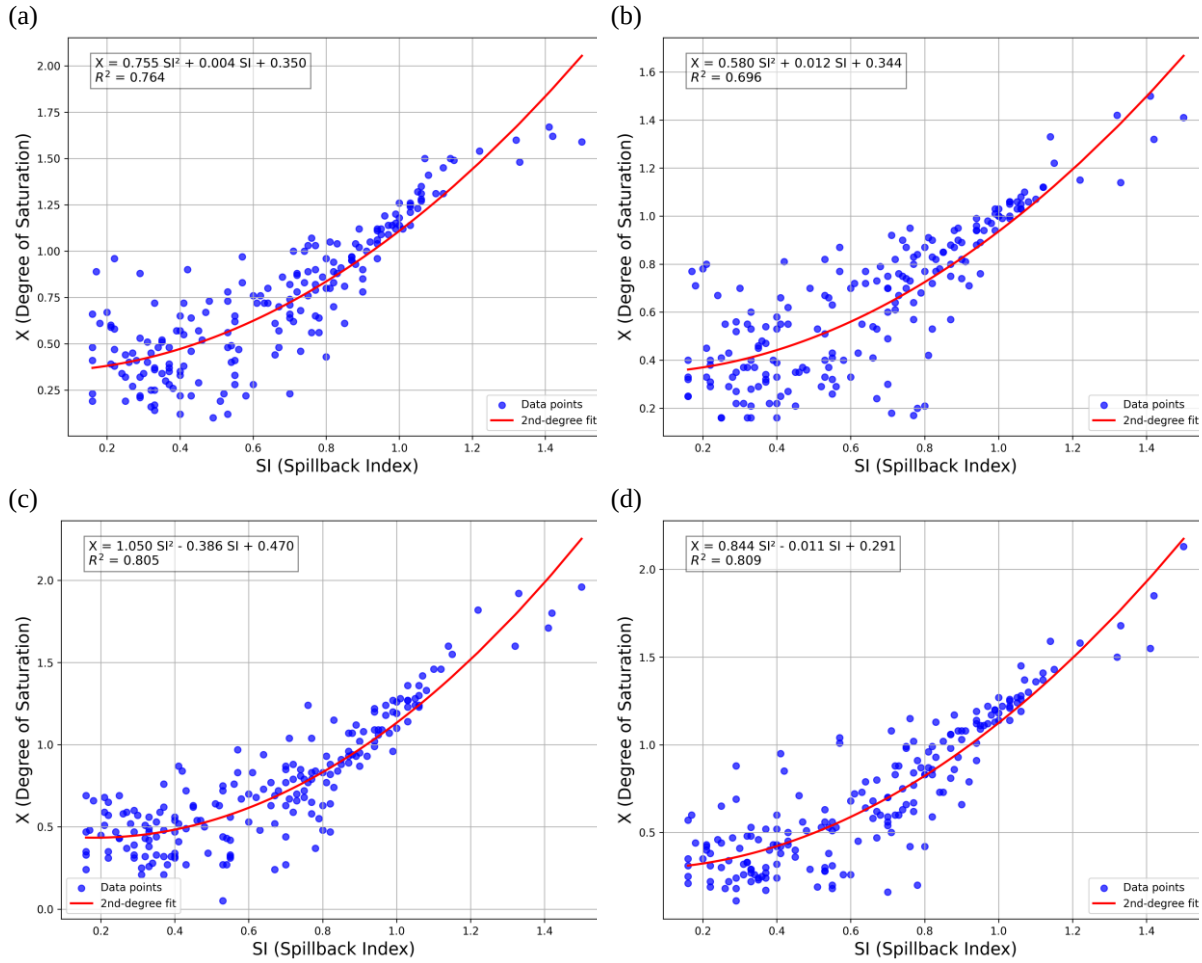


Fig. 2. Relationship between spillback index and degree of saturation for the analysed approaches (a) Group 1 (approaches D-F); (b) Group 2 (approaches C-E); (c) Group 3 (approaches B-H); (d) Group 4 (approaches A-G).

Table 1 Regression coefficients

Approach	α	β	γ	R^2
D-F	0.755	0.004	0.350	0.764
C-E	0.580	0.012	0.344	0.696
B-H	1.050	-0.386	0.470	0.805
A-G	0.844	-0.011	0.291	0.809

4.2 Piecewise regression model

A piecewise regression framework was adopted to capture different traffic regimes. While = 1 represents the theoretical capacity threshold, an optimal breakpoint was also determined through a data-driven approach by minimizing the prediction error across candidate thresholds, which can be seen in Fig. 3. The resulting threshold value indicates a transition between under

and over-saturated conditions. Optimal threshold was determined using a grid search approach by testing multiple candidate values and selecting the one minimizing the total prediction error [9].XX

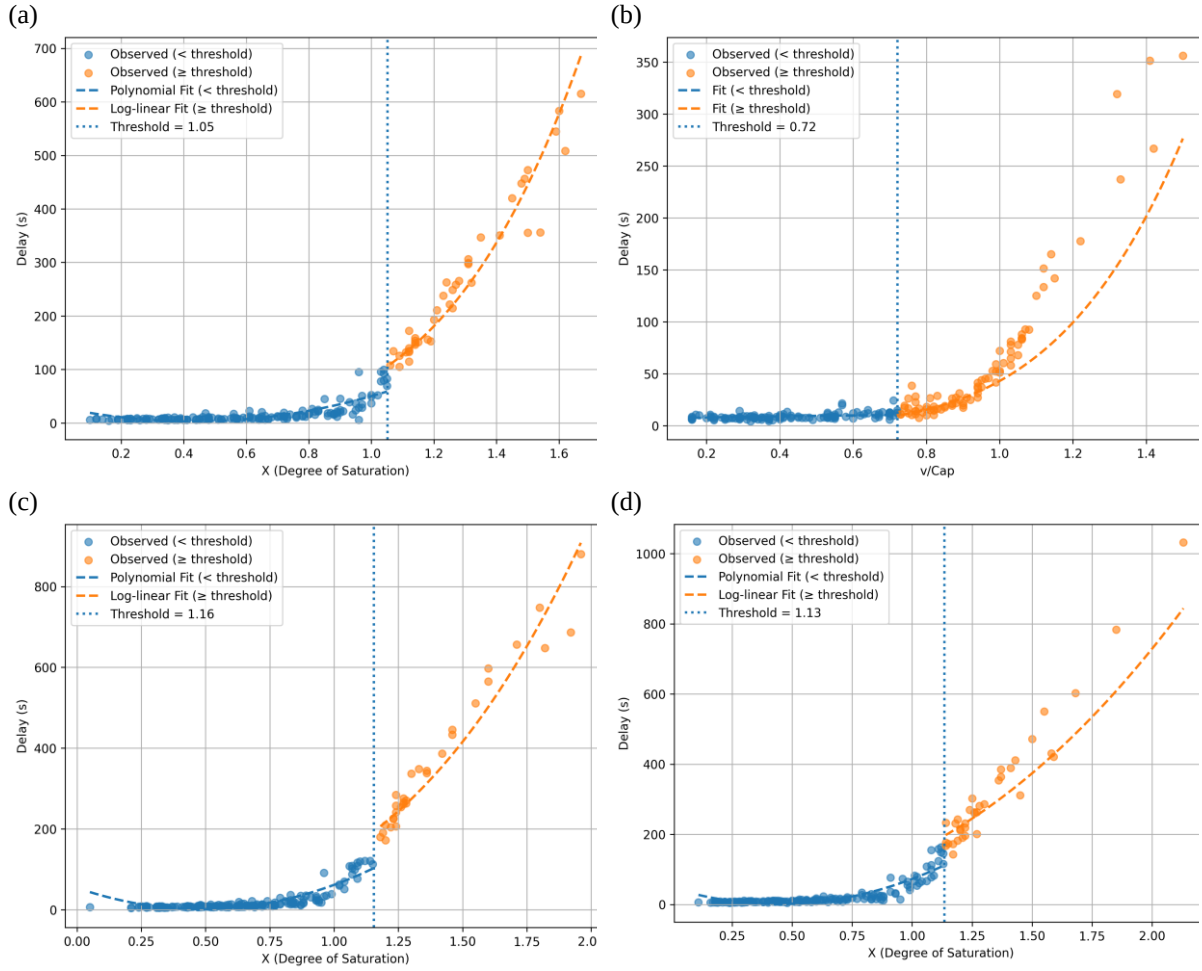


Fig. 3. Piecewise regression fit for (a) Group 1 (approaches D-F); (b) Group 2 (approaches C-E); (c) Group 3 (approaches B-H); (d) Group 4 (approaches A-G).

The approach-specific piecewise regression framework allows for accurate delay prediction across both moderate and high traffic conditions. The model performance significantly improves beyond the identified threshold for B-H approach ($X \approx 1.155$), indicating a transition to a more deterministic delay regime, which can be seen in Fig. 3c. The explanatory power of the oversaturated regime suggests that additional factors, such as geometric interactions and driver behavior, play a more prominent role, in contrast to undersaturated conditions. For the C-E approach (Group 2), the polynomial model could not adequately capture the relationship (low R^2), the log-linear model provides a better fit, which is seen in Fig. 3b.

The coefficients and the corresponding threshold values for each approach were given in Table 2. The C–E approach exhibits a notably low X threshold (0.721), indicating a short-distance segment with generally different congestion levels when compared the effect of other approaches. This segment was difficult to fit using the same model (polynomial), as the characteristic remains different over the range of observed traffic flows. In Model 1, only X was used as the independent variable, captures the main effect of saturation on delay and aligns well with the polynomial assumption, providing a predictable baseline. In Model 2, additional traffic and site variables (Q_{eng}, W_c, n_c, SI) were included to improve predictive accuracy by

accounting for secondary effects. For the C-E approach, the polynomial model could not adequately capture the relationship for model 1, resulting in a low R^2; this was better explained using a log-linear model.

Table 2 Regression coefficients and the threshold values

Approach	Model 1 – Polynomial				Threshold value	Model 2 – Exponential						
	$\beta_2^{(1)}$	$\beta_1^{(1)}$	$\beta_0^{(1)}$	R^2		$\beta_0^{(2)}$	$\beta_1^{(2)}$	$\beta_2^{(2)}$	$\beta_3^{(2)}$	$\beta_4^{(2)}$	$\beta_5^{(2)}$	R^2
D-F	145.144	-125.008	30.045	0.673	1.05	3.246	4.033	0.106	0.371	-0.428	-0.294	0.960
C-E	25.104	-13.140	9.454	0.289	0.721	2.483	4.586	0.531	-1.218	0.765	0.359	0.975
B-H	225.842	-218.320	53.955	0.810	1.16	3.765	2.921	0.076	0.402	-0.562	0.04	0.967
A-G	232.376	-206.798	47.139	0.815	1.13	3.200	2.322	-0.094	1.511	-1.295	0.922	0.957

	$\beta_0^{(2)}$	$\beta_1^{(2)}$	$\beta_2^{(2)}$	$\beta_3^{(2)}$	$\beta_4^{(2)}$	$\beta_5^{(2)}$	R^2
C-E	0.284	0.207	0.329	0.111	-0.120	0.235	0.586

5. Conclusion

This study investigated the relationship between approach-specific, index-based piecewise regression models and delay in closely spaced roundabouts. Optimal thresholds were determined via grid search for each approach, revealing variations linked to segment length and congestion level. The quadratic relationship between SI and X, combined with piecewise fitting for high saturation, provides a practical insight for traffic engineers in operational analysis.

Totally eight approach and four approach groups (D-F, C-E, B-H, and A-G) were analyzed. D-F, B-H, and A-G approaches exhibited higher threshold values (1.05 – 1.16), reflecting sections where congestion significantly affects delay. In contrast, the C-E approach had a notably low threshold point (0.721), consistent with a short-distance segment, which also made fitting more challenging. Furthermore, while polynomial models captured the general trend for most approaches, the C-E approach was better represented by a log-linear model due to the limited fit of the polynomial regression. These findings highlight the importance of approach-specific modeling and threshold selection in accurately predicting delay at closely spaced roundabouts. Future studies may explore multi-roundabout networks and dynamic traffic assignment integration. Future work may extend the approach to larger networks or simulation-based scenarios, also some machine learning models can be adapted to the system to increase the prediction accuracy.

Acknowledgments

The authors would like to thank for the support of The Scientific and Technological Research Council of Turkey (TUBITAK) under Project 2209A.

References

1. Çalışkanelli, P., Özuysal, M., Tanyel, S., Yayla, N.: Comparison of Different Capacity Models for Traffic Circles. Transport 24(4), 257–264 (2009).
2. Klobučar, M., Deluka-Tibljaš, A., Šurdonja, S., Ištoka Otković, I.: A Theoretical Model for Optimizing Signalized Intersection and Roundabout Distance Using Microsimulations. Future Transportation 5(28), 1–24 (2025).
3. Akçelik, R.: Modeling Queue Spillback and Nearby Signal Effects in a Roundabout Corridor. In: Proceedings of the 4th International Roundabout Conference. Transportation Research Board, Seattle, WA, USA (2014).
4. Akçelik, R., Chung, E., Besley, M.: Roundabouts: Capacity and Performance Analysis. ARRB Transport Research Ltd., Vermont South, Australia (1998).
5. Transportation Research Board: Highway Capacity Manual. Transportation Research Board, Washington, DC (2010).
6. Erol, D., Başkan, Ö.: Developing a Capacity Model for Roundabouts Using SIDRA Calibrated via Simulation-Based Optimization. Sustainability 17, 10289 (2025).
7. Ng, C., Susilawati, S., Mei Leng, I.C.: Piecewise Linear Regression: A Statistical Method for the Analysis of the Relationship between Traffic Signal Parameters and Air Pollutant Emissions. In: Australasian Transport Research Forum 2016 Proceedings. Melbourne, Australia (2016).
8. Alsobky, A.: Multiple Piecewise Regression for Trip Generation Models. Alexandria Engineering Journal 61(9), 7417–7428 (2022).
9. Xiao, H., Shen, X., Li, J., Yang, X.: A Method for Filling Traffic Data Based on Feature-Based Combination Prediction Model. Scientific Reports 15(1), 8441 (2025).

Author Contribution Statement

- *Conceptualization:* Nurdan AKBAŞ, Ruti Ruth POLİTİ, Serhan TANYEL
- *Methodology:* Nurdan AKBAŞ, Ruti Ruth POLİTİ, Serhan TANYEL
- *Investigation:* Nurdan AKBAŞ, Ruti Ruth POLİTİ
- *Writing – Original Draft:* Nurdan AKBAŞ, Ruti Ruth POLİTİ
- *Writing – Review & Editing:* Serhan TANYEL

List of Abbreviations

- **d** - control delay
- **L** - ntermediate spacing
- **n_c** - number of circulating lanes
- **n_e** - number of entry lanes
- **Q_c** - circulating flow
- **QLx** - queue length
- **SI** - spillback index
- **W_e** - circulating width
- **W_e** - entry width
- **X** - degree of saturation

.

Publication Note
This paper was peer-reviewed, accepted for presentation, and included in the proceedings of the ACE2026 – International Conference on Advances in Civil Engineering, held on 12–14 October 2026 in Trabzon, Türkiye.

This paper may be cited as follows:
Akbaş N., Politi R., Tanyel S., "Modeling and Prediction of Traffic Delay in Closely Spaced Roundabouts," in Proceedings of the ACE2026 – International Conference on Advances in Civil Engineering, Trabzon, Türkiye, 12–14 October 2026.

Effects of Autonomous Vehicle Driving Strategies on Passenger Car–Heavy Vehicle Interactions in Mixed Traffic Flow

Selim Dündar[1], Ilgin Gokasar[2], Serhan Tanyel[3]
[1] 0000-0003-4433-1998, Civil Engineering Department, İstanbul Okan Üniversitesi, Istanbul, Türkiye
selim.dundar@okan.edu.tr
[2] 0000-0001-9896-9220, Department of Civil Engineering, Boğaziçi University 34342 Bebek, Istanbul, Türkiye
ilgin.gokasar@boun.edu.tr
[3] Civil Engineering Department, Dokuz Eylül University, İzmir, Türkiye
serhan.tanyel@deu.edu.tr

Abstract. This study investigates the effects of autonomous driving strategies on uninterrupted traffic flow, with particular emphasis on heavy vehicle–passenger car interactions. The analysis is based on empirical traffic data collected from multilane urban road sections in İzmir, Türkiye. Observed vehicle speeds and time headways were evaluated together with nine autonomous driving strategies defined in the Research on the Impacts of Connected and Autonomous Vehicles (CAVs) on Traffic Flow report prepared by Atkins Ltd. for the UK Department for Transport, ranging from highly cautious to aggressive driving behavior. The results show that aggressive autonomous driving strategies combined with high CAV penetration rates could theoretically increase lane capacity beyond 4,000 veh/h. In contrast, cautious strategies may reduce capacity where human drivers already maintain short headways. Empirical observations also revealed that drivers frequently follow heavy vehicles at critically short effective reaction times, despite apparently acceptable temporal headways, creating potentially unsafe conditions. Simulation results indicate that cautious autonomous driving substantially increases following headways behind trucks, particularly at CAV penetration rates of 50–70%. Overall, the findings demonstrate that adaptive autonomous driving strategies can improve both traffic safety and flow stability. The study highlights the importance of incorporating heavy vehicle interactions and strategy-dependent autonomous driving behavior into future traffic flow models to balance capacity and safety in mixed traffic environments.

Keywords: Autonomous vehicles, Traffic flow modelling, Heavy vehicle interactions.

1 Introduction

Traffic congestion and road traffic crashes remain among the most significant transportation challenges worldwide, resulting in considerable economic losses, increased travel times, excessive fuel consumption, and severe social consequences. Roadway capacity is commonly defined as the maximum number of vehicles that can pass a specific roadway section within a given period under prevailing traffic and roadway conditions. Among the numerous factors affecting roadway capacity, vehicle time headway plays a fundamental role because it directly reflects the spacing maintained between successive vehicles. Since time headways are largely governed by drivers' perception-reaction times and individual driving behavior, they exhibit substantial variability among drivers

Human factors continue to be recognized as the dominant contributor to road traffic crashes. Both national statistics reported by the Turkish Statistical Institute (TÜİK) and international studies such as the HAVEit project indicate that driver-related factors account for the majority of traffic accidents [1,2]. Consequently, considerable research efforts have focused on reducing the influence of human driving behavior through the development of advanced driver assistance systems and autonomous driving technologies. These developments have accelerated research on connected and autonomous vehicles (CAVs), which are expected to fundamentally reshape future traffic operations.

Among different roadway facilities, uninterrupted traffic environments—including multilane freeways and freeway-like urban arterials—provide one of the most suitable settings for evaluating the operational impacts of connected and autonomous vehicles. In these facilities, vehicles generally travel at relatively stable speeds with short-to-moderate headways, allowing researchers to isolate the effects of car-following behavior from interruptions caused by traffic signals or stop-controlled intersections. Cooperative Adaptive Cruise Control (CACC) and connected vehicle technologies have therefore attracted considerable attention because they enable shorter following distances, coordinated acceleration and deceleration, and platoon formation. These capabilities have been shown to improve roadway capacity while simultaneously reducing fuel consumption and aerodynamic drag [3–6].

Roadway capacity improvements reported in the literature are largely influenced by the penetration rate of connected and autonomous vehicles, platoon size, traffic composition, particularly the proportion of heavy vehicles, and the geometric characteristics of merge and diverge areas [3–7]. Simulation-based studies have demonstrated that, under homogeneous CACC traffic conditions consisting entirely of passenger-car or truck platoons, increasing CAV penetration rate can raise lane capacity from approximately 2,046 veh/h/lane to more than 6,400 veh/h/lane [5,6]. On the other hand, several studies have shown that under high heavy-vehicle platooning rates, dedicated truck lanes or selective lane management strategies may provide greater operational benefits than allowing platoons to operate across all lanes, thereby preserving both capacity and traffic stability [7]. These findings suggest that the maximum operational benefits of autonomous driving technologies can only be achieved under relatively homogeneous traffic conditions. However, such conditions are unlikely to exist in the foreseeable future. Passenger cars and heavy vehicles will continue to coexist with conventional human-driven vehicles for many years, resulting in mixed traffic environments. Consequently, understanding the interaction between autonomous vehicles and conventional heavy vehicles has become one of the key research challenges in future traffic engineering.

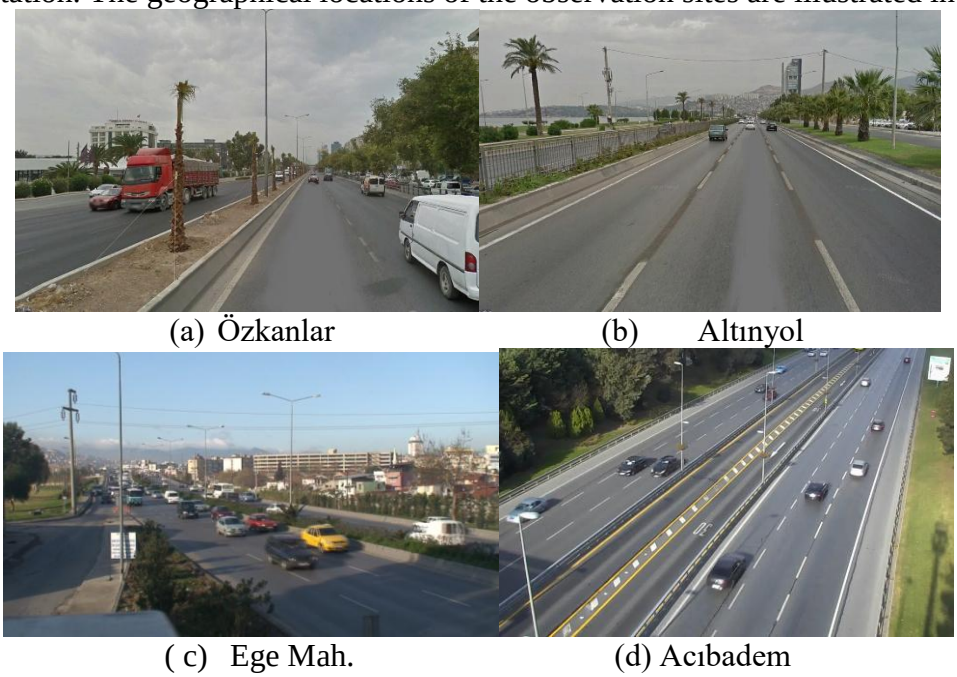
At the end of 2024, approximately 6.2 million medium- and heavy-duty commercial vehicles were in operation across European Union member states. Although the fleet continues to expand, its average age has also increased steadily, indicating that a substantial proportion of heavy vehicles will remain in operation for many years before being replaced by autonomous or highly automated alternatives [8]. A similar situation exists in Türkiye. According to statistics published by the Turkish Statistical Institute (TÜİK), approximately 1.03 million medium and heavy commercial vehicles were registered nationwide in 2024, and nearly 55% of these vehicles were older than 15 years [9]. These statistics clearly indicate that autonomous vehicles are expected to share the road with conventionally driven heavy vehicles equipped with existing technologies for an extended period. Therefore, investigating their operational interaction under mixed traffic conditions is of considerable practical importance.

The primary objective of this study is to investigate the interactions between autonomous vehicles and human-driven heavy vehicles under uninterrupted traffic flow conditions from the perspective of vehicle-following behavior. First, empirical observations collected from three multilane urban arterials in İzmir and one arterial roadway in İstanbul were used to model lane-specific time-headway distributions. Subsequently, autonomous vehicle driving strategies were

incorporated into these empirical headway distributions to estimate lane capacities under different autonomous vehicle penetration rates. Finally, mixed traffic scenarios involving passenger cars, autonomous vehicles, and human-driven heavy vehicles were analyzed to evaluate how autonomous driving strategies influence heavy vehicle interactions, traffic safety, and roadway capacity. The findings are expected to contribute to the development of more realistic mixed traffic flow models capable of representing future transportation systems in which autonomous and conventional vehicles operate simultaneously.

2 Study Sites and Headway Data Collection Procedure

To investigate traffic flow characteristics under uninterrupted traffic conditions, field observations were conducted at four major multilane urban arterial road sections. Three observation sites were located in İzmir, namely Altınyol, Özkanlar (Ankara Street), and Ege District (Mürselpaşa Boulevard), while the fourth site was located in Acıbadem, İstanbul, near the metro station. The geographical locations of the observation sites are illustrated in Fig. 1.



(a) Özkanlar (b) Altınyol

(c) Ege Mah. (d) Acıbadem

Fig. 1. Observation sites used for traffic data collection.

Traffic data were extracted from video recordings obtained under uninterrupted flow conditions. For each observation period, vehicle type, traffic volume, vehicle speed, and individual headways were determined through detailed video analysis. These parameters constituted the primary database used throughout the subsequent analyses. A total of 102 traffic data sets were initially obtained from the right, middle, and left lanes of the four observation sites. Observation periods were established as 15-minute intervals for the İzmir locations and 10-minute intervals for the Acıbadem site in İstanbul. Prior to statistical analysis, all data sets were subjected to a series of quality-control procedures to ensure their suitability for traffic flow modelling.

Trend analysis indicated that only one data set, corresponding to the right lane at the Acıbadem site, exhibited a statistically significant trend. Furthermore, 20 data sets showed evidence of serial dependence, while 17 data sets failed the randomness test. Consequently, these observations were excluded from further analyses, leaving 76 independent data sets suitable for modelling. The final database consisted of 22 right-lane, 27 middle-lane, and 27 left-lane observations.

The analyses demonstrated that vehicle time headways observed in uninterrupted traffic flow can be satisfactorily represented by using the Cowan M3 headway distribution. Originally proposed by Cowan [10], this model has subsequently been applied by several researchers to describe vehicle-following behavior under uninterrupted traffic conditions, including Bunker [11], Akçelik [12, 13] and Ceyhan Yiğiter and Tanyel [14]. The Cowan M3 distribution, also referred to as the deterministic queue model, assumes that a proportion of vehicles travel as followers, maintaining a minimum headway, Δ, behind their respective leading vehicles. The probability density function and cumulative distribution function of the Cowan M3 model are given by Eqs. (1) and (2), respectively.

$$f(t) = \alpha\lambda e^{-\lambda(t-\Delta)} \quad (1)$$

$$F(t) = 1 - \alpha e^{-\lambda(t-\Delta)} \quad (2)$$

where $\boldsymbol{\alpha}$ denotes the proportion of free vehicles, $\boldsymbol{\Delta}$ represents the minimum headway within the traffic stream, and $\boldsymbol{\lambda}$ is the exponential scale parameter. Here a couple of important features of Cowan M3 distribution should be mentioned to have a better understanding of the outcomes of further analysis.

First, it is necessary to discuss the concept of the proportion of free vehicles (α). This parameter is a value that represents the number of vehicles in a traffic flow that do not affect each other in terms of speed and following distance; it can also represent their behavior under different traffic flow conditions. Figure 2 shows the variation of proportion of free vehicles for different lanes, obtained from observations, depending on the traffic flow. Another noteworthy feature of Eqs. (1)–(4) is the repeated appearance of the product Δq. This parameter is directly associated with the minimum time headway, which Akçelik (2003) suggested should correspond to the headway at roadway capacity. Accordingly, Δ can be interpreted as the minimum headway associated with lane capacity as $Q_{cap} = 3600/\Delta$. Consequently, the product Δq represents the degree of saturation of the traffic stream which as an important parameter in traffic flow analysis.

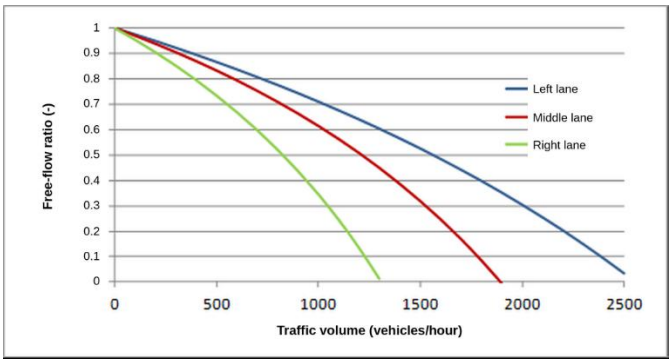


Fig. 2. Variation of the proportion of free vehicles with traffic volume for different lane types.

3. Effects of Autonomous Vehicle Driving Strategies on Traffic Flow Characteristics

Numerous studies have investigated the car-following behavior of autonomous vehicles using microscopic traffic simulation models and theoretical car-following algorithms. The prevailing assumption in the literature is that autonomous vehicles are capable of maintaining considerably shorter and more stable following headways than human-driven vehicles owing to their advanced sensing, communication, and control capabilities. Consequently, higher roadway capacities and improved operational performance are generally expected under increasing autonomous vehicle penetration rates. Martin-Gasulla et al. [15] reported that autonomous vehicles operating under vehicle-to-vehicle (V2V) communication can safely maintain

extremely short following distances when both the leading and following vehicles are autonomous. However, when the leading vehicle is a conventional human-driven vehicle, autonomous vehicle manufacturers may intentionally adopt more conservative following behavior to ensure adequate safety margins. Consequently, the expected capacity improvements may not be fully achieved in mixed traffic environments containing both autonomous and conventional vehicles. This observation suggests that the operational performance of autonomous vehicles depends not only on their penetration rate but also on the driving strategy adopted by their control systems. Friedrich [16] expressed traffic density under uninterrupted traffic conditions as:

$$k = \frac{1}{vT_H + L} \tag{3}$$

where *k* is traffic density (veh/m/lane), *v* is vehicle speed (m/s), *L* is the effective vehicle length consisting of the leading vehicle length plus the clearance between successive vehicles, and T_H is the headway. In autonomous driving applications, the headway may be interpreted as the effective reaction time required by either a human driver or an autonomous driving system.

Although communication among autonomous vehicles may theoretically reduce reaction times to values approaching zero, the strategies adopted while following conventional human-driven vehicles remain uncertain. These strategies primarily determine the desired spacing between the front bumper of the following autonomous vehicle and the rear bumper of the leading vehicle, together with the effective reaction time maintained during vehicle-following operations. Among the available studies, the methodology proposed by Atkins Ltd. [17] provides one of the most comprehensive approaches for representing these behavioural differences. Accordingly, nine autonomous driving strategies were considered in the present study. Strategy TYP1 represents the most cautious behaviour, whereas TYP9 corresponds to the most confident (aggressive) driving strategy. In the study, the recommended safe following distance is expressed as:

$$d_{safe} = CCO + CC1 * v \tag{4}$$

where d_{safe} is the desired following distance (m), *CC0* denotes the minimum standstill distance between the rear bumper of the leading vehicle and the front bumper of the following vehicle (m), *CC*1 represents the desired headway (s), and v is the travelling speed (m/s). The parameter values recommended by Atkins Ltd. [17] are summarized in Table 1.

Table 1. Recommended parameter values for autonomous vehicle driving strategies (adapted from Atkins, 2016).

Autonomous Vehicle Driving Strategy	TYP1	TYP2	TYP3	TYP4	TYP5	TYP6	TYP7	TYP8	TYP9
CC0 (m)	2,5	2,5	2,0	2,0	1,5	1,0	1,0	0,5	0,5
CC1 (sec)	2,1	1,8	1,5	1,2	0,9	0,8	0,7	0,6	0,5

Autonomous Vehicle Driving Strategy	TYP1	TYP2	TYP3	TYP4	TYP5	TYP6	TYP7	TYP8	TYP9
CC0 (m)	2,5	2,5	2,0	2,0	1,5	1,0	1,0	0,5	0,5
CC1 (sec)	2,1	1,8	1,5	1,2	0,9	0,8	0,7	0,6	0,5

Using these parameter values, modified headway distributions were generated for autonomous vehicle penetration rates ranging from 10% to 100%. The headway associated with each observation was calculated using the following equation where t_i is the resulting headway,

t_{CVi} and t_{AVi} denote the headways associated with conventional and autonomous vehicles respectively, while P_{CV} and P_{AV} represent the proportions of conventional and autonomous vehicles within the traffic stream.

$$t_i = \%P_{CV} * t_{CVi} + \%P_{AV} * t_{AVi} \quad (5)$$

Figure 3 presents the probability density functions obtained for the left lane at the Ege District observation site under 50% and 70% autonomous vehicle penetration rates. The distributions clearly demonstrate that increasing autonomous vehicle penetration shifts the headway distribution toward shorter values, particularly for aggressive driving strategies. Consequently, average time headways decrease, leading to substantial increases in theoretical lane capacity. The resulting capacity estimates indicate that, under highly confident autonomous driving strategies (TYP8–TYP9), lane capacities may exceed 4,000 veh/h/lane. Figure 4 illustrates the variation in lane capacity as a function of autonomous vehicle penetration rate for the different driving strategies considered in this study.

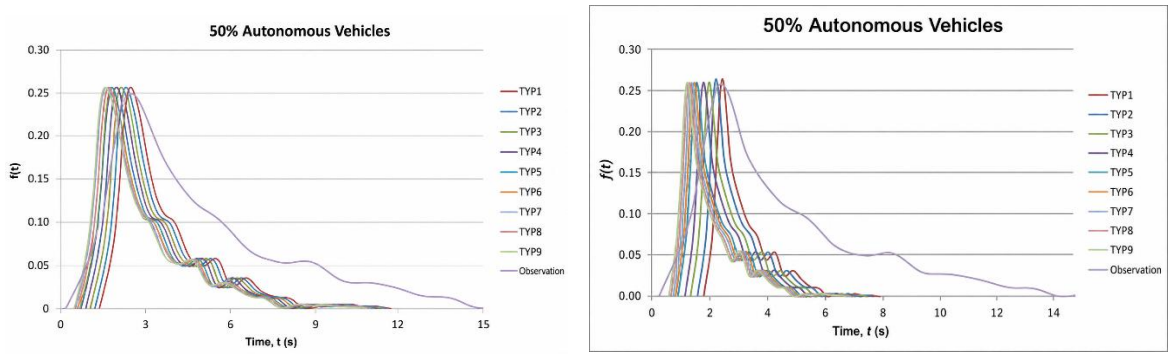


Fig. 3. Probability density functions of vehicle time headways for 50% and 70% autonomous vehicle penetration rate

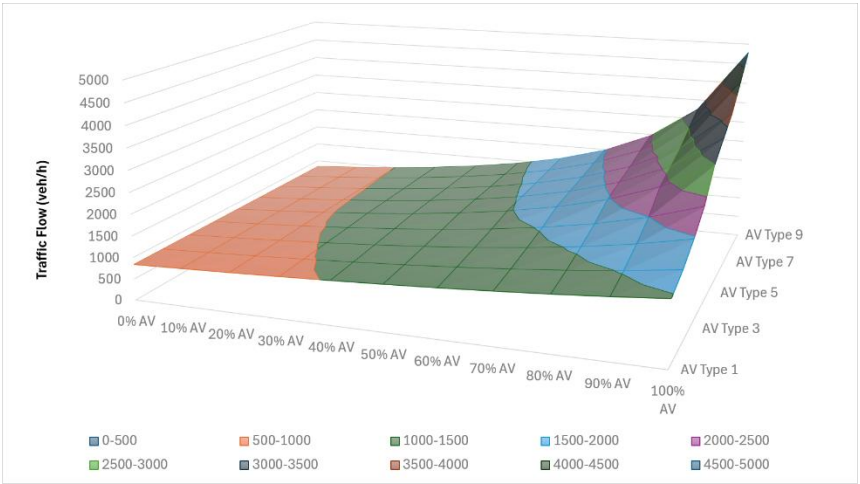


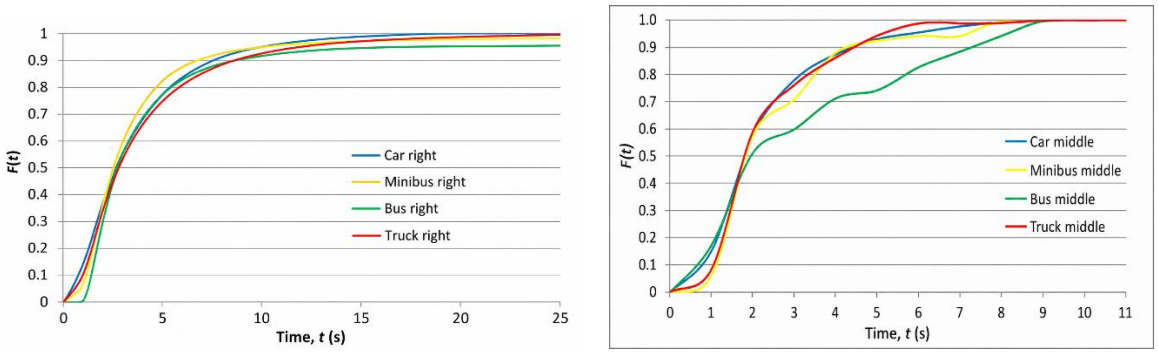
Fig. 4. Variation of lane capacity with autonomous vehicle penetration rate under different autonomous driving strategies.

Results indicate that autonomous driving strategy is at least as influential as autonomous vehicle penetration rate in determining future traffic performance. While aggressive strategies maximize roadway capacity by minimizing following headways, conservative strategies preserve larger safety margins and therefore provide more limited capacity improvements. Consequently, future autonomous driving systems may benefit from adaptive driving strategies

that dynamically adjust their car-following behavior according to prevailing traffic conditions, roadway characteristics, and surrounding vehicle composition.

4. Passenger Car–Heavy Vehicle Interaction under Mixed Traffic Conditions

The introduction of autonomous vehicles into existing traffic streams will inevitably lead to interactions with conventionally driven heavy vehicles. Since heavy vehicles are expected to remain in service for many years, understanding the current behavior of human drivers when following these vehicles provides an essential basis for evaluating future mixed traffic conditions involving autonomous vehicles. To investigate these interactions, traffic observations obtained from the right and middle lanes of the Ege District observation site were analyzed, as this location exhibited the highest proportion of heavy vehicles among all study sites. Heavy vehicle composition at this location consisted of approximately 6% minibuses, 4% buses, and 11% trucks in the right lane, while the corresponding values for the middle lane were 7%, 4%, and 13%, respectively. Initially, the observed time headways maintained by passenger cars while following different vehicle classes were analyzed. Separate cumulative distribution functions were developed for passenger cars following passenger cars, minibuses, buses, and trucks. The resulting distributions are presented in Fig. 5.



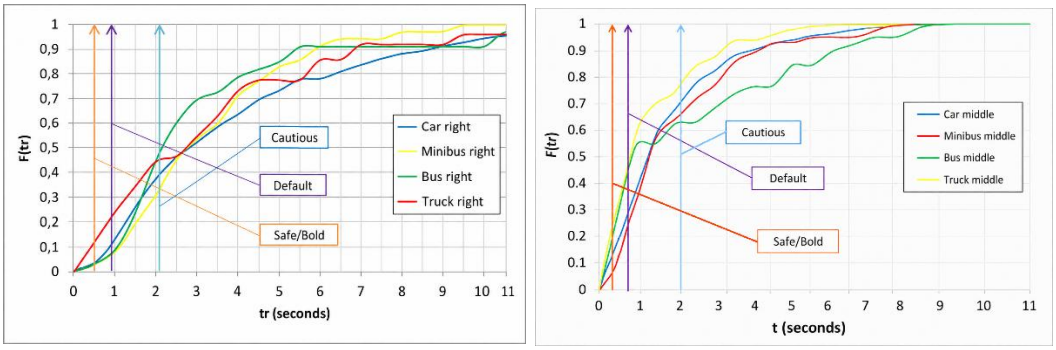
(a) Right Lane (b) Middle Lane

Fig. 5. Cumulative distributions of passenger-car time headways while following different vehicle classes in the right and middle lanes.

The distributions indicate that passenger-car drivers travelling in the right lane generally maintain similar headways regardless of the vehicle type being followed. In contrast, drivers in the middle lane tend to maintain relatively longer headways when following buses. From a traffic safety perspective, however, one would normally expect substantially larger following distances behind all heavy vehicles due to their greater dimensions, reduced acceleration capabilities, and restricted forward visibility. This apparent contradiction arises because headway alone does not adequately represent the actual spacing maintained behind heavy vehicles. Since trucks and buses are considerably longer than passenger cars, identical headways may correspond to significantly shorter effective clearances between the rear bumper of the leading vehicle and the front bumper of the following vehicle. Consequently, evaluations based solely on temporal headways may underestimate the safety risks associated with heavy vehicle following.

A more representative measure of driver behavior is therefore the effective reaction time, which reflects the time interval drivers perceive as sufficient for maintaining safe vehicle-following conditions. Effective reaction times were calculated using Eq. (4), while explicitly accounting for the physical dimensions of the leading vehicle. Following the methodology proposed by Long (2002), effective vehicle lengths were assumed to be 9.6 m for minibuses, 15.8 m for buses, and 18.0 m for trucks. These values include both the vehicle length and the average clearance maintained between successive vehicles. The resulting cumulative

distributions of effective reaction times are presented in Fig. 6. To facilitate comparison with autonomous driving behavior, the recommended CC1 values corresponding to the cautious (TYP1), default (TYP5), and confident (TYP9) autonomous driving strategies were also superimposed on the reaction-time distributions.



(a) Right Lane (b) Middle Lane

Fig. 6. Cumulative distributions of effective reaction times of different types of vehicles

The results reveal a striking behavioral pattern. Passenger-car drivers consistently exhibit the shortest effective reaction times when following trucks, despite the considerably larger dimensions and reduced maneuverability of these vehicles. This behavior suggests that many drivers intentionally travel close behind trucks in anticipation of overtaking opportunities rather than maintaining recommended safety margins. Although the observed headways behind trucks appear comparable to those maintained behind passenger cars, the corresponding effective reaction times are substantially shorter because of the additional vehicle length occupied by trucks. Consequently, the available stopping distance behind heavy vehicles is considerably smaller than temporal headway measurements alone would suggest. These findings indicate that current driving behavior may involve safety margins that are substantially below desirable levels.

To evaluate the potential influence of autonomous vehicles on these interactions, a simulation was performed assuming that autonomous vehicles adopt the most cautious driving strategy (TYP1) when following trucks. Figure 7 illustrates the resulting reaction-time distributions for autonomous vehicle penetration rates of 10%, 50%, and 70%.

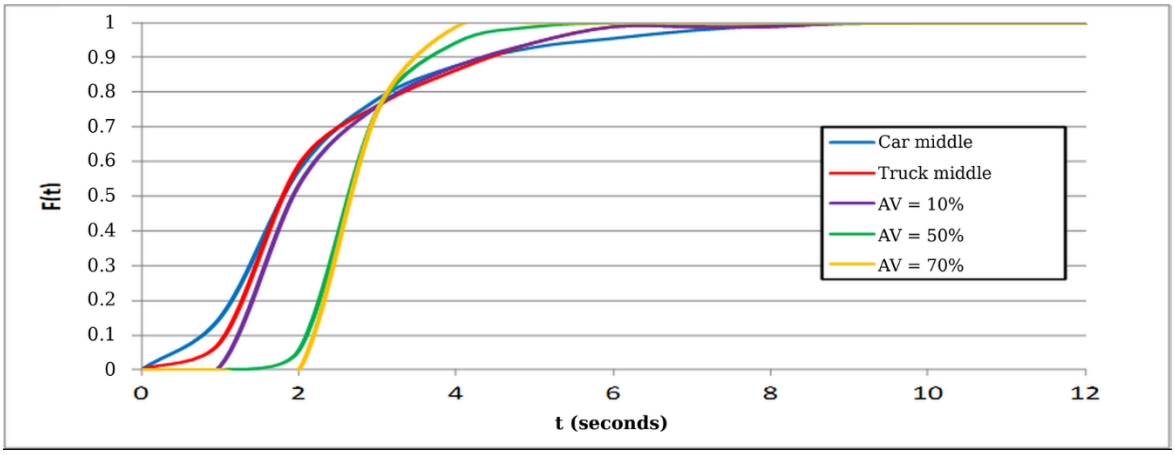


Fig. 6. Effect of autonomous vehicle penetration on passenger car–truck following behavior.

The simulation results indicate that a 10% autonomous vehicle penetration rate produces only marginal changes in the overall headway distribution. However, when the penetration rate reaches 50% and 70%, the distributions shift noticeably toward reaction times between 2 and 3

seconds. This change substantially reduces the proportion of extremely short following headways currently observed behind trucks.

From an operational perspective, this behavioral shift offers two important advantages. First, maintaining longer reaction times significantly improves traffic safety by reducing unsafe close-following conditions and providing greater opportunities for collision avoidance. Second, the reduction in excessively long headways simultaneously mitigates the adverse capacity effects traditionally associated with heavy vehicles. Consequently, autonomous vehicles adopting adaptive and safety-oriented car-following strategies may improve both operational efficiency and traffic safety in future mixed traffic environments.

Overall, the findings demonstrate that the interaction between autonomous vehicles and heavy vehicles cannot be adequately represented using conventional passenger-car-following models alone. Heavy vehicle characteristics must be explicitly incorporated into future traffic flow models to obtain realistic estimates of roadway capacity, traffic stability, and safety performance under mixed traffic conditions.

5. Conclusions

This study investigated the influence of autonomous vehicle driving strategies on uninterrupted traffic flow, with particular emphasis on the interaction between autonomous vehicles and human-driven heavy vehicles under mixed traffic conditions. Unlike many previous studies that primarily focused on capacity improvements resulting from reduced vehicle headways, the present research explicitly considered heavy vehicle–passenger car interactions using empirical traffic observations collected from multilane urban arterials in Türkiye.

The results demonstrate that autonomous vehicle driving strategy is a critical factor influencing both roadway capacity and traffic safety. Under aggressive driving strategies and high autonomous vehicle penetration rates, the theoretical lane capacity may exceed 4,000 veh/h/lane under uninterrupted traffic conditions. Conversely, conservative driving strategies maintain larger following headways, resulting in more modest capacity improvements while providing substantially greater safety margins.

The empirical analyses revealed that human drivers frequently maintain critically short effective reaction times when following trucks, despite apparently acceptable headways. This behavior is largely attributed to drivers' tendency to remain close behind heavy vehicles while preparing for overtaking maneuvers. Consequently, the actual safety margins behind trucks are considerably smaller than those suggested by temporal headway measurements alone.

Results further demonstrated that autonomous vehicles adopting cautious car-following strategies substantially increase following headways behind heavy vehicles, particularly when the autonomous vehicle penetration rate reaches 50–70%. This behavioral adaptation significantly reduces unsafe close-following conditions while simultaneously mitigating the operational impacts traditionally associated with heavy vehicles. Therefore, autonomous vehicles have the potential not only to improve roadway capacity but also to promote safer, more homogeneous, and more stable traffic flow.

Acknowledgments

This study includes the findings obtained from the TUBITAK Research Project No: 217M283. The authors appreciate TÜBİTAK for their support.

References

1. Türkiye İstatistik Kurumu (TÜİK): Trafik Kaza İstatistikleri. http://www.tuik.gov.tr/PreTablo.do?alt_id=1051, last accessed 2017/09/06.
2. HAVEit (Highly Automated Vehicles for Intelligent Transport): Deliverable D61.1. The Future of Driving.

http://www.haveit-eu.org/LH2Uploads/ItemsContent/24/HAVEit_212154_D61.1_Final_Report_Published.pdf, last accessed 2017/09/06.
3. Martínez-Díaz, M., Al-Haddad, C., Soriguera, F., Antoniou, C.: Platooning of Connected Automated Vehicles on Freeways: A Bird's-Eye View. Transportation Research Procedia 58, 479–486 (2021). https://doi.org/10.1016/j.trpro.2021.11.064
4. Lee, S., Oh, C., Lee, G.: Impact of Automated Truck Platooning on the Performance of Freeway Mixed Traffic Flow. Journal of Advanced Transportation, Article ID 8888930 (2021). https://doi.org/10.1155/2021/8888930
5. Zhong, Z., Lee, J., Nejad, M., Lee, E.E.: Clustering Strategies of Cooperative Adaptive Cruise Control: Impacts on Human-Driven Vehicles. In: 2019 IEEE 2nd Connected and Automated Vehicles Symposium (CAVS), Honolulu, HI, USA, pp. 1–7 (2019). https://doi.org/10.1109/CAVS.2019.8887784
6. Wang, X., Lim, A.: Reliable and Efficient Broadcast Routing Using Multipoint Relays over VANET for Vehicle Platooning. arXiv:2205.15648 (2022). https://doi.org/10.48550/arXiv.2205.15648
7. Ibarra, B., Saphores, J.: Lane Management Strategies in a Connected Environment: Analysis of Freight Corridor Scenarios for I-710 in Southern California. Transportation Research Record 2678(2) (2023). https://doi.org/10.1177/03611981231175903
8. ECG Association: Article. https://www.ecgassociation.eu/article/?id=6c400779-3379-4ce9-8067-439e739ae8a8, last accessed 2026/07/22.
9. Türkiye İstatistik Kurumu (TÜİK): Taşıt Cinsi ve Yaş Gruplarına Göre Taşıt-Kilometre. TÜİK Veri Portalı. https://veriportali.tuik.gov.tr/tr/databrowser/tuik/categories/15/15_2/15_2_3/TR,DF_TASIT_KILOMETRE_YAS_GRUP_V2,1.0, last accessed 2026/07/22.
10. Cowan, R.C.: Useful Headway Models. Transportation Research 9(6), 371–375 (1975).
11. Bunker, J.M.: Microscopic Modelling of Freeway Operations. PhD Thesis, School of Civil Engineering, Queensland University of Technology, Brisbane, Australia (1996).
12. Akçelik, R.: Speed-flow and Bunching Relationships for Interrupted Flows. In: Proceedings of the 25th Conference of the Australian Institute of Transportation Research (CAITR 2003), Adelaide, Australia, 3–5 December (2003).
13. Akçelik, R.: Speed-flow and Bunching Models for Uninterrupted Flows. In: Proceedings of the 5th International Symposium on Highway Capacity and Quality of Service, Yokohama, Japan (2006).
14. Ceyhan Yiğiter, Ö., Tanyel, S.: Lane by Lane Analysis of Vehicle Time Headways: Case Study of Izmir Ring Roads in Türkiye. KSCE Journal of Civil Engineering (2015).
15. Martin-Gasulla, M.: Optimizing Signalized Intersections Performance under Conventional and Automated Vehicle Traffic. IEEE Transactions on Intelligent Transportation Systems (2019).
16. Friedrich, B.: The Effect of Autonomous Vehicles on Traffic. In: Maurer, M., Gerdes, J.C., Lenz, B., Winner, H. (eds.) Autonomous Driving, pp. 317–334. Springer, Berlin Heidelberg (2016).
17. Atkins: Research on the Impacts of Connected and Autonomous Vehicles (CAVs) on Traffic Flow. Technical Report, Department for Transport, United Kingdom (2016).
18. Long, G.: Intervehicle Spacings and Queue Characteristics. Transportation Research Record 1796(1), 89–96 (2002).Author 1.: Article title. Journal 2(5), 99–110 (2016).

Author Contribution Statement

- ***Conceptualization:*** Selim Dündar, Serhan Tanyel
- ***Methodology:*** Serhan Tanyel, Ilgın Gökaşar

- ***Data Collection:*** Selim Dündar
- ***Formal Analysis:*** Selim Dündar, Serhan Tanyel
- ***Writing – Original Draft:*** Serhan Tanyel
- ***Writing – Review & Editing:*** Ilgın Gökaşar, Serhan Tanyel

List of Abbreviations

- **AV** — Autonomous Vehicle
- **CAV** — Connected and Autonomous Vehicle
- **CV** — Connected Vehicle
- **HDV** — Human-Driven Vehicle
- **HV** — Heavy Vehicle
- **CACC** — Cooperative Adaptive Cruise Control
- **V2V** — Vehicle-to-Vehicle Communication
- **V2X** — Vehicle-to-Everything Communication
- **CC0** — Minimum Standstill Distance
- **CC1** — Desired Time Headway Parameter
- **PDF** — Probability Density Function
- **CDF** — Cumulative Distribution Function

Publication Note

This paper was peer-reviewed, accepted for presentation, and included in the proceedings of the ACE2026 – International Conference on Advances in Civil Engineering, held on 12–14 October 2026 in Trabzon, Türkiye.

This paper may be cited as follows:

Dündar S., Gokaşar, I., Tanyel S., "Effects of Autonomous Vehicle Driving Strategies on Passenger Car–Heavy Vehicle Interactions in Mixed Traffic Flow," in Proceedings of the ACE2026 – International Conference on Advances in Civil Engineering, Trabzon, Türkiye, 12–14 October 2026.

Analysis of the Ballast Porosity Variations in British A, B, C, and D Gradations using the Discrete Element Method

Huseyin Boler[1] and Hüseyin Köse[2]
[1] 0000-0002-4087-6088, Karadeniz Technical University, Civil Engineering Department, Trabzon, Türkiye, huseyinboler@ktu.edu.tr
[2] 0000-0003-2533-6769, Konya Technical University, Civil Engineering Department, Konya, Türkiye, hkose@ktun.edu.tr

Abstract. In this manuscript, the relationship between several gradation parameters (C_u, C_c, etc.) and ballast layer porosity was investigated through discrete element method (DEM) packing simulations and single- and multiple-linear regression. A total of 108 different gradation variations, all falling into the British A, B, C, and D gradation limits, were used in the simulations. Each gradation case was replicated three times, resulting in a total of 324 simulations. Porosity values were recorded at the end of the simulations. The C_u, C_c, and their components, D_{60}, D_{30}, and D_{10}, were used as predictors in linear regression for the recorded values. The results showed that higher Cu values (finer gradations) were associated with lower porosity values. However, the coefficient of determination (R^2) values were quite low, representing weak relationships. To remedy the situation, C_c was added as a predictor besides C_u, and multiple regression was conducted. No improvements, however, were observed. Consequently, the main components of C_u and C_c (D_{60}, D_{30}, and D_{10}) were investigated as predictors. The results showed that compared to D_{60} and D_{30}, D_{10} had significantly stronger predictor performance, indicating that D_{10} is substantially stronger predictor for ballast porosity compared to traditional parameters, C_u and C_c.

Keywords: Ballast Porosity, Ballast Gradation, DEM Packing

1 Introduction

Railway ballast is designed to have a high porosity (values near 40%) to provide rainwater drainage. Without adequate porosity, as in the case of ballast fouling, water accumulates within the granular structure, resulting in reduced shear strength [1]. Therefore, it is paramount to control the porosity of the ballast layer from initial design to its end of life to prevent failures that might arise from low shear strength. Particle size distribution or gradation is the most important factor that affects the ballast layer's porosity.

There are several ballast specifications, such as the American Railway Engineering and Maintenance of Way Association (AREMA) and British, that provide upper and lower limits for percentage by mass passing through specific sieve ranges [2]. These are all designed to create uniform particle distributions to obtain high ballast layer porosity. The upper and lower limits of these specifications, however, contain wide ranges that could lead to significant differences in layer porosity as reported for AREMA No. 24 gradation [3].

ASTM D2487 (the Unified Soil Classification System) [4] uses two important classification parameters, the coefficient of uniformity (C_u) and the coefficient of curvature (C_c), to determine whether a gradation is uniformly (poorly) or broadly (well) graded. C_u, which is calculated by the ratio of particle sizes at which 60% and 10% of particles are smaller by mass (also expressed as D_{60}/D_{10}), is particularly important. A few studies reported a relationship between C_u and porosity. Tutumluer et al. [5] and Bian et al. [6], for example, reported that more uniformly graded aggregates (lower Cu) contained more air voids. Similarly, Rosa et al. [7] reported

decreasing void ratios, therefore also decreasing porosity, with higher C_u. These studies were all conducted using the discrete element method (DEM), introduced by Cundall et al [8].

British gradation is widely used and also adopted by Turkish Railways (TCDD) for constructing a new ballast layer [9]. The DEM studies discussed earlier demonstrated that ballast gradation has a significant effect on porosity. However, the predictive performance of gradation parameters (C_u and C_c) was not studied across British ballast specifications. In this study, this gap is addressed by conducting DEM packing simulations covering 108 different gradations and evaluating the predictive performance of several parameters using linear regression.

2 Methodology

2.1 British Gradation Variations

The gradations studied were derived from the British ballast specifications (Gradations A, B, C, and D) with particle sizes ranging from 22.4 mm to 80 mm. Details of the specification limits, i.e., the upper and lower gradation bands, can be found in Guo et al. [2]. **Table 1** presents the gradations (108 in total) used in this study. Each cell under the % passing columns in the table represents the different variations used. Since the British B and C specifications overlap, they were merged into a single gradation category. Throughout the rest of the text, this combined gradation is represented as BC. C_u and C_c parameters of the generated gradations ranged from 1.16 to 1.98 and 0.77 to 1.37, respectively. The influence of the variations in these parameters on packing porosity was analyzed and is discussed in the following sections. It should be noted that the data on the British A specification were also used in a previous study to investigate the effects of percent passing across certain sieve ranges on coordination number and porosity [10]. However, that study did not incorporate the relationship between C_u or C_c and the porosity values but focused primarily on coordination number. Therefore, British A specification was added in this study to specifically investigate the relationship between C_u, C_c, and porosity.

Table 1. Gradation Variations Used based on British Specifications

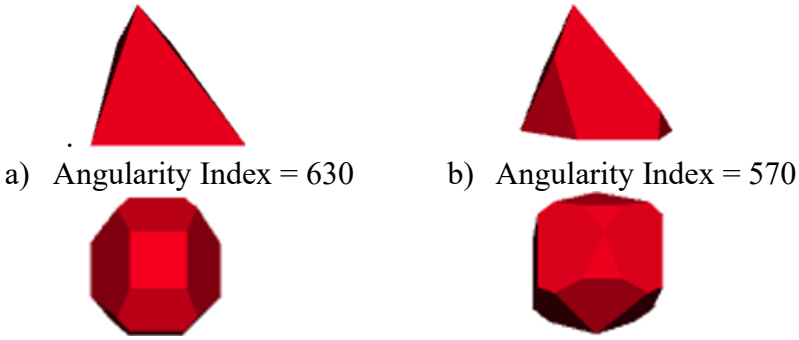
Sieve Size (mm)	A (% Passing)	B and C (% Passing)	D (% Passing)
80		100	100
63	100	95, 100	93, 100
50	70, 85, 99	55, 70, 85	45, 62.5, 70
40	30, 41.5, 53, 65	25, 50, 75	15, 27.5, 40
31.5	1, 13, 25	1, 13, 25	0, 7
22.4	0	0	0
Total Variations	**36**	**36**	**36**

2.2 Particle Shapes and Contact Model Parameters

The packing simulations in this study were conducted using the GranOO open-source DEM software workbench [11, 12]. The workbench comprises a collection of C++ libraries that enable users to tailor simulations for their specific requirements. GranOO supports various particle geometries, including polyhedra, used in this study to represent individual ballast particles.

Fig. 1 presents the polyhedral particle geometries utilized in this study. These particle geometries were previously generated by Huang et al. [13, 14] through scans of real ballast aggregates using the University of Illinois Aggregate Image Analyzer [15-18]. The properties of these particles were provided using object file format in Huang [13] and adopted in this study to represent ballast particles. All particles had a flat and elongation (F&E) ratio of 1. The

angularity index values provided in the Figure quantify the sharpness of the particle corners and edges. Details regarding this index can be found in [17, 18].



a) Angularity Index = 630 b) Angularity Index = 570

c) Angularity Index = 448 d) Angularity Index = 390

Fig. 1. Particle Shapes Used in Simulations (Shapes Regenerated from Huang [13])

GranOO incorporates several models to calculate the forces between the contacting particles. In this study, the Hertz-Mindlin [19] contact model was used. The equivalent Young's modulus and Coulomb's modulus were set to 25 and 10 GPa, respectively, with a restitution coefficient of 0.3. The friction coefficient was varied between 0 and 0.3. In addition, the particle density was assigned to 2650 kg/m^3 to represent a typical aggregate.

2.3 Packing Simulation Steps

Before starting the simulations, the particle shapes, sizes, and initial positions were determined using a Python script [20] and exported to a CSV file. A 40 cm x 40 cm rectangular domain was created in GranOO, and the particles were generated using the CSV file. A compaction plate (40 cm x 40 cm x 5 cm) was created and placed on top of the particles. The time step, gravity, and friction coefficient were initially set to 10^{-6} seconds, 10 g, and 0. The simulation was then conducted using the following steps, as also detailed in [20].

- Drop particles onto the domain with 10 g gravity (Step duration: Varies depending on the number of particles).
- Once the packed particles have stabilized, i.e., not moving excessively, drop the gravity to 5 g (Step duration: 0.1 second).
- Drop the gravity to 1g. Set the friction coefficient to 0.3 (Step duration: 0.1 second).
- Apply an 8 kN vertical force to the compaction plate (Step duration: 0.05 second).

Once these steps were completed, the sample porosity was calculated and recorded. Since the initial particle arrangement can affect the results of a DEM simulation, three different CSV files were generated for each variation case. Therefore, each gradation case had three distinct replicates.

3 Results and Discussions

In this section, the results of single- and multiple-linear regression are presented. The cases studied are listed as follows.

- Linear regression of sample porosity (%) using C_u as predictor.
- Multiple linear regression of sample porosity (%) using C_u and C_c as predictors.
- Linear regression of sample porosity (%) using D_{60}, D_{30}, and D10 (individually) as predictor.
- Linear regression of sample porosity (%) using D_{10} as predictor.

An 80%-20% training-test set split was done before regression. In addition to the train-test split, a 5-fold cross-validation was also conducted on the training set to investigate consistency of the results within the data.

3.1 The relationship between porosity and C_u

Fig. 2 presents the linear regression trends for C_u vs sample porosity for British A, BC, D, and all gradations combined. At first glance, gradations with higher C_u values presented with lower porosity, i.e., denser packing. The test R^2 values, however, were generally quite low, indicating a lack of linear relationship between C_u and porosity. Compared to the other groups, British A presented with relatively higher train (0.635) and test (0.595) R^2 values. However, upon investigating the 5-fold cross-validation results presented in

Table 2, it is evident that test R^2 values were quite low, with high standard deviations across validation folds, for all combinations, including British A. These findings suggest that although a visual trend can be observed between porosity and C_u, it is weak and not reliable. Given that C_c is another important parameter utilized in ASTM D2487, both C_u and C_c were used as predictors for porosity, and the results are presented in the following section.

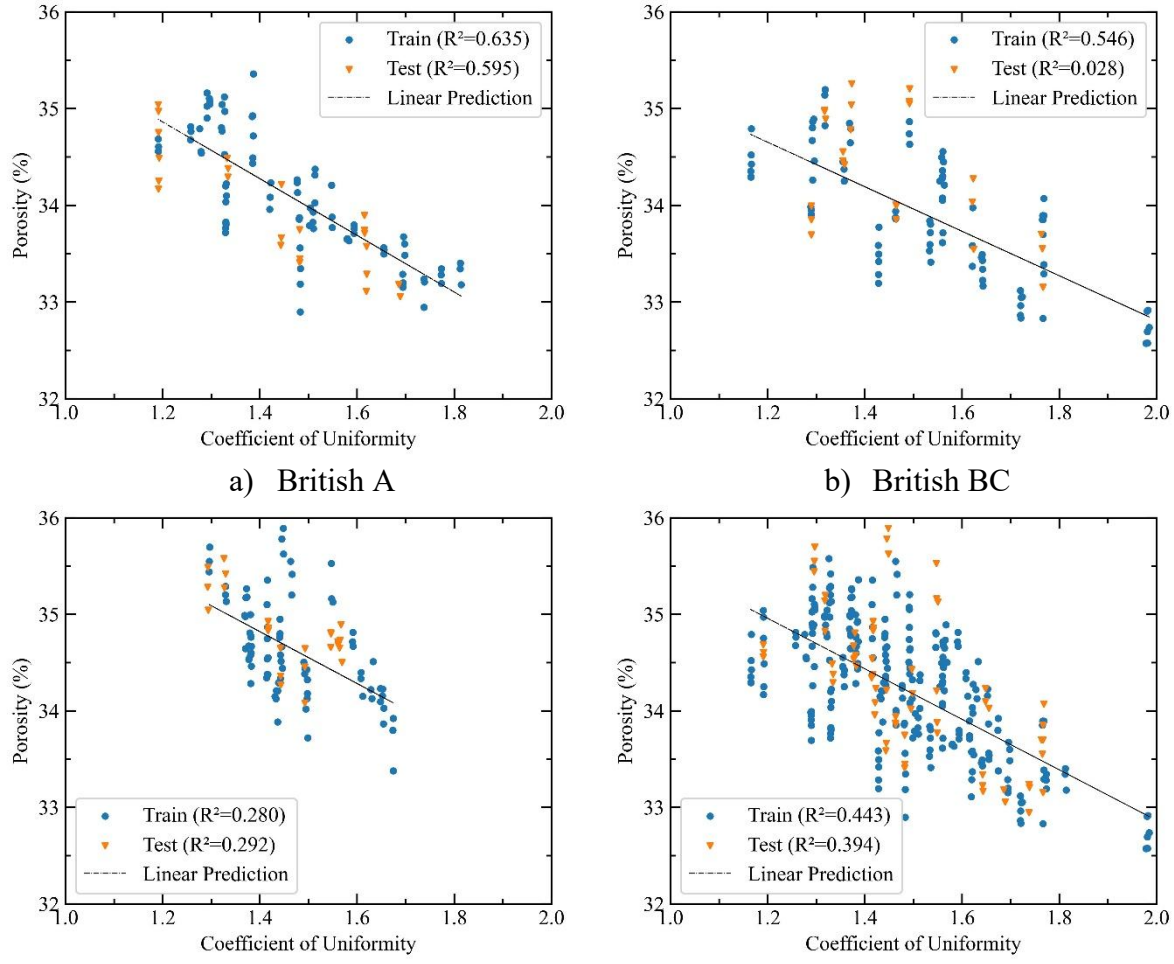


Fig. 2. Coefficient of Uniformity vs Porosity Linear Regression

Table 2. 5-Fold Cross Validation Test R^2 for C_u vs Porosity (%)

Gradation	Test R^2 ± Stdev
British A	.365 ± .369
British B and C	.315 ± .280
British D	.138 ± .319
British A, B, C, and D	.336 ± .284

3.2 The relationship between porosity and C_u combined with C_c

Table 3 presents multiple regression results of C_u and C_c as predictors for porosity. The table also includes the results for the 5-fold cross-validation. As shown in the table, inserting C_c as a predictor besides C_u did not improve the results. Therefore, instead of Cu and Cc, their components, D_{60}, D_{30}, and D_{10}, were individually studied to search for a better trend.

Table 3. Multiple Regression Results Porosity vs C_u and C_c combined

Gradation	Train R^2	Test R^2	CV Test R^2 ± Stdev
British A	.636	.610	.359 ± .357
British B and C	.547	.030	.288 ± .284
British D	.385	.329	.107 ± .315
British A, B, C, and D	.447	.397	.326 ± .274

3.3 The relationship between porosity and D_{60}, D_{30}, and D_{10}

In this section, the individual components of the C_u and C_c equations, D_{60}, D_{30}, and D_{10}, were individually tested as predictors for porosity, and the results are presented in **Table 4**. Note that for brevity, the table includes results for British A, BC, and D combined. As shown in the table, among the 3 components, D_{10} showed significantly higher R^2 values (both in the train-test split and 5-fold CV). Therefore, D_{10} was selected as a promising predictor, and its relationship with porosity was further investigated in the next section.

Table 4. Linear Regression Results Porosity vs D60, D30, and D10

Gradation	Train R^2	Test R^2	CV Test R^2 ± Stdev
D_{60} vs Porosity	.047	.112	.0 ± .086
D_{30} vs Porosity	.407	.426	.321 ± .213
D_{10} vs Porosity	.806	.850	.777 ± .075

3.4 The relationship between porosity and D_{10}

Fig. 3 and **Table 5** present linear regression results with D_{10} vs porosity for British A, BC, D, and all combined. As seen, the higher D10 values, which indicate a coarser gradation, result in higher porosities. What is more, both the train-test split and 5-fold cross-validation R^2 results demonstrated strong predictive performance for porosity across all gradation datasets.

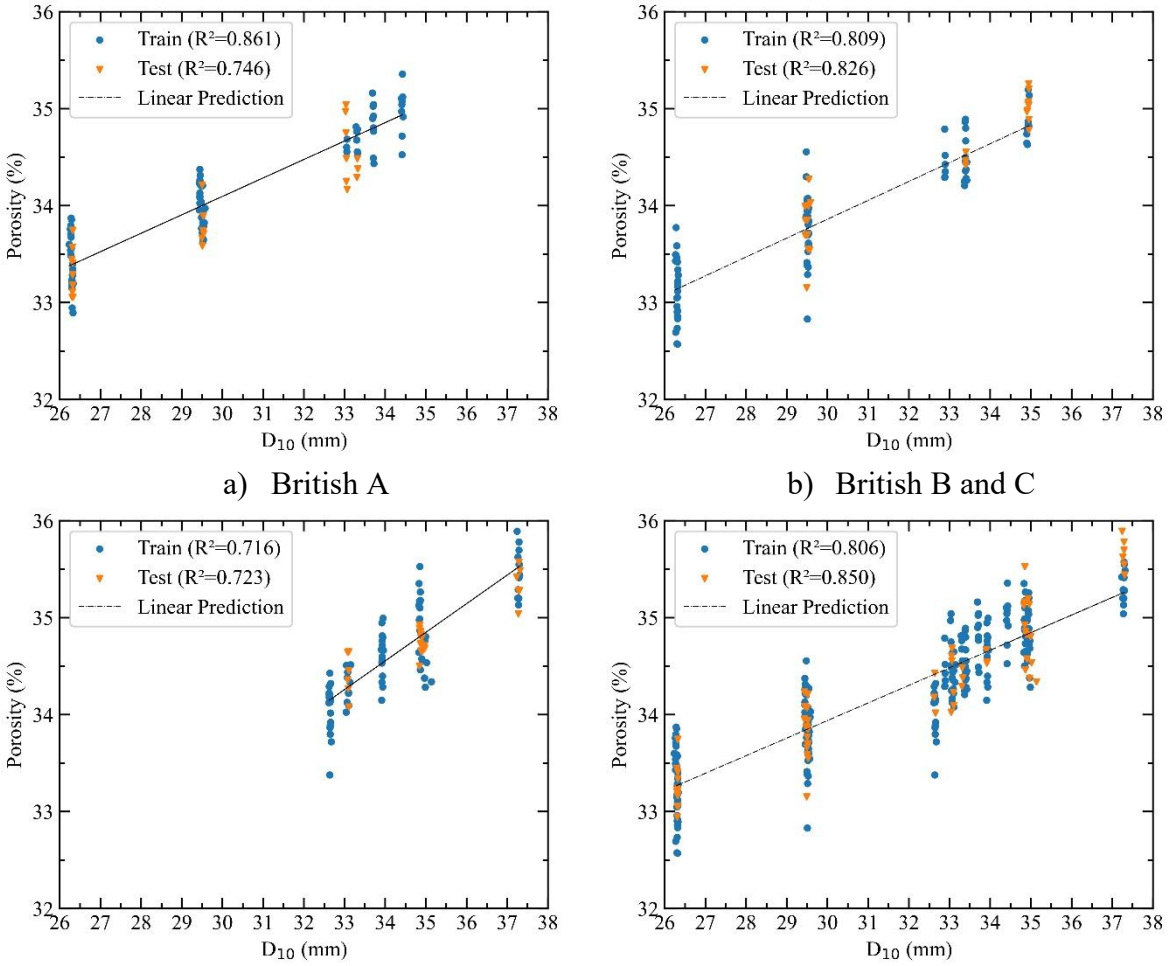


Fig. 3. D_{10} vs Porosity Linear Regression

Table 5. 5-Fold Cross Validation Test R^2 for D_{10} vs Porosity (%)

Gradation	Test R^2 ± Stdev
British A	.799 ± .098
British B and C	.711 ± .140
British D	.631 ± .182
British A, B, C, and D	.777 ± .075

4 Conclusions

In this study, the effect of changes within British ballast gradations (A, B, C, and D) on porosity was investigated using DEM packing simulations with polyhedral shapes and linear regression. A total of 108 unique gradation variations were created within the specification limits, and three replicate DEM packing simulations were conducted for each case. Sample porosities were recorded at the end of the simulations, and linear regressions were conducted between porosities and several predictive parameters, including C_u, C_c, and their components D_{60}, D_{30}, and D_{10}. The findings are summarized as follows.

- While a visual relationship between C_u and porosity was observed, when the R^2 values and five-fold cross-validation results were investigated, it was seen that the relationship was weak and certainly not linear.
- Inserting C_c as an additional predictor besides C_u did not improve the results.

- When D_{60}, D_{30}, and D_{10} were tested as porosity predictors, D_{10} displayed significantly higher performance.
- Increasing D_{10} values, i.e., coarser gradations, resulted in higher porosities with strong linear relationships.

In conclusion, D10 may serve as a design indicator for estimating ballast packing porosity during gradation selection within the British ballast specification.

Acknowledgments
The authors express their gratitude to the National Center for High Performance Computing of Türkiye (UHeM) for the computing resources provided to conduct the DEM simulations.

References

1. Selig, E.T. and J.M. Waters, *Track Geotechnology and Substructure Management*. 1994: Thomas Telford. https://doi.org/10.1680/tgasm.20139.
2. Guo, Y., et al., *Railway ballast material selection and evaluation: A review.* Construction and Building Materials, 2022. **344**: p. 128218.
3. Boler, H., Y. Qian, and E. Tutumluer, *Influence of Size and Shape Properties of Railroad Ballast on Aggregate Packing: Statistical Analysis.* Transportation Research Record: Journal of the Transportation Research Board, 2014(2448): p. 94–104.
4. ASTM, *Standard practice for classification of soils for engineering purposes (unified soil classification system)*, in *D2487*. 2017.
5. Tutumluer, E., et al. *AREMA gradations affecting ballast performance using discrete element modeling (DEM) approach*. in *Proceedings of the AREMA 2009 Annual Conference, Chicago, Illinois, September*. 2009.
6. Bian, X., et al., *"Critical particle size" and ballast gradation studied by discrete element modeling.* Transportation geotechnics, 2016. **6**: p. 38–44.
7. Rosa, A.F., F.T.S. Aragão, and L.M.G. da Motta, *Effects of particle size distribution and lithology on the resistance to breakage of ballast materials.* Construction and Building Materials, 2021. **267**: p. 121015.
8. Cundall, P.A. and O.D. Strack, *A discrete numerical model for granular assemblies.* Géotechnique, 1979. **29**(1): p. 47–65.
9. Yüksel, P., *Demiryolları Malzeme, Yapım, Kontrol ve Bakım Onarım Teknik Esasları*, T.C.U. Bakanlığı, Editor. 2007.
10. Boler, H. and H. Köse, *IMPACT OF VARIATIONS IN PARTICLE SIZE DISTRIBUTION ON PACKING PROPERTIES OF RAILWAY BALLAST: BRITISH A GRADATION CASE*, in *Fifth International Karadeniz Scientific Research and Innovation Congress* 2025: Trabzon, Türkiye (Online). p. 1112–1118.
11. André, D., et al., *The GranOO workbench, a new tool for developing discrete element simulations, and its application to tribological problems.* Advances in Engineering Software, 2014. **74**: p. 40–48.
12. GranOO. *GranOO Open Source DEM Libraries*. 2026 [cited 2026 07/24]; 3.0:[Available from: https://www.granoo.org/.
13. Huang, H., *Discrete element modeling of railroad ballast using imaging based aggregate morphology characterization*. 2010, University of Illinois at Urbana-Champaign.
14. Huang, H. and E. Tutumluer, *Image-aided element shape generation method in discrete-element modeling for railroad ballast.* Journal of Materials in Civil Engineering, 2014. **26**(3): p. 527–535.

15. Rao, C. and E. Tutumluer, *Determination of volume of aggregates: New image-analysis approach.* Transportation Research Record, 2000. **1721**(1): p. 73–80.
16. Rao, C., E. Tutumluer, and J.A. Stefanski, *Coarse aggregate shape and size properties using a new image analyzer.* Journal of testing and evaluation, 2001. **29**(5): p. 461–471.
17. Rao, C.B., *Development of three-dimensional image analysis techniques to determine shape and size properties of coarse aggregate*. 2001, University of Illinois at Urbana, Champaign.
18. Rao, C., E. Tutumluer, and I.T. Kim, *Quantification of coarse aggregate angularity based on image analysis.* Transportation Research Record, 2002. **1787**(1): p. 117–124.
19. Mindlin, R.D. and H. Deresiewicz, *Elastic spheres in contact under varying oblique forces.* 1953.
20. Boler, H. and H. Kose, *Utilization Of Granoo Open-Source Dem Libraries To Simulate Railroad Ballast Particles With Distinct Size Distribution*, in *Sixth Istanbul International Contemporary Scientific Research Congress*. 2024: Istanbul, TURKIYE (Online). p. 144–152.

Author Contribution Statement

- *Conceptualization:* Huseyin Boler
- *Methodology:* Huseyin Boler
- *Investigation:* Hüseyin Köse
- *Writing – Original Draft:* Hüseyin Köse
- *Writing – Review & Editing:* Huseyin Boler

List of Abbreviations

- **DEM** — Discrete Element Method
- **UHeM** — National Center for High Performance Computing of Türkiye
- **F&E** — Flat and Elongation
- **C_u** — Coefficient of Uniformity
- **C_c** — Coefficient of Curvature

Publication Note

This paper was peer-reviewed, accepted for presentation, and included in the proceedings of the ACE2026 – International Conference on Advances in Civil Engineering, held on 12–14 October 2026 in Trabzon, Türkiye.

This paper may be cited as follows:

Hüseyin Böler, Hüseyin Köse, "Analysis of the Ballast Porosity Variations in British A, B, C, and D Gradations using the Discrete Element Method," in Proceedings of the ACE2026 – International Conference on Advances in Civil Engineering, Trabzon, Türkiye, 12–14 October 2026.

Evaluating Fare Structure with Best–Worst Method: Istanbul Metro Example

Ömer Murat Urhan[1] and Mustafa Gürsoy [2]
[1] orcidID: 0000-0003-4640-5858,
Yildiz Technical University, Civil Engineering Department, İstanbul, Türkiye, murat.urhan@std.yildiz.edu.tr

[2] orcidID: 0000-0002-3782-5941,
Yildiz Technical University, Civil Engineering Department, İstanbul, Türkiye, gursoy@yildiz.edu.tr

Abstract. Public transportation (PT) is key to breaking the vicious cycle of private vehicles, a critical challenge in developing countries. The increase in population raises the number of cars, and this trend continues. PT plays a crucial role in reducing car use, traffic congestion, and environmental pollution. PT Fare is vital to the system's ability to encourage passenger's use. It affects mobility, the quality of life, and the sustainability of the system. This study aims to find tailor-made fare system for Istanbul using the BWM (Best–Worst Method) for PT fare for the first time. Moreover, it is the first study for fare structures and criteria for Istanbul, Europe's second-largest city. The most used fare structures and criteria in the literature and practice were weighted by experts using BWM surveys for the Istanbul Metro. The results show that distance-based fare (DBF) (43.7%) is the best fare structure, while flat fare (FF) (12.2%) is the weakest. For the criteria weightings, benefit received (24.4%) and social equity (22.7%) are seen as superior. Finally, the impact of the criterion on the fare structure was demonstrated, and its importance for experts in evaluating PT was highlighted.

Keywords: public transport; fare structure; fare structure criteria; Best–Worst Method.

1 Introduction

In urban areas where the population increases, the importance of transportation planning and decisions also increases. Since these plans and decisions affect not only passengers and operators but also the entire city, they need to be considered from many perspectives [1]. The plans can change where cities will grow, where they will generate profit, which areas will develop, and which areas will lose attractiveness. So, plans and projects in the field of transportation should be long-term and based on a wide range of sources and accurate data.

In modern city's, despite high levels of travel demand, the classic transportation approach, dependent on cars, creates a vicious cycle. This vicious cycle is shown in Figure 1. As a result of increase in demand, congestion begins on the newly built road intended as a solution, and the vicious cycle starts again [1].

In Traffic in Towns, the author argues that this vicious cycle should be broken in cities. Buchanan emphasizes that the car is an expensive mode, therefore, different systems should be developed in cities with populations over 100,000 [1]. One of the main recommendations to break the vicious cycle is on rail systems. Vivier et al. reported that passengers, on average, consume one-quarter as much energy per passenger-kilometer as private cars. Still, increasing congestion on roads and highways in many cities has led to greater investment in car-oriented infrastructure, while relatively few cities have prioritized investments in PT.

H. Mohring emphasizes that this vicious cycle will not occur with an increase in demand for PT and rail systems. An increase in demand creates a positive externality. It is known in the literature as the Mohring effect. The Mohring effect is the observation that if the frequency of a transit service (e.g., trains per hour) increases with demand, then a rise in demand reduces passengers' waiting times at stations [2].

Mohring argued that rail transit can shift passengers' travel behavior by inducing a modal shift, thereby generating a traffic diversion effect. From the user's perspective, this virtuous cycle is explained below (Figure 1) [2].

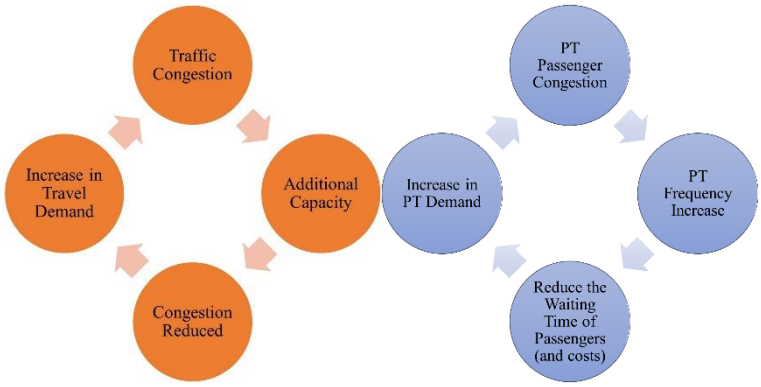


Fig. 1. The vicious cycle of the car-oriented approach (a) and the virtuous cycle of the PT approach (b).

To find a best solution for the Istanbul, need to understand the reason for fare reconstruction. Farebox recovery ratio (FRR) of Metro Istanbul, defined as the share of operating costs covered by passenger revenues, is reported in the Strategic Plan as 68.41% for 2021, 78.23% for 2022, and 75.92% for 2023, with a target of 77.50% set for 2024 [3]. The operating deficit, defined as the proportion of operating costs not covered by fare revenues, was 31.59% in 2021, 21.77% in 2022, 24.08% in 2023, and projected at 22.50% in 2024 [3].

High FRRs are observed in Hong Kong (~107%), Singapore (~101%), and Taipei (~88%), while European systems range from ~30% to ~94%, and North American metros achieve 30–40%. The London Underground exceeds 129%. Istanbul's ratio is moderate, higher than many North American and some European systems, but below top-performing Asian and UK metros [3]. Also, understanding the distribution of trip lengths provides further insight into passenger behavior and system usage patterns. According to 2025 Istanbul Metro data, long-distance trips—journeys of six or more stations—account for 31.7% of all trips. In short-distance trips, the most frequent journey length is three stations, whereas for long-distance trips, seven stations are the most common [3].

2 Conceptual Review

Fares are the core of PT, playing a vital role in ridership patterns and the financial sustainability of transit agencies [4]. When decision-makers target more sustainable city based on PT, an optimal fare strategy can create more intense cities, reduce carbon emissions and maintenance costs [5].

2.1 Fare Structure

Fare structure is pivotal to PT policies, as it significantly affects passengers' socio-economic outcomes, land-use patterns, and the sustainability of systems [5]. Differentiated fare structures are an efficient tool for demand management.

The most used fare structures in theory and practice are given below:

1. Flat fare (FF) does not vary based on any factor. Passengers pay the same fare.

2. Distance-based fare (DBF) determined by the distance or the number of stations crossed.
3. Time-based fare (TBF) determined by when the trip is made.
4. Zone-based fare (ZBF) determined by where the trip is made, and no. zones crossed.

Table 1. Table captions should be placed above the tables.

Fare Structure Type	Advantages	Disadvantages
Flat Fare	Easiest to understand. Simplest and cheapest to implement and administer.	It places an unfair burden on those making short trips. A fare increase will cause the greatest loss of riders. It places an unfair burden on those making short trips.
Distance-Based Fare	It should make the biggest revenue. Considered equitable; longer trip	Difficult to use. Hard to implement and oversee.
Time-Based Fare	Should increase ridership. Allows management of fleet usage through shift to off-peak.	Possibility of fraudulent behavior. Could necessitate new equipment.
Zone-Based Fare	On long PT lines, traveling to more zones allows higher fares to help cover operating costs.	When zone fares vary, it may encourage urban decentralization. Decentralization extends service distances, raising operator costs and fares.

2.2 Fare Structure Assessing Criteria

Seven most used criteria are social equity, benefit received, operator profit, ticket price, number of trips, decentralization, and urban morphology. Although not used as criteria in this study, ability to pay, operator cost/revenue, maximum profitability, complexity, passenger control, implementation difficulty, long trips, payment types, implementation costs, Gini co-efficient, train headway, and social welfare are mentioned in the literature.

This study develops a multi-criteria evaluation (BWM) for comparing fare structures and criteria. The proposed approach incorporates economic, social, and operational criteria, including social equity, benefit received, operator profit, ticket price, travel demand, decentralization, and urban morphology. By integrating these criteria into a structured decision-making framework, the study contributes to the literature by providing a wide approach for assessing fare structures and supporting optimal fare policies.

3 Data and Methodology

Istanbul has experienced significant growth in land use and population over the last five decades. With this growth, Istanbul is now Europe's most populous metropolis. Beyond its population of around 16 million, the ratio of young and working people in the population is also high. For the reasons, the transportation structure has become complicated, and traffic and problems have become the most important issues, with traffic jams every day and millions of dollars of lost time and fuel costs, ultimately leading to people become worse off regarding their quality of life [3].

De Gruyter et al. showed that Eastern Europe has higher overall performance in PT sustainability measures. In the study, eight cities were given in the Eastern European group, and the largest of these cities is Istanbul [6]. However, there are no studies that widely examine PT fares in Istanbul. This study was prepared to address a gap in the literature.

3.1 Transportation in Istanbul

For According to the TomTom Traffic Index Report 2024, the Istanbul metropolitan area ranks fifth in Europe and 19th in the world, with a congestion level of 39% (meaning that, on average, journey times across that area's road network were 39% greater than when traffic is free-flowing). Other metrics of the Traffic Index for Istanbul:

- Average travel time per 10 km = 18 min 51 s;
- Time is lost per year during rush hours = 80 h = 3.3 days [7].

Congestion cause traffic jams across Istanbul, costing more than $1.7 billion annually. Traffic jams have become a critical problem across Istanbul due to a lack of infrastructure to meet demand from rapid growth [6,7].

Public Transport in Istanbul

As of 2026, Metrobus (Bus Rapid Transit), Marmaray (commuter rail), metro (11 lines), tram (5 lines), funicular (2 lines), cable car (2 lines), buses, minibusses, taxi minibusses, and ferries are operated in Istanbul. Metrobus, Marmaray, M11 (metro line of Turkish State Railways Transport-TCDD), and some bus–minibus lines in Istanbul operate with DBF; some bus lines operate with ZBF; and the remaining lines operate with FF.

Ticket Types in Istanbul

In Istanbul, the two most frequently used transit card options are: Istanbulkart and Mavi (Blue) Kart. There are four different Istanbulkart options for passengers: Full fare, the student 30+ card (for students who have reached the age of 30), the social card, and the student card.

The Blue Card is a monthly card. Full fare, the student 30+ card, the social card, and the student card are types of Blue Cards.

All mothers (have children between 0 and 4 years), members of the press, police, veterans, veterans' families, the security service class, disabled people, soldiers, national athletes, mukhtars, martyrs' families, TUİK (TurkStat) personnel use Free Istanbulkart.

An electronic ticket is another option. Passengers can buy single, two, three, four, five, or ten use passes in the form of paper tickets. Passengers can also use their bank cards at PT.

Istanbul Metro Data

The Istanbul Metro is a rail network that serves Istanbul. Except for the M11 line, the system is operated by Metro Istanbul (company), a public enterprise of the Istanbul Metropolitan Municipality (IBB). There is a 380.70 km urban rail system operating in Istanbul. Metro Istanbul serves over 3 million passengers every day, with 18 lines, totaling 241.35 km. Istanbul in 2025:

- According to a recent urban mobility report, 48% of daily trips were made by PT;
- Rail systems account for 20.59% of all trips;
- Metro İstanbul accounts for 10% of all trips;
- The number of trips made by the Istanbul Metro (M lines) 7.4% of the total trips [8].

Metro Istanbul accounts for 63.8% of the total trips made by all rail systems and Metrobus in Istanbul. The number of trips made by the Istanbul Metro is 47.6% of the total trips made by all rail systems and Metrobus in Istanbul [8]. The oldest metro is the M1, which opened in 1989. As of 2026, the system had 11 lines and 159 stations in service, with 36 more under construction [8]. At 243.3 km, the Istanbul Metro network is the fourth-longest in Europe as of 2026. Because of Istanbul's unmatched geography and the Bosporus Strait, its European and Asian metros do not connect directly. The two side of the city are linked through the Marmaray commuter rail line.

Average metro trips in Istanbul cover more or less 5.5 stations and about 18.5 min. The average total travel time, including access to the metro station and the time required to get the

destination, is about 50 min. On average, each passenger makes more than one transfer per trip (1.42 transfers) to get their destination [3,8,9].

Nearly 67.4% of all metro trips in Istanbul during the morning and evening peak hours. The passenger densities for these metro lines are presented in Table 2 [3,8,9]. Peak passenger demand for metro was estimated using the passengers per hour per direction (PPHPD) metric.

Table 2. Peak passenger demand and capacity utilization of the Istanbul metro [5,8].

Metro Line	Avg. Daily Ridership (2024 Data)	Estimated PPHPD	Reference Capacity (PPHPD)	Capacity Utilization (%)
M1	357.116	20.058	60.000	33.4%
M2	445.763	25.037	60.000	41.7%
M3	138.821	7.797	60.000	13.0%
M4	299.659	16.831	60.000	28.1%
M5	292.945	16.454	60.000	27.4%
M6	16.469	925	60.000	1.5%
M7	218.545	12.275	60.000	20.5%
M8	62.925	3.534	60.000	5.9%
M9	49.873	2.801	60.000	4.7%

Average daily ridership data obtained from the 2024 statistics of Metro Istanbul [3,8]. Since 67.4% of trips occur during peak hours, peak demand was distributed across six peak hours and two travel directions to estimate PPHPD:

$$\text{PPHPD} = \frac{\text{Daily Ridership} \times 0.674}{6 \times 2}$$

Capacity use was then calculated by comparing the estimated PPHPD values with a reference metro capacity of 60,000 passengers per hour per direction [3,8]. As shown below M2 line has the highest peak demand, followed by M1, M4, and M5, while newer lines such as M8 and M9 currently operate at lower usage levels [3,8].

To examine Istanbul Metro, data on the week with the most travel in 2024 was get from BELBİM (Electronic Money and Payment Services Inc.). The results of the analyses performed in Excel are presented. Data for the Istanbul Metro (M lines) alone were visualized and presented below (Figures 2 and 3 displays the card type chart, and Figures 4 and 5 display the station charts for weekdays and weekends).

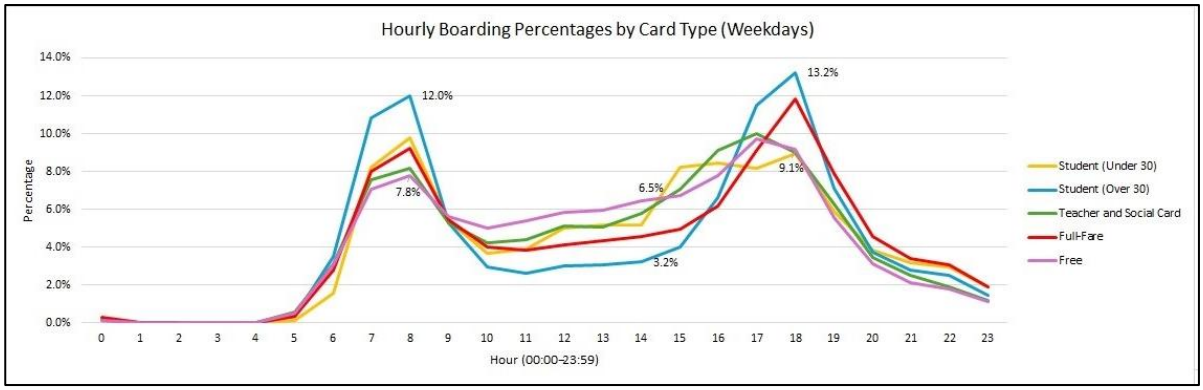


Fig. 2. Hourly boarding percentages by card type—weekdays [9].

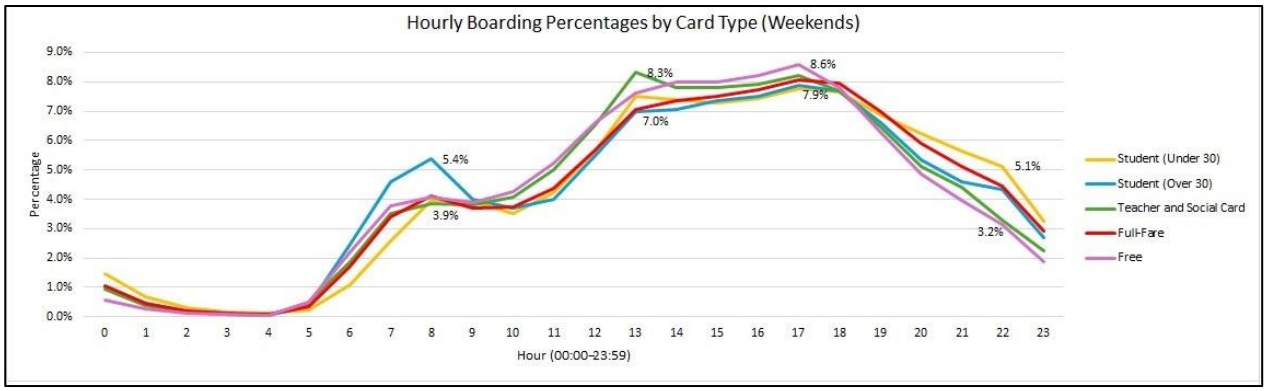


Fig. 3. Hourly boarding percentages by card type—weekends [9].

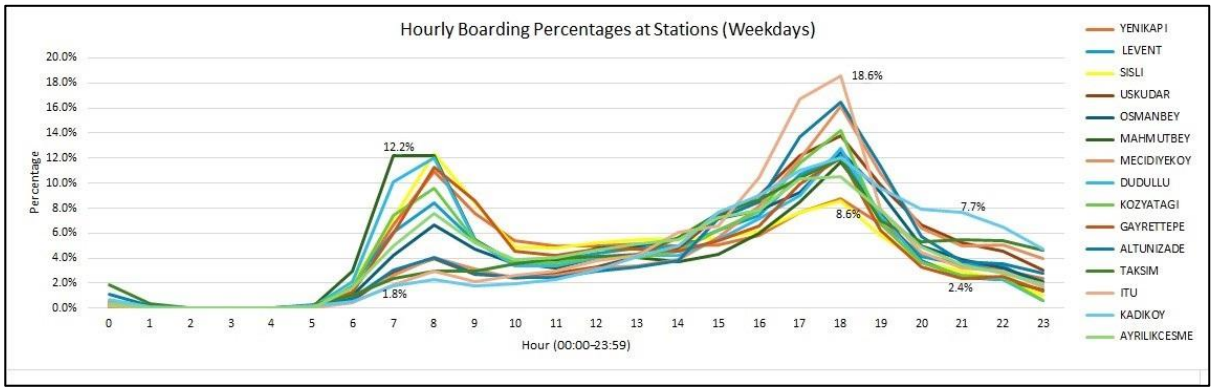


Fig. 4. Hourly boarding percentages at busiest stations—weekdays [9].

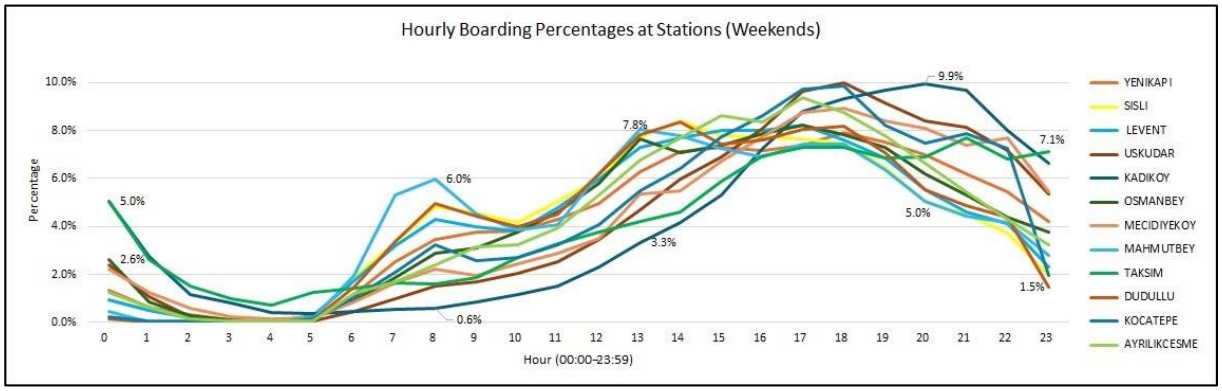


Fig. 5. Hourly boarding percentages at busiest stations—weekends [9].

For more technic analyses, interviewed many experts to collect their opinions on fare structure and criteria. For this reason, proposed using BWM to out a ranking based on fare structure and criteria. The character of Istanbul, along with insights from the literature, guided the selection of the BWM and, accordingly, the determination of the criteria. To the best of the authors' knowledge, there were no empirical studies on PT fare structures and decision criteria for Istanbul.

3.2 Best–Worst Method (BWM)

The BWM, a new and practical MCDM (multiple criteria decision-making) method, was used for the first time in this context. The previous use of AHP (Analytic Hierarchy Process) and MABAC (Multi-Attributive Border Approximation Area Comparison) disclose that MCDM is appropriate for achieving the intended targets and objectives on PT fare [6,7].

The linear BWM model defines the importance and weights of the criteria and alternatives. The BWM requires less comparisons than other MCDM tools; the final weights from the BWM are highly reliable, and the comparisons are more consistent than those in full matrix-based methods. BWM is known for its simplicity, as comparisons are made using only numbers from 1 to 9. This provides a clear benefit from other MCDM methods that require comparison matrices with integers as well as with fractional numbers [10,11]. This work provides additional proof of the method's usability for evaluating technology and its effectiveness in PT fares. Figure 6 shows example of BWM Comparisons.

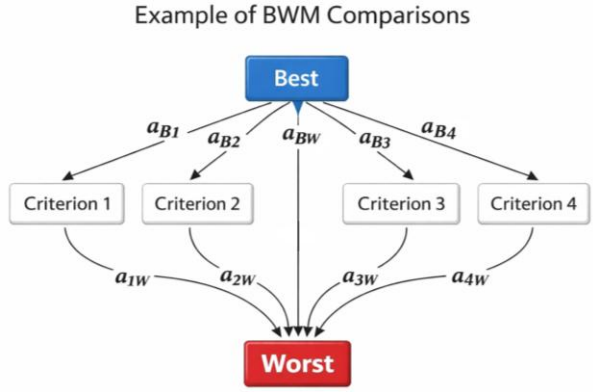


Fig. 6. Example of BWM comparisons [11].

To determine the set of decision criteria, first assessed the factors (social equity, benefit received, operator profit, ticket price, number of trips, decentralization, and urban morphology) and structures (flat fare, distance-based fare, time-based fare, zone-based fare) selected from literature. Then, they conducted a survey to collect data for applying the BWM. The survey was conducted using Microsoft® Excel®. Solver add-in used to calculate the weights in the BWM model for the entire analysis [11].

The survey was sent to more than 150 experts in the field, researchers and practitioners alike, including academics, operators, and government officials with extensive knowledge of PT fare systems. As a result, a total of 22 experts from Türkiye were selected, including 5 practitioners, 17 academics from well-established universities, and a department head.

The experts completed the survey in Excel (Solver add-in). When the Consistency Ratio exceeded 0.10 [12], the experts were asked to revise their responses. A total of 22 experts received the same survey, regardless of the group they were assigned to, and conducted the same analysis for each criterion and structure.

4 Results

The first result emerging from the experts' criteria weightings was the dominance of benefit received (24.4%) and social equity (22.7%). These two criteria represent horizontal and vertical equity, respectively. The experts emphasized that the superiority of these two criteria highlights the importance of equality in PT. The least important criteria were operator profit (8.4%), decentralization (8.8%), and urban morphology (9.4%). The scarce influence of these three criteria say that experts choose a passenger-centric perspective in PT. Even though the number of trips (14.9%) and ticket price (11.4%) showed high values, they were still less effective than the benefit received and social equity criteria.

Experts find DBF (43.7%) as the most dominant fare structure, while FF (12.2%) was the weakest. This choice was likely influenced by the benefit-received criteria—namely, that passengers pay according to their level of use—which is one of the main advantages of DBF over FF. ZBF (23.3%) and TBF (20.8%) outperformed FF, but they were far from DBF. While ZBF and TBF mean fare differentiation and offer benefits based on certain criteria, their

relationship with the benefit-received criterion is not as robust as that of DBF. The results are shown in Table 3.

Table 3. Expert survey results.

	Fare Structure * Weighting				Fare Structure Assessing Criteria Weighting						
Experts	FF	DBF	ZBF	TBF	Social Equity	Benefit Received	Operator Profit	Ticket Price	Number of Trips (Demand)	Decentralization	Urban Morphology
Expert 1	13.5%	27.0%	51.4%	8.1%	18.5%	32.6%	5.6%	12.4%	12.4%	9.3%	9.3%
Expert 2	11.8%	25.7%	7.4%	55.1%	20.9%	34.9%	5.6%	20.9%	7.0%	6.0%	4.7%
Expert 3	25.9%	43.2%	4.9%	25.9%	31.8%	19.1%	3.2%	7.6%	12.7%	12.7%	12.7%
Expert 4	10.8%	40.5%	24.3%	24.3%	33.8%	22.3%	14.9%	11.2%	8.9%	3.3%	5.6%
Expert 5	7.2%	56.2%	13.0%	23.6%	24.3%	24.3%	5.4%	16.2%	12.1%	9.7%	8.1%
Expert 6	14.0%	45.3%	16.3%	24.4%	6.4%	8.0%	27.5%	16.0%	27.5%	10.7%	3.8%
Expert 7	11.8%	41.2%	41.2%	5.9%	20.2%	34.6%	10.1%	10.1%	13.5%	4.8%	6.7%
Expert 8	6.7%	26.2%	49.7%	17.4%	33.7%	19.4%	9.7%	7.8%	12.9%	12.9%	3.6%
Expert 9	9.1%	24.2%	21.2%	45.5%	20.7%	35.2%	4.8%	13.8%	10.3%	6.9%	8.3%
Expert 10	6.8%	63.2%	12.0%	18.0%	23.1%	11.0%	2.2%	5.5%	27.5%	16.5%	14.3%
Expert 11	12.6%	57.7%	21.0%	8.7%	15.0%	11.8%	11.8%	7.1%	5.4%	17.7%	31.3%
Expert 12	22.6%	41.9%	12.9%	22.6%	24.5%	24.5%	5.5%	9.1%	13.6%	9.1%	13.6%
Expert 13	6.5%	16.3%	55.4%	21.7%	32.4%	17.6%	11.8%	8.8%	5.9%	5.9%	17.6%
Expert 14	5.3%	54.3%	20.2%	20.2%	13.8%	34.4%	8.3%	13.8%	20.7%	3.1%	5.9%
Expert 15	10.3%	46.6%	17.2%	25.9%	4.1%	35.3%	8.4%	13.9%	20.9%	10.5%	7.0%
Expert 16	7.4%	48.5%	17.6%	26.5%	29.0%	16.1%	10.8%	10.8%	16.1%	10.8%	6.5%
Expert 17	5.2%	56.4%	21.9%	16.4%	34.4%	20.7%	8.3%	6.9%	20.7%	5.9%	3.1%
Expert 18	11.4%	55.4%	26.9%	6.3%	24.6%	25.3%	2.8%	5.1%	25.3%	11.9%	5.1%
Expert 19	22.2%	44.4%	11.1%	22.2%	34.2%	16.5%	9.7%	13.0%	13.0%	5.9%	7.8%
Expert 20	27.0%	51.4%	13.5%	8.1%	16.8%	32.1%	6.1%	11.2%	16.8%	5.6%	11.2%
Expert 21	9.1%	50.0%	27.3%	13.6%	17.4%	28.6%	4.5%	17.4%	11.6%	8.7%	11.6%
Expert 22	10.3%	46.6%	25.9%	17.2%	19.3%	32.4%	7.7%	12.9%	12.9%	5.3%	9.6%
Average Weights	12.20%	43.70%	23.30%	20.80%	22.70%	24.40%	8.40%	11.40%	14.90%	8.80%	9.40%

As shown in Table 3, DBF is the most appropriate fare structure for the Istanbul Metro. DBF is followed by ZBF, TBF, and FF. The clear dominance of DBF, social equity, and benefit received responses indicates a strong consensus among experts. For twenty out of twenty-two experts DBF as the most superior, while TBF and ZBF were each selected by only one expert. Ten experts assigned the highest weight to the benefit received criterion, whereas eight selected social equity. Only two experts gave the highest weight to the number of trips criterion. The fact that these experts—who were not in communication with one another—have an agreement enhanced the trustworthiness of the results.

There are several reasons why expert opinion is in advantage of DBF:

1. FF is an easy-to-implement, cheap, and simple for the operator. It is also easy for passengers to understand and control. It is the optimal solution for cities with a single center that are not large enough. However, cities where the number of trips increases and distances getting longer (especially in linear cities like Istanbul), it is essential to evaluate a more customized fare structure such as DBF.
2. Istanbul operators' profits decreased because of increases in operating costs, due to the addition of new lines to the end of the metro lines operated with FF in the city in recent years. But even though the lines getting longer, long-distance travelers still pay the same fare. It's unfair for both the operator and the passenger. When DBF is implemented, passengers will pay according to the number of stations, and injustice will be eliminated.

3. In Istanbul, the operating income only covers 30%–35% monthly fixed expenditure. Its similar for the Istanbul Metro [13]. Operations can continue thanks to subsidies. But, the difference between operating income and expenses widens every year, and the subsidies also increase. Li et al. show that DBF can increase operator revenue by 5.88% [14]. DBF, which is applied to suitable fare levels after a thorough analysis of trips, will attract those who chose different modes for short distances with its affordable fares. Also, it will charge much higher fares for long-distance travelers. For sum, operating income will increase, and the need for subsidies will decrease.

From Table 3, it is seen that social equity and benefit received are the most dominant decision criteria. The other five criteria (operator profit, ticket price, number of trips (demand), decentralization, and urban morphology) are far from them. There are reasons why expert opinion is in favor of these two criteria:

1. In Istanbul and similar cities, rising land values and urban renewal in the city center are leading to new housing areas in the outskirts. This increase in land values in the center is rise housing costs. Residents, especially low-income, are moving away from the center and settling in the less-accessible suburbs [15]. This leads to difficulties in accessing urban services for low-income, increased transportation costs, longer travel times, etc. in other words, transportation poverty. For low income, where vehicle ownership rates are low, PT is the only option. With this perspective investments in PT are a useful tool for ensuring social equity.
2. In this study, social equity criteria are used in the sense of vertical, and Benefit Received criteria are used in the sense of horizontal equity. It is stunning that experts outperform the other five criteria on these two equality criteria. With these assessments, they prioritize passengers good over operators good. This can be interpreted as a reflection of the problem of social inequality in Istanbul.
3. Istanbul has the highest income inequality in Türkiye. Based on TÜİK data, the highest income inequality by province was in Istanbul (8.6) [16]. This data strongly emphasizes the importance of social equality in Istanbul. Policies in this direction will reduce social and economic inequalities.
4. The distribution of card types across income groups provides insights into the socio-economic characteristics of Istanbul Metro users. Monthly Mavikart (student and full-fare) and teacher and social cards are predominantly used by higher-income, suggesting that frequent PT usage and monthly fare products are more common among economically stable groups. In contrast, free cards, particularly the 65+ and disabled cards, exhibit relatively higher shares among lower and middle-income groups, highlighting the redistributive role of socially targeted fare policies. These findings demonstrate that fare differentiation and card-type structures serve as key policy tools to improve equity, enabling vulnerable or mobility-dependent groups to maintain access to services. Therefore, analyzing card-type usage patterns alongside income levels provides a framework for evaluating the equity performance of systems.
5. The spatial relationship between income distribution and the metro in Istanbul disclose dimension of transport equity. High-income districts are primarily concentrated along central and coastal areas where metro accessibility is relatively strong due to the presence of major corridors has the highest passenger demand and accessibility. Middle-income districts are served by expanding metro corridors, which improve accessibility between peripheral residential areas and the urban core. In contrast, lower-income districts located mainly on the western and northwestern periphery have historically experienced limited rail access, although recent infrastructure investments have significantly improved connectivity. Overall, the analysis suggests that the expansion of the metro network from M1 to M9 plays a crucial role in lower spatial inequalities in PT accessibility and contributes to the objective of enhancing social equity in urban mobility.

6. Accessible and proper travel should be considered a basic right for all citizens in modern cities. So, operators are required to ensure a minimum level of service to guarantee this. Those with incomes high enough to afford a private car can choose not to use PT. Those without a private car have only two options: PT and taxi. Istanbul has been plagued by a long-standing taxi shortage. In Istanbul, there is only one car for every three people; PT is the only option for millions. Experts recommend providing this service to low-income residents, who have no other option but PT, at a fare proportional to their budget. Higher-income residents, if charged according to their budgets, would pay more per trip than others. This, carries the risk that high-income passengers using PT will opt for their private vehicles in-stead.
7. The benefit received implies that passengers pay in proportion to the benefits they receive. It is no surprise that experts chose DBF as the superior when they chose the benefit received criterion as the superior decision criterion. Paying for the distance traveled in DBF can be interpreted as an application of the benefit received. This ensures passengers pay in proportion to the benefit they receive. Although benefit received and social equity are presented separately in our study, improving benefit received naturally contributes to social equity.

5 Discussion

Rapid urbanization has strengthened the need for PT systems that ensure social equity, economic feasibility and ecological sustainability [17]. Stereotypical fare frameworks primarily prioritize economic performance, often neglecting wider social and environmental implications. This study surveys optimal fare system with BWM for PT fare for the first time. Further, it is the first study to compare PT fare structures and criteria for Istanbul. The main target of this study is to evaluate the best fare system for the Istanbul Metro. To apply the BWM, a survey was conducted among transportation operators, academia, and government officials.

According to BWM result, social equity and benefit received are the most important criteria, with 22.7% and 24.4% [17]. DBF is the most suitable for the Istanbul Metro, while FF is the least. Many of the findings here reflect a common planning approach in developing countries, where short-term, populist measures often take priority over long-term, technically informed solutions. Widely restructuring transportation within metropolitan areas, creating diverse development and employment, and establishing new networks will help resolve the existing issues of an overly centralized system prone to frequent operational disruptions.

Designing a fare system fit to the region's specific characteristics is important for enhancing population mobility and promoting development. Istanbul is known for its lack of, or inadequate, rail systems on the city's peripheries, its planned bus system, and its high fares (relative to average salaries). These force a big portion of passengers to rely on multiple routes and modes of PT, forcing them to pay multiple fares for their daily commute.

One of the reasons for these problems is the lack of collaboration between Istanbul's local and central administrations. Most major metropolitan areas have multiple administrations, often with conflicting political interests, making the full integration of the network and fare system highly challenging. This limits population mobility and embarrass regional development. The outcomes of coordinated efforts presented as outputs for the city of Istanbul, analyzed in this study, demonstrate what can be accomplished through precise planning. This study presents findings that highlight the significance of both vertical and horizontal equity in PT fares. While the FF used in the Istanbul Metro is easy to understand and implement, modern, holistic, and tailored solutions are needed for cities of this scale.

Future research could extend the study in few directions [17]. First, passenger surveys conducted by transit operators or independent researchers could be incorporated to obtain more detailed information on passengers' socio-economic characteristics. Integrating this data into fare policy analyses would enable a more comprehensive understanding of how passenger groups respond to alternative fare structures. Second, future studies could combine survey data

with smart card and automated fare-collection datasets to analyze passenger travel behavior in greater detail. Such integration would provide valuable insights into travel demand patterns and the behavioral impacts of fare policies. Eventually, comparative analyses across different cities could further improve the generalizability of the findings and help identify how variations in urban structure, governance, and PT influence the performance of fare structures. These approaches could support the development of more equitable and efficient fare systems, including targeted discount policies for specific passenger groups such as students, elderly passengers, and disadvantaged.

Acknowledgments
This study was prepared within the scope of the findings from an ongoing Ph.D. dissertation titled 'Developing a Public Transport Pricing Method Using the Best-Worst Method: Istanbul Example' and further draws upon the content of the article 'Evaluating Fare Structure with Best–Worst Method for Improving Sustainable Transit Operations: Istanbul Metro Example', published in the journal named Sustainability.

References

1. Buchanan, C.: Traffic in Towns; Ministry of Transport: London, UK, (1963).
2. Mohring, H.: Optimization and scale economies in urban bus transportation. Am. Econ. Rev., 62, 591–604 (1972).
3. Metro Istanbul. Strategic Plan 2021–2025 (Revised Version).: Available online: https://www.metro.istanbul/Content/assets/uploaded/stratejik%20plan2021-2025_guncel.pdf Metro Istanbul Website, last accessed 2026/06/07.
4. Nuworsoo, C., Golub, A.; Deakin, E.: Analyzing equity impacts of transit fare changes. Eval. Program Plan, 32, 360–368 (2009).
5. Gokasar, I., Karakurt, A., Kuvvetli, Y., Deveci, M., Delen, D., Pamucar, D.: Correction: Sustainable regional rail system pricing using a machine learning-based optimization approach. Ann. Oper. Res., 332, 1315–1316 (2024).
6. De Gruyter, C. Currie, G.; Rose, G.: Sustainability measures of urban public transport. Sustainability, 9, 43 (2017).
7. TomTom.: TomTom Traffic Index Ranking 2024. 2025. Available online: https://www.tomtom.com/traffic-index/ranking/, last accessed 2026/06/08.
8. Metro Istanbul.: Metro Istanbul Lines. 2025. Available online: https://www.metro.istanbul/Hatlarimiz/TumHatlarimiz, last accessed 2026/06/07.
9. BELBİM.: TCDD–IETT–Metro Istanbul Travel Data Details (27 May–2 June 2024); BELBİM: Istanbul, Türkiye, (2025).
10. Rezaei, J.: Best-worst multi-criteria decision-making method. Omega, 53, 49–57 (2015).
11. Rezaei, J.: Best-worst multi-criteria decision-making method: Linear model. Omega, 64, 126–130 (2016).
12. Saaty, T.L.: How to make a decision: The analytic hierarchy process. Eur. J. Oper. Res., 48, 9–26 (1990).
13. Metro Istanbul. Activity Report 2024.: Available online: https://www.metro.istanbul/Content/assets/uploaded/2024_faaliyet_raporu.pdf, last accessed 2026/06/08.
14. Li, N. Mao, B.; Huang, J. Wen, F.; Xu, G.: Fare structure optimization of intercity railway. IET Intell. Transp. Syst, 19, e70041, (2025).
15. Istanbul Transport Poverty Workshop.: From Transportation Poverty to Inclusive Transportation Systems; TÜBİTAK Project No.120K152; Istanbul Transport Poverty Workshop (Istanbul/Türkiye) (2021).

16. Euronews.: Türkiye'nin Yoksulluk ve Gelir Dağılımı Eşitsizliği Haritası. 2019. Available online: https://tr.euronews.com/2019/09/23/a-dan-z-ye-turkiye-nin-yoksulluk-ve-gelir-dagilimi-esitsizligi-haritasi, last accessed 2026/06/09.
17. Murat, U. Ö., Mustafa, G.: Evaluating Fare Structure with Best–Worst Method for Improving Sustainable Transit Operations: Istanbul Metro Example. Sustainability, 18(8), 3715 (2026).

Author Contribution Statement

- *Conceptualization:* Ömer Murat URHAN- Mustafa GÜRSOY
- *Methodology:* Ömer Murat URHAN- Mustafa GÜRSOY
- *Investigation:* Ömer Murat URHAN- Mustafa GÜRSOY
- *Writing – Original Draft:* Ömer Murat URHAN- Mustafa GÜRSOY
- *Writing – Review & Editing:* Ömer Murat URHAN- Mustafa GÜRSOY

List of Abbreviations

- **PT** — Public transportation
- **BWM** — Best-Worst Method
- **DBF** — Distance-Based Fare
- **FF** — Flat Fare
- **FRR** — Farebox Recovery Ratio
- **ZBF** — Zone-Based Fare
- **TBF** — Time-Based Fare
- **TÜİK** — Turkish Statistical Institute
- **IBB** — Istanbul Metropolitan Municipality
- **MCDM** — Multiple-criteria decision making
- **AHP** — Analytic Hierarchy Process
- **MABAC** — Multi-Attributive Border Approximation Area Comparison
- **BELBİM** — Electronic Money and Payment Services Inc.

The authors declare no conflicts of interest.

The study was conducted in accordance with the Declaration of Helsinki, and approved by the Ethics Committee of YILDIZ TECHNICAL UNIVERSITY SOCIAL AND HUMAN SCIENCES RESEARCH ETHICS COMMITTEE (Report No: 20250404491 and date of approval: 3 April 2025).

Publication Note

This paper was peer-reviewed, accepted for presentation, and included in the proceedings of the ACE2026 – International Conference on Advances in Civil Engineering, held on 12–14 October 2026 in Trabzon, Türkiye.

This paper may be cited as follows:

Urhan, Ö.M. and Gürsoy, M, "Evaluating Fare Structure with Best–Worst Method: Istanbul Metro Example," in Proceedings of the ACE2026 – International Conference on Advances in Civil Engineering, Trabzon, Türkiye, 12–14 October 2026.

Lane Changing Behavior at Highway Diverging Areas: A Safety Analysis Based on Time-to-Collision (TTC)

Alpaslan Bozkurt[1], Ali Topal[2], Pelin Önelçin[3], and Serhan Tanyel[4]

[1] 0009-0009-4377-8721, Graduate School of Natural and Applied Sciences, Dokuz Eylül University, İzmir, Türkiye, bozkurtalpaslan0736@gmail.com.tr
[2] 0000-0002-2601-1926, Dokuz Eylül University, Civil Engineering Department, İzmir, Türkiye, ali.topal@deu.edu.tr
[3] 0000-0002-6990-4919, Ege University, Civil Engineering Department, İzmir, Türkiye, pelin.onelcin@ege.edu.tr
[4] 0000-0001-8549-9442, Dokuz Eylül University, Civil Engineering Department, İzmir, Türkiye, serhan.tanyel@deu.edu.tr

Abstract. This study aims to model lane-changing behavior in freeway diverging areas by integrating geometric road data and traffic flow observations. Video-based trajectory extraction was used to analyze driver decisions, lane-change parameters, and safety indicators such as Time to Collision (TTC). The results show that lane changes were generally performed with an adequate safety margin, while a small subset of maneuvers, particularly those with a specific conflict configuration, exhibited lower TTC values. Based on these findings, recommendations are offered for geometric design and traffic management at diverging zones.

Keywords: Lane changing, Diverging area, Time to collision.

1. Introduction

Transportation is the movement of people and goods from one place to another for a specific purpose. In transportation, the goal is to move safely, quickly, economically, and comfortably from a source point to a destination, and this is accomplished through roads [9 - 14].

When traffic flow is disrupted and roads are forced to operate near or beyond their capacity, traffic problems tend to emerge at intersections within urban areas and at diverging and merging zones on ring roads. Particularly in areas with diverging zones, speed reductions and driver confusion caused by sudden lane changes inevitably lead to traffic problems that affect road safety and performance.

Lane changing, defined as a vehicle moving from one lane to an adjacent lane and continuing its travel, is the most critical driver decision that directly affects traffic flow, road performance, and safety. Nearly all traffic collisions are caused by driver errors, and it has been observed that 8.4–13.7% of these are lane-change-related [2]. Furthermore, lane-changing behavior also causes significant performance degradation on roads.

In this study, traffic data obtained through video camera observations at diverging zones on ring roads within the provincial boundaries of Izmir are evaluated to examine the effects of driver behavior on road performance and safety. Vehicle trajectories are extracted and used to calculate Time-to-Collision (TTC) values, which is a quantitative indicator of collision risk during lane-changing maneuvers.

By developing a model that supports and enables vehicles' lane-changing decisions, it is believed that safety and performance will improve, and effective traffic management will be achieved. The findings are intended to inform driver warning systems, as well as geometric

design and traffic management operations at diverging zones, by identifying which lane-changing configurations and conditions are associated with the lowest TTC values and there the highest collision risk.

The aim of the study is to model lane-changing behavior at diverging zones through TTC-based analysis of field-observed trajectories as a function of road geometry and traffic data.

2. Literature Review

This section reviews prior research on collision risk at diverging zones, lane-changing classifications, and the development of Time-to-Collision as a surrogate safety measure to provide the background for the present study. Zhang, Yan, An, and Zhao (2015) [16] collected data from 72 diverging zones at two highway sections in Colorado, USA, to identify the safety influence zone and collision frequencies at highway diverging areas. Traffic and road geometry data, along with fatal, injury, and property-damage collision data from 2006–2010, were obtained from the Pikes Peak Area Council of Governments. A negative binomial regression model was used to explain the relationship between collision and variables. A relationship was observed between collision frequency and ramp clearance values, which were incrementally increased from 30 to 300 ft in 30-ft intervals. The study concluded that collision frequency at diverging zones is directly proportional to the number of ramp lanes, ramp traffic volume, and speed limit, but inversely proportional to ramp length. Collision rates at multi-lane diverging zones were higher than at single-lane diverging zones, due to the confusion caused by more lanes. Additionally, lane changes increase the occurrence of sideswipe collisions.

Aydin (2012) [1] investigated the transverse and longitudinal movements of vehicles within their lanes on a multi-lane road with surface deformations under saturated traffic conditions. From speed and position data, it was observed that vehicles either reduced their speed or changed lanes before reaching the deformation points to avoid being subjected to the deformation effect. Analysis of speed data before, at, and after the deformation points revealed that the most significant parameters influencing speed reduction are driver characteristics (aggressiveness, familiarity with the road, etc.), the position of vehicles in the target lane to which the driver intends to change, and the magnitude of the deformation.

Based on the driver motivation, lane-changing maneuvers are generally grouped into two categories: Mandatory Lane Changes (MLC) and Discretionary Lane Changes (DLC). MLC occurs when the driver has no alternative but to leave the current lane in order to follow the intended route, for instance when merging from an on-ramp or preparing to exit the freeway. DLC, on the other hand, is not dictated by the route itself but is initiated voluntarily, typically to gain a speed advantage, avoid being trapped behind slower vehicles, or move into a lane offering more favorable driving conditions [2-13].

The safety implications of lane-changing activity at special freeway sections have attracted sustained research attention since the early 1970s. Diverging areas are one of the most operationally demanding segments of freeways. Empirical data indicate that crash frequency at diverging areas is typically four to six times higher than on comparable mainline segments, and freeway ramp crashes alone account for more than 30% of total annual freeway crashes [4]. The intensive lane-changing maneuvers between mainline and exiting traffic are the primary source of conflicts and, consequently, crashes at diverging areas remain a persistent safety concern [17].

Time-to-Collision (TTC) remains one of the most widely used surrogate safety measures for identifying near-miss events and quantifying collision risk in traffic conflict analysis. Zürn et al. (2026) [18] analyzed more than 10,000 lane-changing maneuvers using high-resolution drone trajectory data from highways in Germany, China, and the United States. Their analysis showed that only 32% of the maneuvers were risk-free, and they proposed a time-gap redistribution model that could significantly increase the proportion of risk-free lane changes.

Mao et al. (2025) [10] compared lane-changing behavior observed in a real-world weaving section with that reproduced in a driving simulator, using generalized time-to-collision (GTTC). Their results showed that simulated lane changes generally produced larger GTTC values than those observed in the field. Guo et al. (2023) [5] introduced a two-dimensional TTC (2D-TTC) measure to represent the two-dimensional geometry of conflicts during lane changes. They validated the measure using archived crash data from a large-scale connected-vehicle dataset and combined it with deep reinforcement learning to model drivers' evasive behavior in safety-critical lane changes. Yang et al. (2025) [15] proposed a multi-task CNN-LSTM model that jointly predicts lane-change maneuver probability, risk level, and time-to-lane-change using the HighD dataset, while Sheikh and Peng (2024) [12] developed a lane-changing risk index (LCRI) based on probabilistic threat assessment, also using HighD trajectories, combined with a random-parameter ordered logit model to relate risk levels to contributing factors. Most recently, Chen et al. (2025) [3] demonstrated that a real-time crash prediction model based on non-stationary extreme value distributions of the remaining inter-vehicle distance outperformed both traditional TTC and 2D-TTC by 75% and 49%, respectively, revealing that single-value TTC thresholds fall short in reflecting the dynamic risk evolution of lane-changing maneuvers. Focusing specifically on lane-change conflicts, Önelçin (2022) [11] analyzed field-observed lane-changing events to determine a representative TTC threshold for use in driver warning systems. Based on the minimum TTC values observed during conflicts, the study proposed 0.74 s as the most appropriate threshold for identifying critical lane-changing situations.

3. Methodology

The present study adopts a field-based trajectory extraction approach to calculate TTC values at a diverging zone in Izmir, following the TTC-based methods developed by Jimenez et al. (2013) [7]. The methodology consists of four main phases: (1) site selection and video-based field data collection, (2) vehicle trajectory extraction and data pre-processing, (3) microscopic analysis of lane-changing behavior, and (4) calculation and validation of Time-to-Collision (TTC) indicators.

3.1. Study Site

Five criteria were used to select the diverging zone: geometric suitability, traffic volume, site safety, representativeness, and favorable seasonal and lighting conditions. Geometrically, the site had to be sufficiently long to ensure that all lanes were visible from the camera position; according to Turkish standards [8], typical deceleration lane lengths at diverging zones range from 200 to 500 m. The selected site also needed to carry sufficient traffic during peak periods to provide an adequate number of lane-changing events for analysis. To ensure safe data collection, the recording equipment had to be installed without posing risks to personnel or traffic. In addition, the site was required to represent the typical geometric characteristics of the Turkish highway network, including the number of lanes, ramp length, and speed limit. Finally, data collection was conducted under favorable seasonal and lighting conditions to maximize video quality and visibility.

The field study was conducted on 25/03/2025 at the diverging section located in the Gaziemir district. A satellite image of the study area is presented in *Fig. 1*.

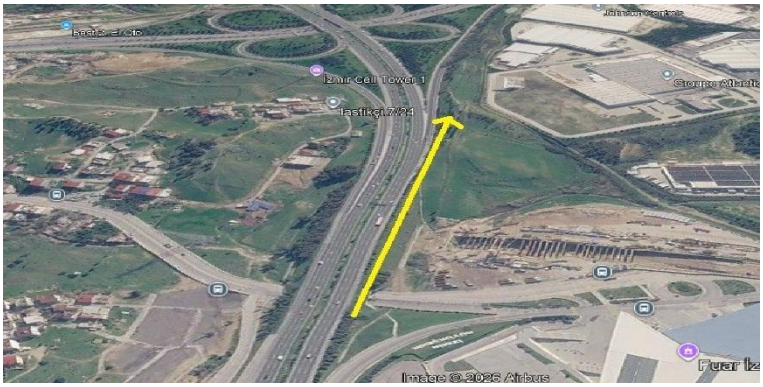


Fig. 1. Satellite image of the study area.

3.2. Data Collection

The field data was collected on 25/03/2025 during the time interval of 08.00-09.00. Observations were conducted during daylight hours to control seasonal variables, ensure consistent weather and visibility conditions, and minimize the effects of light reflections and shadows. The traffic movements were recorded using an unmanned aerial vehicle. The investigated diverging area consisted of 3 lanes, with a mainline width of 3.6 m.

To determine vehicle trajectories, the study area was divided into a series of virtual grids, as illustrated in *Fig. 2*. This grid-based segmentation enabled the precise extraction of vehicle positions and movements throughout the diverging section. By tracking the sequential movement of vehicles across the defined grid cells, trajectory data were obtained and subsequently used to analyze lane-changing behavior.

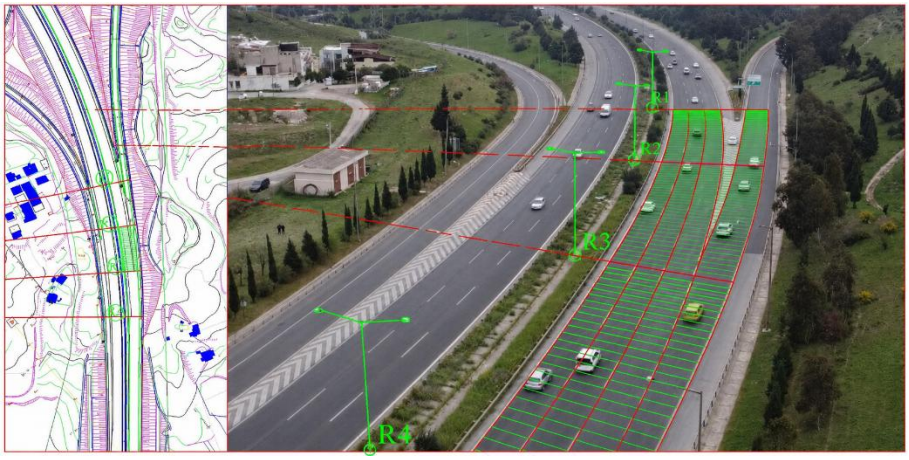


Fig. 2. Grid-based segmentation of the study area.

3.3. Speed Calculation and Surrogate Safety Measures

Longitudinal and lateral velocity components were calculated from consecutive position measurements using the central difference method:

$$v(t) = [x(t + \Delta t) - x(t - \Delta t)]/(2\Delta t) \quad (1)$$

To assess traffic safety, it is necessary to measure not only collisions but also the critical near-miss events preceding them. Traffic Conflict Techniques (TCT), which emerged in the 1970s in response to this need, led to a paradigm shift in traffic safety research. The foundational conceptual contribution in this field was made by Hayward's 1972 article published in Highway Research Record, entitled 'Near-Miss Determination Through Use of a Scale of Danger.' In that study, Hayward introduced the concept of Time to Collision (TTC) as

an objective measure of near-miss events and demonstrated that it could replace subjective observer judgment in traffic safety assessment [6].

Hayward defines TTC as follows: 'TTC is the time remaining until two vehicles collide if their current speeds and directions remain unchanged'[6]. This definition is expressed mathematically as:

$$TTC(t) = [s(t) - L]/[v_f(t) - v_l(t)] \quad (2)$$

In this formula, $s(t)$ denotes the distance between the vehicles, L is the length of the leading vehicle, $v_f(t)$ is the speed of the following vehicle, and $v_l(t)$ is the speed of the leading vehicle. TTC is meaningful only when $v_f > v_l$, i.e., when the following vehicle is traveling faster than the leading vehicle; otherwise, there is no collision risk.

Hayward classified the danger scale according to TTC value as follows: TTC = 0 (collision), 0 < TTC ≤ 1.5 s (serious conflict), 1.5 < TTC ≤ 5.0 s (potential conflict). The threshold value of 1.5 seconds marks a conceptually significant breaking point: below this value, it is anticipated that most drivers would not have sufficient time to complete an emergency evasive maneuver, and therefore TTC_{min} values below this threshold are classified as 'serious conflicts'.

The type and number of collisions vary depending on whether the intersection angle between vehicles is greater than or less than 90 degrees. A total of 32 types of collisions are assumed to be possible depending on the collision angles of the vehicles in question. Of these, only 10 configurations are considered geometrically meaningful for lane-changing conflicts (6 for α < 90° and 4 for α ≥ 90°), and the present study focuses on the former, following Jimenez et al.'s (2013) finding that this configuration yields more realistic results.

Jimenez et al. (2013) [7] calculated TTC values by combining the trajectories of the lane-changing vehicle and the vehicle following it in the target lane to determine the coordinates of the intersection point. The arrival times of both vehicles at the intersection were calculated, and when they were equal, the resulting value was accepted as the TTC.

$$x_+ = \frac{(y_2 - y_1) - (x_2 tan\theta_2 - x_1 tan\theta_1)}{tan\theta_1 - tan\theta_2} \quad (3)$$

$$y_+ = \frac{(x_2 - x) - (y_2 cot\theta_2 y cot\theta_1)}{cot\theta_1 - cot\theta_2} \quad (4)$$

In *Fig. 3*, for the case where angle (a) is less than 90 degrees, the corner points of the lane-changing vehicle and the vehicle behind in the target lane (A1, A2, A3, A4, B1, B2, B3, B4) and the intersection points (Q1, Q2, Q3, Q4) are shown. Table 1. presents the arrival times of the vehicle corner points at the intersection points, and for the case where angle (a) is less than 90 degrees, 6 possible collision types, arrival times at the collision point, and TTC values.

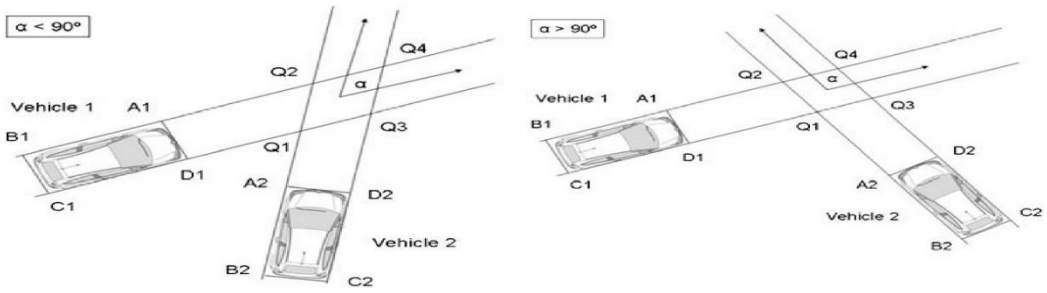
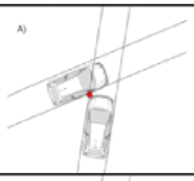
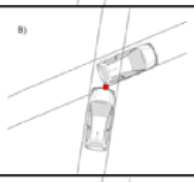
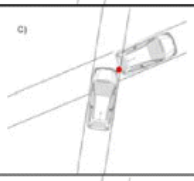
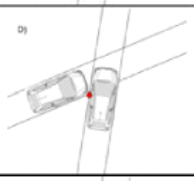
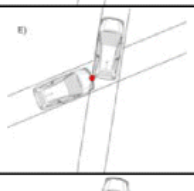
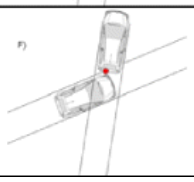


Fig. 3. Collision configuration [7].

Table 1. Collision configurations when α<90° [7].

	Situation	Diagram	Time conditions (Situation in the event the condition is not satisfied)	TTC
A)	Corner Vehicle 2 hits side Vehicle 1		TC11 > TA21 > TD11 / B D	TA21
B)	Front part Vehicle 2 hits corner Vehicle 1		TC13 > TD23 > TA21 > TC11 / C * A	(TA21, TD23)
C)	Corner Vehicle 2 hits rear part Vehicle 1		TB14 > TD24 > TD23 > TC13 / X * B	(TD23, TD24)
D)	Corner Vehicle 1 hits side Vehicle 1		TB21 > TD11 > TA21 / E A	TD11
E)	Front part Vehicle 1 hits corner Vehicle 2		TB22 > TA12 > TD11 > TB21 / F * D	(TD11, TA12)
F)	Corner Vehicle 1 hits rear part Vehicle 2		TC24 > TA14 > TA12 > TB22 / X * E	(TA12, TA14)

*=Always Occurs, X =No Collision

Within the scope of the study, the behavior of the lane-changing vehicle and the vehicle behind it in the target lane at the examined diverging zone was analyzed. The time required for both vehicles to reach the conflict zones, based on their observed and projected linear and lateral positions, was calculated. The likely collision type and Time-to-Collision (TTC) values were estimated

4. Results and Discussions

In this study, data on 40 mandatory lane changes, collected via drone observations conducted on various dates and times at diverging zones in the urban road network of Izmir province, were analyzed. To determine TTC values, starting from the moment the target vehicle's lateral speed exceeded 0.2 m/s as the initial observation time, the TTC values corresponding to the lateral and linear position data taken from the right-rear corners of the lane-changing vehicle and the vehicle behind it in the target lane at 0.5-second intervals were calculated using code written in Python. The obtained data are presented in Table 2.

Table 2. Observed TTC values by collision type.

No	Collision Type	Collision Time	TTC (s)	No	Collision Type	Collision Time	TTC (s)
1	A	TA21	6.67	21	A	TA21	13.34
2	A	TA21	3.50	22	D	TD11	0.52
3	C	TD23-TD24	5.18	23	D	TD11	0.52
4	A	TA21	6.93	24	A	TA21	3.89
5	A	TA21	3.21	25	A	TA21	6.99
6	A	TA21	4.15	26	A	TA21	3.78
7	A	TA21	5.83	27	A	TA21	3.56
8	A	TA21	1.68	28	A	TA21	9.75
9	A	TA21	9.15	29	A	TA21	5.00
10	A	TA21	2.24	30	A	TA21	2.76
11	A	TA21	3.85	31	A	TA21	3.36
12	A	TA21	12.13	32	A	TA21	9.83
13	E	TD11-TA12	1.79	33	A	TA21	3.18
14	A	TA21	6.20	34	A	TA21	10.50
15	A	TA21	6.11	35	B	TA21-TD23	10.29
16	A	TA21	6.15	36	A	TA21	7.19
17	A	TA21	12.26	37	A	TA21	3.00
18	A	TA21	3.98	38	A	TA21	7.96
19	A	TA21	13.00	39	D	TD11	3.92
20	E	TD11-TA12	1.52	40	A	TA21	15.50

Across the 40 observed lane changes, the collision type distribution followed the classification proposed by Jimenez et al. (2013): 33 events were classified as Type A, 1 as Type B, 1 as Type C, 3 as Type D, and 2 as Type E. The high proportion of Type A (82.5% of observations) indicates that most of the lane changes at the observed diverging zone follow a relatively predictable geometry.

TTC values ranged from 0.52 s to 15.50 s, with a mean of 6.32 s. According to Hayward's (1972) danger scale, none of the observed maneuvers reached the collision threshold (TTC = 0), and only Observations 22 and 23 were classified as serious conflicts (TTC $\leq$ 1.5 s). The remaining observations had TTC values either within the potential conflict range (1.5 s < TTC $\leq$ 5.0 s) or above 5.0 s. Despite their low frequency, Type D collisions exhibited the lowest TTC values among the observed lane-change types, indicating a higher collision risk.

The mean TTC of 6.32 s is well above both Hayward's (1972) [6] serious-conflict threshold of 1.5 s and the 0.74 s threshold proposed by Önelçin (2022) [11] for lane-change warning systems, indicating that most lane-changing maneuvers at the study site were performed under relatively safe conditions. However, the minimum TTC value of 0.52 s falls below both thresholds, showing that a small number of maneuvers involved critical conflict situations. A similar pattern was reported by Zürn et al. (2026) [18], who found that although most lane changes were completed safely, critical conflicts still occurred in a small proportion of maneuvers.

It should also be noted that none of the 40 observed lane-changing maneuvers resulted in an actual collision. Instead of relying on actual collisions, TTC-based traffic conflict analysis evaluates near-miss events, since collisions are relatively rare [6].

Overall, the results indicate that the geometric and operational characteristics of the studied diverging zone generally support safe lane-changing behavior. However, a small number of

maneuvers, particularly those classified as Type D, were associated with lower TTC values and therefore deserve particular attention in geometric design and traffic management.

6. Conclusions and Recommendations

This study examined lane-changing safety at a freeway diverging zone in Izmir using field-observed trajectories and Time-to-Collision analysis. Lane changes were generally performed with an adequate safety margin and no actual collisions occurred, though a small subset of maneuvers, particularly those with a Type D conflict configuration, showed lower TTC values.

The findings suggest that improving sight distance and providing sufficient deceleration length may help reduce lane-changing risk. More visible advance signing and longer deceleration lanes could give drivers additional time to assess acceptable gaps, while appropriate speed management within the diverging zone may reduce speed differences between vehicles and contribute to higher TTC values. Since the analysis was based on observations from a single diverging zone over a limited period, these recommendations should be regarded as site-specific. In addition, any increase in the number of lanes should be evaluated carefully, considering the confusion-related crash risk reported for multi-lane diverging zones by Zhang et al. (2015) [16].

Future studies should include a larger number of diverging zones with different geometric characteristics and traffic conditions. Examining the relationship between TTC and geometric variables, such as ramp length and deceleration lane width, would provide a better understanding of how roadway design influences lane-changing safety and help assess whether the findings of the present study are applicable to other diverging zones.

Acknowledgments

The authors would like to express their profound appreciation to the Graduate School of Natural and Applied Sciences at Dokuz Eylül University for its assistance with the doctoral thesis.

References

1. Aydın, M.M.: Modeling Driver Lane Selection Behavior on Multi-Lane Roads. M.Sc. Thesis, Dokuz Eylül University, Institute of Natural and Applied Sciences, İzmir (2012).
2. Balal, E., Cheu, R.L., Sarkodie-Gyan, T.: A binary decision model for discretionary lane-changing move based on fuzzy inference system. Transportation Research Part C: Emerging Technologies 67, 47–61 (2016).
3. Chen, K., Li, Z., Liu, P., Xu, C., Wang, Y.: Real-time lane-changing crash prediction model at the individual vehicle level using real-world trajectories prior to crashes. Transportation Research Part C 176, 105171 (2025).
4. Gao, X., et al.: Driver behavior analysis in diverging area based on driving simulation. In: Proceedings of the Conference on Transportation and Safety, pp. 574–579 (2023).
5. Guo, H., Xie, K., Keyvan-Ekbatani, M.: Modeling driver's evasive behavior during safety-critical lane changes: Two-dimensional time-to-collision and deep reinforcement learning. Accident Analysis and Prevention 186, 107063 (2023).
6. Hayward, J.C.: Near-miss determination through use of a scale of danger. Highway Research Record 384, 24–35 (1972).
7. Jimenez, F., Naranjo, J.E., Garcia, F.: An improved method to calculate the time-to-collision of two vehicles. International Journal of Intelligent Transportation Systems Research 11(1), 34–42 (2013).

8. GDH: Highway Design Manual. General Directorate of Highways, Ankara, pp. 204–232 (2005). (In Turkish) https://kupdf.net/download/karayolu-tasar-305-m-el-kitab-305-2005_59f62e77e2b6f5cb7e17c132_pdf
9. Kutlu, K.: Traffic Engineering. 3rd edition. İTÜ Faculty of Civil Engineering Press, İstanbul (1993). (In Turkish)
10. Mao, S., Lee, J.J., Karimi, A., Lioi, A., Bassani, M.: Validation of lane-changing behaviour in a weaving section using a driving simulator experiment. Transportation Research Part F: Psychology and Behaviour 115, 103364 (2025).
11. Önelçin, P.: A New Safety Measure for Traffic Safety Assessment. Ph.D. Thesis, Ege University, İzmir (2022).
12. Sheikh, M.S., Peng, Y.: Modeling collision risk for unsafe lane-changing behavior: A lane-changing risk index approach. Alexandria Engineering Journal 88, 164–181 (2024).
13. Vechione, M., Balal, E., Cheu, R.: Comparisons of mandatory and discretionary lane changing behavior on freeways. International Journal of Transportation Science and Technology 7(2), 124–136 (2018).
14. Yayla, N.: Highway Engineering. Birsen Publishing, İstanbul (2002). (In Turkish)
15. Yang, L., Zhang, J., Lyu, N., Zhao, Q.: Predicting lane change maneuver and associated collision risks based on multi-task learning. Accident Analysis and Prevention 209, 107830 (2025).
16. Zhang, C., Yan, X., An, M., Zhao, H.: Spatial influence analysis of traffic safety in diverging areas between freeway segments and off-ramps. Discrete Dynamics in Nature and Society 2015, 1–9 (2015).
17. Zhang, Y., Li, Z., Liu, P., Zha, L.: Exploring contributing factors to crash injury severity at freeway diverging areas. Procedia Engineering 21, 178–185 (2011).
18. Zürn, M., Rehborn, H., Querfurth, L., Hayer, R.: Spatial-temporal analysis of lane-changing behavior and time gaps on highways using aerial observations. Transportation Research Procedia 95, 33-40 (2026).

Author Contribution Statement

- *Conceptualization:* Alpaslan Bozkurt, Ali Topal, Serhan Tanyel
- *Methodology:* Alpaslan Bozkurt, Ali Topal, Serhan Tanyel, Pelin Önelçin
- *Investigation:* Alpaslan Bozkurt
- *Writing – Original Draft:* Alpaslan Bozkurt, Ali Topal
- *Writing – Review & Editing:* Alpaslan Bozkurt, Ali Topal, Serhan Tanyel, Pelin Önelçin

Publication Note

This paper was peer-reviewed, accepted for presentation, and included in the proceedings of the ACE2026 – International Conference on Advances in Civil Engineering, held on 12–14 October 2026 in Trabzon, Türkiye.

This paper may be cited as follows:

Bozkurt, A., Topal, A., Onelcin, P., Tanyel, S., "Lane Changing Behavior at Highway Diverging Areas: A Safety Analysis Based on Time-to-Collision (TTC)," in Proceedings

of the ACE2026 – International Conference on Advances in Civil Engineering, Trabzon, Türkiye, 12–14 October 2026.

A Bibliometric Analysis of Asphalt Mixtures Subjected to Short- and Long-Term Aging

Öznur KARADAĞ[1], Gizem KAÇAROĞLU[2], Mehmet SALTAN[3]
[1] 0000-0003-0755-5626, Süleyman Demirel University, Göller Bölgesi Teknokent Coordinatorship, Çünür, Isparta, Türkiye, oznurkaradag@sdu.edu.tr
[2] 0000-0002-5734-7131, Süleyman Demirel University, Civil Engineering Department, Faculty of Engineering and Natural Sciences, Çünür, Isparta, Türkiye, gizemkacaroglu@sdu.edu.tr
[3] 0000-0001-6221-4918, Süleyman Demirel University, Civil Engineering Department, Faculty of Engineering and Natural Sciences, Çünür, Isparta, Türkiye, mehmetsaltan@sdu.edu.tr

Abstract. Aging is a fundamental process affecting the performance characteristics of asphalt mixtures and is generally classified as short-term and long-term aging. Short-term aging is defined as changes in rheological properties occurring during production, hauling/storage, and compaction processes. Long-term aging refers to changes that occur in asphalt pavements throughout their service life. Aging is an inevitable process that influences performance of asphalt mixtures. However, there is still a lack of research on the short- and long-term aging performance of asphalt mixtures incorporating various additives. Therefore, this study aimed to identify existing gaps through a bibliometric analysis of studied investigating the short- and long-term aging performance of asphalt mixtures. A bibliometric analysis was conducted on publications investigating short- and long-term aging performance of asphalt mixtures in accordance with AASHTO R30 standard. The dataset consists of articles and review articles published between 2000 and 2026 and indexed in Web of Science database. A total of 1838 publications were retrieved and analysed. The keywords used for database search was “asphalt” OR “bitumen” OR “bituminous” AND “aging” OR “ageing” AND “short-term” OR “long-term” OR “STOA” OR “LTOA” OR “AASHTO R30”. Obtained data were analysed and visualized using VOSviewer software. Within the scope of bibliometric analysis, co-occurrence, citation, and co-authorship analyses were performed to identify keywords relationships, influential publications, and collaboration patterns. Based on the results of the analysis, key research gaps related to asphalt mixture aging were identified. This study is expected to provide a useful reference for further research on asphalt mixtures aging processes.

Keywords: Asphalt mixtures, short-term aging, long-term aging, bibliometric analysis.

1 Introduction

Asphalt obtained from crude oil through fractional distillation, is widely used in road construction, surfacing, and roofing. The properties of asphalt are altered over time by environmental factors such as oxygen, temperature, moisture and sunlight. Asphalt is composed of organic components such as asphaltene, maltenes, and resins. Asphaltenes are more susceptible to oxidation due to their polar structure, leading to the formation of carbonyl and sulfoxide compounds. These compounds contribute to an increase in the asphaltene fraction, thereby enhancing the stiffness and viscosity of asphalt. These changes in the properties of asphalt are defined as aging. Asphalt is exposed to oxidation at high temperatures during the production, storage, hauling, and paving processes as it mixed with aggregates throughout the construction stage. This process is referred to as the short-term aging of asphalt mixtures. After pavement construction, asphalt continuously reacts with oxygen, and the aging that occurs

throughout its service life is defined as long-term aging. These processes change the rheological properties of asphalt and performance of asphalt mixtures is negatively affected [1,2]. However, according to the reviewed literature, although there are studies on the aging process of asphalt, only a limited number of studies have investigated the aging performance of asphalt mixtures. Since fatigue resistance and moisture susceptibility are commonly used to represent mixture durability, aging performance is often not directly examined. In addition, aging tests of asphalt mixtures are not widely preferred due to their long testing durations [3]. For example, although numerous studies have been conducted on styrene-butadiene-styrene (SBS) and polypropylene (PP) modified asphalt mixtures, the majority have not considered the effect of aging performance. SBS and PP modified mixtures aged long-term were evaluated in terms of stability, rigidity, resilient modulus, indirect tensile strength at two temperatures (25 and 60 °C), tensile strength ratio, and rutting resistance. It has been stated that SBS and PP modified mixtures show higher moisture and rutting resistance than the reference mixtures after long-term aging [4].

The effect of aging on the fatigue performance of asphalt mixtures has been examined under laboratory conditions. Short-term aging of loose mixtures was carried out in a draft oven at 135 °C for 2, 3, and 4 hours, while long-term aging was performed in oven at 85 °C for 3, 5, and 7 days. An increase in the short-term aging duration at the same temperature resulted in an increase in the fatigue life of asphalt mixtures. Asphalt mixtures aged for 7 days under long-term aging conditions exhibited reduced fatigue life due to increased stiffness [5]. The aging behavior of asphalt mixtures incorporating organic warm-mix additives was evaluated, and the results demonstrated that these mixtures may constitute an effective alternative to conventional hot asphalt mixture (HMA) with respect to aging performance [6]. It has been determined that aged and unaged mixtures containing Sasobit and Rheofalt warm-mix additives significantly affect ITS, resilient modulus, and fatigue behavior of mixtures [7]. In addition to this study, the effect of short-term aging temperature (112, 129, and 146 °C) and duration (2, 4, and 8 h) on the moisture susceptibility of asphalt mixtures incorporating Sasobit were evaluated. It was observed that moisture susceptibility of mixtures containing Sasobit subjected to short-term aging at 146 °C for 2 hours decreased [8]. Rad et al. [9] were evaluated the performance of asphalt mixtures subjected to long-term aging at 95 °C and 135 °C temperatures. When the aging temperature increased from 95 °C and 135 °C, significant changes were observed in the rheological and chemical properties of asphalt. The performance of asphalt mixtures aged at 135 °C temperature was adversely affected. Therefore, an aging temperature of 135 °C is not recommended for performance evaluation of asphalt mixtures. The influence of aggregate gradation on the mechanical properties of aged HMA was evaluated. Mixtures prepared with three different gradations (HMA-10, HMA-19, HMA-25) were subjected to short- and long-term aging in accordance with AASHTO R30 standard, after which Marshall, indirect tensile strength (ITS), resilient modulus, permanent deformation, and fatigue were assessed. Mixtures designed in accordance with HMA-19 gradation exhibited the best performance. The results of the tests and measured properties of asphalt mixtures indicate that aggregate gradation has a significant influence on performance [10]. The effects of recycled concrete aggregates (RCAs) ratios (0%, 12%, 21%) on the short-and long-term aging performance of asphalt mixture were investigated. Asphalt mixtures incorporation RCA reduced the aging susceptibility of mixtures while enhancing their strength performance. In particular, asphalt mixtures containing 12% RCA exhibited the highest stiffness, flexibility, and resistance to aging. The use of RCA is beneficial because it reduces the aging sensitivity of asphalt mixtures and improves their strength and performance [11]. The behavior of asphalt mixtures containing glass fibre (0.3%, 0.6% and 6 mm, 12 mm) under short- and long-term aging conditions has been examined. The properties of asphalt mixtures containing glass fibre improved after long-term aging. Therefore, the use of glass fibre in asphalt mixtures contributes to reduced maintenance costs [12]. In

addition, ITS values of mixtures subjected to different aging methods (NCHRP 09-52, NCHRP 09-54, RILEM, and AASHTO R30) were compared with those of field-sampled materials. As no significant differences were observed among the aging methods examined, the ITS values of short-term aged asphalt mixtures were found to be similar. Based on the ITS results, short-term aging in forced draft oven at 135 °C for 2 hours for asphalt mixtures is recommended. Furthermore, the results support the use of AASHTO R30 and NCHRP 09-52 standards for long-term aging [13]. In order to simulate long-term aging, both loose and compacted samples were subjected to oven ageing and pressure ageing vessel ageing in the laboratory. The results indicate that oven aging of loose asphalt mixtures is the most promising method in terms of efficiency, sample integrity, versatility, and cost [14]. Furthermore, aging processes for compacted samples at 85 °C and loose mixtures at 135 °C in laboratory were compared to simulate long-term field aging of asphalt mixtures in Qatar. It was stated that the 5-day oven aging period of compacted samples at 85 °C should be increased to 75 days for the wearing course and 45 days for the base course to better simulate long-term field aging. Conditioning loose mixtures at 135 °C has been suggested an alternative option in terms of time and cost [15]. Consistent with the results of this study, it has been emphasized that further research is required to develop and validate laboratory predictive methodologies capable of accurately representing the initial construction stages of asphalt pavements [16]. Without evaluating laboratory aging tests at different temperatures, it is not possible to accurately predict how the performance of asphalt mixtures will change under varying temperature conditions. Therefore, more dependable results can be achieved by considering the combined effects of time and temperature parameters [17].

The reviewed literature indicated that research on aging of asphalt mixtures is limited. Accordingly, in this study, a bibliometric analysis was conducted on mixtures subjected to short- and long-term aging in accordance with AASHTO R30. The dataset consists of articles and review articles published between 2000 and 2026 and indexed in Web of Science database. A total of 1838 publications were retrieved and analysed. The keywords used for database search was “asphalt” OR “bitumen” OR “bituminous” AND “aging” OR “ageing” AND “short-term” OR “long-term” OR “STOA” OR “LTOA” OR “AASHTO R30”. Obtained data were analyzed and visualized using VOSviewer software. Within the scope of bibliometric analysis, co-occurrence, citation, and co-authorship analyses were performed to identify keywords relationships, influential publications, and collaboration patterns. Based on the results of the analysis, key research gaps related to asphalt mixture aging were identified.

2 Methodology

Bibliometric analysis employs statistical and quantitative methods to evaluate the development of scientific disciplines and structure of knowledge within research fields. This analysis enables identification of relationships among authors, countries, organizations, and keywords, thereby revealing the knowledge structure of subject. In addition, scientific mapping and visualization techniques are used to present these relationships such as VOSviewer [18]. In this study, a bibliometric analysis was conducted on publications investigating short- and long-term aging performance of asphalt mixtures in accordance with AASHTO R30 standard. The dataset consists of articles and review articles published between 2000 and 2026 and indexed in Web of Science database. A total of 1838 publications were retrieved and analyzed. The keywords used for database search was “asphalt” OR “bitumen” OR “bituminous” AND “aging” OR “ageing” AND “short-term” OR “long-term” OR “STOA” OR “LTOA” OR “AASHTO R30”. The obtained data were analyzed and visualized using VOSviewer software. Within the scope of bibliometric analysis, co-occurrence, citation, and co-authorship analyses were performed to identify keywords relationships, influential publications, and collaboration patterns. The present study aims to address following research questions:

1) How has the annual publication trend evolved in studies examining short- and long-term aging performance of asphalt mixtures between 2000 and 2026?

2) Which authors and countries have contributed most significantly to this field, and what are the collaboration patterns among them?

3) Which journals publish the most on aging of asphalt mixtures, and how are these journals interconnected?

4) What are the main research gaps in literature, and what directions can be suggested for future studies?

3 Results of Bibliometric Analysis

This section is discussion the interpretation of graphs obtained using VOSviewer software.

3.1 Publication Year Analysis

Fig. 1 illustrates the annual trend of publications examining short- and long-term aging of asphalt mixtures from 2000 to 2026. A limited number of studies were published between 2000 and 2010, indicating that the topic received relatively little attention during this period. A gradual increase in the number of publications is observed between 2011 and 2019. However, a more pronounced growth trend emerges after 2019, reflecting a rapidly increasing academic interest in the field. The peak in the number of publications in 2025 underscores growing importance of aging performance of asphalt mixtures. The lower number of publications in 2026 may be attributed to the incomplete indexing of the year.

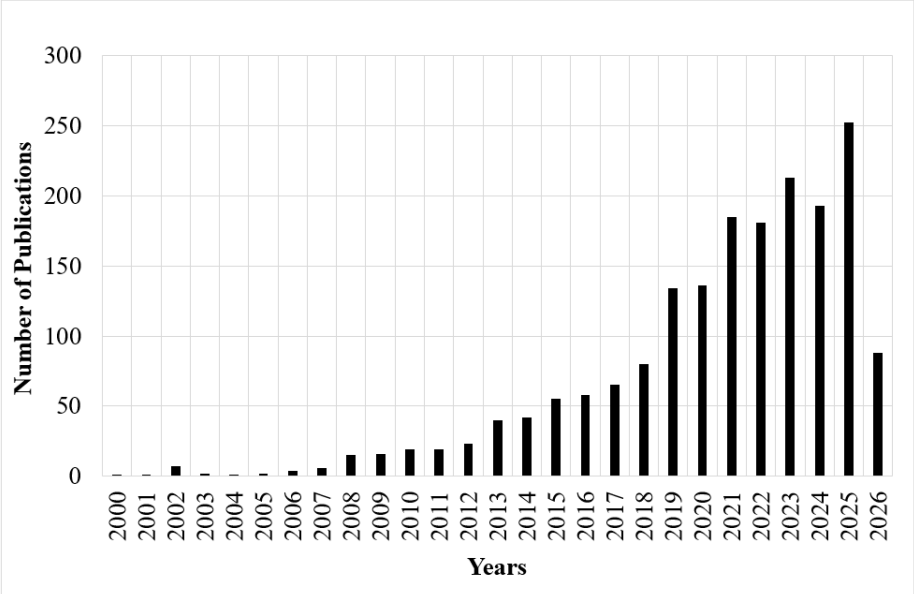


Fig. 1. The trends of annual publications from 2000 to 2026

3.2 Co-authorship Analysis

The authors who have contributed to research on the aging performance of asphalt mixtures and their collaboration patterns were identified (Fig. 2). Authors such as Hofko, Bernhard; Xiao, Feipeng; and Zhang, Henglong stand out in terms of citation impact, while Lee, Soon-Jae exhibits the highest total link strength. In co-authorship networks, a shorter distance between nodes indicates stronger collaborative relationships between authors, whereas a greater distance reflects weaker or more limited collaboration [19].

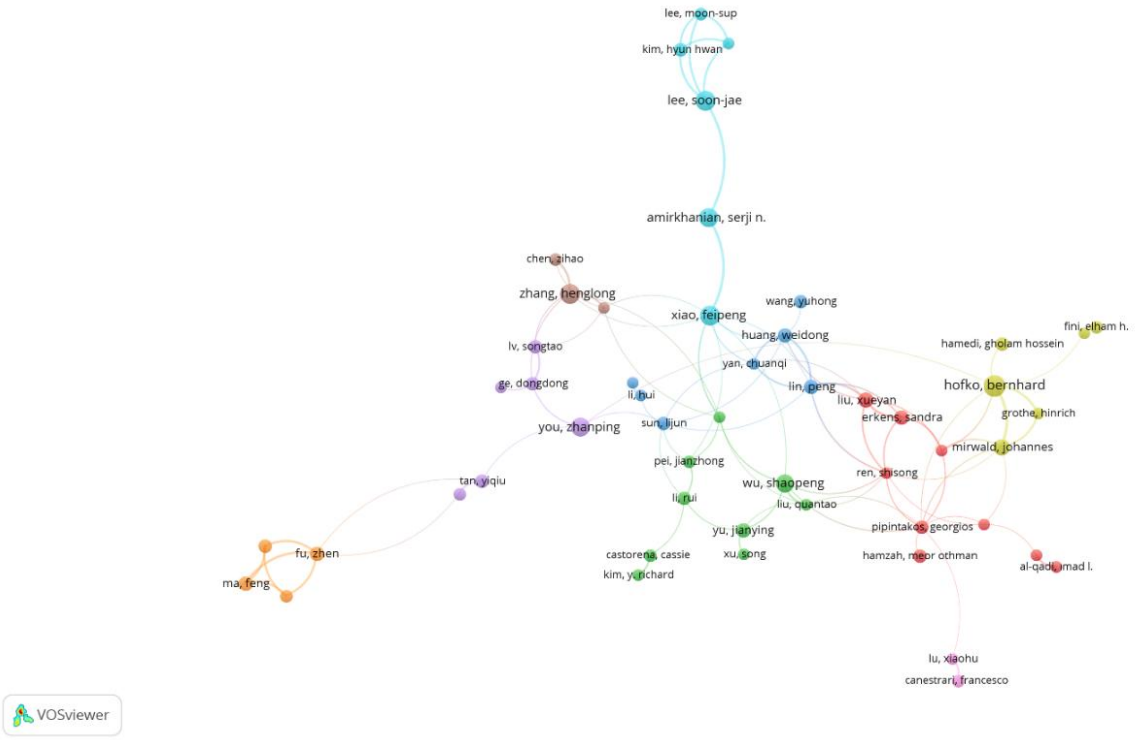


Fig. 2. Co-authorship network of authors in studies on asphalt mixture aging

3.3 Distribution of Publications by Country

Fig. 3 illustrates the international collaboration network among countries in the research field. China and the United States appear as the most prominent and influential countries in the network. Their large node sizes and strong intercountry connections indicate a high level of citation influence and collaboration.

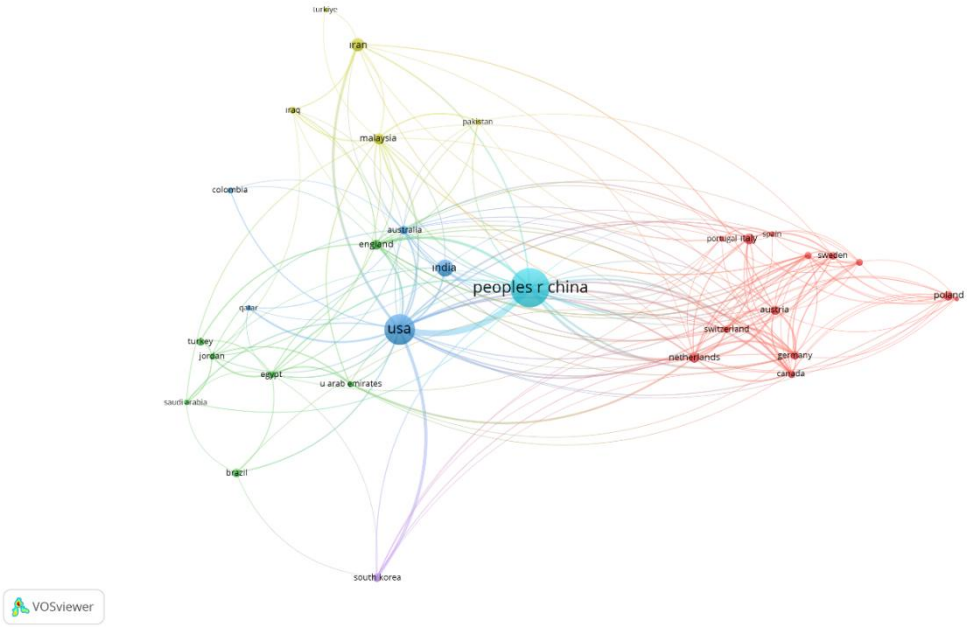


Fig. 3. Visualization of relationships between studies from different countries

3.4 Institutional Collaboration Analysis

The co-authorship network reveals that the literature is clustered around several key centers. In particular, Changan University, Wuhan University of Technology, and Southeast University emerge as the most prominent nodes in the network (Fig. 4). The network structure also highlights the presence of distinct clusters. This indicated that research activities are organized within specific collaborative groups. Moreover, certain institutions act as bridging nodes connecting different clusters, thereby facilitating knowledge exchange across the network.

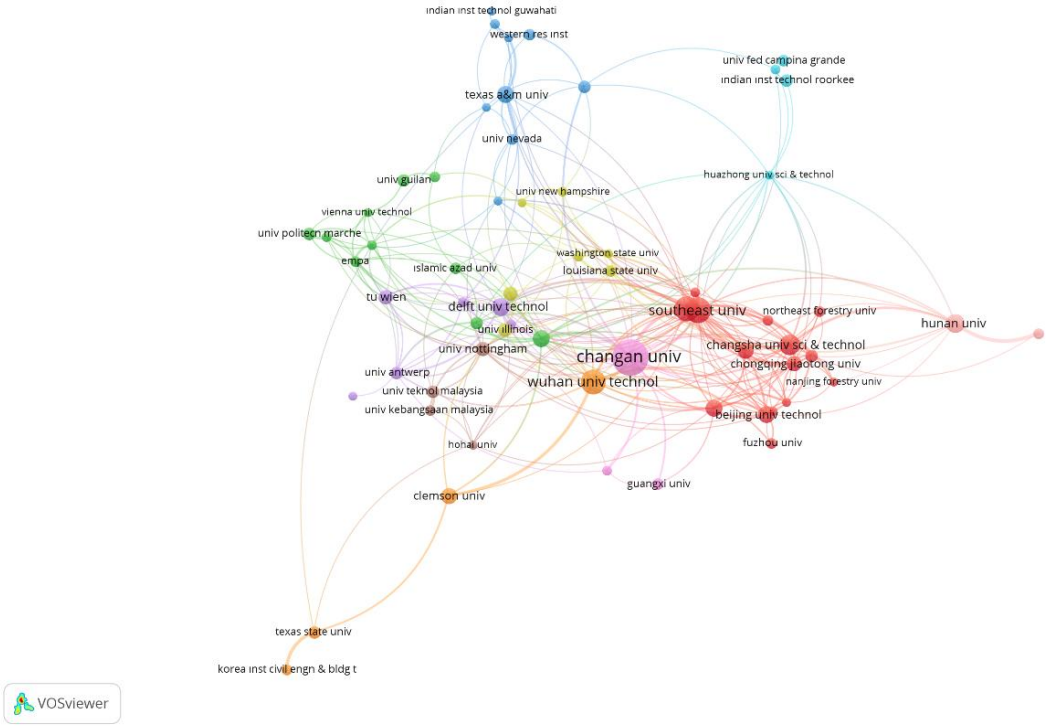


Fig. 4. Co-authorship network of institutions

3.5 Journal Analysis and Impact

The analysis of journals reveals the structural organization and the distribution of scientific publications (Fig. 5). Construction and Building Materials and Journal of Materials in Civil Engineering emerge as the most productive and influential sources in literature. These journals not only publish a higher number of studies but also play a central role in shaping the intellectual structure of the field. Clusters (red, blue, and purple) appear to reflect thematic groupings within the field. The red cluster is primarily associated with construction materials and civil engineering research, as evidenced by core journals such as Construction and Building Materials and Journal of Materials in Civil Engineering. In contrast, the blue cluster is more closely related to transportation infrastructure and pavement engineering, represented by journals such as Road Materials and Pavement Design and Transportation Research Record.

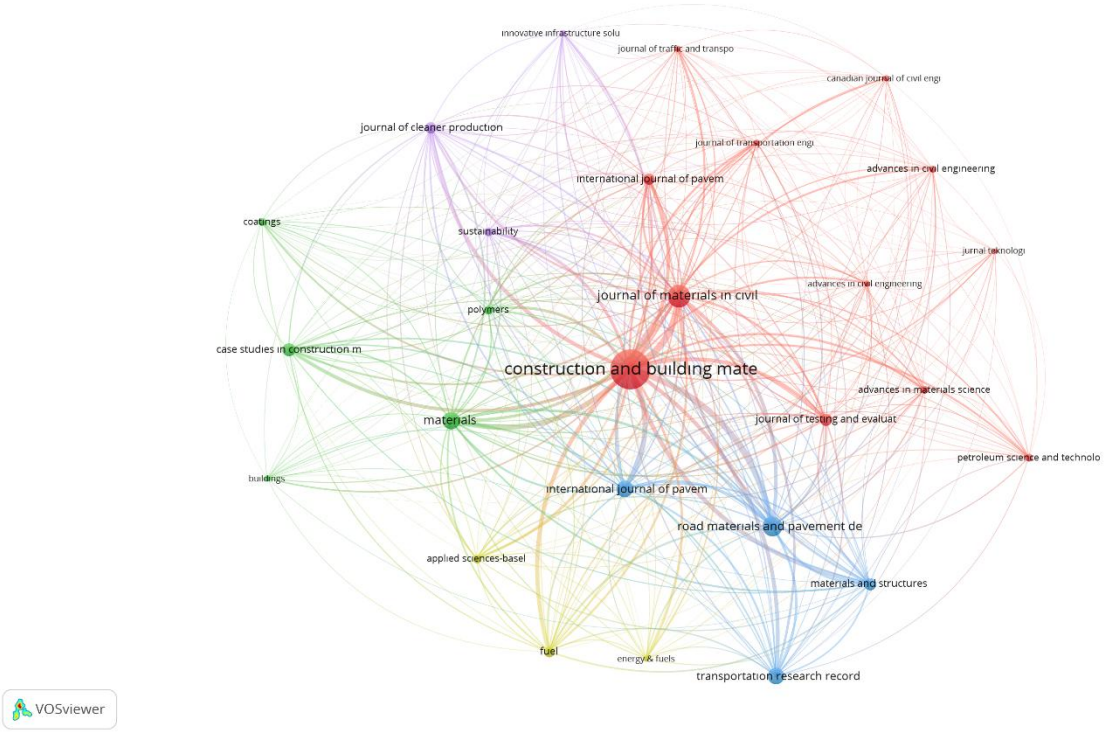


Fig. 5. Distribution of the most influential journals

3.6 Co-occurrence Network of Author Keywords

The co-occurrence network of author keyword reveals the conceptual structure and main research themes within the field (Fig. 6). Nodes represent keywords, while node size is proportional to keyword frequency. The links (edges) indicate co-occurrence relationships between keywords, and the thickness of the links reflects the strength or frequency of co-occurrence [20]. Keywords such as “aging”, “bitumen”, “asphalt”, and “rheology” are characterized by large node size indicating their high frequency of occurrence. The red cluster, which is the largest among the identified clusters, encompasses studies focusing on fatigue, rutting, durability, and rejuvenation which influenced the performance of asphalt mixtures. The green cluster representing aging, demonstrates that bitumen, asphalt binder, and rheology are strongly co-occurring themes. The blue cluster which represents research on rheological properties, demonstrates strong co-occurrence relationships with parameters such as modified asphalt, aging resistance, modification, and oxidation.

The clusters in purple and blue, representing topics such as aging, rheology, rutting, fatigue, asphalt and bitumen, correspond to well-established and extensive studies research themes in the literature (Fig. 6). In contrast, the yellow cluster including rheological properties, aging resistance, asphalt pavement performance, and fatigue resistance reflects more recent and emerging research interests. According to the bibliometric analysis, although the aging behavior and rheological properties of asphalt binders have been extensively investigated, studies addressing the short- and long-term aging performance of asphalt mixtures are comparatively limited. This suggests that the relationship between changes in the rheological properties of asphalt binders and the short-and long-term aging performance of asphalt mixtures has been sufficiently investigated.

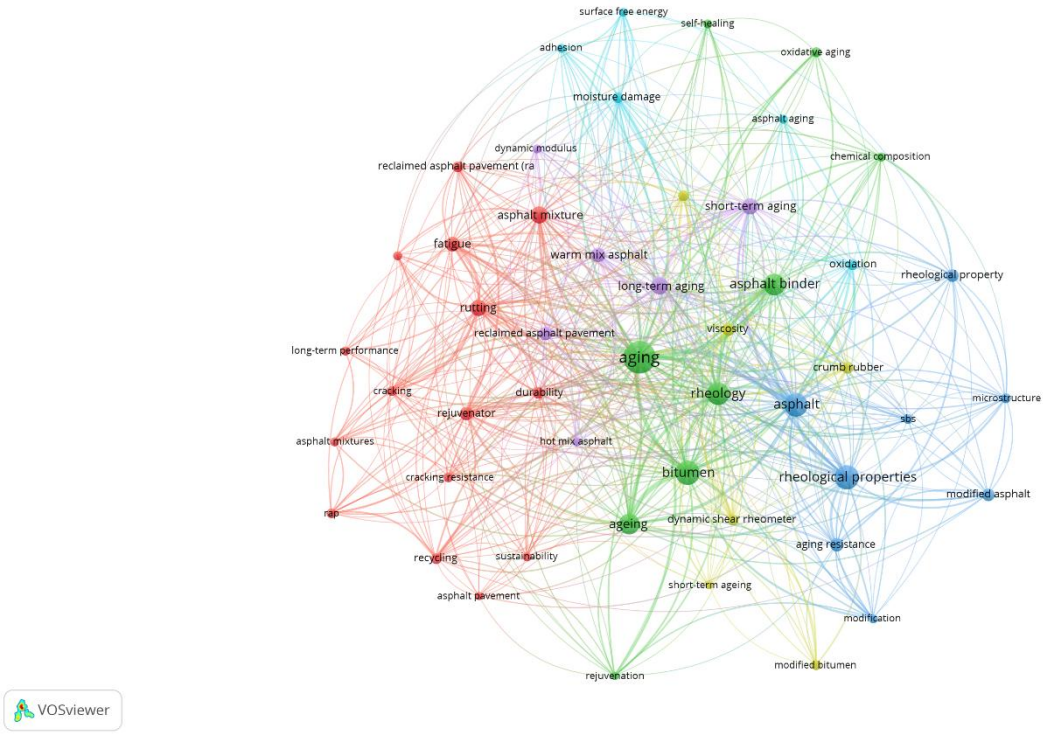


Fig. 6. Co-occurrence network of author keywords

4 Results

A bibliometric analysis was conducted on studies examining the short- and long-term aging performance of asphalt mixtures in accordance with AASHTO R30 standard. Co-occurrence, citation, and co-authorship analyses were performed to identify keyword relationships, influential publications, and collaboration patterns. The results revealed thematic patterns and research trends in literature. The findings indicate that although the aging behavior and rheological properties of asphalt binders have been extensively investigated, studies focusing on the short- and long-term aging performance of asphalt mixtures remain limited. This highlights significant research gaps regarding aging, a critical factor affecting the performance of asphalt mixtures.

References

1. Md Rashadul Islam., Mohammad Imran Hossain., Rafiqul A. Tarefder.: A study of asphalt aging using indirect tensile strength test. Construction and Building Materials, 95, 218-223 (2015). https://doi.org/10.1016/j.conbuildmat.2015.07.159.
2. Priti Rai., Sanjeev Sinha., Bhupendra Singh.: Long-term effectiveness of waste soybean oil (WSO) to rejuvenate aged asphalt binder. International Journal of Pavement Research and Technology, 19(2), 424-437 (2026). https://doi.org/10.1007/s42947-024-00468-2.
3. Qinglin Guo., Li Zhang., Lili Li., Zhiyong Liu., Song Zheng., Shuaipeng Li.: Application of solid waste in asphalt and asphalt mixtures from 2000 to 2024: a review. International Journal of Pavement Research and Technology, 1-25, (2026). https://doi.org/10.1007/s42947-025-00695-1.
4. Al-Hadidy A. Ibrahim.: Effects of long-term aging on asphalt mixes containing SBS and PP-polymer. International Journal of Pavement Research and Technology, 14(2), 153-160 (2021). https://doi.org/10.1007/s42947-020-0089-x.
5. Ghazi Al-Khateeb., Omar Alqudah.: Effect of short-term and long-term aging on fatigue performance of superpave hot-mix asphalt (HMA). Jordan Journal of Civil Engineering, 12(4), (2018).

6. Peyman Aghazadeh Dokandari., Julide Öner., Ali Topal., Burak Şengöz.: A laboratory study of an organic warm mix asphalt additive on aging characteristics of bituminous mixtures. Pamukkale University Journal of Engineering Sciences, 20(9), 332-337 (2014). https://doi.org/10.5505/pajes.2014.02411.
7. Ziari Hasan., Behbahani Hamid., Izadi Amir., Nasr Danial.: Long term performance of warm mix asphalt versus hot mix asphalt. Journal of Central South University, 20(1), 256-266 (2013). https://doi.org/10.1007/s11771-013-1483-1.
8. Bo Li., Jinyu Yang., Xiaohui Li., Xiang Liu., Feng Han., Liangying Li.: Effect of short-term aging process on the moisture susceptibility of asphalt mixtures and binders containing sasobit warm mix additive. Advances in Materials Science and Engineering, 1, 425827 (2015). https://doi.org/10.1155/2015/425827.
9. Farhad Yousefi Rad., Michael D. Elwardany., Cassie Castorena., Y. Richard Kim.: Investigation of proper long-term laboratory aging temperature for performance testing of asphalt concrete. Materials, 147, 616-629 (2017). https://doi.org/10.1016/j.conbuildmat.2017.04.197.
10. Saieth Baudilio Chaves-Pabon., Hugo Alexander Rondon-Quintana., Carlos Alfonso Zafra-Mejia.: Influence of gradation on the mechanical properties of aged hot-mix asphalts. Buildings, 11(12), 632 (2021). https://doi.org/10.3390/buildings11120632.
11. Hugo Alexander Rondon-Quintana., Juan Gabriel Bastidas-Martinez., Saieth Baudilio Chaves-Pabon.: Influence of aging on hot mix asphalt with the incorporation of recycled concrete aggregates. Materials, 19(2), 298 (2026). https://doi.org/10.3390/ma19020298.
12. Mahmoud Enieb., Aboelkasim Diab., Xu Yang.: Short- and long-term properties of glass fiber reinforced asphalt mixtures. International Journal of Pavement Engineering, 22(1), 64-76 (2021). https://doi.org/10.1080/10298436.2019.1577421.
13. Çağla Durmaz., Burak Şengöz., Derya Kaya Özdemir., Ali Topal.: Investigation of different laboratory aging methods of bituminous mixtures. Periodica Polytechnica Civil Engineering, 65(2), 537-545 (2021). https://doi.org/10.3311/PPci.15480.
14. Michael D. Elwardany., Farhad Yousefi Rad., Cassie Castorena., Y. Richard Kim.: Evaluation of asphalt mixture laboratory long-term ageing methods for performance testing and prediction. Road Materials and Pavement Design, 18 (1), 28-61 (2017). https://doi.org/10.1080/14680629.2016.1266740.
15. Okan Sirin., Md Ohiduzzaman., Emad Kassem., Dalim K. Paul.: Comprehensive evaluation of long-term aging of asphalt mixtures in hot climatic condition. Road Materials and Pavement Design, 21(4), 927-949 (2020). https://doi.org/10.1080/14680629.2018.1531777.
16. Safwat F. Said.: Aging effect on mechanical characteristics of bituminous mixtures. Transportation Research Record, 1901(1), 1-9 (2005). https://doi.org/10.1177/0361198105190100101.
17. J. Claine Petersen.: A review of the fundamentals of asphalt oxidation: chemical, physicochemical, physical property, and durability relationships. Transportation Research Circular, 78, (2009).
18. Christiana Adebola Odubela., Haryati Yaacob., Muhammad Naqiuddin Bin Mohd Warid., Khairil Juhanni Binti Abd Karim., Wyom Paul Zakka.: A bibliometric analysis of rejuvenators in reclaimed asphalt pavement. Environmental Science and Pollution Research, 30(11), 28575-28596 (2023). https://doi.org/10.1007/s11356-023-25265-5.
19. Adham Mohammed Alnadish., Madhusudhan Bangalore Ramu., Narimah Kasim., Aawag Mohsen Alawag., Abdullah O. Baarimah.: A bibliometric analysis and review on applications of industrial by-products in asphalt mixtures for sustainable road construction. Buildings, 14(10), 3240 (2024). https://doi.org/10.3390/buildings14103240.

20. Rezvan Babagoli.: Bio-binders in sustainable asphalt technologies: a comprehensive bibliometric analysis. Results in Engineering, 109426 (2026). https://doi.org/10.1016/j.rineng.2026.109426.

Author Contribution Statement

- *Conceptualization:* Mehmet SALTAN
- *Methodology:* Öznur KARADAĞ, Gizem KAÇAROĞLU
- *Investigation:* Öznur KARADAĞ, Gizem KAÇAROĞLU
- *Writing – Original Draft:* Öznur KARADAĞ, Gizem KAÇAROĞLU, Mehmet SALTAN
- *Writing – Review & Editing:* Öznur KARADAĞ, Gizem KAÇAROĞLU

List of Abbreviations

- **AASHTO** — American Association of State Highway and Transportation Officials
- **HMA** — Hot mix asphalt
- **LTOA** — Long-term Oven Aging
- **NCHRP** — National Cooperative Highway Research Program
- **PP** — Polypropylene
- **RILEM** — The International Union of Laboratories and Experts in Construction Materials 206-ATB
- **SBS** — Styrene-butadiene-styrene
- **STOA** — Short-term Oven Aging

Publication Note

This paper was peer-reviewed, accepted for presentation, and included in the proceedings of the ACE2026 – International Conference on Advances in Civil Engineering, held on 12–14 October 2026 in Trabzon, Türkiye.

This paper may be cited as follows:

Öznur KARADAĞ, Gizem KAÇAROĞLU, Mehmet SALTAN "A Bibliometric Analysis of Asphalt Mixtures Subjected to Short- and Long-Term Aging," in Proceedings of the ACE2026 – International Conference on Advances in Civil Engineering, Trabzon, Türkiye, 12–14 October 2026.

Effects of Pedestrian Demand on the Operational Performance of Unsignalized Intersections

Duygu ŞENOL[1,2] and Serhan TANYEL[3]
[1] 0000-0002-6053-2055. Dokuz Eylül University, Graduate School of Natural and Applied Sciences, Transportation Program, PhD Candidate, İzmir, TÜRKİYE, duygusenol@iyte.edu.tr
[2] 0000-0002-6053-2055, İzmir Institute of Technology, Department of Civil Engineering, Research Assistant, İzmir, TÜRKİYE, duygusenol@iyte.edu.tr
[3] 0000-0001-8549-9442, Dokuz Eylül University Faculty of Engineering, Department of Civil Engineering, Professor, Main Campus Adatepe Mah. Dogus Cad. No: 207 / 35390 Buca-İzmir, TÜRKİYE, serhan.tanyel@deu.edu.tr

Abstract. Unsignalized intersections are among the most common at-grade intersections where vehicle–vehicle and vehicle–pedestrian interactions directly affect operational performance. Although STOP and YIELD control are widely used to regulate right-of-way, the effects of pedestrian demand on different traffic movements have received limited attention. This study investigates the effects of pedestrian demand on the operational performance of STOP- and YIELD-controlled three-leg unsignalized intersections.

A total of 100 simulation scenarios, including 50 STOP-controlled and 50 YIELD-controlled intersections with identical geometric characteristics, were developed using SIDRA Intersection. Different combinations of major-road traffic volume, minor-road traffic volume, and pedestrian demand were evaluated. Pearson correlation analysis indicated substantial multicollinearity among the explanatory variables; therefore, Partial Least Squares (PLS) regression was employed to develop prediction models for movement-specific delays.

The developed PLS models were statistically significant and achieved satisfactory predictive performance, with R^2 values ranging from 0.638 to 0.944, demonstrating that delay data obtained from SIDRA simulations could be reliably modelled using the PLS approach. Comparison of paired STOP and YIELD scenarios showed that YIELD control reduced minor-road left-turn, minor-road right-turn, and major-road left-turn delays by approximately 43%, 40%, and 20%, respectively, whereas major-road right-turn delay increased by approximately 79%. Response surface analyses further indicated that increasing pedestrian demand and major-road through traffic increased delays under both control types, although YIELD control generally produced lower delay levels for minor-road movements.

The findings demonstrate that integrating SIDRA simulation with PLS regression provides a reliable framework for evaluating the combined effects of traffic demand, pedestrian demand, and intersection control type, and may support the selection of appropriate control strategies for unsignalized intersections

Keywords: Unsignalized intersections, gap acceptance, pedestrians, traffic delay, delay prediction

1 Introduction

Unsignalized intersections are one of the at-grade intersection types commonly used in urban and rural road networks with low to moderate traffic volumes. Unlike signalized intersections, traffic flow at these intersections is regulated by right-of-way rules rather than traffic signals, with priority assigned through STOP control, YIELD control, or uncontrolled operation. They are widely preferred worldwide due to their low construction and operating costs, the absence of energy requirements, and their ability to provide lower delays under appropriate traffic

conditions. However, since right-of-way decisions must be evaluated instantaneously by drivers, the operational performance of unsignalized intersections largely depends on driver behavior. In particular, the imbalance between major- and minor-road traffic volumes, turning movements, geometric design characteristics, and pedestrian activity play a decisive role in determining the capacity, delay, queue formation, and traffic safety of these intersections. Therefore, understanding drivers' minor-road entry behavior and the decision-making mechanisms governing this behavior is essential for accurately evaluating the operation of unsignalized intersections [1].

Minor-road entry behavior is one of the fundamental processes determining the operational performance of unsignalized intersections. Drivers approaching the intersection from the minor road must enter the intersection by identifying and accepting suitable gaps in the major-road traffic stream. Therefore, this decision-making process is influenced not only by the major-road traffic flow but also by the type of intersection control. At STOP-controlled intersections, drivers are required to come to a complete stop at the stop line and wait until an acceptable gap becomes available. In contrast, at YIELD-controlled intersections, drivers evaluate available gaps while slowing down or stopping only when necessary. These different control types influence drivers' gap acceptance behavior and, consequently, may lead to significant differences in intersection capacity, control delay, queue length, and overall operational performance. Therefore, the operational performance of unsignalized intersections largely depends on drivers' minor-road entry behavior, the gap acceptance mechanism underlying this behavior, and the type of control applied at the intersection. [2-3].

Critical gap is regarded as one of the fundamental performance indicators for describing drivers' gap acceptance behavior under different unsignalized intersection control types. Studies on critical gap estimation are generally classified into two main approaches: empirical and behavioral. Empirical models attempt to estimate the critical gap statistically by evaluating accepted and rejected gaps obtained from field observations. These models treat the minor-road entry process as a "black box" and estimate the critical gap solely based on drivers' acceptance and rejection decisions [4]. In contrast, behavioral models seek to explain the reasons underlying drivers' acceptance or rejection of available gaps. Within these models, the critical gap is not considered a fixed value but rather a dynamic decision variable that may vary depending on drivers' risk perception, experience, waiting time, vehicle type, traffic conditions, and environmental factors [5]. Since empirical models primarily focus on the outcome of the minor-road entry process, whereas behavioral models emphasize the decision-making mechanism, both approaches should be considered together when evaluating critical gap behavior [6].

Classical gap acceptance theory has been the basis of numerous studies assuming that drivers make their entry decisions solely according to the available gaps between vehicles in the major-road traffic stream by considering only vehicle–vehicle interactions. However, the high presence of pedestrians, particularly at urban unsignalized intersections, indicates that this assumption is insufficient. Therefore, pedestrian presence should be considered as a factor that directly influences drivers' minor-road entry decisions [7]. Pedestrian activity not only affects critical gap acceptance behavior but also plays an important role in the operational performance of unsignalized intersections. Consequently, vehicle–pedestrian interactions should be evaluated as an integral component of operational performance assessment [8].

The aim of this study is to investigate the effects of vehicle–pedestrian interactions on the operational performance of STOP- and YIELD-controlled three-leg unsignalized T-intersections under different traffic and pedestrian demand conditions. To this end, STOP- and YIELD-controlled intersection models with identical geometric characteristics were developed using SIDRA Intersection, and a series of scenarios representing different major-road traffic volumes, minor-road traffic volumes, and pedestrian demand levels were analyzed. Major-road

and minor-road delays were evaluated separately for each scenario. In this context, the study considers vehicle–pedestrian interaction as an integral component of the minor-road entry process and evaluates the effects of different intersection control types on operational performance.

2 Methodology

In this study, the operational performance of STOP- and YIELD-controlled unsignalized T-intersections under different traffic and pedestrian demand conditions was comparatively evaluated. The analysis was conducted using the SIDRA Intersection software. Two intersection models with identical geometric characteristics were developed, and their operational performance was compared by varying only the intersection control type. Accordingly, the effects of intersection control type and variations in traffic and pedestrian demand on the operational performance of unsignalized intersections were comparatively assessed. Figure 1 presents the methodological framework of the study.

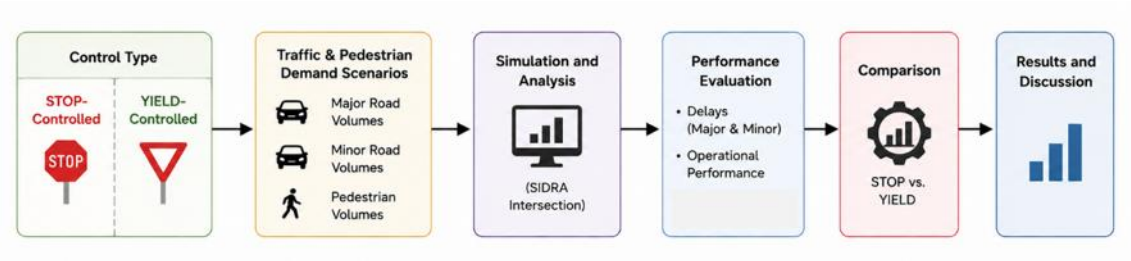


Fig.1. Methodological framework of the study.

2.1 Intersection Geometry and Modeling

The intersection model used in this study was developed as a three-leg unsignalized T-intersection consisting of a two-way major road and a two-way minor road, each providing one lane in each direction. All lane widths were designed as 3.30 m. Without modifying the intersection geometry, the same traffic scenarios were analyzed under two different control types: STOP and YIELD.

Through, right-turn, and left-turn movements were defined for both directions of the major road, whereas only right-turn and left-turn movements were assigned to the minor-road approach in accordance with the T-intersection geometry. To evaluate vehicle–pedestrian interactions, a pedestrian crossing was introduced at the minor-road approach near the intersection entry. This configuration allowed both vehicles entering the intersection from the minor road and vehicles performing right- and left-turn maneuvers from the major road to be affected by pedestrian activity. The intersection geometry and traffic movements adopted in this study are illustrated in Figure 2.

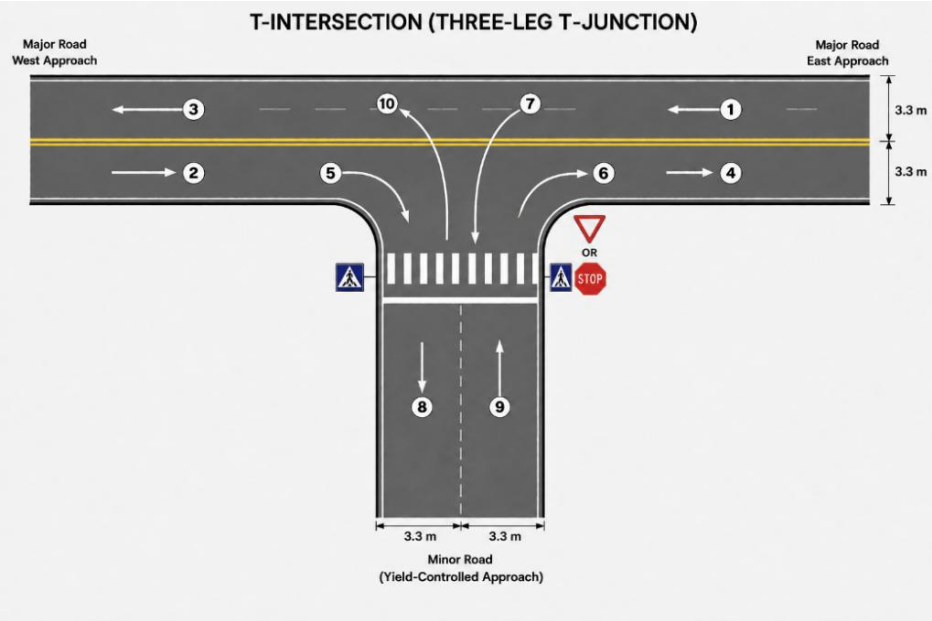


Fig.2. Geometry and traffic movements of the three-leg (T) unsignalized intersections with STOP and YIELD control modeled in SIDRA Intersection.

2.2 Scenarios

A total of 100 simulation scenarios were developed to evaluate the operational performance of STOP- and YIELD-controlled three-leg unsignalized T-intersections. The first 50 scenarios were prepared for the STOP-controlled intersection model, whereas the remaining 50 scenarios were developed for the YIELD-controlled intersection model. Accordingly, each STOP-controlled scenario was replicated under identical geometric and traffic conditions for the YIELD-controlled intersection, enabling the direct comparison of the effects of intersection control type on operational performance.

Table 1. Traffic demand, geometric characteristics, and analysis parameters adopted for the simulation scenarios.

Parameter	**Value / Range**
Intersection control type	STOP / YIELD
Total number of scenarios	100
STOP-controlled scenarios	50
YIELD-controlled scenarios	50
Major-road traffic volume	≤ 1000 veh/h
Minor-road traffic volume	≤ 600 veh/h
Pedestrian volume	50–300 ped/h
Analysis software	SIDRA Intersection 6.1
Intersection geometry	Three-leg (T) unsignalized intersection
Lane configuration	One lane per direction on both major and minor roads
Lane width	3.3 m

During scenario development, major-road traffic volume, minor-road traffic volume, and pedestrian volume were considered as the independent variables. To represent realistic urban traffic conditions, the total major-road traffic volume was limited to 1000 veh/h, while the minor-road traffic volume was restricted to a maximum of 600 veh/h. Pedestrian demand was varied between 50 and 300 ped/h to represent different pedestrian activity levels. This enabled the evaluation of intersection performance under various pedestrian demand conditions. The parameters adopted in the study and their corresponding value ranges are summarized in Table 1.

Considering that individual traffic movements may be affected differently by pedestrian interactions, the analysis results were evaluated separately for delays associated with major-road right-turn and left-turn movements, as well as minor-road right-turn and left-turn movements entering the major traffic stream. The obtained data were transformed into a multi-parameter model using PLS regression. The model used to predict delays in this study was developed based on intersection control type, vehicle and pedestrian demands.

This approach enabled an independent assessment of the effects of intersection control type and pedestrian demand on each turning movement. Movement-specific average delay was adopted as the primary performance measure. Accordingly, delay values for right-turn and left-turn movements on both the major and minor approaches were analyzed separately to compare the effects of pedestrian demand and intersection control type on each traffic movement.

3 Results and Evaluation

Pearson correlation analyses were conducted for the STOP- and YIELD-controlled intersection scenarios to define appropriate regression model for analyzing the simulation outputs considered in this study. Based on Pearson correlation results, PLS regression was identified as the most appropriate method to evaluate the study results. Accordingly, PLS regression analysis was performed to investigate the effects of traffic volume, pedestrian volume, and intersection control type on delays associated with major-road and minor-road movements. The detailed correlation matrices for both intersection control types are presented in Appendix A.

The Pearson correlation analysis revealed strong linear relationships between minor-road traffic volumes and turning movements. In addition, positive correlations were observed between pedestrian volume and delays associated particularly with turning movements. Although some differences in the correlation coefficients were observed between the two intersection control types, both analyses indicated a high degree of correlation among the traffic and pedestrian variables. These findings suggest the presence of substantial multicollinearity among the explanatory variables. Since multicollinearity may reduce the reliability of coefficient estimates in conventional multiple linear regression models, the Partial Least Squares (PLS) regression method, which is capable of producing reliable models in the presence of highly correlated predictors, was adopted in the subsequent analysis.

Table 2. Performance statistics of the developed PLS regression models

Response Variable	Number of Latent Components	R^2	Predicted R^2	F-value	p-value
Major Road Right Delay	4	0.711	0.658	58.53	<0.001
Major Road Left Delay	4	0.874	0.851	164.64	<0.001
Minor Road Left Delay	4	0.638	0.569	41.94	<0.001
Minor Road Right Delay	4	0.944	0.931	397.91	<0.001

Table 2 presents the performance statistics of the PLS regression models developed for the four delay variables. Cross-validation results indicated that four latent components provided the optimum model structure for all models. Furthermore, all developed models were found to be statistically significant ($p < 0.001$).

The explanatory performance of the developed PLS models was evaluated using the coefficient of determination (R^2) and Predicted R^2 values. Among the developed models, the Minor Road Right Delay model exhibited the highest explanatory and predictive performance, with an R^2 value of 0.944 and a Predicted R^2 value of 0.931. This was followed by the Major Road Left Delay ($R^2 = 0.874$), Major Road Right Delay ($R^2 = 0.711$), and Minor Road Left Delay ($R^2 = 0.638$) models. The high explanatory power achieved for the Minor Road Right Delay model indicates that intersection control type, traffic volumes, and pedestrian volume collectively explain a substantial proportion of the variability in this delay component.

These findings suggest that delays experienced by drivers making left-turn movements from the minor road may be influenced not only by traffic and pedestrian volumes but also by behavioral factors that were not included in the model, such as driver behavior, gap acceptance characteristics, and decision-making processes as in this study behavioral approaches are not considered whereas the empirical models are the main concern.

The regression coefficients of the developed PLS models are presented in Table 3. Using these coefficients, prediction equations were established for each delay variable. The sign of each coefficient indicates the direction of the relationship between the corresponding independent variable and the delay component, whereas its magnitude represents the change in the predicted delay associated with a one-unit change in the independent variable while all other variables are held constant.

Prediction equations for the four delay components were developed using the unstandardized regression coefficients presented in Table 3.

Table 3. Regression coefficients of the developed PLS models

Predictor	Major Road Right Delay	Major Road Left Delay	Minor Road Left Delay	Minor Road Right Delay
Constant	1.13546	0.79526	-5444.94	7.00816
Control Type	5.06771	-2.90113	-735.13	-4.18640
Main Road W–E Through	0.00201	0.01504	5.163	0.00373
Main Road W–E Right	-0.00011	0.01281	-1.764	-0.00391
Main Road E–W Through	0.00701	0.00161	4.377	0.00036
Main Road E–W Left	0.00687	0.00657	7.003	-0.00188
Minor Road Left	-0.00144	-0.00054	3.645	0.00028
Minor Road Right	0.00045	0.00308	5.318	0.00143
Pedestrian Volume	0.00162	0.00837	2.937	0.00781

In the developed models, the dependent variables were generally expressed using the linear regression model given in Equation (1). The unstandardized regression coefficients for each model are presented in Table 3, and the prediction equations for Major Road Right Delay, Major Road Left Delay, Minor Road Left Delay, and Minor Road Right Delay can be obtained by substituting the corresponding coefficients into Equation (1).

$$Delay = \beta_0 + \beta_1 CT + \beta_2 V_{WE,T} + \beta_3 V_{WE,R} + \beta_4 V_{EW,T} + \cdots + \beta_5 V_{EW,L} + \beta_6 V_{M,L} + \beta_7 V_{M,R} + \beta_8 P \quad (1)$$

Where, Delay is predicted delay (sec), CT is control type, $V_{WE,T}$ is main road W–E Through Volume (veh/h), $V_{WE,R}$ is Main Road W–E Right-Turn Volume (veh/h), $V_{EW,T}$ is Main Road E–W Through Volume (veh/h), $V_{EW,L}$ is Main Road E–W Left-Turn Volume (veh/h), $V_{M,L}$ is Minor Road Left-Turn Volume (veh/h), $V_{M,R}$ is Minor Road Right-Turn Volume (veh/h), P is Pedestrian Volume (ped/h), β_0 is constant, and β_0-β_8 is Unstandardized Regression Coefficient.

Figure 3 presents the standardized regression coefficients of the developed PLS models, allowing the relative effects of the explanatory variables on the delay components to be directly compared.

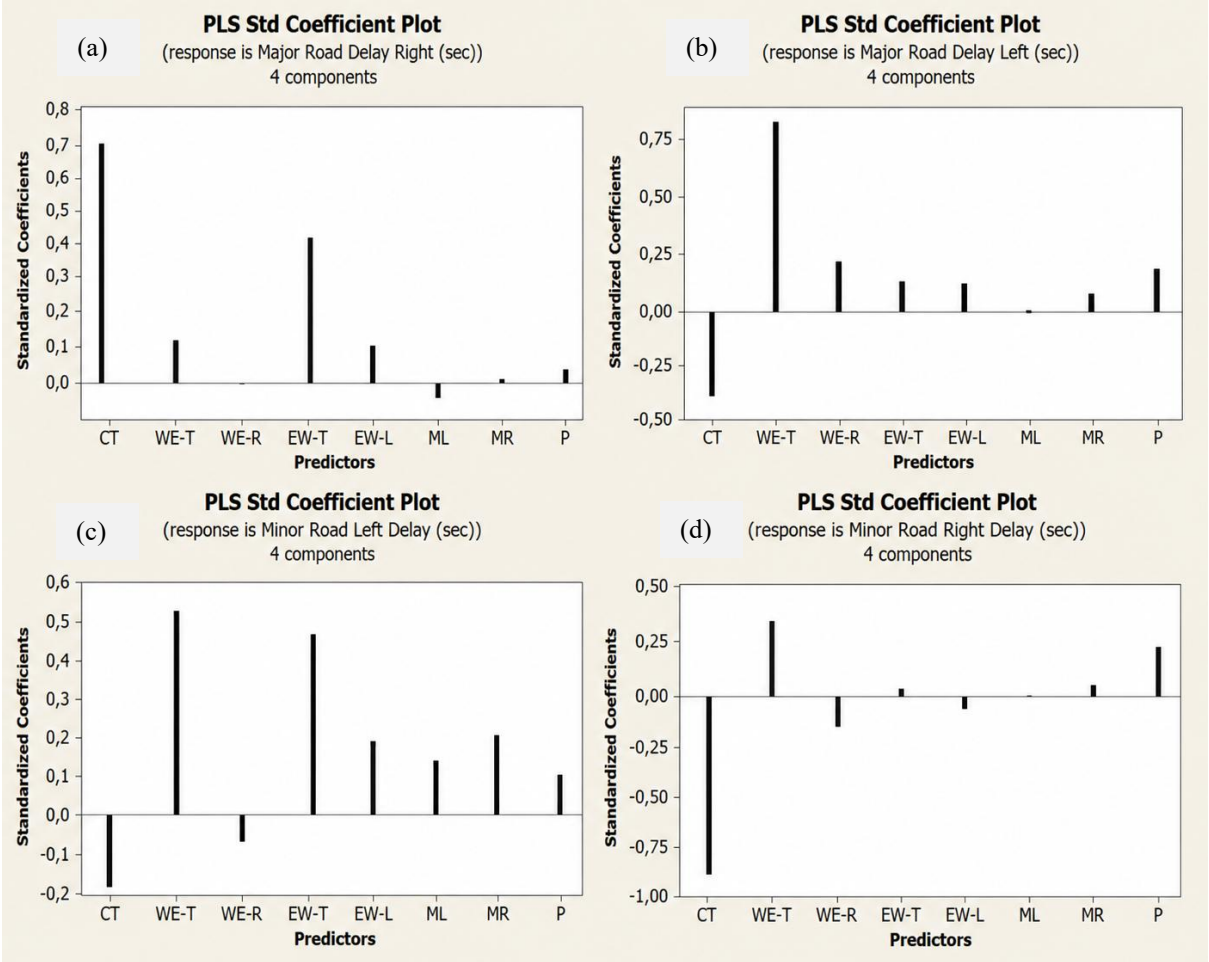


Fig.3. Standardized regression coefficient plots of the developed PLS models for (a) Major Road Right Delay, (b) Major Road Left Delay, (c) Minor Road Left Delay, and (d) Minor Road Right Delay.

For major-road right-turn delays, intersection control type was identified as the most influential variable. In contrast, major-road through traffic volume exhibited the strongest effect

on major-road left-turn delays. For minor-road right-turn delays, the most influential variables were, respectively, intersection control type, major-road through traffic volume, and pedestrian volume. Conversely, major-road through traffic volume was found to be the dominant factor affecting minor-road left-turn delays. Overall, the results indicate that intersection control type is the dominant factor affecting right-turn movements, whereas major-road through traffic volume has a more pronounced influence on left-turn delays.

Figure 4 illustrates the predictive performance of the developed PLS models. Overall, the model predictions and cross-validation results exhibit trends consistent with the observed delay values, indicating reasonable compatibility between the observed and predicted responses. However, the degree of compatibility varies among the developed models. In particular, the Minor Road Left Delay model presented in Figure 4(c) shows a noticeable clustering and wider dispersion of predicted values at relatively low observed delay levels. This behavior may be associated with the wider and more heterogeneous distribution of Minor Road Left Delay values compared with the other delay variables, including considerably high delay values under certain traffic demand conditions. Such a distribution is more difficult to represent using a linear PLS model structure, resulting in greater prediction errors, particularly within the lower-delay range. This observation is consistent with the comparatively lower explanatory and predictive performance of the Minor Road Left Delay model, with R^2 and Predicted R^2 values of 0.638 and 0.569, respectively. Nevertheless, the overall trend between the observed and predicted values is maintained, and the similar distributions of the fitted and cross-validation results indicate that the model is still capable of capturing the general variation in Minor Road Left Delay, despite its lower predictive performance compared with the other delay models.

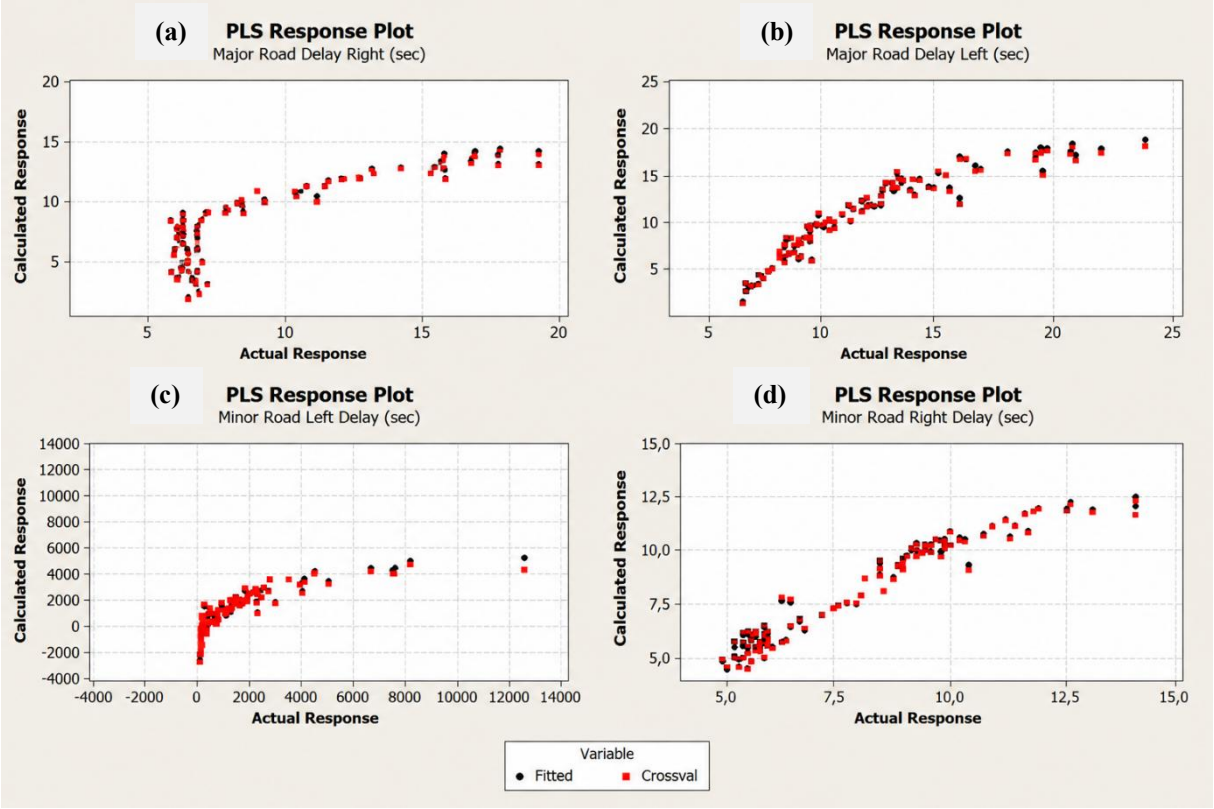


Fig.4. Response plots of the developed PLS regression models for (a) Major Road Right Delay, (b) Major Road Left Delay, (c) Minor Road Left Delay, and (d) Minor Road Right Delay, comparing observed and predicted delay values for both fitted and cross-validation datasets.

Figure 5 illustrates the effects of major-road W–E through traffic volume and pedestrian volume on minor-road left-turn and right-turn delays under STOP- and YIELD-controlled

intersection conditions. For both control types, minor-road delays increased with increasing major-road traffic volume and pedestrian volume. However, the STOP-controlled intersection exhibited substantially higher delay levels, whereas the YIELD-controlled intersection produced lower delays under the same traffic and pedestrian demand conditions. These findings are consistent with the results obtained from the PLS regression analysis and confirm that intersection control type is a key factor influencing delays associated with minor-road movements.

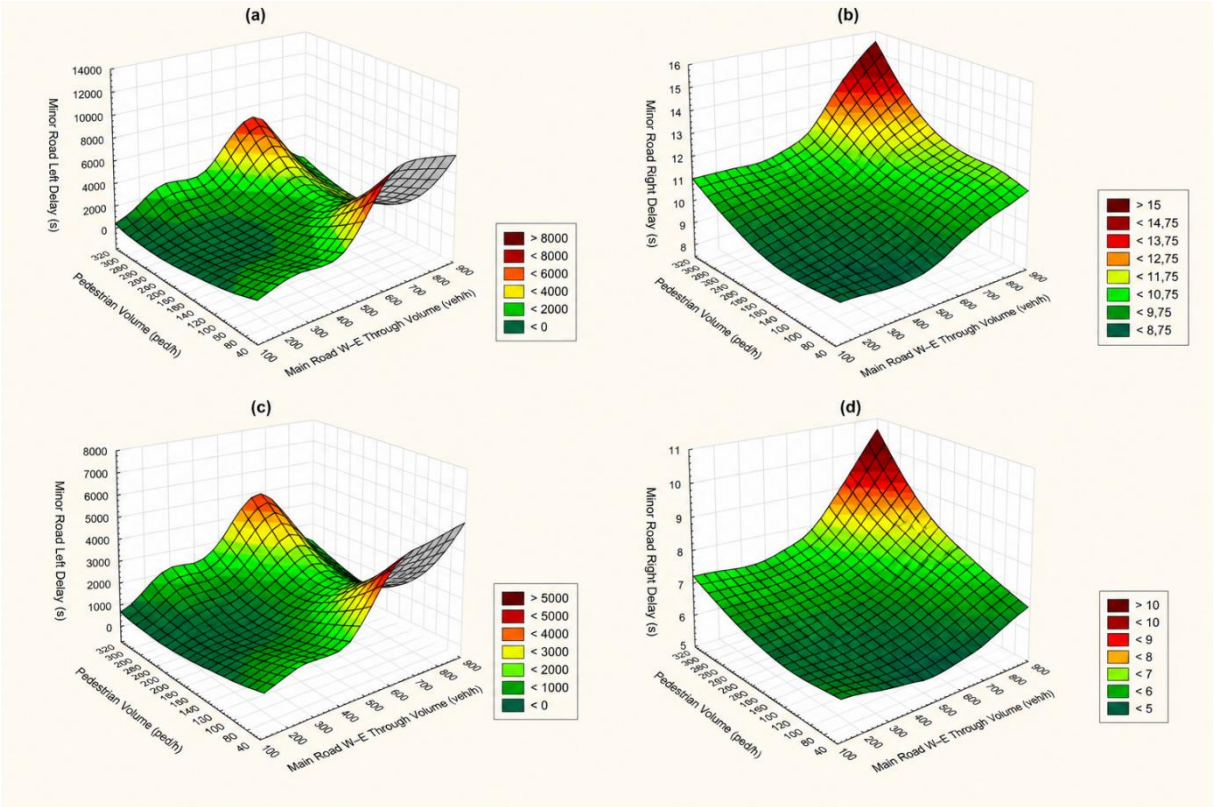


Fig.5. Response surface plots illustrating the combined effects of main-road W–E through traffic volume and pedestrian volume on minor-road left-turn and minor-road right-turn delays under STOP and YIELD control conditions: (a) Minor Road Left Delay under STOP control, (b) Minor Road Right Delay under STOP control, (c) Minor Road Left Delay under YIELD control, and (d) Minor Road Right Delay under YIELD control.

Overall, the developed PLS models provided reliable predictive performance for the different delay components and successfully captured the relationships among intersection control type, traffic volumes, and pedestrian volume. When the standardized regression coefficients and response surface analyses are considered together, the effects of the explanatory variables change according to movement type. In particular, minor-road movements were more sensitive to changes in intersection control type and pedestrian demand, whereas major-road movements were predominantly influenced by major-road traffic volume. Furthermore, the comparative analysis of paired STOP- and YIELD-controlled scenarios (Table 4) revealed substantial differences in operational performance between the two control types.

As presented in Table 4, comparison of the paired scenarios showed that YIELD control reduced minor-road left-turn and minor-road right-turn delays by approximately 43% and 40%, respectively. In addition, major-road left-turn delay decreased by approximately 20%, whereas major-road right-turn delay increased by approximately 79%. These findings indicate that the

effect of intersection control type is movement-dependent and that YIELD control provides considerable operational benefits, particularly for minor-road movements.

Table 4. Comparative delay changes between STOP- and YIELD-controlled intersections

Delay Measure	Mean Change (%)
Average Control Delay	−39.1
Major Road Right Delay	+78.6
Major Road Left Delay	−20.0
Minor Road Left Delay	−43.2
Minor Road Right Delay	−40.2

4 Conclusion and Future Works

In this study, the operational performance of STOP- and YIELD-controlled three-leg unsignalized T-intersections under different traffic and pedestrian demand conditions was evaluated using SIDRA Intersection, and the resulting simulation data were analyzed by means of PLS regression. Pearson correlation analysis revealed a high degree of multicollinearity among the explanatory variables; therefore, PLS regression was adopted to develop delay prediction models.

The developed PLS models were statistically significant for all delay components, with R^2 values ranging from 0.638 to 0.944. The high predictive performance of the models demonstrates that the delay data obtained from SIDRA Intersection simulations can be acceptably modeled using the PLS regression approach, providing a reliable representation of intersection operational performance under varying traffic and pedestrian demand conditions.

Comparison of the paired STOP- and YIELD-controlled scenarios showed that YIELD control reduced minor-road left-turn delays by approximately 43%, minor-road right-turn delays by 40%, and major-road left-turn delays by 20%. In contrast, major-road right-turn delays increased by approximately 79% under YIELD control. Furthermore, the response surface analyses demonstrated that increasing major-road traffic volume and pedestrian demand resulted in higher delays under both control types. However, under the same traffic and pedestrian demand conditions, the YIELD-controlled intersection consistently produced lower delays for minor-road movements than the STOP-controlled intersection. These findings indicate that the effect of intersection control type varies according to movement type and that pedestrian demand has a more pronounced influence on delays associated with minor-road movements.

In conclusion, this study demonstrated that the PLS regression approach provides an effective framework for analyzing data obtained from SIDRA Intersection simulations and for developing reliable models to evaluate the operational performance of unsignalized intersections under varying traffic and pedestrian demand conditions. The findings of this study may contribute to engineering decision-making regarding the selection of appropriate intersection control strategies and the improvement of intersection operational performance. Future research should focus on validating the developed models using field data and incorporating surrogate safety measures, such as Time-to-Collision (TTC) and Post-Encroachment Time (PET), to establish more comprehensive models that jointly evaluate operational performance and traffic safety.

References

1. Aoki, N., Sarker, M. J., Morimoto, A.: Assessment of Congestion Transition and Effectiveness of Measures by Using Micro Simulation. Infrastructure Planning Review, 20, 589–596 (2003).
2. Shimizu, T., MORICHI, S., Hamaya, K.: An Analysis of the Decision Factors at Gap Choice Situation at "Stop-and-go" Merging Section. Infrastructure Planning Review, 21, 861–868 (2004).
3. Bieletska, O., Liubyi, Y., Muzylyov, D., Ivanov, V., Pavlenko, I.: Approach to Determine Transport Delays at Unsignalized Intersections. Communications - Scientific Letters of the University of Zilina, 25(3), A124–A136 (2023).
4. Razzaq, A. K., Shubber, K. H. H.: Effect of Waiting Time on Gap Acceptance Characteristics of Change Direction U-Turn Opening. Mathematical Modelling and Engineering Problems, 9(3), 825–830 (2022).
5. Zhou, H., Ivan, J. N., Gårder, P., Равишанкер, H.: Gap Acceptance for Left Turns From the Major Road at Unsignalized Intersections. Transport, 32(3), 252–261 (2014).
6. Gbologah, F. E., Wei, A., Rodgers, M. O.: Evaluation of Factors Influencing Roundabout Performance in Atlanta. Transportation Research Record Journal of the Transportation Research Board, 2676(9), 216–229 (2022).
7. Asaithambi, G., Anuroop, C.: Analysis of occupation time of vehicles at urban unsignalized intersections in non-lane-based mixed traffic conditions. Journal of Modern Transportation, 24(4), 304–313 (2016).
8. AlKheder, S., Al-Kandari, A. M., Aladwani, B., Alkhamees, W.: Assessment of pedestrian-vehicular interaction at un-signalized intersections to measure the delay caused by crossing pedestrian on platoon vehicles. Smart and Resilient Transport, 5(1), 2–13 (2023).

Author Contribution Statement

- *Conceptualization:* Serhan TANYEL
- *Methodology:* Duygu ŞENOL
- *Investigation:* Duygu ŞENOL, Serhan TANYEL
- *Writing – Original Draft:* Duygu ŞENOL
- *Writing – Review & Editing:* Duygu ŞENOL, Serhan TANYEL

List of Abbreviations

- **HCM— Highway Capacity Manual**
- **PLS—Partial Least Squares**

Appendices

Appendix A. Correlation Matrix for Intersections

This appendix provides tables A1-A2 which are the detailed correlation matrices for STOP-controlled and YIELD-controlled intersection used in the study.

Table A1. Correlation Matrix for the STOP-controlled Intersection

	Main Road Volume W-E (veh/h)	Main Road Volume W-E through (veh/h)	Main Road Volume W-E Right turn (veh/h)	Main Road Volume E-W (veh/h)	Main Road Volume E-W through(veh/h)	Main Road Volume E-W Left turn (veh/h)	Minor Road volume (veh/h)	Minor Road volume Left turn (veh/h)	Minor Road volume Right turn (veh/h)	Pedestrian volume (ped/h)	Major Road Delay Right (sec)	Major Road Delay Left (sec)	Minor Road Left Delay (sec)	Minor Road Right Delay (sec)
Main Road Volume W-E (veh/h)	1.000	0.962	0.495	-0.246	-0.279	-0.103	-0.133	-0.161	-0.094	0.088	0.323	0.917	0.296	0.645
Main Road Volume W-E through(veh/h)	0.962	1.000	0.239	-0.154	-0.216	-0.057	-0.137	-0.150	-0.112	0.036	0.269	0.906	0.354	0.733
Main Road Volume W-E Right turn (veh/h)	0.495	0.239	1.000	-0.383	-0.305	-0.184	-0.037	-0.093	0.021	0.198	0.292	0.378	-0.075	-0.040
Main Road Volume E-W (veh/h)	-0.246	-0.154	-0.383	1.000	0.947	0.427	0.305	0.275	0.306	-0.369	-0.402	-0.170	0.560	-0.130
Main Road Volume E-W through(veh/h)	-0.279	-0.216	-0.305	0.947	1.000	0.266	0.290	0.242	0.311	-0.286	-0.335	-0.230	0.539	-0.109
Main Road Volume E-W Left turn (veh/h)	-0.103	-0.057	-0.184	0.427	0.266	1.000	0.294	0.333	0.228	-0.363	-0.388	0.002	0.320	-0.132
Minor Road volume (veh/h)	-0.133	-0.137	-0.037	0.305	0.290	0.294	1.000	0.952	0.954	-0.276	-0.291	-0.126	0.456	0.013
Minor Road volume Left turn (veh/h)	-0.161	-0.150	-0.093	0.275	0.242	0.333	0.952	1.000	0.817	-0.321	-0.341	-0.159	0.417	-0.054
Minor Road volume Right turn (veh/h)	-0.094	-0.112	0.021	0.306	0.311	0.228	0.954	0.817	1.000	-0.206	-0.215	-0.081	0.451	0.078
Pedestrian volume (ped/h)	0.088	0.036	0.198	-0.369	-0.286	-0.363	-0.276	-0.321	-0.206	1.000	0.965	0.265	-0.156	0.452
Major Road Delay Right (sec)	0.323	0.269	0.292	-0.402	-0.335	-0.388	-0.291	-0.341	-0.215	0.965	1.000	0.479	-0.087	0.590
Major Road Delay Left (sec)	0.917	0.906	0.378	-0.170	-0.230	0.002	-0.126	-0.159	-0.081	0.265	0.479	1.000	0.333	0.750
Minor Road Left Delay (sec)	0.296	0.354	-0.075	0.560	0.539	0.320	0.456	0.417	0.451	-0.156	-0.087	0.333	1.000	0.451
Minor Road Right Delay (sec)	0.645	0.733	-0.040	-0.130	-0.109	-0.132	0.013	-0.054	0.078	0.452	0.590	0.750	0.451	1.000

Table A2. Correlation Matrix for the YIELD-controlled Intersection

	Main Road Volume W-E (veh/h)	Main Road Volume W-E through (veh/h)	Main Road Volume W-E Right turn (veh/h)	Main Road Volume E-W (veh/h)	Main Road Volume E-W through (veh/h)	Main Road Volume E-W Left turn (veh/h)	Minor Road volume (veh/h)	Minor Road volume Left turn (veh/h)	Minor Road volume Right turn (veh/h)	Pedestrian volume (ped/h)	Major Road Delay Right (sec)	Major Road Delay Left (sec)	Minor Road Left Delay (sec)	Minor Road Right Delay (sec)
Main Road Volume W-E (veh/h)	1,000	0,962	0,495	-0,278	-0,279	-0,103	-0,133	-0,161	-0,094	0,088	-0,071	0,931	0,342	0,512
Main Road Volume W-E through(veh/h)	0,962	1,000	0,239	-0,210	-0,216	-0,057	-0,137	-0,150	-0,112	0,036	-0,035	0,923	0,395	0,602
Main Road Volume W-E Right turn (veh/h)	0,495	0,239	1,000	-0,322	-0,305	-0,184	-0,037	-0,093	0,021	0,198	-0,141	0,372	-0,041	-0,095
Main Road Volume E-W (veh/h)	-0,278	-0,210	-0,322	1,000	0,975	0,473	0,333	0,298	0,336	-0,345	0,948	-0,081	0,517	-0,426
Main Road Volume E-W through(veh/h)	-0,279	-0,216	-0,305	0,975	1,000	0,266	0,290	0,242	0,311	-0,286	0,927	-0,114	0,483	-0,386
Main Road Volume E-W Left turn (veh/h)	-0,103	-0,057	-0,184	0,473	0,266	1,000	0,294	0,333	0,228	-0,363	0,436	0,101	0,328	-0,316
Minor Road volume (veh/h)	-0,133	-0,137	-0,037	0,333	0,290	0,294	1,000	0,952	0,954	-0,276	0,267	-0,035	0,462	-0,228
Minor Road volume Left turn (veh/h)	-0,161	-0,150	-0,093	0,298	0,242	0,333	0,952	1,000	0,817	-0,321	0,224	-0,056	0,437	-0,245
Minor Road volume Right turn (veh/h)	-0,094	-0,112	0,021	0,336	0,311	0,228	0,954	0,817	1,000	-0,206	0,285	-0,010	0,443	-0,190
Pedestrian volume (ped/h)	0,088	0,036	0,198	-0,345	-0,286	-0,363	-0,276	-0,321	-0,206	1,000	-0,291	-0,038	-0,177	0,584
Major Road Delay Right (sec)	-0,071	-0,035	-0,141	0,948	0,927	0,436	0,267	0,224	0,285	-0,291	1,000	0,111	0,621	-0,347
Major Road Delay Left (sec)	0,931	0,923	0,372	-0,081	-0,114	0,101	-0,035	-0,056	-0,010	-0,038	0,111	1,000	0,529	0,390
Minor Road Left Delay (sec)	0,342	0,395	-0,041	0,517	0,483	0,328	0,462	0,437	0,443	-0,177	0,621	0,529	1,000	-0,001
Minor Road Right Delay (sec)	0,512	0,602	-0,095	-0,426	-0,386	-0,316	-0,228	-0,245	-0,190	0,584	-0,347	0,390	-0,001	1,000

Publication Note

This paper was peer-reviewed, accepted for presentation, and included in the proceedings of the ACE2026 – International Conference on Advances in Civil Engineering, held on 12–14 October 2026 in Trabzon, Türkiye.

This paper may be cited as follows:

Senol, D., Tanyel, S., "Effects of Pedestrian Demand on the Operational Performance of Unsignalized Intersections," in Proceedings of the ACE2026 – International Conference on Advances in Civil Engineering, Trabzon, Türkiye, 12–14 October 2026.

Evaluation of Physical Properties of POE/Nanoclay Composite Modified Bitumen

Ersoy Kabadayı [1], Erman Çavdar[2], Aytuğ Kumandaş [3], Mahir Kumantaş [4], Neslihan Şahan[5] and Şeref Oruç [6]
[1] 0000-0003-4062-3117, Giresun University, Construction Technology Department, Giresun, Türkiye, ersoy.kabadayi@giresun.edu.tr
[2] 0000-0002-0238-5245, Karadeniz Technical University, Civil Engineering Department, Trabzon, Türkiye, ermancavdar@ktu.edu.tr
[3] 0000-0003-1765-9963, Ondokuz Mayıs University, Civil Engineering Department, Samsun, Türkiye, aytug.kumandas@omu.edu.tr
[4] 0009-0002-7979-7640, Karadeniz Technical University, Civil Engineering Department, Trabzon, Türkiye, mkumantas@ktu.edu.tr
[5] 0000-0003-3904-6527, Kırşehir Ahi Evran University, Civil Engineering Department, Kırşehir, Türkiye, neslihan.sahan@ahievran.edu.tr
[6] 0000-0001-5788-890X, Karadeniz Technical University, Civil Engineering Department, Trabzon, Türkiye, oruc@ktu.edu.tr

Abstract. Asphalt pavements are subjected to various distresses, such as permanent deformation, cracking, and aging, due to increasing traffic loads, temperature variations, and environmental effects throughout their service life. Therefore, improving the physical properties of bituminous binders is considered an important research area for enhancing pavement performance. In this study, the effect of composite modification obtained through the combined use of polyolefin elastomer (POE) and nanoclay additives on the physical properties of 50/70 penetration grade bitumen was investigated. For this purpose, modified bitumen samples coded as P1, P3, P5, and P1N1–P5N3 were prepared using different POE and nanoclay contents. The physical properties of the prepared binders were evaluated through penetration, softening point, and penetration index tests. The experimental results showed that the POE/Nanoclay composite additive had a pronounced effect on the consistency and temperature susceptibility of bitumen. The penetration value of the base bitumen decreased from 53.0 dmm to 24.8 dmm for the P5N3 sample, indicating that the binder became stiffer with the addition of the additive. In contrast, the softening point increased from 50.2 °C to 66.1 °C, demonstrating an improvement in the binder's resistance to softening at elevated temperatures. The penetration index results revealed that temperature susceptibility decreased, particularly in the P3 and P5 groups, and that the modified binders exhibited more stable behavior against temperature variations. Overall, the findings indicate that the POE/Nanoclay composite additive improved the physical stability of bitumen and may provide beneficial effects in terms of high-temperature performance. However, in order to determine the optimum additive content, the physical test results should be supported by further investigations, including aging, storage stability, and mixture performance tests.

Keywords: Bitumen; POE; Nanoclay; Composite additive; Bitumen modification; Penetration; Softening point; Penetration index.

1 Introduction

Asphalt pavements are widely used in highway pavement structures due to their advantages, such as providing comfortable driving conditions, high abrasion resistance, and relatively easy maintenance and repair operations [1, 2]. However, asphalt binders are exposed to

environmental effects such as light, heat, oxygen, and water throughout their service life. These effects cause changes in the physical and chemical structure of the binder, leading to a gradual reduction in pavement performance [3, 4]. Therefore, the modification of bitumen with various additives has become a widely investigated approach to improve the durability of asphalt pavements.

One of the most commonly used polymer additives in bitumen modification is styrene-butadiene-styrene (SBS) block copolymer, which has long held an important place in asphalt engineering [5]. However, the unsaturated double bonds in the molecular structure of SBS are prone to degradation under ultraviolet radiation and high-temperature effects, which may lead to a decrease in binder performance during aging [6, 7]. At this point, polyolefin elastomers (POE) stand out as an alternative polymer additive due to their ability to exhibit elastomeric behavior similar to SBS and the absence of unsaturated bonds in their structure. Owing to these characteristics, POE is reported to provide a more resistant structure against heat, oxygen, and ultraviolet aging [8].

In recent years, studies have increasingly focused on composite additive systems formed with nanomaterials to further enhance the performance of polymer-modified bitumens. In this context, nanoclay is one of the notable nanomaterials due to its potential to improve the performance properties of both asphalt binders and asphalt mixtures [9]. It has been reported that nanoclay, when used at appropriate contents, can have positive effects on the storage stability, aging resistance, and high-temperature performance of polymer-modified bitumens [9]. In addition, the literature indicates that nanoclay can provide significant improvements in bitumen and mixture performance, particularly when used as a composite additive together with polymers [10–18].

In this study, the effect of a composite additive system consisting of POE and nanoclay on the physical properties of 50/70 penetration grade bitumen was experimentally investigated. For this purpose, modified bitumens prepared with different POE and nanoclay contents were evaluated through penetration, softening point, and penetration index tests. The obtained results were comparatively interpreted to reveal the effects of the POE/Nanoclay composite additive on the consistency, resistance to softening at elevated temperatures, and temperature susceptibility of bitumen.

2 Materials and Methods

2.1 Bitumen

In this study, neat bitumen with a 50/70 penetration grade (B 50/70), produced by Tüpraş refineries, was used as the binder material. This bitumen grade was selected because it is one of the commonly used binder types in wearing course mixtures within the scope of the Turkish Highway Technical Specification (KTŞ) and provides a suitable reference for evaluating the stiffening and stabilizing effects of POE/Nanoclay additives.

2.2 POE (Polyolefin Elastomer)

Polyolefin elastomers are elastomeric polymers obtained through the copolymerization of ethylene and an α-olefin. Depending on the ethylene-to-α-olefin ratio, structures with different molecular weights and degrees of crystallinity can be produced. Accordingly, POE exhibits properties such as high elasticity, flexibility at low temperatures, resistance to UV radiation, and good aging resistance. The absence of unsaturated double bonds in its molecular structure makes POE a more resistant alternative polymer additive to heat, oxygen, and ultraviolet aging compared with SBS.

In this study, a polyolefin elastomer commercially coded as ENGAGE™ 8003 (Dow Chemical), based on an ethylene-octene copolymer, was used. The POE used has a density of 0.885 g/cm³ and a Shore A hardness of 84. Owing to its elastomeric structure and processing characteristics, it is considered a suitable material for use with bituminous binders.

2.3 Nanoclay

In this study, a montmorillonite-based organically modified nanoclay was used. Nanoclays have nanoscale layer thickness and a high specific surface area due to their layered silicate structure, and they are widely preferred as reinforcing additives in polymer and bituminous binder systems. In montmorillonite-based nanoclays, the initial interlayer spacing is approximately 15 Å, while this distance can increase to the range of 38–40 Å after organic modification. The increase in interlayer spacing allows the nanoclay to be more homogeneously dispersed within the binder or polymer matrix.

The nanoclay used in this study is a commercial product named esanNANO 1-140, produced by Eczacıbaşı Esan. This additive, obtained by purifying and organically modifying montmorillonite mineral, has been developed particularly for polypropylene (PP)- and polyethylene (PE)-based nanocomposite applications and contains approximately 44 wt.% SiO_2 and 6 wt.% Al_2O_3. Through organic modification, the layered structure is made compatible with polymeric systems.

2.4 Preparation of Modified Bitumens

POE/Nanoclay composite-modified bitumens were prepared using the melt blending approach, which is based on dispersing the additives within the bitumen matrix through mechanical interaction rather than dissolution. For this purpose, 50/70 penetration grade bitumen was heated under controlled conditions before additive incorporation to bring it into a fluid state and enable it to act as the carrier matrix. A Silverson L5M high-shear mixer was used to ensure homogeneous dispersion of the additives within the binder. The modification process was carried out at 170 °C, at a mixing speed of 4000 rpm, for a total duration of 90 min.

In the prepared samples, the POE contents were coded as P1, P3, and P5, while the nanoclay contents were coded as N1, N2, and N3. In the coding system, “P” represents the POE additive, and “N” represents the nanoclay additive. The samples coded as P1, P1N1, P1N2, P1N3, P3, P3N1, P3N2, P3N3, P5, P5N1, P5N2, and P5N3 were evaluated.

2.5 Conventional Bitumen Tests

The consistency of the modified binders was determined using the penetration test. The test was conducted in accordance with the TS EN 1426 standard, in which the depth of penetration of a standard needle into the bitumen sample is measured at 25 °C under a load of 100 g for 5 s [19]. A higher penetration value indicates a softer bitumen consistency, whereas a lower value indicates a stiffer binder.

The change in binder consistency under temperature effects was evaluated using the softening point test. The test was performed in accordance with the TS EN 1427 standard and is based on determining the temperature at which a steel ball placed on the bitumen sample travels a specified distance in a liquid medium heated at a constant rate [20]. A higher softening point indicates that the binder has greater resistance to softening at elevated temperatures.

2.6 Temperature Sensitivity Index

The temperature susceptibility of bitumen was evaluated using the penetration index (PI), which is calculated based on the values obtained from the penetration and softening point tests. The PI value is an important parameter indicating the extent to which the binder can maintain its consistency against temperature variations. An increase in the PI value indicates lower temperature susceptibility and a more stable behavior against temperature changes. The PI value was calculated using Equation (1).

$$PI = \frac{1952 - 500 \times \log(pen) - 20 \times SP}{50 \times \log(pen) - SP - 120} \quad (1)$$

where $\log(pen)$ represents the logarithm of penetration at 25 °C and SP denotes the softening point temperature in degrees Celsius.

3 Results and Discussion

3.1 Penetration Test Results

The penetration test results of the neat and POE/Nanoclay composite-modified bitumens are presented in Figure 1. The penetration value of the neat bitumen was determined as 53.0 dmm. With the incorporation of POE and nanoclay additives, a general decrease in penetration values was observed. This indicates that the additive incorporation increased the consistency of the bitumen and transformed the binder into a stiffer structure.

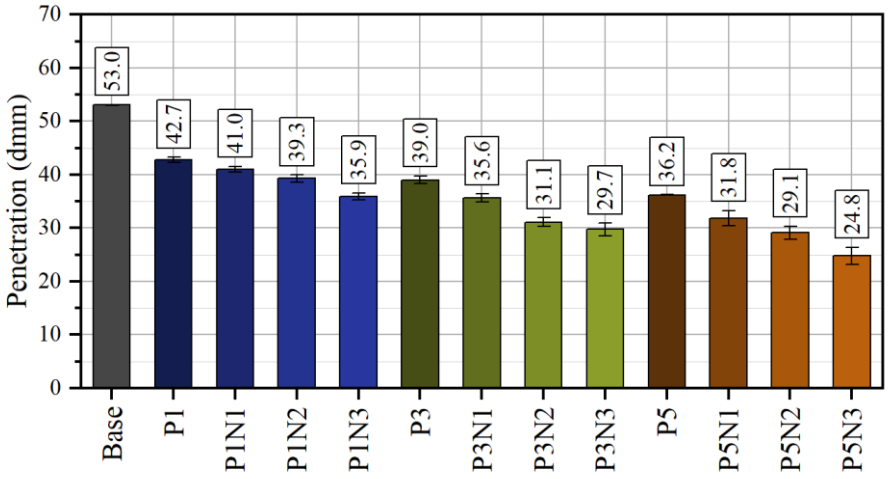


Fig. 1. Penetration test results.

In the P1 group, the penetration value was 42.7 dmm for the P1 sample and decreased to 35.9 dmm for the P1N3 sample with increasing nanoclay content. Similarly, in the P3 group, the penetration value decreased from 39.0 dmm for P3 to 29.7 dmm for P3N3. In the P5 group, the penetration value of 36.2 dmm for the P5 sample decreased to 24.8 dmm for P5N3 with the increase in nanoclay content. These results indicate that increasing both POE and nanoclay contents reduced the penetration value, with the lowest penetration obtained for the P5N3 sample, in which both additives were used at their highest dosages. Compared with the neat bitumen, the penetration value of the P5N3 sample decreased by approximately 53%, indicating that the composite system had a pronounced effect on binder consistency even when evaluated only in terms of penetration.

The reduction in penetration can be explained by two complementary mechanisms. The first is the elastomeric network structure formed by POE within the bitumen. As the polymer phase approaches a more continuous structure within the binder matrix, the resistance against needle penetration increases [8]. The second mechanism is related to the layered silicate structure and high specific surface area of nanoclay, which may promote strong interfacial interactions with bitumen components and stiffen the matrix by restricting the mobility of free-moving fractions [9]. The fact that nanoclay reduced the penetration value at each POE level indicates that this reinforcing effect was maintained within the POE network as well. Similar stiffening behavior has also been reported in the literature for nanoclay-modified binders [10–18].

From an engineering perspective, this reduction in penetration suggests that the binder may exhibit improved resistance to permanent deformation, particularly rutting, at high service temperatures. However, the increase in binder consistency may also make the binder more brittle at low temperatures and increase the risk of thermal cracking. Therefore, the decrease in penetration should not be interpreted as a solely positive indicator; the low-temperature behavior of the modified binders should also be evaluated in subsequent stages.

3.2 Softening Point Test Results

The softening point results of the neat and modified bitumens are presented in Figure 2. The softening point of the neat bitumen was determined as 50.2 °C. With the incorporation of POE and nanoclay additives, a gradual increase in softening point values was observed. This increase indicates that the modified bitumens became more resistant to softening at elevated temperatures.

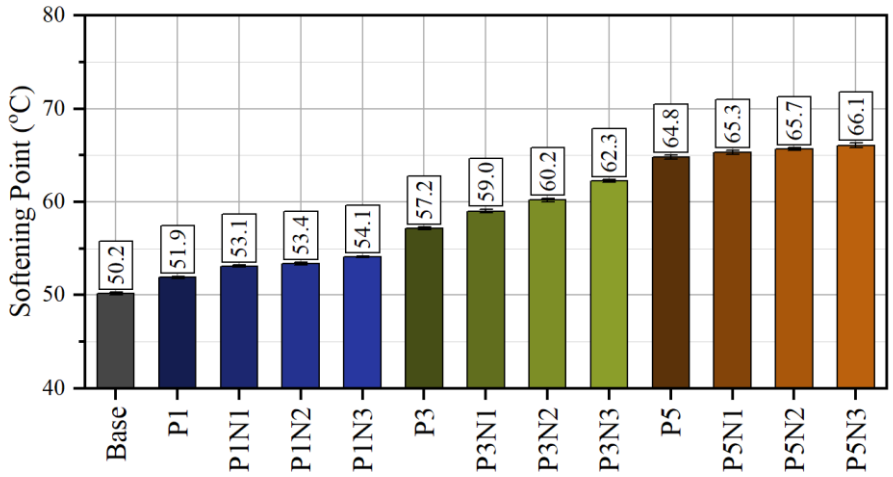


Fig. 2. Softening point test results.

In the P1 group, the softening point was 51.9 °C for the P1 sample and increased to 54.1 °C for P1N3. In the P3 group, the softening point values were obtained as 57.2 °C for P3 and 62.3 °C for P3N3. The highest values were observed in the P5 group, where the softening point increased from 64.8 °C for P5 to 66.1 °C for P5N3. Compared with the neat bitumen, the highest increase was again obtained for the P5N3 sample, with an increase of 15.9 °C.

The findings indicate that the POE content was the dominant component governing the increase in softening point. As the POE level increased from P1 to P5, the improvement in softening point became more pronounced. Nanoclay, on the other hand, played a complementary role by slightly increasing the softening point within each POE group.

However, the contribution of nanoclay remained more limited compared with that of POE; for example, in the P5 group, the increase from N1 to N3 was restricted to only a few degrees Celsius. This suggests that the dominant effect on the softening point originated from the polymer phase, while nanoclay mainly served as a supporting component.

The consistency between the penetration and softening point results indicates that the composite additive consistently improved the high-temperature performance of the binder. A higher softening point suggests the potential of the binder to limit consistency loss under hot climatic conditions and heavy traffic loading. In this respect, the POE/Nanoclay system can be considered a modification approach that enhances the thermal stability of bitumen.

3.3 Penetration Index Results

To evaluate the temperature susceptibility of bitumen in a more comprehensive manner, the penetration index (PI) values calculated from the penetration and softening point results are presented in Figure 3. The PI value of the neat bitumen was calculated as -1.07. The same PI value was also obtained for the P1 sample, while only a limited improvement was observed in the P1N1 and P1N2 samples with the addition of nanoclay. The fact that the PI values of the P1 group remained in the negative range indicates that temperature susceptibility could not be sufficiently reduced at low POE content. This suggests that the polymer network formed at this level was insufficient to balance the temperature-dependent changes in binder consistency.

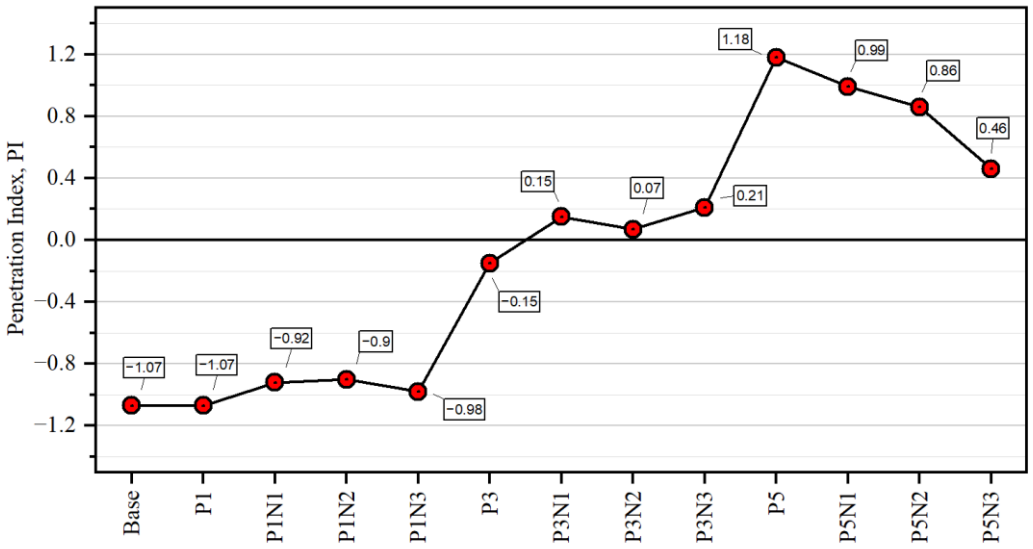


Fig. 3. PI values.

A more pronounced improvement was observed in the P3 group. While the PI value of the P3 sample was -0.15, the PI values of P3N1, P3N2, and P3N3 were calculated as 0.15, 0.07, and 0.21, respectively, shifting into the positive range. The transition of PI from negative to positive indicates that the binder can better maintain its consistency against temperature variations and exhibits a less temperature-susceptible behavior. This finding suggests that the use of POE at an intermediate content, particularly in combination with nanoclay, creates an effective threshold for reducing temperature susceptibility.

The P5 group exhibited the highest PI values. The PI value was determined as 1.18 for the P5 sample, while values of 0.99, 0.86, and 0.46 were obtained for P5N1, P5N2, and P5N3, respectively. Although this group generally showed the lowest temperature susceptibility, a

gradual decrease in PI was notably observed with increasing nanoclay content. Therefore, at high POE dosage, excessive nanoclay addition does not always provide an additional benefit in terms of temperature susceptibility, despite increasing binder stiffness. Similarly, it has been reported in the literature that excessive nanoclay dosage may increase the tendency for interlayer agglomeration, thereby limiting the expected contribution [9].

These findings emphasize the need for a multi-criteria approach in determining the optimum additive content. When the highest stiffness (lowest penetration) or the highest softening point is considered alone as a performance indicator, the composition providing the most balanced behavior in terms of temperature susceptibility may be overlooked. When the three parameters are evaluated together, the most balanced behavior between temperature stability and stiffness improvement appears to be achieved in the P3 group, particularly in the compositions where POE was used together with nanoclay. Although the P5 group provided the lowest temperature susceptibility, it should be further examined in terms of low-temperature performance due to its high stiffness level.

4 Conclusions

In this study, the effect of the POE/Nanoclay composite additive on the physical properties of 50/70 penetration grade bitumen was evaluated through penetration, softening point, and penetration index tests. The modified binders prepared with different POE and nanoclay contents were comparatively examined with the neat bitumen, and the main findings are summarized below:

- The combined use of POE and nanoclay additives caused a significant decrease in penetration values. The penetration value of the neat bitumen, which was 53.0 dmm, gradually decreased with increasing additive content, and the lowest value was obtained as 24.8 dmm for the P5N3 sample. This decrease indicates that the composite additive increased the consistency of the bitumen and transformed the binder into a stiffer structure. The decrease in penetration with increasing nanoclay content in each POE group demonstrates that nanoclay produced a stiffening and structure-reinforcing effect within the composite system.
- The softening point results supported the penetration findings. The softening point of the neat bitumen, which was 50.2 °C, increased steadily with additive incorporation and reached 66.1 °C for the P5N3 sample. This increase indicates that the modified binders softened at higher temperatures compared with the neat bitumen. It was determined that the POE content was the dominant component governing the increase in softening point, while nanoclay played a complementary role.
- The penetration index results more clearly revealed the effect of the composite additive on temperature susceptibility. In the P1 group, the PI values remained in the negative range, indicating that temperature susceptibility could not be sufficiently reduced at this additive level. In contrast, in the P3 group, particularly with the addition of nanoclay, the PI values shifted into the positive range, showing that this level provided a more balanced binder behavior against temperature variations. The P5 group exhibited the highest PI values and, therefore, the lowest temperature susceptibility.
- However, in the P5 group, a gradual decrease in PI values was observed with increasing nanoclay content. This finding indicates that increasing nanoclay content at a high POE level does not always produce a more favorable result and that the optimum additive content should not be determined solely based on the highest stiffness or the highest softening point. Therefore, penetration, softening point, and penetration index results should be considered together when evaluating additive contents.

Overall, the POE/Nanoclay composite additive improved the physical stability of bitumen, increased its stiffness, and enhanced its resistance to softening at elevated temperatures. The results obtained especially in the P3 and P5 groups indicate that composite modification is effective in reducing temperature susceptibility. However, physical test results alone are not sufficient to determine the optimum modification content. In future studies, aging resistance, storage stability, rheological properties, and asphalt mixture performance should be evaluated together. In this context, it was concluded that the POE/Nanoclay composite additive is a usable and promising additive system for bitumen modification.

Acknowledgments
This study was supported by the Scientific Research Projects (BAP) Coordination Unit of Karadeniz Technical University within the scope of a BAP06 – Postgraduate Thesis Project (Project No. FDK-2025-16457). The authors would like to thank Karadeniz Technical University for this support.

References

1. Yang, C., Wu, S., Cui, P., Amirkhanian, S., Zhao, Z., Wang, F., Zhang, L., Wei, M., Zhou, X., Xie, J.: Performance characterization and enhancement mechanism of recycled asphalt mixtures involving high RAP content and steel slag. J. Clean. Prod. 336, 130484 (2022). https://doi.org/10.1016/j.jclepro.2022.130484
2. Zhao, Y., Song, J., Xie, J., Wang, F., Chen, M., Wu, S.: Evaluation of the volume stability and resource benefit of basic oxygen furnace slag and its asphalt mixture based on field application. Adv. Civ. Eng. 2021, 1–10 (2021). https://doi.org/10.1155/2021/6676154
3. Li, Y., Feng, J., Yang, F., Wu, S., Liu, Q., Bai, T., Liu, Z., Li, C., Gu, D., Chen, A., Jin, Y.: Gradient aging behaviors of asphalt aged by ultraviolet lights with various intensities. Constr. Build. Mater. 295, 123618 (2021). https://doi.org/10.1016/j.conbuildmat.2021.123618
4. Zhao, Y., Chen, M., Wu, S., Jiang, Q.: Rheological properties and microscopic characteristics of rejuvenated asphalt using different components from waste cooking oil. J. Clean. Prod. 370, 133556 (2022). https://doi.org/10.1016/j.jclepro.2022.133556
5. Han, X., Mao, S., Xu, S., Yu, J., Cao, Z., Wang, R., He, P., Zeng, S.: Effects of reactive chain extension rejuvenation systems on the viscosity–temperature characteristics, rheological properties, and morphology of aged styrene–butadiene–styrene-modified bitumen. ACS Sustain. Chem. Eng. 9(48), 16474–16484 (2021). https://doi.org/10.1021/acssuschemeng.1c06717
6. Cao, Z., Chen, M., Yu, J., Han, X.: Preparation and characterization of active rejuvenated SBS modified bitumen for the sustainable development of high-grade asphalt pavement. J. Clean. Prod. 273, 123012 (2020). https://doi.org/10.1016/j.jclepro.2020.123012
7. Yang, X., Zhang, H., Zheng, W., Chen, Z., Shi, C.: A novel rejuvenating method for structural and performance recovery of aged SBS-modified bitumen. ACS Sustain. Chem. Eng. 10(4), 1565–1577 (2022). https://doi.org/10.1021/acssuschemeng.1c07035
8. Mahmood, Q., Sun, W.-H.: N,N-chelated nickel catalysts for highly branched polyolefin elastomers: a survey. R. Soc. Open Sci. 5(7), 180367 (2018). https://doi.org/10.1098/rsos.180367
9. Yao, H., You, Z., Li, L., Shi, X., Goh, S.W., Mills-Beale, J., Wingard, D.: Performance of asphalt binder blended with non-modified and polymer-modified nanoclay. Constr. Build. Mater. 35, 159–170 (2012). https://doi.org/10.1016/j.conbuildmat.2012.02.056
10. Ameri, M., Mohammadi, R., Vamegh, M., Molayem, M.: Evaluation the effects of nanoclay on permanent deformation behavior of stone mastic asphalt mixtures. Constr. Build. Mater. 156, 107–113 (2017). https://doi.org/10.1016/j.conbuildmat.2017.07.055

11. Ezzat, H., El-Badawy, S., Gabr, A., Zaki, E.-S.I., Breakah, T.: Evaluation of asphalt binders modified with nanoclay and nanosilica. Procedia Eng. 143, 1260–1267 (2016). https://doi.org/10.1016/j.proeng.2016.06.119
12. Iskender, E.: Evaluation of mechanical properties of nano-clay modified asphalt mixtures. Measurement 93, 359–371 (2016). https://doi.org/10.1016/j.measurement.2016.07.045
13. Martinho, F.C.G., Farinha, J.P.S.: An overview of the use of nanoclay modified bitumen in asphalt mixtures for enhanced flexible pavement performances. Road Mater. Pavement Des. 20(3), 671–701 (2019). https://doi.org/10.1080/14680629.2017.1408482
14. Moussa, G.S., Abdel-Raheem, A., Abdel-Wahed, T.: Effect of nanoclay particles on the performance of high-density polyethylene-modified asphalt concrete mixture. Polymers 13(3), 434 (2021). https://doi.org/10.3390/polym13030434
15. Ren, Z., Zhu, Y., Wu, Q., Zhu, M., Guo, F., Yu, H., Yu, J.: Enhanced storage stability of different polymer modified asphalt binders through nano-montmorillonite modification. Nanomaterials 10(4), 641 (2020). https://doi.org/10.3390/nano10040641
16. Yang, J., Tighe, S.: A review of advances of nanotechnology in asphalt mixtures. Procedia Soc. Behav. Sci. 96, 1269–1276 (2013). https://doi.org/10.1016/j.sbspro.2013.08.144
17. You, Z., Mills-Beale, J., Foley, J.M., Roy, S., Odegard, G.M., Dai, Q., Goh, S.W.: Nanoclay-modified asphalt materials: preparation and characterization. Constr. Build. Mater. 25(2), 1072–1078 (2011). https://doi.org/10.1016/j.conbuildmat.2010.06.070
18. Yu, J., Ren, Z., Yu, H., Wang, D., Svetlana, S., Korolev, E., Gao, Z., Guo, F.: Modification of asphalt rubber with nanoclay towards enhanced storage stability. Materials 11(11), 2093 (2018). https://doi.org/10.3390/ma11112093
19. TS EN 1426: Bitumens and bituminous binders — Determination of needle penetration. Turkish Standards Institution, Ankara (2015).
20. TS EN 1427: Bitumen and bituminous binders — Determination of the softening point — Ring and Ball method. Turkish Standards Institution, Ankara (2015).

Author Contribution Statement

- *Conceptualization:* Ersoy KABADAYI, Şeref Oruç
- *Methodology:* Ersoy Kabadayı, Aytuğ Kumandaş, Neslihan Şahan,
- *Investigation:* Ersoy Kabadayı, Erman Çavdar
- *Writing – Original Draft:* Ersoy Kabadayı, Erman Çavdar, Aytuğ Kumandaş, Neslihan Şahan, Mahir Kumantaş
- *Writing – Review & Editing:* Ersoy Kabadayı, Erman Çavdar, Şeref Oruç

List of Abbreviations

- **POE** — Polyolefin Elastomer
- **SBS** — Styrene-Butadiene-Styrene
- **PI** — Penetration Index
- **SP** — Softening Point
- **Pen_{25}** — Penetration Value at 25 °C
- **KTŞ** — Turkish Highway Technical Specification
- **UV** — Ultraviolet
- **PP** — Polypropylene
- **PE** — Polyethylene

Publication Note
This paper was peer-reviewed, accepted for presentation, and included in the proceedings of the ACE2026 – International Conference on Advances in Civil Engineering, held on 12–13 October 2026 in Trabzon, Türkiye.

This paper may be cited as follows:
Kabadayı, E., Çavdar, E., Kumandaş, A., Kumantaş, M., Şahan, N. and Oruç, Ş., "Evaluation of Physical Properties of POE/Nanoclay Composite Modified Bitumen," in Proceedings of the ACE2026 – International Conference on Advances in Civil Engineering, Trabzon, Türkiye, 12–14 October 2026.

Operational Characteristics of Queue Discharge Flow at Closely Spaced Signalized Intersections

Ruti Politi[1] and Serhan Tanyel[2]
[1] 0000-0001-7851-2506, İzmir University of Economics, Civil Engineering Department, İzmir, Türkiye, ruti.politi@ieu.edu.tr
[2] 0000-0001-8549-9442, Dokuz Eylül University, Civil Engineering Department, İzmir, Türkiye, serhan.tanyel@deu.edu.tr

Abstract. Closely spaced signalized intersections are characterized by strong operational interactions that may lead to queue spillbacks, increased delays, and reduced capacity. Despite the importance of driver behavior in intersection performance, limited attention has been given to start response times in such systems. This study examines driver start response times and queue discharge headways at closely spaced signalized intersections located on an urban arterial in İzmir, Türkiye. Approximately 14 hours of video recordings were analyzed to obtain start response times, traffic volumes, vehicle compositions, cycle lengths, and queue characteristics. A total of 3173 start response time observations were extracted. Statistical analyses were conducted to compare upstream and downstream intersections, evaluate distributional characteristics, and quantify influencing factors. Lane-based t-tests revealed statistically significant differences between upstream and downstream intersections at the 95% confidence level for all lane groups, with downstream drivers exhibiting longer start response times. Distribution fitting results showed that start response times are positively skewed and are best represented by Lognormal distributions in most cases, while Gamma and Weibull distributions provided acceptable fits for selected lane groups. These findings indicate that start response time should be treated as a stochastic variable in capacity analysis and microscopic traffic simulation. Multiple regression analysis further demonstrated that vehicle type, signal location, traffic period, and lane type significantly influence driver start response time. In particular, downstream location and heavy vehicles were associated with increased response times. The findings contribute practical implications for signal coordination, capacity estimation, and simulation modeling of closely spaced signalized intersections.

Keywords: closely spaced intersections; start response time; queue discharge headway; driver behavior.

1 Introduction

Closely spaced intersections are defined as signalized intersections located close to another one such that they may mutually influence traffic operations. These intersections may operate either under a single signal control system utilizing offset timing within the same cycle length or under different signal [1]. In such systems, the short distance between intersections, low travel speeds, and vehicle interactions contribute significantly to increase delays. In addition, queues formed between adjacent intersections may restrict minor street traffic movements, while vehicles entering between upstream and downstream signals from minor approaches may block the progression of major traffic streams [2]. Therefore, coordinated signal control systems should be properly designed to minimize excessive stop-and-go movements and delays while

maximizing uninterrupted vehicle movement through closely-spaced intersections [3]. Recent studies have emphasized that queue spillbacks and downstream congestion can significantly affect the performance of coordinated arterial systems and may reduce the effectiveness of conventional signal timing strategies [4].

The capacity and operational performance of signalized intersections largely depend on driver's behavior. Previous studies have demonstrated that the most critical driver-related parameters at signalized intersections are start-up lost time and saturation headway [5]. Both parameters are directly influenced by the start response time of the leading drivers within a queue [6]. Although these parameters have been extensively investigated for isolated intersections, studies focusing on closely spaced intersections remain limited.

Within the scope of this study, driver start response times and queue discharge headways at closely spaced signalized intersections located on an urban arterial in İzmir, Türkiye, were investigated. Approximately 14 hours of video recordings were analyzed to obtain start response times, queue discharge headways, traffic volumes, vehicle compositions, cycle lengths, and queue lengths. Statistical analyses were conducted to examine differences between upstream and downstream intersections and to evaluate the effects of vehicle type, traffic conditions, and lane characteristics on driver behavior. The findings are expected to contribute to capacity analysis, microscopic traffic simulation, and signal optimization applications for closely spaced signalized intersections.

2 Study Area and Data Collection

2.1 Study Area

This study was conducted on a closely spaced signalized intersection system located in Karabağlar, İzmir, Türkiye. The study area consists of two adjacent signalized intersections operating under coordinated traffic control. The intersections are located on a major urban arterial characterized by high traffic demand and heterogeneous traffic composition. Fig. 1 presents the closely spaced intersection system, where the upstream intersection (K1) and downstream intersection (K2) are indicated. The distance between the stop lines of the upstream and downstream intersections is approximately 50 m, resulting in strong operational interactions between the two signalized junctions.



Fig. 1. Study area of closely spaced signalized intersection system in Karabağlar, İzmir, Türkiye.

The study site was selected due to its high traffic demand and representative urban corridor characteristics. The selected configuration represents a typical closely-spaced intersection system where upstream and downstream signals may interact through queue formation and spillback effects. Detailed geometric and operational characteristics of the study intersections are provided in Table 1.

Table 1 Geometric and operational characteristics of study K1 and K2 intersections.

Intersection	Approach	Volume (veh/h/lane)	Lane Movement	Cycle Length (s)
K1 (Upstream)	Left	1353	Through (TR)	85
	Through	1185	TR	85
	Right	1124	TR / Right-turn (RT)	85
K2 (Downstream)	Left	1342	TR	85
	Through	1132	TR	85
	Right	859	TR / RT	85

2.2 Data Collection Procedure

Traffic data was collected using fixed-positioned video camera recordings under dry weather conditions and during typical weekday traffic operations [7]. A total of approximately 14 hours of continuous video data were recorded, covering morning, midday, and evening peak periods.

The study area consists of two closely spaced signalized intersections, and data were collected from both upstream and downstream approaches. A total of 17 video segments were analyzed, each with an average duration of approximately 53 minutes, ensuring a balanced temporal distribution across different traffic states.

From the recorded videos, the following traffic parameters were extracted for subsequent analysis: driver start response times, queue discharge headways, traffic volumes with turning movement (left, through, right), vehicle composition, signal cycle lengths, phase structures, and queue lengths at each approach. In total, start response time observations were obtained from the analyzed video data, enabling a detailed lane-based and intersection-level evaluation of driver behavior under closely-spaced intersection conditions.

2.3 Data Extraction Process

Microscopic traffic variables were extracted using a frame-by-frame analysis of video recordings. Vehicle movements and signal phase transitions were manually identified, and the occurrence time of each event was determined from the video data. These measurements enabled the derivation of time-dependent traffic parameters, including start response time and vehicle headways, which were subsequently used in the saturation flow analysis [5].

The start response time was defined as the time interval between the onset of the effective green indication and the initiation of movement of the first queued vehicle [5]. Similarly, queue discharge headway was defined as the time difference between successive departing vehicles within the same queue [8].

Although minor measurement errors can be observed in video-based traffic studies, special attention was given to the extraction of traffic variables from the recordings. The collected data were carefully reviewed and cross-checked during the analysis process to improve accuracy and minimize potential observational biases [9].

3 Methodology

The study follows a multi-stage analytical framework. The methodology begins with data preparation, where the dataset is classified according to intersection location (upstream and downstream) and lane type (left, through, right). This classification allows the examination of

driver behavior under different spatial and operational conditions within the closely spaced intersection system.

In the second stage, descriptive statistical analysis and probability distribution fitting are conducted to characterize the statistical properties of driver start response times and queue discharge headways. Common probability distributions, including Lognormal, Gamma, Weibull, and Exponential distributions, are evaluated. The best-fitting distribution for each dataset is selected based on goodness-of-fit measures, including the Kolmogorov-Smirnov, Anderson-Darling, and Chi-square tests.

The third stage involves statistical analysis to examine differences between upstream and downstream intersections across lane groups. Independent samples t-tests are conducted under a 95% confidence level to determine whether statistically significant differences exist between mean start response times.

In the final stage, multiple linear regression analysis is performed to quantify the effects of traffic-related and operational variables on driver start response time. The dependent variable is start response time, while explanatory variables include vehicle type, traffic period (peak/off-peak), lane type, and intersection location. The model is used to quantify behavioral differences and their impact on intersection performance.

3.1 Statistical Analysis

Descriptive statistical analyses were first performed to summarize the characteristics of the collected start response time and queue discharge headway data. Mean, standard deviation, minimum, maximum, skewness, and kurtosis values were calculated to examine the central tendency, variability, and distributional properties of the observations.

3.2 Distribution Fitting

Probability distribution fitting is conducted using EasyFit software to identify distributions that best represent driver start response times [10]. Candidate distributions include Lognormal, Gamma, Weibull, and Exponential distributions. Goodness-of-fit evaluation is performed using Kolmogorov-Smirnov, Anderson-Darling, and Chi-square tests, and the best-fitting distribution is selected based on combined statistical performance.

3.3 Hypothesis Testing

t-tests are conducted to examine whether statistically significant differences exist between upstream and downstream intersections using SPSS software. The analyses are performed separately for left, through, and right lanes. The null hypothesis assumes no difference in mean start response times between intersection locations, while the alternative hypothesis assumes a statistically significant difference at the 95% confidence level.

3.4 Multiple Regression Analysis

Multiple linear regression analysis was employed to evaluate the effects of several explanatory variables on driver start response time. The dependent variable is start response time, while vehicle type, signal location, peak-period category, and lane type were considered as independent variables. The regression model was used to quantify the relative contribution of each factor and to identify the variables significantly influencing driver behavior.

4 Results and Discussion

Within the scope of this study, driver start response times and queue discharge headways at closely-spaced signalized intersections located on an urban arterial in the city center of İzmir, Türkiye, were investigated, and the effects of these parameters on intersection performance were examined. Interactions between upstream and downstream intersections in closely-spaced

systems may result in significant operational consequences, particularly in terms of queue spillbacks, delays, and capacity reductions.

4.1 Queue Discharge Headway

Left-turn lanes generally exhibited shorter discharge headways than through and right-turn lanes. As presented in Table 2, the mean queue discharge headways ranged from 2.30 s to 3.28 s. These findings are consistent with the ranges reported by Jin, et al. [11] and Çalişkanelli and Tanyel [5]. These differences may be attributed to lane-specific saturation behavior and varying driver aggressiveness across turning movements.

Table 2 Mean queue discharge headways by lane and intersection.

Lane	Signal 1 Mean (s)	Signal 2 Mean (s)
Left	2.46	2.30
Through	2.76	2.58
Right	3.15	3.28

4.2 Descriptive Statistics of Start Response Times

The findings indicated that drivers at the downstream signal exhibited longer start response times compared with drivers at the upstream signal. Mean response times ranged between 0.99 s and 1.26 s which can be seen in Table 3. All distributions exhibited positive skewness, indicating that most drivers respond quickly after green onset, while a smaller portion exhibits delayed reactions. The peaks of the distributions correspond to the modal values, indicating the most frequently observed start response times.

Table 3 Descriptive statistics of start response times.

Lane	N	Mean	Std. Dev.	Skewness	Kurtosis	Peak
Left 1	601	1.04	0.50	2.48	10.10	0.80
Left 2	392	1.11	0.47	1.41	2.54	0.82
Through 1	604	0.99	0.40	1.36	2.08	0.95
Through 2	496	1.19	0.57	2.58	12.98	0.90
Right 1	602	0.99	0.44	1.88	5.86	0.82
Right 2	478	1.26	0.55	1.79	5.99	0.98

Based on the results of the t-test conducted to examine differences between groups, statistically significant differences were identified between the two groups (K1 and K2) for each lane type. Therefore, the data from the two signals were analyzed separately. Subsequently, the observations were grouped according to peak periods (morning, midday, and evening), and probability density functions were re-established for each peak period.

4.3 Comparison of Upstream and Downstream Intersections

t-test results confirm statistically significant differences between upstream and downstream intersections for all lane groups at the 95% confidence level (Table 4). Downstream intersections consistently show higher start response times, indicating delayed driver reactions under downstream operational conditions.

These differences may be explained by residual queue effects and upstream platoon dispersion, which increase driver hesitation at downstream intersections.

The presence of two local peaks in the response time distribution which can be seen in Fig. 2 suggests the possibility of heterogeneous driver response behavior. Fig. 2a presents the probability density function (PDF) distributions of start response times, and Fig. 2b, Fig. 2c, and Fig. 2d illustrate the distribution of start response times for the left-turn, through, and right-

turn lanes, respectively. This bimodal tendency may be associated with differences in driver attentiveness, vehicle type, traffic demand conditions, or operational interactions between the upstream and downstream intersections. In closely-spaced signalized systems, residual queue effects and platoon progression may contribute to the formation of distinct response patterns.

Table 4 Lane-based t-test results.

Lane	Mean K1	Mean K2	t-statistic	p-value
Left	1.04	1.11	-2.08	0.038
Through	1.01	1.19	-6.03	<0.001
Right	1.04	1.26	-6.71	<0.001

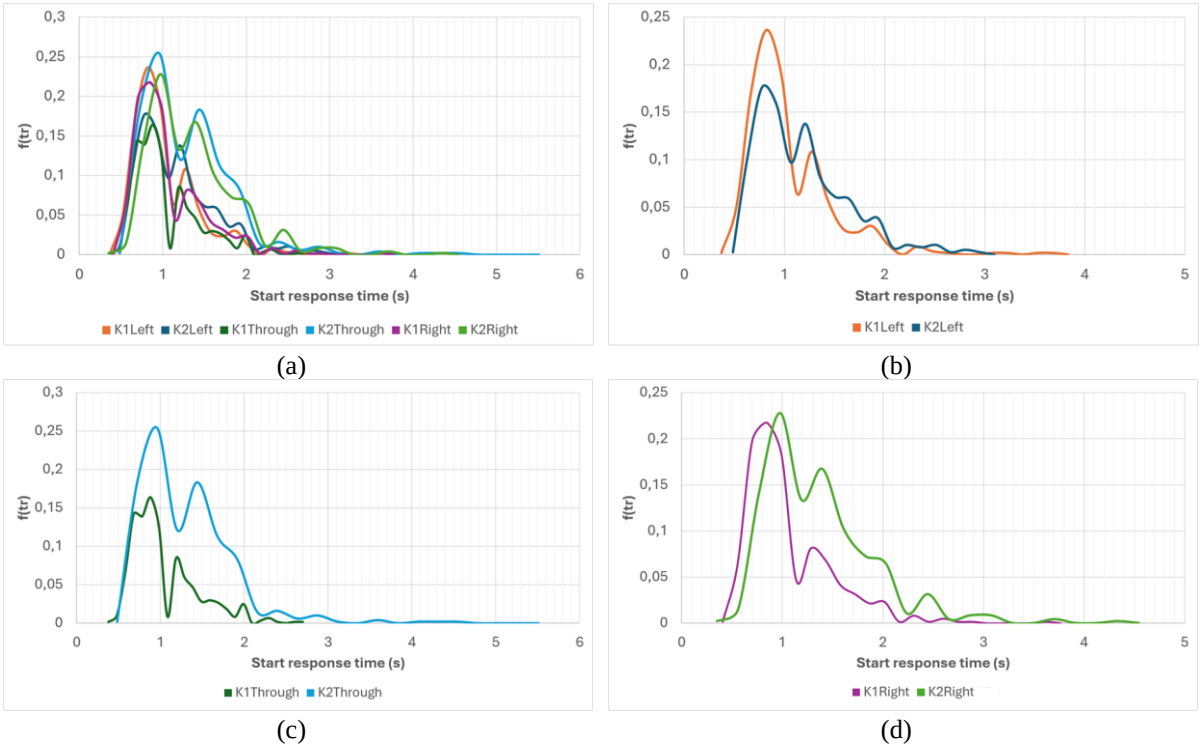


Fig. 2 Probability density functions of start response times for (a) all lane groups, (b) left lane groups, (c) through lane groups, and (d) right lane groups.

As shown in Fig. 3, the probability density functions of start response times vary across peak periods and lane groups. The distributions are presented separately for the K1 and K2 intersections for the left-turn, through, and right-turn movements. The secondary peak becomes more pronounced during the evening peak period, suggesting the presence of heterogeneous driver response behavior under higher traffic demand and more complex operational conditions.

4.4 Distribution Characteristics

Start response time data were found right-skewed. In most lane groups, the Lognormal distribution provided the best fit, while Gamma and Weibull distributions were more suitable for selected cases. These results suggest that driver response behavior is not adequately represented by a normal distribution and is better characterized by asymmetric probability distributions. Table 5 presents the best-fitting distributions obtained for each lane group.

The identification of suitable probability distributions is important because start response times directly affect queue discharge processes and intersection capacity. The results indicate that driver response behavior is generally stochastic and cannot be adequately represented by a

single deterministic value. Therefore, incorporating probabilistic representations of start response times may improve the realism of capacity analyses and microscopic traffic simulation models for closely-spaced signalized intersections.

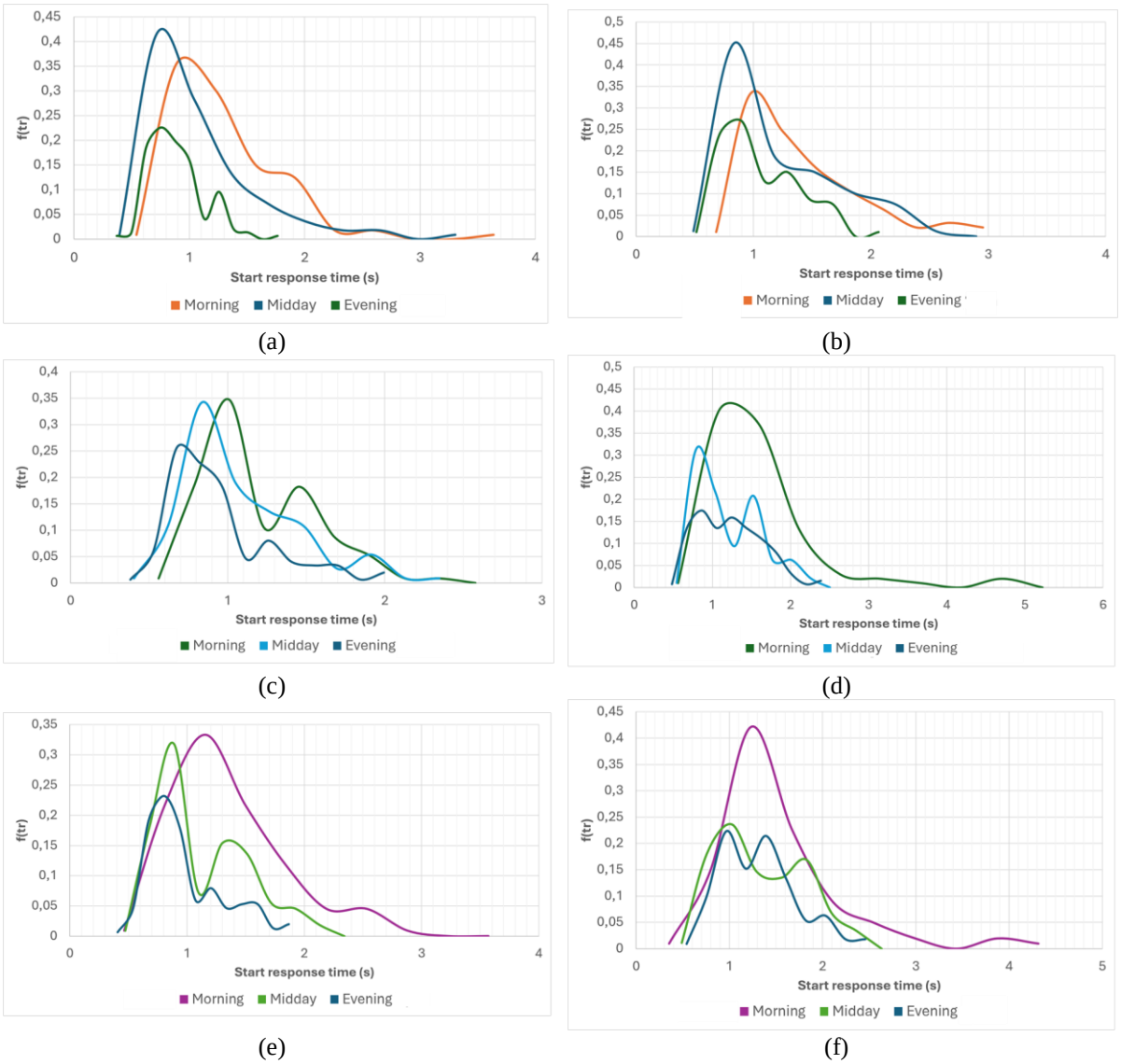


Fig. 3 Probability density functions of start response times during different peak period for (a) K1 left lane group, (b) K2 left lane groups, (c) K1 through lane groups, (d) K2 through lane groups, (e) K1 right lane groups and (f) K2 right lane groups.

Table 5 Best-fitting distributions.

Lane Group	**Best-fitting distribution**
Left 1	Lognormal
Left 2	Gamma
Through 1	Lognormal
Through 2	Weibull
Right 1	Lognormal
Right 2	Lognormal

4.5 Regression Model Results

Previous studies have shown that driver start response time may be affected by both behavioral and operational factors. While Akçelik, et al. [12] treated start response time as a constant parameter, Çalişkanelli and Tanyel [5] demonstrated that factors such as turning movement, driver characteristics, lane geometry, and signal timing may significantly influence driver response behavior. Therefore, multiple regression analysis was employed to investigate the effects of vehicle type, signal location, traffic period, and lane type on start response time. Table 6 presents the descriptive statistics of the variables included in the regression analysis.

Multiple linear regression analysis was conducted to quantify the effects of explanatory variables on start response time. The model is statistically significant, and all included variables were found to be significant predictors ($p < 0.05$).

Table 6 Descriptive statistics of variables used in the regression model.

Variable	**Mean**	**Std. Dev.**
Start response time (t_r) (s)	1.108	0.524
Vehicle type (VT)	1.42	0.875
Signal location (SL)	1.54	0.498
Traffic period (TP)	2.06	0.836
Lane type (LC)	1.79	0.730

Table 7 presents the regression coefficients. Vehicle type, signal location, traffic period, and lane type were all found to be statistically significant predictors of start response time ($p < 0.05$). The independent variables considered in the regression analysis were vehicle type (VT), signal location (SL), traffic period (TP), and lane category (LC). Vehicle type was coded as passenger car = 1, bus = 2, minibus = 3, and truck = 4. Traffic period was coded as morning peak = 1, midday peak = 2, and evening peak = 3, while lane category was coded as left = 1, through = 2, and right = 3. Signal location was used as upstream = 1, and downstream = 2.

Table 7 Multiple regression results.

Variable	**Coefficient**	**p-value**
Vehicle Type	0.065	<0.001
Signal Location	0.178	<0.001
Traffic Period	-0.113	<0.001
Lane Category	0.037	0.046

The estimated regression model is given in Equation (1).

$$t_r = 0.909 + 0.065VT + 0.178SL - 0.113TP + 0.037LC \quad (1)$$

Signal location emerges as the most influential variable, indicating that downstream intersections are associated with systematically higher response times. This may be attributed to cumulative queuing effects and reduced driver expectation consistency in downstream operations. Vehicle type also significantly affects response behavior, with heavy vehicles exhibiting longer reaction times due to increased inertia and lower acceleration capability. Lane category and traffic period show comparatively smaller but still statistically significant effects.

Traffic period exhibits a negative coefficient, suggesting that response times slightly decrease during later peak periods, possibly due to increased driver familiarity and adaptation under congested conditions. Although categorical variables were encoded numerically, sensitivity checks confirm that model stability remains acceptable and multicollinearity effects are not dominant.

4.6 Implications of Start Response Time Variability in Closely-Spaced Signalized Intersections

The findings indicate that downstream intersections consistently exhibit longer start response times, with log-normal distributions best representing driver behavior in most cases. Vehicle type, lane configuration, and traffic period significantly influenced driver response characteristics. These results suggest that start response time should not be treated as a constant parameter in capacity and simulation models, particularly for closely spaced signalized intersections. Instead, it should be modeled as a stochastic and context-dependent variable influenced by traffic composition and spatial signal interactions.

5 Conclusion

Start response time and headway observations were analyzed from a closely spaced signalized intersection system in İzmir, Türkiye, covering different vehicle types and traffic conditions across upstream and downstream locations. The descriptive statistics indicated that drivers at the downstream intersection generally exhibited longer start response times than those at the upstream intersection. This finding suggests that operational interactions between adjacent signalized intersections may influence driver response behavior.

Distribution analyses showed that all start response time datasets were positively skewed. Most datasets were adequately represented by lognormal distributions, while Gamma and Weibull distributions provided satisfactory fits for selected lane groups. These results indicate that start response times should be treated as stochastic variables rather than fixed values in capacity analysis and traffic simulation applications. Therefore, fixed-value assumptions may not fully capture driver start-up behavior in capacity and simulation models.

To investigate differences between the two signal locations, lane-based hypothesis tests were conducted. The results demonstrated statistically significant differences between the upstream and downstream intersections at the 95% confidence level for all analyzed lane groups. This finding supports the hypothesis that closely-spaced signalized intersections may generate distinct driver response characteristics depending on their position within the coordinated intersection system.

Regression results indicated that start response times were influenced by vehicle type, signal location, traffic period, and lane category. Overall, the findings highlight the importance of considering driver response variability when analyzing and coordinating closely-spaced signalized intersections. The results may contribute to more realistic capacity estimation, traffic simulation, and signal timing applications.

These findings demonstrate that start response time is influenced by intersection location within a closely spaced signalized system and can be treated as a stochastic parameter in capacity analysis, traffic simulation, and signal timing applications. Future studies may investigate the effects of additional traffic, geometric, and behavioral factors using more advanced data-driven modeling approaches.

References

[1] A.-B. Shu, D.-B. Liu, Q. Fu, et al.: Optimization of Signal Coordination for Closely Spaced Intersections, In 4th International Conference on Transportation Information and Safety (ICTIS) Banff, Canada, (2017).

[2] K. Ahmed, G. Abu-Lebdeh, and B. Al-Omari: Estimation of Delay Induced by Downstream Operations at Signalized Intersections over Extended Control Time, Journal of Transportation Engineering, 139(1), 8-19, (2013).

[3] F. Ahmed and Y. E. Hawas: An integrated real-time traffic signal system for transit signal priority, incident detection and congestion management, Transportation Research Part C: Emerging Technologies, 60, 52-76, (2015).

[4] Q. Wang, J. Severino, J. Ugirumurera, et al.: Offline Arterial Signal Timing Optimization for Closely Spaced Intersections, In IEEE Green Technologies Conference (GreenTech),pp. 344-350, (2021).

[5] P. Çalişkanelli and S. Tanyel: Investigating the driver's response time at signalized intersections, Transport, 33(2), 380-388, (2016).
[6] S. P. Çalışkanelli, F. Atasever Coşkun, and S. Tanyel: Start-up Lost Time and its Effect on Signalized Intersections in Turkey, Traffic&Transportation, 29(3), 321-329, (2017).
[7] Y. Özinal Avşar, Z. B. Yıldırım, R. R. Politi, et al.: Investigation of the effect of geometric irregularities on capacity of traffic circles by using partial least squares regression method, Canadian Journal of Civil Engineering, 51(12), 1388-1408, (2024).
[8] HCM: Highway Capacity Manual, Washington, D.C. :Transportation Research Board(2000).
[9] H. Li and P. D. Prevedouros: Detailed observations of saturation headways and startup lost time, Transportation Research Board of National Academies, Journal of Transportation Research Board, 1802, 44-53, (2007).
[10] M. M. Harsha and R. H. Mulangi: Probability distributions analysis of travel time variability for the public transit system, International Journal of Transportation Science and Technology, 11(4), 790-803, (2022).
[11] X. Jin, Y. Zhang, F. Wang, et al.: Departure headways at signalized intersections: a log-normal distribution model approach, Transportation Research Part C: Emerging Technologies, 17(3), 318-327, (2009).
[12] R. Akçelik, M. Besley, and R. Roper: Fundemantal relationships for traffic flows at signalized intersections, (1999).

Author Contribution Statement

- *Conceptualization:* Ruti Politi, Serhan Tanyel
- *Methodology:* Ruti Politi, Serhan Tanyel
- *Investigation:* Ruti Politi, Serhan Tanyel
- *Writing – Original Draft:* Ruti Politi, Serhan Tanyel
- *Writing – Review & Editing:* Ruti Politi, Serhan Tanyel

List of Abbreviations

- **LC** – Lane Category
- **RT** – Right-turn
- **SL** – Signal Location
- **TP** – Traffic Period
- **TR** – Through
- **VT** – Vehicle Type
- $\mathbf{t_r}$ – Start response time

Note: Following the conference, this Publication Note will be added to each paper; therefore, authors are kindly requested not to remove the note below and to complete the author(s) and paper title information.

Publication Note

This paper was peer-reviewed, accepted for presentation, and included in the proceedings of the ACE2026 – International Conference on Advances in Civil Engineering, held on 12–14 October 2026 in Trabzon, Türkiye.

This paper may be cited as follows:

Politi R., Tanyel S., "Operational Characteristics of Queue Discharge Flow at Closely-Spaced Signalized Intersections," in Proceedings of the ACE2026 – International Conference on Advances in Civil Engineering, Trabzon, Türkiye, 12–14 October 2026.

The Role of Built Environment Perceptions in University Students' Travel Mode Choices: A Multinomial Logit Analysis

Raziye Peker[1*], Mustafa Sinan Yardım[2], Kadir Berkhan Akalın[3]
[1]*Transportation Program, Department of Civil Engineering, Graduate School of Science and Engineering, Yildiz Technical University, Istanbul 34220, Türkiye*
[2]*Department of Civil Engineering, Yildiz Technical University, Istanbul 34220, Türkiye*
[3]*Department of Civil Engineering, Eskişehir Osmangazi University, Eskişehir 26480, Türkiye*
*Corresponding Author E-mail: raziye.peker@std.yildiz.edu.tr

ABSTRACT

This study investigates university students' travel mode choices and their associations with socio-demographic characteristics, infrastructure conditions, and built-environment perceptions within the context of sustainable urban mobility. Primary data collected through an online survey of 1,087 students from seven universities representing different urban scales in Türkiye were analyzed using a multinomial logit (MNL) model in RStudio. Travel mode was classified into three categories: active transport, public transport, and private vehicle, with private vehicle serving as the reference category. The model results indicate that residing in a dormitory, having access to a personal micromobility vehicle, and holding a public transport subscription are positively associated with the relative likelihood of choosing active or public transport over a private vehicle. Conversely, car availability, higher income, holding a driving license, and residing with family are associated with a greater relative preference for private vehicle use. More favorable perceptions of pedestrian path quality, sidewalk conditions, ramp availability, and route safety are positively associated with active transport choice relative to private vehicle use. Unexpectedly, bicycle infrastructure quality was negatively associated with the relative likelihood of choosing active and public transport over private vehicles. This counterintuitive relationship warrants further investigation and should be interpreted cautiously.

Keywords: University students; Travel mode choice; Pedestrian and bicycle infrastructure; Sustainable transport, Multinomial logit.

1 Introduction

Rapid urbanization, increasing population density, and rising motor vehicle ownership contribute to serious environmental and socio-economic problems in urban areas, such as traffic congestion, air pollution, noise, and greenhouse gas emissions [1]. To reduce these negative externalities and improve urban quality of life, reducing dependence on private vehicles has become a fundamental objective of urban transportation policies [2]. Within

sustainable urban mobility policies, promoting shifts from private car use toward public transport, active modes such as walking and cycling, and emerging micromobility options such as e-scooters and e-bikes has become increasingly important [1], [3]. In particular, using sustainable modes for first- and last-mile trips can improve the accessibility, inclusivity, and efficiency of public transportation systems [3], [4].

Individuals' choices among sustainable transport alternatives depend not only on physical accessibility and travel distance but also on their perceptions of the built environment and available infrastructure [2], [5]. Research in the literature indicates that the quality of pedestrian paths, the presence of standardized sidewalks, ramp accessibility, and the general sense of route safety (perceived safety) have been identified as important factors associated with travel mode choice [5], [6]. Inadequate infrastructure, high levels of motorized traffic, and routes perceived as unsafe may discourage active travel and increase the attractiveness of motorized alternatives [7].

In this process, university students and young adults constitute an important user group of urban transportation networks and micromobility systems due to their vehicle ownership constraints, financial status, propensity for technological innovations, and campus-oriented travel patterns [1], [8]. Students' residential status, access to personal micromobility vehicles, and transit pass ownership have been found to be associated with their travel behavior [1], [9]. Conversely, dissatisfaction with infrastructure and safety concerns may reduce the attractiveness of active transport among current users [7].

This study examines university students' choices among active transport, public transport, and private vehicles and investigates their associations with socio-demographic, travel-related, infrastructural, and perceptual characteristics. Survey data were collected from 1,087 students enrolled at seven universities located in cities of different urban scales in Türkiye: Yildiz Technical University in Istanbul; Eskişehir Osmangazi University, Anadolu University, and Eskişehir Technical University in Eskişehir; Dumlupınar University and the University of Health Sciences in Kütahya; and Bayburt University in Bayburt. A multinomial logit (MNL) model was estimated in RStudio to examine factors associated with the three-category travel mode outcome [10]. By jointly considering individual and travel characteristics together with built-environment and infrastructure perceptions, the study seeks to provide evidence that can support targeted policies aimed at promoting sustainable travel choices in both campus and urban transportation planning.

2 Literature Review

In the transportation planning literature, sustainable urban mobility is commonly understood as the outcome of interactions between the objective characteristics of the built environment and travelers' subjective perceptions of those characteristics [2]. To clarify how these interactions are associated with travel behavior, the following sections review evidence on built-environment perceptions, pedestrian–micromobility interactions, and the travel behavior of university students.

2.1 Sustainable Transportation and Built Environment Perception

Individuals' decisions to use active transport modes are closely associated with how they perceive the opportunities and constraints of the surrounding built environment [2], [3], [11].While active transport modes such as walking and cycling are promoted in the literature as environmentally friendly, economical, and healthy options, whereas private vehicles and

public transport are generally considered motorized or non-active modes [2], [3], [11]. As travel distance increases, active transport generally becomes less attractive, whereas public transport and other motorized alternatives tend to become more competitive [9]. Built-environment characteristics such as population density, land-use mix, and street design can influence the use and integration of active transport and public transport [2]. Mixed land use is generally associated with shorter travel distances and improved accessibility, which can facilitate the use of sustainable transport modes [2]. However, the presence of physical infrastructure alone is not sufficient; perceptions of sidewalk quality, ramp accessibility, and pedestrian infrastructure have also been positively associated with active transport use [2], [3]. In contrast, unplanned neighborhood development, non-standard narrow sidewalks, and infrastructural deficiencies may discourage active transport use [2], [3], [6].

2.2 Pedestrian and Micromobility Interactions

Recent research suggests that perceived safety can be as important as, and in some contexts more influential than, objective crash risk in shaping travel behavior and mode choice Perceived safety, which differs from objective accident statistics, expresses an individual's level of concern about being involved in an accident or getting injured [3], [5]. Particularly in micromobility modes, perceived safety and comfort are directly linked; perceived safety and comfort are closely related and can jointly influence route and mode choice [5] The additional travel distance or time that travelers are willing to accept to avoid unsafe routes and use safer infrastructure is measured by the concept of "Value of Safety" (VoS) Research conducted within this scope shows that while e-bike users are highly willing to extend their travel times for a safer route, e-scooter users may be less willing to accept route extensions and may instead avoid the mode when routes are perceived as unsafe [3]. The proliferation of micromobility vehicles such as e-scooters and e-bikes in urban areas has given rise to new safety and comfort dynamics between pedestrians and these vehicle riders on sidewalks or shared spaces [3], [5]. When examining pedestrian perceptions and behavioral responses regarding the use of shared spaces, pedestrians' sense of safety in these interactions is directly dependent on the speed of the approaching vehicle and the lateral clearance left to the pedestrian [5]. Experiments conducted in a virtual reality environment show that when the micromobility vehicle speed is 10 km/h or less, and a lateral clearance of at least 0.86 m for e-scooters and 1.11 m for bicycles is maintained, high reported levels of comfort and perceived safety (≥99%) [5]. Based on the experimental conditions examined in that study, net sidewalk widths of approximately 2.00 m and 2.30 m, respectively, were suggested for maintaining comfortable interactions [5]. Finally, although shared spaces offer a middle ground that reduces differences in individuals' safety perceptions, it has been found that heavy e-scooter use in mixed traffic decreases pedestrians' subjective safety perception [3].

2.3 University Students' Travel Behaviors and Mode Shift Risk

University students represent a population with considerable potential for sustainable transport use because of their age profile and socio-demographic characteristics. However, infrastructure dissatisfaction may reduce their willingness to continue using active transport modes [3], [9]. Studies conducted to explain these dynamics and behavioral patterns show that socio-demographic characteristics and built environment factors have been found to be significantly associated with individual travel mode choices [2], [9]. When socio-demographic variables are examined: as age increases, students tend to steer toward active transport, while female students, individuals with high-income levels, those with a driving license, automobile or motorcycle ownership, and students living with their families show a

significantly lower propensity to prefer active transport and public transport options [1]. In contrast, students residing in dormitories, having access to personal micromobility vehicles, or holding public transport passes have been found to exhibit a greater propensity to use sustainable modes [1], [8]. As travel distance increases, the likelihood of choosing active transport generally decreases, while some studies have reported no statistically significant association between regional density and travel mode choice. [8] When pedestrian and bicycle infrastructure variables are considered, perceived pedestrian path quality, sidewalk availability, ramp accessibility, and route safety have been positively associated with active transport use [4], [5]. Previous studies also suggest that cyclists' evaluations of infrastructure conditions may be related to their travel behavior, particularly where discontinuous facilities, poor road conditions, or safety concerns reduce the attractiveness of cycling [1], [6]. Such dissatisfaction may discourage continued use of active modes and increase the relative attractiveness of more comfortable or protected motorized alternatives [6]. Therefore, campus and urban transportation planning should prioritize improvements in the continuity, quality, and safety of pedestrian and bicycle infrastructure to support the retention of active transport users and reduce the potential for shifts toward motorized modes [4], [7].

3 Data Description and Methodology

3.1 Study Area and Data Collection Process

Data were collected through an online survey of students from seven universities located in cities with different urban scales and infrastructural characteristics in Türkiye (Fig. 1). Within the scope of the study, Yildiz Technical University (Istanbul), Eskişehir Osmangazi University, Anadolu University, Eskişehir Technical University (Eskişehir), Dumlupınar University, University of Health Sciences (Kütahya), and Bayburt University were selected as the study sites.

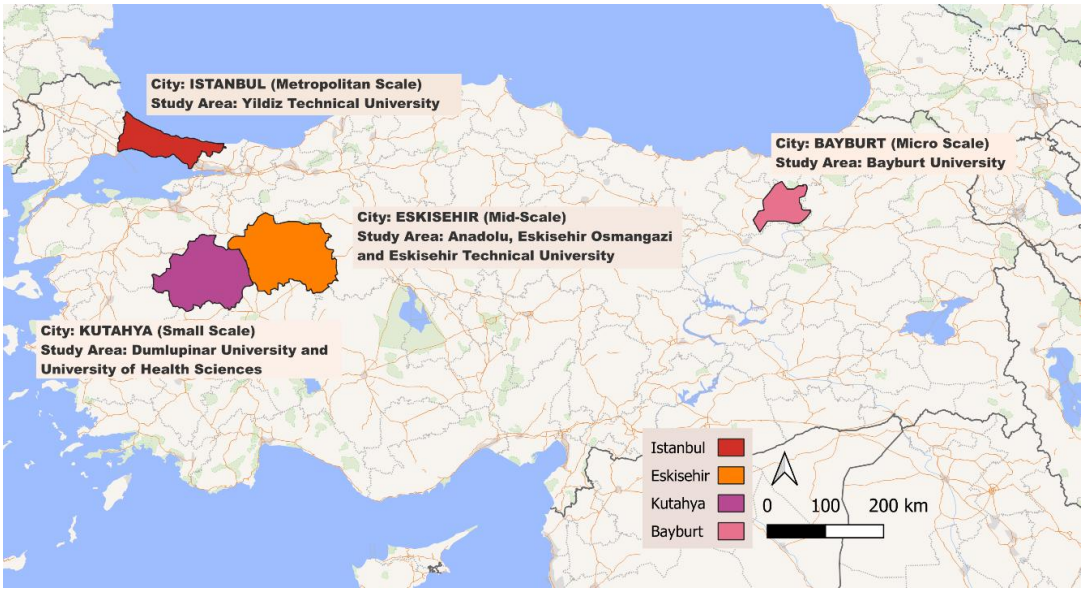


Fig. 1. Geographical distribution and urban scale classification of the seven surveyed universities in Türkiye.

The final analytical sample consisted of 1,087 students enrolled at these universities. The survey collected information on students' socio-demographic characteristics, daily campus

travel and vehicle-access characteristics, and perceptions of pedestrian and bicycle infrastructure and route safety.

Definitions and descriptive statistics of the variables used in the study are presented in Table 1. As the dependent variable, a three-category transportation mode choice was used (active transport, public transport, and private vehicle as the reference category). The independent variables consist of socio-demographic characteristics, transportation characteristics, and perceptual environmental variables.

Table 1. Variable definitions and descriptive statistics

Variable	Mean / Freq.	Type	Description
Dependent Variable			
Mode Choice		**Categorical**	Transportation mode chosen by the traveler.
Active transport	20.06%		Active transport (walking/cycling) is chosen.
Public transport	71.76%		Public transport is chosen.
Private vehicle	8.19%		Private vehicle is chosen (Reference category).
Independent Variables			
Density	1485.32	Numerical	Population or built environment density (×100 persons km^2).
Age	21.04	Numerical	Age of the traveler.
Female	50.69%	Dummy	1 if female, 0 if male.
Income	10.60	Numerical	Monthly income of the traveler (×1000 TL).
Resides with family	38.18%	Dummy	1 if the traveler resides with their family, 0 otherwise.
Resides in dormitory	24.56%	Dummy	1 if the traveler resides in a dormitory, 0 otherwise.
Driving license	54.37%	Dummy	1 if the traveler holds a driving license, 0 otherwise.
Car availability	12.88%	Dummy	1 if the traveler has access to / onws a car, 0 otherwise.
Micromobility availability	11.96%	Dummy	1 if the traveler has access to /owns a micromobility vehicle (e.g. e-scooter), 0 otherwise.
Motorbike availability	3.68%	Dummy	1 if the traveler has access to / owns a motorbike, 0 otherwise.
Travel distance	10.10	Numerical	Travel distance for the trip (km).
Public transport subscription	62.28%	Dummy	1 if the traveler holds a public transport subscription/pass, 0 otherwise.
Bicycle infrastructure quality	3.32	Ordinal	Perception of bicycle infrastructure quality (Likert scale 1-5).
Pedestrian path quality	3.78	Ordinal	Perception of pedestrian path quality (Likert scale 1-5).
Sidewalk quality	3.58	Ordinal	Perception of sidewalk availability and quality (Likert scale 1-5).
Ramp availability	3.14	Ordinal	Perception of ramp availability (Likert scale 1-5).
Safety perception	3.40	Ordinal	Perceived safety level of the route (Likert scale 1-5).

Note: All perception variables were measured on a five-point Likert scale (1 = very poor, 2 = poor, 3 = moderate, 4 = good, and 5 = very good) and were treated as continuous variables in the MNL model.

3.2 Multinomial Logit (MNL) Modeling

In this study, an MNL model was utilized to determine the factors affecting university students' transportation mode choices. The multinomial logit model is widely used to model discrete outcomes with more than two unordered alternatives and is grounded in random utility maximization theory [8], [10].

The MNL model is formulated within a linear utility function framework along with observable attributes and individual-specific characteristics. The systematic utility associated with alternative *j* for individual *i* can be expressed as: [8], [10]:

$$V_{ij} = \beta_{j0} + \Sigma_k \beta_{jk} \cdot x_{ijk} \quad (1)$$

where β_{j0} represents the alternative-specific constant for mode *j*, β_{jk} represents the alternative-specific parameters for mode *j* in the dataset with k explanatory variables, and x_{ijk} represents the vector of explanatory variables. The probability P_{ij} of individual *i* choosing mode *j* is expressed as follows [8], [10]:

$$P_{ij} = e^{(Vij)} / \Sigma_J e^{(ViJ)} \quad (2)$$

The parameters of the MNL model are estimated using the maximum likelihood method. To facilitate the estimation process, the log-likelihood (*LL*) function, which converts the product of probabilities into sums, is utilized [8], [10]:

$$LL = ln(L(\beta)) = \Sigma_i \Sigma_j \delta_{ij} \times ln(P_{ij}(\beta)) \quad (3)$$

where δ_{ij} is the choice indicator; it takes the value of 1 if individual i chooses mode *j*, and 0 otherwise.

The goodness-of-fit of the model is evaluated using the likelihood ratio (*LR*) test and *McFadden's pseudo-R²* metric. The *LR* test compares the estimated model with a reference model containing only the constant term [8], [10]:

$$LR = -2 \times (LLnull - LLmodel) \quad (4)$$

The calculated *LR* value is compared with the critical Chi-square value determined according to the degrees of freedom; if the *LR* value exceeds the critical value, it is concluded that the estimated model performs statistically significantly better than the reference model. *McFadden's pseudo-R²*, used to evaluate the model's goodness-of-fit, is defined as follows [8], [10]:

$$McFadden\text{-}R^2 = 1 - (LLmodel / LLnull) \quad (5)$$

$$Adjusted\ McFadden\text{-}R^2 = 1 - (LLmodel\ -K) / (LLnull) \quad (6)$$

Unlike the traditional R^2, which explains variance, *McFadden's pseudo-R²* values in the range of approximately 0.20–0.40 are often regarded as indicative of a relatively strong fit for discrete choice models, although interpretation is context dependent [8], [10]. All analyses were performed in RStudio using the mlogit package in R.

4 Findings

The estimation results of the MNL model, conducted in R Studio, analyze university students' transportation mode choices (active transport and public transport) compared to the private vehicle option, which was set as the reference group. All findings related to the model are presented in Table 2.

Table 2. Multinomial Logit model results

Variables	Active Transport		Public Transport	
	Estimate	**p-value**	**Estimate**	**p-value**
Constant (Intercept)	3.290 *	<0.001	4.181 *	<0.001
Density (×100 persons/km^2)	0.011	0.516	0.011	0.422
Age	0.052 *	0.002	-0.014	0.376
Female	-0.579 *	<0.001	-0.833 *	<0.001
Income (×1000 TL)	-0.083 *	<0.001	-0.055 *	<0.001
Resides with family	-1.267 *	<0.001	-0.946 *	<0.001
Resides in dormitory	2.318 *	<0.001	1.742 *	<0.001
Driving license	-0.297 *	<0.001	-0.843 *	<0.001
Car availability	-2.499 *	<0.001	-2.765 *	<0.001
Micromobility availability	1.478 *	<0.001	0.743 *	<0.001
Motorbike availability	-3.678 *	<0.001	-2.878 *	<0.001
Travel distance (km)	-0.579 *	<0.001	0.028	0.152
Public transport subscription	1.343 *	<0.001	2.843 *	<0.001
Bicycle infrastructure quality	-0.256 *	<0.001	-0.228 *	<0.001
Pedestrian path quality	0.088 *	<0.001	0.088 *	<0.001
Sidewalk quality	0.027 *	0.004	0.104 *	<0.001
Ramp availability	0.158 *	<0.001	-0.085 *	<0.001
Safety perception	0.271 *	<0.001	0.004	0.691

*Note: * p<0.05. Reference category is Private Vehicle.*

The estimated MNL model provided a substantially better fit than the intercept-only model ($LL = -478.10$ vs. -831.85; $LR\ \chi^2(34) = 707.50$, $p < 0.001$). The model yielded a *McFadden pseudo-R^2* of 0.425 and an adjusted *McFadden pseudo-R^2* of 0.382, indicating a relatively strong model fit.

4.1 Evaluation of The Socio-Demographic and Travel Variables

When the Multinomial Logit model coefficients are examined, it is observed that socio-demographic characteristics have statistically strong and significant effects on university students' sustainable transportation mode preferences. Older students are more likely to choose active transport relative to private vehicles, whereas age is not significantly associated with public transport choice. Female students exhibit significantly lower relative odds of choosing either active or public transport rather than a private vehicle compared with male students. This finding is consistent with previous research highlighting gender differences in perceived safety; however, the present model does not directly test whether safety perceptions mediate the relationship between gender and mode choice.

When students' economic characteristics and vehicle availability are considered, higher income is associated with lower relative odds of choosing both active transport and public transport rather than a private vehicle. Similarly, holding a driving license and having access

to a car or motorcycle are associated with substantially lower relative odds of choosing sustainable transport modes compared with private vehicle use. Students residing with their families also exhibit significantly lower relative odds of choosing active or public transport. In contrast, dormitory residence is strongly and positively associated with both active and public transport choices relative to private vehicle use. Micromobility availability and public transport subscription are likewise associated with greater relative odds of choosing sustainable transport modes. Greater travel distance from home to campus is negatively associated with active transport choice, whereas its association with public transport choice is not statistically significant. Regional population density is also not significantly associated with either active transport or public transport choice.

4.2 Role of Built Environment and Infrastructure Perceptions

Several built-environment perception variables are significantly associated with students' travel mode choices. According to the model results: higher perceived pedestrian path quality is positively associated with both active and public transport choices relative to private vehicles. Similarly, the perception of sidewalk availability in compliance with standards significantly increases active transport and public transit probabilities. Perceived ramp accessibility and barrier-free sidewalk design are positively associated with active transport choice, while the corresponding coefficient for public transport is negative and statistically significant. Similarly, higher perceived route safety is positively associated with active transport choice, whereas its association with public transport is not statistically significant. These findings suggest that perceived accessibility and safety conditions are important correlates of walking and cycling among university students.

4.3 Bicycle Infrastructure Perceptions and Mode Shift

A notable and counterintuitive result concerns the bicycle infrastructure quality variable. Bicycle infrastructure quality exhibited negative coefficients for both active and public transport relative to private vehicle use. This pattern may suggest that current bicycle users are dissatisfied with existing road conditions and infrastructure deficiencies. In light of the findings, discontinuities in bicycle infrastructure and concerns related to safety may increase the likelihood that some active transport users consider shifting toward private vehicles, which may be perceived as more comfortable and protected, particularly if infrastructure conditions are not improved. Although the present analysis does not directly observe future mode switching, the results point to a potential risk of such a transition. Therefore, campus and urban transportation planning should give priority to improving the continuity, quality, and safety of pedestrian and bicycle infrastructure, including the provision of segregated bicycle facilities where appropriate, in order to support the continued use of active transport and reduce the potential shift toward motorized modes.

5 Discussion and Suggestions

The MNL model findings obtained in this study reveal that university students' travel behaviors are strongly shaped by both socio-demographic variables and built environment perceptions. Specifically, older students and students residing in dormitories exhibit a greater relative propensity to choose active transport, while dormitory residence is also positively associated with public transport use. Conversely, holding a driving license and having access to a car or motorcycle are associated with substantially lower relative odds of choosing sustainable transport modes. These findings are consistent with previous studies identifying

vehicle availability as an important barrier to the use and integration of sustainable transport modes.

The significantly lower probability of female students using active transport and public transit compared to male students draws attention to the relationship between gender equality and subjective safety in transportation planning. In the literature, it is frequently emphasized that women feel less safe than men during pedestrian and bicycle travel and are more sensitive to environmental quality. Particularly dim or isolated routes, irregular pedestrian infrastructure, and uncontrolled crossing points create a deterrent effect on female users and steer them toward private vehicle types perceived as more sheltered. In this context, lighting urban and campus travel routes, increasing security measures, and establishing continuous pedestrian connections are primary policy steps for female students to adopt sustainable transport.

The positive association between perceived pedestrian path quality and active transport choice highlights the potential relevance of micro-scale built-environment characteristics to travel behavior. Features such as sidewalk width, ramp accessibility, and pavement condition can influence pedestrian comfort and perceived accessibility. Especially when sidewalks are shared with micromobility vehicles (e-scooters, bicycles, etc.), lateral distances and vehicle speeds must be kept under control to protect pedestrian safety. Virtual reality studies suggest that safe interactions on shared sidewalks may be supported by net sidewalk widths of approximately 2.00–2.30 m and micromobility speeds of no more than 10 km/h. [5]. Therefore, expanding the pedestrian corridors around campus areas in accordance with these standards and making them barrier-free will directly increase active travel rates.

The most critical planning warning of the study is that the perception of bicycle path availability produces negative coefficients. This counterintuitive result indicates that higher bicycle-infrastructure ratings are associated with lower relative odds of active and public transport use. As explained by the concept of “Value of Safety” in the literature, although users are willing to extend their routes to avoid unsafe routes, they completely abandon using sustainable modes when infrastructural inadequacy exceeds a certain threshold [5]. Cyclists feeling unsafe due to the current poor-quality infrastructure triggers the potential for this sensitive user group to shift to other private vehicles in the near future. To prevent users from turning to car dependency due to this dissatisfaction, merely preserving the status quo is insufficient; building bicycle paths physically separated from motorized vehicle traffic and ensuring network continuity is crucial.

6 Conclusion

In this study, the effects of socio-demographic characteristics and built environment perceptions on transportation mode choice were analyzed using an MNL model with data obtained from 1,087 students studying at seven different universities in Türkiye. The results indicate that individual characteristics, vehicle availability, and perceptions of route safety and infrastructure quality are significantly associated with students’ travel mode choices. Dormitory residence, public transport subscription, and micromobility availability are positively associated with the relative likelihood of choosing sustainable transport modes. Conversely, car availability, higher income, and holding a driving license are associated with a greater relative preference for private vehicle use.

To promote sustainable urban mobility and reduce the risk of shifts toward private vehicle use in campus travel, the findings of this study, together with evidence from the literature,

suggest several planning interventions that decision-makers may consider:

- *Keeping Active Transport Users in the System:* To prevent loyal users who currently prefer walking and cycling from shifting to private vehicles due to infrastructure dissatisfaction, existing pedestrian and bicycle paths must be improved.
- *Physical Separation and Standard-Compliant Design:* Bicycle and e-scooter lanes should be physically separated from motorized vehicle traffic and pedestrian sidewalks. The net width of pedestrian sidewalks should be maintained at a minimum of 2.00 meters, and ramp accessibility should be provided continuously.
- *Enhancing Perceived Safety:* To enable female students, in particular, to safely use sustainable transport modes, improved lighting, visibility, and pedestrian-oriented safety measures should be widespread along the routes.

In conclusion, increasing the share of sustainable transportation in university campuses and surrounding urban areas requires not only adequate infrastructure provision but also environments that users perceive as safe, accessible, continuous, and comfortable.

Declaration of Generative AI and AI-assisted technologies in the writing process

During the preparation of this manuscript, the authors used Google NotebookLM, ChatGPT, and Abacus AI for language editing, structural review, clarity checks, translation, and grammar correction. The authors subsequently reviewed and verified all AI-assisted content and assume full responsibility for the final manuscript.

Acknowledgements

This study has been produced from the doctoral research conducted by Raziye PEKER. This work has been supported by Yildiz Technical University Scientific Research Projects Coordination Unit under project number FDK-2025-7231. The authors would like to acknowledge that this paper is submitted in partial fulfilment of the re-quirements for PhD degree at Yildiz Technical University.

References

[1] R. Peker, M. S. Yardım, and K. B. Akalın, “Home-to-Campus Commuting Mode Choice Among University Students in a Small-Scale City: A Mixed Multinomial Logit Analysis of Sustainable Mode Preferences,” *Sustainability*, vol. 18, no. 7, p. 3501, 2026.

[2] Z. Gan, M. Yang, Q. Zeng, and H. J. Timmermans, “Associations between built environment, perceived walkability/bikeability and metro transfer patterns,” *Transportation Research Part A: Policy and Practice*, vol. 153, pp. 171–187, 2021.

[3] P. G. Tzouras, V. Pastia, I. Kaparias, and K. Kepaptsoglou, “Exploring the effect of perceived safety in first/last mile mode choices,” *Transportation*, vol. 52, no. 5, pp. 2145–2183, 2025.

[4] O. Shulika, H. Vasiutina, M. Bujak, F. Ghasemi, and R. Kucharski, “Shifting Car Users To Public Transport: A Utility-Based Approach For Selecting Areas For Feeder Services,” *Transportation Research Procedia*, vol. 95, pp. 744–751, 2026.

[5] A. N. Arshi, C. Dias, W. K. Alhajyaseen, Q. Hussain, C. Samson, and Z. Hussain, “Can pedestrians safely navigate shared sidewalks with e-scooters and bicycles? A behavioral analysis using surrogate safety measures,” *Transportation Research Part F: Traffic Psychology and Behaviour*, vol. 116, p. 103407, 2026.

[6] S. Okafor, C. Bullard, G. Dumedah, E. K. Adanu, C. A. Adams, and S. Jones, “The influence of socio-demographic and neighborhood characteristics on residents’ safety perception of active mobility in Accra, Ghana,” *Urban, Planning and Transport Research*, vol. 11, no. 1, p. 2276398, 2023.

[7] G. Oeschger, P. Carroll, and B. Caulfield, “Micromobility and public transport integration: The current state of knowledge,” *Transportation Research Part D: Transport and Environment*, vol. 89, p. 102628, 2020.

[8] R. Peker, M. S. Yardim, and K. B. Akalin, “Factors influencing transportation mode preferences for educational trips among dormitory resident university students in Kütahya, Türkiye,” *Sustainability*, vol. 16, no. 22, p. 9660, 2024.
[9] D. Tóthová, O. Mikeš, V. Pařil, and P. Tonev, “Children’s and parents’ modal choice when commuting to school and air pollution burden: Is there a healthier way?,” *Transportation Research Part A: Policy and Practice*, vol. 207, p. 104939, 2026.
[10] K. Train and others, *Discrete choice methods with simulation*, vol. 2. Cambridge university press Cambridge, 2003.
[11] L. Klos, J. Fiedler, C. Nigg, C. Niessner, H. Wäsche, and A. Woll, “Walking and non-motorized vehicle use in adolescents: the role of neighborhood environment perceptions across urbanization levels,” *German journal of exercise and sport research*, vol. 54, no. 1, pp. 145–155, 2024.

Publication Note
This paper was peer-reviewed, accepted for presentation, and included in the proceedings of the ACE2026 – International Conference on Advances in Civil Engineering, held on 12–14 October 2026 in Trabzon, Türkiye.

This paper may be cited as follows:
Peker R., Yardım M. S., Akalın K. B., “The Role of Built Environment Perceptions in University Students’ Travel Mode Choices: A Multinomial Logit Analysis,” in Proceedings of the ACE2026 – International Conference on Advances in Civil Engineering, Trabzon, Türkiye, 12–14 October 2026.

Modelling Urban Bicycle Use Intensity Using Penalized Regression Methods: Evidence from Eskişehir

Sıla Cemre Demirci [1] and Çağdaş Kara[2]
[1] 0009-0002-6562-9339, Eskişehir Osmangazi University, Civil Engineering Department, Eskişehir, Türkiye, 503320240029@ogrenci.ogu.edu.tr;
[2] 0000-0002-2520-6561, Eskişehir Osmangazi University, Civil Engineering Department, Eskişehir, Türkiye, ckara@ogu.edu.tr

Abstract
Bicycle transportation is an important component of sustainable urban mobility; however, bicycle use intensity varies across neighborhoods according to their socioeconomic, demographic, mobility-related, and built-environment characteristics. This study investigates neighborhood-level Bicycle Use Intensity (BUI) in Eskişehir and compares the predictive performance of different regression-based modelling approaches. The analysis is based on the 2015 Eskişehir Household Travel Survey conducted for the Eskişehir Transportation Master Plan, using 56 neighborhoods as the unit of analysis. BUI was calculated as the number of bicycle trips made by neighborhood residents divided by the number of surveyed residents. Eleven explanatory variables representing socioeconomic, demographic, mobility-related, and built-environment characteristics were included. Multiple Linear Regression (MLR), Ridge Regression (RR), Least Absolute Shrinkage and Selection Operator (Lasso), and Elastic Net (EN) were compared using 5-fold cross-validation repeated with 100 fixed random seeds. Model tuning was based on the lambda.min criterion, and performance was primarily evaluated using the Cross-Validated Root Mean Squared Error (CV-RMSE). RR achieved the lowest mean CV-RMSE (13.55) and was the best-performing model in all cross-validation runs. A sensitivity analysis using an extended lambda search path produced the same model ranking. Standardized RR coefficients showed positive associations of BUI with driver's license ownership, average age, residential building density, automobile ownership, and population density, whereas workplace building density, employment ratio, homeownership, student ratio, public building density, and average number of trips showed negative associations. The findings demonstrate that RR provides a robust modelling framework for neighborhood-level bicycle use analysis using small-sample zonal transport data.

Keywords: Bicycle use intensity; Ridge Regression; Penalized regression; Neighborhood-level analysis; Sustainable urban mobility

1 Introduction

Bicycle transportation is an important component of sustainable urban mobility because of its environmental, economic, and social benefits. As an environmentally friendly, affordable, and accessible travel mode, cycling contributes to reducing traffic congestion, lowering energy consumption, and promoting physical activity. Increasing bicycle use in urban areas is closely associated with the provision of safe, continuous, and accessible cycling infrastructure. Recent evidence from Türkiye similarly indicates that cycling infrastructure remains fragmented and

insufficiently standardized in many cities, emphasizing the need for continuous and connected networks and the integration of micromobility into transportation master plans [1]. However, the existence of cycling infrastructure alone is insufficient to explain bicycle use. Cycling behaviour is also influenced by individuals' socioeconomic and demographic characteristics, general travel behaviour, and the built-environment characteristics of the neighborhoods in which they live [2, 3].

Previous studies have shown that bicycle use is determined by a wide range of interacting factors. Demographic characteristics such as age, gender, educational attainment, and household composition, together with socioeconomic indicators including income, employment status, automobile ownership, driver's license ownership, and homeownership, have frequently been examined as determinants of bicycle use [2, 4, 5]. Recent research from Türkiye has further shown that cycling is influenced by socio-cultural conditions, including peer effects, concerns related to physical appearance, and perceived societal pressure [6]. In addition, built-environment characteristics play an important role in shaping cycling behaviour. Previous research has identified cycling infrastructure, land-use patterns, residential and employment density, accessibility, network connectivity, travel distance, topography, and street design as important determinants of bicycle use [3, 7-9]. Recent spatially explicit research has also demonstrated that bicycle users' routes, trip durations, and station locations may generate substantial differences in environmental exposure across urban areas [10]. Recent bike-sharing research has also shown that the relative importance of temporal, weather-related, station-level, and nearby spatial characteristics may vary across systems, highlighting the context-dependent nature of bicycle demand [11].

These factors are often interrelated rather than independent. For example, the relationship between urban density and bicycle use may vary depending on automobile ownership, age structure, household characteristics, employment patterns, or the socioeconomic composition of neighborhoods. Consequently, bicycle use should be analysed using modelling approaches that simultaneously consider multiple groups of explanatory variables rather than individual variables in isolation. This issue becomes particularly important in neighborhood-level analyses, where the relatively small sample size and correlations among explanatory variables may lead to coefficient instability in conventional regression models. Penalized regression techniques provide useful alternatives under such conditions. Ridge Regression (RR) improves model stability by shrinking regression coefficients while retaining all variables in the model. The Least Absolute Shrinkage and Selection Operator (Lasso) performs variable selection by shrinking some coefficients exactly to zero. Elastic Net (EN) combines the penalties used in RR and Lasso. In addition, Multiple Linear Regression (MLR) was included as the baseline comparison model in this study [12-14].

The objective of this study is to investigate neighborhood-level bicycle use intensity in Eskişehir using socioeconomic, demographic, mobility-related, and built-environment indicators. To this end, the predictive performance of MLR, RR, Lasso, and EN models is compared to identify the most appropriate modelling approach for small-sample neighborhood-level bicycle use data.

2 Study Area and Data

The study was conducted in the central districts of Odunpazarı and Tepebaşı in Eskişehir, Türkiye. Eskişehir is a medium-sized city where bicycle use is observed in daily urban travel and where cycling infrastructure has been progressively expanded in different parts of the city.

These characteristics make Eskişehir an appropriate case study for examining the factors associated with neighborhood-level bicycle use intensity.

The analysis is based on data obtained from the 2015 Eskişehir Household Travel Survey, which contains information on individuals' daily travel behaviour as well as their socioeconomic and demographic characteristics. Neighborhoods were selected as the unit of analysis. After data aggregation and missing-value screening, the final modelling dataset consisted of 56 neighborhoods.

The dependent variable was defined as resident-based Bicycle Use Intensity (BUI). BUI was calculated by dividing the total number of bicycle trips made by residents of each neighborhood by the number of surveyed individuals living in that neighborhood. Therefore, the indicator represents the relative bicycle use intensity of neighborhood residents rather than bicycle trips attracted to or passing through a neighborhood.

The explanatory variables were generated at the neighborhood level to represent socioeconomic structure, demographic composition, general mobility characteristics, and built-environment conditions. The variables included in the modelling process and their abbreviations are presented in Table 1 and Figure 1 illustrates the study area and the neighborhood boundaries used in the analysis.

Table 1. Variables used in the modelling process and their abbreviations

Variable	Abbreviation	Description	Dimension
Bicycle use intensity	BUI	Number of bicycle trips made by neighborhood residents divided by the number of surveyed individuals	Dependent variable
Automobile ownership	AOW	Neighborhood-level automobile ownership indicator	Socioeconomic/Mobility
Homeownership ratio	HOR	Homeownership ratio	Socioeconomic
Driver's license ownership	DLO	Driver's license ownership ratio	Mobility-related socioeconomic
Average number of trips	ANT	Average daily trip-making indicator	General mobility
Employment ratio	EMP	Share of employed individuals	Socioeconomic
Average age	AAG	Average age of surveyed residents	Demographic
Student ratio	STU	Share of students	Demographic/Socioeconomic
Population density	PDN	Population density indicator	Built environment / Density
Residential building density	RBD	Residential building density	Built environment
Workplace building density	WBD	Workplace building density	Built environment / Land use
Public building density	PBD	Public building density	Built environment / Land use

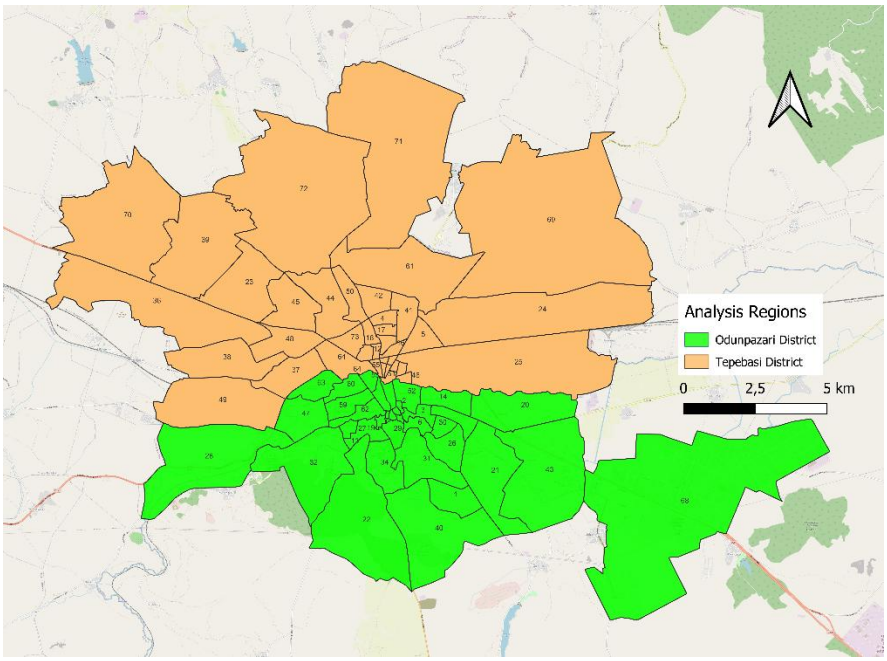


Fig. 1. Study area in Eskişehir and neighborhood boundaries used in the analysis.

3 Methodology

This study compares MLR, RR, Lasso, and EN models to predict BUI. MLR was used as the baseline comparison model, whereas RR, Lasso, and EN were employed to improve coefficient stability and predictive performance in a small-sample dataset with correlated explanatory variables [12-14].

The penalized regression models are based on the following objective function:

$$\min_{\beta_0,\beta}\left\{\frac{1}{N}\sum_{i=1}^{N}(y_i-\beta_0-x_i^T\beta)^2+\lambda\left[\frac{1-\alpha}{2}\sum_{j=1}^{p}\beta_j^2+\alpha\sum_{j=1}^{p}|\beta_j|\right]\right\} \quad (1)$$

The dependent variable is denoted by y_i, x_i represents the vector of explanatory variables, $\beta = (\beta_1, \beta_2, \ldots, \beta_p)$ denotes the vector of regression coefficients, λ is the regularization parameter, and α controls the balance between the RR and Lasso penalties. When $\alpha = 0$, the model corresponds to RR; when $\alpha = 1$, it becomes Lasso; and $0 < \alpha < 1$ represents EN models [9–11]. RR shrinks regression coefficients without performing variable selection, whereas Lasso and EN may set some coefficients exactly to zero, thereby performing variable selection.

All models were estimated in R using the glmnet package [15]. The dependent variable was retained on its original scale, whereas explanatory variables were standardized internally by glmnet during model estimation. This enabled RMSE values to be interpreted in the original units of BUI. The α parameter was evaluated from 0.00 to 1.00 in increments of 0.05, while the default lambda sequence generated by glmnet was adopted.

To reduce the dependence of model performance on a single random data partition, repeated 5-fold cross-validation was performed using 100 fixed random seeds. For each seed, the same fold assignment was used across all α values, ensuring that RR, Lasso, and EN were evaluated under identical training and validation partitions. Model performance was assessed using CV-RMSE, CV-MAE, and CV-R^2, with the mean CV-RMSE adopted as the primary model selection criterion.

To evaluate the adequacy of the lambda search path, an additional sensitivity analysis was conducted using 300 lambda values and a smaller lambda.min.ratio. The ranking of model performance remained unchanged.

Coefficient stability of the best-performing model was evaluated using the results obtained from the 100 repeated cross-validation runs. Since RR does not perform variable selection, the number of selected variables was not reported for the RR model. Instead, the coefficient directions and standardized coefficient magnitudes of all candidate variables were examined. Standardized RR coefficients were calculated as follows:

$$\beta_{std,j} = \bar{\beta}_j \frac{sd(x_j)}{sd(y)} \tag{2}$$

where $\bar{\beta}_j$ denotes the average RR coefficient of the j-th explanatory variable across the 100 repeated cross-validation runs, $sd(x_j)$ is the standard deviation of the corresponding explanatory variable, and sd(y) is the standard deviation of the dependent variable. Standardized coefficients facilitate comparison of the relative contributions of variables measured on different scales. In this study, variable importance was evaluated using the absolute standardized coefficients.

4 Results and Discussion

During model tuning, the lambda.min criterion, which selects the regularization parameter (λ) that minimizes the cross-validation error in each cross-validation run, was adopted.

Table 2 summarizes the representative model performance results obtained from the repeated 5-fold cross-validation procedure. A total of 22 models (RR, 19 EN models, Lasso, and MLR) were evaluated. To improve readability, only the best-performing and representative models are presented.

Table 2. Representative model performance results based on repeated 5-fold cross-validation**.**

Method	Alpha	Median selected λ	Mean CV-RMSE	SD CV-RMSE
RR	0.00	6.70	13.55	0.36
EN	0.05	4.60	13.66	0.37
EN	0.10	3.50	13.73	0.38
EN	0.20	2.54	13.82	0.39
Lasso	1.00	0.85	14.04	0.43
MLR	—	—	15.29	1.02

As shown in Table 2, RR produced the lowest CV-RMSE in all 100 repeated cross-validation runs based on the lambda.min criterion. Although EN models with low alpha values achieved prediction errors close to those of RR, none of them outperformed RR in any repetition. As the alpha value increased, the prediction error of EN models gradually increased, whereas Lasso and MLR produced the highest prediction errors.

These findings indicate that the L2 regularization employed by RR provided more stable predictive performance than the sparser models obtained through variable selection for this dataset.

An additional sensitivity analysis was conducted to examine whether the results depended on the lambda search path. Instead of the default lambda sequence generated by glmnet, an extended search path consisting of 300 lambda values and a wider search range was used. The

ranking of the competing models remained unchanged, and RR was again identified as the best-performing model in all 100 repetitions. This finding confirms that the superior performance of RR was not attributable to the selected lambda search range.

Table 3 presents the standardized RR coefficients. These coefficients were obtained by standardizing the average RR coefficients estimated across the 100 repeated cross-validation runs. Since RR retains all variables in the model, the coefficients should not be interpreted as evidence of variable selection but rather as indicators of the relative direction and magnitude of the associations between the explanatory variables and BUI.

Table 3. Standardized RR coefficients.

Abbreviation	Variable	Standardized coefficient
DLO	Driver's license ownership	0.193
WBD	Workplace building density	-0.183
EMP	Employment ratio	-0.164
AAG	Average age	0.141
RBD	Residential building density	0.121
HOR	Homeownership ratio	-0.104
STU	Student ratio	-0.099
AOW	Automobile ownership	0.074
PDN	Population density	0.065
PBD	Public building density	-0.054
ANT	Average number of trips	-0.047

The coefficients presented in Table 3 were derived from aggregated neighborhood-level data. Therefore, they should be interpreted as spatial associations reflecting the demographic, socioeconomic, mobility, and land-use characteristics of neighborhoods rather than as direct or causal relationships at the individual level.

Positive associations were observed for DLO, AAG, RBD, AOW, and PDN, whereas WBD, EMP, HOR, STU, PBD, and ANT exhibited negative associations with BUI.

The positive coefficient of DLO does not imply that possessing a driver's license directly increases bicycle use at the individual level. One possible explanation is that neighborhoods with higher driver's license ownership in Eskişehir also tend to have lower student concentrations and relatively older populations, reflecting broader neighborhood characteristics rather than individual travel behaviour.

The negative coefficients of WBD and EMP may indicate that neighborhoods characterized by high workplace density and employment concentration function primarily as employment centers. In such areas, mandatory commuting trips may be more frequently made by company shuttle services, public transport, or private automobiles, thereby limiting bicycle use.

The positive association of AAG suggests that cycling in Eskişehir is not limited to younger populations. In several neighborhoods with relatively older or retired residents, bicycle use for short-distance daily trips appears to remain common, which may partly explain this relationship.

The positive coefficient of RBD may reflect the greater prevalence of short-distance local trips in neighborhoods with high residential density. In contrast, the negative coefficient of STU may be explained by the fact that student-dominated neighborhoods are generally located close to universities and the city center, where many short trips can be completed on foot rather than

by bicycle. This finding also suggests that future studies could incorporate explicit spatial indicators representing proximity to universities and the city center.

Similarly, the positive coefficient of AOW should not be interpreted as evidence that automobile ownership promotes bicycle use at the individual level. Rather, neighborhoods with relatively high automobile ownership are often located in outer residential areas where bicycles may still be frequently used for short local trips.

The negative coefficient of PBD may indicate that neighborhoods with high concentrations of public buildings primarily function as service destinations that attract trips rather than generate bicycle trips by residents. Likewise, the negative association of ANT may reflect that individuals making multiple or chained trips throughout the day tend to rely more heavily on public transport or private automobiles than bicycles.

Overall, the findings indicate that neighborhood-level bicycle use intensity is shaped not by a small number of dominant predictors but by the combined influence of demographic, socioeconomic, mobility-related, and built-environment characteristics. The superior performance of RR, which retained all explanatory variables while producing the lowest prediction error, further supports the multidimensional nature of neighborhood-level bicycle use.

5 Conclusions

This study modeled neighborhood-level bicycle use intensity (BUI) in Eskişehir using data from the 2015 Eskişehir Household Travel Survey. Neighborhoods were adopted as the unit of analysis, and BUI was explained using socioeconomic, demographic, mobility-related, and built-environment indicators. MLR, RR, Lasso, and EN models were compared using repeated 5-fold cross-validation with 100 fixed random seeds.

Model tuning was performed using the lambda.min criterion, which selects the lambda value that minimizes the cross-validation error in each repetition. The results demonstrated that RR achieved the lowest and most stable prediction error among the evaluated models. RR attained a mean CV-RMSE of 13.55 on the original scale of the dependent variable and was identified as the best-performing model in all 100 repeated cross-validation runs. Although low-alpha EN models produced prediction errors close to those of RR, their performance gradually deteriorated as the alpha value increased, while Lasso and MLR exhibited weaker predictive performance.

In addition to the default lambda sequence generated by glmnet, an additional sensitivity analysis using 300 lambda values and lambda.min.ratio = 10^{-6} produced the same model ranking. This confirms that the superiority of RR was not attributable to an insufficient lambda search range for EN or Lasso.

Based on the standardized RR coefficients, DLO, AAG, RBD, AOW, and PDN were positively associated with BUI, whereas WBD, EMP, HOR, STU, PBD, and ANT showed negative associations. Since these relationships were obtained from aggregated neighborhood-level data, they should not be interpreted as individual-level causal effects. Instead, they should be understood in the context of neighborhood demographic composition, the spatial distribution of students and workers, centrality, residential structure, and land-use characteristics.

The findings suggest that neighborhood-level bicycle use intensity is influenced by the combined contribution of multiple neighborhood characteristics rather than a small number of dominant predictors. In this context, the L2 regularization employed by RR improved predictive stability by retaining all theoretically relevant variables in the model and outperformed Lasso and high-alpha EN models, which place greater emphasis on variable selection. Consequently,

RR appears to be an appropriate modelling approach for neighborhood-level transportation datasets characterized by relatively small sample sizes and correlated explanatory variables.

The primary limitation of this study is that the analysis was conducted using aggregated neighborhood-level data. Furthermore, the current model does not explicitly include spatial variables such as proximity to universities and the city center, cycling infrastructure availability, terrain slope, pedestrian accessibility, or land-use diversity. Incorporating these variables in future research may provide a more comprehensive explanation of the observed relationships, particularly those involving student concentration, automobile ownership, population density, and driver's license ownership.

Acknowledgments

This paper is based on the master's thesis entitled *"Bicycle Use in Urban Transportation: Demographic Factors and Regional Differences"*, conducted under the supervision of Dr. Çağdaş Kara. The research was financially supported by the Eskişehir Osmangazi University Scientific Research Projects Coordination Unit (Project No. FYL-2026-3870).

Conflict of Interest

The authors declare that they have no conflict of interest.

Data Availability Statement

The data that support the findings of this study are available from the corresponding author upon reasonable request, subject to data-sharing permissions and institutional restrictions.

Author Contribution Statement

• Conceptualization: Çağdaş Kara
• Methodology: Çağdaş Kara
• Data Curation: Çağdaş Kara, Sıla Cemre Demirci
• Formal Analysis: Çağdaş Kara, Sıla Cemre Demirci
• Investigation: Çağdaş Kara, Sıla Cemre Demirci
• Writing – Original Draft: Çağdaş Kara, Sıla Cemre Demirci
• Writing – Review & Editing: Çağdaş Kara
• Supervision: Çağdaş Kara

List of Abbreviations

- AAG — Average Age
- ANT — Average Number of Trips
- AOW — Automobile Ownership
- BUI — Bicycle Use Intensity
- CV — Cross-Validation
- CV-RMSE — Cross-Validated Root Mean Squared Error
- DLO — Driver's License Ownership
- EMP — Employment Ratio
- EN — Elastic Net
- HOR — Homeownership Ratio
- Lasso — Least Absolute Shrinkage and Selection Operator
- MLR — Multiple Linear Regression

- PBD — Public Building Density
- PDN — Population Density
- RBD — Residential Building Density
- RR — Ridge Regression
- SD — Standard Deviation
- STU — Student Ratio
- WBD — Workplace Building Density

Note: Following the conference, this Publication Note will be added to each paper; therefore, authors are kindly requested not to remove the note below and to complete the author(s) and paper title information.

1. Özden, A. and S.B.K. Kün, *Türkiye'de bisiklet ve e-skuter altyapısının kentsel ulaşım bakımından değerlendirilmesi.* Pamukkale Üniversitesi Mühendislik Bilimleri Dergisi, 2025. **31**(1): p. 125-140.https://doi.org/10.5505/pajes.2024.09633
2. Heinen, E., B. Van Wee, and K. Maat, *Commuting by bicycle: an overview of the literature.* Transport reviews, 2010. **30**(1): p. 59-96.https://doi.org/10.1080/01441640903187001
3. Pucher, J. and R. Buehler, *Making cycling irresistible: lessons from the Netherlands, Denmark and Germany.* Transport reviews, 2008. **28**(4): p. 495-528.https://doi.org/10.1080/01441640701806612
4. Handy, S., B. Van Wee, and M. Kroesen, *Promoting cycling for transport: research needs and challenges.* Transport reviews, 2014. **34**(1): p. 4-24.https://doi.org/10.1080/01441647.2013.860204
5. Dill, J. and T. Carr, *Bicycle commuting and facilities in major US cities: if you build them, commuters will use them.* Transportation research record, 2003. **1828**(1): p. 116-123.https://doi.org/10.3141/1828-14
6. Dağ, V. and S. Mansuroğlu, *Bisiklet Kullanımını Etkileyen Sosyo-Kültürel Faktörlerin Belirlenmesi: Denizli Kenti Örneği.* İdealkent, 2024. **16**(43): p. 10-37.https://doi.org/10.31198/idealkent.1392026
7. Winters, M., et al., *Motivators and deterrents of bicycling: comparing influences on decisions to ride.* Transportation, 2011. **38**(1): p. 153-168.https://doi.org/10.1007/s11116-010-9284-y
8. Fraser, S.D. and K. Lock, *Cycling for transport and public health: a systematic review of the effect of the environment on cycling.* The European Journal of Public Health, 2011. **21**(6): p. 738-743.https://doi.org/10.1093/eurpub/ckq145
9. Ewing, R. and R. Cervero, *Travel and the built environment: A meta-analysis.* Journal of the American planning association, 2010. **76**(3): p. 265-294.https://doi.org/10.1080/01944361003766766
10. Hwang, S., et al., *Exploring the inequality of the particulate matter exposure level of public bicycle scheme users using an agent-based model.* Computers, Environment and Urban Systems, 2026. **123**: p. 102367.https://doi.org/10.1016/j.compenvurbsys.2025.102367
11. Cortez-Ordonez, A., P.-P. Vazquez, and J.A. Sanchez-Espigares, *Features that influence bike sharing demand.* Heliyon, 2024. **10**(18).https://doi.org/10.1016/j.heliyon.2024.e37608
12. Zou, H. and T. Hastie, *Regularization and variable selection via the elastic net.* Journal of the Royal Statistical Society Series B: Statistical Methodology, 2005. **67**(2): p. 301-320.https://doi.org/10.1111/j.1467-9868.2005.00503.x
13. Tibshirani, R., *Regression shrinkage and selection via the lasso.* Journal of the Royal Statistical Society Series B: Statistical Methodology, 1996. **58**(1): p. 267-288.https://doi.org/10.1111/j.2517-6161.1996.tb02080.x
14. Hoerl, A.E. and R.W. Kennard, *Ridge regression: Biased estimation for nonorthogonal problems.* Technometrics, 1970. **12**(1): p. 55-67.https://doi.org/10.1080/00401706.1970.10488634
15. Friedman, J., et al., *Package 'glmnet'.* CRAN R Repositary, 2021. **595**: p. 874

Publication Note

This paper was peer-reviewed, accepted for presentation, and included in the proceedings of the ACE2026 – International Conference on Advances in Civil Engineering, held on 12–14 October 2026 in Trabzon, Türkiye.

This paper may be cited as follows:

Demirci, S.C., Kara, C., "Modelling Urban Bicycle Use Intensity Using Penalized Regression Methods: Evidence from Eskisehir," in Proceedings of the ACE2026 – International Conference on Advances in Civil Engineering, Trabzon, Türkiye, 12–14 October 2026.

Influence of CLS Modification on the Conventional Properties and Temperature Susceptibility of Bitumen

Aytuğ Kumandaş[1], Erman Çavdar[2], Mahir Kumantaş[3], Ersoy Kabadayı[4], Neslihan Şahan[5], Erhan Burak Pancar[6] and Şeref Oruç[7]

[1] 0000-0003-1765-9963, Ondokuz Mayıs University, Civil Engineering Department, Samsun, Türkiye, aytug.kumandas@omu.edu.tr

[2] 0000-0002-0238-5245, Karadeniz Technical University, Civil Engineering Department, Trabzon, Türkiye, ermancavdar@ktu.edu.tr

[3] 0009-0002-7979-7640, Karadeniz Technical University, Civil Engineering Department, Trabzon, Türkiye, mkumantas@ktu.edu.tr

[4] 0000-0003-4062-3117, Giresun University, Construction Technology Department, Giresun, Türkiye, ersoy.kabadayi@giresun.edu.tr

[5] 0000-0003-3904-6527, Kırşehir Ahi Evran University, Civil Engineering Department, Kırşehir, Türkiye, neslihan.sahan@ahievran.edu.tr

[6] 0000-0002-7958-3434, Ondokuz Mayıs University, Civil Engineering Department, Samsun, Türkiye, epancar@omu.edu.tr

[7] 0000-0001-5788-890X, Karadeniz Technical University, Civil Engineering Department, Trabzon, Türkiye, oruc@ktu.edu.tr

Abstract. Bitumen is a viscoelastic material whose temperature-dependent behavior directly affects the workability and field performance of asphalt pavements. Therefore, evaluating the conventional properties and temperature susceptibility of modified bitumens provides a practical basis for understanding their suitability for pavement applications. This study investigates the effect of calcium lignosulfonate (CLS) modification on the conventional properties and temperature susceptibility of bitumen. For this purpose, a neat bitumen sample and CLS-modified bitumen samples containing 3%, 5%, 7%, and 9% CLS by weight of bitumen were prepared. The experimental program included penetration, softening point, and rotational viscosity tests at 135 °C. Based on the obtained experimental results, the penetration index (PI) and penetration-viscosity number (PVN) were calculated to evaluate the changes in the temperature susceptibility and consistency characteristics of the samples. The penetration and softening point results were used to assess the effect of CLS addition on bitumen under conventional test conditions, while the rotational viscosity values were considered in terms of high-temperature flow behaviour and workability. In addition, PI and PVN values provided complementary indicators for interpreting the sensitivity of the modified bitumens to temperature changes. Through a comparative evaluation of the neat and CLS-modified samples, this study aims to determine whether CLS primarily acts as a stiffening, stabilizing, or temperature-sensitivity-modifying additive within the investigated dosage range. The findings of this study are expected to contribute to the preliminary assessment of CLS as a potential bitumen modifier and to provide a basis for future rheological and mixture-scale performance investigations.

Keywords: Bitumen Modification; Calcium lignosulfonate; Conventional bitumen tests

1 Introduction

The global transition toward sustainable infrastructure has motivated extensive inquiry into bio-based additives for asphalt binders, primarily to mitigate the environmental impact of petroleum-derived bitumen [1]. As bitumen is a finite, non-renewable resource, the

development of sustainable, high-performance binders has become essential for ensuring long-term road pavement durability [2]. The valorization of industrial waste byproducts as modifiers represents a strategic approach to addressing both resource scarcity and ecological footprints, while simultaneously enhancing the mechanical integrity of asphaltic materials [3-4].

Calcium lignosulfonate, a byproduct derived from the pulp and paper industry, has garnered significant attention as a viable organic modifier [4]. Characterized as a phenylpropane-based polymer with reactive phenolic and hydroxyl functional groups, CLS demonstrates potential compatibility with the bitumen matrix, thereby facilitating structural reinforcement [5]. Furthermore, the integration of CLS into bitumen has been shown to improve consistency and structural rigidity at elevated temperatures, which is critical for mitigating permanent deformation in asphalt pavements [6]. The adoption of this abundant byproduct adheres to circular economy principles, offering a cost-effective and environmentally sound alternative for large-scale engineering applications [7-8].

Despite evidence suggesting that lignin derivatives enhance rutting resistance and oxidative stability, the correlation between additive dosage and binder brittleness necessitates further empirical examination [1, 9-10]. The inherent variability in lignin-based materials, contingent upon their specific source, production methods, and chemical composition, complicates the standardization of these additives [11]. While lignosulfonates are well-established as effective adhesive agents and soil stabilizers [12-13], their systematic application as rheological modifiers in neat bitumen—specifically concerning conventional consistency and temperature susceptibility parameters—remains insufficiently explored in current literature [14-15].

Consequently, this research investigates the mechanical reinforcement and thermal response mechanisms of bitumen binders modified with varying concentrations of CLS. By correlating specific dosage levels with temperature susceptibility indicators, this study aims to refine the binder's physical properties through the utilization of this sustainable industrial byproduct. Ultimately, this investigation underscores the feasibility of employing lignosulfonate as an environmentally benign and cost-effective additive within modern asphalt paving technologies [16-17].

2 Materials and Methods

2.1 Bitumen

The base binder utilized for this experimental program consists of a standard 50/70 penetration grade bitumen. This binder was selected as it represents a widely adopted grade in pavement construction, providing a suitable baseline to evaluate the hardening and stiffening effects of CLS incorporation.

2.2 Calcium Lignosulfonate

The calcium lignosulfonate (CLS) used in this investigation was procured commercially in powder form from Kimya Deposu. This fine-particulate additive was selected for its potential to integrate homogeneously with the bituminous matrix, facilitating a uniform dispersion of the modifier.

2.3 Preparation of CLS Modified Bitumen

The modified binder samples were prepared by incorporating the CLS into the base bitumen at a temperature of 160 °C using a mechanical mixer operating at a constant speed of 1500 rpm for a duration of 30 minutes, ensuring a homogeneous distribution of the additive within the

bituminous matrix. Following the blending process, the samples were subjected to an immediate cooling phase at room temperature to preserve the integrity of the dispersion. The homogeneity of the resulting mixtures was further verified through visual inspection to confirm the absence of modifier agglomeration or phase separation prior to subsequent laboratory testing. Subsequently, these samples were stored in tightly sealed containers to prevent oxidative hardening before undergoing standard penetration, softening point, and rotational viscosity testing.

2.4 Conventional Bitumen Tests

The consistency of the modified binders is characterized through the penetration test, which measures the depth of needle penetration into the sample under specific load and time conditions. This procedure, conducted in accordance with ASTM D5, provides a quantitative assessment of bitumen hardness at a standard temperature of 25 °C. Concurrently, the softening point test, performed as per ASTM D36, is utilized to determine the temperature at which the bitumen reaches a specific state of flow, serving as a primary indicator of its thermal stability.

Furthermore, the flow behavior and workability of the binders at high temperatures were evaluated using rotational viscosity measurements in accordance with ASTM D4402, providing critical data on the binder's resistance to shearing during production and placement. These experimental procedures were performed in triplicate for each specimen to ensure statistical reliability and to minimize the impact of inherent material variability.

2.5 Temperature Susceptibility Indices

Temperature susceptibility refers to the rate at which bitumen consistency varies with fluctuations in service temperature, thus serving as a critical indicator for assessing the binder's performance range. To quantify this sensitivity, the Penetration Index is employed—an empirical metric derived from the relationship between penetration and softening point, which effectively reflects the binder's propensity for thermal deformation. The *PI* values for the CLS-modified bitumen binders are calculated using the following equation:

$$PI = \frac{1952 - 500 \times \log(pen) - 20 \times SP}{50 \times \log(pen) - SP - 120} \tag{1}$$

where $\log(pen)$ represents the logarithm of penetration at 25 °C and *SP* denotes the softening point temperature in degrees Celsius.

Complementing the *PI*, the Penetration-Viscosity Number (*PVN*) is utilized to assess the binder's rheological stability across a broader temperature range by correlating penetration values at 25 °C with rotational viscosity measurements obtained at 135 °C. The *PVN* values for the CLS-modified bitumen binders are calculated using the following equation:

$$PVN = -1.5 \times \frac{4.258 - 0.7967 \times \log P - \log V}{0.795 - 0.1858 \times \log P} \tag{2}$$

where *P* denotes the penetration value at 25 °C and *V* signifies the rotational viscosity at 135 °C.

Collectively, this dual approach provides a comprehensive evaluation of the binder’s consistency. Generally, a higher *PVN* signifies reduced temperature susceptibility and enhanced thermal stability within the service temperature window. Consequently, these indices serve as

essential diagnostic tools for quantifying how the thermoplastic nature of the bitumen is modulated by the addition of CLS.

3 Results and Discussion

3.1 Results of Conventional Bitumen Tests

Fig. 1 illustrates that the base bitumen exhibited a penetration value of 55.6 dmm, whereas the incorporation of calcium lignosulfonate resulted in a pronounced and monotonic reduction in penetration depth. Specifically, the 3CLS, 5CLS, 7CLS, and 9CLS samples yielded penetration values of approximately 52.7, 50.9, 49.1, and 47.6 dmm, respectively. These observations indicate that the CLS additive effectively stiffens the bitumen matrix.

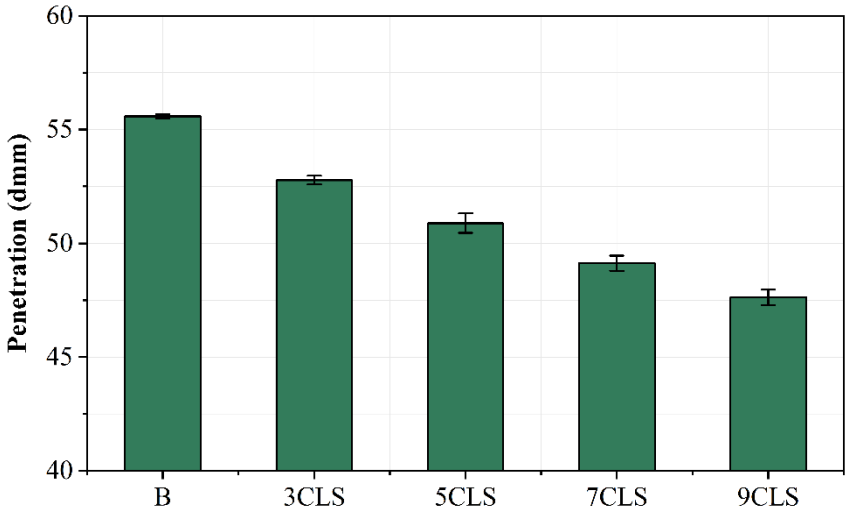


Fig. 1. Penetration test results.

The penetration value decreased by approximately 14.6% at the maximum CLS dosage of 9% compared to the base bitumen. This nearly linear trend suggests a homogeneous dispersion of CLS within the bitumen, underscoring a systematic relationship between additive concentration and binder hardness. Furthermore, this decrease in penetration reflects restricted mobility of the bitumen molecules, likely driven by interactions between the polar functional groups of the lignosulfonate and the asphaltic components [3].

Fig. 2 presents the softening point values of the neat bitumen and the CLS-modified samples. Consistent with the trends observed in the penetration test, the incorporation of CLS led to a monotonic, though modest, upward shift in softening point values. The base bitumen (B) exhibited a softening point of 48.9 °C, while the 3CLS, 5CLS, 7CLS, and 9CLS samples yielded softening points of approximately 49.5, 50.3, 50.3, and 50.4 °C, respectively.

The 9% CLS dosage resulted in a modest increase in the softening point of approximately 1.5 °C compared to the neat binder. This response was significantly more muted in contrast to the penetration test, which demonstrated a 14.6% reduction in penetration depth. This disparity arises because the penetration test is sensitive to near-ambient viscosity, whereas the softening point reflects behavior at elevated temperatures, where the influence of the absorbed maltene fraction is diminished.

Within the tested dosage range, the data reveal two distinct phases. Initially, a moderate increase in the softening point suggests that CLS effectively interacts with asphaltene and resin fractions. Subsequently, this is followed by a plateau phase, which indicates that the stiffening

effect of CLS reaches a saturation point, beyond which additional additive does not significantly alter the binder's flow transition temperature.

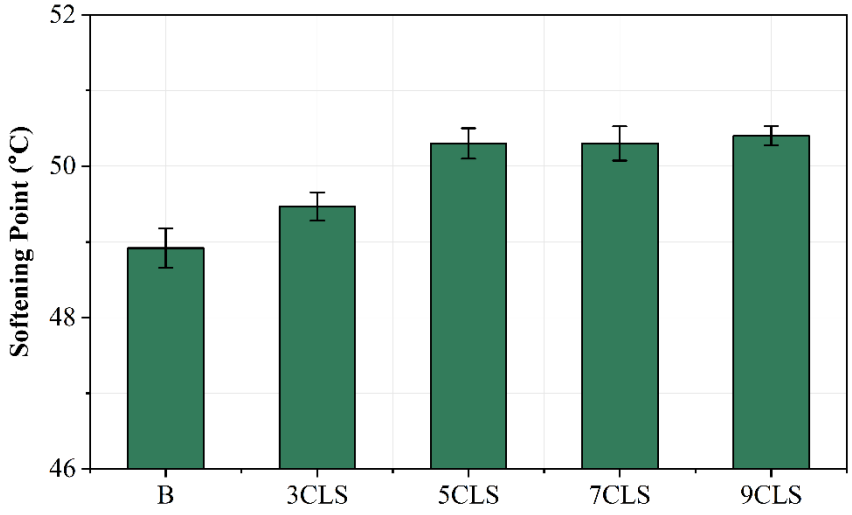


Fig. 2. Softening point test results.

These findings align well with the broader CLS literature. For instance, Fatemi et al. observed a slight upward trend in the softening point of 60/70 penetration-grade bitumen as CLS increased, attributing this limited sensitivity to complex chemical interactions between lignosulfonate and asphaltenes [1]. Furthermore, previous studies indicate that while higher CLS loadings improve high-temperature performance and thermal susceptibility, they offer diminishing returns [1], [5]. Similar trends are reported for kraft lignin modifiers, which can improve softening points but may introduce risks of phase separation and brittleness [10].

Fig. 3 shows the rotational viscosity of the neat and CLS-modified binders. The base bitumen (B) returned an RV of approximately 400 mPa·s, while the 3CLS, 5CLS, 7CLS, and 9CLS samples yielded 440, 463, 490, and 525 mPa·s, respectively. This corresponds to increases of 10%, 15.8%, 22.5%, and 31.3% relative to B.

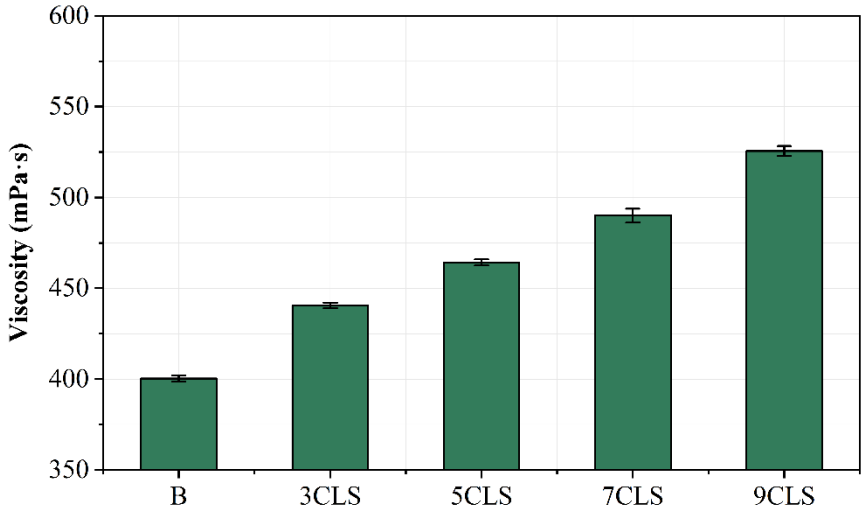


Fig. 3. RV test results at 135 °C.

In contrast to the softening point behavior — where a plateau was observed beyond 5% CLS — RV continued to rise monotonically across the entire dosage range, indicating that CLS

stiffens the binder continuously rather than reaching a saturation threshold. This trend could suggest that CLS acts primarily through maltene absorption, a mechanism that potentially changes the binder's intermediate- and near-ambient viscosity rather than its high-temperature flow onset.

The monotonic RV increase implies a workability penalty: the plant will require higher mixing and compaction temperatures, and the binder becomes more prone to low-temperature cracking [1]. The very small error bars across all samples confirm the repeatability of the measurements.

Taken together, the three conventional tests confirm a consistent picture: CLS acts as a systematic stiffening agent across the 0–9 % dosage window, but the magnitude and shape of the response differ among tests. Penetration decreases monotonically by up to ~14.6 % at 9 % CLS, while softening point rises modestly and plateaus beyond 5 % CLS (~3.1 %), and rotational viscosity climbs more steeply and continuously (~31.3 % at 9 % CLS). This asymmetric response indicates that CLS reinforces the binder predominantly in the intermediate-temperature viscosity regime, consistent with a maltene-absorption mechanism [1], [10]. A practical optimum therefore emerges within the 5–7 % CLS range, where stiffening is largely achieved before the viscosity-related workability penalty becomes dominant [1], [7]. Because the three indices are obtained at different temperatures, they do not yield a single temperature-uniform descriptor of the binder; this motivates the PI and PVN calculations presented in the next section.

3.2 Results of Temperature Susceptibility Indices

The *PI* values calculated from the penetration and softening point results are presented in Fig. 4. All samples exhibited negative *PI* values, ranging from −1.25 to −1.05, which is consistent with conventional paving-grade bitumen and indicates a relatively higher temperature susceptibility compared to oxidized binders.

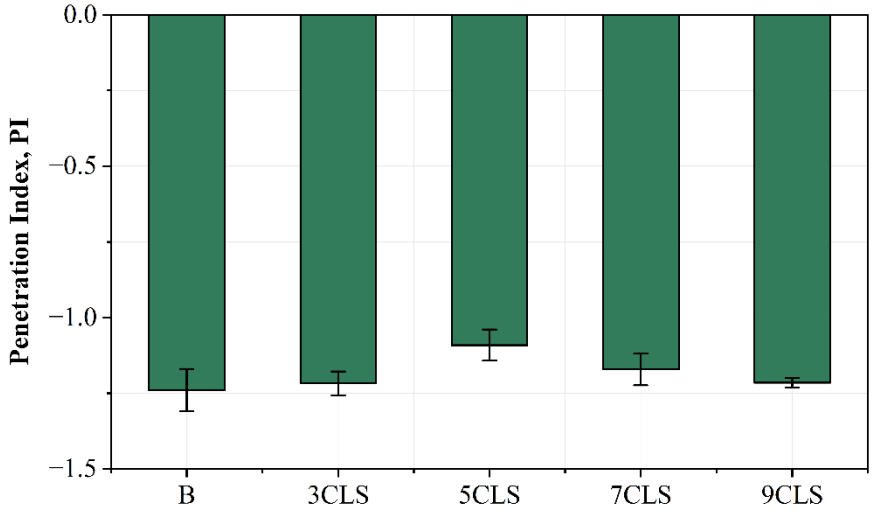


Fig. 4. *PI* values.

The base bitumen (B) yielded the lowest PI value (≈ −1.25), reflecting its higher sensitivity to temperature changes. The incorporation of CLS shifted the PI values towards less negative values, indicating a reduction in temperature susceptibility. Among the modified samples, the 5CLS blend produced the most pronounced improvement, reaching the highest PI value (≈ −1.05) within the tested dosage range. Beyond this optimum, increasing the CLS content to 7% and 9% resulted in a slight reversal of this trend, with PI values decreasing back to

approximately −1.15 and −1.20, respectively. The 3CLS sample (≈ −1.22) showed only a marginal improvement over the base bitumen.

This non-monotonic behavior suggests that 5% represents the optimum CLS dosage for minimizing temperature susceptibility within the investigated range. The narrow error bars across all samples confirm the good repeatability of the measurements. Overall, the PI results indicate that CLS modification enhances the thermal stability of the binder, although the magnitude of improvement remains modest and does not shift the binder outside the range of conventional unmodified bitumen.

The *PVN* values calculated from the penetration, viscosity at 60 °C and viscosity at 135 °C are presented in Figure 5. In line with the *PI* values, all samples yielded negative *PVN* values, indicating that the binders fall within the category of relatively temperature-susceptible bitumens.

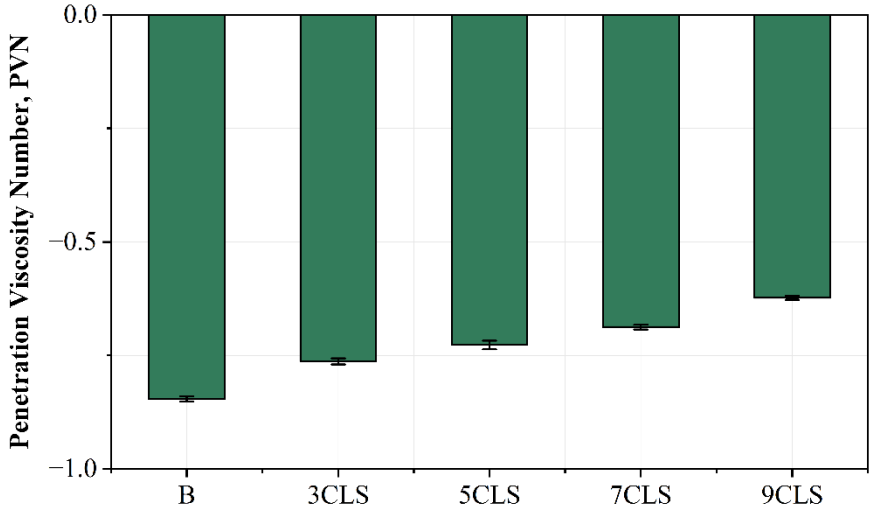


Fig. 5. *PVN* values.

The base bitumen (B) yielded the most negative PVN (≈ −0.85). The addition of CLS shifted *PVN* towards less negative values in a largely monotonic manner as the dosage increased: −0.80 (3CLS), −0.75 (5CLS), −0.70 (7CLS), and the highest value of approximately −0.62 at 9CLS. The narrow error bars again indicate good repeatability of the measurements.

Although both *PI* and *PVN* are derived from the penetration at 25 °C, they incorporate different second parameters: *PI* uses the softening point, whereas *PVN* incorporates the viscosity at 135 °C. This explains the slightly different trends observed for the two indexes. *PI* peaked at 5CLS and then decreased at higher dosages, suggesting that the stiffening effect captured by the softening point does not continue to improve beyond 5% CLS. *PVN*, on the other hand, increased steadily with rising CLS content, indicating that the absolute viscosity at 135 °C, which governs mixing and compaction workability, responds more linearly to CLS addition. In other words, *PI* is more sensitive to high-temperature rheological transitions near the softening point, while *PVN* reflects the progressive increase in viscosity with CLS dosage. Taken together, both indices confirm that CLS reduces the temperature susceptibility of the binder, but *PVN* appears to capture the dosage-dependent improvement more consistently than *PI*.

4 Conclusions

This research investigated the influence of calcium lignosulfonate modification on the conventional properties and temperature susceptibility of bitumen. Bitumen samples modified with 3–9% CLS were subjected to penetration, softening point, and rotational viscosity testing, and the Penetration Index and Penetration Viscosity Number were calculated. Based on these experimental findings, the following conclusions can be drawn:

- CLS acts as a stiffening agent. Adding 3–9 % CLS to a 50/70 penetration grade bitumen produced a monotonic decrease in penetration and a monotonic increase in rotational viscosity at 135 °C, demonstrating a systematic stiffening effect.
- The high-temperature softening response is limited. The softening point increased only modestly and plateaued beyond 5% CLS, indicating that CLS influences the intermediate- and near-ambient viscosity regime more than the high-temperature flow onset.
- The temperature susceptibility is reduced. Both PI and PVN shifted toward less negative values relative to the neat binder, confirming that CLS lowers the binder's sensitivity to temperature variations.
- The two indices show complementary trends. PI peaked at 5CLS and slightly declined at higher dosages. PVN increased monotonically up to 9CLS, reflecting a more linear response of viscosity to CLS dosage.

The conclusions are derived from empirical conventional tests; long-term aging performance and rheological behavior under repeated loading remain to be validated in future studies using RTFOT/PAV aging and DSR-based protocols.

Acknowledgments
The author Aytuğ Kumandaş is supported by The Scientific and Technological Research Council of Türkiye (TÜBİTAK) within the scope of the 2211-A National PhD Fellowship Program. The authors would like to thank TÜBİTAK for this support.

References

1. Fatemi, S., Bazaz, J.B., Ziaee, S.A.: The pros and cons of using calcium lignosulfonate as a recycled anti-aging additive on engineering properties of bituminous mastics. Case Studies in Construction Materials **15**, e00739 (2021).
2. Kataware, A., Suryawanshi, S., Singh, T.: Assessing moisture resistance of calcium lignosulphonate modified bitumen through SFE, BBS, and ITS approaches. International Journal of Adhesion and Adhesives **148**, 104305 (2026).
3. Ziaee, S.A., Fatemi, S., Zarei, M., Fini, E.H.: Introduction of calcium lignosulfonate to delay aging in bituminous mixtures. Construction and Building Materials **400**, 132798 (2023).
4. Ziaee, S.A., Fatemi, S., Shaker, H., Ameri, M., Saadatjoo, S.A., Fatemi, S.S.: Optimization of CLS content of asphalt mixtures based on balanced mix design approach. Advances in Civil Engineering **2023**, 1–14 (2023).
5. Fatemi, S., Bazaz, J.B., Ziaee, S.A., Bolouri Bazaz, J.: Evaluation of rutting and fatigue behaviors of asphalt binders modified with calcium lignosulfonate. Advances in Civil Engineering **2021**(1), 6894514 (2021).
6. Fatemi, S., Bazaz, J.B., Ziaee, S.A.: Laboratory investigation of using calcium lignosulfonate as an oxidation inhibitor in bitumen. Advances in Civil Engineering **2022**(1), 1488958 (2022).

7. Fatemi, S., Bazaz, J.B., Ziaee, S.A.: Investigating the effect of calcium lignosulfonate on the durability and performance of asphalt mixtures. Advances in Materials Science and Engineering **2022**, 1–14 (2022).
8. Zarei, M., Abdi, A.A., Zahedi, M., Akbarinia, F., Khanjari, M.: Evaluation of low and intermediate temperatures fracture indices for modified warm mix asphalt (WMA) using edge notched disc bend (ENDB) specimen. Theoretical and Applied Fracture Mechanics **116**, 103137 (2021).
9. Kamratowsky, E., Fu, C., Leischner, S., Haverkamp, P., Traverso, M., Liu, P.: Technical performance of lignin-modified bitumen and organic bitumen as binders for asphalt considering environmental criteria. Construction and Building Materials **506**, 144801 (2025).
10. Sharma, A., Boora, A., Kumar, Y.: Mechanical and rheological properties evaluation for lignin-modified asphalt mixtures. Proceedings of the Institution of Civil Engineers – Waste and Resource Management **178**(3), 164–182 (2025).
11. Gaudenzi, E., Cardone, F., Lu, X., Canestrari, F.: Chemical and rheological analysis of unaged and aged bio-extended binders containing lignin. Journal of Traffic and Transportation Engineering (English Edition) **10**(6), 947–963 (2023).
12. Dehnad, M.H., Al-Lihyawi, Z.: The impact of lignin as soil stabilizer on the characteristics of treated base through full-depth recycling of pavement. Results in Materials **27**, 100754 (2025).
13. Zarei, M., Abdi, A.A., Zahedi, M.: Pure mode I and pure mode II fracture resistance of modified hot mix asphalt at low and intermediate temperatures. Fatigue & Fracture of Engineering Materials & Structures **44**(8), 2222–2243 (2021).
14. Ziaee, S.A., Fatemi, S., Bazaz, J.B., Shad, R., Saadatjoo, S.A.: Evaluating the cracking resistance of hot mix asphalt modified with calcium lignosulfonate at low and intermediate temperatures. Scientia Iranica (2024).
15. Shah, S.M.R., Min, Y.H., Awang, S.N., Tey, L.-S.: Waste materials as extender of bituminous binder: A review. Jurnal Kejuruteraan **35**(6), 1467–1474 (2023).
16. Gaudenzi, E.: Performance analysis of bio-based asphalt mixtures containing lignin. Università Politecnica delle Marche, pp. 1–12 (2023).
17. Zarei, M., Abdi, A.A., Zahedi, M.: Evaluation of fracture behavior of modified warm mix asphalt (WMA) under modes I and II at low and intermediate temperatures. Theoretical and Applied Fracture Mechanics **114**, 103015 (2021).

Author Contribution Statement

- *Conceptualization:* Aytuğ Kumandaş, Erhan Burak Pancar, Şeref Oruç
- *Methodology:* Aytuğ Kumandaş, Neslihan Şahan, Ersoy Kabadayı
- *Investigation:* Erman Çavdar, Mahir Kumantaş
- *Writing – Original Draft:* Aytuğ Kumandaş, Neslihan Şahan, Mahir Kumantaş
- *Writing – Review & Editing:* Erman Çavdar, Ersoy Kabadayı, Erhan Burak Pancar, Şeref Oruç

List of Abbreviations

- **CLS** — Calcium Lignosulfonate
- **PI** — Penetration Index
- **PVN** — Penetration-Viscosity Number
- **RV** — Rotational Viscosity
- **RTFOT** — Rolling Thin Film Oven Test
- **PAV** — Pressure Aging Vessel
- **DSR** — Dynamic Shear Rheometer

Publication Note
This paper was peer-reviewed, accepted for presentation, and included in the proceedings of the ACE2026 – International Conference on Advances in Civil Engineering, held on 12–14 October 2026 in Trabzon, Türkiye.

This paper may be cited as follows:
Kumandas A., Cavdar E., Kumantas M., Kabadayı E., Sahan N., Pancar E., Oruc, S., "Influence of CLS Modification on the Conventional Properties and Temperature Susceptibility of Bitumen," in Proceedings of the ACE2026 – International Conference on Advances in Civil Engineering, Trabzon, Türkiye, 12–14 October 2026.

Possible User Effects of Sakarya Adapazari - Serdivan Tram Line on Sakarya Transportation

Aykut TOPÇU[1]*, Mustafa GÜRSOY[2,]
Yildiz Technical University, Graduate School of Science and Engineering, Intelligent Transportation Systems, 34210 Davutpasa-Esenler, Istanbul, TURKIYE
aykut.topcu@std.yildiz.edu.tr

Abstract

Urban transportation policies in Turkey have been planned to be mainly in the center of highway for a long time until recent years. This situation, along with rapid urbanization and population growth, has brought problems in many ways, especially traffic density, accessibility problems and environmental impacts. The development of transportation infrastructure has prevented the sustainable planning of public transportation, especially in medium-sized cities; The flexibility of highway-based systems but their inability to provide high capacity has caused urban mobility to be negatively affected in the long term. In recent years, rail systems have started to gain importance thanks to their high passenger capacity, regular operation, relatively low emission production in terms of environmental impact and opportunities to increase the quality of urban life. In line with this trend, Adapazari - Serdivan Tram Line, stands out as an important project that has the potential to create a fundamental transformation in the city's transportation system. The dense student population in Sakarya City, the commercial and socioeconomic dynamics of the center of Adapazari, the rapid development of the Serdivan region and the increasing demand for travel between these two centers pave the way for the Adapazari - Serdivan Tram Line to be a strategic investment in terms of urban transportation. However, many factors such as the integration of a new rail system line planned in the center of the city with the existing minibus and bus transportation, operating efficiency, critical points in route selection, access distances, possible traffic effects, reflections of the construction process on urban life and long-term demand projections need to be evaluated comprehensively. This study was carried out by continuing the studies with the delphi method in order to analyze the possible effects of the planned tram line on the transportation system in Sakarya with a holistic approach. The opportunities, possible risks, integration requirements and demand potential of the line were evaluated. Pre-construction studies are not only the physical infrastructure for the successful implementation of the project; It reveals the necessity of holistic coordination in public transportation, effective integration with alternative modes of transportation, taking into account the behaviors of the people of Sakarya and a planning approach compatible with urban development dynamics. In this respect, the study opens the place of the tram line planned for Sakarya in the transportation system to discussion on a scientific basis and provides evaluations that guide the decision-making processes for rail system investments in similar medium-sized cities in Turkey.

Keywords: *Transportation; Tram; Feasibility; Planning;*

1 Introduction

Transportation can generally be defined as the transportation (mobilization) of people and goods to where they are needed and when they are needed. According to this definition, the impact of the performance of the transportation system on the economic and social life in the city is quite large [1] [2].

Transportation; It is grouped under five subsystems: rail, road, sea, air and pipeline transportation. Among them, railway and road are two systems that can be substituted for each other [3]. Considering the investment costs of transportation projects, the issue of which of these subsystems will be prioritized is of great importance for the economy. Transportation subsystems; It forms an integrity with infrastructure, vehicles, management and all its elements. Compatible with and supporting social and economic development; The necessary transportation policy should be determined in order to achieve the goal of a cheap, fast, regular, safe, non-polluting transportation that does not pollute the environment, in short, a healthy transportation with the lowest cost to the country. [4].

In terms of planning, transportation is considered as ensuring the necessary harmony between different types of transportation on the one hand, and ensuring an effective integrity between economic development and transportation services on the other. Transportation investments; These are investments that should be evaluated not only according to profitability criteria, but also with criteria such as economic development, social, political, security and public transportation. [3].

In our country, the share of the rail system in both urban and intercity transportation is always It is increasing day by day. With the increase in demand for easy and comfortable transportation Both local and central governments increased their new rail system investments continues. Planning, design, Financing needs Rail that needs programming, field applications and long construction processes The development of the systems is also for the lines that are already in operation and are being taken maintenance is needed. With high investment cost and special Maintenance of rail systems with disciplines Line structure, vehicles, signaling, energy systems, etc. prepared. [5].

Trams use the same road surface as road transportation vehicles and have low floors. A city with a relatively low passenger capacity, where vehicles are controlled by a vatman It is an internal rail system. On rails laid at the same level as the road pavement Transition to moving trams according to road vehicles at crossings and intersections right of way priority is ensured. The distance between the platforms on tram lines is higher than in other urban rail systems.

It is short. Tram systems, which generally have a rail gauge of 1435 mm, are 750 V These are systems that work with energy fed from DC voltage catenary. One way The tram, which has a capacity of 10.000 – 20.000 passengers per hour, has an average of The operating speed is 20 km/h [6].

In this study, it is focused to reveal the possible effects of Sakarya Adapazari - Serdivan Tram Line on Sakarya transportation. The necessity of large-scale projects such as rail system investments, their optimal cost, the location or route where they will be built, the possible damage to the environment and other effects that may arise should be carefully examined. Since the proposed system is an at-grade LRT project, potential traffic congestion has raised significant concerns among the public. In this study, the reality of these concerns was investigated by consulting the opinions of Sakarya Metropolitan Municipality Transportation Department officers, academicians and engineers working in the field of transportation.The positive and negative effects of the projects and investments that are the subject of this study on the city were examined with the Delphi technique. In this technique, two rounds of questionnaires were applied to the officers of the Sakarya Metropolitan Municipality Transportation Department, academicians and engineers who are experts in the field of

transportation working in the project, unaware of each other. The responses given at the end of each round of surveys were evaluated with statistical analyses and it was confirmed whether a consensus was reached on each item. As a result of the survey rounds, the questions on which a common decision could not be reached were redirected to the experts in order to reach a consensus.

2 Sakarya Adapazari – Serdivan Tram Line

The planned Sakarya Adapazari - Serdivan Urban Tram Line has a total route length of 15,4 km and 18 stations, and has been designed as the main public transportation backbone in the urban corridor with high travel demand. In order to overcome the topographic thresholds and narrow land use constraints in the city center, the maximum longitudinal slope was designed as 9.0% in the vertical geometric design of the line. This gradient value is within operationally operable limits thanks to the high traction and drive systems of modern very light rail vehicles.

A total of 2,275 meters long engineering structure was designed in order to keep the line within the slope limits, to maintain the operating speed and to minimize surface traffic intersections. These structures are; It consists of 1,070 meters of open U-section and 1,205 meters of cut and cover tunnel structure. The route mainly proceeds in the Right-of-Way Category B type; TCDD, which provides regional train integration, provides direct service to strategic locations such as Adapazari Station and Cark Street, which is the main pedestrian/commercial axis of the city. Thus, the line establishes a seamless and highly accessible transportation link between the historic city center of Adapazari and the thriving residential and education-oriented areas of Serdivan.

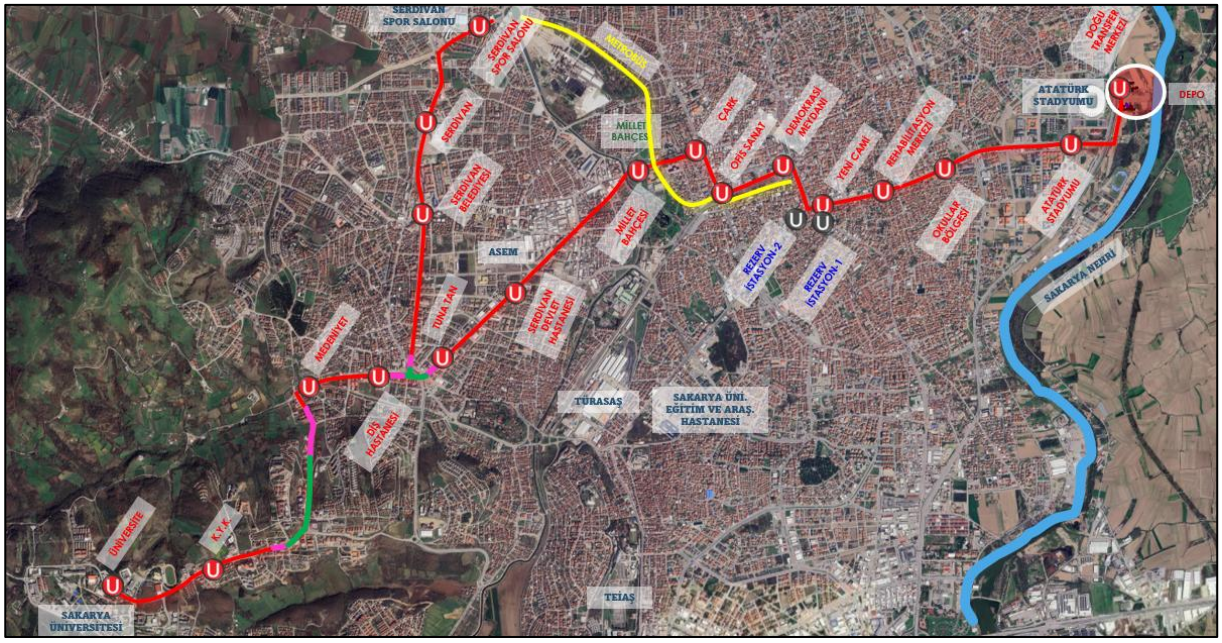


Figure 1- Sakarya Adapazari - Serdivan Tram Line

3 Materials and Methods

The 13-question survey detailed in Table 1 was administered to the expert group

Table 1 - Questions

Possible User Effects of Sakarya Adapazarı - Serdivan Tram Line on Sakarya Transportation

A. Please rate each of the statements compiled below regarding Integration and Competition with Existing Public Transportation (Dolmus/Minibus) on a scale from 1 to 5 (1 = Strongly Disagree, 2 = Disagree, 3 = Undecided, 4 = Agree, 5 = Strongly Agree). **Note: If desired, you may write the rationale for your score in the line provided below each item.**	**Rating**
1)Once the Adapazari–Serdivan tramway line becomes operational, existing dolmus and minibus lines along this corridor should be completely phased out and converted exclusively into 'perpendicular feeder lines'.	**-**
Reason:	
2) In order to ensure the financial sustainability of the tramway system, the service frequencies of road-based public transit vehicles on parallel routes should be reduced.	**-**
Reason:	
3) Considering the mobility habits of the residents of Sakarya, if the access distance to tram stops exceeds 500 meters, passengers will continue to prefer the more flexible dolmus instead of the tramway.	**-**
Reason:	
B. Please rate each of the statements compiled below regarding Risk Analysis on a scale from 1 to 5 (1 = Strongly Disagree, 2 = Disagree, 3 = Undecided, 4 = Agree, 5 = Strongly Agree). **Note: If desired, you may write the rationale for your score in the line provided below each item.**	**Rating**
4) The intersection congestion issues observed in the Sakarya Metrobus (BRT) operation are highly likely to occur on the at-grade (street-running) Tramway line as well.	-
Reason:	
C. Please rate each of the statements compiled below regarding Risk Factors and Reflections of the Metrobus Experience on a scale from 1 to 5 (1 = Strongly Disagree, 2 = Disagree, 3 = Undecided, 4 = Agree, 5 = Strongly Agree). **Note: If desired, you may write the rationale for your score in the line provided below each item.**	**Rating**
5) Traffic congestion stemming from lane reductions in the Metrobus project carries a high risk of causing similar or more severe operational chaos on the at-grade Tramway line.	-
Reason:	
6) The failure to fully integrate the tramway system with existing dolmus and minibus routes (i.e., failing to transform them into feeder routes) is the most critical operational risk that will undermine project efficiency.	-
Reason:	
7) The "door-to-door" travel habits (dolmus culture) of Sakarya residents and students, coupled with resistance to walking distances, will keep demand for a station-based tramway system below expectations.	-
Reason:	

8) Long-term disruptions in the city center during construction (particularly along Cark Street and its feeder roads) will lead to a loss of public support before the project is completed.	-
Reason:	
D. Please rate each of the statements compiled below regarding the Impacts and Travel Demand of the Adapazari – Serdivan Line on a scale from 1 to 5 (1 = Strongly Disagree, 2 = Disagree, 3 = Undecided, 4 = Agree, 5 = Strongly Agree). **Note: If desired, you may write the rationale for your score in the line provided below each item.**	**Rating**
9) The tramway line will reduce private vehicle and private shuttle usage by Sakarya University students for campus access by at least 20% within the next 5 years.	-
Reason:	
10) Retail trade volume along Cark Street and Medeniyet Boulevard will be positively influenced by the pedestrianization effect generated by the tramway.	-
Reason:	
11) The tramway line carries the risk of remaining merely a 'campus line' focused solely on student transport; its contribution to overall urban transit will be limited.	-
Reason:	
E. Please rate each of the statements compiled below regarding the Future Vision and System Expansion on a scale from 1 to 5 (1 = Strongly Disagree, 2 = Disagree, 3 = Undecided, 4 = Agree, 5 = Strongly Agree). **Note: If desired, you may write the rationale for your score in the line provided below each item.**	**Rating**
12) In long-term planning, the existing Metrobus route should be decommissioned, converted into a tramway corridor, and integrated into the rail transit network.	-
Reason:	
13) In long-term planning, rather than planning new tramway lines, the Adapazari–Serdivan Tramway Line should be extended.	-
Reason:	

3.1 Delphi Method

The Delphi technique was developed in the 1950s by researchers Olaf Helmer and Norman Dalkey to systematically elicit expert consensus on military-related issues [7]. Delphi is a "method for structuring a group communication process so that the process is effective in allowing a group of individuals, as a whole, to deal with a com plex problem." The belief is that the group's judgment will have more validity, and will be more complete and accurate than individual points of view [10]

Project designers and technical personnel frequently encounter situations where decision-makers approach a problem from different perspectives, leading to conflicting viewpoints. These differences of opinion may arise regarding the necessary features of a product, the viability of a proposed project, the prioritization of objectives, or the required qualifications of personnel. The Delphi technique is utilized as a consensus-building tool in environments

characterized by such divergent views. It is particularly effective when decisions must be made in political or emotionally charged contexts, or where outcomes risk being influenced by dominant individuals or groups. Defined as a consensus-building mechanism, Delphi systematically solicits expert judgments regarding a specific problem domain. By applying the Delphi technique, individuals and groups with varying perspectives aim to achieve consensus without face-to-face interaction [8], [9].

Anonymity in participation is one of the most critical characteristics of the Delphi technique. The identity behind each proposed opinion is kept confidential throughout the research process. Consequently, ideas are emphasized rather than individuals, preventing unconditional agreement with the views of well-known or highly respected figures within the group. The principle of anonymous participation ensures that diverse and novel ideas can be shared freely without hesitation [8].

Statistical analysis of group responses is conducted after the administration of each Delphi survey round. Participants must thoroughly understand the meaning of the statistics used in these analyses [8]. In this context, the researcher(s) must clearly inform participants regarding the interpretation and significance of the applied statistical analysis results [9].

Controlled feedback; In the Delphi technique, successive questionnaires are used. After the statistical analysis of the survey is completed, the results showing the general trend of the participants are communicated to the participants in the next round. In this way, individuals re-evaluate their own thoughts by comparing them with the results, different opinions and approaches conveyed to them [9].

3.2 Application of the Delphi Method

First, the problem should be identified and described in a few words in a way that all participants can understand [8]. There should be a participant group of at least seven experts who have knowledge and perspective thanks to their experience and qualifications in the work done. The ideal group size consists of 10-20 specialists. Expert groups can be formed from university faculty members in related branches and employers in related fields [8]. First, a 13-question questionnaire containing the problems that may be encountered and possible effects on the project was forwarded to the expert team. All items prepared in the first Delphi questionnaire are forwarded to the participants and they are asked to indicate the level of agreement with each item on a 5-point or 7-point Likert scale. After the second round of survey responses are collected, the 1st quartile, median, 3rd quartile, and interquartile range (IQR) values are calculated for each item [8].

The second Delphi survey is the same as the first round of the survey. In this round, each item is accompanied by the participant's response to that item with the 1st, median, 3rd quartile, and IQR values calculated as a result of the first round. In the second round of the survey, participants are asked to review their responses from the first round, taking into account statistical values. The values calculated in the first round are also calculated for the answers at the end of the second round and evaluated by comparing them with each other. If there is a decrease in the IQR values calculated in the first round for any item in the third round, it can be said that there is a tendency towards consensus for that article. [11].

In this study, while preparing the Delphi survey, the relevant project was meticulously examined and what possible pros and cons there may be in the projects were evaluated. Then, the reservations of the public about the projects were investigated and as a result, it was decided to evaluate the positive and negative aspects of the projects under four main headings (integration management, operational performance and risks, accessibility and social acceptance, socio-economic impact). In the next stage, a participant list consisting of designer engineers (Private Sector), Municipal transportation department officers and academicians from Sakarya University (12 people) working in the Sakarya Adapazari - Serdivan Tram Line

project was prepared. Then, 4 questions were prepared under 13 main headings about the Sakarya Adapazari - Serdivan Tram Line. The questionnaire with the questions was forwarded to each expert in the participant group.

13 experts responded to the first round of the survey. The responses of the experts were evaluated and organized into bullet points to adapt to the format of the second survey. The items prepared in the second questionnaire were adapted to the 5-point Likert scale. Participants were asked to rate each item on a scale of 1 to 5 (1 = strongly disagree, 2 = disagree, 3 = undecided, 4 = agree, 5 = strongly agree). 13 respondents responded to the second round of the survey. The responses were compiled and the 1st quartile, median, 3rd quartile and IQR values were calculated for each item. Having a smaller IQR value means reaching a consensus. In this study, it was accepted that the articles with a IQR value below 1.2 were agreed upon [7].

Then, the second and final round of the questionnaire was conducted and sent to the respondents, who were the respondents of the first round. The second round was conducted in a similar way to the first round of the survey. The 1st quartile, median, 3rd quartile, and IQR values calculated at the end of the first round were added to the second round of the survey, and the participants were asked whether they changed their answers in the second round by taking these values into account. 13 participants responded to the second round of surveys. The responses were recompiled and quartile, median, quartile, 3rd, and IQR values were calculated for each item. Agreed and unagreed articles have been identified.

4 Results

In the last round of the Delphi survey, it was seen that consensus was reached on 11 of the 13 questions.

Possible effects of Sakarya Adapazari - Serdivan Tram Line on Sakarya Transportation:
Integration Management it was examined by 3 items and all of those were agreed upon,
operational performance and risks it was examined by 5 items and 4 of those were agreed upon,
accessibility and social acceptance it was examined by 3 items and 2 of those were agreed upon,
Socio-Economic Impact It was examined by 2 items and all of those were agreed upon.

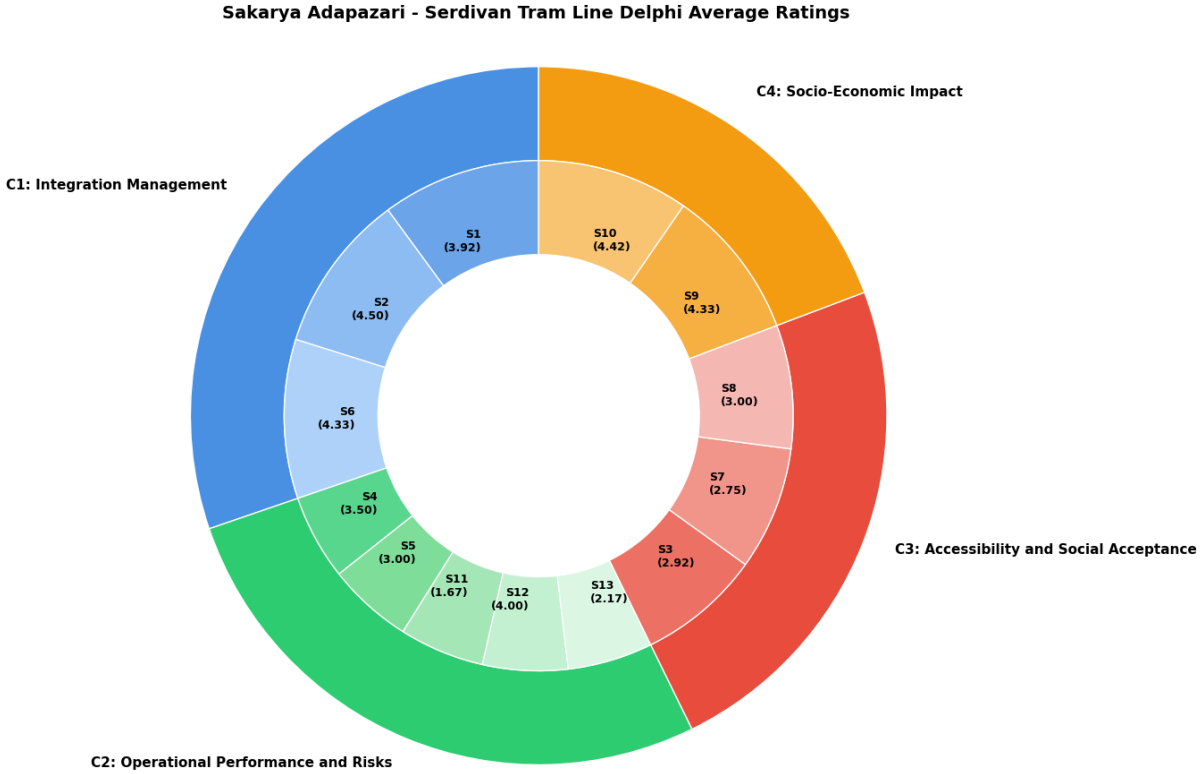


Figure 2 - Average Ratings

In our analyses regarding the detailed examination of the possible effects of the Sakarya Adapazari - Serdivan Tram Line on Sakarya Transportation, it is concluded that a consensus has been reached at the level of "I agree" with the questions about the integration management of the tram line to be made. The decision to organize public transportation vehicles integrated with the tram to be built before the tram is common.

Survey questions on operational performance and risks include the possible effects of the tram line on Sakarya traffic and solutions that can be made to increase tram usage. In the survey responses, it was seen that a consensus was reached in 4 out of 5 questions.

Survey questions were asked about the habits of the people of Sakarya and their adaptation to the use of trams in terms of accessibility and social acceptance. Consensus was reached on 2 of the 3 questions. In the survey responses, it was seen that a consensus was reached at the level of "I am undecided".

Finally, a consensus was reached on 2 questions on socio-economic impact. The possible effects of the tram on the economy of Sakarya and the effects on the places on the route it passes are in the form of the questions conveyed on this subject. The survey responses concluded that a consensus was reached at the level of "agree".

As a result, it is clear that the Sakarya Adapazari - Serdivan Tram Line will be an important part of transportation for Sakarya. However, the issue that has not been agreed upon is the negative effects on Sakarya traffic both during the construction phase and when it becomes operational. The most important issue during the project design phase is that the tram proceeds in traffic at the level and does not increase possible traffic jams. The issues that have been agreed upon are generally their positive effects. There is a common idea that it should revitalize the route it passes, be highly preferred as a use, be designed in a holistic structure with road – based public transit and integrate other public transportation.

References

1. Tanga, K.X., Watersb, N.M. (2005). The internet, GIS and public participation in transportation planning. Progress in Planning, Vol. 64, pp.7–62.
2. Karacasu, M. (2007). Kent içi toplu taşıma yatırımlarının değerlendirilmesinde karar destek modeli (ELECTRE Yöntemi) kullanımı. 7. Ulaştırma Kongresi, İstanbul.
3. Altınok, S. Türkiye'de Ulaştırma Politikaları, Karayolları Ve Demiryollarının Mukayesesi. SÜ İİBF Sosyal ve Ekonomik Araştırmalar Dergisi, pp.73-87
4. Evren, G. Türkiye Ulaştırma Politikalarına Eleştirel Bir Bakış. 10. Ulaşım ve Trafik Kongresi-Sergisi, İstanbul Teknik Üniversitesi
5. ÇINAR, H. (2025). Kentiçi raylı sistemlerde hat bakımı: T1 kabataş bağcılar tramvay hattı örneği (Tez No. 931340) [Yüksek lisans tezi, YILDIZ TEKNİK ÜNİVERSİTESİ]. Ulusal Tez Merkezi.
6. Gunnarsson, A. L. (2001). Light Rail-Experiences from Germany, France and Switzerland. Lulea, İsveç.
7. Dalkey, N., ve Helmer, O., (1962). "An Experimental Application of the Delphi Method to the Use of Experts", RAND CORP SANTA MONICA CA.
8. Sahin, A. E., (2001). "Türkiye'de İlköğretim Okulu Müdürlüğünün Bir Meslek Olarak Mevcut Durumu: Bir Delphi Çalışması", Hacettepe Üniversitesi Eğitim Fakültesi Dergisi, No: (20); 215-220.
9. Arslan, E. S. (2010). Kültürel Peyzaj Kavramı Kapsamında Bir Değerlendirme: Ulus-TBMM Tarihi Aksı (Ankara), Yüksek Lisans Tezi, Ankara Üniversitesi Fen Bilimleri Enstitüsü.
10. Dalkey, N. 1972. Studies in the quality of life: Delphi and decision-making.
11. S. Bacaran And M. Gürsoy, "ANALYZING THE EFFECTS OF NORTHERN MARMARA HIGHWAY AND 3rd BOSPHORUS BRIDGE PROJECT AND 3rd

AIRPORT PROJECT ON ISTANBUL," *International Civil Engineering & Architecture Symposium For Academicans* , İstanbul, Turkey, pp.11-21, 2014

Note: Following the conference, this Publication Note will be added to each paper; therefore, authors are kindly requested not to remove the note below and to complete the author(s) and paper title information.

Publication Note

This paper was peer-reviewed, accepted for presentation, and included in the proceedings of the ACE2026 – International Conference on Advances in Civil Engineering, held on 12–14 October 2026 in Trabzon, Türkiye.

This paper may be cited as follows:

Topcu A., Gürsoy M., "Possible User Effects of Sakarya Adapazari - Serdivan Tram Line on Sakarya Transportation," in Proceedings of the ACE2026 – International Conference on Advances in Civil Engineering, Trabzon, Türkiye, 12–14 October 2026.

Digital Twin Road Corridor Architecture and Maturity Framework in Cooperative Intelligent Transportation Systems

Dilara Usta[1*] and Mustafa Sinan Yardım[2]
[1*] 0009-0005-2342-9541, Transportation Program, Department of Civil Engineering, Graduate School of Science and Engineering, Yildiz Technical University, Istanbul 34220, Türkiye,
[2] 0000-0003-0799-9294, Department of Civil Engineering, Yildiz Technical University, Istanbul 34220, Türkiye
*Corresponding Author E-mail: dilara.usta@std.yildiz.edu.tr

Abstract

Cooperative Intelligent Transportation Systems (C-ITS) enable real-time data exchange among vehicles, infrastructure, and road users. However, most existing Intelligent Transportation Systems (ITS) applications remain focused on traffic monitoring, data collection, and operational control rather than creating dynamic and continuously updated digital representations of road infrastructure. Although digital twin technologies have gained increasing attention in transportation research, corridor-scale approaches integrating real-time data synchronization, roadside units (RSUs), edge AI, V2X communication, and traffic management centers remain limited.

This study examines digital twin road corridors from a C-ITS perspective through a conceptual review of recent literature and selected C-ITS and smart-road initiatives. The roles of sensor networks, AI-supported camera systems, IoT-based data collection, edge computing, and V2X communication are examined, while C-Roads, NordicWay, and selected smart-road initiatives are reviewed to identify relevant practices and implementation approaches. Based on this synthesis, the study proposes a five-stage Digital Twin Corridor Maturity Framework describing the transition from conventional infrastructure toward sensor-enabled, cooperative, digital twin, and adaptive corridor systems. In addition, a C-ITS-based implementation framework for Türkiye is proposed, integrating physical road infrastructure, RSUs, AI-supported perception systems, traffic management centers, cloud/edge computing, and the digital twin platform within a unified architecture.

The analysis suggests that digital twin road corridors can extend beyond conventional traffic monitoring by supporting real-time decision-making, predictive traffic management, and adaptive corridor operations. However, standardization, interoperability, data governance, cybersecurity, and infrastructure compatibility remain key challenges. In view of Türkiye's emerging 5G-supported smart road initiatives, the proposed framework provides a conceptual basis for the future development of C-ITS-enabled digital road corridors.

Keywords: C-ITS; Digital Twin Road Corridors; Predictive Traffic Management

1. Introduction

Cooperative Intelligent Transportation Systems (C-ITS) are emerging as a next-generation transportation approach based on real-time data sharing among vehicles, road infrastructure, and traffic management centers. Through Vehicle-to-Everything (V2X) communication technologies, the goal is for the infrastructure to move beyond being merely a physical component of transportation and actively participate in sensing, communication, and decision-

making processes. This transformation offers significant opportunities for improving traffic safety, optimizing traffic flow, and supporting sustainable transportation policies [1].

However, the majority of Intelligent Transportation Systems (ITS) applications currently in use are limited to functions such as traffic monitoring, incident management, and operational traffic control. Although current systems collect information from various data sources, they are unable to create an integrated digital structure that represents the physical road infrastructure in real time and is continuously updated. In particular, the widespread adoption of connected and autonomous vehicles necessitates the transformation of infrastructure into smart systems capable of not only generating data but also perceiving their surroundings, generating predictions, and providing decision support [2].

Against this background, Digital Twin (DT) technology has attracted increasing attention in transportation research. The DT approach integrates monitoring, analysis, simulation, and decision-support processes by creating digital representations of physical systems synchronized with real-time data. Recent studies indicate that DT technology holds significant potential for the management of transportation infrastructure throughout its lifecycle [3].

However, the existing literature largely focuses on DT applications in building management, industrial production systems, smart cities, and individual transportation infrastructure elements such as bridges, tunnels, and pavements [4]. While European-scale C-ITS initiatives such as C-Roads and NordicWay have demonstrated the feasibility of interoperable V2X services, they do not offer an approach that integrates sensor networks, roadside units (RSUs), artificial intelligence, edge computing, cloud data management, and traffic management centers within a corridor-scale DT architecture [2, 5].

In this context, there is a significant gap in the literature regarding an integrated DT Road Corridor reference architecture applicable at the corridor scale, a systematic maturity framework for assessing technological development levels, and an implementation model for adapting the approach to Türkiye's transportation ecosystem. This study addresses this gap with three key contributions. First, a Digital Twin Road Corridor Reference Architecture that addresses C-ITS components in an integrated manner is proposed. Second, a five-level Digital Twin Road Corridor Maturity Framework is developed to assess the technological transformation of road corridors from static infrastructure to adaptable digital twin corridors. Finally, by jointly evaluating international best practices alongside Türkiye's C-ITS vision and 5G-enabled smart road initiatives, a C-ITS-based DT Road Corridor Implementation Framework is proposed for Türkiye.

2. The Digital Twin Road Corridor Approach and Literature Review

In this section, DT approaches in transportation infrastructure are evaluated in conjunction with C-ITS-based smart road applications, and the theoretical foundations of the proposed corridor architecture are presented.

2.1. Digital Twin in Transportation

DT applications in the transportation sector cover various areas of application, including the lifecycle management of infrastructure assets such as bridges, tunnels, pavements, and highways, as well as structural health monitoring, maintenance planning, traffic operations, and decision support systems [4], [6]. Research conducted particularly in recent years demonstrates that DT technology can be effectively utilized in real-time data collection, the evaluation of operational performance, and predictive maintenance processes [7]. In addition, DT architectures for highway infrastructure highlight the importance of sensor networks, data management, and analysis layers that enable a continuous flow of data between the physical infrastructure and the digital platform [3].

2.2. Current Intelligent Road Projects

The field implementation of C-ITS has gained significant momentum in recent years, particularly in Europe and Asia. The projects developed within this framework demonstrate the

feasibility of implementing key C-ITS components—such as V2X communication, roadside units (RSUs), traffic management centers, and real-time data sharing—at various scales. However, the focus areas, technologies used, and scope of implementation vary depending on each country's transportation policies and technological infrastructure.

The C-Roads Platform, implemented in Europe, is one of the most comprehensive initiatives aimed at developing interoperable C-ITS services across different countries. Within the scope of the project, services such as hazardous road conditions, roadwork, traffic congestion, and variable speed management have been tested using common communication standards, with a strong emphasis on cross-border interoperability [2]. Similarly, the NordicWay project has focused particularly on cross-border data sharing and cooperative traffic services by implementing real-time V2X services over cellular communication infrastructure in the Nordic countries [5].

In applications outside Europe, smart road and connected transportation projects being carried out in China and South Korea demonstrate trends toward the integration of components such as advanced sensing systems, AI-powered data processing, 5G-based communication, and autonomous vehicle testing environments into transportation infrastructure. These applications demonstrate that digital road infrastructure is not limited to communication systems alone; rather, it must be viewed as a comprehensive ecosystem encompassing data collection, analysis, decision support, and traffic management processes [6].

2.3. Literature Review

In transportation infrastructure, DT technology goes beyond the traditional reactive management approach to offer a dynamic, proactive, and data-driven approach that encompasses the entire project life cycle—from planning and design through construction, operation, maintenance, and decommissioning. In a comprehensive literature review conducted by Wu et al. (2025), DT systems for transportation infrastructure were categorized based on their functional scope and data integration methods; a "4 Horizontal + 4 Vertical + N"-based urban transportation architectural framework, comprising data, model, service, and application layers, as shown in Figure 1, was proposed. However, the majority of applications in the existing literature focus on independent components such as traffic flow management or structural health monitoring (SHM) of structures like bridges and tunnels; it is emphasized that critical technical challenges—such as the integration of multi-source heterogeneous data, real-time data processing latency, and a lack of interoperability between systems—persist. This situation underscores the need to advance efforts to establish a standardized road corridor architecture that enables data sharing among heterogeneous devices within the C-ITS ecosystem and to design a maturity framework that evaluates the evolutionary development of these systems [7].

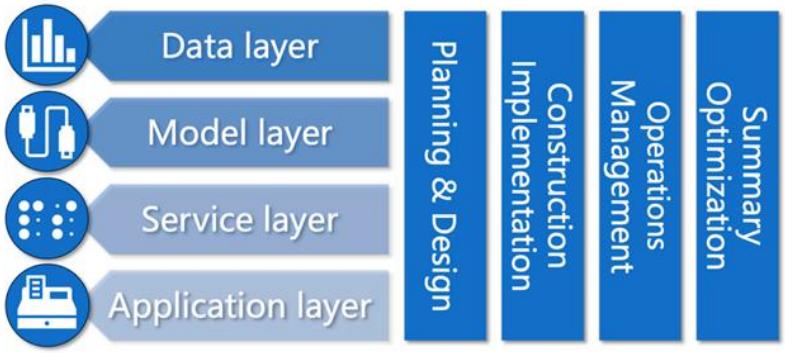


Figure 1. DT framework for urban transportation infrastructure based on the "4 Horizontal + 4 Vertical + N" model [7].

In the literature, theoretical frameworks and general reference architectures for the integration of ITS and DT technologies have begun to be developed. Indeed, Irfan et al. (2024) proposed a hierarchical Transportation DT (TDT) architecture extending from the individual entity level to the network level and comprehensively compiled potential application areas. However, a large portion of existing studies either remain at the conceptual level or are limited to simulation scenarios at the scale of a specific intersection or corridor. In dynamic transportation networks, the real-time synchronization of heterogeneous and large-scale sensor data, the instantaneous estimation of missing information, and the low-latency real-time processing requirements for network-wide proactive optimizations are among the technical challenges on which current research is focusing. Furthermore, the high uncertainty inherent in driver and pedestrian behavior makes it difficult for existing data-driven and physics-based models to generate scalable decisions on their own [8].

Studies on highway infrastructure demonstrate that DT technology must be approached as an integrated framework—encompassing data management, system modeling, and service layers—rather than merely creating a digital representation of the physical infrastructure. In this context, the proposed architectures aim to monitor and manage highway infrastructure throughout its lifecycle via multi-layered structures comprising physical infrastructure, virtual models, data management, connectivity, and service components [3]. Similarly, DT approaches developed for transportation systems focus on enhancing traffic safety, mobility management, and operational decision-support processes by integrating the physical, digital, and communication layers [8].

A comprehensive review of the existing literature reveals that DT technologies are being addressed in an increasingly comprehensive manner within transportation infrastructure. While Wang et al. [3] proposed a multi-layered DT architecture for road infrastructure, Wu et al. [7] comprehensively examined data integration, architectural layers, and decision-support mechanisms in transportation infrastructure. Similarly, Irfan et al. [8] presented a scalable DT reference architecture for transportation systems. Despite these advances, few studies integrate physical road infrastructure, RSUs, V2X communication, sensor networks, AI-based analytics, edge/cloud computing, and Traffic Management Centers (TMCs) within a single corridor-scale operational architecture. Similarly, while existing research focuses on DT architectures or functional layers, maturity models capable of systematically evaluating the technological transformation of corridors are also addressed only to a limited extent. Furthermore, despite international developments, studies on application frameworks that link Türkiye's C-ITS ecosystem, national strategy documents, and 5G-enabled pilot applications to a DT approach are considered an emerging area of research. To address these gaps, an integrated DT Road Corridor Reference Architecture, a five-level maturity framework, and a C-ITS-based implementation framework for Türkiye are proposed.

3. Proposed Digital Twin Corridor Maturity Framework

3.1. Design Approach of the Reference Architecture

Rather than being based on a specific technology or communication infrastructure, the proposed reference architecture is designed as a modular and scalable structure centered on the core functions that a DT-based transportation corridor must fulfill. Three fundamental design principles were adopted in the development of the reference architecture. These design principles align with the physical-digital mapping, continuous data flow, multi-layered architecture, service-oriented usage, and decision-support requirements throughout the lifecycle—all of which are emphasized in the current literature on transportation digital twins. First, the goal is to transfer and update data obtained from the physical road corridor to the digital environment in real time. Second, a flexible architectural structure has been adopted to ensure that different sensing and communication technologies can be integrated into the system in an interoperable manner. Finally, a closed-loop data flow has been established to ensure that

the generated information is used not only for monitoring purposes but also in traffic management and operational decision-support processes. The six-layer reference architecture developed in accordance with these principles is described in the following section.

3.2. Definition of Architectural Layers

The proposed DT Road Corridor Reference Architecture is based on an integrated data lifecycle that enables the sensing, secure transmission, processing, digital representation, and conversion of data generated within the physical road corridor into operational decisions. The architecture consists of six complementary functional layers; while each layer performs a specific task, it also forms part of the data flow that feeds the subsequent layer. Thus, the system transcends the role of a mere data-collecting infrastructure; through a real-time feedback mechanism, it acquires a closed-loop structure that ensures continuous synchronization between the physical corridor and the DT. Figure 2 visualizes the proposed DT road corridor reference architecture and the closed-loop data flow. The architecture also addresses cybersecurity, data governance and privacy, interoperability and standards, and organizational collaboration as cross-cutting enablers that support all six functional layers.

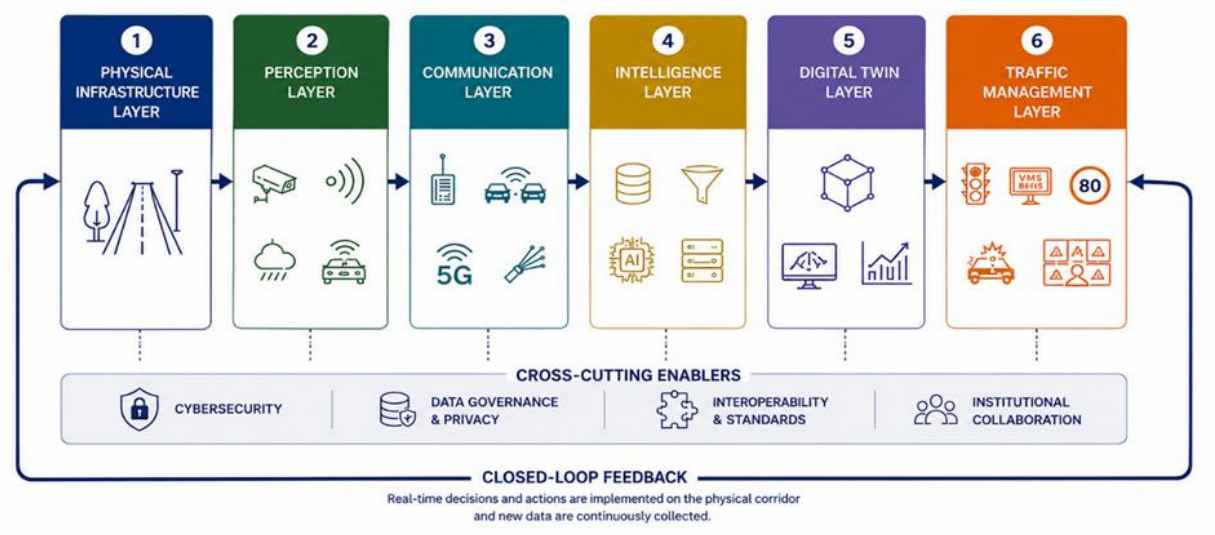


Figure 2. Proposed DT Road Corridor Reference Architecture and Closed-Loop Data Flow

In the proposed architecture, data obtained from the Physical Infrastructure and Perception layers is transmitted to the upper layers via the Communication Layer; it is processed in the Intelligence Layer and used to create a dynamic digital representation of the physical corridor in the Digital Twin Layer. The Traffic Management Layer, in turn, ensures that Digital Twin outputs are converted into operational decisions and fed back to the physical corridor. Thus, the architecture forms a closed-loop structure spanning from perception and data transmission to predictive analysis and operational intervention. The basic functions, components, and data types processed by the layers are summarized in Table 1. In this context, the layers comprising the proposed reference architecture have been defined by considering their basic functions, main components, and the data flow between layers (Table 1). The proposed layers have been designed to seamlessly represent the data, information, and decision lifecycle, extending from the physical system to the generation of operational decisions.

Table 1. Layers of the Proposed DT Road Corridor Reference Architecture

Layer	Basic Function	Main Components	Data Generated/Processed
Physical Infrastructure Layer	Represents the physical route corridor	Roads, intersections, lanes, traffic signals, VMS, vehicles	Physical status information
Perception Layer	Collects data from the physical environment	Cameras, LiDAR, radar, IoT sensors, weather sensors	Raw sensor data
Communication Layer	Transmits data securely and in real time	RSU, OBU, V2X, 5G, fiber-optic network	Communication messages
Intelligence Layer	Analyzes and interprets the data	Edge computing, AI, data fusion, analytics engines	Processed data
Digital Twin Layer	Creates a dynamic digital representation of the physical system	DT platform, simulation, data model	Digital corridor status
Traffic Management Layer	Generates and implements operational decisions	Traffic Management Center (TMC), adaptive signal control, VMS, speed management	Control decisions

3.3. Digital Twin Corridor Maturity Framework

While the DT Corridor Reference Architecture defines the functional structure of the corridor, a systematic assessment approach is needed to compare the levels of digital transformation across different road corridors. The maturity framework developed for this purpose is based not only on the technologies the corridor possesses but also on the operational capability these technologies collectively create. Thus, two different corridors with the same hardware components can be assessed at different maturity levels based on their capabilities in data generation, communication, digital synchronization, and decision-making.

The proposed model consists of five levels (Level 1–Level 5). Each level encompasses all the capabilities of the previous level and progresses by adding new functions. Transition between levels is determined not only by the addition of new technologies to the system but also by advancements in data management, communication infrastructure, DT integration, and operational decision-making capacity. Therefore, for a corridor to be assessed at a specific level, it is expected that the fundamental technical and operational requirements associated with that level are met collectively.

The levels proposed in this study are named Conventional Corridor, Instrumented Corridor, Cooperative Corridor, Digital Twin Corridor, and Adaptive Digital Twin Corridor (Table 2). Each level represents the new capabilities gained by the corridor during its digital transformation process, and the distinct characteristics of the levels are summarized in Table 2. The maturity framework proposed in this study is not an empirical scale statistically validated with direct field data; rather, it is a conceptual assessment tool derived from the literature on transportation digital twins, highway infrastructure, C-ITS communication, and operational decision support. In subsequent phases, the framework must be tested through pilot corridor applications, and measurable performance indicators and threshold values must be determined for each level.

Table 2. DT Road Corridor Maturity Levels

Level	Level Definition	Key Features
Level 1	**Conventional Corridor**	A corridor structure based on physical road infrastructure, where digital data generation is limited and traffic management is largely reactive.
Level 2	**Instrumented Corridor**	A corridor structure capable of generating real-time data using sensors and detection systems, but which uses this data primarily for monitoring purposes.
Level 3	**Cooperative Corridor**	A corridor structure that enables data sharing between vehicles and road infrastructure and facilitates coordinated traffic management through RSU, V2X, and communication infrastructure.
Level 4	**Digital Twin Corridor**	A corridor structure in which continuous synchronization is maintained between the physical corridor and the DT platform, and where simulations and predictive analyses support operational decision-making processes.
Level 5	**Adaptive Digital Twin Corridor**	An adaptive corridor structure in which operational decisions are dynamically optimized through AI-powered analyses and closed-loop feedback mechanisms.

The term "Adaptive Digital Twin Corridor" does not refer to a corridor dedicated to driverless vehicles; rather, it refers to a corridor capable of generating adaptive and largely automated operational decisions by feeding DT outputs into traffic management systems. A conceptual definition of the levels is not sufficient on its own for comparing the maturity levels of corridors. Therefore, the technological and operational capabilities associated with each level must be evaluated together. Table 3 presents a comparative overview of the levels included in the proposed maturity model in terms of technological infrastructure, data processing capacity, communication capabilities, and decision-making capabilities. Thus, the fundamental differences between the levels can be assessed not only based on the technologies used but also based on the functional capabilities these technologies create within the system.

Table 3. Comparative Evaluation of Levels

Evaluation Dimension	L1	L2	L3	L4	L5
Sensor-based data generation	–	✓	✓	✓	✓
Real-time data monitoring	–	✓	✓	✓	✓
RSU and V2X communication	–	–	✓	✓	✓
Multi-source data integration	–	△	✓	✓	✓
DT synchronization	–	–	–	✓	✓
Simulation and scenario analysis	–	–	–	✓	✓
AI-supported decision-making	–	–	△	✓	✓
Closed-loop adaptive management	–	–	–	–	✓

Note: ✓: Fully provided, △: Partially implemented, –: Not available.

While defining and comparing levels within the maturity model helps determine the current status of the corridor, the transition criteria between levels must also be clearly outlined. In this

context, Figure 3 summarizes the fundamental technical and operational requirements that a road corridor must meet in order to reach the next maturity level. Thus, the proposed framework not only provides a conceptual model for classifying the current state but also serves as an assessment tool that defines the development path corridors can follow during their digital transformation process.

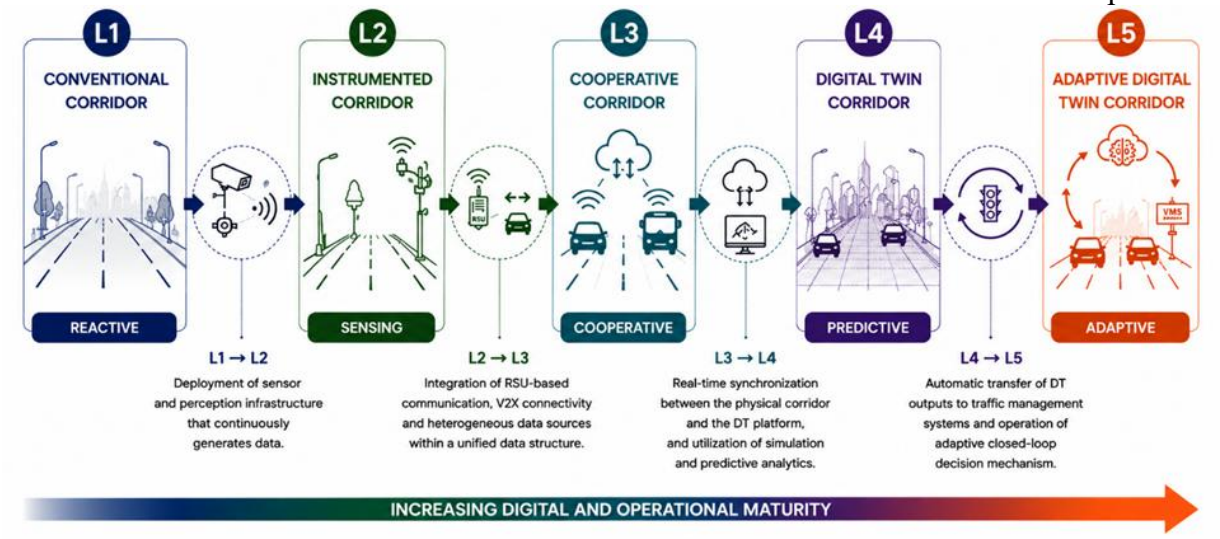


Figure 3. Criteria for Transition Between Levels

This framework makes it possible to compare different road corridors based on common criteria, determine current competency levels, and systematically identify the technical requirements necessary to reach the next level of maturity.

4. Implementation Framework for the Digital Twin Road Corridor in Türkiye

Strategic initiatives carried out in Türkiye in recent years in the field of C-ITS indicate that a significant transformation process has begun for the digitalizing transportation infrastructure. Under the National Intelligent Transportation Systems Strategy Document and the 2024–2030 Action Plan, objectives have been defined for vehicle-to-infrastructure communication, data sharing, standardization, and smart road applications; furthermore, testing of communication- and collaboration-based applications in real-world road environments has begun via a 5G-enabled C-ITS test corridor [9], [10]. However, current efforts are primarily focused on the development of specific technologies and the validation of pilot applications; a systematic implementation approach for evaluating these components within a DT-based integrated corridor management model is still under development.

The reference architecture and five-level maturity framework proposed in this study provide a conceptual implementation framework that enables the evaluation of road corridors at different levels of development in Türkiye using a common methodology. Within this scope, the maturity level of the existing corridor is first determined; then, by identifying gaps in technological and operational capabilities, the transformation steps required to advance to the next level can be planned. Thus, the proposed approach can be used as a decision-support tool not only in the design of new corridors but also in the phased transformation of existing highway infrastructure into DT-based systems.

The proposed framework is compatible with interoperability-focused initiatives such as the C-Roads Platform and NordicWay in Europe, and references the communication and system architecture principles defined in the ETSI TS 103 301 and ISO/TR 7872 standards [1], [11]. However, this study goes beyond these standards by positioning the DT platform as the corridor's central decision-support component and integrating physical infrastructure, communication systems, data processing workflows, and operational management mechanisms under a single evaluation model. In this regard, the proposed implementation framework offers

a common reference approach that can be used for the planning, prioritization, and performance evaluation of future DT road corridors to be established in Türkiye.

5. Conclusion

The analysis indicates that, within the scope of C-ITS, road corridors should be considered not merely as physical infrastructures where traffic data is collected and monitored, but as cyber-physical systems that enable real-time data exchange, digital synchronization, predictive analysis, and operational decision support. A joint evaluation of DT initiatives in transportation infrastructure and C-ITS-based smart road applications has shown that current approaches offer significant contributions in the areas of data collection, communication, infrastructure management, and decision support; however, efforts to address these functions in an integrated manner at the corridor scale remain limited.

Accordingly, as the first contribution of this study, a DT Road Corridor Reference Architecture has been developed that integrates physical infrastructure, sensing, communication, data processing, DT, and traffic management processes under six functional layers. The proposed architecture is based on a closed-loop data flow that enables data obtained from the physical corridor to be processed in upper layers, synchronized within the DT environment, and the resulting decisions to be fed back into the physical system. Thus, DT is positioned not merely as a visualization or monitoring tool, but as a central decision-making and coordination component supporting corridor operations.

The second contribution of this study—the five-level DT Road Corridor Maturity Framework—defines the evolution of corridors from traditional infrastructure levels toward structures equipped with sensors and capable of cooperative, DT-based, and autonomous operation. The levels—named Conventional Corridor, Instrumented Corridor, Cooperative Corridor, Digital Twin Corridor, and Adaptive Digital Twin Corridor—are compared based on technological infrastructure, data processing, communication, and operational decision-making capabilities. The separate definition of transition criteria between levels enables the model to serve not only as a conceptual classification but also as a tool for assessing the current status of different corridors and identifying transformation requirements.

From Türkiye's perspective, national ITS strategies and 5G-supported C-ITS test corridor initiatives provide a significant foundation for implementing the proposed framework. However, validating the reference architecture under field conditions, developing measurable threshold values for maturity levels, and defining data governance, interoperability, cybersecurity, and institutional responsibilities should be key topics for future work. Implementations and performance evaluations conducted in pilot corridors will help test the adaptability of the proposed framework to different road types and operating conditions.

Declaration of Generative AI and AI-assisted technologies in the writing process

During the preparation of this work, the authors used Google NotebookLM, ChatGPT, DeepL and Abacus AI to assist with language editing, structural review, clarity checks, translation, and grammar. Following the use of these tools, the authors carefully reviewed, verified, and edited the content as necessary and take full responsibility for the final manuscript.

References

[1] European Telecommunications Standards Institute (ETSI), Intelligent Transport Systems (ITS); Vehicular Communications; Basic Set of Applications; Facilities Layer Protocols and Communication Requirements, ETSI TS 103 301 V2.2.1, Sophia Antipolis, France, Jul. 2022.

[2] C-Roads Platform, C-Roads Platform – European Cooperative Intelligent Transport Systems (C-ITS) Deployment Platform. [Online]. Available: https://www.c-roads.eu/. Accessed: Jul. 2026.

[3] Wang, Y., Wang, H., Wang, W., Song, S., and Fu, X., “Architecture, application, and prospect of digital twin for highway infrastructure,” Journal of Traffic and Transportation Engineering (English Edition), vol. 11, no. 5, pp. 835–852, 2024, doi: 10.1016/j.jtte.2024.03.003.
[4] Buuveibaatar, M., Shin, S., and Lee, W., "Digital Twin Framework for Road Infrastructure Management," Applied Sciences, vol. 15, no. 10, Art. no. 5765, 2025.
[5] NordicWay, NordicWay 3 – Cooperative Intelligent Transport Systems Deployment. [Online]. Available: https://www.nordicway.net/. Accessed: Jul. 2026.
[6] Yan, Y., Ni, L., Sun, L., Wang, Y., and Zhou, J. "Digital Twin Enabling Technologies for Advancing Road Engineering and Lifecycle Applications," Engineering, vol. 44, pp. 184–206, 2025. https://doi.org/10.1016/j.eng.2024.12.017
[7] Wu, D., Zheng, A., Yu, W., Cao, H., Ling, Q., Liu, J., and Zhou, D., "Digital Twin Technology in Transportation Infrastructure: A Comprehensive Survey of Current Applications, Challenges, and Future Directions," Applied Sciences, vol. 15, no. 4, Art. no. 1911, 2025.
[8] Irfan, M. S., Dasgupta, S., and Rahman, M., “Toward Transportation Digital Twin Systems for Traffic Safety and Mobility: A Review,” IEEE Internet of Things Journal, vol. 11, no. 14, pp. 24581–24603, 2024, doi: 10.1109/JIOT.2024.3395186.
[9] Ulaştırma ve Altyapı Bakanlığı, Ulusal Akıllı Ulaşım Sistemleri Strateji Belgesi ve 2024–2030 Eylem Planı, Ankara, Türkiye, 2024.
[10] Ulaştırma ve Altyapı Bakanlığı, 5G Destekli Kooperatif Akıllı Ulaşım Sistemleri (K-AUS) Test Koridoru Projesi, 2024.
[11] ISO, ISO/TR 7872: Intelligent Transport Systems — Digital Infrastructure Framework and Reference Architecture, International Organization for Standardization, 2023.

List of Abbreviations

- **C-ITS** — Cooperative Intelligent Transportation Systems
- **ITS** — Intelligent Transportation Systems
- **DT** — Digital Twin
- **TDT** — Transportation Digital Twin
- **RSUs** — Roadside Unit
- **VMS** — Variable Message Signs
- **AI** — Artificial Intelligence

Publication Note

This paper was peer-reviewed, accepted for presentation, and included in the proceedings of the ACE2026 – International Conference on Advances in Civil Engineering, held on 12–14 October 2026 in Trabzon, Türkiye.

This paper may be cited as follows:

Dilara Usta, Mustafa Sinan Yardim, “Digital Twin Road Corridor Architecture and Maturity Framework in Cooperative Intelligent Transportation Systems,” in Proceedings of the ACE2026 – International Conference on Advances in Civil Engineering, Trabzon, Türkiye, 12–14 October 2026.

A Review on Physico-Chemical Identity and Performance Evaluation of Recycled Aggregates for Sustainable Pavements

Md. Amin Al Noor[1], Sk. Rakibul Islam[2], Tasnim Mahin[3] and Oishik Majumder[4]
[1] 000-0002-8649-7489, Bangladesh University of Engineering and Technology (BUET), Department of Civil Engineering, Dhaka, Bangladesh, aminalnoor@ce.buet.ac.bd
[2] 0000-0002-5167-1985, Bangladesh University of Engineering and Technology (BUET), Department of Civil Engineering, Dhaka, Bangladesh, rakibulislam@ce.buet.ac.bd
[3] 0009-0003-1712-1394, Bangladesh University of Engineering and Technology (BUET), Department of Civil Engineering, Dhaka, Bangladesh, 2004176@ce.buet.ac.bd
[4] 0009-0006-4530-1992, Bangladesh University of Engineering and Technology (BUET), Department of Civil Engineering, Dhaka, Bangladesh, oishikm76@gmail.com

Abstract. This review synthesizes current knowledge on the physico-chemical identity and pavement performance of four recycled aggregate streams based on literature published between 1978 and 2023. These four streams include- Recycled Concrete Aggregate (RCA), Reclaimed Asphalt Pavement (RAP), Steel Slag Aggregate (SSA), and Crushed Brick (CB). Each material is classified according to its distinct physical and chemical characteristics. The review then examines how these characteristics affect asphalt and concrete mix design including adjustments to optimum bitumen content, the Equivalent Mortar Volume approach, and binder blending for RAP. Conventional index tests, such as Los Angeles Abrasion and Sulfate Soundness, are compared against performance-based methods including Micro-Deval and Resilient Modulus testing. This is done to evaluate their suitability for heterogeneous recycled materials. Mechanistic-empirical evidence shows a trade-off for RCA base layers. These layers can have higher resilient stiffness. But they also show increased susceptibility to permanent deformation. RAP-containing mixtures show a different trade-off. They may improve rutting resistance. But this can come at the cost of reduced fatigue life. Several key research gaps have been identified in this study. RAP binder blending, better mechanistic-empirical representation, performance-based specifications, and life-cycle assessment all need further study. These include source-dependent material variability and the lack of long-term field validation. Additionally, RAP binder blending, better mechanistic-empirical representation, performance-based specifications, and life-cycle assessment all need further study. These findings support a shift in practice. Pavement engineering should move from index-based acceptance toward performance-oriented characterization of recycled aggregates.

Keywords: Recycled aggregates; Pavement engineering; Mix design; Laboratory performance testing; Mechanistic-empirical evaluation; Sustainability.

1 Introduction

The global pavement industry is undergoing a shift in its approach to construction and demolition waste (CDW). These materials are increasingly being recognized as valuable resources rather than landfill waste [1]. Depleting natural aggregate (NA) resources, rising waste generation, and diminishing landfill capacity have created an urgent need to incorporate recycled materials such as Recycled Concrete Aggregate (RCA), Reclaimed Asphalt Pavement (RAP), Steel Slag Aggregate (SSA), and Crushed Brick (CB) into pavement systems [2,3]. Their incorporation can provide substantial environmental benefits. These include reductions of up to 65% in greenhouse gas emissions and 58% in non-renewable energy consumption

versus conventional NA in concrete [1,4]. However, unlike NA, these materials retain "material memory" inherited from their original sources and processing histories. Thus, additional engineering considerations are required [1,4].

Research as well as adoption on recycled aggregates is growing. But characterization and classification remain inconsistent across standards. Conventional testing protocols developed for homogeneous natural aggregates are often applied to recycled aggregates without change. Recycled aggregates, however, are heterogeneous, porous, and chemically reactive. This mismatch creates uncertainty in material selection, specification, and mix design.

This review addresses these gaps by systematically synthesizing current knowledge on RCA, RAP, SSA, and CB to: (1) classify these materials by physico-chemical characteristics and sources; (2) evaluate how these characteristics influence mix design and engineering performance; (3) examine performance-based laboratory testing as alternatives or complements to index testing; and (4) synthesize mechanistic-empirical (ME) evidence to identify key knowledge gaps and research priorities.

2 Methodology

This study used a systematic literature review framework. The framework followed established practice for recycled aggregate research [1]. It synthesized findings on four materials - RCA, RAP, SSA, and CB focusing on their use in pavement applications. Literature was covered from 1978 to 2023 across Google Scholar.

2.1 Search Strategy and Selection Criteria

Database searches combined material-specific terms ("recycled concrete aggregate", "reclaimed asphalt pavement", "steel slag aggregate", "crushed brick") with pavement-engineering terms ("mix design", "resilient modulus", "Micro-Deval", "mechanistic-empirical", "rutting", "cracking") using Boolean AND/OR operators. Studies were included if they were peer-reviewed, English-language journal articles (1978-2023) that investigated at least one target material for pavement applications and reported quantitative or technically interpretable physico-chemical, mix-design, laboratory, or ME performance data. Conference papers, non-English publications, theses, book chapters, technical reports, and studies unrelated to pavement applications, or lacking sufficient engineering detail, were excluded, along with duplicate records.

2.2 Screening and Selection Process

The literature-selection process followed four sequential stages - identification, screening, eligibility assessment, and inclusion. Searches identified more than 500 records; after removing duplicates and clearly irrelevant results, remaining studies were screened by title and abstract, then assessed in full text against the inclusion criteria, with particular emphasis on whether relevant engineering or performance data for RCA, RAP, SSA, or CB were reported. This process, illustrated in Fig. 1, is summarized as:

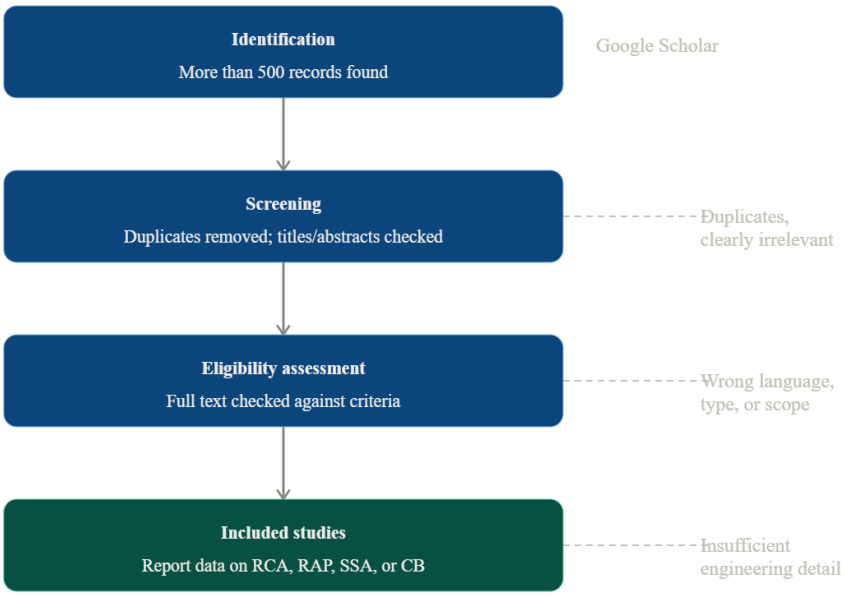


Fig. 1. Systematic literature identification, screening, eligibility assessment, and inclusion process for RCA, RAP, SSA, and CB studies.

2.3 Data Classification and Synthesis

The selected literature was organized by the origin and physico-chemical identity of each material [3], synthesizing source characteristics, physical and mechanical properties, environmental behavior, and pavement-application implications. Conventional index tests were critically compared against performance-based methods such as Resilient Modulus (Mr) and Micro-Deval testing [3], and ME approaches. These tests included tools such as AASHTOWare Pavement ME Design primarily focusing this examination on predicted rutting and cracking outcomes [5]. This synthesis linked three things together – (1) recycled-material characteristics and laboratory-measured properties, (2) laboratory properties and mix-design parameters, and lastly (3) mix-design parameters and pavement performance.

3 Physico-Chemical Properties of Recycled Aggregates

Recycled aggregates exhibit distinct physico-chemical characteristics governed by source material, processing history, contamination, and adhered or residual binder content [3,6]. Unlike relatively homogeneous natural aggregates (NA), recycled aggregates retain characteristics inherited from their parent materials. Properties such as density, porosity, water absorption, surface texture, chemical composition, and binder condition directly influence handling, mix design, and pavement performance. The principal characteristics of RCA, RAP, SSA, and CB are summarized in Table 1.

Recycled Concrete Aggregate (RCA): RCA consists of crushed concrete containing natural aggregate and adhered cement mortar. This mortar is typically porous and alkaline and may constitute 25–35% of RCA mass depending on parent concrete and crushing process [3]. RCA therefore generally shows lower density and substantially higher water absorption than NA (approximately 3–10% versus <1.5% for many conventional aggregates [3]). This directly influences effective water-to-cement ratio and asphalt binder demand, so moisture correction and pre-treatment are important during mix design.

Reclaimed Asphalt Pavement (RAP): RAP consists of mineral aggregate coated with aged, oxidized asphalt binder. This binder is stiffer and less ductile than virgin binder, and

substantially alters mixture rheology [8,9]. Increasing RAP content can increase stiffness and rutting resistance. However, it also increases susceptibility to fatigue or thermal cracking unless the aged binder is balanced by virgin binder or rejuvenators [8,9]. So RAP must be characterized by both aggregate properties and residual binder condition.

Steel Slag Aggregate (SSA): SSA is a dense (3.4–3.5 g/cm³), hard, angular industrial by-product [7]. It offers strong mechanical interlocking, abrasion resistance, and skid resistance, but may contain free CaO and MgO that hydrate and cause volumetric expansion [7]. Thus, SSA requires aging, weathering, or stabilization before use where dimensional stability is critical.

Crushed Brick (CB): CB, from crushed waste masonry, is characterized by high porosity, low density, and high water absorption (approximately 6–19%, well above conventional NA) [10,11]. It contributes to lower mechanical strength and greater degradation susceptibility under loading and environmental exposure. Water-soluble sulfates can create durability concerns in cementitious systems. Besides, capillary action within its porous structure can accelerate soundness-test deterioration [10,11].

Table 1. Physical property comparison of natural and recycled aggregates

Property	NA	RCA	RAP	SSA	CB
Bulk Density (g/cm³)	2.5–2.7	2.1–2.5	~2.4	3.4–3.5	~1.9
Water Absorption (%)	<1.5	3.0–10.0	1.5–2.0	0.7–1.3	6.0–19.0
LA Abrasion Loss (%)	10–30	20–45	~24	10–20	35–40
Porosity (%)	2–3	10–15	~5	4–8	>15

Overall, the four recycled streams exhibit fundamentally different material identities. RCA is primarily governed by adhered mortar and associated porosity; RAP by residual aged asphalt binder; SSA by its dense, angular, and potentially expansive mineral phases; and CB by its highly porous ceramic structure. These differences mean that recycled materials cannot be evaluated solely using the same criteria applied to conventional NA. Their physico-chemical characteristics must instead be explicitly incorporated into material selection, laboratory characterization, and pavement mix design.

4 Mix Design for Pavements

Incorporating recycled aggregates into pavement mixtures requires modifying conventional mix-design procedures. This is because higher absorption, heterogeneous composition, residual binders, and chemical reactivity can substantially alter mixture volumetrics and mechanical behavior [3,8,12]. The necessary adjustments depend on both material and pavement type. For flexible pavements, RCA generally increases optimum bitumen content (OBC). This increase is approximately 0.3–1.7 percentage points versus natural aggregate (NA) mixtures. The reason behind this is the porous adhered mortar because it absorbs part of the binder [3,12]. For this reason, two factors should be explicitly considered. These are aggregate absorption and effective specific gravity. For RAP, aged, oxidized binder is the principal challenge. Higher RAP content can increase stiffness and rutting resistance but reduce low-temperature and fatigue-cracking resistance. Hence, binder selection, blending, and rejuvenators are important for restoring stiffness-ductility balance [8,9].

For rigid pavements, conventional aggregate-volume replacement can overestimate new cement paste needed for RCA concrete. This can be attributed to the fact that adhered mortar already contributes to the mortar phase. Thus, the Equivalent Mortar Volume (EMV) approach accounts for this by proportioning mixtures based on the mortar associated with the recycled aggregate [3]. Treatments such as accelerated CO_2 curing have also been investigated to densify the RCA surface and reduce water absorption via carbonation of alkaline phases. This may

potentially improving early-age performance [13]. But effectiveness depends on RCA characteristics and carbonation degree. This should be verified experimentally rather than assumed universally.

4.1 Asphalt Mix-Design Parameters and Specification Context

Table 2 summarizes representative asphalt mix-design ranges reported for mixtures containing RCA and RAP [8,12]. The values illustrate the changes in mixture properties associated with recycled-material incorporation. They should not be interpreted as universal specification limits, because acceptance criteria depend on the selected mix-design method, nominal maximum aggregate size (NMAS), traffic level, binder grade, and governing agency specification.

Table 2. Representative asphalt mix-design parameters for natural and recycled-aggregate mixtures and their specification context.

Parameter	Natural Mix	RCA Mix (30–60%)	RAP Mix (25–50%)	Relevant specification/interpretation
Optimum Bitumen Content (%)	5.0–5.5	5.3–7.2	4.8–5.4	Project- and material-specific; no universal AASHTO M 323 limit
Marshall Stability (kN)	8–12	10–15	12–18	Marshall-method criterion; commonly ≥8 kN where applicable
Marshall Flow (mm)	2.0–4.0	2.0–3.5	2.5–4.5	Project/agency specific; commonly assessed with stability
Air Voids (%)	3–5	4–6	3–5	Superpave design target is typically 4% at N-design
Specification status	—	Generally compliant except upper-end air voids	Generally within typical ranges	Must be verified against the governing project specification

For Superpave volumetric design, AASHTO M 323 specifies a design air-void target of approximately 4.0% at N-design, with additional requirements for VMA, VFA, and compaction density. Moisture susceptibility is commonly evaluated using AASHTO T 283 with a minimum tensile strength ratio (TSR) of 0.80 [14]. Marshall Stability and Flow, by contrast, are not AASHTO M 323 requirements; where specified (per AASHTO T 245 or ASTM D6927), applicable minimum stability, flow, and air-void limits are set by the relevant agency. This is commonly around 8 kN stability and 3–5% air voids. But these are not universal values. The Asphalt Institute's MS-2 Asphalt Mix Design Methods treats Marshall and Superpave as distinct approaches. Under MS-2, criteria depend on two things. These are the selected design method and the specification framework.

On this basis, the Table 2 values indicate that reported RCA and RAP mixtures generally meet an 8-kN Marshall stability minimum where applicable. RCA mixtures, however, show air-void values up to 6%. This is above the typical 3–5% Marshall range and the 4% Superpave target and requires binder, gradation, or compaction adjustment before being specification-compliant. RAP mixtures (3–5% air voids) generally fall within range. Importantly, improved Marshall stability should not by itself be read as superior pavement performance. Higher stability may reflect increased stiffness. Despite being beneficial for rutting resistance, it is

potentially detrimental to fatigue or thermal-cracking resistance. This is especially true for aged RAP binder. Recycled mixtures should therefore be evaluated using volumetric requirements together with moisture susceptibility, rutting, fatigue, and cracking performance.

5 Laboratory Testing Protocols

Characterizing recycled aggregates requires care because many standardized index tests were developed for relatively homogeneous natural rocks and may not capture the heterogeneous, porous, composite nature of recycled materials [3]. A test result may reflect adhered mortar, residual binder, or pore structure rather than the aggregate skeleton alone. For RCA, the Los Angeles Abrasion test may be dominated by breakdown of the weak adhered mortar rather than the natural aggregate's fragmentation resistance [3]. Again, the Sulfate Soundness test can show comparatively high mass losses for porous materials owing to salt crystallization within interconnected pores [10]. Such results should be interpreted alongside morphology and absorption rather than as direct equivalents of dense natural-aggregate results.

5.1 Performance-Based Testing Framework

A tiered, performance-oriented testing framework is recommended. The first tier establishes fundamental physical and chemical characteristics (particle density, water absorption, gradation, contaminant content, chemical composition) for material classification and mix design. The second tier applies durability and mechanical-performance tests more representative of pavement service conditions. The Micro-Deval test (AASHTO T 327) measures resistance to abrasion and degradation in the presence of water. This is particularly relevant given the moisture-sensitive, porous nature of many recycled materials [3]. The Resilient Modulus (Mr) test (AASHTO T 307) characterizes recoverable deformation under cyclic traffic loading. It provides information more directly relevant to structural and ME design than a single-load index test. It is particularly useful for evaluating whether compositional or moisture differences in recycled base and subbase materials translate into meaningful load-bearing differences.

The resulting testing framework, shown schematically in Fig. 2, can therefore be represented as:

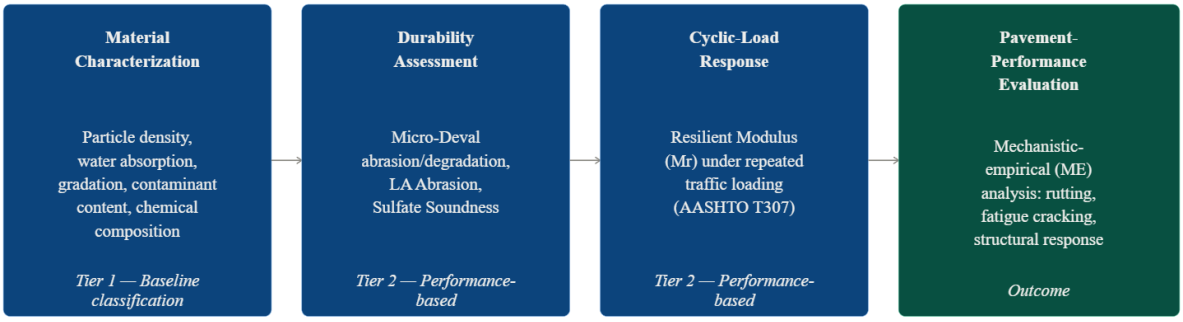


Fig. 2. Tiered, performance-based laboratory testing framework for recycled aggregates

This does not mean conventional index tests should be abandoned. They, however, remain useful for screening, classification, and quality control. But performance-based tests supply the additional evidence needed to establish engineering suitability. This is because two aggregates with similar index properties can behave very differently under repeated traffic loading or environmental exposure.

5.2 Environment and Leaching Assessment

Environmental characterization is a further dimension of assessment. Batch leaching tests provide standardized screening of contaminant release but may not fully reproduce the hydraulic and time-dependent release conditions of pavement systems. This is particularly relevant for materials such as steel slag, which can exhibit high initial alkalinity [5,14]. Column percolation or flow-through leaching tests can complement batch testing by capturing the evolution of contaminant release under controlled, repeated water flow. Thus, it offers a more field-representative assessment of temporal stability [5,14]. Overall, laboratory evaluation should move from isolated index properties toward a multi-level performance-based framework. This framework should combine physical characterization, mechanical durability, cyclic-load response, and environmental stability. Together, these elements would better link laboratory measurement to long-term pavement behavior.

6 Mechanistic-Empirical Performance

Mechanistic-empirical (ME) analysis evaluates whether the laboratory properties of recycled materials translate into acceptable pavement performance under realistic conditions. Pavement structures incorporating RCA in base or subbase layers can achieve performance comparable to natural aggregate (NA). This is only possible under certain conditions. Material quality, gradation, and moisture must be controlled. When they are, RCA's stiffness and particle interlock may permit reduced base-layer thickness. This should not be inferred from laboratory values alone, though. It should instead be confirmed by project-specific ME analysis [3,5]. For flexible pavements, RAP primarily acts as a stiffness modifier. Its aged binder can improve rutting resistance at elevated temperatures. But it may also reduce fatigue and thermal-cracking resistance. This trade-off requires careful control. RAP content, virgin binder grade, and, where necessary, rejuvenation all need attention [9]. RCA asphalt mixtures show a similar pattern. They also show favorable rutting resistance but a greater sensitivity to moisture and compaction. This sensitivity comes from their absorption and porosity [12].

For rigid pavements, recycled aggregate concrete may benefit from residual cementitious activity in the adhered mortar. This can continue hydrating and increase long-term stiffness [1]. However, the magnitude depends strongly on source concrete, carbonation, processing, and replacement level and should not be assumed uniform across RCA sources.

6.1 Mechanistic Performance Indicators

Table 3 summarizes representative mechanistic-performance indicators reported for NA, RCA, and RAP base materials [5]. The values should be interpreted as literature-reported ranges rather than universal design values. This is because resilient modulus, rutting, fatigue life, and permeability are strongly dependent on material gradation, moisture state, compaction, stress conditions, climate, traffic loading, layer thickness, and model calibration.

Table 3. Representative mechanistic-performance indicators for natural- and recycled-aggregate pavement materials.

Performance Metric	NA Base	RCA Base	RAP Base
Resilient Modulus (MPa)	200–350	250–550	300–700
Rutting Depth	Baseline	5–15% higher	10–20% lower
Fatigue Life	Baseline	Similar	15–30% lower
Permeability (cm/s)	(10^{-3})	(10^{-2})–(10^{-4})	(10^{-4})

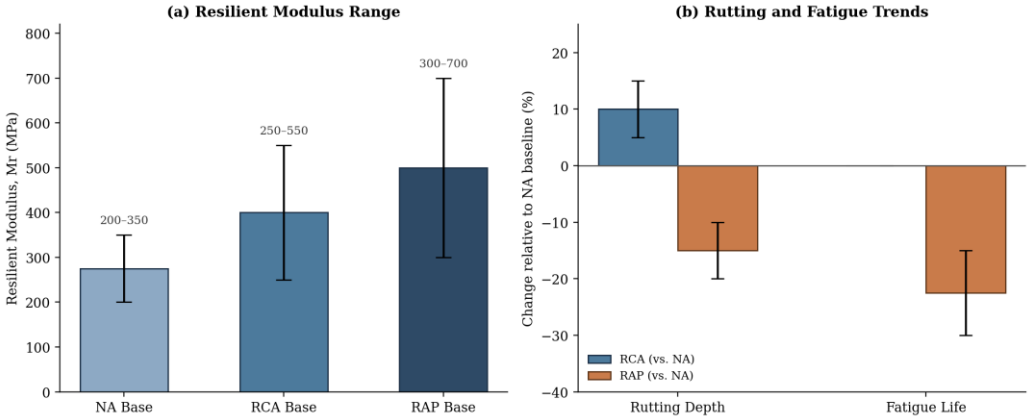


Fig. 3. Schematic comparison of resilient modulus, rutting, fatigue life, and permeability trends for NA, RCA, and RAP base materials.

As summarized schematically in Fig. 3, an important distinction must be made between resilient stiffness and permanent deformation resistance when interpreting Table 3. Although RCA bases may exhibit higher resilient modulus than NA, this recoverable-stiffness gain does not necessarily translate into proportionally lower rutting. Resilient modulus characterizes recoverable deformation under cyclic loading, while rutting reflects accumulated plastic deformation from particle crushing, rearrangement, and moisture-dependent effects. The reported 5-15% increase in RCA rutting is therefore not inconsistent with a higher resilient modulus. The two represent different aspects of pavement response. RCA suitability should be assessed alongside permanent-deformation and moisture-susceptibility indicators, not resilient modulus alone.

The RAP results show a related trade-off: higher stiffness can reduce rutting depth by 10-20%, but the same stiffness may lower fatigue life by approximately 15–30% [9]. Hence, ME evaluation of RAP-containing pavements should weigh rutting and cracking resistance together. It should not treat improvement in one distress as evidence of overall superior performance. Overall, RCA may combine high resilient stiffness with increased permanent-deformation susceptibility. Meanwhile, RAP may trade fatigue-cracking resistance for improved rutting resistance. These trade-offs reinforce the need for ME approaches incorporating multiple distress mechanisms and material-specific behavior.

7 Research Gaps and Recommendations

Despite substantial progress in characterizing and applying recycled aggregates in pavement systems, several limitations continue to restrict their reliable, widespread implementation. The reviewed literature points to five principal gaps: material variability, limited long-term field validation, RAP binder interaction, incomplete representation in mechanistic-empirical (ME) design frameworks, and the absence of performance-based specifications integrated with sustainability assessment.

7.1 Material Variability and Long-Term Field Validation

Recycled-aggregate properties are strongly governed by parent-material characteristics and processing history. For RCA, these are strength, age, and deterioration of the source concrete [6]. Again, for RAP, SSA, and CB, these include binder aging, steelmaking processes, and manufacturing conditions, respectively. This source-dependent variability limits broad material classifications as reliable indicators of performance. Compounding this, most existing evidence derives from laboratory or short-term studies, with comparatively few long-term field observations under realistic traffic and environmental conditions [5]. Future work should

combine two approaches. The first is source-to-performance databases. These link parent-material characteristics to pavement outcomes [1,6]. The second is long-term field monitoring. This monitoring should track resilient modulus, permanent deformation, and degradation. Regional conditions such as freeze–thaw cycling in cold regions and wet–dry and monsoon infiltration in tropical climates should be explicitly accounted for [5].

7.2 RAP Binder Blending and Chemical Interaction

The extent of blending between aged RAP binder and virgin binder remains uncertain. This blending varies with several factors including RAP content, particle size, mixing conditions, and rejuvenator use [9]. Assuming complete blending can be misleading and may misrepresent effective binder properties. Future research addressing this needs to combine three approaches. These are micromechanical characterization, binder rheology, and mixture-level performance testing. This combined approach would quantify RAP–virgin binder interaction and also help establish reliable blending models. Such models could then guide the selection of virgin binder grades and rejuvenator dosages [9].

7.3 Representation of Recycled Materials in ME Design

Current ME pavement design frameworks do not always explicitly represent recycled-material behavior, particularly moisture-dependent response, hydraulic characteristics, and nonlinear stress–strain behavior [5]. Future ME models should incorporate recycled-material-specific parameters such as Soil-Water Characteristic Curves (SWCCs), moisture-dependent resilient modulus, and degradation behavior [5]. This should be done to predict pavement response under changing conditions rather than relying on classifications developed for natural aggregates.

7.4 Performance-Based Specifications and Sustainability Integration

Conventional index tests do not fully capture heterogeneous recycled-material behavior. So, future specifications should combine basic classification with performance indicators such as resilient modulus, permanent deformation, and moisture susceptibility. Acceptance should be allowed based on demonstrated engineering performance rather than similarity to natural aggregates. This effort should be paired with life-cycle assessment (LCA), since additional processing, transport, or treatment can offset environmental savings. Integrating ME performance analysis with LCA would clarify the trade-off between environmental benefit and durability. Overall, future research should progress from isolated laboratory characterization toward source-specific databases, long-term field monitoring, performance-based specifications, and integrated ME–LCA frameworks. The core of this research would be to support the transition of RCA, RAP, SSA, and CB from case-specific use to reliable, scalable components of sustainable pavement infrastructure.

References

1. B. Wang, L. Yan, Q. Fu, and B. Kasal, "A comprehensive review on recycled aggregate and recycled aggregate concrete," Resources, Conservation & Recycling, vol. 171, 105565, 2021.
2. B. Barhmaiah, M. L. Priyanka, and M. Padmakar, "Strength analysis and validation of recycled aggregate concrete," Materials Today: Proceedings, 2020.
3. E. O. Fanijo, J. T. Kolawole, A. J. Babafemi, and J. Liu, "A comprehensive review on the use of recycled concrete aggregate for pavement construction: Properties, performance, and sustainability," Cleaner Materials, vol. 9, 100199, 2023.
4. M. U. Hossain, C. S. Poon, I. M. C. Lo, and J. C. P. Cheng, "Comparative environmental evaluation of aggregate production from recycled waste materials and virgin sources by LCA," Resources, Conservation and Recycling, vol. 109, pp. 67–77, 2016.

5. F. C. G. Martinho et al., "Mechanical and Environmental Performance of Asphalt Concrete with High Amounts of Recycled Concrete Aggregates (RCA)," Sustainability, vol. 16, 248, 2024.
6. A. Azam et al., "Life cycle assessment and pavement performance of recycled aggregates in road construction," Case Studies in Construction Materials, vol. 20, e03062, 2024.
7. P. Ahmedzade and B. Sengoz, "Evaluation of steel slag coarse aggregate in hot mix asphalt concrete," Journal of Hazardous Materials, vol. 165, pp. 300–305, 2009.
8. F. C. G. Martinho, L. G. Picado-Santos, and S. D. Capitão, "Feasibility Assessment of the Use of Recycled Aggregates for Asphalt Mixtures," Sustainability, vol. 10, no. 6, 1737, 2018.
9. A. Arulrajah et al., "Resilient moduli response of recycled construction and demolition materials in pavement subbase applications," Journal of Materials in Civil Engineering, vol. 25, no. 12, pp. 1920–1928, 2013.
10. C. S. Poon and D. Chan, "Feasible use of recycled concrete aggregates and crushed clay brick as unbound road sub-base," Construction and Building Materials, vol. 20, pp. 578–585, 2006.
11. A. Arulrajah, J. Piratheepan, T. Aatheesan, and M. W. Bo, "Geotechnical Properties of Recycled Crushed Brick in Pavement Applications," Journal of Materials in Civil Engineering, vol. 23, no. 10, pp. 1444–1452, 2011.
12. S. Paranavithana and A. Mohajerani, "Effects of recycled concrete aggregates on properties of asphalt concrete," Resources, Conservation & Recycling, vol. 48, no. 1, pp. 1–12, 2006.
13. C. Shi, "CO2 Curing of Concrete," Ph.D. dissertation, Hong Kong Polytechnic Univ., 2012.
14. M. Akbas, B. Ozaslan, and R. Iyisan, "Utilization of recycled concrete aggregates for developing high-performance and durable flexible pavements," Construction and Building Materials, vol. 407, 133479, 2023.

Author Contribution Statement

- *Conceptualization:* Md. Amin Al Noor, Sk. Rakibul Islam
- *Methodology:* Md. Amin Al Noor, Sk. Rakibul Islam
- *Investigation:* Tasnim Mahin, Oishik Majumder
- *Writing – Original Draft:* Tasnim Mahin, Oishik Majumder
- *Writing – Review & Editing:* Md. Amin Al Noor, Sk. Rakibul Islam

List of Abbreviations

- **CDW** - Construction and Demolition Waste
- **RCA** - Recycled Concrete Aggregate
- **SSA** - Steel Slag Aggregate
- **ME** - Mechanistic-Empirical
- **OBC** - Optimum Bitumen Content
- **VMA** - Voids in Mineral Aggregate
- **LCA** - Life-Cycle Assessment
- **NA** - Natural Aggregate
- **RAP** - Reclaimed Asphalt Pavement
- **CB** - Crushed Brick
- **EMV** - Equivalent Mortar Volume
- **NMAS** - Nominal Maximum Aggregate Size
- **Mr** - Resilient Modulus
- **SWCC** - Soil-Water Characteristic Curve

Publication Note
This paper was peer-reviewed, accepted for presentation, and included in the proceedings of the ACE2026 – International Conference on Advances in Civil Engineering, held on 12–14 October 2026 in Trabzon, Türkiye.

This paper may be cited as follows:
Md. Amin Al Noor, Sk. Rakibul Islam, Tasnim Mahin and Oishik Majumder, "A Review on Physico-Chemical Identity and Performance Evaluation of Recycled Aggregates for Sustainable Pavements" in Proceedings of the ACE2026 – International Conference on Advances in Civil Engineering, Trabzon, Türkiye, 12–14 October 2026.

Investigation of the Effect of Service Quality Perception at Public Transport Transfer Centers and Vehicles on Passenger Satisfaction

Handenur Keser[1*] and Yalçın Alver[1]
[1*] 0009-0008-7607-3616, Ege University, Civil Engineering Department, İzmir, Türkiye, 91240000544@ogrenci.ege.edu.tr
[1] 0000-0002-9833-4505, Ege University, Civil Engineering Department, İzmir, Türkiye, yalcin.alver@ege.edu.tr

Abstract. Passenger satisfaction is an important indicator of service quality from the perspective of user experience in public transportation systems. At transfer centers where different transportation modes converge, both transfer conditions and vehicle service quality can influence the overall travel experience. This study examines the effects of passenger satisfaction with transfer center and vehicle services on overall satisfaction and compares satisfaction levels across transportation modes at the Konak, Halkapınar, and Bostanlı transfer centers in İzmir. A survey was conducted with 510 passengers, and 443 usable responses were obtained after data cleaning and excluding passengers making their first boarding at the transfer center. Satisfaction was assessed using a 5-point Likert scale. The data were analyzed using descriptive statistics, Pearson correlation, multiple linear regression, and one-way analysis of variance (ANOVA). The results showed that both transfer center and vehicle satisfaction were positively and significantly associated with overall satisfaction. Together, these variables explained 51.4% of the variance in overall satisfaction, with vehicle satisfaction ($\beta = 0.455$) having a stronger effect than transfer center satisfaction ($\beta = 0.340$). Significant differences in satisfaction levels were also found across transportation modes. Ferry users had the highest mean satisfaction scores across all three measures, while lower satisfaction levels were particularly observed among İZBAN and bus users. The findings highlight the importance of addressing transfer center conditions and vehicle services together through a holistic approach to improve passenger satisfaction.

Keywords: Public transportation, transfer center, passenger satisfaction, vehicle satisfaction, transportation mode.

1 Introduction

Public transportation is one of the fundamental components of urban transportation systems in metropolitan cities. In İzmir, approximately 31% of urban trips are made by public transportation, making it the second most widely used transportation mode after walking [1]. As the use of public transportation becomes more widespread, ensuring that the services provided meet user expectations and improve the travel experience has become increasingly important. In particular, transfer centers, which enable passengers to switch from one transportation mode to another, play an important role in the functioning of urban transportation systems, and the characteristics of these centers can directly affect passenger satisfaction.

When evaluating public transportation systems, it is important to consider not only the provision of transportation services but also how passengers perceive and evaluate these services. Previous studies have indicated that service characteristics such as service frequency, punctuality, waiting time, comfort, cleanliness, safety, accessibility, and passenger information

are associated with passengers' perceptions of service quality and satisfaction [2]. Similarly, the EN 13816 standard provides a framework for defining and measuring public transportation service quality based on passenger expectations and perceptions, identifying eight key quality areas, including accessibility, information, time, comfort, and safety [3]. In this context, passenger satisfaction can be considered an important indicator for evaluating public transportation services from the user's perspective. In addition to vehicle-related service characteristics, such as waiting time, punctuality, onboard comfort, cleanliness, safety, and information provision, factors related to transfer centers—including accessibility to the center, pedestrian connections between different transportation modes, the cleanliness and comfort of waiting areas, safety, accessibility for passengers with disabilities, and the quality of signage and information systems—also shape the overall travel experience. Therefore, evaluating transfer center and vehicle services together allows passenger satisfaction to be assessed from a more comprehensive perspective.

The relationship between public transportation service quality and passenger satisfaction has been examined across different transportation modes and cities. Eboli and Mazzulla [4] investigated the effects of various public transportation service attributes on user satisfaction, while Susilo and Cats [5] examined the factors influencing satisfaction in multimodal journeys. Sil et al. [6] focused on user comfort and satisfaction at transfer points and demonstrated the importance of different service attributes in shaping the user experience. Carvalho and El-Geneidy [7] investigated the key factors determining passenger satisfaction at hubs where road, rail, and maritime transportation intersect, as well as changes in satisfaction over time. In Türkiye, most studies have focused on transfer centers in Istanbul, while user perceptions, experiences, and satisfaction levels have not been directly examined [8-9]. Buran [10], on the other hand, found that "safety and security" was the most critical satisfaction dimension for both passengers and station operators, while passengers ranked "comfort and travel time" second.

Overall, although studies on passenger satisfaction are available in the literature, research examining the combined effects of satisfaction with services provided at transfer centers and the vehicles used on overall passenger satisfaction remains limited. Moreover, recent studies indicate that passenger satisfaction should not be evaluated based on a single service attribute but rather in relation to the different components of the overall travel experience.

The aim of this study is to examine the effect of passenger satisfaction with transfer center and vehicle services on overall satisfaction at the Konak, Halkapınar, and Bostanlı transfer centers in İzmir and to compare satisfaction levels among passengers using different transportation modes.

2 Materials and Methods

2.1 Study Area

The study area consists of the Konak, Halkapınar, and Bostanlı transfer centers located in İzmir city center (Figure 1). These centers were selected as the study area because they are important transportation nodes where different public transportation modes are integrated and where passengers frequently make transfers during their daily journeys.

Konak Transfer Center: Konak is an important transportation hub where metro, tram, ferry, and bus services converge. In addition to providing connections between different transportation modes, its central location contributes to high passenger activity.

Halkapınar Transfer Center: Halkapınar is an important transfer point served by metro, İZBAN, tram, and bus services. It has a particularly important role in providing connections between different rail-based transportation systems.

Bostanlı Transfer Center: Bostanlı is a transfer center where tram, ferry, and bus services converge. It is an important transportation node, particularly for connecting road-based and maritime transportation.

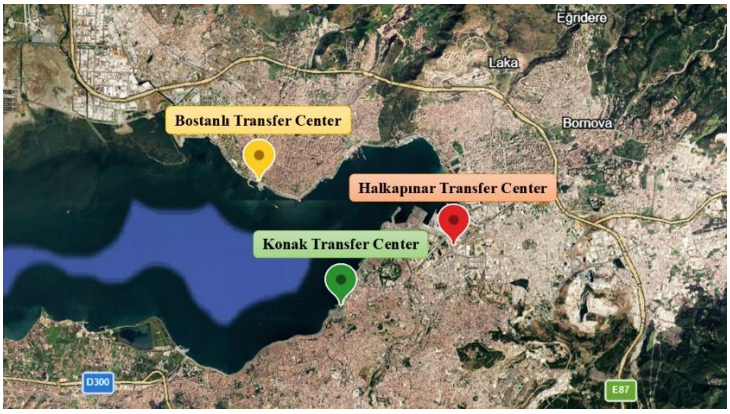


Fig. 1. Study Area and Locations of the Selected Transfer Centers

2.2 Survey Design

A passenger survey was conducted at the Konak, Halkapınar, and Bostanlı transfer centers located in different parts of İzmir, and survey data were collected for use in the study. A total of 510 passengers participated in the survey. After removing incomplete and invalid responses, 497 valid responses remained. Among these, responses from passengers making their first boarding at the transfer center were excluded, resulting in a final sample of 443 survey responses for the analysis.

The questionnaire was developed by adapting items from similar scales in the literature [11-12]. The survey collected the following information:

- Transfer center where the survey was conducted: Konak, Halkapınar, or Bostanlı
- Stage of transfer center use at the time of the survey: first transfer, second transfer, third transfer, or end of journey
- 5-point Likert-scale questions assessing satisfaction levels:
    - Evaluation of the stop/station/ferry terminal being used:
        - Ease of access to the stop at the transfer center
        - Suitability of pedestrian connections between public transportation modes
        - Cleanliness of the waiting area
        - Safety of the waiting area
        - Passenger density and space management
        - Comfort of the waiting area
        - Accessibility for passengers with disabilities
        - Signage and information provision
    - Evaluation of the vehicle most recently used:
        - Service frequency
        - Punctuality
        - Waiting time
        - Onboard cleanliness
        - Onboard safety
        - Onboard comfort
        - Quality of information provided on the vehicle
    - Overall evaluation of the transfer/journey experience.

2.3 Statistical Analysis

All data obtained from the survey were analyzed using IBM SPSS Statistics. To assess the reliability of the scale used in the questionnaire, Cronbach's alpha reliability analysis was performed on the satisfaction items.

Descriptive statistical analyses were conducted on the responses to the satisfaction questions, and the mean and standard deviation values were calculated for each item.

Correlation analysis was performed to examine the relationships between the variables. Pearson correlation analysis was used to assess the linear relationships between the variables and to provide a basis for the subsequent regression analysis. A multiple linear regression analysis was conducted to determine the effects of transfer center satisfaction and vehicle satisfaction on overall satisfaction.

A one-way ANOVA was conducted to examine whether satisfaction levels differed across vehicle types in terms of vehicle satisfaction, transfer center satisfaction, and overall satisfaction. For the analysis, vehicle types were coded as follows:
Bus = 1, Metro = 2, Tram = 3, Ferry = 4, İZBAN = 5.

When statistically significant differences were found between groups, a Tukey post hoc test was performed to determine which specific groups differed significantly from each other.

3 Results

3.1 Reliability Analysis

When the reliability analysis was performed on the 8-item scale assessing the stop/station/ferry terminal at the transfer center, Cronbach's alpha was found to be 0.839. For the 7-item scale assessing the vehicle most recently used at the transfer center, Cronbach's alpha was 0.860. Since both values fall within the range of 0.70–0.90, the scales can be considered reliable and internally consistent (Table 1).

Table 1. Reliability Analysis Results

Scale	Number of Items	Cronbach's α
Transfer Center Satisfaction	8	0.839
Vehicle Satisfaction	7	0.860

3.2 Descriptive Statistics

The analysis of the responses to the satisfaction questions showed that the mean satisfaction score for the transfer center was 3.40, with a standard deviation of 0.86. These values indicate a moderate level of satisfaction, with responses generally concentrated around the mean. Similarly, the mean satisfaction score for the vehicle most recently used at the transfer center was 3.66, with a standard deviation of 0.92. The mean overall satisfaction with the transfer/journey experience was 3.56, with a standard deviation of 0.92 (Table 2).

Table 2. Descriptive Statistics of Satisfaction Measures

Variables	Mean	Std. Deviation
Transfer Center Satisfaction	3.40	0.86
Vehicle Satisfaction	3.66	0.92
Overall Satisfaction	3.56	0.92

Regarding the stop/station/ferry terminal at the transfer center, passengers gave the highest satisfaction score to ease of access to the stop, while the lowest scores were given to accessibility for passengers with disabilities and passenger density and space management.

For the vehicle most recently used at the transfer center, the highest satisfaction score was given to punctuality, while the lowest score was given to onboard comfort.

3.3 Correlation Analysis

The Pearson correlation analysis yielded the results presented in Table 3. The strongest relationship was observed between vehicle satisfaction and overall satisfaction, with a correlation coefficient of 0.666. As passengers' satisfaction with the vehicles they used, including comfort, cleanliness, and overall condition, increased, their overall satisfaction also tended to increase substantially.

The correlation coefficient between transfer center satisfaction and overall satisfaction was 0.623. This indicates that higher satisfaction with transfer center conditions, including waiting areas, signage, and connections between transportation modes, was associated with higher overall satisfaction.

The correlation coefficient between transfer center satisfaction and vehicle satisfaction was 0.622. This suggests that passengers who evaluated the transfer center more positively also tended to evaluate their onboard experience more positively, and vice versa. This may indicate that passengers perceive the quality of the transportation system as a whole rather than as completely separate components.

All correlation coefficients were positive and greater than 0.50, indicating strong positive relationships between the variables. Since the relationships were statistically significant at the 0.01 significance level ($p < 0.01$), the observed associations are statistically significant.

Table 3. Pearson Correlation Analysis Results

Variables	Overall Satisfaction	Transfer Center Satisfaction	Vehicle Satisfaction
Overall Satisfaction	1.000	0.623	0.666
Transfer Center Satisfaction	0.623	1.000	0.622
Vehicle Satisfaction	0.666	0.622	1.000

3.4 Multiple Lineer Regression Analysis

The results presented in Table 4 show that the regression model was statistically significant ($p < 0.001$). This indicates that transfer center satisfaction and vehicle satisfaction have significant effects on overall satisfaction.

The R^2 value was 0.514, indicating that transfer center satisfaction and vehicle satisfaction together explain 51.4% of the variance in overall satisfaction. The remaining 48.6% can be attributed to other factors not included in the model.

The standardized coefficient Beta values were 0.340 for transfer center satisfaction and 0.455 for vehicle satisfaction. Therefore, vehicle satisfaction has a stronger effect on overall satisfaction than transfer center satisfaction.

The regression equation is:

$$OS=0.655+0.363(TCS)+0.457(VS) \quad (1)$$

where *OS* represents overall satisfaction, *TCS* represents transfer center satisfaction, and *VS* represents vehicle satisfaction.

Table 4. Multiple Linear Regression Analysis Results

Variables	Stardardized Coefficients β	t	p value (sig.)
Transfer Center Satisfaction	0.340	8.007	<0.001
Vehicle Satisfaction	0.455	10.717	<0.001

3.5 Comparison of Satisfaction Levels by Transport Mode

When the mean transfer center satisfaction scores were compared across transportation modes, ferry users had the highest satisfaction score, with a mean of 3.68, while bus users had the lowest, with a mean of 3.22.

For vehicle satisfaction, ferry users again had the highest mean satisfaction score (4.03), whereas İZBAN users had the lowest (3.07).

Regarding overall satisfaction, ferry users had the highest mean score (3.87), while İZBAN users had the lowest (3.25) (Figure 2).



Fig. 2. Comparison of Satisfaction Levels Across Transportation Modes

The one-way ANOVA for transfer center satisfaction yielded $F = 3.447$ and $p = 0.009$. Therefore, there was a statistically significant difference in mean transfer center satisfaction across transportation modes. The Tukey post hoc test showed that a statistically significant difference was found only between bus and ferry users.

For vehicle satisfaction, the one-way ANOVA yielded $F = 19.588$ and $p < 0.001$, indicating a statistically significant difference in mean vehicle satisfaction across transportation modes. According to the Tukey post hoc test, significant differences were found between bus and metro, bus and tram, bus and ferry, metro and İZBAN, tram and İZBAN, and ferry and İZBAN users.

For overall satisfaction, the one-way ANOVA yielded $F = 4.592$ and $p = 0.001$, indicating a statistically significant difference in mean overall satisfaction across transportation modes. The Tukey post hoc test showed significant differences between bus and tram users and bus and ferry users (Table 5).

Table 5. One-Way ANOVA Results by Transportation Mode

Variables	**F**	**p**
Transfer Center Satisfaction	3,447	0,009
Vehicle Satisfaction	19,588	<0,001
Overall Satisfaction	4,592	0,001

4 Discussion and Conclusion

This study examined the effects of passenger satisfaction with transfer center and vehicle services on overall journey satisfaction at the Konak, Halkapınar, and Bostanlı transfer centers in İzmir and compared satisfaction levels across different transportation modes. The results showed that satisfaction with both transfer center and vehicle services was positively and significantly associated with overall journey satisfaction. This finding is consistent with studies

indicating that public transportation satisfaction cannot be explained by a single service component and that different dimensions of the travel experience should be considered together [13-14], [10].

The reliability analysis showed that the scales measuring transfer center and vehicle satisfaction were reliable and internally consistent. The descriptive statistics indicated that vehicle satisfaction was higher than transfer center satisfaction. In the evaluation of transfer centers, ease of access to the stop was the most positively rated attribute, whereas accessibility for passengers with disabilities and passenger density and space management emerged as the main areas requiring improvement. Regarding vehicle services, punctuality received the most positive evaluation, while onboard comfort received a comparatively lower rating. These findings are consistent with a systematic review highlighting safety, security, comfort, reliability, and accessibility as key factors shaping public transportation service quality and user satisfaction [14], as well as with the study by Minelgaitė et al. [15], which identified distance to the stop as an important determinant of public transportation use.

The correlation and multiple linear regression results showed that transfer center and vehicle satisfaction together explained 51% of the variance in overall satisfaction. The higher standardized regression coefficient for vehicle satisfaction indicates that this variable has a stronger relationship with overall satisfaction than transfer center satisfaction. This suggests that conditions experienced directly inside the vehicle may play a more influential role in passengers' overall evaluations. This finding is consistent with van Lierop et al. [13], who reported that factors such as onboard cleanliness, comfort, punctuality, and service frequency are associated with overall passenger satisfaction.

The comparison across transportation modes revealed statistically significant differences in satisfaction levels depending on the mode used. Ferry users had the highest mean scores for transfer center, vehicle, and overall satisfaction, whereas bus users had lower transfer center satisfaction and İZBAN users had lower vehicle and overall satisfaction. These differences indicate that mode-specific service conditions should be considered when evaluating public transportation services. Factors such as travel comfort, passenger density, waiting conditions, and service reliability may vary across transportation modes and consequently contribute to differences in satisfaction levels. This finding supports studies emphasizing the importance of considering transportation mode and regional conditions when evaluating public transportation service quality [14], [16]. Therefore, rather than directly generalizing these findings to different transportation systems, the results should be interpreted within the context of the specific service conditions and user profiles of each system.

In conclusion, improving passenger satisfaction requires more than improving only transfer center characteristics or only vehicle-related services. Transfer center attributes, including ease of access to stops, suitability of pedestrian connections, cleanliness, safety and comfort of waiting areas, passenger density and space management, accessibility for passengers with disabilities, and signage and information provision, should be addressed together with vehicle-related factors such as service frequency, punctuality, waiting time, onboard cleanliness, safety, comfort, and the quality of information provided on vehicles. Accordingly, evaluating public transportation service quality through a holistic approach can contribute to improving the overall passenger experience and satisfaction.

Acknowledgments

The authors would like to thank the passengers who participated in the survey and contributed to this study.

References

1. İzmir Büyükşehir Belediyesi: Sürdürülebilir Kentsel Ulaşım Planı (SKUP) Final Raporu. İzmir Büyükşehir Belediyesi, İzmir (2024).
2. Berggren, U., Palmqvist, C.-W., Pyddoke, R.: Measured service reliability and customer satisfaction in public transport. Case Studies on Transport Policy 23, 101669 (2026). https://doi.org/10.1016/j.cstp.2025.101669.
3. Türk Standartları Enstitüsü: TS EN 13816:2002, Ulaştırma-Lojistik ve Hizmetler – Toplu Taşıma – Hizmet Kalitesinin Tarifi, Hedefi ve Ölçümü Standardı. Türk Standartları Enstitüsü, Ankara (2014).
4. Eboli, L., Mazzulla, G.: A new customer satisfaction index for evaluating transit service quality. Journal of Public Transportation 12(3), 21–37 (2009). https://doi.org/10.5038/2375-0901.12.3.2.
5. Susilo, Y.O., Cats, O.: Exploring key determinants of travel satisfaction for multi-modal trips by different traveler groups. Transportation Research Part A: Policy and Practice 67, 366–380 (2014). https://doi.org/10.1016/j.tra.2014.08.002.
6. Sil, E., Chaniotakis, E., Roy, U.K., Antoniou, C.: Exploring satisfaction for transfers at intermodal interchanges: A comparison of Germany and India. Journal of Public Transportation 24, 100005 (2022). https://doi.org/10.1016/j.jpubtr.2022.100005.
7. Carvalho, T., El-Geneidy, A.: Drivers of trip satisfaction over time: A case study across rapid transit systems in Montreal, Canada. Transportation Research Part A: Policy and Practice 210, 105064 (2026). https://doi.org/10.1016/j.tra.2026.105064.
8. Saraçoğlu, B.: Toplu Taşıma Sistemlerinin Entegrasyonunda Aktarma Merkezleri: İstanbul Tarihi Kıyı Bölgeleri Örneği. Yüksek Lisans Tezi, İstanbul Teknik Üniversitesi, Yükseköğretim Kurulu Ulusal Tez Merkezi (2012).
9. Yiğit, S.: Aktarma Merkezlerinin Kent İçi Ulaşıma Etkisi ve Yenibosna Aktarma Merkezi Projesi. Yüksek Lisans Tezi, Yıldız Teknik Üniversitesi, Yükseköğretim Kurulu Ulusal Tez Merkezi (2019).
10. Buran, B.: Assessing the determinants of passenger satisfaction in public bus transport systems: A fuzzy approach. Pamukkale University Journal of Engineering Sciences (2026). DOI: 10.65206/pajes.1903090.
11. Hernandez del Olmo, S.: Assessment Methodology to Make Urban Transport Interchanges Attractive for Users. Doctoral Dissertation, Universidad Politécnica de Madrid (2015).
12. Yahya, N.: Assessment of Service Quality and Satisfaction from Passengers' Perspective to Inform Bus Operator Decision Making. Master's Thesis, University of Leeds (2013).
13. van Lierop, D., Badami, M.G., El-Geneidy, A.M.: What influences satisfaction and loyalty in public transport? A review of the literature. Transport Reviews 38(1), 52–72 (2018). https://doi.org/10.1080/01441647.2017.1298683.
14. Sogbe, E., Susilawati, S., Tan, C.P.: Scaling up public transport usage: A systematic literature review of service quality, satisfaction and attitude towards bus transport systems in developing countries. Public Transport 17, 1–44 (2024). https://doi.org/10.1007/s12469-024-00367-6.
15. Minelgaitė, A., Dagiliūtė, R., Liobikienė, G.: The usage of public transport and impact of satisfaction in the European Union. Sustainability 12(21), 9154 (2020). http://dx.doi.org/10.3390/su12219154.
16. Ojo, T.K.: Quality of public transport service: An integrative review and research agenda. Transportation Letters 11(2), 104–116 (2019). https://doi.org/10.1080/19427867.2017.1283835

Author Contribution Statement

- *Conceptualization:* Handenur Keser, Yalçın Alver
- *Methodology:* Handenur Keser, Yalçın Alver
- *Investigation:* Handenur Keser
- *Writing – Original Draft:* Handenur Keser
- *Writing – Review & Editing:* Handenur Keser, Yalçın Alver

List of Abbreviations

- **SKUP** — Sustainable Urban Mobility Plan
- **İZBAN** — İzmir Suburban Rail System
- **ANOVA** — Analysis of Variance

Note: Following the conference, this Publication Note will be added to each paper; therefore, authors are kindly requested not to remove the note below and to complete the author(s) and paper title information.

Publication Note

This paper was peer-reviewed, accepted for presentation, and included in the proceedings of the ACE2026 – International Conference on Advances in Civil Engineering, held on 12–14 October 2026 in Trabzon, Türkiye.

This paper may be cited as follows:

Keser H., Alver Y., "Investigation of the Effect of Service Quality Perception at Public Transport Transfer Centers and Vehicles on Passenger Satisfaction," in Proceedings of the ACE2026 – International Conference on Advances in Civil Engineering, Trabzon, Türkiye, 12–14 October 2026.

Assessing Campus Travel Behavior and Potential CO_2 Emission Reductions through a Ring Shuttle System: A Case Study of Muğla Sıtkı Koçman University

Ahmet Taha Koçtaş[1] Elif Dağlı[1] Mervegül Uysal[1]
[1] 0009-0004-9008-2392, Muğla Sıtkı Koçman University, Civil Engineering Department, Muğla, Türkiye, ahmettaha2012@hotmail.com
[1] 0009-0002-2011-7567, Muğla Sıtkı Koçman University, Civil Engineering Department, Muğla, Türkiye, elifdagli@posta.mu.edu.tr
[1] 0000-0002-6482-1436, Muğla Sıtkı Koçman University, Civil Engineering Department, Muğla, Türkiye, merveguluysal@posta.mu.edu.tr

Abstract. This study aims to identify the transportation preferences of students and staff at the Muğla Sıtkı Koçman University (MSKU) central campus. Due to their large populations and extensive areas, universities function as small cities and have significant impacts on the surrounding environment. Therefore, transportation is a fundamental component of university sustainability policies. Promoting transportation modes such as carpooling, public transportation, and cycling, reducing the use of private vehicles on campus, and improving pedestrian mobility are among the key objectives within this framework.

On-campus travel, transportation was mostly held by private vehicles, this situation increases traffic congestion and creates environmental problems. In addition, the campus location and local climate conditions limit the use of cycling as a transportation alternative. Therefore, this project aims to support the planning of a new campus shuttle route to reduce on-campus vehicle traffic, encourage the use of public transportation, and improve accessibility, using the data of transportation preferences of campus population that is identified through a questionnaire administered to university students and staff. A binary logistic regression model will be employed to analyze the survey data and determine the factors influencing transportation mode choices and needs while calculating and suggesting improvements for the carbon emission in the campus.

Keywords: Sustainable transportation, Multinominal regression analysis, shuttle route, transportation planning

1 Literature Review

The primary motivation of this research is to establish a stable and optimal transportation profile based on previous empirical studies and methodological frameworks. Accordingly, an extensive body of literature on sustainable transportation and campus shuttle (ring service) planning has been reviewed. Among them, Balsas (2003) emphasized the potential of university campuses to promote sustainable transportation due to their educational environment. The study argued that universities could actively reduce private automobile dependency through educational programs and infrastructure improvements that encourage sustainable mobility alternatives **[1]**. Kaplan (2015) emphasizes that transportation sustainability on university

campuses depends on both the availability of appropriate transportation infrastructure and the travel behavior of campus users. That study empirically evaluated transportation sustainability at a large US university using a mixed-method approach. The author measured pedestrian and bicycle activities during morning and afternoon periods, and conducted surveys involving 668 students. Walking and cycling rates were found to be low, with bicycle usage remaining negligible. Primary barriers included time constraints, lack of convenience, and inadequate infrastructure, showing that existing physical environments heavily constrain active mobility. Furthermore, students' perceptions, together with the campus infrastructure inventory, revealed that the existing transportation environment constituted a significant barrier to sustainable mobility **[2]**.

Whereas more recent studies, analyze the travel mode preferences of students and university personnel through comprehensive survey data and Multinomial Logit (MNL) models. Miralles-Guasch and Domène (2010) examined travel preferences and barriers at the Autonomous University of Barcelona across 5,525 students and staff. Major barriers preventing a shift from private vehicles to walking, cycling, or public transit included insufficient infrastructure, low active travel levels, and prolonged public transport travel times. Owing to its large sample size, this study underscores the necessity of incorporating variables such as "perceived travel time in public transportation" and "adequacy of active transportation infrastructure" into campus survey instruments **[3]**.

Deneke et al. (2024) examined work and school travel choices across seven urban districts in Hawassa, Ethiopia, using the Multinomial Logit (MNL) model. The categorical dependent variable was transportation mode (private car, motorcycle, bus), while independent variables included in-vehicle travel time, out-of-vehicle travel time, travel cost, monthly income, perceived comfort, and socioeconomic factors. Results confirmed that higher income and longer in-vehicle times increased private automobile selection, whereas students preferred public transportation over motorcycles **[4]**. In addition, the study utilized behavioral survey data to estimate future travel demand and modal shares while emphasizing the importance of transportation policy interventions. Similar MNL models could therefore be employed to analyze users' willingness to shift toward the proposed campus shuttle service. The explanatory variables identified in the Hawassa case (such as travel cost, travel time, and income) provide valuable guidance for the development of survey questions and the specification of the analytical model. Given that the present study is conducted within a university campus, the study by Akter and Alam (2024) is particularly relevant, as it examines both campus access and intra-campus mobility at the University of Toledo, Ohio, using descriptive statistics and Multinomial Logit (MNL) modeling. Key determinants included automobile ownership, travel distance, age, gender, academic status, income, perceived safety, travel frequency, and weather conditions. Specific findings demonstrated that; greater travel distance, older age, and staff status increased private car reliance, faculty members walked and cycled more frequently than undergraduate students and higher-income individuals exhibited a higher tendency for intra-campus walking. Which leads us to believe that increased travel frequency promotes car commuting for off-campus trips while increasing walking likelihood for short intra-campus trips **[5]**.

Pun, Zhao, and Liu (2019) proposed a Multiple Linear Regression (MLR) model for traffic flow estimation in Hong Kong. Their study incorporated both topological characteristics

of the road network (e.g., node degree, intersection density, betweenness, closeness, and PageRank indices) and geometric characteristics (road length) to estimate traffic volumes. Three different traffic flow datasets, including vehicle counts, bus routes, and fixed traffic counting stations, were utilized to validate the proposed model. Six explanatory variables, five topological indicators together with road length, were incorporated into the regression analysis to investigate the relationship between road network characteristics and traffic flow **[6]**. Although the methodological framework proposed by Pun et al. does not directly correspond to the objectives of the present study, it provides valuable insights into the application of Multiple Linear Regression for transportation planning. Specifically, the relationship between campus road characteristics (e.g., road length, intersection density, and accessibility) and anticipated shuttle service demand could be investigated using a similar analytical framework. Furthermore, the study demonstrates how heterogeneous transportation datasets can be integrated into a single regression model, providing methodological guidance for estimating campus traffic volumes and expected shuttle passenger demand.

Rybarczyk (2018) analyzed active transportation determinants among residential university students in Michigan using Exploratory Spatial Data Analysis (ESDA), OLS regression, and Geographically Weighted Regression (GWR). Modeling variables included demographics, household automobile ownership, population density, land-use diversity, and network design. Findings revealed that travel distance is not a uniform barrier across geographic space; proximity strongly dictated active travel in certain areas, whereas infrastructural factors dominated in others. This highlights the utility of GWR and GIS spatial visualization for identifying localized demand clusters and accessibility deficiencies on campus **[7].** In some areas, proximity to destinations strongly influenced active transportation, whereas in others, different environmental and infrastructural factors played a more dominant role. These findings emphasize the importance of considering spatial heterogeneity when planning campus shuttle services.

Among the studies conducted in Türkiye, the most relevant examples include Süt, Hamurcu, and Eren (2019) and Keleş, Özgül, and Ulutaş (2024). Süt et al. (2019) applied AHP and TOPSIS methods at Kırıkkale University to select eco-friendly campus shuttle vehicles. Evaluation criteria encompassed engine attributes (fuel type, power, climbing performance), vehicle equipment (capacity, passenger comfort, charging duration), aesthetics, energy efficiency, accessibility, economic cost, and environmental performance **[8]**.

Keleş, Özgül, and Ulutaş (2024) surveyed 60 undergraduate students in Kuşadası, Türkiye, regarding walking, cycling, and shuttle choices. Weather conditions and ambient temperature played critical roles in active travel preferences. Campus shuttles were most frequently preferred during examination periods, whereas walking was restricted to students living near campus. Narrow bicycle lanes were identified across genders as a primary barrier to cycling **[9]**. Although the study was conducted on a relatively small sample, it demonstrates that environmental and infrastructural factors substantially influence transportation behavior even within university campuses such as Kuşadası.

2 Methodology

Based on literature review and preliminary field observations, binary logit regression framework was selected as the primary analytical method for this study. To gather the empirical data required for this framework, a mobile intercept survey comprising 32 questions structured into four distinct sections was developed. The first section gathers demographic and socioeconomic profile data, including gender, age, occupation, and financial status. The second section examines participants' travel habits, covering both off-campus commuting and intra-campus mobility. The third section evaluates user expectations, service requirements, and projected usage rates regarding a potential campus ring shuttle system. The final section incorporates a satisfaction assessment to determine how effectively current municipal bus services fulfill campus transit demand, alongside an open-ended area for participant suggestions and feedback.

Data collection was carried out across the main campus and its immediate surroundings using a mobile survey administration approach, yielding a final sample size of 629 valid respondents. The dataset will be processed, tabulated, and analyzed using IBM SPSS software, followed by binary logit regression modeling to extract behavioral determinants, empirical insights, and policy recommendations. Furthermore, baseline campus-level transportation carbon emissions will be estimated using the survey data. The anticipated environmental improvements resulting from the integration of electric buses and an optimized ring shuttle corridor will be quantified and reported alongside targeted recommendations to reduce the university's carbon emission.

2.1 Survey Results

Regarding the gender distribution of the sample, 51.03% of the participants were male and 48.97% were female. The vast majority of respondents (73.77%) belonged to the age category of 25 and under. The breakdown for the remaining age groups was 7.31% for ages 26–35, 14.47% for ages 36–50, and 4.45% for participants aged 51 and above. Consistent with this age profile, the sample breakdown by institutional status comprised 76.15% students, 12.40% academic personnel, 10.17% administrative staff, and 1.11% private sector employees.

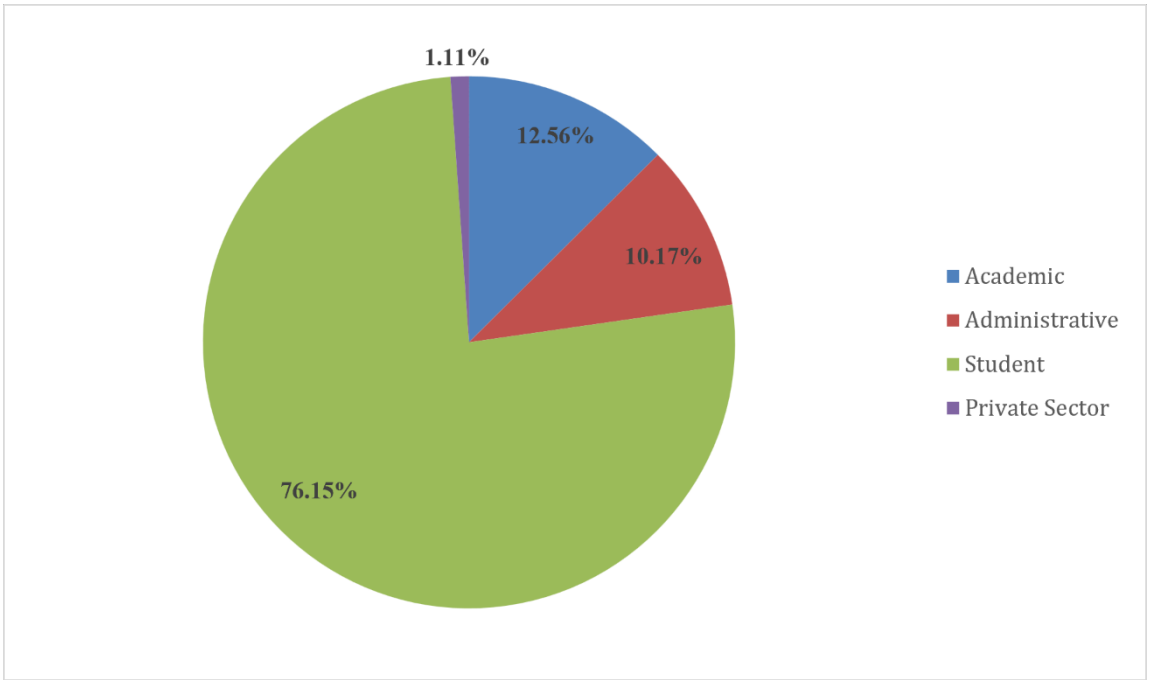


Fig. 1. Pie Chart of Institutional Status of the Campus

Regarding campus entry points, Gate C (which connects the campus to the Kötekli neighborhood area) was identified as the most frequently used entrance, accounting for 54.25% of all access. This was followed by Gate A, leading to the KYK student dormitories, at 29.86%, and Gates B and Gate D, representing 10.43% and 5.46% of campus entries, respectively.

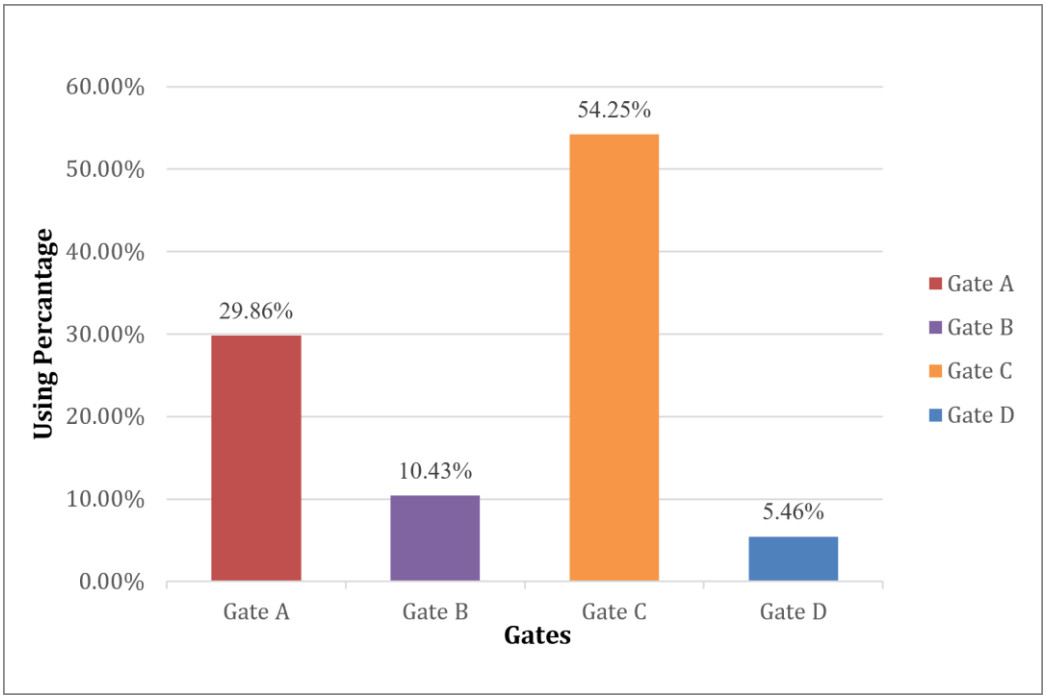


Fig. 2. Chart of Most Used Entrances on MSKU campus

Public transportation was identified as the predominant mode of travel to the campus, accounting for 58.85% of the respondents. Private cars constituted the second preferred mode of transportation, accounting for 26.95% of the respondents. In contrast, bicycle use was remarkably low, representing only 0.16% of all participants. The remaining respondents preferred walking (10.21%) and motorcycles (3.83%) as their primary mode of transportation.

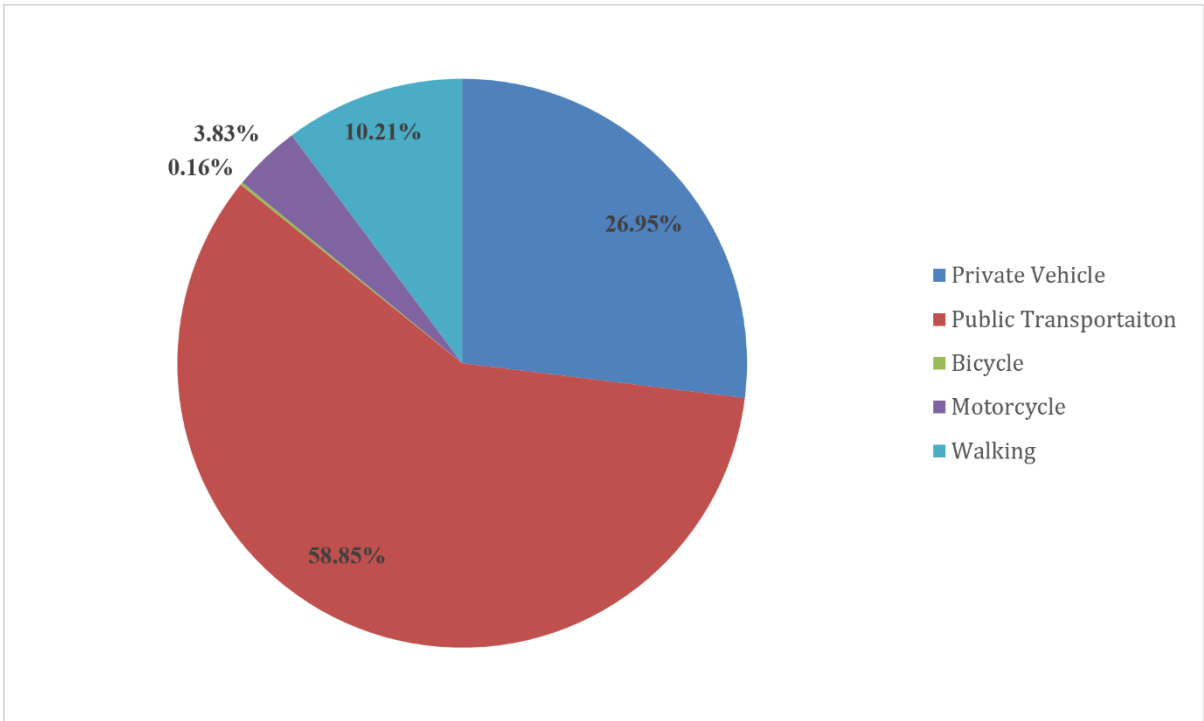


Fig. 3. Preferred Transportation Modes When Coming to the Campus

Private vehicle users prefer 88.21% petrol/diesel, 6.67% hybrid and 5.13% electric vehicles.

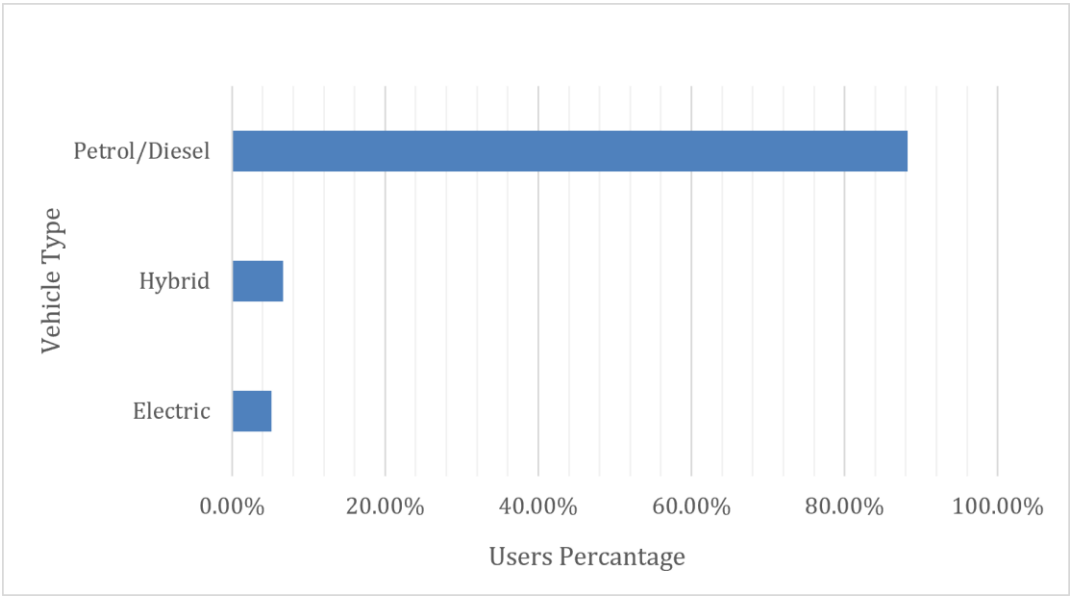


Fig. 4. Chart of Private Vehicle Types Used in the Campus

Compared to travel to the campus from outside, the use of public transportation for on-campus travel decreased slightly to 42.21%. Nevertheless, public transportation remained the dominant

mode of travel within the campus. The proportion of respondents who preferred walking increased substantially, rising from approximately 10% to 39.05%. Meanwhile, the share of private car users declined to 14.71%, whereas the use of bicycles and motorcycles remained at relatively similar levels.

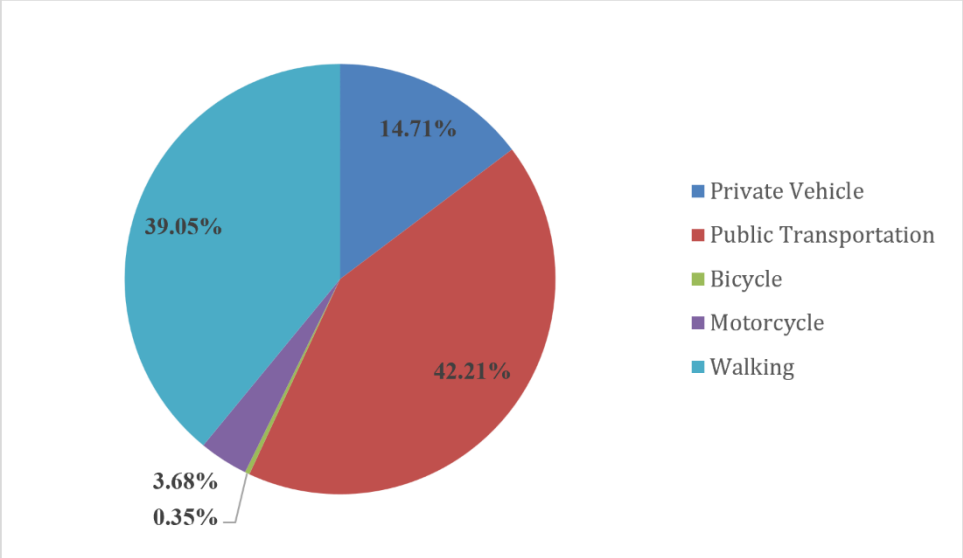


Fig. 5. Preferred Transportation Modes Travelling On-Campus

The findings revealed that 73.44% of the respondents expressed a willingness to use a campus shuttle service if one were provided, while 26.56% reported that they would not utilize such a service. The following table presents the responses to the question of whether the existing municipal bus service (Route 1–48), which currently provides transportation to the campus, adequately meets the transportation needs of the respondents.

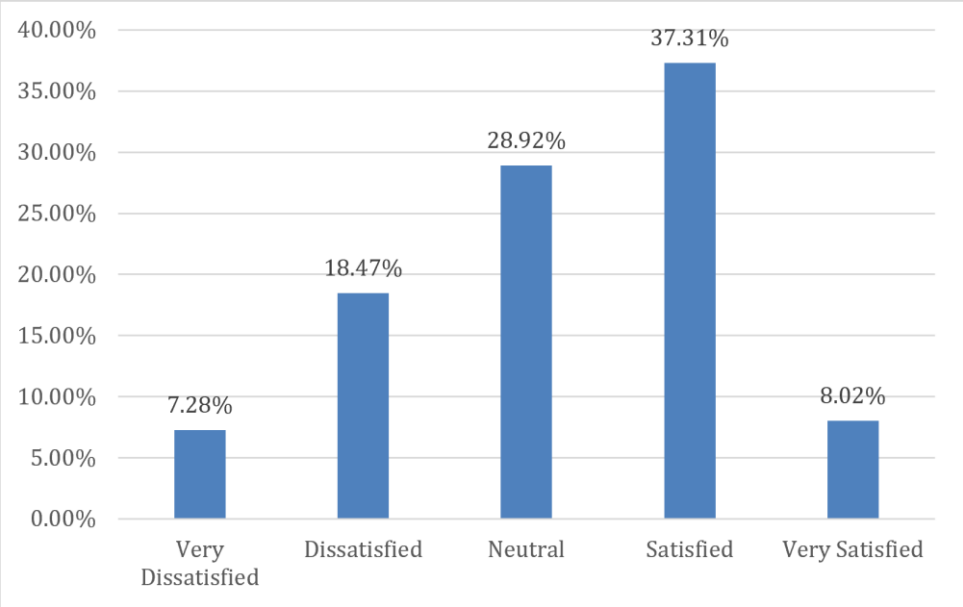


Fig. 6. Thoughts on Current Municipality Public Transportation Route

2.2 Binary Logistic Regression Analysis

A binary logistic regression analysis was conducted to identify the factors associated with participants' intention to use the campus ring shuttle service. The dependent variable was defined based on participants' responses to the question, "Would you use a ring shuttle service if it were available?" Gender, age, occupation, driving licence ownership, income level, preferred campus entrance gate, frequency of travel to the campus, mode of transportation used to access the campus, mode of transportation used within the campus, and awareness of the existing campus ring service were included in the model as independent variables. Due to missing observations, 558 (89.3%) of the 625 valid responses were included in the regression analysis.

The binary logistic regression model provided a statistically significant improvement over the intercept-only model (χ^2 (26) = 81.422, $p < 0.001$). The Cox and Snell pseudo-R^2 and Nagelkerke pseudo-R^2 values were 0.136 and 0.204, respectively. The Hosmer–Lemeshow goodness-of-fit test indicated no statistically significant discrepancy between the observed and model-predicted values (χ^2 (8) = 4.055, $p = 0.852$), suggesting an acceptable fit of the model to the data.

Table 1. Variables in the Equation

	B	S.E.	Wald	df	Sig.	Exp(B)	95% C.I.for EXP(B)	
							Lower	Upper
Driving License	,742	,275	7,288	1	,007	2,099	1,225	3,597
Frequency of travel to campus			9,721	4	,045			
Frequency of travel to campus (1)	1,438	,850	2,858	1	,091	4,212	,795	22,303
Frequency of travel to campus (2)	,623	,427	2,128	1	,145	1,865	,807	4,306
Frequency of travel to campus (3)	,713	,380	3,517	1	,061	2,039	,968	4,294
Frequency of travel to campus (4)	1,050	,360	8,517	1	,004	2,857	1,412	5,783
Awareness of the existing campus ring (1)	-,979	,322	9,246	1	,002	,376	,200	,706
Constant	-1,964	1,408	1,947	1	,163	,140		

An examination of the contributions of the independent variables showed that driving licence ownership ($p = 0.007$), frequency of travel to the campus ($p = 0.045$), and awareness of the existing campus ring service ($p = 0.002$) were significantly associated with the intention to use the ring shuttle service. In contrast, gender ($p = 0.498$), age ($p = 0.927$), occupation ($p = 0.974$), income level ($p = 0.155$), preferred campus entrance gate ($p = 0.713$), mode of transportation used to access the campus ($p = 0.686$), and mode of transportation used within the campus ($p = 0.255$) did not make statistically significant contributions to the model.

Regarding driving licence ownership, participants who held a driving licence had approximately 2.10 times higher odds of reporting that they would not use the ring shuttle service than those without a driving licence ($B = 0.742$, $OR = 2.099$, 95% CI: 1.225–3.597, $p = 0.007$), after controlling for the other variables in the model. This finding indicates that driving licence ownership was associated with a lower intention to use the ring shuttle service.

Frequency of travel to the campus was also significantly associated with the intention to use the ring shuttle service (Wald χ^2 (4) = 9.721, $p = 0.045$). Using participants who travelled to the campus six or more days per week as the reference category, those who travelled to the campus five days per week had approximately 2.86 times higher odds of reporting that they would not use the ring shuttle service ($B = 1.050$, $OR = 2.857$, 95% CI: 1.412–5.783, $p = 0.004$). Differences between the other frequency categories and the reference category were not statistically significant at the 5% significance level.

Awareness of the existing campus ring service was also significantly associated with the intention to use the ring shuttle service. Participants who were aware of the existing ring service had 0.376 times the odds of reporting that they would not use the ring shuttle compared with participants who were unaware of the service ($B = -0.979$, $OR = 0.376$, 95% CI: 0.200–0.706, $p = 0.002$). Expressed in terms of the inverse odds ratio, participants who were aware of the existing ring service had approximately 2.66 times higher odds of intending to use the ring shuttle service than those who were unaware of it. This finding suggests a positive association between awareness of the existing ring service and intention to use the service in the future.

Regarding classification performance, the intercept-only model correctly classified 76.2% of the observations, whereas the all correct classification rate increased to 79.7% after the independent variables were included. The final model correctly classified 95.1% of participants who indicated that they would use the ring shuttle service and 30.8% of those who indicated that they would not use it. Thus, although the inclusion of the independent variables improved the all classification rate, the model showed substantially lower classification performance for participants who did not intend to use the ring shuttle service.

The findings indicate that, rather than most of the demographic characteristics examined, driving licence ownership, frequency of travel to the campus, and awareness of the existing ring service were significantly associated with participants' intention to use the campus ring shuttle service.

Also, a satisfaction score was calculated by averaging the eight items assessing participants' evaluations of the existing campus ring service. The scale demonstrated good internal consistency (Cronbach's $\alpha = .835$), with corrected item-total correlations ranging from .482 to .633. The mean satisfaction score was 3.23 (SD = 0.75) on a five-point scale (N = 532; range = 1–5), indicating a moderate level of satisfaction with the existing campus ring service.

Table 2. Descriptive Statistics

	N	Minimum	Maximum	Mean	Std. Deviation
MEMSKOR	532	1,00	5,00	3,2260	,74566
Valid N (listwise)	532				

3.CO_2 Emission Assessment under the Proposed Electric Ring Shuttle Scenario

A scenario-based CO_2 emission analysis was conducted to assess the potential environmental implications of introducing a battery-electric ring shuttle service for internal trips within the university campus. Since the proposed service is intended exclusively for intra-campus transportation, the analysis focused on the transportation modes currently used by participants within the campus rather than the modes used to access the campus.

The survey results indicated that 83 participants currently used private cars for intra-campus travel, 241 used public transport, 21 used motorcycles, and 223 used active modes, including walking and cycling. Among these groups, 47 private car users (56.6%) and 12 motorcycle users (57.1%) stated that they would use the proposed ring shuttle service. These potential shifts from individual motorised transport to the ring service were considered the primary source of avoided emissions in the scenario analysis. In contrast, shifts from walking and cycling were not considered to generate avoided operational emissions, since these modes were assumed to have zero direct operational CO_2 emissions.

Because detailed operational characteristics of the proposed service have not yet been determined, several assumptions were introduced to establish a baseline scenario. The length of the proposed ring route was assumed to be 3.35 km, which was also adopted as the average distance of an intra-campus trip. The ring service was assumed to operate 20 trips per day using a battery-electric bus. This corresponds to a total daily vehicle distance of 67 km. An average electricity consumption of 1.5 kWh/km was assumed for the electric bus, resulting in an estimated daily electricity demand of 100.5 kWh. Electricity-related emissions were calculated using the emission factor for electricity consumption from the Turkish distribution grid. Private car and motorcycle emissions were estimated using representative vehicle emission factors. Since the latter factors were not specific to the Turkish vehicle fleet, they were treated as proxy values and should therefore be interpreted within the context of a scenario-based assessment.

Under the assumption that each potential mode-shift participant makes one 3.35-km intra-campus trip per day, the avoided emissions associated with the shift of 47 private car users and 12 motorcycle users to the ring service were estimated at approximately 30.90 kg CO_2e/day. In comparison, operation of the proposed electric ring service was estimated to generate approximately 47.13 kg CO_2e/day of indirect emissions associated with electricity generation. Consequently, under the one-trip-per-day scenario, implementation of the ring service would result in a net increase of approximately 16.23 kg CO_2e/day, corresponding to a 52.5% increase relative to the emissions avoided from private car and motorcycle trips.

Given the uncertainty regarding the actual number of daily intra-campus trips, a sensitivity analysis was conducted using one, two, and three trips per person per day. The results are presented in Table 3.

Daily intra-campus trips per person	Avoided private car and motorcycle emissions (kg CO_2e/day)	Electric ring emissions (kg CO_2e/day)	Net change (kg CO_2e/day)	Relative change
1	30.90	47.13	+16.23	+52.5%
2	61.81	47.13	−14.67	−23.7%
3	92.71	47.13	−45.57	−49.2%

The sensitivity analysis demonstrates that the environmental performance of the proposed electric ring service is strongly dependent on the number of motorised intra-campus trips replaced by the service. While the one-trip-per-day scenario does not produce a net reduction in CO_2 emissions, the results change when two or more daily trips per person are assumed. Under the two-trip scenario, the proposed ring service would reduce emissions by approximately 14.67 kg CO_2e/day (23.7%), whereas the three-trip scenario would result in an estimated reduction of 45.57 kg CO_2e/day (49.2%).

Based on the assumptions adopted in the analysis, the break-even point was estimated at approximately 1.53 intra-campus trips per person per day. Thus, the electric ring service becomes advantageous in terms of CO_2 emissions when the average number of private car and motorcycle trips replaced by the service exceeds approximately 1.53 trips per potential mode-shift user per day. This finding highlights that the environmental benefits of an electric shuttle system depend not only on vehicle technology but also on the extent to which the service substitutes existing individual motorised trips.

An additional consideration arises from the potential shift from active transportation modes to the ring service. Of the participants currently using walking or cycling for intra-campus transportation, 162 (72.6%) indicated that they would use the proposed ring service. Since walking and cycling were assumed to generate no direct operational emissions, replacing these trips with motorised shuttle trips would not generate direct emission savings. Although additional passengers may have little effect on the marginal operational emissions of a scheduled electric bus once the service is already operating, a reduction in active-mode use would be undesirable from a broader sustainable mobility perspective. Therefore, the proposed ring service should primarily be designed to substitute private motorised trips rather than compete it walking and cycling for short intra-campus journeys.

The scenario analysis suggests that the introduction of an electric ring shuttle does not automatically guarantee a reduction in transport-related CO_2 emissions. Its environmental effectiveness depends substantially on service frequency, electricity consumption, route length, and, particularly, the number of private car and motorcycle trips replaced. Accordingly, service planning should aim to maximise the modal shift from individual motorised transportation while preserving active transportation for short-distance campus trips. Under sufficiently high substitution of private motorised travel, the proposed electric ring service has the potential to contribute to reducing transport-related CO_2 emissions within the university campus.

4 Results and Conclusion

The findings demonstrate a substantial potential demand for a campus ring shuttle service at Muğla Sıtkı Koçman University. 73.44% of the respondents indicated that they would use such a service if provided, while public transportation was already the predominant mode for both campus access and intra-campus travel. The binary logistic regression model was statistically significant ($\chi^2(26) = 81.422$, $p < 0.001$) and showed an acceptable fit to the data (Hosmer–Lemeshow $\chi^2(8) = 4.055$, $p = 0.852$; Nagelkerke $R^2 = 0.204$). Driving licence ownership ($p = 0.007$), frequency of travel to campus ($p = 0.045$), and awareness of the existing campus ring service ($p = 0.002$) were significantly associated with willingness to use the proposed service, whereas the other demographic and travel-related variables included in the model were not statistically significant. In particular, participants who were aware of the existing ring service had approximately 2.66 times higher odds of intending to use the proposed service than those who were unaware of it. The satisfaction assessment further indicated a moderate level of satisfaction with the existing service ($M = 3.23$, $SD = 0.75$), with the eight-item scale demonstrating good internal consistency (Cronbach's $\alpha = 0.835$).

The environmental assessment indicates that the potential benefits of an electric ring service depend strongly on its ability to substitute private motorised intra-campus trips. Among current intra-campus users, 56.6% of private car users and 57.1% of motorcycle users stated that they would use the proposed service. Under the assumed 3.35-km route, 20 daily services, and battery-electric bus operation, the shuttle was estimated to generate 47.13 kg CO_2e/day from electricity consumption. Sensitivity analysis showed that replacing only one motorised trip per potential user per day would increase net emissions by 16.23 kg CO_2e/day; however, replacing two and three trips would reduce emissions by 14.67 kg CO_2e/day (23.7%) and 45.57 kg CO_2e/day (49.2%), respectively. The estimated break-even point was 1.53 substituted private car or motorcycle trips per person per day, indicating that electrification alone does not guarantee an environmental benefit; sufficient modal shift away from individual motorised transport is also required.

The results support the introduction of a carefully planned electric ring shuttle as part of MSKU's sustainable campus mobility strategy, provided that its operation is designed primarily to reduce private car and motorcycle use rather than replace active travel. This distinction is particularly important because 72.6% of current walking and cycling users also expressed willingness to use the proposed service, suggesting a potential unintended shift away from zero-emission active modes. Accordingly, route and service planning should prioritise locations and periods with high private motorised travel demand, while walking and cycling should remain

attractive alternatives for short intra-campus trips. The proposed ring system should therefore be regarded not simply as an additional transport service, but as a demand-responsive mobility intervention whose effectiveness depends on service design, user awareness, and its capacity to achieve a measurable shift from individual motorised transport toward collective electric mobility.

References

1. Balsas, Carlos JL. "Sustainable transportation planning on college campuses." *Transport Policy* 10.1 (2003).
2. Kaplan, David H. "Transportation sustainability on a university campus." *International Journal of Sustainability in Higher Education* 16.2 (2015).
3. Sustainable transport challenges in a suburban university: The case of the Autonomous University of Barcelona, Miralles-Guasch & Domene (2010).
4. Deneke, Yeshitila, et al. "Transportation mode choice behavior with multinomial logit model: work and school trips." *Transactions on transport sciences* 15.1 (2024).
5. Akter, Taslima, and Bhuiyan Monwar Alam. "Travel mode choice behavior analysis using multinomial logit models towards creating sustainable college campus: a case study of the University of Toledo, Ohio." *Frontiers in Future Transportation* 5 (2024): 1389614.
6. Pun, Lilian, Pengxiang Zhao, and Xintao Liu. "A multiple regression approach for traffic flow estimation." *IEEE access* 7 (2019): 35998-36009.
7. Rybarczyk, Greg. "Toward a spatial understanding of active transportation potential among a university population." *International journal of sustainable transportation* 12.9 (2018).

Author Contribution Statement

- *Conceptualization:* Ahmet Taha Koçtaş, Mervegül Uysal
- *Methodology:*Mervegül Uysal
- *Investigation:* Ahmet Taha Koçtaş, Elif Dağlı
- *Writing – Original Draft:* Ahmet Taha Koçtaş, Mervegül Uysal
- *Writing – Review & Editing:* Mervegül Uysal

Publication Note

This paper was peer-reviewed, accepted for presentation, and included in the proceedings of the ACE2026 – International Conference on Advances in Civil Engineering, held on 12–14 October 2026 in Trabzon, Türkiye.

This paper may be cited as follows:

Ahmet Taha Koçtaş, Elif Dağlı and Mervegül Uysal "Assessing Campus Travel Behavior and Potential CO_2 Emission Reductions through a Ring Shuttle System: A Case Study of Muğla Sıtkı Koçman University," in Proceedings of the ACE2026 – International Conference on Advances in Civil Engineering, Trabzon, Türkiye, 12–14 October 2026.

Smart City and Hospital Location Policy: A Transportation Equity Framework

Zeynep Nur Duman[1*], Mehmet Ali Silgu[2,3] and Mehmet Yılmaz[4]
[1] 0000-0001-9882-0573, Fırat University, Civil Engineering Department, Elazığ, Türkiye, znduman@firat.edu.tr
[2,3] 0000-0002-7667-8796, Bartın University, Civil Engineering Department, Bartın, Türkiye, Koç University, Industrial Engineering Department, İstanbul, Türkiye, masilgu@bartin.edu.tr
[4] 0000-0002-2761-2598, Fırat University, Civil Engineering Department, Elazığ, Türkiye, mehmetyilmaz@firat.edu.tr
* *Corresponding author*

Abstract. Hospital location determines who can reach care, how quickly, and at what cost, yet siting decisions in most health systems still rely on land price and cost rather than population accessibility. This paper develops a policy framework linking hospital location decisions to the transportation intelligence that smart city infrastructure already produces. The framework has three components: an information integration protocol that converts routing-API travel-time matrices, GTFS transit schedules, fleet GPS, smart-card records and mobile-network mobility data into a time-dependent multimodal travel-time matrix; a Transportation Accessibility Impact Assessment (TAIA) that scores accessibility with a two-step floating catchment area method and evaluates fairness with a population-weighted Gini index for elderly, low-income and vehicle-less residents; and an institutional coordination mechanism, grounded in the Health-in-All-Policies approach, requiring joint health-transport review before a hospital siting decision is finalised. Türkiye's City Hospitals programme, which has relocated more than twenty major facilities to urban peripheries since 2017 without a documented accessibility review, supplies the context, and Eastern Anatolian cities such as Elazığ, with below-average car ownership, limited transit coverage, hilly terrain and severe winters, illustrate the equity stakes most sharply. A stylised numerical example shows how the TAIA metrics would flag a peripheral relocation that raises average accessibility while widening the gap between vehicle-owning and vehicle-less residents, a pattern a bed-count criterion cannot detect. The technical barrier to evidence-based hospital siting is now smaller than the institutional one, and closing it requires a few governance instruments rather than new data infrastructure.
Keywords: Smart city; Hospital location policy; Intelligent Transportation Systems; Spatial equity.

1 Introduction

Hospital location affects health outcomes through a channel that can be measured directly: travel time. In acute ischaemic stroke, the treatable brain volume shrinks by roughly two million neurons a minute, so every additional minute of pre-hospital travel carries a quantifiable clinical cost [1]. In out-of-hospital cardiac arrest, a cohort study of the Scottish Ambulance Service found that cutting response time to five minutes could nearly double survival to hospital discharge [2]. For patients managing chronic conditions, the same travel-time channel operates over months rather than minutes: a facility that is hard to reach produces missed appointments and weaker control of the underlying disease. Distance is therefore not an incidental feature of hospital location; it is a determinant of the outcomes that the facility exists to protect.

Despite this evidence, hospital siting is rarely subjected to a formal accessibility test. Decisions are shaped by land availability, construction cost and political negotiation, and the population-level consequence, who can reach the new facility and who cannot, is treated as a byproduct rather than a design criterion. This omission is not a data problem in the way it would have been two decades ago. Contemporary cities operate dense networks of traffic sensors, GPS-tracked transit and emergency fleets, electronic fare systems, navigation platforms and mobile-network infrastructure that jointly constitute what the smart-city literature calls a merger of information and communication technology with traditional urban infrastructure [3]. These systems already expose peak-hour congestion, transit coverage gaps and the neighbourhoods where a short geographic distance translates into a long travel time. The intelligence exists; it simply does not reach the desks where hospital location decisions are made.

This paper argues that the gap between smart-city transportation intelligence and health facility planning is an institutional failure rather than a technical one, and it proposes a framework to close it. The framework couples three components: a protocol for integrating existing smart-city data streams into a usable travel-time input, a quantitative accessibility and equity assessment that health authorities can require before a siting decision is finalised, and a coordination mechanism that gives the assessment institutional force. The remainder of the paper is organised as follows. Section 2 reviews the facility-location, accessibility-measurement and smart-city-data literatures and situates Türkiye's City Hospitals programme within them. Section 3 develops the three-component framework, including a formal accessibility-equity model. Section 4 illustrates the model with a stylised numerical example set in Elazığ. Section 5 discusses implementation barriers, generalisability and limitations, and Section 6 concludes.

2 Background and Related Work

2.1 Hospital location and spatial equity

Facility location research offers a mature toolkit for siting public services. The maximal covering location problem seeks facility positions that maximise the demand served within a coverage radius [4], and a substantial body of covering, median and hierarchical models has since been applied to hospitals, ambulance stations and other health facilities [5]. These models are formally rigorous, but nearly all of them take a distance or travel-time matrix as an exogenous input. They optimise facility positions conditional on that matrix being accurate; they do not address where the matrix comes from or how often it is refreshed. When the underlying travel-time data are static, outdated or based on straight-line distance, the resulting siting recommendation inherits that weakness regardless of how sophisticated the optimisation is.

A parallel literature measures accessibility rather than optimising it. The two-step floating catchment area (2SFCA) method estimates a supply-to-demand ratio around each facility and then sums the ratios reachable from each population zone within a travel-time threshold, combining a floating-catchment logic with a gravity-type distance decay [6]. Subsequent reviews have catalogued the method's sensitivity to threshold choice, zone size and decay-function specification, while confirming its practical advantage of separating the supply side (facility capacity) from the demand side (population distribution) in a single interpretable score [7]. This measurement tradition, rather than the covering-location tradition, is the natural basis for a policy-facing accessibility assessment, because its output is a score that can be mapped, compared across population subgroups and reported to a non-technical decision body.

2.2 Smart-city data infrastructure and transportation intelligence

The travel-time input that both traditions require is exactly what smart-city systems now generate as a byproduct of unrelated operational functions. General Transit Feed Specification (GTFS) schedules make it possible to compute transit accessibility at fine temporal resolution; using GTFS data for Cincinnati, one study showed that accessibility to supermarkets by transit

varies enough across the day that a single representative time-of-day estimate can misstate which residents are actually underserved [8], a finding that applies with at least equal force to hospital access during peak congestion. Automated fare-collection (smart-card) systems, originally deployed for revenue collection, generate detailed records of realised boarding and alighting patterns that a literature review identifies as useful for strategic, tactical and operational transit planning alike [9], making them a source of validated, as opposed to merely scheduled, travel behaviour.

Mobile-network mobility records add a demand-side layer. Analysis of six months of anonymised trajectories from 100,000 mobile-phone users showed that individual mobility is far more regular and predictable than the random-walk models once used to describe it [10], which is precisely the property that allows aggregated, privacy-protected mobile records to approximate where a population actually lives and moves at a spatial and temporal resolution that census data cannot match. Routing platforms complete the picture by supplying time-dependent, multimodal origin-destination travel times on demand. None of these four data streams was designed with hospital planning in mind, and that is the point: the infrastructure investment has already been made for other purposes, so the marginal cost of repurposing it for health facility accessibility is administrative rather than technological [3].

2.3 Institutional context: Türkiye's City Hospitals programme

Türkiye has built more than twenty large City Hospitals through build-lease-transfer public-private partnerships since 2017, consolidating services previously spread across smaller inner-city hospitals into large peripheral campuses. A stakeholder survey of health personnel working in three City Hospitals reported broadly positive views on capacity, service quality and technology, alongside explicit concerns about cost, transparency and management, but access was assessed only qualitatively, through staff perception rather than a measured travel-time distribution across the served population [11]. A separate qualitative study of stakeholders across integrated health campuses reached a similar conclusion: the model was judged on efficiency, quality and financing grounds, with access treated as one perception item among several rather than as a quantitative planning criterion [12].

Neither study, nor the underlying siting process, incorporated a formal transportation accessibility analysis. This is the specific gap the present framework addresses. The facility-location literature supplies models that need accurate travel-time inputs but is silent on how to obtain them at scale; the smart-city literature documents that the required data streams already exist but stops short of connecting them to a health-sector decision procedure; and the Turkish City Hospitals literature documents stakeholder sentiment about an already-built programme without measuring the population-level accessibility change that peripheral relocation produced. Section 3 proposes a framework that closes this three-way gap by turning existing data streams into a standard, auditable input to hospital siting decisions.

3 Proposed Transportation Equity Framework

The framework couples three components, each addressing a distinct point of failure identified in Section 2: an information integration protocol that supplies the travel-time input the facility-location and accessibility literatures require (Component I), a Transportation Accessibility Impact Assessment that turns that input into a decision-relevant accessibility and equity score (Component II), and an institutional coordination mechanism that gives the assessment procedural force (Component III). Figure 1 shows how the three components connect data to decision.

3.1 Component I: information integration protocol

The protocol harmonises four data streams that most municipalities and health authorities already have some access to, either directly or through a commercial or open license. Routing-API queries (for example, Google Maps or HERE) return time-dependent origin-destination travel times for private vehicle, walking and mixed-mode trips and can be sampled at several

representative times of day, including the morning and evening peaks that most affect emergency response and staff commuting. GTFS feeds convert published transit schedules into routable origin-destination transit travel times, which the temporal-variability evidence in Section 2.2 shows should not be collapsed into a single daily average [8]. Fleet GPS and automated fare-collection records validate the schedule-based estimate against realised operating conditions [9], and aggregated mobile-network mobility records supply a demand-side population distribution at a spatial resolution finer than a typical census tract [10]. The integration layer resolves these four streams to a common zonal system and produces a single harmonised, time-dependent multimodal travel-time matrix, refreshed on a fixed cadence, that feeds directly into Component II.

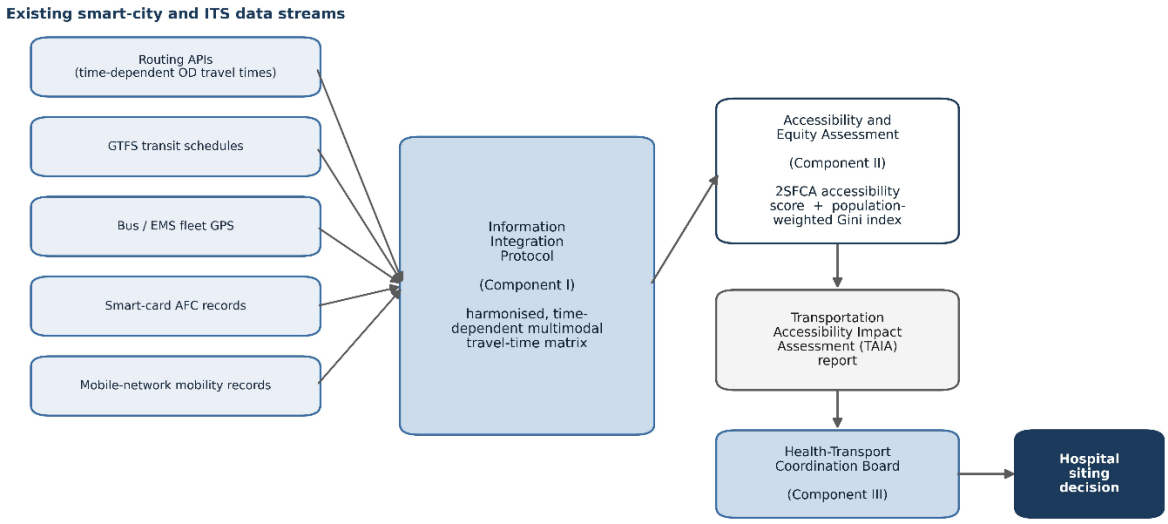


Fig. 1. The three components of the proposed framework, from existing smart-city data streams to a hospital siting decision.

A single data custodian, typically the metropolitan transport authority given its existing ownership of GTFS and fleet data, should be designated to operate the integration layer and to publish the resulting travel-time matrix in a documented, versioned format so that Component II can be audited and reproduced by an independent reviewer.

3.2 Component II: Transportation Accessibility Impact Assessment

The Transportation Accessibility Impact Assessment (TAIA) converts the travel-time matrix from Component I into two decision-relevant quantities for each population subgroup: an accessibility score at each zone and a summary measure of how equally that score is distributed. The model extends the 2SFCA formulation [6] and follows the concept-and-method guidance summarised in [7]. Four assumptions underlie the formulation and are stated explicitly because each has a direct bearing on how the assessment should be interpreted. First, a travel-time matrix built from a small number of representative times of day is taken as an adequate input for comparing siting alternatives at the planning horizon, even though instantaneous travel times fluctuate continuously. Second, licensed bed count, or an equivalent capacity-weighted service unit, is used as a proxy for hospital service availability; this proxy does not capture differences in case mix or medical specialty across facilities. Third, the distance-decay function is assumed to take a negative exponential form, consistent with common 2SFCA practice, with

the decay parameter and catchment threshold calibrated locally rather than imported from another study area. Fourth, population subgroup counts are assumed available at the same zonal resolution as the travel-time matrix, which in practice requires the mobile-network and census inputs from Component I to be reconciled to a common zoning system. Table 1 lists the indicators used in the TAIA model.

Table 1. Notation used in the Transportation Accessibility Impact Assessment model.

Symbol	Definition
I, i	Set and index of population (demand) zones
J, j	Set and index of hospital locations (existing or proposed)
G, g	Set and index of population subgroups (e.g., general, elderly, low-income, vehicle-less)
P_i^g	Population of subgroup g resident in zone i [persons]
P_i	Total population of zone i, Pi = Σg Pi_g [persons]
S_j	Service capacity of hospital j [beds or weighted service units]
t_{ij}	Travel time between zone i and hospital j for a representative time of day [minutes]
d_0	Catchment travel-time threshold [minutes]
β (beta)	Distance-decay (impedance) parameter [1/minute]
W(t)	Distance-decay weight, W(t) = exp(-βt) for t ≤ d0, else 0 [dimensionless, in (0,1]]
R_j	Population-adjusted supply ratio at hospital j [service units per person]
A_i	Spatial accessibility score of zone i, common to all residents of i [service units per person]
$Gini^g$	Gini coefficient of the accessibility scores Ai across zones I, weighted by subgroup g's population [dimensionless, 0-1]
DR^g	Disparity ratio: mean Ai in the top decile of subgroup g's population over the bottom decile, zones ranked by Ai

Equation (1) computes the population-adjusted supply ratio for each hospital by dividing its capacity by the distance-weighted population that falls within its catchment. Equation (2) then sums, for each zone and subgroup, the supply ratios of every hospital reachable from that zone, each discounted by the same distance-decay weight.

$$R_j = S_j / \Sigma_{k \in I} P_k \cdot W(t_{kj}) \qquad (1)$$

$$A_i = \Sigma_{j \in J:\ tij \le d0} R_j \cdot W(t_{ij}) \qquad (2)$$

In Equation (1), Pk is the total population of zone k, summed over subgroups; the denominator therefore represents the effective, distance-discounted population competing for hospital j, so a low value of Rj signals a facility that is either under-capacity or surrounded by dense demand. Equation (2) then aggregates the supply ratios of every hospital within the threshold travel time of zone i into a single accessibility score, Ai, which is a property of the zone itself and is therefore common to every resident of that zone regardless of subgroup: two residents of the same zone face the same geographic accessibility to hospital services. Because Rj and W(t) are both non-negative, Ai is bounded below by zero and increases whenever a new, better-connected or larger facility becomes reachable from zone i, which gives the score the correct sign for use as a planning criterion: higher is better.

Accessibility alone does not reveal whether it is shared or concentrated across population subgroups. Subgroup differentiation enters through the weights used to summarise the distribution of Ai across zones, not through the accessibility score itself. Equation (3) reports the Gini coefficient of Ai across zones I, weighted by the population of subgroup g in each

zone, the same weighted-inequality construction used to assess the equity of public transport supply [13], applied here to ask whether subgroup g's population is disproportionately concentrated in low-accessibility zones.

$$\text{Gini}^{g} = \Sigma_{i\in I} \Sigma_{i'\in I} P_i^{g} P_{i'}^{g} |A_i - A_{i'}| / (2 (\Sigma_{i\in I} P_i^{g})^2 \bar{A}^{g}) \quad (3)$$

where $\bar{A}^{g} = \Sigma_{i\in I} P_i^{g} A_i / \Sigma_{i\in I} P_i^{g}$ is the mean accessibility experienced by subgroup g, weighting each zone's score by how much of subgroup g lives there. Gini^{g} equals zero when subgroup g's population is distributed across zones in exact proportion to accessibility and approaches one as that population concentrates in low-accessibility zones; a companion disparity ratio, DR^{g}, reports the more directly interpretable ratio between the mean accessibility experienced by the best-served and worst-served population deciles of subgroup g. Reporting Gini^{g} and DR^{g} separately for the general population and for the elderly, low-income and vehicle-less subgroups is what allows a Health-Transport Coordination Board to detect a relocation that raises average accessibility while widening subgroup-specific gaps, which Section 4 illustrates numerically.

The formulation inherits two well-documented limitations of the 2SFCA family that any application must manage rather than assume away. Boundary zones near the edge of the study area can appear falsely under-served if hospitals just outside the study boundary are excluded from the catchment search, and the zonal system used to define I is itself a modelling choice that can shift results, the modifiable areal unit problem familiar from the accessibility-measurement literature [7]. Both issues are managed procedurally rather than analytically: the assessment protocol requires the study area to extend at least one catchment radius beyond the municipal boundary, and it requires a documented sensitivity analysis over at least two zonal resolutions and two decay-parameter values before the TAIA report is submitted to Component III.

3.3 Component III: institutional coordination mechanism

A technically sound assessment has no policy effect unless an institutional process requires it to be produced and consulted before a decision is made. The mechanism proposed here adapts the six generic components of the Health-in-All-Policies approach, establishing need and priorities, framing the planned action, identifying supportive structures, facilitating assessment and engagement, ensuring monitoring and reporting, and building capacity [14], to the specific decision point of hospital siting. A Health-Transport Coordination Board, jointly staffed by the health ministry's investment planning unit and the metropolitan transport authority, is convened whenever a proposed hospital investment exceeds a defined capacity or cost threshold, or whenever an inner-city facility is proposed for closure. The Board's sole formal requirement is procedural rather than discretionary: no siting concession may be finalised without a submitted TAIA report, and if the report shows a subgroup-specific Gini or disparity-ratio deterioration relative to the status quo, the responsible health authority must publish a mitigation plan, for example, a dedicated shuttle service or a satellite outpatient clinic, before final approval.

This design deliberately stops short of granting the transport authority a veto over health investment decisions, which would raise the political cost of adoption sharply. It instead makes the accessibility evidence visible and auditable at the point where it can still influence site selection, and it places the burden of response, not the burden of proof, on the health authority when the evidence points to a deterioration in equity.

4 Illustrative Application: A Stylised Scenario for Elazığ

Eastern Anatolian cities such as Elazığ combine below-national-average car ownership, limited public transit coverage, hilly terrain and severe winters, a combination that makes peripheral hospital placement carry a larger accessibility penalty for vehicle-less residents than the same relocation would carry in a flatter, better-motorised city. This section illustrates how the TAIA metrics of Section 3.2 would be read by a Health-Transport Coordination Board facing such a decision. The travel-time matrix, hospital capacities and zonal populations required by

Component I have not yet been assembled for Elazığ as part of this study, so the figures below are explicitly hypothetical (Table 2): they are constructed to be internally consistent with the model of Section 3.2 and to demonstrate how its outputs should be interpreted, not to report a measured outcome of any real siting decision. Assembling and validating the underlying data streams for a real Elazığ catchment is identified as future work in Section 5.4.

Table 2. Illustrative, hypothetical TAIA output comparing a central and a peripheral single-hospital scenario across five stylised zones.

Zone	Vehicle-less population share	Ai, central hospital (illustrative)	Ai, peripheral hospital (illustrative)
Z1 – inner city	38%	1.00	0.55
Z2 – inner-mid ring	29%	0.85	0.70
Z3 – mid ring	22%	0.60	0.80
Z4 – outer ring	17%	0.35	1.05
Z5 – periphery	12%	0.20	1.20
Population-weighted mean	—	0.62	0.83
Gini coefficient (general population)	—	0.29	0.31
Gini coefficient (vehicle-less subgroup)	—	0.24	0.41

The illustrative figures reproduce a pattern that a bed-count-only planning criterion cannot detect. The population-weighted mean accessibility rises from 0.62 to 0.83 after relocation, because the peripheral scenario is built with a larger facility that improves access for the outer, currently under-served zones. The general-population Gini coefficient barely moves, from 0.29 to 0.31, which on its own would read as an acceptable, even a favourable, outcome. The subgroup-specific figure tells a different story: the Gini coefficient for the vehicle-less subgroup rises from 0.24 to 0.41, because the inner-city zones with the highest share of vehicle-less residents, Z1 and Z2, are exactly the zones that lose accessibility under relocation. A TAIA report built only around the general-population average would have cleared this scenario; the subgroup-disaggregated report flags it for the mitigation requirement described in Section 3.3.

5 Discussion

5.1 Policy implications and institutional barriers

Implementing the framework does not require new sensors, new legislation in most jurisdictions, or a new data-collection budget, since Section 2.2 established that the four underlying data streams are already produced for other purposes. The binding constraint is administrative: routing a TAIA through the Health-Transport Coordination Board before a siting concession is signed. In Türkiye, City Hospital concessions are typically negotiated years before a facility opens, and land assembly and financing are locked in early, so the coordination mechanism must intervene at the pre-feasibility stage rather than as a commissioning-stage inspection if it is to have any influence on the final site.

5.2 Generalisability and limitations

The three-component architecture is not specific to Türkiye; it applies to any health system that relies on capital-intensive, centralised hospital campuses and operates in a city with routing-API or GTFS coverage, a condition met by most cities in middle- and high-income countries today. The Turkish City Hospitals programme supplies the motivating and illustrative context because its scale and its peripheral siting pattern make the accessibility question unusually

visible, not because the framework depends on any feature unique to the Turkish institutional setting.

Four limitations qualify these claims. The framework has not yet been validated against a real travel-time matrix and real facility-level outcome data; Section 4 is explicitly illustrative rather than empirical. Mobile-network mobility records raise data-governance and privacy questions, requiring aggregation thresholds and legal agreements with network operators that this paper does not work out in detail. The accessibility score, like any member of the 2SFCA family, is sensitive to zone definition and parameter choice, which is why Section 3.2 requires a documented sensitivity analysis rather than treating a single parameterisation as authoritative. Finally, the framework measures geographic and travel-time access; it does not capture the affordability or clinical-quality dimensions of access, which require complementary assessment instruments outside its scope.

5.3 Future work

Three extensions follow directly from these limitations: a pilot computation of the TAIA model for an existing Turkish City Hospital catchment using open GTFS and routing-API data, an evaluation of institutional uptake through a real pilot of the Health-Transport Coordination Board, and an extension of the accessibility score to incorporate multimodal transfer penalties and the seasonal, winter-specific travel-time degradation that is particularly relevant to Eastern Anatolian cities such as Elazığ.

6 Conclusion

Hospital siting decisions continue to be made without reference to the transportation intelligence that smart-city infrastructure already generates. This paper has proposed a three-component framework, an information integration protocol, a Transportation Accessibility Impact Assessment built on a 2SFCA accessibility score and a population-weighted Gini equity index, and an institutional coordination mechanism, that closes this gap at a low marginal cost, since the underlying data infrastructure is already in place in most cities. Türkiye's City Hospitals programme provided the motivating and illustrative context, and a stylised numerical example showed how the framework would surface a subgroup-specific equity deterioration that an average-accessibility or bed-count criterion would miss. The immediate priority for future research is a pilot application to a real hospital catchment, to establish whether the framework performs as intended once it is exposed to the noise and incompleteness of operational data.

Acknowledgments

The authors thank the Department of Civil Engineering at Fırat University for institutional support during the preparation of this manuscript.

References

1. Saver, J.L.: Time is brain—quantified. Stroke 37(1), 263–266 (2006). https://doi.org/10.1161/01.STR.0000196957.55928.ab
2. Pell, J.P., Sirel, J.M., Marsden, A.K., Ford, I., Cobbe, S.M.: Effect of reducing ambulance response times on deaths from out of hospital cardiac arrest: cohort study. BMJ 322(7299), 1385–1388 (2001). https://doi.org/10.1136/bmj.322.7299.1385
3. Batty, M., Axhausen, K.W., Giannotti, F., Pozdnoukhov, A., Bazzani, A., Wachowicz, M., Ouzounis, G., Portugali, Y.: Smart cities of the future. European Physical Journal Special Topics 214, 481–518 (2012). https://doi.org/10.1140/epjst/e2012-01703-3
4. Church, R.L., ReVelle, C.: The maximal covering location problem. Papers of the Regional Science Association 32, 101–118 (1974). https://doi.org/10.1007/BF01942293

5. Ahmadi-Javid, A., Seyedi, P., Syam, S.S.: A survey of healthcare facility location. Computers & Operations Research 79, 223–263 (2017). https://doi.org/10.1016/j.cor.2016.05.018
6. Luo, W., Wang, F.: Measures of spatial accessibility to health care in a GIS environment: synthesis and a case study in the Chicago region. Environment and Planning B: Planning and Design 30(6), 865–884 (2003). https://doi.org/10.1068/b29120
7. Guagliardo, M.F.: Spatial accessibility of primary care: concepts, methods and challenges. International Journal of Health Geographics 3, 3 (2004). https://doi.org/10.1186/1476-072X-3-3
8. Farber, S., Morang, M.Z., Widener, M.J.: Temporal variability in transit-based accessibility to supermarkets. Applied Geography 53, 149–159 (2014). https://doi.org/10.1016/j.apgeog.2014.06.012
9. Pelletier, M.-P., Trépanier, M., Morency, C.: Smart card data use in public transit: a literature review. Transportation Research Part C: Emerging Technologies 19(4), 557–568 (2011), 10.1016/j.trc.2010.12.003.
10. González, M.C., Hidalgo, C.A., Barabási, A.-L.: Understanding individual human mobility patterns. Nature 453, 779–782 (2008). https://doi.org/10.1038/nature06958
11. Top, M., Sungur, C.: Opinions and evaluations of stakeholders in the implementation of the public-private partnership (PPP) model in integrated health campuses (city hospitals) in Turkey. International Journal of Health Planning and Management 34(1), e241–e263 (2019). https://doi.org/10.1002/hpm.2644
12. Arı, H.O., Şahin, B.: Evaluation of health personnel's views on city hospitals (CHs) as a public-private partnership practice in the Turkish health system. International Journal of Healthcare Management 17(4) (2024). https://doi.org/10.1080/20479700.2023.2235790
13. Delbosc, A., Currie, G.: Using Lorenz curves to assess public transport equity. Journal of Transport Geography 19(6), 1252–1259 (2011). https://doi.org/10.1016/j.jtrangeo.2011.02.008
14. World Health Organization: Health in All Policies (HiAP) framework for country action. Health Promotion International 29(Suppl 1), i19–i28 (2014). https://doi.org/10.1093/heapro/dau035

Author Contribution Statement

- *Conceptualization:* Zeynep Nur Duman, Mehmet Ali Silgu
- *Methodology:* Mehmet Ali Silgu, Zeynep Nur Duman
- *Investigation:* Zeynep Nur Duman, Mehmet Yılmaz
- *Writing – Original Draft:* Zeynep Nur Duman
- *Writing – Review & Editing:* Mehmet Ali Silgu, Mehmet Yılmaz
- *Supervision:* Mehmet Ali Silgu, Mehmet Yılmaz

List of Abbreviations

- **ITS** — Intelligent Transportation System
- **GTFS** — General Transit Feed Specification
- **AFC** — Automated Fare Collection
- **API** — Application Programming Interface
- **2SFCA** — Two-Step Floating Catchment Area
- **TAIA** — Transportation Accessibility Impact Assessment
- **PPP** — Public-Private Partnership
- **HiAP** — Health in All Policies
- **CDR** — Call Detail Records
- **OD** — Origin-Destination

Appendices

Appendix A. Minimum Reporting Fields for a Transportation Accessibility Impact Assessment (TAIA) Report

Table A1 lists the minimum fields a TAIA report must contain before it can be submitted to the Health-Transport Coordination Board described in Section 3.3.

Table A1. Minimum reporting fields for a TAIA report.

Field	Requirement
Study area and zonal system	Boundary definition, zone count and rationale for zone size
Population subgroups covered	At minimum: general population, elderly, low-income, vehicle-less
Travel-time matrix source and date	Data source(s) per Component I, sampling times of day, refresh date
Decay parameters and threshold	Value and justification for β and d0, with source of calibration
Accessibility scores	Ai reported by zone, status quo and proposed scenario
Equity indicators	Gini and DR reported by subgroup, status quo and proposed scenario
Sensitivity analysis	Results under at least two zonal resolutions and two decay parameters
Mitigation plan	Required if any subgroup Gini or DR indicator deteriorates versus status quo
Public disclosure statement	Confirmation that the report has been published prior to Board decision

Conflict of interest: The authors declare no conflict of interest. **Funding:** This research received no dedicated external funding. **Data availability:** This paper presents a conceptual policy framework; the figures reported in Table 2 are hypothetical and illustrative, and no empirical dataset was generated or analysed for a real hospital catchment. **Ethical approval:** Not applicable, as the study involves neither human participants nor personal data.

Note: Following the conference, this Publication Note will be added to each paper; therefore, authors are kindly requested not to remove the note below and to complete the author(s) and paper title information.

Publication Note

This paper was peer-reviewed, accepted for presentation, and included in the proceedings of the ACE2026 – International Conference on Advances in Civil Engineering, held on 12–14 October 2026 in Trabzon, Türkiye.

This paper may be cited as follows:

Duman, Z. N., Silgu, M. A., and Yılmaz, M., "Smart City and Hospital Location Policy: A Transportation Equity Framework," in Proceedings of the ACE2026 – International Conference on Advances in Civil Engineering, Trabzon, Türkiye, 12–14 October 2026.

Micromobility and Placemaking: Rethinking Accessibility in Urban Mobility

Ilgin Gokasar[1], Volkan Yıldız[2], Evinç Doğan[3]
[1] 0000-0001-9896-9220, Boğaziçi University, Department of Civil Engineering, 34342 Bebek, Istanbul, Türkiye, ilgin.gokasar@bogazici.edu.tr
[2] 0009-0000-6709-8768, Boğaziçi University, Department of Civil Engineering, 34342 Bebek, Istanbul, Türkiye, volkan.yildiz@bogazici.edu.tr
[3] 0000-0003-4874-7341, Boğaziçi University, Department of Tourism Administration, 34342 Bebek, Istanbul, Türkiye, evince.dogan@bogazici.edu.tr

Abstract. Micromobility has become an increasingly important component of urban transportation systems, particularly for short-distance trips, first-mile/last-mile connectivity, and flexible daily mobility. While micromobility systems offer several benefits in terms of accessibility, modal integration, and efficient use of urban space, their planning should not be limited to the provision of vehicles alone. The location, design, and management of micromobility stations, parking areas, and mobility hubs directly affect how public space is used and who can benefit from these systems. Therefore, micromobility planning should be considered not only as a transportation issue, but also as a placemaking and fairness in urban mobility issue. This study discusses micromobility through the lens of placemaking, accessibility, and urban transformation. It focuses on how micromobility infrastructure can be integrated into public spaces in a way that supports local needs, improves place quality, and avoids reinforcing existing inequalities. In this context, the study also considers broader fairness-related questions, including gentrification, unequal access, and "accessibility for whom?" Based on a literature-oriented discussion, the paper examines how placemaking can contribute to more inclusive micromobility planning and how station location decisions can shape everyday urban experiences. Finally, the study presents policy implications for Turkey, emphasizing the need to integrate micromobility planning with public space design, pedestrian accessibility, public transport connections, local participation, and context-sensitive urban mobility policies.

Keywords: Micromobility; Placemaking; Fairness in Urban Mobility; Mobility Hubs.

1 Introduction

In recent years, micromobility, which includes lightweight and low-powered personal transport modes often used in shared systems, has rapidly expanded in cities and is expected to continue growing in the coming years [1]. As its use becomes more widespread, micromobility has become an increasingly visible component of urban transportation, particularly for short-distance trips and first-mile/last-mile connections. Micromobility modes, ranging from conventional bicycles to e-scooters, e-bikes, and other small electric vehicles, are increasingly used worldwide and may help address urban transport challenges by encouraging a shift away from private motorized vehicles [2]. As cities seek more sustainable transportation solutions, micromobility is expected to play a growing role in urban mobility.

Dockless micromobility services, particularly bike- and e-scooter-sharing systems, have rapidly expanded worldwide by providing flexible and nearly seamless connections between users and urban activities [3]. Unlike conventional station-based systems, dockless services

allow vehicles to be accessed and left at various locations across the urban environment, providing users with greater flexibility. At the same time, this operational model introduces new spatial challenges, particularly regarding vehicle distribution, parking behavior, pedestrian circulation, and the allocation of public space. A substantial share of conflicts between pedestrians and micromobility users can be attributed to the limited road space allocated to active transport, as most urban road space remains dedicated to motor vehicles [4]. Consequently, the growing presence of micromobility has made its relationship with urban space an increasingly important aspect of transportation planning.

This relationship extends beyond the vehicles themselves to the infrastructure and spaces that support their use. The location and design of stations, parking zones, docking areas, and shared micromobility hubs influence how urban space is used and experienced. Decisions regarding where these facilities are located may determine which users can conveniently access micromobility services while also affecting pedestrian movement and the use of public space. Without designated parking areas, micromobility vehicles may be parked in an uncontrolled manner, potentially blocking sidewalks and reducing the visual quality of public spaces [5]. Beyond their location, the amount of public space allocated to micromobility facilities and the users prioritized in this allocation are equally important, as these decisions may shape who benefits from such interventions and who experiences additional spatial constraints.

Accordingly, micromobility infrastructure should be understood not merely as a transport facility, but as an urban intervention that can reshape the distribution, function, and experience of public space. In this context, placemaking provides a broader perspective for micromobility planning. Rather than considering infrastructure only in terms of transportation efficiency, placemaking emphasizes public space quality, accessibility, social inclusion, and local user needs. Such interventions can also raise questions related to gentrification, unequal access, and "accessibility for whom?" Therefore, integrating placemaking principles into micromobility planning may contribute to transportation systems that are not only efficient but also more inclusive and responsive to their urban context.

2 Literature Review

2.1 Placemaking and Urban Mobility

Placemaking has increasingly emerged as an approach for enhancing the quality of places within neighborhoods, with broader benefits extending to the surrounding community and region, and can be classified into four main types [6]:

- *Standard Placemaking:* Focuses on improving the quality and livability of places through long-term, incremental projects and broad community participation.
- *Strategic Placemaking:* Uses targeted interventions in selected locations to achieve specific objectives, particularly by attracting people, businesses, and economic activity.
- *Creative Placemaking:* Uses arts, culture, and creative activities to shape the physical and social character of places and enhance their vitality.
- *Tactical Placemaking:* Applies low-cost, short-term, and experimental interventions to test potential improvements before committing to larger and more permanent investments.

Beyond these placemaking categories, urbanism can take different forms depending on the level of formality, the degree of design and planning, and the involvement of experts or local communities [7]:

- *Guerrilla Urbanism:* Informal, spontaneous, bottom-up interventions carried out by individuals or local communities, often without formal planning or design procedures.
- *Everyday Urbanism:* Small-scale actions and routines embedded in everyday life that gradually reshape how public spaces are used.
- *Tactical Urbanism:* More deliberate and experimental interventions that may involve temporary design elements and participation by experts or municipalities.

- *Participatory Design / Formal Placemaking:* Structured processes in which professionals and local communities collaborate in planning and designing urban spaces.
- *New Urbanism / Expert Placemaking:* Formally planned and professionally designed interventions led mainly by experts and planning authorities.

Within this broader perspective, space, with its physical characteristics and social features, is a key element of urban development, particularly in its transformation into a meaningful place; therefore, placemaking plays an important role in the planning, management, and experience of urban spaces [8]. Furthermore, as urban neighborhoods are inhabited, their physical and social spaces may gradually transform into meaningful places through everyday interactions, changing residents, and collective actions within the community [9].

Over time, the understanding of placemaking has also evolved. Earlier approaches to placemaking were largely product-oriented, focusing on physical and spatial changes created by designers, whereas more recent perspectives position planners as facilitators and emphasize the involvement of communities and other non-professional actors in the process of shaping places [10].

In addition to these spatial and social dimensions, mobility is also closely connected to how urban places are experienced and transformed. Mobility is neither a new nor a neutral concept, as it has long been intertwined with travel, cultural interaction, globalization, and broader social and political processes [11]. As an integral part of urban life, mobility plays an important role in how people collectively experience and engage with the city [12]. Accordingly, the relationship between mobility and placemaking extends to the infrastructure that supports urban movement. Urban transportation infrastructure can contribute to placemaking not only through its physical presence, but also by generating cultural meanings, shared social interactions, and collective identity within urban space [13].

2.2 Fairness, Gentrification, and "Accessibility for Whom?"

A study investigating residents of traditionally underserved and low-income neighborhoods found that minority respondents faced greater barriers to bikeshare use, particularly regarding membership costs, indicating that spatial access alone may not ensure equitable use [14]. Similarly, in a study on fairness in public transport, autonomous taxis, and bicycle sharing, it is found that simply providing bicycle-sharing infrastructure does not guarantee fair access, since membership procedures, subscription costs, payment requirements, safety concerns, and suitability for different users can continue to exclude women and disadvantaged groups even when stations are spatially accessible [15].

Beyond these user-specific barriers, transportation fairness also requires a clear understanding of what constitutes a fair distribution. In a systematic review of 165 transportation fairness studies, it was shown that assessments of transport fairness often identify disparities without clearly explaining why a particular distribution should be considered fair or unfair, and proposed the 5WH framework to explicitly connect affected groups, benefits and burdens, spatial and temporal context, and fairness standards [16].

Accordingly, fair mobility policies may require differentiated rather than uniform interventions. In a study using European mobility survey data, researchers developed a framework in which socioeconomic characteristics and individual attitudes are used to estimate resistance to sustainable mobility and allocate differentiated incentives to individuals, rather than applying the same incentive to everyone, to maximize adoption while reducing both policy costs and inequalities between groups [17]. Similarly, In a working paper developed within the MyFairShare project, author proposed mobility budgets as a way of distributing limited carbon and street-space resources while accounting for differences in mobility needs, and emphasized that fair allocation may require additional consideration for groups constrained by income, disability, residential location, gender, care responsibilities, or occupational travel needs rather

than assigning identical mobility allowances to everyone [18]. Furthermore, in a paper on fairness and transport sufficiency, it is argued that limited urban street space and carbon-emission capacity should be treated as finite mobility resources, with minimum levels of accessibility guaranteed for users while maximum limits are placed on resource-intensive mobility such as excessive car use [19].

However, fairness concerns in urban mobility extend beyond access to transport services and the allocation of mobility resources, as urban improvements may also influence who is able to remain in and benefit from transformed areas. It is noted that urban regeneration may turn into gentrification when reinvestment leads to displacement or exclusion, including situations in which existing residents are not directly displaced but gradually lose the ability to remain in or access the transformed area [20]. Moreover, it is argued that gentrification should be understood in relation to its geographical and temporal context, since similar regeneration strategies may produce different outcomes depending on the social, economic, and spatial characteristics of cities and neighborhoods [21].

This concern is particularly relevant to transportation investments, which can alter both accessibility and the attractiveness of surrounding areas. It is noted that improvements in transit accessibility can increase land values and attract higher-income residents, potentially displacing lower-income populations and preventing them from benefiting from the new mobility infrastructure [22]. To mitigate such effects, complementary housing policies may therefore be necessary. It is found through an integrated land-use and transportation simulation model in the Washington, DC metropolitan area that affordability requirements targeted at new housing near transit are more effective than housing vouchers or unrestricted increases in housing supply in maintaining low-income households' access to transit and reducing transit-induced gentrification [23].

Nevertheless, the relationship between transportation investment and gentrification is not uniform across different urban contexts. It is found through a systematic review of 35 quantitative studies that, although transit proximity may contribute to gentrification, the relationship is highly context-dependent and is strongly influenced by existing local dynamics, built-environment characteristics, and accompanying policies rather than by transit-oriented development alone [24]. More recently, it is highlighted that transportation investments, including rail, pedestrianization, and improvements in public transport and walking accessibility, can reshape housing markets and neighborhood composition by increasing land values and attracting higher-income groups, while the extent and direction of these effects depend on project design, local socioeconomic conditions, spatial characteristics, and institutional arrangements [25].

2.3 Academic and Real-World Applications of Mobility-Oriented Urban Transformations

A growing number of urban mobility interventions demonstrate how transportation infrastructure and public space transformation can be considered together. Shared micromobility hubs, mobility hubs, tactical urbanism projects, pedestrianization schemes, bicycle-sharing stations, designated e-scooter parking zones, and transit-oriented public space improvements represent different examples of this relationship.

In Brazil, placemaking initiatives have increasingly focused on reclaiming car-oriented urban spaces and transforming them into safer, more inclusive, and people-centered environments that support active mobility and social interaction [26].

- *Eixão de Lazer – Brasília:* The Eixão, originally designed as a high-speed traffic corridor, is closed to vehicles on Sundays and holidays and transformed into a public leisure space for walking, skateboarding, dancing, music, relaxation, and social activities.

- *Paulista Aberta – São Paulo:* Avenida Paulista is closed to motor vehicles on Sundays and holidays, allowing pedestrians and cyclists to use the avenue for recreational, cultural, and sports activities.
- *Minhocão – São Paulo:* The Elevado Presidente João Goulart, originally built to improve traffic flow, has gradually been repurposed for public use and developed toward a park function following concerns over noise, crashes, and community demands.
- *Calçada Viva / Barão do Rio Branco Street – Fortaleza:* Traffic space was reclaimed for pedestrians through wider sidewalks, raised crosswalks, redesigned intersections, kiosks, benches, and outdoor dining areas, increasing pedestrian space from 33% to 60% of the area between façades.
- *João Alfredo Street – Porto Alegre:* The street was redesigned according to Complete Street principles through changes in vehicle-pedestrian flows and the addition of parklets, benches, bike racks, lighting, and green spaces to support active mobility and public-space use.

In the USA, several examples demonstrate how active mobility infrastructure can also contribute to the transformation and improvement of urban public spaces [27].

- *Atlanta BeltLine – Atlanta, USA:* The Atlanta BeltLine combines multi-use trails for walking and cycling with green spaces, public art, transit connections, and community activities, contributing to improved mobility, neighborhood revitalization, and community engagement.
- *Portland Neighborhood Greenways – Portland, USA:* Portland's neighborhood greenways and civic corridors provide safe routes for cyclists and pedestrians while connecting neighborhoods with major transport hubs and key urban functions, improving accessibility and supporting people-oriented streets.
- *Orlando Urban Trail – Orlando, USA:* The Orlando Urban Trail connects parks, cultural sites, and neighborhoods through a multi-use path that supports pedestrian and cyclist mobility while encouraging community engagement and active lifestyles.

In their neighboring continent, Canada, a similar example can be found in Vancouver [27]:

- *Comox–Helmcken Greenway – Vancouver, Canada:* The greenway connects neighborhoods through walking and cycling paths while incorporating landscaped areas and public spaces, contributing to sustainable transportation, improved active mobility infrastructure, community well-being, and environmental sustainability.

3 Discussion

The relationship between placemaking and micromobility becomes particularly important when decisions regarding station and hub locations are considered. Conventional planning approaches may prioritize demand density, expected trip generation, operational efficiency, or technical suitability. Although these factors are necessary, they may not sufficiently explain how micromobility infrastructure interacts with the surrounding public space.

Micromobility infrastructure can either strengthen place quality or create new spatial conflicts. Well-planned stations and hubs can improve connections to public transportation, facilitate short-distance trips, encourage more active street environments, and support more human-oriented mobility networks. In this sense, micromobility facilities may become complementary elements of public space rather than isolated pieces of transportation infrastructure.

In contrast, poorly planned facilities may create sidewalk obstruction, conflicts with pedestrians, or unequal access to mobility opportunities. It is known that, if poorly implemented, micromobility can create additional barriers to public-space access, particularly for people with disabilities whose access is already constrained [28]. Services concentrated

primarily in touristic, central, or high-income areas may also leave peripheral and lower-income neighborhoods relatively underserved. Therefore, the success of micromobility should not be measured only by ridership or vehicle utilization. How the system affects surrounding places, responds to local needs, and distributes accessibility benefits should also be considered.

4 Policy Implications

Placemaking principles can provide practical guidance for integrating micromobility into urban transportation planning. Station and parking locations should therefore not be determined solely by population density, travel demand, and operational data. Public space quality, pedestrian movement, connections with public transportation, social vulnerability, neighborhood characteristics, and local user preferences should also be incorporated into the planning process.

This perspective is particularly relevant for Türkiye, where sidewalk conditions, irregular parking, pedestrian safety, public transportation integration, and municipal access to mobility data can significantly affect the implementation of micromobility systems. Micromobility planning should therefore be coordinated with existing bicycle networks, public transportation transfer points, municipal transportation plans, and local decision-making processes.

Although national regulations establish the broader framework, urban authorities generally hold substantial regulatory influence over local and regional transport through implementation, land-use planning, public transport coordination, and infrastructure provision [29]. In this sense, institutional mechanisms such as UKOME decisions can also be considered together with neighborhood-scale participation and public space planning. Local governments can use participation processes to identify how different groups experience existing micromobility services and whether proposed station locations respond to local mobility needs. In contrast to command planning, which remains widely used, planners should engage directly with neighborhood residents and establish a relationship that recognizes their "right to the city," including their right to participate as local citizens in decisions affecting their communities [30]. Accordingly, micromobility planning in Türkiye should move beyond questions of vehicle numbers and operational permits and incorporate principles of public space fairness and accessibility.

5 Conclusion

Micromobility is likely to become an increasingly important component of urban transportation systems, particularly as cities seek more flexible and sustainable solutions for short-distance mobility. However, its contribution to urban mobility cannot be understood solely through technological development, vehicle availability, or operational performance.

The location and design of micromobility stations and parking areas influence who can access these services, how public space is used, and how transportation benefits are distributed across the city. Placemaking therefore provides a useful framework for connecting micromobility planning with broader questions of accessibility, public space quality, and local needs.

Integrating placemaking into micromobility planning can help cities develop systems that are more accessible, inclusive, and sensitive to their local context. Rather than treating micromobility infrastructure as an independent element of the transportation system, future planning approaches should consider it as part of the wider relationship between mobility, people, and urban space.

Acknowledgments

Acknowledgments will be placed at the end of the text before the references list.

References

1. Y. Zhang, D. Kasraian, and P. van Wesemael, “Built environment and micro-mobility: A systematic review of international literature,” J. Transp. Land Use, vol. 16, no. 1, pp. 293–317, Jan. 2023, doi: 10.5198/JTLU.2023.2266.
2. G. Oeschger, P. Carroll, and B. Caulfield, “Micromobility and public transport integration: The current state of knowledge,” Transp. Res. D Transp. Environ., vol. 89, p. 102628, Dec. 2020, doi: 10.1016/J.TRD.2020.102628.
3. H. Li, Z. Yuan, T. Novack, W. Huang, and A. Zipf, “Understanding spatiotemporal trip purposes of urban micro-mobility from the lens of dockless e-scooter sharing,” Comput. Environ. Urban Syst., vol. 96, p. 101848, Sep. 2022, doi: 10.1016/J.COMPENVURBSYS.2022.101848.
4. C. Zhang, B. Du, Z. Zheng, and J. Shen, “Space sharing between pedestrians and micro-mobility vehicles: A systematic review,” Transp. Res. D Transp. Environ., vol. 116, p. 103629, Mar. 2023, doi: 10.1016/J.TRD.2023.103629.
5. R. Saadati, M. Yildirimoglu, and J. Kim, “Strategic design of hybrid shared micromobility systems with integrated charging and rebalancing,” Transp. Res. Part C Emerg. Technol., vol. 192, p. 105850, Nov. 2026, doi: 10.1016/J.TRC.2026.105850.
6. M. A. Wyckoff, “Definition of Placemaking: Four Different Types,” 2014. Accessed: Aug. 11, 2026. [Online]. Available: https://yieldpro.com/pdf/issues/2024/4typesplacemaking_pzn_wyckoff_january2014.pdf
7. V. Natividade, A. Rivas, B. Büttner, and T. Stojanovski, “The morphology of placemaking – from urban guerrilla and formal street experiments to mobility and metropolitan regions,” pp. 1335–1343, Apr. 2022, doi: 10.17868/80146.
8. K. Dupre, “Trends and gaps in place-making in the context of urban development and tourism: 25 years of literature review,” Journal of Place Management and Development, vol. 12, no. 1, pp. 102–120, Mar. 2019, doi: 10.1108/JPMD-07-2017-0072.
9. J. Friedmann, “Place and Place-Making in Cities: A Global Perspective,” Planning Theory & Practice, vol. 11, no. 2, pp. 149–165, 2010, doi: 10.1080/14649351003759573.
10. W. Strydom, K. Puren, and E. Drewes, “Exploring theoretical trends in placemaking: towards new perspectives in spatial planning,” Journal of Place Management and Development, vol. 11, no. 2, pp. 165–180, May 2018, doi: 10.1108/JPMD-11-2017-0113.
11. A. Sen and J. Johung, “Landscapes of Mobility: Culture, Politics, and Placemaking.” Accessed: Aug. 14, 2026. [Online]. Available: https://books.google.com.tr/books?hl=tr&lr=&id=lNcFDAAAQBAJ&oi=fnd&pg=PP1&dq=placemaking+urban+mobility&ots=T5UWv5cNDp&sig=4ZmIvAgK5YH6srJ4BgvsxTDfhjg&redir_esc=y#v=onepage&q=placemaking%20urban%20mobility&f=false
12. J. Venäläinen, “Senses on/of the move: Mobilities, place-making, and the urban sensory commons,” Sensory Transformations, pp. 123–139, Feb. 2023, doi: 10.4324/9781003131342-9.
13. A. Lee, “Place-Making, Mobility, and Identity: The Politics and Poetics,” 2015, Accessed: Aug. 14, 2026. [Online]. Available: https://academicworks.cuny.edu/cgi/viewcontent.cgi?article=1053&context=jj_pubs
14. A. Yan and B. Howe, “Fairness in Practice: A Survey on Equity in Urban Mobility | NSF Public Access Repository,” A Quarterly bulletin of the Computer Society of the IEEE Technical Committee on Data Engineering, vol. 42, no. 3, Mar. 2020, Accessed: Aug. 15, 2026. [Online]. Available: https://par.nsf.gov/biblio/10188264
15. Y. Hail and R. McQuaid, “The Concept of Fairness in Relation to Women Transport Users,” Sustainability 2021, Vol. 13, Page 2919, vol. 13, no. 5, p. 2919, Mar. 2021, doi: 10.3390/SU13052919.

16. A. Soukhov, I. Tiznado-Aitken, M. Palm, S. Farber, and A. Paez, “Standards of fairness in the transportation literature,” Transportation 2025, pp. 1–44, Nov. 2025, doi: 10.1007/S11116-025-10693-8.
17. C. Quaresmini, E. Villa, V. Breschi, V. Schiaffonati, and M. Tanelli, “Qualification and Quantification of Fairness for Sustainable Mobility Policies,” 2023. Accessed: Aug. 15, 2026. [Online]. Available: https://ceur-ws.org/Vol-3442/paper-29.pdf
18. P. Rode, “Enabling sufficiency: towards an actionable concept of fairness in mobility and accessibility,” 2022. Accessed: Aug. 15, 2026. [Online]. Available: https://www.myfairshare.eu/wp-content/uploads/2023/09/MyFairShare_Working-Paper_Rode_2022_Enabling-sufficiency.pdf
19. P. Rode, “Fairness and the Sufficiency Turn in Urban Transport,” Journal of City Climate Policy and Economy, vol. 2, no. 1, pp. 37–54, Jun. 2023, doi: 10.3138/JCCPE-2023-0006.
20. K. Shaw, “Gentrification: What it is, why it is, and what can be done about it,” Geogr. Compass, vol. 2, no. 5, pp. 1697–1728, Sep. 2008, doi: 10.1111/j.1749-8198.2008.00156.x
21. L. Lees, “A reappraisal of gentrification: Towards a ‘geography of gentrification,’” Prog. Hum. Geogr., vol. 24, no. 3, pp. 389–408, 2000, doi: 10.1191/030913200701540483
22. N. Revington, “Gentrification, transit, and land use: Moving beyond neoclassical theory,” Geogr. Compass, vol. 9, no. 3, pp. 152–163, Mar. 2015, doi: 10.1111/GEC3.12203
23. C. Dawkins and R. Moeckel, “Transit-Induced Gentrification: Who Will Stay, and Who Will Go?,” Hous. Policy Debate, vol. 26, no. 4–5, pp. 801–818, Sep. 2016, doi: 10.1080/10511482.2016.1138986.
24. M. Padeiro, A. Louro, and N. M. da Costa, “Transit-oriented development and gentrification: a systematic review,” Transp. Rev., vol. 39, no. 6, pp. 733–754, Nov. 2019, doi: 10.1080/01441647.2019.1649316.
25. J. J. Lin, K. Chapple, S. Y. He, and T. Schwanen, “Transportation-induced gentrification: new perspectives and evidence,” Transp. Res. D Transp. Environ., vol. 151, p. 105085, Feb. 2026, doi: 10.1016/J.TRD.2025.105085.
26. J. C. M. Ozelim, “The Role of Placemaking Strategies in Urban Spaces and Urban Mobility in Brazilian Cities,” 2024. Accessed: Aug. 15, 2026. [Online]. Available: https://www.academia.edu/170405506/The_Role_of_Placemaking_Strategies_in_Urban_Spaces_and_Urban_Mobility_in_Brazilian_Cities
27. C. Vizmpa, G. Botzoris, P. Lemonakis, and A. Galanis, “Micromobility in Urban Trail Paths: Expanding and Strengthening the Planning of 15-Minute Cities,” Land 2023, Vol. 12, Page 2181, vol. 12, no. 12, p. 2181, Dec. 2023, doi: 10.3390/LAND12122181.
28. C. Bennett, E. Ackerman, B. Fan, J. Bigham, P. Carrington, and S. Fox, “Accessibility and the Crowded Sidewalk: Micromobility’s Impact on Public Space,” DIS 2021 - Proceedings of the 2021 ACM Designing Interactive Systems Conference: Nowhere and Everywhere, pp. 365–380, Jun. 2021, doi: 10.1145/3461778.3462065
29. S. Sareen, D. Remme, and H. Haarstad, “E-scooter regulation: The micro-politics of market-making for micro-mobility in Bergen,” Environ. Innov. Soc. Transit., vol. 40, pp. 461–473, Sep. 2021, doi: 10.1016/J.EIST.2021.10.009.
30. H. Lefebvre, “Writings on Cities.” Accessed: Aug. 11, 2026. [Online]. Available: https://books.google.com.tr/books?hl=en&lr=&id=rT9WiZZzdL8C&oi=fnd&pg=PA214&ots=Lpwoc2KDkC&sig=r6MCBjHLyJnxZLlPgTz_rVbDgjU&redir_esc=y#v=onepage&q&f=falseAuthor 1.: Article title. Journal 2(5), 99–110 (2016).

Author Contribution Statement

- *Conceptualization:* Ilgin Gokasar, Volkan Yildiz, Evinc Dogan
- *Methodology:* Ilgin Gokasar, Volkan Yildiz
- *Investigation:* Ilgin Gokasar

- *Writing – Original Draft:* Volkan Yildiz
- *Writing – Review & Editing:* Ilgin Gokasar, Evinc Dogan

Publication Note
This paper was peer-reviewed, accepted for presentation, and included in the proceedings of the ACE2026 – International Conference on Advances in Civil Engineering, held on 12–14 October 2026 in Trabzon, Türkiye.

This paper may be cited as follows:
Ilgin Gokasar, Volkan Yıldız, Evinç Doğan, "Micromobility and Placemaking: Rethinking Accessibility in Urban Mobility," in Proceedings of the ACE2026 – International Conference on Advances in Civil Engineering, Trabzon, Türkiye, 12–14 October 2026.

Autonomous Public Transport as a Traffic Management Element: A Literature-Based Discussion on Applicability and Feasibility

Ilgin Gokasar[1] and Volkan Yıldız[2]
[1] 0000-0001-9896-9220, Boğaziçi University, Department of Civil Engineering, 34342 Bebek, Istanbul, Türkiye, ilgin.gokasar@bogazici.edu.tr
[2] 0009-0000-6709-8768, Boğaziçi University, Department of Civil Engineering, 34342 Bebek, Istanbul, Türkiye, volkan.yildiz@bogazici.edu.tr

Abstract. Urban traffic congestion has become one of the most challenging problems of daily urban life, affecting travel time, service reliability, accessibility, and overall quality of mobility. One of the key approaches to addressing this problem is the improvement of public transportation systems, which can reduce dependency on private vehicles and support more efficient use of limited urban road space. In this context, the integration of autonomous vehicle technologies into public transportation has introduced the concept of Autonomous Public Transport, particularly through autonomous buses and shuttles. While these systems are often discussed as innovative public transport solutions, their potential role in traffic management also deserves attention. Autonomous Public Transport vehicles may not only operate as mobility service providers but may also contribute to the regulation, coordination, and optimization of traffic flow under certain operational and technological conditions. Therefore, this study reviews the existing literature to examine how Autonomous Public Transport is discussed in relation to traffic management. The review focuses on studies addressing autonomous public transport applications, mixed traffic interactions, traffic flow impacts, and management-oriented approaches associated with autonomous and connected mobility systems. Based on the reviewed literature, the study discusses whether Autonomous Public Transport can be considered applicable and feasible as a traffic management element in urban mobility systems. The findings provide a literature-based understanding of the possible roles, limitations, and future research directions of Autonomous Public Transport in traffic management.

Keywords: Autonomous Public Transport; Autonomous Buses; Traffic Management

1 Introduction

Traffic congestion has become a major challenge in many metropolitan areas, leading cities to implement various measures to reduce its impacts [1]. As travel demand increases, cities need more efficient ways to manage existing transportation systems. It is argued that reducing road congestion requires improving alternatives to private car travel [2]. Public transportation is one of the main alternatives because it can reduce private vehicle use and make better use of urban road capacity.

Recent developments in autonomous vehicle technologies have also created new opportunities for public transportation. Autonomous buses and shuttles are increasingly considered as a part of future public transport systems [3]. These vehicles may improve public transport operations through automation, connectivity, and better coordination with transportation infrastructure.

However, autonomous public transport (APT) may have a role beyond carrying passengers. Autonomous and connected public transport vehicles can interact with traffic signals, infrastructure, and other vehicles. Therefore, they may also contribute to traffic flow and traffic management.

Existing studies mainly focus on the technological, operational, safety, and social aspects of autonomous public transport. Its possible use as a traffic management element has received less attention. Therefore, this study reviews the existing literature to examine the relationship between autonomous public transport and traffic management. It also discusses its potential applications, limitations, and future research needs in urban transportation systems.

2 Literature Review

Recent developments in intelligent transportation systems have expanded the possibilities for traffic management beyond conventional infrastructure-based control. Mulay et al. [4] proposed an urban ITS framework that combines GPS-based public transport tracking, CCTV-based congestion detection, and adaptive traffic signal control, showing how real-time information can be used to support both public transport operations and traffic regulation. El Hamdani & Benamar [5] further discussed autonomous traffic management through V2V and V2I communication, particularly for intersection and road traffic control, and highlighted the potential of cooperative autonomous systems to reduce delay and congestion. Similarly, [Mancino [6] discussed the use of AI for real-time monitoring, dynamic signal control, incident detection, and route optimization, while also emphasizing its potential use in public transport scheduling and routing. Traffic prediction also represents an important part of this development. Manne et al. [7] proposed a traffic-flow prediction model based on Bi-LSTM and reported an average prediction accuracy of 0.951, outperforming SVM, random tree, random forest, and conventional LSTM models. In addition, Ud Din et al. [8] examined AIoT-supported autonomous driving technologies and showed that adaptive cruise control and collision-avoidance systems can improve vehicle-level performance under different traffic environments. Together, these studies indicate that connectivity, automation, real-time data, and intelligent decision-making provide a technological basis for more dynamic forms of traffic management.

Based on these technological developments, several studies have focused on controlling autonomous vehicles at the trajectory and conflict-management level. Lu et al. [9] proposed a trajectory-based traffic management model for an exclusive autonomous vehicle zone. The model uses mixed-integer programming to optimize the trajectories of multiple AVs while resolving inter-vehicle conflicts, together with a rolling-horizon algorithm to improve computational efficiency. Their model was developed for a multi-lane single-link AV environment and was later extended to include scheduling and equity considerations. Martin-Gasulla & Elefteriadou [10] applied a similar vehicle-coordination perspective to single-lane roundabouts. Their centralized Roundabout Manager uses seven priority strategies, including a Shortest-Remaining-Time-First approach, to coordinate CAV trajectories under oversaturated conditions. The simulations showed that a fully CAV traffic environment could increase roundabout capacity by 58–73% and reduce average control delay by 80–97% compared with conventional vehicle operations. Naeem et al. [11] also examined vehicle-level coordination at intersections by applying preemptive and non-preemptive scheduling to autonomous, conventional, and emergency autonomous vehicles in SUMO. Their results showed different delay levels across four tested road networks, with the Washington network producing delays of 4.02 s for AVs, 3.62 s for emergency AVs, and 4.33 s for conventional vehicles in the 50-vehicle scenario.

The coordination of multiple autonomous vehicles has also been examined outside conventional road transportation. Draganjac et al. [12] developed a decentralized traffic management method using state-lattice path planning and local conflict negotiation for

autonomous guided vehicles, demonstrating efficient coordination of fleets with up to 50 vehicles in shared industrial environments.

However, the transition toward autonomous mobility is expected to occur under mixed traffic conditions rather than in fully autonomous environments. Therefore, another group of studies has examined how AVs and CAVs can be integrated into networks shared with human-driven vehicles. Amirgholy et al. [13] developed an optimal lane-management framework for heterogeneous traffic consisting of human-driven vehicles, AVs, and CAVs. Using a macroscopic network fundamental diagram and an optimization model for the San Francisco network, the study dynamically adjusted lane allocation and CAV platoon sizes. The results showed that optimal lane management could reduce corridor delays by up to 78%, while the increase in travel time in the downtown network could be limited to approximately 5%. Yıldırım & Özuysal [14] examined mixed traffic conditions using SUMO simulations based on both the Sioux Falls test network and the İzmir urban transportation network. More than 300 simulations were conducted under different AV penetration rates. Their results showed that dedicated lanes could reduce local density, occupancy, and time loss by 5–35% and improve travel time reliability by 15–25%. In contrast, transitions of control at lower AV penetration levels could reduce traffic performance by up to 10%, showing that the benefits of automation depend strongly on traffic composition and operational conditions.

Beyond managing AVs as part of the traffic stream, recent research has also considered the possibility of using CAVs themselves as active traffic management elements. Gokasar et al. [15] developed the SWSCAV approach, in which CAVs are instructed to reduce their speeds according to the speed of a detected shockwave caused by an incident. The method uses Fused Lasso for smoothing traffic data and Fast Fourier Transform for data upsampling before controlling the speed and acceleration of CAVs. The system was tested in 4800 SUMO scenarios on a three-lane tunnel road network by changing CAV penetration rates, incident characteristics, and control distances. The results showed reductions of 12.68% and 8.15% in the occurrence of density levels above 38 and 28 veh/km/lane, respectively, and the method reduced traffic density more effectively than the tested lane control system even at low CAV penetration rates. Gokasar et al. [16] extended this concept by examining whether traffic could be managed with only a limited number of CAVs rather than relying on a specific penetration rate. A total of 189 SUMO scenarios were tested with a maximum of 12 CAVs. The results showed that the proposed approach could increase mean speed by up to 20.35% and flow by up to 2.45%, while reducing mean density by up to 32.54%. These findings are particularly important because they show that autonomous vehicles can function not only as road users affected by traffic management, but also as actuators that actively influence surrounding traffic flow.

While these studies mainly focus on general AVs and CAVs, autonomous technologies are also increasingly being examined in public transportation. Iclodean et al. [17] reviewed autonomous shuttle bus technologies and reported that current applications are generally more suitable for controlled or low-traffic environments. Autonomous shuttles are typically operated on fixed routes at relatively low speeds, and current applications are concentrated in areas such as airports, industrial parks, commercial areas, and low-traffic night routes. [Fielbaum [18] examined how autonomous vehicle technology could change the design of public transport by developing an autonomous feeder–trunk model. The study showed that automation favors larger fleets of smaller vehicles and more direct routes. Traditional public transport technology was estimated to cost approximately 50% more than autonomous alternatives, although the resulting increase in vehicle numbers could lead to a marginal increase in congestion. Trubia et al. [19], reviewing different autonomous public transport scenarios, similarly emphasized the potential of high-frequency and lower-capacity autonomous services. The reviewed evidence included a MATSim-based Berlin scenario in which at least 50,000 shared autonomous vehicles

would be required to replace the existing public transport system of approximately 1,500 buses and 600 trams, illustrating the possible network-scale implications of replacing conventional public transport with smaller autonomous vehicles.

Autonomous public transport has also been studied from an operational control perspective. Hasebe et al. [20] proposed a last-mile public transportation system based on fleets consisting of manually driven lead vehicles and driverless trailing vehicles. Passenger requests are collected in real time by a central management server, which dynamically determines vehicle schedules and reorganizes vehicle fleets according to demand. The study also proposed provisional routing to maintain transport services in the event of central-server failure, although quantitative traffic-flow improvements were not evaluated. Cao et al. [21] focused more directly on real-time operational control of autonomous public transport vehicles. They developed a simulation-based approach combining discrete-event modeling and a time–space matrix with holding and speed-changing strategies. The method was tested on a 13-km, seven-stop bus route in Auckland, where APTVs were assumed to operate on an exclusive public transport lane without external traffic disturbances. The proposed control strategies eliminated schedule deviations by 100% and improved the overall objective function by approximately 31–33%, demonstrating that APT vehicles can respond dynamically to real-time operational conditions.

Table 1. Literature Review Summary Table

Author(s) / Year	**Traffic Management Role**	**Main Result**
Mulay et al. (2013)	Supporting ITS and congestion management	Integrates real-time public transport information, congestion detection, and congestion-responsive signal timing; no quantitative result reported.
El Hamdani & Benamar (2018)	General autonomous traffic management	Identifies cooperative AVs as potential traffic-management agents through V2V/V2I communication, while highlighting challenges related to complex networks, communication, and mixed road users.
Mancino (2022)	Supporting intelligent traffic management	AI can support dynamic signal control, incident detection, congestion prediction, and route optimization; no quantitative validation was reported.
Manne et al. (2021)	Traffic-flow prediction	The Bi-LSTM model achieved an average prediction accuracy of 0.951, outperforming SVM, RT, RF, and conventional LSTM models.
Din et al. (2024)	Vehicle-level control supporting traffic efficiency	Collision-avoidance accuracy increased from 75% to 90% in urban environments, 80% to 95% on highways, and 65% to 85% under low visibility.
Lu et al. (2019)	Trajectory-based traffic management	The proposed framework successfully coordinated multiple AV trajectories, while the rolling-horizon approach provided computationally efficient approximate solutions.
Martin-Gasulla & Elefteriadou (2021)	Roundabout trajectory and conflict management	Fully CAV traffic increased roundabout capacity by 58–73% and reduced average control delay by 80–97% compared with conventional traffic.
Naeem et al. (2023)	Intersection and priority management	In the best-performing Washington network, average delays were 4.02 s for AVs, 3.62 s for VIP AVs, and 4.33 s for conventional vehicles.

Draganjac et al. (2020)	Decentralized multi-vehicle traffic management	The method demonstrated scalable autonomous fleet coordination, reaching a maximum throughput of 953 missions/h with 30 vehicles.
Amirgholy et al. (2020)	Mixed-traffic lane and network management	Optimal lane management reduced corridor delay by up to 78%, while limiting the downtown travel-time increase to approximately 5%.
Yıldırım & Özuysal (2024)	Mixed-traffic AV integration and lane management	Dedicated lanes reduced density, occupancy, and time loss by 5–35% and improved travel-time reliability by 15–25%, while ToC caused up to a 10% performance decline at low AV penetration.
Gokasar et al. (2023)	CAVs as active traffic-management actuators	SWSCAV reduced occurrences of density above 38 and 28 veh/km/lane by 12.68% and 8.15%, respectively, and remained effective at low CAV penetration rates.
Gokasar et al. (2024)	Limited CAVs as active traffic-management actuators	Using a maximum of 12 CAVs increased mean speed by up to 20.35% and flow by 2.45%, while reducing mean density by up to 32.54%.
Iclodean et al. (2020)	APT deployment and operational feasibility	Current autonomous shuttles are mainly suitable for controlled or low-traffic environments because of their low capacity and operating speed.
Fielbaum (2019)	APT network and service design	Autonomous technology favors larger fleets of smaller vehicles and more direct routes; traditional technology was approximately 50% more costly, although a marginal congestion increase was expected.
Trubia et al. (2021)	APT system-level impacts	Reviewed studies indicate benefits from higher-frequency, lower-capacity autonomous services; a Berlin scenario required at least 50,000 SAVs to replace approximately 1,500 buses and 600 trams.
Hasebe et al. (2017)	Dynamic APT fleet and operational management	The proposed system enables dynamic fleet reorganization and continuation of service through provisional routing after central-server failure; no quantitative traffic-flow result was reported.
Cao et al. (2019)	Real-time APT operational control	Real-time holding and speed-changing reduced schedule deviations from 33 min and 13 min to 0 min under low- and high-demand scenarios, with approximately 31–33% improvement in the objective function.

3 Discussion

The reviewed literature shows that autonomous vehicles can be used not only as road users but also as active elements of traffic management. Existing approaches demonstrate that vehicle speed, trajectory, lane use, and interactions with surrounding traffic can be controlled to influence traffic flow. At the same time, studies on Autonomous Public Transport mainly focus on system design, trajectory control, scheduling, and operational management. Some applications also consider APT vehicles operating on exclusive or dedicated routes. When these two research directions are considered together, a broader role for APT in urban traffic management becomes possible.

Public transportation has an important position in urban mobility because its routes, stops, and operational patterns are generally predefined. This creates a more predictable structure than private vehicle traffic. In conventional traffic, other road users are already expected to follow specific rules around public transport operations, such as respecting bus stops, giving space for buses to enter or leave traffic, or avoiding restricted areas. Autonomous public transport could potentially make these interactions more systematic. Since the location of stops and the movement of APT vehicles are known in advance, these vehicles could interact with surrounding vehicles and infrastructure to support traffic regulation around these locations.

This role could be applied in different traffic environments. In an exclusive or dedicated corridor, APT vehicles could coordinate their trajectories, speeds, and headways to manage traffic within their own operating space. In mixed traffic, their role could extend beyond their own movement. For example, an autonomous bus approaching or leaving a stop could influence the speed or positioning of nearby connected vehicles, support lane organization, or create controlled gaps in traffic. In this sense, APT vehicles could act as mobile traffic management elements while continuing to provide passenger transport.

The fixed nature of public transport routes may also make this approach more feasible than applying the same concept randomly across private AVs. APT vehicles repeatedly travel through the same corridors, intersections, and stops. Therefore, traffic management strategies could be designed specifically for these locations and repeated under similar operational conditions. This could allow APT to contribute to traffic management both through its own controlled operation and through its interaction with surrounding traffic.

However, this concept would require a balance between public transport service objectives and traffic management objectives. An APT vehicle should not significantly delay its passengers simply to improve general traffic conditions. Therefore, its traffic management role would need to operate within predefined limits related to schedule reliability, passenger comfort, and service performance. From this perspective, the applicability of APT as a traffic management element appears possible, particularly in locations where public transport already has a defined operational priority. Its feasibility would depend on how effectively traffic-control functions can be integrated with the primary function of providing reliable public transportation.

4 Conclusion

Urban traffic congestion continues to increase the need for more efficient transportation and traffic management approaches. Public transportation already plays an important role in urban mobility, and autonomous technologies may further expand this role.

The reviewed literature shows that autonomous vehicles can support traffic management through coordinated movement, speed control, and trajectory management. At the same time, APT systems allow more dynamic and controlled operations. Therefore, APT may contribute to traffic management in both dedicated and mixed traffic environments, particularly due to its predefined routes and fixed stops.

Overall, using APT as a traffic management element appears promising. However, its implementation should remain compatible with passenger travel time, service reliability, and public transport performance. Further research is needed to examine its applicability and operational feasibility under different traffic conditions.

Acknowledgments

This study is supported by Bogazici University Research Fund (BAP) with project number 20352 and project code 25A04P1.

References

1. A. M. Rao and K. R. Rao, “Measuring Urban Traffic Congestion - A Review,” International Journal for Traffic and Transport Engineering, vol. 2, no. 4, 2012, doi: 10.7708/ijje.2012.2(4).01.
2. A. Downs, Still Stuck in Traffic: Coping with Peak-Hour Traffic Congestion. The Brookings Institution, 2004. Accessed: Aug. 15, 2026. [Online]. Available: https://books.google.com.tr/books?hl=tr&lr=&id=ckLcxEb5tM8C&oi=fnd&pg=PR7&ots=fJs8MNBJ3Z&sig=CwBO5YhmXdv7Wm_PpC_295UV1Lo&redir_esc=y#v=onepage&q&f=false
3. J. Ainsalu et al., “State of the Art of Automated Buses,” Sustainability 2018, Vol. 10, Page 3118, vol. 10, no. 9, p. 3118, Aug. 2018, doi: 10.3390/SU10093118.
4. S. Mulay, C. Dhekne, R. Bapat, T. Budukh, and S. Gadgil, “Intelligent City Traffic Management and Public Transportation System,” Oct. 2013, Accessed: Aug. 15, 2026. [Online]. Available: https://arxiv.org/pdf/1310.5793
5. S. El Hamdani and N. Benamar, “Autonomous traffic management: Open issues and new directions,” 2018 International Conference on Selected Topics in Mobile and Wireless Networking, MoWNeT 2018, pp. 1–5, Aug. 2018, doi: 10.1109/MOWNET.2018.8428937.
6. G. Mancino, “The Role of Autonomous Vehicles and AI in Smart Transportation Systems: Enhancing Traffic Management, Route Optimization, and Predictive Maintenance,” 2022, doi: 10.13140/RG.2.2.23868.04483.
7. S. Manne, E. L. Lydia, I. V. Pustokhina, D. A. Pustokhin, V. S. Parvathy, and K. Shankar, “An intelligent energy management and traffic predictive model for autonomous vehicle systems,” Soft Computing 2021 25:18, vol. 25, no. 18, pp. 11941–11953, Feb. 2021, doi: 10.1007/S00500-021-05614-7.
8. I. Ud Din, A. Almogren, and J. J. P. C. Rodrigues, “AIoT Integration in Autonomous Vehicles: Enhancing Road Cooperation and Traffic Management,” IEEE Internet Things J., vol. 11, no. 22, pp. 35942–35949, 2024, doi: 10.1109/JIOT.2024.3387927.
9. G. Lu, Y. Nie, X. Liu, and D. Li, “Trajectory-based traffic management inside an autonomous vehicle zone,” Transportation Research Part B: Methodological, vol. 120, pp. 76–98, Feb. 2019, doi: 10.1016/J.TRB.2018.12.012.
10. M. Martin-Gasulla and L. Elefteriadou, “Traffic management with autonomous and connected vehicles at single-lane roundabouts,” Transp. Res. Part C Emerg. Technol., vol. 125, p. 102964, Apr. 2021, doi: 10.1016/J.TRC.2021.102964.
11. A. Bin Naeem, B. Senapati, M. S. Islam Sudman, K. Bashir, and A. E. M. Ahmed, “Intelligent Road Management System for Autonomous, Non-Autonomous, and VIP Vehicles,” World Electric Vehicle Journal 2023, Vol. 14, Page 238, vol. 14, no. 9, p. 238, Sep. 2023, doi: 10.3390/WEVJ14090238.
12. I. Draganjac, T. Petrović, D. Miklić, Z. Kovačić, and J. Oršulić, “Highly-scalable traffic management of autonomous industrial transportation systems,” Robot. Comput. Integr. Manuf., vol. 63, p. 101915, Jun. 2020, doi: 10.1016/J.RCIM.2019.101915.
13. M. Amirgholy, M. Shahabi, and H. Oliver Gao, “Traffic automation and lane management for communicant, autonomous, and human-driven vehicles,” Transp. Res. Part C Emerg. Technol., vol. 111, pp. 477–495, Feb. 2020, doi: 10.1016/J.TRC.2019.12.009.
14. Z. B. Yıldırım and M. Özuysal, “Autonomous Vehicles and Urban Traffic Management for Sustainability: Impacts of Transition of Control and Dedicated Lanes,” Sustainability 2024, Vol. 16, Page 8323, vol. 16, no. 19, p. 8323, Sep. 2024, doi: 10.3390/SU16198323.
15. I. Gokasar, A. Timurogullari, M. Deveci, and H. Garg, “SWSCAV: Real-time traffic management using connected autonomous vehicles,” ISA Trans., vol. 132, pp. 24–38, Jan. 2023, doi: 10.1016/J.ISATRA.2022.06.025.

16. I. Gokasar, A. A. Arisoy, M. Deveci, and A. Mardani, “Evaluation of a New Real-Life Traffic Management Using a Limited Number of Connected Autonomous Vehicles,” IEEE Transactions on Intelligent Transportation Systems, vol. 25, no. 3, pp. 3031–3040, Mar. 2024, doi: 10.1109/TITS.2023.3285913.
17. C. Iclodean, N. Cordos, and B. O. Varga, “Autonomous Shuttle Bus for Public Transportation: A Review,” Energies 2020, Vol. 13, Page 2917, vol. 13, no. 11, p. 2917, Jun. 2020, doi: 10.3390/EN13112917.
18. A. Fielbaum, “Strategic Public Transport Design Using Autonomous Vehicles and Other New Technologies,” International Journal of Intelligent Transportation Systems Research 2019 18:2, vol. 18, no. 2, pp. 183–191, Aug. 2019, doi: 10.1007/S13177-019-00190-5.
19. S. Trubia, S. Curto, A. Severino, F. Arena, and Y. Zuccalà, “Autonomous vehicles effects on public transport systems,” AIP Conf. Proc., vol. 2343, no. 1, Mar. 2021, doi: 10.1063/5.0048036/605990.
20. K. Hasebe, K. Kato, H. Abe, R. Akiya, and M. Kawamoto, “Traffic management for last-mile public transportation systems using autonomous vehicles,” 2017 International Smart Cities Conference, ISC2 2017, Oct. 2017, doi: 10.1109/ISC2.2017.8090821.
21. Z. Cao, A. (Avi) Ceder, and S. Zhang, “Real-time schedule adjustments for autonomous public transport vehicles,” Transp. Res. Part C Emerg. Technol., vol. 109, pp. 60–78, Dec. 2019, doi: 10.1016/J.TRC.2019.10.004.Author 1.: Article title. Journal 2(5), 99–110 (2016).

Author Contribution Statement

- *Conceptualization:* Ilgin Gokasar, Volkan Yildiz
- *Methodology:* Ilgin Gokasar, Volkan Yildiz
- *Investigation:* Ilgin Gokasar
- *Writing – Original Draft:* Volkan Yildiz
- *Writing – Review & Editing:* Ilgin Gokasar

Publication Note

This paper was peer-reviewed, accepted for presentation, and included in the proceedings of the ACE2026 – International Conference on Advances in Civil Engineering, held on 12–14 October 2026 in Trabzon, Türkiye.

This paper may be cited as follows:

Ilgin Gokasar, Volkan Yıldız, “Autonomous Public Transport as a Traffic Management Element: A Literature-Based Discussion on Applicability and Feasibility,” in Proceedings of the ACE2026 – International Conference on Advances in Civil Engineering, Trabzon, Türkiye, 12–14 October 2026.

Autonomous Buses and Their Social Acceptance: A SWOT Analysis

Volkan Yıldız[1] and Ilgin Gokasar[2]
[1] 0009-0000-6709-8768, Boğaziçi University, Department of Civil Engineering, 34342 Bebek, Istanbul, Türkiye, volkan.yildiz@bogazici.edu.tr
[2] 0000-0001-9896-9220, Boğaziçi University, Department of Civil Engineering, 34342 Bebek, Istanbul, Türkiye, ilgin.gokasar@bogazici.edu.tr

Abstract. Urban transportation systems in developing areas experience increasing pressure due to congestion, unreliable service, and operational inefficiencies, creating what several studies describe as a mobility crisis. As cities seek sustainable and long-term solutions, autonomous buses have emerged as a promising alternative, supported by their ability to sense the environment, communicate in real time, and operate with consistent, accurate decision-making. These capabilities offer the potential to improve public transportation efficiency, enhance safety, and strengthen pedestrian connectivity, ultimately contributing to a more accessible and livable urban environment. To better understand the feasibility of autonomous bus deployment in terms of social acceptance, this study conducts a SWOT analysis. The analysis highlights substantial strengths, including operational consistency and long-term cost efficiency, as well as opportunities related to smart city integration and environmental benefits. At the same time, weaknesses such as high initial investment and technical limitations, along with external threats like regulatory uncertainty and cybersecurity risks, underscore the complexity of implementation. Altogether, these factors could explain why social acceptance remains uneven across different socioeconomic and cultural groups. The study further discusses how policymakers interpret these conditions differently from the public, viewing autonomous buses as a strategic long-term investment capable of improving welfare, comfort, and overall mobility performance. Finally, the findings emphasize that awareness campaigns, transparent communication, and user-centered engagement strategies will be essential to improving public trust.

Keywords: Autonomous Buses; Social Acceptance; SWOT Analysis; Urban Mobility

1 Introduction

Public transportation is an essential component of urban mobility, and buses remain one of the most widely used modes of public transport in cities. To support this, the EU transport strategy promotes public passenger transport over individual transport to improve road safety and reduce pressure on road infrastructure [1]. However, conventional bus systems face several operational challenges, particularly in rapidly growing urban areas. In this context, the integration of autonomous buses into public transport systems can provide substantial benefits by reducing traffic accidents, congestion, fuel use, and operating costs, while also improving service quality and environmental sustainability [2].

Autonomous buses combine the conventional role of public transportation with the capabilities of autonomous vehicle technologies. Technology companies, vehicle manufacturers, transit operators, and governments have introduced various AV-based mobility services [3]. A fully autonomous vehicle can be defined as a vehicle that uses sensors,

processors, and mapping data to perceive its surroundings, communicate in real time, make rapid decisions, plan its route, and perform driving tasks with limited or no human intervention [4]. Such capabilities can contribute to more consistent vehicle operations, more reliable public transport services, and improved interaction with the surrounding traffic environment. Therefore, their implementation has the potential to influence not only bus operations but also the overall performance of the urban mobility system. The main reason behind it is the lower operational cost of autonomous buses, which can enable more frequent services [5].

Despite the technological development of autonomous vehicles, the successful implementation of autonomous buses cannot be evaluated solely from an operational perspective. Since passengers are the direct users of public transportation services, social acceptance has an important role in determining whether autonomous buses can become a part of everyday urban mobility. Social acceptability is considered a reciprocal and context-dependent process rather than an isolated phenomenon, particularly because the use of public transportation, including autonomous buses, inherently involves participation in a shared social environment [6]. People's perceptions of autonomous technologies may vary according to socioeconomic, cultural, and individual characteristics. Consequently, users may evaluate the same technology differently in terms of its safety, reliability, usefulness, and potential benefits. This makes public trust an important component of autonomous bus implementation.

Safety is closely related to this issue of trust. In addition to the expected safety benefits of autonomous driving technologies, safety continues to be a major concern, particularly regarding public trust, considering that 316 accidents involving autonomous vehicles were reported in the United States between 2015 and 2020 [7]. Technical uncertainties, possible system failures, cybersecurity risks, and unfamiliarity with automated driving may therefore influence how passengers perceive autonomous buses. As a result, technological improvements alone may not be sufficient to ensure widespread adoption if the public remains uncertain about the reliability and safety of these systems.

Accordingly, this study evaluates autonomous buses through a SWOT analysis from the perspective of policymakers and urban planners. Rather than considering social acceptance as an isolated factor, the study examines how the strengths, weaknesses, opportunities, and threats associated with autonomous buses can collectively influence public perception and acceptance. By evaluating these factors together, the study aims to identify the main issues that policymakers should consider when developing strategies for the successful integration of autonomous buses into urban public transportation systems.

2 Evaluation and SWOT Analysis

The implementation of autonomous buses involves a combination of internal technological characteristics and external conditions. A SWOT analysis provides a useful framework for evaluating these factors by separating them into strengths, weaknesses, opportunities, and threats. In this study, the analysis is conducted primarily from the perspective of policymakers and urban planners, as these actors are responsible for developing regulations, allocating resources, planning infrastructure, and guiding the introduction of autonomous transportation systems.

2.1 Strengths

- *Operational consistency:* Autonomous buses can reduce variations caused by human factors and provide more standardized acceleration, braking, and vehicle operation, supporting regular service intervals and more reliable public transportation [8].
- *Enhanced safety:* Sensors, real-time environmental perception, and automated braking systems can continuously monitor surrounding traffic conditions and reduce some of the risks associated with human error [9].

- *Long-term cost efficiency:* Although autonomous buses require considerable initial investment, reductions in driver-related operational costs and improvements in fuel or energy efficiency may provide economic benefits over the long term [10].
- *Data-driven optimization:* Continuous communication between vehicles and transportation management systems can support improvements in route planning, fleet allocation, capacity management, and service scheduling [11].
- *Accessibility improvements:* More predictable and reliable autonomous bus services may contribute to more inclusive public transportation, particularly for passengers who depend strongly on public transit for daily mobility [12].

2.2 Weaknesses

- *High initial investment requirement:* Autonomous buses require advanced sensors, software, communication systems, digital infrastructure, and possible modifications to existing transportation infrastructure, creating substantial implementation costs.
- *Limited performance in complex urban environments:* Dense traffic, unpredictable pedestrian movements, interactions with conventional vehicles, and complicated intersections can create challenging operating conditions for autonomous buses [13].
- *High maintenance and technical expertise requirements:* Autonomous buses depend on advanced sensors, software, and electronic systems that require specialized maintenance, continuous system updates, and highly trained technical personnel.
- *Dependence on reliable connectivity and infrastructure:* Communication failures and infrastructure disruptions may reduce system performance and limit the potential benefits of automation [14].

2.3 Opportunities

- *Urban mobility transformation:* More reliable and efficient bus operations may increase the attractiveness of public transportation and contribute to reducing dependence on private vehicles [15].
- *Integration with smart city systems:* Smart cities aim to involve all stakeholders in the target area, and autonomous buses can directly support the smart city concept due to their structure, which enables high interaction with the road and communication network [16].
- *Environmental benefits:* When combined with electric propulsion, autonomous buses may support more energy-efficient transportation and contribute to broader sustainability objectives [17].

2.4 Threats

- *Regulatory and legal uncertainty:* The absence of a thorough legal structure to handle liability concerns related to autonomous vehicles is one major worry [18]. Delays in developing operational standards, certification procedures, and liability frameworks may slow or prevent large-scale autonomous bus deployment.
- *High-cost project cancellations:* Economic downturns, changing political priorities, and budget restrictions may lead to the postponement or cancellation of autonomous bus projects.
- *Cybersecurity attacks:* Cyberattacks on automotive systems have increased dramatically as cars become more interconnected, posing a serious threat to data privacy and safety [19]. Unauthorized access to vehicle control systems or transportation data may create significant risks for operational safety and system reliability.

2.5 Evaluation of the SWOT Findings and Social Acceptance

The SWOT analysis indicates that social acceptance cannot be explained by a single characteristic of autonomous buses. Instead, public perceptions are likely to emerge from the interaction between technological benefits, perceived limitations, future opportunities, and external risks.

From the perspective of passengers, several weaknesses and threats may naturally create uncertainty. Potential system malfunctions, cybersecurity risks, complex interactions in urban traffic, and unresolved legal questions may make autonomous buses appear less predictable than conventional buses operated by human drivers. The considerable cost of the technology and the continuing development of regulatory frameworks may further reinforce the perception that autonomous buses are still an emerging rather than fully mature transportation solution. Consequently, it is understandable that some members of the public may perceive autonomous buses as a potential risk or threat despite their expected benefits.

The perspective of policymakers and urban planners, however, is likely to differ because implementation decisions are generally evaluated over a longer time horizon. Autonomous buses may provide economic advantages through lower operational costs and improved resource utilization. At the same time, more reliable and predictable public transportation can enhance accessibility, reduce congestion, and improve the mobility of the wider urban population. Potential improvements in safety, accessibility, and service reliability can also contribute to passenger welfare and comfort.

Therefore, from a policymaker perspective, autonomous buses can be considered not merely as a new vehicle technology but as a long-term strategic investment in the urban transportation system. Their potential benefits extend beyond the operation of individual bus services and may contribute to broader objectives related to mobility, sustainability, efficiency, accessibility, and quality of life.

This difference between short-term public concerns and long-term policy expectations creates an important challenge. The technological and operational advantages of autonomous buses may be significant, but these advantages cannot produce their full societal value if passengers remain unwilling to use the service. Social acceptance therefore acts as a bridge between the technical feasibility of autonomous buses and their actual contribution to urban mobility.

3 Policy Implications

The results of the SWOT analysis suggest that policymakers should consider social acceptance as an integral component of autonomous bus implementation rather than as an issue to be addressed after technological deployment. Policies should therefore aim not only to regulate autonomous bus operations but also to reduce the information and experience gap between policymakers, technology providers, and the public.

One important instrument is the use of awareness campaigns. Many public concerns may originate from limited knowledge about how autonomous buses operate and how their safety systems respond to surrounding traffic conditions. Public information campaigns can explain the basic functioning of the technology, its safety mechanisms, its limitations, and the expected benefits for urban mobility. In addition to that, social media can significantly contribute to the wider acceptance of autonomous vehicles by promoting their advantages through interactive campaigns and engaging content [20].

A second policy option involves the use of incentive mechanisms during the early stages of deployment. Generally, free trial periods, discounted fares, or easier access to pilot services may encourage passengers who would otherwise be hesitant to experience autonomous bus transportation. In order to achieve a more successful outcome, different individual groups should be treated differently, as they could be offered specialized incentives [21]. Direct

experience can help users evaluate the technology based on actual service rather than assumptions or unfamiliarity.

Similarly, hands-on public engagement can be incorporated into pilot projects. Test rides, public demonstrations, informational events, and passenger feedback sessions can create direct interaction between users and the technology. Such activities can also provide policymakers with information about passenger concerns that may not be visible through purely technical evaluations. To evaluate such experiments, questionnaires before, during, and after the trip could be a handful and assist decision-makers in determining key performance indicators [22]. As a result, public engagement can operate in both directions: it can familiarize citizens with autonomous buses while simultaneously helping authorities improve implementation strategies.

Finally, and most importantly, transparent communication and regulatory clarity are essential. Policymakers should clearly communicate safety requirements, monitoring procedures, cybersecurity measures, emergency protocols, and responsibility mechanisms. Transparency may be particularly important following technical failures or incidents, since attempts to minimize or obscure risks can have long-term consequences for public trust. Together, these approaches can help narrow the gap between the long-term benefits identified by policymakers and the uncertainties perceived by passengers.

4 Conclusion

Autonomous buses have the potential to become an important component of future urban public transportation systems. Their technological characteristics may improve safety, operational efficiency, accessibility, and service reliability, while their integration with smart transportation systems may create additional opportunities for urban mobility.

At the same time, their successful implementation depends on more than technological capability. The SWOT analysis demonstrates that weaknesses and external threats can significantly influence how the technology is perceived by the public. Policymakers therefore need to consider the difference between the long-term strategic benefits of autonomous buses and the short-term uncertainties experienced by potential users.

In this context, social acceptance should be treated as a central consideration in autonomous bus implementation. Further research supported by empirical data, passenger surveys, real-world pilot projects, and comparisons between different socioeconomic and cultural groups will be necessary to determine which factors most strongly influence acceptance and which policy interventions are most effective.

Acknowledgments

This study is supported by Bogazici University Research Fund (BAP) with project number 20352 and project code 25A04P1.

References

1. M. Poliak, A. Poliaková, M. Mrníková, P. Šimurková, M. Jaskiewitz, and R. Jurecki, “The competitiveness of public transport,” Journal of Competitiveness, vol. 9, no. 3, pp. 81–97, Sep. 2017, doi: 10.7441/JOC.2017.03.06.
2. J. Weschke, F. J. Bahamonde-Birke, K. Gade, and E. Kazagli, “Asking the Wizard-of-Oz: How experiencing autonomous buses affects preferences towards their use for feeder trips in public transport,” Transp. Res. Part C Emerg. Technol., vol. 133, p. 103454, Dec. 2021, doi: 10.1016/J.TRC.2021.103454.
3. R. Abe, “Introducing autonomous buses and taxis: Quantifying the potential benefits in Japanese transportation systems,” Transp. Res. Part A Policy Pract., vol. 126, pp. 94–113, Aug. 2019, doi: 10.1016/J.TRA.2019.06.003.

4. M. V. Rajasekhar and A. K. Jaswal, “Autonomous vehicles: The future of automobiles,” 2015 IEEE International Transportation Electrification Conference, ITEC-India 2015, Jan. 2016, doi: 10.1109/ITEC-INDIA.2015.7386874.
5. K. Mouratidis and S. Peters, “Autonomous Vehicles as Public Transport: Perceptions of Risks and Opportunities for Mobility, the Environment, and Society,” Journal of Urban Technology, vol. 32, no. 5, pp. 93–114, Oct. 2025, doi: 10.1080/10630732.2025.2509532.
6. N. Hieber, D. Fischer-Pressler, M. Pröbster, J. Kutz, and N. Marsden, “Beyond Acceptance Models: The Role of Social Perceptions in Autonomous Public Transportation Acceptance,” Lecture Notes in Computer Science (including subseries Lecture Notes in Artificial Intelligence and Lecture Notes in Bioinformatics), vol. 14733 LNCS, pp. 26–39, 2024, doi: 10.1007/978-3-031-60480-5_2/FIGURES/4.
7. R. L. Mccarthy, “Autonomous Vehicle Accident Data Analysis: California OL 316 Reports: 2015-2020,” ASCE-ASME Journal of Risk and Uncertainty in Engineering Systems, Part B: Mechanical Engineering, vol. 8, no. 3, Sep. 2022, doi: 10.1115/1.4051779/1114602.
8. Z. Xu and N. Zheng, “Integrating connected autonomous shuttle buses as an alternative for public transport – A simulation-based study,” Multimodal Transportation, vol. 3, no. 2, p. 100133, Jun. 2024, doi: 10.1016/J.MULTRA.2024.100133.
9. J. Wang, L. Zhang, Y. Huang, and J. Zhao, “Safety of Autonomous Vehicles,” J. Adv. Transp., vol. 2020, no. 1, p. 8867757, Jan. 2020, doi: 10.1155/2020/8867757.
10. M. Gusev and S. Gilroy, “The effectiveness of autonomous public transport systems in densely populated urban areas,” Transport Economics and Management, vol. 3, pp. 1–8, Dec. 2025, doi: 10.1016/J.TEAM.2024.11.004.
11. L. Yu, D. Kong, and X. Yan, “A Driving Behavior Planning and Trajectory Generation Method for Autonomous Electric Bus,” Future Internet 2018, Vol. 10, Page 51, vol. 10, no. 6, p. 51, Jun. 2018, doi: 10.3390/FI10060051.
12. A. Millonig and P. Fröhlich, “Where autonomous buses might and might not bridge the gaps in the 4 A’s of Public Transport Passenger Needs - A review,” Proceedings - 10th International ACM Conference on Automotive User Interfaces and Interactive Vehicular Applications, AutomotiveUI 2018, pp. 291–297, Sep. 2018, doi: 10.1145/3239060.3239079
13. H. Yücel and M. Ergün, “Integrating Autonomous Buses into Public Transport Systems: An Assessment of Potential Traffic & Environmental Impacts,” International Journal of Advances in Engineering and Pure Sciences, vol. 37, no. 4, pp. 430–443, Dec. 2025, doi: 10.7240/JEPS.1749662.
14. T. Duvall, E. Hannon, J. Katseff, B. Safran, and T. Wallace, “A new look at autonomous-vehicle infrastructure,” 2019. Accessed: Aug. 11, 2026. [Online]. Available: https://www.mckinsey.com/~/media/McKinsey/Industries/Capital%20Projects%20and%20Infrastructure/Our%20Insights/A%20new%20look%20at%20autonomous%20vehicle%20infrastructure/A-new-look-at-autonomous-vehicle-infrastructure-vF.pdf
15. L. Butler, T. Yigitcanlar, and A. Paz, “Smart urban mobility innovations: A comprehensive review and evaluation,” IEEE Access, vol. 8, pp. 196034–196049, 2020, doi: 10.1109/ACCESS.2020.3034596.
16. C. Latz, V. Vasileva, and M. A. Wimmer, “Supporting Smart Mobility in Smart Cities Through Autonomous Driving Buses: A Comparative Analysis,” Lecture Notes in Computer Science (including subseries Lecture Notes in Artificial Intelligence and Lecture Notes in Bioinformatics), vol. 13391 LNCS, pp. 479–496, 2022, doi: 10.1007/978-3-031-15086-9_31
17. Huber, T. Viere, E. Horschutz Nemoto, I. Jaroudi, D. Korbee, and G. Fournier, “Climate and environmental impacts of automated minibuses in future public transportation,” Transp. Res. D Transp. Environ., vol. 102, p. 103160, Jan. 2022, doi: 10.1016/J.TRD.2021.103160.

18. D. Hafiz, M. AlKhafagy, and I. Zohdy, “Autonomous Public Transport: Evolution, Benefits, and Challenges in the Future of Urban Mobility,” World Electric Vehicle Journal 2025, Vol. 16, Page 482, vol. 16, no. 9, p. 482, Aug. 2025, doi: 10.3390/WEVJ16090482.
19. R. Abreu, F. Branco, M. J. C. S. Reis, and C. Serodio, “Cybersecurity in Connected and Autonomous Vehicles: A Systematic Review of Automotive Security,” IEEE Access, vol. 13, pp. 116818–116855, 2025, doi: 10.1109/ACCESS.2025.3584649.
20. [20] H. Hendra, N. Fadhilah, I. Yani, V. Violin, R. Apramilda, and K. Kushariyadi, “The Role of Marketing Campaigns Through Social Media and Perceived Usefulness on Purchase Intention of Electric Vehicle,” International Journal of Engineering, Science and Information Technology, vol. 5, no. 2, pp. 18–22, Jan. 2025, doi: 10.52088/IJESTY.V5I2.766.
21. B. Liu, Z. Ma, H. Kong, and X. Ma, “How incentives affect commuter willingness for public transport: Analysis of travel mode shift across various cities,” Travel Behav. Soc., vol. 39, p. 100966, Apr. 2025, doi: 10.1016/J.TBS.2024.100966.
22. A. Ariza-Álvarez, M. E. López-Lambas, and J. A. Soria-Lara, “Analysing the acceptance of autonomous buses in real-life traffic environments: pilot project with tourists in Malaga, Spain,” Transportation Planning and Technology, vol. 46, no. 1, pp. 71–92, Jan. 2023, doi: 10.1080/03081060.2022.2159407.

Author Contribution Statement

- *Conceptualization:* Ilgin Gokasar, Volkan Yildiz
- *Methodology:* Ilgin Gokasar, Volkan Yildiz
- *Investigation:* Ilgin Gokasar
- *Writing – Original Draft:* Volkan Yildiz
- *Writing – Review & Editing:* Ilgin Gokasar

Publication Note

This paper was peer-reviewed, accepted for presentation, and included in the proceedings of the ACE2026 – International Conference on Advances in Civil Engineering, held on 12–14 October 2026 in Trabzon, Türkiye.

This paper may be cited as follows:

Volkan Yıldız, Ilgin Gokasar, “Autonomous Buses and Their Social Acceptance: A SWOT Analysis,” in Proceedings of the ACE2026 – International Conference on Advances in Civil Engineering, Trabzon, Türkiye, 12–14 October 2026.

Evaluating Pedestrian Safety and Crossing Preferences Along Urban Arterial Corridors

Beyhan Ipekyuz[1,*] and Funda Ture Kibar[2]
[1]0000-0001-8088-1896, Dicle University, Department of Civil Engineering, Diyarbakır, Türkiye, beyhan.ipekyuz@dicle.edu.tr; * Corresponding author
[2]0000-0001-5700-7033, Başkent University, Department of Civil Engineering, Ankara, Türkiye, ftkibar@baskent.edu.tr

Abstract. Pedestrian safety is a critical concern on high-speed urban arterials where cross-corridor pedestrian demand conflicts with vehicle-oriented road design. This preliminary study investigates reported crossing behaviour, safety perception and infrastructure preferences along the approximately 4-km Mahabad–Seyrantepe section of Elazığ Boulevard in Diyarbakır, Türkiye. The corridor has an 82 km/h posted speed limit, intensive vehicular and pedestrian activity, two pedestrian overpasses, two signalised at-grade crossings and repeated unauthorised openings in the median fencing. Following the required ethical and administrative approvals, a face-to-face questionnaire was administered to 50 corridor users in late July 2026. Among the 47 valid single-choice responses, 25.5% identified a median-barrier opening as their primary crossing method. In addition, 48.0% of all participants reported crossing at road level at least sometimes despite the availability of a designated facility. Although 92.0% considered this behaviour dangerous or dangerous but sometimes understandable, 75.5% of valid respondents perceived vehicle speed as high or very high and 89.8% felt unsafe or only slightly safe while crossing. Existing overpasses were considered difficult to reach by 69.4%, while excessive distance was the most frequently reported reason for avoidance. A safe signalised crossing and an improved, accessible overpass would be used by 71.4% and 69.4% of valid respondents, respectively. The findings suggest that barrier repair alone may be insufficient where formal crossing facilities are poorly aligned with pedestrian movement demand. The results support the consideration of measured speed management, demand-responsive crossing provision and accessible grade separation where warranted.

Keywords: pedestrian crossing behaviour; road safety; pedestrian overpass; urban arterial; risk perception.

1 Introduction

Pedestrians are among the most vulnerable users of the urban transport system because they have little physical protection in the event of a collision. Road traffic injuries therefore remain a major public-health and mobility problem. Approximately 1.19 million people die in road traffic crashes worldwide each year, and pedestrians, cyclists and users of powered two- and three-wheelers together account for more than half of these deaths [1]. In response, the Global Plan for the Decade of Action for Road Safety 2021–2030 calls for at least a 50% reduction in road traffic deaths and injuries by 2030. Its Safe System approach recognises that human error is inevitable and that road infrastructure, speed management and vehicle operation should prevent such errors from resulting in death or serious injury [2].

Pedestrian safety is also an important concern in Türkiye. Official statistics for 2025 recorded 6,035 fatalities and 403,937 injuries in road traffic crashes. Of all fatalities, 57.2% occurred in

crashes within settlements. Crashes classified under the ‘hitting a pedestrian’ category were associated with 1,190 fatalities, corresponding to approximately 19.7% of all road traffic deaths [3]. These national statistics establish the scale of pedestrian-related road trauma but do not explain why unsafe crossing behaviour becomes concentrated at particular road sections. Identification of the underlying behavioural and infrastructure-related factors therefore requires corridor-specific investigation.

Divided urban arterials present a particularly challenging environment for pedestrians because high vehicle speeds, wide cross-sections, central medians and limited crossing opportunities increase both crossing distance and exposure. At the same time, adjacent residential areas, schools, shopping centres, public institutions, commercial frontage and public transport stops generate frequent pedestrian movements between the two sides of the road. Although overpasses, underpasses and median fencing are intended to reduce uncontrolled pedestrian–vehicle interaction, their presence does not necessarily ensure use. When formal facilities impose substantial detour, physical effort or accessibility constraints, pedestrians may prefer shorter at-grade routes. Repeated use of openings in median fencing may therefore indicate not only non-compliance but also a mismatch between formal crossing provision and actual pedestrian desire lines.

The present study examines this problem along Elazığ Boulevard (D885) in Diyarbakır, Türkiye. Preliminary field reconnaissance identified repeated pedestrian crossings through unauthorised openings in the median fencing despite the presence of two pedestrian overpasses and two signalised at-grade crossings within the approximately 4-km section between Mahabad Intersection and the Seyrantepe grade-separated junction. The corridor has a posted speed limit of 82 km/h [4] and accommodates intensive vehicular traffic together with pedestrian demand generated by schools, residential neighbourhoods, commercial and industrial activities, public institutions, public transport stops and a major shopping centre.

Accordingly, the study examines: (i) the crossing methods reported by corridor users; (ii) the traffic, situational and infrastructure-related factors associated with crossing-location choice; (iii) perceptions of vehicle speed, crossing safety, driver attentiveness, lighting and overpass accessibility; and (iv) stated preferences for alternative pedestrian-safety interventions. Particular attention is given to the apparent discrepancy between the recognition of crossing risk and the continued use of informal at-grade crossing locations.

2 Literature Review

Pedestrian crossing behaviour is influenced by the interaction of traffic conditions, road geometry, infrastructure provision and individual decision-making. Vehicle speed, traffic volume, available gaps, crossing distance, waiting time and the number of traffic lanes directly affect pedestrian exposure and gap-acceptance decisions. At the same time, pedestrians evaluate whether the safety benefit of a designated facility compensates for its additional distance, travel time and physical effort. Crossing behaviour should therefore be understood as a balance between perceived risk and the perceived cost of using the formal alternative [5–15].

The location of a crossing facility relative to pedestrian origins and destinations is one of the principal determinants of its use. Pedestrians are less likely to use a designated facility when it requires a substantial deviation from their intended route [5]. The acceptability of signalised crossings, pedestrian overpasses and underpasses is similarly affected by additional walking time, accessibility, convenience and personal security [6]. Accordingly, the spacing and placement of formal crossing facilities should be evaluated in relation to observed pedestrian demand and acceptable detour distances [7].

Studies conducted on wide, multi-lane arterials demonstrate the importance of route directness. Illegal mid-block crossing decisions have been associated with available gap duration, vehicle speed, waiting time, lane position and the walking-distance savings achieved

by selecting a direct route [8]. On high-speed divided arterials, vehicle presence, pedestrian group behaviour, physical obstructions and the pursuit of the shortest route also affect the decision to cross outside designated facilities [9]. Evidence from unmarked road segments further indicates that road-environment characteristics, individual attributes and the behaviour of surrounding pedestrians jointly influence informal crossing [10]. Collectively, these findings indicate that non-designated crossing cannot be attributed solely to deliberate non-compliance [8–10].

Risk perception does not always translate into safe crossing behaviour. Pedestrians may recognise a crossing manoeuvre as hazardous but still accept the risk when the designated alternative is perceived as distant, inconvenient or difficult to access. In addition to observable traffic conditions, route optimisation, individual risk-taking tendencies, detour distance, waiting time, personal security, habitual behaviour and social influence may contribute to crossing decisions [11–15]. Formal facilities should therefore be evaluated not only according to their physical presence but also according to their accessibility, location and correspondence with pedestrian desire lines.

Comparatively limited attention has been given to informal crossings facilitated by unauthorised openings in continuous median fencing, particularly where pedestrian overpasses and signalised crossings are already available. The present study addresses this specific configuration by examining reported crossing behaviour, perceived traffic risk, overpass accessibility and intervention preferences within the same corridor-level framework. This approach enables the study to evaluate whether continued informal crossing is associated primarily with limited risk awareness or with a mismatch between formal infrastructure and actual pedestrian movement demand.

3 Methodology

3.1 Research design and area

A cross-sectional questionnaire study supported by preliminary field reconnaissance was conducted along Elazığ Boulevard in Diyarbakır, Türkiye. The investigated corridor extends approximately 4 km between Mahabad Intersection in the west and the Seyrantepe grade-separated junction in the east. The inbound direction runs from Mahabad towards Seyrantepe and continues towards the city centre and the historic Sur district, while the outbound direction runs from Seyrantepe towards Mahabad. Seyrantepe is a multi-level junction connecting Elazığ Boulevard with Şanlıurfa Boulevard (E99), whereas Ahmed Arif Intersection constitutes an important intermediate connection within the study corridor (see *Fig. 1*).

Elazığ Boulevard is a divided urban arterial carrying intensive vehicular traffic and serving considerable pedestrian activity. The surrounding land uses include residential neighbourhoods, a school zone, Forum Diyarbakır Shopping Centre, industrial and commercial establishments, restaurants, public institutions and public transport stops. The main carriageways generally comprise two through lanes in each direction, while parallel two-lane frontage or service carriageways are present along substantial parts of the corridor. These service carriageways accommodate public transport operations, local traffic and direct property access. The cross-section varies near intersections, access points and merging or diverging areas. At some pedestrian desire lines, the total crossing distance exceeds 40 m when the main carriageways, central median and service roads are considered together. The posted speed limit was 82 km/h [4]. Two pedestrian overpasses and two signalised at-grade crossings are located within the study section. One overpass serves the Forum Diyarbakır Shopping Mall area, while the other is near the State Hydraulic Works (*DSİ*) frontage before the Ahmed Arif Street connection. Median fencing restricts uncontrolled crossings; however, preliminary field reconnaissance identified missing or displaced sections enabling informal pedestrian access to the median.



Fig. 1. Study corridor, principal junctions, surrounding activity areas and formal pedestrian crossing facilities (Google Earth, 2026).

Fig. 2 illustrates representative corridor conditions, including the main and service carriageways, a signalised pedestrian crossing, the Forum pedestrian overpass and an opening in the median fence. *Fig. 2(b)* shows a pedestrian in the crossing area during a vehicular green phase; since the pedestrian signal is not visible, the image is presented as contextual evidence of potential exposure rather than a verified pedestrian signal violation.



Fig. 2. Representative corridor conditions: (a) divided roadway and adjoining service carriageway; (b) signalised pedestrian crossing; (c) Forum pedestrian overpass; and (d) an opening in the median fence used as an informal access point (Google Maps Street View, 2026)

3.2 Questionnaire design and administration

The questionnaire was developed to examine pedestrian crossing behaviour and perceived safety conditions specific to the study corridor. The complete instrument comprised 38 numbered items covering participant characteristics, corridor use, crossing behaviour, perceived traffic conditions, pedestrian-overpass accessibility, risk-related and situational factors, intervention preferences and additional recommendations. It included single-choice categorical questions, multiple-response items, five-point ordinal and Likert-type scales, and one open-ended question. Of the 38 questionnaire items, 29 were included in the present analysis. These items were grouped into six analytical domains, as summarised in *Table 1*.

Following completion of the ethical and administrative approval processes, the questionnaire was administered intermittently at selected locations along the study corridor in late July 2026 using a non-probability intercept sampling approach. Individuals were eligible to participate if they used and were familiar with the study corridor. The questionnaire was administered face-to-face and required approximately 10–12 min to complete. The preliminary analytical sample comprised 50 completed questionnaires.

Ethical approval was granted by the Dicle University Science and Engineering Ethics Committee. The approved research protocol covered both the face-to-face questionnaire and the observational field study. Participation was voluntary, and participants were informed about the purpose and procedures of the research, as well as their right to withdraw at any time without providing a reason. Personal data were kept confidential, and questionnaire responses were anonymised and used exclusively for scientific purposes. For participants below the legal age for independent consent, age-appropriate information and assent procedures were applied, and consent was obtained from a parent or legal guardian in accordance with the approved research protocol. The required administrative permissions for field implementation were obtained separately from the Diyarbakır Governorate, Diyarbakır Provincial Police Department, and other competent public authorities.

Table 1. Questionnaire structure used in the present analysis

Code	Analytical domain	Variables included	Measurement format
A	Participant and travel characteristics	Gender, age, education, corridor-use frequency and usual travel mode	Categorical
B	Crossing behaviour and decision factors	Primary crossing method, informal crossing frequency, crossing considerations, appraisal of informal crossing and reasons for avoiding overpasses	Categorical, ordinal and multiple response
C	Traffic-safety and risk perception	Perceived speed and crossing safety, signage, driver attentiveness, lighting, hazardous-event exposure, median-opening danger, safety problems and crash likelihood	Five-point ordinal, categorical and multiple response
D	Overpass accessibility and personal security	Suitability of overpass location, ease of access and night-time personal security	Five-point Likert-type
E	Preferred pedestrian-safety interventions	Overpass improvements, crossing alternatives, speed-management measures and willingness to use safer facilities	Multiple response and five-point willingness
F	Additional recommendations	Pedestrian-safety and infrastructure recommendations	Open-ended

Note: The complete questionnaire comprised 38 numbered items; 29 items directly related to the objectives of the present study were included in the analysis.

3.3 Data analysis

Questionnaire responses were analysed using descriptive statistics. Categorical variables were summarised using frequencies and item-specific valid percentages. Five-point ordinal and Likert-type responses were retained in their original order and combined only for selected figures. For multiple-response items, each option was coded separately and percentages were based on respondents answering the relevant item; thus, totals could exceed 100%. Multiple selections for single-choice items were excluded only from that item's analysis, and missing responses were not imputed. Open-ended recommendations were coded into non-exclusive descriptive themes. Given the preliminary non-probability sample, no inferential tests or multivariable models were applied.

4 Results

4.1 Participant and travel characteristics

The sample included 45 male participants (90.0%), three female participants (6.0%) and two participants who preferred not to report their gender (4.0%). Twenty-two participants (44.0%) were aged 10–17 years, 13 (26.0%) were aged 18–29 years, 12 (24.0%) were aged 30–44 years and three (6.0%) were aged 45 years or older. High-school education was reported by 30 participants (60.0%). Corridor use was frequent: 24 participants (48.0%) used it every day, seven (14.0%) every weekday and six (12.0%) several times per week. Thus, 74.0% used the corridor at least several times per week. Among the 47 valid single-choice responses for usual travel mode, walking was the most frequently reported mode (40.4%), followed by private car (29.8%) and municipal bus (17.0%).

4.2 Crossing behaviour and perceived causes

Among 47 valid single-choice responses for primary crossing method, 15 (31.9%) reported using an overpass or underpass, 12 (25.5%) reported using an opening in the median barrier, and 11 (23.4%) stated that their choice depended on prevailing conditions. Other marked or unmarked crossing locations accounted for 10.6%, while 8.5% reported primarily using a signalised crossing (*Fig. 3a*). When asked about crossing at road level despite the availability of a designated facility, 16 participants (32.0%) responded "never," 10 (20.0%) "rarely," 10 (20.0%) "sometimes," 9 (18.0%) "often," and 5 (10.0%) "always." Overall, 24 participants (48.0%) reported engaging in this behaviour at least sometimes (*Fig. 3b*).

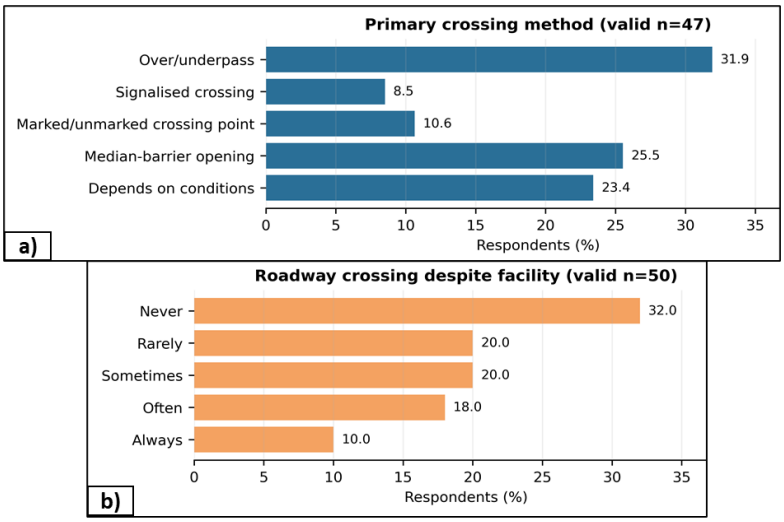


Fig. 3. (a) Reported primary crossing method among unambiguous responses (valid n=47) and (b) frequency of crossing at road level despite an available designated facility (N=50).

Vehicle speed was the most frequently selected factor affecting crossing-location choice (66.0%), followed by traffic volume (18.0%), the availability of a junction or pedestrian overpass (16.0%), signs and markings (12.0%), route directness (10.0%) and the availability of an opening in the median barrier (6.0%). Among the 48 participants who answered the question concerning overpass avoidance, excessive distance to the overpass was the most frequently selected reason (43.8%). Mismatch between crossing demand and facility location and habitual behaviour were each selected by 18.8%, followed by shorter travel time and overpass-design problems (14.6% each) and physical effort (12.5%).

Risk awareness was nevertheless high. 33 participants characterised road-level crossing as definitely wrong and dangerous, and 13 as dangerous but understandable in some circumstances; together these categories represented 92.0% of the sample. Only 3 regarded it as normal and one had no opinion. The coexistence of strong danger recognition and continued informal crossing suggests constrained choice rather than simple risk ignorance.

4.3 Safety perception and overpass evaluation

Of 49 valid responses, 37 (75.5%) rated vehicle speed as high or very high, while 44 (89.8%) felt unsafe or only slightly safe when crossing; none selected “safe” or “very safe”. 32 (65.3%) disagreed that warning signs and markings were adequate, and 42 (85.7%) that drivers were attentive to pedestrians. 41 respondents reported experiencing or witnessing a crash, near miss or hazardous event; 4 answered no, 4 did not remember and one response was missing.

Lighting and access were also evaluated negatively. 34 of 49 respondents (69.4%) considered lighting inadequate, 31 (63.3%) disagreed that overpasses were appropriately located, and 34 (69.4%) that they were easy to reach. Night-time personal security was viewed negatively by 30 of 47 (63.8%). By contrast, only 10 of 49 (20.4%) agreed that overpasses caused excessive time loss and 18 (36.7%) that they were physically tiring, reinforcing the relative importance of access and location.

Crossing risk was rated high or very high by 36 of 47 valid respondents (76.6%), and pedestrian-crash likelihood by 31 (66.0%). Median-fence openings were described as very dangerous by 24 participants (51.1%), dangerous by eight (17.0%) and dangerous but used because pedestrians felt compelled to do so by 14 (29.8%). None considered their use normal. Selected response distributions are presented.

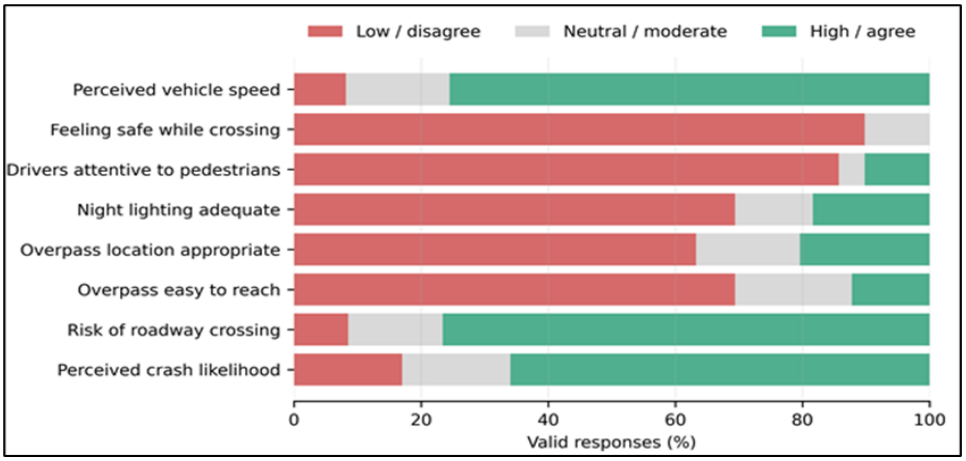


Fig. 4. Distribution of selected responses concerning perceived vehicle speed, crossing safety, driver attentiveness, lighting, overpass location and accessibility, crossing risk and crash likelihood. Percentages are based on the valid responses to each item.

4.4 Preferred pedestrian-safety interventions

Participants selected interventions addressing both overpass conditions and road-level crossing provision. Among the 49 participants answering the overpass-improvement item, escalators were selected by 40.8%, relocation of the overpass by 34.7%, shorter access distance by 28.6%, lifts by 24.5%, and improved lighting and security measures by 20.4% each. Regarding crossing provision, 46.9% selected a new pedestrian overpass, 32.7% a signalised pedestrian crossing, 30.6% an underpass and 22.4% improvement of the existing overpasses. Because these were multiple-response items, the percentages represent endorsement of each measure rather than mutually exclusive preferences.

The most frequently selected traffic-management measure was a reduction in the speed limit (53.1%). Radar-based speed control and speed humps were each selected by 46.9%, followed by electronic enforcement systems (36.7%), pedestrian-priority signalisation (34.7%) and revised signal timing (32.7%). A safe signalised at-grade crossing would be used or definitely used by 35 of the 49 respondents (71.4%), while 34 (69.4%) stated that they would use an improved and accessible pedestrian overpass.

33 participants supplied an open comment. Non-exclusive coding identified requests for more or better-located overpasses in 21 comments, at-grade crossings in 7, lift/escalator provision in 3, speed reduction in 2, enforcement/cameras in 2 and signalisation/lighting. As the thematic categories were non-exclusive, an individual response could be assigned to more than one category. Selected intervention preferences are presented in Fig. 5.

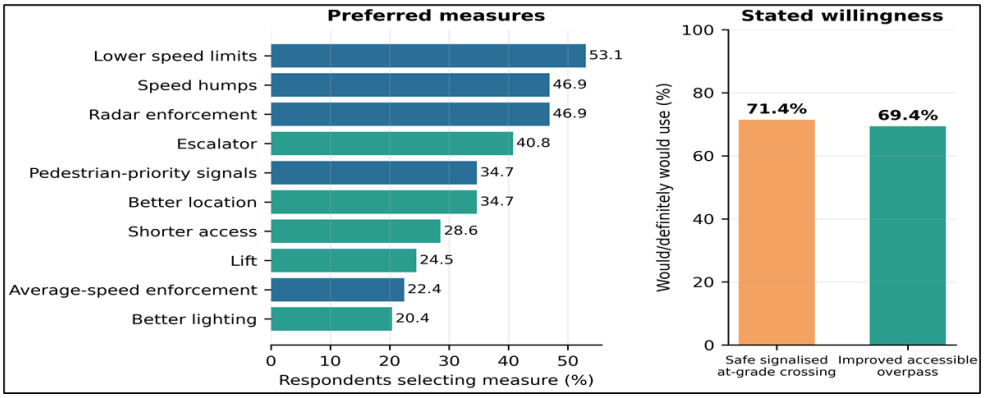


Fig. 5. Preferred overpass improvements, crossing-facility treatments and speed-management measures, together with stated willingness to use safer crossing facilities. Multiple responses were permitted for improvement measures.

5 Discussion

The principal finding was the discrepancy between risk appraisal and reported crossing behaviour. Although 92.0% of participants recognised informal road-level crossing as dangerous or sometimes understandable despite the danger, 48.0% reported doing so at least sometimes. Among those recognising the danger, 47.8% nevertheless crossed informally at least sometimes, indicating that risk awareness alone did not ensure consistent use of designated facilities.

Distance and spatial alignment were the most frequently reported reasons for overpass avoidance. Excessive distance was the leading reason for non-use, while the location and accessibility of existing overpasses were evaluated negatively by most respondents. These findings are consistent with evidence that facility use depends strongly on origin–destination alignment and acceptable detour distance [5–7], and that pedestrians may accept greater traffic exposure for a more direct route [8,9]. Informal crossing may therefore persist or shift if median fencing is restored without addressing pedestrian desire lines.

Most respondents perceived vehicle speeds as high and felt unsafe while crossing. These perceptions should be considered in relation to the corridor's wide cross-section and posted speed limit, although operating speeds were not measured. Direct speed measurements, pedestrian and vehicle counts, trajectory observations, signal compliance and pedestrian–vehicle conflict analysis are needed to establish operational safety conditions.

Similar proportions of respondents stated that they would use a safe signalised crossing or an improved, accessible overpass. The findings therefore do not support a single treatment for the entire corridor. A signalised at-grade crossing could be considered where speed, pedestrian-demand and geometric assessments demonstrate safe operation; otherwise, grade separation may remain necessary if accessible and aligned with pedestrian desire lines. Public transport stops, lighting, maintenance, personal security and approach continuity should also be integrated into crossing-facility planning.

This study has several limitations. First, it used a preliminary non-probability sample of 50 corridor users; the high proportions of male and 10–17-year-old participants limit representativeness and prevent generalisation to all pedestrians in Diyarbakır. Second, crossing behaviour and traffic conditions were self-reported and may be affected by recall and social-desirability bias. Third, some items contained multiple selections despite single-choice wording and were handled using item-specific validity rules. Finally, the study lacked operating-speed measurements, pedestrian and vehicle volumes, accepted gaps, conflict observations and georeferenced crash records. The findings therefore identify reported perceptions and behavioural patterns but do not establish causal relationships or engineering warrants.

6 Conclusions

This study examined reported pedestrian crossing behaviour, perceived safety and crossing-facility preferences along the Mahabad–Seyrantepe section of Elazığ Boulevard. Although most participants recognised the danger of informal road-level crossing, almost half reported engaging in this behaviour at least sometimes. Overpass distance, location and accessibility emerged as the principal infrastructure-related concerns, while perceived vehicle speed and crossing safety were evaluated negatively.

The findings suggest that restoring median fencing alone may be insufficient where formal facilities remain poorly aligned with pedestrian movement demand. Before selecting an intervention, operating-speed measurements, pedestrian and vehicle counts, desire-line mapping, signal-phase observations and accessibility audits of existing overpasses and signalised crossings should be undertaken. These measurements would support location-specific combinations of speed management, formal crossing provision and accessible grade separation where warranted.

Declarations

Ethics approval and consent to participate: Ethical approval was granted by the Dicle University Science and Engineering Ethics Committee on 23 July 2026 (decision item no. 3) and officially communicated by the Dicle University Graduate School of Natural and Applied Sciences on 28 July 2026 (document no. E-56760607-663.05-1191694). Participation was voluntary, and all responses were anonymised. For participants below the legal age for independent consent, age-appropriate information and assent procedures were applied, and consent was obtained from a parent or legal guardian in accordance with the approved research protocol.

Funding: This research received no external funding.

Conflict of interest: The authors declare no conflict of interest.

References

1. World Health Organization. Global status report on road safety 2023. Geneva: World Health Organization; 2023. https://www.who.int/publications/i/item/9789240086517
2. World Health Organization, United Nations Regional Commissions. Global Plan for the Decade of Action for Road Safety 2021–2030. Geneva: World Health Organization; 2021. https://www.who.int/publications/m/item/global-plan-for-the-decade-of-action-for-road-safety-2021-2030
3. Turkish Statistical Institute. Road Traffic Accident Statistics, 2025. Ankara: TurkStat; 2026. https://veriportali.tuik.gov.tr/tr/press/58133
4. Diyarbakır Governorship. Ortalama Hız İhlal Tespit Sistemleri [Average Speed Violation Detection Systems]. 2024. https://diyarbakir.gov.tr/ortalama-hiz-ihlal-tespit-sistemleri
5. Sisiopiku VP, Akin D. Pedestrian behaviors at and perceptions towards various pedestrian facilities: an examination based on observation and survey data. Transp Res Part F Traffic Psychol Behav. 2003;6(4):249–274. https://doi.org/10.1016/j.trf.2003.06.001
6. Anciaes PR, Jones P. Estimating preferences for different types of pedestrian crossing facilities. Transp Res Part F Traffic Psychol Behav. 2018; 52:222–237. https://doi.org/10.1016/j.trf.2017.11.025
7. Chandrappa AK, Bhattacharyya K, Maitra B. Measures for improving pedestrian crossing facilities based on perceptions of urban commuters: an experience in Kolkata. Case Stud Transp Policy. 2021;9(2):965–973. https://doi.org/10.1016/j.cstp.2021.04.017
8. Cherry C, Donlon B, Yan X, Moore SE, Xiong J. Illegal mid-block pedestrian crossings in China: gap acceptance, conflict and crossing path analysis. Int J Inj Contr Saf Promot. 2012;19(4):320–330. https://doi.org/10.1080/17457300.2011.628751
9. Shaaban K, Muley D, Mohammed A. Analysis of illegal pedestrian crossing behavior on a major divided arterial road. Transp Res Part F Traffic Psychol Behav. 2018; 54:124–137. https://doi.org/10.1016/j.trf.2018.01.012
10. Zhang W, Guo H, Wang C, et al. Analysis of pedestrian illegal crossing at unmarked segments: environmental factors, pedestrian characteristics and crossing behaviours. Transp Res Part F Traffic Psychol Behav. 2023; 99:339–355. https://doi.org/10.1016/j.trf.2023.10.022
11. Papadimitriou E, Lassarre S, Yannis G. Introducing human factors in pedestrian crossing behaviour models. Transp Res Part F Traffic Psychol Behav. 2016; 36:69–82. https://doi.org/10.1016/j.trf.2015.11.003
12. Papadimitriou E, Lassarre S, Yannis G. Human factors of pedestrian walking and crossing behaviour. Transp Res Procedia. 2017; 25:2002–2015. https://doi.org/10.1016/j.trpro.2017.05.396
13. Arellana J, Fernández S, Figueroa MA, Cantillo V. Analyzing pedestrian behavior when crossing urban roads by combining RP and SP data. Transp Res Part F Traffic Psychol Behav. 2022; 85:259–275. https://doi.org/10.1016/j.trf.2022.01.012
14. Obeng DA. Pedestrians safety perceptions on midblock crosswalk utilization along urban corridors of developing countries. Int J Inj Contr Saf Promot. 2022; 29(2):152–159. https://doi.org/10.1080/17457300.2021.1969411
15. Osei KK, Obiri-Yeboah AA, Adu-Gyamfi L, Ackaah W. Road crossing behavior and preferences among pedestrians: from the lens of the theory of interpersonal behavior. Traffic Inj Prev. 2024;25(1):91–100. https://doi.org/10.1080/15389588.2023.2271107

Author Contribution Statement

Conceptualization and methodology: B.I. and F.T.K.; *Investigation and data curation*: B.I.; *Analysis and visualization*: B.I.; *Writing*: B.I. and F.T.K. Both authors approved the manuscript.

Publication Note

This paper was peer-reviewed, accepted for presentation, and included in the proceedings of the ACE2026 – International Conference on Advances in Civil Engineering, held on 12–14 October 2026 in Trabzon, Türkiye.

This paper may be cited as follows:

Beyhan Ipekyuz and Funda Ture Kibar, "Evaluating Pedestrian Safety and Crossing Preferences Along Urban Arterial Corridors," in Proceedings of the ACE2026 – International Conference on Advances in Civil Engineering, Trabzon, Türkiye, 12–14 October 2026.

A Framework for Factor Filtering and Algorithm Selection in Highway Alignment Optimization

Özger İnal[1], Mehmet Ali Silgu[2] and Abdullah Hilmi Lav[3]
[1] 0009-0005-0895-7100, Istanbul Technical University, Civil Engineering Department, İstanbul, Türkiye, oinal23@itu.edu.tr
[2] 0000-0002-7667-8796, Bartın University, Civil Engineering Department, Bartın, Türkiye, masilgu@bartin.edu.tr
[3] 0000-0002-7828-7588, Istanbul Technical University, Civil Engineering Department, İstanbul, Türkiye, lav@itu.edu.tr

Abstract. Highway alignment selection involves many interacting criteria spanning technical, environmental, economic, and social dimensions. Most existing methods apply a fixed criteria set regardless of context, and many commit to one optimization algorithm without a clear basis. This study proposes a two-stage decision framework: Stage 1 filters alignment factors against project conditions, and Stage 2 guides algorithm choice through a structured comparison. The filtering stage groups route-selection criteria under seven domains, investor needs, topography and geology, engineering and logistics, traffic demand, economic feasibility, land-use compatibility, and environmental and social constraints, and excludes factors that are not critical in a given context, reducing complexity and focusing the model. The algorithm-selection stage compares genetic algorithms, particle swarm optimization, multi-criteria decision analysis, and GIS-heuristic hybrids on efficiency, multi-objective adaptability, GIS integration, and planning applicability. Fuzzy inference, using Mamdani and Takagi-Sugeno models, drives the decision logic in both stages, with decision-tree and ensemble models tuning the rule bases while keeping them readable. A step-by-step workflow shows how practitioners apply the framework, and implementation challenges and limitations are identified. A case study is planned to validate the framework on a real corridor.

Keywords: Highway Alignment; Multi-Criteria Optimization; Factor Filtering; Fuzzy Inference System.

1 Introduction

Choosing a highway alignment is one of the earliest and most consequential decisions in road planning, since it fixes much of the project's cost, environmental footprint, and service quality; a poor choice is expensive to correct later, and the problem is hard because it involves many criteria that often conflict.

The search space is also vast: an alignment is a continuous path in three dimensions, subject to geometric, geological, and right-of-way constraints. Manual design explores only a few alternatives, while computer-based optimization can explore far more; since the work of Jha and Schonfeld [1], a large body of research has applied search algorithms to this problem.

Two gaps remain. First, most studies use a fixed set of criteria regardless of project context, wasting effort on factors that do not matter locally. Second, most studies commit to a single algorithm, often a genetic algorithm, without a structured reason for that choice [2-3]; the algorithm is treated as given, not selected. This paper addresses both gaps with a two-stage framework: the first stage filters factors to those that matter in a given context, and the second selects an algorithm through a structured comparison. The paper is conceptual, defining the method and decision logic that a planned case study will apply.

Section 2 reviews prior work. Section 3 presents the proposed framework, its decision engine, and its algorithm comparison. Section 4 sets out an application workflow. Section 5 covers the planned case study, challenges, and limitations. Section 6 concludes.

2 Background

2.1 Alignment Optimization Methods

Early alignment optimization minimised total cost as a single objective [1]. Jha and Schonfeld [1] integrated a genetic algorithm with a geographic information system (GIS); this pairing became the dominant approach for a decade. Maji and Jha [2] proposed a multi-objective genetic algorithm returning Pareto-optimal alignments rather than one solution, and Yang et al. [3] extended this with a hybrid algorithm incorporating designer preferences.

Particle swarm optimization (PSO) has also been applied: Shafahi and Bagherian [4] developed a customised PSO for the alignment problem, and Bosurgi et al. [5] added environmental constraints to a PSO-based model. Ant colony optimization has been used mainly for vertical alignment, against earthwork cost [6].

Recent work uses GIS more actively: Al-Hadad et al. [7] used a GIS-derived least-cost path to confine the search to a narrow corridor before the genetic algorithm runs, cutting computation, and Kim et al. [8] used a stepwise strategy to similar effect.

2.2 Multi-Criteria and Fuzzy Methods

Not all alignment decisions reduce to a cost function; many criteria are qualitative, and multi-criteria decision analysis (MCDA) handles these. Liu et al. [9] combined an objective and subjective weighting method with TOPSIS to rank highway route schemes across technical, ecological, social, and economic factors.

Fuzzy inference suits imprecise criteria, representing judgments such as high slope or moderate traffic as fuzzy sets. Mamdani systems produce fuzzy output sets and are easy to interpret [10]; Takagi-Sugeno systems use linear output functions that integrate well with optimization [11], and the two perform similarly on accuracy [12-13]. Machine learning has begun to inform such models: decision trees and ensemble regressors can learn rule bases or output functions from data, and neuro-fuzzy methods combine neural-network learning with fuzzy-system interpretability [14].

3 Proposed Framework

3.1 Two-Stage Decision Process

The framework operates in two sequential stages. Stage 1 filters the candidate factor set against the project context and returns a reduced, context-specific factor set. Stage 2 takes that reduced set, together with the same project priorities, and selects the optimization algorithm best suited to it. Both stages draw on a single fuzzy-inference and machine-learning engine, described in Section 3.2, so one auditable logic governs both what enters the optimization problem and how that problem is solved.

Stage 1: Factor Filtering. Alignment criteria fall into seven domains: investor requirements, topography and geology, engineering and logistics, traffic demand, economic feasibility, land-use compatibility, and environmental and social constraints. Table 1 gives, for each domain, a representative indicator and the project condition that would normally retain or drop it, so every screening decision traces to a named indicator.

Table 1. Taxonomy of route-selection criteria, indicators, and screening conditions.

Domain	Representative factors	Example indicator	Screening condition
Investor requirements	Service level, staged construction, budget ceiling	Target design speed; phasing plan	Retain when funding or schedule constrains the design
Topography and geology	Slope, landslide risk, soil bearing, faulting	Ground slope (%); hazard class	Drop in flat, geotechnically uniform terrain
Engineering and logistics	Earthwork, structures, access, constructability	Cut-and-fill volume; bridge count	Retain where structures or earthwork dominate cost
Traffic demand	Forecast volume, level of service, connectivity	AADT forecast; v/c ratio	Retain on routes serving variable or growing demand
Economic feasibility	Construction cost, life-cycle cost, benefit-cost	Unit cost per km; BCR	Almost always retained as a global objective
Land-use compatibility	Acquisition, severance, zoning conflict	Parcels affected; land-use class	Drop on remote routes far from settlement
Environmental and social	Habitat, noise, emissions, community impact	Protected area overlap; exposed population	Retain near protected or inhabited areas

Table 2 gives examples: for a flat coastal route, steep-grade and landslide factors carry little weight and can be dropped; for a route far from settlements, land-use factors fall away. Filtering cuts the dimensionality of the optimization and focuses the model on the factors that drive alignment performance in the region.

Table 2. Examples of context-based factor exclusion.

Project context	Likely critical factors	Likely excluded factors
Flat coastal corridor	Land use, drainage, traffic demand	Landslide risk, steep grade
Mountain crossing	Slope, geology, earthwork cost	Wide right-of-way acquisition
Peri-urban bypass	Land acquisition, noise, access	Deep cut and fill, tunnelling
Remote rural link	Construction cost, terrain	Dense land-use conflict

Formally, let F be the full factor set and I_j the importance score of factor j, computed by the fuzzy engine of Section 3.2 from the Table 1 indicators and the project priorities. The retained set F* is

$$F^* = \{ j \in F : I_j \geq \tau \} \quad (1)$$

where τ is a retention threshold set by the planning team. A factor tied to a hard regulatory limit is never dropped, and borderline factors are flagged for expert review.

Stage 2: Algorithm Selection. The second stage compares candidate methods, genetic algorithms, particle swarm optimization, MCDA approaches, and GIS-heuristic hybrids, and selects the most suitable one. Each method k receives a suitability score

$$S_k = \Sigma\, v_c\, r_{kc}\,, \quad k^* = arg\ max\ S_k \tag{2}$$

where r_{kc} is the score of method k on criterion c (computational efficiency, multi-objective adaptability, GIS integration, or planning applicability), v_c the weight of that criterion from the project priorities, and k* the selected method; the weights come from the same fuzzy engine, so both stages share one logic. Section 3.3 details the comparison.

3.2 Fuzzy Inference and Machine-Learning Engine

Both stages share a decision engine that turns crisp criterion values into a single score, a factor-importance score in Stage 1 or an algorithm-suitability score in Stage 2, by fuzzification, rule-based inference, and defuzzification. The framework supports Mamdani inference, used where interpretability matters most, such as explaining why a factor was excluded [10], and Takagi-Sugeno inference, used where the output feeds a numerical step, since its linear output functions integrate cleanly [11].

Each retained criterion is mapped to membership grades over linguistic terms, for example low, moderate, and steep for slope, using triangular and trapezoidal membership functions whose breakpoints are easy to set and justify. A triangular function is fixed by three points and returns a grade between zero and one:

$$\mu(x) = max(\ min(\ (x - a)/(b - a),\ (c - x)/(c - b)\ ),\ 0\ ) \tag{3}$$

where a, b, and c are the lower limit, peak, and upper limit of the term, taken from design standards where these exist and from expert judgement otherwise; the common zero-to-one scale lets factors of different units be combined without arbitrary weighting.

Rules take the form: if slope is steep and geology is weak, then earthwork importance is high, with firing strength equal to the minimum input grade for an AND rule. Table 3 shows an illustrative rule base.

Table 3. Illustrative rule base for the factor-filtering stage.

Slope	Geology	Settlement proximity	Earthwork importance	Land-use importance
Low	Strong	Far	Low	Low
Steep	Weak	Far	High	Low
Low	Strong	Near	Low	High
Steep	Weak	Near	High	High

For Mamdani inference the consequents are fuzzy sets, aggregated by union and defuzzified by the centroid of the combined area [10]. For Takagi-Sugeno inference each consequent is a function of the inputs, and the output is the firing-strength-weighted average of the rule outputs [11]:

$$y = (\ \Sigma\, w_i\, f_i(x)\ )\ /\ (\ \Sigma\, w_i\ ) \tag{4}$$

where w_i is the firing strength of rule i and f_i its output function; comparative studies report similar accuracy for both systems [12-13], so the choice is driven by the role of the output.

Decision trees trained on past projects suggest candidate rules and membership-function limits from their split points [18]; ensemble regressors such as random forests estimate the Takagi-Sugeno consequent functions f_i from observed cost and performance [18]; and an ANFIS-type neuro-fuzzy scheme can further tune membership parameters once enough corridor data exist [14-17]. The learned components only adjust an existing, human-readable rule base and are checked against design-standard limits before acceptance, so the result still explains itself as a list of if-then rules.

3.3 Comparison of Candidate Algorithms

Four candidate families cover the search strategies applied to this problem: population-based metaheuristics, swarm methods, ranking-based multi-criteria methods, and spatially driven heuristics. Exact mathematical programming and deep reinforcement learning were considered and set aside, the former for not scaling to the non-convex three-dimensional search in [15], the latter for too thin an alignment record to compare fairly.

Genetic algorithms have the longest record: established by Jha and Schonfeld for the coupled GIS cost model [1], extended to multi-objective search by Maji and Jha [2], refined with preference information and prescreening [3-16], and shown to scale to combined horizontal and vertical alignment [15].

Particle swarm optimisation, customised for alignment search [4] and extended with environmental constraints [5], often converges faster than genetic algorithms on smooth problems; ant colony optimisation appears mainly for vertical alignment [6].

MCDA is retained for problems dominated by qualitative criteria: Liu et al. [9] combined comprehensive weighting with TOPSIS to rank corridors transparently, complementing rather than substituting for the metaheuristics.

GIS-heuristic hybrids confine the search using a least-cost path [7] or a stepwise strategy [8] before a genetic algorithm runs, cutting computation but tying solution quality to the spatial layer.

Table 4 scores the four families on the selection criteria and interpretability. The scores are schematic, illustrating relative strengths drawn from the literature rather than a numerical benchmark from a solved case.

Table 4. Score matrix for the candidate methods (schematic scores, 1 = low, 5 = high, reflecting the reviewed literature).

Method	Computational efficiency	Multi-objective adaptability	GIS integration	Planning applicability	Interpretability
Genetic algorithm	3	5	3	5	2
Particle swarm optimization	4	4	2	3	2
MCDA (AHP / TOPSIS)	5	2	2	4	5
GIS-heuristic hybrid	3	4	5	4	3

Genetic algorithms lead on multi-objective adaptability and planning applicability but are hardest to interpret, since the search is stochastic. Particle swarm optimization is efficient and adapts well but has a shorter highway-planning record. MCDA leads on interpretability and efficiency yet only ranks a fixed set of alternatives. GIS-heuristic hybrids lead on GIS integration but their efficiency depends on the pre-screening step. No method dominates on every criterion, which is why the structured selection of Section 3.1 is needed rather than a default choice.

3.4 Implications for Practice

The common default is to reach for a genetic algorithm and a standard factor list, which is reasonable but not always best: a project dominated by qualitative concerns may be served better by MCDA, and a project with rich terrain data by a GIS-led search. This matters for defensibility as well as quality, since an explainable choice, covering both which factors and which algorithm, is easier to defend in review than one taken by habit; fixing the factor set first also moves analyst time to the cheaper task of agreeing which factors matter, and lets a scoping memo record the retained and dropped factors alongside the algorithm choice and its score.

4 Application Workflow

This section sets out, as a numbered procedure, how a practitioner would apply the framework, connecting the taxonomy, decision engine, and algorithm comparison of Section 3 into a single sequence usable with standard GIS and optimisation tools.

Step 1: Assemble data, priorities, and the criteria taxonomy. Gather corridor endpoints, terrain, geology, land-use, environmental, and traffic data and the investor brief; record project priorities as a short weighting of cost, environment, and service; and populate the seven domains of Table 1 with the indicators available, noting any that are missing.

Step 2: Run factor filtering. Feed the indicators to the fuzzy engine of Section 3.2, retain factors above the threshold, drop those below it, flag borderline factors for expert review, and never drop a factor tied to a hard regulatory limit.

Step 3: Score and select the algorithm. Score the four candidate families against the reduced factor set and the priorities, using the criteria of Section 3.3: a strongly multi-objective problem points to a genetic algorithm, a tight-runtime smooth problem to particle swarm, a qualitative fixed-corridor problem to MCDA, and a data-rich corridor to a GIS-heuristic hybrid.

Step 4: Configure, run, and review the optimisation. Encode only the retained factors as objectives or constraints, run the search, and present the alignment with the rule firings and algorithm score that produced it; if reviewers contest a dropped factor, reinstate it and re-run from Step 2.

Step 5: Record outcomes for learning. Log which factors proved decisive and how the algorithm performed; these records become training data that tune the membership functions and rule bases for the next project.

The workflow is tool-agnostic: each step maps to capabilities already present in commercial GIS and optimisation packages, and its value lies in the order and record it imposes.

5 Planned Case Study and Validation

The framework is now fully specified; what remains is empirical validation. A case study is planned on a real corridor with varied terrain, so that both stages are exercised, in three parts: filtering will be applied and the reduced factor set checked against experienced engineers' judgment; the algorithm-selection stage will be run so that the schematic scores of Table 4 are replaced by measured run time, solution quality, and trade-off spread; and the resulting alignment will be compared with a manually designed alternative to test whether the framework is competitive and whether the effort saved by filtering is real.

5.1 Implementation Challenges and Limitations

The framework assumes a record of past projects to tune the learned components; where history is thin, the machine-learning step degrades to expert-set rules.

A retention threshold set too high discards useful factors, and set too low defeats the purpose of filtering; the safeguards in Section 3.1 reduce but do not remove this sensitivity.

It is easy to check that a retained factor mattered, but harder to prove a dropped factor would not have changed the alignment, since the counterfactual is not run by default.

The four families do not exhaust the method space, and exact and reinforcement-learning methods may suit some problems as their alignment record matures; the framework also asks teams to document decisions they often make by habit, a process change the tool-agnostic design is meant to ease.

6 Conclusions

This paper proposes a two-stage framework for highway alignment optimization. The first stage filters factors to those that matter in a given context; the second selects an optimization algorithm through a structured comparison. A fuzzy inference engine, supported by machine learning, drives the decision logic in both stages.

The framework makes four contributions: it links two steps usually treated separately, which factors to consider and which algorithm to use; it grounds the first in a taxonomy of criteria with named indicators; it specifies the decision engine from membership functions to learned rule tuning; and it sets out a tool-agnostic workflow from raw criteria to a defensible alignment. Filtering first cuts computational load and focuses the model, while comparing algorithms against the filtered set replaces a default choice with a reasoned one.

The paper is conceptual and does not yet report a solved alignment. The planned case study will validate the framework on a real corridor, populate the algorithm comparison with measured outcomes, and test the fuzzy rule bases against expert judgment; the challenges in Section 5.1 define the questions that study must answer.

Acknowledgments

The authors thank their departments for institutional support. No external funding was received. The authors declare no conflict of interest.

References

1. Jha, M.K., Schonfeld, P.: A highway alignment optimization model using geographic information systems. Transportation Research Part A: Policy and Practice 38(6), 455–481 (2004). https://doi.org/10.1016/j.tra.2004.04.001
2. Maji, A., Jha, M.K.: Multi-objective highway alignment optimization using a genetic algorithm. Journal of Advanced Transportation 43(4), 481–504 (2009). https://doi.org/10.1002/atr.5670430405
3. Yang, N., Kang, M.-W., Schonfeld, P., Jha, M.K.: Multi-objective highway alignment optimization incorporating preference information. Transportation Research Part C: Emerging Technologies 40, 36–48 (2014). https://doi.org/10.1016/j.trc.2013.12.010
4. Shafahi, Y., Bagherian, M.: A customized particle swarm method to solve highway alignment optimization problem. Computer-Aided Civil and Infrastructure Engineering 28(1), 52–67 (2013). https://doi.org/10.1111/j.1467-8667.2012.00769.x
5. Bosurgi, G., Pellegrino, O., Sollazzo, G.: A PSO highway alignment optimization algorithm considering environmental constraints. Advances in Transportation Studies 31, 63–80 (2013). https://doi.org/10.4399/97888548663245
6. Sushma, M.B., Roy, S., Maji, A.: Exploring and exploiting ant colony optimization algorithm for vertical highway alignment development. Computer-Aided Civil and Infrastructure Engineering 37(12), 1582–1601 (2022). https://doi.org/10.1111/mice.12814
7. Al-Hadad, B.M.A., Nadir, W.H., Jukil, G.A.M.: Intelligent optimization of highway alignments: A novel approach integrating geographic information system and genetic algorithms. Engineering Applications of Artificial Intelligence 133, 108037 (2024). https://doi.org/10.1016/j.engappai.2024.108037
8. Kim, E., Jha, M.K., Son, B.: Improving the computational efficiency of highway alignment optimization models through a stepwise genetic algorithms approach. Transportation

Research Part B: Methodological 39(4), 339–360 (2005). https://doi.org/10.1016/j.trb.2004.06.001
9. Liu, C., Wang, Q., Cao, Z.: An intelligent optimization method for highway route selection based on comprehensive weight and TOPSIS. PLOS ONE 17(2), e0262588 (2022). https://doi.org/10.1371/journal.pone.0262588
10. Mamdani, E.H., Assilian, S.: An experiment in linguistic synthesis with a fuzzy logic controller. International Journal of Man-Machine Studies 7(1), 1–13 (1975). https://doi.org/10.1016/B978-1-4832-1450-4.50032-8
11. Takagi, T., Sugeno, M.: Fuzzy identification of systems and its applications to modeling and control. IEEE Transactions on Systems, Man, and Cybernetics 15(1), 116–132 (1985). https://doi.org/10.1109/TSMC.1985.6313399
12. Hamam, A., Georganas, N.D.: A comparison of Mamdani and Sugeno fuzzy inference systems for evaluating the quality of experience of Hapto-Audio-Visual applications. In: IEEE International Workshop on Haptic Audio Visual Environments and Games, pp. 87–92. IEEE, Ottawa, Canada (2008). https://doi.org/10.1109/HAVE.2008.4685304
13. Yarar, A., Onucyildiz, M., Copty, N.K.: Modelling level change in lakes using neuro-fuzzy and artificial neural networks. Journal of Hydrology 365(3–4), 329–334 (2009). https://doi.org/10.1016/j.jhydrol.2008.12.006
14. Jang, J.-S.R., Sun, C.-T., Mizutani, E.: Neuro-Fuzzy and Soft Computing: A Computational Approach to Learning and Machine Intelligence. Prentice-Hall, Upper Saddle River (1997).
15. Jong, J.C., Schonfeld, P.: An evolutionary model for simultaneously optimizing three-dimensional highway alignments. Transportation Research Part B: Methodological 37(2), 107–128 (2003). https://doi.org/10.1016/S0191-2615(01)00047-9
16. Kang, M.-W., Schonfeld, P., Yang, N.: Prescreening and repairing in a genetic algorithm for highway alignment optimization. Computer-Aided Civil and Infrastructure Engineering 24(2), 109–119 (2009). https://doi.org/10.1111/j.1467-8667.2008.00574.x
17. Jang, J.-S.R.: ANFIS: adaptive-network-based fuzzy inference system. IEEE Transactions on Systems, Man, and Cybernetics 23(3), 665–685 (1993). https://doi.org/10.1109/21.256541
18. Breiman, L.: Random forests. Machine Learning 45(1), 5–32 (2001). https://doi.org/10.1023/A:1010933404324

Author Contribution Statement

- *Conceptualization:* Mehmet Ali Silgu, Abdullah Hilmi Lav
- *Methodology:* Özger İnal
- *Investigation:* Özger İnal
- *Writing – Original Draft:* Özger İnal, Mehmet Ali Silgu
- *Writing – Review & Editing:* Özger İnal, Abdullah Hilmi Lav

Publication Note

This paper was peer-reviewed, accepted for presentation, and included in the proceedings of the ACE2026 – International Conference on Advances in Civil Engineering, held on 12–14 October 2026 in Trabzon, Türkiye.

This paper may be cited as follows:

İnal, Ö., Silgu, M.A., Lav, A.H., "A Framework for Factor Filtering and Algorithm Selection in Highway Alignment Optimization," in Proceedings of the ACE2026 International Conference on Advances in Civil Engineering, Trabzon, Türkiye, 12- 14 October 2026.

Investigating Urban Mobility Patterns Using Dolmuş Operational Data: The Case of Diyarbakır, Türkiye

Beyhan Ipekyuz*
0000-0001-8088-1896, Dicle University, Department of Civil Engineering, Transportation Division, Diyarbakır, Türkiye, beyhan.ipekyuz@dicle.edu.tr
Corresponding author

Abstract. Urban mobility in rapidly growing cities is shaped not only by conventional public transport but also by flexible services operating through cooperative and semi-formal arrangements. In Türkiye, the dolmuş remains an integral component of this mixed mobility landscape, yet the collective spatial and temporal structure produced by multiple cooperatives has received limited attention. This study examines the supply-side mobility patterns associated with four hub-based dolmuş cooperatives in Diyarbakır. The analysis integrates 50 declared route assignments, verified one-way lengths for 47 regularly documented routes, evidence of period-specific non-dispatch, and 3,433 field-observed vehicle movements aggregated into hourly intervals. Pairwise Jaccard similarity is used to identify the extent to which cooperative route footprints converge on common urban corridors, while hub-normalized hourly profiles reveal differences in the temporal distribution of observed activity. The results indicate a network structure characterized by strong convergence along the Şanlıurfa and Elazığ boulevard approaches and around the Dağkapı central area, followed by hub-specific branching towards peripheral districts. At a 250 m spatial resolution, 69.7% of the declared network footprint is occupied by at least two cooperatives, with the strongest pairwise similarity occurring between Dağkapı and Balıkçılarbaşı ($J = 0.782$). Route lengths are broadly comparable across the four hubs, whereas morning peaks, late-evening activity, and the regular activation of declared routes vary. These findings demonstrate how cooperative organization, shared-corridor use, and temporal differentiation jointly shape the operational geography of dolmuş mobility in Diyarbakır.

Keywords: Dolmuş; urban mobility patterns; cooperative transport; paratransit; route-network overlap; Diyarbakır.

1 Introduction

Urban mobility in rapidly growing cities is rarely produced by a single institutional system. Conventional public transport, walking, private travel, and flexible shared services interact across the same streets and activity centres. Small-vehicle collective transport is particularly important within this mixed landscape because it can extend access beyond high-capacity corridors and respond to spatially uneven demand [1]. Its urban role is therefore expressed not only by individual routes but also by the collective pattern of corridors served and the times at which service is supplied.

The dolmuş is the most established Turkish form of this service. Although vehicles are privately owned, route rights are locally regulated and daily operation is commonly organized through cooperatives [2–6]. This arrangement combines institutional continuity with operating discretion. Declared routes indicate where service is authorized, whereas rotation practices, vehicle assignment, and dispatch decisions influence when that mobility opportunity is produced. A city-scale assessment must consequently consider the spatial and temporal behaviour of the cooperative network rather than treating each route as an independent line.

Diyarbakır provides a revealing case because four hub-based cooperatives connect the historic and contemporary centre with western, northern, and southern districts while repeatedly converging on the same arterial approaches. Their records offer a supply-side view of urban mobility: mapped alignments show how service opportunities are distributed across the road network, and hourly movement records show when observed activity intensifies or persists. Urban mobility patterns are therefore interpreted here as the spatial organization and daily production of collective transport supply, not as individual passenger trajectories.

Against this background, the study addresses three related questions. First, to what extent do the four cooperative route networks converge on common urban corridors? Second, how do the hubs differ in route reach, spatial footprint, and the timing of observed vehicle movements? Third, how does period-specific non-dispatch affect the relationship between the formally declared network and the service that is regularly evidenced in practice? To answer these questions, the study distinguishes four complementary dimensions of the dolmuş system: declared route coverage, verified route extent, period-specific route activation, and the hourly distribution of observed vehicle movements. This distinction makes it possible to identify how an institutionally segmented cooperative system produces a mobility pattern characterized by a shared arterial core, hub-specific peripheral branches, and differentiated operating rhythms.

2 Literature Review and Research Position

Research on dolmuş services in Türkiye has developed along three complementary lines. The first examines passenger preferences and the service attributes through which dolmuş competes or interacts with municipal public transport [2,3]. The second interprets the persistence of the mode through its institutional flexibility, privately organized service production, and capacity to adapt to urban growth and changing regulatory conditions [4–6]. The third addresses integration and digitalization, emphasizing that route coordination, fare technology, operating costs, and organizational feasibility must be considered together rather than as isolated technical issues [7]. Collectively, this literature presents the dolmuş not as a residual transport mode outside the formal urban system, but as a regulated and institutionally embedded component of urban mobility whose operation reflects interactions among passenger demand, cooperative organization, and municipal governance.

Digitalization introduces a related governance issue. Recent research on smart payment in İstanbul shows that technological adoption depends on operating costs, maintenance capacity, and organizational feasibility in addition to technical performance [7]. The same concern extends to operational monitoring: route rights, vehicles, dispatches, and operating responsibility can be linked consistently only when identifiers are standardized across operators and public authorities. For cooperative networks, data standardization is therefore part of institutional integration rather than a purely technical improvement.

International research provides complementary methods for making semi-formal transport networks visible to planning. Mobile-phone and collaborative mapping have translated locally maintained route knowledge into standardized network data [8, 9]. Geometry-based classification has revealed differentiated route roles within apparently irregular systems [10], while studies of stopping behaviour [11], operating efficiency [12], vehicle movement [13], accessibility [14], and Global Positioning System (GPS) traces [15] have connected mapped structure with realized activity. These contributions establish that intended network form and observed operation represent related but analytically distinct dimensions of mobility supply.

A key research gap concerns regulated cooperative systems in which declared route rights, mapped alignments, and operating records exist at different levels of completeness. Existing studies commonly focus on passenger choice, individual routes, network mapping, or vehicle trajectories, whereas the relationship among declared network coverage, documented route

extent, period-specific activation, and hub-level temporal activity remains insufficiently explored. Diyarbakır provides an appropriate setting for addressing this gap because institutionally distinct cooperatives operate through extensively shared metropolitan corridors. The study therefore examines spatial convergence and operational differentiation as simultaneous features of the same cooperative mobility system.

3 Study Area, Network Structure and Data

3.1 Urban Road Structure and Cooperative Mobility Hubs

Diyarbakır's collective transport network is strongly shaped by its radial urban structure. The dense street system surrounding the historic walled city is connected to expanding residential and institutional districts through Şanlıurfa Boulevard from the west and Elazığ Boulevard from the north. These metropolitan approaches converge towards Yenişehir and Dağkapı Square, which functions as a transition between the peripheral arterials and the finer-grained central street network. Consequently, routes associated with separate terminals concentrate along a limited number of central corridors before branching towards different residential, commercial, educational, and peripheral areas (*Fig. 1*).

Balıkçılarbaşı, Dağkapı, Galeria, and Şehitlik serve as the principal operating terminals and spatial anchors of the dolmuş network. Each hub is associated with a registered limited-liability transport cooperative (*Sınırlı Sorumlu in Turkish, S.S.)* that organizes its vehicles and internal operating groups. *Table 1* summarizes the institutional scale and organizational structure of the four cooperatives. Although individual rotation schedules are not examined, the operating-group structure provides relevant context for interpreting hub-level activity. *Fig. 1* and *Fig. 2* further show how these institutionally distinct route portfolios connect hub-specific peripheral branches to a shared central road structure.

Table 1. Institutional scale and declared route inventory of the four cooperative hubs.

Hub/cooperative	Operating organization	Registered vehicles	Declared routes
Balıkçılarbaşı/S.S. 2 Nolu 3. Hat	Three groups (A-C)	109	16
Dağkapı/S.S. 1 Nolu 2. Hat	Four groups (A-D)	111	16
Galeria/S.S. 3 Nolu 1. Hat	Six operating groups	103	10
Şehitlik/S.S. 6 Nolu 4. Hat GAP	Eight operating groups	54	8
System total	Four hub-based cooperatives	377	50

3.2 Route Network and Operational Records

The spatial dataset comprised route geometries and the route inventories maintained for the four cooperatives. The reconciliation of route names, terminal affiliations, and mapped alignments identified 16 declared routes for Balıkçılarbaşı, 16 for Dağkapı, 10 for Galeria, and 8 for Şehitlik. Auxiliary common-trunk geometries, duplicated line segments, and unmatched mapping elements were excluded from the route count. The hub-specific panels in *Fig. 1* display the peripheral reach and branching structure of each cooperative network against the Diyarbakır street system. *Fig. 2* provides a complementary city-wide representation by showing the number of cooperative route networks occupying each 250 m cell. Darker cells therefore indicate corridor-scale spatial convergence rather than traffic volume, passenger demand, service frequency, or vehicle activity. The mapped alignments represent declared route paths and should not be interpreted as reconstructed vehicle trajectories.

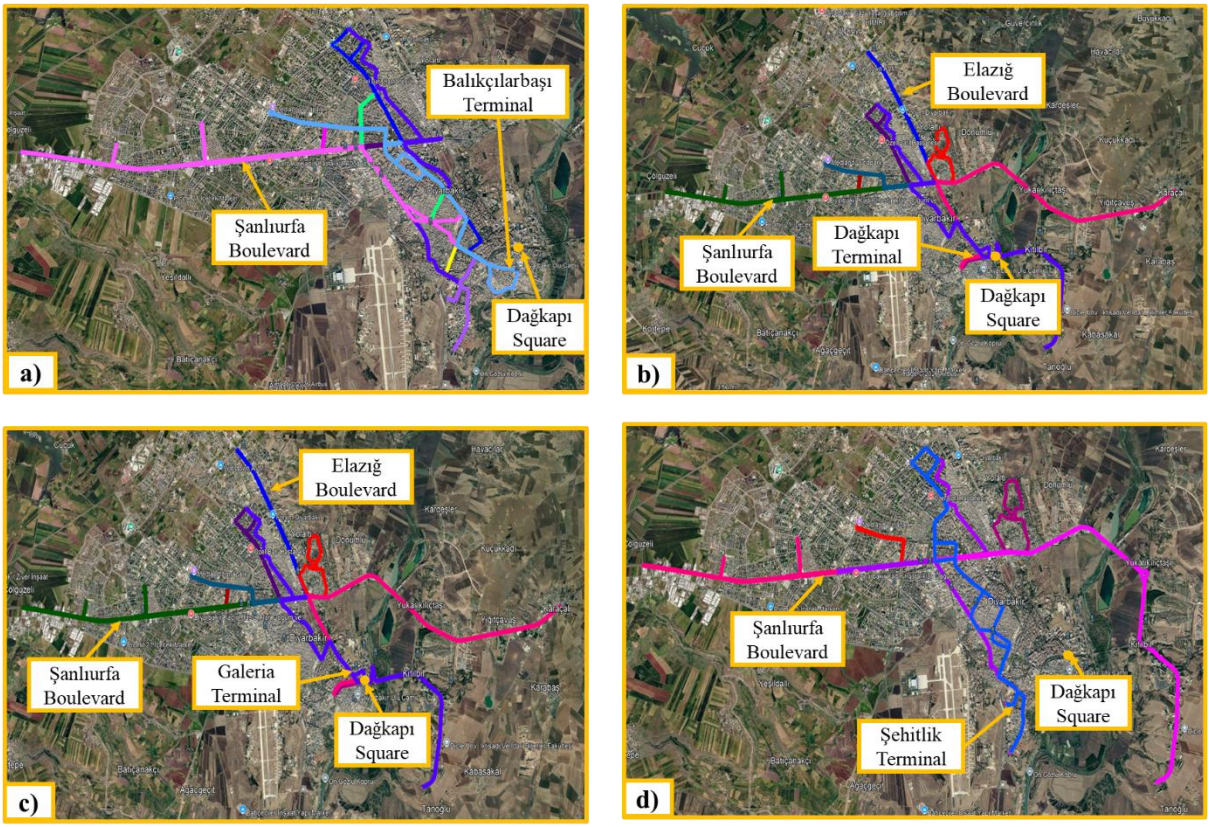


Fig. 1. Hub-specific dolmuş route networks and terminal locations: (a) Balıkçılarbaşı; (b) Dağkapı; (c) Galeria; and (d) Şehitlik; base imagery adopted from Google Earth [16].

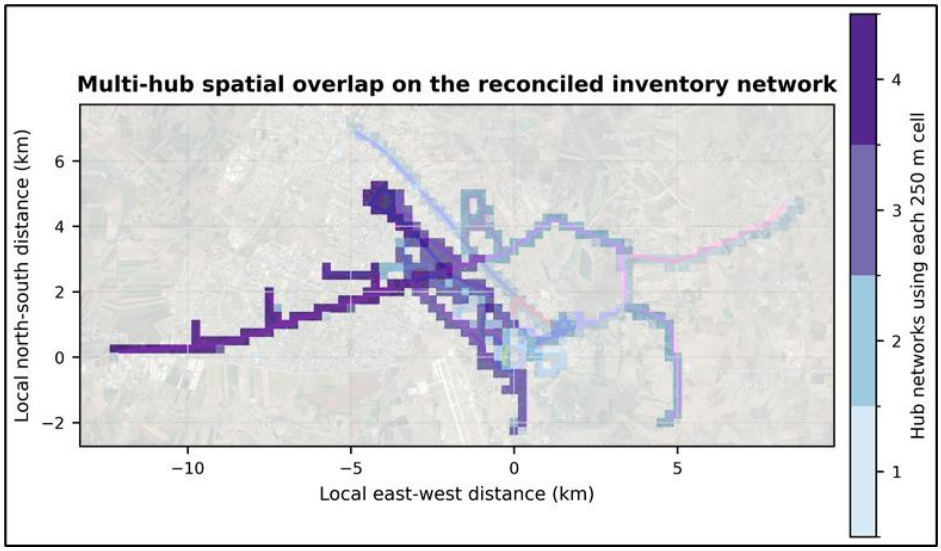


Fig. 2. Spatial convergence of the four cooperative route networks on a 250 m grid.

The declared network and the evidence of regular operation did not coincide fully. Schedule reconciliation and consultation with cooperative representatives indicated that one Balıkçılarbaşı alignment and two Dağkapı alignments received no regular vehicle assignment during some operating periods. These routes remained institutionally recognized but were selectively left without dispatch when anticipated passenger volumes and fare revenues were considered insufficient relative to operating costs. Their status is therefore interpreted as period-specific non-dispatch rather than formal route closure or permanent withdrawal from the

cooperative inventory. All 50 declared alignments were retained in the spatial topology analysis because they represent the formally recognized network footprint. Route-length statistics, however, were restricted to the 47 routes for which both regular operation and one-way length could be documented: 15 from Balıkçılarbaşı, 14 from Dağkapı, 10 from Galeria, and 8 from Şehitlik.

Temporal activity was examined using 3,433 vehicle-movement records collected over 12 survey days between April and June 2026. For the purposes of the analysis, a vehicle movement was defined as an observed departure from the corresponding cooperative hub. Field observations were conducted from 06:00 to 23:00, and the recorded movements were subsequently aggregated into 18 one-hour intervals, extending from 06:00–07:00 to 23:00–24:00. The resulting dataset comprised 927 records for Balıkçılarbaşı, 952 for Dağkapı, 592 for Galeria, and 962 for Şehitlik. Route-code coverage was incomplete and uneven, with identifiable codes available for 13 routes in Balıkçılarbaşı, 13 in Dağkapı, 9 in Galeria, and 7 in Şehitlik. Temporal comparisons were therefore conducted at the hub level rather than at the individual-route level. The absence of a route code from the movement dataset was not interpreted as evidence of route inactivity, because the movement records did not provide complete coverage of every declared route. Accordingly, the observations characterize the temporal distribution of recorded vehicle activity; they do not represent passenger demand, scheduled service frequency, or the number of vehicles simultaneously in operation. Because observation exposure was not identical across all hubs and time intervals, the normalized profiles are interpreted as distributions of observed activity rather than as direct estimates of comparative service frequency.

4 Analytical Framework

4.1 Network Structure and Spatial Convergence

Route geometry represents the spatial opportunity structure associated with the four cooperatives. The declared 50-route inventory was used to characterize the potential spatial footprint of the cooperative system, whereas verified one-way lengths for 47 routes were used to compare the documented scale of route reach. Route length was not treated as a direct measure of service intensity; it was used to determine whether the cooperative hubs differed systematically in the spatial extent of their regularly documented routes.

Spatial convergence among cooperative route networks was quantified with a regular-grid overlay referenced to a common local origin. Geographic coordinates were converted to local east–west and north–south distances relative to 40.22° E and 37.91° N, and the sampled points were assigned to the nearest grid cell. Route polylines were sampled at approximately 50 m intervals, and the resulting points were assigned to 250 m cells. For any pair of cooperative hubs h and k, the similarity between their spatial footprints was calculated using the pairwise Jaccard (J) similarity index as:

$$J(h,k) = |C_h \cap C_k| / |C_h \cup C_k| \quad (1)$$

where h and k represent the two cooperative hubs included in a pairwise comparison; C_h and C_k denote the sets of 250 m grid cells occupied by their respective route networks; $C_h \cap C_k$ is the set of cells shared by both networks; $C_h \cup C_k$ is the complete set of cells occupied by either network; and the vertical bars denote the number of cells in the corresponding set (Eq. (1)).

Jaccard similarity ranges from 0, indicating no shared cells, to 1, indicating identical spatial footprints. Higher values represent stronger corridor-scale convergence, not similarity in service frequency, passenger volume, or route multiplicity. Values in *Fig. 3(b)* are reported as percentages. The 250 m grid limits sensitivity to minor geometric offsets and parallel

carriageways. Network-wide convergence was evaluated from the footprint shared by two or more cooperatives, and the analysis was repeated at 500 m to test the stability of the results.

4.2 Daily Operating Rhythms and Selective Route Activation

To compare the temporal distribution of activity among hubs with different numbers of observations, the count recorded in each hourly interval was divided by the total number of usable movement records for the corresponding hub. The resulting percentages describe how each hub's observed activity was distributed across the operating day; they do not provide direct estimates of absolute service frequency. Morning differentiation was examined from the hourly peak between 06:00 and 10:00, while daytime activity was summarized for 10:00–16:00 and late activity for the period from 20:00 onward.

Selective route activation was interpreted from the relationship between declared route status and period-specific evidence of dispatch. Routes retained in the institutional inventory but not regularly assigned a vehicle during a given period were treated as potential rather than continuously realized coverage. Because continuous digital dispatch and automatic vehicle location records were unavailable, this component remains descriptive and does not support a definitive route-by-route estimate of service reliability.

5 Results

5.1 Spatial Structure of the Dolmuş Mobility Network

Verified one-way route lengths exhibit only modest differences among the four cooperative hubs. Mean route length is 12.22 km for Balıkçılarbaşı, 13.38 km for Dağkapı, 13.72 km for Galeria, and 12.51 km for Şehitlik. The 1.50 km difference between the lowest and highest hub means is smaller than the variation observed within the individual hub distributions shown in *Fig. 3(a)*. The verified-length subset comprises 15 Balıkçılarbaşı, 14 Dağkapı, 10 Galeria, and 8 Şehitlik routes, giving a total of 47 regularly documented routes. These results suggest that the four cooperative networks operate at a broadly comparable scale of route reach. Their mobility roles appear to be differentiated more clearly by their spatial footprints, peripheral branching patterns, and temporal distributions than by systematically longer or shorter routes. Pairwise spatial similarities calculated from the complete 50-route declared inventory are presented in *Fig. 3(b)*.

In contrast to the modest differences in route length, corridor-scale spatial convergence is pronounced. The declared network occupies 432 unique 250 m cells, of which 301 (69.7%) are used by at least two cooperatives, 194 (44.9%) by at least three, and 96 (22.2%) by all four (*Fig. 2*). The strongest pairwise similarity occurs between Dağkapı and Balıkçılarbaşı ($J = 0.782$), followed by Balıkçılarbaşı and Şehitlik ($J = 0.530$; *Fig. 3(b)*). The Dağkapı–Balıkçılarbaşı value means that 78.2% of their combined grid footprint is common to both networks; it is not a common share of trips, vehicles, or passengers. Shared cells cluster along the Şanlıurfa Boulevard approaches, around the Dağkapı central hinge, and on the Elazığ Boulevard spine before routes divide towards peripheral districts. The system therefore exhibits a convergent arterial structure with cooperative-specific branches rather than four independent service territories. The concentration of shared cells around the Şanlıurfa and Elazığ boulevard approaches and the Dağkapı central area indicates that institutional separation among cooperatives does not produce spatially independent networks. Instead, the system combines a common metropolitan movement structure with hub-specific branches serving different peripheral areas.

The dominant relationship remains stable at the 500 m resolution. Dağkapı and Balıkçılarbaşı continue to form the strongest pair ($J = 0.848$), and 73.1% of the coarser spatial footprint is occupied by at least two hubs. As expected, aggregation increases measured overlap; several closely valued secondary pairs change rank. The persistence of the strongest pair and the multi-hub central core, rather than complete rank invariance, supports the robustness of the central-convergence interpretation.

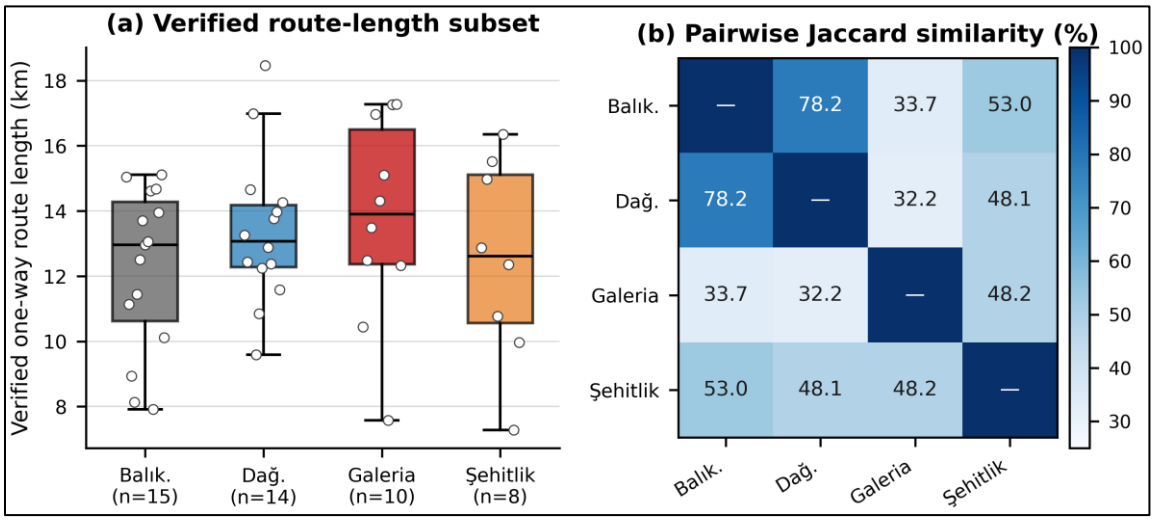


Fig. 3. Route-length distributions and pairwise spatial similarity by cooperative hub.

5.2 Temporal Rhythms and Selective Route Activation

Although the route networks converge spatially, the observed hourly profiles exhibit different morning peak times. Galeria records its largest hourly share between 07:00 and 08:00, Şehitlik between 08:00 and 09:00, and Balıkçılarbaşı and Dağkapı between 09:00 and 10:00 (*Fig. 4*). The period from 10:00 to 16:00 accounts for 35.5–39.4% of the usable observations at each hub, indicating a comparatively sustained distribution of activity during the middle of the operating day. The sequence of morning peaks suggests that the four hubs do not contribute to the city's daily operating pattern in an identical temporal manner, despite their extensive use of common corridors.

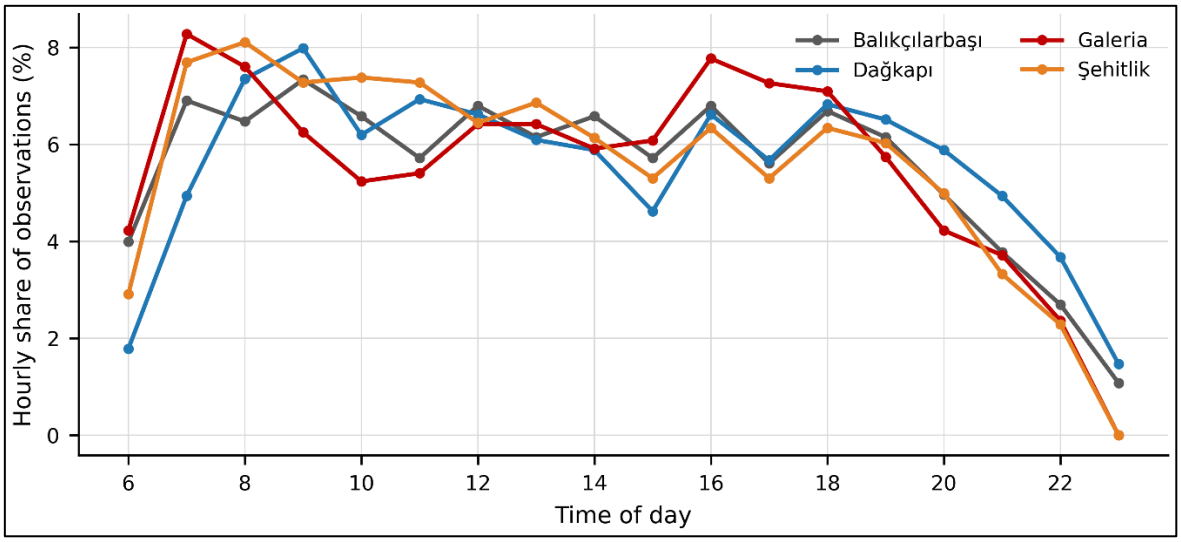


Fig. 4. Hourly distribution of observed vehicle movements by cooperative hub.

Activity from 20:00 onward also varies among the hubs. This period accounts for 16.0% of Dağkapı observations, compared with 12.5% for Balıkçılarbaşı, 10.6% for Şehitlik, and 10.3% for Galeria. These proportions describe the temporal distribution of observed movements within each hub and should not be read as absolute service frequencies. Together with the period-specific non-dispatch of selected alignments, these results show that shared spatial coverage coexists with differentiated operating rhythms and selectively realized route supply.

6 Discussion

The findings reveal a supply-side urban mobility pattern characterized by arterial convergence, hub-specific branching, and temporal differentiation. Diyarbakır's road hierarchy channels institutionally separate cooperative networks through the Şanlıurfa and Elazığ boulevard approaches and the Dağkapı central area before they disperse towards different peripheral districts. The broadly comparable route-length distributions suggest that the hubs are differentiated less by route distance than by their spatial footprints, peripheral branching patterns, and the timing of observed vehicle activity.

Strong convergence along shared corridors highlights the need for coordinated stopping locations, terminal access, dispatch practices, and digital identification of vehicles and route rights. The analysis identifies where such coordination may be required rather than directly measuring congestion, passenger-search behaviour, or roadside stopping. Temporal differences further qualify the shared spatial structure: Galeria exhibits the earliest observed morning peak, whereas Dağkapı records the largest proportion of activity from 20:00 onward. Period-specific non-dispatch also demonstrates that a formally recognized route does not necessarily produce regular service throughout every operating period. Declared network coverage and documented service activation should therefore be monitored as related but distinct characteristics of the dolmuş system.

Unlike paratransit systems whose route structures must first be reconstructed from local knowledge or vehicle traces [8–10], Diyarbakır has institutionally defined route rights and cooperative affiliations, alongside flexible dispatch practices responsive to operating conditions. The study contributes to mobility-pattern research by distinguishing declared network topology, verified route extent, period-specific activation, and observed hourly activity within a common analytical framework. This distinction connects institutional research on Turkish dolmuş operation [3–7] with international studies of paratransit mapping and vehicle activity [8–13, 15], while showing how institutional separation can coexist with spatial convergence and differentiated operating rhythms.

6.1 Limitations and Monitoring Implications

The study relies on supply-side operational evidence and therefore does not support direct inferences about passenger demand, vehicle occupancy, service reliability, commercial speed, or congestion effects. Mapped alignments represent declared routes rather than continuously observed vehicle trajectories. Uneven route-code coverage restricts the temporal analysis to the hub level, while differences in observation exposure require the hourly profiles to be interpreted as within-hub distributions rather than comparative service frequencies. Period-specific non-dispatch was identified through schedule reconciliation and operator consultation rather than independent demand or cost analysis. Grid-cell co-occupation indicates corridor-scale spatial proximity but does not imply identical carriageways, directions, stopping patterns, or service intensity; binary cell occupancy also disregards route multiplicity. Future research should integrate standardized route and vehicle identifiers with digital dispatch records, automatic vehicle location (AVL) data, and passenger observations to examine realized service and accessibility more comprehensively [8, 9, 13, 15].

7 Conclusions

The operational geography of Diyarbakır's dolmuş system is characterized by the coexistence of spatial convergence and institutional differentiation. Although the four cooperatives are organized around separate hubs, 69.7% of the declared network footprint is shared by at least two cooperative networks at the 250 m resolution, and the strongest pairwise relationship occurs between Dağkapı and Balıkçılarbaşı ($J = 0.782$). Comparable route-length distributions indicate that the hubs are not principally distinguished by the distance of their routes. Their roles appear more clearly differentiated through peripheral branching, morning peak timing, late-day activity, and the selective activation of declared alignments.

These findings underline the importance of distinguishing the formally declared network from the service regularly evidenced in operation. The 50-route inventory describes the institutional and spatial potential of the cooperative system, whereas the 47-route verified-length subset and the field-observed movement records represent narrower forms of operating evidence. For urban transport planning, the results support corridor-based coordination, consistent route and vehicle identifiers, and routine monitoring of route activation and operating time. Such measures would provide a stronger basis for integrating regulated cooperative transport into Diyarbakır's wider public-transport planning framework without disregarding the organizational flexibility through which the dolmuş system currently operates.

Acknowledgments

This research was conducted within the "Diyarbakır Urban Public Transportation Network Optimization Project", initiated in November 2025 through cooperation between Dicle University (DU) and Diyarbakır Metropolitan Municipality (DMM). The author acknowledges DMM, the DU Rectorate, the participating dolmuş cooperatives and operators, and the field-survey team.

Data Availability and Conflict of Interest: The analysis uses aggregate operational records and route geometries without personal identifiers. The author declares no conflict of interest.

References

1. Cervero, R., Golub, A.: Informal transport: A global perspective. Transport Policy 14(6), 445–457 (2007). https://doi.org/10.1016/j.tranpol.2007.04.011
2. Ozbilen, B.: Integration of Dolmuş as a Paratransit Mode to the Existing Public Transport Network: Ankara Example. M.S. thesis, Middle East Technical University, Ankara (2016). https://hdl.handle.net/11511/25762
3. Kalpakci, A., Karatas-Unverdi, N.: Integration of paratransit systems with inner-city bus transport: The case of Izmir. Public Transport 8(3), 405–426 (2016). https://doi.org/10.1007/s12469-016-0136-9
4. Aktepe, E.: Kamu Yetersiz Kalınca: Kentsel Ulaşım Hizmetlerinin Sunumunda Küçük Girişimcilik Kesiminin Meşrulaştırılması. Idealkent 11(29), 432–453 (2020). https://doi.org/10.31198/idealkent.684276
5. Zirh, B.C.: Dolmuşun (Uzun) Öyküsü: Basımının Kırkıncı Yılında İlhan Tekeli ve Tarık Okyay'ın Benzersiz Çalışması Üzerine. Idealkent 11(29), 406–431 (2020). https://doi.org/10.31198/idealkent.689860
6. Ekmekcioglu, D., Ozkaraman-Sen, M.: A proposal for a method of the redesign of self-organising systems: The case of minibus transportation in the Istanbul public transport

system. Strategic Design Research Journal 11(3), 230–240 (2018). https://doi.org/10.4013/sdrj.2018.113.07

7. Sahin, O.: Smart payment method evaluation for a cash-based paratransit system. Sustainability 18(7), 3382 (2026). https://doi.org/10.3390/su18073382

8. Williams, S., White, A., Waiganjo, P., Orwa, D., Klopp, J.: The digital matatu project: Using cell phones to create open-source data for Nairobi's semi-formal bus system. Journal of Transport Geography 49, 39–51 (2015). https://doi.org/10.1016/j.jtrangeo.2015.10.005

9. Klopp, J.M., Cavoli, C.: Mapping minibuses in Maputo and Nairobi: Engaging paratransit in transportation planning in African cities. Transport Reviews 39(5), 657–676 (2019). https://doi.org/10.1080/01441647.2019.1598513

10. du Preez, D., Zuidgeest, M., Behrens, R.: A quantitative clustering analysis of paratransit route typology and operating attributes in Cape Town. Journal of Transport Geography 80, 102493 (2019). https://doi.org/10.1016/j.jtrangeo.2019.102493

11. Behal, D., Kumar, S., Tiwari, G.: Determination and analysis of informal public transport stops. IATSS Research 44(1), 36–54 (2020). https://doi.org/10.1016/j.iatssr.2019.05.002

12. Ndibatya, I., Booysen, M.J.: Minibus taxis in Kampala's paratransit system: Operations, economics and efficiency. Journal of Transport Geography 88, 102853 (2020). https://doi.org/10.1016/j.jtrangeo.2020.102853

13. Ndibatya, I., Booysen, M.J.: Characterizing the movement patterns of minibus taxis in Kampala's paratransit system. Journal of Transport Geography 92, 103001 (2021). https://doi.org/10.1016/j.jtrangeo.2021.103001

14. Falchetta, G., Noussan, M., Hammad, A.T.: Comparing paratransit in seven major African cities: An accessibility and network analysis. Journal of Transport Geography 94, 103131 (2021). https://doi.org/10.1016/j.jtrangeo.2021.103131

15. de Beer, L., Venter, C., Snyman, L.: Quantifying informal public transport using GPS data. Journal of Transport Geography 128, 104355 (2025). https://doi.org/10.1016/j.jtrangeo.2025.104355

16. Google LLC: Google Earth. Satellite imagery and map data for Diyarbakır, Türkiye, last accessed 2026/08/10. https://earth.google.com/

Author Contribution Statement

Conceptualization, Methodology, Investigation, Data Curation, Analysis, Visualization, Writing, Editing, and Project Administration: Beyhan Ipekyuz

Publication Note

This paper was peer-reviewed, accepted for presentation, and included in the proceedings of the ACE2026 – International Conference on Advances in Civil Engineering, held on 12–14 October 2026 in Trabzon, Türkiye.

This paper may be cited as follows:

Ipekyuz, B., "Investigating Urban Mobility Patterns Using Dolmuş Operational Data: The Case of Diyarbakır, Türkiye," in Proceedings of the ACE2026 – International Conference on Advances in Civil Engineering, Trabzon, Türkiye, 12–14 October 2026.

Designing a Porous Asphalt Skeleton for Semi-Flexible Pavement Applications

Mert Atakan*[1], Cemalettin Kaplan [2], Yaren Altay [3], Recep Orçun İnce [4], Kürşat Yıldız [5]

[1] 0000-0003-1878-2111, Gazi University, Faculty of Technology, Department of Civil Engineering, Ankara, Turkey, mertatakan@gazi.edu.tr
[2] 0009-0001-5251-800X, Gazi University, Faculty of Technology, Department of Civil Engineering, Ankara, Turkey, cemalettin.kaplan@gazi.edu.tr
[3] 0009-0001-1259-2387, Gazi University, Faculty of Technology, Department of Civil Engineering, Ankara, Turkey, yaren.altay@gazi.edu.tr
[4] 0009-0009-9807-123X, Gazi University, Faculty of Technology, Department of Civil Engineering, Ankara, Turkey, rorcun.ince@gazi.edu.tr
[5] 0000-0003-2205-9997, Gazi University, Faculty of Technology, Department of Civil Engineering, Ankara, Turkey, kursaty@gazi.edu.tr
*Corresponding Author

Abstract. Semi-flexible pavement is produced by filling an open-graded asphalt skeleton with cementitious grout. The asphalt skeleton must therefore remain permeable enough for grout penetration while retaining sufficient stability before grouting. This study evaluated porous asphalt skeleton mixtures for semi-flexible pavement using two aggregate gradations (G1 and G2), and three bitumen contents (3.5%, 4.0%, and 4.5%). Two compaction levels (25X2 and 50X2) were used. Bulk specific gravity, air void content, falling-head permeability, and Cantabro abrasion loss tests were used as screening variables. All tested group means remained above the advised minimum permeability limit of 100 m/day. However, the most open structure did not provide the best overall outcome. The preliminary G1-25X2 -3.5% mixture showed the highest mean permeability, 512.63 m/day, but also the highest mean Cantabro loss which was 40.67%. This result indicated that G1 was too open for the present objective and shifted the optimization effort to the G2 mixtures. Within the G2 series, higher compaction reduced air voids and permeability and improved Cantabro performance. At 4.0% bitumen content, increasing compaction from 25X2 to 50X2 reduced mean permeability by 106.17 m/day and reduced mean Cantabro loss by 15.25 percentage points. The G2-50X2-4.0% group satisfied both screening limits, with mean air voids of 17.82%, mean permeability of 196.73 m/day, and mean Cantabro loss of 15.51%. The results suggest that this porous asphalt skeleton can be a good candidate for semi-flexible pavement production based on a balance between grout penetrability and pre-grouting durability.

Keywords: semi-flexible pavement; porous asphalt skeleton; permeability; Cantabro abrasion loss

1 Introduction

Heavy-duty pavement areas are exposed to severe traffic loading and are vulnerable to rutting and surface distress. Semi-flexible pavement is used for such conditions because it combines an open-graded asphalt skeleton with cementitious grout [1,2]. The grouted layer is intended to retain the continuity of asphalt while gaining the stiffness associated with cement-based materials [1,2].

The porous asphalt skeleton governs the pre-grouting stage of the system. If the skeleton is too dense, grout penetration may be restricted. If it is too open, particle loss and insufficient pre-grouting integrity may occur. Previous studies indicate that connected porosity, pore size,

and permeability control grout infiltration, while open gradations can reduce durability-related performance [1,3,4]. Porous asphalt skeleton design therefore requires a balance between openness and stability.

Permeability and Cantabro abrasion loss provide practical indicators for this balance during laboratory screening. Permeability reflects the continuity of the void network needed for grout infiltration. Cantabro abrasion loss reflects the resistance of the open-graded skeleton to particle loss before grout injection. Studies on porous and open-graded asphalt commonly use Cantabro loss as a durability indicator, and acceptable limits around 20% are frequently reported for unconditioned mixtures [5,6]. Recent studies on semi-flexible pavement also emphasize the coupled influence of pore structure, grout penetration, interface behavior, and mixture durability [8-15]. In addition, previous studies commonly accepted minimum 100 m/day permeability as sufficient for cement grout to penetrate the voids in the porous asphalt [16].

The available literature identifies the governing variables, but it provides limited guidance on selecting the porous asphalt skeleton itself through a stepwise pre-grouting screen that combines gradation, bitumen content, compaction, permeability, and Cantabro loss in one decision framework [8-11,13-15]. More specifically, the literature cited above offers limited detail on how these variables can be used to narrow candidate skeleton mixtures before grout injection under a defined laboratory screening procedure.

Accordingly, this study evaluated porous asphalt skeleton mixtures for semi-flexible pavement by varying aggregate gradation, bitumen content, and compaction level. Marshall-type specimens were prepared using two gradations (G1 and G2), three bitumen contents (3.5%, 4.0%, and 4.5%), and compaction levels of 25X2 and 50X2. Bulk specific gravity, air void content, falling-head permeability, and Cantabro abrasion loss were measured for mixture screening. The screening stage used a minimum permeability limit of 100 m/day and a maximum Cantabro loss of 20%.

2 Materials and Methods

2.1 Materials

The porous asphalt mixtures were produced using 50/70 penetration grade paving bitumen and graded mineral aggregates. The measured softening point was 50.55 °C. The mean penetration was 55.44 (0.1 mm). Bitumen specific gravity was assumed as 1.03 for mixture calculations as common practice. The bitumen properties used in the study are summarized in Table 1.

Aggregate specific gravity and water absorption were determined for the filler, 2 mm, and 4 mm fractions using pycnometer method (EN 1097-6). The 8 mm, 12 mm, 16 mm, and 22 mm fractions were evaluated using Archimedes scale method (EN 1097-6). Table 2 reports the full set of aggregate properties.

Table 1. Basic measured properties of the paving bitumen used in the porous asphalt mixtures.

Property	Unit	n	Mean	Min	Max
Softening point (Ring and Ball)	°C	2	50.55	50.30	50.80
Penetration	0.1 mm	9	55.44	52.00	69.00
Specific gravity	-	0	1.03	1.03	1.03

Table 2. Aggregate specific gravity and water absorption values used in the mixture calculations.

Aggregate Size	Method	Bulk Dry Gsb	Apparent Gsa	Water Absorption (%)
Filler	EN 1097-6	2.760	2.777	0.225
2 mm	EN 1097-6	2.562	2.682	1.736
4 mm	EN 1097-6	2.614	2.657	0.631
8 mm	EN 1097-6	2.594	2.681	1.270
12 mm	EN 1097-6	2.639	2.681	0.594
16 mm	EN 1097-6	2.643	2.682	0.548

2.2 Aggregate Gradations and Mixtures

Two porous asphalt aggregate gradations, designated G1 and G2, were investigated. Both gradations were fully passing the 16 mm sieve, but G2 contained a higher proportion of material in the intermediate and fine sieve range than G1. For example, the percent passing values at 8 mm, 4 mm, and 2 mm were 58.01%, 18.59%, and 10.14% for G2, compared with 50.02%, 11.53%, and 7.15% for G1. The corresponding gradation curves are summarized in Table 3 and illustrated in Fig. 1. The first screening observations indicated that G1 produced a structure that was too open for the current design objective, so the subsequent optimization effort focused on G2.

G1 was tested only at 3.5% bitumen content and 25X2 compaction as an initial gradation-screening case. The G2 series was evaluated at 3.5%, 4.0%, and 4.5% bitumen content under 25X2 compaction, and at 3.5% and 4.0% bitumen content under 50X2 compaction.

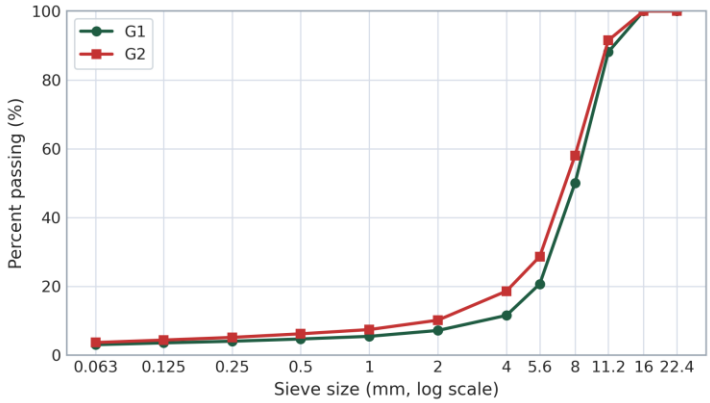


Fig. 1. Aggregate gradation curves for the two porous asphalt gradations used in the study.

Table 3. Aggregate gradation curves expressed as percent passing for gradations G1 and G2.

EN Sieve (mm)	G1 Passing (%)	G2 Passing (%)
22.4	100.00	100.00
16	100.00	100.00
11.2	88.13	91.51
8	50.02	58.01
5.6	20.67	28.65
4	11.53	18.59
2	7.15	10.14
1	5.44	7.40
0.5	4.67	6.17
0.25	4.02	5.13
0.125	3.54	4.36
0.063	3.01	3.64

Specimen Preparation and Bulk Specific Gravity

Marshall-type standard cylindrical porous asphalt specimens were prepared using 25 and 50 blows to each side of the specimens (EN 12697-30). Bulk specific gravity (Gmb) was determined using the ASTM D6752-02 vacuum-sealing method. Each specimen was enclosed in a sealed vacuum bag before weighing so that the connected void structure could be evaluated without uncontrolled water entrance. A representative vacuum-sealed specimen used for the Gmb measurement is shown in Fig. 2. Maximum specific gravity on the other hand was found using EN 12697-5 Procedure C. Then, volumetric properties were calculated according to EN 12697-8 standard.



Fig. 2. Vacuum-sealed porous asphalt specimen used for bulk specific gravity (Gmb) measurement in accordance with ASTM D6752-02.

2.3 Falling-Head Permeability Test

Permeability was evaluated using a falling-head procedure. The test setup consisted of a PVC pipe fitted to the specimen. A transparent tube was attached outside the pipe to monitor the water head, and two level-marks separated by 20 cm were used to define the falling-head interval. The specimen circumference was wrapped with duct tape to reduce leakage, and the connection between the pipe and the specimen was insulated using teflon tape. The custom setup is shown in Fig. 3. Water is filled from the upper side of the pipe quickly to a overfilling level. Then, the time was measured for the water level to fall from the upper level sign to below level sign which was 20 cm height. Permeability was included as a screening variable because prior work indicates that pore connectivity and porosity strongly influence grout penetration in porous asphalt skeletons for semi-flexible pavement [3].

$$k = \frac{(a \cdot L)}{A \cdot t} \cdot \ln \frac{h_1}{h_2} \cdot 86.4 \qquad (1)$$

Permeability was calculated using Eq.1 where k is the permeability (m/day); a is the standpipe cross-sectional area (mm²); A is the specimen cross-sectional area (mm²); L is the specimen height (mm); t is the elapsed time (s); h_1 is the initial head (mm); $h_2 = h_1 - \Delta h$ is the final head (mm); and Δh is the head drop recorded over the measurement interval (mm). The factor 86.4 converts the result from mm/s to m/day.

2.4 Cantabro Abrasion Loss Test and Screening Criteria

Cantabro abrasion loss was used as the pre-grouting durability indicator. Testing followed EN 12697-17. Cantabro loss was calculated as the percentage mass loss after drum rotation from the specimen masses measured before and after testing. Specimens were conditioned at 25 °C for 4 hours prior testing. Each time one Marshall specimen was put in the drum without any additional steel balls, and it was tested using 300 rotations. Rotation speed was 30-33 revolutions per minute, and test was lasted 10 minutes. Representative Cantabro test photographs are shown in Fig. 4.

Two thresholds were used during screening. The first was a minimum permeability of 100 m/day [16]. The second was a maximum Cantabro loss of 20%. The Cantabro limit is consistent with durability-oriented guidance reported for porous and open-graded asphalt mixtures [5,6].

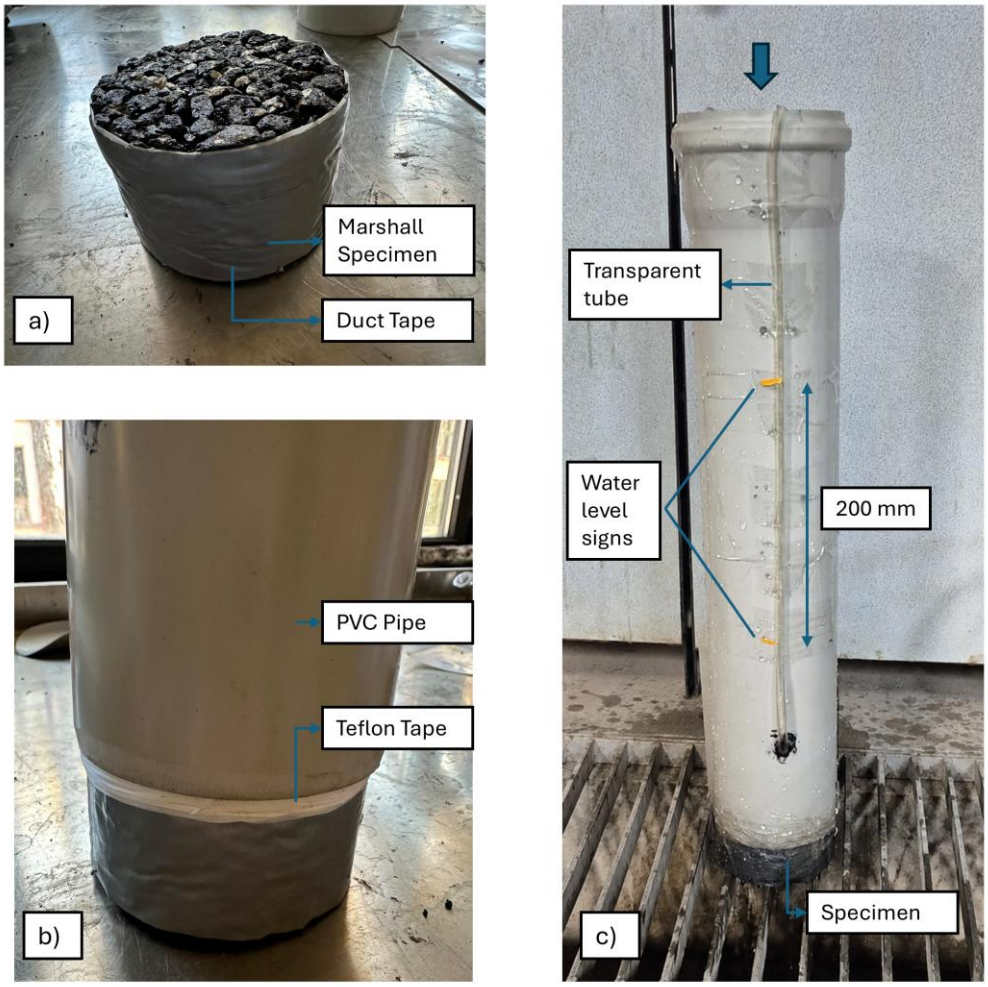


Fig. 3. Custom falling-head permeability setup showing (a) the Marshall specimen wrapped with duct tape, (b) the PVC pipe insulated with teflon tape at the specimen-pipe connection, and (c) the complete assembly with the external transparent tube and the 200 mm falling-head interval used during measurement.

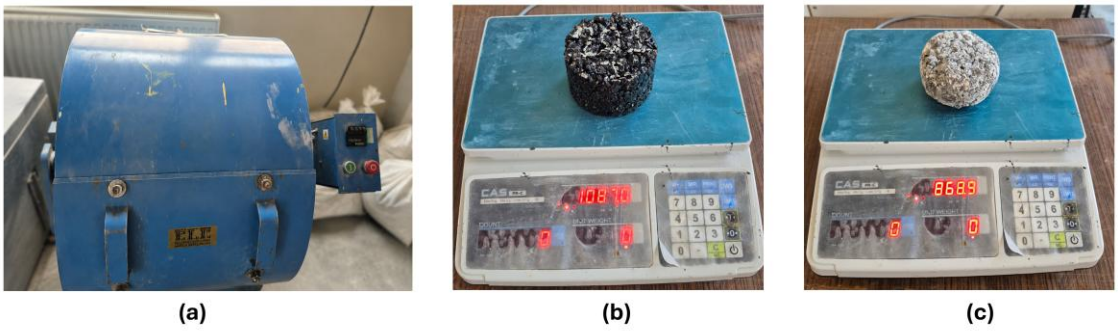


Fig. 4. Cantabro abrasion loss test showing (a) the Los Angeles drum used for abrasion, (b) a representative specimen before testing, and (c) the same specimen after testing.

3 Results and Discussion

3.1 Gradation Screening and Volumetric Behavior

Table 4 summarizes the volumetric and performance results used in the present screening stage. The gradation contrast between G1 and G2 is shown in Fig. 1, whereas the corresponding Gmb and air-void trends are plotted in Fig. 5(a-b). The first screening result from G1 confirmed that

a very open gradation could provide high permeability but remain insufficient in terms of pre-grouting durability. The G1-25X2-3.5% group showed a mean Gmb of 1.946, mean air voids of 22.86%, mean permeability of 512.63 m/day, and mean Cantabro loss of 40.67%. This combination indicated that the void structure was highly connected. It also showed that the abrasion resistance was inadequate for the current screening objective. After this first-stage observation, the optimization effort was directed toward the G2 family.

Within the G2 groups, the volumetric results showed that the higher compaction level produced a denser but still open structure. Under 25X2 compaction, mean air voids remained close to 20%, ranging from 19.85% to 20.30%. Under 50X2 compaction, mean air voids dropped to 17.44% at 3.5% bitumen and 17.82% at 4.0% bitumen. The same trend was reflected in Gmb, which increased from about 2.0 for the 25X2 groups to 2.056-2.082 for the 50X2 groups. These changes indicate that the higher compaction level tightened the internal structure while still maintaining a porous matrix.

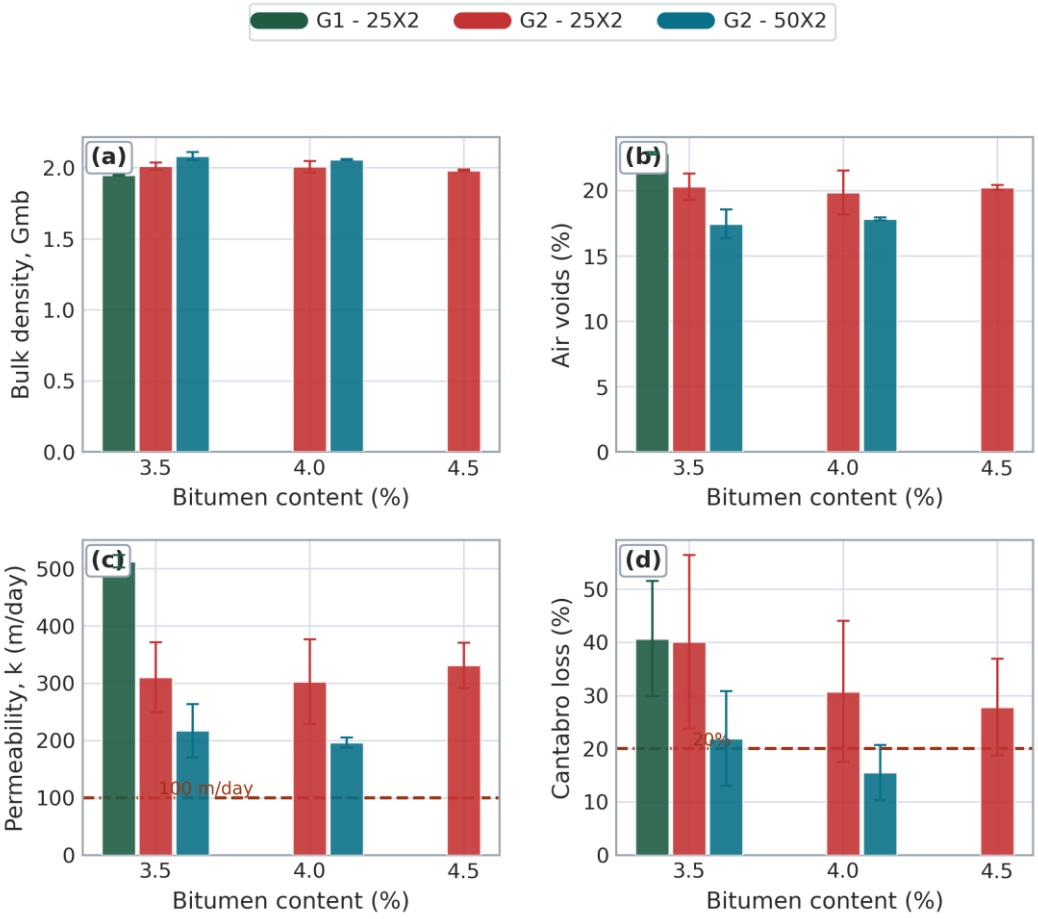


Fig. 5. Four-panel grouped bar charts showing mean values and standard-deviation error bars versus bitumen content for each gradation-compaction group. Panels (a), (b), (c), and (d) show bulk density, air void content, permeability, and Cantabro abrasion loss, respectively.

Table 4. Summary volumetric and pre-grouting performance values reported as mean +/- standard deviation.

Gradation	Compaction	Pb (%)	n	Gmb	Va (%)	Permeability k (m/day)	Cantabro Loss (%)
G1	25X2	3.5	2	1.946 +/- 0.002	22.86 +/- 0.09	512.63 +/- 10.85	40.67 +/- 10.83
G2	25X2	3.5	3	2.009 +/- 0.025	20.30 +/- 1.01	310.71 +/- 60.85	40.07 +/- 16.31
G2	25X2	4.0	3	2.006 +/- 0.042	19.85 +/- 1.67	302.90 +/- 73.99	30.76 +/- 13.27
G2	25X2	4.5	3	1.981 +/- 0.005	20.25 +/- 0.19	331.08 +/- 39.48	27.81 +/- 9.06
G2	50X2	3.5	4	2.082 +/- 0.028	17.44 +/- 1.11	217.24 +/- 46.54	21.93 +/- 8.89
G2	50X2	4.0	3	2.056 +/- 0.003	17.82 +/- 0.11	196.73 +/- 8.74	15.51 +/- 5.15

3.2 Permeability Behavior

Figure 5(c) shows that all group means in the current dataset remained above the working permeability limit of 100 m/day. Even the lowest measured group mean, 196.73 m/day for G2-50X2-4.0%, was still well above the minimum threshold adopted for this screening stage. This result indicates that all tested mixtures retained connected voids that would be expected to support grout infiltration.

However, the permeability results also showed that higher permeability was not automatically desirable. The preliminary G1 group had the highest mean permeability (512.63 m/day), but it also had poor Cantabro performance. Within the G2 mixtures, the 25X2 groups showed higher permeability than the 50X2 groups, with mean values between 302.90 and 331.08 m/day, whereas the 50X2 groups showed lower but still adequate means of 217.24 and 196.73 m/day. At 4.0% bitumen content, increasing compaction from 25X2 to 50X2 reduced mean permeability by 106.17 m/day. A similar reduction of 93.47 m/day was observed at 3.5% bitumen content. These results show that compaction was an effective tool for moderating the openness of the skeleton without eliminating the permeability needed for the next stage of grout injection. This interpretation is consistent with previous porous asphalt studies showing that higher porosity tends to improve permeability while compromising durability-related responses [4,13-15].

3.3 Cantabro Behavior

Figure 5(d) shows that Cantabro loss was the controlling response in the present mixture selection. The 25X2 groups all failed the current 20% target. For G2-25X2, the mean Cantabro loss decreased from 40.07% at 3.5% bitumen to 30.76% at 4.0% and to 27.81% at 4.5%. This trend indicates that increasing bitumen content improved cohesion and reduced aggregate loss, but the improvement was still insufficient to bring the 25X2 mixtures within the target limit.

The effect of higher compaction on Cantabro performance was more pronounced. For G2-3.5%, increasing compaction from 25X2 to 50X2 reduced mean Cantabro loss from 40.07% to 21.93%, an improvement of 18.14 percentage points. At 4.0% bitumen content, the corresponding reduction was from 30.76% to 15.51%, an improvement of 15.25 percentage points. Therefore, although higher compaction reduced permeability, it simultaneously produced a major gain in abrasion resistance.

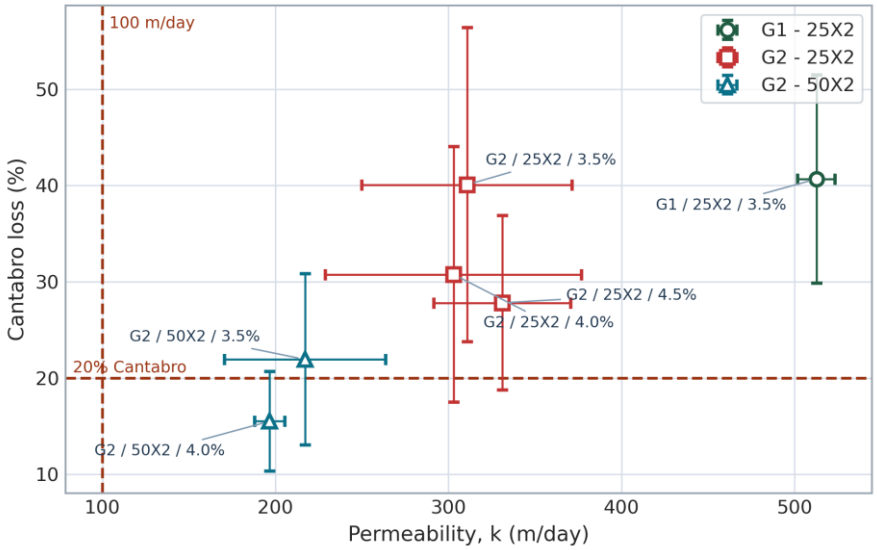


Fig. 6. Trade-off between permeability and Cantabro abrasion loss for the tested mixture groups, shown using group means and standard-deviation error bars. Each averaged point is labeled by gradation, compaction level, and bitumen content, and the current screening limits are shown as reference lines.

3.4 Trade-Off and Candidate Selection

The combined permeability-Cantabro trade-off is plotted in Fig. 6. The permeability and Cantabro results highlight the central design trade-off of the porous asphalt skeleton. A more open structure was beneficial for permeability, but it also tended to be more vulnerable to abrasion loss. Conversely, the denser 50X2 structures had lower permeability, yet their permeability remained above the screening limit and their pre-grouting stability improved substantially. The results indicate that the most permeable mixture is not necessarily the most suitable porous asphalt skeleton. The preferred mixture should preserve sufficient grout penetrability while avoiding excessive Cantabro loss. The screening outcome is summarized in Table 5.

Among the tested groups, G2-50X2-4.0% was the most suitable current candidate. This group had mean air voids of 17.82%, mean permeability of 196.73 m/day, and mean Cantabro loss of 15.51%, making it the only mixture that satisfied both working limits in the current mean-based screening pass. G2-50X2-3.5% was the next most competitive case because its permeability remained adequate at 217.24 m/day, but its mean Cantabro loss of 21.93% exceeded the target slightly. All 25X2 groups failed on Cantabro performance, even though their permeability remained favorable. Selected mixture should be assessed in subsequent mechanical and durability studies after grout injection.

Table 5. Preliminary candidate mixtures screened against the current permeability and Cantabro abrasion criteria.

Gradation	Compaction	Pb (%)	Va (%)	Permeability	Cantabro Loss	Criteria Check	Assessment
G2	50X2	4.0	17.82	196.73	15.51	Pass	Satisfies both screening limits; strongest current recommendation.
G2	50X2	3.5	17.44	217.24	21.93	Near miss	Permeability is sufficient, but Cantabro loss is slightly above the target.
G2	25X2	4.5	20.25	331.08	27.81	Fail	Permeability is sufficient, but abrasion resistance remains inadequate.
G2	25X2	4.0	19.85	302.90	30.76	Fail	Permeability is sufficient, but abrasion resistance remains inadequate.
G2	25X2	3.5	20.30	310.71	40.07	Fail	Permeability is sufficient, but abrasion resistance remains inadequate.

Engineering Implication

The present screening stage indicates that the selected porous asphalt skeleton should be evaluated further through grout injection rather than interpreted as a final field-ready mixture on its own. From that standpoint, G2-50X2-4.0% appears suitable as the primary current candidate for the next phase because it offers a balanced combination of openness and pre-grouting stability. Nevertheless, the final suitability of the semi-flexible system still depends on the behavior of the grouted composite, which

Conclusions

The following conclusions were drawn from the current laboratory screening study.

1. The porous asphalt skeleton for semi-flexible pavement should be selected by balancing permeability and pre-grouting abrasion resistance rather than by maximizing permeability alone.

2. The first screening gradation, G1, produced the highest permeability but also excessive Cantabro loss, which showed that it was too open for the present design objective.

3. All tested group means in the curated dataset remained above the current minimum permeability limit of 100 m/day, indicating that interconnected void paths were maintained throughout the tested range.

4. Cantabro abrasion loss was the controlling constraint in mixture selection. Increasing bitumen content improved Cantabro performance within the G2-25X2 groups, but none of those groups satisfied the 20% target. Increasing compaction from 25X2 to 50X2 reduced permeability but produced a substantial improvement in Cantabro resistance.

5. G2-50X2-4.0% is the most suitable current candidate for the porous asphalt skeleton because it is the only tested group that satisfies both working screening criteria, with mean permeability of 196.73 m/day and mean Cantabro loss of 15.51%.

6. The selected porous asphalt skeleton appears suitable for the next grout-injection stage, but post-grouting mechanical performance still needs to be evaluated before broader engineering conclusions are made.

References

1. Muhammad Imran Khan, M. Sutanto, N. Yusoff, S. Zoorob, Waqas Rafiq, Mujahid Ali, R. Fediuk, and N. Vatin. Cementitious Grouts for Semi-Flexible Pavement Surfaces - A Review. Materials, 2022, 15. https://doi.org/10.3390/ma15155466
2. Alessandra Bonicelli, Jaime Preciado, A. Rueda, and A. Duarte. Semi-Flexible Material: A Solution for High-Performance Pavement Infrastructures. IOP Conference Series: Materials Science and Engineering, 2019, 471. https://doi.org/10.1088/1757-899X/471/3/032062
3. Senlin Ling, Yu Sun, Daquan Sun, and D. Jelagin. Pore characteristics and permeability simulation of porous asphalt mixture in pouring semi-flexible pavement. Construction and Building Materials, 2022. https://doi.org/10.1016/j.conbuildmat.2022.127253
4. T. N. Mansour and B. Putman. Influence of Aggregate Gradation on the Performance Properties of Porous Asphalt Mixtures. Journal of Materials in Civil Engineering, 2013, 25, 281-288. https://doi.org/10.1061/(ASCE)MT.1943-5533.0000602
5. D. Watson, L. Cooley, Kathryn Ann Moore, and K. Williams. Laboratory Performance Testing of Open-Graded Friction Course Mixtures. Transportation Research Record, 2004, 1891, 40-47. https://doi.org/10.3141/1891-06
6. Tommy James, D. Watson, Adam J. Taylor, N. Tran, and Carolina Rodezno. Improving cohesiveness of porous friction course asphalt mixtures. Road Materials and Pavement Design, 2017, 18, 256-272. https://doi.org/10.1080/14680629.2017.1389073
7. I. G. A. A. Putra. Study Characteristics of Porous Asphalt Using Aggregates from Karangasem with 60/70 Penetration Bitumen. Civilla : Jurnal Teknik Sipil Universitas Islam Lamongan, 2022. https://doi.org/10.30736/cvl.v2i2
8. M. Taghipoor, A. Hassani, and Mohammad M. Karimi. Development of procedure for design and preparation of open-graded asphalt mixture used in semi-flexible pavement. Construction and Building Materials, 2021. https://doi.org/10.1016/j.conbuildmat.2021.124884
9. M. Taghipoor, Abolfazl Hassani, and Mohammad M. Karimi. Investigation of material composition, design, and performance of open-graded asphalt mixtures for semi-flexible pavement: A comprehensive experimental study. Journal of Traffic and Transportation Engineering (English Edition), 2024. https://doi.org/10.1016/j.jtte.2023.06.003
10. Zhongbo Chen, Junqiang Qiao, Xiaoyu Yang, Yu Sun, and Daquan Sun. A review of grouting materials for pouring semi-flexible pavement: Materials, design and performance. Construction and Building Materials, 2023. https://doi.org/10.1016/j.conbuildmat.2023.131235
11. A. Huynh, B. Magee, and D. Woodward. A Preliminary Characterisation of Innovative Semi-Flexible Composite Pavement Comprising Geopolymer Grout and Reclaimed Asphalt Planings. Materials, 2020, 13. https://doi.org/10.3390/ma13163644
12. Xiaoyu Liu, Kuanghuai Wu, Xu Cai, Wenke Huang, and Jiandong Huang. Influence of the composite interface on the mechanical properties of semi-flexible pavement materials.

Construction and Building Materials, 2023. https://doi.org/10.1016/j.conbuildmat.2023.132466
13. Haripriya Nekkanti, B. Putman, and B. Danish. Influence of Aggregate Gradation and Nominal Maximum Aggregate Size on the Performance Properties of OGFC Mixtures. Transportation Research Record, 2019, 2673, 240-245. https://doi.org/10.1177/0361198118821628
14. Jeremy P. Wu, P. Herrington, and D. Alabaster. Long-term durability of epoxy-modified open-graded porous asphalt wearing course. International Journal of Pavement Engineering, 2019, 20, 920-927. https://doi.org/10.1080/10298436.2017.1366764
15. Trung Tran, Chen Chen, Nam Tran, Adam Taylor, Fan Yin, D. Watson, J. Musselman, G. Sholar, and Howie Moseley. Improving the Durability of 12.5 mm Open-Graded Friction Course using 9.5 mm Nominal Maximum Aggregate Size Gradation and High Polymer-modified Binder. Transportation Research Record, 2024, 2679, 173-186. https://doi.org/10.1177/03611981241260693
16. Saboo, N., Ranjeesh, R., Gupta, A., & Suresh, M. (2019). Development of hierarchical ranking strategy for the asphalt skeleton in semi-flexible pavement. Construction and Building Materials, 201, 149-158. https://doi.org/10.1016/j.conbuildmat.2018.12.131

Author Contribution Statement

- *Conceptualization:* Mert Atakan
- *Methodology:* Mert Atakan
- *Investigation:* Mert Atakan, Cemalettin Kaplan, Yaren Altay, Recep Orçun İnce
- *Writing – Original Draft:* Mert Atakan
- *Writing – Review & Editing:* Mert Atakan, Kürşat Yıldız

Publication Note

This paper was peer-reviewed, accepted for presentation, and included in the proceedings of the ACE2026 – International Conference on Advances in Civil Engineering, held on 12–14 October 2026 in Trabzon, Türkiye.

This paper may be cited as follows:

M. Atakan, C. Kaplan, Y. Altay, O. İnce, K. Yıldız, "Designing a Porous Asphalt Skeleton for Semi-Flexible Pavement Applications," in Proceedings of the ACE2026 – International Conference on Advances in Civil Engineering, Trabzon, Türkiye, 12–14 October 2026.

CHAPTER 6

Construction Management

19 papers

Construction Management Risk Simulation for Hybrid Renewable Energy EPC Projects: A Probabilistic Framework for Remote Environments

İlkyaz Ceren Güçlü Yavuz[1] and Assoc. Prof. Dr. Gürkan Emre Gürcanlı[2]
[1] 0009-0009-7375-523X, Istanbul Technical University, Civil Engineering Department, Istanbul, Türkiye, guclui@itu.edu.tr
[2] 0000-0002-0807-2020, Istanbul Technical University, Civil Engineering Department, Istanbul, Türkiye, gurcanlig@itu.edu.tr

Abstract. Remote island power plant construction face a combination of engineering, contractual, logistical, and severe weather conditions that are frequently underestimated during the planning phase of Engineering, Procurement, and Construction (EPC) projects. This study introduces a probabilistic Monte Carlo simulation (MCS) framework to quantify cost overrun and schedule delay risks in hybrid energy EPC projects executed in remote environments.

The model is calibrated using project specific technical and contractual specifications derived from a hybrid energy project that integrates natural gas fired engine generation, solar photovoltaic (PV), and battery energy storage systems (BESS). Nine risk parameter structure is adopted to capture critical risk drivers: contract structure, pricing mechanisms, procurement strategy, technology integration, political stability, logistics complexity, foreign currency exposure, regulatory compliance, and extreme climate risks.

This study works on 50,000 iterations with Monte Carlo simulation to modeling cost and schedule data's with the correlation $\rho = 0.65$ log-normal distributions to show the uncertain risks of the energy investment project. The initial results indicates a median (P50) cost overrun of 29.1% and a schedule delay of 20.1%, which is matching usual industry practice. On the other hand, under extreme risk scenarios (P90), cost variation can exceed 100%, which is also shows that planning application in traditional contract management practice does not work for such remote island projects. Main aspects of the cost variations are political stability, foreign exchange volatility, and severe logistics constraints. The assessment which is executed for both risks also shows that 35% outcomes of the simulation, cost and schedule overruns can be expected above median values. This result shows that cost and delay risk are linked each other.

Thanks to this study, contract managers found a practical way to establish realistic contingency allocations to prevent project budget for the expected risks. As a final note, the study helps the construction professional under the such mega contracts to use insights into variation orders, mitigation of claims, and risk assessment mechanisms.

Keywords: Monte Carlo simulation, EPC risk, contractual risk determination, hybrid energy, FIDIC Silver Book, remote island.

1 Introduction

Complexity of the hybrid energy investments on remote island environment is very high. These projects are encounter unique challenges; such as fluctuations and changes on power grids, difficulty with logistics operations, extreme and unexpected climate, and a complete reliance on imported energy. Because these systems operation requires isolated grids for multiple sites, it is not surprising to encounter complex risk environment in such international EPC turnkey contracts.

This study is adopted from a real hybrid energy project which is built across two different locations on isolated islands. The project combines gas based generation system (Genset), solar power, and battery energy storage (BESS) into a single system. At Site A, the production capacities of Gensets are up to 25–35 MW, 10–15 MW for solar, and 15–25 MWh for batteries, while Site B has slightly smaller capacities than Site A.

Execution team projected some several factors which may create high uncertainty during construction. One of them, relying on a single gas source, with LNG storage system, without any backup source creates fuel risks. Secondly, strict environmental standards for example; durability strong winds and corrosion risk due to ocean evaporation, makes the design process much more difficult. Finally, and most generic and serious challenge that several turnkey contracts encountered is that lack of information about the soil data on the Site B creates a risk of working with unexpected soil conditions during construction.

2 Literature Review

With this section, researchers deeply investigate related academic research to finding out why complex projects completed over budget and finish late than scheduled. In the beginning of this section main reasons can be found for these delays and extra budget in traditional projects. Then, it shows how using Monte Carlo simulations helps to manage risks and handle financial uncertainties in latest energy projects.

2.1 Cost Overrun and Schedule Delay in Infrastructure Projects

In real construction projects, especially major energy investments, often exceeds its budget more than expected. Research by Flyvbjerg et al. [1] indicates that construction experts usually underestimate project costs because they are too optimistic or hide the real costs in purpose. On the other hand, when a project duration lasts more than one year, Touran and Lopez [2] used Monte Carlo modeling to show that cost uncertainties increase much faster and become harder to predict in the beginning. In complex environments, such as energy projects, this risk may getting worse because stakeholders of the project has not got the same information. For example, before the signature phase, parties of contract has insufficient data regarding the ground conditions and it causes uncertainty than expected. This often concludes rising the actual costs and contractual disputes during construction execution. Under fixed price contracts like the FIDIC Silver Book, all these risks regarding the soil based are under the contractor responsibility, which heavily increases their financial risk.

2.2 Monte Carlo Simulation in Construction Risk Analysis

To calculate the project risks and contingency, in general practice uses AACE International, and it recommends to use Monte Carlo simulation (MCS). When researcher apply this integration, according to Baghalzadeh Shishehgarkhaneh et al. [3] supply chain and design limits are vital components to analyze. Arnold and Yildiz [4] showed that log-normal distributions work best because cost risks are usually skewed toward higher numbers for especially renewable energy investments.

Another essential part in probabilistic modeling is that project costs and schedules are highly interact with each other. Common suspension during the construction; such as unexpected

weather, failures in supply chain, or delays caused by permits etc., has effect both of them at the same time. In fact, statistics also show a high correlation (ρ between 0.60 and 0.85) between these two, which shows that models must simulate them together.

3 Project Description

This master thesis investigates on a project which has specific technical rules. It uses a lump sum pricing mechanism of an EPC turnkey contract which is also linked to a long term power purchase agreement (PPA) of the owner with the government. Contractor work describing in the contract; install and complete commissioning of the Gensets that can work only on LNG supply, combined with solar PV panels and battery storage system (BESS). Because of the location of the islands, the structures must be resistant strong winds and salty ocean air, requiring high-level (C4 equivalent) rust protection for the whole operation duration which is defined in PPA. The major defined risk here is the soil condition: while Site A has finished all its soil and geology tests on site, Site B lacks complete geotechnical information, which makes the project much riskier. Technical details can be seen in Table 1.

Table 1. Key Project Characteristics (taken from project specification).

Parameter	**Site A**	**Site B**
Genset Capacity	25-35 MWe	15-25 MWe
Solar PV Capacity AC	10-15 MWe	5-10 MWe
BESS Energy Capacity	15-25 MWh	10-20 MWh
BESS Response Time	≤ 200 ms	≤ 200 ms
Fuel Supply	LNG (No backup)	LNG (No backup)
Contract Framework	Bespoke FIDIC Silver Book	Bespoke FIDIC Silver Book
Geotechnical Status	Complete	Incomplete (high risk)

Hybrid projects combine different types of technologies, like this, makes the construction much harder to manage. This complex technology environment becomes a vital problem especially before the facility's commercial operation and most importantly the test and commissioning phases. To achieve commercial operation, the EPC contractor must strictly follow the local grid code and project specification and also pass all grid compliance tests for sure the systems product energy within the feasible levels. Achieving these rules regarding the tests are a mandatory requirement for both provisional acceptance of the EPC contract and the PPA framework.

4 Methodology

Calculation model follows plain and simple process. It takes descriptive, qualitative risks and turns them into mathematical probability curves. This model uses nine separate risk categories (M_1–M_9). Each category uses a specific scale that links risk descriptions to simple multiplier numbers with no units. Depending on the given data of the respective project, researchers assign each of these nine categories a specific rating.

Table 2. Nine Risk Dimensions, Multiplier Ranges, and Base Case Ratings.

#	Risk Dimension	Range	Base Case Rating	ERQ Calibration Basis
M_1	Contract Type	0.85–1.35	1.35	FIDIC Silver Book; contractor risk concentration
M_2	Pricing Mechanism	0.80–1.35	1.35	Fixed Lump Sum; delay damages included
M_3	Procurement Strategy	1.00–1.40	1.40	Owner Furnished Equipment interface risks
M_4	Technology Maturity	0.85–1.80	1.15	Hybrid system integration complexity
M_5	Political Stability	0.80–2.20	1.10	Stable environment with moderate permitting risk
M_6	Logistics Complexity	0.70–1.90	1.45	Extreme remote island; transport restrictions
M_7	FX Volatility	0.85–2.00	1.15	EUR/USD procurement; no currency hedging
M_8	Climate/Hurricane Risk	0.80–1.70	1.35	Exposure to severe tropical storm windows
M_9	Regulatory Complexity	0.80–1.70	1.40	Permitting from several authority and determined grid codes for both sides

To get the cost (Rc) and schedule (Rd) risk factors, it is combined the individual multipliers together. To do this, the model uses a geometric mean formula with fractional exponents. Researchers select this mathematical method because the its advantages regarding the final risk scores from being distorted by extreme numbers:

$$R_c = (M_1 \cdot M_2 \cdot M_3 \cdot M_4 \cdot M_5 \cdot M_6 \cdot M_7 \cdot M_8 \cdot M_9)^{1/3.5} \quad (1)$$

$$R_d = (M_3 \cdot M_4 \cdot M_5 \cdot M_6 \cdot M_8 \cdot M_9)^{1/2.8} \quad (2)$$

In this study, a Cholesky decomposition method is used to show how shared risks has linked cost and schedule together. The model runs the calculation through 50,000 iterations. In each turn, it samples cost overruns (C) and schedule delays (D) together using correlated log-normal formulas, based on a real world correlation coefficient of $\rho = 0.65$. Finally, it has been tested four different situations: Optimistic, Base Case, Conservative, and Stress.

5 Results and Discussion

The probability curves from the simulation lean heavily to the right. When data clustered on the right side of the graph, it shows us that using a log-normal model was the right choice to study on it. Each scenarios tested and results can be seen on the Table 3 below.

Table 3. Monte Carlo Simulation Percentile Results (N = 50,000).

Percentile Metric	Optimistic Scenario	Base Case Scenario	Conservative Scenario	Stress Scenario
P10 Cost %	7.6	13.4	15.6	22.7
P50 Cost %	16.5	29.1	34.2	49.2
P80 Cost %	27.5	48.5	56.9	82.1

P90 Cost %	35.9	63.2	74.1	107.4
P10 Delay %	5.5	8.8	10.3	14.6
P50 Delay %	12.5	20.1	23.4	33.1
P80 Delay %	21.4	34.6	40.2	56.9
P90 Delay %	28.3	45.5	53.3	75.3

According to Base Case results, the median (P50) cost overrun is 29.1%. This is very close to global infrastructure benchmarks of around 28%, which shows our model is accurately calibrated. On the other hand, the P80 cost overrun reaches 48.5%, meaning a standard lump sum pricing risk needs a large and contingency buffer for better risk adjustments. Under Stress conditions, worst-case outcomes (P90) jump past 100% cost escalation. This proves that even more than one problem happen at the same time in remote sites, they multiply each other's risk impact.

When researchers check the one-way sensitivity analysis, it has been found three main drivers behind these cost changes: political stability (M_5, ±8.6 pp range), foreign exchange volatility (M_7, ±7.5 pp range), and logistics constraints (M_6, ±7.4 pp range). Finally, the joint distribution analysis shows that 35% of all simulated cycles suffer from both cost and schedule overruns above their median values. This is clearly proved that cost and time risks are structurally linked.

6 Change Order and Claim Analysis

Study turned these results regarding the risk into practical tools for the contract administration phase. To achieve this, researchers linked a structured change order register directly to the specific EPC contract terms. It can be seen how these commercial risks has been categorized in Table 4.

Table 4. Change Order and Claim Register under EPC Framework.

CO Type	**Probability %**	**Cost Impact**	**Typical Trigger**	**Contractual Basis (FIDIC)**
Fuel Logistics Escalation	90%	8-15% contract	Isolated fuel supply, marine unloading restrictions	Unforeseen physical conditions / Interface risk
Geotechnical Uncertainty	65%	4-12% civil scope	Incomplete site survey data at Site B, latent conditions	Sub-Clause 4.12 Unforeseen Physical Conditions
Grid Connection Scope Variation	75%	5-20% electrical	Grid code compliance adjustments for different Sites	Interconnection and test and commissioning clauses
FX Rate Deviation	60%	5-18% exposure	Currency mismatch in major	Absence of Price

			equipment orders	Adjustment provisions

7 Contract Administration Implications

This section analyses the risk numbers from the Monte Carlo simulation into practical strategies for managing the EPC contract. By comparing probability limits with turnkey delivery rules, project teams can draw a solution and handle uncertainties during construction. Before conclusion, following parts show specific steps to reduce claims, schedule delays, and logistical issues in remote island projects with commercial precautions.

7.1 Geotechnical Uncertainty and Turnkey Risk Allocation

In general, standard lump sum turnkey frameworks, including FIDIC Silver Book [5] Sub-Clause 4.12, financial responsibility of unforeseen ground conditions is on the contractor. Site B geotechnical survey was not completed before the contract execution which is highly common situation to face with multiple claims and brings contractual risks. There is no need to awoke this situation during the negotiation phase, contract administrators can estimate buffer for the geotechnical works, which is approximately 4-12% of civil works or they can determine until the final site data available.

7.2 Performance Guarantees and Sequential Commissioning Milestones

Any delay during the commissioning phase makes delay escalate exponentially because of actions during the commissioning happens because commissioning milestones happen step by step. Not until the hybrid energy production control system satisfies specific grid requirements, ramp rates, and voltage setups under island mode startup can reliability testing even begin. This reliability test phase typically needs 240 uninterrupted hours, approximately 10 days, of operation at a minimum of 99% availability of the energy production equipment. To avoid entire test repetition for the minor interruption cases, project schedules must include sufficient float for those minor interruptions. Additionally, schedule has to be prepared to allow at least two or maximum three failures to avoid possible delay liquidated damages (LDs) executed by the employer.

7.3 Fuel Supply Chain and Environmental Resilience

The facility relying on single LNG shipment route and it creates risks during execution pahse of contract. Additionally, during operation and maintenance period, contract managers should enforce the operators of facility to backup fuel reserve for strategic use (e.g., 72 hours of operation) as a condition for commissioning and prevent un expected cutoffs. Additionally, Construction All Risks (CAR) policies must cover tropical storm damages to protect the facility from extreme weather damages and facility should protective structures during the vulnerable installation and execution phases of construction.

8 Conclusions

In conclusion, this research using a probabilistic Monte Carlo simulation with the data of a hybrid energy EPC investments in remote island. Using 50,000 simulation iterations and a bivariate correlation structure ($\rho = 0.65$), this model demonstrated that fixed budgeting fails to determine the realities of isolated microgrid infrastructures. The Base Case calculated a P50 cost overrun of 29.1% alongside a 20.1% timeline delay.

In the end, external risks like political stability, foreign exchange volatility, and island logistics played a significant role in cost change in comparison of engineering metrics. By using this simulation outputs into contract administration tools, for example given enough float for possible retesting and contingency for the unexpected ground conditions, allows contract

managers to find a proactive solution and/or provide to prevent some disputes during the execution phase for such energy construction projects.

Acknowledgments
I would like to deeply thank Assoc. Prof. Dr. Gürkan Emre Gürcanlı for his guidance and essential academic support during this research.

References
1. Flyvbjerg, B., Holm, M.K.S., Buhl, S.L.: Underestimating Costs in Public Works Projects: Error or Lie? J. Am. Plan. Assoc. 68(3), 279–295 (2002) https://doi.org/10.1080/01944360208976273.
2. Touran, A., Lopez, R.: Modeling Cost Escalation in Large Infrastructure Projects. J. Constr. Eng. Manage. 132(8), 853–860 (2006) https://doi.org/10.1061/(ASCE)0733-9364(2006)132:8(853).
3. Baghalzadeh Shishehgarkhaneh, M., Moehler, R.C., Fang, Y., Aboutorab, H., Hijazi, A.A.: Construction Supply Chain Risk Management. Autom. Constr. 162, 105396 (2024) https://doi.org/10.1016/j.autcon.2024.105396.
4. Arnold, U., Yildiz, Ö.: Economic Risk Analysis of Decentralized Renewable Energy Infrastructures — A Monte Carlo Simulation Approach. Renew. Energy 77, 227–239 (2015) https://doi.org/10.1016/j.renene.2014.11.059.
5. FIDIC: Conditions of Contract for EPC/Turnkey Projects (Silver Book), 2nd edn. International Federation of Consulting Engineers, Geneva (2017).

Author Contribution Statement
- *Conceptualization:* İlkyaz Ceren Güçlü Yavuz
- *Methodology:* İlkyaz Ceren Güçlü Yavuz
- *Investigation:* İlkyaz Ceren Güçlü Yavuz, Assoc. Prof. Dr. Gürkan Emre Gürcanlı
- *Writing – Original Draft:* İlkyaz Ceren Güçlü Yavuz
- *Writing – Review & Editing:* Assoc. Prof. Dr. Gürkan Emre Gürcanlı

List of Abbreviations
- **BESS** — Battery Energy Storage Systems
- **EPC** — Engineering, Procurement and Construction
- **FX** — Foreign Exchange
- **LD** — Liquidated Damages
- **LNG** — Liquefied Natural Gas
- **MCS** — Monte Carlo Simulation
- **PPA**— Power Purchase Agreement
- **PV** — Photovoltaic

Publication Note
This paper was peer-reviewed, accepted for presentation, and included in the proceedings of the ACE2026 – International Conference on Advances in Civil Engineering, held on 12–14 October 2026 in Trabzon, Türkiye.

This paper may be cited as follows:
İlkyaz Ceren GÜÇLÜ YAVUZ, Gürkan Emre GÜRCANLI, "Construction Management Risk Simulation for Hybrid Renewable Energy EPC Projects: A Probabilistic Framework

for Remote Environments” in Proceedings of the ACE2026 – International Conference on Advances in Civil Engineering, Trabzon, Türkiye, 12–14 October 2026.

Information Compliance and Quantity Consistency in IFC-Based Quantity Take-Off: A Focused Review and Conceptual Verification Workflow

Mahdis Motamedi [1] and Hasan Basri Başağa [2]
[1] 0009-0007-6386-3646, Karadeniz Technical University, Civil Engineering Department, Trabzon, Türkiye, motamedi.mahdis@gmail.com
[2] 0000-0002-6964-3309, Karadeniz Technical University, Civil Engineering Department, Trabzon, Türkiye, Türkiye, hasanbb@ktu.edu.tr
[2] Earthquake and Structural Health Application and Research Center, Karadeniz Technical University, Trabzon, Türkiye
[2] Northsign Design Software Construction Trade Ltd. Co., Trabzon, Turkey

Abstract. Building Information Modelling (BIM) can reduce manual effort in quantity take-off (QTO) and cost estimation, but model-derived quantities remain sensitive to modelling practice, object representation, software behaviour, and measurement assumptions. This focused review examines the relationship between IFC-based QTO, IDS-based information compliance, and BIM quantity verification. Three focused searches were conducted in the Web of Science Core Collection for the 2013–2026 period, and nine peer-reviewed studies were included in the qualitative synthesis. The review shows that IFC-based quantity extraction and IDS-based compliance checking address related but distinct problems. IDS can verify predefined information requirements, but it does not independently establish whether stored IFC BaseQuantities are geometrically consistent. Based on this distinction, the paper proposes a wall-focused conceptual workflow that separately reports information compliance, geometric assessability, quantity consistency or discrepancy, non-assessable cases, and human-review needs. The proposed structure aims to prevent information compliance from being interpreted as proof of quantity reliability in downstream cost-estimation workflows.

Keywords: BIM; IFC; IDS; Quantity Take-Off; Model Checking

1 Introduction

Quantity take-off (QTO) extends beyond the measurement of building components. In construction projects, quantity information supports tendering, cost estimation, procurement, progress valuation, and cost control. Consequently, quantity errors may extend beyond the modelling environment and affect contractual and financial decisions. Although BIM-based QTO can reduce repetitive manual measurement, the availability of a digital model does not eliminate the need to examine how quantities are generated, represented, exported, and verified [1, 2].

Research on BIM-based QTO presents two complementary findings. On the one hand, IFC-based openBIM workflows demonstrate that quantities can be extracted from vendor-neutral model data and integrated into cost-estimation processes [3–6]. On the other hand, empirical and methodological studies show that model-derived quantities may vary according to modelling practices, object representation, software interpretation, parameter completeness, and checking procedures [1, 2, 7]. The central issue is therefore not whether BIM can support QTO, but under which modelling, information, and verification conditions model-derived quantities can be considered sufficiently reliable for cost-related use.

The Information Delivery Specification (IDS) introduces an important information-compliance layer to this discussion. buildingSMART defines IDS as a standard for expressing information requirements in a computer-interpretable form and checking their delivery in IFC models [8]. IDS can specify requirements concerning IFC entities or objects, classifications, materials, properties, quantities, and permitted values. However, buildingSMART also states that IDS is limited to alphanumeric information and does not address geometrical aspects [8]. This limitation is particularly important for QTO. A wall may comply with IDS requirements concerning its classification, material, or the presence of a quantity field while the numerical value stored in that field remains inconsistent with the wall geometry or with the intended measurement basis.

Recent studies have begun to integrate IDS into cost-estimation workflows. Cassandro et al. connected structured cost data, IFC, IDS, and model validation within cost-estimation data management [9], while Dias et al. proposed an IDS-based openBIM verification workflow for construction cost estimation [10]. These studies demonstrate the potential of IDS to verify whether predefined information requirements have been satisfied before QTO. Nevertheless, information compliance alone does not establish whether a stored IFC quantity is consistent with the corresponding model geometry.

This paper therefore treats information compliance and geometric quantity consistency as complementary but analytically distinct verification dimensions. Compliance with task-essential information requirements may be necessary to perform a particular quantity comparison. However, general IDS compliance neither proves quantity consistency nor necessarily determines whether a geometry-based comparison can be conducted. Building on this distinction, the paper reviews relevant IFC-, IDS-, and BIM-QTO studies and proposes a wall-focused conceptual workflow that separately reports information compliance, geometric assessability, quantity discrepancies, non-assessable cases, and the need for human review.

Throughout the paper, information compliance refers to conformity with predefined information requirements, whereas quantity consistency refers to agreement between a stored IFC quantity and an independently derived comparison value under equivalent measurement assumptions. Accuracy and correctness are reserved for comparisons against an accepted reference or authoritative measurement rule. A discrepancy therefore indicates a difference requiring interpretation rather than automatically implying an error.

2 Scope and Methodological Position

2.1 Review Aim and Research Questions

This paper aims to clarify how research on IFC-based quantity take-off (QTO), IDS-based information compliance, and BIM verification can be connected to support the reliability of wall quantity take-off. Walls are selected as a focused demonstrator because their quantity assessment may involve semantic and classification requirements, material and layer information, stored IFC BaseQuantities, gross and net quantity definitions, openings, joins and intersections, composite or decomposed representations, and differences arising from modelling and export procedures.

The review is guided by the following research questions:

1. How has IFC been used in BIM-based quantity take-off and cost-estimation workflows?
2. What reliability problems have been reported for BIM-derived quantities?
3. What types of information checking can IDS support in IFC-based workflows?
4. How can IDS-based information compliance be coordinated with geometry-based quantity-consistency assessment for wall elements?

2.2 Review Method and Scope

This study adopts a focused review approach supported by qualitative thematic synthesis. It is not intended as a PRISMA-based systematic review, meta-analysis, or exhaustive review of the BIM-QTO literature, but focuses on the intersection of IFC-based quantity extraction, IDS-based information checking, and quantity-consistency concerns relevant to cost-estimation workflows.

The literature search was conducted in the Web of Science Core Collection between 25 and 29 June 2026 for publications from 2013 to 2026. Three focused search strings addressed IFC-based QTO and cost estimation, IDS-based information checking, and geometry- or quantity-related verification. The search strategy and initial retrieval results are summarised in Table 1. The three searches returned 142 records in aggregate before consideration of possible overlap among the search sets.

Table 1. Web of Science search strategy and initial retrieval results

Search focus	Search string	Records
IFC-based QTO and cost estimation	("Building Information Modeling" OR BIM) AND (IFC OR "Industry Foundation Classes") AND ("quantity take-off" OR QTO OR "quantity surveying" OR "cost estimation")	47
IDS-based information checking	("Information Delivery Specification" OR IDS) AND (BIM OR IFC OR "Industry Foundation Classes") AND ("compliance checking" OR validation OR "information requirements")	26
Geometry/quantity verification	(IFC OR BIM OR openBIM) AND ("quantity take-off" OR QTO OR BaseQuantities OR "cost estimation") AND ("geometry-based" OR "geometric verification" OR "quantity validation" OR accuracy)	69

The search and initial screening were conducted by the first author. Candidate records were screened by title and abstract, and nine peer-reviewed studies were retained for qualitative synthesis [1–7, 9, 10]. Studies were included when they directly addressed IFC-based quantity extraction, BIM-QTO reliability, quantity- or cost-related model checking, IDS-based information requirements, or IFC-based cost-data structuring. Studies without a direct relationship to IFC, IDS, QTO, or cost estimation were excluded. The selected full texts were examined for research aim, method, model or project scope, IFC/IDS context, comparator or checking basis, key findings, and limitations.

Official buildingSMART documentation was reviewed separately for technical definitions of IFC, IDS, quantity sets, and wall BaseQuantities [8, 11–13]. These sources were not counted among the nine peer-reviewed studies. The synthesis focused on four themes: IFC-based QTO and interoperability, BIM-QTO reliability, IDS-based information compliance, and IFC/IDS-supported verification for cost estimation.

The review is limited to one bibliographic database, three focused search strings, a 2013–2026 publication period, nine peer-reviewed studies, single-author screening, and heterogeneous study designs. Accordingly, the findings should be interpreted as a focused qualitative synthesis rather than a comprehensive review of the BIM-QTO literature.

3 Scope and Methodological Position

3.1 IFC-Based Quantity Take-Off

Industry Foundation Classes (IFC) provide a vendor-neutral schema for exchanging building objects, properties, relationships, geometry, and quantity information across software

environments [12]. Within QTO research, IFC is used primarily as an interoperable data source rather than as a costing method. The reviewed IFC-based studies employ IFC data for specification-compliant tender estimation, schematic-stage estimation, and interoperable QTO algorithm development [3–6]. Although these studies collectively demonstrate that IFC can support quantity extraction, computation, classification, and linkage between model objects and cost items, their comparison and validation bases differ. Ma et al. use formal measurement rules as the basis for quantity calculation; Choi et al. combine model-quality checking with comparison against commercial software; and Akanbi et al. examine the robustness of QTO algorithms across different IFC representations and authoring-tool outputs [3–6]. These approaches provide evidence of implementation feasibility, interoperability, and rule-based processing, but they do not directly address whether stored IFC BaseQuantities are numerically consistent with quantities independently derived from the corresponding geometry. This distinction is particularly relevant to wall QTO. A quantity may be successfully extracted from IFC, agree with commercial software output, or satisfy a formal measurement specification while still requiring explicit interpretation of openings, intersections, boundaries, material layers, and gross or net definitions. Consequently, IFC-based QTO methods support traceable extraction and rule-based calculation, but a separate comparison basis is required when the objective is to assess the consistency of a stored quantity with model geometry.

3.2 Reliability Problems in BIM-QTO

Research on BIM-QTO reliability shows that quantity outcomes are influenced not only by the availability of model data but also by how building elements are represented, parameterized, and processed. Wahab and Wang, Kim et al., and Valinejadshoubi et al. investigate this issue using different comparison bases, including project reference quantities and workflow comparisons, study-defined target representations, and internal parameter-consistency checks [1, 2, 7]. Their findings are therefore complementary rather than directly comparable. Across these studies, quantity variation is associated with workflow selection, object composition, material representation, missing or inconsistent parameters, alternative parameter-based calculations, and differences between manual and automated checking procedures [1, 2, 7]. Ma et al. further demonstrate that formal measurement rules concerning openings, accessories, and intersections can alter quantities calculated from model information [3]. Taken together, these studies indicate that BIM-based QTO depends on four closely related factors: model representation, information completeness, measurement rules, and computational procedure.

An important implication is that neither a stored model quantity nor a geometry-derived quantity should be treated as inherently correct without first defining a common measurement basis. Differences may arise from actual modelling or export errors, but they may also reflect legitimate differences in quantity definitions, deduction rules, object decomposition, or measurement conventions. Quantity comparison therefore requires explicit alignment of the quantity definition and the assumptions under which each value has been produced.

3.3 IDS and Information Compliance

The Information Delivery Specification (IDS) provides a computer-interpretable mechanism for defining information requirements and checking their delivery in IFC models [8]. Depending on the specified requirement, IDS checks may concern IFC entities and predefined types, attributes, properties, quantities, classifications, materials, relationships, and permitted values. This capability is relevant to QTO because cost-estimation workflows often depend on information that is not guaranteed to be present or consistently structured in every IFC model. IDS can make such expectations explicit and support repeatable compliance checking before model information is used downstream. However, IDS is designed for alphanumeric information requirements, while geometrical definitions and spatial calculations fall outside its

scope [8]. For example, an IDS requirement may verify that a wall contains a NetVolume quantity and that the value satisfies the specified information requirement. It does not reconstruct the wall geometry, calculate deductions for openings, resolve wall intersections, or independently determine whether the stored value corresponds to the intended gross or net geometric volume. The presence and formal compliance of a quantity field therefore constitute a different type of evidence from geometric consistency.

Information compliance and geometric quantity consistency should consequently be treated as related but analytically distinct dimensions. An element may fail an IDS requirement unrelated to the selected quantity while remaining geometrically assessable. Conversely, an element may satisfy all required classifications, properties, materials, and quantity fields while its stored quantity differs from an independently derived geometric value. IDS results should therefore be interpreted as evidence of information conformance and readiness for a defined workflow, rather than as proof of quantity accuracy, correctness, or geometric consistency.

3.4 IFC/IDS-Based Verification for Cost Estimation

Recent research has begun to operationalize IDS within cost-estimation workflows. Cassandro et al. and Dias et al. connect formalized information requirements with IFC-based cost processes, although their principal contribution is information control rather than independent geometric verification of stored quantities [9, 10]. Cassandro et al. show how IDS can formalize cost-workflow requirements and how IFC cost entities can structure relationships between model objects and cost items [9]. Dias et al. demonstrate the use of IDS-based requirements for assessing information readiness, supporting semantic enrichment and remediation, and communicating non-conformities before QTO [10]. These studies strengthen the role of explicit and machine-readable information requirements in cost-estimation workflows. However, they should not be interpreted as demonstrating independent geometric recalculation of stored wall quantities. Their contribution lies primarily in ensuring that required information is present, structured, and suitable for downstream use.

The reviewed literature therefore reveals a specific gap at the intersection of information compliance and quantity verification. IFC-based QTO studies explain how model information can be extracted, interpreted, and computationally processed [3–6]. BIM-QTO reliability studies demonstrate how quantities may vary according to representation, model detail, parameter completeness, workflow, and measurement procedure [1, 2, 7]. IDS-related cost-estimation studies show how cost-related information requirements can be formalized and checked before QTO [9, 10].

What remains insufficiently addressed is the coordinated reporting of these two verification dimensions at the level of individual model elements. Checking that a stored wall quantity exists, is located in the expected quantity set, or satisfies an IDS requirement does not establish that its numerical value is consistent with the IFC geometric representation under equivalent measurement assumptions. Conversely, failure of an information requirement does not necessarily make a selected geometric quantity comparison impossible. Within the studies included in this review, no approach was identified that explicitly combines IDS-based information-conformity reporting with an independently derived wall-quantity comparison while also distinguishing assessable, discrepant, and non-assessable cases. This coordination gap provides the basis for the conceptual verification workflow proposed in Section 4. The methodological roles and comparison bases of the nine studies included in the review are summarised in Table 2.

Table 2. Methodological focus of the studies included in the qualitative synthesis

Ref.	Main focus	Comparison/checking basis	Relevance to the present study
[1]	BIM-based vs. traditional QTO	Project/reference quantities and workflow comparison	Shows workflow-related quantity variation
[2]	BIM QTO discrepancy analysis	Study-defined representation/comparison basis	Shows effects of modelling representation
[3]	IFC-based tender cost estimation	Formal measurement rules	Demonstrates rule-based IFC quantity processing
[4]	openBIM schematic QTO	Model-quality checking and commercial-software comparison	Demonstrates interoperable QTO feasibility
[5]	Interoperable QTO algorithm development	IFC representations and authoring-tool variation	Addresses robustness across model representations
[6]	Automated IFC-based QTO	IFC-based architectural model case study	Demonstrates automated quantity extraction/calculation
[7]	High-accuracy BIM QTO	Parameter and quantity consistency checking	Highlights model-information consistency issues
[9]	IFC/IDS-supported cost information	Information requirements and IFC cost structures	Connects IDS with cost-workflow readiness
[10]	IDS-based openBIM cost verification	Information requirement compliance	Demonstrates IDS-supported pre-QTO information checking

4 Proposed Conceptual Verification Workflow

Building on the review synthesis, this section proposes a conceptual, wall-focused verification workflow rather than an implemented or empirically validated software system. Walls are selected as a manageable analytical case because their quantity assessment may involve stored BaseQuantities, classifications, properties, material layers, openings, joins and intersections, gross and net quantity definitions, and alternative geometric representations. Although the workflow is illustrated through wall elements, the underlying distinction between information compliance and quantity consistency is not limited to walls.

The initial scope is restricted to ordinary IFC wall instances and selected stored wall BaseQuantities. IFC quantity sets provide standardised structures for storing quantity information [12], and Qto_WallBaseQuantities may include quantities such as Length, Width, Height, GrossSideArea, NetSideArea, GrossVolume, and NetVolume [13]. The treatment of more complex cases, including curved, layered, decomposed, curtain, covering, hosted, and irregular wall configurations, is outside the initial conceptual scope and should be addressed during implementation.

4.1 IFC Information Layer

The workflow begins by identifying the relevant wall instance and the specific stored quantity to be assessed. For each wall, the IFC information layer records the element identifier, object type, quantity-set name, quantity name, stored value, unit, available properties, material information, classifications, and geometric representation.

This element-level traceability is necessary because quantity assessment should not be performed independently of the object and quantity definition from which the value originates. In particular, the stored quantity must be explicitly associated with its quantity name and unit before any geometric comparison is attempted.

4.2 IDS Information-Compliance Layer

The IDS layer evaluates predefined information requirements associated with the intended QTO or cost-estimation task. A distinction is made between task-essential information and broader workflow information. Task-essential information comprises the data required to perform the selected quantity comparison, such as the wall identifier, selected quantity, unit, quantity definition, and information necessary to establish an equivalent measurement basis. If such information is unavailable or incompatible, a meaningful geometric comparison may not be possible. Broader workflow information may include cost classification, material naming, load-bearing status, or other attributes required for downstream cost-estimation activities. Failure to satisfy such requirements may affect overall workflow readiness without necessarily preventing a selected quantity from being geometrically assessed.The IDS result is therefore recorded as an information-compliance outcome and is not interpreted as evidence that the numerical quantity value is geometrically consistent.

4.3 Quantity-Consistency Layer

The quantity-consistency layer compares a specifically identified stored IFC quantity with an independently derived geometric value, provided that an equivalent measurement basis can be established.

Before the comparison is performed, the following conditions must be defined:

- whether the stored quantity represents a gross or net measurement;
- how openings are treated;
- how joins and intersections are treated;
- which geometric boundaries are included;
- whether material layers are evaluated collectively or separately; and
- whether the stored and independently derived values use compatible units and quantity definitions.

These conditions are essential because a numerical difference does not necessarily indicate an error. It may instead result from different measurement rules, geometric interpretations, deduction procedures, or model representations. Once an equivalent comparison basis has been established, units are normalised and an independent geometric value is derived. The numerical difference between the stored quantity and the independently derived value is then reported. A tolerance threshold is applied only where a technically justified threshold is available. The geometry-derived value is treated as an independent comparison value rather than as automatic ground truth.

4.4 Outcome Classification and Reporting

The result of the assessment is classified according to the information-compliance and quantity-consistency outcomes. Four principal situations may occur:

1. *Information-compliant and quantity-consistent:* the required information is available and the stored quantity agrees with the independently derived value within the defined comparison basis and, where applicable, tolerance.
2. *Information-compliant and quantity-discrepant:* the required information is available, but the stored and independently derived quantities differ beyond the accepted comparison condition.
3. *Information-non-compliant but quantity-comparison-assessable:* one or more broader IDS requirements are not satisfied, while the information required for the selected geometric quantity comparison remains available.
4. *Quantity-comparison-non-assessable:* an equivalent comparison cannot be established because essential quantity, unit, geometry, or measurement-basis information is missing, unsupported, or incompatible.

The reporting structure should therefore maintain separate fields for information-compliance status, quantity-comparison assessability, stored quantity, independently derived comparison value, numerical discrepancy, applied assumptions, tolerance where applicable, and the need for human review. This separation is important because it prevents IDS compliance from being interpreted as proof of quantity consistency and prevents the failure of an unrelated information requirement from automatically stopping a geometrically valid comparison. The proposed workflow does not prescribe a specific geometry-processing engine, support every IFC wall representation, establish universal tolerance thresholds, modify IFC files, or automatically determine which quantity value is correct. Its purpose is instead to provide a traceable conceptual structure for coordinating information-compliance checking with independent quantity-consistency assessment.

5 Discussion

The reviewed literature indicates that IFC-based QTO, BIM-QTO reliability research, and IDS-supported information checking address related but distinct verification problems. As summarised in Table 2, IFC-based studies demonstrate that vendor-neutral model information can support quantity extraction, calculation, interoperability, and linkage with cost-estimation workflows [3–6]. However, their comparison bases differ, including formal measurement rules, commercial-software outputs, and alternative model representations. Therefore, successful extraction or agreement within a particular workflow should be interpreted as evidence of feasibility or consistency under a defined comparison basis, rather than as independent proof of quantity accuracy.

The reliability studies further show that BIM-derived quantities are influenced by modelling representation, object composition, parameter completeness, software workflows, and measurement assumptions [1, 2, 7]. Although these studies use different comparators, their findings are complementary in showing that quantity results depend on both model content and the rules used to interpret that content. Quantity assessment should therefore explicitly define what is being compared, how the quantity has been produced, and which measurement basis or comparator is being applied.

IDS contributes primarily to information compliance by formalising and machine-checking predefined requirements concerning model entities, classifications, properties, materials, quantities, and related information [8–10]. This provides an important control layer before QTO, but IDS does not independently reconstruct geometry or determine whether a stored quantity is numerically consistent with the corresponding geometric representation. Information compliance and quantity consistency should therefore be coordinated as separate verification dimensions.

The proposed workflow addresses this distinction by separating task-essential information, broader cost-estimation readiness, geometric assessability, quantity discrepancy, and professional interpretation. This separation represents the main conceptual contribution of the study. Rather than treating model quality as a single pass-or-fail condition, the framework allows an element to be information-compliant but quantity-discrepant, information-non-compliant yet still assessable, or non-assessable when an equivalent measurement basis cannot be established.

The non-assessable category is particularly important. A numerical difference should not automatically be classified as an error when the stored and independently derived quantities are based on different assumptions. Differences may arise from the treatment of openings, intersections, layers, boundaries, gross or net definitions, or software-export behaviour. In such cases, withholding a consistency judgement may be more appropriate than forcing a binary result.

The framework is intended to support, rather than replace, professional judgement. It does not automatically identify which quantity is correct, modify IFC files, or guarantee the accuracy of a downstream cost estimate. Instead, it structures the available evidence so that discrepancies and non-assessable cases can be traced to specific elements, assumptions, and comparison conditions.

The findings should be interpreted within the limits of the review, which is based on nine peer-reviewed studies, a single-author screening process, and heterogeneous study designs. In addition, the proposed workflow remains conceptual and has not yet been empirically validated. Future research should therefore implement the approach using real IFC wall models, explicit quantity-specific measurement rules, and alternative modelling and export conditions, and evaluate whether the resulting reports improve traceability and decision support for BIM-based QTO.

6 Conclusion

This focused review examined how IFC-based quantity take-off, BIM-QTO reliability research, and IDS-supported information checking can be coordinated for wall quantity assessment. The evidence indicates that IFC enables interoperable extraction and processing of quantity information, while quantity outcomes remain sensitive to modelling representation, information completeness, software workflows, and measurement definitions. IDS can formalise and verify information requirements, but such compliance does not independently demonstrate that a stored IFC quantity is geometrically consistent.

The principal contribution of the study is a conceptual verification workflow that treats information compliance, geometric assessability, and quantity consistency as related but separate dimensions. The framework distinguishes information-compliant and quantity-consistent cases, information-compliant but discrepant cases, information-non-compliant yet assessable cases, and cases in which an equivalent geometric comparison cannot be established. This structure avoids treating either IDS compliance or an independently derived geometric value as automatic proof of quantity correctness.

The workflow remains conceptual and requires empirical implementation. Future work should test it using real IFC wall models, explicitly defined measurement rules, alternative modelling and export conditions, and element-level discrepancy reports. Such testing will determine whether the proposed reporting structure improves traceability and supports professional decisions concerning the suitability of BIM-derived quantities for cost-estimation use.

References

1. Wahab, A., Wang, J.: Factors-driven comparison between BIM-based and traditional 2D quantity takeoff in construction cost estimation. Engineering, Construction and Architectural Management 29(2), 702–715 (2022). https://doi.org/10.1108/ECAM-10-2020-0823
2. Kim, S., Chin, S., Kwon, S.: A discrepancy analysis of BIM-based quantity take-off for building interior components. Journal of Management in Engineering 35(3), 05019001 (2019). https://doi.org/10.1061/(ASCE)ME.1943-5479.0000684
3. Ma, Z., Wei, Z., Zhang, X.: Semi-automatic and specification-compliant cost estimation for tendering of building projects based on IFC data of design model. Automation in Construction 30, 126–135 (2013). https://doi.org/10.1016/j.autcon.2012.11.020
4. Choi, J., Kim, H., Kim, I.: Open BIM-based quantity take-off system for schematic estimation of building frame in early design stage. Journal of Computational Design and Engineering 2(1), 16–25 (2015). https://doi.org/10.1016/j.jcde.2014.11.002

5. Akanbi, T., Zhang, J., Lee, Y.-C.: Data-driven reverse engineering algorithm development method for developing interoperable quantity takeoff algorithms using IFC-based BIM. Journal of Computing in Civil Engineering 34(5), 04020036 (2020). https://doi.org/10.1061/(ASCE)CP.1943-5487.0000909
6. Akanbi, T., Zhang, J.: IFC-based algorithms for automated quantity takeoff from architectural model: Case study on residential development project. Journal of Architectural Engineering 29(4), 05023007 (2023). https://doi.org/10.1061/JAEIED.AEENG-1447
7. Valinejadshoubi, M., Moselhi, O., Iordanova, I., Valdivieso, F., Bagchi, A.: Automated system for high-accuracy quantity takeoff using BIM. Automation in Construction 157, 105155 (2024). https://doi.org/10.1016/j.autcon.2023.105155
8. buildingSMART International: Information Delivery Specification (IDS). https://www.buildingsmart.org/standards/bsi-standards/information-delivery-specification-ids/, last accessed 2026/07/07.
9. Cassandro, J., Mirarchi, C., Zanchetta, C., Pavan, A.: Enhancing accuracy in cost estimation: Structured cost data integration and model validation. Journal of Information Technology in Construction 29, 1293–1325 (2024). https://doi.org/10.36680/j.itcon.2024.058
10. Dias, D.C., Miceli Junior, G., Pellanda, P.C.: Information requirement-driven BIM verification for construction cost estimation: openBIM workflow based on Information Delivery Specification (IDS). Automation in Construction 189, 107043 (2026). https://doi.org/10.1016/j.autcon.2026.107043
11. buildingSMART International: Industry Foundation Classes (IFC). https://www.buildingsmart.org/standards/bsi-standards/industry-foundation-classes/, last accessed 2026/07/07.
12. buildingSMART International: IFC 4.3.2 documentation: Quantity sets. https://ifc43-docs.standards.buildingsmart.org/IFC/RELEASE/IFC4x3/HTML/concepts/Object_Definition/Quantity_Sets/content.html, last accessed 2026/07/07.
13. buildingSMART International: IFC 4.3.2 documentation: Qto_WallBaseQuantities. https://ifc43-docs.standards.buildingsmart.org/IFC/RELEASE/IFC4x3/HTML/lexical/Qto_WallBaseQuantities.htm, last accessed 2026/07/07.

Author Contribution Statement

- *Conceptualization:* Mahdis Motamedi, Hasan Basri Başağa
- *Methodology:* Mahdis Motamedi, Hasan Basri Başağa
- *Investigation:* Mahdis Motamedi
- *Writing – Original Draft:* Mahdis Motamedi
- *Writing – Review & Editing:* Hasan Basri Başağa, Mahdis Motamedi

Publication Note

This paper was peer-reviewed, accepted for presentation, and included in the proceedings of the ACE2026 – International Conference on Advances in Civil Engineering, held on 12–14 October 2026 in Trabzon, Türkiye.

This paper may be cited as follows:

Mahdis Motamedi, Hasan Basri Başağa, "Information Compliance and Quantity Consistency in IFC-Based Quantity Take-Off: A Focused Review and Conceptual Verification Workflow," in Proceedings of the ACE2026 – International Conference on Advances in Civil Engineering, Trabzon, Türkiye, 12–14 October 2026.

Identifying Key Business Survey Indicators to Predict Construction Production and Cost Indices

Serkan Aydınlı[1]
[1] https://orcid.org/0000-0002-2897-4144, Çukurova University, Civil Engineering Department, Adana, Türkiye, saydinli@cu.edu.tr

Abstract. The construction sector is characterized by long project durations, which necessitates the precise forecasting of changes in sectoral parameters. Business surveys, such as sector confidence indicators and sentiment surveys, are widely monitored as leading indicators for the sector. However, determining which surveys accurately predict future actual construction indicators presents a complex analytical challenge. Construction-related production and cost indexes are frequently delayed indicators, published a month subsequent to actual occurrences. Conversely, business surveys serve as high-frequency, leading indicators. Establishing a mathematically valid causal relationship between them enables policymakers, investors, and contractors to anticipate macroeconomic fluctuations and pricing shocks months in advance. The primary goal of this study is to determine the causal relationships between business/consumer surveys and critical construction sector indicators (production and cost indexes). To achieve these objectives, this research utilizes PCMCI (Peter-Clark and Momentary Conditional Independence) algorithm. This study demonstrates genuine causal relationships—from the business surveys to production and cost indexes in the construction industry—through the application of the PCMCI framework. The results will yield data-driven early warning signals, allowing sector stakeholders, investors, and regulators to precisely anticipate developments in the construction industry based on the most statistically robust survey indicators.

Keywords: Construction industry; business surveys; production in construction; construction costs.

1 Introduction

The construction industry has substantial significance for the global economy. Global research indicates that the sector represents a significant portion of Gross Domestic Product (GDP). An analysis of European Union statistics reveals that the construction sector's gross value added is approximately 5.5 percent [1]. The high level of added value naturally places the sector among those that countries consider to be of great importance. An additional reason for the sector's significance arises from its connections with other sectors [2], [3]. For example, a building construction project promotes the construction material industry. Upon the sale of the finished residences, industries including furnishings, household appliances, and finance have heightened activity. This connection is also reflected in employment. This industry is inherently labor-intensive. Labor constitutes a fundamental element of project resources. According to Eurostat data, approximately 8.6% of total employment is directly in the construction sector [4].

Another consideration that requires monitoring of the construction-related business is the magnitude of expenses within the sector. Business operations in this sector necessitate a robust capital framework and consistent liquidity over time. Unexpected fluctuations in material and energy prices have a direct impact on project costs [5]. Therefore, analyzing and forecasting the prices of inputs of construction activities is crucial for achieving the project's financial

objectives. Since construction projects are normally long-term, it is important to monitor not only the costs, but also the risks of domestic and global crises. The construction industry is very sensitive to crises (e.g. COVID-19 pandemic or the war of Ukraine and Russia). These crises decrease the predictability of the sector [6]. This induces a decrease of the production [7].

The dynamic industry structure of today's world requires data-driven decisions and not intuitive ones. By monitoring the production and costs at the macro level with the help of various indicators, decision-makers and policymakers can formulate data-driven strategies and reduce risks, while efficiently planning long-term investment decisions. The paper analyses the relation between sectoral indices (cost and production indices) and construction business surveys. The rest of the paper is organized as follows. In section "2. Importance of Business Surveys", the importance of business surveys specific to each industry, produced and disseminated by statistical agencies, is discussed. The variables and the analytical approach are discussed in the "3. Methodology" section. In "4. Findings & Discussion", the results are presented and discussed in relation to existing literature. Finally, the findings are summarized in section "5. Conclusion".

2 Importance of Business Surveys

Qualitative business surveys have been regarded as significant resources for sectoral and economic assessment, policy development, and macroeconomic forecasting [8], [9]. One of the most significant advantages of business surveys is that they are published earlier than other sectoral indicators [10]. On the other hand, the results of business surveys are generally published shortly after the end of the relevant period [11]. Thus, business surveys serve as early indicators for decision-makers.

A further characteristic that enhances the significance of business surveys is their direct representation of the observations and insights of industry experts. The surveys offer a comprehensive insight into various fields from diverse viewpoints such as current situation and expectations via industry experts [8]. For example, while the "Construction Confidence Index" and "Evolution of the Current Overall Order Books" are indicators that provide an analysis of the current situation, "Employment Expectations over the next 3 months," "Building Activity Development over the past 3 months," and "Price Expectations over the next 3 months" are indicators that reflect future expectations. In contrast to macroeconomic measures, these indicators enable us to monitor qualitative aspects related to the sector.

Business surveys provide substantial insights to the literature, especially within the realm of econometrics. Survey indicators perform particularly effectively in forecasting short-term GDP growth and industrial production [12-13]. The studies show that the "production expectations for the next three months" of enterprises are the most effective leading indicator for forecasting GDP growth [14]. In addition, consumer and confidence indices also stand out as key variables in GDP forecasts [15]. The studies also show that order book levels, export orders, finished goods inventories, and employment expectations are frequently used in econometric forecasts ([13], [16]).

Business surveys are also employed in inflation forecasting models. A study performed in Germany indicates that the "IFO Price Expectations" indicator is a crucial factor in predicting both producer and consumer inflation (CPI) [17]. Furthermore, the literature has found that price-based surveys alone are not sufficient to explain CPI inflation; survey questions regarding capacity constraints, real economic activity, and the labor market also have a very strong additional explanatory power for CPI inflation. It is believed that inquiries concerning the evaluation of the prevailing economic conditions are factors that substantially improve the accuracy of CPI estimates [12].

The literature confirms that business surveys make significant contributions to forecasting models. Nonetheless, the relationship between business surveys and industry-specific indicators

in the construction sector remains untested. This study aims to identify potential variables for forecasting models by examining the relationships between the construction sector business surveys—which are published by statistical offices—and, in particular, production and cost indices.

3 Methodology

3.1 Data

Data employed in this paper has been obtained from the official database of the European Union's statistical office (EUROSTAT) [18]. The statistical agencies of European Union nations perform several business surveys on a monthly basis and submit the findings to Eurostat. Eurostat, thereafter, publishes the data following the verification process. The key business surveys and sectoral indicators examined in this study are presented in Table 1.

Table 1. Construction Sector Business Surveys and Industrial Indicators

Variables	**Reference**
Construction Confidence Index (CONF)	[19]
Evolution of the Current Overall Order Books (Construction) (ECOOB)	
Employment Expectations over the next 3 months (Construction) (EE)	
Building Activity Development over the past 3 months (BAD)	
Price Expectations over the next 3 months (Construction) (PE)	
Factors Limiting Building Activity – None (FLBA-N)	
Factors Limiting Building Activity – Insufficient Demand (FLBA-ID)	
Factors Limiting Building Activity – Weather Conditions (FLBA-WC)	
Factors Limiting Building Activity – Shortage of Labour (FLBA-SOL)	
Factors Limiting Building Activity – Shortage of Material and/or Equipment (FLBA-SOM)	
Factors Limiting Building Activity – Other (FLBA-O)	
Construction Cost Index (CCI)	[20]
Production in Construction (PiC)	[21]

Business surveys are fundamentally structured as balance-type questionnaires. In balance-type surveys, participants can respond to the questions in three ways: increased/positive, unchanged/stable, and decreased/negative [22]. Surveys measure current conditions and future expectations. FLBA-N signifies the absence of impediments to construction efforts, whereas FLBA-O denotes the presence of additional difficulties beyond those indicated. Survey statistics are derived by computing a difference between the proportion of positive responses, and the proportion of negative responses [22]. The investigation covered countries that have fully reported all variables from 2000 to 2026; in this regard, Austria, Finland, and the Netherlands were included as part of the study.

3.2 Peter-Clark and Momentary Conditional Independence (PCMCI)Algorithm

The PCMCI algorithm [23] is a causal inference method designed to detect underlying causal relationships and lagged interactions in multivariate time series [24]. In contrast to econometric causality models, the algorithm is highly effective at controlling for autocorrelations and potential confusing correlations in multidimensional time-series data [25].

The algorithm consists of two stages: PC and MCI. In the PC phase, potential variables are identified from the time series. At this stage, an independence test is conducted for each variable up to the designated lag value [24]. The MCI (Momentary Conditional Independence) phase performs more focused tests using the set of candidate parent-child pairs obtained from the PC phase. The primary goal here is to eliminate all remaining false relationships [26].

In this study, the approach was used to explore the causal relationships between all job surveys and the CCI and PiC variables. Prior to identifying causal relationships between the variables, all variables were standardized utilizing Z-scores. Subsequently, the relationships up to a 6-month lag in the surveys were examined.

4 Findings & Discussion

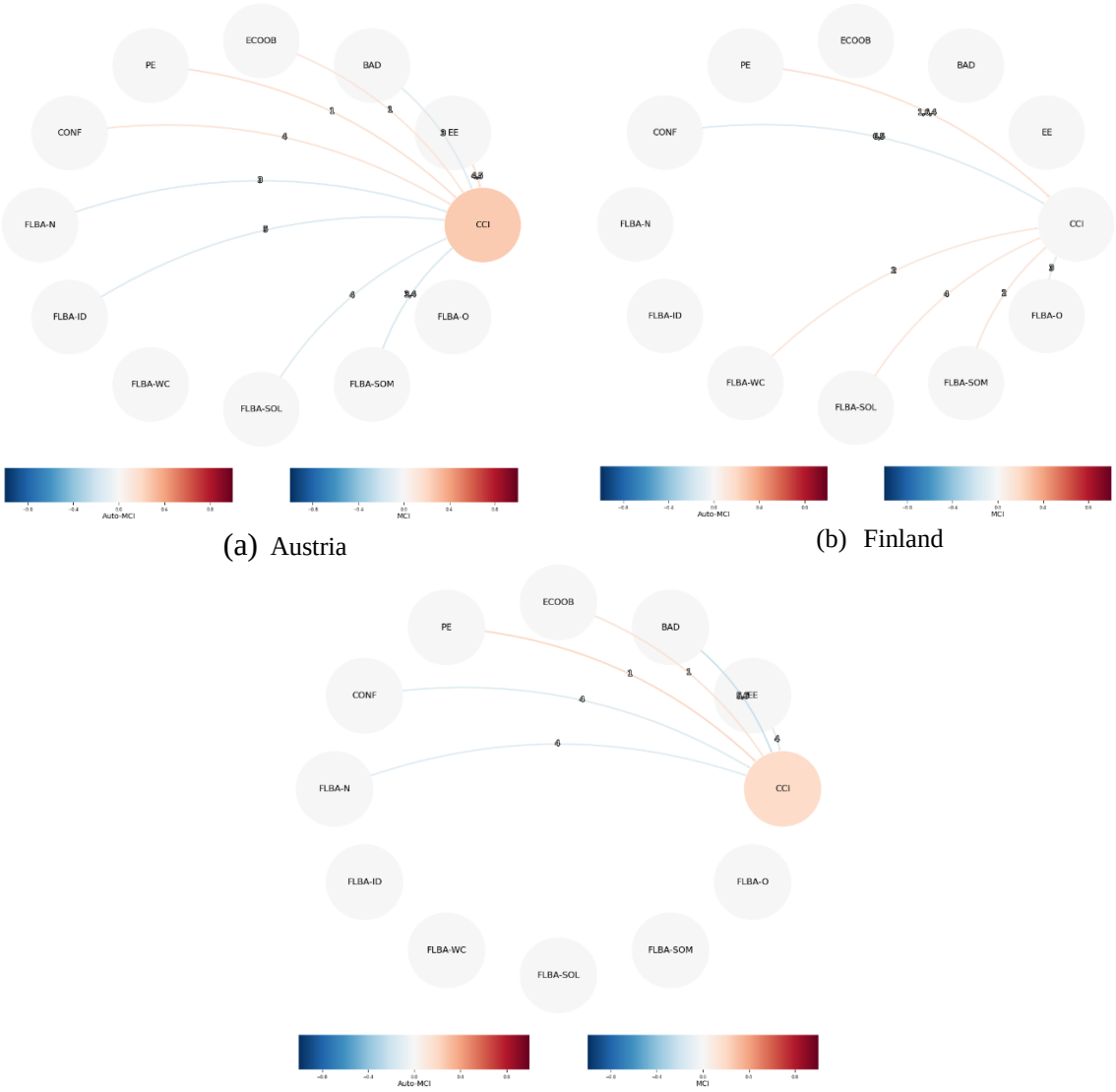
The measures of central tendency for the variables analyzed in this study are presented in Table 2.

Table 2. Mean and Std. Deviations of Variables

Variables	Austria		Finland		Netherlands	
	Mean	Std. Dev.	Mean	Std. Dev.	Mean	Std. Dev.
CONF	-8.93	18.35	-10.42	19.47	1.03	20.71
ECOOB	-14.72	19.70	-16.75	19.73	-2.87	22.94
EE	-3.13	25.50	-4.09	25.42	4.92	19.25
BAD	3.90	24.90	1.54	21.73	1.82	17.65
PE	6.34	21.02	-3.68	26.84	25.61	25.18
FLBA-N	48.78	15.44	33.74	12.34	62.06	12.29
FLBA-ID	16.25	9.23	39.04	18.64	15.60	12.81
FLBA-WC	11.64	13.78	3.98	5.02	5.51	8.11
FLBA-SOL	15.40	12.38	23.30	14.43	9.33	9.86
FLBA-SOM	3.17	7.34	4.97	5.40	4.42	7.53
FLBA-O	2.69	5.18	7.19	5.85	9.07	7.26
CCI (%)	0.26	0.63	0.18	0.37	0.23	0.48
PiC	2.92	19.64	1.78	15.80	6.40	42.43

According to comparing the cost and production indices of countries, Austria exhibits the highest volatility in costs, whereas the Netherlands has the greatest volatility in its production index. Surveys generally show a pessimistic outlook concerning order books. For the CONF, EE, BAD, and PE variables, it is noted that perspectives fluctuate over time; thus, the survey means tend to be low, followed by larger standard deviations. It is also evident that participants in all three countries generally stated that there were no factors limiting construction activity.

The analysis results show that many business surveys explain the change in the CCI (Fig. 1). The results show that, despite not being strong, there is a statistically significant causal relationship between survey data and the CCI in each country. In Austria, the EE and PE surveys were identified as exerting the most influence on the CCI (Fig. 1(a)). The effect coefficients of EE (lag 4) and PE (lag 1) on the CCI were determined to be 0.192 (p-value: 0.001) and 0.169 (p-value: 0.004) respectively. In Finland, similarly, the PE (lag 1) variable stands out as the variable with the highest explanatory power for the CCI, with a MCI coefficient of 0.171 (p-value: 0.003) (Fig. 1(b)). In the case of the Netherlands, the BAD (lag 6) and PE (lag 1) variables are the most significant variables, with MCI coefficients of -0.222 (p-value: 0.000) and 0.213 (p-value: 0.000), respectively (Fig. 1(c)). The results show that there is a significant causal relationship between the price expectation survey and cost index in all three countries. The notable relationship between a price expectations and the cost index suggests that the prior period's price expectations survey has the potential to be regarded as a predictive indicator. In addition, it has been found that the employment survey in Austria and the construction activity survey in the Netherlands show causal relationships with cost index. The findings indicate, in particular, that the PE variable has the potential to contribute to CCI forecasts.



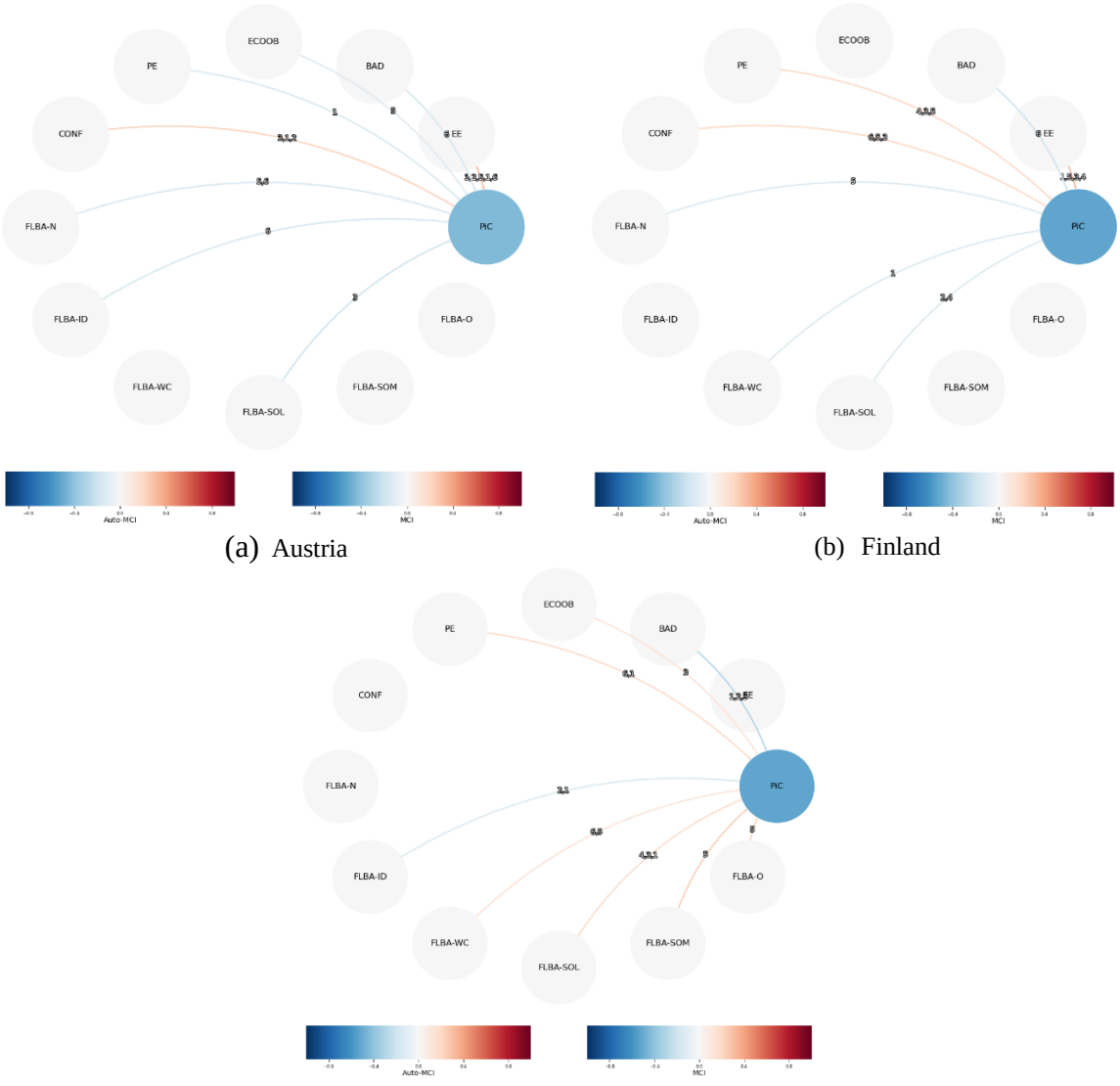
(a) Austria (b) Finland

(c) Netherlands

Fig. 1. PCMCI Results on CCI

In the second phase of the study, the causal relationships between the survey data and the construction production index were explored. The causal relationships between the business surveys and PiC are shown in Fig. 2. The findings indicate that the surveys show much stronger relationship with PiC. In Austria, the strongest causal relationships with PiC are EE (lag 3) and EE (lag 2) (Fig. 2(a)). The MCI coefficients for these two variables with respect to PiC are 0.313 (p-value: 0.000) and 0.300 (p-value: 0.000), respectively. On the other hand, there is a relatively weaker but still significant causal relationship between CONF (lag 3) and PiC (MCI: 0.222, p-value: 0.000). The data from Finland also confirms that there is a strong causal relationship between the EE (lag 1) variable and PiC with MCI: 0.309 (p-value: 0.000) (Fig. 2(b)). The findings indicate that the most appropriate business survey indicator for identifying changes in production in the construction sector in Austria and Finland is employment expectations. However, the findings have not been confirmed in the Netherlands. Unlike in other countries, the variables BAD (lag 1, 2 and 3) stand out as having a significant and strong causal relationship with the PiC variable. Interestingly, while a negative MCI coefficient (-0.283, p-value: 0.000) was observed between BAD (lag 1) and PiC, positive causal relationships were identified between BAD (lag 2 and 3) and PiC, with coefficients of 0.195 and 0.187, respectively (p-value: 0.001). It is believed that this situation indicates that, particularly with

the development of new projects, a decline in production was observed in the short term as a result of the shift in the workforce, but that the decline recovered in later periods and production increased. Finally, a moderate causal relationship was found in the Netherlands between the FLBA-SOM (lag 5) variable and PiC (MCI: 0.239, p-value: 0.000). This shows that the increase in production was reflected in a rise in demand for machinery and materials.



(a) Austria (b) Finland

(c) Netherlands

Fig. 22. PCMCI Results on PiC

5 Conclusion

This study was conducted to investigate the potential of business survey time-series data in construction project management. The study identified causal relationships between the construction cost and production indices and the construction business surveys published monthly by statistical offices. The time-series data were obtained from the Eurostat database. Causal relationships between the lagged values of each survey and the sector indices were identified using the PCMCI algorithm. The results indicate that there exist notable relationships among the variables, even in the absence of strong connections. The EE and PE variables have a causal relationship with the CCI. In one of the three countries, it was found that the BAD variable also has a causal relationship with the CCI. Analysis of the causal relationships

between the surveys and production revealed that the EE and BAD variables have a significant causal relationship with PiC.

The research findings provide important insights for future CCI and PiC forecasting studies. The integration of the specified variables into forecasting models possesses the ability to aid in model advancement. However, validation of the results across different economies would strengthen the findings.

References

[1] Eurostat, Housing in Europe – 2025 edition, (2025). doi: 10.2785/1681390.

[2] Naderpajouh N., Choi J., and Hastak M., Exploratory framework for application of analytics in the construction industry. J. Manag. Eng., 32(2), (2016). doi: 10.1061/(ASCE)ME.1943-5479.0000409.

[3] Ofori G., Indicators for measuring construction industry development in developing countries. Build. Res. Inf. 29(1), pp. 40–50, (2001). doi: 10.1080/09613210150208787.

[4] Eurostat, Businesses in the construction sector. 2026. [Online]. Available: https://ec.europa.eu/eurostat/statistics-explained/index.php?title=Businesses_in_the_construction_sector#Context last accessed 2026/08/05.

[5] Naderpajouh N., Boppana A., and Hastak M., The need for indices to assess the health of the construction industry. in Construction Research Congress 2012, Reston, VA: American Society of Civil Engineers, May 2012, 1510–1519. doi: 10.1061/9780784412329.152.

[6] Aydinli S., Impact of unexpected conditions on construction cost forecasting performance: evidence from Europe. Constr. Manag. Econ. 42(9), 787–801, (2024). doi: 10.1080/01446193.2024.2328700.

[7] Shiha A. and Dorra E. M., Resilience index framework for the construction industry in developing countries. J. Constr. Eng. Manag. 149(4), 2023. doi: 10.1061/JCEMD4.COENG-12942.

[8] Adamowicz E., Dudek S., and Walczyk K., The use of business survey data in macroeconomic analysis and forecasting. Pr. i Mater. Inst. Rozw. Gospod. SGH 74, pp. 357–375, (2004).

[9] Cesaroni T. and Iezzi S., The predictive content of business survey indicators: evidence from SIGE," J. Bus. Cycle Res. 13(1), 75–104, (2017). doi: 10.1007/s41549-017-0015-8.

[10] Giannone D., Reichlin L., and Small D., Nowcasting: The real-time informational content of macroeconomic data. J. Monet. Econ. 55(4), 665–676, (2008). doi: 10.1016/j.jmoneco.2008.05.010.

[11] Lemmens A., Croux C., and Dekimpe M. G., On the predictive content of production surveys: A pan-European study. Int. J. Forecast. 21(2), 363–375, (2005). doi: 10.1016/j.ijforecast.2004.10.004.

[12] Kaufmann D. and Scheufele R., Business tendency surveys and macroeconomic fluctuations. Int. J. Forecast. 33(4), 878–893, (2017). doi: 10.1016/j.ijforecast.2017.04.005.

[13] Klein L. R. and Özmucur S., The use of consumer and business surveys in forecasting. Econ. Model. 27(6), 1453–1462, (2010). doi: 10.1016/j.econmod.2010.07.005.

[14] Claveria O., Monte E., and Torra S., Economic forecasting with evolved confidence indicators. Econ. Model. 93, 576–585, (2020). doi: 10.1016/j.econmod.2020.09.015.

[15] Hansson J., Jansson P., and Löf M., Business survey data: Do they help in forecasting GDP growth?. Int. J. Forecast. 21(2), 377–389, (2005) doi: 10.1016/j.ijforecast.2004.11.003.

[16] Claveria O., Monte E., and Torra S., A genetic programming approach for estimating economic sentiment in the Baltic countries and The European Union, Technol. Econ. Dev. Econ. 27(1), 262–279, (2021). doi: 10.3846/tede.2021.13989.
[17] Lehmann R., The forecasting power of the IFO business survey. J. Bus. Cycle Res. 19(1), 43–94, (2023). doi: 10.1007/s41549-022-00079-5.
[18] Eurostat, "Eurostat Database." [Online]. Available: https://ec.europa.eu/eurostat/data/database, last accessed 2026/08/05.
[19] Eurostat, "Construction confidence indicator and survey results - monthly data." [Online]. Available: https://ec.europa.eu/eurostat/databrowser/view/ei_bsbu_m_r2__custom_21723004/default/table, last accessed 2026/08/05.
[20] Eurostat, "Construction producer prices or costs, new residential buildings - monthly data." [Online]. Available: https://ec.europa.eu/eurostat/databrowser/view/sts_copi_m__custom_22076289/default/table, last accessed 2026/08/05.
[21] Eurostat, "Production in construction - monthly data." [Online]. Available: https://ec.europa.eu/eurostat/databrowser/view/sts_copi_q/default/table?lang=en, last accessed 2026/08/05.
[22] European Commission, The Joint Harmonised EU Programme of Business and Consumer Surveys - User Guide. (2021).
[23] Runge J., Nowack P., Kretschmer M., Flaxman S., and Sejdinovic D., Detecting and quantifying causal associations in large nonlinear time series datasets. Sci. Adv. 5(11), (2019). doi: 10.1126/sciadv.aau4996.
[24] Chen Z. *et al.*, Intelligent temporal causal inference framework for wastewater treatment plant nitrogen removal: Multi-stage spurious causal elimination. Bioresour. Technol., 439, 133394, (2026). doi: 10.1016/j.biortech.2025.133394.
[25] Mustofa Irawan A. *et al.*, Multiparameter causal models for the estimation and explainability of wildfire burned area. IEEE J. Sel. Top. Appl. Earth Obs. Remote Sens. 18, 14501–14516, (2025). doi: 10.1109/JSTARS.2025.3573263.
[26] Yang J. and Zhang M., Data-driven causal networks for pork supply chain risk analysis in Sichuan Province. Sci. Rep. (2026). doi: 10.1038/s41598-026-60441-w.

Publication Note
This paper was peer-reviewed, accepted for presentation, and included in the proceedings of the ACE2026 – International Conference on Advances in Civil Engineering, held on 12–14 October 2026 in Trabzon, Türkiye.

This paper may be cited as follows:
Aydınlı S., "Identifying Key Business Survey Indicators to Predict Construction Production and Cost Indices," in Proceedings of the ACE2026 – International Conference on Advances in Civil Engineering, Trabzon, Türkiye, 12–14 October 2026.

Artificial Intelligence Adoption in Construction Management: A Bibliometric Analysis of Emerging Trends, Opportunities, and Future Directions

Özge ALBOĞA*
0000-0002-2848-8373, Independent Scholar, Adana, Türkiye
*albogaozge@gmail.com

Abstract. In recent years, the acceleration of digital transformation has led to a notable increase in academic research on the application of artificial intelligence (AI) technologies in construction management. Machine learning, deep learning, and AI-enabled decision making systems, in particular, have been increasingly applied in many construction management applications, such as project management, risk management, process optimization, and resource planning. This study aims to investigate research trends, development patterns, and future directions for the integration of artificial intelligence in construction management through bibliometric analysis. A total of 249 academic publications published between 2020 and 2026 and indexed in the Web of Science Core Collection were examined. VOSviewer software was used for bibliometric mapping and visualization. The analyses included keyword co-occurrence analysis, overlay visualization, and density analysis. The results show that artificial intelligence has emerged as a central research focus in the construction management literature. Recent studies have expanded from earlier research concentrating on machine learning-based risk prediction and safety management applications toward AI-supported construction project management, integrated decision-support systems, and intelligent project management approaches. A significant increase in publication volume has been observed since 2024. The findings are expected to contribute to understanding the current state of research on artificial intelligence adoption in construction management and to provide guidance for future studies.

Keywords: Artificial intelligence, construction management, bibliometric analysis, project management, VOSviewer.

1 Introduction

Construction projects are, by their very nature, socio-technical production systems in which numerous stakeholders work simultaneously and where site conditions, the supply chain, contractual relationships, and project objectives constantly interact. Project data is generated from various sources, including BIM models, work schedules, cost records, contracts, progress reports, images, sensors, and enterprise information databases [1]–[3]. In addition to increasing the amount of data, this diversity calls for the fast, accurate, and context-sensitive interpretation of data in a variety of formats and levels of detail in order to support choices about cost, schedule, safety, quality, and resource management. The sector's project-based, multi-stakeholder structure and low digitalization level further complicate translating this data into timely decisions. However, today’s advancing Artificial Intelligence (AI) technologies offer

capabilities such as classification, prediction, optimization, natural language processing, and computer vision that can support this decision-making burden [3]–[5].

Therefore, the maturation of the field depends not only on model accuracy but also on the integration of these components within project workflows. Previous studies have shown that AI has expanded through methods such as genetic algorithms, neural networks, machine learning (ML), natural language processing, and computer vision; the primary application contexts are project planning, optimization, progress tracking, and risk management [4]–[6]. Pan and Zhang [3] categorized the roles of AI in civil engineering and management in terms of data generation, knowledge extraction and decision-making/action processes. Taboada et al. [7] studied automation and decision support in project management and, as shown by Datta et al. [2] the application of AI/ML is mostly on planning and construction phases within the whole project life cycle. Recent reviews also indicate that cost, schedule, and safety management form a common, data-intensive, and interdependent axis of project management [8]. On the other hand, Aladağ et al. [9] used a scope-definition method to classify AI's contribution to construction project management processes in terms of planning, scheduling, cost estimation, and quality control; Savaş [10], expanded these findings to include organizational, cultural, and strategic dimensions, emphasizing that factors such as resistance to change and skill gaps can often take precedence over technical performance.

Technical model success, however, does not automatically lead to organizational adoption. Implementing AI in construction requires simultaneously managing technological suitability, data quality, business-process alignment, cost, competence, trust, and regulatory responsibilities. Watfa et al. [11] associated the adoption of automation with the on-site feasibility and low-cost proof-of-concept demonstrations, whereas Igwe et al. [12] reported that digital instruments are adopted unevenly in the area of cost management. Wider reviews find that barriers like data access, interoperability, upfront costs, skills gap, explainability, privacy and resistance to change slow down the scalability [13], [14]. The emergence of generative AI and Large Language Models (LLMs) offers opportunities in education, information access and contextual decision support, but has also brought issues such as accuracy, source reliability, hallucination and accountability into sharper focus [15]–[19].

Previous bibliometric studies have focused mostly on machine learning methods or AI-Building Information Modeling (BIM) integration [1], [4], [6]. In contrast, during the 2024–2026 period, there are only a limited number of studies that directly address the rapidly growing literature on generative AI, LLMs, explainable AI, and decision support within the context of construction management by updating it with record-level compliance checks and normalized author keywords. This study offers three complementary contributions: quantitatively determining the current publication momentum, analyzing the field's conceptual structure through eight thematic clusters and the relationships between them, and synthesizing the findings in terms of applicability and the requirements for responsible use. The study focuses on three research questions: (RQ1) How has publication output changed during the 2020–2026 period? (RQ2) Around which core concepts and thematic clusters are author keywords organized? (RQ3) What do temporal trends reveal about the opportunities, limitations, and future research agenda of AI in construction management?

2 Materials and Methods

The study is based on a three-phase design consisting of bibliometric performance analysis, keyword-based science mapping, and contextual thematic interpretation. As part of the performance analysis, changes in the number of publications over the years were examined; the

relationships between keywords and the resulting clusters were evaluated through science mapping. In the contextual thematic interpretation phase, the identified patterns were discussed within the framework of construction management functions, debates regarding the adoption of artificial intelligence, and potential future research directions. This approach allows bibliometric findings to be evaluated not only through numerical distributions but also within the scope of the relevant literature.

2.1. Data source, search, and selection

The data were obtained in August 2026 from the Web of Science Core Collection database, within the scope of accessible indexes. The search query used in the "Topic" field is as follows: ("artificial intelligence" OR "AI" OR "machine learning") AND ("construction management" OR "construction project management"). The search results were limited to studies published between 2020 and 2026, with the document types "Article" and "Review Article," and published in English. The Web of Science was selected because it presents bibliographic records in a standardized format and allows author keywords and citation information to be imported into the VOSviewer software. The initial search yielded 299 records. Since the presence of search terms in the title, abstract, or keywords does not necessarily mean that each record is directly relevant to the scope of the study, the titles and abstracts of the studies were also reviewed. Studies were included if AI/ML served as a method or decision-support tool for cost, time, risk, safety, quality, contracts, planning, training, or asset management.

Conversely, 48 studies were excluded from the scope because the terms "construction" or "management" appeared only in a limited or indirect manner; these studies focused primarily on materials science, medicine, urban planning, or cultural heritage and did not establish a sufficient connection to construction management. Additionally, two retracted publications were not included in the analysis set. The review revealed no duplicate Web of Science entries, and the final analysis set consisted of 249 publications. Since data for 2026 included only publications indexed in Web of Science through August 2026, the number of publications for that year was evaluated with caution when compared directly to complete years.

2.2. Bibliometric analysis

Bibliometric analysis enables the examination of development and relationship patterns within large sets of publications through performance indicators and science mapping [20], [21]. VOSviewer is one of the tools widely used in the literature for bibliometric analysis [22]. Therefore, VOSviewer 1.6.20 was used in this study as well. Author keywords were selected as the unit of analysis because they directly reflect the conceptual focus highlighted by the authors of the studies. In the full count, the presence of a keyword in each record is weighted equally. Node size represents the number of occurrences (Occurrence-O); a link indicates the co-occurrence of two terms in the same record; and Total Link Strength (TLS) represents the sum of all co-occurrence links for a term in the network. In the "Overlay" view, colors represent the occurrence-weighted average publication year, while in the "Density" view, they represent local neighborhood density weighted by term weight [21], [23].

The author keyword is present in 239 of the 249 records. The 843 unique terms in the raw data were normalized using a canonical thesaurus file to prevent plural/singular forms, abbreviations, and spelling variants from fragmenting the network. This involved (i) merging spelling/abbreviation variants (e.g., AI, ML, BIM, LLM), (ii) standardizing singular/plural forms, and (iii) removing generic methodological terms (e.g., "systematic literature review"). The minimum occurrence threshold was set at three, and all 50 terms meeting this threshold were included in the analysis. The software's default settings were retained for clustering and

visualization. Cluster names were not automatically assigned by VOSviewer; instead, they were carefully assigned by the researchers based on term composition and reported in Table 1 along with representative terms.

3 Results and Discussion

3.1. The Chronological Development of Publications

The annual distribution of the final 249 publications is as follows: 11 in 2020, 16 in 2021, 25 in 2022, 17 in 2023, 37 in 2024, 62 in 2025, and 81 in 2026 (Fig. 1). Following a temporary decline in 2023, a marked acceleration occurred during the 2024–2026 period. These three years' account for 72.3% of total publications, while 2025–2026 alone accounts for 57.4%. When comparing full years, the number of publications in 2025 is 5.64 times that of 2020. Although the 2026 data covers only records indexed through August 5, it has already surpassed the 2025 level. However, due to the partial year, indexing delays, and the query's sensitivity to specific terms, this value should be interpreted not as a growth estimate but as a descriptive indicator of the field's current research intensity.

This acceleration is consistent with the association of AI with project management, BIM-based digital ecosystems, text analytics, and generative AI applications, beyond individual prediction problems [1], [17], [24], [25]. The broadening of the research focus brings to the forefront the combined use of images, text, and structured data within the same project problem, as well as the integration of prediction outputs into workflows such as decision support and automated reporting [19], [26], [27].

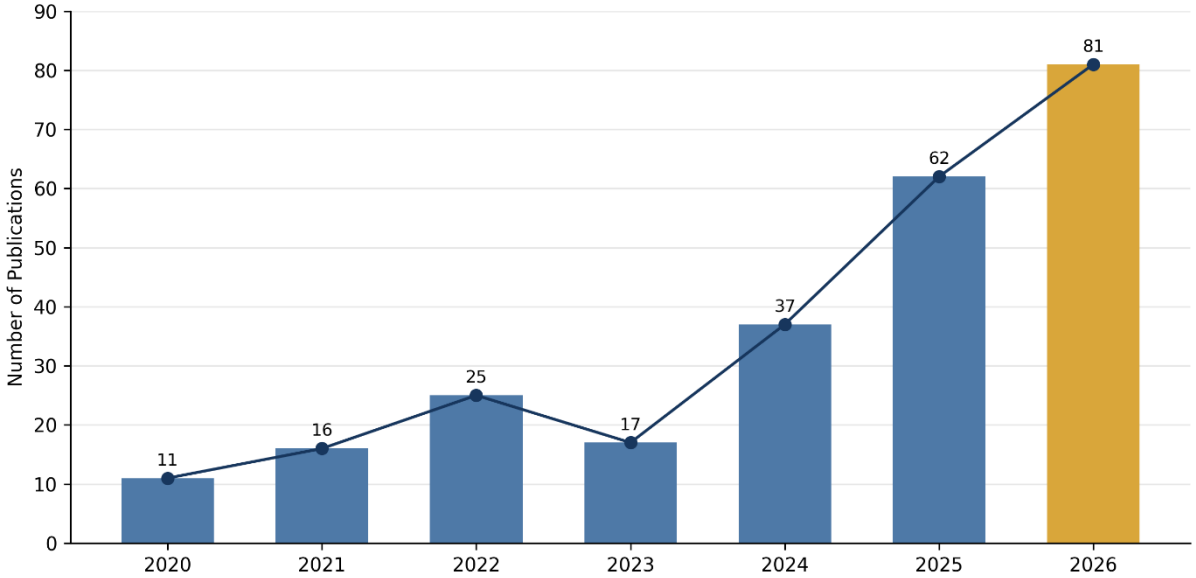


Fig. 1. Number of publications by year in the final sample

3.2. The Core of the Keyword Network and Thematic Clusters

Visualizations of the network based on author keywords, temporal overlap, and density are presented in Figure 2. In Figure 2a, "construction management" (O=85; TLS=157) is the largest node; "artificial intelligence" (O=75; TLS=153) and "machine learning" (O=68; TLS=111) follow. Building information modeling (O=24; TLS=53), deep learning (O=22; TLS=49), construction project management (O=21; TLS=30), and project management (O=16; TLS=42) are other prominent terms. The strongest relationships were found between construction management and machine learning (29), artificial intelligence and construction management

(26), artificial intelligence and building information modeling (14), and artificial intelligence and machine learning (11).

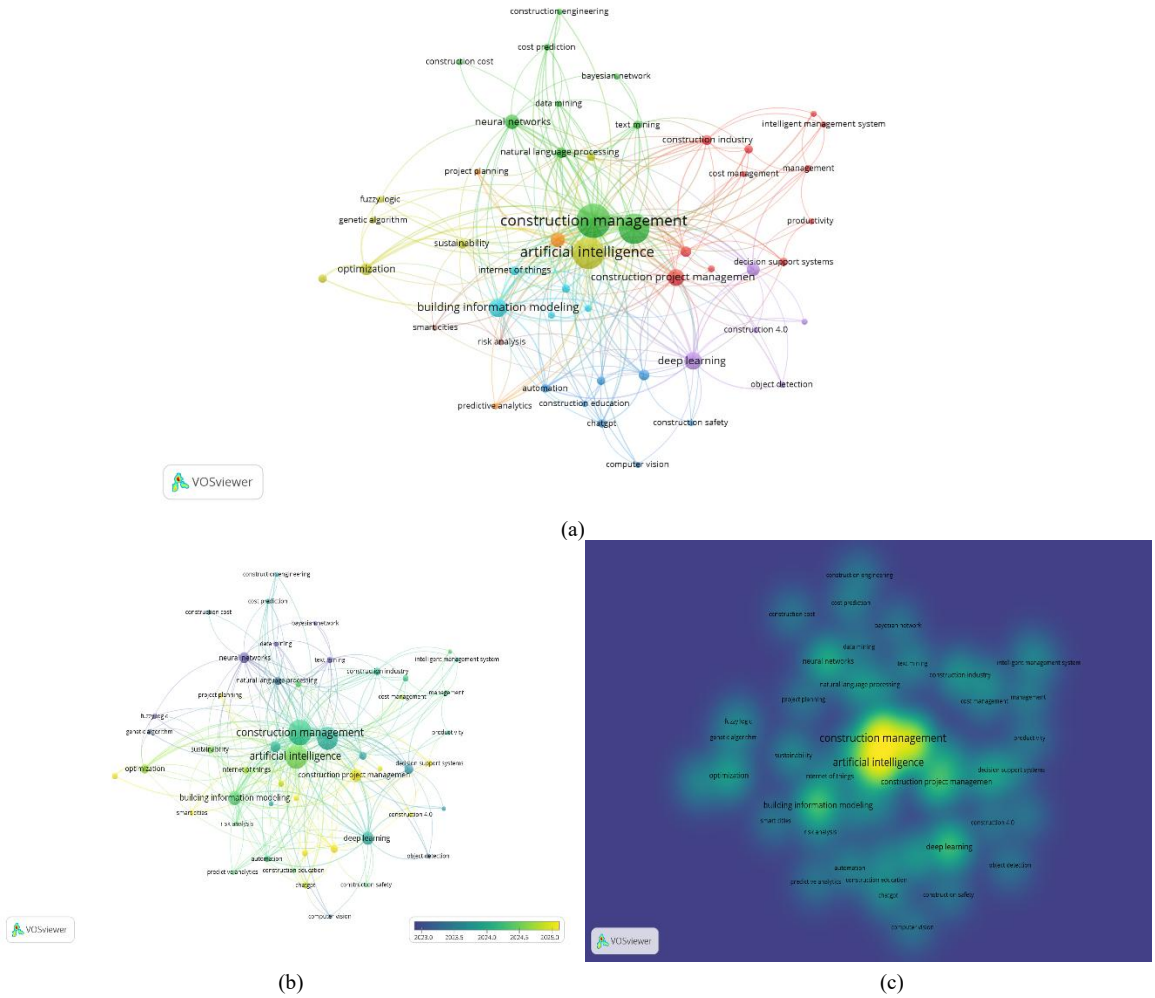


Fig. 2. Visualizations of author keywords showing (a) network, (b) temporal overlap, and (c) density

Tablo 1. Thematic Summary of VOSviewer Keyword Clusters

Cluster	Proposed theme	n	Representative terms (O; TLS)
1	Project management and decision support	11	construction project management (21; 30); risk management (9; 23); decision support systems (5; 9)
2	Machine learning and text/data analytics	10	construction management (85; 157); machine learning (68; 111); neural networks (15; 36)
3	Generative AI, automation, education, and safety	7	large language models (9; 19); automation (5; 21); ChatGPT (5; 15)
4	AI-supported optimization and sustainability	7	artificial intelligence (75; 153); optimization (11; 23); sustainability (6; 21)
5	Deep learning and visual/technical prediction	5	deep learning (22; 49); construction (12; 25); object detection (3; 7)
6	BIM-integrated connected and smart construction	5	building information modeling (24; 53); internet of things (6; 20); smart construction (5; 18)
7	Project planning and predictive analytics	3	project management (16; 42); predictive analytics (3; 8); project planning (3; 6)
8	Risk analysis in the smart city context	2	risk analysis (3; 14); smart cities (3; 8)

Note: O = occurrences; TLS = total link strength.

The keyword network presented in Figure 2a, when evaluated in conjunction with Table 1, shows that the eight-cluster solution space does not consist of a single technical axis. Cluster K2 forms the methodological core by combining machine learning with text/data analytics in construction management, while Cluster K4 forms the performance and objective functions layer through the integration of AI, optimization, and sustainability. In Figure 2a, the closeness of these two clusters to the center of the network, and their dense interconnection, indicates that methodological and managerial themes are not developing independently of each other. Prediction and information extraction are often related to the optimization of resources, time, cost, or environmental performance, as can be seen by the fact that the total inter-cluster connection strength between these two clusters is 69, the largest value in the network. The co-occurrence of construction project management, risk management, cost management and decision support systems in K1 indicates that AI has shifted from a technical model to managerial decision support [3], [7], [28]. The combination of project management, predictive analytics and project planning in K7 represents a more limited but management-oriented subfield, where foresight is brought into the planning and control cycle.

Terms such as deep learning, object detection and cost estimation in K5 are indicative of technical applications based on automatic feature extraction from images and high-dimensional data. As shown in Figure 2a, the fact that K5 operates within a more limited but distinct subnetwork in the deep learning environment suggests that these applications, while connected to the main network, are more specialized. This approach has shown promise for applications such as site monitoring, quality defect detection and cost estimation, but it is sensitive to issues like data volume, class imbalance and explainability [5], [29], [30]. The convergence of BIM, Internet of Things (IoT), smart construction, digital transformation and digital twins in K6, in contrast, is indicative of the interconnected data infrastructure that powers these models [1], [24]. The connections between K5 and K6 on the network map indicate that sensing and prediction methods are considered in conjunction with technologies that provide digital representation and data flow.

In K3, LLMs, ChatGPT, generative AI, automation, construction training, and safety are grouped under the same theme. The fact that the terms “large language models,” “ChatGPT,” and “generative artificial intelligence” appear in more contemporary color tones in Figure 2b indicates that this cluster represents one of the trends that gained prominence in the final years of the period under review. The occurrence-weighted average year for the cluster is 2024.79, making K3 one of the network’s most recent trends [16], [17]. Empirical studies show that progress is not merely conceptual but is highly dependent on the task and dataset. Lee et al. [15] found that RAG and fine-tuned models provided improvements of 21.5% and 26%, respectively, over the general-purpose GPT-4 in accessing construction safety information; Zhou et al. [27] reported that a multimodal knowledge graph incorporating domain-specific knowledge increased the accuracy of general-purpose LLMs in project management question-answering by an average of 30%. Xiao et al. [30] validated the use of ChatGPT with computer vision for the automatic generation of daily reports at a real construction site over the course of one month. Ray et al. [31], Smetana et al. [32] and Al Omari et al. [33] reported similarly high performance in extracting and classifying accident-narrative text at scale. These findings support the potential of LLMs for information retrieval, reporting, and safety analytics, but also indicate that performance depends on domain knowledge, verified sources, task design, and human supervision. The fact that K8 appears in Figure 2a as a small, peripheral cluster consisting of only two terms suggests that risk analysis within the framework of smart cities is underrepresented in the dataset under examination. When assessed together, the field can be divided into three high-level strata. The first layer is the data/representation infrastructure, such

as BIM, IoT, digital twins, images, and text. The second layer generates predictions, classifications, and options through machine learning, deep learning, natural language processing, and optimization.

These results provide evidence of the potential of LLMs in information retrieval, reporting and safety analytics, but also show that performance is dependent on domain knowledge, verified sources, task design and human supervision. The fact that K8 appears in Figure 2a as a small, peripheral cluster with only two terms suggests that risk analysis in the setting of smart cities is underrepresented in the dataset under examination. When assessed together, the field can be divided into three high-level strata. The first layer is the data/representation infrastructure, such as BIM, IoT, digital twins, images and text. The second layer generates predictions, classifications and options through machine learning, deep learning, natural language processing and optimization. The third layer bridges analytical results with human decision-making and organizational workflows using project management, decision support systems, explainable AI, and LLM interfaces. Concepts associated with the top-two layers are more prevalent in the literature, as demonstrated by the unique core around "construction management," "artificial intelligence," and "machine learning" in the density visualization of Figure 2c. The link between data infrastructure, technical analysis, and management tasks is instead reflected by the secondary density clusters around "BIM," "deep learning," and "construction project management." The presence of "generative AI," "explainable AI," and "decision support" in the more recent color tones of Figure 2b also suggests that research on the third layer has been more prevalent in recent years.

3.3. Temporal orientation, intensity, and research agenda

Theoretically, the findings indicate that AI research in construction management has expanded from an algorithm-centered approach toward a system- and human-centered integration. From a managerial perspective, the findings indicate that AI investments should be managed as a phased implementation portfolio rather than a single-step transformation beginning with technology procurement. This should proceed in phases: evaluating data ownership and quality; selecting bounded use cases with clear success metrics (e.g., cost estimation, reporting, contract screening); and embedding human approval, explanation, and audit trails into the workflow. The decision to scale up should only be made after external validation has been achieved using project performance indicators such as accuracy, time savings, error costs, decision quality, user trust, and field safety. This approach can reduce the risk of early and uncontrolled deployment of high-visibility technologies into processes with low readiness levels [11], [13], [28].

4 Conclusion

This study examined the development, conceptual structure, and current trends of 249 Web of Science (WoS) publications on the adoption of AI in construction management during the 2020–2026 period. The fact that 72.3% of the publications were published in the last three years and that 2026 reached the highest number of publications demonstrates the rapid expansion of this research field. The keyword network generated 50 terms, 8 clusters, 265 connections, and 550 TLS; "construction management," "artificial intelligence," and "machine learning" formed the core of the field. The eight clusters revealed a multi-layered research structure in which AI extends from machine learning and forecasting to optimization, sustainability, BIM-IoT-digital twin integration, project planning, decision support, and generative AI. The strongest inter-cluster link—between machine learning/text analytics and AI-supported optimization/sustainability—indicates that technical methods are increasingly being linked to managerial objectives and performance metrics.

The study's key contribution lies in presenting both classical technical methods and new managerial and generative AI themes within the same contemporary framework and maintaining a clear distinction between bibliometric visibility and actual organizational adoption. Going forward, producing more models will not be sufficient; reliable data infrastructure, explainable outputs, human oversight, and measurable field impact must be addressed collectively. Success should therefore be measured not only by prediction accuracy but also by decision quality, accountability, and contribution to project performance. This approach offers a more realistic research and application framework for the transition of AI in construction management from experimental tools to reliable and institutionalized decision support. Since this study covers co-occurrence analysis based solely on articles and reviews published in English and indexed in the Web of Science Core Collection, the results are sensitive to the choice of database, language, and keywords. For future studies, it is recommended to include different databases such as Scopus and to conduct sensitivity analyses using alternative thresholds and clustering settings. Furthermore, it may be beneficial to support the bibliometric findings with surveys, case studies, and field validation research that examine the actual use of artificial intelligence at the project and organizational levels.

References

1. Peng, X.: Digitalization of the construction industry driven by AI and BIM: A bibliometric study using CiteSpace and VOSviewer. Engineering 17(11), 582–599 (2025).
2. Datta, S.D., Islam, M., Rahman Sobuz, M.H., Ahmed, S., Kar, M.: Artificial intelligence and machine learning applications in the project lifecycle of the construction industry: A comprehensive review. Heliyon 10(5), e26888 (2024).
3. Pan, Y., Zhang, L.: Roles of artificial intelligence in construction engineering and management: A critical review and future trends. Automation in Construction 122, 103517 (2021).
4. Darko, A., Chan, A.P.C., Adabre, M.A., Edwards, D.J., Hosseini, M.R., Ameyaw, E.E.: Artificial intelligence in the AEC industry: Scientometric analysis and visualization of research activities. Automation in Construction 112, 103081 (2020).
5. Baduge, S.K., et al.: Artificial intelligence and smart vision for building and construction 4.0: Machine and deep learning methods and applications. Automation in Construction 141, 104440 (2022).
6. Garcia, J., et al.: Machine learning techniques applied to construction: A hybrid bibliometric analysis of advances and future directions. Automation in Construction 142, 104532 (2022).
7. Taboada, I., Daneshpajouh, A., Toledo, N., de Vass, T.: Artificial intelligence enabled project management: A systematic literature review. Applied Sciences 13(8), 5014 (2023).
8. Gao, Y., Antwi-Afari, M.F., Huang, Y., Chen, Z.-S., Manzoor, B.: Artificial intelligence in construction project management: A systematic literature review of cost, time, and safety management. Buildings 16(5), 1061 (2026).
9. Aladağ, H.: Contribution of artificial intelligence (AI) to construction project management processes: State of the art with scoping review method. Sigma Journal of Engineering and Natural Sciences 42(5), 1654–1669 (2024).
10. Savaş, S.: Artificial intelligence in construction project management: Trends, challenges and future directions. Journal of Design for Resilience in Architecture and Planning 6(2), 221–238 (2025).
11. Watfa, M., Bykovski, A., Jafar, K.: Testing automation adoption influencers in construction using light deep learning. Automation in Construction 141, 104448 (2022).
12. Igwe, U.S., Mohamed, S.F., Azwarie, M.B.M.D., Ugulu, R.A., Ajayi, O.: Acceptance of

contemporary technologies for cost management of construction projects. Journal of Information Technology in Construction 27, 864–883 (2022).
13. Regona, M., Yigitcanlar, T., Xia, B., Li, R.Y.M.: Opportunities and adoption challenges of AI in the construction industry: A PRISMA review. Journal of Open Innovation: Technology, Market, and Complexity 8(1), 45 (2022).
14. Salimimoghadam, S., et al.: The rise of artificial intelligence in project management: A systematic literature review of current opportunities, enablers, and barriers. Buildings 15(7), 1130 (2025).
15. Lee, J., Ahn, S., Kim, D., Kim, D.: Performance comparison of retrieval-augmented generation and fine-tuned large language models for construction safety management knowledge retrieval. Automation in Construction 168, 105846 (2024).
16. Jelodar, M.B.: Generative AI, large language models, and ChatGPT in construction education, training, and practice. Buildings 15(6), 933 (2025).
17. Alwashah, Z., Xiao, B., Liu, H., Mueller, S.T., Shao, X.: Generative artificial intelligence for construction: Use cases, trends, challenges, and opportunities. Journal of Building Engineering 112, 113802 (2025).
18. Naderi, H., Shojaei, A.: Large-language model (LLM)-powered system for situated and game-based construction safety training. Expert Systems with Applications 283, 127887 (2025).
19. Wang, Y., Luo, H., Fang, W.: An integrated approach for automatic safety inspection in construction: Domain knowledge with multimodal large language model. Advanced Engineering Informatics 65, 103246 (2025).
20. Zupic, I., Čater, T.: Bibliometric methods in management and organization. Organizational Research Methods 18(3), 429–472 (2015).
21. Donthu, N., Kumar, S., Mukherjee, D., Pandey, N., Lim, W.M.: How to conduct a bibliometric analysis: An overview and guidelines. Journal of Business Research 133, 285–296 (2021).
22. Aria, M., Cuccurullo, C.: Bibliometrix: An R-tool for comprehensive science mapping analysis. Journal of Informetrics 11(4), 959–975 (2017).
23. van Eck, N.J., Waltman, L.: Software survey: VOSviewer, a computer program for bibliometric mapping. Scientometrics 84(2), 523–538 (2010).
24. Pan, Y., Zhang, L.: Integrating BIM and AI for smart construction management: Current status and future directions. Archives of Computational Methods in Engineering 30(2), 1081–1110 (2023).
25. Shamshiri, A., Ryu, K.R., Park, J.Y.: Text mining and natural language processing in construction. Automation in Construction 158, 105200 (2024).
26. Wu, C., et al.: Natural language processing for smart construction: Current status and future directions. Automation in Construction 134, 104059 (2022).
27. Zhou, S., et al.: Augmenting general-purpose large-language models with domain-specific multimodal knowledge graph for question-answering in construction project management. Advanced Engineering Informatics 65, 103142 (2025).
28. Zhu, H., Hwang, B.-G., Ngo, J., Tan, J.P.S.: Applications of smart technologies in construction project management. Journal of Construction Engineering and Management 148(4), 04022010 (2022).
29. Davila Delgado, J.M., Oyedele, L.: Deep learning with small datasets: Using autoencoders to address limited datasets in construction management. Applied Soft Computing 112, 107836 (2021).
30. Xiao, B., Wang, Y., Zhang, Y., Chen, C., Darko, A.: Automated daily report generation from construction videos using ChatGPT and computer vision. Automation in Construction 168, 105874 (2024).

31. Ray, U., Arteaga, C., Ahn, Y., Park, J.: Enhanced identification of equipment failures from descriptive accident reports using language generative model. Engineering, Construction and Architectural Management 33(3), 2298–2313 (2026).
32. Smetana, M., Salles de Salles, L., Khazanovich, L.: Improving large language model assisted categorization and classification of highway construction accidents. Engineering Applications of Artificial Intelligence 176, 114798 (2026).
33. Al Omari, M., Itair, M., Eslahi, M., Loywick, J., El Meouche, R.: An integrated analytics method for structured accident analysis and safety decision support in construction. Decision Analytics Journal 19, 100711 (2026)

Author Contribution Statement

- *Conceptualization:* Özge ALBOĞA
- *Methodology:* Özge ALBOĞA
- *Investigation:* Özge ALBOĞA
- *Writing – Original Draft:* Özge ALBOĞA
- *Writing – Review & Editing:* Özge ALBOĞA

Note: Following the conference, this Publication Note will be added to each paper; therefore, authors are kindly requested not to remove the note below and to complete the author(s) and paper title information.

Publication Note

This paper was peer-reviewed, accepted for presentation, and included in the proceedings of the ACE2026 – International Conference on Advances in Civil Engineering, held on 12–14 October 2026 in Trabzon, Türkiye.

This paper may be cited as follows:

ALBOGA O, "Artificial Intelligence Adoption in Construction Management: A Bibliometric Analysis of Emerging Trends, Opportunities, and Future Directions," in Proceedings of the ACE2026 – International Conference on Advances in Civil Engineering, Trabzon, Türkiye, 12–14 October 2026.

Integrated Decision Support Model for Project Management Software Selection Using DEMATEL, TODIM, and CODAS

Büşra Ziypak[1], Ümit Bahadır[2], Fatemeh Mostofi[3] and Vedat Toğan[4]
[1] https://orcid.org/0009-0005-7043-1353, Karadeniz Technical University, Civil Engineering Department, Trabzon, Türkiye, ziypakbusra@gmail.com
[2] https://orcid.org/0000-0002-9878-8769, Karadeniz Technical University, Civil Engineering Department, Trabzon, Türkiye, umitbahadir@ktu.edu.tr
[3] https://orcid.org/0000-0003-0974-1270, Karadeniz Technical University, Civil Engineering Department, Trabzon, Türkiye, fatemee.mostofi@gmail.com
[4] https://orcid.org/0000-0001-8734-6300, Karadeniz Technical University, Civil Engineering Department, Trabzon, Türkiye, togan@ktu.edu.tr

Abstract. The effective use of project management software capable of supporting planning, coordination, resource management, and real-time decision-making processes can support the successful execution of construction and engineering projects. However, selecting the most appropriate software remains a challenging problem because decision makers must evaluate multiple technical, operational, and organizational criteria simultaneously. This study develops an integrated multi-criteria decision-making model based on decision-making trial and evaluation laboratory (DEMATEL), TODIM (Portuguese acronym for interactive multi-criteria decision-making), and combinative distance-based assessment (CODAS) methods for project management software selection. The DEMATEL method is first applied to identify the interdependencies among evaluation criteria and determine their significance weights. Subsequently, TODIM is used to rank software alternatives by considering the behavioral tendencies and preferences of decision makers. In the final phase, the CODAS method is employed to validate and re-rank alternatives according to their distance from the negative ideal solution. The study adopts a group decision-making approach involving five academicians and five project managers. The evaluation criteria are established through the integration of literature findings and expert judgments, including emerging considerations such as artificial intelligence functionalities, automation features, and field usability performance. The findings show that functionality (K1) received the highest DEMATEL weight (0.1121), TODIM ranked MS Project first, and CODAS ranked Asana first, indicating that the final recommendation depends on the decision logic adopted.

Keywords: Project management software selection; Multi-criteria decision-making; DEMATEL; TODIM; CODAS.

1 Introduction

A project is a set of activities conducted to achieve planned objectives by delivering a unique product or service within a specified timeframe [1]. Project management is the planning, execution, monitoring, and control of a project within defined scope, time, cost, and quality constraints to achieve project objectives [2]. Activities such as cost estimation, resource planning, budget control, team management, documentation, and reporting, carried out from project design to final delivery, generate a large volume of data. As a result, manually managing project processes becomes increasingly difficult. Today, engineers and project managers extensively use project management software to facilitate project processes and improve project performance [1,3].

Project management software plays a critical role in effectively managing project scope within predefined time and budget constraints [4]. Accordingly, selecting the most appropriate software is an important process that directly contributes to project success [5,6]. However, the wide range of software products available on the market, with different functionalities and costs, makes selecting the most appropriate software a challenging task for project managers and requires the simultaneous evaluation of multiple factors [1,7]. Consequently, selecting software that satisfies the requirements of engineers, project managers, and experts becomes a multi-criteria decision-making (MCDM) problem [1]. Although various MCDM techniques have been applied to the project management software selection problem, studies addressing this problem remain limited in the existing literature [4,7].

In this study, MS Project, Primavera, and Asana were ranked using TODIM and CODAS according to ten DEMATEL-weighted criteria under a group decision-making approach.

2 Literature Review

Studies on the selection of enterprise and project management software and tools using MCDM methods have been examined in the literature. These studies can be classified into two groups: studies employing individual MCDM methods and studies adopting integrated MCDM frameworks.

Studies based on individual MCDM methods have employed techniques such as AHP, ANP, and MARCOS for software selection problems. Puska et al. [6] evaluated 4 software alternatives (MS Project, Asana, Primavera, and Basecamp) using the MARCOS method based on 6 criteria and identified Smartsheet as the best software alternative. Akbar et al. [4] applied the ANP method using 3 main criteria and 18 sub-criteria to evaluate OpenProject, Redmine, and MS Project, identifying Redmine as the most appropriate software. Kutlu et al. [5] evaluated three software alternatives (HP-PPM, MS Project, and Primavera) using the AHP method based on 4 main criteria and 17 sub-criteria. Based on expert evaluations from 3 sectors, HP-PPM was identified as the most appropriate alternative.

Studies based on integrated MCDM frameworks have combined different MCDM methods within a single decision-making framework. Ömürbek et al. [1] applied the AHP and TOPSIS methods using 4 main and 13 sub-criteria to evaluate 4 enterprise project management software alternatives, identifying Alternative A as the most suitable software. Ünal and Çetin [8] addressed CRM software selection using the Delphi technique together with the DEMATEL and TODIM methods based on 6 criteria and identified Alternative 5 as the most suitable CRM software. Karaatlı et al. [9] evaluated 23 Turkish sugar factories using the DEMATEL and Fuzzy TOPSIS methods based on 7 criteria. The criteria weights were determined by DEMATEL, and Ereğli, Ilgın, and Eskişehir were identified as the best-performing alternatives.

The existing literature indicates that software selection studies have mainly focused on traditional MCDM methods, whereas integrated decision-making frameworks and the consideration of interrelationships among criteria remain limited. Furthermore, recent technological developments and AI-related evaluation criteria have not been adequately considered. Therefore, this study proposes a hybrid framework in which the criteria are weighted using DEMATEL and the software alternatives are ranked using TODIM and CODAS. Since TODIM and CODAS are based on different decision-making principles, they were employed together to provide behavioural-based and distance-based evaluations of the software alternatives.

3 Methodology

In this section, the application procedures of the DEMATEL, TODIM, and CODAS methods employed in this study are presented with the corresponding mathematical formulation.

3.1 DEMATEL

DEMATEL is one of the MCDM methods developed to analyze and solve complex problems [9]. The method analyzes the cause-and-effect relationships among interdependent criteria and ranks them according to their relative importance [8,9]. By revealing the strength of the relationships among the criteria, DEMATEL enables the calculation of criterion weights [9]. The application steps of the DEMATEL method are presented below.

Step 1. Construction of the direct-relation matrix. In the first step, the influence of each criterion on the others is evaluated by the experts using the scale presented in Table 1. Based on the evaluations provided by the expert group, an $n \times n$ matrix is constructed for each expert. The direct-relation matrix (**A**) is then obtained from these matrices using Eq. (1), as shown in Eq. (2).

$$a_{ij} = \frac{1}{H}\sum_{k=1}^{H} x_{ij}^{ex} \quad i,\ j \in \{1, 2, 3, \ldots, n\} \tag{1}$$

in which, H denotes the number of experts participating in the study; x_{ij}^{ex} denotes the evaluation score assigned by the ex^{th} expert to represent the influence of criterion (i) on criterion (j); and a_{ij} denotes the average of the expert evaluations.

$$\mathbf{A} = \begin{bmatrix} a_{11} & \cdots & a_{1n} \\ \vdots & \ddots & \vdots \\ a_{n1} & \cdots & a_{nn} \end{bmatrix} \tag{2}$$

where, n denotes the number of criteria. Since the influence of a criterion on itself is not evaluated, the diagonal elements of matrix **A** are equal to zero.

Table 1. The measurement scale for DEMATEL (Karaatlı et al. [9]).

Numerical Value	Description
0	No influence
1	Low influence
2	Medium influence
3	High influence
4	Very high influence

Step 2. Normalization of the direct-relation matrix. In the second step, the normalized direct-relation matrix (**M**) is obtained from matrix **A** using Eqs. (3) and (4)

$$\mathbf{M} = k \times \mathbf{A} \tag{3}$$

$$k = min\left[\frac{1}{\max\limits_{1 \le i \le n} \sum_{j=1}^{n} |a_{ij}|}, \frac{1}{\max\limits_{1 \le i \le n} \sum_{j=1}^{n} |a_{ij}|}\right] \tag{4}$$

where, k denotes the normalization factor determined based on the maximum row and column sums of the direct-relation matrix.

Step 3. Construction of the total-relation matrix. In the third step, the identity matrix (**I**) is first constructed. Matrix **M** is then subtracted from identity matrix **I** and the total-relation matrix (**S**) is obtained using Eq. (5).

$$\mathbf{S} = \mathbf{M} \times (\mathbf{I} - \mathbf{M})^{-1} \tag{5}$$

Step 4. Determination of the cause-and-effect groups. In the fourth step, the cause-and-effect groups are determined using Eqs. (6) and (7). The row sums and column sums of the **S** are denoted by, respectively. The $D - R$ value indicates whether a criterion belongs to the cause or effect group. Criteria with positive $D - R$ values are classified as the cause group, whereas those with negative values belong to the effect group. The $D + R$ value represents the total level of interaction of each criterion within the system.
where $\mathbf{S} = [S_{i,j}]_{\mathrm{n}\times\mathrm{n}}$; $i, j \in \{1, 2, 3, \ldots, n\}$

$$D = \left[\sum_{j=1}^{n} S_{i,j}\right]_{n*1} \tag{6}$$

$$R = \left[\sum_{i=1}^{n} S_{i,j}\right]_{1*n} \tag{7}$$

An influence diagram is constructed using the obtained values. In the diagram, the horizontal axis represents the $D + R$ values, whereas the vertical axis represents the $D - R$ values.

Step 5. Calculation of the criterion weights. In the final step, the relative weight (w_i) representing the relative importance of each criterion within the system and the normalized weight (W_i) of each criterion are calculated using the $D + R$ and $D - R$ values through Eqs. (8) and (9).

$$w_i = \{(D_i + R_i)^2 + (D_i - R_i)^2\}^{1/2} \tag{8}$$

$$W_i = \frac{w_i}{\sum_{i=1}^{n} w_i} \tag{9}$$

3.2 TODIM

TODIM is a multi-criteria decision-making method based on Prospect Theory, proposed by Kahneman and Tversky in the 1970s, which explains how individuals make decisions under risk [8,10]. In this method, the alternatives are evaluated by considering the decision makers' behavior toward gains and losses [8,10]. For this purpose, the dominance values between the alternatives are calculated with respect to a criterion selected as reference, and the total dominance of each alternative over the other alternatives is determined [8,10]. The alternatives are ranked according to the obtained overall performance values [10]. The application steps of the TODIM method are presented below.

Step 1. Construction of the decision matrix. In the first step, the performance values of the alternatives under each criterion are determined by the decision makers, and the decision matrix (**X**) given in Eq. (10) is constructed.

$$\mathbf{X} = [x_{uc}]_{q\times p} = \begin{bmatrix} x_{11} & \cdots & x_{1p} \\ \vdots & \ddots & \vdots \\ x_{q1} & \cdots & x_{qp} \end{bmatrix} \tag{10}$$

where, q denotes the number of alternatives; p denotes the number of criteria; and x_{uc} denotes the performance value of alternative A_u with respect to criterion C_c.

Step 2. Construction of the normalized decision matrix. In the second step, the values of the **X** are normalized according to the benefit and cost type criteria using Eq. (11) and the normalized decision matrix $\mathbf{P} = [p_{uc}]_{q\times p}$ is obtained.

$$p_{uc} = \begin{cases} \frac{x_{uc} - min_u\, x_{uc}}{max_u\, x_{uc} - \min_u x_{uc}} & c \in C^+ \\ \frac{\max_u x_{uc} - x_{uc}}{\max_u x_{uc} - \min_u x_{uc}} & c \in C^- \end{cases} \quad (11)$$

in which, p_{uc} denotes the normalized performance value, whereas $C^+$and C^- denote the benefit and cost criteria, respectively.

Step 3. Calculation of the relative criteria weights. In the third step, a reference criterion is selected by the decision maker by considering the criterion weights obtained using DEMATEL. The criterion with the highest weight may be selected as the reference criterion [8]. The relative weights of the criteria with respect to the reference criterion are calculated using Eq. (12).

$$w_{cr} = \frac{w_c}{w_r} \quad (12)$$

here, w_c denotes the criterion weight; $w_r = \max\{ w_c | \, c = 1,2, \dots, p\}$ denotes the weight of the reference criterion; and w_{cr} denotes the relative criterion weight.

Step 4. Calculation of the dominance performances of the alternatives. In the fourth step, the dominance value of alternative A_u over alternative A_v with respect to criteria C_c is obtained using Eq. (13).

$$\phi(A_u, A_v) = \begin{cases} \sqrt{\frac{w_{cr}(P_{uc} - P_{vc})}{\sum_{c=1}^{p} w_{cr}}} & \text{if } P_{uc} - P_{vc} > 0 \\ 0 & \text{if } P_{uc} - P_{vc} = 0 \\ \frac{-1}{\theta} \sqrt{\frac{(\sum_{c=1}^{p} w_{cr})(P_{vc} - P_{uc})}{w_{cr}}} & \text{if } P_{uc} - P_{vc} < 0 \end{cases} \quad (13)$$

where θ is the attenuation factor of losses. When $\theta = 1$, losses affect the result in proportion to their actual values [10]. Accordingly, θ was set to 1 in this study.

The total dominance value of alternative A_u over alternative A_v across all criteria C_c is obtained using Eq. (14).

$$\delta(A_u, A_v) = \sum_{c=1}^{p} \phi_c\,(A_u, A_v) \quad (14)$$

Step 5. Calculation of the overall performances of the alternatives. In the final step, the dominance performance is normalized using Eq. (15) and the overall performance value is calculated.

$$\xi_u = \frac{\sum_{v=1}^{q} \delta(A_u, A_v) - min_u\{\sum_{v=1}^{q} \delta(A_u, A_v)\}}{max_u\{\sum_{v=1}^{q} \delta(A_u, A_v)\} - min_u\{\sum_{v=1}^{q} \delta(A_u, A_v)\}} \quad (15)$$

The alternatives (A_u) are ranked by ordering the overall performance values (ξ_u) from highest to lowest.

3.3 CODAS

CODAS is a distance-based multi-criteria decision-making method introduced by Ghorabaee et al. [11]. The method primarily uses the Euclidean distance [11,12]. When the Euclidean distances of the alternatives are close to each other, the Taxicab distance is additionally considered [11,12]. Accordingly, alternatives farther from the negative ideal solution are ranked higher [11,12]. Since CODAS evaluates alternatives based on their distances from the negative

ideal solution, it provides an additional perspective for assessing the software alternatives in this study. The application steps of the CODAS method are presented below.

Step 1. Construction of the decision matrix. In the first step, the performance values of the alternatives under each criterion are determined by the decision makers, and the decision matrix (**X**) given in Eq. (10) is constructed.

Step 2. Construction of the normalized decision matrix. In the second step, the values of **X** are normalized according to the benefit and cost type criteria using Eq. (16) and the normalized decision matrix $\mathbf{N} = [n_{uc}]_{q\times p}$ is obtained.

$$n_{uc} = \begin{cases} \dfrac{x_{uc}}{max_u\, x_{uc}} & c \in C^+ \\ \dfrac{\min_u x_{uc}}{x_{uc}} & c \in C^- \end{cases} \tag{16}$$

here, n_{uc} denotes the normalized performance value, whereas C^+ and C^- denote the benefit and cost criteria, respectively.

Step 3. Construction of the weighted normalized decision matrix. In the third step, the normalized values are multiplied by the criterion weights obtained using DEMATEL, as shown in Eq. (17), to obtain the weighted normalized decision matrix $\mathbf{R} = [r_{uc}]_{q\times p}$.

$$r_{uc} = w_c \times n_{uc} \tag{17}$$

in which, w_c denotes the criterion weight; r_{uc} denotes the weighted normalized value.

Step 4. Determination of the negative ideal solution. In the fourth step, the negative-ideal solution vector is obtained by selecting the minimum value in each column of the weighted normalized decision matrix using Eq. (18).

$$s_c^- = \min_u (r_{uc}) \tag{18}$$

where, s_c^- denotes the negative-ideal solution value for criterion C_c.

Step 5. Calculation of the Euclidean and Taxicab distances. In the fifth step, the distances of the alternatives from the negative ideal solution are calculated using Eqs. (19) and (20).

$$E_u = \sqrt{\sum_{c=1}^{p}(r_{uc} - s_c^-)^2} \tag{19}$$

$$T_u = \sum_{c=1}^{p}|r_{uc} - s_c^-| \tag{20}$$

here, E_u denotes the Euclidean distance of alternative A_u from the negative-ideal solution, whereas T_u denotes its Taxicab distance.

Step 6. Construction of the relative assessment matrix. In the sixth step, the relative assessment matrix ($\boldsymbol{R_a}$) is obtained using Eq. (21).

$$\mathbf{R_a} = [h_{uv}]_{q\times q} \tag{21}$$

$$h_{uv} = (E_u - E_v) + [\psi(E_u - E_v) \times (T_u - T_v)] \tag{22}$$

where, h_{uv}, obtained using Eq. (22), denotes the relative assessment value of alternative A_u with respect to alternative A_v. Eq. (23) defines the threshold function ψ for considering the Taxicab distance based on the difference between the Euclidean distances of the alternatives.

$$\psi(x) = \begin{cases} 0 & if \quad |x| < \tau \\ 1 & if \quad |x| \geq \tau \end{cases} \tag{23}$$

here, τ denotes the threshold parameter of the CODAS method used to determine whether the Taxicab distance should be taken into consideration based on the difference between the Euclidean distances. Its value ranges from 0.01 to 0.05 [11]. In this study, τ = 0.02.

Step 7. Calculation of the assessment scores. In the final step, the assessment scores (H_u) obtained using Eq. (24) are ranked from highest to lowest, and the alternative with the highest assessment score is selected as the best alternative.

$$H_u = \sum_{v=1}^{q} h_{uv} \tag{24}$$

4 Application and Results

In this study, an integrated DEMATEL, TODIM, and CODAS model was developed to determine the most suitable project management software for construction projects. Ten evaluation criteria identified through the literature review and expert opinions are presented in Table 2. Among these criteria, Mobility and Field Usability and AI and Automation were included based on expert opinions to reflect current industry needs and recent technological developments. Based on the literature review and expert evaluations, MS Project, Primavera, and Asana were selected. The expert group consisted of five academicians specializing in construction management with at least 10 years of academic experience and five project managers with at least 7 years of professional experience in different engineering companies. Before the evaluation, the criteria and software alternatives were explained to the experts. For the DEMATEL, a common direct-relation matrix was constructed by calculating the arithmetic mean of the experts' evaluations. For the TODIM and CODAS, the experts evaluated the alternatives using a nine-point scale (1 = worst, 9 = best), and a common decision matrix was obtained by calculating the arithmetic mean of their evaluations. All calculations were performed using Microsoft Excel; the main intermediate matrices should be provided as supplementary material to support reproducibility.

Table 2. List of criteria used in this study.

Code	Criteria	Description
K1	Functionality	Support for project planning, monitoring, reporting and control functions
K2	Installation and Maintenance	Ease of installation, maintenance, software updates and sustainability
K3	Cost	License, subscription and total cost of ownership (USD)
K4	Reliability	System stability, data security, fault tolerance and operational continuity
K5	Vendor Evaluation	Vendor experience, support capability, market position and references
K6	User-Friendly Interface	Ease of use, learnability and interface simplicity
K7	Compatibility and Integration	Integration with CAD, office software and other systems
K8	Service and Support	Technical support, training, online assistance and consulting services

K9	Mobility and Field Usability (Expert Opinion)	Mobile access, field usability, offline operation and field data transfer
K10	AI and Automation (Expert Opinion)	AI-based forecasting, automated reporting and resource optimization support

The $D + R$, $D - R$ and criterion weights obtained from the DEMATEL analysis are presented in Table 3. According to the results, K1 had the highest $D + R$ value and was identified as the most important criterion, indicating the greatest level of interaction within the system, while its W_i value represents its normalized criterion weight. In contrast, K4 had the lowest $D - R$ value and was identified as the main effect criterion, indicating that it is influenced more by the other criteria than it influences them. As shown in Figure 1, K1, K6, K9, and K10 belong to the cause group, whereas K2, K3, K4, K5, K7, and K8 belong to the effect group.

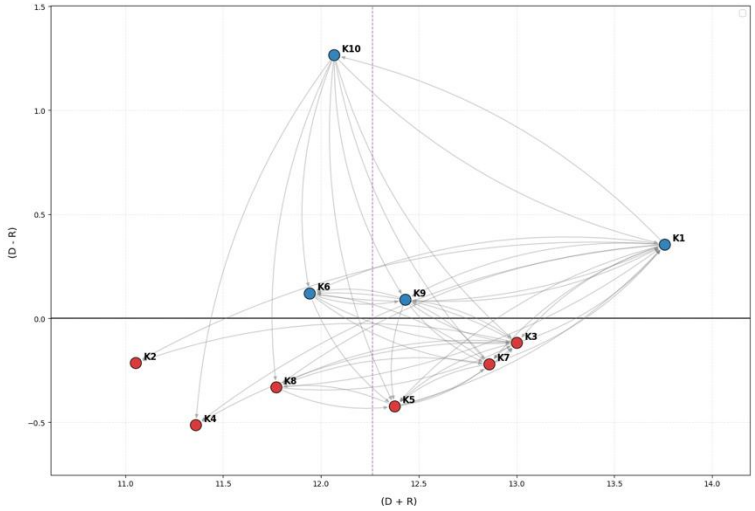


Fig. 1. DEMATEL cause-effect diagram

Table 3. DEMATEL results.

Criteria	**D + R**	**D - R**	W_i
K1	13,7583	0,3537	0,1121
K2	11,0538	-0,2154	0,0901
K3	13,0019	-0,1184	0,1059
K4	11,3607	-0,5140	0,0927
K5	12,3777	-0,4240	0,1009
K6	11,9430	0,1186	0,0973
K7	12,8614	-0,2215	0,1048
K8	11,7722	-0,3323	0,0960
K9	12,4320	0,0888	0,1013
K10	12,0680	1,2645	0,0989

The software rankings obtained using the TODIM and CODAS methods are presented in Table 4. The results show that the two methods produced different ranking results. According

to the results, MS Project ranked first in TODIM (score = 1.0000), whereas Asana ranked first in CODAS (score = 0.0488). The CODAS scores of Asana and MS Project were very close, indicating that the CODAS evaluation distinguished only a small performance difference between these two software alternatives.

Table 4. Comparison of TODIM and CODAS results.

Alternative	TODIM Score(ξ_u)	TODIM Rank	CODAS Score(H_u)	CODAS Rank
MS Project	1,0000	1	0,0439	2
Primavera	0,4720	2	-0,0927	3
Asana	0,0000	3	0,0488	1

5 Discussion

The TODIM and CODAS methods produced different software rankings: TODIM ranked MS Project first, whereas CODAS ranked Asana first. The different rankings obtained from the two methods can be attributed to their different decision-making mechanisms. While TODIM evaluates the alternatives based on their relative dominance by considering the behavioral preferences of decision makers, CODAS ranks the alternatives according to their distances from the negative-ideal solution. These findings indicate that the final choice is sensitive to the decision logic embedded in the selected MCDM method. Therefore, considering the results obtained from different MCDM methods enables decision makers to evaluate software alternatives from different decision-making perspectives.

Since studies integrating the DEMATEL, TODIM, and CODAS methods for project management software selection remain limited, the proposed hybrid framework is expected to contribute to the existing literature. Future studies may increase the number of software alternatives, include a larger and more diverse expert group, perform sensitivity analysis, and integrate additional MCDM methods.

6 Conclusion

This study developed and demonstrated an integrated DEMATEL–TODIM–CODAS decision-making framework for project management software selection, showing that different MCDM methods may lead to different software selection outcomes. In this study, project management software selection was carried out in three main stages. First, the evaluation criteria and software alternatives were identified based on the literature review and expert opinions. Second, the criterion weights were calculated using the DEMATEL method, which identified Functionality (K1) as the most important criterion with a criterion weight of 0.1121. Finally, the software alternatives were ranked using the TODIM and CODAS methods, where MS Project ranked first with a TODIM score of 1.0000, whereas Asana ranked first with a CODAS score of 0.0488. The proposed integrated decision-making framework provides a systematic approach for evaluating project management software from different decision-making perspectives.

References

1. Ömürbek, N., Makas, Y., Ömürbek, V.: AHP ve TOPSIS yöntemleri ile kurumsal proje yönetim yazilimi seçimi. Süleyman Demirel Üniversitesi Sosyal Bilimler Enstitüsü Dergisi (21), 59-83 (2015).
2. Kostalova, J., Tetrevova, L.: Project management and its tools in practice in the Czech Republic. Procedia-Social and Behavioral Sciences 150, 678-689 (2014).

3. Gharaibeh, H.: Evaluating project management software packages using a scoring model—A comparison between MS project and Primavera. Journal of Software Engineering and Applications 7(7), 249-258 (2018). https://doi.org/ 10.4236/jsea.2014.77050
4. Akbar, S., Ullah, R., Khan, R., Asghar, I., Zubair, M., Zheng, Z.: A Multi-Criteria Decision-Making Framework for Software Project Management Tool Selection. In: 9th International Conference on Computer Technology Applications, pp. 184–191. ACM, USA (2023).
5. Kutlu, B., Bozanta, A., Ates, E., Erdogan, S., Gokay, O., Kan, N.: Project management software selection using analytic hierarchy process method. International Journal of Applied 4(6), 113-119 (2014).
6. Puška, A., Stojanović, I., Maksimović, A., Osmanović, N.: Project management software evaluation by using the measurement of alternatives and ranking according to compromise solution (MARCOS) method. Operational Research in Engineering Sciences: Theory and Applications 3(1), 89-102 (2020). https://doi.org/ 10.31181/oresta2001089p
7. Ahmad, N., Laplante, P. A.: Software project management tools: making a practical decision using AHP. In: 30th Annual IEEE/NASA Software Engineering Workshop, pp. 76–84. IEEE, USA (2006). https://doi.org/10.1109/SEW.2006.30
8. Ünal, Z. C., Çetin, E. I.: Selection of CRM software in hospitality industry by integrated DEMATEL and TODIM method. Pamukkale University Journal of Engineering Sciences 26(4), 779-788 (2020). https://doi.org/10.5505/pajes.2020.08455
9. Karaatlı, M., Ömürbek, N., Işık, E., Yılmaz, E.: Performans değerlemesinde DEMATEL ve bulanık TOPSIS uygulaması. Ege Academic Review 16(1), 49-64 (2016).
10. Gomes, L. F. A. M., Machado, M. A. S., Rangel, L. A. D.: Behavioral multi-criteria decision analysis: the TODIM method with criteria interactions. Annals of Operations Research 211(1), 531-548 (2013). https://doi.org/10.1007/s10479-013-1345-0
11. Ghorabaee, M. K., Zavadskas, E. K., Turskis, Z., Antucheviciene, J.: A new combinative distance-based assessment (CODAS) method for multi-criteria decision-making. Economic Computation and Economic Cybernetics Studies and Research 50(3), 25-44 (2016).
12. Ulutaş, A.: SWARA tabanlı CODAS yöntemi ile kargo şirketi seçimi. MANAS Sosyal Araştırmalar Dergisi 9(3), 243-256 (2018). https://doi.org/ 10.33206/mjss.559351

Author Contribution Statement

- *Conceptualization:* Büşra Ziypak, Ümit Bahadır, Fatemeh Mostofi, Vedat Toğan
- *Methodology:* Büşra Ziypak, Ümit Bahadır, Fatemeh Mostofi, Vedat Toğan
- *Investigation:* Büşra Ziypak
- *Writing – Original Draft:* Büşra Ziypak
- *Writing – Review & Editing:* Büşra Ziypak, Ümit Bahadır, Fatemeh Mostofi, Vedat Toğan

Publication Note

This paper was peer-reviewed, accepted for presentation, and included in the proceedings of the ACE2026 – International Conference on Advances in Civil Engineering, held on 12–14 October 2026 in Trabzon, Türkiye.

This paper may be cited as follows:

Ziypak, B., Bahadır, Ü., Mostofi, F., and Toğan, V., "Integrated Decision Support Model for Project Management Software Selection Using DEMATEL, TODIM, and CODAS," in Proceedings of the ACE2026 – International Conference on Advances in Civil Engineering, Trabzon, Türkiye, 12–14 October 2026.

Automatic Brick Wall Quantity Estimation from Construction Site Images Using YOLO-Based Object Detection and Multiple Regression

Sertaç Alperen Koçak[1,*] and Hasan Basri Başağa[1,2]
[1] https://orcid.org/0009-0004-9568-4528, Karadeniz Technical University, Civil Engineering Department, Trabzon, Türkiye, alperenskocak@ktu.edu.tr
[2] https://orcid.org/0000-0002-6964-3309, Earthquake and Structural Health Monitoring Research Center, Karadeniz Technical University, Trabzon, Turkey.
Northsign Design Software Construction Trade Ltd. Co., Trabzon, Turkey.
hasanbb@ktu.edu.tr

Abstract. This study proposes a multi-stage framework for automatic brick wall quantity estimation from real construction site images using YOLO-based object detection and multiple linear regression. First, individual bricks are detected using a YOLO-based object detection model. Instead of directly using the detected brick count for quantity estimation, the detection outputs are transformed into physically meaningful quantity variables based on brick count, bounding box geometry, equivalent brick count, and area representations. Based on these variables, eleven parametric quantity estimation approaches are developed and comparatively evaluated. The best parametric approach achieved a Mean Absolute Percentage Error (MAPE) of 7.00%. To further improve estimation accuracy, the outputs of the eleven parametric approaches were integrated into a multiple linear regression model. Variable reduction was performed to obtain a compact regression model while maintaining high prediction accuracy. The final regression model achieved a MAPE of 5.19%, a Mean Absolute Error (MAE) of 0.1408 m², and an adjusted R^2 of 0.9796. The proposed framework demonstrates that combining YOLO-based object detection with parametric quantity estimation and regression provides an accurate, interpretable, and practical solution for automated brick wall quantity estimation from construction site images.

Keywords: Brick wall quantity estimation; YOLO; object detection; regression analysis; automated quantity takeoff.

1 Introduction

The rapid advancement of digital technologies has accelerated the adoption of data-driven approaches in the architecture, engineering, and construction (AEC) industry. Among these technologies, computer vision and deep learning have become increasingly important for automating construction site monitoring, progress assessment, and quantity surveying. Compared with traditional manual measurements, image-based methods offer significant advantages in terms of efficiency, repeatability, and reduced labor requirements, particularly under dynamic construction site conditions.

Recent studies have successfully applied deep learning-based object detection methods to various construction applications, including worker and equipment monitoring (Nath and Behzadan, 2020), personal protective equipment detection (Kurniawan et al., 2025), and automated material recognition and counting (Li et al., 2021). In addition, advances in YOLO architectures have further improved the accuracy and efficiency of real-time object detection for construction-related tasks (Ding et al., 2025). Despite these developments, research on automated quantity takeoff from construction site images remains limited. Existing studies

primarily rely on image segmentation or pixel-based measurements, while object detection outputs are generally used only for counting detected objects. One of the few studies addressing brick wall quantity estimation was conducted by Başağa and Hacıefendioğlu (2024), who estimated wall areas using a U-Net-based image segmentation approach. However, the direct use of object detection outputs for quantity estimation has received limited attention.

To address this gap, this study proposes a multi-stage framework for automatic brick wall quantity estimation from real construction site images using YOLO-based object detection and multiple linear regression. First, individual bricks are detected using a YOLO model. Subsequently, the detection outputs are transformed into physically meaningful quantity variables through eleven parametric quantity estimation approaches developed under different assumptions regarding brick visibility and bounding box geometry. Finally, the outputs of these parametric approaches are integrated into a multiple linear regression model to improve wall quantity estimation accuracy.

The main contributions of this study are as follows:

- A YOLO-based object detection model is developed for automatic brick detection using images collected from real construction sites.
- Eleven parametric quantity estimation approaches are proposed to estimate brick wall quantities under different geometric assumptions.
- A multiple linear regression model is developed by integrating the outputs of the parametric approaches to improve estimation accuracy.
- The proposed framework is validated using independent test images, demonstrating its applicability for automated brick wall quantity estimation under real construction site conditions.

2. Methodology

2.1. Overall Framework

This study proposes a multi-stage framework for automatic brick wall quantity estimation from real construction site images. The proposed framework consists of five main stages: image acquisition, brick annotation, YOLO-based brick detection, parametric quantity estimation, and regression-based quantity prediction. Rather than directly using the detected number of bricks as the final quantity estimate, the proposed framework transforms the detection outputs into different parametric quantity estimates, which are subsequently integrated through a multiple linear regression model to improve estimation accuracy. The overall workflow of the proposed framework is illustrated in Fig. 1.

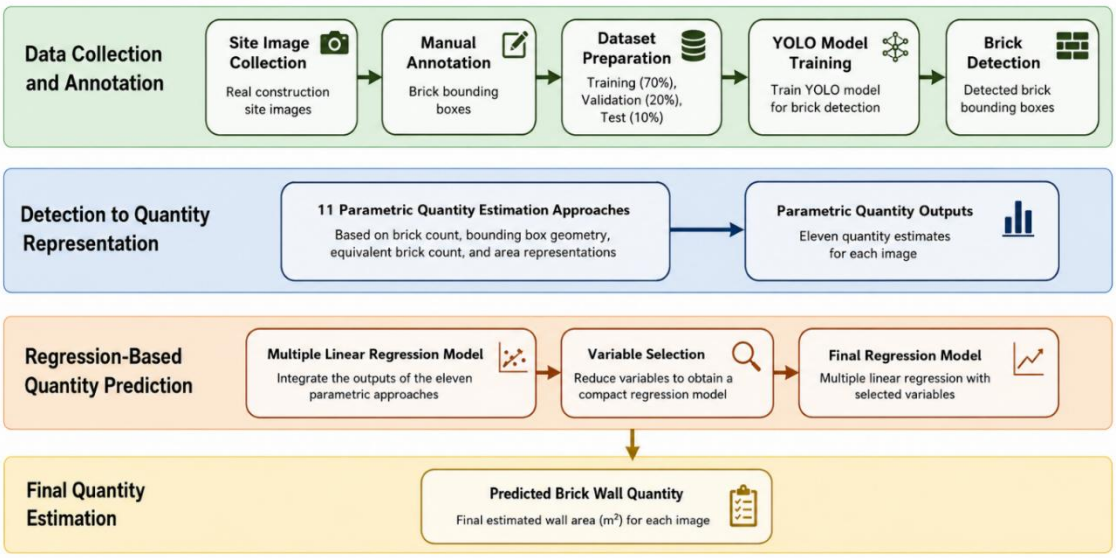


Fig. 1. Overall workflow of the proposed multi-stage brick wall quantity estimation framework

2.2. Data Collection and Annotation

Brick wall images were collected from active construction sites, primarily representing interior masonry works. To ensure that the proposed framework reflects realistic construction environments, images were captured under different lighting conditions, viewing angles, shooting distances, and wall configurations using a smartphone without any stabilizing equipment. The dataset includes flat walls, walls with openings, and walls adjacent to sloped ceilings. All images have a resolution of 2160 × 3840 pixels.

The dataset consists of 300 images, which were divided into training (70%), validation (20%), and test (10%) subsets for object detection.

Representative examples of the collected images are shown in Fig. 2.



Fig. 2. Representative samples of brick wall images collected from real construction sites under varying conditions

All brick instances were manually annotated using the Roboflow platform. Each brick was assigned to a single object class (*brick*) by drawing a bounding box around the visible brick region. Approximately 40,000 brick instances were annotated. To improve the robustness of the detection model, rotational data augmentation (±20°) was applied while preserving the corresponding annotation coordinates.

An example of the annotated images is presented in Fig. 3.

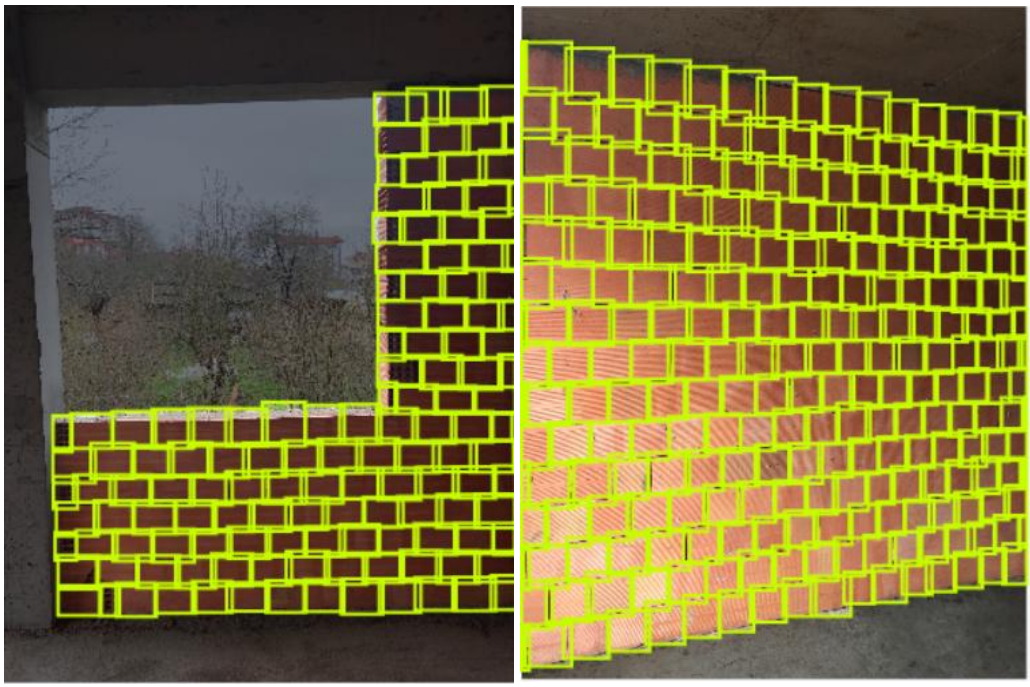


Fig. 3. Example of annotated brick wall images with bounding boxes used for YOLO training

2.3. YOLO-Based Brick Detection

Brick detection was performed using a YOLO-based object detection model trained on the annotated dataset. The trained model predicts the location of each brick by generating bounding boxes, which subsequently provide the geometric information required for quantity estimation. Model training was carried out using the Google Colab platform with NVIDIA T4 GPU acceleration.

Unlike conventional counting approaches, the proposed framework does not directly convert the detected brick count into wall quantities. Instead, the detection outputs serve as the basis for generating multiple quantity estimation scenarios.

2.4. Parametric Quantity Estimation

To estimate brick wall quantities from YOLO detections, four groups of parametric quantity estimation approaches were developed. These approaches progressively consider different assumptions regarding brick visibility and bounding-box geometry. In total, eleven quantity estimation scenarios were generated, including one full-brick approach, four threshold-based partial-brick approaches, one multi-level area-based approach, and five area-reduction approaches.

2.4.1. Full-Brick Assumption

In the first approach, all detected bricks are assumed to be complete bricks. The estimated wall area is calculated as

$$Q = N \times A_{brick} \tag{1}$$

where Q denotes the estimated wall area, N is the number of detected bricks, and A_{brick} is the physical area of a single brick.

2.4.2. Threshold-Based Partial-Brick Estimation

This approach classifies detected bricks as either full or partial according to their bounding-box areas relative to the average bounding-box area. The estimated wall area is computed as

$$Q = N_{full}A_{brick} + N_{partial}(A_{brick}\alpha) \tag{2}$$

where α represents the partial-brick coefficient. Four different coefficient values (0.50, 0.40, 0.30, and 0.20) were evaluated to investigate the influence of partially visible bricks on quantity estimation.

2.4.3. Multi-Level Area-Based Estimation

Instead of using a binary classification, this approach assigns each detected brick to one of four area categories according to the ratio between its bounding-box area and the average bounding-box area:

$$r_i = \frac{A_i}{A_{average}} \tag{3}$$

The estimated wall area is then calculated as

$$Q = \sum_{k=1}^{4} N_k \, A_{brick} \omega_k \tag{4}$$

where ω represents the weighting factor assigned to each area category (0,25, 0,50, 0,75, and 1,00).

2.4.4. Area Reduction-Based Estimation

In the final approach, all detected bricks are considered complete, while reduction coefficients are introduced to compensate for overestimation caused by partial brick visibility and geometric uncertainties.

The estimated wall area is calculated as

$$Q = NA_{brick}\beta \tag{5}$$

where β denotes the reduction coefficient. Five reduction coefficients (0.95, 0.90, 0.85, 0.80, and 0.75) were comparatively evaluated.

2.5. Regression Model

The eleven quantity estimation outputs obtained from the parametric approaches were used as independent variables in a multiple linear regression model to improve wall quantity estimation. The regression model can be expressed as

$$y = \beta_0 + \beta_1 x_1 + \beta_2 x_2 + \cdots + \beta_{11} x_{11} + \varepsilon \tag{6}$$

where y represents the measured wall area, x_1–x_{11} denote the outputs of the eleven parametric quantity estimation approaches, β represents the regression coefficients, and ε is the error term. A multiple linear regression model was developed using the outputs of the eleven parametric quantity estimation approaches as independent variables. Stepwise variable elimination was then performed to identify a simpler model while maintaining prediction accuracy. The final regression model was evaluated using an independent test dataset, and its performance was assessed using Mean Absolute Error (MAE), Root Mean Square Error (RMSE), Mean Absolute Percentage Error (MAPE), adjusted coefficient of determination (Adjusted R^2), and bias.

3. Results and Discussion

3.1. YOLO Detection Performance

The performance of the trained YOLO model was evaluated using the independent test dataset. Detection performance was assessed in terms of precision, recall, F1-score, and mAP, which are widely used metrics for object detection tasks. The confusion matrix of the final model is presented in Fig. 4, while the corresponding performance metrics are summarized in Table 1.

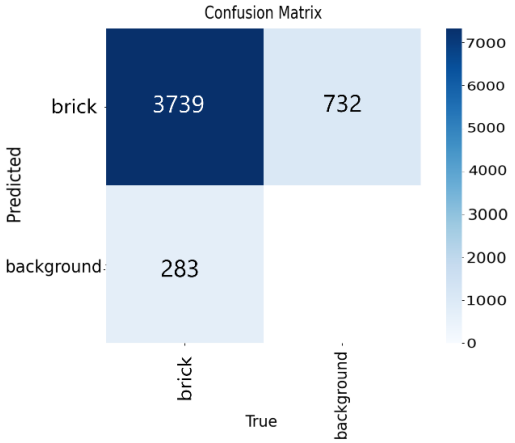


Fig. 4. Confusion matrix results

Table 1. Model metrics

Precision	0,8758
Recall	0,9114
F1 Score	0,8932
mAP@50	0,9260

The results indicate that the proposed model successfully detected individual bricks under varying construction site conditions, including different viewing angles, illumination levels, and wall geometries. Accurate brick localization provides the foundation for the subsequent quantity estimation process, as the detected bounding boxes are directly used to generate the parametric quantity estimation outputs.

3.2. Performance of Parametric Quantity Estimation Approaches

The eleven parametric quantity estimation approaches developed from the YOLO detection outputs were compared using the measured wall areas as reference values. The average error of each approach is illustrated in Fig. 5.

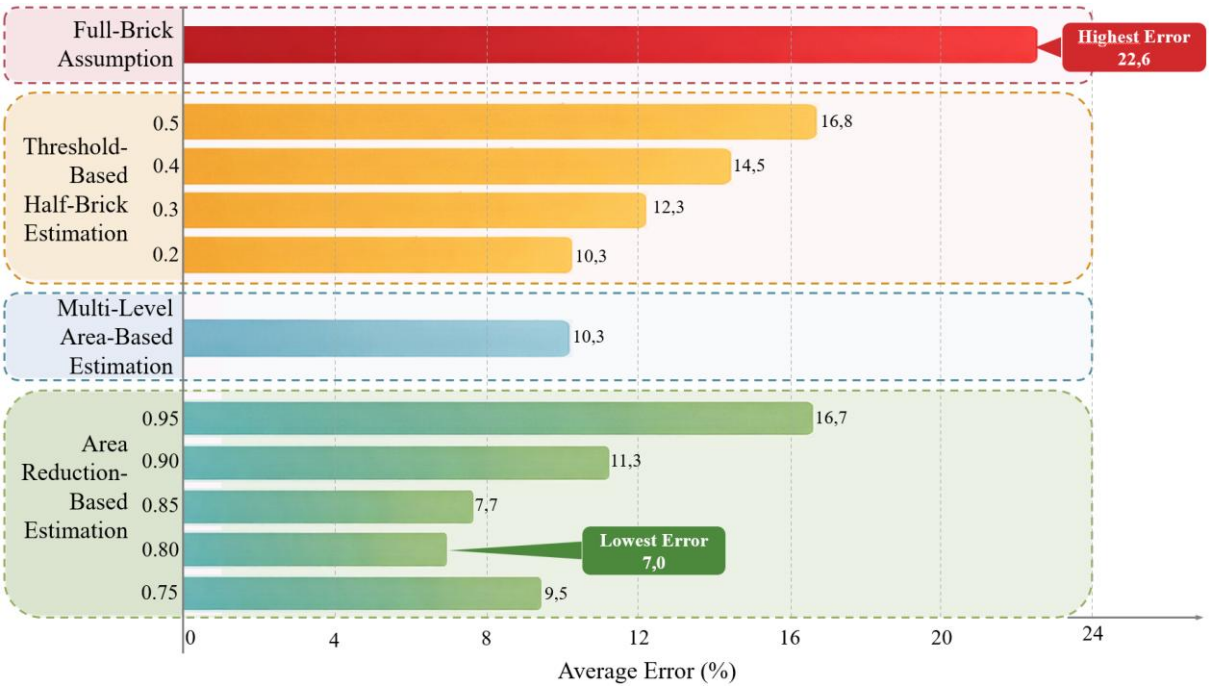


Fig. 5. Comparison of average error rates for different parametric quantity estimation approaches

The full-brick assumption produced the largest estimation error because all detected bricks were considered complete, resulting in systematic overestimation of the wall area. Introducing partial-brick assumptions substantially reduced the estimation error by accounting for partially visible bricks. The performance of the threshold-based approaches varied depending on the selected partial-brick coefficient.

The multi-level area-based approach provided more balanced estimations by assigning different weighting factors according to the relative bounding-box area of each detected brick. However, the lowest estimation errors were obtained using the area reduction approaches. In particular, reduction coefficients between 0,80 and 0,85 yielded the most accurate quantity estimates among all parametric approaches.

These findings demonstrate that incorporating geometric information derived from the detected bounding boxes significantly improves quantity estimation compared with simple object counting.

3.3. Regression Results

To improve the accuracy of wall quantity estimation, a multiple linear regression model was developed using the outputs of the eleven parametric quantity estimation approaches. The initial model, which included all variables, achieved an R^2 value of 0.9835, indicating a strong relationship between the parametric estimates and the measured wall area. To reduce model complexity, a stepwise variable elimination procedure was performed. At each step, the least significant variable was removed, and the resulting models were evaluated using R^2, Adjusted R^2, MAE, MAPE, and Bias. The performance of the regression models during the variable elimination process is summarized in Table 2.

Following the variable elimination process, the regression performance improved compared with the initial model. As shown in Table 2, the initial model containing all eleven variables achieved a MAPE of 6.58% and an MAE of 0.1716, whereas the reduced models yielded lower prediction errors. The lowest error was obtained using the eight-variable model (MAPE = 5.19%, MAE = 0.1408). A similar performance was achieved with the seven-variable model, while reducing the number of variables below seven resulted in a gradual increase in prediction error. Therefore, the seven-variable model was selected as the final regression model because it provided comparable accuracy with a simpler model structure.
The bias values remained close to zero for all regression models, indicating the absence of significant systematic prediction errors. Although a slight increase in bias was observed as the number of variables decreased, the overall prediction performance remained stable. The final regression equation is given below.

$$y = 0{,}0558 - 0{,}0906x_1 - 0{,}5491x_2 + 1{,}0956x_3 - 0{,}7018x_5 + 1{,}9199x_6 + 49{,}1126x_9 - 47{,}1925x_{10} \quad (7)$$

The final regression model achieved a MAPE of 5.19%, an MAE of 0.1408 m², and an Adjusted R^2 of 0.9796. These results demonstrate that integrating the outputs of the eleven parametric quantity estimation approaches through multiple linear regression significantly improves wall quantity estimation compared with individual parametric approaches. The proposed regression model provides an effective balance between prediction accuracy and model simplicity, making it suitable for automated brick wall quantity estimation from real construction site images.

Table 2. Stepwise variable elimination results and performance metrics of regression models

Removed	Remaining Features	R^2	Adj. R^2	MAPE	MAE	Bias
----	$x_1, x_2, x_3, x_4, x_5, x_6, x_7, x_8, x_9, x_{10}, x_{11}$	0,9835	0,9805	6,58%	0,1716	-0,0101
x_7	$x_1, x_2, x_3, x_4, x_5, x_6, x_8, x_9, x_{10}, x_{11}$	0,9819	0,9790	5,41%	0,1472	0,0364
x_4	$x_1, x_2, x_3, x_5, x_6, x_8, x_9, x_{10}, x_{11}$	0,9818	0,9792	5,24%	0,1420	0,0332
x_{11}	$x_1, x_2, x_3, x_5, x_6, x_8, x_9, x_{10}$	0,9816	0,9793	5,19%	0,1408	0,0294
x_8	$x_1, x_2, x_3, x_5, x_6, x_9, x_{10}$	0,9816	0,9796	5,19%	0,1408	0,0293
x_1	$x_2, x_3, x_5, x_6, x_9, x_{10}$	0,9816	0,9799	5,21%	0,1413	0,0292
x_5	$x_2, x_3, x_6, x_9, x_{10}$	0,9809	0,9795	5,30%	0,1446	0,0573
x_9	x_2, x_3, x_6, x_{10}	0,9808	0,9797	5,49%	0,1500	0,0664
x_3	x_2, x_6, x_{10}	0,9804	0,9795	5,73%	0,1572	0,0774
x_2	x_6, x_{10}	0,9803	0,9797	5,85%	0,1602	0,0820

4. Discussion

This study proposed a multi-stage framework for automatic brick wall quantity estimation from real construction site images by integrating YOLO-based object detection, parametric quantity estimation, and multiple linear regression. Unlike conventional object counting approaches, the proposed framework transforms YOLO detection outputs into physically meaningful quantity estimates using different assumptions regarding brick visibility and bounding-box geometry. This detection-to-quantity strategy enables a more reliable estimation of wall quantities under real construction site conditions.

The results demonstrate that directly converting detected brick counts into wall quantities is insufficient for accurate quantity estimation. The full-brick assumption produced the highest estimation error (22,6%), indicating that partial brick visibility, openings, and geometric variations significantly affect quantity estimation. Incorporating geometric corrections through the proposed parametric approaches substantially reduced the estimation error, with the best parametric approach achieving a MAPE of 7.00%. These findings confirm that bounding-box geometry provides valuable information beyond simple object counting.

Further improvements were achieved by integrating the outputs of the eleven parametric quantity estimation approaches into a multiple linear regression model. The final regression model reduced the prediction error to a MAPE of 5.19% while maintaining a high Adjusted R^2 of 0.9796, demonstrating that combining complementary parametric estimates provides more accurate wall quantity predictions than any individual approach.

Compared with the segmentation-based approach proposed by Başağa and Hacıefendioğlu (2024), the proposed framework eliminates the need for pixel-level segmentation and reference area measurements by directly utilizing object detection outputs for quantity estimation. This demonstrates the feasibility of object detection as an alternative framework for automated brick wall quantity estimation from construction site images.

Despite these promising results, the proposed framework has several limitations. The regression model was developed and evaluated using a limited number of wall images with measured reference areas, and its generalization to different masonry types and construction environments requires further investigation. In addition, the estimation accuracy depends on the quality of YOLO detections, particularly in images containing occlusions, irregular brick arrangements, or inaccurate bounding boxes. Future studies should evaluate the proposed framework using larger datasets collected from different construction sites and investigate its applicability to other masonry materials and building components.

5. Conclusions

This study presented a multi-stage framework for automatic brick wall quantity estimation from real construction site images by integrating YOLO-based object detection, parametric quantity estimation, and multiple linear regression. Rather than directly converting detected brick counts into wall quantities, the proposed framework transforms object detection outputs into physically meaningful quantity estimates using eleven parametric approaches developed under different geometric assumptions.

The experimental results showed that the full-brick assumption resulted in the highest estimation error (22.6%), whereas the best parametric approach reduced the error to a MAPE of 7.00%. By combining the outputs of the eleven parametric approaches, the proposed multiple linear regression model further improved the estimation accuracy, achieving a MAPE of 5.19%, an MAE of 0.1408 m^2, and an Adjusted R^2 of 0.9796.

Overall, the proposed framework demonstrates that transforming YOLO detection outputs into physically meaningful quantity estimates provides an effective and interpretable solution for automated brick wall quantity estimation. The proposed methodology has the potential to support digital quantity surveying and construction site management and may be extended to other masonry elements and image-based quantity estimation applications in future studies.

References

1. Nath, N. D. and Behzadan, A. H. (2020). Deep convolutional networks for construction object detection under different visual conditions. *Frontiers in Built Environment*, 6, 97. https://doi.org/10.3389/fbuil.2020.00097
2. Naufaldihanif, R., Kurniawan, D. and Tania, K. D. (2025). Performance analysis of YOLO, Faster R-CNN, and DETR for automated personal protective equipment detection. *Journal of Applied Informatics and Computing*, 9(6), 3810–3820. https://doi.org/10.30871/jaic.v9i6.11593
3. Li, Y., Lu, Y. and Chen, J. (2021). A deep learning approach for real-time rebar counting on the construction site based on YOLOv3 detector. *Automation in Construction*, 124, 103602. https://doi.org/10.1016/j.autcon.2021.103602
4. Ding, D., Deng, Z. and Yang, R. (2025). YOLO-TC: An optimized detection model for monitoring safety-critical small objects in tower crane operations. *Algorithms*, 18(1), 27. https://doi.org/10.3390/a18010027
5. Başağa, H. B. and Hacıefendioğlu, K. (2024). An approach for brick wall quantity take-off by U-Net method based on deep learning. *Turkish Journal of Civil Engineering*, 35(1). https://doi.org/10.18400/tjce.1214798

Author Contribution Statement

- *Conceptualization:* Sertaç Alperen Koçak, Hasan Basri Başağa
- *Methodology:* Sertaç Alperen Koçak, Hasan Basri Başağa
- *Investigation:* Sertaç Alperen Koçak, Hasan Basri Başağa
- *Writing – Original Draft:* Sertaç Alperen Koçak, Hasan Basri Başağa
- *Writing – Review & Editing:* Sertaç Alperen Koçak, Hasan Basri Başağa

List of Abbreviations

- **YOLO** — You Only Look Once
- **MAE** — Mean Absolute Error
- **MAPE** — Mean Absolute Percentage Error
- **RMSE** — Root Mean Square Error

Note: Following the conference, this Publication Note will be added to each paper; therefore, authors are kindly requested not to remove the note below and to complete the author(s) and paper title information.

Publication Note

This paper was peer-reviewed, accepted for presentation, and included in the proceedings of the ACE2026 – International Conference on Advances in Civil Engineering, held on 12–14 October 2026 in Trabzon, Türkiye.

This paper may be cited as follows:

Kocak S.A., Basağa H.A., "Automatic Brick Wall Quantity Estimation from Construction Site Images Using YOLO-Based Object Detection and Multiple Regression" in Proceedings of the ACE2026 – International Conference on Advances in Civil Engineering, Trabzon, Türkiye, 12–14 October 2026.

A Conceptual Analysis of the Need for Prescriptive Digital Tools and Dynamic Decision Partners in Lean Construction Management in Light of Global Literature

İlkim Güven Balli[1]*, Elçin Filiz Taş[2]
[1]0000-0001-9203-8302, Istanbul Technical University, Graduate School, Architecture Department, Project and Construction Management PhD Program, İstanbul, Türkiye, guveni23@itu.edu.tr
[2]0000-0002-8688-9618, Istanbul Technical University, Graduate School, Architecture Department, Project and Construction Management Program, İstanbul, Türkiye, tase@itu.edu.tr
*Corresponding Author

Abstract. On a global scale, the construction industry struggles with chronic issues such as project delays, cost overruns, and productivity losses due to its intrinsic dynamic nature, multi-stakeholder organizational structures, and high-uncertainty factors. International literature and field practices demonstrate that these chronic problems are fundamentally rooted in disruptions in on-site information flow, labor mismatches, and operational wastes (muda). Although the Lean Construction approach offers a robust methodological framework for waste elimination and continuous improvement (kaizen), the lack of practical, accessible, and guiding digital tools to ensure the sustainable implementation of these principles, particularly in the field environment, is felt as a global problem. Existing construction management tools and Building Information Modeling (BIM) solutions primarily remain at descriptive ("What happened?") or diagnostic ("Why did it happen?") analysis layers in terms of their data processing capacities. However, in dynamic and chaotic jobsite environments where field crews must make decisions within seconds, the need for a prescriptive guidance mechanism to answer the question "What should I do now?" stands as a critical gap in the literature.

This study adopts Systematic Literature Review (SLR) and conceptual analysis methods to systematically examine operational efficiency barriers and information flow interruptions in the global construction industry. Accordingly, a large-scale review covering the years 2020-2026 was conducted across the Scopus, IEEE Xplore, and ScienceDirect databases, through which 138 qualified academic publications screened within the framework of determined criteria were analyzed in depth. By synthesizing these theoretical and practical findings in the international literature, coordination problems in the field, interruptions in real-time information flow, and delays in decision-making processes were identified as the primary global structural impediments to lean efficiency. Unlike traditional data storage systems, this study demonstrates the conceptual and theoretical necessity of an interactive decision support structure capable of directly interacting with field personnel, interpreting signals from the jobsite, and generating prescriptive action recommendations. Consequently, through an in-depth literature analysis and theoretical modeling, this research constructs the theoretical infrastructure for a novel mechanism that will enable the proactive forecasting of field wastes and convert complex field data into instant action planning. The proposed approach contributes theoretically and methodologically to the global sectoral digitalization vision by arguing that digital tools in construction management must transform

from passive archiving centers into dynamic "decision partners" that think alongside project managers.

Keywords: Lean Construction, Operational Efficiency, Decision Support Systems, Prescriptive Analytics, Construction Management.

1 Introduction

The global construction industry frequently experiences chronic issues such as budget overruns, delays, and stagnant productivity due to its fragmented nature, multi-stakeholder organizational structures, and complex project dynamics (Kissi et al., 2022). International literature and field practices demonstrate that these failures generally stem from the accumulation of daily micro-disruptions -such as disconnections in information flow, spatial conflicts, and operational inefficiencies- rather than a single major event (Görsch et al., 2024).

To eliminate these non-value-adding activities (Ohno, 1988), termed as "muda" (waste) in production theory, and to ensure "kaizen" (continuous improvement), the Lean Construction approach adapted from the Toyota Production System was developed (Koskela, 1992). Lean tools such as the Last Planner System (LPS), Value Stream Mapping (VSM), and Just-in-Time (JIT) delivery possess the potential to stabilize workflows (Ballard, 2000; Bamana et al., 2019). However, the disconnect between high-level planning and the volatile dynamics in the field hampers the sustainable implementation of these principles. This bottleneck originates from the lack of dynamic, accessible, and prescriptive digital tools tailored to real-time field conditions, thereby causing jobsite management to remain reactive rather than proactive (Dave et al., 2016; Görsch et al., 2024).

Today, the construction industry is undergoing a profound digital transformation led by Building Information Modeling (BIM), the Internet of Things (IoT), and sensor technologies (Dave et al., 2016). Nevertheless, while these technologies enhance visualization and data collection capacities, they fall short in dynamic and short-interval decision-making processes on site; they generally function as passive administrative archives that report what has already occurred in the past (Salhab et al., 2026). Yet, in fast-paced and chaotic jobsite environments, managers and engineers urgently require not only descriptive or diagnostic analyses but also actionable, instantaneous, and prescriptive guidance that answers the question, "What should I do now?"

In this context, it is a critical requirement on a global scale for digital systems to evolve from passive data repositories into proactive "decision partners" that think alongside managers. Utilizing a comprehensive literature review and conceptual analysis method, this study systematically examines the operational efficiency barriers and real-time information flow interruptions in the global construction industry. By addressing the integration of lean construction philosophy with modern data analytics solutions, the research aims to establish the conceptual framework for more advanced and holistic models that will enable the proactive management of operational wastes in the field.

2 Systematic Literature Review Methodology

This study adopts Systematic Literature Review (SLR) and conceptual analysis methods to reveal the barriers to operational efficiency in the global construction industry and to demonstrate the need for prescriptive digital tools in overcoming these barriers. Moving beyond a random literature review, the objective is to filter and categorize the global body of knowledge regarding the research question in accordance with specified criteria, and to establish a conceptual and theoretical foundation for future digital tools.

2.1 Data Collection and Screening Strategy

In this study, an initial search conducted across the relevant databases (Scopus, IEEE Xplore, ScienceDirect) based on the determined keywords yielded a total of 1,280 academic publications. During the search process, combinations of keywords including "Lean Construction," "Muda," "BIM," "Decision Support Systems," and "Industry 4.0" were utilized to capture the intersection of operational efficiency, digitalization, and lean principles in construction management. Studies belonging to disciplines outside of construction management that did not directly align with the focus of the research, as well as duplicate records across different databases, were systematically excluded from the pool.

Following the initial screening stage, 659 publications that maintained relevance to the topic were subjected to a second evaluation based on title, publication year, and contextual suitability criteria. At this stage, articles failing to meet the recency and scoping limitations of the research were eliminated, reducing the number of publications to be reviewed to 531.

In the final stage, all of the remaining 531 publications were analyzed in depth using the full-text analysis method. Studies that did not provide a direct theoretical or practical contribution to the intersection of lean construction philosophy, jobsite digitalization, and prescriptive decision support systems were excluded. As a result of this rigorous and multi-stage methodological elimination process, 138 references were ultimately included in the analysis to construct the conceptual framework of the study and to substantiate its theoretical foundation.

This large-scale literature pool has allowed for the mapping of a universal, rather than merely regional, landscape of operational efficiency barriers in the global construction industry. The distribution of the relevant publications according to their databases, methodologies, and thematic focuses is comprehensively summarized in Table 1. The methodological synthesis of the analyzed ~140 studies clearly validates the global necessity for prescriptive digital mechanisms that will allow the industry to break away from static archiving processes and function as dynamic "decision partners."

Table 1. Database and Thematic Distribution of the Analyzed Literature

Database	**Reviewed Period**	**Number of Articles (N)**	**Most Frequently Encountered Methods**	**Dominant Thematic Focus Areas**
Scopus	2020–2025	~65	Structural Equation Modeling (SEM), Quantitative Survey Analyses, Bibliometric and Critical Reviews, Conceptual Model Development	Lean construction implementation barriers, awareness and knowledge obstacles, process improvement in mega projects, Industry 4.0, and operational efficiency.
IEEE Xplore	2021–2025	~45	Discrete Event Simulation (DES), Algorithm Modeling, Knowledge Graphs, Statistical Analyses (ANOVA, RII), Case Studies	Digital twin and 4D/5D BIM applications, smart supply chain constraint management, intelligent communication, and visual jobsite management mechanisms.
ScienceDirect	2020–2026	~30	Delphi Technique, Systematic Literature	Decision support systems, computer vision-based

			Reviews (SLR), Fuzzy Systems, Computer Vision, Interviews	proactive site/field management, lean construction knowledge (LCK) frameworks, and sustainability integration.
TOTAL	2020–2026	~140		General Trend: Shift from root causes of operational inefficiencies toward prescriptive and dynamic decision support systems.

2.2 Synthesis of Literature Findings and Operational Barriers

The global construction industry suffers from chronic inefficiencies due to its highly fragmented structure, multi-stakeholder organizational charts, dynamic field conditions, and high-uncertainty factors (Ghassemi & Becerik-Gerber, 2011; Ibrahim et al., 2026). These systematic inefficiencies lead to significant project delays, budget overruns, and stagnant productivity rates (Pourrahimian et al., 2026). Systematically classifying these barriers and determining the need for "prescriptive" digital tools to overcome them constitutes one of the most critical areas of study in the construction management literature. Listed below are the barriers compiled within the framework of available references through the Systematic Literature Review (SLR) and Conceptual Analysis methods, along with the necessity of prescriptive tools.

According to the literature, operational barriers in the sector can be grouped into four main categories: organizational, process-based, spatial, and technological-information-driven.

2.2.1. Organizational and Behavioral Barriers

Managerial and Cultural Resistance: The preservation of traditional "command and control" oriented hierarchical structures and the failure to adopt a Lean Construction culture (Ibrahim et al., 2026). Resistance to change and the inability to decentralize decision-making authority on site slow down decision-making processes (Bidhendi et al., 2026; Ghassemi & Becerik-Gerber, 2011).

Fragmented Contractual and Project Delivery Models: Temporary, transactional, and adversarial short-term relationships among designers, main contractors, and subcontractors lead to a "silo mentality" (Ghassemi & Becerik-Gerber, 2011). This fragmentation creates a governance gap where risks and responsibilities are inequitably distributed among stakeholders (Ibrahim et al., 2026).

2.2.2. Process and Supply Chain Barriers

Workflow Unreliability and Volatility: Uncertainties in the material supply chain, unplanned downtimes, and the inability to manage interdependencies between sequential activities disrupt the continuity of workflow (Babanagar et al., 2024).

Retrospective Performance Tracking: The industry's heavy reliance on the static Critical Path Method (CPM) and retrospective (post-mortem) progress reports prevents the instantaneous resolution of micro-disruptions emerging in real time on site, such as material delays or handover cleanups (Aboelmagd, 2020; Salhab et al., 2026).

2.2.3. Spatiotemporal and Spatial Barriers

Workspace Conflicts and Congestion: Distinct subcontractor crews attempting to utilize the same physical space within the same time frame constitutes a severe spatial constraint

(Salhab et al., 2026). Studies indicate that congested and uncoordinated workspaces reduce labor productivity by up to 65% and lead to project delays of up to 30% (Salhab et al., 2026). This barrier is further exacerbated by the inability of static 2D layout plans to capture dynamic field realities.

2.2.4. Technological and Information-Driven Barriers

Lack of Digital Literacy and Integration: The insufficiency of field technical personnel and foremen in utilizing complex digital tools (digital literacy gap) and the non-user-friendly nature of software applications (Bidhendi et al., 2026).

Data and Communication Disconnection: The inability to integrate systems such as Building Information Modeling (BIM), computer vision (CV), and the Internet of Things (IoT) with on-site decision support systems (DSS), which causes data to remain isolated in silos and leads to information loss (Salhab et al., 2026).

2.3. The Need for Prescriptive Digital Decision Support Tools

The majority of digital tools in construction management currently operate solely at the descriptive ("What happened?") and diagnostic ("Why did it happen?") layers of data analytics (Pourrahimian et al., 2026). These tools do not go beyond being passive digital archives that report retrospective data. However, chaotic and fast-changing jobsite environments require managers and field crews to make decisions within seconds. This situation renders the transition to prescriptive analytics ("What should I do now?") a theoretical and practical necessity (Salhab et al., 2026).

By processing unstructured field data (site logs, voice recordings, etc.) via natural language processing (NLP) and machine learning, prescriptive systems forecast lean wastes such as waiting and rework before they even occur, and simulate alternative scenarios to prevent them (Maciel et al., 2026; Pourrahimian et al., 2026). Digital twins and artificial intelligence-based decision support systems transform from being passive displays for managers into proactive "decision partners" that think alongside them (Liu & Liu, 2026). These systems generate optimized, context-specific, and actionable operational plans to resolve instantaneous constraints on site. In this manner, complex office planning is successfully translated into short-interval visual work instructions that foremen and craftsmen working directly in the field can easily understand (Görsch et al., 2026). Consequently, a bidirectional, real-time feedback loop is established between the workers and the decision engine, triggering continuous improvement (kaizen) directly at the point of production.

2.4. Conceptual Analysis

When the "future research directions" obtained from the systematic literature review were examined, it was observed that the literature clearly points toward decision support structures and the lean integration of advanced technologies. Pioneers in the literature emphasize the necessity of simulation-based virtual test environments and decision support tools (Sreram & Thomas, 2023) to detect non-value-adding (NVA) activities and accelerate process improvement, knowledge graph-based intelligent evaluation systems, or the integration of computer vision with fuzzy logic (Salhab et al., 2026). Accordingly, the ultimate methodological output of this study is to establish the philosophical and theoretical foundation for the vision of utilizing novel digital tools capable of proactivity forecasting wastes by processing heterogeneous data from the field, thereby closing the gaps identified in the literature (static archiving, reactive management, and information barriers). The research aims to

systematically define the conceptual boundaries upon which future dynamic decision mechanisms will be built.

3 Prescriptive Digital Tools in Lean Construction Management

3.1. Analytical Layers and Limitations of Existing Digital Systems

The transition from labor-intensive traditional processes to technological solutions in the construction industry fundamentally shapes operational control mechanisms. This transformation process evolves from the stage of digitization, where manual practices are replaced by integrated digital systems, toward the level of digitalization, where data analytics, artificial intelligence, and cyber-physical systems are utilized to optimize decision-making processes (Salhab et al., 2026). Today, digital technologies used in construction management are divided into five main functional categories: data collection, analytical processes, visualization, communication, and design and execution automation (Chen et al., 2022). However, the major operational limitation of existing digital systems is that, due to their information-centric building blocks, they do not allow project teams to communicate effectively at the field level and coordinate activities instantaneously (Guerriero et al., 2017).

Widely used lean production control mechanisms, such as the Last Planner System (LPS), primarily ensure coordination at the team or workgroup level, yet they cannot directly respond to the daily and dynamic decision-making needs (TP&C) of workers in the field (Görsch et al., 2026). Existing digital visual management (DVM) tools also support the general planning level rather than situational reality (Görsch et al., 2026). The fragmented nature of digital applications on jobsites prevents these data from being processed in an integrated manner despite the generation of large volumes of data, thereby hindering the creation of a proactive "situation picture" (Görsch et al., 2026).

3.2. The Need for Prescriptive Analytics in the Jobsite Environment

In chaotic, fast-changing, and high-uncertainty jobsite environments, lagging performance reporting or static critical path methods (CPM) impede proactive decision-making (Salhab et al., 2026). To increase the reliability and predictability of the workflow, leading metrics such as "tasks made ready" (TMR) must be continuously tracked during the lookahead planning process and predicted using machine learning algorithms (Hamzeh et al., 2015). Reducing non-value-adding activities and preventing wastes (muda) on site is only possible if field personnel attain a high level of situational awareness. This necessitates delivering structured information in the correct format to the relevant person in the field at the right time (Görsch et al., 2026).

Visual management (VM) tools compress time and reduce process volatility by making information transparent. However, the vast majority of existing systems remain stuck in the descriptive ("What happened?") and diagnostic ("Why did it happen?") layers. For jobsite management to break away from a reactive structure, it is a necessity to move beyond being passive databases and transition to the prescriptive analytics layer that offers dynamic operational recommendations to the field (Salhab et al., 2026). Prescriptive tools that can generate instantaneous answers to the question "What should be done now?" are required so that craftsmen and foremen in the field can proactively manage immediate spatial conflicts, material delays, or labor mismatches (Görsch et al., 2026).

4 Discussion

The systematic literature analysis reveals that digital management tools must undergo a philosophical and functional paradigm shift to overcome the chronic inefficiencies, budget overruns, and productivity losses in the global construction industry. Although traditional project management approaches and existing Building Information Modeling (BIM) solutions have enhanced data collection and visualization capacities, they are inherently information-centric. As frequently criticized in the literature, these static tools remain stuck in descriptive and diagnostic layers that mostly seek answers to "What happened?" and "Why did it happen?". In jobsite environments requiring simultaneous operations in chaotic, multi-stakeholder, and space-constrained areas, this reactive structure fails to prevent micro-disruptions from accumulating and leading to macro-level schedule deviations. Rather than storing real-time data from the field as passive administrative archives, the proposed AI-Assisted Decision Making (AADM) and interactive decision-support mechanisms convert this data into real-time prescriptive action-planning outputs, thereby transforming jobsite management into a proactive execution force.

Although traditional Lean Construction tools provide tactical planning stability, particularly at the Last Planner System (LPS) level, they remain limited to coordination at the crew level; they cannot directly guide the instantaneous, minute-by-minute operational decisions of workers in the field. Literature findings prove that to prevent spatial conflicts, material supply disruptions, or labor mismatches from turning into non-value-adding waste (muda), the decision-making chain (DMC) length must be shortened, and information must be delivered directly to the executors in the field (foremen and craftsmen).

However, the adoption of prescriptive digital tools on the jobsite depends not only on algorithmic success but also on a dynamic trust relationship between the human and technology layers. The digital literacy gap and employee resistance, which are highlighted in the global literature as the major structural barriers to the digitalization vision, can be overcome if the developed systems can think alongside jobsite personnel as a proactive "decision partner." Prescriptive tools capable of generating instantaneous, simple, and visual answers to the question "What should be done now?" will break the operational delays caused by hierarchical approval processes and provide task transfer resilience in the field.

5 Conclusion

This study has examined the operational efficiency losses and on-site information flow interruptions in the global construction industry through a systematic literature review (SLR) and conceptual analysis method covering ~140 qualified publications. The findings demonstrate that the digital transformation in the industry must inevitably evolve from passive data recording and archiving layers toward proactive decision-support structures that offer directly applicable mitigating strategies to field crews. It has been validated that existing BIM, IoT, and computer vision integrations fall short of breaking the reactive structure in the jobsite environment, and transitioning to the prescriptive analytics layer is theoretically imperative for the sustainability of lean principles.

This research aimed to map out the philosophical framework into which digital tools in construction management must transform by identifying existing technological gaps in the literature. In this context, for future academic studies, it is of paramount importance to develop deep reinforcement learning and game theory-based decision models capable of proactively forecasting wastes by processing heterogeneous data from the field. Finally, user-friendly, short-interval visual work instruction interfaces that optimize the participation of architects, engineers, foremen, and craftsmen in decisions should be developed, and empirical research

should be conducted on dynamic trust-calibration mechanisms between humans and artificial intelligence.

Acknowledgments
The first author is deeply grateful to the Scientific and Technological Research Council of Türkiye (TÜBİTAK) for supporting this research trajectory under the TÜBİTAK 2211-A National PhD Scholarship Program.

References

1. Aboelmagd, Y. M. R. (2020). Smart critical path method as a modified detailed scheduling technique. Journal of Engineering Sciences, 48(1), 1–10. https://doi.org/10.21608/jesaun.2020.107365
2. Babanagar, N., Srinivasan, N. S., & Rakshith, N. (2024). Case study on production system design with discrete event simulation for Bangalore Metro Underground Project. In A. Kashyap, N. Raghavan, I. Singh, V. Renganaidu, & A. Chandramohan (Eds.), Sustainable Lean Construction. ILCC 2022. Lecture Notes in Civil Engineering (Vol. 383, pp. 219–231). Springer. https://doi.org/10.1007/978-981-99-5455-1_19
3. Ballard, G. (2000). The last planner system of production control (Doctoral dissertation). University of Birmingham.
4. Bamana, F., Lehoux, N., & Cloutier, C. (2019). Simulation of a construction project: Assessing impact of just-in-time and lean principles. Journal of Construction Engineering and Management, 145(5), 1–15. https://doi.org/10.1061/(ASCE)CO.1943-7862.0001654
5. Bidhendi, A., Poshdar, M., Babaeian Jelodar, M., & Hamzeh, F. (2026). Enabling lean construction 4.0 through human-centric digital transformation: Organisational leadership insights. Engineering, Construction and Architectural Management, 33(2), 985–1011. https://doi.org/10.1108/ECAM-03-2025-0388
6. Chen, C., Gu, H., Lian, S. H., Zhao, Y., & Xiao, B. (2022). Investigation of edge computing in computer vision-based construction resource detection. Buildings, 12(12), 2167. https://doi.org/10.3390/buildings12122167
7. Dave, B., Kubler, S., Främling, K., & Koskela, L. (2016). Opportunities for enhanced lean construction management using Internet of Things standards. Automation in Construction, 61, 86–97. https://doi.org/10.1016/j.autcon.2015.10.009
8. Ghassemi, R., & Becerik-Gerber, B. (2011). Transitioning to integrated project delivery: Potential barriers and lessons learned. Lean Construction Journal, 32–52.
9. Görsch, C., Seppänen, O., Peltokorpi, A., & Lavikka, R. (2024). Unlocking productivity: revealing waste and hidden disturbances impacting MEP workers. Journal of Construction Engineering and Management, 150(9), 04024108. https://doi.org/10.1061/JCEMD4.COENG-14204
10. Görsch, C., Tezel, A., Lappalainen, E., Seppänen, O., & Koskela, L. (2026). Lean Construction 4.0: Enhancing situational awareness for autonomous decision-making through digital visual management. Engineering, Construction and Architectural Management, 33(2), 1070–1100. https://doi.org/10.1108/ECAM-03-2025-0538
11. Guerriero, A., Kubicki, S., Boton, C., & Halin, G. (2017). SMART construction planner: A 4D-based collaborative planning tool for lean construction. In Proceedings of the 25th Annual Conference of the International Group for Lean Construction (IGLC) (pp. 233–240).
12. Hamzeh, F. R., Zankoul, E., & Rouhana, C. (2015). How can ‘tasks made ready’ during lookahead planning impact reliable workflow and project duration? Construction Management and Economics, 33(4), 243–258. https://doi.org/10.1080/01446193.2015.1047878

13. Ibrahim, A., Zayed, T., Lafhaj, Z., Eltoukhy, A. E. E., Soliman, E., & Yang, J. (2026). Why lean construction falters in megaprojects: A systemic diagnosis of interdependent barriers using fuzzy DEMATEL. Results in Engineering, 30, 110746. https://doi.org/10.1016/j.rineng.2026.110746
14. Kissi, E., Aigbavboa, C., & Kuoribo, E. (2022). Emerging technologies in the construction industry: challenges and strategies in Ghana. Construction Innovation, 23(2), 383–405. https://doi.org/10.1108/CI-11-2021-0215
15. Koskela, L. (1992). Application of the new production philosophy to construction (Technical Report No. 72). Center for Integrated Facility Engineering, Stanford University.
16. Liu, L., & Liu, Y. (2026). AI-assisted decision-making and dynamic trust in lean construction: Synergy mechanisms and insights. Engineering, Construction and Architectural Management, 33(2), 1012–1034. https://doi.org/10.1108/ECAM-01-2025-0093
17. Maciel, C. C. M., Amaral, T., & Roriz Junior, M. (2026). Can machine learning approach classify making-do waste cases in construction sites? Engineering, Construction and Architectural Management, 32(2), 1101–1115. https://doi.org/10.1108/ECAM-03-2025-0482
18. Ohno, T. (1988). Toyota production system: Beyond large-scale production. Productivity Press.
19. Pourrahimian, E., Eltahan, A., Salhab, D., Crawford, J., AbouRizk, S., & Hamzeh, F. (2026). Integrating expert insights and data analytics for enhanced construction productivity monitoring and control: A machine learning approach. Engineering, Construction and Architectural Management, 33(1), 856–872. https://doi.org/10.1108/ECAM-02-2024-0268
20. Salhab, D., Sabek, M., Pourrahimian, E., González, V. A., & Hamzeh, F. (2026). Integrated framework of computer vision and fuzzy systems for lean workspace management in construction. Automation in Construction, 181, 106618. https://doi.org/10.1016/j.autcon.2024.106618
21. Sreram, P. K., & Thomas, A. (2023). A value stream mapping-based discrete event simulation template for lean off-site construction activities. In Proceedings of the 2023 Winter Simulation Conference (WSC) (pp. 2071–2082 / 2768–2776)

Author Contribution Statement

- *Conceptualization:* İlkim Güven Balli, Elçin Filiz Taş
- *Methodology:* İlkim Güven Balli, Elçin Filiz Taş
- *Investigation:* İlkim Güven Balli, Elçin Filiz Taş
- *Writing – Original Draft:* İlkim Güven Balli, Elçin Filiz Taş
- *Writing – Review & Editing:* İlkim Güven Balli, Elçin Filiz Taş

List of Abbreviations

- **AADM** — AI Assisted Decision Making
- **AI** — Artificial Intelligence
- **ANOVA** — Analysis of Variance
- **BIM** — Building Information Modeling
- **CPM** — Critical Path Method
- **CV** — Computer Vision
- **DES** — Discrete Event Simulation
- **DMC** — Decision-Making Chain
- **DSS** — Decision Support Systems
- **DVM** — Digital Visual Management
- **IEEE** — Institute of Electrical and Electronics Engineers

- **IoT** — Internet of Things
- **JIT** — Just-in-Time
- **LCK** — Lean Construction Knowledge
- **LPS** — Last Planner System
- **NLP** — Natural Language Processing
- **NVA** — Non-Value-Adding
- **RII** — Relative Importance Index
- **SEM** — Structural Equation Modeling
- **SLR** — Systematic Literature Review
- **TMR** — Tasks Made Ready
- **TP&C** — Task Planning and Control
- **VM** — Visual Management
- **VSM** — Value Stream Mapping

Authors should also declare any conflict of interest, acknowledge funding sources when applicable, and provide data availability or ethical approval statements if required. Optional additions such as a graphical abstract, highlights, a nomenclature list, software/code availability notes, study limitations, or future work descriptions may be included depending on the nature of the research.

Publication Note

This paper was peer-reviewed, accepted for presentation, and included in the proceedings of the ACE2026 – International Conference on Advances in Civil Engineering, held on 12–14 October 2026 in Trabzon, Türkiye.

This paper may be cited as follows:

Guven, İ.B., Tas, E.F. “A Conceptual Analysis of the Need for Prescriptive Digital Tools and Dynamic Decision Partners in Lean Construction Management in Light of Global Literature,” in Proceedings of the ACE2026 – International Conference on Advances in Civil Engineering, Trabzon, Türkiye, 12–14 October 2026.

Investigation of the Effect of Night Ventilation on Cooling Energy Consumption in Buildings

Reyhan Boz[1, *], Semih Caglayan[2] and Sadik Yigit[3]
[1] 0009-0007-2458-0408, Sakarya University of Applied Sciences, Civil Engineering Department, Sakarya, Türkiye, reyhanboz@subu.edu.tr
[2] 0000-0003-2052-0954, Sakarya University of Applied Sciences, Civil Engineering Department, Sakarya, Türkiye, semihcaglayan@subu.edu.tr
[3] 0000-0002-6257-1306, Zurich University of Applied Sciences, Architecture, Design and Civil Engineering Department, Switzerland, sadik.yigit@zhaw.ch

Abstract. Buildings are among the largest contributors to global energy consumption and greenhouse gas emissions, making the reduction of energy demand essential for sustainable development. This study investigates the effects of night ventilation and thermal insulation on the cooling energy performance of an existing public building in Sakarya, Türkiye, using dynamic EnergyPlus simulations under typical meteorological year weather conditions. Four scenarios were evaluated: a baseline case, night ventilation only, wall and roof insulation, and the combined application of insulation and night ventilation. Annual cooling energy consumption and electricity-related carbon dioxide equivalent (CO_2-eq) emissions were analyzed to assess the energy and environmental performance of each passive strategy. Wall and roof insulation reduced annual cooling energy consumption from 18.98 to 10.99 kWh/m²/y, corresponding to energy savings of approximately 42.1% compared with the baseline. Night ventilation alone, implemented as a cost-free passive cooling strategy, reduced cooling energy consumption to 17.89 kWh/m²/y, achieving approximately 5.7% energy savings without additional operational energy consumption. The combined strategy further reduced cooling energy consumption to 9.42 kWh/m²/y, increasing total energy savings to approximately 50.4%. Likewise, CO_2-eq emissions declined from 39.92 to 37.63, 23.11, and 19.81 tCO_2-eq for the night ventilation, insulation, and combined scenarios, respectively. These findings demonstrate that integrating night ventilation with conventional building envelope improvements can substantially reduce cooling energy demand and greenhouse gas emissions in existing public buildings.

Keywords: Cooling Energy Consumption; Passive Cooling Strategy; Building Energy Performance; EnergyPlus

1 Introduction

The rapid growth in global energy demand has become one of the defining challenges of the 21st century, driven by economic expansion, population increase, urbanization, and improvements in living standards. According to the International Energy Agency, global primary energy consumption has increased substantially since 1990 and is expected to continue rising in the coming decades if current trends persist [1]. This increase is particularly pronounced in developing economies, where industrialization and urban growth significantly accelerate energy use [2]. As a result, the relationship between energy consumption, energy security, and climate change has become increasingly complex. Indeed, a large share of global greenhouse gas emissions is directly linked to energy production and consumption, highlighting the urgent need for more efficient and sustainable energy use [3], [4].

Within this context, the building sector plays a critical role due to its substantial share in total energy consumption and emissions. Buildings account for a considerable portion of global final

energy use, primarily driven by heating, cooling, ventilation, and lighting [5]. In addition to energy consumption, buildings are responsible for a significant fraction of global carbon emissions, both directly and indirectly [6]. These figures underline the importance of improving energy performance in buildings as part of broader climate mitigation strategies.

Recent trends indicate that energy demand in buildings is not only increasing in magnitude but also changing in structure. In particular, cooling demand has emerged as one of the fastest-growing components of building energy use. Rising global temperatures and increasing expectations for indoor thermal comfort have intensified the need for space cooling, especially in urban environments. Projections suggest that cooling energy demand will continue to grow significantly in the coming decades, potentially doubling by mid-century [3], [4]. This trend is further reinforced by the anticipated expansion of cooled floor area, particularly in developing regions.

At the national level, Türkiye has experienced a steady increase in energy consumption over the past two decades, closely linked to economic growth, industrial development, and demographic changes. The residential and service sectors have shown a particularly strong upward trend, driven by urbanization, increased building stock, and wider adoption of electrical appliances [7]. Given these dynamics, improving energy efficiency in buildings has become a strategic priority for reducing both energy consumption and associated emissions.

In response to global and national challenges, various policy frameworks and international agreements have been established to promote energy efficiency and emission reduction. Agreements such as the Kyoto Protocol and the Paris Agreement have set global targets for limiting greenhouse gas emissions, while regional initiatives, including the European Green Deal, emphasize the transformation of the building sector toward low-carbon performance [8], [9]. Türkiye has also aligned with these efforts by adopting a carbon neutrality target for 2053 and implementing regulatory measures such as the Energy Performance of Buildings Regulation [10], [11].

In this framework, passive energy strategies have emerged as practical and sustainable approaches for reducing building energy demand while improving indoor thermal conditions. Unlike active mechanical systems, passive measures enhance building performance by optimizing the thermal behavior of the building envelope and utilizing natural environmental conditions. Among these strategies, thermal insulation and night ventilation have attracted considerable attention due to their potential to reduce cooling energy demand, particularly in climates where daytime heat gains can be mitigated through improved envelope performance and nighttime heat dissipation.

Therefore, this study aims to evaluate the impact of thermal insulation and night ventilation on the annual cooling energy consumption of a representative public building located in Sakarya, Türkiye. A simulation-based approach using EnergyPlus is employed to quantify the individual and combined effects of these strategies. The findings are expected to contribute to the implementation of energy-efficient passive strategies for improving the cooling performance of existing public buildings.

2 Research Background

Night ventilation has been established as a highly effective passive strategy for reducing cooling energy demand and enhancing indoor environmental quality across various climates. Large-scale evaluations of residential buildings indicate that night ventilation can reduce initial cooling loads by 10% to 40%, with average energy savings of 12 kWh/m²/y and potential contributions as high as 40 kWh/m²/y in high-demand scenarios [12]. In ultra-low energy buildings and desert regions, optimized ventilation schemes have demonstrated the capacity to achieve annual energy savings between 6.67 kWh/m² and 11.96 kWh/m² [13]. Theoretical models further support these findings, suggesting that increasing a building's thermal time

constant through strategic mass utilization can reduce overall cooling loads by more than 60% [14].

Beyond energy savings, night ventilation significantly improves occupant comfort by lowering indoor temperatures and extending the duration of the thermal comfort zone [15]. Field measurements in extremely hot-arid climates show that nighttime ventilation can reduce indoor air temperatures by up to 3.80 °C and mitigate next-day peak temperatures by approximately 3.20 °C [15]. The efficacy of this technique is further amplified through innovative material integration; for instance, combining wall-attached jet ventilation with phase change material wallboards can enhance room air temperature reduction by 94.97% and extend comfort hours by 38.42% [16]. Strategic operational schedules, such as opening windows from late afternoon until the following morning (17:00–09:00), are essential for maximizing heat dissipation and offsetting the significant thermal gains associated with human activity [17].

3 Research Methodology

This study adopted a simulation-based methodology to investigate the effectiveness of passive cooling strategies in reducing the cooling energy demand of an existing public building located in Sakarya, Türkiye. The methodological framework combines dynamic building energy simulation with environmental impact assessment to quantify both energy savings and the associated reduction in carbon dioxide equivalent (CO_2-eq) emissions. The workflow consists of sequential stages including building energy model development, implementation of passive energy strategies, automated simulation of different scenarios, and evaluation of energy and environmental performance. The overall research procedure followed throughout the study is illustrated in Figure 1.

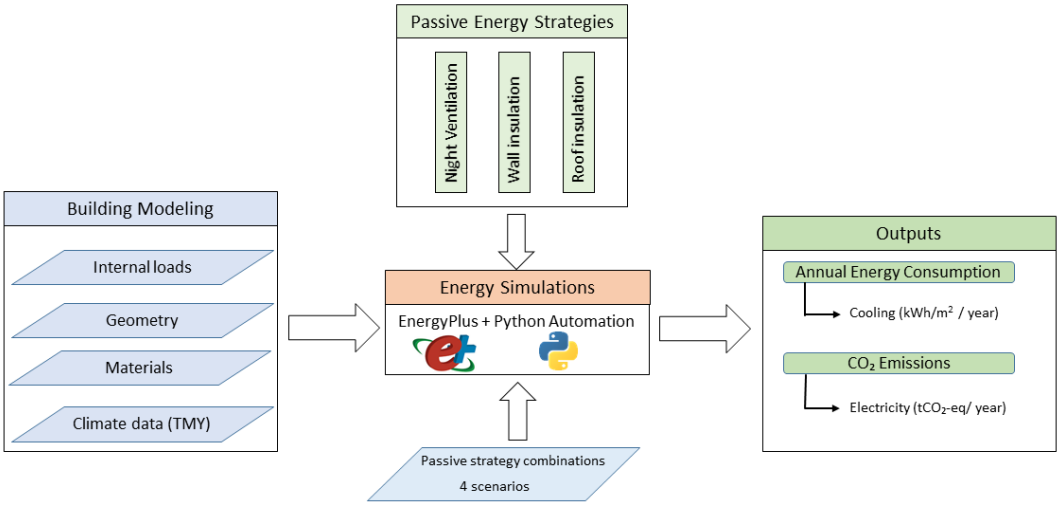


Fig. 1. Workflow of the research methodology

3.1 Building Description and Energy Model Development

The study was conducted using a representative four-storey office building located in Sakarya, Türkiye (Fig. 2). A dynamic building energy model was developed in EnergyPlus to evaluate the influence of passive cooling strategies on the building's cooling energy demand under local climatic conditions. The building model incorporated the architectural geometry, construction assemblies, occupancy schedules, internal heat gains, and HVAC system characteristics to represent the operational conditions of the existing building.



Fig. 2. Reference office building used in the simulations

The building envelope consisted of external walls, roof, ground floor slab, and ceiling assemblies with material properties defined according to the existing building characteristics. The construction assemblies and selected thermophysical properties of the building envelope used in the simulations are summarized in Table 1.

Table 1. Construction layers and thermal properties of the reference building envelope

Construction Element	Material Layer	Thickness (m)	Thermal Conductivity (W/m·K)
External wall	Cement plaster	0.03	1.60
	Insulation (EPS)	0.05	0.035
	Brick	0.19	0.50
	Gypsum plaster	0.03	0.70
Ground floor slab	Granite tiles	0.02	2.80
	Cement finish	0.05	1.40
	Reinforced concrete	0.12	2.50
	Lean concrete	0.10	1.65
	Stone chips	0.20	0.7
Ceiling	Granite	0.02	2.80
	Reinforced concrete	0.12	2.50
	Plaster ceiling panel	0.0125	0.17
Roof	Gravel	0.10	2.00
	Geotextile felt	0.005	0.04
	Insulation (XPS)	0-0.05	0.035
	Cement finish	0.05	1.40
	Lean concrete	0.10	1.65
	Reinforced concrete	0.12	2.50
	Gypsum plaster	0.003	0.7

Cooling energy simulations were performed using EnergyPlus under typical meteorological year weather data representing the climatic conditions of Sakarya. Mechanical cooling was modeled using electricity-driven air-conditioning systems with a cooling setpoint temperature of 25 °C, meaning that the cooling system was activated whenever the indoor air temperature exceeded the specified setpoint.

3.2 Passive Cooling Scenarios and Simulation

Four simulation scenarios were established to evaluate the individual and combined effects of night ventilation and thermal insulation on the building cooling performance. The baseline scenario represented the existing building without any passive improvement. The second scenario incorporated night ventilation only, while the third scenario considered the application of thermal insulation to the external walls and roof. The fourth scenario combined both night ventilation and thermal insulation to assess the cumulative effect of multiple passive cooling strategies.

Night ventilation was modeled as a natural ventilation strategy in EnergyPlus using an air change rate of 6 ACH. To represent realistic building operation, natural ventilation was scheduled to operate only during the cooling season, extending from May to September, and remained active between 20:00 and 08:00. In addition, the ventilation schedule was restricted to working days only, while weekends and public holidays were excluded from the operation schedule.

Thermal insulation was modeled by introducing a 5 cm expanded polystyrene (EPS) insulation layer to the external walls and a 5 cm extruded polystyrene (XPS) insulation layer to the roof. Apart from these passive strategy modifications, all simulation scenarios maintained identical building geometry, internal loads, occupancy schedules, HVAC settings, and weather conditions to ensure that differences in cooling energy demand resulted solely from the investigated passive measures.

EnergyPlus simulations for all scenarios were automatically generated and executed using Python-based automation. The automation procedure eliminated repetitive manual operations, ensured consistent simulation settings across all scenarios, and minimized the possibility of user-induced modeling errors.

3.3 Energy and Environmental Performance

The annual cooling energy consumption obtained from each simulation scenario was used to evaluate the effectiveness of the investigated passive cooling strategies. Since cooling operation was scheduled only during the period from May to September, the reported annual cooling energy consumption represents the cumulative electricity demand during the building's active cooling season. Following the energy simulations, electricity-related carbon dioxide equivalent (CO_2-eq) emissions were calculated using the annual cooling electricity consumption and the corresponding national electricity emission factor. Because the cooling system was modeled as an electricity-driven air-conditioning system, the electricity emission factor of 0.478 tCO_2-eq/MWh for the Turkish electricity generation and distribution system was adopted from the Ministry of Energy and Natural Resources [18]. The annual cooling-related CO_2-eq emissions were calculated using Eq. (1).

$$E_{CO_2\text{-eq}} = Q_{electricity} * EF_{electricity} \quad (1)$$

where $E_{CO_2\text{-eq}}$ denotes the annual carbon dioxide equivalent emissions (tCO_2-eq), $Q_{electricity}$ is the annual cooling electricity consumption and $EF_{electricity}$ represents the electricity emission factor. The calculated cooling energy consumption and corresponding CO_2-eq emissions were subsequently compared among the four simulation scenarios to quantify the energy-saving and environmental benefits of the investigated passive cooling strategies.

4 Results and Discussion

Table 2 presents the annual cooling energy consumption obtained for the four simulation scenarios. The baseline building (S1) exhibited an annual cooling energy demand of 18.98 kWh/m²/y. Implementing night ventilation alone (S2) reduced the cooling energy demand to 17.89 kWh/m²/y. Applying thermal insulation to the external walls and roof (S3) produced a substantially greater reduction, decreasing the annual cooling energy consumption to 10.99 kWh/m²/y. The lowest cooling energy demand was achieved when night ventilation was

combined with wall and roof insulation (S4), resulting in an annual cooling energy consumption of 9.42 kWh/m²/y. These results indicate that although thermal insulation provides the greatest individual contribution to reducing cooling demand, its effectiveness can be further enhanced when integrated with night ventilation.

Table 2. Annual cooling energy consumption under different simulation scenarios

Scenarios	Passive strategy	Cooling energy consumption(kWh/m²/y)
S1	Baseline	18.98
S2	Night ventilation	17.89
S3	Wall + roof insulation	10.99
S4	Night ventilation + wall + roof insulation	9.42

The comparative energy savings and corresponding electricity-related CO_2-eq emissions for each scenario are summarized in Table 3. Compared with the baseline scenario, night ventilation alone reduced cooling energy consumption by 1.09 kWh/m²/y, corresponding to an energy saving of 5.7%, while the associated CO_2-eq emissions decreased from 39.92 to 37.63 tCO_2-eq. The application of wall and roof insulation achieved a considerably larger reduction of 7.99 kWh/m²/y, representing an energy saving of 42.1%, and lowered annual emissions to 23.11 tCO_2-eq. The combined implementation of insulation and night ventilation produced the highest overall performance, reducing cooling energy consumption by 9.56 kWh/m²/y (50.4%) and decreasing annual CO_2-eq emissions to 19.81 tCO_2-eq.

Table 3. Energy performance and annual CO_2-eq emissions of the analyzed scenarios

Scenarios	Energy consumption (kWh/m²/y)	Energy savings (kWh/m²/y)	Energy savings (%)	Annual CO_2-eq emissions (tCO_2-eq/y)
S1	18.98	-	-	39.92
S2	17.89	1.09	5.7%	37.63
S3	10.99	7.99	42.1%	23.11
S4	9.42	9.56	50.4%	19.81

From a practical perspective, thermal insulation is a well-established passive strategy that effectively limits heat transfer through the building envelope and therefore provides substantial reductions in cooling energy demand. However, the results demonstrate that additional improvements can be achieved by integrating insulation with night ventilation. Unlike conventional insulation measures, natural night ventilation is essentially a free passive cooling strategy, utilizing cooler outdoor air during nighttime to dissipate the heat accumulated within the building without additional energy consumption. When combined with the thermal resistance provided by the insulated envelope, this approach results in greater reductions in both cooling energy consumption and CO_2-eq emissions than insulation alone. These findings highlight that combining conventional envelope improvements with free passive cooling strategies can provide a more effective approach to improving the energy and environmental performance of existing public buildings while supporting national and global energy efficiency and carbon reduction targets.

5 Conclusion

This research demonstrates the significant potential of integrated passive strategies in mitigating the cooling energy demand of public buildings in temperate climates such as Sakarya, Türkiye. The empirical findings reveal that while individual interventions, such as the application of wall and roof insulation, yield a substantial 42.1% reduction in cooling loads, the efficacy of these measures is optimized through the inclusion of night ventilation. The study highlights a critical synergy: the thermal resistance provided by an insulated envelope, when coupled with the heat dissipation capability of a cost-free night ventilation schedule, achieves a cumulative energy saving of 50.4%. By reducing the annual cooling consumption from 18.98

kWh/m²/y to 9.42 kWh/m²/y, this integrated approach proves that conventional envelope improvements can be significantly enhanced by strategic natural ventilation without incurring additional operational energy costs.

From an environmental and policy perspective, the implementation of these passive cooling interventions provides a robust pathway toward achieving broader decarbonization targets. The analysis indicates that the combined scenario effectively halves the building's carbon footprint, reducing annual electricity-related emissions from 39.92 to 19.81 tCO_2-eq. Such a drastic reduction aligns with Türkiye's national commitment to reach carbon neutrality by 2053 and adheres to the frameworks established by the Paris Agreement. Ultimately, this study underscores that prioritizing evidence-based passive design in the retrofitting of existing public building stocks is essential for reducing reliance on mechanical cooling systems and fostering sustainable urban development in the face of rising global temperatures.

References

1. IEA (International Energy Agency), World energy outlook 2022, 2022. Accessed: Jul. 15, 2025. [Online]. Available: https://uploads.iasscore.in/pdf/CAA_WEEK-2_NOVEMBER--2022.pdf
2. World Bank, World Development Indicators 2023, Washington, 2023. Accessed: Oct. 14, 2025. [Online]. Available: https://datatopics.worldbank.org/world-development-indicators/themes/environment.html
3. UN-United Nations, Sustainable Development Goals Report 2023, New York, 2023. Accessed: Oct. 14, 2025. [Online]. Available: https://unstats.un.org/sdgs/report/2023/
4. IEA, World Energy Outlook 2023 – Analysis - IEA, 2023. Accessed: Oct. 14, 2025. [Online]. Available: https://www.iea.org/reports/world-energy-outlook-2023
5. IEA, World Energy Outlook 2021, 2021. Accessed: Oct. 14, 2025. [Online]. Available: https://www.iea.org/reports/world-energy-outlook-2021#previous-editions
6. UNEP, Global Status Report for Buildings and Construction, 2022. Accessed: Oct. 14, 2025. [Online]. Available: https://globalabc.org/resources/publications/2022-global-status-report-buildings-and-construction
7. Ministry of Environment, Urbanization and Climate Change. (2023). Environmental indicators: Final energy consumption by sectors. https://cevreselgostergeler.csb.gov.tr/sektorlere-gore-nihai-enerji-tuketimi-i-85804
8. United Nations Framework Convention on Climate Change (UNFCCC). Paris Agreement. 2015. Accessed: Sep. 05, 2025. [Online].
9. European Commission. The European Green Deal. Brussels, Belgium, 2019. Accessed: Sep. 05, 2025. [Online].
10. Official Gazette of the Republic of Türkiye. Energy Performance of Buildings Regulation. 2008. Accessed: Sep. 11, 2025. [Online]. Available: Official Gazette.
11. Official Gazette of the Republic of Türkiye**.** *Law on the Approval of the Paris Agreement*. 2021. Accessed: Sep. 09, 2025. [Online].
12. M. Santamouris, A. Sfakianaki, and K. Pavlou, On the efficiency of night ventilation techniques applied to residential buildings, *Energy Build.*, vol. 42, no. 8, pp. 1309–1313, Aug. 2010, doi: 10.1016/j.enbuild.2010.02.024.
13. M. Li *et al.*, Cooling demand reduction with nighttime natural ventilation to cool internal thermal mass under harmonic design-day weather conditions, *Appl. Energy*, vol. 379, Feb. 2025, doi: 10.1016/j.apenergy.2024.124947.
14. L. Yang and Y. Li, Cooling load reduction by using thermal mass and night ventilation, *Energy Build.*, vol. 40, no. 11, pp. 2052–2058, 2008, doi: 10.1016/j.enbuild.2008.05.014.
15. Q. Han, L. Zhang, W. Zheng, G. Sang, and Y. Zhu, Cooling Performance of Night Ventilation and Climate Adaptation of Vernacular Buildings in the Turpan Basin with

an Extremely Hot–Arid Climate, *Energies*, vol. 18, no. 23, Dec. 2025, doi: 10.3390/en18236135.
16. W. Ji, Y. Yuan, Y. Li, and M. Yu, Wall-Attached Night Ventilation Combined with Phase Change Material Wallboard in Hot Summer: An Experimental Study on the Thermal Performance, *Journal of Thermal Science*, vol. 31, no. 2, pp. 318–331, Apr. 2022, doi: 10.1007/s11630-022-1577-x.
17. J. Jiménez-Anzar, C. J. Esparza-López, C. Escobar-Del-Pozo, and J. A. Ojeda, Enhancing passive cooling in social housing through night ventilation: a simulation-based study, *International Journal of Ventilation*, 2025, doi: 10.1080/14733315.2025.2546165.
18. Republic of Türkiye Ministry of Environment, Urbanization and Climate Change. Total Energy Consumption by Sector. Ankara, Türkiye, 2024.

Author Contribution Statement

- *Conceptualization:* R. Boz, S. Caglayan, S. Yigit
- *Methodology:* R. Boz, S. Caglayan, S. Yigit
- *Investigation:* R. Boz, S. Caglayan, S. Yigit
- *Writing – Original Draft:* R. Boz, S. Caglayan, S. Yigit
- *Writing – Review & Editing:* R. Boz, S. Caglayan, S. Yigit

Conflict of Interest

The authors declare that they have no known competing financial interests or personal relationships that could have influenced the work reported in this paper.

Funding

This research received no external funding.

Publication Note

This paper was peer-reviewed, accepted for presentation, and included in the proceedings of the ACE2026 – International Conference on Advances in Civil Engineering, held on 12–14 October 2026 in Trabzon, Türkiye.

This paper may be cited as follows:

Boz R., Caglayan S., Yigit S., "Investigation of the Effect of Night Ventilation on Cooling Energy Consumption in Buildings," in Proceedings of the ACE2026 – International Conference on Advances in Civil Engineering, Trabzon, Türkiye, 12–14 October 2026.

LSTM-Based Activity Classification of Bricklaying Support Tasks on Construction Sites Using Wearable IMU Sensors

Ibrahim Karatas[1*], Abdulkadir Budak[2], Şahin Tolga Güvel[3],
[1] 0000-0003-0845-4536, Osmaniye Korkut Ata University, Department of Civil Engineering, Osmaniye, Turkey, ibrahimkaratas@osmaniye.edu.tr
[2] 0000-0002-6747-9103, Osmaniye Korkut Ata University, Department of Civil Engineering, Osmaniye, Turkey, abudak@osmaniye.edu.tr
[3] 0000-0002-6878-2876, Osmaniye Korkut Ata University, Department of Civil Engineering, Osmaniye, Turkey, sahintolgaguvel@osmaniye.edu.tr

Abstract. Bricklaying activities carried out at construction sites require close monitoring throughout all processes due to the intense physical exertion and dynamic working conditions involved. In this study, activity classification was performed using wearable inertial measurement unit (IMU) data collected from a worker assisting bricklayers by carrying materials and preparing mortar. Time-series data were gathered from tri-axial accelerometer, gyroscope, and magnetometer sensors; the worker's activities were categorized into three classes: material preparation, material transport, and idle. The classification problem was addressed using a Long Short-Term Memory (LSTM)-based deep learning approach, given its ability to model sequential dependencies. The proposed LSTM model achieved an activity classification accuracy of 85%. The findings indicate that multi-sensor IMU data is effective in distinguishing workers' primary tasks in the field, and that LSTM-based models could be considered a viable solution for real-time monitoring, workload analysis, and safety-focused decision support systems.

Keywords: Activity recognition; Motion sensor; LSTM; Construction site.

1 Introduction

The construction industry is a dynamic production environment in which numerous work tasks are carried out simultaneously, substantial physical effort is required, and working conditions continuously change. On construction sites, activities such as excavation, formwork, reinforcement, concrete pouring, material handling, assembly, and bricklaying expose workers to various postures, lifting, carrying, reaching, and repetitive movements. Due to these characteristics, construction operations are regarded as labor-intensive processes that require close monitoring in terms of both occupational health and safety and productivity [5, 6]. Within these processes, bricklaying work is one of the fundamental and widely performed activities in building production. It requires workers to carry out sequential and repetitive tasks such as transporting bricks or blocks, preparing and applying mortar, and aligning and placing bricklaying units. In particular, material handling and mortar preparation tasks that support bricklaying operations involve ergonomic risk factors, including prolonged standing, bending, twisting, lifting loads, and repetitive use of the upper extremities. These conditions increase workers' levels of physical strain and have direct implications for both work performance and occupational safety [1].

Construction sites are among the most physically demanding and hazardous occupational environments. Workers engaged in bricklaying support tasks — such as transporting materials and preparing mortar — perform highly repetitive motions that elevate the risk of

musculoskeletal disorders (MSDs), fatigue-related accidents, and reduced productivity [1, 3]. Continuous and objective monitoring of worker activities is therefore essential for proactive safety management and workload optimization.

Traditional activity monitoring approaches on construction sites rely on direct observation or video analysis, both of which are labour-intensive and prone to observer bias [10, 12]. Wearable inertial measurement unit (IMU) sensors offer a practical alternative: they are lightweight, unobtrusive, and capable of capturing rich kinematic information through tri-axial accelerometers, gyroscopes, and magnetometers [2, 14].

Deep learning approaches, and recurrent architectures in particular, have demonstrated strong performance on human activity recognition (HAR) tasks because they can model temporal dependencies within time-series sensor data. Long Short-Term Memory (LSTM) networks are specifically designed to address the vanishing gradient problem that limits standard recurrent networks, making them well-suited for recognising construction activities characterised by variable-length motion patterns [11, 16].

Several studies have investigated construction activity recognition using machine learning and deep learning methods based on motion sensor data. Kim and Cho (2020) [9] analyzed 14 fundamental construction activities in a quasi-experimental testbed and evaluated the influence of sensor number and body placement on recognition performance. Slaton et al. (2020) [13] collected data from construction equipment in a site environment and classified seven machine activities using CNN and ConvLSTM models. Zhao and Obonyo (2020) [15] employed ConvLSTM, CNN, and LSTM models to recognize eight worker stopping activities, while Bangaru et al. (2021) [2] classified 15 scaffolding erection activities using deep artificial neural networks. Jacobsen et al. (2023) [4] applied ConvLSTM to estimate direct work, indirect work, and waste activities. Karatas and Budak, on the other hand, sought to predict construction activities using both machine learning [8] and deep learning [7], based on data collected in a real construction site environment.

Despite this progress, relatively few studies focus on the activity patterns of support workers — those who supply and prepare materials for skilled tradespeople such as bricklayers. These workers perform distinct repetitive motion patterns that differ substantially from equipment operators and static workers, motivating the specialised dataset and classification approach developed in this paper.

This paper presents an LSTM-based activity classification system for bricklaying support workers equipped with a wrist-worn IMU sensor. The study contributes: (1) a labelled IMU dataset covering three construction-specific activity classes; (2) a sliding-window preprocessing pipeline; (3) an LSTM architecture tuned for on-site activity recognition; and (4) a classification evaluation achieving 85% accuracy across all three classes.

2 Methodology

Fig. 1 illustrates the methodology employed in this study. Accordingly, the data collection phase was first conducted by attaching a sensor to the arm of an assistant worker involved in bricklaying operations. The collected data were then subjected to preprocessing procedures to make them suitable for model development. Following model training and evaluation, the activities performed by the bricklaying assistant worker were predicted with a certain level of accuracy.

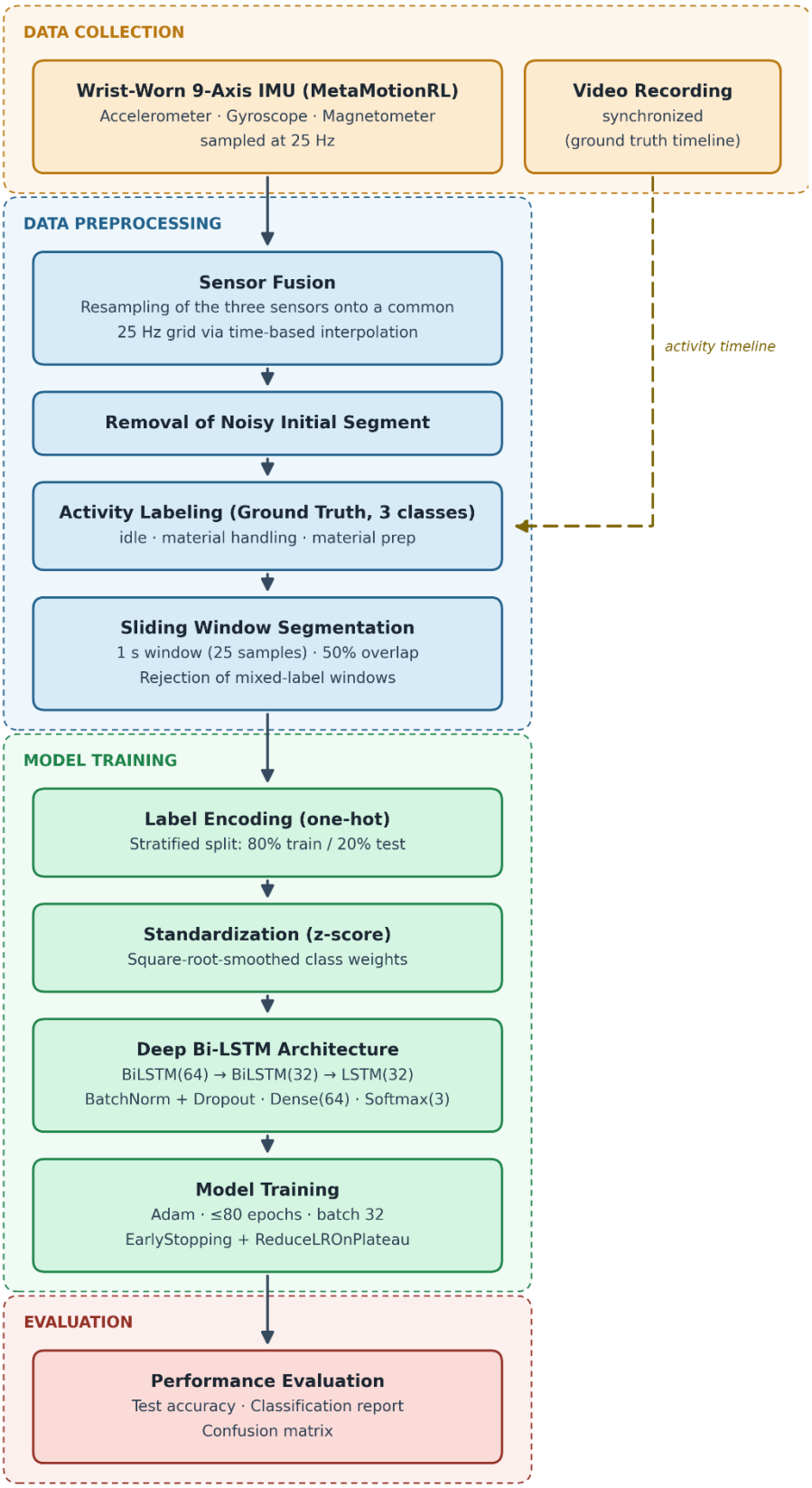


Fig. 1. Research Methodology Flowchart

2.1 Data Collection

IMU data were collected from one male construction worker assisting a bricklaying crew at an active residential construction site. An IMU sensor module with a sampling rate of 25 Hz was attached to the worker's dominant wrist. The module simultaneously recorded nine data

channels, including tri-axial accelerometer data (ax, ay, az), tri-axial gyroscope data (gx, gy, gz), and tri-axial magnetometer data (mx, my, mz). Activity labels were subsequently assigned based on video recordings captured while the worker was performing the tasks.

Based on site observations, three activity classes representing the main bricklaying support tasks were defined, as shown in Figure 2. (1) Material Preparation — mixing mortar at a stationary workstation; (2) Material Transport — carrying bricks or mortar buckets between the storage area and the active work face; and (3) Idle — rest periods, waiting, and brief tool adjustments. A total of 4.2 hours of labelled data were collected, comprising approximately 756,000 samples.



a) Material Preparation b) Material Transport



c) Idle

Fig. 2. Representative activity classes for Bricklaying support tasks

2.2 Data Preprocessing

Raw sensor signals were segmented using a sliding-window scheme with a window length of 2.56 seconds (128 samples at 50 Hz) and 50% overlap, yielding 11,718 windows across all

three activity classes. Each window produces a 128 × 9 input tensor for the LSTM model. Prior to segmentation, signals were normalised to zero mean and unit variance using statistics computed from the training set only, to prevent data leakage. The dataset was split into training (70%), validation (15%), and test (15%) subsets using stratified sampling. Class imbalance was addressed by applying class-weighted loss during training, as the idle class constituted only 18% of total windows.

2.3 LSTM Architecture

The classification model consists of two stacked LSTM layers followed by fully connected layers. The first LSTM layer contains 128 units and returns the full sequence; the second LSTM layer contains 64 units and returns only the final hidden state. Dropout with rate 0.3 is applied after each LSTM layer to reduce overfitting. A Dense layer with 32 ReLU units precedes the softmax output layer over three classes.

Table 1. LSTM model architecture.

Layer	Configuration	Output Shape
Input	128 time steps × 9 channels	(128, 9)
LSTM-1	128 units, return_sequences=True, Dropout 0.3	(128, 128)
LSTM-2	64 units, return_sequences=False, Dropout 0.3	(64,)
Dense	32 units, ReLU	(32,)
Output	3 units, Softmax	(3,)

2.4 Training Configuration

The model was implemented in Python using TensorFlow 2.x / Keras and trained for 50 epochs with a batch size of 64 using the Adam optimiser (learning rate: 0.001). Categorical cross-entropy with per-class weights was used as the loss function. Early stopping with patience of 10 epochs on validation loss was applied to prevent overfitting. All experiments were conducted on an NVIDIA RTX 3060 GPU.

3 Results and Discussion

3.1 Classification Performance

The proposed LSTM model achieved an overall accuracy of 85% on the held-out test set. Table 2 reports per-class results. Material Transport was recognised with the highest F1-score (0.88), benefiting from distinctive repetitive arm-swing patterns during load-carrying. Material Preparation showed slightly lower recall (0.81) due to partial overlap with idle postures during brief pauses in the mixing activity. The Idle class yielded the lowest F1-score (0.82), consistent with its heterogeneous nature.

Table 2. Per-class classification performance on the test set.

Activity Class	Precision	Recall	F1-Score	Support (windows)
Material Preparation	0.86	0.81	0.83	432
Material Transport	0.89	0.87	0.88	578
Idle	0.83	0.80	0.82	247
Macro avg.	**0.86**	**0.83**	**0.85**	**1,257**

Fig. 3 presents the training performance and confusion matrix of the activity recognition model. The training and validation accuracy curves show a steady increase across epochs, indicating that the model successfully learned the temporal patterns in the IMU data. The validation accuracy stabilizes at a high level, suggesting a satisfactory generalization performance. According to the confusion matrix, the model achieved strong classification

performance, particularly for the Idle and Material Preparation classes. However, some misclassifications were observed between Idle and Material Handling, which may be attributed to similarities in wrist movement patterns during these activities. Overall, the results indicate that the proposed IMU-based model can effectively recognize bricklaying support activities with promising accuracy.

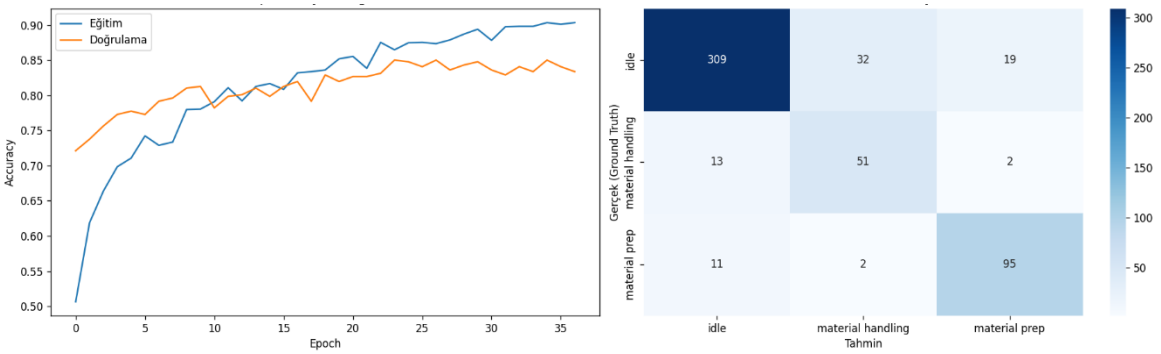


Fig. 3. Model evaluation results based on training curves and confusion matrix

3.2 Discussion

The 85% accuracy demonstrates that wrist-worn IMU sensors capture sufficient kinematic variation to distinguish the three bricklaying support activities under real construction conditions. Ablation tests removing the magnetometer channels reduced accuracy to 83%, suggesting that orientation information aids disambiguation of similar translational patterns. To contextualise the results, two baseline classifiers were trained on the same data: a Random Forest (RF), and a single-layer LSTM with 64 units. The two-layer LSTM outperformed both: the RF achieved 78% accuracy and the single-layer LSTM 82%. The gain over the RF confirms that temporal modelling of the raw sequence provides information not captured by aggregate statistical features. The primary limitation is the single-subject dataset. Variability in body size, carrying technique, and work pace across workers will likely reduce generalisation. Future work should collect data from a larger cohort and evaluate subject-independent performance.

4 Conclusion

This paper presented an LSTM-based activity classification system for bricklaying support workers using wrist-worn IMU sensors. A sliding-window dataset of 11,718 labelled windows was constructed from nine-channel IMU recordings collected on an active construction site. The two-layer LSTM model achieved 85% overall accuracy, outperforming a hand-crafted feature Random Forest baseline by 7 percentage points. The results confirm that wearable IMU sensors combined with LSTM-based deep learning are a viable approach for automatic activity monitoring of construction support workers.

Future research will address cross-worker generalisation through transfer learning, extend the activity taxonomy to include additional support tasks, and investigate edge deployment of the model on low-power microcontrollers for real-time on-body inference.

References

1. Antwi-Afari, M.F., Li, H., Umer, W., Yu, Y., Xing, X.: Construction Activity Recognition and Ergonomic Risk Assessment Using a Wearable Insole Pressure System. J. Constr. Eng. Manage. **146**(7), 4020077 (2020). doi: 10.1061/(ASCE)CO.1943-7862.0001849

2. Bangaru, S.S., Wang, C., Busam, S.A., Aghazadeh, F.: ANN-based automated scaffold builder activity recognition through wearable EMG and IMU sensors. Automation in Construction **126**, 103653 (2021). doi: 10.1016/j.autcon.2021.103653
3. Ding, L., Fang, W., Luo, H., Love, P.E., Zhong, B., Ouyang, X.: A deep hybrid learning model to detect unsafe behavior: Integrating convolution neural networks and long short-term memory. Automation in Construction **86**, 118–124 (2018). doi: 10.1016/j.autcon.2017.11.002
4. Jacobsen, E.L., Teizer, J., Wandahl, S.: Work estimation of construction workers for productivity monitoring using kinematic data and deep learning. Automation in Construction **152**, 104932 (2023). doi: 10.1016/j.autcon.2023.104932
5. Karatas, I.: Deep learning-based system for prediction of work at height in construction site. Heliyon **11**(2), e41779 (2025). doi: 10.1016/j.heliyon.2025.e41779
6. Karatas, I., Budak, A.: Prediction of Labor Activity Recognition in Construction with Machine Learning Algorithms. ICONTECH INTERNATIONAL JOURNAL OF SURVEYS, ENGINEERING, TECHNOLOGY **5**(3), 38–47 (2021). doi: 10.46291/ICONTECHvol5iss3pp38-47
7. Karatas, I., Budak, A.: Deep learning-based recognition of construction activities in real construction site environment. Engineering, Construction and Architectural Management **33**(2), 1536–1555 (2026). doi: 10.1108/ECAM-08-2024-1036
8. Karataş, İ., Budak, A.: Sensor-based activity recognition for construction activities on site using stacking ensemble method. RDLC **24**(2), 235–255 (2025). doi: 10.7764/RDLC.24.2.235
9. Kim, K., Cho, Y.K.: Effective inertial sensor quantity and locations on a body for deep learning-based worker's motion recognition. Automation in Construction **113**, 103126 (2020). doi: 10.1016/j.autcon.2020.103126
10. Luo, H., Xiong, C., Fang, W., Love, P.E., Zhang, B., Ouyang, X.: Convolutional neural networks: Computer vision-based workforce activity assessment in construction. Automation in Construction **94**, 282–289 (2018). doi: 10.1016/j.autcon.2018.06.007
11. Mekruksavanich, S., Jitpattanakul, A.: Smartwatch-based Human Activity Recognition Using Hybrid LSTM Network. IEEE Sensors, 1–4 (2020). doi: 10.1109/SENSORS47125.2020.9278630
12. Roberts, D., Golparvar-Fard, M.: End-to-end vision-based detection, tracking and activity analysis of earthmoving equipment filmed at ground level. Automation in Construction **105**, 102811 (2019). doi: 10.1016/j.autcon.2019.04.006
13. Slaton, T., Hernandez, C., Akhavian, R.: Construction activity recognition with convolutional recurrent networks. Automation in Construction **113**, 103138 (2020). doi: 10.1016/j.autcon.2020.103138
14. Sungkook Hong, Youngjib Ham, Jaeyoul Chun and Hyunsoo Kim: Productivity Measurement through IMU-Based Detailed Activity Recognition Using Machine Learning: A Case Study of Masonry Work. Sensors **23**(7635), 1–22 (2023). doi: 10.3390/s23177635
15. Zhao, J., Obonyo, E.: Convolutional long short-term memory model for recognizing construction workers' postures from wearable inertial measurement units. Advanced Engineering Informatics **46**, 101177 (2020). doi: 10.1016/j.aei.2020.101177
16. Zhao, Y., Wang, X., Luo, Y., Aslam, M.S.: Research on Human Activity Recognition Algorithm Based on LSTM-1DCNN. CMC, 1–10 (2023). doi: 10.32604/cmc.2023.040528

Author Contribution Statement

- *Conceptualization:* İ.K, A.B., Ş.T.G
- *Methodology:* İ.K.
- *Investigation:* A.B., Ş.T.G., İ.K.

- *Writing – Original Draft:* İ.K., Ş.T.G.
- *Writing – Review & Editing:* A.B.

List of Abbreviations

- **IMU** — Inertial Measurement Unit
- **LSTM** — Long Short-Term Memory
- **HAR** — Human Activity Recognition
- **MSD** — Musculoskeletal Disorder
- **RF** — Random Forest

Publication Note

This paper was peer-reviewed, accepted for presentation, and included in the proceedings of the ACE2026 – International Conference on Advances in Civil Engineering, held on 12–14 October 2026 in Trabzon, Türkiye.

This paper may be cited as follows:

Karatas, I., Budak, A., Guvel, Ş.T., "LSTM-Based Activity Classification of Bricklaying Support Tasks on Construction Sites Using Wearable IMU Sensors," in Proceedings of the ACE2026 – International Conference on Advances in Civil Engineering, Trabzon, Türkiye, 12–14 October 2026.

AI-Based Decision Support Systems in Construction Management: From Technical Capability to Managerial Decision Quality

Yasemin Bayrakkaya[1], Ali Erkan Karaman[2]
[1]0000-0003-0852-8363, Balıkesir University, Bigadic Vocational School, Balıkesir, Türkiye
ymenekse@balikesir.edu.tr
[2]0000-0003-1958-9743, Balıkesir University, Faculty of Engineering, Department of Civil Engineering, Balıkesir, Türkiye
ekaraman@balikesir.edu.tr

ABSTRACT

Artificial intelligence (AI) is increasingly used to support planning, monitoring, risk analysis, forecasting and other decision-intensive activities in construction management. Recent research demonstrates substantial progress in the technical capabilities of AI-based decision support systems (DSS), yet technical performance alone does not explain whether these systems improve managerial decisions in practice. This literature-based discussion examines the transition from AI capability to managerial decision quality by bringing together research on technical AI applications in construction, substantive system use, explainability and trust, and human-AI interaction. Recent construction studies combine predictive analytics with explainability, structured decision methods and expert involvement, while broader DSS research highlights the importance of system use, human judgement and appropriate reliance. The paper distinguishes organisational adoption from the substantive incorporation of AI capabilities into managerial work and uses this distinction to examine how technical capability may acquire practical decision value. The discussion identifies a need for construction-specific empirical research on how managers use, question and combine AI-generated information with professional judgement, and how these patterns of use relate to managerial decision quality.

Keywords: AI-based decision support systems; construction management; managerial decision quality; explainability; trust; substantive system use; human-AI interaction

1 Introduction

Construction management involves interdependent decisions concerning planning, scheduling, cost, resources, risk, safety and project control. These decisions are often made under uncertainty, time pressure and incomplete information. As construction projects generate increasing volumes of digital data, artificial intelligence (AI) has extended conventional decision support through prediction, pattern recognition, optimisation and real-time analysis [1-3,6].

Recent research demonstrates substantial growth in the technical capabilities of AI in construction. Machine learning, deep learning, computer vision and related techniques are increasingly applied to safety management, cost estimation, scheduling, monitoring and risk assessment [1-3]. Systematic reviews also show a growing role for AI-based decision support systems (DSS), although much of the literature remains concentrated on prediction and technically oriented applications [3,6]. Construction-specific systems illustrate this progress: Zorrilla et al. [7] combine machine learning and explainable AI (XAI) to support proactive risk identification, while Mlybari and Elgohary [8] integrate predictive analytics, multi-criteria decision-making and XAI within a construction value-management framework.

However, technical capability alone does not establish managerial value. Construction AI research continues to report problems related to fragmented implementation, data quality,

interoperability, interpretability and organisational readiness [3,4]. Construction decisions also depend on contextual knowledge, professional judgement and project-specific conditions that cannot always be represented completely by algorithmic models [3,9]. Predictive accuracy or analytical sophistication therefore does not by itself demonstrate that AI-generated information is understood, accepted or incorporated into managerial decisions.

This distinction directs attention to the difference between technology adoption and substantive system use. The Technology Acceptance Model (TAM) and Unified Theory of Acceptance and Use of Technology (UTAUT) explain important determinants of technology acceptance and behavioural intention [14,15]. Yet organisational adoption does not necessarily indicate how available system capabilities are used in practice. Drawing on the broader conceptualisation of system usage proposed by Burton-Jones and Straub [16], this paper uses substantive system use to refer to the extent to which available AI capabilities are incorporated into managerial decision processes.

A further issue concerns how managers interpret and evaluate AI-generated recommendations. Research on XAI and trust shows that high predictive performance may be insufficient when users cannot understand the basis of an output or do not consider it sufficiently reliable for use in a decision [10-13]. Recent AI-DSS research also indicates that transparency and trust can influence adoption and decision outcomes [19,20]. In construction, Mlybari and Elgohary [8] report improved decision consistency and greater stakeholder satisfaction with decision transparency when predictive analytics, structured decision methods and XAI are integrated in a construction decision-support environment.

Human-AI interaction therefore becomes central to AI-supported managerial decision-making. Research on hybrid intelligence and human-AI symbiosis emphasises complementary roles for computational analysis and human expertise [17,18]. Construction-specific work is beginning to reflect this perspective. Sarkheyli-Hagele et al. [9], for example, propose an expert-in-the-loop DSS for megaproject risk management in which AI-generated analysis is combined with domain knowledge and continuous human feedback.

The central question in this paper is therefore how technical AI capability becomes meaningful input to managerial decision-making. Construction research has begun to integrate technical AI capability, explainability and stakeholder-centred decision support in specific applications [7-9]. Nevertheless, the broader process through which organisational adoption becomes substantive system use, and how such use interacts with explainability, trust and human-AI interaction to shape managerial decision quality, remains insufficiently explained across construction management contexts. The purpose of this paper is not to propose or validate a causal model, but to clarify these conceptual connections and identify where further construction-specific empirical evidence is required. The contribution of this paper lies in reframing the managerial value of AI-based DSS as a transition from technical capability to substantive system use and, ultimately, managerial decision quality, while positioning explainability, trust and human-AI interaction as conditions shaping this transition.

2 Literature-Based Analytical Perspective

This study uses a narrative literature-based approach to examine how AI-based decision support moves from technical capability to managerial use in construction. The discussion draws on construction management, information systems and human-centred AI research because no single literature adequately captures this transition. Construction studies provide evidence on AI applications and implementation challenges [1-9], while information systems and human-centred AI research offers concepts for examining technology use, trust and the role of human judgement in decision support [10-23].

Sources were selected purposively for their relevance to the analytical relationships examined in this paper rather than through a systematic-review protocol. Priority was given to

construction-specific reviews and applications, complemented by established studies from information systems and human-centred AI where construction literature did not provide sufficient conceptual grounding. The selected studies are used to develop an analytical interpretation rather than an exhaustive classification of the literature. Particular attention is given to findings that help explain the gap between what an AI-based DSS is technically capable of doing and how its outputs become part of managerial decisions. The resulting discussion focuses on connections across the literature and on questions that remain insufficiently examined in construction-specific settings.

3 From Technical Capability to Managerial Decision Quality

3.1 Technical AI Capability in Construction Management

AI applications in construction management have expanded from relatively specific predictive tasks to a broader range of project functions. Machine learning, deep learning, computer vision and optimisation are now used in areas including cost estimation, scheduling, safety, progress monitoring and risk management [1-3]. AI is also increasingly integrated with digital environments such as BIM, enabling project data to support more responsive forms of analysis and decision support [5].

Recent reviews confirm both the scale of this development and its continuing technical orientation. Razi et al. [3], in a systematic review of 191 studies published between 2020 and 2025, identify risk and safety management, decision support, and monitoring and control among the main areas of AI application in construction management. Smith and Wong [6] similarly show that a substantial share of construction AI-DSS research has focused on prediction, particularly in early project stages. Together, these studies indicate a field with growing analytical capability but a strong emphasis on what AI systems can predict, detect or optimise.

More recent applications show a gradual move towards decision-oriented systems. Zorrilla et al. [7] combine machine learning with XAI to identify emerging construction risks and provide interpretable information for proactive intervention. Mlybari and Elgohary [8] go further by combining predictive analytics, multi-criteria decision-making and XAI in a construction value-management framework, reflecting the broader integration of machine learning and structured multi-criteria methods in intelligent DSS [23].

These developments also reveal a distinction that is sometimes blurred in discussions of AI in construction. Analytical performance describes the capability of the system; decision support describes what happens when that capability enters a managerial process. Construction projects involve changing site conditions, multiple stakeholders and forms of professional knowledge that cannot always be reduced to model inputs [3,4]. Technical performance is therefore an important starting point, but it cannot on its own indicate how much managerial value an AI-based DSS creates. The question then becomes whether useful analysis is actually incorporated into managerial work.

3.2 Adoption and Substantive System Use

The adoption of an AI-based DSS is an important organisational step, but it says relatively little about what happens afterwards. TAM and UTAUT explain technology acceptance through factors influencing behavioural intention and use [14,15]. For the present discussion, however, the more relevant question is not simply whether managers accept a system, but how they engage with its capabilities once it becomes available.

This distinction follows the broader information systems view that system usage should be understood in relation to the user, the technology and the task being performed [16]. Accordingly, substantive system use is used here to describe the extent to which available AI capabilities are incorporated into managerial decision processes. The term does not represent a

new measurement construct; it provides a way of distinguishing meaningful engagement with AI-based DSS from their organisational presence alone.

This is particularly relevant in construction because implementation remains uneven and project organisations differ substantially in digital maturity, data availability and managerial routines [3,4]. Conceptually, an organisation may introduce an AI-enabled system without its analytical functions becoming a regular part of project decisions. Conversely, substantive use implies that relevant outputs, such as forecasts, risk indicators or alternative scenarios, are considered when managers evaluate a problem or choose a course of action. The issue is therefore not the number of times a system is accessed, but the role its analytical capabilities play in the work being performed.

Evidence from the broader AI-DSS literature suggests that this role may also depend on how users evaluate the system. Bondac et al. [19] found that transparency and data quality were associated with trust and that trust influenced adoption intention. Their results also linked adoption intention with decision-making efficiency. Although these findings come from outside the construction context, they show that adoption-related attitudes towards AI-DSS are shaped by how users evaluate the system and the information it provides [19]. They do not, however, establish how extensively the system is subsequently incorporated into managerial work.

3.3 Explainability and Trust in AI-Based Decision Support

The increasing use of complex AI models introduces a practical problem for decision support: a useful prediction may still be difficult for a manager to evaluate. Explainable AI addresses this problem by providing information about how an output was produced, which factors influenced it or why a particular recommendation was generated [10,11]. In a DSS context, this matters because managers are not only recipients of predictions; they must decide whether those predictions are relevant and credible enough to influence action.

Explainability should therefore not be treated simply as an additional technical feature. Coussement et al. [11] argue that the strong emphasis on predictive performance in AI can come at the expense of explainability, creating difficulties for decision-makers who need to understand and evaluate model outputs. Kostopoulos et al. [10] similarly identify transparency and interpretability as central concerns in XAI-based DSS. The practical purpose of an explanation is not to expose every technical detail of a model, but to provide information that helps the user evaluate its output.

Trust is closely related to this process, but the two concepts are not interchangeable. Lee and See [12] argue that effective automation depends on appropriate reliance rather than simply increasing trust. Too little trust may lead users to disregard useful recommendations, whereas excessive trust can result in uncritical acceptance. Research on human trust in AI likewise shows that trust depends on system performance, transparency, user characteristics and the context in which the system is used [13]. Explainability may contribute to trust, but an explanation does not automatically make an AI recommendation trustworthy.

This distinction is especially relevant in construction, where managerial decisions often require information to be interpreted against site conditions, stakeholder requirements and professional experience. Mlybari and Elgohary [8] integrate XAI into an AI-supported value-management framework and report greater stakeholder satisfaction with decision transparency alongside improved decision consistency. Their findings suggest that explanations can have practical value when they are incorporated into a structured decision process rather than presented as isolated technical outputs. Explainability and trust therefore help clarify why the availability of an AI capability does not guarantee its substantive use.

3.4 Human-AI Interaction and Managerial Decision Quality

AI-based decision support does not remove the need for professional judgement. Research on hybrid intelligence and human–AI symbiosis suggests that computational and human capabilities can play complementary roles in decision-making [17,18]. AI can process large datasets, identify patterns and generate forecasts, while managers contribute contextual knowledge, experience and an understanding of constraints that may not be represented in the data.

This complementary view is particularly relevant to construction projects. Sarkheyli-Hagele et al. [9] propose an expert-in-the-loop approach to megaproject risk management in which AI analysis is combined with domain expertise and continuous feedback. Their framework allows experts to validate, correct and contextualise machine-generated insights, keeping the system aligned with human judgement and changing project conditions. Mlybari and Elgohary [8] similarly place AI-generated analysis within a structured construction decision process involving multiple criteria and stakeholder input.

Managerial decision quality should be distinguished from the technical quality of the information produced by an AI system. Earlier DSS research demonstrates that improvements in information quality do not necessarily translate directly into better decisions because the relationship also depends on the quality of the decision-making process [21]. Raghunathan [21], for example, shows that the effect of information quality on decision quality varies with decision-maker quality. This distinction is particularly important in construction, where forecasts and recommendations must be interpreted in relation to project conditions, stakeholder requirements and professional experience.

The contribution of a DSS may therefore extend beyond supplying information. Nemati et al. [22] argue that decision-support effectiveness can also be understood in terms of how well a system improves the decision-maker's knowledge, mental models and understanding, and thereby supports better decision-making. AI-based DSS should therefore not simply generate more accurate outputs; they should also help managers understand and evaluate those outputs within the decision context.

Construction-specific evidence provides some support for this view. Mlybari and Elgohary [8] report improved decision consistency when predictive analytics, multi-criteria evaluation and explainability are combined within an integrated decision-support process. Their case validation showed an increase in decision consistency from 0.67 to 0.82, alongside greater stakeholder satisfaction with decision transparency. These findings suggest that decision-support value can emerge from the combination of analytical capability, structured evaluation and transparent interaction rather than from predictive performance alone.

Evidence from human-centred AI-DSS research provides a similar indication. Zalfani et al. [20] compared an explainable, human-centred DSS with a functionally equivalent black-box system and reported improvements in trust, transparency, usability and decision accuracy. Their system also incorporated structured user feedback, human oversight and user-override functionality, allowing users to retain meaningful control over final decisions. This pattern is consistent with the principle of appropriate reliance [12]: effective decision support does not require managers to defer automatically to AI, but to judge when its output should be accepted, questioned or supplemented by professional judgement.

The managerial value of an AI-based DSS can therefore be located neither in the algorithm alone nor in human judgement alone. It emerges from the way analytical capability is brought into the decision process, interpreted by the user and combined with contextual knowledge. Fig. 1 summarises this analytical perspective. The figure is intended to organise the relationships discussed in the literature rather than to represent an empirically validated causal model [8,9,12,17,18,20-22].

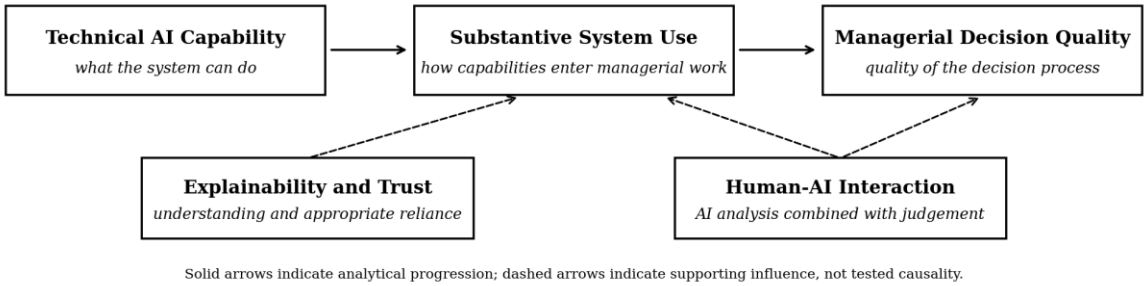


Fig. 1. Analytical perspective on AI-based decision support and managerial decision quality in construction management. Arrows indicate analytical relationships discussed in the literature rather than empirically established causal effects.

4 Research Gap and Future Research Direction

The literature reviewed here points to a broader issue than the limited adoption of AI in construction. Construction research has already demonstrated increasingly sophisticated AI applications and, more recently, has begun to combine predictive analysis with explainability, structured decision methods and human expertise [7-9]. These developments indicate that the field is moving beyond purely technical applications. However, the process through which technical AI capability becomes sustained and meaningful input to managerial decision-making remains insufficiently understood across construction contexts.

One part of this problem concerns the transition from adoption to substantive system use. Existing research provides considerable evidence on AI applications and implementation barriers [1-6], while recent reviews continue to report fragmented and inconsistent adoption in practice [3,4]. Organisational adoption, however, does not reveal which AI capabilities are actually incorporated into managerial work or how strongly they influence project decisions. The distinction between technology availability and substantive system use therefore requires greater attention in construction management research [16].

A related issue concerns explainability and trust. General AI-DSS research increasingly links transparency, explainability and trust with acceptance, reliance and decision outcomes [10-13,19,20]. Construction-specific studies also show growing interest in transparent and human-centred decision support [8,9]. Nevertheless, the literature reviewed here provides limited construction-specific empirical evidence on how explainability and appropriately calibrated trust affect managers' actual use of AI-generated information in managerial decision processes.

The literature reviewed here also provides limited evidence on the connection between substantive use and managerial decision quality. Construction applications demonstrate that AI, XAI and structured decision methods can improve particular aspects of decision support [7,8]. Broader DSS research, however, shows that better information does not automatically produce better decisions and that decision-maker quality and understanding remain important [21,22]. What is still unclear in construction is how AI-generated information is interpreted alongside professional judgement, project conditions and stakeholder requirements, and under what circumstances this interaction improves managerial decision quality.

These issues point to a research direction centred on the transition from technical capability to substantive system use and managerial decision quality, with explainability, trust and human-AI interaction shaping that transition. This perspective is analytical rather than causal. Future empirical research could examine which AI capabilities project managers actually use, how they assess and challenge AI-generated outputs, and whether different patterns of human-AI interaction are associated with differences in decision quality.

5 Conclusion

AI has substantially expanded the analytical capabilities available for decision support in construction management. Current applications demonstrate increasingly sophisticated uses in prediction, monitoring, risk analysis and structured decision-making [1-8]. However, the practical value of an AI-based DSS cannot be inferred from technical performance or organisational adoption alone. The central issue is how AI-generated information becomes part of managerial decision-making.

The literature reviewed in this paper suggests that substantive system use provides an important link between technical capability and managerial practice. Explainability and appropriately calibrated trust may affect whether AI-generated information is considered credible and usable, while human-AI interaction shapes how that information is interpreted alongside professional judgement [10-13,17-20]. More fundamentally, DSS research indicates that improvements in information quality do not necessarily translate directly into improvements in decision quality and that the knowledge and judgement of the decision-maker remain important [21,22]. Construction-specific studies are beginning to reflect this more interactive view of decision support [8,9], but evidence across project and organisational settings remains limited.

Future research should therefore examine AI-based DSS as part of the managerial decision process rather than evaluating them primarily through technical performance or adoption. Empirical studies are needed to establish which AI capabilities project managers actually use, how they evaluate and challenge AI-generated outputs, and how those outputs are combined with contextual knowledge and professional judgement. Such research would help clarify the conditions under which AI-based DSS contribute to higher-quality managerial decisions in construction management.

References

[1] Pan, Y., Zhang, L. Roles of artificial intelligence in construction engineering and management: A critical review and future trends. *Automation in Construction*. 2021;122:103517. doi:10.1016/j.autcon.2020.103517.

[2] Abioye, S.O., Oyedele, L.O., Akanbi, L., Ajayi, A., Davila Delgado, J.M., Bilal, M., Akinade, O.O., Ahmed, A. Artificial intelligence in the construction industry: A review of present status, opportunities and future challenges. *Journal of Building Engineering*. 2021;44:103299. doi:10.1016/j.jobe.2021.103299.

[3] Razi, N., Badhan, S.J., Samsami, R. Artificial Intelligence (AI) in Construction Management (CM): A systematic review of models and methods. *Buildings*. 2026;16(11):2225. doi:10.3390/buildings16112225.

[4] Regona, M., Yigitcanlar, T., Xia, B., Li, R.Y.M. Opportunities and adoption challenges of AI in the construction industry: A PRISMA review. *Journal of Open Innovation: Technology, Market, and Complexity*. 2022;8(1):45. doi:10.3390/joitmc8010045.

[5] Pan, Y., Zhang, L. Integrating BIM and AI for smart construction management: Current status and future directions. *Archives of Computational Methods in Engineering*. 2023;30(2):1081-1110. doi:10.1007/s11831-022-09830-8.

[6] Smith, C.J., Wong, A.T.C. Advancements in artificial intelligence-based decision support systems for improving construction project sustainability: A systematic literature review. *Informatics*. 2022;9(2):43. doi:10.3390/informatics9020043.

[7] Zorrilla, J., Seijo, S., Arenal, U., Mena, J.R. AI-driven decision support system for proactive risk management in construction projects. *Intelligent Infrastructure and Construction*. 2026;2(2):4. doi:10.3390/iic2020004.

[8] Mlybari, E.A., Elgohary, H.A. AI-driven value management in construction: A theoretically-grounded framework with empirical validation. *Journal of Umm Al-Qura*

University for Engineering and Architecture. 2025;16:1686-1705. doi:10.1007/s43995-025-00203-3.

[9] Sarkheyli-Hagele, A., Sarkheyli, A., Sarkheyli, E., Shahbazi, Z., Johnsson, M. An interactive and adaptive AI-based decision support system for dynamic risk management in megaprojects. In: *2025 3rd International Conference on Federated Learning Technologies and Applications (FLTA)*. IEEE; 2025. p. 479-483. doi:10.1109/FLTA67013.2025.11336661.

[10] Kostopoulos, G., Davrazos, G., Kotsiantis, S. Explainable artificial intelligence-based decision support systems: A recent review. *Electronics*. 2024;13(14):2842. doi:10.3390/electronics13142842.

[11] Coussement, K., Abedin, M.Z., Kraus, M., Maldonado, S., Topuz, K. Explainable AI for enhanced decision-making. *Decision Support Systems*. 2024;184:114276. doi:10.1016/j.dss.2024.114276.

[12] Lee, J.D., See, K.A. Trust in automation: Designing for appropriate reliance. *Human Factors*. 2004;46(1):50-80. doi:10.1518/hfes.46.1.50_30392.

[13] Glikson, E., Woolley, A.W. Human trust in artificial intelligence: Review of empirical research. *Academy of Management Annals*. 2020;14(2):627-660. doi:10.5465/annals.2018.0057.

[14] Davis, F.D. Perceived usefulness, perceived ease of use, and user acceptance of information technology. *MIS Quarterly*. 1989;13(3):319-340. doi:10.2307/249008.

[15] Venkatesh, V., Morris, M.G., Davis, G.B., Davis, F.D. User acceptance of information technology: Toward a unified view. *MIS Quarterly*. 2003;27(3):425-478. doi:10.2307/30036540.

[16] Burton-Jones, A., Straub, D.W. Reconceptualizing system usage: An approach and empirical test. *Information Systems Research*. 2006;17(3):228-246. doi:10.1287/isre.1060.0096.

[17] Dellermann, D., Ebel, P., Sollner, M., Leimeister, J.M. Hybrid intelligence. *Business & Information Systems Engineering*. 2019;61(5):637-643. doi:10.1007/s12599-019-00595-2.

[18] Jarrahi, M.H. Artificial intelligence and the future of work: Human-AI symbiosis in organizational decision making. *Business Horizons*. 2018;61(4):577-586. doi:10.1016/j.bushor.2018.03.007.

[19] Bondac, G.-T., Stanescu, S.-G., Ionescu, C.A., Duica, A., Uzlau, M.C. Decision-making in complex systems using AI-based decision support: The role of trust, transparency, and data quality. *Electronics*. 2026;15(2):372. doi:10.3390/electronics15020372.

[20] Zalfani, M., Sule, E., Bakar, M. Human-centered AI for decision support systems: Enhancing usability and trustworthiness. *Systems*. 2026;14(6):651. doi:10.3390/systems14060651.

[21] Raghunathan, S. Impact of information quality and decision-maker quality on decision quality: A theoretical model and simulation analysis. *Decision Support Systems*. 1999;26(4):275-286. doi:10.1016/S0167-9236(99)00060-3.

[22] Nemati, H.R., Steiger, D.M., Iyer, L.S., Herschel, R.T. Knowledge warehouse: An architectural integration of knowledge management, decision support, artificial intelligence and data warehousing. *Decision Support Systems*. 2002;33(2):143-161. doi:10.1016/S0167-9236(01)00141-5.

[23] Ali, R., Hussain, A., Nazir, S., Khan, S., Khan, H.U. Intelligent decision support systems-An analysis of machine learning and multicriteria decision-making methods. *Applied Sciences*. 2023;13(22):12426. doi:10.3390/app132212426.

Author Contribution Statement

- *Conceptualization:* Yasemin Bayrakkaya
- *Methodology:* Yasemin Bayrakkaya
- *Investigation:* Yasemin Bayrakkaya, Ali Erkan Karaman
- *Writing - Original Draft:* Yasemin Bayrakkaya
- *Writing - Review & Editing:* Yasemin Bayrakkaya, Ali Erkan Karaman
- *Supervision:* Ali Erkan Karaman

List of Abbreviations

- AI - Artificial Intelligence
- BIM - Building Information Modelling
- DSS - Decision Support System
- TAM - Technology Acceptance Model
- UTAUT - Unified Theory of Acceptance and Use of Technology
- XAI - Explainable Artificial Intelligence

Publication Note

This paper was peer-reviewed, accepted for presentation, and included in the proceedings of the ACE2026 – International Conference on Advances in Civil Engineering, held on 12–14 October 2026 in Trabzon, Türkiye.

This paper may be cited as follows:

Bayrakkaya, Y., Karaman, A. E., "AI-Based Decision Support Systems in Construction Management: From Technical Capability to Managerial Decision Quality," in Proceedings of the ACE2026 – International Conference on Advances in Civil Engineering, Trabzon, Türkiye, 12–14 October 2026.

Engineered Stone Restrictions and Trade: A Comparative Assessment Focused on Turkish Natural Stone

Selahattin Armağan Vurdu[1] and Bahri Akyüz[2*]
[1] 0000-0002-5836-876X, Istanbul Mineral and Metals Exporters' Association, armagan.vurdu@immib.org.tr
[2] 0009-0008-0632-8871, Istanbul Mineral and Metals Exporters' Association, bahri.akyuz@immib.org.tr
*corresponding author

Abstract. This paper examines how restrictions on high-silica engineered stone are reshaping international trade for building and surface materials. Focusing on Australia as the most developed prohibition regime and comparing emerging approaches in the United States, Great Britain and New Zealand, the study evaluates how regulatory change affects import patterns, material substitution, customs classification and supplier competition. The analysis combines regulatory review with a descriptive assessment of Australian trade data for engineered-stone-associated product groups and natural stone. The findings indicate a clear contraction in trade categories linked to engineered stone, accompanied by stronger demand for natural stone and other alternatives, including porcelain, sintered surfaces and low-silica composite products. However, substitution is not certain and not evenly distributed among exporting countries. For Turkey, the changing market creates opportunities for natural stone exporters, particularly in higher-value finished and project-ready products. The paper concludes that engineered-stone restrictions can be perceived as a broader reshaping of the building materials market, in which regulatory compliance, product identity and supply-chain positioning increasingly shape international competitiveness.

Keywords: engineered stone; building material trade; natural stone; material substitution; Australia; Turkey; HS Code; market access

1 Introduction

Engineered stone is an industrially produced surface material that has become more and more popular over the last 20 years. It is made with the bonding of quartz and various types of aggregates through polymer resins, pigments and other additives. The success of the material in the global market can be attributed to wide range of uniform colour and pattern choices as well as the production cost efficiency along with the ability to mass produce granting competitive pricing [16]. Furthermore, the material has increasingly become a primary work safety concern in a few countries. As with other worktop materials engineered stones arrive at the area of construction as bulk slabs and are processed and cut to the shape desired. This situation causes silica in these materials to form tiny particles that can be inhaled by the workers [15].

Engineered stone commonly contains a substantially higher proportion of crystalline silica than most natural stones, with some products containing more than 90%, compared with much lower levels in marble and lower but variable levels in granite [15]. Cutting, grinding and polishing can release respirable particles that penetrate deep into the lungs and cause inflammation and irreversible fibrosis. Among engineered-stone workers, silicosis may develop after comparatively short and intense exposure histories and may continue to progress even after occupational exposure has ended. Advanced cases can result in severe respiratory impairment, lung transplantation or death, and no curative treatment is currently available [1,15,17]. The combination of high silica content, dust-intensive fabrication and rapidly

progressive disease helps explain why the regulatory response has moved beyond conventional workplace controls towards the elimination of particular products from the market.

The health effects associated with respirable crystalline silica generated during fabrication triggered the current regulatory response [1-4]. For trade analysis, the main development is that this response moved beyond workshop rules/basic safety measures. Australia removed a major category of slabs from domestic supply and then prohibited imports, converting an occupational health concern into a direct restriction on the trade and production of a building material. Other jurisdictions have not uniformly adopted a ban, but tighter rules, inspections and possible product restrictions are increasing compliance costs and regulatory uncertainty [5-11].

This paper analyses the extent of these regulations and how they have the potential to alter international trade for surface materials. It asks three questions: how a product restriction is transmitted to import flows; which substitute materials and supplier countries capture the displaced demand; and how Turkey can respond given its competitive advantage in natural stone. [14] The paper sees regulation as the initiator, while placing market substitution, customs classification, supplier competition and industrial adjustment at the centre of the analysis.

2 Engineered Stone in the Surface-Materials Market

Engineered stone occupies a specific segment between geologically formed natural stone and manufactured ceramic or sintered surfaces. Its industrial production permits large batches with controlled appearance, while the slab format allows the product to enter established worktop and interior design supply chains. The value chain extends from mineral aggregates, pigments and unsaturated polyester or other resins to slab producers, international distributors, local fabricators, installers and project contractors. A restriction at the slab stage therefore affects several upstream and downstream industries.

The relevant substitutes are not commercially identical. Natural marble, travertine, granite and quartzite offer variation and established premium or architectural identities, but may differ in weight, finishing requirements, maintenance and price. Resin-free porcelain and sintered surfaces can offer large formats and consistent appearance and are excluded from the Australian engineered-stone definition, while low-silica or silica-free composites attempt to preserve the standardisation advantages of engineered surfaces. Buyers can also move towards laminates, wood or stainless steel in specific price and design segments. Substitution is therefore a product range decision shaped by application, technical specification, consumer preference and the capabilities of local fabricators.

A restriction on silica heavy engineered stone redistributes demand. Importers replace prohibited or commercially risky product lines; retailers change catalogues and display ranges; architects revise material specifications; fabricators invest in new tooling or processing knowledge; and upstream suppliers reformulate products or seek other end uses. The final distribution of demand depends on relative prices, available colours and formats, fabrication costs, delivery times, warranty practices, brand recognition and access to contractors and designers. Regulatory status is one variable within this broader competition, but once market access is lost it can dominate the others.

3 Methodology and Limitations

Terminology in the manufactured-surface industry is not internationally uniform. In this paper, “engineered stone” is retained as the principal term because it is the terminology used in the Australian regulatory framework that forms the main case study. Commercial or regulatory expressions such as “quartz surface”, “engineered quartz” and “artificial stone” may overlap

with this category in other markets, but are not treated as legally interchangeable unless the relevant jurisdiction defines them as such.

The study uses a descriptive and comparative design updated through July 2026. It aims to depict the current issues and recent developments in the surface material trade through official regulations/stances and trade indicators. Primary sources include Safe Work Australia and Australian border-control materials, California legislation and Standards Board releases, British Health and Safety Executive guidance and enforcement communications, and New Zealand consultation documents. These sources are used only to establish the scope and timing of measures that can affect market access, product ranges and purchasing behaviour [2-12].

The trade component uses quarterly Australian import series compiled from ITC Trade Map [13]. Headings commonly associated with artificial, reconstituted or mineral stone products are combined as an engineered-stone proxy basket, while selected natural-stone groups are assessed separately. This approach reveals directional change but does not produce an exact measure of engineered-stone trade. Products can appear under headings such as 6810.11.90, 6810.99.90 and 6815.99, which also contain cement, concrete, other artificial-stone articles, mineral products and substitutes. A recovery in the engineered stone basket can consequently reflect alternative products rather than the return of prohibited slabs. The usage of the terms like countertops, worktops and benchtops vary between different geographies refer to the same function. Different terminology for engineered stone also may apply in different countries ie. in the US terms like quartz surfaces are widely used.

The analysis is not a causal estimate. Construction activity, exchange rates, prices, inventories and supplier strategy may also influence imports. Nor does a rise in natural-stone imports prove that all displaced engineered-stone demand moved to natural stone. The series is interpreted as evidence of a market break and subsequent reallocation across a wider building material product range.

4 Regulation and Market Access Shock

4.1 Australian Case of Ban

Australia provides the clearest trade case. From 1 July 2024, work involving the manufacture, supply, processing or installation of engineered-stone benchtops, panels and slabs was prohibited. For the purposes of the Australian model WHS Regulations, engineered stone is defined as at least 1% crystalline silica by weight, combines natural stone materials with chemical constituents such as resins or pigments, and is hardened into a product. Natural stone, concrete and cement products, ceramic tiles, resin-free sintered stone and resin-free porcelain are among the exclusions [2-4].

The decisive border measure followed on 1 January 2025, when engineered-stone benchtops, panels and slabs became prohibited imports under the Customs (Prohibited Imports) Regulations 1956 [4,5]. Safe Work Australia states that the import prohibition was designed to complement the domestic prohibition [4]. Commercially, this removed the principal route through which foreign slab producers supplied the Australian fabrication market. Importers and distributors had to replace affected stock-keeping units, verify whether alternatives fell outside the definition and redirect procurement towards natural stone, porcelain, sintered products or reformulated composites.

The 2025 review and January 2026 implementation plan show that the Australian market has entered a post-ban adjustment phase rather than returning to the pre-ban structure [6,7]. Questions concerning alternative materials, product classification, legacy stock and exemptions affect buyer confidence and the documentation expected from overseas suppliers. The result is

a lasting change in market organisation even where the immediate legal question appears settled.

4.2 Regulatory Diffusion and Market Behaviour

Outside Australia, regulation currently influences trade mainly through cost, uncertainty and anticipatory product range changes. California law prohibits dry methods for specified high-exposure tasks, requires effective wet methods and introduced annual training attestation from 1 July 2026 [8]. On 21 May 2026, the California Occupational Safety and Health Standards Board initiated a process towards a possible prohibition on artificial stone containing more than 1% crystalline silica [9]. This was not a final ban by 14 July 2026, but manufacturers, importers and retailers have an incentive to prepare for stricter market access before a final rule is adopted.

The regulatory pressure is supported by an increasingly severe public-health record. By 13 November 2025, the California Department of Public Health had confirmed 432 silicosis cases among countertop workers, including at least 25 deaths and 48 lung transplants. The median age at diagnosis was 46 and the median age at death was 48, while the identified workers were predominantly immigrant men from Mexico and Central America [17]. Enforcement evidence also indicates the practical limits of a control-only approach. An April 2026 Cal/OSHA evaluation reported that 94% of inspected fabrication shops had been cited for violations and that 20% had required emergency shutdown orders. The approximately 140 inspected shops represented only about one tenth of the estimated fabrication operations in the state [20]. These findings help explain why California has progressed from stricter fabrication rules towards consideration of a material-specific prohibition.

Great Britain has retained product availability but issued dedicated guidance, launched a nationwide inspection campaign and served prohibition notices on firms that failed inspections [10,11]. New Zealand has pursued consultation rather than a final ban [12]. These models differ legally, yet all can alter purchasing decisions by raising the expected cost of conventional engineered stone, increasing distributor caution and encouraging suppliers to introduce low-silica or alternative product lines.

The British debate is also supported by emerging clinical evidence. The first published UK case series documented eight male artificial-stone workers with a median age of only 34 and a median exposure history of 12.5 years; one of the patients had died by the time the cases were reported [18]. The relatively young age of the affected workers reinforced calls for intervention despite the continued availability of the product. New Zealand illustrates an earlier stage of the same policy process. Its consultation considered both an Australian-style prohibition and strengthened control-based approaches for work involving engineered stone and other crystalline-silica materials [12]. Consequently, the present trade effect in New Zealand is primarily anticipatory, whereas Australia has already created direct exclusion at the border and Great Britain is generating commercial pressure through enforcement.

Table 1. Regulatory models and principal trade effects as of July 2026

Jurisdiction		Market-access instrument	Principal trade and market effect
Australia		Domestic prohibition from July 2024 and import prohibition from January 2025.	Direct removal of conventional engineered-stone slabs from new supply; rapid substitution and border-classification requirements.
United States	California	Material-specific duties and rulemaking towards a possible >1% silica prohibition.	Higher compliance costs and anticipatory product supply shifts in a major U.S. building material market.
	Federal	Process-based silica rules and enforcement; no federal product ban.	Product remains tradable, but fabrication costs and liability concerns affect downstream demand.
Great Britain		Dedicated guidance, inspections and prohibition notices rather than a product ban.	Commercial pressure on fabricators and suppliers without formal exclusion from the market.
New Zealand		Consultation and policy development.	Regulatory uncertainty encourages suppliers and buyers to evaluate substitutes and lower-silica products.

5 Australian Trade Effects and Supplier Reallocation

The Australian import series shows a pronounced break before and after the prohibition. The engineered-stone basket averaged USD 50.6 million per quarter in 2023. Its average fell to USD 35.6 million in 2024, a decline of 29.7%. The basket then reached USD 18.4 million in the first quarter of 2025, 63.6% below the 2023 quarterly average. Although values recovered to USD 23.7 million in the second quarter and USD 30.3 million in the third, the mixed content of the HS headings means that this rebound cannot be interpreted as a return of prohibited engineered-stone slabs.

Natural-stone imports moved in the opposite direction. Their quarterly average rose from USD 49.4 million in 2023 to USD 58.1 million in 2024, an increase of 17.6%. Imports remained above USD 60 million in each of the first three quarters of 2025 and reached USD 71.0 million in the third quarter, 43.7% above the 2023 quarterly average. The timing and direction are compatible with substitution, particularly because the natural-stone series moved to a higher range from the second quarter of 2024. Nevertheless, the figures also incorporate construction demand, price effects and inventory decisions.

The increase was not uniform across natural-stone product groups. The principal upward movement was concentrated in processed marble and travertine products and in other worked monumental or building stone, while worked granite displayed a comparatively stable pattern and certain simply cut granite categories weakened. This composition suggests that the reallocation favoured finished or application-ready products rather than producing an equal expansion across all quarry-based exports. The product pattern is therefore consistent with demand emerging from worktop, surface and building applications, although the HS data cannot identify the final use of each imported product [13].

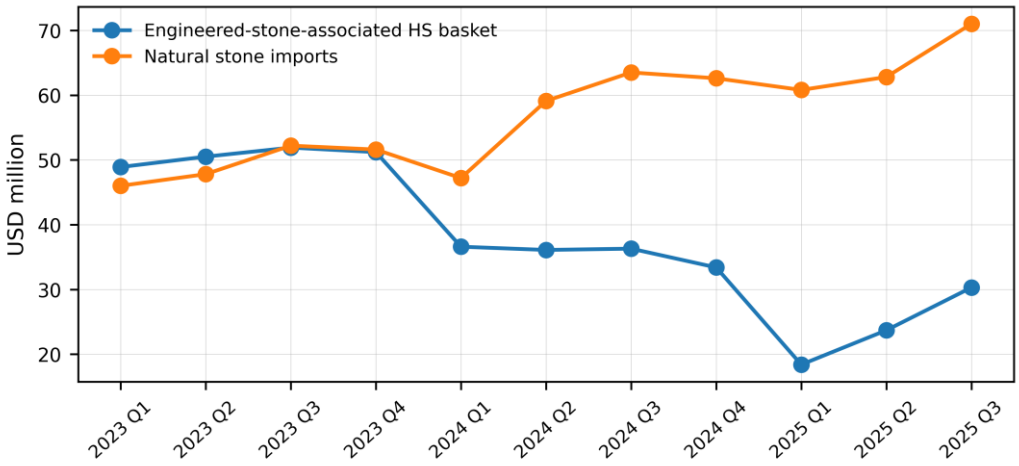


Fig. 1. Australian quarterly imports: engineered-stone-associated HS basket and natural-stone groups, 2023 - 2025. Source: ITC Trade Map [13].

Substitution demand is not distributed evenly among exporting countries as demonstrated by the data divided by natural stone exporters. In fact, it seems to be almost completely absorbed by China and Italy. China maintained a clear lead throughout the period and expanded its share of the four-country total from 50.7% in the fourth quarter of 2023 to 55.0% in the third quarter of 2025. Italy also strengthened its relative position, increasing its share from 22.4% to 25.7%. Turkey, by contrast, remained an established supplier but saw its share decline from 20.3% to 14.1%, as its import value remained broadly stable while Chinese and Italian exports expanded. The absolute import values make this divergence more visible. Between the fourth quarter of 2023 and the third quarter of 2025, Australian imports of the selected marble and granite products from China increased from USD 21.5 million to USD 31.9 million, while imports from Italy rose from USD 9.5 million to USD 14.9 million. Imports from Turkey remained broadly stable, moving from USD 8.6 million to USD 8.2 million, and imports from India changed only slightly, from USD 2.8 million to USD 3.0 million [13]. The additional demand observed in this comparison was therefore captured primarily by China and Italy, while Turkey maintained its market presence without participating proportionately in the expansion. These figures cover the four suppliers examined and should not be interpreted as their shares of Australia's total natural-stone imports.

It can be drawn out from product distinction that the relevant competitive unit is often not a quarry block or unfinished slab but a project-ready surface. Engineered stone was sold through a system built around predictable slab dimensions, colour continuity and rapid fabrication. Natural-stone exporters capture more of the displaced value when they can supply calibrated slabs, worktops, vanities, wall panels, edge finishing, packaging, technical support and reliable delivery. Otherwise, the substitution may favour Chinese processed stone, Italian premium products, porcelain, sintered surfaces or reformulated composites rather than raw or semi-processed natural stone.

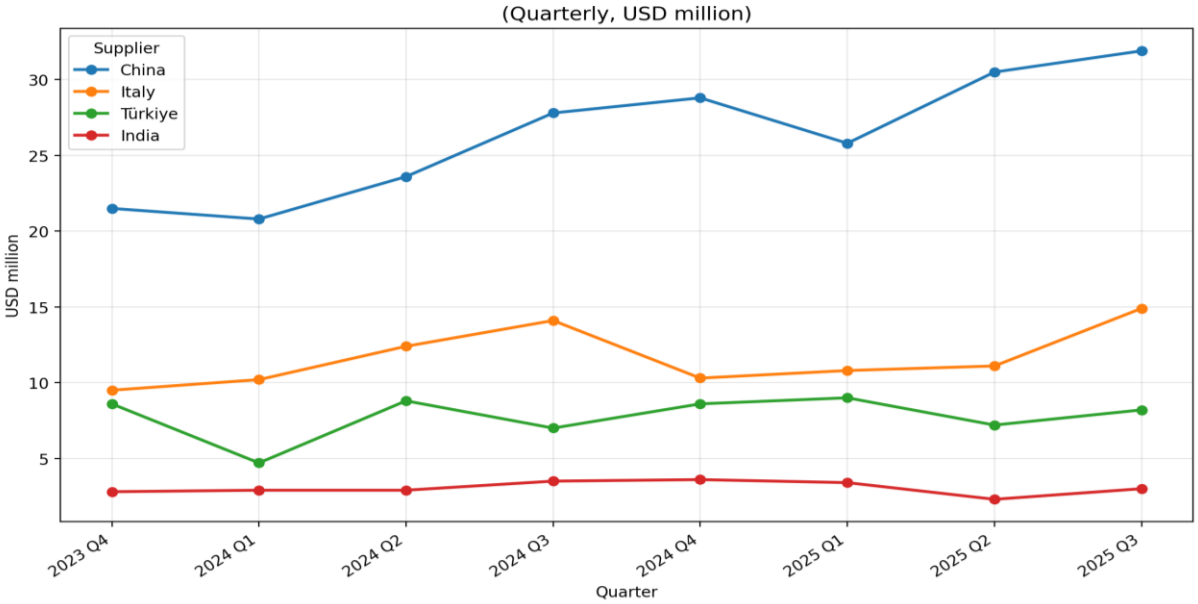


Fig. 2. Australian natural stone imports divided by exporter. Source: ITC Trade Map [13].

The same HS ambiguity that limits statistical analysis also creates commercial friction. Engineered stone is not represented by a single globally uniform code, while broad headings can contain prohibited slabs, excluded alternatives and unrelated mineral articles. Marketing expressions such as quartz surface, artificial stone, mineral surface or composite slab do not by themselves establish legal treatment. Importers may therefore request composition declarations, resin-status information, silica-content data, technical sheets and product photographs before shipment.

Documentary identity becomes part of the traded product. Natural-stone exporters must demonstrate that the material is geologically formed rather than reconstituted; producers of porcelain and sintered surfaces must document the absence of resin where this determines exclusion; and low-silica composite producers must show that the formulation meets relevant thresholds. Firms that standardise these documents can reduce customs delay and buyer hesitation, while vague classification increases the risk of rejected orders or lost specifications.

6 Wider Building Materials Trade Implications

The Australian case cannot only be read as a simple transfer from engineered stone to natural stone. A product prohibition changes the relative position of several materials at once. Natural stone gains access to where was left unoccupied by restrictions, however it is usually considered more expensive and less flexible than other substitutes. Porcelain and sintered surfaces compete for buyers that prioritise consistent design and manufactured specifications. Low and no-silica composites allow established engineered-surface firms to retain some of their technology, branding and distributor relationships. Lower-cost applications may move towards laminates or other non-stone surfaces. The recovery of the engineered stone associated HS coded products in the Fig.1 might be associated with more substitutes like silica free engineered stone, that is classified under these HS codes, being introduced to the market.

The shift also redistributes value within the supply chain. Conventional engineered-stone slab producers lose direct access to prohibition markets. Importers and wholesalers suffer the cost of replacing product lines. Fabricators may need different cutting, handling or installation methods. Kitchen and bathroom retailers must revise displays and warranties, while architects and contractors update specifications. At the upstream level, suppliers of quartz aggregate,

pigments, unsaturated polyester resins and other binders face reduced demand from affected formulations unless they diversify into new products or markets.

Regulatory hurdles favour firms with broad product ranges and strong documentation. A producer that can offer natural stone, porcelain or low-silica composites can redirect customers more easily than a single-product supplier. Larger firms may also absorb testing, certification and compliance costs more readily. The emerging trade pattern may consequently involve both material substitution and supplier consolidation, particularly where distributors prefer fewer vendors capable of serving multiple specifications.

7 Implications for Turkey

Turkey faces a dual exposure. Its natural-stone industry can benefit when engineered-stone demand shifts towards marble, travertine and other geological materials. A national or sectoral strategy should therefore avoid presenting the transition as an unqualified natural-stone gain.

Turkey's response can be considered through three separate trade and industrial channels. First, natural-stone producers can target direct exports of finished and project-ready products to Australia and other markets affected by restrictions. Second, block and slab exporters may benefit indirectly where processing centres, particularly China, capture a larger share of the additional demand for finished natural-stone products [13].

For natural stone, competing in the product forms that engineered stone previously supplied is the goal. This means moving beyond blocks and generic slabs towards calibrated and polished slabs, worktops, vanities, wall panels, edge profiles and project packages. The Australian supplier comparison indicates that Turkey is present but faces strong Chinese and Italian competition. Higher market share requires reliable delivery, consistent finishing, local distributor relationships and early involvement with architects, kitchen-bath designers and contractors.

Classification and technical documentation can also be a prime concern. Common templates should identify the geological material, commercial name, quarry origin, resin or mesh treatment where applicable, recommended HS classification, product dimensions and relevant composition information. This is important not because natural stone is part of the Australian prohibition, but because border authorities and buyers need to distinguish it quickly from reconstituted products and from resin-containing alternatives.

Finally, occupational compliance should be treated as a supporting market-access capability rather than the central commercial message. Buyers increasingly expect evidence of responsible fabrication and clear product information across all mineral surfaces. Turkish suppliers can meet that expectation through process documentation and credible supply-chain practices without reducing the trade strategy to a health-and-safety campaign.

8 Conclusion

Restrictions on engineered stone are reorganising international trade in a group of competing building materials. Australia converted the issue into a direct market-access shock by combining a domestic prohibition with an import prohibition. The engineered-stone import basket fell sharply, while natural-stone imports moved to a higher range. This provides strong descriptive evidence of market reallocation, although mixed HS headings and wider construction-market conditions prevent a one-to-one causal interpretation.

The commercial outcome is more than natural-stone substitution. Demand is being divided among natural stone, porcelain, sintered surfaces, low-silica composites and other materials. Supplier countries gain according to their ability to provide finished products, competitive prices, design compatibility, logistics, documentation and access to distribution and project

channels. Product restrictions also transmit upstream to aggregate and resin suppliers and downstream to importers, fabricators, retailers and contractors.

For Turkey, the appropriate response is a strategy that encapsulates the substitute market. The natural-stone sector should target higher-value finished applications and strengthen its position in architectural and distribution networks. Future research should extend the trade series through 2026, separate price and quantity changes, and compare the import performance of natural stone with porcelain, sintered surfaces and new composite formulations. The central transformation is the reallocation of a building material value chain under changing rules of market access.

9 References

1. Rose, C., Heinzerling, A., Patel, K., et al.: Severe silicosis in engineered stone fabrication workers - California, Colorado, Texas, and Washington, 2017-2019. MMWR Morb. Mortal. Wkly. Rep. 68, 813-818 (2019). https://doi.org/10.15585/mmwr.mm6838a1.
2. Safe Work Australia: Decision Regulation Impact Statement: Prohibition on the Use of Engineered Stone. Australian Government, Canberra (2023a).
3. Safe Work Australia: Report on the Prohibition on the Use of Engineered Stone. Australian Government, Canberra (2023b).
4. Safe Work Australia: Silica - Engineered Stone Ban. Australian Government, https://www.safeworkaustralia.gov.au/safety-topic/hazards/silica/engineered-stone-ban,
5. Australian Border Force: Engineered Stone - Prohibited Goods. Australian Government, https://www.abf.gov.au/importing-exporting-and-manufacturing/prohibited-goods/categories/engineered-stone
6. Safe Work Australia: Review of the Engineered Stone Prohibition. Australian Government, Canberra (2025).
7. Safe Work Australia: Engineered Stone Prohibition Review: Safe Work Australia Implementation Plan. Australian Government, Canberra (2026).
8. California Legislative Information: Senate Bill No. 20, Chapter 734 - Occupational Safety: High-Exposure Trigger Tasks on Artificial Stone. Approved 13 October 2025 (2025), https://leginfo.legislature.ca.gov/faces/billTextClient.xhtml?bill_id=202520260SB20
9. California Department of Industrial Relations: Standards Board Advances Efforts to Protect Workers from Silicosis. News Release 2026-45, 22 May 2026 (2026), https://www.dir.ca.gov/DIRNews/2026/2026-45.html, last accessed 2026/07/14.
10. Health and Safety Executive: HSE Says No Dry Cutting of Engineered Stone Ahead of Inspection Crackdown. 11 May 2026 (2026), https://press.hse.gov.uk/2026/05/11/hse-says-no-dry-cutting-of-engineered-stone-ahead-of-inspection-crackdown/, last accessed
11. Health and Safety Executive: Businesses Ordered to Stop Work with Engineered Stone after Failing Safety Inspections. 25 June 2026 (2026), https://press.hse.gov.uk/2026/06/25/businesses-ordered-to-stop-work-with-engineered-stone-after-failing-safety-inspections/
12. Ministry of Business, Innovation and Employment: Summary of Submissions - Work with Engineered Stone and Materials Containing Crystalline Silica. New Zealand Government, Wellington (2025).
13. International Trade Centre: Trade Map - Trade Statistics for International Business Development. Australian quarterly import series, 2023 Q1-2025 Q3 (2026), https://www.trademap.org
14. Akyüz, B., Uslu, M.: Türkiye Doğaltaş Sektörünün Küresel Rekabetçiliği: 2024 Yılı Perspektifinde Fırsatlar, Zorluklar ve Stratejiler. In: The 12th International Marble and Natural Stone Congress and Exhibition (MERSEM'2025) (2025).

15. Ramkissoon, C., Gaskin, S., Song, Y., Pisaniello, D. and Zosky, G.R. (2024). “From Engineered Stone Slab to Silicosis: A Synthesis of Exposure Science and Medical Evidence.” International Journal of Environmental Research and Public Health, 21(6), 683. doi:10.3390/ijerph21060683.
16. Özodabaş, A., Yıldız, B. and Tayçu, A. (2024). “Mermer, Granit ve Kompozit Kuvars Mutfak Tezgâhlarının Teknik Özelliklerinin Karşılaştırılması.” International Journal of Engineering Research and Development, 16(2), 813–831. doi:10.29137/umagd.1464925.
17. California Department of Public Health: Silicosis Cases in Countertop Workers Continue to Rise, as Silicosis Becomes a Reportable Disease in California. Health Advisory, 17 November 2025 (2025), https://www.cdph.ca.gov/Programs/OPA/Pages/CAHAN/Silicosis-Becomes-a-Reportable-Disease-in-California-.aspx
18. Feary, J., Devaraj, A., Burton, M., et al.: Artificial stone silicosis: a UK case series. *Thorax* 79(10) (2024). https://doi.org/10.1136/thorax-2024-221715

Publication Note

This paper was peer-reviewed, accepted for presentation, and included in the proceedings of the ACE2026 – International Conference on Advances in Civil Engineering, held on 12–14 October 2026 in Trabzon, Turkey.

This paper may be cited as follows:

Vurdu S. A., Akyüz B., “Engineered Stone Restrictions and Trade: A Comparative Assessment Focused on Turkish Natural Stone” in Proceedings of the ACE2026 – International Conference on Advances in Civil Engineering, Trabzon, Turkey, 12–14 October 2026.

Investigation of COPRAS and ARAS Methods in Trade-Off Problems of Construction Project Scheduling

Nur Sena Kınalı[1], Tayfun Dede[1], H. Abdullah Uçan[2]
[1] 0009-0006-2982-5307 Karadeniz Technical University, Department of Civil Engineering, Trabzon, Turkey
nursenakinali61@gmail.com
[1] 0000-0001-9672-2232 Karadeniz Technical University, Department of Civil Engineering, Trabzon, Turkey
dtayfun@ktu.edu.tr
[2] 0000-0001-9049-8858 Republic of Türkiye, Ministry of Environment, Urbanization and Climate Change, General Directorate for Protection of Natural Assets, 06510 Ankara, Türkiye
habdullah.ucan@csb.gov.tr

Abstract. In the planning process of construction projects, determining and simultaneously evaluating the time, cost, and quality values of activities is one of the most important stages. In this process, the primary objective is to minimize time and cost while maximizing quality. However, alternative selection problems arise when criteria such as time-cost-quality (TCQ) take different values. To solve these problems, a holistic evaluation of the criteria is necessary. Decision Support Systems (DSS) stand out for evaluating all these criteria holistically and determining the best solution. In this study, a MATLAB-based Decision Support System (DSS) has been developed to solve TCQ trade-off problems and determine the best alternatives. In the developed MATLAB-based DSS, the Additive Ratio Assessment (ARAS) and Complex Proportional Assessment (COPRAS) methods, which are multi-criteria decision-making methods, are designed to work together with the Jaya, which is based on the principle of convergence to the best solution and divergence from the worst solution. By using multi-criteria decision-making methods, decision-makers are actively involved in the process by determining the criterion weights. The developed MATLAB-based DSS approach aims to introduce a new approach to the literature for the optimization of multi-criteria problems.

Keywords: DSS; Construction Project Planning; ARAS method; COPRAS method

1 Introduction

For construction projects to be successfully completed under multiple criteria such as TCQ, the planning process must be carried out systematically and in detail. Through the comprehensive work conducted during the planning phase, it is aimed to complete the project on time, keep the project cost to a minimum, and achieve the desired quality level. Decisions made during the planning phase of the project significantly affect the subsequent phases of the project [1].

Construction projects consist of multiple activities that are interconnected in a predetermined sequence. Each project activity has different values for criteria such as time, cost, and quality. The combination of these different values results in different TCQ values at the project level, presenting the decision-maker with numerous alternatives. The goal is to minimize the time and cost criteria and maximize the quality criterion. However, trade-off relationships exist among these criteria, and an improvement in one criterion may negatively affect the others. For example, reducing the cost criterion may lead to an increase in the time criterion and a decrease in the quality criterion. This makes it difficult to achieve the desired balance among the TCQ criteria simultaneously. Therefore, decision-makers have difficulty deciding among the alternatives [2]. In such trade-off problems, the criteria need to be evaluated holistically. In trade-off problems, DSS are utilized to determine the alternative that provides the most

appropriate balance among the criteria. DSS are computer-based systems used to support decision-makers in making more effective decisions in the solution of complex problems [3]. In the literature, multi-objective optimization (MOO) methods are used to solve such problems. There are two main approaches to solving multi-objective problems within the scope of MOO. One of these approaches is to reduce the objective functions to a single objective function or to incorporate the other objective functions into the model through certain constraints while one objective function is taken as the basis. The other approach is to determine the entire Pareto optimal solution set or a subset that represents this set. The Pareto optimal solution set consists of solutions that do not dominate one another and provides the decision-maker with a set of good solutions [4]. In the literature, another method used in solving decision problems by evaluating criteria holistically is Multi-Criteria Decision Making (MCDM). These methods help in evaluating alternatives according to multiple criteria and making the appropriate decision according to the objective of the decision problem.

When the literature is examined, there are also studies in which Pareto-based approaches and MCDM methods are addressed in a hybrid manner in construction projects. Zhan et al. [5] developed an MOO model including time-cost-safety-carbon emissions (TCSE). They obtained solution sets using the Nondominated Sorting Genetic Algorithm-II (NSGA-II) and Nondominated Sorting Genetic Algorithm-III (NSGA-III) methods. To determine the most appropriate solution from the solution set obtained by the NSGA-III method, they used the entropy-weighted VIKOR method. Bingöl et al. [6] developed an MOO model that holistically considers the cost-duration-quality-safety-environmental impact criteria for subcontractor selection in a construction project. In the study, subcontractor candidates were evaluated using the Grey Relational Analysis (GRA) method. NSGA-II was used to determine the Pareto set of the best subcontractor plans. The selection of the most appropriate subcontractor plan was carried out using the Technique for Order Preference by Similarity to Ideal Solution (TOPSIS) method.

Within the scope of this study, the trade-off relationship among TCQ criteria in the planning of a construction project consisting of 13 activities was analyzed through a DSS developed in the MATLAB environment. Within the developed system, ARAS and COPRAS, which are MCDM methods, were integrated into the system to work together with Jaya.

2 Problem formulation for time–cost–quality

In this study, the total project duration, project cost, and overall project quality were calculated in the MATLAB environment based on the approaches adopted by Mohammadi et al. [7]. The total project duration was determined using the Critical Path Method (CPM), developed by Kelley and Walker [8]. CPM is a method that calculates the project completion time by identifying the critical activities in the project. The total project cost was calculated using Equation (1), considering the direct cost, indirect cost, penalty cost and incentive cost. In calculating the overall project quality, quality indicators are used for each project activity. The quality of each activity is determined through these indicators, and the weighted total project quality is calculated by considering the quality weights of the activities within the overall project.

$$C = \sum_{i=1}^{N} DC_i^{(k)} + D \cdot ICR + u(D - D_{PD})(D - D_{PD})C_{pen} - u(D_{PD} - D)(D_{PD} - D)C_{inc} \quad (1)$$

In Equation (1), C represents the total project cost, $DC_i^{(k)}$ the direct cost of the i^{th} activity, N the number of activities, D the total project duration, ICR the indirect cost rate, D_{PD} the project deadline, and C_{pen} and C_{inc} the penalty cost and incentive cost of the project, respectively. In

addition, the function u(x) takes a value of 1 for positive x and 0 for negative x.

3 Description of Selected 13-Activity Construction Project

In this study, a 13-activity bridge construction project was investigated. This construction project example was first introduced by Zhang and Xing [13] and was subsequently used separately by ElBassuony [14] and Mohammadi et al. [7]. Zhang and Xing [13] expressed the TCQ values of the activities using fuzzy numbers. Subsequently, Mohammadi et al. [7] transformed the fuzzy numbers into expected TCQ values using Equations (2), (3), and (4), respectively. This bridge construction project consists of one preliminary work, three foundation excavations, three foundation piling, three pier concreting, two beam constructions, and one deck pavement. The activities, their corresponding numbers, and the precedence relationships among the activities are presented in Table 1. A maximum of three alternatives is available for the expected TCQ values of each activity. The expected TCQ values of the activities are presented in Tables 2, 3, and 4, respectively. The CPM network showing the precedence relationships among the activities is presented in Fig. 1.

$$T_e = \frac{T_o + 4T_m + T_p}{6} \tag{2}$$

$$C_e = \frac{C_{op} + 4C_{ml} + C_{pe}}{6} \tag{3}$$

$$Q_e = \frac{Q_{op} + 4Q_{ml} + Q_{pe}}{6} \tag{4}$$

Table 1. Activities and their corresponding numbers [13].

Activity No	Pre activity	Activity Name
1		Preliminary work
2	1	Foundation excavation 1
3	1	Foundation excavation 2
4	1	Foundation excavation 3
5	2	Foundation piling 1
6	3	Foundation piling 2
7	4	Foundation piling 3
8	5	Pier concreting 1
9	6	Pier concreting 2
10	7	Pier concreting 3
11	8,9	Beam construction 1
12	9,10	Beam construction 2
13	11,12	Deck pavement

Table 2. Expected time values for the selected 13-Activity construction project [7].

Activity No	Time of activity (DAYS)		
	T_e1	T_e2	T_e3
1	28	25	19
2	42.33	37	33
3	45	40.167	35
4	44	38.33	33
5	38	34	30
6	50	42	36
7	40	35	30
8	85	82	75
9	90	84	78
10	85	80	76
11	20	18	16
12	22	17	14
13	25	22	15

Table 3. Expected Cost Values for the Selected 13-Activity Construction Project [7].

Activity No	Cost of activity $*10^3$ (Chinese Yuan)		
	C_e1	C_e2	C_e3
1	18	20.167	22
2	170	190	220
3	175	200	225
4	170	200	220
5	134	164	220
6	190	230	270
7	140	170	180
8	220	248.333	275
9	240	260	300
10	230	250	280
11	120	145	160
12	130	140	165
13	65	75	80

Table 4. Expected Quality Values for the Selected 13-Activity Construction Project [7].

Activity No	Quality weight of the activity	Quality of activity		
		Q_e1	Q_e2	Q_e3
1	1	0.983333	0.883333	0.783333
2	8	0.983333	0.783333	0.403333
3	9	0.983333	0.583333	0.4
4	8	0.983333	0.583333	0.4
5	11	0.983333	0.783333	0.4
6	11	0.983333	0.583333	0.4
7	11	0.983333	0.883333	0.783333
8	8	0.883333	0.783333	0.583333
9	8	0.883333	0.783333	0.583333
10	8	0.883333	0.783333	0.583333
11	6	0.983333	0.583333	0.4
12	6	0.983333	0.583333	0.4
13	5	0.983333	0.883333	0.783333

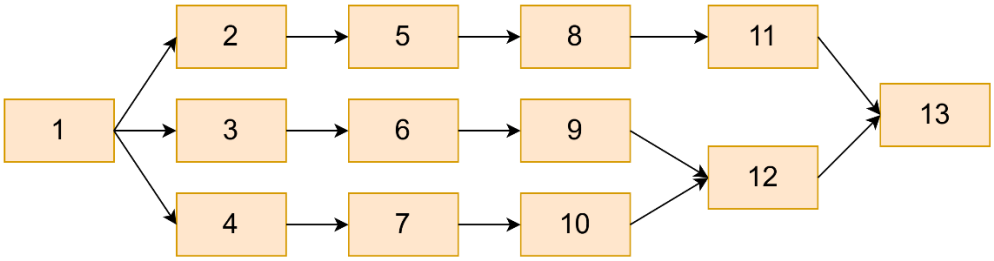


Fig. 1. CPM Activity Network for the Selected Construction Project [13]

4 Jaya-COPRAS and Jaya-ARAS Approaches

4.1 Jaya Algorithm

The Jaya algorithm, developed for solving constrained and unconstrained optimization problems, was first proposed by Rao. Only common control parameters are used in the Jaya algorithm. The flowchart of the algorithm is given in Figure 2. The basic approach of the algorithm is to update the obtained solutions in such a way that they approach the best solution while moving away from the worst solution [9]. The obtained solutions are updated using Equation (5) in the flowchart.

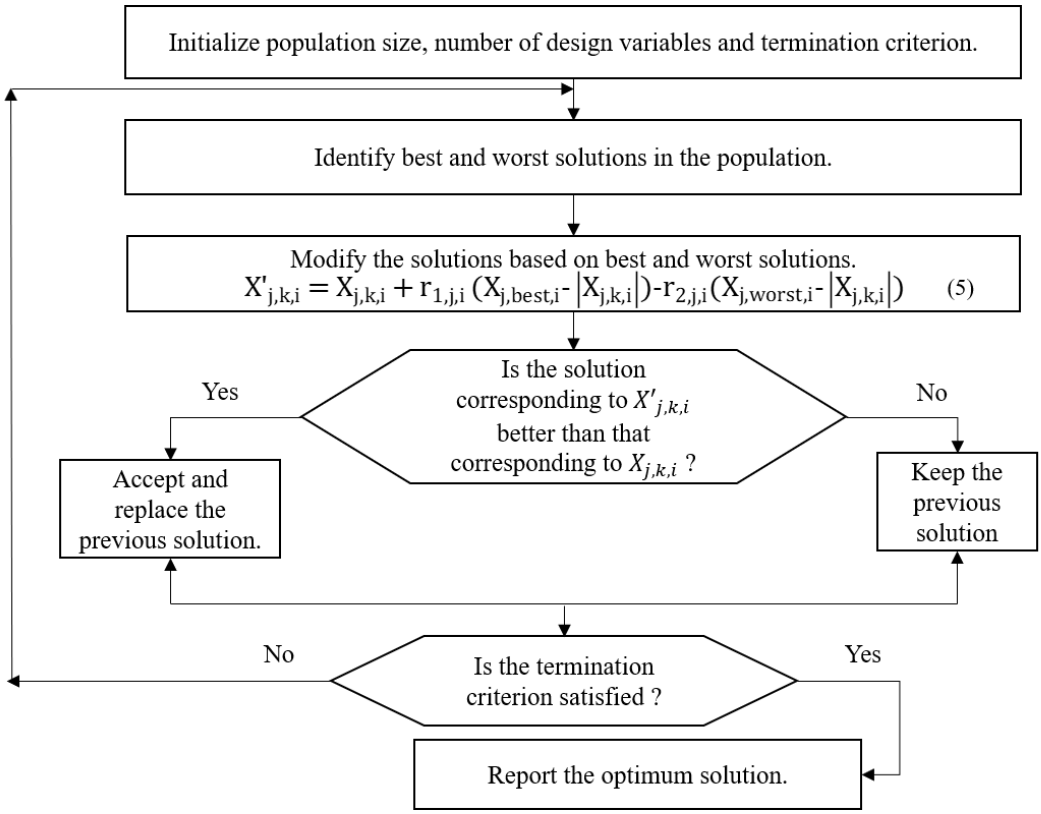


Fig. 2. The Jaya algorithm's flowchart [9]

In Equation (5), $X_{j,k,i}$ represents the value of the j^{th} variable for the k^{th} candidate in the i^{th} iteration. The new value obtained by updating this variable is represented by $X'_{j,k,i}$. $X_{j,best,i}$ and $X_{j,worst,i}$ represent the j^{th} variable values of the best and worst candidate solutions, respectively, in the i^{th} iteration. $r_{1,j,i}$ and $r_{2,j,i}$ are randomly generated numbers within the range [0,1].

4.2 COPRAS

First developed by Zavadskas and Kaklauskas, COPRAS is an MCDM method. The primary goal of COPRAS is to evaluate and rank alternative solutions by considering utility-oriented and cost-oriented criteria. This method uses the following steps to solve the problem [10-11].

Step 1: A decision matrix is created where columns correspond to criteria and rows correspond to alternatives.

Step 2: Each value in the decision matrix is divided by the sum of its respective columns to obtain the normalized decision matrix.

Step 3: The decision-maker assigns a weight value for each criterion. Then, the values in the normalized decision matrix are multiplied by their respective criterion weights to obtain the weighted normalized decision matrix.

Step 4: Using the values in the weighted normalized decision matrix, the sum of the utility-oriented criteria and the sum of the cost-oriented criteria are calculated separately for each alternative.

Step 5: The relative significance value of each alternative is calculated using the values obtained from the sums of the utility-oriented and cost-oriented criteria.

Step 6: The performance index value of each alternative is calculated by multiplying the ratio of its relative significance value to the highest relative significance value by 100. The alternative with the highest performance index value is considered the best option.

4.3 ARAS

The ARAS method was first developed by Zavadskas and Turskis. The main objective of this method is to determine the complex relative efficiency of each alternative by simultaneously considering the values and weights of the criteria. This method uses the following steps to solve the problem [12].

Step 1: First, the decision matrix is constructed. An optimal value is determined for each criterion and added to the decision matrix as a separate row. If the optimal value is unknown, the highest value among the alternatives is considered the optimal value for utility-oriented criteria, while the lowest value is considered the optimal value for cost-oriented criteria.

Step 2: The normalized decision matrix is constructed. To construct the normalized decision matrix, for utility-oriented criteria, each value is divided by the sum of all alternative values for the corresponding criterion. For cost-oriented criteria, the reciprocal of each value is first taken, and the resulting values are then divided by the total value in the column containing the corresponding criterion.

Step 3: A weight is assigned to each criterion by the decision-maker. The normalized values are then multiplied by their corresponding criterion weights to construct the weighted normalized decision matrix.

Step 4: The optimality function value for each alternative is calculated by summing the weighted normalized values of all criteria for that alternative. The alternative with a higher optimality function value is considered more effective.

Step 5: The optimality function value of each alternative is divided by the best optimality function value to determine the utility degrees of the alternatives. The utility degrees are ranked in ascending order, and the alternative with the highest utility degree is determined as the best alternative.

5 Analysis results

The selected bridge project was analyzed through the Jaya-COPRAS and Jaya-ARAS methods, with equal weights given to the criteria. The analysis was conducted using a population size of 50, 100 iterations, and 10 runs. The analysis results are presented in Table 5. In the analysis conducted using the Jaya-COPRAS method, two dominant solutions were identified. The first solution was obtained in 9 of the 10 runs, while the second solution was obtained only once. In the analysis conducted using the Jaya-ARAS method, a single optimal solution was obtained in all 10 runs.

Table 5. Analysis results

Jaya-COPRAS				
Solution	**Total time**	**Total cost**	**Total quality**	**Frequency**
(3,1,1,1,1,1,1,1,2,1,1,1,3)	235	2041	93.9333	9
(3,1,1,1,1,1,1,1,1,1,1,1,3)	241	2046	94.7333	1
Jaya-ARAS				
Solution	**Total time**	**Total cost**	**Total quality**	**Frequency**
(3,1,1,1,1,1,1,1,2,1,1,1,3)	235	2041	93.9333	10

6 Conclusion

The primary objective of this study is to comprehensively evaluate the TCQ trade-off in the planning of a 13-activity bridge construction project. To achieve this objective, a MATLAB-based computer program integrating the Jaya-COPRAS and Jaya-ARAS methods was

developed. The developed MATLAB-based DSS presents the decision-maker with the best alternatives among the available alternative solutions.

- In the analysis performed using the Jaya-COPRAS method, the solution (3,1,1,1,1,1,1,1,2,1,1,1,3) was repeated 9 times and became the most dominant alternative. The solution (3,1,1,1,1,1,1,1,1,1,1,1,3) was repeated 1 time.
- In the analysis performed using the Jaya-ARAS method, the solution (3,1,1,1,1,1,1,1,2,1,1,1,3) was obtained as the single best solution.
- Analysis results obtained using Jaya-COPRAS and Jaya-ARAS methods showed that solution (3,1,1,1,1,1,1,1,2,1,1,1,3) provided a more consistent and balanced result.

Acknowledgments

This study is supported by The Scientific and Technological Research Council of Türkiye (TÜBİTAK), Directorate of Science Fellowships and Grant Programmes (BİDEB), under the 2210/A National MSc/MA Scholarship Program. TÜBİTAK's support, provided to the author Nur Sena Kınalı, is gratefully acknowledged.

References

1. Yılmaz, M.: Yapı Projelerinde Karar Verme Süreçlerinin İncelenmesi ve Bu Süreçleri Yönetebilen Bir Yazılım Programı Oluşturulması. Doktora Tezi, K.T.Ü., Fen Bilimleri Enstitüsü, Trabzon (2025).
2. Işıkyıldız, S.: İnşaat Projelerinde Meta-sezgisel Yaklaşımla Süre-Maliyet-Kalite Optimizasyonu. Yüksek Lisans Tezi, İstanbul Üniversitesi-Cerrahpaşa, Lisansüstü Eğitim Enstitüsü, Türkiye (2019).
3. Yılmaz, E. A. G., Tüfekci, A.: Zeki Karar Destek Sistemleri: Bir Sistematik Literatür Haritalaması. Kastamonu Education Journal 28(2), 1044–1053 (2020). https://doi.org/10.24106/kefdergi.702944
4. Konak, A., Coit, D. W., Smith, A. E.: Multi-objective optimization using genetic algorithms: A tutorial. Reliability Engineering & System Safety 91(9), 992–1007 (2006). https://doi.org/10.1016/j.ress.2005.11.018
5. Zhan, Z., Hu, Y., Xia, P., Ding, J.: Multi-objective optimization in construction project management based on NSGA-III: Pareto front development and decision-making. Buildings 14(7), 2112 (2024). https://doi.org/10.3390/buildings14072112
6. Bingol, B. N., Arditi, D., Polat, G.: Subcontractor Selection for a Construction Project: Optimal Plan. Journal of Construction Engineering and Management 151(12), 04025205 (2025). https://doi.org/10.1061/JCEMD4.COENG-16409
7. Mohammadi, M.O., Dede, T., Grzywiński, M.: Solving a stochastic time-cost-quality trade-off problem by meta-heuristic optimization algorithms. Construction of Optimized Energy Potential 11, 41–48 (2022). https://doi.org/10.17512/bozpe.2022.11.05
8. Kelley, J. E., Jr., Walker, M. R.: Critical-path planning and scheduling. In: Papers presented at the December 1–3, 1959, Eastern Joint IRE-AIEE-ACM Computer Conference, pp. 160–173 (1959). https://doi.org/10.1145/1460299.1460318
9. Rao, R.: Jaya: A simple and new optimization algorithm for solving constrained and unconstrained optimization problems. International Journal of Industrial Engineering Computations 7(1), 19–34 (2016). https://doi.org/10.5267/j.ijiec.2015.8.004
10. Gül, A., Kaygın, C. Y.: Analysis of the financial performances of real estate investment trusts critic aras and copras methods: the case of BIST. İşletme Araştırmaları Dergisi 16(4), 2062–2076 (2024). https://doi.org/10.20491/isarder.2024.1902
11. Zavadskas, E. K., Kaklauskas, A., Peldschus, F., Turskis, Z.: Multi-attribute assessment of road design solutions by using the COPRAS method. The Baltic Journal of Road and Bridge Engineering 2(4), 195–203 (2007).

12. Zavadskas, E. K., Turskis, Z.: A new additive ratio assessment (ARAS) method in multicriteria decision-making. Technological and Economic Development of Economy 16(2), 159–172 (2010). https://doi.org/10.3846/tede.2010.10
13. Zhang, H., Xing, F.: Fuzzy-multi-objective particle swarm optimization for time–cost–quality tradeoff in construction. Automation in Construction 19(8), 1067–1075 (2010). https://doi.org/10.1016/j.autcon.2010.07.014
14. ElBassuony, M.: Time-cost-quality trade-off analysis for construction projects. Master's Thesis, School of Sciences and Engineering, American University in Cairo (2010).

Author Contribution Statement

- *Conceptualization:* Tayfun Dede, Nur Sena Kınalı
- *Methodology:* Tayfun Dede, Nur Sena Kınalı
- *Investigation:* Tayfun Dede, Nur Sena Kınalı, H. Abdullah Uçan
- *Writing – Original Draft:* Tayfun Dede, Nur Sena Kınalı
- *Writing – Review & Editing:* Tayfun Dede, Nur Sena Kınalı, H. Abdullah Uçan

Publication Note

This paper was peer-reviewed, accepted for presentation, and included in the proceedings of the ACE2026 – International Conference on Advances in Civil Engineering, held on 12–14 October 2026 in Trabzon, Türkiye.

This paper may be cited as follows:

Kınalı N.S., Dede T., Uçan H.A., "Investigation of COPRAS and ARAS Methods in Trade-Off Problems of Construction Project Scheduling," in Proceedings of the ACE2026 – International Conference on Advances in Civil Engineering, Trabzon, Türkiye, 12–14 October 2026.

Adaptive Mold Technology in Precast Concrete Panel Facilities: Optimization and Analysis

Bedirhan Enes Kelek[1,*], Gökçen Karakol[2], Beni Kohen[3], Muhammed Maraşlı[4], Necati Aras[5], Nilüfer Özyurt[6]

[1] 0009-0005-4294-1479, Bogazici University, Civil Engineering Department, Istanbul, Türkiye, bedirhan.kelek@bogazici.edu.tr
[2] 0009-0000-7305-5908, Bogazici University, Industrial Engineering Department, Istanbul, Türkiye, gokcennkarakol@gmail.com
[3] 0000-0002-8497-6857, Fibrobeton Corp., Istanbul, Türkiye, beni@fibrobeton.com.tr
[4] 0000-0003-2684-1003, Fibrobeton Corp., Istanbul, Türkiye, muhammed@fibrobeton.com.tr
[5] 0000-0002-1485-730X, Bogazici University, Industrial Engineering Department, Istanbul, Türkiye, arasn@bogazici.edu.tr
[6] 0000-0003-4533-8702, Bogazici University, Civil Engineering Department, Istanbul, Türkiye, nilufer.ozyurt@bogazici.edu.tr

Abstract. Shell structures have excited architects and engineers with their astonishing aesthetics and fascinating structural behavior. Advances in 3D modeling techniques have allowed designers to expand their creativity with elegant free-form shell designs but a significant gap remains between the design and physical realization of such structures. One of the key barriers is the formwork requirement since they require a rigid, custom, and in most cases, geometry-specific formworks. This results in too much time, labor work and a tremendous amount of waste. A novel technology for the feasible construction of the shells is adaptive molding. In this technology, desired single or doubly curvature formwork can be obtained in a short time by deforming the surface with the help of the actuators. In this study, we analyze the manufacturing process of the concrete shell panels by focusing on an existing precast concrete panel facility. The major production processes are represented in the model using discrete-event simulation software Simio and validated based on the real production data. To investigate the adoption of the adaptive mold technology, we analyze the modified production process in a simulation model. The number of adaptive molds in the system emerged as a critical factor to fulfill the desired capacity for the panel production with this technology. The proposed methodology can be employed to determine this number and also can be utilized as a decision-support tool to test the viability of the integration of the emerging novel technologies and guide the decision-making process.
Keywords: Shell structures, adaptive mold, formwork, facility design, digital construction.

1. Introduction

Shell structures have excited architects and engineers with their astonishing aesthetics and fascinating structural behavior. They are special structures that can resist loads by virtue of their forms. That is why they are often called form-resistant structures. In recent years, advances in 3D modeling techniques of geometries have allowed designers to expand their creativity with elegant and appealing free-form shell designs. Today, curved and complex free-forms can be

easily created with the aid of modern CAD software, making innovative architectural designs more accessible than ever.

Despite development in design tools, there is still a significant gap between the design and physical realization of such structures [1]. The manufacturing of individual free-form shell components is a challenging task because of the lack of defined standardized methods that are applicable to the varying shapes of shell components. The conventional method in the industry requires a rigid formwork and, in most cases, formwork is specifically generated for only one shell geometry. This results in too much time, labor work and a tremendous amount of waste to construct the structural element mainly related to the formwork [2], [3]. The impractical and inefficient erection of this method is therefore one of the most important barriers against the extensive usage of shell concrete panels despite their aesthetics and engineering value.

Traditional formwork systems, despite being primarily designed for regular shapes, utilize rigid materials such as wood and metal to achieve curved surface. Wooden formwork is frequently employed in the construction of curved shells and arches, often requiring a skeleton frame to support the desired geometry, while steel formwork can be more efficient to produce curved surfaces due to multiple uses. However, the difficulty of shaping rigid materials has led to the development of flexible formwork systems, which offer a fundamentally different approach to casting non-standard shapes [4], [5]. Within this category, fabric formwork utilizes synthetic textile sheets that can be tensioned by external factors to create irregular forms. Additionally, digitally fabricated formwork leverages the methods—such as CNC milling of polystyrene blocks to realize concrete elements with full geometric freedom and high precision.

A novel technology for the feasible construction of the shells is adaptive molding. In this technology, desired single or doubly curvature formwork can be obtained in a short time by deforming the surface with the help of the actuators or pistons of the device, as demonstrated in Fig. 1. The construction sector, especially for free-form shell concrete panels, needs such cost-effective and time-saving technology for molding [6], [7] and necessary standards and guidelines should be established.

This study addresses the challenges in the production of geometrically complex concrete shell panels first by identifying production processes and then creating the facility model using Simio which is an object-based discrete-event simulation modeling framework [8], [9]. To enhance the efficiency of the production lines of the free-form shell components, it is essential to optimize operational efficiency, and ensure the cost-effective manufacturing by simulating the production process. The simulation model can serve as a crucial tool to understand and evaluate the integration of the novel technologies such as adaptive molds into the manufacturing line of existing facilities.

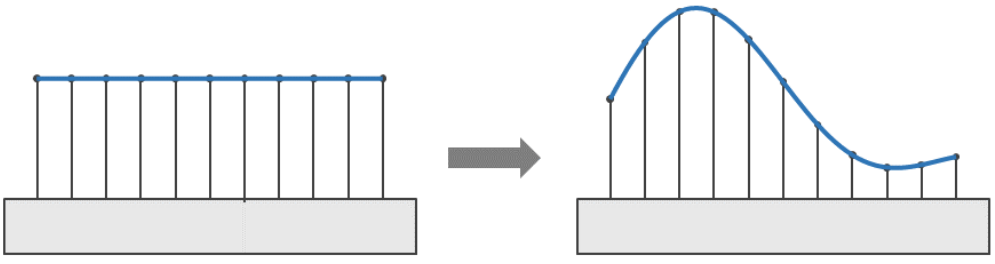


Fig. 1. Adaptive mold schematics.

1.1 Description of the Precast Concrete Panel Production Process

The production process of an existing precast concrete panel facility is examined to understand the production process of the existing plants. Accordingly, the workflow is classified into the phases while focusing on the manufacturing phase of the concrete panels, as shown in Fig. 2.

The first phase in the system is design and planning in which the type of formwork and manufacturing order of the panels are determined according to multiple factors, including the

geometric complexity of the product, the intended surface texture, and the number of repetitions required for the same mold and availability of the production line. The concrete panel manufacturing process starts with the production of the mold. The mold preparation stage plays a decisive role in determining the quality and efficiency of the manufacturing process. At the concrete facility investigated in this research, four primary mold types are utilized: wooden, polyester, styrofoam, and rubber molds. Each of these types has distinct properties and usage contexts.

Once a mold has been produced, the manufacturing process proceeds to the concrete casting stage where the concrete mixture is poured into the mold. After approximately one day, the panels are demolded and cured under controlled conditions. A typical curing period of seven to eight days is allocated to ensure proper strength development and to reduce the risk of cracking. If required, surface treatments such as sanding or polishing are carried out during post-processing. These operations are essential to meet aesthetic and functional requirements. The final stage of the production involves quality control inspection. Each panel is examined for dimensional accuracy, surface quality, and structural integrity. Based on the inspection results, the panels are either approved for shipment or returned for reprocessing.

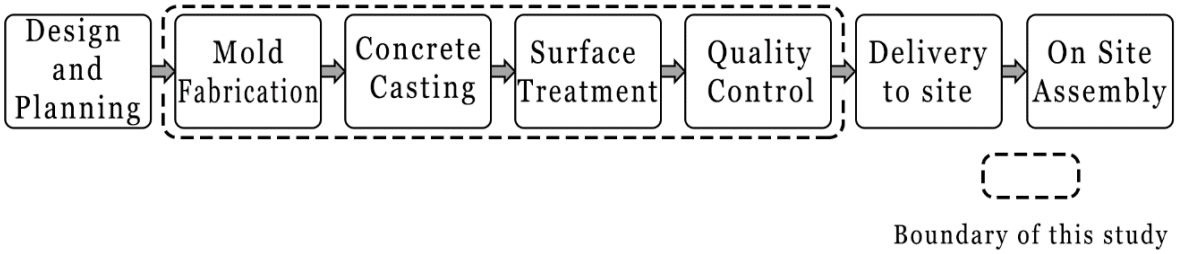


Fig. 2. Production phases in a concrete precast panel facility.

2. Methodology and Design of the Facility Model

1.2 Facility Design and Modeling in Simio

In the Simio model, each production process is represented as a separate server. The model is mainly composed of two parts that are the production of the molds and the concrete casting to represent the actual production line. Because of the insufficient data for the sub-processes of the mold production, they are modeled using a single aggregated server considering that it contains all of the sub-processes in the manufacturing process.

Figs. 3 and 4 illustrate the overview of the discrete-event simulation model. The production orders in the model are represented by *MoldEntity*. These entities first enter one of the mold production servers according to the specified selection weights. After erection of the molds, the mold entities proceed to the concreting and related processes as shown in Fig. 3. It is processed in the server *ConcreteCasting* that corresponds to the concreting process (either spraying or casting). The server *CuringOnMold* represents the curing time on the mold before reaching adequate hardening for removal from the formwork. Once curing is completed, the separator object, called *Demolding* in the model, removes the concrete panel from the mold. The *MoldEntity* returns back to *MoldRework* server for repairing and re-casting if the mold can be still used. The separator object, *Demolding*, creates a new entity, called as *Panel* in the model, and it goes to *Curing* server. After the panel entity passes through the servers *SurfaceTreatment*, *QualityControl*, and *Rework* if necessary, it leaves the production process at the server *Sink*. At this point, the panel is considered finished and ready for transportation to the construction site.

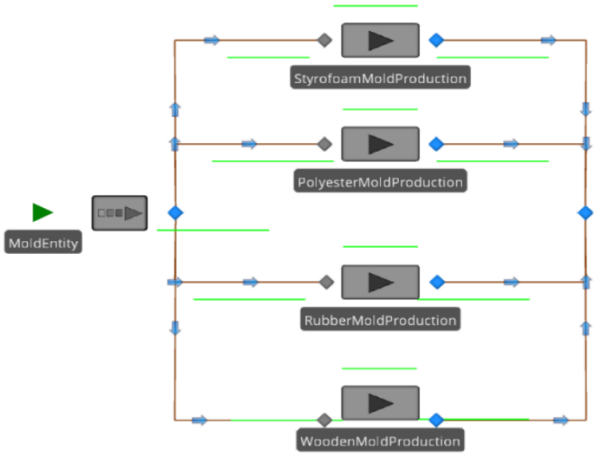


Fig. 3. Production of molds in Simio model.

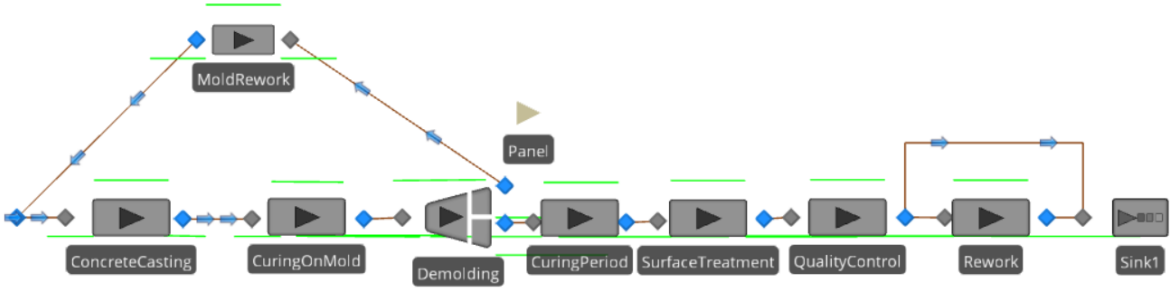


Fig. 4. Concreting and panel production in discrete-event simulation model.

1.3 Distribution Fitting and Data Analysis of the Processes

Production data are obtained from the Fibrobeton precast concrete panel facility and includes the mold production and concrete casting processes. The raw data were first cleaned by removing missing values, correcting inconsistencies and filtering outliers. Consequently, about 2750 and 4500 data were utilized for mold production and concrete casting processes, respectively. The mold production data consist of the observations of styrofoam (n=745), polyester (n=258), rubber (n=524), and wooden (n=1223). Then, the Chi-square method was used as the primary measure to fit the appropriate statistical distribution for each process. The resulting distributions were then incorporated into the simulation model developed in the Simio software. Furthermore, Q-Q plot of the fitted statistical distributions were presented as a diagnostic tool to evaluate the goodness-of-fit.

The triangular distribution was employed for the processes that do not have recorded data, namely *Demolding*, *CuringPeriod*, *SurfaceTreatment*, *Quality Control* and *Rework* processes. The minimum, median and maximum values of the triangular distributions were provided by the experts working in the facility.

1.4 Production System Specifications

The server capacities such as mold production and concrete casting processes were provided by facility's chief engineer and inserted into the model. Additionally, in order to reflect realistic mold usage in the model, a selection weight was assigned to the path between the source and mold production servers based on the one year period of production data.

In the production system, each mold can be used multiple times by repairing or modifying after the concrete panel is removed from the formwork. The company provided the median, maximum, and minimum allowable uses of each mold type. These parameters are employed to

assign maximum life span to each formwork applying triangular distributions. This approach considers the fact that not all molds are used until failure. They may be removed if they are not needed further or if they are critically damaged earlier.

The lifespan values are assigned to each mold entity when the entity exits the mold production server. Fig. 5 illustrates the add-on process to track the number of usage of the molds. Each time a mold returns to the *MoldRework* server (see Fig. 4), its count use is increased by one. In *Decide* stage, it checks whether the mold has reached its lifespan. If it does, the model destroys the entity and removes it from the model.

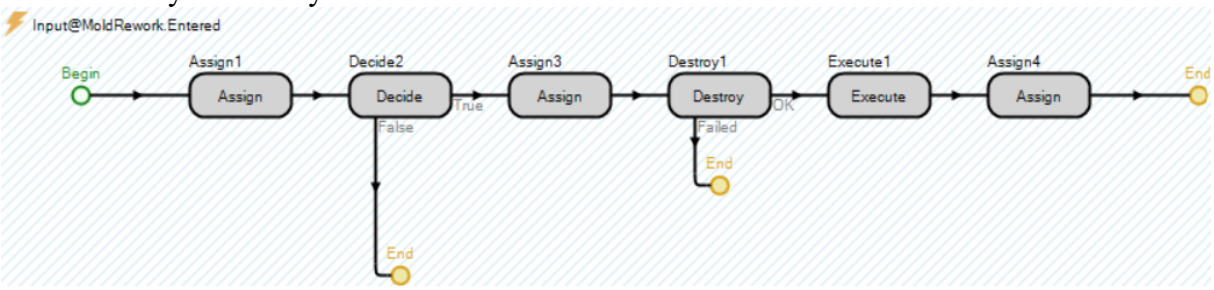


Fig. 5. Add-on process for lifespan check of the molds.

The concrete casting area has a fixed physical capacity in the facility. To check the availability of the concrete casting process in the model, a pseudo station was created in Simio model to hold molds when the casting server is full. The molds are directly transported to the concreting processes if *ConcreteCasting* server has available capacity. Otherwise, the mold entities are sent to the station, where they are stored until a mold is removed from the concreting process. An add-on process is triggered whenever a mold is removed from the casting server, which releases the next mold from the station into the concreting server.

Arrival rate is defined as the frequency at which new production orders enter the system. To be able to capture variability observed in the historical data, the arrival process was modeled using an exponential distribution based on the production data.

The warm-up period in the facility design refers to the initial phase of the simulation during which no data are collected. The aim is to make the model reach a stationary state before collecting the data to overcome unrealistic results and eliminate initialization bias. The performance indicator that is daily panel production was monitored for 1-year period to identify the point at which the system reached steady-state behavior.

After the quality control phase in the facility, concrete panels may need additional work such as surface treatment. Extra treatments are applied to these panels to meet the quality standards. In the model, this stage was represented with the server *Rework* at the end. Based on the data, about 25% of the panels needed extra surface treatment before the final approval. To implement this in the model, the selection weights of the paths were adjusted according to this proportion. The panels that do not require extra surface treatment directly proceed to *Sink* and destroyed from the system, which corresponds to the delivery to site phase in the concrete panel life cycle phases.

1.5 Integration of Adaptive Mold Systems

To integrate adaptive mold production systems, the model was modified as depicted in Fig.6. The initial model was retained and a parallel path representing adaptive mold system was added. In this setup, a specified percentage of the concrete panels, except for the panels produced with styrofoam molds, is manufactured using adaptive mold systems. The reason why styrofoam molds are excluded is that the panels produced with the styrofoam molds typically include complex and highly curved geometry, whose production with the adaptive molds is not quite

possible because of the technical limitations. However, as adaptive mold technology advances rapidly, this limitation is expected to disappear in the near future.

A server called *AdaptiveMoldShaping* was created to represent the process for shaping the surface of the adaptive mold with the help of the actuators. The statistical process time distribution is assigned triangular distribution with mean of 30 min. The servers for the casting, curing and demolding were assigned same processing time with the conventional process since the work being done does not change for these parts of the manufacturing.

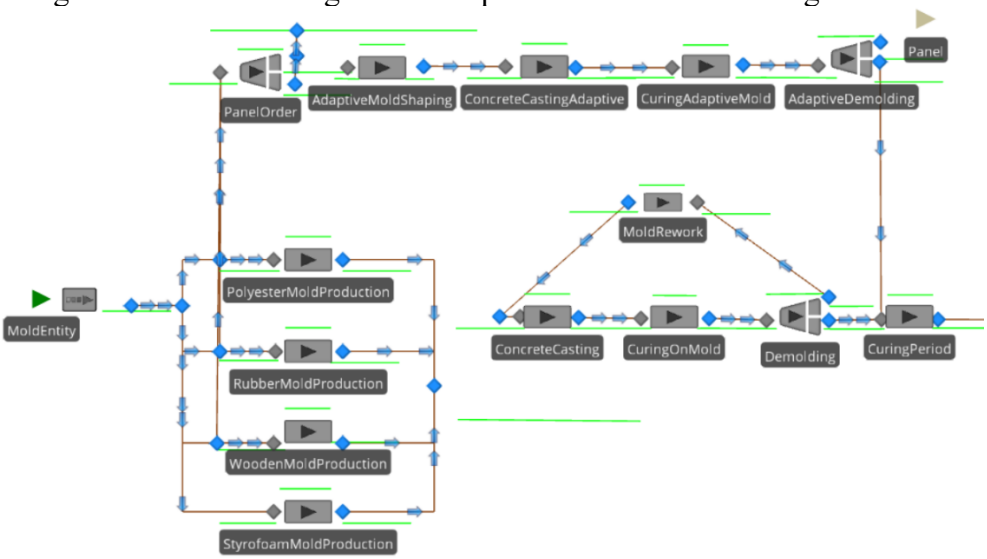


Fig. 6. Adaptive mold integrated model.

The aim of this adaptive-mold integrated model is to determine the optimum number of adaptive molds that fulfill a designated percentage of annual panel production. By simulating the scenarios where 5% and 10% of the total panel production are realized with the adaptive molds, this analysis identifies how many adaptive molds is required to meet the demand. Ultimately, these findings can provide critical insights into the feasibility of integrating this technology into the existing precast concrete facilities.

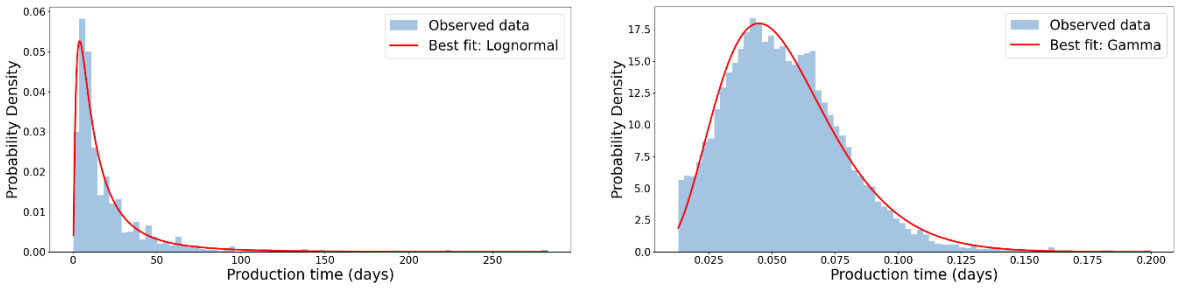
3. Results

2.1 Data Distribution Fitting

The outcomes of the distribution fitting analysis for each mold type and casting stage are presented in Table 1, which includes the fitted distribution and its parameters.

Table 1. Data distributions of the processes.

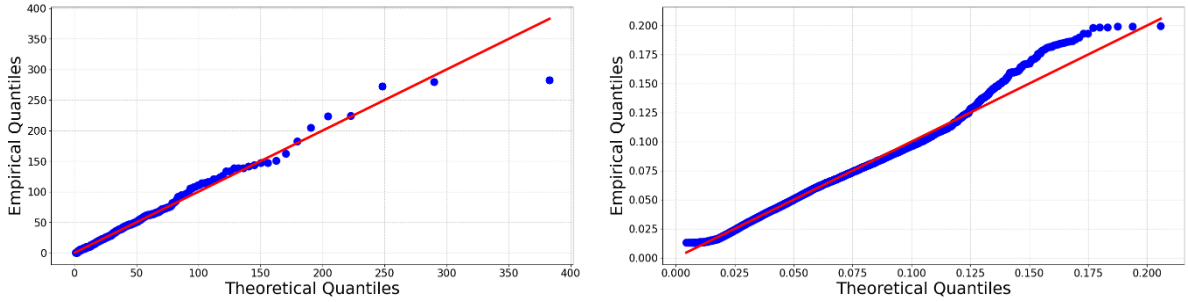
Process	Distribution Type	Parameters
Styrofoam Mold	Gamma Distribution	$\alpha = 2.057$, $\beta = 24.298$
Polyester Mold	Lognormal Distribution	$\alpha = 1.177$, $\beta = 2.737$
Rubber Mold	Gamma Distribution	$\alpha = 0.810$, $\beta = 36.456$
Wooden Mold	Lognormal Distribution	$\alpha = 1.067$, $\beta = 2.528$
Concrete Casting	Gamma Distribution	$\alpha = 5.254$, $\beta = 0.0106$



(a) **(b)**

Fig. 7. Distribution fitting for the production time data; (a) process of wooden mold, (b) process of concrete casting.

The production process histogram and fitted distribution are plotted for the wooden mold and concrete casting processes as representative in Fig 7. For these production process time data, Q-Q plots are provided in Fig. 8 to further validate the goodness-of-fit.



(a) **(b)**

Fig. 8. Q-Q plots for production time distribution fitting; (a) process of wooden mold, (b) process of concrete casting.

2.2 Model Verification

The warm-up period of the production system was determined based on the daily panel production. Accordingly, it was observed that the system starts to stabilize after approximately 105 days, corresponding to 15 weeks. As a result, the warm-up period of 15 weeks was selected for this facility model.

To ensure the reliability of the simulation model, a verification process was conducted by comparing key model outputs with real data. Two main outputs which are number of concrete panel and formwork production per year were calculated and the mean values are reported by running 10 simulation replications, as given in Table 2.

Table 2. Verification of simulation model.

	Model Output	**Real Data**	**Error (%)**
Concrete Panel Production (per year)	30492	30000	1.64%
Formwork Production (per year)	2616	2700	3.11%

Panel entities are the final output product of the system, created upon successful casting on a mold. The expected number of panels was 30,000. The simulation result reported a total of 30,492 panel entities, resulting in 1.64% deviation from the expected value. The simulation output produced total 2616 units of the formwork, resulting in an error of 3.11% compared to the expected value of 2700. This can be considered reasonable and within acceptable bounds for validation purposes.

2.3 Evaluation of Adaptive Mold Integration

The number of adaptive molds required was analyzed for the case in which 5% and 10% of the panels produced with the conventional molds are produced with the adaptive molds. The simulations were carried out using different numbers of adaptive molds with ten replications for each scenario. The results are illustrated in Fig. 9.

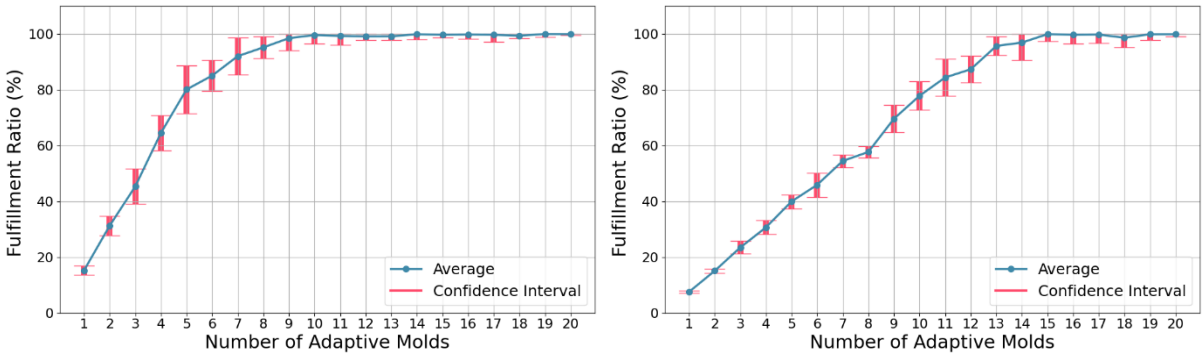


Fig. 9. The adaptive mold capacity analysis; (a) 5% replacement, (b) 10% replacement.

To evaluate the system performance, the fulfillment ratio is defined as the ratio of the number of panels produced to the number of panels ordered. The results in Fig. 9 indicate that achieving a full fulfillment ratio for the 5% and 10% panel production scenarios requires about 10 and 15 adaptive molds, respectively. Notably, this finding reveals that doubling the production with the adaptive molds leads to approximately 50% increase in the adaptive mold capacity, which suggest the non-linear scaling effects in the manufacturing process.

4. Discussion

This research presents the development and analysis of a discrete-event simulation model of a precast concrete panel production facility using the Simio software. The modeling process includes major stages of production line which are mold production and concrete casting. The objective of this study was not only to analyze an existing precast concrete panel production facility but also to evaluate the adaptability of the emerging technologies specifically, adaptive mold integration.

The integration of the adaptive molds into the facility in the simulation model can reveal significant insights for the efficient application of this prominent technology. In this analysis, number of adaptive molds in the system emerged as a critical factor to fulfill the assumed capacity for the panel production with this technology. This can be critically analyzed to decide on the number of the adaptive molds to incorporate into the facility. This simulation framework can be utilized as a decision-support tool to test the viability of the integration of the emerging novel technologies.

In future works, the mold production process can be modeled considering the sub-processes to enhance the accuracy, which leads to more detailed analysis of the manufacturing line. Furthermore, the adaptive mold integration can be further analyzed based on the complexity of the panel geometry, the type of formwork and costs. When deciding the optimum number of the adaptive molds, the cost of adopting of this technology into the existing facilities should be taken into account for a more comprehensive analysis. Accordingly, the optimum number can be explored for a more sustainable and cost-efficient solution for the thin-section concrete shell panel production.

5. Conclusion

In this study, an existing precast concrete panel production facility was modeled using Simio simulation software to investigate an emerging and novel adaptive mold technology. This technology has a great potential to transform the molding of the curved shell components into more cost-effective and time-efficient process. However, the integration of adaptive molds into the existing precast concrete panel facilities requires a detailed analysis to maximize the efficiency and decide on the optimum number of adaptive molds.

The simulation model was constructed based on the real process data provided by a precast concrete panel manufacturer. The major production processes were represented in the model and the parameters such as processing time or capacities were assigned according to the production process data. The model also was verified to validate its representativeness of the existing facility.

Various scenarios were explored for the integration of the adaptive molds, assuming a specific percentage of total panel production would be manufactured using this technology. This analysis allows to identify how many adaptive molds is required to meet the target panel production. Critically, doubling the panel production with the adaptive molds increases the required number of the adaptive molds by only 50%, which reveals a crucial nonlinear relationship. Ultimately, this simulation model can serve as a strategic tool to assess the integration of emerging technologies and guide the decision-making process for more feasible and sustainable production of curved shell structures.

Acknowledgments

The authors greatly acknowledge the grant from TUBITAK within the framework of the Collective Research Networking (CORNET) project (Grant number: 222N097). The authors would like to acknowledge the contribution of all the project partners Fibrobeton, ITA RWTH Aachen University, Attec Design, IMSAD, Hidropar Hareket Kontrol Sistemleri, Plustechno.

References

1. J. Schwartz.: Graphic statics and their potential for digital design and fabrication with concrete. Cement and Concrete Research (112), 122–135 (2018). doi: https://doi.org/10.1016/j.cemconres.2018.06.015.
2. J. Nilimaa, Y. Gamil, and V. Zhaka.: Formwork Engineering for Sustainable Concrete Construction. CivilEng (4), 1098–1120 (2023). doi: 10.3390/civileng4040060.
3. W. Li, X. Lin, D. W. Bao, and Y. Min Xie.: A review of formwork systems for modern concrete construction. Structures (38), 52–63 (2022). doi: https://doi.org/10.1016/j.istruc.2022.01.089.
4. T. Wangler, N. Roussel, F. P. Bos, T. A. M. Salet, and R. J. Flatt.: Digital Concrete: A Review. Cement and Concrete Research (123), 105780 (2019). doi: https://doi.org/10.1016/j.cemconres.2019.105780.
5. Hawkins, W.J., Herrmann, M., Ibell, T.J., Kromoser, B., Michaelski, A., Orr, J.J., Pedreschi, R., Pronk, A., Schipper, H.R., Shepherd, P., Veenendaal, D., Wansdronk, R. and West, M.: Flexible formwork technologies – a state of the art review. Structural Concrete (17), 911–935 (2016). doi: https://doi.org/10.1002/suco.201600117.
6. R. Schipper.: Double-Curved Precast Concrete Elements - Research into Technical Viability of the Flexible Mould Method. PhD Thesis, Delft University of Technology (2015).

7. M. Michel.: Electronic controlled adaptive formwork for freeform concrete walls and shells. in *Proceedings of the 9th fib International PhD Symposium in Civil Engineering: Karlsruhe Institute of Technology (KIT),* pp. 281, KIT Scientific Publishing (2012).
8. J. S. Smith, D. T. Sturrock, and W. D. Kelton.: *Simio and Simulation: Modeling, Analysis, Applications*, 7th ed. Simio LLC (2018).
9. C. D. Pegden, "Introduction to Simio," In: *Winter Simulation Conference*, pp. 229–235 (2008).

Author Contribution Statement

- *Conceptualization:* Bedirhan Enes Kelek, Beni Kohen, Muhammed Maraşlı, Necati Aras, Nilüfer Özyurt
- *Methodology:* Bedirhan Enes Kelek, Gökçen Karakol, Necati Aras, Nilüfer Özyurt
- *Investigation:* Bedirhan Enes Kelek, Gökçen Karakol
- Supervision: Necati Aras, Nilüfer Özyurt
- Project Administration: Nilüfer Özyurt
- *Writing – Original Draft:* Bedirhan Enes Kelek
- *Writing – Review & Editing:* Gökçen Karakol, Beni Kohen, Muhammed Maraşlı, Necati Aras, Nilüfer Özyurt

Publication Note

This paper was peer-reviewed, accepted for presentation, and included in the proceedings of the ACE2026 – International Conference on Advances in Civil Engineering, held on 12–14 October 2026 in Trabzon, Türkiye.

This paper may be cited as follows:

Kelek B. E., Karakol G., Kohen B., Maraslı M., Aras N., Ozyurt N., "Adaptive Mold Technology in Precast Concrete Panel Facilities: Optimization and Analysis," in Proceedings of the ACE2026 – International Conference on Advances in Civil Engineering, Trabzon, Türkiye, 12–14 October 2026.

Barriers in adoption of Circular Economy in Construction and Demolition Waste Management in Developing Countries

Dr Manjari Chakraborty[1], Pooja Singh[2], Dr Rizwan Kazmi[3]

[1]0000-0002-2313-9473, BIT Mesra, Ranchi, Department of Architecture & Planning, India

dr_manjari@bitmesra.ac.in

[2] 0009-0006-6934-5244, BIT Mesra, Ranchi, Department of Architecture & Planning, India

poojasingh1692ps@gmail.com

[3]0000-0001-7297-9762, BIT Mesra, Ranchi, Department of Architecture & Planning, India

rizwan@bitmesra.ac.in

ABSTRACT

The rapid growth of the construction industry has significantly increased construction and demolition waste (C&DW) generation, creating a critical global environmental challenge. Traditionally, the construction sector has followed a linear "take-make-dispose" model, resulting in resource depletion, waste generation, and environmental pollution. Circular Economy (CE) offers an alternative approach by promoting resource efficiency, waste minimization, reuse, recycling, and recovery. This study presents a comprehensive literature review examining the major barriers to CE adoption in construction and demolition waste management (C&DWM) in developing countries. The review identifies key barriers related to policy and regulation, economic conditions, technical capacity, institutional governance, infrastructure, stakeholder knowledge, and social acceptance. Findings indicate that inadequate infrastructure for waste segregation, collection, recycling, and material recovery remains a major constraint. Limited access to appropriate recycling technologies and technical expertise further reduces the effective utilization of C&DW as secondary construction materials. Weak regulatory frameworks, unclear institutional responsibilities, high investment costs, limited financial incentives, and insufficient demand for recycled products also hinder CE implementation. In addition, limited stakeholder awareness, fragmented governance, inadequate C&DW databases, and the predominance of informal recycling systems create further challenges. Despite these barriers, opportunities exist through stronger policy incentives, improved regulatory frameworks, capacity building, public–private partnerships, and the application of digital and assessment tools such as Building Information Modeling (BIM) and Life Cycle Assessment (LCA). The study highlights the need for context-specific and integrated strategies that consider the socio-economic, institutional, and infrastructural conditions of developing countries to accelerate the transition towards sustainable and circular C&DWM systems.

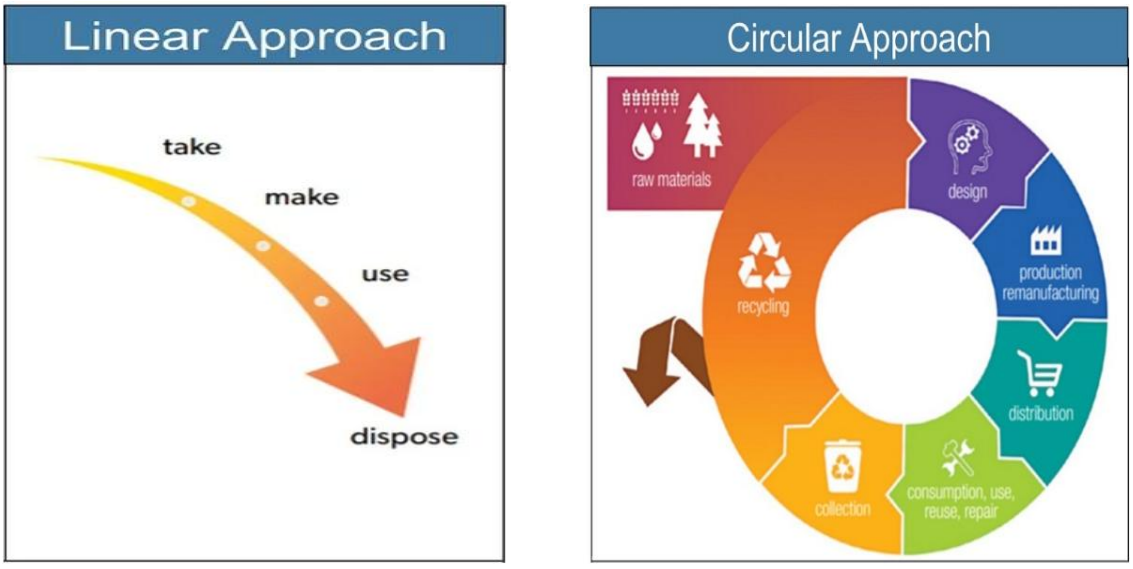
Keywords: Construction and Demolition Waste; Circular Economy; Waste Management Barrier

1. Introduction

The construction industry is a major contributor to economic development through infrastructure expansion, urbanization, and employment generation. However, it is also one of

the most resource-intensive sectors, consuming substantial quantities of raw materials, energy, and water while generating significant C&DW. Rapid urbanization, population growth, and infrastructure development have further increased C&DW generation, particularly in developing countries. The conventional linear "take–make–dispose" model has contributed to resource depletion, landfill disposal, greenhouse gas emissions, and environmental degradation [1, 2].

The CE provides an alternative to this linear model by seeking to retain products, materials, and resources within the economic system for as long as possible through reduction, reuse, repair, refurbishment, remanufacturing, repurposing, recycling, and recovery [3, 4]. Unlike the conventional disposal-oriented approach, CE aims to minimize waste generation while improving resource efficiency and creating opportunities for secondary-material markets. The transition from the linear to circular approach is illustrated in Figure 1. The linear model follows a one-way pathway from resource extraction to disposal, whereas the circular model seeks to maintain material flows through recovery and reuse.



a) Linear "take–make–use–dispose" b) Circular approach for resource retention and recovery

Figure 1. Comparison of linear and circular economic approaches: (a) linear "take–make–use–dispose" model and (b) circular approach for resource retention and recovery. (Source: https://www.wsp.com/en-GL/insights/building-a-circular-economy)

Within the construction sector, CE extends beyond the recycling of C&DW and incorporates circular principles throughout the building life cycle. Strategies such as design for disassembly, adaptability, modular construction, adaptive reuse, selective demolition, material passports, BIM, and LCA can support material recovery and reduce waste generation[3, 5, 6]. Previous research indicates that applying circular strategies from the early design stage can improve the recovery potential of building materials and reduce environmental impacts at later stages of the building life cycle [7].

Despite these potential benefits, the practical adoption of CE in C&D waste management (C&DWM) remains limited, particularly in developing countries. Existing literature identifies weak regulatory enforcement, inadequate recycling infrastructure, high implementation costs, limited technical expertise, fragmented institutional responsibilities, and insufficient stakeholder awareness as important barriers to circular construction [4, 8]. Developing countries may also face limited waste segregation and recovery facilities, inadequate C&DW

databases, and difficulties in establishing reliable markets for recycled construction materials. The literature on India further highlights economic constraints, stakeholder awareness, institutional coordination, and the need for stronger enabling mechanisms for circular construction.

Although several studies have examined CE and C&DWM, the existing literature remains fragmented, with studies often focusing on individual countries, specific barriers, or particular circular strategies. There is a need for a broader synthesis of the interconnected barriers affecting CE adoption in developing-country contexts. Differences in economic conditions, institutional capacity, regulatory enforcement, technological readiness, and stakeholder awareness make it difficult to directly transfer circular practices developed in advanced economies to developing countries. Therefore, context-specific approaches are necessary to facilitate the transition from linear to circular construction systems [7, 9].
Accordingly, this review aims to synthesize the existing literature on the barriers affecting CE adoption in C&DWM in developing countries, examine the relationships among these barriers, and identify strategies and future research directions that can support circular construction. The review particularly focuses on policy and regulatory, economic, technical, institutional, infrastructural, and socio-cultural dimensions.

The objectives of this review are to:

a) Identify the major barriers affecting the adoption of CE practices in C&DWM in developing countries.
b) Classify these barriers into policy and regulatory, technical, economic, institutional, infrastructural, and socio-cultural dimensions.
c) Critically analyze the interrelationships among these barriers based on existing literature.
d) Propose recommendations and future research directions to facilitate the transition towards circular construction systems in developing countries.

2. Research Methodology

This study adopts a Systematic Literature Review (SLR) approach to identify, synthesize, and critically analyze the barriers affecting the adoption of CE practices in C&DWM in developing countries. A systematic approach was selected to ensure transparency and consistency in the identification and selection of relevant literature [10]. The review process was guided by the PRISMA 2020 framework, which provides a structured procedure for identification, screening, eligibility assessment, and inclusion of studies [11].

2.1 Literature Search and Selection

Relevant literature was searched using Scopus and Web of Science, focusing on peer-reviewed publications related to CE, C&DWM, barriers, challenges, and developing countries. The search employed combinations of keywords such as *"Circular Economy," "Construction and Demolition Waste," "Construction Waste Management," "Barriers," "Challenges,"* and *"Developing Countries"* using Boolean operators.
Studies published in English and directly addressing CE implementation, C&DWM, or barriers and enabling factors in developing countries were considered. Duplicate records, conference abstracts, editorials, and studies unrelated to construction or C&DW were excluded. The screening process involved title and abstract assessment followed by full-text evaluation of potentially relevant studies.

2.2 Data Extraction and Thematic Analysis

The selected studies were then analyzed thematically to identify recurring barriers and their relationships.
Based on the literature, the barriers were classified into six major categories:

1. Policy and regulatory barriers
2. Economic and financial barriers
3. Technical and technological barriers
4. Institutional and governance barriers
5. Infrastructure barriers
6. Social and behavioral barriers

The systematic review provides a structured basis for understanding the existing research on CE adoption in C&DWM. Before examining the barriers that constrain CE implementation, it is important to establish the role of CE within the construction sector and understand how circular strategies can be applied across the building life cycle. Therefore, the following section briefly discusses the concept of CE in C&DWM, its major circular strategies, the role of digital technologies, and the specific challenges associated with its implementation in developing countries.

3. Circular Economy in Construction and Demolition Waste Management

3.1 Concept of CE in the Construction Sector

The conventional construction sector largely follows a linear economic model based on the extraction of raw materials, production, construction, use, and eventual disposal. This “take–make–consume–dispose” model results in substantial resource consumption and waste generation. In contrast, the CE seeks to maintain the value of materials and products for as long as possible through strategies such as reducing, reusing, repairing, refurbishing, remanufacturing, repurposing, recycling, and recovering resources [3, 12].
The construction sector is particularly important for CE because buildings contain large quantities of materials that can potentially be reused or recovered. CE in construction, therefore, involves more than recycling demolition waste at the end of a building's life. It requires circular thinking throughout the building life cycle, beginning with planning and design and continuing through construction, operation, maintenance, renovation, demolition, and material recovery [1, 9].
Circular construction strategies include DfD, design for adaptability, adaptive reuse, modular construction, material reuse, selective demolition, recycling, and recovery. Such strategies can reduce the consumption of virgin materials and increase the possibility of recovering components and materials at the end of a building's service life [13–15].
The CE concept can therefore be understood as a shift from “waste management” to “resource management.” Instead of treating C&DW as an unwanted output requiring disposal, circular construction considers buildings and infrastructure as material stocks from which resources can be recovered and returned to productive use.

3.2 Circular Strategies Across the Building Life Cycle

Circularity can be incorporated at different stages of the building life cycle. Early-stage decisions are particularly important because design and material-selection decisions influence

future waste generation and the potential for reuse and recovery. Table 1 and Figure 2 below show CE strategies across the building life cycle

Table 1 Circular Economy strategies across the building life cycle (Source: The Authors)

S.no	Building life-cycle stage	Major circular strategies	Potential contribution
1.	Planning and design	Design for disassembly, adaptability, and durability	Facilitates future reuse and recovery
2.	Material selection	Recycled and reusable materials	Reduces demand for virgin resources
3.	Construction	Prefabrication, modular construction, and waste minimization	Reduces material waste
4.	Operation and maintenance	Repair, maintenance, and adaptive reuse	Extends building service life
5.	Demolition	Selective demolition and deconstruction	Improves component recovery
6.	End-of-life	Reuse, recycling, and material recovery	Reduces landfill disposal

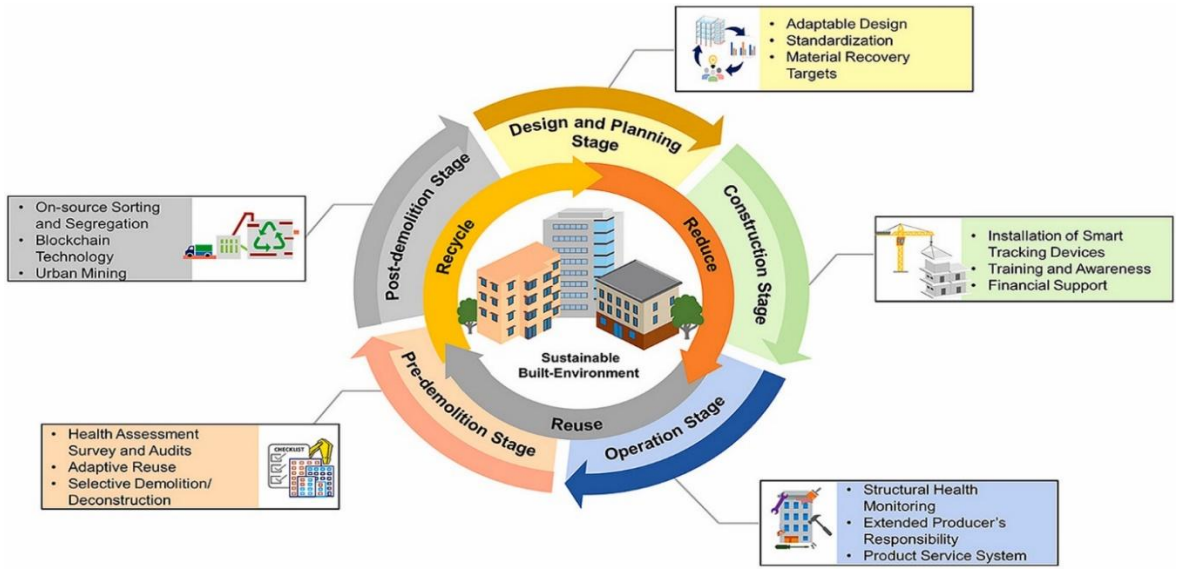


Figure 2 Circular Economy strategies across the building life cycle [16]

The literature indicates that circular strategies should not be considered independently because decisions at one stage affect opportunities at subsequent stages. For example, designing connections that can be dismantled rather than permanently bonded can make components easier to recover during demolition. Similarly, documenting materials and components during design and construction can support their identification and reuse in the future [5, 17].

Adaptive reuse is another important CE strategy because retaining an existing building can avoid the material consumption and waste generation associated with complete demolition and new construction. Life-cycle studies have consequently emphasized the importance of

considering whether an existing building can be repurposed before selecting demolition and replacement as the preferred option [18, 19].

3.3 Role of Digital Technologies in Circular Construction

These technological means can enable CE processes through better management of information and traceability of materials in the construction process. BIM can be used to identify and document building components, estimate the amount of material and waste production, plan for demolition, and design for disassembly [6].

In addition, the material passport can give information about materials used in building constructions. The information can help identify reusable materials during the renovation or demolition of buildings [5]. However, the implementation of these technologies requires appropriate digital infrastructure, standardized data, trained professionals, and institutional support.

The use of LCA will enhance such digital techniques in assessing the environmental impacts of different materials, as well as waste management options. The use of LCA together with CE will enable the identification of whether the use of reuse, recycling, or recovery options is environmentally beneficial in a certain situation. According to the literature, however, it is difficult to integrate such techniques in practice, especially in developing countries [6, 20, 21]. Thus, digital technologies should be regarded as enabling tools rather than standalone solutions. Their effectiveness depends on the availability of reliable material data, institutional capacity, technical expertise, and supportive regulatory frameworks.

4. Circular Economy in Developing Countries

The transition towards CE becomes particularly important for developing nations since the process of urbanization and infrastructural development is resulting in increased use of construction materials on one hand, while simultaneously producing huge amounts of C&DW [4, 9]. However, the conditions for implementation of the transition in developing nations are quite different from those in developed nations due to differences in institutional capacity, infrastructure, regulatory framework, and market development [7].

Developing nations generally suffer from a lack of waste management infrastructure, ineffective regulation enforcement, a lack of funding, technical know-how, institutional fragmentation, and a lack of awareness amongst stakeholders. Such conditions tend to hinder the process of segregation, recycling, material recovery, and circular design [4, 22]. The current review also finds the lack of segregation, collection, recycling, and material recovery infrastructure, economic constraints, weak regulation, technical knowledge, and institutional fragmentation as significant barriers to the transition [7, 23].

The literature also indicates that CE practices cannot simply be transferred from developed countries without considering local socio-economic and institutional conditions [3, 9]. For example, circular systems based on sophisticated digital platforms, advanced recycling technologies, or highly developed secondary-material markets may be difficult to implement where basic collection, segregation, and recycling systems are still developing [4]. Therefore, context-specific CE strategies are required for developing economies.

This is particularly relevant for countries such as India, where rapid construction activity is accompanied by increasing C&D waste generation, while challenges remain in terms of regulatory implementation, recycling infrastructure, stakeholder coordination, and market development for recovered materials [7, 20, 24]. Strengthening the alignment between CE objectives, construction policies, and C&DWM practices is therefore essential for establishing a more circular construction sector in India [7].

Consequently, the successful adoption of CE in developing countries requires simultaneous

attention to policy, economic viability, infrastructure, technical capacity, institutional coordination, and stakeholder behavior [4, 22]. These interconnected factors form the basis for the barrier analysis presented in the following section.

The above discussion clearly shows that CE presents a chance for changing the paradigm of C&DWM from the traditional disposal process into a process of conserving, reusing, recycling, and recovering resources. Yet, the application of circular approaches is inconsistent between countries, and developing nations have unique obstacles to overcome in terms of regulation capability, financial ability, infrastructure, technology, and collaboration among stakeholders. The literature also shows that such obstacles are interrelated instead of being independent, and the weakness in one factor tends to exacerbate the problems in other areas. Hence, in order to understand why CE has not been adopted by developing nations, this section will examine the barriers to the implementation of circular C&DWM through critical analysis.

5. Barriers to the Adoption of CE in Construction and Demolition Waste Management

The adoption of CE in C&DWM in developing countries is constrained by interconnected policy, economic, technical, institutional, infrastructural, and social factors. These barriers often reinforce one another, making it difficult to establish effective circular material flows [4, 22].

5.1 Policy and Regulatory Barriers

Lack of a proper regulatory framework and enforcement is still one of the challenges to the implementation of CE. The regulations of C&DW in the developing nations tend to concentrate on only collection and disposal, and not on waste prevention and recycling [4, 7, 22, 23, 25]. Lack of clear-cut roles of the various parties involved, lack of monitoring, and lack of recycled building material standards hinder the CE process [7].

5.2 Economic and Financial Barriers

The transition to circular construction often involves higher initial costs for waste segregation, transportation, processing, recycling facilities, and workforce training. At the same time, low demand for recycled materials and competition from relatively inexpensive virgin materials can reduce the economic attractiveness of recycling [7, 20, 25]. Limited access to finance further restricts investment, particularly among small and medium-sized construction enterprises. Subsidies, tax incentives, landfill charges, and development of stable markets for recovered materials can improve the economic feasibility of CE.

5.3 Technical and Technological Barriers

Poor source segregation, heterogeneous waste streams, limited recycling technologies, and inadequate technical expertise reduce the quality and quantity of recovered materials. Developing countries may also lack appropriate testing facilities and standards for assessing recycled construction products [4]. Digital tools such as BIM and material passports can improve material identification, tracking, and recovery, but their implementation requires reliable data, technical skills, and supporting infrastructure [5, 6]. Thus, technology adoption needs to be aligned with local technical capacity.

5.4 Institutional and Governance Barriers

Implementation gaps may arise because of fragmented roles in the different agencies of government and inadequate coordination between the public entities and construction actors. The lack of accurate C&DW databases poses further challenges with regard to the estimation

of waste generation, planning for recycling facilities, and monitoring the recovery efficiency [4, 7]. It is thus necessary to enhance institutional capability at the local level and coordination efforts among the various stakeholders.

5.5 Infrastructure Barriers

Inadequate infrastructure for collection, segregation, transportation, sorting, and recycling is a major constraint in developing countries. Limited availability of recycling facilities can increase transportation and processing costs and encourage disposal rather than recovery [4]. Infrastructure development should therefore be supported by reliable information on waste quantities, composition, and geographical distribution to ensure that recycling facilities are appropriately located and sized.

5.6 Knowledge and Capacity Barriers

Low levels of awareness and technical expertise on the part of architects, engineers, contractors, laborers, and local government bodies can serve as impediments to the implementation of circular practices. CE principles, such as deconstruction, recycling, selective demolition, and the use of recycled materials, involve a set of skills that might not have been taught during traditional construction [3, 7]. Professional training, academic programs, and demonstration projects can help build the required capacity.

5.7 Informal Sector and Social Barriers

The presence of an informal recycling system is a problem as well as an advantage for C&DWM. First of all, informal recycling could take place outside the waste management system and be accompanied by a fragmentation of flows of materials; nevertheless, such informal recyclers can provide a significant contribution to material recycling [4]. Secondly, the quality of recycled material may cause reluctance from construction contractors and customers [7]. Appropriate integration of informal recovery networks, quality certification, and stakeholder awareness can help address these challenges.

5.8 Interrelationship Among Barriers

These barriers are not mutually exclusive but are interconnected, creating a system where each one reinforces the other. For instance, poor regulation can hinder infrastructure development; poor infrastructure can cause higher recycling costs; high costs may result in lower demand for recyclables; and reduced demand can hinder private sector investments. In the same way, poor technical capacity may hinder the effectiveness of both regulatory and technological interventions [13, 19, 20, 22]. Therefore, there is a need for a holistic strategy for overcoming such barriers to ensure the success of CE. Seven main categories of barriers have been identified in the literature review. They include: policy and regulatory barriers; economic and financial barriers; technical and technological barriers; institutional and governance barriers; infrastructure barriers; knowledge and capacity barriers; and informal-sector and social barriers. These barriers are discussed in detail in Table 2 below.

Table 2 Major barriers to CE adoption in C&DWM (Source: The Authors)

S.no	Barrier category	Key issues
1.	Policy & regulatory	Weak enforcement, fragmented regulations, lack of standards
2.	Economic & financial	High costs, limited finance, and weak recycled-material markets
3.	Technical & technological	Poor segregation, limited technology, and technical expertise
4.	Institutional & governance	Poor coordination, weak local capacity, and limited data
5.	Infrastructure	Inadequate collection, sorting, and recycling facilities
6.	Knowledge & capacity	Limited CE awareness and professional skills
7.	Informal & social	Informal recovery, low acceptance of recycled materials

The analysis of the preceding section demonstrates that the adoption of CE in C&DWM is constrained by a combination of policy, economic, technical, institutional, infrastructural, and social barriers. These challenges are interconnected, and addressing them individually is unlikely to achieve effective circularity. Therefore, a coordinated set of strategies and enabling measures is required to create a supportive environment for CE adoption. The following section discusses the key strategies and enablers that can help overcome these barriers and facilitate the transition towards sustainable and circular C&DWM in developing countries.

6. Suggestive Measures & Recommendations

The barriers discussed in Section 5 indicate that CE adoption requires coordinated interventions across policy, economic, technical, institutional, and social dimensions. The following strategies can help create an enabling environment for circular C&DWM in developing countries.

6.1.Policy and Economic Measures

C&DW management regulations need to be strengthened through the formulation of proper waste prevention measures, waste source segregation, waste reuse, and recycling practices, accompanied by proper monitoring and enforcement [4, 8]. Standards for recycled construction products may promote market trust, whereas circular procurement can create demand for recovered waste [7].

Financial tools like subsidies, taxes, low interest rates, and landfill fees may make recovery and recycling more economically feasible [26]. Equally important is the development of a consistent market for recycled construction waste, since a lack of demand would deter private sector recycling investments.

6.2 Infrastructure, Technology, and Capacity Building

Adequate facilities for collection, segregation, sorting, and recycling are essential for establishing circular material flows. Infrastructure should be planned according to local waste quantities and composition [4, 13]. Appropriate technologies such as BIM, GIS, material passports, and LCA can further support material identification, tracking, waste estimation, and environmental assessment [5, 6]. However, technology adoption should be aligned with local

financial and technical.
Training and capacity building for architects, engineers, contractors, local authorities, and waste workers are also necessary to improve the implementation of circular practices. Greater awareness can increase acceptance of recycled materials and encourage the adoption of circular design and waste-management practices [3, 27].

6.3 Institutional and Stakeholder Collaboration

Effective CE implementation requires coordination among government agencies, construction professionals, developers, contractors, recyclers, and material suppliers. Public–private partnerships can support investment in recycling infrastructure and facilitate knowledge and technology transfer [17]. In developing countries, the informal recovery sector should also be considered within CE strategies, where appropriate, because its existing material-recovery networks can contribute to resource recovery.

6.4 Integrated Approach

The literature indicates that no single intervention can overcome the barriers to CE adoption. Policy support creates the enabling environment, economic incentives improve feasibility, infrastructure enables material recovery, technology supports efficient management, and capacity building facilitates implementation. Therefore, these measures should be implemented in an integrated and context-specific manner to support the transition from conventional waste disposal towards circular C&DWM.
The strategies discussed in Section 5 demonstrate that overcoming barriers to CE adoption requires coordinated interventions across policy, economics, infrastructure, technology, and stakeholder participation. However, the effectiveness of these measures depends on their integration and adaptation to the specific conditions of developing countries. The following section discusses the key findings of the review, the interrelationships among the identified barriers and enablers, and their implications for achieving circular C&D waste management.

7. Conclusion

The reviewed literature demonstrates that the transition towards CE in C&DWM in developing countries is influenced by a combination of policy, economic, technical, institutional, infrastructural, and social factors. These barriers are interconnected, indicating that CE adoption cannot be achieved through isolated interventions.
A key finding is that policy and institutional support provide the foundation for circular transformation. Regulations can establish requirements for segregation, recycling, and recovery; however, their effectiveness depends on enforcement, institutional capacity, and stakeholder coordination. Economic conditions are equally important because high recycling costs and limited demand for secondary materials can discourage investment, even when appropriate regulations exist.
The review also indicates that infrastructure and technical capacity act as critical enabling conditions. Without adequate collection, segregation, and recycling facilities, the practical implementation of CE remains limited. Similarly, technologies such as BIM, material passports, and LCA can support circular construction, but their effectiveness depends on data availability, technical skills, and institutional readiness.
An important implication is that CE strategies developed in developed economies cannot be directly transferred to developing countries. Differences in infrastructure, governance, financing, construction practices, and informal recovery systems require context-specific approaches. Therefore, developing countries should initially strengthen basic waste-

management systems, regulatory enforcement, and local capacity while progressively introducing advanced circular technologies and market mechanisms.
Overall, the findings suggest that successful CE adoption requires a system-level approach in which policy, finance, infrastructure, technology, and stakeholder participation reinforce one another. This integrated perspective provides a basis for developing practical and context-specific C&DWM frameworks for developing countries.

8. Future Research Direction

Based on the identified barriers and gaps, future research should focus on:

a) Standardized C&DW Quantification**:** Develop consistent and locally adaptable methods for estimating C&DW generation at city and project levels.
b) City-Level Waste Databases**:** Establish reliable databases on waste quantity, composition, material flows, and recycling rates to support evidence-based planning.
c) Integration of CE and LCA**:** Combine CE strategies with LCA to evaluate the environmental benefits of reuse, recycling, and material recovery.
d) Economic Feasibility of Circular Practices**:** Assess recycling costs, transportation, market demand, and financial incentives to develop economically viable circular business models.
e) Informal-Sector Integration**:** Investigate appropriate approaches for integrating informal material-recovery networks into formal C&DWM systems.
f) Context-Specific CE Frameworks**:** Develop and validate CE frameworks that reflect the institutional, economic, infrastructural, and socio-cultural conditions of developing countries.
g) Digital Technology Adoption: Explore affordable and scalable applications of BIM, GIS, and material passports for waste estimation, material tracking, and recovery planning.
h) Stakeholder Collaboration**:** Examine effective mechanisms for improving coordination among governments, designers, contractors, recyclers, and other stakeholders.

References

1. Benachio GLF, Freitas M do CD, Tavares SF (2020) Circular economy in the construction industry: A systematic literature review. J Clean Prod 260:121046. https://doi.org/10.1016/J.JCLEPRO.2020.121046

2. United Nations Environment Program (UNEP) (2023) UNEP Report 2023

3. Pomponi F, Moncaster A (2017) Circular economy for the built environment: A research framework. J Clean Prod 143:710–718. https://doi.org/10.1016/J.JCLEPRO.2016.12.055

4. Ghaffar SH, Burman M, Braimah N (2020) Pathways to circular construction: An integrated management of construction and demolition waste for resource recovery. J Clean Prod 244:118710. https://doi.org/10.1016/j.jclepro.2019.118710

5. Honic M, Kovacic I, Aschenbrenner P, Ragossnig A (2021) Material Passports for the end-of-life stage of buildings: Challenges and potentials. J Clean Prod 319:128702. https://doi.org/10.1016/J.JCLEPRO.2021.128702

6. Charef R, Emmitt S (2021). Uses of building information modeling for overcoming barriers to a circular economy. J Clean Prod 285:124854. https://doi.org/10.1016/J.JCLEPRO.2020.124854

7. Kazmi R, Chakraborty M (2025) Barriers and Enablers Towards Integrating Circular Economy in the Construction Industry in India. Journal of The Institution of Engineers (India): Series A 106:953–964

8. Yuan H (2013) Critical management measures contributing to construction waste management: Evidence from construction projects in China. Project Management Journal 44:101–112. https://doi.org/10.1002/pmj.21349

9. López Ruiz LA, Roca Ramón X, Gassó Domingo S (2020) The circular economy in the construction and demolition waste sector – A review and an integrative model approach. J. Clean. Prod. 248:119238

10. Tranfield D, Denyer D, Smart P (2003) Towards a methodology for developing evidence-informed management knowledge by means of systematic review. Wiley Online Library 14:207–222. https://doi.org/10.1111/1467-8551.00375

11. J. Page M, E. McKensie J, M. Bossuyt P, Boutron I, C. Hoffmann T, D. Mulrow C, Shamseer L, M. Tetzlaff J, A. Akl E, E. Brennan S, Chou R, Glanville J, M. Grimshaw J, Hrobjartsson A, M. Lalu M, Li T, W. Loder E, Mayo-Wilson E, McDonald S, A. McGuinness L, A. Stewart L, Thomas J, C. Tricco A, A. Welch V, Whiting P, Moher D (2021) The PRISMA 2020 statement: an updated guideline for reporting systematic reviews. BMJ 372:790–799. https://doi.org/10.1136/BMJ.N71

12. Potting J, Hekkert M, Worrell E, Hanemaaijer A (2017) Circular Economy: Measuring Innovation in the Product Chain

13. Guerra BC, Leite F (2021) Circular economy in the construction industry: An overview of United States stakeholders' awareness, major challenges, and enablers. Resour Conserv Recycl 170:. https://doi.org/10.1016/j.resconrec.2021.105617

14. Eberhardt LCM, Birkved M, Birgisdottir H (2022) Building design and construction strategies for a circular economy. Architectural Engineering and Design Management 18:93–113. https://doi.org/10.1080/17452007.2020.1781588

15. Akhimien NG, Latif E, Hou SS (2021) Application of circular economy principles in buildings: A systematic review. Journal of Building Engineering 38:102041. https://doi.org/10.1016/j.jobe.2020.102041

16. Sharma N, Kalbar PP, Salman M (2022) Global review of circular economy and life cycle thinking in building Demolition Waste Management: A way ahead for India. Build Environ 222:109413. https://doi.org/10.1016/J.BUILDENV.2022.109413

17. Leising E, Quist J, Bocken N (2018) Circular Economy in the building sector: Three cases and a collaboration tool. J Clean Prod 176:976–989. https://doi.org/10.1016/J.JCLEPRO.2017.12.010

18. Assefa G, Ambler C (2017) To demolish or not to demolish: Life cycle consideration of repurposing buildings. Sustain Cities Soc 28:146–153. https://doi.org/10.1016/J.SCS.2016.09.011

19. Oluleye BI, Chan DWM, Olawumi TO (2022) Barriers to circular economy adoption and concomitant implementation strategies in building construction and demolition waste management: A PRISMA and interpretive structural modeling approach. Habitat Int 126:102615. https://doi.org/10.1016/J.HABITATINT.2022.102615

20. Al-Otaibi A, Bowan PA, Abdel Daiem MM, Said N, Ebohon JO, Alabdullatief A, Al-Enazi E, Watts G (2022) Identifying the Barriers to Sustainable Management of Construction and Demolition Waste in Developed and Developing Countries. Sustainability 14:7532. https://doi.org/10.3390/su14137532

21. Butera S, Christensen TH, Astrup TF (2015) Life cycle assessment of construction and demolition waste management. Waste Management 44:196–205. https://doi.org/10.1016/j.wasman.2015.07.011

22. Yuan H (2017) Barriers and countermeasures for managing construction and demolition waste: A case of Shenzhen in China. J Clean Prod 157:84–93. https://doi.org/10.1016/j.jclepro.2017.04.137

23. Mahpour A (2018) Prioritizing barriers to adopt circular economy in construction and demolition waste management. Resour Conserv Recycl 134:216–227. https://doi.org/10.1016/j.resconrec.2018.01.026

24. Agamuthu P (2008) Challenges in sustainable management of construction and demolition waste. Waste Management and Research 26:491–492

25. Ooa D, Ioe D (2017) Barriers to Implementation of Sustainable Construction Techniques

26. Ghisellini P, Ripa M, Ulgiati S (2018) Exploring environmental and economic costs and benefits of a circular economy approach to the construction and demolition sector. A literature review. J Clean Prod 178:618–643. https://doi.org/10.1016/j.jclepro.2017.11.207

27. Kazmi R, Chakraborty M (2024) Status and probable direction of circular economy in the construction industry in India through a systematic literature review. International Journal of Green Economics 18:61–86. https://doi.org/10.1504/IJGE.2024.138514

Publication Note

This paper was peer-reviewed, accepted for presentation, and included in the proceedings of the ACE2026 – International Conference on Advances in Civil Engineering, held on 12–14 October 2026 in Trabzon, Türkiye.

This paper may be cited as follows:

Chakraborty M., Singh P., Kazmi R., “Barriers in adoption of Circular Economy in Construction and Demolition Waste Management in Developing Countries,” in Proceedings of the ACE2026 – International Conference on Advances in Civil Engineering, Trabzon, Türkiye, 12–14 October 2026.

Environmental Implications of Formwork Systems: A Comprehensive Review from a Circular Economy Perspective

Serkan KARALI[1], Gülben ÇALIŞ[2,*]
[1] *Department of Civil Engineering, Graduate School of Natural and Applied Sciences, Ege University, Bornova 35040 Izmir, Turkey*
[2] *Ege University, Faculty of Engineering, Department of Civil Engineering, 35040, İzmir, Türkiye*
*Corresponding Author E-mail: gulben.calis@ege.edu.tr

Abstract. Formwork systems represent a significant proportion of the cost, material consumption, and environmental footprint in reinforced concrete construction. As the industry accelerates its transition toward net-zero emissions, evaluating the environmental profiles of commonly utilized formwork materials such as timber, steel, aluminum, and plastic becomes essential. Each material exhibits a distinct ecological impact driven by factors like embodied carbon, reusability, and end-of-life recyclability. This study presents a comprehensive literature review investigating these systems through the perspectives of sustainability, carbon footprint reduction, and circular economy principles. The primary objective is to synthesize empirical data from recent peer-reviewed research to assess the environmental implications of various materials and identify key decision criteria for sustainable formwork selection. Ultimately, the findings indicate that formwork materials should be selected based on their full life-cycle performance and circularity rather than solely on their initial environmental impacts.

Keywords: Carbon footprint, Circular economy, Formwork systems, Sustainability.

1 Introduction

The building industry is responsible for a considerable share of resource consumption worldwide, as well as the associated waste generation and emissions [12]. Notably, CO_2 emissions from the construction sector account for almost 40% of the industry's annual emissions. Operating at the core of this highly resource-intensive environment, reinforced concrete (RC) structures constitute the backbone of global infrastructure. Within this supply chain, formwork systems are fundamental to the structural formation process. Despite being temporary elements, formwork constitutes the predominant financial and environmental burden in RC projects, accounting for up to 60% of the concrete structure's unit cost, 15% of the overall construction expenses, and a massive portion of the embodied carbon load ([9, 10]). Advances in construction technology have introduced a wide range of formwork materials, including conventional timber and alternative systems made of steel, aluminum, and plastic.

As the construction industry moves toward net-zero emission targets, formwork selection needs to consider more than initial investment cost. Existing Life Cycle Assessment (LCA) studies of conventional and modern formwork materials generally focus on cradle-to-gate environmental impacts. However, this approach may not fully account for factors such as on-site reusability, occupational health and safety (OHS) conditions during erection, and end-of-life recyclability.

This study systematically reviews the existing literature to identify the main findings and research gaps related to the environmental performance and circularity of formwork systems. It also outlines future research directions for integrating extended service life, wear-out coefficients, end-of-life recyclability, and practical site-related factors, including labor

efficiency and OHS risks, into formwork selection. The study aims to support future construction management research in developing more comprehensive, life-cycle-based decision-making approaches.

2 Methodology

To examine the environmental implications and circular economy potentials of formwork systems, this study adopted a comprehensive review methodology guided by Systematic Literature Review (SLR) principles. The data collection process was conducted through Scopus and Web of Science (WoS), the most prominent and prestigious databases in academic literature.

To effectively filter the vast literature towards the specific research objective, the search string was formulated based on three main concepts: System Focus, Environmental/Economic Impact and Circularity, and Analyzed Material Types. Accordingly, the following Boolean search string was executed in the databases: ("formwork") AND ("circular economy" OR "life cycle assessment" OR "LCA" OR "embodied carbon" OR "carbon footprint" OR "sustainability" OR "sustainable") AND ("timber" OR "wood" OR "steel" OR "aluminum" OR "plastic").

To capture the most recent technological advancements and sustainability paradigms, the search was limited to peer-reviewed journal articles and conference proceedings published in English from 2010 to the present. The initial search yielded 218 potential records from Scopus and 211 from Web of Science, resulting in a total pool of 429 publications.

The initial pool of 429 articles was subjected to a rigorous screening process to maintain the strict focus of the study. First, duplicate records across the two databases were removed. Subsequently, a title and abstract screening was conducted. Studies that evaluated formwork systems solely based on structural strength, concrete mechanics (e.g., load-bearing capacity), or those that focused on whole-building Life Cycle Assessments without isolating formwork as a specific analytical unit were excluded from the scope.

Due to the rigid nature of search engine algorithms, it was identified that several fundamental studies analyzing the site dynamics (e.g., occupational health and safety, operational speed) and eco-efficiency of formwork systems using alternative terminologies (e.g., "wear-out coefficient", "jump formwork") were filtered out during the initial search. To eliminate this literature blind spot and enhance analytical depth, the Backward Snowballing technique was integrated into the methodology.

The reference lists of the core articles filtered through the standard Boolean search were manually screened. Crucial studies that fell outside the primary keyword syntax but were vital for a comprehensive circular economy perspective were included. As a result of this meticulous PRISMA-based screening and synthesis process, a final set of 10 highly relevant core studies—comparing formwork systems across environmental, economic, and operational (workforce/safety) dimensions—was selected for the critical review. Ultimately, these selected studies established the empirical foundation to identify critical research gaps and outline strategic future research directions for the industry.

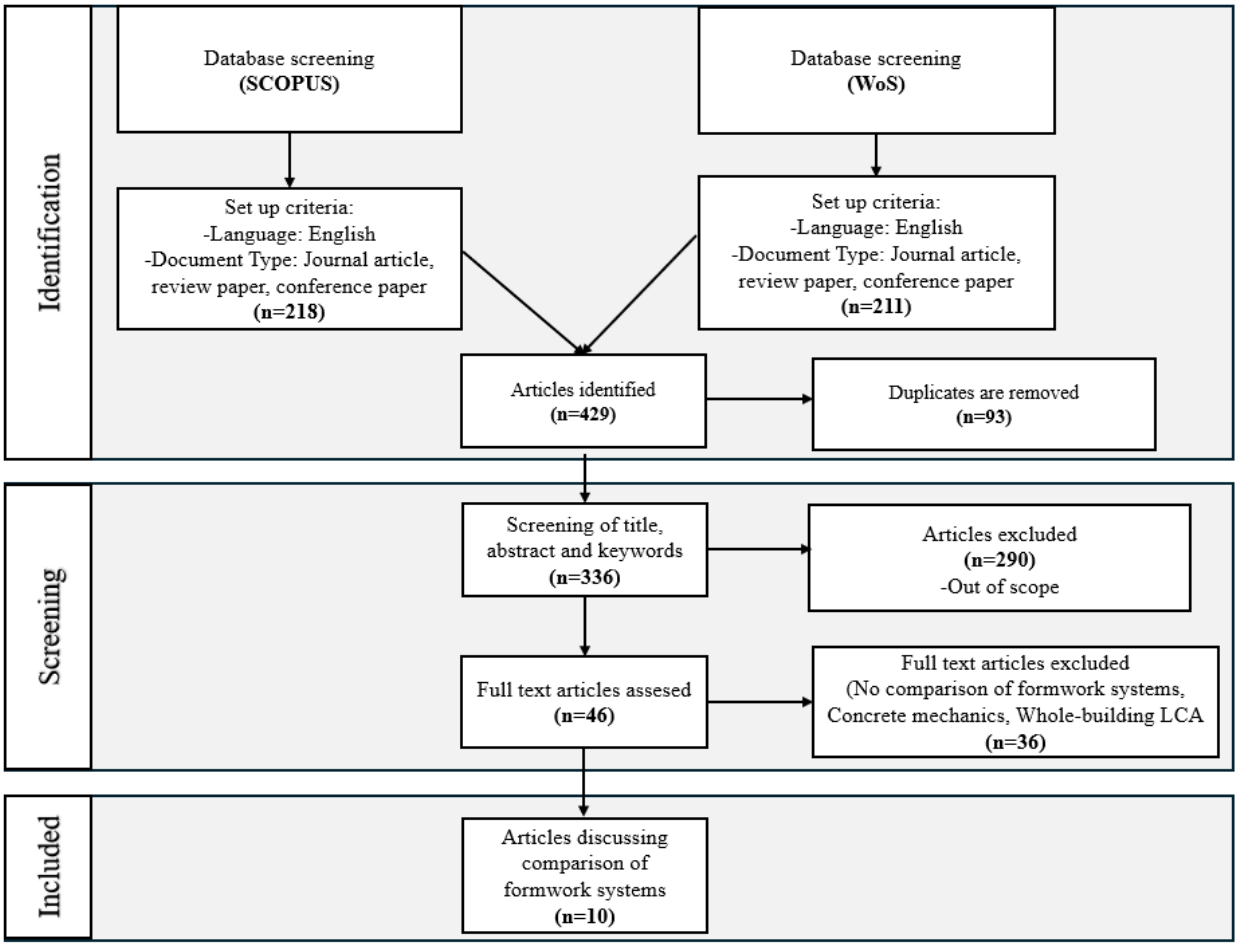


Fig. 1. The PRISMA flow diagram of the literature selection process

3 Review of Existing Literature

The reviewed literature indicates a gradual shift in the evaluation of formwork systems. While earlier studies mainly examined initial costs and material properties, recent research considers a wider range of environmental, economic, and operational factors. Table 1 summarizes the methods, findings, and limitations of the selected studies and provides a basis for identifying the main research gaps.

Table 1. Critical synthesis of the selected literature

Author and Year	Examined Systems	Core Focus & Methodology	Key Findings
Rahim & Haron, 2013	Timber vs. IBS (Lightweight Steel) Formwork	Case Study (Cost, Labor, and Wastage in High-Rise Buildings)	Timber causes massive wastage and demands high skilled labor. Conversely, steel IBS reduces overall costs and construction time via high reusability.
Parekh, 2015	Timber, Aluminum, Steel Formwork	Feasibility and Performance Analysis in Mass Construction	Aluminum formwork delivers rapid, high-quality, and low-maintenance construction, but its cost-effectiveness strictly depends on mass construction and highly repetitive projects.

Author and Year	Examined Systems	Core Focus & Methodology	Key Findings
Kazi & Parkar, 2015	Timber, Plastic (PLASTECH) and Steel (DOKA, PERI, RMD, MIVAN) Formwork	Cost, Quality, and Speed Comparison in Fast-Track Construction	Plastic minimizes idle costs in highly uncertain projects, whereas MIVAN is economically viable exclusively in mass housing.
Asadi et al., 2017	Timber and Steel (DOKA, MIVAN) Formwork	Comparative Analysis based on Site Constraints and Repetition	MIVAN reduces cost/time in repetitive projects, but wood remains preferred in non-repetitive projects facing severe space and storage restrictions.
Gaddam & Achuthan, 2020	Timber, Aluminum, Jump Formwork	Multi-Project Case Analysis (Cost and Duration Comparison)	Advanced systems like jump formwork generate significant indirect cost savings by reducing project duration, overcoming initial cost barriers.
Donkor et al., 2022	Timber and Steel Formwork	Field Survey (Quantitative Questionnaire Study)	While timber has initial cost benefits, steel shows better performance in durability, surface finish, and labor productivity.
Bakırhan & Kayılı, 2023	Timber, Steel and Aluminum Formwork	Scenario-Based Environmental and Economic LCA	While timber is economical for single-use scenarios, factoring in actual multi-use service lives reveals that steel systems show better performance for mass housing, achieving a 70% cost reduction and a 60.6% lower global warming potential.
Balasbaneh et al., 2024	Plastic, Steel, Plywood, Timber Formwork	LCA, LCC, and MCDM (1-use vs. 50-use scenarios)	While timber is optimal for a single use, MCDM analysis ultimately identifies plastic as the best overall formwork material after 50 cycles regarding embodied energy and economic cost.
Apdeni et al., 2024	Aluminum and Timber Formwork	Site Case Study (Eco-Efficiency and Cost Analysis)	Despite being initially 2.25 times more expensive, aluminum's 200-cycle reusability and zero waste achieved significantly higher eco-efficiency than timber.
Baskaran et al., 2025	Steel, Timber, Aluminum, Plastic Hybrid Formwork	LCA integrated with Material Wear-Out Coefficients	Hybrid systems provide the most sustainable solutions by offsetting the high environmental burdens of short-lived timber with the extreme durability of aluminum (250 cycles), thereby minimizing overall material depletion.

The reviewed studies show a gradual shift from basic cost comparisons to life-cycle-based sustainability assessments.

Initial studies in the literature heavily prioritized operational speed, direct costs, and physical on-site wastage. Rahim and Haron [14] compared conventional timber formwork with lightweight steel Industrialized Building Systems (IBS). They reported that the limited reusability of timber increases skilled-labor requirements and material waste, whereas steel systems can reduce overall costs and labor demand. Parekh [13] found that aluminum formwork supports faster erection and higher construction quality, although its economic performance depends largely on mass construction and repetitive project designs. Kazi and Parkar [8] examined fast-track formwork technologies, including Plastech, Doka, and MIVAN. Their study showed that industrialized systems may lead to substantial idle costs when construction is interrupted, indicating that operational flexibility should also be considered in formwork selection.

As the literature progressed, researchers began to increasingly factor in site restrictions and indirect economic benefits. Asadi et al. [1] reported that MIVAN can reduce construction time and cost in highly repetitive projects, while conventional timber may remain more suitable for non-repetitive projects with limited site and storage space. Gaddam and Achutam [7] indicated that jump formwork and aluminum systems can shorten project duration and generate indirect cost savings that help offset their higher initial costs. Donkor et al. [6] found through a quantitative field survey that, although timber is often selected because of its lower acquisition cost, steel performs better in terms of durability, surface finish, and labor productivity.

In recent years, the analytical focus has fundamentally shifted toward Life Cycle Assessment (LCA), reusability dynamics, and the "initial carbon fallacy." Bakırhan and Kayılı [3] mathematically demonstrated that evaluating formwork without accounting for its service life leads to flawed decisions. Under a hypothetical single-use scenario, steel exhibited carbon emissions 19 times higher than timber; however, when actual multi-use lifespans were factored in, timber's global warming potential was 60.6% higher. This paradigm shift is extensively supported by Balazbaneh et al. [4], who utilized a Multi-Criteria Decision-Making (MCDM) model. Their findings revealed that at a 1-use scenario, timber is the optimal choice, but at a 50-use scenario, the hierarchy completely reverses, crowning plastic and steel as the most sustainable options. Similarly, a site case study by Apdeni et al. [2] reported that despite aluminum being 2.25 times more expensive initially, its extraordinary 200-cycle reusability and zero material waste yield far higher eco-efficiency than conventional systems.

Recent research has also examined the potential benefits of combining different formwork materials. Baskaran et al. [5] evaluated hybrid formwork systems and identified the wear-out coefficient as an important assessment criterion. Their findings suggest that combining durable materials such as aluminum or steel with lower-impact materials such as timber or plastic may provide a more balanced solution by reducing overall material consumption and distributing environmental impacts over a longer service life.

4 Discussion and Conclusion

Despite the progress from operational comparisons to life-cycle-based assessments, an important research gap remains. Current sustainability models account for physical wear-out coefficients and theoretical carbon impacts, but they often overlook practical construction-site conditions. Future construction management studies should therefore combine material-level environmental assessments with economic and operational criteria through multi-criteria decision-making approaches.

Future research should also move beyond traditional cradle-to-gate assessments and single-use carbon metrics. Initial embodied carbon values may be misleading when the service life and repeated use of formwork materials are not considered. Life Cycle Assessment (LCA) studies should therefore incorporate the wear-out coefficient and report environmental impacts on a per-use basis over the service life, rather than only on a per-kilogram basis. The maximum number of reuse cycles and end-of-life recovery options, including recyclability and scrap value, should also be considered to provide a more accurate assessment of eco-efficiency and circularity.

Environmental performance should be evaluated together with social and operational factors. Relevant site-related criteria include occupational health and safety (OHS) risks, storage requirements, workforce demand, labor productivity, erection speed, crane dependency, and waste generation during construction. Project repetition and site constraints should also be considered because they may significantly influence the economic and operational performance of a formwork system. Including these criteria would allow future assessment models to better reflect actual construction conditions.

A formwork system may show favorable environmental performance in theory but still create practical difficulties if it requires substantial skilled labor, increases material-handling risks, or causes operational bottlenecks. The reviewed literature indicates that the suitability of a formwork system depends on both its material characteristics and the conditions under which it is used. Therefore, environmental, economic, social, and operational indicators should be considered together when evaluating the sustainability and circularity of formwork systems.

References

1. Asadi, S.S., Praneeth, P.V.: A comparative study for evaluation of different form work systems utilization in construction projects. International Journal of Mechanical Engineering and Technology 8(11), 21–29 (2017).
2. Apdeni, R., Hellyward, J., Syihab S.R., D.L.: Comparative study of cost and eco-efficiency factors of aluminum and conventional formwork in the AYOMA apartment construction project. CIVED 11(1), 174–184 (2024).
3. Bakırhan, E.K., Kayili, M.T.: Evaluation of the environmental impact of formwork systems depending on the service life and cost analysis. CRPASE: Transactions of Civil and Environmental Engineering 9(2), 1–10 (2023).
4. Balasbaneh, A.T., Sher, W., Ibrahim, M.H.W.: Life cycle assessment and economic analysis of reusable formwork materials considering the circular economy. Ain Shams Engineering Journal 15(4), 102585 (2024).
5. Baskaran, D., Chockkalingam, U., Muthalvan, R.S.: Assessment of sustainable hybrid formwork systems using life cycle assessment and the wear-out coefficient—a case study. Buildings 15(10), 1630 (2025).
6. Donkor, D.K., Mahamud, S.: Comparative assessment of formwork systems used in construction projects in the Tamale metropolis of northern Ghana. SSRG International Journal of Civil Engineering 9(2), 44–50 (2022).
7. Gaddam, M.S., Achuthan, A.: A comparative study on newly emerging type of formwork systems with conventional type of form work systems. Materials Today: Proceedings 33, 736–740 (2020).
8. Kazi, A., Parkar, F.: Comparative study and decision making for a formwork technique to be adopted on a construction site in Mumbai. International Journal of Research in Engineering and Technology 4(12), 234–238 (2015).
9. Krawczyńska-Piechna, A.: Comprehensive approach to efficient planning of formwork utilization on the construction site. Procedia Engineering 182, 366–372 (2017).

10. Ko, C.H., Wang, W.C., Kuo, J.D.: Improving formwork engineering using the Toyota way. Journal of Engineering, Project, and Production Management 1(1), 13–27 (2011).
11. Li, W., Lin, X., Bao, D.W., Xie, Y.M.: A review of formwork systems for modern concrete construction. Structures 38, 52–63 (2022).
12. Minunno, R., O'Grady, T., Morrison, G.M., Gruner, R.L.: Exploring environmental benefits of reuse and recycle practices: A circular economy case study of a modular building. Resources, Conservation & Recycling 160, 104855 (2020).
13. Parekh, N.M., Marvadi, B.M., Patel, U.: Comparative studies of construction techniques (conventional technique vs aluminium formwork techniques). Journal of Information, Knowledge and Research in Civil Engineering 3(2), 279–287 (2015).
14. Rahim, M.S.M., Haron, N.A.: Construction cost comparison between conventional and formwork system for condominium project. IJASCSE 2(5) (2013).

Note: Following the conference, this Publication Note will be added to each paper; therefore, authors are kindly requested not to remove the note below and to complete the author(s) and paper title information.

Publication Note

This paper was peer-reviewed, accepted for presentation, and included in the proceedings of the ACE2026 – International Conference on Advances in Civil Engineering, held on 12–14 October 2026 in Trabzon, Türkiye.

This paper may be cited as follows:

Karali, S., Calis, G., "Environmental Implications of Formwork Systems: A Comprehensive Review from a Circular Economy Perspective " in Proceedings of the ACE2026 – International Conference on Advances in Civil Engineering, Trabzon, Türkiye, 12–14 October 2026.

Modeling Bid/No-Bid Decisions in International Infrastructure Projects Using Graph Neural Networks and Natural Language Processing: A Pilot Study

Uğur Günay[1] and Onur Behzat Tokdemir[2,3]
[1] 0000-0002-2820-0886, Department of Civil Engineering, Istanbul Technical University, 34467 Istanbul, Türkiye,
gunayu@itu.edu.tr
[2] 0000-0002-4101-8560, Department of Civil Engineering, Istanbul Technical University, 34467 Istanbul, Türkiye,
[3] Artificial Intelligence and Data Science Research Center, Istanbul Technical University, 34467 Istanbul, Türkiye,
otokdemir@ itu.edu.tr

Abstract. Bidding decisions in international construction represent a strategically significant and resource-intensive process, requiring contractors to evaluate multiple competing criteria under time pressure and organisational constraints. Firms operating in large-scale infrastructure markets must rapidly screen hundreds of opportunities against limited organizational capacity, weighing financial scale, geographic risk, technical fit, and strategic alignment simultaneously. The continued reliance on expert scoring systems leaves rich information sources, particularly unstructured project description texts, largely outside the decision-making process.

This paper presents a pilot study developing and evaluating a machine learning based Decision Support System (DSS) for bidding decisions in international transportation (road and railway) infrastructure projects. A proprietary dataset of 2259 infrastructure project records was used, combining structured project attributes with Natural Language Processing (NLP) derived features extracted from text descriptions. The study's primary focus is the applicability of GraphSAGE to the bid/no-bid decision problem, chosen for its capacity to model inter-project relationships through graph-based aggregation and to generalise to new project nodes through inductive learning. Logistic Regression, Random Forest, and XGBoost serve as baseline models. A dual strategy graph was constructed connecting projects through shared Region values and text embedding cosine similarity, and SHAP analysis was applied to interpret model decisions.

Logistic Regression achieved the highest overall accuracy at 98.33% with an AUC-ROC of 0.9976, while GraphSAGE recorded the highest precision of 96.24%, demonstrating its value as a conservative and reliable bid recommender. SHAP analysis applied to the best-performing model revealed that text embedding features account for 72.5% of total feature importance, substantially exceeding the 24.6% contribution of structured features. This demonstrates that project description texts carry decision-relevant signals far beyond what structured project attributes alone can capture.

Keywords: Bidding decisions; Machine learning; GraphSAGE; NLP.

1 Introduction

International construction contractors are routinely confronted with extensive project screening processes that require the simultaneous evaluation of competing criteria, including financial scale, geographic risk profile, technical fit, and strategic priority [12]. Poor management of the bid/no-bid decision carries significant consequences on both ends. Misallocated resources and weakened market position when unsuitable projects are pursued, and the loss of strategically viable opportunities when promising ones are overlooked, each outcome with direct implications for a firm's long term-competitive standing.

A fundamental limitation of current practice is the heavy reliance on expert scoring systems and the resulting inability to systematically exploit the rich informational content embedded in project databases, particularly written project descriptions. This gap represents not merely a methodological shortcoming but a tangible efficiency loss arising from the failure to translate available institutional knowledge into the decision-making process.

Recent advances in machine learning and NLP offer promising pathways to address this limitation. Graph neural networks allow structural and semantic relationships between projects to be incorporated into the model, enabling access to contextual information that conventional flat classifiers cannot capture. GraphSAGE, introduced by Hamilton et al. [1], extends this capability through inductive learning, generating representation vectors for project nodes not encountered during training. This feature offers a significant practical advantage when modeling new datasets to which new project records are continuously added.

This study takes the applicability of GraphSAGE to bid/no-bid decision making as its primary research objective and makes four original contributions in this direction. First, a multimodal feature engineering data-pipeline is developed that integrates structured project attributes with Sentence-BERT based text embeddings. Second, a dual strategy graph construction method is proposed, connecting projects based on shared Region data and text embedding cosine similarity. Third, a comparative experimental design against three baseline models is established to enable a meaningful evaluation of GraphSAGE's independent contribution. Fourth, SHAP analysis is employed to reveal the dominant influence of text embedding features on model decisions. This finding underpins a two-stage DSS architecture capable of generating meaningful preliminary recommendations even in the absence of expert scoring criteria. The empirical basis for the study is a proprietary dataset drawn from a contractor operating across multiple sectors, filtered to transportation infrastructure projects. Full details of the dataset composition, feature engineering pipeline, and model configurations are described in the sections that follow.

2 Literature Review

The growing adoption of artificial intelligence in construction has attracted substantial scholarly attention, resulting in several broad-scope reviews that provide the conceptual backdrop for this study. Pan and Zhang [2] conducted a systematic review combining scientometric and qualitative analysis of 4,473 journal articles published between 1997 and 2020, documenting the progression of AI applications in construction engineering and management and identifying six key future research directions, among them NLP and intelligence optimization, and process mining. García et al. [3] extended this synthesis with a hybrid bibliometric analysis covering studies from 2015 to 2022, using a BERT-based topic modelling methodology to identify principal application clusters, which include construction management, tunnelling, concrete technology, and pavement engineering. Xu et al. [4] complemented these surveys by tracing the theoretical transition from shallow to deep learning in construction contexts, evaluating the relative strengths and limitations of each generation of models and proposing directions for domain-specific deep network development.

Within the construction project management domain, machine learning has been applied most extensively to cost estimation, schedule prediction, and risk classification. Gondia et al. [5] developed ML-based predictive models for construction project delay risk using a multivariate dataset drawn from 51 historical projects, finding that decision tree and Naive Bayes classifiers effectively captured the interdependencies among delay-inducing factors. Mahmoodzadeh et al. [6] applied four optimized ML models, namely Gaussian Process Regression, Support Vector Regression, Linear Regression, and Decision Tree, to a dataset of 350 historical tunnel projects from 34 sites worldwide, using the Grey Wolf Optimisation algorithm for hyperparameter tuning and finding that Linear Regression delivered the strongest prediction performance for both construction cost and duration. At the building level, Alshboul et al. [7] demonstrated the superiority of XGBoost over deep neural networks and Random Forest for green building cost prediction, with XGBoost achieving an R^2 of 0.96, outperforming the neural network baseline by 5% and Random Forest by 9.4%.

A separate body of work applies machine learning to legal and contractual dimensions of construction project management, where structured project data intersects with complex dispute histories and procurement records. Ayhan et al. [8] developed a data-driven dispute occurrence prediction model using empirical survey data from construction experts, finding that the C5.0 decision tree algorithm achieved a validation accuracy of 83.92%, and identifying the most influential variables contributing to dispute risk. Un et al. [9] extended this line of enquiry to dispute outcome prediction, training five ML classifiers on a dataset of arbitration cases from Turkey and finding that Support Vector Machine achieved the highest accuracy at 71.65%, with twelve significant project and contractual variables identified as the most predictive features. Jacques de Sousa et al. [10] applied ML classification algorithms to a dataset of over 5000 public construction procurement contracts from the Portuguese national repository, evaluating the effect of data balancing strategies including oversampling, undersampling, and SMOTE on the prediction of budget compliance, and demonstrating the practical viability of ML-driven compliance forecasting in public procurement contexts.

Natural language processing has emerged as a complementary analytical tool in construction, enabling the extraction of structured information from the large volumes of unstructured text generated across project lifecycles. Moon et al. [11] developed a Named Entity Recognition model for automated construction specification review, training a Word2Vec-embedded BiLSTM-CRF architecture on road project specifications and achieving a mean F1 score of 0.917, with precision and recall of 0.919 and 0.914 respectively, demonstrating that NLP can support contractors in systematically understanding specification requirements during the bidding phase.

Graph neural networks represent a more recent development in construction informatics. Wu et al. [12] applied a domain-adapted graph-based deep learning model to the knowledge base completion problem in package-based constraint management, arguing that general-purpose knowledge base completion methods fail to capture the semantic specificity of construction constraint networks and demonstrating that construction-domain knowledge embedding substantially improves link prediction performance over general-purpose baselines. While this application differs from the classification task examined in the present study. Mostofi et al. [13] developed a Graph Convolutional Network model for construction safety risk assessment by restructuring a historical accident dataset into a network in which accidents were connected based on shared project type, enabling the model to learn from relational dependency information rather than treating each incident in isolation. The GCN severity predictor achieved a prediction accuracy of 94.47%, outperforming conventional feedforward neural network baselines and demonstrating that graph-structured representations of construction records carry predictive signal beyond what independent feature vectors alone can capture.

Against this background, quantitative bidding decision modelling has remained an underexplored area, and the published work that does exist tends to rely on structured project attributes alone. Araújo et al. [14] proposed a classification model that uses a fuzzy preferential procedure adapted from ELECTRE TRI-C to assign construction opportunities to ordinal attractiveness categories,

demonstrating that multi-criteria classification can provide contractors with a systematic and consistent basis for bid/no-bid decisions. However, no prior study has combined graph neural networks with transformer-based NLP embeddings for this problem, and none has empirically examined the relative contribution of unstructured project description text to model decisions. The present study addresses both gaps.

3 Data and Methodology

3.1 Dataset

The dataset used in this study is drawn from the proprietary project tracking database of an international construction contractor, filtered to include only transportation infrastructure projects, yielding a working dataset of 2259 project records. All data was recorded as of July 2023, and project names and web addresses were excluded from the analysis to protect commercial confidentiality. Each project record contains two types of features. The first comprises structured attributes covering numerical and categorical data such as project value, geographic region, and construction stage. The second consists of text features in the form of written project descriptions, organized across four columns (Project Overview, Project Scope, Project Background, and Latest Update).

The dataset includes scoring columns assigned by tender evaluation experts. Each of these columns has a specific weight percentage, and numerical evaluations for each project are provided under the headings Project Status Score, Project Value Score, Country Grade, Risk Level, and Business Development Rating (BD Rating). A weighted formula combines these five numerical values into a single total score called TOTAL POINT. A binary target variable named Bid_Label has been created from the TOTAL POINT score. To produce the most balanced class distribution, a threshold value of 4.7 is applied to the TOTAL POINT score, resulting in 50.1% of the projects being labeled as BID and 49.9% as NO BID. This near-perfect balance does not require a special correction technique for class imbalance. The dataset is summarized in Table 1.

Table 1. Dataset Summary

Attribute	**Value**
Total projects	2259
Training set (80%)	1807 projects
Test set (20%)	452 projects
Structured features	309 columns
Free-text description columns	4 (Project Overview, Project Scope, Project Background, Latest Update)
Target variable	Bid_Label (1=BID, 0=NO BID, threshold=4.7/7.4)
Class balance	50.1% BID / 49.9% NO BID

3.2 Data Preparation and Feature Engineering

Seven columns were removed from the dataset, including database identifiers, privacy-sensitive fields, and a sector column with a constant value following the initial filtering step. The Latest Momentum Score column contained non-numeric entries such as "X" and "x", which were treated as zero-momentum signals and recoded as 0. A binary indicator, Is_Eliminated, was created to record whether a project had been flagged for elimination under the original scoring system. Categorical columns were converted to numerical format through one-hot encoding, which generates a separate binary column for each possible category value. The Country and

Secondary Sector columns, which could contain multiple values per cell, were processed using multi-label binary encoding.

Date and quarter columns were decomposed into numerical components. An estimated project duration feature was also derived, along with a months-since-last-update variable capturing the recency of project information. The five expert scoring criteria and the Is_Eliminated indicator were excluded from the feature set prior to model training, as these variables directly compose the TOTAL POINT score from which Bid_Label is derived. Following all processing steps, the structured feature matrix comprised 309 columns. The dataset was then split into a training set of 1807 projects (80%) and a test set of 452 projects (20%) using stratified sampling to preserve the class distribution in both subsets.

3.3 NLP Processing Data Pipeline

A three-stage processing data pipeline was applied to the four free-text description columns to extract numerical features from the written content. In the first stage, sentence embeddings were generated using the all-MiniLM-L6-v2 model based on Sentence-BERT. Each text column was transformed into a 384-dimensional vector, and the four vectors were concatenated to produce a 1536-dimensional text feature matrix per project.

In the second stage, topic modelling was performed using Latent Dirichlet Allocation (LDA). Eight thematic clusters were extracted from the corpus, covering topics such as highway expansion, railway development, and bridge rehabilitation, contributing eight additional numerical features per project. In the third stage, a pre-trained DistilBERT model was applied to the Latest Update column to produce a signed sentiment score capturing the overall tone of recent project updates. The final feature matrix combines 309 structured features, 8 topic scores, 1 sentiment score, and 1536 text embedding dimensions, yielding a total of 1,845 features per project.

3.4 Graph Construction

GraphSAGE requires a graph in which each project is represented as a node and relationships between projects are encoded as edges. A dual-strategy approach was adopted. The first strategy connects projects sharing the same geographic region, capturing shared market conditions and regulatory environments. The second connects projects whose sentence embedding vectors exhibit a cosine similarity above 0.80, linking projects with comparable technical descriptions regardless of geographic location.

The resulting training graph comprises 2132 nodes and 1536042 edges, with an average degree of approximately 1440 connections per node. Graph construction parameters are detailed in Table 2. Figure 1 provides a visual representation of a 50-node sample, where blue nodes denote BID-labelled projects and red nodes denote NO BID-labelled projects.

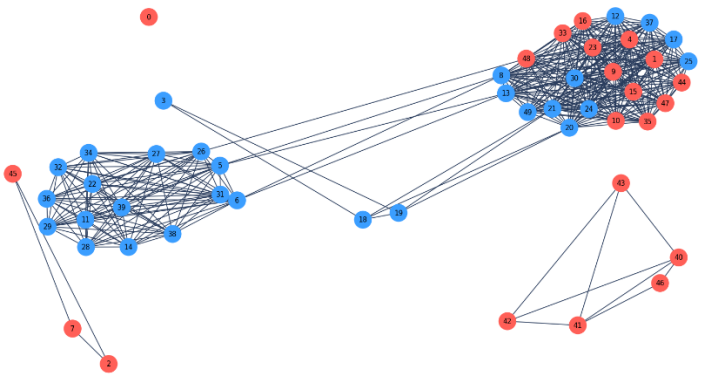


Figure 1: 50-node project similarity graph (Blue = BID, Red = NO BID.)

Table 2. Graph Construction Parameters

Parameter	Value	Description
Total nodes	2,132	Training projects
Total edges	1,536,042	Combined from both strategies
Average node degree	~1,440	Average connections per project
Strategy A	Shared Region	Geographic similarity
Strategy B	Cosine similarity > 0.80	Semantic text similarity
Node features	1,845 dimensions	Structured features + NLP embeddings

4 Model Development

Four machine learning models were developed and evaluated, one serving as the primary model under investigation and three as performance baselines. The adoption of a multi-model experimental design is not solely motivated by performance comparison but reflects a methodological necessity. The independent contribution of graph structure and NLP-derived features to the decision process can only be isolated and quantified through systematic comparison against models of varying complexity.

Logistic Regression, at the baseline hierarchy, models the linear decision boundary between two classes within the 1845-dimensional feature space. L2 regularization was applied to prevent overfitting, with the added benefit of stable convergence under high-dimensional input. The second baseline, Random Forest, targets non-linear relationships in the feature space through an ensemble architecture of decision trees. With 200 trees and a minimum of 5 observations per split, the configuration provides both variance reduction and natural resistance to overfitting. The third baseline, XGBoost, represents the gradient boosting paradigm in which each successive tree is built to minimize the residual error of the previous model. Configured with 300 trees, a learning rate of 0.05, and a maximum depth of 6, the model is widely regarded as the current best-practice standard for structured tabular data.

GraphSAGE generates each node's representation by sampling and transforming features from its local neighborhoods, enabling the production of generalizable embeddings for nodes not encountered during training. The architecture employed consists of two SAGEConv layers with 128 hidden dimensions and a dropout rate of 30%, trained over 200 epochs using the Adam optimizer, with a total of 505,602 learnable parameters.

Standard SHAP approximation methods for GNNs require perturbing individual features independently of the graph structure, which introduces numerical instability in dense graph settings. SHAP analysis was therefore applied to the best-performing Logistic Regression model using a Linear SHAP explainer, which derives exact Shapley values directly from the model’s coefficient matrix without approximation, providing stable explanations across the 1,845-dimensional feature space. Explanations were computed for all test projects. This analysis constitutes the methodological backbone of the study, not only producing a feature importance ranking but numerically establishing which feature group dominates model decisions.

5 Results

5.1 Model Performance on the Test Set

Table 3 reports the performance of all four models on the 452-project test set. Logistic Regression achieved the strongest overall results with 98.33% accuracy, an F1 Score of 0.9828, and an AUC-ROC of 0.9976. F1 Score provides a balanced measure of precision and recall across both classes. Precision quantifies the proportion of predicted BID projects that are

correctly classified, while recall measures what fraction of actual BID projects were successfully identified. GraphSAGE reached 87.89% accuracy and an AUC-ROC of 0.9332, but achieved the highest precision of 0.9624 across all four models, indicating that its BID recommendations are highly reliable.

Table 3. Model Performance on Test Set (n = 452)

Model	Accuracy	Precision	Recall	F1 Score	AUC-ROC
Logistic Regression	0.9833	0.9703	0.9957	0.9828	0.9976
Random Forest	0.8455	0.7932	0.9174	0.8508	0.9410
XGBoost	0.9165	0.8831	0.9522	0.9163	0.9861
GraphSAGE	0.8789	0.9624	0.7783	0.8606	0.9332

The ROC curves for all four models are presented in Figure 2. Each curve illustrates the trade-off between the true positive rate and the false positive rate. As shown in Figure 2, Logistic Regression produces the curve nearest to that corner.

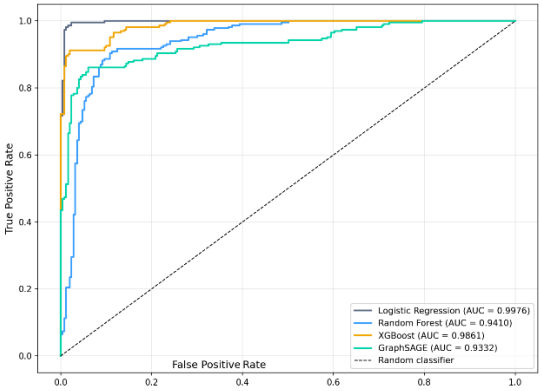


Figure 2: ROC curves for all four models.

The confusion matrices, presented in Figure 3, report the number of correct and incorrect predictions for each class. Logistic Regression produced approximately 8 total errors across the 452 test projects, with only 1 false negative and 7 false positives, confirming near-perfect recall. GraphSAGE produced approximately 55 total errors, with a high false negative count consistent with its lower recall of 0.7783, but only 7 false positives, consistent with its leading precision of 0.9624.

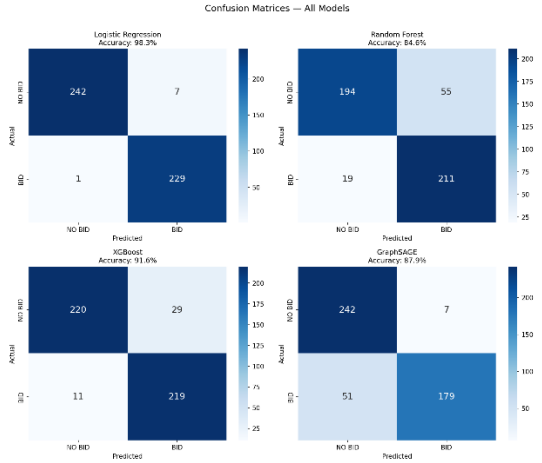


Figure 3: Confusion matrices for all four models.

Five-fold cross-validation was additionally conducted to confirm result stability. Logistic Regression achieved a mean F1 Score of 0.9858 with a standard deviation of 0.0026, confirming highly consistent performance across different data partitions. XGBoost returned a mean F1 of 0.9626 (SD = 0.0066) and Random Forest 0.9151 (SD = 0.0141).

5.2 SHAP Feature Importance Analysis

SHAP analysis applied to the best-performing Logistic Regression model showed that text embedding features derived from written project descriptions account for 72.5% of total feature importance, with topic model scores and sentiment contributing a further 2.9%. Structured features contribute 24.6%, with NLP-derived features thus dominating model decisions by a substantial margin, as illustrated in Figure 4. This result suggests that project description texts carry decision-relevant signals beyond what structured attributes alone reflect.

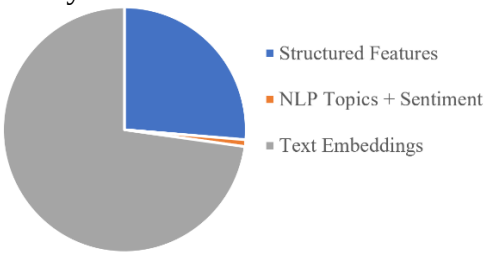


Figure 4: NLP vs. structured feature contribution (72.5% vs. 24.6%).

Among structured features, country-level and regional indicators are the strongest predictors, with Country_India and Region_Europe leading the ranking, followed by Country_China, Region_North America, and Region_Asia, suggesting that geographic exposure plays a notable role in historical bid decisions.

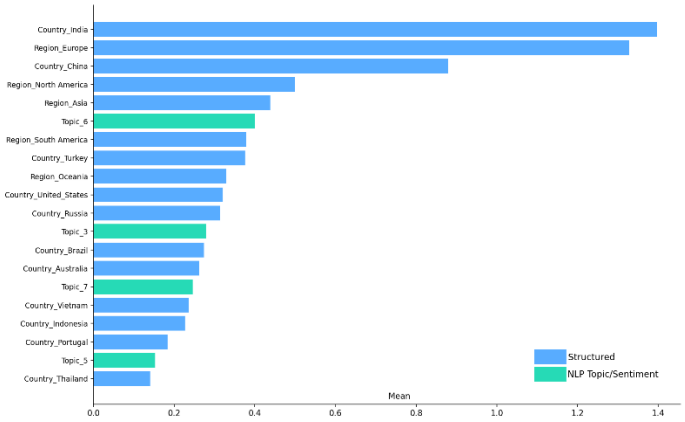


Figure 5: Top 20 features by mean (SHAP value).

Figure 5 presents the top 20 features ranked by mean absolute SHAP value. Most high-ranking features are text embedding dimensions, displayed in orange, while structured features, shown in blue, appear lower in the ranking. Although individual embedding dimensions carry small SHAP values, their collective contribution across 1536 dimensions exerts a dominant influence on model output.

6 Discussion

The variation in model performance across the four models warrants careful interpretation. Logistic Regression's leading accuracy of 98.33% suggests that the feature space, combining geographic signals with high-dimensional text embeddings, is largely linearly separable, which is broadly consistent with the structured nature of historical contractor bid decisions.

A notable result from the SHAP analysis is that text embedding features account for 72.5% of total feature importance, with structured features contributing 24.6%, suggesting that written project descriptions carry more decision-relevant signal than structured attributes alone. GraphSAGE achieves lower overall accuracy than Logistic Regression (87.89% vs. 98.33%), but records the highest precision of 0.9624 across all four models, meaning its BID recommendations are rarely incorrect. The lower recall is consistent with known characteristics of GNNs under dense graph conditions and self-loop inference at test time.

The proposed two-stage DSS translates these findings into a practical framework, generating text-based preliminary recommendations without expert scoring in Stage 1 and incorporating full evaluation in Stage 2. Figure 6 presents the DSS output for three representative projects, illustrating how each project receives an ensemble probability score and a final recommendation derived from all four models.

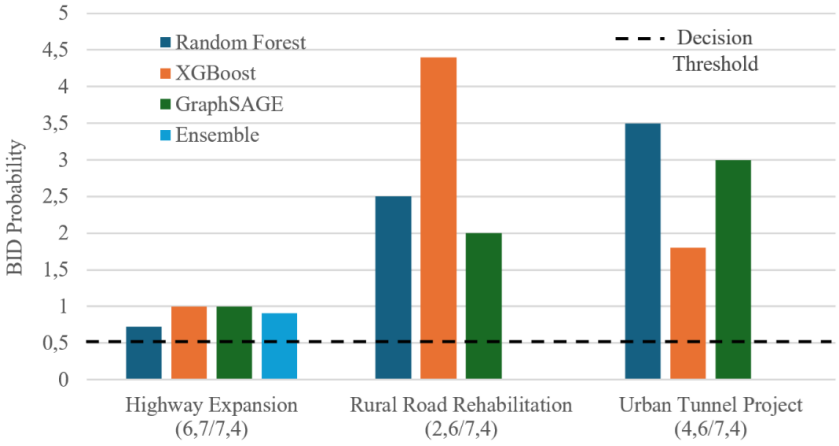


Figure 6: DSS bid recommendation dashboard for three example projects

This study is subject to several limitations. The dataset originates from a single company in one sector, which limits generalizability. The exclusion of the five expert scoring criteria, while necessary to avoid target leakage, removes signals whose independent predictive value remains untested. The self-loop inference configuration at test time additionally prevents a fully inductive evaluation of GraphSAGE's graph-learning capability

7 Conclusion

This study demonstrates that machine learning and graph-based representation learning can be effectively combined to support bid/no-bid decision-making in international infrastructure construction.

All four models produced competitive results on the test set. Logistic Regression achieved the highest overall accuracy at 98.33%, while GraphSAGE recorded the highest precision of 96.24%. SHAP analysis revealed that text embedding features account for 72.5% of total feature importance, substantially exceeding the 24.6% contribution of structured features, suggesting that project descriptions carry decision-relevant signals beyond what structured attributes alone capture. The two-stage DSS proposed in this study operationalises these findings, enabling preliminary text-based recommendations before full expert scoring is applied.

Acknowledgments

During the preparation of this study, the author used Grammarly and DeepL to assist with English language editing. All outputs were reviewed and edited by the author, who take full responsibility for the content of this publication.

References

[1] Hamilton, W., Ying, Z., & Leskovec, J. (2017). Inductive representation learning on large graphs. Advances in neural information processing systems, 30. https://doi.org/10.48550/arXiv.1706.02216

[2] Pan, Y., & Zhang, L. (2021). Roles of artificial intelligence in construction engineering and management: A critical review and future trends. Automation in Construction, 122, 103517. https://doi.org/10.1016/j.autcon.2020.103517

[3] García, J., Villavicencio, G., Altimiras, F., Crawford, B., Soto, R., Minatogawa, V., Franco, M., Martínez-Muñoz, D., & Yepes, V. (2022). Machine learning techniques applied to construction: A hybrid bibliometric analysis of advances and future directions. Automation in Construction, 142, 104532. https://doi.org/10.1016/j.autcon.2022.104532

[4] Xu, Y., Zhou, Y., Sekula, P., & Ding, L. (2021). Machine learning in construction: From shallow to deep learning. Developments in the Built Environment, 6, 100045. https://doi.org/10.1016/j.dibe.2021.100045

[5] Gondia, A., Siam, A., El-Dakhakhni, W., & Nassar, A. H. (2019). Machine learning algorithms for construction projects delay risk prediction. Journal of Construction Engineering and Management, 146(1), 04019085. https://doi.org/10.1061/(ASCE)CO.1943-7862.0001736

[6] Mahmoodzadeh, A., Nejati, H. R., & Mohammadi, M. (2022). Optimized machine learning modelling for predicting the construction cost and duration of tunnelling projects. Automation in Construction, 139, 104305. https://doi.org/10.1016/j.autcon.2022.104305

[7] Alshboul, O., Shehadeh, A., Almasabha, G., & Almuflih, A. S. (2022). Extreme gradient boosting-based machine learning approach for green building cost prediction. Sustainability, 14(11), 6651. https://doi.org/10.3390/su14116651

[8] Ayhan, M., Dikmen, I., & Birgonul, M. T. (2021). Predicting the occurrence of construction disputes using machine learning techniques. Journal of Construction Engineering and Management, 147(4), 04021022. https://doi.org/10.1061/(ASCE)CO.1943-7862.0002027

[9] Un, B., Erdis, E., Aydınlı, S., Genc, O., & Alboga, O. (2024). Forecasting the outcomes of construction contract disputes using machine learning techniques. Engineering, Construction and Architectural Management, 32(10), 6421–6444. https://doi.org/10.1108/ECAM-05-2023-0510

[10] Jacques de Sousa, L., Poças Martins, J., & Sanhudo, L. (2024). Predicting construction project compliance with machine learning model: Case study using Portuguese procurement data. Engineering, Construction and Architectural Management, 31(13), 285–302. https://doi.org/10.1108/ECAM-09-2023-0973

[11] Moon, S., Lee, G., Chi, S., & Oh, H. (2020). Automated construction specification review with named entity recognition using natural language processing. Journal of Construction Engineering and Management, 147(1), 04020147. https://doi.org/10.1061/(ASCE)CO.1943-7862.0001953

[12] Wu, C., Li, X., Jiang, R., Guo, Y., Wang, J., & Yang, Z. (2023). Graph-based deep learning model for knowledge base completion in constraint management of construction projects. Computer-Aided Civil and Infrastructure Engineering, 38(6), 702–719. https://doi.org/10.1111/mice.12904

[13] Mostofi, F., Toğan, V., Ayözen, Y. E., & Tokdemir, O. B. (2022). Construction safety risk model with construction accident network: A graph convolutional network approach. Sustainability, 14(23), 15906. https://doi.org/10.3390/su142315906

[14] Araújo, M. C. B., Alencar, L. H., & de Miranda Mota, C. M. (2022). Classification model for bid/no-bid decision in construction projects. International Transactions in Operational Research, 29(2), 1025–1047. https://doi.org/10.1111/itor.13037

Author Contribution Statement

- *Conceptualization:* Uğur Günay
- *Methodology:* Uğur Günay
- *Investigation:* Uğur Günay, Onur Behzat Tokdemir
- *Writing – Original Draft:* Uğur Günay
- *Writing – Review & Editing:* Onur Behzat Tokdemir

List of Abbreviations

- **AI** — Artificial Intelligence
- **ML** — Machine Learning
- **BD** — Business Development
- DSS — Decision Support System
- SHAP — SHapley Additive exPlanations
- NLP — Natural Language Processing

Publication Note

This paper was peer-reviewed, accepted for presentation, and included in the proceedings of the ACE2026 – International Conference on Advances in Civil Engineering, held on 12–14 October 2026 in Trabzon, Türkiye.

This paper may be cited as follows:

Uğur GÜNAY and Onur Behzat TOKDEMIR, "Modeling Bid/No-Bid Decisions in International Infrastructure Projects Using Graph Neural Networks and Natural Language Processing: A Pilot Study" in Proceedings of the ACE2026 – International Conference on Advances in Civil Engineering, Trabzon, Türkiye, 12–14 October 2026.

BIM Integrated Risk Simulation and Management for Data Center Projects

Şeyma Türkmen[1] and Gürkan Emre Gürcanlı[2]
[1] 0009 0005 8382 1385, İstanbul Technical University, Architecture Department, İstanbul, Türkiye, turkmens24@itu.edu.tr
[2] 0000 0002 0807 2020, İstanbul Technical University, Civil Engineering Department, İstanbul, Türkiye, gurcanlig@itu.edu.tr

Abstract. In a world of advancing technology and digitalization, data centers have become digital economic assets for organizations and governments. Unlike traditional buildings they feature high electrical system density, multi layered mechanical redundancy, and the need for uninterrupted operation. Furthermore, these buildings require tight interdisciplinary coordination, with virtually zero margin of error. Therefore, risk management must be an integral part of these processes. A literature review indicates limited research on the role of BIM in risk management for data center projects.
This study examines eight previously defined BIM value domains under a single BIM maturity parameter linked to four probabilistic risk modules. PERT is used for planning risk, the log normal for cost overrun, the normal PUE uncertainty, and the Poisson for design conflicts. The aim is to compare "BIM off/on" scenarios at the commonly used P80 confidence level for project risk targeting, and a browser based decision support platform has been developed that combines deterministic EVM monitoring with a 10,000 iteration Monte Carlo simulation. The results show that raising BIM maturity from a low to a high level resulted in improvements of 15.0% in schedule duration (P80), 1.3% in cost, 18.9% in PUE, and 86.8% in expected clash count. Consequently, since all results share a common maturity factor, it is argued that the benefits of BIM should be evaluated as a composite and multidimensional impact rather than a single metric. This perspective is particularly relevant to data centers due to their high coordination requirements, low error tolerance, long operational lifespans, and increasing industry demand.

Keywords: Building Information Modeling; Data Center; Monte Carlo Simulation; Project Risk Management; Earned Value Management; Digital Twin

1 Introduction

Digital infrastructure now underpins nearly every critical sector of the global economy. Data centers have consequently become nationally strategic assets, supporting AI workloads, cloud platforms, financial transaction systems, healthcare data infrastructure, telecommunications, and e commerce, while also constituting a security critical element for defense and public systems. Global data center electricity consumption is projected to reach approximately 415 TWh in 2024 and approach 945 TWh by 2030 [16]. Türkiye's position bridging Europe and Asia, together with its young, technology oriented population, points to its potential as an emerging regional hub for this growth.

Data center construction projects are fundamentally more complex than conventional buildings, with unusually demanding design and construction phases driven by their critical role. Unlike an approach that traditional project management tools struggle to support, high density electrical infrastructure, sensitive cooling systems, uninterruptible power supplies, and

layered N+1/2N redundancy require a multidisciplinary and tightly coordinated approach in both the design and implementation phases. Over the past two decades, BIM has reshaped construction practice more broadly through its documented benefits in coordination, planning, and cost control [1,2]; its role is arguably even more decisive in data center projects, where coordination failures, planning drift, and energy inefficiencies carry more severe consequences than in typical construction.

This study examines where and how BIM generates value in data center construction, arguing that this value is best assessed through the lens of risk management, a strategic necessity rather than an optional enhancement. Section 2 reviews the relevant literature; Section 3 outlines the strategic and technical profile of data center projects; Section 4 addresses the BIM value domains associated with this profile; Section 5 presents the simulation methodology; Section 6 discusses limitations; and Section 7 reports the results.

2 Literature Review

BIM is useful not only for geometric modeling but also for managing project information. Previous studies show that it can improve coordination, cost management, and clash reduction across different building types [1,2]. Industry organizations have also reported the operational costs of design failures under the Uptime Institute's Tier framework. However, research focused specifically on data centers is still limited [17].

A parallel literature links BIM to digital twin development, treating BIM models as the structural basis from which real time facility twins can be derived, and extending this to BIM IoT integration for asset tracking [8,9] and the conceptual transition from static models to construction phase digital twins. A third approach applies Monte Carlo simulation to construction risk, including integrated BIM Monte Carlo planning frameworks [5], Monte Carlo based planning risk simulation in a BIM environment [6], structured reviews of BIM related project risk [3], and prioritization of AHP based BIM risk factors [4]. However, none of these studies combine planning, cost, energy, and collision frequency risk into a single BIM maturity as a focused probabilistic framework calibrated to the technical profile of data center projects. This study addresses this gap.

A recurring limitation in the literature in this area is the lack of BIM skills, particularly due to the limited availability of device specific BIM object libraries and the slow adaptation of manufacturers. This leads to unfavorable outcomes for data centers, considering the dependencies on specialized mechanical and electrical devices. This study aims to create an integrated framework specific to data centers by leveraging the literature in BIM, digital twin, and Monte Carlo risk modeling.

3 Data Center Projects: Strategic and Technical Profile

The growing importance of digital infrastructure has made data centers critical assets with major economic and national security implications, rather than simply technology investments. The rapid growth of AI and machine learning has increased demand for GPU clusters, high-density racks, and advanced cooling systems. At the same time, cloud computing, digital healthcare, and financial technologies have increased the need for reliable, low-latency data processing and storage.Türkiye's geographical position between Europe, the Middle East, and Asia, combined with its expanding digital economy, gives it strong potential to develop as a regional data center hub making operational continuity, data sovereignty, and cybersecurity increasingly significant at the national level.

Data centers are more technically complex than typical construction projects. Their electrical systems include medium voltage distribution, transformers, UPS units, power distribution units, and extensive cable management. Mechanical systems also require close coordination. CRAC/CRAH units, chillers, cooling towers, and airflow systems must meet PUE requirements to support energy efficiency and long term sustainability [12,20]. These systems need careful

coordination, especially in high-density areas. N+1 and 2N redundancy configurations also affect design decisions and project costs from the early stages.

Data centers differ from traditional buildings in terms of the need for continuous operation, high system availability, minimal error tolerance, and strict timelines. Commissioning, in particular, is one of the most critical project phases. The goal is to ensure that the facility operates safely, reliably, and in accordance with specified performance requirements. The process involves systematically testing and validating critical systems and their integrated performance prior to handover. Given the complexity and operational importance of these systems, commissioning represents a particularly challenging and unique phase of data center construction.

4 BIM Concept and Value Areas in Data Center Projects

Building Information Modeling (BIM) is a structured digital modeling approach in which a construction project's geometric data are integrated with associated information on materials, costs, scheduling, and operational processes. The conventional dimensional classification of this approach extends from 3D geometric representation, through 4D scheduling and 5D cost analysis, to 6D sustainability assessment and 7D facility/operations management [12] BIM supports the project throughout its lifecycle by allowing architectural, structural, and mechanical, electrical, and plumbing (MEP) teams to work within the same digital environment instead of relying on separate discipline specific documents.

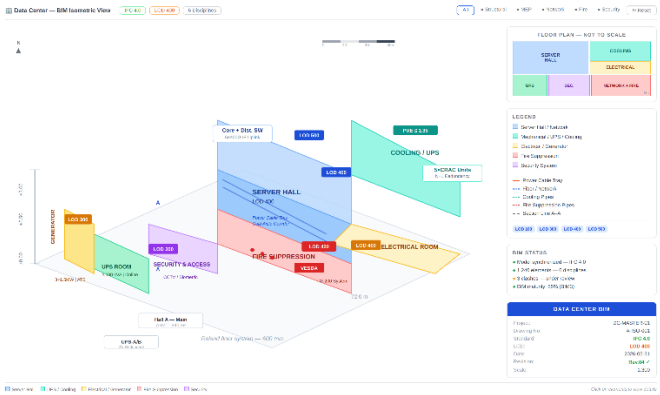


Fig. 1. The integration of architectural, MEP etc. disciplines into a single federated model (LOD 400, IFC 4.0) in an isometric BIM coordinating perspective of a data center facility.

This capability translates into eight interlocking value areas in data center projects especially, which are outlined below.

4.1 Interdisciplinary Coordination and Clash Detection

Data centers have inherently limited space, and cable trays, cooling pipes, sprinkler systems, and structural elements often overlap. Physical conflicts, unnoticed until construction begins, can bring work to a complete standstill. BIM's conflict detection feature solves this problem by revealing these conflicts long before installation, during the design phase. This reduces conflicts by up to 40% [2] and greatly limits rework, material waste, and on site design revisions.

4.2 4D Scheduling and Program Control

Linking the project schedule to the BIM model produces a 4D simulation that renders the timeline visible and manageable, enabling more precise planning of critical equipment deliveries, specialized infrastructure works, and phased commissioning. Overlapping activities can be identified in advance, and resources can be planned more effectively. In addition, stakeholders are ensured to work from the same plan. As a result, the timeline becomes more than just a record; it transforms into an active management tool.

4.3 5D Cost Control and Take off Accuracy

Using the BIM model for quantity take offs and cost estimates can speed up procurement and improve accuracy. When the model is updated, quantities such as cable lengths, piping runs, and the number of equipment units are also updated, reducing the risk of incorrect orders and keeping the project budget under control.

4.4 Equipment Layout Optimization

Heavy equipment such as UPS systems, generators, CRAC/CRAH units, transformers, and server racks should be positioned to allow efficient operation and easy maintenance access. The BIM model tests multiple 3D layout scenarios to identify the optimal configuration, while integrated airflow simulation reveals how hot aisle/cold aisle arrangements affect energy consumption before construction begins.

4.5 Commissioning Readiness

Commissioning is arguably the most demanding phase of data center delivery. Because the BIM model consolidates every system component, connection, and operating parameter into a single dataset, it provides a direct foundation for comprehensive, accurate commissioning plans, test procedures, and checklists allowing missing or faulty installations to be caught early.

4.6 Facility Management Handover and Digital Twin Enablement

Traditionally filing the documents on paper like equipment specifications, material data, maintenance schedules, and warranty records can easily lost. This is a risk of missing data. BIM allows this information to be transferred directly to CMMS/CAFM systems. When the model is linked to live sensor data, the model can also be developed into a digital twin for real time energy monitoring, predictive maintenance, and capacity planning [8,9,19].

4.7 Energy Efficiency and Sustainability

Energy analysis with a BIM model during the design phase enables evaluation of cooling strategies. It also supports PUE improvements by assessing natural ventilation and heat gains through the building facade. In addition, BIM assists in material selection and documentation for LEED and BREEAM certifications, which are becoming increasingly important for owners and investors [13, 14, 15].

4.8 Project Risk Management

Project information with a large scale BIM model allows teams to identify and assess the risks in the design review. Visual simulations allow teams to discuss potential problems before construction begins. This is particularly important given the long lead times and complex supply chains of critical data center equipment. Adoption of BIM has been shown to reduce Information Requests (RFI) by 30–50% [2,18]. This is a significant efficiency gain at the data center scale.

5 Methodology

5.1 Simulation Platform

An HTML/JavaScript based decision support platform was developed to translate the eight BIM value domains identified in Section 4 into a quantitative risk assessment framework. The platform integrates deterministic tracking based on physical progress, Earned Value Management indices (Equations 1–3), PUE, and 5D cost analysis with four independent Monte Carlo modules covering duration (PERT), cost (lognormal), energy (normal), and clash count (Poisson). Each module was run for 10,000 iterations to derive the P10, P50, P80, and P95 percentiles. A single BIM maturity variable (μ_BIM) drives all four modules through the impact ratios defined in Equations (6)– (7), enabling comparison between "BIM off" and "BIM on" scenarios.

$$CPI = BCWP / ACWP,\ SPI = BCWP / BCWS\ (1),\ (2)$$
$$EAC = BAC / CPI\ (3)$$

5.2 Risk Modules

Duration risk was modeled using a PERT distribution to represent the characteristic right skewness of construction activity durations (Equation 4). Three point duration estimates for five construction phases are presented in Table 1. MEP installation, which carries the widest uncertainty range, was found to contribute most to schedule risk in the sensitivity analysis. The BIM effect is applied multiplicatively to each simulation sample (Equation 5):

$$\mu = (a + 4m + b) / 6\ (4) \qquad T_{on} = T_{off} \times (1 - \rho_duration \times r)\ (5)$$

Cost risk was modeled using a lognormal distribution, consistent with its strictly positive and right skewed structure. The BIM effect is applied to the distribution parameters prior to sampling, reducing both the expected cost overrun and the spread of the distribution. PUE risk was modeled using a normal distribution, consistent with the Central Limit Theorem under the assumption of independent contributing factors [20]. BIM lowers the mean PUE value while narrowing the standard deviation by a factor of 0.7. Clash risk was modeled using a Poisson distribution, appropriate for representing independent and comparatively rare coordination conflicts within a fixed project scope.

The effect of BIM maturity on duration and cost is defined by Equations (6)–(7); the same ρ_duration and ρ_cost ratios are applied proportionally, as a function of μ_BIM, to the target PUE mean and to the Poisson λ_on parameter: the BIM on PUE mean is shifted from the BIM off baseline toward the target value by this ratio, while λ_on is obtained as λ_on = λ_off × (1 − ρ_clash), where ρ_clash follows the same functional form as ρ_duration but is scaled with coefficients specific to clash reduction. This approach ensures that all four risk modules are governed consistently by a single maturity score.

$$\rho_duration = 0.05 + 0.0015 \times \mu_BIM\ (6) \qquad \rho_cost = 0.04 + 0.0012 \times \mu_BIM\ (7)$$

At 85% BIM maturity, these equations yield an approximate 18% duration impact and a 14% cost impact.

Table 1. Three point PERT duration estimates by construction phase (weeks)

Phase	Optimistic	Most Likely	Pessimistic
Foundation works	6	8	12
Structural steel	7	9	14
MEP installation	10	14	22
Equipment installation	6	8	13
Testing & commissioning	5	8	14

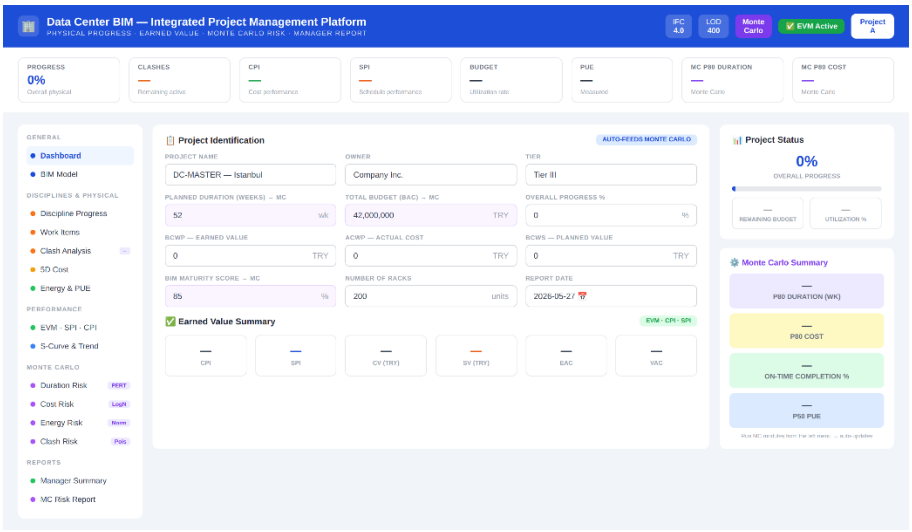


Fig. 2. Main dashboard of the integrated simulation platform, showing project definition fields, the BIM maturity input ("BIM Maturity Score"), Earned Value summary cards, and the Monte Carlo summary panel.

Table 2. Monte Carlo module specifications and BIM maturity linkage

Module	Distribution	Parameters	BIM Effect
Duration	PERT	5 phases (Table 1)	Equations 5–6
Cost	Lognormal	Mean overrun 10%; σ = 8% of BAC	μ, σ reduction via Equation 7
PUE	Normal	Off: μ=1.65, σ=0.12; On: μ=1.35	0.7σ reduction + mean shift
Clash count	Poisson	λ_off=47; λ_on=5; unit rework cost 75,000 TRY	λ reduction with maturity

5.3 Percentile Based Risk Assessment

For each module, P10, P50, P80, and P95 percentiles were obtained after 10,000 iterations. P80 was selected as the primary comparison metric, offering a balanced approach between the limited operational confidence provided by P50 and the excessive contingency cost implied by P95. A supplementary tornado sensitivity analysis, based on 2,000 independent samples per phase, identified MEP coordination as the most effective intervention area for reducing schedule risk.

6 Results and Discussion

Table 3 reports the P80 outcomes for all four modules under the BIM off and BIM on scenarios at 85% BIM maturity.

Table 3. Monte Carlo simulation results: P80 values and the effect of BIM integration.

Risk Factor	Distribution	BIM off (P80)	BIM on (P80)	Improvement	Improvement (%)	Unit
Duration	PERT	52.47	44.59	7.88	15.03	weeks
Cost	Lognormal	48.96	48.32	0.64	1.30	million TRY
Energy (PUE)	Normal	1.75	1.42	0.33	18.90	PUE
Clashes	Poisson	53	7	46	86.79	clash count

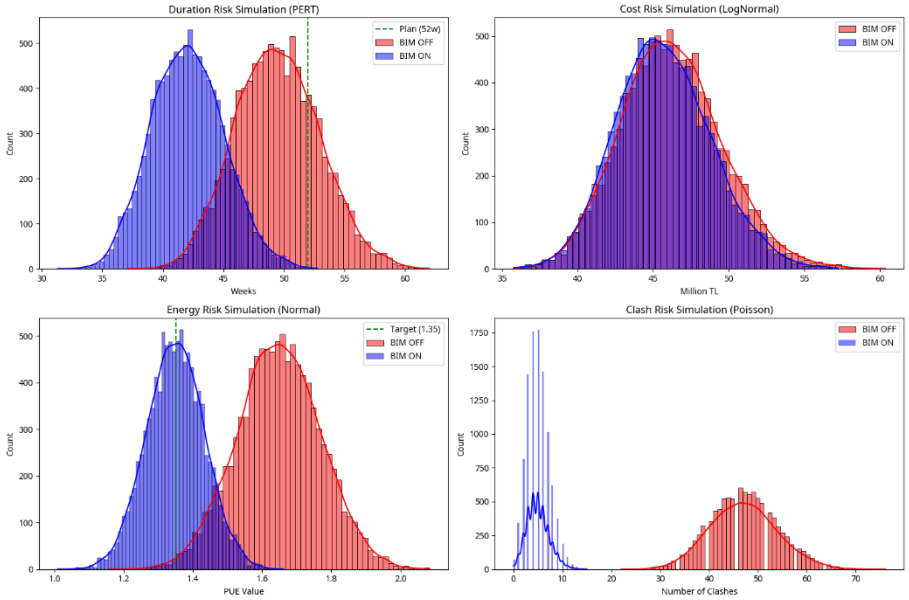


Fig. 3. Monte Carlo simulation results (10,000 iterations) for the BIM off and BIM on scenarios: (a) project duration (PERT), (b) total project cost (lognormal), (c) Power Usage Effectiveness (normal), and (d) number of design clashes (Poisson).

6.1 Duration Risk

The simulation results indicate that improving the schedule is one of the biggest advantages of using BIM. Without BIM, the P80 project duration is 52.47 weeks. With BIM, this decreases to 44.59 weeks. This means the project is completed 15.0% faster. This result is consistent with previous studies showing that BIM can reduce uncertainty on the critical path by improving MEP coordination and delivery planning [5,6]. A sensitivity analysis shows that MEP installation, with an estimated duration of 10–22 weeks, is the most significant source of planning uncertainty (Table 1). Therefore, BIM-based MEP coordination provides a significant advantage in reducing planning risk.

6.2 Cost Risk

BIM reduces the P80 cost by 1.3%, from TRY 48.96 million to TRY 48.32 million. Considering the right skewed lognormal cost distribution, this result shows that BIM primarily reduces the risk of excessive cost overruns rather than significantly reducing the average cost [2]. This finding is also consistent with the advantages of 5D quantity surveying discussed in Chapter 4.3, where BIM enables the prevention of quantity errors and rework.

6.3 Energy Risk (PUE)

Under BIM integration, the P80 PUE value improves from 1.75 to 1.42 an 18.9% gain accompanied by a tighter distribution overall. This narrowing points to reduced operational variability, suggesting that BIM supported equipment layout, airflow modeling, and cooling optimization (Sections 4.4, 4.7) improve not just average energy performance but its consistency across seasonal and load conditions [20]. Because PUE compounds across a multi decade operational life, even this improvement translates into substantial cumulative savings.

6.4 Clash Risk

Coordination conflicts reveal the greatest impact of BIM by far. The P80 number drops from 53 to 7; this is an 86.8% reduction and exceeds the single stage figures of up to 40% often cited in the literature [2]. This difference stems from the scope difference. The simulation reflects the cumulative effect of BIM across MEP, structural and architectural disciplines rather than a

single coordination phase. Since each conflict leads to rework, delay and safety risk, the near complete elimination of high conflict results in P80 directly increases site efficiency [7]. Given that unresolved conflicts are the main cause of delays in the MEP phase, this explains a large part of the time improvement reported in 6.1.

6.5 Synthesis: The Cumulative Value of BIM Integration

The four P80 results in Table 3 vary considerably, from 1.3% for cost to 86.8% for clashes. However, these improvements are not independent. All four modules are driven by the same BIM maturity parameter (Section 5.2). As BIM maturity increases, cost uncertainty decreases, project duration becomes shorter, PUE uncertainty is reduced, and fewer clashes are expected. Therefore, BIM benefits should be considered together across schedule, cost, energy, and coordination rather than through a single metric [3,4].

The construction profile of data centers as described in Section 3 is coordination intensive, has low error tolerance and long operating lifespans. These results illustrate the value of BIM driven risk mitigation. Any building project would be interested in a 15% reduction of P80 duration or 87% reduction of expected clashes. But in data centers, delays can impact hyperscale tenant revenue, while conflicts identified during commissioning can threaten Tier certification. So the effect of these improvements may be greater than the percentages imply.

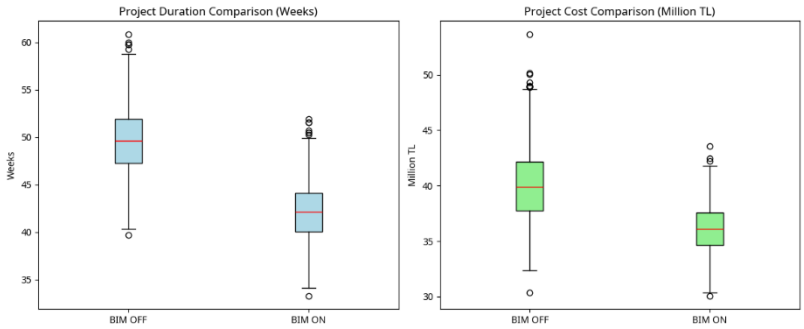


Fig. 4. Box plot comparison of (a) project duration and (b) total project cost between BIM off and BIM on scenarios.

There are two industry constraints that affect the interpretation of these findings. First, BIM object libraries are limited for specific equipment and manufacturers' slow adaptation process continue to limit modeling accuracy [10,11]. This limitation is more important for data centers because they rely on specialized MEP equipment, and it is also evident in the simulation itself. At low BIM maturity, all four percentile ranges become wider and the BIM on and BIM off scenarios move closer together. This shows that maturity affects the overall risk profile rather than simply indicating model quality [3,4]. Further improvements are also possible. AI based clash detection can reduce the λ_on value better than manual coordination [7]. Broader IoT adoption could increase digital twin applications [8,9]. As BIM standards keep evolving, this approach presented here may be more generally applied.

7 Limitations and Conclusion

Several limitations should be considered when interpreting the results. The input values used in the platform were derived from conceptual estimates informed by the literature rather than from a single audited case study. Therefore, the reported percentages (e.g., 15.0% improvement in duration) should be interpreted as indicators of the direction and relative magnitude of BIM's impact rather than definitive benchmarks.

The connections between BIM maturity and its effects in Equations (6) and (7) were determined using intuitive calibration instead of statistical analysis. Although the four Monte Carlo

modules are considered independent, interactions may occur in real situations. For example an open issue may lead to schedule delay as well as additional costs. This implies that the model may not be capturing risks that influence both sectors at once. The study has not been compared to a completed project or validated by professionals. The results therefore mainly illustrate the promise of the suggested method as a decision support tool, while still requiring further refinement and validation.

This study investigated the multidimensional value of BIM in data center construction through a conceptual, simulation based framework covering eight value areas. The developed platform integrates deterministic EVM tracking with four BIM maturity driven Monte Carlo risk modules. Increasing BIM maturity from low to high results in P80 improvements of 15.0% in duration, 1.3% in cost, 18.9% in PUE, and 86.8% in expected clash count. Since these four indicators are driven by a common maturity variable, their benefits should be evaluated cumulatively rather than independently. Considering the intensive coordination requirements, low error tolerance, and long operational lifespan that distinguish data centers from conventional buildings, the practical value of BIM investment extends beyond the reported percentages. This supports positioning BIM not as an optional enhancement but as a strategic necessity for reliable and competitive data center delivery.

Future research should focus on empirically calibrating the framework using real projects with varying scales, geographical contexts, and BIM maturity levels; modeling correlations among the four risk modules to capture joint tail risk; further integrating BIM models with commissioning processes; and extending this integration toward digital twin validation. In addition, industry specific investigation of equipment manufacturers' adoption of BIM compatible object libraries could directly address a structural constraint identified in the literature [10,11].

8 References

[1] Eastman C, Teicholz P, Sacks R, Liston K (2011) BIM Handbook: A Guide to Building Information Modeling for Owners, Managers, Designers, Engineers and Contractors, 2nd edn. John Wiley & Sons, Hoboken, NJ.

[2] Azhar S (2011) Building information modeling (BIM): trends, benefits, risks, and challenges for the AEC industry. Leadersh Manag Eng 11(3):241–252. https://doi.org/10.1061/(ASCE)LM.1943 5630.0000127

[3] Numan M (2024) BIM and risk management: a review of strategies for identifying, analysing and mitigating project risks. J Eng Res Sci 3(1):20–26. DOI:10.55708/js0301004

[4] Aladayleh KJ, Aladaileh MJ (2024) Applying analytical hierarchy process (AHP) to BIM based risk management for optimal performance in construction projects. Buildings 14(11):3632. https://doi.org/10.3390/buildings14113632

[5] Sharma R, Iyer KC, Gandhi P (2025) Risk integrated scheduling for commercial building construction: a BIM and Monte Carlo simulation approach. Asian J Civ Eng.

[6] Kadume NH, Naji HI (2021) Building schedule risks simulation by using BIM with Monte Carlo technique. IOP Conf Ser Earth Environ Sci 856:012059. DOI:10.1088/1755 1315/856/1/012059

[7] Lopes J, Ferreira B, Neves J, Cachadinha N (2025) Automating clash relevance filtering in BIM based multidisciplinary coordination using machine learning. Autom Constr.

[8] Quaquero E, Rubiu G, Gatto G, Perra C (2021) BIM and IoT sensors integration: a framework for consumption and indoor conditions data monitoring of existing buildings. Sustainability 13(8):4496. https://doi.org/10.3390/su13084496

[9] Biagini C, Donato V, Orlando M, Ferretti F (2024) From BIM to digital twin: IoT data integration in asset management platform. J Inf Technol Constr 29:1104–1125.

[10] Ghaffarianhoseini A, Tookey J, Ghaffarianhoseini A, Naismith N, Azhar S, Efimova O, Raahemifar K (2017) Building information modelling (BIM) uptake: clear benefits, understanding its implementation, risks and challenges. Renew Sustain Energy Rev 75:1046–1053. DOI: 10.1016/j.rser.2016.11.083
[11] Papadonikolaki E, van Oel C, Kagioglou M (2019) Organising and managing boundaries: a structurational view of collaboration with BIM. Int J Proj Manag 37(3):378–394. DOI:10.1016/j.ijproman.2019.01.010
[12] Succar B (2009) Building information modelling framework: a research and delivery foundation for industry stakeholders. Autom Constr 18(3):357–375. 10.1016/j.autcon.2008.10.003
[13] Kivits R, Duke C (2012) BIM: enabling sustainability and asset management through knowledge management. Sci World J 2012:1–14.
[14] Vanlande R, Nicolle C, Cruz C (2008) IFC and buildings lifecycle management. Autom Constr 18(1):70–78. 10.1016/j.autcon.2008.05.001
[15] Wong JKW, Zhou J (2015) Enhancing environmental sustainability over building life cycles through green BIM: a review. Autom Constr 57:156–165. 10.1016/j.autcon.2015.06.003
[16] International Energy Agency (2025) Electricity 2025: Analysis and Forecast to 2027. IEA, Paris.
[17] Uptime Institute (2024) Global Data Center Survey Results 2024. Uptime Institute Intelligence, New York.
[18] Muhamad Halil F, Sipan I, Mohamad Salleh N, Shafie M, Awang H (2024) Contractor selection risk in building construction through BIM and Monte Carlo simulation. J Constr Dev Ctries 29(1):211–235.
[19] Kabir G, Teng SY, Rangasamy T, Hossain MS (2024) IoT enabled digital twin framework for energy optimization in smart buildings. Energy Build 310:114098. DOI:10.1109/ACTEA58025.2023.10194071
[20] Zhang L, Liu Q, Meng X, Cai M (2021) Data center cooling strategies and their impact on power usage effectiveness (PUE): a comprehensive review. Energy Convers Manag 241:114298. DOI:10.9734/jenrr/2025/v17i7438

Note: Following the conference, this Publication Note will be added to each paper; therefore, authors are kindly requested not to remove the note below and to complete the author(s) and paper title information.

Publication Note

This paper was peer reviewed, accepted for presentation, and included in the proceedings of the ACE2026 – International Conference on Advances in Civil Engineering, held on 12–14 October 2026 in Trabzon, Türkiye.

This paper may be cited as follows:

Türkmen, Ş., and Gürcanlı, G. E., "BIM Integrated Risk Simulation and Management for Data Center Projects," in Proceedings of the ACE2026 – International Conference on Advances in Civil Engineering, Trabzon, Türkiye, 12–14 October 2026.

Development of an Automation-Based Smart Curing Cover for Optimizing the Concrete Curing Process

İpek Naz Semercioğlu Akbulut[1], Seyedehdorsa Akhtarian[2], Aleyna Özdemir[3], Bartuğhan Uzun[4], Yunus Emrahan Akbulut[5], Hasan Basri Başağa[6,7,8*]

[1] 0000-0001-5927-8785, Karadeniz Technical University, Civil Engineering Department, Trabzon, Türkiye, ipeknaz@ktu.edu.tr

[2] Karadeniz Technical University, Civil Engineering Department, Trabzon, Türkiye, akhtariand@gmail.com

[3] Karadeniz Technical University, Civil Engineering Department, Trabzon, Türkiye, aleynazdmrr@gmail.com

[4] Karadeniz Technical University, Computer Science Department, Trabzon, Türkiye, bartughan@gmail.com

[5] 0000-0001-5704-4432, Karadeniz Technical University, Civil Engineering Department, Trabzon, Türkiye, emrahan@ktu.edu.tr

[6] 0000-0002-6964-3309, Karadeniz Technical University, Civil Engineering Department, Trabzon, Türkiye, hasanbb@ktu.edu.tr

[7] 0000-0002-6964-3309, Karadeniz Technical University, Earthquake and Structural Health Application and Research Center, Trabzon, Türkiye, hasanbb@ktu.edu.tr

[8] 0000-0002-6964-3309, Northsign Design Software Construction Trade Ltd. Co., Trabzon, Türkiye, hasanbb@ktu.edu.tr

Abstract. An automation-based smart curing cover was developed in this study to reduce water use and automate the concrete curing process through controlled water release based on relative humidity data. The system integrated an automatic control infrastructure consisting of a DHT11 temperature and humidity sensor, an Arduino Uno microcontroller, a relay module, and a solenoid valve with a physical cover comprising hydrophobic upper and hydrophilic lower layers. Water was automatically released when the relative humidity beneath the cover fell below 95%. The performance of the developed system was evaluated against water-spraying curing and wet-burlap curing in terms of water consumption and 7- and 28-day compressive strength. The smart curing cover reduced water consumption by approximately 53.6-57.1% compared with the conventional methods. The mean equivalent standard cylinder compressive strengths obtained with the smart curing cover were 31.73 MPa at 7 days and 40.45 MPa at 28 days, demonstrating compressive strength performance comparable to that of the conventional curing methods. The findings indicate that the developed system can reduce water consumption while maintaining concrete strength development and eliminating the need for periodic human intervention in the watering process, thereby providing an automated and water-efficient alternative for concrete curing.

Keywords: Concrete curing; Smart Curing Cover; Automated curing; Moisture control.

1 Introduction

Concrete curing is intended to maintain the moisture required for hydration by limiting water loss from the concrete or providing an external water supply [1]. Appropriate moisture and temperature conditions, particularly at early ages, are required for cement hydration to continue and for concrete to develop the desired mechanical and durability-related properties. Excessive moisture loss from the concrete surface may hinder cement hydration and contribute to shrinkage, cracking, and inadequate strength development. Maintaining adequate moisture conditions during the early stages of concrete hardening is therefore a fundamental requirement for effective curing [1].

Water spraying and wet coverings are among the conventional curing methods widely used to maintain moisture at the concrete surface [1, 2]. However, the effectiveness of these methods depends on the continuity and frequency of water application, as well as on the amount of water supplied and the timing of application [2, 3]. In conventional manual curing practices, water application may not be directly controlled according to the actual moisture condition of the concrete, which can result in either excessive or insufficient watering [3]. Excessive application may lead to unnecessary water consumption, whereas insufficient or discontinuous application may compromise the continuity of surface moisture; moreover, reliance on repeated human intervention increases labor requirements [2, 3].

To overcome these limitations, automated concrete curing systems employing sensors, microcontrollers, and Internet of Things (IoT) technologies have been developed. Taffese and Nigussie [3] proposed a conceptual IoT-based automated curing system in which temperature and relative humidity within the concrete are monitored in real time and a smart valve and sprinkler system are controlled according to a predefined moisture threshold. Yang et al. [4] developed an automated curing system in which spraying intervals are determined through a programmable logic controller (PLC) by considering hydration-related behavior together with real-time temperature and relative humidity data, while curing water is applied through fog spraying. Lo et al. [5] developed an IoT-based system that monitors variables including air temperature, relative humidity, wind speed, concrete temperature, and concrete moisture content to evaluate environmentally induced water loss and applies water to the concrete surface through a microcontroller-controlled pump when required. Reddy and Hamsalekha [6] developed a microcontroller-based curing system in which the moisture detected within the concrete is compared with a predefined threshold to automatically switch a water pump on and off. More recently, Feng et al. [7] developed a robotic system in which plastic-film placement and water spraying are performed by separate modules, while computer vision is used to classify the curing condition of the concrete surface and automatically determine whether spraying is required. Ascona García et al. [8] integrated temperature and humidity sensors embedded in concrete elements with an Arduino-based control system to perform automated irrigation cycles, reporting a 20% reduction in water consumption compared with conventional curing. Nevertheless, the active water-application components of these studies predominantly rely on spraying, fogging or sprinkler mechanisms. Consequently, limited attention has been given to curing approaches that integrate sensor-controlled water release, retention of the released water at the concrete surface, and its distribution across the surface within a physical cover.

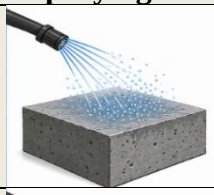
In this study, an automation-based smart curing cover was developed to provide controlled water release in response to the relative humidity adjacent to the concrete surface. The developed system integrates a hydrophobic upper layer designed to limit moisture loss and a hydrophilic lower layer that distributes the supplied water across the concrete surface through capillary action with a sensor-controlled automatic water-release mechanism. Its curing performance was comparatively evaluated against conventional water-spraying and wet-burlap curing methods in terms of water consumption and 7- and 28-day compressive strength.

2 Methodology

To evaluate the developed smart curing cover system experimentally, the study comprised three curing methods (water-spraying curing, wet-burlap curing, and curing with the smart curing cover) and two test ages (7 and 28 days), using a total of six concrete specimens. Accordingly, the overall experimental arrangement is presented in Table 1. The experimental study began with the development of the technical infrastructure of the smart curing cover, which was subsequently integrated with a physical cover system designed to retain water on the concrete surface and promote its uniform distribution. In addition, a main reservoir was connected to the

smart curing cover via a hose to store and deliver the water required by the system in a controlled manner. Concrete specimens were then produced and subjected to the three mentioned curing methods. Throughout the curing period, the amount of water consumed was recorded. To evaluate the 7-day early-age and 28-day compressive strength development of the concrete, core specimens were extracted from the relevant specimens and subjected to uniaxial compression tests. The methodological details of the study, including the technical infrastructure and physical design of the smart curing cover, specimen production, curing processes and compressive strength testing, are presented in the following subsections.

Table 1. Experimental groups and curing methods considered in the study.

		Conventional wet-curing methods		**Developed curing method**
		Water-spraying curing	**Wet-burlap curing**	**Smart curing cover**
Compressive strength groups	**7-day**			
	28-day			

2.1 Technical Infrastructure of the Smart Curing Cover

The technical infrastructure of the smart curing cover was developed based on sensing the relative humidity in the environment adjacent to the concrete surface, evaluating the acquired data using a microcontroller, and automatically controlling water flow in response to the predefined humidity condition. For this purpose, the system was configured as an integrated control circuit comprising a sensing unit (DHT11 temperature and humidity sensor), a data-processing control unit (Arduino Uno microcontroller), a switching element for regulating water flow (relay module), a solenoid valve controlling water passage, a 12 V power supply, a breadboard, and jumper wires providing the electrical connections between the components. The main technical components of the system and the circuit connections between them are illustrated in Fig. 1.

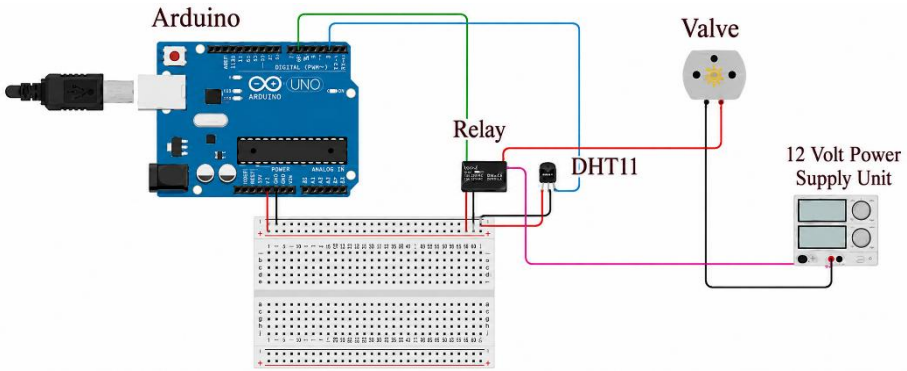


Fig. 1. Wiring diagram of the technical infrastructure of the smart curing cover

As shown in Fig. 1, the Arduino Uno microcontroller serves as the central control unit of the system. Temperature and relative humidity in the region adjacent to the concrete surface were measured using the DHT11 sensor and transmitted digitally to the Arduino. Although the sensor

simultaneously measured both temperature and relative humidity, relative humidity was selected as the primary control variable governing automatic water release. The relative humidity threshold used in the decision mechanism was set at 95%, taking into account the minimum relative humidity condition specified in TS EN 12390-2 [9] for curing concrete specimens. Accordingly, the control algorithm continuously evaluated the relative humidity measured by the sensor and compared it with this threshold. When the measured relative humidity fell below 95%, the Arduino activated the relay module, thereby opening the solenoid valve powered by the 12 V power supply and allowing water to flow from the reservoir to the smart curing cover. When the relative humidity reached or exceeded 95%, the relay was deactivated, causing the solenoid valve to close and the water flow to cease. Through this configuration, the system functioned as a closed-loop automatic control mechanism operating through a measurement–evaluation–decision–actuation cycle. Accordingly, the developed technical infrastructure enabled water application, which in conventional curing methods depends on periodic manual intervention, to be automatically controlled on the basis of sensor data. In addition, a Python-based data-logging system was developed to enable the temperature, relative humidity and relay-status data obtained through the Arduino to be monitored and stored on a computer. The data were recorded together with date and time information, allowing the operating behavior of the system to be monitored throughout the curing period.

2.2 Physical Design of the Smart Curing Cover

Following the development of the technical infrastructure of the smart curing cover, the system components were integrated with a physical cover system designed to retain moisture at the concrete surface and distribute the released water over the surface. Accordingly, the smart curing cover was designed to consist of two main layers with hydrophobic and hydrophilic properties from the outer to the inner surface. The side view and layered structure of the smart curing cover are shown in Fig. 2. As shown in the figure, a vinyl/PVC-based hydrophobic covering material was used as the upper layer to limit the uncontrolled transfer of water to the external environment and contribute to moisture retention beneath the cover. The lower layer, which was in contact with the concrete surface, consisted of a hydrophilic capillary irrigation mat with a high water-absorption capacity and the ability to distribute water across the entire surface through capillary action. Owing to these properties, the water supplied from the center of the cover was absorbed by the hydrophilic layer rather than remaining confined to the inlet region and was distributed toward the edges and corners of the cover.

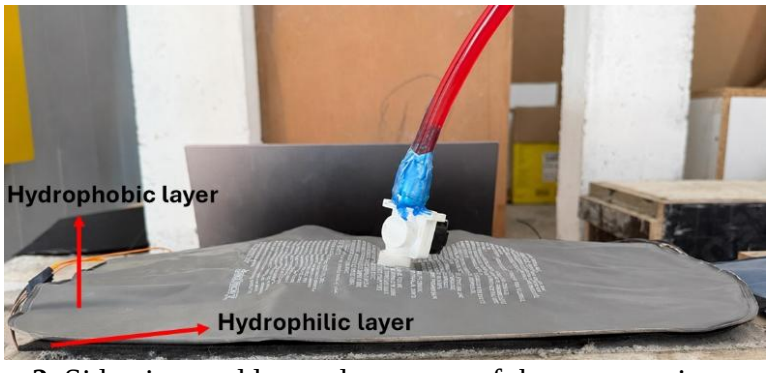


Fig. 2. Side view and layered structure of the smart curing cover

The solenoid valve responsible for water release was positioned at the center of the hydrophobic upper layer, allowing the water supplied from the main reservoir to be transferred directly to the hydrophilic lower layer. The central position of the valve was selected to enable water supplied from a single point to be distributed across the cover by utilizing the absorption and capillary-spreading properties of the hydrophilic layer. The central placement of the solenoid

valve on the cover is shown in Fig. 3a. Meanwhile, the DHT11 temperature and humidity sensor was placed within the hydrophilic layer using a specially designed protective housing to enable measurements beneath the cover while protecting the sensor from direct contact with water. The sensor was positioned in the lateral region opposite to the water-discharge direction of the solenoid valve. This arrangement was intended to prevent the water released when the valve was opened from directly contacting and wetting the sensor, thereby avoiding any misleading effect of direct wetting on the measurements. The physical placement of the sensor within the hydrophilic layer is shown in Fig. 3b.



(a) Top view (b) Bottom view

Fig. 3. Physical arrangement of the water-release and sensing components of the curing cover

A main reservoir positioned outside the cover was incorporated into the system to supply the water required by the smart curing cover. The main reservoir was connected to the solenoid valve through a hose, enabling water to be conveyed from the reservoir to the cover system. In addition, the reservoir was graduated to determine the total amount of water consumed by the smart curing cover during the curing process. The connection between the smart curing cover and the main reservoir and the graduated configuration of the reservoir are shown in Fig. 4a and Fig. 4b, respectively. Through these arrangements, the hydrophobic upper layer, hydrophilic lower layer, solenoid valve, DHT11 sensor and its protective housing, main reservoir, and hose connection were integrated into a single curing system.



a) Connection between the cover and reservoir b) Graduation of the reservoir

Fig. 4. Details of the main reservoir supplying the smart curing cover

2.3 Specimen Production

A total of six concrete specimens were produced in accordance with the experimental arrangement presented in Table 1. All specimens were prepared with dimensions of 26×42×12 cm, and the same dimensions were used for all experimental groups to limit the influence of specimen geometry on the experimental results. C30/37 ready-mixed concrete was used for specimen production; thus, variability arising from the concrete mixture was reduced to enable a more reliable comparison of the effects of the different curing methods on strength development. Following completion of the production process and the initial setting of the specimens, the curing procedures specified in the experimental plan were initiated.

2.4 Curing Processes

Following the initial setting of the specimens, three curing methods -water-spraying curing, wet-burlap curing, and curing with the smart curing cover- were applied simultaneously in accordance with the experimental groups defined in Table 1. The amount of water used for each method was specifically recorded throughout the curing processes. An overall view of the concrete specimens, divided into two different groups and subjected to the three curing methods, is presented in Fig. 5.



Fig. 5. Curing of the concrete specimens using three different methods

Water-spraying curing and wet-burlap curing, which were considered conventional curing methods, were applied at 12 hours intervals during the first 7 days. In each application, 200 mL of water was used to maintain the amount of water applied in a controlled and constant manner. In the water-spraying curing method, the measured water was applied directly to the concrete surface, whereas in the wet-burlap curing method, the concrete surface was covered with burlap and the burlap was rewetted with the same amount of water at each application interval. In the smart curing cover method, the developed covers were placed on the concrete surfaces following the initial setting of the specimens, and no periodic manual watering was applied during the curing process; instead, the process was governed entirely by the automatic control system. Water release was automatically performed according to the relative-humidity-based control mechanism described in Section 2.1 and the required water was supplied from the graduated main reservoirs connected to the smart curing cover system. The total amount of water used during curing with the smart curing cover was determined from the changes in the water levels in the reservoirs. This enabled comparison between the amount of water used in

the conventional methods and the amount of water used by the smart curing cover under sensor-based control. Following the curing applications, the specimens were maintained until the 7- and 28-day test ages specified for compressive strength evaluation.

2.5 Compressive Strength Testing

Following the curing processes, core specimens were extracted from the corresponding concrete specimens to determine the 7- and 28-day compressive strengths of the concrete. Core extraction was performed on the 7th and 28th days after concrete casting in accordance with the experimental groups defined in Table 1. At each test age, three core specimens were extracted from the corresponding concrete specimen for each of the three curing methods. The core extraction locations were selected from similar regions to maintain consistent sampling conditions among the specimens; the cores were positioned along the longitudinal direction of the concrete specimen and on the centerline of its short axis. The core specimens used in the compression tests were prepared with a diameter of 95 mm and a height of 90 mm, corresponding to a length-to-diameter ratio of 0.95. Fig. 6 shows the specimens considered for the 7-day compressive strength evaluation and the core specimens extracted from them.



Fig. 6. Core specimens extracted from the concrete specimens

The extracted core specimens were subjected to uniaxial compression tests using a 300-ton-capacity compression testing machine at a loading rate of 0.6 MPa/s. In accordance with TS EN 13791 [10], the length-to-diameter ratio of the core specimens was 0.95, which falls within the range of 0.90–1.10 specified for 1:1 core specimens. Therefore, the maximum compressive strength values obtained from the tests were considered equivalent standard cube strengths. The corresponding equivalent standard cylinder strengths were calculated by multiplying these values by a factor of 0.82, in accordance with the cube-to-cylinder strength conversion specified in TS EN 13791 [10]. Thus, the equivalent standard cylinder strengths obtained for both test ages and all three curing methods were used for comparative evaluation.

3 Results and Discussion

The performance of the developed smart curing cover was comparatively evaluated against conventional water-spraying and wet-burlap curing methods based on the amount of water used during the curing process and the 7- and 28-day compressive strengths of the concrete.

3.1 Water Consumption Performance

In the conventional curing methods, the concrete specimens received 200 mL of water at 12 hours intervals during the first 7 days, resulting in a total water consumption of approximately 2800 mL per specimen. For the two concrete specimens cured with the smart curing cover, the total amounts of water consumed from the main reservoirs over the same period were measured as approximately 1300 mL and 1200 mL, respectively. Based on these values, the smart curing cover reduced water consumption by approximately 53.6% and 57.1%, respectively, compared

with the 2800 mL used in the conventional methods. This reduction in water consumption can be attributed to the fact that, whereas water was continuously applied at predetermined intervals in the conventional methods regardless of the existing moisture condition, the smart curing cover released water only when the relative humidity fell below the 95% threshold. Once the threshold was reached again, the water flow was stopped, further limiting unnecessary water application. In addition, the automatic operation of the watering process eliminated the need for periodic user intervention. Thus, the smart curing cover provided advantages in terms of both reducing water consumption and automating the curing process independently of manual labor.

3.2 Compressive Strength Performance

The compression test results obtained from the core specimens extracted from the 7- and 28-day concrete specimens subjected to the three curing methods are presented in Tables 2 and 3, respectively. For each curing method and test age, the mean equivalent standard cylinder compressive strength was calculated from the three core specimens, and these mean values were additionally visualized in Fig. 7 to facilitate a clearer comparison among the methods. In the figure, the dashed lines represent the mean strength values obtained with the smart curing cover, whereas the bars represent the mean values obtained with the conventional curing methods. The percentage values shown above the bars indicate the relative differences between the mean strengths obtained with the conventional curing methods and the corresponding mean strength obtained with the smart curing cover, which was taken as the reference at each test age. Positive values indicate a higher mean strength than the smart curing cover, whereas negative values indicate a lower mean strength. The mean 7-day equivalent standard cylinder compressive strengths were determined as 31.73, 29.90, and 32.20 MPa for the smart curing cover, water-spraying curing, and wet-burlap curing, respectively. Taking the smart curing cover as the reference, the mean value obtained with water-spraying curing was approximately 5.7% lower, whereas that obtained with wet-burlap curing was approximately 1.5% higher. Accordingly, the 7-day mean strength obtained with the smart curing cover fell between those of the two conventional methods and exhibited comparable early-age strength performance. At 28 days, the mean equivalent standard cylinder compressive strengths were calculated as 40.45, 38.76, and 39.87 MPa for the smart curing cover, water-spraying curing, and wet-burlap curing, respectively. Relative to the mean value obtained with the smart curing cover, the mean strengths achieved with water-spraying curing and wet-burlap curing were approximately 4.2% and 1.5% lower, respectively. In terms of 28-day strength development, the smart curing cover achieved a higher mean compressive strength than both conventional curing methods and effectively sustained the development of the 28-day strength. Considering the 7- and 28-day results together, the findings demonstrate that the developed smart curing cover system was able to provide effective curing performance without causing any reduction in concrete compressive strength development, despite its substantially lower water consumption.

Table 2. 7-day compressive strength values

Curing Method	**Core No**	**Maximum Load (kN)**	**Maximum Compressive Strength (MPa)**	**Equivalent Standard Cylinder Compressive Strength (MPa)**
Curing with the Smart Curing Cover	1	273.97	38.65	31.69
	2	259.89	36.67	30.07
	3	288.86	40.75	33.42
Water-Spraying Curing	4	265.63	37.48	30.73
	5	245.72	34.67	28.43
	6	264.01	37.25	30.55
	7	270.42	38.15	31.28

Wet-Burlap Curing	8	280.95	39.64	32.50
	9	283.73	40.03	32.82

Table 3. 28-day compressive strength values

Curing Method	**Core No**	**Maximum Load (kN)**	**Maximum Compressive Strength (MPa)**	**Equivalent Standard Cylinder Compressive Strength (MPa)**
Curing with the Smart Curing Cover	1	334.27	48.17	39.50
	2	346.80	49.97	40.98
	3	345.97	49.85	40.88
Water-Spraying Curing	4	326.73	47.08	38.61
	5	329.78	47.52	38.97
	6	327.60	47.21	38.71
Wet-Burlap Curing	7	335.95	48.41	39.70
	8	345.36	49.77	40.81
	9	330.38	47.67	39.09

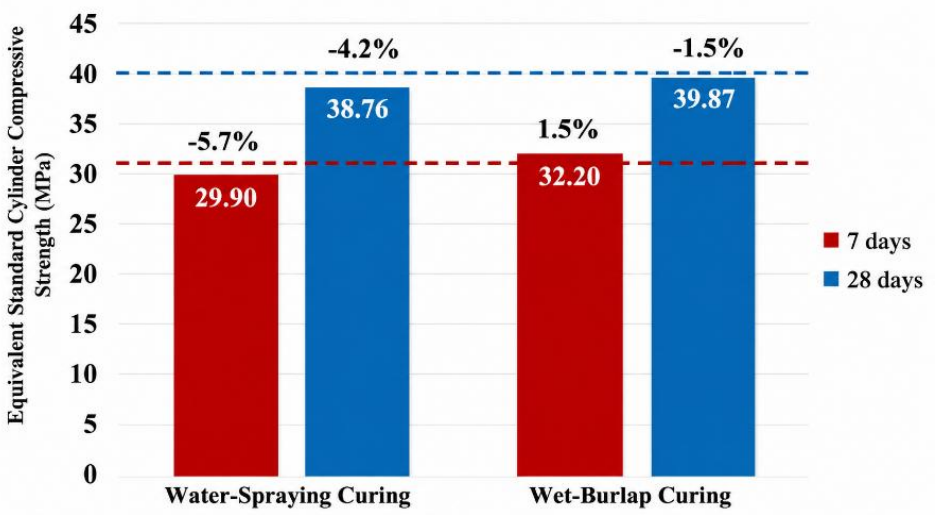


Fig. 7. Comparison of mean equivalent standard cylinder compressive strengths obtained with the three curing methods.

4 Conclusions

The smart curing cover developed within the scope of this study reduced water consumption by 53.6–57.1% while maintaining 7- and 28-day compressive strength performance comparable to conventional water-spraying and wet-burlap curing methods. The results indicate that controlling water release in response to relative humidity can limit unnecessary water application and reduce the need for periodic human intervention without adversely affecting strength development. By combining automatic water release, moisture retention, and a more uniform distribution of the supplied water across the concrete surface, the developed smart curing cover provides a water-efficient and automation-based alternative to conventional wet-curing practices. Further validation using a larger number of independent specimens and under field conditions is recommended for a more comprehensive assessment of the system.

Acknowledgments

This research was financially supported by the Scientific and Technological Research Council of Türkiye (TÜBİTAK) under the grant number [1919B012403311], as part of the 2209-A Research Project Support Programme for Undergraduate Students.

References

1. Gereziher Atsbha, T., Zhutovsky, S.: The effect of external curing methods on the development of mechanical and durability-related properties of normal-strength concrete. Construction and Building Materials 324, 126706 (2022).
2. Yao, J.-L., Wang, Z.-Q., Tang, D.-H.: Development and application of water-saving and moisture-retaining membrane made from controllable high polymer materials for concrete curing. Journal of Performance of Constructed Facilities 33(1), 04018104 (2019).
3. Taffese, W.Z., Nigussie, E.: Automated concrete curing and assessment of strength and durability using IoT system. Materials Today: Proceedings 121, 295–300 (2026).
4. Yang, J., Fan, J., Kong, B., Cai, C.S., Chen, K.: Theory and application of new automated concrete curing system. Journal of Building Engineering 17, 125–134 (2018).
5. Lo, K.-C., Kwok, H.-W.T., Siu, M.-F.F., Shen, Q.G., Lau, C.-K.: Internet of Things-based concrete curing invention for construction quality control. Advances in Civil Engineering 2021, Article ID 9933615 (2021). https://doi.org/10.1155/2021/9933615.
6. Reddy, V.M., Hamsalekha, S.: Smart concrete curing system. E3S Web of Conferences 184, 01086 (2020). https://doi.org/10.1051/e3sconf/202018401086.
7. Feng, J., Jia, H., Pei, H., Zhai, H., Xu, J., Lacidogna, G.: Research on the application of residual networks considering attention mechanism in concrete curing robot. Developments in the Built Environment 17, 100350 (2024). https://doi.org/10.1016/j.dibe.2024.100350.
8. Ascona García, P.P., Ordoñez Carpio, G.E., Zelada Zamora, W.M., Aguirre Camacho, M.A., Rojas Pintado, W., Cuadros Rojas, E.J., Mundaca Ramos, H.M., Arce Fernández, N.: Intelligent automated monitoring and curing system for cracks in concrete elements using integrated sensors and embedded controllers. Technologies 13(7), 284 (2025).
9. TS EN 12390-2. Testing hardened concrete—Part 2: Making and curing specimens for strength tests. Turkish Standards Institution, Ankara (2019).
10. TS EN 13791. Assessment of in-situ compressive strength in structures and precast concrete components. Turkish Standards Institution, Ankara. (2019).

Author Contribution Statement

- *Conceptualization:* Seyedehdorsa Akhtarian, İpek Naz Semercioğlu Akbulut, Hasan Basri Başağa
- *Methodology:* Bartuğhan Uzun, Seyedehdorsa Akhtarian, Aleyna Özdemir, Yunus Emrahan Akbulut, İpek Naz Semercioğlu Akbulut
- *Investigation:* Seyedehdorsa Akhtarian, Aleyna Özdemir, Yunus Emrahan Akbulut
- *Writing – Original Draft:* İpek Naz Semercioğlu Akbulut
- *Writing – Review & Editing:* Hasan Basri Başağa

Publication Note

This paper was peer-reviewed, accepted for presentation, and included in the proceedings of the ACE2026 – International Conference on Advances in Civil Engineering, held on 12–14 October 2026 in Trabzon, Türkiye.

This paper may be cited as follows:

Semercioğlu Akbulut İN, Akhtarian S, Özdemir A, Uzun B, Akbulut YE, Başağa HB, "Development of an Automation-Based Smart Curing Cover for Optimizing the Concrete Curing Process," in Proceedings of the ACE2026 – International Conference on Advances in Civil Engineering, Trabzon, Türkiye, 12–14 October 2026.

Evaluation of Construction Contract Disputes Through Supreme Court Decisions

Eda Bayram[1] and Ömer Giran[2]
[1]0000-0003-1414-3638, Independent Researcher, Istanbul, Türkiye, eda.bayram@gmail.com
[2] 0000-0003-4135-393X, Istanbul University - Cerrahpasa, Civil Engineering Department, Istanbul, Türkiye, ogiran@iuc.edu.tr

Abstract. Construction contracts constitute one of the most common contractual relationships in the construction industry and frequently lead to legal disputes due to the complex nature of construction projects. In Türkiye, these contracts are evaluated within the scope of work contracts under the Turkish Code of Obligations and are mainly regulated by Article 470 of the Code of Obligations No. 6098, with Article 355 of the former Code No. 818 serving as a comparative legal reference. This study aims to establish a comprehensive database for the evaluation of construction contract disputes in Türkiye between 2000 and 2021 through Supreme Court decisions. The Supreme Court of Appeals, functioning as the highest judicial review authority under Turkish law, provides final legal interpretations regarding construction-related disputes and therefore represents a reliable source for identifying recurring contractual problems in practice. Within the scope of the research, all Supreme Court decisions associated with work contracts under Articles 355 and 470 were examined and categorized according to their dispute subjects. The analyzed case files were classified under specific headings, enabling the development of dispute classification tables reflecting real judicial cases in the construction sector. The findings reveal the most frequent sources of disputes encountered in construction contracts and provide valuable insights for risk identification and management processes in construction project management. The study is expected to contribute to the development of more realistic risk assessment approaches by utilizing judicial case analyses as a practical reference for construction managers, legal professionals, and researchers.

Keywords: Construction Contract; Construction Disputes; Supreme Court Decisions; Risk Management.

1 Introduction

The construction sector operates in an environment characterized by high financial exposure, long project durations, and considerable technical complexity [1]. These characteristics make construction projects particularly vulnerable to disagreements among project stakeholders. In Türkiye, construction agreements are generally classified as work contracts. Their legal framework is primarily governed by Article 470 of the Turkish Code of Obligations (TCO) No. 6098 and, historically, by Article 355 of the former Code No. 818 [2]. Under these provisions, the contractor undertakes to create and deliver a work, while the employer undertakes to pay the agreed compensation.

Despite contractual provisions established at the outset of a project, actual project conditions frequently differ from those originally anticipated. Unforeseen site conditions, design modifications, delays in material delivery, payment defaults, and other changes during project execution may create conflicts between the parties [3, 4]. When contractual or alternative

dispute resolution mechanisms fail to resolve these conflicts, disputes may proceed to litigation. In the Turkish judicial system, the Supreme Court of Appeals (Yargıtay) serves as the highest judicial review authority for the relevant decisions. Its case law therefore provides an important empirical source for examining recurring contractual problems in the construction industry [5].

Previous research has largely focused on dispute causes, claim management, proactive risk management, and contractual analysis. Although these studies provide valuable insights, empirical analyses based on actual judicial decisions remain relatively limited [6, 7]. Historical litigation data can provide additional evidence regarding the contractual and administrative problems that repeatedly develop into formal disputes.

Accordingly, this study analyzes Supreme Court decisions concerning construction-related work contracts rendered between 2000 and 2021. The decisions were systematically categorized according to their principal dispute subjects in order to identify recurring sources of construction litigation in Türkiye. The findings are subsequently interpreted from a construction risk management perspective.

The main objective of the study is to demonstrate how judicial case analysis can contribute to the identification of contractual risks and support the development of more proactive dispute prevention strategies. By linking recurring dispute categories with construction risk management practices, the study seeks to provide practical insights for construction managers, contract administrators, legal professionals, and researchers.

2 Legal and Methodological Framework

2.1 Statutory Context of Work Contracts

Under Article 470 of TCO No. 6098, a work contract is a bilateral agreement under which the contractor undertakes to produce a work or achieve a specific result, while the employer undertakes to pay the agreed price [8]. This result-oriented nature distinguishes work contracts from contractual relationships based primarily on the provision of services or effort.

The contractor is generally expected to perform the work with due care, use appropriate materials, and deliver the work in accordance with contractual and legal requirements. The employer, on the other hand, is primarily responsible for accepting the completed work when it conforms to the contract and paying the agreed compensation [9].

When disputes arise, courts evaluate the parties' performance and obligations under the relevant statutory provisions governing issues such as defective performance, delay, acceptance, payment, and price adjustments. Article 480 of the TCO, for example, may become relevant in disputes involving price adjustments arising from circumstances that could not reasonably have been foreseen by the parties [10]. The interpretation of these provisions in Supreme Court decisions therefore provides an important basis for examining litigation exposure in construction projects.

2.2 Data Collection and Qualitative Categorization Methodology

The study collected judicial decisions from public and legal databases covering the period from January 2000 to December 2021. The search primarily focused on decisions rendered by the 15th Civil Chamber of the Supreme Court (Yargıtay 15. Hukuk Dairesi), which dealt extensively with disputes arising from work contracts during the study period.

The evaluation followed a structured qualitative process:

Filtering: Decisions were screened using search terms and legal references associated with Articles 355 and 470, construction contracts, defective work, additional works, and contractual termination.

Relevance screening: Decisions concerning non-construction work contracts, procedural dismissals, and repetitive precedents that did not provide additional information regarding the nature of the dispute were excluded.

Qualitative categorization: The selected decisions were examined to identify their underlying dispute subjects. The cases were subsequently classified into functional categories based on their principal contractual themes.

Pattern mapping: The categorized cases were evaluated to identify the relative frequency of the principal dispute categories and their relationship with recurring project and contractual risks.

3 Findings and Dispute Analysis

The qualitative analysis established a descriptive profile of construction litigation in Türkiye. The examined disputes were grouped into five core categories: scope changes and additional works, defective execution, contractual delay and time extensions, payment and price adjustments, and contract termination and damages.

3.1 Distribution of Dispute Categories

Table 1 presents the classification of the analyzed construction contract disputes and summarizes the principal legal issues associated with each category.

Table 1. *Classification of construction contract disputes.*

Primary Dispute Subject	Applicable TCO Article	Relative Frequency (%)	Key Contested Issue
Additional Work & Scope Changes	Arts. 470, 481	28.5	Lack of written variation orders
Defective Work & Workmanship	Arts. 474, 475	24.2	Latent defects and inspection timing
Contractual Delay & Time Extension	Arts. 473, 478	21.0	Force majeure and concurrency of delays
Payment & Price Adjustments	Arts. 480, 482	16.8	Unexpected cost increases and unit price disputes
Contract Termination & Damages	Arts. 484, 486	9.5	Unilateral termination and its consequences

The results indicate that additional work and scope changes constituted the largest single dispute category, accounting for 28.5% of the analyzed cases. Defective work and workmanship followed at 24.2%, while contractual delays and time extensions represented 21.0%. Together, these three categories accounted for more than 70% of the disputes examined.

Payment and price adjustment disputes represented 16.8% of the cases, while contract termination and damages constituted the smallest category at 9.5%. Although less frequent, termination disputes often involve significant legal and financial consequences because they may affect the continuation of the project and the parties' subsequent rights and obligations.

3.2 Key Findings and Judicial Interpretations

Scope Changes and Additional Work: Disputes concerning scope variations represented the largest category in the dataset. A recurring issue in these disputes involved instructions for additional work that were not adequately documented through formal written change orders. The Supreme Court decisions examined in this category demonstrate the importance of contractual procedures and evidentiary requirements when parties claim additional compensation for work that is alleged to fall outside the original scope [11, 12].

From a construction management perspective, these findings highlight the importance of systematic change management. Verbal instructions, informal requests, and undocumented changes may create uncertainty regarding both entitlement and valuation. Therefore, changes should be recorded in writing and formally evaluated with respect to their cost and time consequences.

Defective Work and Inspection: Defective performance constituted the second-largest dispute category. These disputes frequently involved questions regarding the identification of defects, the timing of inspections, and notification to the contractor. Under Article 474 of the TCO, the employer is required to inspect the completed work and notify the contractor of defects within the legally required framework [13].

The findings demonstrate that technical inspection and contractual administration are closely related. Delayed inspection or inadequate documentation may complicate the determination of whether a defect existed at the time of delivery and whether the relevant rights were preserved. Effective inspection procedures and written defect notifications can therefore play an important role in preventing disputes.

Delays and Time Extensions: Delay disputes represented 21.0% of the analyzed cases. These disputes may arise from various causes, including contractor-related delays, late site handover, delayed design approvals, external events, and concurrent delays involving more than one party. Determining responsibility is particularly important because the outcome may affect extensions of time, compensation, or the application of delay-related contractual consequences [14].

The findings emphasize that delay management should not be limited to schedule monitoring. Detailed site records, project correspondence, progress documentation, and timely notices are also essential for establishing the factual and contractual basis of delay claims.

Payment and Price Adjustments. Payment and price adjustment disputes accounted for 16.8% of the analyzed cases. These disputes generally involve disagreements concerning the valuation of work, unit prices, additional costs, or the financial consequences of changed project conditions. The findings illustrate the importance of maintaining transparent procedures for measuring completed work and determining the applicable contractual price.

Contract Termination and Damages: Contract termination and related damage claims represented 9.5% of the cases. These disputes involve questions concerning the termination of the contractual relationship and the legal and financial consequences of incomplete or disputed

performance. Clear contractual provisions concerning termination procedures and the documentation of performance are therefore essential for reducing uncertainty when serious disagreements arise.

3.3 Qualitative Risk Exposure Evaluation

Rather than applying a strict mathematical risk model, the findings were interpreted through a qualitative risk perspective. The relative frequency of dispute categories provides an indication of recurring areas of contractual exposure, while the nature of the disputes provides information regarding their potential legal and operational consequences.

Scope variations and defective performance represent particularly significant risk areas because they combine relatively high frequency with substantial evidentiary requirements. Delay disputes may similarly create considerable exposure when project records are insufficient to establish responsibility for the delay.

The analysis suggests that construction disputes should not be considered only as isolated legal events. They can also be interpreted as indicators of recurring weaknesses in project planning, contract administration, communication, documentation, and risk allocation.

4 Discussion and Strategic Risk Management Implications

The findings reveal an important connection between construction management practices at the project level and the issues that later emerge in litigation. Many disputes do not necessarily result from a single technical failure or deliberate misconduct. Instead, they may develop through inadequate documentation, unclear communication, inconsistent contractual procedures, or the failure to manage changes and delays systematically.

4.1 Implications for Project Management

The analysis provides several practical implications for construction project managers:

Formalize communication: The recurrence of disputes concerning additional works demonstrates the importance of eliminating ambiguity in site instructions. Change orders, requests for extensions of time, project correspondence, and meeting decisions should be documented in writing and communicated through the contractual procedures established for the project [15].

Establish structured inspection procedures: Formal inspection and handover procedures can help clarify whether the work conforms to contractual requirements. Written inspection records and timely notification of defects are particularly important for preserving the parties' rights and reducing uncertainty concerning defective performance.

Maintain comprehensive delay records: Contractors and project teams should maintain detailed site records to document the occurrence, duration, and causes of delay events. Daily site records, correspondence, progress reports, and schedule updates may become essential when determining responsibility for delays and their consequences [16, 17].

4.2 Contract Drafting and Systemic Controls

The findings also have implications for contract drafting and administration. Construction contracts should establish clear procedures for variations, site instructions, payment, inspection, delay notices, extensions of time, and termination.

A contract alone cannot prevent all disputes. However, well-defined procedures can reduce uncertainty and provide a framework for addressing disagreements before they develop into

formal litigation. Effective contract administration is equally important because even detailed contractual provisions may lose their practical value when project participants do not follow them during project execution.

An integrated dispute prevention framework should therefore combine clear contractual provisions with systematic documentation and project-level monitoring [18]. Such an approach can support earlier identification of potential conflicts and reduce the need to rely on judicial interpretation after a dispute has escalated.

5 Conclusion

This study evaluated construction contract disputes in Türkiye through the analysis of Supreme Court decisions rendered between 2000 and 2021. The decisions were examined and categorized according to their principal dispute subjects, revealing five recurring areas of litigation: additional work and scope changes, defective work and workmanship, contractual delays and time extensions, payment and price adjustments, and contract termination and damages.

The findings show that disputes concerning scope variations, defective workmanship, and performance delays account for more than 70% of the analyzed cases. These results indicate that construction litigation is strongly associated with recurring contractual and administrative problems related to scope, quality, time, payment, and performance.

Although construction disputes and claim management have been extensively discussed in previous research, the systematic analysis of Supreme Court decisions provides an additional empirical perspective. Judicial cases reflect disputes that have developed beyond ordinary project-level disagreements and have required formal legal evaluation. For this reason, they provide valuable evidence regarding the types of contractual problems that repeatedly emerge in practice.

The results further suggest that a considerable proportion of disputes may be associated with weaknesses in project administration, particularly inadequate documentation of changes, delays in identifying and notifying defects, and insufficient records concerning delay events. Aligning day-to-day project administration with contractual requirements can therefore support earlier resolution of disagreements and reduce litigation exposure.

Overall, the findings indicate that construction disputes are repetitive rather than entirely random, while Supreme Court decisions provide valuable empirical evidence regarding the recurring causes and characteristics of such disputes. The systematic analysis of judicial cases can therefore contribute to the identification of contractual and project-related risks at an earlier stage. In this respect, judicial case analysis may support the development of more realistic risk identification and management approaches in construction projects.

Future research may extend the existing dispute database and use larger judicial datasets to investigate the relationships between dispute categories, project characteristics, and contractual variables. Moreover, the database developed in this study may provide a foundation for future machine learning and artificial intelligence-supported dispute prediction systems in construction contract management. Such systems could support a transition from the retrospective analysis of disputes toward more proactive and predictive approaches to risk identification and dispute prevention.

Acknowledgments

The authors express their gratitude to legal scholars and industry experts who offered guidance on legal database navigation and Supreme Court case indexing during the preliminary data collection phase.

Conflict of Interest

The authors declare no conflict of interest.

Funding

The authors received no specific financial support for the research, authorship, or publication of this study.

Data Availability Statement

The data supporting the findings of this study consist of judicial decisions examined within the scope of the research. The classified dataset may be made available by the corresponding author upon reasonable request.

References

1. Love, P.E.D., Davis, P.R., Ellis, J.M., Cheung, S.O.: Dispute causation: Identification of pathogenic structures in construction networks. Journal of Legal Affairs and Dispute Resolution in Engineering and Construction 2(2), 82–89 (2010). https://doi.org/10.1061/(ASCE)LA.1943-4170.0000013
2. Dayınlaç, K.: Borçlar Hukuku Özel Borç İlişkileri. 12th edn. Yetkin Yayınları, Ankara (2021).
3. Cheung, S.O., Yiu, T.W.: Are construction disputes inevitable? IEEE Transactions on Engineering Management 53(3), 456–470 (2006). https://doi.org/10.1109/TEM.2006.877445
4. Ilter, D.: Identification of the relations between dispute factors and dispute categories in construction projects. International Journal of Law in the Built Environment 4(1), 45–59 (2012). https://doi.org/10.1108/17561451211211732
5. Yargıtay Kararları Dergisi: Eser Sözleşmesinden Doğan Uyuşmazlıklar ve Yargıtay İçtihatları. Yargıtay Yayınları, Ankara (2019).
6. Cakmak, P.I., Cakmak, E.: An analysis of causes of disputes in the construction industry using analytical hierarchy process. Procedia - Social and Behavioral Sciences 109, 183–187 (2014). https://doi.org/10.1016/j.sbspro.2013.12.441
7. Gündüz, M., Nielsen, Y., Özdemir, M.: Quantification of delay factors using the relative importance index method for construction projects in Turkey. Journal of Management in Engineering 29(2), 133–139 (2013). https://doi.org/10.1061/(ASCE)ME.1943-5479.0000129
8. Tandoğan, H.: Borçlar Hukuku Özel Borç İlişkileri Cilt II. 5th edn. Vedat Kitapçılık, İstanbul (2010).
9. Zevkliler, A., Gökyayla, K.E.: Borçlar Hukuku Özel Borç İlişkileri. 20th edn. Turhan Kitabevi, Ankara (2020).

10. Aral, F., Ayrancı, H.: Borçlar Hukuku Özel Borç İlişkileri. 14th edn. Yetkin Yayınları, Ankara (2022).
11. Yates, D.J., Epstein, A.: Cause-and-effect relationships of changes in construction contracts. Journal of Construction Engineering and Management 132(11), 1185–1193 (2006). https://doi.org/10.1061/(ASCE)0733-9364(2006)132:11(1185)
12. Ergezen, M.: Eser Sözleşmesinde Uygulanacak Hüküm ve Yargıtay Uygulaması. Seçkin Yayıncılık, Ankara (2018).
13. Kostakoğlu, C.: İçtihatlı İnşaat Hukuku ve Eser Sözleşmesi. 10th edn. Beta Yayıncılık, İstanbul (2015).
14. Ibbs, C.W., Nguyen, L.D., Lee, S.: Quantified impacts of project change. Journal of Professional Issues in Engineering Education and Practice 133(1), 45–52 (2007). https://doi.org/10.1061/(ASCE)1052-3928(2007)133:1(45)
15. Diekmann, J.E., Girard, M.J.: Are contract disputes predictable? Journal of Construction Engineering and Management 121(4), 355–363 (1995). https://doi.org/10.1061/(ASCE)0733-9364(1995)121:4(355)
16. Braimah, N.: Construction delay analysis techniques: A review of application issues and improvement needs. Buildings 3(3), 506–531 (2013). https://doi.org/10.3390/buildings3030506
17. Öztaş, A., Ökmen, Ö.: Judgmental risk analysis process development in construction projects. Building and Environment 41(9), 1244–1254 (2006). https://doi.org/10.1016/j.buildenv.2005.05.009
18. Semple, C., Hartman, F.T., Jergeas, G.: Construction claims and disputes: Causes and cost/time overruns. Journal of Construction Engineering and Management 120(4), 785–795 (1994). https://doi.org/10.1061/(ASCE)0733-9364(1994)120:4(785)
19. Turkish Ministry of Justice: Judicial Statistics Database and Case Records. Turkish Ministry of Justice, https://adliistatistik.adalet.gov.tr, last accessed 2026/02/15.

Author Contribution Statement

Conceptualization: Eda Bayram, Ömer Giran
Methodology: Eda Bayram, Ömer Giran
Investigation: Eda Bayram
Data Curation: Eda Bayram
Formal Analysis: Eda Bayram
Writing – Original Draft: Eda Bayram
Writing – Review & Editing: Eda Bayram, Ömer Giran
Supervision: Ömer Giran

List of Abbreviations

TCO — Turkish Code of Obligations
Yargıtay — Supreme Court of Appeals of Türkiye

Note: Following the conference, this Publication Note will be added to each paper; therefore, authors are kindly requested not to remove the note below and to complete the author(s) and paper title information.

Publication Note

This paper was peer-reviewed, accepted for presentation, and included in the proceedings of the ACE2026 – International Conference on Advances in Civil Engineering, held on 12–14 October 2026 in Trabzon, Türkiye.

This paper may be cited as follows:

Bayram, E., Giran, O., (2026). "Evaluation of Construction Contract Disputes Through Supreme Court Decisions," in Proceedings of the ACE2026 – International Conference on Advances in Civil Engineering, Trabzon, Türkiye, 12–14 October 2026.

Author Index

Paper code (page number)

Farid Abed
ACE-STR-007 (117)

Reşat Acar
ACE-HYD-017 (1130)

Mehmet Ada
ACE-STR-037 (400)

Gökhan Adıyaman
ACE-STR-039 (419)

Gulmira Adzhygulova
ACE-CME-002 (517)

Siamak Aghaei
ACE-STR-037 (400)

Reza Saleh Ahari
ACE-CME-011 (598), ACE-CME-012 (609), ACE-CME-013 (620)

Cihan Tayyar Ahı
ACE-CME-015 (640)

Muhammad Ahmad
ACE-CME-036 (832), ACE-CME-037 (844)

Kadir Berkhan Akalın
ACE-TRA-014 (1286)

Nurdan Akbaş
ACE-TRA-005 (1194)

İpek Naz Semercioğlu Akbulut
ACE-COM-018 (1604)

Yunus Emrahan Akbulut
ACE-COM-018 (1604)

Ahmet Akif Akcora
ACE-STR-040 (429)

Kutalmış Recep Akça
ACE-CME-001 (507)

Burak Akçay
ACE-GEO-014 (986)

Barış Akdemir
ACE-TRA-003 (1174)

O. Burak Akgun
ACE-HYD-008 (1050)

Seyedehdorsa Akhtarian
ACE-COM-018 (1604)

Hassan Aknouche
ACE-STR-042 (452)

Kaan Aksoy
ACE-CME-021 (699)

Yusuf Buğra Aksoy
ACE-HYD-016 (1118)

Cenk Aksoylar
ACE-STR-010 (142)

Nihan Doğramacı Aksoylar
ACE-STR-010 (142)

Muhammed Emin Akyürek
ACE-STR-010 (142)

Bahri Akyüz
ACE-COM-011 (1534)

Aroob Alateyat
ACE-STR-007 (117)

Özge Alboğa
ACE-COM-004 (1469)

Hussein Abdullahi Ali
ACE-CME-017 (658)

Ola Aljumaili
ACE-CME-016 (648)

Alaaddin Aljuneed
ACE-STR-045 (479)

Abdulrezzak Alkan
ACE-CME-020 (690)

Emre Alpaslan
ACE-STR-012 (162)

Vahiddin Alperen
ACE-CME-034 (814)

Hasan Altawil
ACE-GEO-003 (878)

Yaren Altay
ACE-TRA-043 (1432)

Ahmet Can Altunışık
ACE-GEO-014 (986)

Yalçın Alver
ACE-TRA-022 (1347)

Huseyin Okan Anadut
ACE-STR-022 (255)

Zekai Angin
ACE-GEO-005 (896)

Tuğçe Anılan
ACE-HYD-003 (1017)

Dina Aqra
ACE-GEO-011 (955)

Zülal Akbay Arama
ACE-GEO-007 (914)

Necati Aras
ACE-COM-013 (1553)

M. Kemal Ardoğa
ACE-CME-025 (734), ACE-CME-028 (760)

Yeşim Arslantürk
ACE-CME-016 (648)

Tunahan Aslan
ACE-STR-029 (326)

Sina Atabey
ACE-STR-021 (245)

Hakan Nuri Atahan
ACE-CME-006 (546)

Mert Atakan
ACE-TRA-043 (1432)

Şevket Ateş
ACE-STR-043 (462), ACE-STR-046 (490)

Barbaros Atmaca
ACE-STR-017 (210), ACE-STR-043 (462)

Esin Ertürk Atmaca
ACE-GEO-014 (986)

Rümeysa Atmaca
ACE-CME-019 (676)

Yaşar Avcı
ACE-STR-019 (230)

Ceydanur Aydın
ACE-HYD-013 (1089)

Serkan Aydınlı
ACE-COM-003 (1461)

Beyza Aygun
ACE-CME-007 (557), ACE-CME-008 (568)

Muhammed Emin Aytekin
ACE-GEO-010 (942)

Fatma Ayvaz
ACE-CME-036 (832), ACE-CME-037 (844)

Yusuf Ayvaz
ACE-STR-037 (400)

Badawi B.
ACE-CME-009 (579)

Irem Bagca
ACE-CME-001 (507)

Author Index (cont.)

Ümit Bahadır
ACE-COM-005 (1479)

Osman Tuğrul Baki
ACE-HYD-010 (1072)

Vahiddin Alperen Baki
ACE-CME-036 (832), ACE-CME-037 (844)

İlkim Güven Balli
ACE-COM-007 (1499)

Mehmet Baran
ACE-CME-017 (658)

Hasan Basri Başağa
ACE-COM-002 (1451), ACE-COM-006 (1489), ACE-COM-018 (1604)

Esra Ece Bayat
ACE-GEO-014 (986)

Bilgin Furkan Bayrak
ACE-HYD-016 (1118)

Yasemin Bayrakkaya
ACE-COM-010 (1525)

Eda Bayram
ACE-COM-019 (1614)

Hakim Bechtoula
ACE-STR-042 (452)

Kaan Beyazkılıç
ACE-CME-003 (524)

Sidar Nihat Bıçakçı
ACE-CME-006 (546)

Perihan Biçer
ACE-GEO-009 (932)

Senem Bilici
ACE-CME-015 (640), ACE-CME-023 (718)

Turhan Bilir
ACE-CME-007 (557), ACE-CME-008 (568)

Eray Birinci
ACE-GEO-010 (942)

Huseyin Boler
ACE-TRA-007 (1213)

Gökçen Bombar
ACE-HYD-026 (1148)

Abdullah Bostanci
ACE-STR-021 (245)

Nouredine Bourahla
ACE-STR-042 (452)

Reyhan Boz
ACE-COM-008 (1509)

Alpaslan Bozkurt
ACE-TRA-009 (1233)

Sercan Bozkurt
ACE-GEO-009 (932)

Zafer Bozkuş
ACE-HYD-015 (1108)

Abdulkadir Budak
ACE-COM-009 (1517)

Murathan Bulut
ACE-CME-036 (832), ACE-CME-037 (844)

Osman Bulut
ACE-STR-032 (356), ACE-CME-014 (630)

Rumeysa Bulut
ACE-GEO-004 (886)

Zeynep Başaran Bundur
ACE-CME-021 (699)

Zehra Büyüker
ACE-HYD-026 (1148)

Semih Caglayan
ACE-COM-008 (1509)

Ferhun C. Caner
ACE-STR-016 (203)

Kağan Cebe
ACE-HYD-016 (1118)

Fatih Cebir
ACE-STR-020 (238)

Amal Chakir
ACE-CME-036 (832), ACE-CME-037 (844)

Manjari Chakraborty
ACE-COM-014 (1563)

Kazım Burç Civelek
ACE-STR-003 (79)

Mustafa Comert
ACE-STR-001 (57)

Turgay Cosgun
ACE-CME-007 (557), ACE-CME-008 (568)

Omer Canbey Cucemen
ACE-STR-032 (356), ACE-CME-014 (630)

Gülben Çalış
ACE-COM-015 (1576)

Ayten Çaputcu
ACE-CME-036 (832), ACE-CME-037 (844)

Erman Çavdar
ACE-TRA-012 (1266), ACE-TRA-017 (1307)

Haşim Çayır
ACE-STR-010 (142)

Muhammed Çeçen
ACE-CME-029 (770), ACE-CME-031 (787)

Erkan Çelebi
ACE-STR-033 (366), ACE-STR-034 (378)

T. Kutay Çelebioğlu
ACE-HYD-015 (1108)

Damla Nur Çelik
ACE-CME-019 (676)

Kemal Önder Çetin
ACE-GEO-010 (942), ACE-GEO-014 (986)

Oğuzhan Çetindemir
ACE-STR-026 (297), ACE-STR-027 (306)

Burak Çırağ
ACE-HYD-017 (1130)

Erdal Çokça
ACE-GEO-002 (868)

Halit Erdem Çolakoğlu
ACE-STR-023 (265)

Elif Dağlı
ACE-TRA-023 (1356)

Gizem Çağlar Dal
ACE-STR-013 (173)

Yakup Darama
ACE-HYD-009 (1060)

Tayfun Dede
ACE-STR-017 (210), ACE-COM-012 (1544)

Attila Dedeoğlu
ACE-HYD-003 (1017)

Kaveh Dehghanian
ACE-GEO-006 (905)

Cem Demir
ACE-STR-001 (57)

Muhammed Sungur Demir
ACE-HYD-018 (1141)

Author Index (cont.)

Nira Nur Demir
ACE-HYD-013 (1089)

Nur Demir
ACE-CME-018 (665)

Serhat Demir
ACE-STR-020 (238)

Yunus Emre Demir
ACE-CME-016 (648)

Şenol Demirbaş
ACE-HYD-027 (1158)

Rüya Kılıç Demircan
ACE-CME-019 (676)

Sıla Cemre Demirci
ACE-TRA-016 (1297)

Said Derbane
ACE-GEO-012 (965)

Inci Develioglu
ACE-GEO-004 (886)

Berk Dikmenoğlu
ACE-GEO-014 (986)

Beste Koçak Dinç
ACE-GEO-006 (905)

Aleyna Dinçer
ACE-CME-022 (709)

Evinç Doğan
ACE-TRA-025 (1380)

Gamze Doğan
ACE-STR-015 (195)

Ünal Anıl Doğan
ACE-CME-018 (665), ACE-CME-022 (709)

Cemile Duman
ACE-STR-029 (326)

Zeynep Nur Duman
ACE-TRA-024 (1370)

Ebru Dural
ACE-STR-011 (151), ACE-CME-002 (517)

Selim Dündar
ACE-TRA-003 (1174), ACE-TRA-004 (1184), ACE-TRA-006 (1202)

Julia Eberl
ACE-STR-033 (366), ACE-STR-034 (378)

Tamer El-Maaddawy
ACE-STR-007 (117)

M.A. Erberik
ACE-STR-009 (132)

Ali Ercan
ACE-HYD-007 (1040)

Elif Erdem
ACE-HYD-002 (1007)

Elcin Kentel Erdogan
ACE-HYD-002 (1007)

Sinan T. Erdoğan
ACE-CME-032 (796)

Ayşe Erdölen
ACE-CME-033 (805)

Ozgur Eren
ACE-STR-040 (429)

Teoman Erenoğlu
ACE-CME-023 (718), ACE-CME-026 (744)

Hasan Ergin
ACE-CME-026 (744)

Büşra Çınar Ernek
ACE-CME-023 (718)

Hasan Eser
ACE-STR-044 (472)

Selin Esfendiyar
ACE-STR-015 (195)

Ehsan Etminan
ACE-GEO-006 (905)

Mutlu İ. F.
ACE-CME-009 (579)

Maziar Fahimi Farzam
ACE-STR-002 (69), ACE-STR-031 (346)

Chiraz Fazzaa
ACE-STR-043 (462)

Seyhan Fırat
ACE-GEO-010 (942)

Onur Gedik
ACE-STR-008 (123)

Ömer Giran
ACE-COM-019 (1614)

Alara Girgin
ACE-CME-021 (699)

Zehra Canan Girgin
ACE-CME-030 (779)

Ilgin Gokasar
ACE-TRA-006 (1202), ACE-TRA-025 (1380), ACE-TRA-026 (1389), ACE-TRA-027 (1397)

Beste Seyla Göçkün
ACE-GEO-006 (905)

İsmail Gökalp
ACE-CME-022 (709), ACE-CME-023 (718), ACE-CME-026 (744)

Feyzullah Gulsen
ACE-GEO-013 (976)

Arife Günay
ACE-HYD-003 (1017)

Gürkan Günay
ACE-TRA-004 (1184)

Uğur Günay
ACE-COM-016 (1583)

Murat Günaydın
ACE-GEO-014 (986)

Tuba Gündoğdu
ACE-CME-022 (709)

Yunus Gündüz
ACE-CME-020 (690)

Beyza Güngör
ACE-CME-006 (546)

Mahmut Güngör
ACE-HYD-017 (1130)

Gürkan Emre Gürcanlı
ACE-COM-001 (1443), ACE-COM-017 (1594)

Mustafa Gürsoy
ACE-TRA-001 (1165), ACE-TRA-008 (1221), ACE-TRA-018 (1317)

Şahin Tolga Güvel
ACE-COM-009 (1517)

Kemal Hacıefendioğlu
ACE-STR-029 (326), ACE-STR-030 (336)

Omer Faruk Halici
ACE-STR-001 (57)

Enes Hamidoğlu
ACE-CME-018 (665)

Oğuzhan Hasançebi
ACE-STR-044 (472)

Mustafa Hatipoğlu
ACE-GEO-001 (859)

Semiha Hayrioğlu
ACE-STR-028 (316)

Author Index (cont.)

Çağlayan Hızal
ACE-STR-024 (276)

Metin Hüsem
ACE-STR-020 (238)

Pelin İlker
ACE-HYD-012 (1079)

Alper Ilki
ACE-STR-001 (57)

Özger İnal
ACE-TRA-029 (1414)

Recep Orçun İnce
ACE-TRA-043 (1432)

Ahmet Faruk İpek
ACE-HYD-006 (1034)

Muhammet Ali İpekçi
ACE-STR-010 (142)

Beyhan Ipekyuz
ACE-TRA-028 (1404), ACE-TRA-031 (1422)

Sk. Rakibul Islam
ACE-TRA-021 (1336)

Berna İstegün
ACE-STR-033 (366), ACE-STR-034 (378)

Nihat Sinan Işık
ACE-GEO-010 (942)

Rabia Izol
ACE-STR-036 (390)

Ersoy Kabadayı
ACE-TRA-012 (1266), ACE-TRA-017 (1307)

Gizem Kaçaroğlu
ACE-TRA-010 (1243)

Ercan Kahya
ACE-HYD-006 (1034)

Volkan Kahya
ACE-STR-039 (419)

Cemalettin Kaplan
ACE-TRA-043 (1432)

Gökhan Kaplan
ACE-CME-019 (676)

Alperhan Kapucu
ACE-GEO-006 (905)

Çağdaş Kara
ACE-TRA-016 (1297)

Mehmet Kara
ACE-CME-030 (779)

Nihat Can Karabulut
ACE-TRA-001 (1165)

Öznur Karadağ
ACE-TRA-010 (1243)

Gulnara Karadeniz
ACE-CME-002 (517)

Mehmet Karadeniz
ACE-CME-002 (517)

Olguhan Şevket Karahasan
ACE-GEO-005 (896)

Gökçen Karakol
ACE-COM-013 (1553)

Serkan Karali
ACE-COM-015 (1576)

Ali Erkan Karaman
ACE-COM-010 (1525)

Ibrahim Karatas
ACE-COM-009 (1517)

Muhammed Furkan Kart
ACE-HYD-007 (1040)

Elifsu Kayrak
ACE-STR-003 (79)

Rizwan Kazmi
ACE-COM-014 (1563)

Bedirhan Enes Kelek
ACE-CME-035 (822), ACE-COM-013 (1553)

M. Kubilay Keleşoğlu
ACE-GEO-014 (986)

Onur Kemalli
ACE-HYD-015 (1108)

Elcin Kentel
ACE-HYD-008 (1050)

Handenur Keser
ACE-TRA-022 (1347)

Erdal Kesgin
ACE-HYD-027 (1158)

Aslı Ülke Keskin
ACE-HYD-016 (1118)

Meysam Khalilzadeh
ACE-CME-013 (620)

Derya Kılıç
ACE-HYD-014 (1098)

Havvanur Kılıç
ACE-GEO-009 (932)

Nur Sena Kınalı
ACE-COM-012 (1544)

Funda Ture Kibar
ACE-TRA-028 (1404)

Muslum Kilinc
ACE-STR-025 (286)

Adnan Kiral
ACE-STR-002 (69), ACE-STR-031 (346)

Esat Selim Kocaman
ACE-CME-035 (822)

Serhan Koç
ACE-STR-039 (419)

Ali Koçak
ACE-STR-041 (439)

Sertaç Alperen Koçak
ACE-COM-006 (1489)

Ahmet Taha Koçtaş
ACE-TRA-023 (1356)

Beni Kohen
ACE-COM-013 (1553)

Fuat Koksal
ACE-STR-022 (255)

Hideo Komine
ACE-GEO-013 (976)

Ayşegül Koyunlular
ACE-CME-022 (709)

Sedat Kömürcü
ACE-STR-016 (203)

Hüseyin Köse
ACE-TRA-007 (1213)

Hurmet Kucukgoncu
ACE-STR-005 (97)

Aytuğ Kumandaş
ACE-TRA-012 (1266), ACE-TRA-017 (1307)

Mahir Kumantaş
ACE-TRA-012 (1266), ACE-TRA-017 (1307)

Şirin Kurbetci
ACE-CME-010 (589)

Derya Kurt
ACE-CME-029 (770), ACE-CME-031 (787)

Tugba Kuru
ACE-CME-014 (630)

Mesut Küçük
ACE-CME-006 (546)

Author Index (cont.)

Abdullah Hilmi Lav
ACE-TRA-029 (1414)

Ramazan Livaoğlu
ACE-STR-020 (238)

Yılmaz M.
ACE-CME-009 (579)

Tasnim Mahin
ACE-TRA-021 (1336)

Oishik Majumder
ACE-TRA-021 (1336)

Mouloud Mansouri
ACE-GEO-012 (965)

Muhammed Maraşlı
ACE-COM-013 (1553)

Hiba Meddah
ACE-STR-042 (452)

Ali Danandeh Mehr
ACE-CME-003 (524)

Akbar Mikaeelnezhad
ACE-CME-011 (598)

Mohammad Mahdi Milani
ACE-CME-012 (609)

Fatemeh Mostofi
ACE-COM-005 (1479)

Ali Motamedi
ACE-STR-029 (326), ACE-STR-030 (336)

Mahdis Motamedi
ACE-COM-002 (1451)

Ziya Muderrisoglu
ACE-STR-019 (230)

Abdullah Muratoğlu
ACE-HYD-018 (1141)

İbrahim Fırat Mutlu
ACE-GEO-007 (914)

Mehmet Nadir
ACE-CME-027 (752)

Memduh Nas
ACE-CME-034 (814), ACE-CME-036 (832), ACE-CME-037 (844)

Safa Nayır
ACE-CME-034 (814), ACE-CME-036 (832), ACE-CME-037 (844)

Md. Amin Al Noor
ACE-TRA-021 (1336)

Mehmet Sefa Orak
ACE-STR-038 (411), ACE-CME-027 (752)

Şeref Oruç
ACE-TRA-012 (1266), ACE-TRA-017 (1307)

Mustafa Ozdemir
ACE-STR-025 (286)

Halit Ozen
ACE-TRA-001 (1165)

Mehmet Selim Ökten
ACE-STR-010 (142)

Pelin Önelçin
ACE-TRA-009 (1233)

Erdal Önkol
ACE-CME-015 (640)

Özgür Özçelik
ACE-STR-014 (184)

Emircan Özçelikci
ACE-CME-017 (658)

Burak Özçörekçi
ACE-GEO-001 (859)

Aleyna Özdemir
ACE-COM-018 (1604)

Ecmel Eylül Naz Özdoğan
ACE-STR-014 (184)

Emine Özdoğru
ACE-CME-016 (648)

Sevgi Özen
ACE-CME-040 (853)

İffet Gamze Mütevelli Özkan
ACE-STR-018 (220)

Sadi Özsaraç
ACE-STR-006 (107)

Buse Öztürk
ACE-CME-032 (796)

G.B.O. Öztürk
ACE-STR-011 (151)

Hamdi Öztürk
ACE-STR-004 (89)

Hasan Tahsin Öztürk
ACE-STR-028 (316), ACE-HYD-014 (1098)

İsmail Onur Öztürk
ACE-CME-006 (546)

Muhammed Mustafa Öztürk
ACE-STR-012 (162)

Nurcan Öztürk
ACE-HYD-013 (1089), ACE-HYD-014 (1098)

Ziya Cem Öztürk
ACE-HYD-012 (1079)

Nilüfer Özyurt
ACE-COM-013 (1553)

Tarık İlyas Özyurt
ACE-CME-022 (709)

Eren Pamuk
ACE-GEO-010 (942)

Erhan Burak Pancar
ACE-TRA-017 (1307)

Raziye Peker
ACE-TRA-014 (1286)

Clifford Phiri
ACE-STR-024 (276)

Hülya Pir
ACE-STR-017 (210)

Yasemen Polat
ACE-CME-028 (760)

Ruti Politi
ACE-TRA-005 (1194), ACE-TRA-013 (1276)

Sm Arifur Rahman
ACE-KEY-001 (27)

Bilici S.
ACE-CME-009 (579)

Anas Saber
ACE-STR-007 (117)

Mehmet Saltan
ACE-TRA-010 (1243)

Arif Tufan Salva
ACE-CME-015 (640)

Mihriban Sarı
ACE-CME-021 (699)

Prabir Sarker
ACE-KEY-001 (27)

Mahmut Cenk Sayil
ACE-CME-010 (589)

Y. Semerdoken
ACE-STR-009 (132)

Serhan Sensoy
ACE-STR-040 (429)

İzel Yıldız Sertgöz
ACE-GEO-007 (914)

Author Index (cont.)

Özer Sevim
ACE-CME-028 (760)

Kağan Sevinç
ACE-CME-022 (709)

Faiz Shaikh
ACE-KEY-001 (27)

Mehmet Ali Silgu
ACE-TRA-024 (1370), ACE-TRA-029 (1414)

Pooja Singh
ACE-COM-014 (1563)

Oguz K. Sivri
ACE-GEO-008 (925)

Osman Sivrikaya
ACE-GEO-014 (986)

Hussien Alkasim Soalih
ACE-STR-020 (238)

Mehmet Sorgun
ACE-HYD-004 (1024), ACE-HYD-012 (1079)

Kurtuluş Soyluk
ACE-STR-013 (173)

Merve Arli Sönmez
ACE-STR-041 (439)

Alexander Stark
ACE-STR-033 (366), ACE-STR-034 (378)

Fezayil Sunca
ACE-GEO-014 (986)

Harun Yahya Sündü
ACE-CME-033 (805)

Erol Şadoğlu
ACE-GEO-011 (955)

Neslihan Şahan
ACE-TRA-012 (1266), ACE-TRA-017 (1307)

Oğuzhan Şahin
ACE-CME-016 (648)

Yuşa Şahin
ACE-CME-020 (690)

Doğukan Şahiner
ACE-CME-034 (814)

Mustafa Şahmaran
ACE-CME-028 (760)

Emin Şengün
ACE-CME-016 (648)

Duygu Şenol
ACE-TRA-011 (1253)

Sebahat Şimşek
ACE-STR-048 (498)

Ertuğrul Taciroğlu
ACE-GEO-014 (986)

Özcan Tan
ACE-GEO-003 (878)

Serhan Tanyel
ACE-TRA-005 (1194), ACE-TRA-006 (1202), ACE-TRA-009 (1233), ACE-TRA-011 (1253), ACE-TRA-013 (1276)

İsmail Hakkı Tarhan
ACE-CME-029 (770), ACE-CME-031 (787)

Muhittin Tarhan
ACE-CME-015 (640)

Yeşim Tarhan
ACE-CME-029 (770), ACE-CME-031 (787)

Elçin Filiz Taş
ACE-COM-007 (1499)

İlteriş Taşkolu
ACE-HYD-017 (1130)

Erhan Tekin
ACE-GEO-010 (942)

Vedat Toğan
ACE-COM-005 (1479)

Onur Behzat Tokdemir
ACE-COM-016 (1583)

Fatma Zehra Toker
ACE-CME-026 (744)

Mustafa Tokyay
ACE-CME-025 (734)

Mustafa Tolun
ACE-GEO-008 (925)

Makoto Tone
ACE-GEO-013 (976)

Zeliha Tonyali
ACE-STR-002 (69), ACE-STR-031 (346)

Ali Topal
ACE-TRA-009 (1233)

Aykut Topçu
ACE-TRA-018 (1317)

Sarp Toprakkale
ACE-HYD-009 (1060)

Muhittin Turan
ACE-STR-039 (419)

Ahmet Turer
ACE-STR-035 (46), ACE-STR-036 (390)

İhsan Türkel
ACE-STR-018 (220)

Temel Türker
ACE-STR-045 (479)

Şeyma Türkmen
ACE-COM-017 (1594)

Hasan Nuri Türkmenoğlu
ACE-CME-006 (546), ACE-CME-014 (630)

Tüten
ACE-CME-026 (744)

H. Abdullah Uçan
ACE-COM-012 (1544)

Koray Ugurlu
ACE-STR-001 (57)

Ömer Murat Urhan
ACE-TRA-008 (1221)

Beyza Uslu
ACE-CME-022 (709)

Dilara Usta
ACE-TRA-020 (1326)

Mervegül Uysal
ACE-TRA-023 (1356)

Mucteba Uysal
ACE-CME-007 (557), ACE-CME-008 (568), ACE-CME-024 (726)

Pınar Uysal
ACE-CME-026 (744)

Ergun Uzlu
ACE-HYD-001 (999)

Bartuğhan Uzun
ACE-COM-018 (1604)

Hasan Ahmet Uzunoğlu
ACE-CME-026 (744)

Kadircan Varan
ACE-CME-022 (709), ACE-CME-023 (718), ACE-CME-026 (744)

Furkan Varinlioglu
ACE-STR-022 (255)

Büşra Yakak Vatandaş
ACE-STR-017 (210), ACE-STR-043 (462)

Author Index (cont.)

Selahattin Armağan Vurdu
ACE-COM-011 (1534)

Magd Abdel Wahab
ACE-STR-048 (498)

Naoya Watanabe
ACE-GEO-013 (976)

İ. Özgür Yaman
ACE-CME-025 (734)

Mustafa Sinan Yardım
ACE-TRA-014 (1286), ACE-TRA-020 (1326)

Shahab Yasrebi
ACE-KEY-002 (36)

Yasin Yataganbaba
ACE-HYD-004 (1024)

İlkyaz Ceren Güçlü Yavuz
ACE-COM-001 (1443)

Murat Yegin
ACE-HYD-008 (1050)

Emirhan Yener
ACE-CME-003 (524)

Pınar Yıldırım
ACE-CME-005 (536)

Sefa Yıldırım
ACE-GEO-002 (868)

Yıldız Yıldırım
ACE-CME-026 (744)

Kürşat Yıldız
ACE-TRA-043 (1432)

Volkan Yıldız
ACE-TRA-025 (1380), ACE-TRA-026 (1389), ACE-TRA-027 (1397)

Fatih Yılmaz
ACE-STR-006 (107)

İhsan Yılmaz
ACE-GEO-010 (942)

Mazem Yılmaz
ACE-CME-024 (726)

Mehmet Yılmaz
ACE-TRA-024 (1370)

Meryem Yılmaz
ACE-GEO-007 (914)

Sadik Yigit
ACE-COM-008 (1509)

Kutay Yilmaz
ACE-HYD-009 (1060)

Meric Yilmaz
ACE-HYD-009 (1060)

Yilmaz Yilmaz
ACE-CME-034 (814), ACE-CME-036 (832), ACE-CME-037 (844)

Gökçe Yurtseven
ACE-TRA-004 (1184)

Umut Yüksel
ACE-CME-006 (546)

Nabi Yüzer
ACE-CME-033 (805)

Akbay Arama Z.
ACE-CME-009 (579)

Arda Ziya
ACE-CME-006 (546)

Büşra Ziypak
ACE-COM-005 (1479)